

HANDBOOK OF **CRYSTAL GROWTH**  
**SECOND EDITION**



# **FUNDAMENTALS:** THERMODYNAMICS AND KINETICS, AND TRANSPORT AND STABILITY



EDITED BY **TATAU NISHINAGA**



# Handbook of Crystal Growth

Fundamentals: Thermodynamics  
and Kinetics

VOLUME I, Part A

Second Edition

Editor-in-Chief and  
Volume Editor

**Tatau Nishinaga**

The University of Tokyo  
Hongo, Bunkyo-ku, Tokyo, Japan



ELSEVIER

Amsterdam • Boston • Heidelberg • London  
New York • Oxford • Paris • San Diego  
San Francisco • Singapore • Sydney • Tokyo



# Handbook of Crystal Growth

Fundamentals: Transport and Stability

VOLUME I, Part B

Second Edition

Editor-in-Chief and  
Volume Editor

**Tatau Nishinaga**

The University of Tokyo  
Hongo, Bunkyo-ku, Tokyo, Japan



ELSEVIER

Amsterdam • Boston • Heidelberg • London  
New York • Oxford • Paris • San Diego  
San Francisco • Singapore • Sydney • Tokyo

Elsevier

Radarweg 29, PO Box 211, 1000 AE Amsterdam, The Netherlands  
The Boulevard, Langford Lane, Kidlington, Oxford OX5 1GB, UK  
225 Wyman Street, Waltham, MA 02451, USA

First edition 1993

Second edition 2015

Copyright © 2015, 1993 Elsevier B.V. All rights reserved.

The crystals on the front cover are high-quality synthetic diamond crystals grown by Sumitomo Electric Industries, LTD by a temperature gradient method under high pressure and high temperature. The yellowish crystals are ordinary synthetic diamonds containing nitrogen impurity of several tens of ppm (type Ib). The colorless ones are high-purity synthetic diamonds free of impurities (type IIa). The size of the largest high-purity crystal (lower left) is about 12 mm in diagonal length. The photo was provided by Dr. Hitoshi Sumiya.

No part of this publication may be reproduced or transmitted in any form or by any means, electronic or mechanical, including photocopying, recording, or any information storage and retrieval system, without permission in writing from the publisher. Details on how to seek permission, further information about the Publisher's permissions policies and our arrangements with organizations such as the Copyright Clearance Center and the Copyright Licensing Agency, can be found at our website: [www.elsevier.com/permissions](http://www.elsevier.com/permissions).

This book and the individual contributions contained in it are protected under copyright by the Publisher (other than as may be noted herein).

#### Notices

Knowledge and best practice in this field are constantly changing. As new research and experience broaden our understanding, changes in research methods, professional practices, or medical treatment may become necessary.

Practitioners and researchers must always rely on their own experience and knowledge in evaluating and using any information, methods, compounds, or experiments described herein. In using such information or methods they should be mindful of their own safety and the safety of others, including parties for whom they have a professional responsibility.

To the fullest extent of the law, neither the Publisher nor the authors, contributors, or editors, assume any liability for any injury and/or damage to persons or property as a matter of products liability, negligence or otherwise, or from any use or operation of any methods, products, instructions, or ideas contained in the material herein.

#### British Library Cataloguing in Publication Data

A catalogue record for this book is available from the British Library

#### Library of Congress Cataloging-in-Publication Data

A catalog record for this book is available from the Library of Congress

SET Volume ISBN: 978-0-444-56369-9

Volume 1, Part A–978-0-444-63322-4

Volume 1, Part B–978-0-444-63323-1

For information on all Elsevier publications  
visit our website at [www.store.elsevier.com](http://www.store.elsevier.com)

Printed and bound in the UK.



Working together  
to grow libraries in  
developing countries

[www.elsevier.com](http://www.elsevier.com) • [www.bookaid.org](http://www.bookaid.org)



# Contents

General Preface	ix
Preface to Volume I	xi
List of Contributors	xiii

## Part A. Thermodynamics and Kinetics

1. Crystal Growth through the Ages: A Historical Perspective <i>Robert S. Feigelson</i>	1
2. Phase Equilibria <i>Detlef Klimm</i>	85
3. Atomistic Calculation of Defect Thermodynamics in Crystalline Silicon <i>Talid Sinno</i>	137
4. Stoichiometry of Oxide Crystals <i>Satoshi Uda</i>	175
5. Equilibrium Shape of Crystals <i>Theodore L. Einstein</i>	215
6. Rough–Smooth Transition of Step and Surface <i>Noriko Akutsu, Takao Yamamoto</i>	265
7. Theory of Nucleation <i>Christo N. Nanev</i>	315
8. Growth Kinetics: Basics of Crystal Growth Mechanisms <i>Makio Uwaha</i>	359
9. Structure of Melt and Liquid Alloys <i>Jean-Pierre Gaspard</i>	401

10.	Monte Carlo Simulations of Crystal Growth <i>Luis A. Zepeda-Ruiz, George H. Gilmer</i>	445
11.	Ab initio-Based Approach to Crystal Growth: Chemical Potential Analysis <i>Tomonori Ito, Yoshihiro Kangawa</i>	477
12.	Simulation of Epitaxial Growth by Means of Density Functional Theory, Kinetic Monte Carlo, and Phase Field Methods <i>Wolfram Miller</i>	521
13.	Controlled Colloidal Assembly: Experimental Modeling of Crystallization <i>Tian Hui Zhang, Xiang Yang Liu</i>	561
Part B. Transport and Stability		
14.	Morphological Stability <i>Robert F. Sekerka, Sam R. Coriell, Geoffrey B. McFadden</i>	595
15.	Phase-Field Models <i>Mathis Plapp</i>	631
16.	Dendritic Growth <i>Martin E. Glicksman</i>	669
17.	Grain Growth in the Melt <i>Kozo Fujiwara</i>	723
18.	Growth of Semiconductor Nanocrystals <i>Katsuhiko Tomioka, Takashi Fukui</i>	749
19.	Crystallization of Proteins <i>Peter G. Vekilov</i>	795
20.	Biological Crystallization <i>Jaime Gómez-Morales, Giuseppe Falini, Juan Manuel García-Ruiz</i>	873
21.	Crystallization of Pharmaceutical Crystals <i>Stéphane Veesler, François Puel</i>	915

22.	Crystallization of Chiral Molecules <i>Cristóbal Viedma, Gérard Coquerel, Pedro Cintas</i>	951
23.	In Situ Observation of Crystal Growth by Scanning Electron Microscopy <i>Yoshikazu Homma</i>	1003
24.	In Situ Observation of Crystal Growth and Flows by Optical Techniques <i>Katsuo Tsukamoto</i>	1031
25.	Snow and Ice Crystal Growth <i>Yoshinori Furukawa</i>	1061
26.	Crystal Growth of Quasicrystals <i>An-Pang Tsai, Can Cui</i>	1113
	Index	1157



# General Preface

The history of crystal growth is long as those of the universe and the earth. Meteorites contain pyrites and olivine crystals which indicate these crystals were grown when the planets were born. Crystals naturally produced are used as gems from the early time of the human history. In Exodus, it is written that breast-piece was decorated by ruby, emerald, sapphire, amethyst, and other gems.

There are a lot of crystals around us. As examples, we can find snowflakes falling down from the sky, ice crystals in a lake in winter, salt and sugar crystals in the pots of our kitchen. But, it was after the invention of point contact and junction transistors, respectively in 1947 and 1948, that the industry paid a great interest on the crystal growth. Without the growth of high purity and highly perfect single-crystal semiconductor, at that time of Ge, the invention of the transistors will never happen.

It is well known that the modern information society will be not realized without electronic and optical devices. One finds large-scale integrated circuits of Si in every computer from laptop to super computers. For high speed and mass transmission of information, compound semiconductor devices are indispensable.

These devices are fabricated almost all by using single crystals of semiconductors and oxides. When we look into the history of the devices, we always see that an invention of crystal growth technique makes it possible to bring out new device. As we saw, the invention of transistor was possible only after the growth of high-quality Ge single crystal. The growth of large-diameter dislocation-free Si crystal has enabled the production of large-scale integrated circuit. Due to the invention of liquid-phase epitaxy, it became possible to realize light-emitting diode (LED) and laser diode (LD) in real use. Drastic technological improvement in highly lattice mismatch heteroepitaxy made it possible to realize blue ~ ultraviolet LED and LD and it can be said that the success in the growth of high-quality nitride semiconductor gave the blue light all over the world. Hence, we should understand that new technology of crystal growth has always created new electronic and optical devices.

It is extremely good news for the community of crystal growth that 2014 Nobel Prize in Physics was awarded to Professors Isamu Akasaki, Hiroshi Amano and Shuji Nakamura for the invention of efficient blue light-emitting diodes which has enabled bright and energy-saving white light sources. This invention is basing on the growth of nitride semiconductors employing a low-temperature buffer layer on sapphire substrate in heteroepitaxy. We are happy that Professor Hiroshi Amano, one of the winners, is contributing to this Handbook as an author of Chapter 16 in Vol. IIIA.

The first edition of the Handbook of Crystal Growth was edited by D.T.J. Hurlé. This Handbook was composed of three volumes and published in 1993–1994. The present second edition of the Handbook also consists of three volumes. Each volume was edited by separate editors. Volume I is edited by T. Nishinaga and the volume covers the basic aspects of crystal growth. In Volume IA, fundamentals and kinetics of crystal growth are described and in IB, advanced problems of transport and stability are discussed. Volume II is edited by P. Rudolph and this volume covers bulk crystal growth. Volume IIB presents basic technologies of bulk growth and IIB does growth mechanism and dynamics. Volume III was edited by T. F. Kuech and the volume covers thin film growth and epitaxy. Volume IIIA discusses basic techniques and IIIB does growth mechanisms and dynamics.

Present Handbook project was created in March, 2011 and six advisors were appointed. They are T. F. Kuech, G. B. Stringfellow, J. B. Mullin, J. J. Derby, R. Fornari, and K. H. Ploog. I am very much grateful for their important and valuable suggestions.

Finally, all editors would like to express their sincere thanks to Shannon Stanton, Elsevier, for her strong and well cared support to this work.

Tatau Nishinaga  
(Editor in Chief)



# Preface to Volume I

Crystal growth has three faces. One is the face of science, the second is that of art, and the final one is of technology. For a long time in the human history, people have wondered how snowflakes grow in such beautiful shapes and tried to understand the mechanism. The curiosity is the driving force for the growth science. Crystal growth is an important tool to obtain useful crystals for human life and industry use. The growth of ruby is one of the examples. People have developed the art of the growth and the art was improved by many workers and finally Verneuil has arrived at an elegant growth method called as Verneuil method.

For a long time, science and art of crystal growth have been developed separately such as in school and in small factory in town. However, after the crystal growth has been employed to fabricate advanced electronic and optoelectronic devices, the art based on science is strongly required. For the control of the accurate structure and dimension of such devices, the growth should be carried out with deep understandings of growth science.

A half century ago, nobody thought that the real-time observation of 2D nucleation is possible in molecular beam epitaxy (MBE) during the growth of quantum well laser by reflection high-energy electron diffraction (RHEED). It was only in recent years that growth spirals were found on the surface of GaN grown by metal organic chemical vapor deposition (MOCVD) to be used for the fabrication of blue light-emitting diode (LED) and laser diode (LD). It was shown that the relationship between growth rate and surface supersaturation of GaN MOCVD is explained very well by classical Burton–Cabrera–Frank (BCF) theory. In this experiment, a mask epitaxy using photolithography was employed.

In the history of crystal growth, there has been no age when the art and the science of crystal growth are so closely combined like today. However, there is still strong contribution of art required in the crystal growth technology. For instance, to grow the advanced devices by MBE, one should be very skillful to manipulate the machine, however, with advanced knowledge of growth science. This is what is different from the old art of crystal growth.

The purpose of the Volume I is to show the recent advances in the growth science and to give scientific bases for the technologies to be developed in the following Volumes II and III, which are devoted to the bulk crystal growth and thin film growth and epitaxy, respectively.

Volume Ia describes thermodynamics and kinetics and Volume IIb does the transport and stability. The first chapter of Volume Ia gives a historical introduction of the crystal growth especially for the beginners. This chapter is followed by those of phase equilibria,

defect thermodynamics, and stoichiometry. Then, Chapter 5 discusses the equilibrium shape of crystal and Chapter 6 does rough–smooth transition of step and surface. Both chapters aim at giving the true picture of the crystal surface. Chapters 7 and 8 will cover the most fundamental and basic aspects of crystal growth, nucleation and growth kinetics, respectively. Chapter 9 is devoted to explain the structure of melt and liquid alloys. To understand the growth from the melt, one should have the knowledge about the atomistic structure of the melt. Next three chapters discuss the simulation of crystal growth employing classical and quantum mechanically calculated potentials. The final chapter presents the colloid crystal growth, which provides the experimental modeling for the crystal growth.

The first chapter of Volume Ib gives a general introduction to morphological stability that is followed by Chapter 15, in which the modern theory of morphological stability, i.e., phase-field model, is explained and applied to solidification to understand micro-structure formation processes. The next two chapters describe the experiments related to the morphological stability. In Chapter 16, the detailed theoretical and experimental studies of dendritic growth are presented. On the other hand, in Chapter 17, grain growth in the melt is discussed and it is demonstrated that the dendritic growth is often observed in grain growth. Nanocrystal growth is one of the rapidly expanding fields. Growth of nanocrystals from vapor is discussed as an example in Chapters 18. Crystal growth of protein and other biological molecules are studied very extensively to facilitate the advancement of life science. Chapters 19 and 20 are devoted to this subject. The following two chapters discuss the problems which one encounters in producing medicine. Chapter 21 describes the fundamental growth process of pharmaceutical crystallization, which is exactly the same as ordinary crystal growth. Chapter 22 discusses the growth of chiral molecules. Selective growth of one type is especially important for pharmacy production.

Chapters 23–25 describe in situ observation of crystal growth in vacuum, solution, and melt. Chapters 24 and 25 are devoted some parts to the growth in space. The final chapter describes the growth of quasicrystal which shows symmetries forbidden in ordinary crystallography. It is possible to grow single-grained quasicrystals and their properties were studied in detail.

The present editor wishes to acknowledge deeply all authors of Volume I for their excellent articles. The mails of the request were sent in the autumn of 2012 and the deadline was the end of October 2013. But, the most of authors only could send their manuscript by March of 2014 and some did in the beginning of July, 2014. I would like to thank all authors for sacrificing many hours of their important official and private time.

Tatau Nishinaga  
Editor of the Volume I  
July, 2014



# List of Contributors

**Noriko Akutsu** Faculty of Engineering, Osaka Electro-Communication University,  
Neyagawa, Osaka, Japan

**Pedro Cintas** Depto. Química Orgánica e Inorgánica, Universidad de Extremadura,  
Badajoz, Spain

**Gérard Coquerel** Normandie Université, Université de Rouen, Mont-Saint-Aignan,  
Cedex, France

**Sam R. Coriell** National Institute of Standards and Technology, Gaithersburg, MD, USA

**Can Cui** Department of Physics, Center for Optoelectronic Materials and Devices,  
Zhejiang Sci-Tech University, Hangzhou, China

**T.L. Einstein** Department of Physics and Condensed Matter Theory Center, University of  
Maryland, College Park, MD, USA

**Giuseppe Falini** Dipartimento di Chimica "G. Ciamician," Alma Mater Studiorum  
Università di Bologna, Bologna, Italy

**Robert S. Feigelson** Geballe Laboratory for Advanced Materials, Stanford University,  
Stanford, CA, USA

**Kozo Fujiwara** Institute for Materials Research, Tohoku University, Sendai, Miyagi,  
Japan

**Takashi Fukui** Graduate School of Information Science and Technology, Hokkaido  
University, Sapporo, Japan; Research Center for Integrated Quantum Electronics (RCIQE),  
Hokkaido University, Sapporo, Japan

**Yoshinori Furukawa** Institute of Low Temperature Science, Hokkaido University,  
Sapporo, Hokkaido, Japan

**Juan Manuel García-Ruiz** Laboratorio de Estudios Cristalográficos, Instituto  
Andaluz de Ciencias de la Tierra, CSIC-Universidad de Granada, Granada, Spain

**Jean-Pierre Gaspard** Solid state physics, interfaces and nanostructures, University of  
Liege, Sart-Tilman, Belgium

**George H. Gilmer** Mechanical Engineering Department, Colorado School of Mines, Golden, CO, USA

**Martin E. Glicksman** Department of Mechanical and Aerospace Engineering, Florida Institute of Technology, Melbourne, FL, USA

**Jaime Gómez-Morales** Laboratorio de Estudios Cristalográficos, Instituto Andaluz de Ciencias de la Tierra, CSIC-Universidad de Granada, Granada, Spain

**Yoshikazu Homma** Department of Physics, Tokyo University of Science, Shinjuku, Tokyo, Japan

**Tomonori Ito** Department of Physics Engineering, Mie University, Kurima-Machiya, Tsu, Japan

**Yoshihiro Kangawa** Research Institute for Applied Mechanics, Kyushu University, Kasuga-Koen, Kasuga, Japan

**Detlef Klimm** Leibniz Institute for Crystal Growth, Berlin, Germany

**Xiang Yang Liu** Department of Physics and Department of Chemistry, National University of Singapore, Singapore

**Geoffrey B. McFadden** National Institute of Standards and Technology, Gaithersburg, MD, USA

**Wolfram Miller** Leibniz Institute for Crystal Growth, Numerical Modelling, Max-Born-Str. 2, 12489 Berlin

**Christo N. Nanev** Rostislav Kaischew Institute of Physical Chemistry, Bulgarian Academy of Sciences, Acad. G. Bonchev Str. Bl. 11, 1113 Sofia, Bulgaria

**Mathis Plapp** Physique de la Matière Condensée, École Polytechnique, CNRS, Palaiseau, France

**François Puel** LAGEP UMR CNRS 5007, Université de Lyon, ESCPE Lyon, Villeurbanne Cedex, Lyon, France

**Robert F. Sekerka** Department of Physics, Carnegie Mellon University, Pittsburgh, PA, USA

**Talid Sinno** Department of Chemical and Biomolecular Engineering, University of Pennsylvania, Philadelphia, PA, USA

**Katsuhiro Tomioka** Graduate School of Information Science and Technology, Hokkaido University, Sapporo, Japan; Research Center for Integrated Quantum Electronics (RCIQE), Hokkaido University, Sapporo, Japan; Japan Science and Technology Agency (JST), PRESTO, Kawaguchi, Japan

**An-Pang Tsai** Institute of Multidisciplinary Research for Advanced Materials, Tohoku University, Sendai, Japan; National Institute for Materials Science, Tsukuba, Japan

**Katsuo Tsukamoto** Graduate School of Science, Tohoku University, Aramaki Aoba, Sendai, Japan

**Satoshi Uda** Institute for Materials Research, Tohoku University, Katahira, Aoba-ku, Sendai, Miyagi, Japan

**Makio Uwaha** Department of Physics, Nagoya University, Chikusa-ku, Nagoya, Japan

**Stéphane Veesler** CINaM-CNRS, Aix-Marseille Université, Marseille, France

**Peter G. Vekilov** Department of Chemical and Biomolecular Engineering, and Department of Chemistry, University of Houston, Houston, Texas, USA

**Cristóbal Viedma** Depto. de Cristalografía y Mineralogía, Universidad Complutense, Madrid, Spain

**Takao Yamamoto** Division of Pure and Applied Science, Faculty of Science and Technology, Gunma University, Kiryu, Gunma, Japan

**Luis A. Zepeda-Ruiz** Physical and Life Sciences Directorate, Lawrence Livermore National Laboratory, Livermore, CA, USA

**Tian Hui Zhang** Center for Soft Condensed Matter Physics and Interdisciplinary Research, Soochow University, Suzhou, China; School of Physical Science and Technology, Soochow University, Suzhou, China



# Crystal Growth through the Ages: A Historical Perspective

Robert S. Feigelson

GEBALLE LABORATORY FOR ADVANCED MATERIALS,  
STANFORD UNIVERSITY, STANFORD, CA, USA

Excerpt from Pliny the Elder's, *Natural History*, AD 77, "... I have prefaced these volumes with the names of my authorities. I have done so because it is, in my opinion, a pleasant thing and one that shows an honourable modesty, to own up to those who were the means of one's achievements..."

Trans. H. Rackham

## CHAPTER OUTLINE

<b>1.1 Introduction</b> .....	<b>2</b>
<b>1.2 Evolution of Crystal Growth Theories</b> .....	<b>4</b>
1.2.1 Early Developments (Before the Nineteenth Century) .....	4
1.2.2 The Nineteenth Century .....	5
1.2.3 The Twentieth Century.....	6
<b>1.3 Crystal Growth Methods</b> .....	<b>16</b>
1.3.1 Melt Growth .....	17
1.3.1.1 The Nineteenth Century and the Verneuil Process .....	18
1.3.1.2 The Twentieth Century .....	20
1.3.1.3 The Czochralski Crystal Pulling Method.....	20
1.3.1.4 Bridgman–Stockbarger/Gradient Freeze Methods.....	25
1.3.1.5 Nacken–Kyropoulos Methods.....	28
1.3.1.6 Stöber/Heat Exchanger Methods .....	30
1.3.1.7 Kapitza's Method .....	30
1.3.1.8 Zone Melting .....	31
1.3.1.9 Shaped Growth .....	33
1.3.1.10 Skull Melting .....	37
1.3.2 Solution Growth.....	38
1.3.2.1 Introduction .....	38

## 2 HANDBOOK OF CRYSTAL GROWTH

1.3.2.2 Aqueous Solution Growth.....	38
1.3.2.3 Growth of Biological Macromolecules.....	41
1.3.2.4 Growth from Gels.....	43
1.3.2.5 Nonaqueous Solution Growth.....	44
1.3.2.6 High Temperature Solution (Flux) Growth.....	44
1.3.2.7 Hydrothermal Growth.....	49
1.3.2.8 Electrochemical Crystal Growth.....	52
<b>1.3.3 Vapor Growth.....</b>	<b>53</b>
1.3.3.1 Introduction.....	53
1.3.3.2 Bulk Growth.....	55
1.3.3.3 Vapor Phase Epitaxy.....	58
1.3.3.4 The VLS Method.....	63
1.3.3.5 Artificial Epitaxy (Graphoepitaxy).....	64
<b>1.3.4 Synthetic Diamond Crystals.....</b>	<b>65</b>
<b>1.3.5 Solid State Recrystallization.....</b>	<b>70</b>
<b>1.4 Epilogue.....</b>	<b>72</b>
<b>Acknowledgments.....</b>	<b>72</b>
<b>References.....</b>	<b>73</b>

## 1.1 Introduction

Most scientists and engineers are aware that the basic tools they use in their daily research activities were developed by groups of researchers working in series or parallel over decades, in some cases centuries. It was often in an incremental way, one study building on another. As time went on, these earlier ideas became more refined and practical, providing future workers with a more thorough understanding of the physics and chemistry involved in different materials systems and leading to innovative new processes for making materials and devices that have affected everyone's lives. They helped define the world we live in and used their newly gained knowledge to stoke the technological revolution.

The crystal growth field (a branch of materials science, physics, chemistry and crystallography) has a rich historical background that goes back at least several millennia. It basically deals with understanding the underlying mechanisms involved in the crystallization process and the technology to produce a single crystal from some medium in a controlled fashion. One of the earliest written accounts documenting work on methods for preparing crystals was given by the Roman Pliny the Elder in 77–79 AD [1]. His collected work was a summary of knowledge going back to even more ancient times. It is probable that even prehistoric man engaged in the recrystallization of materials like salt. Among other topics, Pliny discussed the preparation of Vitriol (iron,

copper and zinc sulfate hydrates). The process involved evaporating mine or spring waters obtained from the Mediterranean region. About 1500 years later, in medieval times, Pliny's work was referred to by both Biringuccio [3] and Agricola [2]. They concentrated on preparing crystals of these compounds for medicines, dyes, fluxes and acids. The various methods employed generally began with the purification of mineral deposits, followed by recrystallization of the remaining solutions by evaporation.

The field of crystal growth encompasses a wide spectrum of scientific disciplines and includes (1) experimental and theoretical studies of crystallization processes, (2) the growth of crystals under controlled conditions for both scientific purposes and industrial applications and (3) crystal characterization. It also covers almost all classes of materials, i.e., inorganic and organic compounds, elemental materials as well as biological macromolecules. Many methods have been developed over the years for producing single crystals, the size range for which varies from the nanometer to meter scale. These crystals have in common an atomic ordering that persists throughout their bulk and without the presence of grain boundaries. The two principal scientific pillars upon which the field of crystal growth depends are thermodynamics and kinetics. The thermodynamic properties of a system describe how solid, liquid and gaseous phases behave with respect to state variables such as temperature, pressure and composition. They provide a road map, so to speak, which crystal growers use to plan growth strategies. For the preparation of crystals of a size, purity and composition required for a specific application, one needs to know what material phases will exist under various conditions of temperature,  $T$ , and pressure,  $P$ , etc., and how these phases will form under dynamic solidification processing conditions. Kinetic factors, on the other hand, influence our ability to produce a crystal at a desired growth rate and with a degree of perfection and uniformity suited to the intended application. We will explore below how interface stability and segregation behavior are influenced both by thermodynamic and kinetic factors.

In the beginning, crystal growth was not the well-defined field it is today. Work was carried out by chemists, physicists, etc., and research results were reported in various conferences and journals of these societies. The first conference to concentrate on the topic was at a Faraday Society meeting in 1949, held in Bristol, England. In spite of the growing importance of crystals for solid-state electronic applications in the early 1950s, it was almost a decade later before a second meeting concerning issues in crystal growth arose. That conference, held in Cooperstown, New York in 1958 [4], gathered together some of the most eminent crystal growth researchers to discuss a wide range of topics of interest to the crystal growth community. Conferences were also started in the Soviet Union (Moscow) as early as 1956. However, the major consolidation of the field into a viable entity was the formation in 1966 of the International Organization of Crystal Growth (IOCG) and under their aegis, the subsequent International Conferences on Crystal Growth (ICCG). These conferences have been held every three years since 1966.

The local organizers of the first ICCG conference held in Boston, Massachusetts immediately founded the American Association for Crystal Growth (AACG) under the joint chairmanship of Doctor Robert (Bob) Laudise and Doctor Kenneth (Ken) Jackson.

The AACG held their own national conferences soon afterward and other national groups formed around the world. The *Journal of Crystal* was established in 1967 under the leadership of Professor Michael Schieber, along with Sir Charles Frank and Dr Nicholas Cabrera as co-editors. Although papers on crystal growth topics are published elsewhere as well, the *Journal of Crystal Growth* has remained the major venue for papers on crystal growth theory, practice and characterization and has published related proceedings of conferences focused on various aspects of the field.

Many of the topics discussed in this introductory history are covered in much more detail in various chapters in this comprehensive, updated version of the *Handbook of Crystal Growth*. This treatment is designed to focus mainly on their historical context.

## 1.2 Evolution of Crystal Growth Theories

Although crystals can be grown by purely empirical means, control of their rate of growth, perfection, dimensions, composition and physical properties is greatly facilitated by having a good grasp of the fundamentals underlying crystal growth processes. Over the past century, a sound theoretical foundation has been built up through the efforts of many different scientists and engineers working in materials-related fields such as chemistry, physics and crystallography. The approach is generally two-fold: first to understand the nature of material systems (crystal structure and morphology, phase equilibrium, etc.), and second, to determine the factors that affect the crystallization process (nucleation, growth kinetics, segregation behavior, interface stability, heat and mass transport, etc.). Although remarkable progress has been made, the complex nature of the field and its changing emphasis on newer materials and structures keeps providing a constant source of challenges to our understanding of crystallization processes.

### 1.2.1 Early Developments (Before the Nineteenth Century)

The earliest scientific studies important to the field of crystal growth were made by natural scientists trying to understand the morphologies of mineral crystals. One of these early pioneers was the Swiss naturalist Conrad Gesner (1516–1565) who in 1564, after studying different crystals, reported that one crystal differs from another by its angles and form [5]. Later in the sixteenth century, Andreus Caesalpinus (1519–1603) wrote in “De Metallicis” [6] that the shape of crystals grown from water solution (e.g., salt, sugar and alum) were a characteristic of the material. Ichiro Sunagawa [7] proposed, however, that the science of crystal growth started with the treatise of N. Steno. Nicolas Steno, also known as Niels Stensen, (1638–1686) was a well-known Danish scientist specializing in the fields of geology and anatomy. He was also one of the founders of crystallography. In his treatise, published in 1669 [8], he observed that, although quartz crystals differ in appearance from one to another, the angles between corresponding faces are always the same. In addition, he noted that they grew by an inorganic hydrothermal process rather than through the action of bacteria [7]. Years later, Steno’s law of *constant interfacial*

*angles* in crystals was confirmed, first by the Italian Domenico Guglielmini (1665–1710) [9] who asserted, like Casealpinus, that every salt has its own particular shape. A century later, the Frenchman Jean Baptiste Romé de l'Isle (1736–1790) [10], concluded from his study of many hundreds of different crystals that every crystalline substance with a specific composition had a similar and particular crystal shape (1772) See Figure 1.1(A)). He found six different fundamental forms from which all others could be derived. Although the above work, and that of other researchers not mentioned, set the stage for our improved understanding of the nature of crystals, it was not until much later that attention turned seriously to the question of how crystals grew and which mechanisms were involved. Figure 1.1(B) shows the internal structure of a lithium niobate crystal revealed by partial melting.

## 1.2.2 The Nineteenth Century

French physicist Auguste Bravais (1811–1853), building on l'Isle's previous work, determined in 1848 that there are 14 unique “Bravais” lattices comprising three-dimensional crystalline systems [11]. This work provided the basis for understanding symmetry, crystal morphology and crystalline anisotropy. The morphology of a crystal is influenced by (1) external factors, e.g., the surrounding nutrient phase and (2) internal features, e.g., cell dimensions, atom sizes, positions, and bond energies.

Contemporary quantitative crystal growth science originated with the thermodynamic studies of the American scientist J. Willard Gibbs (1839–1903). Gibbs studied how various phases behaved in heterogeneous systems under the influence of state variables such as temperature and pressure. His seminal work, *On the Equilibrium of*

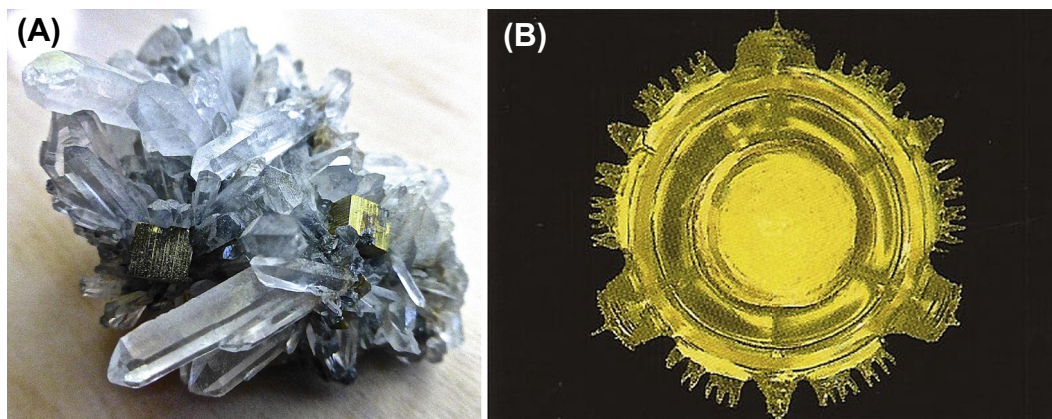


**FIGURE 1.1** (A) Naturally occurring crystals of quartz ( $\text{SiO}_2$ ) interspersed with pyrite ( $\text{FeS}_2$ ) crystals. Their different morphologies reflect their internal crystal structures, trigonal and cubic respectively. (B) The bottom side of a c-axis Czochralski grown lithium niobate crystal that was rapidly heated to cause it to separate from the melt surface. The resulting dendritic-like structure reveals the internal three-fold symmetry along the axis of this rhombohedral crystal.

*Heterogeneous Substances* (1876 and 1878) [12], included both the first and second laws of thermodynamics and thermodynamic reaction tendencies in any thermodynamic system. His graphical representations, the earliest phase diagrams, have been expanded through the years to include numerous chemical systems of both academic and industrial interest. These were derived largely by experimental studies but also in recent years by numerical simulations. These “phase diagrams” are vital data sources for the crystal grower, enabling him or her to select the most appropriate growth method and produce a crystal with the desired composition and properties.

To form a crystal, a nutrient phase (i.e., liquid, gas or solid) must be in a metastable state. In other words, the free energy (at constant volume) or the Gibbs potential (at constant pressure) of this phases must exceed that of the crystal. This excess is the driving force for crystallization. This metastability is accomplished by either supercooling a melt or supersaturating a solution or vapor phase. During crystallization, latent heat is evolved. Among other remarkable contributions made by Gibbs was that nucleation phenomena resulted from heterophase fluctuations in metastable homogeneous phases. Nucleation can be either homogeneous (from within the pure matrix phase) or heterogeneous (on a foreign substance such as particles or substrates within the matrix phase or the container walls). The maximal amount of supercooling or supersaturation required depends on the thermodynamic properties of the material system, various external forces such as mechanical vibrations, and of course, the nature of the crystal surface, etc. In practice, the initial nucleation stage is often bypassed by using oriented seed crystals.

### 1.2.3 The Twentieth Century

In the opinion of K. Jackson [13], our modern understanding of crystal growth processes began with the research work of Harold Wilson (1874–1964) [14] and Martin Knudsen (1871–1949) [15]. Wilson’s work in 1900 concerned the velocity of solidification and viscosity of supercooled liquids, whereas Knudsen’s work involved kinetic molecular theory that much later played an important role in molecular beam epitaxy. One of the most important early growth theories was proposed in 1921 by the German physical chemist Max Volmer (1885–1965) and his student Immanuel Estermann (1900–1973) [16]. Their adsorption-layer theory (i.e., layer-by-layer growth) was deduced from measuring the tangential growth rate of plate-like mercury crystals from the vapor state at low temperatures. The proposed adsorption-layer lies between the crystal and nutrient phase, with the crystallizing species losing only part of their latent heat, while maintaining some surface mobility in the layer parallel to the crystal surface. The species are incorporated into the crystal lattice at the edges of the incomplete atomic layers (steps on the growing crystal face). Volmer was also the first to consider the role of ad-atoms (or molecules) and holes on the crystal surface under equilibrium and nonequilibrium conditions.

Walther Kossel (1888–1956) [17], a German physicist known for his theory of chemical bonding, proposed in 1928 an atomistic view of crystal growth (kinetic theory), as

opposed to a “continuum” thermodynamic interpretation. It was similar to that independently proposed by Iwan N. Stranski (1897–1979), [18] a Bulgarian physical chemist, and was based on earlier diffusion theories concerning mass transport of the crystallizing species to the growth interface with the distinction that what went on in the interface region (how the species found an appropriate lattice site) was *not* a negligible effect. Their work is often linked together as the Kossel–Stranski model. They both concluded from early work on the rock salt structure that no other planes but the cubic ones are possible and that other planes (110, 111, etc.) are not present on the surface as complete planes but are made up of alternating (001) and (100) faces several atoms thick (kinetic roughening). This work led to what is commonly referred to as the TLK (terrace-ledge-kink) model where Kossel [19] suggested that incorporation of an atom required that the steps spread laterally across the surface. Somewhat later came the work of Stranski’s younger colleague Rostislav Kaishev (1908–2002) linking the equilibrium crystal shape, i.e., the facets making this shape, with the average work required to detach a molecule from that facet, and thereby accounting for different structural positions on that facet and its edge. Stranski and Kaishev founded the famous Bulgarian school of nucleation and crystal growth (see Ref. [20]). Much of their work was on low-temperature aqueous solution growth and the crystallization of metals at room temperature in electrolyte solutions. An extensive discussion of Kossel and Stranski’s work, together with other contemporaries, is given in Buckley’s book *Crystal Growth* [21] and numerous other more recent publications.

The goal of scientific studies is the development of effective models that can explain observable physical phenomena and direct practical crystal growing via generalized predictive relationships. These activities were both based on scientific inquisitiveness and to provide guidelines for practitioners to produce material for the benefit of mankind. Basic studies on nucleation and crystal growth have greatly expanded over the years. Older theories and concepts have been refined and new concepts proposed and tested. Basic understanding has greatly benefited from important advances in crystal characterization technologies. They have provided direct evidence of crystal perfection and growth behavior down to the atomic scale. Two examples are the transmission electron microscope and in situ atomic force microscopy. The former technology makes possible the imaging of atomic structures of real crystals, allowing a study of their perfection and the nature of their imperfection. Atomic force microscopy can be used, to great effect, both to study the formation and kinetics of growth layers during solution growth (particularly biological macromolecules) and how they change upon post-growth heat treatments (surface reconstruction). Reflected beam electron microscopy has also been very useful.

The discovery of crystalline imperfections such as edge and screw dislocations, stacking faults, point defects and inclusions in an otherwise uniform crystal lattice, has had a strong impact on our understanding of crystal properties, on the one hand, and crystal growth mechanisms on the other. They are also of great technological importance for the influence they have on the electronic and mechanical properties of a material.

In 1934, Sir Geoffrey Taylor (1886–1975), a noted British physicist and mathematician, proposed that the *plastic* deformation of ductile materials could be explained in terms of the theory of dislocations developed by Vito Volterra in 1905. Some years later, the subject of dislocations occupied the thoughts of Sir Charles Frank (1911–1998), an eminent British crystallographer who spent much of his career at Bristol University. His fundamental contributions to the field of crystal growth include the laws governing dislocation branching, the existence and properties of dislocation networks, and in 1950, the Frank-Read mechanism for the generation of dislocations. In a well-documented account, the idea for this latter mechanism occurred to both Sir Charles and to W.T. Read (an American working at the General Electric Co.) independently and at the same time. Frank had shown the year before [22] that two-dimensional nucleation theory failed significantly to explain observed high crystal growth rates at low supersaturation. This discrepancy could, however, be readily reconciled if the growth face contained a screw dislocation outcrop. That this dislocation should lead to continuous step generation in the form of a “growth spiral” step on the growth face was immediately validated by experimentally observed growth spirals formed on actual crystals (i.e., Refs [23,24]).

Some of the important work on crystal symmetry in modern times was done by Donnay and Harker in 1937 [25] and later by Hartman and Perdok [26]. Hartman and Perdok’s theory [26] classified different types of faces, with only one type forming crystal facets. For ionic crystals, they defined the energy released during growth of a layer as  $E(hkl)$  and were able to generate growth forms by assuming that  $E(hkl)$  was proportional to the growth rate. These calculated forms were similar to natural or manmade crystals such as zircon, garnets, etc. Many researchers before and since have also observed variations from predicted or expected crystal morphologies due to impurity adsorption on a growth face. That led to methods to alter the morphologies for a specific application, one example being the purposeful poisoning of a fast-growing needle axis to make a more equiaxed crystal. Other notable contributions to our understanding of growth shapes include those of Sunagawa (1960) [7] and Bennema (1980) [27].

A major effort to control the purity and dopant uniformity in Si and Ge electronic devices was begun at Bell Laboratories in the early 1950s. The research team of Burton, Prim and Slichter came up with a relationship that described how impurities and dopants are distributed along an as-grown boule (the now well-known BPS equation). Their work was first reported in 1952, but not openly published until 1953 [28]. Measuring solute concentrations, solid–liquid distribution coefficients, diffusion coefficients and solute distributions in actual crystals, they derived equations describing what the concentration of a dopant or impurity would be in an as-grown crystal as a function of its initial melt concentration and growth rate  $R$ .

$$K_e = K_o/K_i + (1 - K_o)\exp(-R\delta_D/D) \quad (1.1)$$

where  $K_e$  is the effective segregation coefficient,  $K_o$  is the interface or equilibrium segregation coefficient,  $R$  the growth rate,  $\delta_D$  is the diffusion boundary layer thickness and

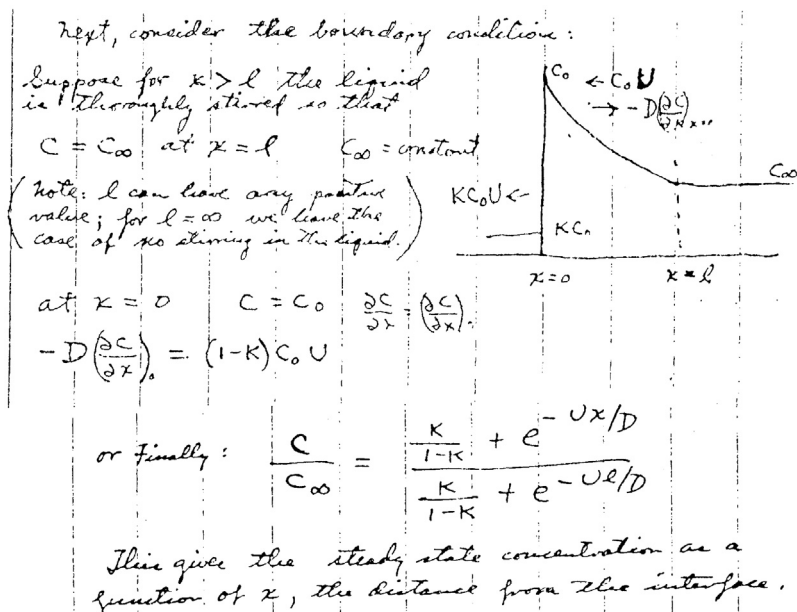


FIGURE 1.2 One of the diagrams in J.A. Burton's laboratory notebook (1951) explaining the concept of the BPS theory. The plot shows the variation of solute concentration in the solid and melt during unidirectional solidification. The  $x = 0$  position is the growth interface while  $x = l$  defines the width of the solute boundary layer [29].

$D$  is the solute diffusion coefficient. Figure 1.2 shows a sketch and notes from Burton's laboratory notebook illustrating the features of the now famous segregation relationship.

This research was part of a larger effort amongst various semiconductor scientists and engineers at Bell Laboratories [29,30]. Since then, BPS segregation theory has become a particularly valuable tool for crystal growth practitioners, allowing them to control the compositional uniformity in single- and multi-component material systems via control of growth velocity, melt composition, fluid convection, etc. While BPS theory is useful for well-behaved systems, it does not work in all cases. A critical analysis of the limitations of the BPS theory and later modifications by various scientists was given by Carruthers [31] (from the standpoint of the mother liquor hydrodynamics) and by Chernov [32] (from the standpoint of equilibrium and nonequilibrium processes at the growing interface). See also Handbook chapter "Segregation and Component Distribution" for a description of the limitations of BPS segregation theory.

As mentioned in the introduction, the Faraday Society in 1949 convened one of its meetings for the sole purpose of presenting and discussing papers on crystal growth. This was the first scientific conference devoted to this topic as a separate subject. Subsequently, the proceedings of this conference, entitled *Crystal Growth*, were published in the Discussions of the Faraday Society. During that meeting, Burton and Cabrera [33] presented their research on the influence of surface structure on the rate of

growth of a perfect crystal. They considered two types of surface structures, one ordered (atomically flat) and the other disordered (stepped, containing terraces, ledges and kinks with ledge heights of atomic dimensions). Burton and Cabrera made use of the analogy between the existence of these two surface structure types and two possible states in two-dimensional systems—ordered and disordered *phases*, transferring from one to another as the temperature/binding energy ratio changes. This concept followed the 1945 suggestion by Yakov I. Frenkel that the step should be disordered and possess a kink configuration at nearly each atomic site. As a result, these steps should grow much faster than a step-free terrace. Indeed, only at the kink configuration can an atom join the crystal lattice, and thereby reduce its Gibbs potential to that of any of the bulk atoms in the crystal. In the simple cubic system, for example, only the (110) and (111) faces are flat, all others are stepped [17]. The growth proceeds by the attachment of atoms at Kossel–Stranski kinks along the step ledges [34], but not on the terraces, which do not participate in the growth phenomena. Therefore, on the flat, ordered surface of a perfect crystal, growth will not proceed until a small island or cluster nucleates on the surface, thus producing a step loop that is kinked by thermal fluctuations. The stability of such a cluster is given by the Gibbs–Thomson relationship that describes the cluster’s solubility. If the cluster reaches the critical size, it may expand, generating a new lattice layer. Thus the nucleation frequency (very low at low supersaturations) determines the ordered face propagation rate. If one considers a nonperfect lattice, where the surface contains defects, such as screw dislocations [22], twins, etc., growth can proceed without the necessity for surface nucleation due to the defect providing growth steps.

Burton and Cabrera also examined the kinetics of vapor phase growth on these surfaces, considering the diffusion of the adsorbed atoms across the close-packed crystal surfaces (terraces), where secondary nucleation is required. This was a refinement of the earlier two-dimensional nucleation model proposed by Becker and Döring in which surface diffusion [35] was not taken into account. Combining their results with Frank’s theory concerning the presence of spiral dislocations that can act as growth steps on otherwise atomically flat surfaces, they published together a seminal paper from which the well-known BCF theory derives [36]. In this theory, developed for vapor growth but later extended to solution growth, the boundary between the crystal and nutrient phase was considered to be sharp (interface of zero thickness), i.e., as proposed by Kossel–Stranski, rather than by Gibbs’s finite layer thickness model. In this case, atoms or molecules belonged to only one or the other phase. The BCF theory of layer-by-layer growth of the crystal lattice on smooth surfaces was quantitatively confirmed in numerous studies of growth from solutions, including electrocrystallization.

In the ensuing years, interface structure and surface kinetics models have been refined to include more complex interfaces, including material systems such as biological macromolecules [37]. These and other crystals with large lattice spacings grown from room-temperature solutions have made it possible for in situ atomic force microscopy to capture spiral dislocation sources generating new layers during solution growth, as well as the important phenomena of step bunching, low kink density at steps,

etc. Nevertheless, this theory provided the crystal growth field with a more sound theoretical foundation together with a better understanding of experimental results. It formed an important base from which future studies could be built upon.

The roughening concept was employed in 1958 by Jackson [38] to consider the problem of why many melt-grown crystals of nonmetals had specific faceted, euhedral shapes, whereas metal crystals did not. He derived an elegantly simple theory for the solid–liquid interface structure that could successfully explain and predict experimental results. Jackson used a two-layer Bragg-Williams statistical model (rather than the BCF Onsager model) taking into account nearest neighbor bonds into the solid and lateral bonds within the solid–melt interface. The free energy for adding atoms to a singular (or atomically smooth) interface is calculated until a complete monolayer is formed. Starting with the change in excess free energy associated with randomly adding atoms to such a surface, Jackson found the following relationship for solid–liquid transitions.

$$\alpha = (L/KT_e)(\eta/\nu) \quad (1.2)$$

where  $L$  is the change in internal energy associated with the transfer of one atom from the bulk liquid to the bulk solid (latent heat),  $\eta$  is the maximum number of adatom nearest neighbors on the surface,  $\nu$  is the total number of nearest neighbors of an atom in the crystal, and  $T_e$  is the equilibrium temperature for the phase change. This so-called Jackson “ $\alpha$  factor” consists of two terms: the first is essentially the entropy of melting divided by the gas constant and is a materials parameter, and the second depends on the crystal structure and specific surface under consideration. The crystallographic term is maximum for close-packed planes, and always  $<1$ . It has values of  $2/3$  for a (100) simple cubic, structure and  $1/2$  for (111) fcc and (110) bcc structures. Materials with  $\alpha < 2$  grow with nonsingular interfaces, whereas materials with  $\alpha > 2$  exhibit facets on the growing interface. The former are often metals, with simple centro-symmetric crystal structures, whereas the latter are materials with more complex crystal structures. Using transparent systems having different values of  $\alpha$ , Jackson and Hunt [39] were able to demonstrate experimentally the efficacy of their model. Figure 1.3 shows the crystalline morphologies observed for high and low  $\alpha$  factor materials. A comparison of the BCF and Jackson models was given by Woodruff [40]. In 2004, Chernov [37] discussed how interface growth kinetics has advanced during the past 50 years.

In the years following, interface structure and surface kinetics models were refined to include more realistic interfaces where each interfacial atom cannot be ascribed to one or the other phase. Instead, this disordered interface is viewed as a layer several atomic spacings thick, where all atoms move randomly and, on average over time, realizes continuous transition between the fully ordered crystal bulk and the disordered melt. This approach allowed for the prediction of a kinetic coefficient linearly connecting the supercooling  $\Delta T$  at the rough crystal–melt interface to its growth rate  $V$  for simple liquids, like metals.

$$V = A\sqrt{kT/m\Delta T}/T_e. \quad (1.3)$$

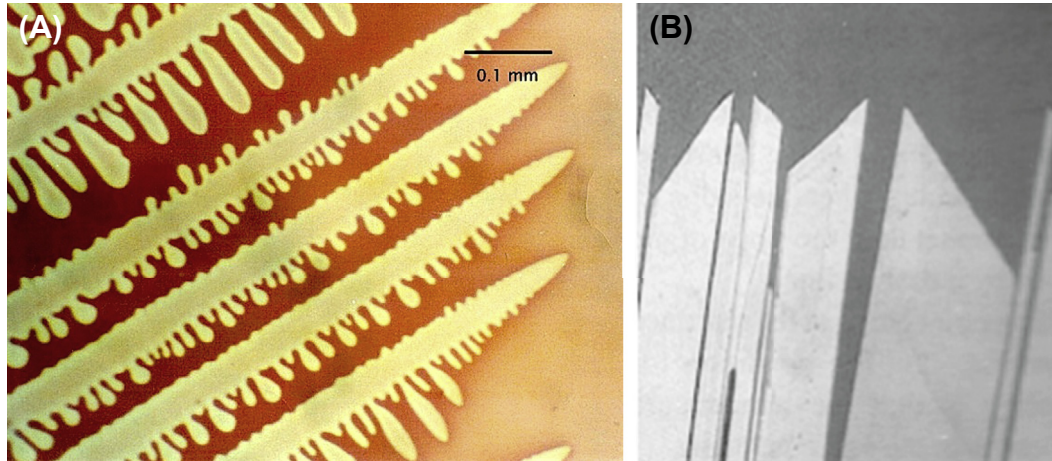


**FIGURE 1.3** Comparison of crystal morphologies for (A) a transparent metal analog with an  $\alpha$ -factor less than 2. This material grows with a dendritic structure and (B) a benzyl crystal with an  $\alpha$ -factor greater than two showing well-developed facets.

Here  $m$  is the mass of the atom while the numerical coefficient  $A$  is determined by the structure of the liquid and is close to unity. All in all, the BCF theory and its further development provided the crystal growth field with a more stable theoretical foundation together with a better understanding of experimental results. It formed an important base from which future studies could be built upon.

In 1953, research to elucidate and quantify the nature of interface instabilities during crystal growth began with the work of Canadian metallurgists Rutter and Chalmers [41]. They postulated that the cellular (honeycomb-like) substructure that formed in solidifying metals containing a small concentration of impurities (as revealed by rapid melt decanting) was due to some type of instability at the growth interface. This led to the idea that a boundary layer containing rejected impurities develops at a growing solid–liquid interface, depressing the melting point of the liquid in that region so that it became supercooled, but at a higher temperature than the interface. The now well-known term “constitutional supercooling” was derived from Chalmers studies.<sup>1</sup> Shortly thereafter, William Tiller, observed banding in lead crystals arising from unintentional variations in the translation rate (hence growth rate). The structural banding was also found to be associated with the boundary layer composition. Professor Chalmers charged his group to develop a mathematical expression for what was happening at the interface to cause these interesting interfacial instabilities. Their discovery was published later the same year [42]. Their simple

<sup>1</sup>G.P. Ivantsov working independently in Russia in the late 1940s postulated the same concept, calling it “concentrational” supercooling (Dokl. Akad.Nauk. SSSR 81 (1951) 179).

relationship for constitutional supercooling provides one of the most useful tools in the crystal grower's arsenal. The relationship, Eqn (1.4) below, shows how the ratio of temperature gradient in the liquid ( $G$ ) to the growth velocity ( $R$ ) must remain above some critical value to achieve stable growth. That value depends upon the material properties of the growth system, i.e., the initial melt concentration  $C_o$  (far away from the interface), the slope of the liquidus curve ( $m$ ), the segregation coefficient ( $k_o$ ) and the diffusion coefficient. To maintain stable growth and avoid constitutional supercooling one requires that

$$G/R > mC_o(1/k_o - 1)/D \quad (1.4)$$

For the crystal grower this means that to produce a crystal without second phases and cellular structure one *must* either decrease the growth rate for a given temperature gradient or increase the temperature gradient. Faster growth rates are typically very desirable, and so many efforts were undertaken to build special furnaces, sometimes incorporating baffling, localized cooling, etc., to achieve steep thermal gradients.

The early roughening transitions models were two-dimensional models based on the Onsager (BCF) or Bragg-Williams (Jackson) models. It was found that computer modeling was needed to study the problem in more complex three-dimensional systems. Leamy and Gilmer [43] were the first to produce simulated computer images both above and below the surface roughening transition. They also determined the free energy ( $F$ ) of a growth step for various values of Jackson's  $\alpha$ -factor [44]. They showed that  $F$  for the step goes to zero at the roughening transition and therefore does not require an energy barrier for new layer formation.

Molecular dynamic simulations have provided detailed information about the process of crystal growth at the atomic level. Its use in morphological stability problems was taken up by numerous groups over the ensuing years which, coupled with experimental work, has led to a significantly greater understanding of the crystallization process (see Figure 1.4).

Modern concepts of interfacial and morphological stability are largely based on the 1963 work of Mullins and Sekerka [45]. Whereas previous researchers knew that various perturbations during growth such as mechanical vibrations, temperature fluctuations, etc., could lead to interface instabilities such as cells and dendrites, they were unable to explain the dynamic mechanisms that were responsible. Mullins and Sekerka developed a mathematical theory of linear morphological interface stability. This was based on small perturbations (sinusoidal ripples) on the growth plane in an unstirred melt that either decay or grow with time. Their analysis led to a more refined relationship that considered the destabilizing effect of the diffusion field and the influence of surface free energy on the boundary conditions. Their results extend the constitutional supercooling criterion described in Eqn (1.3), with several extra terms affecting interface stability [42]. Linear stability theory proves that constitutional supercooling is the correct criterion in the limit of disturbances with small wavenumbers (long wavelengths). The important

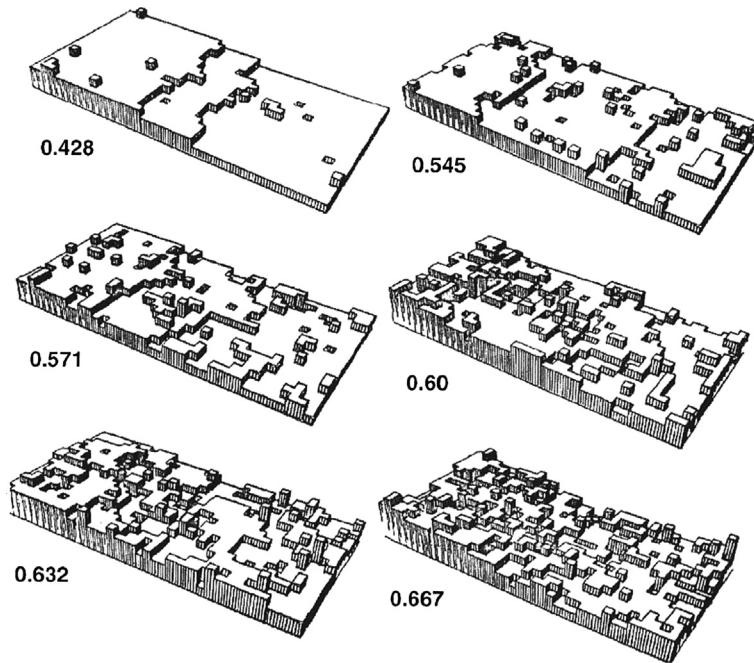


**FIGURE 1.4** Monte Carlo simulations of equilibrium surface structures (microstates) for a simple cubic crystal as a function of temperature (as  $KT/\epsilon$ ) [44]. The surface orientation is the  $(20,1,0)$  and at the lowest temperature,  $KT/\epsilon = 0.428$ , the step edge is clearly rough. As the temperature increases, the roughness increases. At a critical value, the thermal roughening transition, the steps become indistinguishable.

crystal growth/materials parameters affecting interface stability are the temperature gradient normal to the growing interface, the slope of the liquidus from the phase diagram, the growth velocity, latent heat, mass and interfacial energy densities and the thermal conductivities of the liquid and solid. It was also found that stability depends on whether the thermal conductivity of the melt is greater or less than that of the solid. Other researchers expanded on this research to include molecular attachment kinetic effects, interface energy anisotropy, nonlinear effects, etc., among them V. Voronkov [46] whose independent investigation on mosaic and cellular structures actually predated that of Mullins & Sekerka. John Cahn [47] was the first to treat anisotropic surface tension and interface attachment kinetics (for a spherical geometry). Coriell and Serkeka [48] studied the same types of anisotropies for a planar interface. Chernov [49] treated the case of strong anisotropies and Hurlle [50] analyzed the influence of melt convection.

Historically, understanding crystal morphology has provided much of the impetus driving theoretical crystal growth studies. Aside from the regular crystalline forms found in nature (e.g., quartz) or produced during solution or vapor growth in the laboratory, other more complex crystalline morphologies such as dendrites and multiphase eutectic systems have stimulated researchers to uncover the underlying mechanisms involved in their creation.

Dendrites are “tree-like” branched crystal structures that grow in various media under unstable growth conditions. The earliest humans were sure to have noticed and pondered the reason behind the large variety and symmetry of the beautiful snowflake. Snowflakes form when microscopic supercooled cloud droplets freeze and their morphology is dependent on the ambient conditions during their growth. Dendrites also can form during the crystallization of metals, inorganic and organic compounds and even biological macromolecules from melts and solutions. They are common in metals and alloys grown from the melt in shallow temperature gradients.

Dendrites typically contain a stem terminating in a tip and side branches along the stem (see Fig 1.3a). Growth proceeds by steady-state propagation of the tip and a time-dependent crystallization of secondary and tertiary side branches. In 1947, G.P. Ivantsov [357] was the first to identify these self-reproducing crystal shapes—like paraboloids, the basis of the dendrite tip. In pure materials, growth is controlled by diffusion of latent heat away from the advancing growth interface, and in impure systems and alloys it is driven by solute buildup at the interface and where chemical diffusion dominates over thermal transport. In 1960, Temkin [51], and shortly afterward Bolling and Tiller [52], described the role of thermodynamic and kinetic driving forces in the dendritic growth of pure materials. From that time onward, theoretical and experimental dendritic growth studies have proceeded, relying on newer mathematical and computational approaches. Hamilton and Seidensticker [53] examined the role of twin planes in the rapid dendritic propagation of germanium crystals on the basis of re-entrant corner nucleation. In 2004, Glicksman and Lupulescu [54] reviewed 40 years of progress toward understanding the mechanisms involved in the dendritic growth of pure materials including low gravity experiments. An update on this subject is provided in the Handbook chapter “Dendritic Growth.”

Growth of polyphase alloys or compounds by unidirectional solidification has also been the subject of much interest to crystal growth researchers. These structures can be produced from eutectic ( $L \rightarrow \alpha + \beta$ ), monotectic ( $L_1 \rightarrow \alpha + L_2$ ) and peritectic ( $L + \alpha \rightarrow \beta$ ) three-phase melt systems. A eutectic crystal can contain four types of structures within a matrix phase (1) parallel lamellar, (2) parallel rods, (3) globular particles of regular shape and (4) irregularly shaped particles. Researchers were interested in the relationship between growth velocity on lamellar spacing and interface undercooling. R. Vogel [55], in 1912, was the first to postulate that growth occurred by both phases growing simultaneously. Eutectic growth theory, however, remained largely qualitative until 1957 when Tiller [56] introduced his diffusion model of eutectic growth. This development was based on the earlier theory on eutectoid growth by Clarence Zener (1905–1993). Tiller’s work was used as a basis for Jackson and Hunt’s model of 1966 [57], a well-known model and one often used as the basis for later papers. Readers interested in this topic are directed to Glicksman’s book [58] that provides, among other crystal growth topics, an excellent review on progress in eutectic solidification.

The transport of heat and mass during crystal growth is of great importance in the design of a growth process and in understanding the resulting features found in the

crystals produced. In melt growth, the dominant factor is often heat transport, whereas in solution and vapor growth, mass transport normally dominates. As to which transport mechanism dominates, it is a matter of degree and an important consideration is what happens in the boundary layer near the interface. As a crystal grows, latent heat is evolved and the allowable growth speed depends on its removal. Therefore, the geometry of the system, the thermal properties of the crystal, the ambient atmosphere and the growth rate all comprise important factors. In addition, the growing crystal needs fresh nutrient to sustain its growth and the rates at which various species reach the interface will partly determine the maximum allowable growth rate and crystal perfection. The concentration of dopant and/or impurity species are often different in the interface region than in the bulk medium, thus influencing mass transport. Instabilities in heat and mass flow can lead to defects such as striations and interface breakdown. The degree and nature of melt convection will strongly affect both the growth process itself and the crystal produced. Many processes, for example Czochralski growth, use forced convection (crystal rotation) to enhance the growth rate and improve thermal and crystal homogeneity, whereas in other methods, for example, vertical and horizontal Bridgman growth, natural buoyant convection occurs from thermally and solutally induced density gradients. In Czochralski growth, the crystal is rotated and sometimes the crucible as well. W. Wilcox [59] and J. Carruthers and K. Nassau [60] studied the fluid dynamic behavior of such systems, as did many other researchers. The effect of fluid flow and flow instabilities are also important in other melt growth processes such as unidirectional solidification, vapor deposition and solution growth. See also Handbook chapter “Segregation and Component Distribution.”

Defects, inhomogeneities, segregation, and interface effects during crystal growth have all been the subject of numerous studies. Some useful reviews have been provided by D. Hurlé and P. Rudolph [61] and C. Wang et al. [62].

### 1.3 Crystal Growth Methods

Crystal growth technology is mainly an applications-driven field. In the last 60 years or so, the major applications have been in the fields of electronic and optical materials. Crystals, however, can be prepared from all types of materials including elements, alloys and inorganic, organic and biological compounds. The compounds can vary from simple binary mixtures to multicomponent systems having numerous components and complex molecular or crystal structures. As a result, crystal growth methods vary widely depending on the thermodynamic and kinetic properties of the system of interest. The starting point for developing a viable crystal growth process begins with a thorough knowledge of the phase relations of the system under investigation. For example, we need to know whether the compound melts congruently, has a phase transformation below its melting temperature, has a high vapor pressure, etc. The most appropriate strategy for producing a crystal depends on the size required, purity and an ability to

control its defect structure (either by elimination, neutralization or incorporation). Crystal dimension requirements (size and shape) are a very important issue in determining the methodology. Single crystals can be grown in bulk, thin film, particulate and fiber form and from the nanometer scale up to meter dimensions. During the last decade, nanoscale wires, whiskers and quantum dots have been found to have unique properties, and this has opened up the possibility for new and improved devices for advanced applications. Classical single crystal growth methods and newer techniques have been used to create a variety of desired nanostructures.

The number of crystal growth methods available to the crystal grower is quite large and varied. The simplest approach to categorizing them is by the nutrient phase from which the crystal is grown. Single crystals can be grown from (1) a liquid phase (melt or solution), (2) from a vapor phase (condensation, sublimation or reaction) or (3) from within a strained solid. Each method has certain advantages and disadvantages that depend on both the properties of the material system involved and the application requirements. Melt growth methods are generally preferred to other methods wherever possible, while solid-state growth methods are the least useful from a commercial point of view.

The growth of a crystal from any nutrient phase requires either a seed crystal or the creation of a solid interface within the growth medium by homogeneous or heterogeneous nucleation. Homogeneous nucleation requires additional energy in the form of supercooling in melt growth or supersaturation in solution and vapor growth methods. Wherever possible, however, the use of a seed crystal or a compatible substrate (as in thin film growth) is desirable. We will explore some of the strategies that have been employed by growers to prepare very high quality, high performance materials.

The theoretical studies mentioned above range from fundamental questions about the mechanisms involved in various crystallization environments to computer simulations of actual growth systems. Issues such as growth rate anisotropy, component segregation, interface faceting, stability and morphology, fluid dynamics, thermal stability and gradient effects, etc., have been extensively studied. During the last decade in particular, computer modeling has helped growers design and modify growth systems in a more systematic way to create thermal and fluid flow environments to enhance interface shape, stability and growth rates.

### 1.3.1 Melt Growth

When a material melts under nearly congruent conditions and has no low-temperature destructive phase transformations, it is usually desirable to prepare a single crystal of it directly from its melt. Often seed crystals are used to control the orientation and to take advantage of growth rate and thermal anisotropies (heat and expansion). The most useful methods include the Czochralski, Bridgman–Stockbarger, Kyropoulos, Verneuil (flame fusion), and float zone methods. There are innumerable variations to these

general techniques such as the heat exchanger method (an inverted Kyropoulos configuration) and the pedestal growth and micro pull-down techniques to name a few. The discussion of melt growth will begin with the oldest technique for growing large crystals from a melt: Verneuil's flame fusion method.

### 1.3.1.1 *The Nineteenth Century and the Verneuil Process*

Alchemists were not only trying to transmute base metals into gold, they were also attempting to grow gemstones in the laboratory. From the beginning of the nineteenth century, various researchers were attempting to grow crystals of diamond, emerald, ruby and sapphire by various techniques, particularly by melting various oxide mixtures. These early methods, however, only produced small crystallites. A really viable commercial process did not appear until the work of Auguste Victor Louis Verneuil (1856–1913) on the growth of large ruby crystals was made public in 1902. Actually, he developed the now well-know flame fusion process a decade earlier and spent the next decade improving the method before making it public knowledge. A very thorough description of the life and work of Verneuil was given by K. and J. Nassau [63]. Verneuil (see Figure 1.5(A) below) was a French “renaissance” man and well-beloved teacher, actively interested in music performance and art and whose accomplishments spanned many different areas of chemistry. He became interested in chemistry working in his father's photography shop (his father changed careers after meeting Mr Deguerre (Louis Jacques Maude, 1787–1851), the inventor of photography. In 1873, at age 17, Verneuil went to study in the chemical laboratory of the distinguished Professor Edmund Frémy

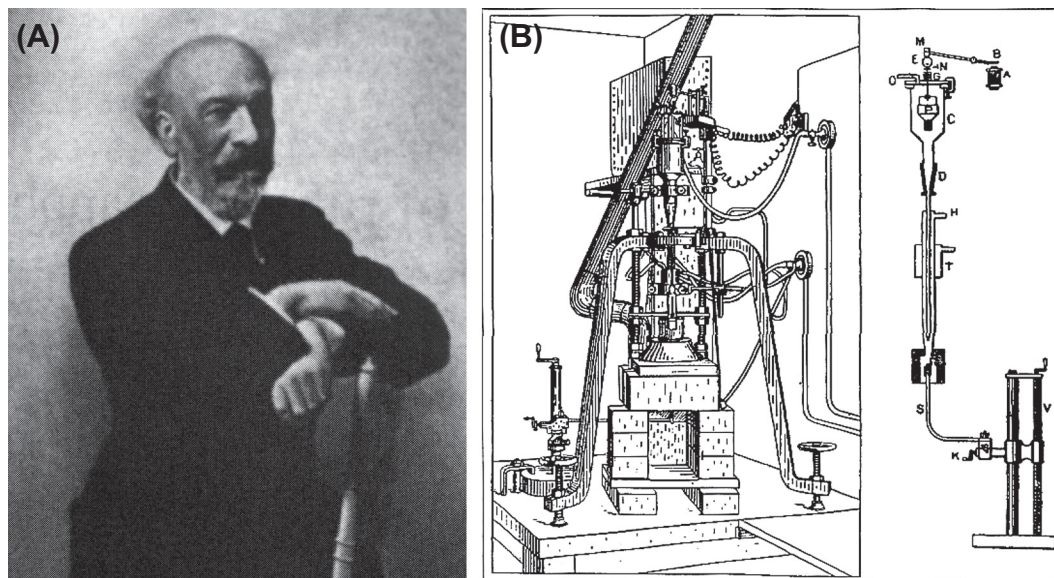


FIGURE 1.5 (A) A photograph of Dr. A.V.L. Verneuil, and (B) a schematic diagram of Verneuil's crystal growth apparatus [63].

(1817–1894). He eventually earned his doctoral degree in 1886. In his earlier years in the Frémy laboratory, he participated in research on ruby crystal growth by a melting technique using porous alumina crucibles. He also became friends with Henri Moissan (1852–1902) who worked on diamond crystallization in Frémy's laboratory.

In 1886, an unknown group from Geneva started selling larger synthetic ruby crystals than were available elsewhere. It is now believed that these so-called “Geneva Rubies” were actually grown by an early version of the flame fusion process [63]. Verneuil was intrigued by these samples, and it stimulated him to develop the method for which he became famous. The mysterious group from Geneva ceased operation in 1905, not long after the Verneuil Process had gone into commercial production. Such groups have appeared from time to time trying to pass off synthetic crystals for natural stones that garner much greater value.

The flame fusion method was first developed to produce large, high-quality ruby for the gemstone market and also for watch bearings. The process, which is still in use today, involves passing a powder of the compound through a vertically aligned oxy-hydrogen flame. Molten droplets descend by gravity onto a rotating alumina pedestal containing the growing crystal and the crystal grows upward on the pedestal. The basic apparatus used by Verneuil is shown in [Figure 1.5\(B\)](#). Temperature gradients are steep, boules are prone to cracking and the early powder delivery systems were often unreliable. Important processing refinements were made by Verneuil over his lifetime to improve the process reliability and crystal quality. The first problem he solved was the severe cracking problem. He accomplished this by reducing the contact area of the boule with the pedestal. While preventing cracking, the boules after growth were still highly strained. This strain was relieved naturally when the boules split in half or were split by hand. Powder delivery was done by mechanical tapping mechanism mounted on a hopper containing the charge powder. For ruby growth, the powder Verneuil used was a mixture of ammonium and chrome alums. The chromium oxide concentration in the boules was  $\sim 2.5\%$ . The oxygen content in the ambient gas phase was critical for achieving the appropriate oxidation state in the crystal. A flame rich in hydrogen and carbon was necessary to prevent introduction of gas bubbles in the molten ruby melts.

In 1909, Verneuil worked with L. Heller & Son of New York and Paris on developing his process for making blue sapphire. Instead of chromium additions, the sapphire was doped with a mixture of iron and titanium oxides, two impurities found in natural minerals. He suggested that the titanium in the crystal gave the deep blue color by converting the ferrous ions created by the flame back to ferric ions. Another pioneer of the flame fusion growth method was Leon Merker (1917–2007). He also worked with the Heller Co. starting during the early days of World War II, after he escaped fascism in Europe and came to the U.S. to study at the University of Michigan. Based on a friend's recommendation, he met Mr Heller from France. After some fruitful discussions, Heller assigned Merker the task of setting up the Verneuil Process for ruby and sapphire in New Jersey. The venture was successful and the General Synthetics Corporation was formed

in 1941 to provide ruby to the military and for the gem industry [64]. Merker also worked on barium, calcium and strontium titanates; the latter two with greater success.

Since Verneuil dedicated much of his career to the successful development of a commercial process for growing sizable crystals with controllable properties, he might be considered the father of the commercial crystal growth industry.

### 1.3.1.2 *The Twentieth Century*

Even while Verneuil was improving on his method, other researchers at the turn of the century were beginning to produce crystals in the laboratory to study both their solidification behavior and physical properties.

One of the earliest was Gustav Tammann (1861–1938). He was born in Russia of Baltic and German parents and spent most of his life in Germany. Among other notable achievements, he established the first Institute of Inorganic Chemistry in Germany at Göttingen University in 1903. Tammann's interests led him to study the solidification of metal alloys and their nucleation behavior. He made important contributions to the fields of heterogeneous equilibria, crystallization and metallurgy. One of his important contributions to crystal growth involved the solidification of metal alloys in long narrow tubes tapered to a point to both confine nucleation and supercooling to a small volume and thereby promoting the propagation of a single crystal along the tube [65]. He was probably one of the first to understand the relationship between grain selection and growth rate anisotropy and the concept of confining the melt to control the number of grains that form. His method would be classified today as the gradient freeze method. He also grew crystals of a number of organic compounds and studied their crystallization behavior.

Within the same time period, Obreimov and Schubnikov from Saint Petersburg, Russia, [66] published a paper describing the growth of metal crystals using a modification of Tammann's method, i.e., in a long glass tube with an imposed temperature gradient along its length. They also briefly discuss the easy to operate Czochralski process (to be discussed below) but rejected it in favor of the Tammann's method because the free-standing Czochralski crystals were not of uniform shape and some of the low-melting metals could deform during growth without being supported. In their experiments, they used a vertical cylindrical tube tapered at the bottom like Tammann. Nucleation was achieved by cooling the tapered tip with cold air and then, after crystallization in this region was accomplished, slowly cooled the furnace to propagate the crystal up the length of the tube. Both these methods distinguish themselves from the Bridgman and Stockbarger methods (also to be discussed later) in that growth is not achieved by moving either the ampoule or furnace to solidify the melt.

### 1.3.1.3 *The Czochralski Crystal Pulling Method*

#### 1.3.1.3.1 **The Invention**

Following Verneuil's pioneering work, a number of other researchers began to grow metal and alkali halide crystals for property studies. In 1918, Jan Czochralski, a well-known young Polish metallurgist (head of AEG's metals laboratory in Berlin), published a

paper [67] that would describe a technique that quickly became one of the most powerful methods for growing crystals in use today. In a story related by Tomaszewski [68], Czochralski, while working late at night in his laboratory, discovered by accident the crystal pulling method for which he became famous. His studies concerned the crystallization rate of metals and while working on his experimental notes, instead of dipping his pen tip into the ink well, dipped it instead into a crucible of molten tin on his desk. When he pulled it out he found a long filament of solidified tin on the end. He subsequently found it to be a single crystal. He then realized the value of studying crystallization rates using such a device. His early apparatus (see Figure 1.6(A)) consisted of a clock-motor-driven lifting mechanism. Replacing the pen tip, a short tapered glass rod with a hook on the end was held on a silk thread connected to the pull mechanism. The rod could be raised or lowered in a continuous fashion. By dipping this rod into the surface of the melt, he was able to solidify metal onto it and pull out crystals of tin, lead and zinc in a continuous and controlled fashion. Czochralski later modified the glass rod, incorporating a capillary at the bottom to draw up the molten metal. This had the effect of restricting nucleation to the limited volume of melt in the capillary. With this apparatus he produced 1 mm thick single crystal wires at maximum crystallization velocities of up to 140 mm/min and in lengths up to 19 cm. Czochralski's life and research accomplishments can be found in Tomaszewski's monograph [68].

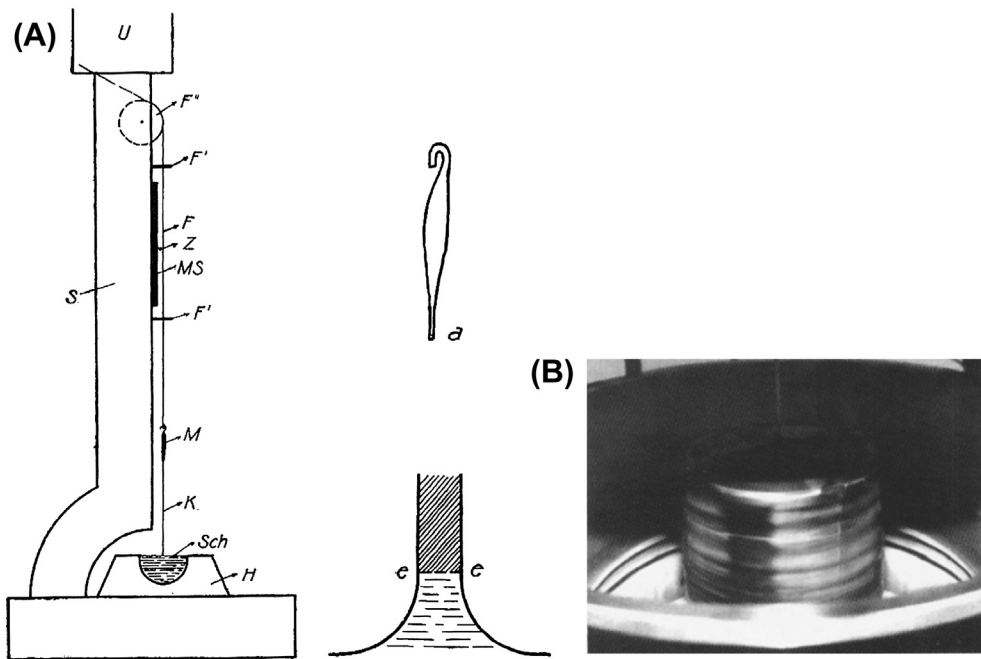


**FIGURE 1.6** (A) Czochralski's original experimental setup [67], and (B) a photograph of a five-inch diameter commercial single crystal silicon boule growing by Czochralski's method. (From the front cover of the ACG Newsletter 13 (1983)—photo courtesy of the Siltec Corp).

Czochralski's pulling method was almost immediately put to use by von Wartenberg [69] to grow zinc single crystal wires onto oriented seed crystals. Somewhat later, Von Gomperz [70] pulled single crystal fibers of metals through a hole in a mica plate floating on the surface of the melt. He also used a capillary for seeding. His work was the forerunner of the edge-defined film-fed growth (EFG) and the laser heated pedestal fiber growth methods. In 1928 E.P.T. Tyndall [71] wrote a paper on the *Factors Governing the Growth of Zinc Crystals by the Czochralski-Gomperz Method*. In 1937, Henry Walther of Bell Laboratories published the first paper on the use of Czochralski's method for the growth of nonmetals [72]. He rejected other methods such as the Kyropoulos method because he was intent on growing long, uniform, cylindrical bars of NaCl single crystals for property measurements. He therefore was attracted to the pulling methods that Czochralski and von Gomperz used to grow low-melting metals. He used a quartz crucible to hold the melt and dipped a platinum rod or closed tube into its surface, sometimes with an oriented seed attached. In the beginning, he used Kyropoulos's method of pulling the tube up slightly after the first melt solidified on the rod to reduce melt contact with the crystalline solid that formed. He placed an air-cooled coil containing small holes above the melt to cool the growing crystal and pulled up at rate of 5 cm/hr while rotating the crystal at 10 rpm. He was the first to apply rotation to the Czochralski method and produced the first bulk crystals of a high melting point compound by this method. Walther successfully produced NaCl boules 2 cm in diameter and 30 cm long. It is rather amazing that this paper, although published in a prominent journal and referenced twice a few years after its publication, was only found very recently (by Reinhard Uecker [73]). Strangely, even many Bell Laboratories researchers from that period to the present time seem to have been unaware of Walther's work, and it was not mentioned in the rather extensive review of engineering and science research in the Bell system during the period 1925–1980 [30]. In 1940 Evans [74] used Walther's method to grow single crystals of NaCl, KCl and KBr.

#### 1.3.1.3.2 Semiconductors

Bardeen and Brattain discovered the transistor in 1947 using large-grained Ge samples produced by unidirectional solidification [30]. Shortly afterward, it was demonstrated that single crystals were better, and this led to a dramatic expansion of the crystal growth field in general, and the Czochralski method in particular. This versatile technique has been applied to a wide variety of materials of commercial importance—particularly semiconductors and optical materials.

According to [30] (p. 422), “A single crystal growth technique, first used by J. Czochralski in 1917, was adapted and improved in 1950 by G.K. Teal and J. B. Little for the growth of single crystals of germanium” [75]. They dipped an oriented Ge seed crystal into the melt surface and, while rotating, pulled modest sized crystals (by today's standards) of 2.5 cm diameter and 10 cm in length. The minority carrier lifetimes were significantly better than in polycrystalline materials, and therefore the semiconductor researchers shifted their efforts to producing bigger and better crystals with control of

the dopant concentrations and uniformity. In addition, the single crystal technique allowed for the creation, during growth, of n-p-n junctions by perturbing the growth conditions [76]. While this junction technique was eventually superseded, it was an important step in transistor technology. The importance of homogeneity in semiconductor devices led many researchers to study the thermodynamic and kinetic aspects of impurity and dopant incorporation. One such seminal study, as mentioned earlier, was that of Burton, Prim and Slichter [28,29]. Shortly after the germanium research activities began, the focus shifted to silicon whose properties were deemed to be superior. In 1952, Teal and Buehler [77] reported on the Czochralski growth of silicon crystals—a much higher melting compound (1414 °C compared with 938 °C for Ge) and more difficult to grow due to its reactivity. Over the years, crystal sizes have constantly increased (see Figure 1.6(B) above), and today commercial systems are available to grow Si boules 12 in in diameter and 6 ft long from which substrates can be cut for the preparation of integrated circuits. In situ recharging to grow longer crystals and controlling melt flows using magnetic fields were added over the years to boost production rates and quality. One of the most important factors in producing high quality crystals was not only to control impurities and other point defects but their complex interactions with each other, as well as with dislocations. Removal of one defect can lead to the redistribution of other defects to lower the overall energy of the system.

It was recognized early on that purity of the starting material was critical to semiconductor performance. In 1951, William Pfann [78] invented the zone refining method for ultrapurifying Ge. This very important method, in wide use today, has been successfully adapted to the purification of all classes of materials. Shortly afterward, Theuerer [30] invented the crucible-free float zone process to grow O<sub>2</sub>-free silicon. Oxygen incorporation during Czochralski growth was due to the use of SiO<sub>2</sub> crucibles. Theuerer's method is still in commercial use today to produce O<sub>2</sub>-free Si for special device applications. It also has been used with other materials for which melt-crucible interactions are problematic. With the use of optical heating systems (such as lasers or xenon lamps), its simplicity makes it very useful for growing crystals of numerous materials for physical property studies. Pfann [79] also invented the zone leveling crystal growth method that is a combination of horizontal Bridgman growth coupled with zone refining. In this case a seed and a dopant are placed at one end of a horizontal tube and by moving a molten zone along the tube, the dopant could be uniformly distributed along the boule. This method was used early on to produce transistors and diodes.

It became apparent that dislocations were affecting the electrical properties of Si single crystals and the need for zero-dislocation material arose. In 1959, William Dash [80] developed a method for doing this during Czochralski growth. Since dislocations propagate mainly from the seed, he used high-quality seeds together with careful control of the initial growth conditions. He was able to produce dislocation-free crystals by “necking” down the growing boule to a very small diameter before widening it back out to the desired size.

Important advances in both purification and control of crystalline perfection has led to the improved performance of Si devices.

When compound semiconductor materials such as GaAs, InP and their alloys became important to the electro-optic field, special Czochralski techniques had to be developed because they have high vapor pressures at elevated temperatures. In 1962, Metz et al. [81] were the first to report the use of molten  $B_2O_3$  as a melt encapsulant for the Czochralski growth of PbTe. Both Pb and Te are volatile at the compounds melting temperature, and they successfully sought to cap the melt to prevent losses. In 1965, Mullins et al. [82] demonstrated that molten  $B_2O_3$  was also a useful encapsulant for the growth of GaAs and InAs. They were able to adapt a commercial low-pressure Czochralski system for the growth of these compounds. This method is now known as the liquid encapsulation Czochralski (LEC) method. A few years later, Mullins et al. [83] extended their work to include the growth of GaP and InP in high-pressure furnace systems. One problem with group V elements was that when the crystal emerges from the encapsulating layer, it starts to lose P or As from its surface. In 1983, Azuma [84] came up with an innovative approach to inhibit these losses. He used a pressure balancing system to control the partial pressure of P in the InP growth chamber. In the upper chamber was extra  $P_4$ , maintained at a pressure such as to prevent evaporative losses at the crystal surface.

### 1.3.1.3.3 Oxide Growth

Following the success of the Czochralski method for growing elemental Si and Ge single crystal boules at Bell Laboratories, they and other laboratories started to use this method extensively for growing bulk single crystals of oxide compounds for laser, nonlinear optical, scintillator and numerous other applications.

The laser was predicted by Arthur L. Schawlow and Charles H. Townes in 1958 [30, 358, 359] but not actually demonstrated until the work of Maiman in 1960 [85] with a single crystal ruby rod prepared at the Union Carbide company. In the same year, Nassau and Van Uitert [86] were the first to use the Czochralski's method to grow a high-quality oxide crystal. They prepared laser crystals of Nd:CaWO<sub>4</sub>. During the following decade, the Czochralski method was vigorously pursued in many research and industrial laboratories around the World. A wide variety of important optical materials were grown, including LiNbO<sub>3</sub> [87,88], LiTaO<sub>3</sub> [89], Bi<sub>12</sub>Ge(or Si)O<sub>20</sub> and Sr<sub>x</sub>Ba<sub>1-x</sub>Nb<sub>2</sub>O<sub>6</sub> [90], YAG (Y<sub>3</sub>Al<sub>5</sub>O<sub>12</sub>) [91], Nd:YAG [92], Sapphire [93,94], and Gd<sub>3</sub>Ga<sub>5</sub>O<sub>12</sub> (GGG) [95]. Many of these materials are still commercially important. A concise history of oxide crystal growth by the Czochralski method was given by C. D. Brandle [96].

Many improvements to the method were made over the succeeding decades. Compositional variations along the length and diameter were of major importance and stimulated the construction and analysis of related phase diagrams. It was found, for example, that the stoichiometric composition was not always the congruent composition [97] and to get uniformity one needed to shift the composition to the off-stoichiometric congruent composition to achieve homogeneity. Another problem often

encountered was that the shape of the phase field boundary of the compound might be curved instead of straight leading to precipitation of a second phase.

During the 1960s, very little was known about how the growth interface shape could influence crystal quality. This was very important in Si growth where zero-dislocation crystals rely on a particular interface shape. Cockayne et al. [98] were the first to show that interface shape could be modified and controlled by crystal rotation. Nominally, crystals growers find that a slightly convex interface toward the melt is most desirable. Another factor of major importance in melt and solution growth is fluid convection. It affects mass and heat transport and therefore interface shape, boundary layer and growth rate instabilities, etc. In Czochralski growth natural convection and crystal rotation can interact to modify both the interface shape and the composition in the melt near the growth interface (boundary layer). Various researchers have achieved significant improvements in crystal quality by controlling these parameters.

The application of computer modeling to help solve crystal growth problems was begun in the 1980s by Robert Brown and his group at MIT. One example is a paper written by Derby and Brown [99] on the dynamics of Czochralski growth. One of the major tasks of computer simulations is to model the flow regimes in a system in which the thermal configurations are adjustable. In recent years, facilitated by the dramatic increase in computing power, almost all types of crystal growth processes (Bridgman, float zone, etc.) have been modeled. Simulations performed have been very successful in helping design and guide refinements to laboratory and commercial crystal growth process.

During Czochralski growth, the melt level in the crucible drops as the crystal grows. This changes a number of factors including the thermal gradients and convection patterns. Often the temperature has to be changed during growth or some other parameters modified. Whiffin and Brice [100] have shown that melt height can affect thermal oscillations in the melt. These thermal fluctuations can lead to growth rate variations and crystalline imperfections such as striations. A striation is a compositional variation parallel to the growth interface, usually caused by poor temperature control and/or melt oscillations. In the 1960s most growth was carried out manually, i.e., the temperature was changed or the crucible position altered by analog temperature and motor controllers. With commercialization came the need for automated diameter control systems. These were based on either crucible or crystal weighing or by controlling the meniscus position optically.

#### 1.3.1.4 *Bridgman–Stockbarger/Gradient Freeze Methods*

Little did Percy Bridgman (1882–1961) or Donald Stockbarger (1895–1952) know at the time of their respective discoveries that their names would become historically intertwined in describing one of the most popular techniques for growing crystals. Their versatile method(s) made possible the growth of many different types of materials including metals and their alloys, semiconductors, and both inorganic and organic compounds. It was also a method that allowed the preparation of some of the largest manmade crystals ever produced.

Percy Williams Bridgman was a Noble Prize-winning American physicist working at Harvard University, only a few miles away from MIT where Donald C. Stockbarger worked as an Associate Professor of Physics. His prize (1946) was for his work in the field of high pressure physics. The crystal growth method he developed and published in 1925 [101] departed from the work of Tammann [65] and Obreimov and L. Schubnikov [66] in that the vertical tube containing the melt was not stationary during growth. Growth was initiated in a capillary tube at the bottom end of a larger cylindrical ampoule and propagated upward along the tube by lowering it down through a single zone vertical tube furnace and out the bottom. The capillary was used for seed selection and was further enhanced by reducing the capillary diameter at the juncture between the capillary and the larger bore container. His first experiments were done using bismuth melts. Not long afterward, various other researchers used his method or variants of his method to grow other metal crystals, such as copper, and zinc.

In the late 1920s Stockbarger started his work on the growth of large, high-optical-quality crystals of LiF and later CaF. At first, he tried Bridgman's method [101] for CaF but it required more careful atmosphere control to prevent hydrolysis, better starting material purity and temperature stability to produce useful crystals. This led Stockbarger to modify Bridgman's method [102,103]. He used a so-called vertical "elevator furnace" that had two graphite heaters separated by a Mo baffle through which a covered crucible containing the melt could be passed from the upper higher temperature region into a lower temperature section by a motorized translation device. The use of a two-zone furnace led to better control of the thermal gradient at the growth interface. The crucible, support rod and pedestal were graphite. The V-shaped crucible bottom rested in the pedestal. There was no capillary region below the tapered region for seed selectivity, and the included angle was much larger than those used in the Bridgman and other earlier methods. So it is speculated that seed selection was controlled by the locally steep gradient at the tip created by the thermally conducting graphite support rod coupled with the baffle, thereby limiting the volume of super-cooled melt that can form.

The Bridgman–Stockbarger method (shown in Figure 1.7 below) has been widely used to grow crystals of varying sizes from its development in the 1920s until the present day. It has also been used extensively in a horizontal configuration. While initially used for metals and then shortly afterward for inorganic optical materials, it has since been used to grow hundreds of other compounds including semiconductors (GaAs, CdTe, HgCdTe, and chalcopyrite compounds such as CdGeAs<sub>2</sub>, ZnGeP<sub>2</sub>), organic materials, oxides such as Pb(Mg<sub>1/3</sub>Nb<sub>2/3</sub>)O<sub>3</sub>–PbTiO<sub>3</sub> (PMNT) and halides such as Tl:CsI and Tl:NaI, and Eu:SrI<sub>2</sub> etc. Process improvements include the use of the accelerated crucible rotation technique to improve melt homogeneity and interface boundary conditions [104], vibroconvective mixing [105], baffles in the melt near the interface, growth under high pressure, etc.

The gradient freeze (GF) method of Tammann [65] differs from the Bridgman–Stockbarger approach in that there are no moving parts. Neither the ampoule nor furnace

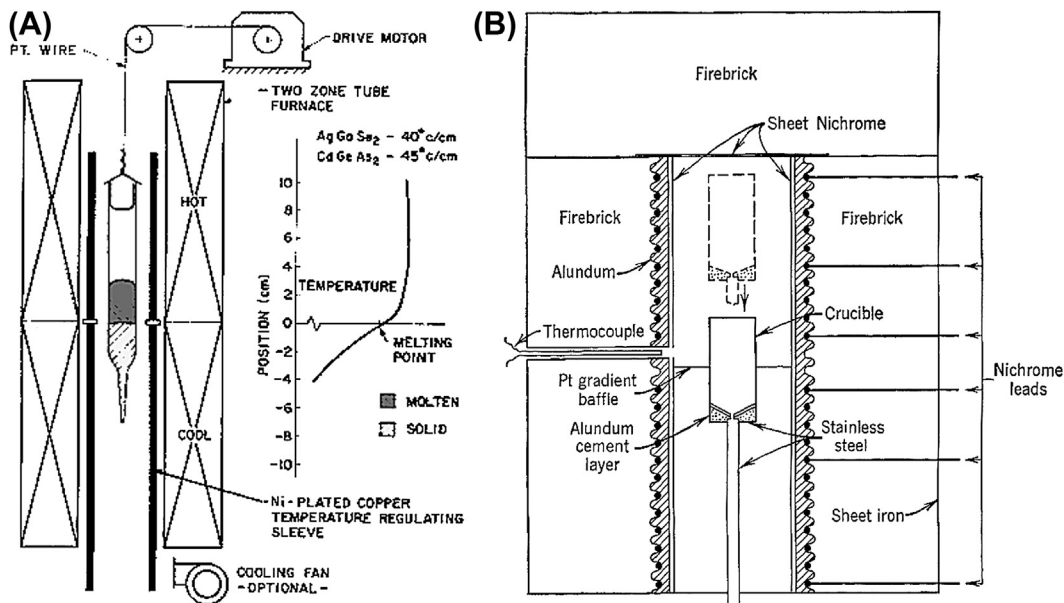


FIGURE 1.7 (A) Drawing of a Bridgman apparatus showing a tapered crucible being lowered through a stationary furnace having a steep gradient at the growth interface. In Bridgman's experiments the crucible is lowered out of the furnace. (B) A schematic diagram of Stockbarger's growth apparatus. Note the platinum baffle that separates the two furnace zones for gradient control and the crucible pedestal.

is translated with respect to the fixed thermal gradient in the furnace. Instead, a temperature gradient is maintained across the melt-containing crucible such that when the temperature of the furnace is lowered, the cool end of the melt solidifies first, and the rest of the melt solidifies layer by layer as the freezing point moves across the melt. This method is simple to implement and was used for the growth of a number of materials. Its big disadvantage was that as the furnace temperature decreased, so did the gradient across the remaining melt. Under constant cooling conditions this change in gradient could lead to changes in growth velocity and thereby variable crystal properties along its length due to component segregation and perhaps interface breakdown. One method used to solve this problem was by continuously changing the furnace-cooling rate to maintain constant freezing rate in the melt. In 1986, Gault et al. [106] successfully applied the vertical gradient freeze method (VGF) to the growth of large diameter GaP, InP, and GaAs crystals.

Attempts to grow some important III-V compounds by the vertical Bridgman and gradient freeze methods were complicated by the fact that these compounds expand on cooling and can aggressively stick to the walls of many crucible materials [107]. These methods both exist in horizontal versions that are applicable to certain important commercial crystals. While many different types of crystals have been grown by the horizontal Bridgman and gradient freeze techniques, their sizes are limited compared their vertical counterparts, and the boules have noncircular cross-sections.

### 1.3.1.5 Nacken–Kyropoulos Methods

During the early decades of the twentieth century, many new developments in crystal growth technology came out of Germany. During the 1920s in particular, a burst of activity in the field led to numerous growth techniques being developed, many of which are being used today in either their original or modified form.

One of the most important crystal growth pioneers of this period was the German mineralogist Richard Nacken (1884–1971). A few years before Czochralski's discovery, he reported on a process for growing crystals from the surface of a melt using a cooled copper rod with a rounded end and a seed attached [108]. Nacken's apparatus is illustrated in Figure 1.8(B) below. The general idea was to locally supercool the melt adjacent to the rod and initiate growth under controlled conditions. After growth started, the furnace temperature could be lowered to keep the seed growing. No pulling was involved. As the crystal grows, the melt level drops due to the higher density of the crystal. The method was later used by J. M. Adams and W. Lewis [109] to grow very large ice crystals. Nacken also developed a viable hydrothermal process for growing quartz crystals. His unpublished work was found in secret WW II German reports. E. Buehler and A.C. Walker at Bell Laboratories [110] based their successful hydrothermal quartz growth technology on Nacken's process.

About 10 years later, Spyro Kyropoulos (1887–1967), a student of Tammann and professor of Applied Physics at the Gottingen University (later he taught at the California

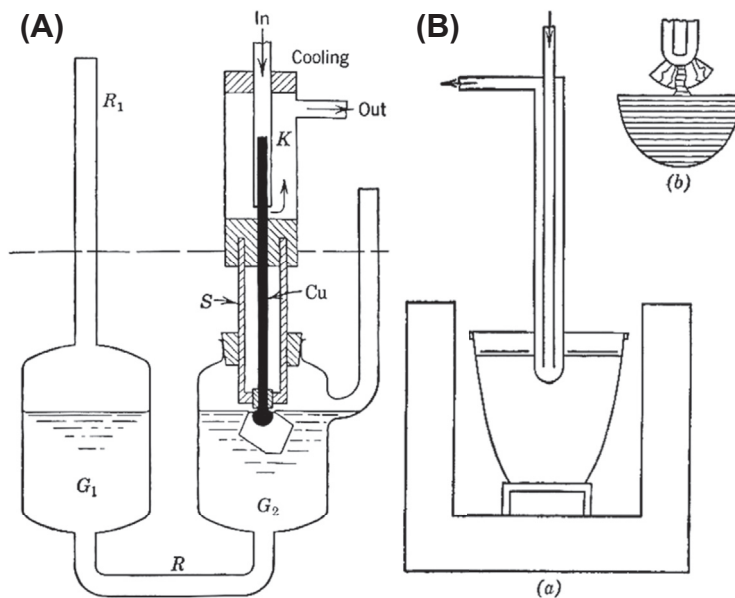


**FIGURE 1.8** (A) A drawing of Nacken's apparatus illustrating the growth of a faceted crystal using a seeded cold "finger" inserted into the melt's surface. (B) A schematic diagram of Kyropoulos's experimental setup where, unlike Nacken, a cold rod is placed in the melt surface without a seed. The inset shows how seed selection can be accomplished using a rounded seed rod.

Institute of Technology) took up Nacken's melt growth method to grow crack-free alkali halide crystals for precision optics. The advantage of Nacken's method is that the crystal is grown within the melt rather than being confined to a container that can induce strain in the crystal during cooling. Instead of using a seed, Kyropoulos [111], using an air-cooled platinum tube, nucleated a few crystallites on the end of his tube and then lifted it up slightly so that the melt stayed in contact with only one grain. Kyropoulos's apparatus is shown in Figure 1.8(B) above. This seeding method had to be carefully controlled so that the tube did not break free from the melt surface. After the seeding stage, the furnace is slowly cooled to allow the crystallite with the fastest growing direction of heat flow to grow to cm-size crystals before being pulled out of the melt. The thermal gradients in the melt are generally quite small. As mentioned before, the melt level drops in systems where the density of the solid is greater than the melt density. Kyropoulos used this process for growing many alkali halide crystals [112]. The method is attractive because of its general simplicity, reliability and low operating costs. Two other advantages of the method are (1) the ability to see what was going on and to make adjustments to enhance the crystal quality and (2) its use of lower thermal gradients than in the Czochralski method. On the other hand, the lower gradients lead to faceting at the interface and thus chemical inhomogeneities in the crystals. Several years later, Korth [113] took up this method but used a seed attached to the cooled rod as did Nacken many years earlier. He grew crystals as large as  $6 \times 8$  cm. A few years later, Katherine Chamberlain in the United States used this method to grow very large KBr crystals up to five inches in diameter and weighing up to seven pounds [114]. Typically Kyropoulos's method does not involve continuous pulling or rotation as in the Czochralski method. Growth rates are of the order of mm's/hr with cooling rates below  $1^\circ\text{C/hr}$ . The crystal diameters usually are up to 90% of the crucible diameter. Bliss [115] gave a detailed review of Kyropoulos's life and method.

The Kyropoulos method has been in commercial use for over 75 years. From its inception until the present time, the method has been used to grow large alkali halide crystals for windows, prisms and scintillators (e.g., Tl:NaI and Tl:CsI) compounds. Due to the development of GaN-based light emitting diodes, there has sprung up a very large industry around the growth of large sapphire crystals for use as substrates. The Kyropoulos method is one of the most widely used methods today for this applications. Up to 12 inch-long crystals have been produced. It is also used in the commercial production of Ti:Sapphire laser crystals. A variety of other materials have been grown by the Kyropoulos method in laboratory settings, including organic materials, semiconductors such as Si, ZnSe, and InP and other types of laser crystals. For the growth of InP crystals [116], liquid encapsulation together with magnetic fields has been applied to the Kyropoulos configuration to improve crystalline perfection. This has been called the MLEK method. Over the years, furnaces have become much more complex. Heat shields are now used to control thermal profiles. Numerical analysis has helped to define the optimal conditions for growth of specific materials through proper baffling and positioning of the crucible in the heater. Other improved capabilities include the ability to weigh the crystal or crucible during growth to control the rate of mass increase with time.

### 1.3.1.6 *Stöber/Heat Exchanger Methods*

In 1925, F. Stöber [117] reported on the growth of large crystals of anisotropic materials such as sodium nitrate, zinc and bismuth by removing the latent heat of crystallization from the bottom of a stationary bowl-shaped crucible containing a melt (growth from the bottom upward). A heater plate was placed above the surface of the melt and a water-cooled plate at the bottom creating an axial temperature gradient. The radial heat flow, present in most other growth systems, was minimal. Stöber's method, along with one of Tammann's techniques, were perhaps the first gradient freeze methods (i.e., moving the gradient along the melt rather than by moving the crucible or furnace). Stöber also found that crystal singularity was enhanced when the thermal conductivity in one crystallographic orientation was significantly greater than in other directions. One attractive feature of Stöber's method was that you could produce very large crystals in near-net shape, i.e., in the exact shape of the container. In addition the method is very simple to implement since there are no moving parts, and lower thermal gradients employed help reduce stresses in the final boule. He grew crystals of  $\text{NaNO}_3$  up to 10 pounds by his method. He also grew ice crystals by inverting the cooler and immersing it into the liquid surface.

In 1970, Frederick Schmid and Dennis Viechnicki [118] from the Army Research Laboratory at the Watertown Arsenal, reported on a new method to produce large-diameter sapphire crystals from the melt. This work was stimulated by the need by the military for very large transparent armor plates. They called their new technique the heat exchanger method (HEM). The method is similar to the Stöber process in that the crystal grows upward from the bottom filling the crucible and taking its shape. Neither the furnace, crucible nor crystal moves during growth. A He-cooled cold finger (similar to the water-cooled bottom plate used by Stöber) extracts heat from the crucible bottom in a controlled manner and independent of the heat input. A furnace that surrounds the crucible replaced the upper pancake heater. In addition, the technique allows for a small-diameter seed to be centered over the cold spot created by the He heat extraction tube. Heat can be removed from the crucible bottom by increasing the He flow rate. Since then (1975), a He recirculation system was developed along with the technology to grow large-diameter, flat-bottom crystals free of light scatter from the small seed centered over the heat exchanger. High-quality sapphire crystals have been grown commercially up to 44 cm in diameter and weighing 160 kg [119]. In situ annealing in shallow gradients is used to relieve stresses. The crystals produced are competitive with commercial Kyropoulos sapphire. The method has also been used to produce single crystal ingots of spinel, ruby, Ti:sapphire, Nd:Y<sub>3</sub>Al<sub>5</sub>O<sub>12</sub> and silicon. Commercial growth systems are available.

### 1.3.1.7 *Kapitza's Method*

Piotr Kapitza (1894–1984) was an important Russian physicist who spent many years in England before returning to Stalinist Russia. He was awarded a Nobel Prize for his work in low-temperature physics. He used the Bridgman method to prepare metal single

crystals for his experiments, but when it came to preparing Bi rods of a specific orientation, he found that its expansion on cooling was sufficient to cause enough strain to prevent the seeded orientation from propagating down the rod. To solve this problem, he developed a method in which the crystal was not completely constrained [120]. He placed a bismuth rod on a copper plate and covered it with loose-fitting glass plates to reduce drafts and then melted the rod. At one end, an oriented seed was attached and by unidirectionally solidifying the rod by cooling he was able to produce an oriented Bi single crystal at rates up to 5 cm per hour. This method was taken up and modified by others, and today it might be considered the forerunner of the horizontal Bridgman method which is widely used today for growing materials like GaAs for LED's [121] and ZnGeP<sub>2</sub> and CdGeAs<sub>2</sub> [122] for nonlinear optical applications.

#### 1.3.1.8 Zone Melting

Zone melting methods have played an important part in (1) purification of materials for crystal growth and other materials processing (zone refining), (2) for producing crystals with uniform composition (zone leveling) and (3) for growing crystals without crucibles (the float zone method). There are a number of variants to all these methods including different methods of heating, horizontal and vertical arrangements, traveling mechanisms, etc. The first reported use of zone melting was by Kapitza in 1928 [120]. In his experiments, he passed a short resistance heater along a Bi filled tube to produce a single crystal. In 1937, Andrade and Roscoe [123] used zone melting (also a traveling heater) to grow lead and cadmium single crystals having low strain. By far the most important and extensive work on zone melting for purification (zone refining) and zone leveling was that of William Pfann [78]. In 1952, Pfann conceived of the zone refining method when asked by the transistor researchers at Bell Laboratories (where he had worked since the late 1930s) to develop a method to produce higher purity Si and Ge for use in growing crystals with better electronic properties. Toward this end, it was used with great success in the early days of semiconductor processing. This very versatile method was found applicable to numerous other materials, including inorganic and organic compounds, metals and semiconductors. Many papers on its adaptation to different materials and operational improvements have been published since then, and it has become an important tool for both research laboratories and industry. Pfann's book on zone melting [124] is the seminal publication on the method, comprehensively covering both the theory and practice involved.

The method consists of moving a molten zone through a bar of material. Two solid interfaces are created. As the zone moves (by moving the heater or furnace), material from one interface dissolves in the zone and is recrystallized at the other interface. Purification occurs for those impurities whose solubility in the liquid is different than that in the solid (segregation coefficients,  $K$ , greater or less than one). Materials with  $K < 1$  will be rejected at the growth interface and will build up in the last to freeze region. Those with  $K > 1$  will tend to congregate at the start of the ingot. It is also a very useful method for growing crystals from materials that melt incongruently.

Various types of heaters have been used with the zone melting method, including resistance, RF, electron beam, plasmas, lasers and xenon lamps. Refining can be done with one zone moved through the ingot many times (passes) or by moving multiple zones simultaneously. The ends of a sample can be removed and the sample zone refined again as many times as needed. More passes are needed when  $K$  for a particularly detrimental impurity is close to 1. Volatile species can complicate the process but techniques to control or minimize melt losses have been developed.

Zone leveling is a way to produce material with uniform composition along its length. It has many of the features of zone refining. Once the zone has reached a steady-state composition, the species of interest will transfer from one interface to the other. The composition will be the same on both the melting interface and the solidifying interface. In both zone methods, crystal growth can be carried out during the purification or leveling procedures.

The floating zone technique is a very important variant of the zone melting method. It allows for crucible-free growth and eliminates possible contamination from the crucible material and also stresses due to differential expansion between the crystal and container. The method was invented and patented by H. Theuerer [125], a close colleague of Pfann, to grow ultra pure Si. For better uniformity, the rods can be rotated during growth. As mentioned before, the method is used commercially today for growing low or oxygen-free silicon. In recent years, automated commercial optical lamp heated float zone systems have become available and have permitted researchers from a variety of disciplines to grow crystals of a wide variety of materials for physical property studies [126].

The pedestal growth method is essentially a floating zone process. However, because the pull rate of the crystal (smaller diameter) is different from the push rate of the source rod (larger diameter) it has some characteristics of the Czochralski method. Parenthetically, one might classify the Verneuil method as a pedestal growth method since the crystal is grown on a pedestal and the molten zone is fed by molten powder rather than a solid rod. The first use of a pedestal growth technique was in 1958 by F. Horn [127] at the General Electric Corp. His method was a hybrid technique between the Czochralski and float zone methods. The charge in the crucible was only melted near the top surface and the crystal, of smaller diameter, pulled from this melt. As the crystal grew he changed the heater position to melt some more of the solid below. He grew boules of Sb-doped Ge having a more uniform composition than achievable by the Czochralski technique where the entire charge was melted. Dash [128], and Poplawski and Thomas [129] used this method to grow dislocation-free crystals of Si and Ge.

Two techniques that have been found particularly useful for producing small-diameter crystals for property studies are the *laser-heated* pedestal fiber growth (LHPG) [130] and micro pull-down ( $\mu$ -PD) [131,132] methods. The LHPG method is a zone melting method in which, rather than a zone traversing a bar of material of uniform diameter, a fiber is grown from a source rod of larger diameter. The pedestal configuration was first used by Horn [127] and Poplawsky [129]. The source rod forms a pedestal

whose upper surface is melted with a small spatially fixed laser beam. A seed crystal is lowered into the melt and is withdrawn at a rate faster than the rate at which the source rod is pushed upward to maintain constant melt volume. It is a crucible-less method, minimizing contamination; the growth rates are much faster than bulk growth (mm/min) because the temperature gradients at the interface are very large ( $>1000\text{ }^{\circ}\text{C}/\text{cm}$ ). These high-growth velocities can lead to greater dopant incorporation and to the growth of metastable phases. The method is useful for incongruently as well as congruently melting compounds, although it is limited to systems where the vapor pressures are modest and dissociation is not a problem. The small diameter fibers were often found to have better crystalline perfection than bulk materials. The LHPG method has been used to grow fibers of a vast array of materials including oxides, halides, borides, carbides, and metals. Haggerty [133] was the first to use the pedestal method with laser heating. He grew  $\text{LaB}_6$  single crystal fibers. A few years later, it was used to grow single crystal Nd:YAG fiber lasers [134]. One of the big advances in LHPG growth was the replacement of individual laser beams (two or four) with reflexicon optics [135] giving a circular beam and a much more uniformly heated molten zone. An interesting discovery came about during the growth of  $\text{LiNbO}_3$  fibers. Lithium niobate is a ferroelectric material whose as-grown bulk crystals contain numerous parallel and antiparallel domains. To be useful in nonlinear and other device applications, these have to be aligned after growth in an electric field at elevated temperatures. During the growth of  $\text{LiNbO}_3$  fibers using a two-beam laser system, however, the small diameters and steep gradients led to single domain fibers when grown along the c-axis and a bi-domain fiber of opposing  $180^{\circ}$  domains when grown along the a-axis [136]. The axial gradients were responsible for the single domain c-axis fibers and the radial gradient a-axis fibers. These observations later led to a method to produce fibers with periodically poled domain structures by periodically shuttering one of the laser beams during growth [137]. Later, other periodically poled structures for quasiphase matching applications were produced by other methods.

In 1980, Mimura et al. [131] published a paper on the growth of KRS-5 fiber crystals using an inverted pulling system (modified floating zone technique). They had a crucible filled with melt on the top with a feed rod continuously feeding the melt as the fiber grew. At the bottom of the crucible was a long heated capillary tube with a shaper at the end. The growth interface was below the shaper. The growing crystal was pulled downward. This method was taken up by D. Yoon et al. [132] and called the micro-pull down method. It has been used successfully for many materials, and growth systems are available commercially. This method was reviewed by V. Chani [138].

#### 1.3.1.9 Shaped Growth

Shaped growth generally means a method for producing a crystal with a predetermined cross-sectional configuration. The quest to develop such methods is associated with a need to reduce product cost and/or improve crystal quality. Notable savings can be achieved in device fabrication, such as cutting and polishing, reducing the loss of expensive material and reducing mechanical damage. In addition, the method usually

allows significantly higher than normal growth velocities, thereby increasing production rates. In a very real sense, shaped growth is a hybrid method that borrows from other more established methods. For example, some are simple modifications of the crystal pulling or directional freezing methods.

One might consider the Bridgman–Stockbarger method to be one of the first shaped growth processes because the crystal retains the shape of the ampoule used. It is not quite so obvious since almost all Bridgman crystals are grown from cylindrical ampoules. One of several recent exceptions being a paper by Feigelson and Route [139] on the growth of square cross-section crystals of  $\text{AgGaSe}_2$  in vacuum-formed quartz crucibles. Using oriented seeds, they grew crystals not only aligned along the c-axis, but also so that the flat crystal side faces would be normal to the [110] planes in which light propagates during type 1 phase-matched nonlinear interactions. A comprehensive review of the various shaped crystal growth methods is given in Ref. [140] and elsewhere.

Perhaps the earliest attempt at shaped crystal growth is attributed to the 1921 work of von Gomperz [70] at the Institute of Fiber Chemistry in Berlin-Dahlem. He worked in Michael Polyani's group. Polyani [141], reminiscing some 40 years later, recalled "Some metallurgists, interested in my work on the hardening of single crystals, told me of a method invented by Czochralski for producing metal crystals in the form of wires. It consisted in pulling out a thread from a pool of molten metal, so that the thread continued to solidify at the rate at which you were pulling it out. Erwin von Gomperz, who was doing his thesis with me, was put to growing single crystals of tin and zinc in this way. Unfortunately, the metal tended to come out in lumps, and the project was saved only by the intervention of Hermann Mark who covered the liquid metal by a sheet of mica with a hole in the middle, through which the thread came out as a smooth cylindrical wire. But for this ingenious intervention, our subsequent investigations of the plastic flow of metals might not have come about" [142].

In 1938, Stepanov at the Ioffe Institute in St. Petersburg began his extensive studies on shaping crystals during growth using wetted and nonwetted dies [143,144]. These dies have one or more capillaries or slots to transport melt from the crucible to the growth interface. The shape and height of the melt column is dependent on capillary properties such as surface tension, density, melt viscosity, impurities and wetting angle. Over many years, Stepanov's group produced a wide variety of shaped crystals including single and multibore tubes, rectangular bars, sheets, discs, etc. Shaped crystals of a number of different types of materials were grown, including oxides, metals and compound semiconductors.

Shaped growth in the United States began in the late 1960s with the preparation of sapphire filaments (later sapphire tubes for Na-vapor lights) by the edge-defined film-fed growth method (EFG) and single crystal superalloy turbine blades by directional solidification in complex molds [145,146]. The EFG process is in effect one of Stepanov's techniques, but it specifically focused on the advantages of wetted dies. It was discovered independently by LaBelle [147] who made a significant observation during his early attempts to pull sapphire fibers from a die placed in the melt surface. He noticed that the

melt wet the die and instead of being the diameter of the capillary within the die was the shape of the outer rim of the die. This was recognized by Mlavsky [148] as being of significant benefit and thus began extensive work on the EFG method. A sketch of the EFG method is shown in Figure 1.9. In a relatively short time after its discovery, it became a commercially viable technology. This was due to the early recognition that concurrent with experimental work, theoretical studies were needed to thoroughly understand the mechanisms involved in the process and ways to maintain better shape stability and rapid growth rates [149,150]. In 1980, an entire volume of the *Journal of Crystal Growth* was devoted to the subject of shaped growth methods. The EFG method has been successfully used in the commercial production of sapphire single fibers, tubes and ribbons and other materials. Today, the EFG method has gained an increasingly greater market share in the production of sapphire ribbons for GaN substrates used in lighting applications. Automated commercial EFG equipment can now be readily obtained, permitting companies to produce such wafers themselves.

The Stepanov and EFG methods are a meniscus-controlled process like Czochralski growth, and like it, growth is driven by crystal pulling. However, instead of pulling directly off the melt surface, the crystal is pulled from a suitable die face located above the melt surface. It can either float on the surface, like in von Gomperz's early experiments [70], held in a fixed position with respect to the crucible or moved during growth. The die position leaves the growth interface some distance above the hot melt surface and the thermal gradients are much steeper permitting enhanced growth velocities. The die material is chosen on the basis of its wettability with the melt and its reactivity. For sapphire, Mo dies have been used. In commercial systems the die can be moved during growth to maintain constant conditions and be equipped with an automatic monitoring system based on crystal weighing.

During the 1970s, the oil energy crisis led to serious efforts to produce silicon solar cells at a much lower cost than using cut wafers from Czochralski boules. This led to a robust effort to produce Si sheet at high growth rates. One of the most promising methods at the time was the EFG process. Extensive efforts went into adapting it to produce low-cost Si solar cells, but with limited success. Other innovative Si shaped crystal growth methods were studied during this time period, including the dendritic web process [151] in which a silicon dendrite is used a seed. It grows out laterally

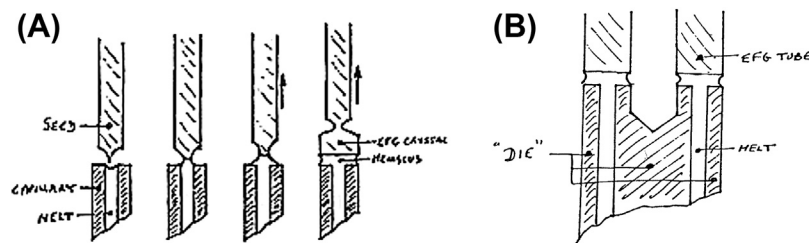
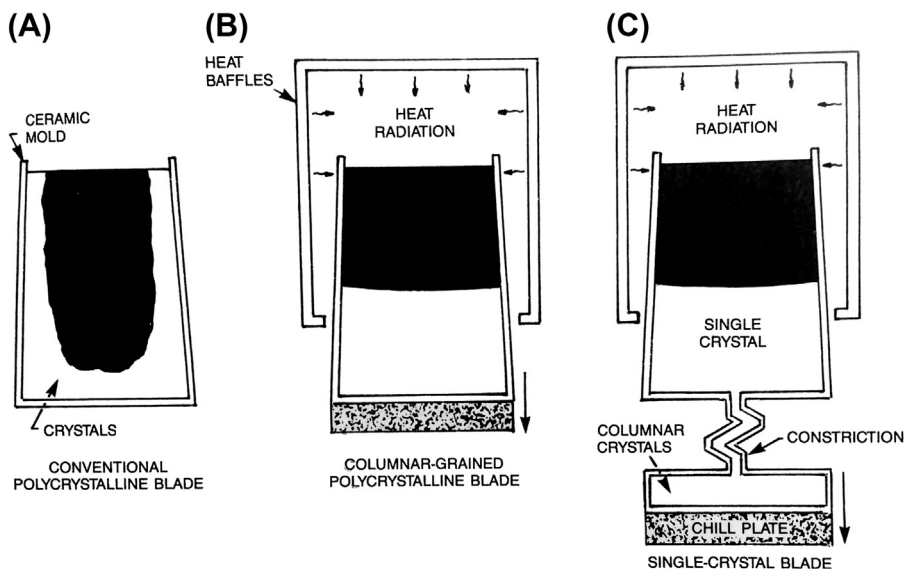


FIGURE 1.9 Illustration of the EFG shaped growth process. (A) the sequential steps involved in seeding and growing a crystal from a cylindrical die. (B) a die used to grow a hollow tubular crystal [148].

forming a thin sheet of silicon bounded by two new dendrites that define the width of the sheet. Some other methods include the ribbon against drop (RAD) method [152], where silicon is deposited as aligned grains on a carbon substrate, and the silicon on ceramic process [153], which is similar to the RAD process except that the substrate is a ceramic material. Two other methods of note are the ribbon to ribbon (RTR) [154] and horizontal ribbon (HRG) [155] growth methods. The former is a laser heated float-zone technique using a poly ribbon as the source and the latter involves pulling a ribbon (cooled from the top) horizontally from a free melt surface. The growth rates achievable in these processes are in the 5–10 cm/min range except for the HRG method where controlled cooling of the upper surface permitted growth rates of 10–40 cm/min. These methods are reviewed in Ref. [140].

The unidirectional casting method used for making single crystal jet engine turbine blades, as mentioned above, has had an important influence on aircraft performance. These blades, made from nickel-based superalloys, were found to have superior creep resistance if they have aligned grains [140] or better yet be one single crystal [156]. The method is like a Bridgman technique with the mold having the shape of the blade and extending down below is a zig-zag-shaped capillary tube mounted on a hollow pedestal that sits on a chill plate (see Figure 1.10). Growth is upward, initiated first from the melt in the pedestal by cooling the chill plate. This produces elongated grains along the mold's vertical axis, one of which will be in line with the capillary to provide seed selection. If by chance more than one grain makes it into the capillary from the pedestal, the crooked capillary will aid in seed selection.



**FIGURE 1.10** Schematic diagrams showing various methods for making jet engine turbine blades. (A) original casting method (polycrystalline), (B) single crystal growth by unidirectional solidification and (C) unidirectional growth with grain selection [146].

### 1.3.1.10 Skull Melting

The skull melting method is a quasi-crucible-less crystal growth method that was developed in the late 1960s in Russia, especially for growing large, high-purity oxide crystals for laser and gemstone production [157]. Since the 1970s it has become an important method for manufacturing cubic zirconia gemstones in a variety of colors (J.F. Wenckus et al. at the Arthur D. Little Company [158]). The method is adaptable to Czochralski and Bridgman growth methods using seed crystals and also in centrifugal casting.

In skull melting, a relatively large powder charge is contained within a water-cooled cylindrical Cu crucible surrounded by an RF heating coil. The RF field generates a magnetic field that in turn generates eddy currents due to ohmic losses in the material within the crucible. The process works for materials whose electrical conductivity increases with temperature, even through the melting stage. Due to the cold crucible wall, a skin (skull) of unmelted materials surrounds the melt and keeps it from coming into direct contact with the crucible, thus preventing contamination. Temperatures of over 3000 °C can be achieved and a wide selection of gas atmospheres are possible. Unless coupled with seeding, it is impossible to grow one single crystal due to the seeding effect of grains in the skull. For the gem industry, large slabs of crystals are retrieved from large-grained poly masses. The nature of the heat flow encourages the grains to grow along the vertical direction.

Cubic zirconia ( $\text{ZrO}_2$ ) is used in the gem industry as a substitute for diamond since its optical properties, hardness, and fracture toughness are similar. Pure zirconia, however, undergoes a number of destructive phase transformations upon cooling. In order to grow single crystals from the melt, therefore, its composition has to be modified (stabilized) by doping to allow the high temperature cubic phase to persist to room temperature. The most common stabilizer is yttrium (YCZ), but CaO and MgO are also used. Concentrations of dopants vary from 10 to 40 mol%. These stabilizers work by creating many vacancies on the oxygen sublattice that prevent the cubic phase from transforming to phases of lower symmetry. Partially stabilized zirconia (PSZ) can be produced by reducing the dopant concentrations to less than 6 mol%. In these materials, part of the material transforms into the tetragonal phase creating a composite structure with excellent mechanical properties, making them attractive for applications such as drilling, threading, medical instruments such as scalpels, etc. [157]. The wide range of colors possible in zirconia gemstones are created using rare earth or transition metal element dopants.

Recently a Ukrainian group [159] developed a technique for growing large Tl:NaI scintillator crystals by a method similar to skull melting. Since the melting temperatures are quite low ( $\sim 661$  °C), they did not need RF heating and reconfigured the system from horizontal heating to vertical resistance heating. Basically, they hold a heater plate about 1 cm over the charge, which is held in a rectangular aluminum tray sitting on the bottom of water-cooled vacuum chamber. Since the heater is smaller in area than the container, only the center part of the charge is melted leaving a skull 5–10 mm thick surrounding

the melt and keeping it out of contact with the aluminum. Growth is achieved by slow cooling from the bottom up by lowering the temperature of the upper heater. It is not clear what the grain structure of the resulting slab is like, since seeding is not used and the plates produced are quite large. However, the scintillator properties are in line with those of single crystals produced by other methods and in a more cost-effective manner.

## 1.3.2 Solution Growth

### 1.3.2.1 Introduction

Solution growth methods involve dissolving material in a liquid (or gel) medium and then recrystallizing it under controlled conditions to produce a crystal of a desired size, shape and perfection for a specific application. The control of crystal shape and size can extend from very large crystals for optical applications down to fine powders for pharmaceutical, agricultural, or specialty chemical uses. The solvent media may be a low-temperature solvent like water or a high-temperature flux like PbO. Pressure-enhanced solution growth (the hybrid hydrothermal growth method) has also been a commercial success for the preparation of large crystals of quartz. The most common solvent used is water, and an impressive number of inorganic salts have been converted into single crystals using this technique, some weighing over 50 pounds. Other solvents include organic liquids (for the growth of organic crystals) and liquid ammonia.

Growing crystals from water solutions was undoubtedly the earliest effort by early man to replicate what he observed in nature. Natural salt ponds drying up in the hot summer months and then redissolving during winter rains assuredly piqued his interest and led him to experiment. Since salt became such an important commercial product, it is not surprising that this material and method became one of the first industrial crystal growth activities. Sugar was another material of early commercial interest. Through trial and error, a rudimentary understanding of saturation and supersaturation began to develop and, along with techniques such as seeding and solution homogenization (via stirring), better control of nucleation, crystal size and purity was achieved. Later, the role of additives to enhance growth behavior and tailor crystal properties was incorporated into the growth procedures. The eventual use of solubility diagrams greatly aided crystal growers in choosing appropriate growth conditions, i.e., temperature and composition regions. In these early days, as today, control of purity and size were of great commercial significance. Several basic methodologies are employed in solution growth: (1) controlled evaporation, (2) temperature programming, (3) mass transport in a concentration gradient at constant T and (4) changing the composition of the solution (salting out method).

### 1.3.2.2 Aqueous Solution Growth

Like all other crystal growth methods, a variety of modifications have been made over the years to facilitate the growth of a specific type of material, and to achieve an appropriate dimension and degree of crystalline perfection (purity, homogeneity, strain,

etc.) required for the application intended. Materials vary so widely in their thermodynamic and kinetic properties that even the growth of related materials of similar composition and structure can require changes in growth procedure or even in overall methodology.

In 1901, G. Wulff [160] published his famous theorem on the influence of surface energy on equilibrium shape of a crystal (morphology). It established a relationship between the crystal habit and the structure of crystals. It was derived from studies on the growth rates on different faces of crystals grown in water solutions. He used a rotating cylindrical crystallizer, in which a seed crystal was placed along the axis of the cylinder at its center-point. This allowed the crystal to grow out of contact with the vessel walls and be exposed to nutrient equally on all faces. Other early pioneers advancing the development of water solution methods during the first half of the twentieth century included Kruger and Finke [161], and Valetton [162]. Kruger and Finke were the first to investigate growth under constant temperature and supersaturation conditions. Their apparatus, shown in Figure 1.11, had in common two vertical chambers connected by upper and lower tubes through which solution passed in a specific way. One chamber contained source material and the other a stirring paddle (growth chamber) to move nutrient and depleted solution from one to the other. After equilibration of the growth chamber in a slightly undersaturated state, a seed crystal was added. Valetton's apparatus had a more precise way to control temperature in each bath. These methods utilized mass transported from the source chamber to the growth chamber to control the growth process. Crystals of potash alum and potassium sulfate were grown in these early experiments. In 1916, Nacken [163] developed a similar but more sophisticated apparatus using a vertical configuration for solute transport. Some 30 years later, Walker and Kohman [164] at Bell Laboratories developed a large-scale commercial crystallizer similar to these earlier methods known as the constant temperature process. Together with Holden's contributions on seed mounting [165], this apparatus was capable of growing four large EDP (ethylene diamine tartrate) piezoelectric crystals at a time. These crystals were used to replace natural quartz in telephone circuits. Crystals weighing up to 40 pounds could be

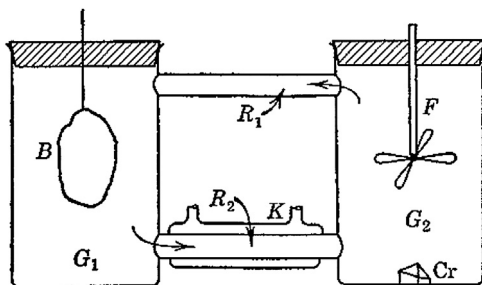


FIGURE 1.11 The aqueous solution crystallizer used by Kruger and Finke [161]. The nutrient was contained in a porous bag in heated beaker  $G_1$ . The stirrer in beaker  $G_2$  recirculates saturated from  $G_1$  through a water-cooled tube  $K$ , where it becomes supersaturated, into beaker  $G_2$  where the crystals grow. Large potassium sulfate crystals 2 cm in size were produced in this reactor.

grown by this method. The method involved several large chambers with solution in one chamber saturated at one temperature being continuously fed into the crystallizer chamber being held at a slightly lower temperature, thereby providing the supersaturation conditions necessary for growth.

In 1919, R.W. Moore [166] working at the General Electric Company needed large Rochelle salt crystals for electrical property studies. Since suitable material was not available commercially, he was forced to develop his own method. At first he started with the method of Kruger and Finke [161]. This proved unsuccessful. After thoroughly studying the available literature he came up with a new and simple approach based on the temperature lowering method. First, a saturated solution was formed 10–15 °C above room temperature, the solution decanted to separate it from the excess salt and then filtered. After heating the saturated solution 7–8° above its saturation point, it was poured into a vessel containing small seeds suspended on silk threads or metal wires, covered with a glass plate and then placed in water bath at 0.5 °C above the saturation temperature. From that point onward, the temperature was lowered to cause the seeds to grow. No means of stirring the solution was provided in these early experiments.

Moore's temperature lowering method was eventually modified to supply some fluid movement and distribute nutrient more uniformly to all the faces. The so-called rocking tank method was applied in 1947 by Walker [167] to the growth of large ammonium dihydrogen phosphate (ADP) crystals needed for submarine detection. The tanks were large rectangular trays that were gently rocked to replace depleted solution at the growth interfaces with fresh supersaturated material. Like EDP, crystals as large as  $6 \times 6 \times 20$  in were produced by this method. Many crystals could be grown in each tray and for production (Western Electric Co.) rooms were filled with many rocking trays. Evaporation was inhibited and the room temperature had to be carefully controlled. One famous name associated with water solution growth was Alan Holden [165]. Aside from his research at Bell Laboratories, he also wrote a very popular book on the subject [168]. Numerous amateurs have used it to initiate crystal growth experiments. In 1949, he introduced the "rotary crystallizer" originally to grow EDP and then later for ADP crystals. It consisted of a large, one-foot-diameter cylindrical vessel holding the solution. It was heated from the bottom by two concentric heaters, an inner one to keep the bottom center somewhat under saturated. In this way, errant crystallites that have fallen to the bottom would dissolve. The outer heater controlled the overall solution temperature. The important feature introduced by Holden was the rotating seed holder (called a "spider"). The seed crystals were mounted on spokes emanating from the rotation shaft. Several sets of spokes holding the seeds were used along the vertical axis. The seeds were rotated first in one direction for a selected period of time and then in the other direction. The system was sealed and some water condensed on the upper lid forming droplets. When large enough, the droplets fell to the solution surface keeping it under saturated and thus preventing the nucleation of spurious grains.

Most of the growth methods mentioned above have inherently slow growth rates (0.5–1 mm/day) due to low solution supersaturation. The higher supersaturation

needed to yield increased growth rates were hard to achieve and control. In 1983, Loiacono et al. [169], using a three-stage crystallizer (modeled after Walker and Kohman's growth system from 1948 [164]), and under conditions of constant temperature and supersaturation were able to achieve 5 mm/day growth rates for large potassium dihydrogen phosphate (KDP) crystals. KDP is an important nonlinear optical material for modulating lasers. It has been grown commercially for many decades using aqueous methods similar to the ones described above. The need for even larger crystals of KDP for electro-optic switch and frequency converter plates in inertial confinement fusion research led to a big advance in solution growth methodology. It started in 1982 in Rashkovich's group at Moscow University. There they developed a rapid growth process for KDP from water solutions [170]. Over the next several decades, that work was taken up by Zaitseva and colleagues at the Lawrence Livermore National Laboratories in California [171]. They demonstrated that the standard Holden [165] crystallizer with temperature reduction could be used to grow large high-optical-quality KDP and deuterated KDP (DKDP) crystals up to 50 cm on a side at rates 10–100 times faster than older methods and without spontaneous nucleation and macroscopic defects. From their research on growing large crystals under fast growth conditions, they were able to develop a more thorough understanding of the mechanisms involved in solution growth. In addition to the influence of temperature, supersaturation and dislocations on growth rates, they realized the importance of impurities, mass transport (via high solution velocities) and in having a highly stable growth system. It was found imperative to control secondary nucleation. The most important feature of their rapid growth process was using highly supersaturated solutions (70–76 °C) coupled with elaborate techniques for preventing spontaneous nucleation. Toward that end a continuous filtration system and a seed protector were important modifications to the growth system.

### 1.3.2.3 Growth of Biological Macromolecules

Determining the crystal structure of complex biological molecules such as DNA, proteins, enzymes, etc., is important to both our understanding of animal and plant biology and functionality and our ability to develop pharmaceutical products to combat various illnesses that afflict these species. During the past century, protein crystallographers have slowly worked out the structures of a myriad of important species using X-ray diffraction methods. To accomplish this, researchers needed small, high-quality single crystals of controlled composition.

The first recorded protein crystallization experiments were done by German scientist F.L. Hunfeld in 1840. He prepared acicular crystals of earthworm hemoglobin by pressing blood between glass slides and allowing it to slowly evaporate. Since then, many techniques have been developed to prepare such crystals and the quality and size of the crystals produced were essential to the success of the structural detail obtained. The working out of the structures of myoglobin (1950) and hemoglobin (1955) using heavy metals covalently bonded to the protein led to the Nobel Prize for their researchers.

Another Nobel Prize winner who grew crystals in order to study their crystal structures was crystallographer Dorothy Crowfoot Hodgkin (1910–1994) [172]. As a child, Hodgkin was influenced by books that described how to grow crystals and on the interaction of X-rays with crystals. She won her prize in 1962 for her part in unraveling the crystal structure of the Vitamin B-12 molecule [173]. She also, together with Kathleen Lonsdale, grew crystals of penicillin and potassium and rubidium benzyl-penicillin. One of her major accomplishments was deciphering the structure of insulin.

While the crystal growth of biological macromolecules was primarily the domain of protein crystallographers and biologists during most of the century, in the 1980s the effort expanded to include experts more familiar with the theoretical and practical aspects of crystal growth (albeit small molecule materials). This came about in two ways. First, NASA had received requests from the crystallography community to fund protein crystal growth experiments in the low gravity environment of outer space. It was believed that the quality and size might be enhanced under these conditions. At the same time, NASA had been funding a variety of small molecule crystal growth experiments in low gravity with some promising results. NASA decided to try to engage some of the small molecule crystal growth community in the protein growth field. Several such programs were funded, one of which was my group at Stanford University. I immediately realized that we did not know enough about biological species to carry out his program successfully, and so when I found out that protein crystal growers did not have their own forum to discuss growth problems of mutual interest, I decided to bring them to Stanford basically to teach us about the field. Together with Alex McPherson [174], and with support from the American Association of Crystal Growth and NASA, we organized the first international conference on protein crystal growth at Stanford University in 1985. It not only brought together protein crystal growers for the first time, it also included well-known scientists and engineers from the small molecule crystal community. A total of 140 attendees were present. It was a somewhat contentious meeting at first, but as it proceeded, both sides, who spoke quite a different scientific language, came to understand more clearly the relevant issues, i.e., the physics behind the growth process and the influence of various processing parameters on the size and quality of the crystals produced. This international conference series has been held regularly every since.

Crystals of proteins and other biological species can be grown by a number of techniques including dialysis, sequential extraction, interface diffusion, vapor diffusion (plates, hanging or sitting drops), via pH and temperature changes, evaporation and in thermal (concentration) gradients. McPherson's original book, *Preparation and Analysis of Protein Crystals* [175], gives a comprehensive review of growth methods (see also Ref. [176]). Purification of starting materials and the composition of the growth solutions, like in most small molecule systems, are critically important to produce suitable crystals for X-ray structural analysis. Most of the growths are done in small batches. To establish the correct crystallizing conditions, a matrix approach is often used. Here, small samples with a systematically varied concentration of protein, salting agent,

solvent, etc., are placed within many cells and crystallized under the same conditions. Regions in the matrix that contain crystals are then regrown on a more refined compositional scale to enhance the results. In effect, this is the combinatorial chemistry approach and one that lends itself to automation using robotics to meter out the desired quantities into each cell. This latter approach was pioneered by Ward et al. [177] during the mid-1980s and is in wide use today.

One final comment worthy of mentioning again (see Scientific Study section) is that the large size of the growth units in biological macromolecules gave crystal growth scientists a unique opportunity to dynamically study the morphology and kinetics of step and ledge movement (including step bunching) during growth using the relatively new atomic force microscopy technique. The first such in situ studies were carried out in 1995 by Land et al. [178] and Malkin et al. [179].

#### 1.3.2.4 Growth from Gels

In 1896, the German chemist Raphael E. Liesegang slowly put a drop of silver nitrate-water solution onto a thin gel layer containing potassium dichromate, and in doing so discovered the precipitation ring phenomena named after him [180]. This initial discovery stimulated a strong interest in understanding how the process worked. A gel is a semisolid containing small pores of angstrom dimensions in which a variety of salts can be dissolved. Early efforts on growing crystals in gels include the work of Hatschek [181] in 1911 and Dreaper [182] in 1913. The former grew small crystals of gypsum by letting sulfate ions diffuse in a gelatin containing a dilute solution of calcium chloride and the latter lead chloride crystals in a test-tube-shaped vessel. The idea for growing crystals in a gel media was stimulated by the research work of Fisher and Simons [183] in 1926. They were intrigued by some earlier work with gold and copper crystals produced by the reduction of their metal salts in a silica gel and the coincident occurrence of gold in quartz veins. From their early experiments, they predicted that this method would be “far-reaching” and this enthusiasm caught the attention of later researchers and became an area of vigorous research, particularly from the early 1960s onward. The work by Heinz Henisch’s group at Pennsylvania State University stimulated researchers around the world and was summarized in his book *Crystals in Gels* [184].

The gel growth method has been used to prepare an impressively wide range of inorganic and organic crystals, including proteins. Gels provide a medium where mass transport is by the slow diffusion of suitable ions to a region where they can react during crystallization. It is a convection-free method and the crystals, when nucleated under carefully controlled conditions, are suspended from one another. These factors, plus the near room-temperature growth conditions purportedly result in higher crystal quality. Crystal dimensions can vary from micron to centimeter sizes depending on the system under study, but typically they only reach mm sizes. Like other solution growth crystals, they exhibit growth rate anisotropy and faceting. Typical gels used are silica hydrogel (sodium metasilicate), agar (derived from seaweed) and gelatin; however, many other gel compositions have been used as well. Crystals can be grown within gels by a number of

techniques, including (1) chemical reaction, (2) complex dilution, (3) chemical reduction and (4) solubility reduction. An extensive list of crystals grown is given in Ref. [185]. During the last decade or so, interest in gel growth has diminished along with the number of publications.

#### 1.3.2.5 *Nonaqueous Solution Growth*

Organic crystals are useful for a number of applications including semiconductors and scintillator devices. Organic materials, like other substances, vary widely with respect to their thermodynamic and physical properties. Therefore it is not surprising that a suitable crystal growth method will depend on the specific properties of the material in question. They can be grown by a variety of common crystal growth techniques including vapor, melt and solution methods. Organic materials that melt without dissociation are prime candidates for melt growth methods. Others have been grown in solution or by vapor phase techniques. Solution growth methods usually involve organic solvents such as ethyl alcohol, acetone, hexane, and carbon tetrachloride. The techniques used are similar to water solvent methods and include solvent evaporation, slow cooling or heating, vapor diffusion and liquid-liquid diffusion and are nicely summarized in Ref. [186]. One of the recent examples of solution growth using organic solvents is the work at the Lawrence Livermore Laboratories on the growth of large, high-quality crystals of trans-stilbene ( $C_{14}H_{12}$ ) for fast neutron detectors [187]. The solvents used were toluene or anisole, the latter preferred due to its lower evaporation rate. Melt growth techniques did not yield large, high-quality crystals. Building crystallization systems to withstand the organic solvents and by using the temperature reduction method together with rotation, very high-quality crystals in dimensions up to four inches have been produced.

#### 1.3.2.6 *High Temperature Solution (Flux) Growth*

##### 1.3.2.6.1 **Bulk Crystals**

As with other solution growth methods, the high temperature flux growth method also relies on the careful control of the supersaturation and melt composition. Like the low temperature processes, there are three general methods for controlling supersaturation: (1) slow cooling, (2) evaporation and (3) transport in a concentration gradient. In its early incarnations, the method was unseeded and crystals grew on the surface of the melt where supersaturation is usually greatest (due to volatility) or on the crucible walls where heterogeneous nucleation is favored. Later, the use of seeds or cooled probes helps facilitate growth. Generally solvents are classified as common ion or noncommon ion fluxes. An example of the former is the growth of  $(Ba,Sr)TiO_3$  from excess  $TiO_2$  melt [188], and the latter, the growth of  $Y_3Fe_5O_{12}$  from  $BaO-B_2O_3$  based fluxes [189]. The  $BaO-B_2O_3$  flux, while used early on, was not nearly as successful as  $PbO-B_2O_3$  or  $PbO-PbF_2-B_2O_3$  fluxes that form ionic solutions. The 1975 book *Crystal Growth from High Temperature Solutions* by Elwell and Scheel [190] still remains the most thorough, encyclopedic treatment on the history, theory and methodology of flux growth.

Crystal growth from high-temperature solutions probably began during the nineteenth century. One of the earliest documented studies (1823) was by Friedrich Wöhler (1800–1882), a famous German chemist who used a flux-reaction technique to grow sodium tungsten bronze ( $\text{Na}_x\text{WO}_3$ , where  $x$  is  $\leq 1$ ) crystals by passing  $\text{H}_2$  gas over a  $\text{Na}_2\text{WO}_4$  flux [191]. He is also famous for his synthesis of urea and the codiscovery of Be, Si and silicon nitride. By mid-century, early experiments were of a similar nature and a variety of materials were produced including CdS (using a  $\text{CdCl}_2$  solvent and  $\text{H}_2\text{S}$  reactant), alkaline earth and transition metal oxides, silicates and sapphire [190]. Later in the century, more traditional flux methods were used to grow a variety of binary, ternary and higher order compounds using chemically compatible solvents. Some examples include Doelter [192], who in 1886 grew  $\text{Ag}_2\text{S}$  by dissolving and recrystallizing it from  $\text{AgCl}$  or  $\text{SbCl}_3$  melts.  $\text{AlB}_{12}$  crystals were grown from  $\text{B}_2\text{O}_3$  melts by Wöhler and Deville in 1857 [193], and ruby was grown by Fremy and Feil in 1877 [194] using  $\text{PbO}$  as the flux (which from the 1950s onward became a popular flux for growing oxide crystals for optical applications). The results varied from laboratory to laboratory, and generally the crystal sizes were on the small side. Over 100 flux-grown compounds and their solvent phases are listed in Ref. [190]. In this time period this was probably the most important method used for preparing crystals of non water-soluble materials.

Solvent requirements include (1) a suitable melting temperature and solubility in the temperature range of interest, (2) a temperature coefficient of solubility, (3) low volatilization (an issue with  $\text{PbO}$  and halide fluxes), (4) compatibility with available crucible materials (reactivity and wettability) and (5) a relatively low viscosity. In the 1950s, the flux growth method again became an important adjunct to other developing crystal growth methods such as the Czochralski and Bridgman methods. It was particularly important for compounds that melt incongruently, have high vapor pressures at their melting temperatures, are refractory with excessive melting temperatures or have destructive phase transformations, etc.

After World War II, the flux growth method gained interest commensurate with device researchers' interests in finding new and better materials for optical, electronic and magnetic applications. The use of this method was very extensive during the 1950s through about 1980 and took place in many laboratories around the world. As a result, it is only possible to cite a few illustrative examples in this brief historical review to give a sense of what growth activities were like during this period. In 1964, Edward Giess [195] successfully prepared  $\text{Cr}:\text{Al}_2\text{O}_3$  (ruby) using a  $\text{PbF}_2$  flux. Lead fluoride is quite volatile, and so it was often combined with  $\text{PbO}$  with some added  $\text{B}_2\text{O}_3$  to stabilize it. At about the same time, Stanley Austerman [196] used the flux growth method to grow  $\text{BeO}$  crystals.  $\text{BeO}$  substrates were of interest because of its very high thermal conductivity and therefore its ability to remove heat from electronic devices. This would permit higher power operation. Austerman grew  $\text{BeO}$  from a  $\text{Li}_2\text{MoO}_4$ -based flux. Later, Newkirk and Smith [197] grew  $\text{BeO}$  from  $\text{PbO}$ -based fluxes. In Russia, V.A. Timofeeva's group was very active during this time period, studying the flux growth of many different oxide compounds including  $\text{Al}_2\text{O}_3$ ,  $\text{Cr}_2\text{O}_3$ ,  $\text{Fe}_2\text{O}_3$ , rare earth oxides and the garnets  $\text{Y}_3\text{Fe}_5\text{O}_{12}$ , (YIG)

and  $\text{Y}_3\text{Al}_5\text{O}_{12}$  (YAG). In the latter case, she investigated how growth defects formed as a function of the flux growth conditions and solvent composition [198].

Single crystal garnets ( $\text{A}_3\text{B}_5\text{O}_{12}$ ) were of great interest for laser, microwave and ultrasonic applications. In 1958, Nielsen and Dearborn at Bell Laboratories were the first to report on the flux growth of  $\text{Y}_3\text{Fe}_5\text{O}_{12}$  (YIG) [199]. Major improvements in size and quality were achieved by adding impurities such as CaO to a  $\text{PbF}_2\text{-PbO-B}_2\text{O}_3$  flux. Van Uitert et al. [200] worked on the growth of large, optical-quality  $\text{Y}_3\text{Al}_5\text{O}_{12}$  (YAG) crystals in very large platinum crucibles. Remeika, whose extensive crystal growth activities also included the flux growth of YIG, found that pure YIG crystals contained small amounts of  $\text{Fe}^{4+}$ , which resulted in reduced optical quality [201]. By adding small additions of tetravalent ions such as Si, Sn and Ge to the flux, the problem was eliminated. Some examples of flux grown crystals are shown in Figure 1.12.

Flux growth methods vary from simply slow cooling a melt without seeding (self-nucleation) to more complicated seeded growth techniques. The bottom cooling method helps control nucleation in unseeded melts. A small supersaturated region is created in the melt to limit the volume in which nucleation can take place. This can also be used to prevent a seed from dissolving before it starts to grow (like in the heat exchanger method). In 1955 and 1956, Reisman and Holtzberg were the first to prepare single crystals of potassium niobate  $\text{KNbO}_3$  (KN) and potassium tantalate  $\text{KTaO}_3$  (KT). These compounds were of interest for ferroelectric and piezoelectric applications [203]. A  $\text{K}_2\text{O}$  flux was found suitable for this purpose. KN in particular became a very important material for efficient direct diode doubling and other NLO frequency conversion processes, such as generating blue light from a Ti:Sapphire laser via critical phase matching. Over the years, large-scale

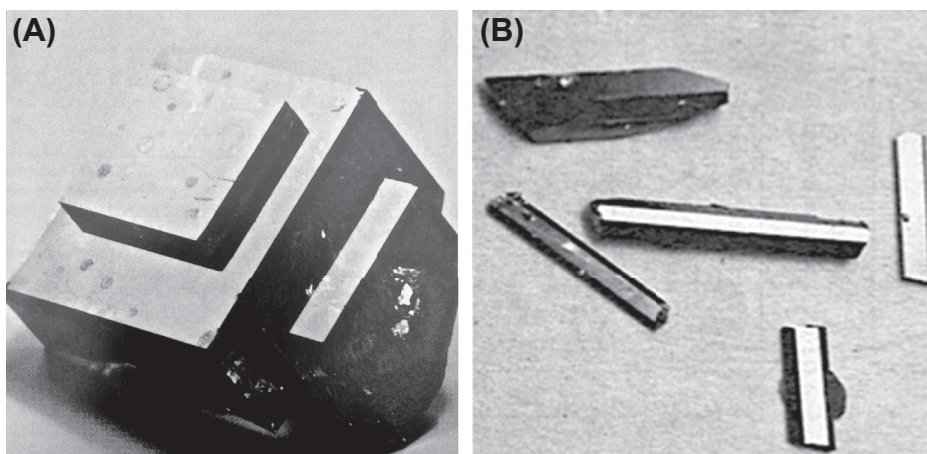


**FIGURE 1.12** (A) A photograph of a large ( $3.5 \times 3 \times 2.5$  cm), flux-grown crystal of  $\text{GdAlO}_3$ . It contained large inclusion-free regions. A  $\text{PbO-PbF}_2\text{-B}_2\text{O}_3$  flux containing some other minor additives was used. The large size and quality is attributed to ACRT stirring method [202]. (B) Photograph of some highly faceted acicular crystals of  $\text{CdGeAs}_2$  grown from a Bi flux (author). Some are solid, others contain a core of solidified Bi solvent. Strong growth rate anisotropy is evident.

crystal growth methods capable of producing 100 gm crystals were developed [204,205]. While the  $K_2O$  flux was still used, top seeding was added later to control nucleation and growth conditions. This seeding technique, now known as the top-seeded solution growth method (TSSG), became a very important flux growth method. The first description of this method was in a 1958 paper by Miller [206]. He used a seed crystal mounted on a rod that rotated in a reciprocating fashion. Without pulling, he grew KN crystals up to 15 gm from a charge containing  $K_2CO_3$  and  $Nb_2O_5$ . He also used an electrical circuit between the crucible and seed to determine the exact moment when the seed touched the melt. The method was used later by Linares for YIG growth [207] and at MIT by Belruss et al. [208] for the growth of  $SrTiO_3$  and  $BaTiO_3$  crystals from melts containing excess  $TiO_2$  and  $GeO_2$ . More recently, the method has been used for growing beta barium borate crystals ( $\beta$ - $BaB_2O_4$ , BBO) from melts containing some  $Na_2O$  [209] or other solvents to lower the  $\eta$  viscosity and to permit growth at temperatures below the  $\alpha$ - $\beta$  phase transformation temperature. BBO and other similar compounds like  $LiB_3O_5$  (LBO) and  $CsLiB_6O_{10}$  (CLBO) are very useful for optical applications in the visible and ultraviolet regions.

As seen with aqueous solution growth, stirring during growth is very beneficial to the enhancement of crystal quality and growth rates. In addition to top seeding with rotation that provides some fluid flow, other methods have been devised. One useful approach is the accelerated crucible rotation technique (ACRT). It was first used by Nelson and Remeika [210] in 1964 for pregrowth stirring. Scheel and Schultz-Dubois first demonstrated its usefulness during growth in 1971 [104]. The method is very helpful with growth from volatile melts that need to be grown in sealed crucibles. No moving parts, like stirring rods, need to be placed in the melt. The method relies on acceleration and deceleration of the crucible, thereby decoupling the fluids movement from the crucible's trajectory in a periodic fashion. Two major flow mechanisms, spiral shearing distortion and Ekman-layer flow, are operative during acceleration and deceleration. It has been found to limit nucleation and to help produce large, inclusion-free crystals. It was first applied to the growth of  $GdAlO_3$  crystals from a  $PbO$ - $PbF_2$ - $B_2O_3$  flux and yielded the largest such crystal to date [202].

One other method worth mentioning was that devised by Tolksdorf [211] at the Phillips Central Laboratories in Hamburg. In the past, one of the problems with growing YIG crystals from the volatile  $PbO$ - $PbF_2$  flux was that it redissolves below 950 °C. To prevent this, Nielsen [212] poured off the flux at 1040 °C outside the furnace. Unfortunately, the crystals cracked due to thermal shock. An improvement on this method was by Grodkiewicz, Dearborn and Van Uitert [213]. They punctured the bottom of their large platinum crucibles draining off the melt. This was expensive, as the flux material could not be reused. In Tolksdorf's method he used a sealed crucible that could be rotated on its axis. It was half filled with a  $PbO/PbF_2$ /YIG melt and, after the crystals were grown by slow cooling, the crucible was spun 180° separating the crystals from the melt. In a similar way, he could mount a seed on the empty side, and when the melt was saturated, could rotate the seed into the melt, slow cool to initiate growth onto the seed, and when done, rotate the crucible back to its original position to remove the flux from

the crystal. Toldsdorf's method and apparatus was later used to grow  $\text{KTiOPO}_4$  (KTP) crystals (an important nonlinear optical material) using the flux method.

#### 1.3.2.6.2 Thin Film Liquid Phase Epitaxy

In addition to bulk crystal growth, high-temperature solutions have also been used to grow thin films of semiconductors, oxides (magnetic and electro-optic) and various other compounds. The method is known as liquid phase epitaxy (LPE). The LPE method involves the crystallization of a single crystal or crystallographically oriented layer on a substrate in contact with a liquid phase. The substrate (usually a single crystal wafer) may be either of the same base composition (homoepitaxy) or a different composition (heteroepitaxy). The field of epitaxial growth extends well beyond the LPE method to include numerous vapor phase depositions techniques to be discussed later. While these other methods are very important, the LPE has certain advantages including (1) greater crystalline perfection due to the near equilibrium growth conditions and use of a near perfect substrate template, (2) better stoichiometry control, (3) higher growth rates due to higher solutes concentrations and (4) lower cost compared to other methods. A comprehensive review of LPE field is given in Ref. [214].

Epitaxial deposits have been found in various natural mineral formations. One example is rutile crystals growing on hematite facets [215]. In 1836, Moritz Frankenheim (1801–1869), a German physicist, was the first of many researchers to observe epitaxial growth in the laboratory when he produced oriented crystals of sodium nitrate on a cleaved surface of calcite crystals [216]. In 1906 Baker did some experiments on the orientation of crystals growing from droplets crystallizing on cleaved surfaces [217]. In 1928, Royer followed this line of research [218] and using X-ray diffraction analysis, was the first to describe the requirements for lattice matching between the film and substrate to achieve epitaxy (an orientation relationship between the layer and the substrate).

In the 1960s, attention turned to thin film semiconductor devices. At the RCA Laboratories, H. Nelson [219] was the first to develop an effective LPE method for growing epilayers of GaAs on GaAs substrates (homoepitaxy). He used a horizontal graphite boat system with a GaAs + Sn melt at one end. When the substrate, located at the other end was at  $640^\circ\text{C}$ , the boat was tilted and the melt flowed over the substrate. After cooling for a period of time the melt was poured back off, leaving the substrate covered by a single crystal layer of GaAs. Other LPE techniques involved dipping substrates (either vertically or horizontally) into an appropriate solution and then, after deposition, withdrawing them back out. Substrate rotation has also been used to achieve better uniformity. By using these various methods p-n junctions could be produced using doped layers. These epilayers were used in a number of important device applications including GaAs [220] and  $\text{Al}_x\text{Ga}_{(1-x)}\text{As}$  [221] lasers and the extensive commercial production of light emitting diodes (LED's). The LPE method has also been used to prepare thin film structures from silicon, germanium and their solid solutions, II–VI compounds such as ZnSe, CdTe,  $\text{Hg}_{1-x}\text{Cd}_x\text{Te}$  (MCT), SiC, the III–V nitrides (AlN and GaN) and many other alloy compositions [214]. As with any flux growth method, the solvents have to be tailored to the specific film

composition to be grown and the substrate and its orientation carefully chosen. The requirement for high-quality substrates for both LPE and vapor phase epitaxy have kept the bulk crystal growth industry very active.

In addition to semiconductor research, various applications for magnetic garnet crystals (e.g.,  $\text{Y}_3\text{Fe}_5\text{O}_{12}$  and  $\text{Ca}_{2x}\text{Bi}_{3-2x}\text{Fe}_{5-x}\text{V}_x\text{O}_{12}$ ) were developing during this same time period. LPE became an important method for the preparation of various types of microwave, magneto-optic and bubble memory thin film devices. One of the first attempts to use the LPE method for YIG film deposition on garnet substrates was in 1965 by Linares et al. [222]. In 1968 Linares [223] grew high quality YIG films on GGG using the tilting boat method and a lead borate flux. Magnetic bubble memory thin film devices became an important research activity during the 1970s [224]. These thin film structures were once expected to replace Si-based memory chips and various groups extensively studied both their preparation and properties. Magnetic garnet single crystal LPE films were typically grown from  $\text{PbO-B}_2\text{O}_3$  fluxes. The substrates used were nonmagnetic  $\text{Gd}_3\text{Ga}_5\text{O}_{12}$  (GGG). It is a very good lattice match with YIG. Various techniques such as substrate dipping and rotation during growth were studied. Withdrawal after growth could be problematic due to cracking and film peeling. The process gave high growth rates and crystalline perfection, film thickness uniformity, and compositional homogeneity. Over time, ever more complex film compositions evolved to enhance their properties [225,226]. The technology reached its zenith with the growth of bismuth-doped rare earth iron garnet thick films up to one-half mm thick from  $\text{Bi}_2\text{O}_3\text{-PbO-B}_2\text{O}_3$  fluxes onto large lattice parameter-matched Ca-Mg-Zr substituted GGG substrates.

In 1986, Bednorz and Müller discovered  $\text{H}_i\text{-Tc}$  superconductivity while working at the IBM research laboratories near Zurich [227]. The ceramic material they produced was an oxygen-deficient Ba-doped Lanthanum cuprate ( $\text{La}_{2-x}\text{Ba}_x\text{CuO}_4$ ), a perovskite-like compound that exhibited zero electrical resistance at 35 K, twice the highest transition temperature achieved to date. This set off a whirlwind of research activities to find other cuprates with even higher  $T_c$ 's including  $\text{YBa}_2\text{Cu}_3\text{O}_{7-x}$  (92 K) followed by  $\text{Bi}_2\text{Sr}_2\text{Ca}_{n-1}\text{Cu}_n\text{O}_{4+2n+x}$  ( $n = 1, 2$  and  $3$ ) with a  $T_c$  between 85 and 110 K. Thallium- and mercury-based cuprates had even high  $T_c$ 's, the latter a record at 134 K. At this point a great effort was made to grow single crystals of these compounds for physical property studies and to enhance their properties. Due to the complex nature of the phase equilibria in these systems, crystal growth was very complicated, making difficult the preparation of large, high-quality single crystals. All manner of bulk and film deposition methods were tried with varying success. In Scheel et al. [228], the LPE method was used to prepare very flat, high quality epitaxial layers of  $\text{YBa}_2\text{Cu}_3\text{O}_{7-x}$  on  $\text{NdGaO}_3$  substrates. Step heights were between 1.2 and 7.2 nm and did not exhibit the spiral islands found using vapor phase deposition techniques.

### 1.3.2.7 Hydrothermal Growth

Hydrothermal growth is a solution growth method operated at modest temperatures and elevated pressures. Byrappa and Yoshimura [229] authored an exhaustive treatise on the

history and technology behind the hydrothermal growth process. The subject has also been discussed to a lesser extent in numerous other books and journal articles, for example [230]. The process involves the controlled growth of crystals in an autoclave (see Figure 1.13(A)) onto seeds immersed in a water solution containing the nutrient and usually a mineralizing agent. The driving force for growth is the solubility difference generated by a temperature gradient. The method has several advantages. Growth takes place below the material's melting temperature and often below a destructive phase transformation (e.g.,  $\alpha$ -quartz, the low-temperature polymorph of  $\text{SiO}_2$ ). Since the growth process takes place in a sealed system, the atmosphere can be modified to suit the material being grown (i.e., maintaining an oxidizing or reducing environment). In addition, the method generally produces less stress on the crystal and can lead to an increased crystalline perfection. Another attractive feature of hydrothermal growth is that the growth rates are relatively fast compared to other solution growth methods. High-pressure vessels can be made of various materials depending on the temperature and pressures required.

Hydrothermal growth's principal use has been for the commercial growth of large, highly perfect (dislocation-free)  $\alpha$ -quartz crystals for piezoelectric applications. A rack of crystals produced from one large-scale commercial autoclave is shown in Figure 1.13(B). Piezoelectric materials such as quartz generate an electrical polarization when subjected

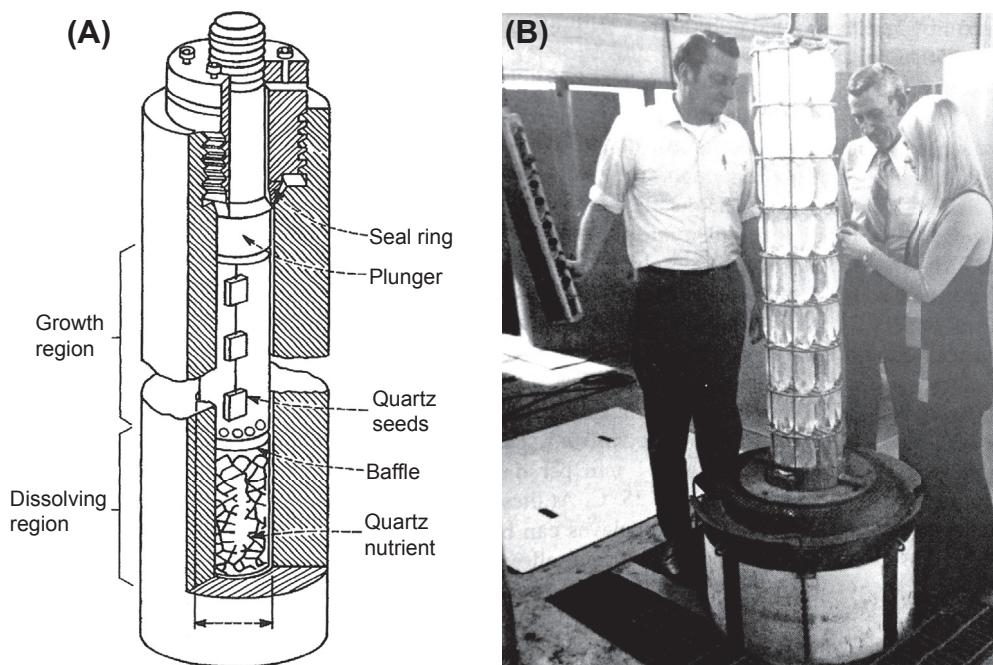


FIGURE 1.13 (A) A schematic diagram of a hydrothermal quartz autoclave. (B) The commercial harvesting of quartz crystals at AT&T's factory in Massachusetts [30].

to a mechanical stress. The hydrothermal method has also been used to successfully grow a variety of crystals of many different classes of compounds from simple binary compounds, such as ZnO, ZnS and GaN, to more complex compounds, such as the phosphates (AlPO<sub>4</sub>, and KTiOPO<sub>4</sub>), calcite, hydroxyapatite, zeolites, silicates, metal borates, vanadates, tungstates, and rare earth garnets (e.g., YIG and YAG).

Geologists trying to understand how crystals grew in nature (in an aqueous media under high pressures and temperatures) were the first to carry out hydrothermal phase equilibria studies. Experiments have been traced back to the twelfth century. Their main interest was in phase relationships rather than the growth of large crystals. One of the first published papers on hydrothermal crystallization was by Karl Emil von Schafhäütl in 1845. He prepared microcrystals of quartz. A short time later, in 1848, Robert Bunsen prepared some of the alkaline earth carbonates. The first attempt to grow large crystals hydrothermally was by Henri De Sénarmont in 1851 [231]. He introduced the use of seed plates. It was one of his many studies on the hydrothermal crystallization of minerals. Fifty years later, Giorgi Spezia (1905) published one of the seminal papers on the seeded growth of  $\alpha$ -quartz [232]. These early research efforts in Europe eventually formed the basis of the commercial quartz crystal industry.

The modern synthetic quartz crystal growth industry arose during World War II. Supplies of natural Brazilian quartz were not getting to the U.S. due to German submarine attacks on allied shipping. Ironically, one of the applications for quartz crystals was for submarine detection. Piezoelectric materials are needed in single crystal form to take advantage of their anisotropic properties. In oscillators for example, the frequency depends on crystal orientation and devices require precisely oriented parts. Quartz is also used for watches and clocks for precision time management and in signal processing applications.

Major developments in the hydrothermal growth technology were centered on the growth of quartz crystals at the Bell Telephone Laboratories and the Western Electric Company during the 1950s. Walker and Buehler [233] developed a hydrothermal growth method capable of producing very large crystals. They used a welded steel autoclave that was capable of temperatures of 450 °C and pressures up to 3000 atm. Improvements in autoclave designs were based on some early high pressure studies by Bridgman. Over the following years, improvements were made by the Western Electric Company that led to its successful commercialization. It was in large part due to the efforts of Laudise and Sullivan [234]. Systematic kinetic studies by Laudise [235] led to significant improvements in crystal growth rates. An effort to improve the resonance of quartz oscillators was undertaken by Bell Laboratory scientists and other researchers. Lithium and nitrite ions added to the growth solutions led to improved mechanical Q values [30].

Important hydrothermal growth parameters include (1) operating temperature, (2) temperature gradient, (3) pressure, (4) percent fill, (5) impurity and mineralizer concentration, and (6) seed orientation and surface area. Using quartz as an example, the autoclave is placed in a two-zone furnace with the upper section, containing the oriented seed plates, being cooler than the bottom in which the nutrient, SiO<sub>2</sub>, is placed.

A perforated metal disc serves as a baffle between the two zones. The vessel is then filled with solvent to a desired level. The nutrient dissolves in the hot region of the furnace and the upper becomes supersaturated and deposits crystal layers on the seed plates. Convective currents generated by the temperature gradients help move saturated solutions to the seed chamber. For commercial quartz production (see [Figure 1.13\(B\)](#) above), a typical set of conditions might include a hot zone temperature of 400 °C, a seed zone temperature of 360 °C, a fill factor of 80% and a solution containing 1.0 M NaOH, a baffle opening of 5% and a pressure of 21 kpsi (144 MPa) [230].

An important more recent application of hydrothermal growth has been in the preparation of ZnO crystals. ZnO is a transparent, wide bandgap semiconductor (n- or p-type when doped) with a range of useful properties. It is piezoelectric, ferroelectric, exhibits room temperature ferromagnetism, has a large magneto-optic response, etc. It is useful for chemical sensors, catalysis and optoelectronic applications. When doped, its conductivity can vary from insulating to metallic. Bulk crystals, thin films and various nanostructures can be produced using this method. Nanostructures, in the form of platelets, rods, columns, and complex bilayer (column-to-rod), have recently been prepared using hydrothermal methods [236–239].

#### 1.3.2.8 *Electrochemical Crystal Growth*

Another useful solution growth technology is electrodeposition. It can be carried out in both aqueous and molten salts solutions, and both bulk and thin film single crystals can be grown in this way. The process involves introducing an anode and cathode into either type of solution (of appropriate composition) and applying a suitable voltage across the cell. The driving force for crystallization is the passage of current between the electrodes. The electrode can be a single crystal substrate (wafer or seed), a wire or a more complex structure. Electrodeposition has recently become an attractive method for use in preparing nano-, bio- and micro-structures. It can be used to make functional materials with the aid of three-dimensional masks and scaled up from the deposition of a few atoms to thick deposits.

The first use of electrolysis in chemical processing is attributed to the famous English chemist Sir Humphry Davy (1778–1829). Davy, who was responsible for the discovery of several alkali and alkaline earth metals, separated K from KOH in 1807, the first metal isolated by electrolysis. It has been used since then for the synthesis of a variety of materials. The Hall process, developed in the 1930s for separating Al metal from bauxite (dissolved in a molten salt), is one of its most important industrial applications of electrodeposition. It has also been used to produce many refractory compounds such as borides, phosphides, silicides and carbides. The application of this technology to crystal growth had a late start, surprising since Kunnmann [240] observed that “materials electrochemically precipitated from fused melts can almost always be obtained in the form of reasonably large crystal when sufficiently low current densities are employed.”

The potential advantages of electrocrystallization for crystal growth include (1) growth can be accurately controlled solely by electrochemical parameters (current

density and electric potential), (2) the process is isothermal (thermal gradients and temperature ramps are unnecessary), (3) its insensitivity to temperature fluctuations, (4) low growth temperatures minimize thermal decomposition and stresses, as well as vapor losses, (5) purification can be achieved electrochemically and (6) growth features can be studied quantitatively by varying electrochemical parameters [241]. On the other hand, the material to be grown and substrate have to be electrically conducting, and the growth rates are typically slow due to the generally low solute concentrations in the solution. An interesting hybrid method, developed by DeMattei et al. [242], combined molten salt electrodeposition with the Czochralski pulling technique. They demonstrated the method by growing long [110] oriented crystals of sodium tungsten bronze from [110] oriented seed crystals.

Silicon was first electrodeposited in 1854 by Claire-Deville [243]. He used a  $\text{NaAlCl}_4$ -Si molten salt solution. This work was followed a decade later by Ullik [244] who used a  $\text{K}_2\text{SiF}_6$ -KF flux. Cohen and Huggins [245], using a similar flux, were the first to produce coherent epitaxial layers of Si on Si substrates. Metal substrates yielded polycrystalline films. Other semiconductors electrodeposited from molten salt fluxes include the III-V compounds GaP, GaAs and InP. A review of molten salt electrochemical crystal growth was given by Feigelson in 1980 [246].

In the 1990s, an active research area developed around the growth of heteroepitaxial thin films of chalcogenide semiconductors using the low temperature aqueous solution electrodeposition method [247]. Large-scale solar cells were made from electrodeposited polycrystalline CdTe films [248]. Epitaxial films of CdTe can be electroplated from solutions containing cadmium sulfate and  $\text{TeO}_2$  onto an InP substrate [249]. In addition, epitaxial films of PbS [250], CdS [251], ZnSe [252] and other related compounds have been electrodeposited. Schlesinger et al. [253] presented a comprehensive review on the subject of semiconductor electrodeposition.

As mentioned above, ZnO is an important and versatile material of great interest to the research and industrial communities. The electrodeposition of ZnO was first demonstrated by Izaki et al. [254] and later Peulon et al. [255]. The growth of oriented rods and flat, disc-shaped crystals were described in Refs. [256–258]. Xu et al. [259] electrodeposited well-defined nano- and micro-structures onto to indium-doped tin oxide substrates using low molecular weight salts in the solutions to control crystal shape. They produced hexagonally shaped tapered ZnO rods and platelets and rhombohedral rods by using amine and other inorganic ions in their solutions.

### 1.3.3 Vapor Growth

#### 1.3.3.1 Introduction

Vapor phase crystal growth methods have been used extensively for the preparation of both bulk crystals and single crystal thin films. The latter, called vapor-phase epitaxy, are usually deposited on single crystal substrates and have found their greatest utility in the preparation of films and patterned nanostructures for electronic and electro-optic devices.

Important film deposition techniques include OMVPE, MBE, sputtering, etc. In most of these techniques the crystalline lattice of the film needs to be tailored to the substrate upon which it is deposited. Their properties depend not only on their composition, but also on lattice matching between the film and substrate and the crystalline defects that might arise from any misorientation. The substrates are typically thin, crystallographically oriented wafers cut from bulk crystals usually grown by melt growth techniques. The process can be homoepitaxial (growth on a substrate of the same material) or heteroepitaxial (growth on a different substrate material). Some common examples being Si integrated circuits, GaAs LED devices and more recently GaN on sapphire for lighting applications. Artificial epitaxy, to be discussed later, involves the creation of a geometric pattern (containing some orientational relationship with the film lattice) on a substrate by etching or deposition. The base substrate can be an amorphous material like glass.

Vapor growth technology does not have as long a history as other crystal growth methods. Most research and development work began mainly from 1960 onward. However, it has been traced back a bit further to the German chemist Robert Bunsen (1811–1899) [260]. In 1852, Bunsen observed that  $\text{Fe}_2\text{O}_3$  crystals formed together with HCl in volcanic gases through a reaction between ferric chloride and water vapor, i.e., a chemical vapor deposition (CVD) process [261]. Not long afterward, in 1861, French chemist Henri Claire-Deville (1818–1881) became the first person to put a CVD process to use preparing artificial oxide minerals of magnesium, titanium and tin [262].

The first commercial CVD process was inaugurated in 1880 for the fabrication of filaments for the new incandescent lamp industry [263]. In 1914, F.C. Brown, studied the crystal habits of Se crystals deposited by sublimation of its vapor in a closed tube under either vacuum or atmospheric pressure [264]. He held the Se at  $270^\circ\text{C}$  for up to a week and the crystals formed along the tube where the temperature was lower. The largest crystals always formed at the higher condensation temperatures ( $\sim 210^\circ\text{C}$ ). During the 1920s, Fritz Koref and immediately afterward Anton Eduard Van Arkel used  $\text{WCl}_4$  to deposit W on single crystal tungsten wires. Koref [265] used a hydrogen reduction method to dissociate  $\text{WCl}_4$  gas near the wire, which was heated to between 110 and  $1000^\circ\text{C}$ . This led to a W deposit containing oriented grains. In Van Arkel's process [266],  $\text{H}_2$  was not needed as the process was operated at much higher temperatures (1600–1700  $^\circ\text{C}$ ). In 1921, research began on growing metal crystals by sublimation. Gross [267] and Gross and Volmer [268] grew leaflet crystals of Zn and Cd by directing vapors onto cool glass plates. This work led Volmer to his adsorption-layer theory discussed earlier. In 1932 Straumanis [269] grew Mg, Zn, and Cd crystals by a similar technique. The metals were held at temperatures somewhat below their melting points.

Three basic techniques have been used to grow crystals from the vapor phase: (1) direct sublimation or evaporation of material followed by condensation, (2) chemical transport reaction and (3) chemical vapor deposition. Chemical thermodynamics (shifts in vapor–solid equilibrium) and mass transport are some basic differentiating features between these methods. The process relies on mass transport of species from the source through the gas phase to its incorporation onto the crystal surface. The sublimation and

chemical vapor deposition methods have been operated in either an open system, using an inert carrier gas, or in a closed growth chamber containing vacuum or higher gas pressures. The chemical vapor deposition method, most often used in thin film epitaxy, involves the decomposition of molecular species (precursors). The chemical transport reaction method, a reversible process, converts nonvolatile species into volatile ones prior to crystallization in closed systems.

Crystals can usually be grown by vapor growth techniques at lower temperatures than from melts of the same composition. Vapor phase methods are especially useful when a compound is difficult to grow because of a high vapor pressure, dissociation prior to melting, etc., or where a thin film is required. While these methods are used more extensively to grow epitaxial thin films, bulk crystals of a wide variety of elements and compounds (inorganic and organic) have also been prepared in useful sizes. Seeds are often used but many studies have involved heterogeneous nucleation on the walls of an ampoule. Vapor grown bulk crystals have been particularly useful for the preparation of small crystals for physical property studies, and in a few cases larger crystals, such as SiC and CdS, have found commercial markets. Crystals prepared by vapor techniques include halides, chalcogenides, oxides, pnictides and organic compounds. Growth rates vary for different materials systems and process details, but generally tend to be slower than melt growth methods. Comprehensive reviews of vapor growth theory and methods have been given by Kaldis [270], Faktor and Garrett [271], and Wilke [272].

### 1.3.3.2 Bulk Growth

#### 1.3.3.2.1 Physical Vapor Transport

A volatile compound that congruently sublimates (or evaporates from the liquid state) can form crystals when it condenses in a cooler region of a furnace. In its simplest form, a closed glass ampoule containing the source at one end is placed in a temperature gradient. The source sublimates at a selected temperature and condenses at the cooler end either as self-nucleated crystallites or on a seed crystal. When no seed is used, many nuclei usually form and some may outgrow the others due their temperature of deposition or their orientation with respect to the heat flow in the system. In 1954, Pizzarello [273] made an important modification to the method that helped improve crystal size and quality. It involved translating the ampoule in the furnace gradient and has some similarities to zone melting with the source and crystal separated by the gas phase rather than the melt. The amount of vaporization at the source end is balanced by amount deposited on the crystal [274]. This “zonal sublimation method” has been used to grow doped crystals of Cd and Zn chalcogenides (see Ref. [275]). Both vertical and horizontal methods have evolved. By controlling the nutrient flux toward the growth interface, seeded growth is possible. This was demonstrated both by Fochs in 1960 with CdS [276] and by Prior in 1961 with PbSe [277].

Some refractory materials such as SiC and ZnO require high temperatures to achieve useful vapor pressures. SiC and ZnO are important wide bandgap, high-temperature/high-voltage semiconductors. Large crystals are sought-after for the

fabrication of substrates. Since melt growth would require pressures of 100,000 atm and 3200 °C, other growth methods were sought. Various novel growth chambers and heating methods were developed for the vapor growth of these crystals. One of the earliest was by Frisch [278] in 1935. He grew ZnO needles by sublimation of a ZnO pellet heated to very high temperatures. In 1955, Jan Anthony Lely [279] developed a sublimation process for growing SiC single crystals that forms the basis of all commercial processes today. In his method, silicon carbide was placed in a graphite crucible and heated to 2500 °C in an argon atmosphere. Large hexagonal platelets of 6H-SiC formed. The crystals were of different sizes up to  $2 \times 2 \text{ cm}^2$  and were of very high quality. In 1978, Tairov and Tsverkov [280] modified the process to include seeding. They placed the source at the bottom of the reactor and the seed at the top. Growth rates of 0.5–1 mm/h were achieved. Further modifications have been made since then, and now crystals greater than 50 cm in diameter can be produced. The formation of defects in these crystals, in particular micro-pipes has been a challenging problem [281]. Much effort has gone into their reduction or elimination.

Large crystals of organic compounds such as urea have also been grown by sublimation techniques [282]. However, the formation of gaseous byproducts such as ammonia during growth were problematic. To remove these unwanted species, which either slowed down or stopped the growth process, a vacuum pumped effusion hole was incorporated into the ampoule. Large cm-size high-optical-quality boules of urea were grown on [001] seeds at rates of 2.5 mm/day (by comparison growth from methanol solutions was 0.3 mm/day). The reactor used for the PVT growth of large urea crystals is shown in Figure 1.14.

#### 1.3.3.2.2 Chemical Transport Reaction

When a material is nonvolatile under convenient processing conditions, it can often be chemically converted into a volatile species. Crystal growth can then proceed in a reversible process. This method is called the chemical transport reaction method (CRT). For example, ZnSe crystals can be grown in a sealed ampoule in the presence of a small amount of  $\text{I}_2$  vapor (the transport medium). The ZnSe charge at the hotter end will react to form  $\text{ZnI}_2 (v) + \text{Se} (v)$ . These gaseous species will then be transported to the cooler end reforming ZnSe on the growing crystal and thereby releasing  $\text{I}_2$ . The freed iodine can then react with more ZnSe source material and return to the growth zone. In this case, for deposition at the cold end, the required conditions are that the enthalpy ( $\Delta H$ ) and entropy ( $\Delta S$ ) are  $<0$ . For materials where  $\Delta H$  and  $\Delta S$  are  $>0$  deposition takes place in the hot zone.

The chemical transport method is based upon the pioneering work of Van Arkel and de Boer [283]. In 1925, they prepared the refractory metals titanium, hafnium and thorium using this iodine transport technique with deposition taking place on a heated wire. By 1963, the field had expanded to encompass many different materials using a variety of transporting agents. Harold Schafer's book entitled *Chemical Transport*

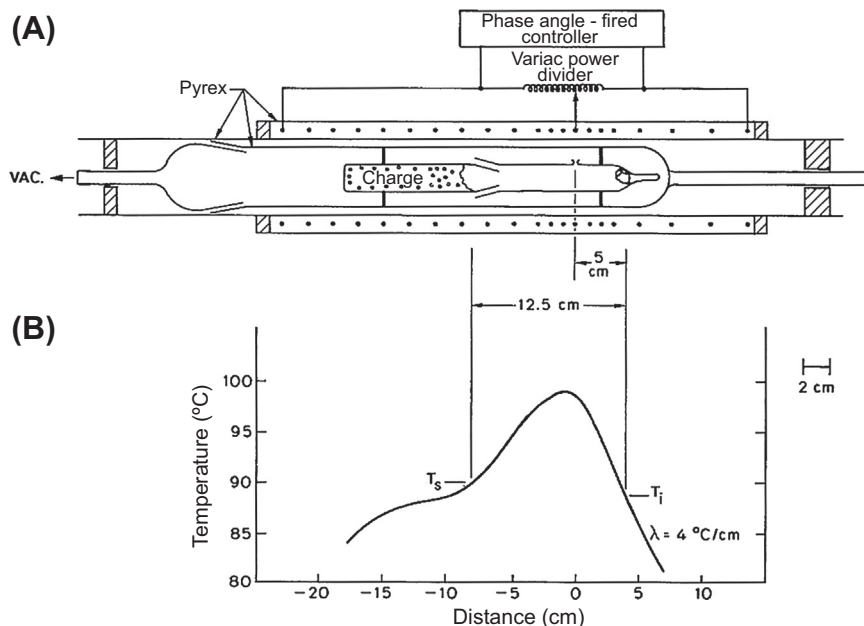
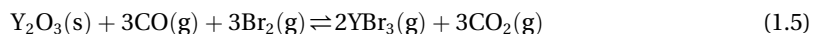


FIGURE 1.14 An example of a physical vapor transport bulk crystal growth apparatus. This growth system was used for growing urea crystals [282].

*Reactions* [284] has been an invaluable reference source for workers in the field since 1964.

Some important process requirements include (1) a chemical reaction that produces only one stable phase, (2) a free energy close to zero to facilitate reversibility, (3) a non-zero  $\Delta H^\circ$  and (4) the ability to control nucleation and the growth kinetics via crystallization zone temperature, temperature gradients, etc. Dopants have been added by incorporating volatile species of the desired element(s) into the growth ampoule. The choice of transporting agent is based on the thermodynamic propensity for the volatile species to form and dissociate in a useful temperature range. Sometimes additional species such as CO are added to the ampoule to facilitate the desired reaction. Sagal showed in 1966 that the growth of  $Y_2O_3$  crystals solely by halogen transport was not favored due to relatively high values of  $\Delta G^\circ$  (near 60 kcal/mol for the  $Cl_2$  gas and higher for  $Br_2$  and  $I_2$ ) [285]. However, by adding CO to Br the  $\Delta G^\circ$  value could be shifted closer to zero. The reaction therefore would be:



During the 1950s and 1960s, considerable research work was in progress using the CTR method. Metals such as iron, cobalt, copper and nickel crystals were produced, as well as classical semiconductors such as silicon, gallium arsenide and gallium phosphide. In addition, various oxide crystals such as alumina, beryllia and silica were grown.

### 1.3.3.2.3 Chemical Vapor Deposition

The same basic chemical transport process can be used in open systems; however, the process is not reversible. This method is typically known as chemical vapor deposition (CVD). Its most important application by far is the growth of epitaxial thin films to be discussed later. Bulk crystals or thin oriented films are grown by reacting and/or decomposing one or more volatile precursors in the vapor state and depositing them onto the crystal or substrate. These sources can be in many forms; gases, liquids, solutions and aerosols. Any unwanted reaction byproducts can exit the system in the gas stream. Very pure crystals can be produced by this method depending on the type of precursor used. Perhaps the earliest example of this technique was reported by Lorenz in 1891 [286]. He reacted Cd vapor with H<sub>2</sub>S gas to form fairly large crystals of CdS. In 1947, Frerichs [287] modified the technique by using a slow stream of H<sub>2</sub> gas to drive the H<sub>2</sub>S over Cd metal that was heated to 800–1000 °C. His open tube system produced crystals up to 2 cm<sup>2</sup>. An extensive discussion of bulk crystal growth from the vapor phase is given by Schönherr [288]. He provides many useful and practical details including the various methods used, ampoule designs and furnace systems, etc. Bulk growths can be grown in vertical or horizontal configurations or any angle inbetween. Translating the growth chamber or ampoule in a temperature gradient is an often-used procedure. The reactors can be operated at pressures ranging from atmospheric to ultra-high vacuum. Materials produced by the CVD method include refractory metals (such as tungsten), semiconductors (such as silicon and III-V compounds), oxides (such as SiO<sub>2</sub>), silicon carbide, nitride and oxynitride, and various carbon structures, including diamond as discussed later. Since the late 1990s, it has found use in the preparation of nanocrystals, one important example being carbon nanotubes and fibers. The nanotubes can be produced by a number of methods including the catalytic decomposition method [289], a CVD technique using metal catalysts together with hydrocarbon precursors. Depending on the details of the process, i.e., the metal catalysts used, etc., aligned single- or multi-walled nanotubes can be produced.

### 1.3.3.3 Vapor Phase Epitaxy

#### 1.3.3.3.1 Organometallic Vapor Phase Epitaxy

Organometallic vapor phase epitaxy (OMVPE aka MOCVD) is a subset of the more general Chemical Vapor Deposition (CVD) method. It uses at least one organometallic precursor (OM) but may also be combined with other types of volatile species to produce films of many different II-VI and III-V semiconductor compounds and their solid solutions. Like other methods, there are lots of variations in technique. One of the earliest recorded descriptions of the OMVPE process was in Scott et al.'s little known 1957 United Kingdom patent [290]. In it, he describes the deposition of InSb in a cold wall reactor by the pyrolysis of a Group III alkyl (i.e., triethylindium) and a Group V hydride (i.e., stibine-SbH<sub>3</sub>). The second, in a 1965 U.S. patent, described the pyrolysis of a Group III alkyl (i.e., triethylindium or trimethylgallium) and a Group V reactant such as arsine to produce a III-V semiconductor [291]. However, the first published work in the

scientific literature was in 1969 in a paper by Harold Manasevit and W. Simpson [292]. They grew single crystal Ga-group V compounds on insulating, GaAs, GaP or Ge single crystal substrates. Either trimethylgallium or triethylgallium in the presence of arsine, phosphine and arsine-phosphine or arsine-stibine gas phases was used in these experiments. In 2004, Manasevit, now considered one of the founders of OMVPE technology, published his recollections on how the OMVPE field developed [293]. A schematic drawing of his apparatus is shown in Figure 1.15. Along with his colleagues at the Autonetics Division of North American Rockwell, Manasevit published numerous other papers on this topic. In 1975, Seki et al. [294] produced the first important device quality (i.e., very high mobility) GaAs layers. This advancement was due to the enhanced purity and crystalline perfection of the films. Other major technological advancements followed soon afterward.

One of the important virtues of the OMVPE method is that it can be used to grow epitaxial semiconductor alloy films. In 1977, Dupuis and Dapkus [295] grew low oxygen and carbon films of AlGaAs by the OMVPE method. This material had excellent minority carrier lifetimes making them useful for light-emitting diode devices. In 1978, Gerald Stringfellow, from the Hewlett-Packard Laboratories, both proposed [296] and demonstrated [297] that with OMVPE one could grow very bright LEDs from AlInP and AlGaInP epitaxial films.

In the 1960s, Isamu Akasaki's group at Nagoya University started working on GaN-based LED's devices. In 1989, his work culminated in the invention of a bright gallium nitride p-n junction by using the low temperature OMVPE method with an AlN buffer layer on sapphire [298]. A major step was in creating p-type GaN using magnesium as the dopant and n-type with silicon. In 1994, Nakamura et al. [299] grew the first very bright InGaN/AlGaN double-heterostructure blue-light-emitting diodes also on

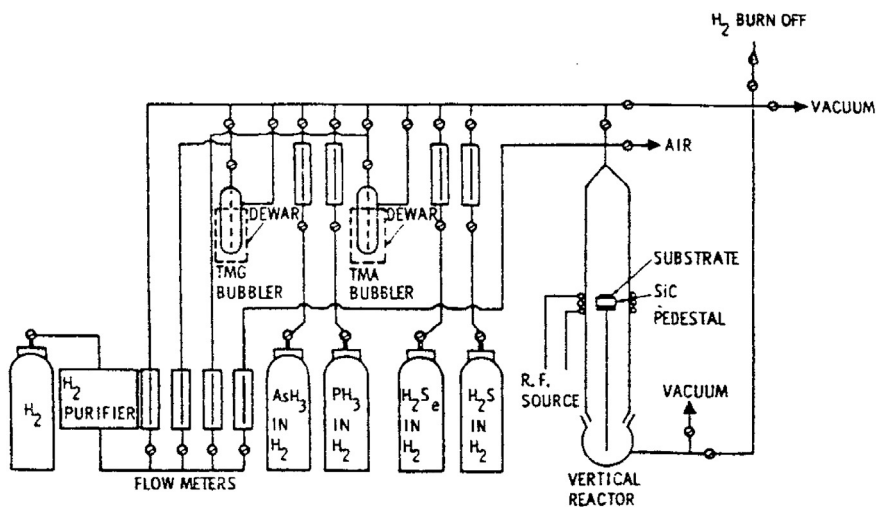


FIGURE 1.15 Schematic drawing of Manasevit's MOCVD deposition system [293].

sapphire substrates using a two-flow OMVPE method. The work of Nakamura's group at the Nichia Chemical Company, as summarized in Ref. [300], was a pivotal step in the development of the now multibillion dollar industry centered on the fabrication of highly efficient GaN-based/sapphire epitaxial films for optoelectronic devices. OMVPE development since then has been continuous with emphasis not only on improving the quality and properties of the epilayers, but also the quality and cost of the sapphire substrates. In an example of a more recent work (2002), Liu et al. [301] grew GaN single crystal epitaxial layers on sapphire in a three-step process using the low-pressure OMVPE method together with an AlN buffer layer and via atomic layer epitaxy (to be discussed later).

Stringfellow reviewed the development and status of the OMVPE method several times (e.g., Refs [297,302]). In the latter, he commented "One reason that OMVPE is so widely used today is that it is the most versatile technique for the growth of materials and structures for a wide range of devices."

#### 1.3.3.3.2 Molecular Beam Epitaxy (MBE)

Molecular beam epitaxy (MBE) is a process in which a thin single crystal layer is deposited on a single crystal substrate using atomic or molecular beams generated in Knudsen cells contained in an ultra-high vacuum chamber. The source beams can be created in a number of ways, including (1) melting and evaporation of solids or liquids contained in crucibles (2) solid sublimation from a crucible, (3) ion beam bombardment, and (4) cracking various chemical species, etc. Its greatest use is for making multilayer semiconductor device structures. Details of the MBE method, as well as other bulk and thin film growth techniques used to prepare compound semiconductors, are given in Ref. [303].

One of the earliest published studies on the use of the MBE method for single crystal film growth was that of Joyce and Bradley [304]. In the mid-1960s they grew homoepitaxial layers of Si from SiH<sub>4</sub>. The growth rates were very low comparative to other Si film methods and therefore not competitive in a market that needed 10 μm-thick films. A few years later, J. Davey and T. Pankey [305] from the Naval Research Laboratory, and J. Arthur [306] and A. Cho et al. [307] from Bell Laboratories expanded the MBE method for the deposition of GaAs. Arthur focused on surface kinetic studies, Davey and Pankey grew large-area GaAs epitaxial films on GaAs and Ge substrates using the three temperature technique, while Cho focused on device applications. The MBE technique is a powerful method both for film deposition and in situ analysis. It has yielded, in addition to device structures, a wealth of data on the surface atomistic phenomena such as surface reconstruction. It has also been applied to other semiconductor material systems such as the nitrides and has facilitated the construction of novel structures such as periodically poled GaAs for IR nonlinear applications and quantum dots. Today, it is a very important research tool and is used extensively in commercial optoelectronic device processing. A historical review of the MBE method was given by Joyce and Joyce in Ref. [308].

### 1.3.3.3 Sputtering

In 1852, Sir William Robert Grove (1811–1896), a noted Welsh judge, physical scientist and inventor of the fuel cell, was the first to discover the deposition process now known as sputtering [309]. He was able to deposit material from the tip of a wire in a chamber at a pressure of 0.5 Torr onto a polished silver surface when the latter was the positive electrode in an electrical circuit. An interesting factoid is that the first commercial application of the sputtering method may be attributable to Thomas Edison who early in the development of his wax phonograph cylinders using a sputtering methodology for plating them.

The sputtering method, as used to prepare thin films, became popular and of commercial importance from the mid-1960s onward. It has the advantage of not requiring high temperatures to deposit materials, even very refractory ones. The films have compositions similar to the target material and large areas can be deposited. While this physical vapor deposition method is more often used to deposit polycrystalline and amorphous films, single crystal films have been produced by carefully controlling the processing parameters. The method is used for fabricating integrated circuits, antireflection coatings, solar cells and optical waveguides, etc. Typical materials sputtered include metals, semiconductors, oxides, and nitrides, etc.

The simplest sputtering process involves just a temperature-controlled cathode and anode, a source of energetic particles, i.e., ions or atoms, and a vacuum chamber. A DC potential of several thousand volts is usually maintained across the electrodes. Radio frequency sputtering, where the sign of the electrodes is varied at a high rate, has also been found beneficial. The material to be deposited is ejected from the target (at the cathode) by bombarding it with ions or atoms, and the ejected material is transported in the plasma formed to the substrate (at the anode). In addition to the ions released from the target, electrons are also produced and they play an important role in maintaining the plasma. However at the same time they can cause excessive heating of the substrate. The transport mechanism within the gap between the two electrodes is complicated and depends to a great extent on the background gas pressure. For efficient ejection, the sputtering gas should have a similar atomic weight as the target elements. Nonreactive gases such as argon, krypton and neon are often used to eject atoms from the target, but reactive sputtering, using oxygen or nitrogen gas, has been employed to deposit oxide and nitride films (e.g., ZnO and TaN). In the latter process a chemical reaction takes place between the gas and the sputtered ions near the cathode before being transported to the substrate. Higher substrate temperatures encourage the deposition of single crystal films. Williams has given an extensive overview of the sputtering field and sputtered ion emission [310].

Conventional sputtering has some disadvantages including low deposition rates, low ionization efficiencies and substrate heating. One major improvement to this technology was the introduction of magnetron sputtering [311]. In this process a magnetic field is incorporated into the sputtering apparatus with the magnetic field positioned parallel to the target and confining the secondary electron movement close to the target. This

maximizes the probability of electron–atom interactions, increasing ionization efficiency. The result is higher sputtering and deposition rates. It also permits the use of lower operating pressures and voltages. The magnetron was originally conceived by P.M. Penning in 1936 [312]. In 1980, Naoe et al. [313] were the first to use it in a sputtering application. Over the years magnetron sputtering configurations have been modified, and these developments have led to improved film quality and device performance [311].

#### 1.3.3.3.4 Atomic Layer Deposition

In 1977, Dr Tuomo Suntola from Helsinki University in Finland patented a novel technique to prepare highly oriented compound thin films [314]. The method was called atomic layer epitaxy (ALE). More recently, the nomenclature atomic layer deposition (ALD) has been favored. The ALD technique provides precise control of the film thickness and composition and with the proper substrate composition, orientation and temperature, can produce single crystal thin films. It involves the periodic (alternating) pulse deposition of a film's components in a vacuum chamber. In between pulses there is an equilibration period during which the excess components can desorb from the surface and exit the growth chamber. This leaves just one atomic layer on the substrate surface. The next atomic species is then deposited, and a controlled chemical reaction at the surface between these two layers creates the desired film composition or composite structure. By way of example, to produce an epitaxial ZnS film by this technique, a single Zn atomic layer is first deposited on the substrate surface. This layer is then exposed to  $S_2(g)$  or  $H_2S(g)$ , either of which react with the Zn layer to form the compound ZnS. Following equilibration, another Zn layer is deposited and then reacted again with the sulfur-containing gas. The thickness is determined by the number of cycles employed.

Historically, the idea for a sequential layering film deposition process was first mentioned in the 1952 thesis of Professor V. B. Aleskovskii as molecular layering. And years later, (during the 1970s) his group in Russia worked on the developing this concept further [315]. The efficacy and implementation of the method into a commercially viable process derived from the work of Suntola's group during the years prior to their patent application. For a definitive review of all aspects of the methodology, see Suntola [316].

The ALD technique can produce atomically flat films with almost perfect stoichiometry and surface conformity through the self-limiting reaction mechanism. It can be used with many of the chemical vapor deposition methods described above that normally deposit the requisite phases simultaneously. It can be used to produce layered films with abrupt interfaces (e.g.,  $TiO_2/Al_2O_3$  films [317]), and M. Ritala and M. Leskela [318] reviewed the method's features and its potential role in nanotechnology. One of the drawbacks of the ALD method is the slow deposition rates. This has been somewhat overcome by increasing the substrate areas during deposition. The use of bias sputtering has given the best stoichiometry to date. Besides oxides and chalcogenides, as mentioned above, the method has also been used for the preparation of various semiconductors, nitrides, and metal films.

### 1.3.3.4 The VLS Method

Another interesting and useful growth method is the vapor-liquid-solid (VLS) technique. This hybrid method combines chemical vapor deposition with solution growth. Deposition takes place at localized positions on a single crystal substrate to yield a nanostructure, particularly whiskers, rods and nanowires. It starts with a single crystal substrate patterned with an array of small dots made from a solid metal solvent phase (the “catalyst”). The patterning can be done using lithography or by converting a solvent film deposited on the substrate surface to droplets. The growth procedure is simple. When the substrate is heated, the solvent phase melts. The liquid phase rapidly super-saturates by adsorption of nutrient species from the gas phase. Growth subsequently takes place at the substrate–liquid interface and not on the bare substrate surface. The solvent region rises up, as a mass is deposited below it, thus propagating the growth feature. The molten zone remains on the fiber tip during growth. As an example, silicon nanowires have been produced from a Au–Si alloy droplet and with a gas phase containing  $\text{SiCl}_4$  and  $\text{H}_2$  (see Figure 1.16 below). The VLS method has been used in conjunction with CVD, MBE, laser ablation and carbothermic reduction.

The VLS method was first described in 1964 in the pioneering work of Bell Laboratories scientists R. Wagner and W. Ellis [319] (see Figure 1.16). The VLS

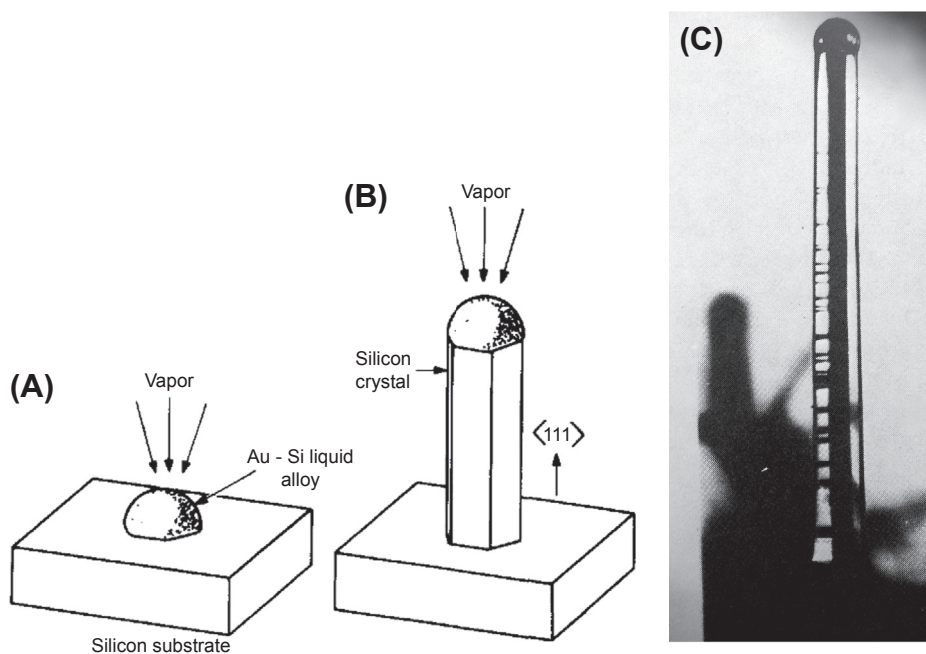


**FIGURE 1.16** Original schematic diagram of the VLS process for Si whisker growth on a silicon substrate, (A) Au–Si alloy catalyst droplet on substrate surface before growth. (B) A growing whisker. A photograph of an actual Si whisker (0.5 mm diameter) grown on a  $\{111\}$  Si substrate is shown in (C). It has 12 side facets alternating between the  $\{211\}$  and  $\{110\}$  [318].

mechanism they proposed explained the growth of silicon whiskers on silicon substrates in the absence of the axial screw dislocation growth model described by Frank [22]. Some advantages to the VLS growth process include a lower reaction energy than with regular vapor growth techniques, the structures only grow where the solvent is located, and anisotropic-shaped columns can be produced. Important process parameters include (1) the wettability of the liquid droplet and its reactivity with the substrate, (2) the substrate orientation and surface roughness, (3) the processing temperature, etc. It is also very important and obvious that the solvent phase has to have a low equilibrium vapor pressure.

Some of the popular semiconductor materials grown by VLS include Si, Ge, GaAs, GaN, SiC and ZnO. Gold is most often used as the solvent phase, but other materials such as Ni, Pt have been successfully used. The substrates may be of the same or similar composition as the growth pillars (homoepitaxy) or on different material (heteroepitaxy). One example of the latter is the growth of densely aligned GaN wires grown on sapphire, LiAlO<sub>2</sub> or MgO substrates [320]. Schmidt et al. discussed various aspects of the growth of silicon nanowires and their electrical properties, including use of the VLS method [321].

The VLS method has been easily adapted to the growth of nanostructures. This has become a very important active area of research and should lead to exciting new commercial applications in the foreseeable future. One of the leading groups in this area is Lars Samuelson's group at Lund University. They have reviewed the fundamental mechanisms involved in the VLS processing of nanowires and the prognosis for further development of this technology [322]. Many new and unique structures have been created using the VLS process. One example being a decade old study that showed that certain material systems can phase separate into cored nanofibers. In a one-step VLS process, Choi et al. [323] grew GaN cored nanowires with a thick AlGaIn skin. Other techniques have also been used to coat the nanowires. An excellent review of the VLS method was given by Choi [324].

#### 1.3.3.5 Artificial Epitaxy (Graphoepitaxy)

Up to now, we have discussed the epitaxial growth of single crystal thin films on substrates made from materials of related composition and/or structure. The usefulness of high-quality single crystal or highly oriented films is well-known and crystalline perfection of the film depends on various attributes of the substrate and its quality. However, it would be highly desirable to be able to grow oriented films on inexpensive amorphous substrates or on substrate layers important to device function. In the early 1970s, Prof. N.N. Sheftal from the Russian Institute of Crystallography first described the concept of growing films on an artificial lattice. The paper, which described the technique as "artificial epitaxy," was translated into English three years later [325]. In 1982, the technique was renamed "graphoepitaxy" [326], and this more catchy term has gained favor in much of the subsequent literature.

Graphoepitaxy involves inscribing a micro-relief pattern onto a flat amorphous substrate surface. The surface patterns consist of only four symmetries, two-, three- four- and

six-fold (i.e., arrays of stripes, triangles, squares and hexagons). The walls of the relief pattern simulate the kinks and ledges associated with a crystal growth surface as described by the Kossel-Stranski model. Rather than atoms or molecules, however, the growth units that attach to these relatively large steps are microcrystallites of nanometer or micron sizes. The pattern chosen is determined by the crystal structure of the material to be deposited. For example, the three-fold relief would be used for the growth of the diamond lattices of Si and Ge. The reliefs can be achieved by a number of techniques including photolithography and etching, etc.

Graphoepitaxy can be accomplished using a variety of gas phase, melt or solution growth techniques, including the VLS method mentioned above. Like other methods described in this chapter many different materials have been prepared by graphoepitaxy, including very large-molecule biological materials [327]. By way of illustration, Figure 1.17 shows two crystals of catalase (an enzyme) that were deposited from an aqueous solution onto a silicon substrate that contained a striated micro-relief [327]. The pattern used here had a 5  $\mu\text{m}$  periodicity and a groove depth of 1–2  $\mu\text{m}$ . The crystals are clearly aligned with the micro-relief. Deposited on an unpatterned substrate, the crystals would have no orientational relationship with one another.

Graphoepitaxy has also been used to prepare oriented single crystal nanowires of semiconductor oxides such as ZnO, SnO<sub>2</sub>, In<sub>2</sub>O<sub>3</sub>. The method has been exhaustively covered in a book by Givargizov [328]. Since this book was written, the technique has become very popular, particularly in the semiconductor field. For example, so-called nano-graphoepitaxy has been used to prepare semiconductors for three-dimensional integration devices [329].

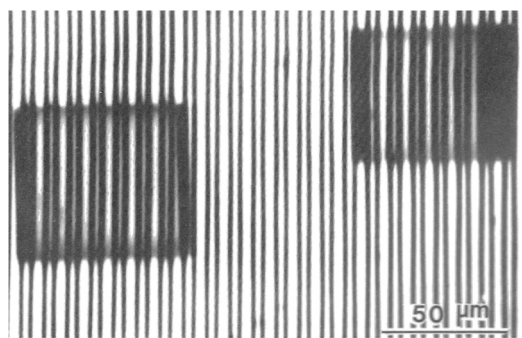


**FIGURE 1.17** Two catalase crystals grown from solution onto an oriented Si substrate having an etched micro-relief pattern. The crystals, which are aligned with the pattern, grew by artificial or graphoepitaxy [327].

### 1.3.4 Synthetic Diamond Crystals

Diamond, while highly sought after as a gemstone, also has a unique combination of properties that make it very useful in industrial applications. Diamond not only has the highest known hardness, it also has a very high thermal conductivity and electron mobility, low thermal expansion coefficient and excellent optical transmission over a

broad spectral range. In addition to its major commercial market, i.e., cutting tools and polishing powders, diamond has a myriad of other uses. Diamond-based devices include high-power electronic devices, high-frequency field effect transistors, LED's, ultraviolet and high-energy particle detectors, substrates and optical windows. The two principal methods used to grow synthetic diamonds are (1) crystallization of bulk crystals from solution at high pressures and temperatures (HPHT) and (2) deposition at low pressures and relatively low temperatures using the chemical vapor deposition (CVD) method. Both were developed during the early 1950s within a few years of each other and are still in use today to manufacture synthetic diamond products.

The earliest known reference to diamond can be found in the Old Testament [330]. It was not until near the end of eighteenth century that it was realized that diamond, while transparent and colorless, was made up solely of carbon atoms like graphite. The discovery came from the French chemist Antoine Lavoiser (1743–1794), who shortly before his death, decomposed a diamond by heating it in oxygen and found  $\text{CO}_2$  as the only byproduct. Thereafter, a number of credible researchers tried to synthesize diamond, one of the first being Scottish chemist James Hannay (1855–1931). His attempts in 1879 [331], later questioned, were followed in 1895 by the French Noble Prize-winning chemist Henri Moissan (1852–1907). He tried to synthesize diamond in the laboratory [332] starting with charcoal and iron heated to temperatures as high as  $3500^\circ\text{C}$  using an electric arc furnace. The heated mixture was then quenched in water to hopefully create the high pressures under which diamond formed in nature. Other researchers who tried to duplicate these studies either failed or had their various claims discredited. Sir Charles Algernon Parsons (1882–1922), the inventor of the steam turbine, spent considerable time and energy over many years trying to duplicate the work of Hannay and Moissan. He also tried to develop his own method to produce diamond. In 1928, as reported by Desch [333], Parsons concluded that synthetic diamonds had not been produced. Kathleen Lonsdale used X-ray diffraction methods to study some of Hannay's "diamonds" held at the British Museum. She concluded in a 1962 paper [334] that they were natural diamonds and doubted that "... neither Hannay, Moissan or Parsons ever, in fact, made diamonds by their respective methods." Percy Bridgman, who as mentioned before won a Nobel Prize for his high pressure work, spent the better part of 50 years (from 1905 to 1955) trying to synthesize diamond. His efforts were apparently unsuccessful as well [330]. In addition to the researchers mentioned above, the nineteenth century was littered with numerous unsuccessful attempts to synthesize diamonds by various means. One particularly engaging and well-researched book on the history and growth of diamond crystals is *The Diamond Makers* by Robert Hazen [335].

In 1941, the General Electric Research Laboratories, in conjunction with the Norton and Carborundum companies, set about to develop a process to synthesize industrial diamonds. The effort was suspended during WW II but started up again in 1951. While GE put together a large staff charged with designing a furnace that could go to both high pressures and high temperatures, it was not until H. Tracy Hall, came

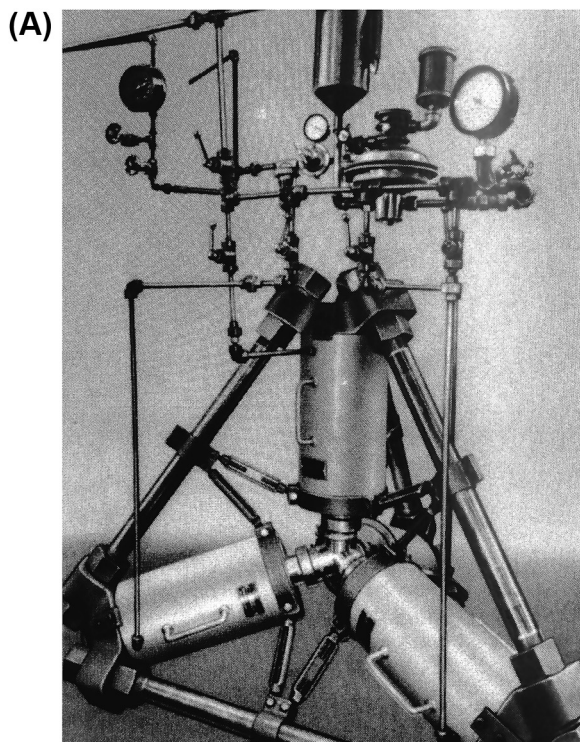


**FIGURE 1.18** Early diamond crystal growth (A) Schematic of the belt high-pressure, high-temperature apparatus built at the General Electric Corp., and (B) the first synthetic diamonds produced using this apparatus [330].



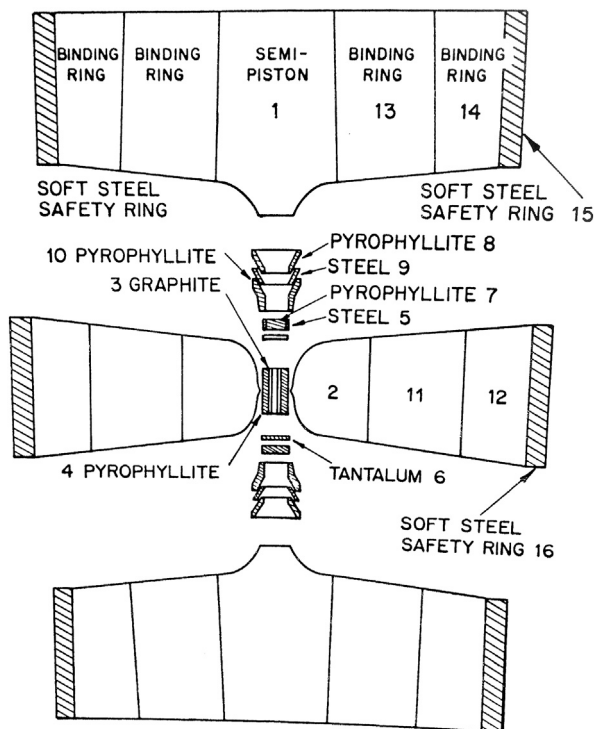
up with the “Belt” press (see [Figure 1.18\(A\)](#)) that a breakthrough was imminent. This device exceeded the original specifications of 35,000 atm and 1000 °C to achieve 250,000 atm and 1800 °C [336]. The growth chamber consisted of a graphite tube surrounded by a pyrophyllite container. Inside were placed Ni, Fe, or Co to act as a solvent-catalyst in which the graphite dissolved. The bottom was in contact with a Ta disc. However, even with this capability, diamond was not readily produced. It was

not until the end of 1954, after much experimentation and frustration, that the first small, micron-sized faceted diamond crystals were produced (see [Figure 1.18\(B\)](#)). The addition of FeS to the container did the trick. These were not gem-quality stones but appropriate for abrasive applications. Hall's personal reminiscences, given in Ref. [330], describe how the process was invented and the subsequent events that led to his other important invention—the tetrahedral anvil press shown in [Figure 1.19](#). Oddly, just before the GE success, the Swedish company ASEA, also managed to produce small diamonds in a top-secret project that only went public in 1980 [337].

The first successful preparation of gem-quality diamonds by HPHT was in 1970, again accomplished by GE. The process was similar to that described above with the addition of thin diamond seeds. The first crystals were 5 mm (1 carat) in size and took a week to grow. Longer growth times were required to produce larger crystals. These early crystals were yellow or brown in color due to nitrogen contamination and contained inclusions. By adding nitrogen getters such as Al and Ti, clear colorless crystals could be produced. On the other hand, other dopants have been used to modify the color of synthetic diamonds (e.g., boron gives it a blue color). A variety of colored stones have been produced.

The inherent technological difficulty in preparing diamonds or other materials at high pressures and temperatures and the high cost of equipment led many researchers,

**FIGURE 1.19** The original tetrahedral press for producing synthetic diamond [330].



particularly in the U.S. and the Soviet Union, to try to find a low-pressure method. Not many scientists, however, thought this would be possible. Nevertheless, in 1952–1953, William Eversole, at the Union Carbide Corporation, became the first person ever to prepare synthetic diamonds [338] by the chemical vapor deposition technique. It involved slowly depositing carbon atoms on clean diamond particle surfaces (i.e., substrates) in a vacuum at temperatures in the 800 °C range. Carbon monoxide (CO) or methane (CH<sub>4</sub>) was used as the source of carbon. Due to the propensity for graphite formation under these conditions, the residual graphite had to be removed after a period of time. This involved removing the crystals from the deposition chamber and cleaning them in an autoclave at 1000 °C and 50 atm of H<sub>2</sub> gas. Numerous such cycles were required. While he accomplished this feat about two years before General Electric and just a few months before ASEA in Sweden [337], his work (described in a patent only) was not published until 1962. In 1968, John Angus [339] independently verified Eversole's work, as did Deryagin and Fedoseev in 1970 [340]. While Angus also deposited diamond on single-crystal diamonds, Deryagin and Fedoseev made epitaxial films on other substrate materials such as Si and metals. From this point onward this very versatile method was aggressively pursued and refined by a number of groups in the USSR (Russia), the U.S. and Japan for the growth of both bulk crystals and homoepitaxial films on diamond substrates and by heteroepitaxial growth on suitably oriented materials like Si. A useful review of diamond growth by the chemical vapor deposition method was written by Garcia et al. [341].

One of the initial problems with the commercialization of CVD bulk diamond was the slow growth rates. In 1969, the former USSR scientists Spitsyn and Dervagin, who had been working on this problem since 1956, were finally able to increase the growth rates reported by Eversole by an order of magnitude. The improvement over their own previous work was due to the use of methane at higher pressures (13–40 Pa), together with an increased deposition temperature (950–1050 °C). Just a year later, a significant breakthrough was made independently by J. Angus (USA) and V. Varnin (USSR) [342]. They found that the use of atomic hydrogen in the growth chamber would remove the graphite co-deposits that form along with diamond due to a large difference in etching rates. A decade later, a group of researchers at Japan's National Institute for Research in Inorganic Materials made a series of important process improvements. They developed the microwave plasma, hot filament, and RF-Plasma CVD methods, new ways to dissociate the carbon-containing gases into reactive species [343–345]. Growth rates up to several μm/hr were achieved. This in turn led to the development of a variety of other processes and process refinements by this and other groups, leading the commercial success of the CVD method for a variety of diamond products including gemstones and coatings for various types of electronic and optical devices.

Two other methods have been employed for growing small-size diamonds. One is the explosive detonation method in which a carbon-based explosive is detonated inside a metal tube containing graphite [346]. The procedure, an HPHT process, produces

nanoscale diamonds. The diamonds are prevented from reconvertng to the more stable graphite form due to the quenching effect of a surrounding water-filled chamber. However, they have to be separated from the remaining carbon by dissolution in acid. The second method is the ultrasonic cavitation technique [347]. This more recent process is carried out at room temperature and atmospheric pressure. It involves the application of ultrasonic energy to a suspension of graphite particles in an organic liquid and results in micron-sized diamond crystals.

### 1.3.5 Solid State Recrystallization

The next to last topic to be covered in this chapter is the growth of sizable single crystals from the solid phase. This technology has a much smaller impact on the crystal growth field than the other methods described above. First, it is mainly limited to metals, and second, there are various processing difficulties associated with controlling nucleation and growth over extended length scales. The mechanisms involved are related to ceramic and powder metallurgy processing, where control of crystallite (grain) size and morphology in polycrystalline structures is a major concern. There are a myriad of important industrial applications for these polycrystalline materials (piezoelectric elements, magnets, etc.) and all aspects from theory to sample preparation are covered in various books on ceramics and powder metallurgy. The use of solid-state methods for crystal growth is covered in the book by R. Laudise [285].

At the heart of solid-state crystal growth (recrystallization) is grain growth. As mentioned before, the method is mainly used with metals such as aluminum, tungsten and iron. The material from which the crystal is grown contains grains of varying sizes and morphologies, plus grain boundaries and dislocations. Single crystals can be formed by controlling the growth of preexisting grains or by nucleating new grains with lower free energies. Wilhelm Ostwald's pioneering work in 1896–1897 explained how crystallites behave at elevated temperatures [348]. He showed that smaller particles adjacent to larger ones would decrease in diameter while the larger grains increased in size (an effect now known as Ostwald ripening). When the more energetic surface atoms on the smaller crystallites redeposit on the larger grains, the total energy of the system decreases. The driving force for grain growth can also be related to orientation differences between grains.

The principal method used to grow large metal crystals involves strain annealing techniques. A suitable polycrystalline sample, a bar, rod, plate, etc., is strained by one of a number of techniques such as rolling, drawing and extrusion. It then may be fabricated into a suitable shape to facilitate growth. The amount of strain induced is usually between 1 and 10% and the amount is critical in controlling the nucleation of strain-free grains. Growth is most often done in a temperature gradient and nucleation control is similar to other growth methods. In some respects, it is related to the Bridgman–Stockbarger method where the sample can be a rod with a tapered

end that is translated through the gradient. The gradients, however, are reversed from melt growth. The polycrystalline charge is heated until the tapered end reaches the recrystallization temperature and strain free grains are created in a localized region at the tip. Further movement propagates the strain-free grain(s) along the axis of the sample consuming the strained grains. If nucleation creates several strain-free grains, the sample can be notched somewhere along the length to permit only one grain to propagate through into the main part of the charge. Seeds can also be used. Suppressing nucleation ahead of the growth front has been a concern, and generally slow translation rates and sharp gradients minimize this problem (e.g., Ref. [348]).

The concept for strain-annealed crystal growth can be traced to Robert Anderson in 1918 [349]. This led, in 1921, to Carpenter and Elam's demonstration of the growth of large aluminum crystals by the strain-anneal method [350]. Over the ensuing years, various other metals have been grown by this method. One technique used to prevent random nucleation ahead of the growth interface during the strain-annealed growth of alpha iron crystals was the incorporation of pulsed heating [351]. Large, 25cm-long oriented single crystal rods and strips could be produced in a few hours using this method.

The solid-state recrystallization method has also been applied to semiconductor fabrication (e.g., Si and Ge). One technique of note is the solid phase epitaxial growth method. In 1968, L. Kulper at IBM, patented a process for the growth of aluminum-doped silicon films by the migration of silicon through an aluminum thin film during a heat treatment process [352]. The solid-state growth process provided doped layers with a maximum amount of aluminum in silicon. Later Mayer et al. [353], from the California Institute of Technology, patented a similar but more general process for doping with other species. In this process, a single crystal substrate is coated with a thin metal film having such properties that it will permit the migration of material through it to form an epitaxial layer without acting as an active dopant itself. Upon this film a dopant layer is deposited followed by an amorphous or polycrystalline layer of the material that will make up the doped epilayer. This sandwich structure is first heated to a temperature that permits the metal layer to dissolve some of the dopant, amorphous film and part of the substrate. After a time, the temperature is raised to allow the transport and epitaxial deposition of the doped layer onto the substrate. For the solid-state epitaxial growth of silicon, for example, the substrate and amorphous or polycrystalline layers would be silicon, the dopant layer might be phosphorous, aluminum, or boron, and the metal film palladium, vanadium, or nickel. A review of this technology is included in the book by Mayer and Lau [354].

Another application for solid-state crystal growth was in the preparation of piezoelectric single crystals, such as lead magnesium niobium-titanate (PMNT) [355]. The principal motivations were its potential cost advantage and enhanced

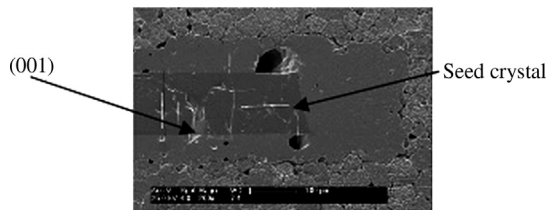


**FIGURE 1.20** An example of template growth. Shown is a micrograph of a polished and thermally etched ( $1080\text{ }^{\circ}\text{C}$  for 30 min) sample of  $\text{BiScO}_3\text{-PbTiO}_3$  (BS-PT) that was heat-treated with an embedded barium titanate (BT) seed crystal ( $5\text{ mm}^2 \times 100\text{ }\mu\text{m}$  thick). A 5% excess of PbO was used in the mixture to enhance diffusion. An overgrowth of a BS-PT crystal onto the surrounding BT seed can be clearly seen [355].

manufacturing throughput over conventional crystal growth methodologies. Two techniques were explored, conventional grain growth and templated growth in which seed crystals were embedded into a powdered matrix and processed at elevated temperatures. An example of the templated growth of  $\text{BiScO}_3\text{-PbTiO}_3$  is shown in Figure 1.20.

## 1.4 Epilogue

Crystal growth is a field that has had a major impact on modern society. The devices we have come to rely on today were made possible through the contributions of numerous scientists and engineers from a variety of disciplines. These devices are based on single crystals prepared in various ways and in forms and compositions reflecting the application intended. The foundations upon which our understanding of a crystal's structure, thermochemistry, growth mechanisms and methods is based on work from earlier centuries and dramatically expanded on all fronts (theory, growth and characterization) just after World War II. The book by Buckley in 1950 was the first comprehensive treatment (in English) of the prior art and science of crystal growth. Today, there are well over 100 books covering the topic, from surveys of the entire field to various specialized topics. This historical review of the crystal growth field is not comprehensive but was designed to highlight the major achievements. While I have tried to be as inclusive as possible, I apologize in advance if I have left out any major contributors to this field or important theories and growth methods. As a final comment, I must mention that a selection of some pioneering crystal growth papers were collected and reprinted in their original languages by D. Hurle [356].

## Acknowledgments

The author is indebted to Alex Chernov, Vince Fratello, Gabe Loiacono, and Jerry Stringfellow for critiquing specific sections of this chapter, and for discussions with Al Ballman, Bill Tiller and others.

## References

- [1] Pliny the Elder (Gaius Plinius Secundus). Volume 9 (Books 33–35), [H. Rackham, Trans.]. *Naturalis Historia circa AD 77–79*. Loeb Classical Library/Harvard University Press; 1958. p. 430.
- [2] Agricola G. *De Re Metallica* [L. Hoover and H. Hoover, Trans.]. Dover Publications; 1950.
- [3] Biringuccio V. *The Pirotechnia* [C. Smith and M. Gnudi, Trans.]. Dover Publications; 1990. p. 477.
- [4] Doremus RH, Roberts BW, Turnbull D. *Proc. int. conf. on crystal growth: growth and perfection of crystals*. New York: Wiley; 1958.
- [5] Gessner C. *De omni rerum fossilium*; 1565.
- [6] Caesalpinus A. *De metallicis libri tres*. Rome; 1596.
- [7] Sunagawa I. In: Feigelson RS, editor. *50 years progress in crystal growth*. Amsterdam: Elsevier; 2004. p. 35.
- [8] Steno N. *De solido intra solidum naturaliter contento*; 1669.
- [9] Guglielmini D. Philosophical reflections deducted from figures of salts from Doctor Domenico Guglielmini expressed in a speech recited in academy philosophical experimental affirmations. Archdeacon Marsigli; the evening of March 21, 1688. Bologna.
- [10] Romé de l'Isle JB. *Essay of crystallography or description of geometric figures*. L'Academie Electorale des Sciences Utiles de Mayence; 1772.
- [11] Bravais A. *Mémoire sur les systèmes formés par des points distribués régulièrement sur un plan ou dans l'espace*. *J De l'Ecole Polytech* 1848;19:1.
- [12] Gibbs JW. *The collected works of J. Willard gibbs, in two volumes*. In: Longley WR, Van Name RG, editors. New Haven: Yale University Press; 1993. 1957 (1928).
- [13] Jackson KA. In: Feigelson RS, editor. *50 years progress in crystal growth*. Amsterdam: Elsevier; 2004. p. 35.
- [14] Wilson HA. *Phil Mag* 1900;50:238.
- [15] Knudsen M. *Ann Phys* 1909;29:179.
- [16] Volmer M, Estermann I. *Z Phys* 1921;7:13.
- [17] Kossel W, *Nachr. Gesell. Wiss. Gottingen. Math-Phys. K1* 1927;135.
- [18] Stranski IN. *Phys Chem* 1928;136:259.
- [19] Kossel W. In: Falkenhagen H, editor. *Quantentheorie und Chemie*, Leipzig; 1928. p. 46.
- [20] Stranski IN, Kaishev R. *Z Krist* 1931;78:373.
- [21] Buckley HE. *Crystal growth*. New York: John Wiley; 1951.
- [22] Frank FC. *The influence of dislocations on crystal growth*. *Discuss Faraday Soc* 1949;5:48.
- [23] Heck CM. *Phys. Rev* 1937;51:686.
- [24] G.G. Lemmlein, *Vestn. Akad. Nauk SSSR* 4, 119 (1945)
- [25] Donnay JDH, Harker D. *Am Mineral* 1937;22:44.
- [26] Hartman P, Perdok W. *Acta Cryst* 1955;8:495.
- [27] Bennema P. *Growth and morphology of crystals*. In: Hurlé DTJ. *Handbook of crystal growth*, Parat 1a. North Holland (Amsterdam); 482.
- [28] Burton JA, Prim RC, Slichter WP. *J Chem Phys* 1953;21:1987.
- [29] Burton JA, Slichter WP. In: Feigelson Robert S, editor. *50 years progress in crystal growth*. Amsterdam: Elsevier; 2004. p. 43.

- [30] Millman S, editor. A history and of engineering and science in the Bell system, physical sciences (1925–1980). AT&T Bell Laboratories; 1983.
- [31] Carruthers JR. In: Bardsley W, Hurle DTJ, Mullin JB, editors. Crystal growth: a tutorial approach. Amsterdam: North Holland; 1979. p. 157.
- [32] Chernov AA. In: Feigelson Robert S, editor. 50 years progress in crystal growth. Amsterdam: Elsevier; 2004. 47 and Sov. Phys. Uspekhi 4 (1961) 116.
- [33] Burton WK, Cabrera N. Discuss Faraday Soc 1949;5:33.
- [34] Frenkel J. Phys J USSR 1932;1:498.
- [35] Becker R, Döring W. Ann Phys 1935;24:719.
- [36] Burton WK, Cabrera N, Frank FC. Philos Trans R Soc London Ser A 1951;243:299.
- [37] Chernov AA. J Cryst Growth 2004;264:499.
- [38] Jackson KA. Interface structure. In: Doremus RH, Roberts BW, Turnbull D, editors. Growth and perfection of crystals. London: Chapman and Hill; 1958. p. 319.
- [39] Jackson KA, Hunt JD. Acta Met 1965;13:1212.
- [40] Woodruff DP. The solid-liquid interface. Cambridge solid state science series. London: Cambridge University Press; 1973.
- [41] Rutter JW, Chalmers B. Can J Phys 1953;31:15.
- [42] Tiller WA, Jackson KA, Rutter JW, Chalmers B. Acta Met 1953;I:428.
- [43] Leamy HJ, Gilmer GH, Jackson KA. In: Blakely JM, editor. Surface physics on materials, vol. 1. New York: Academic Press; 1975. p. 121.
- [44] Leamy HJ, Gilmer GH. J Cryst Growth 1974;24/25:499.
- [45] Mullins WW, Sekerka RF. J Appl Phys 1963;34:323; 35 (1964):444.
- [46] Voronkov VV. Sov Phys Solid State 1965;6:2378.
- [47] Cahn JW. Crystal growth. In: Steffen Peiser H, editor. Proceedings of the international conference on crystal growth. Oxford: Pergamon Press; 1967. p. 681.
- [48] Coriell SR, Sekerka RF. J Cryst Growth 1976;34:157.
- [49] Chernov AA. J Cryst Growth 1974;24/25:11.
- [50] Hurle DTJ. J Cryst Growth 1969;5:162.
- [51] Temkin DE. Dokl Akad SSR 1960;132:1307.
- [52] Bolling GF, Tiller WA. J Appl Phys 1961;32:2587.
- [53] Hamilton DR, Seidensticker RG. J Appl Phys 1960;31:1165.
- [54] Glicksman ME, Lupulescu A. In: Feigelson Robert S, editor. 50 years progress in crystal growth. Amsterdam: Elsevier; 2004. p. 97.
- [55] Vogel R. Z Anorg Chem 1912;76:425.
- [56] Tiller WA. Liquid metals and solidification. Cleveland (OH): ASM; 1958. p. 276.
- [57] Jackson KA, Hunt JD. Trans Metall Soc AIME 1966;236:1129.
- [58] Glicksman ME. Principles of solidification. New York: Springer; 2010.
- [59] Wilcox WR. J Appl Phys 1964;35:636.
- [60] Carruthers JR, Nassau K. J Appl Phys 1968;39:5205.
- [61] Hurle DTJ, Rudolph P. In: Feigelson Robert S, editor. 50 years progress in crystal growth. Amsterdam: Elsevier; 2004. p. 109.

- [62] Wang CA, Carlsen D, Motakef S, Wiegel M, Wargo MJ, for Witt AW. In: Feigelson Robert S, editor. 50 years progress in crystal growth. Amsterdam: Elsevier; 2004. p. 125.
- [63] Nassau K, Nassau J. In: Feigelson Robert S, editor. 50 years of progress in crystal growth. Amsterdam: Elsevier; 2004. p. 9.
- [64] Merker L. In: Feigelson Robert S, editor. 50 years of progress in crystal growth. Amsterdam: Elsevier; 2004. p. 23.
- [65] Tammann G. Metallography [Dean and Swenson, New York, Trans.]. N.Y: The Chemical Catalog Co.; 1925. p. 26.
- [66] Obreimov J, Schubnikov L. Z Phys 1924;25:31.
- [67] Czochralski J. Z Phys Chem 1918;92:219.
- [68] Tomaszewski P. Jan czochralski and his method. Wroclaw-Keynia; 2003.
- [69] von Wartenberg H. Verh Dtsch Phys Ges 1918;20:113.
- [70] von Gomperz E. Z Phys 1921;8:184.
- [71] Tyndall EPT. Phys Rev 1928;31:313.
- [72] Walther H. Rev Sci Insts 1937;8:406.
- [73] Uecker R. JCG 2014;401:7–24.
- [74] Evans J. Phys Rev 1940;57:47.
- [75] Teal GK, Little JB. Phys Rev 1950;78:647.
- [76] Shockley W, Sparks M, Teal GK. Phys Rev 1951;83:139.
- [77] Teal GK, Buehler E. Phys Rev 1952;87:190.
- [78] Pfann WG. J Met 4, Trans AIME 194 (1952):747.
- [79] Pfann WG, Olsen KM. Phys Rev 1953;89:322.
- [80] Dash WC. J Appl Phys 1959;30:459.
- [81] Metz EPA, Miller RC, Mazelsky R. J Appl Phys 1962;33(6):2016.
- [82] Mullins JB, Straughan BW, Bickel WS. J Phys Chem Solids 1965;26:82.
- [83] Mullins JB, Heritage RJ, Holiday CH, Straughan BW. J Cryst Growth 1968;3–4:261.
- [84] Azuma K. Japanese Patent 60–111299, Furukawa Ind.; 1983.
- [85] Maiman. Nature 1960;187:493.
- [86] Nassau K, Van Uitert LG. J Appl Phys 1960;31:1508.
- [87] Ballman AA. J Am Ceram Soc 1965;48:112.
- [88] Nassau K. In: Feigelson Robert S, editor. 50 years of progress in crystal growth. Amsterdam: Elsevier; 2004. p. 155.
- [89] Fedulov SA, Shapiro ZI, Ladyshinskii PB. Kristallografia 1965;10(22):268.
- [90] Ballman AA. J Cryst Growth 1967;1:109.
- [91] Bardsley W, Cockayne B. In: Peiser HS, editor. Crystal growth. Oxford: Pergamon; 1967. p. 109.
- [92] Kestigian M, Holloway WW. In: Peiser HS, editor. Crystal growth. Oxford: Pergamon; 1967. p. 451.
- [93] Cockayne B, Chesswas M, Gasson DB. J Mater Sci 1967;2:7.
- [94] Charvat FR, Smith JC, Nestor OH. In: Peiser HS, editor. Crystal growth. Oxford: Pergamon; 1967. p. 45.
- [95] Brandle CD, Valentino AJ. J Cryst Growth 1972;12:3.

- [96] Brandle CD. *J Cryst Growth* 2004;264:593.
- [97] Carruthers JR, Peterson GE, Grasso M. *J Appl Phys* 1971;42:1846.
- [98] Cockayne B, Chesswas B, Gasson DB. *J Mater Sci* 1968;3:224.
- [99] Derby JJ, Brown RA. *J Cryst Growth* 1987;83:137.
- [100] Wiffen PAC, Brice JC. *J Cryst Growth* 1976;13:13.
- [101] Bridgman PW. *Proc Am Acad Arts Sci* 1914;49:625.
- [102] Stockbarger DC. *Am Mineral* 1927;12:26.
- [103] Stockbarger DC. *Rev Sci Instr* 1936;7:133.
- [104] Scheel HJ, Schultz-Dubois EO. *J Cryst Growth* 1971;8:304.
- [105] Zawilski KT, Custodio MCC, DeMattei RC, Feigelson RS. *J Cryst Growth* 2005;282:236.
- [106] Gault WA, Monberg EM, Clemens JE. *J Cryst Growth* 1986;74:491.
- [107] Mullins JB. In: Feigelson Robert S, editor. 50 years of progress in crystal growth. Amsterdam: Elsevier; 2004. p. 141.
- [108] Nacken R. *Neues Jahrb Mineral Geol* 1915;2:133.
- [109] Adams JM, Lewis W. *Rev Sci Instrum* 1935;5:400.
- [110] Buehler E, Walker AC. *Growing quartz*. Bell Telephone Publication; 1949.
- [111] Kyropoulos S. *Z Anorg Chem* 1926;154:308.
- [112] Kyropoulos S. *Z Phys* 1930;63:849.
- [113] Korth K. *Z fur Phys* 1933;8:677.
- [114] Chamberlain K. *Rev Sci Instrum* 1938;9:322.
- [115] Bliss D. In: Feigelson Robert S, editor. 50 years of progress in crystal growth. Amsterdam: Elsevier; 2004. p. 29.
- [116] Bryant GG, Bliss DF, Gabbe DR, Zach FX, Iseler GW. Photonic device engineering for dual-use applications, 2481. *SPIE*; June 30, 1995. 232.
- [117] Stober F. *Z Krist* 1925;61:299.
- [118] Schmid F, Viechnicki D. *J Am Ceram Soc* 1970;53(9):528.
- [119] Kattik C, Schmid F. *J Cryst Growth* 2001;225:572.
- [120] Kapitza P. *Proc R Soc London* 1928;A 119:358–442.
- [121] Mullin JB. In: Miller LS, Mullin JB, editors. *Electronic materials: from silicon to organics*. New York: Plenum Press; 1991. p. 118.
- [122] Schunemann PG, Pollak TM. *MRS Bull* 1998;23(7):23.
- [123] da C. Andrade EN, Roscoe R. *Proc Phys Soc London* 1937;49:152.
- [124] Pfann William G. *Zone melting*. Wiley series on the science. New York (NY): John Wiley & Sons; 1958.
- [125] Theuerer HC. *J Met* 8, *Trans AIME* 206(1956):1316.
- [126] Poplawsky RP. *J Appl Phys* 1962;33:1616.
- [127] Horn FH. *J Electrochem Soc* 1958;105:393.
- [128] Dash WC. *J Appl Phys* 1960;31:736.
- [129] Poplawski RP, Thomas Jr JE. *Rev Sci Instr* 1960;31:1303.
- [130] Feigelson RS. *Mater Sci Eng* 1988;B1:67.

- [131] Mimura Y, Okamura Y, Komazawa Y, Ota C. *Jpn J Appl Phys* 1980;19:269.
- [132] Yoon DH, Yonenaga I, Fukuda T, Ohnishi N. *J Cryst Growth* 1994;144:339.
- [133] Haggerty JS, Menashi P. Prod fibers by floating zone fiber drawing technique. Final Rep. NASA-CR-120948; 1971.
- [134] Burris CA, Stone J. *Appl Phys Lett* 1975;26:318.
- [135] Fejer MM, Nightingale JL, Magid GA, Byer RL. *Rev Sci Inst* 1984;55:1791.
- [136] Luh Y, Feigelson RS, Fejer MM. *J Cryst Growth* 1986;78:135.
- [137] Magel GA, Fejer MM, Byer RL. *Appl Phys Lett* 1990;56:108.
- [138] Chani VI. In: Fukuda T, Chani VI, editors. *Advances in materials research-shaped crystals*, vol. 8. Berlin: Springer; 2007. p. 3.
- [139] Feigelson RS, Route RK. *J Cryst Growth* 1990;104:789.
- [140] Feigelson RS. Growth of shaped crystals. In: Arend H, Hulliger J, editors. *Crystal growth in science and technology*. Plenum Publishing Corp; 1989. p. 275.
- [141] Polanyi M. My time with X-rays and crystals. In: Ewald PP, editor. *50 years of X-ray diffraction*. Utrecht: International Union of Crystallography; 1962. p. 629.
- [142] Mark H, Polanyi M, Schmid E. *Z Phys* 1923;12:58.
- [143] Stepanov AV. *Zh Tech Fiz* 1959;29:382.
- [144] Antonov PI, Nikandrov SP. *J Cryst Growth* 1980;50:3.
- [145] LaBelle Jr HE, Mlavsky AI. *Mater Res Bull* 1971;6:581.
- [146] VerSnyder FL, Shank ME. *Mater Sci Eng* 1970;6:231.
- [147] LaBelle HE. In: Feigelson Robert S, editor. *50 years of progress in crystal growth*. Amsterdam: Elsevier; 2004. p. 179.
- [148] Mlavsky AI. In: Feigelson Robert S, editor. *50 years of progress in crystal growth*. Amsterdam: Elsevier; 2004. p. 177.
- [149] Surek T, Coriell SR, Chalmers B. *J Cryst Growth* 1980;50:21.
- [150] Tatarchenko VA, Brener EA. *J Cryst Growth* 1980;50:126.
- [151] Seidensticker RG. *J Cryst Growth* 1977;39:17.
- [152] Belouet C, Brissot JJ, Martres R, Ngo-Tich Phuoc. In: *Proc. photovoltaic solar energy conf. Luxembourg*; 1977. p. 164.
- [153] Zook J, Koepke BG, Grung BL, Leipold MH. *J Cryst Growth* 1980;50:260.
- [154] Baghdadi A, Gurtler RW. *J Cryst Growth* 1980;50:236.
- [155] Bleil CE. *J Cryst Growth* 1969;5:99.
- [156] Kear BH, Pearcey BJ. *Trans AIME* 1967;238:1209.
- [157] Leomonova EE, Osiko VV. Growth of zirconia crystal by skull-melting technique. In: Scheel HJ, Fukuda T, editors. *Crystal growth technology*. John Wiley & Sons, Ltd; 2003. p. 461.
- [158] Castonguay RA, Menashi WF, Wenckus JF, Arthur D. Little, Inc., U.S. Patent 4049384, (September 20, 1977).
- [159] Kisil II, Taranyuk VI, Yaroslavkin SV. *Funct Mater* 2008;15:600.
- [160] Wulff G. *Z Krist* 1901;34:449.
- [161] Kruger F, Finke W. *Dtsch Reich Patent*. 228, 246, K1, 120, Gr2 (November 5, 1910).
- [162] Valetton JJP, Sachs K. *Math-physik Klasse*, 67. Leipzig: Ges. Wiss; 1915. p. 1.

- [163] Nacken R. *Z Instrumentenk* 1916;36:12.
- [164] Walker AC, Kohman GT. *Trans Am Inst Elec Engrs* 1949;68:222.
- [165] Holden AN. *Discuss Faraday Soc* 1949;5:312.
- [166] Moore RW. *J Am Chem Soc* 1919;41:1060.
- [167] Walker AC. *Bell Lab Rec* 1947;25:35.
- [168] Holden AN, Singer Phylis. *Crystals and crystal growing*. New York: Anchor Press/MIT Press; January 1, 1982. p. 318.
- [169] Loiacono GM, Zola JJ, Kostescky G. *J Cryst Growth* 1983;62:545.
- [170] Rashkovich LN. Rapid growth of large crystals for nonlinear optics from solution. *Bull Acad Sci USSR* 1984;9:15.
- [171] Zaitseva N, Carmen L. Rapid growth of KDP-type crystals, progress in crystal growth and characterization of materials. Pergammon 2001;1.
- [172] Glusker JP, Dorothy crowfoot hodgkin (1910–1994). *Protein Sci* 1994;3:2465.
- [173] Brink C, Hodgkin DC, Lindsey J, Pickworth J, Robertson JH, White JG. *Nature* 1954;174:1169.
- [174] Protein crystal growth. In: Feigelson RS, editor. *Proc. first int. conf. on crystal growth*. Stanford (CA): Stanford University; August 1985. North Holland, Amsterdam (1986).
- [175] McPherson A. *Preparation and analysis of protein crystals*. New York: John Wiley and Sons; 1982.
- [176] McPherson A. *Crystallization of biological macromolecules*. NY: Cold Spring Harbor Lab. Press, Cold Spring Harbor Press; 1999.
- [177] Ward KB, Perozzo MA, Zuk WM. *J Cryst Growth* 1988;90:325.
- [178] Land TA, Malkin AJ, Kuznesov YG, McPherson A, DeYoreo JJ. *Pus Rev Lett* 1995;75:2774.
- [179] Malkin AJ, Land TA, Kuznetsov YG, McPherson A, DeYoreo JJ. *Phys Rev Lett* 1995;75:2778.
- [180] Liesegang RE. *Nat Wochschr* 1896;11:221.
- [181] Hatschek E. *J Soc Chem Ind* 1911;30:276.
- [182] Dreaper WP. *J Soc Chem Ind* 1913;32:678.
- [183] Fisher LW, Simons FL. *Am Mineral* 1926;11:124 and 200.
- [184] Henisch HK. *Crystal growth in gels*. University Park (PA): The Pennsylvania State University Press; 1970.
- [185] Patel AR, Verikateswara Rao A. *Bull Mat Sci* 1982;4:527.
- [186] Jiang H, Kloc C. *MRS Bull* 2013;38:28.
- [187] Carman L, Zaitseva N, Martinez HP, Rupert B, Pawelczak I, Glenn A, et al. *J Cryst Growth* 2013; 368:56.
- [188] Bethe K, Weltz F. *Mat Res Bull* 1971;6:209.
- [189] Linares RC. *J Am Ceram Soc* 1962;45:307.
- [190] Elwell D, Scheel HJ. *Crystal growth from high temperature solutions*. London: Academic Press; 1975.
- [191] Wöhler F. *Ann Chim Phys* 1823;29(2):43.
- [192] Doelter C. *Z Krist* 1886;11(29):40.
- [193] Wöhler F, St Claire Deville H. *Ann Chem Pharm* 1857;101(113):347.
- [194] Fremy E, Feil C. *Compt Rend* 1877;85:1029.
- [195] Giess EA. *J Am Ceram Soc* 1964;47:388.

- [196] Austerman SB. *J Am Ceram Soc* 1963;46:6.
- [197] Newkirk HW, Smith DK. *Am Min* 1965;50:44.
- [198] Timofeeva VA. *J Cryst Growth* 1968;3/4:496.
- [199] Nielsen JW, Dearborn EF. *Phys Chem Solids* 1958;5:202.
- [200] Van Uitert LG, Grodkiewicz WH, Dearborn EF. *J Am Ceram Soc* 1965;48:105.
- [201] Wood DL, Remeika JP. *J Appl Phys* 1966;37:1232.
- [202] Scheel HJ. In: Feigelson Robert S, editor. *50 years progress in crystal growth*. Amsterdam: Elsevier; 2004. p. 173.
- [203] Reisman A, Holtzberg F. *J Am Chem Soc* 1955;77:2115.
- [204] Mizell GJ, Fay WR, Alekel III T, Rytz D, Garrett M. *Visible and UV lasers*, 2115. SPIE; 1994.
- [205] Fluckiger U, Arend H. *J Cryst Growth* 1978;43:406.
- [206] Miller CE. *J Appl Phys* 1958;29:233.
- [207] Linares RC. *J Appl Phys* 1964;35:433.
- [208] Belruss V, Kalnajs J, Linz A, Foweiler R. *Mat Res Bull* 1971;6:899.
- [209] Chen CT, Wu B, Jiang A, You G. *Sci Sin Ser B* 1985;28:235.
- [210] Nelson DF, Remeika JP. *J Appl Phys* 1964;35:522.
- [211] Tolksdorf W. *J Cryst Growth* 1968;3/4:463.
- [212] Nielsen JW. *Electronics* 1964;37:44.
- [213] Grodkiewicz WH, Dearborn EP, Van Uitert LG. In: Steffen Peiser H, editor. *Crystal growth, proceedings of the international conference on crystal growth*. Oxford: Pergamon Press; 1967. p. 441.
- [214] Capper P, Mauk M, editors. *Liquid phase epitaxy of electronic, optical, and optoelectronic materials*. Chicester (England): John Wiley; 2007.
- [215] Rakovan J. *Rocks Miner* 2006;81:317.
- [216] Frankenheim ML. *Ann Phys* 1836;3(7):516.
- [217] Baker TV. *J Chem Soc Trans* 1906;89:1120.
- [218] Royer L. *Bull Soc Franc Mineral* 1928;51:7.
- [219] Nelson H. *RCA Rev* 1963;24:603.
- [220] Rupprecht H. *Symposium on GaAs, Reading (England)*. (1966) 57.
- [221] Panish MB, Sumski S, Hayashi I. *Metall Trans* 1971;2:795.
- [222] Linares RC, McGraw RB, Schroeder JB. *J Appl Phys* 1965;36:2884.
- [223] C. Linares R. *J Cryst Growth* 1968;3/4:443.
- [224] Bobeck AH, Della Torre E. *Magnetic bubbles*. Amsterdam: North-Holland; 1975.
- [225] Hibiya T. *J Cryst Growth* 1983;64:400.
- [226] Fratello VJ, Wolfe R. In: Francombe MH, Adam JD, editors. *Magnetic film devices*. Academic Press; 2000.
- [227] Bednorz JG, Müller KA. *Z Phys-Condensed Matter* 1986;64:189.
- [228] Scheel HJ, Klemenz C, Reinhart FK, Lang HP, Güntherodt HJ. *Appl Phys Lett* 1994;65(7):901.
- [229] Byrappa K, Yoshimura M. *Handbook of hydrothermal technology*. Norwich (NY): Noyce Publications; 2000.

- [230] Ballman AA, Laudise RA. In: Gilman JJ, editor. *The art and science of growing crystals*. New York: Wiley; 1963. p. 231.
- [231] Senarmont H. *Ann chem phys* 1851;32:129.
- [232] Spezia G. *Acad Sci Torino Atti* 1905;40:254.
- [233] Walker AC, Buehler E. *Indust Eng Chem* 1950;42:1369.
- [234] Laudise RA, Sullivan RA. *Chem Eng Prog* 1959;55:55.
- [235] Laudise RA. *J Am Chem Soc* 1959;81:562.
- [236] Tian ZR, Voigt JA, Liu J, Mckenzie B, Mcdermott MJ. *J Am Chem Soc* 2002;124:12954.
- [237] Vayssieres L, Keis K, Lindquist SE, Hagfeldt AJ. *Phys Chem B* 2001;105:3350.
- [238] E Greene L, Law M, Goldberger J, Kim F, Johnson JC, F Zhang Y, et al. *Angew Chem Int Ed* 2003;42:3021.
- [239] Zhang J, Sun LD, Liao CS, Yan CH. *Chem Commun* 2002:262.
- [240] Kunnmann W. In: Lefever RA, editor. *Preparation and properties of solid state materials*. New York: Dekker; 1971. p. 1.
- [241] Bostanov V. *J Cryst Growth* 1977;42:194.
- [242] DeMattei RC, Huggins RA, Feigelson RS. *J Cryst Growth* 1976;34:1.
- [243] St Claire-Deville H. *Compt Rend* 1854;39:323.
- [244] Ullik F. *Ber Akad Wien* 1865;52:115.
- [245] Cohen U, Huggins RA. *J Electrochem Soc* 1976;123:381.
- [246] Feigelson RS. In: Holt SL, Milstein JB, Robbins M, editors. *Solid state chemistry, a contemporary overview*; 1980. p. 243. Am. Chem. Soc. Washington, DC.
- [247] Hodes G. In: Rubinstein I, editor. *Electrodeposition of II–VI semiconductors, physical electrochemistry*. New York: M. Dekker Inc.; 1995. p. 515.
- [248] Turner AK, Woodcock JM, Ozsan E, Summers JG. In: Luque A, Sala A, Palz W, Dos Santos A, Helm P, editors. *Proceedings of the 10th European Solar Energy Conference, held at Lisbon Portugal*: Springer [Netherlands]; April, 1991 8–12, p.791.
- [249] Isshiki M, Endo T, Masumoto K, Usui Y. *J Electrochem Soc* 1990;137:2697.
- [250] Lincot D, Ortega-Borges R, Froment M. *Appl Phys Lett* 1994;64:569.
- [251] Chaudary GN, Sardesai SN, Sathaye SD, Rao VJ. *J Mat Sci* 1992;27:4647.
- [252] Lincot D, Furlong MJ, Froment M, Cortes R, Bernard MC. *Mat Res Soc Symp Proc* 1997;451:223.
- [253] Schlesinger TE, Rajeshwar K, De Tacconi NR. *Electrodeposition of semiconductors*. In: Schlesinger M, Paunovic M, editors. *Modern electroplating*. New York: John Wiley & Sons; 2010.
- [254] Izaki M, Omi T. *Appl Phys Lett* 1996;68:2439.
- [255] Peulon S, Lincot DJ. *J Electrohem Soc* 1998;145:864.
- [256] Liu R, Vertegel AA, Bohannan EW, Sorenson TA, Switzer JA. *Chem Mater* 2001;13:508.
- [257] Vanheusden K, Warren WL, Seager CH, Tallant DR, Voigt JA, Gnade BE. *J Appl Phys* 1996;79:7983.
- [258] Yshida T, Tochimoto M, Schlettwein D, Wöhrle D, Sugiura T, Minoura H. *Chem Mater* 1999;11:2657.
- [259] Xu L, Guo Y, Liao Q, Zhang J, Xu D. *J Phys Chem B* 2005;109:13519.
- [260] Allendorf M. *From Bunsen to VLSI*. *Electrochem Soc Interface* 1998. Spring.
- [261] Bunsen R. *J Prakt Chem* 1852;56:53.

- [262] St Claire-Deville H. *Annals* 1861;120:176.
- [263] Tietjen JJ. *Ann Rev Mater Sci* 1973;3:317.
- [264] Brown FC. *Phys Revs* 1914;4:85.
- [265] Koref F. *Z Electrochem* 1922;28:511.
- [266] Van Arkel AE. *Physica* 1923;3:76.
- [267] Gross R. *Z Krist* 1921;56:421.
- [268] Gross R, Volmer M. *Z Phys* 1921;5:188.
- [269] Straumanis M. *Z Phys Chem* 1932;B19:63.
- [270] Kaldis E. In: Goodman CHL, editor. *Crystal growth, theory, and techniques*, vol. 1. England: Plenum Press; 1974.
- [271] Faktor MM, Garrett J. *Growth of crystals from the vapor*. London: Chapman and Hall; 1974.
- [272] Wilke KT. *Kristall-zuchtung*. Berlin: VEB Deutscher Verlag d. Wissenschaften; 1973.
- [273] Pizzarello F. *J Appl Phys* 1954;25:804.
- [274] Avinor M. *Philips Res Rep* 1959;14:211.
- [275] Piper WW, Polich SJ. *J Appl Phys* 1961;32:1278.
- [276] Fochs PD. *J Appl Phys* 1960;31:1733.
- [277] Prior AC. *J Electrochem Soc* 1961;108:82.
- [278] Frisch O. *Ann Phys* 1935;22:375.
- [279] Lely JA. *Ber Dtsch Keram Ges* 1955;32:229.
- [280] Tairov TM, Tsvetkov VF. *Neorg Mater (USSR)* 1977;13:448.
- [281] Heindl J, Strunk PH, Heydemann VD, Pensl G. *Phys Stat Sol (A)* 1997;167:251.
- [282] Feigelson RS, Route RK, Kao TM. *J Cryst Growth* 1985;72:585.
- [283] Van Arkel AE, de Boer JH. *Zeit anorg Allgem chem* 1925;148:345.
- [284] Schäfer H. *Chemical transport reactions*. New York: Academic Press; 1963.
- [285] Laudise RA. *The growth of single crystals*. New Jersey: Prentice-Hall; 1970. 234.
- [286] Lorenz R. *Chem Ber* 1891;24:1509.
- [287] Frerichs R. (1996) 1701. *Phys Rev* 72 (1947) 594.
- [288] Schönherr H. *The growth of large crystals from the vapor state*. In: *Crystals, growth, properties and applications*. Berlin: Springer-Verlag; 1980. p. 51.
- [289] WZ Li, SS Xie, LX Qian, BH Chang, BS Zhou, WY Zhou, et al. *Science*;274.
- [290] Scott TR, King G, Wilson JM. UK Patent 778,383 (1957).
- [291] Miederer W, Ziegler G, Dotzer R. US Patent 3,226,270 (1965).
- [292] Manasevit HM, Simpson WJ. *J Electrochem Soc* 1969;12:1725.
- [293] Manasevit HM. In: Feigelson Robert S, editor. *50 years progress in crystal growth*. Amsterdam: Elsevier; 2004. p. 217.
- [294] Seki Y, Tanno K, Iida K, Ichiki E. *J Electrochem Soc* 1975;122:1108.
- [295] Dupuis RD, Dapkis PD. *Appl Phys Lett* 1978;32:40.
- [296] Stringfellow GB. *Annu Rev Mater Sci* 1978;8:73.
- [297] Stringfellow GB. *Organometallic vapor phase epitaxy: theory and practice*. 2nd ed. Boston: Academic Press; 1999.

- [298] Akasaki I, Amano H. *Jpn J Appl Phys* 2006;45:9001.
- [299] Nakamura S, Mukai T, Senoh M. *Appl Phys Lett* 1994;64:1687.
- [300] Nakamura S, Fasol G. *The blue laser diode*. Berlin: Springer; 1997.
- [301] Liu BL, Lachab M, Jia A, Yoshikawa A, Takahashi K. *J Cryst Growth* 2002;234:637.
- [302] Stringfellow GB. *J Cryst Growth* 2004;264(4):620–30.
- [303] Holloway PH, McGuire GE. *Handbook of compound semiconductors; growth, processing, characterization and devices*. Noyes Publications; 1995.
- [304] Joyce BA, Bradley RR. *Phils Mag* 1966;14:289.
- [305] Davey JE, Pankey T. *J Appl Phys* 1968;39:1941.
- [306] Arthur JR. *J Appl Phys* 1968;39:4032.
- [307] Cho AY, Panish MB, Hayashi J. In: *Proceedings of the symposium on GaAs and related compounds*. Inst. of physics, vol. 2. Germany: Aachen; 1970. p. 118.
- [308] Joyce BA, Joyce TB. In: Feigelson Robert S, editor. *50 years progress in crystal growth*. Amsterdam: Elsevier; 2004. p. 203.
- [309] Grove WR. *Trans R Soc* 1852;142:87.
- [310] Williams P. *Surf Sci* 1979;90:588.
- [311] Kelly PJ, Arnell RD. *Vacuum* 2000;56:159.
- [312] Penning PM. *Physica* 1936;3:873.
- [313] Naoe M, Yamanaka S, Hoshi Y. *IEEE Trans Magn* 1980;Mag-16:646.
- [314] Suntola T. *US Patent* 4058430 (1977).
- [315] Aleskovskii VB. *J Appl Chem USSR* 1974;47:2207.
- [316] Suntola T. *Mater Sci Rep* 1989;4:261.
- [317] Triani G, Evans PJ, Mitchell DRG, Attard DJ, Finnie KS, James M, et al. *Proc SPIE* 2005;5870:9.
- [318] Ritala M, Leskela M. *Nanotechnology* 1999;10:19.
- [319] Wagner RS, Ellis WC. *Appl Phys Lett* 1964;4:89.
- [320] Kuykendall T, Pauzauskie PJ, Zhang Y, Goldberger J, Sirbuly D, Denlinger J, et al. *Nat Mater* 2004; 3:524.
- [321] Schmidt V, Wittemann JV, Senz S, Gösele U. *Adv Mater* 2009;21:2681.
- [322] Wacaser BA, Dick KA, Johansson J, Borgstrom MT, Deppert K, Samuelson L. *Adv Mater* 2009; 21:153.
- [323] Choi HJ, Johnson JC, He R, Lee SK, Kim F, Pauzauskie P, et al. *Chem B* 2003;107:8721.
- [324] Choi HJ. Vapor-liquid-solid growth of semiconductor nanowires. In: Yi GC, editor. *Semiconductor nanostructures for optoelectronic applications*, vol. 1. Berlin: Springer-Verlag; 2012.
- [325] Sheftal NN. Trends in real crystal formation and some principles for single crystal growth. In: *Growth of crystals*, vol. 10. New York: Consultants Bureau; 1976. p. 185.
- [326] Geis MW, Tsaour BY, Flanders DC. *Appl Phys Lett* 1982;41:526.
- [327] Givargizov EI, Kliya MO, Melik-Adamyany VR, Grebenko AI, DeMattei RC, Feigelson RS. *J Cryst Growth* 1991;112:758.
- [328] Givargizov EI. *Oriented crystallization on amorphous substrates*. New York: Plenum Oress; 1991.
- [329] Crnogorac F, Witte DJ, Pease RFW. *J Vac Sci Technol B* 2008;26:2520.

- [330] Tracy Hall H. In: Feigelson Robert S, editor. 50 years progress in crystal growth. Amsterdam: Elsevier; 2004. p. 193.
- [331] Hannay JB. Proc R Soc London 1879;30:450.
- [332] Moissan H. Comptes Rendus 1894;118:320.
- [333] Desch CH. Nature 1928;121:799.
- [334] Lonsdale K. Nature 1962;196:104.
- [335] Hazen RM. The diamond makers. Cambridge: Cambridge University Press; 1999.
- [336] Tracy Hall H. Rev Sci Instrum 1960;31:125.
- [337] Barnard AS. The diamond formula: diamond synthesis: a gemological perspective. Oxford: Butterworth-Heinemann; 2000.
- [338] Eversole WG. Synthesis of diamond, US Patent 3,030,188, (April 17, 1962).
- [339] Angus JC. J Appl Phys 1968;39:2915.
- [340] Deryagin BV, Fedoseev DV. Rus Chem Rev 1970;39:783.
- [341] Gracio JJ, Fan QH, Madaleno JC. J Phys D Appl Phys 2010;43:1.
- [342] Angus JC. A short history of diamond synthesis. In: Asmussen J, Reinhard DK, editors. Diamond films handbook. New York: Marcel Dekker Inc.; 2002.
- [343] Matsumoto S, Sato Y, Kamo M, Setaka N. Jpn J Appl Phys 1982;21L:183.
- [344] Kamo M, Sato Y, Matsumoto S, Setaka N. J Cryst Growth 1983;62:642.
- [345] Matsui Y, Matsumoto S, Setaka N. J Mater Sci 1983;2:532.
- [346] Decarli P, Jamieson J. Science 1961;133:1821.
- [347] Galimov ÉM, Kudin AM, Skorobogatskii VN, Plotnichenko VG, Bondarev OL, Zarubin BG, et al. Dokl Phys 2004;49:150.
- [348] Ostwald W. Zeit Phys Chem 1897;22:289.
- [349] Anderson RJ. J Frankl Inst 1919;187:1.
- [350] Carpenter HCH, Elam CF. Proc R Soc London 1921;100:329.
- [351] Bailey DJ, Brewer EG. Metal Trans A 1975;6A:403.
- [352] Kulper LL. U. S. Patent 3413157, November 26, 1968.
- [353] Mayer JK, Nicolet MA, Lau SS. U. S. Patent 4012235, March 17, 1977.
- [354] Mayer JK, Lau SS. Electronic materials science: for integrated circuits in Si and GaAs. New Jersey: Prentice Hall; 1989.
- [355] Kwon S, Hackenberger WS, Rehrig PW, Lee J-B, Heo T-M, Kim D-H, Lee H-Y. In: Proceedings 2004 IEEE international ultrasonics, ferroelectrics and frequency control conference; 2004. p. 153.
- [356] Hurler DTJ, editor. A perspective on crystal growth: a historical collection in celebration of 25 years of the journal of crystal growth. Elsevier Science Publishers; 1992.
- [357] Ivantsov GP. Dokl Akad Nauk SSSR 1947;58:567.
- [358] Schawlow AL, Townes CH. Phys Rev 1958;112:1940.
- [359] Dunn CG, Nonken GC. Metal Prog 1953;71:71.

# Phase Equilibria

Detlef Klimm

LEIBNIZ INSTITUTE FOR CRYSTAL GROWTH (IKZ), BERLIN, GERMANY

## CHAPTER OUTLINE

<b>2.1 Introduction</b> .....	<b>86</b>
2.1.1 Basic Terms .....	86
2.1.1.1 Components and Concentrations .....	86
2.1.1.2 Phases and Phase Rule .....	88
2.1.1.3 System .....	89
2.1.2 Thermodynamic Functions and Potentials .....	90
2.1.2.1 Specific Heat Capacity .....	90
2.1.2.2 Enthalpy .....	91
2.1.2.3 Entropy .....	94
2.1.2.4 Gibbs Free Energy .....	96
2.1.3 Phase Transitions .....	98
2.1.4 Calculation of Phase Diagrams .....	103
2.1.4.1 Miscibility .....	103
2.1.4.2 Analytical Expressions .....	106
2.1.4.3 Minimization of the Gibbs Energy .....	109
<b>2.2 Equilibria Between Condensed Phases</b> .....	<b>110</b>
2.2.1 One Component .....	110
2.2.1.1 Pressure–Temperature Diagrams .....	110
2.2.1.2 Other Fields .....	111
2.2.2 Two Components .....	112
2.2.2.1 Total Miscibility in 2 Phases .....	113
2.2.2.2 Eutectics and Eutectoids .....	117
2.2.2.3 Segregation and Lever Rule .....	119
2.2.2.4 Intermediate Compounds .....	121
2.2.2.5 Peritectics and Peritectoids .....	122
2.2.2.6 Syntectics and Monotectics .....	124
2.2.3 Three and More Components .....	124
2.2.3.1 $x - y$ Diagrams .....	124
2.2.3.2 Concentration Triangles .....	126

2.2.3.3 <i>Isoleth Sections</i> .....	127
2.2.3.4 <i>Reciprocal Salt Pairs</i> .....	128
<b>2.3 Equilibria Including Gas Phase</b> .....	<b>129</b>
2.3.1 Volatile Species.....	130
2.3.2 Ellingham Type Diagrams.....	131
<b>References</b> .....	<b>133</b>

## 2.1 Introduction

In this chapter, phase diagrams will be introduced as basic tools for the development and understanding of crystal growth processes. The focus will be on reading diagrams that can be found in the literature, or that can be calculated with commercial or freeware computer programs such as described later in [Section 2.1.4.3](#). If nothing else is written explicitly, equilibrium phase diagrams are presented. The crystal growth process itself, however, is a nonequilibrium process, where some nutrient phase (e.g., a melt, a solution, or a gas) is transformed to the desired solid (crystal) phase. The relevance of equilibrium phase diagrams for the description of crystal growth is given if the growth process is performed not too far from equilibrium conditions. This condition is typically fulfilled for most slow growth processes from the melt or from melt solutions such as Czochralski, Bridgman, Verneuil, top seeded solution growth (TSSG), micro-pulling-down ( $\mu$ -PD), heat exchanger method (HEM), or vertical gradient freeze (VGF) technique. Also, growth processes from hot gas phases with sufficient density (not too far below ambient pressure 1 bar, such as chemical vapor transport (CVD) or physical vapor transport (PVT) can usually be described well by equilibrium phase diagrams. For further reading and for refereed collections of phase diagrams, some web sites prove to be helpful, e.g., [\[1–3\]](#).

### 2.1.1 Basic Terms

#### 2.1.1.1 *Components and Concentrations*

A *component* is a substance that, under the given conditions, cannot be further divided into parts. A chemical element can always be chosen as component; but often it is more convenient to choose compounds instead, because a smaller number of components makes the description easier. It must be possible to create all compounds that may be found in equilibrium by chemical reactions between the components! If two or three compounds instead of elements are chosen to set up a phase diagram, the system is sometimes called *pseudobinary* or *pseudoternary*, respectively.

It is not always straightforward to decide whether a chemical compound can be used as component for the description of a specific system. For instance, vanadium(V) oxide  $V_2O_5$  and molybdenum(VI) oxide  $MoO_3$  are reacting upon heating to an intermediate phase [\[4\]](#). This intermediate phase was initially described as  $V_2MoO_8$ , and binary phase diagrams similar to [Figure 2.1](#) left, with  $V_2O_5$  and  $MoO_3$  as components, were published.

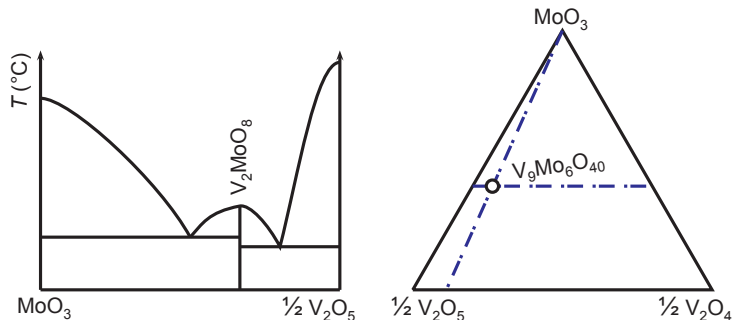


**FIGURE 2.1** Left: Simplified binary phase diagram  $V_2O_5$ – $MoO_3$  under the incorrect assumption that the intermediate phase is  $V_2MoO_8$  [6], entry 4467. Right: Correct phase triangle demonstrating that intermediate  $V_9Mo_6O_{40}$  is ternary.

Further studies showed that  $\frac{1}{9}$  of the  $V^{5+}$  ions are reduced to  $V^{4+}$  during the reaction, and the compound should rather be written as  $V_9Mo_6O_{40} = 4 V_2O_5 \cdot \frac{1}{2} V_2O_4 \cdot 6MoO_3$  [5]. Consequently, three components are required to give an appropriate description of the system, such as shown in the right panel of Figure 2.1. Of course, a description in terms of the chemical elements V–Mo–O would be valid too.

The share of the  $i$ -th component in the system is called its *concentration*. If not mentioned explicitly, concentrations  $x_i$  are given in molar fractions, or atomic fractions,

$$x_i = \frac{n_i}{\sum_{i=1}^C n_i} \quad (2.1)$$

where  $C$  is the number of components and  $n_i$  is the number of moles of component  $i$ . It is obvious that  $\sum_i x_i = 1$ , and hence in two-component systems only one concentration  $x$  is necessary. Mol-% or At-% values can be obtained by multiplying  $x_i$  with 100%.

For a specific chemical composition, the  $x_i$  depend on the choice of the components  $Y_i$  ( $i = 1 \dots C$ ). In dielectric systems (e.g., oxides, halides) often compounds  $A_mB_n$  (A: cation, B: anion) are chosen as components. Then it may be useful to scale them in such a way that all components bear the same number of cations (often one). The benefit of such scaling is that the resulting phase boundaries are often more symmetrical around invariant compositions. An example is given in Figure 2.1 for the system  $V_2O_5$ – $MoO_3$  where the right component is written as  $VO_{2.5}$ .

In systems with many intermediate compounds, the choice of components is ambiguous. Figure 2.2 demonstrates this for a system of the chemical elements (or basic

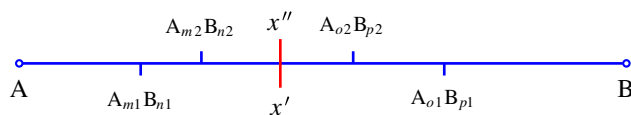


**FIGURE 2.2** A specific composition  $x = x' = x''$  can be expressed in terms of basic components (e.g., elements) A, B. Alternative descriptions are in terms of compounds  $A_{m1}B_{n1}$ ,  $A_{o1}B_{p1}$  ( $x'$ ) or  $A_{m2}B_{n2}$ ,  $A_{o2}B_{p2}$  ( $x''$ ), respectively.

compounds such as simple oxides) A and B, with four intermediate compounds; the stoichiometry is expressed by indices. If a composition  $x$  is given in terms of  $A_{m1}B_{n1}$  and  $A_{o1}B_{p1}$  (below the concentration axis), the amounts of the basic compounds can be calculated by

$$\begin{aligned} [A] &= (1 - x') \frac{m1}{m1 + n1} + x' \frac{o1}{o1 + p1} \\ [B] &= (1 - x') \frac{n1}{m1 + n1} + x' \frac{p1}{o1 + p1} \end{aligned} \quad (2.2)$$

from the concentration  $x'$  and the stoichiometric indices of the components. The concentration with respect to the basic components is then easily expressed by

$$x = \frac{[B]}{[A] + [B]} \quad (2.3)$$

as a molar fraction. Rescaling of concentration data to  $A_{m2}B_{n2}$ ,  $A_{o2}B_{p2}$  ( $x''$ , above the concentration axis) is given by

$$x'' = \frac{x - \frac{n2}{m2+n2}}{\frac{p2}{o2+p2} - \frac{n2}{m2+n2}} \quad (2.4)$$

where the molar fraction  $x$  with respect to the basic components is given by Eqn (2.3). For the general case of component transformation in a multicomponent system ( $C > 2$ ), the reader is referred to the literature, e.g., Ref. [7].

### 2.1.1.2 Phases and Phase Rule

A phase is a homogeneous part of a system, on scales that are large compared to atoms. This means that all physical quantities, and composition, are no function of the position  $\vec{r}$ , except differential fluctuations or gradients. Usually systems contain only one gas phase. Liquids (melts) of similar substances are often forming one liquid phase (molten slag, molten alloy, solution in a liquid). Dissimilar, nonmixing liquids form several phases (water and oil, molten slag and metal). Each solid compound is often forming a separate phase, with a specific crystal structure. Only if the components of a solid phase have identical crystal structure and are otherwise similar, they may intermix each other in arbitrary ratio. Such mixtures are one phase, called mixed crystal, or solid solution ( $\text{Ge}_{1-x}\text{Si}_x$ ,  $\text{Ag}_{1-x}\text{Au}_x$ ,  $\text{K}_{1-x}\text{Rb}_x\text{Cl}$ ;  $0 \leq x \leq 1$ ). More details on phase miscibility will be given in Section 2.1.4.1.

For a given system with  $C$  components, Gibbs phase rule

$$P + F = C + 2 \quad (2.5)$$

limits the number  $P$  of coexisting phases and the number  $F$  of degrees of freedom that the system has in equilibrium. This means that in a one-component system, never more than three phases may exist at the same time. This is, e.g., demonstrated in Figure 2.3, where never more than three phase fields are touching each other in one point. Such triple points “ $T_i$ ” describe conditions where  $P = 3$  phases are in equilibrium.

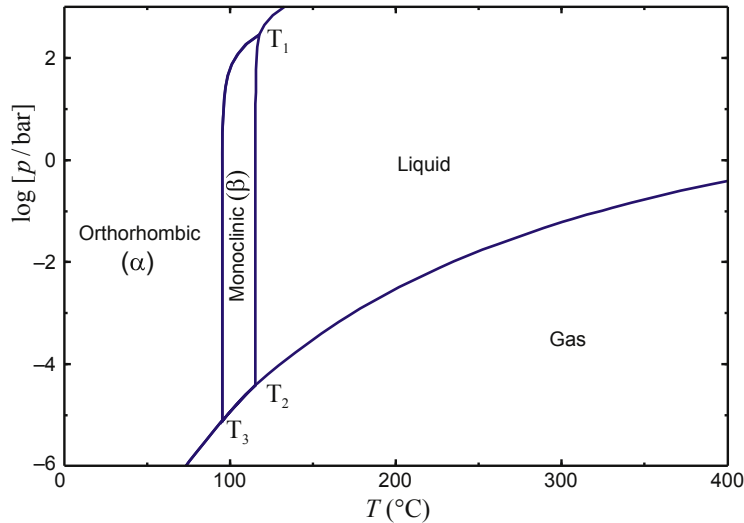


**FIGURE 2.3** Phase diagram of sulfur in coordinates  $T - \log[p]$ .  $T_i$  are the invariant triple points where three phases are in equilibrium.

Often, experiments are performed under isobar conditions  $p = 1$  bar, which consumes 1 degree of freedom. Then Eqn (2.5) simplifies to

$$P + F = C + 1 \quad (2.6)$$

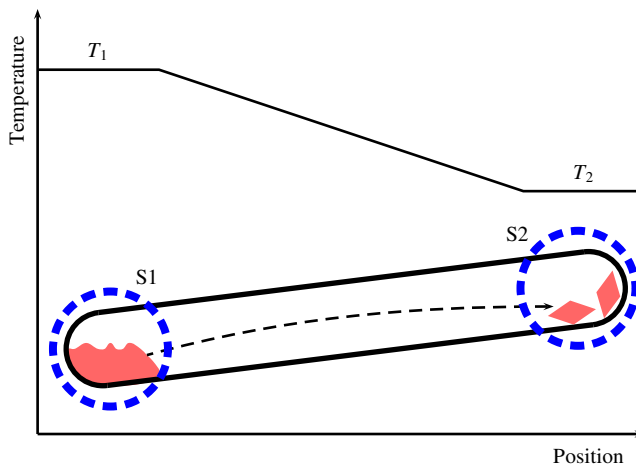
which means that, e.g., in two-component systems, never more than three phases may coexist under isobar conditions. In the left panel of Figure 2.1, this is the case in the two “eutectic points” on both sides of  $V_2MoO_8$  where the liquid phase (stable at high  $T$ ) is in equilibrium with solid  $V_2O_5 + V_2MoO_8$  or  $V_2MoO_8 + MoO_3$ , respectively. Both eutectic points are invariant, because any deviation would result in the disappearance of at least one phase. In phase fields where only one phase is stable (e.g., within the liquid phase field of Figure 2.1), one obtains from Eqn (2.6)  $F = C - P + 1 = 2 - 1 + 1 = 2$ . Indeed, one can move somewhat up or down (freedom of  $T$ ) and left or right (freedom of  $x$ ) without leaving the phase field.

### 2.1.1.3 System

If a specific volume  $V$  contains a limited amount of matter with mass  $m$ , and is characterized by some intensive properties, such as pressure  $p$  or temperature  $T$ , it may set up a system. Intensive properties do not change if two identical systems are united. Often, closed systems are considered, with no exchange of matter or energy with the surroundings. Then, in equilibrium  $T$  is constant for all parts of the system. However,  $p$  may be a function of the position  $\vec{r}$  as a result of surface tension, e.g., in epitaxial layers. In contrast  $V$  and  $m$  are extensive properties. Their value depends on the system size.

Crystal growth is a dynamic process and matter is transported from a reservoir to a seed, where crystallization takes place as a result of supersaturation. Figure 2.4

**FIGURE 2.4** Crystal growth by sublimation in an ampoule. Feedstock is transported from a hot reservoir (temperature  $T_1$ ) to the colder end ( $T_2$ ).



demonstrates this for sublimation growth (physical vapor transport (PVT)) from the hot part of an ampoule ( $T_1$ ) to the cold part ( $T_2$ ). Under such conditions, it is not possible to define overall intensive conditions  $p$ ,  $T$  for the whole ampoule. It may be useful, however, to consider separately system S1 where the solid feed is at  $p$ ,  $T_1$  in equilibrium with the surrounding gas, and system S2 where at  $p$ ,  $T_2$  gas is in equilibrium with the seed. Then, the growth process can be divided to three parts: (1) equilibration in S1, (2) transport of gas under cooling, (3) equilibration in S2.

## 2.1.2 Thermodynamic Functions and Potentials

### 2.1.2.1 Specific Heat Capacity

The specific heat capacity  $c$  is the basic thermodynamic quantity that can be measured. Typically, lattice vibrations (phonons) are the major contributors to the internal energy  $U$  of a substance, and  $U$  is a function of  $T$ . If an amount of heat energy  $Q$  is transferred to 1 mol of a sample, its temperature increases under isochor (volume  $V = \text{const.}$ ) or isobar (pressure  $p = \text{const.}$ ) conditions by

$$\Delta T_V = \frac{\Delta Q}{c_V} \quad (2.7)$$

$$\Delta T_p = \frac{\Delta Q}{c_p} \quad (2.8)$$

where  $c_V$  or  $c_p$  is the specific heat capacity of the material under the given conditions. Especially for technical purposes, the amount of substance is often given by the mass  $m = nM$  ( $n$ , number of mol;  $M$ , molar mass). The difference

$$c_p - c_V = \frac{T}{n} \left( \frac{\partial V}{\partial T} \right)_p \left( \frac{\partial p}{\partial T} \right)_V \quad (2.9)$$

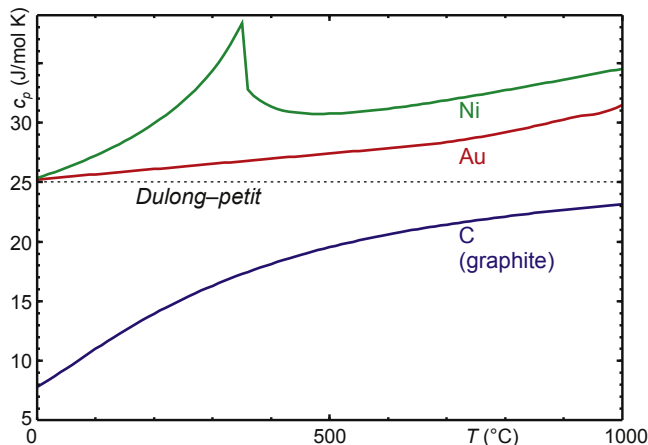


FIGURE 2.5  $c_p(T)$  functions for three chemical elements compared to the Dulong–Petit law (Eqn (2.10)).

is usually small, (but  $> 0$ ) for condensed phases with small thermal expansion  $\partial V/\partial T$  (solids, liquids). For ideal gases, one has  $c_p - c_V = R$  (gas constant).

Dulong and Petit found that, for many solid chemical elements, the specific heat capacity approaches 25 J/(mol K) at room temperature (ref. Eqn (2.10) and Figure 2.5). For very low temperature  $c_p(T)$  follows a  $T^3$  law (see Figure 2.6) and vanishes at absolute zero (Eqn (2.11)). Neumann and Kopp found that  $c_p(T)$  of a chemical compound  $A_mB_n$  is nearly the sum of the  $c_p(T)$  of its composing chemical elements (Eqn (2.12)).

$$\lim_{T \rightarrow 298\text{K}} c_p \approx 25 \text{ J/mol} \cdot \text{K} \quad (\text{Dulong–Petit}) \quad (2.10)$$

$$\lim_{T \rightarrow 0} c_p = 0 \quad (2.11)$$

$$c_p^{(A_mB_n)}(T) \approx mc_p^{(A)}(T) + nc_p^{(B)}(T) \quad (\text{Neumann–Kopp}) \quad (2.12)$$

For most substances, the function  $c_p(T)$  rises monotonously with  $T$ ; the slope is steep at low  $T$  and becomes flatter near room temperature. Anomalies arise near phase transitions (see Section 2.1.3). Distant from phase transitions, the functions  $c_p(T)$  are usually smoothly rising, which can be expressed, e.g., by polynoms

$$c_p = A + BT + CT^2 + DT^3 + E/T^2 \quad (2.13)$$

and data for many substances are compiled in commercial databases, on the web (e.g., <http://webbook.nist.gov>), or in printed reference books [9].

### 2.1.2.2 Enthalpy

The internal energy  $U$  that was mentioned in Section 2.1.2.1 describes the potential and vibrational energy that is contained in the material itself. In a real system, the material has a certain volume  $V$  and is exposed to a pressure  $p$ . It should be noted that for systems

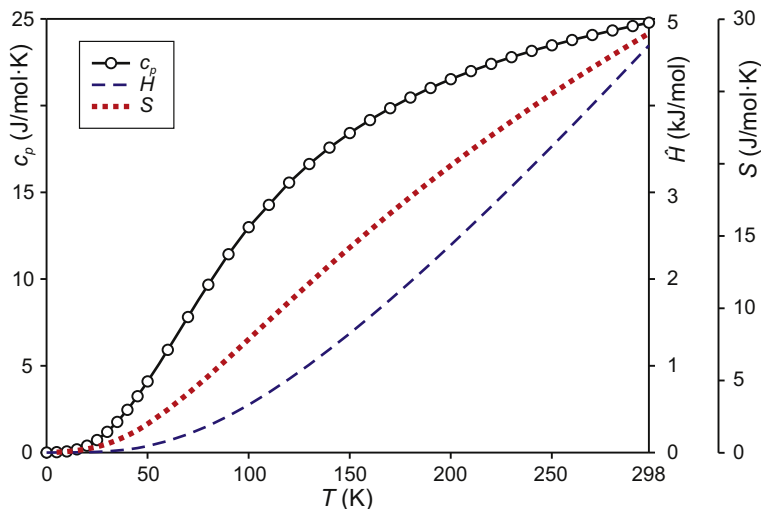


**FIGURE 2.6** Measured  $c_p(T)$  data for lithium below room temperature [8].  $\hat{H} = H - H(0\text{ K})$  is the “real” enthalpy that starts from 0 at absolute zero. The entropy  $S(T)$  was calculated with (Eqn (2.21)).

where surface energy can be neglected (phases sufficiently large and phase boundaries with low curvature),  $p$  is constant over the whole system, such as  $T$ . The quantity

$$H = U + pV \quad (2.14)$$

is called *enthalpy* and is the sum of the internal energy and the amount of work (“volume work”) that must be performed to create the phase volume  $V$  against the system pressure  $p$ . Such as  $U$  itself,  $H$  is a thermodynamic potential (=state function) because it depends only on the current status of the system, and not on how this status was reached.

It is usually difficult, if not impossible, to measure the total amount of  $\hat{H}$  stored inside a phase, because the energy balance of all contributions to  $U$  is often unknown. Contrarily, the enthalpy change of a system from an initial state  $i$  to a final state  $f$

$$\Delta H = H_f - H_i = Q \quad (2.15)$$

can usually be measured because it equals the heat  $Q$  added to the system provided that  $p = \text{const.}$ , and no other work except volume expansion work is done by the system.

To circumvent the problem of absolute  $H$  measurements, it is useful to determine “standard conditions” and a set of basic substances where the  $H$  values are determined at these standard conditions. For this purpose, the U.S. National Bureau of Standards defined  $T_0 = 25\text{ }^\circ\text{C} = 298.15\text{ K}$  and  $p_0 = 1 \times 10^5\text{ Pa} = 1\text{ bar}$  as “standard ambient temperature and pressure” [10]. Under these conditions  $H_i = H_0 = 0$  (Eqn (2.15)) is defined for every chemical element in the phase state that is stable under these conditions (Figure 2.7). The function  $H(T)$  is usually smooth, except at first-order phase transitions (cf. Section 2.1.3) where it jumps by an amount that is called *heat of fusion* ( $\Delta H_f$ ), *heat of vaporization* ( $\Delta H_v$ ), or in general *heat of transition* ( $\Delta H_t$ ). Some first-order

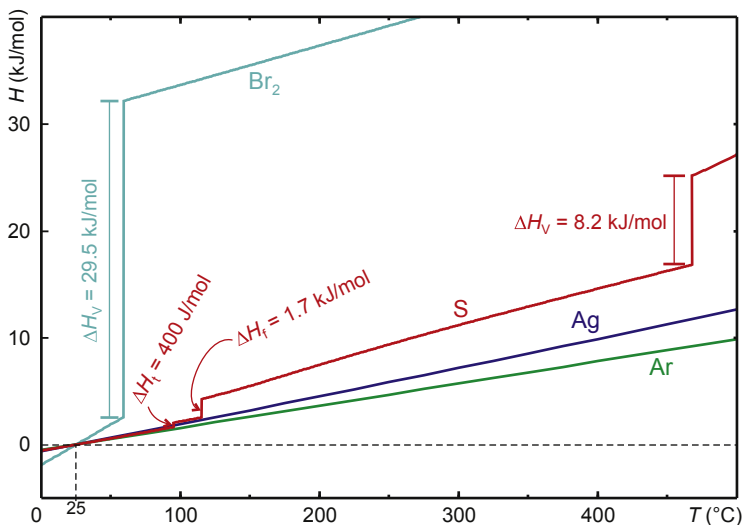


**FIGURE 2.7**  $H(T)$  functions for four chemical elements at 1 bar. Bromine vaporizes at 59 °C. Sulfur undergoes a monoclinic  $\rightleftharpoons$  orthorhombic phase transition at 95 °C, melts at 115 °C, and vaporizes at 469 °C. Silver and argon show no transformations in this  $T$  range.

transitions for bromine and sulfur are shown in [Figure 2.7](#). In contrast to this, [Figure 2.6](#) shows “absolute”  $\hat{H}(T)$  data for Li metal below room temperature.

For other temperatures, the enthalpy can be calculated by

$$H(T) = H_0 + \int_{T_0}^T c_p(T) dT \quad (2.16)$$

from experimental  $c_p(T)$  data. If one starts with  $\hat{H}(0 \text{ K}) = 0$ , then [Eqn \(2.16\)](#) represents the area under the  $c_p(T)$  curve in [Figure 2.6](#).  $c_p(T)$  rises with  $T^3$  only for low  $T \lesssim 50 \text{ K}$  and quickly approaches the Dulong–Petit value 25 J/(mol K) ([Eqn \(2.10\)](#)) and is slowly changing then; consequently,  $H(T)$  is an almost a linear function for high  $T$ .

As mentioned above,  $H$  is a thermodynamic potential. Hence, the enthalpy produced or consumed during a chemical reaction does not depend on the path of the reaction ([Figure 2.8](#)). Hess’s Law can be used also for changes in entropy  $S$  and in Gibbs free energy  $G$ , which are state functions, such as  $H$ . With Hess’s Law, the dependence of

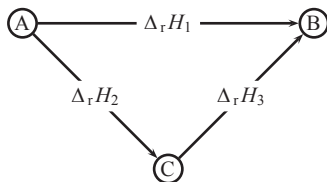


**FIGURE 2.8** Hess’s Law: the reaction enthalpy does not depend on the path of the reaction:  $\Delta_r H_1 = \Delta_r H_2 + \Delta_r H_3$ .

reaction enthalpies on  $T$  can be calculated, and also transition enthalpies under nonequilibrium conditions.

### 2.1.2.3 Entropy

The term *entropy* describes another thermodynamic potential that can be defined either statistically or from a thermodynamic viewpoint. The statistical interpretation is related to the Shannon entropy [11], which is used in information theory, and corresponds to the average information density in a system of symbols (or atoms). In the statistical interpretation, entropy  $S$  is a measure of “uncertainty” of a given state, that is, a measure of the number of equivalent arrangements of elements setting up the system. This is shown in Figure 2.9(A) for the case of a planar lattice where all possible sites are occupied by atoms. Another equivalent possibility for the atoms does not exist, and the probability for this state is  $P = 1$ . This is not so in Figure 2.9(B) where two atoms are missing. There are 48 options for selecting the first missing atom, and 47 options remain for the second missing atom, but it is indistinguishable which atom was missing first. This means  $48 \times 47/2 = 1128$  equivalent microstates exist that result in the same macrostate “plane lattice” with 48 sites. If  $P_i$  is the probability of the  $i$ -th microstate, then

$$S = -k_B \sum_i P_i \ln P_i \quad (2.17)$$

is the entropy of the corresponding macrostate.

For the arrangement from Figure 2.9, this is demonstrated in Figure 2.10. The system has  $N$  atom sites that are either “faulty” (number  $f$ ) or occupied (number  $N - f$ ). The number of possible arrangements of faulty sites (=number of microstates) is

$$\frac{1}{P} = \Omega = \frac{N!}{(N-f)!f!} \quad (2.18)$$

and grows drastically with  $f$  until a maximum value that is obtained for  $f = N/2$ .

In closed systems in equilibrium,  $P$  is often identical for all microstates and Eqn (2.17) simplifies to

$$S = k_B \ln \Omega \quad (2.19)$$

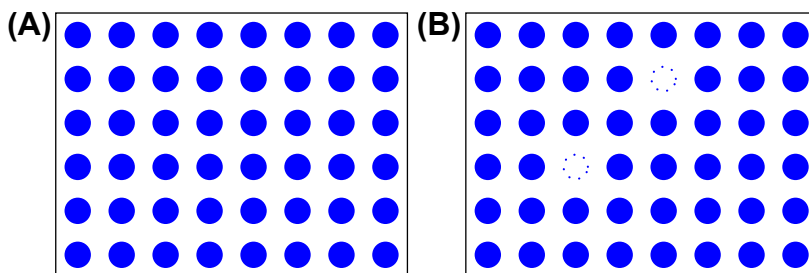


**FIGURE 2.9** Statistical interpretation of entropy. (A) One option is possible to distribute  $6 \times 8 = 48 = n$  atoms on  $n$  lattice sites. (B) This figure shows one of  $48 \times 47/2 = 1128$  equivalent options to arrange  $f = 2$  faults (e.g., unoccupied sites or vacancies) on 48 lattice sites.

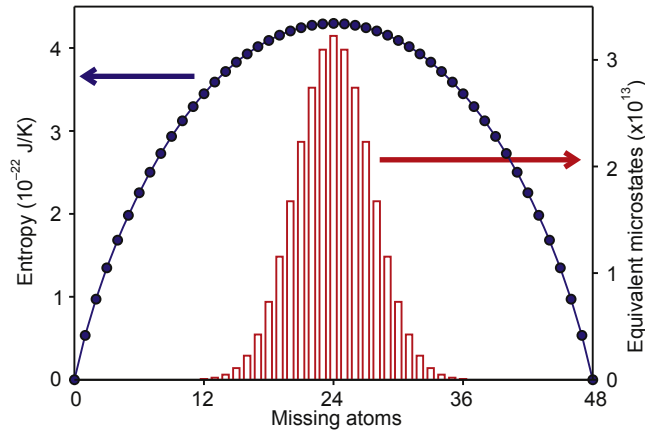


**FIGURE 2.10** Derivation of entropy  $S$  for the ensemble that is shown in Figure 2.8 with different numbers of missing atoms. The number  $\Omega$  of equivalent microstates is maximum if 50% of the sites are faulty.

where  $S(f)$  is shown by the box plot in Figure 2.10. If in a real system with  $f > 0$  and at  $T > 0$  all faulty sites are initially ordered ( $\Omega(t=0) = 1$ ), this ordering will drop with time  $t$ . It will be shown in Section 2.1.2.4 that the growth of  $S$  is the driving force for increasing the “uncertainty” of the system.

The thermodynamic interpretation of  $S$  does not depend on the atomistic nature of matter, but can be related to it. Figure 2.11(A) shows an ideal lattice where the atoms are connected by chemical bonds. One can assume that this solid is formed because the creation of every bond reduces the internal energy of the material (compared with sole atoms) by a certain amount  $E$ . In Figure 2.11(B), some vacancies are introduced that increase the disorder, or the “uncertainty,” of the system, and increase its entropy  $S$ . If for this purpose  $n$  bonds had to be broken, the energy  $Q = n \cdot E$  was used. Assuming that this process is performed under equilibrium conditions, it is reversible, and the relation

$$\Delta S = \frac{Q_{\text{rev}}}{T} \quad (2.20)$$

describes the entropy change of the system.

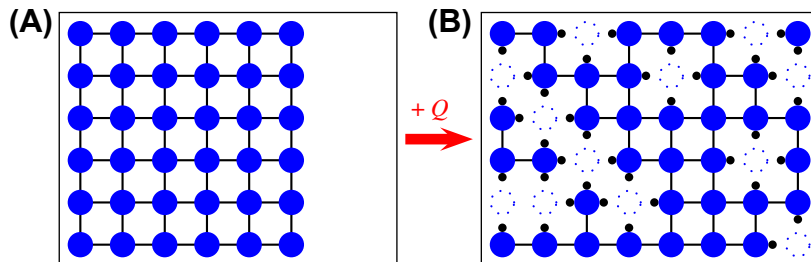


**FIGURE 2.11** Thermodynamic interpretation of entropy: In (A) all atoms occupy lattice sites and form ideal bonds. In (B) faults (here vacancies) are introduced and some bonds are “dangling.” For this process, a certain amount of energy  $Q$  was used.

In analogy to Eqn (2.16), the entropy can be derived from the specific heat capacity by

$$S(T) = S_0 + \int_{T_0}^T \frac{c_p(T)}{T} dT \quad (2.21)$$

and one has  $S_0(0 \text{ K}) = 0$ . Figure 2.6 shows, together with  $H(T)$ , the function  $S(T)$  for Li metal down to absolute zero.

#### 2.1.2.4 Gibbs Free Energy

The enthalpy  $H$  introduced in Section 2.1.2.2 is a measure for the amount of energy that is added (or extracted) from a system. This process is, however, usually not reversible: Even if lattice vibrations are considered undamped (contribution  $U$  in Eqn (2.14)) and if volume work can be restored (contribution  $pV$ ), the entropy  $S$  of the system is increased upon heating. Once the disorder of a system became larger, it is in general an irreversible process.

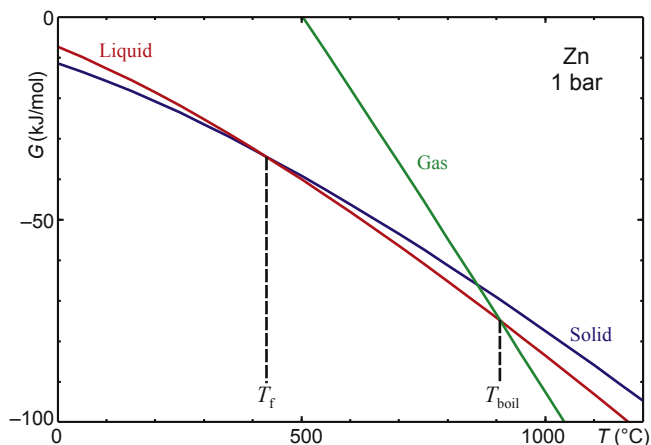
It is useful to define the “free energy” (or Gibbs energy)

$$G = H - TS = U + pV - TS \quad (2.22)$$

which is the amount of energy that can reversibly be added or extracted from the system. Such as  $H$  and  $S$ ,  $G$  is a thermodynamic potential. This means that for a given state  $x_i$ ,  $T$ ,  $p$  of a system,  $G$  does not depend on how this state was reached.

At elevated  $T$  (room temperature or beyond),  $H$  changes only weakly (see, e.g., Figure 2.7), and the same holds for  $S$ . From Eqn (2.22) it is obvious that  $G(T)$  is a function that drops nearly linearly for most phases and systems. Figure 2.12 demonstrates this for the three aggregation states of zinc metal. The solid phase develops most stable binding forces between atoms, this way reducing  $H$  and resulting in the most negative  $G^{\text{sol}}[0 \text{ }^\circ\text{C}] = -11.42 \text{ kJ/mol}$ . The energy gain by binding is less significant in the liquid

**FIGURE 2.12**  $G$  as a function of  $T$  for the solid, liquid, and gaseous phases of zinc.  $T_f$ , fusion point;  $T_{\text{boil}}$ , boiling point.



( $G^{\text{liq}}[0\text{ °C}] = -7.38\text{ kJ/mol}$ ) or even smaller in the gas with much weaker attractive forces between atoms ( $G^{\text{gas}}[0\text{ °C}] = +86.42\text{ kJ/mol}$ ). On the other hand, the degree of disorder, and consequently the slope  $-S$  of the  $G$  functions becomes larger from solid over liquid to gas. The result is that, in this order, these phases have the lowest  $G$ , and become stable one after the other with larger  $T$ .

For all curves in [Figure 2.12](#),  $p = 1\text{ bar}$  was assumed. The influence of  $p$  on  $S$  and  $H$  is usually small for condensed phases (solids, liquids). Contrary gases show high compressibility, which leads to a high dependency of atomic interactions on pressure. For lower  $p$ ,  $G^{\text{gas}}(T)$  shifts to bottom left ([Eqn \(2.14\)](#)), leading to an intersection with  $G^{\text{liq}}(T)$  at lower  $T$ —this means  $T_{\text{boil}}$  drops with  $p$ . If for sufficient small  $p$  the intersection is below  $T_f$ , the liquid phase is never stable and the substance undergoes sublimation, which is a first-order phase transition from the solid to the gas, and vice versa.

Many chemical elements can react with each other under the formation of compounds. The stability of compounds depends on the binding forces between components, hence on the lattice energy. Typically, compounds with prevalent ionic bonding consist of electropositive cations (often metals) and electronegative anions, and are named, for instance,

- pnictides (compounds with negative N, P, As ions)
- oxides (oxygen) or chalcogenides (compounds with negative S, Se, Te ions)
- halides (compounds with negative F, Cl, Br, I ions).

These anion-forming elements are gases or at least volatile already at moderate temperatures  $T$ . The partial molar Gibbs energy (= chemical potential) of an ideal gas can be written as

$$\mu_i = \mu_i^0 + RT \ln p_i \quad (2.23)$$

where  $\mu_i^0$  is the Gibbs energy at standard pressure (1 bar) and  $p_i$  is the partial pressure of this gas. As a consequence of [Eqn \(2.23\)](#), functions  $G(\log p_i)$  are linear for  $T = \text{const.}$  For different phases, the slopes  $G(\log p_i)$  are different, and the resulting intersections are the limits of stability ranges for these phases. This is demonstrated in [Figure 2.13](#) for the system Fe–O<sub>2</sub>.

From [Eqn \(2.23\)](#) it is obvious that for  $T = \text{const.}$  the  $\mu_i$  are linear functions of the logarithmic vapor pressures  $p_i$ . [Figure 2.14](#) shows this for equilibria between iron, oxygen, and sulfur. Only if both  $p_i$  are low, metallic iron is stable. If the oxygen pressure becomes larger, oxides FeO, Fe<sub>3</sub>O<sub>4</sub>, Fe<sub>2</sub>O<sub>3</sub> appear in the same order as in [Figure 2.13](#). If only the sulfur pressure becomes larger, the sulfides FeS or FeS<sub>2</sub> are formed. In an intermediate region where oxygen and sulfur have significant  $p_i$ , iron(II) sulfate FeSO<sub>4</sub> or iron(III) sulfate Fe<sub>2</sub>(SO<sub>4</sub>)<sub>3</sub> are formed. Phase diagrams of this type are valuable, e.g., for predictions, whether interfaces between a substrate and an epitaxial layer are stable. Under the given conditions, FeS<sub>2</sub> (“pyrite”) can exist in equilibrium with FeSO<sub>4</sub> as well as Fe<sub>2</sub>(SO<sub>4</sub>)<sub>3</sub>. This means that from the thermodynamic point of view, epitaxial growth of both sulfates on a pyrite substrate might be feasible. FeS (“pyrrhotite”), in contrast,

**FIGURE 2.13**  $G$  as a function of the oxygen partial pressure  $p_{O_2}$  for 1 mol iron in equilibrium with  $\frac{3}{2}$  mol  $O_2$ . From left to right, the solid phases  $Fe(bcc) \rightarrow FeO \rightarrow Fe_3O_4 \rightarrow Fe_2O_3$  have the lowest  $G$  and are stable.

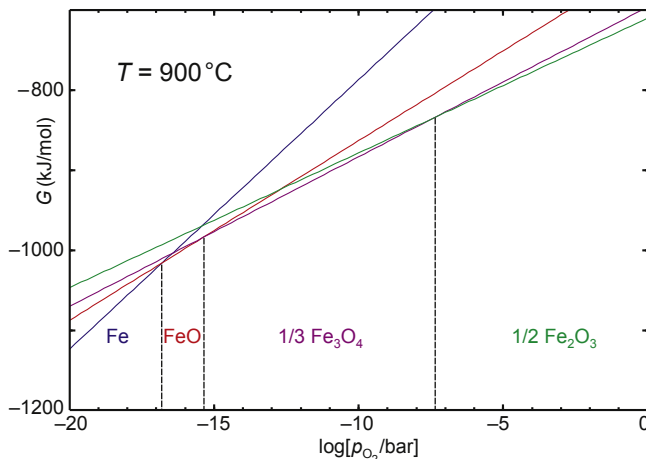
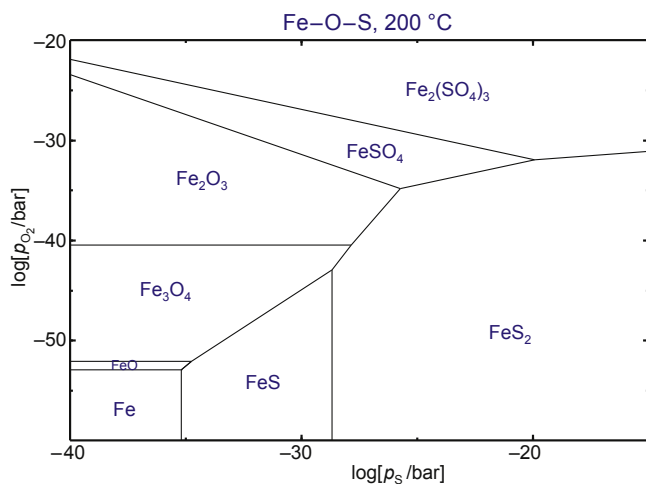


**FIGURE 2.14** Predominance diagram for  $FeO_xS_y$  phases in coordinates  $p_s, p_{O_2}$  (decadic logarithms) for the constant temperature 200 °C.



cannot exist in equilibrium with both sulfates. This means that epitaxy of both sulfates on pyrrhotite, if possible at all, can create only a metastable layer.

### 2.1.3 Phase Transitions

If water ice is heated under ambient pressure with constant heat flux per time unit  $dQ/dt = \dot{Q}$  from low temperatures  $T \ll 0$  °C it first increases its temperature until the melting point (fusion point)  $T_f = 0$  °C is reached. Then  $T$  remains constant for some holding time  $t_f^{hold} = \Delta H_f / \dot{Q}$ . The heat of fusion  $\Delta H_f = 6$  kJ/mol is a thermodynamic property of the substance water. During  $t_f^{hold}$  the solid (ice) and the liquid (water) are in

equilibrium; just their mass ratio drops from unity to zero. Upon further heating, the water temperature rises again until  $T_v = 100\text{ }^\circ\text{C}$  where water vaporizes. A second holding time  $t_v^{\text{hold}} = \Delta H_v / \dot{Q}$  appears where liquid water continuously evaporates, and the heat of vaporization  $\Delta H_v = 40.87\text{ kJ/mol}$  is another thermodynamic property of water. The chemical substance water ( $\text{H}_2\text{O}$ ) remains unchanged during the whole process, but the physical properties are changing abruptly at  $T_f$  and  $T_v$ . Melting and vaporization are phase transitions.

At phase transitions, some structural properties of a substance are changing. Usually, these are the positions of atoms, but in some cases only minor changes (electric or magnetic polarization, electronic spins) undergo variations. For the above-mentioned processes of melting and evaporation, the structural changes are very obvious; in other cases, the changes are smaller. Equation (2.15) showed that the heat  $Q = \dot{Q} \cdot t$  increases the enthalpy  $H$  of the system. In Figure 2.7 the chemical elements Ar and Ag show smooth  $H(T)$  functions, and the slopes  $\partial H / \partial T = c_p$  are the specific heat capacities. Bromine melts at  $-8\text{ }^\circ\text{C}$  and is liquid until  $T_v = 59\text{ }^\circ\text{C}$  where a step with height  $\Delta H_v = 29.5\text{ kJ/mol}$  follows. Sulfur shows steps in the  $H(T)$  functions not only at  $T_v$  and  $T_f$ , but additionally a smaller step  $\Delta H_t = 400\text{ J/mol}$  at  $T_t = 95\text{ }^\circ\text{C}$ . At this temperature, the crystal structure of the solid changes from  $\alpha$ -S (low  $T$ ) to  $\beta$ -S (high  $T$ ).  $\Delta H_t$  for this transition is small, because structural similarities are significant (see also Section 2.2.1.1).

Phase transitions can be classified from the thermodynamic as well as from the structural point of view; both schemes are, of course, related to each other. Paul Ehrenfest proposed a classification of phase transitions based on the discontinuity in derivatives of the Gibbs free energy. This classification says that a phase transition is of  $n$ -th order if the  $n$ -th derivative of  $G$  with respect to a system variable such as  $p$  or  $T$  is discontinuous. Figure 2.12 shows  $G(T)$  for the three phases of zinc. The system will always minimize  $G$ , hence the lowermost curve is valid for the system. This is replotted in Figure 2.15 for Zn and for Ni (see also Figure 2.5). Only  $G(T)$  for Zn shows significant bends at  $T_f$  and especially at  $T_v$ , consequently the first derivative  $G'(T)$  has discontinuities there (arrows from top) and both transitions are of first order.  $G(T)$  for Ni is much smoother, and only  $G'(T)$  has a small (but hard to recognize) bend near  $354\text{ }^\circ\text{C}$ . In the second derivative  $G''(T)$  a discontinuity appears, which resembles the shape of the Greek letter  $\lambda$ —the transition is of second order. The  $\lambda$  shape is typical for transitions from a ferromagnetic or ferroelectric state where the material has low crystal symmetry to a paramagnetic (paraelectric) state with high symmetry.

Melting and vaporization are always first-order transitions (sometimes called *transitions of the first kind*), and like all first-order transitions characterized by a “latent heat”  $\Delta H_t$  that must be added to the system at  $T_t$  without changing the temperature. Second-order transitions bear no latent heat, and the introduction of heat into the system always increases its temperature. Experimentally, the discrimination between first- and second-order transitions is not straightforward, if  $\Delta H_t$  is very small (below a few  $10\text{ J/mol}$ ). The ferro-/paraelectric transition of  $\text{BaTiO}_3$  is sometimes described as second order, but bears nevertheless a small  $\Delta H_t \approx 200\text{ J/mol}$  [3].

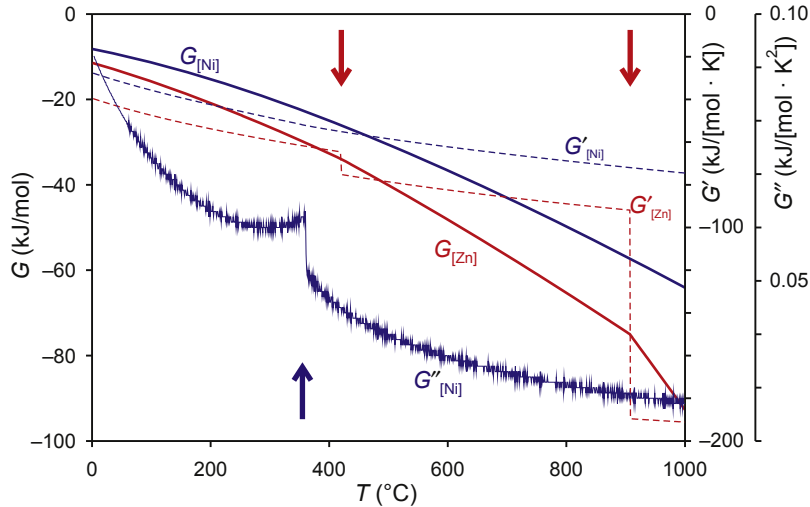


**FIGURE 2.15** Solid lines:  $G(T)$  for Zn and Ni at 1 bar, dashed lines:  $G'(T) = \partial G/\partial T$ , scattered line:  $G''(T) = \partial^2 G/\partial T^2$  (for Ni only). The arrows from top mark first-order transitions of Zn (melting, evaporation). The arrow from the bottom marks a second-order transition of Ni (Curie temperature  $T_c$  where a ferromagnetic material loses intrinsic magnetization).

A thermodynamic approach for second-order transitions was introduced by Lew Landau [12], where an order parameter  $Q$  results in an excess Gibbs energy term

$$G = H - TS = \frac{1}{2}A(T - T_c)Q^2 + \frac{1}{4}BQ^4 + \frac{1}{6}CQ^6 \quad (2.24)$$

( $A$ ,  $T_c$ ,  $B$ ,  $C$ —constants), which describes the behavior of measurable physical quantities  $M$  such as specific heat capacity, polarization, or atomic positions near second-order phase transitions by expressions of the type

$$M \propto |T_c - T|^{-\alpha} \quad (2.25)$$

where  $T_c$  is the transition (Curie) temperature and  $\alpha \approx \frac{1}{2}$  is the “critical exponent”. For a comprehensive introduction to Landau theory, the reader is referred to Salje [13].

From the structural point of view, second-order transitions often proceed by smooth, continuous shifts of atoms (“displacement type”). Typically, the crystal structure in the high  $T$  phase has a high symmetry, and after the shift, at lower  $T$ , the crystal symmetry is lowered. Other second-order transitions are of the “order–disorder” type. The  $\beta/\beta'$  brass phase in Figure 2.16 is an example. At high  $T \approx 800^\circ\text{C}$ ,  $\beta$ -brass has a wide homogeneity range from ca. 44% to ca. 64% Cu, which includes the 1:1 composition CuZn. Under these conditions, Cu and Zn atoms form a body-centered cubic structure (structural type  $\alpha$ -Fe, space group  $Im\bar{3}m$ ) where both atom types are distributed statistically across the corners and centers of cube unit cells. It should be noted that corners and centers of the cubic unit cells are symmetrically equivalent.

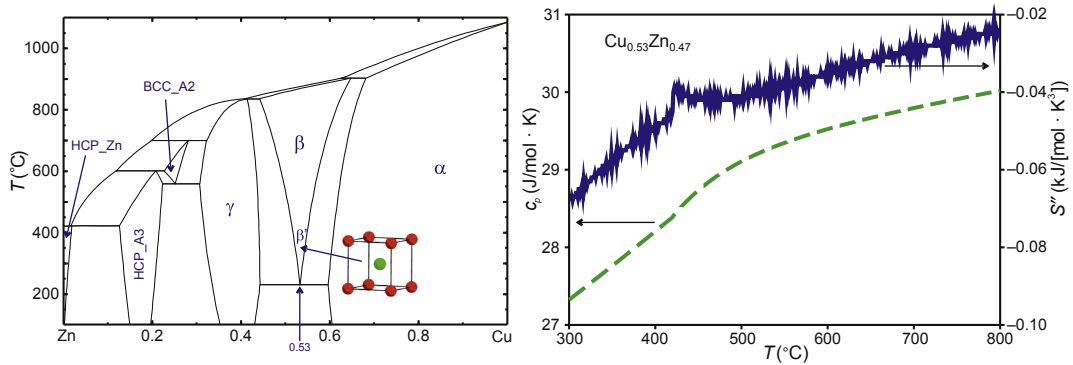


**FIGURE 2.16** Left: Binary phase diagram Cu–Zn; the phase fields with one solid phase are labeled. The crystal structure of  $\beta'$  brass is shown in the insert. Right: Specific heat capacity (dashed line) and  $S'' = \partial^2 S / \partial T^2$  of the mixed crystal 53% Cu + 47% Zn.

If the temperature becomes lower, it is energetically more favorable if every atom has more opposite type atoms as neighbors. This is reached by placing one atom type preferably on the corner positions, and the other type on the center positions. Ordering does not happen suddenly and is not complete; just the initially fully random distribution gets partially lost if  $T$  drops. The totally ordered case with different atom types at the corners or centers, respectively, is shown in the insert of the phase diagram. It corresponds to the CsCl structure type with  $Pm\bar{3}m$  space group. The ordered case is called the  $\beta'$ -brass phase.

The phase width of  $\beta/\beta'$  brass becomes smaller for lower  $T$  and degenerates to one point  $x = 0.53$  at  $530^\circ\text{C}$ , which implies that ordering cannot be perfect resulting from a slight Cu excess. The right panel of [Figure 2.16](#) shows the  $c_p(T)$  function of the  $\text{Cu}_{0.53}\text{Zn}_{0.47}$  alloy, which is calculated [\[3\]](#) between  $300$  and  $800^\circ\text{C}$ . The broad anomaly around  $450^\circ\text{C}$  results from this “continuous” phase transition [\[14\]](#). The anomaly results from the change of ordering mentioned above, and this change of ordering is reflected by a minor change of slope for the  $S(T)$  function, which becomes obvious in the second derivative  $S''$ .

Both panels of [Figure 2.16](#) are calculated for equilibrium conditions. It should be noted that the redistribution of atoms on lattice sites is a diffusion process, and diffusion is time dependent. Correspondingly, the width of the transition depends not only on thermodynamic, but also on kinetic parameters. Generally, second-order and higher order transitions are characterized by a certain transition range from the low  $T$  to the high  $T$  phase. Often, only the upper limit is characterized by a critical temperature  $T_c$  (see [Figures 2.15](#) and [2.17](#)). Besides, the transition proceeds in a smooth way, usually without mechanical disintegration of samples such as crystals during growth. Ferroelectric lithium niobate  $\text{LiNbO}_3$  is a good example: This material is grown on an industrial scale, and it grows from the melt in a paraelectric  $R\bar{3}c$  phase [\[15\]](#). The Li:Nb ratio is not fixed, and the formula should rather be written as  $(1-x)\text{Nb}_2\text{O}_5 \cdot x\text{Li}_2\text{O} = \text{Li}_x\text{Nb}_{1-x}\text{O}_{2.5-2x}$ . [Figure 2.18](#) shows the dependence  $T_c(x)$  of the Curie temperature

**FIGURE 2.17** Measured X-ray intensity data for the  $11\bar{2}3$  reflections of calcite [17] fitted with a Landau expression (2.25) gives  $T_c = 1254^\circ\text{C}$  and  $\alpha = 0.51$ . See also Ref. [13], p. 11.

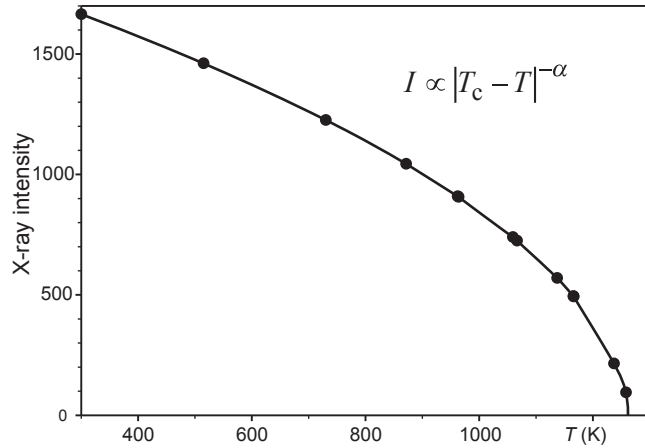
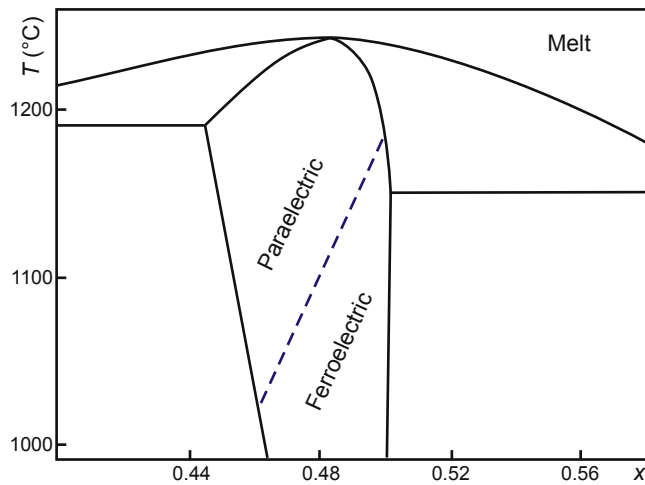


**FIGURE 2.18** Dependence of the Curie temperature  $T_c$  (dashed line) across the stoichiometry width of lithium niobate  $\text{Li}_x\text{Nb}_{1-x}\text{O}_{2.5-2x}$  on the lithium concentration  $x$  [18]. Reprinted with permission from AIP Publishing LLC.



where the second-order transition to the ferroelectric  $R3c$  phase occurs. Similar to the  $\beta/\beta'$  transition of brass (Figure 2.16 right), the para-/ferroelectric transition of lithium niobate is accompanied by a  $c_p$  anomaly that can be observed, e.g., by differential scanning calorimetry (DSC) [16].

Only briefly “glass transitions” shall be mentioned here, because the glass state is metastable, hence, cannot be found in (equilibrium) phase diagrams. Nevertheless,  $x - T$  regions where glass states are easily formed are sometimes marked. Often, glass formation is connected with immiscibility of two liquid phases below some critical temperature  $T_m$ , which usually depends on  $x$ . If at least one of these liquids contains a “network builder” such as  $\text{SiO}_2$ ,  $\text{B}_2\text{O}_3$ , or  $\text{P}_2\text{O}_5$ , a glass can be formed that initially

(at high  $T$ ) has a rubberlike behavior. Upon further cooling, at the glass transition  $T_g < T_m$ , the glass becomes more brittle. Such behavior can be observed, e.g., in binary systems  $B_2O_3$ – $A_2O$  ( $A = Li, Na, K, Rb, Cs$ ) [19]. The softening of glass if heated above  $T_g$  can be measured by thermomechanical analysis (TMA); in addition, it is connected with a  $c_p$  anomaly, shifting a DSC curve to the endothermal direction [20].

## 2.1.4 Calculation of Phase Diagrams

### 2.1.4.1 Miscibility

If in one specific phase  $\phi$  several components show miscibility, this mixing increases disorder hence the entropy  $S$  (Eqn (2.19)). Increasing  $S$ , however, reduces the Gibbs free energy  $G$  (Eqn (2.22)) and makes the mixed phase thermodynamically more stable, compared to the unmixed (or “mechanically mixed”) state (Figure 2.19). If mixing does not occur, one has the simple case of a pure substance with fixed stoichiometry. Then  $c_p$  and the derived thermodynamic potentials  $H$ ,  $S$ ,  $G$  are only functions of  $T$ , and data for many substances can be found in the literature.

$\phi$  is a mixed phase if it has a variable composition  $x_1, x_2, \dots, x_{C-1}$  ( $C$ —number of components). Assuming that the mixture is ideal, one has

$$G^\phi = \underbrace{\sum_i^C x_i \mu_i^0}_{G^0} + RT \underbrace{\sum_i^C x_i \ln x_i}_{G^{id}} \quad (2.26)$$

where the first expression  $G^0$  results from the weighed contributions of the pure components (dashed line in Figure 2.19), and the second expression  $G^{id}$  from the ideal entropy of mixing. Often, especially if  $T$  is very high and chemical interaction forces between components are weak, Eqn (2.26) gives a realistic approximation for real systems too. If energetic ( $H^{ex}$ ) or entropic ( $S^{ex}$ ) excess contributions must be taken into account, a term ( $G^{ex}$ ) must be added to Eqn (2.26).

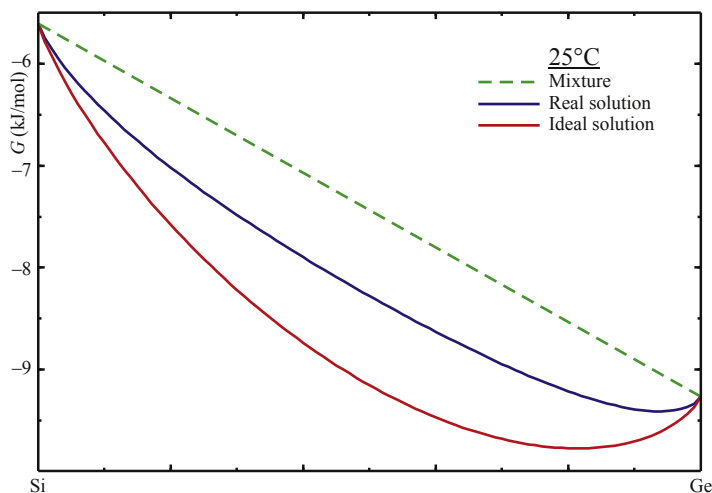


**FIGURE 2.19** The functions  $G(x)$  for a mechanical mixture of silicon and germanium (dashed line), and for the solid solution  $Si_{1-x}Ge_x$  with real data (upper solid curve) and assuming an ideal solid solution (lowest solid curve).

Often this  $G^{\text{ex}}$  is described by the subregular solution model (Redlich–Kister [21]), which is expressed by

$$G^{\text{ex}} = x_A x_B \sum_{j=0}^N L_j (x_A - x_B)^j \quad (2.27)$$

where  $x_A$  and  $x_B$  are the molar fractions of components  $A$  and  $B$ , respectively. (Only the binary case is described here,  $x_A + x_B = 1$ .)  $L_j$  terms represent the interaction coefficients between the basis compounds, and they are often given as a linear function of temperature, e.g.,  $L_j = L_j^{(0)} + L_j^{(1)} T$ . Other models, e.g., the “two-sublattice ionic solution” [22], take into account that anions and cations are intermixing only on separate sublattices, and an anion usually cannot jump to a cation site and vice versa.

The  $G^{\text{ex}}$  of a specific phase can be determined experimentally, e.g., by measuring phase diagrams, electrical potential differences, or by vapor pressure measurements. Such data are available not only in the original literature, but also from databases. Often, the theoretical estimation is possible if interatomic potentials between the constituents (atoms, ions) are known. Then the total energy of a pure phase (e.g., a stoichiometric crystal) can be compared to the total energy of the distorted phase (the mixed crystal). The difference is the energy of mixing. It should be noted that the determination of  $G^{\text{ex}}$  is often elaborate.

The topology of phase diagrams depends substantially on the extent to which the components can mix in the different phases. The following rules of thumb for gases, liquids, and solids can be given.

*Gases:* Unless under extreme conditions [23], gases are mixing in arbitrary ratio. Moreover, ideal mixing ( $G^{\text{ex}} = 0$ ) can be assumed if the pressure does not approach the critical pressure and if the temperature is not too low. Both requirements are fulfilled for most crystal growth processes, except hydrothermal growth or high-pressure synthesis.

*Liquids:* Liquids (melts) of different components are miscible if chemically similar. Certainly, this statement is not very definite: It simply means that, if all components belong to one group of substances such as metals, oxides, halides, hydrocarbons, alcohols, sugars, there is a good chance that mixing is possible for all compositions. For technical applications, and especially for crystal growth, many relevant systems fulfill this condition and just one liquid phase is formed. Nevertheless, exceptions exist, and Figure 2.20 shows that, e.g., below ca. 1900 °C CaO–SiO<sub>2</sub> melts with ca. 85% SiO<sub>2</sub> decompose under formation of two liquids with different SiO<sub>2</sub> concentration. In a closer look, phase transition or demixing phenomena in melts seem not uncommon, especially under conditions close to the crystallization of solid phases: Crystal growth of HgTe was observed from demixed melts [24], melts of CdTe undergo a structural transition under formation of associates near  $T_f$  [25], and even if CaCO<sub>3</sub> crystallizes from aqueous Ca(HCO<sub>3</sub>)<sub>2</sub> solutions, separation of the liquid was observed in theory and experiment [26,27].

*Solids:* The condition of chemical similarity for complete miscibility is valid also for crystalline materials. Yet another precondition makes the formation of mixed crystals

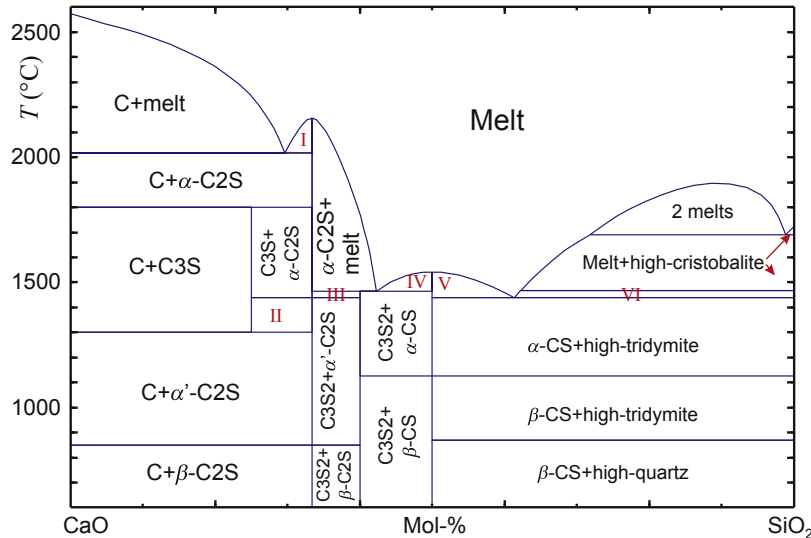


**FIGURE 2.20** Phase diagram CaO–SiO<sub>2</sub> with a region of liquid immiscibility for SiO<sub>2</sub> rich melts. The abbreviations are common in the construction material industry; these are the definitions: C = CaO, C2S = Ca<sub>2</sub>SiO<sub>4</sub>, CS = CaSiO<sub>3</sub>, C3S2 = Ca<sub>3</sub>Si<sub>2</sub>O<sub>7</sub>, C3S = Ca<sub>3</sub>SiO<sub>5</sub>. All phase fields are labeled, and the roman letters stand for: I = α-C2S + melt, II = C3S + α'-C2S, III = C3S2 + α'-C2S, IV = V = CS + melt, VI = high-tridymite + melt.

(=solid solutions) less probable compared to liquids: If two components A and B form a solid solution, their atoms must be able to substitute each other in the corresponding crystals in a complete chain of constitutions. This is possible only if A and B belong to the same crystal structure type. The left panel of [Figure 2.21](#) demonstrates this for silicon and germanium. Both crystallize in the diamond structure type (space group  $Fd\bar{3}m$ ), and the lattice constants of their cubic unit cells are  $a_0^{\text{Si}} = 0.543$  nm or  $a_0^{\text{Ge}} = 0.566$  nm, respectively. The similarities are so significant that Si and Ge can replace each other, and a continuous row of solid solutions is formed. The lens-shaped binary phase diagram shown there is typical for such “mixed crystal” systems (see [Section 2.2.2.1](#)). The right panel of [Figure 2.21](#) shows the binary system lead–tin, both elements follow immediately after Si and Ge in the fourth group of the periodic table, and are similar from the chemical point of view. However, at ambient temperature, Sn crystallizes in a tetragonal structure (space group  $I4_1/amd$ , lattice constants  $a_0^{\text{Sn}} = 0.582$  nm,  $c_0^{\text{Sn}} = 0.317$  nm). The lead structure instead is a face-centered cubic lattice (space group  $Fm\bar{3}m$ ,  $a_0^{\text{Pb}} = 0.495$  nm). The large Pb atoms can replace only ca. 2% of Sn in its structure; on the other side, the small tin atoms can substitute ca. 20% of Pb. A continuous solubility range cannot exist because continuous transformation between both structures is impossible. Hence, a eutectic system is formed (see [Section 2.2.2.2](#)).

As a result of the  $G^{\text{id}}$  term in [Eqn \(2.26\)](#), the slope of the  $G^\phi(x)$  functions becomes infinite near the pure components at  $x = 0$  or  $x = 1$ . This means that  $G^\phi(x)$  drops

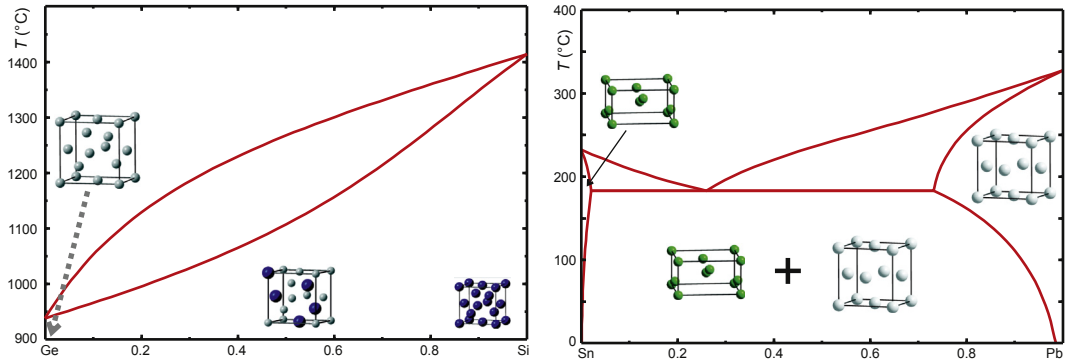


**FIGURE 2.21** Left: Phase diagram Si–Ge with formation of a solid solution for  $0 < x < 1$  because both end members have identical (diamond) crystal structure and can replace each other (inserts). Right: Phase diagram Pb–Sn with limited mutual solubility at the rims, resulting from different crystal structures of both end members.

considerably for every phase if minor amounts of arbitrary impurities are added. In other words, a minor “rim” solubility always exists. Minor impurity concentrations in the order of parts per million (ppm) or even less may be important, e.g., for doping semiconductors, but are irrelevant for many other applications. All solid phases in Figure 2.20 have a negligible phase width and are represented by vertical lines. Such phases with fixed stoichiometry are called “line compounds” or “daltonides.” The opposite is either a mixed crystal spanning all concentrations  $0 < x < 1$  of a phase diagram (Figure 2.21 left), or a “berthollide” phase where the composition is a variable within certain limits. Lithium niobate (Figure 2.18) is an example where the concentrations of Li and Nb can shift by a few percent, consequently  $\text{Li}_x\text{Nb}_{1-x}\text{O}_{2.5-2x}$  shows a finite phase width (=“homogeneity range”). In the Cu–Zn system (Figure 2.16(left)), all solid phases are berthollides.

#### 2.1.4.2 Analytical Expressions

Often, for practical purposes, binary phase diagrams with two components A, B are used. Then one has  $x_B = 1 - x_A = x$  and one concentration value  $x$  describes the composition completely.  $x$  and temperature  $T$  are often used as coordinates for A–B phase diagrams, and some types of such diagrams will be presented in Section 2.2.2. It was stated in Section 2.1.4.1 that the topology of phase diagrams is determined by the mutual miscibility of A and B in different phases  $\phi^i$ . For the three limit cases in Figure 2.22, the shape of phase boundaries can be given analytically.

There and in the following, fixed chemical compositions will be described by Latin letters or combinations of them: A, B, AB,  $\text{AB}_2$ ,  $\text{A}_m\text{B}_n$ . Phases will be described by  $\phi'$ ,  $\phi''$ ,.... If necessary, the chemical composition of a phase can be denoted in brackets.  $\text{A}(\phi')$  means pure A in the phase state  $\phi'$ .  $\text{A}_{1-x}\text{B}_x(\phi'')$  means a mixture with molar concentration  $x$  of B in the phase state  $\phi''$ .

For all diagrams in Figure 2.22, phase fields are separated by lines. Component A undergoes a first-order transition  $\phi' \leftrightarrow \phi''$  at  $T_A$ , and B an analog transition at  $T_B$ . Often

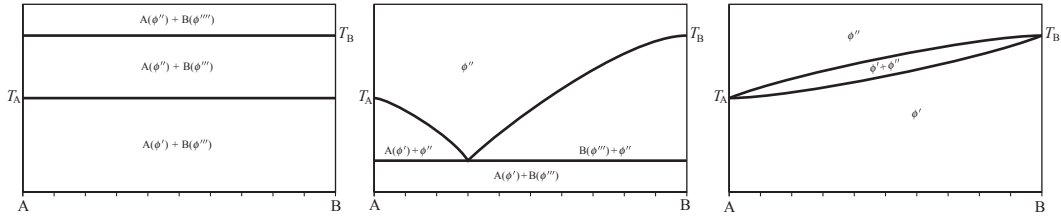


**FIGURE 2.22** Three basic topologies of binary phase diagrams where both components undergo a transition from a low  $T$  phase  $\phi'$  to a high  $T$  phase  $\phi''$ . Left: No mixing in  $\phi'$  and  $\phi''$ . Middle: no mixing in  $\phi'$ , but mixing in  $\phi''$ . Right: mixing in  $\phi'$  and  $\phi''$ .

$\phi''$  is the liquid (melt), and then the lower phase boundary where only melt(s) appear(s) is named *liquidus*. The maximum temperature at which all phases remain solid is marked by the *solidus* line, and is below the liquidus. The shape of these phase boundaries, however, depends only on the corresponding transition temperatures  $T_A$ ,  $T_B$  and on the enthalpy changes at these temperatures (=heat of transition)  $Q_A$ ,  $Q_B$ . This means that diagrams such as shown in Figure 2.22 can be valid for melting transitions ( $\phi'' = \text{liquid}$ ) as well as for other first-order transitions, e.g., between liquids and gas, or between different solid phases. The following cases can be distinguished:

Figure 2.22 Left: No mixing at all, such with water and mercury. Then  $T_A = -39^\circ\text{C}$  is the melting point of Hg, and  $T_B = 0^\circ\text{C}$  is the melting point of  $\text{H}_2\text{O}$ . At low  $T$  we have a mixture of pure solid Hg with pure solid  $\text{H}_2\text{O}$ . At high  $T$  both components are liquid, but immiscible. Consequently, pure water and pure Hg form separate phases. At intermediate  $T$ , solid pure  $\text{H}_2\text{O}$  (ice) floats on pure liquid Hg. For the liquidus and solidus, one has

$$T^{\text{sol}} = T_A \quad (2.28)$$

$$T^{\text{liq}} = T_B \quad (2.29)$$

if B melts higher, or vice versa.

Figure 2.22 Middle: Mixing only in the high  $T$  phase  $\phi''$ , which is often the liquid. The resulting  $G^{\text{id}}$  (Eqn (2.26)) lowers  $G$  for this phase, and makes it more stable. The left panel of Figure 2.1 is an example if one considers only the part between  $\text{V}_2\text{O}_5$  and  $\text{V}_2\text{MoO}_8$ , or only the part between  $\text{V}_2\text{MoO}_8$  and  $\text{MoO}_3$ . Assuming ideal and unlimited mixing of the components in phase  $\phi''$  and no solubility of B in  $A(\phi')$  or A in  $B(\phi''')$ , respectively, the bent phase lines (liquidus of A or B, respectively) can be described analytically by the expressions

$$x^{\text{liq}} = 1 - \exp\left[-\frac{Q_A}{R}\left(\frac{1}{T} - \frac{1}{T_A}\right)\right] \quad (2.30)$$

$$x^{\text{liq}'} = \exp \left[ -\frac{Q_B}{R} \left( \frac{1}{T} - \frac{1}{T_B} \right) \right] \quad (2.31)$$

where Eqn (2.30) describes the A-rich and Eqn (2.31) describes the B-rich side. Both branches meet at the eutectic point and the third phase boundary (eutectic line) is a horizontal through that point, representing the solidus. This is a *eutectic system* (see Section 2.2.2.2). Figure 2.23 shows a calculated eutectic phase diagram for two different sets  $Q_A$ ,  $Q_B$ . It should be noted that a change of one  $Q_i$  influences only the slope on the side of the corresponding component  $i$ . Consequently, for the case  $Q_A = 10$  kJ/mol,  $Q_B = 20$  kJ/mol one had to elongate in Figure 2.23 the B liquidus (solid line) until it meets the dashed A liquidus, resulting in  $x_{\text{eut}} \approx 0.32$  and  $T_{\text{eut}} \approx 760$  K.

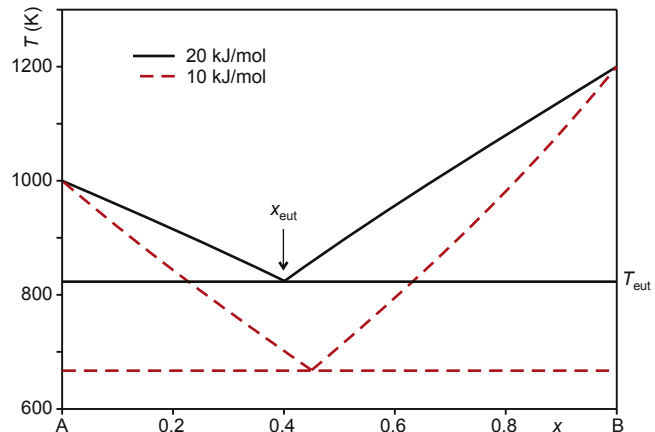
Figure 2.22 Right: If complete mixing of A and B is possible in phases  $\phi''$  and  $\phi'$ , both phases are stabilized by the Gibbs free energy of mixing. One-phase fields appear at very low and very high  $T$ . Both one-phase fields are separated by a two-phase field  $\phi' + \phi''$ . Assuming again ideal behavior in both phases, solidus and liquidus can be expressed analytically

$$x^{\text{sol}} = \frac{\exp \left[ -\frac{Q_A}{R} \left( \frac{1}{T} - \frac{1}{T_A} \right) \right] - 1}{\exp \left[ -\frac{Q_A}{R} \left( \frac{1}{T} - \frac{1}{T_A} \right) \right] - \exp \left[ -\frac{Q_B}{R} \left( \frac{1}{T} - \frac{1}{T_B} \right) \right]} \quad (2.32)$$

$$x^{\text{liq}} = \exp \left[ -\frac{Q_B}{R} \left( \frac{1}{T} - \frac{1}{T_B} \right) \right] \times x^{\text{sol}} \quad (T_A \leq T \leq T_B) \quad (2.33)$$

if heat  $Q$  and temperature  $T$  of the phase transformation are known for both pure substances. The two-phase lens is symmetrical for  $Q_A = Q_B$ , and it becomes

**FIGURE 2.23** Calculated hypothetical eutectic phase diagram with  $T_A = 1000$  K,  $T_B = 1200$  K. The solid and dashed lines were calculated with Eqns (2.30) and (2.31), and  $Q_A = Q_B = 20$  or  $Q_A = Q_B = 10$  kJ/mol, respectively.



broader for large  $Q$  values. Even for ideal mixing, the lens can bend upward or downward if  $Q_A$  and  $Q_B$  are significantly different. However, both liquidus and solidus are for ideal mixtures monotonous rising or falling, respectively. Local minima may occur only if excess Gibbs free energy of mixing occurs.

### 2.1.4.3 Minimization of the Gibbs Energy

In Section 2.1.2.4, the Gibbs free energy  $G$  was introduced, which has a minimum for every system in thermodynamic equilibrium. The contributions of several phases  $\phi$  ( $i = 1 \dots P$ ) are additive

$$G = \sum_{i=1}^P G_{\phi_i} \quad (2.34)$$

and each phase may consist of several constituents. The number  $C_\phi$  of constituents of a phase  $\phi$  may be unity—then one has a *pure phase*. For pure phases,  $G_\phi$  is basically a function of  $T$ , and sometimes other intensive quantities such as  $p$ , but not on concentration. Instead,  $G(T)$  is given by Eqn (2.22), with  $H(T)$  from Eqn (2.16) and  $S(T)$  from Eqn (2.21). Alternatively, formation enthalpy  $\Delta H_f$ , entropy  $S_0$  (at standard conditions) and coefficients for the  $c_p(T)$  function (2.13) are a sufficient dataset for the description of pure phases.

Mixed phases bear additional contributions  $G^{\text{id}}$ , and possibly  $G^{\text{ex}}$ , to  $G_\phi$  that depend on the concentrations of species present in this phase. Usually, the number of species is much larger than the component number of the system, as already single-phase chemical elements may form several species: gaseous oxygen exists as O, O<sub>2</sub>, and O<sub>3</sub>. For the whole system, the mass balance for all elementary components must be fulfilled; this means that the number of atoms of one chemical element that are present in all phases may not change.

Knowing the  $G(T, x, p, \dots)$  functions for all possible phases that can be formed from a given starting composition, and taking into account the mass balance for all chemical elements that are present, numerical minimization of  $G$  (Eqn (2.34)) allows to calculate the equilibrium state of the system for the given conditions  $T, p, \dots$  [28]. The task of numerical minimization of  $G$  is not straightforward, as equation systems with many unknowns (the concentrations of all species in the stable phases) have to be solved. For doing this, commercial software packages such as FactSage [3] or Thermo-Calc [29] as well as some free software, are available. The journal *Calphad* (CALculation of PHase Diagrams) is a forum for work devoted to such calculation efforts, and an overview of available software can be found there [30]. Commercial software packages are often integrated with databases for thermodynamic data at least for pure substances, and partially also for mixture phases. Free data collections can be found in the literature (e.g., [8–10] or on the internet [31,32]). Many phase diagrams for real systems in this chapter were calculated with FactSage.

## 2.2 Equilibria Between Condensed Phases

### 2.2.1 One Component

#### 2.2.1.1 Pressure–Temperature Diagrams

For systems with only one component ( $C = 1$ ), Gibbs phase rule (Eqn (2.5)) gives a sum  $F + P = 3$  degrees of freedom + phases. The concentration is fixed to be unity, and often pressure and temperature are used for constructing phase diagrams. Figure 2.3 shows this for sulfur as an example, where the four different phase fields are separated by lines (phase boundaries). Under ambient conditions, sulfur is a soft but brittle yellow solid, with orthorhombic crystal structure ( $\alpha$ -S). It melts at 115 °C to a dark liquid, but if cooled quickly (e.g., by pouring into water), an almost rubberlike solid with monoclinic crystal structure is obtained ( $\beta$ -S), which transforms slowly back to  $\alpha$ -S under ambient conditions. A detailed investigation reveals that at 1 bar  $\beta$ -S is stable for  $95 \leq T$  (°C)  $\leq 115$ .

$F + P = 3$  can be obtained in three ways, as follows, which can be seen from Figure 2.3:

$F = 0$ : No degree of freedom means a fixed point with as much as three coexisting phases. This is the case in the three “triple points”  $T_1$  ( $\alpha + \beta + \text{liq}$ ; 117 °C, 283 bar),  $T_2$  ( $\beta + \text{liq} + \text{gas}$ ; 115 °C,  $3.8 \times 10^{-5}$  bar),  $T_3$  ( $\alpha + \beta + \text{gas}$ ; 95 °C,  $7.6 \times 10^{-6}$  bar).

$F = 1$ : One degree of freedom does exist along lines separating phase fields in the diagram. Along these lines, the neighboring phases are coexisting. The slope of the lines is given by the Clausius–Clapeyron equation

$$\frac{dp}{dT} = \frac{\Delta H}{\Delta V_m \cdot T} \quad (2.35)$$

where  $\Delta H$  is the enthalpy difference between the two neighboring phases. For melting events this is, e.g., the heat of fusion  $\Delta H_f$ , and first-order phase transformations (see Section 2.1.3) are characterized by the heat of transition  $\Delta H_t$ . Both sulfur structures are characterized by  $S_8$  rings and differ mainly in the arrangement of these rings. The corresponding phase transition does not rearrange too many bonds, hence  $\Delta H_t = 0.4$  kJ/mol is small for the  $\alpha \rightleftharpoons \beta$  transition of S. In other cases, where the crystal structure undergoes a complete rearrangement, the enthalpy of solid-state transitions may approach the heat of fusion.  $\text{BaCl}_2$  undergoes, at 37 K below its melting point, a strong structural transition from orthorhombic to cubic [33] with  $\Delta H_t = 16.9$  kJ/mol, and  $\Delta H_f$  (at 962 °C) is 16.0 kJ/mol. Generally, one can assume that a few kJ/mol to several 10 kJ/mol are typical values for  $\Delta H$  to be entered in Eqn (2.35).  $\Delta V_m$  is the difference between molar volumes in both phases, which are inverse proportional to the mass density  $\rho$ . This is for most solids and liquids in the range  $1 \leq \rho \leq 20$  g/cm<sup>3</sup>: Under ambient conditions extreme values are lithium (0.535 g/cm<sup>3</sup>) and osmium or iridium with  $\rho \approx 22.6$  g/cm<sup>3</sup>. For most transitions between condensed phases,  $\rho$  does not change much,

and  $\Delta V_m$  is small. Consequently, the slope  $dp/dT$  is large, which is shown by the almost perpendicular phase boundaries  $\alpha/\beta$  and  $\beta/\text{liquid}$  in [Figure 2.3](#). For transitions between condensed phases and gases, however, the molar volume changes remarkably. The large  $\Delta V_m$  results in significantly smaller slopes of the phase boundaries. If the volume of the condensed phase is neglected in comparison to the volume of the gas phase  $V_g$ ,  $\Delta V_m$  in ([Eqn \(2.35\)](#)) can be replaced by the volume of an ideal gas  $V = RT/p$ . This gives

$$\frac{d \ln p}{dT} = \frac{\Delta H}{R \cdot T^2} \quad (2.36)$$

which corresponds to the parabolic behavior of the gas phase boundary in [Figure 2.3](#).

$F = 2$ : Two degrees of freedom are available inside the four phase fields of [Figure 2.3](#), and always only one phase is stable there. Two degrees of freedom means that two independent parameters (here  $p$  and  $T$ ) can be changed within the limits of the corresponding phase field independently.

### 2.2.1.2 Other Fields

$T$  and  $p$  are typical intensive parameters that are used as axes, but generally the Gibbs free energy may depend on other fields requiring more terms to be added to [Eqn \(2.22\)](#), e.g.,

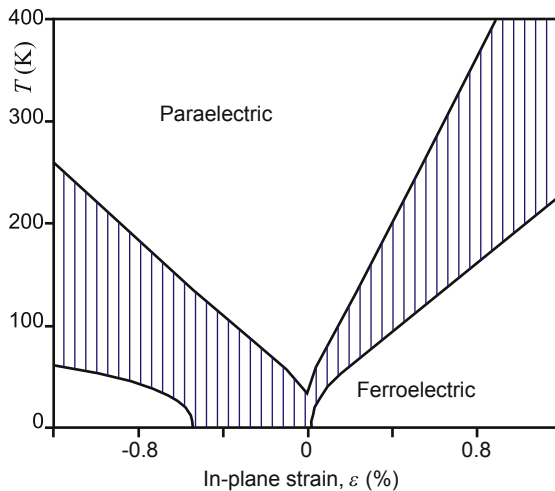
$$G = H - TS - V_m \vec{E} \cdot \vec{D} - V_m {}^2\vec{\sigma} : {}^2\vec{\epsilon} \quad (2.37)$$

where  $W_{el} = \vec{E} \cdot \vec{D}$  is the electric work density of a polarized crystal ( $\vec{E}$ ,  $\vec{D}$ —electric field or displacement, respectively) and  $W_{elast} = {}^2\vec{\sigma} : {}^2\vec{\epsilon}$  is the elastic energy stored in a deformed solid ( ${}^2\vec{\sigma}$ —elastic stress,  ${}^2\vec{\epsilon}$ —strain). Notations such as  ${}^2\vec{\epsilon}$  express that the corresponding physical property is described by a second rank tensor, a construct having in general  $3 \times 3$  components [\[34\]](#).

Such alternative contributions to  $G$  can be significant, especially for epitaxial layers. Strontium titanate  $\text{SrTiO}_3$  is an example: The substance crystallizes at high  $T$  in a cubic perovskite paraelectric phase, which has no permanent moments. If cooled below the Curie temperature  $T_C$ , it lowers crystal symmetry and becomes in a second-order transition (see [Section 2.1.3](#)) ferroelectric.  $T_C$  depends on the  $G(T, \epsilon)$  functions of the paraelectric and ferroelectric phases, and  $\epsilon$  can be manipulated by growing titanate layers on substrates that are almost, but not perfectly, lattice matched. Distorted perovskite substrates such as  $\text{REScO}_3$  allow “strain engineering” to manipulate the ferroelectric properties of  $\text{SrTiO}_3$  layers [\[35\]](#).

Gibbs phase rule ([Eqn \(2.5\)](#)) in its classical form relies on the expression  $G = H - TS = U + pV - TS$ . This means that pressure  $p$  and temperature  $T$  are independent variables. If under isobar conditions  $p = \text{const.}$ , the number of independent variables is reduced, the phase rule has to be altered to [Eqn \(2.6\)](#), with 1 instead of 2 as integer constant. Contrarily, a larger number of independent variables such as shown in [Eqn \(2.37\)](#) can increase the integer in [Eqn \(2.5\)](#) from two to larger values. This is

**FIGURE 2.24** Phase diagram of SrTiO<sub>3</sub> with  $\varepsilon = (a_{\parallel} - a_0)/a_0$  as abscissa.  $a_{\parallel}$ ,  $a_0$  is the lattice constant of SrTiO<sub>3</sub> in stressed (=epitaxially grown) or free-standing state, respectively. After Ref. [37], reprinted by permission from Macmillan Publishers Ltd.



demonstrated in Figure 2.24 for the one-component system SrTiO<sub>3</sub>, which can be grown on several substrates, causing strain within the thin single crystalline SrTiO<sub>3</sub> layer. Only for small  $\varepsilon$  or high  $T$  the material remains in its normal paraelectric cubic phase. For large  $\varepsilon$ , the material lowers its symmetry completely and becomes ferroelectric. In the intermediate region, paraelectric and ferroelectric states coexist: a phenomenon that is not found in typical one-component phase diagrams with  $p$ ,  $T$  as coordinates (Figure 2.3). For vanadium(IV) oxide VO<sub>2</sub> a triple point between two isolating monoclinic and a metallic rutile type phase was found in coordinates strain  $\varepsilon$  (or stress  $\sigma \propto \varepsilon$ , respectively) versus temperature at  $T = (65.0 \pm 0.1)^\circ\text{C}$ ,  $\varepsilon = 0$  [36].

## 2.2.2 Two Components

The pressure dependence of phase transitions can be described by the Clausius–Clapeyron Eqn (2.35). Many phase transitions are influenced only to a small extent by the total pressure  $p$  of the system. This is the case, e.g., for the melting of solids and for transitions between different crystal structures of one chemical compound where  $|\Delta V|$  is usually small. Besides, the variation of  $x$  and  $T$  can, under usual experimental conditions, be more easily performed than variations of  $p$ , which require experiments within pressure cells or sealed ampules. For both reasons, the phase composition of the system depends nearly exclusively on  $T$  and on the composition  $x_i$  of all components  $i$ . As  $\sum x_i = 1$ , one concentration value  $x$  is sufficient in the case of binary systems with only two components.

The topology of the binary phase diagram in the  $x - T$  plane (often called A–B phase diagram) depends on the miscibility of A and B in the different  $\phi^i$ . Some typical (limit) cases will be presented in the next sections. One should note that transients between these limit cases can be found often, if a limited but non-negligible miscibility

between A and B occurs in one or more phases. The same syntax that was introduced in Section 2.1.4.2 will be used for the description of phases with fixed or variable composition  $x$ .

### 2.2.2.1 Total Miscibility in 2 Phases

This case of total mixing in a high  $T$  and low  $T$  phase was already described analytically Eqns (2.32) and (2.33). Pure A undergoes at  $T_A$  a first-order phase transition, such as melting, from  $\phi'$  to  $\phi''$ , and pure B undergoes at  $T_B$  an analog first-order transition from  $\phi'$  to  $\phi''$ . If the necessary but not sufficient conditions

1. identical space symmetry groups (requiring at least identical point symmetry groups, which again requires at least identical crystal system)
2. similar lattice parameters  $a, b, c$  (should not be different by more than  $\approx 15\%$ )
3. similar nature of chemical bonds (ionic, covalent, van der Waals, or metallic)

are fulfilled for both phases, each of them can adopt any composition  $0 \leq x \leq 1$  (complete miscibility). Accordingly, for low  $T$ , only one phase  $\phi'$  is stable for all  $x$ . This means that this combination of system variables corresponds to a one-phase room (or one-phase field) in the diagram. For high  $T$ , only  $\phi''$  is stable, resulting in another one-phase field. For intermediate  $T$  both phases  $\phi'$  and  $\phi''$  may exist in equilibrium that is represented by a two-phase field that typically has the shape of a lens. The two-phase field  $\phi' + \phi''$  spreads from the composition A to the composition B in the binary phase diagram (Figure 2.25). It should be noted that the first-order transition happening at one point on the  $T$  scale for the pure substances A and B is spread over a  $T$  range which is spanned by the lines limiting the two-phase field for intermediate compositions. This  $T$  range becomes broader for larger heats of transformation (Figure 2.26).

Often,  $\phi''$  is simply the melt (liquidus). In this case, the first condition for miscibility is usually fulfilled, as liquids (except “liquid crystals”) are isotrope. Isotropy is described by the limit point symmetry group (Curie group)  $\infty \infty m$ , which is the highest symmetry group at all. Condition 2 does not apply to liquids; hence, only condition 3 decides

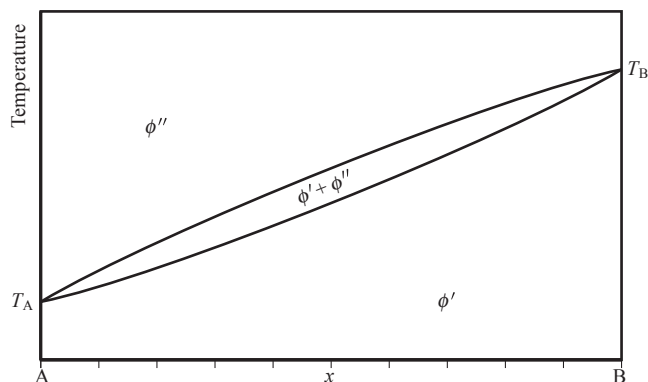
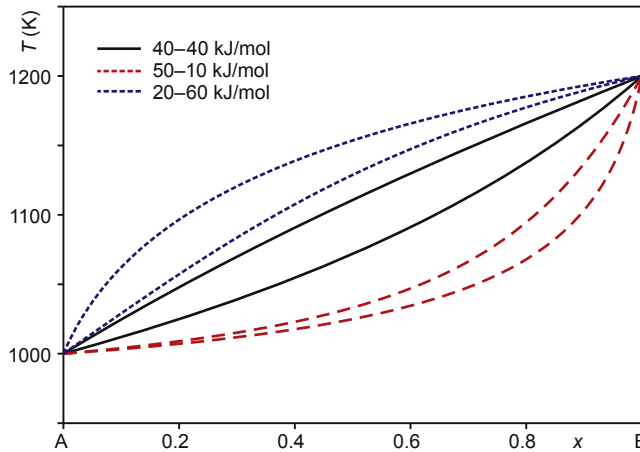
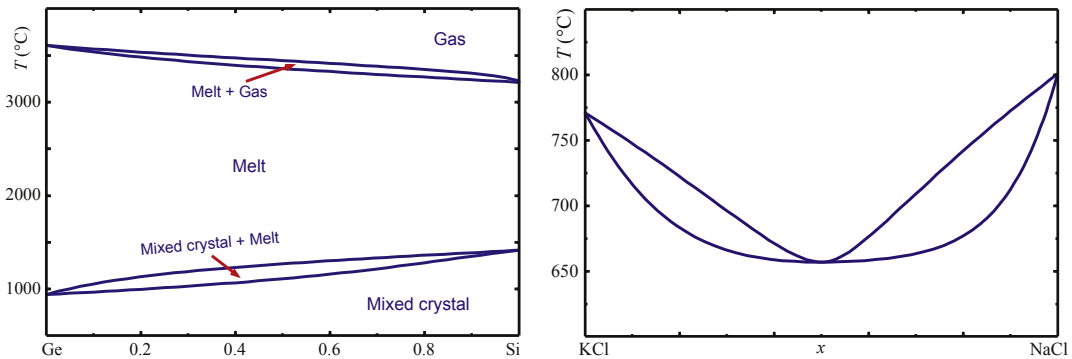


FIGURE 2.25 Binary phase diagram with ideal mixing both (low  $T$  and high  $T$ ) phases  $\phi'$  and  $\phi''$ .



**FIGURE 2.26** Calculated hypothetical mixed crystal phase diagram with  $T_A = 1000$  K,  $T_B = 1200$  K. The three sets of solidus and liquidus lines were calculated with Eqns (2.32) and (2.33) for the  $Q_A - Q_B$  pairs given in the legend.



**FIGURE 2.27** Left: Binary phase diagram Si-Ge for an extended  $T$  range (compare to Figure 2.20) where one-phase fields "mixed crystal," "melt," "gas," are separated by two-phase fields. Right: The binary phase diagram NaCl-KCl shows an azeotropic point where liquidus and solidus are coincident.

whether or not the phases  $\phi''$  of both components A or B can mix. In such cases where  $\phi''$  is the melt, the lower boundary line of the two-phase field  $A_{1-x}B_x(sol) + melt$  is called solidus and the upper boundary line is called liquidus. Like melting, evaporation is a first-order transition and liquid-vapor equilibria are similar to solid-liquid equilibria. This is demonstrated in the left panel of Figure 2.27. Similar topologies with subsequent one-phase fields can also be observed for systems with first-order transitions between different solid phases. The zirconium-hafnium system is an example in which both components undergo transitions (h.c.p)  $\rightleftharpoons$  (b.c.c)  $\rightleftharpoons$  melt. The abbreviations in brackets stand for the identical hexagonal closed packed or body centered cubic crystal structures of both metals, respectively. For zirconium and hafnium, the solid-state transition appears at 865 or 1950 °C and melting at 1860 or 2230 °C, and complete miscibility is

observed in all phases [38]. Consequently, a narrow two-phase field appears between h.c.p. and b.c.c., and a broader one ( $\Delta H_f \approx 5\Delta H_f$  for both metals) between b.c.c. and melt.

If  $G^{\text{ex}}$  is small for both phases with total miscibility, the phase boundaries (e.g., liquidus and solidus; see Figure 2.26) are monotonous rising or falling. The right panel of Figure 2.27 shows in contrast the case NaCl–KCl, where the melt extends for intermediate  $x$  below the  $T_f$  of the components, forming a local minimum. If such minimum occurs, both phase boundaries must meet there in one common “azeotropic” point, where  $\phi'$  and  $\phi''$  have identical composition  $x_{\text{az}}$ . This is remarkable because  $x_{\text{az}}$  is the only composition, except the pure components, for which crystal growth from the melt is possible without segregation (cf. Section 2.2.2.3). The system  $\text{CaF}_2$  ( $T_f = 1418^\circ\text{C}$ )– $\text{SrF}_2$  ( $T_f = 1477^\circ\text{C}$ ) has an azeotropic point at  $x_{\text{az}} \approx 0.418$ ,  $T_{\text{az}} = 1374^\circ\text{C}$ , where homogeneous single crystals with 30 mm diameter and 50 mm length could be grown by the Czochralski method [39]. Principally azeotropic points could also be common maxima of liquidus and solidus, but this case is not very realistic: It requires a relative stabilization of the solid with respect to the liquid (negative  $G^{\text{ex}}$ ). This, however, results rather in the formation of an intermediate compound. In the system Cu–Au, where both components have face-centered cubic structures, solid solutions exist for all concentrations with an azeotrope near 60% gold. Below ca.  $400^\circ\text{C}$ , the interaction between Cu and Au atoms becomes so strong that their distribution on lattice sites is partially ordered. Depending on the Cu/Au ratio, compounds with approximate compositions  $\text{Cu}_3\text{Au}$ ,  $\text{CuAu}$ , or  $\text{CuAu}_3$  are formed, and all of them show some flexibility of composition around the ideal values 25, 50, or 75% Au.

Other examples for intermediate compounds are  $\text{Sr}_x\text{Ba}_{1-x}\text{Nb}_2\text{O}_6$  (SBN) with a liquidus/solidus maximum at  $x = 0.61$  [40–42] or  $\text{Ca}_x\text{Ba}_{1-x}\text{Nb}_2\text{O}_6$  (CBN) with a liquidus/solidus maximum at  $x = 0.281$  (see Figure 2.28) [43]. Sometimes, SBN and CBN are called mixed crystals, but this denomination might cause errors because it suggests mixing from the end members  $\text{EANb}_2\text{O}_6$  (EA = Ca, Sr, Ba), which is wrong. Instead, both systems are pseudobinary with an intermediate congruently melting compound, and eutectics on both sides of this compound (see Section 2.2.2.4). It is just remarkable that the homogeneity width of these compound is rather large: from ca. 0.2 to 0.8 for SBN, and from ca. 0.15 to 0.4 for CBN.

The Gibbs energy gain from mixing becomes smaller for low  $T$  as the second term of Eqn (2.26) vanishes. Consequently, mixed phases do not exist in equilibrium at very low  $T$ . Of course, demixing of solid solutions (in contrast to liquid solutions) requires diffusion steps that need time, and are consequently often hindered kinetically. Not always demixing results in the formation of intermediate compounds, like in the Cu–Au system above mentioned. No intermediate compounds exist between antimony and bismuth. Both are crystallizing in identical structures belonging to the rhombohedral  $R\bar{3}c$  space group with lattice constants  $a_{0,\text{rh}}^{\text{Sb}} = 0.45067\text{ nm}$  and  $a_{0,\text{rh}}^{\text{Bi}} = 0.47458\text{ nm}$  [44]. This difference of ca. 5% is rather small, and allows the formation of solid solutions  $\text{Sb}_{1-x}\text{Bi}_x$  for  $0 \leq x \leq 1$  at sufficiently high temperature. The binary phase diagram in Figure 2.29

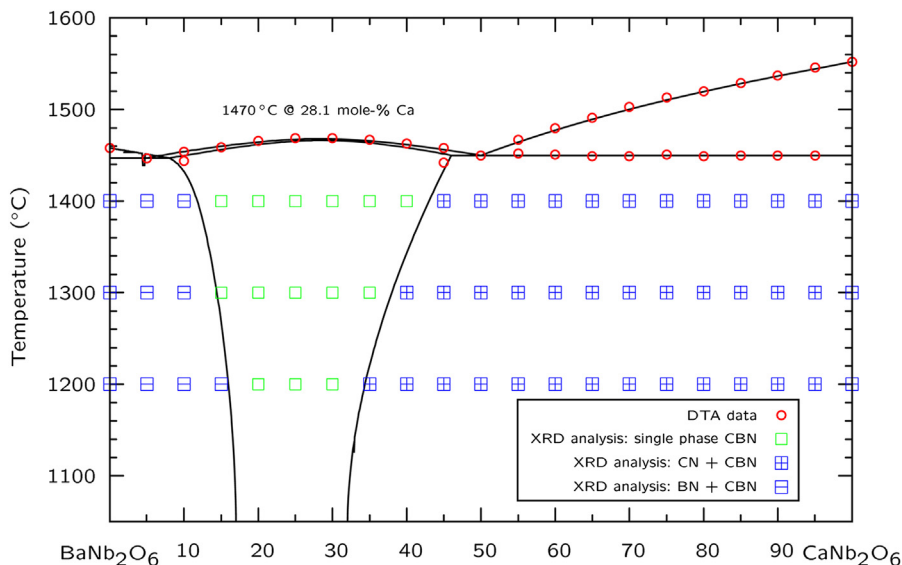


**FIGURE 2.28** Pseudobinary phase diagram  $\text{CaNb}_2\text{O}_6$ - $\text{BaNb}_2\text{O}_6$  with congruently melting intermediate  $(\text{Ca,Ba})\text{Nb}_2\text{O}_6$  ("CBN"). The CBN phase field is single phase, in contrast to the neighboring fields. Reprinted with permission from Elsevier [43].

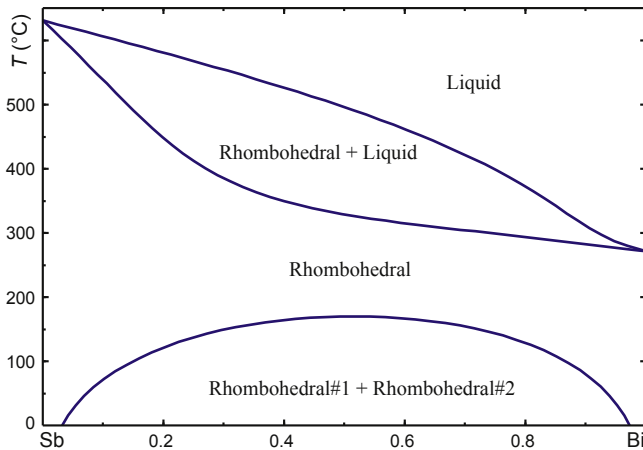


**FIGURE 2.29** Phase diagram bismuth-antimony with complete miscibility at high  $T$  in the rhombohedral A7 structure. Below the miscibility gap, decomposition to a Sb-rich and a Bi-rich phase occurs, both with identical A7 crystal structure like that above the gap.

shows, however, that near  $x = 0.5$ , such mixed crystals become unstable at  $T \lesssim 170^\circ\text{C}$ . Then the initially homogeneous solid solution (one phase) becomes unstable and decomposes under conservation of the crystal structure to volume elements, which are enriched in Sb or Bi, respectively (two phases). It should be mentioned that such

miscibility gaps, even if theoretically expected for all mixed crystal systems, are practically not observed very often for kinetic reasons.

### 2.2.2.2 Eutectics and Eutectoids

A eutectic phase diagram is formed if the components are immiscible in their solid phases, but exhibit complete miscibility in their molten (liquid) phases. This case was described analytically by Eqns (2.30) and (2.31). If a melt with composition  $x_{\text{eut}}$  in the hypothetical phase diagram Figure 2.23 is cooled, then it crystallizes completely at  $x_{\text{eut}}$  under formation of the solid phases A and B. In other words, a *eutectic reaction* liquid  $\rightarrow$  A (sol) + B (sol) takes place, where one phase decomposes and forms two other different phases. The crystallization of two phases at the same time close together results typically in a fine-grained, interpenetrated structure. Such eutectic solids sometimes show metamaterial properties that might differ considerably from the properties of its constituents [45]. If in Figure 2.23 the initial composition of the cooling melt deviates from  $x_{\text{eut}}$ , the crystallization of a solid phase starts already at another  $T_{\text{liq}} > T_{\text{eut}}$  and continues until  $T_{\text{eut}}$ . The first crystallizing phase left from the eutectic composition is solid A, and right from  $x_{\text{eut}}$  solid B. All phase fields are labeled correspondingly in Figure 2.30.

It is not a requirement that the high  $T$  phase is liquid. Figure 2.30 shows the more general case where, during heating, the component A undergoes at  $T_A$  the transformation  $\phi' \rightarrow \phi'''$ , and B at  $T_B$  a transformation  $\phi'' \rightarrow \phi'''$ . This means that at low  $T$ , A and B show a different phase state, and are therefore immiscible, but have identical phase states  $\phi'''$  with unlimited miscibility at high  $T$ . If  $\phi'''$  is a solid phase, then the composition  $x_{\text{eut}}$  undergoes at  $T_{\text{eut}}$  a eutectoid reaction.

Figure 2.31 shows as an example of high technical relevance the iron-rich part of the Fe–C system. It should be noted that this system is drawn here for true equilibrium. Under the technical conditions of iron and steel metallurgy, often cementite phase  $\text{Fe}_3\text{C}$  appears [46], which is not an equilibrium phase in the Fe–C system (but see Figure 2.32

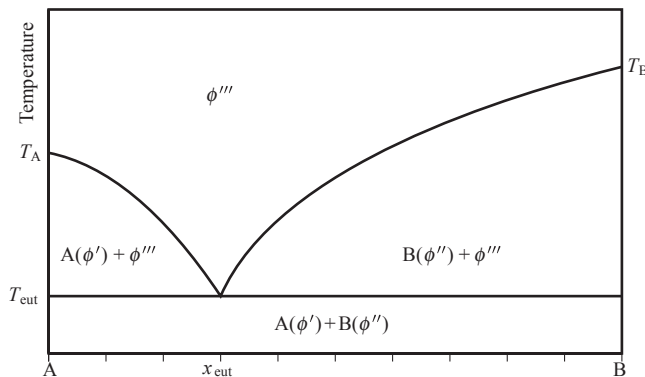


**FIGURE 2.30** Binary phase diagram with ideal mixing in the high  $T$  phase  $\phi'''$  only. Below  $T_A$  pure component A exists in the phase  $\phi'$  and below  $T_B$  pure component B exists in the phase  $\phi''$ .  $\phi'$  and  $\phi''$  are immiscible.

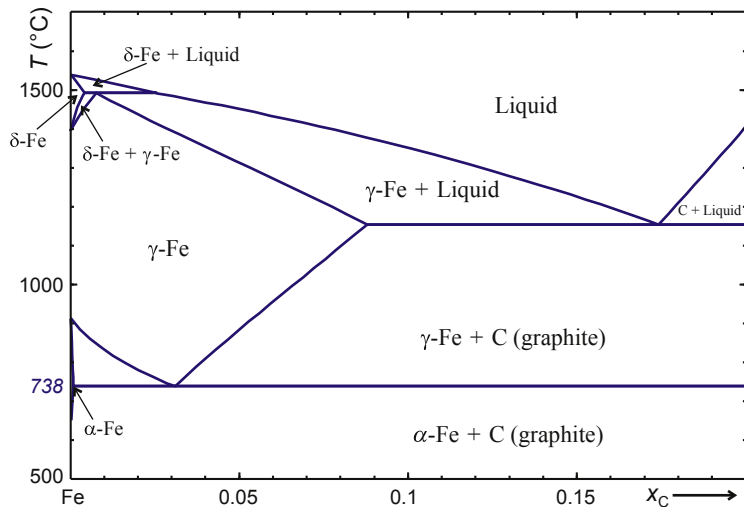


**FIGURE 2.31** The iron-rich part ( $x_C \leq 0.2$ ) of the iron–carbon phase diagram. Pure iron undergoes transitions  $\alpha$ -Fe  $\rightarrow$   $\gamma$ -Fe  $\rightarrow$   $\delta$ -Fe  $\rightarrow$  melt. The maximum solubility of carbon in the solid phases is (in this order) 0.001, 0.09, 0.004. Single-phase  $\gamma$ -Fe with  $x_{Fe} = 0.03$  is stable down to 738 °C, where it undergoes eutectoid decomposition to  $\alpha$ -Fe and graphite.

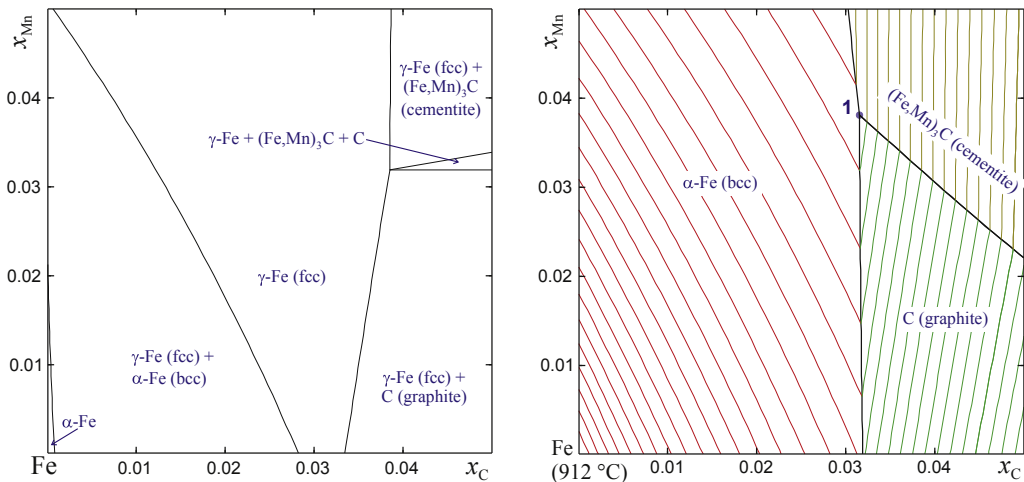


**FIGURE 2.32** Left: Isothermal section  $T = 750$  °C through the ternary system Fe–Mn–C near the Fe-rich corner (bottom left) up to 5 mol-% Mn and C. Only for minor concentrations of the additives ( $x_C \leq 0.001$ ;  $x_{Mn} \leq 0.02$ ) iron remains single-phase  $\alpha$ -Fe; otherwise, a large range of single-phase  $\gamma$ -Fe exists. Right: Polythermal projection of the same concentration range on the  $\gamma$ -Fe (f.c.c.) phase field with 10 K isotherms. The four phase invariant point “1” is at  $x = 0.032$ ,  $y = 0.038$ ,  $T = 693$  °C.

for Fe–Mn–C). Nevertheless, the appearance of  $Fe_3C$  results only in minor amendments to the phase diagram part that is shown in [Figure 2.31](#): the rightmost liquidus becomes flatter—it is then the liquidus of  $Fe_3C$  instead of C, and the lowest stability limit of  $\gamma$ -Fe drops from 738 °C by ca. 12 K. Pure Fe has below 911 °C a body-centered cubic structure

(such as tungsten) and is comparably hard. This structure can dissolve only minor amounts of carbon. For  $911 < T \text{ (}^\circ\text{C)} < 1395$ ,  $\gamma$ -Fe is stable, which has a face-centered cubic structure (such as copper) and can dissolve large amounts  $\leq 9\%$  C. Dissolved carbon stabilizes  $\gamma$ -Fe down to the eutectoid temperature  $T_{\text{eutectoid}} = 738 \text{ }^\circ\text{C}$  at  $x_{\text{eutectoid}} = 0.03$ . If such  $\text{Fe}_{0.97}\text{C}_{0.03}$  is cooled from the  $\gamma$  phase field below  $T_{\text{eutectoid}}$ , it decomposes to the  $\alpha$ -Fe phase and graphite. This transformation from one phase to two phases has analogy with a eutectic, but proceeds only with solid phases. It is therefore called a eutectoid.

### 2.2.2.3 Segregation and Lever Rule

Many solidification and crystal growth processes are performed by cooling melts or melt solutions. Such crystallization is often accompanied by *segregation*. This means that a solid (e.g., the just-formed part of the crystal) and a liquid (e.g., the rest of the melt) of different composition are in equilibrium. During heating, the same observation is often called *incongruent melting*, as melting solid and created liquid have no identical composition. The appearance of segregation is very different in systems with or without mixed crystals. The left panel of Figure 2.33 shows the case of a simple mixed crystal system. If a melt with composition  $x_0$  is cooled, the first solid is formed at the temperature  $T'$  where the liquidus touches  $x_0$ . The system is in equilibrium, and consequently every part of it is at  $T'$  now (isothermal conditions). The composition of the solid phase is shown by the solidus, and this curve gives at  $T'$  the composition  $x'_{\text{sol}} \neq x_0$ . The dashed horizontal line at  $T'$  connecting  $x_0$  (liquid) and  $x'_{\text{sol}}$ , which are in equilibrium, is called the *tie-line*. During further slow cooling, the system reaches  $T''$ , and now a melt  $x''_{\text{liq}}$  is in equilibrium with a solid  $x''_{\text{sol}}$ . Reaching such state, however, is an extremely time-consuming process, as all solid material that was crystallized before with  $x > x'_{\text{sol}}$  had to be transformed by solid-state diffusion to the new composition. Practically, this seldom happens, even during geological times: The mineral olivine is a crystal mixed between forsterite  $\text{Mg}_2\text{SiO}_4$  and fayalite  $\text{Fe}_2\text{SiO}_4$ , and shows locally different Fe/Mg ratio in artificial as well as natural crystals [47]. Theoretically, under perfect equilibrium, the

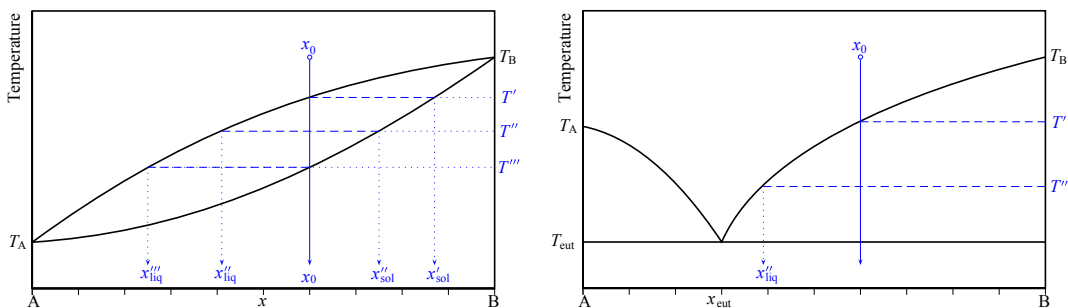


**FIGURE 2.33** Crystallization of a starting composition  $x_0$ : Left: Crystallization processes in a mixed crystal system result in a solid concentration  $x_{\text{sol}}(T)$  that depends on the current temperature. Right: In a eutectic system, the solid body has a fixed concentration (here B with  $x = 1$ ).

crystallization process is finished at  $T'''$  when the two-phase field is left. As material may not disappear, the resulting crystal had the initial composition  $x_0$  then.

Practically, the initially crystallized part will often be too far from the residual melt to reach equilibration. Depending on the geometrical conditions, the first fraction crystallized with  $x'_{\text{sol}}$  may then be surrounded by subsequently crystallized material with smaller B-composition (“gradient crystal”). In crystal-pulling processes, such as Czochralski, the B-rich material crystallizes first close to the seed, and is closer to the tail followed by material with lower B concentration. In systems such as shown in [Figure 2.33](#) left, the higher melting component will always be enriched in the first crystallized fractions. Often, a segregation coefficient

$$k_0 = \frac{x_{\text{sol}}}{x_{\text{liq}}} \approx \text{const.} \quad (2.38)$$

is defined that approximates the solidus and liquidus to be linear near the pure components. This case was discussed first by Gulliver [\[48\]](#), and results in a dependence on the position given by

$$x_{\text{sol}}(g) = k_{\text{eff}} x_0 (1 - g)^{k_{\text{eff}} - 1} \quad (2.39)$$

where  $0 < g < 1$  is the crystallized part of the melt with initial composition  $x_0$ . The effective distribution coefficient  $k_{\text{eff}}$  depends on  $k_0$  (for crystallization that is not too quick, one often has  $k_{\text{eff}} \approx k_0$ ) and several parameters of the crystallization process itself [\[49\]](#).

Segregation appears always in mixed crystal systems, except at azeotropic points (see [Figure 2.27](#) right) and often significantly impedes crystal growth, because large volumes with constant composition cannot then be easily grown. If the concentration, hence the properties of the mixed crystal, depend too strongly on position, even a stable crystal growth process may become impractical.

Also in systems where the solid phase has a fixed composition, such as the eutectic system in [Figure 2.33](#) right, segregation can occur. If a melt  $x_0$  is cooled, at  $T'$  the pure solid B ( $x = 1$ ) crystallizes. The crystallization of B (sol) continues until  $T_{\text{eut}}$  is reached where the whole system becomes solid. Such behavior may be beneficial if for some reason (too high volatility, phase transition, or another destructive process below  $T_{\text{B}}$ , technical restrictions for very high  $T_{\text{B}}$ ) the crystal B (sol) cannot be grown from a pure B melt. This is the basis for melt solution growth processes, such as TSSG [\[50\]](#).

For one-phase fields, a point  $(x, T)$  gives the composition and temperature of this phase at this specific point. From the tie-line constructions mentioned above, it is clear that this is not the case for two-phase fields. There, the tie-line crossing this point connects two phases with different compositions that are in equilibrium at this  $T$ . Not only can both compositions, but also the shares of both phases, be read directly from the phase diagram, following the *lever rule*. According to this rule, the quantities of both equilibrium phases are indirectly proportional to the “levers” that are spanned from the given composition to the corresponding phase boundaries. For instance, in [Figure 2.33](#)

right, one has at  $T'$  solid B ( $x = 1$ ) in equilibrium with a melt composition  $x''_{\text{liq}}$ . The quantities are

$$\text{melt} : \frac{1 - x_0}{1 - x''_{\text{liq}}} \quad (2.40)$$

$$\text{B(sol)} : \frac{x_0 - x''_{\text{liq}}}{1 - x''_{\text{liq}}} \quad (2.41)$$

With further lowering of  $T$ ,  $x''_{\text{liq}}$  finally approaches  $x_{\text{eut}}$ , and this gives the maximum yield (expressed as share of the starting material) that can be reached with crystal growth processes from melt solution with

$$Y_{\text{max}} = \frac{x_0 - x_{\text{eut}}}{x_{\text{sol}} - x_{\text{eut}}} \quad (2.42)$$

where  $x_{\text{sol}}$  is the composition of the phase which has to be grown (in Figure 2.33 right  $x = 1$ ), and  $x_0$  is the initial composition of the melt.

#### 2.2.2.4 Intermediate Compounds

Sometimes the components of a thermodynamic system can interact so strongly that intermediate compounds are formed. This is usually the case if one component easily creates cations (such as most metals), and the other easily creates anions (such as halogens, oxygen, or sulfur). Then simple salts, oxides, or sulfides are built. Also, however, systems set up from comparably similar components can form intermediate compounds if a sufficiently large Gibbs free energy reduction can be reached; see, e.g., the CaO–SiO<sub>2</sub> system in Figure 2.20.

Figure 2.34 shows two similar pseudobinary systems LiF–AF ( $A = \text{Cs, Rb}$ ), and both of them contain an intermediate compound LiAF<sub>2</sub>. It should be noted that for  $A = \text{K, Na}$  the

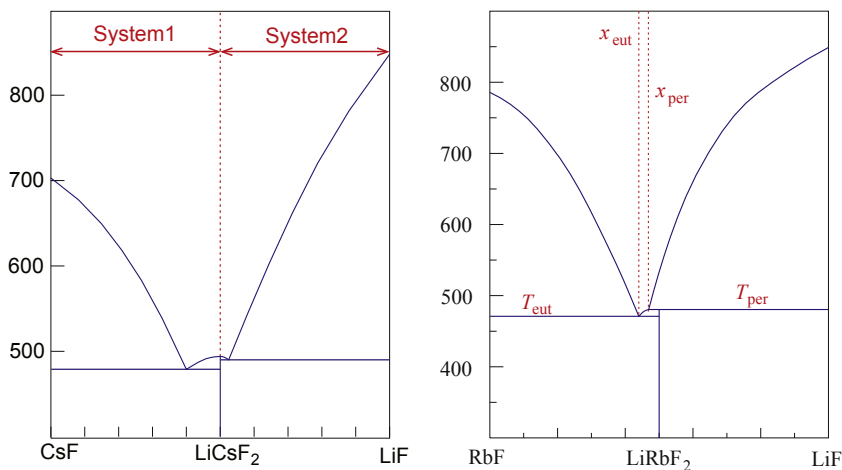


FIGURE 2.34 Both systems LiF–CsF (left) and LiF–RbF (right) contain an intermediate 1:1 compound. LiCsF<sub>2</sub> has a larger formation enthalpy, and melts congruently. This is the precondition for constructing independent partial systems.

systems form simple eutectics (for Na with some rim solubility on the NaF side), but no intermediate compounds. Obviously the larger radius difference between the A ions, in octahedral coordination Li (90), Na (116), K (152), Rb (166) Cs (181 pm), makes the Gibbs energy gain upon compound formation stronger.

From the lever rule introduced in Section 2.2.2.3, it is obvious that every melt composition from the left half of the LiF–CsF system (Figure 2.34 left,  $0 \leq x_{\text{LiF}} \leq 0.5$ ) forms during crystallization only CsF and/or LiCsF<sub>2</sub>. Otherwise, from melts  $0.5 \leq x_{\text{LiF}} \leq 1$ , only LiCsF<sub>2</sub> and/or LiF are crystallizing. This means that both halves of the LiF–CsF system are independent, and consequently form subsystems. But this is not so for the LiF–RbF system shown in the right panel of Figure 2.34: The intermediate LiRbF<sub>2</sub> at  $x_{\text{LiF}} = 0.5$  undergoes at  $T_{\text{per}}$  peritectic decomposition (see Section 2.2.2.5) and the lever rule shows that from melts  $x_{\text{per}} < x \leq 1$ , LiF (sol) crystallizes first. But  $x_{\text{per}}$  is  $< 0.5$ , in the left half of the system! This means that some compositions in the left half of the system have LiF from the right half as first crystallizing solid. In other words, it is impossible to define independent partial systems with peritectically melting compounds as (rim) components. Otherwise, congruently melting intermediate compounds in binary systems, such as LiCsF<sub>2</sub> in the LiF–CsF system, can be used as rim components for partial systems.

This is sometimes helpful if a complete system is on the one side sophisticated and difficult to measure, but on the other side in some regions not really interesting for a specific purpose. The CaO–SiO<sub>2</sub> system in Figure 2.20 is a good example: For CaO-rich compositions, the liquidus goes up beyond 2500 °C, which is considerably higher than the  $T$  limit of typical devices for thermal analysis such as differential thermal analysis (DTA). The binary phase diagram shows the congruently melting phases C2S = Ca<sub>2</sub>SiO<sub>4</sub> at 33% SiO<sub>2</sub> (belite) and CS = CaSiO<sub>3</sub> at 50% SiO<sub>2</sub> (wollastonite). Consequently, C2S and CS may be used as end members of a partial system, and it becomes clear that CaO–SiO<sub>2</sub> mixtures between 33.33% and 50% SiO<sub>2</sub> may contain in equilibrium only C2S, CS, and the intermediate C3S2 (Ca<sub>3</sub>Si<sub>2</sub>O<sub>7</sub>, rankinite). For some of them, high- and low  $T$  phases ( $\alpha, \alpha', \beta$ ) do exist, but phases with different chemical composition such as “free chalk” CaO or alite C3S are not permitted in this concentration range.

### 2.2.2.5 Peritectics and Peritectoids

Every compound A<sub>x</sub>B<sub>y</sub> disintegrates at some specific temperature  $T_{\text{AxBy}}$ . Often, a liquid phase is the result, and then the composition of this liquid phase is the same as of the initial solid: A<sub>x</sub>B<sub>y</sub> (sol) → (x A + y B) (liq). This process is called *congruent melting* and is shown by LiCsF<sub>2</sub> (sol) in Figure 2.34. The behavior of LiRbF<sub>2</sub> in the right panel of the figure is different, because at its disintegration temperature  $T_{\text{per}}$  not only a liquid, but additionally solid LiF is formed. One can formulate the peritectic reaction LiRbF<sub>2</sub> (sol) → [ $x_{\text{per}}$ LiF + (1 –  $x_{\text{per}}$ )RbF] (liq) + LiF (sol) with  $x_{\text{per}} \approx 0.47$ . Peritectic decomposition (= peritectic melting) is one form of incongruent melting, because the melting compound is not in equilibrium with a liquid of the same composition. But not every incongruent melting requires a peritectic reaction—instead it was shown in

Section 2.2.2.3 that already in simple mixed crystal systems the liquid and solid phase in equilibrium have different composition, hence the solid shows incongruent melting.

Figure 2.35 shows the typical case where an intermediate compound (here assumed to have the composition  $AB_2$ ) undergoes peritectic melting and solid B is the higher melting neighbor phase that is formed. At  $T_{\text{per}}$ , three phases are in equilibrium, which is the maximum for a two-component system (Eqn (2.6)), and there is no degree of freedom left. The point where B liquidus,  $AB_2$  liquidus, and peritectic line meet is called the *peritectic point* and has the peritectic composition  $x_{\text{per}}$ . Solid  $AB_2$  crystallizes only from melts with initial composition  $x_{\text{eut}} < x_0 < x_{\text{per}}$ . If one sets for the left diagram in Figure 2.35  $x_0$  as close as possible to  $x_{\text{per}}$  (but not beyond it!), one obtains with Eqn (2.42) the maximum yield  $Y_{\text{max}} = 54.5\%$  for the growth of AB crystals from the melt ( $x_0 = x_{\text{per}} = 0.5$ ,  $x_{\text{eut}} = 0.3$ ,  $x_{\text{sol}} = 0.6667$ ).

Also, compounds showing peritectic melting may have a finite phase width, and an example  $A_{1\pm\delta}B_2$  is given in the right panel of Figure 2.35. The left and right phase boundaries of  $A_{1\pm\delta}B_2$  are the solidus of this phase and are limiting a one-phase field. The upper limit of this field must be a point on the peritectic line; if both phase boundaries met not in one point, the composition of  $A_{1\pm\delta}B_2$  would be left as a degree of freedom, which infringes the phase rule. Not only can intermediate compounds melt peritectically, but also rim compounds if a solid solution is formed that melts higher compared to the pure component. The system ZnO–MgO is an example where doping by  $\leq 7\%$  Mg increases the melting temperature of ZnO by ca. 45 °K [51].

In a peritectic reaction, a low  $T$  solid phase  $\beta$  is in equilibrium with another solid phase and a liquid:  $\beta$  (sol)  $\rightleftharpoons$   $\alpha$  (sol) + liq. A peritectoid reaction is an analog with the difference that a third solid phase replaces the liquid. Examples are  $\text{MoNi}_4$  (sol), which decomposes peritectoid to  $\text{MoNi}_3$  (sol) + Ni:Mo (f.c.c.), and subsequently  $\text{MoNi}_3$ , which decomposes to  $\text{MoNi}(\delta)$  + Ni:Mo (f.c.c.), or  $\text{FeAlO}_3$  in the  $\text{FeO}$ – $\text{Fe}_2\text{O}_3$ – $\text{Al}_2\text{O}_3$  system [52].

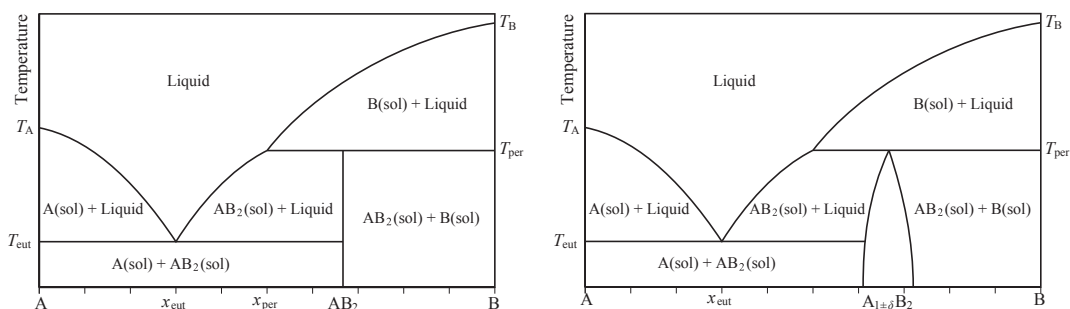


FIGURE 2.35 Two types of A–B phase diagrams with an intermediate compound  $AB_2$  showing peritectic decomposition at  $T_{\text{per}}$ . Left:  $AB_2$  is a line compound (daltonide, Section 2.1.4.1) with fixed composition  $x_B = 0.6667$ . Right:  $AB_2$  is a berthollide with finite homogeneity width  $\delta$ .

### 2.2.2.6 Syntectics and Monotectics

Both phenomena are related to demixing in the liquid phase. An example was given in [Figure 2.20](#) where in the CaO–SiO<sub>2</sub> system SiO<sub>2</sub>-rich melts are single phase only above ca. 1900 °C. The maximum of the “two melts” phase field near 89% SiO<sub>2</sub> is a critical point, and below it, more silicatelike melt is in equilibrium with another more oxidelike melt. Such behavior is called *monotectic*. The system iodine–lead even has two regions with immiscibility of liquid phases: For  $x_1 \leq 0.1$  and  $T > 368$  °C, a monotectic miscibility gap occurs. Besides the intermediate phase PbI<sub>2</sub> ( $x_1 = 0.6667$ ) is at 406° in a syntectic equilibrium with two immiscible melts of slightly different composition ( $x_1 \approx 0.53$  or  $\approx 0.7$ , respectively) [53].

## 2.2.3 Three and More Components

In the previous sections, thermodynamic systems with either one or two components were considered. With the Gibbs phase rule ([Eqn \(2.6\)](#)), one has in the easiest case of constant pressure (often  $p = 1$  bar) for fields with only one phase ( $P = 1$ )  $F = C$ , hence two degrees of freedom in two-component systems, which can be well represented in 2D drawings. For systems with three or more components, this is not so straightforward, and three options remain:

1. 3D diagrams can be constructed for systems with  $C = 3$ , and drawn in a suitable perspective. Although such procedure is instructive, a severe drawback appears, because quantitative data are hard to read from perspective representations.
2. The number of degrees of freedom is reduced by keeping some quantities constant (e.g.,  $T$ , or some  $x_i$ ), or by defining dependencies between several of these parameters (e.g.,  $x_i/x_j = \text{const.}$ ). For quantitative representations, this method is preferred and will be used almost exclusively in this section.
3. Projections onto the surface of a specific phase (often the liquid) are performed.

### 2.2.3.1 $x - y$ Diagrams

If  $x_A$ ,  $x_B$ ,  $x_C$  are the corresponding molar fractions of a ternary system, one has  $x_A + x_B + x_C = 1$  and thus two independent concentrations. It is a reasonable option to set  $p = \text{const.}$ ,  $T = \text{const.}$  and choose, e.g.,  $x_A/x_B$  and  $x_C/x_B$  as coordinates. This type of plot can be useful if one of the components may be distinguished, e.g., the main component of an alloy. In [Figure 2.32](#), this is shown for iron and the two important steel additives carbon and manganese. The left panel shows an isothermal section through the ternary system near the Fe-rich corner, and the right panel is a projection of the same concentration range on the boundaries of one specific phase (here: face-centered cubic iron,  $\gamma$ -Fe). This means that the viewer looks from inside the  $\gamma$ -Fe phase field, which is not shown in the diagram, down to the boundaries of neighboring phases, which are differently shaded. For pure Fe, the f.c.c. phase is stable  $>912$  °C and it transforms to  $\alpha$ -Fe for lower  $T$ . By adding C ([Figure 2.31](#)) and/or Mn, the transition temperature can be

lowered. For C concentrations that are too high, free carbon separates as graphite, and for C + Mn concentrations that are too high, an iron–manganese carbide, cementite, is formed. The phase rule (Eqn (2.6)) says for  $C = 3$  (Fe, C, Mn) under isobar conditions  $P + F = 4$ . Consequently, up to four phases can exist in equilibrium at nonvariant points ( $F = 0$ ). “1” in the right panel of Figure 2.32 is such point where  $\gamma$ -Fe,  $\alpha$ -Fe, graphite, and cementite are in equilibrium. Analogous diagrams can be constructed for  $C > 3$  if for every additional component beyond three, one restriction (constant concentration, or constant concentration ratio) is implemented.

Such  $x - y$  diagrams with two concentration ratios (or concentrations) as Cartesian axes are often appropriate for the presentation of systems where one component is clearly prevailing, such as alloys with a main component, or semiconductor systems with their dopants. For other systems with equivalent weighed components, Cartesian diagrams are not so well suited. The example LiCl–NaCl–KCl is shown in Figure 2.36. These substances exhibit unlimited solubility in the liquid phase and form solid solutions (halite structure). In the solid phase, however, the miscibility is unlimited only for the partial systems KCl–NaCl and LiCl–NaCl. Both partial systems have an azeotrope point, whereas KCl–LiCl is eutectic (insert). Along the abscissa of Figure 2.36, right, the composition shifts from pure NaCl (KCl/NaCl = 0) to KCl/NaCl = 5, which corresponds to  $x_{\text{KCl}} = \frac{5}{6}$ . The isotherms show there is a common minimum near KCl/NaCl = 1, which corresponds with the azeotrope point in Figure 2.27 right. The liquidus minimum of the ternary system appears at the composition  $x_{\text{LiCl}} = 0.51$ ,  $x_{\text{NaCl}} = 0.12$ ,  $x_{\text{KCl}} = 0.37$ , close to the binary eutectic KCl–LiCl. This composition is located inside the 360 °C isotherm close to the top rim of the ternary  $x - y$  diagram (Figure 2.36). From the construction of both axes in this diagram, it is obvious that the limit system KCl–LiCl can never be reached, which is a severe drawback of this diagram type. A concentration triangle of this system, such as shown in Figure 2.37 can solve this problem.

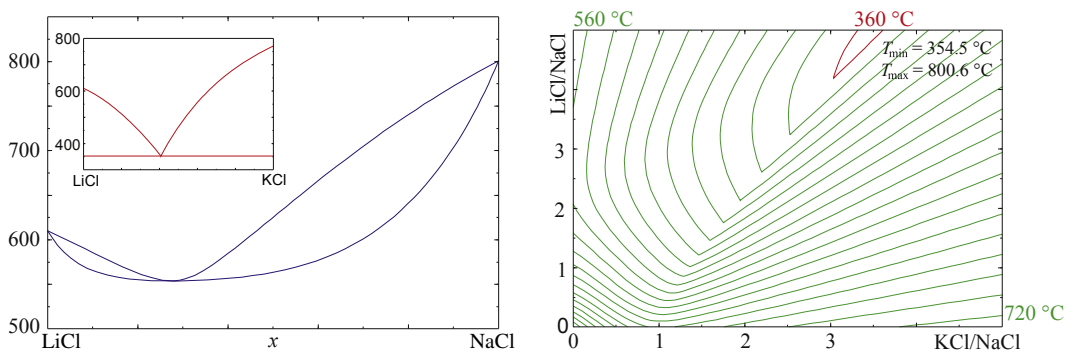


**FIGURE 2.36** Left: The binary system NaCl–LiCl shows complete miscibility with an azeotrope, such as NaCl–KCl (Figure 2.27). In contrast, KCl–LiCl form a eutectic (insert). Right: The system NaCl–LiCl–KCl with a projection onto the liquidus surface. NaCl at the origin has the highest melting point  $T_f = 801$  °C. The isotherms have 20 K difference, and three of them are labeled. See also Figure 2.37.

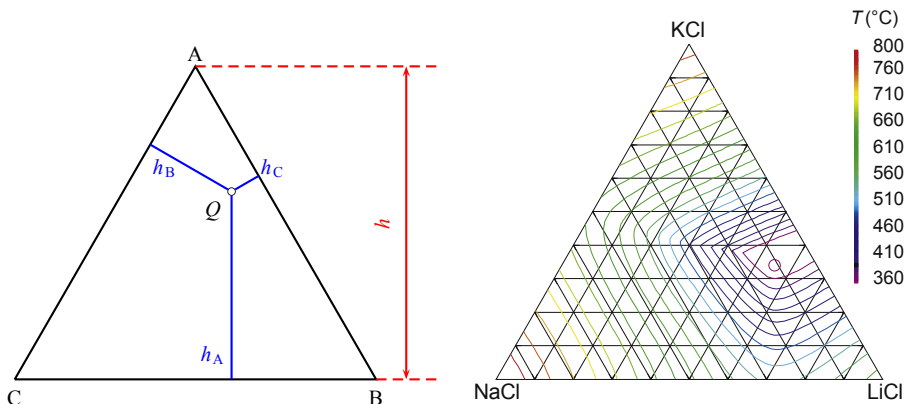


**FIGURE 2.37** Left: Gibbs triangle A–B–C with one intermediate composition  $x_A = 0.6$ ,  $x_B = 0.3$ ,  $x_C = 0.1$ . For every composition one has  $x_A + x_B + x_C = h$  (Eqn (2.43)). Right: The system NaCl–LiCl–KCl (see Figure 2.36) right as Gibbs triangle in polythermal projection. The eutectic point is marked by a circle, 20 K isotherms.

### 2.2.3.2 Concentration Triangles

The example Figure 2.36 right demonstrates a disadvantage of Cartesian presentations for ternary systems: The component on the bottom left corner of the diagram is always distinguished. This is reasonable if the other components are only minor additives to the main component, as in Figure 2.32. If, however, all components are to be treated similarly, the “concentration triangle” (Gibbs triangle) is suitable for three-component systems of components A, B, C.

This construction is shown in Figure 2.37 and consists of a regular triangle where the pure components “A,” “B,” “C” are represented by the corners. The concentration triangle relies on Viviani’s theorem that in a regular triangle, for every point  $Q$  the sum of the distances of this point from the three sides equals the height of the triangle

$$h_A + h_B + h_C = h \quad (2.43)$$

and is therefore constant. If  $h = 1.0$  (100%) is chosen,  $h_A$ ,  $h_B$ ,  $h_C$  can represent the concentration of one component, that add up to unity. The following holds:

- All compositions where the concentration of one component is constant are represented by lines parallel to the triangle side opposite to the corner of this component. For example, in Figure 2.37, left, a horizontal line through  $Q$  represents all compositions  $x_A = 0.6$ ,  $x_B = 0 \dots 0.4$ ,  $x_C = 0.4 - x_B$ .
- All compositions where the ratio between two components is constant are represented by straight lines that start from the corner of the third component. For example, in Figure 2.37, left, a line from the top corner “A” through  $Q$  to the bottom line represents all compositions  $x_A = 1 \dots 0$ ,  $x_B/x_C = 3$ .

For another system in Figure 2.38, right, the four regions of primary crystallization are distinguished by different shadings. From NaCl-rich compositions, NaCl crystallizes first

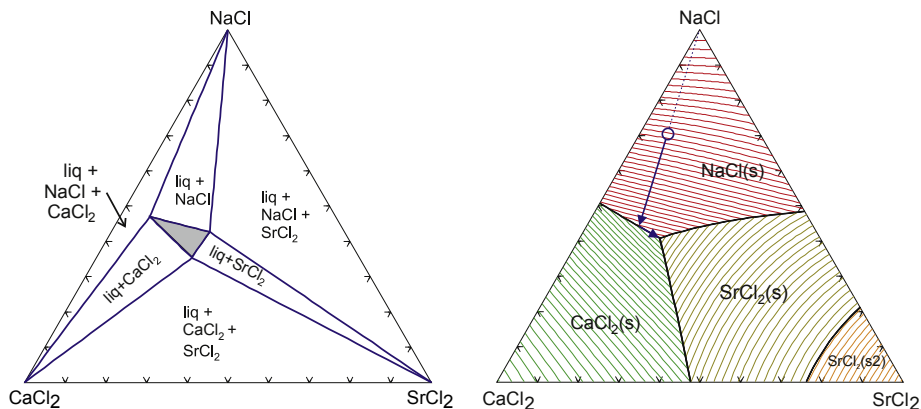


**FIGURE 2.38** The ternary system NaCl–CaCl<sub>2</sub>–SrCl<sub>2</sub> under the (somewhat simplifying) assumption that no mixing occurs in the solid phases. The melt shows complete mixing. NaCl:  $T_f = 801\text{ }^\circ\text{C}$ , CaCl<sub>2</sub>:  $T_f = 772\text{ }^\circ\text{C}$ , SrCl<sub>2</sub>:  $T_f = 874\text{ }^\circ\text{C}$ ,  $T_t = 727\text{ }^\circ\text{C}$ . Left: isothermal section at  $460\text{ }^\circ\text{C}$ , “liq” field shaded. Right: Projection on the liquidus surface with 10 K isotherms and crystallization path for a NaCl-rich melt.

(top); and from CaCl<sub>2</sub>-rich compositions, CaCl<sub>2</sub> crystallizes (bottom left). Solid SrCl<sub>2</sub> undergoes a solid-state phase transition s/s<sub>2</sub> at  $T_t \approx 727\text{ }^\circ\text{C}$ . Only from melts with  $\geq 80\%$  SrCl<sub>2</sub> does the high  $T$  phase s<sub>2</sub> crystallize, because the liquidus temperature is  $>T_t$  there (bottom right corner); for smaller SrCl<sub>2</sub> concentrations, the low  $T$  “s” phase crystallizes first.

The thick black line between the s<sub>2</sub> and s field is the intersection of the  $T_t$ -isotherm with the liquidus surface. Most regions of primary crystallization are separated by three “eutectic valleys” represented by black lines. The eutectic valleys meet in the ternary eutectic point, where NaCl(s), CaCl<sub>2</sub>(s), SrCl<sub>2</sub>(s), and liq are in equilibrium.

If a molten sample of an arbitrary composition inside one of the primary crystallization fields is cooled, first the corresponding pure component phase crystallizes. The melt is depleted from this component, and its composition shifts to the opposite direction until it touches one of the eutectic valleys. There, the parallel crystallization of a second (pure component) phase starts, together with the previous one. This way, the melt composition moves downward (to lower  $T$ ) along the valley, until it reaches the ternary eutectic point. There, the rest of the melt crystallizes isothermally. The crystallization path for a NaCl-rich melt (blue circle) is shown in the polythermal projection. In the left panel of [Figure 2.38](#), the same system is shown in an isothermal section ca. 25 K above the eutectic temperature, where only in a small region around the eutectic composition a single phase field for the liquid remains.

### 2.2.3.3 Isopleth Sections

If  $T$  is requested as coordinate for systems with three or more components, instructive sections can be used where either one concentration is kept constant, or where the ratio of two concentrations is kept constant. Both cases are demonstrated in [Figure 2.39](#) for the same system that is shown in [Figure 2.38](#).

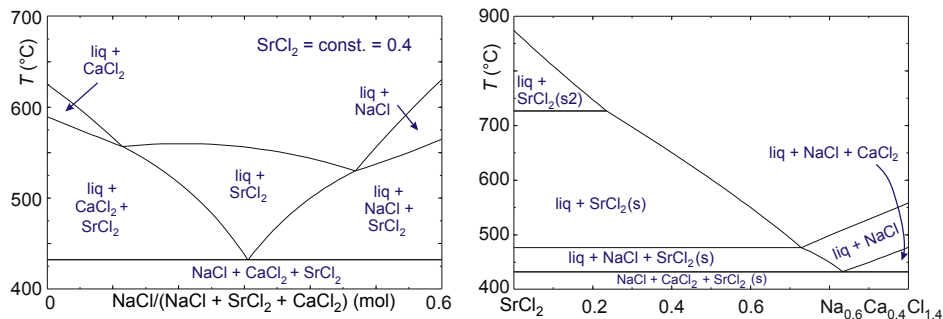


**FIGURE 2.39** Sections through the ternary system NaCl–CaCl<sub>2</sub>–SrCl<sub>2</sub>. Left panel: for a constant SrCl<sub>2</sub> concentration  $x_{\text{Sr}} = 0.4$ . Right panel: for a constant concentration ratio NaCl/CaCl<sub>2</sub> = 1.5.

Figure 2.38, right, was a projection on the liquidus surface of the ternary system. The left panel of Figure 2.39 is a section through this concentration triangle perpendicular to the projection plane and parallel to the left side of the triangle, at  $x_{\text{Sr}} = 0.4$ . This section starts (from bottom) in the CaCl<sub>2</sub> field, crosses the SrCl<sub>2</sub> field, and terminates in the NaCl field. If the crystallization starts, e.g., inside the NaCl field, later the eutectic valley with SrCl<sub>2</sub> is reached and this phase crystallizes parallel until the ternary eutectic point. There, all three component phases are crystallizing.

The right panel of Figure 2.39 is a section through Figure 2.38 perpendicular to the projection plane and from the SrCl<sub>2</sub> corner to a point Na<sub>0.6</sub>Ca<sub>0.4</sub>Cl<sub>1.4</sub>, which is a small distance above the middle of the NaCl/CaCl<sub>2</sub> side of Figure 2.38. Starting from SrCl<sub>2</sub>, high  $T$  SrCl<sub>2</sub> crystallizes first. Subsequently, with lower liquidus temperature, low  $T$  SrCl<sub>2</sub> crystallizes first, and in the end NaCl crystallizes first.

It is very important to note that horizontal lines ( $T = \text{const.}$ ) in such isopleth sections through ternary systems are in general not connecting phases which are in equilibrium! Practically, this means that the composition of all coexisting phases does not remain on such sections. Hence, the isothermal lines are not tie-lines, and the lever rule (Section 2.2.2.3) cannot be used.

#### 2.2.3.4 Reciprocal Salt Pairs

Pairs of compounds with well-defined and interchangeable cations C1, C2, and anions A1, A2 are called *reciprocal salt pairs*. In such systems, C1 and C2 or A1 and A2 can replace each other in arbitrary ratio, but the relation  $(C1 + C2)/(A1 + A2)$  must be constant for maintaining charge neutrality. The presentation is typically done as square diagrams with the possible compounds C1A1, C1A2, C2A1, and C2A2 at the corners. An example is given in Figure 2.40 and shows that the mutual substitution



leads to the presence of four compounds in the system if only two are supplied. Nevertheless, the system can be considered to be ternary, due to the dependency

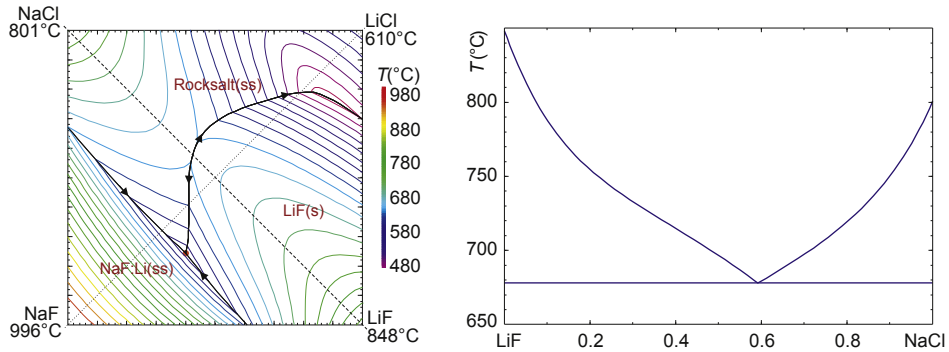


**FIGURE 2.40** Left: The reciprocal salt pair (Li,Na)(F,Cl) in polythermal projection with 20 K isotherms. At  $T_{eut} = 608$  °C (red dot) rocksalt(ss), NaF:Li(ss), LiF(s) and the melt are in equilibrium. Right: The eutectic of the NaCl–LiF subsystem corresponds with the saddle point in the left panel, on the dashed line.

Eqn (2.44), and according to the phase rule (Eqn (2.6)) four phases are in equilibrium at the (invariant) eutectic point.

In Figure 2.40, all rim systems except NaCl–LiCl are eutectic, which somewhat contradicts “Phase Diagrams for Ceramists” No. 3622, [6] where another eutectic and the compound  $\text{LiNaCl}_2$  were claimed to exist in the upper rim system. The more recent Figure 2.36 [54], however, shows that this system forms solid solutions over the whole concentration range instead. Eutectic valleys connect the eutectic points at the rims and run to the ternary eutectic. NaCl–LiF (dashed line) can be treated as a pseudobinary system and the eutectic composition near 59% NaCl (Figure 2.40 right) is a saddle point in the liquidus projection of the left panel. This is necessary because otherwise the pseudobinary eutectic composition  $(\text{NaCl})_{0.59}(\text{LiF})_{0.41}$  would, upon crystallization, leave the pseudobinary dashed line in the reciprocal salt pair diagram. It should be noted that the other pair NaF and LiCl (dotted line) cannot set up a pseudobinary system, because the melting point of LiCl is too low compared to the liquidus in the middle of the system (ca. 695 °C).

## 2.3 Equilibria Including Gas Phase

The transformations solid–gas (sublimation) as well as liquid–gas (evaporation, boiling) are first-order transitions, and consequently the gas phase can be shown in phase diagrams without further precautions. This is demonstrated in Figure 2.3 for sulfur (one component) or in Figure 2.27, left, for Si–Ge (two components). But very often the gas phase is not shown because evaporation plays no role in a specific process. In other cases, the gas phase must be taken into account, namely if at least one main species in the system has a significant volatility, if chemical or physical gas phase transport is performed, or if the gas phase equilibria determine the valency of species in the condensed phases. These cases will be considered in the following subsections.

### 2.3.1 Volatile Species

If a chemical element such as iodine, the heavier chalcogens (Figure 2.3), the heavier pnictogens, or even some metals such as Zn or Hg are heated, their vapor pressure quickly approaches ambient pressure and volatility becomes significant. Also, some compounds that are academically or technically interesting (e.g.,  $\text{NH}_4\text{Cl}$ ,  $\text{AlN}$ ,  $\text{SiC}$ ) can be transferred completely to the gas phase, and recrystallized at a colder seed. This process is called *sublimation* or *physical vapor transport* (PVT). For some other compounds, the sublimation temperature is so high that PVT is not straightforward ( $\text{ZnO}$ ), or the fugacities of constituents are so different that only the more volatile component evaporates sufficiently ( $\text{GaN}$ ). Then, transport agents may be added to create an intermediate state where the desired compound can be transported from the feed to the seed.

Figure 2.41 demonstrates the CVT growth of  $\text{ZnO}$  crystals where the chemical transport is described by the equilibrium



which is shifted to the product side upon heating. The calculated diagram shows that mixtures of  $\text{ZnO}$  and carbon (graphite) are stable only below ca.  $900^\circ\text{C}$ . For intermediate compositions, a gas phase is formed consisting mainly of  $\text{Zn}(\text{g}) + \text{CO}(\text{g})$ , which reacts at low  $T$  back to  $\text{ZnO}(\text{s})$  (Eqn (2.45)). From the diagram, it is obvious that if thermal gradients are too large, this can lead the process to the “C +  $\text{ZnO}$ ” phase field, which means that graphite inclusions may occur [56].

The left panel of Figure 2.42 shows the binary diagram gallium–arsenic with the intermediate 1:1 compound gallium arsenide.  $\text{GaAs}$  forms eutectics with both of its components; the eutectic to the Ga side is degenerate, as the melting temperature of gallium is low ( $30^\circ\text{C}$ ). Gallium arsenide is a basic material in the semiconductor industry, mainly for solid-state lighting and high-frequency devices. Unfortunately, this  $x$ – $T$  diagram does not

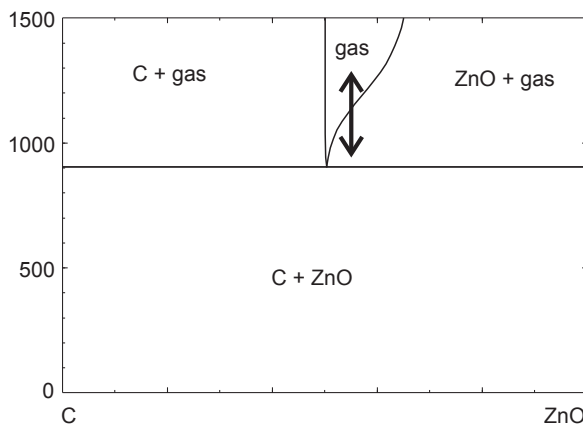
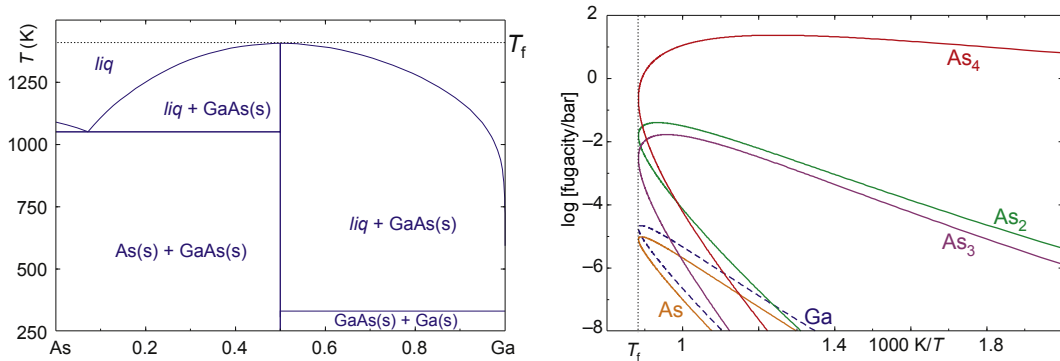


FIGURE 2.41 Phase diagram for the system  $\text{ZnO}$ – $\text{C}$  for a system pressure  $p = 1$  bar. The arrow shows the conditions under which chemical vapor transport can be performed. Reprinted with permission from Elsevier [55].



**FIGURE 2.42** Left: The phase diagram Ga–As with the intermediate compound GaAs considering condensed phases only. Right: Fugacities of gas species along the GaAs liquidus.

express the high volatility, mainly of arsenic, which results in the decomposition of GaAs to arsenic gas and gallium liquid before melting under ambient pressure.

The GaAs liquidus spans almost the complete phase diagram, consequently GaAs(s) can be grown from a wide range of  $\text{Ga}_x\text{As}_{1-x}$  compositions. The liquidus temperature at which crystallization starts will depend on  $x$ . Besides, the chemical composition can be varied slightly if the melt has an excess of one component [57]. For the control of crystal growth, it is desirable to know the equilibrium vapor pressure ( $\approx$  fugacity  $f$ ) of both components along the GaAs liquidus. The right panel of Figure 2.42 shows this for several species occurring in the gas phase in a plot  $\log(\text{fugacity})$  versus  $1/T$ . The curves there have two branches, and the upper and lower branches for the  $\text{As}_i$  ( $i = 1 \dots 4$ ) curves show  $f_{\text{As}_i}(1/T)$  on the As-rich or Ga-rich side the GaAs liquidus, respectively. Vice versa for  $f_{\text{Ga}}(1/T)$ , where the higher values are reached on the Ga-rich side. All curves have an apex at the melting point  $T_f$  of GaAs.

### 2.3.2 Ellingham Type Diagrams

Some chemical elements, especially many transition metals, tend to form oxides, sulfides, and other compounds in multiple valency states. Then, chemical equilibria of the kind



describe the transition from valency state  $m$  to the higher state  $m + 1$ . The Gibbs free energy balance  $\Delta G^0 = \Delta H^0 - T\Delta S^0$  of this reaction determines which valency (here, oxidation) state is stable. If the metal oxides show no significant volatility, the chemical equilibrium (Eqn (2.46)) is determined by  $T$  and the chemical potential of oxygen (Eqn (2.23)). For the case  $T = \text{const.}$  and two different volatiles  $V_1, V_2$  in the system linear predominance diagrams were already constructed above from plots  $\log p_{V_2}$  versus  $\log p_{V_1}$  (Figure 2.14). Plots  $RT \ln p_{\text{O}_2}$  versus  $T$  for redox reactions of the type (Eqn (2.46))

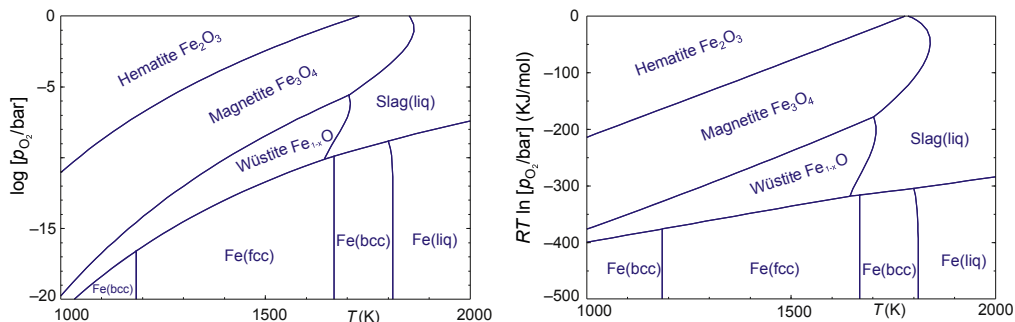


FIGURE 2.43 Predominance diagrams of the system Fe–O<sub>2</sub> in coordinates  $T$ ,  $\log p_{\text{O}_2}$  (left) or  $T$ ,  $RT \ln p_{\text{O}_2}$  (right, Ellingham type), respectively.

are also straight lines. Such Ellingham diagrams can be used as predominance phase diagrams showing the stability fields of several oxides under the given conditions  $T$ ,  $p_{\text{O}_2}$  [28].

Figure 2.43 shows the system iron–oxygen in two representations. In the right panel (Ellingham type), the phase boundaries are often almost straight lines. The “slag” phase covers a wide composition range of iron oxides where the melting temperature depends on the oxygen partial pressure, hence on the composition of condensed phases. Vertical lines at the bottom describe the phase transitions of metallic iron up to its melting (cf. Figure 2.31).

For practical purposes, often the simpler diagram type from the left panel is useful, as the important experimental parameter  $p_{\text{O}_2}$  is plotted directly. Then, phase boundaries between neighboring  $\text{FeO}_x$  are bend lines. Obviously, oxidation states with lower valency become more stable if  $T$  rises and if  $p_{\text{O}_2}$  drops, and this behavior is typical as oxidation reactions (Eqn (2.46)) are mainly exothermic. Phase boundaries with negative slope occur only in scarce cases (e.g.,  $\text{Re}_2\text{O}_7$ ,  $\text{CrO}_2$ ).

Predominance diagrams such as shown in Figure 2.43 can easily be computed for systems with more than one metallic component. If mixed oxides



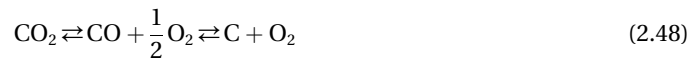
are formed, these compounds appear with separate phase fields in the diagrams. In cases where  $G(T)$  for  $\text{Me}'\text{Me}''\text{O}_{x+y}$  are unknown, the calculation of stability fields for the simple oxides  $\text{Me}'\text{O}_x$ ,  $\text{Me}''\text{O}_y$  often gives a good approximation, because energetic contributions of reactions between oxides (Eqn (2.47)) are typically small compared to the formation enthalpies (Eqn (2.46)).

For narrow phase fields, such as  $\text{Fe}_{1-x}\text{O}$  in the left panel of Figure 2.43, often no constant  $p_{\text{O}_2}$  can be found that lies totally inside this predominance field. For every process where temperature gradients occur—which is always the case for crystal growth—every specific  $p_{\text{O}_2} = \text{const.}$  then crosses several phase fields, which means that different oxides are stable at different  $T$ . Fortunately, several gaseous oxides of

**Table 2.1** Oxygen Fugacities ( $p_{\text{O}_2}$  in bar) in Different Atmospheres (Total Pressure 1 bar)

Gas	500 °C	1000 °C	1500 °C	2000 °C	2500 °C
CO <sub>2</sub>	$1.24 \times 10^{-10}$	$1.23 \times 10^{-5}$	$1.79 \times 10^{-3}$	$2.67 \times 10^{-2}$	$1.14 \times 10^{-1}$
10% CO <sub>2</sub> +90% CO	$1.76 \times 10^{-27}$	$9.30 \times 10^{-17}$	$2.87 \times 10^{-10}$	$1.14 \times 10^{-6}$	$2.13 \times 10^{-4}$
CO	$1.76 \times 10^{-27}$	$3.97 \times 10^{-19}$	$1.87 \times 10^{-16}$	$6.49 \times 10^{-15}$	$5.46 \times 10^{-13}$

nonmetals, such as H<sub>2</sub>O (as humidity in carrier gases), or CO<sub>2</sub> and CO, decompose upon heating, e.g., by



similarly to metal oxides, and under suitable conditions may result in a “self-adjusting oxygen partial pressure”  $p_{\text{O}_2}(T)$  that runs for all  $T$  through the stability field of a desired oxide. Table 2.1 shows that  $p_{\text{O}_2}$  changes over several orders of magnitude upon heating, and often the right choice of such “reactive atmosphere” allows to keep  $p_{\text{O}_2}(T)$  over the whole  $T$  range of interest inside the stability field of the desired oxide [58].

A similar approach of reactive atmospheres is feasible not only for oxides but also for other anions where a suitable carrier can be found. For sulfides, e.g., H<sub>2</sub>S can be used to adjust the sulfur (S<sub>2</sub>) partial pressure from 1.4 mbar (500 °C) to 270 mbar (2000 °C) under ambient total pressure. Then, a predominance diagram for the corresponding Me–S phases must be created in analogy to Figure 2.43, left, with  $T$  and  $\log(p_{\text{S}_2})$  as coordinates. A suitable growth atmosphere should give a  $p_{\text{S}_2}(T)$  that runs completely through the stability field of the desired sulfide.

## References

- [1] Alloy Phase Diagrams Center, Villars P. In: Okamoto H, Cenzua K, editors. ASM alloy phase diagram database. Materials Park, OH: ASM International; 2006–13. <http://www1.asminternational.org/AsmEnterprise/APD/>.
- [2] Villars P. Pauling file – inorganic materials database; 2013. <http://paulingfile.com/>.
- [3] GTT Technologies, Kaiserstr. 100, 52134 Herzogenrath, Germany, FactSage 6.4; 2013. <http://www.factsage.com/>.
- [4] Magnéli A, Blomberg B. Studies on the vanadium pentoxide—molybdenum trioxide system. II. Phase analysis. Acta Chem Scand 1951;5:585–9.
- [5] Eick HA, Kihlberg L. The crystal structure of V<sub>2</sub>MoO<sub>8</sub>. Acta Chem Scand 1966;6:1658–66.
- [6] American Ceramic Society. NIST, phase equilibria diagrams 3.4; 2013. <http://ceramics.org/publications-and-resources/phase-equilibria-diagrams>.
- [7] Paufler P. Phasendiagramme (in German). Braunschweig; Wiesbaden: Vieweg; 1981.
- [8] Alcock CB, Chase MW, Itkin VP. Thermodynamic properties of the group Ia elements. J Phys Chem Rev Data 1994;23:385–497.

- [9] Barin I. Thermochemical data of pure substances. Weinheim: Wiley-VCH; 2008.
- [10] Chase JMW, Curnutt JL, Downey JJR, McDonald RA, Syverud AN, Valenzuela EA. JANAF thermochemical tables, 1982 supplement. *J Phys Chem Rev Data* 1982;11:695–940.
- [11] Shannon CE. A mathematical theory of communication. *Bell Syst Tech J* 1948;27:379–656.
- [12] Landau L. The theory of phase transitions. *Nature* 1936;138:840–1.
- [13] Salje EKH. Phase transitions in ferroelastic and co-elastic crystals. Cambridge: University Press; 1990.
- [14] Yeomans JM. Statistical mechanics of phase transitions. Oxford: University Press; 1992.
- [15] Boysen H, Altorfer F. Neutron powder investigation of the high-temperature structure and phase transition in  $\text{LiNbO}_3$ . *Acta Cryst B* 1994;50:405–14.
- [16] Dohnke I, Trusch B, Klimm D, Hulliger J. A study on the influence of ytterbium and impurities on lattice parameters and the phase transition temperature of Czochralski-grown  $\text{LiNbO}_3$ . *J Phys Chem Solids* 2004;65:1297–305.
- [17] Dove MT, Powell BM. Neutron diffraction study of the tricritical orientational order/disorder phase transition in calcite at 1260 K. *Phys Chem Miner* 1989;16:503–7.
- [18] Carruthers JR, Peterson GE, Grasso M, Bridenbaugh PM. Nonstoichiometry and crystal growth of lithium niobate. *J Appl Phys* 1971;42:1846–51.
- [19] Shaw RR, Uhlmann DR. Subliquidus immiscibility in binary alkali borates. *J Am Ceram Soc* 1968;51:377–82.
- [20] Nitsch K, Cihlár A, Klimm D, Nikl M, Rodová M. Na–Gd phosphate glasses – preparation, thermal and scintillating properties. *J Therm Anal Calor* 2005;80:735–8.
- [21] Redlich O, Kister AT. Algebraic representation of thermodynamic properties and the classification of solutions. *Ind Eng Chem* 1948;40:345–8.
- [22] Hillert M, Jansson B, Sundman B, Ågren JA. A two-sublattice model for molten solutions with different tendency for ionization. *Met Trans A* 1985;16:261–6.
- [23] Gray CG, Gubbins KE, Joslin CG. Theory of molecular fluids, vol. 2. Oxford: University Press; 2011 [Chapter 7].
- [24] Delves RT. Constitutional supercooling and two-liquid growth of HgTe alloys. *Br J Appl Phys* 1965;16:343–51.
- [25] Mühlberg M, Rudolph P, Laasch M, Treser E. The correlation between superheating and supercooling in CdTe melts during unseeded Bridgman growth. *J Cryst Growth* 1993;128:571–5.
- [26] Pouget EM, Bomans PHH, Goos JACM, Frederik PM, de With G, Sommerdijk NAJM. The initial stages of template-controlled  $\text{CaCO}_3$  formation revealed by cryo-TEM. *Science* 2009;323:1455–8.
- [27] Wallace AF, Hedges LO, Fernandez-Martinez A, Raiteri P, Gale JD, et al. Microscopic evidence for liquid–liquid separation in supersaturated  $\text{CaCO}_3$  solutions. *Science* 2013;341:885–9.
- [28] Cahn RW, Haasen P, Kramer EJ. Materials science and technology. In: Cahn, et al., editors. Thermodynamics and phase diagrams of materials (Arthur D. Pelton), vol. 5. Multivolume ed. Weinheim: VCH; 1991. p. 1–73.
- [29] Thermo-Calc Software. Norra Stationsgatan 93, Plan 5, 113 64 Stockholm, Sweden, Thermo-Calc 3.0, 2013. <http://www.thermocalc.se/>.
- [30] Hallstedt B, Liu Z-K. Software for thermodynamic and kinetic calculation and modelling. *Calphad* 2009;33:265.
- [31] NIST Standard Reference Database Number 69. NIST chemistry webbook; 2011. <http://webbook.nist.gov/chemistry/>.

- [32] Springer materials—the Landolt-Börnstein database. Heidelberg: Springer-Verlag GmbH; 2013. <http://www.springermaterials.com>.
- [33] Hull S, Norberg ST, Ahmed I, Eriksson SG, Mohn CE. High temperature crystal structures and superionic properties of SrCl<sub>2</sub>, SrBr<sub>2</sub>, BaCl<sub>2</sub> and BaBr<sub>2</sub>. *J Solid State Chem* 2011;184:2925–35.
- [34] Nye JF. Physical properties of crystals. Oxford: Clarendon Press; 1951.
- [35] Schlom DG, Chen L-Q, Eom C-B, Rabe KM, Streiffer SK, Triscone J-M. Strain tuning of ferroelectric thin films. *Annu Rev Mater Res* 2007;37:589–626.
- [36] Park JH, Coy JM, Kasirga TS, Huang C, Fei Z, Hunter S, et al. Measurement of a solid-state triple point at the metal-insulator transition in VO<sub>2</sub>. *Nature* 2013;500:431–4.
- [37] Haeni JH, Irvin P, Chang W, Uecker R, Reiche P, Li YL, et al. Room-temperature ferroelectricity in strained SrTiO<sub>3</sub>. *Nature* 2004;430:758–61.
- [38] Fast JD. The allotropic transformation of hafnium and a tentative equilibrium diagram of the system zirconium–hafnium. *J Appl Phys* 1952;23:350–1.
- [39] Klimm D, Rabe M, Bertram R, Uecker R, Parthier L. Phase diagram analysis and crystal growth of solid solutions Ca<sub>1-x</sub>Sr<sub>x</sub>F<sub>2</sub>. *J Cryst Growth* 2008;310:152–5.
- [40] Carruthers JR, Grasso M. Phase equilibria relations in the ternary system BaO–SrO–Nb<sub>2</sub>O<sub>5</sub>. *J Electrochem Soc* 1970;117:1426–30.
- [41] Megumi K, Nagatsuma N, Kashiwada Y, Furuhashi Y. The congruent melting composition of strontium barium niobate. *J Mater Sci* 1976;11:1583–92.
- [42] Ulex M, Pankrath R, Betzler K. Growth of strontium barium niobate: the liquidus–solidus phase diagram. *J Cryst Growth* 2004;271:128–33.
- [43] Muehlberg M, Burianek M, Joschko B, Klimm D, Danilewsky A, Gelissen M, et al. Phase equilibria, crystal growth and characterization of the novel ferroelectric tungsten bronzes Ca<sub>x</sub>Ba<sub>1-x</sub>Nb<sub>2</sub>O<sub>6</sub> (CBN) and Ca<sub>x</sub>Sr<sub>y</sub>Ba<sub>1-x-y</sub>Nb<sub>2</sub>O<sub>6</sub> (CSBN). *J Cryst Growth* 2008;310:2288–94.
- [44] Schiferl D, Barrett CS. The crystal structure of arsenic at 4.2, 78 and 299 K. *J Appl Cryst* 1969;2:30–6.
- [45] Pawlak DA, Turczynski S, Gajc M, Kolodziejek K, Diduszko R, Rozniatowski K, et al. How far are we from making metamaterials by self-organization? The microstructure of highly anisotropic particles with an SRR-like geometry. *Adv Funct Mater* 2010;20:1–9.
- [46] Gulyaev AP. On the iron–carbon diagram. *Metal Sci Heat Treat* 1990;32:493–4.
- [47] Ganschow S, Klimm D. Shaped crystals—growth by micro-pulling-down technique. In: Fukuda T, Chani VI, editors. *Ch. Growth of olivine and Wüstite crystals*. Heidelberg: Springer, Berlin; 2007. p. 265–74.
- [48] Gulliver GH. The quantitative effect of rapid cooling upon the constitution of binary alloys. *J Inst Met* 1913;9:120–57.
- [49] Burton JA, Prim RC, Slichter WP. The distribution of solute in crystals grown from the melt. *J Chem Phys* 1953;21:1987–91. 1991–1996.
- [50] Ellwell D, Scheel HJ. *Crystal growth from high-temperature solutions*. London: Academic Press; 1975.
- [51] Schulz D, Bertram R, Klimm D, Schulz T, Thiede E. Segregation of Mg in Zn<sub>1-x</sub>Mg<sub>x</sub>O single crystals grown from the melt. *J Cryst Growth* 2011;334:118–21.
- [52] Muan A, Gee CL. Phase equilibrium studies in the system iron oxide–Al<sub>2</sub>O<sub>3</sub> in air and at 1 atm. O<sub>2</sub> pressure. *J Am Ceram Soc* 1956;39:207–14.
- [53] Okamoto H. I–Pb (iodine–lead). *J Phase Equilibria Diffusion* 2010;31:320–1.
- [54] Sangster J, Pelton AD. Phase diagrams and thermodynamic properties of the 70 binary alkali halide systems having common ions. *J Phys Chem Ref Data* 1987;16:509–61.

- [55] Klimm D, Schulz D, Ganschow S. Growth of bulk ZnO. In: Bhattacharya P, Fornari R, Kamimura H, editors. *Comprehensive semiconductor science and technology*. Amsterdam: Elsevier; 2011. p. 302–38.
- [56] Ntep J-M, Hassani SS, Lusson A, Tromson-Carli A, Ballutaud D, Didier G, et al. ZnO growth by chemical vapour transport. *J Cryst Growth* 1999;207(1–2):30–4.
- [57] Wenzl H, Dahlen A, Fattah A, Petersen S, Mika K, Henkel D. Phase relations in GaAs crystal growth. *J Cryst Growth* 1991;109:191–204.
- [58] Klimm D, Ganschow S, Schulz D, Bertram R, Uecker R, Reiche P, et al. Growth of oxide compounds under dynamic atmosphere composition. *J Cryst Growth* 2009;311:534–6.

# Atomistic Calculation of Defect Thermodynamics in Crystalline Silicon

Talid Sinno

DEPARTMENT OF CHEMICAL AND BIOMOLECULAR ENGINEERING,  
UNIVERSITY OF PENNSYLVANIA, PHILADELPHIA, PA, USA

## CHAPTER OUTLINE

<b>3.1 Introduction .....</b>	<b>138</b>
<b>3.2 Theoretical Infrastructure for Analysis of Point Defect and Cluster Thermodynamics .....</b>	<b>139</b>
3.2.1 Point Defects.....	139
3.2.2 Point Defect Clusters.....	140
<b>3.3 Theoretical Estimation of Ground State Point Defect Formation Properties .....</b>	<b>142</b>
3.3.1 Empirical Potential Atomistic Simulations.....	142
3.3.2 Quantum Mechanical Estimates for Point Defect Thermodynamics .....	145
<b>3.4 Ground State Point Defect Cluster Thermodynamics .....</b>	<b>147</b>
3.4.1 Vacancy Clusters .....	147
3.4.2 Small Compact Self-Interstitial Clusters .....	149
3.4.3 Large Planar Self-Interstitial Clusters .....	152
<b>3.5 Inherent Structure Theory and Potential Energy Landscapes .....</b>	<b>153</b>
3.5.1 Inherent Structure Landscape (ISL) Theory for Defects in Crystals.....	155
3.5.2 Sampling Inherent Structures with Molecular Dynamics Simulation .....	156
<b>3.6 High Temperature Defect Thermodynamics .....</b>	<b>158</b>
3.6.1 The Single Vacancy .....	158
3.6.2 Vacancy Clusters .....	159
3.6.3 Self-Interstitial Clusters .....	163
3.6.3.1 Landscape Roughness and the Effect of Pressure.....	165
<b>3.7 Conclusions .....</b>	<b>167</b>
<b>References.....</b>	<b>169</b>

## 3.1 Introduction

Intrinsic point defects, namely vacancies and self-interstitials, in crystalline silicon have been the subject of an enormous number of studies over the last several decades. The driving force for this intense research effort stems from the fact that intrinsic point defects are responsible for a staggering range of fundamentally interesting phenomena and play important roles in the formation of almost all known microstructural features found in dislocation-free, single-crystal silicon. This material, most commonly in the form of thin wafers sliced from melt-grown ingots, underpins much of the (silicon-based) microelectronics and photovoltaics industries.

To this day, almost all single-crystal silicon is still grown by the venerable Czochralski (CZ) technique in which a seed of single-crystal is dipped into a highly pure silicon melt contained in a rotating, quartz-lined crucible and then slowly pulled away from the melt under tightly controlled thermal conditions to produce a cylindrical ingot [1]. Currently, silicon boules 300 mm in diameter are routinely grown weighing well over 250 kg, and next-generation 450 mm ingots remain under development. While dislocations and grain boundaries are completely suppressed in the CZ growth process, the formation of a range of point defect–impurity complexes and intrinsic point defect aggregates remains technologically relevant in spite of decades of research. With that said, current emphasis is principally on process optimization because while much of the basic mechanisms are well understood, established defect microstructure reduction measures usually come at a cost of reduced throughput and increased process expense.

Unlike impurities and intentionally introduced dopants, intrinsic point defect generation in growing crystals is a consequence of fundamental thermodynamic forces that cannot be avoided. Simply put, the minimum free energy state of any crystal at finite temperature does not correspond to crystalline perfection, but rather is one that includes a (temperature-dependent) distribution of point defects and small defect clusters. Fortunately, intrinsic point defects and very small clusters comprised of them are not directly associated with deleterious effects such as reduced charge carrier lifetimes; rather, it is how they interact with each other and with other species that ultimately leads to reduced material quality. The aim for most silicon crystal growers, therefore, is not to circumvent point defect formation altogether, but rather to cleverly design process conditions so that point defects do not subsequently lead to undesirable microstructure in the form of large aggregates. This target is not a static one: the very definition of “large” is continuously evolving due to improvements in detection techniques and increased sensitivity to ever-smaller defects as CMOS scaling continues and feature lengths decrease. Nonetheless, for this endeavor to be successful, a quantitatively accurate mechanistic picture of intrinsic defect thermodynamics must be available.

The goal of this chapter is to provide a (highly selective and necessarily incomplete) overview of intrinsic point defect and defect cluster thermodynamics that is relevant to the formation of vacancy and self-interstitial microdefects during silicon crystal growth and wafer annealing. The present emphasis is on predictions from molecular

simulations based on empirical interaction potentials. When appropriate, comparisons are made with results from more accurate quantum mechanical methods. Note that this chapter does not seek to provide a comprehensive quantitative summary of point defect and cluster formation energies and entropies, although whenever appropriate, literature references to such studies will be provided. The remainder of the chapter is structured as follows. In [Section 3.2](#), the basic theoretical elements for describing point defect and cluster thermodynamics are briefly described. In [Section 3.3](#), approaches for estimating ground state point defect formation energies are summarized; these include atomistic simulations based on quantum mechanical and empirical potential descriptions. In [Section 3.4](#), analysis of ground-state defect cluster thermodynamics is presented. A more general theoretical framework for finite temperature defect thermodynamics then is presented in [Section 3.5](#) and applied to single point defects and clusters in [Section 3.6](#). Finally, conclusions and outlook are presented in [Section 3.7](#).

## 3.2 Theoretical Infrastructure for Analysis of Point Defect and Cluster Thermodynamics

### 3.2.1 Point Defects

The materially open system equilibrium concentration of a particular point defect species is one of the most essential properties underlying any quantitative analysis of defect formation and evolution. This is because the equilibrium concentration directly dictates the extent of any point defect supersaturation (or undersaturation) present, which in turn dictates the extent of clustering. Here, “open system” denotes that the crystal domain is connected to a sink/source for point defects that allows an unconstrained equilibrium to be established everywhere in the domain—the crystal surface typically serves this purpose.

Consider the free energy of a crystal domain with  $N$  distinct lattice sites containing one type of point defect species,

$$G = G_0 + nG^f - k_B T \ln \frac{N!}{(N-n)!n!}, \quad (3.1)$$

where  $n$  is the number of point defects,  $G^f$  is the free energy of formation of a single point defect, and  $G_0$  is the perfect crystal (reference) free energy. The last term in [Eqn \(3.1\)](#) represents the contribution of translational entropy to the total free energy, where it is assumed that each lattice site can accommodate a single point defect and no proximity effects are present, i.e., point defects do not interact with each other. The equilibrium concentration of point defects is obtained by minimizing [Eqn \(3.1\)](#) with respect to  $n$ , i.e.,

$$C^{eq}(T) = gC_s \exp\left(-\frac{G^f}{k_B T}\right) = gC_s \exp\left(\frac{S^f}{k_B}\right) \exp\left(-\frac{H^f}{k_B T}\right), \quad (3.2)$$

where,  $C_s$  is the density of lattice sites ( $\sim 5 \times 10^{22}/\text{cm}^3$  for Si),  $g$  is a configurational degeneracy factor, and  $H^f$ ,  $S^f$  represent the formation enthalpy and entropy, respectively, of a single point defect. The configurational degeneracy factor is usually taken to be the symmetry of the point defect structure and therefore is a number that is  $O(1)$  in magnitude; it is often ignored in analyses of point defect thermodynamics. We will return to the issue of defect degeneracy in [Section 3.4](#) and show that the entropy arising from configurational degeneracy can in fact be quite significant. The remaining entropic term in [Eqn \(3.2\)](#) then corresponds to the vibrational entropy of formation. The conventional approach for calculating the equilibrium concentration of a point defect species using atomistic simulations is to first find the lowest energy configuration and then compute its formation energy and vibrational entropy, usually under the assumption that these are constants, i.e., that the equilibrium concentration is an Arrhenius function of temperature.

### 3.2.2 Point Defect Clusters

The thermodynamics of defect clusters can be formulated in a similar manner as for point defects. The total free energy of a system containing a distribution of a single point defect species and its aggregates is given by

$$G(T) = G_0 + \sum_i n_i G_i^f(T) - k_B T \ln \Omega, \quad (3.3)$$

here  $G_i^f(T)$  is the formation free energy of a cluster of size  $i$ ,  $n_i$  is the number of such aggregates, and  $\Omega$  is the number of ways that a distribution of clusters can be distributed across lattice sites. For an open system (i.e., one with accessible surfaces) in which each cluster size can reach equilibrium independently of the others and assuming that the cluster site density is equal to lattice site density,  $\Omega$  is the same as for the point defect case ([Eqn \(3.1\)](#)) and the cluster equilibrium concentrations are given by

$$C_i^{eq}(T) = g_i C_s \exp\left(-\frac{G_i^f}{kT}\right), \quad \forall i. \quad (3.4)$$

In many situations the crystal cannot be assumed to be materially open and the cluster size distribution is established via a constrained free energy minimization subject to a fixed total number of point defects. Such a situation is typical in crystal growth where the nearest surface is much further away than the point defect diffusion distance. Now,  $\Omega$  is given by [\[2\]](#)

$$\Omega = \prod_i \frac{(i)^{n_i} (N/i)!}{(N/i - n_i)! (n_i)!} \quad (3.5)$$

which represents the number of ways of distributing  $\{n_i\}$  clusters over the  $N$  lattice sites. The closed system equilibrium cluster concentration at each size is now obtained by minimizing the augmented free energy function

$$\begin{aligned} \widehat{G} = G_0 + \sum_i n_i G_i^f - k_B T \sum_i \left\{ n_i \ln i + \frac{N}{i} \ln \frac{N}{i} - \left[ \frac{N}{i} - n_i \right] \ln \left[ \frac{N}{i} - n_i \right] - n_i \ln n_i \right\}, \\ + \lambda \left( \sum_i i \cdot n_i - n_{tot} \right) \end{aligned} \quad (3.6)$$

with respect to the number of each cluster size [3], i.e.,

$$\frac{\partial \widehat{G}}{\partial n_i} = G_i^f - k_B T \ln \frac{N - i \cdot n_i}{n_i} + i\lambda = 0, \quad \forall i. \quad (3.7)$$

The last term in Eqns (3.6) and (3.7) represents the constraint of a fixed total number of point defects and  $\lambda$  is a Lagrange multiplier. An immediate implication of Eqn (3.7) is that the equilibrium concentrations of all cluster sizes are coupled to each other. Under the physically reasonable assumption that clusters exist in dilute concentrations,  $i \cdot n_i \ll N$ , the closed system cluster equilibrium concentrations are given by solving Eqn (3.7) for each size

$$\widehat{C}_i^{eq}(T) = g_i C_s \exp \left( - \frac{\widetilde{G}_i^f}{k_B T} \right) = g_i C_s \left( \frac{C}{C^{eq}} \right)^n \exp \left( - \frac{G_i^f}{k_B T} \right), \quad \forall i \quad (3.8)$$

where

$$\widetilde{G}_i^f(T) = -ik_B T \ln \left( \frac{C}{C^{eq}(T)} \right) + G_i^f(T), \quad \forall i \quad (3.9)$$

and  $C$  and  $C^{eq}$  represent the actual and equilibrium concentrations of point defects, respectively. Note that the assumption of diluteness effectively decouples the equilibrium concentration of each cluster size from other sizes—the concentration is only a function of the extent of point defect local supersaturation,  $C/C^{eq}$ . Finally, applying Eqn (3.7) to the monomer point defect species gives an expression for the equilibrium monomer point defect concentration in the presence of a cluster of size  $i$ , i.e.,

$$C^{eq}|_i = C^{eq} \exp \left( \frac{\partial G_i^f / \partial i}{k_B T} \right), \quad \forall i. \quad (3.10)$$

The enhancement of the point defect equilibrium concentration in the vicinity of a cluster as specified in Eqn (3.10) is a statement of the Gibbs–Thompson effect [4]; alternatively, this equilibrium concentration can be thought of as the cluster “vapor pressure” in which the vapor phase consists of a monomer point defect “fluid” surrounding a cluster.

All equilibrium concentrations defined above, whether for point defects or for clusters, require the estimation of free energies of formation. There are two principal approaches for carrying out this task. The first is to directly compute free energies using atomistic calculations based either on quantum mechanical or empirical descriptions for the interatomic interactions. The second is to measure experimentally some property or phenomenon and extract the free energies using a model. Both approaches have

inherent limitations and advantages. Atomistic scale calculations are the most direct path for free energy estimation: the system is completely defined and the free energy can be unambiguously accessed. On the other hand, empirical atomistic calculations, which are computationally very efficient, are completely dependent on the specification of a good interatomic potential function. The issue of accuracy is mostly (but not completely) resolved with quantum mechanical calculations, but the immense computational requirements of these methods limit the system sizes that can be considered and also largely preclude the use of statistical sampling approaches commonly employed for free energy estimation. In the following section, we describe the salient features of each approach for computing point defect thermodynamic properties.

## 3.3 Theoretical Estimation of Ground State Point Defect Formation Properties

### 3.3.1 Empirical Potential Atomistic Simulations

Empirical potentials are constructed beginning with an ansatz for the functional form of the interaction energy between pair, triplet, and higher-order (many-body) interaction functions. The resulting potential function is usually characterized by several parameters that are regressed to a number of material properties that are either experimentally measured or computed using more accurate quantum mechanical calculations. The challenge for accurate modeling of covalently bonded materials such as silicon is the directionality of the bonds, leading to structures (such as the diamond lattice) that typically require many-body interaction terms to stabilize. Arguably, silicon has served as the prototypical system for the development of potential models for covalently bonded materials and there exists a large number of potentials and parameterizations in the literature.

In an excellent early review, Balamane et al. [5] defined two main types of empirical formalisms, “cluster potentials” in which pair and triplet interactions terms were separately defined, and “cluster functionals” or bond-order formulations, in the which the pair interaction is modified by many-body (usually three) environment terms. The Stillinger–Weber (SW) potential [6] was the first “comprehensive” model to address both solid and liquid phases, interfaces and surfaces, and defects. The potential was represented by separate two- and three-body terms with the tetrahedral angle built explicitly into the latter. Similar cluster potentials include the Pearson, Takai, Halicioglu, Tiller (PHTT) [7] and Biswas–Hamann (BH) [8] potentials, although these are less popular than the SW. The Tersoff model [9,10] followed soon after with similar capabilities as the SW potential but was based on a bond-order formulation. The SW and Tersoff potentials have since been applied in countless studies, being reparameterized several times [11–14] and extended to Group IV alloy systems [10,12,15,16] and continue to be popular to this day. Another popular class of potentials is the modified embedded-atom model (MEAM) [17–20], in which the embedded-atom model for metals was extended to

include directionality for covalent materials such as silicon. The MEAM potential framework is attractive because parameters have been generated for a wide range of materials and compounds making it quite versatile. The Lenosky potential (LP) is a derivative of the MEAM class of potentials that was specifically optimized for silicon [21]. Finally, the so-called environment-dependent interatomic potential (EDIP) [22,23] represents another formulation in the bond-order class of potentials.

The most common metrics for potential validation include crystal phase stability order, elastic constants, surface energetics and reconstructions, point defect thermodynamics and structure, dislocation and stacking-fault energetics, and amorphous/liquid phase structure [14,16] and melting characteristics [11]. Finally, although isolated clusters have also been considered in potential evaluation, the energetics of such structures are generally quite poorly reproduced unless the potential parameters are specifically tuned using these highly undercoordinated structures [20]. There is no single clear winner among silicon potentials and each has been shown to have strengths and weaknesses, some of which may be traced to the database that was used to establish the parameters. Even different parameterizations of the same potential function have been shown to provide rather different results.

Before proceeding with a comparative analysis of point defect formation energies, which we focus on here, it is important to note that empirical potentials cannot account for different point defect charge states. As mentioned previously, the lowest energy configuration for a given point defect is not necessarily the electrically neutral one, making a comparison between DFT and empirical potential results somewhat ambiguous. Here, we take the point of view that an empirical potential is a coarse-grained representation of atomic bonding in which the electronic states have been somehow (not formally) “averaged out.” In this view, comparisons between empirical potential and DFT predictions for point defect formation energies should be made on the basis of the lowest energy charge state at zero temperature, and a Boltzmann-weighted average of the different charge states at finite temperatures. In other words, there is nothing in the empirical potential formulation to necessarily suggest that the “equivalent” configuration in the DFT case is the neutral state.

A representative list of empirical potential predictions for the single vacancy formation energies at zero temperature is provided in Table 3.1. Apart from some outliers, there is general consensus in the range of  $E_V^f \sim 3 - 4$  eV, in good agreement with the DFT range 3.2–3.6 eV (see Section 3.2). In all cases, the basic ground state configuration is a missing atom with some localized relaxation of the surrounding atoms. Note that few of these studies report the precise configurational details of the relaxed vacancy such as inward/outward relaxation, symmetry, and bond angles and lengths of neighboring atoms. This is largely due to the fact that such high-resolution information is not likely to be meaningfully reproduced by most empirical potentials. Again, the notion that an empirical potential function represents some kind of a coarse-grained representation of the full bonding environment can be invoked to suggest that empirical potentials may be good at describing certain, but not all, features of a point defect configuration.

**Table 3.1** Zero-Temperature Vacancy Formation Energies Predicted by Selected Empirical Potentials for Silicon

Potential Model	Vacancy Formation Energy (eV)	Ref.
SW	2.59, 2.82	[5,24]
SW-Pizzagalli	3.27	[13]
BH	2.12	[5,8]
Tersoff (T3)	3.70	[5]
Tersoff-ARK	3.70	[11]
MEAM-Baskes	3.19	[25]
MEAM-Timonova	3.14	[20]
MEAM-Lenosky	3.30	[21]
EDIP	3.22	[21]
Bond-order	2.76	[26]

**Table 3.2** Selected Zero-Temperature Formation Energies for Ground State Configurations of Self-Interstitials, as Predicted by Selected Empirical Potentials for Silicon

Potential Model	Self-interstitial Formation Energy (eV)	Lowest Energy Configuration	Ref.
SW	3.61	<110>-dumbbell	[24]
SW-Pizzagalli	5.92	<110>-dumbbell	[13]
BH	1.56	Tetrahedral	[5,8]
Tersoff (T3)	3.45	Tetrahedral	[5,27]
Tersoff-ARK	2.20	Tetrahedral	[11]
MEAM-Baskes	4.81	Tetrahedral	[25]
MEAM-Timonova	3.84	Tetrahedral	[20]
MEAM-Lenosky	3.00	Tetrahedral distorted	[21]
EDIP	3.35	<110>-dumbbell	[21]
Bond-order	2.64	Tetrahedral	[26]

The assessment of self-interstitial formation energies is more nuanced, where several distinct configurations may exist in a relatively narrow energy range. The most reported configurations include the tetrahedral, hexagonal bond-centered, and some form of the <110>-dumbbell configuration. Shown in Table 3.2 are formation energies for the reported lowest-energy configurations found for several empirical potentials. It should be noted that, unlike the vacancy case, significant “scatter” exists in the reported self-interstitial formation energy values for a given configuration and with a given potential model. In addition, the lowest-energy configuration is not always the same across potentials, with the tetrahedral and <110>-dumbbell geometries most often being reported as the ground state configurations. These observations are likely to be at

least partially due to the presence of multiple closely spaced local minima that correspond to different interstitial configurations and even different relaxations of a single configuration. In fact, as we will show in [Section 3.5](#), the notion of a “rough energy landscape” with multiple local minima is a generic feature that introduces a significant amount of configurational entropy at elevated temperature, necessitating a somewhat different approach for thinking about finite temperature point defect and cluster thermodynamics.

Comparison of the self-interstitial formation energy predictions in [Table 3.2](#) to the results of DFT calculations, whose consensus gives a range of about 3.3–3.8 eV for the  $\langle 110 \rangle$ -dumbbell, highlights the limitations of using (currently available) empirical potentials for quantitative estimation of point defect parameters—it is not yet possible to do this without strict a posteriori validation of the results against more accurate approaches. More importantly, the potentials that appear to provide the best agreement with specific DFT calculations were fitted to the DFT results, and the quantitative accuracy of the potential for any other properties therefore is in question (until explicitly tested). Nonetheless, the most commonly employed potentials such as SW, Tersoff and EDIP all appear to provide good estimates in the range of 3.3–3.9 eV.

### 3.3.2 Quantum Mechanical Estimates for Point Defect Thermodynamics

Atomistic simulations that explicitly consider electronic interactions between ions, frequently referred to as *ab initio* or *first-principles* calculations, are indisputably the gold standard for theoretically estimating silicon defect thermodynamic and transport properties. The vast majority of quantum mechanical atomistic simulations are based on the application of density function theory (DFT), in which the many-electron problem is reduced to that of a single electron moving in an effective potential specified either through the local density approximation (LDA) or generalized gradient approximation (GGA) [28]. More accurate treatments of the many-electron problem are available (e.g., quantum Monte Carlo and Hartree-Fock), but these are currently very infrequently applied to defects in silicon because of their extreme computational intensity [29].

Not only are DFT calculations obviously important in their own right, but they are also crucial for (1) parameterizing empirical potentials for silicon, and (2) validating the predictions of these empirical potentials by providing reference calculations. On the other hand, despite the relative efficiency of DFT, such calculations still remain *much* more computationally intensive than corresponding empirical potential simulations. This is particularly true when considering larger defects such as clusters and when free energies at finite temperature are required. The computational expense of DFT has led to continued interest in simplified quantum mechanical approximations, such as the tight-binding method [30], in addition to empirical potential development. Although tight-binding simulations have in some instances been shown to be demonstrably better than some empirical potentials [31], it is difficult to unequivocally make the case that

their added computational expense necessarily improves accuracy relative to empirical potentials.

A detailed treatise of quantum mechanical models is well beyond the scope of this chapter. Instead, the aim here is to provide a brief discussion of the principal outcomes and outstanding issues related to such calculations, specifically in the context of point defect formation thermodynamics in silicon. The history of silicon point defect formation energy calculations with electronic DFT dates back over three decades. Arguably, the formation energy and relaxation structure of the neutral single vacancy have served as the principal benchmarks during this period [32–43]. The reason for this stems from the deceptive simplicity of the calculation; indeed, definitive convergence criteria for the calculation have only recently emerged [41–43]. Remarkably, the numerous reported DFT calculations of the neutral vacancy formation energy have ranged from over 4 eV to just below 3 eV. Even the qualitative nature of the surrounding atomic relaxation (inward vs. outward, symmetry) has been the subject of debate. The reasons for the long-standing challenge associated with this particular calculation are in fact quite straightforward. First, several choices and parameter selections must be made when performing any DFT simulation, some of which are constrained by computational expense. These choices include (i) supercell size, (ii) exchange-correlation functional, (iii) basis set type (plane waves or orbitals) and energy cutoff, and (iv) Brillouin zone integration mesh. As shown recently in refs. [41,43], the particular combination of these parameters and functionals can lead to errors that interact in nonlinear ways and make it difficult to perform convergence tests without a complete (and very expensive) parametric analysis. For example, it appears that a system size of about 256 atoms is required to sufficiently isolate the neutral vacancy and allow it to relax into the  $D_{2d}$  symmetry via the expected Jahn-Teller distortion [43]. This is not surprising given the long-ranged elastic relaxation fields around vacancies found in both DFT and empirical potential simulations [44,45]. In addition, electrostatic and wave-function interactions across the periodic boundaries are likely to play roles in the slow convergence with respect to system size. One example of the nonlinear coupling among the various parametric selections was observed in Ref. [43] in which a sparser sampling of the Brillouin zone was more likely to exhibit the correct relaxed vacancy symmetry when the system size was small.

The long history of convergence notwithstanding, there is little doubt that the state-of-the-art DFT calculations have now reached the point where they can be reliably used to compute a variety of point defect and small cluster thermodynamics. For the neutral vacancy formation energy, the range between 3.2 and 3.6 eV almost certainly includes the “correct” value. The neutral self-interstitial is much less well studied but the  $\langle 110 \rangle$ -split dumbbell configuration is well established as the ground state with the formation energy range 3.3–3.8 eV [36,46–48].

Note that the neutral charge state is simply used here as a basis for discussion—it is not necessarily the charge state with the lowest formation energy. In fact, under extrinsic conditions corresponding to finite doping levels, charged states are usually lower in formation energy and may even possess different structures than the neutral

configuration. This poses some ambiguity in the comparison of defect structures and energies between DFT and empirical potential calculations. While it is customary to compare to the neutral defect structure when validating empirical potential predictions, one may also consider the structures predicted by empirical potentials as coarse-grained entities that represent some kind of “average” over the various charge states. In other words, given the complete absence of explicit charge consideration in most empirical potentials for silicon, the use of the neutral configuration as a reference is not necessarily meaningful—one could just as well use the lowest energy configuration, irrespective of its charge, as a basis for validation.

## 3.4 Ground State Point Defect Cluster Thermodynamics

There are far fewer atomistic simulation studies of point defect cluster thermodynamics due to the larger simulation cells and longer relaxation times required. The principal difficulty in computing cluster thermodynamics is the identification of the ground state configuration. For quantum mechanical calculations, in particular, a good initial guess for the cluster structure is required before static relaxation can be applied. Nonetheless, certain features of small vacancy and self-interstitial clusters are now well established. For example, both types of clusters exhibit magic sizes that are particularly stable relative to neighboring sizes [49–51]. In addition, both cluster species are characterized by overall decreasing trends in their per-point defect formation energies. The latter trend is a consequence of the ability of larger clusters to achieve reconstructions that are not possible for very small ones.

### 3.4.1 Vacancy Clusters

Vacancy cluster ground state configurations are relatively straightforward to derive on the basis of broken-bond minimization. Using this approach, Chadi and Chang [52] were able to predict magic sizes for clusters up to size 12. The 6-vacancy hexagonal ring structure and 10-vacancy “adamantine cage” configuration were found to be the key building blocks for all cluster sizes, see Figure 3.1. These conclusions were subsequently supported by quantum mechanical (LDA-DFT) [53], tight-binding [50], and empirical potential (EDIP) atomistic calculations [51].

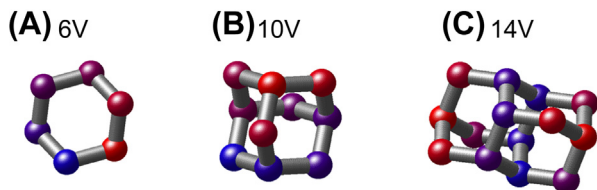


**FIGURE 3.1** Ground state configurations of vacancy clusters generated on the basis of closed ring and adamantane cage configurations. From left: (A) 6-vacancy ring, (B) 10-vacancy adamantane cage, and (C) 14-vacancy cluster comprised entirely of closed rings and cages. All three configurations correspond to specially stable “magic” sizes.

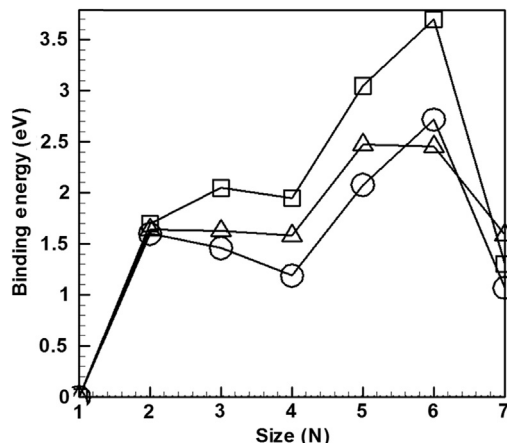


FIGURE 3.2 Binding energies as a function of size for vacancy clusters computed using LDA-DFT (squares), tight-binding (circles), and the empirical EDIP potential (triangles). Binding energies,  $E_n^b$ , are defined according to the relationship  $E_n^b = E_{n+1}^f - (E_n^f + E_1^f)$ , where  $E_n^f$  is the formation energy of a cluster of size  $n$ .

Shown in Figure 3.2 are zero-temperature binding energies for vacancy clusters up to size seven for the three different interaction models. Overall, the agreement between the three representations is very good, clearly showing the special stability of the 6-vacancy hexagonal ring configuration. The agreement across calculations also demonstrates the validity of using empirical potentials such as EDIP for defect thermodynamic property estimation. More recently, divacancy and hexavacancy formation energies computed with GGA-DFT and several empirical potentials (SW, EDIP and Tersoff) were compared and once again shown to be quite consistent across the various potentials [49].

Calculations for larger cluster sizes with tight-binding and EDIP potentials also show similar special stability for sizes 10, 14, and 18—all sizes that correspond to completed hexavacancy rings and/or adamantine cages [45,51,54]. Interestingly, the hexavacancy ring and adamantine cage building blocks naturally lead to octahedral cluster shapes bounded by (111) planes at larger cluster sizes—the octahedral geometry being the most common experimentally observed one for large vacancy aggregates present in CZ-grown silicon crystals [1]. The formation energies for vacancy clusters that follow the octahedral motif have been calculated using the EDIP potential for sizes as large as 1000 [45,51,54]. The overall vacancy cluster energetics were found to be described very well by a power-law function that scales as  $n^{2/3}$ , where  $n$  is the number of vacancies in the cluster. In other words, vacancy clusters, as expected, are energetically defined by their surfaces. Deviation from this power-law scaling was only observed for very small clusters, which are unable to arrange into closed rings and cages. Approximating the cluster surface area by assuming a spherical shape, the EDIP potential was found to predict a zero-temperature effective surface energy of 1.24 J/m<sup>2</sup>. This value is in excellent agreement with several experimental measurements of the Si(111) surface energy at cryogenic temperatures [55,56].

Finite temperature formation free energies (including vibrational entropy) for vacancy clusters computed with the EDIP potential suggest that the overall trends observed with the zero-temperature calculations are preserved with increasing temperature [57]. Near the melting temperature, the effective surface free energy including vibrational entropy is reduced to about  $0.9 \text{ J/m}^2$ . Unfortunately, the validity of this estimate is more difficult to verify against experimental measurements, although one indirect experimental measurement places the melting temperature (111) surface energy right around  $0.89 \text{ J/m}^2$  [58]. The issue of effective void surface energies at finite temperature is revisited more comprehensively in Section 3.6, where the influence of configurational entropy is also included.

### 3.4.2 Small Compact Self-Interstitial Clusters

The analysis of self-interstitial clusters is complicated by bonding reconstructions associated with the presence of multiple self-interstitials in close proximity. While vacancy clusters are characterized by the octahedral morphology across all sizes, no single morphological motif describes self-interstitial clusters. Nonetheless, several broad features of self-interstitial clusters are now well established both experimentally and by various types of calculations. Small clusters containing up to about 15 self-interstitials are compact and three-dimensional and exhibit magic sizes, particularly at sizes that are integer multiples of four (i.e., 4, 8, and 12) [46,50,59]. Evidence for special stability of these sizes has been demonstrated not only theoretically but also experimentally. Cowern et al. [60], in particular, used inverse modeling of boron diffusion profiles to extract effective formation free energies for interstitial clusters as a function of size and found that the best agreement was obtained when 4- and 8-interstitial clusters were assumed to be particularly stable relative to adjacent sizes. Larger interstitial clusters are observed experimentally in several types of planar structures including {113}-oriented rod-like defects, {111} partial and perfect dislocation loops, and possibly also {100}-oriented plate-like structures; example studies include refs. [61–72]. These structures are most commonly observed in ion-implanted samples. Evidence for the {100} planar defects is not as well established as for the other types of planar defects. The transitions between small compact clusters and the various larger planar structures are still not fully understood, and the dependence of these transitions on temperature and other variables (e.g., local stress) even less so.

Here, we summarize a selection of theoretical estimates for the ground state formation thermodynamics of self-interstitial clusters and defer discussion of finite temperature thermodynamics to Section 3.5. A large number of computational studies of interstitial clusters have focused specifically on the 4-interstitial ( $I_4$ ) cluster, which is the smallest magic cluster size. The ground state structure predicted by most of these studies consists of 5- and 7-membered bond rings with no dangling bonds; see Figure 3.3 (taken from Ref. [73]). We henceforth refer to this structure as the Humble/Arai configuration after refs. [74,75]. Various estimates for the formation energy of this cluster are

**FIGURE 3.3** Schematic representation of the 4-interstitial cluster (right) relative to the perfect silicon lattice (left). The four [001] split-interstitial pairs are represented by atoms labeled "c" and the reconstructed bonds which link the interstitial pairs are shaded. Taken from Ref. [73].

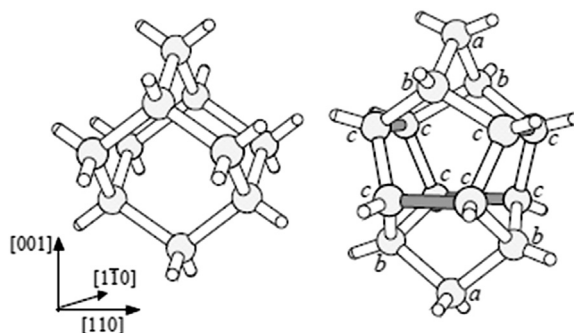


**Table 3.3** Ground State 4-Interstitial ( $I_4$ ) Formation Energies Predicted by Various Interaction Models

Model	$I_4$ Formation Energy (eV)	Ref.
LDA-DFT	8.7	[73]
LDA-DFT	5.96	[76]
LDA-DFT	7.28	[46]
GGA-DFT	7.40	[46]
Tight-binding	9.41	[50]
Tight-binding	9.84	[75]
Empirical SW	8.40	[75]
Empirical EDIP	8.75	[77]

summarized in Table 3.3. With few exceptions, the formation energy estimates are remarkably consistent across the various studies, and the per-interstitial formation energy is tightly clustered in the range 1.8–2.4 eV/atom. It is notable, however, that not all studies show the  $I_4$  to be a magic size. For example, the tight-binding calculations in Ref. [50] and the LDA-DFT results in Ref. [48] both indicate that the per-interstitial formation energy varies monotonically with size and that  $I_4$  is no more stable than adjacent sizes. Moreover, the tight-binding results generally lead to systematically higher formation energies than the DFT predictions.

Shown in Figure 3.4 are formation energies per interstitial for a range,  $2 \leq n_I \leq 9$ , of small compact self-interstitial clusters computed using the EDIP empirical potential and two different sets of DFT calculations [46,48,77]. Overall the agreement between the three sets of calculations is quite good. The EDIP formation energies are higher than both of the DFT results although the difference in the two sets of DFT predictions is of similar magnitude as the difference between the EDIP results and those in Ref. [46].

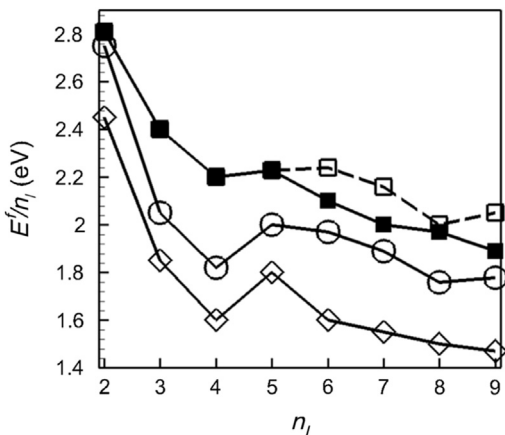


**FIGURE 3.4** Formation energies per interstitial as a function of cluster size,  $n_I$ . Squares—EDIP results for compact (open) and elongated (filled) [77]; circles—DFT [46]; diamonds—DFT [48].

While the special stability of the 4-interstitial cluster (Humble/Arai configuration) is found in all three studies, the picture is somewhat murkier for the 8-interstitial cluster. The interpretation of the formation energy calculations is complicated by the fact that two different morphologies for  $n_I \geq 5$  can be identified. The first, which is denoted as “compact” is based on the Humble/Arai motif; thus a 5-interstitial cluster is a Humble/Arai 4-mer plus an additional interstitial and so on. The second structural motif, “elongated”, refers to [110]-aligned configurations that serve as the building blocks for the {113}-oriented planar configurations (see next section).

The relative stability of compact and elongated configurations in the size range  $n_I < 12$  is not conclusive: Refs [77] and [46] seem to indicate that the elongated structures are more stable but ref. [48] finds the opposite trend. In either case, the difference is not large and the 8-interstitial cluster is only weakly favored over neighboring sizes, if at all. A possible explanation for this apparent discrepancy with the experimental inference in Ref. [60] is provided in Figure 3.5. Here, cluster formation free energies that include vibrational entropy are estimated using the EDIP potential. Interestingly, the vibrational entropies are such that the free energies of compact and elongated configurations become almost identical. Moreover, for the compact 8-interstitial cluster, which is comprised of two Humble/Arai 4-interstitial cluster, a rather large configurational entropy for the compact structure also is suggested due to the large number of (almost degenerate) ways that the two 4-interstitial clusters can be placed [77]. With these entropic factors included, strong “magicness” at size eight emerges. These results suggest that the consideration of entropic contributions might be necessary to fully understand cluster thermodynamics and that conclusions based on ground state configurations may be misleading or at least incomplete. In Sections 3.5 and 3.6, the calculation of entropic contributions is generalized and further evidence is provided for the importance of entropy in defect thermodynamic analysis.

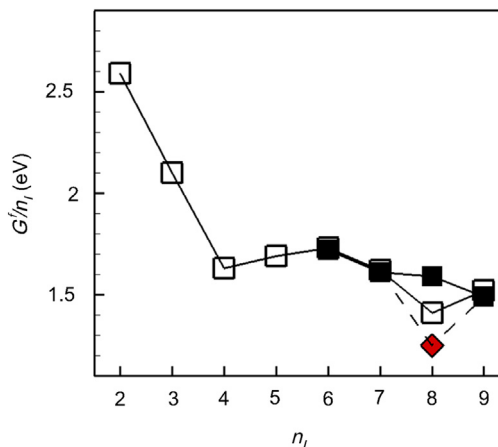


**FIGURE 3.5** EDIP-predicted formation free energies as a function of interstitial cluster size at 1100 K (EDIP melting temperature is 1520 K). Open squares—compact structures; filled squares—elongated structures. Single diamond symbol shows free energy including estimated configurational entropy for 8-interstitial compact cluster. Adapted from Ref. [77].

### 3.4.3 Large Planar Self-Interstitial Clusters

Formation energy estimates have also been computed for the various types of planar defects found in ion-implanted silicon wafers. The most intensively studied is the {113}-oriented family of planar structures, which are characterized according to how densely interstitial chains are packed along the [332] direction. Briefly, the notation /I/ represents a sequence of adjacent self-interstitial chains (highest density packing) while /IO/ and /IIO/ represent sequences along the defect (in the [332] direction) in which some chains are missing—a missing chain is denoted by “O”; see Ref. [62] for more notational details. A summary of per-interstitial formation energies for the {113} family of planar is shown in Table 3.4 assuming infinitely long interstitial chains (in the [110] direction). It is notable that the lowest energy configuration on a per-interstitial basis is not the densest (/I/) but rather one that consists of about 66–75% occupancy of interstitial chains along the [332] direction, i.e., /IIO/ or /IIIO/.

It has been suggested that {113}-oriented defects grow and eventually transform into {111}-oriented dislocation loops, namely Frank partial loops (FDLs) and perfect dislocation loops (PDLs). There is also some direct experimental evidence for such a transformation [66]. The transformation size has been estimated to be approximately 20 nm, or when clusters contain on the order of 500 self-interstitials [67]. The formation energies for large {111}-oriented planar defects can be estimated on the basis of continuum mechanical arguments because of the relatively simple structures. For small loop sizes, FDLs have lower per-interstitial formation energy than PDLs but the trend is reversed when the loop radius is greater than about 40 nm [79]. The limiting FDL formation energy is 0.027 eV/atom (the stacking-fault energy), while PDL formation energies tend

**Table 3.4** Ground State Formation Energies for {113}-Oriented Planar Self-Interstitial Clusters

Model	Configuration	Formation Energy (eV/atom)	Ref.
LDA-DFT	/110/	0.68	[75]
SW	/110/	0.88	
LDA-DFT	/10/	0.49	[76]
LDA-DFT	//	0.63	[68]
	/10/	0.72	
	/110/	0.46	
	/1110/	0.48	
Tight-binding	/10/	1.35	[78]
LDA-DFT	//	0.71	[48]
	/10/	0.76	
	/1110/	0.55	

to zero (on a per-interstitial basis) in the limit of large loop size. These very small energies suggest that if sufficient self-interstitials are present to allow growth and coarsening to produce large cluster sizes, dislocation loops will be the predominant structures. Claverie et al. [67,70,79–81] have summarized comprehensively self-interstitial cluster morphologies as a function of annealing history in a series of papers.

### 3.5 Inherent Structure Theory and Potential Energy Landscapes

As described in the previous section, the “conventional” strategy for computing point defect (or cluster) free energies is to locate the ground state (minimum energy) configuration, compute its formation energy and vibrational entropy, and if possible estimate a degeneracy factor based on symmetry considerations. These elements are then combined in Eqn (3.2) or (3.4) to provide the “open-system” equilibrium concentration for that particular defect. The implicit assumption in this picture is that no other configurations of the defect are energetically close to the ground state and thus do not contribute in any way to the stability of the defect. In this section, a framework is described for including the contributions of higher-energy configurations into the defect free energy. It will be shown that the configurational entropy contribution from higher formation energy configurations can be significant at the high temperatures associated with silicon crystal growth and wafer annealing. As a result, defect free energies based on ground state analyses can overestimate the true free energy and, in some cases, lead to qualitatively incorrect predictions for defect thermodynamics.

In the following, the notion of the Inherent Structure Landscape (ISL) is used to develop a quantitative theory for describing high-temperature defect thermodynamics. While ISL theory has since been applied successfully to a variety of systems, including

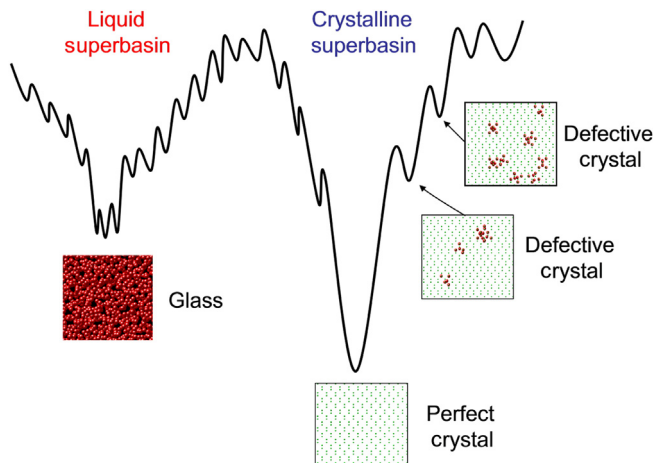


**FIGURE 3.6** One-dimensional schematic representation of the potential energy landscape for a model atomic material showing two “superbasins” corresponding to liquid/glass/amorphous solid and crystal macro-states. Within each superbasin, many local minima correspond to distinct inherent structures—the global minimum corresponds to the perfect crystal configuration. Insets show example configurations in which large red spheres qualitatively correspond to disordered (i.e., noncrystalline) atoms and small green ones denote atoms in crystalline positions. Taken from Ref. [92].

atomic clusters [82–84], glasses [85–87] and polymers [83,88], it has not received much attention in the arena of crystal defect thermodynamic analysis since the early work of Stillinger and Weber [89]. Inherent structures, as first introduced by Stillinger and Weber [89,90], correspond to local minima in the  $3N$ -dimensional potential energy (or enthalpy) landscape defined by the three-dimensional coordinates of an  $N$ -atom system [91]. Shown in Figure 3.1 is a schematic one-dimensional projection of a potential energy landscape for some hypothetical material. On the left is a “superbasin” that contains all micro-configurations that are macroscopically noncrystalline, including the liquid phase (higher energy) and amorphous solid phase (lower energies). On the right is the crystal superbasin that includes the perfect crystal ground state and higher-energy levels that correspond to configurations that include defects. In all cases, “inherent structures” correspond to mechanically stable configurations and are represented by local minima in Figure 3.6. In turn, each local minimum is surrounded by a basin that defines the region of phase space from which a local minimum is always reached upon downhill energy minimization (e.g., steepest descent or conjugate-gradient) [82].

Under certain conditions, the total phase space of the system is well approximated by the collection of basins surrounding inherent structures, i.e., the system spends most of its time in the vicinity of one or more of the inherent structures and very little time in transition between them. Under these conditions, the partition function that describes the system becomes much simpler to approximate and enables a direct route for estimating various thermodynamic properties. In the following section, a summary of the

ISL framework is provided in a form that is appropriate for the analysis of defect thermodynamics in crystalline materials.

### 3.5.1 Inherent Structure Landscape (ISL) Theory for Defects in Crystals

Consider the constant particle-volume-temperature (NVT) statistical ensemble, in which the Helmholtz free energy is related to the classical canonical partition function,  $Z$ , by the relation

$$\beta F = -\ln Z(N, \beta, V), \quad (3.11)$$

where  $\beta = 1/kT$ ,  $V$  is the system volume, and

$$Z = \frac{1}{N!} \frac{1}{\Lambda^{3N}} \int \exp(-\beta E(\mathbf{r}^N)) d\mathbf{r}^N. \quad (3.12)$$

In the above equation,  $\Lambda$  is the thermal de Broglie wavelength and  $E(\mathbf{r}^N)$  represents the potential energy of the  $N$ -atom system. Within the ISL approximation, the partition function is rewritten in terms of an integral over inherent structure basins so that [90]

$$Z = \frac{1}{\Lambda^{3N}} \int g(E_\alpha) \exp(-\beta E_\alpha) \exp(-\beta F_{vib}(\beta, E_\alpha)) dE_\alpha, \quad (3.13)$$

where  $E_\alpha$  is the (local ground state) potential energy of inherent structure  $\alpha$  and  $g(E_\alpha)$  is the configurational density-of-states (DOS), or degeneracy function, for the distribution of basins within the landscape. In other words,  $g(E_\alpha)$  is the number of basins present that possess minimum potential energy  $E_\alpha$ . Note that the configurational degeneracy function is a property of the potential energy landscape and is independent of temperature. The vibrational free energy,  $F_{vib} = -TS_{vib}$ , of each basin is a measure of the basin size where the vibrational entropy of a basin,  $S_{vib} \equiv k \ln N_{vib}$ , can be regarded as representing the number of vibrational states contained in that basin.

We now define a combined vibrational and configurational degeneracy in a single function, i.e.,

$$G'(\beta, E_\alpha) \equiv g(E_\alpha) \exp(-\beta F_{vib}(\beta, E_\alpha)). \quad (3.14)$$

Noting that the perfect crystal has unit configurational degeneracy, i.e.,  $g(E^P) = 1$  where  $E^P$  is the perfect crystal energy, the combined DOS function may be expressed in terms of formation energies, i.e.,

$$G''(\beta, \Delta E_\alpha) \equiv \frac{G'(\beta, E_\alpha)}{G'(\beta, E^P)} = g(E_\alpha) \exp(-\beta \Delta F_{vib}(E_\alpha)), \quad (3.15)$$

where  $\Delta E_\alpha \equiv E_\alpha - E^P$  is the formation energy of basin  $\alpha$  and

$$\Delta F_{vib}(E_\alpha) \equiv F_{vib}(\beta, E_\alpha) - F_{vib}(\beta, E^P), \quad (3.16)$$

is the formation vibrational free energy. Note that all reference perfect crystal properties are scaled to refer to the same number of atoms as in the defective crystal. Within the

harmonic approximation [93], the combined DOS function in Eqn (3.15) can be further simplified into the form [92,94]

$$G'(\beta, \Delta E_\alpha) = G(\Delta E_\alpha) \Omega^P(\beta), \quad (3.17)$$

where

$$\Omega^P(\beta) = G'(\beta, E^P) \exp(-\beta E^P), \quad (3.18)$$

is a temperature-dependent constant defined only on the perfect crystal configuration. The DOS distribution,  $G(\Delta E_\alpha)$ , is now independent of temperature and will be used as the basis for computing defect thermodynamic properties in the following sections. Using Eqns (3.17) and (3.18), the partition function in Eqn (3.13) can be written entirely in terms of formation energy as

$$Z = \frac{\Omega^P(\beta)}{\Lambda^{3N}} \int G(\Delta E_\alpha) \exp(-\beta \Delta E_\alpha) d\Delta E_\alpha. \quad (3.19)$$

Finally, the formation (Helmholz) free energy for a defect is given by

$$\Delta G = -k_B T \ln \int G(\Delta E_\alpha) \exp(-\beta \Delta E_\alpha) d(\Delta E_\alpha). \quad (3.20)$$

The above formalism readily can be extended to the isobaric-isothermal (NPT) ensemble which is characterized by an *enthalpy* landscape [95,96]. The key result is that the isothermal-isobaric partition function can be written in an analogous form to Eqn (3.13), i.e.,

$$Y(N, P, T) \propto \int g(H_\alpha) \exp(-\beta H_\alpha) \exp(-\beta \tilde{F}_{vib}(\beta, H_\alpha)) dH_\alpha \quad (3.21)$$

where  $P$  is the pressure,  $H_\alpha$  is the enthalpy of inherent structure  $\alpha$ , and  $\tilde{F}_{vib}(\beta, H_\alpha)$  is the vibrational free energy of basin  $\alpha$  within the NPT ensemble. Similar considerations used to derive Eqn (3.19) can be applied to give

$$Y \sim \int G(\Delta H_\alpha) \exp(-\beta \Delta H_\alpha) d\Delta H_\alpha. \quad (3.22)$$

In Eqn (3.22), the formation enthalpy is calculated as  $\Delta H_\alpha = \Delta E_\alpha + P \Delta V_\alpha$ , where  $\Delta V_\alpha \equiv V_\alpha - V^P$  is the formation volume of a particular configuration that corresponds to basin  $\alpha$  relative to the volume of the perfect crystal,  $V^P$ .

### 3.5.2 Sampling Inherent Structures with Molecular Dynamics Simulation

In order to apply ISL theory to defect thermodynamics, the potential energy landscape (PEL) must be appropriately sampled. Standard molecular dynamics (MD) is used to perform all PEL sampling described in this chapter, although any suitable variant of the Monte Carlo method is equally applicable. For example, prior studies have employed a number of highly efficient methods, notable examples being the basin hopping

technique [82] and the minima hopping method [97]. Although certainly not the most efficient approach, the principal advantage of direct MD sampling is that it automatically accounts for all configurational and vibrational degrees of freedom.

The procedure for locating potential energy basins for the various defect configurations is as follows. First, the defect is inserted into the simulation cell and a short MD simulation is used to relax the structure before data is collected. Next, the probability distribution of the inherent structure minimum energies is accumulated by periodically taking snapshots of the MD trajectory and quenching them using conjugate-gradient energy minimization (or any other quenching method). Here, minimization was performed every 200 MD time steps. The result from each quench gives the local inherent structure formation energy,  $\Delta E_\alpha$ , of the current basin. A formation energy (or enthalpy) histogram is then collected into energy/enthalpy bins (width is typically 0.1–1.0 eV). The result of this procedure is a temperature-dependent probability distribution of basin energies, which is related to the configurational-vibrational density-of-states distribution by [87,88,98]

$$P(\Delta E, \beta_{sim}) = G(\Delta E) \exp(-\beta_{sim} \Delta E) \quad (3.23)$$

where  $\beta_{sim}$  is the temperature at which the simulation is performed. Note that in Eqn (3.23) and in all subsequent discussion, the subscript “ $\alpha$ ” is omitted for notational brevity.

In the following sections, all MD simulations for PEL sampling were carried out in either the constant atom-volume-temperature (NVT) or the constant atom-pressure-temperature (NPT) ensembles using the EDIP empirical potential unless otherwise stated. It should be noted here that there is recent evidence [99] that potential energy landscapes predicted by empirical potentials such as EDIP tend to be significantly rougher than landscapes generated by more accurate representations such as DFT and tight-binding potentials. While such discrepancies, which are not yet fully characterized, can alter the quantitative estimates of entropic contributions obtained from inherent structure theory, that the qualitative conclusions generated on the basis of empirical potentials are useful for understanding the mechanisms of high-temperature microstructural evolution.

The LAMMPS software [100] was used for all MD simulations and conjugate-gradient energy minimizations. In the case of NVT simulations, the system volume was chosen using short NPT simulations to provide the desired value of the hydrostatic pressure. MD time steps of 1.0 fs were used to integrate the particle trajectories. Generally,  $O(10^5)$  inherent structures are needed to produce a converged probability distribution at a specified temperature. The exact number of inherent state visits required for convergence depends on the least visited states within the distribution; the  $10^5$  estimate is sufficient to converge distributions down to probabilities in the  $10^{-3}$ – $10^{-4}$  range (with increasing error at lower probabilities). Convergence was checked by comparing distributions as the number of inherent structure samples increased.

## 3.6 High Temperature Defect Thermodynamics

In this section, the ISL framework outlined in [Section 3.5](#) is used to compute point defect and cluster thermodynamics at finite temperature. The single vacancy is considered first to illustrate the key features of the theoretical framework followed by vacancy and self-interstitial cluster analyses.

### 3.6.1 The Single Vacancy

The inherent structure probability distribution for the single vacancy near the melting temperature (1600 K) was computed using the EDIP potential according to the method outlined in [Section 3.5.2](#). Shown in [Figure 3.7\(A–F\)](#) are example mechanically stable structures with increasing formation energy. Several configurations (e.g., (a), (b), and (d))

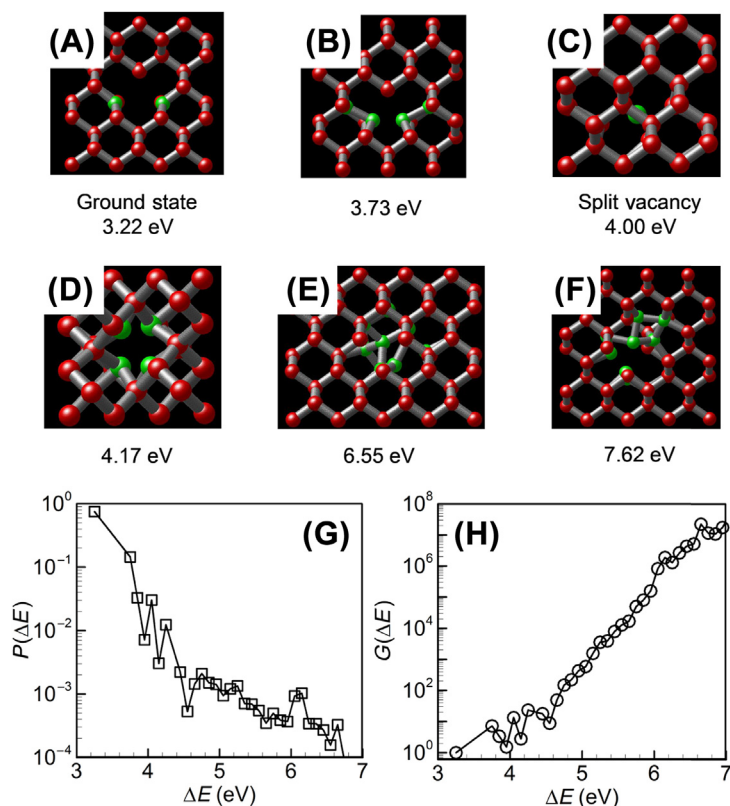


**FIGURE 3.7** (A–F) Example inherent structures of the single vacancy including the ground state (A), the split vacancy (C) and several other higher energy configurations. Red spheres denote silicon atoms that are within a threshold distance of their perfect lattice positions, while green spheres correspond to atoms that are displaced by more than 3% of a bond length. (G) Probability density distribution (PDF) for the EDIP vacancy; (H) Corresponding density-of-states (DOS) distribution.

are qualitatively similar but, in fact, correspond to completely distinct relaxations of the atoms surrounding the vacant site. Higher energy configurations (e.g., (e) and (f)) correspond to increasingly disordered structures.

The plots in (g) and (h) show the PDF and DOS for the vacancy. The PDF is normalized to unit probability, while the DOS, computed from the PDF using Eqn (3.23), is shifted so that  $G(\Delta E) = 1$  for the ground state configuration. While the probability of observing the ground state is highest, the system quenches to other configurations approximately 20% of the time at the temperature considered here. Note that there is no fundamental limit on the formation energies that can be accessed in these simulations; the range of energies accessed is limited by the extent of sampling. In other words, larger inherent structure samples would show progressively higher energy (and rarer) configurations. More frequent access to even higher energy configurations can be achieved simply by increasing the simulation temperature. In fact, as with almost all simulations of crystalline systems with periodic boundary conditions, significant superheating is possible and much higher energy inherent structures can be found. While such configurations do not play much of a role at temperatures below the melting point, they are important in the context of melting [88,92,94,101].

Most significantly, application of Eqn (3.20) at the melting temperature of EDIP silicon results in a formation free energy that is about 20% lower than that obtained by only considering the ground state configuration. In other words, at or near the melting point of EDIP silicon the (open system) equilibrium concentration of single vacancies is actually about a factor of two higher than would be expected based only on the ground state. This result starkly demonstrates the potential impact of configurational entropy at high temperature and suggests that it must be considered when high-temperature properties are required. As will be shown in the following sections, this is even more the case for point defect clusters.

### 3.6.2 Vacancy Clusters

The extension of the preceding analysis to vacancy clusters is straightforward. In this case, several vacancies are placed in close proximity, the system allowed to equilibrate at some temperature, and periodic quenches applied to isolate inherent structures. The only additional consideration here is that any configurations that correspond to “broken” clusters, in which not all vacancies are connected to each other in a single cluster, are discarded because these are not relevant to the PDF or DOS distributions for the single cluster. Here, the atomic energy is used to identify atoms that are near vacancies, and then the Stillinger criterion [102] is used to assess whether or not they are connected.

Shown in Figure 3.8 are PDFs (A) and DOS distributions (B) for several vacancy cluster sizes at 1600 K. Most significantly, the PDFs (A) for clusters larger than size three become peaked at formation energies that are substantially higher than the ground state configuration. In fact, at the temperature considered here, the ground state

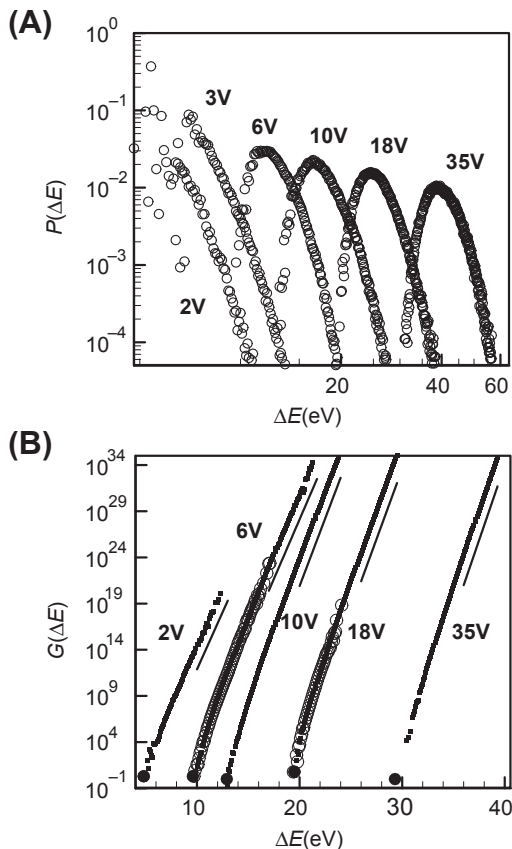


**FIGURE 3.8** (A) Probability distribution function for EDIP vacancy clusters at 1600 K. (B) Selected corresponding anchored density-of-states functions—thick lines; exponential fits—thin short lines; density-of-states for hexagonal ring configurations (see Section 3.4) used to anchor the distributions—solid circles. Adapted from Ref. [98].

configurations are never observed. Simply, the enormous configurational and vibrational degeneracy present at higher energy levels overwhelms the energetic favorability of the ground state at elevated temperature. This phenomenon becomes progressively more pronounced for larger clusters, whereby the difference between the energies of the ground state and the most likely states increases with cluster size.

The PDFs in Figure 3.8, which have been normalized to unit area, are known only to within a multiplicative constant, which is required for computing cluster free energies of formation using Eqn (3.20). The process by which these constants are obtained is as follows. First, the PDFs are converted to the corresponding DOS distributions as shown in Figure 3.8(B). The DOS curves are formed using simulations at multiple temperatures in order to properly sample low energy states and in particular the ground states (shown by the large solid circles). Recall that the ground state configurations for vacancy clusters are derived from hexagonal rings and adamantine cages as shown in Figure 3.1. Once the

DOS distributions are obtained, the degeneracy for the bin containing the ground state (and only the ground state) is calculated. To do this, the vibrational spectrum for the ground state configuration is computed using the quasi-harmonic approximation (QHA) [103,104] or some equivalent approach. The configurational degeneracy of the ground state then is estimated using symmetry arguments (see configurations in Figure 3.1) and the product of the two contributions (vibrational and configurational) is used to obtain  $G(\Delta E_{GS})$ , where “GS” represents the ground state. The rest of the DOS is then shifted accordingly for each cluster size.

The impact of configurational and vibrational entropy on vacancy cluster free energies is shown as a function of temperature and size in Figure 3.9. Shown in Figure 3.9(A) are cluster free energies as a function of size and temperature expressed as effective surface energies, i.e.,  $\sigma = \Delta G(n, T)/2.224n^{2/3}$ , where the numeric factor represents the surface area of a sphere with volume equal to  $n$  vacancies. The top surface in Figure 3.9(A) represents the free energy for the ground state configuration and includes the vibrational entropy which leads to the linear decrease of the free energy with

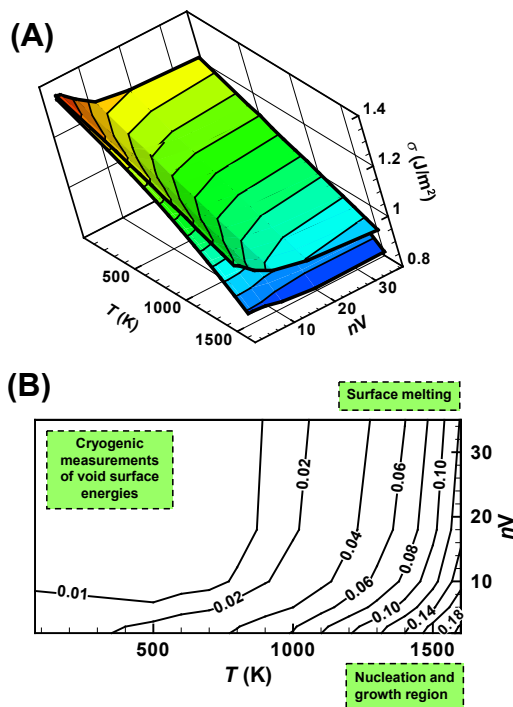


**FIGURE 3.9** (A) Temperature–size dependence of the formation free energy for small vacancy clusters. The free energy is expressed as an effective surface free energy for convenience (see text). Top surface corresponds to ground state (GS) analysis (vibrational entropy only) while lower surface corresponds to ISL analysis (ISL) that includes both vibrational and configurational entropic contributions. (B) Normalized difference,  $|\sigma_{GS} - \sigma_{ISL}|/\sigma_{ISL}$ , between the two analyses. Adapted from Ref. [98].

temperature. The lower surface was obtained using Eqn (3.20) and the data shown in Figure 3.8, i.e., including both vibrational and configurational entropy. While the agreement between the two curves is excellent at low temperature, they diverge significantly at higher temperature due to the rapid increase in configurational entropy.

A more transparent view of the difference between the two results is shown in Figure 3.9(B) in which the normalized difference between the two free energies is plotted on a line plot. Several important points are highlighted. The largest difference is apparent in the lower right corner, corresponding to small clusters at high temperature. These clusters are significantly different in morphology from the expected compact octahedral structures observed experimentally (which are large and have cooled to low temperature). Instead of assuming the compact hexagonal ring and adamantine cage constructs depicted in Figure 3.1, these clusters tend to be in loosely bound, extended configurations with capture radii that are significantly larger than those of the compact configurations. Given that this small size-high temperature regime is crucial in the initial stages of void nucleation during silicon crystal growth, the omission of configurational entropy in any nucleation-growth model for voids is likely to cause large errors.

In the opposite corner, i.e., larger clusters at low temperature, the agreement between the ground state and ISL analyses is perfect because configurational entropy does not play a role. Recall from Section 3.4.1 that in this region, where void formation energies are well described by the (111) surface energy, the EDIP predictions are in excellent agreement with experimental measurements. Finally, in the top right corner of Figure 3.9(B), corresponding to larger clusters at high temperature, a moderate but persistent error between the ground state and ISL analysis exists. This size-temperature regime corresponds to surface melting of voids, in which the overall void shape may be compact, but configurational entropy is sufficient to lead to a melted surface layer at the void-matrix interface. In fact, this feature is directly connected to the phenomenon of defect-induced melting, which is beyond the scope of the present discussion.

In summary, the ISL picture for vacancy cluster thermodynamics shows surprisingly rich behavior. At high temperatures, configurational entropy drives small clusters into mobile, loosely bound structures that have lower free energy than corresponding compact configurations. These effects play major roles in the nucleation and early growth phase of small vacancy clusters. As the crystal cools, the impact of configurational entropy gradually decays, leading to the well-known compact octahedral structures observed experimentally. The action of configurational entropy is therefore somewhat insidious—although it materially impacts the final distribution of voids in silicon crystals, it is hard (or even impossible) to observe it directly in action. However, there is some indirect evidence for the validity of this overall picture. In ref. [57], the ISL-based free energy function obtained in Figure 3.9 was employed in a continuum model for void nucleation and growth during CZ growth of silicon crystals [1,58,105,106]. While these models have been quite successful at predicting void size distributions as a function of crystal growth conditions, they have relied on some degree of empirical parameter fitting in order to attain quantitative agreement with experimental

measurements of void size, void density, and the nucleation temperature at which voids suddenly nucleate during crystal cooling. A long-standing issue in particular was the fact that the (111) surface model for octahedral voids, while intuitively appealing, gave free energies that were too high and resulted in insufficient void formation. The ISL free energy picture resolves this issue with no empirical parameter fitting. At high temperatures where nucleation and growth take place, the free energy is much lower than the octahedral model would predict, and at low temperatures it naturally becomes consistent with it.

In concluding this section, it should be noted once again that the above results are strictly only valid for the EDIP potential. As mentioned earlier, there is some evidence that PEL roughness is somewhat overpredicted by empirical potentials as compared to DFT calculations [99]. If this is indeed the case, the results presented here are likely to overestimate the impact of configurational entropy. On the other hand, similar calculations with multiple empirical potentials (data not shown) seem to show that the presence of a noisy PEL with many closely spaced, mechanically stable inherent structures is fairly ubiquitous, with only quantitative deviations across the various potential models. Clearly, further work aimed at analyzing the nature of empirical potential and DFT PELs is required before more formal conclusions regarding this issue can be made.

### 3.6.3 Self-Interstitial Clusters

The ISL-based analysis of self-interstitial clusters is essentially identical to that for vacancy clusters. Given the higher degree of morphological complexity associated with self-interstitial clusters as mentioned earlier in Sections 3.4.2 and 3.4.3, only a few of the major features are described here and the reader is referred to refs. [92,107,108] for more details. Shown in Figure 3.10 are PDFs for several interstitial cluster sizes computed

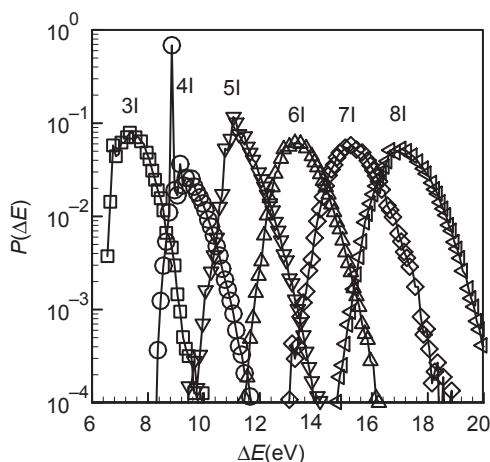
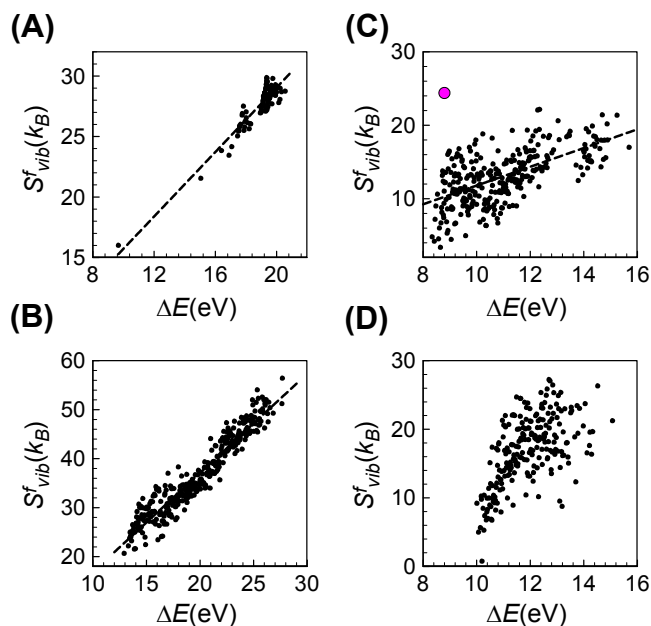


FIGURE 3.10 Probability distribution functions for EDIP self-interstitial clusters at 1100 K. Adapted from Ref. [108].

using the EDIP potential at 1100 K. Most of the distributions are qualitatively similar to the vacancy cluster PDFs, except for a striking feature in the 4-interstitial case. Here, a sharp peak is observed in the probability distribution at 8.75 eV formation energy that corresponds to the Humble/Arai configuration discussed in Section 3.4.2. Note that the peak does not correspond to the lowest energy configuration, i.e., the EDIP potential predicts slightly lower formation energy configurations, although these are observed quite rarely. Thus, while the Humble/Arai configuration, which is the known ground state configuration for the 4-interstitial cluster, is not predicted to be the absolute EDIP ground state, it is by far the most favored configuration. Other cluster sizes do not appear to exhibit similar special configurations.

The special favorability of the Humble/Arai configuration arises from a single unusual feature—it possesses very high vibrational entropy relative to energetically neighboring configurations [108]. Shown in Figure 3.11 are vibrational entropies computed using the QHA for large numbers of inherent structures for two vacancy clusters (left) and two interstitial clusters (right). Qualitatively, all clusters exhibit the same behavior in which the vibrational entropy increases roughly linearly with increasing inherent structure energy, although the dispersion is larger for the interstitial clusters. The vibrational entropy of formation corresponding to the Humble/Arai configuration is denoted by the large shaded sphere in Figure 3.11(C) and is notably higher (by about 5–6  $k_B$ ) than the surrounding values. This anomalous vibrational entropy readily accounts for the approximately  $O(10^2)$  increase in probability for the Humble/Arai configuration. Thus, although some configurations are predicted by the EDIP potential to be slightly more

**FIGURE 3.11** Vibrational entropy of formation for (A) 6-vacancy, (B) 10-vacancy, (C) 4-interstitial, and (D) 5-interstitial clusters as a function of formation energy. Each symbol represents a QHA calculation for a single inherent structure of a given cluster species. The large circle in (C) represents the Humble/Arai configuration. Dashed lines are guides and do not represent linear fits. Taken from Ref. [108].



energetically favorable than the Humble/Arai structure, it is entropically stabilized at finite temperature. In the language of potential energy landscapes, the basin that corresponds to the Humble/Arai configuration is particularly “wide” rather than being exceptionally “deep”.

The fact that the source of the stability is entropic leads to fundamentally different temperature dependence. Recall that for the vacancy cluster case, the ground state and other low energy/low entropy configurations become progressively less important as the system temperature rises. This is because as the temperature increases, the higher configurational entropy associated with higher energy configurations begins to dominate the free energy shifting the system toward sampling higher energy configurations. Here, however, due to the fact that the Humble/Arai configuration is vibrationally stabilized, it remains important even at elevated temperature.

### 3.6.3.1 Landscape Roughness and the Effect of Pressure

The prior discussion of small interstitial clusters in Section 3.4.2 suggests that similar entropic effects should be observed for the 8-interstitial cluster whose ground state is essentially two interacting Humble/Arai clusters in close proximity. However, no anomalous peak is obviously apparent in Figure 3.10 in the PDF for 8-interstitial case; this was also found to be the case at all temperatures at which ISL sampling was performed [108]. While temperature appears to have a simple and predictable influence on the PDFs shown in Figure 3.10—they shift to the right and become wider with increasing temperature—the impact of hydrostatic pressure was found to be much more subtle and provides insight into the complex interplay between energy and configurational and vibrational entropies in these systems.

PDFs at 1100 K are shown in Figure 3.12 for the 4- and 8-interstitial clusters at different applied hydrostatic pressures. The base-case zero pressure PDFs are denoted

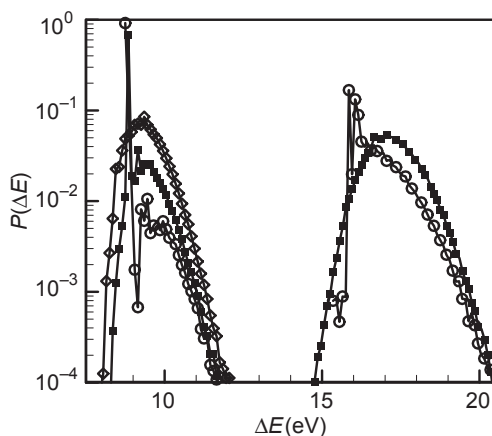


**FIGURE 3.12** PDFs for the 4 (left) and 8 (right) interstitial clusters at 1100 K. Filled squares—zero pressure; open circles—3 GPa tension; open diamonds (4-interstitial only)—3 GPa compression.

by the filled square symbols and correspond to the PDFs shown previously in [Figure 3.10](#). The open circles show the PDFs computed under 3 GPa of applied tension, which corresponds to about 1% tensile strain. The 4-interstitial PDF is modified in two important ways—first the dominance of the Humble/Arai peak increases, and second, the inherent structures previously found to the left of the peak are no longer mechanically stable and disappear so that the Humble/Arai configuration becomes the lowest energy configuration. The change in 8-interstitial PDF is even more striking. Whereas the zero pressure distribution was the usual smoothly rounded distribution, the PDF under tension now exhibits sharp peaks near the minimum energy, much like the 4-interstitial case. In fact, these spikes correspond to the well-known “compact” and “elongated” configurations identified in refs. [46,48]. Once again, their probabilities are enhanced by their high vibrational entropies relative to neighboring configurations. Finally, the 4-interstitial PDF obtained under compression is shown by the open diamond symbols. Here, the peak corresponding to the Humble/Arai configuration is no longer visible.

It is tempting to interpret the trends in [Figure 3.12](#) by considering the effect of hydrostatic pressure on the Humble/Arai configuration. However, as shown in ref. [108] applied pressure (compressive or tensile) does not alter the formation energy or vibrational entropy of the Humble/Arai configuration. Instead, the behavior in [Figure 3.12](#) arises from a collective phenomenon across the entire PEL of the system. In [Figure 3.13](#), the DOS distributions for the 4-interstitial cluster at each of the three applied pressures are plotted so that they are equal at the energy bin that contains the Humble/Arai configuration. The effect of hydrostatic pressure is immediately evident. Simply put, compression tends to increase the density of states while tension reduces it. Given that

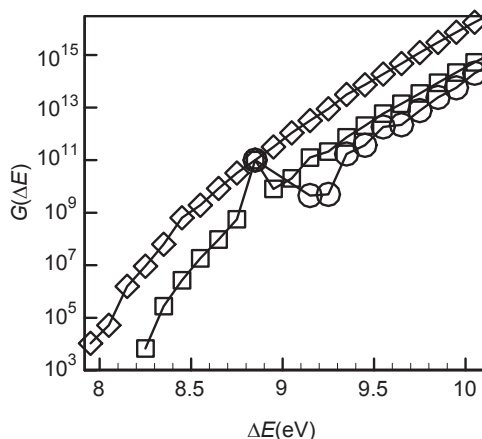


**FIGURE 3.13** 4-interstitial DOS as a function of pressure. Squares—zero pressure; circles—3 GPa tension; diamonds—3 GPa compression. Taken from Ref. [108].

the vibrational entropy of a given configuration is unaltered by hydrostatic pressure (at least at the levels applied here), the effect on the DOS is largely configurational. Thus, when compression is applied, the Humble/Arai configuration does not become altered; it simply loses its dominance over other configurations because the total number of alternative configurations is now much greater. The opposite effect is present under tension—as inherent structures are lost, the dominance of the Humble/Arai configuration becomes even stronger. Thus, whether the Humble/Arai configuration is dominant or not, depends on a competition between its high vibrational entropy and the collective configurational entropy of all other configurations.

A very simple, yet conceptually appealing, interpretation of the effect of hydrostatic pressure is that compression acts to roughen the potential energy landscape, while tension acts to smooth it, much like pushing and pulling on a sheet of paper. Subsequent analysis with other potentials such as Tersoff has shown that this is not unique to EDIP, and appears to be a common feature of empirical potentials (or at least bond-order type potentials). One possible explanation for this behavior is that as the system is compressed, the number of neighbors within interaction range of a given atom increases, leading to increased landscape roughness.

Finally, it is interesting to note that while the EDIP potential predicted the existence of apparently spurious stable configurations with formation energies below that of the Humble/Arai configuration, these minima in the PEL quickly disappear under the application of tension. Consider a situation in which the EDIP potential is being tested using the 4-interstitial cluster. Performing the defect in the Humble/Arai configuration would show that, indeed, this is a stable structure with a predicted formation energy that is in good agreement with DFT values. On the other hand, a global minimization over the PEL, with no initial knowledge of the Humble/Arai configuration, would identify a ground state that looks nothing like the Humble/Arai configuration with slightly lower formation energy. In this case, the potential would be considered as invalid when compared to DFT. The present analysis shows that the potential is largely in excellent agreement with DFT results but appears to predict some spurious local minima some of which lie at lower energy than the Humble/Arai configuration. The collective impact of these spurious minima on the overall configurational entropy predicted by EDIP is an open question. Answering it may help identify new ways to think about empirical potential design and validation.

### 3.7 Conclusions

The aim of this chapter was to provide evidence, through several vignettes, for the utility of atomistic simulations of intrinsic defect physics in silicon. The identification of the energetic ground state and the subsequent calculation of its structure and formation thermodynamics has been the subject of many studies, yet the ability to do this with complete quantitative confidence remains elusive. In the second portion of the chapter,

an example application of atomistic simulation to the study of entropic effects at elevated temperature was used to demonstrate the potential for such simulations to provide mechanistic information that is generally very difficult to come by with experimental measurements.

Overall, it is safe to say that atomistic calculations are, as a collective tool kit, extremely powerful and versatile tools for studying the thermodynamics of point defect and defect clusters in crystalline silicon. Indeed, there are now countless examples of successful studies in the literature and there is little doubt that they have greatly increased our understanding of defect physics, thermodynamics and transport in silicon. However, numerous challenges remain and these must be clearly identified when deciding on how to apply this tool kit to a particular situation. First and foremost, it is important to state at the outset that the notion of employing atomistic calculations in a “plug-and-play” fashion to compute defect properties on demand has not yet been realized. Ironically, the temptation to treat simulations in this manner has been exacerbated by the increased availability of sophisticated, user-friendly and very powerful open-source codes. However, in both empirical potential and electronic structure calculations, there are many parameters that need to be carefully specified (and are problem specific) and many validation steps that need to be undertaken each time. This is especially true when the properties being computed are not well studied. In the case of empirical potential calculations, it is clear that the choice of potential is crucial—while there is no one single potential that works best for everything, some are clearly better for particular aspects. Even for so-called *ab initio* calculations, the proper choice of model parameters such as sampling points for integration, system size, and exchange-correlation functional can make surprisingly large impacts on the computed property. This can lead to an overestimate of the accuracy of the results.

On the whole, and particularly for silicon, it can therefore be argued that much of the success achieved with atomistic simulation of defect physics in silicon has not been related to the calculation of quantitative estimates for specific thermophysical properties. Instead the success has stemmed in large part from an improved mechanistic understanding of processes that are otherwise extremely difficult to probe experimentally. As mentioned above, part of the reason for this is the large scatter in the predicted properties with respect to a number of model parameters and choices. Moreover, coupled with this is the fact that many observable defect-related phenomena in silicon crystal growth and wafer annealing arise from a highly sensitive balance between self-interstitials and vacancies requiring tremendous (and presently unattainable) accuracy to predict without some amount of parametric regression. As a result, the most successful applications of this tool kit have been to establish a semi-quantitative picture, which is then further refined by detailed comparisons to experimental measurements. Given the tremendous progress in the quality and scope of atomistic simulations over the last few decades, there is no doubt that the role of such calculations will only grow.

## References

- [1] Sinno T, Dornberger E, von Ammon W, Brown RA, Dupret F. Defect engineering of Czochralski single-crystal silicon. *Mater Sci Eng R* 2000;28:149–98.
- [2] Katz JL, Wiedersi H. Nucleation of voids in materials supersaturated with vacancies and interstitials. *J Chem Phys* 1971;55:1414.
- [3] Prasad M, Sinno T. Internally consistent approach for modeling solid-state aggregation. I. Atomistic calculations of vacancy clustering in silicon. *Phys Rev B* 2003;68:045206.
- [4] Lifshitz IM, Slyozov VV. The kinetics of precipitation from supersaturated solid solutions. *J Phys Chem Solids* 1961;19:35–50.
- [5] Balamane H, Halicioglu T, Tiller WA. Comparative-study of silicon empirical interatomic potentials. *Phys Rev B* 1992;46:2250–79.
- [6] Stillinger FH, Weber TA. Computer-simulation of local order in condensed phases of silicon. *Phys Rev B* 1985;31:5262–71.
- [7] Pearson E, Takai T, Halicioglu T, Tiller WA. Computer modeling of Si and Sic surfaces and surface processes relevant to crystal-growth from the vapor. *J Cryst Growth* 1984;70:33–40.
- [8] Biswas R, Hamann DR. Interatomic potentials for silicon structural energies. *Phys Rev Lett* 1985;55:2001–4.
- [9] Tersoff J. Empirical interatomic potential for silicon with improved elastic properties. *Phys Rev B* 1988;38:9902–5.
- [10] Tersoff J. Modeling solid-state chemistry – interatomic potentials for multicomponent systems. *Phys Rev B* 1989;39:5566–8.
- [11] Agrawal PM, Raff LM, Komanduri R. Monte Carlo simulations of void-nucleated melting of silicon via modification in the tersoff potential parameters. *Phys Rev B* 2005;72.
- [12] Erhart P, Albe K. Analytical potential for atomistic simulations of silicon, carbon, and silicon carbide. *Phys Rev B* 2005;71.
- [13] Pizzagalli L, Godet J, Guérolé J, Brochard S, Holmstrom E, Nordlund K, et al. A new parametrization of the Stillinger–Weber potential for an improved description of defects and plasticity of silicon. *J Phys Condens Matter* 2013;25:055801.
- [14] Vink RLC, Barkema GT, van der Weg WF, Mousseau N. Fitting the Stillinger–Weber potential to amorphous silicon. *J Non-Cryst Solids* 2001;282:248–55.
- [15] Kelires PC, Tersoff J. Equilibrium alloy properties by direct simulation – oscillatory segregation at the Si–Ge(100) 2x1 surface. *Phys Rev Lett* 1989;63:1164–7.
- [16] Cook SJ, Clancy P. Comparison of semiempirical potential functions for silicon and germanium. *Phys Rev B* 1993;47:7686–99.
- [17] Baskes MI. Atomistic potentials for the molybdenum-silicon system. *Mat Sci Eng A* 1999;261:165–8.
- [18] Thijsse BJ. Silicon potentials under (ion) attack: towards a new MEAM model. *Nucl Instrum Meth B* 2005;228:198–211.
- [19] Lee BJ. A modified embedded atom method interatomic potential for silicon. *Calphad-Computer Coupling Phase Diagrams Thermochem* 2007;31:95–104.
- [20] Timonova M, Thijsse BJ. Optimizing the MEAM potential for silicon. *Model Simul Mater Sci Eng* 2011;19.
- [21] Lenosky TJ, Sadigh B, Alonso E, Bulatov VV, de la Rubia TD, Kim J, et al. Highly optimized empirical potential model of silicon. *Model Simul Mater Sci Eng* 2000;8:825.

- [22] Bazant MZ, Kaxiras E, Justo JF. Environment-dependent interatomic potential for bulk silicon. *Phys Rev B* 1997;56:8542–52.
- [23] Justo JF, Bazant MZ, Kaxiras E, Bulatov VV, Yip S. Interatomic potential for silicon defects and disordered phases. *Phys Rev B* 1998;58:2539–50.
- [24] Sinno T, Jiang ZK, Brown RA. Atomistic simulation of point defects in silicon at high temperature. *Appl Phys Lett* 1996;68:3028–30.
- [25] Baskes MI, Nelson JS, Wright AF. Semiempirical modified embedded-atom potentials for silicon and germanium. *Phys Rev B* 1989;40:6085–100.
- [26] Gillespie B, Zhou X, Murdick D, Wadley H, Drautz R, Pettifor D. Bond-order potential for silicon. *Phys Rev B* 2007;75:155207.
- [27] Marqués LA, Pelaz L, Castrillo P, Barbolla J. Molecular dynamics study of the configurational and energetic properties of the silicon self-interstitial. *Phys Rev B* 2005;71:085204.
- [28] Argaman N, Makov G. Density functional theory: an introduction. *Am J Phys* 2000;68:69–79.
- [29] Estreicher SK. Structure and dynamics of point defects in crystalline silicon. *Phys Status Solidi B* 2000;217:513–32.
- [30] Colombo L. Tight-binding molecular dynamics: a primer. *Riv Nuovo Cimento* 2005;28:1–59.
- [31] Lenosky TJ, Kress JD, Kwon I, Voter AF, Edwards B, Richards DF, et al. Highly optimized tight-binding model of silicon. *Phys Rev B* 1997;55:1528.
- [32] Antonelli A, Bernholc J. Pressure effects on self-diffusion in silicon. *Phys Rev B* 1989;40:10643–6.
- [33] Scheffler M, Vigneron JP, Bachelet GB. Total-energy gradients and lattice-distortions at point-defects in semiconductors. *Phys Rev B* 1985;31:6541–51.
- [34] Car R, Kelly PJ, Oshiyama A, Pantelides ST. Microscopic theory of impurity-defect reactions and impurity diffusion in silicon. *Phys Rev Lett* 1985;54:360–3.
- [35] Nichols CS, Vandewalle CG, Pantelides ST. Mechanisms of dopant impurity diffusion in silicon. *Phys Rev B* 1989;40:5484–96.
- [36] Blochl PE, Smargiassi E, Car R, Laks DB, Andreoni W, Pantelides ST. 1st-principles calculations of self-diffusion constants in silicon. *Phys Rev Lett* 1993;70:2435–8.
- [37] Pino AD, Rappe AM, Joannopoulos JD. Abinitio investigation of carbon-related defects in silicon. *Phys Rev B* 1993;47:12554–7.
- [38] Zhu J, delaRubia TD, Yang LH, Mailhot C, Gilmer GH. Ab initio pseudopotential calculations of B diffusion and pairing in Si. *Phys Rev B* 1996;54:4741–7.
- [39] Mercer JL, Nelson JS, Wright AF, Stechel EB. Ab initio calculations of the energetics of the neutral Si vacancy defect. *Model Simul Mater Sci Eng* 1998;6:1–8.
- [40] Puska MJ, Poykko S, Pesola M, Nieminen RM. Convergence of supercell calculations for point defects in semiconductors: vacancy in silicon. *Phys Rev B* 1998;58:1318–25.
- [41] Probert MIJ, Payne MC. Improving the convergence of defect calculations in supercells: an ab initio study of the neutral silicon vacancy. *Phys Rev B* 2003;67.
- [42] Wright A. Density-functional-theory calculations for the silicon vacancy. *Phys Rev B* 2006;74:165116.
- [43] Corsetti F, Mostofi AA. System-size convergence of point defect properties: the case of the silicon vacancy,”. *Phys Rev B* 2011;84.
- [44] Dai JG, Kanter JM, Kapur SS, Seider WD, Sinno T. On-lattice kinetic Monte Carlo simulations of point defect aggregation in entropically influenced crystalline systems. *Phys Rev B* 2005;72.
- [45] Prasad M, Sinno T. Internally consistent approach for modeling solid-state aggregation. I. Atomistic calculations of vacancy clustering in silicon. *Phys Rev B* 2003;68.

- [46] Lee S, Hwang GS. Structure and stability of small compact self-interstitial clusters in crystalline silicon. *Phys Rev B* 2008;77:085210.
- [47] Kim J, Kirchhoff F, Aulbur WG, Wilkins JW, Khan FS, Kresse C. Thermally activated reorientation of di-interstitial defects in silicon. *Phys Rev Lett* 1999;83:1990–3.
- [48] Kim J, Kirchhoff F, Wilkins JW, Khan FS. Stability of Si-interstitial defects: from point to extended defects. *Phys Rev Lett* 2000;84:503–6.
- [49] Wang C, Wang Z, Meng Q. Comparative study of the empirical interatomic potentials and density-functional simulations of divacancy and hexavacancy in silicon. *Phys B: Condens Matter* 2011;406:467–70.
- [50] Bongiorno A, Colombo L, Cargnoni F, Gatti C, Rosati M. Evolution of energetics and bonding of compact self-interstitial clusters in Si. *Europhys Lett* 2000;50:608–14.
- [51] Prasad M, Sinno T. Atomistic-to-continuum description of vacancy cluster properties in crystalline silicon. *Appl Phys Lett* 2002;80:1951–3.
- [52] Chadi DJ, Chang KJ. Magic numbers for vacancy aggregation in crystalline Si. *Phys Rev B* 1988;38:1523–5.
- [53] Estreicher SK, Hastings JL, Fedders PA. The ring-hexavacancy in silicon: a stable and inactive defect. *Appl Phys Lett* 1997;70:432–4.
- [54] Prasad M, Sinno T. Internally consistent approach for modeling solid-state aggregation. II. Mean-field representation of atomistic processes. *Phys Rev B* 2003;68.
- [55] Jaccodine RJ. Surface energy of germanium and silicon. *J Electrochem Soc* 1963;110:524–7.
- [56] Gilman JJ. Direct measurements of the surface energies of crystals. *J Appl Phys* 1960;31:2208–18.
- [57] Frewen TA, Kapur SS, Haeckl W, von Ammon W, Sinno T. A microscopically accurate continuum model for void formation during semiconductor silicon processing. *J Cryst Growth* 2005;279:258–71.
- [58] Voronkov VV, Falster R. Vacancy-type microdefect formation in Czochralski silicon. *J Cryst Growth* 1998;194:76–88.
- [59] Kapur SS, Sinno T. Entropic origins of stability in silicon interstitial clusters. *Appl Phys Lett* 2008;93:221911.
- [60] Cowern NEB, Mannino G, Stolk PA, Roozeboom F, Huizing HGA, van Berkum JGM, et al. Energetics of self-interstitial clusters in Si. *Phys Rev Lett* 1999;82:4460–3.
- [61] Madden PK, Davidson SM. Nature of rod-like defects observed in boron-irradiated silicon. *Radiat Eff* 1972;14:271–3.
- [62] Kohyama M, Takeda S. Atomic-structure and energy of the {113} planar interstitial defects in Si. *Phys Rev B* 1992;46:12305–15.
- [63] Jones KS, Liu J, Zhang L, Krishnamoorthy V, DeHoff RT. Studies of the interactions between {311} defects and type I and II dislocation loops in Si<sup>+</sup> implanted silicon. *Nucl Instrum Methods Phys Res Sect B* 1995;106:227–32.
- [64] Pan GZ, Tu KN. Transmission electron microscopy on {113} rodlike defects and {111} dislocation loops in silicon-implanted silicon. *J Appl Phys* 1997;82:601–8.
- [65] Muto S, Takeda S. New stable defect structure on the {001} plane in germanium formed by deuteron irradiation. *Philos Mag Lett* 1995;72:99–104.
- [66] Li JH, Jones KS. {311} defects in silicon: the source of the loops. *Appl Phys Lett* 1998;73:3748–50.
- [67] Claverie A, Colombeau B, De Mauduit B, Bonafos C, Hebras X, Ben Assayag G, et al. Extended defects in shallow implants. *Appl Phys A* 2003;76:1025–33.

- [68] Goss JP, Eberlein TAG, Jones R, Pinho N, Blumenau AT, Frauenheim T, et al. Planar interstitial aggregates in Si. *J Phys: Condens Matter* 2002;14:12843–53.
- [69] Fedina L, Gutakovskii A, Aseev A, Van Landuyt J, Vanhellefont J. On the mechanism of {111}-defect formation in silicon studied by in situ electron irradiation in a high resolution electron microscope. *Philos Mag A* 1998;77:423–35.
- [70] Cristiano F, Colombeau B, Bonafos C, Altibelli A, Ben Assayag G, Claverie A. Thermal evolution of extrinsic defects in ion implanted silicon: current understanding and modelling. *Gettering and defect engineering semiconductor technology*, vol. 82–84; 2002. 201–206.
- [71] Chaudhry S, Liu J, Jones KS, Law ME. Evolution of dislocation loops in silicon in an inert ambient 2. *Solid-State Electron* 1995;38:1313–9.
- [72] Claverie A, Colombeau B, Cristiano F, Altibelli A, Bonafos C. Modeling of the Ostwald ripening of extrinsic defects and transient enhanced diffusion in silicon. *Nucl Instrum Methods Phys Res Sect B* 2002;186:281–6.
- [73] Coomer BJ, Goss JP, Jones R, Oberg S, Briddon PR. Identification of the tetra-interstitial in silicon. *J Phys-Condens Matter* 2001;13:L1–7.
- [74] Humble P. The structure and mechanism of formation of platelets in natural type Ia Diamond. *Proc R Soc London Ser A* 1982;381:65.
- [75] Arai N, Takeda S, Kohyama M. Self-interstitial clustering in crystalline silicon. *Phys Rev Lett* 1997; 78:4265–8.
- [76] Kohyama M, Takeda S. First-principles calculations of the self-interstitial cluster I-4 in Si. *Phys Rev B* 1999;60:8075–80.
- [77] Kapur SS, Sinno T. Entropic origins of stability in silicon interstitial clusters. *Appl Phys Lett* 2008;93.
- [78] Alippi P, Colombo L. Lattice-strain field induced by {311} self-interstitial defects in silicon. *Phys Rev B* 2000;62:1815–20.
- [79] Cristiano F, Grisolia J, Colombeau B, Omri M, de Mauduit B, Claverie A, et al. Formation energies and relative stability of perfect and faulted dislocation loops in silicon. *J Appl Phys* 2000;87:8420–8.
- [80] Claverie A, Giles LF, Omri M, de Mauduit B, Ben Assayag G, Mathiot D. Nucleation, growth and dissolution of extended defects in implanted Si: impact on dopant diffusion. *Nucl Instrum Methods Phys Res Sect B* 1999;147:1–12.
- [81] Cristiano F, Hebras X, Cherkashin N, Claverie A, Lerch W, Paul S. Clusters formation in ultralow-energy high-dose boron-implanted silicon. *Appl Phys Lett* 2003;83:5407–9.
- [82] Bogdan TV, Wales DJ, Calvo F. Equilibrium thermodynamics from basin-sampling. *J Chem Phys* 2006;124.
- [83] Calvo F, Doye JPK, Wales DJ. Collapse of Lennard-Jones homopolymers: size effects and energy landscapes. *J Chem Phys* 2002;116:2642–9.
- [84] Farrell JD, Lines C, Shepherd JJ, Chakrabarti D, Miller MA, Wales DJ. Energy landscapes, structural topologies and rearrangement mechanisms in clusters of dipolar particles. *Soft Matter* 2013;9: 5407–16.
- [85] Sciortino F, Kob W, Tartaglia P. Inherent structure entropy of supercooled liquids. *Phys Rev Lett* 1999;83:3214–7.
- [86] Debenedetti PG, Stillinger FH. Supercooled liquids and the glass transition. *Nature* 2001;410: 259–67.
- [87] Buchner S, Heuer A. Potential energy landscape of a model glass former: thermodynamics, anharmonicities, and finite size effects. *Phys Rev E* 1999;60:6507–18.

- [88] Nakagawa N, Peyrard M. The inherent structure landscape of a protein. *Proc Natl Acad Sci USA* 2006;103:5279–84.
- [89] Stillinger FH, Weber TA. Point-defects in Bcc crystals – structures, transition kinetics, and melting implications. *J Chem Phys* 1984;81:5095–103.
- [90] Stillinger FH, Weber TA. Hidden structure in liquids. *Phys Rev A* 1982;25:978–89.
- [91] Wales DJ. The energy landscape as a unifying theme in molecular science. *Philos Trans R Soc A* 2005;363:357–75.
- [92] Nieves AM, Chuang CY, Sinno T. Inherent structure analysis of defect thermodynamics and melting in silicon. *Mol Simul* 2012;38:659–70.
- [93] Mishin Y, Sorensen MR, Voter AF. Calculation of point-defect entropy in metals. *Philos Mag A* 2001;81:2591–612.
- [94] Nieves AM, Sinno T. An enthalpy landscape view of homogeneous melting in crystals. *J Chem Phys* 2011;135.
- [95] Mauro JC, Loucks RJ, Balakrishnan J, Raghavan S. Monte Carlo method for computing density of states and quench probability of potential energy and enthalpy landscapes. *J Chem Phys* 2007;126.
- [96] Potuzak M, Mauro JC, Kiczinski TJ, Ellison AJ, Allan DC. Communication: resolving the vibrational and configurational contributions to thermal expansion in isobaric glass-forming systems. *J Chem Phys* 2010;133.
- [97] Goedecker S. Minima hopping: an efficient search method for the global minimum of the potential energy surface of complex molecular systems. *J Chem Phys* 2004;120:9911–7.
- [98] Kapur SS, Prasad M, Crocker JC, Sinno T. Role of configurational entropy in the thermodynamics of clusters of point defects in crystalline solids. *Phys Rev B* 2005;72.
- [99] Ghasemi SA, Amsler M, Hennig RG, Roy S, Goedecker S, Lenosky TJ, et al. Energy landscape of silicon systems and its description by force fields, tight binding schemes, density functional methods, and quantum Monte Carlo methods. *Phys Rev B* 2010;81:214107.
- [100] Plimpton SJ. Fast parallel algorithms for short-range molecular dynamics. *J Comp Phys* 1995;117:1.
- [101] Wales DJ, Berry RS. Melting and freezing of small argon clusters. *J Chem Phys* 1990;92:4283–95.
- [102] Stillinger FH. Rigorous basis of Frenkel-Band theory of association equilibrium. *J Chem Phys* 1963;38:1486.
- [103] Bian Q, Bose SK, Shukla RC. Vibrational and thermodynamic properties of metals from a model embedded-atom potential. *J Phys Chem Solids* 2008;69:168–81.
- [104] Della Valle RG, Venuti E. Quasiharmonic lattice-dynamics and molecular-dynamics calculations for the Lennard-Jones solids. *Phys Rev B* 1998;58:206–12.
- [105] Sinno T, Brown RA. Modeling microdefect formation in Czochralski silicon. *J Electrochem Soc* 1999;146:2300–12.
- [106] Sinno T. A bottom-up multiscale view of point-defect aggregation in silicon. *J Cryst Growth* 2007;303:5–11.
- [107] Kapur SS, Sinno T. Detailed microscopic analysis of self-interstitial aggregation in silicon. I. Direct molecular dynamics simulations of aggregation. *Phys Rev B* 2010;82.
- [108] Kapur SS, Nieves AM, Sinno T. Detailed microscopic analysis of self-interstitial aggregation in silicon. II. Thermodynamic analysis of single clusters. *Phys Rev B* 2010;82.

# Stoichiometry of Oxide Crystals

Satoshi Uda

INSTITUTE FOR MATERIALS RESEARCH, TOHOKU UNIVERSITY, KATAHIRA, AOBA-KU, SENDAI, MIYAGI, JAPAN

## CHAPTER OUTLINE

<b>4.1 General Overview of Conventional Stoichiometry and Related Point Defects.....</b>	<b>176</b>
4.1.1 Brief Overview of Stoichiometry and Point Defects in Oxide Compounds .....	176
4.1.2 Crystal Sites in Oxide Crystals .....	179
4.1.3 Partitioning Behavior of Ionic Solutes in an Oxide Melt.....	180
<b>4.2 Extended Concept of Stoichiometry in Oxide Crystals .....</b>	<b>182</b>
4.2.1 The Thermodynamic Definition of Stoichiometry Associated with the Activity of Constituent Elements.....	183
4.2.2 Conventional Stoichiometric Compositions and the Law of Multiple Proportions....	184
4.2.2.1 Activities of the Constituent Elements in a Conventional Stoichiometric Crystal .....	185
4.2.3 Extended Stoichiometric Compositions Including Impurities and Vacancies.....	188
4.2.3.1 Degrees of Freedom in a Crystal Site.....	188
4.2.3.2 Activity of the Constituent Elements in an Extended Stoichiometric Crystal.....	189
<b>4.3 Growth Characteristics of Stoichiometric Crystals.....</b>	<b>192</b>
4.3.1 Crystallization Electromotive Force .....	193
4.3.2 Activities of Constituent Elements in the Melt and Solid States for an Oxide Crystal that is Both Stoichiometric and Congruent.....	196
<b>4.4 Oxide Crystals Having a Stoichiometric Composition Coincident with the Congruent Point .....</b>	<b>200</b>
4.4.1 MgO-Doped LiNbO <sub>3</sub> .....	201
4.4.1.1 Distribution of the Melting Temperatures of MgO-Doped LiNbO <sub>3</sub> .....	201
4.4.1.2 Crystallization Electromotive Force.....	202
4.4.1.3 Bulk Crystal Growth of <i>cs</i> -MgO:LiNbO <sub>3</sub> and Its Nonlinear Optical Characterization	203
4.4.2 MgO-Doped LiTaO <sub>3</sub> .....	207
4.4.2.1 Distribution of Melting Temperatures of MgO-Doped LiTaO <sub>3</sub> .....	207
4.4.2.2 Crystallization Electromotive Force.....	208
4.4.2.3 Bulk Crystal Growth and Curie Temperature of <i>cs</i> -MgO:LiTaO <sub>3</sub> .....	208
4.4.3 Thermodynamic Requirements for Impurity Doping .....	210
<b>4.5 Summary .....</b>	<b>212</b>
<b>References.....</b>	<b>212</b>

## 4.1 General Overview of Conventional Stoichiometry and Related Point Defects

### 4.1.1 Brief Overview of Stoichiometry and Point Defects in Oxide Compounds

A conventional stoichiometric compound is characterized as one that has an exact and fixed composition with a small integer ratio among its atomic components. This concept is related to Dalton's so-called law of multiple proportions [1]. The atoms in such a compound are located precisely at the appropriate crystal lattice points, and neither impurities nor defects are allowed to exist. Nonstoichiometry represents a deviation from the well-defined stoichiometry, by the introduction of point defects such as impurities and vacancies, when forming a solid solution. As such, the definition of a nonstoichiometric oxide material often refers to a structure that may be formed within a certain range of anion-to-cation ratios. Stoichiometric materials are used in electronic, optic, and optoelectronic devices [2,3] because of their excellent uniformity and high efficiency, which are attributed to the perfect ordering of the atoms in the crystal lattice. For an ideal stoichiometric structure, defects should be avoided. On the other hand, because their compositional variation enables the optimization of piezoelectric, ferroelectric, ferromagnetic, and other physical properties, nonstoichiometric materials with certain ranges of solid solutions often attract more attention than stoichiometric materials from the viewpoint of potential applications, given their greater ability to meet the requirements for different devices. Therefore, point defects, such as impurities or vacancies, are often intentionally added to a host material for such a purpose. Semiconducting materials, in which only a small amount of dopant in the range of  $10^{14}$ – $10^{18}$  /cm<sup>3</sup> is sufficient to cause drastic changes in the electronic properties, are typical examples [4–7]. Color change in the oxides [8] is another. However, it is difficult to experimentally show the exactness of a stoichiometric composition; it is also challenging to precisely determine the solid solution range in nonstoichiometric materials.

When discussing the characteristics of point defects, it is vital to have an understanding of the structure of the host material. Conventionally, the bonding state between the constituent elements, that is, the major components (the cations and anions) and any impurities and vacancies, forms the basis for discussing the generation, morphology, and mode of distribution of defects. Pauling [9] introduced the theoretical concepts of bond ionicity and bond strength parameters for a stable coordination polyhedron based on his second principle, the electrostatic valence rule. Since then, many modifications to the second principle have been suggested, including those of Brown and Shannon [10] and Brown [11,12]. The result has been the development of a concept proposing a bond-valence model in which static bond energy is a function of bond length, i.e., the distance between an oxygen ion and an associated cation. However, this concept is largely restricted to ionic compounds, and the parameters evaluated to date are not necessarily effective when applied to oxides, since the bonding state of many oxides represents a

mixture of ionic and covalent characteristics. As an example, MgO represents a typical ionic compound while SiO<sub>2</sub> is covalent. The degree of ionicity of the oxide is important and dominates its ionization behavior in the melt, as will be discussed in [Section 4.4.3](#).

The defect structure is uncertain for many oxide compounds, due to an inadequate understanding of issues related to the crystal structure, including the coordination sites for metal cations, ionic-covalent bonding states, oxygen-to-oxygen interactions, degree of oxidation, effect of the size ratio of metal to oxygen on crystal deformation, defect interactions, population of point defects and their configurations associated with ordering and disordering, solid solution ranges, and so on. For instance, the balance between ionic and covalent bonding depends on the individual oxide, which leads to variable energy states associated with defect generation and makes it difficult to predict bond length, lattice size, and the mode of deformation associated with defects and defect interactions. The oxide object of a defect study can vary from simple cubic to more complex perovskite and other crystal types. Many oxides show significant deviations from stoichiometry; depending on the oxygen pressure, the transition metals form numerous nonstoichiometric oxide phases with ions of differing valences, resulting in varying metal ion-to-oxygen ratios. Among these are the Magnéli phases, such as V<sub>n</sub>O<sub>2n-1</sub> and Ti<sub>n</sub>O<sub>2n-1</sub> [13,14]. The general form of two-element cubic compounds can be addressed as M<sub>a/b</sub>O crystals, where a/b is the ratio of metal (M) to oxygen (O) per mole of O atoms. The transition metal monoxides, such as NiO and CoO, are representative examples of M<sub>a/b</sub>O. For these materials, the ratio of metal to oxygen varies; NbO and VO have ratios both greater and less than one (NbO<sub>1.9975</sub> to NbO<sub>2.003</sub> and VO<sub>0.8</sub> to VO<sub>1.27</sub>), while CoO and CdO have ratios less than or equal to one (Co<sub>0.99</sub>O to Co<sub>1.00</sub>O) and equal to or greater than one (Cd<sub>1.00</sub>O to Cd<sub>1.0005</sub>O) [15]. The a/b ratio affects the physical properties of oxides, which are dominated by conventional factors, such as the ionic size, electronegativity, ionic-covalent character, attractive and repulsive interactions, and various oxidation states of the metal. The molar volume is one characteristic of oxide structures that is indicative of their crystalline properties and changes with the a/b ratio [16].

LiNbO<sub>3</sub> is a ferroelectric material with a more complex ilmenite structure belonging to the perovskite family, and it has a wide compositional range as a solid solution [17]. However, its composition deviates from stoichiometric only toward the Nb-rich side, since Li does not replace Nb at the Nb site. This behavior cannot be simply explained in terms of the ionic radius or electronegativity of the elements but is rather related to the inhibition of oxygen deficiency formation as a means of charge compensation due to the replacement of Nb<sup>5+</sup> by Li<sup>+</sup>. In extreme cases, the stoichiometric composition of some semiconducting materials, such as SnTe, does not belong to its solid solution range [18]. The oxidation of such materials is thought to be governed by the growth atmosphere, although the ease or difficulty of oxidation may also depend on the structure and the composition of the oxides. Coloring due to the presence of impurities or oxygen vacancies that act as color centers is also often observed in oxide crystals when they are grown or annealed in an insufficient oxygen atmosphere.

A simple consideration of the presence of interstitial impurities and/or oxygen vacancies may not be sufficient to confirm defect structures in oxides, since point defects in nonstoichiometric materials are not necessarily randomly distributed but rather may be ordered at high concentrations in cases where this ordering reduces the free energy of the structure. These point defects may also interact with one another [19], and one consequence of this interaction may be the formation of clusters. As an example, vacancy clustering has been proposed for Fe vacancies in a  $\text{Fe}_{1-x}\text{O}$  phase [20] (Figure 4.1). Interactions between defects can also form a superlattice; a 13:4 Koch–Cohn cluster is an example of one such superlattice [21]. On the other hand, vacancies, interstitials, and clusters, including their origins and formation mechanisms, have been well studied during Si crystal growth on both a theoretical and experimental basis [22–26].

Regarding analytical studies of point defects, thermodynamics and statistical thermodynamics are useful for understanding the generation and distribution of point defects from the energetic point of view, not only with regard to the random distribution of defects at low defect densities but also as a means of understanding the ordering and clustering of highly populous defects by taking into account the interactions between defects [27,28].

It is thus important to be aware of and to consider the quantity of impurities or vacancies. In this chapter, point defects will be discussed in association with the solid solution. Impurities or vacancies replacing the host elements at lattice points are often  $10^{-4}$  to  $10^{-2}$  mol or more in quantity if vacancies are required for charge compensation due to valence differences between the host element and the impurity. A thermally

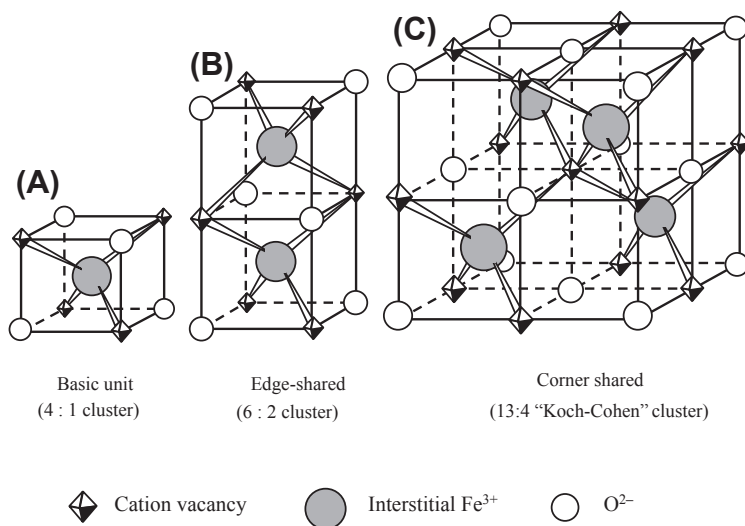


**FIGURE 4.1** Vacancy clustering and cluster association of iron-deficient  $\text{Fe}_{1-x}\text{O}$ . (A) The basic unit: a so-called 4:1 cluster consisting of four vacancies and one interstitial  $\text{Fe}^{3+}$  ion. (B) Two basic units combined to form an edge-shared 6:2 cluster complex. (C) Four basic units combined to form a corner-shared 13:4 cluster complex representing a superlattice known as a Koch–Cohn cluster [21].

activated vacancy is one of the intrinsic vacancies and can become enriched, depending on the band gap of the material, near the melting temperature of the material. However, the amount of vacancies of this type or of color-causing impurity centers is much smaller than the quantity of defects replacing the host element, by at least two orders of magnitude at high temperatures. For this reason, intrinsic point defects are disregarded in the following discussion.

### 4.1.2 Crystal Sites in Oxide Crystals

An oxide crystal consists of an oxygen framework that provides space for a metal cation based on its coordination number. For descriptive purposes, the space is often referred to as a crystal site, as in *tetrahedral* (4-coordination), *octahedral* (6-coordination), and *decahedral* (8-coordination) sites. Each of the constituent cations of the crystal is located in its specific site depending on its radius, valence, and electronegativity, such that attractive and repulsive forces between oxygen atoms and cations are in equilibrium. Each site in a conventional stoichiometric compound is completely filled with a specific element without any foreign elements or vacancies, so that a simple atomic ratio may be used to describe the relative quantities of the constituent elements; this is the law of multiple proportions [1]. Stoichiometric compositions of this type are readily described and understood without any uncertainties. The conventional stoichiometric compound  $\text{LiNbO}_3$  (s-LN), for example, contains three crystal sites: the Li, Nb, and O sites, each of which is completely filled with Li, O, and Nb, without any foreign elements or vacancies. In contrast, conventional congruent-melting  $\text{LiNbO}_3$  (c-LN) has completely filled Nb and O sites, while the Li site is occupied not only by Li but also by Nb (antisite Nb) as well as by vacancies necessary for charge compensation. Therefore, the components of this material consist of Li, Nb, and vacancies.

There are always issues concerning the extent to which an oxide crystal changes its oxygen content when it is grown or annealed in a different oxygen atmosphere. In cubic crystals, such as FeO, NiO, ZnO, and  $\text{VO}_5$ , and tetragonal crystals, such as  $\text{TiO}_2$ , the metal-to-oxygen ratio varies readily, concomitant with a change in the metal ion oxidation states. The oxygen quantity varies significantly, and this variation is explicitly reflected in the chemical formula of the substance. Although many questions remain unanswered regarding the oxygen deficiency mechanism associated with the defect structures, the formation energies of metal oxides available in the Ellingham diagram provide a good indication of whether these oxides easily lose oxygen upon exposure to a reduction atmosphere. The oxidation states of iron, nickel, and copper change readily according to the oxygen atmosphere because the transition energies between different oxidation states are small for these metal oxides. In contrast, once oxidized, lithium, magnesium, aluminum, and titanium cannot be reduced because they have elevated oxidation energies.  $\text{LiNbO}_3$  alone barely loses 0.01–0.1 mol of oxygen when annealed under reducing atmosphere. However, when doped with  $\text{Fe}^{3+}$  ions and annealed under reducing atmosphere,  $\text{LiNbO}_3$  easily loses oxygen in an amount equivalent to the oxygen

loss obtained for the reduction of  $\text{Fe}_2\text{O}_3$  to  $\text{FeO}$  contained in  $\text{LiNbO}_3$ . The reverse process (oxidation) is also the case. Metal oxides containing elements that evaporate readily exhibit more complex defect structures because mass conservation rules do not hold. These materials include  $\text{PbTiO}_3$ , PZNT ( $\text{Pb}(\text{Zn}_{1/3}\text{Nb}_{2/3})\text{O}_3\text{-PbTiO}_3$ ), PMNT ( $\text{Pb}(\text{Mg}_{1/3}\text{Nb}_{2/3})\text{O}_3\text{-PbTiO}_3$ ) [29–31], and  $\text{La}_3\text{Ga}_5\text{SiO}_{14}$  [32,33].

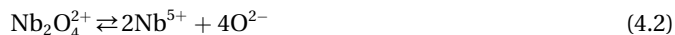
It is also well known that some of oxides exhibit a color change from colorless to yellow, orange, or even black when they are grown or annealed in an oxygen-poor atmosphere. However, the amount of oxygen that must be lost to yield a color center is often on the order of ppm or less, whereas the quantity of point defects associated with forming a solid solution will range from 0.01 to 0.1 mol. This chapter focuses on oxides with relatively complex structures, such as garnet, langasite, and perovskites involving ilmenite, such as  $\text{LiNbO}_3$  or  $\text{LiTaO}_3$ , in which oxygen is assumed to form a rather stable framework and the oxygen sites are fully saturated with oxygen, although they may still contain a small quantity of oxygen deficiencies that act as color centers.

#### 4.1.3 Partitioning Behavior of Ionic Solutes in an Oxide Melt

Typically, defect structures have been reviewed and discussed in association only with the solid state. Many excellent articles and books have been published concerning point defects in oxides [15,34–38], however, almost all of these regard defects only as a solid state issue; few publications have discussed defects in relation to crystallization from the melt, with the exception of some works regarding Si [22–26]. Since impurities or even vacancies are partitioned from the melt into the crystal during crystallization, it is imperative to discuss defects by relating their formation, characteristics, and thermodynamic stability to the coexistence of solid and liquid during crystallization.

Solute partitioning behavior is generally investigated using an equilibrium phase diagram. However, most oxide phase diagrams are pseudo-phase diagrams where the stoichiometry of oxygen to metal always holds and the oxygen is not considered an independent component. For this reason, conventional oxide phase diagrams do not take into account the ionization of neutral species that actually occurs in the oxide melt. Ionic species, which represent one of the major sources of point defects, are present in the melt [39] and are partitioned into the solid during crystallization [40–43]. Point defects, therefore, should be discussed in association with crystallization, and the oxygen in the melt should be considered as an independent component in the phase diagram. As will be discussed in detail in Section 4.3.1, the oxygen ions and metal ionic species behave independently, which has been experimentally demonstrated by the observation of crystallization electromotive force (c-EMF) generated by the segregation of ionic species at the solid–liquid interface, even in the case of c- $\text{LiNbO}_3$ . Therefore, although the  $\text{LiNbO}_3$  congruent point in the pseudo-binary diagram of  $\text{Li}_2\text{O-Nb}_2\text{O}_5$  is invariant, it is not invariant in the ternary diagram of  $\text{Li-Nb-O}$ , and thus a variety of population ratios among the ionic species are allowed.

If we simply assume that  $\text{LiNbO}_3$  is dissociated into  $\text{Li}_2\text{O}$  and  $\text{Nb}_2\text{O}_5$  and then ionized into further species, such as  $\text{Li}^+$ ,  $\text{OLi}^-$ ,  $\text{Nb}^{5+}$ ,  $\text{Nb}_2\text{O}_4^{2+}$ , and  $\text{O}^{2-}$  [39], in the ternary diagram of Li-Nb-O, all of these species can be regarded as components rather than just  $\text{Li}_2\text{O}$  and  $\text{Nb}_2\text{O}_5$  that are valid in the pseudo-binary diagram of  $\text{Li}_2\text{O}$ - $\text{Nb}_2\text{O}_5$ . The number of components therefore increases from two to five. However, even this is not entirely correct since we also have ongoing chemical reactions such as those shown in Eqns (4.1) and (4.2) following:



Accordingly, we can write the chemical potential relationships

$$\mu^{\text{OLi}^-} = \mu^{\text{O}^{2-}} + \mu^{\text{Li}^+} \quad (4.3)$$

and

$$\mu^{\text{Nb}_2\text{O}_4^{2+}} = 2\mu^{\text{Nb}^{5+}} + 4\mu^{\text{O}^{2-}}. \quad (4.4)$$

Equations (4.3) and (4.4) represent constraints that reduce the number of independent components to three species:  $\text{Li}^+$ ,  $\text{Nb}^{5+}$ , and  $\text{O}^{2-}$ . The above chemical species are hypothetical so that the general forms of the Li-bearing species and Nb-bearing species may be written as

$$\text{Li}(1), \text{Li}(2), \dots, \text{Li}(k) \quad (4.5)$$

and

$$\text{Nb}(1), \text{Nb}(2), \dots, \text{Nb}(l). \quad (4.6)$$

The oxygen ion,  $\text{O}^{2-}$ , is also a constituent chemical species. It therefore appears that the number of components is  $k + l + 1$ , however, the independent components are only  $\text{Li}^+$ ,  $\text{Nb}^{5+}$ , and  $\text{O}^{2-}$  since other components are complexes of Li and O or Nb and O so that constraints are in effect similar to those presented in Eqns (4.3) and (4.4), meaning that

$$\mu^{\text{Li}(i)} = m\mu^{\text{Li}^+} + n\mu^{\text{O}^{2-}} \quad (4.7)$$

and

$$\mu^{\text{Nb}(j)} = s\mu^{\text{Nb}^{5+}} + t\mu^{\text{O}^{2-}}. \quad (4.8)$$

Since there are three components instead of two, one more degree of freedom is available in the melt, which enables the population ratio to vary among the ionic species even for a congruent-melting composition. This population ratio will in turn depend on the growth conditions, such as growth velocity and temperature gradient. Although it initially seems strange that the ratio between ionic species changes with growth velocity while the congruent melt composition does not, this occurs because the congruent composition is defined on the basis of the  $\text{Li}_2\text{O}$ - $\text{Nb}_2\text{O}_5$  pseudo-binary associated with  $\text{LiNbO}_3$ , and this is invariant regardless of the growth velocity. In contrast, the presence of ionic species requires the oxygen ion to be considered as an

independent component, which adds one more degree of freedom to the ternary system and enables population change among the ionic species with growth velocity.

However, when these ionic species are partitioned into the solid, this one degree of freedom in the melt phase must be consumed in such a way that the partition coefficient for each ionic species is determined. Otherwise, the solid composition cannot be fixed in the pseudo-phase diagram. It should be noted that the physical phenomenon with a higher degree of freedom does not surpass the one governed by the lower degree of freedom. Thus, the same number of constraints as that for the melt species is required to solve the partition coefficient for each species. The constraint that consumes the one degree of freedom must then be determined. Because the composition of the solid phase is determined in the pseudo-phase diagram, a stoichiometric ratio between the metal and oxygen atoms in the solid is required, which is the last constraint necessary to achieve zero degrees of freedom.

## 4.2 Extended Concept of Stoichiometry in Oxide Crystals

Nonstoichiometric compounds often demonstrate interesting physical properties that may be induced by tuning their chemical compositions. Examples include variation of the Curie temperature and dielectric constant of ferroelectric materials used in ceramic capacitors such as  $(\text{Ba,Sr})\text{TiO}_3$  with the addition of small amounts of Y, Nd, and Sm [44,45] and the large piezoelectric constant associated with the Curie temperature of PZNT or PMNT [29–31] at compositions near the polymorph phase boundary (MPB), which enable applications in ultrasonic sensors and other piezoelectric applications.

Due to its ordered configuration of constituent elements on the lattice points, the stoichiometric compound will exhibit certain superior physical properties to the nonstoichiometric compound. Stoichiometric  $\text{LiNbO}_3$  (s-LN) or  $\text{LiTaO}_3$  (s-LT) crystals [2,3], for instance, show a higher conversion efficiency for secondary harmonic generation (SHG) in nonlinear optical applications and much lower coercive electric fields associated with poling compared to c-LN and congruent  $\text{LiTaO}_3$  (c-LT) crystals. However, these stoichiometric compositions are rigid, and only a small number of stoichiometric crystals are available that correspond to the law of multiple proportions [1]. Thus, it would be beneficial from both scientific and technological perspectives if stoichiometric compounds could be obtained over a wider compositional range. In this chapter, by considering the essential concept of stoichiometry, we redefined *stoichiometry* in such a way that a material in which the activities of all the constituent elements can be unity is stoichiometric [46,47]. The constituent elements in this definition include not only the primary constituent atoms but also the impurities and vacancies that replace these primary atoms. This revised concept of stoichiometry expands the current definition of stoichiometric composition from a single point to a range described by a line.

### 4.2.1 The Thermodynamic Definition of Stoichiometry Associated with the Activity of Constituent Elements

The application of thermodynamic principles throughout a broad spectrum of scientific and engineering disciplines may be considered to fall into two categories. One approach is related to solving practical problems regarding the conversion efficiency between different kinds of energy and is concerned with the reaction constant, the activity of elements during the chemical reaction process and so on. The other involves analytical considerations and is more conceptual in nature. Our development of an extended stoichiometry will use the latter approach.

One of the thermodynamic principles used for this purpose is *activity*, a term that is associated with the standard-state chemical potential. The chemical potential of component  $j$  (termed  $\mu^j$ ) in a nonstoichiometric material is given by Eqn (4.9):

$$\mu^j = \mu_0^j + RT \ln a^j, \quad (4.9)$$

where  $\mu_0^j$  is the standard-state chemical potential and  $a^j$  is the activity for  $j$  that indicates mixing with another solute. It should be noted that the chemical potential,  $\mu^j$ , has a definite value, while the activity,  $a^j$ , is variable. Once  $\mu_0^j$  is chosen,  $a^j$  is determined accordingly using the relationship

$$\ln a^j = \frac{\mu^j - \mu_0^j}{RT}. \quad (4.10)$$

The value of the standard-state chemical potential,  $\mu_0^j$ , is essentially chosen based on one's preference, although in most cases it represents the chemical potential of a pure substance at 1 atm and 298.15 K. This is because the energy of formation of pure substances is typically readily available, which is helpful for many thermodynamic calculations associated with practical applications.

The essence of “stoichiometry” may be elucidated by comparing it with “non-stoichiometry” from a thermodynamic perspective. A nonstoichiometric composition is derivative from a stoichiometric composition by the addition of impurities, which implies that the activity of the chemical species or element  $j$  is not unity,

$$a^j \neq 1. \quad (4.11)$$

In contrast, the chemical potential of the stoichiometric composition has no mixing term, and thus

$$\mu^j = \mu_0^j, \quad (4.12)$$

which is equivalent to saying that the activity of species  $j$  is unity,

$$a^j = 1. \quad (4.13)$$

We should note here that the statement  $a^j = 1$  also implies that the mole fraction is unity ( $x^j = 1$ ), which means that the standard-state composition about  $j$  reflects the bulk composition,  $j$  of the material itself regardless of the quantity of  $j$  in the material. It should be noted again that the standard-state composition does not have to be purely  $j$ .

In order for the material to be stoichiometric, Eqn (4.13) must be valid for any component,  $j$ . That is, the activity of all constituent components in the stoichiometric material is unity. Conversely, if the activity of all constituent components is unity, the material can be considered to be stoichiometric [46,47]. Following, we will demonstrate the validity of an extended stoichiometry concept by comparing this concept with the conventional understanding of stoichiometry.

#### 4.2.2 Conventional Stoichiometric Compositions and the Law of Multiple Proportions

The composition of a conventional stoichiometric crystal is represented by a small integer that gives the ratio of constituent elements, representing the so-called law of multiple proportions [1]. Here we use two kinds of stoichiometric crystals to demonstrate different types of compositions: (1)  $\text{Li}_2\text{B}_4\text{O}_7$ , which is a line-compound, and (2) s-LN, which belongs to a solid solution with a wide compositional range.

$\text{Li}_2\text{B}_4\text{O}_7$  has a very limited solid solution range, therefore it can be considered as a line compound (Figure 4.2(A)). This solid solution range is determined by investigating the limits of the compositional shift from the stoichiometric composition [48], using XRD or DTA to determine whether or not the secondary phase is present in the residual melt after normal freezing under vigorous mixing of the melt. The solid solution was found to vary around the stoichiometric composition by a margin of  $\pm 0.3$  mol%  $\text{Li}_2\text{O}$  [48]. However, the observation of zero c-EMF, which will be explained in Section 4.3.1, revealed that  $\text{Li}_2\text{B}_4\text{O}_7$  is a line compound with almost zero solid solution range. It should be noted here that there may still be some limited compositional variation in this

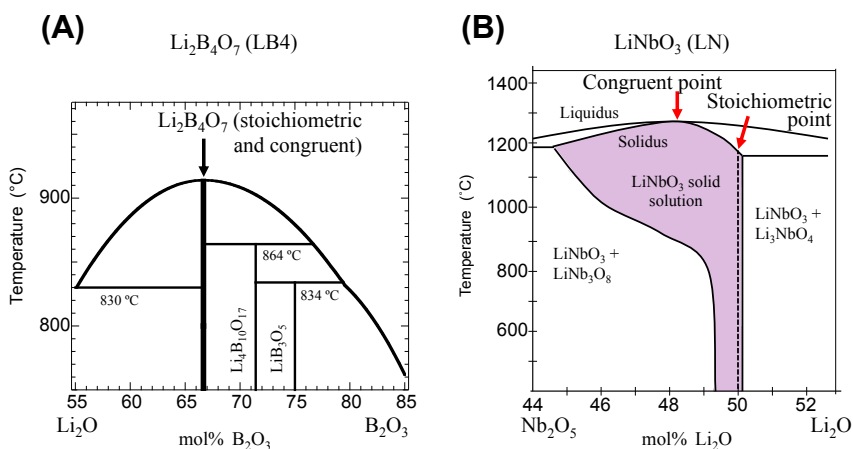


FIGURE 4.2 Equilibrium phase diagrams of pseudo-binary systems. (A)  $\text{Li}_2\text{O}$ – $\text{B}_2\text{O}_3$  around  $\text{Li}_2\text{B}_4\text{O}_7$  (after Ref. [48]) and (B)  $\text{Li}_2\text{O}$ – $\text{Nb}_2\text{O}_5$  around  $\text{LiNbO}_3$  (after Ref. [17]). Note that the stoichiometric composition and the congruent point coincide in  $\text{Li}_2\text{B}_4\text{O}_7$  but not in  $\text{LiNbO}_3$ .

material due to the presence of thermally activated vacancies. However, this small amount of compositional variation is neglected in the present discussion. The most important feature of this line-compound stoichiometric crystal is that it is coincident with the congruent point.

The phase diagram of the pseudo-binary system of  $\text{Li}_2\text{O}-\text{Nb}_2\text{O}_5$  is presented [17] in Figure 4.2(B), in which conventional stoichiometric  $\text{LiNbO}_3$  (s-LN) and conventional congruent-melting  $\text{LiNbO}_3$  (c-LN) are indicated. In contrast to the stoichiometric line-compound  $\text{Li}_2\text{B}_4\text{O}_7$ , s-LN is separate from c-LN and is located at the far end of  $\text{Li}_2\text{O}$  composition in the  $\text{LiNbO}_3$  solid solution. Although both  $\text{Li}_2\text{B}_4\text{O}_7$  and s-LN are stoichiometric,  $\text{Li}_2\text{B}_4\text{O}_7$  is coincident with the congruent point while s-LN is not, which reflects the different equilibrium partitioning of their constituent elements. This will be discussed in detail in Section 4.3.2.

#### 4.2.2.1 Activities of the Constituent Elements in a Conventional Stoichiometric Crystal

In the following discussion, we will demonstrate that the activities of all constituent elements in a conventional stoichiometric compound are unity [46]. The composition of a conventional stoichiometric compound is represented by a small integer ratio between constituent elements, and as such the line-compound  $\text{Li}_2\text{B}_4\text{O}_7$  may be employed as a conventional stoichiometric material.

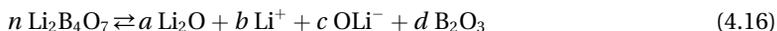
In both the  $\text{Li}_2\text{B}_4\text{O}_7$  melt and the solid at its crystallization temperature, the most likely possibility would be for  $\text{Li}_2\text{B}_4\text{O}_7$  to dissociate into  $\text{Li}_2\text{O}$  and  $\text{B}_2\text{O}_3$  [46], as shown by Eqn (4.14), which is analogous to the dissociation of  $\text{LiNbO}_3$  [39], since the  $\text{Li}_2\text{B}_4\text{O}_7$  crystal consists of firm B-O frameworks with Li in the pore spaces.



Subsequently, each species would be expected to ionize. For instance,  $\text{Li}_2\text{O}$  may ionize at high temperature, as shown in Eqn (4.15):



In the following discussion, the chemical species  $j$  are differentiated in two ways:  $\bar{j}$  is the net chemical species that normally appears as a component in the pseudo-binary phase diagram, while  $j$  is the actual chemical species existing in the solid or melt and that forms the net chemical species  $\bar{j}$ .  $\overline{\text{Li}_2\text{O}}$  and  $\overline{\text{B}_2\text{O}_3}$  are thus the net species while  $\text{Li}_2\text{O}$ ,  $\text{Li}^+$ ,  $\text{O}^{\text{Li}^-}$ , and others represent the proposed real chemical species,  $j$ , that form  $\overline{\text{Li}_2\text{O}}$ . Thus,  $\text{Li}_2\text{B}_4\text{O}_7$  may be decomposed into several chemical species as indicated by Eqn (4.16):



At this time, we do not take into account the further decomposition of  $\text{B}_2\text{O}_3$ . The chemical potential of  $\text{Li}_2\text{B}_4\text{O}_7$  is written as Eqn (4.17):

$$n \mu^{\text{Li}_2\text{B}_4\text{O}_7} = a \mu^{\text{Li}_2\text{O}} + b \mu^{\text{Li}^+} + c \mu^{\text{O}^{\text{Li}^-}} + d \mu^{\text{B}_2\text{O}_3}, \quad (4.17)$$

and

$$n \mu^{\text{Li}_2\text{B}_4\text{O}_7} = n \mu^{\overline{\text{Li}_2\text{O}}} + 2n \mu^{\overline{\text{B}_2\text{O}_3}}. \quad (4.18)$$

Equation (4.19) then describes  $\text{B}_2\text{O}_3$ :

$$2n \mu^{\overline{\text{B}_2\text{O}_3}} = d \mu^{\text{B}_2\text{O}_3} \quad (4.19)$$

The relationship between the net chemical species and the real chemical species for the  $\text{Li}_2\text{O}$  component can then be written for both the solid and liquid assuming that all chemical species in the melt are partitioned into the solid so that the discussion can be made based on the equilibrium partitioning of each chemical species. Equations (4.17), (4.18), and (4.19) yield Eqn (4.20):

$$n \mu_{\beta}^{\overline{\text{Li}_2\text{O}}} = a \mu_{\beta}^{\text{Li}_2\text{O}} + b \mu_{\beta}^{\text{Li}^+} + c \mu_{\beta}^{\text{OLi}^-}, \quad (4.20)$$

where  $\beta$  is either the solid (S) or liquid (L) phase. This describes the relationship in chemical potential between the net  $\overline{\text{Li}_2\text{O}}$  and Li-bearing species, and a similar relationship can be made between the net  $\overline{\text{B}_2\text{O}_3}$  and B-bearing species. Thus, hereon we will deal exclusively with  $\text{Li}_2\text{O}$ .

The above chemical species are hypothetical, and it is not clear that they actually exist. Thus, Eqn (4.21) is hereafter used for the general discussion instead of Eqn (4.20):

$$n \mu_{\beta}^{\overline{\text{Li}_2\text{O}}} = m_1 \mu_{\beta}^{\text{Li}(1)} + m_2 \mu_{\beta}^{\text{Li}(2)} + m_3 \mu_{\beta}^{\text{Li}(3)} + \cdots + m_k \mu_{\beta}^{\text{Li}(k)}, \quad (4.21)$$

where  $\text{Li}(i)$  are the chemical species containing Li and for which  $m_i \geq 0$ . It is important to note that the Li-bearing species in Eqn (4.21) are assumed to be common to both the solid and liquid states since all the chemical species in the melt are partitioned into the solid during growth. Specifically, the chemical potential of the net  $\overline{\text{Li}_2\text{O}}$  in the solid at a given temperature  $T$  may be written as

$$n \mu_{S(T)}^{\overline{\text{Li}_2\text{O}}} = m_1 \mu_{S(T)}^{\text{Li}(1)} + m_2 \mu_{S(T)}^{\text{Li}(2)} + m_3 \mu_{S(T)}^{\text{Li}(3)} + \cdots + m_k \mu_{S(T)}^{\text{Li}(k)}, \quad (4.22)$$

and this equation may be rewritten as Eqn (4.23) by breaking down the chemical potential into the standard-state chemical potential and the mixing term as

$$\begin{aligned} n \mu_{S(T,0)}^{\overline{\text{Li}_2\text{O}}} + n RT \ln a_{S(T)}^{\overline{\text{Li}_2\text{O}}} - \left( m_1 \mu_{S(T,0)}^{\text{Li}(1)} + m_2 \mu_{S(T,0)}^{\text{Li}(2)} + m_3 \mu_{S(T,0)}^{\text{Li}(3)} + \cdots + m_k \mu_{S(T,0)}^{\text{Li}(k)} \right) \\ = \Delta \mu_{S(T,0)}^{\text{Li}^+} + n RT \ln a_{S(T)}^{\overline{\text{Li}_2\text{O}}} = RT \left( m_1 \ln a_{S(T)}^{\text{Li}(1)} + m_2 \ln a_{S(T)}^{\text{Li}(2)} + m_3 \ln a_{S(T)}^{\text{Li}(3)} + \cdots + m_k \ln a_{S(T)}^{\text{Li}(k)} \right) \end{aligned} \quad (4.23)$$

where  $\mu_{S(T,0)}^j$  is the standard-state chemical potential of the solid about  $j$  at a temperature  $T$ , and  $\Delta \mu_{S(T,0)}^{\text{Li}^+}$  is the difference in standard-state chemical potentials between  $\overline{\text{Li}_2\text{O}}$  and the dissolved species,  $\text{Li}(i)$ , which is written as

$$\Delta \mu_{S(T,0)}^{\text{Li}^+} = n \mu_{S(T,0)}^{\overline{\text{Li}_2\text{O}}} - \left( m_1 \mu_{S(T,0)}^{\text{Li}(1)} + m_2 \mu_{S(T,0)}^{\text{Li}(2)} + m_3 \mu_{S(T,0)}^{\text{Li}(3)} + \cdots + m_k \mu_{S(T,0)}^{\text{Li}(k)} \right). \quad (4.24)$$

Here, the standard-state chemical potential is defined for  $\mu_{S(T,0)}^{\overline{\text{Li}_2\text{O}}}$  and  $\mu_{S(T,0)}^{\text{Li}(i)}$  ( $1 \leq i \leq k$ ), individually:  $\mu_{S(T,0)}^{\overline{\text{Li}_2\text{O}}}$  is defined as the chemical potential of the solid for the exact  $\text{Li}_2\text{O}$

concentration in the stoichiometric composition of  $\text{Li}_2\text{B}_4\text{O}_7$  at a temperature  $T$ . The activity,  $a_{S(T)}^{\overline{\text{Li}_2\text{O}}}$ , is then written as

$$\ln a_{S(T)}^{\overline{\text{Li}_2\text{O}}} = \frac{\left(\mu_{S(T)}^{\overline{\text{Li}_2\text{O}}} - \mu_{S(T,0)}^{\overline{\text{Li}_2\text{O}}}\right)}{RT}. \quad (4.25)$$

The term  $\mu_{S(T,0)}^{\text{Li}(i)}$  can be defined at a given temperature  $T$  in such a way that the  $\Delta\mu_{S(T,0)}^{\text{Li}(i)}$  term in Eqn (4.24) becomes zero. This is allowed because the Li, B, and O sites are fully occupied by their own specific elements in stoichiometric  $\text{Li}_2\text{B}_4\text{O}_7$ , which provides one degree of freedom to define  $\mu_{S(T,0)}^{\text{Li}(i)}$ . This freedom associated with the crystal sites and its usage is discussed in more detail in Section 4.2.3.1. Thus  $\mu_{S(T,0)}^{\text{Li}(i)}$  is defined as in Eqn (4.26):

$$n \mu_{S(T,0)}^{\overline{\text{Li}_2\text{O}}} = m_1 \mu_{S(T,0)}^{\text{Li}(1)} + m_2 \mu_{S(T,0)}^{\text{Li}(2)} + m_3 \mu_{S(T,0)}^{\text{Li}(3)} + \cdots + m_k \mu_{S(T,0)}^{\text{Li}(k)}, \quad (4.26)$$

where the appropriate value can be assigned to each  $\mu_{S(T,0)}^{\text{Li}(i)}$  term such that the equation is satisfied at temperature  $T$ , even though  $\mu_{S(T,0)}^{\text{Li}(i)}$  is not individually specified. Combining Eqn (4.26) with Eqn (4.23) gives

$$n \ln a_{S(T)}^{\overline{\text{Li}_2\text{O}}} = m_1 \ln a_{S(T)}^{\text{Li}(1)} + m_2 \ln a_{S(T)}^{\text{Li}(2)} + m_3 \ln a_{S(T)}^{\text{Li}(3)} + \cdots + m_k \ln a_{S(T)}^{\text{Li}(k)}, \quad (4.27)$$

and thus

$$\left(a_{S(T)}^{\overline{\text{Li}_2\text{O}}}\right)^n = \left(a_{S(T)}^{\text{Li}(1)}\right)^{m_1} \left(a_{S(T)}^{\text{Li}(2)}\right)^{m_2} \left(a_{S(T)}^{\text{Li}(3)}\right)^{m_3} \cdots \left(a_{S(T)}^{\text{Li}(k)}\right)^{m_k}. \quad (4.28)$$

$\text{Li}_2\text{B}_4\text{O}_7$  is peculiar in that the solid solution range of  $\text{Li}_2\text{B}_4\text{O}_7$  is sufficiently small such that the composition of the solid  $\text{Li}_2\text{B}_4\text{O}_7$  coexisting with the liquid can be assumed to be nearly constant and equal to the stoichiometric composition at any given temperature,  $T$ , which is coincident with the congruent composition. Thus, Eqns (4.29) and (4.30) hold true at any temperature. As such, the chemical potential for the bulk  $\text{Li}_2\text{O}$ ,  $\mu_{S(T)}^{\overline{\text{Li}_2\text{O}}}$ , is assigned to the standard-state chemical potential,  $\mu_{S(T)}^{\overline{\text{Li}_2\text{O}}}$ , as in Eqn (4.29):

$$\mu_{S(T)}^{\overline{\text{Li}_2\text{O}}} = \mu_{S(T,0)}^{\overline{\text{Li}_2\text{O}}} \quad (4.29)$$

Combining this equation with Eqn (4.25), Eqn (4.30) is obtained:

$$a_{S(T)}^{\overline{\text{Li}_2\text{O}}} = X_{S(T)}^{\overline{\text{Li}_2\text{O}}} = 1, \quad (4.30)$$

where  $X_{S(T)}^{\overline{\text{Li}_2\text{O}}}$  is the net concentration of  $\text{Li}_2\text{O}$  in the solid  $\text{Li}_2\text{B}_4\text{O}_7$  at a temperature,  $T$ .

Combining with Eqn (4.28), the product of  $a_{S(T)}^{\text{Li}(i)}$  is unity as shown by Eqn (4.31):

$$\left(a_{S(T)}^{\text{Li}(1)}\right)^{m_1} \left(a_{S(T)}^{\text{Li}(2)}\right)^{m_2} \left(a_{S(T)}^{\text{Li}(3)}\right)^{m_3} \cdots \left(a_{S(T)}^{\text{Li}(k)}\right)^{m_k} = 1. \quad (4.31)$$

Equation (4.31) holds at any temperature,  $T$ , and thus we can write Eqns (4.32) and (4.33):

$$a_{S(T)}^{\text{Li}(1)} = a_{S(T)}^{\text{Li}(2)} = a_{S(T)}^{\text{Li}(3)} = \cdots = a_{S(T)}^{\text{Li}(k)} = 1 \quad (4.32)$$

$$X_{S(T)}^{\text{Li}(1)} = X_{S(T)}^{\text{Li}(2)} = X_{S(T)}^{\text{Li}(3)} = \dots = X_{S(T)}^{\text{Li}(k)} = 1 \quad (4.33)$$

As in Eqn (4.25),  $a_{S(T)}^{\text{Li}(i)}$  is defined as

$$\ln a_{S(T)}^{\text{Li}(i)} = \frac{\left( \mu_{S(T)}^{\text{Li}(i)} - \mu_{S(T,0)}^{\text{Li}(i)} \right)}{RT}. \quad (4.34)$$

The value of  $\mu_{S(T,0)}^{\text{Li}(i)}$  in Eqn (4.34) is determined in order to satisfy Eqn (4.26), and  $a_{S(T)}^{\text{Li}(i)} = 1$  leads to  $\mu_{S(T)}^{\text{Li}(i)} = \mu_{S(T,0)}^{\text{Li}(i)}$  for any temperature. This same process also applies to the B-bearing species. Overall, then, the activity of all constituent elements in the stoichiometric compound  $\text{Li}_2\text{B}_4\text{O}_7$  is unity [46],

$$a_{\text{Li site}}^{\text{Li}} = a_{\text{B site}}^{\text{B}} = a_{\text{O site}}^{\text{O}} = 1. \quad (4.35)$$

### 4.2.3 Extended Stoichiometric Compositions Including Impurities and Vacancies

In the previous section, we demonstrated that a material in which the activity of each constituent element can be unity represents a stoichiometric material, by assigning each chemical potential,  $\mu^j$ , to the standard-state chemical potential,  $\mu_0^j$ . In other words, if we are allowed to assign  $\mu^j$  to  $\mu_0^j$  for any component,  $j$ , such that  $\mu_0^j = \mu^j$ , the material can be considered stoichiometric. Stoichiometric materials by this definition may include impurities and vacancies and so may be more stable in terms of entropy than conventional stoichiometric substances. This raises an important objection—if an assignment such as this is possible in any material, then every material could potentially be considered stoichiometric, which is certainly not the case. The question is how we can know whether or not  $\mu^j$  can be assigned to  $\mu_0^j$ . To make such an assignment, we require a degree of freedom, since the standard-state chemical potential,  $\mu_0^j$ , can have any value if one degree of freedom is present in the crystal site where the element  $j$  is present.

#### 4.2.3.1 Degrees of Freedom in a Crystal Site

It is important to determine the element occupancy of each crystal site. These elements include constituent cations, impurity ions, antisite defects, and vacancies. The possible element occupancy at a site is examined by considering the associated degrees of freedom, and we can explain the degrees of freedom of a crystal site by employing  $\text{LiNbO}_3$  as an example. Here the vacancy is a defect that forms in order to compensate for the charge imbalance due to the difference between the valences of the impurity ions and that of the host ion present in a site. The quantity of vacancies will be on the order of  $10^{-4}$  to  $10^{-2}$  mol or more depending on the population of impurity ions or antisite defects. In the following discussion, we assume that the oxygen sites are saturated with oxygen and that no oxygen vacancies are present even when  $\text{LiNbO}_3$  is exposed to an

oxygen-reduced atmosphere during the growth or annealing processes. Such a reduced atmosphere is known to generate a color center in the crystal, with a concurrent change from colorless to yellow or orange, but the accompanying extent of oxygen deficiency is much less than the degree of oxygen vacancy required for the charge compensation, by at least two orders of magnitude. Thus, the possible presence of elements at each cation site will be discussed, assuming that oxygen saturation is maintained.

The degrees of freedom are obtained by subtracting the number of constraints from the number of parameters. In this case, the number of parameters at a site is the number of elements, based on the following three constraints:

1. Mass conservation holds at each site. That is, the sum of the mole fractions of each constituent element,  $j$  (where  $j = 1$  to  $C$ ), is unity, as in Eqn (4.36):

$$X^1 + X^2 + \cdots + X^C = 1 \quad (4.36)$$

2. If an element is present at multiple sites in a crystal, its chemical potentials at those sites are equal, thus

$$\mu_{\text{site } 1}^j = \mu_{\text{site } 2}^j = \cdots \quad (4.37)$$

3. The vacancy population is calculated in such a way that overall charge neutrality is maintained in the bulk crystal.

These three constraints are necessary conditions, although additional restrictions may be added to decrease the degree of freedom at a given site.

#### 4.2.3.2 Activity of the Constituent Elements in an Extended Stoichiometric Crystal

Based on our newly defined “stoichiometry,” referring to a material in which the activity of all the constituent elements can be unity, we extend the stoichiometric composition from a single point to a linear series. Introducing impurities and vacancies is necessary in this case, which is not allowed in a conventional stoichiometric compound. As an example, we may consider MgO-doped LiNbO<sub>3</sub> in the pseudo-ternary system of Li<sub>2</sub>O–Nb<sub>2</sub>O<sub>5</sub>–MgO, shown in Figure 4.3. The isoconcentration line at 50 mol% Nb<sub>2</sub>O<sub>5</sub> is termed line *A*, and the MgO-doped LiNbO<sub>3</sub> on line *A* is termed 50Nb-LN. The conventional stoichiometric compound LiNbO<sub>3</sub> (s-LN), the conventional congruent-melting LiNbO<sub>3</sub> (c-LN) on the pseudo-binary line of Li<sub>2</sub>O–Nb<sub>2</sub>O<sub>5</sub>, and c-LN doped with 5 mol% MgO (5MgO:LN) are also indicated.

The site structures of these crystals are presented in Figure 4.3(B). All the sites of conventional s-LN are filled with Li, Nb, and O, without any excess atoms or deficiencies. Thus, it is readily understood that the activity of each site as well as the activity of the element at each site is unity. The site structures of c-LN and 50Nb-LN are similar in that both have fully occupied Nb and O sites, and their Li sites are occupied with vacancies or cations other than Li, such as antisite Nb in c-LN and Mg in 50Nb-LN. Although the elements present in their Li sites are much the same, c-LN is not

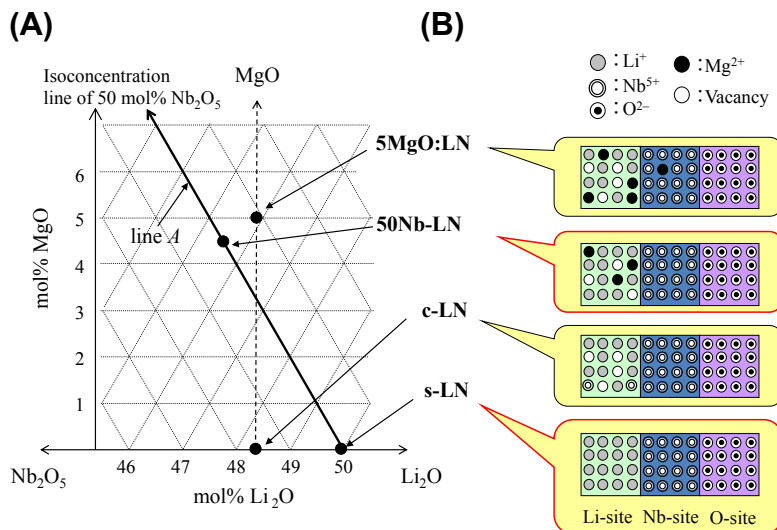


**FIGURE 4.3** (A) Composition diagram of various  $\text{LiNbO}_3$  compositions in the pseudo-ternary system of  $\text{Li}_2\text{O}-\text{Nb}_2\text{O}_5-\text{MgO}$ . The isoconcentration line of 50 mol%  $\text{Nb}_2\text{O}_5$  line is termed line A and represents an O-to-Nb ratio of exactly 3.0. Legend: s-LN = stoichiometric  $\text{LiNbO}_3$  on the  $\text{Li}_2\text{O}-\text{Nb}_2\text{O}_5$  line, c-LN = congruent  $\text{LiNbO}_3$  on the  $\text{Li}_2\text{O}-\text{Nb}_2\text{O}_5$  line, 50Nb-LN = MgO-doped  $\text{LiNbO}_3$  on line A, 5MgO:LN = c-LN doped with 5 mol% MgO. (B) Crystal site structures for each of the various  $\text{LiNbO}_3$  crystals.

stoichiometric while 50Nb-LN is [47], a phenomenon that will be discussed subsequently. In 5MgO:LN, the Mg is located at both Li and Nb sites, but no antisite Nb is present at the Li sites.

Whether a crystal is stoichiometric or not is determined by examining the possibility of each of the constituent elements in the crystal having an activity of unity. This question directly applies to the activities of the elements at Li sites in c-LN and 50Nb-LN.

Firstly, we can examine the degrees of freedom associated with the Li sites in c-LN. These sites have three parameters: Li, Nb, and vacancies. The constraints on the Li site include conservation of mass, the exchange of equilibrium Nb between Li and Nb sites, and the vacancy population required for charge compensation. Since the overall number of constraints is three, zero degrees of freedom are available for assigning  $\mu^j$  to the standard-state chemical potential,  $\mu_0^j$ . Therefore, the activity of the elements at the Li sites cannot be unity, and it has been proven on a thermodynamic basis that c-LN is not stoichiometric.

The degrees of freedom of the Li sites in 50Nb-LN can subsequently be examined using a similar process. Here the number of parameters is three while the number of constraints is two, since we are only concerned with conservation of mass and the vacancy population. As a consequence, the Li sites have one degree of freedom, which allows unrestricted choice of the standard-state chemical potential,  $\mu_0$ . It should be noted that, in the 50Nb-LN crystal, each element, including Mg and vacancies, belongs

only to one specific site. However,  $\mu_0^j = \mu^j$  must be valid for all three of the elements that may be present at the Li sites ( $j = \text{Li, Mg, and vacancy}$ ) in order for the activities of these elements to be unity. Thus, it appears that three degrees of freedom are required, and hence the challenge is to use one degree of freedom to assign  $\mu$  to  $\mu_0$  for each of the three elements. To address this, one can consider the chemical potentials and activities of the crystal sites as well as the constituent elements in 50Nb-LN. The Nb site is fully occupied by Nb and Nb does not enter into any other site, which is also the case for the O sites and O atoms. Hence, the activity of the Nb and O sites is unity, and simultaneously the activity of Nb at the Nb sites and O at the O sites is unity. Since the Li sites preserve the overall charge neutrality with regard to the Nb and O sites, the Li site must also be neutral and the activity of the Li site must be unity. Thus,

$$a_{\text{Li site}} = a_{\text{Nb site}} = a_{\text{O site}} = 1, \quad (4.38)$$

and

$$a_{\text{Nb site}}^{\text{Nb}} = a_{\text{O site}}^{\text{O}} = 1. \quad (4.39)$$

The chemical potential of the Li sites in 50Nb-LN is calculated by summing that of each element, as follows:

$$\mu^{\text{Li site}} = p\mu_{\text{Li site}}^{\text{Li}} + q\mu_{\text{Li site}}^{\text{Mg}} + r\mu_{\text{Li site}}^{\text{Va}} \quad (4.40)$$

where Va denotes a vacancy and  $p$ ,  $q$ , and  $r$  are real numbers. By differentiating the chemical potential into the standard-state chemical potential and the mixing term, Eqn (4.40) may be rewritten as:

$$\mu_0^{\text{Li site}} + RT \ln a_{\text{Li site}} = p(\mu_0^{\text{Li}} + \ln a_{\text{Li site}}^{\text{Li}}) + q(\mu_0^{\text{Mg}} + \ln a_{\text{Li site}}^{\text{Mg}}) + r(\mu_0^{\text{Va}} + \ln a_{\text{Li site}}^{\text{Va}}) \quad (4.41)$$

One degree of freedom allows the standard-state chemical relationship between the Li site and its constituent elements, which is shown in Eqn (4.42):

$$\mu_0^{\text{Li site}} = p\mu_0^{\text{Li}} + q\mu_0^{\text{Mg}} + r\mu_0^{\text{Va}} \quad (4.42)$$

Subsequently, the activity relationship between the Li site and its constituent elements is obtained by combining with Eqn (4.41) to give Eqn (4.43):

$$a_{\text{Li site}} = (a_{\text{Li site}}^{\text{Li}})^p (a_{\text{Li site}}^{\text{Mg}})^q (a_{\text{Li site}}^{\text{Va}})^r = 1 \quad (4.43)$$

Equation (4.43) is valid for any combination of  $p$ ,  $q$ , and  $r$  that lies on the isoconcentration line of 50 mol% Nb<sub>2</sub>O<sub>5</sub> (line A in Figure 4.3). Therefore, the activity of all three elements is unity [47], expressed as

$$a_{\text{Li site}}^{\text{Li}} = a_{\text{Li site}}^{\text{Mg}} = a_{\text{Li site}}^{\text{Va}} = 1. \quad (4.44)$$

Combining this equation with Eqn (4.39), the activity of all elements in 50Nb-LN can be shown to equal unity, and so it is proven on a thermodynamic basis that 50Nb-LN, a Mg-doped LN on the isoconcentration line of 50 mol% Nb<sub>2</sub>O<sub>5</sub>, is stoichiometric.

### 4.3 Growth Characteristics of Stoichiometric Crystals

A line-compound stoichiometric crystal is always congruent, but the conventional stoichiometric oxide crystal accompanying the solid solution is often not congruent. Although both types of crystals have an activity equal to unity for each of their constituent elements, the partitioning of constituent elements from the liquid to the solid during growth differs between the two. This indicates that there is a close relationship between the partitioning behavior of an ionic species, stoichiometry, and the congruency of the growing crystal.

Most oxide melts are electrically conductive [39,49,50], therefore they are considered to contain ionic constituent species in addition to neutral species, as illustrated in Figure 4.4. The existence of ionic species in the oxide melt is easily demonstrated when one considers that molten salts are used as electrolyte solutions in electrochemical studies. The populations of these ionic species are dependent on the composition and temperature of the oxide melt. We have seen that pseudo-oxide phase diagrams, in which the stoichiometry between the metal and oxygen holds, only address the oxide components of the material and do not provide any information concerning ionic species. It is generally believed that the partition coefficients are unity at the congruent composition since the solidus line coincides with the liquidus line at that point, meaning that the solid and liquid compositions are the same. However, this is true only for the oxide components appearing in the pseudo-phase diagram; it is not true when one considers that oxygen ions represent one of the ionic species present in the melt. As an example, the pseudo-binary diagram of  $\text{Li}_2\text{O}-\text{Nb}_2\text{O}_5$  is not sufficient to explain the partitioning of ionic species in the  $\text{LiNbO}_3$  melt. In this case, oxygen should be treated as an independent component, and the ternary Li-Nb-O diagram should be used instead of the pseudo-binary  $\text{Li}_2\text{O}-\text{Nb}_2\text{O}_5$  diagram. Each of the constituent species, including ionic species, has its own equilibrium partition coefficient, and it can be shown that the equilibrium partition coefficient of any element in the exact line-compound melt is unity, meaning that there is no segregation of ionic species near the interface during growth. This arises from the fact that the line compound is both stoichiometric and

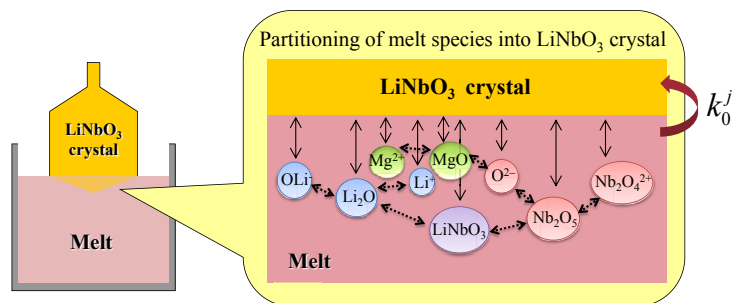


FIGURE 4.4 Neutral and ionic chemical species possibly present in the  $\text{LiNbO}_3$  melt. Each species,  $j$ , is partitioned into the solid based on its own unique equilibrium partition coefficient,  $k_0^j$ .

congruent. In contrast, even a congruent crystal that is not consistent with the stoichiometric point grows in such a manner that the ionic solutes have nonunity partition coefficients. Consequently, the ionic species in the solute boundary layer undergo segregation, resulting in the accumulation or depletion of these species and generating a c-EMF at the interface, which in turn produces an interface electric field that complicates the growth process.

In this section, c-LN is employed as an example of a congruent crystal that generates a nonzero c-EMF during growth, which demonstrates that the partition coefficients of the ionic species present in the congruent melt are nonunity [51–53], even though the partition coefficients of the net  $\overline{\text{Li}_2\text{O}}$  or  $\overline{\text{Nb}_2\text{O}_5}$  are unity. However, an extended stoichiometric crystal including both impurities and vacancies could coincide with the congruent point at a certain composition, in which case no segregation will occur even if the material is not a line compound. This process will be discussed further in Section 4.3.2.

### 4.3.1 Crystallization Electromotive Force

Each ionic species,  $j$ , is partitioned based on its own equilibrium partitioning coefficient,  $k_0^j$ , and is accumulated or depleted at the growth interface due to solute segregation depending on the value of  $k_0^j$ , the diffusivity,  $D^j$ , and the growth rate, which results in the differential segregation of ions of opposing valences to generate a net charge in the liquid boundary layer as well as a charge of the opposite sign in the crystal, thus producing the c-EMF [40,47,51–53],  $\Delta\phi_{\text{EMF}}$ . This process is illustrated in Figure 4.5. D'yakov et al. [54] first measured the c-EMF generated by c-LN, and

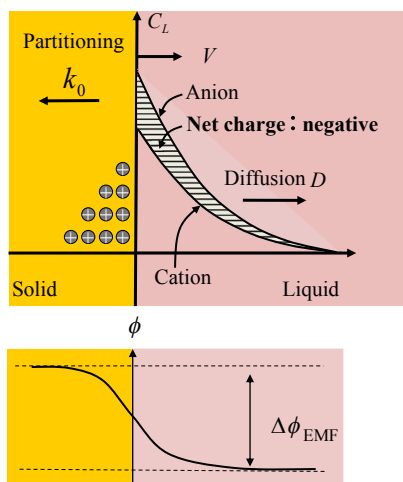


**FIGURE 4.5** Schematic illustration of the segregation of ionic species in the liquid boundary layer (above) and the generation of crystallization electromotive force (c-EMF),  $\Delta\phi_{\text{EMF}}$  (below) during the growth of the  $\text{LiNbO}_3$  crystal. The horizontal axis shows the distance from the growth interface; the vertical axis shows the net concentrations of anions and cations (above) and electric potential (below) [47].

Aleksandrovskii et al. [55] reported similar measurements using the Czochralski method but did not investigate its origin. The c-EMF is useful not only in terms of growth equilibrium, as discussed herein, but also since it allows the study of growth dynamics.  $\Delta\phi_{\text{EMF}}$  is easily measured using a micro-pulling down ( $\mu$ -PD) system, as shown in Figure 4.6 [47]. The furnace in this apparatus consists of a small platinum (Pt) crucible with a capillary nozzle attached to its base. A sintered material is charged into the Pt crucible and is melted by sending an electric current through the crucible, such that the crucible serves as a resistance heater. Two thermocouples (TC<sub>1</sub>, TC<sub>2</sub>) are set in the liquid and solid phases; TC<sub>1</sub> is fixed in the liquid, while TC<sub>2</sub> is mobile. During the pulling down (crystal growth stages: 1, 2, and 3), halt and pulling up (crystal melting stages: 4, 5, and 6) of TC<sub>2</sub>,  $T_1$  and  $T_2$  (the temperatures of TC<sub>1</sub> and TC<sub>2</sub>, respectively) and the potential difference,  $\Delta\phi$ , between TC<sub>1</sub> and TC<sub>2</sub> are measured. During pulling down and pulling up, the rate of movement of TC<sub>2</sub> is constant. When a *c*-oriented crystal is used to seed the crystal nucleation, the resulting crystal has the same (*c*-) orientation as the seed crystal. During all stages,  $T_1$  is kept nearly constant and only  $T_2$  and  $\Delta\phi$  vary. Figure 4.7 depicts an example of a  $\Delta\phi - T_2$  curve acquired during the crystal growth process, showing the halt and melting of *c*-LN [47]. The  $\Delta\phi$  term may be represented by Eqn (4.45) [47,51,54]:

$$\Delta\phi = \alpha_L(T_1 - T_i) + \alpha_S(T_i - T_2) + \Delta\phi_{\text{EMF}}, \quad (4.45)$$

where  $\alpha_L$  and  $\alpha_S$  are the Seebeck coefficients of the liquid and solid phase, and correspond to the slopes of the  $\Delta\phi - T_2$  curve in the liquid (stages 1–2 and 5–6 in Figure 4.6) and solid regions (stage 2–3 and 4–5 in Figure 4.6), respectively. The value of  $\alpha_L$  is 0.27 mV/K, while  $\alpha_S$  is  $-0.85$  mV/K [47], both of which are nearly constant for all compositions.  $T_i$  is the temperature at the solid/liquid interface, and  $\Delta\phi_{\text{EMF}}$  is the c-EMF that is obtained from the extent of hysteresis generated in the solid region during the

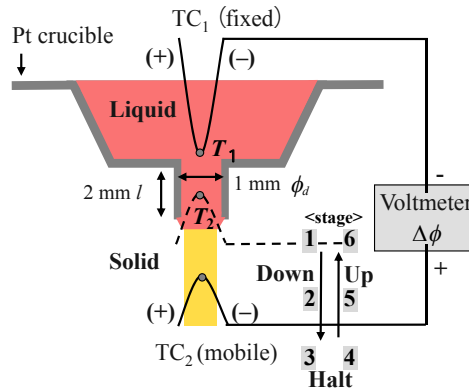


**FIGURE 4.6** The micro-pulling-down ( $\mu$ -PD) system for the measurement of crystallization electromotive force (c-EMF). TC<sub>1</sub> is fixed, while TC<sub>2</sub> is mobile.  $\Delta\phi$  is measured by the difference in electric potentials measured at  $T_1$  and  $T_2$  during the pulling down (growth stage 1–3), halt and pulling up (melting stage 4–6) processes. After Ref. [47].

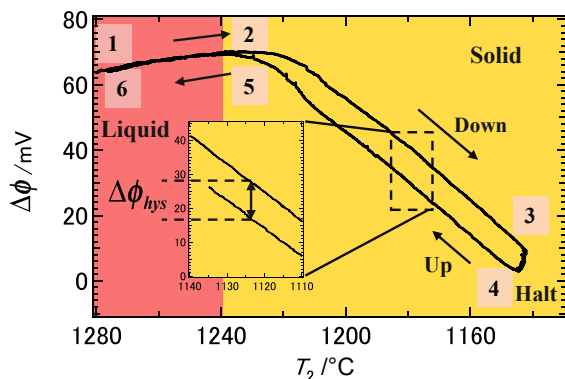


**FIGURE 4.7** The  $\Delta\phi - T_2$  curve obtained during the growth, halt and melting processes of c-LN [47]. The slope of the  $\Delta\phi - T_2$  curve may be used to obtain the Seebeck coefficient of the liquid ( $\alpha_L$ ) and the solid ( $\alpha_S$ ), while  $\Delta\phi_{EMF}$  is obtained from the hysteresis potential ( $\Delta\phi_{hys}$ ) in the solid region.

solidification and melting process. It should be noted that, in Eqn (4.45), both  $\alpha_L$  and  $\alpha_S$  are fixed values specific to the material being examined, whereas  $\Delta\phi_{EMF}$  is completely growth-system dependent. The value of this term is normally in the range of several mV and can be measured with reasonable accuracy.

The generation of a c-EMF during the growth of  $\text{LiNbO}_3$  from melts with various compositions demonstrates that the EMF has a nonzero value at the conventional stoichiometric point and even at the congruent point (Figure 4.8) [52]. This EMF arises during growth as the result of the segregation of ionic solutes in the liquid boundary layer in a congruent melt in which the equilibrium partition coefficients are not unity, even though the coefficients of the net  $\overline{\text{Li}_2\text{O}}$  and  $\overline{\text{Nb}_2\text{O}_5}$  are unity, based on interpretation of the conventional pseudo-phase diagram. In contrast, Figure 4.9 shows that the c-EMF observed during the growth of  $\text{Li}_2\text{B}_4\text{O}_7$  is zero at the stoichiometric-congruent point but nonzero during growth from the off-stoichiometric melt [52]. The

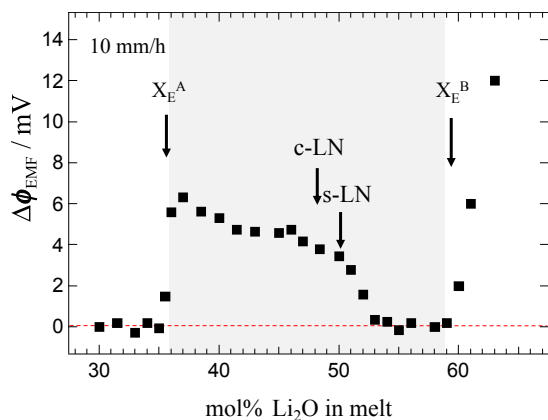
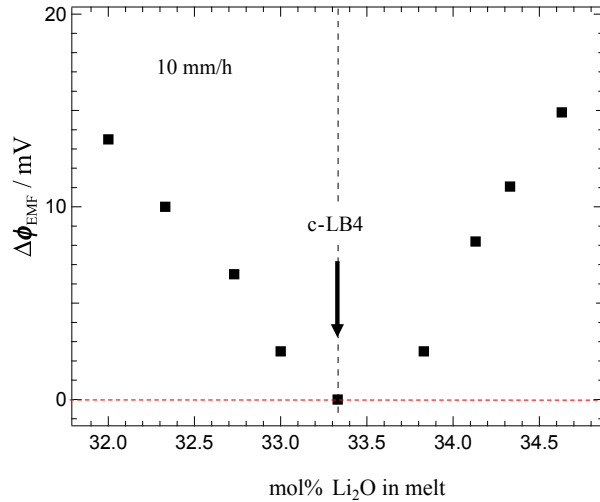


**FIGURE 4.8** The c-EMF ( $\Delta\phi_{EMF}$ ) values obtained during the growth of  $\text{LiNbO}_3$  via a  $\mu$ -PD measurement system plotted as a function of the  $\text{Li}_2\text{O}$  composition of the melt in the pseudo-binary  $\text{Li}_2\text{O}-\text{Nb}_2\text{O}_5$  system at a growth rate of 10 mm/h.  $X_E^A$  and  $X_E^B$  are the eutectic points in the Nb-rich and Li-rich regions, respectively, while c-LN is the congruent point and s-LN is the stoichiometric composition. Note that  $\Delta\phi_{EMF} \neq 0$  even for the c-LN composition. After Ref. [52].

**FIGURE 4.9** The c-EMF ( $\Delta\phi_{\text{EMF}}$ ) values obtained during the growth of  $\text{Li}_2\text{B}_4\text{O}_7$  via a  $\mu$ -PD measurement system plotted as a function of the  $\text{Li}_2\text{O}$  composition of the melt in the pseudo-binary  $\text{Li}_2\text{O}$ - $\text{B}_2\text{O}_3$  system at a growth rate of 10 mm/h. The congruent point of  $\text{Li}_2\text{B}_4\text{O}_7$  is c-LB4, which is coincident with its stoichiometric composition. Note that  $\Delta\phi_{\text{EMF}} = 0$  at the composition for which the congruent point coincides with the stoichiometric composition. After Ref. [52].



zero-EMF exhibited by the stoichiometric-congruent composition will always occur during growth at various growth rates, although different growth rates normally result in varying degrees of segregation of the ionic species at the interface if their partition coefficients are not unity. Therefore, no segregation of ionic species occurs at the stoichiometric-congruent point, leading to the conclusion that every ionic species in the  $\text{Li}_2\text{B}_4\text{O}_7$  melt has an equilibrium partition coefficient of unity [46]. On this basis, we may conclude that the value of c-EMF will be zero during growth when the crystal is simultaneously stoichiometric and congruent. The opposite is equally true; the crystal is stoichiometric and congruent if no segregation of any constituent species occurs (c-EMF = 0) or if, in other words, the equilibrium partition coefficient of any constituent species is unity. These statements will be proven on a thermodynamic basis in the following sections.

#### 4.3.2 Activities of Constituent Elements in the Melt and Solid States for an Oxide Crystal that is Both Stoichiometric and Congruent

In the previous section, it was demonstrated on an experimental basis that a crystal presents zero c-EMF when it is simultaneously stoichiometric and congruent. The thermodynamic requirement for the coincidence of stoichiometry and congruency in the solid can be analyzed only when one sees that the activities of the constituent species in both the melt and the solid are unity.

The activity of a chemical species,  $i$ , in liquid  $\text{Li}_2\text{B}_4\text{O}_7$ ,  $a_{L(T)}^{\text{Li}(i)}$ , coexisting with the stoichiometric solid has been discussed [46]. It should be noted again that all the species in the liquid are assumed to be identical to those in the solid since they are partitioned from the liquid into the solid during growth. The chemical

potentials of both phases in equilibrium about the net  $\overline{\text{Li}_2\text{O}}$  are therefore equal and we may write

$$\overline{\mu}_{L(T)}^{\overline{\text{Li}_2\text{O}}} = \overline{\mu}_{S(T)}^{\overline{\text{Li}_2\text{O}}}. \quad (4.46)$$

Since  $a_{S(T)}^{\overline{\text{Li}_2\text{O}}} = 1$  at any temperature,  $T$ , it is also true that

$$a_{L(T)}^{\overline{\text{Li}_2\text{O}}} = \exp \left[ \frac{\Delta\mu_{(T,0)}^{\overline{\text{Li}_2\text{O}}}}{RT} \right], \quad (4.47)$$

where  $\Delta\mu_{(T,0)}^{\overline{\text{Li}_2\text{O}}} = \overline{\mu}_{S(T,0)}^{\overline{\text{Li}_2\text{O}}} - \overline{\mu}_{L(T,0)}^{\overline{\text{Li}_2\text{O}}}$  and  $\overline{\mu}_{L(T,0)}^{\overline{\text{Li}_2\text{O}}}$  is the standard-state chemical potential of the liquid phase associated with  $\overline{\text{Li}_2\text{O}}$ . Similar to the  $\overline{\mu}_{S(T,0)}^{\overline{\text{Li}_2\text{O}}}$  term,  $\overline{\mu}_{L(T,0)}^{\overline{\text{Li}_2\text{O}}}$  is defined as the chemical potential of the liquid associated with the exact  $\text{Li}_2\text{O}$  concentration in the stoichiometric composition of  $\text{Li}_2\text{B}_4\text{O}_7$  at a temperature,  $T$ . Concerning the equilibrium at the congruent point,  $a_{L(T)}^{\overline{\text{Li}_2\text{O}}} = 1$  in Eqn (4.47), and thus  $\Delta\mu_{(T,0)}^{\overline{\text{Li}_2\text{O}}} = 0$  and  $\overline{\mu}_{S(T,0)}^{\overline{\text{Li}_2\text{O}}} = \overline{\mu}_{L(T,0)}^{\overline{\text{Li}_2\text{O}}}$ . Furthermore,  $\overline{\mu}_{L(T)}^{\overline{\text{Li}_2\text{O}}}$  is transitioned into a linear coupling of the chemical potential of the real liquid chemical species,  $\mu_{L(T)}^{\text{Li}(i)}$ , in the same manner as Eqn (4.22) regarding  $\overline{\mu}_{S(T)}^{\overline{\text{Li}_2\text{O}}}$  and  $\mu_{S(T)}^{\text{Li}(i)}$ , such that the relationship shown in Eqn (4.48) holds.

$$p \overline{\mu}_{L(T)}^{\overline{\text{Li}_2\text{O}}} = q_1 \mu_{L(T)}^{\text{Li}(1)} + q_2 \mu_{L(T)}^{\text{Li}(2)} + q_3 \mu_{L(T)}^{\text{Li}(3)} + \cdots + q_k \mu_{L(T)}^{\text{Li}(k)} \quad (4.48)$$

Based on the above relationship between the chemical potentials, the appropriate standard-state chemical potential,  $\overline{\mu}_{L(T,0)}^{\text{Li}(i)}$ , may be chosen to satisfy Eqn (4.49):

$$n \overline{\mu}_{L(T,0)}^{\overline{\text{Li}_2\text{O}}} = m_1 \overline{\mu}_{L(T,0)}^{\text{Li}(1)} + m_2 \overline{\mu}_{L(T,0)}^{\text{Li}(2)} + m_3 \overline{\mu}_{L(T,0)}^{\text{Li}(3)} + \cdots + m_k \overline{\mu}_{L(T,0)}^{\text{Li}(k)}. \quad (4.49)$$

It should be noted that  $\overline{\mu}_{L(T,0)}^{\text{Li}(i)}$  is represented in the molar free energy diagram by the intersection of the molar free energy curve of the  $\text{Li}(i)$  species in the liquid with the principal axis ( $X_L^{\text{Li}(i)} = 1$ ). The axis in this diagram is the same as that associated with the  $\text{Li}(i)$  species in the solid, where  $X_S^{\text{Li}(i)} = 1$ , and  $\overline{\mu}_{L(T,0)}^{\text{Li}(i)}$  does not necessarily have to equal to  $\overline{\mu}_{S(T,0)}^{\text{Li}(i)}$ . Combining Eqn (4.49) with Eqn (4.26) and taking into account the equivalency  $\overline{\mu}_{S(T,0)}^{\overline{\text{Li}_2\text{O}}} = \overline{\mu}_{L(T,0)}^{\overline{\text{Li}_2\text{O}}}$  at the congruent point, Eqn (4.50) is obtained:

$$\begin{aligned} & m_1 \left( \overline{\mu}_{S(T,0)}^{\text{Li}(1)} - \overline{\mu}_{L(T,0)}^{\text{Li}(1)} \right) + m_2 \left( \overline{\mu}_{S(T,0)}^{\text{Li}(2)} - \overline{\mu}_{L(T,0)}^{\text{Li}(2)} \right) + m_3 \left( \overline{\mu}_{S(T,0)}^{\text{Li}(3)} - \overline{\mu}_{L(T,0)}^{\text{Li}(3)} \right) + \cdots + m_k \left( \overline{\mu}_{S(T,0)}^{\text{Li}(k)} - \overline{\mu}_{L(T,0)}^{\text{Li}(k)} \right) \\ & = m_1 \Delta\mu_{(T,0)}^{\text{Li}(1)} + m_2 \Delta\mu_{(T,0)}^{\text{Li}(2)} + m_3 \Delta\mu_{(T,0)}^{\text{Li}(3)} + \cdots + m_k \Delta\mu_{(T,0)}^{\text{Li}(k)} = 0, \end{aligned} \quad (4.50)$$

where  $\Delta\mu_{(T,0)}^{\text{Li}(i)} = \overline{\mu}_{S(T,0)}^{\text{Li}(i)} - \overline{\mu}_{L(T,0)}^{\text{Li}(i)}$ . At this point, we can discuss the sign of  $\Delta\mu_{(T,0)}^{\text{Li}(i)}$ , which determines whether or not the liquid can coexist with the solid. The molar free energy of  $\text{Li}(i)$  in the solid is actually represented by a point on the principal axis (Figure 4.10) [46]

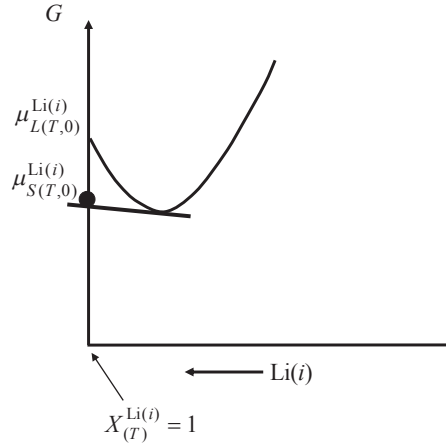


**FIGURE 4.10** Relationship between the standard-state chemical potentials of the liquid,  $\mu_{L(T,0)}^{\text{Li}(i)}$ , and solid,  $\mu_{S(T,0)}^{\text{Li}(i)}$ , about Li-bearing chemical species,  $\text{Li}(i)$  [46]. Due to the limited solid solution range, the molar free energy of the solid  $\text{Li}(i)$  is represented by a dot on the principal axis corresponding to  $\mu_{S(T,0)}^{\text{Li}(i)}$ .  $\mu_{S(T,0)}^{\text{Li}(i)}$  should be greater than or equal to  $\mu_{L(T,0)}^{\text{Li}(i)}$  in order to draw a common tangent between the molar free energies,  $G$ , of the liquid and solid. Note that both free energy curves have a common principal axis at  $X_{(T)}^{\text{Li}(i)} = 1$ .

at which  $\mu_{S(T)}^{\text{Li}(i)} = \mu_{S(T,0)}^{\text{Li}(i)}$ , since  $\text{Li}_2\text{B}_4\text{O}_7$  is a line compound, and, as discussed previously, the activity of any species in the solid,  $a_{S(T)}^{\text{Li}(i)}$ , is unity at any temperature. When drawing a common tangent to the molar free energy curve between the solid and the liquid, Eqn (4.51) should always hold since the tangent point on the solid molar free energy curve always lies on the principal axis corresponding to  $\mu_{S(T,0)}^{\text{Li}(i)}$ , while the tangent point on the liquid molar free energy curve moves away from the axis, such that

$$\mu_{S(T,0)}^{\text{Li}(i)} \leq \mu_{L(T,0)}^{\text{Li}(i)}. \quad (4.51)$$

This is illustrated in Figure 4.10 and leads to Eqn (4.52):

$$\Delta\mu_{(T,0)}^{\text{Li}(i)} \leq 0. \quad (4.52)$$

Combining Eqn (4.50) with  $m_i \geq 0$  and  $\Delta\mu_{(T,0)}^{\text{Li}(i)} \leq 0$ , the value of the  $\Delta\mu_{(T,0)}^{\text{Li}(i)}$  term at the congruent point is zero, as in Eqn (4.53):

$$\Delta\mu_{(T,0)}^{\text{Li}(i)} = 0. \quad (4.53)$$

At the liquidus temperature,  $T$ , the chemical potentials of all real chemical species,  $\text{Li}(i)$ , will be identical in either the solid or the liquid, such that

$$\mu_{S(T)}^{\text{Li}(i)} = \mu_{L(T)}^{\text{Li}(i)}. \quad (4.54)$$

Then, since  $a_{S(T)}^{\text{Li}(i)} = 1$ ,

$$\ln a_{L(T)}^{\text{Li}(i)} = \frac{\Delta\mu_{(T,0)}^{\text{Li}(i)}}{RT}. \quad (4.55)$$

At the congruent point,  $\Delta\mu_{(T,0)}^{\text{Li}(i)} = 0$  (from Eqn (4.53)), and so

$$a_{L(T)}^{\text{Li}(i)} = X_L^{\text{Li}(i)} = 1. \quad (4.56)$$

Finally, the equilibrium partition coefficient of  $\text{Li}(i)$ ,  $k_0^{\text{Li}(i)}$ , is given by

$$k_0^{\text{Li}(i)} = \frac{X_S^{\text{Li}(i)}}{X_L^{\text{Li}(i)}} = \frac{1}{1} = 1. \quad (4.57)$$

The equilibrium partition coefficient,  $k_0^{\text{Li}(i)}$ , for each of the Li-bearing species is found to be unity in the composition associated with a material that is simultaneously stoichiometric and congruent, such as  $\text{Li}_2\text{B}_4\text{O}_7$  [46]. The partition coefficients of the B-bearing chemical species can be discussed in a similar manner, and all of these species can be shown to also have coefficients of unity at the congruent point. Therefore, no segregation of any constituent species, including ionic species, takes place and a c-EMF value of zero will be apparent.

In contrast, in the case of a material for which the stoichiometric composition is located somewhere other than the congruent point, such as holds true for  $\text{LiNbO}_3$ , the constituent species do not necessarily have partition coefficients equal to unity. Although the activity of the bulk liquid in equilibrium with the stoichiometric solid could be unity, i.e.,  $a_{L(T)}^{\overline{\text{Li}_2\text{O}}} = 1$ , the principal axis ( $X = 1$ ) cannot be common to the solid and the liquid since the equilibrium compositions are different between these two phases, such that  $a_{S(T)}^{\overline{\text{Li}_2\text{O}}} = 1$  and  $a_{L(T)}^{\overline{\text{Li}_2\text{O}}} = 1$  do not both hold true in the same coordination system. As a result, Eqns (4.48) to (4.57) cannot be used to analyze a stoichiometric crystal with a composition that differs from the congruent point. Thus, Eqn (4.53) is not valid, meaning that

$$\Delta\mu_{(T,0)}^{\text{Li}(i)} \neq 0, \quad (4.58)$$

and

$$\ln \left( \frac{a_{L(T)}^{\text{Li}(i)}}{a_{S(T)}^{\text{Li}(i)}} \right) = \frac{\Delta\mu_{(T,0)}^{\text{Li}(i)}}{RT} \neq 0.$$

Therefore, Eqn (4.59), below, can be written

$$\frac{a_{L(T)}^{\text{Li}(i)}}{a_{S(T)}^{\text{Li}(i)}} = a_{L(T)}^{\text{Li}(i)} \neq 1. \quad (4.59)$$

The partition coefficients,  $k_0^{\text{Li}(i)}$ , for the constituent melt species of a stoichiometric crystal that is not congruent will not equal unity and so segregation will occur, which in turn leads to a nonzero value of c-EMF. This is demonstrated on an experimental basis in Figure 4.8.

## 4.4 Oxide Crystals Having a Stoichiometric Composition Coincident with the Congruent Point

As discussed in the previous section, when a compound has a stoichiometric structure at the congruent point, the equilibrium partitioning coefficients of all chemical species become unity and segregation does not occur. With regard to conventional c-LN or c-LT, the segregation of ionic species is observed during growth because these materials are not stoichiometric. A unique relationship between the unity of the partitioning coefficients of ionic species and the coincidence of stoichiometry and congruency is quite beneficial in terms of developing LN or LT crystals that are superior to conventional LN and LT. The congruent compositions are found on the stoichiometric line of 50 mol% Nb<sub>2</sub>O<sub>5</sub> (line A in Figure 4.3) in the Li<sub>2</sub>O–Nb<sub>2</sub>O<sub>5</sub>–MgO system and on the stoichiometric line of 50 mol% Ta<sub>2</sub>O<sub>5</sub> (line B in Figure 4.11) in the Li<sub>2</sub>O–Ta<sub>2</sub>O<sub>5</sub>–MgO system. Using Kröger–Vink notation, these materials may be written as  $(\text{Li}_{\text{Li}}^{\times})_{0.906}(\text{Mg}_{\text{Li}}^{\cdot})_{0.047}(\text{V}_{\text{Li}}^{\prime})_{0.047}(\text{Nb}_{\text{Nb}}^{\times})(\text{O}_{\text{O}}^{\times})_3$ , termed cs-MgO:LN [47], and  $(\text{Li}_{\text{Li}}^{\times})_{0.816}(\text{Mg}_{\text{Li}}^{\cdot})_{0.092}(\text{V}_{\text{Li}}^{\prime})_{0.092}(\text{Ta}_{\text{Ta}}^{\times})(\text{O}_{\text{O}}^{\times})_3$ , termed cs-MgO:LT [56], respectively. These compounds show no segregation of ionic species during growth, which demonstrates that the equilibrium partition coefficients,  $k_0$ , are unity for all constituent chemical species in the melt, and thus cs-MgO:LN and cs-MgO:LT are congruent and stoichiometric simultaneously. Therefore, the conventional congruent materials LiNbO<sub>3</sub> and LiTaO<sub>3</sub>, both of which are nonstoichiometric, are converted to congruent,

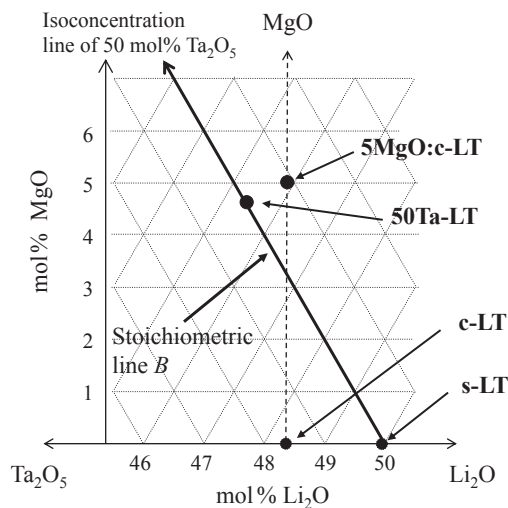


**FIGURE 4.11** Composition diagram of various LiTaO<sub>3</sub> compositions in the pseudo-ternary Li<sub>2</sub>O–Ta<sub>2</sub>O<sub>5</sub>–MgO system. The isoconcentration line of 50 mol% Ta<sub>2</sub>O<sub>5</sub> is termed line B and represents a ratio of O to Ta of exactly 3.0. Legend: s-LT = stoichiometric LiTaO<sub>3</sub> on the Li<sub>2</sub>O–Ta<sub>2</sub>O<sub>5</sub> line; c-LT = congruent LiTaO<sub>3</sub> on the Li<sub>2</sub>O–Ta<sub>2</sub>O<sub>5</sub> line; 50Ta-LT = MgO-doped LiTaO<sub>3</sub> on line B; 5MgO:LT = c-LT doped with 5 mol% MgO.

stoichiometric crystals based on our extended concept of stoichiometry. Both materials, however, contain impurities and vacancies that are not allowed under the conventional definition of stoichiometry.

#### 4.4.1 MgO-Doped LiNbO<sub>3</sub>

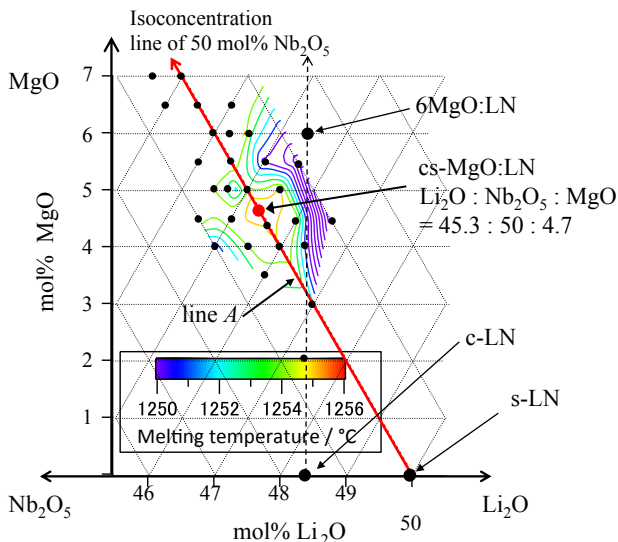
In a conventional stoichiometric crystal, each element occupies only its own unique site in the crystal lattice, and no defects arising from nonstoichiometry are allowed. Thus, a conventional stoichiometric crystal usually shows good optical properties. However, the stoichiometric composition often does not coincide with the congruent composition. In such a case, growth of the stoichiometric compound is difficult due to the compositional deviation caused by the segregation of constituent species in the melt during growth. LiNbO<sub>3</sub> (LN) is one such compound. As shown in Figure 4.2(B) [17], the stoichiometric composition (s-LN; Li<sub>2</sub>O = 50 mol%) does not coincide with the congruent composition (c-LN; Li<sub>2</sub>O = 48.38 mol% [57]). Although it can easily be grown from the melt, the optical properties of c-LN, such as conversion efficiency of SHG, photoconductivity, and transparency in the short-wavelength region, are inferior to those of s-LN [2], and so impurity doping of c-LN is performed to improve its optical properties. MgO is considered to be an effective impurity for LN, because MgO-doped s-LN exhibits high photoconductivity and has a high threshold for optical damage [2]. However, these crystals are no longer congruent nor are they stoichiometric. In the following section, the growth and characterization of cs-MgO:LN, a crystal that is simultaneously congruent and stoichiometric, is described.

First, the distribution of the melting temperatures of sintered materials with various compositions was determined for the Li<sub>2</sub>O–Nb<sub>2</sub>O<sub>5</sub>–MgO ternary system via DTA. The composition possessing the highest melting temperature is the congruent point of the MgO-doped LN. Next, this composition was confirmed to be the exact ternary congruent composition by confirming that c-EMF was not generated. Such a composition is found on the 50 mol% Nb<sub>2</sub>O<sub>5</sub> stoichiometric line, where the congruent point meets the stoichiometric composition. The compound cs-MgO:LN (Li<sub>2</sub>O:Nb<sub>2</sub>O<sub>5</sub>:MgO = 45.3:50:4.7) is such a compound and is expected to be easily grown and to exhibit superior optical properties compared to those of conventional c-LN, MgO-doped c-LN, and s-LN.

##### 4.4.1.1 Distribution of the Melting Temperatures of MgO-Doped LiNbO<sub>3</sub>

The ternary phase diagram for the MgO–Li<sub>2</sub>O–Nb<sub>2</sub>O<sub>5</sub> system is illustrated in Figure 4.12. The isoconcentration line for 50 mol% Nb<sub>2</sub>O<sub>5</sub> is also drawn as a stoichiometric line on this diagram (line A). Every LN crystal on this line (50Nb-LN) could potentially be stoichiometric. The melting temperatures of sintered versions of this material with various compositions were measured by high-temperature DTA around line A. The distribution of melting points is plotted in Figure 4.12, which represents the solidus surface of the Mg-doped LN in this region. The congruent composition, which

**FIGURE 4.12** Distribution of the melting temperatures of sintered compounds with various compositions around the isoconcentration line of 50 mol%  $\text{Nb}_2\text{O}_5$  (line A) in the pseudo-ternary system of  $\text{Li}_2\text{O}-\text{Nb}_2\text{O}_5-\text{MgO}$ . Isothermal contours showing the solidus plane around cs-MgO:LN are also included. The highest melting temperature corresponding to the congruent point is found on line A, and this represents the cs-MgO:LN composition at which the congruent point is coincident with the stoichiometric composition:  $\text{Li}_2\text{O}:\text{Nb}_2\text{O}_5:\text{MgO} = 45.3:50:4.7$ . After Ref. [58].



corresponds to the highest melting point, was found at the composition  $\text{Li}_2\text{O}:\text{Nb}_2\text{O}_5:\text{MgO} = 45.3:50:4.7$  on line A [58]. This represents a new LN composition, termed cs-MgO:LN, equal to the congruent point coincident with the stoichiometric composition. Although several studies concerning Mg-doped LN have been reported [59–61], none of these has discussed this unique composition. In the pseudo-binary system of  $\text{Li}_2\text{O}-\text{Nb}_2\text{O}_5$ , c-LN does not coincide with s-LN, and the ionic species segregate during growth. Although 5MgO:LN exhibits improved optical properties [62], it is neither congruent nor stoichiometric, and thus segregation of bulk components as well as ionic species occurs during growth, yielding an inhomogeneous compositional distribution in the crystal.

#### 4.4.1.2 Crystallization Electromotive Force

The c-EMF measurement methods are described in detail in Section 4.3.1. The c-EMF is represented as a hysteresis gap on the potential curve in Figure 4.7 during the melting and solidification processes and has a magnitude of several mV. The value of c-EMF is also growth-rate dependent and not specific to the material itself. Furthermore, because a high temperature gradient is present in the melt near the interface in a  $\mu$ -PD measurement system, an intrinsic interface electric field is generated due to a thermoelectric process (via the Seebeck effect), and this in turn influences the distribution of ionic species in the solute boundary layer. Thus, an extrapolation of c-EMF toward the zero temperature gradient is drawn in Figure 4.13 for the compositions c-LN, s-LN, c-LN doped with 6 mol% MgO (6MgO:LN), and cs-MgO:LN. In the case of each of these compositions, the amplitude of c-EMF ( $\Delta\phi_{\text{EMF}}$ ) decreases with decreasing temperature gradient. The exact value of  $\Delta\phi_{\text{EMF}}$  can be obtained at  $0^\circ\text{C}/\text{cm}$  where no electric field

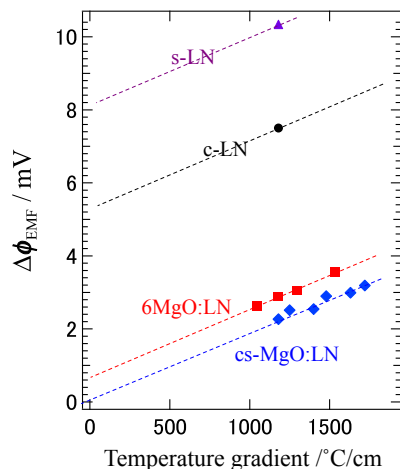


**FIGURE 4.13** Temperature gradient dependence of  $\Delta\phi_{\text{EMF}}$  for s-LN, c-LN, 6MgO:LN, and cs-MgO:LN. For each composition,  $\Delta\phi_{\text{EMF}}$  decreases as the temperature gradient decreases. The  $\Delta\phi_{\text{EMF}}$  value of cs-MgO:LN becomes 0 mV at 0 °C/cm, while the values of the other materials become nonzero. Modified from Ref. [47].

exists, and cs-MgO:LN is the only composition that attains zero c-EMF at 0 °C/cm [47]. These data also confirm that no segregation occurs during growth at any growth rate, demonstrating that the partition coefficients of all the solute components, including the ionic species, are unity and thus assuring the true congruency of cs-MgO:LN [47]. In the previous section, it was shown on a thermodynamic basis that partition coefficients equal to unity of the solute components leads to activity values equal to unity in both the solid and liquid states, and this in turn results in cs-MgO:LN simultaneously having a stoichiometric structure. The converse is also true—based on thermodynamic arguments, in a compound that has a stoichiometric structure at the congruent composition, the equilibrium partition coefficient of all chemical species, including ionic species, becomes unity. In other words, the activities of all constituent elements both in the melt and the solid will be unity in the case of a compound that exhibits the simultaneous occurrence of stoichiometry and congruency, as described in Section 4.3.2.

In contrast, the conventional congruent material  $\overline{\text{LiNbO}_3}$  (c-LN) requires the partition coefficient to equal unity only for the bulk  $\overline{\text{Li}_2\text{O}}$  and  $\overline{\text{Nb}_2\text{O}_5}$  components, and its crystallization EMF has a nonzero value, suggesting that the ionic species in the c-LN melt have nonunity partition coefficients. The values obtained for activity,  $a^j$  ( $j = \text{O}, \text{Nb}, \text{Li}, \text{Mg}$ , and vacancy) and equilibrium partition coefficient,  $k_0^j$ , are summarized in Table 4.1 for the growth of s-LN (stoichiometric), c-LN (congruent), and cs-MgO:LN (stoichiometric and congruent) crystals.

#### 4.4.1.3 Bulk Crystal Growth of cs-MgO:LiNbO<sub>3</sub> and Its Nonlinear Optical Characterization

Only cs-MgO:LN has no segregation of ionic species [47] and therefore is truly congruent, easy to grow, and is expected to have a higher compositional homogeneity

**Table 4.1** Activity,  $a^j$ , and Equilibrium Partition Coefficient,  $k_0^j$ , Crystallization Electromotive Force (c-EMF),  $\Delta\phi_{EMF}$ , Values Associated with the Growth of s-LN (Stoichiometric), c-LN (Congruent) and cs-MgO:LN (Stoichiometric and Congruent) Crystals

	Activity, $a^j$ ( $j = \text{Li, Nb, Mg, O, Vacancy}$ )	Equilibrium Partition Coefficient, $k_0^j$ ( $j = \text{Li, Nb, Mg, O, Vacancy}$ )	c-EMF, $\Delta\phi_{EMF}$
s-LN	$a_S^j = 1, a_L^j \neq 1$	$k_0^j \neq 1$	$\Delta\phi_{EMF} \neq 0$
c-LN	$a_S^j \neq 1, a_L^j \neq 1$	$k_0^j \neq 1^*$	$\Delta\phi_{EMF} \neq 0$
cs-MgO:LN	$a_S^j = 1, a_L^j = 1$	$k_0^j = 1$	$\Delta\phi_{EMF} = 0$

\* $k_0^j$  is unity for the bulk component  $\overline{\text{Li}_2\text{O}}$  and  $\overline{\text{Nb}_2\text{O}_5}$  in the pseudo-binary system of  $\text{Li}_2\text{O}-\text{Nb}_2\text{O}_5$ .

than the conventional crystals of c-LN and MgO-doped c-LN. It is also expected to exhibit a SHG conversion efficiency as high as that of s-LN because of its stoichiometric structure. Bulk crystals of cs-MgO:LN were therefore grown, and its superiority in both compositional homogeneity and nonlinear optical properties were demonstrated by comparing its SHG properties with those of c-LN, s-LN, and 5MgO:LN.

A bulk single crystal of cs-MgO:LN was grown at a rate of 2 mm/h via the Czochralski method along the Z-axis in an air atmosphere. The resulting crystal was colorless and inclusion-free, as shown in Figure 4.14 [58]. The crystal was about 22 mm in diameter and 40 mm long, and its solidified melt fraction,  $g$ , was 0.25 after the completion of growth. The Czochralski technique was also used to grow c-LN, 5MgO:LN, and s-LN,



**FIGURE 4.14** A cs-MgO:LN single bulk crystal grown along the Z-axis by the Czochralski method [58].

although the s-LN was produced using the double-crucible method [63]. The SHG properties of these bulk single crystals were measured. In preparation, all crystals were poled and subsequently sliced into  $5 \times 5 \times 5$  mm blocks (the solidified melt fraction value was  $g = 0.13$  in the case of cs-MgO:LN along the  $x[1\bar{2}10]$ ,  $y[10\bar{1}0]$ ,  $z[0001]$  directions and the  $x$ -planes were polished to a mirror finish to form the incident plane. An optical parametric oscillator (OPO) pumped by the third harmonic wave of a Q-switched Nd:YAG laser (1064 nm) was used to evaluate the SHG properties associated with noncritical phase matching, using  $d_{31}$  of the LN crystal in the infrared region from 800 to 1200 nm.

Since the phase-matching wavelength is sensitive to the crystal composition [64], its distribution in a crystal test plate was used to evaluate the compositional homogeneity of the crystal. Figure 4.15 shows the in-plane distribution of the noncritical phase-matching wavelength for a  $4 \times 4$  mm area on each crystal. It should be noted that the vertical direction in each test plate in Figure 4.15 was parallel to the growth axis, while the horizontal direction was parallel to the radial direction. The phase-matching wavelength of the cs-MgO:LN was almost constant over the whole test plate ( $\Delta g = 0.024 \sim 0.025$ ) [58]. This homogeneity was surprisingly sustained during growth even with possible variations in the growth rate due to the changing crystal diameter,

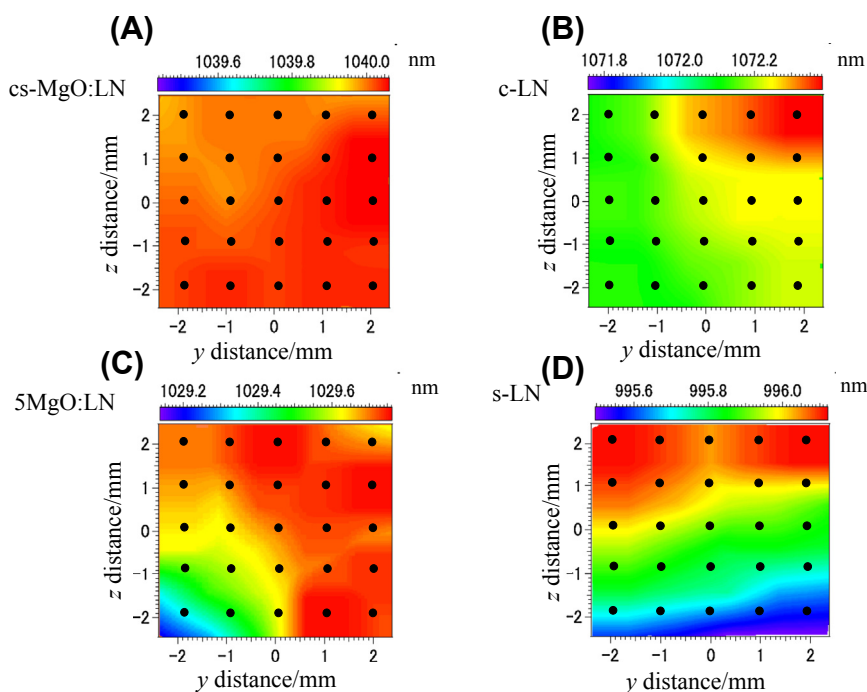


FIGURE 4.15 The in-plane distribution ( $4 \times 4$  mm) of the noncritical phase-matching wavelength [58]. Solid circles indicate the measured points: (A) cs-MgO:LN, (B) c-LN, (C) 5MgO:LN, and (D) s-LN.

which was attributed to the complete unity of the partition coefficients of all the melt species. To confirm the compositional homogeneity over the entire length of the cs-MgO:LN crystal, its Curie temperature was measured via differential scanning calorimetry (DSC) at the top and the base. The Curie temperature difference between the top and bottom portions was  $0.8\text{ }^{\circ}\text{C}$ , which corresponds to a  $0.02\text{ mol}\%$   $\text{Li}_2\text{O}$  variation [65] when neglecting the effect of MgO incorporation. This variation was sufficiently small as to demonstrate the congruency of cs-MgO:LN. The c-LN crystal was slightly less homogeneous than the cs-MgO:LN, but was much more homogeneous than both the s-LN and 5MgO:LN materials. These results are consistent with the partitioning behavior of the solute components, since both c-LN and cs-MgO:LN have congruent-melting crystals and bulk components, such as  $\text{Li}_2\text{O}$ ,  $\text{Nb}_2\text{O}_5$ , and/or MgO, which are not segregated but rather partitioned into the crystal with partition coefficients of unity. In the case of cs-MgO:LN, neither the bulk components nor the ionic species are segregated, so its composition would be expected to be more homogeneous than that of c-LN. In contrast, the phase-matching wavelengths of s-LN and 5MgO:LN varied drastically within the test plate since these compounds were not congruent. The maximum compositional deviations of s-LN and c-LN within the measured areas were estimated to be  $0.0092\text{ mol}\%$   $\text{Li}_2\text{O}$  and  $0.0042\text{ mol}\%$   $\text{Li}_2\text{O}$ , respectively. The observed variation in the phase-matching wavelength in s-LN might reflect the compositional variation along the growth axis during growth. This indicates the difficulty of growing homogeneous s-LN using the double-crucible method [63].

The SHG conversion efficiency was measured at the center of each test plate ( $z: 0\text{ mm}$ ,  $y: 0\text{ mm}$  in Figure 4.15) at a constant value of the fundamental beam power. As shown in Figure 4.16, the conversion efficiency of cs-MgO:LN is slightly lower than those obtained with 5MgO:LN and s-LN [58], however, these values are almost equal in magnitude, while the value measured for the c-LN sample is considerably lower. These experiments demonstrated that cs-MgO:LN has been generated, based on our extended concept of stoichiometry, and that this material, due to its congruent state, is superior to

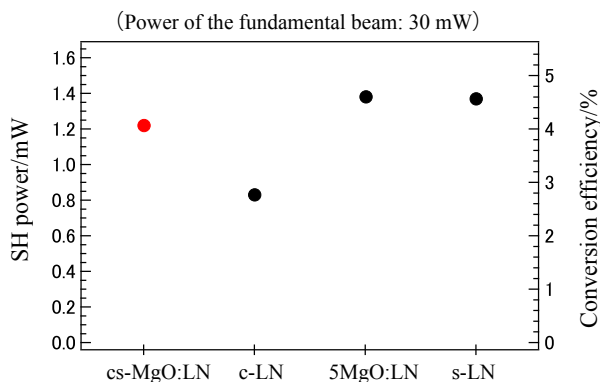


FIGURE 4.16 Plots of the secondary harmonic generation conversion efficiency obtained from cs-MgO:LN, c-LN, 5MgO:LN, and s-LN.

conventional  $\text{LiNbO}_3$  crystals having a highly homogeneous composition. This substance also exhibits a high conversion efficiency of secondary harmonic generation due to its stoichiometric structure.

#### 4.4.2 MgO-Doped $\text{LiTaO}_3$

Lithium tantalate (LT), like lithium niobate (LN), is an oxide material whose congruent composition differs from its stoichiometric composition in the binary  $\text{Li}_2\text{O}-\text{Ta}_2\text{O}_5$  system. By employing our extended concept of stoichiometry, a new lithium tantalate incorporating MgO doping, cs-MgO:LT ( $\text{Li}_2\text{O}:\text{Ta}_2\text{O}_5:\text{MgO} = 40.8:50.0:9.2$ ), has been developed [56]. As in the case of cs-MgO:LN, this material is stoichiometric and congruent. Because of this coincidence, cs-MgO:LT does not exhibit any c-EMF and does not show any segregation during growth, even in the case of ionic species. A bulk crystal was grown from a cs-MgO:LT melt via the Czochralski method and showed excellent compositional homogeneity, as demonstrated by the constant distribution of the Curie temperature throughout the crystal.

##### 4.4.2.1 Distribution of Melting Temperatures of MgO-Doped $\text{LiTaO}_3$

The ternary phase diagram for the system of  $\text{MgO}-\text{Li}_2\text{O}-\text{Ta}_2\text{O}_5$  is illustrated in Figure 4.17. The isoconcentration line of 50 mol%  $\text{Ta}_2\text{O}_5$  is also drawn as a stoichiometric line (line B). Every LT crystal on this line (50Ta-LT) could potentially be stoichiometric. The melting temperatures of sintered materials with various compositions were measured by high-temperature DTA around line B. The distribution of melting points is

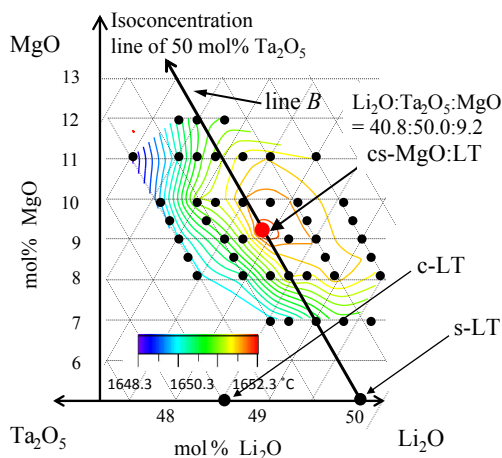


**FIGURE 4.17** Distribution of the melting temperatures of sintered compounds with various compositions around the isoconcentration line of 50 mol%  $\text{Ta}_2\text{O}_5$  (line B) in the pseudo-ternary system of  $\text{Li}_2\text{O}-\text{Ta}_2\text{O}_5-\text{MgO}$ . Isothermal contours showing the solidus plane around cs-MgO:LT are also drawn. The highest melting temperature corresponding to the congruent point is found on line B. This is the cs-MgO:LT composition at which the congruent point is coincident with the stoichiometric composition:  $\text{Li}_2\text{O}:\text{Ta}_2\text{O}_5:\text{MgO} = 40.8:50.0:9.2$ . After Ref. [56].

plotted in Figure 4.17, which represents the solidus surface of the Mg-doped LT in this region. The congruent composition, which corresponds to the highest melting point, was found at the composition corresponding to  $\text{Li}_2\text{O}:\text{Ta}_2\text{O}_5:\text{MgO} = 40.8:50.0:9.2$  on line B [56]. This represents a new LT composition, cs-MgO:LT, that exists at the congruent point coincident with the stoichiometric composition.

Since cs-MgO:LT has a composition that lies well within the solid solution range in the  $\text{Li}_2\text{O}-\text{Ta}_2\text{O}_5-\text{MgO}$  ternary system, it can be grown without any compositional constraints, similar to the case of cs-MgO:LN. In contrast, conventional s-LT has a composition located near the solubility limit of  $\text{Li}_2\text{O}$  so that the practical upper limit for the  $\text{Li}_2\text{O}$  content in this material is 49.8 mol% [66,67]. Thus cs-MgO:LT is more tolerant than s-LT from a compositional perspective, which offers a significant advantage with regard to crystal growth.

#### 4.4.2.2 Crystallization Electromotive Force

Measurement of c-EMF was carried out for cs-MgO:LT and for conventional c-LT using the same  $\mu$ -PD technique as was applied in the case of LN. The furnace apparatus used during these measurements was composed of Pt containing 20% Rh rather than pure Pt because of the high melting temperature of LT. Growth via the  $\mu$ -PD technique is accompanied by a large temperature gradient near the interface that leads to an intrinsic electric field due to the Seebeck effect, as is observed during LN growth. An intrinsic electric field such as this significantly affects the segregation of ionic species at the interface [40,68], and thus the  $\Delta\phi_{\text{EMF}}$  values obtained for cs-MgO:LT and c-LT were corrected by extrapolation to the temperature gradient at  $0^\circ\text{C}/\text{cm}$ . Following this correction, it was found that the  $\Delta\phi_{\text{EMF}}$  of c-LT was nonzero, while that of cs-MgO:LT was zero [56]. These results demonstrate experimental verification that the partition coefficient,  $k_0$ , of the ionic species in the cs-MgO:LT melt is unity. Consequently, the activity of all constituent elements both in the melt and in the solid state of cs-MgO:LT is unity, meaning that cs-MgO:LT is both stoichiometric and congruent.

#### 4.4.2.3 Bulk Crystal Growth and Curie Temperature of cs-MgO:LiTaO<sub>3</sub>

A bulk single crystal was grown along the Z-axis from the cs-MgO:LT melt under an atmosphere composed of 99 vol% Ar/1 vol%  $\text{O}_2$  via the CZ method. The resulting crystal is shown in Figure 4.18 [56]. Since the cs-MgO:LT composition is congruent, a homogeneous compositional distribution was expected in this material. The Curie temperatures of this crystal were measured via DSC at the top, middle, and bottom of the sample along its central axis. Figure 4.19 summarizes the distribution of the Curie temperature over the cs-MgO:LT crystal as well as the temperature of the residual melt. The maximum difference in Curie temperature over the cs-MgO:LT crystal was  $0.4^\circ\text{C}$  [56], corresponding to a 0.03 mol%  $\text{Li}_2\text{O}$  difference [69] when neglecting the effect of MgO doping. This result demonstrates the superior homogeneity of the cs-MgO:LT crystal and shows that the cs-MgO:LT is congruent. It should be noted that growth from the melt of



FIGURE 4.18 A cs-MgO:LT single bulk crystal grown along the Z-axis by the Czochralski method [56].

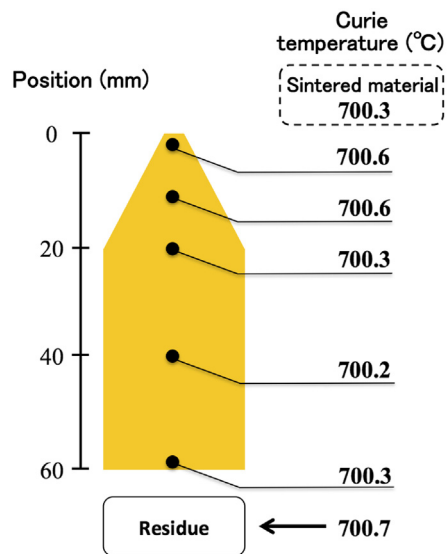


FIGURE 4.19 Distribution of the Curie temperatures of as-grown cs-MgO:LT along the growth axis, the seed crystal, and the residual melt [56].

the cs-MgO:LT composition does not accompany segregation of any ionic melt species. This material thus represents a true congruent state, whereas conventional c-LT in the  $\text{Li}_2\text{O}-\text{Ta}_2\text{O}_5$  binary system does not since its  $\Delta\phi_{\text{EMF}}$  value is not zero, meaning that segregation of ionic species takes place. Therefore, cs-MgO:LT contains essentially no uncoupled ionic species in the crystal and is expected to have superior nonlinear optical properties as compared to conventional LT crystals.

#### 4.4.3 Thermodynamic Requirements for Impurity Doping

MgO is a suitable doping oxide for the preparation of high quality LN and LT crystals exhibiting the concurrent occurrence of stoichiometry and congruency in the ternary system. It is natural to inquire as to whether any other oxides produce a similar effect when added to LN or LT such that the resulting crystals become simultaneously stoichiometric and congruent and whether there are any specific requirements for an oxide to behave as an effective dopant. Figure 4.20 illustrates the ternary  $\text{Li}_2\text{O}-\text{Nb}_2\text{O}_5-\text{ZnO}$  diagram, in which the distribution of melting points is drawn around the stoichiometric line of 50 mol%  $\text{Nb}_2\text{O}_5$  (line C). The highest melting point that corresponds to the congruent point does not lie on the stoichiometric line C, and thus it is not possible to make LN simultaneously congruent and stoichiometric by adding ZnO. We may then ask ourselves, what is the difference between MgO and ZnO that renders MgO effective but ZnO ineffective?

In order to develop an LN or LT composition, the crystals must have a zero c-EMF value. In other words, the activity of every constituent element in both the solid and

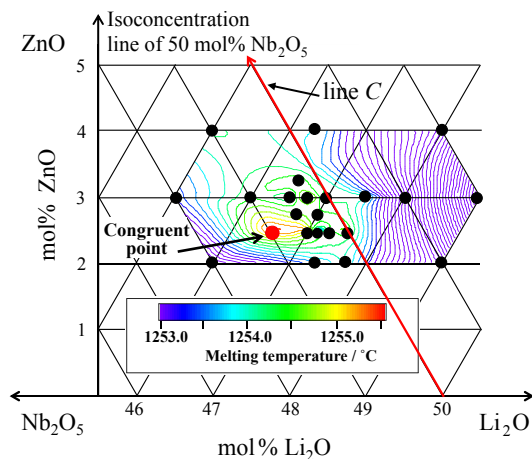
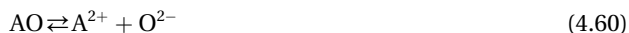


**FIGURE 4.20** Distribution of the melting temperatures of sintered compounds with various compositions around the isoconcentration line of 50 mol%  $\text{Nb}_2\text{O}_5$  (line C) in the pseudo-ternary  $\text{Li}_2\text{O}-\text{Nb}_2\text{O}_5-\text{ZnO}$  system. Isothermal contours showing the solidus plane around line C are also drawn. The highest melting temperature corresponding to the congruent point is located apart from line C.

liquid states is required to be unity. Suppose that a divalent oxide, AO, is doped into LN and subsequently ionized in the melt according to the following equation:



The congruent point is assumed to form at a certain composition in the ternary diagram of  $\text{Li}_2\text{O}-\text{Nb}_2\text{O}_5-\text{AO}$ . At the congruent melt composition, the partition coefficients of the three bulk components will be unity, such that

$$k_0^{\overline{\text{AO}}} = k_0^{\overline{\text{Li}_2\text{O}}} = k_0^{\overline{\text{Nb}_2\text{O}_5}} = 1, \quad (4.61)$$

where the bar over a species indicates a bulk component. Accordingly, the activities of these three bulk components in both the solid and liquid are unity, meaning that

$$a_\beta^{\overline{\text{AO}}} = a_\beta^{\overline{\text{Li}_2\text{O}}} = a_\beta^{\overline{\text{Nb}_2\text{O}_5}} = 1, \quad (4.62)$$

where  $\beta$  indicates solid (S) or liquid (L) phases. Because the value of c-EMF is zero, one degree of freedom is available to establish the appropriate relationship between the standard-state chemical potentials of AO,  $\text{A}^{2+}$ , and  $\text{O}^{2-}$  in both the solid and liquid, as follows:

$$a_\beta^{\overline{\text{AO}}} = a_\beta^{\text{A}^{2+}} a_\beta^{\text{O}^{2-}} = 1 \quad (4.63)$$

Likewise,

$$a_\beta^{\overline{\text{Li}_2\text{O}}} = \left(a_\beta^{\text{Li}^+}\right)^2 a_\beta^{\text{O}^{2-}} = 1, \quad (4.64)$$

and

$$a_\beta^{\overline{\text{Nb}_2\text{O}_5}} = \left(a_\beta^{\text{Nb}^{5+}}\right)^2 \left(a_\beta^{\text{O}^{2-}}\right)^5 = 1. \quad (4.65)$$

At this point, we also wish to determine the thermodynamic criteria that produce activities of unity for the species  $\text{A}^{2+}$ ,  $\text{O}^{2-}$ ,  $\text{Li}^+$ , and  $\text{Nb}^{5+}$ . If AO is completely ionized, the partitioned AO in the solid is attributed only to  $\text{A}^{2+}$  in the melt. Thus,

$$k_0^{\text{A}^{2+}} = 1, \quad (4.66)$$

and so

$$a_\beta^{\text{A}^{2+}} = 1. \quad (4.67)$$

Inserting Eqn (4.67) into Eqn (4.63) leads to  $a_\beta^{\text{O}^{2-}} = 1$ , and combining this with Eqns (4.64) and (4.65) gives

$$a_\beta^{\text{Li}^+} = a_\beta^{\text{Nb}^{5+}} = 1. \quad (4.68)$$

Thus, the activity of every constituent element in the AO-doped LN is unity in both the liquid and solid states. This composition is found on the stoichiometric line of 50 mol%  $\text{Nb}_2\text{O}_5$  and can be termed cs-AO:LN, since it is both congruent and stoichiometric. This scenario occurs in the case of MgO doping, which is understandable when one considers that MgO is an almost completely ionic oxide. In contrast, if AO is only partially ionized, both AO and  $\text{A}^{2+}$  will be partitioned into the crystal. As a result, even

if  $\overline{a_{\beta}^{AO}} = 1$  (Eqn (4.63)) is true, neither  $a_{\beta}^{A^{2+}}$  nor  $a_{\beta}^{O^{2-}}$  will necessarily equal unity, and so the congruent point will not lie on the stoichiometric line for this material. In general, then, a dopant that is only partially ionized in the melt will not generate a compound LN in which stoichiometry and congruency are coincident. In contrast, when the oxide dopant AO is completely ionized, the congruent point can appear on the stoichiometric line.

## 4.5 Summary

An extended concept of a *stoichiometric* oxide has been developed. The chemical potential of this new stoichiometric compound has no mixing term, and thus the activities of all its constituent elements will equal unity. The opposite is equally true—when the activities of all the constituent elements can be unity, the material is stoichiometric. In this definition, the term *constituent element* is expanded to potentially include both impurities and vacancies, neither of which is allowed in the conventional definition of stoichiometry. An activity of unity for a species is possible only when one degree of freedom is available at the crystal site, so as to assign the chemical potential of each species,  $j$ , to the standard-state chemical potential, such that  $\mu_0^j = \mu^j$ . Based on this extended understanding of stoichiometry, new LiNbO<sub>3</sub> and LiTaO<sub>3</sub> crystals have been developed by doping with MgO. These materials are simultaneously stoichiometric and congruent and are therefore easy to grow and exhibit excellent nonlinear optical properties. Thermodynamic arguments demonstrate that the concurrent occurrence of stoichiometry and congruency requires activity values of unity for all the constituent elements of the substance, not only in the solid but also in the liquid state at equilibrium. This means that the partition coefficients of all the chemical species in the melt must also be unity such that no segregation occurs; this has been demonstrated experimentally by the observation of zero c-EMF. It is very important that the stoichiometry of an oxide crystal and its relevant point defects are discussed in association with solute partitioning during crystal growth. This is because the point defects are partitioned with other elements from the liquid to the solid state as the crystal is formed, and the associated partitioning is related to the activity of the constituent elements in terms of their respective equilibrium partition coefficients, which in turn determines the stoichiometry or nonstoichiometry of the material.

## References

- [1] Dalton J. A new system of chemical philosophy part 1. Manchester: S. Russell; 1808.
- [2] Furukawa Y, Kitamura K, Takekawa S. Opt Lett 1998;23:1892.
- [3] Nakamura M, Takekawa S, Terabe K, Kitamura K, Usami T, Nakamura K, et al. Ferroelectrics 2002; 273:199.
- [4] Bube R. Electrons in solids: an introductory survey. Academic Press; 1988.
- [5] Sze SM. Semiconductor devices: physics and technology. 3rd ed. John Wiley & Sons; 2012.

- [6] Oda O. Compound semiconductor bulk materials and characterizations. World Scientific Pub Co Inc; 2003.
- [7] Rudolph P, Jurisch M. *J Cryst Growth* 1999;198–199:325.
- [8] Dhar A, Mansingh A. *J Appl Phys* 1990;68:5804.
- [9] Pauling L. *J Am Chem Soc* 1929;51:1010.
- [10] Brown ID, Shannon RD. *Acta Cryst A* 1972;29:266.
- [11] Brown ID. *Acta Cryst B* 1992;48:553.
- [12] Brown ID. *The chemical bond in inorganic chemistry. The bond valence model.* New York: Oxford Univ. Press; 2002.
- [13] Andersson J, Collen B, Kuylenstierna U, Magnéli A. *Acta Chem Scand* 1957;11:1641.
- [14] Magnéli A. *Pure Appl Chem* 1978;50:1261.
- [15] Tilley RJD. *Defect crystal chemistry and its applications.* Blackie & Son Limited, Glasgow and London. Published in USA by Chapman and Hall, New York; 1987.
- [16] Stokořsa A, Laskowska B. *J Chem Crystallogr* 2008;38:913.
- [17] Svaasand LO, Eriksrud M, Nakken G, Grande AP. *J Cryst Growth* 1974;22:179.
- [18] Rogacheva EL, Gorne GV, Zhigareva NK, Ivanova AB. *Inorg Mater* 1991;27:194.
- [19] Collongues R. *Jpn J Appl Phys* 1993;32:442.
- [20] Roth WL. *Acta Cryst* 1960;13:146.
- [21] Koch F, Cohen JB. *Acta Cryst B* 1969;25:275.
- [22] Nakamura K, Saishoji T, Kubota T, Iida T, Shimanuki Y, Kotooka T, et al. *J Cryst Growth* 1997;180:61.
- [23] Voronkov VV, Falster R. *J Cryst Growth* 1998;194:76.
- [24] Falster R, Voronkov VV. *Mater Sci Eng B* 2000;73:87.
- [25] Abe T, Takahashi T. *J Cryst Growth* 2011;334:16.
- [26] Voronkov VV, Falster R. *J Cryst Growth* 2012;351:115.
- [27] Catlow CRA, Fender BEF. *J Phys C* 1975;8:3267.
- [28] Catlow CRA, Fender BEF, Muxworthy DG. *J Phys (Paris) C* 1977;7:67.
- [29] Ye ZG, Dong M. *J Appl Phys* 2000;87:2312.
- [30] Xu GS, Luo HS, Xu HQ, Yin ZW. *Phys Rev B* 2001;64:020102.
- [31] Yamashita Y, Hosono Y, Harada K, Yasuda N. *IEEE Trans Ultrason Ferroelectr Freq Control* 2002;49:184.
- [32] Gotalskaya N, Drezin DI, Bezdelkin VV, Stassevich VN. *Proc IEEE Freq Symp* 1993:339.
- [33] Uda S, Buzanov OA. *J Cryst Growth* 2000;211:318.
- [34] Kröger FA. *The chemistry of imperfect crystals.* 2nd rev. Amsterdam: North-Holland Publishing Company; 1974.
- [35] ToftSørensen O, editor. *Nonstoichiometric oxides.* New York: Academic Press Inc.; 1981.
- [36] Agullo-Lopez F, Catlow CRA, Townsend PD. *Point defects in materials.* London: Academic Press Limited; 1988.
- [37] Gellings PJ, Bouwmeester HJM, editors. *The CRC handbook of solid state chemistry.* London: CRC Press; 1997.
- [38] Innocenti A, editor. *Stoichiometry and materials science – when numbers matter.* In Tech; 2012.
- [39] Uda S, Tiller WA. *J Cryst Growth* 1992;121:155.

- [40] Uda S, Tiller WA. *J Cryst Growth* 1992;121:93.
- [41] Uda S, Kon J, Ichikawa J, Inaba K, Shimamura K, Fukuda T. *J Cryst Growth* 1997;179:567.
- [42] Uda S, Kon J, Shimamura K, Ichikawa J, Inaba K, Fukuda T. *J Cryst Growth* 1997;182:403.
- [43] Uda S, Tsubota T. *J Cryst Growth* 2010;312:3650.
- [44] Boikov YA, Goltsman BM, Yarmarkin VK, Lemanov VV. *Appl Phys Lett* 2001;78:3866.
- [45] Surowiak Z, Margolin AM, Zakharchenko IN, Biryukov SV. *Thin Solid Films* 1989;176:227.
- [46] Uda S. *J Cryst Growth* 2008;310:3864.
- [47] Kimura H, Uda S. *J Cryst Growth* 2009;311:4094.
- [48] Uda S, Komatsu R, Takayama K. *J Cryst Growth* 1997;171:458.
- [49] Uda S, Koh S, Huang X. *J Cryst Growth* 2006;292:1.
- [50] Azuma Y, Uda S. *J Cryst Growth* 2007;306:217.
- [51] Koh S, Uda S, Nishida M, Huang X. *J Cryst Growth* 2006;297:247.
- [52] Koh S, Uda S, Huang X. *J Cryst Growth* 2007;306:406.
- [53] Kimura H, Koizumi H, Uchida T, Uda S. *J Cryst Growth* 2009;311:1553.
- [54] D'yakov VA, Shumov DP, Rashkovich LN, Aleksandrovskii AL. *Bull Acad Sci USSR, Phys Ser* 1985;49:117.
- [55] Aleksandrovskii AL, Shumov DP. *Cryst Res Technol* 1990;25:1239.
- [56] Fujii S, Uda S, Maeda K, Nozawa J, Koizumi H, Fujiwara K, et al. *J Cryst Growth* 2013;383:63.
- [57] Bourdi PF, Norwood RG, Bird CD, Calvert GD. *J Cryst Growth* 1991;113:61.
- [58] Kimura H, Taniuchi T, Iida S, Uda S. *J Cryst Growth* 2010;312:3425.
- [59] Grabmaier BG, Otto F. *J Cryst Growth* 1986;79:682.
- [60] Zhou YF, Wang JC, Wang PL, Tang LA, Zhu QB, Wu YA, et al. *J Cryst Growth* 1991;114:87.
- [61] Dakki A, Ferriol M, Cohen-Adad MT. *Eur J Solid State Inorg Chem* 1996;33:19.
- [62] Bryan DA, Gerson R, Tomaschke HE. *Appl Phys Lett* 1984;44:847.
- [63] Kitamura K, Yamamoto JK, Iyi N, Kimura S. *J Cryst Growth* 1992;116:327.
- [64] Jundt DH, Fejer MM, Byer RL. *IEEE J Quant Electron* 1990;26:135.
- [65] O'Bryan HM, Gallagher PK, Brandle CD. *J Am Ceram Soc* 1985;68:493.
- [66] Kitamura K, Furukawa Y, Niwa K, Gopalan V, Mitchell TE. *Appl Phys Lett* 1998;73:3073.
- [67] Tian L, Gopalan V, Galambos L. *Appl Phys Lett* 2004;85:4445.
- [68] Uda S, Tiller WA. *J Cryst Growth* 1993;126:396.
- [69] Kushibiki J, Ohashi Y. *IEEE Trans Ultrason Ferroelectr Freq Control* 2006;53:385.

# Equilibrium Shape of Crystals

T.L. Einstein

DEPARTMENT OF PHYSICS AND CONDENSED MATTER THEORY CENTER,  
UNIVERSITY OF MARYLAND, COLLEGE PARK, MD, USA

## CHAPTER OUTLINE

<b>5.1 Introduction</b> .....	<b>216</b>
<b>5.2 From Surface Free Energies to Equilibrium Crystal Shape</b> .....	<b>217</b>
5.2.1 General Considerations .....	217
5.2.2 More Formal Treatment.....	220
<b>5.3 Applications of Formal Results</b> .....	<b>224</b>
5.3.1 Cusps and Facets .....	224
5.3.2 Sharp Edges and Forbidden Regions .....	225
5.3.3 Experiments on Lead Going beyond Wulff Plots .....	227
<b>5.4 Some Physical Implications of Wulff Constructions</b> .....	<b>229</b>
5.4.1 Thermal Faceting and Reconstruction .....	229
5.4.2 Types A and B.....	231
5.4.3 2D Studies .....	233
<b>5.5 Vicinal Surfaces—Entrée to Rough Regions Near Facets</b> .....	<b>234</b>
<b>5.6 Critical Behavior of Rough Regions Near Facets</b> .....	<b>239</b>
5.6.1 Theory .....	239
5.6.2 Experiment on Leads .....	241
5.6.3 Summary of Highlights of Novel Approach to Behavior Near Smooth Edges .....	243
<b>5.7 Sharp Edges and First-Order Transitions—Examples and Issues</b> .....	<b>245</b>
5.7.1 Sharp Edges Induced by Facet Reconstruction.....	245
<b>5.8 Gold—Prototype or Anomaly of Attractive Step—Step Interaction?</b> .....	<b>250</b>
<b>5.9 Well-Established Attractive Step—Step Interactions Other Than <math>\ell^{-2}</math></b> .....	<b>253</b>
5.9.1 Atomic-Range Attractions .....	253
5.9.2 Attractions at Periodic Ranges of Separation via Oscillatory Friedel-Type Interactions .....	255
<b>5.10 Conclusions</b> .....	<b>257</b>
<b>Acknowledgments</b> .....	<b>257</b>
<b>References</b> .....	<b>258</b>

## 5.1 Introduction

The notion of equilibrium crystal shape (ECS) is arguably the platonic ideal of crystal growth and underpins much of our thinking about crystals. Accordingly, it has been the subject of several special reviews and tutorials [1–4,215] and is a prominent part of most volumes and extended review articles and texts about crystals and their growth [5–9]. In actual situations, there are many complications that thwart observation of such behavior, including kinetic barriers, impurities, and other bulk defects like dislocations. Furthermore, the notion of a well-defined equilibrium shape requires that there is no contact of the crystal with a wall or surface, since that would alter its shape. By the same token, the crystal cannot then be supported, so gravity is neglected. For discussions of the effect of gravity or contact with walls, see, e.g., Ref. [7].

Gibbs [10] is generally credited with being the first to recognize that the equilibrium shape of a substance is that which, for a fixed volume, minimizes the (orientation-dependent) surface free energy integrated over the entire surface; the bulk free energy is irrelevant since the volume is conserved, while edge or corner energies are ignored as being higher order effects that play no role in the thermodynamic limit. Herring [11,12] surveys the early history in detail: The formulation of the problem was also carried out independently by Ref. [13]. The solution of this ECS problem, the celebrated Wulff construction, was stated by Ref. [14]; but his proof was incorrect. Correct proofs were subsequently given by Ref. [15–17], who presented a critical review. However, these proofs, while convincing of the theorem, were not general (and evidently applied only to  $T = 0$ , since they assumed the ECS to be a polyhedron and, compared the sum over the facets of the surface free energy of each facet times its area with a similar sum over a similar polyhedron with the same facet planes but slightly different areas (and the same volume)). Dinghas [18] showed that the Brunn–Minkowski inequality could be used to prove directly that any shape differing from that resulting from the Wulff construction has a higher surface free energy. Although Dinghas again considered only a special class of polyhedral shapes, Herring [11,12] completed the proof by noting that Dinghas' method is easily extended to arbitrary shapes, since the inequality is true for convex bodies in general. In their seminal paper on crystal growth, Burton, Cabrera, and Frank [19] present a novel proof of the theorem in two dimensions (2D).

Since equilibrium implies minimum Helmholtz free energy for a given volume and number, and since the bulk free energy is ipso facto independent of shape, the goal is to determine the shape that minimizes the integrated surface free energy of the crystal. The prescription takes the following form: One begins by creating a polar plot of the surface free energy as a function of orientation angle (of the surface normal) and draws a perpendicular plane (or line in 2D) through the tip of each ray. (There are many fine reviews of this subject in Refs [20–23].) Since the surface free energy in three dimensions (3D) is frequently denoted by  $\gamma$ , this is often called a  $\gamma$  plot. The shape is then formed by the interior envelope of these planes or lines, often referred to as a pedal. At zero

temperature, when the free energy is just the energy, this shape is a polyhedron in 3D and a polygon in 2D, each reflecting the symmetry of the underlying lattice. At finite temperature, the shapes become more complex. In 2D, the sharp corners are rounded. In 3D, the behavior is richer, with two possible modes of evolution with rising temperature. For what Wortis terms type-A crystals, all sharp boundaries smooth together, while in type-B, first the corners smooth, then above a temperature denoted  $T_0$ , the edges also smooth. The smooth regions correspond to thermodynamic rough phases, with height–height correlation functions that diverge for large lateral separation  $l$ —like  $l^\alpha$ , with  $\alpha$  (typically  $0 < \alpha < 1$ ) called the roughening exponent—in contrast to facets, where they attain some finite value as  $l \rightarrow \infty$  [5]. The faceted regions in turn correspond to “frozen” regions. Pursuing the correspondence, sharp and smooth edges correspond to first-order and second-order phase transitions, respectively.

The aim of this chapter is primarily to explore physical ideas regarding ECS and the underlying Wulff constructions. This topic has also attracted considerable interest in the mathematics community. Readers interested in more formal and sophisticated approaches are referred to two books, Refs [24,25] and to many articles, including [26–36]. Particular attention is devoted to the origin of sharp edges on the ECS, the impact of reconstructed or adsorbed surface phases coexisting with unadorned phases, and the role and nature of possible attractive stepstep interactions.

## 5.2 From Surface Free Energies to Equilibrium Crystal Shape

### 5.2.1 General Considerations

To examine this process more closely, we examine the free energy expansion for a vicinal surface, that is, a surface misoriented by some angle  $\theta$  from a facet direction. Cf. Figure 5.1. Unfortunately, this polar angle is denoted by  $\phi$  in much of the literature on vicinal surfaces, with  $\theta$  used for in-plane misorientation; most reviews of ECS use  $\theta$  for the polar angle, as we shall here. The term *vicinal* implies that the surface is in the vicinity of the orientation. It is generally assumed that the surface orientation itself is rough (while the facet direction is below its roughening temperature and so is smooth). We consider the projected surface free energy  $f_p(\theta, T)$  [37] (with the projection being onto the low-index reference, facet direction of terraces):

$$f_p(\theta, T) = f_0(T) + \beta(T) \frac{|\tan \theta|}{h} + g(T) |\tan \theta|^3 + c(\tan \theta)^4. \quad (5.1)$$

The first term is the surface free energy per area of the terrace (facet) orientation; it is often denoted  $\sigma$ . The average density of steps (the inverse of their mean separation  $\langle \ell \rangle$ ) is  $\tan \theta/h$ , where  $h$  is the step height. In the second term,  $\beta(T)$  is the line tension or free energy per length of step formation. (Since 2D is a dimension smaller than 3D, one uses  $\beta$  rather than  $\gamma$ . Skirting over the difference in units resulting from the dimensional

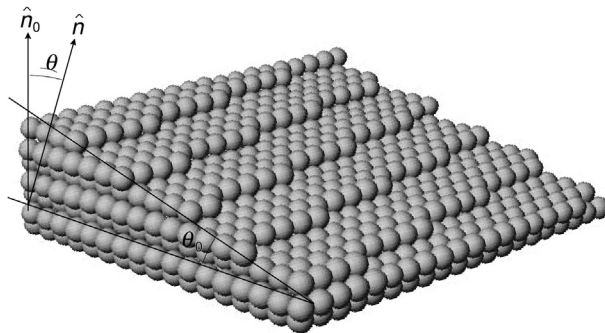


**FIGURE 5.1** Portion of a  $(3, \bar{2}, 16)$  surface, vicinal to an fcc (001), to illustrate a misoriented, vicinal surface. The vicinal surface and terrace normals are  $\hat{n} = (3, -2, 16)/\sqrt{269}$  and  $\hat{n}_0 = (0, 0, 1)$ , respectively. The polar angle  $\theta$  [with respect to the (001) direction], denoted  $\phi$  in the original figure (consistent with most of the literature on vicinal surfaces), is across  $(16/\sqrt{269})$ , while azimuthal angle  $\varphi$  (denoted  $\theta$  in most of the literature on vicinal surfaces), indicating how much  $\hat{n}$  is rotated around  $\hat{n}_0$  away from the vertical border on which  $\theta_0$  is marked, is clearly  $\arctan(1/5)$ ;  $\tan \theta_0 = \tan \theta \cos \phi$ . Since  $h$  is  $a_1/\sqrt{2}$ , where  $a_1$  is the nearest-neighbor spacing, the mean distance  $\ell$  (in a terrace plane) between steps is  $a_1/(\sqrt{2}\tan \theta) = 8\sqrt{2}/13a_1 = 3.138a_1$ . While the average distance from one step to the next along a principal, (110) direction looks like  $3.5a_1$ , it is in fact  $a_1/(\sqrt{2}\tan \theta_0) = 3.2a_1$ . The “projected area” of this surface segment, used to compute the surface free energy  $f_p$ , is the size of a (001) layer:  $20a_1 \times 17a_1 = 340a_1^2$ ; the width is  $20a_1$ . In “Maryland notation” (see text),  $z$  is in the  $\hat{n}_0$  direction, while the normal to the vicinal,  $\hat{n}$ , lies in the  $x$ - $z$  plane and  $y$  runs along the mean direction of the edges of the steps. In most discussions,  $\phi = 0$ , so that this direction would be that of the upper and lower edges of the depicted surface. Adapted from Ref. [38].

difference, many use  $\gamma$  in both cases.) While step free energy per length and line tension are equivalent for these systems, where the surface is at constant (zero) charge, they are inequivalent in electrochemical systems, where it is the electrode potential conjugate to the surface charge that is held fixed [39]. The third term is associated with interactions between steps, in this case assumed to be proportional to  $\ell^{-2}$  (so that this term, which also includes the  $\ell^{-1}$  density of steps, goes like  $\ell^{-3}$ ). The final term is the leading correction.

The  $\ell^{-2}$  interaction is due to a combination (not a simple sum) of two repulsive potential energies: the entropic repulsion due to the forbidden crossing of steps and the elastic repulsions due to dipolar strains near each step. An explicit form for  $g(T)$  is given in Eqn (5.27) below. The  $\ell^{-2}$  of the entropic interaction can be understood from viewing the step as performing a random walk in the direction between steps (the  $x$  direction in “Maryland notation”<sup>1</sup> as a function of the  $y$  direction (which is timelike in the fermion transcription to be discussed later), cf. Figure 5.1, so the distance ( $y$ ) it must go until it touches a neighboring step satisfies  $\ell^2 \propto y$ . To get a crude understanding of the origin of the elastic repulsion, one can imagine that since a step is unstable relative to a flat surface, it will try to relax toward a flatter shape, pushing atoms away from the location of the step by a distance decaying with distance from the step. When two steps are close

<sup>1</sup>This term was coined by a speaker at a workshop in Traverse City in August 1996—see Ref. [43] for the proceedings—and then used by several other speakers.

to each other, such relaxation will be frustrated because atoms on the terrace this pair of steps are pushed in opposite directions, so they relax less than if the steps are widely separated, leading to a repulsive interaction. Analyzed in more detail [7,40,41], this repulsion is dipolar and so proportional to  $\ell^{-2}$ . However, attempts to reconcile the prefactor with the elastic constants of the surface have met with limited success. The quartic term in Eqn (5.1) is due to the leading ( $\ell^{-3}$ ) correction to the elastic repulsion [42], a dipole-quadrupole repulsion. It generally has no significant consequences but is included to show the leading correction to the critical behavior near a smooth edge on the ECS, to be discussed below.

The absence of a quadratic term in Eqn (5.1) reflects that there is no  $\ell^{-1}$  interaction between steps. In fact, there are some rare geometries, notably vicinals to (110) surfaces of fcc crystals (Au in particular) that exhibit what amounts to  $\ell^{-1}$  repulsions, which lead to more subtle behavior [44]. Details about this fascinating idiosyncratic surface are beyond the scope of this chapter; readers should see the thorough, readable discussion by van Albada et al. [45].

As temperature increases,  $\beta(T)$  decreases due to increasing entropy associated with step-edge excitations (via the formation of kinks). Eventually,  $\beta(T)$  vanishes at a temperature  $T_R$  associated with the roughening transition. At and above this  $T_R$  of the facet orientation, there is a profusion of steps, and the idea of a vicinal surface becomes meaningless. For rough surfaces, the projected surface free energy  $f_p(\theta, T)$  is quadratic in  $\tan \theta$ . To avoid the singularity at  $\theta = 0$  in the free energy expansion that thwarts attempts to proceed analytically, some treatments, notably Bonzel and Preuss [46], approximate  $f_p(\theta, T)$  as quadratic in a small region near  $\theta = 0$ . It is important to recognize that the vicinal orientation is thermodynamically rough, even though the underlying facet orientation is smooth. The two regions correspond to incommensurate and commensurate phases, respectively. Thus, in a rough region, the mean spacing  $\langle \ell \rangle$  between steps is not in general simply related to (i.e., an integer multiple plus some simple fraction) the atomic spacing.

Details of the roughening process have been reviewed by Weeks [216] and by van Beijeren and Nolden [9]; the chapter by Akutsu in this Handbook provides an up-to-date account. However, for use later, we note that much of our understanding of this process is rooted in the mapping between the restricted body-centered (cubic) solid-on-solid (BCSOS) model and the exactly solvable [47,48] symmetric 6-vertex model [49], which has a transition in the same universality class as roughening. This BCSOS model is based on the BCC crystal structure, involving square net layers with ABAB stacking, so that sites in each layer are lateral displaced to lie over the centers of squares in the preceding (or following) layer. Being an SOS model means that for each column of sites along the vertical direction, there is a unique upper occupied site, with no vacancies below it or floating atoms above it. Viewed from above, the surface is a square network with one pair of diagonally opposed corners on A layers and the other pair on B layers. The restriction is that neighboring sites must be on adjacent layers (so that their separation is the distance from a corner to the center of the BCC lattice). There are then six possible

configurations: two in which the two B corners are both either above or below the A corners and four in which one pair of catercorners are on the same layer and the other pair are on different layers (one above and one below the first pair). In the symmetric model, there are three energies,  $-\epsilon$  for the first pair, and  $\pm\delta/2$  for the others, the sign depending on whether the catercorner pair on the same lattice is on A or B [50]. The case  $\delta = 0$  corresponds to the  $F$ -model, which has an infinite-order phase transition and an essential singularity at the critical point, in the class of the Kosterlitz-Thouless [51] transition [52]. (In the “ice” model,  $\epsilon$  also is 0.) For the asymmetric 6-vertex model, each of the six configurations can have a different energy; this model can also be solved exactly [53,54].

## 5.2.2 More Formal Treatment

To proceed more formally, we largely follow [1]. The shape of a crystal is given by the length  $R(\hat{\mathbf{h}})$  of a radial vector to the crystal surface for any direction  $\hat{\mathbf{h}}$ . The shape of the crystal is defined as the thermodynamic limit of this crystal for increasing volume  $V$ , specifically.

$$r(\hat{\mathbf{h}}, T) \equiv \lim_{V \rightarrow \infty} \left[ R(\hat{\mathbf{h}}) / \alpha V^{1/3} \right], \quad (5.2)$$

where  $\alpha$  is an arbitrary dimensionless variable. This function  $r(\hat{\mathbf{h}}, T)$  corresponds to a free energy. In particular, since both independent variables are fieldlike (and so intrinsically intensive), this is a Gibbs-like free energy. Like the Gibbs free energy,  $r(\hat{\mathbf{h}}, T)$  is continuous and convex in  $\hat{\mathbf{h}}$ .

The Wulff construction then amounts to a Legendre transformation<sup>2</sup> to  $r(\hat{\mathbf{h}}, T)$  from the orientation  $\hat{\mathbf{m}}$ -dependent interfacial free energy  $f_i(\hat{\mathbf{m}}, T)$  (or in perhaps the more common but less explicit notation,  $\gamma(\hat{\mathbf{m}}, T)$ , which is  $f_p(\theta, T)/\cos(\theta)$ ). For liquids, of course,  $f_i(\hat{\mathbf{m}}, T)$  is spherically symmetric, as is the equilibrium shape. Herring [12] mentions rigorous proofs of this problem by Schwarz in 1884 and by Minkowski in 1901. For crystals,  $f_i(\hat{\mathbf{m}}, T)$  is not spherically symmetric but does have the symmetry of the crystal lattice. For a system with cubic symmetry, one can write

$$f_i(\hat{\mathbf{m}}, T) = \gamma_0(T) \left[ 1 + a(T) (m_x^4 + m_y^4 + m_z^4) \right], \quad (5.3)$$

where  $\gamma_0(T)$  and  $a(T)$  are constants. As illustrated in Figure 5.2, for  $a = 1/4$  the asymmetry leads to minor distortions, which are rather inconsequential. However, for

<sup>2</sup>As explicated clearly in Ref. [55], one considers a [convex] function  $y = y(x)$  and denotes its derivative as  $p = \partial y / \partial x$ . If one then tries to consider  $p$  instead of  $x$  as the independent variable, there is information lost: one cannot reconstruct  $y(x)$  uniquely from  $y(p)$ . Indeed,  $y = y(p)$  is a first-order differential equation, whose integration gives  $y = y(x)$  only to within an undetermined integration constant. Thus,  $y = y(p)$  corresponds to a family of displaced curves, only one of which is the original  $y = y(x)$ . The key concept is that the locus of points satisfying  $y = y(x)$  can be equally well represented by a family of lines tangent to  $y(x)$  at all  $x$ , each with a  $y$ -intercept  $\psi$  determined by the slope  $p$  at  $(x, y(x))$ . That is,  $\psi = \psi(p)$  contains all the information of  $y = y(x)$ . Recognizing that  $p = (y - \psi) / (x - 0)$ , one finds the transform  $\psi = y - px$ . Readers should recall that this is the form of the relationship between thermodynamic functions, particularly the Helmholtz and the Gibbs free energies.

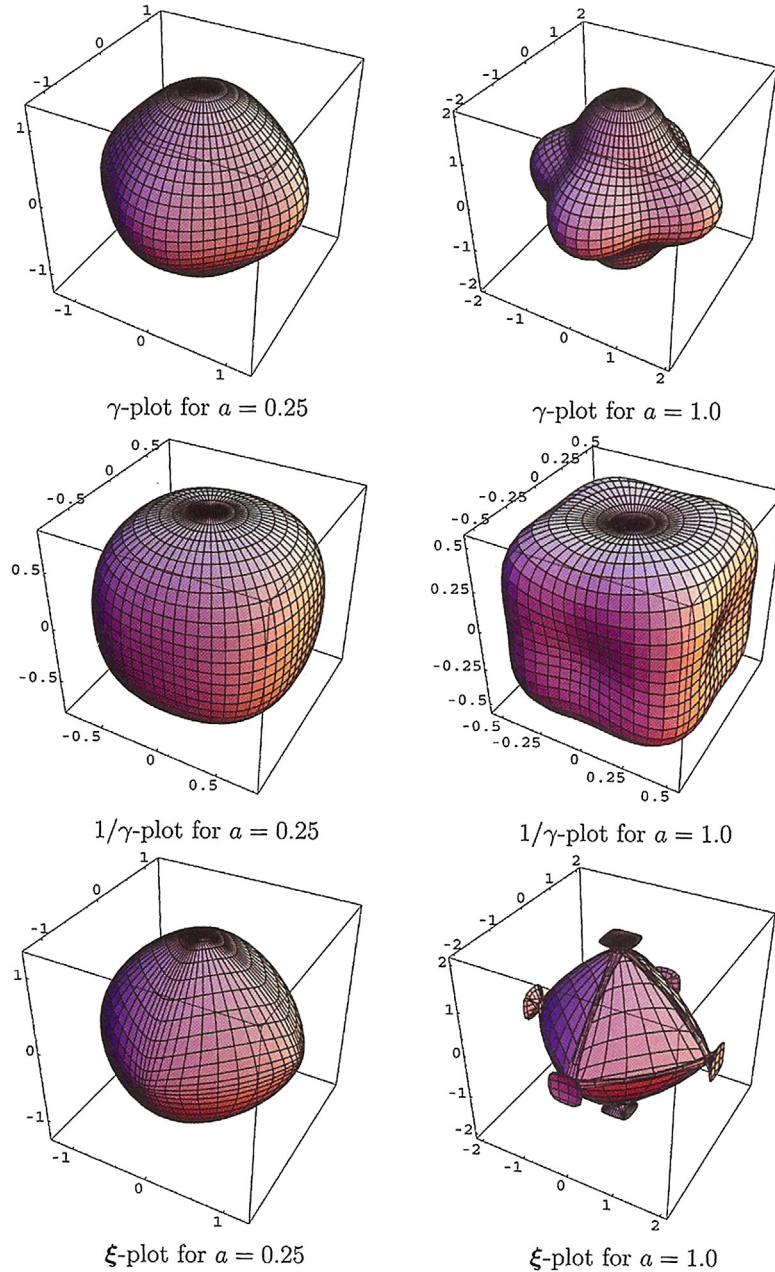


**FIGURE 5.2**  $\gamma$ -plots (plots of  $f_i(\widehat{\mathbf{m}})$ ),  $1/\gamma$ -plots and  $\xi$ -plots for Eqn (5.3) for positive values of  $a$ ). For  $a = 1/4$ , all orientations appear on the ECS. For  $a = 1.0$ , the  $1/\gamma$ -plot has concave regions, and the  $\xi$ -plot has ears and flaps that must be truncated to give the ECS essentially an octahedron with curved faces. From Ref. [8], which shows in a subsequent figure that the  $\gamma$ - and  $1/\gamma$ -plots for  $a = -0.2$  and  $-0.5$  resemble the  $1/\gamma$ - and  $\gamma$ -plots, respectively, for  $a = 1/4$  and 1.

$a = 1$ , the enclosed region is no longer convex, leading to an instability to be discussed shortly.

One considers the change in the interfacial free energy associated with changes in shape. The constraint of constant volume is incorporated by subtracting from the change in the integral of  $f_i(\widehat{\mathbf{m}}, T)$  the corresponding change in volume, multiplied by a Lagrange multiplier  $\lambda$ . Herring [11,12] showed that this constrained minimization problem has a unique and rather simple solution that is physically meaningful in the limit that it is satisfactory to neglect edge, corner, and kink energies in  $f_i(\widehat{\mathbf{m}}, T)$ , that is, in the limit of large volume. In this case  $\lambda \propto V^{-1/3}$ ; by choosing the proportionality constant as essentially the inverse of  $\alpha$ , we can write the result as

$$r(\widehat{\mathbf{h}}, T) = \min_{\widehat{\mathbf{m}}} \left( \frac{f_i(\widehat{\mathbf{m}}, T)}{\widehat{\mathbf{m}} \cdot \widehat{\mathbf{h}}} \right) \quad (5.4)$$

The Wulff construction is illustrated in Figure 5.3. The interfacial free energy  $f_i(\widehat{\mathbf{m}})$ , at some assumed  $T$  is displayed as a polar plot. The crystal shape is then the interior envelope of the family of perpendicular planes (lines in 2D) passing through the ends of the radial vectors  $\widehat{\mathbf{m}} f_i(\widehat{\mathbf{m}})$ . Based on Eqn (5.4) one can, at least in principle, determine  $\widehat{\mathbf{m}}(\widehat{\mathbf{h}})$  or  $\widehat{\mathbf{h}}(\widehat{\mathbf{m}})$ , which thus amounts to the equation of state of the equilibrium crystal shape. One can also write the inverse of Eqn (5.4):

$$\frac{1}{f_i(\widehat{\mathbf{m}}, T)} = \min_{\widehat{\mathbf{h}}} \left( \frac{1/f_i(\widehat{\mathbf{h}}, T)}{\widehat{\mathbf{m}} \cdot \widehat{\mathbf{h}}} \right) \quad (5.5)$$

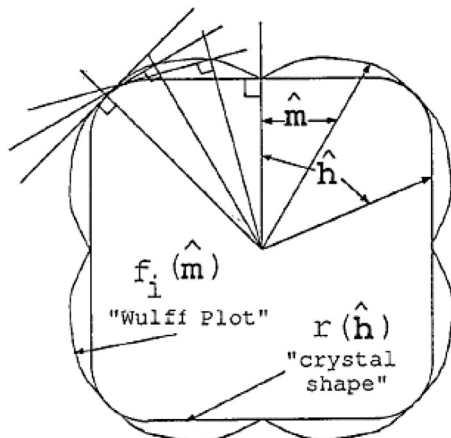


**FIGURE 5.3** Schematic of the Wulff construction. The interfacial free energy per unit area  $f_i\widehat{\mathbf{m}}$  is plotted in polar form (the "Wulff plot" or " $\gamma$ -plot"). One draws a radius vector in each direction  $\widehat{\mathbf{m}}$  and constructs a perpendicular plane where this vector hits the Wulff plot. The interior envelope of the family of "Wulff planes" thus formed, expressed algebraically in Eqn (5.4), is the crystal shape, up to an arbitrary overall scale factor that may be chosen as unity. From Ref. [1].

Thus, a Wulff construction using the inverse of the crystal shape function yields the inverse free energy.

To be more explicit, consider the ECS in Cartesian coordinates  $z(x,y)$ , i.e.,  $\hat{\mathbf{h}} \propto (x, y, z(x,y))$ , assuming (without dire consequences [1]) that  $z(x,y)$  is single-valued. Then, for any displacement to be tangent to  $\hat{\mathbf{h}}$ ,  $dz - p_x dx - p_y dy = 0$

$$\hat{\mathbf{h}} = \frac{1}{\sqrt{1 + p_x^2 + p_y^2}} (-p_x z, -p_y z, 1), \quad (5.6)$$

where  $p_x$  is shorthand for  $\partial z / \partial x$ .

Then the total free energy and volume are

$$\begin{aligned} F_i(T) &= \iint f_p(p_x, p_y) dx dy \\ V &= \iint z(x, y) dx dy \end{aligned} \quad (5.7)$$

where  $f_p$ , which incorporates the line-segment length, is  $f_p \equiv [1 + p_x^2 + p_y^2]^{1/2} f_i$ . Minimizing  $F_i$  subject to the constraint of fixed  $V$  leads to the Euler–Lagrange equation

$$\frac{\partial}{\partial x} \frac{f_p(\partial_x z, p_y)}{p_x} + \frac{\partial}{\partial y} \frac{f_p(p_x, p_y)}{p_y} = -2\lambda \quad (5.8)$$

(Actually, one should work with macroscopic lengths, then divide by the  $V^{1/3}$  times the proportionality constant. Note that this leaves  $p_x$  and  $p_y$  unchanged [1].) On the right-hand side,  $2\lambda$  can be identified as the chemical potential  $\mu$ , so that the constancy of the left-hand side is a reflection of equilibrium. Equation (5.8) is strictly valid only if the derivatives of  $f_p$  exist, so one must be careful near high-symmetry orientations below their roughening temperature, for which facets occur. To show that this highly nonlinear second-order partial differential equation with unspecified boundary conditions is equivalent to Eqn (5.4), we first note that the first integral of Eqn (5.8) is simply

$$z - xp_x - yp_y = f_p(p_x, p_y) \quad (5.9)$$

The right-hand side is just a function of derivatives, consistent with this being a Legendre transformation. Then, differentiating yields

$$x = -\partial f_p / \partial (p_x), \quad y = -\partial f_p / \partial (p_y) \quad (5.10)$$

Hence, one can show that

$$z(x, y) = \min_{p_x, p_y} (f_p(p_x, p_y) + xp_x + yp_y) \quad (5.11)$$

## 5.3 Applications of Formal Results

### 5.3.1 Cusps and Facets

The distinguishing feature of Wulff plots of faceted crystals compared to liquids is the existence of (pointed) cusps in  $f_i(\widehat{\mathbf{m}}, T)$ , which underpin these facets. The simplest way to see why the cusp arises is to examine a square lattice with nearest-neighbor bonds having bond energy  $\epsilon_1$ , often called a 2D Kossel [56,57] crystal; note also [210]. In this model, the energy to cleave the crystal is the Manhattan distance between the ends of the cut; i.e., as illustrated in Figure 5.4, the energy of severing the bonds between (0,0) and (X,Y) is just  $+\epsilon_1 (|X| + |Y|)$ . The interfacial area, i.e., length, is  $2(X^2 + Y^2)$  since the cleavage creates *two* surfaces. At  $T = 0$ , entropy plays no role, so that

$$f_i(\theta) = \frac{\epsilon_1}{2} (|\sin \theta| + |\cos \theta|) \sim \frac{\epsilon_1}{2} (1 + |\theta| + \dots) \quad (5.12)$$

At finite  $T$  fluctuations and attendant entropy do contribute, and the argument needs more care. Recalling Eqn (5.1), we see that if there is a linear cusp at  $\theta = 0$ , then

$$f_i(\theta, T) = f_i(0, T) + B(T)|\theta|, \quad (5.13)$$

where  $B = \beta(T)/h$ , since the difference between  $f_i(\theta)$  and  $f_p(\theta)$  only appears at order  $\theta^2$ . Comparing Eqns (5.12) and (5.13), we see that for the Kossel square  $f_i(0,0) = \epsilon_1/2$  and  $B(0) = \epsilon_1/2$ . Further discussion of the 2D  $f_i(\theta)$  is deferred to Section 5.4.3 below.

To see how a cusp in  $f_i(\widehat{\mathbf{m}}, T)$  leads to a facet in the ECS, consider Figure 5.5: the Wulff plane for  $\theta \gtrsim 0$  intersects the horizontal  $\theta = 0$  plane at a distance  $f_i(0) + d(\theta)$  from the vertical axis. The crystal will have a horizontal axis if and only if  $d(\theta)$  does not

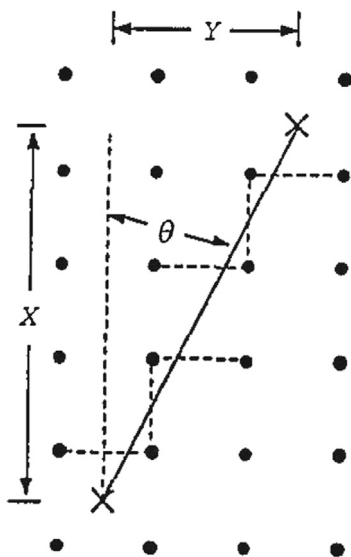
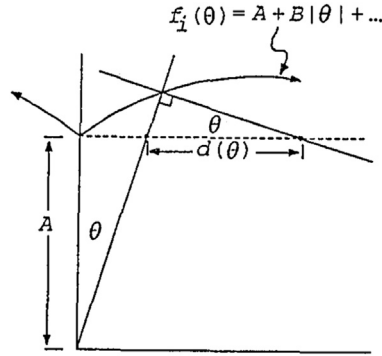


FIGURE 5.4 Kossel crystal at  $T = 0$ . The energy to cleave the crystal along the depicted slanted. Interface ( $\tan \theta = Y/Z$ ) is  $\epsilon_1 (|X| + |Y|)$ . From Ref. [1].



**FIGURE 5.5** Wulff plot with a linear cusp at  $\theta = 0$ . If  $d(\theta) \rightarrow 0$  as  $\theta \rightarrow 0$ , then there is no facet corresponding to  $\theta = 0$ , and the  $\theta = 0$  Wulff plane (dotted line) is tangent to the crystal shape at just a single point. Since  $d(\theta) = B$ , a cusp in the Wulff plot leads to a facet of the corresponding orientation on the equilibrium crystal shape. From Ref. [1].

vanish as  $\theta \rightarrow 0$ . From Figure 5.5, it is clear that  $\theta \approx \sin \theta \approx B\theta/d(\theta)$  for  $\theta$  near 0, so that  $d(0) = B > 0$ . For a weaker dependence on  $\theta$ , e.g.,  $B|\theta|^\zeta$  with  $\zeta > 1$ ,  $d(0) = 0$ , and there is no facet. Likewise, at the roughening temperature,  $\beta$  vanishes and the facet disappears.

### 5.3.2 Sharp Edges and Forbidden Regions

When there is a sharp edge (or corner) on the ECS  $r(\hat{\mathbf{h}}, T)$ , Wulff planes with a range of orientations  $\hat{\mathbf{m}}$  will not be part of the inner envelope determining this ECS; they will lie completely outside it. There is no portion of the ECS whose surface tangent has these orientations. As in the analogous problems with forbidden values of the “density” variable, the free energy  $f_i(\hat{\mathbf{m}}, T)$  is actually not properly defined for forbidden values of  $\hat{\mathbf{m}}$ ; those unphysical values should actually be removed from the Wulff plot. Figure 5.6 depicts several possible ECSs and their associated Wulff plots. It is worth emphasizing that, in the extreme case of the fully faceted ECS at  $T = 0$ , the Wulff plot is simply a set of discrete points in the facet directions.

Now if we denote by  $\hat{\mathbf{m}}_+$  and  $\hat{\mathbf{m}}_-$ , the limiting orientations of the tangent planes approaching the edge from either side, then all intermediate values do not occur as stable orientations. These missing, not stable, “forbidden” orientations are just like the forbidden densities at liquid–gas transitions, forbidden magnetizations in ferromagnets at  $T < T_c$  [58], and miscibility gaps in binary alloys. Herring [11,12] first presented an elegant way to determine these missing orientations using a spherical construction. For any orientation  $\hat{\mathbf{m}}$ , this tangent sphere (often called a Herring sphere) passes through the origin and is tangent to the Wulff plot at  $f_i(\hat{\mathbf{m}})$ . From geometry, he invoked the theorem that an angle inscribed in a semicircle is a right angle. Thence, if the orientation  $\hat{\mathbf{m}}$  appears on the ECS, it appears at an orientation that points outward along the radius of that sphere. Herring then observes that only if such a sphere lies completely inside the plot of  $f_i(\hat{\mathbf{m}})$  does that orientation appear on the ECS. If some part were inside, its Wulff

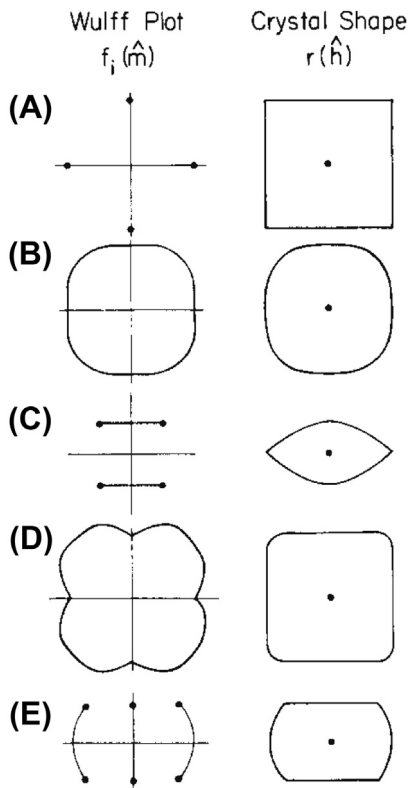


**FIGURE 5.6** Some possible Wulff plots and corresponding equilibrium crystal shapes. Faceted and curved surfaces may appear, joined at sharp or smooth edges in a variety of combinations. From Ref. [4]; the equilibrium crystal shape are also in Ref. [12].

plane would clip off the orientation of the point of tangency, so that orientation would be forbidden.

The origin of a hill-and-valley structure from the constituent free energies [59,221,222] is illustrated schematically in Figure 5.7. It arises when they satisfy the inequality

$$f_i(\widehat{\mathbf{m}} = \mathbf{n}_1)A_1 + f_i(\mathbf{n}_2)A_2 < f_i(\mathbf{n})A, \quad (5.14)$$

where  $A_1$  and  $A_2$  are the areas of strips of orientation  $\mathbf{n}_1$  and  $\mathbf{n}_2$ , respectively, while  $A$  is the area of the sum of these areas projected onto the plane bounded by the dashed lines in the figure. This behavior, again, is consistent with the identification of the misorientation as a density (or magnetizationlike) variable rather than a fieldlike one.

The details of the lever rule for coexistence regimes were elucidated by Wortis [1]: As depicted in Figure 5.8, which denotes as P and Q the two orientations bounding the region that is not stable, the lever rule interpolations lie on segments of a spherical surface. Let the edge on the ECS be at R. Then an interface created at a forbidden  $\widehat{\mathbf{m}}$  will

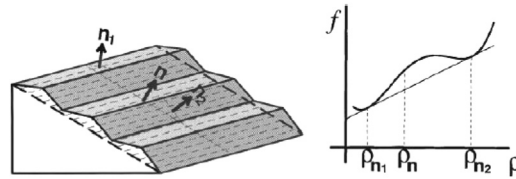


**FIGURE 5.7** Illustration of how orientational phase separation occurs when a “hill-and-valley” structure has a lower total surface free energy per area than a flat surface as in Eqn (5.14). The sketch of the free energy versus  $\rho \equiv \tan \theta$  shows that this situation reflects a region with negative convexity which is accordingly not stable. The dashed line is the tie bar of a Maxwell or double-tangent construction. The misorientations are the coexisting slatlike planes, with orientations  $\mathbf{n}_1$  and  $\mathbf{n}_2$ , in the hill-and-valley structure. From Ref. [59].

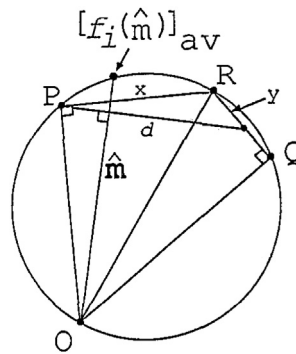


**FIGURE 5.8** Equilibrium crystal shape (ECS) analogue of the Maxwell double-tangent construction. O is the center of the crystal. Points P and Q are on the (stable) Wulff plot, but the region between them is unstable; hence, the ECS follows PRQ and has an edge at R. An interface at the intermediate orientation  $\widehat{\mathbf{m}}$  breaks up into the orientations P and Q with relative proportions  $x:y$ ; thus, the average free energy per unit area is given by Eqn (5.15), which in turn shows that  $f_i(\widehat{\mathbf{m}})_{avr}$  lies on the circle. From Ref. [1].

evolve toward a hill-and-valley structure with orientations P and Q with a free energy per area of

$$[f_i(\widehat{\mathbf{m}})]_{avr} = \frac{xf_i(P) + yf_i(Q)}{d}. \quad (5.15)$$

It can then be shown that  $\widehat{\mathbf{m}}[f_i(\widehat{\mathbf{m}})]_{avr}$  lies on the depicted circle, so that the Wulff plane passes through the edge at R.

### 5.3.3 Experiments on Lead Going beyond Wulff Plots

To determine the limits of forbidden regions, it is more direct and straightforward to carry out a polar plot of  $1/f_i(\widehat{\mathbf{m}})$  [20] rather than  $f_i(\widehat{\mathbf{m}})$ , as discussed in Sekerka’s review chapter [8]. Then a sphere passing through the origin becomes a corresponding plane; in particular, a Herring sphere for some point becomes a plane tangent to the plot of  $1/f_i(\widehat{\mathbf{m}})$ . If the Herring sphere is inside the Wulff plot, then its associated plane lies outside the plot of  $1/f_i(\widehat{\mathbf{m}})$ . If, on the other hand, if some part of the Wulff plot is inside a

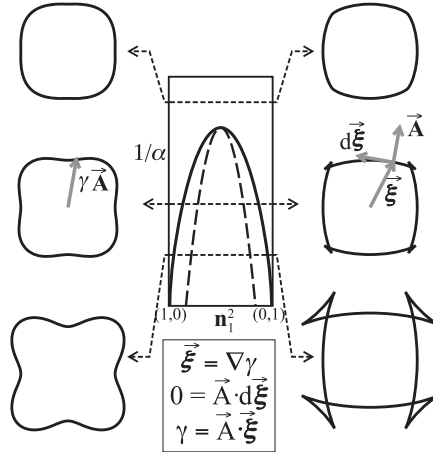


**FIGURE 5.9** Graphical constructions for an anisotropic  $f_i(\widehat{\mathbf{m}})$  for various values of an anisotropy parameter  $\alpha$ , where  $f_i \propto 1 + \alpha \cos^2 \theta \sin^2 \theta$ . In the left column  $f_i(\theta)$  is plotted from top to bottom for  $\alpha = 1/2, 1, 2$ . Anisotropy increases with positive  $\alpha$ , so  $1/\alpha$  corresponds in some sense to a temperature in conventional plots. In the center panel,  $\mathbf{n}_1^2$  is  $\cos^2 \theta$ . The shape resulting from the gradient construction with the ears removed is the Wulff equilibrium crystal shape. *From Ref. [60].*

Herring sphere, the corresponding part of the  $1/f_i(\widehat{\mathbf{m}})$  plot will be outside the plane. Thus, if the plot of  $1/f_i(\widehat{\mathbf{m}})$  is convex, all its tangent planes will lie outside, and all orientations will appear on the ECS. If it is not convex, it can be made so by adding tangent planes. The orientations associated with such tangent planes are forbidden, so their contact curve with the  $1/f_i(\widehat{\mathbf{m}})$  plot gives the bounding stable orientations into which forbidden orientations phase separate.

Summarizing the discussion in Ref. [8], the convexity of  $1/f_i(\widehat{\mathbf{m}})$  can indeed be determined analytically since the curvature  $1/f_i(\widehat{\mathbf{m}})$  is proportional (with a positive-definite proportionality constant) to the stiffness, i.e., in 2D,  $\gamma + \partial^2 \gamma / \partial \theta^2 = \tilde{\gamma}$ , or preferably  $\beta + \partial^2 \beta / \partial \theta^2 = \tilde{\beta}$  as in Eqn (5.1) to emphasize that the stiffness and (step) free energy per length have different units in 2D from 3D. Hence,  $1/f_i(\widehat{\mathbf{m}})$  is not convex where the stiffness is negative. The very complicated generalization of this criterion to 3D is made tractable via the  $\xi$ -vector formalism of Refs [30,61], where  $\xi = \nabla(r f_i(\widehat{\mathbf{m}}))$ , where  $r$  is the distance from the origin of the  $\gamma$  plot. Thus,

$$f_i(\widehat{\mathbf{m}}) = \xi \cdot \widehat{\mathbf{m}}, \quad \widehat{\mathbf{m}} \cdot d\xi = 0, \quad (5.16)$$

which is discussed well by Refs [8,62]. To elucidate the process, we consider just the 2D case [60].

The solid curve in Figure 5.10 is the  $\xi$  plot and the dashed curve is the  $1/\gamma$ -plot for  $f_i(\widehat{\mathbf{m}}) \equiv \gamma \propto 1 + 0.2 \cos 4\theta$ . For this case, the  $1/\gamma$ -plot is not convex and the  $\xi$  plot forms “ears.” The equilibrium shape is given by the interior envelope of the  $\xi$  plot; in this case it exhibits four corners.

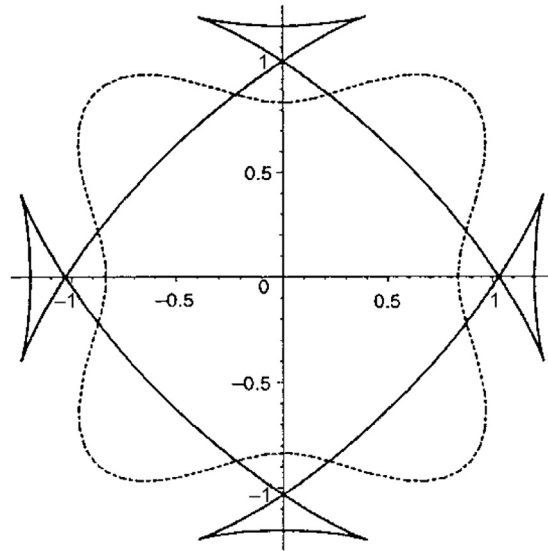


**FIGURE 5.10** The solid curve is the  $\xi$  plot, while the dashed curve is the  $1/\gamma$ -plot for  $f_i(\hat{m}) \equiv \gamma \propto 1 + 0.2 \cos 4\theta$ . For this case (but not for small values of  $a$ ), the  $1/\gamma$ -plot is not convex, and the  $\xi$  plot forms “ears.” These ears are then removed, so that the equilibrium shape is given by the interior envelope of the  $\xi$  plot, in this case having four corners. From Ref. [62].

Pursuing this analogy, we see that if one cleaves a crystal at some orientation  $\hat{m}$  that is not on the ECS, i.e., between  $\hat{m}_+$  and  $\hat{m}_-$ , then this orientation will break up into segments with orientations  $\hat{m}_+$  and  $\hat{m}_-$  such that the net orientation is still  $\hat{m}$ , providing another example of the lever rule associated with Maxwell double-tangent constructions for the analogous problems. The time to evolve to this equilibrium state depends strongly on the size of energy barriers to mass transport in the crystalline material; it could be exceedingly long. To achieve rapid equilibration, many nice experiments were performed on solid hcp  $^4\text{He}$  bathed in superfluid  $^4\text{He}$ , for which equilibration occurs in seconds [63–66], and many more (see Ref. [67] for a comprehensive recent review). Longer but manageable equilibration times are found for Si and for Au, Pb, and other soft transition metals.

## 5.4 Some Physical Implications of Wulff Constructions

### 5.4.1 Thermal Faceting and Reconstruction

A particularly dramatic example is the case of surfaces vicinal to Si (111) by a few degrees. In one misorientation direction, the vicinal surface is stable above the reconstruction temperature of the (111) facet, but below that temperature,  $f_i(111)$  decreases significantly so that the original orientation is no longer stable and phase separates into reconstructed (111) terraces and more highly misoriented segments [68,69]. The

correspondence to other systems with phase separation at first-order transitions is even more robust. Within the coexistence regime, one can in mean field determine a spinodal curve. Between it and the coexistence boundary, one observes phase separation by nucleation and growth, as for metastable systems; inside the spinodal, one observes much more rapid separation with a characteristic most-unstable length [70]. This system is discussed further below.

Wortis [1] describes “thermal faceting” experiments in which metal crystals, typically late-transition or noble metal elements like Cu, Ag, and Fe, are cut at a high Miller index direction and polished. They are then annealed at high temperatures. If the initial plane is in a forbidden direction, optical striations, due to hill-and-valley formation, appear once these structures have reached optical wavelengths. While the characteristic size of this pattern continues to grow as in spinodal decomposition, the coarsening process is eventually slowed and halted by kinetic limitations.

There are more recent examples of such phenomena. After sputtering and annealing above 800 K, Au(4,5,5) at 300 K forms a hill-and-valley structure of two Au(111) vicinal surfaces, one that is reconstructed and the other not, as seen in Figure 5.11. This seems to be an equilibrium phenomenon: It is reversible and independent of cooling rate [77]. Furthermore, while it has been long known that adsorbed gases can induce faceting on bcc (111) metals [72], ultrathin metal films have also been found to produce faceting of W(111), W(211), and Mo(111) [73,74].

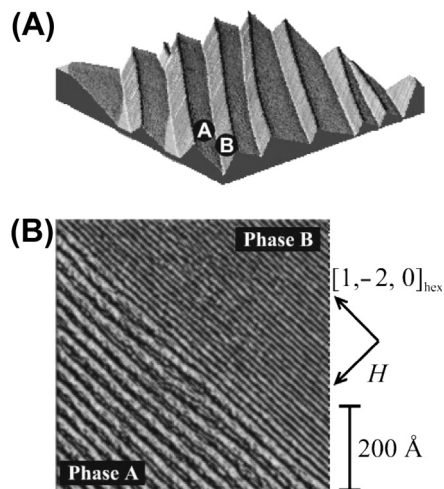


**FIGURE 5.11** Morphology of the faceted Au(4,5,5) surface measured at room temperature. (A) 3D plot of a large-scale (scan area:  $1.4 \times 1.4$  mm) scanning tunneling microscopy (STM) image. Phases A and B form the hill-and-valley morphology. (B) STM image zoomed in on a boundary between the two phases. All steps single-height, i.e.,  $2.35\text{\AA}$  high. Phase B has smaller terraces,  $13\text{\AA}$  wide, while phase A terraces are about  $30\text{\AA}$  wide. This particular surface has (2,3,3) orientation. From Ref. [71].

### 5.4.2 Types A and B

The above analysis indicates that at  $T = 0$ , the ECS of a crystal is a polyhedron having the point symmetry of the crystal lattice, a result believed to be general for finite-range interactions [75]. All boundaries between facets are sharp edges, with associated forbidden nonfacet orientation; indeed, the Wulff plot is just a set of discrete points in the symmetry directions. At finite temperature, two possibilities have been delineated (with cautions [1], labeled nonmnemonically) A and B. In type A, there are smooth curves between facet planes rather than edges and corners. Smooth here means, of course, that not only is the ECS continuous, but so is its slope, so that there are no forbidden orientations anywhere. This situation corresponds to continuous phase transitions. In type B, in contrast, corners round at finite  $T$  but edges stay sharp until some temperature  $T_0$ . For  $T_0 < T < T_1$ , there are some rounded edges and some sharp edges, while above  $T_1$  all edges are rounded.

Rottman and Wortis [4] present a comprehensive catalog of the orientation phase diagrams, Wulff plots, and ECSs for the cases of nonexistent, weakly attractive, and weakly repulsive next-nearest-neighbor (NNN) bonds in 3D. Figures 5.12 and 5.13 show the orientation phase diagrams and the Wulff plots with associated ECSs, respectively, for weakly attractive NNN bonds. As indicated in the caption, it is easy to describe what then happens when  $\epsilon_2 = 0$  and only  $\{100\}$  facets occur. Likewise, Figures 5.14 and 5.15 show the orientation phase diagrams and the Wulff plots with associated ECSs, respectively, for weakly repulsive NNN bonds.

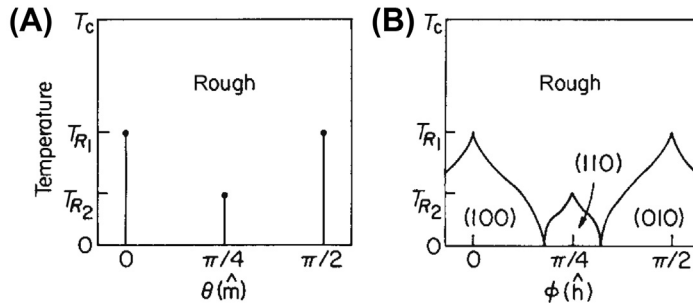


**FIGURE 5.12** Interfacial phase diagrams for simple-cubic nearest-neighbor Kossel crystal with nearest-neighbor as well as (weak) next nearest-neighbor (NNN) attractions. The angular variables  $\theta$  and  $\phi$  (not to be confused with  $\varphi$ , cf. Section 5.2.1) interfacial orientation ( $\hat{\mathbf{m}}$ ) and equilibrium crystal shape ( $\hat{\mathbf{h}}$ ), respectively, in an equatorial section of the full 3D phase diagram. (A) The  $T$ - $\theta$  phase diagram (b) shows the locus of cusps in the Wulff plot along the symmetry directions below the respective roughening temperatures. For no NNN interaction ( $\epsilon_2 = 0$ ), there are only cusps at vertical lines at 0 and  $\pi/2$ . (B) The  $T$ - $\hat{\mathbf{h}}$  phase diagram gives the faceted areas of the crystal shape. The NNN attraction leads to additional (111) (not seen in the equatorial plane) and (110) facets at low enough temperature. Thus, for  $\epsilon_2 = 0$  the two bases of the (100) and (010) phases meet and touch each other at (and only at)  $\phi = \pi/4$  (at  $T = 0$ ), with no intervening (110) phase. Each type of facet disappears at its own roughening temperature. Above the phase boundaries enclosing those regions, the crystal surfaces are smoothly curved (i.e., thermodynamically “rough”). This behavior is consistent with the observed phase diagram of hcp  $^4\text{He}$ . From Ref. [4].

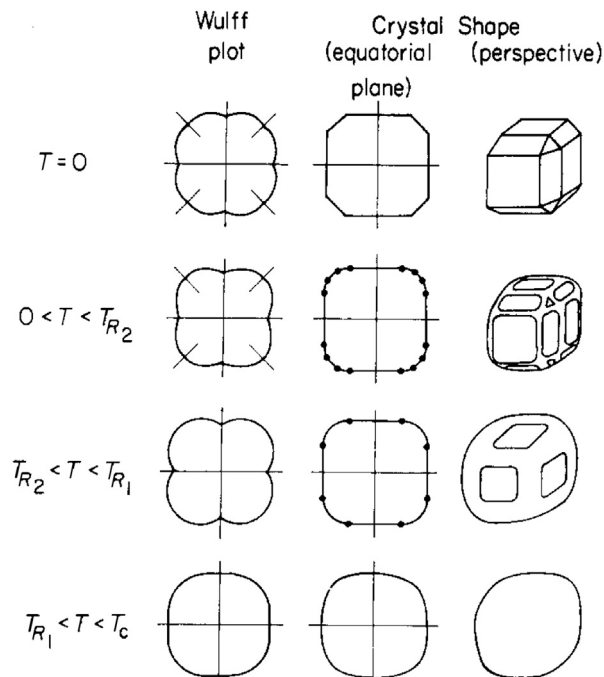


**FIGURE 5.13** Representative Wulff plots and equilibrium crystal shapes for the crystal with weak next nearest-neighbor attractions whose phase diagram is shown in Figure 5.12. At low enough temperature there are (100), (110), and (111) facets. For weak attraction, the (110) and (111) facets roughen away below the (100) roughening temperature. For  $\epsilon_2 = 0$ ,  $T_{R2} = 0$ , so that the configurations in the second row do not occur; in the first row, the octagon becomes a square and the perspective shape is a cube. Facets are separated at  $T > 0$  by curved surfaces, and all transitions are second order. Spherical symmetry obtains as  $T$  approaches melting at  $T_c$ . From Ref. [4].

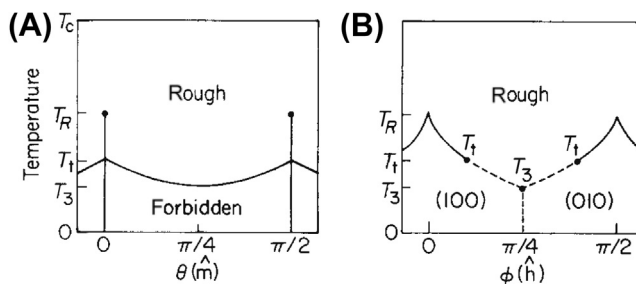


**FIGURE 5.14** Interfacial phase diagram with (weak) next nearest-neighbor (NNN) repulsion rather than attraction as in Figure 5.12. The NNN repulsion stabilizes the (100) facets. Curved surfaces first appear at the cube corners and then reach the equatorial plane at  $T_3$ . The transition at the equator remains first order until a higher temperature  $T_t$ . The dotted boundaries are first order. A forbidden (coexistence) region appears in the  $T - \hat{h}$  phase diagram. From Ref. [4].

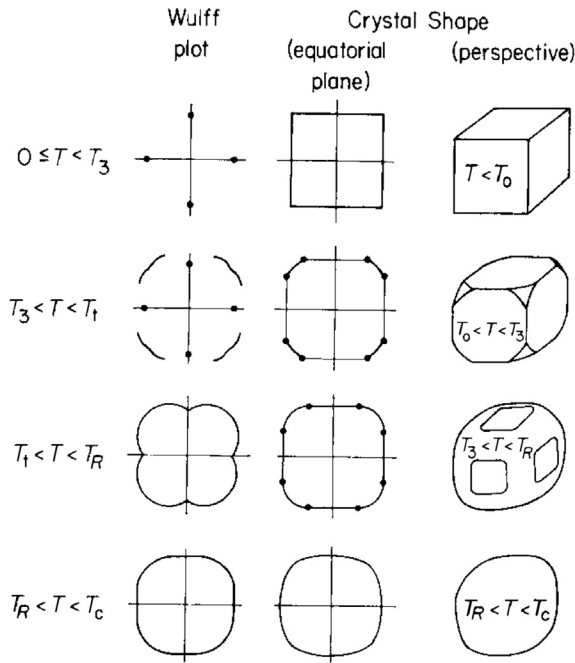


**FIGURE 5.15** Representative Wulff plots and equilibrium crystal shapes for the crystal with weak next nearest-neighbor repulsions whose phase diagram is shown in Figure 5.14. Curved surfaces appear first at the cube corners. Junctions between facets and curved surfaces may be either first or second order (sharp or smooth), depending on orientation and temperature. From Ref. [4].

### 5.4.3 2D Studies

Exploring the details is far more transparent in 2D than in 3D. The 2D case is physically relevant in that it describes the shape of islands of atoms of some species at low fractional coverage on an extended flat surface of the same or another material. An entire book is devoted to 2D crystals [76]. The 2D perspective can also be applied to cylindrical surfaces in 3D, as shown by Ref. [7]. Formal proof is also more feasible, if still arduous, in 2D: An entire book is devoted to this task [25]; see also Refs [34,35].

For the 2D nearest-neighbor Kossel crystal described above [1] notes that at  $T = 0$  a whole class of Wulff planes pass through a corner. At finite  $T$ , thermal fluctuations lift this degeneracy and the corner rounds, leading to type A behavior. To gain further insight, we now include a next nearest-neighbor (NNN) interaction  $\epsilon_2$ , so that

$$f_i(\theta) = \frac{\epsilon_1 + \epsilon_2}{2} (|\cos \theta| + |\sin \theta|) + \frac{\epsilon_2}{2} (|\cos \theta| - |\sin \theta|) \quad (5.17)$$

For favorable NNN bonds, i.e.,  $\epsilon_2 > 0$ , one finds new  $\{11\}$  facets but still type A behavior with sharp edges, while for unfavorable NNN bonds, i.e.,  $\epsilon_2 < 0$ , there are no new facets but for finite  $T$ , the edges are no longer degenerate so that type B behavior obtains. Again recalling that  $f_i(\theta) = f_p(\theta) |\cos \theta|$ , we can identify  $f_0 = \epsilon_2 + \epsilon_1/2$  and  $\beta/h = \epsilon_1/2$ , as noted in other treatments, e.g., Ref. [77]. That work, however, finds that such a model cannot adequately account for the orientation-dependent stiffness of islands on Cu(001).

Attempts to resolve this quandary using 3-site non-pairwise (trio) interactions [78,79] did not prove entirely satisfactory. In contrast, on the hexagonal Cu(111) surface, only NN interactions are needed to account adequately for the experimental data [79,80]. In fact, for the NN model on a hexagonal grid, [81] found an exact and simple, albeit implicit, expression for the ECS. However, on such (111) surfaces (and basal planes of hcp crystals), lateral pair interactions alone cannot break the symmetry to produce a difference in energies between the two kinds of step edges, viz. {100} and {111} microfacets (A and B steps, respectively, with no relation to types A and B!). The simplest viable explanation is an orientation-dependent trio interaction; calculations of such energies support this idea [79,80].

Strictly speaking, of course, there should be no 2D facet (straight edge) and accompanying sharp edges (corners) at  $T > 0$  (see Refs [82–85] and references therein) since that would imply 1D long-range order, which should not occur for short-range interactions. Measurements of islands at low temperatures show edges that appear to be facets and satisfy Wulff corollaries such as that the ratio of the distances of two unlike facets from the center equals the ratio of their  $f_i$  [86]. Thus, this issue is often just mentioned in passing [87] or even ignored. On the other hand, sophisticated approximations for  $f_i(\theta)$  for the 2D Ising model, including NNN bonds, have been developed, e.g., Ref. [88], allowing numerical tests of the degree to which the ECS deviates from a polygon near corners of the latter. One can also gauge the length scale at which deviations from a straight edge come into play by using that the probability per atom along the edge for a kink to occur is essentially the Boltzmann factor associated with the energy to create the kink [89].

Especially for heteroepitaxial island systems (when the island consists of a different species from the substrate), strain plays an important if not dominant role. Such systems have been investigated, e.g., by Liu [90], who points out that for such systems the shape does not simply scale with  $\lambda$ , presumably implying the involvement of some new length scale[s]. A dramatic manifestation of strain effects is the island shape transition of Cu on Ni(001), which changes from compact to ramified as island size increases [91]. For small islands, additional quantum-size and other effects lead to favored island sizes (magic numbers).

## 5.5 Vicinal Surfaces—Entrée to Rough Regions Near Facets

In the rough regions, the ECS is a vicinal surface of gradually evolving orientation. To the extent that a local region has a particular orientation, it can be approximated as an infinite vicinal surface. The direction perpendicular to the terraces (which are densely packed facets) is typically called  $\hat{\mathbf{z}}$ . In “Maryland notation” (cf. Section 5.2.1) the normal to the vicinal surface lies in the  $x$ – $z$  plane, and the distance  $\ell$  between steps is measured along  $\hat{\mathbf{x}}$ , while the steps run along the  $\hat{\mathbf{y}}$  direction. In the simplest and usual approximation, the repulsions between adjacent steps arise from two sources: an entropic or

steric interaction due to the physical condition that the steps cannot cross, since overhangs cannot occur in nature. The second comes from elastic dipole moments due to local atomic relaxation around each step, leading to frustrated lateral relaxation of atoms on the terrace plane between two steps. Both interactions are  $\propto 1/\ell^2$ .

The details of the distribution  $\check{P}(\ell)$  of spacings between steps have been reviewed in many works [60,92,93,97]. The average step separation  $\langle \ell \rangle$  is the only characteristic length in the  $\hat{x}$  direction. N.B.,  $\langle \ell \rangle$  need not be a multiple of, or even simply related to, the substrate lattice spacing. Therefore, we consider  $P(s) = \langle \ell \rangle^{-1} \check{P}(\ell)$ , where  $s \equiv \ell/\langle \ell \rangle$ , a dimensionless length. For a “perfect” cleaved crystal,  $P(s)$  is just a spike  $\delta(s - 1)$ . For straight steps placed randomly at any position with probability  $1/\langle \ell \rangle$ ,  $P(s)$  is a Poisson distribution  $\exp(-s)$ . Actual steps do meander, as one can study most simply in a terrace step kink (TSK) model. In this model, the only excitations are kinks (with energy  $\epsilon$ ) along the step. (This is a good approximation at low temperature  $T$  since adatoms or vacancies on the terrace cost several  $\epsilon_1$  ( $4\epsilon_1$  in the case of a simple-cubic lattice)). The entropic repulsion due to steps meandering dramatically decreases the probability of finding adjacent steps at  $\ell \ll \langle \ell \rangle$ . To preserve the mean of one,  $P(s)$  must also be smaller than  $\exp(-s)$  for large  $s$ .

If there is an additional energetic repulsion  $A/\ell^2$ , the magnitude of the step meandering will decrease, narrowing  $P(s)$ . As  $A \rightarrow \infty$ , the width approaches 0 ( $P(s) \rightarrow \delta(s - 1)$ , the result for perfect crystals). We emphasize that the energetic and entropic interactions do not simply add. In particular, there is no negative (attractive) value of  $A$  at which the two cancel each other (cf. Eqn (5.30) below.) Thus, for strong repulsions, steps rarely come close, so the entropic interaction plays a smaller role, while for  $A < 0$ , the entropic contribution increases, as illustrated in Figure 5.16 and explicated below. We emphasize that the potentials of both interactions decay as  $\ell^{-2}$  (cf. Eqn (5.27)

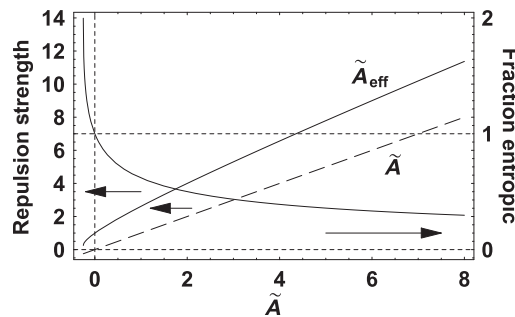


**FIGURE 5.16** Illustration of how entropic repulsion and energetic interactions combine, plotted versus the dimensionless energetic interaction strength  $\tilde{A} \equiv A\tilde{\rho}/(k_B T)^2$ . The dashed straight line is just  $\tilde{A}$ . The solid curve above it is the combined entropic and energetic interactions, labeled  $\tilde{A}_{\text{eff}}$  for reasons explained below. The difference between the two curves at any value of the abscissa is the dimensionless entropic repulsion for that  $\tilde{A}$ . The decreasing curve, scaled on the right ordinate, is the ratio of this entropic repulsion to the total dimensionless repulsion  $\tilde{A}_{\text{eff}}$ . It falls monotonically with  $\tilde{A}$ , passing through unity at  $\tilde{A} = 0$ . See the discussion accompanying Eqn (5.26) for more information and explicit expressions for the curves. From Ref. [92].

below), in contrast to some claims in the literature (in papers analyzing ECS exponents) that entropic interactions are short range while energetic ones are long range.

Investigation of the interaction between steps has been reviewed well in several places [60,94–97]. The earliest studies seeking to extract  $A$  from terrace-width distributions (TWDs) used the mean-fieldlike Gruber–Mullins [96] approximation, in which a single active step fluctuates between two fixed straight steps  $2\langle\ell\rangle$  apart. Then the energy associating with the fluctuations  $x(y,t)$  is

$$\Delta\mathcal{E} = -\beta(0)L_y + \int_0^{L_y} \beta(\theta(y)) \sqrt{1 + \left(\frac{\partial x}{\partial y}\right)^2} dy, \quad (5.18)$$

where  $L_y$  is the size of the system along the mean step direction (i.e., the step length with no kinks). We expand  $\beta(\theta)$  as the Taylor series  $\beta(0) + \beta'(0)\theta + 1/2\beta''(0)\theta^2$  and recognize that the length of the line segment has increased from  $dy$  to  $dy/\cos\theta \approx dy(1 + 1/2\theta^2)$ . For close-packed steps, for which  $\beta'(0) = 0$ , it is well known that (using  $\theta \approx \tan\theta = \partial x/\partial y$ )

$$\Delta\mathcal{E} \approx \frac{\tilde{\beta}(0)}{2} \int_0^{L_y} \left(\frac{\partial x}{\partial y}\right)^2 dy, \quad \tilde{\beta}(0) \equiv \beta(0) + \beta''(0), \quad (5.19)$$

where  $\tilde{\beta}$  is the step stiffness [97]. N.B., the stiffness  $\tilde{\beta}(\theta)$  has the same definition for steps with arbitrary in-plane orientation—for which  $\beta'(\theta) \neq 0$ —because to create such steps, one must apply a “torque” [98] which exactly cancels  $\beta'(\theta)$ . (See Refs [88,99] for a more formal proof.)

Since  $x(y)$  is taken to be a single-valued function that is defined over the whole domain of  $y$ , the 2D configuration of the step can be viewed as the worldline of a particle in 1D by recognizing  $y$  as a timelike variable. Since the steps cannot cross, these particles can be described as spinless fermions in 1D, as pointed out first by de Gennes [100] in a study of polymers in 2D [220]. Thus, this problem can be mapped into the Schrödinger equation in 1D:  $\partial x/\partial y$  in Eqn (5.19) becomes  $\partial x/\partial t$ , with the form of a velocity, with the stiffness playing the role of an inertial mass. This correspondence also applies to domain walls of adatoms on densely covered crystal surfaces, since these walls have many of the same properties as steps. Indeed, there is a close correspondence between the phase transition at smooth edges of the ECS and the commensurate-incommensurate phase transitions of such overlayer systems, with the rough region of the ECS corresponding to the incommensurate regions and the local slope related to the incommensurability [101–105]. Jayaprakash et al. [37] provide the details of the mapping from a TSK model to the fermion picture, complete with fermion creation and annihilation operators.

In the Gruber–Mullins [96] approximation, a step with no energetic interactions becomes a particle in a 1D infinite-barrier well of width  $2\langle\ell\rangle$ , with well-known groundstate properties:

$$\psi_0(\ell) \propto \sin\left(\frac{\pi\ell}{2\langle\ell\rangle}\right); \quad P(s) = \sin^2\left(\frac{\pi s}{2}\right); \quad E_0 = \frac{(\pi k_B T)^2}{8\tilde{\beta}\langle\ell\rangle^2} \quad (5.20)$$

Thus, it is the kinetic energy of the ground state in the quantum model that corresponds to the entropic repulsion (per length) of the step. In the exact solution for the free energy expansion of the ECS [106], the numerical coefficient in the corresponding term is 1/6 rather than 1/8. Note that  $P(s)$  peaks at  $s = 1$  and vanishes for  $s \geq 2$ .

Suppose, next, that there is an energetic repulsion  $U(\ell) = A/\ell^2$  between steps. In the 1D Schrödinger equation, the prefactor of  $-\partial^2\psi(\ell)/\partial\ell^2$  is  $(k_B T)^2/2\tilde{\beta}$ , with the thermal energy  $k_B T$  replacing  $\hbar$ . (Like the repulsions, this term has units  $\ell^{-2}$ .) Hence,  $A$  only enters the problem in the dimensionless combination  $\tilde{A} \equiv A\tilde{\beta}/(k_B T)^2$  [107]. In the Gruber–Mullins picture, the potential (per length) experienced by the single active particle is (with  $\tilde{\ell} \equiv \ell - \langle \ell \rangle$ )

$$\tilde{U}(\tilde{\ell}) = \frac{\tilde{A}}{(\tilde{\ell} - \langle \ell \rangle)^2} + \frac{\tilde{A}}{(\tilde{\ell} + \langle \ell \rangle)^2} = \frac{2\tilde{A}}{\langle \ell \rangle^2} + \frac{6\tilde{A}\tilde{\ell}^2}{\langle \ell \rangle^4} + \mathcal{O}\left(\frac{\tilde{A}\tilde{\ell}^4}{\langle \ell \rangle^6}\right) \quad (5.21)$$

The first term is just a constant shift in the energy. For  $\tilde{A}$  sufficiently large, the particle is confined to a region  $|\tilde{\ell}| \ll \langle \ell \rangle$ , so that we can neglect the fixed walls and the quartic term, reducing the problem to the familiar simple harmonic oscillator, with the solution:

$$\psi_0(\ell) \propto e^{-\tilde{\ell}^2/4w^2}; \quad P_G(s) \equiv \frac{1}{\sigma_G \sqrt{2\pi}} \exp\left[-\frac{(s-1)^2}{2\sigma_G^2}\right] \quad (5.22)$$

where  $\sigma_G = (48\tilde{A})^{-1/4}$  and  $w = \sigma_G \langle \ell \rangle$ .

For  $\tilde{A}$  of 0 or 2, the TWD can be computed exactly (See below). For these cases, Eqns (5.20) and (5.22), respectively, provide serviceable approximations. It is Eqn (5.22) that is prescribed for analyzing TWDs in the most-cited resource on vicinal surfaces [58]. Indeed, it formed the basis of initial successful analyses of experimental scanning tunneling microscopy (STM) data [108]. However, it has some notable shortcomings. Perhaps most obviously, it is useless for small but not vanishing  $\tilde{A}$ , for which the TWD is highly skewed, not resembling a Gaussian, and the peak, correspondingly, is significantly below the mean spacing. For large values of  $\tilde{A}$ , it significantly underestimates the variance or, equivalently, the value of  $\tilde{A}$  one extracts from the experimental TWD width [109]: in the Gruber–Mullins approximation the TWD variance is the same as that of the active step, since the neighboring step is straight. For large  $\tilde{A}$ , the fluctuations of the individual steps on an actual vicinal surface become relatively independent, so the variance of the TWD is the *sum* of the variance of each, i.e., twice the step variance. Given the great (quartic) sensitivity of  $\tilde{A}$  to the TWD width, this is problematic. As experimentalists acquired more high-quality TWD data, other approximation schemes were proposed, all producing Gaussian distributions with widths  $\propto \tilde{A}^{-1/4}$ , but with proportionality constants notably larger than  $48^{-1/4} = 0.38$ .

For the “free-fermion” ( $\tilde{A} = 0$ ) case, [110] developed a sequence of analytic approximants to the exact but formidable expression [111,112] for  $P(s)$ . They, as well as a slightly earlier paper [113], draw the analogy between the TWD of vicinal surfaces and

the distribution of spacings between interacting (spinless) fermions on a ring, the Calogero–Sutherland model [113,114], which, in turn for three particular values of the interaction—in one case repulsive ( $\tilde{A} = 2$ ), in another attractive ( $\tilde{A} = -1/4$ ), and lastly the free-fermion case ( $\tilde{A} = 0$ )—could be solved exactly by connecting to random matrix theory [92,111,115]; Figure 5.5 of Ref. [117] depicts the three resulting TWDs.

These three cases can be well described by the Wigner surmise, for which there are many excellent reviews [111,117,118]. Explicitly, for  $\varrho = 1, 2$ , and 4:

$$P_\varrho(s) = a_\varrho s^\varrho \exp(-b_\varrho s^2), \quad (5.23)$$

where the subscript of  $P$  refers to the exponent of  $s$ . In random matrix literature, the exponent of  $s$ , viz. 1, 2, or 4, is called  $\beta$ , due to an analogy with inverse temperature in one justification. However, to avoid possible confusion with the step free energy per length  $\beta$  or the stiffness  $\tilde{\beta}$  for vicinal surfaces, I have sometimes named it instead by the Greek symbol that looked most similar,  $\varrho$ , and do so in this chapter. The constants  $b_\varrho$ , which fixes its mean at unity, and  $a_\varrho$ , which normalizes  $P(s)$ , are

$$b_\varrho = \left[ \frac{\Gamma\left(\frac{\varrho+2}{2}\right)}{\Gamma\left(\frac{\varrho+1}{2}\right)} \right]^2 \quad a_\varrho = \frac{2 \left[ \Gamma\left(\frac{\varrho+2}{2}\right) \right]^{\varrho+1}}{\left[ \Gamma\left(\frac{\varrho+1}{2}\right) \right]^{\varrho+2}} = \frac{2b_\varrho^{\varrho+1/2}}{\Gamma\left(\frac{\varrho+1}{2}\right)} \quad (5.24)$$

Specifically,  $b_\varrho = \pi/4, 4/\pi$ , and  $64/9\pi$ , respectively, while  $a_\varrho = \pi/2, 32/\pi^2$ , and  $(64/9\pi)^3$ , respectively.

As seen most clearly by explicit plots, e.g., Figure 4.2(a) of Haake’s text [118],  $P_1(s)$ ,  $P_2(s)$ , and  $P_4(s)$  are excellent approximations of the exact results for orthogonal, unitary, and symplectic ensembles, respectively, and these simple expressions are routinely used when confronting experimental data in a broad range of physical problems [118,119]. (The agreement is particularly outstanding for  $P_2(s)$  and  $P_4(s)$ , which are the germane cases for vicinal surfaces, significantly better than any other approximation [120].)

Thus, the Calogero–Sutherland model provides a connection between random matrix theory, notably the Wigner surmise, and the distribution of spacings between fermions in 1D interacting with dimensionless strength  $\tilde{A}$ . Specifically:

$$\tilde{A} = \frac{\varrho}{2} \left( \frac{\varrho}{2} - 1 \right) \quad \Leftrightarrow \quad \varrho = 1 + \sqrt{1 + 4\tilde{A}}. \quad (5.25)$$

For an arbitrary system, there is no reason that  $\tilde{A}$  should take on one of the three special values. Therefore, we have used Eqn (5.28) for arbitrary  $\varrho$  or  $\tilde{A}$ , even though there is no symmetry-based justification of distribution based on the Wigner surmise of Eqn (5.26), and refer hereafter to this formula, Eqns (5.26, 7.27), as the generalized Wigner distribution (GWD). Arguably the most convincing argument is a comparison of the predicted variance with numerical data generated from Monte Carlo simulations. See Ref. [92] for further discussion.

There are several alternative approximations that lead to a description of the TWD as a Gaussian [109]; in particular, focus on the limit of large  $\varrho$ , neglecting the entropic

interaction in that limit. The variance  $\sigma^2 \propto \tilde{A}^{-1/2}$ , the proportionality constant is 1.8 times that in the Gruber–Mullins case. This approximation is improved, especially for repulsions that are not extremely strong, by including the entropic interaction in an average way. This is done by replacing  $\tilde{A}$  by

$$\tilde{A}_{\text{eff}} = \left(\frac{\varrho}{2}\right)^2 = \tilde{A} + \frac{\varrho}{2}. \quad (5.26)$$

Physically,  $\tilde{A}_{\text{eff}}$  gives the full strength of the inverse-square repulsion between steps, i.e., the modification due to the inclusion of entropic interactions. Thus, in Eqn (5.1)

$$g(T) = \frac{(\pi k_B T)^2}{6h^3 \tilde{\beta}} \tilde{A}_{\text{eff}} = \frac{(\pi k_B T)^2}{24h^3 \tilde{\beta}} \left[1 + \sqrt{1 + 4\tilde{A}}\right]^2. \quad (5.27)$$

From Eqn (5.29) it is obvious that the contribution of the entropic interaction, viz. the difference between the total and the energetic interaction, as discussed in conjunction with Figure 5.16, is  $\varrho/2$ . Remarkably, the ratio of the entropic interaction to the total interaction is  $(\varrho/2)/(\varrho/2)^2 = 2/\varrho$ ; this is the fractional contribution that is plotted in Figure 5.16.

## 5.6 Critical Behavior of Rough Regions Near Facets

### 5.6.1 Theory

Assuming (cf. Figure 5.17)  $\hat{\mathbf{z}}$  the direction normal to the facet and  $(x_0, z_0)$  denote the facet edge,  $z \sim z_0 - (x - x_0)^\vartheta$  for  $x \geq x_0$ . We show that the critical exponent  $\vartheta^3$  has the value  $3/2$  for the generic smooth edge described by Eqn (5.1) (with the notation of Eqn (5.13)):

$$f_p(p) = f_0 + Bp + gp^3 + cp^4. \quad (5.28)$$

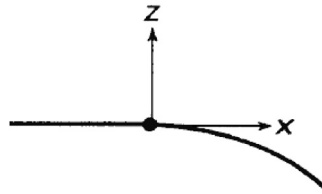


**FIGURE 5.17** Critical behavior of the crystal shape near a smooth (second-order) edge, represented by the dot at  $(x_0, z_0)$ . The temperature is lower than the roughening temperature of the facet orientation, so that the region to the left of the dot is flat. The curved region to the right of the dot correspond to a broad range of rough orientations. In the thermodynamic limit, the shape of the smoothly curved region near the edge is described by the power law  $z \sim z_0 - (x - x_0)^\vartheta$ . Away from the edge there are “corrections to scaling”, i.e., higher order terms (cf. Eqn (5.33)). For an actual crystal of any finite size, there is “finite-size rounding” near the edge, which smooths the singular behavior. Adapted from Ref. [120].

<sup>3</sup>The conventional designation of this exponent is  $\lambda$  or  $\theta$ . However, these Greek letters are the Lagrange multiplier of the ECS and the polar angle, respectively. Hence, we choose  $\vartheta$  for this exponent.

Then we perform a Legendre transformation [55] as in Refs [125,126]; explicitly:

$$\frac{f_p(p) - \tilde{f}(\eta)}{p} = \left[ \frac{df_p}{dp} \equiv \eta \right] = B + 3gp^2 + 4cp^3 \quad (5.29)$$

Hence:

$$\tilde{f}(\eta) = f_0 - 2gp^3(\eta) - 3cp^4(\eta) \quad (5.30)$$

But from Eqn (5.29):

$$p = \left( \frac{\eta - B}{3g} \right)^{1/2} \left[ 1 - \frac{2c}{3g} \left( \frac{\eta - B}{3g} \right)^{1/2} + \dots \right] \quad (5.31)$$

Inserting this into Eqn (5.30) gives

$$\tilde{f}(\eta) = f_0 - 2g \left( \frac{\eta - B}{3g} \right)^{3/2} + c \left( \frac{\eta - B}{3g} \right)^2 + \mathcal{O} \left( \frac{\eta - B}{3g} \right)^{5/2} \quad (5.32)$$

for  $\eta \geq B$  and  $\tilde{f}(\eta) = f_0$  for  $\eta \leq B$ . (See Refs [9,120,122].) Note that this result is true not just for the free-fermion case but even when steps interact. Jayaprakash et al. [37] further show that the same  $\vartheta$  obtains when the step-step interaction decreases with a power law in  $\ell$  that is greater than 2. We identify  $\tilde{f}(\eta)$  with  $r(\hat{\mathbf{h}})$ , i.e., the magnetic-fieldlike variable discussed corresponds to the so-called Andreev field  $\eta$ . Writing  $z_0 = f_0/\lambda$  and  $x_0 = B/\lambda$ , we find the shape profile

$$\begin{aligned} \frac{z(x)}{z_0} = 1 - 2 \left( \frac{f_0}{g} \right)^{1/2} \left( \frac{x - x_0}{z_0} \right)^{3/2} \\ + \frac{cf_0}{g^2} \left( \frac{x - x_0}{z_0} \right)^2 + \mathcal{O} \left( \frac{x - x_0}{z_0} \right)^{5/2} \end{aligned} \quad (5.33)$$

Note that the edge position depends only on the step free energy  $B$ , not on the step repulsion strength; conversely, the coefficient of the leading  $(x - x_0)^{3/2}$  term is independent of the step free energy but varies as the inverse root of the total step repulsion strength, i.e., as  $g^{-1/2}$ .

If, instead of Eqn (5.31), one adopts the phenomenological Landau theory of continuous phase transitions [121] and performs an analytic expansion of  $f_p(p)$  in  $p$  [123, 124] (and truncate after a quadratic term  $f_2 p^2$ ), then a similar procedure leads  $\vartheta = 2$ , which is often referred to as the “mean-field” value. This same value can be produced by quenched impurities, as shown explicitly for the equivalent commensurate-incommensurate transition by [125].

There are some other noteworthy results for the smooth edge. As the facet roughening temperature is approached from below, the facet radius shrinks like  $\exp[-\pi^2 T_R/4 \{2\ln 2(T_R - T)\}^{1/2}]$  [122], in striking contrast to predictions by mean field theory. The previous discussion implicitly assumes that the path along  $x$  for which  $\vartheta = 3/2$  in Eqn (5.36) is normal to the facet edge. By mapping the crystal surface onto the asymmetric 6-vertex model, using its exact solution [53,54], and employing the Bethe ansatz to

expand the free energy close to the facet edge [127], find that  $\vartheta = 3/2$  holds for any direction of approach along the rounded surface toward the edge, *except* along the tangential direction (the contour that is tangent to the facet edge at the point of contact  $x_0$ ). In that special direction, they find the new critical exponent  $\vartheta_y = 3$  (where the subscript  $y$  indicates the direction perpendicular to the edge normal,  $x$  [128]). Also, Akutsu and Akutsu [128] confirmed that this exact result was universally true for the Gruber–Mullins–Prokrovsky–Talapov free-energy expansion. (The Prokrovsky–Talapov argument was for the equivalent commensurate-incommensurate transition.) They also present numerical confirmation using their transfer-matrix method based on the product-wave-function renormalization group (PWFRG) [129,130]. Observing  $\vartheta_y$  experimentally will clearly be difficult, perhaps impossible; the nature and breadth of crossover to this unique behavior has not, to the best of my knowledge, been published. A third result is that there is a jump (for  $T < T_R$ ) in the curvature of the rounded part near the facet edge that has a universal value [106,131], distinct from the universal curvature jump of the ECS at  $T_R$  [122].

## 5.6.2 Experiment on Leads

Noteworthy initial experimental tests of  $\vartheta = 3/2$  include direct measurements of the shape of equilibrated crystals of  $^4\text{He}$  [132] and Pb [133]. As in most measurements of critical phenomena, but even harder here, is the identification of the critical point, in this case the value of  $x_0$  at which rounding begins. Furthermore, as is evident from Eqn (5.36), there are corrections to scaling, so that the “pure” exponent  $3/2$  is seen only near the edge and a larger effective exponent will be found farther from the edge. For crystals as large as a few mm at temperatures in the range 0.7–1.1 K,  $^4\text{He}$   $\vartheta = 1.55 \pm 0.06$  was found, agreeing excellently with the Prokrovsky–Talapov exponent. The early measurements near the close-packed (111) facets of Pb crystallites, at least two orders of magnitude smaller, were at least consistent with  $3/2$ , stated conservatively as  $\vartheta = 1.60 \pm 0.15$  after extensive analysis. Sáenz and García [134] proposed that in Eqn (5.31) there can be a quadratic term, say  $f_2 p^2$  (but neglect the possibility of a quartic term). Carrying out the Legendre transformation then yields an expression with both  $x - B$  and  $(x - B + f_2^2/3g)^{3/2}$  terms, which they claim will lead to effective values of  $\vartheta$  between  $3/2$  and 2. This approach provided a competing model for experimentalists to consider but in the end seems to have produced little fruit.

As seen in Figure 5.18, STM allows detailed measurement of micron-size crystal height contours and profiles at fixed azimuthal angles. By using STM to locate the initial step down from the facet, first done by Surnev et al. [135] for supported Pb crystallites,  $x_0$  can be located independently and precisely. However, from the 1984 Heyraud–Métois experiment [133] it took almost two decades until the Bonzel group could fully confirm the  $\vartheta = 3/2$  behavior for the smooth edges of Pb(111) in a painstaking study [137]. There were a number of noteworthy challenges. While the close-packed 2D network of spheres has six-fold symmetry, the top layer of a (111) facet of an fcc crystal (or of an (0001) facet

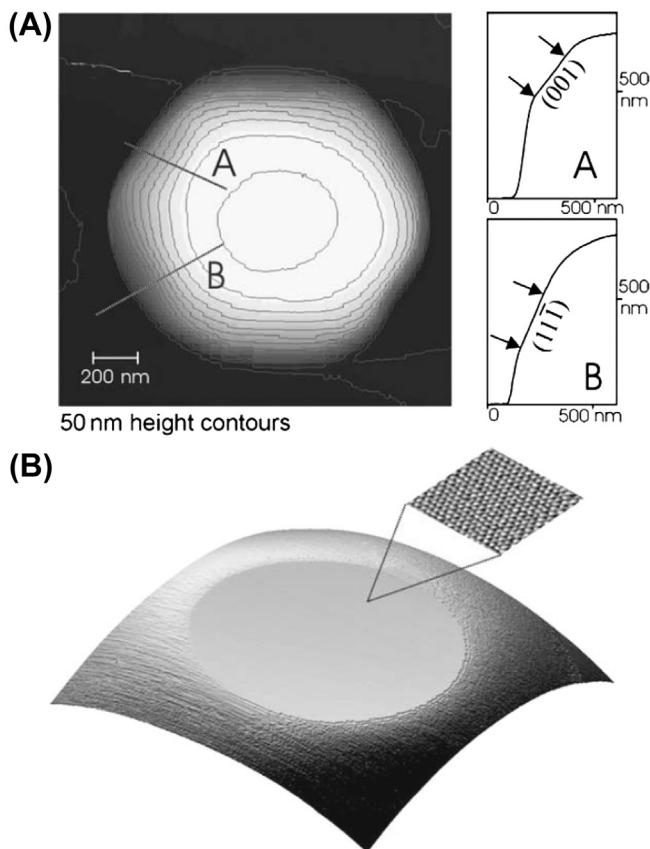


**FIGURE 5.18** (A) Micron-size lead crystal (supported on Ru) imaged with a variable-temperature scanning tunneling microscopy at  $T = 95^\circ\text{C}$ . Annealing at  $T = 95^\circ\text{C}$  for 20 h allowed it to obtain its stable, regular shape. Lines marked A and B indicate location of profiles. Profile A crosses a (0 0 1)-side facet, while profile B a (1 1 1)-side facet. (B)  $770 \times 770$  nm section of the top part of a Pb crystal. The insert shows a  $5.3 \times 5.3$  nm area of the top facet, confirming its  $(11\bar{1})$ -orientation. Both the main image and the insert were obtained at  $T = 110^\circ\text{C}$ . From Ref. [141].

of an hcp crystal) has only three-fold symmetry due to the symmetry-breaking role of the second layer. There are two dense straight step edges, called A and B, with  $\{100\}$  and  $\{111\}$  microfacets, respectively. In contrast to noble metals, for Pb there is a sizable (of order 10%) difference between their energies. Even more significant—when a large range of polar angles is used in the fitting—is the presence of small (compared to  $\{111\}$ )  $\{112\}$  facets for equilibration below 325 K. Due to the high atomic mobility of Pb that can lead to the formation of surface irregularities, Bonzel's group [135] worked close to room temperature. One then finds strong (three-fold) variation of  $\vartheta$  with azimuthal angle, with  $\vartheta$  oscillating between 1.4 and 1.7. With a higher annealing temperature of 383 K, [137] report the azimuthal averaged value  $\vartheta = 1.487$  (but still with sizable oscillations of about  $\pm 0.1$ ); in a slightly earlier short report [137], they give a value  $\vartheta = 1.47$  for annealing at

room temperature. Their attention shifted to deducing the strength of step–step repulsions by measuring  $g$  [138,139]. In the most recent review of the ECS of Pb [140], the authors rather tersely report that the Prokrovsky–Talapov value of  $3/2$  for  $\vartheta$  characterizes the shape near the (111) facet and that imaging at elevated temperature is essential to get this result; most of their article relates to comparison of measured and theoretically calculated strengths of the step–step interactions.

Few other systems have been investigated in such detail. Using scanning electron microscopy (SEM) [142] the researchers considered In, which has a tetragonal structure, near a (111) facet. They analyzed the resulting photographs from two different crystals, viewed along two directions. For polar angles  $0^\circ \leq \theta < \sim 5^\circ$  they find  $\vartheta \approx 2$  while for  $5^\circ \leq \theta \leq 15^\circ$  determine  $\vartheta \approx 1.61$ , concluding that in this window  $\vartheta = 1.60 \pm 0.10$ ; the two ranges have notably different values of  $x_0$ . This group [143] also studied Si, equilibrated at  $900^\circ\text{C}$ , near a (111) facet. Many profiles were measured along a high-symmetry  $\langle 111 \rangle$  zone of samples with various diameters of the order a few  $\mu\text{m}$ , over the range  $3^\circ \leq \theta \leq 17^\circ$ . The results are consistent with  $\vartheta = 3/2$ , with an uncertainty estimated at 6%. Finally, [144] studied large (several mm) spherical cuprous selenide ( $\text{Cu}_{2-x}\text{Se}$ ) single crystals near a (111) facet. Study in this context of metal chalcogenide superionic conductors began some dozen years ago because, other than  $^4\text{He}$ , they are the only materials having sub-cm size crystals with an ECS form that can be grown on a practical time scale (viz. over several days) because their high ionic and electronic conductivity enable fast bulk atomic transport. For  $14.0^\circ \leq \theta \leq 17.1^\circ$  [144] find  $\vartheta = 1.499 \pm 0.003$ . (They also report that farther from the facet  $\vartheta \approx 2.5$ , consistent with the Andreev mean field scenario.)

### 5.6.3 Summary of Highlights of Novel Approach to Behavior Near Smooth Edges

Digressing somewhat, we note that Ferrari, Prähofer, and Spohn [145] found novel static scaling behavior of the equilibrium fluctuations of an atomic ledge bordering a crystalline facet surrounded by rough regions of the ECS in their examination of a 3D Ising corner (Figure 5.19). This boundary edge might be viewed as a “shoreline” since it is the edge of an islandlike region—the crystal facet—surrounded by a “sea” of steps [146].

Spohn and coworkers assume that there are no interactions between steps other than entropic, and accordingly the step configurations can be mapped to the worldlines of free spinless fermions, as in treatments of vicinal surfaces [37]. However, there is a key new feature that the step number operator is weighted by the step number, along with a Lagrange multiplier  $\lambda^{-1}$  associated with volume conservation of the crystallite. The asymmetry of this term leads to the novel behavior found by the researchers. They then derive an exact result for the step density and find that, near the shoreline:

$$\lim_{\lambda \rightarrow \infty} \lambda^{1/3} \rho_\lambda(\lambda^{1/3}x) = -x(\text{Ai}(x))^2 + (\text{Ai}'(x))^2, \quad (5.34)$$

where  $\rho_\lambda$  is the step density (for the particular value of  $\lambda$ ).

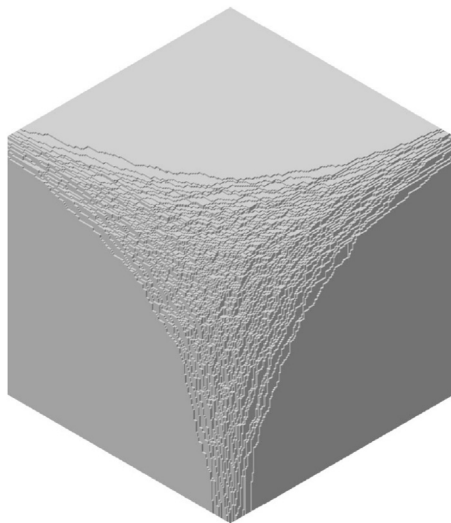


FIGURE 5.19 Simple-cubic crystal corner viewed from the  $\{111\}$  direction. From Ref. [145].

The presence of the Airy function  $\text{Ai}$  results from the asymmetric potential implicit in  $\mathcal{H}_F$  and preordains exponents involving  $1/3$ . The variance of the wandering of the shoreline, the top fermionic worldline in Figure 5.20 and denoted by  $b$ , is given by

$$\text{Var} [b_\lambda(t) - b_\lambda(0)] \cong \lambda^{2/3} g(\lambda^{-2/3} t) \quad (5.35)$$

where  $t$  is the fermionic “time” along the step;  $g(s) \sim 2|s|$  for small  $s$  (diffusive meandering) and  $\sim 1.6264 - 2/s^2$  for large  $s$ . 1.202... is Apery’s constant and  $N$  is the number of atoms in the crystal. They find:

$$\text{Var} [b_\ell(\ell\tau + x) - b_\ell(\ell\tau)] \cong (\mathcal{A}\ell)^{2/3} g\left(\mathcal{A}^{1/3}\ell^{-2/3}x\right), \quad (5.36)$$

where  $\mathcal{A} = (1/2)b'_\infty$ . This leads to their central result that the width  $w \sim \ell^{1/3}$ , in contrast to the  $\ell^{1/2}$  scaling of an isolated step or the boundary of a single-layer island and to the  $\ln \ell$  scaling of a step on a vicinal surface, i.e., in a step train. Furthermore, the

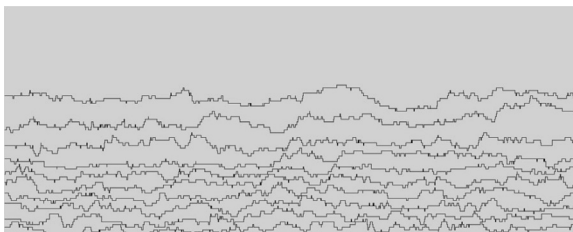


FIGURE 5.20 Snapshot of computed configurations of the top steps (those near a facet at the flattened side portion of a cylinder) for a terrace-step-kink (TSK) model with volume constraint. From Ref. [145].

fluctuations are non-Gaussian. The authors also show that near the shoreline, the deviation of the equilibrium crystal shape from the facet plane takes on the Pokrovsky–Talapov [101,104] form with  $\nu = 3/2$ .

From this seminal work, we could derive the dynamic exponents associated with this novel scaling and measure them with STM, as reviewed in Ref. [150].

## 5.7 Sharp Edges and First-Order Transitions— Examples and Issues

### 5.7.1 Sharp Edges Induced by Facet Reconstruction

Si near the (111) plane offers an easily understood entry into sharp edges [68,69]. As Si is cooled from high temperatures, the (111) plane in the “(1 × 1)” phase reconstructs into a (7 × 7) pattern [150] around 850 °C, to be denoted  $T_7$  to distinguish it clearly from the other subscripted temperatures. (The notation “(1 × 1)” is intended to convey the idea that this phase differs considerably from a perfect (111) cleavage plane but has no superlattice periodicity.) For comparison, the melting temperature of Si is  $\sim 1420$  °C, and the  $T_R$  is estimated to be somewhat higher. As shown in Figure 5.21, above  $T_7$ , surfaces of

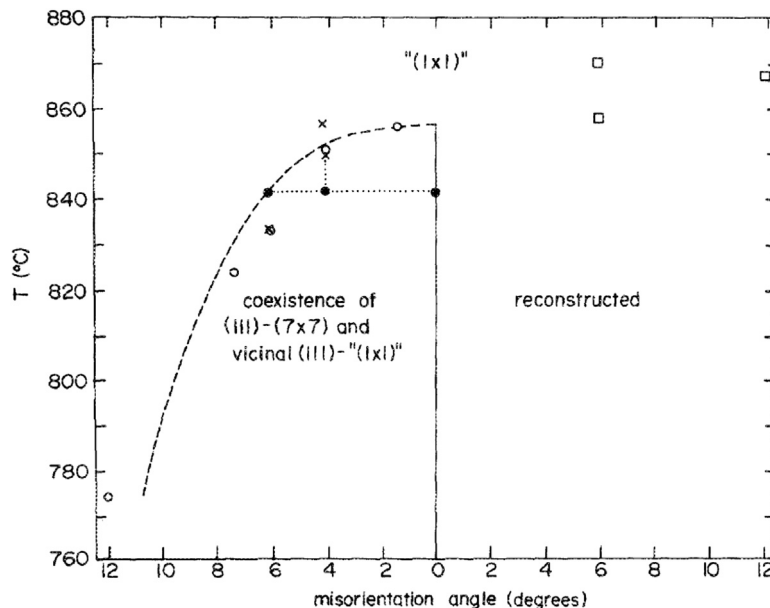


**FIGURE 5.21** Summary of experimental results for vicinal Si (111) surface: ○ denotes the temperature at which faceting begins for surfaces misoriented toward the (110) direction, × the faceting temperatures for surfaces misoriented toward the  $[11\bar{2}]$ , and □ the temperatures at which the step structure of surfaces misoriented toward the  $[\bar{1}\bar{1}2]$  direction change. The dashed line displays a fit of the  $[\bar{1}\bar{1}0]$  data to Eqn (5.43). The dotted lines show how a four sample phase separates into the states denoted by ● as it is further cooled. From Ref. [69].

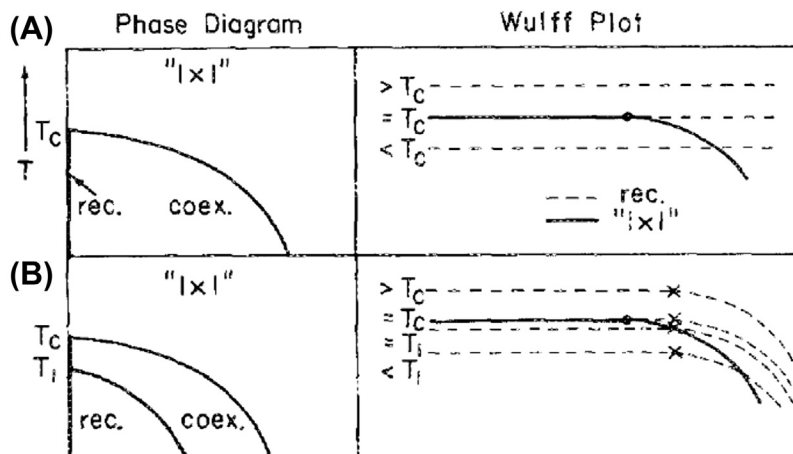


**FIGURE 5.22** Wulff plots illustrating the effect of a reconstructive transition on the equilibrium crystal shape (ECS), and corresponding temperature-[mis]orientation phase diagrams. The solid curves represent the ECS with an unreconstructed [" $(1 \times 1)$ "] facet, while the dashed curves give the ECS with a reconstructed facet. As temperature decreases, the free energy of the reconstructed facet, relative to that of the unreconstructed facet, decreases. Below the transition temperature  $T_c$  (called  $T_7$  in the text), the two shapes intersect, giving a "net" ECS that is the inner envelope of the two. The phase diagram shows regions where all orientations  $\tan \theta$  (or  $\hat{\mathbf{m}}$ ) are allowed for the unreconstructed crystal [" $(1 \times 1)$ "], regions of phase separation (labeled "coex."), and regions where the reconstruction (labeled "rec.") is allowed for ranges of orientation. The relative size of the reconstructed and unreconstructed facets depends on the free energy to create a step on the reconstructed (111) face, compared to its unreconstructed counterpart: (A) the behavior for extremely large energy to create steps on the  $(7 \times 7)$  terrace and (A) a smaller such energy. Solid circles mark the sharp edge at the temperature at which the crystal shapes cross. Crosses show the intersection of the facet and the curved part (i.e., the smooth edge) of the crystal shape for the reconstructed phase. *From Ref. [69].*

all orientations are allowed and are unreconstructed. At  $T_7$ , a surface in the (111) direction reconstructs but all other orientations are allowed and are unreconstructed. Below  $T_7$ , surfaces misoriented toward  $[\bar{1}\bar{1}\bar{2}]$  remain stable during cooling (although the step structure changes). On the other hand, on surfaces misoriented toward  $[\bar{1}10]$  and  $[11\bar{2}]$ , the temperature at which the  $(7 \times 7)$  occurs decreases with increasing misorientation angle  $\hat{\mathbf{m}}$ . Furthermore, just as the  $(7 \times 7)$  appears, the surface begins to separate into two phases, one a perfectly oriented  $(7 \times 7)$  plane  $\hat{\mathbf{m}} = 0$  and the second an unreconstructed phase with a misorientation greater than that at higher temperature. As the temperature further decreases, the misorientation of the unreconstructed phase increases. Figure 5.21 depicts this scenario with solid circles and dotted lines for a  $4^\circ$  misoriented sample at  $840^\circ\text{C}$ . This behavior translates into the formation of a sharp edge on the ECS between a flat  $(7 \times 7)$  line and a rounded " $(1 \times 1)$ " curve.

To explain this behavior, one coplots the ECS for the two phases, as in Figure 5.22 [69]. The free energy to create a step is greater in the  $(7 \times 7)$  than in the " $(1 \times 1)$ " phase. In the top panels (A), the step energy for the  $(7 \times 7)$  is taken as infinite, i.e., much larger than that of the " $(1 \times 1)$ " phase, so its ECS never rounds. At  $T_7$  ( $T_c$  in the figure), the free energies per area  $f_0$  of the two facets are equal, call them  $f_7$  and  $f_1$ , with associated

energies  $u_7$  and  $u_1$  and entropies  $s_7$  and  $s_1$  for the  $(7 \times 7)$  and “ $(1 \times 1)$ ” phases, respectively, near  $T_7$ . Then  $T_7 = (u_1 - u_7)/(s_1 - s_7)$  and, assuming the internal energies and entropies are insensitive to temperature:

$$f_1 - f_7 = (T_7 - T)(s_1 - s_7). \quad (5.37)$$

Since  $s_1 > s_7$  because the  $(7 \times 7)$  phase is so highly ordered, we find that  $f_1 - f_7 > 0$  below  $T_7$ , as illustrated in [Figure 5.22](#). Making connection to thermodynamics, we identify

$$\frac{L}{T_7} = (s_1 - s_7)_{T_7} = \left(\frac{\partial f_7}{\partial T}\right)_{T_7} - \left(\frac{\partial f_1}{\partial T}\right)_{T_7} \quad (5.38)$$

where  $L$  is the latent heat of the first-order reconstruction transition.

Corresponding to the minimum of a free energy as discussed earlier, the ECS of the system will be the inner envelope of the dashed and solid traces: a flat  $(7 \times 7)$  facet along the dashed line out to the point of intersection, the sharp edge, beyond which it is “ $(1 \times 1)$ ” with continuously varying orientation. If one tries to construct a surface with a smaller misorientation, it will phase separate into flat  $(7 \times 7)$  regions and vicinal unreconstructed regions with the orientation at the curved (rough) side of the sharp edge. Cf. [Figure 5.23](#).

Using the leading term in [Eqn \(5.35\)](#) or [\(5.36\)](#), we can estimate the slope of the coexisting vicinal region and its dependence on temperature<sup>4</sup>: First we locate the sharp edge (recognizing  $f_0$  as  $f_1$  and  $z_0$  as  $z_1$ ) by noting

$$\begin{aligned} z_7 &= z_1 - 2(\lambda/g)^{1/2}(x - x_0)^{3/2} \\ (T_7 - T)\Delta s &\approx (f_1 - f_7)_T = \lambda^{3/2}g^{-1/2}(x - x_0)^{3/2} \end{aligned} \quad (5.39)$$

Since the slope  $m$  there is  $-3\lambda(\lambda/g)^{1/2}(x - x_0)^{1/2}$ , the temperature dependence of the slope is

$$m = -3\left(\frac{L}{2g}\right)^{1/3}\left(1 - \frac{T}{T_7}\right)^{1/3} \quad (5.40)$$

If the step free energy of the reconstructed phase were only modestly greater than that of the “ $(1 \times 1)$ ”, then, as shown in the second panel in [Figure 5.22](#), the previous high- $T$  behavior obtains only down to the temperature  $T_1$  at which the “ $(1 \times 1)$ ” curve intersects the  $(7 \times 7)$  curve at its [smooth] edge. For  $T < T_1$  the sharp edge associated with the interior of the curves is between a misoriented “ $(1 \times 1)$ ” phase and a differently misoriented  $(7 \times 7)$  phase, so that it is these two which coexist. All orientations with smaller misorientation angles than this  $(7 \times 7)$  plane are also allowed, so that the forbidden or coexistence regime has the depicted slivered crescent shape. Some other, but physically improbable, scenarios are also discussed by Bartelt et al. [\[69\]](#). Phaneuf and Williams [\[68\]](#) show (their Figure 3) the LEED-beam splitting for a surface misoriented by  $6.4^\circ$  is  $\propto (T_7 - T)^{1/3}$  once the surface is cooled below the temperature (which is  $< T_7$ ) when this orientation becomes unstable to phase separation; however, by changing the

<sup>4</sup>There are some minor differences in prefactors from Ref. [\[69\]](#).

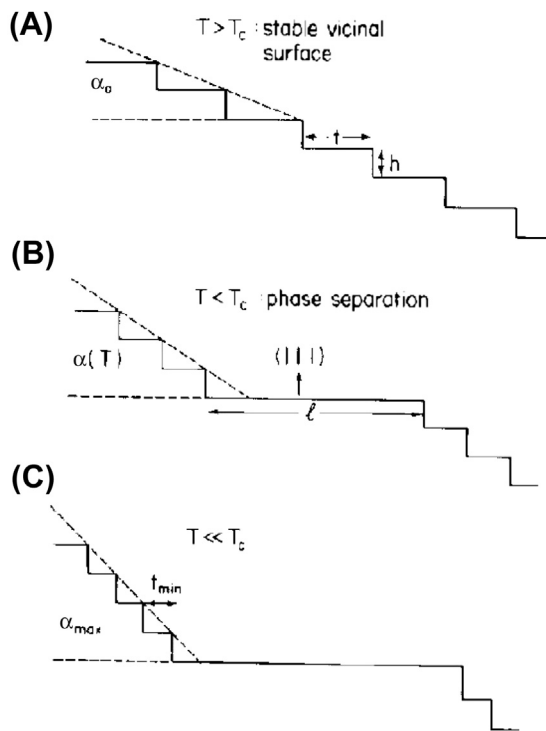


**FIGURE 5.23** Microscopic view of what happens to a misoriented surface in Figure 5.22 as temperature decreases. (A) At high temperature, the Si(III) vicinal surface is a single, uniform phase. Initial terrace widths  $t$  are typically a few nm, as determined by the net angle of miscut  $\alpha_0$  (i.e.,  $\theta_0$ ), and the step-height  $h$ , which is one interplanar spacing ( $\sim 0.31$  nm). (B) Below the  $(7 \times 7)$  reconstruction temperature ( $\sim 850^\circ\text{C}$ ), the steps cluster to form a new surface of misorientation angle  $\alpha(T)$  (i.e.,  $\theta$ ). A facet of  $(111)$  orientation with  $(7 \times 7)$  reconstruction forms simultaneously. The width of the  $(111)$  facet,  $l$ , is larger than the experimentally resolvable width of 500 Å. (C) Well below the transition, the step separation reaches a minimum distance,  $t_{\min} \sim 1$  nm. No further narrowing occurs, perhaps because surface diffusion is too slow  $T \leq 600^\circ\text{C}$ . From Ref. [3].

range of fitting, they could also obtain agreement with  $(T_7 - T)^{1/2}$ , i.e.,  $\vartheta = 2$ . With high-resolution LEED, [151] conclude that the exponent  $\bar{\vartheta} \equiv (\vartheta - 1)/\vartheta = 0.33 \pm 0.05$  (i.e., that  $\vartheta = 3/2$ ). The result does depend somewhat on what thermal range is used in the fit, but they can decisively rule out the mean-field value  $\vartheta = 2$ . Williams et al. [152] give a more general discussion of vicinal Si, with treatment of azimuthal in addition to polar misorientations. In contrast, synchrotron X-ray scattering experiments by Noh et al. [153,154] report the much larger  $\vartheta = 2.3^{+0.8}_{-0.3}$ . However, subsequent synchrotron X-ray scattering experiments by [155] obtain a decent fit of data with  $\vartheta = 3/2$  and a best fit with  $\vartheta = 1.75$  (i.e.,  $\bar{\vartheta} = 0.43 \pm 0.07$ ). (They also report that above 1159 K, the surface exists as a single, logarithmically rough phase.) The origin of the curious value of  $\vartheta$  in the Noh et al. experiments is not clear. It would be possible to attribute the behavior to impurities, but there is no evidence to support this excuse, and indeed for the analogous behavior near the reconstructing  $(331)$  facet of Si (but perhaps a different sample), Noh

et al. [156] found  $\vartheta = 1.47 \pm 0.1$ . It is worth noting that extracting information from X-ray scattering from vicinal surfaces requires great sophistication (cf. the extensive discussion in Ref. [157]) and attention to the size of the coherence length relative to the size of the scattering region [158], as for other diffraction experiments.

Similar effects to reconstruction (viz. the change in  $f_0$ ) could be caused by adsorption of impurities on the facet [159]. Some examples are given in a review by Somorjai and Van Hove [160]. In small crystals of dilute Pb-Bi-Ni alloys, cosegregation of Bi-Ni to the surface has a similar effect of reversibly changing the crystal structure to form {112} and {110} facets [161]. There is no attempt to scrutinize the ECS to extract an estimate of  $\vartheta$ . Meltzman et al. [162] considered the ECS of Ni on a sapphire support, noting that, unlike most fcc crystals, it exhibits a faceted shape even with few or no impurities, viz. with {111}, {100}, and {110} facets; {135} and {138} emerged at low oxygen pressure and additionally {012} and {013} at higher pressure.

The phase diagram of Pt(001), shown in Figure 5.24 and studied [163] using synchrotron X-ray scattering, at first seems similar to that of Si near (111) [223,224,225], albeit with more intricate magic phases with azimuthal rotations at lower temperatures, stabilized by near commensurability of the period of their reconstruction and the separation of their constituent steps. In the temperature-misorientation (surface slope) phase diagram, shown in Figure 5.24, the (001) facet undergoes a hexagonal reconstruction at  $T_6 = 1820$  K (well below the bulk melting temperature of 2045 K). For samples misoriented from the (100) direction (which are stable at high temperature), there is coexistence between flat reconstructed Pt(001) and a rough phase more highly

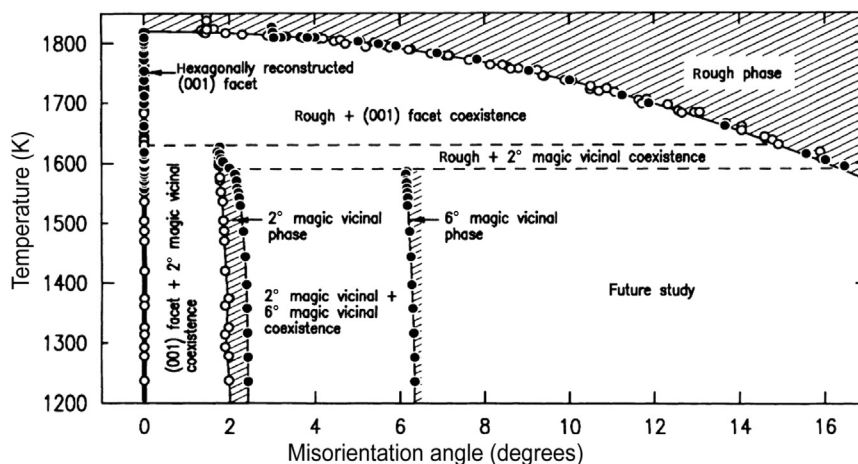


**FIGURE 5.24** Orientational phase diagram of vicinal Pt (001) misoriented toward the [110] direction. Single-phase regions are hatched, and two-phase coexistence regions are unhatched. Solid lines are boundaries between two phases. Dashed lines mark triple points. Open circles show misorientation angles measured for a sample miscut by  $1.4^\circ$  toward the [110] direction, while solid circles show tilt angles measured for a sample miscut by  $3.0^\circ$ . From Ref. [163].

misoriented than it was at high temperature, with a misorientation that increases as temperature decreases. However, they find  $\bar{\beta} = 0.49 \pm 0.05$ , or  $\vartheta = 1.96$ , consistent with mean field and inconsistent with  $\bar{\beta} = 1/3$  or  $\vartheta = 3/2$  of Prokrovsky–Talapov. The source of this mean-field exponent is that in this case the (001) orientation is rough above  $T_6$ . Hence, in Eqn (5.31)  $B$  vanishes, leaving the expansion appropriate to rough orientations. Proceeding as before, Eqn (5.35) becomes

$$f_p(p) = f_0 + Dp^2 \Rightarrow \tilde{f}(\eta) = f_0 - \eta^2/4D, \quad (5.41)$$

where the result for  $\tilde{f}(\eta)$  is reached by proceeding as before to reach the modification of Eqn (5.35). Thus, there is no smooth edge take-off point (no shoreline) in the equivalent of Figure 5.22, and one finds the reported exponent  $\vartheta$  near 2.

The effect of reactive and nonreactive gases metal catalysts has long been of interest [211]. Various groups investigated adsorbate-induced faceting. Walko and Robinson [164] considered the oxygen-induced faceting of Cu(115) into O/Cu(104) facets, using Wulff constructions to explain their observations. The researchers found three temperature regimes with qualitatively different faceting processes. Szczepkowicz et al. [165] studied the formation of {211} facets by depositing oxygen and paladium on tungsten, both on (111) facets and on soherical crystals. While the shape of the facets is different for flat and curved surfaces, the distance between parallel facet edges is comparable, although the area of a typical facet on a curved surface is an order of magnitude greater. There is considerable information about facet sizes, width of the facet-size distribution, and surface rms roughness.

For 2D structures on surfaces, edge decoration can change the shape of the islands. A well-documented example is Pt on Pt(111). As little as  $10^{-3}$  ml of CO produces a  $60^\circ$  rotation of the triangular islands by changing the balance of the edge free energies of the two different kinds of steps forming the island periphery [166]. Stasevich et al. [167] showed how decoration of single-layer Ag islands on Ag(111) by a single-strand “necklace” of  $C_{60}$  dramatically changes the shape from hexagonal to circular. With lattice-gas modeling combined with STM measurements, they could estimate the strength of  $C_{60}$ -Ag and  $C_{60}$ - $C_{60}$  attractions. Generalizations to decoration on systems with other symmetries is also discussed [167].

## 5.8 Gold–Prototype or Anomaly of Attractive Step–Step Interaction?

Much as  $^4\text{He}$  and Pb are the prototypical materials with smooth edges, Au is perhaps the prime example of a surface with sharp edges, around (1111) and (100) facets (cf. e.g., Ref. [1]). Care must be taken to ensure that the surface is not contaminated by atoms (typically C) from the supporting substrate [168]. (See similar comments by Handwerker et al. [169] for ceramics, which have a rich set of ECS possibilities.) To describe these systems phenomenologically, the projected free energy expansion in Eqn (5.1) requires a negative term to generate a region with negative curvature, as in Figure 5.7, so that the

two orientations joined by the Maxwell double-tangent construction correspond to the two sides of the sharp edge. Thus, for sharp edges around facets, the more-left minimum must be in the high-symmetry facet direction.

In a mean field-based approach, Wang and Wynblatt [168] included a negative quadratic term, with questionable physical basis. Emundts et al. [170] instead took the step–step interaction to be attractive ( $g < 0$ ) in Eqn (5.1). Then, proceeding as above, they find

$$x_0 = \frac{1}{\lambda} \left[ B - \frac{4}{27} |g| \left( \frac{g}{c} \right)^2 \right], \quad p_c = \frac{2|g|}{3c}, \quad (5.42)$$

where  $p_c$  is the tangent of the facet contact angle. Note that both the shift in the facet edge from  $B$  and the contact slope increase with  $|g|/c$ . Emundts et al. [170] obtain estimates of the key energy parameters in the expansion for the sharp edges of both the (111) and (100) facets. They also investigate whether it is the lowering of the facet free energy  $f_0$  that brings about the sharp edges, in the manner of the case of Si(111) discussed above. After reporting the presence of standard step–step repulsions (leading to narrowing of the TWD) in experiments on flame-annealed gold, Shimoni et al. [171] then attribute to some effective long-range attraction—with undetermined dependence on  $\ell$ —the (nonequilibrium) movement of single steps toward step bunches whose steps are oriented along the high-symmetry  $\langle 110 \rangle$ .

Is it possible to find a generic long-range attractive  $A\ell^{-2}$  step–step interaction ( $A < 0$ ) for metals and elemental semiconductors (where there is no electrostatic attraction between oppositely charged atoms)? Several theoretical attempts have only been able to find such attractions when there is significant alternation between “even” and “odd” layered steps. Redfield and Zangwill consider whether surface relaxation can produce such an attraction, pointing out a flaw in an earlier analysis assuming a rigid relaxation by noting that for large step separations, the relaxation must return to its value for the terrace orientation. Since atomic displacements fall off inversely with distance from a step, the contribution to the step interaction can at most go like  $\ell^{-2}$  and tend to mitigate the combined entropic and elastic repulsion. They argue that this nonlinear effect is likely to be small, at least for metals. It is conceivable that on an elastically highly anisotropic surface, the elastic interaction might not be repulsive in special directions, although I am not aware of any concrete examples.

By observing that the elastic field mediating the interaction between steps is that of a dipole applied on a stepped rather than on a flat surface, Kukta et al. [172] deduce a correction to the  $\ell^{-2}$  behavior of the Marchenko–Parshin [41] formula that scales as  $\ell^{-3} \ln \ell$ . Using what was then a state-of-the-art semiempirical potential, the embedded atom method (EAM) [228], the authors find that this can lead to attractive interactions at intermediate values of  $\ell$ . However, their “roughness correction” term exists only when the two steps have unlike orientations (i.e., one up and one down, such as on opposite ends of a monolayer island or pit). For the like-oriented steps of a vicinal surface or near a facet edge, the correction term vanishes. The oft-cited paper then invokes three-step

interactions, which are said to have the same size as the correction term, as a way to achieve attractive interactions. Although the authors discuss how this idea relates to the interaction between an isolated step and a step bunch, they do not provide the explicit form of the threefold interaction; their promise that it will be “presented elsewhere” has not, to the best of my searching, ever been fulfilled. Prévot and Croset [173] revisited elastic interactions between steps on vicinals and found that with a buried-dipole model (rather than the surface-dipole picture of Marchenko and Parshin), they could achieve “remarkable agreement” with molecular dynamics simulations for vicinals to Cu and Pt (001) and (111), for which data is fit by  $E_2^{MD}\ell^{-2} + E_3^{MD}\ell^{-3}$ . The tabulated values of  $E_2^{MD}$  indeed agree well with their computed results for their improved elastic model, which includes the strong dependence of the interaction energy on the force direction. While there is barely any discussion of  $E_3$ , plots of the interaction are always repulsive. Hecquet [174] finds that surface stress modifies the step–step interaction compared to the Marchenko–Parshin result, enhancing the prefactor of  $\ell^{-2}$  nearly threefold for Au(001); again, there is no mention of attractive interactions over any range of step separations.

In pursuit of a strictly attractive  $\ell^{-2}$  step interaction to explain the results of Shimoni et al. [171], Wang et al. [175] developed a model based on the SSH model [176] of polyacetylene (the original model extended to include electron–electron interaction), focusing on the dimerized atom rows of the  $(2 \times 1)$  reconstruction of Si(001). The model produces an attractive correction term to the formula derived by Alerhand et al. [177] for interactions between steps on Si(001), where there is ABAB alternation of  $(2 \times 1)$  and  $(1 \times 2)$  reconstructions on neighboring terraces joined at single-height steps. For this type of surface, the correction has little significance, being dwarfed by the logarithmic repulsion. It also does not occur for vicinals to high-symmetry facets of metals. However, for surfaces such as Au(110) with its missing row morphology [178] or adsorbed systems with atomic rows, the row can undergo a Peierls [179] distortion that leads to an analogous dimerization and an  $\ell^{-2}$  attraction. There have been no tests of these unsung predictions by electronic structure computation.

Returning to gold, applications of the glue potential (a semiempirical potential rather similar to EAM), Ercolessi et al. [180] were able to account for reconstructions of various gold facets, supporting that the sharp edges on the ECS are due to the model used for Si(111) rather than attractive step interactions. Studies by this group found no real evidence for attractive step interactions [181].

In an authoritative review a decade ago, Bonzel [2]— the expert in the field who has devoted the most sustained interest in ECS experiments on elemental systems— concluded that it was not possible to decide whether the surface reconstruction model or attractive interactions was more likely to prove correct. In my view, mindful of Ockham’s razor, the former seems far more plausible, particularly if the assumed attractive interaction has the  $\ell^{-2}$  form.

The phase diagram of surfaces vicinal to Si(113) presents an intriguing variant of that vicinal to Si(111). There is again a coexistence regime between the (113) orientation and progressively more highly misoriented vicinals as temperature is reduced below a

threshold temperature  $T_b$ , associated with a first-order transition. However, for higher temperatures  $T > T_t$  there is a continuous transition, in contrast to the behavior on (111) surfaces for  $T > T_7$ . Thus, Song and Mochrie [182] identify the point along (113) at which coexistence vanishes, i.e.,  $T_b$ , as a tricritical point, the first such point seen in a misorientation phase diagram. To explain this behavior, Song and Mochrie invoke a mean-field Landau theory argument in which the cubic term in  $p$  is proportional to  $(T - T_t)$ , so negative for  $T < T_b$ , with a positive quartic term. Of course, this produces the observed generic behavior, but the exponent  $\bar{\beta}$  is measured as  $0.42 \pm 0.10$  rather than the mean-field value 1. Furthermore, the shape of the phase diagram differs from the mean-field prediction and the amplitude of the surface stiffness below  $T_t$  is larger than above it, the opposite of what happens in mean field. Thus, it is not clear in detail what the interactions actually are, let alone how an attractive interaction might arise physically.

## 5.9 Well-Established Attractive Step–Step Interactions Other Than $\ell^{-2}$

For neutral crystals, there are two ways to easily obtain interactions that are attractive for some values of  $\ell$ . In neither case are the interactions monotonic long range. The first is short-range local effects due to chemical properties of proximate steps, while the other is the indirect Friedel-like interaction.

### 5.9.1 Atomic-Range Attractions

At very small step separations, the long-range  $\ell^{-2}$  monotonic behavior is expected to break down and depend strongly on the local geometry and chemistry. Interactions between atoms near step edges are typically direct, thus stronger than interactions mediated by substrate elastic fields or indirect electronic effects (see below). We saw earlier that a  $\ell^{-3}$  higher order term arises at intermediate separations [42], and further such terms should also appear with decreasing  $\ell$ . On TaC(910) [vicinal to (001) and miscut toward the [010] direction], Zuo et al. [183] explained step bunching using a weak  $\ell^{-3[\pm 0.5]}$  attraction in addition to the  $\ell^{-2}$  repulsion. (The double-height steps are electrically neutral.) Density-functional theory (DFT) studies were subsequently performed for this system by Shenoy and Ciobanu [184]. Similarly, Yamamoto et al. [185] used an attractive  $\ell^{-3}$  dipole-quadrupole interaction to explain anomalous decay of multilayer holes on SrTiO<sub>3</sub>(001).

More interesting than such generic effects are attractions that occur at very short step separations for special situations. A good example is Ciobanu et al. [186], who find an attraction at the shortest separation due to the cancellation of force monopoles of two adjacent steps on vicinal Si(113) at that value of  $\ell$ .

As alluded to above, most of our understanding of the role of  $\ell^{-2}$  step interactions comes from the mapping of classical step configurations in 2D to the worldlines of spinless fermions in 1D. Unlike fermions, however, steps can touch (thereby forming double-height steps), just not cross. Such behavior is even more likely for vicinal fcc or

bcc (001) surfaces, where the shortest possible “terrace,” some fraction of a lateral nearest-neighbor spacing, amounts to touching fermions when successive layers of the crystal are described with simple-cubic rather than layer-by-layer laterally offset coordinates. Sathiyarayanan et al. [187] investigated some systematics of step touching, adopting a model in which touching steps on a vicinal cost an energy  $\epsilon_t$ . Note that  $\epsilon_t = \infty$  recoups the standard fermion model. For simplicity, the short study concentrates on the “free-fermion” case  $\tilde{A} = 0$ , i.e.,  $\varrho = 2$  (cf. Eqn (5.28)). Even for  $\epsilon_t = 0$ , there is an effective attraction, i.e.,  $\varrho < 2$ , since the possibility of touching broadens the TWD. This broadening is even more pronounced for  $\epsilon_t < 0$ . In other words, such short-range effects can appear, for a particular system, to contribute a long-range attraction. Closer examination shows that this attraction is a finite-size effect that fades away for large values of  $\langle \ell \rangle$ . In our limited study, we found that fits of simulated data to the GWD expression could be well described by the following finite-size scaling form, with the indicated three fitting parameters:

$$\varrho_{\text{eff}} = 2 - (0.9 \pm 0.1) \langle \ell \rangle^{-0.29 \pm 0.07} \exp \left[ - (3.3 \pm 0.2) \epsilon_t / k_B T \right]. \quad (5.43)$$

While Eqn (5.43) suggests that making the step touching more attractive (decreasing  $\epsilon_t$ ) could decrease  $\beta_{\text{eff}}$  without limit, instabilities begin to develop, as expected since Lässig [188] showed that for  $\tilde{A} < -1/4$ , i.e.,  $A < -(k_B T)^2 / 4\tilde{\beta}$ , a vicinal surface becomes unstable (to collapse to step bunches). Correspondingly, the lowest value tabulated in Sathiyarayanan et al. [187] is  $\epsilon_t / k_B T = -0.2$ .

To distinguish true long-range ( $\ell^{-2}$ ) attractions on vicinal surfaces requires measurements of several different vicinalities (i.e., values of  $\langle \ell \rangle$ ). Likewise, in analyses of ECS data, consideration of crystallites of different sizes would seem necessary. Wortis [1] noted the importance of size dependence in other contexts.

Along this theme, an instructive specific case is the “sticky-step” or, more formally, the p-RSOS (restricted solid-on-solid with point-contact attractions between steps) model explored in detail by Akutsu [189] using the product wavefunction renormalization group (PWFRG) method, calculating essentially the ECS (see Figure 5.25) and related properties. Steps are zig-zag rather than straight as in the preceding Sathiyarayanan model, so her “stickiness” parameter  $\epsilon_{int}$  is similar but not identical to  $\epsilon_t$ . She finds that in some temperature regimes, nonuniversal non-Prokrovsky–Talapov values of  $\vartheta$  occur. Specifically, let  $T_{f,111}(\epsilon_{int}/\epsilon, \phi_0)$  and  $T_{f,001}(\epsilon_{int}/\epsilon, \phi_0)$  be the highest temperature at which a first-order phase transition (sharp edge) occurs for the (111) and (001) facets, respectively, where  $\phi_0$  indicates the position along the ECS. Note  $T_{f,111}(\epsilon_t/\epsilon, \phi_0) = (0.3610 \pm 0.0005)\epsilon/k_B > T_{f,111}(\epsilon_{int}/\epsilon, \phi_0) = (0.3585 \pm 0.0007)\epsilon/k_B$ . For  $k_B T/\epsilon = 0.37$ , so  $T > T_{f,111}(-0.5, \pi/4)$ , Akutsu recovers Prokrovsky–Talapov values for  $\vartheta$  and  $\vartheta_t$ , but for  $k_B T/\epsilon = 0.36$  (shown in Figure 5.26), so  $T_{f,111}(-0.5, \pi/4) > T > T_{f,001}(-0.5, \pi/4)$ , the values are very different:  $\vartheta = 1.98 \pm 0.03$  and  $\vartheta_t = 3.96 \pm 0.08$ , more like mean field. For  $\phi_0 = 0$  (tilting toward the  $\langle 100 \rangle$  direction), only standard Prokrovsky–Talapov exponents are found. Upon closer examination with Monte Carlo simulations, Akutsu finds large step bunches for  $T < T_{f,100}$  but step droplets for  $T_{f,001} < T < T_{f,111}$ . The details are beyond the

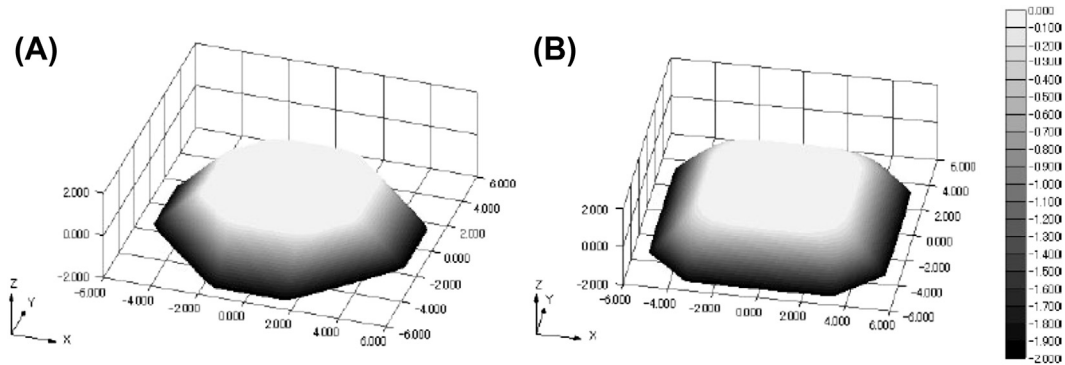


**FIGURE 5.25** Perspective views of essentially the equilibrium crystal shape (actually the Andreev surface free energy divided by  $k_B T$ ) around the (001) facet calculated by the transfer-matrix method with the product-wavefunction renormalization group algorithm at  $k_B T/\epsilon_1 = 0.3$ . (A) Restricted solid-on-solid with point-contact attractions between steps (p-RSOS) model ( $\epsilon_{int}/\epsilon_1 = -0.5$ ). (B) For comparison, the original unsticky RSOS model ( $\epsilon_{int} = 0$ ). From Ref. [189].

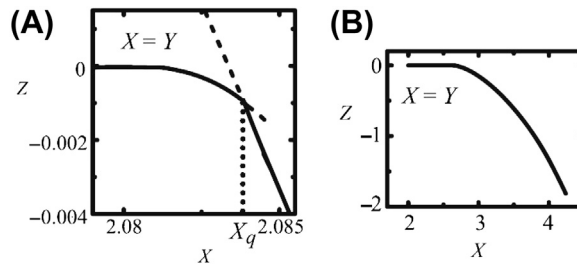


**FIGURE 5.26** Profiles in the diagonal direction of the surface in Figure 5.25, still at  $k_B T/\epsilon_1 = 0.3$ . Broken lines represent metastable lines. (A)  $k_B T/\epsilon_1 = 0.36$ ,  $\epsilon_{int}/\epsilon_1 = -0.5$ , on a very fine length scale. The edge of the (111) facet is denoted by  $X_q$ . (B) The original RSOS model ( $\epsilon_{int} = 0$ ) on a much coarser scale. On this scale (and on an intermediate scale not included here), the profiles are flat until the edge. On the intermediate scale, the region beyond  $X_q$  starts deviating rather smoothly for  $k_B T/\epsilon_1 = 0.35$  but looks straight for  $k_B T/\epsilon_1 = 0.36$  and  $0.37$ . See text and source. From Ref. [189].

scope of this review, but eventually Akutsu deduces an expansion of the projected free energy that includes either a quadratic term or a term after the linear term that has the form  $|p|^\zeta$ , with  $\zeta > 1$ .

### 5.9.2 Attractions at Periodic Ranges of Separation via Oscillatory Friedel-Type Interactions

Oscillatory (in sign) interactions, mediated by substrate conduction electrons, between steps ipso facto lead to attractive interactions between steps. As reviewed by Einstein [94], such interactions have been known for many decades to account for the ordered patterns of adsorbates on metal surfaces [190]. While at short range, all electrons

contribute, asymptotically the interaction is dominated by the electron(s) at the Fermi surface or, from another perspective, the nonanalyticity in the response function at the nesting vector. The interaction energy has the form

$$E_{\text{pair}}^{\text{asympt}} \propto \ell^{-n} \cos(2k_F \ell + \Phi) \quad (5.47)$$

This, or its analogue for interacting local magnetic species, is called the RKKY [191,192] interaction. (The community studying magnetism now labels as RKKY any interaction mediated by substrate electrons, not just the asymptotic limit written down in the RKKY papers.) The phase factor  $\Phi$  is the nonperturbative result is the scattering phase shifts at the two atoms that are interacting; it is absent in the perturbational approach to this problem used in the RKKY papers. The exponent  $n$  indicates the decay envelope. For interacting bulk entities,  $n = 3$ , the standard RKKY results. On metal surfaces, the leading term in the propagator is canceled by the image charge, leading to  $n = 5$ , with very rapid decay [94,190]. Such effects are insignificant for adatom interactions but can be more potent when a whole step participates. Redfield and Zangwill [193] show that a line of localized perturbations will generate an interaction with  $n$  reduced by subtracting  $1/2$  and  $\Phi$  augmented by  $\pi/4$ . They used this result, with  $n = 9/2$ , to account for Frohn et al.'s [194] remarkable experimental results on vicinal Cu(001): from their observed bimodal TWD, Frohn et al. deduced that the step–step interaction is attractive for intermediate distances three to five atoms. Indeed, it was their striking observation that led to several of the previously discussed theory papers that claimed to find long-range step attractions.

When there are metallic surface states (i.e., surface states for which their 2D band dispersion relation crosses the Fermi energy  $E_F$ ) of Shockley nature (lying in a 2D band gap containing  $E_F$ ), the indirect interaction has a much slower decay, with  $n = 2$  [94,195–199]. Furthermore, the Fermi wavevector typically is much smaller than that of bulk states, so the period of the oscillation in real space is much larger. Perhaps the most familiar metallic surface on metals is that at the center of the surface Brillouin zone ( $\bar{\Gamma}$ ) of the (111) surfaces of noble metals, which exist inside the necks of the Fermi surface, discussed in textbooks, e.g. [200]. This is the state that produces the famous wave structure in Eigler's group's dramatic STM images [201] of atoms on metal surfaces. However, there is a less well-known metallic surface state on Cu(001), discovered relatively late (compared to other surface states) by Kevan [202]; it is centered at the zone-edge center  $\bar{X}$  rather than  $\bar{\Gamma}$ , and may provide a better explanation of the Frohn et al. results in the Redfield–Zangwill framework. For surface-state mediated interactions between steps, their formula indicates  $n = 3/2$ , comparable to the entropic and elastic repulsions.

The effect of surface-state mediated interactions on TWDs was elucidated by Pai et al. [203] in combined experimental and theoretical examination of vicinal Ag(110), which has a metallic surface state centered at  $\bar{Y}$ , the middle of the shorter edge of the rectangular surface Brillouin zone [204]. In essence, the surface state introduces a second length scale, the Fermi wavelength  $\lambda_F$ , in addition to  $\langle \ell \rangle$ , with the major consequence that the TWD is no longer a function of the single scaled dimensionless variable  $s$  but depends

also on  $\langle \ell \rangle$ . With a suitable model potential, Pai et al. [203] could then account for the different TWDs at a few different misorientations (i.e., mean step spacings). Indeed, to establish convincingly that this Friedel-like effect is significant, one must measure several different values of  $\langle \ell \rangle$ . While this paper has been cited with regard to other modifications of TWDs (cf. e.g., Refs [205,206]), I have found no other investigations of Friedel-like effects on TWDs for several misorientations of the same substance.

Patrone and Einstein [207] discuss other issues related to possible anisotropic surface state dispersion as well as showing the insensitivity to the point in the surface Brillouin zone about which the state is centered.

## 5.10 Conclusions

An aspect of ECS studies on which there has been substantial progress since the 1980s, but which has received little attention in this chapter, is comparing and reconciling the values of the characteristic energies (surface free energy per area, step free energy per length, and step–step repulsion strength) that are extracted from experimental measurements with ever-improving calculations (using density functional theory) of these energies. Bonzel’s review [2], as well as Nowicki and Bonzel [140], Bonzel et al. [139], Barreateau et al. [226], Yu et al. [227], contain extensive coverage of this issue for the soft metals to which his group has devoted exhaustive attention. Williams [59] review most results for silicon. Such efforts to find absolute energies has also taken place in studies of island shapes, e.g., of TiN(001) [208] and (111) [209].

There are several significant advances in generic understanding of ECS since the 1980s. The Prokrovsky–Talapov ( $\nu = 3/2$ ) critical phenomena near the edge of the smoothly curved region near a facet has proved to be far more robust and general than originally realized, while novel behavior is predicted in a very special direction. Even though invoked in many accounts of sharp edges, long-range attractive  $\ell^{-2}$  do not have an apparent physical basis, except perhaps in idiosyncratic cases. The likely cause is a reconstruction or adsorption that changes the surface free energy of the facet orientation. On the other hand, hill-and-valley structures are widely seen, and the possibility of azimuthal in addition to polar misorientation can lead to astonishingly rich phase diagrams. Of course, nonequilibrium considerations open up a whole new universe of behavior. Furthermore, at the nanoscale, cluster shape is very sensitive to the particulars of a system, with the addition or removal of a single atom leading to a substantial change in shape, rather like biological systems, in contrast to the macroscale phenomena that have been treated in this chapter.

## Acknowledgments

My research related to this subject was long supported by the UMD-NSF MRSEC; it is now supported partially by NSF-CHE 13-05892. Much of this paper is based on extensive collaboration with the experimental surface physics group at the University of Maryland, led by Ellen D. Williams until 2010,

with ongoing guidance by Janice Reutt-Robey and William G. Cullen, as well as with Margret Giesen and Harald Ibach, and Hans P. Bonzel, at FZ-Jülich, partially sponsored by a Humboldt Senior U.S. Scientist Award, and, over the last decade, with Alberto Pimpinelli. I also benefited from fruitful interactions at Maryland with John D. Weeks, theory postdocs Olivier Pierre-Louis, Howard L. Richards, Ferenc Szalma, and Kwangmoo Kim, and graduate students Norman C. Bartelt, Raymond C. Nelson, Sanjay V. Khare, Hailu Gebremarian, Timothy J. Stasevich, Rajesh Sathiyarayanan, Paul N. Patrone, and Josue R. Morales-Cifuentes.

## References

- [1] Wortis M. Equilibrium crystal shapes and interfacial phase transitions. In: Vanselow R, Howe R, editors. *Chemistry and physics of solid surfaces*, VII. Berlin: Springer-Verlag; 1988. p. 367–405.
- [2] Bonzel HP. *Phys Rep* 2003;385:1.
- [3] Williams ED, Bartelt NC. *Ultramicroscopy* 1989;31:36.
- [4] Rottman C, Wortis M. *Phys Rep* 1984;103:5979.
- [5] Pimpinelli A, Villain J. *Physics of crystal growth*. Cambridge (England): Cambridge University Press; 1998.
- [6] Landau LD, Lifshitz EM. *Statistical physics, part 1*. revised and enlarged by Lifshitz EM and Pitaevskii LP. 3rd ed. Oxford: Pergamon Press; 1980. pp. 155.
- [7] Nozières P. Shape and growth of crystals. In: Godrèche C, editor. *Solids far from equilibrium*. Cambridge: Cambridge University Press; 1992.
- [8] Sekerka RF. Theory of crystal growth morphology. In: Müller G, Métois J-J, Rudolph P, editors. *Crystal growth – from fundamentals to technology*. Amsterdam: Elsevier; 2004. p. 55.
- [9] van Beijeren H, Nolden I. “The roughening transition”, structure and dynamics of surfaces II: phenomena, models, and methods. In: Schommers W, von Blanckenhagen P, editors. *Topics in current physics*, vol. 43. Berlin: Springer; 1987. p. 299.
- [10] J. W. Gibbs, “On the equilibrium of heterogeneous substances”, *Transactions of the Connecticut academy of arts and sciences*, 3, 108 248, 343 524, (1874–1878). Reproduced in both the *Scientific Papers*. 1906; 55–353 and *The Collected Works of Gibbs JW*. 1928; 55–353. *The Collected Works of Gibbs JW*, in two volumes, Longley WR, Van Name RG, editors. New Haven: Yale University Press; 1957 (1928).
- [11] Herring C. *Phys Rev* 1951;82:87–93.
- [12] Herring C. The use of classical macroscopic concepts in surface energy problems. In: Gomer R, Smith CS, editors. *Conference arranged by National Research Council, Lake Geneva, 1952*. Chicago: University of Chicago Press; 1953b. p. 5–81 [Chapter 1].
- [13] Curie P. *Bull Soc Min Fr* 1885;8:145.
- [14] Wulff G. *Z für Kryst Mineral* 1901;34:449.
- [15] Hilton H. *Mathematical crystallography*. Oxford; 1903.
- [16] Liebmann H. *Z Krist* 1914;53:171.
- [17] von Laue M. Der Wulffsche Satz für die Gleichgewichtsform von Kristallen. *Z Krist* 1943;105:124.
- [18] Dinghas A. *Z Krist* 1944;105:303–14.
- [19] Burton WK, Cabrera N, Frank FC. *Phil Trans R Soc A* 1951;243:299.
- [20] Frank FC. Metal surfaces. *Metals Park (OH): American Society for Metals; 1962/3* [Chapter 1]p. 1–15.

- [21] Mullins WW. In: Metal surfaces. Metals Park (OH): American Society for Metals; 1962/3. p. 17–62 [Chapter 2].
- [22] Jackson KA. In: Ueda R, Mullin JB, editors. Crystal growth and characterization. Amsterdam: North-Holland; 1975. p. 21.
- [23] Chernov AA. Sov Phys Uspekhi 1961;4:116.
- [24] Cerf R, Picard J. The Wulff crystal in ising and percolation models. Berlin: Springer; 2006.
- [25] Dobrushin RL, Kotecký R, Shlosman S. The Wulff construction: a global shape from local interactions. Providence (RI): AMS; 1992. preprint: <http://www.cpt.univ-mrs.fr/dobrushin/DKS-book.pdf>.
- [26] Almgren F, Taylor JE. Fractals 1996;3:713.
- [27] Peng D, Osher S, Merriman B, Zhao H-K. The geometry of Wulff crystal shapes and its relation with Riemann problems. In: Nonlinear partial differential equations. Contemp. Math, vol. 238. Providence (RI): AMS; 1999. p. 251–303.
- [28] Dobrushin RL, Kotecký R, Shlosman SB. J Stat Phys 1993;12:1.
- [29] Dacorogna B, Pfister CE. J Math Pures Appl 1992;71:97–118.
- [30] Fonseca I. Proc R Soc Lond A 1991;432:125.
- [31] De Coninck J, Dunlop F, Rivasseau V. Commun Math Phys 1989;121:401.
- [32] Miracle-Sole S. In: Miracle-Sole S, Ruiz J, Zagrebnov V, editors. Mathematical results in statistical mechanics. Singapore: World Scientific; 1999. p. 83 [arXiv:1206.3736v1].
- [33] Miracle-Sole S. Wulff shape of equilibrium crystals. 2013 [arXiv:1307.5180v1].
- [34] Pfister CE. Helv Phys Acta 1991;64:953.
- [35] Miracle-Sole S, Ruiz J. On the Wulff construction as a problem of equivalence of statistical ensembles. In: Fannes M, Verbeure A, editors. On three levels: micro, meso and macroscopic approaches in physics. New York: Plenum Press; 1994. p. 295–302 [arXiv:1206.3739v1].
- [36] Fonseca I, Müller S. Proc R Soc Edinb 1991;119:125.
- [37] Jayaprakash C, Rottman C, Saam WF. Phys Rev B 1984;30:6549. in the Hamiltonian in their Eqn 3, the factor  $t/2$  should have been  $t$ . See erratum in Ref. [152].
- [38] Nelson RC, Einstein TL, Khare SV, Rous PJ. Surf Sci 1993;295:462–84.
- [39] Ibach H, Schmickler W. Phys Rev Lett 2003;91:016106.
- [40] Stewart J, Pohland O, Gibson JM. Phys Rev B 1994;49:13848.
- [41] Marchenko VI, Parshin A Ya. Sov. Phys. JETP 1980;52:129 [Zh Eksp Teor Fiz 1980;79:257].
- [42] Najafabadi R, Srolovitz DJ. Surf Sci 1994;317:221–34.
- [43] Duxbury PM, Pence TJ, editors. Dynamics of crystal surfaces and interfaces. New York: Plenum; 1997.
- [44] Carlon E, van Beijeren H. Phys Rev E 2000;62:7646.
- [45] van Albada SB, Rost MJ, Frenken JWM. Phys Rev B 2002;65:205421.
- [46] Bonzel HP, Preuss E. Surf Sci 1995;336:209.
- [47] Lieb EH, Wu FY. In: Domb C, Green MS, editors. Phase transitions and critical phenomena, vol. 1. London: Academic Press; 1972. p. 331.
- [48] Lieb EH. Phys Rev Lett 1967;19:108.
- [49] van Beijeren H. Phys Rev Lett 1977;38:993.
- [50] Nolden IM, van Beijeren H. Phys Rev B 1994;49:17224.
- [51] Kosterlitz JM, Thouless DJ. J Phys C 1973;6:1181.
- [52] Kosterlitz JM. J Phys C 1974;7:1046.

- [53] Yang CP. *Phys Rev Lett* 1967;19:586.
- [54] Sutherland B, Yang CN, Yang CP. *Phys Rev Lett* 1967;19:588.
- [55] Callen HB. *Thermodynamics and an introduction to the mostatistics*. 2nd ed. New York: Wiley; 1985.
- [56] Kossel W. *Nachr Ges Wiss Göttingen* 1927;143.
- [57] Kossel W. *Ann Phys* 1934;21:457–80.
- [58] García N, Sáenz JJ, Cabrera N. *Physica* 1984;124B:251.
- [59] Jeong H-C, Williams ED. *Surf Sci Rep* 1999;34:171.
- [60] Cahn JW, Carter WC. *Metall Mater Trans A Phys Metall Mater Sci* 1996;27:1431–40 [arXiv:cond-mat/0703564v1].
- [61] Hoffman DW, Cahn JW. *Surf Sci* 1972;31:368. Cahn JW, Hoffman DW. *Acta Met* 1974;22:1205.
- [62] Wheeler AA. *J Stat Phys* 1999;95:1245–80.
- [63] Balibar S, Castaing B. *J Phys Lett* 1980;41:L329.
- [64] Keshishev KO, Parshin AY, Babkin AV. *Sov Phys JETP* 1981;53:362.
- [65] Wolf PE, Balibar S, Gallet F. *Phys Rev Lett* 1983;51:1366.
- [66] Wolf PE, Gallet F, Balibar S, Rolley E, Nozières P. *J Phys Fr* 1985;46:1987.
- [67] Balibar S, Alles H, Parshin A Ya. *Rev Mod Phys* 2005;77:317.
- [68] Phaneuf RJ, Williams ED. *Phys Rev Lett* 1987;58:2563.
- [69] Bartelt NC, Williams ED, Phaneuf RJ, Yang Y, Das Sarma S. *J Vac Sci Technol A* 1989;7:1898.
- [70] Phaneuf RJ, Bartelt NC, Williams ED, Swiech W, Bauer E. *Phys Rev Lett* 1993;71:2284.
- [71] Rousset S, Berroir JM, Repain V, Garreau Y, Etgens VH, Lecoeur J, et al. *Surf Sci* 1999;443:265.
- [72] Bonczek F, Engel T, Bauer E. *Surf Sci* 1980;97:595.
- [73] Madey TE, Guan J, Nien C-H, Tao H-S, Dong C-Z, Campbell RA. *Surf Rev Lett* 1996;3:1315.
- [74] Madey TE, Nien C-H, Pelhos K, Kolodziej JJ, Abdelrehim IM, Tao H-S. *Surf Sci* 1999;438:191.
- [75] Fisher DS, Weeks JD. *Phys Rev Lett* 1983;50:1077.
- [76] Lyuksyutov I, Naumovets AG, Prokrovsky V. *Two-dimensional crystals*. San Diego: Academic Press; 1992.
- [77] Dieluweit S, Ibach H, Giesen M, Einstein TL. *Phys Rev B* 2003;67:121410(R).
- [78] Stasevich TJ, Einstein TL, Zia RKP, Giesen M, Ibach H, Szalma F. *Phys Rev B* 2004;70:245404.
- [79] Stasevich TJ, Einstein TL, Stolbov S. *Phys Rev B* 2006;73:115426.
- [80] Stasevich TJ, Gebremariam H, Einstein TL, Giesen M, Steimer C, Ibach H. *Phys Rev B* 2005;71:245414.
- [81] Zia RKP. *J Stat Phys* 1986;45:801.
- [82] Avron JE, van Beijeren H, Schulman LS, Zia RKP. *J Phys A Math Gen* 1982;15:L81–6.
- [83] Gallavotti G. *Commun Math Phys* 1972;27:103.
- [84] Abraham DB, Reed P. *Phys Rev Lett* 1974;33:377.
- [85] Abraham DB, Reed P. *Commun Math Phys* 1976;49:35.
- [86] Kodambaka S, Khare SV, Petrov I, Greene JE. *Surf Sci Rep* 2006;60:55–77.
- [87] Michely T, Krug J. Berlin: Springer; 2004 [Chapter 3].
- [88] Stasevich TJ, Einstein TL. *[SIAM-]Multiscale Model Simul* 2007;6:90.

- [89] Weeks JD. Private discussions, 2014.
- [90] Liu F. Modeling and simulation of strain-mediated nanostructure formation on surface. In: Rieth M, Schommers W, editors. Handbook of theoretical and computational nanotechnology, vol. 4. American Scientific Publishers; 2006. p. 577–625.
- [91] Müller B, Nedelmann L, Fischer B, Brune H, Barth JV, Kern K. Phys Rev Lett 1998;80:2642.
- [92] Einstein TL. Appl Phys A 2007;87:375384 [cond-mat/0612311].
- [93] Einstein TL, Richards HL, Cohen SD, Pierre-Louis O. Surface Sci 2001;493:460.
- [94] Einstein TL. Interactions between adsorbate particles. In: Unertl WN, editor. Physical structure of solid surfaces. Handbook of surface science, vol. 1. Amsterdam: Elsevier; 1996. Holloway S, Richardson NV, series editors, 577–650.
- [95] Giesen M. Prog. Surface Sci. 2001;68:1.
- [96] Gruber E, Mullins WW. J Phys Chem Solids 1967;28:875.
- [97] Fisher MPA, Fisher DS, Weeks JD. Phys Rev Lett 1982;48:368.
- [98] Leamy HJ, Gilmer GH, Jackson KA. Statistical thermodynamics of clean surfaces. In: Blakely JM, editor. Surface physics of materials, vol. 1. New York: Academic Press; 1975. p. 121 [Chapter 3].
- [99] Stasevich TJ. 2006 [Ph.D. dissertation]. University of Maryland [unpublished].
- [100] de Gennes PG. J Chem Phys 1968;48:2257.
- [101] Prokrovsky VL, Talapov AL. Phys Rev Lett 1979;42:65. Sov Phys-JETP 1980;51:134.
- [102] Haldane FDM, Villain J. J Phys Paris 1981;42:1673.
- [103] Schulz HJ, Halperin BI, Henley CL. Phys Rev B 1982;26:3797.
- [104] Prokrovsky VL, Talapov AL. Theory of incommensurate crystals, soviet scientific reviews supplement series physics, vol. 1. Chur: Harwood Academic Publishers; 1984 [and references therein].
- [105] Villain J. In: Riste T, editor. Ordering in strongly fluctuating condensed matter systems. New York: Plenum; 1980. p. 221.
- [106] Akutsu Y, Akutsu N, Yamamoto T. Phys Rev Lett 1988;61:424.
- [107] Jeong H-C, Weeks JD. Surf Sci 1999;432:101 [and references therein].
- [108] Wang X-S, Goldberg JL, Bartelt NC, Einstein TL, Williams ED. Phys Rev Lett 1990;65:2430.
- [109] Ihle T, Misbah C, Pierre-Louis O. Phys Rev B 1998;58:2289.
- [110] Joós B, Einstein TL, Bartelt NC. Phys. Rev. B 1991;43:8153.
- [111] Mehta ML. Random matrices. 3rd ed. New York: Academic; 2004.
- [112] Dyson FJ. Statistical Theory of the Energy Levels of Complex Systems. III. J. Math. Phys. 1962;3:166.
- [113] Bartelt NC, Einstein TL, Williams ED. Surf Sci 1990;240:L591.
- [114] Calogero F. J Math Phys 1969;10:2191. 2197.
- [115] Sutherland B. J Math Phys 1971;12:246. Phys Rev A 1971;4:2019.
- [116] Dyson FJ. Commun. Math. Phys. 1970;19:235.
- [117] Haake F. Quantum signatures of chaos. 2nd ed. Berlin: Springer; 1991.
- [118] Guhr T, Müller-Groeling A, Weidenmüller HA. Phys. Rept 1998;299:189.
- [119] Gebremariam H, Cohen SD, Richards HL, Einstein TL. Phys Rev B 2004;69:125404.
- [120] Jayaprakash C, Saam WF. Phys Rev B 1984;30:3916.
- [121] Andreev AF. Sov. Phys.-JETP 1982;53:1063 [Zh. Eksp. Teor. Phys 1981;80:2042].
- [122] Jayaprakash C, Saam WF, Teitel S. Phys Rev Lett 1983;50:2017.

- [123] Cabrera N, García N. *Phys Rev B* 1982;25:6057.
- [124] Cabrera N. The equilibrium of crystal surfaces. *Surf Sci* 1964;2:320.
- [125] Kardar M, Nelson DR. *Phys Rev Lett* 1985;55:1157.
- [126] Dahmen SR, Wehefritz B, Albertini G. A novel exponent in the equilibrium shape of crystals. 1998. arXiv:cond-mat/9802152.
- [127] Akutsu Y, Akutsu N, Yamamoto T. Universality of the tangential shape exponent at the facet edge of a crystal. 1998. arXiv:cond-mat/9803189.
- [128] Akutsu Y, Akutsu N. *Prog Theor Phys* 2006;116:983.
- [129] Nishino T, Okunishi K. *J Phys Soc Jpn* 1995;64:4084.
- [130] Okunishi K, Hieida Y, Akutsu Y. *Phys Rev B* 1999;59:6806. 1999;60:R6953.
- [131] Sato R, Akutsu Y. *J Phys Soc Jpn* 1995;64:3593.
- [132] Carmi Y, Lipson SG, Polturak E. *Phys Rev B* 1987;36:1894.
- [133] Rottman C, Wortis M, Heyraud JC, Métois JJ. *Phys Rev Lett* 1984;52:1009.
- [134] Saénz JJ, García N. *Surf Sci* 1985;155:24.
- [135] Surnev S, Arenhold K, Coenen P, Voigtländer B, Bonzel HP. *J Vac Sci Technol A* 1998;16:1059.
- [136] Nowicki M, Bombis C, Emundts A, Bonzel HP, Wynblatt P. *New J Phys* 2002;4:60.
- [137] Nowicki M, Bombis C, Emundts A, Bonzel HP, Wynblatt P. *Eur Phys Lett* 2002;59:239.
- [138] Nowicki M, Bombis C, Emundts A, Bonzel HP. *Phys Rev B* 2003;67:075405.
- [139] Bonzel HP, Nowicki M. *Phys Rev B* 2004;70:245430.
- [140] Bonzel HP, Yu DK, Scheffler M. *Appl Phys A* 2007;87:391.
- [141] Thürmer K, Reutt-Robey JE, Williams ED. *Surf Sci* 2003;537:123.
- [142] Métois JJ, Heyraud JC. *Surf Sci* 1987;180:647.
- [143] Bermond JM, Métois JJ, Heyraud JC, Floret F. *Surf Sci* 1998;416:430.
- [144] Gladić J, Vučić Z, Lovrić D. *J Cryst Growth* 2002;242:517–32.
- [145] Ferrari PL, Prähofer M, Spohn H. *Phys Rev E* 2004;69:035102.
- [146] Pimpinelli A, Degawa M, Einstein TL, Williams ED. *Surf Sci* 2005;598:L355.
- [147] Degawa M, Stasevich TJ, Cullen WG, Pimpinelli A, Einstein TL, Williams ED. *Phys Rev Lett* 2006;97:080601.
- [148] Degawa M, Stasevich TJ, Pimpinelli A, Einstein TL, Williams ED. *Surface Sci.* 2007;601:3979 [Proc. ECOSS 2006].
- [149] Einstein TL, Alberto Pimpinelli. *J Statistical Phys* 2014;155:1178. longer version posted at arXiv <http://arxiv:1312.4910v1>.
- [150] Farnsworth HE, Schlier RE. *J Chem Phys* 1959;31:89.
- [151] Hwang RQ, Williams ED, Park RL. *Phys Rev B* 1989;40:11716.
- [152] Williams ED, Phaneuf RJ, Wei Jian, Bartelt NC, Einstein TL. *Surface Sci* 1993;294:219. Erratum 1994;310:451.
- [153] Noh DY, Blum KI, Ramstad MJ, Birgeneau RJ. *Phys Rev B* 1991;44:10969.
- [154] Noh DY, Blum KI, Ramstad MJ. *Phys Rev B* 1993;48:1612.
- [155] Held GA, Goodstein DM, Brock JD. *Phys Rev B* 1995;51:7269.
- [156] Noh DY, Liang KS, Hwu Y, Chandavarkar S. *Surf Sci* 1995;326:L455.
- [157] Dietrich S, Haase A. *Phys Rep* 1995;260:1.

- [158] Ocko B. Private discussion, 2014.
- [159] Cahn JW. *J de Physique* 1982;43(C6):199–213. Proceedings of Conference on the Structure of Grain Boundaries, Caen, France.
- [160] Somorjai GA, Van Hove MA. *Prog Surf Sci* 1989;30:201.
- [161] Cheng W-C, Wynblatt P. *Surf Sci* 1994;302:185.
- [162] Meltzman H, Chatain D, Avizemer D, Besmann TM, Kaplan WD. *Acta Mater* 2011;59:3473.
- [163] Yoon M, Mochrie SGJ, Zehner DM, Watson GM, Gibbs D. *Phys Rev B* 1994;49:16702.
- [164] Walko DA, Robinson IK. *Phys Rev B* 2001;64:045412.
- [165] Szczepkowicz A, Ciszewski A, Bryl R, Oleksy C, Nien C-H, Wu Q, et al. *Surf Sci* 2005;599:55.
- [166] Kalf M, Comsa G, Michely T. *Phys Rev Lett* 1998;81:1255.
- [167] Stasevich TJ, Tao C, Cullen WG, Williams ED, Einstein TL. *Phys Rev Lett* 2009;102:085501.
- [168] Wang Z, Wynblatt P. *Surf Sci* 1998;398:259.
- [169] Handwerker CA, Vaudin MD, Blendell JE. *J Phys Colloq* 1988;49:C5-367.
- [170] Emundts A, Bonzel HP, Wynblatt P, Thrmmer K, Reutt-Robey J, Williams ED. *Surf Sci* 2001;481:13.
- [171] Shimoni N, Ayal S, Millo O. *Phys Rev B* 2000;62:13147.
- [172] Kukta RV, Peralta A, Kouris D. *Phys Rev Lett* 2002;88:186102.
- [173] Prévot G, Croset B. *Phys Rev Lett* 2004;92:256104.
- [174] Hecquet P. *Surf Sci* 2008;602:819.
- [175] Wang G, Webb JF, Zi J. *Surf Sci* 2007;601:1944.
- [176] Su WP, Schrieffer JR, Heeger AJ. *Phys Rev Lett* 1979;42:1698. *Phys Rev B* 1980;22:2099.
- [177] Alerhand OL, Vanderbilt D, Meade RD, Joannopoulos JD. *Phys Rev Lett* 1988;61:1973.
- [178] Copel M, Gustafsson T. *Phys Rev Lett* 1986;57:723.
- [179] Peierls RF. *Quantum theory of solids*. Oxford: Clarendon; 1955. p. 108 [Also Fröhlich H. *Proc R Soc A* 1954;223:296].
- [180] Ercolessi F, Bartolini A, Garofalo M, Parrinello M, Tosatti E. *Surf Sci* 1987;189/190:636.
- [181] Tosatti E. Private communication, March 2014.
- [182] Song S, Yoon M, Mochrie SGJ. *Surf Sci* 1995;334:153.
- [183] Zuo J-K, Zhang T, Wendelken JF, Zehner DM. *Phys Rev B* 2001;63:033404.
- [184] Shenoy VB, Ciobanu CV. *Phys Rev B* 2003;67(081402).
- [185] Yamamoto M, Sudoh K, Iwasaki H, Williams ED. *Phys Rev B* 2010;82:115436.
- [186] Ciobanu CV, Tambe DT, Shenoy VB, Wang CZ, Ho KM. *Phys Rev B* 2003;68:201302R.
- [187] Sathyanarayanan R, Hamouda ABH, Einstein TL. *Phys Rev B* 2009;80:153415.
- [188] Lässig M. *Phys Rev Lett* 1996;77:526.
- [189] Akutsu N. *J Phys Condens Matter* 2011;23:485004.
- [190] Einstein TL, Schrieffer JR. *Phys Rev B* 1973;7:3629.
- [191] Ruderman MA, Kittel C. *Phys Rev* 1954;96:99.
- [192] Yosida K. *Phys Rev* 1957;106:893.
- [193] Redfield AC, Zangwill A. *Phys Rev B* 1992;46:4289.
- [194] Frohn J, Giesen M, Poensgen M, Wolf JF, Ibach H. *Phys Rev Lett* 1991;67:3543.

- [195] Lau KH, Kohn W. *Surf Sci* 1978;75:69.
- [196] Repp J, Moresco F, Meyer G, Rieder K-H, Hyldgaard P, Persson M. *Phys Rev Lett* 2000;85:2981.
- [197] Hyldgaard P, Persson M. *J Phys Condens Matter* 2000;12:L13.
- [198] Knorr N, Brune H, Epple M, Hirstein A, Schneider MA, Kern K. *Phys Rev B* 2002;65:115420.
- [199] Hyldgaard P, Einstein TL. *J Cryst Growth* 2005;275:e1637 [cond-mat/0408645].
- [200] Ashcroft NW, Mermin ND. *Solid state physics*. Cengage Learning; 1976.
- [201] Crommie MF, Lutz CP, Eigler DM. *Nature* 1993;363:524. *Science* 1993;262:218.
- [202] Kevan SD. *Phys Rev B* 1983;28:2268(R).
- [203] Pai WW, Ozcomert JS, Bartelt NC, Einstein TL, Reutt-Robey JE. *Surf Sci* 1994;309:747.
- [204] Liu SH, Hinnen C, van Huong CN, de Tacconi NR, Ho K-M. *J Electroanal Chem* 1984;176:325.
- [205] Mugarza A, Schiller F, Kuntze J, Cordón J, Ruiz-Osés M, Ortega JE. *J Phys Condens Matter* 2006;18:S27.
- [206] Li F, Allegretti F, Surnev S, Netzer FP. *Surf Sci* 2010;604:L43.
- [207] Patrone PN, Einstein TL. *Phys Rev B* 2012;85:045429.
- [208] Kodambaka S, Khare SV, Petrova V, Vailionis A, Petrov I, Greene JE. *Surf Sci* 2002;513:468474.
- [209] Kodambaka S, Khare SV, Petrova V, Johnson DD, Petrov I, Greene JE. *Phys Rev B* 2003;67:035409.
- [210] Stranski I. Z. *Phys Chem Leipz* 1928;136:259.
- [211] Flytzani-Stephanopoulos M, Schmidt LD. *Prog Surf Sci* 1979;9:83.
- [212] Rottman C, Wortis M. *Phys Rep* 1984;103:5979.
- [214] Gibbs JW. *Trans Conn Acad* 1877;3:108–248. see *Collected Works* 1928, p. 343–524.
- [215] Zia RKP. Anisotropic surface tension and equilibrium crystal shapes. In: Hu CK, editor. *Progress in Statistical Mechanics*. Singapore: World Scientific; 1988. p. 303–57.
- [216] Weeks JD. In: Riste T, editor. *Ordering in strongly fluctuating condensed matter systems*. New York: Plenum; 1980. p. 293.
- [217] Rottman C, Wortis M. *Phys Rev B* 1984;29:328.
- [218] von Laue M. *Z. Krist Min* 1944;105:124.
- [219] Andreev AF. *Sov Phys-JETP* 1982;53:1063.
- [220] For a review of fermionic methods, see den Nijs M. In: Domb C, Lebowitz JL, editors. *Phase transitions and critical phenomena*, vol. 12. London: Academic; 1989.
- [221] Williams ED, Bartelt NC. Thermodynamics and statistical mechanics of surfaces. In: Unertl WN, editor. *Physical structure of solid surfaces*. Holloway S, Richardson NV, editors. *Handbook of surface science*, vol. 1. Amsterdam: Elsevier; 1996. p. 51–99.
- [222] Einstein TL, Pimpinelli A. Dynamical scaling implications of Ferrari, Prähofer, and Spohn's remarkable spatial scaling results for facet-edge fluctuations, arXiv 1312.4910.
- [223] Song S, Mochrie SGJ. *Phys Rev Lett* 1994;73:995.
- [224] Song S, Mochrie SGJ. *Phys Rev B* 1995;51:10068.
- [225] Shimoni N, Ayal S, Millo O. *Phys Rev B* 2000;62:13147.
- [226] Barreteau C, Raouafi F, Desjonquères MC, Spanjaard D. *J Phys Condens Matter* 2003;15:3171.
- [227] Yu DK, Bonzel HP, Scheffler M. The stability of vicinal surfaces and the equilibrium crystal shape of Pb by first principles theory. *New J Phys* 2006;8:65.
- [228] Daw MS, Foiles SM, Baskes MI. *Mater Sci Rep* 1993;9:251.

# Rough–Smooth Transition of Step and Surface

Noriko Akutsu<sup>1</sup>, Takao Yamamoto<sup>2</sup>

<sup>1</sup>FACULTY OF ENGINEERING, OSAKA ELECTRO-COMMUNICATION UNIVERSITY, NEYAGAWA, OSAKA, JAPAN; <sup>2</sup>DIVISION OF PURE AND APPLIED SCIENCE, FACULTY OF SCIENCE AND TECHNOLOGY, GUNMA UNIVERSITY, KIRYU, GUNMA, JAPAN

## CHAPTER OUTLINE

<b>6.1 Introduction: Universal Features</b> .....	<b>266</b>
<b>6.2 Background</b> .....	<b>270</b>
6.2.1 Rough Surface in Crystal Growth—Viewpoint of BCF .....	270
6.2.2 Entropy Effect—Jackson’s Argument .....	271
6.2.3 “Drumhead Wandering” due to Capillary Waves .....	272
<b>6.3 Rough Surface</b> .....	<b>275</b>
6.3.1 Definition of an Interface .....	275
6.3.1.1 Existence of a Roughening Transition Temperature .....	275
6.3.1.2 Ising Model and the Equivalent Lattice Gas Model .....	276
6.3.1.3 Definition of Interface Tension .....	277
6.3.2 Definition of Surface Roughness .....	279
6.3.2.1 Surface Width—Variance of Surface Height .....	279
6.3.2.2 Height–Height Correlation Function of a Surface .....	280
6.3.2.3 Thin Film-Like Surface in the Macroscopic Scale .....	281
6.3.3 Relationship between Energy and Shape .....	281
6.3.4 Roughness of a Single Step .....	282
<b>6.4 Roughening Transition and Faceting Transition as Critical Phenomena</b> .....	<b>284</b>
6.4.1 Microscopic Models for Studying Surface Roughness .....	284
6.4.1.1 BCSOS Model .....	285
6.4.1.2 ASOS Model and RSOS Model .....	286
6.4.2 Summary of KT-Type Critical Phenomena of Surfaces .....	286
6.4.3 Diffuseness for Atomically Rough Surfaces .....	290
6.4.3.1 New Picture of Roughening .....	290
6.4.3.2 Intrinsic Width of a Step .....	291
6.4.3.3 Preroughening Phenomena .....	291

6.4.4	Changes in the Roughening Temperature on Complex Surfaces .....	292
6.4.4.1	<i>Inverse Roughening</i> .....	292
6.4.4.2	<i>Surface Modified by Langmuir Adsorption</i> .....	292
<b>6.5</b>	<b>Vicinal Surface</b> .....	<b>294</b>
6.5.1	Rough or Smooth? The Terrace-Step-Kink Picture .....	294
6.5.2	1D Free-Fermion Universal Features—Gruber-Mullins-Pokrovsky-Talapov Behavior .....	295
6.5.3	Logarithmic Behavior on the Width of a Single Step .....	296
6.5.3.1	<i>Height–Height Correlation Function of a Single Step</i> .....	296
6.5.3.2	<i>Elastic Step–Step Repulsion</i> .....	297
<b>6.6</b>	<b>Step Faceting</b> .....	<b>298</b>
6.6.1	Stability of a Macrostep .....	298
6.6.2	Discontinuous Surface Tension .....	300
6.6.2.1	<i>p-RSOS Model</i> .....	300
6.6.2.2	<i>Discontinuity in Surface Tension</i> .....	300
<b>6.7</b>	<b>Summary</b> .....	<b>302</b>
	<b>Appendix A. Transfer Matrix Method</b> .....	<b>303</b>
	<b>Appendix B. Driving Force for Crystal Growth</b> .....	<b>304</b>
	<b>Appendix C. Example of the Anisotropy of the Entropy of a Step</b> .....	<b>304</b>
	<b>Appendix D. IPW Method</b> .....	<b>304</b>
	<b>Appendix E. Calculation of Surface Width</b> .....	<b>306</b>
	<b>Appendix F. Derivation of the Capillary Wave Hamiltonian</b> .....	<b>307</b>
	<b>Appendix G. Other Microscopic Models</b> .....	<b>308</b>
	Appendix G.1. Discrete Gaussian Model .....	308
	Appendix G.2. RSOS-I Model .....	308
	<b>Acknowledgment</b> .....	<b>309</b>
	<b>References</b> .....	<b>309</b>

## 6.1 Introduction: Universal Features

During the years 1970–2000, much progress was made in understanding roughening and faceting transitions [1–39]. Roughening transitions are particularly notable because they are a typical example of the Kosterlitz–Thouless (KT) transition [40–43]. The KT transition was first presented as a magnetic phase transition of the two-dimensional (2D) XY model [40]. Later, 2D crystals [40,41], a 2D Coulomb gas [42], and a superfluid film [43] of helium ( $^4\text{He}$ ) were also shown to exhibit KT transitions.

Van Beijeren provided the correct understanding of the roughening transition by his exact calculation of the body-centered cubic solid-on-solid (BCSOS) model [1]. The

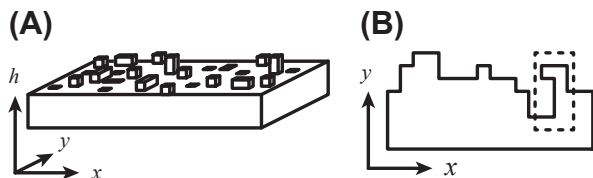


**FIGURE 6.1** Microscopic diagram of a crystal surface. (A) Perspective view of a solid-on-solid model; (B) top view of a step. The pattern inside the broken rectangle shows the overhanging structure.

solid-on-solid (SOS) model, [Figure 6.1\(A\)](#), is a model for studying surface roughness when it is inhibited by an overhanging structure (the overhang structure is shown in the dotted square of [Figure 6.1\(B\)](#)).<sup>1</sup> Van Beijeren showed by exact calculations that the step internal energy  $e_{\text{step}}$  reduces to zero at the roughening transition temperature  $T_R$  as  $e_{\text{step}} \propto \exp(-C/\sqrt{T_R - T})$ . This also means that the step tension decreases to zero at  $T_R$  as  $\gamma_{\text{step}} \propto \exp(-C'/\sqrt{T_R - T})$ . It had not been known previously if the step tension became zero at  $T_R$ . His exact calculation showed us, for the first time, the close connection between surface roughening and the KT transition. Soon after, Knops [\[10\]](#) and Jose et al. [\[11\]](#) showed that any 2D SOS models in 3D can be mapped to the XY model. In [Figure 6.2](#), we show this observed singular property of the step tension on Si(001) [\[32\]](#).

Without the long-range order in 2D, the KT phase transition has special characteristics. When the number of dimensions is less than or equal to two, thermal fluctuations destroy the long-range order [\[47\]](#). In the XY model, the KT transition occurs at the temperature  $T_{\text{KT}}$ , where the entropy of forming a special spin configuration called a “vortex” exceeds the excitation energy of the vortex [\[43\]](#). For  $T < T_{\text{KT}}$ , the 2D XY model forms a quasi-long-range order for the pairs of +1 and -1 vortices; for  $T > T_{\text{KT}}$ , the proliferation of the vortex monomers destroys the quasi-long-range order. The correlation length  $\xi_{\text{KT}}$ , which characterizes the size of the coherent domain, is infinite for  $T < T_{\text{KT}}$ , and  $\xi_{\text{KT}} \propto \exp(A/\sqrt{T - T_{\text{KT}}})$  for  $T > T_{\text{KT}}$ . Thus, the critical exponents are infinite, and  $\xi_{\text{KT}}$  depends on temperature differently than does a typical phase transition, such as that in the 2D Ising model.<sup>2</sup>

The KT transition, however, is such a subtle phase transition that it is difficult to directly detect the singularity. Fortunately, in the roughening transition, the universal quantities specific to the KT transition are measurable as geometrical quantities on an equilibrium crystal shape (ECS) [\[48–58\]](#), which is the shape of a crystal droplet with the least surface free energy. The shape change accompanied by the roughening transition is

<sup>1</sup>From several numerical studies of a 2D interface in the 3D Ising model, the roughening transition temperature  $T_R$  is estimated to be almost half of the transition temperature  $T_c$  of the 3D Ising model. Hence, up to around  $T_R$ , the frequency at which the overhang structure forms is thought to be sufficiently low. As a step, however, an overhang such as the one shown within the broken line in [Figure 6.1\(B\)](#) frequently appears near  $T_c$  in the 2D Ising model.

<sup>2</sup>The correlation lengths of the 2D and 3D Ising models diverge only at the temperature of the phase transition.

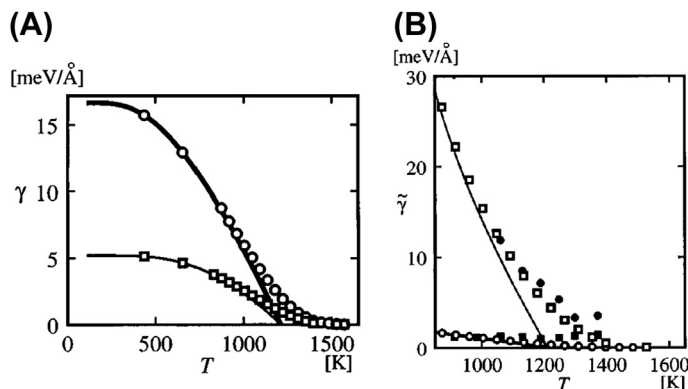


**FIGURE 6.2** Step tension  $\gamma$  and step stiffness  $\tilde{\gamma}$  of an Si(001) surface [32]. (A) Step tension; (B) step stiffness. Open squares: values of the  $S_A$  step calculated by the PWFRG method [44] (see Appendix A). Open circles: values of the  $S_B$  step calculated by the PWFRG method. Thick and thin solid curves: one-dimensional (1D) interface in a two-dimensional (2D) next-nearest-neighbor Ising model for the  $S_B$  step and  $S_A$  steps, respectively [31]. Solid circles: low-energy electron microscopy (LEEM) [45] results for the  $S_A$  step. Solid squares: LEEM results for the  $S_B$  step [46]. From Ref. [32].

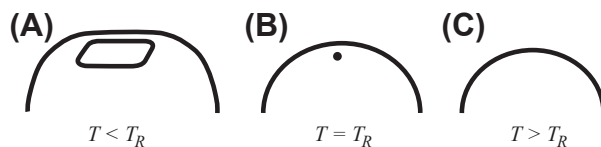


**FIGURE 6.3** Faceting transition on an equilibrium crystal shape.

called the faceting transition [18] (Figure 6.3). A facet is a plane with a low Miller index that appears on the ECS (Figure 6.3(A)). The facet appears at  $T < T_R$ , where  $T_R$  represents that of the facet plane. The shape of the facet represents the 2D ECS with respect to the step tension [24,33]. The area of the facet shrinks as the temperature increases. At  $T_R$ , the area of the facet becomes zero (Figure 6.3(B)). For  $T > T_R$ , the facet disappears (Figure 6.3(C)).

The exact study of the vicinal surface in the BCSOS model [18] again leads to correct understanding of the faceting transition. When the temperature rises to just above  $T_R$ , the Gaussian curvature<sup>3</sup>  $K_G$  [59] at the topmost point in Figure 6.3(B) jumps from 0 to  $\Delta K_G = [\lambda a_z^2 / (k_B T_R)]^2 K_R^2$ , where  $a_z$  represents the height of a single step,  $\lambda$  represents the Lagrange multiplier relating to the volume of the crystal droplet,  $T$  represents the temperature, and  $k_B$  represents the Boltzmann constant. It is surprising that the *universal quantity*  $K_R = 2/\pi$  appears in the expression of the Gaussian curvature jump, where  $K_R$  is proportional to the inverse of the KT transition temperature of the XY

<sup>3</sup>The Gaussian curvature is defined as  $K_G = \kappa_1 \kappa_2$ , where  $\kappa_1$  and  $\kappa_2$  are the principal values of the curvature.

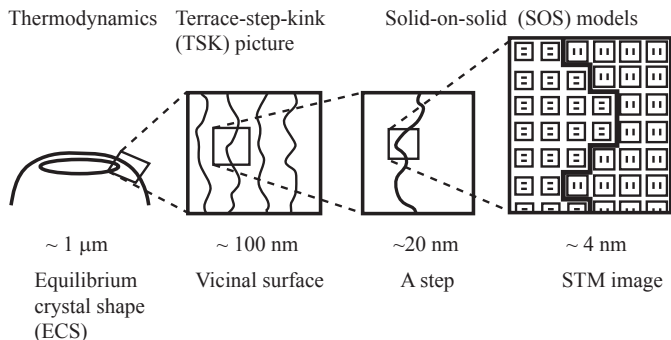


FIGURE 6.4 Models in various scales. From Ref. [86].

model:  $K_R = J/(k_B T_{KT})$ , where  $J$  is the coupling constant of the XY model [18]. This relation is a result of the duality relationship between the XY model and the SOS model, which Knops [10] and Jose et al. [11] pointed out.

The vicinal surface for  $T < T_R$ , where  $T_R$  represents the roughening transition temperature of the *terrace* plane, is also interesting because the system can be mapped to a 1D system of free fermions [13–33]. For  $T < T_R$ , the vicinal surface is described by a regular train of steps with a zigzag structure (Figure 6.4). This image of the vicinal surface is called the terrace-step-kink (TSK) or the terrace-ledge-kink (TLK) picture [60–63]. The free energy of the vicinal surface  $f(\rho)$  can be obtained by the ground-state energy of the 1D free fermion (FF), as follows [13–33]:

$$f(\rho) = f(0) + \gamma\rho + B\rho^3 + \dots \quad (6.1)$$

where  $\rho$  represents the step density,  $\gamma$  represents the step tension, and  $B$  represents the step interaction coefficient. This correspondence of the surface steps to quantum particles provides another universal type of surface; in the field of surface studies, a surface for which the energy is described in Eqn (6.1) is said to be of the Gruber-Mullins-Pokrovsky-Talapov (GMPT) type [13]. In addition, for  $T < T_R$ , the vicinal surface near a facet edge has another universal quantity reminiscent of the KT transition: the universal Gaussian curvature jump at the facet edge [25,26]. The Gaussian curvature jump can be expressed exactly in the 1D FF system, independent of the orientation of the vicinal surface:  $\Delta K'_G = [\lambda a_z^2 / (k_B T)]^2 (K_R/2)^2$ . We will discuss this in detail in Section 5. We add here that these singularities on the ECS are observed in systems of  $^4\text{He}$  [64–72], Pb [73–76], Ag<sub>2</sub>S [77], Si [78–82], and other materials [83–85].

This chapter gives an overview of the universal features of the roughening and smoothing phenomena of surfaces and steps. As background, we mention the treatment of a surface by Burton, Cabrera, and Frank (BCF) [87] for vapor growth, the treatment of the surface for melt growth by Jackson [88,89], and the “drumhead wandering” [90–92] that is caused by capillary waves. We begin with surfaces at temperatures higher than  $T_R$  and then consider those at lower temperatures. This also means that we begin with models at macroscopic scales and proceed to those at microscopic scales. We do this

because surfaces and their interfaces are so complex that many models in various scales need to be considered (Figure 6.4). We begin with an explanation of the surface thermodynamic quantities, including definitions of surface, interface, and surface roughness (Section 3). Next, we show the critical phenomena when the surface is near the temperature  $T_R$  (Section 4), after which we mention several topics concerning roughening transitions. We then discuss the vicinal surface when  $T < T_R$  (Section 5). Finally, we mention the smoothing of steps and the formation of macrosteps, which is due to an anomalous polar-angle dependence of the surface tension (Section 6).

## 6.2 Background

### 6.2.1 Rough Surface in Crystal Growth—Viewpoint of BCF

Before we proceed further, we briefly review the classical but important work of Burton, Cabrera and Frank [87], and Jackson [88].

BCF discussed the importance of the roughening transition of a surface<sup>4</sup> [87], and they showed that the growth mechanisms are very different on a rough surface than they are on a smooth surface.

The growth rate of a rough surface is proportional to the driving force  $\Delta\mu$  of the crystal growth ( $\Delta\mu$  is the difference between the chemical potentials of the bulk crystal phase and the ambient phase<sup>5</sup>). A smooth surface, however, does not grow linearly with  $\Delta\mu$ . Hence, BCF had to introduce the 2D nucleation process, a surface with a regular train of steps (a vicinal surface), and a surface with screw dislocations [87,93] in order to explain a realistic growth rate of a crystal (for example, see Figure 6.5). To see this, let us consider a curved step on a surface that is near equilibrium. As mentioned in Appendix D.12 in BCF [87], the normal velocity of a step  $v_n$  on a surface is described as follows:

$$v_n = \nu \left[ \frac{\Delta\mu}{\Omega} - \frac{\tilde{\gamma}}{R} \right], \quad \tilde{\gamma} = \gamma + \frac{\partial^2 \gamma}{\partial \phi^2}, \quad (6.2)$$

where  $\nu$  represents a kinetic coefficient,  $\Delta\mu$  represents the driving force,<sup>6</sup>  $\Omega$  represents a unit volume,  $R$  represents the radius of curvature,  $\tilde{\gamma}$  represents the step stiffness,  $\gamma$  represents the step tension, and  $\phi$  represents the tilt angle of the mean tangential line of a step, relative to the  $y$ -axis (Figure 6.5(B)). Equation (6.2) is known as the Gibbs-Thomson equation for a curved step.

<sup>4</sup>BCF studied the roughening transition by adopting a two-dimensional (2D) Ising model by means of the Bethe approximation. The limits of this approximation method misled them to thinking that the step tension had a finite value at the temperature of the roughening transition.

<sup>5</sup>For vapor growth,  $\Delta\mu = k_B T \ln \alpha = k_B T \ln P/P_0$ , in the BCF notation, where  $k_B$  represents the Boltzmann constant,  $T$  represents the temperature,  $P$  represents the pressure in the ambient phase, and  $P_0$  represents the equilibrium pressure at some temperature  $T_0$ . For other cases, please see Appendix B [94].

<sup>6</sup> $\Delta\mu/\Omega = kT \ln \alpha$  in equation D.12 of BCF, and it expresses the case of  $v_n = 0$ .

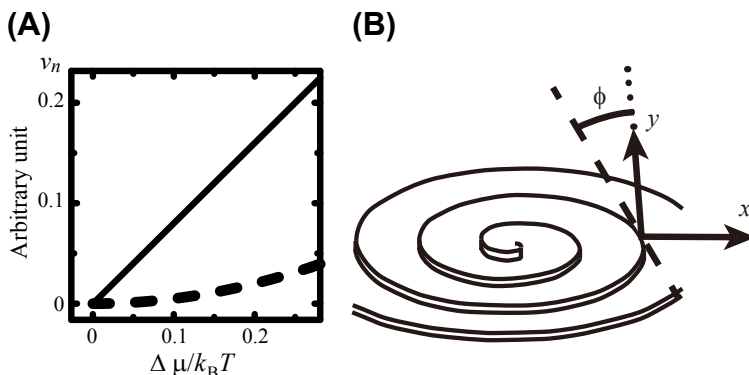


**FIGURE 6.5** (A) Example of crystal growth at a surface at a normal velocity  $v_n$ . Solid line: a rough surface. Broken line: a smooth surface with a screw dislocation. (B) Schematic illustration of a screw step on a surface (perspective view) [87].

As a natural extension of Eqn (6.2), the normal velocity of a surface  $v_n$  is described as follows [95,96]:

$$v_n = v \left[ \frac{\Delta \mu}{\Omega} - \frac{f_1}{R_1} - \frac{f_2}{R_2} \right], \quad (6.3)$$

where  $R_1$  and  $R_2$  represent the radii of curvature in the principal direction, and  $f_1$  and  $f_2$  represent the surface stiffness tensors in the principal direction. It should be noted that the surface of the crystal whose growth behavior is expressed by Eqn (6.3) is implicitly assumed to be rough. For a smooth surface, the value of  $f_1 \times f_2$  diverges [23], so Eqn (6.3) cannot be applied to describe the growth velocity. On a smooth surface, crystal growth occurs under conditions that are far from equilibrium. Hence, the growth process of a smooth surface depends on the microscopic details of the surface.

### 6.2.2 Entropy Effect—Jackson’s Argument

In 1958, Jackson [88] pointed out the relationship between the surface roughness and the entropy of melting, and introduced the parameter  $\alpha$ , which is called Jackson’s parameter. Jackson’s parameter indicates the relative degree to which the surface energy contributes to the free energy, compared to the contribution of the surface entropy. In this subsection, we discuss the surface entropy of roughness.

According to the calculations on the two-level (Jackson) model [55,88,94], in which the interface is considered in the “atomic” scale,<sup>7</sup> the interface between the liquid and the crystal is described by a 2D lattice. The free energy of the interface between the liquid and the crystal  $G(C, T)$  is given by a mean-field approximation, as follows:

$$G(C, T_m) / (Nk_B T_m) \approx \alpha C(1 - C) + C \ln C + (1 - C) \ln(1 - C), \quad (6.4)$$

<sup>7</sup>What was meant by the “atomic” scale in 1958 is equivalent to a scale that is more than a unit cell of a crystal.

where  $T_m$  represents the melting temperature,  $N$  represents the total number of lattice points in the 2D lattice,  $k_B$  represents the Boltzmann constant,  $C$  represents the concentration of the “solid-like atom,” and  $\alpha = z' \phi_{eff} / (2k_B T_m)$  represents Jackson’s  $\alpha$ . Here,  $z'$  represents the number of nearest-neighbor (nn) sites for a 2D lattice on a surface,  $\phi_{eff}$  represents the effective bond energy. Since the bond energy is approximately measured by the heat of melting per molecule  $\Delta h$ , Jackson’s  $\alpha$  can be rewritten using the entropy of melting, as follows:

$$\alpha = \frac{z' \Delta h}{z k_B T_m} = \frac{z' \Delta s}{z k_B}, \quad (6.5)$$

where  $z$  represents the number of nn sites in a 3D lattice and  $\Delta s$  represents the entropy of melting per molecule. Using the roughening transition temperature  $T_R$ , Jackson’s  $\alpha$  can be rewritten as follows:  $\alpha \approx 2T_R/T_m$  [97]. Therefore,  $\alpha$  can be used to estimate the roughening transition temperature of a specific surface.

The original idea of introducing  $\alpha$  in Eqn (6.4) was to consider the relative contributions of the energy and the entropy to the interface free energy (Figure 6.6). The first term on the right-hand side (r.h.s.) of Eqn (6.4) represents the energy cost due to interface roughness, and the second and the third terms on the r.h.s. represent the contributions of the interface entropy. Hence, for large  $\alpha$ , energy wins and the interface is smooth, while for small  $\alpha$ , entropy wins and the interface becomes rough. Usually, the entropy does not depend on the substance,<sup>8</sup> but the bond energy strongly depends on the substance. Therefore, for each substance, Jackson’s  $\alpha$  parameter gives us information about whether the roughening transition will be observable.<sup>9</sup>

The anisotropy of interface entropy due to the interface roughness is sometimes ignored, and we note that there is also anisotropy due to the structure of the crystal lattice. As shown in C, the ground-state structure of the interface is generally degenerated except for the several interfaces that have a low Miller index. When there is an in-plane bond network that connects all of the atoms, the interface will have a unique structure [51].

### 6.2.3 “Drumhead Wandering” due to Capillary Waves

In Figure 6.7, we show an intuitive picture of phase coexistence for a bulk crystal and a bulk ambient phase. The two phases are separated by a narrow interface region of width  $w$ .

<sup>8</sup>We recall Trouton’s rule for the vaporization of a liquid. This rule states that the entropy of vaporization is almost constant, irrespective of the substance.

<sup>9</sup>If the loss of the long-range periodicity of a crystal has a dominant contribution to the increase of entropy, as in metals, the melting of entropy will be small and so  $\alpha$  is small (2–3). The interface is rough near the melting temperature. On the other hand, in the case of orientational molecules, for example, the entropy of melting is large because disordering of the molecular orientation occurs together with the disordering of the periodicity of the crystal. In this case,  $\alpha$  becomes large ( $\sim 10$ ). Then, the surfaces at several azimuths become facets at the melting temperature.

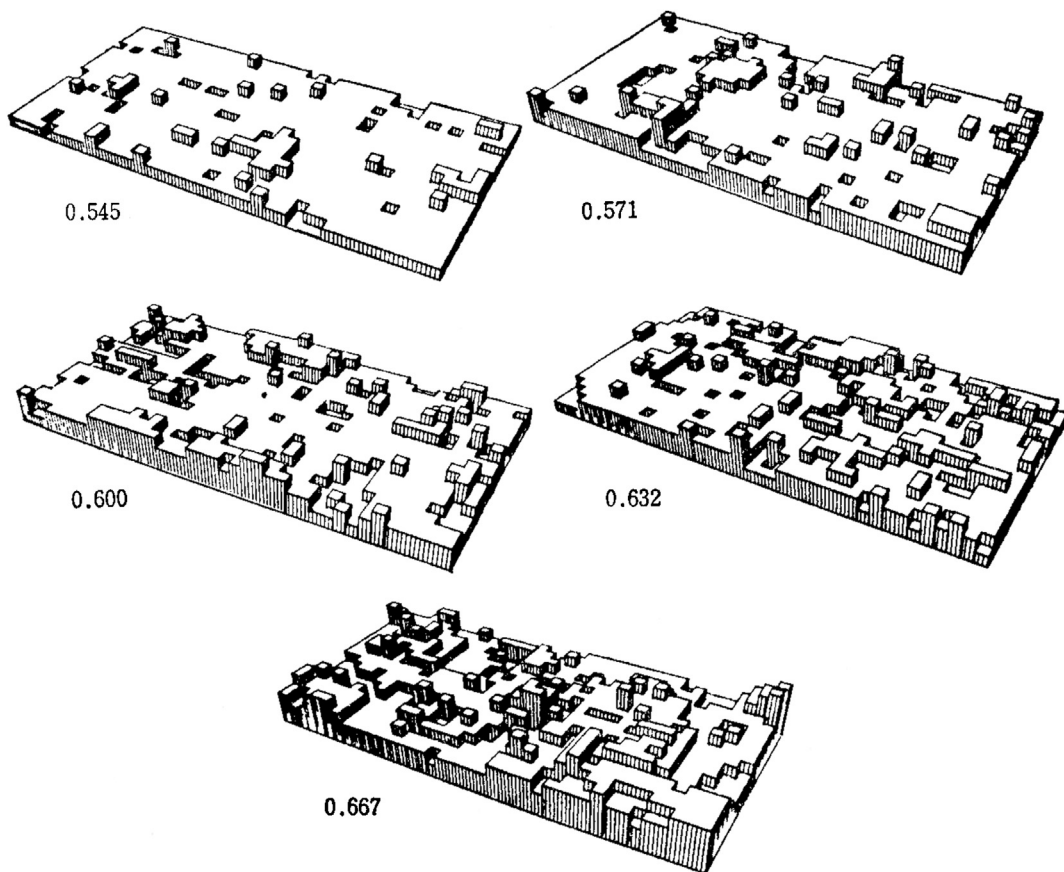


FIGURE 6.6 Snapshots of a computer simulation of the roughening transition on a solid-on-solid model [89]. From Ref. [55].

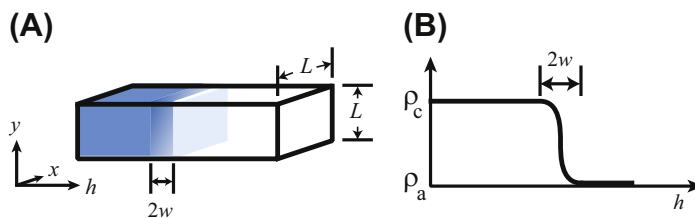


FIGURE 6.7 Schematic illustration of crystal-vapor coexistence, showing the diffuse interfacial region. (A) Shaded area: crystal;  $w$ : width of interface. (B) Density profile.  $\rho_c$ : density of crystal;  $\rho_a$ : density of the ambient phase (vapor phase).

If we try to consider the interface/surface precisely, we find that the definition of an interface (surface) is not trivial. At a crystal-melt interface, for example, the location of the interface is rather ambiguous when we consider the model at a microscopic scale. The liquid phase is generally distinguished from the crystal phase by the lack of a

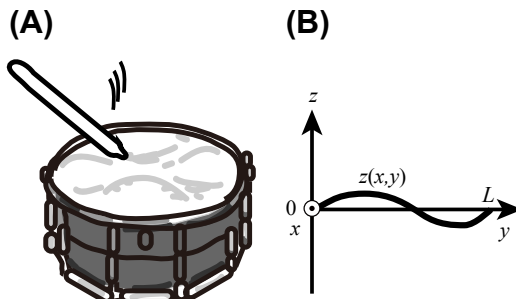


FIGURE 6.8 (A) A drum with a drumhead. (B) Surface height of the drumhead.

long-range periodic structure. This means that we cannot tell the difference between “liquid” and “crystal” by observing only a single atom. The same situation occurs in the magnetic domain walls of the XY model and the Heisenberg model. The microscopic parameters at the interface or in the domain wall change continuously, as shown in Figure 6.7. In this case, the interface (or the crystal surface) is unstable against the long-wavelength distortions that are excited by thermal fluctuations with infinitesimal energy costs [90–92]. That is, the interface is rough.

In this subsection, using the drumhead model (Figure 6.8), we explain how the long-wavelength distortions called “capillary wave” destabilize the continuous interface/surface.

The work functional against the surface tension for the instantaneous distortion of the surface dividing phase 1 from phase 2 is given by Buff, Lovett, and Stillinger in the following equation [90–92]:

$$\mathcal{H}_{DH} = \int \gamma_0 \sqrt{g} dx dy + \frac{1}{2} m_0^2 \int z(x,y)^2 dx dy, \quad (6.6)$$

where  $z(x,y)$  represents the instantaneous “dividing surface” between phases 1 and 2 (the surface of the drumhead),  $\sqrt{g} dx dy$  represents a small surface area  $dA$ ,  $\gamma_0$  represents the surface tension, and  $m_0$  represents the force necessary to stabilize the surface (e.g., gravity for a liquid–gas interface). Here,  $g$  represents a geometrical factor and is defined by  $g = 1 + p_x^2 + p_y^2$ , where  $p_x = \partial z / \partial x$  and  $p_y = \partial z / \partial y$ . This work functional is also called the “drumhead” Hamiltonian [92]. The thermodynamic equations and the correlations follow from  $Z_{DH} = \int Dz [\exp\{-\beta \mathcal{H}_{DH}\}]$  with  $\beta = 1/k_B T$ , where  $\int Dz$  describes the integral of all possible surface distortions. The surface area term in Eqn (6.6) can be expanded as

$$\sqrt{g} = 1 + \frac{1}{2} (p_x^2 + p_y^2) + \mathcal{O}[(p_x^2 + p_y^2)^2] + \dots \quad (6.7)$$

The Hamiltonian of Eqn (6.6) is usually approximated by the term that has lowest order with respect to  $\sqrt{g} : 1 + (1/2)(p_x^2 + p_y^2)$ .

The local strength of the fluctuations from the mean shape of the surface  $\langle z(x, y) \rangle = 0$  is measured by the variance, where  $\langle \cdot \rangle$  represents the thermal average. This becomes

$$\langle z(x, y)^2 \rangle = \frac{k_B T}{(2\pi)^2} \int \frac{dq_x dq_y}{\gamma_0 (q_x^2 + q_y^2) + m_0^2}, \quad (6.8)$$

where  $q_x$  and  $q_y$  are the wave numbers introduced by the Fourier decomposition (similar to the argument in Appendix E). In the thermodynamic limit ( $L \rightarrow \infty$ ), this integral becomes

$$\langle z(x, y)^2 \rangle = \frac{k_B T}{4\pi\gamma_0} \ln \frac{\gamma_0 \Lambda^2 + m_0^2}{\gamma_0 k_0^2 + m_0^2}, \quad (6.9)$$

where  $\Lambda = 2\pi/a$  represents the upper cutoff,  $a$  is the lattice spacing, and  $k_0 = 2\pi/L$  represents the low-wavenumber (infrared) cutoff for the integral. Therefore, for  $m_0^2 = 0$ , the variance diverges logarithmically in the thermodynamic limit  $L \rightarrow \infty$ , as follows:

$$\langle z(x, y)^2 \rangle = \frac{k_B T}{4\pi\gamma_0} \ln L. \quad (6.10)$$

The long-wavelength fluctuations, the capillary waves, destabilize the surface. This surface instability is referred to as “drumhead wandering” [92].

It is important to note that the drumhead wandering depends on the dimensionality of the space. Extending the above argument to a general  $(d - 1)$ -dimensional interface in a  $d$ -dimensional space, the variance of the interface fluctuations Eqn (6.8) becomes as follows:

$$\langle z^2 \rangle = \frac{k_B T}{(2\pi)^{d-1}} \int \frac{d^{d-1}q}{\gamma_0 q^2 + m_0^2} \propto \int_{k_0}^{\Lambda} \frac{q^{d-2} dq}{\gamma_0 q^2 + m_0^2}. \quad (6.11)$$

In the thermodynamic limit ( $L \rightarrow \infty$ ),  $\langle z^2 \rangle$  becomes  $(m_0^2)^{\frac{1}{2}(d-3)}$ . Hence, for  $d < 3$ ,  $\langle z^2 \rangle$  obeys a power law, and for  $d = 3$ ,  $\langle z^2 \rangle$  becomes  $\sim -\ln m_0^2$ . While for  $d > 3$ , there is no divergence around  $k_0 = 0$ . As for the surface with  $m_0 \rightarrow 0$ ,<sup>10</sup> for  $d = 2$ , the 1D surface (a step) is always rough; for  $d = 3$ , the surface is marginal; and for  $d > 3$  (if it exists), the surface is always smooth [4,5].

## 6.3 Rough Surface

### 6.3.1 Definition of an Interface

#### 6.3.1.1 Existence of a Roughening Transition Temperature

Rigorously speaking, at equilibrium, the crystal surface is an interface between the crystal phase and the ambient phase. However, we will use the terms *surface* and *interface* interchangeably. We begin this section with the definition of an interface.

<sup>10</sup>As a candidate of  $m_0$  on a surface, we may consider the potential to form a lattice structure. Such an effect can be taken into consideration by the discrete Gaussian model [98]. In the case of metals, a quantum effect with respect to the electrons may be a candidate for the case of  $m_0$ .

When a crystal is surrounded by a vapor phase, the microscopic separation between the crystal phase and the vapor phase is relatively clear.<sup>11</sup> The discrete order parameter, therefore, can be used to describe the configuration of the interface.<sup>12</sup> In this case, the surface of the crystal can be described as the interface in a 3D Ising model. For the interface in a 3D Ising model, it has been rigorously proven that the interface causes a roughening transition at a temperature less than the transition temperature of the bulk 3D Ising model  $T_{c,3D}$  [4,5]. In addition, the roughening transition temperature  $T_R$  is near the transition temperature of the 2D Ising model  $T_{c,2D}$ , but has been rigorously proven to be higher than  $T_{c,2D}$  [4]. Since the existence of the roughening transition is guaranteed by these rigorous results for the interface in a 3D Ising model, several solid-on-solid (SOS) models, which are specialized for surfaces, will be used to study surface roughness.

A coarse-grained rough surface of a crystal is diffuse, and it will have a surface profile that appears similar to that shown in Figure 6.7. In the following subsections, we will give a brief overview of how to assign tension to a coarse-grained interface when using the Ising model. To simplify this, we will use the 2D Ising model.

### 6.3.1.2 Ising Model and the Equivalent Lattice Gas Model

The 2D and the 3D Ising models are often adopted for the microscopic study of surface roughness. The Hamiltonian of the Ising model is written as follows<sup>13</sup>:

$$\mathcal{H}_{\text{Ising}} = -J \sum_{\langle i,j \rangle} \sigma_i \sigma_j - H \sum_{i=1}^{\mathcal{N}} \sigma_i, \quad (6.12)$$

where  $\sigma = \{\pm 1\}$  represents the Ising spin,  $J$  represents the coupling constant between spins,  $H$  represents an external magnetic field, and  $\mathcal{N}$  represents the total number of lattice points. The summation of  $\langle i,j \rangle$  is taken over all the nearest-neighbor (nn) pairs. The equivalent Hamiltonian of the lattice gas model is written as follows:

$$\mathcal{H}_{\text{LG}} = -\widehat{\phi} \sum_{\langle i,j \rangle} C_i C_j - (\mu_{2D} - \mu_{\text{ambient}}) \sum_{i=1}^{\mathcal{N}} C_i, \quad (6.13)$$

where  $\widehat{\phi}$  represents the bond energy between nn atoms,  $C = \{0,1\}$  indicates the presence of lattice gas ( $C=1$  when it is present and  $C=0$  otherwise),  $\mu_{2D}$  represents the chemical potential of the atoms in the 2D lattice, and  $\mu_{\text{ambient}}$  represents the chemical potential of the atoms in the ambient phase.  $\mu_{2D}$  is approximately written by  $\mu_{2D} = -\widehat{\phi}/2 + \mu_{\text{crystal}}$ , where  $\mu_{\text{crystal}}$  represents the chemical potential of the atoms in the bulk crystal. The Ising

<sup>11</sup>Even in the case of a crystal-vapor interface, the location of the phase separation sometimes becomes ambiguous for multicomponent crystals, such as can be seen in stones.

<sup>12</sup>The crystal-melt interface can be described by the discrete order parameter when another parameter, such as one for dielectric polarization, accompanies the crystal-melt transition. It is possible to identify melt or crystal at the microscopic scale by observing the dielectric polarization parameter.

<sup>13</sup>Figure 6.13(A) shows a side view of a 2D lattice gas model that is equivalent to the 2D Ising model.

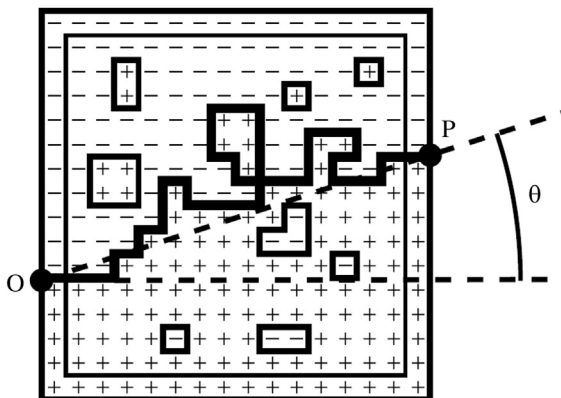


**FIGURE 6.9** A 1D interface as a phase separation line under an antiphase boundary condition in the 2D Ising model [4,6–8,38,39]. In the lattice gas model that is equivalent to this 2D Ising model, the phase separation line corresponds to a step on the surface. From Ref. [39].

Hamiltonian (6.12) is translated into the lattice gas Hamiltonian by substituting  $\sigma = 2C - 1$ , as follows:

$$\begin{aligned} \mathcal{H}_{\text{Ising}} &= \mathcal{H}_{\text{LG}} + \Delta E \\ \Delta E &= \left(2H - zJ\right)\mathcal{N}/2, \quad 4J = \widehat{\phi}, \quad 2H = \mu_{\text{crystal}} - \mu_{\text{ambient}}, \end{aligned} \quad (6.14)$$

where  $z$  represents the number of nn sites.<sup>14</sup>

In the case of  $J = 0$ , the Ising model (the lattice gas model) reduces to a two-level model with independent elements (Jackson’s model).

### 6.3.1.3 Definition of Interface Tension

The partition function of the Ising system is obtained as  $Z_{\text{Ising}} = \sum_{\{\sigma_i\}} \exp[-\beta\mathcal{H}_{\text{Ising}}]$ , where  $\beta = 1/k_{\text{B}}T$ . The summation  $\{\sigma_i\}$  is taken over all possible spin configurations. The free energy (density) of the system is obtained as  $f(T) = -(k_{\text{B}}T/\mathcal{N})\ln Z_{\text{Ising}}$ . The exact form of  $f(T)$  was given by Onsager for the 2D Ising model with  $H = 0$  [99].

The free energy of an interface is generally defined as the *excess* free energy due to the coexistence of the two phases. We will consider an example of this for a 1D interface in a 2D Ising model. For a temperature  $T < T_{c,2\text{D}}$ , where  $T_{c,2\text{D}}$  represents the Curie temperature of the 2D Ising model, a finite magnetized spin configuration will be self-organized. A phase separation line, such as the one between end points O and P in Figure 6.9, can be formed by applying a special boundary condition called an antiphase boundary condition (Figure 6.9). We denote the partition function of the Ising model system with a uniform boundary condition by  $Z_{++}$ , and the partition function with the antiphase boundary condition by  $Z_{+-}(\theta)$ . The 1D interface free energy per length (in the horizontal direction) is defined as follows [4]:

$$f_{\text{1D}}(\theta) = \lim_{N_x \rightarrow \infty} \frac{-k_{\text{B}}T}{N_x a} \ln \frac{Z_{+-}(\theta)}{Z_{++}}, \quad (6.15)$$

<sup>14</sup>This  $zJ(= z\widehat{\phi}/4)$  relates to the “half crystal site.”

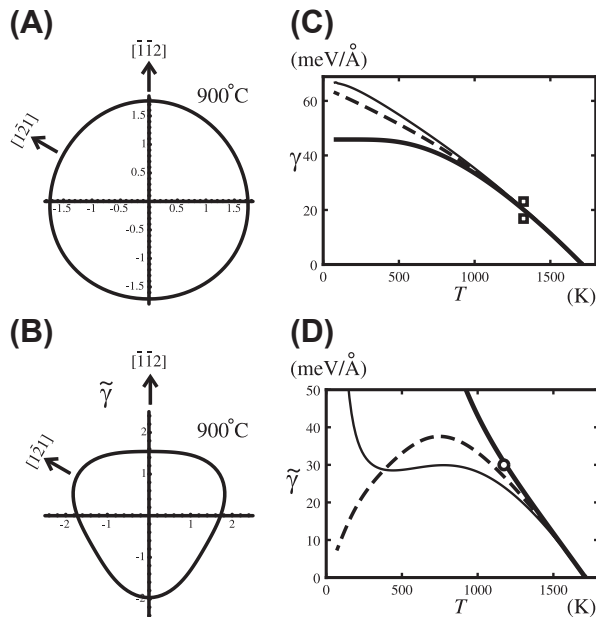


**FIGURE 6.10** Step quantities for a double layer of a (111) surface of a diamond structure [39]. The microscopic coupling constants were chosen to reproduce the experimental observations [81,101] on Si(111), which are denoted by open squares and an open circle. (A) The equilibrium shape of an island at 900 °C; (B) a polar graph of the step stiffness at 900 °C; (C) temperature dependence of the step tension; (D) temperature dependence of the step stiffness. In (C) and (D), the thick lines correspond to the  $\{21\bar{1}\}$  step and the thin lines to the  $\{10\bar{1}\}$  step. From Ref. [39].

where  $N_x$  is the number of lattice points in the horizontal direction. The interface tension of a 1D interface is given by

$$\gamma_{1D}(\theta) = f_{1D}(\theta)|\cos \theta| = f_{1D}(\theta) / \sqrt{1 + p_x^2}, \quad (6.16)$$

where  $p_x = \tan \theta$  [6,94].

In the case of the 1D interface, we can go further by using the imaginary-path-weight random walk (IPW) method (Appendix D) [100]. In Figure 6.2, the calculated step quantities for Si(001) are shown [31]. The Ising values were calculated by the IPW method. As seen from Figure 6.2, the Ising model provides good approximations for the step tensions and step stiffness at low temperatures. Figure 6.10 shows the step tension and step stiffness for the Si(111) surface, as calculated by using the honeycomb Ising model with a staggered magnetic field [39]. The calculated values were obtained by the IPW method.

The random walk picture of the interface that connects O and P locates the 1D interface at the line connecting O and P in the limit of  $L \rightarrow \infty$ . The existence of the limit is guaranteed by the central limit theorem. Similarly, a 2D interface in the 3D Ising model can be introduced under the antiphase boundary condition. The idea of the phase separation line can be easily extended to that of a phase separation surface in the 3D

**Table 6.1** Surface Width and Surface Roughness ( $d = 3$ )

Squared Surface Width $W_{\text{surf}}^2$	Squared Surface Roughness $w_{\text{surf}}^2$	Remarks
$\frac{k_B T}{2\pi\sqrt{\det(f^{ij})}} \ln L$	$\frac{k_B T}{2\pi\sqrt{\det(f^{ij})}}$	$T > T_R$ (Section 3.2.1, Section 3.3, Appendix E)
$\frac{a_z^2}{2\pi} K_R \ln L$	$\frac{a_z^2}{2\pi} K_R$	$T = T_R$ , $K_R = \frac{2}{\pi}$ (Section 3.2.1, Section 4.2)
$w^2$	0	$T < T_R$ smooth surface (Section 3.2.1) $w^2$ : a finite value of the variance of the surface height
$\frac{a_z^2}{2\pi} \left(\frac{K_R}{2}\right) \ln L$	$\frac{a_z^2}{2\pi} \left(\frac{K_R}{2}\right)$	$T < T_R$ for vicinal surface with small slope limit (Section 5.2)
$\frac{k_B T}{2\pi\sqrt{\det(f^{ij})}} \ln L$	$\frac{k_B T}{2\pi\sqrt{\det(f^{ij})}}$	$T < T_R$ for vicinal surface with large slope (Section 3.3)
$\frac{a_z^2}{2\pi\tilde{\lambda}(g)} \left(\frac{K_R}{2}\right) \ln L$	$\frac{a_z^2}{2\pi\tilde{\lambda}(g)} \left(\frac{K_R}{2}\right)$	$T < T_R$ for vicinal surface with small slope and with elastic step–step repulsion (Section 5.3)

Ising model. Therefore, the location of the interface as a mathematical plane  $h(x,y)$  is determined by the boundary condition in the Ising model.<sup>15</sup>

### 6.3.2 Definition of Surface Roughness

#### 6.3.2.1 Surface Width—Variance of Surface Height

The variance of the surface height is defined as the *squared surface width*, as follows:

$$W_{\text{surf}}^2 = \langle [h(\mathbf{x}) - \langle h(\mathbf{x}) \rangle]^2 \rangle, \quad (6.17)$$

where  $\langle \cdot \rangle$  represents the thermal average. Examples of the squared surface width in the limit as  $L \rightarrow \infty$  are listed in Table 6.1, where  $a_z$  represents the unit height of a step and  $d$  is the number of space dimensions.<sup>16</sup> When  $T < T_R$ , the squared surface width becomes a certain finite value in the limit of  $L \rightarrow \infty$ . Let the finite value be denoted by  $w^2$ . Hence, we have

$$w^2 = \lim_{L \rightarrow \infty} \langle [h(\mathbf{x}) - \langle h(\mathbf{x}) \rangle]^2 \rangle. \quad (6.18)$$

<sup>15</sup>For more general cases, the location of the interface within the area  $w$  in Figure 6.7 is ambiguous. For simplicity, however, we will consider that the interface is located at the Gibbs' dividing surface, and we will denote it by  $h(x,y)$ . In the case of multicomponent materials, the interface may have multiple dividing surfaces.

<sup>16</sup>This is done in accordance with the customary notation of the statistical mechanics of an interface [92].

When  $T \geq T_R$ , the surface width diverges logarithmically as the limit of  $L \rightarrow \infty$ , as follows (Appendix E, Eqn (E.6)) [23]:

$$W_{\text{surf}}^2 = \frac{k_B T}{2\pi \sqrt{\det(f^{ij})}} \ln L, \quad (6.19)$$

where  $(f^{ij})$  ( $i, j = x, y$ ) represents the surface stiffness tensor, which will be explained in the following subsection (Section 3.3). This divergence is caused by the “drumhead wandering” explained in Section 2.3. Though the surface is well defined in the microscopic scale, a rough surface behaves like the liquid–vapor interface in macroscopic scale. That is, long-wavelength distortions of the surface, called capillary waves, destabilize the surface.

Keeping in mind Eqn (6.19), a nondivergent measure of the surface roughness  $w_{\text{surf}}$  can be defined as follows:

$$w_{\text{surf}} = \left[ W_{\text{surf}}^2 / \ln L \right]^{1/2} \quad (L \rightarrow \infty), \quad (6.20)$$

which we call a *scaled surface width*. The scaled surface width is suitable for defining the “surface roughness.” Hence, the squared surface roughness is expressed as follows:

$$w_{\text{surf}}^2 = \begin{cases} \frac{k_B T}{2\pi \sqrt{\det(f^{ij})}} & T > T_R \\ a_z^2 K_R / 2\pi & T = T_R \\ 0 & T < T_R \end{cases}, \quad (d = 3), \quad (6.21)$$

where we use the universal relationship  $\sqrt{\det(f^{ij})} = k_B T / (K_R a_z^2)$  at  $T_R$  (Section 4.2) with the universal value  $K_R = 2/\pi$ .

### 6.3.2.2 Height–Height Correlation Function of a Surface

There is another quantity that may be suitable for defining the surface roughness. The height–height correlation function is defined as follows:

$$G(\mathbf{r}) = \langle [h(\mathbf{x} + \mathbf{r}) - h(\mathbf{x})]^2 \rangle. \quad (6.22)$$

Similarly, after some calculations, in the limit of  $r = |\mathbf{r}| \rightarrow \infty$ , we obtain [22]

$$G(\mathbf{r}) = \begin{cases} \frac{k_B T}{\pi \sqrt{\det(f^{ij})}} \ln r & T > T_R \\ (a_z^2 K_R / \pi) \ln r & T = T_R \\ 2w^2 & T < T_R \end{cases}, \quad (d = 3). \quad (6.23)$$

where  $w^2$  represents a finite value calculated by Eqn (6.18). Hence, we can also define the surface roughness as  $[G(\mathbf{r})/\ln r]^{1/2}$ , which is the value multiplied by  $\sqrt{2}$  of the value defined by Eqn (6.20).

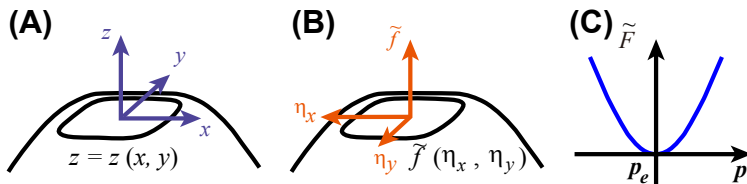


FIGURE 6.11 (A) An equilibrium crystal shape; (B) Andreev free energy [57]; (C) Extended free energy for the Hamiltonian of the capillary wave.

### 6.3.2.3 Thin Film-Like Surface in the Macroscopic Scale

It should be noted that the macroscopic appearance of a rough surface looks like a continuous thin surface. The surface width  $W_{\text{surf}}$ , the square root of the variance of the surface height, diverges at the rough surface. The ratio of the volume of the surface region ( $\sim L^2 \times W_{\text{surf}}$ ) and the bulk ( $\sim L^3$ ) becomes  $W_{\text{surf}}/L$  and converges to zero in the limit as  $L \rightarrow \infty$ . Therefore, in the thermodynamic limit, a rough surface looks like a thin elastic film.

## 6.3.3 Relationship between Energy and Shape

In this subsection, we show how the thermodynamic quantities on the surface relate to the geometry of the equilibrium crystal shape, which is the shape of a crystal droplet that has the least surface free energy (Figure 6.11(A)). The final relationship we would like to present in this subsection is the following [23]:

$$w_{\text{surf}}^2 = \frac{1}{2\pi} \frac{k_B T}{\sqrt{\det(f^{ij})}} = \frac{1}{2\pi} \frac{k_B T}{\lambda} g \sqrt{K_G}, \quad g = 1 + |\mathbf{p}|^2, \quad (6.24)$$

where  $g$  is the geometrical constant<sup>17</sup> and  $K_G$  is the Gaussian curvature [59] of the surface.

The quantities defined on crystal surfaces are anisotropic; this is because of the structure of the crystal lattice. The ECS can be obtained by using the polar graph of the surface tension and the Wulff construction method [49–55]. Andreev and Landau [56,57] proposed another method in which the ECS may be obtained analytically [56,57]; in their method, the ECS and the surface gradient  $\mathbf{p}$  are described by  $z(x,y)$  and  $\mathbf{p}=(\partial z(x,y)/\partial x, \partial z(x,y)/\partial y)$ , respectively. Andreev introduced the Andreev free energy  $f(\boldsymbol{\eta})$  [57] as the Legendre transformed thermodynamic potential of a surface with respect to the surface gradient  $\mathbf{p}$ , as follows:  $f(\boldsymbol{\eta}) = f(\mathbf{p}) - \mathbf{p} \cdot \boldsymbol{\eta}$ , where  $f(\mathbf{p}) = \gamma_{\text{surf}}(\mathbf{n})\sqrt{g}$  represents the surface free energy per projected  $xy$  area,  $\gamma_{\text{surf}}(\mathbf{n})$  represents the surface tension,  $\mathbf{n}$  represents the surface normal unit vector (see Eqn (F.1)). Hereafter, we will call  $f(\mathbf{p})$  the vicinal surface free energy. Here,  $\boldsymbol{\eta}$  is the Andreev field, the thermodynamic force conjugate to the surface gradient, which causes the surface to tilt.

<sup>17</sup>More precisely,  $g = \det(g_{\mu\nu})$ , where  $g_{\alpha\beta} = \delta_{\alpha\beta} + p_\alpha p_\beta$  ( $\alpha, \beta = \{x,y\}$ ),  $p_x = \partial z(x)/\partial x$ , and  $p_y = \partial z(x)/\partial y$  [59].

For the least free energy condition on the crystal droplet, the thermodynamic equations for the ECS [57] are obtained as follows:

$$\begin{aligned}\tilde{f}(\eta_x, \eta_y) &= \lambda z(x, y), \quad \eta_x = -\lambda x, \quad \eta_y = -\lambda y \\ p_{e,\alpha} &= -\frac{\partial \tilde{f}(\eta_x, \eta_y)}{\partial \eta_\alpha}, \quad \eta_\alpha = \frac{\partial f(p_x, p_y)}{\partial p_\alpha}, \quad (\alpha = x, y),\end{aligned}\quad (6.25)$$

where  $\mathbf{p}_e$  ( $p_{e,x}$ ,  $p_{e,y}$ ) is the surface gradient in equilibrium

It is interesting that the shape of the Andreev free energy as a function of  $\boldsymbol{\eta}$  is similar to the ECS (Figure 6.11(A) and (B)). Therefore, determining a thermodynamic quantity on a surface can be transformed to the problem of determining the geometry of the ECS.

Next, let us consider the fluctuations around the ECS. The Gaussian-type capillary-wave Hamiltonian is obtained from the extended free energy with respect to the slope fluctuations around the equilibrium surface slope (Appendix F) [23,102]:

$$\mathcal{H}_{CW} = \frac{1}{2} \int_0^L dx \int_0^L dy \left[ f^{xx}(\mathbf{p}_e) \Delta p_x^2 + f^{yy}(\mathbf{p}_e) \Delta p_y^2 + (f^{xy}(\mathbf{p}_e) + f^{yx}(\mathbf{p}_e)) \Delta p_x \Delta p_y \right], \quad (6.26)$$

where  $(f^{ij})$  represents the surface stiffness tensor and is defined as follows:

$$(f^{ij}) = \begin{pmatrix} f^{xx}(\mathbf{p}_e) & f^{xy}(\mathbf{p}_e) \\ f^{yx}(\mathbf{p}_e) & f^{yy}(\mathbf{p}_e) \end{pmatrix} = \left. \begin{pmatrix} \frac{\partial^2 f(\mathbf{p})}{\partial p_x^2} & \frac{\partial^2 f(\mathbf{p})}{\partial p_y \partial p_x} \\ \frac{\partial^2 f(\mathbf{p})}{\partial p_x \partial p_y} & \frac{\partial^2 f(\mathbf{p})}{\partial p_y^2} \end{pmatrix} \right|_{\mathbf{p}=\mathbf{p}_e}. \quad (6.27)$$

Using this capillary-wave Hamiltonian, we can determine the thermal average explicitly (Appendix E), and then we obtain

$$W_{\text{surf}}^2 = \frac{k_B T}{2\pi \sqrt{\det(f^{ij})}} \ln L. \quad (6.28)$$

Further, from the definition of the Gaussian curvature and Eqn (6.25), we can obtain an expression for the Gaussian curvature  $K_G$ , as follows:

$$\begin{aligned}K_G &= \frac{1}{g^2} \det \left( \frac{\partial^2 z}{\partial x^\mu \partial x^\nu} \right) = \frac{\lambda^2}{g^2} \frac{1}{\det(f^{ij})}, \\ (\mu, \nu &= 1 \text{ or } 2, \quad x^1 = x, \quad x^2 = y).\end{aligned}\quad (6.29)$$

From Eqns (6.20), (6.28), and (6.29), we obtain the final equation, Eqn (6.24).

Equation (6.24) connects the quantities of the surface roughness (the scaled surface width), the surface stiffness tensor, and the Gaussian curvature of the surface.

### 6.3.4 Roughness of a Single Step

In this subsection, we consider the roughness of a single step on a surface when  $T < T_R$ . As shown in Figure 6.9 [6] for the Ising model, we will consider a step for which the mean running direction is  $\overline{OP}$ . We assign the height of the step  $h(x)$  in the vertical

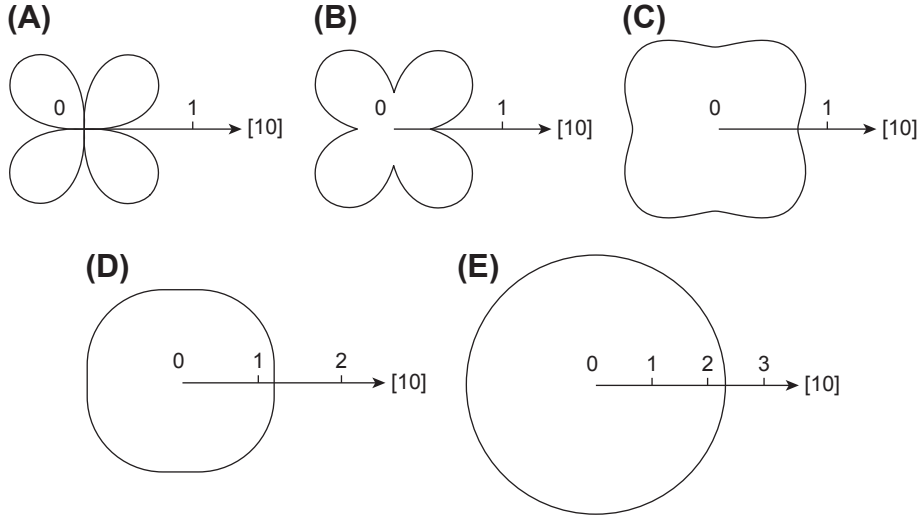


**FIGURE 6.12** Polar graphs of  $w_{\text{step}}(\phi)\sqrt{\cos\phi} = W_{\text{step}}(\phi)\sqrt{\cos\phi/L}$  for the 2D square-lattice Ising model. The temperatures are chosen as (A)  $T/T_c = 0.1$ ; (B)  $T/T_c = 0.3$ ; (C)  $T/T_c = 0.5$ ; (D)  $T/T_c = 0.7$ ; and (E)  $T/T_c = 0.9$ . From Ref. [6].

direction. Similar to Eqn (6.17), we define the width of the step as the variance of the height of the step, as follows:

$$W_{\text{step}}^2 = \langle [h(x) - \langle h(x) \rangle]^2 \rangle. \quad (6.30)$$

We can then obtain, for  $T < T_R$ :

$$W_{\text{step}}^2 = (k_B T / \tilde{\gamma}) L, \quad \tilde{\gamma} = \gamma + \frac{\partial^2 \gamma}{\partial \phi^2} \quad (6.31)$$

for an isolated step, where  $\tilde{\gamma}$  represents the step stiffness, and  $\phi$  represents tilt angle of the step. Hence, it is natural to define the step roughness as  $w_{\text{step}} = W_{\text{step}}/\sqrt{L}$ . In Figure 6.12, examples are shown of  $w_{\text{step}}$  for a 1D interface in the 2D Ising model [6]. The 1D interface in the 2D Ising model is considered to be an approximate model of a step on a (001) surface of a cubic Kossel crystal (Figure 6.2). As seen from Figure 6.12, the roughness of a step is strongly anisotropic at low temperatures. This is because of the degeneracy of the ground states with respect to the configuration of a step.

We can obtain a relationship similar to Eqn (6.24) between the step stiffness, the step roughness, and the curvature of the 2D ECS [6,7]:

$$w_{\text{step}}^2 = \frac{k_B T}{\tilde{\gamma}} = \frac{k_B T}{\lambda} \kappa, \quad (6.32)$$

where  $\kappa$  represents the curvature at a point of the 2D ECS.

It should be noted that the variance of a step in the *vicinal surface* is different from Eqn (6.31) but becomes as follows [103–105]:

$$W_{\text{step,vicinal}}^2 = \begin{cases} \frac{k_B T}{2\pi\alpha_z^2\rho^2\sqrt{\det(f^{ij})}} \ln L & (L \rightarrow \infty) \\ \frac{1}{2\pi^2\rho^2} \ln L & (\rho \rightarrow 0, L \rightarrow \infty) \end{cases}, \quad (6.33)$$

where  $\rho$  represents the step density on a vicinal surface. Since a single step collides with the adjacent steps, the step width here diverges more weakly than for an isolated step. In this case, the squared “roughness of a step”  $w_{\text{step,vicinal}}^2$  should be defined as  $w_{\text{step,vicinal}}^2 = W_{\text{step,vicinal}}^2 / \ln L$ . We will return to this below in Section 5.3.

## 6.4 Roughening Transition and Faceting Transition as Critical Phenomena

### 6.4.1 Microscopic Models for Studying Surface Roughness

In this subsection, we will demonstrate some typical microscopic models for studying the surface roughness of the (001) surface of a crystal (Figure 6.13). The known roughening transition temperatures  $T_R$  are listed in Table 6.2. Since the transition temperature  $T_c$  of the 2D Ising model gives a lower bound for  $T_R$ ,  $T_c$  for several lattice structures are also given in Table 6.2.

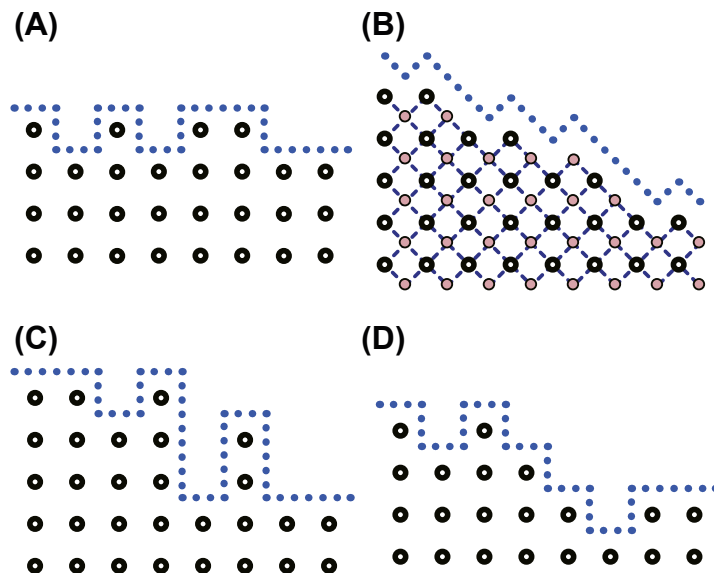
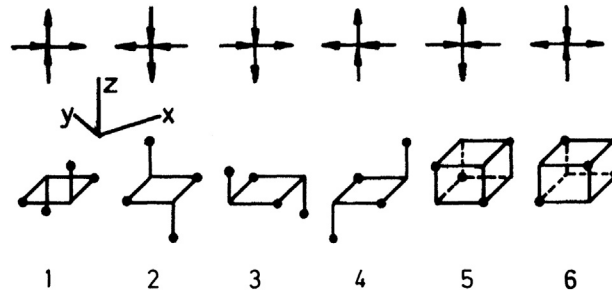


FIGURE 6.13 Side view of surfaces. (A) 2D lattice gas model equivalent to the 2D Ising model, (B) BCSOS model, (C) ASOS model, (D) RSOS model.

**Table 6.2** Phase Transition Temperatures

Model	$T_R$ or $T_c$	Hamiltonian	Remarks
2D Ising model	$k_B T_c / J = 2 / \ln(1 + \sqrt{2})$ $\approx 2.269$	Equation (6.12)	Exact. Square lattice.
	$k_B T_c / J = 2 / \cos h^{-1}(2)$ $\approx 1.519$	Equation (6.12)	Exact. Honeycomb lattice [106].
	$k_B T_c / J = 4 / \ln(3)$ $\approx 3.641$	Equation (6.12)	Exact. Triangular lattice [106].
	$k_B T_c / J = 4 / \ln(3 + 2\sqrt{3})$ $\approx 2.143$	Equation (6.12)	Exact. Kagome lattice [106].
	$k_B T_c / J = 4 / \ln(3)$ $\approx 2.405$	Equation (6.12)	Exact. Diced lattice [106].
3D Ising model	$T_R > T_{c,2D}$	Equation (6.12)	
BCSOS model	$k_B T_R / \varepsilon = 1 / \ln 2$ $\approx 1.443$	Equation (6.34)	Exact [1].
ASOS model	$k_B T_R / \varepsilon \approx 1.21$	Equation (6.37)	Square lattice [2].
RSOS model	$k_B T_R / \varepsilon \approx 1.580$	Equation (6.38)	Square lattice [3,107].
Discrete Gaussian model	$k_B T / J \approx 1.44$	Equation (G.1)	Square lattice [2].


**FIGURE 6.14** Mapping of the body-centered cubic solid-on-solid model to a 6-vertex model [1]. From Ref. [1].

#### 6.4.1.1 BCSOS Model

In **Figure 6.13(B)**, the BCSOS model [1] is shown. The BCSOS model is a microscopic model of the (001) surface of the body-centered cubic crystal. This model is usually described by the 6-vertex model (**Figure 6.14**). The Hamiltonian is as follows:

$$\mathcal{H}_{\text{BCSOS}} = \varepsilon_1 / 2 \sum_{(n,m)} \sum_{\delta} [|h_A(n,m) - h_B\{(n,m) + \delta\}|] + \varepsilon_2 \sum_{\langle i,j \rangle} [|h_{A,i} - h_{A,j}| + |h_{B,i} - h_{B,j}|], \quad (6.34)$$

where  $\varepsilon_1$  represents half of the nn bond energy, and  $\varepsilon_2$  represents half of next nn (nnn) bond energy. Since the crystal structure of the model is body-centered cubic (BCC), the lattice points can be divided into two cubic lattices, the A-sublattice and B-sublattice. We will distinguish the sites in the A- and B-sublattices by adding an A or B to the variables. The summation  $(n,m)$  is taken over all A-sublattice points, and the summation  $\langle i,j \rangle$  is taken over all pairs of the nn sublattice points.

In the BCSOS model,  $\varepsilon_1$  is set to infinity in order to avoid the overhang structure. Hence, the height difference between the nn sites,  $|\Delta h| = |h_{A,i} - h_{B,j}|$ , is fixed to be 1/2. The partition function of the BCSOS model  $Z_{\text{BCSOS}}$  is defined as

$$Z_{\text{BCSOS}} = \sum_{\{h_A(m,n)\}} \sum_{\{h_B(m,n)\}} \exp[-\beta \mathcal{H}_{\text{BCSOS}}], \quad (6.35)$$

where  $\beta = 1/k_B T$ , and the summation with respect to  $\{h_A(m,n)\}$  and  $\{h_B(m,n)\}$  means the summation over all possible surface configurations. This partition function is usually calculated for the equivalent 6-vertex model (Figure 6.14), and it was obtained exactly by van Beijeren [1]. The surface tension  $\gamma_{\text{surf}}(0)$  and the surface free energy per area  $f_{\text{surf}}(0)$  for the (001) surface are calculated as follows:

$$\gamma_{\text{surf}}(0) = f_{\text{surf}}(0) = \lim_{N \rightarrow \infty} \frac{k_B T}{N a^2} \ln Z_{\text{BCSOS}}, \quad (6.36)$$

where  $a$  represents the lattice constant of a cubic lattice. As mentioned in Section 1, the exact calculations for the BCSOS model greatly contributed to the understanding of roughening and faceting transitions.

#### 6.4.1.2 ASOS Model and RSOS Model

Figure 6.13(C) shows a side view of the absolute SOS (ASOS) model [89]. A perspective view of the ASOS model was already shown in Figure 6.1(A). This ASOS model is a natural model and is based on the Kossel crystal [108]. The height variable  $h(x,y)$  takes an integer. The Hamiltonian of the ASOS model is given by

$$\mathcal{H}_{\text{ASOS}} = \varepsilon \sum_{m,n} [|h(m+1, n) - h(m, n)| + |h(m, n+1) - h(m, n)|], \quad (6.37)$$

where  $\varepsilon$  represents the microscopic energy cost required to make the nearest-neighbor (nn) height difference  $\Delta h$ . The summation of  $(m,n)$  covers all lattice points on the square lattice. Since  $\varepsilon$  is half of the lateral bond energy,  $\varepsilon$  corresponds to  $2J$  in the 2D Ising model.

Figure 6.13(D) shows a side view of the restricted SOS (RSOS) model [109], where “restricted” means that the nn height difference is restricted to  $\{0, \pm 1\}$ . The Hamiltonian of the RSOS model is similar to that of the ASOS model, as follows:

$$\mathcal{H}_{\text{RSOS}} = \varepsilon \sum_{m,n} [|h(m+1, n) - h(m, n)| + |h(m, n+1) - h(m, n)|]. \quad (6.38)$$

The RSOS restriction is implicitly assumed.

The partition function of the ASOS model  $Z_{\text{ASOS}}$  and the RSOS model  $Z_{\text{RSOS}}$  are defined in a way similar to Eqn (6.35). The exact solutions for these models, however, have not yet been obtained.

### 6.4.2 Summary of KT-Type Critical Phenomena of Surfaces

According to Knops’ correspondence [10,11] that was based on the duality arguments,  $T_{\text{KT}}^*$  is related to the roughening transition temperature  $T_{\text{R}}$ ; the quasi-long-range ordered

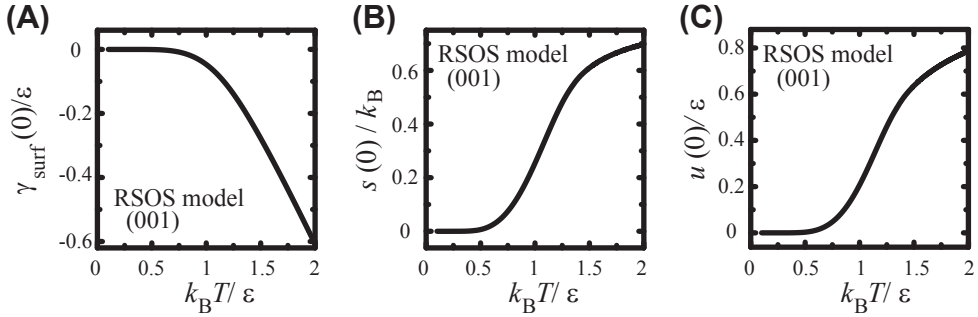


**FIGURE 6.15** Thermodynamic quantities of the (001) surface of a cubic lattice: RSOS model and PWFRG calculations (Appendix A).  $k_B T_R/\epsilon = 1.580$ . (A) Surface free energy per unit cell area. (B) Surface entropy per unit cell area. (C) Surface internal energy per unit cell area [110]. From Ref. [110].

phase for  $T^* < T_{KT}^*$  in the XY model corresponds to the rough phase for  $T > T_R$  in the surface model, and the phase for  $T^* > T_{KT}^*$  in the XY model corresponds to the smooth phase for  $T < T_R$ . The transition temperature of the XY model is given by the zero of the free energy for a single vortex creation as follows:  $k_B T_{KT}^*/J = 1/K_R = \pi/2$  [11,40].<sup>18</sup> The surface structure corresponding to the vortex in the XY model is not easily seen.

The features of the roughening transition are listed below [18,22,25,26]:

### 1. Correlation length

$$\xi(T) = \begin{cases} \infty & T \geq T_R \\ \xi_0 \exp\left(\frac{A}{\sqrt{T_R - T}}\right) & T < T_R \end{cases}, \quad (6.39)$$

where  $T_R$  (Table 6.2),  $\xi_0$ , and  $A$  are nonuniversal constants.

### 2. Surface tension: The singular part of the surface tension becomes

$$\gamma_{\text{surf,sing}} \approx B \exp\left(-\frac{C}{\sqrt{|T - T_R|}}\right), \quad (6.40)$$

where  $B$  and  $C$  are nonuniversal constants. In Figure 6.15(A), we show the surface tension of the (001) surface for the RSOS model. We also show the surface entropy and the surface internal energy in Figure 6.15(B) and (C), respectively. The singularity around  $T_R$ , however, is too subtle to be discerned. The steep increase of the surface entropy occurs near at  $T_{c,\text{Ising}}$ <sup>19</sup> of the 2D Ising model. This increase of the surface entropy results from the increase of the kink density on the surface.

<sup>18</sup> $J$  represents the coupling constant of the XY model.

<sup>19</sup> $k_B T_{c,\text{Ising}}/\epsilon = 1/\ln(1 + \sqrt{2}) \sim 1.135$ .

### 3. Height–height correlation function:

$$G(\mathbf{r}) = \begin{cases} \frac{k_B T}{\pi \sqrt{\det(f^{ij})}} \ln r & T > T_R \\ (a_z^2 K_R / \pi) \ln r & T = T_R \\ 2w^2 & T < T_R \end{cases} \quad (d=3), \quad (6.41)$$

where  $w^2$  represents a finite value calculated by Eqn (6.18).

### 4. Step free energies: Near $T_R$ , the step free energy behaves as follows:

$$f_{\text{step}}(T) = \begin{cases} 0 & T \geq T_R \\ f_{\text{step},0} \exp\left(-\frac{A}{\sqrt{T_R - T}}\right) & T < T_R \end{cases} \quad (6.42)$$

where  $f_{\text{step},0}$  and  $A$  are nonuniversal constants. For the BCSOS model,  $A = \pi^2 / (4\sqrt{2} \ln 2) \approx 2.52$  [18]. Since the 2D ECS obtained by the step tension coincides with the facet shape of the ECS [24], a decrease in the step tension leads to a faceting transition (Figure 6.3).

In Figure 6.16, we show the step tension  $\gamma_{\text{step}}$  and the step stiffness  $\tilde{\gamma}_{\text{step}}$ . As expected, the behavior of step tension at high temperature is well described by Eqn (6.42). Unexpectedly the value of  $A$  for the BCSOS model could fit the data for the RSOS model, though the value of  $A$  is thought to be nonuniversal.

We also show the step entropy and the step internal energy for the RSOS model in Figure 6.17. Both the step internal energy and the step entropy reduce to zero in the manner of Eqn (6.42). Here, a step entropy of zero does not mean a smooth surface. From Eqn (6.32), a step stiffness of zero causes a divergence in the step

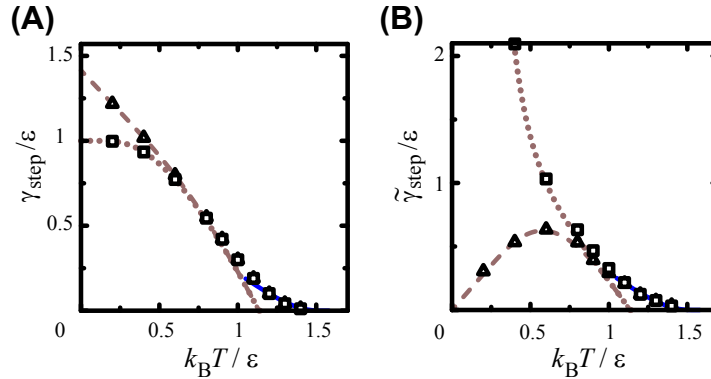


**FIGURE 6.16** Thermodynamic quantities of a step on a (001) surface [110]. (A) Step tension. (B) Step stiffness. Open squares:  $\phi = 0, (01)$  step. Open triangles:  $\phi = \pi/4, (11)$  step. Dotted line: 1D interface for the 2D nn Ising model  $\phi = 0$ , Broken line: 1D interface for the 2D nn Ising model  $\phi = \pi/4$ . Solid line: (A)  $\gamma_{\text{step}} / \epsilon = 6 \times \exp(-2.52 / \sqrt{1.580 - k_B T / \epsilon})$ ; (B)  $\tilde{\gamma}_{\text{step}} / \epsilon = 8 \exp(-2.52 / \sqrt{1.580 - k_B T / \epsilon})$ .  $k_B T_R / \epsilon$  is assumed to be 1.580. From Ref. [110].

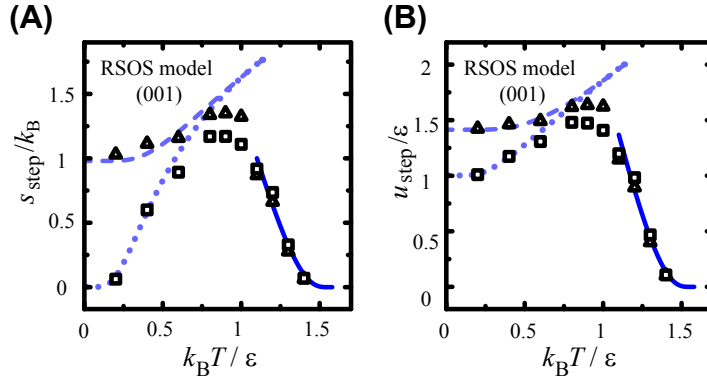


**FIGURE 6.17** Thermodynamic quantities of a step on the (001) surface [110]. (A) Step entropy. (B) Internal energy of a step. Open squares:  $\phi = 0$  ((01) step). Open triangles:  $\phi = \pi/4$  ((11) step). Dotted line: 1D interface for the 2D nn Ising model  $\phi = 0$ . Broken line: 1D interface for the 2D nn Ising model  $\phi = \pi/4$ . Solid line: (A)

$s_{\text{step}}/k_B = 38 \exp(-2.52/\sqrt{1.580 - k_B T/\epsilon})$ ; (B)  $u_{\text{step}}/\epsilon = 52 \exp(-2.52/\sqrt{1.580 - k_B T/\epsilon})$ .  $k_B T_R/\epsilon$  is assumed to be 1.580. From Ref. [110].

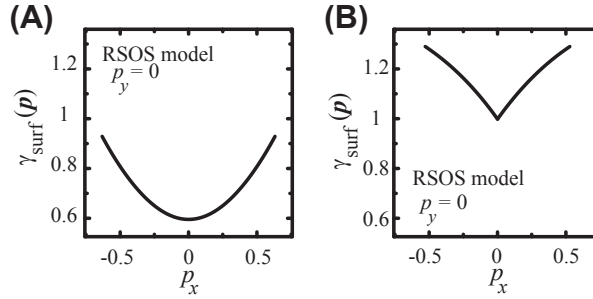


**FIGURE 6.18** Profile of surface tension: RSOS model and PWFRG calculations (A)  $k_B T/\epsilon = 1.7$  ( $T > T_R$ ). (B)  $k_B T/\epsilon = 0.6$  ( $T < T_R$ ).

roughness (the scaled step width)  $u_{\text{step}}$  at  $T_R$ . Hence, the steps dissolve into the bulk, as will be discussed in the following Section 4.3.2 for the 2D Ising model. Since the step free energy is defined as the excess part of the free energy from the bulk (Section 3.1.3), the step free energy decreases to zero as the temperature increases to  $T_R$ .

5. Surface free energy: Just above  $T_R$ , the vicinal surface free energy density and the Andreev free energy become as follows (Figure 6.18(A)) [18]:

$$f(\mathbf{p}) = f(0) + \frac{k_B T_R}{2K_R a_z^2} |\mathbf{p}|^2 + \mathcal{O}(|\mathbf{p}|^3), \quad (6.43)$$

$$\tilde{f}(\boldsymbol{\eta}) = f(0) - \frac{a_z^2 K_R}{2k_B T_R} |\boldsymbol{\eta}|^2 + \mathcal{O}(|\boldsymbol{\eta}|^3), \quad (6.44)$$

where  $K_R = 2/\pi$  and  $f(0) = \gamma_{\text{surf}}(0)$ . Hence, we have,

$$|\boldsymbol{\eta}| = \frac{k_B T}{K_R a_z^2} |\mathbf{p}|. \quad (6.45)$$

Using this equation, we can determine  $T_R$  numerically [3].

6. Universal curvature jump: The faceting transition on the ECS (Figure 6.3) accompanies a jump in the Gaussian curvature at the faceted surface as follows:

$$K_G = \begin{cases} \left( \frac{\lambda a_z^2}{k_B T_R} \right)^2 K_R^2 & T = T_R \\ 0 & T < T_R \end{cases}. \quad (6.46)$$

The Gaussian curvature is expressed as  $K_G = \kappa_1 \kappa_2$ , where  $\kappa_1$  and  $\kappa_2$  are the principal values of the curvature at that point on the surface.

7. Universal jump in the surface stiffness tensor: The faceting transition also accompanies a jump in the determinant of the surface stiffness tensor at the faceted surface as follows:

$$\det(f^{ij}) = \begin{cases} \left( \frac{k_B T_R}{a_z^2} \right)^2 \left( \frac{1}{K_R} \right)^2 & T = T_R \\ \infty & T < T_R \end{cases}. \quad (6.47)$$

### 6.4.3 Diffuseness for Atomically Rough Surfaces

#### 6.4.3.1 New Picture of Roughening

Since the step tension becomes zero at  $T \geq T_R$  (Eqn (6.42)), surface roughening is said to occur as a result of the step proliferation without any excess cost of free energy (Figure 6.19). According to this picture, some finite structures of the excited states, such as the adatoms and islands that form on the surface, do not significantly contribute to the free energy of the surface (i.e., they are irrelevant).

As shown in Figure 6.6, however, a surface simulated by Monte Carlo calculations with an ASOS model at high temperature is slightly different from the picture in Figure 6.19. The surface appears rough in the small scale. Hence, the terms *surface diffuseness* or *atomically rough surface* have been used in order to describe the roughness in the small scale. This difference is considered to be important in dynamic phenomena such as crystal growth, but it seems that the problem has not yet been clarified

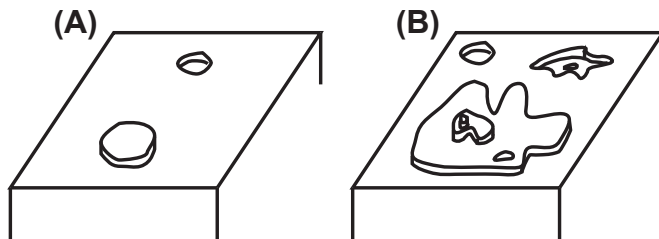


FIGURE 6.19 Proliferation of steps. (A)  $T < T_R$ . (B)  $T > T_R$ .

sufficiently. However, the following two approaches may help us to connect an atomically rough structure and the rough phase with drumhead wandering.

One approach is to study the intrinsic interface width [4,111,112], and the other approach is to study the preroughening phenomena [113]. We will discuss them briefly in the following subsections.

#### 6.4.3.2 Intrinsic Width of a Step

To understand the microscopic structure of a phase separation line (1D interface) in the 2D Ising model, Bricomont, Lebowitz, and Pfister [111] presented the notion of “deformations.” They decomposed a 1D interface into a bone-line and “blobs.” In Figure 6.20(A), the blobs are shown. The blobs are replaced by kinks of size  $D$  (Figure 6.20(B)). The kinks are deformations in the phase separation line. Then,  $d_n$ , which is  $n$ -th moment of  $|D|$ , is defined as follows [112]:

$$d_n = \lim_{N_x \rightarrow \infty} \frac{1}{N_x} \sum_i \langle |D_i|^n \rangle, \quad (6.48)$$

where  $N_x$  represents the number of lattice points in the direction of the bone-line. Based on the results of a Monte Carlo study [112],  $d_1$  is kept finite for  $T \leq T_c$  and  $d_2$  coincides with  $w_{\text{step}}^2 = k_B T / \tilde{\gamma}$ . Since  $\tilde{\gamma} \propto T_c - T$ ,  $d_2$  and  $w_{\text{step}}^2$  diverge as  $[(T_c - T)/T_c]^{-1}$ . Therefore, due to the effect of the local structures of the small domains of flipped spins (Figure 6.9), both  $W_{\text{step}}$  and  $w_{\text{step}}$  diverge at  $T_c$ .

For a surface step, we expect a similar divergence. In this case, however,  $\tilde{\gamma} \propto \exp[-A/\sqrt{T_R - T}]$ , and then from Eqn (6.32),  $w_{\text{step}}^2$  diverges as  $\exp[A/\sqrt{T_R - T}]$ . Therefore, when  $T = T_R$ , steps roughen the surface, and, at the same time, the steps dissolve into the surface. The excited structures such as adatoms and islands contribute to the values of the step tension and step stiffness.

#### 6.4.3.3 Preroughening Phenomena

Den Nijs and Rommels [113] predicted *preroughening phenomena* on surfaces where a short-range step–step repulsion exists.

When the temperature is near  $T_c$  for the 2D Ising model, the relatively large blobs are excited. Due to repulsion, the steps are kept apart from other steps. As a result, when the temperature is in the region  $T_c < T < T_R$ , the surface seems to be rough, but the steps are confined to two levels on the surface. This phase was named the “disordered flat phase”

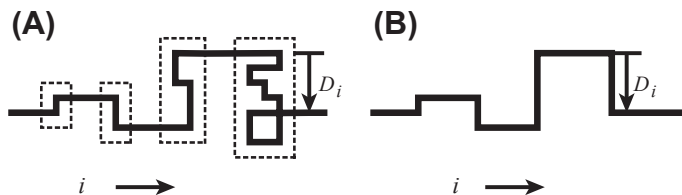


**FIGURE 6.20** Schematic diagram of deformations. (A) An example of a 1D interface (phase separation line) in a 2D Ising model. The configurations in the dotted squares are “blobs” [4,111,112]. A blob at the site  $i$  is replaced by a kink, which is called a deformation with size  $D_i$ . (B) 1D converted interface with kinks.

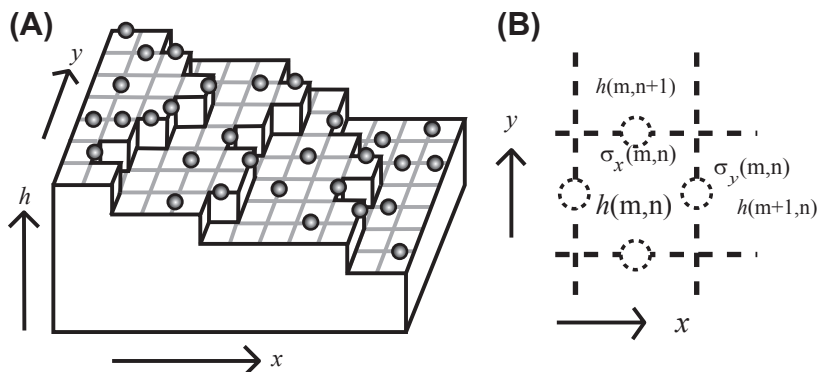


**FIGURE 6.21** A “decorated” RSOS model for the Langmuir adsorption; the coverage is less than 1 [107]. (A) Perspective view. (B) Adsorption site. From Ref. [107].

(DFP) by den Nijs and Rommels. The DFP seems to be a candidate for the atomically rough phase.<sup>20</sup>

## 6.4.4 Changes in the Roughening Temperature on Complex Surfaces

### 6.4.4.1 Inverse Roughening

In 1994, Luijten et al. [114] predicted the “inverse roughening” phenomena on the (001) surface of a CsCl-type crystal structure. The model that Luijten et al. adopted is the staggered BCSOS model, which has a uniform field (stoichiometric chemical potential) that favors the Cs component on the surface of the BCSOS model. In the inverse roughening phenomena, the surface is rough when the temperature is zero; as the temperature increases, it becomes smooth; with further increases, the step tension begins to decrease; finally, at sufficiently high temperature, a second transition occurs and the surface again becomes rough [33,114].

Using this type of model with different statistical weights for the vertices, the disordered flat phase [115–117] and the reconstructed rough phase [116,117] can also be studied. Details of these models are not discussed in this article.

### 6.4.4.2 Surface Modified by Langmuir Adsorption

Adsorbed materials on a surface are empirically known to change the thermodynamic behavior of that surface [94]. Using a lattice model named the “decorated” RSOS model (Figure 6.21), Akutsu et al. [107] showed the change of surface tension in a case of Langmuir adsorption. They also showed that Langmuir-type adsorbed materials with coverage less than one changes the roughening transition temperature. In this subsection, we explain how the roughening transition temperature is changed by a small amount of adsorbed materials.

<sup>20</sup>The DFP can be translated to an  $S = 1/2$  quantum spin system as the resonating valence bond (RVB) state relating to the Haldane gap.

The Hamiltonian of the decorated RSOS model consists of an RSOS model ( $\mathcal{H}_{\text{RSOS}}$ ), a lattice gas model for adsorption ( $\mathcal{H}_L$ ), and their coupling parts, as follows:

$$\mathcal{H} = \mathcal{H}_{\text{RSOS}} + \mathcal{H}_L + \mathcal{H}_{\text{int}}, \quad (6.49)$$

where

$$\begin{aligned} \mathcal{H}_{\text{RSOS}} + \mathcal{H}_{\text{int}} &= \sum_{m,n} \{ \varepsilon [1 - \alpha \sigma_y(m, n)] \cdot |h(m+1, n) - h(m, n)| \\ &\quad + \varepsilon [1 - \alpha \sigma_x(m, n)] \cdot |h(m, n+1) - h(m, n)| \} \\ \mathcal{H}_L &= -H \sum_{m,n} [\sigma_x(m, n) + \sigma_y(m, n)]. \end{aligned} \quad (6.50)$$

$\mathcal{H}_L$  is expressed by the Ising spin variables  $\sigma = \pm 1$ .<sup>21</sup> The spin variables are put on the bridge site, as shown in [Figure 6.21\(B\)](#), because we consider that an adsorbed material on the RSOS ledge changes the microscopic ledge energy. The parameter  $\alpha$  in  $\mathcal{H}_{\text{int}}$  describes the coupling between the RSOS model and the lattice gas model of the adsorbed materials. For  $\alpha > 0$ , the adsorbed materials favor the edge of the step, while for  $\alpha < 0$ , the adsorbed materials favor the terrace sites.

The partition function is calculated as  $Z = \sum_{\{h_i\}} \sum_{\{\sigma_i\}} \exp[-\beta \mathcal{H}]$ , where  $\beta = 1/k_B T$ . After taking the partial sum with respect to  $\{\sigma_i\}$ , we obtain the exact RSOS Hamiltonian with the effective ledge energy  $\varepsilon^{\text{eff}}$ , as follows:

$$\varepsilon^{\text{eff}}(T, H) = \varepsilon - k_B T \ln \left[ \frac{\cosh(\beta \alpha \varepsilon + \beta H)}{\cosh \beta H} \right]. \quad (6.51)$$

The mean coverage of the materials of adsorption at the step ledge  $C_y$  is given by the following equation:

$$M_y = 2C_y - 1 \approx \tanh \beta H + [\tanh \beta(H + \varepsilon \alpha) - \tanh \beta H] p_x, \quad (6.52)$$

where  $M_y$  represents the mean magnetization of  $\langle \sigma_y \rangle$ . [Equation \(6.51\)](#) says that the effective ledge energy depends on the temperature and the chemical potential of the adsorbed materials in the ambient phase.

Since the roughening temperature is given by  $k_B T_R / \varepsilon^{\text{eff}} = 1/\zeta_R \approx 1.580$  for the RSOS model, where  $\zeta_R = 0.6330$ , we have

$$\frac{H}{k_B T_R} = \frac{1}{2} \ln \frac{\exp[\zeta_R - (1 + \alpha)\varepsilon/(k_B T_R)] - 1}{1 - \exp[\zeta_R - (1 - \alpha)\varepsilon/(k_B T_R)]}, \quad (6.53)$$

which allows us to draw the critical line in the  $H - T$  plane, as shown in [Figure 6.22](#). In the case of  $\alpha \approx 1$ , there is a region of  $H$  where the inverse roughening occurs. We can see the region of  $H$  where the inverse roughening occurs in [Figure 6.22\(B\)](#) and [\(C\)](#).

<sup>21</sup>To obtain the expression for the lattice gas variables, replace  $\sigma$  with  $2C - 1$  as in section 3.1.2.  $H = \mu/2 = (k_B T/2) \ln(P/P_e)$  where  $P$  represents the vapor pressure of the adsorbed materials and  $P_e$  represents the vapor pressure of the adsorbed materials with the coverage being 50%.

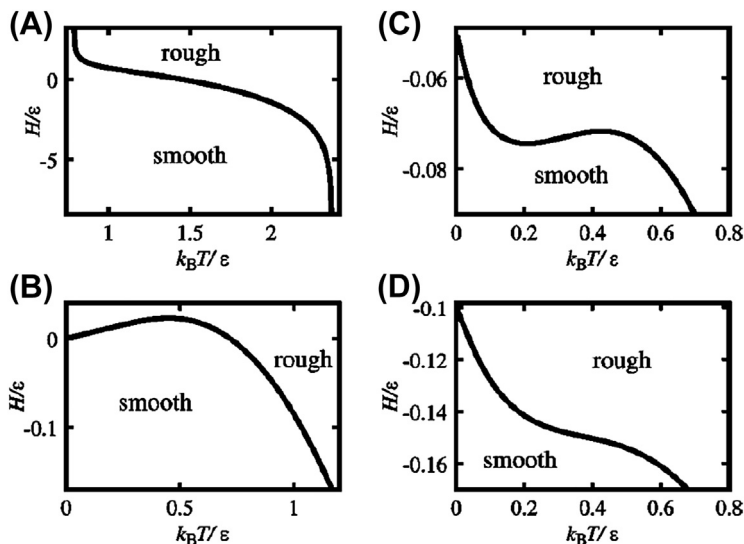


FIGURE 6.22 Change of the roughening transition temperature. (A)  $\alpha = 0.1$ . (B)  $\alpha = 1.0$ . (C)  $\alpha = 1.1$ . (D)  $\alpha = 2.0$ . From Ref. [107].

## 6.5 Vicinal Surface

### 6.5.1 Rough or Smooth? The Terrace-Step-Kink Picture

As mentioned in Section 1, studying the vicinal surface by using the BCSOS model [18] gave us a correct understanding of the faceting transition. In addition, the vicinal surface for  $T < T_R$  is itself interesting because the system can be mapped to a 1D free fermion (FF) system by using a terrace-step-kink (TSK) picture of the vicinal surface. This characteristic of the 1D FF, as in Eqn (6.1), is the GMPT [13] type of universal character.

A vicinal surface is a slightly tilted surface from a plane with a low Miller index. Figure 6.23 shows a typical vicinal surface for which the temperature  $T$  is lower than  $T_R$  of the terrace surface. As mentioned in the previous section, the excited structures such as adatoms and islands contribute to changes in the step tension and the step interaction coefficients of the step.<sup>22</sup> Hence, in the mesoscopic scale, a vicinal surface is well described by terraces, steps, and kinks in a step. This is called the TSK picture.

Since the terrace is smooth, a vicinal surface seems to be a smooth surface. In fact, as mentioned in the work of BCF [87], the growth rate of a surface that has a regular train of steps is different from that of a surface with  $T > T_R$ . The linear dependence on the driving force  $\Delta\mu$  concerning the growth rate, however, is similar to a rough surface. The vicinal surface grows in the “step flow growth” mode, and the growth rate of a vicinal surface is proportional to  $\Delta\mu$ . According to the definition of the surface roughness in Section 3.2.1,

<sup>22</sup>Recall that islands and negative islands on a terrace are irrelevant.

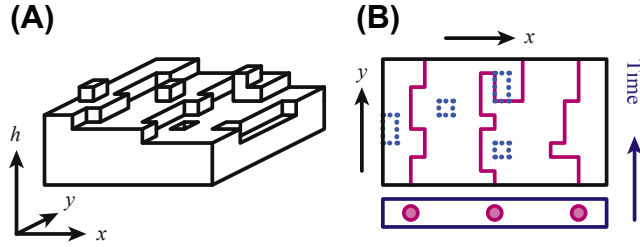


**FIGURE 6.23** (A) A perspective view of a vicinal surface. (B) A terrace-step-kink picture of a vicinal surface. Solid line: steps on the vicinal surface shown in (A) (top view). Dotted rectangles: islands or negative islands on the surface.

the vicinal surface is rough, because the variance of the surface height diverges logarithmically as the area  $L^2$  increases (Eqn (6.28)).

Therefore, we can say that a vicinal surface has characteristics of both a rough surface and a smooth surface. Statically, a vicinal surface has the characteristics of a rough surface; dynamically, it has the characteristics of a smooth surface.

### 6.5.2 1D Free-Fermion Universal Features—Gruber-Mullins-Pokrovsky-Talapov Behavior

In the TSK picture (Figures 6.4 and 6.23), the steps can be regarded as linear excitations buried in a 2D planar lattice. Since overhang structures are inhibited in SOS models, the linear excitations are impenetrable by adjacent excitations. Due to the impenetrability, the vicinal surface can be exactly described by a 1D spinless free fermion (FF) at temperature  $T = 0$  [26]. The zigzag structure of a step corresponds to the quantum zero-point oscillations. Hence, as previously shown in Eqn (6.1), the free energy of the vicinal surface  $f(\rho)$  can be obtained by the ground-state energy of the 1D FF, as follows:

$$f(\rho) = f(0) + \gamma_{\text{step}}\rho + B\rho^3 + \dots, \quad (6.54)$$

where  $\rho$  represents the step density,  $f(0) = \gamma_{\text{surf}}(0)$  represents the surface tension of the terrace plane,  $\gamma_{\text{step}}$  represents the step tension, and  $B$  represents the step interaction coefficient. In the case of the 1D FF [25,26],

$$B = \frac{\pi^2}{6} k_B T w_{\text{step}}^2. \quad (6.55)$$

Recalling Eqn (6.32), we have the following relationship:

$$\beta B = \frac{\pi^2}{6\beta\tilde{\gamma}}, \quad (6.56)$$

where  $\beta = 1/k_B T$  and  $\tilde{\gamma} = \gamma_{\text{step}} + \partial^2 \gamma_{\text{step}} / \partial \phi^2$  represents the step stiffness. Substituting Eqn (6.56) into Eqn (6.54) with  $|\mathbf{p}| = \rho a_z$ , we have

$$f(\mathbf{p}) = \gamma_{\text{surf}}(0) + \gamma_{\text{step}} \frac{|\mathbf{p}|}{a_z} + \frac{\pi^2}{6} \frac{(k_B T)^2}{\tilde{\gamma}} \left( \frac{|\mathbf{p}|}{a_z} \right)^3 + \dots \quad (6.57)$$

The surface tension for the RSOS model is calculated from  $f(\mathbf{p})$  as  $\gamma_{\text{surf}}(\mathbf{p}) = f(\mathbf{p})/\sqrt{1 + |\mathbf{p}|^2}$  at  $k_B T/\varepsilon = 0.6$ , and it is shown in Figure 6.18(B).

In addition, applying Eqn (6.57) to the stiffness tensor (Eqn (6.27)), we have another universal jump of  $\det(f^{ij})$  at the facet edge, as follows [25,26]:

$$\det(f^{ij}) = \begin{cases} \left(\frac{2}{K_R}\right)^2 \left(\frac{k_B T}{a_z^2}\right)^2 = \pi^2 \left(\frac{k_B T}{a_z^2}\right)^2, & (|\mathbf{p}| \rightarrow 0) \\ \infty, & (|\mathbf{p}| = 0) \end{cases} \quad (6.58)$$

for small  $|\mathbf{p}|$ , where  $K_R = 2/\pi$ . Similarly, for the surface roughness and the Gaussian curvature on the ECS, we have a jump, as follows:

$$w_{\text{surf}} = \begin{cases} \sqrt{\frac{K_R a_z^2}{4\pi}} = \frac{a_z}{\sqrt{2\pi}}, & (|\mathbf{p}| \rightarrow 0) \\ 0, & (|\mathbf{p}| = 0) \end{cases} \quad (6.59)$$

$$K_G = \begin{cases} \left(\frac{\lambda a_z^2}{k_B T}\right)^2 \left(\frac{K_R}{2}\right)^2, & (|\mathbf{p}| \rightarrow 0) \\ 0, & (|\mathbf{p}| = 0) \end{cases} \quad (6.60)$$

Therefore,  $\det(f^{ij})$ , the Gaussian curvature, and the surface roughness are constant near a facet edge.

### 6.5.3 Logarithmic Behavior on the Width of a Single Step

#### 6.5.3.1 Height–Height Correlation Function of a Single Step

As mentioned in Section 3.4, we have shown that the variance  $W_{\text{step}}^2$  of the “height” of a step on a surface is proportional to  $L$ , where  $L$  is the linear size of the system. In this subsection, we will show that the variance of the “height” of a single step on a vicinal surface is not proportional to  $L$  because the step collides with adjacent steps on the vicinal surface.

We now consider the height–height correlation function  $\Delta^2(r)$  for a single step on a vicinal surface, as follows [103–105]:

$$\Delta^2(r) = \left\langle (x(y+r) - x(y))^2 \right\rangle, \quad (6.61)$$

where, without loss of generality, the  $y$ -axis can be chosen to lie along the mean running direction of the steps. Here we introduce the probability  $Q(x,y)$  that two points  $(0,0)$  and  $(x,y)$  lie in the same terrace:

$$Q(x,y) = C \langle \delta(h(0,0) - h(x,y)) \rangle, \quad (6.62)$$

where  $C$  is a normalization factor. Using the capillary wave Hamiltonian (Eqn (6.26)), we obtain

$$Q(x,y) \propto \exp\left(\frac{-p^2 x^2}{2G(x,y)}\right), \quad (6.63)$$

where  $G(x,y)$  represents the height–height correlation function of the surface (Eqn (6.22)). Equation (6.63) shows that  $Q(x,y)$  is identical to the probability that a step passes the two points  $(0,0)$  and  $(x,y)$ . Using the probability in Eqn (6.63), Eqn (6.61) then becomes the following:

$$\Delta^2(r) = \int Q(x,y)x^2 dx = \frac{1}{p^2} G(0,r) \quad (r \rightarrow \infty). \quad (6.64)$$

Since  $G(0,y) = [k_B T / (\pi \sqrt{\det(f^{ij})})] \ln r$  (Eqn (6.23)), we have the relation

$$\begin{aligned} \Delta^2(r) &= \left[ k_B T / \left( \pi \rho^2 a_z^2 \sqrt{\det(f^{ij})} \right) \right] \ln r \\ &= \frac{1}{\pi \rho^2} \ln r \quad (\rho \rightarrow 0). \end{aligned} \quad (6.65)$$

The Eqn (6.65) on  $\Delta^2(r)$  is also derived exactly in the limit  $\rho \rightarrow 0$  for the TSK model on a lattice [103,104]. The variance of the height of a single step on the vicinal surface  $W_{\text{step,vicinal}}^2$  becomes exactly [104].

$$\begin{aligned} W_{\text{step,vicinal}}^2 &= \left[ k_B T / \left( 2\pi \rho^2 a_z^2 \sqrt{\det(f^{ij})} \right) \right] \ln L \\ &= \frac{1}{2\pi \rho^2} \ln L \quad (\rho \rightarrow 0). \end{aligned} \quad (6.66)$$

### 6.5.3.2 Elastic Step–Step Repulsion

On a crystal surface, elastic repulsion such as  $g_0/(x_i - x_{i+1})^2$  [118,119] sometimes exists. Here,  $g_0$  represents the coupling constant, and  $x_i$  represents the location of the  $i$ -th step (Figure 6.23(B)). By adding this term to the capillary wave Hamiltonian, we have the surface free energy for this system, as follows [103,120]:

$$f_{\text{elastic}}(p) = f(0) + \gamma(\phi) \frac{p}{a_z} + \frac{\pi^2}{6} \frac{(k_B T)^2}{\tilde{\gamma}(\phi)} \tilde{\lambda}^2(g) \frac{p^3}{a_z^3}, \quad (6.67)$$

where

$$g = 2\beta^2 \tilde{\gamma}(\phi) g_0, \quad \tilde{\lambda}(g) = \left[ 1 + \sqrt{1 + 2g} \right] / 2. \quad (6.68)$$

Here, we used the exact result of Sutherland [121]. Therefore, we have this new relationship around the facet edge:

$$\det(f^{ij}) = [k_B T \pi \tilde{\lambda}(g)]^2, \quad G(0,r) = \frac{1}{\pi^2 \tilde{\lambda}(g)} \ln r, \quad \Delta^2(r) = \frac{1}{\pi^2 \rho^2 \tilde{\lambda}(g)} \ln r. \quad (6.69)$$

The jump of the Gaussian curvature at the facet edge  $\Delta K_G(g)$  becomes

$$\Delta K_G(g) = \Delta K_G(0) / \tilde{\lambda}^2(g) = \frac{1}{\tilde{\lambda}^2(g)} \left( \frac{\lambda a_z^2}{k_B T} \right)^2 \left( \frac{K_R}{2} \right)^2. \quad (6.70)$$

## 6.6 Step Faceting

### 6.6.1 Stability of a Macrostep

In this section, we discuss the faceting of a macrostep.

Since faceted steps [122] are often observed on real surfaces, it seems natural to consider the roughening transition of an isolated step. Empirically, some impurities or materials of adsorption are known to induce faceted steps, and surface reconstructions are also known to do so [94,123]. As mentioned in Section 2.3, however, the drumhead wandering of a 1D surface (a step) activated by thermal fluctuations destabilizes a smooth surface. Hence, a step on a 2D surface is always rough when  $T < T_R$ , due to drumhead wandering. This seems to be contradicted by the observation of faceted steps in equilibrium.

Cabrera [62,63] presented the special polar angular dependence of the surface tension and its profile for the ECS<sup>23</sup> (Figure 6.24). Cabrera and Coleman [62] discussed the stability of a macrostep by assuming the surface free energy shown in Figure 6.24. If the surface free energy has the Type-II slope dependence, as shown on the left-hand side of Figure 6.24, a macrostep stabilizes as the two surfaces coexist under equilibrium.

The profile of the Type-II ECS, Figure 6.24, is called a first-order shape transition [20,34–36]. Rottman and Wortis [34] showed the first-order shape transition on the ECS for the 3D cubic Ising models with the negative second nearest-neighbor interaction using mean field approximation. Jayaprakash and Saam [20] showed the first-order shape transition on the ECS for the fcc lattice models with the negative second-nearest-neighbor interaction, using the mean-field approximation. Jayaprakash et al. [35] studied the vicinal surface between the (100) surface and the (110) surface by using a TSK model. Assuming an attractive step–step interaction, such as  $g_0/(x_i - x_j)^2$ , they obtained the first-order shape transition between the (100) surface and the (110) surface using the mean-field approximation. In the 1980s, the phase transition on the ECS attracted attention, but not much attention was paid to the stability of macrosteps.

Recently, various microscopic models that show an ECS similar to Type II in Figure 6.24 have been presented; these include the p-RSOS model [86,96,124,125], the RSOS-I model [126–128], and a modified RSOS-I model [129]. The p-RSOS model (Figure 6.25), explained in the following subsection, is the RSOS model with a point-contact type of step–step attraction. This type of step–step attraction works at the meeting point of adjacent steps. It was introduced to describe the energy gain that arises from the formation of a bonding state between steps due to the overlapping of orbitals. The RSOS-I model (the RSOS model coupled with the Ising system; see Appendix G.2) is used to study the effects of adsorption on the surface thermodynamic quantities. The

<sup>23</sup>In Figure 6.24,  $\beta(\mathbf{p})$  represents a vicinal surface free energy  $f(\mathbf{p})$  of this article. Later, the shape shown as type II in Figure 6.24 was called a “first-order shape transition” [22,36,57] because the surface slope jumps at the facet edge. The surface slope is given by the first derivative of the vicinal surface free energy with respect to  $\eta$  (Eqn (6.25)), and at the facet edge, it converges to  $\eta_1$  from the left but converges to 0 from the right.

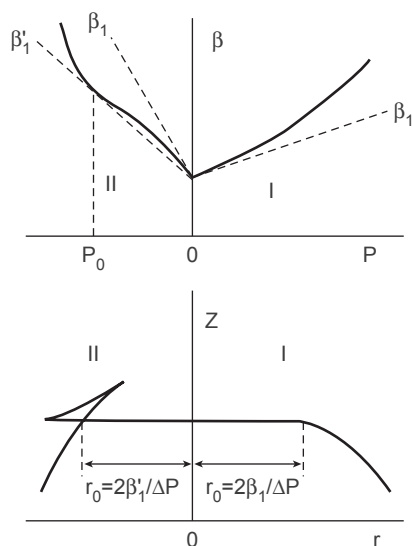


**FIGURE 6.24** Top figure: the vicinal surface free energy denoted by  $\beta$  as a function of  $p = p_x$ . Type I (right-hand side of the figure): the case of  $\partial^2\beta/\partial p^2 > 0$ . Type II (left-hand side of the figure): the case of  $\partial^2\beta/\partial p^2 < 0$ . Bottom figure: The profile of the ECS. Type I (right-hand side) and Type II (left-hand side). From Ref. [63].

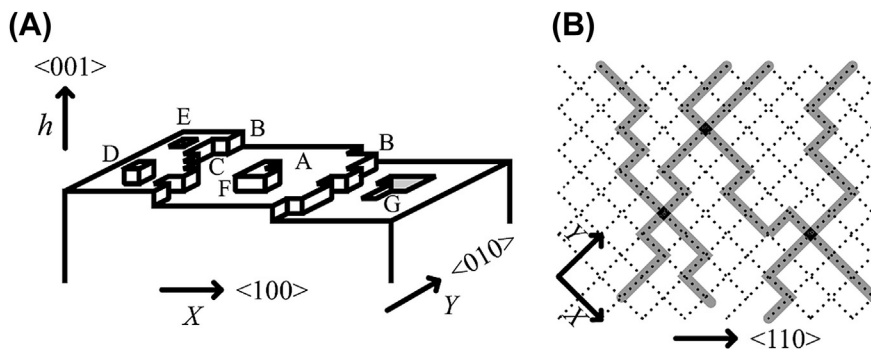


**FIGURE 6.25** An example of a vicinal surface on the p-RSOS model. (A) Perspective view. (B) Top view. From Ref. [86].

modified RSOS-I model is the RSOS-I model in which a relaxation of stress at the step edge is taken into consideration.

The faceted steps are obtained in these models at low temperatures, where the two surfaces coexist at equilibrium. The key quantity for these phenomena was found to be the microscopic step–step attraction [86,96,124–128]. This attractive step–step interaction causes a discontinuity in the surface tension [96] at low temperatures. The temperature dependence of the phenomena is understood to be due to the competition

between the attractive energy between the steps and the entropy of the step wandering. These phenomena can also be understood as 1D Bose gas condensation at  $T=0$  [86].

## 6.6.2 Discontinuous Surface Tension

### 6.6.2.1 *p*-RSOS Model

One of the microscopic models showing step faceting is the RSOS model with the point-contact type of step–step attraction (*p*-RSOS model) [86,96,124,125]. The Hamiltonian of the *p*-RSOS model is written as follows:

$$\begin{aligned} \mathcal{H}_{\text{p-RSOS}} = & \sum_{ij} \varepsilon[|h(i+1, j) - h(i, j)| + |h(i, j+1) - h(i, j)|] \\ & + \sum_{ij} \varepsilon_{\text{int}}[\delta(|h(i+1, j+1) - h(i, j)|, 2) \\ & + \delta(|h(i+1, j-1) - h(i, j)|, 2)], \end{aligned} \quad (6.71)$$

where  $\varepsilon$  is the microscopic ledge energy,  $\varepsilon_{\text{int}}$  is the microscopic step–step interaction energy, and  $\delta(a, b)$  is the Kronecker delta. The summation with respect to  $(i, j)$  is performed over all of the sites on the square lattice. The RSOS restriction is required implicitly. In the case of  $\varepsilon_{\text{int}} < 0$ , the interaction between the steps becomes attractive.

For a vicinal surface, we add the terms of the Andreev field [57]  $\boldsymbol{\eta} = (\eta_x, \eta_y)$  to the Hamiltonian in Eqn (6.71) as an external field. The model Hamiltonian given in Eqn (6.71) for the vicinal surface then becomes

$$\mathcal{H}_{\text{vicinal}} = \mathcal{H}_{\text{p-RSOS}} - \eta_x \sum_{ij} [h(i+1, j) - h(i, j)] - \eta_y \sum_{ij} [h(i, j+1) - h(i, j)]. \quad (6.72)$$

The partition function  $\mathcal{Z}$  for the *p*-RSOS model is given by  $\mathcal{Z} = \sum_{\{h(i, j)\}} \exp[-\beta \mathcal{H}_{\text{vicinal}}]$ . The Andreev surface free energy  $\tilde{f}(\boldsymbol{\eta})$  is the thermodynamic potential calculated from the partition function  $\mathcal{Z}$  by using the expression  $\beta \tilde{f}(\boldsymbol{\eta}) = -\lim_{\mathcal{N} \rightarrow \infty} (1/\mathcal{N}) \ln \mathcal{Z}$ , where  $\mathcal{N}$  is the number of points on the square lattice.

### 6.6.2.2 Discontinuity in Surface Tension

In Figure 6.26, we show the Andreev free energy calculated by the PWFRG method (Appendix A) [86,96,124,125]. The model is found to have two transition temperatures  $T_{f,1}$  and  $T_{f,2}$ ,<sup>24</sup> where for  $T < T_{f,1}$ , the surface tension of the (111) surface becomes discontinuous, and when  $T < T_{f,2}$ , the surface tension of the (001) surface becomes discontinuous. The shape of the equilibrium (001) facet is shown in Figure 6.27. As seen from this figure, the (001) facet directly contacts the (111) facet at  $T < T_{f,2}$ .

From the Legendre transformation of  $f(\mathbf{p}) = \tilde{f}(\boldsymbol{\eta}) + \mathbf{p} \cdot \boldsymbol{\eta}$ , we obtain the vicinal surface free energy and the surface tension  $\gamma_{\text{surf}}(\mathbf{p}) = f(\mathbf{p}) / \sqrt{1 + |\mathbf{p}|^2}$ . In Figure 6.28, we show the vicinal surface free energy and the surface tension calculated by the PWFRG

<sup>24</sup> $k_{\text{B}} T_{f,1}/\varepsilon = 0.3610 \pm 0.0005$  and  $k_{\text{B}} T_{f,2}/\varepsilon = 0.3585 \pm 0.0007$ .

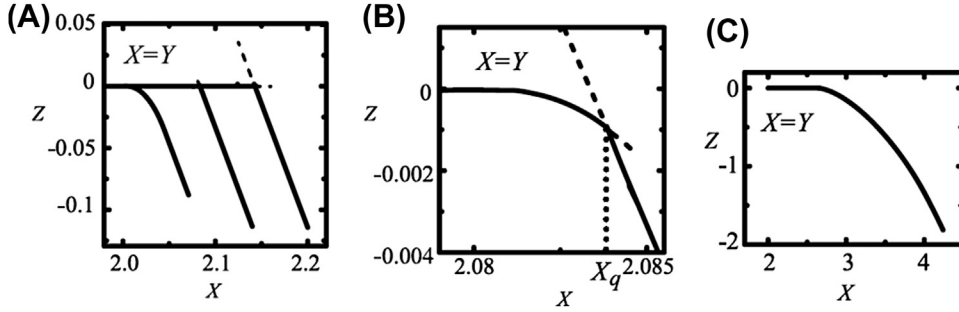


**FIGURE 6.26** Profile of the reduced equilibrium crystal shape calculated by the PWFRG method.  $X = \eta_x/k_B T = -\lambda x/k_B T$ ,  $Y = \eta_y/k_B T = -\lambda y/k_B T$ , and  $Z = \tilde{f}(\eta)/k_B T = \lambda z(x, y)/k_B T$ .  $\varepsilon_{\text{int}}/\varepsilon = -0.5$ . Broken lines represent metastable lines. (A) From right to left,  $k_B T/\varepsilon = 0.35, 0.36$ , and  $0.37$ . (B)  $k_B T/\varepsilon = 0.36$ . The edge of the (111) facet is denoted by  $X_q$ . (C) Original RSOS model ( $\varepsilon_{\text{int}} = 0$ );  $k_B T/\varepsilon = 0.3$ . From Ref. [96].

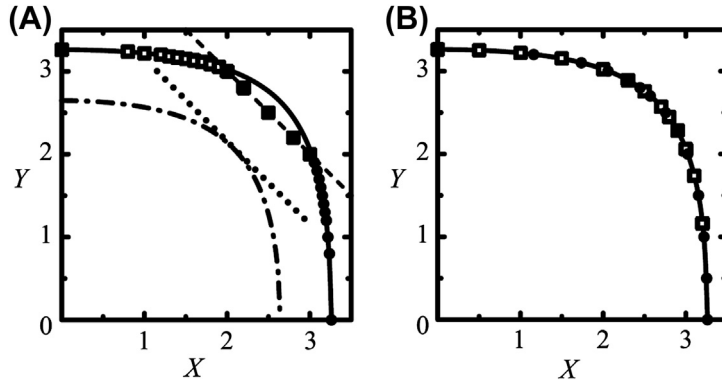


**FIGURE 6.27** Equilibrium facet shape (EFS) for  $X > 0$  and  $Y > 0$ . Filled circles:  $(X_c, Y_c)$  values calculated by the PWFRG method [44] (Appendix A) for  $k_B T/\varepsilon = 0.3$ . Open squares:  $(Y_c, X_c)$  values. Solid lines: EFS of the 2D square nn Ising model for  $k_B T/\varepsilon = 0.3$ . Dash-dotted lines: EFS of the 2D Ising model for  $k_B T/\varepsilon = 0.361$ . EFS of 2D Ising model is calculated by  $\cosh(X_c) + \cosh(Y_c) = [\cosh^2(\varepsilon/(k_B T))]/[\sinh(\varepsilon/(k_B T))]$ . Dashed lines:  $Y = -X + 5.0$ . Dotted lines:  $Y = -X + 4.1551$  ( $Y = -X + (2\varepsilon + \varepsilon_{\text{int}})/k_B T$ ). (A)  $\varepsilon_{\text{int}}/\varepsilon = -0.5$ ; (B)  $\varepsilon_{\text{int}} = 0$ . From Ref. [86].

method. For  $T_{f2} < T < T_{f1}$ , we have obtained a non-GMPT form for the vicinal surface free energy, as follows [86]:

$$f_{\text{eff}}(\mathbf{p}) = f(0) + \gamma_{\text{step}}(\phi) \left| \frac{\mathbf{p}}{a_z} \right| + A_{\text{eff}}(\phi) \left| \frac{\mathbf{p}}{a_z} \right|^2 + B_{\text{eff}}(\phi) \left| \frac{\mathbf{p}}{a_z} \right|^3 + \mathcal{O}\left( \left| \frac{\mathbf{p}}{a_z} \right|^4 \right). \quad (6.73)$$

Here, the quadratic term with respect to  $|\mathbf{p}|$  has reappeared.

It should be noted that the metastable lines in Figure 6.26 converge to points when  $T < T_{f2}$ . This means that there are no Gaussian-type capillary wave fluctuations (Figure 6.11(C)) with respect to the surface slope. This lack of slope fluctuations

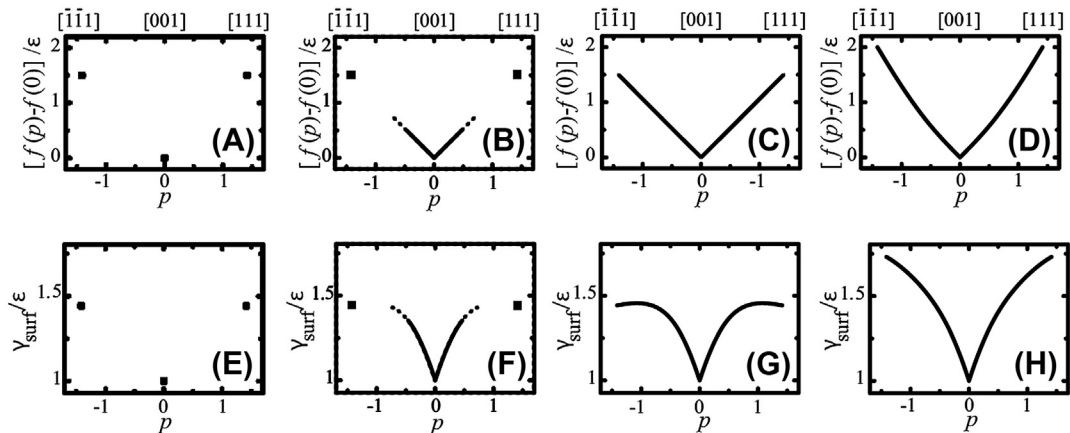


**FIGURE 6.28** The surface tilted toward the (110) direction, as calculated by the PWFRG (DMRG) method. (A)–(D) Slope dependence of the vicinal surface free energy  $[f(p_x, p_y) - f(0, 0)]/\epsilon$ ; and (E)–(H) surface tension  $\gamma_{\text{surf}}(p, p)/\epsilon$ . For (A)–(C) and (E)–(G),  $\epsilon_{\text{int}}/\epsilon = -0.5$ ; and for (D) and (H),  $\epsilon_{\text{int}} = 0$ , the original RSOS model. Temperatures:  $k_B T/\epsilon = 0.35$  for (A), (D), (E), and (H);  $k_B T/\epsilon = 0.36$  for (B) and (F);  $k_B T/\epsilon = 0.37$  for (C) and (G). Closed squares: (A) and (B),  $(0, 0)$  and  $[f(1, 1) - f(0, 0)]/\epsilon$ ; (E) and (F),  $\gamma_{\text{surf}}(0, 0)/\epsilon$  and  $\gamma_{\text{surf}}(1, 1)/\epsilon$ . Broken lines: (B) and (F), the curves for the metastable states. From Ref. [96].

stabilizes the flat plane of the side surface of the macrostep. This faceted macrostep formation was confirmed by a Monte Carlo calculation [86].

In addition to the above properties, the movements of a macrostep are inhibited near equilibrium [96]. When a macrostep is faceted ( $T < T_{f,2}$ ), the kink density at the side surface of the macrostep is extremely small because the side surface is flat and smooth. The macrostep moves by way of 2D nucleation, and thus there is intermittent motion of the macrostep near equilibrium. When the driving force is large enough to frequently create new 2D nuclei, kinetic roughening occurs on the side surfaces of the macrosteps. Hence, the macrostep dissolves into a homogeneous vicinal surface.

In the temperature region  $T_{f,2} < T < T_{f,1}$ , the steps merge locally, forming “step droplets” with a finite lifetime [86,96]. Due to the discontinuity in the surface tension around the (111) surface, the kink density decreases on the merged steps. The movements of the vicinal surface with step droplets, therefore, become smaller than what would be expected for the vicinal surface with regular train of steps.

## 6.7 Summary

Roughening and faceting transitions of surfaces and steps have been reviewed from the point of view of statistical mechanics. We paid attention to the crystal surfaces expressed by the distinct border in the microscopic scale between the crystal phase and the ambient phase such as in the case of vapor growth or solution growth. The definition of the surface free energy (or the interface free energy) was introduced. We have also shown how to define and calculate the surface free energy and step tension.

The microscopic surface shape is well described by the SOS model. Analysis of the statistical mechanics of the SOS model shows that the roughening transition is the Kosterlitz–Thouless type phase transition. In the rough phase, the variance of the surface heights becomes large and diverges logarithmically with the linear size of the surface due to the drumhead wandering. The surface size dependence of the variance is attributed to the lower *cutoff* of the wave number of the drumhead wandering. The universal features associated with the KT transition were reviewed concerning the roughening and faceting transitions. We have presented a brief description of other systems that have complex phase diagrams for the roughening transition temperature.

Universal features on the vicinal surface have been also discussed for temperatures lower than the roughening temperature of the terrace surface. The logarithmic behavior with respect to the length of the step has been explained for the variance of a single step height.

Finally, we discussed the faceting of a macrostep and its stability.

## Appendix A. Transfer Matrix Method

PWFRG is an acronym for the product wave-function renormalization group method [44]. The PWFRG method is a transfer matrix [130] version of the White’s density matrix renormalization group (DMRG) method [131,132] for 1D quantum spin systems. The 1D quantum system can be mapped to a 2D classical system through the transfer matrix with the Suzuki–Trotter formula [133].

In order to apply the PWFRG method to the RSOS systems, we construct the transfer matrix  $\hat{T}(t_1, t_2, \dots, t_N; s'_1, s'_2, \dots, s'_N)$  (Figure A.29(C)) by using the 19-vertex model [32,113] (Figure A.29(B)). The partition function  $\mathcal{Z}$  is then rewritten by  $\hat{T}$  as follows:

$$\mathcal{Z} = \text{Tr} \left[ \hat{T}(t_1, t_2, \dots, t_N; s'_1, s'_2, \dots, s'_N)^M \right], \quad (\text{A.1})$$

where  $N$  is the number of the linked vertices, and  $M$  is the linear size of the system in the vertical-direction in Figure A.29(D). Then the transfer matrix is expressed by use of the statistical weight denoted by  $V(s, t; s', t')$  as follows:

$$\hat{T}(t_1, t_2, \dots, t_N; s'_1, s'_2, \dots, s'_N) = \sum_{\{q_1\}, \{q_2\}, \dots} V(s_1, t_1; s'_1, q_1) V(q_1, t_2; s'_2, q_2) \cdots V(q_{N-1}, t_N; s'_N, q'_N). \quad (\text{A.2})$$

In the limit of  $M, N \rightarrow \infty$ , only the largest eigenvalue of the transfer matrix  $\Lambda(N)$  contributes to the partition function. The Andreev surface free energy, therefore, is obtained from the partition function (Eqn (A.1)) as

$$\beta \tilde{f}(\boldsymbol{\eta}) = - \lim_{M, N \rightarrow \infty} \frac{1}{NM} \ln \Lambda(N)^M, \quad (\text{A.3})$$

The transfer matrix is diagonalized efficiently by the PWFRG method. In the PWFRG calculation, the number of the so-called “retained bases”  $m$  are set from 7 to 37. The iteration number for the diagonalization is set to be  $1500 - 1 \times 10^5$ .

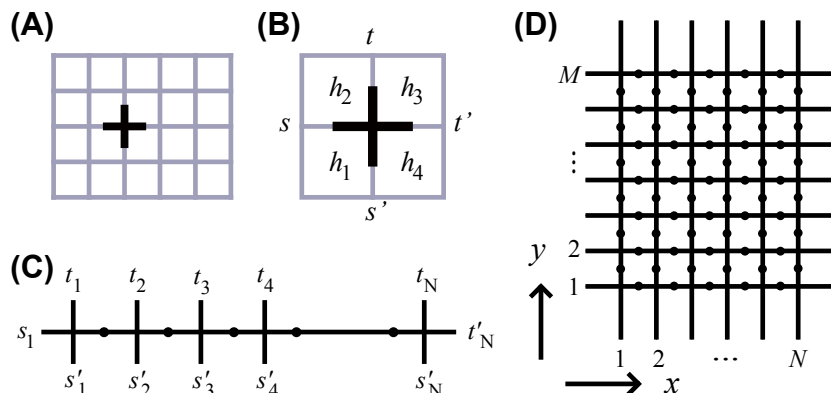


**FIGURE A.29** (A) Top view of the (001) surface of a cubic lattice. (B) Quadruplet of squares surrounding a vertex. In the figure,  $s = h_2 - h_1$ ,  $t = h_3 - h_2$ ,  $s' = h_4 - h_1$ ,  $t' = h_2 - h_1$  with  $s, s', t,$  and  $t'$  being  $\{0, \pm 1\}$ . (C) The transfer matrix assembled by the vertices. (D) Products of the transfer matrices.

## Appendix B. Driving Force for Crystal Growth

The driving force for crystal growth  $\Delta\mu$  is defined as the difference of the bulk chemical potential between the crystal phase and the ambient phase. Examples of the driving force are shown in [Table B.3](#) [94].

## Appendix C. Example of the Anisotropy of the Entropy of a Step

Let us consider a step on the (001) surface of cubic lattice ([Figure C.30](#)). The ground-state structure of a (010) step is uniquely determined. In [Figure C.30\(A\)](#), the step has six broken bonds, and eight in (B). Hence, the structure in (A) is the ground state, and the structure in (B) is in an excited state. On the other hand, (C), (D), and (E) also have eight broken bonds. There are 67 other structures with the same number of broken bonds. These 70 structures are all in the ground state, but they are degenerated. Hence, the ground-state structure of the (110) step cannot be determined uniquely. Since the entropy  $S$  is given by  $S = k_B \ln W$ , where  $W$  represents the degeneracy, the entropy of a step depends on the azimuth of the step.

## Appendix D. IPW Method

In this section, we explain how to derive the 1D interface tension from a rough phase separation line in the 2D Ising model [100]. The 1D interface as the phase separation line is made by an antiphase boundary condition, as shown in [Figure 6.9](#). We regard the

**Table B.3** Equation of Driving Force

Vapor growth	$\Delta\mu = k_B T \ln P/P_0^a$
Solution growth	$\Delta\mu = k_B T \ln C/C_0^b$
Melt growth	$\Delta\mu = \mu_{\text{liquid}} - \mu_{\text{crystal}} \approx \Delta s_{\text{melting}}(T_m - T)^c$
Electrocrystallization of metals	$\Delta\mu = ze\eta^d$

<sup>a</sup> $k_B$  represents the Boltzmann constant,  $T$  represents the temperature,  $P$  represents the pressure in the ambient phase, and  $P_0$  represents the equilibrium pressure at some temperature  $T_0$ . <sup>b</sup> $C$  and  $C_0$  are the real and the equilibrium concentrations of the solute, respectively. <sup>c</sup> $T_m$  represents the melting temperature, and  $\Delta s_{\text{melting}}$  represents the entropy of melting. <sup>d</sup> $z$  represents the valence of the neutralizing ions,  $e$  represents the elementary electric charge, and  $\eta = E - E_0$  represents the over-voltage given by the difference of the equilibrium potential  $E_0$ .

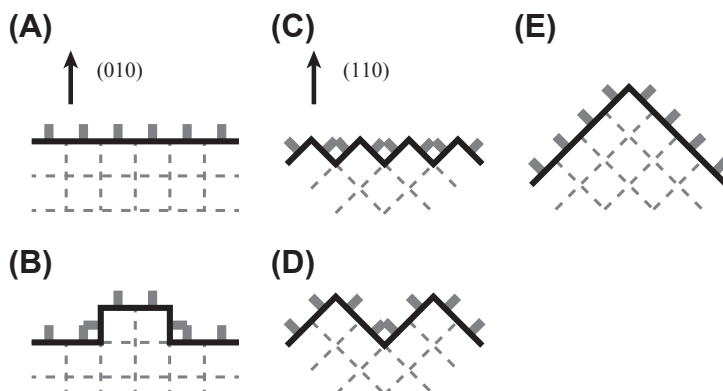


**FIGURE C.30** Microscopic configuration of a step on a cubic lattice with both ends being fixed. Black solid line: the edge of a step. Gray line: a broken bond. (A) and (B): (010) steps. (C), (D), and (E): (110) steps.

phase separation line as a random walk connecting the ends O and P. The main idea for obtaining  $\gamma_{1D}(\theta, T)$  is to use the “duality” between the interface tension and the correlation length [134]. The asymptotic form of the correlation function becomes

$$G(\mathbf{R}) \sim \exp[-|\mathbf{R}|/\xi(\theta, T^*)], \quad (|\mathbf{R}| \rightarrow \infty), \quad (\text{D.1})$$

where  $T^*$  represents the temperature in the world of  $\xi(\theta, T^*)$ . From the duality relation, we have  $\gamma_{1D}(\theta, T)/k_B T = 1/\xi(\theta, T^*)$ , and

$$\mathcal{G}(\mathbf{R} + \mathbf{r}, \beta|\mathbf{R}, \alpha) \sim \exp[-\gamma_{1D}(\theta, T)|\mathbf{r}|/k_B T], \quad (|\mathbf{r}| \rightarrow \infty), \quad (\text{D.2})$$

We will only give a brief review of the derivation of the final equations, Eqns (D.6)–(D.8) [100].

Let us label each elementary path by a pair  $(\mathbf{R}, \alpha)$ , where  $\mathbf{R}$  represents the starting position of the path and  $\alpha$  represents its direction, such as  $\{\rightarrow, \leftarrow, \uparrow, \downarrow\}$ . We denote the weighted sum over all possible  $N$ -step walks by  $\mathcal{G}_N(\mathbf{R}, \alpha|\mathbf{R}_0, \alpha_0)$ , where the random walk

starts at  $\mathbf{R}_0$  with direction  $\alpha_0$  and ends at  $\mathbf{R}$  with direction  $\alpha$ . Using the connectivity matrix  $A(\mathbf{R}, \alpha | \mathbf{R}', \beta)$ ,  $\mathcal{G}_N$  satisfies the following recursion relation:

$$\mathcal{G}_{N+1}(\mathbf{R}, \alpha | \mathbf{R}_0, \alpha_0) = \sum_{\mathbf{R}', \beta} A(\mathbf{R}, \alpha | \mathbf{R}', \beta) \mathcal{G}_N(\mathbf{R}', \beta | \mathbf{R}_0, \alpha_0). \quad (\text{D.3})$$

Writing in matrix form, Eqn (D.3) becomes  $\mathcal{G}_{N+1} = A\mathcal{G}_N$ . Let us introduce  $\mathcal{G}$  as  $\mathcal{G} = \sum_{N=0}^{\infty} \mathcal{G}_N$ . Then with initial condition  $\mathcal{G}_0 = 1$ , we have  $\mathcal{G} = [1 - A]^{-1}$ . Then, evaluating  $Z^{++}$  and  $Z^{+-}(\theta)$  by Vdovichenko's method [135], we have

$$\frac{Z^{+-}(\theta)}{Z^{++}} \propto \mathcal{G}(\mathbf{R} + \mathbf{r}, \beta | \mathbf{R}, \alpha). \quad (\text{D.4})$$

From Eqns (D.2)–(D.4),

$$\gamma_{1\text{D}}(\theta, T) = -k_{\text{B}}T \lim_{|r| \rightarrow \infty} \frac{1}{|r|} \ln \left[ \int_{-\pi}^{\pi} \int_{-\pi}^{\pi} dk^2 \frac{e^{ikr}}{D(\mathbf{k})} \right], \quad (\text{D.5})$$

where  $D(\mathbf{k})$  represents  $D(\mathbf{k}) = \det[1 - A(\mathbf{k})]$  and  $A(\mathbf{k})$  represents the matrix of the Fourier components of  $A(\mathbf{R}, \alpha | \mathbf{R}', \beta)$ .

We estimate the right-hand side of Eqn (D.5) by the saddle-point method, and denote the saddle-point  $\mathbf{k}^* = (i\omega_1, i\omega_2)$ . Then, we have a set of equations as follows [39,86,100]:

$$\gamma_{1\text{D}}(\theta, T) = k_{\text{B}}T(\omega_1 \cos \theta + \omega_2 \sin \theta) \quad (\text{D.6})$$

$$D(\omega) = 0 \quad (\text{D.7})$$

$$[\partial D(\omega) / \partial \omega_2] / [\partial D(\omega) / \partial \omega_1] = \tan \theta. \quad (\text{D.8})$$

From the thermodynamics of ECS, we have  $-\eta = \lambda x = k_{\text{B}}T\omega_2$  and  $\tilde{f}(\eta) = \lambda y = k_{\text{B}}T\omega_1$ .

It should be noted that  $D(\mathbf{k})$  also appears in the bulk free energy of the 2D Ising model.

## Appendix E. Calculation of Surface Width

In this section, we derive an explicit equation for the variance of the surface height, Eqn (E.6) [23].

The variance of the surface height,

$$W^2 = \left\langle [h(\mathbf{x}) - \langle h(\mathbf{x}) \rangle]^2 \right\rangle, \quad (\text{E.1})$$

can also be written as

$$W^2 = \sum_{\mathbf{k}} \langle h(\mathbf{k}) h(-\mathbf{k}) \rangle \quad (\text{E.2})$$

where

$$\begin{aligned} h(\mathbf{x}) &= \sum_{\mathbf{k}} h(\mathbf{k}) \exp(i\mathbf{k}\mathbf{x}), \quad \mathbf{k} = (k_1, k_2), \\ k_1 &= (2\pi m)/L, \quad k_2 = (2\pi m')/L. \quad (m, m' = \pm 1, \pm 2, \pm 3, \dots) \end{aligned} \quad (\text{E.3})$$

Using Eqn (6.26) for the thermal average, we obtain the following equation:

$$W^2 = \frac{k_B T}{L^2} \sum_{\mathbf{k}} \left[ \sum_{\alpha, \beta} f^{\alpha\beta} k_\alpha k_\beta \right]^{-1}, \quad (\text{E.4})$$

where  $f^{\alpha\beta}$  represents  $f^{xx}(\mathbf{p}_e)$ ,  $f^{yy}(\mathbf{p}_e)$ ,  $f^{xy}(\mathbf{p}_e)$ , and  $f^{yx}(\mathbf{p}_e)$ , and they are the components of the surface stiffness tensor defined by Eqn (6.27). Applying a continuous approximation to the r.h.s. of the above summation with respect to  $\mathbf{k}$ , we have

$$W^2 = \frac{k_B T}{2\pi \sqrt{\det(f^{\alpha\beta})}} \int_{k_0}^{\Lambda} dq \frac{1}{q}, \quad (\text{E.5})$$

where  $\Lambda = 2\pi/a$  represents the upper cutoff, and  $k_0 = 2\pi/L$  represents the lower cutoff. In this way, we have in the limit of  $L \rightarrow \infty$ ,

$$W^2 = \frac{k_B T}{2\pi \sqrt{\det(f^{\alpha\beta})}} \ln L. \quad (\text{E.6})$$

## Appendix F. Derivation of the Capillary Wave Hamiltonian

In this section, we derive Eqn (6.26).

The total surface free energy  $\Phi$  of a crystal droplet surrounded by rough surfaces is described as follows:

$$\Phi = \int \gamma_{\text{surf}}(\mathbf{n}) dA = \int f(\mathbf{p}) dx dy, \quad f(\mathbf{p}) = \gamma_{\text{surf}}(\mathbf{n}) \sqrt{g} \quad (\text{F.1})$$

where  $\gamma_{\text{surf}}(\mathbf{n})$  represents the surface tension,  $\mathbf{n}$  represents the surface normal unit vector,  $dA$  represents a small surface area, and  $f(\mathbf{p})$  represents the surface free energy per projected  $xy$  area. For an inclined surface of area  $L^2$ , a generalized free energy  $\tilde{F}(\mathbf{p}, \boldsymbol{\eta})$  [23] is considered from Eqn (F.1) as follows:

$$\tilde{F}(\mathbf{p}, \boldsymbol{\eta}) = L^2 [f(\mathbf{p}) - \mathbf{p} \cdot \boldsymbol{\eta}], \quad (\text{F.2})$$

where  $\boldsymbol{\eta}$  and  $\mathbf{p}$  are assumed to be independent variables. The equilibrium orientation of the surface is obtained by minimizing  $\tilde{F}(\mathbf{p}, \boldsymbol{\eta})$  with respect to  $\mathbf{p}$ . After some calculations, we have the following equation near the equilibrium surface slope  $\mathbf{p}_e$ , Figure 6.11(C):

$$\tilde{F}(\mathbf{p}, \boldsymbol{\eta}) = L^2 \tilde{f}(\boldsymbol{\eta}) + \frac{1}{2} L^2 \left[ f^{xx}(\mathbf{p}_e) \Delta p_x^2 + f^{yy}(\mathbf{p}_e) \Delta p_y^2 + (f^{xy}(\mathbf{p}_e) + f^{yx}(\mathbf{p}_e)) \Delta p_x \Delta p_y \right], \quad (\text{F.3})$$

where  $\tilde{f}(\boldsymbol{\eta})$  represents the Andreev free energy [57]; and  $f^{xx}(\mathbf{p}_e)$ ,  $f^{yy}(\mathbf{p}_e)$ ,  $f^{xy}(\mathbf{p}_e)$ , and  $f^{yx}(\mathbf{p}_e)$  are the components of the surface stiffness tensor defined by Eqn (6.27).

Hence, the capillary wave Hamiltonian of the inclined crystal surface becomes Gaussian (Figure 6.11(C)) as follows:

$$\mathcal{H}_{CW} = \frac{1}{2} \int_0^L dx \int_0^L dy \left[ f^{xx}(\mathbf{p}_e) \Delta p_x^2 + f^{yy}(\mathbf{p}_e) \Delta p_y^2 + (f^{xy}(\mathbf{p}_e) + f^{yx}(\mathbf{p}_e)) \Delta p_x \Delta p_y \right]. \quad (\text{F.4})$$

## Appendix G. Other Microscopic Models

### Appendix G.1. Discrete Gaussian Model

The discrete Gaussian (DG) model introduced by Chui and Weeks [42] is one of the SOS models, and the Hamiltonian of the DG model is given as follows:

$$\mathcal{H}_{DG} = \frac{J}{2} \sum_{j,\delta} (h_j - h_{j+\delta})^2, \quad (\text{G.1})$$

where  $\{h_j\}$  represents the surface height at a site  $j$  and  $J$  represents the energy cost to create the height difference on the surface between  $i$  and  $i + \delta$  as the nn lattice sites. The summation with respect to  $i$  runs over all lattice points, and the summation with respect to  $\delta$  runs over all the nn sites around  $i$ . Note that  $\{h_j\}$  in the DG model is a continuous variable.

Since the DG model is a Gaussian-type model, it is easy to analyze theoretically. The model, therefore, contributes to establishing an essential connection between the roughening transition on the surface and the XY model in two dimensions.

### Appendix G.2. RSOS-I Model

The image of the RSOS model and the materials of adsorption for the RSOS-I model are similar to Figure 6.21. The Hamiltonian for the RSOS-I model [126,128] is written as follows:

$$\begin{aligned} \mathcal{H}_{\text{RSOS-I}} &= \mathcal{H}_{\text{RSOS}} + \mathcal{H}_{\text{Ising}} + \mathcal{H}_{\text{int}} \\ &= \sum_{m,n} [\varepsilon(1 - \alpha\sigma_y(m, n)) |h(m+1, n) - h(m, n)| + \varepsilon(1 - \alpha\sigma_x(m, n)) |h(m, n+1) - h(m, n)|] \\ &\quad - J \sum_{m,n} [\sigma_x(m, n)\sigma_y(m, n) + \sigma_x(m, n)\sigma_y(m-1, n) \\ &\quad + \sigma_x(m, n-1)\sigma_y(m, n) + \sigma_x(m, n-1)\sigma_y(m-1, n)] \\ &\quad - H \sum_{m,n} [\sigma_x(m, n) + \sigma_y(m, n)]. \end{aligned} \quad (\text{G.2})$$

In the case of  $J = 0$ , the model reduces to the decorated RSOS model in Section 4.4.2 (Eqn (6.50)).

## Acknowledgment

This work is supported by the Japan Society for Promotion of Science (JSPS) KAKENHI Grant Number 25400413.

## References

- [1] van Beijeren H. *Phys Rev Lett* 1977;38:993.
- [2] Swendsen RH. *Phys Rev B* 1982;25:2019.
- [3] den Nijs M. *J Phys A Math Gen* 1985;18:L549.
- [4] Abraham DB. In: Domb C, Lebowitz JL, editors. *Phase transition and critical phenomena*, vol. 10, 1. London: Academic Press; 1986.
- [5] Aizenman M, Fernandez R. *J Stat Phys* 1986;44:383.
- [6] Akutsu Y, Akutsu N. *J Phys A* 1986;19:2813.
- [7] Fisher MPA, Fisher DS, Weeks JD. *Phys Rev Lett* 1982;48:368. de Coninck J, Ruiz J. *J Phys* 1988;A21:L147. Abraham DB, Upton PJ. *Phys Rev* 1988;B37:3835.
- [8] Rottman C, Wortis M. *Phys Rev B* 1981;24:6274. Avron JE, van Beijeren H, Schulman LS, Zia RKP. *J Phys* 1982;A15:L81.
- [9] Müller-Krumbhaar H. In: Kaldis E, editor. *Current topics in materials science*, vol. 1. Amsterdam: North-Holland Publishing; 1978. Ch. 1, 1.
- [10] Knops HJF. *Phys Rev Lett* 1977;39:766.
- [11] Jose JV, Kadanoff LP, Kirkpatrick S, Nelson DR. *Phys Rev B* 1977;16:1217.
- [12] Weeks JD. In: Riste T, editor. *Ordering in strongly fluctuation condensed matter systems*. Plenum, New York and London; 1980. p. 293.
- [13] Gruber EE, Mullins WW. *J Phys Chem Solids* 1967;28:6549. Pokrovsky VL, Talapov AL. *Phys Rev Lett* 1979;42:65; *Zh Eksp Teor Fiz* 1980;78:269 [*Sov Phys JETP* 1980;51:134].
- [14] Haldane FDM, Villain J. *J Phys Paris* 1981;42:1673.
- [15] Villain J. In: Riste T, editor. *Ordering in strongly fluctuation condensed matter systems*. Plenum, New York and London; 1980. p. 222. Villain J, Bak P. *J Phys Paris* 1981;42:657.
- [16] Cabrela N, Garcia N. *Phys Rev B* 1982;25:6057.
- [17] Izuyama T, Akutsu Y. *J Phys Soc Jpn* 1982;51:50. Yamamoto T, Izuyama T. *J Phys Soc Jpn* 1987;56:632.
- [18] Jayaprakash C, Saam WF, Teitel S. *Phys Rev Lett* 1983;50:2017.
- [19] Rottman C, Wortis M. *Phys Rep* 1984;103:59. Wortis M. *Chemistry and physics of solid surface VII*. In: Vanselow R, Howe R, editor. Berlin, Heidelberg: Springer-Verlag; 1988. p. 367.
- [20] Jayaprakash C, Saam WF. *Phys Rev B* 1984;30:3916.
- [21] Schultz HJ. *J Phys* 1985;46:257.
- [22] van Beijeren H, Nolden I. In: Schommers W, von Blanckenhagen P, editors. *Structure and dynamics of surfaces II*. Berlin, Heidelberg: Springer-Verlag; 1987. p. 259.
- [23] Akutsu N, Akutsu Y. *J Phys Soc Jpn* 1987;56:1443.
- [24] Akutsu N, Akutsu Y. *J Phys Soc Jpn* 1987;56:2248 [Uwaha M, unpublished].
- [25] Akutsu Y, Akutsu N, Yamamoto T. *Phys Rev Lett* 1988;61:424.

- [26] Yamamoto T, Akutsu Y, Akutsu N. *J Phys Soc Jpn* 1988;57:453.
- [27] Mikheev LV, Pokrovsky VL. *J Phys* 1991;1:373.
- [28] Saam WF. *Phys Rev Lett* 1989;62:2636.
- [29] Akutsu Y, Akutsu N, Yamamoto T. *Phys Rev Lett* 1989;62:2637.
- [30] Yamamoto T, Akutsu Y, Akutsu N. *J Phys Soc Jpn* 1989;58:3531. Yamamoto T, Akutsu N, Akutsu Y. *J Phys Soc Jpn* 1990;59:3831; *J Phys Soc Jpn* 1991;60:3600.
- [31] Akutsu N, Akutsu Y. *Surf Sci* 1997;376:92.
- [32] Akutsu N, Akutsu Y. *Phys Rev B* 1998;57:R4233.
- [33] Akutsu N, Akutsu Y. *Prog Theor Phys* 2006;116:983.
- [34] Rottman C, Wortis M. *Phys Rev B* 1984;29:328.
- [35] Jayaprakash C, Rottman C, Saam WF. *Phys Rev B* 1984;30:6549.
- [36] Nozières P. In: Godrèche C, editor. *Solids far from equilibrium*. Cambridge, New York, Port Chester, Mellbourne, Sydney; 1991. p. 1.
- [37] Pimpinelli A, Villain J. *Physics of crystal growth*. Cambridge University Press; 1998.
- [38] Akutsu N, Akutsu Y. *J Phys Soc Jpn* 1990;59:3041. *J Phys* 1990;A23:L217. Akutsu N. *J Phys Soc Jpn* 1992;61:477. Akutsu N, Akutsu Y. *J Phys Soc Jpn* 1995;64:736; *J Phys Soc Jpn* 1996;65:1233.
- [39] Akutsu N, Akutsu Y. *J Phys Condens Matter* 1999;11:6653.
- [40] Kosterlitz JM, Thouless DJ. *J Phys C* 1973;6:1181. Kosterlitz JM. *J Phys C* 1974;7:1046.
- [41] Young AP. In: Riste T, editor. *Ordering in strongly fluctuation condensed matter systems*. Plenum Press, New York and London; 1980. p. 271. Wegner FJ. *Phase transition and critical phenomena*, vol. 6, Domb C, Green MS, editors. London: Academic Press; 1976. p. 7.
- [42] Chui ST, Weeks JD. *Phys Rev B* 1976;14:4978.
- [43] Bishop DJ, Reppy JD. *Phys Rev Lett* 1978;40:1727. Nelson DR. *Phase transition and critical phenomena*, vol. 7, p. 1. Domb C, Lebowitz JL, editors. London: Academic Press; 1983.
- [44] Nishino T, Okunishi K. *J Phys Soc Jpn* 1995;64:4084. Hieida Y, Okunishi K, Akutsu Y. *Phys Lett* 1997; A233:464; *New J Phys* 1999;1:7.1.
- [45] Bauer E, Teliëps W. *Ultramicroscopy* 1985;17:57. *Scan Microsc* 1987;(suppl. 1):99; In: *The study of surfaces and interfaces by electron optical techniques*, Howie A, Valderé U, editors. Plenum, New York, 1988; p. 195.
- [46] Bartelt NC, Tromp RM, Williams ED. *Phys Rev Lett* 1994;73:1656.
- [47] Mermin ND, Wagner H. *Phys Rev Lett* 1966;17:1133.
- [48] Wulff G. *Kristallogr Z. Miner* 1901;34:449.
- [49] von Laue M. *Kristallogr Z. Miner* 1943;105:124.
- [50] Herring C. *Phys Rev* 1951;82:87.
- [51] Hartman P, Pedok WG. *Acta Cryst* 1955;8:49. *Acta Cryst* 1955;8:521; *Acta Cryst* 1995;8:525.
- [52] MacKenzie JK, Moore AJW, Nicholas JF. *J Chem Phys Solids* 1962;23:185.
- [53] Frank FC. *Metal surfaces*, ASM. 1963. 1.
- [54] Toschev S. In: Hartman P, editor. *Crystal growth, an introduction*; 1973. p. 328. North-Holland.
- [55] Ookawa A. *Crystal growth*. Syōkabō, Tokyo. 1977 [in Japanese].
- [56] Landau LD, Lifshitz EM. *Statistical physics*. 2nd ed. Oxford, Pergamon; 1968. Landau LD, Lifshitz EM. *Statistical physics, Part 1 (Course of theoretical physics vol. 5)*, 3rd ed., Elsevier, Butterworth-Heinemann, Amsterdam; 1980).

- [57] Andreev AF. *Zh Eksp Theor Fiz* 1981;80:2042. *Sov Phys JETP* 1981;53:1063.
- [58] Kern R, Le Ley G, Métois JJ. In: Kaldis E, editor. *Current topics in materials science*, vol. 3. Amsterdam: North-Holland Publ.; 1979. Ch. 3, 131. Kern R. *Morphology of crystals*. Sunagawa I, editor. Tokyo: Terra Scientific Publishing; 1987. p. 77.
- [59] Kreyszig E. *Introduction to differential geometry and Riemannian geometry*. University of Toronto Press; 1968.
- [60] Ehrenfest P. *Ann Phys* 1915;48:360.
- [61] Yamada M. *Phys Zeit* 1923;24:364. 1924;25:52; 1924;25:289.
- [62] Cabrera N, Coleman RV. In: Gilman JJ, editor. *The art and science of growing crystals*. New York, London: John Wiley & Sons; 1963. p. 3.
- [63] Cabrera N. *Surf Sci* 1964;2:320.
- [64] Balibar S, Edwards DO, Laroche C. *Phys Rev Lett* 1979;42:782.
- [65] Landau J, Lipson SG, Maattanan LM, Balfour LS, Edwards DO. *Phys Rev Lett* 1980;45:31.
- [66] Avron JE, Balfour LS, Kuper CG, Landau J, Lipson SG, Schulman LS. *Phys Rev Lett* 1980;45:814.
- [67] Wolf PE, Gallet GF, Balibar S, Rolley E, Nozières P. *J Phys* 1985;46:1987.
- [68] Nozières P, Gallet F. *J Phys* 1987;48:35. Gallet GF, Nozières P, Balibar S, Rolley E. *Europhys Lett* 1986;2:701.
- [69] Babkin AV, Keshishev KO, Kopeliovich DB, Ya Parshin A. *Sov Phys JETP Lett* 1984;39:633.
- [70] Carmi Y, Lipson SG, Polturak E. *Phys Rev B* 1987;36:1894.
- [71] Balibar S, Guthmann C, Rolley E. *J Phys I* 1993;3:1475.
- [72] Balibar S, Alles H, Parshin AY. *Rev Mod Phys* 2005;77:318.
- [73] Pavlovskaya A, Bauer E. *Europhys Lett* 1989;9:797. Pavlovskaya A, Faulian K, Bauer E. *Surf Sci* 1989; 221–233.
- [74] Bonzel HP, Dücker K. In: Vanselow R, Howe RF, editors. *Chemistry and physics of solid surfaces VII*. Berlin, Heidelberg: Springer-Verlag; 1988. p. 429.
- [75] Cheng W-C, Wynblatt P. *Surf Sci* 1996;364:417. Arenhold K, Surnev S, Bonzel HP, Wynblatt P. *Surf Sci* 1999;424:271.
- [76] Nowicki M, Bombis C, Emundts A, Bonzel HP, Wynblatt P. *Europhys Lett* 2002;59:239. *New J Phys* 2002;4:60.
- [77] Ohachi T, Taniguchi I. *J Cryst Growth* 1983;65:84.
- [78] Rottman C, Wortis M, Heyraud JC, Métois J. *Phys Rev Lett* 1984;52:1009.
- [79] Heyraud JC, Métois JJ. *Surf Sci* 1986;177:213. Métois JJ, Heyraud JC. *Surf Sci* 1987;180:647.
- [80] Eaglesham DJ, Unterwald FC, Jacobson DC. *Phys Rev Lett* 1993;70:966.
- [81] Bermond JM, Métois JJ, Egea X, Floret F. *Surf Sci* 1995;330:48.
- [82] Suzuki T, Métois JJ, Yagi K. *Surf Sci* 1995;339:105. Suzuki T, Minoda H, Tanishiro Y, Yagi K. *Surf Rev Lett* 1999;6:985.
- [83] Pavlovskaya A, Nenow D. *J Cryst Growth* 1971;8:209. *Surf Sci* 1971;27:211. Pavlovskaya A. *J Cryst Growth* 1979;46:551.
- [84] Nenow D, Stoyanova V. *J Cryst Growth* 1979;46:779.
- [85] Görnert P, Voigt F. In: Kaldis E, editor. *Current topics in materials science*, vol. 11. Amsterdam: North-Holland Publ; 1984. Ch. 1, 1.
- [86] Akutsu N. *J Phys Condens Matter* 2011;23:485004.

- [87] Burton WK, Cabrela N, Frank FC. *Philos Trans R Soc Lond A* 1951;243:299.
- [88] Jackson KA. In: Doremus RH, editor. *Growth and perfection of crystals: proceedings*. New York, London: John Wiley & Sons; 1958. p. 319.
- [89] Leamy HJ, Gilmer GH, Jackson KA. In: Blakely JM, editor. *Surface physics of crystalline materials*. New York: Academic Press; 1975. p. 121.
- [90] Buff FP, Lovett RA, Stillinger FH. *Phys Rev Lett* 1965;15:621.
- [91] Weeks JD. *J Chem Phys* 1977;67:3106.
- [92] Jasnow D. *Rep Prog Phys* 1984;47:1059. Jasnow D. *Phase transition and critical phenomena*, vol. 10, Domb C, Lebowitz JL, editors. London: Academic Press; 1986. p. 269.
- [93] Frank FC. *Discuss Faraday Soc* 1949:48. No.5.
- [94] Markov IV. *Crystal growth for beginners*. 2nd ed. World Scientific, New Jersey, London, Singapore, Hong Kong; 2003.
- [95] Müller-Krumbhaar H, Burkhardt TW, Kroll DM. *J Cryst Growth* 1977;38:13.
- [96] Akutsu N. *Phys Rev E* 2012;86:061604. *Phys Rev E*, "Kaleidoscope," December 2012 (<http://pre.aps.org/>). Akutsu N, *J Cryst Growth* 2014;401:72. (<http://dx.doi.org/10.1016/j.jcrysgro.2014.01.068>).
- [97] Saito Y. *Statistical physics of crystal growth*. World Scientific, New Jersey, London, Singapore, Hong Kong; 1996.
- [98] Saito Y. In: Riste T, editor. *Ordering in strongly fluctuation condensed matter systems*. Plenum, New York and London; 1980. p. 319.
- [99] Onsager L. *Physical review*, series II, vol. 65; 1944. 117.
- [100] Akutsu Y, Akutsu N. *Phys Rev Lett* 1990;64:1189. Holzer M. *Phys Rev Lett* 1990;64:653; *Phys Rev B* 1990;42:10570.
- [101] Bartelt NC, Goldberg JL, Einstein TL, Williams ED, Heyraud JC, Métois JJ. *Phys Rev B* 1993;48:15453.
- [102] Barabasi A-L, Stanley HE. *Fractal concepts in surface growth*. Cambridge; 1994.
- [103] Yamamoto T, Akutsu Y, Akutsu N. *J Phys Soc Jpn* 1994;63:915. Akutsu Y, Akutsu N, Yamamoto T. *J Phys Soc Jpn* 1994;63:2032.
- [104] Yamamoto T, *Phys J. Soc Jpn* 1996;65:3810.
- [105] Yamamoto T, Akutsu N, Akutsu Y. *Advances in the understanding of crystal growth mechanisms*, part I. In: Nishinaga T, Nishioka K, Harada J, Sasaki A, Takei H, editors. *Crystal growth theory and simulations*. Amsterdam, New York: Elsevier Science; 1997. p. 19.
- [106] Syoji I. In: Domb C, Green MS, editors. *Phase transitions and critical phenomena*, vol. 1. London: Academic Press; 1972. p. 270.
- [107] Akutsu N, Akutsu Y, Yamamoto T. *Phys Rev B* 2001;64:85415–21.
- [108] Kossel W. *Nach Ges Wiss Gottingen* 1927:135. *Naturewissenschaften* 1930;18:901.
- [109] Sogo K, Akutsu Y, Abe T. *Prog Theor Phys* 1983;70:739. Truong TT, den Nijs M. *J Phys A* 1986;19:L645.
- [110] <http://noriko-akutsu.com/data/>.
- [111] Bricmont J, Lebowitz J, Pfister Ch. *J Stat Phys* 1981;26:313.
- [112] Akutsu Y, Akutsu N. *J Phys A* 1987;20:5981.
- [113] den Nijs M, Rommelse K. *Phys Rev B* 1989;40:4709.
- [114] Luijten E, van Beijeren H, Blöte HWJ. *Phys Rev Lett* 1994;73:456.

- [115] Mazzeo G, Carlon E, van Beijeren H. Surf Sci 1996;352–354:960. Carlon E, Mazzeo G, van Beijeren H. Phys Rev B 1997;55:757.
- [116] Davidson D, den Nijs M. Phys Rev E 1997;55:1331.
- [117] Carlon E, van Beijeren H. Phys Rev E 2000;62:7646.
- [118] Marchenko VI, Ya Parshin A. Sov Phys JETP 1980;52:129.
- [119] Alerhand OL, Vanderbilt D, Meade RD, Jonnopoulos JD. Phys Rev Lett 1988;61:1973.
- [120] Williams ED, Phaneuf RJ, Wei J, Bartelt NC, Einstein TL. Surf Sci 1993;294:219. Surf Sci 1994;310:451.
- [121] Sutherland B. J Math Phys 1971;12:246.
- [122] Mullins WW. Philos Mag 1961;6:1313.
- [123] Bartelt NC, Einstein TL, Rottman C. Phys Rev Lett 1991;66:961.
- [124] Akutsu N. Appl Surf Sci 2009;256:1205.
- [125] Akutsu N. J Cryst Growth 2011;318:10.
- [126] Akutsu N, Akutsu Y, Yamamoto T. Surf Sci 2001;493:475. Prog Theor Phys 2001;105:361.
- [127] Akutsu N, Akutsu Y, Yamamoto T. J Cryst Growth 2002;237.
- [128] Akutsu N, Akutsu Y, Yamamoto T. Phys Rev B 2003;67:125407–11.
- [129] Akutsu N, Hibino H, Yamamoto T. e-J Surf Sci Nanotech 2009;7:39.
- [130] Lieb E. In: Domb C, Green MS, editors. Phase transitions and critical phenomena, vol. 1. London, New York: Academic Press; 1972. p. 331. Baxter RJ. Exactly solved models in statistical mechanics, Section 2 and Section 8. London, New York: Academic Press; 1982).
- [131] White SR. Phys Rev Lett 1992;69:2863. Nishino T. J Phys Soc Jpn 1995;64:3598.
- [132] Peschel I, Wang X, Kaulke M, Hallberg K. In: Density-matrix renormalization, a new numerical method in physics. Berlin, Heidelberg: Springer-Verlag; 1999.
- [133] Trotter HF. Proc Am Math Soc 1959;10:545. Suzuki M. Comm Math Phys 1976;51:183.
- [134] Zia RKP. Phys Lett A 1978;64:345.
- [135] Vdovichenko NV. Zh Eksp Theor Fiz 1964;47:715 [Sov Phys JETP 1965;20:477]. Feynman RP. Statistical mechanics (Benjamin/Cummings, Reading, Mass., 1972). Morita T. J Phys A 1986;19:1197.

# Theory of Nucleation

Christo N. Nanev

*ROSTISLAW KAISCHEW INSTITUTE OF PHYSICAL CHEMISTRY, BULGARIAN ACADEMY OF SCIENCES, ACAD. G. BONCHEV STR. BL. 11, 1113 SOFIA, BULGARIA*

## CHAPTER OUTLINE

<b>7.1 Introduction</b> .....	<b>316</b>
<b>7.2 Classical (Capillary) Nucleation Theory and Nucleation in Vapors</b> .....	<b>317</b>
7.2.1 Nucleation Driving Force.....	318
7.2.2 Thermodynamics of Homogeneous Nucleation, Energy Barriers for Homogeneous Nucleation, and the Critical Nucleus Size.....	319
7.2.3 Rate of Homogeneous Nucleation: Steady-State Nucleation Rate.....	322
7.2.4 Non-Steady-State Nucleation Rate .....	326
7.2.5 Induction Time for Nucleation.....	327
<b>7.3 Nucleation in some other systems, Nucleation of Gas Bubbles from Superheated Liquids and Boiling</b> .....	<b>328</b>
7.3.1 Crystal Nucleation in Melts .....	330
7.3.2 Crystal Nucleation in Solutions .....	331
<b>7.4 Earlier Corrections of the CNT</b> .....	<b>331</b>
7.4.1 Some Recent Nucleation Theories.....	333
<b>7.5 Molecular-Kinetic Approach to Crystal Nucleation</b> .....	<b>335</b>
<b>7.6 Equilibrium Shape of Crystals</b> .....	<b>339</b>
<b>7.7 Two-Dimensional Crystal Nucleation</b> .....	<b>339</b>
<b>7.8 Heterogeneous (Substrate) Nucleation, the Equilibrium Shape of Crystals on Supports, and Energy Barriers for Heterogeneous Nucleation</b> .....	<b>342</b>
7.8.1 Saturation Density of Nuclei during Mass Crystallization in Solutions and Melts.....	345
<b>7.9 Nucleation Theorem</b> .....	<b>346</b>
<b>7.10 Probabilistic Features of the Nucleation Process</b> .....	<b>347</b>
<b>7.11 Use of Burst Nucleation for Producing Equally-Sized Nanoparticles</b> .....	<b>348</b>
<b>7.12 Nucleation of Protein Crystals</b> .....	<b>348</b>
7.12.1 Bond Selection Mechanism .....	349
7.12.2 Shape of the Protein Crystal Nucleus .....	350
7.12.3 Energy Barrier for Protein Crystal Nucleation .....	351
7.12.4 Protein Cluster–Cluster Aggregation on Diffusional Encounter .....	352
<b>7.13 Concluding Remarks</b> .....	<b>354</b>

7.14 Perspectives .....	355
Frequently Used Abbreviations .....	355
References .....	355

## 7.1 Introduction

Any phase transformation starts with a new phase appearing inside the supersaturated old (mother) phase. Because the thermodynamic stability of the system requires continuity of the thermodynamic functions during the entire course of phase transformation, the change in system thermodynamic potential occurring infinitely close to the transition point has to be infinitely small. Two possibilities correspond to this postulate: either an infinitely small amount of the new phase would appear, with properties distinctly different from the properties of the old phase, or an “infinitesimal” new property would appear simultaneously in the entire phase volume. The first case is denoted as a *first-order phase transition* because first derivatives of the thermodynamic potential are changed, whereas the second case is denoted as a *second-order phase transition* because second derivatives of the thermodynamic potential are changed.

Nucleation is a first-order phase transition. It is a widespread phenomenon in both nature and technology. Rain, fog, ice and snow, salt crystallization by evaporation of sea water, and gas bubble formation in mineral water—just to mention some—begin with the nucleation of a new phase. Nucleation predetermines some basic properties of the new phases created in chemical technology processes (e.g., during evaporation, condensation, and crystallization), metallurgy, deposition of epitaxial layers in electronics, purification (including pharmaceutical substances) by crystallization, formation of nanocrystals, etc. Even in some processes of biological matter crystallization, such as in protein crystallization, nucleation plays a central role. The questions to be answered here are: Why is nucleation required for new phase formation in so many phenomena and processes? Why is it ubiquitous?

Qualitative consideration of the simplest case of a first-order phase transition, namely the transition from single molecules randomly scattered in vapor to a new condensed liquid phase, comes in evidence to nucleation inevitability. Vapor condensation starts with the formation of a sequence of molecule clusters: pairs, triplets, etc. (Figure 7.1). However, because they have a highly convex shape, such clusters tend to dissolve into the ambient mother phase rather than continue to grow. According to the Young–Laplace equation, the smaller the droplet is (i.e., the higher its surface curvature), the higher the droplet vapor pressure is. Although evaporation of a single molecule from a large (flat) liquid surface does not change its curvedness, the same process with very small droplets results in a noticeable curvature increase, and thus in vapor pressure augmentation and further droplet evaporation. In 1878, J.W. Gibbs [1] assumed that repeated density fluctuations in the mother phase were the only reason to oppose such a course of events. He stipulated that a series of density fluctuations were responsible for the formation of an entire set of differently sized undercritical molecule clusters (Figure 7.1(b)) and the critical nucleus itself.

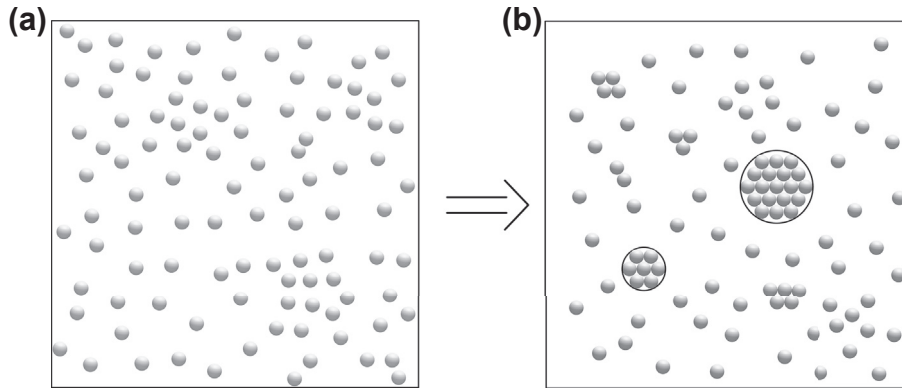


**FIGURE 7.1** Snapshots of the dynamic process of new phase formation. (a) The initial state of the vapor phase. Although some very small molecule clusters (e.g., pairs) may appear randomly, they exist only temporarily, decay, and new pairs are born. (b) The start of the transition to the new phase formation.

As is very well known, fluctuations are not limited to metastable system conditions only. Under equilibrium conditions, there already exist locally different and temporally fluctuating numbers of variously sized molecule clusters (Figure 7.1(a)). Gibbs' notion suggests that the probability of sufficiently large fluctuations leading to a stable new phase is infinitesimal in view of the processes occurring near equilibrium. This suggestion is attributed to the large barrier to phase transition arising from the energy cost for creating an interface between the new born cluster and the original phase. Moreover, the larger the critical nucleus is, the larger density fluctuation that is needed for its formation; also, the larger the fluctuation, the less probable (and rarer) is its appearance. Therefore, the prerequisite for the occurrence of a noticeable nucleation process is the establishment of sufficiently high supersaturation, when small fluctuations are required for critical nuclei appearance. Conversely, a limit on metastability is set when, due to a supersaturation increase, fluctuations leading to the new phase become comparable in number to the equilibrium thermodynamic fluctuations in the original phase [2]. This means that the system needs to be brought sufficiently deep into the metastable region to reduce the phase transition barrier until it becomes of the same order as the thermal energy,  $k_{\text{B}}T$  (where  $k_{\text{B}}$  is the Boltzmann constant and  $T$  is the absolute temperature).

## 7.2 Classical (Capillary) Nucleation Theory and Nucleation in Vapors

Despite nucleation inevitability, even direct observation of critical nuclei has proven elusive.<sup>1</sup> That is why theoretical explanations of nucleation processes have been developed. As already

<sup>1</sup>The protein crystal nuclei make no exception. Although formed by huge protein molecules, being still nanosized particles they remain invisible by optical microscopy. In addition, the critical nuclei are not labeled; it is impossible to distinguish them in the whole assembly of undercritical, critical, and supercritical molecule clusters. In addition, the number of the critical nuclei changes dynamically because of the constant growth/decay of differently sized clusters.

mentioned, Gibbs [1] has given a thermodynamic description of the condensation of supersaturated vapors into liquid droplets. His ideas represent the cornerstone of the classical nucleation theory (CNT), also called the capillary theory or fluctuation theory. Unfortunately, the significance of Gibbs' ideas on nucleation was largely ignored until 1926, when Volmer and Weber [3] acknowledged their importance.

Evidently, when the phase transition is thermodynamically favored, the molecules in the bulk of sufficiently large clusters of the new phase have to be of a lower free energy than the same molecules residing in the parent phase. However, when a nucleus of a new phase with distinctly different properties is formed within the original phase, the two have to be separated by an interface region with intermediate structure and properties; the interfacial width is determined by the structures of the two phases and the interactions between the molecules within these phases. In addition, the smaller the cluster of the new phase, the larger is the percentage of building units that reside in the interfacial region. In his fundamental work, Gibbs [1] introduced the notion of a dividing surface between the old and new phase, and he assumed it was sharp.

Interface matter bonding is less strong than the one in the bulk of the new phase cluster, which is why molecules in the interface region possess more energy compared to the one they would have in the macroscopic new phase. Therefore, the interface, appearing between small clusters and parent phase, is associated with definite interface energy. That is why the creation of small clusters of the new phase requires work to be done; a free energy cost has to be paid, which is the key barrier to nucleation (establishment of sufficiently high supersaturation being *condicio sine qua non* for creation of small clusters).

## 7.2.1 Nucleation Driving Force

The thermodynamic supersaturation, which is the nucleation driving force, is generally given as the difference in the chemical potentials of the parent and new phases,  $\Delta\mu > 0$ . Respectively, equilibrium is characterized by  $\Delta\mu = 0$  and undersaturation (overheating, undervoltage) by  $\Delta\mu < 0$ . The thermodynamic supersaturation for vapor condensation is expressed as

$$\Delta\mu = k_{\text{B}}T \ln (p/p_{\infty}) \quad (7.1)$$

where  $p$  is the actual vapor pressure and  $p_{\infty}$  is the equilibrium pressure (where the infinitely large condensed phase stands in equilibrium). An analogous expression holds true for the bubble formation driving force (see [Section 7.3](#)). For the vapor deposition of thin films,  $\Delta\mu$  is expressed by replacing the actual and equilibrium vapor pressures through the corresponding impingement rates of vapor atoms on the substrate.

In the case of crystallization from solutions,

$$\Delta\mu = k_{\text{B}}T \ln (a/a_{\infty}) \approx k_{\text{B}}T \ln (c/c_{\infty}) \quad (7.2)$$

where  $a$  and  $a_{\infty}$  are the corresponding solute activities. Because the activity coefficients are usually taken as equal to 1,  $\Delta\mu$  is expressed in this case by the concentration ratio  $c/c_{\infty}$ , with  $c$  being the actual concentration and  $c_{\infty}$ , being the equilibrium concentration.

For crystallization from melts,  $\Delta\mu$  is expressed as

$$\Delta\mu \approx Q_M \Delta T / T_M \quad (7.3)$$

where  $Q_M$  is the molar heat of fusion and the undercooling  $\Delta T = T_M - T$ , with  $T_M$  being the melting temperature and  $T$  being the actual temperature.

Most nucleation processes do not involve chemical transformations; rather, they are purely physical events. However, a few exceptions do exist, such as crystallization of chemical reaction products and electrochemical nucleation. In the case of electrocrystallization of metals, the nucleation driving force is

$$\Delta\mu = zF\eta \quad (7.4)$$

where  $z$  denotes the number of exchanged charges (e.g., the valence of the neutralizing ions);  $F = 96,500$  C/mol, which is the so-called Faraday equivalent; and  $\eta = e - e_0$  is the overpotential (overvoltage), which is given by the difference between the electrical potential  $e$  that is applied on the electrochemical system and the equilibrium potential  $e_0$  of the deposited ion in the solution [4].

## 7.2.2 Thermodynamics of Homogeneous Nucleation, Energy Barriers for Homogeneous Nucleation, and the Critical Nucleus Size

The spontaneous formation of nuclei in the bulk of a supersaturated system where the probability of the process is equal throughout the whole system, commonly known as *homogeneous nucleation*, usually marks the beginning of any consideration regarding the process. The reason is that the basic physics of nucleation is best illustrated with the help of this (simplest) theory.

The formation of molecule clusters of the new phase in an isothermal and isobaric system consisting of  $N$  molecules is to be considered for a one-component system. Gibbs [1] has defined the change in free energy (or thermodynamic potential,  $\Delta G$ ), required for the new phase formation as a sum of two terms: (1) the free energy gain resulting from the transfer of  $n$  molecules (atoms, ions) from the supersaturated phase to the new phase cluster, and (2) the free energy penalty  $\Phi$  imposed due to the formation of the new interface.

If we denote the starting thermodynamic potential by  $G_{\text{start}}$ , and the final thermodynamic potential by  $G_{\text{fin}}$ , we can write  $G_{\text{start}} = N\mu_{\text{mother}}$ , and  $G_{\text{fin}} = (N - n)\mu_{\text{mother}} + n\mu_{\text{new}} + \Phi$ , where  $\mu_{\text{mother}}$  and  $\mu_{\text{new}}$  are the chemical potentials of the mother and the new phase. Thus,

$$\Delta G = G_{\text{fin}} - G_{\text{start}} = -n\Delta\mu + \Phi \quad (7.5)$$

where  $\Delta\mu = \mu_{\text{mother}} - \mu_{\text{new}} > 0$ . The first term in Eqn (7.5) is negative because the new phase is more stable than the old one. This term decreases the system thermodynamic potential and indicates a tendency toward a spontaneous phase transition.

Consideration of droplet nucleation in the vapor phase, with droplets assumed to be of spherical shape, is an important basis to analyze other cases. So,  $n$  depends on the third power of droplet radius  $r$ , and the second term in the sum is proportional to the

interface area (i.e., it depends on droplet radius in power 2). Initially, with very small cluster sizes, the surface-to-volume ratio is large and the second term prevails. That is why the smallest liquid clusters tend to evaporate. Rising cluster size leads to the volume term increasing faster than the surface term. Thus, the competition between these two terms determines the energy barrier for nucleus formation as the maximum in total free energy change,  $\Delta G^* = \max$ , which is reached at the *critical cluster size* (Figure 7.2).

In large and/or open systems, the critical nucleus stands in an unstable equilibrium with the surrounding parent phase.<sup>2</sup> The equilibrium is unstable because even an infinitesimal increase in the critical nucleus size leads to a decrease in thermodynamic potential (Figure 7.2), and nucleus growth becomes favorable. With further growth, droplet vapor pressure decreases continuously. Because the external pressure remains unchanged in such systems, the growth process becomes irreversible. On the contrary, if the critical nucleus radius decreases, its vapor pressure will augment and the droplet will evaporate. A mechanical analog of unstable equilibrium is depicted in Figure 7.3.

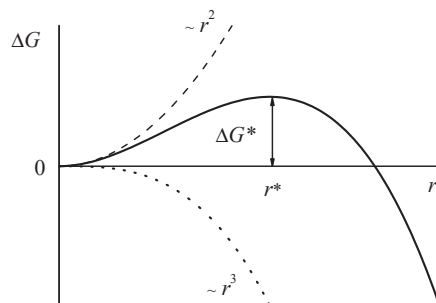


FIGURE 7.2 Plot of the free energy (Gibbs' thermodynamic potential),  $\Delta G$ , versus droplet radius,  $r$ .  $\Delta G^* = \max$  determines the radius of the critical nucleus  $r^*$ .

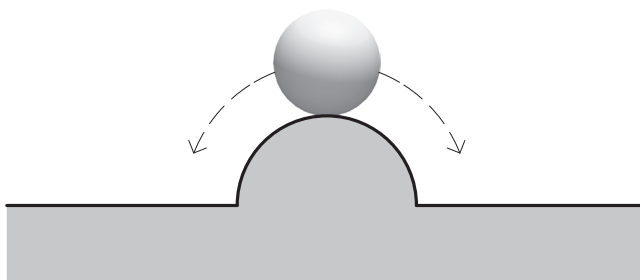


FIGURE 7.3 Mechanical analog of unstable equilibrium. Even an extremely small push exerted on the ball causes it to roll down, either to the right (which corresponds to growth) or to the left (which corresponds to dissolution).

<sup>2</sup>Stable equilibrium is achievable only in sufficiently small closed systems, when any droplet evaporation increases appreciably the vapor pressure and leads to back condensation. Vice versa, if the droplet grows above the critical size, the vapor pressure will decrease below the equilibrium value, which inevitably leads to some droplet back evaporation.

A unified consideration of liquid droplet and crystal nucleation is presented here. For homogeneous crystal nucleation, the total surface free energy (of various shapes) is  $\Phi = \Sigma(S^{\text{hkl}} \gamma^{\text{hkl}})$ , where  $S^{\text{hkl}}$  denotes the surface area of the crystal face with Miller indices hkl and  $\gamma^{\text{hkl}}$  are the corresponding specific interface energies. Basically,  $\Phi$  also includes the binding energy of crystal edges and apexes. However, edge energy is negligibly small as compared to surface free energy (see Section 7.7), whereas apex number is constant; it changes only with the change in crystal shape. Then, we have for crystals of any shape

$$\Delta G = -n\Delta\mu + \Sigma(S^{\text{hkl}}\gamma^{\text{hkl}}) \quad (7.6)$$

From the postulate that the critical crystal nucleus is determined by the maximum of the total free energy,  $d(\Delta G)/dn = 0$ , with  $\Delta\mu$  and  $\gamma^{\text{hkl}}$  being independent on  $n$ , one obtains

$$\Delta\mu = \Sigma[\gamma^{\text{hkl}}(dS^{\text{hkl}}/dn)], \quad (7.7)$$

which is a general expression of the Gibbs–Thomson equation for crystals, in which edge and apex energies are neglected.

For combinations of crystallographically equivalent faces, Eqn (7.6) simplifies to

$$\Delta G = -n\Delta\mu + S\gamma, \quad (7.8)$$

where  $S$  is the total surface of the new phase and  $\gamma$  is the specific interphase energy. The graphical plot of Eqn (7.8) for spherical crystals is the same one as the presented in Figure 7.2.

It should be emphasized here that Eqns (7.5), (7.6), and (7.8), which also hold true for the energy barrier for nucleus formation, are meaningful for  $n \gg 1$  only; otherwise, these equations would assign nonphysical, nonzero work for formation of the monomer,  $n = 1$ .

Again from the condition for a maximum of the thermodynamic potential, we have

$$dS^*/dn = \Delta\mu/\gamma \quad (7.9)$$

The two simplest cases are usually considered as examples. Firstly, the same Gibbs–Thomson equation is obtained for liquid droplets and spherical crystals:

$$r^* = 2\Omega\gamma/\Delta\mu \quad (7.10)$$

where  $r^*$  is the critical nucleus radius and  $\Omega$  is the volume of a crystal building block (CBB).

Secondly, a convenient model is the so-called Kossel crystal, which is a crystal built by tiny cubic building blocks that are held together by equal forces in a cubic primitive lattice. With an edge length  $\delta$  of a building block in the crystal lattice, the surface  $S^*$  of the critical nucleus constituted of  $n^*$  molecules is  $S^* = 6\delta^2 n^{2/3}$ , and  $\Omega = \delta^3$ . Then, Eqn (7.9) yields

$$n^* = 64\Omega^2\gamma^3/\Delta\mu^3 \quad (7.11)$$

The radius  $r_3^*$  of the sphere inscribed in the crystal nucleus is  $r_3^* = (n^*\Omega)^{1/3}/2 = r^*$ .

Combining Eqns (7.8) and (7.9), one obtains the energy barrier  $\Delta G_{\text{homo}}^*$  for homogeneous crystal nucleation:

$$\Delta G_{\text{homo}}^* = \gamma[S^* - n^*(dS/dn)] \quad (7.12)$$

Using Eqn (7.10),  $\Delta G_{\text{homo}}^*$  is calculated as

$$\Delta G_{\text{homo}}^* = K\Omega^2\gamma^3/\Delta\mu^2 \quad (7.13)$$

with a coefficient  $K = 16\pi/3$  for a sphere and  $K = 32$  for the Kossel crystal. (Consideration of fully completed crystals is an implicit assumption in the latter case.) Comparing Eqns (7.13) and (7.11), one sees that for the Kossel crystal

$$\Delta G_{\text{homo}}^* = n^*\Delta\mu/2 \quad (7.14)$$

Gibbs found that the energy barrier for nucleus formation  $\Delta G_{\text{homo}}^*$  amounts to one third of the surface free energy. Now, substituting  $\Delta\mu$  from Eqn (7.10) in Eqn (7.8), and with  $n^* = 4\pi r^{*3}/3\Omega$ , one obtains the energy for reversible isothermal-isobaric formation of a spherical nucleus:

$$\Delta G_{\text{homo}}^* = 4\pi r^{*2}\gamma/3 = S^*\gamma/3 \quad (7.15)$$

Two other expressions can be obtained by substituting  $\Delta\mu$  from Eqn (7.10) in Eqn (7.8):

1. For spheres,

$$\Delta G(r) = \Delta G^* \left[ 3(r/r^*)^2 - 2(r/r^*)^3 \right], \quad (7.16)$$

2. For the Kossel crystal, substituting  $n\Omega = 4\pi r^3/3$

$$\Delta G(n) = \Delta G^* \left[ 3(n/n^*)^{2/3} - 2(n/n^*) \right] \quad (7.17)$$

Equation (7.17) will be used for deriving expressions for the nucleation rate in the next subsection.

### 7.2.3 Rate of Homogeneous Nucleation: Steady-State Nucleation Rate

One of nucleation theory's main purposes is to provide expressions for the nucleation rate,  $J$ , which is the number of nuclei that appear in unit volume,  $1 \text{ cm}^3$  per unit time,  $t = 1 \text{ s}$ . Using a statistical-thermodynamic approach, Volmer [5] further developed the Gibbs thermodynamic nucleation theory. He introduced and popularized the notion of two- and three-dimensional nuclei. By treating the nucleation barrier as activation energy, Volmer derived expressions for the rates of both kinds of nuclei formation. On the basis of Boltzmann's relationship between entropy and probability, taken in the form used by Einstein, Volmer wrote [5]

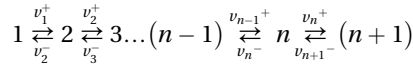
$$J = A \exp(-\Delta G^*/k_{\text{B}}T) \quad (7.18)$$

where  $A$  is a pre-exponential factor. Although  $A$  remained unknown in Volmer's statistical-thermodynamic derivation, Eqn (7.18) shows why the nucleation rate  $J$  is extremely sensitive to  $\Delta\mu$  and  $\gamma$  (compare Eqn (7.13)).

The pre-exponential factor  $A$  is revealed by the kinetic derivation of Eqn (7.18). After Volmer and Weber [3] formulated the core kinetic ideas, Frakas [6] looked into the details of the process mechanism. Using the chain reaction idea of Leo Szilard, he attempted to derive the nucleation rate. This basic notion is the root of theoretical considerations made later by Kaischew and Stranski [7], Becker and Döring [8], and Volmer [5].

For the sake of simplicity, steady-state liquid droplet formation from supersaturated vapors is examined further. Evidently, no steady-state process can be realized in a closed supersaturated system because irreversible growth of supercritical nuclei exhausts the monomers. To overcome this obstacle, a feasible physical model has been developed [5,8]. According to this model, all droplets that become larger than the critical size are removed from the system and an equivalent amount of vapors is added immediately, so that the number  $N$  of the molecules in the vapor phase is maintained constant. This secures constant supersaturation at all times. The assumption is valid in some practical cases because the number of molecules involved in forming the nuclei is sufficiently small, and the single-molecule depletion has a negligible effect in the earliest stages of nucleation.

The model excludes the possibility for molecule clusters to coalesce and produce larger size aggregates and/or disintegrate in smaller clusters. The clusters can grow or decay by attachment/detachment of single molecules only. In other words, the classical kinetic model describes cluster formation through a succession of steps, each leading to a cluster of slightly (merely by one molecule) larger size. Then, a stationary flux of rising size clusters will flow throughout the system:



where  $\nu^+$  and  $\nu^-$  are the corresponding probabilities (rate constants) for attachment and detachment of single molecules. Taking into account the birth and decay processes of clusters of size  $n$ , one obtains the time dependence of the concentration  $c_n$  of clusters constituted by  $n = 2, 3, \dots$  molecules:

$$dc_n/dt = (v_{n-1}^+ c_{n-1} + v_{n+1}^- c_{n+1}) - (v_n^+ c_n + v_n^- c_n) \quad (7.19)$$

Evidently, the net flux  $J_n$  of clusters through the size  $n$  is

$$J_n = v_{n-1}^+ c_{n-1} - v_n^- c_n \quad (7.20)$$

Thus,

$$dc_n/dt = J_n - J_{n+1} \quad (7.21)$$

Considering the steady-state process,  $dc_n/dt = 0$ ,  $J_n = J_{n+1} = J_{st}$ , where  $J_{st}$  denotes the steady-state rate (that is frequency) of formation of clusters, which is independent on the cluster size, and thus, includes the formation of critically sized nuclei as well. Therefore, the rate of nucleation  $J$  is defined by the flux  $J^*$  through the critical size, and the steady state is characterized by

$$\begin{aligned} J_{st} &= v_1^+ c_1 - v_2^- c_2, \\ J_{st} &= v_2^+ c_2 - v_3^- c_3, \\ &\dots\dots\dots \\ J_{st} &= v_n^+ c_n - v_{n+1}^- c_{n+1} \\ &\dots\dots\dots \\ J_{st} &= v_{\Lambda-1}^+ c_{\Lambda-1}. \end{aligned} \quad (7.22)$$

To totally exclude any probability of cluster evaporation, the chain is cut off at some upper limit  $\Lambda \gg n^*$ , where all supercritical nuclei leave the system,  $c_\Lambda = 0$ . Becker and Döring [8] multiplied each equation of this system by an appropriate rate constant ratio: the first equation is multiplied by  $1/v_1^+$ , the second one by  $v_2^-/v_1^+v_2^+$ , and the  $n$ -th by  $v_2^-v_3^- \dots v_n^-/v_1^+v_2^+ \dots v_n^+$ . Then, they summed up the equation system. In doing so, Becker and Döring got rid of the intermediate terms on the right-hand side of the equation. Because  $c_\Lambda = 0$ , the right-hand side of the sum becomes equal to  $c_1$  (molecules per  $\text{cm}^3$ ), and

$$J_{\text{st}} = c_1 \left/ \left[ \sum_{n=1}^{\Lambda-1} (v_2^-v_3^- \dots v_n^-)/v_n^+(v_1^+v_2^+ \dots v_{n-1}^+) \right] \right. \quad (7.23)$$

It is well known that the probability  $v_{n-1}^+$  for the attachment of a molecule from the vapor phase to the surface of a liquid droplet of size  $(n-1)$  is determined by the number of collisions per  $1 \text{ cm}^2$ , times the surface area  $S_{n-1}$ :

$$v_{n-1}^+ = pS_{n-1}/(2\pi mk_B T)^{1/2} \quad (7.24)$$

where  $m$  is the atomic (molecular) mass.

Taking into account the fact that the molecules have a nonzero size, Volmer scrutinizes the crossing of a molecule through the spherical intermolecular-interaction boundary that surrounds the droplet [5]. Evidently, a molecule is finally detached from the droplet only after its mass center crosses the said boundary; just then, the liquid surface of a cluster consisting of  $n$  molecules shrinks to  $S_{n-1}$ :

$$v_n^- = p_n S_{n-1}/(2\pi mk_B T)^{1/2} \quad (7.25)$$

Using the Gibbs–Thomson equation,

$$p/p_\infty = \exp(2v\gamma/k_B T r) \quad (7.26)$$

where  $v$  is the specific volume of a liquid molecule, we have for the critical nucleus,  $n^* = n-1$ ,

$$v_n^-/v_{n-1}^+ = p_n/p = \exp\{(2v\gamma/k_B T)[(1/r_n) - (1/r^*)]\} \quad (7.27)$$

Keeping in mind that  $n\nu = 4\pi r^3/3$ , we obtain

$$(v_2^-v_3^- \dots v_n^-)/(v_1^+v_2^+ \dots v_{n-1}^+) = \exp\left\{(2\gamma/k_B T)(4\pi\nu^2/3)^{1/3} \sum_1^n [(1/n^{1/3}) - (1/n^{*1/3})]\right\} \quad (7.28)$$

In the framework of the CNT,  $n^* \gg 1$ , and the sum in the right-hand side of this equation can be replaced by an integral. Then, integrating from 0 to  $n$ , we obtain

$$(v_2^-v_3^- \dots v_n^-)/(v_1^+v_2^+ \dots v_{n-1}^+) = \exp\left\{(\gamma/k_B T)(4\pi\nu^2 n^{*2}/3)^{1/3} [3(n/n^*)^{2/3} - 2(n/n^*)]\right\} \quad (7.29)$$

The comparison with Eqns (7.15) and (7.17) leads to

$$(v_2^-v_3^- \dots v_n^-)/(v_1^+v_2^+ \dots v_{n-1}^+) = \exp[\Delta G(n)/k_B T] \quad (7.30)$$

Let us now note that the equilibrium distribution of heterophase fluctuations can be calculated considering the metastable equilibrium in a slightly supersaturated system,

where no critical nuclei can arise,  $J = 0$ . Evidently, the condition for (both steady-state process and) equilibrium is a time-independent cluster-size distribution. However, the concentration of clusters of category  $n$  is constant only provided the appearance and disappearance rates are equal. Thus, the equilibrium concentration  $C_n$  of clusters in the absence of molecular flux in the system is

$$v_{n-1}^+ C_{n-1} = v_n^- C_n \quad (7.31)$$

Equation (7.31) represents the so-called *detailed balance*, according to which at equilibrium, each elementary process should be equilibrated by its reverse process. Rewriting Eqn (7.31) as  $C_n/C_{n-1} = v_{n-1}^+/v_n^-$  and multiplying the ratios  $C_n/C_{n-1}$  from  $n = 2$  to  $n$  gives

$$C_n/C_1 = \prod_{i=2}^n (v_{i-1}^+/v_i^-) = 1/[(v_2^- v_3^- \dots v_n^-)/(v_1^+ v_2^+ \dots v_{n-1}^+)] \quad (7.32)$$

Thus, Eqns (7.30) and (7.32) tell us that the metastable equilibrium concentration of droplets consisting of  $n$  molecules is

$$C_n = C_1 \exp[-\Delta G(n)/k_B T] \quad (7.33)$$

where  $C_1$  is the number of single atoms when the system is in equilibrium.

Bearing in mind that the nucleation rate  $J_{\text{st}}$  can be roughly estimated from the number density of critical clusters multiplied by the attachment probability (frequency)  $v^{*+}$  of a molecule to the critical cluster, we can write (with  $C_1 \cong c_1$ )

$$J_{\text{st}} = C_n^* v^{*+} = c_1 v^{*+} \exp[-\Delta G^*/k_B T] \quad (7.34)$$

The next step is to specify the expression. With this end in view, we replace the sum in the denominator of Eqn (7.23) with an integral:

$$\left[ \sum_{n=1}^{\Lambda-1} (v_2^- v_3^- \dots v_n^-)/v_n^+ (v_1^+ v_2^+ \dots v_{n-1}^+) \right] \approx \int_1^{\Lambda} (1/v_n^+) \exp\left\{(\Delta G^*/k_B T) [3(n/n^*)^{2/3} - 2(n/n^*)]\right\} dn \quad (7.35)$$

The function  $(\Delta G^*/k_B T)[3(n/n^*)^{2/3} - 2(n/n^*)]$  possesses a sharp maximum in the vicinity of  $n^*$  and can be expanded in Taylor series. Thus, following the known procedure (e.g., [9,10]) and after some approximations (including the assumption that  $v_n^+$  is constant, equal to the attachment probability to the nucleus, and thus it can be placed in front of the integral), the integration from  $-\infty$  to  $+\infty$  (instead from 1 to  $n$ ) yields

$$J_{\text{st}} = c_1 v^{*+} Z \exp(-\Delta G^*/k_B T) \quad (7.36)$$

where

$$Z = (1/n^*)(\Delta G^*/3\pi k_B T)^{1/2} \quad (7.37)$$

In the literature,  $Z$  is known as the Zeldovich factor, which accounts for the difference between the equilibrium and the actual steady-state numbers of critical nuclei. Zeldovich [11] assumed that only variation by  $k_B T$  in both sides around the maximum  $\Delta G^*$  are of interest. The width of the energy barrier maximum is of special interest

because, evidently, only the near-critical clusters contribute the most to the nucleation rate. (For a more rigorous treatment of the problem, see Ref. [12].) In fact,  $Z$  is not a large correction; its value is on the order of  $10^{-2}$  for water (see Table 1.1 in Toshew's work [9]).

To conclude, it should be noted that vapor droplet formation is one of the oldest nucleation study topics. The literature on it is extensive and there is not space to review it all here. I will note only that condensation of water droplets is of considerable practical interest as well in view of its technological importance; for instance, to prevent energy efficiency losses, it is essential to calculate the onset of water droplet nucleation in steam turbines [13].

## 7.2.4 Non-Steady-State Nucleation Rate

Basically, steady-state nucleation can occur only for a short period of time in sufficiently large systems and under the condition that concentration and/or temperature are altered by supercritical nuclei growth in nuclei nearest proximity only, while remaining unchanged in the bulk. Following that short period of time, supersaturation and nucleation rate constantly drop until they finally approach zero—the reason being the growth of supercritical nuclei. Zeldovich [11], Frenkel [14], Turnbull and Fisher [15], Kashchiev [12] and many others have explored the transition periods of the non-steady-state nucleation process,  $dc_n/dt \neq 0$ . For such a process, Zeldovich and Frenkel regarded the number  $n$  of molecules constituting clusters as a continuous variable and replaced the discrete cluster concentration dependence, expressed by Eqn (7.21), with a new differential equation to satisfy the continuity condition:

$$dc(n, t)/dt = -dJ(n, t)/dn \quad (7.38)$$

where  $c(n, t)$  and  $J(n, t)$  are the size- and time-dependent cluster concentration and rate of cluster formation, respectively.

Correspondingly, Eqn (7.20) is replaced in this case by

$$J(n, t) = v_{n-1}^+ c(n-1, t) - v_n^- c(n, t) \quad (7.39)$$

Again for  $J=0$ , the detailed balance equation is changed for the non-steady-state case:

$$v_{n-1}^+ C(n-1) = v_n^- C(n) \quad (7.40)$$

where  $C(n)$  denotes the equilibrium concentration of clusters of size  $n$  [14].

Thus, we can replace the detachment probability  $v_n^-$  to obtain

$$J(n, t) = v_{n-1}^+ C(n-1) [c(n-1, t)/C(n-1) - c(n, t)/C(n)] \quad (7.41)$$

Using the approximation  $v_{n-1}^+ C(n-1) \cong v_n^+ C(n)$ , we can write for the continuous case

$$J(n, t) \cong -v_n^+ C(n) \partial [c(n, t)/C(n)] / \partial n \quad (7.42)$$

Combining Eqns (7.38) and (7.42), we obtain the partial differential equation that describes the non-steady-state nucleation process:

$$\partial c(n, t) / \partial t = \partial \{ v_n^+ C(n) \partial [c(n, t)/C(n)] / \partial n \} / \partial n \quad (7.43)$$

Many authors attempted to solve this equation, but most of them made more or less physically acceptable assumptions and approximations. Perhaps one of the most rigorous solutions was given by Kashchiev [12]. Conducting a profound mathematical examination of the non-steady-state nucleation problem, he concluded that only within the critical region introduced by Zeldovich (of  $k_B T$  in both sides around the maximum  $\Delta G^*$ ) does the non-steady-state distribution  $c(n, t)$  differ essentially from the steady-state distribution,  $C_n$ . Thus, he wrote:

$$J(n, t) = J_{\text{st}} \left[ 1 + 2 \sum_{i=1}^{\infty} (-1)^i \exp(-i^2 t / \tau_N) \right] \quad (7.44)$$

where the parameter  $\tau_N$  is called *induction time* or *nonstationary time lag*. It characterizes the ability of the system to reorganize itself until producing a steady flow of nuclei

$$\tau_N = 8k_B T / \pi^2 \lambda v^{*+} \quad (7.45)$$

where  $\lambda = -[d^2 \Delta G(n) / dn^2]_{n=n^*} > 0$ . After  $t > 5\tau_N$ , the sum in Eqn (7.44) can be neglected and the steady-state nucleation rate is achieved [12].

## 7.2.5 Induction Time for Nucleation

The nucleation process cannot become stationary immediately after setting the conditions rendering a steady state. The reason is that when supersaturation is established in the system, cluster size distribution changes first from the equilibrium distribution to that corresponding to the metastable state. The larger the cluster, the longer it takes for the cluster to emerge; hence, an equilibrium distribution of clusters smaller than the critical size has to be attained before the appearance of the first critical nucleus. Furthermore, any supersaturation change provokes an entirely new set of stationary populations of subcritical and critical clusters; the inherited cluster size distribution has to accommodate the new steady state.

Keeping in mind that the total number of nuclei  $C_n^*(t) = \int_0^t J dt$  and substituting  $J(n, t)$  from Eqn (7.44), Kashchiev [12] showed that the integral renders

$$C_n^*(t) = J_{\text{st}} \left\{ t - (\pi^2 \tau_N / 6) - 2\tau_N \sum_{i=1}^{\infty} [(-1)^i / i^2] \exp(-i^2 t / \tau_N) \right\} \quad (7.46)$$

Again, the sum in the above equation can be neglected after  $t > 5\tau_N$  [12], and  $C_n^*$  augments further linearly with time:

$$C_n^*(t) = J_{\text{st}} [t - (\pi^2 \tau_N / 6)] \quad (7.47)$$

When  $\tau_N$  is smaller than the observation time  $t$ , that can be neglected:

$$C_n^*(t) = J_{\text{st}} t \quad (7.48)$$

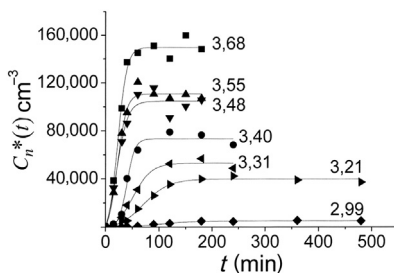


**FIGURE 7.4** Number densities  $C_n^*(t)$  of nucleated insulin crystals versus nucleation time  $t$  (Nanev, unpublished work). Because the nucleation rate  $J$  cannot be determined directly, the figure plots experimentally determined number densities of critical nuclei formed per the corresponding nucleation time. The numbers for the curves give concentration ratios,  $\ln(c/c_\infty) = \Delta\mu/k_B T$ . The measurements plotted were carried out by separation of crystal nucleation and growth stages (e.g., [16]).

Induction time  $\tau_N$  depends mainly on the attachment probability  $\nu^{*+}$  to the clusters of critical size (Eqn (7.45))—that is, on the mechanism of molecule supply from the mother phase. Therefore, the system type strongly influences  $\tau_N$ ; induction time can be a small fraction of a second in vapor condensation, but can take many years in a process such as glass crystallization. Moreover,  $\tau_N$  is inversely proportional to the square of supersaturation or undercooling [9]; that is, the higher the supersaturation, the shorter is the induction time. This is confirmed experimentally (see the intersections of the curves in Figure 7.4 with the  $x$ -axis).

Induction time determination is of special interest because  $\tau_N$  represents the inverse of the frequency of critical nuclei formation,  $\tau_N \sim 1/J$ . The temptation to measure  $\tau_N$  might be so irresistible that some authors tend to use the time for observing the first new phase particles as a substitute for the true nucleation induction time. However, the time for observing the first new phase particles is longer than the authentic induction time for nucleation. Induction time per se includes only the time needed to achieve a stationary size distribution of undercritical clusters and the time required for forming nuclei of critical size. In contrast, the time for observing the first new phase particles includes additionally the time for their growth to visible sizes. However loosely defined, the latter depends on the growth rate and on the resolution capability of the observation method used. Only by capturing nuclei at their birth by means of, for instance, laser light scattering, can one render reliable data. Another possibility to directly measure the supersaturation dependence of  $\tau_N$  has been proposed [16,17]. Nucleation in some other systems will be considered in the following sections.

### 7.3 Nucleation in some other systems, Nucleation of Gas Bubbles from Superheated Liquids and Boiling

Although evaporation is taking place from any free liquid surface, boiling is a common property of liquids. Therefore, nucleation of gas bubbles is of considerable technological interest. It appears also in aerated waters (including carbonated beverages) and magma.

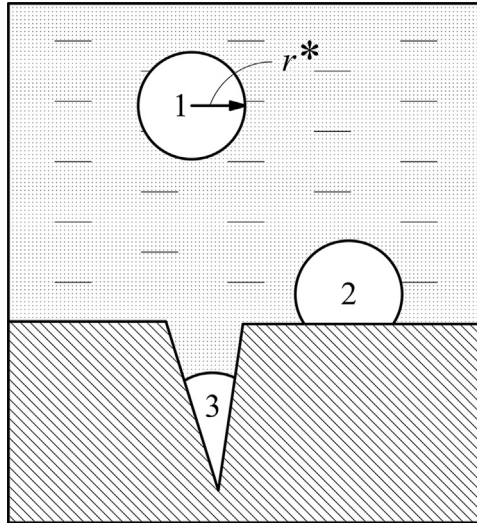


**FIGURE 7.5** Homogeneous (1), heterogeneous (2), and nucleation at preexisting gas microcavities (3) are depicted. A finite nucleation energy barrier must be overcome for each nucleus, but significantly less dissolved gas supersaturation is required for the third kind of bubble formation; increasing the supersaturation, a point is reached at which the radius of curvature of each meniscus equals the critical radius,  $r^*$ . Due to the smaller volumes of the heterogeneous nuclei, the nucleation threshold for heterogeneous nucleation is significantly lower than the one in the homogeneous case; this is most pronounced with preexisting gas cavities. *Courtesy of Elsevier; license Nr 3377621150350.*

If bubbles of nitrogen form in divers' blood while surfacing too fast, they suffer decompression sickness and may die.

Liquids can be superheated easily. This fact points unequivocally to the existence of a barrier to the formation of a new vapor phase inside the liquids. Although heterogeneous bubble nucleation occurs more easily than the homogeneous one, the basic principles of the homogeneous process are discussed here because they represent a general scientific platform for the phenomenon. For the impact of preexisting gas cavities in surfaces (Figure 7.5), of container walls, of suspended particles, or in the form of metastable microbubbles—called *heterogeneous nucleation*—interested readers may refer to Ref. [18].

In contrast to a liquid droplet, a gas bubble in a bulk liquid is compressible. Therefore, the thermodynamically derived Gibbs–Thomson equation for the vapor pressure of bubbles is expressed again with the liquid molecule volume  $v$ :

$$k_B T \ln(p_b/p_\infty) = -2v\gamma/r_b, \quad (7.49)$$

where  $p_b$  is the gas pressure inside the bubble and  $r_b$  is bubble radius. The *significant* difference with respect to droplet formation is constituted in the negative sign of equation's right-hand side.

It is seen that  $p_b$  is lower than the equilibrium pressure  $p_\infty$  of the plane vapor–liquid interface. The evident equilibrium condition refers to  $p_b$  withstanding the sum of

external (usually barometric) pressure  $p_{\text{ex}}$ , capillary pressure  $2\gamma/r_b$ , and hydrostatic liquid pressure  $\hat{h}\zeta g$ :

$$p_b^* = p_{\text{ex}} + 2\gamma/r_b + \hat{h}dg \approx p_{\text{ex}} + 2\gamma/r_b \quad (7.50)$$

where  $\hat{h}$  is the height of the liquid column above the bubble,  $d$  is liquid density, and  $g$  is the gravity acceleration of Earth.

According to Eqn (7.49),  $p_b^* < p_\infty$ . Hence, gas bubble formation inside the liquid may proceed merely under the condition  $p_{\text{ex}} < p_\infty$ , but still positive:  $p_{\text{ex}} > 0$ .<sup>3</sup> Therefore, the bubble nucleus stands in equilibrium with a supersaturated liquid, with the equilibrium being also unstable. With bubble formation driving force  $\Delta\mu = (p_b^* - p_{\text{ex}})v$ , we obtain the expression

$$\Delta G_{\text{homo}}^* = 16\pi\gamma^3 v^2 / 3\Delta\mu^2 \quad (7.51)$$

which is analogous to Eqn (7.13).

Noting that CNT describes fairly well the gas bubble formation during boiling, Hirth and Pound [20] supposed that the contradictions appearing in the case of droplet formation in vapors may be attributed to the incomplete molecule accommodation on the surface of the arising cluster of the new liquid phase.

### 7.3.1 Crystal Nucleation in Melts

Crystal nucleation in melts is important from a technological point of view because the nucleation rate predetermines grain size and, hence, the important mechanical properties of cast metal wares. The liquid-to-solid transition involves the appearance of new periodic structure and density changes. Once periodic order appears, the molecules become differently packed (in most cases, more closely) than in the liquid.

It is convenient to use Eqn (7.36) as a basis for the calculation of nucleation rates of melt crystallization. Evidently, the attachment probability  $\nu^{*+}$  of a molecule from the melt to the (spherical) critical crystal nucleus does not depend on molecule transport, but only on molecule rearrangement in the crystal lattice

$$\nu^{*+} = c_1 4\pi r^{*2} \zeta \exp[-\Delta E_{\text{re}}/k_B T] \quad (7.52)$$

where  $\zeta$  is the product of a frequency factor times the molecule's mean free path in the melt,  $\Delta E_{\text{re}}$  is usually identified with the activation energy for viscous flow, and

$$J_{\text{st}} = c_1^2 4\pi r^{*2} \zeta Z \exp[-\Delta E_{\text{re}}/k_B T] \exp[-\Delta G^*/k_B T] \quad (7.53)$$

In this case, temperature plays a more significant role than in vapor condensation. When  $T$  decreases, it causes simultaneous augmentation of undercooling (Eqn (7.3)) and melt viscosity, and vice versa. The difficulties in the comparison of theoretical and experimental results stem from the presence of impurity particles and from the temperature history of the crystallizing system (*memory effects* [2] and presence of *athermal nuclei* [9]).

<sup>3</sup>Bubble formation under negative external pressure exerted on the liquid is called *cavitation*. This is a mechanical rupture of a liquid; similar to solids, liquid cavitation occurs abruptly (for more details, see Ref. [19]).

### 7.3.2 Crystal Nucleation in Solutions

Crystal nucleation in solutions is another case of new phase formation for which it is convenient to use Eqn (7.36). In this case, the attachment probability  $\nu^{*+}$  of a molecule from the solution to the spherical critical crystal nucleus depends on both molecule transport and rearrangement in the crystal lattice. Being a relatively slow process, diffusion is usually the rate-limiting stage in the process. However, before attachments to the nucleus, the species (ions or molecules) also have to become free of their immediate solvent surroundings

$$\nu^{*+} = 4\pi r^{*2} \zeta c_s \exp[-\Delta E_{\text{dis}}/k_B T] \quad (7.54)$$

where  $\Delta E_{\text{dis}}$  is the dissolution energy and  $\zeta$  is the product of vibration frequency times the molecule's mean free path in the solution. Thus,

$$J_{\text{st}} = c^2 4\pi r^{*2} \zeta Z \exp[-\Delta E_{\text{dis}}/k_B T] \exp[-\Delta G^*/k_B T] \quad (7.55)$$

## 7.4 Earlier Corrections of the CNT

Operating with lucid and easily understandable ideas, and being relatively simple and easy to use, CNT properly explains the origins of the nucleation barrier and nucleation rate. However, the difficulties with CNT arise mainly because it assumes that data derived from property measurements on macroscopic phases, such as surface tension, structure, and density, can be applied to microscopic clusters containing a limited number of molecules; CNT treats such clusters as small phases cut out of large macroscopic phases. Capillarity—that is, the assumption of the interface between the arising small cluster of the new phase and the parent phase being sharp—is another drawback of CNT. The interface is described simply by a surface with a specific (per unit area) free energy,  $\gamma$ . However,  $\gamma$  is usually not available from direct measurements; for nanosizes, it is experimentally quantifiable only to a very limited extent (e.g., [21,22]). Besides, the  $\gamma$ -value for a curved boundary is relatively independent on the position chosen for the dividing surface, only when its radius of curvature is much larger than the width of the interface transition region. In contrast, the size of the smallest critical clusters is similar to the thickness of the molecularly diffuse interface, so that the dividing surface cannot be sharp. The interfacial width increases toward much larger values near the thermodynamic critical point, which finally brings about spinodal transformation in the unstable regions of the free energy; then, the work of formation for the fluctuation vanishes [2].

Tolman was the first to realize the extent by which the surface tension of a small liquid droplet,  $\gamma_R$ , deviates from its planar value,  $\gamma_\infty$ . Using thermodynamic considerations to account for this circumstance, he introduced a curvature correction  $\delta_T$  [23]:

$$\gamma_R = \gamma_\infty / (1 + 2\delta_T/R_e) \quad (7.56)$$

where  $\delta_T$  is the difference in the radii of the equimolecular dividing surface [1] and the so-called surface of tension [24];  $R_e$  is the equimolar radius of the liquid droplet.  $\delta_T$  is also

known as the *Tolman length*. Tolman's correction represents the first term of the expansion in power series of the surface energy, Eqn (7.56), in terms of surface curvature:

$$\gamma_R \approx \gamma_\infty (1 - 2\delta_T/R_e) \quad (7.57)$$

Equations (7.56) and (7.57) show that the surface energy starts to deviate appreciably from its planar value when the droplet radius is on the order of  $\delta_T$ . It should be noted here that, according to Eqns (7.13) and (7.18), a variation of only 10% in  $\gamma$  can alter the nucleation rate by many orders of magnitude. Due to this tremendous effect, the issue is still of enormous interest; using the keyword *Tolman length*, many dozens of papers devoted to the topic can be found online. Despite the large number of works concerned with Tolman's correction, there is hardly a generally accepted view on the problem; the topic is still debated [25] and a plethora of experimental techniques have been employed to perform nucleation rate measurements (e.g., see the first 12 references listed in Ref. [26]). Basically, they show that although CNT is valid near equilibrium where the critical fluctuation and the work required for it are large, a different behavior is observed moving further away from equilibrium.

Mutaftschiev [19] also studied the surface energy size dependence and the limits of capillary approximation applicability. Taking into account the corrections needed for this dependence in view of the discrete (atomic) constitution of extremely small clusters, he added a constant in the classical expression for the thermodynamic potential of the new condensed phase [19]. It is remarkable that, being a constant, this correction term does not change the derivation of the Thomson–Gibbs equation (Section 7.2.2).

Another disadvantage of CNT is its intrinsic feature to allow for a miscalculation of the degree of freedom of nucleating clusters. Because for homogeneous nucleation the nucleus can form around any one of the molecules present, it can appear anywhere in the homogeneous system with the same probability. Moreover, a free cluster is not static but translates and rotates freely in the entire volume of the parent phase, thus contributing to a higher system disorder. It has higher entropy than the one ascribed by CNT and, therefore, lower free energy than a small phase cut out of a large condensed phase. Thus, classical thermodynamics overestimates the cluster's excess free energy. With this in mind, Lothe and Pound [27] introduced the so-called Lothe and Pound (correcting) factor,  $I$ . In the case of a homogeneous water droplet nucleation from vapors, the calculations yield  $I \approx 10^{17}$ , but it turns out that it affects only the pre-exponential factor in the nucleation rate equation [28].

A typical assumption used in the kinetic models of CNT is that cluster–cluster interactions can be neglected because of their rarity. An alternative to this assumption is the so-called chemical approach presented by Frenkel [14]. He considered the molecule clusters as polymer molecules that obey chemical reaction laws. His approach allows aggregation of clusters of any size, but not only attachment/detachment of single molecules to/from the clusters. Mutaftschiev [29] discussed the merits and inconsistencies of the chemical approach. With this approach, it becomes clear why the critical nucleus plays the role of an “activated complex” in the theory of the chemical

reactions; the critical nucleus is the “molecule” of maximum energy and minimum concentration.

However, CNT is not an anachronism. Firstly, a quite surprising validity of the capillary approximation has been noticed by Bonissent and Mutaftschiev, even for particles of only a few atoms [30]. In the authors’ opinion, this seems to be due to a kind of compensation effect between energy and entropy (for closer look at the topic, see Ref. [30]). As far as the cluster coagulation effect on the nucleation rate is concerned, it should be noted that it is not only too infrequent to be concurrent with single molecule attachment, but at least for one case—namely, the diffusion controlled aggregation of protein crystalline clusters—it is highly improbable (see Section 7.12.4 and Ref. [31]).

### 7.4.1 Some Recent Nucleation Theories

Due to space limitations, only some novel ideas will be mentioned here in addition to the corrections mentioned above. For instance, contrary to the CNT assumption that crystal embryo structure and properties are the same as that of the bulk macroscopic crystal phase, some authors assumed that the embryo’s structure differs significantly (e.g., Ref. [32]). A fractal structure of the heterogeneous nucleus has been suggested as well [33]. However, polyhedral nuclei of apoferritin crystals have been observed by atomic force microscopy [34]; the authors have shown that crystals of near-nucleus size exhibit the same *fcc* structure as the bulk apoferritin crystals.

Numerous investigations have been carried out to solve specific nucleation problems, the recent methods of choice being predominantly molecular dynamic and Monte Carlo computer simulations (e.g., [26,35]), just to mention a few. McGraw and Laaksonen [36] considered a diffusive liquid droplet of changing density. Using the Gibbs surface dividing method [24] and density functional theory, the authors found a temperature-dependent correction to the nucleation barrier  $\Delta G^*$ , which, however, is independent of the nucleus size (the latter is assumed to be the same as the one found in CNT). The surface energy  $\gamma_d$  correction introduced by the authors [36,37] is considered to be an alternative to the Tolman correction (Eqn (7.56)):

$$\gamma_d = \gamma_\infty + f(T)/S^* \quad (7.58)$$

where  $f$  is an arbitrary function.

Walton and Rhodin pointed out that although the CNT is capable of describing the nucleation phenomenon at low supersaturations, an atomistic approach is more common at high supersaturations [38–40]. They developed a statistical nucleation theory for vapor deposition of thin films, according to which, at high impingement rates of atoms on the substrate, even a single atom can be a critical nucleus. Moreover, point defects on the crystal surface can trap adatoms, which then appear as supercritical centers of irreversible growth [41].

Milchev and Stoyanov [42,43] (see also Ref. [44]) have adopted the atomistic approach for the case of electrochemical nucleation, where high overvoltages are applied as well. Scrutinizing the discrete character of the cluster size alteration for single-digit molecule

numbers, they pointed out that the  $n^*$  versus  $\Delta\mu$  relationship is not continuous, but a stepwise one (Figure 7.6). It was shown, too, that a supersaturation interval, not a fixed supersaturation, corresponds to each critical nucleus; the smaller the nuclei, the wider the intervals and vice versa. Also, the supersaturation dependence of the steady-state nucleation rate is altered for extremely small nuclei. A broken line is observed in the atomistic case with high  $\Delta\mu$ , while according to CNT  $\ln J_{st}$  should change smoothly (Figure 7.7).

Using numerical simulations, ten Wolde and Frenkel [45] have shown that density fluctuations in a protein solution located near the liquid–liquid boundary may induce the formation of a high-density protein drops surrounded by low-concentration solution. On this basis arises the so-called two-stage nucleation mechanism of protein crystal nucleation. The first step in this mechanism consists of the separation of dense protein liquid drops from the bulk of the solution of the nucleating substance. The second step is crystal nuclei formation inside the high-concentrated regions,

**FIGURE 7.6** Critical nucleus size  $n^*$  versus  $\Delta\mu$ . The smooth line is the plot of the Gibbs–Thomson equation. *Courtesy of Elsevier; license Nr 3375810205283.*

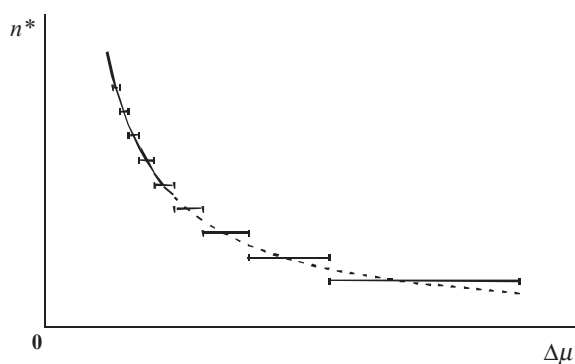
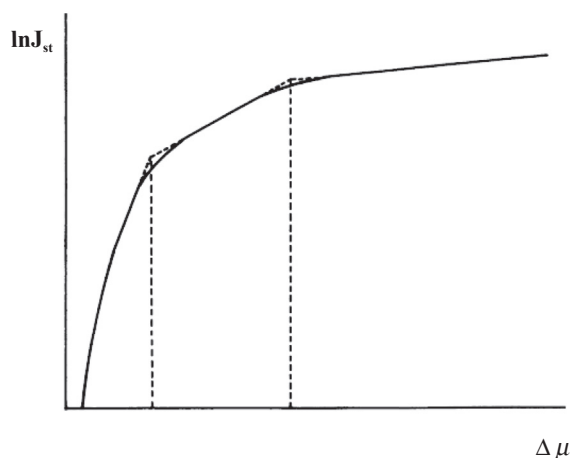


**FIGURE 7.7** Schematic representation of the  $\ln J_{st}$  vs.  $\Delta\mu$  relationship. The slope of each straight line section of the curve gives the number of atoms in the critical nuclei. *Courtesy of Elsevier; license Nr 3375800275481.*



which proceeds at a reduced energy barrier. Because of the slow ordering kinetics of the crystalline phase, this step determines the nucleation process rate [46]. Based also on experimental observations, the two-step nucleation mechanism remarkably resembles Ostwald's rule of stages (e.g., [19]). The topic is considered in full detail by Vekilov in Chapter 19 of Volume 1B.

## 7.5 Molecular-Kinetic Approach to Crystal Nucleation

A significant advancement in CNT has been marked by the molecular-kinetic approach to crystal nucleation, equilibrium, growth, and dissolution developed by Stranski and Kaischew [47–49]. First, Kossel [50] and Stranski [51] recognized, simultaneously and independently from each other, the importance of the unique position on the crystal surface known nowadays as a kink (kink site). Kossel called it a *repeatable step* because no change in surface geometry and energy takes place if an individual CBB is added to/or detached from the kink on an “infinitely” large crystal face. For the same position, Stranski used the notion of *half-crystal position* (Figure 7.8). This position on the crystal face determines the thermodynamic equilibrium with the ambience of a sufficiently large crystal (i.e., its chemical potential) because, evidently, under equilibrium the statistical probabilities for its occupation or nonoccupation are equal. Thus, with a sufficiently large crystal—so large that the energy contributions of the particles situated at the ends of its faces can be ignored—any crystal can be grown or dissolved reversibly by repetitively attaching/detaching CBB at the kink site; this proceeds with the same attachment or detachment energy, respectively, which is measured as the work of separation  $\varphi_{1/2}$ . Indeed,  $\varphi_{1/2}$  depends on crystal lattice structure. For instance,

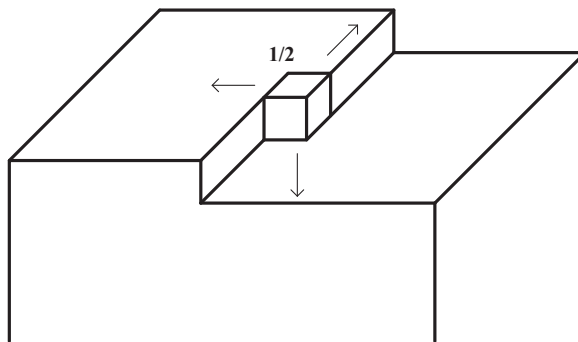


**FIGURE 7.8** Schematic presentation of a half-crystal position ( $1/2$ ) on a face of “infinitely” large crystal. CBB in this position is as follows (see the arrows): (1) at the end of a half CBB row (starting backwards); (2) connected to the ledge of a half-crystal lattice plane (situated on the left); and (3) standing on the half of the “infinite” crystal (beneath). To complete the crystal, one has to add the three missing crystal half-parts. Then, the atom (ion, molecule) under consideration would stand in crystal bulk. Hence, CBB in the half-crystal position is bound exactly two times less strongly than the atom (ion, molecule) standing in the crystal bulk and has an equal number of saturated and dangling bonds.

CBB at the kink site in the Kossel crystal is connected to three first-nearest neighbors (Figure 7.8). Taking into account only this kind of interaction, its bond energy is  $\varphi_{1/2} = 3\psi$ , where  $\psi$  denotes the energy of a single bond between two CBBs.

Kaischew [52] revealed the quantitative relationship between chemical potential, vapor pressure of the “infinitely” large crystal face,  $p_\infty$ , and  $\varphi_{1/2}$  for monoatomic vapors and for temperatures for which crystal energy is negligible:

$$\mu_\infty^c = \mu_0 + k_B T \ln p_\infty = -\varphi_{1/2} + k_B T \ln \left[ (2\pi m)^{3/2} (k_B T)^{5/2} / \hbar^3 \right] \quad (7.59)$$

where  $\mu_\infty^c$  is the chemical potential of an “infinitely” large crystal,  $\mu_0$  is the standard chemical potential, and  $\hbar$  is Planck’s constant. Thus, at  $T = 0$ ,  $\mu_\infty^c = -\varphi_{1/2}$ .

The situation with small crystals is completely different. The smaller the crystal, the greater are the deviations in the work of separation at the beginning and the end of the crystal face as compared with the work of separation from the half-crystal position. Taking into account this fact (and the principle of detailed balance), Stranski and Kaischew [47–49] suggested that, under equilibrium conditions, the probability of attachment of a whole new lattice plane on a crystal face should be equal to the probability of its detachment. Consequently, they calculated the energetic parameter that determines the equilibrium of small crystals with the surrounding media as the mean value of the work of separation (MWS),  $\varphi$ , averaged per building block of the corresponding crystal face. In doing so, Stranski and Kaischew divided the total work of separation involved in disintegrating the uppermost lattice layer of any face belonging to the crystal equilibrium form by the total number of blocks in that layer. Being equal for every face of the crystal, MWS determines its equilibrium shape (see Section 7.6).

Figure 7.9 depicts the procedure for calculating MWS with a (100) face of a Kossel crystal. CBBs are removed successively, one by one ( $n_3 - 1$ )<sup>2</sup> CBB (namely all white cubes in Figure 7.9(a)), starting with the atom situated on the right-hand front crystal apex. Detaching each of them from its three neighboring cubic CBB, a separation work amounting  $3\psi$  is performed per each single cube. Then, the two rows of  $2(n_3 - 1)$  dashed cubes in Figure 7.9(b) are separated, performing work  $2\psi$  for each. Finally, the last remaining cube (the black one at the left-behind crystal apex in Figure 7.9(c)) is

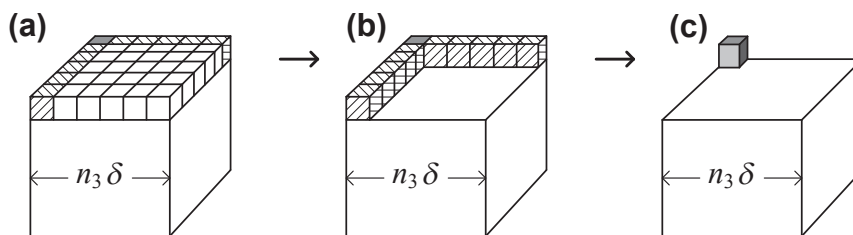


FIGURE 7.9 Three stages of detachment from a Kossel crystal of a whole (100) lattice plane, constituted of  $n_3^2$  building blocks.

separated, performing work  $\psi$ . Now, dividing the sum of those three works by the total number of  $n_3^2$  particles, we obtain the MWS for that crystal plane:

$$\varphi = \left[ 3\psi(n_3 - 1)^2 + 2\psi 2(n_3 - 1) + \psi \right] / n_3^2 = 3\psi - (2\psi/n_3) = \varphi_{1/2} - (2\psi/n_3) \quad (7.60)$$

It is seen that the smaller the crystal, the lower the MWS. In contrast,  $\varphi$  approaches  $\varphi_{1/2}$  with a crystal size increase.

Keeping in mind the analogy with Eqn (7.58), Kaischew [52] has shown that in the case of finite size crystals, MWS appears instead of  $\varphi_{1/2}$ . Thus, MWS determines the vapor pressure,  $p$ , of such crystals (see also [10]):

$$\mu_f^c = \mu_o + k_B T \ln p = -\varphi + k_B T \ln \left[ (2\pi m)^{3/2} (k_B T)^{5/2} / h^3 \right] \quad (7.61)$$

The supersaturation is

$$\Delta\mu = \mu_f^c - \mu_\infty^c = k_B T \ln(p/p_\infty) = \varphi_{1/2} - \varphi = 2\psi/n_3 \quad (7.62)$$

Stranski and Kaischew [47–49] conceived the concept of MWS to establish a link between the molecular kinetic theory of crystal nucleation and growth and the thermodynamic-statistical treatment of the problems, given by Gibbs [1] and Volmer [5]. To demonstrate this link, the specific surface energy  $\gamma$ , limited to energetic interaction between first-nearest neighbors in the Kossel crystal, is defined as

$$\gamma = \psi/2\delta^2 \quad (7.63)$$

Thus,  $\psi = 2\gamma\delta^2$ , and

$$\Delta\mu = 4\delta^2\gamma/n_3 \quad (7.64)$$

Keeping in mind that the diameter of the sphere inscribed in the Kossel crystal is  $2r^* = n_3^*\delta$ , and  $\Omega = \delta^3$ , Eqn (7.64) represents the Gibbs–Thomson equation (compare Eqn (7.10)).

The molecular-kinetic approach also enables the calculation of the energy barrier for crystal nucleation,  $\Delta G_{\text{hom}o}^*$ . Stranski [53] has defined the free energy  $\Phi$  as the difference between the total binding energy of a cluster as if all its building blocks are in the bulk of the infinitely large crystal, expressed by the term  $n_3^3\varphi_{1/2}$ , and the energy of the bonds in the real small cluster,  $U$ :

$$\Phi = n_3^3\varphi_{1/2} - U, \quad (7.65)$$

where  $U = \sum_{i=1}^n \varphi_i$  is the disintegration energy of the entire crystalline cluster into  $n = n_3^3$  individual building blocks. Evidently, this difference gives the number of unsaturated dangling bonds on the outside of the cluster, multiplied by the energy necessary to break a bond. Note that Stranski's relationship is universal, in the sense that it applies equally well to large and one-digit molecule crystal clusters. Replacing Eqn (7.65) with Eqn (7.5) and using the Gibbs–Thomson equation presented in the form of Eqn (7.62),  $\Delta\mu = \varphi_{1/2} - \varphi$ , one obtains the energy barrier for crystal (including nucleus) formation:

$$\Delta G_{\text{hom}o}^* = n_3^3\varphi - \sum_{i=1}^n \varphi_i. \quad (7.66)$$

Taking into account only the first-nearest neighbor interactions in a Kossel crystal, one can see that the separation work of a CBB situated on the eight cube vertices is  $3\psi = \varphi_{1/2}$  (Figure 7.9(a)); that is, the cubic shape is stable [54]. The total binding energy of a Kossel crystal possessing  $n_3$  CBB in the edge is

$$\sum_{i=1}^n \varphi_i = 3n_3^2(n_3 - 1)\psi \quad (7.67)$$

Using Eqns (7.66) and (7.60), Kaischew [54] obtained

$$\Delta G_{\text{homo}}^* = n_3^3[3\psi - (2\psi/n_3)] - 3n_3^2(n_3 - 1)\psi = n_3^2\psi \quad (7.68)$$

Replacing  $n_3$  from Eqn (7.62),  $n_3 = 2\psi/\Delta\mu$ , yields

$$\Delta G_{\text{homo}}^* = 4\psi^3/\Delta\mu^2 \quad (7.69)$$

Thus, one finally obtains [54]:

$$\Delta G_{\text{homo}}^* = 32\Omega^2\gamma^3/\Delta\mu^2 \quad (7.70)$$

Generally, applying the MWS method, Stranski and Kaischew arrived at the same conclusions for crystal nucleation that have already been known from CNT, and they have been able to develop further kinetic notions for the process. Moreover, operating with interaction energies in the crystal lattice only (thus avoiding the use of macroscopic surface tension values for small clusters), the MWS approach overcomes one of the deficiencies of CNT. Indeed, the absolute values of the intralattice interactions are known merely for limited crystal types (e.g., for ionic crystals [55]), but Stranski and Kaischew required to have their relative strength only. Hence, they considered the problems of crystal nucleation from a more realistic standpoint than CNT.

Perhaps the single shortcoming of the Stranski–Kaischew’s theory is that it is limited to complete and highly symmetrical crystals. Excluded from the considerations remain vicinal surfaces on crystals. However, these limitations are not of principle importance. Firstly, the incomplete clusters would have an increased number of dangling bonds, which would be attractive sites for subsequent attachments until a complete shape would be attained. Secondly, even using the simplest models, such as the Kossel crystal, Stranski–Kaischew’s considerations reveal the general features and trends of the nucleation phenomenon (and crystal growth and evaporation as well). This is shown here taking into account only the first-nearest neighbor interactions, but the same results have been obtained using first-, second- and third-neighbor interactions.

Although rarely used nowadays, as seen from the brief introduction provided here (see also Ref. [56]), the MWS approach is not obsolete. Based on this approach, a consideration of protein crystals equilibrium shapes is presented in Section 7.12.2 (see also Ref. [57]). Another example for an MWS application is the calculation of the energy barrier for protein crystal nucleation (Section 7.12.3). As seen in the next three sections, the predictive and explanatory power of the MWS approach should not be underestimated. However, the original works of Stranski and Kaischew are not very accessible (they are in Bulgarian and German). Therefore, the brief introduction provided above may be useful to the reader.

## 7.6 Equilibrium Shape of Crystals

Gibbs [1] showed thermodynamically that, at a constant crystal volume, the equilibrium crystal shape is established under a minimum in the total surface free energy,  $\Phi = \Sigma(S^{\text{hkl}} \gamma^{\text{hkl}}) = \text{minimum}$ . His idea has been elaborated further in a geometric construction, now known as the Gibbs–Curie–Wulff theorem. According to this theorem, the equilibrium shape of a crystal can be depicted by putting crystal faces at distances  $h_i$  from a central crystal (so-called Wulff's) point, with  $h_i$  being strictly proportional to the specific surface free energies  $\gamma_i$  of the corresponding crystal face. Then, the innermost body obtained is the equilibrium crystal shape. Wulff's theorem is expressed as

$$\gamma_i/h_i = \text{const, or } \gamma_1:\gamma_2:\gamma_3\dots = h_1:h_2:h_3\dots \quad (7.71)$$

The derivation is simple (e.g., see Ref. [10]) but lengthy and is omitted here.

Chapter 5 (this volume) by Einstein is devoted to a thorough consideration of the issue. Therefore, it will not be reviewed here in any detail, but the underlying physical ideas of Stranski and Kaischew's determination of the equilibrium shapes of crystals will be discussed; the reason is their simplicity [58]. The principle is that *no* CBB whose bonding with the crystal is looser than the MWS can belong to the equilibrium shape because the vapor pressure of such crystals would be higher than the equilibrium pressure. From this standpoint, Stranski and Kaischew started with an arbitrary crystal shape and successively removed all CBB—the separation work of which is smaller than MWS. In doing so, they revealed the equilibrium shape faces. However, depending on the starting crystal shape, some nonequilibrium faces may still remain. Therefore, the areas of all faces have been varied until the same MWS is reached for all of them. Due to the disappearance of all nonequilibrium faces, this procedure leads to the true equilibrium crystal shape (see also Ref. [59]). In addition, Stranski and Kaischew showed [58] that, with an increase in the supersaturation, the equilibrium shape becomes simpler because some faces disappear from it; due to the diminishing nucleus size, the latter shrinks to a CBB size.

The equilibrium shapes of crystals nucleated on a foreign substrate are considered in Section 7.8.

## 7.7 Two-Dimensional Crystal Nucleation

Although he did not systematically consider nucleation kinetic problems, Gibbs noticed that the growth of a face on a crystal must be a periodic process, which is accomplished by a successive formation and spreading of crystal layers. Moreover, he pointed out that the formation of every new lattice layer is associated with surmounting an energetic barrier (although it is not high). In 1927, Brandes reconsidered the possibility of two-dimensional (2D) nuclei formation and found that the energy cost,  $\Delta G_2^*$  was precisely half of the total edge energy:

$$\Delta G_2^* = (1/2)\Sigma(\chi_i \ell_i) \quad (7.72)$$

where  $\chi_i$  is the specific edge energy of the  $i$ -th edge and  $\ell_i$  is its length.

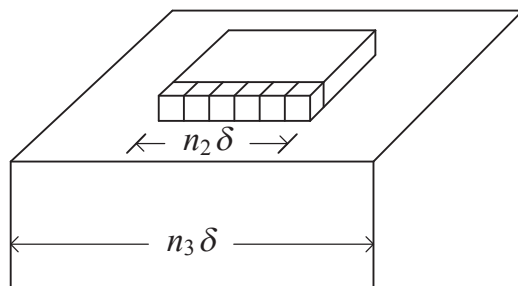


**FIGURE 7.10** 2D crystal on the (100) face of the Kossel crystal.  $n_2$  is the number of CBBs in the edge row of the 2D crystalline cluster;  $n_3$  is the number of CBBs in the Kossel crystal edge.

There are several different ways to obtain this result [5,8]. To demonstrate how fruitful the MWS method can be, we use it here. In analogy with deriving the MWS method for three-dimensional (3D) crystals, Stranski and Kaischew [48] suggested that, under equilibrium conditions, the probability for evaporation of all CBB that form the edge of a 2D crystalline cluster has to be equal to the probability for their deposition. Using as a model a 2D crystalline cluster of length  $\ell_2 = n_2\delta$ , formed onto (100) face of the Kossel crystal (Figure 7.10) and denoting the corresponding MWS as  $\varphi_2$ , Stranski and Kaischew determined it to be

$$\varphi_2 = 3\psi - \psi/n_2 = \varphi_{1/2} - \psi/n_2 \quad (7.73)$$

Analogically to Eqn (7.62) for the 2D case,

$$\Delta\mu = k_B T \ln(p/p_\infty) = \varphi_{1/2} - \varphi_2 = \psi/n_2 \quad (7.74)$$

Stranski and Kaischew [60] realized that the condition for a simultaneous equilibrium between the 3D-nucleus, 2D-nucleus, and vapor phase is the equality of the two MWS,  $\varphi = \varphi_2$ , or for the Kossel crystal  $n_2 = n_3/2$  (compare Eqns (7.62) and (7.74)). From this standpoint, the work for the formation of a 2D nucleus upon a completed (100) face of a Kossel crystal is calculated by a conceivable separation of the process in three stages (Figure 7.11), with the first step being the attachment of a single atom from the vapor phase (Figure 7.11(a)). From an energy perspective, it is the most difficult step because the required separation work, equal to  $\psi$ , is substantially lower than  $\varphi_2$ , and the single atom should be removed. Therefore, a free energy fluctuation amounting  $\varphi_2 - \psi = 2\psi - \psi/n_2$  is required for the deposition of the first CBB on the

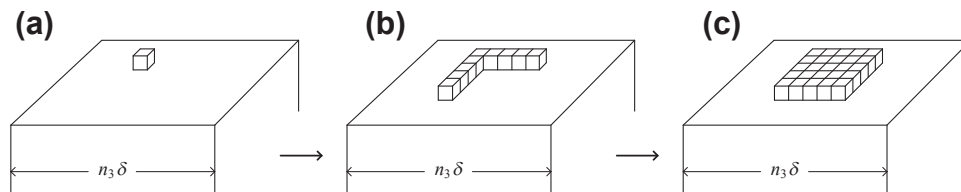


**FIGURE 7.11** Formation of a 2D nucleus upon a completed (100) face of a Kossel crystal.

completed (100) face of a Kossel crystal (Figure 7.11(a)). The next step is the formation of two edge rows of the arising 2D nucleus (Figure 7.11(b)). It requires binding energy of  $2\psi$  per CBB, so that the necessary energy fluctuation is  $\varphi_2 - 2\psi = \psi - \psi/n_2$ . Multiplying by the number  $2(n_2 - 1)$  of such particles, one obtains the total energy fluctuation as  $2(n_2 - 1)(\psi - \psi/n_2)$ . Finally, the attachment of  $(n_2 - 1)^2$  CBB that complete the 2D nucleus (Figure 7.11(c)) requires binding energy of  $3\psi$  per CBB, and the necessary energy fluctuation is  $\varphi_2 - 3\psi = -\psi/n_2$ . Thus, the total energy fluctuation for this stage is minus  $(n_2 - 1)^2(\psi/n_2)$ . Summing all that up, Stranski and Kaischew show that the total energy fluctuation needed for the formation of the complete 2D nucleus is  $\Delta G_2^* = n_2\psi$ . Using the definition for the specific edge energy  $\chi$  as  $\chi = \psi/2\delta$  and with  $\ell_2 = n_2\delta$ , the authors [60] obtained:

$$\Delta G_2^* = 2\chi\ell_2 \quad (7.75)$$

This is Brandes' Eqn (7.72) for the Kossel crystal. Note that exactly the same result is obtained considering the formation of the 2D nucleus in an alternative way, such as dissolving its surrounding crystal lattice plain [60]. It should be emphasized that combining  $\chi = \psi/2\delta$  with  $\gamma = \psi/2\delta^2$ , from Eqn (7.62) yields  $\chi = \delta\gamma$ . Because  $\delta$  is on the order of  $10^{-7}$  cm, we see that  $\chi \ll \gamma$ .

Burton, Cabrera, and Frank [61] have pointed out that in calculating  $\Delta G_2^*$  Volmer [5] and Becker and Döring [8] neglected the conformational entropy. This is equivalent to an assumption that the nucleus shapes are independent of temperature, and that all shapes are like the nucleus shape at  $T=0$  K. A more rigorous treatment of the problem [61] shows that the inclusion of the conformational entropy rendered only a small correction of  $\Delta G_2^*$  (multiplication by a factor of 0.8), and that the equilibrium nucleus shape depends on the temperature only, but not on the supersaturation. The shape is completely polygonized at  $T=0$  K and becomes increasingly rounded with temperature increase [61]. As a matter of fact, this circumstance was already known to Gibbs, who noticed that the apexes of a crystal at equilibrium with the surrounding media should be slightly rounded on a molecular scale.

Before the knowledge that real crystals are imperfect, Volmer suggested that 2D nucleation is a mandatory requirement for the growth process [5]. Frank's idea that the self-perpetuating steps originating from screw-dislocation emergence points make the nucleation mechanism unnecessary for crystal growth [62] sparked a new era in modern crystal growth theory, in which the interest in 2D nucleation declined significantly. However, the physical reality of 2D nucleation has been proven by experiments performed with free of screw-dislocation emergence points silver (100) and (111) crystal faces [63] and the (0001) face of cadmium crystals [64]; such faces grow by means of the so-called capillary technique for electrocrystallization.

Volmer also considered the formation of negative 2D nuclei (*Lochkeime* in German), which have to appear on sufficiently large close-packed crystal faces under considerable undersaturation. His suggestion has been confirmed experimentally with perfect faces of *p*-toluidine crystals; local undersaturation has been evoked using a directed sharp

air-blow, and the evaporation depressions created on the crystal faces were attributed to negative 2D nucleation [65]. However, even easier than on a perfect crystal faces, 2D nuclei arise also on emergence points of edge dislocations. The reason is that, due to the accumulated dislocation strain energy  $E_d$ , the chemical potential increases locally on such places. To elucidate the problem, Cabrera [66] described the change in the thermodynamic potential as

$$\Delta G = -\pi r_e^2 \delta \Delta \mu / \Omega + 2\pi r_e \delta \gamma' - h E_d \quad (7.76)$$

where  $r_e$  is the radius of the empty disc that arises on the emergence point of the dislocation,  $\delta$  is the hollow depth, and  $\gamma'$  is the energy of hollow periphery, which is usually set as  $\gamma' \approx \gamma$ . With the elastic strain energy,  $E_{el}$  and dislocation core energy,  $E_{core}$ , the total edge dislocation energy per unit length is  $E_d = E_{el} + E_{core} = \check{G} b_B^2 \ln(r_e / \rho_o) / 4\pi(1 - \xi) + E_{core}$ , where  $\check{G}$  is the shear modulus (modulus of rigidity),  $b_B$  is the Burgers vector of the dislocation,  $\rho_o$  is the radius of the so-called core of the dislocation, and  $\xi \approx 0.3$ , being Poisson's cross-contraction ratio. From the condition for a maximum of  $\Delta G$  and keeping in mind that  $E_{core}$  is a constant, two equilibrium radii arise [66]:

$$r_{\min, \max}^* = \left[ 1 \mp (1 - 4\rho_F / r_2^{-*})^{1/2} \right] r_2^{-*} / 2 \quad (7.77)$$

where  $\rho_F = \check{G} b_B^2 / 8\pi^2 \gamma' (1 - \xi)$  is Frank's hollow core radius and  $r_2^{-*}$  is the radius of the negative 2D nucleus on the perfect crystal face. Because  $r_{\min}^*$  rises and  $r_{\max}^*$  diminishes with an undersaturation increase (the latter diminishing  $r_2^{-*}$ ), a critical undersaturation can be reached when  $r_{\min}^* = r_{\max}^*$ , and  $r_2^{-*} = 4\rho_F$ . The energy barrier for nucleation disappears and a spontaneous formation of hollow disks on the edge dislocation emergence points proceeds with further undersaturation augmentation.

## 7.8 Heterogeneous (Substrate) Nucleation, the Equilibrium Shape of Crystals on Supports, and Energy Barriers for Heterogeneous Nucleation

Homogeneous nucleation occurs very rarely. Much more frequent is heterogeneous nucleation, occurring on foreign surfaces of different origins, such as impurity particles, container walls, etc. (Ions also activate nucleation, the most famous example being droplet formation in the so-called Wilson camera [5].) The reason for the highly predominating heterogeneous nucleation is that  $\Delta G_{\text{heter}}^*$  can be very much less than  $\Delta G_{\text{homo}}^*$ .

Again, Gibbs [1] laid the foundations of the theory describing how liquid droplets nucleate on interfaces between two bulk liquids and on a solid support. The theory has been further developed by Volmer [5]. The expression for the heterogeneous nucleation work is

$$\Delta G_{\text{heter}}^* = \Delta G_{\text{homo}}^* (0.5 - 0.5 \cos \beta - 0.25 \sin^2 \beta \cos \beta) \quad (7.78)$$

where  $\Delta G_{\text{homo}}^*$  is given for spherical drops from Eqn (7.13) and  $\beta$  is the wetting angle. For  $\beta = 0$ , meaning complete wetting,  $\Delta G_{\text{heter}}^* = 0$  and vapor condensation requires only a relatively small barrier for 2D liquid nucleation. For  $\beta = \pi$ , meaning complete non-wetting,  $\Delta G_{\text{heter}}^* = \Delta G_{\text{homo}}^*$ —that is, the substrate has no effect on droplet nucleus formation. For any  $\beta$  value between 0 and  $\pi$ , nucleation of liquid droplets proceeds heterogeneously in an easier manner than in a bulk vapor phase.

Due to its enormous practical significance, theoretical consideration of heterogeneous crystal nucleation has been provided by many authors (e.g., [67–69], just to mention some). Using the MWS method (Section 7.5) and the Kossel crystal model, Kaischew calculated equilibrium crystal shapes and energy barriers for crystal nucleation on foreign substrates [54,70]. Later, his significant contribution was called the Wulf–Kaischew theorem [68]. Here, Kaischew’s work is presented in brief because his original papers [54,70] are in Bulgarian and are not accessible to the general scientific audience.

Because any molecule on a nucleus surface has to occupy an equilibrium position, at a given supersaturation the kind and size of nucleus faces contacting the ambient phase only have to remain the same (Figure 7.12). As for the four faces in Figure 7.13(a) contacting with the support, each built by  $n'n_3$  CBB (with  $n'$  being the number of CBBs in the normal to the support crystal edges) Kaischew calculated the MWS,  $\phi'$ , as

$$\psi' = [n'n_3\psi + n'(n_3 - 1)\psi + n_3(n' - 1)\psi + n_3\psi'] / n'n_3 = 3\psi - [(\psi - \psi')/n' + \psi/n_3] \quad (7.79)$$

where  $\psi'$  is the detachment energy of a single CBB from the support. Because under equilibrium the MWS of these faces must be equal to the MWS of the topmost crystal face contacting with the vapor phase only, it follows according to Eqns (7.62) and (7.79) that

$$\Delta\mu = 2\psi/n_3 = (\psi - \psi')/n' + \psi/n_3 \quad (7.80)$$

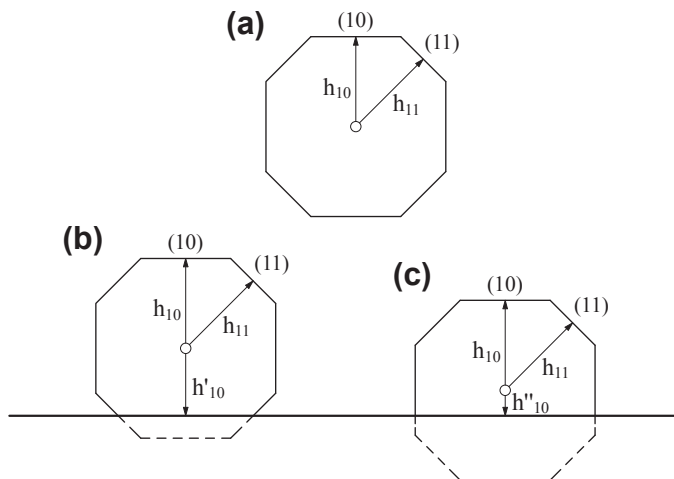
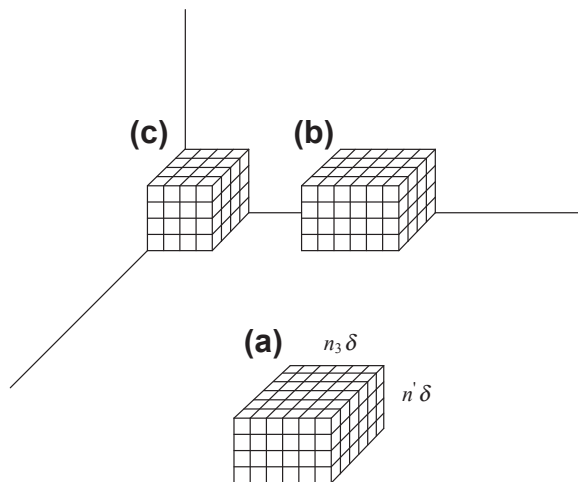


**FIGURE 7.12** Three combined crystal shapes: a homogeneous nucleus (a) and heterogeneously formed nuclei (b) and (c). Wulff’s points are shown by small circles, while the support is represented by the straight line. From Ref. [54].

**FIGURE 7.13** 3D models of Kossel-crystals nucleated on (a) one substrate, (b) two equal substrates, and (c) three equal substrates.



Thus, the equilibrium crystal shape (Figure 7.13(a)) is determined by

$$n'/n_3 = 1 - \psi'/\psi. \quad (7.81)$$

To calculate the energy barrier  $\Delta G_{\text{heter}}^*$ , Kaischew used Eqn (7.63), which relates  $\psi$  with  $\gamma$ ; analogically, he expressed  $\psi'$  by the specific adhesion energy,  $\omega = \psi'/\delta^2$  (this expression reflects the fact that only one crystal surface is appearing by detachment of a CBB from the support). In the case under consideration,

$$\sum_{i=1}^n \varphi_i = 2n_3 n' (n_3 - 1) \psi + n_3^2 (n' - 1) \psi + n_3^2 \psi', \quad (7.82)$$

Again, Eqn (7.66) is used to establish the energy barrier for heterogeneous crystal nucleation,  $\Delta G_{\text{heter}}^*$ . With Eqn (7.60), Kaischew obtained

$$\begin{aligned} \Delta G_{\text{heter}}^* &= n_3^2 n' [3\psi - (2\psi/n_3)] - \sum_{i=1}^n \varphi_i = n_3^2 (\psi - \psi') = n_3^2 \psi (1 - \psi'/\psi) = \Delta G_{\text{homo}}^* (1 - \psi'/\psi) \\ &= \Delta G_{\text{homo}}^* (1 - \omega/2\gamma). \end{aligned} \quad (7.83)$$

In a similar manner, he considered nucleation in concave edges (Figure 7.13(b)), where the crystal reclines on two support plains, and in concave vertices (Figure 7.13(c)), where the crystal sits on three support plains [54]. In doing so, Kaischew showed that in the former case

$$\Delta G_{\text{heter}}^* = \Delta G_{\text{homo}}^* (1 - \omega/2\gamma)^2, \quad (7.84)$$

In the second case,

$$\Delta G_{\text{heter}}^* = \Delta G_{\text{homo}}^* (1 - \omega/2\gamma)^3, \quad (7.85)$$

It is seen that the equilibrium crystal shapes (Figure 7.13(a)), energy barriers, and thus rates of crystal nucleation on substrates depend on the differing nucleation activity of

foreign surfaces, expressed by the corresponding specific adhesion energies,  $\omega$ . Furthermore, Kaischew also calculated thermodynamically the ratio  $\Delta G_{\text{heter}}^*/\Delta G_{\text{homo}}^*$  (for the same supersaturation) [70]:

$$\Delta G_{\text{heter}}^*/\Delta G_{\text{homo}}^* = V_{\text{heter}}^*/V_{\text{homo}}^*. \quad (7.86)$$

The physical explanation of this result is simple: depending on the substrate nucleation activity, the nucleus volume is decreased (see Figure 7.12), and the nucleation energy barrier is proportionally decreased.

Kaischew considered only the simplest case of nucleation on structureless (or isomorphous) substrate. Clearly, on a lattice-mismatched substrate, the deposited crystal as well as some part of the underlying substrate are strained. In such cases, the elastic strain energy arising due to the misfit with the support has to be added to the change in thermodynamic potential. In doing so, Mueller and Kern [68] concluded that, owing to the strain, the equilibrium crystal shape changes; some facets decrease while some others increase in size.

### 7.8.1 Saturation Density of Nuclei during Mass Crystallization in Solutions and Melts

Particularly active sites for nucleation are present on the substrates themselves as well. Assuming equal activity of the sites, the rate  $d\tilde{N}/dt$  at which they are consumed has been calculated by Robins and Rhodin [41]. Evidently, this rate depends on the number ( $\tilde{N}_a - \tilde{N}^*$ ) of the still unoccupied active sites:

$$d\tilde{N}^*/dt = J'_{\text{st}}(\tilde{N}_a - \tilde{N}^*) \quad (7.87)$$

where  $J'_{\text{st}}$  ( $\text{s}^{-1}$ ) is the nucleation frequency per active site and  $\tilde{N}_a$  and  $\tilde{N}^*$  denote the density of the active sites and nuclei numbers, respectively. Taking into account the initial condition that for  $t = 0$ ,  $\tilde{N}^* = 0$ , the integration from  $\tilde{N}_a$  to  $\tilde{N}_a - \tilde{N}^*$  yields

$$\tilde{N}^* = \tilde{N}_a [1 - \exp(-J'_{\text{st}}t)] \quad (7.88)$$

As seen, at  $t \rightarrow \infty$ ,  $\tilde{N}^* \rightarrow \tilde{N}_a = \text{const}$ . Due to the exponential dependence, the ratio  $\tilde{N}^*/\tilde{N}_a = 0.98$  to  $0.99$  is attained at  $t > 4/J'_{\text{st}}$  to  $5/J'_{\text{st}}$ ,  $1/J'_{\text{st}}$  being the time constant of the process.

However, the active sites on the support can possess different activity in respect to the nucleation phenomenon [63]. Even when the substratum is a single crystal, its surface is not homogeneous; there are always emergence points of (both edge and screw) dislocations, tilt and twist boundaries, foreign inclusions embedded in the crystal lattice, point defects, and surface steps, which, due to the locally increased chemical potential or/and relief change, can become the preferred nucleation sites. Evidently, any different kind of site can become active in the nucleation process, provided the system's supersaturation rises higher than some characteristic threshold. Correspondingly, these kinds of sites can be classified with respect to the said critical supersaturation. In such a case, the maximal nuclei density does not exceed the

number of corresponding kind of active sites. However, with the increase in the system's supersaturation, less active sites will be involved in the nucleation process. The limit to this stepwise activation process is set by the critical supersaturation that is sufficient for homogeneous nucleation. This issue has been quantitatively looked into by Kaischew and Mutaftschiev [71].

Similar to CNT, matter and heat transport in the mother phase are neglected by Stranski and Kaischew's theory. However, they are of importance in condensed systems. As already noted (Section 7.2.4), depending on the matter and heat transport in the parent phase, nuclei growth may substantially change the concentration and/or temperature in their immediate surroundings. The so-called excluded nucleation zones appear when supersaturation falls below the critical nucleation limit (e.g., see Ref. [10]). Then, the exhaustion of the active particles/centers and/or the overlap of the excluded nucleation zones sets the upper limit of the nuclei number.

## 7.9 Nucleation Theorem

Gibbs [1] was the first to notice that the thermodynamic nucleation theory proposed by him leads to a simple relationship between the critical work and critical size; the relationship between  $\Delta G^*$ ,  $n^*$ , and  $\Delta\mu$  is given by Eqn (7.14) (see also Ref. [72]). Perhaps the famous nucleation theorem, given by Kashchiev and Oxtoby [73–76], was a result of this argument. This nucleation theorem is very valuable for experimenters because it reveals how the critical nucleus size is related to the supersaturation dependence of nucleation rate. Using experimental data for the nucleation rate  $J_{st}$ , the number of molecules  $n^*$  constituting critically sized nuclei<sup>4</sup> can be calculated by means of the following equation:

$$n^* \approx k_B T d(\ln J_{st})/d(\Delta\mu) + \alpha_1 \quad (7.89)$$

where  $\alpha_1$  is a small correction taking values between 0 and 1 [74].

It should be emphasized that nucleation theorem validity is not restricted by nucleus shape or size [73,74]. Moreover, nucleus size can be established without knowing the molecular mechanism details of its formation. An in-depth theoretical analysis [74] has shown that Eqn (7.89) provides a high degree of certainty; it “can be used to give  $n^*$  with an accuracy of 1–2 molecules” [73]. A statistical mechanical–kinetic derivation of the nucleation theorem, which takes into account the kinetic prefactor in the rate expression as well as the exponential term, has been proposed by Ford [77]. The nucleation theorem has also been checked thoroughly by Schmelzer [78], who expanded its application.

Kashchiev [75] gave strict phenomenological and thermodynamic proof of the nucleation theorem and provided some generalizations. Although oversimplified, a

<sup>4</sup>In concentrated systems, this is the excess number of molecules in the critical nucleus, which is given by the difference between the number of molecules in the nucleus and the number of molecules there would be in the same volume without the nucleus.

simple derivation of Eqn (7.89) is presented here, starting from the logarithmic form of Volmer's equation (Eqn (7.18)) for the nucleation rate:

$$\ln J = \ln A - \Delta G^*/k_B T \quad (7.90)$$

Then, replacing the  $\Delta G^*$  value from Eqn (7.8), Eqn (7.90) is derived with respect to  $\Delta\mu$ , under the assumption that  $A$  and  $\gamma$  are constants. In doing so, an equivalent form of Eqn (7.89) is obtained:

$$n^* \approx k_B T d(\ln J)/d(\Delta\mu) - [dn^*/d(\ln\Delta\mu) - \gamma(dS^*/d(\Delta\mu))] \quad (7.91)$$

Then, with Eqn (7.10) for spherical crystals, one obtains

$$n^* \approx k_B T d(\ln J)/d(\Delta\mu) \quad (7.92)$$

Using Eqn (7.9) and with  $dS^*/d(\Delta\mu) = (dS^*/dn^*)[dn^*/d(\Delta\mu)]$ , Eqn (7.92) is yielded for the Kossel crystal as well.

## 7.10 Probabilistic Features of the Nucleation Process

Both molecule attachment and detachment are random processes, which means that any cluster smaller than the critically sized one performs a random size-walk forth and back on the time axis, until it eventually reaches the critical size [9]. Therefore, the nucleation rate itself is a random quantity as well. Thus, the formal probability laws govern the statistical distribution of the nucleation rates, whereas the kinetic nucleation theory predicts their average values only. This fact is reflected in the inherent data scatter of the measured nucleation rates.

The probabilistic features of the nucleation process have been discussed thoroughly by Toshev and co-workers [9,79]. Following these authors, only the simplest case of steady-state nucleation will be considered here because it is more lucid than the nonsteady case and renders a clear result.

Toshev [9] considered nucleation as a sequence of independent random events occurring during a fixed time interval. Using the Poisson expression, he calculated the probability  $P_M$  of finding  $M$  events within the time interval from 0 to  $t$ :

$$P_M = [\check{N}^M \exp(-\check{N})]/M! \quad (7.93)$$

where  $\check{N}$  is the average number of expected nucleation events, which should appear in the chosen time interval.

Following the calculus of probability, Toshev [9] derivates Poisson's formula to obtain a relationship between the probability and nucleation rate  $d\check{N}/dt$ :

$$dP_{\geq M} = (d\check{N}/dt) [(\check{N}^{M-1})/(M-1)!] \exp(-\check{N}) dt \quad (7.94)$$

Integrating Eqn (7.94), he obtained the probability of formation of minimum  $M$  nuclei before time  $t$  is elapsed. Introducing the total number of nuclei according to Eqn (7.48), he considered  $\check{N}$  and  $J = d\check{N}/dt$  as representative for the whole system and assumed that the supersaturation remains constant. To obtain an expression for appearance of at least

one nucleus,  $M = 1$ , Toshev assumed as a limiting case the rate equation for steady-state nucleation and reached

$$dP_{\geq 1} = J_{st} \exp(-J_{st}t)dt \quad (7.95)$$

This formula expresses the probability of occurrence of the first nucleus within the time interval between  $t$  and  $t + dt$ . By integrating, the probability  $P_{\geq 1}$  (that at least one nucleus has arisen before the time  $t$  is elapsed) was obtained:

$$P_{\geq 1} = 1 - \exp(-J_{st}t) \quad (7.96)$$

According to the theorem for average values of a function, the mean expectation time  $T_1$  for the appearance of at least one nucleus is

$$T_1 = \int_0^{\infty} t dP_{\geq 1} = 1/J_{st} \quad (7.97)$$

It is seen that the mean expectation time  $T_1$  needed to form at least one nucleus is reciprocal to the steady-state nucleation rate. Although the time of first nucleus formation in the system is also a random quantity, Toshev and co-workers had shown that it yields valuable information concerning the kinetics of the process [79].

*Some novel applications of the nucleation theory* will be considered in the following sections.

## 7.11 Use of Burst Nucleation for Producing Equally-Sized Nanoparticles

A detailed understanding of the mechanisms responsible for formation of metallic particles with carefully tailored properties is indispensable to many contemporary technology areas, such as photovoltaics, catalysis, electronics, and medicine. In this respect, burst nucleation of metal colloids and nanoparticles in solutions, followed by diffusional growth and aggregation, or their combinations, represents an interesting development [80]. Burst nucleation is initiated by chemically generating (or introducing) monomers. By burst nucleation and further growth, molecule clusters reach sizes up to a couple of tens of nanometers. In many cases, nanocrystals of ZnS, CdS, Fe<sub>2</sub>O<sub>3</sub>, Au, Ag (and other metals) can begin to aggregate, becoming “monomers” for the formation of (crystalline) colloids. A modification of CNT has been used to explain the burst nucleation [80].

## 7.12 Nucleation of Protein Crystals

Protein crystal nucleation is a special case of spontaneous highly precise self-assembly of biological macromolecules into stable clusters, formed as a result of selective and appropriately directed interactions. It is a mandatory requirement that biological macromolecules have to be arranged in a geometry that is appropriate for creating

crystallographically symmetrical molecular structures. On the basis of reliable statistic data, Wukovitz and Yeates [81] revealed a tendency for proteins to crystallize in a small number of preferred space groups, where it is the easiest to achieve connectivity. The specificity of protein crystal nucleation will be considered in the following section.

### 7.12.1 Bond Selection Mechanism

It is known that only the structure of the protein molecule surface dictates a molecule's ability to bind to partners during protein crystallization. Evidence comes from the entirely analogous crystallization behavior of apo- and holoferritin, observed to occur due to the same molecule surface structure, regardless of the dramatically different molecule core. Recall that apoferritin is an empty shell, while a mineral core is present in the holoferritin. Nevertheless, when forming under the same conditions, the crystals of both proteins have exactly the same shape; the crystals differ only in their color: apoferritin crystals are yellowish, whereas holoferritin is reddish-brown [82]. Taking that into account and the experimental observations that protein crystal nucleation is rather slow, a bond selection mechanism (BSM) has been suggested [83,84]. It represents an attempt to describe the most important features of the extremely complex molecular-kinetic mechanism of protein crystal nucleation.

As is well known, there is a fundamental difference between small inorganic and large protein molecules. Small molecules possess spherical interaction fields with constant interaction potential. In supersaturated media, every hit between them, independently of molecules' spatial orientation, has the potential to contribute to a crystal bond formation. In contrast, the surface of the protein molecule is highly patchy and heterogeneous. The rationale behind BSM rests on the concept that patch–patch recognition is mandatory for the formation of lattice contacts in protein crystals.

Although it is impossible to observe the elementary acts of protein crystal bond formation, knowledge about lattice contacts (e.g., see Protein Data Bank, (PDB) data in Refs [85–88]), resulting in protein crystallization, lay a sound basis to suggest a mechanism of protein crystal bonding. It has been evidenced by PDB-structure statistics [85] that protein lattice contacts are not random; they occur through strict selection of amino-acid residues situated on the protein molecule surface. Only two (arginine and glutamine) predominate in crystal lattice contacts, of the 20 proteinogenic amino-acid residues that the vast multitude of living organisms rely on. In contrast, the least likely residues to be found in the crystal lattice contacts are lysine and glutamate residues [85].

Such a bond selection imposes severe steric restriction to protein molecule association, leading to crystal nucleus formation. In addition, it should be emphasized that only amino-acid residues situated in proper positions on the molecule surface are able to participate in producing crystal lattices. Even though potentially active, some residues that are out of crystallographically symmetrical positions (if, for instance, they are situated too close) can remain unused. Therefore, over their surface, protein molecules exhibit a highly limited number of discrete patches, which are the authentic bonding

sites under the actual crystallization conditions. Because such a patch occupies only a small fraction of the total surface of the protein molecule [82], BSM dramatically decreases the chance for a crystalline lattice bond formation and postpones the nucleation process significantly.

Indeed, the steric restriction effect is somewhat mitigated by rotational diffusion, which involves multiple collisions. The latter increases the chance for fine-tuning of the proper spatial positioning of crystallization patches on the two meeting protein molecules [89]. However, the rotational diffusion is highly effective only for protein pair formation. Its impact decreases strongly with larger complexes, following the order of pair  $\gg$  trimer  $\gg$  ...  $n$ -mer ...  $\rightarrow 0$ . The reason is that random rotation slows down very fast with larger complexes; for spheres, it is inversely proportional to their volume [89,90]. Therefore, it is highly improbable that the rotational diffusion may effectively assist a reasonably frequent formation of critical clusters constituted of large number of protein molecules (see also Section 7.12.4).

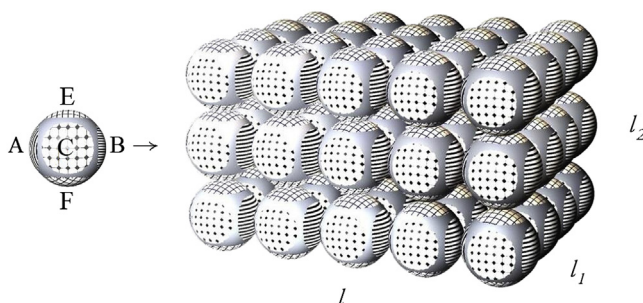
The reasons for BSM and its impact on protein crystal nucleation are considered in full detail in a review paper [91].

### 7.12.2 Shape of the Protein Crystal Nucleus

Crystal nucleation kinetics is studied intensively with globular proteins, but the experimental determination of the shape of the crystal nucleus still remains a challenge. The evident reason is the principal impossibility to see the critical nuclei directly. As already mentioned (see Section 7.4.1), the shape of the critical crystal nucleus has been deduced from the observed nearly critical apoferritin crystallites [34]. Surprisingly, the crystallites had a raft-like form. This observation is rather puzzling [92,93] because the apoferritin molecule is quite symmetrical in shape, almost spherical, and crystallizes in *fcc* lattice. Using the classical approach of the MWS method, the observation of Yau and Vekilov has been explained on the basis of the hypothesis for different crystal lattice bond strengths [57].

A Kossel-like crystal nucleus model was considered for globular proteins [83,84], in which spheres replaced the cubic building blocks of the said crystal (Figure 7.14). Keeping in mind the nature of the lattice binding forces between the huge biomolecules,

**FIGURE 7.14** Cubic primitive lattice model of a 3D crystal, formed due to six sticky patches (not to scale): A, B, C, E, F, and the patch just behind C that is not seen.  $l$ ,  $l_1$  and  $l_2$  are the numbers of molecules in the corresponding rows.



only the first-nearest neighbors were taken into account. A diametrical opposition of the sticky patches was assumed because it simplified substantially the quantitative consideration of the nucleus shape (Figure 7.14).

The crystal model shown in Figure 7.14 is constructed from three rows of molecules. The bond strength of the most stable contact between two molecules, the one in the horizontal front row in Figure 7.14, is denoted as  $\psi_1$ ,  $\psi_1 = \max$ . Then, a second type of weaker bond of strength  $\psi_2$  is added horizontally at the back. And finally, a third type of bond  $\psi_3$  is necessary to construct the three-dimensional cluster; those are the weakest bonds. Using this model, it is easy to calculate the corresponding MWS,  $\varphi$ , for the three types of faces:

$$\varphi_1 = \psi_1 + \psi_2 + \psi_3 - \psi_1/l - \psi_2/l_1 \quad - \text{ for the top (or bottom) face in Figure 5.14.} \quad (7.98)$$

$$\varphi_2 = \psi_1 + \psi_2 + \psi_3 - \psi_1/l - \psi_3/l_2 \quad - \text{ for the front (or back) face in Figure 5.14.} \quad (7.99)$$

$$\varphi_3 = \psi_1 + \psi_2 + \psi_3 - \psi_2/l_1 - \psi_3/l_2 \quad - \text{ for the side – faces in Figure 5.14.} \quad (7.100)$$

At equilibrium, all three MWSs have to be equal. Hence:

$$l/l_1 = \psi_1/\psi_2, \quad l_1/l_2 = \psi_2/\psi_3 \text{ and } l/l_2 = \psi_1/\psi_3 \quad (7.101)$$

Because  $\psi_1 > \psi_2 > \psi_3$ , the three-dimensional crystal is a parallelepiped, but not cube. It is worth showing here that this result obeys the Gibbs–Curie–Wulff law. According to Eqn (7.101) we have:  $ll_1 > 1$ ,  $ll_2 > 1$  and  $l_1/l_2 > 1$ , and hence:

$$ll_2 > l_1 l_2, \quad ll_1 > l_1 l_2, \text{ and } ll_1 > ll_2 \quad (7.102)$$

Thus, the smallest are the left- and right-hand side faces in Figure 7.14, which are situated normally to the strongest connecting force; the largest (top and bottom) faces are normal to the weakest bonding force. Keeping in mind Eqn (7.63) for the specific surface free energy  $\gamma_i$ , one sees that the equilibrium crystal face with the largest specific surface free energy  $\gamma_1 \approx \psi_1/2s$  is the smallest in size, and the one possessing the lowest energy  $\gamma_3 \approx \psi_3/2s$  (having the weakest dangling bonds) is the largest in size. Thus, the model obeys the Gibbs–Curie–Wulff law.

Closely packed 3D-crystal nuclei models built of spherical protein molecules, including those similar to the raft-like apoferritin crystal shapes of Yau and Vekilov, have been considered as well [57]. It should be noted that the formation of nonequilibrium shaped clusters is feasible but its energy cost is higher [94].

### 7.12.3 Energy Barrier for Protein Crystal Nucleation

Applying the MWS method to calculate the energy barrier for homogeneous protein crystal nucleation [84], using Eqn (7.66), gives

$$\Delta G_{\text{homo}}^* = ll_1 l_2 \varphi - \sum_1^{n^*} \varphi_i \quad (7.103)$$

The total binding energy of the crystal, built of  $n^* = ll_1 l_2$  individual molecules, is

$$\sum_1^{n^*} \varphi_i = (l-1)l_1 l_2 \psi_1 + (l_1-1)ll_2 \psi_2 + (l_2-1)ll_1 \psi_3, \quad (7.104)$$

and thus,

$$\Delta G_{\text{homo}}^* = l_1 \psi_3 (= l_2 \psi_2 = l_1 l_2 \psi_1) \quad (7.105)$$

From Eqn (7.62),  $l$ ,  $l_1$ , and  $l_2$  are expressed by  $\psi_1$ ,  $\psi_2$ , and  $\psi_3$  and the supersaturation  $\Delta\mu$ :  $l = 2\psi_1/\Delta\mu$ ,  $l_1 = 2\psi_2/\Delta\mu$  and  $l_2 = 2\psi_3/\Delta\mu$ . Then, an analog to Eqn (7.13) is obtained expressing  $\psi_1$ ,  $\psi_2$ , and  $\psi_3$  by the corresponding surface free energies  $\gamma_1$ ,  $\gamma_2$ ,  $\gamma_3$ , according to Eqn (7.63):

$$\Delta G_{\text{homo}}^* = 32\gamma_1\gamma_2\gamma_3\Omega^2/(\Delta\mu)^2 \quad (7.106)$$

The numerical estimation, performed by means of Eqn (7.106) and with  $\gamma \approx 1$  erg/cm<sup>2</sup> [95],  $\Omega \approx 3 \times 10^{-20}$  cm<sup>3</sup>, and  $\Delta\mu \approx 3k_B T$ , yields  $\Delta G_{\text{homo}}^* = 2 \times 10^{-12}$  erg. In view of Eqn (7.83), and taking into account the experimental data obtained for heterogeneous insulin crystal nucleation,  $\Delta G_{\text{heter}}^* = (3.8 - 6.8) \times 10^{-13}$  erg [84], the result is encouraging.

#### 7.12.4 Protein Cluster–Cluster Aggregation on Diffusional Encounter

Despite the unusually high supersaturations applied in protein crystal nucleation studies, the nucleation kinetics is rather slow [84,31]. One possible explanation of this observation may be that successive series of multiple coalescences of critical and/or near-critical clusters could reduce the observed crystal yield. Because there is no technique to track the destiny of the individual undercritically, critically, and supercritically sized clusters, it is particularly difficult to give any confident statement regarding the intermediate processes that may occur before and after the onset of crystal nucleation. In addition to the complexity of the issue is the fact that, while coalescence of clusters equal or larger than the critical size would diminish the crystal nucleation rate, coalescence of smaller sized clusters would augment it.

Firstly, due to the patchy and highly inhomogeneous surface of the protein molecules constituting the clusters, it is reasonable to expect that BSM should affect protein molecule clusters as well. In other words, when such clusters meet, their proper spatial orientation provides an inevitable coalesce condition. Because crystalline protein clusters are polyhedrons in shape [34], the simplest model is coalescence of two clusters with a Kossel-like lattice that consists of eight molecules each (i.e., two dice; Figure 7.15). Evidently, the facets on the two dice that correspond to the strongest intermolecular binding are most prone to bind together [31].

The probability for a proper meeting of two such dice in space is equal to the probability for the simultaneous appearance of just the same number on both dice by crap-shooting—that is,  $\sim 0.028$ . This probability is about 3 times smaller than that one for formation of protein molecule dimmers, which has been estimated to be 0.09–0.13 [84].

Note that the dice-meeting probability also includes partial coincidence, when merely one or two molecules on each dice become associated. Such a construction would hardly have sufficient stability; complete stability could only be achieved by

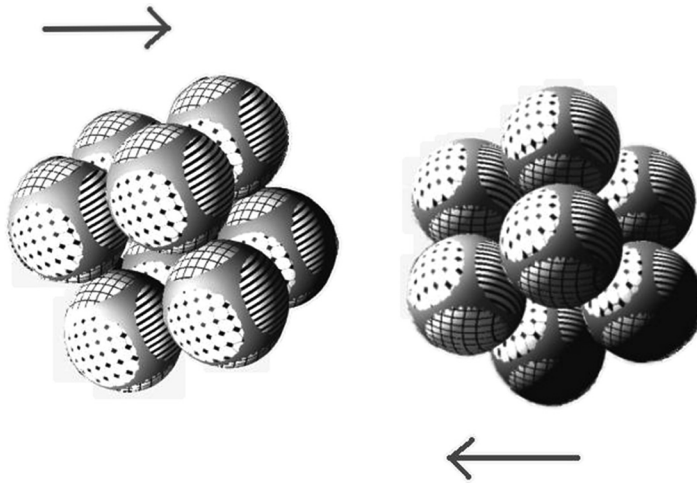


**FIGURE 7.15** Accidental meeting in space of two clusters (two dice) that consist of eight protein molecules each.

bonding of all eight molecules on both preferred dice faces. Thus, an additional spatial adjustment is required, which may be provided by rotational diffusion. However, because of the Brownian motion, the dice also may be separated in the meantime, which additionally decreases the coalescence probability.

Coalescence of clusters larger than eight molecules has also been discussed [31]. Obviously, the attachment of a ninth (and also tenth and eleventh) protein molecule to the dice in Figure 7.15 will create bulges. Bulges appear also on clusters consisting of 13–15 protein molecules, etc. However, flat faces bind together much stronger than bulges do, thus reducing coalescence probability even further. As already mentioned (see Section 7.12.2), in complete parallelepiped clusters, the side faces normal to the strongest connecting forces are of the smallest area (this holds true also for completed clusters consisting of 12, 60, etc. molecules), which decreases their coalescence probability.

Only coalescence of equally sized protein clusters has been considered so far. Indeed, differently sized clusters coalesce as well, but their coalescence does not change the general trend [31]. The reason is that smaller clusters rotate diffusionally and accommodate faster than larger particles. This is especially pronounced with clusters of highly differing sizes. In such a case, only the smaller cluster rolls about the larger one, like a ball on a floor. The larger cluster is almost immovable.

A general conclusion can be drawn that, due to the spatial adjustment via rotational diffusion, coalescence of critical and/or supercritically sized crystalline clusters of protein molecules is less probable than that for clusters smaller than the critical nucleus size. Moreover, due to the decreasing effect of the rotational diffusion, any successive (multiple) cluster coalescence resulting in a large-scale conglomeration is improbable.

The protein cluster coalescence problem has been given some quantitative considerations as well [31]. Using Smoluchowski's approach to rapid coagulation of spherical colloids, the dynamic process of the single coalescence of clusters composed of  $n$  protein molecules, which are consumed to produce larger size of clusters, is described by the rate equation for second-order bimolecular reactions written for every category of equally sized clusters:

$$dZ_n/dt = -k_n Z_n^2, \quad (7.107)$$

where  $k_n$  is the coalescence rate constant and  $Z_n$  is the concentration of clusters in the category  $n$ . Our implicit assumption is based on the predominating process of monomer attachment/detachment to/from the clusters; thus, no cluster size is missing. In other words, a quasi-equilibrium cluster distribution (Szillard chain) is established sufficiently fast.

Coalescence balance is estimated by integrating Eqn (7.107) from  $Z_n^o$  at  $t = 0$  to  $Z_n$ :

$$Z_n^o/Z_n = 1 + Z_n^o k_n t = R_n, \quad (7.108)$$

Note that  $Z_n^o k_n t$  is dimensionless, likely  $R_n$ ;  $Z_n^o k_n$  has the meaning of reciprocal half-life time, and larger  $R_n$  means a faster coagulation for the particles in the category  $n$ .

It has been suggested [31] that the cluster coalescence rate constant  $k_n$  represents the coalescence probability. Whether the change in  $k_n$  is monotonous or not is rather uncertain; that is why the following logical scheme has been applied: denoting  $j = n^*/2$  for even  $n^*$  numbers and  $j = (n^* + 1)/2$  for odd  $n^*$  numbers, it follows from the qualitative consideration presented above that the coalescence probability  $P_j$  for clusters in the category  $j$ , is much larger than the coalescence probability  $P_{n^*}$  for the clusters in the category  $n^*$ . Respectively,  $P_{j+1} > P_{n^*+1}$ ,  $P_{j+2} > P_{n^*+2}$ , ... ,  $P_{n^*-1} > P_{n^*+j-1}$ . Thus, the rate constants  $k_{n < n^*}$  have to be systematically larger than the rate constants  $k_{n \geq n^*}$ . In addition, it is logical to assume that the initial concentrations of the clusters  $Z_{n < n^*}^o$ , for every cluster category  $n = 2, 3, \dots, n^* - 1$ , is at least equal to  $Z_{n \geq n^*}^o$ ; for instance, the critical nuclei are of minimum concentration (Section 7.4). Finally, summing up the system of equations of the type of Eqn (7.108) for the different cluster categories and for the same time  $t$ , and knowing that  $k_{n < n^*} Z_{n < n^*}^o > k_{n \geq n^*} Z_{n \geq n^*}^o$ , we see that the coalescence probability for clusters in the range from  $j$  to  $n^* - 1$ , which may produce critical and supercritical nuclei, should be larger as compared with the coalescence of clusters of critical and supercritical size. Taking into account the rotational diffusion effect as well, the general conclusion is that being too slow, cluster coalescence does not play any role in the process of bulk protein crystal nucleation.

## 7.13 Concluding Remarks

The study of nucleation is the subject of a huge number of papers. The literature also comprises more than 70 books and reviews. (For an extended list of books and reviews, see the preface of Kashchiev's book [75].) A number of excellent books (e.g., [2]) and

papers have been published subsequently (e.g., [46,80,96–99]), and the scientific and technological interest in the topic is not declining. Due to the large body of literature on the subject, this chapter is not intended to be exhaustive. I outlined some of the basic physics that is believed to underlie this phenomenon. With the intention of making the topic more comprehensible to a broader readership, heavy mathematics was omitted. In addition, the limited space permits consideration of nucleation in a one-component system only. (Readers interested in nucleation in multicomponent systems may refer to Ref. [2].) In view of the author's background and preferences, the chapter focuses on some cases that seem underestimated in contemporary literature, such as the almost forgotten but fruitful MWS method.

## 7.14 Perspectives

In a constant quest to improve the nucleation theory, many corrections have been suggested, some of which were mentioned in Sections 7.4 and 7.4.1. Except for the most basic notions of CNT, such as the necessity of fluctuative nucleus formation under a sufficiently high driving force, almost all remaining postulates have been questioned in recent decades. Nevertheless, CNT remains the essence of nucleation theory. Although it is particularly difficult to give any confident statement as to how the theory will develop in the coming years, it is possible to predict that improvement will most likely be centered on explanations of specific cases, such as nanoparticle and protein crystal nucleation.

## Frequently Used Abbreviations

<b>BSM</b>	bond selection mechanism
<b>CBB</b>	crystal building block
<b>CNT</b>	classical nucleation theory
<b>MWS</b>	mean work of separation

## References

- [1] Gibbs JW. *Trans Connect Acad* 1876;3:108. 16(1878) 343 (Russian translation, Nauka, Moscow, 1982, 61).
- [2] Kelton KF, Greer AL. *Nucleation in condensed matter, applications in materials and biology*. Elsevier; 2010.
- [3] Volmer M, Weber A. *Z phys Chem* 1926;119:277.
- [4] Kaischew R. *Ann Sofia Univ Fiz Math (Chem)* 1946/1947;63:53.
- [5] Volmer M. *Kinetik der Phasenbildung*. Dresden-Leipzig: Theodor Steinkopff Verlag; 1939.
- [6] Farkas L. *Z Phys Chem* 1927;125:236.
- [7] Kaischew R, Stranski I. *Z Phys Chem* 1934;B26:317.
- [8] Becker R, Döring W. *Ann Phys* 1935;24:719.

- [9] Toshev S. Homogeneous nucleation. In: Hartman P, editor. *Crystal growth: an introduction*. North-Holland Publ. Co.; 1973.
- [10] Markov I. *Crystal growth for beginners, fundamentals of nucleation, crystal growth and epitaxy*. 2nd ed. New Jersey, London, Singapore, Hong Kong: World Scientific; 2003.
- [11] Zeldovich JB. *Acta Physicochim URSS* 1943;18:1.
- [12] Kashchiev D. *Surf Sci* 1969;14:209.
- [13] Wölk J, Strey R, Heath CH, Wusloulzil BE. *J Chem Phys* 2002;117:4954.
- [14] Frenkel JI. *Kinetik theory of liquids*. Oxford: Oxford University Press; 1946.
- [15] Turnbull D, Fisher JC. *J Chem Phys* 1949;17:71.
- [16] Penkova A, Chayen N, Saridakis E, Nanev CN. *Acta Crystallogr D* 2002;D58:1606.
- [17] Penkova A, Dimitrov I, Nanev Chr N. *Ann N Y Acad Sci* 2004;1027:56.
- [18] Jones SF, Evans GM, Galvin KP. *Adv Colloid Interface Sci* 1999;80:27.
- [19] Mutaftschiev B. Nucleation theory. In: Hurlle DTJ, editor. *Handbook of crystal growth*, vol. 1. Amsterdam: Elsevier; 1993. p. 187–247 [Chapter 4].
- [20] Hirth JP, Pound GM. Condensation and evaporation; nucleation and growth kinetics. In: Chalmers B, editor. *Progress in materials science*, vol. 11. Oxford: Pergamon Press; 1963.
- [21] Mutaftschiev B, Zell J. *Surf Sci* 1968;12:317.
- [22] Chernov SF, Fedorov YV, Zakharov VN. *J Phys Chem Solid* 1993;54:963.
- [23] Tolman RC. *J Chem Phys* 1949;17:333–7.
- [24] Ono S, Kondo S. In: Flüggé S, editor. *Handbuch der Physik*, vol. 10. Berlin-Göttingen-Heidelberg: Springer Verlag; 1960.
- [25] Xiao W, Ru-Zeng Z. *Chin Phys B* 2013;22:1–3. 036801.
- [26] Nellas RB, Keasler SJ, Siepmann JI, Chen B. *J Chem Phys* 2010;132:1–9. 164517.
- [27] Lothe J, Pound GM. *J Chem Phys* 1962;36:2080.
- [28] Abraham FF. *J Atmos Sci* 1968;25:47.
- [29] Mutaftschiev B. The atomistic nature of crystal growth. In: *Springer series in materials science*, vol. 43. Berlin, Heidelberg, New York: Springer-Verlag; 2001.
- [30] Bonissent A, Mutaftschiev B. *J Phys Chem* 1973;56:3727.
- [31] Nanev CN. *Cryst Res Technol* 2009;44:7.
- [32] ten Wolde PR, Frenkel D. *Phys Chem Chem Phys* 1999;1:2191.
- [33] Liu X-Y. *J Cryst Growth* 2002;237–239:106.
- [34] Yau S-T, Vekilov PG. *Nature* 2000;406:494.
- [35] Merikanto J, Zapadinsky E, Laury A, Vehkamäki H. *Phys Rev Lett* 2007;98:1–4. 145702.
- [36] McGraw R, Laaksonen A. *J Chem Phys* 1997;106:5284.
- [37] McGraw R, Laaksonen A. *Phys Rev Lett* 1996;76:2754.
- [38] Walton D. *J Chem Phys* 1962;37:2182.
- [39] Walton D. *Phil Mag* 1962;7:1671.
- [40] Walton D, Rhodin TN, Rollins R. *J Chem Phys* 1963;38:2695.
- [41] Robins JL, Rhodin TN. *Surf Sci* 1964;2:346.
- [42] Milchev A. *Contemp Phys* 1991;32:321.

- [43] Stoyanov S. *Current topics in mat. sci.*. Amsterdam: North-Holland; 1974.
- [44] Milchev A, Malinovski J. *Surf Sci* 1985;156:36.
- [45] ten Wolde PR, Frenkel D. *Science* 1997;277:1975.
- [46] Vekilov PG. *Cryst Growth Des* 2010;10:5007–19 [and the references therein].
- [47] Stranski I, Kaischew R. *Z Phys Chem A* 1934;170:295.
- [48] Stranski I, Kaischew R. *Z Phys Chem B* 1934;26:100.
- [49] Stranski I, Kaischew R. *Z Phys Chem B* 1934;26:114.
- [50] [a] Kossel W. *Göttinger Nachrichten* 1927:135;  
[b] Debye P, editor. *Leipziger Vorträge*, p.1; *Probleme der modernen Physik*, Leipzig 1928.
- [51] Stranski IN. *Z Phys Chem* 1928;136:259.
- [52] Kaischew R. *Z Phys* 1936;102:684 [and the reference of O. Stern therein].
- [53] Stranski IN. *Ann Sofia Univ* 1936/37;30:367.
- [54] Kaischew R. *Commn Bulg Acad Sci Phys Ser Bulg* 1950;1:100.
- [55] Madelung E. *Phys Zs* 1918;19:524.
- [56] Tassev VL, Bliss DF. *J Cryst Growth* 2008;310:4209.
- [57] Nanev CN. *J Cryst Growth* 2012;361:171.
- [58] Stranski IN, Kaischew R. *Ann Phys* 1935;23:330.
- [59] Honnigmann B. *Gleichgewichts- und Wachstumsformen von Kristallen*. Darmstadt: Theodor Steinkopff Verlag; 1958.
- [60] Stranski IN, Kaischew R. *Ann Sofia Univ, Fiz-Mat Faculty, Chem (Bulgarian)* 1935/36;32:171.
- [61] Burton W, Cabrera N, Frank FC. *Phil Trans* 1951;A243:299.
- [62] Frank FC. *Disc Faraday Soc* 1949;5:48.
- [63] Kaischew R, Budevski E. *Contemp Phys* 1967;8:489.
- [64] Bostanov V, Naneva R. *J Electroanal Chem Interfacial Electroch* 1986;208:153.
- [65] Sears G. *J Chem Phys* 1956;24:868.
- [66] Cabrera N. *J Chem Phys* 1956;53:675.
- [67] Fletcher NH. *J Chem Phys* 1958;29:572–6.
- [68] Mueller P, Kern R. *Surf Sci* 2000;457:229.
- [69] Liu X-Y. In: Sato K, Nakajima K, Furukawa Y, editors. *Advances in crystal growth research*. Amsterdam: Elsevier Science; 2001. p. 42–61.
- [70] Kaischew R. *Commn Bulg Acad Sci Phys Ser Bulg* 1951;2:191.
- [71] Kaischew R, Mutaftschiev B. *El Acta* 1965;10:643.
- [72] Nielsen AE. *Kinetics of precipitation*. International series of monographs on analytical chemistry, vol. 18. New York: Macmillan; 1964.
- [73] Kashchiev D. *J Chem Phys* 1982;76:5098.
- [74] Oxtoby DW, Kashchiev D. *J Chem Phys* 1994;100:7665.
- [75] Kashchiev D. *Nucleation, basic theory with application*. Oxford: Butterworth-Heinemann; 2003.
- [76] Kashchiev D. *J Chem Phys* 2006;125:014502.
- [77] Ford IJ. *Phys Rev E* 1997;56:5615.
- [78] Schmelzer J. *J Colloid Interface Sci* 2001;242:354.

- [79] Toshev S, Milchev A, Stoyanov S. *J Cryst Growth* 1972;13/14:123.
- [80] Sevonkaev I, Privman V, Goia D. *J Solid State Electrochem* 2013;17:279 [and references therein].
- [81] Wukovitz SW, Yeates TO. *Nat Struct Biol* 1995;2:1062.
- [82] Nanev CN. *Cryst Res Technol* 2008;43:914.
- [83] Nanev CN. *Cryst Res Technol* 2007;42:4.
- [84] Nanev CN. *Cryst Growth Des* 2007;7:1533.
- [85] Dasgupta S, Iyer GH, Bryant SH, Lawrence CE, Bell JA. *Proteins Struct Funct Genet* 1997;28:494.
- [86] Dale GE, Oefner C, D'Arcy AJ. *J Struct Biol* 2003;142:88.
- [87] Bahadur RP, Chakrabarti P, Rodier F, Janin J. *J Mol Biol* 2004;336:943.
- [88] Janin J, Rodier F, Chakrabarti P, Bahadur RP. *Acta Crystallogr D Biol Crystallogr* 2007;63:1.
- [89] Northrup SH, Erickson HP. *Proc Natl Acad Sci USA* 1992;89:3338 [and references therein].
- [90] Shoup D, Lipary G, Szabo A. *Biophys J* 1981;36:697.
- [91] Nanev CN. *Prog Cryst Growth Character Mater* 2013;59:133.
- [92] Oxtoby DW. *Nature* 2000;406:464–5.
- [93] Gorman J. *Sci News Week* 2000;158:84.
- [94] Kaischew R. *Growth Cryst Russ* 1965;5:45.
- [95] Chernov AA. *J Struct Biol* 2003;142:3.
- [96] Revalor E, Hammadi Z, Astier J-P, Grossier R, Garcia E, Hoff C, et al. *J Cryst Growth* 2010;312:939.
- [97] Garcia-Ruiz JM. *J Struct Biol* 2003;142:22.
- [98] Sear RP. *J Phys Condens. Matter* 2007;19:033101.
- [99] Sleutel M, Van Driessche AES. *PNAS* 2014;111:E546 [and the references therein].

# Growth Kinetics: Basics of Crystal Growth Mechanisms

Makio Uwaha

DEPARTMENT OF PHYSICS, NAGOYA UNIVERSITY, CHIKUSA-KU, NAGOYA, JAPAN

## CHAPTER OUTLINE

<b>8.1 Introduction: Purpose of This Chapter .....</b>	<b>360</b>
<b>8.2 Crystal Growth as a Process of Phase Transition.....</b>	<b>361</b>
8.2.1 Equilibrium and Transition to Solid Phase .....	361
8.2.2 Linear Kinetics .....	363
8.2.3 Transport and Chemical Potential.....	363
<b>8.3 Growth from Various Mother Phases .....</b>	<b>364</b>
8.3.1 Growth from the Vapor .....	364
8.3.2 Growth from the Melt.....	365
8.3.2.1 Sharp Interface Picture.....	366
8.3.2.2 Diffuse Interface Picture.....	368
8.3.3 Growth from a Solution .....	369
<b>8.4 Normal Growth and Lateral Growth .....</b>	<b>370</b>
8.4.1 Adhesive Growth on Rough Faces .....	370
8.4.2 Growth via Two-Dimensional Nucleation on a Facet.....	371
8.4.2.1 Single-Nucleation versus Multinucleation .....	373
8.4.2.2 Growth of a 2D Circular Island.....	374
8.4.2.3 Change of Coverage by Nucleation and Spread.....	375
8.4.2.4 Velocity of Multinucleation Growth.....	376
8.4.3 Spiral Growth with Screw Dislocations.....	377
8.4.3.1 Velocity of Spiral Growth.....	377
8.4.3.2 Growth of a Facet with Many Dislocations .....	378
8.4.3.3 Change of Growth Mode and Kinetic Roughening.....	379
8.4.3.4 Formation of Mounds.....	380
<b>8.5 Growth of Vicinal Faces .....</b>	<b>380</b>
8.5.1 A Model of Solution Growth: Bulk Diffusion .....	381

8.5.2 Vapor Growth and Surface Diffusion .....	382
8.5.2.1 The BCF Model .....	383
8.5.2.2 Asymmetric Kinetics at the Step .....	384
8.5.2.3 A Simple Example of Growth Kinetics .....	385
8.5.3 Growth of Vicinal Faces and Morphology of the Stepped Surface .....	387
8.5.3.1 Wandering of Steps .....	388
8.5.3.2 Bunching of Steps .....	390
<b>8.6 Crystal Growth in a Diffusion Field .....</b>	<b>391</b>
8.6.1 Melt Growth and Solution Growth .....	391
8.6.1.1 Evacuation of Latent Heat in Melt Growth .....	391
8.6.1.2 Supply of Matter in Solution Growth .....	394
8.6.2 Growth of a Planar Interface in a Diffusion Field .....	394
<b>8.7 Various Simulation Models of Crystal Growth .....</b>	<b>395</b>
8.7.1 Atomistic Model and Simulation .....	395
8.7.2 Continuum Models .....	396
<b>References .....</b>	<b>397</b>

## 8.1 Introduction: Purpose of This Chapter

We know that the ground state of many identical particles (e.g., atoms and molecules) is a state of a crystal in which particles form a periodic array. [Figure 8.1](#) shows an example: a tiny 1- $\mu\text{m}$  crystal of Pb shows a perfect array of atoms [\[1\]](#). If a Pb atom were as large as

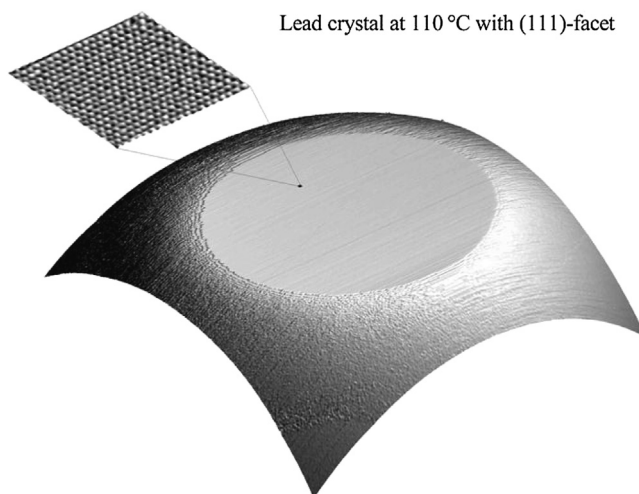


**FIGURE 8.1** A 750 nm  $\times$  750 nm scanning tunneling microscope image of a Pb crystal acquired at a temperature of 383 K. The inset shows the atomically resolved (111) surface zooming into the top facet. *Reprinted from Ref. [1], with permission from AIP.*

a golf ball, the size of the facet would be several tens of meters. It is not evident at all, however, that the particles can really form such a structure spontaneously. Merely by reducing temperature or increasing pressure, atoms or molecules in a liquid/gas aggregate and organize themselves to form a crystal. The purpose of this chapter is to explain the basic mechanism of this self-organization of atoms for beginners who have some basic knowledge of physics.<sup>1</sup>

The present chapter is not intended to give a comprehensive view of growth mechanisms but rather to explain the simple typical pathways of crystal growth on such a level that beginners can understand the physical mechanism. As a result, topics are limited and a comprehensive biography is not supplied.

## 8.2 Crystal Growth as a Process of Phase Transition

Crystallization is the process of the phase transition from a liquid or a gas to a solid. Crystal growth is a synonym of crystallization, and the word suggests that the crystal is becoming larger and larger. The birth of a crystal is called *nucleation*, which is explained in Chapter 7 of this book. This chapter discusses how small crystals grow.

### 8.2.1 Equilibrium and Transition to Solid Phase

The mother phase is the uniform isotropic phase and the solid phase has a periodic atomic structure and therefore is anisotropic (no spherical symmetry). Because of the difference in symmetry, the two phases can be distinguished clearly. In [Figure 8.2](#), a

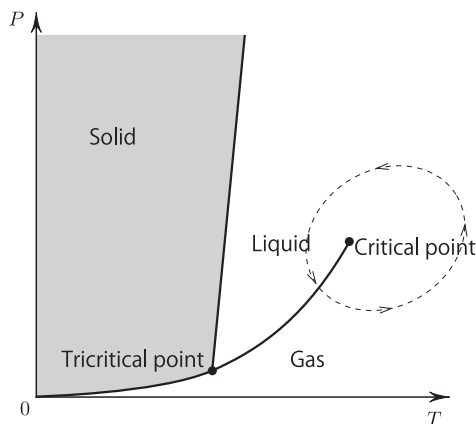


**FIGURE 8.2** A typical form of the phase diagram of simple material. Continuous transition from the gas to the liquid is realized along the dashed curve.

<sup>1</sup>There are already many textbooks available in bookstores. Some of the books the author noted and consulted to write the present chapter are Refs [3–9].

typical phase diagram is shown. In contrast to the solid–liquid (or gas) transition, a continuous transition between the gas and the liquid is possible, as indicated by the dashed curve in Figure 8.2, because there is not any change in symmetry. Liquid and gas can be distinguished clearly only when they exist at the same time with an interface.

If one changes the temperature  $T$  and/or pressure  $P$  of the system, the state of matter may change so as to lower the Gibbs free energy  $G(T, P)$ . The most important quantity is the chemical potential  $\mu(T, P)$ , which is the Gibbs free energy per particle<sup>2</sup>:  $\mu = G/N$ . Figure 8.3 shows chemical potentials of solid and liquid (or gas). Figure 8.3(A) corresponds to the change of  $\mu$  along a horizontal cut in Figure 8.2, and Figure 8.3(B) is along a vertical cut. If one decreases the temperature or increases the pressure beyond the coexisting point, the chemical potential  $\mu_L$  of the liquid becomes higher than that of the solid,  $\mu_S$ . Their difference,  $\Delta\mu = \mu_L - \mu_S$  is the *driving force of solidification*. Note that we have assumed the entropy in solid  $s_S$ , which is the down slope in Figure 8.3(A), is smaller than that in liquid  $s_L$ . Otherwise, the solid phase appears at the high-temperature side.<sup>3</sup> Also, we have assumed the atomic volume in solid  $v_S$ , which is the slope in Figure 8.3(B), is smaller than that in liquid  $v_L$ . A well-known counterexample is water ( $\text{H}_2\text{O}$ ): ordinary ice melts when pressure is applied. For simplicity, we always assume the standard behavior, as in Figure 8.3. Similarly, if the mother phase is a gas,  $\Delta\mu = \mu_G - \mu_S$  is the corresponding driving force.

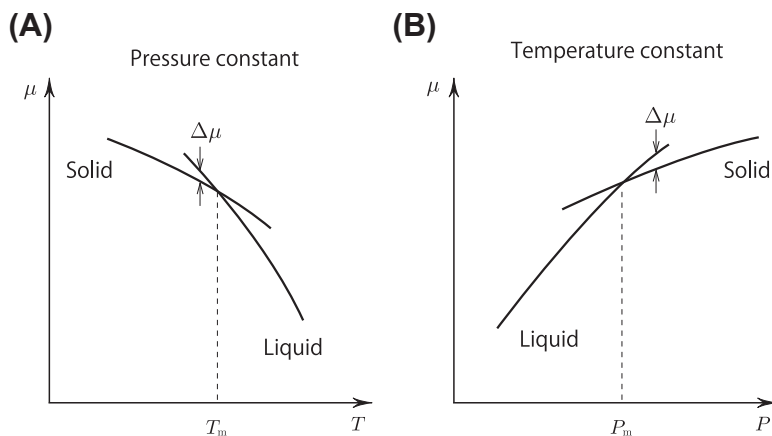


FIGURE 8.3 Change of chemical potentials of the solid and the liquid (gas) as a function of temperature  $T$  (A) and pressure  $P$  (B).

<sup>2</sup>Unless explicitly mentioned, we always deal with the simplest case—that is, one-component simple atoms/molecules.

<sup>3</sup>This case is rare but is seen in He [6].

## 8.2.2 Linear Kinetics

If a solid and a liquid are in equilibrium, temperature  $T$ , pressure  $P$ , and chemical potential  $\mu$  are equal in both phases. When these quantities are shifted from equilibrium, the pressure balance is related to mechanical equilibrium and restored at once. An imbalance of temperature produces heat flow, and an imbalance of chemical potential produces mass flow. When the shift is not too large, the corresponding response is proportional to the amount of shift. Such a linear response relationship usually holds true. In crystal growth, however, nonlinear behavior sometimes controls the system.

## 8.2.3 Transport and Chemical Potential

The process of crystallization is like constructing a brick building. Bricks that make up the building are transported from other places by various ways to the construction site. There, bricks are piled up one by one, and the building becomes larger and larger. Waste from construction is in turn transported by trucks from the site and discarded somewhere in the environment. Crystallization processes are categorized into two types: transport of materials and waste (transport processes) from/to remote places and assembling at the construction site (kinetics at the interface). In both processes, free energy is consumed. In crystallization at given temperature and pressure, chemical potential is consumed in such processes.

If convection is neglected, transport is controlled by *diffusion*, and the local mass current  $\mathbf{j}$  at the position  $\mathbf{r}$  is determined by

$$\begin{aligned}\mathbf{j}(\mathbf{r}) &= -D_\mu \nabla \mu(\mathbf{r}) \\ &= -D \nabla n(\mathbf{r}),\end{aligned}\tag{8.1}$$

where  $D_\mu$  and  $D$  are the diffusion coefficients and  $n(\mathbf{r})$  is the local number density of atoms. In a dilute system, chemical potential is proportional to density  $n$  and the second line holds.<sup>4</sup> Material is transported to the interface by the gradient of chemical potential. At the interface, with consumption of chemical potential  $\Delta\mu$ , transformation from liquid (gas) to solid—crystallization—occurs. Such process is called *interface kinetics* (surface kinetics), and it consists of several atomic processes. Macroscopically, the speed of liquid–solid transformation is measured by the velocity of the solid surface  $V$  and can be written as

$$V = K \Delta\mu,\tag{8.2}$$

where  $\Delta\mu$  is the difference of the chemical potential of the liquid at the interface and that of the solid. The proportionality coefficient  $K$  is called the kinetic coefficient. The proportionality is expected, except for a singular surface called a facet. A distinction between the facet and nonsingular faces is essential to understand the crystal growth mechanism, as explained in detail in Chapters 5 and 6 of this book.

<sup>4</sup>Because  $\mu = k_B T \ln n + \text{const.}$ , for a small change  $\delta\mu = (k_B T/n)\delta n \propto \delta n$ , and  $D = D_\mu k_B T/n$ .

## 8.3 Growth from Various Mother Phases

Crystallization occurs not only from the liquid phase but also from various other phases: from the vapor (from a gas, pure or mixture), from the solution (from a liquid mixture), and from other solid or amorphous phases. This section explains the characteristic features of several basic cases.

### 8.3.1 Growth from the Vapor

Growth of a solid directly from a gas is called *vapor growth*. It is the reverse process of evaporation (sublimation, more specifically). Growth of snow crystals in the sky and growth of frost on the window glass are examples from everyday life. Because observation of the surface is relatively easy, one can see what is happening there to find the growth mechanism better than in other cases. In a dilute gas, each elementary process contains only a few atoms (molecules), which also helps our understanding. As a result, we have relatively good control of the system.

Features of the vapor growth include the following:

1. Because the crystal grows from a dilute phase, the growth velocity is low. It is convenient for the surface manipulation (e.g., of semiconductor crystals) to make a device but is inefficient for making a big bulk crystal.
2. Unless the crystal is very large, the growth environment can be regarded as uniform, and local difference of the growth conditions is usually negligible.
3. The difference of density in solid and in gas is large, and the anisotropy of the surface is strong. As a consequence, large facets appear on the surface of the crystal.
4. Because most of the surface of a crystal consists of facets, where immediate solidification is usually difficult, various surface processes limit the growth velocity and the growth velocity is slow. These surface processes are very important and will be explained in the following sections.

Let us estimate the *maximum* growth velocity expected for growth from the vapor. If all atoms (or molecules) coming onto the crystal surface are taken into the crystal and solidify, the incoming flux will give the growth rate when evaporation is absent. At finite temperatures, evaporation occurs, and the evaporating flux should be subtracted from the incoming flux to obtain the net flux of solidification. If we denote the incoming current (flux density: number of atoms per unit area per unit time) by  $j_{\text{in}}$ , the outgoing current by  $j_{\text{out}}$  and atomic volume in the solid by  $\nu_{\text{S}}$ , the growth velocity, which is the advancing velocity of the surface, is given by

$$V = \nu_{\text{S}}(j_{\text{in}} - j_{\text{out}}). \quad (8.3)$$

For a classical ideal gas, which in an equilibrium state takes the Maxwell–Boltzmann distribution function,

$$f(\mathbf{p})d^3p = \frac{n_{\text{G}}}{(2\pi mk_{\text{B}}T)^{3/2}} e^{-p^2/2mk_{\text{B}}T} d^3p, \quad (8.4)$$

where  $n_G$  is the number density of the gas,  $j_{\text{in}}$  is easily calculated. The number of atoms incident to a unit surface area in the  $x - y$  plane within a time  $\Delta t$  from the above<sup>5</sup> is expressed as

$$\begin{aligned} j_{\text{in}}(T, P) &= \int_{-\infty}^0 dp_z \int_{-\infty}^{\infty} dp_y \int_{-\infty}^{\infty} dp_x \left( \frac{p_z}{m} \right) f(\mathbf{p}) \\ &= \frac{n_G k_B T}{\sqrt{2\pi m k_B T}} = \frac{P}{\sqrt{2\pi m k_B T}} \end{aligned} \quad (8.5)$$

because atoms of the velocity  $v_z = p_z/m$  ( $<0$ ) within the distance  $|v_z|\Delta t$  collide with the surface irrespective of the velocity  $v_x$  and  $v_y$ . The rate of evaporation, in contrast, must be a function of temperature  $T$  and is independent of the atmosphere. Calculating the evaporation current  $j_{\text{out}}(T)$  is difficult, but we know that under the equilibrium vapor pressure  $P_{\text{eq}}(T)$ , with which the solid neither grows nor sublimates, the two currents must balance:  $j_{\text{out}}(T) = j_{\text{in}}(T, P_{\text{eq}}(T))$ . Therefore, we can write the growth velocity (Eqn (8.3)) as

$$V_{\text{max}} = \frac{1}{\sqrt{2\pi m k_B T}} v_s (P - P_{\text{eq}}(T)). \quad (8.6)$$

Because we have assumed that all incoming atoms solidify, this equation, called the *Hertz-Knudsen formula*, gives the maximum growth velocity from the vapor [10,11]. The sticking coefficient—that is, the ratio of atoms captured by the solid surface to all incoming atoms—is less than unity (only at a very rough surface is it close to unity), and the growth is considerably slower.

If supersaturation is not too high, we can obtain a linear relation, as in Eqn (8.2). From the relationship between chemical potential and pressure for an ideal gas:

$$\mu = k_B T \ln P + (\text{function of } T). \quad (8.7)$$

$\Delta\mu$  is related to the pressure difference as

$$\Delta\mu = k_B T \ln \left( \frac{P}{P_{\text{eq}}} \right) \approx k_B T \frac{P - P_{\text{eq}}}{P_{\text{eq}}} = (P - P_{\text{eq}}) v_G, \quad (8.8)$$

where  $v_G$  is the volume per atom in gas. Equation (8.6) can be rewritten as

$$V_{\text{max}} = \frac{v_s}{v_G \sqrt{2\pi m k_B T}} \Delta\mu = \frac{n_G}{n_s} \frac{1}{\sqrt{2\pi m k_B T}} \Delta\mu. \quad (8.9)$$

Therefore, the maximum value of the kinetic coefficient is

$$K_{\text{max}}^{\text{vapor}} \approx \frac{v_s}{v_G} \frac{1}{m v_{\text{therm}}}. \quad (8.10)$$

### 8.3.2 Growth from the Melt

When a crystal grows from a liquid phase of the same material, it is called *melt growth*. This is the reverse process of melting.

<sup>5</sup>The space  $z \leq 0$  is assumed to be the solid.

Features of melt growth include the following:

1. Because the density difference between the two phases is small, the interfacial free energy and its anisotropy is usually small, and the interface tends to be rough.
2. There is no need for material transport, and a rough interface brings about rapid growth.
3. The velocity of growth is limited by transport of the latent heat. The transport of heat is carried out by heat conduction in the material and/or convection in the liquid. As a result, nonuniformity of the system is usually relevant, and stability of the growth form should be always taken care of.

### 8.3.2.1 Sharp Interface Picture

One can estimate the growth velocity from the melt as in the vapor growth. When the interface is rough, the growth velocity is determined by the balance of the solidifying current  $j_{\text{sol}}$  and the melting current  $j_{\text{mel}}$ . For a rough surface, kink sites, where solidification and melting take place, are everywhere, and the solidifying current is

$$j_{\text{sol}} \approx N_{\text{kink}} \nu_0 W_S e^{-E_b/k_B T}, \quad (8.11)$$

where  $N_{\text{kink}} \sim a^{-2}$  ( $a$ : lattice constant) is the number of kinks in a unit area,  $\nu_0$  is a characteristic frequency of molecular motion (such as the Debye frequency),  $W_S$  is the number of possible molecular configurations in a solid, and  $E_b$  is the height of the energy barrier to enter a kink site of the crystal. The energy barrier  $E_b$  is about the same magnitude as the energy barrier  $E_d$  for atomic diffusion in the liquid.  $W_S$  is related to the configuration entropy as  $W_S = e^{s_S/k_B}$  and is unity for an isotropic molecule, such as a rare gas atom. For molecules whose orientation in solid is limited, the difference of the number of allowed molecular orientations in liquid,  $W_L = e^{s_L/k_B}$ , and in solid may be significant. The current of the inverse process is

$$j_{\text{mel}} \approx N_{\text{kink}} \nu_0 W_L e^{-(E_b + \Delta h)/k_B T}, \quad (8.12)$$

where  $\Delta h = h_L - h_S$  is the difference of enthalpy (note that the two processes occur under a given pressure).

At the equilibrium temperature  $T_m$ , the two currents  $j_{\text{sol}}$  and  $j_{\text{mel}}$  must be equal and, from Eqns (8.11) and (8.12), we have  $h_L - T_m s_L = h_S - T_m s_S$ —that is,  $\mu_L = \mu_S$ . If temperature deviates from  $T_m$ , the net solidifying current is

$$\begin{aligned} j_{\text{sol}} - j_{\text{mel}} &\approx N_{\text{kink}} \nu_0 W_S e^{-E_b/k_B T} (1 - e^{\Delta s/k_B} e^{-\Delta h/k_B T}) \\ &= N_{\text{kink}} \nu e^{-\Delta s/k_B} e^{-E_b/k_B T} (1 - e^{-\Delta \mu/k_B T}), \end{aligned} \quad (8.13)$$

where  $\nu = \nu_0 W_L$  and  $\Delta s = s_L - s_S$ . In the last line, we take the motion in liquid as the standard and write the equation in a form that emphasizes reduction of the growth rate by the difference of configurational entropy  $\Delta s$ . If supersaturation is not too large, the growth velocity is written as

$$\begin{aligned} V &\approx \nu_S(j_{\text{sol}} - j_{\text{mel}}) \\ &\approx \nu_S N_{\text{kink}} \nu e^{-\Delta s/k_B} e^{-E_b/k_B T} \frac{\Delta\mu}{k_B T}, \end{aligned} \quad (8.14)$$

and is proportional to the driving force  $\Delta\mu$ . The temperature dependence of the kinetic coefficient

$$K^{\text{melt}} \approx \frac{\nu_S N_{\text{kink}} \nu}{k_B T} e^{-\Delta s/k_B} e^{-E_b/k_B T} \quad (8.15)$$

$$\approx \frac{a\nu}{k_B T} e^{-\Delta s/k_B} e^{-E_b/k_B T} \quad (8.16)$$

is controlled by the energy barrier  $E_b$ . Note that, in the last line, we have assumed that  $N_{\text{kink}} \approx a^{-2}$ : kinks cover the rough surface. Otherwise, a reduction factor  $N_{\text{kink}} a^2$  is necessary.

In terms of supercooling  $\delta T = T_m - T$ , the linear relation is written as

$$V = K\Delta\mu = K_T \delta T, \quad (8.17)$$

$$K_T = a\nu e^{-E_b/k_B T} e^{-\Delta s/k_B} \frac{\Delta s}{k_B T}, \quad (8.18)$$

where we have used  $\Delta\mu = (s_L - s_S)\delta T = \Delta s\delta T$ . The entropy gap is related to the latent heat per molecule,  $l$ , as  $\Delta s = l/T_m$ . Because the diffusion coefficient is given by  $D \approx a^2 \nu e^{-E_b/k_B T}$ , the first three factors of Eqn (8.18) are simply  $D/a$ , and  $K^{\text{melt}} \approx (D/k_B T a) e^{-\Delta s/k_B}$ . The equation for the growth velocity from the melt is called the *Wilson-Frenkel formula* [12,13]. With the Einstein–Stokes relation<sup>6</sup>  $D = k_B T / (3\pi\eta a)$ , the diffusion coefficient is related to the viscosity  $\eta$ , which is easily measured. Thus, the kinetic coefficient  $K_T$  is essentially determined by the viscosity of the liquid, but reduced by a factor  $e^{-\Delta s/k_B}$  if the entropy gap is not negligible. By lowering the temperature, the growth velocity first increases linearly with  $\delta T$ . When the temperature becomes too low, however, the viscosity increases exponentially ( $\eta \propto e^{E_b/k_B T}$ ) and solidification stops: in extreme cases, amorphous material may appear instead of crystal.

For metals, the values of kinetic coefficients are estimated as  $K_T \approx 1\text{--}50$  cm/s K ( $K_T \approx 10^{15\text{--}17}$  s/g cm) [3]. In real systems, because the transport of latent heat is the rate-limiting process, the apparent kinetic coefficient is much smaller if one uses the values of  $\Delta\mu$  or  $\delta T$  measured far<sup>7</sup> from the interface.

<sup>6</sup>We put the molecular radius as  $a/2$ , half the lattice constant.

<sup>7</sup>Macroscopically close sometimes means microscopically far.

It is known from molecular dynamics simulations that the activation type behavior of the kinetic coefficient (Eqn (8.18)) is not true for simple materials, such as molecules with van der Waals interactions [14]. It seems that crystallization proceeds without an energy barrier and  $av e^{-E_b/k_B T}$  is replaced by  $av_{\text{therm}}/l_{\text{mf}}$ , where  $v_{\text{therm}} = \sqrt{3k_B T/m}$  is the thermal velocity and  $l_{\text{mf}}(\sim a)$  is the mean free path of an atom. To understand such behavior, the image of melt growth must be modified.

### 8.3.2.2 Diffuse Interface Picture

The kinetic coefficient given above is derived with the assumption that the incorporation of an individual atom to the solid is the elementary process of crystallization. In this viewpoint, each atom belongs to the solid or to the liquid, and the boundary between solid and liquid is sharply defined, although it may be very rough. In reality, as indicated by many molecular dynamics simulations, it is not always possible to divide liquid and solid sharply at a rough interface, and collective motion in the liquid is significant. The periodic arrangement of atoms in the solid penetrates into the liquid phase with rather slow decay. Then, growth of crystal is nothing but advancement of such an order to the region previously considered as liquid. In this process, many atoms shift their average positions only slightly, and the crystalline order grows simultaneously in several atomic layers. Therefore, the growth velocity can be much faster than that in the growth of single atoms.

Historically, a continuum model of a diffuse interface was introduced by van der Waals [15] and has been studied in the context of a first-order phase transition as the Ginzburg-Landau model [16]. The important conclusion derived from the continuum model is that the kinetic coefficient is essentially given by the interface width divided by the relaxation time of the local order. (A modern continuum model is the phase field model. Various versions of it are used in many other fields, and the models in crystal growth are explained in Chapter 15 in Volume IB.) Cahn studied the growth of a periodic structure in a diffuse interface with the use of a lattice model [17]. More recently, an estimation of the real kinetic coefficient based on a picture of the diffuse interface was given by Mikheev and Chernov [18]. In this picture, the relevant quantity to describe the system is the order parameter  $\eta$ , which changes continuously at the interface. The local number density may be represented as follows (Figure 8.4):

$$n(\mathbf{r}, t) = n_c + \sum_{\mathbf{G}} \eta_{\mathbf{G}}(z - Rt) e^{i\mathbf{G} \cdot \mathbf{r}}, \quad (8.19)$$

where  $\mathbf{G}$  is the reciprocal lattice vector and  $R$  is the velocity of the interface. With a detailed theoretical analysis, the following formula for the kinetic coefficient is proposed [19,20]:

$$K \approx \frac{n_L^2 S(G_1)}{k_B T \tau_{G_1}} \left[ \sum_{|\mathbf{G}|=G_1} \int \left( \frac{d\eta_{\mathbf{G}}}{dz} \right)^2 dz \right]^{-1}, \quad (8.20)$$

where  $S(G_1)$  is the structure factor of the liquid for the smallest  $\mathbf{G}$  ( $G_1$  is assumed to be approximately equal to the wave number at the peak of  $S(\mathbf{k})$  in the liquid). The relaxation time of the density fluctuation,  $\tau_{G_1}$ , is determined from the half-width of the peak  $S(\mathbf{k}, \omega)$ .

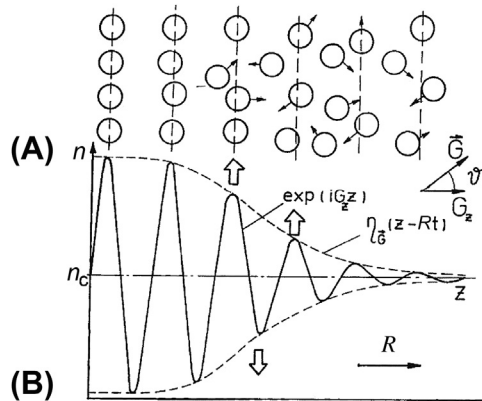


**FIGURE 8.4** Diffuse interface between solid (left) and liquid (right) propagating during growth [18,19]. (A) Atoms are ordered in the crystal and disordered in the melt. (B) Profile of the number density is assumed to have the form  $n(z) = n_c + \eta_G(z - Rt)e^{iG_z z}$ , with  $n_L \approx n_S \equiv n_c$ . Reprinted from Ref. [19], with permission from Elsevier.

The last factor with  $n_L^2$  roughly corresponds to the interface width, which is larger than the atomic distance and contributes to the increase in  $K$  as expected from the simple continuum theory [16]. The Eqn (8.20) can be estimated with measurable quantities,<sup>8</sup> and gives a good values of  $K$  for simple metals [19]. It provides the correct hierarchy of  $K$  for different faces. The order of magnitude of the estimated values  $K \sim (mv_{\text{therm}})^{-1}$  agrees reasonably with the experimental data. The analysis also suggests that the growth is limited by formation of the lateral order in the interface plane.

### 8.3.3 Growth from a Solution

Although the major pathways of crystal growth are from the melt and from the vapor, growth from a solution is also very important. A crystal, simple substance or compound, can grow from a liquid phase with additional components, which is called *solution growth*.<sup>9</sup> Many kinds of crystals, such as salt and quartz, are grown from solutions. Salt (NaCl) crystals are easily produced from seawater at room temperature despite that the melting temperature is 800 °C. The melting temperature of quartz (SiO<sub>2</sub>) is very high as 1610 °C, but industrial quartz is produced from an alkaline solution under high pressure at approximately 350 °C (hydrothermal synthesis).

Solution growth is similar to vapor growth in the respect that growth occurs with an excess of solute concentration  $c$ . Solidification proceeds via incorporation of an atom, which exists at the probability  $ca^3 \approx cv_S$  in an atomic volume of the solution, into a kink site by passing over an energy barrier. In solution growth, it is sometimes necessary for an atom (or a molecule) to break bonds with solvent molecules in solidification, which is

<sup>8</sup>The interface width is identified as the half width of the peak of  $S(\mathbf{k})$  in the liquid.

<sup>9</sup>Sometimes, it is called flux growth when inorganic compounds are used as solvents.

called desolvation. Therefore, by a similar argument that led to Eqn (8.14), we obtain the growth velocity from the solution

$$\begin{aligned} V &\approx v_S(j_{\text{sol}} - j_{\text{mel}}) \\ &\approx v_S^2 N_{\text{kink}} \nu e^{-\Delta s/k_B} e^{-(E_b + E_{\text{des}})/k_B T} (c - c_{\text{eq}}), \end{aligned} \quad (8.21)$$

where  $E_{\text{des}}$  is the extra energy barrier for desolvation. In a dilute solution, the chemical potential  $\mu_{\text{sol}}$  is related to the concentration as  $\mu_{\text{sol}} = k_B T \ln c + (\text{function of } T)$ , and chemical potential  $\mu_S$  in the solid is the equilibrium value  $\mu_{\text{eq}}$ . Then,  $\Delta\mu = \mu_{\text{sol}} - \mu_S = \mu_{\text{sol}} - \mu_{\text{eq}} = k_B T \ln(c/c_{\text{eq}})$ , and we obtain

$$\begin{aligned} V &\approx N_{\text{kink}} \nu v_S^2 c_{\text{eq}} e^{-\Delta s/k_B} e^{-(E_b + E_{\text{des}})/k_B T} (e^{\Delta\mu/k_B T} - 1) \\ &\approx N_{\text{kink}} \nu v_S^2 \frac{c_{\text{eq}}}{k_B T} e^{-\Delta s/k_B} e^{-(E_b + E_{\text{des}})/k_B T} \Delta\mu. \end{aligned} \quad (8.22)$$

The linear relation in the last line, with the kinetic coefficient

$$K \approx N_{\text{kink}} \nu v_S^2 \frac{c_{\text{eq}}}{k_B T} e^{-\Delta s/k_B} e^{-(E_b + E_{\text{des}})/k_B T} \quad (8.23)$$

is valid for small supersaturation. Compared with the melt growth in Eqn (8.16), there is an extra factor  $v_S c_{\text{eq}} e^{-E_{\text{des}}/k_B T}$ , which is very small for a dilute solution and for a high desolvation energy barrier. Solution growth is much slower than melt growth.

## 8.4 Normal Growth and Lateral Growth

Except for faceted faces, the surface of a crystal is rough and there are kinks everywhere.<sup>10</sup> The surface can grow in the direction normal to the local surface orientation, on a microscopic scale, by incorporating surrounding atoms or molecules. The growth is called *normal growth* or *adhesive growth*. On the other hand, if the surface is faceted, an atom or a molecule needs to find a kink site to crystallize stably. Kinks are present along a step on the faceted surface, and steps on the facet move forward along the surface so that the surface advances. Because the crystal grows by the lateral motion of steps, the growth is called *lateral growth* or *layer growth*.

### 8.4.1 Adhesive Growth on Rough Faces

For adhesive growth to occur, the surface must be rough—that is, temperature must be higher than the roughening temperature of the face. As we have seen in Eqn (8.3), the normal growth velocity  $V$  of the surface is proportional to the supersaturation  $\Delta\mu$  near

<sup>10</sup>Meanings of rough and smooth faceted faces are explained in Chapters 5 and 6 and depicted schematically in Figure 8.5.

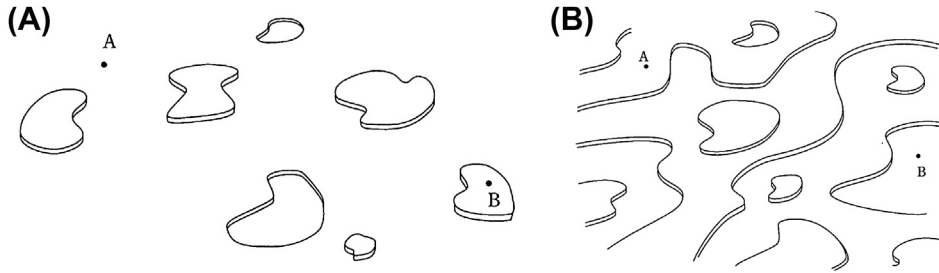


**FIGURE 8.5** Smooth (A) and rough (B) faces. The height difference of A and B is within the lattice constant  $a_z$  in (A). The height difference is expected to increase logarithmically with the distance between A and B in (B).

the kink sites. Because kinks are everywhere,  $\Delta\mu$  is practically the same all over the surface. Such a linear relationship between the growth velocity and the supersaturation,  $V = K\Delta\mu$ , is characteristic for rough surfaces. Thus, the kinetic coefficient  $K$  is a well-defined quantity for rough surfaces.

The linearity does not hold for a facet because supersaturation is not uniform on the surface and the local supersaturation at the growth site differs depending on the configuration of kinks (or steps). To understand the growth of a faceted surface, we should consider the generation mechanism of steps and the motion of steps, of which kinks are present at the edge.

## 8.4.2 Growth via Two-Dimensional Nucleation on a Facet

On a facet of a perfect crystal at very low temperatures, there are no steps, so the facet cannot grow at all. At finite temperatures, there are small two-dimensional (2D) islands or holes that are thermally excited, as shown in [Figure 8.5\(A\)](#). For a 2D island of typical radius  $R$ , the step edge costs energy typically  $2\pi R\beta$ , where  $\beta$  is the step free energy per unit length.<sup>11</sup> Near equilibrium,  $\Delta\mu \approx 0$ , as a result of thermal fluctuation, islands whose energy is of the order of  $k_B T$  or smaller may be created. Thus, the typical size of the thermally created islands is  $\xi \sim k_B T / (2\pi\beta)$ , which is the correlation length of the height. If such a thermally excited island grows, the energy will increase. Most islands tend to lower their energy and disappear soon.

If the environment becomes supersaturated, the free energy of a circular 2D island is given by ([Figure 8.6](#)):

$$G_2(R) = -\frac{\pi R^2}{\Omega_2} \Delta\mu + 2\pi R\beta, \quad (8.24)$$

<sup>11</sup>Roughly speaking, the free energy density of a step,  $\beta$ , vanishes above the roughening transition temperature, and the formation of an island does not require any extra free energy on a rough surface.

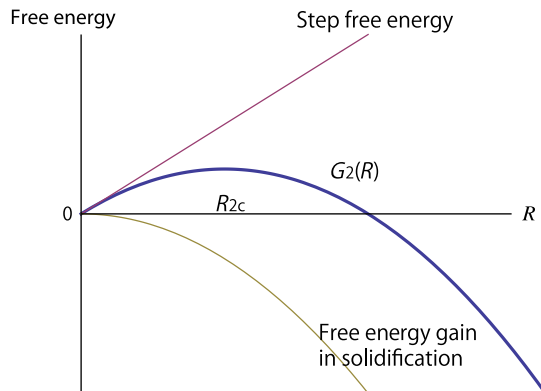


FIGURE 8.6 Free energy of a circular two-dimensional nucleus as a function of the radius.

where  $\Omega_2 = 1/(a_z n_S) = v_S/a_z$  is the atomic area and  $a_z$  is the atomic height. The first term is the free energy gain by the solidification of  $\pi R^2/\Omega_2$  atoms. In a supersaturated state,  $\Delta\mu > 0$ ,  $G_2$  increases with the size and takes a maximum value

$$G_2(R_{2c}) = \pi \frac{\Omega_2 \beta^2}{\Delta\mu} \equiv G_{2c} \quad (8.25)$$

at the radius

$$R_{2c} = \frac{\Omega_2 \beta}{\Delta\mu}, \quad (8.26)$$

and decreases beyond this point. The 2D island of the size  $R_{2c}$  is at unstable equilibrium with the environment, called the *critical 2D nucleus*.  $R_{2c}$  is called the radius of a critical nucleus, and  $G_{2c}$  is its free energy. According to the nucleation theory described in Chapter 7, if an island larger than the critical radius appears as a result of thermal fluctuation, it most likely grows forever. This growth of an island is *nucleation* of the new layer of the crystal.

The frequency of the appearance of a critical nucleus by thermal fluctuation [20] is determined by the critical free energy  $G_{2c}$ . From the nucleation theory, the steady-state nucleation rate per unit area per unit time is given by the product of three quantities [4,5,21]:

$$j_{\text{nuc}} \approx Z w_c^+ n_c^{\text{eq}}. \quad (8.27)$$

The last factor,  $n_c^{\text{eq}}$ , is the equilibrium density of critical islands expressed as

$$n_c^{\text{eq}} \approx n_1 e^{-G_{2c}/k_B T} \sim \frac{e^{-G_{2c}/k_B T}}{\Omega_2}, \quad (8.28)$$

where  $n_1$  is the density of atoms on the surface and is  $\sim \Omega_2^{-1}$  for melt growth. This quantity is controlled by the critical free energy  $G_{2c}$  and the most sensitive factor to  $\Delta\mu$  in  $j_{\text{nuc}}$ . The second factor,  $w_c^+$ , is the attachment rate of atoms to the critical island; it is proportional to the edge length  $2\pi R_c = 2\pi\Omega_2\beta/\Delta\mu$  and to the incoming current  $j_{\text{in}}$ . Its

explicit expression depends on systems we consider. For surface diffusion with diffusion length  $x_s$ , it is the number of impinging atoms onto a zone near the step edge of the width  $2x_s$  (assuming  $R_c \gtrsim x_s$ ):

$$w_c^+ \approx 4\pi x_s R_c f = \frac{4\pi x_s \Omega_2 \beta}{\Delta\mu} f, \quad (8.29)$$

where  $f$  is the impingement rate of atoms onto the surface per unit area. For simple melt growth,

$$w_c^+ \approx \frac{av_0 e^{-E_b/k_B T}}{\Omega_2} 2\pi R_c = 2\pi av_0 e^{-E_b/k_B T} \frac{\beta}{\Delta\mu}. \quad (8.30)$$

The first factor  $Z$  is the Zeldovich factor, which appears as a result of stochastic nature of nucleation (see Chapter 7), representing broadness of the peak of the free energy (Eqn (8.24)):

$$Z = \sqrt{\frac{(\Delta\mu)^3}{4\pi^2 \Omega_2 k_B T \beta^2}}. \quad (8.31)$$

From Eqns (8.28), (8.30), and (8.31), the nucleation rate (Eqn (8.27)) is estimated as [21,22]

$$j_{\text{nuc}} \sim \frac{\bar{\nu}}{\Omega_2} \left( \frac{\Delta\mu}{k_B T} \right)^{1/2} e^{-\pi\Omega_2\beta^2/(\Delta\mu k_B T)}, \quad (8.32)$$

where  $\Omega_2^{-1} = a^{-2}$  is the number of sites where nucleation is possible, and  $\bar{\nu} = \nu_0 e^{-E_b/k_B T}$  is a typical frequency of the atomic attachment to the island edge per site.

#### 8.4.2.1 Single-Nucleation versus Multinucleation

When supersaturation is weak,  $G_{2c}$  is large so that  $e^{-G_{2c}/k_B T}$  is extremely small: the nucleation rate is practically zero. If supersaturation is increased, nucleation may occur within the observation period, and the facet starts to grow. For a very small facet, the nucleated supercritical 2D island spreads to cover the whole facet, which means that the growth stops until a new supercritical island is born on the new layer. Such intermittent growth is called *single-nucleation growth* (Figure 8.7(A)). The growth velocity of a facet of the size  $R_f$  is the lattice constant times the nucleation rate:

$$V \approx \pi a R_f^2 j_{\text{nuc}} = a \bar{\nu} \frac{\pi R_f^2}{\Omega_2} \left( \frac{\Delta\mu}{k_B T} \right)^{1/2} e^{-\pi\Omega_2\beta^2/\Delta\mu k_B T}. \quad (8.33)$$

For a large facet, many nucleation events occur before a single island covers the whole facet. Many islands coalesce to form a new atomic layer. The growth is continuous and called *multinucleation growth* (Figure 8.7(B)).

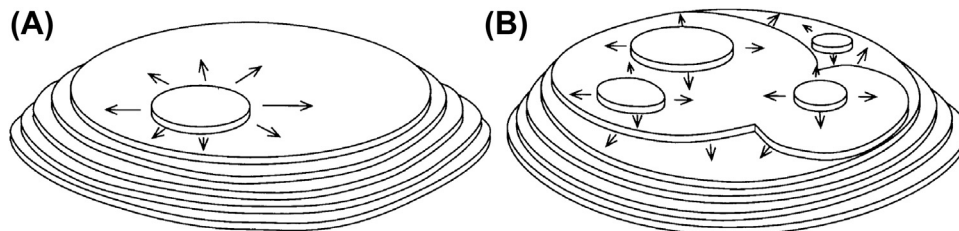


FIGURE 8.7 (A) Single-nucleation growth. (B) Multinucleation growth.

#### 8.4.2.2 Growth of a 2D Circular Island

To find the growth velocity in multinucleation growth, we need to know the growth of a 2D island under constant supersaturation. For a circular island bound by an isotropic step, the effective driving force of the step edge is

$$\Delta\mu_{\text{eff}} = \Delta\mu - \frac{\Omega_2 \tilde{\beta}}{R}, \quad (8.34)$$

where the second term is the retraction force due to the *step stiffness*<sup>12</sup>  $\tilde{\beta}$ . Because the step is always rough at a finite temperature, the velocity is proportional to the driving force:

$$\begin{aligned} V_{\text{st}} &= K_{\text{st}} \left( \Delta\mu - \frac{\Omega_2 \tilde{\beta}}{R} \right) \\ &= K_{\text{st}} \Delta\mu \left( 1 - \frac{R_{2c}}{R} \right), \end{aligned} \quad (8.35)$$

where  $K_{\text{st}}$  is the kinetic coefficient of the step. The second line is expressed in terms of the critical radius  $R_{2c}$ , and it is valid if the crystal anisotropy in the plane can be neglected.<sup>13</sup> The island is then circular, and the radius at time  $t$  is obtained by integrating Eqn (8.35) as

$$\frac{K_{\text{st}} \Delta\mu}{R_{2c}} t = \frac{R}{R_{2c}} + \ln \left| \frac{R}{R_{2c}} - 1 \right| + \text{const.} \quad (8.36)$$

If the initial radius is smaller than the critical radius  $R < R_{2c}$ , the island will disappear. When  $R \ll R_{2c}$ , it shrinks as

$$R(t) \approx R_{2c} \left[ \frac{2K_{\text{st}} \Delta\mu}{R_{2c}} (t_0 - t) \right]^{1/2} = [2K_{\text{st}} \Omega_2 \tilde{\beta} (t_0 - t)]^{1/2}, \quad (8.37)$$

where  $t_0$  is the time it vanishes. If the initial radius is larger than the critical radius  $R > R_{2c}$ , the island expands. When the island becomes much larger than the critical radius,  $R \gg R_{2c}$ , the step stiffness may be neglected and move at a constant

<sup>12</sup>The stiffness of a step,  $\tilde{\beta}(\phi)$ , is the most important quantity to characterize the step when crystal anisotropy is relevant. It is the sum of  $\beta(\phi)$ , which is now a function of the azimuthal angle  $\phi$ , and its second derivative  $\beta''(\phi)$ :  $\tilde{\beta} = \beta + \beta''$ .

<sup>13</sup>For an isotropic step, the stiffness is constant and the same as the free energy density:  $\tilde{\beta} = \beta$ .

speed:  $R(t) = K_{st}\Delta\mu t$ . Except for a very early stage, the radius of an island created by 2D nucleation grows at a constant speed:

$$V_{st} = K_{st}\Delta\mu. \quad (8.38)$$

### 8.4.2.3 Change of Coverage by Nucleation and Spread

To estimate the velocity of multinucleation growth, let us first consider the change of coverage of a new layer on a flat facet by nucleation and spread of 2D islands [16,23,24]. For simplicity, we consider the growth of a single layer. We assume that nucleation occurs randomly at constant probability and circular islands spread at the constant step velocity  $V_{st}$ . At time  $t$ , an arbitrary point P located at  $\mathbf{x}$  is still on the initial facet surface with a probability  $p$ —that is, the ratio  $p$  of the facet area is not covered by the new layer. The point P is covered by the new layer if there was a nucleation event at the location  $\mathbf{x}'$  and the time  $t'$  that satisfies the following:

$$V_{st}(t - t') > |\mathbf{x} - \mathbf{x}'|.$$

If we denote  $t - t' = \bar{t}$  and  $\mathbf{x}' - \mathbf{x} = \bar{\mathbf{x}}$ , the probability  $p$  is given by the product of probabilities that nucleation does not occur at the point satisfying the condition  $V_{st}\bar{t} > |\bar{\mathbf{x}}|$ . That is,

$$p = \prod_{0 < |\bar{\mathbf{x}}| < V_{st}\bar{t}, 0 < \bar{t} < t} (1 - j_{nuc} d^2\bar{\mathbf{x}} d\bar{t}). \quad (8.39)$$

Because the second term in the bracket is infinitesimal, this equation can be written as

$$\begin{aligned} p &= \exp\left[\ln \prod (1 - j_{nuc} d^2\bar{\mathbf{x}} d\bar{t})\right] \\ &= \exp\left(-\sum j_{nuc} d^2\bar{\mathbf{x}} d\bar{t}\right) \\ &= \exp\left(-j_{nuc} \int_0^t d\bar{t} \int_0^{V_{st}\bar{t}} 2\pi\bar{x} d\bar{x}\right) \\ &= \exp\left(-\frac{\pi}{3} j_{nuc} V_{st}^2 t^3\right). \end{aligned}$$

Therefore, the coverage of the new layer  $\Theta_{2D}$  changes as

$$\Theta_{2D}(t) = 1 - p = 1 - \exp\left(-\frac{\pi}{3} j_{nuc} V_{st}^2 t^3\right). \quad (8.40)$$

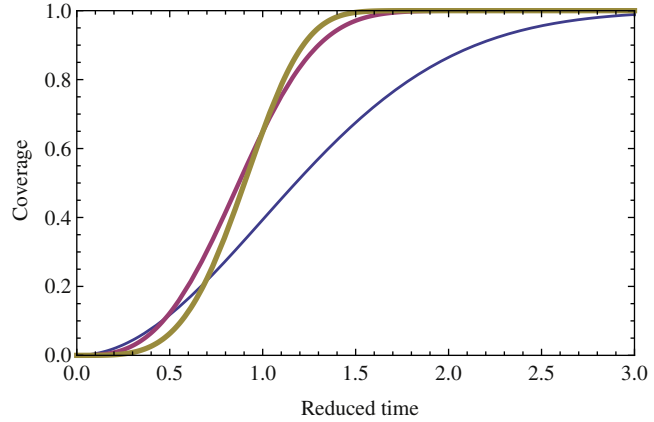
As shown in Figure 8.8, it initially increases as

$$\Theta_{2D}(t) \approx \frac{\pi}{3} j_{nuc} V_{st}^2 t^3, \quad (8.41)$$

and approaches unity at about  $j_{nuc}^{1/3} V_{st}^{2/3} t \approx 1.5$ . A similar calculation in one and three spatial dimensions gives the following results for the advancement of a straight step and volume occupation of a new phase:

$$\Theta_{1D}(t) = 1 - \exp\left(-\frac{1}{2} j_{nuc} V_k t^2\right), \quad (8.42)$$

**FIGURE 8.8** Coverage of the new phase, in one, two, and three dimensions (thin line to thick line). The reduced time is  $t$  multiplied by  $(j_{\text{nuc}}V_k)^{1/2}$ ,  $(j_{\text{nuc}}V_{\text{st}}^2)^{1/3}$  and  $(j_{\text{nuc}}V^2)^{1/4}$ , respectively.



$$\Theta_{3D}(t) = 1 - \exp\left(-\frac{\pi}{3}j_{\text{nuc}}V^3t^4\right), \quad (8.43)$$

where  $V_k$  is the velocity of a kink and  $V$  is the velocity of the interface.

#### 8.4.2.4 Velocity of Multinucleation Growth

Because one atomic layer is covered in a period  $\tau \sim (j_{\text{nuc}}V_{\text{st}}^2)^{-1/3}$ , the velocity of a facet growing by multinucleation growth is

$$\begin{aligned} V &= \frac{a}{\tau} \approx aj_{\text{nuc}}^{1/3}V_{\text{st}}^{2/3} \\ &= a\left(\frac{\bar{v}}{\Omega_2}\right)^{1/3}\left(\frac{\Delta\mu}{k_B T}\right)^{1/6}e^{-G_{2c}/3k_B T}(K_{\text{st}}\Delta\mu)^{2/3} \\ &\sim (\Delta\mu)^{5/6}e^{-\pi\Omega_2\beta^2/(3k_B T\Delta\mu)}. \end{aligned} \quad (8.44)$$

Note that the energy of a critical nucleus in the exponential factor is divided by three compared with Eqn (8.32). In the case of step growth limited by surface diffusion, the step velocity is proportional to  $c - c_{\text{eq}} = c_{\text{eq}}(e^{\Delta\mu/k_B T} - 1) \approx \Delta\mu/k_B T$ , and the prefactor becomes proportional to  $(\Delta\mu/k_B T)^{5/6}$ . The result is consistent with the Monte Carlo simulation [25], which demonstrates the sharp contrast of the  $\Delta\mu$  dependence of growth velocity below and above the roughening transition. In the experiment, the growth velocity of a  $^4\text{He}$  crystal below the roughening transition temperature was measured with changing<sup>14</sup>  $\Delta\mu$  [26]. The data were analyzed with a simpler formula<sup>15</sup>:  $V \sim V_{\text{st}}e^{-G_{2c}/3k_B T} = K_{\text{st}}\Delta\mu e^{-\pi\Omega_2\beta^2/(3k_B T\Delta\mu)}$ . The plots  $\ln(V/\Delta\mu)$  versus  $(\Delta\mu)^{-1}$  at various temperatures show clear linear dependence, and from their slopes the step free energy density  $\beta(T)$  was determined. The result showed a singular temperature dependence and supported the theory of roughening transition (see Chapter 6) [6].

<sup>14</sup>Although this is a melt growth experiment, the temperature is fixed and  $\Delta\mu$  is varied by the change of pressure.

<sup>15</sup>The present system is a quantum system, and the pre-exponential factor is different from Eqn (8.44).

In real growth of a macroscopic facet, there are steps originating from dislocations exposed on the facet, and the growth proceeds via spiral growth, which is explained in the following section. The 2D nucleation growth becomes important only under high supersaturation.

### 8.4.3 Spiral Growth with Screw Dislocations

If a crystal is perfect without any defect, its facets cannot grow under weak supersaturation because the free energy of a critical 2D island is much larger than the thermal energy,  $\delta G_{2c} \gg k_B T$ , and nucleation never occurs during the observation period. In real crystals, however, facets certainly grow under weak supersaturation. This puzzle was solved by Frank's proposal that facets grow with the help of screw dislocations that always exist in a macroscopic crystal [27–29].

A screw dislocation is a topological defect of a crystal lattice. If one moves around the dislocation, the lattice plane shifts by one layer (or more layers), like a spiral staircase. The Burgers vector of a screw dislocation is parallel to the dislocation line. If the screw dislocation is exposed on a facet, a step emerges at the end of the dislocation and stretches to an edge of the facet (Figure 8.9(B)). When the chemical potential of the environment is changed, the step advances or recedes according to the sign of  $\Delta\mu$ , as shown in Figure 8.9(A) and (C). Because the end of the step is pinned at the dislocation,<sup>16</sup> the shape of the step becomes spiral. Such growth helped by a dislocation is called *spiral growth*. The advantage of spiral growth is that the step does not disappear, and the growth continues without the creation of a new step.

#### 8.4.3.1 Velocity of Spiral Growth

The velocity of a step is proportional to supersaturation,  $V_{st} = K_{st}\Delta\mu_{eff}$ , and growth is possible under small supersaturation. If the distance between steps is  $l$  (Figure 8.9(C)), the growth velocity  $V$  perpendicular to the facet is  $V_{st}(a_z/l)$ . Because, far apart from the dislocation, the curvature of the step is very small, the step velocity is  $V_{st}^\infty = K_{st}\Delta\mu$ , and the growth velocity is given by

$$V = \frac{a_z}{l} K_{st} \Delta\mu. \quad (8.45)$$

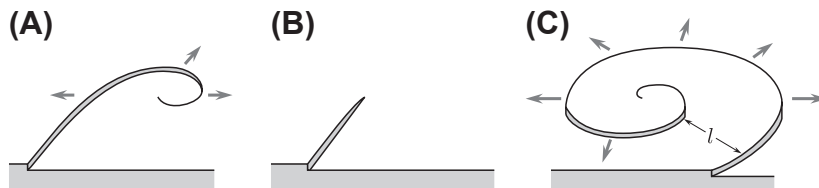


FIGURE 8.9 Spiral step with a dislocation: (A) in melting,  $\Delta\mu < 0$ ; (B) in equilibrium,  $\Delta\mu = 0$ ; (C) in growth,  $\Delta\mu > 0$ .

<sup>16</sup>Dislocations may be moved with elastic stress, but not with  $\Delta\mu$ .

The shape of the spiral step is similar to an Archimedean spiral, whose expression in the polar coordinates is  $r(\phi) = A\phi$ . In the polar coordinates, the curvature of the Archimedean spiral is

$$\frac{1}{R} = \frac{r^2 + 2(r')^2 - rr''}{(r^2 + (r')^2)^{3/2}} = \frac{A^2\phi^2 + 2A^2}{(A^2\phi^2 + A^2)^{3/2}}. \quad (8.46)$$

Near the origin (dislocation), where  $\phi \rightarrow 0$ , the curvature is  $R^{-1} = 2/A$ . Because the step advances little at the center of the spiral, the curvature there must be  $R_c$ , which means  $A = 2R_{2c}$ . Thus, with one rotation, the distance from the center increases by  $2\pi A = 4\pi R_{2c} = l$ . For a more accurate calculation, one must solve Eqn (8.35) with Eqn (8.46) numerically. The result is  $l \approx 19R_{2c}$  [30], and the growth velocity is

$$V \approx \frac{a_z}{19R_{2c}} K_{st} \Delta\mu = K_{st} \frac{a_z}{19\Omega_2 \bar{\beta}} (\Delta\mu)^2. \quad (8.47)$$

Because the step distance is inversely proportional to  $\Delta\mu$ , the growth velocity is proportional to  $(\Delta\mu)^2$ , which is the characteristic feature of spiral growth.

Here, we have assumed that the step is isotropic. If a step is anisotropic, the spiral is also anisotropic and the coefficient differs from 1/19. For example, if the equilibrium shape of the 2D island is square, the coefficient becomes  $(4L_{2c})^{-1}$  instead of  $(19R_{2c})^{-1}$ , where  $L_{2c} = 2\bar{\beta}/\Delta\mu$  is the side length of the square critical island. This relationship is derived by assuming the straight step can grow only when the length exceeds  $L_{2c}$  [5].

#### 8.4.3.2 Growth of a Facet with Many Dislocations

It is important to note that the growth velocity of a facet does not depend on the number of dislocations as long as they are nonzero [28]. Figure 8.10(A) shows spiral growth with a pair of screw dislocations of the opposite sign. If the Burgers vector of the dislocation is opposite, the spiral winds in the opposite direction. The two spirals originating from the opposite dislocations collide and merge to form concentric circles asymptotically. The distance of successive steps is the same as the original spiral, and the growth velocity remains the same as that with a single step. For two dislocations of the same sign (the same Burgers vector), a similar recombination of steps occur if the centers of the spirals

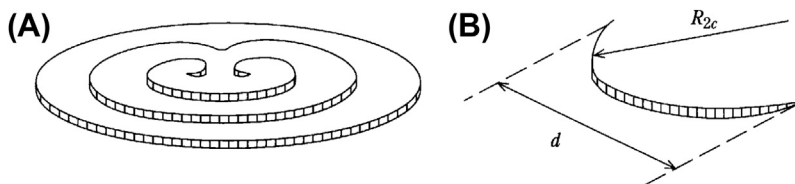


FIGURE 8.10 (A) Spiral growth with a pair of screw dislocations. (B) A step pinned by a pair of screw dislocations.

are not too close. If their distance  $d$  is smaller than the period of the spiral  $l$ , they operate additively, and the efficiency as a step source can be twice as that of a single dislocation, at the best.<sup>17</sup> Therefore, the growth velocity of the whole facet is not much larger than that with a single dislocation.

Although we find the growth velocity is proportional to  $(\Delta\mu)^2$ , there is a small threshold value of supersaturation for spiral growth to work. If there is a pair of dislocations of the opposite sign as shown in Figure 8.10(B), the distance  $d$  should be larger than  $2R_{2c}$  for the pair to operate as a step source. Otherwise, the advancement of the step is blocked. Therefore, for growth of a facet, supersaturation should be stronger than the threshold value

$$\Delta\mu_{\text{th}} = \frac{2\Omega_2\tilde{\beta}}{d}, \quad (8.48)$$

where  $d$  is the narrowest channel for the step on the facet.<sup>18</sup> For a small facet, growth is sensitive to the configuration of dislocations: their number and location, the magnitude of Burgers vector, etc. [31].

#### 8.4.3.3 Change of Growth Mode and Kinetic Roughening

In thermal equilibrium, only small islands of the size  $\xi \sim k_B T / \tilde{\beta}$  appear temporarily as fluctuations, and the position of a facet is locked at a single atomic layer: the surface is atomically smooth (Figure 8.5(A)). Under weak supersaturation, the 2D nucleation rate is so low that the facet never grows without dislocations. A facet under weak supersaturation is thermodynamically in a *metastable equilibrium* state. With screw dislocations, the facet grows above the threshold supersaturation  $\Delta\mu_{\text{th}}$ . If  $\Delta\mu \gg \Delta\mu_{\text{th}}$ , the growth velocity is proportional to  $(\Delta\mu)^2$ . By increasing supersaturation, 2D nucleation growth occurs in parallel to the spiral growth and eventually dominates the growth (Figure 8.11). The successive nucleation of islands blurs the flat facet. Under high supersaturation, the free energy of the critical nucleus, as in Eqn (8.25), becomes small and comparable to the thermal energy  $k_B T$ . The condition  $\delta G_{2c} \sim k_B T$  is equivalent to the condition  $R_{2c} \sim \xi$ , which means that the critical radius is of the same order of the characteristic length of step fluctuation. There, so many steps appear on the facet and distinction between steps originating from dislocations versus 2D nucleation is no longer possible. The facet is atomically rough and its growth velocity becomes as fast as rough faces. The gradual crossover phenomenon, with increasing supersaturation, from a facet to a rough face is called *kinetic roughening*.<sup>19</sup>

<sup>17</sup>In fact, a dislocation with a large Burgers vector works very efficiently as a step source.

<sup>18</sup>Like dislocations, impurities may pin down steps on a facet. As a result, scattered impurities on a facet can retard the motion of steps and the growth. If the concentration of impurities on a facet becomes too high, they may completely block the growth of the facet and hysteresis may be observed in the relationship between the supersaturation and the growth velocity [32,33].

<sup>19</sup>The concept of kinetic roughening has been used in a wider field of study than crystal growth. Some of the reviews describing crystal growth are Refs [34–36].

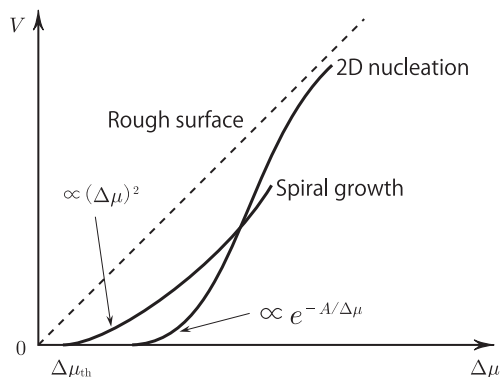


FIGURE 8.11 Change of growth mode by increasing supersaturation.

#### 8.4.3.4 Formation of Mounds

We estimated the characteristic time  $\tau$  necessary to cover one layer by considering a single layer system. In reality, nucleation occurs on a new layer before the new layer covers the whole surface: growth proceeds on many layers simultaneously. During growth from a vapor, transport along the surface–surface diffusion is important.<sup>20</sup> On a growing 2D island, nucleation of the new layer is likely to occur near the center of the island because atoms landing near the step edge are consumed by the step growth and the density of atoms near the center is higher. By successive nucleation in the central area of new layers, a nearly concentric multilayer island is formed when supersaturation is sufficiently high. Such a multilayer island is called a mound. Note that in growth at low temperatures, evaporation is weak and nonuniformity of the height can be produced only when the transport of material along the surface occurs. Thus, surface diffusion is necessary for the formation of mounds. Mounds are formed by several ways; detailed explanations are given in Refs [34,37,38].

## 8.5 Growth of Vicinal Faces

A face slightly tilted from a facet consists of an array of parallel steps and terraces bound by the steps. Such a face is called a *vicinal face*. A vicinal face grows by layer growth—that is, lateral advancement of parallel steps. Unlike the growth of a facet, the average distance  $l$  of parallel steps is determined by external conditions, such as the tilt angle in cutting the crystal.<sup>21</sup>

The growth velocity in the normal direction to the terrace is

$$V_z = \frac{a_z}{l} V_{st} = a_z n_{st} V_{st}, \quad (8.49)$$

<sup>20</sup>The role of surface diffusion in vapor growth is explained in Section 8.5.2.

<sup>21</sup>If a cone formed by a spiral step is large, its side face can be regarded as a vicinal face.

where  $l$  is the distance between steps and  $V_{st} = K_{st}\Delta\mu_{eff}$  is the velocity of a step. The growth velocity in the direction normal to the face is

$$V = V_z \cos \theta = V_{st} \sin \theta. \quad (8.50)$$

The tilt angle  $\theta$  (or the slope  $p$ ) and the step density  $n_{st}$  are related as  $a_z n_{st} = \tan \theta$  ( $=p$ ). If  $\theta$  is very small, the distance between steps is very large and each step can move independently. If the distance of neighboring steps becomes shorter, the steps compete each other for obtaining material or evacuating heat via overlapping diffusion fields. Here, we consider two typical cases in which the step velocity changes with the distance  $l$  depending on the transport mechanism.

### 8.5.1 A Model of Solution Growth: Bulk Diffusion

In solution growth, flow of the solution (either artificial or natural) makes the solute concentration and the temperature uniform. Because of the viscosity of the liquid, however, the solution near the crystal surface is usually stagnant and diffusion in the bulk liquid is important. A simple model representing this situation is shown in Figure 8.12 [29]. At a distance  $\lambda_0$  from the surface, the solute is regarded as static and uniform with the bulk concentration  $c_\infty$ . This hypothetical layer of the thickness  $\lambda_0$  is called the *diffusion boundary layer*. Diffusion of the solute to the equidistant parallel steps conveys the material for growth of the crystal. A growing step is a sink of the solute, and the diffusion flow brings up the advancement of the step. Approximating the step of the height  $a$  with a half cylinder with the radius  $a/\pi$ , the step velocity is related to the diffusion flow as

$$\frac{aV_{st}}{v_s} = D \left. \frac{\partial c}{\partial r} \right|_{r=a/\pi} a. \quad (8.51)$$

Solving the diffusion equation  $\nabla^2 c = 0$  with the boundary conditions (Eqn (8.51)) and  $c(x, y = \lambda_0) = c_\infty$ , the step velocity is calculated as [3,29]:

$$V_{st} = v_s \frac{\delta c_\infty}{\frac{1}{K_{st}} + \frac{a}{\pi D} \ln \left[ \frac{l}{a} \sinh \left( \frac{\pi \lambda_D}{l} \right) \right]}, \quad (8.52)$$

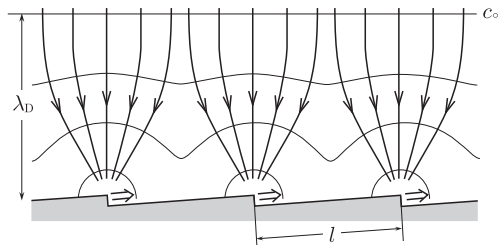


FIGURE 8.12 Contours of the solute concentration and flow-lines to the steps of the solute [29].

where  $\delta c_\infty \equiv c_\infty - c_{\text{eq}}$ , and the kinetic coefficient of the step is defined as<sup>22</sup>

$$\mathcal{K}_{\text{st}} = \frac{V_{\text{st}}}{v_{\text{S}} \delta c_{\text{st}}}, \quad (8.53)$$

where  $\delta c_{\text{st}} = c(r_{\text{step}}) - c_{\text{eq}}$  is the supersaturation at the step position. The structure within the boundary layer is difficult to observe, and the experimentally observable kinetic coefficient of the step,  $\mathcal{K}_{\text{st}}^{\text{eff}} = V_{\text{st}}/(v_{\text{S}} \delta c_\infty)$ , is related to  $\mathcal{K}_{\text{st}}$  as

$$\frac{1}{\mathcal{K}_{\text{st}}^{\text{eff}}} = \frac{1}{\mathcal{K}_{\text{st}}} + \frac{a}{\pi D} \ln \left[ \frac{l}{a} \sinh \left( \frac{\pi \lambda_{\text{D}}}{l} \right) \right]. \quad (8.54)$$

The first term represents the resistance of attachment and detachment at the step, and the second term represents the growth resistance of bulk diffusion. If the step distance is larger than the thickness of the boundary layer, the second term becomes independent of the step distance. Then, the growth velocity of the vicinal face is proportional to the slope of the face,  $p = a/l$ , and  $K \sim \mathcal{K}_{\text{st}}^{\text{eff}}(p \rightarrow 0)p$ . On the other hand, if the step distance is small, the diffusion field interferes strongly and the growth velocity becomes insensitive to the slope  $p$ . If the step distance is close to the lattice constant  $l \sim a$ , the second term of Eqn (8.54) is  $\lambda_{\text{D}}/D$ , which means the growth resistance of the diffusion is proportional to the thickness of the boundary layer: the face we consider is no longer a vicinal face but practically a rough face.

The kinetic coefficient defined by Eqn (8.53) is intrinsic to the step and does not depend on the surrounding conditions. Its magnitude can be estimated with the use of Eqn (8.23).  $N_{\text{kink}} a^2$  in the surface kinetic coefficient is replaced by the corresponding kink density  $a/l_{\text{kink}}$  ( $l_{\text{kink}}$  is the average kink distance along the step) for a step, and  $k_{\text{B}}T/(v_{\text{S}} c_{\text{eq}}^0)$  is multiplied to convert  $K$  to  $\mathcal{K}$ :

$$\mathcal{K}_{\text{step}} \approx \frac{a}{l_{\text{kink}}} a v e^{-\Delta s/k_{\text{B}}} e^{-(E_{\text{b}}+E_{\text{des}})/k_{\text{B}}T}. \quad (8.55)$$

For simple molecules  $\Delta s \approx 0$ , and  $E_{\text{des}} = 0$  if desolvation is not necessary at the step. Then we obtain

$$\mathcal{K}_{\text{step}} \approx \frac{a}{l_{\text{kink}}} a v e^{-E_{\text{b}}/k_{\text{B}}T}. \quad (8.56)$$

To some extent, a similar argument will apply to melt growth if the concentration field of solute is replaced by a temperature field that evacuates the latent heat.

## 8.5.2 Vapor Growth and Surface Diffusion

In vapor growth, atoms landing on the surface migrate on a flat terrace and crystallize at a kink position along the step. It is important to make a proper model of the surface to understand the growth of a vicinal face.

<sup>22</sup>Here,  $\mathcal{K}$  is defined in terms of the concentration  $c$  and the current  $j$ , and not in terms of the chemical potential  $\mu$  and the velocity  $V$ . Because  $\Delta\mu = k_{\text{B}}T \ln(c/c_{\text{eq}}^0) \approx k_{\text{B}}T(\delta c/c_{\text{eq}}^0)$ , they are related as  $K = (v_{\text{S}} c_{\text{eq}}^0/k_{\text{B}}T)\mathcal{K}$ .

### 8.5.2.1 The BCF Model

The classical model of vapor growth is the BCF model studied by Burton, Cabrera, and Frank [28]. Atoms enter from a uniform gas environment onto the crystal surface at a constant rate:  $f$  atoms per unit area per unit time. Those atoms adsorbed on the surface are called *adatoms*. An adatom migrates on the crystal surface and evaporates into the gas with a lifetime  $\tau$ . Therefore, the number density  $c$  of adatoms at the position  $\mathbf{x}$  ( $\mathbf{x}$  is a two-dimensional vector) obeys the diffusion equation

$$\frac{\partial c(\mathbf{x})}{\partial t} = D_s \nabla^2 c(\mathbf{x}) - \frac{c(\mathbf{x})}{\tau} + f. \quad (8.57)$$

If adatoms are uniformly distributed, then the balance of evaporation and impingement, the last two terms, determines the adatom density as  $c_\infty = f\tau$ . In the model, atoms (molecules) consisting of the crystal and atoms migrating on the surface are distinguished. Adatoms cannot solidify without steps, where kink sites are found.

If there is a step on the surface, the adatoms join the crystal there or the solid atoms “melt” from the step onto the surface. Exchange of atoms between the solid and the adatom layer occurs at the step. If the exchange is very fast, the adatom density at the step becomes the equilibrium density:

$$c_{\text{st}} \equiv c(\mathbf{x}_{\text{step}}) = c_{\text{eq}}. \quad (8.58)$$

The equilibrium density at the step is given by

$$c_{\text{eq}} = c_{\text{eq}}^0 \exp\left(-\frac{f_{\text{st}}\Omega_2}{k_B T}\right) \approx c_{\text{eq}}^0 \left(1 - \frac{f_{\text{st}}\Omega_2}{k_B T}\right), \quad (8.59)$$

where  $c_{\text{eq}}^0$  is the equilibrium density for a straight step. The exponential factor represents the Boltzmann factor for the extra work necessary if a force  $f_{\text{st}}$  is acting on the step<sup>23</sup> when an atom of the area  $\Omega_2$  solidifies. If  $c_\infty > c_{\text{st}}$ , adatoms flow into the step and the step becomes a sink of adatoms: solidification occurs. If  $c_\infty < c_{\text{st}}$ , adatoms flow out from the step and the step becomes a source of adatoms: melting occurs.

As for the force  $f_{\text{st}}$  acting on the step, two origins are well known. One is the capillary force due to the step stiffness:  $-\tilde{\beta}/R$  corresponding to the second term in Eqn (8.34).<sup>24</sup> The other is a force due to elastic stress, which drives the step to the direction of lower elastic energy [7]. If there are two parallel steps of the same sign (both up or both down steps) at a distance  $d$ , a repulsive force proportional to  $d^{-3}$  arises to make them move apart [39].

The simple BCF model assumes fast step kinetics—that is, the adatom density takes the equilibrium value  $c_{\text{eq}}$  at the step. Then, Eqn (8.58) is the boundary condition for the diffusion Eqn (8.57). Usually the density of adatoms is low,  $c_{\text{eq}}\Omega_2 \ll 1$ , and the movement of steps is slower than relaxation of the adatom density. Under such conditions, one may use the static approximation of Eqn (8.57), in which the left-hand side is neglected and

<sup>23</sup> $f_{\text{st}}$  is defined as positive in the direction of the outward normal of the step.

<sup>24</sup>As the driving force of solidification, the extra work  $\delta\mu = f_{\text{st}}\Omega_2$  is written as  $\delta\mu = (\partial\mu/\partial c)\delta c = (k_B T/c)\delta c$  because  $\mu = k_B T \ln c$  for an adatom. Then, the shift  $\delta c$  corresponds to  $f_{\text{st}}\Omega_2 c/k_B T$  as in Eqn (8.59).

the solution with a given boundary condition at each instance is used. The diffusion equation is cast into the form

$$\left(\nabla^2 - \frac{1}{x_s^2}\right)(c(\mathbf{x}) - c_\infty) = 0, \quad (8.60)$$

where

$$x_s = \sqrt{D_s \tau}$$

is the *surface diffusion length*. It represents the characteristic length scale that an atom entering on a large facet can move within the lifetime  $\tau$ .

### 8.5.2.2 Asymmetric Kinetics at the Step

In general, solidification at the step proceeds at a finite rate as on a rough surface. Supersaturation at the step is finite, and the solidification current is

$$j_s = \mathcal{K}_{st} \delta c_{st}, \quad (8.61)$$

from Eqn (8.53). Adatoms may come to the step either from the upper or from the lower side of the step. We may write the solidification current separately for each side of the step (Figure 8.13(A)):

$$j_{s-} = \mathcal{K}_{st}^- \delta c_{st}^-, \quad j_{s+} = \mathcal{K}_{st}^+ \delta c_{st}^+, \quad (8.62)$$

where  $j_{s-}$  ( $j_{s+}$ ) indicates the solidification current on the left (right) side terrace of the step, and  $c_{st}^\pm = c(\mathbf{x}_{step} \pm 0)$  is the adatom density on each side of the step. The corresponding kinetic coefficients for the upper terrace  $\mathcal{K}_{st}^-$  and for the lower terrace  $\mathcal{K}_{st}^+$  may be different

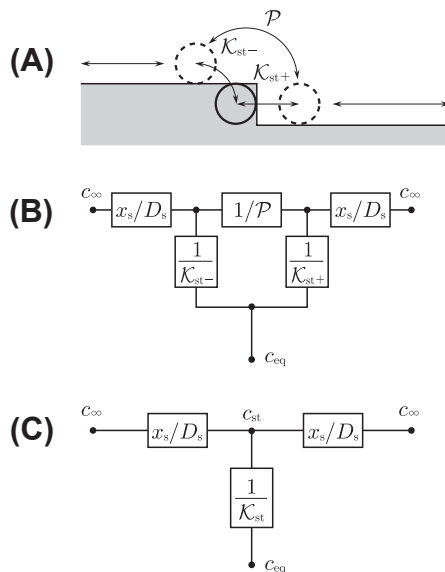


FIGURE 8.13 (A) Transport processes around the step and their resistances. (B, C) Paths of solidification current from far on the terrace,  $c_\infty$ , to the solid,  $c_{eq}$ .

because there is an extra energy barrier for hopping over the step edge:  $\mathcal{K}_{\text{st}}^+$  is usually larger than  $\mathcal{K}_{\text{st}}^-$ . The extra energy barrier is called the *Ehrlich-Schwoebel barrier* (ES barrier) and may have significant influence on the morphology of stepped surfaces in growth [40,41]. In addition, if the kink density along the step is very low, adatoms may pass through the step without solidification or melting. Such a step is *permeable* (or transparent).

Figure 8.13(A) and (B) shows schematically the general boundary condition at the step for the diffusion equations, Eqns (8.57) or (8.60). The adatom density at the step site (in the solid),  $c_{\text{eq}}$ , is related to that at the upper side of the step,  $c_{\text{st}}^+$ , and that at the lower side of the step,  $c_{\text{st}}^-$ , by the resistance  $(\mathcal{K}_{\text{st}}^\pm)^{-1}$ . The latter two sites are connected by the resistance  $\mathcal{P}^{-1}$  ( $\mathcal{P}$ : permeability of the step), and also with the environment away from the step,  $c_\infty$ , by the resistance of the surface diffusion on the terrace  $x_s/D_s$ . Like an electric circuit, the current between these positions are related to satisfy the conservation law:

$$j_- = j_{s-} + j_p, \quad j_+ = -j_{s+} + j_p, \quad (8.63)$$

where  $j_-$ , and  $j_+$  are the diffusion current on both terraces, and  $j_p$  is the current that passes through the step. The step velocity is given by the solidification current from both terraces as

$$V_{\text{st}} = \Omega_2(j_{s-} + j_{s+}) = \Omega_2(j_- - j_+), \quad (8.64)$$

which is also expressed by the difference of the diffusion currents. These currents are proportional to the differences of the corresponding adatom densities (Eqn (8.62); equivalently, proportional to the chemical potentials) and [42]

$$j_p = \mathcal{P}(c(\mathbf{x}_{\text{st}-}) - c(\mathbf{x}_{\text{st}+})). \quad (8.65)$$

### 8.5.2.3 A Simple Example of Growth Kinetics

As an example for the growth of a vicinal face, let us consider the simple BCF model—that is, the case with  $\mathcal{K}_{\text{st}+} = \mathcal{K}_{\text{st}-}$ ,  $\mathcal{P} = \infty$  (Figure 8.13(C)). Because  $c(\mathbf{x}_{\text{st}+}) = c(\mathbf{x}_{\text{st}-}) = c_{\text{st}}$ , the solution of the diffusion Eqn (8.60) for an array of equidistant steps at  $y = 0$  and  $y = l$  is Figure 8.14

$$c(y) = \frac{e^{-y/x_s} + e^{(y-l)/x_s}}{1 + e^{-l/x_s}} (c_{\text{st}} - c_\infty) + c_\infty \quad (8.66)$$

for  $0 < y < l$ . From the density profile in Eqn (8.66), the diffusion current that flows into the step at the origin is

$$j_- - j_+ = -2D_s \left. \frac{\partial c}{\partial y} \right|_{y=0} = 2 \frac{D_s}{x_s} (c_\infty - c_{\text{st}}) \tanh\left(\frac{l}{2x_s}\right), \quad (8.67)$$

which should be the same as the solidification current  $j_{s-} + j_{s+}$  obtained from Eqn (8.62). This condition determines the density at the step  $c_{\text{st}}$ . With  $c_{\text{st}}$  so determined, the velocity of the step is easily calculated as

$$V_{\text{st}} = \Omega_2 \frac{1}{\mathcal{K}_{\text{st}}} + \frac{\delta c_\infty}{1 + \frac{2D_s}{x_s} \tanh\left(\frac{l}{2x_s}\right)}, \quad (8.68)$$

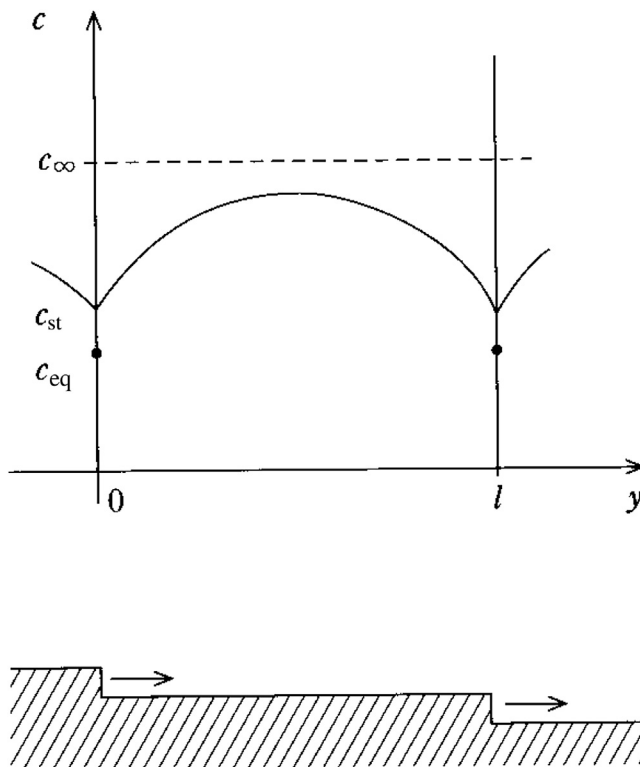


FIGURE 8.14 Adatom density on a terrace of the width  $l$  in a growing vicinal face.

where the kinetic coefficient is  $\mathcal{K}_{\text{st}} = 2\mathcal{K}_{\text{st}+} = 2\mathcal{K}_{\text{st}-}$ . This equation corresponds to the step velocity in Eqn (8.52) in solution growth.

If the step distance  $l$  is much larger than the diffusion length ( $l \gg x_s$ ), the step incorporates adatoms within distance  $x_s$  of its both sides. From Eqn (8.68) with  $\tanh(l/x_s) \rightarrow 1$ , the effective kinetic coefficient, defined by  $\mathcal{K}_{\text{st}}^{\text{eff}} = V_{\text{st}}/(\Omega_2 \delta c_\infty)$ ,

$$\frac{1}{\mathcal{K}_{\text{st}}^{\text{eff}}} = \frac{1}{\mathcal{K}_{\text{st}}} + \frac{x_s}{2D_s} \quad (8.69)$$

is constant. If the step distance is small,  $l \ll x_s$ , the territory for a step decreases by a factor  $l/x_s$ ; the second term increases as

$$\frac{1}{\mathcal{K}_{\text{st}}^{\text{eff}}} = \frac{1}{\mathcal{K}_{\text{st}}} + \frac{x_s^2}{D_s l} = \frac{1}{\mathcal{K}_{\text{st}}} + \frac{\tau}{l}. \quad (8.70)$$

If the exchange of atoms at the step is fast (relatively to the diffusion), we may put  $\mathcal{K}_{\text{st}} \rightarrow \infty$  in Eqn (8.68), and the growth velocity of the surface becomes

$$V_z = \frac{a_z}{l} \Omega_2 \frac{2D_s}{x_s} \tanh\left(\frac{l}{2x_s}\right) \delta c_\infty. \quad (8.71)$$

For a vicinal face with a very small tilt,  $n_{\text{st}}x_s = x_s/l \ll 1$ , the velocity is proportional to the step density  $n_{\text{st}}$ :

$$V_z = n_{\text{st}}a_z\Omega_2 \frac{2D_s}{x_s} \delta c_\infty. \quad (8.72)$$

With a large tilt,  $n_{\text{st}}x_s = x_s/l \gg 1$ , since  $x_s^2 = D\tau$ , it becomes

$$V_z = a_z\Omega_2 \frac{\delta c_\infty}{\tau} = a_z\Omega_2 (f - f_{\text{eq}}^0) = \nu_s \delta f. \quad (8.73)$$

The growth velocity is given by the impingement rate that exceeds the evaporation rate. When steps are closely distributed, atoms entering onto the terrace always reach the step, and the growth rate is given by the balance of impingement and evaporation as on the rough surface (Eqn (8.6)).

For general cases, the static diffusion equation,<sup>25</sup> Eqn (8.60), is solved with the boundary conditions for a given configuration of steps. Then, the solution  $c(\mathbf{x})$  determines the diffusion currents at the step

$$j_\pm = -D_s \hat{\mathbf{n}} \cdot \nabla c(\mathbf{x}_{\text{st}\pm}), \quad (8.74)$$

where  $\hat{\mathbf{n}}$  is the unit normal vector of the step pointing downward. The difference of the diffusion current gives the local step velocity from Eqn (8.64), and that determines the change of the step configuration. Thus, the time evolution of the step-adatom system can be calculated (in principle, numerically).

### 8.5.3 Growth of Vicinal Faces and Morphology of the Stepped Surface

In equilibrium, a vicinal face consists of equidistant parallel steps, whose configuration is stabilized by the stiffness of each step and by repulsion between the steps. For a face with a small tilt  $\mathbf{p} = \left( \frac{\partial z}{\partial x}, \frac{\partial z}{\partial y} \right)$ , the free energy per unit projected area  $f(\mathbf{p})$  can be written as<sup>26</sup>

$$f(\mathbf{p}) = \alpha(0, 0) + \frac{\beta}{a_z} |p| + \frac{\phi}{a_z^3} |p|^3 + \dots \quad (8.75)$$

where  $\alpha(0, 0)$  is the surface free energy per unit area without steps, and isotropy in the  $xy$ -plane has been assumed (therefore,  $\tilde{\beta} = \beta$ ). The second term is the free energy of noninteracting steps, and the third term is the interaction energy, which is proportional

<sup>25</sup>The full time-dependent diffusion in Eqn (8.57) is seldom used because of the difficulty of solving it.

<sup>26</sup>Note the relationship between  $\alpha(\mathbf{p})$  and  $f(\mathbf{p})$ :  $\alpha(\mathbf{p}) = f(\mathbf{p})/\sqrt{1 + p^2}$ .

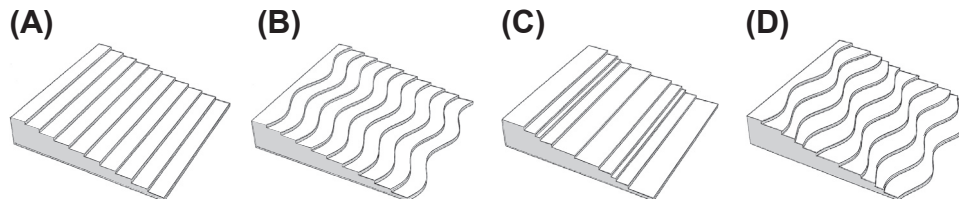


**FIGURE 8.15** Deformation of a vicinal face: (A) ideal vicinal face, (B) in-phase wandering of steps, (C) bunching of steps, and (D) wandering with a phase shift. Reprinted from Ref. [43], with permission from Elsevier.

to the repulsion energy<sup>27</sup>  $\phi l^{-2}$  times the step density  $p = a_z/l$ . The surface stiffness of the two orthogonal directions are calculated from Eqn (8.75) as follows [4]:

$$\tilde{\alpha}_{\perp}(p) \approx \frac{\beta}{a_z} \frac{1}{p}, \quad (8.76)$$

$$\tilde{\alpha}_{\parallel}(p) \approx 6 \frac{\phi}{a_z^3} p. \quad (8.77)$$

Equation (8.76) represents stiffness of the surface against deformation, such as Figure 8.15(B), and is determined by the stiffness of each step. Equation (8.77) represents stiffness against deformation, such as Figure 8.15(C), and is determined by the step repulsion. By approaching the facet, a vicinal surface becomes stiffer in one direction and softer in the orthogonal direction because the number density of steps decreases: the surface deformation becomes more difficult and the step repulsion becomes weaker.

When a vicinal surface is growing or sublimating, surface diffusion tends to produce deformation of the surface against the stabilizing effect of the surface stiffness. If the destabilizing effect wins, the vicinal face becomes unstable and sinusoidal deformation develops [45–47].

### 8.5.3.1 Wandering of Steps

If step kinetics is not symmetric (i.e., kinetic coefficients for the upper and the lower terraces differ), a step may become unstable. If  $\mathcal{K}_{st+} > \mathcal{K}_{st-}$ , the step incorporates more atoms from the lower terrace than from the upper terrace during growth. If a small bump is formed along the straight step as a result of fluctuation, the bump has an advantage for further growth because it has moved into an area of higher adatom density. The bump grows faster when the step stiffness is not strong enough to pull it back. The initially straight step becomes wavy, and the instability is called *step wandering* (or meandering). This is a kind of two-dimensional Mullin-Sekerka instability (see Chapter 14 of Volume IB) [48]. The stability of the step is characterized by the amplification rate of sinusoidal step fluctuation of wave number  $q$ ,  $\delta y_q(t) = \delta y_0 e^{-iqx + \omega_q t}$ . It is given by<sup>28</sup> [49,50]

<sup>27</sup>Two types of repulsive interactions exist rather generally: the elastic repulsion originated from elastic deformation near the steps [40] mentioned before, and an entropic repulsion due to thermal wandering fluctuation of steps with the coefficient  $\phi = (\pi^2/6)((k_B T)^2/\beta)$  [44].

<sup>28</sup>The growth rate of fluctuation,  $\omega_q$ , given here is the formula for  $l \rightarrow \infty$ .

$$\begin{aligned}\omega_q &= -D_s\Omega_2 \left[ \frac{c_\infty - c_{\text{eq}}^0}{x_s^2} - \Lambda_q \left( \frac{c_\infty - c_{\text{eq}}^0}{x_s} - \Gamma q^2 \right) \right] \\ &= V_{\text{st}}^0 (\Lambda_q - x_s^{-1}) - D_s\Omega_2 \Gamma \Lambda_q q^2,\end{aligned}\quad (8.78)$$

where  $V_{\text{st}}^0$  is the velocity of the straight step,  $\Gamma = \Omega_2 c_{\text{eq}}^0 \tilde{\beta} / k_B T$  and  $\Lambda_q \equiv \sqrt{q^2 + x_s^{-2}}$ . The coefficient of  $q^2$  in the series expansion of Eqn (8.78) becomes positive when  $V_{\text{st}}^0 \geq 2D_s\Omega_2\Gamma/x_s^2$ ,<sup>29</sup> and long wavelength fluctuations grow. When evaporation is negligible,  $x_s \rightarrow \infty$   $\Lambda_q \rightarrow q$ , and the amplification rate becomes

$$\omega_q = V_{\text{st}}^0 q - D_s\Omega_2 \Gamma q^3. \quad (8.79)$$

Now, the step is always unstable under growth ( $V_{\text{st}}^0 > 0$ ). The fastest-growing mode is given by the largest  $\omega_q$  in Eqn (8.79), with the wave number

$$q_{\text{max}} = \sqrt{\frac{V_{\text{st}}^0}{3D_s\Omega_2\Gamma}}. \quad (8.80)$$

The characteristic wavelength  $\lambda_{\text{max}} = 2\pi/q_{\text{max}}$  is inversely proportional to the square root of the step velocity. Once the instability sets in, the pattern of the step is controlled by the nonlinearity of the system. The time evolution of the destabilized step with evaporation is found to be chaotic [49,50]: bumps of the wavy pattern of the wavelength  $\lambda_{\text{max}}$  arise, move, and annihilate randomly. In a vicinal face, the motion of neighboring steps is correlated, and in-phase step wandering (Figure 8.15(B)) is observed [51]. Troughs perpendicular to the steps appear.

The cause of the wandering instability is the front and back asymmetry in step kinetics resulting from the step edge energy barrier. Other such asymmetry may induce a similar instability. When an Si(111) surface is heated by direct electric current perpendicular to the step, wandering instability is observed [46]. The current produces drift of adatoms in the same direction as the current. Theoretically, the drift of adatoms modifies the effective diffusion length in the upper terrace and that in the lower terrace differently, and the instability may occur when the drift direction is opposite to the step motion [52]. Also, in the growth of Si(111), wandering instability is seen near the structural phase transition from the low-temperature  $7 \times 7$  surface structure to the high-temperature  $1 \times 1$  structure [53]. The phase transition starts at the step; near the transition temperature, the structures of the upper terrace and the lower terrace of a step are different, which makes strong asymmetry to induce step wandering.

<sup>29</sup>In terms of the impingement rate, this condition is  $f \geq f_c \equiv f_{\text{eq}}^0 (1 + (2\tilde{\beta}\Omega_2)/(x_s k_B T))$ .

### 8.5.3.2 Bunching of Steps

In equilibrium, the distance between parallel steps is kept equal by the step repulsion. If an ES barrier is present (suppose  $\mathcal{K}_{st+} > \mathcal{K}_{st-}$ ), equidistant steps become unstable during sublimation. When a step recedes slightly faster than other steps by fluctuation, its lower side terrace is wider than that of other steps, so it recedes even faster. If this effect is stronger than the step repulsion that stabilizes the equidistant steps, the steps tend to bunch and the vicinal face deforms like Figure 8.15(C). The instability is called *step bunching*. If the step repulsion is short-range or very weak, pairing of steps will occur [54]. With the existence of the power law repulsive interaction, bunching instability occurs at a long wavelength; that is, a density wave of steps is seen (Figure 8.16(A)).

Bunching of steps occurs with various causes. In Figure 8.17, several examples are shown. The velocity of a step is, in many cases, a function of the widths of its upper and lower terraces, and the relationship determines the stability of the vicinal face [8]. If the contribution of the lower terrace to the step velocity is dominant, the face is unstable during growth. The impurity effect shown in Figure 8.17(A), in addition to the ES barrier effect (Figures 8.17(B) and (C)), is an example. A considerable amount of impurities exist in many systems, and they accumulate on terraces during growth to reduce the velocity of steps. The density of impurities on the lower terrace is proportional to the exposure time of the surface, which is proportional to the width of the terrace. Thus, impurity accumulation causes instability of equidistant steps as shown in Figure 8.17(A) and the formation of step bunches [56,57]. An external field may play a similar role to induce step bunching. In Si(111) vicinal faces, direct electric current perpendicular to the steps for heating the crystal induces step bunching [46,58,59] (Figure 8.17(D)). In solution growth,

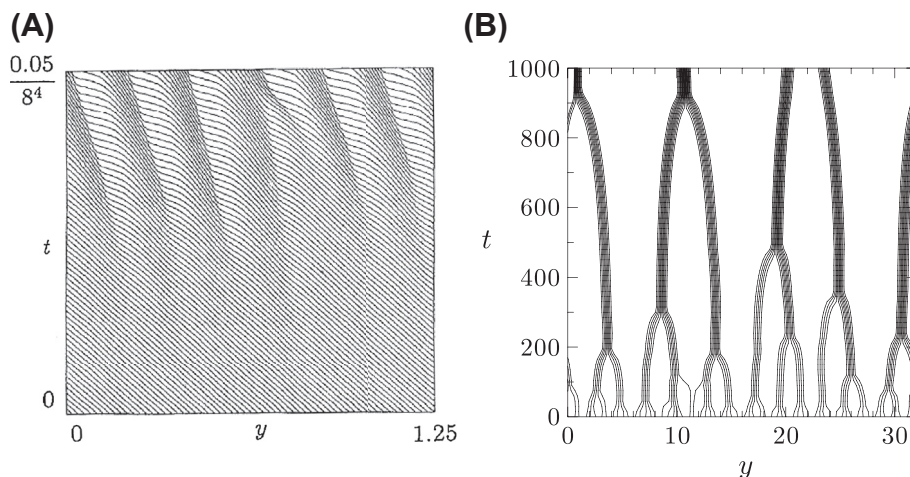


**FIGURE 8.16** Evolution of step bunching (A) in sublimation and (B) with drift of adatoms. (A) Step bunching develops as a density wave of steps. [32]. (B) Hierarchical pairing results in large bunches. Reprinted from Ref. [53], with permission from AIP; and Ref. [55], with permission from Elsevier.

like the drift of adatoms, external flow of solution induces step bunching in growth, as shown in Figures 8.17(E) and (F) [60,61]. In this case, the velocity of a step is not locally determined but is influenced by more distant conditions: growth/dissolution of a part of the vicinal face is correlated with growth/dissolution of an upstream area.

## 8.6 Crystal Growth in a Diffusion Field

As discussed in the previous section, the growth of a vicinal face is possible through the transport of atoms from the environment by bulk and/or surface diffusion followed by incorporation of atoms at the steps. The series of transport processes is a general feature of crystal growth. The flow of matter is controlled by the difference (or spatial gradient) of chemical potential. The difference of chemical potential between the solid and the environment,  $\delta\mu_\infty$ , is consumed by each step of the transport: several processes work in series (or sometimes in parallel) as resistances in an electric circuit (as in Figures 8.13(B) and (C)). The diffusion current at the interface must be the same as the solidification current. These conditions give relationships that determine the growth velocity.

Also, in general, heat released in solidification needs to be evacuated to the environment. Heat transport should work in parallel with the transport of matter. Usually in melt growth, heat transport is the rate-limiting process; in solution growth, material transport is the rate-limiting process. We may neglect the faster process—material transport in melt growth and heat transport in solution growth, respectively.

### 8.6.1 Melt Growth and Solution Growth

For simplicity, we neglect convection in the following discussion. Then, we can formulate the two problems—evacuation of the latent heat by heat diffusion (synonym of heat conduction) in melt growth and supply of matter by diffusion in solution growth—in a similar way.

#### 8.6.1.1 Evacuation of Latent Heat in Melt Growth

In growth from the melt, the growth velocity is proportional to supercooling at the interface:

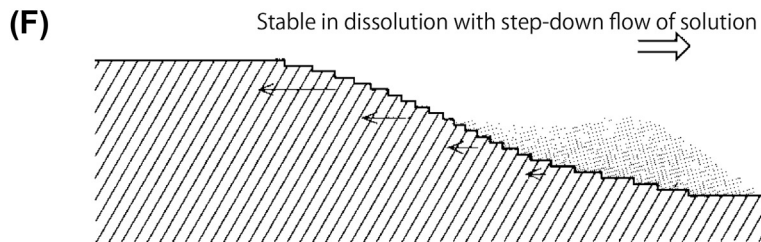
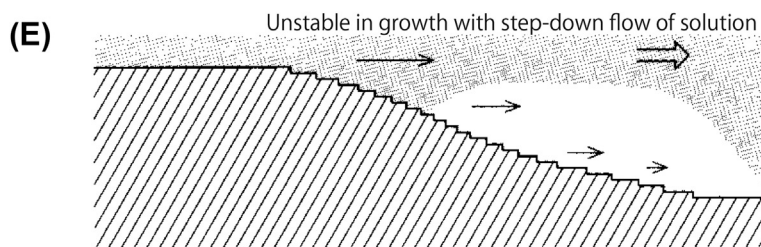
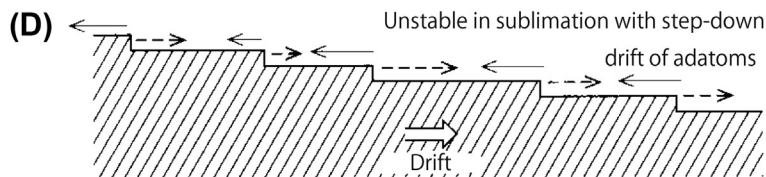
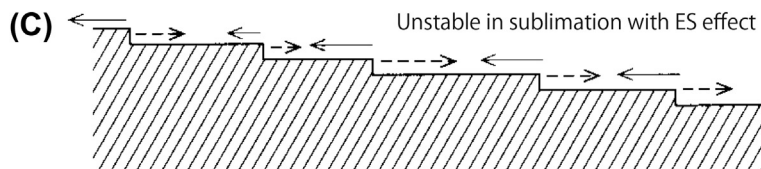
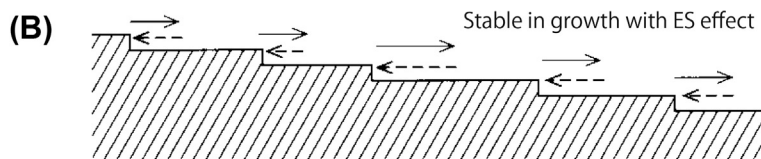
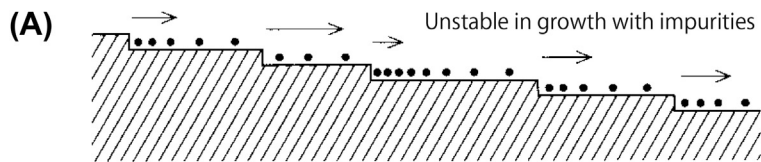
$$V = K_T(T_m - T_i), \quad (8.81)$$

where  $T_m$  is the melting temperature (the equilibrium temperature),  $T_i$  is the temperature at the interface,<sup>30</sup> and  $K_T$  is a kinetic coefficient. Because the latent heat ( $L$  per unit volume of a solid) should be evacuated from the interface by heat diffusion,

$$LV = -\kappa_T \hat{\mathbf{n}} \cdot \nabla T \quad (8.82)$$

must hold. Here,  $\kappa$  is heat conductivity in the melt, and we have assumed that the heat is evacuated into the bulk liquid phase. In general, heat goes to both phases depending on

<sup>30</sup>Here, we assume a solid is the low-temperature phase.



boundary conditions. The simple model here is called a one-sided model. The heat diffusion is described by the diffusion equation

$$\frac{\partial T}{\partial t} = D_T \nabla^2 T, \quad (8.83)$$

where the thermal diffusion coefficient (diffusivity)  $D_T$  is related to the thermal conductivity  $\kappa_T$  and the heat capacity per unit volume  $c_P$  as  $D_T = \kappa_T/c_P$ .

It is convenient to use a dimensionless supercooling, in which temperature increase from the far environment is measured by the temperature increase by the latent heat,  $L/c_P$ ,

$$u = \frac{T - T_\infty}{L/c_P}. \quad (8.84)$$

With the dimensionless supercooling  $u$ , Eqns (8.83) and (8.82) are cast into the simple forms

$$\frac{\partial u}{\partial t} = D_T \nabla^2 u, \quad (8.85)$$

$$V = -D_T \hat{\mathbf{n}} \cdot \nabla u. \quad (8.86)$$

The other expression of the growth velocity, Eqn (8.81), with the Gibbs–Thomson effect, is written as

$$V = \tilde{K}_T (\Delta - u_i - d_T \kappa), \quad (8.87)$$

where  $\tilde{K}_T = KL/c_P$ , and

$$\Delta = u_m^0 = \frac{(T_m^0 - T_\infty) c_P}{L} \quad (8.88)$$

is the value of  $u$  for a flat equilibrium interface (i.e., the dimensionless supercooling of the environment). In Eqn (8.87),  $\kappa = 1/R_1 + 1/R_2$  is the curvature of the interface and  $d_T$  is the *capillary length*, which expresses the strength of the surface stiffness  $\tilde{\alpha}$

$$d_T = \frac{\tilde{\alpha} c_P T_m^0}{L^2}. \quad (8.89)$$

The capillary length is a length scale at which temperature increase by the latent heat,  $L/c_P$ , and the change of the equilibrium temperature due to the Gibbs–Thomson effect,  $(\alpha/d)(T_m^0/L)$ , become comparable.

←

**FIGURE 8.17** Various causes of step bunching. (A) Accumulation of impurities on terraces decreases the velocity of steps. The step behind the wider terrace moves slower, and the step behind the narrower terrace moves faster: a step pair is formed. (B) With Schwoebel barrier in growth, the retarded step has a wide lower terrace and moves faster to recover the delay. (C) With Schwoebel barrier in sublimation, the advanced step has a wide lower terrace and moves faster to amplify the advantage. (D) With step-down drift in sublimation, the advanced step has a wide lower terrace and moves faster to amplify the advantage. (E) With step-down flow in growth, the diluted part of solution moves to the lower area and hinders growth of the lower steps: the slope becomes steeper. (F) With step-down flow in dissolution, the concentrated part of solution moves to the lower area and decelerates dissolution of the lower steps: the slope becomes gentler.

### 8.6.1.2 Supply of Matter in Solution Growth

Equations (8.81)–(8.83) have their counterparts in solution growth:

$$V = v_S \mathcal{K}(c_i - c_{\text{eq}}), \quad (8.90)$$

$$V = v_S D \hat{\mathbf{n}} \cdot \nabla c, \quad (8.91)$$

$$\frac{\partial c}{\partial t} = D \nabla^2 c. \quad (8.92)$$

Equation (8.90) is derived from the relationship between the solidification current and the interface velocity,  $(c_S - c_i)V = \mathcal{K}(c_i - c_{\text{eq}})$ ; by neglecting the solute density  $c_i$  compared to the solid density,  $c_S = v_S^{-1}$  because we assume that the solution is dilute. In a dilute solution,  $\partial \mu / \partial c = k_B T / c_{\text{eq}}^0$  is also valid. By defining a new dimensionless variable

$$u = \frac{c_\infty - c}{c_S - c_{\text{eq}}^0} \quad (8.93)$$

as in Eqn (8.84). Equations (8.90)–(8.92) turn into the same forms as Eqns (8.85)–(8.87), except for the diffusion and kinetic coefficients. The dimensionless supercooling and the capillary length are now defined by

$$\begin{aligned} \Delta &= \frac{c_\infty - c_{\text{eq}}^0}{c_S - c_{\text{eq}}^0} \approx v_S (c_\infty - c_{\text{eq}}^0), \\ d_c &= \frac{c_{\text{eq}}^0 \tilde{\alpha}}{k_B T (c_S - c_{\text{eq}}^0)^2} \approx \frac{v_S^2 c_{\text{eq}}^0 \tilde{\alpha}}{k_B T}. \end{aligned} \quad (8.94)$$

Therefore, the two problems are treated in the same way.<sup>31</sup>

## 8.6.2 Growth of a Planar Interface in a Diffusion Field

For a simple example of growth in a diffusion field, we consider a planar solid in a solution, which is initially uniform, and the solute concentration is  $c_\infty$ . The interface is parallel to the  $xy$ -plane and growing in the  $z$ -direction. The diffusion equation and the solidifying current  $j = (c_S - c_i)V$  are

$$\frac{\partial c}{\partial t} = D \frac{\partial^2 c}{\partial z^2}, \quad (8.95)$$

$$(c_S - c_i)V = \mathcal{K}(c_i - c_{\text{eq}}^0), \quad (8.96)$$

$$(c_S - c_i)V = D \left. \frac{\partial c}{\partial z} \right|_{z=\zeta}. \quad (8.97)$$

where  $z = \zeta$  is the position of the interface. We may put  $c_S - c_i \approx c_S = v_S^{-1}$ .

<sup>31</sup>The length  $\Omega_2 \Gamma = \Omega_2^2 c_{\text{eq}}^0 \tilde{\beta} / k_B T$ , which appeared in Eqn (8.78), is the two-dimensional analogue of  $d_c$ .

When the solid grows at a constant speed  $V$ , the diffusion equation in the reference frame moving with the interface is written as

$$\frac{1}{D} \frac{\partial c}{\partial t} = \frac{\partial^2 c}{\partial z'^2} + \frac{1}{l_D} \frac{\partial c}{\partial z'} = 0, \quad (8.98)$$

where  $z' = z - Vt$  is the new coordinate of the moving system, and  $l_D = D/V$  is the *diffusion length*, which characterizes the spatial change of the diffusion field.<sup>32</sup> Because the system is steady in the moving frame of reference, the time derivative is put at zero.

The solution of Eqn (8.98), with the boundary conditions  $c = c_i$  at  $z' = 0$  and  $c = c_\infty$  at  $z' = \infty$ , is

$$c(z') = (c_i - c_\infty)e^{-z'/l_D} + c_\infty. \quad (8.99)$$

From the solution (8.99), the velocity in Eqns (8.96) and (8.97) is written as

$$V = \frac{c_i - c_{\text{eq}}^0}{c_s - c_i} \mathcal{K} = -\frac{1}{c_s - c_i} D \frac{c_i - c_\infty}{l_D} = \frac{c_\infty - c_i}{c_s - c_i} V, \quad (8.100)$$

which requires  $c_\infty = c_s$ . Steady growth is possible only if this condition is satisfied. In melt growth, the corresponding condition is  $\Delta = 1$ .

These conditions are the result of the conservation laws (mass and energy) in one dimension. Because the solute density in a solution is always lower than that in a solid, the condition  $c_\infty = c_s$  is never satisfied, so that steady growth is not possible. In reality, when a planar solid is placed in a supersaturated solution, it grows fast at the beginning with a short  $l_D = D/V$ , and the solute concentration near the solid decreases to make  $l_D$  longer and longer. A simple solution of the time-dependent one-dimensional diffusion equation shows that the growth velocity decreases in time as  $V = D/l_D \sim 1/\sqrt{t}$ : the growth speed approaches zero [4].

In melt growth, fine tuning of the liquid temperature to realize  $\Delta = 1$  is in principle not forbidden. If this condition is satisfied, the above solution with any value of  $l_D$  is allowed, and the growth velocity is not determined. This is not physical: nature must choose one particular growth speed.<sup>33</sup> Problems related to the growth velocity and the growth form in a diffusion field will be explained in the first three chapters in Volume IB.

## 8.7 Various Simulation Models of Crystal Growth

With our understanding of the kinetics of crystal growth, various models have been developed for calculating the time evolution of crystal growth. They will be explained in some detail in chapters 10, 11, 12, and 15. Here, we give only a short overview.

### 8.7.1 Atomistic Model and Simulation

In principle, the properties of matter can be understood with the use of quantum mechanics. Because the crystal growth process is repetition of simple elementary processes,

<sup>32</sup>In many studies, the diffusion length is defined as  $l_D = 2D/V$ .

<sup>33</sup>The planar interface is not stable, in fact.

we only need to understand the elementary process in terms of quantum mechanics. Such microscopic theory based on quantum mechanics is called an *ab initio* calculation. What we need in practice is the energies of various atomic configurations and characteristic frequencies of the change of states. Although it is a formidable task to know these parameters in a system consisting of many ions and electrons, density functional theory calculation with various approximation methods makes it possible. These calculations can predict the pathways for an atom to be incorporated in a crystal and the values of various parameters in each process.

With information on possible pathways, energy parameters, and frequency parameters, atomistic models are constructed and numerical simulation is performed. The standard method is solving Newton's equation of motion for atoms or molecules interacting with potentials calculated by the quantum mechanical calculation, or with simpler semiempirical potentials. This is called *molecular dynamics simulation* (MD simulation). Increasing the efficiency and capacity of a computer enables one to follow the time evolution of a fairly large system: we may watch a small region, say tens of nanometers in size, of a growing crystal. MD simulation is generally very useful for growth from the melt because the collective motion of atoms/molecules at the interface is complicated and we have no other way to know their behavior. The limitation of this method is, of course, that the manageable system size is still not so large.

For growth from a solution or from a gas, the important stable atomic configuration is limited by the substrate crystal, and the evolution of the system can be approximated by the change of configurations on the lattice sites. Instead of tracing all orbits of atoms, the transition between the possible atomic configurations on the lattice is traced. The transition occurs stochastically according to the Boltzmann factor  $e^{-\Delta E/k_{\text{B}}T}$ , where  $\Delta E$  is the difference of energy in the transition state<sup>34</sup> and that in the initial state (i.e., the energy barrier from the beginning configuration to the ending configuration). The stochastic dynamics is believed to represent time evolution of many microscopically equivalent systems.<sup>35</sup> Such simulation is called a Monte Carlo simulation, named after the famous town where probability plays a major role in the economy.

### 8.7.2 Continuum Models

Macroscopic behavior of crystals may be more adequately described by models of large length scales. The basic model is the thermodynamic description of crystal growth in terms of a continuum solid phase and an environmental phase with a sharp interface. Each phase is characterized by thermodynamic quantities, such as density  $\rho$ , heat capacity  $c_p$ , thermal conductivity  $\kappa$ , etc., which may not be uniform and may be anisotropic reflecting the anisotropy of the crystal. The interface is regarded as sharp and

<sup>34</sup>The transition state is the state of maximum energy in the path between the initial and the final configurations.

<sup>35</sup>The Boltzmann factor, under certain conditions, assures that the system represents the equilibrium system mathematically accurately in the long run.

characterized by the anisotropic surface tension  $\alpha$ , or the stiffness  $\tilde{\alpha}$ , and the kinetic coefficient  $K$ . For studying smooth interface (facets) or vicinal faces, the interface itself may be further divided by flat terrace and dividing sharp continuum steps. Such models may be called *sharp interface models*. This is the traditional description of the system, and it has a solid physical basis. Quantum mechanics and statistical mechanics can supply the values of physical parameters. Phenomenological equations, such as the diffusion equation and various kinetic equations, determine the time evolution of the system.

The sharp interface model is manifestly physical, and useful to understand the changes in crystal morphology. It is, however, computationally not simple because of the existence of the singular interface. The surface may merge or break up: these processes bring up mathematical problems. To avoid difficulties, the interface is treated as a region of smoothly changing phase fields. The phase field is nothing but a local order parameter representing the solid order. The model is called the *phase field model* and contains at least two fields<sup>36</sup>: one is the phase field and the other is a field representing a conserved quantity such as energy (heat) or density. The two fields are coupled in a physically consistent way, as explained in Eqn (8.6). The model is flexible to include more degrees of freedom of the system, such as elastic stress, composition of the material, crystal orientation, etc. Thanks to the fast development of computation capacity, phase field models are now standard tools in materials science. The phase field theory is explained in Chapter 15 of Volume IB.

## References

- [1] Thürmer K, Reutt-Robey JE, Williams ED, Uwaha M, Emundts A, Bonzel HP. Step dynamics in 3D crystal shape relaxation. *Phys Rev Lett* 2001;87:186102.
- [3] Chernov AA. Crystallization processes. In: Chernov AA, editor. *Modern crystallography III*. Berlin: Springer-Verlag; 1984. p. 1–297.
- [4] Saito Y. *Statistical physics of crystal growth*. Singapore: World Scientific; 1996.
- [5] Markov I. *Crystal growth for beginners: fundamentals of nucleation, crystal growth, and epitaxy*. 2nd ed. Singapore: World Scientific; 2004.
- [6] Balibar S, Alles H, Parshin A Ya. The surface of helium crystals. *Rev Mod Phys* 2005;77:317–70.
- [7] Jackson KA. *Kinetic processes*. 2nd ed. Weinheim: Wiley-VCH; 2012.
- [8] Bennema P, Gilmer GH. Kinetics of crystal growth. In: Hartman P, editor. *Crystal growth: an introduction*. Amsterdam: North-Holland; 1973. p. 263–327.
- [9] Pimpinelli A, Villain J. *Physics of crystal growth*. Cambridge: Cambridge University; 1998.
- [10] Hertz H. *Ann Phys Lpz* 1882;17:193.
- [11] Knudsen M. *Ann Phys* 1915;352:697.
- [12] Wilson HA. *Philos Mag* 1900;50:238.
- [13] Frenkel J. *Phys Z. Sowjetunion* 1932;1:498.

<sup>36</sup>A single field model of the smooth interface was introduced by van der Waals in 1893 [15].

- [14] Broughton JQ, Gilmer GH, Jackson KA. Crystallization rates of a Lennard-Jones liquid. *Phys Rev Lett* 1982;49:1496–500.
- [15] Rowlinson JS, Translation of J.D. van der Waals. The thermodynamic theory of capillarity under the hypothesis of a continuous variation of density. *J Stat Phys* 1979;20:197–244.
- [16] For a brief review Langer JS. An introduction to the kinetics of first-order phase transition. In: Godrèche C, editor. *Solids far from equilibrium*. Cambridge: Cambridge University Press; 1991. p. 297–363.
- [17] Cahn JW. Theory of crystal growth and interface motion in crystalline materials. *Acta Metal* 1960;8: 554–62.
- [18] Mikheev LV, Chernov AA. Mobility of a diffuse simple crystal-melt interface. *J Cryst Growth* 1991; 112:591–6.
- [19] Chernov AA. Notes on interface growth kinetics 50 years after Burton, Cabrera and Frank. *J Cryst Growth* 2004;264:499–518.
- [20] Kaischew R, Stranski IN. *Z. Phys Chem A* 1934;170:295.
- [21] Hillig WB. A derivation of classical two-dimensional nucleation kinetics and the associated crystal growth laws. *Acta Metall* 1966;14:1868–9.
- [22] Gilmer GH, Bennema P. Simulation of crystal growth with surface diffusion. *J Appl Phys* 1972;43: 1347–60.
- [23] Kolmogorov AN. Statistical theory of crystallization of metals. *Bull Acad Sci USSR Mat Sci* 1937;1:355–9.
- [24] Avrami M. Kinetics of phase change. I general theory. *J Chem Phys* 1939;7:1103–12.
- [25] Gilmer GH, Jackson KA. Computer simulation of crystal growth. In: Kaldis E, Scheel HJ, editors. *Crystal growth and materials*. Amsterdam: North Holland; 1977. p. 80–114.
- [26] Wolf PE, Gallet F, Balibar S, Rolley E, Nozières P. Crystal growth and crystal curvature near roughening transitions in hcp  $^4\text{He}$ . *J Phys* 1985;46:1987–2007.
- [27] Frank FC. The influence of dislocation on crystal growth. *Disc Faraday Soc* 1949;5:48–54.
- [28] Burton WK, Cabrera N, Frank FC. The growth of crystals and the equilibrium structure of their surfaces. *Phil Trans R Soc Lond* 1951;243:299–358.
- [29] Chernov AA. The spiral growth of crystals. *Usp Fiz Nauk* 1961;73:277–331 [*Sov Phys-USPEKHI* 4, 116–148 (1961)].
- [30] Cabrera N, Levine MM. On the dislocation theory of evaporation of crystals. *Phil Mag* 1956;1:450–8.
- [31] Uwaha M, Nozières P. The behaviour of steps on a crystal facet under small supersaturation. *J Phys Fr* 1987;48:407–12.
- [32] Ranganathan M, Weeks JD. Theory of impurity induced step pinning and recovery in crystal growth from solutions. *Phys Rev Lett* 2013;110:055503.
- [33] Miura H, Tsukamoto K. Role of impurity on growth hysteresis and oscillatory growth of crystals. *Cryst Growth Des* 2013;13:3588–95.
- [34] Barabási A-L, Stanley HE. *Fractal concepts in surface growth*. Cambridge: Cambridge University Press; 1995.
- [35] Krug J, Spohn H. Kinetic roughening of growing surfaces. In: Godrèche C, editor. *Solids far from equilibrium*. Cambridge: Cambridge University Press; 1991. p. 479–582.
- [36] Halpin-Healy T, Zhang Y-C. Kinetic roughening phenomena, stochastic growth, directed polymers and all that. Aspects of multidisciplinary statistical mechanics. *Phys Rep* 1995;254:215–414.
- [37] Politi P, Grenet G, Marty A, Ponchet A, Villain J. Instabilities in crystal growth by atomic or molecular beams. *Phys Rep* 2000;324:271–404.

- [38] Michely T, Krug J. Islands, mounds and atoms. Berlin: Springer; 2004.
- [39] Marchenko VI, Parshin AY. Elastic properties of crystal surfaces. *Sov Phys JETP* 1980;52:129. *Zh Eksp Teor Fiz* 1980;79:257–260.
- [40] Ehrlich G, Hudda FG. Atomic view of surface self-diffusion: tungsten on tungsten. *J Chem Phys* 1966;44:1039–49.
- [41] Schwoebel RL, Shipsey EJ. Step motion on crystal surfaces. *J Appl Phys* 1966;37:3682–6.
- [42] Ozdemir M, Zangwill A. Morphological equilibration of a faceted crystal. *Phys Rev B* 1992;45:3718–29.
- [43] Uwaha M. Surface step dynamics: basic concepts, theory and simulation. *Adv Cryst Growth Res* 2001:78.
- [44] Akutsu Y, Akutsu N, Yamamoto T. Universal jump of Gaussian curvature of the facet edge of a crystal. *Phys Rev Lett* 1988;61:424–7.
- [45] Jeong H-C, Williams ED. Steps on surfaces: experiment and theory. *Surf Sci Rep* 1999;34:171–294.
- [46] Yagi K, Minoda H, Degawa M. Step bunching, step wandering and faceting: self-organization at Si surfaces. *Surf Sci Rep* 2001;43:45–126.
- [47] Misbah C, Pierre-Louis O, Saito Y. Crystal surfaces in and out of equilibrium: a modern view. *Rev Mod Phys* 2010;82:981–1040.
- [48] Bales GS, Zangwill A. Morphological instability of a terrace edge during step-flow growth. *Phys Rev B* 1990;41:5500–8.
- [49] Bena I, Misbah C, Valance A. Nonlinear evolution of a terrace edge during step flow growth. *Phys Rev B* 1993;47:7408–19.
- [50] Saito Y, Uwaha M. Fluctuation and instability of steps in a diffusion field. *Phys Rev B* 1994;49:10677–92.
- [51] Maroutian T, Douillard L, Erns H-J. Morphological instability of Cu vicinal surfaces during step-flow growth. *Phys Rev B* 2001;64:165401.
- [52] Sato M, Uwaha M. Wandering instability of an isolated step with direct electric current. *J Phys Soc Jpn* 1996;65:2146–51.
- [53] Hibino H, Homma Y, Uwaha M, Ogino T. Step wandering induced by homoepitaxy on Si(1 1 1) during “1 × 1”-7 × 7 phase transition. *Surf Sci* 2003;527:L222–8.
- [54] Sato M, Uwaha M. Hierarchical bunching of steps in a conserved system. *J Phys Soc Jpn* 1998;67:3675–8.
- [55] Sato M, Uwaha M. Growth of step bunches formed by the drift of adatoms. *Surf Sci* 1999;442:318.
- [56] Frank FC. On the kinematic theory of crystal growth and dissolution processes. In: Doremus RH, Roberts BW, Turnbull D, editors. *Growth and perfection of crystals*. New York: Wiley; 1958. p. 411–9.
- [57] van der Eerden JP, Müller-Krumbhaar H. Dynamical coarsening of crystal surfaces by formation of macrosteps. *Phys Rev Lett* 1986;57:2431–3.
- [58] Latyshev AV, Aseev AL, Krasilnikov AB, Stenin SI. Transformations on clean Si(111) stepped surface during sublimation. *Surf Sci* 1989;213:157–69.
- [59] Stoyanov S. Electromigration induced step bunching on Si surfaces—how does it depend on the temperature and heating current direction? *Jpn J Appl Phys* 1991;30:1–6.
- [60] Chernov AA, Kuznetsov YG, Smol'sky IL, Rozhanskii VN. *Sov Phys Crystallogr* 1986;31:705.
- [61] Chernov AA. How does the flow within the boundary layer influence morphological stability of a vicinal face? *J Cryst Growth* 1992;118:333–47.

# Structure of Melt and Liquid Alloys

Jean-Pierre Gaspard

PHYSICS DEPARTMENT, UNIVERSITY OF LIEGE, BELGIUM

## CHAPTER OUTLINE

<b>9.1 Introduction: Structure of the Liquid State</b> .....	<b>402</b>
9.1.1 The Liquid State .....	404
9.1.2 Pair Correlation Function .....	404
<b>9.2 Scattering: of Neutrons and X-rays</b> .....	<b>405</b>
9.2.1 Scattering: Generalities .....	405
9.2.2 Master Equation .....	408
9.2.3 Coherent and Incoherent Scattering.....	408
9.2.4 Scattering by Liquid and Amorphous Structures.....	410
9.2.5 Static Approximation .....	410
9.2.6 Diffraction by a Crystal, Scherrer Broadening and SAS .....	412
9.2.7 Coherence Volume .....	413
9.2.8 Neutrons and X-rays [7, 28, 33, 37, 48, 72] .....	414
<b>9.3 Case Studies</b> .....	<b>416</b>
9.3.1 Monoatomic Liquids .....	416
9.3.1.1 First Characterization of $S(q)$ .....	417
9.3.1.2 Pair Correlation Function .....	419
9.3.2 Polyatomic Liquids .....	420
9.3.2.1 Partial Structure Factors .....	420
9.3.2.2 Partial Pair Correlation Functions .....	424
9.3.3 Normal and Anomalous Melting.....	425
9.3.3.1 Liquid Metals and Rare Gases .....	425
9.3.3.2 Liquid Semiconductors.....	427
<b>9.4 X-ray Absorption: EXAFS</b> .....	<b>427</b>
<b>9.5 Production of Beams</b> .....	<b>430</b>
9.5.1 X-ray Sources .....	430
9.5.2 Neutron Sources .....	431
9.5.2.1 Fission Reactors.....	432
9.5.2.2 Spallation Sources.....	432

<b>9.6 Experimental Setups</b> .....	<b>433</b>
9.6.1 Diffractometer .....	433
9.6.2 Sample Environment.....	433
<b>9.7 Computer Simulations of Liquids</b> .....	<b>434</b>
9.7.1 Direct Techniques: Monte Carlo and Molecular Dynamics.....	434
9.7.2 Inverse Techniques: RMC and EPSR.....	435
9.7.2.1 Reverse Monte Carlo .....	435
9.7.2.2 Empirical Potential Monte Carlo .....	435
<b>9.8 Characterizations Beyond <math>g(r)</math></b> .....	<b>436</b>
9.8.1 Distribution of first, second...neighbors .....	436
9.8.2 3-Body Correlations.....	437
9.8.3 Angular Distributions.....	438
<b>9.9 Supramolecular Liquid Structures</b> .....	<b>438</b>
<b>9.10 Quasielastic and Inelastic Scattering</b> .....	<b>440</b>
9.10.1 Quasielastic Scattering.....	440
9.10.2 Inelastic Scattering .....	440
<b>9.11 Conclusions</b> .....	<b>440</b>
<b>Acknowledgments</b> .....	<b>441</b>
<b>References</b> .....	<b>441</b>

## 9.1 Introduction: Structure of the Liquid State

In the study of the nucleation and growth of crystals from the melt, it is mandatory to determine as accurately as possible the structure of the liquid phase down to the atomic level.

The liquid state is complicated because it is halfway between the perfect crystal and the ideal gas [20]. Table 9.1 compares the structure and dynamics of gas, liquid, amorphous, and crystalline states of matter. A crystal is simple to describe because of its numerous symmetry properties that reduce drastically the number of independent parameters. At the opposite, the (perfect) gas phase of pointlike atoms is simplified by the

**Table 9.1** Comparison of the Structure and Dynamics of the Different States of Matter

Gas	Liquid	Amorphous	Crystal
Random positions	Dynamic SRO	Static SRO	LRO
Ballistic motion	Diffusion	No diffusion	Collective modes

SRO, short range order; LRO, long range order.

fact that it is completely random. The liquid has a density close to that of the crystal with, generally, a fairly similar short range order (SRO) but without long range order (LRO). Schematically, from the structural point of view, the liquid resembles a crystal at short distances (a few shells of neighbors) and a gas at long distances. Due to its partial randomness, the liquid has to be described in a statistical way, by its correlation functions. The most important one is the distribution of interatomic separations  $r$ , the pair correlation function  $g(r)$  (Figure 9.1).

The most widely used technique for the structural analysis of liquids is the scattering of neutrons and X-rays. If the diffraction techniques enable complete solution of the structure of crystals, this is no longer valid for disordered systems. Indeed, the diffraction pattern of liquids contains a limited amount of information on a structure that requires, in principle, many parameters to be described, in contrast with crystalline materials, which show a rich collection of sharp diffraction peaks (see Figure 9.6). The scattered intensity  $I(\theta)$  of liquid, amorphous or glassy materials, gives, by Fourier transformation, the pair correlation function  $g(r)$ . B. Warren [79] conducted pioneering work on X-ray scattering of glasses that can be considered as frozen liquids. As the pair correlation function is far from being a complete description of the structure, the diffraction analysis has to be complemented by measurements of density, electrical conductivity, thermal properties, inelastic neutron and X-ray scattering spectra, and X-ray absorption fine structure (EXAFS) technique. Large-scale facilities (neutron sources and synchrotrons) contributed a great deal to the study of liquids and disordered materials in general, in particular under extreme conditions of temperature and pressure. The pioneering work of J. Enderby and P. Egelstaff by neutron scattering of the structural and chemical analysis of liquid alloys is a landmark in this field [21]. In addition, computer simulations of the structure of liquids (Monte Carlo simulation, ab initio molecular dynamics, reverse Monte Carlo analysis) bring a wealth of relevant information and enhance our understanding of the liquid phases. We review the different approaches of the study of liquids and amorphous structures, from the simplest metallic structures to the more complex semiconducting alloys and even up to supramolecular liquid structures.

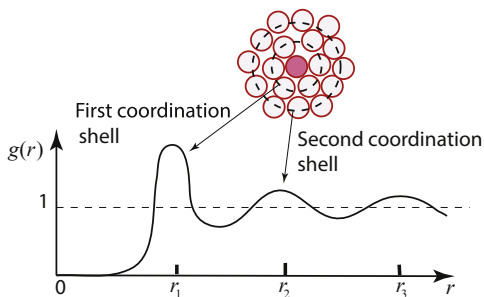


FIGURE 9.1 Pair correlation function  $g(r)$ .

### 9.1.1 The Liquid State

Due to the randomness of a liquid, its description is statistical by nature and is expressed in term of the correlation functions [38]. The simplest (2- body) correlation function is the pair correlation function  $g(r)$ , which plays a crucial role because it allows computing the average interatomic distance and the number of nearest neighbors, and it is directly related to scattering experiments.

In principle, the liquid structure should be described by a full set of N-body correlation functions but the higher (triplet...) correlation functions  $g(\vec{r}_1, \vec{r}_2, \vec{r}_3\dots)$  are functions of many variables and they cannot be measured experimentally. One can have access to them only by computer simulation (see Section 7).

### 9.1.2 Pair Correlation Function

By definition, the number  $dN(r)$  of atoms contained between two concentric shells of radii  $r$  and  $r + dr$  centered on an atom at the origin is

$$dN(r) = 4\pi\rho_0g(r)r^2 dr \quad (9.1)$$

where  $\rho_0$  is the average density.

The pair correlation function characterizes the probability of having an atom at distance  $r$  from a reference atom located at the origin. Figure 9.1 shows the pair correlation function  $g(r)$ .

By construction,  $g(r)$  is dimensionless and approaches 1 for large  $r$  values in a liquid. For a perfect gas with total disorder,  $g(r)$  is equal to 1 everywhere; the departure from unity is a measure of the order that is less and less present when  $r$  increases. Below some cutoff value (roughly the diameter of the atom), the steric hindrance imposes that  $g(r) = 0$ .

The position  $r_1$  of the first maximum of  $g(r)$  gives the average distance of the first nearest neighbors and its width characterizes the dispersion of nearest neighbors' distances. For a crystal at  $T=0$ , it is a  $\delta$ -peak.

The **radial distribution function**  $RDF(r) = 4\pi\rho_0r^2g(r)$  is a useful function that allows counting the number of neighbors by integration. The average number of neighbors around an atom, its coordination number  $\bar{N}$ , is obtained by integrating Eqn (9.1) from 0 to  $R = r_{\min}$ , the first minimum of  $g(r)$ .

$$\bar{N} = 4\pi\rho_0 \int_0^{r_{\min}} g(r)r^2 dr \quad (9.2)$$

The coordination number is not an integer number in a noncrystalline structure; e.g., a coordination number of, say, 5.1 may be a weighted average of atoms with local coordinations 4, 5, 6 and 7. The dispersion of coordination numbers around their mean is of great interest but unfortunately scattering experiments do not give access to this value that can be obtained by computer simulation (Section 7).

The coordination number is subject to some arbitrariness. Indeed, the minimum  $r_{\min}$  after the first peak may be ill-defined in some liquid structures and, in addition, alternative definitions of the coordination number have been suggested (e.g., fitting the first peak by various bell-shaped functions). A fluctuation of about 1 on the coordination numbers may occur depending on the calculation technique. However, the evolution of the coordination numbers with temperature and composition is more accurate than its absolute value provided that one keeps the same definition.

## 9.2 Scattering: of Neutrons and X-rays

The main technique of structural analysis of condensed matter, whether crystalline or disordered, is the coherent scattering (diffraction) of quanta (particles/waves) [45,2,68] with a wavelength of the order of magnitude of the interatomic separation (i.e., Å). The most used analyzing beams are the photons (X-rays), neutrons, and electrons. Due to their charge neutrality, the photons and neutrons penetrate deeply inside the materials (order of magnitude of mm) and are then qualified for the analysis of bulk materials [2]. At the opposite, the electrons have a very small mean free path in the material (as small as  $\leq 10$  Å at 100 eV) due to their charge; as a consequence, they are restricted to the analysis of surfaces or very thin films. In the following, we will concentrate on the structural analysis with neutrons and X-rays. For the study of liquids, the neutrons are especially interesting, as their long mean free path is compatible with a complex sample environment (sample holder, furnace, high pressure cell). Neutrons, and to some extent X-rays, weakly perturb the structure. As a consequence, the analysis is fairly simple: a first-order perturbation (Fermi golden rule or kinematical approximation) is valid and leads to the well-established Fourier transform formalism. As a rule of thumb, under normal conditions less than 10% of the neutrons are scattered, hence multiple scattering is marginal.<sup>1</sup> This is true also for X-rays to a lesser extent.

### 9.2.1 Scattering: Generalities

The interference pattern is a fingerprint of the structure. Figure 9.2 shows a schematic view of the scattering setup with the triplet: source, sample, and detector, with some additional optics. The production and characteristics of the beams are postponed in Section 5.

Assuming that the source and the detector are at long distances from the sample, a plane wave falls on the sample and on the detector; the relevant parameter is the sample size to distance ratio.

Neutrons are chargeless massive particles that are scattered by the pointlike nuclei via strong nuclear interactions. X-rays are massless particles scattered by the extended

<sup>1</sup>One calibrates the thickness of the sample such that at most 10% of the neutrons are scattered, leaving 90% of the beam unperturbed. The probability of a double scattering is then of the order of 1%. This “waste” of the incoming particles is necessary to get clean and easy-to-interpret diffraction patterns.

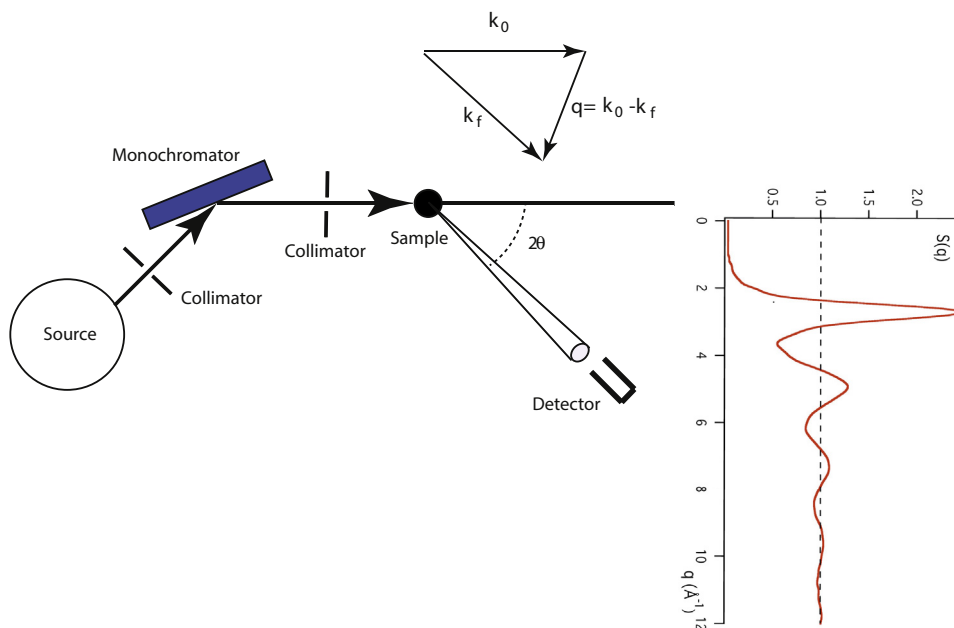


FIGURE 9.2 Diffraction setup (schematic),  $\vec{k}_0$  is the incident wave vector and  $\vec{q} = \vec{k}_0 - \vec{k}_f = \frac{4\pi}{\lambda} \sin(\theta)$ .

electron clouds via electromagnetic interactions. We do not consider here the magnetic scattering of neutrons by the electrons.

The strength of the interaction is given by a single parameter, the scattering length  $b_i$  (possibly complex if the material is absorbing) that has the dimension of a length [16],17. The scattering length of the neutrons for the various isotopes is experimentally measured and tabulated [16]. In Figure 9.3, the values of the  $b_i$  for neutrons look randomly

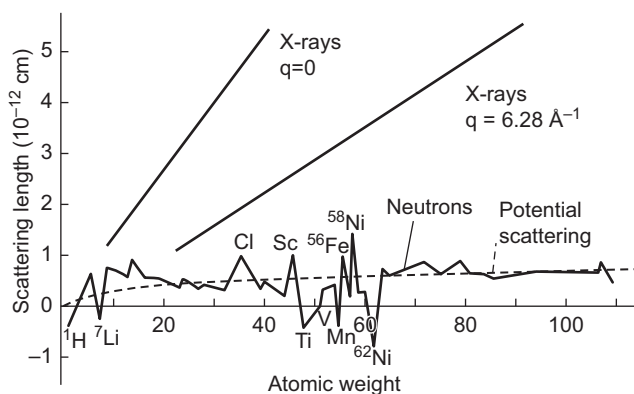


FIGURE 9.3 Coherent scattering lengths for X-rays and neutrons ( $b$ ) as a function of atomic number. Note the dependence on  $q = \frac{4\pi}{\lambda} \sin(\theta)$  only for X-rays. Figure after Ref. [4].

distributed around a mean value of about  $6 \cdot 10^{-12}$  cm as a consequence of the complexity of the neutron–nucleus strong interaction.<sup>2</sup>

The orders of magnitude of the scattering lengths of X-rays and neutrons are comparable, by chance.

In the X-ray community, the analogous of the scattering length is called the atomic form factor  $f(q)$ ; it is  $q$ -dependent because of the spatial extension of the diffracting electron cloud. Its value at  $q = 0$  is  $Zr_c$ , where  $Z$  is the number of electrons of the element and  $r_c$  is the classical radius of the electron ( $r_c = e^2/mc^2 = 0.282 \cdot 10^{-12}$  cm). The values of  $f(q)$  are tabulated [64].

For the sake of homogeneity, we try to give a unified description of the X-ray and neutron scattering formalism, keeping the same notation  $b_i$  for X-rays and neutrons, as far as possible, except when a specific distinction has to be done (Table 9.2).

Table 9.3 shows the scattering lengths of selected isotopes and atoms.

**Table 9.2** Labeling of the Scattering Lengths and Intensities for Neutrons and X-rays

	Neutrons		X-rays	
Scattering length	$b_i$	Form factor	$f_x(q)$	
Scattered intensity	$F_N(q)$	Scattered intensity	$I_x(q)$	

**Table 9.3** Scattering Lengths of Some Elements and Isotopes

	Atomic Number	$b_{coh}$ ( $10^{-12}$ cm)	$b_{inc}$ ( $10^{-12}$ cm)	$f_x(q = 0)$ ( $10^{-12}$ cm)	$f_x(q = 2\pi\text{Å}^{-1})$ ( $10^{-12}$ cm)
<sup>1</sup> H	1	−0.374	2.52	0.28	0.02
<sup>2</sup> D	1	0.667	0.403	0.28	0.02
C	6	0.665	0.009	1.69	0.48
N	7	0.936	0.197	1.97	0.562
O	8	0.580	0	2.25	0.68
Si	14	0.415	0.020	3.95	1.72
<sup>23</sup> Na	11	0.363	0.222	3.08	1.19
<sup>nat</sup> Cl	17	0.958	0.649	4.80	2.0
<sup>35</sup> Cl	17	1.171	0.611	4.80	2.0
<sup>37</sup> Cl	17	0.309	0.009	4.80	2.0
<sup>nat</sup> Ni	28	1.030	0.648	7.90	3.6
<sup>58</sup> Ni	28	1.440	0	7.90	3.6
<sup>60</sup> Ni	28	0.280	0	7.90	3.6
Zr	40	0.716	0.014	11.29	5.6

<sup>2</sup>The same holds also for inelastic scattering.

## 9.2.2 Master Equation

The **double differential scattering cross section**  $\frac{d^2\sigma}{d\Omega dE}$  (see Figure 9.2) is the intensity (number of quanta, neutrons, or photons) scattered per second in a solid angle  $d\Omega$  in an energy domain between  $E$  and  $E + dE$ . Usually, the energy is converted in frequency according to Planck's relation  $E = \hbar\omega$ .

Following van Hove [78], the double differential scattering cross section for a collection of  $N$  atoms centered at positions  $r_i(t)$  at time  $t$  writes

$$\frac{d^2\sigma}{d\Omega d\omega} = \frac{1}{2\pi} \frac{k_f}{k_0} \int_{-\infty}^{\infty} dt e^{-i\omega t} \left\langle \sum_{i,j} \overline{b_i b_j} e^{-i\vec{q} \cdot \vec{r}_i(0)} e^{i\vec{q} \cdot \vec{r}_j(t)} \right\rangle \quad (9.3)$$

where  $\vec{k}_0$  and  $\vec{k}_f$  are the incident and diffracted wave vectors and  $\vec{q} = \vec{k}_f - \vec{k}_0$  (Figure 9.2). The horizontal bar is **the configurational average**, and  $\langle \rangle$  is the thermal average. It has the dimension of an area (in  $\text{cm}^2$  or in  $\text{fm}^2$  or in barn [ $10^{-24} \text{cm}^2$ ]).

## 9.2.3 Coherent and Incoherent Scattering

In the double sum of Eqn (9.3), we consider separately the cases where the two sites are either distinct ( $i \neq j$ ) or identical ( $i = j$ ). Assuming the absence of correlation between the  $b_i$  values of distinct scatterers, we have

$$\overline{b_i b_j} = \overline{b}^2 \quad i \neq j \quad (\text{distinct}) \quad (9.4)$$

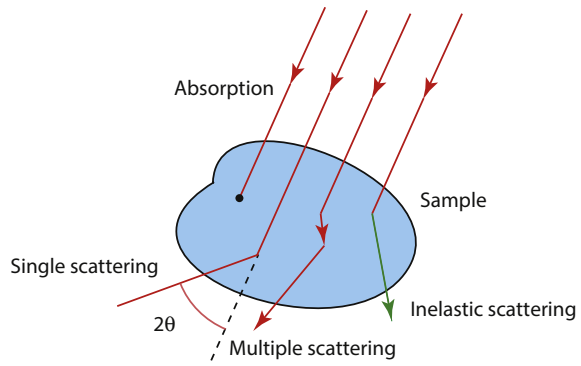
$$\begin{aligned} \overline{b_i b_j} &= \overline{b}^2 \quad i = j \quad (\text{self}) \\ &= \sum_{\alpha} c_{\alpha} |b_{\alpha}|^2 \end{aligned} \quad (9.5)$$

where  $c_{\alpha}$  is the concentration in element  $\alpha$ . The upper term is called *distinct* and the second term ( $i = j$ ) is called *self*.

The *coherent* and *incoherent* scattering lengths are defined as

$$b_{coh} = \overline{b} = \sum_{\alpha} c_{\alpha} b_{\alpha} \quad (9.6)$$

FIGURE 9.4 Possible scattering events (schematic).



$$b_{inc} = \sqrt{\bar{b}^2 - \bar{b}^2} \quad (9.7)$$

and the coherent and incoherent cross sections are

$$\sigma_{coh} = 4\pi\bar{b}^2 \quad (9.8)$$

$$\sigma_{inc} = 4\pi(\bar{b}^2 - \bar{b}^2) \quad (9.9)$$

The double differential scattering cross section Eqn (9.3) is a sum of two terms:

$$\begin{aligned} \frac{d^2\sigma}{d\Omega d\omega} &= \frac{d^2\sigma}{d\Omega d\omega_{distinct}} + \frac{d^2\sigma}{d\Omega d\omega_{self}} \\ &= \frac{1}{2\pi} \frac{k_f}{k_0} \left[ \int_{-\infty}^{\infty} dt e^{-i\omega t} \bar{b}^2 \sum_{i \neq j}^N \langle e^{-i\vec{q} \cdot \vec{r}_i(0)} e^{i\vec{q} \cdot \vec{r}_j(t)} \rangle \right. \\ &\quad \left. + \int_{-\infty}^{\infty} dt e^{-i\omega t} \bar{b}^2 \sum_i^N \langle e^{-i\vec{q} \cdot \vec{r}_i(0)} e^{i\vec{q} \cdot \vec{r}_i(t)} \rangle \right] \quad (9.10) \end{aligned}$$

The first term  $\frac{d^2\sigma}{d\Omega d\omega_{distinct}}$  is sensitive to the structure as it is related to the interferences between two different scattering sites, whereas the second term  $\frac{d^2\sigma}{d\Omega d\omega_{self}}$  is structure insensitive, as it involves a single site ( $i = j$ ).

The two terms of Eqn (9.10) are usually rearranged in a coherent and an incoherent contribution. In the **coherent** term  $\frac{d^2\sigma}{d\Omega d\omega_{coh}}$  the sum is performed on all the sites, without exclusion, and in the remaining part, the incoherent term  $\frac{d^2\sigma}{d\Omega d\omega_{inc}}$ , the variance of the scattering lengths occurs (Eqn (9.7)). The double differential scattering cross section writes

$$\begin{aligned} \frac{d^2\sigma}{d\Omega d\omega} &= \frac{d^2\sigma}{d\Omega d\omega_{coh}} + \frac{d^2\sigma}{d\Omega d\omega_{inc}} \\ &= \frac{1}{2\pi} \frac{k_f}{k_0} \int_{-\infty}^{\infty} dt e^{-i\omega t} \left[ \bar{b}^2 \sum_{i,j}^N \langle e^{-i\vec{q} \cdot \vec{r}_i(0)} e^{i\vec{q} \cdot \vec{r}_j(t)} \rangle \right. \\ &\quad \left. + (\bar{b}^2 - \bar{b}^2) \sum_i^N \langle e^{-i\vec{q} \cdot \vec{r}_i(0)} e^{i\vec{q} \cdot \vec{r}_i(t)} \rangle \right] \quad (9.11) \end{aligned}$$

or in a more compact form

$$\frac{d^2\sigma}{d\Omega d\omega} = N \frac{k_f}{k_0} \left[ b_{coh}^2 S(\vec{q}, \omega) + b_{inc}^2 S_s(\vec{q}, \omega) \right] \quad (9.12)$$

where  $S_s(\vec{q}, \omega)$  is the self (incoherent) dynamic structure factor and  $S(\vec{q}, \omega)$  is the full (coherent) dynamic structure factor  $S(\vec{q}, \omega)$  that contains the structural and dynamical information on the system. Its properties are developed in many textbooks [2,13,68,73,32,7]. See Figure 9.5 for a schematic view of coherent and incoherent contributions to the neutron scattering cross section  $\frac{d\sigma}{d\Omega}(q)$  of a liquid.

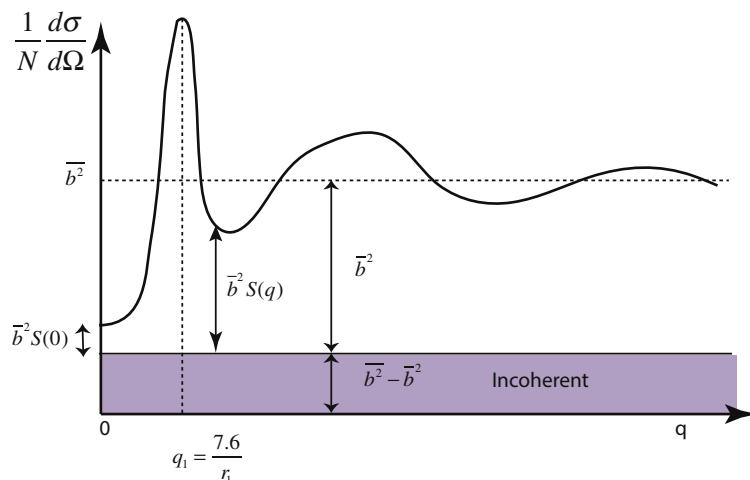


FIGURE 9.5 Coherent and incoherent contributions to the neutron scattering cross section  $\frac{d\sigma}{d\Omega}(\mathbf{q})$  of a liquid.

## 9.2.4 Scattering by Liquid and Amorphous Structures

Equations (9.3)–(9.12) are valid for any structure, crystalline or disordered. In a liquid, the atoms diffuse and vibrate, whereas in a solid, whether crystalline or amorphous, they only vibrate along their equilibrium positions. As a consequence of the diffusive motion, there is no coherent elastic scattering in a liquid except at  $\vec{q} = 0$  [73]. Indeed, because of the spectral (sometimes called Heisenberg) inequality, a strict conservation of the energy (or frequency  $\Delta\omega = 0$ ) requires an infinite time of measurement as  $\Delta\omega\Delta t \geq \frac{1}{2}$ . During this time interval, the atoms diffuse, and at  $t = \infty$  the memory of their original positions is completely lost. The time averaged density is a constant in space and its Fourier transform gives a delta peak  $\delta(\vec{q})^2$ . In conclusion, in a liquid, there is no elastic scattering, except in the uninteresting case of forward scattering ( $\vec{q} = 0$ ).

However, in a short time period, an atom of a liquid vibrates in the cage of its neighbors. The scattering spectrum is then an average of the instantaneous snapshots of the configurations of the liquid. Consequently, the scattered intensity shows damped oscillations, contrary to a gas (Figure 9.6).

The case of amorphous structures is different: the atoms undergo a thermal motion about their time-independent mean positions. It is then possible to measure the elastic part of the spectrum that differs from the static approximation by the Debye-Waller factor, as in crystals.

## 9.2.5 Static Approximation

In most scattering experiments, especially in diffuse scattering setups, there is no energy filtering; all the energies are collected by the detector with an efficiency  $\varepsilon(E)$  that will be

<sup>2</sup>The same holds also for inelastic scattering.

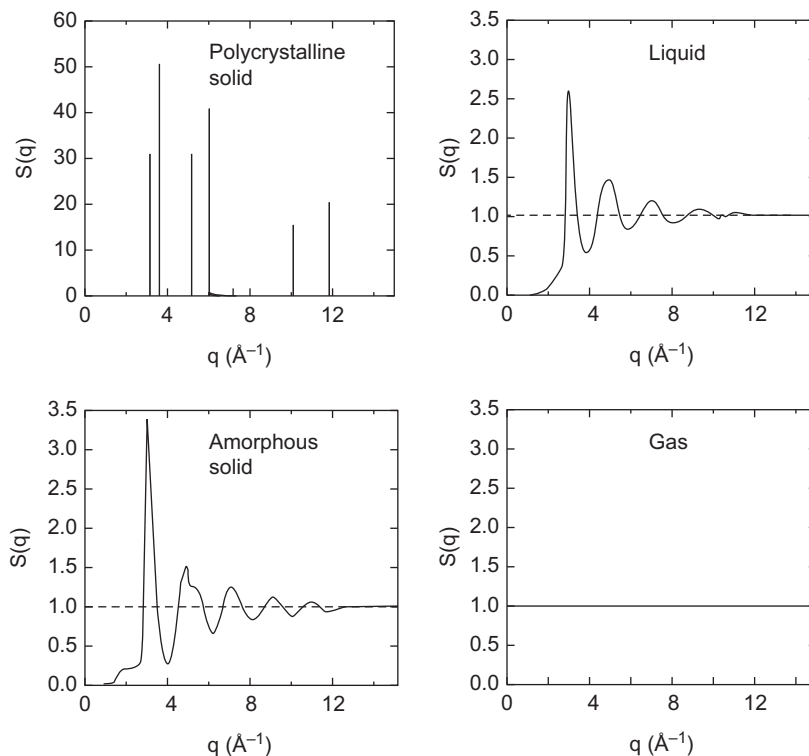


FIGURE 9.6 Structure factor  $S(q)$  of a polycrystal, an amorphous sample, a liquid, and a gas for comparison.

assumed to be equal to 1 (or to a constant) for simplicity. Integrating Eqn (9.12) over all the energy exchanges corresponds to taking snapshots ( $\Delta t = 0$ ) of the structure. It is called the *static approximation*. The  $\omega$ - (or  $E$ -) independent measured differential scattering cross section is given by

$$\frac{d\sigma}{d\Omega}(\vec{q}) = \int_{-\infty}^{\infty} \frac{d^2\sigma}{d\Omega dE}(\vec{q}, E) \varepsilon(E) dE = \frac{d\sigma}{d\Omega_{coh}}(\vec{q}) + \frac{d\sigma}{d\Omega_{inc}}(\vec{q}) \quad (9.13)$$

In practice, for X-rays, the incident energy (several kiloelectron volts) exceeds the maximum energy transfers between the wave/particle and all the excitations of the sample (several millielectron volts). For thermal neutrons, whose energies are of the same order of magnitude as the vibrations (i.e.,  $k_B T$ ), the integration cannot be done upon the energies of all the possible excitations and, to get a reliable value of  $\frac{d\sigma}{d\Omega}$ , an inelastic correction is needed (Placzek correction), particularly important for light atoms [62,14].

The static approximation ( $\Delta t = 0$ ) of the structure is different from an elastic scattering ( $\Delta\omega = 0$ ) that corresponds to an average over an infinite time.

Combining (Eqn 9.3) and (Eqn 9.13), with the assumption that  $k_f=k_0$ , the differential scattering cross section is given by

$$\begin{aligned} \frac{1}{N} \frac{d\sigma}{d\Omega}(q) &= b_{coh}^2 S(q) + b_{inc}^2 \\ &= \bar{b}^2 [S(q) - 1] + \bar{b}^2 \end{aligned} \quad (9.14)$$

where  $S(q)$  is the static structure factor.

In noncrystalline materials (liquids, glasses), the system is isotropic in the average and the scattering pattern depends only on the modulus  $q = |\vec{q}|$ , related to the scattering angle  $2\theta$  (Figure 9.2) by

$$q = \frac{4\pi}{\lambda} \sin \theta \quad (9.15)$$

For isotropic liquids, the limiting values of  $S(q)$  have simple expressions.

The limit value of  $S(q)$  for  $q \rightarrow 0$  is the second derivative of the free energy  $G$  with respect to the volume  $V$  and is related to the isothermal compressibility  $\kappa_T$  and to the density  $\rho_0$ .

$$\begin{aligned} \lim_{q \rightarrow 0} S(q) &= \rho_0 \kappa_T k_B T \\ \lim_{q \rightarrow \infty} S(q) &= 1 \end{aligned} \quad (9.16)$$

This is valid for homogeneous liquids and obviously for gases (for which  $S(q) = 1$  everywhere). If the structure is inhomogeneous, one observes an increase of  $S(q)$  at low  $q$  values, the small angle scattering (SAS).

### 9.2.6 Diffraction by a Crystal, Scherrer Broadening and SAS

The elastic scattering of a monochromatic wave by a perfect crystal is well known and abundantly documented [45,2,63,13,68]. The diffraction pattern, described by  $S(\vec{q}, 0)$ , gives the Bragg peaks when the Laue conditions are fulfilled [45,2]. Some additional remarks are worth being done in relation to the scattering by liquids.

1. For a perfect crystal (of infinite volume, by definition), with an infinite volume of coherence of the beam (see Section 2.7), the peak widths are zero ( $\Delta \vec{q} = 0$ ) as a consequence of the LRO extending to infinity. If the crystal has a finite extension (microcrystallites, defective crystals, etc.), the diffraction peaks have a nonzero width  $\Delta q$  given by Scherrer's formula that can be simply obtained by dimensional analysis:

$$\Delta q = a \frac{2\pi}{D} \quad (9.17)$$

where  $D$  is the size of the crystal or the extent of the translational order and  $a$  is a dimensionless parameter close to unity. For a sphere of diameter  $D$ ,  $a = 0.91$ .

This equation has a wider range of applications than expected.

2. Equation (9.17) can be adapted to liquids. In this case,  $D$  is the extent of the SRO, usually a few shells of neighbors. The widths of the diffraction peaks are large and, when  $q$  increases, they merge and give a constant asymptotic value.
3. In any case, crystalline or disordered, a coherent scattering exists at  $\theta = 0$  (or  $q = 0$ ) as all the beams are in phase. The analysis of the shape and the width of the central peak led to important developments: the small angle scattering, SAS<sup>3</sup> [68,76,75] (cf. Section 9). Both SAS and Scherrer's broadening are driven by the same formula: the SAS is the Scherrer's broadening of the central peak. It gives information on the size of the diffracting object, provided it has some contrast (i.e., difference in scattering lengths) with respect to the surrounding medium.

## 9.2.7 Coherence Volume

A monochromatic plane wave is an idealization. An actual beam deviates from the ideal case in two ways: it is not perfectly monochromatic and it has some angular divergence.

The **longitudinal coherence** length depends on the departure from monochromaticity (dispersion  $\Delta\lambda$  around the average wavelength  $\lambda$ ).

From the spectral (or Heisenberg) equality, the longitudinal coherence length  $L_L$  is given by [2,28]

$$L_L = \frac{1}{2} \frac{\lambda^2}{\Delta\lambda} \quad (9.18)$$

The longitudinal coherence length is the wavelength  $\lambda$  multiplied by an enhancement factor  $\frac{\lambda}{2\Delta\lambda}$ . The better the monochromatization, the longer the longitudinal coherence. Typically for a liquid diffractometer,  $\frac{\Delta\lambda}{\lambda} \cong .01$ . The longitudinal correlation length is then  $50 \cdot \lambda$ , about  $100 \text{ \AA}$ , far larger than the extent of the local order in a liquid or an amorphous material. Typical values are given in Table 9.4.

The **lateral or transverse coherence** lengths originate from the beam divergence. The beam is not perfectly collimated; the source is not a point, as it has some spatial extension  $D_x$  in the  $x$  direction (Figure 9.7) and an angular divergence  $D_x/R$  where  $R$  is

**Table 9.4** Orders of Magnitude of the Coherence Parameters.  $R$  is the Diameter of the Source,  $D$  the Source-Sample Distance

	$\lambda(\text{\AA})$	$\Delta\lambda(\text{\AA})$	$L_L(\text{\AA})$	$R(m)$	$D(m)$	$L_{t,x}(\text{\AA})$
X-rays	1	0.01	50	0.001	10	5000
Neutrons	1	0.01	50	0.05	5	50
SAS	10	0.1	1000	0.05	10	1000

SAS, small angle scattering.

<sup>3</sup>SAXS for X-rays and SANS for neutrons.

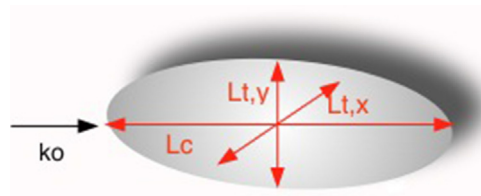


FIGURE 9.7 Coherence volume (schematic).

the source-sample distance and similarly for the  $y$  direction. The lateral or transverse coherence length  $L_{t,x}$  ( $L_{t,y}$ ) writes [2]

$$L_{t,x} = \frac{\lambda}{2} \frac{R}{D_x} \quad (9.19)$$

The enhancement factor is now half the inverse of the angular opening of the source seen from the sample  $\frac{R}{2D}$ . This value is of the order of  $2^\circ$  ( $35 \text{ mrad}$ ) for neutrons and considerably smaller for X-rays (cf. Table 9.4).

The ellipsoid-like coherence volume (Figure 9.7) is proportional to the product of the three coherence lengths

$$V_{coh} \cong L_L L_{t,x} L_{t,y} \quad (9.20)$$

Inside the coherence volume, the *amplitudes* of the waves add and give rise to interferences (Eqn (9.3)) that are the cornerstone of the structural analysis. Outside the coherence volume, the partial *intensities* add and give an average picture.

In practice, the quality of monochromatization and collimation results from a compromise between intensity and resolution. Due to their low brilliance, neutrons cannot be as monochromatic and as well collimated as the X-rays, but for liquids, this is not important because the diffraction spectra have no sharp peaks. The intensity is favored with respect to the resolution. There is no need to have a sharp monochromatization.

In the study of mesoscopic liquids (e.g., liquid of micelles, Section 9) in the SAS regime,  $\frac{\Delta\lambda}{\lambda}$  may be as large as about 10–20% in order to enhance still further the intensity of the incoming beam. The coherence volume should be decreased, but it is compensated by a larger wavelength, e.g., 10–20 Å (Table 9.4). More details can be found in [56].

In the extreme case of a single coherence volume of the sample, which can be achieved in modern X-ray sources (synchrotrons, free electron lasers), one has diffraction-limited speckle scattering [42]. Ultrafast pulses of coherent hard X-rays open new opportunities for studies of atomic-scale dynamics in liquid and amorphous materials on times scales down to the femtosecond range [5].

### 9.2.8 Neutrons and X-rays [7, 28, 33, 37, 48, 72]

We particularize Eqn (9.13). We assume that the very first corrections have been done: subtraction of the parasitic signals from the ambient background, from the sample

environment (container, furnace if any), correction for absorption of the different constituents [58], including the sample itself, correction of multiple scattering [10, 71], and normalization to the (multi)detector sensitivity. Finally, the remaining signal is the signal of the sample itself.

As shown in Section 2.3, the scattered intensity is the sum of a self term (incoherent) and a distinct term that contains the structural information. Additional terms are specific to each type of radiation. In summary, we have, for the neutron case:

$$\frac{1}{N} \frac{d\sigma}{d\Omega}(q)|_N = \left( \sum_{\alpha} c_{\alpha} b_{\alpha} \right)^2 (S_N(q) - 1) + \sum_{\alpha} c_{\alpha} (b_{\alpha})^2 + P(\theta) \quad (9.21)$$

where  $P(\theta)$  is the inelastic (Placzek [62]) correction, which is moderate, as most neutrons are elastically scattered. This is still more true for the X-ray photons because their energies (10 keV) are six orders of magnitude larger than the energies of the excitations (e.g., up to several tens of meV for the phonons). For the X-ray case

$$\frac{1}{N} \frac{d\sigma}{d\Omega}(q)|_X = \left( \sum_{\alpha} c_{\alpha} f_{\alpha}(q) \right)^2 (S_X(q) - 1) + \sum_{\alpha} c_{\alpha} (f_{\alpha}(q))^2 + C_X(q) \quad (9.22)$$

where  $C_X(q)$  is the Compton scattering.

Figure 9.8 shows the scattered intensities in a neutron and an X-ray experiment. In brief, in the neutron case, the intensity oscillates around a constant. To obtain  $S(q)$ , one subtracts the incoherent contribution and makes correction due to inelasticity. In the X-ray case, one divides by the atomic form factor that is decreasing a function of  $q$  because it is the Fourier transform of the charge density. Note that in the case of magnetic neutron scattering by the electron spins, a magnetic structure factor is present, analogous to the atomic form factor.

For the X-rays, in a monoatomic system,  $b_{inc} = 0$ . For the neutrons, the  $b_i$  are dependent on the isotope and the nuclear spin. The latter plays an important role. For

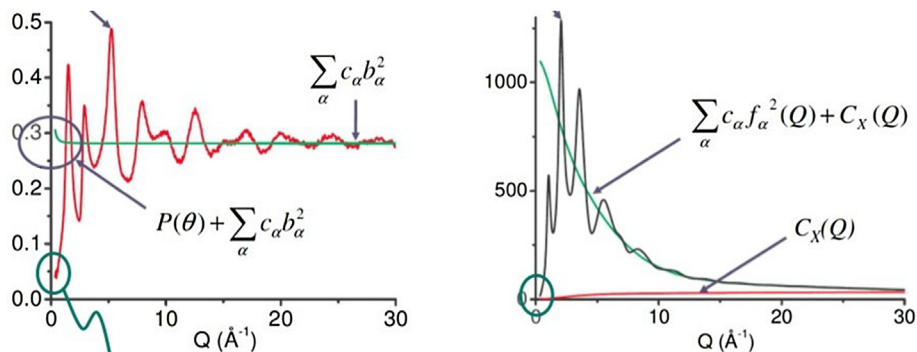


FIGURE 9.8 Scattered intensities of a liquid in a neutron (left) and X-ray (right) scattering experiment, respectively.

**Table 9.5** Advantages and Disadvantages of the X-ray and Neutron Scattering Techniques

	X-rays	Neutrons
Advantages	Availability (lab.) High flux (synchrotron) Sensitivity to heavy element Single sample (anomalous scatt.)	Isotopes Nuclear scattering Sensitivity to hydrogen Relatively easy data treatment
Disadvantages	$q$ -dependent form factor Strong sample environment scattering	Low flux Cost and availability of isotopes

instance, in normal hydrogen ( $^1\text{H}$ ), the up and down spin gives different scattering lengths, so that  $b_{inc}$  is large, whereas for deuterium (D)  $b_{inc} = 0$ . Hence, one deuteriates the sample to lower the incoherent scattering, in addition the contrast is modified.

Let us finally remark that the structure factors  $S_N(q)$  and  $S_X(q)$  are not identical because the neutrons are scattered by the pointlike nuclei while the X-rays are scattered by the diffuse electron cloud. Even after division by the X-ray form factor  $\sum_{\alpha} c_{\alpha} f_{\alpha}(q)$ , the X-ray structure factor is slightly different because the chemical bond rearranges the electron cloud (covalency effect). A deconvolution of the electron cloud effects is possible.

Table 9.5 shows the advantages and disadvantages of the X-ray and neutron scattering techniques. In short, the main differences between neutrons and X-rays are as follows.

1. The scattering length  $b_i$  is constant for the neutrons (neglecting the magnetic scattering) while the X-ray form factor  $f_i(q)$  is strongly  $q$ -dependent.
2. The correction factors are
  - a. for neutrons: absorption, inelastic correction (Placzek), multiple scattering
  - b. for X-rays: absorption, Compton scattering, multiple scattering. Ideally, the correction terms should not exceed 10% of the scattered intensity.

## 9.3 Case Studies

### 9.3.1 Monoatomic Liquids

For a monoatomic liquid, with identical scattering lengths, the static coherent structure factor  $S(q)$  simplifies and writes in term of the interatomic separations  $r_{ij} = |\vec{r}_{ij}|$  [15]

$$S(q) = 1 + \frac{1}{N} \sum_{i,j \neq i} \frac{\sin(qr_{ij})}{qr_{ij}} \quad (9.23)$$

This formula was the sole formula in P. Debye's Nobel speech (1936). It is also a valuable first approximation for an alloy for which the scattering lengths of the elements are assumed to be identical.

9.3.1.1 First Characterization of  $S(q)$ 

A first look at  $S(q)$  allows to characterize the gross features of the structure prior to performing a full analysis using the Fourier transform.

1. The position of the first main peak of  $S(q)$ ,  $q_1$  gives a fair approximation of the nearest-neighbor distance

$$r_1 = \frac{7.6}{q_1} \quad (9.24)$$

The numerator is 20% larger than the expected  $2\pi$ . Indeed, the interatomic separation of spheres is twice the radius  $r_1 = 2R$ , whereas the (repetitive) distance between the successive shells of neighbors is slightly smaller because the shells interpenetrate (Figure 9.1).

For an FCC structure,  $r_1 q_1 = 2\pi\sqrt{1.5} \approx 7.695$ .

2. The ratio of the positions of the two first peaks  $q_2/q_1$  is correlated to the type of structure and coordination number. For “normal” liquids (metals, rare gases, and transition metals), for which the atoms are linked by fairly isotropic forces, the ratio  $q_2/q_1$  falls in the range [1.80, 1.86] (Figure 9.9 and Table 9.6).

For liquid rare earth metals,  $q_2/q_1$  is in the range [1.86, 1.90], due to the bonding by  $d$  and  $f$  electrons.

For liquid covalent structures, generally liquid semiconductors,  $q_2/q_1$  has higher values, in the range [1.96, 2.07] (Figure 9.10 and Table 9.6). This corresponds to directional bonds driven by the  $p$  orbitals. The coordination numbers (around 6–7) are smaller than in the compact structures and the maximum  $S(q_1)$  is smaller than in compact liquids. Liquid Si (Figure 9.10) and Ge are relevant examples, with metallic conductivities.

3. The latter have the peculiarity that their melting entropy is high and their densities increase at the melting. We classify them as “anomalous” liquids. The local

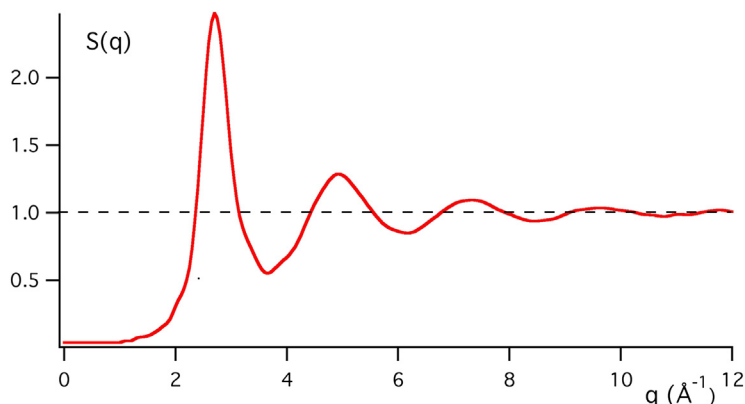
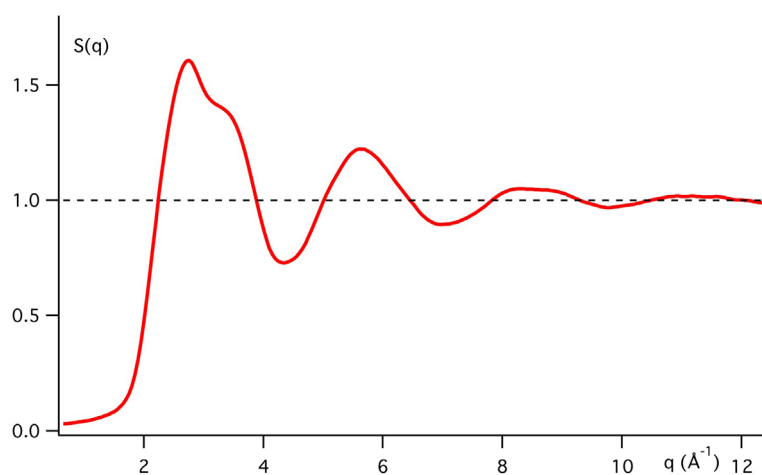


FIGURE 9.9 Structure factor  $S(q)$  of liquid Al.

**Table 9.6** Positions of the Two First Diffraction Peaks of Selected Liquids and Nearest-Neighbor Separations

	$q_1$ ( $\text{\AA}^{-1}$ )	$q_2$ ( $\text{\AA}^{-1}$ )	$q_2/q_1$	$r_1$ ( $\text{\AA}$ )	$q_1 r_1$
Na	2.03	3.75	1.85	3.81	7.73
Al	2.68	4.96	1.85	2.82	7.56
Fe	2.98	5.46	1.83	2.58	7.69
Ni	3.10	5.70	1.84	2.53	7.84
Si	2.72	5.62	2.07	2.50	6.80
Ge	2.56	5.11	2.00	2.82	7.22
Sn	2.15	4.38	2.04	–	–

**FIGURE 9.10** Structure factor  $S(q)$  of liquid Si.

structure of the liquid is very different from that of the solid. The coordination number is higher and the interatomic distances are larger.

4. The coherence length (Table 9.7) of the local order is estimated from the width of the diffraction peak:  $L_{ord}$  is equal to  $2\pi$  divided by the width of the first diffraction peak. It amounts to about three shells for normal liquids and less than two for anomalous liquids.
5. In covalently bonded liquids, the ratio  $S(q_2)/S(q_1)$  characterizes the type of environment of an atom: It is greater than one for a tetrahedral liquid and smaller than one for an octahedral liquid [74].
6. For large  $q$  values, the structure factor is asymptotically a sine function damped by an exponential  $S(q) \cong A \sin(qr_1 + \varphi)e^{-ar}$  where  $r_1$  is the nearest-neighbor distance [43].

**Table 9.7** Estimated Values of the Correlation Length of the Local Order in Liquid Elements. The Width is Arbitrarily Measured at  $S(q) = 1$ 

	$q_1$ ( $\text{\AA}^{-1}$ )	$\Delta q_1$ ( $\text{\AA}^{-1}$ )	$L_{ord}$ ( $\text{\AA}$ )	Nb Shells
Na	2.03	0.53	11.9	3.1
Al	2.68	0.78	8.1	3.5
Fe	2.98	0.90	6.9	2.7
Ni	3.10	0.78	8.1	3.2
Si	2.72	1.63	3.85	1.5
Ge	2.56	1.30	4.83	1.7
Sn	2.15	0.95	6.6	1.9
Crystal	–	0	$\infty$	$\infty$

### 9.3.1.2 Pair Correlation Function

The pair correlation is directly related to the structure factor  $S(q)$  by Fourier transformation [38,73]:  $r(g(r)-1)$  is proportional to the sine Fourier transform of  $q(S(q)-1)$ .

$$g(r) = 1 + \frac{1}{2\pi^2\rho_0 r} \int_0^\infty [S(q) - 1] q \sin(qr) dq \quad (9.25)$$

Equation (9.25) needs some warnings.

In practice,  $S(q)$  is not measured up to infinity but up to a maximum value  $q_{max} = \frac{4\pi}{\lambda}$ . Usually,  $S(q)$  shows oscillations up to possibly 20  $\text{\AA}$ , implying that the wavelength should be as low as  $\lambda = 0.5 \text{\AA}$ . This is easily achieved by X-ray synchrotrons, but for neutrons it requires a hot source. Indeed, thermal neutrons ( $\lambda \approx 1.7 \text{\AA}$ ) give only  $q_{max} \approx 7 \text{\AA}^{-1}$ .

The truncation of the  $S(q)$  spectrum has two effects: it broadens the peaks of  $g(r)$  and it produces spurious oscillations. The broadening of the peaks is negligible with respect to the natural width in liquids, but it may be of some relevance in amorphous substances. The oscillations of the Fourier transform, with a period  $2\pi/q_{max}$ , is a more difficult issue as the oscillations are enhanced at short distances because of the  $r$  factor in the denominator of Eqn (9.25) [44]. There are different ways to circumvent this artifact. The most popular technique consists of hiding the low  $r$  part of the function  $g(r)$ ! The *apodization* technique is a gentle damping of the oscillations of  $S(q)$  [47] at large  $q$ . The price to pay is an extra broadening of the peaks of  $g(r)$ .

As  $g(r)$  and its successive derivatives vanish at the origin by steric hindrance, a set of sum-rules on the even moments of  $S(q)-1$  are deduced [21]. They can be used for normalization, coherence, or fine tuning corrections of the data.

$$\int_0^\infty q^2 [S(q) - 1] dq = -2\pi^2\rho_0 \quad (9.26)$$

$$\int_0^\infty q^{2n} [S(q) - 1] dq = 0 \quad (n \geq 2)$$

### 9.3.2 Polyatomic Liquids

In the case of polyatomic systems, not only the position matters but also the chemical nature of the elements. In direct space, the structure is described by the **partial** (i.e., element sensitive) **pair correlation functions**  $g_{\alpha\beta}(r)$  where  $\alpha$  and  $\beta$  designate the chemical element. They are the Fourier transforms of the **partial structure factors**  $S_{\alpha\beta}(q)$  similarly to (Eqn (9.25)).

#### 9.3.2.1 Partial Structure Factors

The partial structure factors  $S_{\alpha\beta}(q)$  are named according to Faber and Ziman [22], but the original definition is due to Fournet [29]. For an  $n$ -component system, there are  $n(n+1)/2$  partial structure factors.

For a system with  $n$  components, the measured diffracted intensity is decomposed into a distinct and a self contribution. The former is a linear combination of the  $S_{\alpha\beta}(q)$ . The case is complicated by the fact that the different partial contributions to scattering are weighted by the scattering lengths of the various elements,

$$\frac{1}{N} \frac{d\sigma}{d\Omega}(q) = \sum_{\alpha\beta=1}^n c_{\alpha} c_{\beta} \bar{b}_{\alpha} \bar{b}_{\beta}^* [S_{\alpha\beta}(q) - 1] + \sum_{\alpha} c_{\alpha} \bar{b}_{\alpha}^2 \quad (9.27)$$

where the partial structure factors  $S_{\alpha\beta}(q)$  result from the interference of the  $\beta$  atoms around an  $\alpha$ -type atom and  $\bar{b}_{\alpha}^2 = b_{coh,\alpha}^2 + b_{inc,\alpha}^2$ .

Let us remark that the Fourier transform of the coherent part of (Eqn (9.27)) gives a weighted average of the pair correlation functions, sometimes called the *total pair correlation function*  $G_T(r)$ ; the weighting factor includes the scattering lengths so that  $G_T(r)$  has the dimension of an area

$$G_T(r) = \sum_{\alpha,\beta} c_{\alpha} c_{\beta} \bar{b}_{\alpha} \bar{b}_{\beta}^* (g_{\alpha\beta}(r) - 1) \quad (9.28)$$

A variant of the partial structure factors, better adapted to computer simulation, is the Ashcroft-Langreth definition [3]

$$S_{\alpha\beta}^{AL}(q) = \delta_{\alpha\beta} + \sqrt{c_{\alpha} c_{\beta}} [S_{\alpha\beta}(q) - 1] \quad (9.29)$$

Alternatively, in the Bhatia-Thornton [5] formalism, three sets of partial structure factors are defined for a binary alloy  $S_{NN}(q)$ ,  $S_{CC}(q)$ , and  $S_{NC}(q)$ ,  $N$  for number and  $C$  for concentration. They are, respectively, the distribution of the atomic number density, of concentration, and their cross correlation.  $S_{NN}(q)$  is a concentration weighted combination of the partial structure factors

$$S_{NN}(q) = c_1^2 S_{11}(q) + 2c_1 c_2 S_{12}(q) + c_2^2 S_{22}(q) \quad (9.30)$$

$S_{NN}(q)$  is the structure factor of the alloy if both chemical species have identical coherent scattering lengths.  $S_{NN}(q)$  characterizes the geometric structure, independent of the chemical order. The latter is described by  $S_{CC}(q)$  and  $S_{NC}(q)$  defined as

$$S_{CC}(q) = c_1 c_2 [1 + c_1 c_2 (S_{11}(q) - 2S_{12}(q) + S_{22}(q))] \quad (9.31)$$

$$S_{NC}(q) = c_1 c_2 [c_1 (S_{11}(q) - S_{12}(q)) - c_2 (S_{22}(q) - S_{12}(q))] \quad (9.32)$$

$S_{NN}(q)$  and  $S_{CC}(q)$  are positive and  $S_{CC}(q)S_{NN}(q) \geq S_{NC}(q)^2$ .

$S_{CC}(q)$  is equal to  $c_1 c_2$  if the three  $S_{\alpha\beta}(q)$  are identical.

If  $S_{CC}(q)$  is greater than  $c_1 c_2$  in average, homoatomic correlations are preferred.

If  $S_{CC}(q)$  is smaller than  $c_1 c_2$ , then heteropolar correlations are favored;  $S_{CC}$  plays the same role as the Warren–Cowley parameter in substitutional alloys [18].

In addition, in the case of a zero alloy,  $\bar{b} = 0$ , the signal measures directly  $S_{CC}(q)$ .

In the following, we will restrict ourselves to binary alloys.

When a single experiment is performed, one gets a single  $S(q)$ , which is a linear combination of the partials  $S_{11}$ ,  $S_{12} = S_{21}$ , and  $S_{22}$ . To obtain the individual  $S_{\alpha\beta}$ , one needs three independent equations for the three unknown functions.

Information at the partial structure factor level is important to reveal details of the local and intermediate-range orders.

Three independent experiments can be done in one of the following ways:

### 1. Neutron diffraction with isotopic substitution (NDIS) [28, 6]

The NDIS technique consists of measuring the coherent scattered intensity  $F(q)$  of three samples with the same chemical composition but different isotopic compositions. Their structures are the same as the cohesive properties are insensitive to the nature of the isotopes. Three sets of isotopes are used with the scattering lengths  $(b_\alpha^{(1)}, b_\beta^{(1)})$ ,  $(b_\alpha^{(2)}, b_\beta^{(2)})$ , and  $(b_\alpha^{(3)}, b_\beta^{(3)})$ . Usually, one set is made of natural isotopes and is labeled *nat*. We then have three sets of equations.

$$\begin{pmatrix} F_1(q) \\ F_2(q) \\ F_3(q) \end{pmatrix} = \begin{pmatrix} c_\alpha^2 b_\alpha^{(1)2} & 2c_\alpha c_\beta b_\alpha^{(1)} b_\beta^{(1)} & c_\beta^2 b_\beta^{(1)2} \\ c_\alpha^2 b_\alpha^{(2)2} & 2c_\alpha c_\beta b_\alpha^{(2)} b_\beta^{(2)} & c_\beta^2 b_\beta^{(2)2} \\ c_\alpha^2 b_\alpha^{(3)2} & 2c_\alpha c_\beta b_\alpha^{(3)} b_\beta^{(3)} & c_\beta^2 b_\beta^{(3)2} \end{pmatrix} \begin{pmatrix} S_{\alpha\alpha}(q) - 1 \\ S_{\alpha\beta}(q) - 1 \\ S_{\beta\beta}(q) - 1 \end{pmatrix} \quad (9.33)$$

The NDIS technique can only be performed if isotopes with sufficient contrast exist and are affordable. In any case, the huge cost of the isotopes (in grams) restricts the technique to selected fundamental studies. In compact matrix notation, Eqn (9.33) can be written as

$$\vec{F}(q) = A(\vec{S}(q) - 1) \quad (9.34)$$

The system can be inverted if the determinant of  $A$  is not too small, i.e., if the contrast is sufficient. Very often, the relative differences between the  $S_{\alpha\beta}(q)$  values may be as small as 1%, and the system (Eqn (9.33) or Eqn (9.34)) is poorly conditioned. The error bars on the  $S_{\alpha\beta}(q)$  functions are then large and the partial pair correlation functions  $g_{\alpha\beta}(r)$  are inaccurate.

An interesting illustration of this method, in relation to crystal growth, is the study of the structure of liquids in the undercooled regime. Indeed, to prevent crystallization, different containerless techniques have been developed: electromagnetic levitation [40]

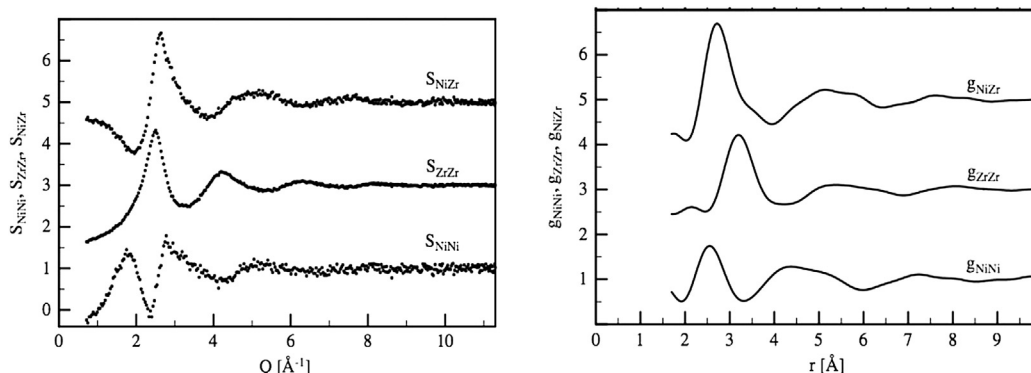


FIGURE 9.11 Partial structure factors and pair correlation functions of undercooled liquid  $\text{Ni}_{36}\text{Zr}_{64}$  at 1375 K [40].

and aerodynamic levitation [41]. The local order of undercooled liquid  $\text{Ni}_{36}\text{Zr}_{64}$  has been studied by neutron scattering with isotopic substitution. Three compositions have been analyzed:  $^{nat}\text{Ni}_{36}\text{Zr}_{64}$ ,  $^{58}\text{Ni}_{36}\text{Zr}_{64}$ , and  $^{60}\text{Ni}_{36}\text{Zr}_{64}$ . From the partial structure factors (Figure 9.11), it is shown that the melt exhibits a pronounced chemical short range: the Ni-Zr nearest neighbors are preferred as shown by the heteroatomic pair correlation function  $g_{\text{NiZr}}$  [40] (see Section 9.3.2.2). By contrast to some other metallic melts, no indications for the existence of an icosahedral SRO is found in the undercooled liquid. This may result from the comparatively larger difference of the atomic radii of Ni and Zr.

## 2. Anomalous X-ray Scattering

With X-rays, it is possible to do three independent experiments on the same sample by varying the wavelength, as the scattering lengths  $f(q)$  are significantly wavelength dependent in the vicinity of an absorption edge [2]. See Figure 9.12.

$$f(q, E_0) = r_e [Zf_{\text{mod}}(q) + f'(E_0) + if''(E_0)] \quad (9.35)$$

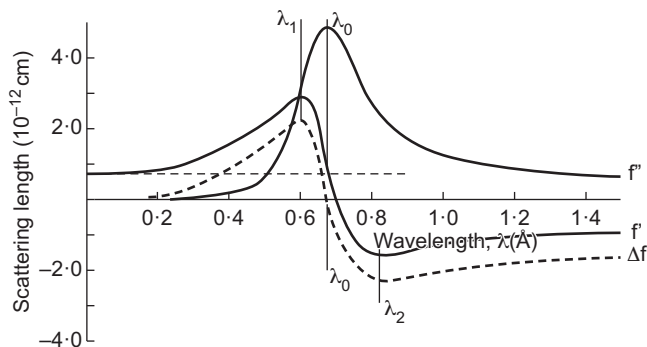


FIGURE 9.12 Scattering lengths as a function of the wavelength  $\lambda$  in the vicinity of an absorption edge ( $\lambda_0$ ). Three measurements should be done: below the edge ( $\lambda_2$ ), at the edge and above the edge ( $\lambda_1$ ).

where  $Z$  is the atomic number,  $r_e$  the classical radius of the electron, and  $f_{mod}(q)$  a modulation factor that goes from 1 at  $q = 0$  to 0 at  $q = \infty$ . The additional contributions  $f' + if''$  are the so-called anomalous terms that involve inner electrons of small radii and, consequently, their  $q$ -dependence can be neglected. The real part contributes to the scattering and the imaginary part represents the absorption.

$$\begin{pmatrix} F_1(q) \\ F_2(q) \\ F_3(q) \end{pmatrix} = \begin{pmatrix} c_{\alpha}^2 f_{\alpha 1}^2(q) & 2c_{\alpha} c_{\beta} f_{\alpha 1}(q) f_{\beta 1}(q) & c_{\beta}^2 f_{\beta 1}^2(q) \\ c_{\alpha}^2 f_{\alpha 2}^2(q) & 2c_{\alpha} c_{\beta} f_{\alpha 2}(q) f_{\beta 2}(q) & c_{\beta}^2 f_{\beta 2}^2(q) \\ c_{\alpha}^2 f_{\alpha 3}^2(q) & 2c_{\alpha} c_{\beta} f_{\alpha 3}(q) f_{\beta 3}(q) & c_{\beta}^2 f_{\beta 3}^2(q) \end{pmatrix} \begin{pmatrix} S_{\alpha\alpha}(q) - 1 \\ S_{\alpha\beta}(q) - 1 \\ S_{\beta\beta}(q) - 1 \end{pmatrix} \quad (9.36)$$

This technique is interesting and far less expensive than NDIS. However, the data reduction has to be done with great care because the electronic processes are markedly different before and after an absorption edge. Typical K-edges are given in [Table 9.8](#).

### 3. Combination of neutron and X-ray scattering

In principle, it is possible to perform three independent experiments combining X-rays with or without anomalous effects, and neutron scattering possibly with isotopic substitution [31]. As the neutron scattering length—due to strong nuclear interactions and the X-ray scattering length, purely electromagnetic—are totally independent, the matrix  $A$  can be inverted. The X-rays are more sensitive to the heavy elements. Despite its benefits, the combined method suffers from several difficulties. Some contributions are specific to X-rays (Compton) and some are specific to neutrons (inelasticity). The two techniques differ on many aspects: absorption, inelasticity, size of the beam, and this adds difficulty in the data reduction. There is no automatic canceling out by subtraction. The data treatment is therefore difficult. In addition, the diffraction process itself is different. As X-rays are diffracted by the electron clouds that may have a sizable departure from sphericity when the atoms are linked by a covalent or a metallic bond [69], the X-ray-neutron mixed method needs some special care in the case of covalent liquids. As we will see further on, the combination scattering data with computer simulation is of great help.

**Table 9.8** K-edge of Selected Elements (Groups IV and V and Transition Metals)

Element	K-Edge (keV)
Si	1.84
Ge	11.10
As	11.87
Sn	29.20
Pb	88.00
Fe	7.11
Ni	8.33
Pd	24.35
Pt	78.39

## 9.3.2.2 Partial Pair Correlation Functions

From the partial structure factors  $S_{\alpha\beta}(q)$ , the partial pair correlation functions  $g_{\alpha\beta}(r)$  can be obtained by Fourier transformation, the same way as for the pure elements.

$$g_{\alpha\beta}(r) = 1 + \frac{1}{2\pi^2\rho r} \int_0^\infty [S_{\alpha\beta}(q) - 1]q \sin(qr) dq \quad (9.37)$$

Special care has to be taken regarding the continuation, normalization, etc., of the  $S(q)$ .

Let us consider liquid NaCl that is a physically and historically important case. In ionic liquid alloys, there are two conflicting effects: the electrostatic energy favors the charge alternation whereas the entropic term favors a random distribution of ions as we are at high temperature in the liquid state.

Using neutron scattering with isotopic substitution on the Cl atoms, Enderby et al. [19] performed three independent experiments with three samples  $\text{Na}^{37}\text{Cl}$ ,  $\text{Na}^{35}\text{Cl}$ , and  $\text{Na}^{\text{nat}}\text{Cl}$  measured at  $875^\circ\text{C}$  just above the melting point. Figure 9.13 shows, after data reduction, the homoatomic  $S_{\text{NaNa}}(q)$  and  $S_{\text{ClCl}}(q)$  structure factors and the cross function  $S_{\text{NaCl}}(q)$ . As the A matrix (Eqn (9.33)) has a determinant as small as 0.03 after normalization, the partials are subject to large error bars, in particular  $S_{\text{NaCl}}(q)$ . The partial pair correlation functions  $g_{\text{NaNa}}(r)$ ,  $g_{\text{ClCl}}(r)$ , and  $g_{\text{NaCl}}(r)$  are shown in Figure 9.13. We observe that the homoatomic pair correlation functions  $g_{\text{NaNa}}(r)$  and  $g_{\text{ClCl}}(r)$  are nearly identical

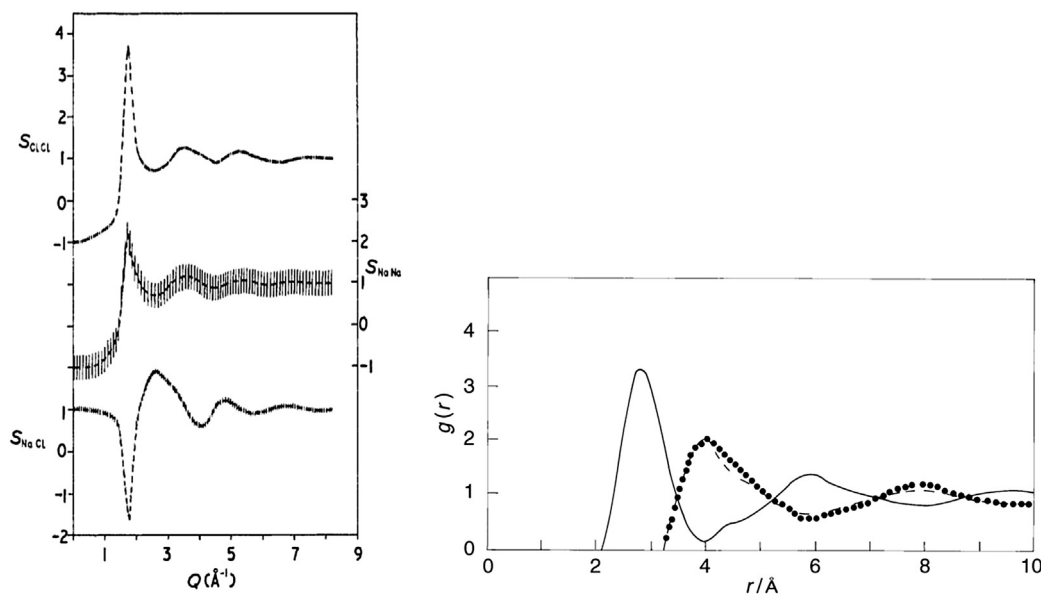


FIGURE 9.13 Partial structure factors  $S_{\alpha\beta}(q)$  (left) and pair correlation functions  $g_{\alpha\beta}(r)$  (right) of liquid NaCl at  $875^\circ\text{C}$ . The homoatomic pair correlation functions are in phase (dotted lines) and in phase opposition with the heteroatomic pair correlation function (full line).

**Table 9.9** Maxima and Minima of the Pair Correlation Functions of Liquid NaCl at 875 °C from [19]

Pair Corr. Function	1st Max (Å)	1st Min (Å)	2nd Max (Å)
$g_{\text{NaNa}}(r)$	3.8	5.8	7.7
$g_{\text{ClCl}}(r)$	3.7	6.0	7.7
$g_{\text{NaCl}}(r)$	2.6	3.8	5.7

with their maxima and minima in phase, whereas the heteroatomic pair correlation function  $g_{\text{NaCl}}(r)$  is in phase opposition. Table 9.9 shows the positions of the maxima and minima of the  $g_{\alpha\beta}(r)$ . The liquid shows an alternation of  $\text{Na}^+$  and  $\text{Cl}^-$  shells of ions like in crystalline NaCl. In conclusion, the ionic forces dominate the structure at the melting temperature. At higher temperatures or in less ionic systems, the balance between enthalpic and entropic terms may be different, and the conclusions are altered. This is the case, e.g., for liquid CuCl [59]. See, e.g., the review papers [54,55].

### 9.3.3 Normal and Anomalous Melting

Is there a qualitative difference between the SRO of a crystal and a liquid? In a large majority of cases, the chemical bond and the local structure of the liquid are similar to the crystal, and we define this as the normal melting. The liquid is, to a first approximation, similar to a high temperature crystal with 5–10 % of vacancies and, of course, no LRO. In some rare cases, mainly in group IV semiconductors and III-V compounds, qualitative and quantitative variations of the chemical bond and the local structure are observed. The melting is anomalous. In the normal melting, one observes a volume expansion, whereas in anomalous melting a contraction occurs. Let us recall the Clausius-Clapeyron formula:

$$\frac{dp}{dT} = \frac{L_f}{T(V_L - V_S)} \quad (9.38)$$

As the heat of fusion  $L_f$  is positive, the slope  $\frac{dp}{dT}$  is defined by the variation of volume at melting. For most systems,  $V_L - V_S$  is positive (normal melting) but there are important exceptions such as water, silicon, and germanium. See Figure 9.14. As we will see, their liquid structure is different from the crystalline structure, which has some consequences on the crystallization and amorphization. This difference can be characterized at the level of the structure factor  $S(q)$ .

#### 9.3.3.1 Liquid Metals and Rare Gases

In this case, the bonding is mainly isotropic and described by a pair potential  $V(r)$ , giving rise to compact structures with a high coordination number, e.g., 12 in FCC or HCP structures. The structure is mainly the result of steric hindrance: it is not possible to put more than 12 spheres in close contact with a central sphere. The liquid structure at short distances shows only small quantitative differences with respect to the crystal. The ratio  $q_2/q_1$  is in the range [1.80,1.86], and it has some similarities with the scattering of a

compact FCC structure. The  $q_1$  peak is a broadening of the (111) and (200) Bragg peak, whereas the  $q_2$  peak comes from the (220), (113), and (222) peaks. The interatomic distance is marginally the same and the number of nearest neighbors  $\bar{N}$  is lower than in a crystal by 5–10 %. Of course,  $\bar{N}$  is subject to uncertainties and, in addition, the comparison is difficult with semicompact structures (e.g., BCC) because there are two types of nearest neighbors. The main difference with the crystal is the dispersion of the interatomic separations shown in the first peak of  $g(r)$ .

The entropy of melting is the sum of two contributions due, respectively, to the disorder and to the volume variation at melting  $\Delta S_{melting} = S_{disorder} + S_{volume}$ . The configurational entropy of the disorder is equal to  $R \ln 2 \approx 1.4 \text{ cal/k}_B/\text{mole/K}$  [66], a value a little smaller than those observed in Table 9.10 for metals; the remaining entropy is due to the volume expansion.

**Table 9.10** Physical Parameters of Selected Elements and Binary Alloys

	Crystal Structure	$Z_C$	$T_m \cdot K$	$Z_I$	$\Delta V/V\%$	$\Delta r/r\%$	$q_2/q_1$	$S_{melt}$ cal/K/mole
Li	BCC	8(+6)	454	9.5	5	–	1.83	2.3
Na	BCC	8(+6)	371	10.4	2.5	2.7	1.85	1.7
Mg	HCP	12	923	10.9	4.1	0.6	1.82	2.3
Al	FCC	12	933	11.5	4.1	–1.4	1.85	2.7
Fe	BCC	8(+6)	1811	10.6	3.6	4	1.83	2.0
Cu	FCC	12	1358	11.3	4.2	0.82	1.82	2.3
Si	Diamond	4	1687	6.4	–10	6	2.07	7.1
Ge	Diamond	4	1212	6.8	–4.8	15	2.00	7.0
As	Trigonal	3(+3)	1090	3.5	10	0.0	1.53	–
Sb	Trigonal	3(+3)	904	6.3	1	–	1.96	5.3
Bi	Trigonal	3(+3)	544	8.8	–3.3	–	1.95	–
GaAs	Blende	4	1511	5.5	–11	–	2.1	4.7
InSb	Blende	4	800	6.3	–3.7	–	2.1	7.1
ZnTe	Blende	4	1512	3.7	8.0	–	1.7	3.9
CdTe	Blende	4	1314	3.7	0.7	–	1.72	3.8
HgTe	Blende	4	943	6.3	–3.3	–	2.11	4.5

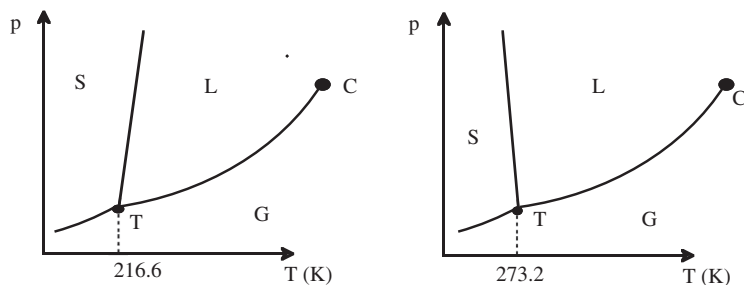


**FIGURE 9.14** Normal (left) and anomalous (right) melting.

### 9.3.3.2 Liquid Semiconductors

The case of covalent structures, mainly semiconductors, is totally different from the previous section. The most remarkable examples are Si and Ge. Their four-coordinated diamond structure is related to the directionality of the  $sp^3$  chemical bond, and their packing fraction is as low as  $\eta = 0.34$ . When melting, their interatomic separation increases by a value of the order of 10%, their coordination number increases by more than 50%, and their liquid density is higher than the solid. Indeed, the expected decrease of the density on the basis of the increased interatomic separations is more than compensated by the denser packing of the structure. The liquid structure is about six-coordinated with some similarities with the simple cubic or the  $\beta$ -Sn structure. The ratio  $q_2/q_1$  is higher than 2. The entropy of melting is three to four times higher than for metals. This seems contradictory at the first sight. Indeed, a decrease of the volume would give a higher order and a decrease in entropy. The increase of the interatomic distances and the loss of angular rigidity dramatically increases the entropy.

The III-V compounds are isoelectronic to Si and Ge. They have a four-coordinated zincblende crystalline structure. These compounds behave like Si or Ge (see [Table 9.10](#)); their coordination number increases also by about 50%, their ratio  $q_2/q_1$  is above 2, and their density increases upon melting. They undergo a transition from an  $sp^3$ -type bonding to a  $p$  bonding mechanism in the liquid.

By contrast, the II-VI compounds (ZnTe, CdTe) behave differently because of their higher ionicity. They melt by keeping their four-coordinated structure with a slight dilation. However, HgTe, which is less ionic, behaves the same way as silicon or GaAs.

In summary, the great majority of elements and compounds melt normally: The liquid keeps approximately the local order of the crystal with a decrease of both the coordination number and the density. The exceptions are the  $sp^3$ -bonded semiconductors, for which the open structure (diamond, zincblende, or wurtzite) shrinks upon melting into a denser structure.

## 9.4 X-ray Absorption: EXAFS

The absorption spectroscopy of X-rays (XAS) is an interesting alternative technique to analyze the local structure, particularly in noncrystalline materials [67,2,23,24]. It is a combination of photoemission and scattering of the photoelectron by the surrounding atoms. This X-ray technique has been developed almost exclusively on synchrotrons. A beam of X-rays of energy  $E$  is shined on the sample; the absorption coefficient  $\mu(E)$  is recorded as a function of the photon energy  $E$ . In condensed matter, above an ionization edge, usually a K- (or L-)edge, oscillations of the absorption coefficient are observed (see [Figure 9.15](#)). In the close vicinity of the absorption edge  $E_0$ , the structure is due to electronic transitions, it is called X-ray absorption near edge structure (XANES). About 100 eV above  $E_0$ , the domain of EXAFS oscillations starts. The XANES spectrum is sensitive to local site symmetry, charge state, and orbital occupancy. As the mean free path of the photoelectron is very small in condensed matter, EXAFS is sensitive to the local

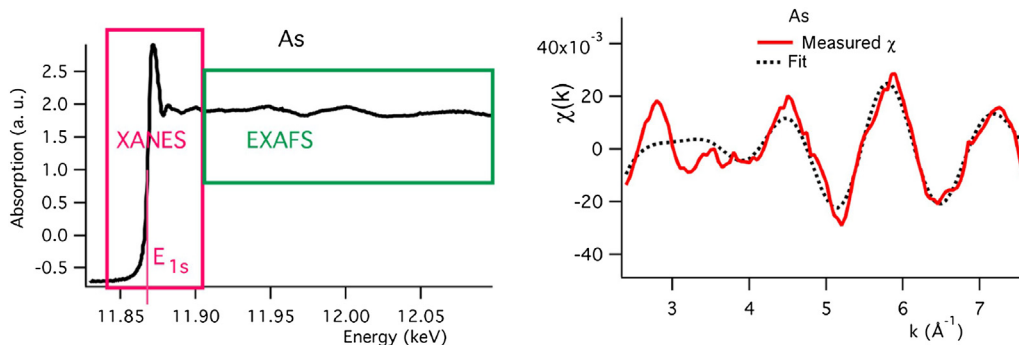


FIGURE 9.15 Left: Absorption spectrum of crystalline arsenic. Right, the EXAFS function  $\chi(k)$  versus the photoelectron wave vector  $k = \sqrt{2m(E - E_{1s})}/\hbar$  and a fit to Eqn (9.40).

environment (one or two shells of neighbors); consequently, the technique is well adapted to the study of noncrystalline materials [24]. The EXAFS spectroscopy exploits the interference of photoelectrons interacting with the potential of the surrounding atoms. From the interference pattern, it is possible to determine the distance and coordination number of the nearest neighbors of the photoabsorbing atomic species. The EXAFS spectroscopy is therefore an ideal element-selective local structural probe for investigating the average environment of specific elements in a liquid. However, the analysis of the X-ray absorption signal remains a challenging theoretical and numerical problem.

The EXAFS oscillations (Figure 9.15) originate from interferences of the photoelectron wave function along its various paths in the material. The simplest path (back and forth) is represented in Figure 9.16; its length is twice the interatomic separation  $2R$ . A photoelectron is emitted by an atom  $\alpha$ , backscattered on a neighboring atom  $\beta$  with a backscattering amplitude  $A_{\alpha\beta}(k)$ , which is element and energy (or  $k$ ) dependent, and

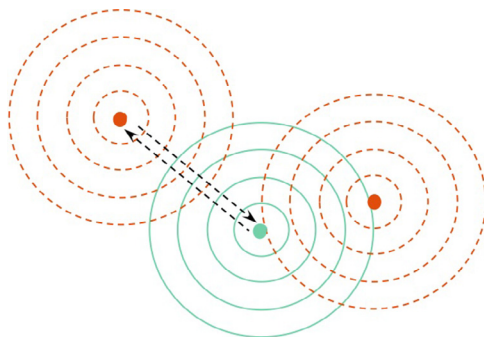


FIGURE 9.16 An EXAFS path (back and forth). An electron is photoemitted by the green atom  $\alpha$ , backscattered on a neighboring red atom  $\beta$  and reabsorbed by atom  $\alpha$ . The total length of the path of the electron is  $2R_{\alpha\beta}$ , twice the interatomic separation  $R_{\alpha\beta}$ .

comes back to the emitting atom  $\alpha$ .  $k$  is the modulus of the wave vector of the photoelectron,  $k = \sqrt{2m(E - E_{1s})}/\hbar$ . Longer paths also occur with a smaller amplitude but they will be neglected here for the sake of simplicity. The EXAFS equation is rather complex, and we present a compact version at the level of pair path. The EXAFS function  $\chi(k)$  is the normalized difference between the absorption coefficient  $\mu(E)$  in the condensed phase and the gaseous (or atomic) phase  $\mu_0(E)$ , generally a calculated or interpolated value.

$$\chi(k) = \frac{\mu(E) - \mu_0(E)}{\mu_0(E)} \Big|_{E = E(k)} \quad (9.39)$$

For a photoemitting atom of  $\alpha$  type and its neighbors  $\beta$ ,  $\chi(k)$  writes, to a first approximation:

$$\chi_\alpha(k) = \sum_{\text{neighbours } \beta} A_{\alpha\beta}(k) \sin[2kR_{\alpha\beta} + \phi_{\alpha\beta}(k)] \quad (9.40)$$

It looks like a Fourier sum (transform), with two differences: the wave number is  $q = 2k$  and a  $k$ -dependent phase shift  $\phi_{\alpha\beta}(k)$  appears. In most cases,  $\phi(k)$  has roughly a linear dependence in  $k$ :  $\phi(k) \sim -2ka$ , where  $a$  is a length of about 0.3–0.4 Å. Accurate calculations of the backscattered amplitude and the phase shift can be obtained by using various data reduction softwares [67]. From Eqn (9.40), the interatomic separations can be obtained with a good accuracy; they are related to the frequency of  $\chi(k)$ , but the coordination numbers, related to the amplitude of the signal, have larger standard deviations (of the order of units). Fortunately, the evolution of the structural parameters with external parameters (pressure, temperature) are safer as a cancellation of the errors takes place. The configurational average of Eqn (9.40), gives [24]

$$\chi_\alpha(k) = \sum_{\beta} 4\pi\rho_{\beta} \int_0^{\infty} r^2 g_{\alpha\beta}(r) A_{\alpha\beta}(k, r) \sin[2kr + \phi_{\alpha\beta}(k, r)] dr \quad (9.41)$$

where  $\rho_{\beta}$  is the atomic density of element  $\beta$ . By back Fourier transformation, the partial pair correlation functions  $g_{\alpha\beta}(r)$  are determined.

In summary, the EXAFS directly probes the interatomic distances; it is a local element sensitive technique of structural and chemical analysis that is well adapted to the study of noncrystalline materials. However, the analysis of the EXAFS spectra is difficult and needs some experience.

Using hard X-rays of synchrotrons, the EXAFS technique has been widely developed and applied to the investigations of liquid metals, semiconductors, molecular fluids, and solutions, e.g., the nucleation and crystal growth of Ni particles on an SiO<sub>2</sub> support has been successfully investigated by EXAFS [80].

In addition, thanks to the high brilliance of the synchrotrons, it is possible to focus the beam down to several tens of  $\mu m$  or less. This allows to perform EXAFS experiments under extreme pressures with a diamond anvil cell and to heat with a laser. Nearly six million times the atmospheric pressure (560 GPa) and 5000 K are now reachable by dynamic compression. This is of considerable interest for earth science

and for our understanding of the chemical bond under extreme conditions. We are now on the way to reproducing the thermodynamic conditions of the center of the earth [61]. In particular, the results provide first-hand information on the melting line of iron.

## 9.5 Production of Beams

Table 9.11 shows the different wavelengths of the quanta used in structural analysis.

### 9.5.1 X-ray Sources

The X-rays used in structural analysis have a wavelength of the order of the interatomic distances, more widely between 0.1 Å and 10 Å.

The relation between wavelength and energy of the photon is given by

$$\lambda(\text{Å}) = \frac{12.4}{E(\text{keV})} \quad (9.42)$$

A photon energy of 12.4 keV gives a wavelength of 1 Å, which is a relevant value for structural analysis.

X-rays are produced by accelerating electric charges (usually electrons) either in an X-ray tube in a lab (since Röntgen in 1896) or by using third-generation synchrotrons dedicated to structural analysis and spectroscopy [2].

In laboratory experiments, the  $\text{CuK}\alpha$  or  $\text{MoK}\alpha$  characteristic radiations are used with photons energies of 8.04 and 17.44 keV, respectively.

The brilliance (number of photons/s/mm<sup>2</sup>/steradian<sup>2</sup>/0.1%bandwidth) of synchrotrons is an ever-increasing function (Figure 9.17); roughly, it doubles every year. This opens many new possibilities (coherent beams, fast measurements and kinetics, small sample down to the nanometer range). A new field of research opens up every time another order of magnitude is gained! Hard X-rays allow using complex environments (high pressure cells, laser heating) that are interesting for studying liquids under extreme conditions. This is of great importance, e.g., in earth sciences.

Most synchrotrons produced many documents, including videos, that explain their operations (e.g., [http://www.aps.anl.gov/video/APS\\_Producing\\_Xrays/](http://www.aps.anl.gov/video/APS_Producing_Xrays/)).

**Table 9.11** Energies and Wavelengths of X-ray and Neutron Beams

Beam	Energy Range $E$	Wavelengths $\lambda$ (Å)
X-rays	1–100 keV	0.12–12
Hot neutrons	100–700 meV	0.35–0.9
Thermal neutrons	10–100 meV	0.9–3
Cold neutrons	0.2–10 meV	3–20

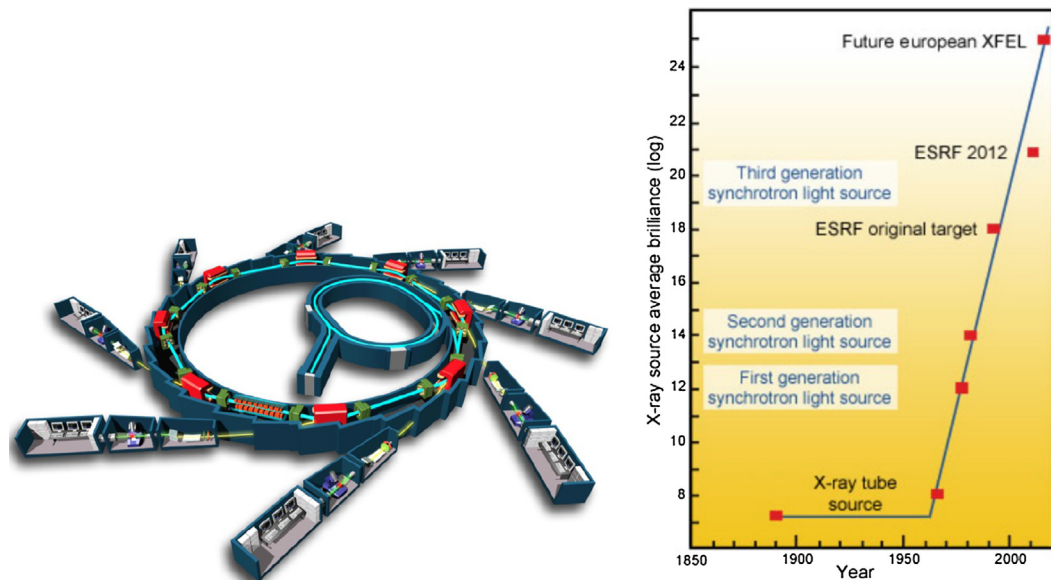


**FIGURE 9.17** Left: Schematic view of a synchrotron (Soleil, Paris). Starting from the center: linear accelerator, booster, storage ring, and experimental setups. Right: brilliance of X-ray sources in photons/s/mm<sup>2</sup>/steradian<sup>2</sup>/0.1% bandwidth along the years.

In the study of the structure of liquids, X-rays were the pioneers, then the neutrons took the advantage in the 1970s. More recently, synchrotron X-rays allow new opportunities because of their huge brilliance.

## 9.5.2 Neutron Sources

Neutrons are the most abundant elementary particles on earth in mass, but the production of free neutrons is not easy. Unlike X-rays, neutrons are produced almost only in large-scale facilities, national or international. There are two main production tools: fission reactors and spallation sources. Once produced, free neutrons have a lifetime of about a quarter of an hour (886 s), enough to perform scattering experiments. There are many neutron sources for research worldwide. A list is given in <http://www.ncnr.nist.gov/nsources.html>. The sources of neutrons are fully incoherent and their brilliance is orders of magnitude smaller than the synchrotron sources. At the Laue-Langevin Institute (ILL), the brightest steady-state source in the world, the unperturbed flux is  $1.5 \cdot 10^{15} \text{ n s}^{-1} \text{ cm}^{-2}$ .

The relation between energy  $E$ , wave vector  $k$  and wavelength  $\lambda$  is

$$E(\text{meV}) = 2.073k^2(\text{\AA}^{-2}) = \frac{81.82}{\lambda^2(\text{\AA}^2)} \quad (9.43)$$

The neutrons are massive particles and their de Broglie associated wavelength depends on their velocity, hence on their temperature. The average wavelength, in the Maxwellian distribution, follows the relation

$$\bar{\lambda}(\text{\AA}) = \frac{0.28}{\sqrt{E(\text{eV})}} = \frac{30.8}{\sqrt{T(\text{K})}} \quad (9.44)$$

where  $\bar{\lambda}$  is the average wavelength of the Maxwellian spectrum. Usually, neutrons are thermalized either in heavy water at room temperature (thermal neutrons) or in liquid hydrogen or deuterium at 20 K (cold neutrons) or heated on a block of graphite at 2000 K (hot neutrons). Table (9.11) shows the different wavelengths.

For the study of liquids and amorphous materials, the k-range should extend up to about  $10 \text{\AA}^{-1}$ , i.e., an energy of the order of 200 meV. Because neutrons penetrate deeply into matter, it is rather straightforward to use them even in complex and bulky sample environments. This is the case of high-temperature liquids that require a sample holder, a furnace, and possibly a vacuum vessel.

#### 9.5.2.1 Fission Reactors

Neutrons are produced by fission of  $^{235}\text{U}$ . The excited nucleus decays in a cascade of fission products, producing an average of 2.5 neutrons of about 2 MeV per  $^{235}\text{U}$  nucleus. Using a moderator (e.g.,  $\text{D}_2\text{O}$ ), the fast neutrons are slowed down to meV energies in order to sustain the nuclear chain reaction and to get neutrons with suitable wavelengths. The production of neutrons is at a constant rate. A schematic of neutron production in a fission reactor, slowed by  $\text{D}_2\text{O}$ , is shown in Figure 9.18.

#### 9.5.2.2 Spallation Sources

For different reasons (brilliance, safety), the new trend is to produce neutrons by spallation. High-energy protons generated in a linear accelerator hit a target of heavy metal: mercury, lead, uranium, or tungsten. The excited nucleus emits a wealth of particles, among others, 20 high-energy neutrons that are moderated. Unlike the reactors, the spallation source produces pulsed neutrons, because the protons are generated in

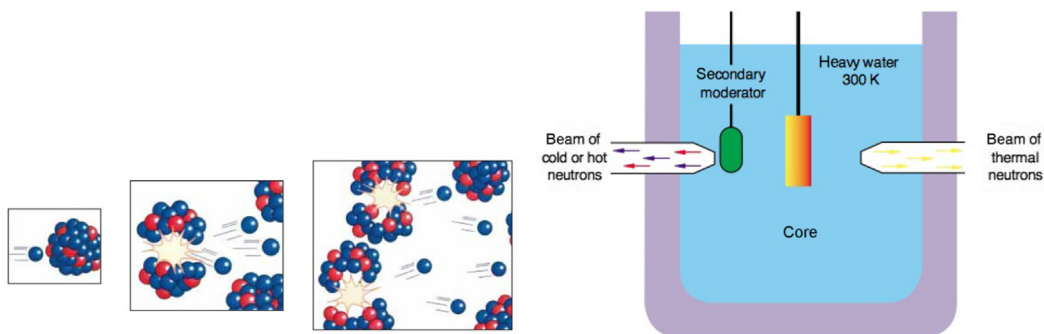


FIGURE 9.18 Neutrons are produced in the core of a steady-state reactor by the fission of  $^{235}\text{U}$ . The fast neutrons are slowed down by a moderator (here  $\text{D}_2\text{O}$ ).

bunches. Thanks to their time structure, the neutron energies are simply measured by a time of flight method. Spallation sources are operated in the United Kingdom (ISIS), the United States (SNS), Japan (J-SNS), and Switzerland (SINQ). Currently, in Lund, Sweden, a European spallation source (ESS) is being built, which will be around 30 times brighter than today's leading facilities. The ESS investment cost is estimated at approximately €1900 million (2013), with €140 million annual operations cost.

All these facilities are well documented, and a virtual tour of their operations can be found at <http://www.ill.eu/about/movies/presentation-movie/>.

## 9.6 Experimental Setups

### 9.6.1 Diffractometer

A liquid diffractometer is similar to a 2-axis powder diffractometer optimized to collect the maximum intensity at the expense of the angular or  $q$  resolution. Typically, it spans about  $150^\circ$  with an angular resolution of  $0.1^\circ$ – $0.2^\circ$ . In a steady-state reactor, wavelengths of  $0.7 \text{ \AA}$  and  $0.5 \text{ \AA}$  ( $q_{\text{max}} = 18 \text{ \AA}^{-1}$  and  $25 \text{ \AA}^{-1}$ ) are available from a hot source (Table 9.11) with a reasonable flux at the sample ( $5 \cdot 10^7 \text{ n cm}^{-2} \text{ s}^{-1}$ ). For special purposes, a wavelength of  $0.35 \text{ \AA}$  ( $q_{\text{max}} = 36 \text{ \AA}^{-1}$ ) can be obtained at the expense of the flux.

D4c at ILL [27] (Figure 9.19) is equipped with nine  $^3\text{He}$ -gas one-dimensional position-sensitive detectors. Typical counting statistics of 0.1% per  $0.125^\circ$  cell can be obtained in about three hours for a sample of average dimensions and scattering cross section.

### 9.6.2 Sample Environment

The sample environment is fairly complex for liquids, as one needs a sample holder, a furnace, most of the time, and possibly a pressure cell. All these materials diffract and absorb, and their contribution has to be subtracted.

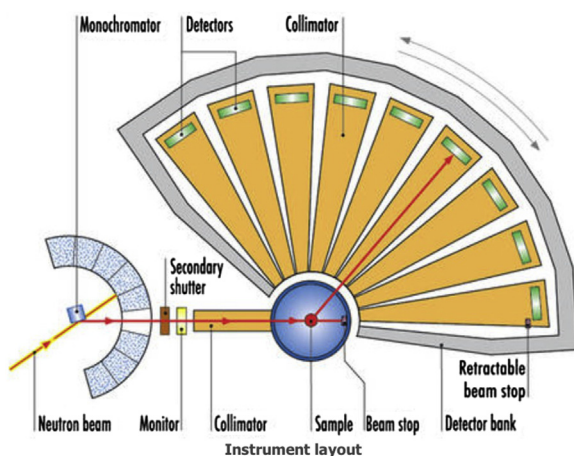


**FIGURE 9.19** The D4c diffractometer at the Laue-Langevin Institute ILL, (Grenoble) devoted to liquid and amorphous diffuse scattering. The  $2\theta$  range is  $[1.5^\circ, 140^\circ]$  with a resolution of  $0.125^\circ$ . The flux at the sample is  $5 \cdot 10^7 \text{ n cm}^{-2} \text{ s}^{-1}$ .

Still more complex sample environments are required if one needs high pressures. It opens new fields of research. For example, the complexity of the phase behavior above 100 GPa suggests extraordinary liquid and solid states of sodium [36,65] and has implications for other seemingly simple metals.

At the opposite, one may require the absence of container in order to avoid interfacial interactions and to get undercooled liquids, this is achieved e. g. by electromagnetic levitation [40].

## 9.7 Computer Simulations of Liquids

The use of computers to explore the structure and thermodynamic properties of liquids is almost as old as computers themselves [52,53]. First in two dimensions with hard sphere interactions, then in three dimensions with soft potentials, and now using ab initio quantum mechanical calculations, computer simulations contributed considerably to our understanding of liquids. Indeed, a system of interacting particles has no exact analytical solution: Many approximations (Percus-Yevick, hypernetted chain [38]) of such complicated systems needed to be tested by “computer experiments” to bridge the gap between scattering experiments and approximate theories. The ever-increasing computational power and memory of computers allowed considering more and more realistic descriptions at the atomic level. In addition, because of their time evolution, liquids demand huge computer resources. Some issues (large fluctuations, slow processes) are even now beyond the capabilities of existing computers. Crystal nucleation (and growth) remains still a difficult problem with current computers.

Many textbooks [1,30,46], review papers, and software packages have been published; here, we just recall some elementary facts. In this handbook, the field is covered in the chapters written by G. Gilmer, T. Ito, and W. Miller.

As we have seen, scattering experiments give access only to the pair correlation function. It is difficult, if not impossible, to go beyond experimentally.

Here, computers come into play. The strategy is in principle obvious. One generates atomic configurations at a given temperature, above the melting point for liquids or below for amorphous structures. The pair correlation function and the structure factor are computed and compared to the experimental results. If the agreement is fair, the structure is analyzed in detail, and higher order correlations (above the pair) are computed. If the agreement is unsatisfactory, other energetic models are tried up to satisfaction. The generation of configurations can be made either by a direct approach (Monte Carlo and molecular dynamics) or by the inverse approach (reverse Monte Carlo, RMC) and (empirical potential Monte Carlo, EPMC).

### 9.7.1 Direct Techniques: Monte Carlo and Molecular Dynamics

The interaction potential can be either an empirical isotropic 2-body potential, or a 3-body potential including angular forces or even higher order potentials. The so-called ab

initio methods involve interaction energies that are computed by solving the Schrödinger equation, with some assumption and hypothesis. The atoms are moved either randomly (Monte Carlo technique) or the equations of motion are solved (molecular dynamics).

As these methods are developed in detail in various chapters of this handbook, we limit ourselves to a short list of references [1,12,30,46] and some comments.

## 9.7.2 Inverse Techniques: RMC and EPSR

### 9.7.2.1 Reverse Monte Carlo

The idea is to generate atomic configurations that agree with the diffraction data to finely analyze the local orders. Earlier attempts were made in the study of substitutional disordered alloys [70,35]. An initial structure is guessed, in general not in agreement with experimental structure factor  $S(q)$ . Atoms are moved and exchanged, and the result is compared again with the experimental data. The move is accepted or rejected according to the Metropolis recipe [53] based on  $\chi^2$  test. If  $\chi^2$  is improved, the move is accepted; if not, it is accepted with some probability linked to the Boltzmann factor. For liquids, the technique has been developed by McGreevy et al. [49–51] and is widely used in various fields: atomic and molecular liquids, aqueous solutions, amorphous structures. X-ray, neutrons, and/or EXAFS data can be simultaneously handled. The technique is relatively simple, easy to use, and the software is freely available.<sup>4</sup> It can be used to determine the partial structure factors by combining neutron and an X-ray measurement without recourse to the cost-effective isotopic substitution.

In addition, RMC can be used to Fourier transform  $S(q)$ : by construction a clean  $g(r)$  is obtained without spurious cutoff oscillations in the small  $r$  domain. Some discussion arose concerning the uniqueness of the solution and the relevance of the solution in the absence of interaction energy or static hindrance.

Indeed, the number of data points (hundredths) is far smaller than the number of coordinates (thousands of atoms). More recent versions include constraints (distance of closest approach, condition on the valence angles) and bonded and nonbonded potentials.

### 9.7.2.2 Empirical Potential Monte Carlo

This technique, previously called empirical potential structure refinement (EPSR), has been developed by Soper [71]. It has some similarities to RMC but it includes an extra loop so as to allow a refinement of the interatomic potentials. One begins with a structure obtained via Monte Carlo simulation at the experimental density and temperature with realistic trial reference potential  $U_{\alpha\beta}^{ref}(r)$  that is generally a linear combination of a Lennard-Jones potential and an electrostatic term. The partial pair correlation functions are computed and compared to the data and the starting potentials refined. This procedure is continued until convergence of simulation with data occurs. It is straightforward to use with molecular systems. This technique has been applied

<sup>4</sup><http://www.szfi.hu/nphys/rmc++/downloads.html>

successfully to water, whether liquid or amorphous [26], ionic liquids, or organic molecules (e.g., butanol) in water [11–13].

## 9.8 Characterizations Beyond $g(r)$

The scattering experiments give information at the level of the pair with, in favorable cases, a possible access to the partial pair correlation functions  $g_{\alpha\beta}(r)$ ; with the help of computer simulations, one can go far beyond that description as all the positions of the atoms are known. As an example, we consider a system that requires an analysis above the pair. Many covalent elements or alloys have a low coordination due to a quantum mechanical symmetry breaking mechanism (Peierls distortion) that leads to the octet rule [34]. For instance, As has a coordination 3 and Te has a coordination 2. The Peierls distortion or spontaneous symmetry breaking mechanism is well known in crystals [60].

### 9.8.1 Distribution of first, second...neighbors

We show in Figure 9.20 the temperature evolution of liquid  $\text{As}_2\text{Te}_3$ . To analyze in great detail the structural evolution of the liquid with temperature or pressure, it is interesting to decompose the first peak of  $g(r)$  into its series of nearest neighbors (not in the common sense). This is done as follows. An atom is chosen and its distance to its (single) first neighbor is determined. The process is repeated for all the atoms at any time step in the course of the simulation. One has, in such a way, the distribution of the (very) first neighbors. The same can be done for the second, third...neighbors. The first peak of  $g(r)$

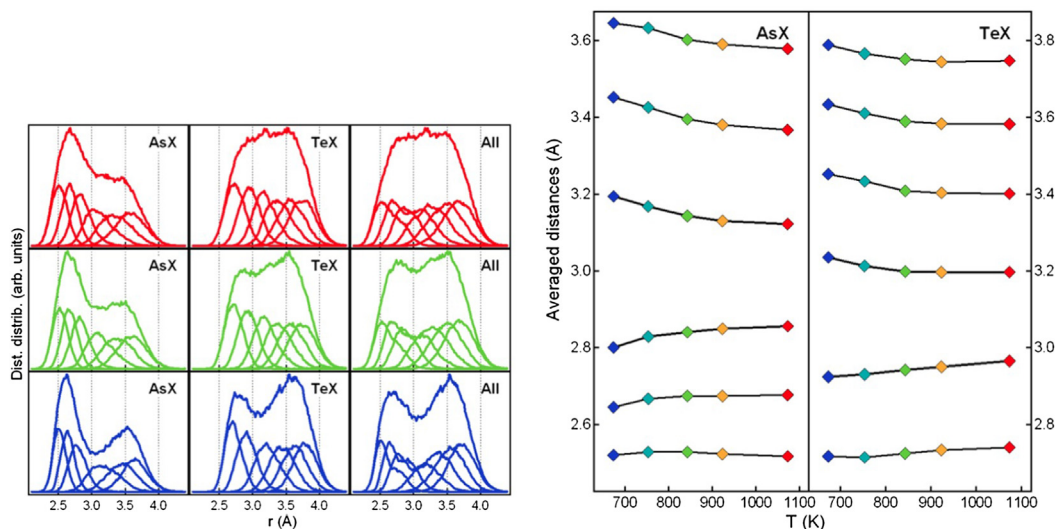


FIGURE 9.20 Distribution of first, second...neighbors in liquid  $\text{As}_2\text{Te}_3$  as a function of the temperature. The evolution of the maxima of the different curves is shown in the right panel. We see the continuous evolution of the Peierls distorted structure (3 short and 3 long neighbors for the As atoms, 2 and 4 neighbors for Te) to a nondistorted structure (six neighbors continuously distributed).

is decomposed into subpeaks (Figure 9.20). The position and width of the subpeaks are determined.

We show that the Peierls distortion may survive in liquids. Indeed, in the right panel of Figure 9.20, just above the melting point, the As atoms are 3 (+3) coordinated and the Te atoms are 2 (+4) coordinated. For As, we observe one bundle of three short nearest neighbors and a complementary bundle of three longer nearest neighbors. When the temperature increases, the distribution of neighbor changes and the two bundles of three atoms merge into a continuous distribution of the six distances. The same holds for Te atoms. This occurs when  $k_B T$  exceeds the Peierls distortion energy. In addition, a negative thermal expansion of liquid  $\text{As}_2\text{Te}_3$  is observed in this temperature range [57].

### 9.8.2 3-Body Correlations

In the crystal of  $\text{As}_2\text{Te}_3$ , one observes an alternation of short and long bonds nearly aligned. Is this effect, attributed to the periodicity, still present in a liquid? To analyze

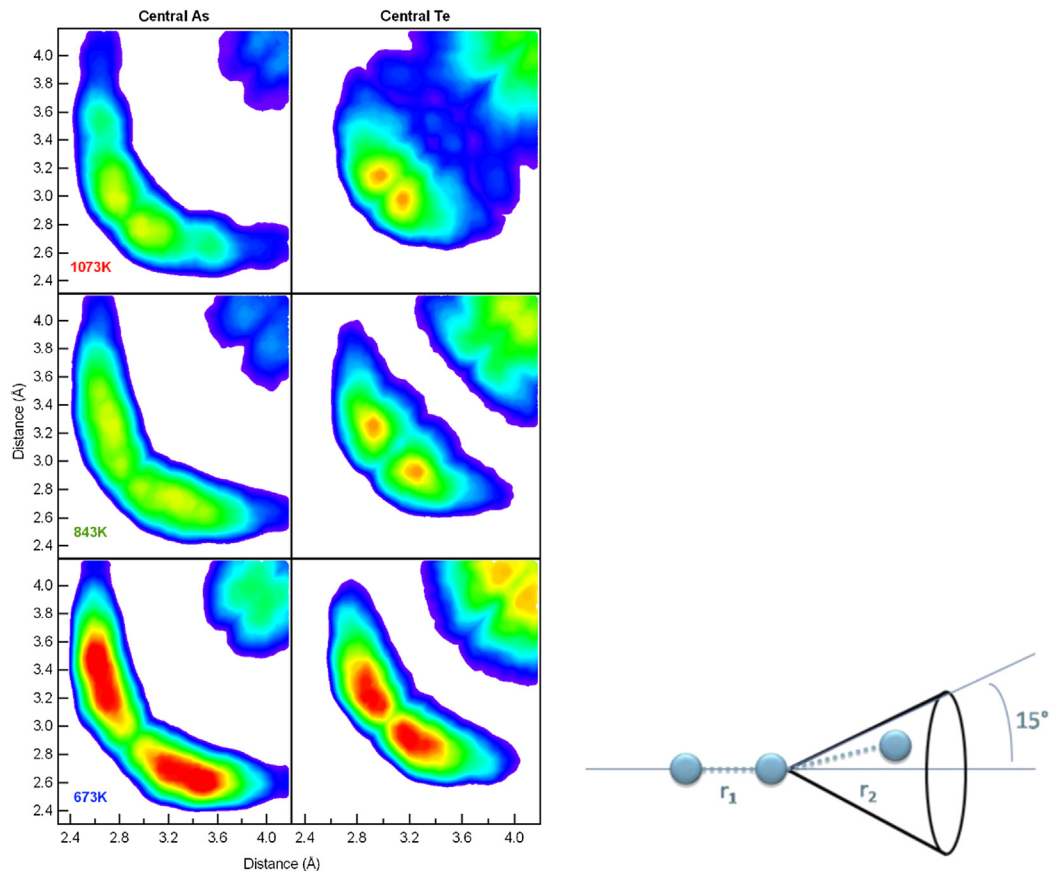


**FIGURE 9.21** Probability density of the occurrence of a pair of distances  $(r_1, r_2)$  nearly aligned. At “low” temperature, a clear symmetry breaking is observed (alternation of short and long bonds) while at higher temperatures, the two-peak structure vanishes (As) or is strongly reduced (Te).

this effect, the correlation of the distance of two successive bonds is analyzed. Based on a density functional theory (DFT) calculation, Figure 9.21 shows the probability of having a pair of distances  $(r_1, r_2)$  nearly aligned in  $\text{As}_2\text{Te}_3$  alloys. We see that at low temperatures the distortion exists, but at higher temperatures it disappears [57], in agreement with Figure 9.20. In conclusion, if the thermal energy  $k_B T$  is lower than the Peierls energy (the energy gained in the symmetry breaking process), then the system is still distorted in the liquid phase.

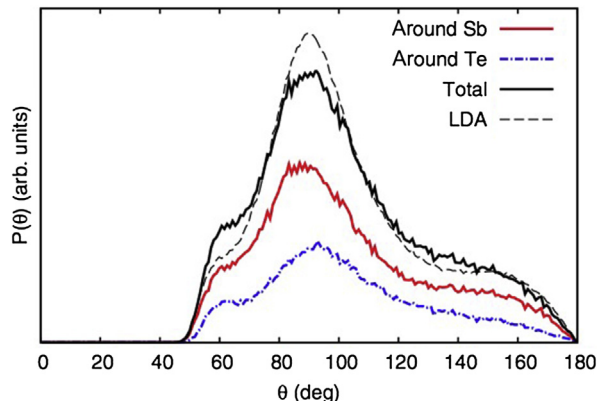
### 9.8.3 Angular Distributions

In computer simulations, from the atomic coordinates, it is possible to compute any correlation function. The limitation comes from the number of parameters and the possibility to represent a picture. The 3-body correlation function  $g(\vec{r}_1, \vec{r}_2, \vec{r}_3)$  contains, in principle, nine variables! The distribution of valence angles is easy to obtain in simulated structures: one selects an atom and two of its neighbors. The distance cutoff is a crucial parameter. Whether the central atom in an octahedral ( $\theta \sim 90^\circ$ ) or in a tetrahedral ( $\theta \sim 120^\circ$ ) environment is an interesting issue, in particular in covalent amorphous structures like liquid  $\text{Sb}_2\text{Te}_3$ . The broad peaks at 90 and around 170 indicate the presence of an octahedral-like geometry similar to that of the crystalline phase, in agreement with the criterion  $S(q_2)/S(q_1)$  of Ref. [74] (Figure 9.22).

## 9.9 Supramolecular Liquid Structures

Up to now, we discussed the structure of liquids at the atomic level, with the Å as a unit. During the last decades, soft condensed matter grew fantastically with particular emphasis on complex systems such as polymers, colloids, and liquid crystals. In this field, one finds similar issues and problematics to the atomic liquids but at different (larger) length scales [8,39]. For instance, in the semidiluted solution of identical spherical micelles schematized in Figure 9.23, the total coherent scattered intensity  $I(q)$

FIGURE 9.22 Angle distribution functions of  $l\text{-Sb}_2\text{Te}_3$ .



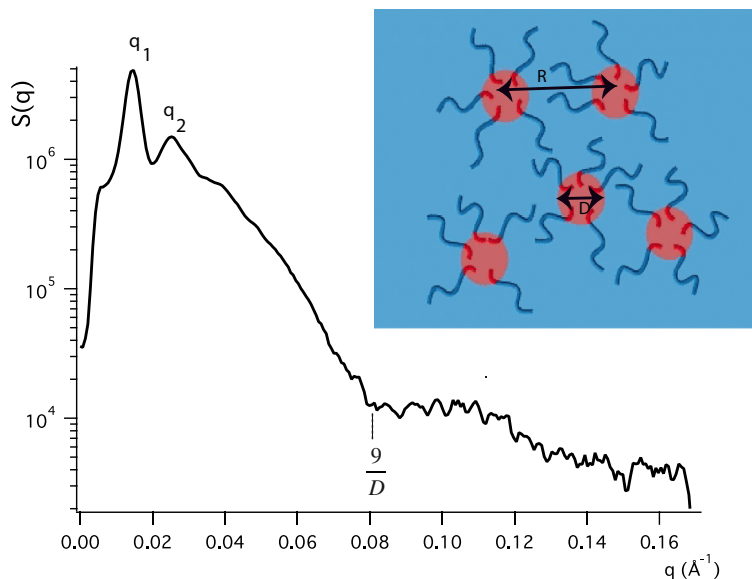


FIGURE 9.23 Diffraction pattern of a semidilute (10%) solution of inverted micelles of PS-PAACs.

is the product of the scattered intensity  $I_{mic}(q)$  of a single micelle by the structure factor  $S(q)$  of the center of the micelles (Eqn 9.45). Two reference lengths are present: the diameter  $D$  of the micelles and the intermicellar spacing  $R$ . Typical values are tens or hundredths of  $\text{\AA}$ , consequently the structures in the  $q$  domain are scaled to  $2\pi/D$  and  $2\pi/R$ , respectively. We are in the so-called small angle scattering regime (SAXS), in fact it is a small  $q$  regime [68].

$$I(q) = S(q)I_{mic}(q) \quad (9.45)$$

We illustrate this in Figure 9.23 by a 10% solution in toluene of the diblock copolymer polystyrene-*b*-polyacrylate of Cs. This gives rise to an inverted micelle. The core is made of polyacrylate of Cs and the hair is polystyrene, which shows nearly no contrast with toluene.

The structure factor  $S(q)$  of the supramolecular liquid is similar to the structure factor of an atomic liquid, and the form factor of a single micelle  $I_{mic}(q)$  is analogous to the atomic form factor of an atom in X-ray scattering. Of course, the  $r$  and  $q$  scales differ by orders of magnitude. The wavelength has to be adapted to this new length scale and, for neutron scattering, one has to use long wavelength neutrons thermalized in a cold source (Table 9.5 and Eqn 9.44). The diameter  $D$  of the core of the micelle is determined by the first minimum occurring at  $q_{min} = \frac{9}{D}$  while the fast oscillations are related to the intermicellar separations  $R$ . Here,  $D \cong 110 \text{ \AA}$  and  $R = \frac{2\pi}{q_2 - q_1} \cong 600 \text{ \AA}$ .

In addition, SAS allows to determine the degree of crystallinity, e.g., in semicrystalline polymers [68].

Furthermore, SAXS is an interesting tool for following the changes induced by the crystallizing agents in different physicochemical conditions, mainly in protein

crystallization. Furthermore, the coupling of SAXS and numerical simulations characterizes the interaction potential of biological molecules [25,77].

## 9.10 Quasielastic and Inelastic Scattering

The total scattering (static approximation) gives an average of snapshots of the structure. In favorable cases, the partial pair correlation functions are determined and the study is complemented by computer simulations. Inelastic scattering adds interesting information on the dynamics of the liquid in two energy regimes:

- Quasielastic scattering
- Inelastic scattering

### 9.10.1 Quasielastic Scattering

Quasielastic scattering involves very small energy transfers (tens of  $\mu\text{eV}$ ) that are related to the diffusion of atoms in the liquid state. With a time of flight spectrometer, it is possible to measure energy changes even very close to the elastic peak. Diffusion is described by the self incoherent structure factor  $S_s(q, \omega)$  [9,10]. At short length and time scales, a free ballistic motion of the atom is observed; at intermediate length and time scales, the motion of the atoms is governed by Fick's law and a diffusion coefficient  $D$  can be measured from the quasielastic signal. Finally, the long-time behavior is governed by the confinement effects.

### 9.10.2 Inelastic Scattering

The true inelastic scattering corresponds to vibrations (of the order of tens of  $\text{meV}$ ). In a liquid, an atom vibrates in the cage of its neighbors. By contrast to the crystal where extended eigenmodes, the phonons, are described by dispersion relations  $\omega(q)$ , the liquid shows localized modes with a finite lifetime. However, a density of vibrational modes  $g(\omega)$  can be defined and measured. It gives information on the strength of the interaction potential as  $\omega \sim \sqrt{k/m}$  where  $k$  is a force constant and  $m$  a mass. The inelastic signal in liquids is mostly due to the self incoherent contribution  $S_s(q, \omega)$ . The coherent inelastic scattering exists in principle in liquids but it is strongly damped except in quantum liquids due to the superfluid LRO. The distribution of vibrational modes can be measured by neutron or X-ray inelastic techniques.

## 9.11 Conclusions

The study of the structure of liquids at the atomic level is a difficult issue because of the disorder inherent to liquids and because of the poverty of the information content of the scattering signal. However, by a combination of different techniques, and the crucial help of computer simulations, it is possible to gather important information on the local

structure of liquids, its spatial extent, and its variations as a function of the external parameters such as the temperature or the pressure.

## Acknowledgments

The author thanks the Belgian Fonds National de la Recherche Scientifique for support, the Institut Laue–Langevin for hospitality during the writing of the manuscript, and Dr. Christophe Bichara for a critical reading of the manuscript.

## References

- [1] Allen MP, Tildesley DJ. *Computer simulation of liquids*. Oxford: Oxford University Press; 1987.
- [2] Als-Nielsen J, McMorrow D. *Elements of modern X-Ray physics*. New York: Wiley; 2001 [Weinheim: Wiley-VCH].
- [3] Ashcroft NW, Langreth DC. *Phys Rev* 1967;156(3):685–92. *Phys Rev*, 159(3):500–510(1967), *Phys Rev*, 166(3):934 (1968).
- [4] Bacon GE. *Neutron diffraction*. 3rd ed. Oxford: Clarendon; 1975.
- [5] Bhatia AB, Thornton DE. *Phys Rev B* 1970;2(8):3004–12.
- [6] Barnes AC, Lague SB, Salmon PS, Fischer HE. *J Phys Condens Matter* 1997;9:6159.
- [7] Hippert F, Geissler E, Hodeau JL, Lelievre-Berna E, Regnard JR. *Neutron and X-ray Spectroscopy*, Grenoble Sciences and Springer. 2006.
- [8] Barrat JL, Hansen JP. *Basic concepts for simple and complex liquids*. Cambridge University Press; 2003.
- [9] Bee M. *Quasielastic neutron scattering*. Bristol: Adam Hilger; 1988.
- [10] Blech IA, Averbach BL. *Phys Rev* 1965;137:1113.
- [11] Bowron DT, Moreno SD. *J Phys Condens Matter* 2003;15:S1217.
- [12] Car R, Parrinello M. *Phys Rev Lett* 1985;55:2471.
- [13] Chen SH, Kotlarchyk M. *Interactions of photons and neutrons with matter*. World Scientific; 2002.
- [14] Dahlborg U, Kunsch B. On the Placzek correction for simple liquids and gases. *Phys Chem Liq* 1983; 12(3):237–54.
- [15] Debye P. *Ann Phys* 1915;46:809.
- [16] Dianoux A-J, Lander G. *Neutron data booklet*. 2nd ed. OCP Science; 2003. <http://www.ill.eu/quick-links/publications/>.
- [17] Dore JC, Webber B, Hartl M, Behrens P, Hansen T. Neutron diffraction studies of structural phase transformation for water-ice in confined geometry. *Phys A* 2002;314:501–7.
- [18] Ducastelle F. *Order and phase stability in alloys*, vol. 3. Amsterdam (New York): North-Holland; 1991.
- [19] Edwards FG, Enderby JE, Howet RA, Page DI. *Phys C Solid State Phys* 1975;8.
- [20] Egelstaff PA. *An introduction to the liquid state*. 2nd ed. Oxford: Oxford University Press; 1992.
- [21] Enderby JE, North DM, Egelstaff PA. The partial structure factors of liquid Cu-Sn. *Philos Mag* 1966; 14:961.

- [22] Faber TE, Ziman JM. *Philos Mag* 1965;11:153–73.
- [23] Filippini A, Di Cicco A, Natoli CR. X-ray absorption spectroscopy and n-body distribution functions in condensed matter. *Phys Rev B* 1995;52(21):15122–48.
- [24] Filippini A. *J Phys Condens Matter* 2001;13:R23–60.
- [25] Finet S, Tardieu A. *J Cryst Growth* 2001;232:40–9.
- [26] Finney JL, Hallbrucker A, Kohl I, Soper AK, Bowron DT. *Phys Rev Lett* 2002;88:225–503.
- [27] Fischer HE, Cuello GJ, Palleau P, Feltin D, Barnes AC, Badyal YS, et al. *Appl Phys A* 2002;74:S160–2.
- [28] Fischer HE, C Barnes A, Salmon PS. *Rep Prog Phys* 2006;69:233–99.
- [29] *Handbuch der Physik*, vol. 32. Berlin: Springer; 1957. p. 238–320.
- [30] Frenkel D, Smit B. *Understanding molecular simulation*. New York: Academic Press; 2002.
- [31] Furrer A, editor. *Complementarity between neutron and synchrotron X-Ray scattering*. Singapore: World Scientific; 1998.
- [32] Furrer A, Mesot J, Strässle T. *Neutron scattering in condensed matter physics*. World Scientific; 30 June 2009. p. 301.
- [33] Egelstaff PA. In: Price DL, Sko K, editors. *Methods of experimental physics. Neutron scattering*, vol. 23. London and New York: Academic; 1987. p. 40570. part B, [chapter 14].
- [34] Gaspard JP, Pellegatti A, Marinelli F, Bichara C. *Philos Mag B* 1998;77:727.
- [35] Gerold V, Kern J. *Acta Metall* 1987;35:3939.
- [36] Gregoryanz E, Lundegaard LF, McMahon MI, Guillaume C, Nelmes RJ, Mezouar M. *Science* 2008; 320(5879):1054–7. 23.
- [37] Gurman SJ. In: Fairbanks MC, et al., editors. *Neutron and X-Ray scattering: complementary techniques*. IOP conference series, vol. 101. Bristol: IOP Publishing; 1990. p. 2540.
- [38] Hansen JP, McDonald I. *Theory of simple liquids*. 4th ed. Academic Press; 2013.
- [39] Hansen JP, Levesque D, Zinn-Justin J. *Liquides, cristallisation et transition vitreuse*. NATO Advanced Study Institute North Holland; 1991.
- [40] Holland-Moritz D, Stber S, Hartmann H, Unruh T, Hansen T, Meyer A. *Phys Rev B* 2009;79(064204).
- [41] Hennem L, Thiaudiere D, Landron C, Melin P, Price DL, Berar J-F, et al. *Appl Phys Lett* 2003;83:3305.
- [42] Hruszkewycz SO, Sutton M, Fuoss PH, Adams A, Rosenkranz S, Ludwig KF, et al. *Phys Rev Lett* 2012; 109:185502.
- [43] Jal JF, Mathieu C, Chieux P, Dupuy J. *Philos Mag B* 1990;62:351.
- [44] Johnson PAV, Wright AC, Sinclair RN. *J Non-Cryst Solids* 1983;58:109.
- [45] Kittel C. *Introduction to solid state physics*. 8th ed. Wiley; 2005.
- [46] Krauth W. *Statistical mechanics, algorithms and computations*. Oxford: Oxford University Press; 2006.
- [47] Lorsch E. *J Phys C Solid State Phys* 1969;2:229.
- [48] Lovesey SW. *Theory of neutron scattering from condensed matter*, vol. 1; 1984. 310 pages.
- [49] McGreevy RL, Pusztai L. *Mol Simul* 1988;1:359–67.
- [50] McGreevy RL, Pusztai L. *Proc R Soc London A* 1990;430:241.
- [51] McGreevy RL. Reverse monte carlo modelling. *J Phys Condens Matter* 2001;13:R877–913.
- [52] Metropolis N, Ulam S. The Monte-Carlo method. *J Am Stat Assoc* 1949;44:335–41.
- [53] Metropolis N, Rosenbluth AW, Rosenbluth MN, Teller AH, Teller E. Equation of state calculation by fast computing machines. *J Chem Phys* 1953;21:1087–92.

- [54] Neilson GW, AK Adya. *Annu Rep Prog Chem Sect C Phys Chem* 1996.
- [55] Neilson GW, Adya AK, Ansell S. *Annu Rep Prog Chem Sect C Phys Chem* 2002;98:273–322.
- [56] Nugent KA. Coherent methods in the X-ray sciences. *Adv Phys* 2010;59(1):1–99.
- [57] Otjacques C, Raty JY, Hippert F, Schober H, Johnson M, Ceolin R, et al. *Phys Rev B* 2010;82(054202).
- [58] Paalman HH, Pings CJ. *J Appl Phys* 1962;33:2635.
- [59] Page DI, Mika K. *J Phys C* 1971;4:30–4.
- [60] Peierls RE. *Quantum theory of solids*. Oxford: Clarendon; 1955. viii, 229 pp.
- [61] Ping Y, Coppari F, Hicks DG, Yaakobi B, Fratanduono DE, Hamel S, et al. *Phys Rev Lett* 2013; 111(065501).
- [62] Placzek G. *Phys Rev* 1952;86:377.
- [63] Poirier J-P. *Introduction to the physics of the Earth's interior*. 2nd ed. 2000.
- [64] Brown PJ, Fox AG, Maslen EN, O'Keefe MA and Willis BTM. *International Tables for Crystallography* (2006). Vol. C, ch. 6.1, pp. 554–595.
- [65] Raty J-Y, Schweigler E, Bonev SA. *Nature* 2007;449:448–51.
- [66] Rivier N, Duffy DM. *J Phys C* 1982;15:2867.
- [67] Rehr JJ, Albers RC. Theoretical approaches to X-ray absorption fine structure. *Rev Mod Phys* 2000; 72:621–54. <http://www.feffproject.org>.
- [68] Roe RJ. *Methods of X-Ray and neutron scattering in polymer science*. Oxford University Press; 2000.
- [69] Salmon PS, Petri I, de Jong PHK, Verkerk P, Fischer HE, Howells WS. *J Phys Condens Matter* 2004;16: 195–222.
- [70] Schweika W, Haubold H-G. *Phys Rev B* 1988;37:92408.
- [71] Soper AK. *Chem Phys* 1996;202:295–306.
- [72] Soper AK, Egelstaff PA. *Nucl Instr Meth* 1980;178:415–25.
- [73] Squires GL. *Introduction to the theory of Thermal neutron scattering*. Cambridge: Cambridge University Press; 1978.
- [74] Steimer C, Coulet V, Welnic W, Dieker H, Detemple R, Bichara C, et al. *Adv Mater* 2008;20:4535.
- [75] Svergun DI, J Koch MH. *Rep Prog Phys* 2003;66:1735–82.
- [76] Svergun DI, Koch MHJ, Timmins PA, May RP. *Small angle X-Ray and neutron scattering from solutions of biological*. Oxford Scholarship Online; 2013.
- [77] Tardieu A, Finet S, Bonnetè F. *J Cryst Growth* 2001;232:19.
- [78] Van Hove L. *Phys Rev* 1954;95:1374–84.
- [79] Warren BE. X-ray determination of the structure of Glass. *J Am Ceram Soc* 1934;17:249.
- [80] Yanga JC, Shula YG, Louis C, Che M. *Catal Today* September 30, 1998;44(14):315–25.

# Monte Carlo Simulations of Crystal Growth

Luis A. Zepeda-Ruiz<sup>1</sup>, George H. Gilmer<sup>2</sup>

<sup>1</sup>PHYSICAL AND LIFE SCIENCES DIRECTORATE, LAWRENCE LIVERMORE NATIONAL LABORATORY, LIVERMORE, CA, USA; <sup>2</sup>MECHANICAL ENGINEERING DEPARTMENT, COLORADO SCHOOL OF MINES, GOLDEN, CO, USA

## CHAPTER OUTLINE

<b>10.1 Introduction</b> .....	<b>445</b>
<b>10.2 Monte Carlo Model Description</b> .....	<b>448</b>
<b>10.3 Deposition on a Spherical Crystal Seed</b> .....	<b>450</b>
10.3.1 Faceting during Deposition of Metals .....	450
10.3.2 Effect of Deposition Rate .....	451
<b>10.4 Nucleation of Films on Foreign Substrates</b> .....	<b>452</b>
10.4.1 Effect of Wetting .....	452
10.4.2 Effect of Temperature .....	453
10.4.3 Effect of Inhibited Diffusion over Steps .....	454
<b>10.5 Film Growth</b> .....	<b>455</b>
10.5.1 Effect of Wetting .....	455
10.5.2 Effect of Temperature .....	457
10.5.3 Effect of Inhibited Diffusion over Steps .....	457
10.5.4 Strategy to Grow a Smooth Film .....	459
<b>10.6 Texture Development</b> .....	<b>460</b>
<b>10.7 Physical Vapor Deposition and Step Coverage</b> .....	<b>462</b>
<b>10.8 Size and Habit Evolution of Molecular Crystals</b> .....	<b>466</b>
<b>Auspices</b> .....	<b>472</b>
<b>References</b> .....	<b>472</b>

## 10.1 Introduction

In the last several decades, atomistic simulations have contributed enormously to our understanding of crystal growth mechanisms. In most cases, elucidating these mechanisms involves simulating the motion of a large number of atoms. Heavy computational

power is required to bridge the gap between the atomistic length scale and mesoscopic regions that are large enough to accommodate the basic crystal growth mechanisms. An example is growth on a facet, requiring the nucleation of two-dimensional (2D) clusters. The computational cell must contain the critical nucleus and a region surrounding it sufficiently large so that boundary effects are negligible. On one hand, the size of the critical nucleus depends on the driving force, and increases without limit as the driving force approaches zero. But deposition rates close to equilibrium can often be obtained by extrapolation from data obtained using higher driving forces. On the other hand, extremely high driving forces are often employed in magnetron sputtering chambers used in industrial manufacturing. In this case, the critical nuclei are small, but morphological instabilities often produce mounding and columnar growth structures that can reach sizes of several microns. A limiting factor with atomistic simulations is the efficiency of computers. During the last three decades, the efficiency of computers measured in computations per kilowatt hour has increased by a factor of  $10^4$  [1–3]. Simulations that were impossible several years ago are now common at many universities and laboratories.

In this chapter, we discuss physical vapor deposition (PVD) of crystals and films under a variety of conditions, using Monte Carlo (MC) simulations. We treat a small number of specific materials, but the mechanisms involved are often similar to crystallization phenomena observed in a large number of materials. Atomistic models of thin-film deposition and crystal growth have the advantage that the crystal lattice structure and atomic interactions are implicit in the models. For this reason, important phenomena such as faceting, grain-boundary grooves at growing surfaces, and polycrystalline microstructures are natural consequences of the simulations and do not require artificial constraints. Results of these models have played a central role in the understanding of the surface roughening transition and its effect on crystal growth kinetics. In addition, the influence of dewetting of films deposited on a foreign substrate, the formation of pinholes, have been successfully investigated using these simulations. In this chapter, we review some of these applications and discuss MC modeling of sputter deposition of thin films based on materials parameters derived from first principles and molecular dynamics (MD) methods. Our models of deposition are large enough to exhibit clustered, columnar, and polycrystalline film structures. Applications to device fabrication are discussed based on simulations of film deposition onto substrates with topologies that include vias and trenches and their extension to the length scale of real devices.

The morphology of a thin film is influenced by the structure and properties of the substrate, the conditions that prevail during deposition, and transport properties such as diffusion rates on different crystallographic orientations. One of the most effective models that can match these diverse properties is based on MC simulations of kinetic lattice models. This approach has been used to study crystal growth and surface roughening on close-packed surfaces [4–6], the formation of 2D and 3D islands during the initial stages of film growth by PVD [7–14], the columnar microstructure formed at

low-temperature PVD [15], and the trapping of defects, impurities, and of concentrations of the different species in a growing alloy [16,17]. Complex crystals, such as urea growth from solution, have also been modeled using MD and MC simulations [18,19]. This type of model has the advantage of fast computation because of the simplicity of the MC events, but at the same time it can include accurate rates for atomic diffusion and other mechanisms based on more detailed simulations by MD or first principles methods (details of our implementation of the model are given in the bibliography [20]). The MD simulations can be used to obtain rates for processes that control and limit the growth process: diffusion rates, defect production, sputtering yields, and other information needed to match real materials. The book “Kinetic Processes” by K. A. Jackson has excellent discussions of MC modeling of the kinetics of crystal growth, together with experiments [21], and “Physics of Crystal Growth” by Pimpinelli and Villain treats theoretical aspects of crystal growth phenomena [22].

Most of the models developed to simulate the evolution of surfaces in three dimensions are based on continuum equations. Level set continuum models are treated in a book by J. A. Sethian [23]. Models have been developed specifically for the morphology of step coverage for various amounts of surface diffusion and angular distributions (EVOLVE [24,25]). The thickness of barrier layer films can be assessed by the use of these models, and this can be crucial for applications involving features with high aspect ratios; other continuum models are the level set method [26], SPEEDIE [27], and the grain-growth model [28]. These models allow fast exploration of conditions and are able to treat structure development on macroscopic length scales. Discrete atomistic and cluster models have also been applied to study issues related to metallization [29,30].

Although the continuum models incorporate 3D features, complete simulations with microstructure development during growth including micro-voids and grain boundaries are dependent on data from atomistic modeling or detailed data from experiments. This is a difficult task because of the large number of parameters controlling mass transport, interface properties affecting wetting, and surface faceting. Atomistic models have the advantage that most of these parameters are implicit in the interatomic potential, and are not dependent on other simulations or experiments. An example of modifying a level set model to treat bread loafing correctly is discussed below in the section on deposition on substrates containing vias and trenches. Bread loafing is the formation of a bulge overhanging the edges of trenches and vias; it is a universal result of low-pressure vapor deposition of thin films since it is caused by the finite size of atoms. Bread loafing can lead to void formation inside vias during the metallization step of silicon device fabrication. Also, stochastic effects of deposition and random nucleation events have not been included in most continuum models. For studies on this level of complexity, it seems appropriate to also apply atomistic models. After obtaining a detailed understanding of the atomistic processes and some values for macroscopic parameters, the most important atomistic effects can often be included in the continuum models. Some processes are implicit in an atomistic model: for example, nucleation, statistical

fluctuations in the deposition of atoms, and diffusion. The MC models require detailed energies for a number of atomic configurations, but recent improvements in first principles methods have enabled the development of good interatomic potentials for a large number of materials.

We discuss the application of MC models to faceting during growth, nucleation, and growth during deposition of metal layers, and molecular crystals. In particular, we describe the general aspects of our Monte Carlo model in [Section 10.2](#). [Section 10.3](#) treats some of the consequences of faceting during deposition. [Sections 10.4 and 10.5](#) show the effect of materials properties and processing conditions on the nucleation and growth of films, respectively. [Section 10.6](#) is concerned with the important issue of texture and the influence of deposition conditions on grain orientation. [Section 10.7](#) has a brief discussion of step coverage results. Finally, [Section 10.8](#) describes some results for habit evolution of a molecular crystal.

This is a brief description of the method and a set of applications to crystal and film growth. We suggest that the reader goes to the references for more detail of the examples shown here.

## 10.2 Monte Carlo Model Description

MC models of film deposition and crystal growth are based on the repetition of several basic events. In the general case, the simulation proceeds by selecting one of three events: (1) insertion of a sputtered particle (atom or molecule), (2) selecting a surface particle for a diffusion jump, or (3) evaporation. This type of model has the advantage of fast computation because of the simplicity of the MC events, while including accurate diffusion rates and other mechanisms based on more detailed data (i.e., MD or first principles calculations). Here, we describe a basic form of the model; modifications of more complex systems are described below.

Deposition of particles on a substrate is accomplished by randomly selecting launching points in a plane above all occupied sites. Then, the particles are moved along the chosen trajectories in small increments until they reach a lattice site that has at least one occupied neighboring site. In cases where the site at the point of contact corresponds to an unstable position, the particle is moved to a stable site. Equilibrium deposition rate  $r^+$  per surface site corresponds to zero driving force and is given by

$$r^+ = \nu \exp[-(E_g - E_k)/k_B T], \quad (10.1)$$

where  $E_g$  is the internal energy of a particle in the gas phase relative to that in the crystal,  $E_k$  is the energy of a particle at a kink site,  $k_B$  is the Boltzmann constant,  $T$  is the temperature, and  $\nu$  is an effective vibrational frequency. Note that the difference in free energy between a particle at a kink site and a particle in the gas phase,  $(E_k - E_g)$ , is the cohesive energy.

For the materials and temperatures we treat in this chapter, the deposition rate is typically many orders of magnitude larger than that of [Eqn \(10.1\)](#), and evaporation

events can be neglected. Starting from an initial configuration, all particles are assigned to different lists based on their evaporation and surface diffusion rates. These lists are used to calculate a set of probabilities for picking a particle to execute an evaporation or diffusion event. The evaporation rate  $r_i^-$  and diffusion rate  $r_i^d$  depend on the number of nearest neighbors and are given by

$$r_i^- = \nu \exp[-(E_g - E_i)/k_B T] \quad (10.2)$$

and

$$r_{i \rightarrow j}^d = \nu \exp[-(E_i - E_j)/k_B T], \quad (10.3)$$

where  $E_i$  and  $E_j$  are the energies of the particles with  $i$  and  $j$  nearest neighbors, respectively. Now, the total event rate for the system is

$$R = \sum_i (N_i r_i^- + N_i r_{i \rightarrow j}^d), \quad (10.4)$$

where  $N_i$  is the number of surface particles in each of the  $i$  energy lists. Normalizing the weighted individual rates,  $r_i^-$  and  $r_{i \rightarrow j}^d$ , by the total event rate,  $R$ , we obtain that an evaporation event is chosen with probability

$$P_i^- = \frac{N_i r_i^-}{R} \quad (10.5)$$

and a diffusion event (assuming a vacant neighboring site where the atom would have equal or lower potential energy) with probability

$$P_{i \rightarrow j}^d = \frac{N_i r_{i \rightarrow j}^d}{R}. \quad (10.6)$$

The elapsed time  $\Delta t$ , for an event attempted in a system with this set of  $N_i$  particles, is  $R^{-1}$ , and the sum of these values for each event gives the elapsed time. The product of the elapsed time and the deposition rate determines the insertion of new atoms in the vapor.

A random number is used to select an event based on the above probabilities. After an event is chosen, a particle in that energy category is chosen, with a second random number, to perform the corresponding evaporation/diffusion event. When a diffusion event is chosen, a third random number is used to select a vacant nearest neighbor site. Finally, the corresponding energy categories are updated. Since surface diffusion events are chosen in a way that satisfies the condition for microscopic reversibility [4], a system evolving under surface diffusion alone will approach the equilibrium structure for the simulated temperature. Kinetic effects resulting from the deposition process become less pronounced for systems with a large surface diffusion mobility. The relative probabilities for selecting these events depend on the conditions being simulated. In particular, they depend on the ratio of the impingement frequency of sputtered particles to the hop frequency at the surface. A full description and variations of the MC model can be found elsewhere [20,31].

## 10.3 Deposition on a Spherical Crystal Seed

The early work using MC models has shown that close-packed surfaces in equilibrium tend to be atomically flat at low temperatures [32], provided that there are bond chains parallel to the surface orientation along two different directions [33]. This has consequences for the kinetics of crystal growth on these faces at low temperatures, since the generation of new layers on atomically flat surfaces requires the nucleation of stable 2D clusters of atoms. As is typical of nucleation processes, the growth rate on the surface drops exponentially as the driving force is reduced to small values. These results were observed in the MC simulations of the (001) face of a simple cubic Ising model [32,34]. Because of the very low growth rate on the facet of a perfect crystal, deposition on different crystallographic orientations can be highly anisotropic. At higher temperatures, in equilibrium, the free energies of steps in the surface may drop to zero and the surfaces roughen. If this is the case for all close-packed orientations, the growth rate becomes nearly isotropic. This surface roughening transition has large consequences for crystal morphology, and for the morphological stability of surfaces during growth. As the temperature is increased the equilibrium density of steps increases until, at the transition temperature, the 2D islands percolate and form a connected structure across the entire surface. In this situation, the growth rate is linear in the chemical potential driving force, since nucleation is not required.

### 10.3.1 Faceting during Deposition of Metals

The influence of crystallographic anisotropies on the growth of crystals is most clearly observed in the case of full three-dimensional (3D) systems in which all crystallographic orientations are accessible for deposition. For example, the fcc (111) and (001) orientations of Al crystals are atomically flat right up to the melting point, and only the (110) face exhibits a roughening transition [35]. Therefore, we can expect some degree of faceting during growth on both the (111) and (001) faces at all temperatures.

The growth of an Al crystal with the initial shape of a sphere is shown in Figure 10.1. Starting from a spherical crystal seed that is 4 nm, as shown in Figure 10.1(A), we inject atoms onto the crystal seed along the radial direction. The temperature was maintained at 200 K throughout the simulation. The initial sphere grows out to form an octahedron bounded by (111) faces. After the crystal reaches a critical size, the (001) faces appear, as shown in Figure 10.1(B). The surface is covered with 111 and 100 facets, with 111 being dominant. Near equilibrium, the 100 and 111 facets are comparable in size. However, the high adatom potential energy on the 111 surface causes it to become the dominant facet during growth. For the small initial sphere, the diffusion rate is sufficient for adatoms to diffuse to neighboring faces and to congregate on the faces with the lower adatom potential energies. As a result, these faces can nucleate new layers and grow rapidly until they disappear from the growth form, as shown in Figure 10.1(C). Because of the small size of the initial sphere (4 nm initial diameter), there is little kinetic roughening induced

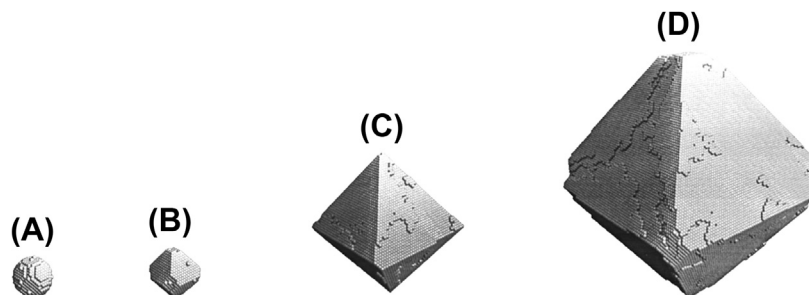


**FIGURE 10.1** Simulation of deposition on a spherical seed of 4 nm diameter at 200 K with a deposition rate of  $1 \mu\text{m}/\text{min}$ . All particles are injected from a shell surrounding the crystal with velocities toward the crystal along the radial direction. Snapshots are taken at the start, (A); after deposition of  $2 \times 10^3$ , (B); after  $5 \times 10^4$ , (C); and after  $5 \times 10^5$  atoms (D).

by the deposition at the start. We found that 111 facets smaller than about 12 nm in diameter are not able to nucleate new layers because the adatoms diffuse too quickly to the edges where they attach in sites of low potential energy, such as step edges. As the crystal grows larger, the 111 facets reach the critical size, and multiple clusters can form. The steps from these clusters act as sinks for the adatoms impinging on the 111 face, so that fewer adatoms from these facets can reach neighboring 100 orientations. This effect slows the growth of 100 relative to 111 to the point that 100 facets remain on the growth form. This can be seen in [Figure 10.1\(D\)](#).

### 10.3.2 Effect of Deposition Rate

The effect of high deposition rates on the morphology of the crystal formed by deposition on a small spherical seed is shown in [Figure 10.2](#). With increasing deposition rate, the facets shrink and eventually disappear. At the higher rates, there are not enough diffusion hops to move more than a few angstroms from the impinging point. Atoms that stick where they land tend to maintain the spherical shape. However, because of the small numbers involved, the fluctuations produce a rough surface, and as time goes on, a shadowing instability. A higher region on the surface intercepts more of the subsequent

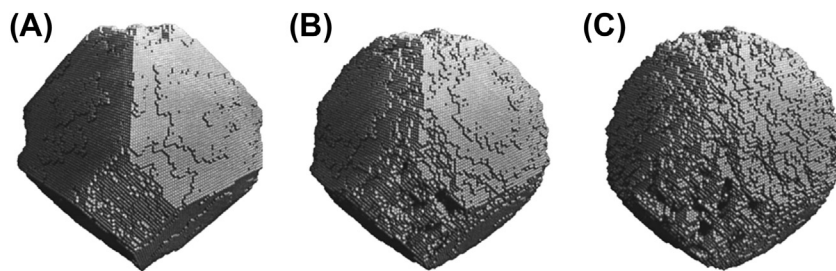


**FIGURE 10.2** Comparison of deposited films on a spherical crystal seed as in [Figure 10.1](#). (A) with deposition rates of  $10 \mu\text{m}/\text{min}$ ; (B)  $100 \mu\text{m}/\text{min}$ , and (C) at  $1000 \mu\text{m}/\text{min}$ .

flux of atoms and grows faster than its surroundings, which are being shadowed. This instability is an undesirable surface roughening mechanism.

Clearly, the (111) facet will have a relatively small growth rate if most atoms arriving on it have time to escape to sites with lower energies. If the facet is sufficiently large, however, then there is time for other atoms to arrive and interact with others to form clusters. In this case, each atom is more likely to stick on the same facet close to the point where it arrived, and the growth would be less sensitive to crystallographic orientation. The transition from highly anisotropic growth (Figure 10.1) to growth rates that are more nearly independent of orientation (Figure 10.2) occurs at a critical facet radius  $R_c$ . A similar situation arises in the theory of kinetic roughening on “infinite” surfaces [22]. Rapid deposition onto close-packed orientations that are atomically flat in equilibrium will lead to some degree of kinetic roughening. This is a result of the nucleation and growth of the 2D islands. The average radius of atomically flat regions will have a magnitude approximately equal to  $R_c$ , since the flat regions larger than this value are likely to nucleate new 2D clusters and, thus, have their size reduced. This radius also gives a measure of the step spacing on a kinetically roughened surface. More information on how to calculate  $R_c$  can be found in Ref. [36].

## 10.4 Nucleation of Films on Foreign Substrates

The early stages of thin film growth usually involve the nucleation of islands on a foreign substrate. Our purpose is to explore the influence of materials properties and processing conditions on cluster morphology. The initial islands have an important role in determining the initial orientations and density of the grains in the polycrystalline film [37]. For this purpose, we model the substrate as a single crystal, but with reduced interaction energies with the deposited material (the reduction being 0.15 eV per bond). In addition to having a reduced film/substrate bond energy, there is, in most cases, strain due to lattice mismatch that weakens the bonding compared to simple film/substrate bond energies. Furthermore, we explore the effect of temperature and inhibited diffusion at steps on cluster morphology. The latter was achieved by including different values of the Ehrlich-Schwoebel barrier ( $\phi_{ES}$ ), which assigns an extra activation energy for diffusion hops over a step edge for an adatom on the upper terrace [38,39]. A large  $\phi_{ES}$  inhibits adatoms from hopping into surface vacancy clusters and grooves, thereby slowing surface smoothing processes.

### 10.4.1 Effect of Wetting

As a result of the difference in the interfacial energy between the film and the substrate, there is a tendency for the deposited material to cluster and form islands on top of the substrate. This effect is called dewetting and is present in most film/substrate systems [40]. We will treat a system with weaker film/substrate interactions and define the wetting parameter,  $w$ , as the ratio of the film/substrate interfacial energy to the film/film

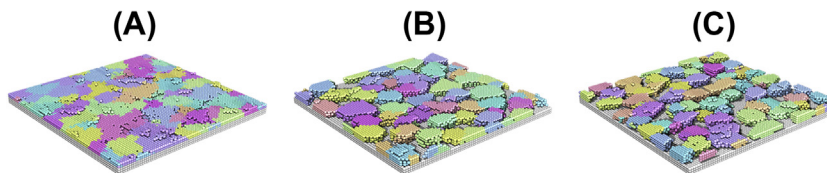


**FIGURE 10.3** Comparison of cluster morphology during deposition of two monolayers (ML) of Be atoms at different values of the wetting parameter. (A)  $w = 0$ , (B)  $w = 0.2$ , and (C)  $w = 0.4$ . Other values are  $T = 20^\circ\text{C}$  and  $\phi_{ES} = 0$ .

bonding energy ( $w = [0,1]$ ; 0 for homoepitaxy). Perfect wetting would require matching of both the substrate surface lattice spacing and interatomic forces to the film.

A comparison of clusters for different values of the wetting parameter is shown in [Figure 10.3](#). All three cases were produced by deposition of two monolayers of Be atoms with  $\phi_{ES} = 0$  at a temperature of  $20^\circ\text{C}$ . For the case of  $w = 0$  ([Figure 10.3\(A\)](#)) (perfect wetting), the clusters are thin and flat; as  $w$  increases ([Figure 10.3\(B\)](#) and [\(C\)](#)), they tend to be taller and, for the same amount of deposited atoms, cover less area. The voids between the 3D clusters resulting from strong dewetting may initiate pinholes in the film that traverse the entire thickness. This is most likely to happen when the growth conditions are favorable for morphological instabilities. For example, a flux of atoms at grazing incidence, together with low mobility of atoms on the surface, will deposit preferentially on the tallest clusters. This is an unstable process since the taller clusters will intercept the most material and will grow faster shadowing more of the surrounding surface. A similar situation occurs if there is a significant barrier to cross over the steps,  $\phi_{ES}$ ; the lower surface regions are surrounded by steps going down, and the barrier impedes the filling in of this region by surface diffusion. This is called Schwoebel instability and is shown below. [Figure 10.3\(A\)](#) shows a simulation of deposition with perfect wetting. A large region of the deposited crystal is fully dense, whereas in [Figure 10.3\(B\)](#) and [\(C\)](#), the deposited material has void regions starting at the interface with the substrate and extending a few layers, clearly a consequence of dewetting. The effect of dewetting can be quantified by plotting the number of grains per layer vs. layer height. This is shown in [Figure 10.4](#) for the films shown in [Figure 10.3](#). Height = 1 correspond to the first layer above the substrate. Here we can see that the number of 3D clusters that nucleate and expand into grains during the early stages of deposition have a strong dependency on the wetting parameter  $w$ .

## 10.4.2 Effect of Temperature

At higher deposition temperatures, the increased atom mobility reduces the number of grains, as shown in [Figure 10.5](#). This is a result of increased ripening during deposition. The area of the substrate left bare increases with temperature because of the diffusion of atoms from the substrate to the clusters, where a stronger bonding is favored. As can be seen from [Figure 10.6](#), the number of grains in all layers decreased a large amount in changing temperature from  $61^\circ\text{C}$  to  $145^\circ\text{C}$ .

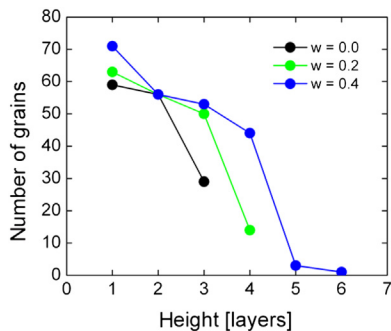


FIGURE 10.4 Plot of the number of grains per layer vs. layer height for the films shown in Figure 10.3.

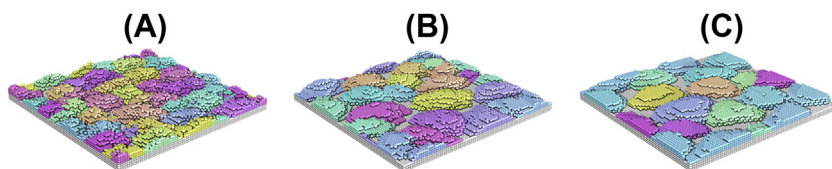


FIGURE 10.5 Comparison of cluster morphology during deposition of two monolayers (ML) of Be atoms at different temperatures. (A)  $T = 61\text{ }^{\circ}\text{C}$ , (B)  $T = 102\text{ }^{\circ}\text{C}$ , and (C)  $T = 145\text{ }^{\circ}\text{C}$ . Other values are  $w = 0.1$  and  $\phi_{ES} = 0.1$ .

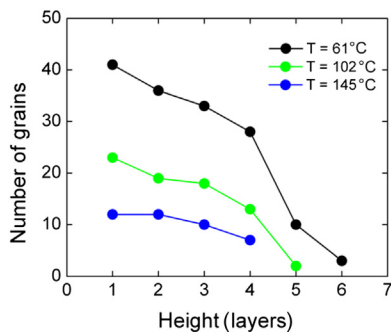
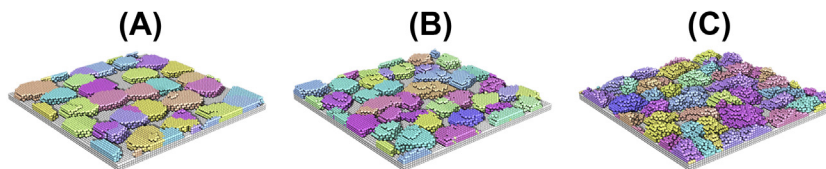


FIGURE 10.6 Plot of the number of grains per layer vs. layer height for the films shown in Figure 10.5.

### 10.4.3 Effect of Inhibited Diffusion over Steps

Figure 10.7 shows the resulting morphologies after deposition of two monolayers (ML) of Be atoms at a temperature of  $60\text{ }^{\circ}\text{C}$  and the same wetting parameter  $w = 0.8$  but with different values of  $\phi_{ES}$ . The effect of  $\phi_{ES}$  on the surface morphology is evident. Most of the islands that have coalesced in the  $\phi_{ES} = 0$  case have formed a flat surface, without steps or grooves at the grain boundaries (Figure 10.7(A)). As the magnitude of  $\phi_{ES}$  increases, more grain boundaries have developed grooves, resulting in a more disordered configuration (Figure 10.7(C)). The increase in the number of grains (see Figure 10.8) and surface roughness with increasing  $\phi_{ES}$  occurs because of a reduction in the flux of



**FIGURE 10.7** Comparison of cluster morphology during deposition of two monolayers (ML) of Be atoms at different values of the Ehrlich-Schwoebel barrier. (A)  $\phi_{ES} = 0$ , (B)  $\phi_{ES} = 0.05$  eV, and (C)  $\phi_{ES} = 0.20$  eV. Other values are  $w = 0.2$  and  $T = 61^\circ\text{C}$ .

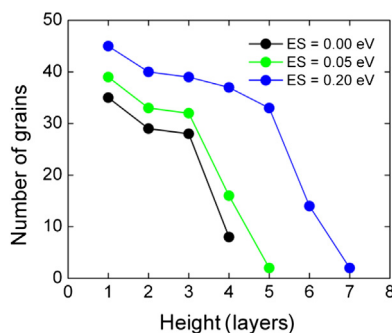


**FIGURE 10.8** Plot of the number of grains per layer versus layer height for the films shown in [Figure 10.2](#).

adatoms from the upper terraces. This produces a greater probability to nucleate new layers on top of an island, and bias it to grow vertically instead of in the lateral directions.

## 10.5 Film Growth

The growth of uniform thin films on foreign substrates is impeded by several morphological instabilities. Hill-and-valley structures are formed and enhanced during sputter deposition where surface height perturbations have an opportunity to grow to large amplitudes [41]. While surface roughness can be partially controlled by changing growth conditions (such as deposition rate, substrate temperature, and angular distribution of impinging particles), the diffusion of particles over step edges plays a very important role in determining both surface roughness and the density of the films. During the initial stages of growth, each nucleation event creates an island with a random crystalline orientation. When two islands coalesce, grain boundaries are formed with reduced bonding between two atoms belonging to different grains.

### 10.5.1 Effect of Wetting

As more atoms are deposited, and the clusters continue to grow vertically, some will attach to the lateral walls of the clusters and will be stabilized by the strong film/film bonds. Eventually, the clusters may coalesce completely with their neighbors, resulting

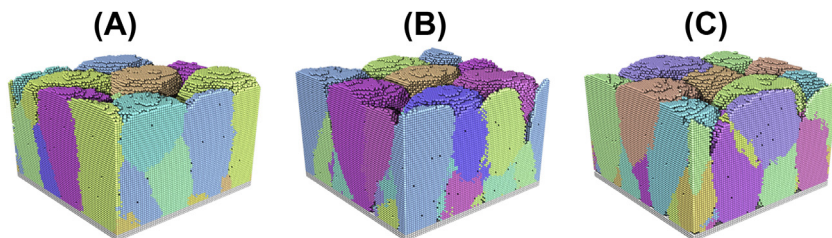


**FIGURE 10.9** Simulated surfaces after deposition of 50 monolayers (ML) of Be atoms at different values of the wetting parameter. (A)  $w = 0$ , (B)  $w = 0.2$ , and (C)  $w = 0.4$ . Other values are  $T = 60^\circ\text{C}$  and  $\phi_{ES} = 0.05\text{ eV}$ .

in full density above this point. This depends on the degree of wetting, the Ehrlich-Schwoebel barrier ( $\phi_{ES}$ ), and the presence of grain boundaries. In [Figure 10.9\(A\)](#) the film had a weak  $\phi_{ES}$  barrier, but perfect wetting ( $w = 0$ ). In this case, the region of the film close to the substrate has full density, without pinholes. The combination of  $\phi_{ES}$  and grain boundaries has caused grooves to form after the deposition of several nanometers of material. The presence of a finite  $\phi_{ES}$  inhibits atoms diffusing on the surface from filling the grooves. The formation of grooves is delayed until, (1) the deposited film is thick enough to have formed steps, and (2) sufficient flux has crossed the steps to affect the growth on the downward sides of the steps. The grooves are located preferentially along grain boundaries since the bonds crossing the boundaries are weaker as a result of the grain boundary energy.

The effect of dewetting, [Figure 10.9\(B\) and \(C\)](#), is to reduce the thickness of the region without pinholes and grooves, but the diameter of the columns is not sensitive to the degree of wetting. The magnitude of  $\phi_{ES}$  is the primary factor controlling the column diameters in this case. The grooves form closer together as  $\phi_{ES}$  increases, since the downward flux across the step is reduced ([Figure 10.10](#)).

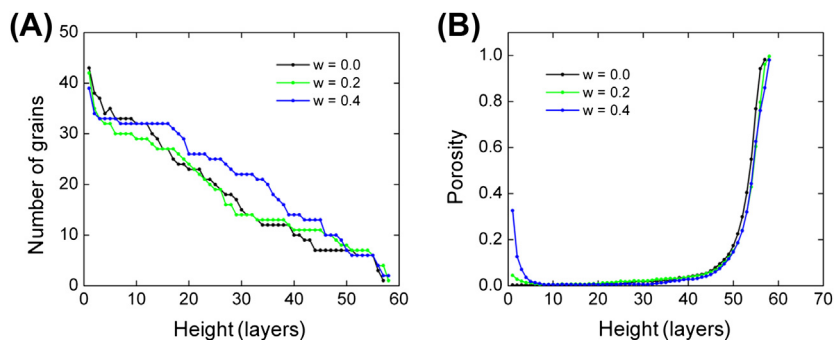


**FIGURE 10.10** (A) Number of grains versus height and (B) Porosity for each crystalline layer after deposition of 50 monolayers (ML) of Be atoms for different values of the Ehrlich-Schwoebel barrier. In all three cases the substrate temperature is  $200^\circ\text{C}$  and the wetting parameter is  $w = 0.9$ .

## 10.5.2 Effect of Temperature

The effect of temperature in the film growth is illustrated in Figure 10.11. The growth conditions, including the temperatures, are the same as in Figure 10.5 (showing the nucleation of the first two layers) except that the dewetting parameter has been increased from  $w = 0.1$  in Figure 10.5 to  $w = 0.3$ . The stronger dewetting is sufficient to produce pinholes extending through the entire film at all three temperatures. The effects of the higher temperatures are similar to those in Figure 10.5, in that it increases the diameters of the columnar-shaped grains. However, higher temperatures increase the densities of the films, whereas the densities in Figure 10.5 are reduced. This seems to be a transient effect during the initial growth, where high mobility causes atoms to diffuse to the higher levels and thereby to increase the height of the clusters at the expense of their girth.

The tops of the columnar grains become flat, with only a few steps at the higher temperatures. Again, this is very similar to the clusters in Figure 10.5. At the lowest temperature, the nucleation of a 2D island on top of the surface requires only a few atoms, and the density of the 2D islands is high, producing a rough top to the columnar grains. The larger diffusion coefficient of adatoms and the large critical nucleus greatly decreases the density of stable 2D islands.

The number of grains in 2D horizontal layers is given in Figure 10.12, as a function of the height of the layer. The values for the lowest temperature (61 °C) deposition are much higher than those for the two higher temperatures.

## 10.5.3 Effect of Inhibited Diffusion over Steps

Further growth of a film beyond the first few monolayers shows that  $\phi_{ES}$  also has a strong effect on the morphology in this regime. Figure 10.13 shows three different films obtained after deposition of 50 ML of Be atoms at a temperature of 200 °C, a wetting parameter  $w = 0.9$ , and  $\phi_{ES} = 0, 0.05$ , and  $0.15$  eV in (A), (B), and (C), respectively. In the case where  $\phi_{ES} = 0$ , a smooth surface forms, with only a few steps surrounding two-dimensional islands (Figure 10.13(A)), as expected for layer-by-layer growth. On the

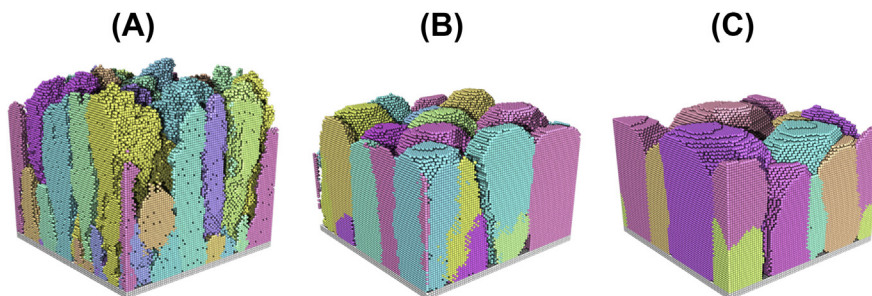
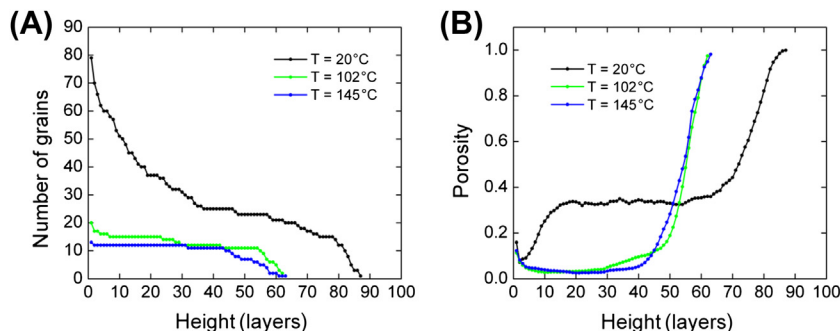
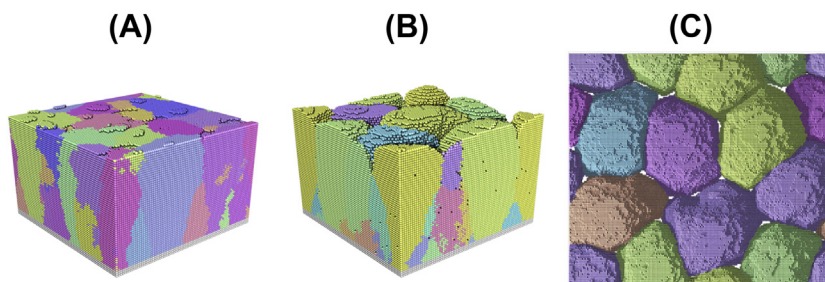


FIGURE 10.11 Simulated surfaces after deposition of 50 monolayers (ML) of Be atoms at different temperatures. (A)  $T = 61$  °C, (B)  $T = 102$  °C, and (C)  $T = 145$  °C. Other values are  $w = 0.3$  and  $\phi_{ES} = 0.10$  eV.



**FIGURE 10.12** (A) Number of grains vs. height and (B) porosity for each crystalline layer after deposition of 50 monolayers (ML) of Be atoms for different temperatures, from configurations in Figure 10.11. In all three cases, the Ehrlich-Schwoebel barrier is  $\phi_{ES} = 0.10$  eV and the wetting parameter is  $w = 0.9$ .



**FIGURE 10.13** Resulting surfaces after deposition of 50 monolayers (ML) of Be atoms at different values of the Ehrlich-Schwoebel barrier. (A)  $\phi_{ES} = 0$  and (B)  $\phi_{ES} = 0.05$  eV, (C)  $\phi_{ES} = 0.15$  (top view). Other values are  $T = 145^\circ\text{C}$  and  $w = 0.1$ .

other hand, the  $\phi_{ES} = 0.05$  eV case shows deep grooves, even with a relatively small barrier (Figure 10.13(B)). Note that the grooves developed during deposition may not extend all the way down to the substrate. This can be seen in the plot of porosity vs. height of Figure 10.13(C). We defined porosity as the number of vacancies at each layer of the film normalized to full coverage. In the simulations shown in Figure 10.13(A) and (B), we use an almost perfect wetting between the film and the substrate ( $w = 0.1$ ). This results in a fully dense film (0 porosity) close to the substrate since the Ehrlich-Schwoebel instability requires some time to develop and to produce the grooves that cause the reduction in film density. Approximately a 25% reduction in density is produced with  $\phi_{ES} = 0.15$  eV, after the initial transient. Even the film with  $\phi_{ES} = 0.05$  eV shows some signs of reaching a steady-state reduction of several percent in density. Further growth would be required to confirm this. Increasing of Figure 10.13(B) from 0.05 to 0.10 eV, and strengthening dewetting, from  $w = 0.1$  to 0.3, as in Figure 10.11(C), results in pinholes that penetrate through the film to the substrate, as shown in Figure 10.14. Methods to control these pinholes are important for controlling the magnitude of stress in the film [42].

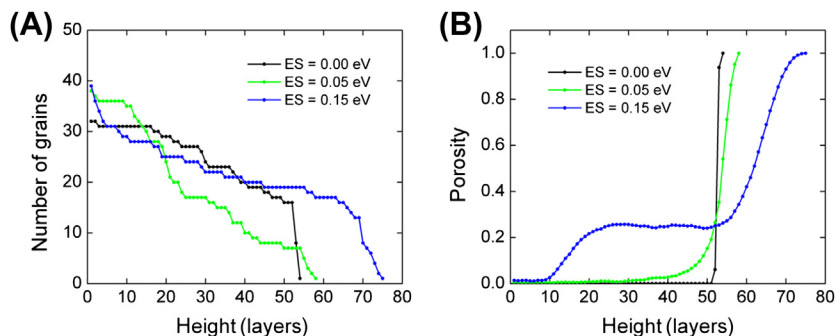


**FIGURE 10.14** (A) Number of grains versus height and (B) porosity for each crystalline layer after deposition of 50 monolayers (ML) of Be atoms for different values of the Ehrlich-Schwoebel barrier from configurations in Figure 10.13. In all three cases, the substrate temperature is 200 °C and the wetting parameter is  $w = 0.9$ .

### 10.5.4 Strategy to Grow a Smooth Film

Temperature has a well-known effect on thin film morphologies, i.e., a low-density irregular columnar microstructure is formed at low temperature where the impinging atoms do not have sufficient mobility to diffuse more than a few Ångströms from the point where they contact the surface. This effect is crucial for the processing of metallic interconnects in the silicon device manufacturing industry. Pore formation will create nonuniform film thickness and regions likely to fail during device operation.

Our MC simulations show that the uniformity of a nonwetting film may be improved by depositing the film at two temperatures. When a few monolayers are deposited with a low substrate temperature, as shown in Figure 10.15(A), surface diffusion rates are small, and atoms stick close to the point where they impinge. A dense array of small 3D islands are formed and coalesce. Once percolation occurs, the 3D islands form single, connected layers, with low density and containing Ångstrom-sized pores, extending through the film. As shown in Figure 10.15(B), increasing the temperature does not improve things, since the extra mobility causes dewetting of the film from the substrate. As the initial atoms are deposited on the substrate, they diffuse and cluster together to form small islands that grow vertically because of the stronger bonding of the Al atoms with other Al atoms than those between the Al atoms and the substrate. This causes them to grow into large 3D islands, with bare substrate between them.

Our method will take advantage of the low temperature deposition to prevent the deposited atoms from forming 3D islands and yet provide mobility to fill the small pores that form at the low temperature; we can deposit a few layers at 175 K, and then once percolation occurs, increase the substrate temperature to 250 K so that the atoms in the film are mobile. Then the deposition is continued until the desired thickness is obtained. The initial uniform film is metastable against dewetting, since the small holes in the percolated film will fill in because of the negative curvature of the holes, and it provides a perfect wetting surface for the high-temperature deposition. The simulation can provide information on the optimum values of the parameters (e.g., the temperatures) for formation of a smooth film.

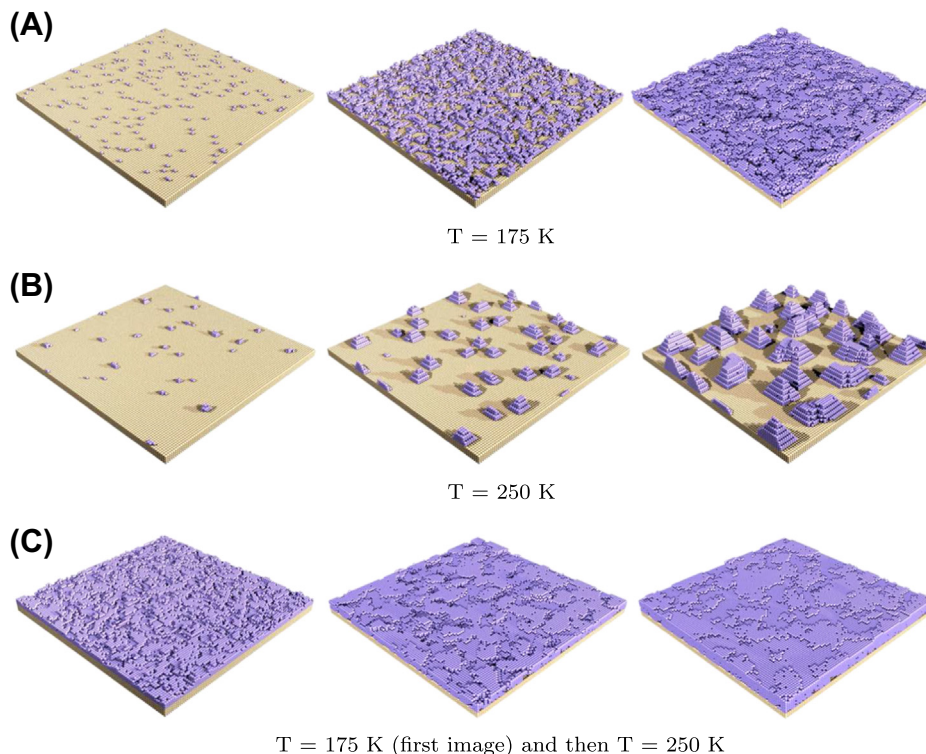


**FIGURE 10.15** Control of substrate temperature during deposition is used to obtain uniform Al film on a plastic substrate. (A) Deposition on substrate at 175 K, (B) deposition on substrate at 250 K, and (C) initial deposition with substrate at 175 K, and continued deposition at substrate temperature of 250 K.

## 10.6 Texture Development

One of the most important aspects of the growth of polycrystalline films is the tendency for the grains to develop a preferred orientation. This occurs even in the case of amorphous substrates and is, therefore, not likely to result from atomic alignment or “template” effects at the substrate–film interface. In most cases, a particular crystal axis of the grains is aligned within a few degrees of the normal to the plane of the substrate. In-plane crystal axes are generally rotated in random directions; although in some cases, there are more low-angle grain boundaries than would be present for random in-plane orientations.

A number of mechanisms have been proposed to explain the appearance of texture, but most apply to growth at relatively high temperatures. In that case, high atomic mobility is thought to permit the expansion of grains oriented in such a way as to minimize either strain energy or surface energy [43,44]. Texture in refractory materials is thought to be a result of competitive growth; crystallites oriented with a fast-growing surface parallel to the substrate will incorporate a disproportionately large fraction of

the deposited atoms and eventually encompass the grains with slower growing surface orientations. Some materials such as TiN can exhibit different textures if the conditions are changed. At room temperature, TiN grows with the fast-growing (111) face parallel to the substrate, but at 800 V, the texture is that of the slow-growing (001). This change also occurs at room temperature if a beam of low-energy ions is directed toward the surface, thus increasing the mobility of the surface atoms [45]. This change is thought to be a result of the high mobility since the surface energy is reduced.

We first consider the deposition of Al at 100 K. At this temperature, only adatoms on (111) faces have high mobility because of their small activation energy (0.08 eV) for diffusion. Some configurations generated by the model during the initial growth of the film are shown in Figure 10.16. Crystallites with (001) faces parallel to the substrate normal have much higher 2D nucleation rates than those with (111) parallel. This is result of a higher adatom potential energy on the (111) faces, resulting in lower adatom concentrations. Rapid 2D nucleation causes faster vertical growth rates on the (001) surfaces. These crystals grow higher, and because of their height, they intercept more flux than do the (111) oriented crystals, resulting in even faster growth. As the film grows thicker, the (001) crystals dominate, although the region near the substrate has both orientations present.

Figure 10.17 shows the film during growth at a temperature of 300 K, where the mobility is much higher. In this case, the crystallites with the larger lateral growth rate dominate. The density of clusters is lower because of Ostwald ripening; at the higher mobility, small clusters will dissolve and supply larger, more stable clusters. Adatoms on the (111) face can diffuse even farther and stick preferentially at the edges of the cluster. As a result, the (111) grains spread laterally over larger distances. The (001) grains are

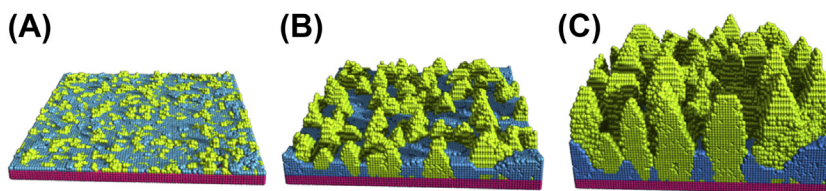


**FIGURE 10.16** Simulated growth of Al deposited at  $1 \mu\text{m}/\text{min}$  at a temperature of 100 K onto a flat substrate and with a cosine angular distribution for the impinging Al atoms. Clusters with (001) and (111) are permitted to nucleate and grow simultaneously using the multilattice model. The substrate is dark grey, the (111) clusters an intermediate shade, and the (001) clusters are light grey. Configurations (A), (B), and (C) correspond to the film at different times during the deposition.

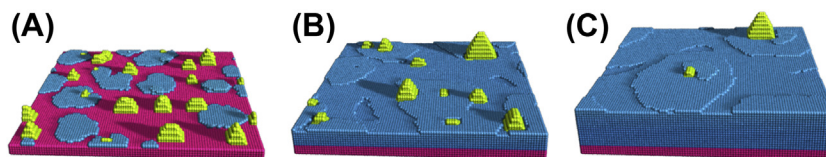


**FIGURE 10.17** Simulated growth of Al deposited at  $1 \mu\text{m}/\text{min}$  at a temperature of 300 K onto a flat substrate. The angular distribution is cosine, and the cluster orientations are indicated as in Figure 10.16.

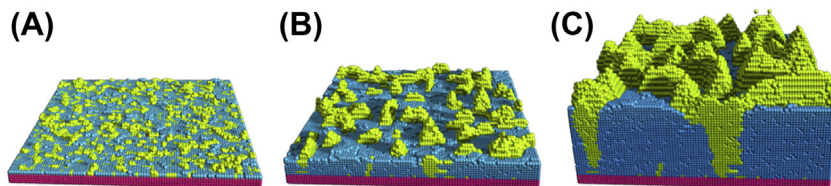


**FIGURE 10.18** Simulated growth of Al deposited at  $1 \mu\text{m}/\text{min}$  at a temperature of 100 K onto a flat substrate. The angular distribution is cosine as modified by a 1:1 collimator. Cluster orientations are indicated as in [Figure 10.16](#).

again higher and intercept more flux, but in this case, the higher mobility allows significant atomic exchange between (001) and (111) grains. Because of the higher radius of curvature of the (001) crystals (smaller cross-sections), they have a higher chemical potential and lose material in the exchange. This loss of material is greater than the gain resulting from the height advantage of the (001) crystals, and as a result, the (111) crystals eventually cover the entire surface of the film.

The flux to the (001)-oriented crystals, relative to those at other orientations, can be altered by changing the angular distributions of the impinging atoms. Atoms arriving at oblique angles to the substrate are most likely to strike one of the higher crystals; whereas, atoms arriving at normal incidence should impinge on (001) and (111) crystals with equal probability. Thus, the use of a collimator would be expected to reduce the growth rates of (001) crystals more than the (111). To test this conjecture, we examine the result of collimated growth under low mobility conditions. This is shown in [Figure 10.18](#). Only the angular distribution is changed from the simulation shown in [Figure 10.16](#). It is apparent that the amount of material with (111) texture is considerably thicker than in the uncollimated case. The angular distribution of the impinging atoms clearly has a large effect on the film structure, and at a somewhat higher temperature, it can make the difference between depositing films of (111) and (001) texture. Film texture has a strong effect on the density of thin films of refractory materials, and methods to control texture have important technological applications.

## 10.7 Physical Vapor Deposition and Step Coverage

Thin films of metal are a crucial part of current on-chip interconnection technology. The films serve as diffusion barrier layers—e.g., Ta and Ti and seed layers of Cu, among others. These layers are typically deposited over substrate topography for integrated circuit fabrication using low-pressure magnetron sputtering. The step coverage on trenches and vias is usually the region of minimum film thickness inside a feature, and this thickness is a key quantity that indicates the future integrity of the layer. Both surface tracking and atomistic models have been applied to treating this important step in the fabrication of devices [9,46–48].

Although continuum models are used extensively in the software employed in the fabrication of electronic devices, these models have serious shortcomings. The surface

evolution resulting from the deposition of discrete particles is intrinsically different from that produced by continuum processes. The atomistic effects have major consequences, even when observed at macroscopic length scales. The MC model represents the physics of the deposition process a great deal more faithfully than the continuum model. Monte Carlo codes can fairly easily be used to simulate the kinetics of surface impingement and are, by their nature, stochastic.

An interplay between continuum and atomistic simulation approaches led to the development of a continuum model that mimics a key mechanism that is represented in the atomistic model, but absent in the usual continuum model. It turns out that the effect is quite pronounced in certain cases, namely collimated and low-energy ionized PVD. In these regimes of deposition, the film can exhibit a “catastrophic” shadowing instability at the upper corners of the feature profiles, leading to exceedingly low film coverage at these locations. The usual continuum model almost completely fails to capture this phenomenon, thereby undermining confidence in its predictions of minimum step coverage under these deposition conditions. The MC model, on the other hand, does reproduce the behavior observed in experiments.

Films simulated by the MC model of deposition onto a via and a trench are shown in [Figure 10.19](#). The thickness of the deposit in the bottom of the via is greater than that of the trench. This results from the fact that the via walls shadow the center more effectively. Trajectories of atoms arriving at large angles of incidence are all blocked and cannot reach the bottom of the via, whereas some large angle trajectories arriving at the trench can reach the bottom. The high temperature of 390 °C redistributes the sputtered material by surface diffusion, and for this reason, the overhang produced by the bread loafing effect is not as large as that typically observed during manufacturing. Note that the thinnest film on the sidewalls is at the bottom, a characteristic of high surface diffusion. (The name “bread loafing” is derived from the shape of baked bread rising out of the pan and bulging out over the edges.)

An experiment showing more pronounced bread loafing was performed, with deposition at room temperature of a Ta layer on a substrate containing vias, and is shown in [Figure 10.20](#). The mobility of Ta at room temperature is extremely low, and as a result, the thickness increases with depth, just the opposite of [Figure 10.19](#). The overhang expands with the amount of material deposited, blocking a region on the sidewalls that increases with further deposition. This gives rise to the taper of the sidewall film, which decreases in thickness with height. At the corner, the sidewall thickness is

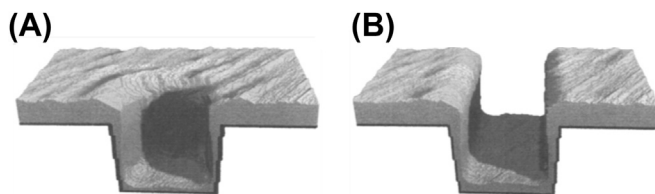


**FIGURE 10.19** Configurations generated by the MC model with a substrate containing a 0.025  $\mu\text{m}$  (A) via and a (B) trench. Here the temperature during deposition was held at 390 °C, and the deposition rate was scaled to correspond to 0.25  $\mu\text{m}/\text{min}$  for a 1  $\mu\text{m}$  trench (the actual deposition rate was  $1.6 \times 10^4 \mu\text{m}/\text{min}$ ).

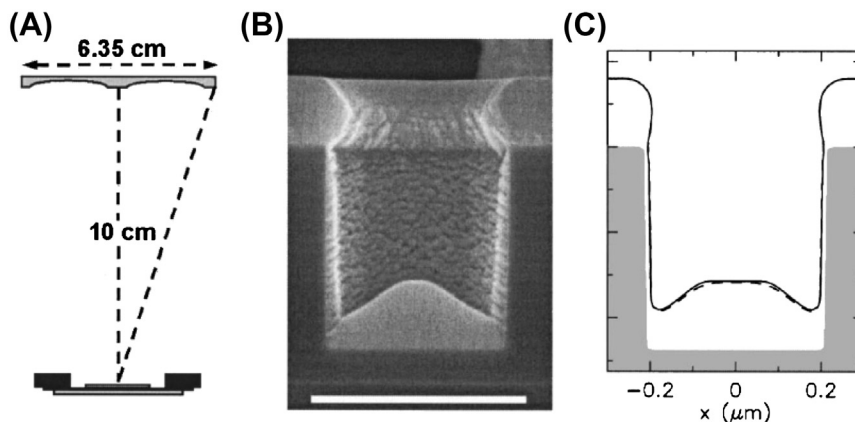


**FIGURE 10.20** (A) Sketch of Ta deposition experiment. (B) Cross-sectional scanning electron micrograph of an axis symmetry contact via with Ta barrier layer. Dark areas indicate  $\text{SiO}_2$  substrate and light areas indicate Ta. Via depth 460 nm, width at top 430 nm, width at bottom of via is 415 nm, scale bar is 500 nm wide. (C) Numerical simulations using continuum model. Solid line: ballistic deposition with cosine angular distribution from target. Dashed line: simulation utilizing angular distribution obtained from gas scattering code, mean free path is 5 cm.

essentially zero, since that region is blocked with the initial film deposition. The sputter gas was Ar at a pressure 1 mTorr, and no electrical bias was applied to the substrate. A scanning electron micrograph of one deposition is shown in [Figure 10.20\(B\)](#). A corresponding simulation is shown in [Figure 10.20\(C\)](#). The throw distance is 10 cm while the target diameter is 6.35 cm. Hence, at low pressure where there is negligible scattering, the flux at the substrate is confined to a cone of angles less than  $18^\circ$ —a moderately collimated beam. The agreement of the standard level set model with the experiment is poor, with only a slight bulge where the experiment shows a large overhang. The sidewalls have uniform thickness in the level set model; whereas, the experiment shows a taper with the thick region at the bottom of the via.

In [Figure 10.20\(B\)](#), we see three important features of the film morphology. First, the sidewalls exhibit a highly columnar microstructure. This is a consequence of the high angles of incidence of the largely collimated flux of Ta, together with the extremely low surface mobility of Ta. Second, the film appears to be fully dense on those parts of the via that are approximately normal to the incident flux, namely on the bottom of the via and on the field. The film in these places is very smooth, which is a consequence of the almost-normal incidence, but also perhaps because of the energy of the impinging atoms. The energy of the sputtered Ta is 25 eV on average. Third, the minimum step coverage occurs at the upper end of the sidewall rather than the more usual location at the bottom of the sidewall in less collimated deposition. Immediately above this “pinched” region, the film bulges sideways, forming an almost semicircular overhang. The overhang shadows the wall from the collimated beam and causes the pinch at the upper sidewall.

The drastic difference between the experiment and continuum model can be understood by the crucial difference between the behavior of particles of an atomic flux and

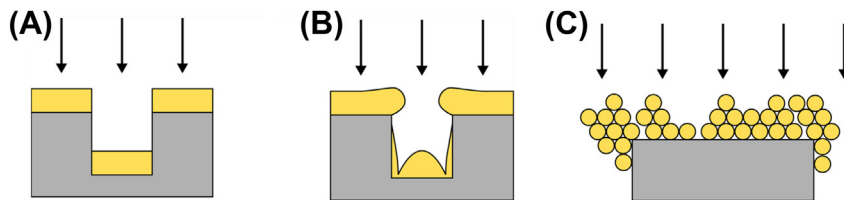


**FIGURE 10.21** Schematics showing: (A) a film deposited on a trench simulated by a continuum model, compared to (B) a typical MC simulation of a film resulting from a collimated beam of atoms, and (C) a diagram from MD simulations indicating how atoms extend over the edge. As the film grows thicker, it extends farther at the overhang. This angle is independent of the atomic size.

that assumed in the continuum model. This difference affects the shape of thin films in a number of different applications. [Figure 10.21](#) shows a schematic comparison of atomistic with continuum models.

Each segment of the film surface is assumed to receive a flux from the source(s) that are visible from the source, corrected for the orientation of the segment relative to the direction of the source. The collimated flux, therefore, has no interaction with the vertical walls, in the schematic [Figure 10.21\(A\)](#). (Numerical errors cause a small amount of material to attach to the walls in [Figure 10.20\(C\)](#).) But the particles in [Figure 10.21\(B\)](#) will not simply slide down the vertical walls if they come within an atomic interaction range of the walls. Some of the particles will stick on the wall just because they are within several Ångströms of the wall. Also, particles that impinge near the edge of the trench will diffuse over the corner and find stable sites on the vertical walls, as illustrated in [Figure 10.21\(C\)](#). Although the deposition of a single layer of particles will not cause significant overhanging material, the second layer will, on the average, extend farther out over the via by a distance proportional to the atomic diameter. A film will extend out in Ångstrom-sized increments as each layer is deposited and will extend out a distance proportional to the film thickness. This overhang is essentially zero for the continuum model, no matter what film thickness is deposited, but it may be significant for particles.

Although the discussion has assumed that the film thickness is only a fraction of the diameter of the via or the trench width, there are applications where the deposited material is expected to fill the via, and therefore, a layer is deposited that is at least as thick as the via diameter or trench width. In this case, the overhangs of the bread loafing effect can coalesce from both sides of the trench (or via) and seal off a void. Again, the continuum models are unable to predict the occurrence of void creation, although they may have a deleterious effect on the long-term performance of the device.

Other applications where continuum modeling yields erroneous results are illustrated in [Figure 10.22](#). A shadowing instability can produce low-density porous material; one example where low diffusion coefficients and the flux of atoms impinge at a glancing angle is the deposition on the sidewalls of the via of collimated Ta, mentioned above, [Figure 10.22\(B\)](#). Again, there is a large difference between the morphology predicted by a

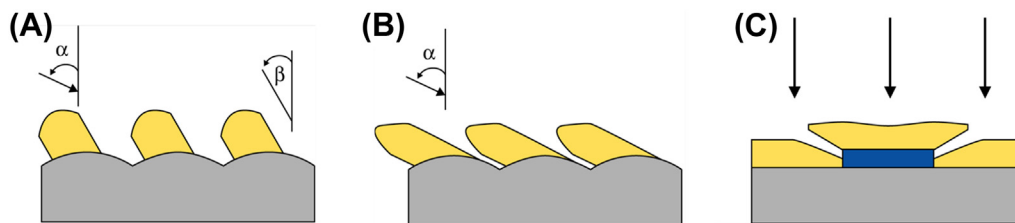


**FIGURE 10.22** Atomic size affects the morphology of the deposited film on a macroscopic length scale; each layer of atoms deposited extends in the same direction, so the displacement accumulates. Here  $\alpha$  is the incident angle of the atoms in the beam, and  $\beta$  is the average angle of the columns. (A) A schematic of columns formed by atomic beams (experiment or MC atomistic simulation) and (B) schematic of columns simulated using level set continuum model. (C) Typical piezoelectric film deposited onto an electrode in a filter arrangement in a cell phone. The material deposited on top of the electrode is not connected to the film on the substrate.

continuum model and an atomistic model. In most cases, the continuum models predictions are more favorable to the application than the real atomic flux. Finally, deposition of piezoelectric films onto a substrate containing an electrode leaves a gap between the electrode with a film on top and the film on the substrate, as shown in [Figure 10.22\(C\)](#).

We have developed a continuum model that incorporates finite atomic length scales. The model incorporates effects of atomic interactions, which lead to the capture of impinging atoms that pass near a point on the film. The effect of this capture process results in bread loafing at corners and convex regions of a surface with large curvature. The model employs the same calculation for the flux and its interaction with the surface of the substrate or film, but includes a calculation of the distance between the atoms flux from all sources. But, instead of requiring that the flux impinge on a surface, it can also contribute to surface regions in close proximity to the path of the flux. The results for deposition onto a via are shown in [Figure 10.23](#). This model does not take into account the details of the atomic displacements on collision with a surface, but it does detect situations where impinging particles would come within the capture radius of the film, causing them to stick.

## 10.8 Size and Habit Evolution of Molecular Crystals

The size and shape distribution of crystallites controls important materials properties, such as chemical, mechanical, thermal, and optical properties that can be quite different from the bulk. It is, therefore, not surprising that many studies exist in the literature, both experimental and theoretical, of how crystallites grow and change shape and how such evolution is affected by external factors like stress, temperature, solvent, additives, and so on [\[49,50\]](#). General theories for predicting crystal morphology based on considerations of geometry [\[51,52\]](#), surface free energy [\[53\]](#), and attachment energy [\[54–56\]](#) have been around for several decades. Using empirical interatomic potentials, such theories have been used to predict the “average” morphology of crystallites belonging to

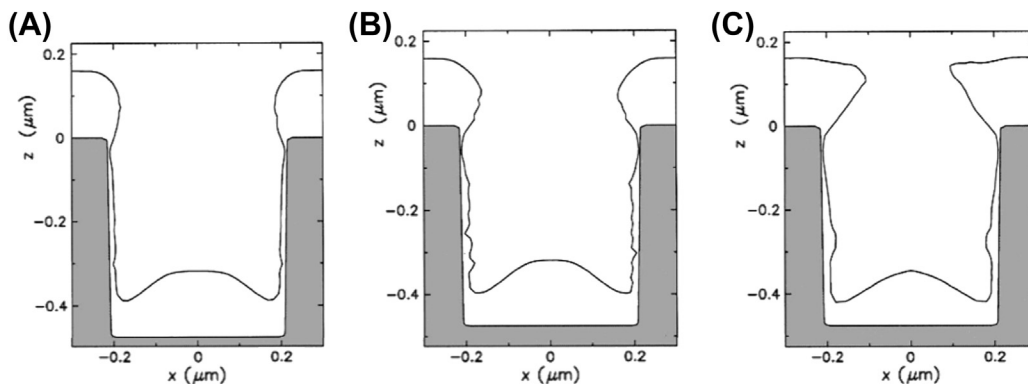


**FIGURE 10.23** Cross-sectional views of sputter deposition into axisymmetric contact vias corresponding to the modified level set model. Capture distances are 5, 20, and 120 Å.

a wide variety of materials types: metallic, semiconductors, ionic, organic, etc. However, such approaches yield morphologies where kinetics are included only in a very approximate way. Real systems typically consist of a distribution of crystallite shapes and sizes. For an understanding of how such a distribution depends on various external factors, it is desirable to create a simulation method that takes important kinetic processes into account, such as the ratio between diffusion and incorporation of molecules.

A typical PETN (Pentaerythritol Tetranitrate) crystal is shown in [Figure 10.24\(A\)](#). Although this crystal was grown from solution, it exhibits the primary facets that are observed during growth from the vapor. This crystal was grown by slow recrystallization from acetone, yielding colorless crystals at 4 °C, and had an average aspect ratio of 5:2 for the length:width. [Figure 10.24\(B\)](#) shows the predicted growth morphology or crystal “habit” of a PETN crystal obtained by a standard Wulff construction, but using the so-called attachment energies instead of surface free energies [54]. A Wulff construction based on the surface free energies yields the equilibrium morphology, which for the PETN crystal looks very similar to the growth morphology of [Figure 10.24\(B\)](#) and, therefore, is not shown. In the computed morphology, the crystal habit matches the experimentally grown crystal of [Figure 10.24\(A\)](#), where four {110} facets are shown along the length (long axis), while the end caps are faceted by eight planes belonging to the {101} family. However, most of the experimental particles deviate from the nice symmetry of [Figure 10.24\(B\)](#).

These solution-grown crystals are compressed to 50% of their theoretical maximum density, and the resulting powder is stored for several years. At room temperature, the powder is stable, showing no rearrangement over a period of several days. The rate of recrystallization and the aspect ratio of the crystallites are strongly dependent on the temperature at which the PETN is kept. The change in aspect ratio may result by changing the supersaturation of the environment where the PETN powder is maintained. Although the particle size distribution can be measured experimentally, there is little

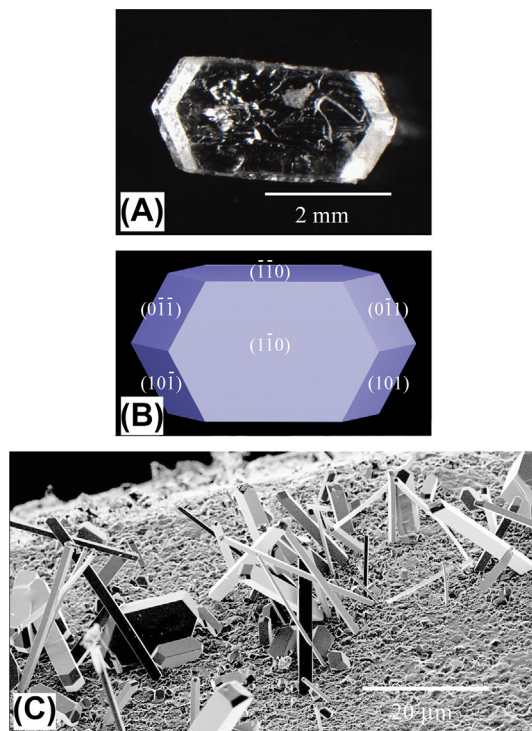


**FIGURE 10.24** (A) Microscope image of a typical PETN crystal grown from solution. (B) Hartman-Perdok (HP) growth morphology of PETN as computed by the COMPASS force field via the attachment energy method. Two types of facets are prominent, four elongated faces of the  $\{110\}$  family and eight end faces of the  $\{101\}$  family. (C) Microscope image of typical PETN crystallites illustrating a variety of aspect ratios after aging.

information on the mechanism associated with the change in surface area. The resulting morphology during aging also appears to be dominated by the two families of facets shown in Figure 10.24(B). Figure 10.24(C) is a SEM micrograph of PETN crystallites resulting from subliming PETN powder followed by aging at  $80\text{ }^{\circ}\text{C}$  for 90 days at ambient pressure. These crystallites in Figure 10.24(C) show a clear propensity for elongation along the (001) axis, with aspect ratio in excess of 100:3 for some of the crystallites. Although crystallites are elongated along the crystal (001) axis, the ratios of surface area of the  $\{110\}$  to the  $\{101\}$  facets vary significantly from crystallite to crystallite, and the areas of the end  $\{101\}$  faces are typically unequal within the same crystallite.

For this study, we substitute the entire PETN molecule,  $\text{C}(\text{CH}_2\text{ONO}_2)_4$ , by a single unit whose interaction depends on its local environment, i.e., number and type of neighbors. This allows us to substitute the complexity of the 29 atoms that form a PETN molecule by an equivalent unit that is packed on a body center tetragonal lattice [31], and to study the unit–unit interaction on a lattice in a manner similar to the crystal graph theory of Hartman-Perdok [54]. Starting from a given initial configuration, each MC step consists of choosing a particle at random and moving it to a randomly chosen unoccupied site

within a given cutoff radius. Next, we calculate the change of energy,  $\Delta E$ , due to this move. The new configuration is accepted with probability 1 if the resulting energy change  $\Delta E$  is less than zero, and accepted with a probability  $\exp(-\Delta E/k_B T)$  otherwise. This local random walk can be interpreted as the result of a few successive neighboring hops. Such a procedure ensures that all possible configurations can be sampled. Also, since all attempted atomic displacement steps obey detail balance, it implies that the system approaches an equilibrium configuration as the simulation time approaches infinity. A more accurate simulation of the kinetics of the morphology evolution would involve neighboring diffusional steps weighted by factors determined by the activation barriers and changes in energy. This would require the calculation of a large number of possible diffusion pathways, the corresponding transition states, and hopping rates.

The influence of crystallographic anisotropy on the growth and evolution of PETN crystals is most clearly observed in the case of a full three-dimensional system in which all crystallographic orientations are accessible for diffusive transport. As a first step in our analysis of size and habit evolution, we decided to study the evolution of the shape of a PETN crystal starting from an arbitrary initial shape. [Figure 10.25\(A\)](#) displays the specific example of a spherical crystallite of diameter 16 nm, which was equilibrated for  $2 \times 10^6$  MC steps. The reason for choosing a sphere was to eliminate any directional bias or artificial anisotropy that might influence the resulting crystallite shape. The resulting configuration, [Figure 10.25\(B\)](#) shows the presence of 101 and 110 facets, also present in the Hartman-Perdok-predicted morphology. In addition, four small 100 faces are also present. Note the comparable surface energies (obtained by COMPASS calculations) between these three faces: 0.21, 0.27, and 0.27 kcal/(molÅ<sup>2</sup>) for the 101, 110, and 100 surface, respectively. Thus, the appearance of these facets in the equilibrated structure gave us confidence not only in the accuracy of the intermolecular lattice potential, but also its ability to mimic realistic crystallite shapes when used with the MC procedure described above.

The morphology in [Figure 10.25\(B\)](#) results from the “local rearrangement” of a fixed number of particles (the ones that formed the initial spherical crystallite) driven by the tendency of the system energy to reach a local minimum. However, the experimentally observed morphologies are a result of growth through particle addition and diffusion,

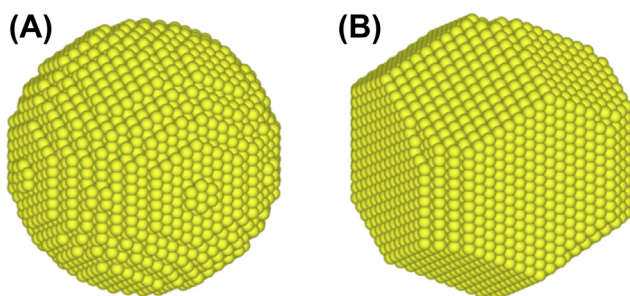


**FIGURE 10.25** Resulting equilibrium configuration obtained from a spherical PETN crystal of 16 nm in diameter that was annealed for  $2 \times 10^6$  MC steps.

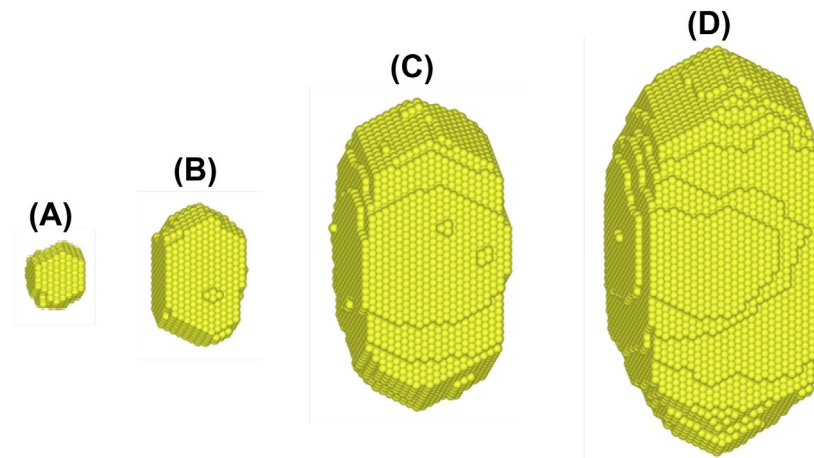


**FIGURE 10.26** Snapshots of the simulation of deposition on a spherical PETN seed of 5 nm in diameter at 300 K. (A) after deposition of  $2 \times 10^2$  molecules, (B)  $2 \times 10^3$  molecules, (C)  $1.5 \times 10^4$  molecules, and (D)  $3 \times 10^4$  molecules.

whose rates strongly depend on experimental conditions. To this end, we have studied the change in morphology during growth in a similar way as described in Ref. [20]. Thus, we start from an initial spherical seed and add particles to the surface of the growing crystallite along a randomly selected radial direction. Following each particle addition, we perform a predefined number of MC steps, aimed at representing surface diffusion. Thus, the above number of MC steps between two successive particle addition events represents, on average, the ratio of the diffusion hop rate to the crystallite growth rate.

Figure 10.26 shows the evolution of an initial spherical seed of 5 nm in diameter at 300 K. We performed 17 MC steps per insertion and particles were allowed to move within a cutoff radius of 5 nm. After insertion of only 200 particles, as shown in Figure 10.26(A), the surface of the crystal is bounded by 101 and 110 facets of approximately the same size. As more material is added to the crystal, 110 facets become dominant as shown in Figure 10.26(B). This is a result of the difference in adatom potential energy between these two faces. The 101 faces have a lower adatom potential energy ( $-28.7$  kcal/mol) than the 110 faces ( $-18.7$  kcal/mol), thus making the nucleation of a new layer easier and leading to a faster growth, as shown in Figure 10.26(C). As the crystal grows larger, the 110 facets can nucleate stable, two-dimensional islands that allow these faces to grow through the motion of monatomic steps, as shown in Figure 10.26(D).

Controlling the ratio between the sizes of the 101 and 110 facets can be achieved by varying experimental conditions such as deposition rate and growth temperature. Experimental data suggest that at lower temperatures crystallites tend to be more round with a 110/101 aspect ratio being close to unity, while elevated temperatures tend to yield needle-like crystals [31]. Temperature clearly affects all the important kinetic processes, i.e., adsorption, desorption, and diffusion rates on each surface. Although we

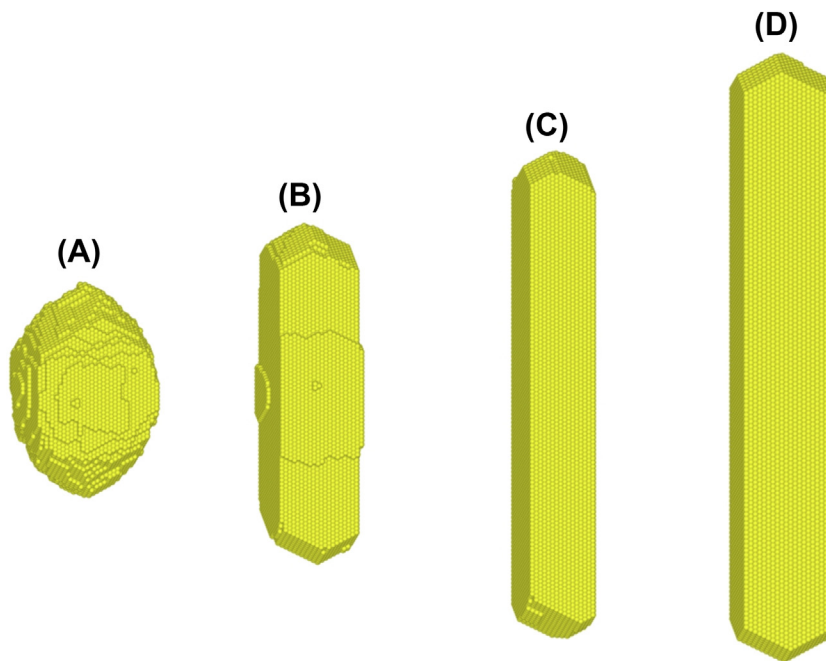


**FIGURE 10.27** Comparison of the final configurations obtained after deposition of  $3.5 \times 10^4$  particles on a spherical seed with (A) 10 MC steps, (B) 25 MC steps, (C) 50 MC steps, and (D) 100 MC steps between particle insertion.

eventually plan on computing and implementing the important rates into our MC, as a first approximation, we decided to incorporate the temperature effects simply by varying the number of MC steps between insertions of new particles. Figure 10.27(A)–(D) show the resulting configurations following  $3.5 \times 10^4$  particle insertions, respectively, at the rates of 10, 25, 50, and 100 MC diffusion steps between insertions. This variation can be interpreted either as an increase in surface diffusivity (e.g., by increasing the growth temperature) or as a decrease in growth rate. Therefore, the progressively needle-like evolution in going from Figure 10.27(A)–(D) is a clear manifestation of what is seen experimentally [31]. It is apparent that the results shown in Figure 10.27 have little relationship to the equilibrium shape of the crystal shown in Figure 10.25(B). To explain the long needle-like shapes based on equilibrium morphologies would require large ratios between the surface free energies—ratios corresponding to the aspect ratios of the crystal shapes. The wide variation in morphologies observed in real crystals of PETN is direct evidence of the predominance of kinetics in this system, even though these crystals are not formed under highly nonequilibrium conditions.

The change in the morphology from the rounded shapes at low temperatures (few diffusion hops) to the anisotropic shapes at high temperatures can also be understood in terms of the surface diffusion occurring between molecule additions. If a molecule makes only a few diffusion hops before another molecule arrives in its vicinity, then

nucleation is favored by the high probability of the association of the two molecules into a small cluster. The high nucleation probability means that molecules are likely to stick close to the point where they originate, and the various crystal faces will advance at approximately the same rate. At high temperatures, where the molecules execute a large number of diffusion hops between molecule additions, they diffuse over larger distances as a mobile unit before joining a surface cluster or encountering another molecule to form a new cluster. Some of the molecules will be able to diffuse across the surface of the crystallite to another facet. The exchange of molecules between facets will result in higher concentrations of mobile species on the facets where the potential energy is lower, and this will in turn result in a disparity in growth rates on the facets. Thus, the higher diffusion rates at high temperature result in large variations in the growth rates as a consequence of different rates of the nucleation of clusters on the faces. Equilibrium forms based on Wulff plots, where the anisotropies in surface free energies cause only a relatively small variation in the facet sizes, cannot explain this kinetic effect.

## Auspices

This work was performed under the auspices of the U.S. Department of Energy by Lawrence Livermore National Laboratory under Contract DE-AC52- 07NA27344.

## References

- [1] Koomey JG, Berard S, Sanchez M, Wong H. Implications of historical trends in the electrical efficiency of computing. *IEEE Ann Hist Comput* 2011;33(3):46–54. <http://doi.ieeecomputersociety.org/10.1109/MAHC.2010.28>.
- [2] Liddle DE. The wider impact of Moore's law. *IEEE Solid-State Circ News* 2006;20:28–30.
- [3] Moore GE. Cramming more components onto integrated circuits. *Electronics* 1965;38(8):114–7. <http://dx.doi.org/10.1109/jproc.1998.658762>.
- [4] Gilmer GH, Bennema P. Simulation of crystal growth with surface diffusion. *J Appl Phys* 1972;43(4):1347–60.
- [5] Abraham FF, White GM. Computer simulation of vapor deposition on two-dimensional lattices. *J Appl Phys* 1970;41(4):1841–9.
- [6] Chernov AA. Growth of copolymer chains and mixed crystals – trial-and- error statistics. *Sov Phys Uspekhi* 1970;13(1):101–28.
- [7] Adams JB, Wang Z, Li Y. Modeling cu thin film growth. *Thin Solid Films* 2000;365(2):201–10. [http://dx.doi.org/10.1016/S0040-6090\(99\)01047-0](http://dx.doi.org/10.1016/S0040-6090(99)01047-0).
- [8] Evans JW, Thiel P, Bartelt MC. Morphological evolution during epitaxial thin film growth: formation of 2d islands and 3d mounds. *Surf Sci Rep* 2006;61(1–2):1–128.
- [9] Voter AF, Interatomic potentials for atomistic simulations. *MRS Bull* 21. 1996
- [10] Bhuiyan AK, Dew SK, Stepanova M. Controlled self-assembly of nanocrystalline arrays studied by 3d kinetic Monte Carlo modeling. *J Phys Chem C* 2001;115:19557–68.
- [11] Akis R, Ferry DK, Musgrave CB. Kinetic lattice Monte Carlo simulations of processes on the silicon (100) surface. *Phys E Low-Dimensional Syst Nanostruct* 2003;19(1–2):183–7. Fourth International Symposium on Nanostructures and Mesoscopic Systems.

- [12] Landau DP, Pal S. Monte Carlo simulation of simple models for thin film growth by {MBE}. *Thin Solid Films* 1996;272(2):184–94.
- [13] Zhang P, Zheng X, Wu S, Liu J, He D. Kinetic Monte Carlo simulation of cu thin film growth. *Vacuum* 2004;72(4):405–10.
- [14] Jackson KA. Computer modeling of atomic scale crystal growth processes. *J Cryst Growth* 1999; 198–199(Part 1(0)):1–9.
- [15] Guenther KH. Microstructure of vapor-deposited optical coatings. *Appl Opt* 1984;23(21):3806–16.
- [16] Jackson KA, Gilmer GH, Temkin DE. Monte Carlo simulation of the rapid crystallization of bismuth-doped silicon. *Phys Rev Lett* 1995;75:2530–3.
- [17] Beatty KM, Jackson KA. Monte Carlo modeling of dopant segregation. *J Cryst Growth* 2004;271(3–4): 495–512. <http://dx.doi.org/10.1016/j.jcrysgro.2004.07.074>.
- [18] Piana S, Reyhani M, Gale JD. Simulating micrometre-scale crystal growth from solution. *Nature* 2005;438(7064):70–3.
- [19] Gale JD, Piana S. Three-dimensional kinetic Monte Carlo simulation of crystal growth from solution. *J Cryst Growth* 2006;294:46–52.
- [20] Huang H-C, Gilmer GH, de la Rubia TD. An atomistic simulator for thin film deposition in three dimensions. *J Appl Phys* 1998;84(7):3636–49. <http://dx.doi.org/10.1063/1.368539>.
- [21] Jackson KA. Kinetic processes: crystal growth, diffusion, and phase transitions in materials. WILEY-VCH Verlag; 2005. <http://dx.doi.org/10.1002/anie.200485247>.
- [22] Pimpinelli A, Villain J. *Physics of crystal growth*. Cambridge University Press; 1999.
- [23] Sethian JA. *Level set methods and fast marching methods*. Cambridge University Press; 1999.
- [24] Cale TS, Raupp GB, Gandy TH. Ballistic transport-reaction prediction of film conformality in tetraethoxysilane O<sub>2</sub> plasma enhanced deposition of silicon dioxide. *J Vac Sci Technol A* 1992;10(4, 1): 1128–34. <http://dx.doi.org/10.1116/1.578214>.
- [25] Cale TS, Jain MK, Taylor DS, Duffin RL, Tracy CJ. Model for surface-diffusion of aluminum-(1.5-percent) copper during sputter deposition. *J Vac Sci Technol B* 1993;11(2):311–8. <http://dx.doi.org/10.1116/1.586676>.
- [26] Adalsteinsson D, Sethian JA. A level set approach to a unified model for etching, deposition, and lithography. 1. Algorithms and 2-dimensional simulations. *J Comput Phys* 1995;120(1):128–44. <http://dx.doi.org/10.1006/jcph.1995.1153>.
- [27] Li JL, Mcvittie JP, Ferziger J, Saraswat KC, Dong J. Optimization of intermetal dielectric deposition module using simulation. *J Vac Sci Technol B* 1995;13(4):1867–74. 2nd Topical Conference on Manufacturing Science and Technology, at the 41st National Symposium of the American-Vacuum-Society, Denver, CO, Oct 24–28, 1994.
- [28] Frost HJ, Thompson CV, Walton DT. Simulation of thin-film grain structures.1. Grain-growth stagnation. *Acta Metall Mater* 1990;38(8):1455–62. [http://dx.doi.org/10.1016/0956-7151\(90\)90114-V](http://dx.doi.org/10.1016/0956-7151(90)90114-V).
- [29] Yang Y, Johnson R, Wadley H. A Monte Carlo simulation of the physical vapor deposition of nickel. *Acta Mater* 1997;45(4):1455–68. [http://dx.doi.org/10.1016/S1359-6454\(96\)00256-X](http://dx.doi.org/10.1016/S1359-6454(96)00256-X).
- [30] Chang CY, Sze SM. *ULSI devices*. Wiley; 1996.
- [31] Zepeda-Ruiz LA, Maiti A, Gee R, Gilmer GH, Weeks BL. Size and habit evolution of PETN crystals – a lattice Monte Carlo study. *J Cryst Growth* 2006;291(2):461–7. <http://dx.doi.org/10.1016/j.jcrysgro.2006.02.052>.
- [32] Weeks JD, Gilmer GH. Pair approximation equations for interfaces and free surfaces in ising-model. *J Chem Phys* 1975;63(7):3136–43. <http://dx.doi.org/10.1063/1.431742>.
- [33] Hurlé DTJ. *Handbook of crystal growth*. vol. 1, Fundamentals: transport and stability; vol. 2, Bulk crystal growth: growth mechanism and dynamics, Amsterdam: Elsevier; 1993.

- [34] Weeks JD, Gilmer GH, Leamy HJ. Structural transition in ising-model interface. *Phys Rev Lett* 1973; 31(8):549–51. <http://dx.doi.org/10.1103/PhysRevLett.31.549>.
- [35] Polcik M, Wilde L, Haase J. Partial order of the quasiliquid during surface melting of Al(110). *Phys Rev Lett* 1997;78(3):491–4.
- [36] Gilmer GH, Huang H-C, de la Rubia TD, Dalla Torre J, Bau-mann F. Lattice Monte Carlo models of thin film deposition. *Thin Solid Films* 2000;365(2):189–200.
- [37] Rubio JE, Jaraiz M, Martin-Bragado I, Hernandez-Mangas JM, Barbolla J, Gilmer GH. Atomistic Monte Carlo simulations of three- dimensional polycrystalline thin films. *J Appl Phys* 2003;94(1): 163–8.
- [38] Ehrlich G, Hudda FG. Atomic view of surface self-diffusion – tungsten on tungsten. *J Chem Phys* 1966;44(3):1039.
- [39] Schwoebel RL, Shipsey EJ. Step motion on crystal surfaces. *J Appl Phys* 1966;37(10):3682.
- [40] Dalla Torre J, Gilmer GH, Rouhani MD. Imperfect wetting of vapor- deposited thin films: Monte Carlo simulations and nucleation model. *Phys Rev B* 2004;69:195414. <http://dx.doi.org/10.1103/PhysRevB.69.195414>.
- [41] Zepeda-Ruiz LA, Gilmer GH, Walton CC, Hamza AV, Cha-son E. Surface morphology evolution during sputter deposition of thin films: lattice Monte Carlo simulations. *J Cryst Growth* 2010;312(8): 1183–7. the 17th American Conference on Crystal Growth and Epitaxy/The 14th {US} Biennial Workshop on Organometallic Vapor Phase Epitaxy/The 6th International Workshop on Modeling in Crystal Growth.
- [42] Zepeda-Ruiz LA, Chason E, Gilmer GH, Wang Y, Xu H, Nikroo A, et al. Understanding the relation between stress and surface morphology in sputtered films: atomistic simulations and experiments. *Appl Phys Lett* 2009;95(15):151910.
- [43] Floro JA, Thompson CV, Carel R, Bristowe PD. Competition between strain and interface energy during epitaxial grain-growth in Ag films on Ni(001). *J Mater Res* 1994;9(9):2411–24.
- [44] Thompson CV, Carel R. Stress and grain growth in thin films. *J Mech Phys Solids* 1996;44(5):657–73. Engineering Foundation Conference on Mechanics and Physics of Layered and Graded Materials, Davos, Switzerland, Aug 21–25, 1995.
- [45] Greene JE, Sndgren JE, Hultman L, Petrov I, Bergstrom DB. Development of preferred orientation in polycrystalline tin layers grown by ultrahigh-vacuum reactive magnetron sputtering. *Appl Phys Lett* 1995;67(20):2928–30.
- [46] Vogl P, Hansen U, Fiorentini V. Multiscale approaches for metal thin film growth. *Comput Mater Sci* 2002;24(1–2):58–65.
- [47] Sheergar MK, Smy T, Dew SK, Brett MJ. Simulation of three dimensional refractory metal step coverage over contact cuts and vias. *J Vac Sci Technol B* 1996;14(4):2595–602.
- [48] Jensen KF, Rodgers ST, Venkataramani R. Multiscale modeling of thin film growth. *Curr Opin Solid State Mater Sci* 1998;3(6):562–9.
- [49] Mullin JW. *Crystallization*. 4th ed. Oxford: Butterworth-Heinemann; 2001.
- [50] Scheel HJ, Fukuda T. *Crystal growth technology*. Wiley; 2003.
- [51] Bravais A. *Etudes crystallographiques*. Paris: Acedemie des Sciences; 1913.
- [52] Donnay JDH, Harker D. A new law of crystal morphology extending the law of bravais. *Am Mineralog* 1937;22(5):446–67.
- [53] Gibbs JW. *The collected works*. New York: Longman; 1928.
- [54] Hartman P, Perdok WG. On the relations between structure and morphology of crystals.1. *Acta Crystallogr* 1955;8(1):49–52.

- [55] Docherty R, Clydesdale G, Roberts KJ, Benemma P. Application of Bravais-Friedel-Donnay-Harker, attachment energy and ising-models to predicting and understanding the morphology of molecular-crystals. *J Phys D-Appl Phys* 1991;24(2):89–99.
- [56] Brunsteiner M, Price SL. Morphologies of organic crystals: sensitivity of attachment energy predictions to the model intermolecular potential. *Cryst Growth Des* 2001;1(6):447–53.

# Ab initio-Based Approach to Crystal Growth: Chemical Potential Analysis

Tomonori Ito<sup>1</sup>, Yoshihiro Kangawa<sup>2</sup>

<sup>1</sup>DEPARTMENT OF PHYSICS ENGINEERING, MIE UNIVERSITY, KURIMA-MACHIYA,  
TSU, JAPAN; <sup>2</sup>RESEARCH INSTITUTE FOR APPLIED MECHANICS, KYUSHU UNIVERSITY,  
KASUGA-KOEN, KASUGA, JAPAN

## CHAPTER OUTLINE

<b>11.1 Introduction</b> .....	<b>477</b>
<b>11.2 Computational Methods</b> .....	<b>479</b>
11.2.1 Chemical Potential .....	479
11.2.2 Monte Carlo Simulations .....	483
<b>11.3 GaAs</b> .....	<b>484</b>
11.3.1 Surface Structures of GaAs .....	485
11.3.2 Growth on GaAs Surfaces .....	488
<b>11.4 InAs on GaAs</b> .....	<b>493</b>
11.4.1 Surface Structures of the InAs Wetting Layer .....	493
11.4.2 Growth on InAs Wetting Layer Surfaces .....	496
<b>11.5 GaN</b> .....	<b>502</b>
11.5.1 Surface Structure of GaN .....	504
11.5.2 Growth on GaN Surfaces .....	507
<b>11.6 InGaN on GaN</b> .....	<b>510</b>
11.6.1 Surface Structure of the InGaN Wetting Layer .....	511
11.6.2 Growth on InGaN Wetting Layer Surfaces .....	513
<b>11.7 Summary</b> .....	<b>515</b>
<b>References</b> .....	<b>517</b>

## 11.1 Introduction

The development of advanced techniques for crystal growth has played an important role in the progress of modern technology. During the last several decades, improvements in bulk- and thin film-growth techniques have provided scientists and engineers

with opportunities to fabricate substantially improved devices and to prepare novel device structures, particularly in the field of semiconductor technology. In particular, crystal growth processes during molecular beam epitaxy (MBE) and metal-organic vapor-phase epitaxy (MOVPE) have been paid much attention for semiconductor crystal growth; these thin film-growth techniques realize highly nonequilibrium conditions where the growth is governed by the diffusive kinetics of the source atoms within the crystalline surfaces, in contrast with bulk-growth processes that proceed near thermodynamic equilibrium conditions. Furthermore, these growth techniques have made it possible to create artificial materials with physical properties on the atomic scale, such as various nanostructures including quantum dots and nanowires. Thus, a fundamental understanding of the growth processes in these techniques not only leads to better growth techniques, but it also gives guiding principles for the fabrication of the novel materials that are not found in nature.

As a physical process, the growth of thin films is controlled by various growth processes that involve adsorption of atoms or molecules onto a surface, their subsequent diffusion across the surface, dissociation of molecules, and desorption at the gas–solid interface in the growth front. It is well known that reconstructed structures appear on the growth front (surfaces) of semiconductor materials [1]. Therefore, we have to understand the atomic structures on the surfaces to control the interface mass transfer. To this end, so far a lot of theoretical work has been carried out to investigate the surface structures of semiconductors using *ab initio* calculation, which is a promising tool for clarifying the complicated growth processes because of its ability to calculate electronic structures and total energy [2–4]. Kaxiras et al. [2] studied the lowest-energy geometry for GaAs(111) with different stoichiometries. Qian et al. [3] discussed the relationship between the stoichiometry and the surface reconstruction on GaAs(001) by means of chemical potentials. Northrup [4] classified the stable structures on Si(001)H using H chemical potential. All of these approaches discussed the static structural stability on the surfaces at 0 K, although the methodologies are different.

Generally, vapor-phase epitaxy, such as MBE and MOVPE, is performed under finite temperatures and gas pressures. This implies that it is indispensable to consider the ambient conditions to predict the reconstructed structures on the growth surfaces. We [5,6] proposed an *ab initio*-based chemical potential approach that incorporates the free energy of gas phase. Therefore, the theoretical approach is useful to analyze the influence of temperatures and gas pressure on the stability of reconstructed surfaces. By the application of this method, growth kinetics and processes can be investigated. In this article, we discuss the feasibility of the chemical potential approach to the actual growth system, such as MBE growth and MOVPE growth for GaAs, GaN, lattice-mismatched InAs, and InGaN. Surface-phase diagram calculations as functions of temperature and gas pressure are performed for GaAs(001), GaAs(111), InAs(001), InAs(111), GaN(0001), GaN(000-1), GaN(1-100), GaN(11-20), GaN(1-101), GaN(11-22),  $\text{In}_{0.25}\text{Ga}_{0.75}\text{N}(0001)$ ,  $\text{In}_{0.25}\text{Ga}_{0.75}\text{N}(1-100)$ , and  $\text{In}_{0.25}\text{Ga}_{0.75}\text{N}(2-201)$ . Furthermore, kinetic growth processes on

these surfaces are also investigated using kinetic Monte Carlo (kMC) simulations on the basis of the results of adsorption, desorption, and migration energies obtained by the ab initio calculations. Comparative studies between GaAs and lattice-mismatched InAs on GaAs and among polar, nonpolar, and semipolar surfaces of GaN and  $\text{In}_{0.25}\text{Ga}_{0.75}\text{N}$  are shown to check the versatility of the chemical potential approach to adatom behavior on various semiconductor surfaces.

## 11.2 Computational Methods

### 11.2.1 Chemical Potential

To investigate the reconstructed structures on semiconductor surfaces under a certain growth condition, we carried out a step-by-step theoretical approach. First, the relative stability among various surface reconstructions was discussed to select the candidate surfaces. Then, the  $p$ - $T$  surface phase diagram was calculated, in which  $p$  is the partial pressure of source gas and  $T$  is the growth temperature. The relative stability among various surfaces was studied using the surface formation energy according to the conventional thermodynamic formalism [7]. The surface formation energy,  $E_f$ , is estimated by the following equation:

$$E_f = E_{\text{tot}} - E_{\text{ref}} - \sum_i N_i \mu_i, \quad (11.1)$$

where  $E_{\text{tot}}$  and  $E_{\text{ref}}$  are the total energy of the surface under consideration and of the reference surface, respectively;  $\mu_i$  is the chemical potential of the  $i$ th species; and  $N_i$  is the number of excess or deficit  $i$ th atoms with respect to the reference. In the present article, we considered the surface stability of prototypical semiconductors, such as GaAs, InAs, GaN, and InGaN. In these cases, the surface is assumed to be in equilibrium with bulk semiconductor expressed as

$$\mu_{\text{III}} + \mu_{\text{V}} = \mu_{\text{III-V}}^{\text{bulk}}, \quad (11.2)$$

where  $\mu_{\text{III}}$ ,  $\mu_{\text{V}}$  and  $\mu_{\text{III-V}}^{\text{bulk}}$  are the chemical potential of a group-III element, group-V element, and bulk semiconductor, respectively. The allowable range for  $\mu_{\text{III}}$  is

$$\mu_{\text{III}}^{\text{bulk}} - \Delta H_f < \mu_{\text{III}} < \mu_{\text{III}}^{\text{bulk}}, \quad (11.3)$$

where  $\mu_{\text{III}}^{\text{bulk}}$  is the chemical potential of a group-III element in the condensed phase and  $\Delta H_f [= \mu_{\text{III}}^{\text{bulk}} + \mu_{\text{V}}^{\text{bulk}} - \mu_{\text{III-V}}^{\text{bulk}}]$  is the heat of formation. The allowable range for  $\mu_{\text{V}}$  is given in the same manner. Moreover, Eqn (11.1) is applicable to the discussion of hydrogen coverage. In the case of MOVPE growth, there are hydrogen atoms around the growth surface. This implies that a number of dangling bonds on the growth surface would be terminated by hydrogen. To examine the hydrogen coverage on the surface, Eqn (11.1) is modified as

$$E_f = E_{\text{tot}} - E_{\text{ref}} - \sum_i N_i \mu_i - N_{\text{H}} \mu_{\text{H}}, \quad (11.4)$$

where  $N_{\text{H}}$  and  $\mu_{\text{H}}$  are the number and the chemical potential of hydrogen, respectively. Using these equations, we can discuss the relative stability of surface reconstructions as functions of  $\mu_i$  and/or  $\mu_{\text{H}}$ .

By the theoretical analyses described above, we can select the candidate structures appearing on the growth surface. Next, we investigate the stability of these surface structures under certain growth conditions, such as gas pressure and growth temperature. To study the issues, we proposed an ab initio-based chemical potential approach that incorporates free energy of gas phase [5]. The concept of this theoretical approach is shown in Figure 11.1. An impinging atom (molecule) can adsorb on the surface if the free energy of an atom (molecule) in the gas phase is larger than the adsorption energy of it. On the other hand, the desorption of an impinging atom (molecule) occurs if the free energy of it in the gas phase is smaller than the adsorption energy. Here, the free energy of an atom (molecule), which called a chemical potential,  $\mu_{\text{gas}}$ , can be computed by using quantum statistical mechanics [8]. The adsorption energy,  $E_{\text{ad}}$ , can be obtained by ab initio calculations. By comparing  $\mu_{\text{gas}}$  with  $E_{\text{ad}}$ , we can discuss the adsorption–desorption behavior, as shown in Figure 11.1.

The chemical potential  $\mu_{\text{gas}}$  for the ideal gas is given by

$$\mu_{\text{gas}} = -k_{\text{B}}T \ln(gk_{\text{B}}T/p \times \zeta_{\text{trans}}\zeta_{\text{rot}}\zeta_{\text{vibr}}), \quad (11.5)$$

$$\zeta_{\text{trans}} = (2\pi mk_{\text{B}}T/h^2)^{3/2}, \quad (11.6)$$

$$\zeta_{\text{rot}} = (1/\pi\sigma) \left\{ 8\pi^3 (I_{\text{A}}I_{\text{B}}\dots)^{1/n} k_{\text{B}}T/h^2 \right\}^{n/2}, \quad (11.7)$$

$$\zeta_{\text{vibr}} = \prod_i^{3N-3-n} \{1 - \exp(-h\nu_i/k_{\text{B}}T)\}^{-1}, \quad (11.8)$$

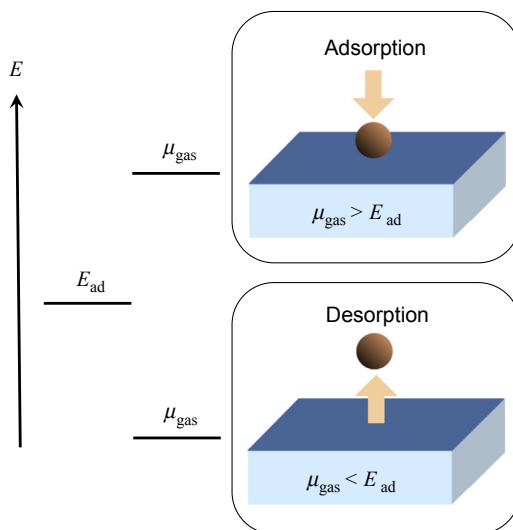


**FIGURE 11.1** Concept of the theoretical approach for discussing the adsorption–desorption behavior of adatoms impinging on the surface. If the chemical potential,  $\mu_{\text{gas}}$  is larger than adsorption energy,  $E_{\text{ad}}$ , net adsorption would occur. If  $\mu_{\text{gas}} < E_{\text{ad}}$ , net desorption would occur.

**Table 11.1** Degeneracy of the Electron Energy Levels of the Various Elements

	Element	$g$
I	H, Li, Na, K, Rb, Cs, Cu, Ag, Au	2
II	Be, Mg, Ca, Sr, Ba, Zn, Cd, Hg	1
III	B, Al, Ga, In, Tl	2
IV	C, Si, Ge, Sn, Pb	3
V	N, P, As, Sb, Bi	4
VI	O, S, Se, Te, Po	3
VII	F, Cl, Br, I	2
0	He, Ne, Ar, Kr, Xe, Rn	1

where  $\zeta_{\text{trans}}$ ,  $\zeta_{\text{rot}}$ , and  $\zeta_{\text{vibr}}$  are the partition functions for the translational motion, the rotational motion, and the vibrational motion, respectively. Here,  $k_B$  is Boltzmann's constant,  $T$  is the temperature,  $g$  is the degree of degeneracy of the electron energy level (see Table 11.1),  $p$  is the partial pressure of the particle,  $m$  is the mass of one particle,  $h$  is Planck's constant,  $\sigma$  is the symmetric factor,  $I_1$  is the moment of inertia,  $n$  is the degree of freedom of the rotation,  $N$  is the number of atoms in the particle,  $i$  is the degree of freedom for the vibration, and  $\nu$  is the frequency.  $I_1$  is written as

$$I_1 = m_1 r^2, \quad (11.9)$$

where  $m_1$  is the reduced mass and  $r$  is the radius of gyration.

The adsorption energies of adatoms (molecules) were obtained by ab initio calculations. In the total energy calculations for the compound semiconductor surfaces with various atomic arrangements, we used the ab initio pseudopotential method based on the local-density functional formalism [9] within the generalized gradient approximation [10]. The detailed procedure in the total energy calculations has been reported elsewhere [11–30]. Using these chemical potentials  $\mu$  and adsorption energies  $E_{\text{ad}}$ , the adsorption–desorption behavior or the relative stability of reconstructions on the compound semiconductor surfaces is clarified as functions of  $p$  and  $T$ .

Equations (11.5)–(11.9) are applicable for an ideal gas. Here, we discuss the pressure range in the application of this approach. Under the low-pressure conditions seen in MBE, atoms (or molecules) in the gas phase have almost no interaction with each other. In such cases, we can consider an ideal gas approximation. On the other hand, atoms (or molecules) in a real gas would interact with each other. For instance, the pressure dependence of the chemical potential for the real gas might resemble that shown in Figure 11.2. To adapt Eqns (11.5)–(11.9) to this case, the true pressure,  $p$ , should be replaced by an effective pressure,  $f$ , called the fugacity [31]. The fugacity is represented as.

$$f = \gamma p, \quad (11.10)$$

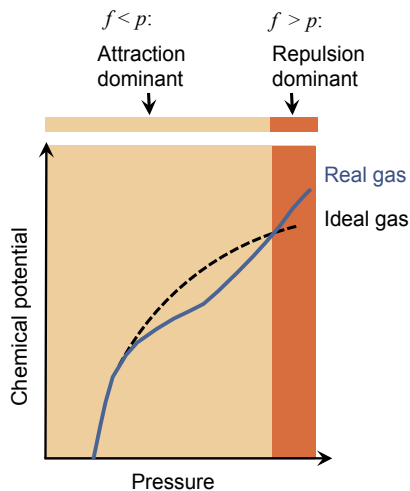


**FIGURE 11.2** The chemical potential of a real gas. As  $p \rightarrow 0$ , the chemical potential coincides with the value for an ideal gas. If attractive forces are dominant, the chemical potential is less than that of the ideal gas. At high pressures, when repulsive forces are dominant, the chemical potential is greater than that of an ideal gas.

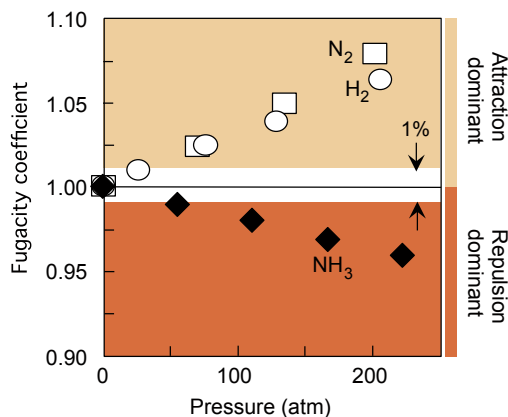


**FIGURE 11.3** Fugacity coefficient of  $N_2$ ,  $H_2$ , and  $NH_3$  at 800 K (523 °C) as a function of pressure,  $p$ . The fugacity coefficient is almost unity at  $p = 1$  atm, which is a typical total pressure of MOVPE.

where  $\gamma$  is the dimensionless fugacity coefficient. Figure 11.3 shows the fugacity coefficient of  $H_2$ ,  $N_2$ , and  $NH_3$  at 800 K (527 °C) as a function of pressure [31]. These molecules are typically used in the III-nitride MOVPE. In Figure 11.3, the fugacity coefficient of these gases are within  $1.00 \pm 0.01$  at  $p < 25$  atm. That is, the deviations from the ideal systems are within 1% at  $p < 25$  atm in case of  $T = 800$  K, which is a conventional MOVPE growth temperature of In-related semiconductors. This implies that the theoretical approach is applicable to investigate the surface structures in the conventional MOVPE performed at  $p = 1$  atm. When we discuss the stability of surface structures in a

high-pressure growth performed at  $p > 25$  atm, the fugacity coefficients should be incorporated in the approach. In this article, we studied the stability of the various surfaces in the MBE or conventional MOVPE. Therefore, we considered the ideal gas approximation in the following analyses.

## 11.2.2 Monte Carlo Simulations

We employ two Monte Carlo simulation methods in the present study. One of those is an electron-counting Monte Carlo (ECMC) simulation based on the Metropolis Monte Carlo (MMC) simulation [5,32,33]. The ECMC simulations were carried out to investigate the transition process among the surface reconstructions. For example, we found that Ga atoms can replace the topmost As atoms on the  $c(4 \times 4)$  surface to form Ga–As dimers. We performed ECMC simulations to study the stability of disordered dimer arrangements for the  $c(4 \times 4)$  surface with Ga–As dimers, which would appear in the transition process. In the ECMC simulation, we employ the energy of various disordered dimer arrangements in the  $c(4 \times 4)$  surface unit cell obtained by the ab initio calculations to equilibrate the surface. The dimer arrangements are recorded for a lattice size of  $100 \times 100$  surface unit cell of  $c(4 \times 4)$ . Periodic boundary conditions are imposed on the  $x$ - $y$  plane.

Another simulation method used in this study is kMC simulation. The kMC simulation is used for investigating the surface lifetime  $\tau$  and diffusion length  $L$  of one adatom while staying on the surface [32]. In the simulation procedure, specific lattice sites for an adatom on the surface are assumed—that is, a discrete lattice-gas model is employed. The site-correlated adsorption probability  $P_{\text{ad}}(x)$  is written, assuming the local-thermal equilibrium approximation, by

$$P_{\text{ad}}(x) = \frac{\exp(-\Delta\mu(x)/k_{\text{B}}T)}{\{1 + \exp(-\Delta\mu(x)/k_{\text{B}}T)\}}, \quad (11.11)$$

where  $\Delta\mu(x)$  is the difference of chemical potentials between the cases of an atom on the site  $x$ ,  $\mu_{\text{ad}}(x)$ , and in the gas phase,  $\mu_{\text{gas}}$ . That is,  $\Delta\mu(x) = \mu_{\text{ad}}(x) - \mu_{\text{gas}}$ . Here, the chemical potential of an atom on the surface  $\mu_{\text{ad}}(x)$  corresponds to minus desorption energy  $E_{\text{de}}(x)$ . The chemical potential of the atom in the gas phase  $\mu_{\text{gas}}$  is given by Eqn (11.5). The diffusion probability  $P_{\text{diff}}(x \rightarrow x')$  is assumed to be in the Arrhenius form of

$$P_{\text{diff}}(x \rightarrow x') = \nu_{\text{lattice}} \exp\left(-\frac{\Delta E(x \rightarrow x')}{k_{\text{B}}T}\right), \quad (11.12)$$

where the diffusion prefactor  $\nu_{\text{lattice}}$  is  $2k_{\text{B}}T/h$  [34] and  $\Delta E(x \rightarrow x')$  is the local activation energy involving the adatom hopping from site  $x$  to  $x'$ . The desorption probability  $P_{\text{de}}(x)$  is written by

$$P_{\text{de}}(x) = \nu_{\text{lattice}} \exp\left\{-\left(\frac{E_{\text{de}}(x) - \Delta\mu(x)}{k_{\text{B}}T}\right)\right\}, \quad (11.13)$$

This equation implies that the difference  $\Delta\mu(x) [= \mu_{\text{ad}}(x) - \mu_{\text{gas}}]$  of chemical potentials between the cases of an atom on the surface and in the gas phase influences the activation energy for desorption of the atom. That is, the adatom easily desorbs if  $\mu_{\text{gas}}$  is

lower than  $\mu_{\text{ad}}(x)$ , while the atom prefers to stay on the surface if  $\mu_{\text{gas}}$  is higher than  $\mu_{\text{ad}}(x)$ . More precisely, the probability  $\exp\{-E_{\text{de}}(x)/k_{\text{B}}T\}$  for surmounting the activation energy of  $E_{\text{de}}(x)$  is reduced (or enhanced) by a weighting function of  $\exp\{\Delta\mu(x)/k_{\text{B}}T\}$ , which corresponds to the local-thermal equilibrium desorption probability. On the basis of the above-mentioned stochastic differential equation, we carried out the kMC random-walk simulations and estimated the  $\tau$  and  $L$  of one adatom on the surface. The diffusion coefficient  $D$  is also computed by  $D = L^2/(2\tau)$ .

## 11.3 GaAs

Atomic structure of the reconstructions during and after MBE growth on the compound semiconductor surfaces has been the subject of a number of experimental investigations. GaAs(001) surfaces have attracted much attention in general technological fields as well as in the field of surface science; these surfaces are the most popular for epitaxial growth and reveal a large variety of surface superstructures depending on the substrate temperature and As pressure, as shown in Figure 11.4 [1]. In particular, GaAs(001)-c(4 × 4) and -(2 × 4) surfaces have been intensively studied because of their technological importance for thin film fabrications and scientific interest in surface phase transition between c(4 × 4) and (2 × 4) when the substrate temperature and As pressure are changed [35–40]. GaAs(111)B surfaces have also received considerable attention due to their advantages in fabricating nanostructures such as nanodots and nanowires [41–44]. As for the structural and physical properties of the GaAs(111)B surface, experimental and theoretical studies [45–55] have found that GaAs(111)B surfaces take various surface reconstructions, such as (2 × 2) and  $(\sqrt{19} \times \sqrt{19})R 23.4^\circ$ , depending on temperature and As pressure. The scanning tunneling microscopy (STM) observations have shown that the change from the  $(\sqrt{19} \times \sqrt{19})R 23.4^\circ$  to the (2 × 2) reconstruction occurs below 560 °C in MBE [54]. From theoretical viewpoints, surface energy calculations for various surface

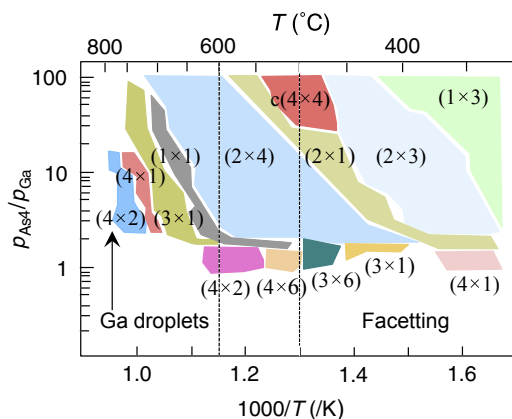


FIGURE 11.4 Surface-phase diagram of GaAs(001).

structures have revealed that the stable surface reconstruction depends on the chemical potential of As. The  $(2 \times 2)$  surface with As trimer is stable over a wide range of As chemical potential [47,50]. Therefore, these results indicate that the GaAs(111)B- $(2 \times 2)$  surface with As trimer appears in the growth condition of the MBE ( $\sim 500^\circ\text{C}$ ) [51,54].

In this section, the adsorption–desorption behavior of Ga and As atoms on these GaAs surfaces such as (001)- $c(4 \times 4)$ , (001)- $(2 \times 4)$ , and (111)B- $(2 \times 2)$  are investigated as functions of growth conditions, such as temperature and pressure, of Ga, As<sub>2</sub>, and As<sub>4</sub> using chemical potential approach. On the basis of the calculated adsorption energy and chemical potential of Ga, As<sub>2</sub>, and As<sub>4</sub>, phase diagrams of these surfaces are shown to identify the stable surface structures at certain growth conditions. Furthermore, growth processes on these surfaces are discussed in terms of the self-surfactant effect, where Ga adatoms act as self-surfactant atoms to maintain layer-by-layer growth without antisite defect formation on the compound semiconductor surfaces. Phase transitions between the GaAs(001)- $c(4 \times 4)$  and  $-(2 \times 4)$  surfaces are also successfully clarified by investigating relative stability between the GaAs(001)- $c(4 \times 4)$  surfaces with various surface dimers predicted by the surface phase diagram calculations and  $-(2 \times 4)$  surfaces with Ga deposition predicted by ECMC simulations.

### 11.3.1 Surface Structures of GaAs

Figure 11.5 shows various GaAs(001) surface structures, including  $c(4 \times 4)_\alpha$ ,  $c(4 \times 4)_\beta$ , and  $(2 \times 4)_\beta 2$  surfaces, which are considered in this section. It was believed for a long time that the  $c(4 \times 4)$  surface was composed of three As–As dimers per surface unit cell, as shown in Figure 11.5(B). However, Ohtake et al. [35] proposed the new structure model of the  $c(4 \times 4)$  surface with three Ga–As dimers per surface unit cell, as shown in

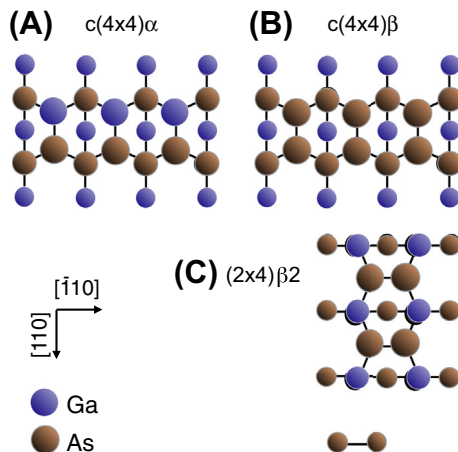


FIGURE 11.5 Schematic of the GaAs(001) surfaces: (A)  $c(4 \times 4)_\alpha$  with Ga–As dimer, (B)  $c(4 \times 4)_\beta$  with As–As dimer, and (C)  $(2 \times 4)_\beta 2$ .

Figure 11.5(A). Using the chemical potential and adsorption energy, the change in the stable structure of the  $c(4 \times 4)$  surfaces is clarified by considering adsorption or desorption of surface dimers as functions of temperature and As pressure. Figure 11.6 shows the surface phase diagram of the  $c(4 \times 4)$  with different dimer constituents under  $\text{As}_2$  and  $\text{As}_4$  [56,57]. Under  $\text{As}_2$ , the  $c(4 \times 4)$  surface with As dimers is stable at low temperatures less than  $\sim 400$  K, whereas the surface with Ga–As dimers is stabilized at relative high temperatures in the range of  $\sim 400$ – $700$  K. This is because the desorption energy of the As dimer (1.78 eV) is smaller than that of the Ga–As dimer (4.31 eV). These results agree with the previous reported STM measurements, which imply that the  $c(4 \times 4)\alpha$  surface with the Ga–As dimer is stable in the temperature range of 473–723 K [35]. On the other hand, it should be noted that the  $c(4 \times 4)\beta$  surface with As dimer does

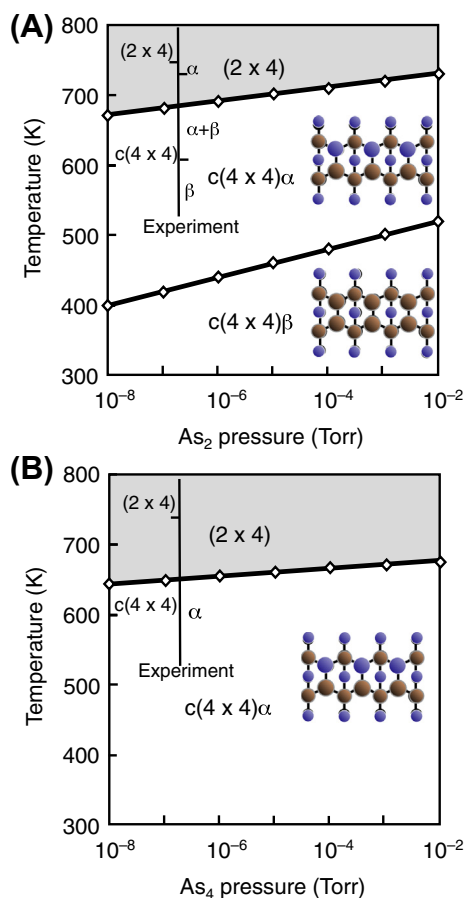
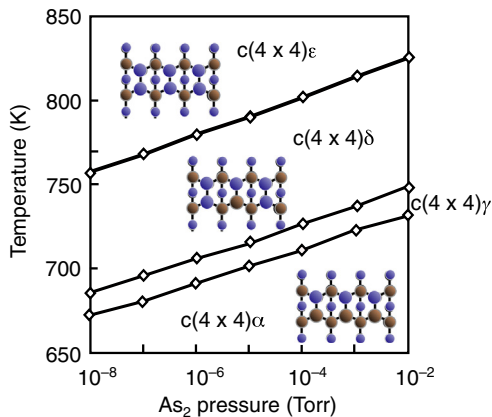


FIGURE 11.6 Calculated surface phase diagrams of the GaAs(001)- $c(4 \times 4)$  as functions of temperature and (A)  $\text{As}_2$  pressure and (B)  $\text{As}_4$  pressure. Blue and orange circles denote Ga and As atoms, respectively. Inserted bar indicates the temperature range of the  $c(4 \times 4)$  surface with various surface dimers observed by experiments.



**FIGURE 11.7** Calculated surface-phase diagram of the GaAs(001)- $c(4 \times 4)$  with various surface dimers as functions of temperature and As pressure. Blue and orange circles denote Ga and As atoms, respectively.

not appear even at low temperatures under  $\text{As}_4$ , as shown in Figure 11.6(B). This is because the desorption energy of the As dimer becomes almost zero (0.12 eV) in contrast with the still large value of Ga–As dimer (3.48 eV) under  $\text{As}_4$ . This is also consistent with experimental results [37,58]. If we increase the temperatures, more various combinations of As, Ga–As, and Ga dimers appear in the surface unit, as seen in Figure 11.7. Co-existence of two Ga–As and one Ga dimers in the  $c(4 \times 4)$  unit cell denoted by  $c(4 \times 4)\gamma$  is found within the temperature range of approximately 700–710 K. The surface with one Ga–As and two Ga dimers denoted by  $c(4 \times 4)\delta$  appears beyond  $\sim 710$  K because of large desorption energy of Ga dimers (6.40 eV). The temperature range around 710 K is almost the same with phase transition temperature between  $c(4 \times 4)$  and  $(2 \times 4)\beta 2$ . This suggests that these  $c(4 \times 4)$  surfaces with different dimers are candidates for the phase transition state.

Sasaki and Yoshida investigated the surface reaction of trimethylgallium (TMG) on the  $c(4 \times 4)$  and  $(2 \times 4)$  surfaces using quadrupole mass spectroscopy (QMS) and reflection high-energy electron diffraction (RHEED) measurements at 738 K [40]. The QMS intensity variation for the surface of  $c(4 \times 4)$  with a 0.46 monolayer (ML) of Ga is identical to that for the surface of  $(2 \times 4)$  with 0.018 ML of Ga. These results suggest that predepositing Ga has a crucial role for the phase transition between  $c(4 \times 4)$  and  $(2 \times 4)$  surfaces. Our previous studies also clarified that preexisting of Ga on the  $c(4 \times 4)$  is closely related to the phase transition from the  $c(4 \times 4)$  to  $(2 \times 4)$  surfaces using ECMC simulation, ab initio calculations, and STM [59–61]. On the grounds of these aspects, we discuss the phase transition from  $c(4 \times 4)$  to  $(2 \times 4)$  under the existence of excess Ga on the surfaces. Figure 11.8 shows the schematic of ECMC simulation results for resultant  $(2 \times 4)$  surface structure (type 1 and 2) via deposition of a 0.5 ML of Ga from three kinds of  $c(4 \times 4)$  initial surfaces. This figure implies that a type 2 structure similar to  $(2 \times 4)\beta 2$

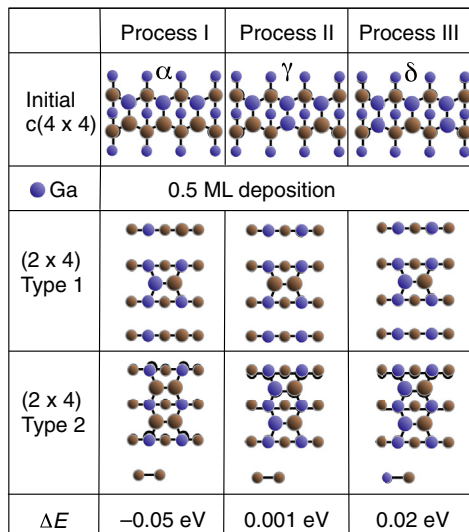


**FIGURE 11.8** Schematic of the simulated results for the surface phase transition from three kinds of  $c(4 \times 4)$  to  $(2 \times 4)$  surfaces (type 1 and 2) appearing via a 0.5 ML of Ga deposition. Blue and orange circles denote Ga and As, respectively. The relative energy differences between type 1 and 2 structures obtained by ab initio calculations are also shown.

appears when phase transition is initiated from the  $c(4 \times 4)$  with Ga–As dimers (process I), whereas the  $c(4 \times 4)$  with two Ga dimers in the surface unit favors the type 1 structure (process III). In case of process II, the  $c(4 \times 4)$  with two Ga–As and one Ga dimers in the surface unit might lead its structure to both type 1 and 2 structures because of very small energy difference between them (0.001 eV/atom). That is, the phase transition from  $c(4 \times 4)$  to  $(2 \times 4)$  would proceed by process I or II. This seems to be reasonable because the stable temperature range of these two initial surfaces around 700 K agree with phase transition temperatures observed experimentally. Moreover, this finding is qualitatively consistent with STM analyses, where the  $c(4 \times 4)$  with Ga–As dimers initiates the phase transition from the  $c(4 \times 4)$  to  $(2 \times 4)$  with As-dimers [37].

### 11.3.2 Growth on GaAs Surfaces

To clarify the growth processes of semiconductors, we have to understand each elementary process that progresses on the growth surfaces. In this section, we discuss the migration and adsorption–desorption behavior of adsorbate on the GaAs(001)- $c(4 \times 4)$ . Figure 11.9 shows the calculated migration potentials for Ga and As adatoms on the  $c(4 \times 4)$  $\alpha$  surface with Ga–As dimers. The results suggest that Ga and As adatoms prefers the lattice sites E and L, respectively. In general, adatoms on the compound semiconductor surfaces prefer the lattice site to lower strain energy and suppress the number of electrons remaining in the surface dangling bonds [62]. The

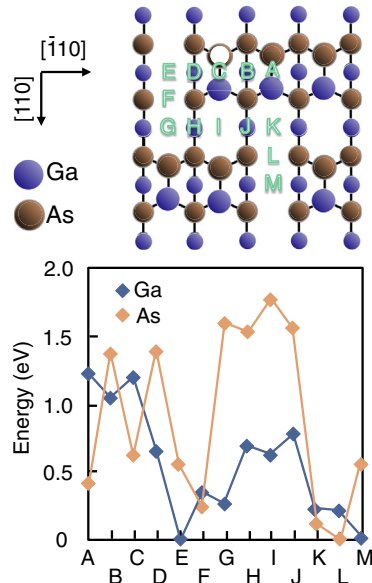


**FIGURE 11.9** Calculated migration potentials for Ga (blue diamond) and As (orange diamond) adatoms on the GaAs(001)- $c(4 \times 4)$  surface with Ga–As dimers.

lattice sites E and L do not suppress the number of electrons in the dangling bonds but lower the strain energies because of the formation of interatomic bonds with As atoms at the regular fcc sublattice sites in the second layer. Moreover, these preferable lattice sites for adatoms can be simply interpreted by the coordination number. Ga adatom at the E site is stabilized by forming Ga–As bonds with an ideal coordination number of 4 for GaAs, whereas As adatoms at the L site with As–As bonds have the coordination number 2, which is close to ideal coordination number 3 for As. Figure 11.10 shows the adsorption–desorption transition curve for the Ga adatom (Figure 11.10(A)) and As adatom (Figure 11.10(B)) on the  $c(4 \times 4)\alpha$  surface, with Ga–As dimers as functions of temperature and pressures. The calculated results reveal that Ga adatoms can adsorb even at high temperatures, while desorption of As adatoms occurs even at low temperatures. This is because the desorption energy of the Ga adatom ( $\sim 3$  eV) is much larger than that of the As adatom ( $\sim 0.4$  eV). The difference in desorption energy between Ga and As adatoms is due to the fact that the Ga adatom at the preferable E site forms strong Ga–As bonds in contrast with the formation of weak As–As bonds for As adatom at the L site. Thus, these results reveal that Ga atoms can adsorb and migrate on the surfaces while desorption of As adatoms proceeds without sufficient migration. Therefore, Ga adatoms play a crucial role for the epitaxial growth of GaAs on the  $c(4 \times 4)$  surfaces.

Figure 11.11(A) depicts the structure of the GaAs(111)B- $(2 \times 2)$  surfaces with excess As-trimer on the ideal (111) surface. To fabricate GaAs thin films, a monolayer of Ga and

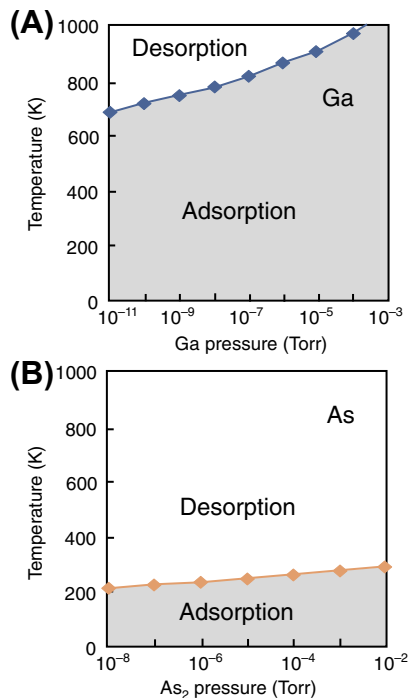


FIGURE 11.10 Calculated adsorption-desorption transition curve for the (A) Ga adatom and (B) As adatom as functions of temperature and pressure.

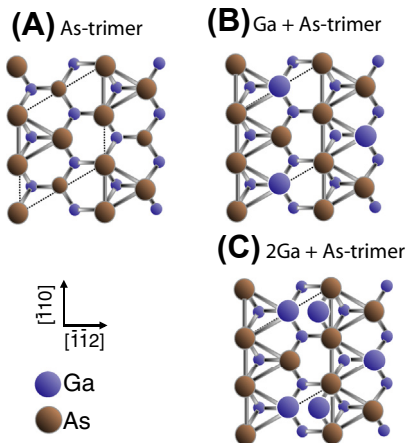
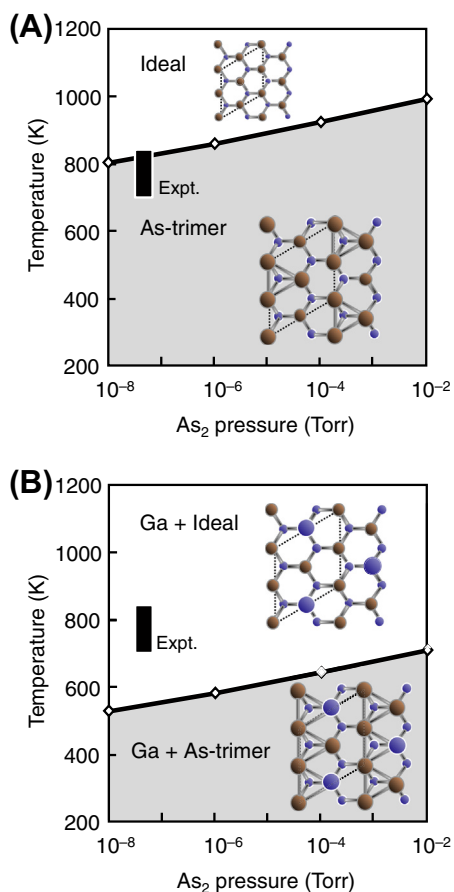


FIGURE 11.11 Schematic of the GaAs(111)B-( $2 \times 2$ ) surfaces (A) with As-trimer, (B) Ga + As-trimer with one Ga adatom, and (C) 2Ga + As-trimer with two Ga adatoms.

As has to be alternatively incorporated on the surface with excess As-trimer. Therefore, clarifying how layer-by-layer growth is maintained on the  $(2 \times 2)$  surface by controlling the excess As-trimer is one of fundamental problems in GaAs MBE growth. To this end, we also employ the GaAs(111)B- $(2 \times 2)$  surfaces with Ga + As-trimer with one Ga adatom (Figure 11.11(B)), and  $2\text{Ga} + \text{As-trimer}$  with two Ga adatoms (Figure 11.11(C)) in this section. The surface structures with Ga adatoms are obtained due to the relaxation to form Ga–As bonds between the Ga adatom and top As atoms. The additional Ga adatom forms two Ga–As bonds between top As atoms constituting the neighboring As trimer. Because the Ga–As bond is basically the most energetically favorable configuration among Ga–Ga, Ga–As and As–As bonds, the stable positions of Ga adatoms can be understood by stable Ga–As bond formation. Using these stable structures, the phase diagrams of the  $(2 \times 2)$  surfaces under  $\text{As}_2$  flux are calculated as shown in Figure 11.12.



**FIGURE 11.12** Calculated surface phase diagrams of GaAs(111)B- $(2 \times 2)$  surfaces: (A) without Ga adatom and (B) with one Ga adatom as functions of temperature and  $\text{As}_2$  pressure. In the shaded regions, the As trimer is stable on the surface. Inserted bars with Expt. denote the temperature range of GaAs(111)B- $(2 \times 2)$  surface.

Figure 11.12(A) indicates that the  $(2 \times 2)$  surface with As trimer is stable at temperatures less than  $\sim 800$  K, whereas that without As trimer is stabilized beyond  $\sim 800$  K. In contrast, the  $(2 \times 2)$  surface without As trimer is stable beyond  $\sim 560$  K for the Ga + As-trimer surface with one Ga adatom (Figure 11.12(B)). Similar results were obtained for the  $2\text{Ga} + \text{As}$ -trimer with two Ga adatoms [12]. The low transition temperatures from the  $(2 \times 2)$  surfaces with As trimer to those without As trimer in the Ga adsorbed cases suggest that the As-trimer desorption is promoted by Ga adatoms. This is because the desorption energy of As trimer with Ga adatoms (3.6–3.8 eV) is much lower than that without Ga adatom (5.4 eV). The decrease in the desorption energy clearly manifests a self-surfactant effect, where Ga adatoms induce As rearrangement during GaAs epitaxial growth, as clarified in GaAs(001) [63] and GaAs(111)A surfaces [64]. Moreover, it should be noted that the difference in the transition temperature for the As-trimer desorption between the  $(2 \times 2)$  surfaces with one and two Ga adatoms is less than 20 K. This reflects the small energy difference in  $E_{\text{de}}$  (within 0.2 eV), implying that the growth can be promoted even if one Ga atom is adsorbed on the  $(2 \times 2)$  surface unit. Consequently, Ga deposition during MBE growth promotes As-trimer desorption to realize layer-by-layer growth of GaAs on the GaAs(111)B- $(2 \times 2)$  surface, as schematically shown in Figure 11.13.

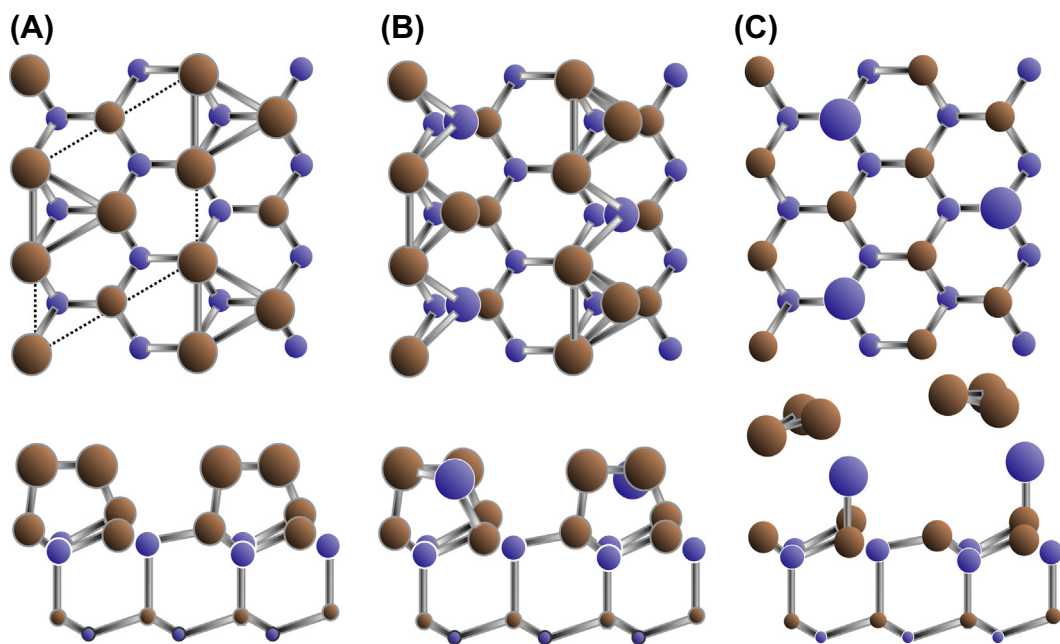


FIGURE 11.13 Schematic of the  $(2 \times 2)$  surface: (A) with As-trimer, (B) with As-trimer and Ga adatom, and (C) with Ga adatom without As-trimer. Change in surface structure from (A) to (C) shows the self-surfactant effect.

## 11.4 InAs on GaAs

InAs/GaAs heteroepitaxial systems grown by MBE are crucial for fabricating low-dimensional semiconductor nanostructures, including quantum dots (QDs). Due to the 7% lattice mismatch between InAs and GaAs, many shapes of self-assembled QDs can be fabricated depending on growth orientations. The InAs on the GaAs(001) produces a three-dimensional island shape on the InAs with Stranski-Krastanov growth mode [65], whereas the InAs stacking-fault tetrahedrons (SFT) as a QD is also fabricated on the GaAs(111)A [66]. Because of the successful fabrication of the InAs QDs on the GaAs(001), there have been some experimental studies for investigating microscopic growth processes of the InAs on the GaAs(001) using STM and in situ scanning tunneling microscopy [67–70].

Many studies have been also done for surface structures and In adatom diffusion on the InAs/GaAs(001) from theoretical viewpoints [71–79]. For the InAs/GaAs(111), Yamaguchi et al. reported experimental measurements using STM on the mechanisms of strain relaxation in InAs/GaAs(111)A heteroepitaxy to propose a possible model for the resulting semicoherent interface structure [80]. Ohtake et al. studied strain-relaxation processes in the InAs/GaAs(111)A using a rocking-curve analysis of RHEED [81]. Zepeda-Ruiz et al. theoretically analyzed the strain relaxation at the semicoherent interface structure consisting of a network of interacting misfit dislocations [82]. Joe et al. have also investigated the SFT formation in InAs/GaAs(111) using empirical interatomic potentials to clarify the contribution of strain relaxation stabilizing it [83]. These previous studies have mainly focused on the strain relaxation at the InAs/GaAs(111) interface without incorporating surface-related phenomena. From the viewpoint of surface phenomena, Taguchi and Kanisawa have studied the surface structures and adsorption–desorption behavior on the InAs(111)A surface using ab initio calculations [84].

In this section, we systematically investigate adsorption–desorption behavior on the InAs heteroepitaxially grown on GaAs(001) and GaAs(111)A. Using these results, a surface-phase diagram of the InAs wetting layer (WL) is obtained to compare the fully relaxed InAs surface. The contribution of the heterointerface to the structural change is discussed as functions of temperature and gas pressure. On the basis of the calculated results, distinctive features in the InAs wetting layers are clarified.

### 11.4.1 Surface Structures of the InAs Wetting Layer

To clarify the effect of the lattice constraint and the heterostructures, we consider the InAs(001) surface without lattice constraints (hereafter InAs(001)), the InAs(001) surface with an in-plane lattice parameter of bulk GaAs (hereafter InAs(001)-S), and a GaAs(001) surface covered with approximately two layers of InAs (hereafter InAs-W), as shown in Figure 11.14. Figure 11.15(A) shows the calculated surface-phase diagrams of InAs(001), InAs(001)-S, and InAs(001)-W as functions of temperature  $T$  and gas pressure of As<sub>2</sub> molecule  $p_{\text{As}_2}$ . The phase boundary between  $(2 \times 4)\alpha_2$  and  $(2 \times 4)\beta_2$  structures on

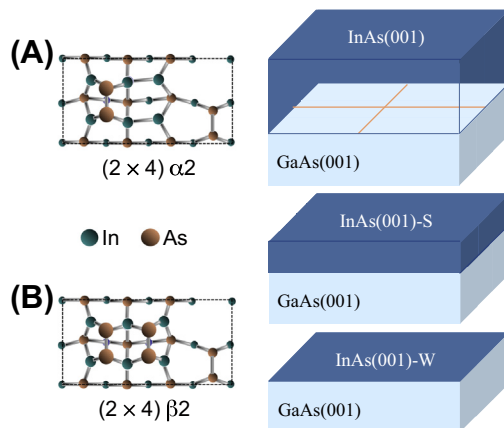


**FIGURE 11.14** Top views of InAs(001)- $(2 \times 4)$  surface structures, such as (A)  $(2 \times 4) \alpha 2$  and (B)  $(2 \times 4) \beta 2$  considered in this study. Computational models, such as InAs(001), InAs(001)-S, and InAs(001)-W used in this study, are also schematically shown in this figure.

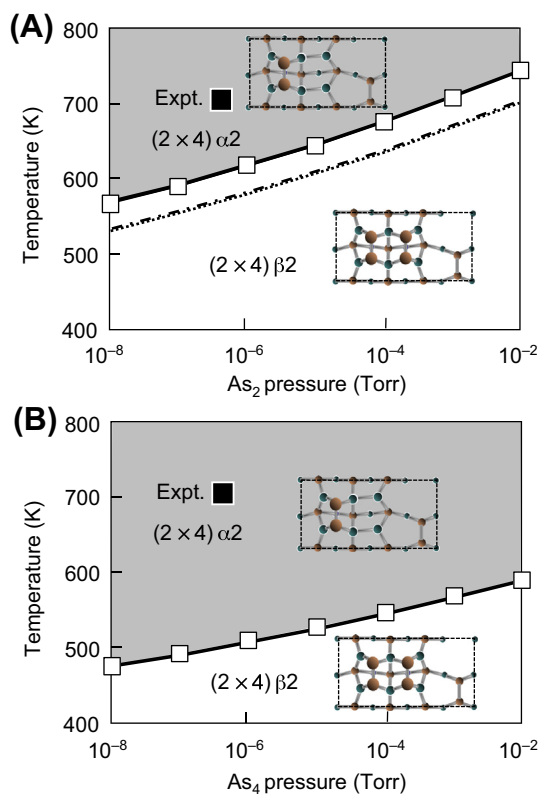


**FIGURE 11.15** Calculated surface phase diagrams of InAs(001)- $(2 \times 4)$  surfaces as functions of temperature and (A)  $\text{As}_2$  pressure and (B)  $\text{As}_4$  pressure. The solid, dashed, and dotted lines show the boundaries of the stable surface structure regions for InAs(001)-W, InAs(001), and InAs(001)-S, respectively. Experimental growth conditions are also shown as Expt. in this figure.

InAs(001) is in the range of 530–710 K (dashed line in Figure 11.15(A)). The stable temperature range of these structures is consistent with the temperature range of the MBE growth (613 K) at which both  $(2 \times 4)\alpha 2$  and  $(2 \times 4)\beta 2$  structures are observed [69]. We also find that the phase boundary on InAs(001)-S (dotted line in Figure 11.15(A)) is identical to that on InAs(001), indicating that the lattice constraint has little effect on the relative stability between  $(2 \times 4)\alpha 2$  and  $(2 \times 4)\beta 2$  structures. This is because the strain induced by in-plane lattice constraint is effectively released by the relaxation along the [001] direction in these structures. In contrast, the phase boundary on InAs-W (560–750 K, solid line in Figure 11.15(A)) is slightly higher than those on InAs(001) and InAs(001)-S. The higher phase boundary implies that the entity of InAs/GaAs interface affects the relative stability between  $(2 \times 4)\alpha 2$  and  $(2 \times 4)\beta 2$  structures. Figure 11.15(B) shows the calculated surface phase diagram for the InAs(001)-W surfaces as functions of temperature  $T$  and gas-pressure of  $\text{As}_4$  molecule  $p_{\text{As}_4}$ . Here, we employ the WL surface structure with  $\text{In}_{1/3}\text{Ga}_{2/3}\text{As}$  at the interface [70,85–87]. The phase boundary between the  $(2 \times 4)\alpha 2$  and  $(2 \times 4)\beta 2$  ranges from 470 to 600 K, which is lower than that under  $\text{As}_2$ , because the  $\text{As}_4$  molecule is more stable than  $\text{As}_2$  in the gas phase. The stable temperature range of these structures is consistent with experimental conditions during MBE growth [86,88]. This reveals that  $(2 \times 4)\alpha 2$  is stable at conventional growth conditions, such as  $T$  of  $\sim 700\text{--}750$  K and  $p_{\text{As}_4}$  of  $\sim 10^{-7}\text{--}10^{-6}$  Torr.

Figure 11.16 shows the top view of the InAs(111)A- $(2 \times 2)$  surface structures with In-vacancy ( $V_{\text{In}}$ ) (Figure 11.16(A)) and As-trimer ( $T_{\text{As}}$ ) (Figure 11.16(B)), and the three computational models considered in this study. Here, the in-plane lattice parameters

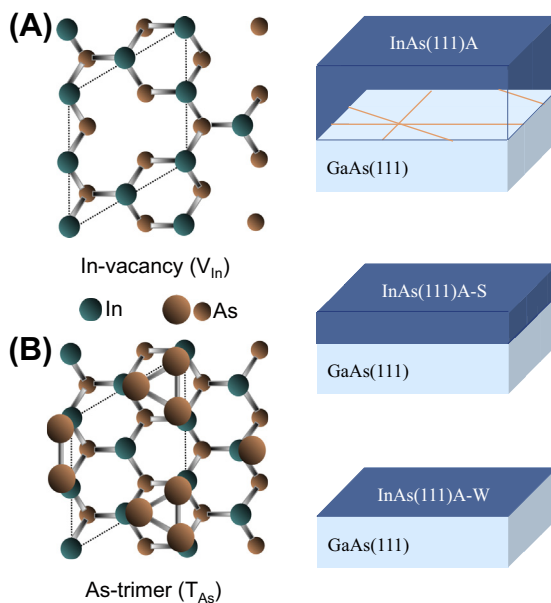


**FIGURE 11.16** Top views of InAs(111)A- $(2 \times 2)$  surface structures with (A) In-vacancy ( $V_{\text{In}}$ ) and (B) As-Trimer ( $T_{\text{As}}$ ) considered in this study. A  $(2 \times 2)$  unit cell is represented by dashed line. Computational models, such as InAs(111)A, InAs(111)A-S, and InAs(111)A-W used in this study, are also schematically shown in this figure.

$\sqrt{2}a$  ( $a$  is the lattice constant) of InAs without lattice constraint (hereafter InAs(111)A) and with lattice constraint from the GaAs substrate (hereafter InAs(111)A-S) are those in bulk InAs and GaAs, respectively. Furthermore, we also employ the InAs(111)A- $(2 \times 2)$  surface with one atomic double layer grown on the GaAs(111) substrate (hereafter InAs-W), consisting of two atomic double layers of GaAs. These models correspond to the InAs surfaces at the initial growth stage of InAs (InAs(111)A-W), at coherent growth with a large film thickness that is enough for neglecting the contribution of the InAs/GaAs interface (InAs(111)A-S), and after relaxing the lattice constraint due to misfit dislocation formation at the interface (InAs(111)A), as schematically shown in Figure 11.16. Figure 11.17 shows the calculated surface-phase diagrams for the  $(2 \times 2)$  surfaces of InAs(111)A (Figure 11.17(A)), InAs(111)A-S (Figure 11.17(B)), and InAs(111)A-W (Figure 11.17(C)) as functions of temperature and  $\text{As}_4$  pressure. Here, we assume that the gas pressure of the In atom is  $p_{\text{In}} \sim 10^{-7}$  Torr. The stable temperature ranges for  $V_{\text{In}}$  are consistent with the MBE growth temperature range of 723–773 K (shaded area), at which  $V_{\text{In}}$  is observed experimentally [80,89,90].

Figure 11.17(A) indicates that the transition temperature of 500–590 K between  $V_{\text{In}}$  and  $T_{\text{As}}$  on the InAs(111)A is larger than that on the InAs(111)A-S by  $\sim 30$  K, as shown in Figure 11.17(B) for the InAs(111)A-S. The enlargement of  $V_{\text{In}}$  stable region on the InAs(111)A-S is due to the fact that the In-vacancy allows large displacements of atoms near the surface to relieve the compressive strain in the InAs(111)A-S. On the other hand, an As-adatom surface in InAs(111)A-W newly appears between stable regions of  $V_{\text{In}}$  and  $T_{\text{As}}$ , as shown in Figure 11.17(C), where the As adatom stably resides in the interstitial site bonding with three substrate In atoms. Figure 11.18 shows the calculated difference in charge density between the InAs(111)A and the InAs(111)A-W. Here, Figure 11.18(A) and (B) denote the results for the In-vacancy and As-adatom surfaces, respectively. Figure 11.18(A) reveals that the large decrease in the charge density (red-colored region) is found at surface As atoms on the In-vacancy surface (arrow). This is because the electronegativity of In on the surface is smaller than that of Ga at the interface [91,92]. This results in breaking the electron counting model to destabilize the In-vacancy surface. The As-adatom surface makes up this deficiency in charge density as shown in Figure 11.18(B), where the charge density around the As adatom is transferred to the substrate In atom to strengthen the interatomic bond between the In and As atoms. Consequently, the As-adatom surface appears as a stable phase between  $V_{\text{In}}$  and  $T_{\text{As}}$  in the InAs(111)A-W.

## 11.4.2 Growth on InAs Wetting Layer Surfaces

On the  $(2 \times 4)\alpha 2$  WL surface (InAs(001)-W), the adsorption–desorption boundary of In is shown in Figure 11.19 as functions of  $T$  and  $p_{\text{In}}$ . It is compared with boundaries on the fully relaxed InAs(001) and fully strained InAs(001)-S surfaces without interface structure of InAs/GaAs. The calculated lifetime  $\tau$  and diffusion length  $L$  of an In adatom were estimated to be small, such as  $\tau = 1.59 \times 10^{-3}$  s and  $L = 6.18 \times 10^2$  nm on the  $(2 \times 4)\alpha 2$

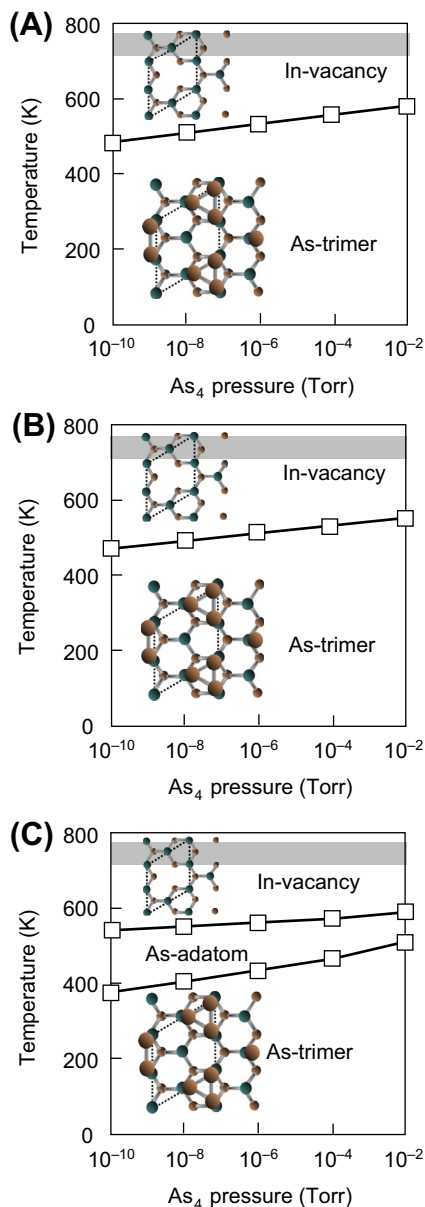


**FIGURE 11.17** Calculated surface-phase diagrams of (A) InAs(111)A, (B) InAs(111)A-S, and (C) InAs(111)A-W as functions of temperature and  $As_4$  pressure. The solid lines show the boundaries of the stable surface structure regions. The shaded area denotes the temperature range of the conventional molecular beam epitaxy growth.

WL surface. This elucidates that In adsorption does not occur on the InAs(001)-W and InAs(001)-S surfaces but is allowed on the InAs(001) surface. Similar results were obtained in InAs(001)-(1 × 3) and -(2 × 3) WL surfaces, where In atoms do not adsorb at

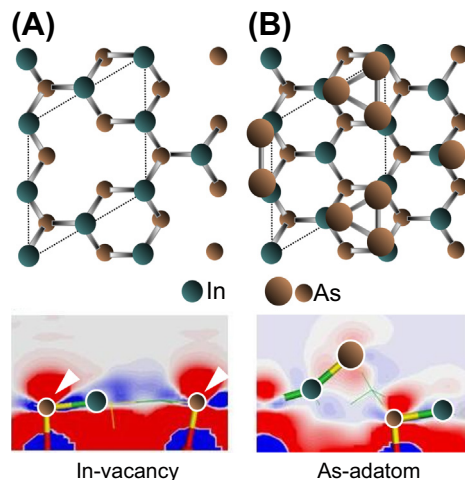


**FIGURE 11.18** Decrease (in red color) and increase (in blue color) in charge density on the (A) In-vacancy and the (B) As-atom surfaces in the InAs-5. The large decrease around surface As atoms are indicated by white arrows. Schematic of the top views of the In-vacancy and As-atom surfaces are also shown in this figure.

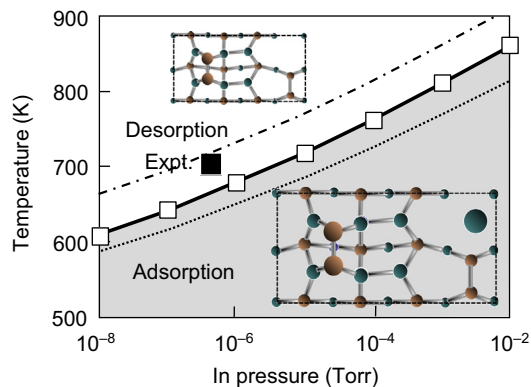


**FIGURE 11.19** Calculated adsorption–desorption boundaries for In on an InAs(001)-(2 × 4) × 2 wetting layer (solid line), fully strained layer (dotted line), and fully relaxed layer (dashed line) surfaces as functions of temperature and In pressure, respectively. Inserted bar with Expt. denotes experimental growth conditions.

equilibrium under growth conditions. This is because the adsorption energies for In atom are fairly large, such as  $-1.97$  eV on the  $(1 \times 3)$  surfaces,  $-1.68$  eV on the  $(2 \times 3)$  WL surfaces, and greater than  $-2.38$  eV on the  $(2 \times 4) \times 2$  surfaces. Considering the fact that In atoms can easily adsorb on the GaAs(001)- $c(4 \times 4)$  substrate surface, these results suggest that In adsorption proceeds InAs growth on the initial GaAs(001) and the final InAs(001) surfaces, while the growth process on the InAs(001) WL surfaces is more complex. RHEED and STM observations for InAs on GaAs(001) have clarified that the surface changes its structure from the initial GaAs(001)- $c(4 \times 4) \alpha$  surface to the final

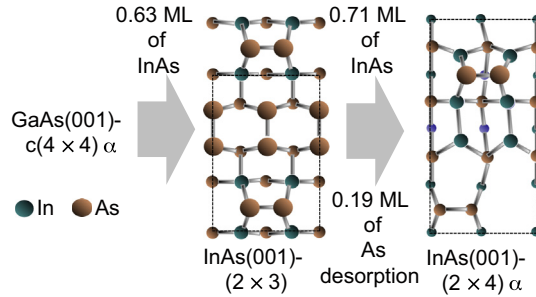


**FIGURE 11.20** Schematic of InAs wetting layer formation process on GaAs(001). The initial GaAs(001)-c(4 × 4)α surface changes its structure to the final InAs(001)-(2 × 4)α<sub>2</sub> via InAs(001)-(2 × 3) with increase of InAs coverage.

InAs(001)-(2 × 4)α<sub>2</sub> surface via InAs(001)-(1 × 3)/(2 × 3), with an increase of InAs coverage [70]. On the basis of these results, the surface structural change is schematically shown in Figure 11.20, as obtained by counting the number of deposited In and As atoms on the initial GaAs(001)-c(4 × 4)α. This suggests that the (2 × 3) surface with In<sub>0.375</sub>Ga<sub>0.625</sub>As at the interface reasonably appears after 0.63 ML of InAs deposition on the GaAs(001)-c(4 × 4)α. This is consistent with experimental findings where 2/3 ML of InAs deposition creates the (2 × 3) surface with In<sub>1/3</sub>Ga<sub>2/3</sub>As [70,85–87]. Further deposition with 0.71 ML of InAs realizes the (2 × 4)α<sub>2</sub> surface, which is also consistent with the RHEED observations where the (2 × 4) surface appears supplying ~1.3–1.4 ML of InAs on the GaAs(001)-c(4 × 4)α [70]. Here, it should be noted that the desorption of 0.19 ML of As is indispensable to realize the (2 × 4) surface during the structural change from the (2 × 3) to the (2 × 4) surface.

Figure 11.21(A) shows the calculated surface-phase diagram for the InAs(001)-(2 × 3) and (n × 3) WL surfaces (n = 4, 6, and 8) as functions of temperature and As<sub>4</sub> pressure. Here, the (2 × 3) surface is fully covered by As-dimers on the surface, while one As-dimer is missing every n As-dimer on the (n × 3) surfaces to approach satisfying the electron counting model at n = 8. This implies that the (2 × 3) surface is unstable at growth conditions because the desorption energy of the As-dimer on the (2 × 3) surface is very small (e.g., 1.12 eV); therefore, it can easily desorb from the WL surface to change its structure from (2 × 3) to (8 × 3), even at low temperatures. Instead of the (2 × 3) surface, the (6 × 3) surface was found to be preferable for InAs(001) WL surface at growth conditions. This is consistent with STM observations where the trench dimer row has high stability and is missing one or two top As-dimers locally, which forms either a (4 × 3) or a (6 × 3) surface unit cell [71].

The adsorption–desorption boundary of In on the (6 × 3) WL surface is shown in Figure 11.21(B) as functions of T and p<sub>In</sub>, which is compared with boundaries on the (2 × 3) and the (4 × 3) WL surfaces. This indicates that In adsorption does not occur on the (2 × 3) WL surface but is allowed on the (4 × 3) and the (6 × 3) WL surfaces at growth conditions. This is because the adsorption energy for the In atom is very large, such as −1.68 eV on the (2 × 3) WL surface in contrast with −3.87 eV on the (4 × 3)

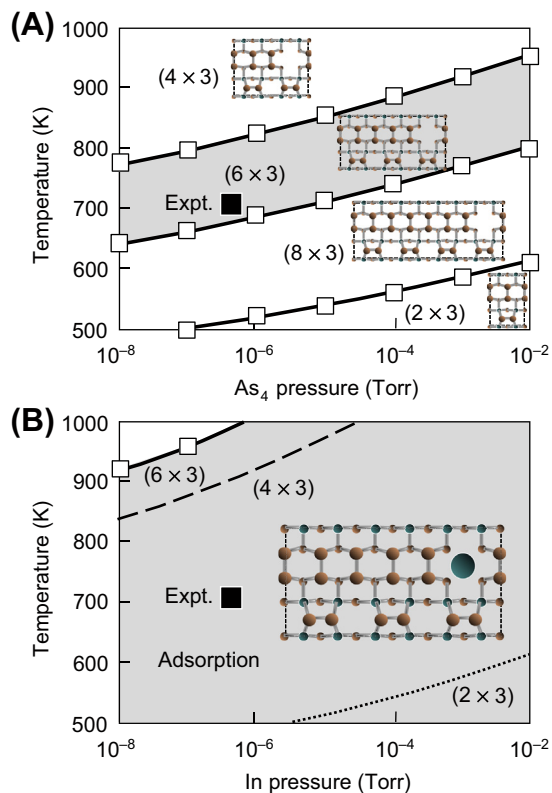


**FIGURE 11.21** (A) Calculated surface-phase diagram for InAs(001)-( $n \times 3$ ) wetting layer surfaces as functions of temperature and  $\text{As}_4$  pressure and (B) adsorption-desorption boundaries for In on InAs(001)-( $6 \times 3$ ) wetting layer (solid line),  $-(4 \times 3)$  wetting layer (dashed line), and  $-(2 \times 3)$  wetting layer (dotted line) surfaces as functions of temperature and In pressure, respectively. Inserted bars with Expt. denote experimental growth conditions.

WL,  $-3.66$  eV on the  $(6 \times 3)$  WL, and  $-3.33$  eV on the  $(8 \times 3)$  WL surfaces. This is because the stable adsorption site of In on the  $(2 \times 3)$  WL surface is around the center position between upper As-dimer and lower As-dimer, which is quite different from the missing As-dimer site on the  $(n \times 3)$  WL surface as shown in Figure 11.21(B). Therefore, it was concluded that In atoms impinging on the InAs(001)- $(2 \times 3)$  WL surfaces tend to desorb, and the growth on the  $(2 \times 3)$  WL proceeds with the aid of As desorption on the basis of the self-surfactant effect [63].

Figure 11.22 summarizes the adsorption energy differences for In atom on the  $(2 \times 2)$  In-vacancy surface of the InAs(111)A, the InAs(111)A-S, and the InAs(111)A-W. The stable lattice site for In adatom on the InAs(111)A is V site, consistent with the previous ab initio calculations [84]. On the other hand, In adatom favors interstitial sites (C and D sites) on the InAs(111)A-S. This can be interpreted by considering the In atomic position on the surfaces. For the InAs(111)A, the In adatom is located  $1.44 \text{ \AA}$  above the V site, while the positions at the C and D sites are  $2.19$  and  $1.88 \text{ \AA}$

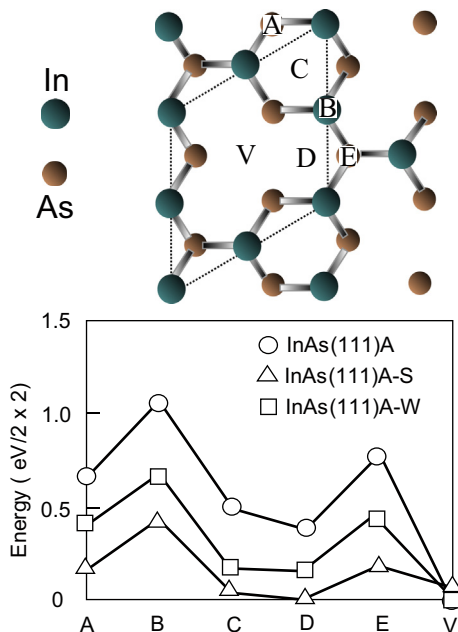


**FIGURE 11.22** Energy difference (in  $\text{eV}/(2 \times 2)$ ) for the In atom in the InAs(111)A (open circles), the InAs(111)A-S (open triangles), and the InAs(111)A-W (open squares). The origin of energy is set to the total energy of the most stable sites in each system. Adsorption sites considered in this study are indicated by letters A, B, C, D, E, and V shown in this figure.

higher than the substrate, respectively. Due to the close distance between the In adatom and surface As atoms at the V site in the InAs(111)A, its adsorption energy ( $-1.76$  eV) is lower than those at the C and D sites ( $-1.38$  eV). For the InAs(111)A-S, the height of the In adatom drastically increases at the V site ( $2.24$  Å) and then the adsorption energy ( $-1.21$  eV) becomes higher than that for the InAs(111)A. These changes are caused by large displacements of surface As atoms around the V site. In contrast with the results for the InAs(111)A-S, the V site is also favored for In adatom on the InAs(111)A-W, similarly to the InAs(111)A. Our calculated charge density in the InAs(111)A-W implies that the charge density around In adatom decreases due to its smaller electronegativity [91,92]. The decrease in charge density induces electrostatic interaction between In adatom and surface atoms to stabilize the In adatom at the V site. Therefore, the lattice constraint in the InAs(111)A-S and the charge redistribution in the InAs(111)A-W crucially contribute to the stable adsorption for In atom on the InAs(111)A- $(2 \times 2)$  surface.

Figure 11.23 shows the calculated adsorption–desorption transition curve for an In atom without and with simultaneous As adsorption on the  $(2 \times 2)$  In-vacancy surface of the InAs(111)A, the InAs(111)A-S, and the InAs(111)A-W as functions of temperature and In pressure. These figures reveal that In adsorption on the In-vacancy surface does not occur without simultaneous As adsorption under conventional growth temperatures in

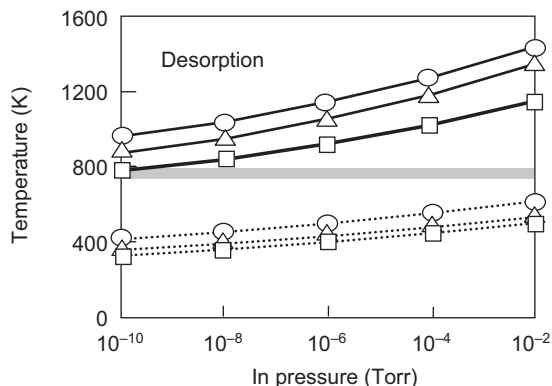


**FIGURE 11.23** Calculated adsorption–desorption transition curve for In atom without (dotted line) and with simultaneous As adsorption (solid line) on the  $(2 \times 2)$  In-vacancy surface of InAs(111)A (open circles), InAs(111)A-S (open triangles), and InAs(111)A-W (open squares) as functions of temperature and In pressure. Shaded area denotes the temperature range of the conventional molecular beam epitaxy growth.

the range of 723–773 K. The calculated lifetime  $\tau$  of In without simultaneous As adsorption was estimated to be very small, such as  $\tau = 4.35 \times 10^{-14}$  s on the InAs(111)A- $(2 \times 2)$  WL surface. After As adsorption, In adsorption energies on the In-vacancy surface dramatically decrease such as  $-1.76$  eV without As to  $-4.17$  eV with As in the InAs(111)A,  $-1.29$  to  $-3.80$  eV in the InAs(111)A-S, and  $-1.46$  to  $-3.27$  eV in the InAs(111)A-W. These findings thus imply that In adsorption is promoted only when As atoms are adsorbed on the InAs(111)A- $(2 \times 2)$  surface and the InAs growth proceeds with the adsorption of As atoms. This reveals that the self-surfactant effect is crucial for the growth processes similar to the GaAs growth [12,63]. Considering the fact that the computational models considered in this study correspond to individual growth stage, these distinctive features in the calculated results suggest that adsorption–desorption behavior on the InAs(111)A- $(2 \times 2)$  surface strongly depends on film thickness of InAs heteroepitaxially grown on GaAs.

## 11.5 GaN

III-nitride semiconductors, such as GaN, have a wurtzite structure, as shown in Figure 11.24. Generally, blue light-emitting diodes (LEDs) and laser diodes (LDs) using III-nitrides are fabricated on the (0001)-polar surface. Recently, III-nitrides growth on nonpolar and semipolar surfaces has attracted increasing attention. This is because there are large internal piezoelectric fields in the III-nitride layers grown on the (0001) heterosubstrates. The large internal piezoelectric fields separate electrons and holes to opposite interfaces of the layer. This spatial separation of electrons and holes in the III-nitride layer affects the quantum efficiency of optical devices. To avoid the problem, III-nitride should be grown on the surfaces with nonpolar (11-20), semipolar (1-101), and semipolar (11-22) orientations, where the piezoelectric field is negligible

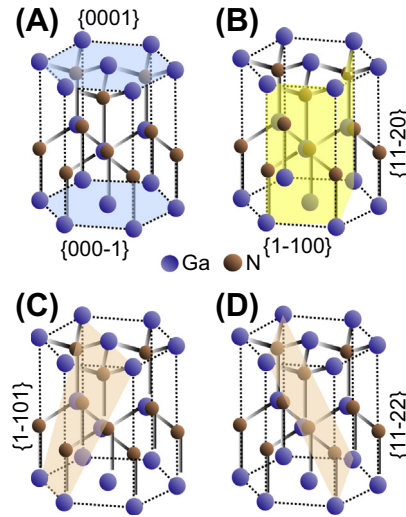


**FIGURE 11.24** Schematic of wurtzite structure and various planes such as (A) (0001) and (000-1), (B) (1-100) and (11-20), (C) (1-101), and (D) (11-22) considered in this study.

[93]. Since the demonstration of InGaN/GaN LEDs on semipolar (11-22) bulk GaN [94,95], the (11-22) plane has been the most promising among the semipolar orientations. Unlike the conventional GaN growth along the [0001] direction, lower temperatures (870–975 °C) are found to be required to obtain atomically flat (11-22) surfaces in MOVPE [7] and hydride vapor-phase epitaxy [95]. It has been also shown that one Ga monolayer can be stabilized on a GaN(11-22) surface under Ga-rich conditions in plasma-assisted MBE, and this surface is necessary to optimize the surface morphology [96]. Despite these experimental studies, little is known about the incorporation behavior on semipolar surfaces in nitride semiconductors. To clarify the growth processes on various semipolar surfaces, investigations not only for adsorption–desorption behavior but also for the reconstructions on the semipolar surfaces are necessary from theoretical viewpoints, taking growth conditions into account.

In this section, we present a review of our recent achievements for clarifying the reconstruction, adsorption–desorption behavior, and growth processes of various GaN surfaces, including polar, nonpolar, and semipolar surfaces using the chemical potential approach. Surface-phase diagrams as functions of temperature and pressure are shown for various GaN surfaces, exemplified by those with the polar (0001), polar (000-1), nonpolar (1-100), nonpolar (11-20), semipolar (1-101), and semipolar (11-22) orientations shown in Figure 11.24. Furthermore, the growth processes on the polar (0001) and semipolar (11-22) orientations are systematically discussed on the basis of the surface-phase diagrams. Comparative studies among polar, nonpolar, and semipolar surfaces are shown to check the versatility of our approach to incorporation behavior on various surfaces with different polarities.

### 11.5.1 Surface Structure of GaN

Many researchers have fabricated LED and LD devices on GaN(0001) surfaces. In the case of MBE, the  $(2 \times 2)$  and pseudo- $(1 \times 1)$  surfaces have been observed on the GaN(0001) by STM [97,98]. There have been several theoretical studies based on ab initio calculations for the atomic arrangements on the surfaces. Northrup et al. [99] have proposed that pseudo- $(1 \times 1)$  is the most stable structure under Ga-rich conditions among various surface structures. Ishii [100] has investigated the favorable adsorption behavior on the  $(2 \times 2)$  surface.

Figure 11.25(A) shows a calculated surface-phase diagram of GaN(0001) as a function of temperature and Ga pressure [13,14,25]. The pseudo- $(1 \times 1)$  surface is stable in the temperature range less than 684 K at  $10^{-8}$  Torr and less than 973 K at  $10^{-2}$  Torr. These temperature ranges are consistent with experimental results [101]. This surface-phase diagram also reveals that the  $(2 \times 2)$  with Ga adatom is stable in the temperature range between 767 and 1017 K at  $10^{-8}$  Torr and between 1078 and 1420 K at  $10^{-2}$  Torr. These are consistent with experimental stable temperature ranges for the  $(2 \times 2)$  surface with Ga adatom [102,103]. On the other hand, it has been clarified by STM observations that Ga atoms deposit onto the GaN(000-1)- $(1 \times 1)$  surface and form  $(3 \times 3)$ ,  $(6 \times 6)$ , and  $c(6 \times 12)$  structures [104]. On the basis of ab initio calculations, the  $(1 \times 1)$  surface is determined to consist of a monolayer of Ga atoms bonded in atop sites above the topmost N atoms of an N-terminated bilayer. The  $(3 \times 3)$  surface consists of Ga adatoms

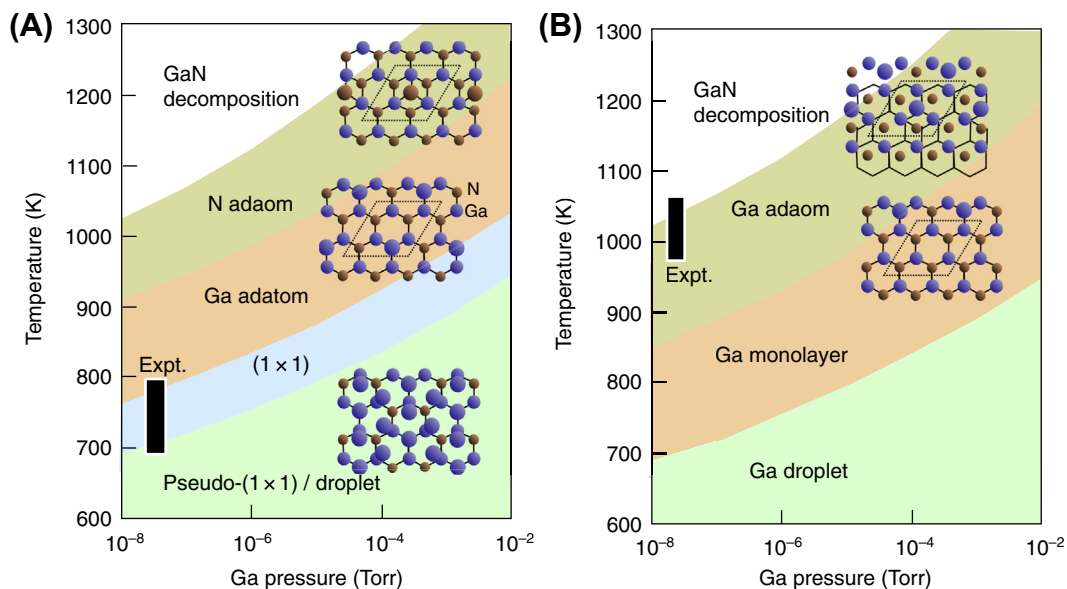


**FIGURE 11.25** Surface-phase diagram of (A) GaN(0001) and (B) GaN(000-1) as functions of temperature and Ga vapor pressure. Inserted bar in (A) denotes the temperature range for submonolayer deposition of GaN. Inserted bar in (B) shows the typical temperature range of GaN MBE on GaN(000-1). MBE, molecular beam epitaxy.

bonded on top of this adlayer. Figure 11.25(B) shows the surface phase diagram for GaN(000-1) as functions of temperature and Ga pressure. The  $(2 \times 2)$  surface with Ga adatom is stabilized in the temperature range less than 850 K at  $10^{-8}$  Torr and less than 1190 K at  $10^{-2}$  Torr. The  $(1 \times 1)$  surface with a monolayer of Ga atoms is also observed beyond 850 K at  $10^{-8}$  Torr and 1190 K at  $10^{-2}$  Torr. The surface phase diagram suggests that both surfaces can appear in the typical temperature ( $\sim 1070$  K) for MBE of GaN. Because the homoepitaxial growth of GaN on GaN(000-1) have been performed under Ga-rich conditions, the calculated result is consistent with the experimental stable temperature range for the  $(1 \times 1)$  surface [105].

Previous ab initio calculations have clarified that the ideal surface is most stable over a large range of chemical potentials, and the surfaces with Ga adlayers are stabilized for Ga-rich conditions [106,107]. The reconstructions on nonpolar (1-100) and (11-20) surfaces are very simple, as shown in Figure 11.26(A) and (B), respectively [23,25]. The ideal surface appears beyond the temperature range between 725 and 1030 K and between 770 and 1080 K on (1-100) and (11-20) surfaces, respectively, whereas the Ga adlayer surfaces are stable only at lower temperatures. For the ideal surfaces, the N atom relaxes outward, whereas the Ga atom relaxes inward, accompanied by a charge transfer from the Ga dangling bond to the N dangling bond. As a result of this charge transfer, the ideal surface satisfies the EC rule [108] to be stabilized without any adsorption or desorption in the surface. That is, the ideal surface itself is stable because the number of dangling bond of cation and anion on the surface unit cell is the same in case of

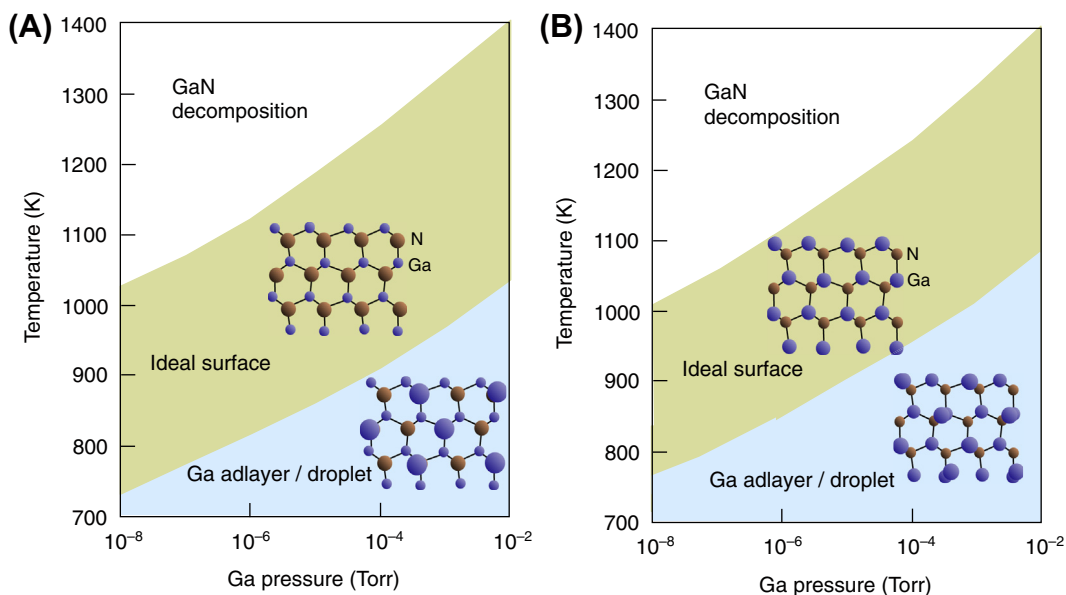


FIGURE 11.26 Surface phase diagram of (A) GaN(1-100) and (B) GaN(11-20) as functions of temperature and Ga vapor pressure.

nonpolar GaN surfaces. Therefore, the MBE growth proceeds on the ideal GaN(1-100) and (11-20) surfaces regardless of Ga vapor pressure at the conventional growth temperatures.

The surface-phase diagram of the semipolar GaN(1-101) surface is shown in Figure 11.27(A) [22]. With increasing temperatures, the metallic reconstruction with a Ga bilayer, which is stabilized at low temperatures, changes its structure to that with Ga dimers by way of that with Ga monolayer. The stabilization of metallic reconstruction under Ga-rich conditions is similar to that found in the GaN(0001) surface. Therefore, many types of reconstructions could appear around a typical MBE growth temperature ( $\sim 1100$  K), depending on Ga vapor pressure. This suggests that the growth kinetics on the GaN(1-101) surface depends on the growth temperatures owing to temperature-dependent surface reconstructions. Figure 11.27(B) shows the surface phase diagram of a semipolar GaN(11-22) surface [19]. This implies that the metallic reconstructions with a Ga adlayer and a Ga monolayer emerge only at low temperatures and high Ga-rich conditions. On the other hand, the Ga adatom surface is favored over the wide temperature range. The calculated surface-phase diagram agrees with the results obtained by experiments where the Ga monolayer surface is formed under high Ga fluxes close to the onset of Ga accumulation (droplet) in the plasma-assisted MBE ( $T \sim 1000$  K) [96]. The calculated phase diagram thus suggests that the growth kinetics on the GaN(11-22) surface depends on growth temperatures similar to that on the GaN(1-101) surface.

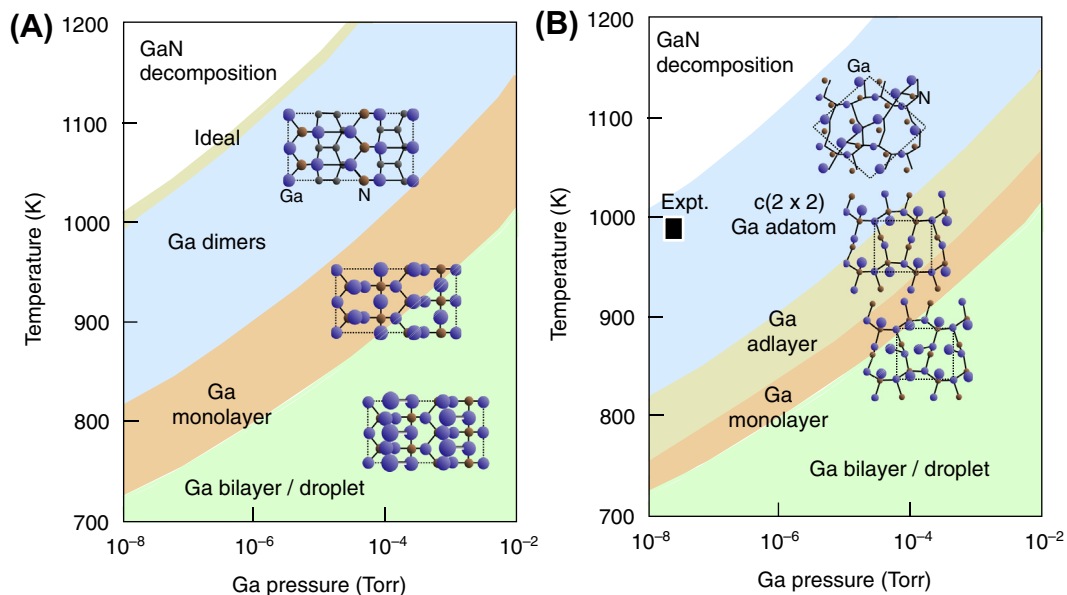
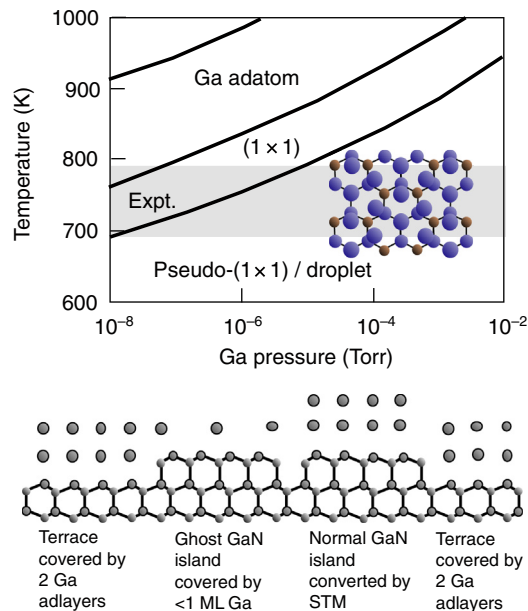


FIGURE 11.27 Surface phase diagram of (A) GaN(1-101) and (B) GaN(11-22) as functions of temperature and Ga vapor pressure. Inserted bar in (B) shows typical growth temperature range.

## 11.5.2 Growth on GaN Surfaces

Ishii [100] has investigated the favorable adsorption behavior on the GaN(0001)-(2 × 2) surface using ab initio calculations. The calculated results imply that an N-rich condition is not suitable for the MBE growth of GaN, because N atoms impinging on the GaN(0001)-(2 × 2) surface tend to reside in a lattice site that is different from the original wurtzite lattice site. On the other hand, a Ga-rich condition is helpful for the epitaxial growth to fabricate a high-quality GaN crystal. This is because a preadsorbed Ga atom on the GaN(0001)-(2 × 2) surface changes the stable lattice site for a subsequent N adatom to the wurtzite lattice site. Therefore, a surface-phase diagram as a function of Ga pressure shown in Figure 11.25(A) is useful for interpreting the growth process of GaN on the polar (0001) surface. On the basis of Figure 11.25(A), we discuss the growth process on the (0001) surface observed by the STM, where Xie et al. clarified that the pseudo-(1 × 1)-like normal and the (2 × 2)-like ghost islands coexist during the submonolayer deposition of GaN at ~673–773 K by MBE [101] as schematically shown in Figure 11.28.

It should be noted that the deposition temperature range of submonolayer GaN corresponds to the stable region of the pseudo-(1 × 1), (1 × 1), and the (2 × 2)-Ga. The calculated surface phase-diagram of the GaN(0001) reveals that the pseudo-(1 × 1) consisting of two monolayers of excess Ga on the GaN(0001) appears below 700–950 K. The pseudo-(1 × 1) surface changes its structure to the (2 × 2)-Ga with submonolayer of Ga adatoms at higher temperatures, such as ~800–1000 K via the newly found (1 × 1) with two adlayers of Ga. These results are consistent with the stable temperature range of



**FIGURE 11.28** Surface phase diagram of GaN(0001) and schematic of the formation of ghost island observed by STM during MBE growth at conditions denoted by shaded area. MBE, molecular beam epitaxy.

both the pseudo-(1 × 1) and (2 × 2)-Ga obtained experimentally [102,103]. The (1 × 1) and (2 × 2) surfaces with another coverage of Ga do not appear as stable structures of GaN(0001). It is clear that the deposition temperature range of GaN includes the stable regions of the pseudo-(1 × 1), (1 × 1), and the (2 × 2)-Ga. These results suggest that Ga adsorption or desorption during GaN MBE growth can easily change the pseudo-(1 × 1) to the (2 × 2)-Ga or (1 × 1), and vice versa depending on Ga BEP. This is consistent with their STM observations, where a ghost island with submonolayer Ga coexists with a normal island on the terrace and can be easily converted by STM.

To elucidate migration behavior, the potential-energy surface (PES) of Ga and N on the semipolar GaN(11-22) surface was calculated by fixing the adatom laterally at various positions and allowing relaxation along vertical direction. First, we investigated the growth kinetics of Ga and N on the  $c(2 \times 2)$  surface, which appeared under typical  $c$ -plane growth conditions. The PES of N (not shown here) demonstrates that the N adatom prefers the site close to the topmost N atom, resulting in the formation of strong N–N bonds that desorb as an N<sub>2</sub> molecule. The stabilization of the N-desorbed surface thus suggests that the adsorption of Ga attached to the outermost N is necessary to proceed with GaN growth on the  $c(2 \times 2)$  surface. Our calculations for an additional Ga atom on the  $c(2 \times 2)$  surface show that the Ga easily desorbs from the surface under typical  $c$ -plane growth conditions. Figure 11.29(A) shows the PES of Ga on  $c(2 \times 2)$  surface. The most stable Ga adsorption site indicated by the cross is close to the Ga-lattice site above the topmost N atom.

Figure 11.30(A) shows the adsorption–desorption boundary for Ga adsorption on the  $c(2 \times 2)$  surface with a Ga adatom as functions of temperature and Ga pressure. It is found that the transition temperature varies from 770 to 1100 K depending on the Ga pressure. This implies that most of the additional Ga desorbs from the surface under the MBE growth conditions at  $\sim 1000$  K [96]. However, due to the small energy difference between the adsorption energy  $E_{\text{ad}}$  and vapor phase chemical potential  $\mu_{\text{Ga}}$ , some of them are likely to be eventually adsorbed. That is, the adsorbed Ga would not be entirely eliminated, even in the MBE conditions. In Figure 11.30(A), the dashed line shows the adsorption–desorption transition conditions for the Ga adatom at a saddle point in Figure 11.29(A). The high migration energy barrier results in low adsorption energy at the saddle point, leading to notably low desorption temperatures compared to those at the stable sites. This suggests that even though Ga atoms eventually adsorbed at the stable sites, they desorb during their surface migration. The desorption propensity of additional Ga atoms on the  $c(2 \times 2)$  surface also provides a possible explanation for inhibiting the formation of the atomically flat (11-22) surface [109].

To verify the growth process under the low-temperature/high Ga vapor pressure condition, we now focus on the kinetics of Ga and N adatoms on the (1 × 1) surface with a Ga monolayer. Figure 11.29(B) and (C) show the PES for Ga and N adatom on the (1 × 1) surface with Ga monolayer. The stable adsorption site for Ga is located at the Ga-lattice site above the Ga monolayer, as indicated by the cross in Figure 11.29(B). On the other hand, the N adatom is stabilized at the N-lattice site between the Ga monolayer

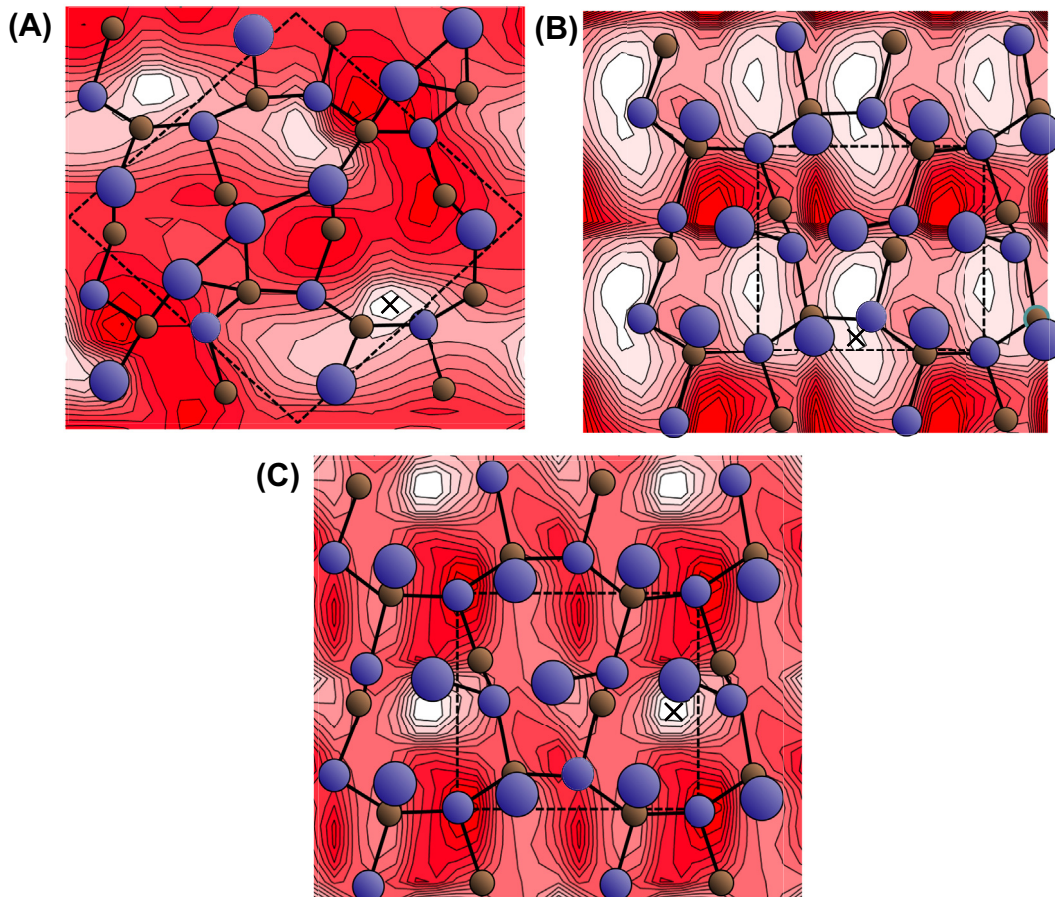


**FIGURE 11.29** Contour plots of the PES for (A) additional Ga atom on the GaN(11-22)- $c(2 \times 2)$  with Ga adatom, (B) Ga adatom, and (C) N adatom on the  $(1 \times 1)$  surface with Ga monolayer. Large and small circles represent Ga and N atoms, respectively. Crosses represent stable adsorption sites of the PES in the dashed rectangles denoting the  $c(2 \times 2)$  and  $(1 \times 1)$  surface unit cells.

and outermost Ga atom of the substrate, as shown in [Figure 11.29\(C\)](#), resulting in the formation of four Ga–N bonds. The adsorption–desorption transition boundaries for Ga and N adatoms on the  $(1 \times 1)$  surface with a Ga monolayer are shown in [Figure 11.30 \(B\) and \(C\)](#), respectively. Due to the smaller adsorption energy ( $-5.82$  eV) of the N adatom on the  $(1 \times 1)$  with Ga monolayer, the desorption temperature of N at the stable site exceeds 1500 K, although the Ga desorption temperature appears in the range between 700 and 1000 K ( $E_{\text{ad}} = -2.73$  eV at the stable adsorption site). In the latter case, the desorption temperature of N from the saddle point appears to be in the range of 1200–1500 K depending on N pressure. This implies that the N adatom diffuses on the  $(1 \times 1)$  with a Ga monolayer surface without desorption. Because these desorption temperatures are higher than that in the MBE growth ( $\sim 1000$  K), it is thus concluded

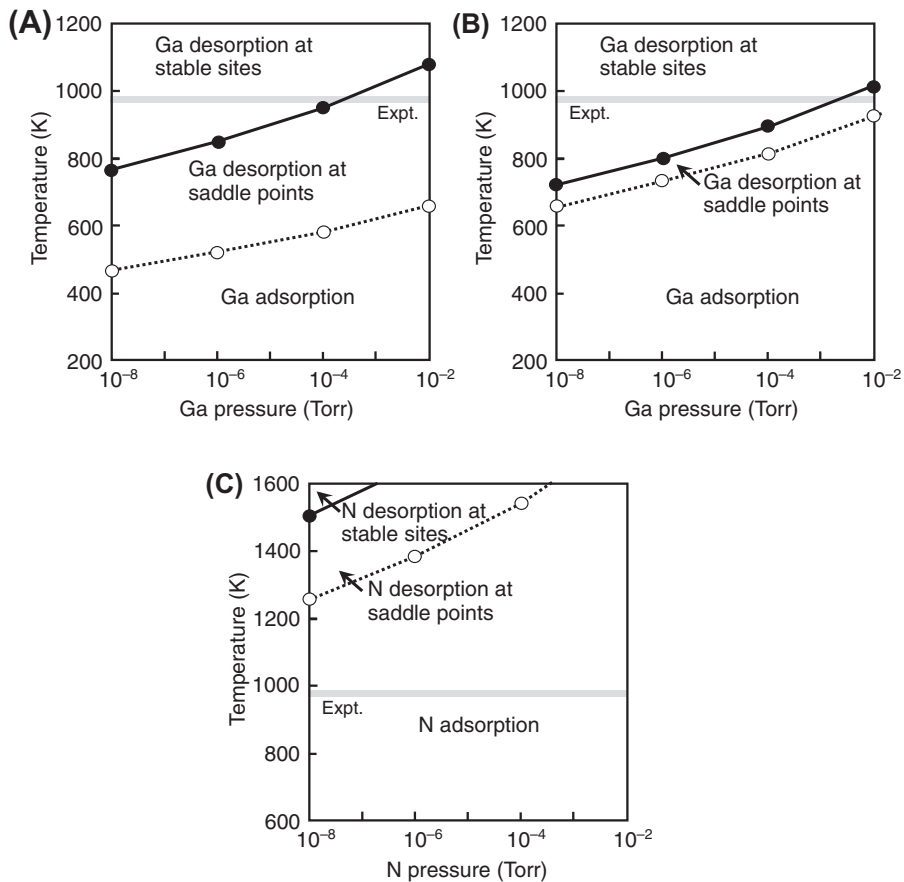


**FIGURE 11.30** Calculated surface phase diagrams for (A) Ga adsorption on the  $c(2 \times 2)$  surface with Ga adatom, (B) Ga adsorption on the  $(1 \times 1)$  surface with Ga monolayer, and (C) N adsorption on the  $(1 \times 1)$  surface, as functions of temperature and vapor pressure. The typical temperature for (0001) growth is attached by horizontal line.

that both Ga and N adatoms can be incorporated into the surface and the formation of GaN layers proceeds under high Ga-pressure conditions, consistent with the experimental results by MBE [109]. Furthermore, considering that the  $(1 \times 1)$  with Ga monolayer also appears under low-temperature conditions [19], the crystal growth on GaN(11-22) surface can be realized for low temperatures. This reasonably agrees with the experimental results in the MOVPE [109–112].

## 11.6 InGaN on GaN

The fabrication of green LDs with emission wavelengths of approximately 500 nm [113–117] has received considerable attention due to their application for light sources in full-color laser projectors. To achieve the green lasing, there is an increasing interest in

crystal growth of  $\text{In}_x\text{Ga}_{1-x}\text{N}$  alloy system with an In incorporation of approximately 25% in InGaN/GaN quantum wells. High-quality  $\text{In}_{0.25}\text{Ga}_{0.75}\text{N}$  epitaxial layers can be grown on polar (0001) and semipolar (20-21) orientations, whereas the incorporation efficiency of In on a nonpolar (1-101) surface is lower than that on a polar (0001) surface [116,117].

During InGaN growth, it is well known that abrupt InN/GaN interfaces are rarely obtained due to a large lattice mismatch between InN and GaN. Using the method of droplet elimination by radical beam irradiation (DERI), a metal-rich condition, and subsequent N irradiation, InN/InGaN heterostructures can be successfully achieved using surface segregation of In during InGaN growth [118]. Despite the importance of these phenomena, the effects of surface orientation on the stability and kinetics of In atoms on the InGaN surfaces cannot be taken into account in the previous theoretical studies. Thermodynamic analyses by Koukitsu et al. clarified that the solid composition of InGaN alloy grown by MOVPE deviates from that of vapor phase [119] in addition to some first-principle calculations for the structures of InGaN surfaces. However, these theoretical investigations cannot be directly related to growth conditions [120,121].

In this section, we systematically investigate the adsorption–desorption behavior of In, Ga, and N on GaN with various orientations, such as polar (0001), semipolar (20-21), and nonpolar (10-10). Using these results, a surface-phase diagram of the  $\text{In}_{0.25}\text{Ga}_{0.75}\text{N}$  wetting layer is obtained. The adsorption of In and Ga adatoms on these reconstructed surfaces will clarify the orientation dependence of In incorporation at growth conditions. Moreover, the formation of InN/GaN(0001) heterostructures in the DERI method is discussed, taking into account N incorporation on the metallic surfaces as functions of temperature and N pressure in conjunction with In surface segregation.

### 11.6.1 Surface Structure of the InGaN Wetting Layer

The calculated surface phase diagrams of  $\text{In}_{0.25}\text{Ga}_{0.75}\text{N}$  surfaces are shown in Figure 11.31. Here, the adsorption of hydrogen is not taken into account because the amount of incorporated In is known to be reduced by the presence of  $\text{H}_2$  molecules [122]. Our calculations correspond to the growth conditions in which the chemical potential of hydrogen is maintained at low values. The surface phase diagrams clearly show that the stable reconstructions are notably altered by growth conditions. At high temperatures, cations of the topmost layer consist of only Ga atoms, regardless of the orientation. The stabilization of these structures is due to a strong Ga–N bond (2.3 eV) in comparison to the In–N bond (2.0 eV); In atoms easily desorb from the surfaces. The stabilization of such reconstructions implies that the amount of incorporated In is reduced for high temperatures, consistent with published experiments [122–124]. At low temperatures, the surfaces are covered by In adatoms, such as an In bilayer and In adlayers. Another striking feature of these reconstructions is the orientation dependence of In composition at the topmost layer.

For (0001) and (20-21) orientations, respectively shown in Figure 11.31(A) and (C), the surfaces incorporating an In atom at the topmost layer are stabilized below 1010 and

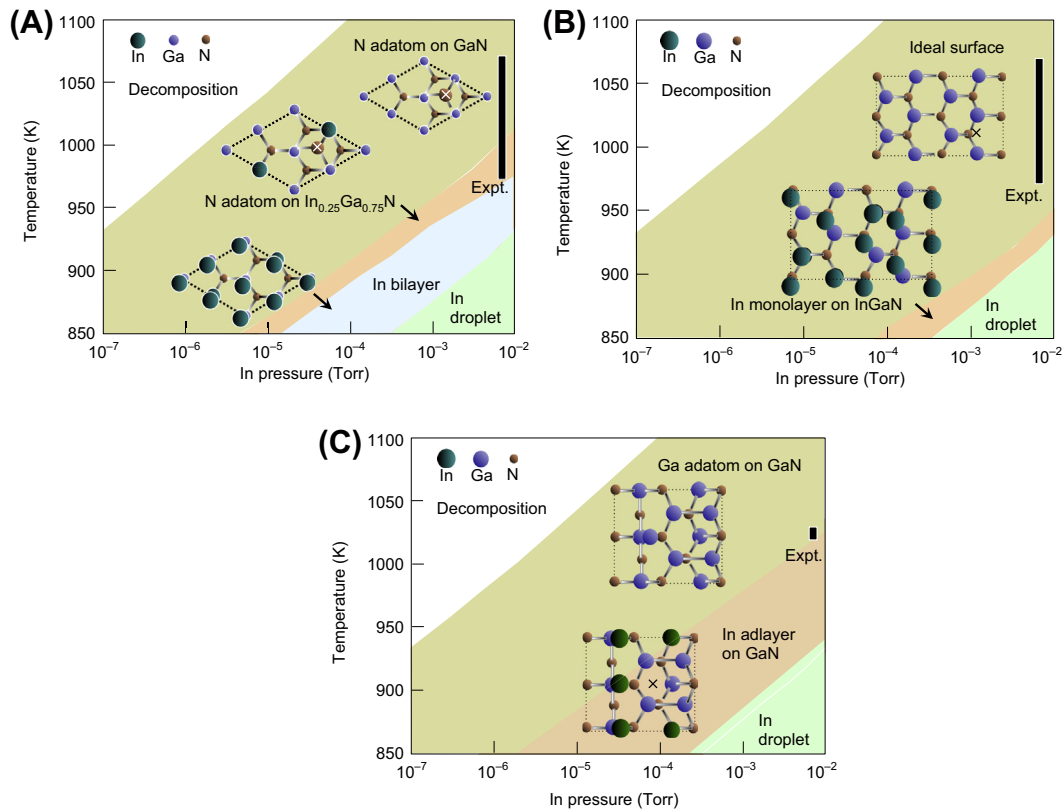


**FIGURE 11.31** Calculated surface phase diagrams of  $\text{In}_{0.25}\text{Ga}_{0.75}\text{N}$  surfaces on (A) polar (0001), (B) nonpolar (1-100), and (C) semipolar (2-201) orientations under N-rich limit as functions of temperature and pressure. Schematic top views of stabilized surfaces under growth conditions are also shown. The adsorption sites of In and Ga adatoms are indicated by crosses. Experimental growth conditions are also shown as inserted bars with Expt. in these figures.

1040 K, respectively. Because there are four cation-lattice sites at the topmost layer, the incorporation of an In atom results in surfaces with In concentration of 25%. In contrast, the surfaces corresponding to 25% In concentration do not appear, and a surface with In concentration of 50% is stabilized below 950 K for the (10-10) orientation, as shown in [Figure 11.31\(B\)](#). This implies that the surfaces with In concentrations of 25% can be stabilized for (0001) and (20-21) orientations, whereas such types of surfaces are unavailable for (10-10) orientation under growth conditions of the MOVPE. From the viewpoint of structural stability, these calculated results reasonably agree with the experiments, in which the InN molar fraction in InGaN films on the (10-10) is lower than that on the (0001) [123]. The analysis of reconstructed surfaces provides a clue for the stabilization of the surfaces with In concentration of 25%. Our calculations reveal that the energy deficits for substituting an In atom at the topmost layer by a Ga atom for (10-10) orientation (1.1–1.2 eV) are much higher than those for (0001) and (20-21) orientations (0.4–0.5 eV). Because the large energy deficits result in low adsorption energy,

the surfaces with In at the topmost layer become unstable only for the (10-10) orientation as shown in [Figure 11.31\(B\)](#). Accordingly, In–N and Ga–N bond lengths in the (10-10) surfaces with an In atom at the topmost layer are 0.12 Å shorter than bulk ones. Although we are currently unable to figure out why such structural differences occur depending on the orientation, the formation of strained bonds might cause the destabilization of (10-10) surfaces with In at the topmost layer [\[125\]](#).

## 11.6.2 Growth on InGaN Wetting Layer Surfaces

To address the growth processes of InGaN films, we now consider the adsorption of In and Ga adatoms on the reconstructed surfaces. [Figure 11.32](#) shows the estimated InN molar fraction using  $P_i$  in [Eqn \(11.11\)](#) for various orientations. Here, we assume the values of In and Ga pressures in  $\mu_{\text{gas}}$  as  $p_{\text{In}} = 1 \times 10^{-2}$  and  $p_{\text{Ga}} = 3 \times 10^{-2}$  Torr, respectively. The stable adsorption sites are explored and determined, as shown in [Figure 11.32](#). It should be noted that the InN molar fraction on (20-21) surface is close to 0.5, as estimated from the In adlayer on InGaN(20-21) in [Figure 11.31\(C\)](#). The stable adsorption site on the surface with In at the topmost layer is located between In–Ga dimer and Ga–Ga dimer rows, which corresponds to the stable adsorption site of a Ga adatom on the ideal GaN(0001) surface (T4 site). Owing to this adsorption site, the adsorption-energy difference between In and Ga adatoms is small (less than 0.01 eV). Furthermore, most of Ga and In adatoms adsorb on the surfaces at temperatures less than 1030 K. Both  $p_{\text{Ga}}$  and  $p_{\text{In}}$  are almost unity, leading to the estimated InN molar fraction close to 0.5.

At high temperatures, in contrast, the adsorption energy of an In adatom on the surface without In at the topmost layer (Ga adatom on GaN(20-21) in [Figure 11.31\(C\)](#)) becomes small (–2.80 eV) compared with that of Ga adatom (–2.87 eV), because the adsorption site is located above the topmost N atom. The lower adsorption energy of the In atom results in low  $p_{\text{In}}$ , and then the estimated InN molar fraction at high temperatures becomes lower than that at low temperatures. Because both In and Ga adatoms are attached to the topmost N adatom in the (0001) surfaces with an N adatom (N adatom on InGaN(0001) and N adatom on GaN(0001) shown in [Figure 11.31\(A\)](#)), the energy difference of –0.4 eV between the adsorption energy of In adatom and that of Ga adatom is also apparent. However, the adsorption energies (–2.5 eV) are still low enough for the adsorption less than 950 K. Therefore, the InN molar fraction takes a higher value, especially at low temperatures. In contrast, the values of adsorption energy (–2.02 and –2.38 eV for In and Ga adatoms, respectively) and their differences are quite large for (1-100) orientation (GaN(1-100) in [Figure 11.32](#)). The adsorption of the In adatom is inhibited due to higher adsorption energy, leading to the small values in the InN molar fraction. Although the adsorption processes of one-monolayer InGaN film should be verified to obtain the InN molar fraction quantitatively, the estimated molar fraction manifests the orientation dependence of adsorption behavior, which is qualitatively consistent with the experiments [\[123\]](#).

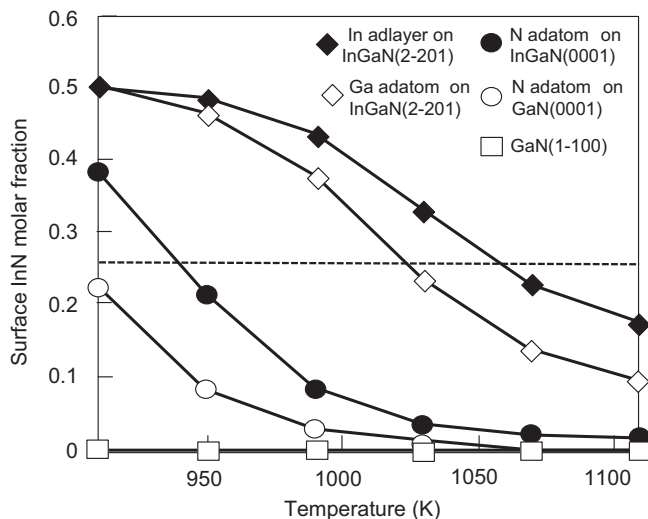


**FIGURE 11.32** Calculated InN molar fraction on polar (0001) (circles), nonpolar (1-100) (squares), and semipolar (2-201) (diamonds) surfaces obtained by the adsorption probability  $P_{\text{In}}$  ( $P_{\text{Ga}}$ ) in Eqn (11.11) for In (Ga) pressure  $p_{\text{In}} = 1 \times 10^{-2}$  ( $p_{\text{Ga}} = 3 \times 10^{-2}$ ) Torr as a function of temperature. Filled and empty symbols represent the InN molar fraction using the adsorption energies of In and Ga adatoms at low and high temperatures, respectively. Dashed line denotes InN molar fraction  $x = 0.25$  of bulk  $\text{In}_{0.25}\text{Ga}_{0.75}\text{N}$ .

Under the metal-rich condition employed in the DERI method, our ab initio calculations reveal that the (0001)-pseudo- $(1 \times 1)$  surface, analogous to droplets consisting of In topmost and Ga subsurface layers, is more stable than that with the topmost Ga and subsurface In layers, even under Ga-rich conditions. Figure 11.33 shows the calculated adsorption-desorption boundaries for various N supplies on the pseudo- $(1 \times 1)$  surface

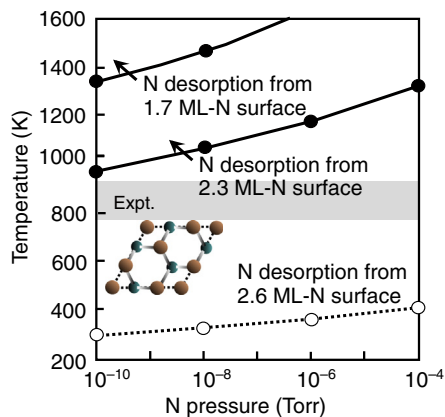


**FIGURE 11.33** Calculated adsorption-desorption boundaries for various N supplies on the pseudo- $(1 \times 1)$  surface as functions of temperature and N pressure. The shaded area denotes the temperature range of the conventional growth.

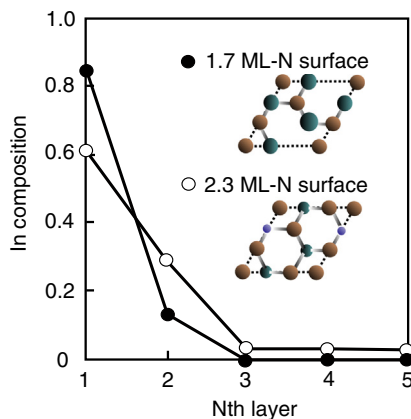


**FIGURE 11.34** Calculated results for In composition in each layer, varying the amount of N deposition obtained by the MMC simulation using ab initio data. Closed and open circles denote the results for 1.7 and 2.3 ML depositions of N on the pseudo- $(1 \times 1)$  surface, respectively.

as functions of temperature and N pressure. This suggests that N atoms can be incorporated on the pseudo- $(1 \times 1)$  surface by 2.3 ML at growth conditions. Moreover, excess In atoms in the topmost layer desorb with adsorption of the N atoms that are preferentially incorporated between the topmost In and subsurface Ga layers to form an InN layer on GaN at growth conditions, as schematically shown in Figure 11.33. The results for the In composition in each layer, varying the amount of N deposition obtained by the MMC simulation using ab initio data, are shown in Figure 11.34 for 1.7 and 2.3 ML depositions of N to elucidate the formation of InN/GaN heterostructures. The results for 1.0 and 2.0 ML depositions of N also investigated are similar to those for 1.7 and 2.3 ML depositions, respectively. This implies that the smaller the N deposition, the larger the surface composition of In. This is because the strained In-N interatomic bonds are effectively relaxed at the surface with small amounts of N deposition such as 1.7 ML, whereas N covering the surface induces the substitution between the topmost In and subsurface Ga to decrease strain in both Ga-N and In-N bonds [126]. Considering the fact that small amounts of N deposition correspond to metal-rich conditions and accumulation of excess metal on the surface, these calculated results are qualitatively consistent with experimental findings—not only in the DERI method [118] but also by Mosely et al. [127], who found that In surface segregation only occurs after a threshold excess metal is accumulated.

## 11.7 Summary

Computer-aided calculation methods enable us to interpret and predict various material properties from a quantum mechanical viewpoint. Assuming atomic arrangements in materials, this facilitates computer-aided materials science such that any property for material can be systematically predicted by using a few elementary input parameters.

In this article, we have shown the power and applicability of ab initio calculations and chemical potential analysis to the crystal growth for semiconductors, such as GaAs, InAs on GaAs, GaN, and InGaN on GaN, in understanding their surface reconstructions through predicting surface-phase diagrams and growth processes, including adsorption–desorption and migration behavior of atoms and molecules on the surfaces with the aid of the MC simulations. Success with the chemical potential analysis will lead to more realistic simulations of crystal growth for various materials to predict atomic arrangements themselves as functions of growth conditions, such as temperature and gas pressure.

For example, polytypism in AlN grown on 4H-SiC(11-20) as a function of III/V ratio in addition to temperature and gas pressure has been clarified by using the chemical potential analysis [128]. The distinctive atomic arrangements were found to appear in subsequent adsorption of Al and N atoms after N and Al predepositions, respectively. After the N deposition, the subsequent Al adatom occupies the 4H lattice site similarly to the results for single Al on the surface. On the other hand, the N adatom tends to form a dimer structure with the predeposited Al. Reflecting these results, Al adatoms can easily occupy the 4H lattice sites to form the 4H-AlN layer at a III/V ratio greater than 10. In the range of a III/V ratio less than 0.1, the N adatoms reside in the stable interstitial sites to form the Al-N dimer layer or intermittently migrate to the 2H lattice site to form the 2H-AlN layer. Moreover, we have successfully applied the chemical potential analysis to more complicated investigations, such as elemental nitridation processes of corundum  $\text{Al}_2\text{O}_3$ (0001) and (1-102) surfaces [129]. The calculations reveal that the structures with substitutional N atoms beneath the surface are stabilized under nitridation conditions. We also found that the desorption of O atoms at the topmost layer induces outward diffusion of O atoms as well as inward diffusion of N atoms, leading to the transformation into AlN films. The kMC simulations in conjunction with density functional theory results indeed demonstrate a dependence of these chemical and structural changes on temperature and gas pressure.

The results presented here are just an example of future prospects in the ab initio-based approach to crystal growth. The ab initio-based approach with chemical potential analysis has been successfully applied to investigate a wide range of problems, such as the surface structures of InP(111)A [130], AlN [26,27], GaN, and InN with hydrogen [23] with various orientations; the incorporation of Si on GaAs(111)A [131], Mg [22], and C [24] on GaN(1-101); Bi [132] and N on GaAs(001) [133]; and the formation of InP nanowires [134]. Recent progress in fabrication techniques will make it possible to create various new nanomaterials, including nanodots, nanowires, and nanocolumns, by controlling the atomic arrangements during crystal growth. Under these circumstances, the chemical potential analysis on the basis of ab initio calculations will be an essential technique in the future of materials design to interpret and predict the dynamic changes of these materials' properties because of its availability of predicting atomic arrangements during the crystal growth. We believe that the ab initio-based approach with chemical potential analysis will lead to great advances in crystal growth for various materials.

## References

- [1] Däweriz L, Hey R. *Surf Sci* 1990;236:15.
- [2] Kaxiras E, Bar-Yam Y, Joannopoulos JD, Pandey KC. *Phys Rev B* 1987;35:9625.
- [3] Qian GX, Martin RM, Chadi DJ. *Phys Rev Lett* 1998;60:1962.
- [4] Northrup JE. *Phys Rev B* 1991;44:1419.
- [5] Kangawa Y, Ito T, Taguchi A, Shiraishi K, Ohachi T. *Surf Sci* 2001;493:178.
- [6] Kangawa Y, Ito T, Hiraoka YS, Taguchi A, Shiraishi K, Ohachi T. *Surf Sci* 2002;507:285.
- [7] Vande Walle CG, Neugebauer J. *Phys Rev Lett* 2002;88:066103.
- [8] For example Glasstone S, Laidler KY, Eyring H. *The theory of rate processes*. New York: McGraw-Hill Book Company, Inc.; 1964.
- [9] Hamman DR, Schluter M, Chiang C. *Phys Rev Lett* 1979;43:1494.
- [10] Perdew JP, Burke K, Ernzerhof M. *Phys Rev Lett* 1996;77:3865.
- [11] Kangawa Y, Matsuo Y, Akiyama T, Ito T, Shiraishi K, Kakimoto K. *J Cryst Growth* 2007;300:62.
- [12] Tatematsu H, Sano K, Akiyama T, Nakamura K, Ito T. *Phys Rev B* 2008;77:233306.
- [13] Ito T, Akiyama T, Nakamura K. *J Cryst Growth* 2009;311:698.
- [14] Ito T, Akiyama T, Nakamura K. *J Cryst Growth* 2009;311:3093.
- [15] Kangawa Y, Akiyama T, Ito T, Shiraishi K, Kakimoto K. *J Cryst Growth* 2009;311:3106.
- [16] Akiyama T, Nakamura K, Ito T, Song JH, Freeman AJ. *Phys Rev B* 2009;80:075316.
- [17] Akiyama T, Ammi D, Nakamura K, Ito T. *Jpn J Appl Phys* 2009;48:100201.
- [18] Akiyama T, Ammi D, Nakamura K, Ito T. *Jpn J Appl Phys* 2009;48:110202.
- [19] Yamashita T, Akiyama T, Nakamura K, Ito T. *Jpn J Appl Phys* 2009;48:120201.
- [20] Akiyama T, Yamashita T, Nakamura K, Ito T. *Jpn J Appl Phys* 2009;48:120218.
- [21] Akiyama T, Yamashita T, Nakamura K, Ito T. *Jpn J Appl Phys* 2010;49:030212.
- [22] Akiyama T, Ammi D, Nakamura K, Ito T. *Phys Rev B* 2010;81:245317.
- [23] Akiyama T, Yamashita T, Nakamura K, Ito T. *J Cryst Growth* 2011;318:79.
- [24] Akiyama T, Nakamura K, Ito T. *Jpn J Appl Phys* 2011;50:080216.
- [25] Ito T, Akiyama T, Nakamura K. *Semicond Sci Technol* 2012;27:024010.
- [26] Akiyama T, Obara D, Nakamura K, Ito T. *Jpn J Appl Phys* 2012;51:018001.
- [27] Akiyama T, Saito Y, Nakamura K, Ito T. *Jpn J Appl Phys* 2012;51:048002.
- [28] Akiyama T, Nakamura K, Ito T. *Appl Phys Lett* 2012;100:251601.
- [29] Ito T, Ogasawara K, Sugitani T, Akiyama T, Nakamura K. *J Cryst Growth* 2013;362:2.
- [30] Ito T, Hirai K, Akiyama T, Nakamura K. *J Cryst Growth* 2013;378:13.
- [31] Atkins P, De Paula J. *Physical chemistry*. Oxford University Press; 2002.
- [32] Kangawa Y, Ito T, Taguchi A, Shiraishi K, Irisawa T, Ohachi T. *Appl Surf Sci* 2002;190:517.
- [33] Kangawa Y, Ito T, Hiraoka YS, Taguchi A, Shiraishi K, Ohachi T. *Surf Sci* 2002;507–510:285.
- [34] Clarke S, Vvedensky DD. *Phys Rev Lett* 1987;58:2235.
- [35] Ohtake A, Nakamura J, Tsukamoto S, Koguchi N, Natori A. *Phys Rev Lett* 2002;89:206102.
- [36] Ohtake A, Koguchi N. *Appl Phys Lett* 2003;83:5193.
- [37] Ohtake A, Kocan P, Nakamura J, Natori A, Koguchi N. *Phys Rev Lett* 2004;92:236105.

- [38] Hashizume T, Xue QK, Ichimiya A, Sakurai T. *Phys Rev B* 1995;51:4200.
- [39] Takahashi M, Yoneda Y, Yamamoto N, Mizuki J. *Phys Rev B* 2003;68:085321.
- [40] Sasaki M, Yoshida S, Vac J. *Sci Technol B* 1992;10:1720.
- [41] Hiruma K, Morgan GP, Katsuyama T, Ogawa K, Koguchi M, Kobayashi H. *Appl Phys Lett* 1991;59:431.
- [42] Ohlsson BJ, Björk MT, Magnusson MH, Deppert K, Samuelson L, Wallenberg LR. *Appl Phys Lett* 2001;79:3335.
- [43] Motohisa J, Noborisaka J, Takeda J, Inari M, Fukui T. *J Cryst Growth* 2004;272:180.
- [44] Noborisaka J, Motohisa J, Fukui T. *Appl Phys Lett* 2005;86:21302.
- [45] Kaxiras E, Pandey KC, Bar-Yam Y, Joannopoulos JD. *Phys Rev Lett* 1986;56:2819.
- [46] Kaxiras E, Bar-Yam Y, Joannopoulos JD, Pandey KC. *Phys Rev B* 1986;33:4406.
- [47] Biegelsen DK, Bringans RD, Northrup JE, Swartz L-E. *Phys Rev Lett* 1990;65:452.
- [48] Fu J, Kim J, Gallagher MC, Willis RF, Miller DL. *Surf Sci* 1994;318:349.
- [49] Thornton JMC, Weightman P, Woolf DA, Dunscombe CJ. *Phys Rev B* 1995;51:14459.
- [50] Moll N, Kley A, Pehlke E, Scheffler M. *Phys Rev B* 1996;54:8844.
- [51] Avery AR, Tok ES, Jones TS. *Surf Sci* 1997;376:L397.
- [52] Setzer C, Platen J, Bludau H, Gierer M, Over H, Jacobi K. *Surf Sci* 1998;402–404:782.
- [53] Deng BC, Yu ZX, Xu G, Mrstik BJ, Tong SY. *Phys Rev B* 1999;59:9775.
- [54] Ohtake A, Nakamura J, Komura T, Hanada T, Yao T, Kuramochi H, et al. *Phys Rev B* 2001;64:045318.
- [55] Woolf DA, Sobiesierski Z, Westwood DI, Williams RH. *J Appl Phys* 1992;71:4908.
- [56] Ito T, Tsutsumida K, Nakamura K, Kangawa Y, Shiraishi K, Taguchi A, et al. *Appl Surf Sci* 2004;237:194.
- [57] Ito T, Ishizaki H, Akiyama T, Nakamura K. *e-J Surf Sci Nanotech* 2005;3:488.
- [58] Ohtake A. *Surf Sci Rep* 2008;63:295.
- [59] Ito T, Shiraishi K. *Surf Sci* 1996;357/358:486.
- [60] Ito T, Shiraishi K. *Jpn J Appl Phys* 1998;37:262.
- [61] Shiraishi K, Ito T, Suzuki Y, Kageshima H, Kanisawa K, Yamaguchi H. *Surf Sci* 1999;433/435:382.
- [62] Ito T, Shiraishi K. *Jpn J Appl Phys* 1998;37:4234.
- [63] Shiraishi K, Ito T. *Phys Rev B* 1998;57:6301.
- [64] Taguchi A, Shiraishi K, Ito T. *Appl Surf Sci* 2000;162–163:354.
- [65] Wang YQ, Wang ZL, Shen JJ, Brown AS. *Solid State Commun* 2002;122:553.
- [66] Kanisawa K, Butcher MJ, Tokura Y, Yamaguchi H, Hirayama H. *Phys Rev Lett* 2001;87:196804.
- [67] Krzyzewski TJ, Joyce PB, Bell GR, Jones TS. *Surf Sci* 2003;532–535:822.
- [68] Tsukamoto S, Honma T, Bell GR, Ishii A, Arakawa Y. *Small* 2006;2:587.
- [69] Tsukamoto S, Bell GR, Arakawa Y. *Microelectron J* 2006;37:1498.
- [70] Belk JG, McConville CF, Sudijono JL, Jones TS, Joyce BA. *Surf Sci* 1997;387:213.
- [71] Grabrowski J, Prohl C, Höpfner B, Dähne M, Eisele H. *Appl Phys Lett* 2009;95:233118.
- [72] Ito T, Shiraishi K. *Jpn J Appl Phys* 1997;36:1525.
- [73] Ishii A, Fujiwara K, Arisaka T. *Appl Surf Sci* 2003;216:478.

- [74] Kratzer P, Penev E, Scheffler M. *Appl Phys A* 2002;75:79.
- [75] Penev E, Stojkovic S, Kratzer P, Scheffler M. *Phys Rev B* 2004;69:115335.
- [76] Liu E-Z, Wang C-Y. *Surf Sci* 2006;600:2007.
- [77] Hammerschmidt T, Kratzer P, Scheffler M. *Phys Rev B* 2008;77:235303.
- [78] Rosini M, Kratzer P, Magri R. *J Phys Condens Matter* 2009;21:355007.
- [79] Rosini M, Kratzer P, Magri R. *Phys Status Solidi C* 2010;7:181.
- [80] Yamaguchi H, Belk JG, Zhang XM, Sudijono JL, Fay MR, Jones TS, et al. *Phys Rev B* 1997;55:1337.
- [81] Ohtake A, Ozeki M, Nakamura J. *Phys Rev Lett* 2000;84:4665.
- [82] Zepeda-Ruiz LA, Maroudas D, Weinberg WH. *Surf Sci* 1998;418:L68.
- [83] Joe H, Akiyama T, Nakamura K, Kanisawa K, Ito T. *J Cryst Growth* 2007;837:301.
- [84] Taguchi A, Kanisawa K. *Appl Surf Sci* 2006;252:5263.
- [85] Kita T, Wada O, Nakayama T, Murayama M. *Phys Rev B* 2002;66:195312.
- [86] Patella F, Nufri S, Arciprete F, Fanfoni M, Placidi E, Sgarlata A, et al. *Phys Rev B* 2003;67:205308.
- [87] Xu C, Temko Y, Suzuki T, Jacobi K. *Surf Sci* 2005;580:30.
- [88] Yamaguchi H, Horikoshi Y. *Jpn J Appl Phys* 1994;33:L1423.
- [89] Yamaguchi H, Homma Y, Kanisawa K, Hirayama Y. *Jpn J Appl Phys* 1999;38:635.
- [90] Yamaguchi H, Sudijono JL, Joyce BA, Jones TS, Gatzke C, Stradling RA. *Phys Rev B* 1998;58:4219.
- [91] Phillips JC. *Rev Mod Phys* 1970;42:2147.
- [92] Villars P, Hullinger F. *J Less Common Met* 1987;132:289.
- [93] Takeuchi T, Lester S, Basile D, Girolami G, Twist R, Mertz F, et al. *Proc Int Workshop Nitride Semicond* 2000;1:137.
- [94] Funato M, Ueda M, Kawakami Y, Narukawa Y, Kosugi T, Takahashi M, et al. *Jpn J Appl Phys* 2006;45:L659.
- [95] Suzuki N, Uchida T, Tanikawa T, Hikosaka T, Honda Y, Yamaguchi M, et al. *J Cryst Growth* 2009;311:2875.
- [96] Lahourcade L, Renard J, Gayral B, Monroy E, Chaivat MP, Ruterana P. *J Appl Phys* 2008;103:93514.
- [97] Xue QK, Xue QZ, Bakhtizin RZ, Hasegawa Y, Tsong IS, Sakurai T, et al. *Phys Rev Lett* 1999;82:3074.
- [98] Smith AR, Feenstra RM, Greve DW, Shin MS, Skowronski M, Neugebauer J, et al. *Surf Sci* 1999;423:70.
- [99] Northrup JE, Neugebauer J, Feenstra RM, Smith AR. *Phys Rev B* 2000;61:9932.
- [100] Ishii A. *Appl Surf Sci* 2003;216:447.
- [101] Xie MH, Zheng LX, Dai XQ, Wu HS, Tong SY. *Surf Sci* 2004;558:195.
- [102] Ramachandran V, Lee CD, Feenstra RM, Smith AR, Northrup JE, Greve DW. *J Cryst Growth* 2000;209:355.
- [103] Vézian S, Semond F, Massies J, Bullock DW, Ding Z, Thibado PM. *Surf Sci* 2003;541:242.
- [104] Smith AR, Feenstra RM, Greve DW, Neugebauer J, Northrup JE. *Phys Rev Lett* 1997;79:3934.
- [105] Feenstra RM, Northrup JE, Neugebauer J. *MRS Internet J Nitride Semicond Res* 2002;7:1.
- [106] Segev D, Van de Walle CG. *Surf Sci* 2007;601:L15.
- [107] Northrup JE, Neugebauer J. *Phys Rev B* 1996;53:R10477.
- [108] Pashley MD, Haberer KW, Friday W, Woodall JM, Kirchner PD. *Phys Rev Lett* 1988;60:2176.

- [109] Funato M, Kotani T, Kondou T, Kawakami Y, Narukawa Y, Mukai T. *Appl Phys Lett* 2006;88:261920.
- [110] Marchand H, Ibbetson JP, Fini PT, Keller S, Den Baars SP, Speck JS, et al. *J Cryst Growth* 1998;195:328.
- [111] Hiramatsu K, Nishiyama K, Motogaito A, Miyake H, Iyechika Y, Maeda T. *Phys Status Solidi A* 1999;176:535.
- [112] Hiramatsu K, Nishiyama K, Onishi M, Mizutani H, Narukawa M, Motogaito A, et al. *J Cryst Growth* 2000;221:316.
- [113] Kim KS, Son JK, Lee SN, Sung YJ, Paek HS, Kim HK, et al. *Appl Phys Lett* 2008;92:101103.
- [114] Okamoto K, Kashiwagi J, Tanaka T, Kubota M. *Appl Phys Lett* 2009;94:071105.
- [115] Queren D, Avramescu A, BruÅNderl G, Breidenassel A, Schillgalies M, Lutgen S, et al. *Appl Phys Lett* 2009;94:081119.
- [116] Miyoshi T, Masui S, Okada T, Yanamoto T, Kozaki T, Nagahama S, et al. *Appl Phys Express* 2009;2:062201.
- [117] Enya Y, Yoshizumi Y, Kyono T, Akita K, Ueno M, Adachi M, et al. *Appl Phys Express* 2009;2:082101.
- [118] Yamaguchi T, Nanishi Y. *Phys Status Solidi A* 2010;207:19.
- [119] Koukitu A, Takahashi N, Taki T, Seki H. *Jpn J Appl Phys* 1996;35:L673.
- [120] Northrup JE. *Phys Rev B* 2009;79:041306.
- [121] Northrup JE. *Appl Phys Lett* 2009;95:133107.
- [122] Piner EL, Behbehani MK, El-Masry NA, McIntosh FG, Roberts JC, Boutros KS, et al. *Appl Phys Lett* 1997;70:461.
- [123] Chichibu SF, Yamaguchi H, Zhao L, Kubota M, Onuma T, Oakamoto K, et al. *Appl Phys Lett* 2008;93:151908.
- [124] Matsuoka T, Yoshimoto N, Sasaki T, Katsui A. *J Electron Mater* 1992;21:157.
- [125] Gil B, Bigenwald P, Briot O. *Phys Status Solidi Rapid Res Lett* 2007;1:268.
- [126] Ito A, Akiyama T, Nakamura K, Ito T. *e-J. Surf Sci Nanotech* 2014;12:136.
- [127] Moseley M, Gunning B, Greenlee J, Lowder J, Namkoong G, Doolittle WA. *J Appl Phys* 2012;112:014909.
- [128] Ito T, Ito T, Akiyama T, Nakamura K. *e-J Surf Sci Nanotech* 2010;8:52.
- [129] Akiyama T, Saito Y, Nakamura K, Ito T. *Phys Rev Lett* 2013;110:026101.
- [130] Akiyama T, Kondo T, Tatematsu H, Nakamura K, Ito T. *Phys Rev B* 2008;78:205318.
- [131] Akiyama T, Tatematsu H, Nakamura K, Ito T. *Surf Sci* 2010;604:171.
- [132] Murase I, Akiyama T, Nakamura K, Ito T. *J Cryst Growth* 2013;378:21.
- [133] Sugitani T, Akiyama T, Nakamura K, Ito T. *J Cryst Growth* 2013;378:29.
- [134] Yamashita T, Akiyama T, Nakamura K, Ito T. *Surf Sci* 2013;609:207.

# Simulation of Epitaxial Growth by Means of Density Functional Theory, Kinetic Monte Carlo, and Phase Field Methods

Wolfram Miller

LEIBNIZ INSTITUTE FOR CRYSTAL GROWTH, NUMERICAL MODELLING,  
MAX-BORN-STR. 2, 12489 BERLIN

## CHAPTER OUTLINE

<b>12.1 Overview on Methods and Goals</b> .....	<b>522</b>
<b>12.2 Density Functional Theory Calculations</b> .....	<b>524</b>
12.2.1 Basics of the Method .....	524
12.2.1.1 Surfaces .....	527
12.2.1.2 Order of Computations .....	528
12.2.2 Surface Structure and Reconstruction .....	529
12.2.3 Adatoms .....	531
12.2.4 Adsorption, Dissociation and Diffusion .....	533
12.2.5 Ab Initio Thermodynamics .....	535
<b>12.3 Kinetic Monte Carlo Simulations</b> .....	<b>538</b>
12.3.1 Introduction of the Method .....	538
12.3.2 Kinetic Monte Carlo Simulation of Deposition from Gas Phase .....	538
12.3.3 On-Lattice KMC .....	540
12.3.4 Kinetic Monte Carlo with Elastic Strain .....	544
12.3.5 Growth of Quantum Dots .....	548
<b>12.4 Phase Field Methods</b> .....	<b>550</b>
12.4.1 Philosophy of Phase Field Approaches .....	550
12.4.2 Phase Field Crystal—Structures and Defects .....	551
12.4.3 Phase Field Simulation—Step Growth and Beyond .....	553
<b>References</b> .....	<b>555</b>

## 12.1 Overview on Methods and Goals

Today, most of the devices in electronics and optoelectronics exploit their functionality by layers and structures deposited from the gas phase on a substrate. Usually, the functionality depends critically on the structure of the material deposited. To gain better understanding of the deposition process, a wide range of numerical tools has been developed and applied. On the production scale, global heat and mass transport are considered, resulting in the computation of the variation in layer thickness on a wafer. Such simulations as, e.g., [1,2] are not the subject of this chapter. These global calculations are based on the knowledge of the kinetic processes at the surface or at least on realistic assumptions (a good overview on linking different scales is given in [3]). In this chapter, an overview on numerical methods will be given, aiming to gain a basic understanding of the surface kinetics in epitaxial growth processes. The results of such computations will help to interpret the experimental results in terms of physics and surface chemistry, and will eventually provide realistic input parameters for the aforementioned global simulations.

The most fundamental calculations are based on *ab initio* methods, which are free of input parameters. However, all *ab initio* methods include certain approximations. Depending on the final goal of the computations, they might be simple or sophisticated, resulting in low or high demand for computational time. *Ab initio* methods are divided in two major groups: *quantum chemical* and *solid-state physics* simulations. Methods of the first category are based on the Hartree–Fock method, and used for computing the electronic structure of molecules or agglomerates of molecules; they can also be used to study reactions from a thermodynamic point of view (see, e.g., [4]). As indicated by the name, the second category is for computing the electronic structure of solids and with an extension also for surfaces. This so-called density functional theory (DFT) method is subject of the next section. The name refers to the electron density, which is subject to computation. In the context of phase field crystal (PFC) methods, the term *density functional method* often appears with the meaning of a particle density such as atoms in liquid and solid. This DFT should be not mixed with the one we discuss in this chapter. The outcome of DFT calculations is the electronic structure (band structure) and the total energy of the configuration considered. Energy barriers, e.g., for diffusion processes are the result of differences in energies of two configurations such as the initial one and the one of an intermediate state along the diffusion pathway. Because total energies might be rather large (depending on the size of the system) but barriers might be small, this presents challenges for the accuracy of the computations.

As a next step, one can include dynamics by performing molecular dynamics (MD) calculations. The task is to solve Newton's equation of motion for every particle in a potential field. The first question is how to obtain the potential field. The most accurate way would be to obtain the potential from *ab initio* calculations. This *ab initio* MD became attractive after the important step by Car and Parinello toward an efficient computational scheme [5]. Nevertheless, the method is very time-consuming and more appropriate for

the computation of configurations of large molecules or dynamics of single defects rather than for surface growth dynamics. The other possibility is to use interatomic potentials, which are a function of the distance between two respective atoms. Still, the achievable real time is quite short, because every vibration of the particles is included in the computations. Because vibrational frequencies are about  $10^{12}$ – $10^{13}$  1/s, one can imagine the computational cost. Kinetic Monte Carlo (KMC) methods circumvent this by ignoring the vibrations and using a fixed prefactor for rates of particle movements. Still, they are statistical methods and can treat processes far from thermodynamical equilibrium.

In this chapter, we will introduce only KMC but not MD methods. KMC can use interatomic potentials in the same way as MD. In this case, one can use the so-called off-lattice KMC as applied by some groups for specific problems [6,7]. More recently, for off-lattice KMC, on-the-fly techniques for computing saddle points of transitions have also been applied [8]. However, in this chapter we will restrict our discussion to on-lattice KMC. This means all particles/atoms sit on fixed positions of a lattice (often a simple cubic one) and obey certain rules for movements, including definitions for their energy barriers.

All types of KMC have the commonality of being serial in time, i.e., one event is computed after the other. Thus, in case of fast kinetics, one needs to compute a huge number of events in a given physical time. Some approaches have been developed to circumvent these lengthy computations if one type of the processes has very fast kinetics compared to all the others (see, e.g., [9,10]). The other drawback of the serial character of KMC is that one cannot make use of the modern computer architectures in terms of running the code in parallel. Contrary to KMC in lattice gas automata (LGA), all particles sit on the nodes of a regular lattice and hop synchronously from one site to another according to a site- and time-dependent probability (see, e.g., [11]). The time step is fixed and defined by a reference process. The major appeal of LGA dynamics, besides natural parallelism, is its mathematical and computational simplicity and efficiency. On the other hand, it is based on a very simple description of the dynamics, which have to be deduced from possibly very complex surface phenomena. LGA has been applied, e.g., to nanowhisker growth [12]. We will not discuss this method.

A step further toward macroscopic scale is the use of phase field models. Here, the term *phase field* is linked to the layer height. The height is still resolved on the atomic scale but the lateral direction is not. Phase field models are continuous models and have a smooth transition from one layer to the next. Phase field models have been used for studying step dynamics. Based on the same thermodynamic concept, PFC models have been developed. Once again, we have an atomic resolution, but in contrast to the discrete method discussed above (MD and KMC), all fluctuations are integrated out. Thus, the time scale is diffusive and processes can be followed for longer times than with KMC. The main restriction of PFC models today is the limited number of currently available energy functionals. This means a very limited number of structures, which can be handled by this method.

Numerical simulations are not a standalone field but have to be compared to experimental results and verified by well-defined experiments. The latter is, in general, not an easy task, because the required tools for measurements do not work under the

conditions of processing as they are used in numerical simulations. For instance, the investigation of surface structures on microscopic and atomic scale is often possible only under low-pressure/vacuum conditions. The same is true for in situ observations of the growth process. Because of the controlled deposition of atoms, molecular beam epitaxy (MBE) is well suited for this purpose, whereas pulsed laser deposition and the technologically more interesting chemical vapor deposition are too complex in the arriving particles on the surface to be a good tool for comparison with fundamental numerical investigations. The classical method for in situ investigation of growth is reflection high-energy electron diffraction (RHEED). Also, scanning probe techniques such as scanning tunneling microscopy (STM) and atomic force microscopy (AFM) have been used for in situ investigations of growth (see, e.g., [13]). However, growth kinetics must be slow compared to the scan times. Very recently, transmission electron microscope (TEM) has been adapted for in situ investigations (growth of nanowires [14], structural reorganization of graphene [15]).

## 12.2 Density Functional Theory Calculations

### 12.2.1 Basics of the Method

When we want to describe solids or surfaces by quantum mechanical methods, we are confronted with solving the many-body Schrödinger equation, which is challenging. However, we can circumvent this due to the important theorem by Hohenberg and Kohn<sup>1</sup> in 1964 that, for the ground-state of an electron gas system, the many-body system can be replaced by many one-electron systems with wave functions  $\psi_i$  and single electron energies  $\varepsilon_i$  [16]. Thus, we get the equation [17]:

$$\left(-\frac{1}{2}\nabla^2 + V_{\text{eff}}(\mathbf{r})\right)\psi_i(\mathbf{r}) = \varepsilon_i\psi_i(\mathbf{r}) \quad \text{with} \quad V_{\text{eff}}(\mathbf{r}) = V_{\text{ext}}(\mathbf{r}) + V_{\text{H}}(\mathbf{r}) + V_{\text{XC}}(\mathbf{r}), \quad (12.1)$$

where the effective one-electron potential  $V_{\text{eff}}$  is represented by three terms, namely the charged cores of the atoms ( $V_{\text{ext}}(\mathbf{r})$ ), the electron–electron repulsion (Hartree potential  $V_{\text{H}}$ ), and the exchange–correlation potential ( $V_{\text{XC}}$ ). The ground-state charge density is given by  $n(\mathbf{r}) = \sum_{i=1}^N |\psi_i(\mathbf{r})|^2$ , where  $N$  is the number of electrons  $N = \int d\mathbf{r} n(\mathbf{r})$ .  $V_{\text{ext}}$  does not depend on  $n(\mathbf{r})$ , but is given by the charge and positions of the core of the atoms. The two other potentials are given by

$$V_{\text{H}}(\mathbf{r}) = \frac{1}{2} \int d\mathbf{r}' \frac{n(\mathbf{r}')}{|\mathbf{r} - \mathbf{r}'|}, \quad V_{\text{XC}}(\mathbf{r}) = \frac{\delta E_{\text{XC}}[n(\mathbf{r})]}{\delta n(\mathbf{r})}. \quad (12.2)$$

The exchange–correlation energy  $E_{\text{XC}}$  contains the many-particle corrections (correlation energy) and the correction because of Pauli’s principle (exchange energy). In particular,  $E_{\text{XC}}$  has to be approximated (see below), which is the only weakness at this point. A self-

<sup>1</sup>Walter Kohn received the Nobel Prize for Chemistry in 1998 for his pioneering work in density functional theory.

consistent solution to the problem can be obtained by solving Eqn (12.1), getting the energies and wave functions, and from the latter, the electron density  $n(\mathbf{r})$ . With this  $n(\mathbf{r})$ , new potentials  $V_H$  and  $V_{XC}$  can be computed and Eqn (12.1) can be solved again. This is repeated until there is no change up to numerical accuracy. The total energy of the system is given by

$$E = \sum_{i=1}^N \varepsilon_i + \frac{1}{2} \sum_{j \neq i} \frac{Z_i Z_j}{|\mathbf{R}_i - \mathbf{R}_j|} - \frac{1}{2} \int \frac{n(\mathbf{r})n(\mathbf{r}')}{|\mathbf{r}_i - \mathbf{r}_j|} d\mathbf{r}d\mathbf{r}' + \left( E_{XC} + \int d\mathbf{r} V_{XC}n(\mathbf{r}) \right). \quad (12.3)$$

$Z_i$  and  $R_i$  are the charge and the position of the core of the  $i$ -th atom, respectively.

In a pure bulk crystal, we have a periodicity of unit cells in all three spatial directions represented by translational vectors  $\mathbf{a}_i$ . Thus, we have a translational invariance for the effective potential in Eqn (12.1) as  $V_{eff}(\mathbf{r} + \mathbf{R}_T) \equiv V_{eff}(\mathbf{r})$  employing the lattice vector  $\mathbf{R}_T = n_1\mathbf{a}_1 + n_2\mathbf{a}_2 + n_3\mathbf{a}_3$ , where  $n_i$  is any integer number. This means that any one-electron wave function can be represented by the product of an exponential factor with the wave vector  $\mathbf{k}$  and a periodic function  $u_{i,\mathbf{k}}(\mathbf{r} + \mathbf{R}_T) \equiv u_{i,\mathbf{k}}(\mathbf{r}_T)$ :

$$\psi_{i,\mathbf{k}}(\mathbf{r}) = e^{i\mathbf{k}\mathbf{r}} u_{i,\mathbf{k}}(\mathbf{r}). \quad (12.4)$$

This function is named the Bloch function, and it fulfills:

$$\psi_{i,\mathbf{k}}(\mathbf{r} + \mathbf{R}_T) = e^{i\mathbf{k}\mathbf{r}} \psi_{i,\mathbf{k}}(\mathbf{r}). \quad (12.5)$$

Equation (12.1) can be rewritten as:

$$\left[ \frac{1}{2} (\mathbf{K} - i\nabla^2) + V_{eff}(\mathbf{r}) \right] u_{i,\mathbf{k}}(\mathbf{r}) = \varepsilon_{i,\mathbf{k}} u_{i,\mathbf{k}}(\mathbf{r}). \quad (12.6)$$

The energy eigenvalues  $\varepsilon_{i,\mathbf{k}}$  of each level  $i$  changes smoothly with increasing wave number  $\mathbf{k}$ . The entire volume can be separated into polyhedral cells (Voronoi cells) around each atom, called Wigner–Seitz cells. Such a cell is defined by polygons, which intersect the connection from the atom considered with an adjacent one.

Now, we wish to shift to the reciprocal space and introduce the reciprocal lattice vector  $\mathbf{G} = l_1\mathbf{b}_1 + l_2\mathbf{b}_2 + l_3\mathbf{b}_3$ , where  $\mathbf{a}_i \cdot \mathbf{b}_j = 2\pi\delta_{ij}$ . Then, by expanding  $u_{i,\mathbf{k}}$  in a Fourier series, the wave function can be expressed as

$$\psi_{i,\mathbf{k}} = \frac{1}{\sqrt{\Omega}} \sum_{\mathbf{G}} \tilde{u}_i(\mathbf{k} + \mathbf{G}) e^{i(\mathbf{k} + \mathbf{G})\mathbf{r}}, \quad (12.7)$$

where  $\Omega$  is the volume of the unit cell and

$$\tilde{u}_i(\mathbf{k} + \mathbf{G}) = \frac{1}{\sqrt{\Omega}} \int_{\text{cell}} e^{-\mathbf{G}\mathbf{r}} u_{i,\mathbf{x}}(\mathbf{r}) d\mathbf{r} \quad (12.8)$$

The Kohn–Sham equation in the reciprocal space reads:

$$\sum_{\mathbf{G}'} \left[ \left( \frac{1}{2} (\mathbf{k} + \mathbf{G}')^2 - \varepsilon_j \right) \delta_{\mathbf{G}\mathbf{G}'} + \tilde{V}_{eff}(\mathbf{G}' - \mathbf{G}) \right] \tilde{u}_j(\mathbf{k} + \mathbf{G}') = 0, \quad (12.9)$$

where the effective potential in real and reciprocal space are related via  $V_{eff}(\mathbf{r}) = \sum_{\mathbf{G}} \tilde{V}_{eff}(\mathbf{G}) e^{i\mathbf{G}\mathbf{r}}$ .

Since  $\psi_{i,\mathbf{k}}(\mathbf{r}) \equiv \psi_{i,\mathbf{k}+\mathbf{G}}(\mathbf{r})$ , one can confine the wave vector  $k$  to the Wigner–Seitz cell, also called *first Brillouin zone* in this context. Formally, the Kohn–Sham equation has to be solved in the entire Brillouin zone and, e.g., the charge density must be obtained by integrating over the Brillouin zone:

$$n(\mathbf{r}) = \sum_j \int_{\text{BZ}} d\mathbf{k} \psi_{j,\mathbf{k}}^*(\mathbf{r}) \psi_{j,\mathbf{k}}(\mathbf{r}). \quad (12.10)$$

The integral must be replaced by a finite sum choosing a representative set of  $\mathbf{k}$ -points ( $S(\mathbf{k})$ ) and associate a specific weight  $f(\mathbf{k})$ :

$$n(\mathbf{r}) = \sum_j \sum_{s(\mathbf{k})} \sum_{\mathbf{G}} f(\mathbf{k}) |\tilde{u}_j(\mathbf{k} + \mathbf{G})|^2. \quad (12.11)$$

Monkhorst and Pack set up rules for  $S(\mathbf{k})$  and  $f(\mathbf{k})$  as a function of the number of integration points, which are commonly used [18].

One also wishes to limit the number of plane waves used in the expansion (12.7), which is done by choosing a maximum kinetic energy  $1/2(\mathbf{k} + \mathbf{G})^2$ , normally called cutoff energy.

For many properties, only the valence electrons are of interest. In the “pseudopotential” approach, the core electrons are completely ignored in the self-consistent computational scheme. Thus, instead having a core potential in Eqn (12.1),  $V_{\text{ext}}(\mathbf{r})$  is represented by the superposition of individual, nonoverlapping atomic pseudopotentials  $V_i(\mathbf{r})$  as  $V_{\text{ext}}(\mathbf{r}) = \sum_l w_l(\mathbf{r} - \mathbf{R}_l)$ , where  $\mathbf{R}_l$  are the coordinates of atom  $l$ . A further step toward saving computation time was the introduction of ultrasoft pseudopotentials by Vanderbilt [19]. However, with increasing computer power, full potential codes have become more attractive.

A different approach for solving the Kohn–Sham equations is to divide the space into a potential spherical part around each atom (muffin-tin region), where the Schrödinger equation can be written in spherical coordinates. Out of this region the potential is constant. This introduces an adjustable parameter, namely the radius of the muffin-tin region. The wave function expansion (augmented plane waves) depends on the region:

$$\psi_{\mathbf{k}}^{\text{MT,in}}(\mathbf{r}) = e^{i\mathbf{k}\mathbf{r}} \sum_{lm} A_{lm} Y_{lm}(\theta_{\mathbf{r}}, \phi_{\mathbf{r}}) R_l(|\mathbf{r} - \mathbf{R}|) \quad (12.12)$$

$$\psi_{\mathbf{k}}^{\text{MT,out}}(\mathbf{r}) = \sum_{\mathbf{G}} C_{\mathbf{k}}(\mathbf{G}) e^{i(\mathbf{k}+\mathbf{G})\mathbf{r}}. \quad (12.13)$$

By this definition, the augmented-planewave method (APW) is an all-electron method but not a full potential one. Within the muffin-tin radius, the symmetry of the potential is fixed; it is spherical. The APW method is suitable to study excited states, where the inner electrons might contribute, but it is not as computationally heavy as the full-potential planewave method.

A subject of research and controversy is the proper definition of the exchange-correlation potential  $E_{\text{XC}}[n(\mathbf{r})]$ . The choice depends on the system of investigation (metallic, ionic, covalent, van der Waals character) and the properties to be computed (energy barriers, band gaps, optical properties, etc.). The most straightforward approach is to use a

homogeneous electron gas, which gives the local density approach (LDA). This is good for systems with smoothly changing electron density. In the generalized gradient approximation (GGA), also the local gradient of the electron density is taken into account for the functional. In most cases, GGA underestimates bond strengths, whereas LDA overestimates them. Therefore, LDA gives smaller lattice constants and GGA larger ones than experimentally observed. Because LDA and GGA are available in parameterized form, the computational effort is negligible. Another approach stemming from the world of quantum chemical calculations is the hybrid functional B3LYP [20]. It contains an exact exchange potential from Hartree–Fock ( $E_x^{\text{HF}}$ ) but on the other hand has three mixing parameters for different contributions (the subscripts  $c$  and  $e$  denote correlation and exchange, respectively):

$$E_{xc}^{\text{B3LYP}} = E_{xc}^{\text{LDA}} + a_0(E_x^{\text{HF}} - E_x^{\text{LDA}}) + a_x(E_x^{\text{GGA}} - E_x^{\text{LDA}}) + a_c(E_c^{\text{GGA}} - E_c^{\text{LDA}}). \quad (12.14)$$

The B3LYP functional became fashionable during the last years, but exhibits severe problems for certain systems (see, e.g., [21]). Another approach is the self-interaction correction (sic), which is useful for systems with spatially localized electron charges, as it is especially the case for  $d$ - and  $f$ -states (see, e.g., [22]). Depending on the approach in detail the method can be computationally extremely heavy.

Another approach does not add much computational cost, but introduces another parameter: the Hubbard parameter  $U$ . It might be difficult to find a proper value.

Corrections to LDA and GGA are of great importance for systems with impurities as, e.g., hydrogen on the surface. For instance, the position of the electron impurity level below or above the conduction band minimum will define the character of the surface. In the latter, it will become metallic as it was predicted, e.g., for H/SrTiO<sub>3</sub> [24]. Because the band gap is over- and underestimated in LDA and GGA, respectively, the conclusion might be different (and wrong) depending on the method used. At the end, we shall mention that recently the random phase approximation has been used and tested for crystalline solids [25].

### 12.2.1.1 Surfaces

So far, the method can be applied to bulk material with periodic boundary conditions in all three directions. To treat surfaces, one has to introduce a vacuum, represented by plane waves. The system is still periodic in  $z$ -direction but now with a slab of certain number of atomic layers and a vacuum of certain thickness on both sides of the slab. In this supercell approach, two new parameters are introduced: the number of layers in the slab  $N_L$  and the thickness of the vacuum  $D_{\text{vac}}$ . In principle, one likes to obtain the result for a quasi-infinitely thick slab and vacuum. From a computational point of view, the vacuum is not the problem, but the slab. A typical procedure is to run the job for an increasing number of atomic layers and plot the energy versus the number of layers. One also has to keep in mind that the atoms near the surface will rearrange their positions because of the symmetry breaking by the surface. Thus, one needs to let the position of the atoms in a certain number of surface layers free to relax at least in  $z$ -direction. However, atoms might change their positions also in the  $x/y$ -direction, as is the case for surface reconstructions. In other words, one has to perform several runs of DFT

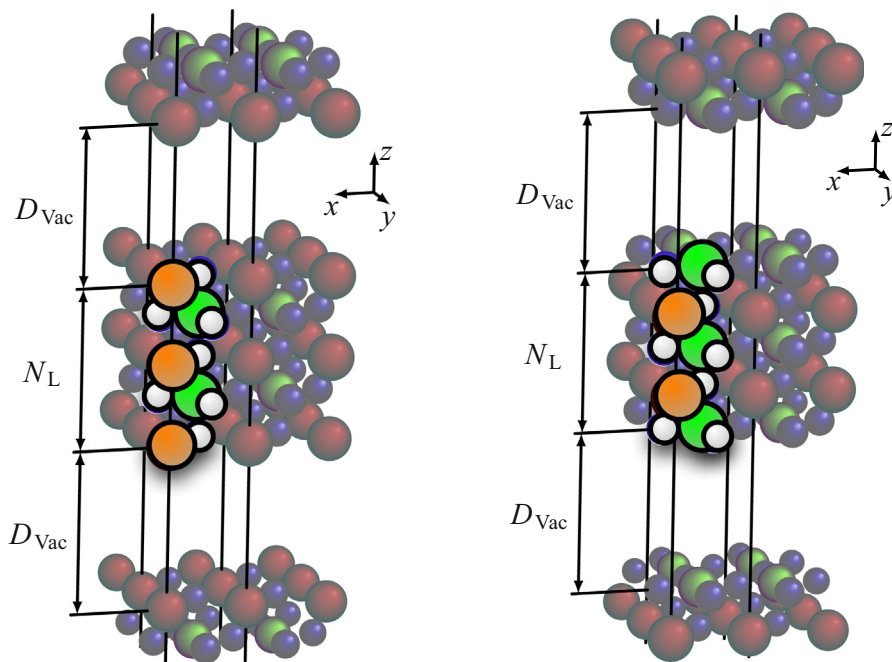


**Figure 12.1** Model for SrO-terminated (left) and TiO<sub>2</sub>-terminated (right) SrTiO<sub>3</sub>(001) surface. The model is periodic in all three directions. In the slab, there are five layers. On the left side, three SrO and two TiO<sub>2</sub> layers and on the right side, three TiO<sub>2</sub> and two SrO layers. The atoms in the inner three layers are fixed in their positions according to the bulk calculations. All other atoms can relax into the positions of minimum total energy. For a  $1 \times 1$  surface cell, only the rimmed atoms are in the supercell (10 atoms left and 13 atoms right). Sketch based on Figure 3.5 in [23].

calculations to obtain the configuration of minimum energy. This makes these types of computations rather time consuming.

As an example for a configuration of surface computation in Figure 12.1, the situation for SrTiO<sub>3</sub> is shown. In contrast to, e.g., Si, where for low index surface planes upper and lower surfaces are identical, for SrTiO<sub>3</sub> it becomes more complicated. In (001) direction, SrTiO<sub>3</sub> consists of alternating layers of SrO and TiO<sub>2</sub> (see also Figure 12.2). Thus, the surface can either be SrO-terminated or TiO<sub>2</sub>-terminated. From a stoichiometric point of view, the upper surface should be SrO-terminated and the lower TiO<sub>2</sub>-terminated or vice versa. However, the electron density is different over the SrO layer than over TiO<sub>2</sub> layer. Consequently, when defining the slab in the above-mentioned manner, an artificial dipole moment will be the result. Therefore, a mirror symmetry should be used with the same termination on both sides, as shown in Figure 12.1.

### 12.2.1.2 Order of Computations

Exact quantities of bulk properties, such as, e.g., the lattice constant, depend critically on the details of the method used. For instance, the choice of the exchange-correlation

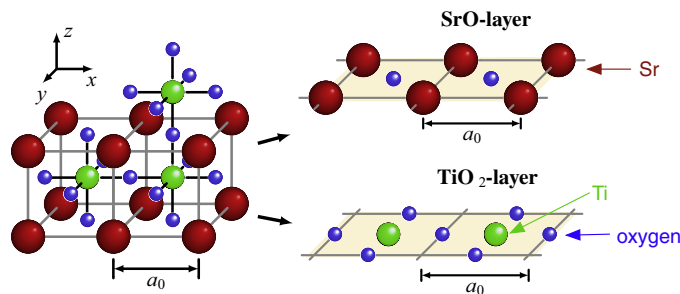


Figure 12.2 Structure of  $\text{SrTiO}_3$  at room temperature ( $Pm\bar{3}m$ ).

functional might have a significant influence on the results. For this reason, it is necessary to perform calculations for the bulk prior to start with computations for the surface. In this step, properties of the bulk should be tested against the number of  $\mathbf{k}$ -points and the cutoff energy for plane waves. For our purposes, the most important properties are the formation energy and the lattice constant.

In the following, we will consider  $\text{SrTiO}_3$  as the substrate material. For this particular material, the formation energy is given by:

$$E_{\text{SrTiO}_3}^{\text{Form}} = E_{\text{SrTiO}_3}^{\text{Bulk}} - E_{\text{Sr}} - E_{\text{Ti}} - \frac{3}{2}E_{\text{O}_2}^{\text{Gas}} \quad (12.15)$$

Thus, one needs to compute a Sr and Ti bulk crystal as well as an oxygen molecule in vacuum. For all these three computations, one uses a fixed structure, i.e., a fixed lattice constant (may be taken from literature data) and a fixed bond length for the oxygen.

Because the bulk modulus depends on the spatial derivatives, it is more sensitive than the lattice parameter itself. One can also test the influence of the cutoff energy on the forces in the oxygen molecule; the bond length is kept fixed by definition. In Figure 12.3, one can see their dependence on the cutoff energy. The convergence behavior is different for different exchange-correlation functions as, in particular, for LDA (left side) and PBE (right side). PBE is one type of GGA functional. This underlines the necessity to test the convergence once again when changing the exchange-correlation function.

The output of the bulk calculations is the lattice constant  $a_0$ , which should be used for all subsequent calculations with surfaces and adatoms. Furthermore, one knows the minimum number of  $\mathbf{k}$  points and plane waves.

## 12.2.2 Surface Structure and Reconstruction

The first point to be investigated is the structure of the pure surface. The surface atoms have only a part of the bondings as in the bulk and will therefore rearrange with respect to their bulk positions. In the simplest case, there will be a shift of the positions only in the vertical direction. But it might also be necessary to rearrange atoms in the lateral direction to minimize the energy of the system. This can lead to a reconstruction of the surface.

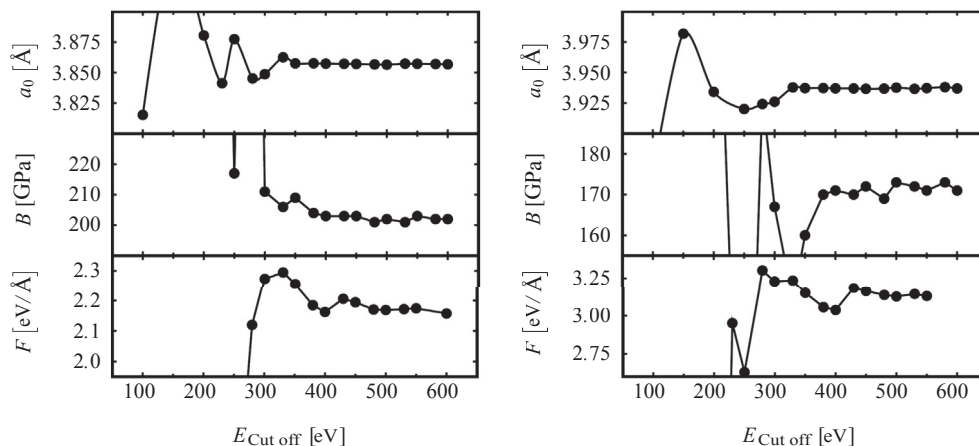


**Figure 12.3** Lattice constant  $a_0$  and bulk modulus  $B$  of the SrTiO<sub>3</sub> crystal, as well as the force  $F$  on one oxygen atom of the oxygen molecule as a function of the plane-wave basis set. Two different exchange-correlation potentials were used: LDA (left), and GGA-PBE (right). Reprinted from Figure 3.3 in [23].

One of the classical examples in semiconductors is the  $7 \times 7$  reconstruction of Si(111) surface. Many models have been developed and many experiments have been performed. However, the latter were exclusively experiments in the Fourier space and the large unit cell, which contains 49 atoms at the surface for a  $7 \times 7$  reconstruction, represents a challenge both for resolution and for analyzing the data. The first real-space determination was done in 1982 [26]. It became possible by the invention of the scanning tunneling microscope (STM) by Binnig and Rohrer<sup>2</sup> a year before [27]. The investigation of the Si(111) surface was one of the first applications of the new equipment, which underlines the importance of this kind of reconstruction during that time. The large unit cell also presented a major challenge for density functional calculations. Nearly 10 years after the experimental clarification of the structure, the system was investigated by means of ab initio molecular dynamics [28]. The breakthrough was due to the emergence of massively parallel computers. Brommer et al. considered 1,000 atoms and used 16,384 one-bit processors in a Thinking Machines CM-2.

Another example is the investigation of the complex surface structure of Fe<sub>3</sub>O<sub>4</sub>(001). A quantitative analysis is a big challenge due to the large number of atoms involved, and interpretation of the outcome of low-energy electron diffraction (LEED) is very difficult. In this case, DFT was used to support the data analysis from LEED measurements [29]. Through repeated cycles of DFT and LEED refinement, the researchers obtained a good overall agreement between the two methods, both with respect to size and direction of the relaxations. Now, we return to our example SrTiO<sub>3</sub> and consider the (001) plane. Thus, we have a stack of SrO and TiO<sub>2</sub> layers as shown in Figure 12.2 and the surface can

<sup>2</sup>Gerd Binnig and Heinrich Rohrer received the Nobel Prize in 1986 for the development of STM together with Ernst Ruska for his invention of the electron microscope.

**Table 12.1** DFT Computations for the SrTiO<sub>3</sub>(001) Surface. Change of Vertical Cation–Cation Distances with Respect to Bulk Values ( $\Delta d_{ij}$ . Shifting  $s_i$  (“Rumpling”) of the Oxygen Atoms with Respect to the Cations of the Same Layer

SrO-term			$\Delta d_{12}$ [%]	$\Delta d_{23}$ [%]	$\Delta d_{34}$ [%]	$s_1$ [Å]	$s_2$ [Å]
	LDA	[30]	−14	+5	−3	0.23	−0.05
	PBE	[30]	−15	+5	−5	0.22	−0.05
	LDA	[31]	−14	+5		0.22	
TiO <sub>2</sub> -term			$\Delta d_{12}$ [%]	$\Delta d_{23}$ [%]	$\Delta d_{34}$ [%]	$s_1$ [Å]	$s_2$ [Å]
	LDA	[30]	−9	+5	−3	0.07	−0.12
	PBE	[30]	−13	+5	−2	0.09	−0.14
	LDA	[31]	−7	+3		0.07	

be either SrO-terminated or TiO<sub>2</sub>-terminated. The outmost cations move toward the bulk, so that the distance between the cations of the topmost layer and the layer below decreases with respect to the bulk distance ( $\Delta d_{12}$  is negative, see Table 12.1). The distance between the cations of the second and third layer is increased ( $\Delta d_{23}$  is positive), and even on the layer below an effect on the positions is detected. Furthermore, the oxygen atoms and cations of one layer are no longer at the same height as in the bulk. The oxygen atoms are shifted, in the top layer outward, and in the second layer inward. These shifts are called “rumplings” and are denoted by  $s_i$  (see Table 12.1). There has been some discussion on surface reconstruction of SrTiO<sub>3</sub> surfaces, because the interpretation of some experiments suggests such rearrangement of atoms [32,33]. However, almost all DFT calculations exhibit unreconstructed surfaces as the ones with lowest energy. It has to be noted that DFT calculations have been performed for a surface versus vacuum and formally at 0 K. In experiments, the deviation from these ideal conditions might have an impact on the results.

### 12.2.3 Adatoms

When we wish to investigate the growth kinetics in epitaxial growth, the first step is to consider adatoms on the surface. This implies the next challenge in computation because we might need many unit cells in  $x$ - $y$ -direction depending on the adatom density. The simplest situation occurs for a full layer of atoms—the system can be restricted to one unit cell in  $x$ - $y$ -direction.

As an example, we consider an oxygen atom adsorbed on a SrTiO<sub>3</sub>(001) surface. As already seen, there are two possibilities of terminations: TiO<sub>2</sub> and SrO termination. In Figure 12.4, the configuration with lowest energy is shown for the case of a  $2 \times 2$  cell. The first thing to be observed is the different position of the oxygen atom with respect to that in the bulk (the bulk position is indicated by a light grey atom with dotted rim). The bonding is very similar to that in an O<sub>2</sub> molecule. This behavior holds for both terminations. In Table 12.2 the binding energy  $\frac{1}{2}(E_{\text{O@SrTiO}_3}^{\text{surf}} - E_{\text{SrTiO}_3}^{\text{surf}} - E_{\text{O}_2}^{\text{gas}})$  is listed for different

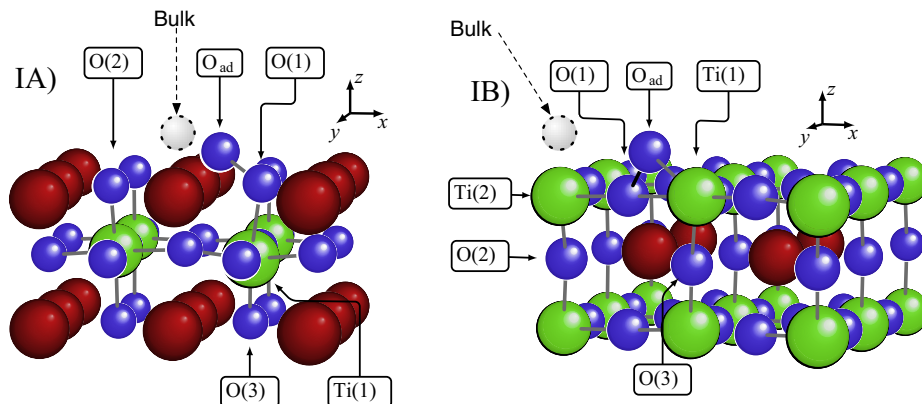


**Figure 12.4** Positions of an adsorbed oxygen atom on both terminations of  $\text{SrTiO}_3$ . The adsorbed oxygen is bonded to the oxygen of the topmost layer in a similar way as in an oxygen molecule. The dotted grey ball indicates the position of an oxygen atom in the bulk. The situation is plotted for a  $2 \times 2$  surface cell. *Figure 4.1 from [23], slightly extended.*

**Table 12.2** Binding energies for O on  $\text{SrTiO}_3(001)$  as a function of coverage and slab thickness

Surface Unit Cells	$N_L$	$E^{\text{IA}}$	bridge I	$E^{\text{IB}}$	Bridge II
$1 \times 1$	7	0.28	—	0.69	—
	9	0.28	—	0.69	—
	11	0.27	—	0.70	—
$2 \times 2$	7	-0.10	0.26	0.54	0.66
	9	-0.11	—	0.45	—
	11	-0.13	—	0.38	—
$3 \times 3$	7	-0.10	—	0.33	—
	9	-0.15	—	0.30	—
	11	-0.20	—	0.29	—
	13	-0.22	—	—	—

Taken from Table 4.1 in [23].

configurations.  $E_{\text{O@SrTiO}_3}^{\text{surf}}$  and  $E_{\text{SrTiO}_3}^{\text{surf}}$  are the total energies of the surface with and without the oxygen adatom.  $E_{\text{O}_2}^{\text{gas}}$  is the total energy of the gas phase molecule computed in an  $18 \times 18 \times 18 \text{ \AA}$  supercell with the experimentally measured bond length. The factor 1/2 accounts for the fact that we have a surface on both sides of the slab. For the  $\text{TiO}_2$ -termination ( $E^{\text{IB}}$ ), the binding energy is always positive, i.e., a reaction of the  $\text{SrTiO}_3$  surface with  $\text{O}_2$  is endothermic. For the  $\text{SrO}$ -termination, the binding energy is slightly negative except for a full coverage ( $1 \times 1$  unit cell). The influence of the slab thickness can be clearly seen.

To find the most stable surface configuration, i.e., the configuration with minimal energy, one has to perform runs for different positions. From the results, one can

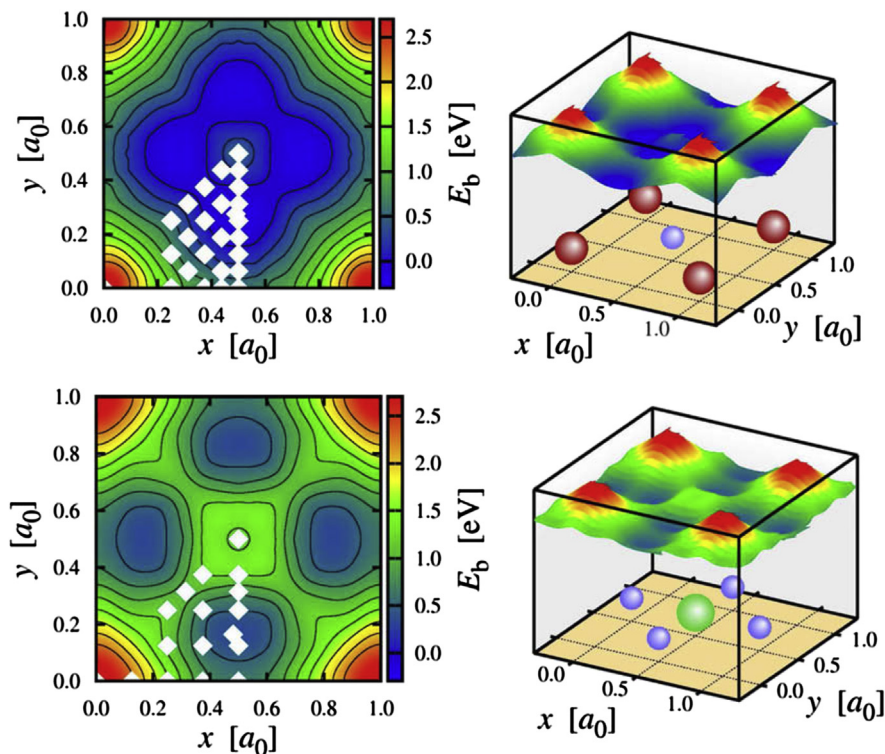


**Figure 12.5** Potential energy surface for an oxygen atom on a SrO-terminated (top) and a TiO<sub>2</sub>-terminated (bottom) surface. The white rhombs indicate the positions of the oxygen adatom, for which calculations have been performed. *Reprinted from [30] with permission of Elsevier.*

construct a potential energy surface. The potential energy surfaces are shown in [Figure 12.5](#) for both terminations. On the left hand, the white rhombs indicate the position of oxygen atoms for which calculations have been performed. It is noteworthy that, at least in this case, it is essential to compute the potential energy surface (PES) by means of many runs to find the most stable surface structure. As shown in [Figure 12.4](#), the oxygen atom on top is not found in a position of high-symmetry. Thus, a restriction of computing the structure for adatoms in highly symmetric positions might lead to invalid conclusions as occurred, e.g., in [\[34\]](#). An accurate PES is even more important if one likes to identify the diffusion path and its energy barrier (see next subsection).

#### 12.2.4 Adsorption, Dissociation and Diffusion

Adsorption, desorption, dissociation, and diffusion are dynamical processes and therefore cannot be tackled by DFT directly. However, DFT computations can

provide an energetic landscape, which helps to identify pathways for the dynamical processes.

In the last subsection, it was shown that the binding energy for an oxygen atom is only slightly negative for the SrO-termination and even positive for the TiO<sub>2</sub>-termination. Thus, it is very unlikely that an O<sub>2</sub> molecule will dissociate on a perfect SrTiO<sub>3</sub> surface. On the other hand, in reality, an atomically perfect surface is rather unusual. According to DFT calculations of oxygen vacancies in bulk SrTiO<sub>3</sub>, the energy of such defects is quite high [35]. Thus, one can expect that an oxygen molecule can easily stick to a vacancy position on the surface.

A similar behavior has been observed for oxygen adsorption on rutile TiO<sub>2</sub>(110) [36]. Adsorption on a perfect surface is strongly endothermic (binding energy is positive), whereas on a surface with one vacancy per unit cell, the adsorption is exothermic (binding energy is negative). From the viewpoint of growth kinetics, it would be desirable to compute the adsorption at a step edge. For instance, adsorption at step edges might be preferred with respect to that on terraces, which would drive the system toward a step growth mode. However, because of the periodic boundaries in DFT calculations, one needs a large lateral cell to mimic a step edge, which requires considerable computer resources. Atoms can also diffuse on the terrace and finally attach a step edge. The computation of a diffusion barrier by DFT is by far not as computationally heavy as the adsorption at a step edge. We continue with oxygen on a SrTiO<sub>3</sub>(001) surface. In Figure 12.5, the potential energy surface for an oxygen adatom on a 2 × 2 surface unit cell is plotted. The surface was constructed by computing the binding energy for a set of predefined locations (see white rhombs). From this figure, the minimum saddle point of a diffusion path can be found. By this method, one gets 0.81 and 0.67 eV for the diffusion barrier of an oxygen atom to its neighboring stable position for SrO- and TiO<sub>2</sub>-terminated surfaces, respectively.

Instead of searching the diffusion path by hand after constructing the PES, one can employ the so-called nudge elastic band method [37]. The algorithm is searching the path of minimal energy between two surface configurations. This reduces the amount of computations if the surface processes are more complex than the diffusion of a single atom like oxygen. As an example, we consider the diffusion of an OH molecule on the SrO-terminated surface of SrTiO<sub>3</sub> (see Figure 12.6). Starting point is an adsorbed H<sub>2</sub>O molecule (reaction coordinate 0.0). One H atom of the water molecule is binding to a surface oxygen atom. The binding energy is negative and therefore adsorption of a water molecule on a perfect SrO-terminated SrTiO<sub>3</sub>(001) surface is very likely, in contrast to the adsorption of an oxygen molecule. Afterward, the water molecule can dissociate, leaving one hydroxyl group in place and another moving to the neighboring site (IIA2) in Figure 12.6. For this diffusion, an energy barrier of about 1 eV has to be overcome ( $\Delta E_{IIA12}$ ). The energy barriers for a further diffusion of the hydroxyl group are significantly smaller than the very first one.

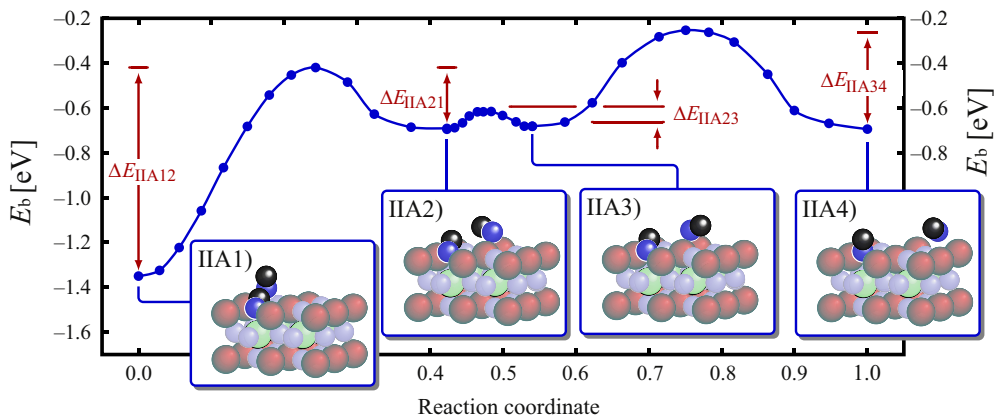


**Figure 12.6** Energy profile for surface diffusion of the protruding O1-H1 hydroxyl group over the SrO-terminated surface. Reprinted from [38] with permission of APS.

### 12.2.5 Ab Initio Thermodynamics

In DFT calculations, neither the surrounding atmosphere (partial pressures, temperature) nor the temperature of the substrate itself is considered. This gap to real systems can be tried to be closed by ab initio thermodynamics.

The interfacial energy per unit area is given by

$$\gamma_{\text{int}} = \left[ G_{\text{int}}(T, p) - \sum_{A,B,\dots} N_n \mu_n(T, p) \right] / 2S. \quad (12.16)$$

$G_{\text{int}}$  is the Gibbs energy of the contents of a supercell containing two interfaces,  $\mu_n$  is the chemical potential of component  $n$ , and  $N_n$  is the number of atoms of component  $n$  in the supercell. The termination on both sides of the slab is expected to be identical with a surface area  $S$ . As an example, we consider the adsorption of water on  $\text{SrTiO}_3$ . In this case we have

$$\gamma_{\text{int}} = \frac{1}{S} [G_{\text{H}_2\text{O@surf}} - G_{\text{surf}} - N_{\text{H}_2\text{O}} \mu_{\text{H}_2\text{O}}]. \quad (12.17)$$

$G_{\text{H}_2\text{O@surf}}$  and  $G_{\text{surf}}$  are the Gibbs free energies of the surface covered with  $N_{\text{H}_2\text{O}}$  water molecules per surface area  $S$  and of the corresponding clean surface, respectively. The difference in these Gibbs free energies can be identified with the difference in the total energies obtained from the DFT calculations. By this procedure, we neglect differences in the vibrational energy and in the configurational entropy. We are left with the computation of the chemical potential  $\mu_{\text{H}_2\text{O}}$  of the water vapor, which can be written as:

$$\mu_{\text{H}_2\text{O}} = E_{\text{H}_2\text{O}(\text{gas})} + \Delta\mu_{\text{H}_2\text{O}}(T, p_{\text{H}_2\text{O}}). \quad (12.18)$$

The total energy contribution  $E_{\text{H}_2\text{O}(\text{gas})}$  can be computed by DFT and the relative potential  $\Delta\mu_{\text{H}_2\text{O}}$  is split in the relative potential at the standard condition of

$p_{\text{H}_2\text{O}} = 1 \text{ bar} \equiv p^0$  and the change due to different pressure according to the ideal-gas relation:

$$\Delta\mu_{\text{H}_2\text{O}}(T, p_{\text{H}_2\text{O}}) = \Delta\mu_{\text{H}_2\text{O}}(T, p^0) + k_B T \ln\left(\frac{p_{\text{H}_2\text{O}}}{p^0}\right). \quad (12.19)$$

The relative potential at the standard condition can be derived from tabulated values for the enthalpy  $H$  and entropy  $S$ :

$$\Delta\mu_{\text{H}_2\text{O}}(T, p^0) = [H(T, p^0) - H(0 \text{ K}, p^0)] - T[S(T, p^0) - S(0 \text{ K}, p^0)]. \quad (12.20)$$

Data for standard enthalpies and entropies for many elements and compounds are provided by, e.g., the National Institute of Standards and Technology (NIST) also via internet: <http://kinetics.nist.gov/janaf/>.

In Figure 12.7 the surface energy is plotted as a function of the chemical potential of water, which can be translated into a partial pressure at a fixed temperature. The dotted grey boxes indicate the region above the  $\text{H}_2\text{O}$ -rich limit, i.e., where the present approach assuming equilibrium with water vapor is no longer strictly applicable. For a SrO-termination (left), the surface energy becomes negative before reaching this region; i.e., the calculations predict that a coverage with  $\text{H}_2\text{O}$  is stable up to a coverage of 25%. A full coverage is unstable (line for  $[1 \times 1]$ ). The plain blue background boxes mark the region of gas-phase conditions probed by Iwahori et al. in their friction force microscope (FFM) experiments [39]. On a  $\text{TiO}_2$ -termination, water adsorption is not stable even at a coverage of only 11%. This observation corresponds with the results of Iwahori et al.

Another example is the stability of the  $\text{SrTiO}_3$  and its surfaces under different vapor conditions of oxygen and different chemical potentials of Sr. In experiments, the latter is provided by atomic sources (MBE), by fragments of a target (PLD), or metalorganic compounds (MOCVD). In all these cases, no direct link between experimental conditions and chemical potential can be made. Only qualitatively a low chemical potential

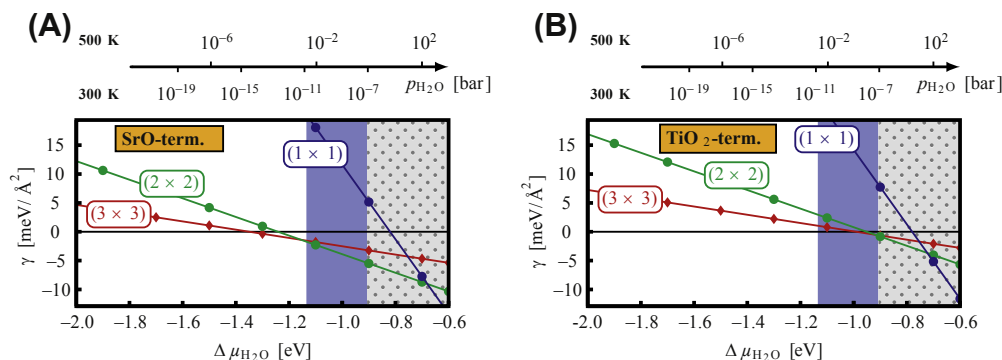
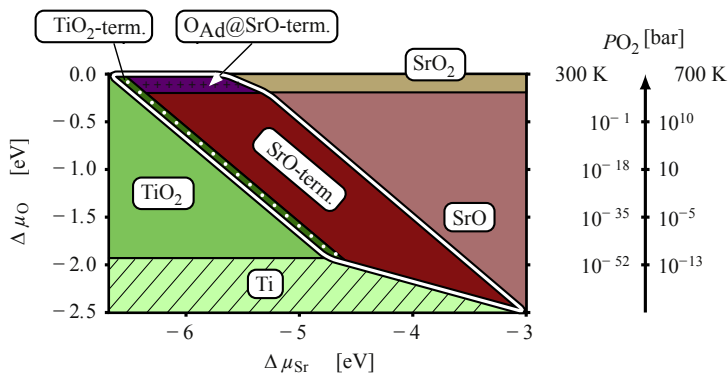


Figure 12.7 Stability of water adsorption on the two terminations of  $\text{SrTiO}_3$ . Reprinted from [38] with permission of APS.



**Figure 12.8** Phase diagram as a function of the oxygen pressure and the chemical potential of strontium. Low values of the latter means Ti-rich conditions. *Figure 4.6 (slightly modified) of [23].*

$\Delta\mu_{\text{Sr}}$  means poor Sr and Ti rich conditions. In [Figure 12.8](#), the phase diagram for the system Sr, Ti, and oxygen is shown. At low oxygen pressures, a titanium crystal is stable as long as the Sr is not provided in excess. In an intermediate region,  $\text{SrTiO}_3$  is stable (region boundary is marked by a white line). Interestingly, the  $\text{TiO}_2$ -termination is thermodynamically stable only in a very narrow region (area with white dots) in contrary to the SrO-termination. Nevertheless, the preparation of  $\text{SrTiO}_3$  surfaces using buffered HF solution yields a  $\text{TiO}_2$ -terminated surface [\[40\]](#). Strontium reacts much easier with the solution than Ti does. The SrO-terminated surface is stable at atmospheric pressure and the conditions of typical deposition experiments. This is not necessarily in contradiction to the theoretical study, because the conversion from a SrO- to a  $\text{TiO}_2$ -terminated surface might be kinetically hindered. Kinetics were not taken into account in the considerations above. In principle, one can go beyond this equilibrium situation by employing the KMC method (see next section), and using this, kinetic effects can be included. Using the data obtained by DFT for the KMC calculations, one replicates the phase diagram by DFT. For instance, this was shown for the surface of  $\text{LnMnO}_3$  in an oxygen atmosphere [\[41\]](#). The results are shown in [Figure 12.9](#): the left is the result of DFT thermodynamics, where (B) and (C) represent equilibrium and metastable situation, respectively.

DFT, the middle of KMC at equilibrium, and the right with KMC representing a metastable situation. At low temperatures, a coverage with oxygen atoms is stable over wide range of  $\text{O}_2$  pressure. However, the dissociation is kinetically hindered and, in reality, one will have a metastable situation as in case (C). The surface is covered by molecular oxygen at low temperatures.

The gas atmosphere might not influence only the surface termination but also the surface structure, i.e., different reconstructions can occur depending on the partial pressures. As an example, we refer to Wang et al. and their calculations for  $\alpha\text{-Fe}_2\text{O}_3$  (0001) [\[42\]](#).

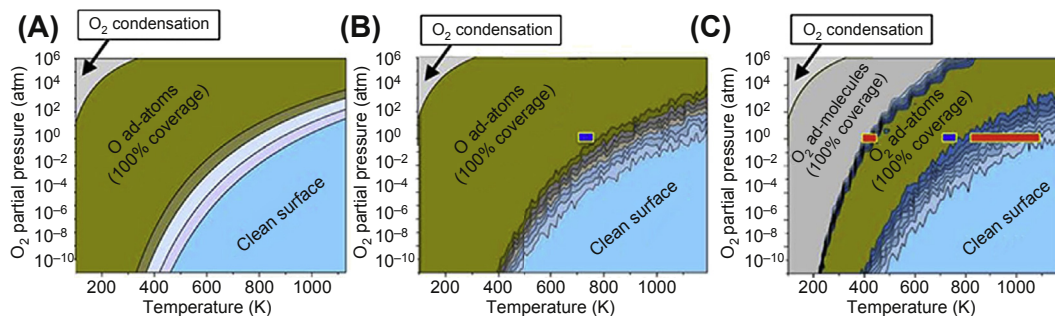


**Figure 12.9** Phase diagram for the  $\text{MnO}_2$ -terminated  $\text{LnMnO}_3$  surface in oxygen atmosphere. Three different kinds of computations have been applied: (A) DFT thermodynamics (B) and (C) kinetic Monte Carlo, whereas (B) and (C) represents equilibrium and *metastable* situation, respectively. Reprinted from [41] with permission of ACS.

## 12.3 Kinetic Monte Carlo Simulations

### 12.3.1 Introduction of the Method

With the help of KMC methods, one can study the dynamics of a system on atomistic scale, typically in situations far away from equilibrium. First of all, one has to distinguish between off-lattice and on-lattice methods. In the latter, a fixed grid is given and atoms can only move from one site to another. Such an on-lattice approach is not the best choice for treating defects. In an off-lattice approach, the atoms are not sitting on a rigid grid but can rearrange within a potential field. As in MD simulations, potential models are used to define the interaction of the atoms. Also, the treatment of heteroepitaxy, i.e., including effects of strain, is much more natural as in the case of on-lattice KMC (see, e.g., [7,43]). However, the use of a potential has two drawbacks. First, the computational requirements are drastically increased, and often calculations are restricted to 1 + 1 dimensions. Second, potentials like Lennard–Jones or Buckingham are good approaches to reproduce bulk properties, but often fail for surfaces. In on-lattice KMC, rules are set up for defining movements and their energy barriers. In principle, there is no limit in complexity, but the crucial point is to relate the heuristic model to reality. Data for the input might come from DFT calculations as described in the previous section, or from experimental measurements. A different procedure is to perform a parameter study and compare the results with experimentally observed ones to find the realistic set of parameters.

### 12.3.2 Kinetic Monte Carlo Simulation of Deposition from Gas Phase

The KMC method is a statistical method taking into account all possible processes at the surface at a certain time. Let us assume that the entire system (substrate + adatoms) has the configuration  $c_{itl}$  at iteration  $itl$ . In the next update, the configuration will change to  $c_{itl+1}$ . The transition from  $c_{itl}$  to  $c_{itl+1}$  has a probability  $P(c_{itl} \rightarrow c_{itl+1})$ . As mentioned

above, all possible processes are taken into account, therefore the new configuration  $c_{itl+1}$  has to be picked up from a large set of different configurations. For instance, an adatom might diffuse in four different directions by moving from an adsorption site to another, or it can desorb. Thus, in total there will be five new configurations, and each transition might have its own probability. If there are  $N$  new possible configurations, we have  $N$  probabilities  $P_n(c_{itl} \rightarrow c_{itl+1})$ , where  $n$  denotes the process. The probability is given by the activation energy for the process  $E^n$  and the thermal energy:

$$P_n = \exp\{-E^n/k_B T\}. \quad (12.21)$$

The concept of configurations  $c$  has roots in classical Monte Carlo simulation and its master equation. The basics of the dynamical Monte Carlo methods can be found in [44,45]. In the original concept, there was only one time scale; in all processes, the particles had the same frequency  $\nu$  in their potential wells. Typically, it is  $\nu \approx 10^{12} - 10^{13} \text{ s}^{-1}$ . In principle,  $\nu$  can be computed by DFT calculations. However, the frequencies might not be unique. Therefore, we proceed using rates  $R_n = \nu_n P_n$  rather than probabilities.

To pick up a process, one introduces the relative rate

$$\delta R_n = R_n / \sum_{n'=1}^N R_{n'}, \quad 0 \leq \delta R_n \leq 1. \quad (12.22)$$

The process ( $\tilde{n}$ ) is chosen randomly by

$$\sum_{n'=0}^{\tilde{n}-1} R_{n'} < \mathcal{N}_{\text{rand}} \leq \sum_{n'=0}^{\tilde{n}} R_{n'}, \quad (12.23)$$

where  $0 < \mathcal{N}_{\text{rand}} < 1$  is a random number. Formally,  $R_0 \equiv 0$ . This procedure is visualized in Figure 12.10. It should be noted that also processes with a high activation barrier and consequently low rate might occur by this procedure, which underlines the statistical character of KMC. Adsorption can be also treated in this framework. If  $F$  is the rate of particle impingement from the gas phase on the surface, the rate for the adsorption process is

$$R_{\text{ads}} = F S, \quad (12.24)$$

where  $S$  is the sticking coefficient. The sticking coefficient can be defined locally,

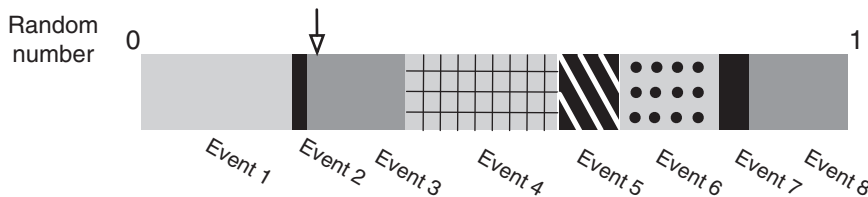


**Figure 12.10** Selection of an event in KMC calculations. The arrow indicates the number computed by the random number generator. It is more probable that the arrow hits an event with a high rate than one with a low rate. However, an event with a very small rate might also occur.

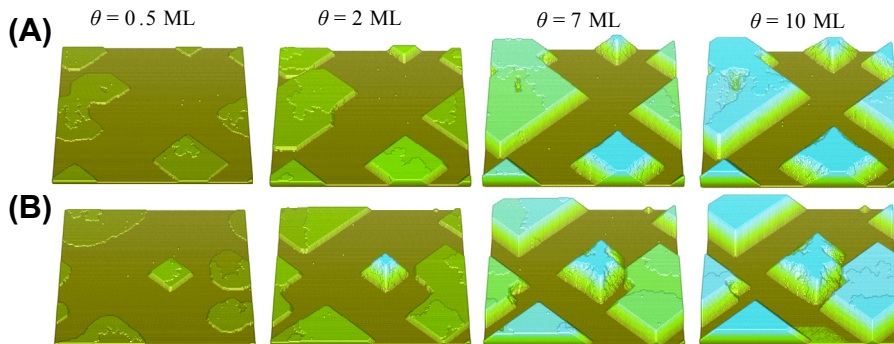


**Figure 12.11** The results of two runs with the same physical parameters but different initializations of the random number generator (A) and (B) are shown at different stages. In case (B), a small island is formed, which is growing fast in height. Visualization was done by VESTA [47].

depending on the local configuration. For instance, if the adsorption of an  $O_2$  molecule is not possible at a certain site,  $S = 0$  and thus  $R_{\text{ads}} = 0$  at this site.

Once a process is picked up, the particle will be moved according to this process and the new configuration is stored. This is one Monte Carlo step. We still have to access a time to this process and link it to the real world. The time is incremented by  $\Delta t = -(1/\sum R_n) \ln \mathcal{N}'_{\text{rand}}$ , where  $0 < \mathcal{N}'_{\text{rand}} < 1$  is a random number.

In practice, the random numbers will be generated numerically by so-called random number generators. For realistic results, the quality of the random generator is essential; see, e.g., discussions in [46]. One run of a KMC will give one possible evolution of the system. For a reasonable statistic, one has to perform several runs using different initializations for the random number generator. Depending on the system, the outcome of different runs might be quite different, at least at intermediate stages when the system is far from equilibrium. An example is shown in Figure 12.11 for a system InAs/GaAs, as two runs with the same parameters but different initialization.

### 12.3.3 On-Lattice KMC

As mentioned in the introduction, we will deal only with on-lattice KMC. In this model, particles sit on predefined sites of a regular lattice. The simplest case is a simple cubic lattice. The energy for a process  $E^n$  is defined in terms of the neighboring atoms. A typical definition reads

$$\text{Diffusion: } E_{\text{diff}} = E_S + E_{\text{neigh}} + E_{\text{ES}} \quad (12.25)$$

$$\text{Desorption: } E_{\text{des}} = E_S + E_{\text{neigh}} + \Delta E_{\text{des}}. \quad (12.26)$$

$E_S$  is the binding energy to substrate, thus defines the diffusion coefficient on a bare terrace.  $E_{\text{neigh}}$  is the energy to neighbor atoms in the same layer, which can be set in

simplest version as  $E_{\text{neigh}} = NE_n$ , where  $N$  is the number of neighbors and  $E_n$  is the binding energy between two neighbor atoms. At steps, there might be in addition an Ehrlich–Schwoebel barrier, represented by  $E_{\text{ES}}$ . The Ehrlich–Schwoebel barrier lowers the probability for a particle on a terrace to hop down at a step edge to the lower terrace, compared to the diffusion on the terrace itself. For desorption, one needs to overcome an additional energy  $\Delta E_{\text{des}}$ . Typically, on-lattice KMC is restricted to the solid-on-solid (SOS) model, i.e., no overhanging is allowed. In the SOS model, particles move to the adjacent grid site occupying the position on the topmost particle. Thus, no vacancy can be created.

KMC handles nucleation on a plane or terrace intrinsically. All surface energies are defined by the interaction energies between the particles. Because normally only nearest neighbors and partly next-nearest neighbors are taken into account, the interaction is short range. However, this is a question of defining the particular model and not a problem of the KMC method in general.

Homoepitaxial growth of silicon is a simple example, because only one type of atom is involved. However, the Si(001) surface obeys a  $2 \times 1$  surface reconstruction, i.e., the Si atoms are arranged in dimer rows. Hence, the energy contributions are different for atoms along the row ( $E_{\parallel}$ ) and normal to the row ( $E_{\perp}$ ):  $E_{\text{diff}} = E_{\text{S}} + N_{\parallel}E_{\parallel} + N_{\perp}E_{\perp} + E_{\text{dim}}$  [49].  $E_{\text{dim}}$  is the additional energy for atoms arranged in dimers. By comparing computed and measured island densities Cavalotti et al. optimized the energy parameters [48]. For different substrate temperatures, different growth modes can be observed, as depicted in Figure 12.12. The simulations started from a surface with two steps of one atom distance. Still, there are periodic boundary conditions in both lateral directions. When an atom is leaving the domain at the right-hand side on a lower terrace, it will reenter on the left-hand side on the upper terrace and vice versa. For the two cases with high temperature, a step-flow mode is observed and the steps prevail throughout the deposition. For lower temperatures, diffusion is too slow for the deposition rate of 1 ML/s and the surface becomes rough. In a technical process, silicon is not provided by an atomic source as in MBE but as silane ( $\text{SiH}_4$ ). Consequently, also hydrogen will adsorb on the surface. Configurations and energies have been computed by DFT calculations (for details, see [3]). KMC calculations showed that at low temperatures, the surface is mostly covered by hydrogen, which will hinder further growth of the silicon layer. One outcome of the KMC calculations is the growth rate, which can enter a global simulation. A global simulation comprises the reactor aiming to compute the change of the layer thickness on a wafer as a function of the process time. Vice versa, temperature and deposition rates enter the KMC model. Such a coupled model can recover the experimentally observed growth rates of runs with different process parameters very well [3].

So far, we have dealt with a system of one atom type only. For instance, treating III-V compounds such as GaAs, we have two types of atoms. However, in most KMC simulations, GaAs is treated as one particle. This reflects the phenomenological nature of KMC, which in the end should mimic the real growth dynamics. Systems of III-V

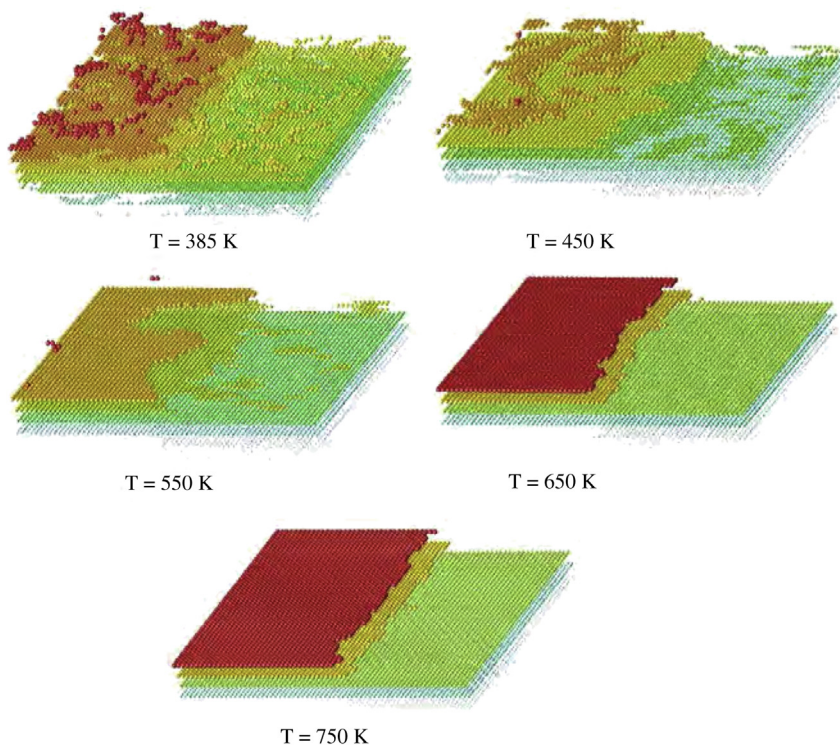


**Figure 12.12** KMC simulation of Si(001) homoepitaxy on-lattice  $64 \times 69$  atoms. The influence of temperature on the growth is shown. Reprinted from [48] with permission of Elsevier.

compounds have been mainly investigated, aiming at understanding the formation of quantum dots. The 3D growth is induced by strain and will be discussed in the next subsection.

Oxides are another interesting system with a variety of applications. One example in which KMC was applied is the homoepitaxy of MgO. In this system, the atoms O and Mg and their movements in terms of diffusion and rotation are considered [50]. The latter results in a vacancy diffusion. The energies for the processes have been computed before by DFT calculations. With such a KMC model, one can, e.g., study how perfect the layers are in terms of filling up under different process conditions such as surface temperature and pressure (see Figure 12.13). The higher the pressure, the higher the impingement rate on the surface and, consequently, the filling ratio is lower. A higher temperature enhances the diffusion and leads to a higher filling rate.

For perovskites like  $\text{SrTiO}_3$ , the situation is even more complex. Zhang et al. considered three types of particles:  $\text{SrTiO}_3$ ,  $\text{SrO}$ , and  $\text{TiO}_2$  [52].  $\text{SrO}$  and  $\text{TiO}_2$  are deposited with a certain rate and can diffuse on the surface. If  $\text{SrO}$  and  $\text{TiO}_2$  collide,

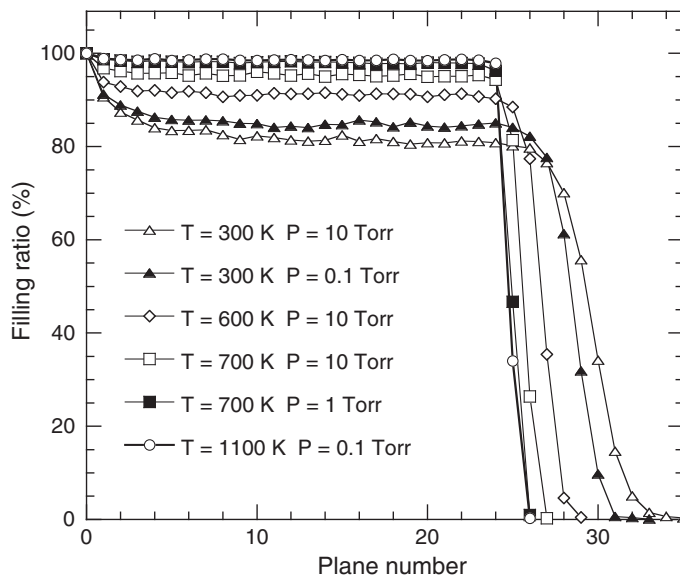


**Figure 12.13** Influence of temperature and pressure during homoepitaxy of MgO on the filling ratio as a function of the plane number. All data correspond to averages over 10 KMC runs. For each run, 30,000 molecules were deposited on a perfect substrate of  $50 \times 50$  atoms. Reprinted from [50] with permission of Elsevier.

$\text{SrTiO}_3$  will be formed, which will be fixed at this site. In this model, the perovskite structure is not recognized.

Handling the atoms separately needs a more complex model. However, the perovskite structure can be mapped on a simple cubic lattice by defining two types of layers, one for SrO and one for  $\text{TiO}_2$  [51]. Also, in one layer the sites of the lattice are not equivalent: sites with odd numbers in both  $x$ - and  $y$ -direction may be defined as sites for Sr; sites with even numbers in both  $x$  and  $y$ -direction may be defined as sites for O. The other sites are unoccupied. In the other layer, sites with even number in one direction and odd in the other are the ones for O, and sites with even numbers in both  $x$ - and  $y$ -direction are the ones for Ti. The principal mapping can be figured out from the right-hand side in Figure 12.2.

From the DFT, we know that a single oxygen adatom will sit on the oxygen of the layer below instead of the site in bulk. Thus, one should allow an oxygen atom to sit on these sites and should give other values for  $E_S$  and  $E_{\text{neigh}}$ . In particular,  $E_S$  on this site should be larger than on the bulk site such that an oxygen atom will preferentially sit on the site, which has minimum energy according to DFT. Once the layer is filled up and the oxygen atom has metal atoms as neighbors, the bulk position should become favorable, which can be reached by setting  $E_{\text{neigh}}$  properly. On the bulk position for oxygen, the value should be high, whereas on the other position it should be low or even negative to enhance diffusion. The rules and barriers for KMC might have a strong impact on the

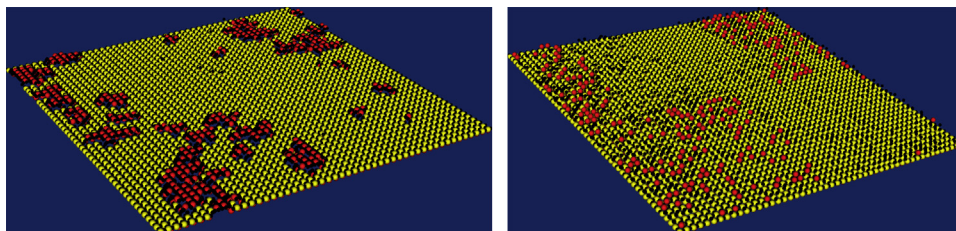


**Figure 12.14** Kinetic Monte Carlo (KMC) simulation for the deposition of  $\text{Na}_{0.5}\text{Bi}_{0.5}\text{TiO}_3$  on  $\text{SrTiO}_3$  with a simple parameter set (left) and parameter set partly based on DFT calculations (right). Na and Bi atoms are not distinguished and are colored in red. The small black atoms are oxygen and the yellow atoms are Ti atoms of the topmost substrate layer. Reprinted from [51] with permission of Wiley-VCH.

resulting surface structure, as seen in the example for the deposition of  $\text{Na}_{0.5}\text{Bi}_{0.5}\text{TiO}_3$  on  $\text{SrTiO}_3$  in Figure 12.14. The left part was observed was obtained by simple rules, whereas the right part is based on the outcome of the DFT calculations as discussed in the previous section [53].

There is one additional point if the processing is in PLD or metalorganic chemical vapor deposition (MOCVD). In both cases, it is unlikely that pure metal atoms arrive at the surface. In PLD, the target is often the same as the layer to be grown, and different fractures of the material will arrive at the surface, as, e.g., when depositing  $\text{SrTiO}_3$  there might arrive  $\text{SrO}$ ,  $\text{TiO}_2$ ,  $\text{SrTiO}_3$ , or clusters. In MOCVD, complex precursors are used, where the metal atom is bonded to several oxygen atoms. Thus, it is more likely that  $\text{SrO}$ ,  $\text{TiO}$ , or  $\text{TiO}_2$  will arrive on the surface. This has to be taken into account in KMC simulations, in particular when defining the sticking coefficient  $S$  in Eqn (12.24).

### 12.3.4 Kinetic Monte Carlo with Elastic Strain

Most of the interesting systems are not homo- but heterosystems with layer material different from that of the substrate. In general, this means different bulk lattice constants of the two materials, which implies an elastic strain in the layers. In an off-lattice KMC, these effects are intrinsically included by using potential models. However, the outcome of such computations depends critically on the applicability of the used potentials. In the phenomenological ansatz of the on-lattice KMC, the effect of strain has to be introduced explicitly. The elastic strain will change the diffusion barriers, which is typically included in KMC by another energy term  $\Delta E_{\text{strain}}$ . Thus, Eqn (12.25) becomes:

$$E_{\text{diff}} = E_{\text{S}} + E_{\text{n}} + E_{\text{ES}} + \Delta E_{\text{strain}} \quad (12.27)$$

Three approaches have been developed and used for computing  $\Delta E_{\text{strain}}$ :

- $\Delta E_{\text{strain}} = \frac{1}{2} [\sum_j \gamma / r_{i_2j}^3 - \sum_j \gamma / r_{i_1j}^3]$ , where  $r_{ij}$  is the distance between the considered adatom  $i$  and an island atom  $j$ . The initial and final positions are sites  $i_1$  and  $i_2$ , respectively [54].

- Green's function formalism [55].
- Ball and spring model introduced by Orr [56] and Lam [57].

The first one is a simple method and by this, the calculation of  $\Delta E_{\text{strain}}$  is rather quick. Such a procedure is obviously isotropic and does not account for different elastic constants in different directions.

The second approach is also an isotropic formalism. It has been used for the computation of the formation of GaAs quantum dots [58] and SiGe pyramids [59]. These computations were intended to study the self-assembling of quantum dots without any wetting layer. Investigating a transition from layer-by-layer growth to island growth was not the subject of these calculations.

For the rest of this section, the ball and spring model will be described, and applications will be presented. This approach was originally introduced by Orr et al. [56] and more than 10 years later it was applied to the system Ge/Si (100) [57,60,61]. Further developments focus on a higher efficiency of the method [62] and island growth [63]. Elastic effects are taken into account by assuming that the bonds will act as springs between the atoms. It is assumed that the mass-spring system is always in mechanical equilibrium. In the following, two types of springs are considered, a lateral one with constant  $k_L$  and a diagonal one with constant  $k_D$ . In the case of a cubic lattice, the two spring constants are related to the elastic constants (in Voigt notation) via  $k_L = a(C_{11} - 2C_{12})$  and  $k_D = aC_{12}$ .  $C_{11}$  and  $C_{44}$  cannot be distinguished in the approach with two spring constants.  $a$  is the lateral distance of atoms in the material. In the following, we denote the lateral distance of atoms in the substrate and the film by  $a_s$  and  $a_f$ , respectively. An adsorbed layer (full coverage) will be in equilibrium if the vertical distance of atoms is  $a_z = a_f + a_s \varepsilon k_D / (k_L + k_D)$ . This relation can be derived from the balance of forces on the surface atoms. Such a system of complete layers acts as a reference system. For a general system of  $N$  adatoms, the displacements of atoms with respect to this reference system are computed solving a matrix equation:

$$\mathbf{F} = \mathcal{A}\mathbf{U} + \mathbf{B} \quad (12.28)$$

The contributions  $\mathbf{B} = (\mathbf{b}_1, \mathbf{b}_2, \dots, \mathbf{b}_N)$  are the forces due to the fact that a layer might be not complete. The matrix  $\mathcal{A}$  includes the contributions from the interaction with the substrate and the film. The resulting forces  $\mathbf{F} = (\mathbf{f}_1, \mathbf{f}_2, \dots, \mathbf{f}_N)$  should be zero in equilibrium, i.e., the left-hand side in Eqn (12.28) is a zero vector. Obviously, the matrix increases by time because particle adsorption leads to an increase of the value  $N$ . Therefore, the cost of computing the displacements  $\mathbf{U} = (\mathbf{u}_1, \mathbf{u}_2, \dots, \mathbf{u}_N)$  increases with progressing time and is quite considerable. Once the displacements have been computed, the energy stored in all springs can be computed via:

$$E_{\text{strain}} = \frac{1}{2} \sum \varepsilon_{ijk}, \quad (12.29)$$

where the sum is over all sites and  $e_{ijk}$  is the total energy stored in all the bonds associated to the atom located at site  $(i, j, k)$ . The 1/2 accounts for double counting of the summation.  $e_{ijk}$  is composed as  $e_{ijk} = e_{ijk}^x + e_{ijk}^y + e_{ijk}^z$ , where  $e_{ijk}^x$  is given by:

$$\begin{aligned}
 e_{ijk}^x = & \frac{k_L}{2} \left( [u_x(i+1, j, k) - u_x(i, j, k) + d_x]^2 + [u_x(i-1, j, k) - u_x(i, j, k) - d_x]^2 \right) \\
 & + \frac{k_D}{2} \left( [u_x(i+1, j, k+1) - u_x(i, j, k) + d_x]^2 + [u_x(i-1, j, k+1) - u_x(i, j, k) - d_x]^2 \right) \\
 & + \frac{k_D}{2} \left( [u_x(i+1, j, k-1) - u_x(i, j, k) + d_x]^2 + [u_x(i-1, j, k-1) - u_x(i, j, k) - d_x]^2 \right) \\
 & + \frac{k_D}{2} \left( [u_x(i+1, j+1, k) - u_x(i, j, k) + d_x]^2 + [u_x(i-1, j+1, k) - u_x(i, j, k) - d_x]^2 \right) \\
 & + \frac{k_D}{2} \left( [u_x(i+1, j-1, k) - u_x(i, j, k) + d_x]^2 + [u_x(i-1, j-1, k) - u_x(i, j, k) - d_x]^2 \right).
 \end{aligned} \tag{12.30}$$

Because the values  $u_x(i, j, k)$  were computed with respect to the reference system, the difference  $d_x = a_f - a_s$  enters Eqn (12.30). So, finally we get the contribution for Eqn (12.27):

$$\Delta E_{\text{strain}} = E_{\text{strain}}(\text{with adatom}) - E_{\text{strain}}(\text{without adatom}). \tag{12.31}$$

The method has been used to study the transition from layer-by-layer to 3D growth. At this point some general remarks on epitaxial growth are in order. Layer-by-layer (Frank van der Merwe) growth is observed if the lattice mismatch is small. If the lattice mismatch is large, 3D (Vollmer–Weber) growth will occur. In the atomistic view, it means that now the adatom–adatom bond is stronger than the adatom–surface bond, in contrast to the Frank van der Merwe mechanism, where it is opposite. In reality, often a mixture is observed: the Stranski–Krastanov growth mode. For a few layers, a layer-by-layer takes place before 3D growth starts.

For a given set of parameters, one can scan the misfit  $\varepsilon = (a_f - a_s)/a_f$  and check the growth mode. Here,  $a_f$  and  $a_s$  are the bulk lattice constants of the film and substrate, respectively. By this procedure, one obtains either the Frank van der Merwe or the Vollmer–Weber mode. Stranski–Krastanov growth is not observed.

There is an ongoing discussion on the origin of the Stranski–Krastanov growth mode. One reason might be the occurrence of interdiffusion. Atoms supplied to the surface will diffuse to bulk and, in reverse, atoms of the substrate will diffuse to the surface. This will reduce the lattice mismatch, hence a layer-by-layer growth is possible. With progressing time and layer height, the composition will change by decreasing the amount of atoms from the substrate, hence the lattice misfit will increase. Eventually, this leads to 3D growth. However, the strain may be also relaxed by defects like vacancies. For SiGe nanostructures, the current status is discussed in [64]. This kind of nanostructure is of interest for electronic applications, therefore has been the focus of KMC simulations. For instance, Xiang et al. studied the spontaneous

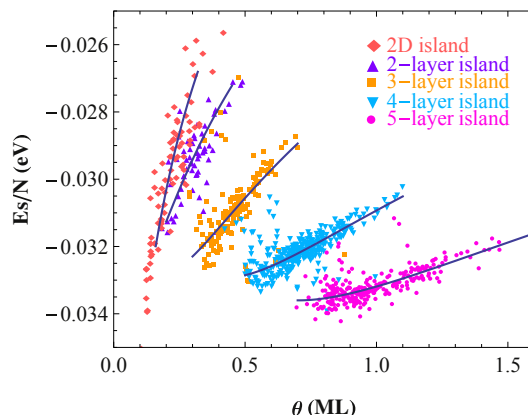


**Figure 12.15** Plot of the strain relaxation energy per atom  $E_s/N$  against coverage  $\theta$  from simulations at deposition rates 1, 3, and 10 MLs<sup>-1</sup>. The island height is inferred from the measured maximum surface height. *Reprinted from [65] with permission of APS.*

formation of Ge quantum dots on Si [65]. They applied a misfit of  $\varepsilon = 0.08$ . Spontaneously, there is a 3D island growth without any stage of layer-by-layer growth. In Figure 12.15, the strain relaxation energy  $E_s$  is plotted as a function of the coverage. This energy is defined as the difference between the strain energy stored in all springs at mechanical equilibrium and the strain in the homogeneously strained state. In the latter, all atoms are sitting at their bulk positions, i.e., the atoms did not relax to new positions out of the bulk ones. By this definition,  $E_s$  is always negative.  $E_s$  was measured at various times and in the plot, its values were indicated by the maximum height in the system (2D island, two-layer island, etc.). The plot can be understood as follows: After nucleation of the first island, this island spreads and the strain is increased. With increasing size, the probability of nucleation of a new layer on top is increasing. Once formed, it results in a drop of strain energy.

Baskaran et al. introduced an intermixing in their KMC model for computing Ge pyramids on a Si substrate [63]. They simply allowed the Si atoms of the underlying substrate to hop. For this reason they introduced a certain number of layers for the substrate. Strictly speaking, they allow surface diffusion for the substrate atoms, but not a bulk diffusion for the Ge atoms. The main result of their computation was showing the different evolutions of the Ge pyramids in cases with and without intermixing. In the latter, no wetting layer was formed, whereas in the case of intermixing, first a layer-by-layer growth was observed before the 3D growth has overtaken. Another system with a Stranski–Krastanov mode is  $\text{In}_x\text{Ga}_{1-x}\text{As}/\text{GaAs}$ . Experimental measurements and theoretical attempts have been made to find the critical layer thickness at which the transition occurs from a layer-by-layer to a 3D growth.

This transition depends on the composition of the incoming fluxes  $x$ , which can be tuned with high precision in MBE experiments. Such a system can be studied by KMC

[66]. Intermixing is not taken into account explicitly but indirectly, by using an effective lattice misfit  $\varepsilon_{\text{eff}}$ , which is given by

$$\varepsilon_{\text{eff}} = \frac{x - \xi}{1 - \xi} \frac{H}{H_{c,1}} \varepsilon_{x_1}. \quad (12.32)$$

$\xi$  is the composition for which holds: if  $x > \xi$  there is 3D growth at finite thickness. Only for this case Eqn (12.32) is valid – otherwise  $\varepsilon_{\text{eff}} = 0$ .  $\varepsilon_{x_1}$  is the critical effective misfit in the case  $x = 1$  and  $H_{c,1}$ , the corresponding apparent critical layer thickness. This equation can be derived from the fact that  $E_{\text{strain}} = \varepsilon^2 \Delta W$ , where  $\Delta W$  does not depend on the misfit. Relating everything to the case of a flux composition of  $x = 1$  (corresponding misfit  $\varepsilon_1 = 0.07$ ), we obtain:

$$\Delta W(H, x) = x_{\text{eff}}^2 \Delta W_{\varepsilon_1} \quad \text{with} \quad x_{\text{eff}} = \frac{\varepsilon_{x_1}}{\varepsilon_1} \frac{x - \xi}{1 - \xi} \frac{H}{H_{c,1}} \quad (12.33)$$

$\Delta W_{\varepsilon_1}$  will be computed during the run. The two parameters  $H_{c,1}$  and  $\xi$  have to be determined beforehand. Because  $H_{c,x} \approx H_{c,1}(1 - \xi)/(x - \xi)$ , one can use two experimental points to obtain both  $H_{c,1}$  and  $\xi$ . In Figure 12.16, the prediction of the KMC is shown together with experimental results and a curve from theoretical considerations. It shows that the KMC runs reproduce the experimental data. Once validated by this comparison, the KMC can be used to study the details of the growth process such as quantum dot formation and growth.

### 12.3.5 Growth of Quantum Dots

Quantum dots have become of great interest because of the new physics in such confined systems. In contrary to a typical film growth, where one likes to have layer-by-layer growth, for quantum dots one needs a 3D growth mode. For applications, quantum

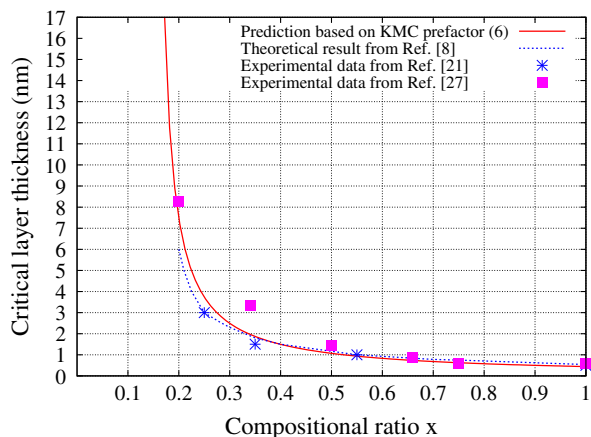


Figure 12.16 Critical layer thickness as a function of the composition of the particle flux. Ref. [8], Ref. [21], and Ref. [27] are [68, 69, 70], respectively. Reprinted from [66] with permission of Elsevier.

dots should be of the same size and arranged in a regular manner, which might be achieved by a self assembling of the system. This has been the subject of research and, in this context, KMC has been used. Meixner et al. studied the size distribution under different process conditions such as deposition rate and substrate temperature [58]. They used the Greens function formalism and performed calculations in the submonolayer regime.

Ideally, quantum dots are clearly separated and have a well-defined shape. However, in 3D growth, instabilities in the shape of the 3D object might occur or a growth with shallow mounds between the objects. KMC can provide better insight into the processes (see overview [71]).

Sometimes, peculiar structures occur in 3D growth mode. For instance, when growing GaSb nanostructures on Si doped GaAs(100) by droplet epitaxy, ring structures of GaSb were observed. Such structures could be revisited by means of KMC [72].

For certain applications, quantum dots are not freestanding but packed in a matrix. For instance, the quantum dots are overgrown by the same material as the substrate. Taking interdiffusion into account, such processing might not result in the structure wanted. One can use KMC to study the process in detail; in experiments, the intermediate stages cannot be investigated. This has been done for InAs quantum dots on a GaAs substrate embedded in  $\text{In}_x\text{Ga}_{1-x}\text{As}$  [73]. The evolution in time can be seen in Figure 12.17. Two different distributions of quantum dots have been used for following capping processes. For every stage the situation is shown for an  $\text{In}_x\text{Ga}_{1-x}$  capping with a consecutive increasing  $x$  (two top lines) and for a GaAs capping (two bottom lines). InAs particles are in yellow, GaAs particles are in blue. As already mentioned, the computation of the elastic strain in every Monte Carlo step is very time consuming, because the matrix of the entire system has to be solved. Several simplifications have been introduced. One approach is to compute the elastic strain, not for every adatom but only for those at step edges. This is based on the fact that the largest strain is felt by atoms at the step edges and the elastic energy is decreasing with increasing height of the 3D object (see, e.g., Figure 2 in [59]). Consequently, one can restrict the additional term  $\Delta E_{\text{strain}}$  to atoms at step edges, which will reduce the computational requirements dramatically [74]. As a consequence, runs for a larger number of monolayers are possible. We consider the system InAs/GaAs employing the relevant input data from [75] [58], and [76]. In Figure 12.18, the mean height as a function of the substrate temperature and the deposition rate is shown. A large value means a few pyramids with large height, which are preferentially formed at low deposition rate and high temperature because the surface diffusion is fast. Climbing up a step edge is enhanced by strain ( $\Delta W_1 = 0.3$  eV) but hopping down is hindered by the Ehrlich–Schwoebel barrier (0.08 eV). The relation of these two barriers has a large influence on the size and distribution of quantum dots. If there is no strain energy applied ( $\Delta E_{\text{strain}} = 0$ ), one needs an unrealistically high Ehrlich–Schwoebel barrier to obtain 3D structures ( $\Delta E_{\text{ES}} > 0.15$  eV). On the other hand, for  $\Delta W_1 = 0.05$  eV, the growth is already 3D.

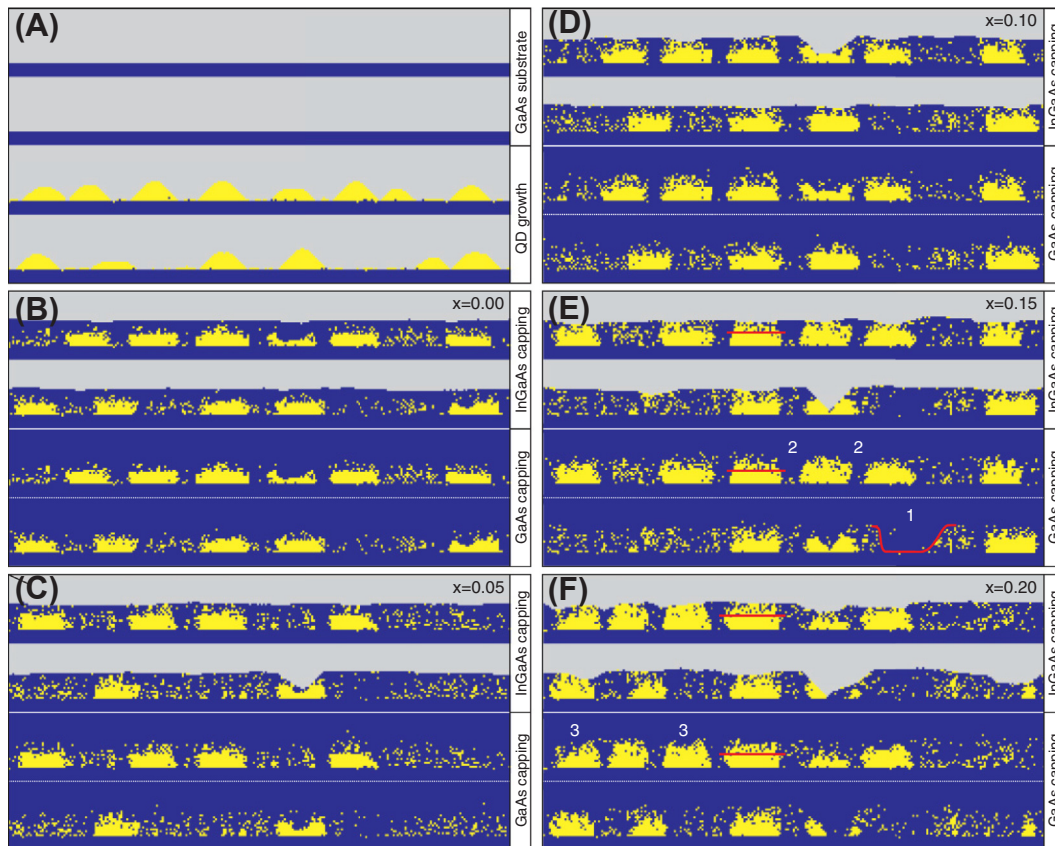


**Figure 12.17**  $140 \times 20 \text{ nm}^2$  cross sections through the KMC data set. Each window shows two stretches and two situations. These uncapped QDs represent the initial configuration for all performed KMC simulations of the capping process. (A)–(F) The indium fraction  $x$  is increased in the consecutive windows, which show the situation after the growth of the InGaAs capping layer (top two panes), and after the growth of the pure GaAs spacer layer (bottom two panes). (E), (F) The horizontal red line marks, for an exemplary QD, the boundary between the pure InAs region and the region of phase separation. Examples of the three observed peculiarities are marked: (1) variation in the thickness of the InGaAs layer between the QDs (solid red line), (2) indium-depleted regions, and (3) asymmetrically shaped QDs. *Reprinted from [73] with permission of APS.*

## 12.4 Phase Field Methods

### 12.4.1 Philosophy of Phase Field Approaches

Phase field methods are devoted for phase transitions, i.e. at least we have two different phases, which are described by different values of an order parameter  $\phi(x, t)$ .

For instance, in the solidification/melting transition, one introduces  $\phi = 0$  for melt and  $\phi = 1$  for solid. The important point is that the order parameter is a continuous variable. Formally, this enables us to write a free energy functional  $F$  as a function of  $\phi$ . Then, the equation of motion can be obtained by the variational principle, i.e., taking the

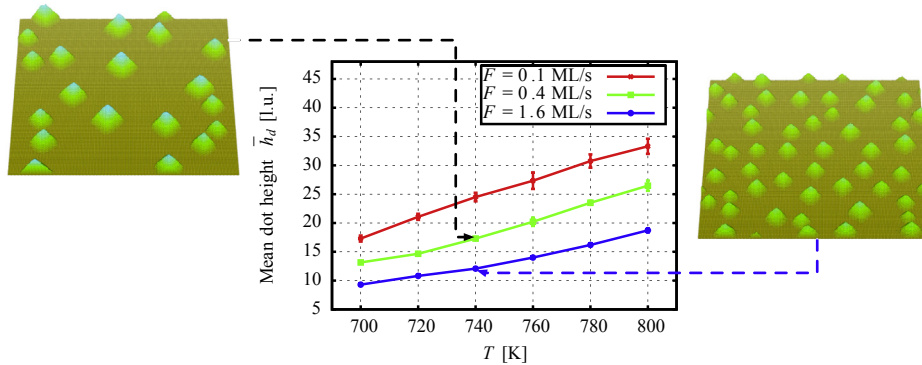


**Figure 12.18** KMC simulations of depositing InAs on GaAs [74]. Mean island height  $\bar{h}_d$  is shown as a function of temperature  $T$  for different deposition rates  $F$ . For two parameter points, a representation of the surface configuration is shown. *Extended figure from [74] with permission of Elsevier.*

derivative of  $\mathcal{F}$  with respect to  $\phi$ . It also means that there is no sharp interface and there are regions that are partly one phase and partly the other. J. S. Langer was the first who proposed the use of this Ginzburg–Landau approach to the liquid/solid transition. The first publication was by G. Caginalp [77] (see also “Phase Field Models” by M. Plapp in Volume 1b). Afterward, Liu and Metiu were the first who introduced this concept for layer growth [78]. They used it for computing a 1D step motion. Such simulations are based on the concept of Burton, Cabrera, and Frank (BCF) [79], which is described in more detail below. The phase field measures the layer height such as  $\phi = 0, 2, 4, 6, \dots$ . The steps are smeared out in the lateral direction where the value of  $\phi$  changes from one integer value to the next. Karma and Plapp applied this kind of model in full 3D calculation and considered spiral growth [80].

Since  $\phi$  measures the layer height, it has an atomistic resolution in the stack direction. One can go one step further and apply the phase field variable, a purely atomistic meaning, i.e.,  $\phi = 1$  means particle and  $\phi = 0$  means no particle.  $\phi$  becomes an atomistic density. Elder et al. introduced this concept in 2002 giving (2D) examples for grain growth, ordering of a binary alloy, and epitaxial growth [81]. The length scale is atomic and, thus, the same as in molecular dynamics or KMC calculations, but the time scale is diffusive. This allows the study of slow processes.

## 12.4.2 Phase Field Crystal—Structures and Defects

As mentioned above, the PFC model was introduced by Elder and coworkers [81] by defining a free energy as a function of the particle density  $\phi$  with a periodic hexagonal structure as its minimum. Recent overviews can be found in [67,82,83]. The simplest form of a free energy is:

$$\mathcal{F} = \int_V \left( \frac{1}{2} \phi [(q_0^2 + \nabla^2)^2 + a] \phi + \frac{1}{4} \phi^4 \right) dV. \quad (12.34)$$

$q_0$  and  $a$  are two phenomenological parameters.  $a$  can be considered as the driving force.

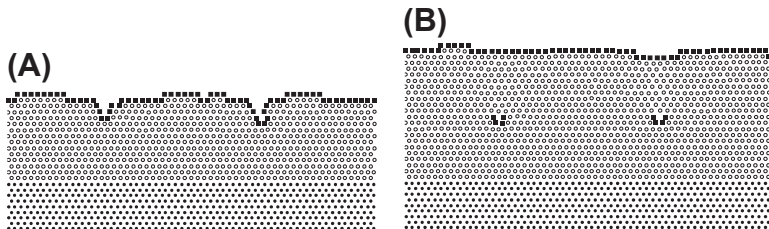


**Figure 12.19** Two-dimensional phase field crystal simulation of epitaxial growth. Situation (A) and (B) are after a deposition of an average of 13 and 21 layers. *Reprinted from [81] with permission of APS.*

$q_0$  defines the lattice spacing in the bulk. Because  $\phi$  is conserved (closed system with the mass conserved), the dynamics are given by

$$\frac{\partial \phi}{\partial t} = \nabla^2 \frac{\delta \mathcal{F}}{\delta \phi} + \nabla \zeta = \nabla^2 \left[ \left( a(q_0^2 + \nabla^2) \right) \phi - \phi^3 \right] + \nabla \zeta, \quad (12.35)$$

where  $\zeta$  is a stochastic noise field of particle fluxes.<sup>3</sup>

A phase diagram can be derived as a function of the driving force  $a$  and the mean value of  $\psi$ , i.e., the density of the system. For low densities, a system of stripes will have the minimum free energy, at medium densities a hexagonal system, and at high densities a constant state. The latter is the liquid phase. Equation (12.34) can be modified to obtain also fcc and bcc phase in a certain range of density and driving force [84]:

$$\mathcal{F} = \int_V \left( \frac{1}{2} \phi \left[ \lambda (q_0^2 + \nabla^2)^2 \left[ (q_1^2 + \nabla^2)^2 + r_1 \right] + a \right] \phi + \frac{1}{4} \phi^4 \right) dV. \quad (12.36)$$

In their original paper, Elder et al. gave one example of epitaxial growth. They used two different values of  $q$  for the substrate (small circles in Figure 12.19) and for the adlayer (larger circles). It is a 2D simulation exhibiting the development of two bulk defects. Going to a specific system, Xu and Liu proposed another free energy [85]. Their aim was to describe the dimerization on Si(001) or Ge(001) surfaces. It is a 2D model, thus they consider only the surface and looking on the surface structure as a function of the temperature. Computation of epitaxial growth is not yet possible for such a system.

Chen et al. studied the influence of vicinal angles of the substrate on the emerging structure of the deposited layers [86]. They employed the original 2D model of Elder plus an external potential of the form  $V = V_S [\cos(q_s x) + \cos(q_s y)] + \bar{\psi}$ . The additional potential represents the influence of the substrate and  $q_s = 2\pi/a_s$  with  $a_s$  as the lattice constant of substrate. The lattice constant of the film is entering  $q_0$  of Eqn (12.35).  $\bar{\psi}$  is the average value of  $\psi$ . The lattice mismatch in their<sup>3</sup> calculations was  $\varepsilon = 0.065$  and  $0.11$  and the vicinal angle was varied between  $4.5^\circ$  and  $14.5^\circ$ . Facetted growth, columnar growth, and occurrence of defects were observed, depending on the two parameters varied.

PFC methods are promising, but currently the type of systems to be handled is very limited, and free energy definitions for the variety of realistic systems are lacking.

<sup>3</sup>Please note that sometimes you will find equations with a stochastic noise  $\eta$  instead of  $\nabla \zeta$ . This is incorrect, because the mass is not conserved in every time step but may be conserved only as an average over time.

### 12.4.3 Phase Field Simulation—Step Growth and Beyond

The phase field model was introduced to tackle the problem of step motion by numerical simulations. At this point, we give a short description of the governing equations, which are based on the BCF model. We do not consider atoms as in the PFC model but have an atom density  $\rho$  on terraces, i.e., a density per area. On a terrace,  $\rho$  obeys the following diffusion equation:

$$\partial_t \rho = \nabla(D(r)\nabla\rho) + F - \tau_{\text{des}}^{-1}\rho. \quad (12.37)$$

$F$  is the flux from gas phase, i.e., how many particles per area and time will attach to the surface of the terrace.  $\tau_{\text{des}}^{-1}$  is the desorption rate. Terraces end at steps, which are sinks or sources of adatoms. In equilibrium, the step edge will not move and there is neither a release nor a consumption of atoms. For this situation, the adatom density at the step edge is  $\rho^{\text{eq}}$ . If the actual density is different, there a flux to or from the steps, and we have the following boundary conditions at the step edge, one for the lower terrace and for the upper one:

$$D \frac{\partial \rho^+}{\partial n} = k^+ (\rho^+ - \rho^{\text{eq}}), \quad \text{from the lower terrace} \quad (12.38)$$

$$-D \frac{\partial \rho^-}{\partial n} = k^- (\rho^- - \rho^{\text{eq}}), \quad \text{from the upper terrace.} \quad (12.39)$$

$k^+$  and  $k^-$  are the rates for incorporating atoms at the step. Because in most real cases we have an Ehrlich–Schwoebel barrier for atoms hopping from the upper terrace to the lower one,  $k^+ > k^-$  for many real systems. The equilibrium adatom density at the step edges depends on the energy due to the curvature  $\kappa$  and the thermal energy  $k_B T$ :

$$\rho^{\text{eq}} = \rho_0^{\text{eq}} \left( 1 + \frac{\Omega \gamma \kappa}{k_B T} \right) = \rho_0^{\text{eq}} (1 + d_0 \kappa). \quad (12.40)$$

$\gamma$  is the energy of the step edge,  $d_0$  the capillary length, and  $\Omega$  is the atomic area.  $\rho_0^{\text{eq}}$  is the equilibrium adatom density for a straight step. This is given by the relation between the energy gain of an atom by attaching to the step edge  $E_{\text{attach}}$  and the thermal energy:

$$\rho_0^{\text{eq}} = 1 / (1 + e^{E_{\text{attach}}/k_b T}) \quad (12.41)$$

The velocity of the step is given by:

$$v_{\text{step}} = -D \left( \frac{\partial \rho^+}{\partial n} - \frac{\partial \rho^-}{\partial n} \right). \quad (12.42)$$

The set of equations is difficult to solve in a sharp interface approach, where the boundary conditions have to be applied to a moving step edge, which requires a moving grid or a clever approach of interpolation. The problem becomes even worse if new steps occur by 2D nucleation on a terrace. To overcome these problems, the phase field concept has been applied to epitaxial growth by introducing an order parameter  $\phi$ , where an even integer value of  $\phi$  denotes the layer height. The phase field evolves via

$$\tau_\phi(\mathbf{r}, t) \partial_t \phi = W^2 \nabla^2 \phi + \partial_\phi f + \lambda_{\rho g_\phi \rho}, \quad (12.43)$$

with

$$f(\phi) = -\frac{1}{\pi}(\cos(\pi[\phi - \phi_s]) + 1), \quad \partial_\phi f = \sin(\pi[\phi - \phi_s]) \quad (12.44)$$

$$g(\phi) = -\frac{1}{\pi}(\sin(\pi[\phi - \phi_s]) + \phi), \quad \partial_\phi g = \cos(\pi[\phi - \phi_s]) + 1. \quad (12.45)$$

$\phi_s$  is the height of the substrate. The equation for the adatom density becomes:

$$\partial_t \rho = \nabla(D(r)\nabla\rho) + F - \tau_{\text{des}}^{-1}\rho - \frac{1}{2}\frac{\partial\phi}{\partial t}. \quad (12.46)$$

On the terraces,  $\phi$  has even integer value, and in the region of the step edge it is smoothly changing from one even integer value to another. The width of this transition region is  $W$ . The parameters  $\lambda$ , and  $\tau_\phi$  are related to the capillary length and diffusion constant via  $d_0 = a_1 W/\lambda$  and  $\lambda = \tau_\phi D/a_2 W^2$ .  $a_1$  and  $a_2$  are 0.718,348 and 0.510,442 obtained by a 1D stationary profile solution. Karma and Plapp employed this model to compute a spiral growth on the surface. Shortly after their publication, spiral growth was studied by the so-called level-set method, a method similar to phase field methods [87]. A further extension was made by the inclusion of heat transport in the layers [88].

Going toward a real system, Yu et al. applied the phase field model to the anomalous spiral step growth on Si(001) surfaces [89]. Such a behavior has been previously observed by in situ low-energy electron microscopy [90]. In the phase field simulations, the two terraces, namely  $(2 \times 1)$  and  $(1 \times 2)$ , are indicated by  $\phi = 1, 3, 5, \dots$  and  $\phi = 2, 4, 6, \dots$

The functions in Eqn (12.43) are now given by:

$$f(\phi) = \frac{1}{\pi}[-\cos(2\pi\phi) \pm \Delta\gamma(\pi\phi)] \quad (12.47)$$

$$g(\phi) = \frac{1}{\pi}[\sin(2\pi\phi) - 2\pi\phi \pm \Delta\gamma(\pi\phi)], \quad (12.48)$$

where the parameter  $\Delta\gamma$  is the difference of the surface energy of the  $(2 \times 1)$  and  $(1 \times 2)$  termination. By this parameter, a strain field at the screw dislocation is introduced, which is considered to be related to the anomalous spiral motion. Setting  $\Delta\gamma = 0$ , one can compute the regular spiral motion on Si(111).  $\delta\gamma$  on Si(001) depends on the location around the dislocation, which acts as a source for the spiral growth (see Figure Z3B in [90]). The differences in the spiral structure for finite and zero  $\Delta\gamma$  can be clearly seen in Figure 12.20.

Hitherto, step growth was treated by the phase field model. The concept is quite flexible and so one can, e.g., also deal with island growth. The phase field simply distinguishes between island ( $\phi = +1$ ) and nonisland ( $\phi = -1$ ). Xu and Liu derived a free energy to describe the evolution of metal islands on insulators [91]. This kind of calculation allows overhanging as it is observed at higher temperatures. An example for island shapes at different temperatures is shown in Figure 12.21. The diffuse interface region defined by the phase field model is clearly seen in this figure by the grey regions. A direct comparison to experiment was not yet made. However, these kinds of shapes for the crystallites were observed some time ago for Pb/graphite(00.1) [92].

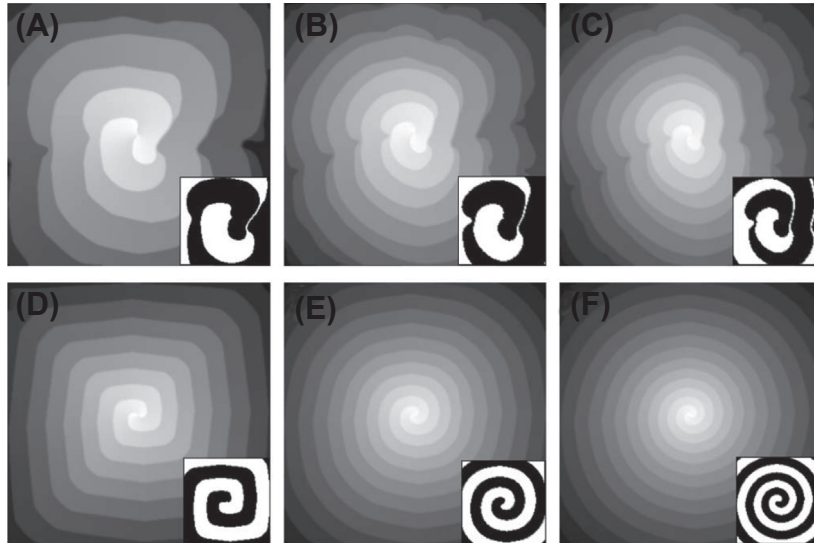


**Figure 12.20** Images of the spiral growth at the steady-state regime simulated using  $F = 0.005$  ML/s (left),  $0.02$  ML/s (middle), and  $0.04$  ML/s (right). In the upper row, strain effects are included in the lower row not ( $\Delta\gamma = 0$ ). From left to right, the coverage was 105, 187, and 224 ML. The lightest grey corresponds to the highest surface height, being around 109, 193, 231, 111, 200, and 233 ALs. The sharp change in grey indicates the position of the step. Reprinted from [89] with permission of APS.

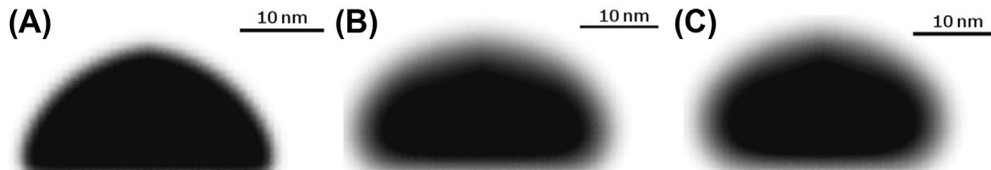


**Figure 12.21** Island shapes for a metal-on-insulator system computed by a phase field model. The temperature is increasing from left to right. Reprinted from [91] with permission of Elsevier.

## References

- [1] Mitrovic B, Gurary A, Kadinski L. On the flow stability in vertical rotating disc MOCVD reactors under a wide range of process parameters. *J Cryst Growth* 2006;287:656–63.
- [2] Martina C, Dauelsberg M, Protzmann H, Boyd AR, Thrush EJ, Heuken M, et al. Modelling of group-III nitride MOVPE in the closed coupled showerhead reactor and planetary reactor<sup>®</sup>. *J Cryst Growth* 2006;303:318–22.
- [3] Barbato A, Cavallotti C. Challenges of introducing quantitative elementary reactions in multiscale models of thin film deposition. *Phys Status Solidi B* 2010;247:2127–46.
- [4] Gadzhiev OB, Sennikov PG, Petrov AI, Gogova D, Siche D. Gas-phase reactions regarding GaN crystal growth in a carbon-based transport system: a quantum chemical study. *Cryst Growth Des* 2013;13:1445–57.
- [5] Car R, Parrinello M. Unified approach for molecular dynamics and density-functional theory. *Phys Rev Lett* 1985;55:2471–4.

- [6] Guo WD, Schulze TP, E W. Simulation of impurity diffusion in a strained nanowire using off-lattice KMC. *Commun Comp Phys* 2007;2:164–76.
- [7] Volkmann T, Much F, Biehl M, Kotrla M. Interplay of strain relaxation and chemically induced diffusion barriers: nanostructure formation in 2D alloys. *Surf Sci* 2005;586:157–73.
- [8] Xu H, Osetzky YN, Stoller RE. Simulating complex atomistic processes: on-the-fly kinetic Monte Carlo scheme with selective active volumes. *Phys Rev B* 2011;84:132103.
- [9] Zhenga Z, Stephens RM, Braatz RD, Alkire RC, Petzold LR. A hybrid multiscale kinetic Monte Carlo method for simulation of copper electrodeposition. *J Comput. Phys* 2008;227:5184–99.
- [10] Mandreoli L, Neugebauer J, Kunert R, Schöll E. Adatom density kinetic Monte Carlo: a hybrid approach to perform epitaxial growth simulations. *Phys Rev B* 2003;68:155429.
- [11] Kosturek R, Malarz K. New cellular automaton designed to simulate epitaxial films growth. *Phys A* 2005;345:538–46.
- [12] Miller W, Succi S. Lattice gas modeling of nanowhisker growth. *Phys Rev E* 2007;76. pp. 031601–1–12.
- [13] Kroll M, Köhler U. Small Cu-clusters on ZnO(001)-Zn: nucleation and annealing behavior. *Surf Sci* 2007;601:2182–8.
- [14] Kallesøe C, Wen C-Y, Booth TJ, Hansen O, Bøggild P, Ross FM, et al. In situ TEM creation and electrical characterization of nanowire devices. *Nano Lett* 2012;12:2965–70.
- [15] Westenfelder B, Meyer JC, Biskupek J, Kurasch S, Scholz F, Krill CE, et al. Transformations of carbon adsorbates on graphene substrates under extreme heat. *Nano Lett* 2011;11:5123–7.
- [16] Hohenberg P, Kohn W. Inhomogeneous electron gas. *Phys Rev* 1964;136:B864–71.
- [17] Kohn W, Sham LJ. Self-consistent equations including exchange and correlation effects. *Phys Rev* 1965;140:A1133–8.
- [18] Monkhorst J, Pack JD. Special points for Brillouin-zone integrations. *Phys Rev B* 1976;13:5188–92.
- [19] Vanderbilt D. Soft self-consistent pseudopotentials in a generalized eigenvalue formalism. *Phys Rev B* 1990;41:7892–5.
- [20] Becke AD. Density-functional thermochemistry. III. the role of exact exchange. *J Chem Phys* 1993; 98:5648–52.
- [21] Paier J, Marsman M, Kresse G. Why does the B3LYP hybrid functional fail for metals? *J Chem Phys* 2007;127. pp. 024103–1–10.
- [22] Filippetti P, Spaldin NA. Self-interaction-corrected scheme for magnetic and strongly-correlates systems. *Phys Rev B* 2003;67. pp. 125109–1–15.
- [23] Guhl H. Density functional theory study of oxygen and water adsorption on SrTiO<sub>3</sub>(001) [Ph.D. thesis]. Humboldt-Universität zu Berlin; 2010.
- [24] Lin F, Wang S, Zheng F, Zhou G, Wu J, Gu B-L, et al. Hydrogen-induced metallicity of SrTiO<sub>3</sub>(001) surfaces: a density functional theory study. *Phys Rev B* 2009;79. pp. 035311–1–7.
- [25] Ren X, Rinke P, Joas C, Scheffler M. Random-phase approximation and its applications in computational chemistry and materials science. *J Mater Sci* 2012;47:7447–71.
- [26] Binnig G, Rohrer H, Gerber C, Weibel E.  $7 \times 7$  reconstruction on Si(111) resolved in real space. *Phys Rev Lett* 1983;50:120–3.
- [27] Binnig G, Rohrer H, Gerber C, Weibel E. Surface studies by scanning tunneling microscopy. *Phys Rev Lett* 1982;49:57–60.
- [28] Brommer KD, Needels N, Larson BE, Joannopoulos JD. Ab initio theory of the Si(111)-(7 × 7) surface reconstruction: a challenge for massively parallel computation. *Phys Rev Lett* 1992;68:1355–9.
- [29] Pentcheva R, Moritz W, Rundgren J, Frank S, Schrupp D, Scheffler M. A combined DFT/LEED-approach for complex oxide surface structure determination: Fe<sub>3</sub>O<sub>4</sub>(001). *Surf Sci* 2008;602:1299–305.

- [30] Guhl H, Miller W, Reuter K. Oxygen ad-atoms on SrTiO<sub>3</sub> (001) - a density functional study. *Surf Sci* 2010;604:372–6.
- [31] Padilla J, Vanderbilt D. Ab initio study of SrTiO<sub>3</sub> surfaces. *Surf Sci* 1998;418:64–70.
- [32] Lanier CH, van de Walle A, Erdman N, Landree E, Warschkow O, Kazimirov A, et al. Atomic-scale structure of the SrTiO<sub>3</sub>(001)-c(6 × 2) reconstruction: experiments and first-principles calculations. *Phys Rev B* 2007;76. pp. 045421–1–9.
- [33] Jiang QD, Zegenhagen J. c(6 × 2) and c(4 × 2) reconstructions of SrTiO<sub>3</sub>(001). *Surf Sci* 1999;425: 343–54.
- [34] Piskunov S, Zhukovskii YF, Kotomin EA, Heifets E, Ellis DE. Adsorption of atomic and molecular oxygen on the SrTiO<sub>3</sub> (001) surfaces: predictions by means of hybrid density functional calculations. *Mater Res Soc Symp Proc* 2006;894:295–300.
- [35] Carrasco J, Illas F, Lopez N, Kotomin EA, Zhukovskii YF, Evarestov RA, et al. First- principle calculations of the atomic and electronic structure of f centers in the bulk and on the (001) surface of SrTiO<sub>3</sub>. *Phys Rev B* 2006;73:06410601–11.
- [36] Rasmussen MD, Molina LM, Hammer B. Adsorption, diffusion, and dissociation of molecular oxygen at defected TiO<sub>2</sub>(110): a density functional theory study. *J Chem Phys* 2004;120:988–97.
- [37] Henkelman BP, Uberuaga BP, Jonsson H. A climbing image nudged elastic band method for finding saddle points and minimum energy paths. *J Chem Phys* 2000;113:9901–3.
- [38] Guhl H, Miller W, Reuter K. Water adsorption and dissociation on SrTiO<sub>3</sub>(001): a density functional study. *Phys Rev B* 2010;81. pp. 155455–1–8.
- [39] Iwahori K, Watanabe S, Kawai M, Mizuno K, Sasaki K, Yoshimoto M. Nanoscale composition analysis of atomically flat SrTiO<sub>3</sub>(001) by friction force microscopy. *J Appl Phys* 2000;88:7099–103.
- [40] Koster G, Kropman BL, Rijnders GJHM, Blank DHA. Quasi-ideal strontium titanate crystal surfaces through formation of strontium hydroxide. *Appl Phys Lett* 1998;73:2920–2.
- [41] Pilania G, Gao P-X, Ramprasad R. Establishing the LaMnO<sub>3</sub> surface phase diagram in an oxygen environment: an ab initio kinetic Monte Carlo simulation study. *J Phys Chem C* 2012;116:26349–57.
- [42] Wang X-G, Weiss W, Shaikhutdinov SK, Ritter M, Petersen M, Wagner F, et al. The hematite (α-Fe<sub>2</sub>O<sub>3</sub>) (0001) surface: evidence for domains of distinct chemistry. *Phys Rev Lett* 1998;81:1038–41.
- [43] Biehl M, Ahr M, Kinzel W, Much F. Kinetic Monte Carlo simulations of heteroepitaxial growth. *Thin Solid Films* 2003;428:52–5.
- [44] Fichthorn KM, Weinberg WH. Theoretical foundations of dynamical Monte Carlo simulations. *J Chem Phys* 1991;95:1090–6.
- [45] Kang HC, Weinberg H. Dynamic Monte Carlo with a proper energy barrier: surface diffusion and two-dimensional domain ordering. *J Chem Phys* 1989;90:2824–30.
- [46] L'Ecuyer P, Simard R. Testu01: a c library for empirical testing of random number generators. *ACM Trans Math Softw* 2007;33:22.
- [47] Momma K, Izumi F. Vesta 3 for three-dimensional visualization of crystal, volumetric and morphology data. *J Appl Crystallogr* 2011;44:1272.
- [48] Cavallotti C, Barbato A, Cavalotti A. A combined three- dimensional kinetic Monte Carlo and quantum chemistry study of CVD of Si on Si(100) surfaces. *J Cryst Growth* 2004;266:371–80.
- [49] Cavallotti C, Stanislao MD, Moscatelli D, Veneroni A. Materials computation towards technological impact: the multiscale approach to thin films deposition. *Electrochem. Acta* 2005;50:4566–75.
- [50] Antoshchenkova E, Hayoun M, Finocchi F, Genestec G. Kinetic Monte-Carlo simulation of the homoepitaxial growth of MgO{001} thin films by molecular deposition. *Surf Sci* 2012;606:605–14.
- [51] Petrov P, Guhl H, Miller W. First atomistic studies of epitaxial growth of Na<sub>0.5</sub>Bi<sub>0.5</sub>TiO<sub>3</sub> on SrTiO<sub>3</sub>. *Phys Status Solidi B* 2008;245:2649–56.

- [52] Zhang Q, Zhu J, Tan J, Yu G, Wu J, Zhu J, et al. Monte Carlo simulation of the growth of SrTiO<sub>3</sub> thin film with molecular source. *Vacuum* 2006;81:539–44.
- [53] Petrov P, Miller W. A new kinetic Monte Carlo method for the thin film growth of perovskites. *Surf Rev Lett* 2009;16:909–16.
- [54] Nandipati G, Amar JG. Effects of strain on island morphology and size distribution in irreversible submonolayer growth. *Phys Rev B* 2006;73. pp. 045409–1–6.
- [55] Meixner M, Schöll E, Shchukin VA, Bimberg D. Self-assembled quantum dots: crossover from kinetically controlled to thermodynamically limited growth. *Phys Rev Lett* 2001;87. pp. 236101–1–4.
- [56] Orr BG, Kessler DA, Snyder CW, Sander LM. A model for strain-induced roughening and coherent island growth. *Europhys Lett* 1992;19:33.
- [57] Lam C-H, Lee C-K, Sander LM. Competing roughening mechanisms in strained heteroepitaxy: a fast kinetic Monte Carlo study. *Phys Rev Lett* 2002;89. pp. 216102–1–4.
- [58] Meixner M, Kunert R, Scholl E. Control of strain-mediated growth kinetics of self-assembled semiconductor quantum dots. *Phys Rev B* 2003;67. pp. 195301–1–12.
- [59] Gaillard P, Aqua J-N, Frisch T. Kinetic Monte Carlo simulations of the growth of silicon germanium pyramids. *Phys Rev B* 2013;87. pp. 125310–1–6.
- [60] Lung MT, Lam C-H, Sander LM. Island, pit, and groove formation in strained heteroepitaxy. *Phys Rev Lett* 2005;95. pp. 086102–1–4.
- [61] Russo G, Smereka P. Computation of strained epitaxial growth in three dimensions by kinetic Monte Carlo. *J Comput. Phys* 2006;214:809–29.
- [62] Schulze T, Smereka P. An energy localization principle and its application to fast kinetic Monte Carlo simulation of heteroepitaxial growth. *J Mech Phys Solids* 2009;57:521–38.
- [63] Baskaran A, Devita J, Smereka P. Kinetic Monte Carlo simulation of strained heteroepitaxial growth with intermixing. *Contin Mech Thermodyn* 2010;22:1–26.
- [64] Aqua J-N, Berbezier I, Favre L, Frisch T, Ronda A. Growth and self-organization of SiGe nanostructures. *Phys Rep* 2013;522:59–189.
- [65] Xiang R, Lung MT, Lam C-H. Layer-by-layer nucleation mechanism for quantum dot formation in strained heteroepitaxy. *Phys Rev E* 2010;82. pp. 021601–1–8.
- [66] Petrov PP, Miller W. Kinetic Monte Carlo simulation of Stranski–Krastanov heteroepitaxial growth. *Comp Mater Sci* 2012;60:176–80.
- [67] Emmerich H, Gránásy L, Löwen H. Erratum to: selected issues of phase-field crystal simulations. *Eur Phys J Plus* 2011;128:113.
- [68] Cullis G, Norris DJ, Walther T, Migliorato MA, Hopkinson M. Stranski–Krastanow transition and epitaxial island growth. *Phys Rev B* 2002;66. pp. 081305(R)–1–4.
- [69] Tersoff J, LeGoes FK. Competing relaxation mechanisms in strained layers. *Phys Rev B* 1994;72: 3570–3.
- [70] Tu Y, Tersoff J. Origin of apparent critical thickness for island formation in heteroepitaxy. *Phys Rev Lett* 2004;93. pp. 216101–1–4.
- [71] Evans JW, Thiel PA, Bartelt MC. Morphological evolution during epitaxial thin film growth: formation of 2D islands and 3D mounds. *Surf Sci Rep* 2006;61:1–128.
- [72] DeJarld M, Reyes K, Smereka P, Millunchick JM. Mechanisms of ring and island formation in lattice mismatched droplet epitaxy. *Appl Phys Lett* 2013;102. pp. 133107–1–5.
- [73] Keizer JG, Koenraad PM, Smereka P, Ulloa JM, Guzman A, Hierro A. Kinetic Monte Carlo simulations and cross-sectional scanning tunneling microscopy as tools to investigate the heteroepitaxial capping of self- assembled quantum dots. *Phys Rev B* 2012;85. pp. 155326–1–8.

- [74] Petrov PP, Miller W. Fast kinetic Monte Carlo simulation and statistics of quantum dot arrays. *Surf Sci* 2014;621:175–83.
- [75] Zhu R, Pan E, Chung PW. Fast multiscale kinetic Monte Carlo simulations of three-dimensional self-assembled quantum dot islands. *Phys Rev B* 2007;75. pp. 205339–1–7.
- [76] Lee C-H, Noordhoek MJ, Smereka P, McKay H, Mil-lunchick JM. Filling of hole arrays with InAs quantum dots. *Nanotechnology* 2009;20. pp. 285305–1–6.
- [77] Caginalp G. Surface tension and supercooling in solidification theory. In: Garrido L, editor. *Applications of field theory to statistical mechanics. Lecture notes in physics*, vol. 216. Berlin: Springer-Verlag; 1985. p. 216–26.
- [78] Liu F, Metiu H. Stability and kinetics of step motion on crystal surfaces. *Phys Rev E* 1994;49:2601–16.
- [79] Burton WK, Cabrera N, Frank FC. The growth of crystals and the equilibrium structure of their surfaces. *Philos Trans R Soc Lond Ser A* 1951;243:299–358.
- [80] Karma A, Plapp M. Spiral surface growth without desorption. *Phys Rev Lett* 1998;81:4444–7.
- [81] Elder KR, Katakowski M, Haataja M, Grant M. Modeling elasticity in crystal growth. *Phys Rev Lett* 2002;88. pp.245701–1–4.
- [82] Emmerich H, Gránásy L, Löwen H. Selected issues of phase-field crystal simulations. *Eur Phys J Plus* 2011;126. pp.102–1–18.
- [83] Emmerich H, Löwen H, Wittkowski R, Gruhn T, Töth GI, Tegge G, et al. Phase-field-crystal models for condensed matter dynamics on atomic length and diffusive time scales: an overview. *Adv Phys* 2012;61:665–743.
- [84] Wu K-A, Adland A, Karma A. Phase-field-crystal model for fcc ordering. *Phys Rev E* 2010;81. pp. 061601–1–16.
- [85] Xu Y-C, Liu B-G. Phase-field-crystal modelling of the  $(2 \times 1)$ – $(1 \times 1)$  phase transitions of Si(001) and Ge(001) surfaces. *J Phys D Appl Phys* 2009;42. pp. 035402–1–4.
- [86] Chen C, Chen Z, Zhang J, Du X. Phase-field crystal modeling of shape transition of strained islands in heteroepitaxy. *Sci China* 2012;55:2042–8.
- [87] Smereka P. Spiral crystal growth. *Phys D* 2000;138:282–301.
- [88] Emmerich H, Eck C. Microstructure morphology transitions at meso- scopic epitaxial surfaces. *Contin Mech Thermodyn* 2006;17:373–86.
- [89] Yu Y-M, Voigt A. Phase-field modeling of anomalous spiral step growth on Si(001) surface. *Phys Rev B* 2009;79:235317.
- [90] Hannon JB, Shenoy VB, Schwarz KW. Anomalous spiral motion of steps near dislocations on silicon surfaces. *Science* 2006;313:1266–9.
- [91] Xu Y-C, Liu B-G. Unified phase-field model for epitaxial growth of multi-scale three- dimensional islands on insulating surfaces. *Phys B* 2009;404:4303–7.
- [92] M $\acute{e}$ tois JJ, Lay GL. Complementary data obtained on the metal- semiconductor interface by LEED, AES, and SEM Pb/Ge(111). *Surf Sci* 1983;133:422–42.

# Controlled Colloidal Assembly: Experimental Modeling of Crystallization

Tian Hui Zhang<sup>2,3</sup>, Xiang Yang Liu<sup>1</sup>

<sup>1</sup>DEPARTMENT OF PHYSICS AND DEPARTMENT OF CHEMISTRY, NATIONAL UNIVERSITY OF SINGAPORE, SINGAPORE; <sup>2</sup>CENTER FOR SOFT CONDENSED MATTER PHYSICS AND INTERDISCIPLINARY RESEARCH, SOOCHOW UNIVERSITY, SUZHOU, CHINA; <sup>3</sup>SCHOOL OF PHYSICAL SCIENCE AND TECHNOLOGY, SOOCHOW UNIVERSITY, SUZHOU, CHINA

## **CHAPTER OUTLINE**

<b>13.1 Introduction</b> .....	<b>562</b>
<b>13.2 Colloidal Assembly under Control</b> .....	<b>563</b>
<b>13.3 Thermodynamic Driving Force for Crystallization</b> .....	<b>568</b>
13.3.1 Classical Nucleation Theory .....	568
13.3.1.1 Nucleation Kinetics .....	572
13.3.1.2 Equilibrium State .....	572
13.3.1.3 Stationary (or Steady) State .....	573
13.3.1.4 Nonsteady State .....	573
13.3.2 Experimental Verification of Classical Nucleation Theory .....	574
13.3.3 Discrepancies between CNT and Observations .....	575
<b>13.4 Nonclassical Nucleation</b> .....	<b>576</b>
13.4.1 Structure Evolution of Precritical Nuclei .....	576
13.4.2 Multistep Crystallization .....	578
13.4.3 CNT and Ostwald's Rule .....	579
<b>13.5 Kinetics of Crystal Growth</b> .....	<b>580</b>
13.5.1 Step Kinetics .....	580
13.5.2 Cluster Adsorption .....	582
13.5.3 Surface Roughening .....	583
<b>13.6 Interfacial Structural Mismatch and Network Formation</b> .....	<b>586</b>
<b>13.7 Crystal Defects</b> .....	<b>588</b>
<b>13.8 Concluding Remarks</b> .....	<b>589</b>
<b>Acknowledgment</b> .....	<b>590</b>
<b>References</b> .....	<b>591</b>

## 13.1 Introduction

Crystallization plays a crucial role in the preparing of functional materials [1–4], the structural characterization of natural and synthetic molecules [5,6], and the development of advanced technologies [7–9]. However, crystallization has in many ways continued to be more like an art than a science, mainly because there is no sufficient knowledge on its critical early stages and the atomic processes [10–17]. In this regard, the kinetics of the transition from metastable phases to stable phases has so far been open to question. The key challenge is the in situ imaging of the atomic/molecular dynamic process, which is limited by both the spatial and the temporal definition of current technologies and the absence of direct observations on the transition process in real space, except for some local events of crystallization/quasi-crystallization of large species, namely proteins [18–24] and colloidal particles [25–27]. Computer simulations have been applied to acquire the information [28–30]. Nevertheless, due to the constraint of computation power and the methodologies, the knowledge obtained is still limited [31]. It is therefore of critical importance to develop a new methodology to “simulate” or “monitor” the atomic/molecular dynamic process of the nucleation and growth of crystals.

Colloids refer to solid/liquid/gas particles of a size ranging from 1 nm to 10  $\mu\text{m}$ , which disperse in an ambient phase. In solutions, colloidal particles are small enough to exhibit Brownian motion and have a well-defined thermodynamic temperature. Colloidal assembly from a disordered to an ordered state is of broad interest in developing advanced materials [32]. In physics, the self-assembly of colloidal particles from dilute dispersions to crystalline structures is a typical first-ordered phase transition, the so-called crystallization. In addition to crystallization, colloids exhibit rich phase transitions between gas, liquid, and solids. These transitions are analogous to that occurring in atomic systems [33]. Based on these features, colloidal particles can be regarded as big atoms to model phase transitions. Compared with atoms, colloidal particles are large enough for direct observation using normal microscopy and their relatively much slower movement can be monitored in real time at the single-particle level. In addition, the interactions between colloidal particles can be tailored from attractive to repulsive, from short-range to long-range, from hard to soft, and from symmetric to directional. As model systems, colloids have been widely employed to study phase transitions including crystallization [34], glass transition [35], and melting [36], among others.

This chapter introduces the most recent developments in the kinetics of crystallization, simulated by colloidal systems. This will cover the dynamics of nucleation, step kinetics, and surface roughening. Section 13.2 discusses the interactions between colloidal particles and the ways of controlling colloidal crystallization. In Section 13.3, the thermodynamics in a colloidal system and the classical nucleation theory are addressed. In Section 13.4, the atomic process of nucleation will be examined in terms of colloidal nucleation. In Sections 13.5 and 13.6, the attention will be focused on the interfacial processes of crystallization. In Section 13.7, we will discuss the defect formation dynamics in the colloidal model system. Finally, some general remarks will be given in Section 13.8.

## 13.2 Colloidal Assembly under Control

The type of phase diagram in colloidal model systems is determined by the feature of interactions between colloidal particles [33]. For example, in hard sphere systems, there are only two stable phases (Figure 13.1(A)): fluid and solid [37]. As hard spheres are complemented with a long-range attractive interaction, the system displays three phases (Figure 13.1(B)): gas, liquid, and solid. If the effective range of the attraction is shorter than 15% of the hard core diameter, the system exhibits only two stable phases: gas and crystal. The critical point where gas and liquid become identical moves to the metastable region, which is below the freezing curve, and a metastable liquid–liquid transition may occur (Figure 13.1(C)).

The interaction between colloidal particles in solutions is generally a combination of attractions and repulsions. The attractive interactions may be depletion attractions, van der Waals attractions, and attractive dipole–dipole interactions. The repulsive interactions are usually induced by electrostatic repulsions and electric/magnetic dipole–dipole interactions. The overall interactions between colloidal particles can be described by the Deryagin–Landau–Verwey–Overbeek (DLVO) theory [38]. In DLVO theory, the overall interaction between colloidal particles is simplified as a combination of short-range van der Waals attractions and long-range electrostatic repulsions.

Figure 13.2 presents three typical cases of DLVO theory. At low ionic strengths (Figure 13.2(A)), the electrostatic repulsion is relatively strong and long-range. The overall interaction is then repulsive at a large distance and attractive at a short distance. At an intermediate distance, there is an energy barrier for colloids to overcome before they can close into each other for aggregation. At intermediate ionic strengths (Figure 13.2(B)), the energy barrier for colloids to aggregate becomes small and a secondary potential minimum exits. At high ionic strengths (Figure 13.2(C)), the long-range coulomb repulsion is greatly screened; the overall interaction is then dominated by the short-range attraction. In the first situation (Figure 13.2(A)), the competition between the short-range attraction and the long-range repulsion leads to an intriguing phase

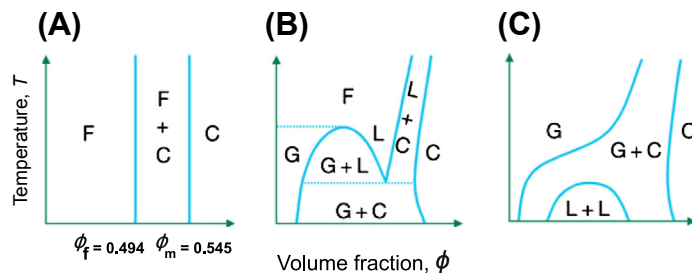


**FIGURE 13.1** Phase diagrams in colloidal systems. (A) Hard spheres. (B) Systems with a long-range attraction. (C) Systems with a short-range attraction. Atomic systems are often modeled by hard spheres with long-range attractions. Reprinted with permission from Ref. [33]. Copyright (2002) Nature Publishing Group.

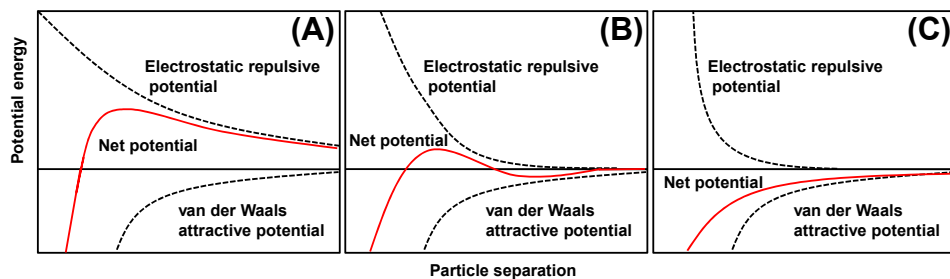


FIGURE 13.2 Interactions between colloids of DVLO theory. From left to right, electrolytes concentration increases.

behavior: equilibrium clusters with an optimum size formed through microphase separations are more stable with respect to an infinite bulk crystal [39].

To examine the underlying mechanism of colloidal phase transitions, the ability of controlling colloidal phase behavior by tuning colloidal interactions is critical. So far, a variety of strategies have been developed to control the behavior of colloidal particles [32,40,41]. Because colloidal particles in solutions are generally charged, external electric fields have been widely used in controlling colloidal aggregation [32] for various applications [42]. For example, Figure 13.3(A) illustrates an experimental colloidal system controlled by an alternating electric field (AEF). In this system, as the AEF is applied, two-dimensional (2D) colloidal self-assembly will occur on electrodes [43]. In comparison with other stimuli, the electric stimulus therein can be switched on/off instantly without disturbing the original solutions after experiments. As a number of experimental results summarized in this chapter are from this 2D colloidal system, a brief introduction to this AEF-controlled system may help in going through the rest of the sections.

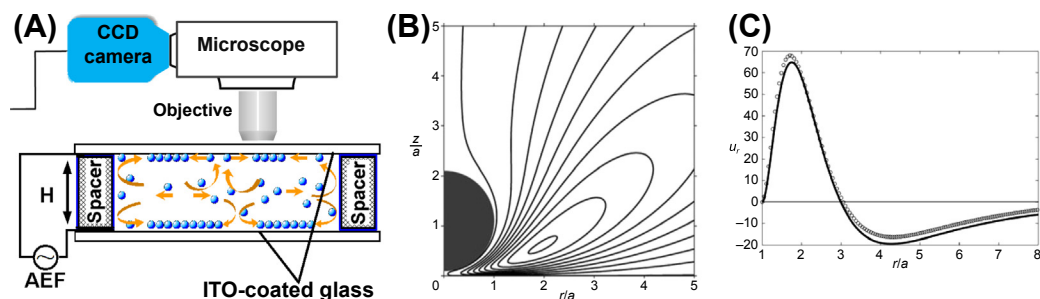


FIGURE 13.3 Alternating electric field (AEF)-induced colloidal aggregation. (A) The schematic of the experimental setup. The colloidal suspension is sandwiched between two Indium tin oxide (ITO)-coated glass plates separated by insulating spacers. (B) Electrohydrodynamic (EHD) flow around colloidal particles near the electrodes. For  $C'_0 < 0$ , the flow direction is clockwise and counterclockwise for  $C'_0 > 0$ . (C) A representative plot of the radial EHD velocity around a colloid near the electrode. For negative  $u_r$ , the EHD flow brings another particle close and, vice versa, the flow carries another distinct colloid away.  $\circ$ , numerical solution with a volumetric body force;  $—$ , analytical solution with slip conditions specified at the boundaries. Parts (b) and (c): Reprinted with permission from Ref. [44]. Copyright (2007) Cambridge University Press.

The driving force for the 2D colloidal aggregation in the AEF-controlled system arises from the so-called electrohydrodynamic (EHD) flow [44]. The mechanism is that the dissolved ionic species build up an electric double layer adjacent to the electrode surface. The double layer is then disrupted due to the presence of charged colloidal particles, giving rise to a spatially varying free charge distribution. At the same time, the presence of charged colloidal particles also distorts the applied field, resulting in a lateral electrical field. The interaction between the free charges and the lateral electric field leads to a fluid flow around the particles (Figure 13.3(B)). The studies by Ristenpart et al. [45] show that the tangential EHD flow velocity along the electrode surface scales as follows:

$$u_t \sim \frac{3\varepsilon\varepsilon_0 E_\infty^2}{\mu\kappa} \left\{ C'_0 \left\{ C'_0 + \frac{DK^2}{\omega} C''_0 \right\} \right\} \quad (13.1)$$

where  $\varepsilon_0$  is the permittivity of free space,  $\kappa$  is the reciprocal Debye length, and  $E_\infty$  is the strength of the incident electric field.  $D$  denotes the ionic diffusion coefficient and  $\omega$  is the angular frequency of the applied oscillating electric field. The parameters  $C'_0$  and  $C''_0$  are associated with the dipole coefficient. The strength and the direction of the EHD flow depends on frequency: within a frequency window, the flow velocity is negative (flowing toward the particles), leading to an attractive Stokes force between the colloidal particles. Beyond this frequency window, the EHD flow becomes essentially zero or even positive (flowing away from the particles).

In addition to the EHD flow-induced attraction, repulsive electrostatic screened Coulomb interactions and dipole–dipole interactions also play key roles in this system [46]. The competition between the attractive force and repulsive force determines whether the 2D colloidal aggregation occurs or not. According to Eqn (13.1), increasing the frequency will reduce the EHD flow-induced attractive force. However, dipolar interactions between identical particles are not sensitive to the frequency, although it strongly depends on the strength of AEF [44]. Consequently, upon increasing the frequency ( $f > 500$  Hz), the overall interaction between colloidal particles becomes dominated increasingly by the repulsive component; thus, the normalized equilibrium distance  $r_{eq}$  in a 2D colloidal crystal increases correspondingly (Figure 13.4(A)). The frequency window for 2D colloidal crystals, as Figure 13.4(A) shows, becomes wider at a higher temperature. The mechanism is that increasing temperature increases the ionic diffusion coefficient  $D$  and thus enhances the EHD flow-induced attraction (Eqn (13.1)) [47]. Moreover, Eqn (13.1) suggests that both the flow-induced attraction and the dipolar repulsion will be enhanced upon increasing the strength of the AEF. Therefore, the equilibrium distance  $r_{eq}$  is independent of the field strength (Figure 13.4(B)) as the frequency is above hundreds of hertz. However, at low-frequency regions, the behavior of  $r_{eq}$  deviates from the prediction of the EHD flow mechanism. First, because the frequency is below 500 Hz, the equilibrium distance decreases upon increasing frequency (Figure 13.4(A)); in the frequency window of 100–200 Hz, (Figure 13.4(B)),  $r_{eq}$  increases with the field strength. At a very low frequency of 40 Hz,  $r_{eq}$  can even be tuned from

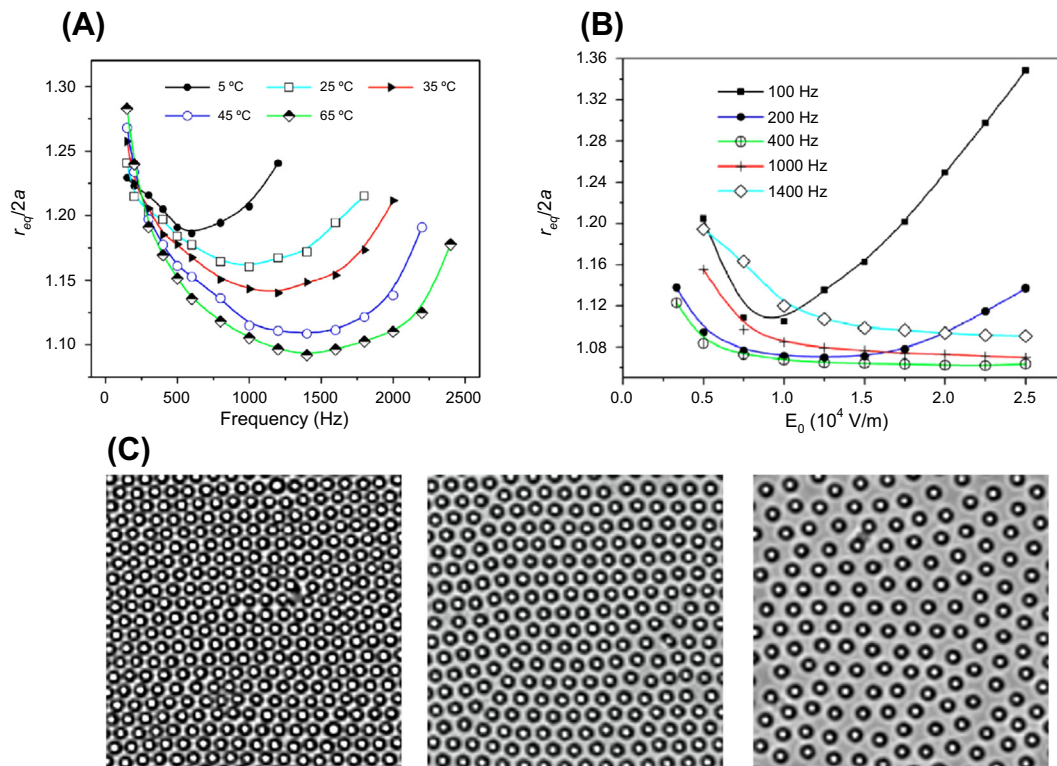


**FIGURE 13.4** (A) Variation of dimensionless equilibrium distance  $r_{eq}/2a$  with frequency at different temperatures at field strength  $E_\infty = 1.5 \times 10^4$  V/m. (B)  $r_{eq}/2a$  as a function of the field strength at different frequencies with temperature of 25 °C. (C) Colloidal aggregations at different field strengths (from left to right) of  $5.8 \times 10^4$ ,  $7.5 \times 10^4$ , and  $8.3 \times 10^4$  V/m. The measured equilibrium distance  $r_{eq}/2a$  (from left to right) is 1.34, 1.66, and 2.23. Adapted with permission from Ref. [47]. Copyright (2007) AIP Publishing LLC.

$1.05 \times 2a$  to  $2.23 \times 2a$  by increasing the field strength (Figure 13.4(C)). The discrepancy between the observation of  $r_{eq}$  and the EHD mechanism suggests that, at low frequencies, the 2D colloidal aggregation is dominated by a different mechanism other than the EHD flow.

Risterpart et al. suggested [48] that, in steady electric fields, both electroosmotic flow (EOF) and EHD mechanism are responsible for the 2D aggregation on electrodes. The EOF stems from the influence of the incident steady electric field on the equilibrium diffuse layers of particles. The strength of EOF,  $u_{EOF}$ , is dependent on the field strength  $E_\infty$  and the particle surface potential  $\zeta$  by  $u_{EOF} \sim \zeta E_\infty$ . In a steady field, the EHD flow scales as  $u_t \sim E_\infty \cdot \log E_\infty$ . The EHD flow-induced attraction works at a distance far from the particles, whereas the EOF-induced attraction is valid near the particles. The EOF mechanism is based on a steady electric field. However, if the frequency is not high ( $<1000$  Hz), the EOF mechanism is still valid for an oscillating field. At a low-frequency region, increasing the field strength will enhance both the EHD flow and the EOF.

Simultaneously, increasing field strength enhances the repulsive dipolar interaction. Because the repulsive dipolar interaction is proportional to the square of field strength [49], the increase of repulsion will overwhelm the increase of attraction, giving rise to a larger equilibrium separation, as seen in Figure 13.4(C). Nevertheless,  $r_{eq}$  becomes larger at a lower frequency ( $<500$  Hz), as Figure 13.4(A) shows. This behavior so far is still not well understood. It follows that, at low frequencies, the mechanism underlying the 2D colloidal aggregation becomes complex. Experimentally, the related studies usually were conducted in the frequency window where the EHD mechanism is valid.

Figure 13.5 presents the phase diagram of the 2D colloidal systems in the space of field strength  $E_\infty$  and frequency  $f$ . The structures observed range from oscillating vortex rings to interlinked chains and from 2D crystals to three-dimensional (3D) aggregation [50]. This phase diagram is obtained at room temperature with colloidal particles of 1  $\mu\text{m}$  (diameter). However, it is important to mention that the phase boundaries in Figure 13.5 may shift if a different particle size or ionic concentration is employed.

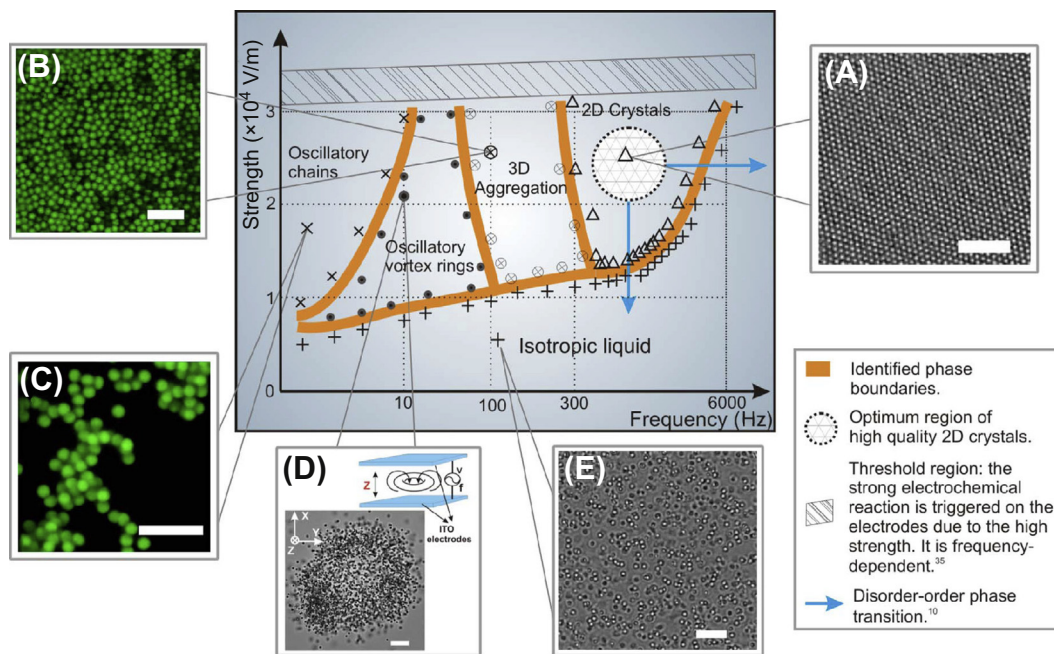


**FIGURE 13.5** The phase diagram and typical colloidal patterns induced by an AEF. (A) A 2D colloidal crystal at field strength  $\sigma_E = 2.6 \times 10^4$  V/m and  $f = 800$  Hz. (B) 3D aggregation of colloidal particles, as captured by the Laser scanning confocal microscope (LCSM) at  $\sigma_E = 2.4 \times 10^4$  V/m and  $f = 100$  Hz. (C) Static snapshot of colloidal chains by the LCSM at  $\sigma_E = 1.8 \times 10^4$  V/m and  $f = 0.1$  Hz. (D) Snapshot of oscillatory vortex rings at  $2.3 \times 10^4$  V/m and  $f = 1$  Hz. (E) The isotropic liquid state of colloidal suspension. Scale bars in (B) and (C) represent 5  $\mu\text{m}$ ; scale bars in (A), (D), and (E) represent 10  $\mu\text{m}$ . Colloidal suspension (0.1% in volume fraction) of monodisperse charged polystyrene spheres (1  $\mu\text{m}$  in diameter) is confined to a horizontal layer between two conductive glass microscope slides. Glass spacers set the layer thickness in the cells at  $2H = 120 \pm 5$   $\mu\text{m}$  across the  $1.5 \times 1.5$   $\text{cm}^2$  observation area. The AEF was supplied by a waveform generator. The motions of the colloidal particles were recorded with a computer-driven digital Charge coupled device (CCD) camera. Reprinted with permission from Ref. [50]. Copyright (2009) AIP Publishing LLC.

## 13.3 Thermodynamic Driving Force for Crystallization

Thermodynamically, phase transitions are driven by the trend to minimize the free energy of metastable systems. For example, the chemical potentials of a growth unit in the ambient mother phase and a crystal phase are represented by  $\mu_i^{\text{ambient}}$  and  $\mu_{\text{crystal}}$ , respectively. The difference between the chemical potentials  $\mu_i^{\text{ambient}}$  and  $\mu_{\text{crystal}}$  is given by:

$$\Delta\mu = \mu_i^{\text{ambient}} - \mu_{\text{crystal}} \quad (13.2)$$

Subscript *i* denotes the solute in the ambient phase. For  $\Delta\mu > 0$ , the chemical potential in the ambient mother phase is higher than that in the crystal phase; the system is then said to be supersaturated and crystallization will occur. Conversely, if  $\Delta\mu < 0$ , the system is undersaturated and crystals will dissolve. For  $\Delta\mu = 0$ , the ambient phase can coexist with the crystal phase. For the crystallization from solutions, the chemical potential of species *i* is often associated with the activity  $a_i$  or concentration  $C_i$  by [51]

$$\mu_i = \mu_i^0 + k_B T \ln a_i \approx \mu_i^0 + k_B T \ln C_i \quad (13.3)$$

where  $\mu_i^0$  denotes the standard state ( $a_i = 1$ ) of the chemical potential. Correspondingly, the thermodynamic driving force for crystallization can be quantified by:

$$\frac{\Delta\mu}{k_B T} = \ln \frac{a_i}{a_i^{\text{eq}}} \approx \ln \frac{C_i}{C_i^{\text{eq}}} \quad (13.4)$$

$a_i^{\text{eq}}$  and  $C_i^{\text{eq}}$  are, respectively, the equilibrium activity and concentration of species *i*. With the definition of supersaturation  $\sigma$ :

$$\sigma = (a_i - a_i^{\text{eq}}) / a_i^{\text{eq}} \approx (C_i - C_i^{\text{eq}}) / C_i^{\text{eq}} \quad (13.5)$$

Equation (13.4) can be simplified as

$$\Delta\mu / k_B T = \ln(1 + \sigma) \cong \sigma \quad (\text{in the case of } \sigma \ll 1) \quad (13.6)$$

### 13.3.1 Classical Nucleation Theory

Any crystallization process contains two subsequent stages: nucleation and crystal growth. By nucleation, initial embryos of crystals are created from metastable mother phases. After nucleation, the resulted nuclei grow into bulk crystals by incorporating growth units. The quality of crystals to a large extent is determined by nucleation. To apply control on nucleation, a full understanding of nucleation is critical. Currently, the most widely used theory about nucleation is the so-called classic nucleation theory (CNT), which was initially developed in the 1920s [2]. CNT suggests that by transferring a growth unit from the metastable liquid phase to the stable crystalline phase, the free energy of the system is lowered by  $\Delta\mu$ , as indicated by Eqn (13.2). However, the formation of a crystalline nucleus creates a surface at the same time. On the surface, a growth unit has less bonded neighbors than a bulk unit does, giving rise to the so-called interfacial free energy or surface tension. As a result, the formation of a surface contributes a positive addition to the free energy. The total free energy change  $\Delta G$  associated

with the formation of a crystalline nucleus is a sum of the decreasing bulk free energy and the increasing surface free energy, namely:

$$\Delta G = -n\Delta\mu + \Phi_n \quad (13.7)$$

where  $n$  is the number of the growth unit contained by the nucleus and  $\Phi_n$  is the total surface energy of the nucleus. For spherical nuclei with a radius  $R$ , one has  $n = 4\pi R^3 \rho_c / 3$  and  $\Phi_n = 4\pi R^2 \gamma$ . Here,  $\rho_c$  is the particle number density in nuclei and  $\gamma$  is the surface free energy area density. Alternatively, Eqn (13.7) can be expressed as

$$\Delta G = -\frac{4}{3}\pi R^3 \rho_c \Delta\mu + 4\pi R^2 \gamma \quad (13.8)$$

During the growth of nuclei, the decreasing bulk free energy has to compete with the increasing surface free energy. As a result of the competition,  $\Delta G$  experiences a maximum  $\Delta G^*$  at a critical size  $R_c$  (Figure 13.6(A)).  $\Delta G^*$  is the so-called nucleation barrier. Mathematically, the nucleation barrier and the critical size can be calculated by setting  $0 = d\Delta G(R)/dR|_{R_c}$ . The results are represented by:

$$\Delta G^* = \frac{16\pi\gamma^3}{3(\rho_c\Delta\mu)^2} \quad (13.9)$$

$$R_c = \frac{2\gamma}{\rho_c\Delta\mu} \quad (13.10)$$

For subcritical nuclei smaller than the critical size  $R_c$ , most of the growth units reside at the surface and the overall free energy change  $\Delta G$  is dominated by the positive interfacial free energy. Therefore, the formation of subcritical nuclei is not thermodynamically favored; thus, they have to be created by fluctuation. Before they reach the critical size, subcritical nuclei can dissolve or grow by chance (Figure 13.6(B)); only after they cross over the critical size, nuclei become stable and can grow stably. Figure 13.6(C) represents a nucleation process observed in the 2D AEF-controlled system. There, two subcritical nuclei are created and grow almost simultaneously. However, only one of them eventually develops into a stable nucleus, while the other one vanishes finally.

In deriving Eqns (13.7)–(13.10), the effect of foreign bodies on nucleation is not taken into account, and the probability of forming a critical nucleus is assumed to be uniform in space throughout the system, the so-called homogeneous nucleation. However, foreign bodies, such as the wall of solution container, foreign particles, or substrates, often occur in nucleating systems. In many cases, a foreign body can effectively lower the interfacial (or surface) free energy and thus reduce the nucleation barrier. In this case, nucleation occurs preferentially near or on the foreign bodies, namely heterogeneous nucleation. The effect of foreign bodies in lowering the nucleation barrier can be depicted by an interfacial correlation factor  $f$ :

$$f = \Delta G_{\text{heter}}^* / \Delta G_{\text{homo}}^* \quad (13.11)$$

where  $\Delta G_{\text{homo}}^*$  is the homogeneous nucleation barrier as defined by Eqn (13.9) and  $\Delta G_{\text{heter}}^*$  is the heterogeneous nucleation barrier. According to Gibbs-Thomson effect [54],

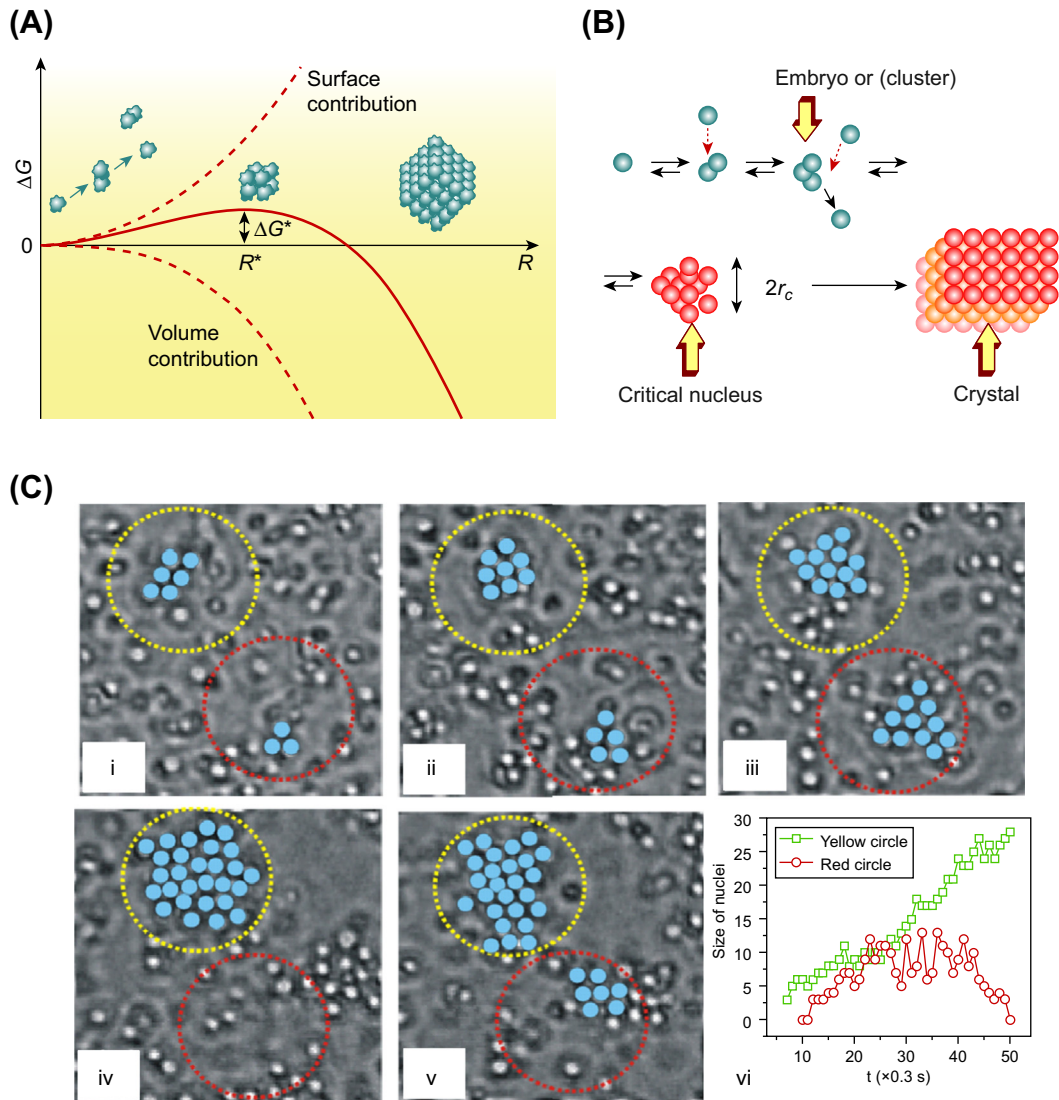


**FIGURE 13.6** (A) Nucleation barrier and critical size for nuclei [52]. (Reprinted with permission from Ref. [52]. Copyright (2013) Elsevier.) (B) Nuclei have to require a critical size before they become thermodynamically stable. (C) Subcritical nuclei dissolve or grow by chance. i–v: Experimental observation. vi: Size of the nuclei as a function of time. (Reprinted with permission from Ref. [53]. Copyright (2004) Nature Publishing Group.)

given the thermodynamic condition, the size of the critical nucleus in a homogeneous nucleation is the same as that in a heterogeneous nucleation. As a result, the interfacial correlation factor can be given by:

$$f(m, R) = \frac{1}{2} + \frac{1}{2} \left( \frac{1 - mR'}{w} \right)^2 + \frac{1}{2} R^3 \left[ 2 - 3 \left( \frac{R' - m}{w} \right) + \left( \frac{R' - m}{w} \right)^2 \right] + \frac{3}{2} m R^2 \left( \frac{R' - m}{w} - 1 \right) \quad (13.12)$$

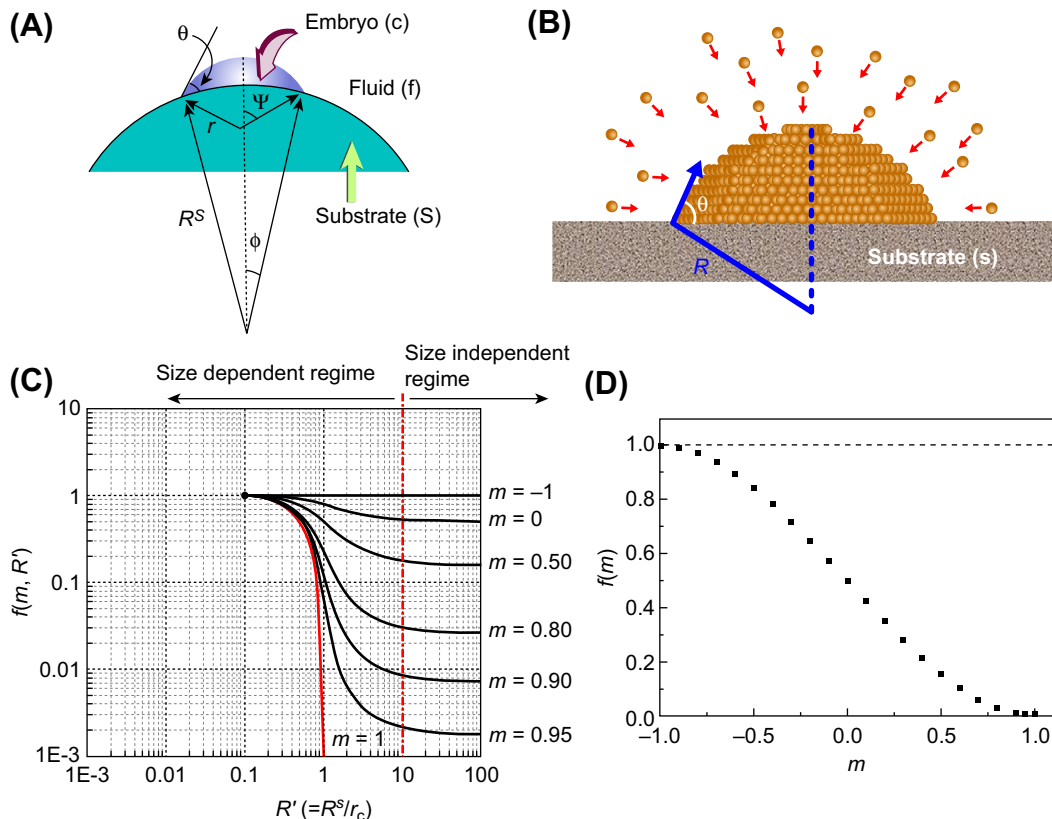


**FIGURE 13.7** Heterogeneous nucleation and the interfacial correlation factor. (A) Schematic illustration of the nucleation on a curved foreign body. (B) Nucleation on a flat substrate. (C) The interfacial correlation function as a function of  $m$  and  $R'$ . (D) The interfacial correlation function in the case of a flat substrate.

Here,  $m = (\gamma_{sf} - \gamma_{sc}) / \gamma_{cf} \sim \cos \theta$  (Figure 13.7(A)) and  $w = [1 + (R')^2 - 2R'm]^{1/2}$ .  $R'$  is the dimensionless radius of a curved substrate in reference to the radius of the critical nucleus  $R_c$ .  $\gamma_{ij}$  is the surface free energy between phases  $i$  and  $j$ . The subscripts  $f$ ,  $c$ , and  $s$  denote the fluid, crystalline phases, and the foreign body, respectively. As a function of  $m$  and  $R'$ , the value of  $f(m, R')$  ranges from 1 to 0 (Figure 13.7(C)). When  $R' \rightarrow 0$ ,  $f(m, R') = 1$ , implying that the foreign body does not act as a nucleating substrate. This is true if foreign bodies are too small with respect to the critical radius, such that they play no role in lowering the nucleation barrier. On the other hand, if  $R' \gg 1$ , the foreign body is large enough to be treated as a flat substrate with respect to the critical nuclei (Figure 13.7(B)). In this case,  $f(m, R')$  depends only on the parameter  $m$ , and Eqn (13.12) is then simplified as:

$$f(m, R') = f(m) = \frac{1}{4}(2 - 3m + m^2) \quad (13.13)$$

### 13.3.1.1 Nucleation Kinetics

Nucleation is a dynamic process by which atoms or molecules aggregate to form clusters. The most widely employed kinetic model of nucleation (within the cluster approach) was established by Farkas [3] in 1927. In this model, nucleation is a process of successive “chain reaction” from monomer to  $n$ -sized clusters and can be depicted by a group of continuity equations [12]:

$$dZ_n/dt = J_{n-1} - J_n \quad (13.14)$$

where  $Z_n(t)$  is the concentration of  $n$ -sized clusters at time  $t$  and  $J_n$  is the flux through point  $n$  on the size axis. The flux through the critical nucleus size  $n^*$ ,  $J_{n^*}(t)$ , defines the nucleation rate, which is time dependent. A basic problem in studying nucleation kinetics is to determine the nucleation rate by solving the master Eqn (13.14). In principle, there are three distinct states in nucleation (Figure 13.8): the equilibrium, the stationary (or steady) state, and the nonstationary states.

### 13.3.1.2 Equilibrium State

In an equilibrium state, the size distribution of nuclei follows the Boltzmann law,  $Z_n = C_n$  ( $C_n$  is the equilibrium concentration of  $n$ -sized clusters). The distribution does not change with time anymore,  $dZ_n/dt = 0$  and  $J_n = 0$ . According to the Boltzmann law, one can easily obtain:

$$C_n/Z = (C_1/\Sigma)^n \exp(-\Delta G_n/kT) \quad (13.15)$$

where  $n = (2, 3, 4, \dots)$  with the effective total number of “molecules” per unit volume. At the critical size  $n = n^*$ ,  $\Delta G(\Delta\mu)$  reaches the maximum; correspondingly,  $C_n$  experiences a minimum at  $n^*$ . The increasing of  $C_n$  at  $n > n^*$  is not a physical scenario; it just reflects the fact that the mother phase is saturated.

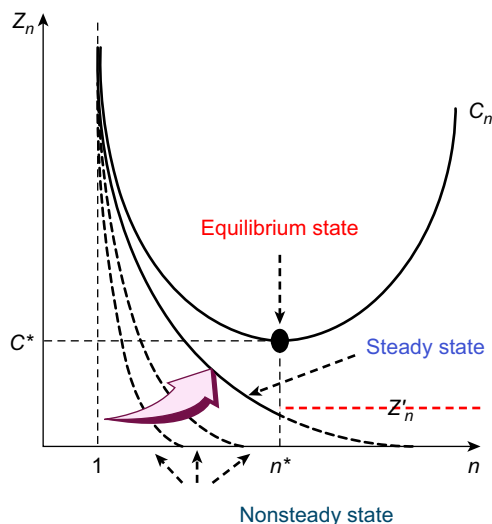


FIGURE 13.8 Possible states of nucleation.

### 13.3.1.3 Stationary (or Steady) State

In the stationary state, the fluxes through all sizes are the same,  $J_n = \text{constant} = J_{n^*} = J$ , and thus  $dZ_n/dt = 0$ . The stationary nucleation rate for homogeneous nucleation is given by the Becker-Doering formula [55]:

$$J = \frac{zK^*}{\nu_m} \exp\left(-\frac{\Delta G_{\text{hom}}^*}{k_B T}\right) \quad (13.16)$$

with

$$z = Z'_{n^*}/C_{n^*} - Z'_{n^*+1}/C_{n^*+1} \quad (13.17)$$

where  $Z'_n$  ( $\sim Z_n$ ) is the steady-state cluster size distribution,  $z$  is the so-called Zeldovich factor [56],  $K^* = K_{n^*}$  depicts the frequency of monomer attachment to the critical nucleus, and  $\nu_m$  denotes the average volume of structural units in the ambient phase. At the steady state,  $J'$ , the number of new formed critical nuclei per unit volume-time around a foreign body is equal to the steady growth rate of clusters on the surface of the foreign body. Taking into account the effect of the substrate on both the nucleation barrier and the transport process, the nucleation rate is given by [56]:

$$J = 4\pi a(R^*)^2 N^0 f''(m, R)^{1/2} \left[ -\frac{16\pi\gamma_{cf}^3 \Omega^2}{3k_B T [k_B T \ln(1+\sigma)]^2} f(m, R) \right] \quad (13.18)$$

where  $N^0$  denotes the number density of the substrates (or “seeds”) and  $B$  is the kinetic constant. Due to the presence of the substrate, the growth units from the side of the substrate (Figure 13.7(B)) are screened from colliding the surfaces of nuclei. In Eqn (13.18), the shadow effect of the substrate on nuclei growth is reflected by the prefactor  $f''(m, R)$ , which is the ratio between the average effective collision in the presence of substrates and that of homogeneous nucleation. For homogeneous nucleation, Eqn (13.18) can be simplified to:

$$J = B \exp\left[-\frac{16\pi\gamma_{cf}^3 \Omega^2}{3k_B T [k_B T \ln(1+\sigma)]^2}\right] \quad (13.19)$$

For a 2D nucleation, the nucleation rate has a similar form [56]:

$$J_{2D} = \left\{ \frac{2D_s n_1^2}{\pi} \left[ \frac{\Omega \ln(1+\sigma)}{h} \right]^{1/2} \exp\left[-\frac{\pi\Omega h \gamma^2}{(k_B T)^2 \ln(1+\sigma)^2}\right] \right\} \beta_{\text{link}} \quad (13.20)$$

where  $D_s$  denotes the surface diffusivity,  $n_1$  is the number of single particles (monomers), and  $\beta_{\text{link}}$  is the sticking possibility. In general, although 3D and 2D nucleation are not exactly the same, they share many common features in almost all aspects [57]. Therefore, the principles obeyed by 3D nucleations can be applied to understand 2D nucleation, and vice versa.

### 13.3.1.4 Nonsteady State

In a nonsteady state, the size distribution  $Z_n$  changes with time,  $dZ_n/dt \neq 0$ ; thus, the flux  $J_n$  is dependent on  $n$  and  $t$ . The nucleation rate  $J_{\text{nonst}}(t)$  will change with time.

### 13.3.2 Experimental Verification of Classical Nucleation Theory

Classical nucleation theory and its predictions have been established for a long time. However, direct experimental verification had been absent until recently, when it was performed by Liu et al. in the AEF-controlled 2D colloidal system [53]. In their study, the size distribution of 2D subcritical nuclei was obtained and the predictions of CNT were quantitatively examined. It was found that the nucleation starts from a nonstationary state (Figure 13.9(A)  $t > 0$  s) and gradually approaches a stationary state (Figure 13.9(A),  $t > 20$  s)

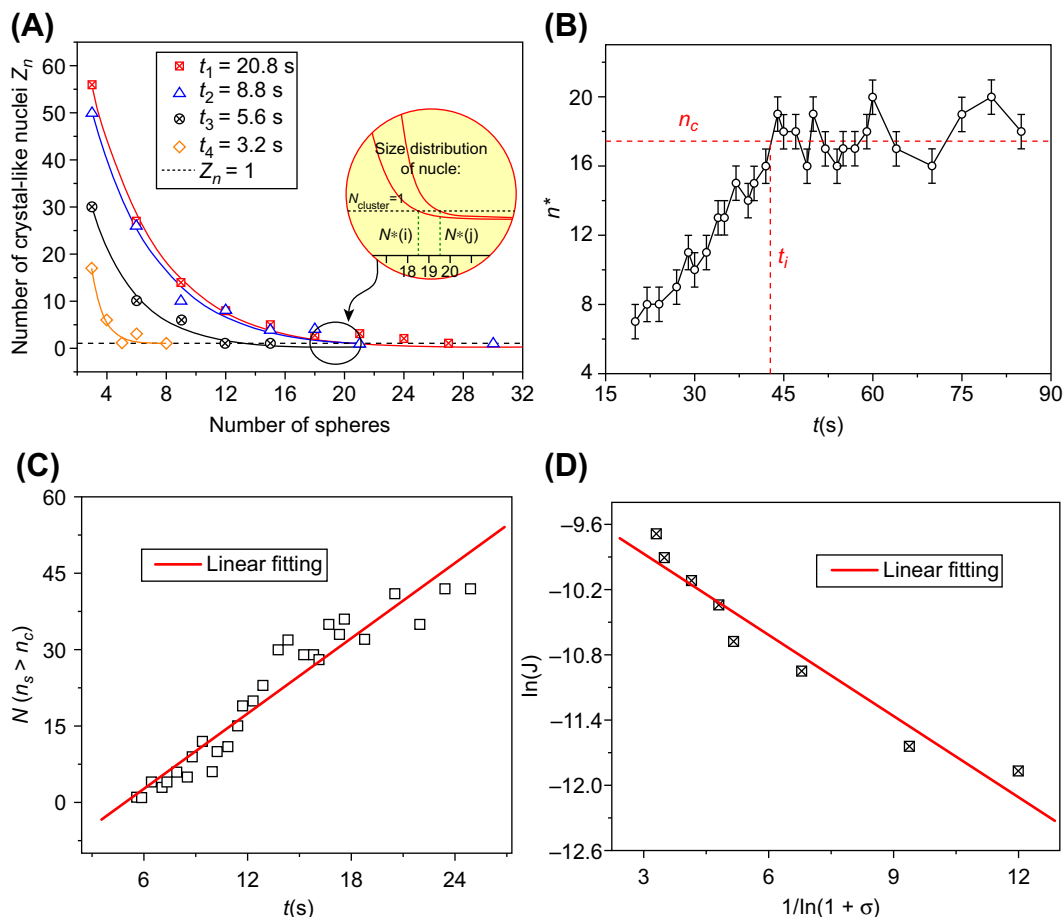


**FIGURE 13.9** Statistical measurement of nucleation kinetics. (A) The typical size distribution of subcritical nuclei versus time ( $E_\infty = 2.6 \times 10^4$  V/m  $f = 600$  Hz). (B)  $n^*(t)$  versus time. After the induction time,  $n^*(t)$  becomes stable. The critical size can be determined. (C) The number of nuclei with a size larger than the critical size in different times. We can measure the nucleation rate in the unit area according to the slope of linear fitting of this curve. (D) The nucleation rate under the different supersaturation (driving force). The straight fitting line is based on Eqn (13.20). From Eqn (13.20), we also can get the line tension of interface. The value of  $\gamma_{step}$  is  $0.50kT/a$  ( $a$  is the diameter of colloidal particles), which is agreement with the measurements. Reprinted with permission from Ref. [53]. Copyright (2004) Nature Publishing Group.

in which the distribution of nucleating clusters  $Z_n$  is independent of time. A critical nuclei size  $n_c$  at time  $t$  is defined by  $Z_{n^*}(t) = 1$ . In the experiments,  $n_c$  is time-dependent at the beginning and becomes constant until the nucleation goes into the stationary state (Figure 13.9(B)). Therefore, the critical size of nuclei is definite only at a stationary state. Figure 13.9(C) shows that the number  $N_c$  of supercritical nuclei ( $n > n_c$ ) increases with time. The slope of linear fitting of  $N_c \sim t$  gives the nucleation rate  $J_{2D}$ , the average number of newly formed supernuclei per unit time in a unit area. Figure 13.9(D) shows that the nucleation rate is dependent on the driving force and the plot of  $\ln(J) \sim 1/\ln(1 + \sigma)$  can be well fitted with a linear relationship, agreeing with the prediction (Eqn (13.20)) of CNT under the genuine steady state.

### 13.3.3 Discrepancies between CNT and Observations

The observation presented in Figure 13.9 offers an example indicating that CNT is successful in describing nucleation processes. However, there are also a growing amount of discrepancies between the predictions of CNT and the actual observations from experiments and simulations. For example, Gasser et al. found that crystal nucleus is not necessarily spherical and may be anisotropic (elliptic) [25]. Moreover, in apoferritin protein solutions, planar nuclei were observed as well [58]. These observations are in contrast to the spherical nuclei assumption of CNT. More intriguingly, the experimentally measured nucleation rate undergoes a maximum upon increasing supersaturations [59] and the nucleation rate derived from CNT can be 10 orders higher than what experimentally measured [60]. There are also remarkable discrepancies between the experimentally observed and predicted kinetic factors [61]. These discrepancies suggest that CNT has intrinsic limitations. The limitations may stem from the fundamental assumptions of CNT, such as the following [62]:

1. Nuclei are spherical. The physics of this assumption is that nuclei tend to minimize the surface free energy.
2. Nuclei are identical to an infinite bulk crystal (in the case of crystallization) in structure.
3. The surface tension of crystal nuclei is exactly the same as that of an infinite bulk crystal and is independent of the size and shape of nuclei.
4. During the growth, nuclei incorporate one monomer at a time. Coalescence of nuclei and clusters are neglected.
5. The stationary distribution of subcritical nuclei is established instantaneously once the system is supersaturated. The nucleation rate is thus time-independent.

There is increasing evidence suggesting that the basic assumptions adopted by CNT are not valid in many cases. For example, ten Wolde et al. [28] found that nuclei structure can be size-dependent. Initially, nuclei with a metastable body-centered cubic (BCC) structure are created and, subsequently, a structure transition from BCC to face-centered cubic occurs as nuclei reach the critical size. In another work, ten

Wolde and Frenkel found that nucleation in systems with short-range attractions, such as granular proteins, may proceed through a two-step process: First, amorphous droplets are formed from a supersaturated solution and crystalline structures are subsequently nucleated from the amorphous droplets. It is becoming increasingly clear that the properties, such as the shape and the structure, of nuclei in many cases are dependent on nuclei size. Nucleation may proceed through intermediate states or structures, being in contradiction to the assumptions of CNT. However, these deviations from CNT can be well understood in the framework of the so-called Ostwald's rule, which suggests that the first nucleated phase is not necessarily the thermodynamically most stable one, but the one closest to the metastable liquid phase in terms of free energy [63]. Alternatively, Stranski and Totomanow argued that the first nucleated phase should be the one that has the lowest free energy barrier [64]. Although Ostwald's rule offers an interpretation to nonclassical nucleation routes, the kinetics involved are still open to question. It is in colloidal model systems that a lot of insights were obtained in past decades.

## 13.4 Nonclassical Nucleation

Classical nucleation theories assume that crystal nuclei are created with a thermodynamically stable crystalline structure. However, severe deviations occur frequently in actual observations. Therefore, more details concerning nucleation under different conditions should be acquired. In this context, the application of the experimental modeling not only verified observed events (e.g., multistep crystallization, templating) but also identified some new phenomena, such as supersaturation-dependent nucleation routes and supersaturation-driven interface mismatch, shedding new light on the understanding of crystallization.

### 13.4.1 Structure Evolution of Precritical Nuclei

Applying new image techniques, it is now possible to visualize 3D nuclei by confocal microscopes. However, nucleation process is a fast dynamic process; even with confocal microscopes, it is still a challenge to track moving nuclei and identify their structures at the same time. Although 3D and 2D nucleation share common physical features [57], 2D nucleation offers the better experimental accessibility in identifying the structure of nuclei and studying the dynamic evolution of nuclei. To quantitatively study the structure of a 2D nucleus, a local two-dimensional bond-order parameter  $\psi_6(r_i)$  is widely used. It is defined as follows [26]:

$$\psi_6(r_i) = M^{-1} \sum_j e^{-i6\theta_{ij}} \quad (13.21)$$

where  $M$  is the number of nearest neighbors of particle  $i$  and  $r_i$  denotes the center position of particle  $i$ . All its neighbor particles are characterized by an angle  $\theta_{ij}$ , which is defined by the vector connecting the particle  $i$  to its  $j$ th nearest neighbor in reference to

the arbitrary axis. The order degree of a particle is measured by  $|\psi_6(r_i)|$ . The average value  $\langle |\psi_6(r_i)| \rangle$  in typical 2D crystals is taken as the criterion for crystal-like particles.

In the AEF-controlled 2D colloidal system, it was found that at a relatively high frequency (low supersaturation), nuclei are created with a liquid-like structure (Figure 13.10(A), top left). As the nuclei grow, their structure becomes more ordered simultaneously (Figure 13.10(A), top middle and right) [27]. The transition from the initial liquid-like structure to the final stable crystalline structure is a continuous process. This can be seen clearly in terms of  $\langle |\psi_6(r_i)| \rangle$  (Figure 13.10(A), bottom): the average bond-order parameter of the nuclei increases with the size and becomes essentially constant ( $\sim 0.8$ ) as the nuclei is beyond a critical size.

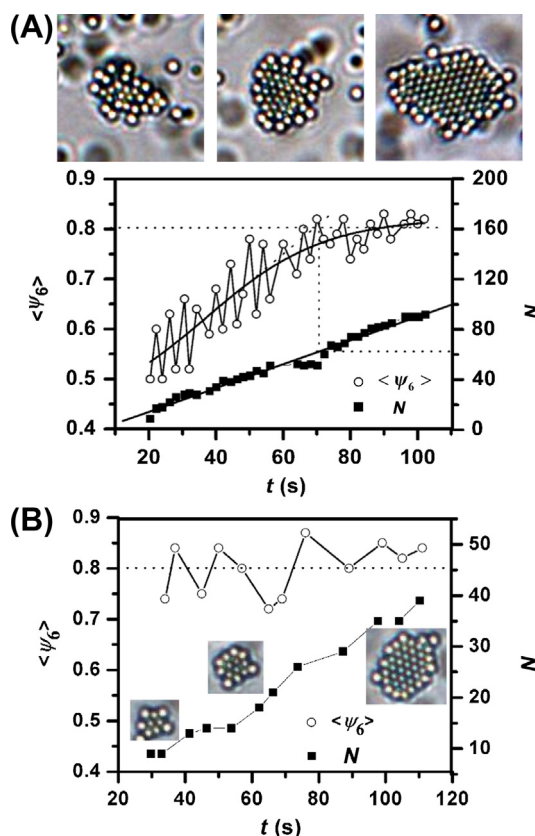


**FIGURE 13.10** (A) Top: Snapshots of a growing nucleus under conditions of  $V_{pp} = 2.5$  V,  $f = 5000$  Hz. In the schematic representations, red particles represent crystal-like particles with  $|\psi_6(r_i)| > 0.8$  and blue particles represent the liquid-like particles. The average bond-order parameter  $\langle |\psi_6(r_i)| \rangle$  of nuclei increases gradually as a function of the size of nuclei and reaches the plateau at a critical size. (B)  $\langle |\psi_6| \rangle$  as a function of nuclei size  $N$  under conditions of  $V_{pp} = 2.5$  V,  $f = 1000$  Hz. Nuclei are created with a crystalline structure from the beginning. Salt ( $\text{Na}_2\text{SO}_4$ ) concentration:  $2 \times 10^{-4}$  M. Reprinted with permission from Ref. [27]. Copyright (2009) Wiley-VCH Verlag GmbH & Co. KGaA, Weinheim.

At a high supersaturation, a distinct nucleation as shown in Figure 13.10(B) is observed. In this case, nuclei are created with a crystalline structure, which is stable in the following growth. Consistently, the average bond-order parameter is measured as  $\sim 0.8$  from the early beginning and remains stable during the whole growth (Figure 13.10(B)). At an intermediate supersaturation (Figure 13.3 in Ref. [27]), the structure of subcritical nuclei becomes flexible: the structure is crystalline at one time and then in the subsequent seconds it becomes disordered. Only when the size is beyond a critical size is the crystalline structure adopted stably. It is concluded from the above observations that the structure of subcritical nuclei is supersaturation dependent. At low supersaturation, a metastable liquid-like structure is likely to occur first. At higher supersaturations, stable crystalline structures are preferred from the beginning. The understanding is that at low supersaturations, nucleation barriers are high for stable crystalline structures, while for a metastable liquid-like structure it is much lower. Therefore, the occurrence of a metastable liquid-like structure can significantly reduce the nucleation barrier and enhance the nucleation [65].

Upon increasing supersaturation, the nucleation barriers decrease, both for stable crystal structure and metastable liquid-like structures. When the supersaturation is high enough, the difference between the nucleation barriers for stable crystalline structures and metastable liquid-like structures becomes so small that it is comparable to (or even smaller than)  $k_B T$ . As a result, the effect of metastable structures on the lowering nucleation barrier becomes subtle and nuclei can adopt the stable crystalline structure from the beginning. In other words, at low supersaturations, the nucleation barrier is lower than that predicted by CNT due to the presence of metastable structures. At high supersaturations, as the nucleation barrier becomes substantially low, adopting metastable structures is not energetically favorable anymore. Therefore, the nucleation processes follow CNT.

### 13.4.2 Multistep Crystallization

In systems with short-range attractions, such as proteins, ten Wolde and Frenkel found by simulations that nucleation for crystals may proceed through a two-step processes, namely two-step crystallization (TSC) [66]. Sense amorphous droplets are formed first through liquid-liquid phase separation; within the amorphous droplets, crystalline nuclei are subsequently nucleated. The occurrence of a metastable amorphous phase has also been found in biomineralization, by which organisms form a variety of crystalline structures [67]. The crystalline structures created by organisms are ubiquitously well-defined in size and shape. There is increasing evidence that metastable amorphous phases in biomineralization play a key role in controlling the size and the shape [68]. Although TSC has been extensively studied [69], the mechanism of TSC remains unclear because of the absence of direct observations. In this case, the experimental studies conducted in the AEF-controlled 2D colloidal system offer a direct demonstration of TSC on a single-particle level.

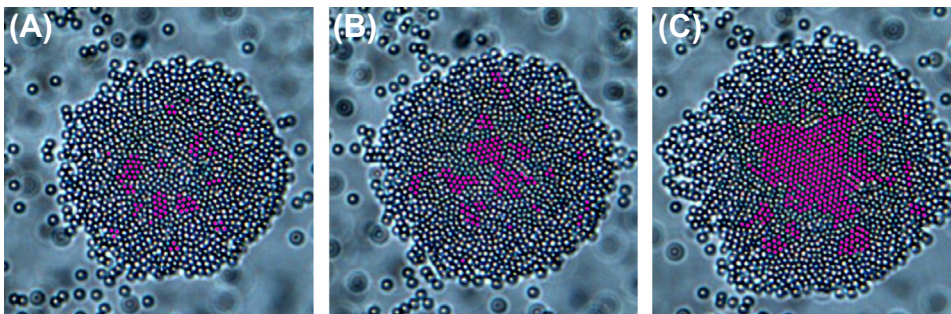


**FIGURE 13.11** Multistep crystallization observed in the 2D colloidal system. The crystal-like particles defined by  $\langle |\psi_6| \rangle > 0.8$  are colored. (A) Amorphous dense droplets are first created from the mother phase and small subcrystalline nuclei are then created in the droplets by fluctuation. (B) Subcrystalline nuclei are not stable. (C) A stable mature crystalline nucleus is created from the dense droplet. Adapted with permission from Ref. [26]. Copyright (2007) American Chemical Society.

Figure 13.11 presents a typical multistep crystallization (MSC) process, as observed by Zhang et al. [26] In MSC, 2D dense amorphous droplets are created first from the supersaturated solution. As the amorphous droplets grow up, a few subcrystal nuclei are created by fluctuation from the droplets (Figure 13.11(A)). However, the subnuclei are not stable and usually dissolve soon; new subnuclei are created somewhere randomly again (Figure 13.11(B)). The crystalline nuclei in the droplets have to acquire a critical size  $N_{\text{cry}}^*$  before they become stable in the droplets (Figure 13.11(C)). Experimentally, every droplet can produce only one stable crystal. To form a stable crystal beyond  $N_{\text{cry}}^*$ , the droplets have to acquire a critical size  $N^*$ . Although many small dense droplets are created at the beginning, only a small fraction of them can reach the critical size  $N^*$  and accommodate a stable crystal. In MSC, the overall nucleation rate  $J_c$  of crystal nuclei can be determined by measuring the local nucleation rate  $j_c$  in individual dense droplets [70].

### 13.4.3 CNT and Ostwald's Rule

The observations of the metastable structures of nuclei and MSC are in contrast to CNT. However, these observations can be well understood in the framework of the Ostwald step rule [63]. The liquid-like structure of subnuclei and the amorphous droplets in MSC have a smaller surface tension because of their liquid-like structure and thus a lower energy barrier. Kinetically, they will be created faster than observed. Increasing evidence shows that Ostwald's rule may underlie most of crystallization processes in physical, chemical, and biological systems. However, although the Ostwald step rule offers a framework in understanding stepwise nucleation, it is a challenge to establish a theoretical model that can quantitatively take into account the effect of the metastable structures on nucleation barrier and nucleation rate. So far, CNT is still widely used because quantitative analysis is necessary. A quantitative model including the Ostwald step rule is highly expected in this field.

## 13.5 Kinetics of Crystal Growth

After nucleation, crystal growth, which is the second stage of crystallization, occurs. The growth of crystals proceeds through a number of dynamic processes, such as surface diffusion, island nucleation, and incorporation. Figure 13.12(A) illustrates the surface of a growing crystal. At the surface, there are flat regions (the so-called terrace), steps, and diffusing adatoms. New terraces can be created by 2D nucleation on an existing terrace. The steps are usually zigzagged due to the presence of kink sites, which are the most stable positions for incoming atoms or molecules to attach because more bonds can be formed there. Kink sites can be created by thermally activated detachment or adatom absorption. During the growth, surface morphology, such as island density and terrace width, is critical in determining the quality of resulted crystals. Surface morphology is generally a result of interplay between dynamic processes, including surface diffusion, step diffusion, and mass transfer between terraces. For the mass transfer between terraces, there is a step-edge barrier, namely the Ehrlich-Schwoebel (ES) barrier (Figure 13.12(B)). So far, a rich variety of phenomenon have been observed during the growth of crystals; such phenomenon, such as surface roughening, defect formation, and polymorphism, have been studied for decades in atomic systems [53]. In the last decade, this kind of study was extended into colloidal systems; it was found that the dynamic processes included in colloidal crystal growth follow the same principles obeyed by atoms [71]. However, in a crystallizing colloidal system, direct observation of crystal growth on single-particle level is allowed, while it is limited in atomic systems.

### 13.5.1 Step Kinetics

For thin-film materials, a smooth surface is extensively required. In epitaxial growth, smooth growth or two-dimensional growth is usually observed at high temperatures when adatoms have enough kinetic energy to overcome the ES barrier. At low

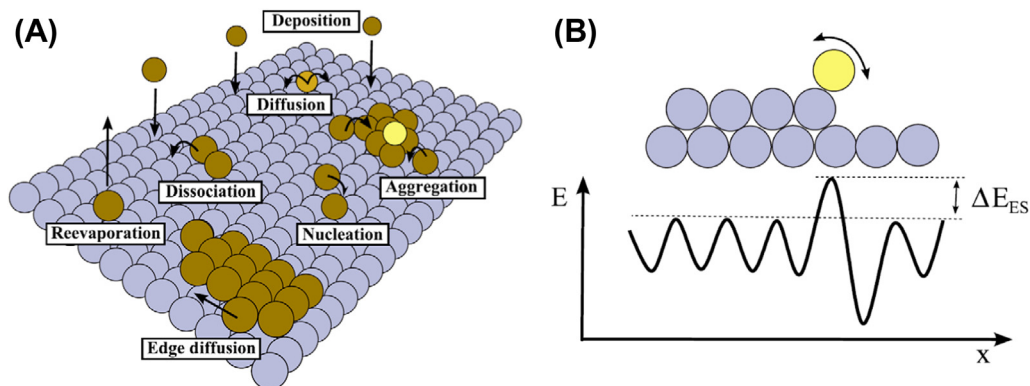
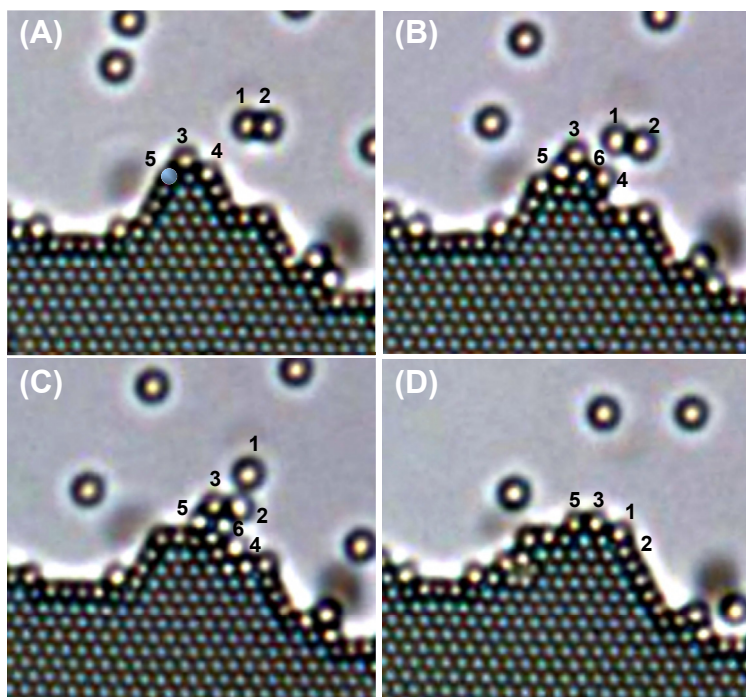


FIGURE 13.12 (A) Surface of a growing crystal. (B) Step-edge barrier.

temperatures when the interlayer transport is inhibited by the ES barrier, rough surface occurs [72]. However, when the temperature is lower than a critical value, smooth growth occurs unexpectedly [73]. To address the reentrant smooth growth at low temperatures, downward funneling (DF) was suggested [74]. The DF mechanism argues that atoms deposited beyond a step edge would like to funnel down to lower layers with their condensation energy. However, van Dijken et al. found that if the attraction between growing fronts and incoming atoms is taken into account [75], incoming atoms would be directed to the top of exiting islands in a steering effect. The steering effect and the DF mechanism are competing with each other [76]. Therefore, it is still a challenge to interpret the smooth growth at low temperatures as the steering effect is present.

Direct observations of incorporation processes in the AEF-controlled 2D colloidal system revealed that the steering effect suggested in previous studies reflects only one side of the attraction's role [75]. Figure 13.13 presents a typical process of adsorbing incoming dimers. Particles 3–6 form a step protrusion of a growing 2D crystal. The incoming dimer consisting of particles 1–2 is approaching the step (Figure 13.13(A)). As the attraction between the incoming dimer and the particles at the protrusion peak



**FIGURE 13.13** Smoothing effect of the attraction between incoming clusters and step protrusions. (A)–(D) Step particles are pulled down by the incoming dimer, resulting in a reduction of the local roughness. Reprinted with permission from Ref. [77]. Copyright (2007) American Chemical Society.

begins to work, the trajectory of the dimer is directed toward the protrusion (Figure 13.13(B)). Simultaneously, step particles 3–6 are accelerated to move. Particles 4 and 6, with their excess kinetic energy, descend to the lower layers (Figure 13.13(C)). In the end, the incoming dimer incorporates into the protrusion. At the same time, the protrusion is remarkably smoothed, ready to accept more incoming particles [77]. From this observation, it is concluded that the role of the attraction between the incoming particles and the step particles is twofold: it can induce a steering effect and, simultaneously, can also activate a smoothing process. The attraction-induced smoothing effect can effectively fill up the gaps between step protrusions and leads to smooth steps. The smoothing effect would become more significant if the incoming units are large clusters.

### 13.5.2 Cluster Adsorption

In crystal growth, as Figure 13.13 shows, the growth often happens through cluster adsorption. Using the AEF-controlled 2D colloidal system, the structure evolution of absorbed clusters was studied by Xie et al. [78]. In their studies, a line template was fabricated first on the electrodes to control the crystallization (Figure 13.14(A)). The

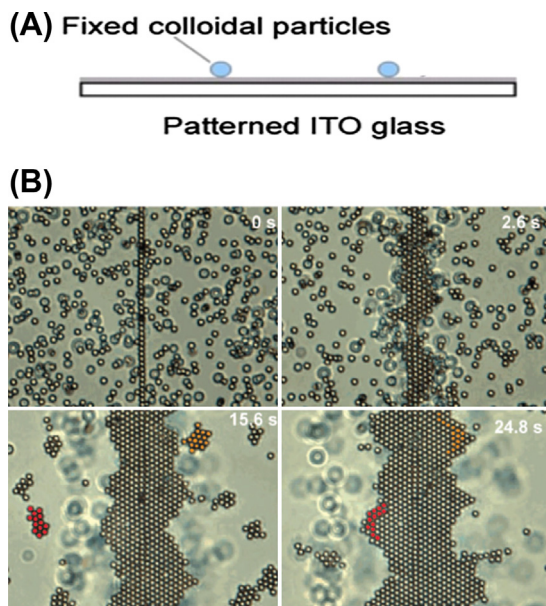


**FIGURE 13.14** (A) Schematic illustration of the epitaxial assembly of 2D colloidal crystals under an AEF. (B) High-resolution time snapshots of the epitaxial crystallization of 1.8- $\mu\text{m}$  colloidal particles using a 1.8- $\mu\text{m}$  colloidal particle line as a template, under the AEF of frequency  $f = 800$  Hz and field strength  $E_{\infty} = 4.0 \times 10^4$  V/m. The bright dots correspond to the well-focused spheres that are assembled on the bottom electrode. The dark dots correspond to the ill-focused spheres, which are suspended in the bulk solution. (A) Reprinted with permission from Ref. [40]. Copyright (2012) Wiley-VCH Verlag GmbH & Co. KGaA, Weinheim. (B) Reprinted with permission from Ref. [78]. Copyright (2009) American Chemical Society.

colloidal solution was loaded after the templating (Figure 13.14(B), 0 s). Upon the application of AEF of a frequency 800 Hz and a field strength  $E_{\infty} = 4.0 \times 10^4$  V/m, crystallization occurs preferentially near the line templates. At the same time, a large number of colloidal clusters are formed (Figure 13.14(B),  $t = 2.6$  s). During the growth of the crystal, clusters adsorption occurs frequently. In the absorption, the clusters exhibit high structure flexibility (Figure 13.14(B): 15.6 s, 24.8 s) and the occurrence of defects is rare. It is believed that the local melting induced by the impact of incoming clusters plays a key role in annealing the growing fronts [79]. Nevertheless, if the incoming flux of clusters is too high, voids or grain boundaries can be formed and frozen in the crystals.

### 13.5.3 Surface Roughening

The growth of crystals occurs at the boundaries/interfaces between the crystal phase and the fluid phase; the boundaries keep moving toward the fluid phase [80]. The morphology of the crystal surface results from a certain growth model, which in turn will affect the growth kinetics of crystal faces. There are two types of crystal surfaces: flat surface (Figure 13.15(A) left) and roughened surface (Figure 13.15(A), right) [80].

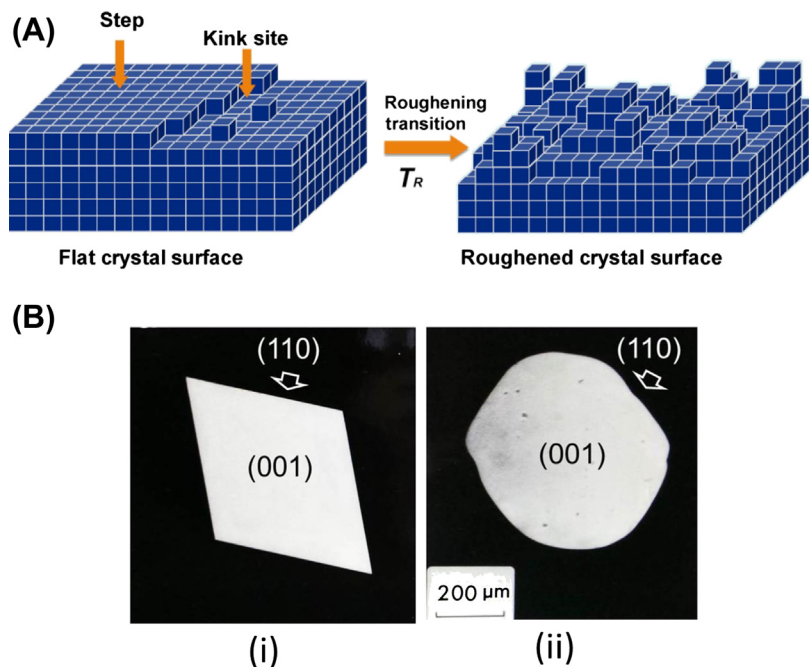


**FIGURE 13.15** Surface roughening by the solid-on-solid model. (A) Schematic illustration of flat (left) and roughened (right) crystal surfaces. (B) Paraffin crystal grown from a hexane solution below the roughening temperature (i) and above the roughening temperature (ii) of the faces {110}; the faces {110} (side faces) are straight.

Flat surfaces generally result from layer-by-layer growth or faceted growth. In this case, the overall crystallographic orientation is well maintained during the growth (Figure 13.15(B), left; the (110) face of  $n\text{-C}_{23}\text{H}_{48}$  crystals). In a roughened growth or normal growth mode, the growing crystal faces lose the overall crystallographic orientation and the surface becomes round (Figure 13.15(B), right; the (110) face of  $n\text{-C}_{23}\text{H}_{48}$  crystals) [81]. A faceted crystal surface may experience a transition from the flat mode to the rough mode at a critical temperature, the so-called roughening temperature  $T_R$  [81] (Figure 13.15(A)). The mechanism is that, below the roughening temperature, there is a nonzero free energy—the so-called step free energy associated with the creation of a step of unit length at the surface [82]. Consequently, the creation of a new layer on existing layers at crystal surfaces has to overcome a free energy barrier, the so-called two-dimensional nucleation barrier. Therefore, below the temperature  $T_R$ , the creation of new islands is not preferred, giving rise to an overall flat surface [83]. Above  $T_R$ , the step free energy vanishes; the energy cost to form new steps or kinks is small. As a result, the surface microscopically becomes rough and crystallographic orientation is lost.

The roughening transition has been investigated extensively by computer simulations [83]. In these simulations, the so-called solid-on-solid interfacial model was widely used. This model is a generalization of Ising model, which assumes that crystal surface is a collection of interacting columns. The corresponding Hamiltonian is given by:

$$H = \gamma_E \sum_{ij} |h_i - h_j|^2 \quad (13.22)$$

Here,  $\gamma_E$  is the step energy per unit length and  $h_i$  is the column height; the step free energy  $\gamma$  is dependent on temperature by:

$$\gamma \sim \exp\left[-\alpha(T_R - T)^{-1/2}\right] \text{ as } T \rightarrow T_R (T < T_R) \quad (13.23)$$

As the temperature approaches  $T_R$ ,  $\gamma$  vanishes continuously. Therefore, the roughening transition can be regarded as a type of Kosterlitz-Thouless transition (an infinite-order transition) [84]. However, the experimental observations in the AEF-controlled 2D colloidal system show that a roughening transition can be of infinite order or first order [85].

The 2D colloidal crystals can be regarded as the top layer of atoms or molecules on a crystal surface. In this system, a phase transition from a highly ordered colloidal monolayer to an isotropic suspension can be induced by decreasing the field strength or increasing frequency [85]. Intriguingly, the transition induced by decreasing field strength as shown in Figure 13.16(A) is an infinite-order transition, while the frequency-induced transition is a typical second-order phase transition. We notice that both the infinite-order and the second-order phase transition (Figure 13.16(B)). We notice that both the infinite-order and the second-order surface roughening have so far not been recognized in previous studies.

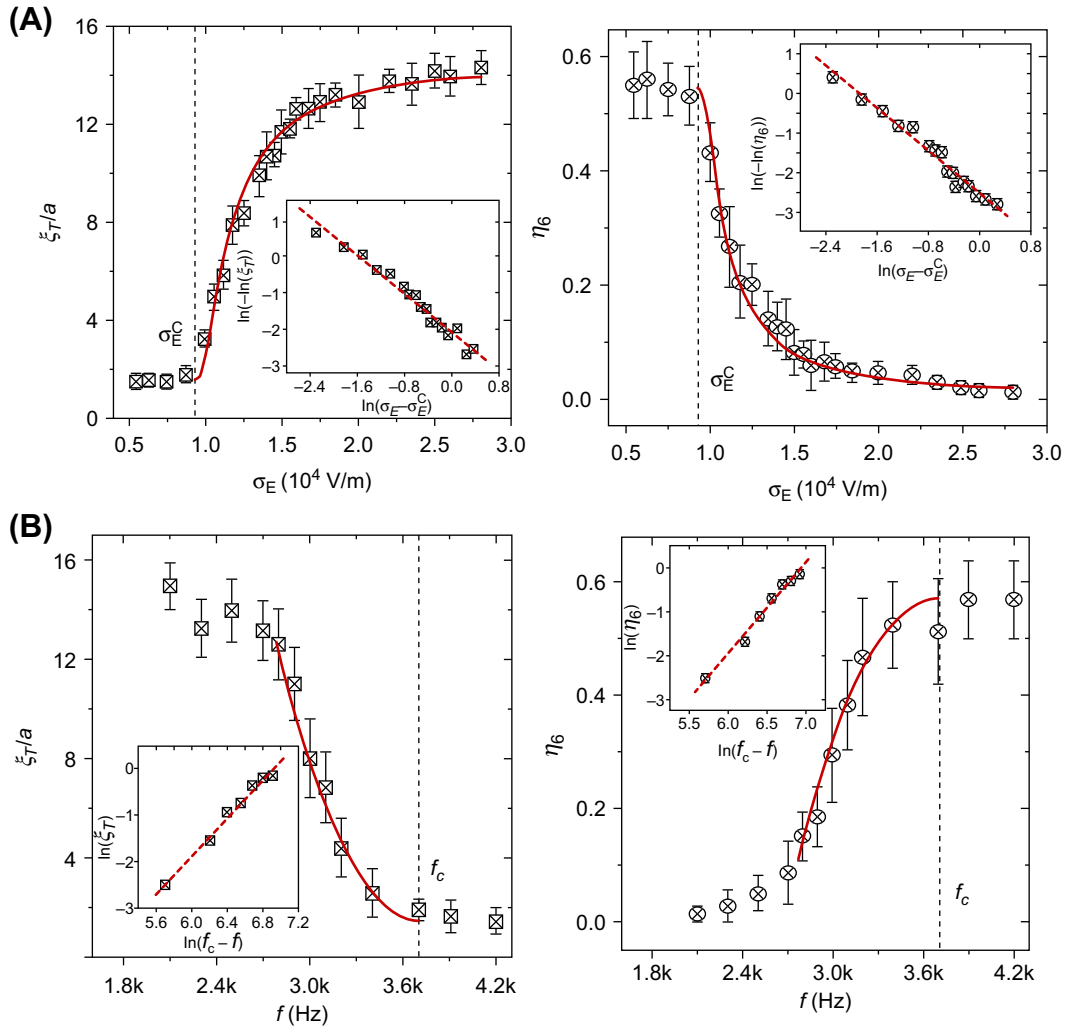


**FIGURE 13.16** (A) The change of order parameters of the transition induced by the field strength. Left: The translational correlation length  $\xi_T$ . Right: the bond-orientational order  $\eta_6$  change with the external field strength from  $2.8 \times 10^4$  V/m to  $0.5 \times 10^4$  V/m at a fixed frequency of  $f = 0.8$  kHz. Here, the position of the vertical dotted line is the critical strength  $\sigma_E^c = 0.9 \pm 0.05 \times 10^4$  V/m. The  $\ln \sim \ln$  plots of the normalized order parameters  $\xi_T'$  and  $\eta_6'$  against  $\ln(\sigma_E - \sigma_E^c)$  are shown in the right-corner insets. The straight dotted line in each inset is the least-squares fit of the data, resulting in the values of the fitting parameters of  $\ln(\alpha) = -2.055 \pm 0.058$ ,  $\beta = -1.33 \pm 0.061$  for the left and  $\ln(\alpha) = -2.518 \pm 0.057$ ,  $\beta = -1.350 \pm 0.058$  for the right. The red curves are the best fits of the exponential function with the given fitting parameters. (B) The change of the order parameters of the transition induced by the frequency.  $\xi_T$  (left) and  $\eta_6$  (right) change with the frequency of the electric field from 2.1 to 4.2 kHz at a fixed strength  $\sigma_E = 2.8 \times 10^4$  V/m. The position of the vertical dotted line is the critical frequency  $f_c = 3.7 \pm 0.1$  kHz. The  $\ln$  plots of the normalized order parameters  $\xi_T'$  and  $\eta_6'$  against  $\ln(f_c - f)$  are shown in the left-corner insets. The straight dotted lines in the insets are the least-squares fits of the data, resulting in the values of the fitting parameters of  $\lambda = 2.04 \pm 0.07$  for the left and  $\lambda = 2.09 \pm 0.11$  for the right. The red curves are the best fits of the power-law function with the given fitting parameters. Reprinted with permission from Ref. [85]. Copyright (2006) by the American Physical Society. (For interpretation of the references to color in this figure legend, the reader is referred to the online version of this book.)

## 13.6 Interfacial Structural Mismatch and Network Formation

On one hand, substrates can lower nucleation barriers in a supersaturated solution. On the other hand, they also exert a negative impact on the surface integration, the so-called *shadow effect*, as illustrated in [Figure 13.7\(B\)](#). The shadow effect will slow the nucleation kinetics and weaken the effect of reduced nucleation barrier. These two competing effects play different roles in different regimes ([Figure 13.17\(A\)](#) up). At low supersaturations, the nucleation barrier is high; thus, nucleation will be substantially enhanced if the nucleation barrier is lowered effectively ( $f(m) \rightarrow 0$ ). In this case, the interaction between the substrate and the nucleating phase is important and heterogeneous nucleation is kinetically favored. Under this condition, nucleation barrier can be most effectively reduced if the structural synergy between the nucleating phase and the substrate is optimal, giving rise to self-epitaxial nucleation [86]. At higher supersaturations, nucleation barrier becomes low and the effect of substrates in reducing nucleation barrier becomes less important. Instead, the shadow effect of the substrate becomes significant.

Nuclei on the substrates with larger  $f(m)$  and  $f''(m)$  (or  $m \rightarrow 0, -1$ ; see [Eqn \(13.18\)](#)) will have a higher freedom in orientation (or a larger entropy) and thus have more chance to grow. It follows that as the supersaturation is too high, the epitaxial templating relationship between substrates and nucleating phases cannot be maintained, even if substrates have an excellent structural match with the new phase, leading to a supersaturation-driven interfacial structural mismatch. [Figure 13.17\(A\)](#) (bottom) illustrates a typical example of the self-epitaxial nucleation induced assembly and the supersaturation-driven interfacial structural mismatch. As shown, in a solution growth, calcite crystals evolve from single crystals to polycrystals upon increasing supersaturation. At relatively low supersaturations, the polycrystals are well aligned with each other (self-epitaxial nucleation induced assembly). As the supersaturation increases, the structural match between the adjacent crystallites in the assembly are lost gradually, namely supersaturation-driven interfacial structural mismatch.

The supersaturation-driven interfacial structural mismatch plays a very important role in pattern formation, crystallite network formation, and supermolecule soft material formation [9]. Although it has been studied theoretically for a long time, a direct experimental verification of the supersaturation-driven interfacial structural mismatch has been missing. Recently, such direct observations was realized in the AEF-controlled 2D colloidal system by Xie and Liu [78]. In their study, one-dimensional colloidal templates were fabricated on the electrodes first. As the AEF was switched on, 2D crystallizations occurred preferentially along the line templates ([Figure 13.17\(B\)](#), left). To examine the ordering degree of the colloidal crystals, an orientational order parameter  $S = 1/2\langle 3 \cos^2 \theta - 1 \rangle$  was used to quantify the uniaxial ordering of the colloidal assembly. The misfit angle  $\theta$  of a crystal domain was measured in reference to the epitaxial colloidal line templates. The brackets denote an overall average of the particles in the assembly.  $S = 1$  means that the orientation of a crystalline domain is parallel to the line

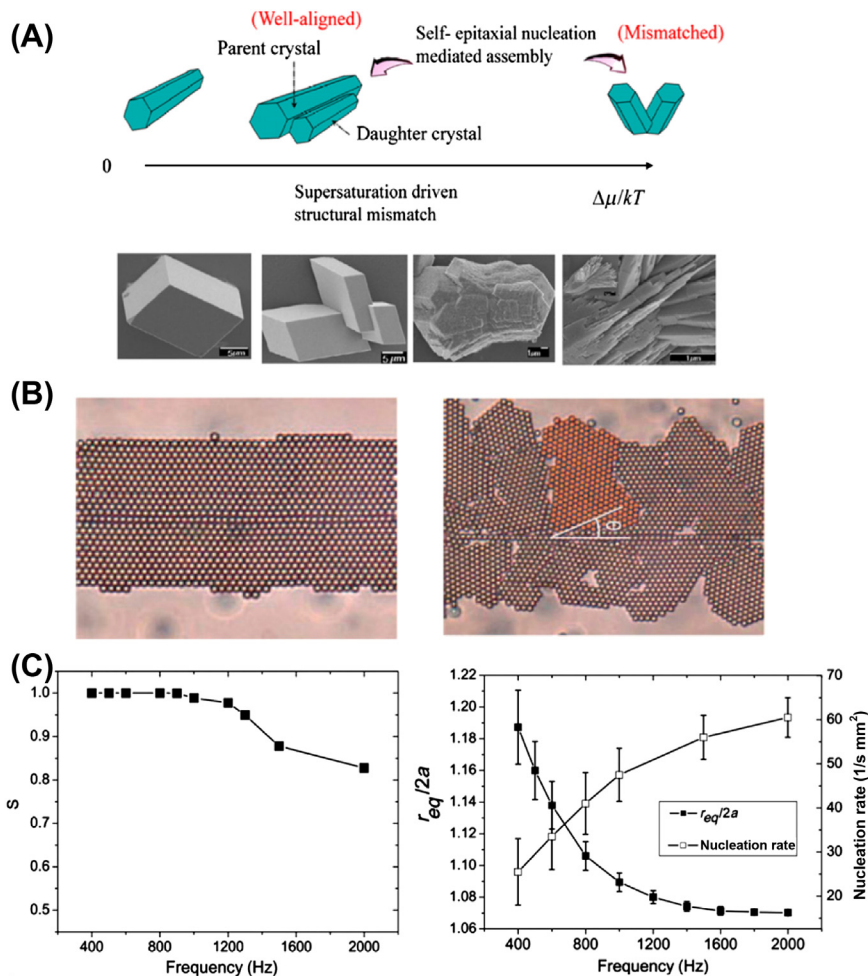


**FIGURE 13.17** (A) Self-epitaxial nucleation-induced assembly and supersaturation-driven interfacial structure mismatch nucleation. The structural match between the daughter crystals and the parent crystal will become poor as supersaturation increases. An example in calcite crystallization is demonstrated. (B) Heterogeneous 2D colloidal crystallization. Left: Orientational order parameter  $S = 1$  at 800 Hz. Right:  $S = 0.83$  at 1000 Hz. (C) Variation of the orientational order parameter, the equilibrium distance, and nucleation rate as a function of frequency. The diameter of the colloidal particles is 1.8  $\mu\text{m}$ . (a) Reprinted with permission from Ref. [40]. Copyright (2012) Wiley-VCH Verlag GmbH & Co. KGaA, Weinheim. (b)–(c) Reprinted with permission from Ref. [78]. Copyright (2009) American Chemical Society.

template. This was observed in the low-frequency range (400–800 Hz), where the resulting crystals are free of defects. At high frequencies (1000–2000 Hz), the quality of crystals in terms of  $S$  gradually decreases (Figure 13.17(C), left). The interparticle separation  $r_{eq}$  in the crystalline domains (Figure 13.17(C), right) decreases with frequency at the low-frequency region and reaches its minimum in the range of 1000–2000 Hz. This implies that the attractive force between particles becomes stronger as the frequency

increases. In other words, the supersaturation for crystallization is stronger at high frequencies. The reduced ordering degree of the colloidal crystals and the decreased  $S$  can be regarded as a direct reflection of a supersaturation-driven interfacial structural mismatch at high supersaturations.

## 13.7 Crystal Defects

Defects exist ubiquitously in crystals. There are several different types of defects: vacancy, dislocation, and grain boundary. These defects have great impact on the properties of crystals. For example, the presence of dislocation can strongly change the electrical and optical properties of crystals; vacancies can enhance atom diffusion in crystals [87]. Understanding the diffusion of defects and the interaction between defects are of great importance in condensed-matter physics and material sciences [88]. The development of colloidal model systems allows the direct observation of defects at the single-particle level [89].

In the AEF-controlled 2D colloidal systems, configurations and diffusion of vacancies were studied by Zhang and Liu [90]. Figure 13.18(A) shows that, in the 2D system, both

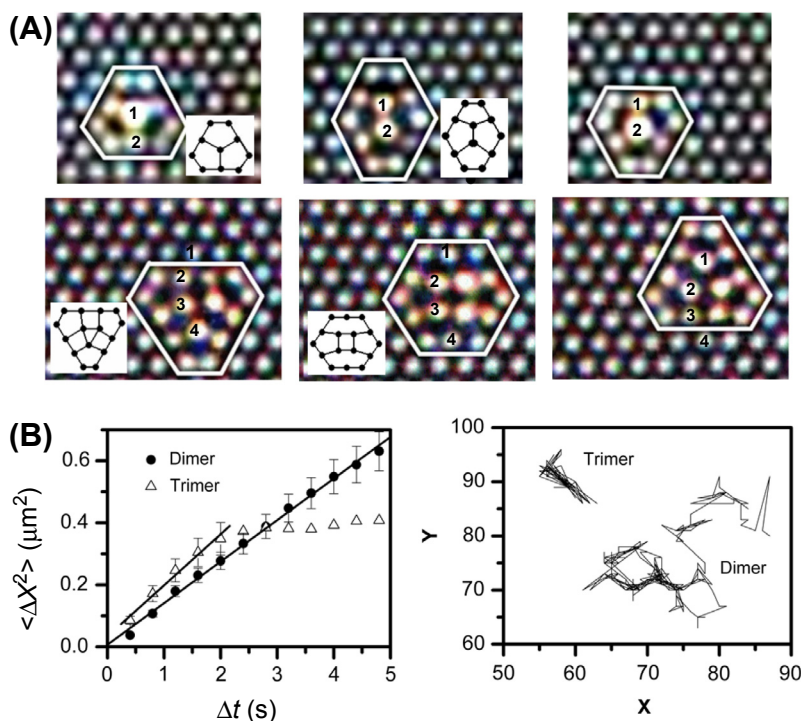


**FIGURE 13.18** Configurations of vacancies in 2D colloidal crystals. (A) Configurations of dimer vacancies and trimer vacancies. (B) Average squared displacement and trajectories of the mass center of vacancies. *Reprinted with permission from Ref. [90]. Copyright (2006) AIP Publishing LLC.*

dimer and trimer vacancies exhibit two stable configurations—threefold symmetric ( $D_3$ ) and twofold symmetric ( $D_2$ ), respectively. For dimer vacancies, the relative occurrence probabilities for  $D_2$  and  $D_3$  are  $0.47 \pm 0.01$  and  $0.53 \pm 0.01$ , respectively, being slightly different. The free energy difference  $\Delta\varepsilon$  between configurations  $D_2$  and  $D_3$  can be estimated from the occurrence probabilities. It was found that the  $\Delta\varepsilon$  for dimer vacancies is about  $0.12k_B T$ . Experimentally, dimer vacancies keep hopping between the two stable configurations (Figure 13.18(A) up). For trimer vacancies, the relative occurring probabilities of  $D_3$  and  $D_2$  are  $0.68 \pm 0.01$  and  $0.32 \pm 0.01$  respectively, being significantly different. The corresponding energy difference is around  $0.75k_B T$ .

In the experiments, monomer vacancies are immobile, whereas dimer/trimer vacancies keep hopping from one configuration to another configuration. Accompanying the configuration transformation, the mass center of vacancies undergoes a displacement. The linear fitting of the average squared displacements  $\langle \Delta r^2 \rangle$  of the mass center of vacancies shows that the diffusion coefficient of the dimer vacancies is around  $0.13 \pm 0.03 \mu\text{m}^2/\text{s}$ . However, as Figure 13.18(B) (left) shows, the average squared displacements of trimer vacancies reaches a plateau as the observation is beyond 2 s, suggesting that the trimer vacancies do not experience global diffusion in the 2D crystal. This is more clearly demonstrated by the trajectory plot (Figure 13.18(B), right). For dimer vacancies, the trajectory of the mass center exhibits a global Brownian motion in the crystal, whereas the mass center of trimer vacancies experiences only a local oscillation between two positions. The limited diffusion of trimer vacancies can be attributed to the significant energy difference between its two stable configurations: trimer vacancies prefer to adopt the  $D_3$  configuration, and hopping between  $D_2$  and  $D_3$  is not energetically favored.

In previous studies [91], both monomer vacancies and dimer vacancies in colloids with repulsive interactions are mobile and can diffuse globally. Moreover, dimer vacancies can dissociate into a dislocation pair. All these observations are distinct from the observations presented in Figure 13.18. These discrepancies may be due to the different interactions between colloidal particles [90]. In repulsive colloids, the particles adjacent to the missing particle of monomer vacancies tend to be pushed out from their equilibrium positions, leading to the deformation and diffusion of monomer vacancies. However, in AEF-controlled 2D colloidal systems, the electrostatic repulsion between two particles inside the clusters is balanced by an attraction. A small displacement from the equilibrium positions will produce a recovering force to pull the particle back. Therefore, the hopping of colloidal particles next to the missing particles of monomer vacancies is inhibited.

## 13.8 Concluding Remarks

In this chapter, we summarized recent progresses in understanding the mechanism of crystallization, which were achieved in colloidal modeling systems. In the modeling systems, almost all fundamental aspects of crystallization can be examined. It follows from these studies that classical nucleation theories provide a reasonable good

description for the main feature of nucleation dynamics in the steady state. On the other hand, the actual nucleation deviates from CNT in many cases. For example, in contrast to the assumption of CNT about the structure of crystal embryos, the structures of the embryos are usually supersaturation-dependent; in some cases, nucleation can occur through metastable phases or structures. These nonclassical nucleation routes can effectively reduce the overall nucleation barrier, hence speeding up the kinetics. Alternatively, the occurrence of substrates can also effectively reduce nucleation barriers. However, the effect of a substrate on nucleation is supersaturation dependent as the templated 2D colloidal nucleation reveals: supersaturation-driven structural mismatch may happen at high supersaturations.

Colloidal experimental modeling also demonstrates that a cluster of a few growth units can be incorporated into the steps without causing any defect. In the context of surface roughening, one can have both the infinite-order and the second-order surface roughening transition at the two layer solid–fluid interface as different parameter sets were chosen. This is in contrast to the two-dimensional Ising models, which only predict a second-order phase transition. Moreover, as demonstrated, the colloidal modeling technique has been successfully applied to examine many other crystallization processes, such as atomic step integration, defect generation, and migration kinetics, which have never been understood before at the single-particle level.

In the future, numerous important phenomena should be further examined using controlled colloidal modeling:

1. The formation and diffusion of grain boundaries in crystals.
2. Oriented attachment, which has been suggested as another important mechanism for nuclei/nano-crystal growth [92,93]. So far, in situ observations for this mechanism are rare, and the underlying mechanism is still open to discussion [94].
3. Heterogeneous nucleation. Although there are a plenty of discussions about the mechanism of heterogeneous nucleation, to the best of our knowledge, there is still limited direct experimental evidence available. By pinning colloidal clusters on the surfaces where crystallization occurs, we can examine systematically how the size and the shape of the clusters as nucleation centers will affect nucleation processes.
4. Interaction between defects. How defects, such as dislocations, interact with each other is intriguing. Direct observations may improve our understanding of it.

There are still many other problems to be added to the list. It is certain that a comprehensive understanding of these subjects will significantly improve the ability to fabricate advanced materials.

## Acknowledgment

T.H. Zhang acknowledges the financial support from National Natural Science Foundation of China NOS. 11374218.

## References

- [1] Gibbs JW. The collected works of J. Willard Gibbs, Volume I: Thermodynamics. New York: Longmans and Green; 1928.
- [2] Volmer M, Weber A. Nuclei formation in supersaturated states. *Z Phys Chem* 1925;119:277–301.
- [3] Farkas L. The speed of germinative formation in over saturated vapours. *Z Phys Chem* 1927;125: 236–42.
- [4] Kaischew R, Stranski IN. Zur kinetischen ableitung der keimbildungs-geschwindigkeit. *Z Phys Chem B* 1934;26:317.
- [5] Becker R, Döring W. Kinetic treatment of germ formation in supersaturated vapour. *Ann Phys* 1935; 24:719–52.
- [6] Zeldovich JB. On the theory of new phase formation. *Acta Physicochim URSS* 1943;18:1–22.
- [7] Hirth JP, Pound GM. Condensation and evaporation. Oxford: Pergamon Press; 1963.
- [8] Nielsen AE. Kinetics of precipitation. Oxford: Pergamon; 1964.
- [9] Liu XY. From solid-fluid interfacial structure to nucleation kinetics: principles and strategies for micro/nanostructure engineering. In: Liu XY, De Yoreo JJ, editors. *Nanoscale structure and assembly at solid-fluid interface*, vol. 1. Kluwer Academic Publishers; 2004. p. 109.
- [10] Lewis VB, Anderson JC. Nucleation and growth of thin films. London/New York/San Francisco: Academic Press; 1978.
- [11] Söhnel O, Garside J. *Precipitation: basic principles and industrial applications*. Oxford: Butterworth-Heinemann; 1992.
- [12] Zettlemoyer AC. *Nucleation*. New York: Dekker; 1969.
- [13] Toschev S. In: Hamm P, editor. *Crystal growth: an introduction*. Amsterdam: North Holland; 1973. p. 1.
- [14] Gutzow I. *Contemp Phys* 1980;21(121):243.
- [15] Jiang H, Liu X-Y, Zhang G, Li Y. Kinetics and template nucleation of self-assembled hydroxyapatite nanocrystallites by chondroitin sulfate. *J Biol Chem* 2005;280:42061–6.
- [16] Jiang H, Liu X-Y, Lim CT, Hsu CY. Ordering of self-assembled nanobiominerals in correlation to mechanical properties of hard tissues. *Appl Phys Lett* 2005;86:163901.
- [17] Jiang H, Liu XY. Principles of mimicking and engineering the self-organized structure of hard tissues. *J Biol Chem* 2004;279:41286–93.
- [18] Vekilov PG, Galkin O. In: Liu XY, De Yoreo JJ, editors. *Nanoscale structure and assembly at solid-fluid interfaces*, vol. II. London: Springer; 2004. p. 105–44. chs 4.
- [19] Jia YW, Narayanan J, Liu XY, Liu Y. Investigation of the mechanism of crystallization of soluble protein in the presence of nonionic surfactant. *Biophys J* 2005;89:4245.
- [20] Jia YW, Liu XY. Self-assembly of protein at aqueous solution surface in correlation to protein crystallization. *Appl Phys Lett* 2005;86:023903.
- [21] Jia YW, Liu XY. Prediction of protein crystallization based on interfacial and diffusion kinetics. *Appl Phys Lett* 2005;87:103902.
- [22] Jia Y, Liu XY. From surface self-assembly to crystallization: prediction of protein crystallization conditions. *J Phys Chem B* 2006;110:6949.
- [23] Zhang J, Liu XY. Effect of protein-protein interactions on protein aggregation kinetics. *J Chem Phys* 2003;119:10972–6.
- [24] Wang L, Liu X-Y. Kinetic analysis of protein crystal nucleation in gel matrix. *Biophys J* 2008;95:5931–40.
- [25] Gasser U, Weeks ER, Schofield A, Pusey PN, Weitz DA. Real-space imaging of nucleation and growth in colloidal crystallization. *Science* 2001;292:258–62.

- [26] Zhang TH, Liu XY. How does a transient amorphous precursor template crystallization. *J Am Chem Soc* 2007;129:13520–6.
- [27] Zhang TH, Liu XY. Nucleation: what happens at the initial stage? *Angew Chem Int Ed* 2009;48:1308.
- [28] ten Wolde PR, Ruiz-Montero MJ, Frenkel D. Numerical evidence for bcc ordering at the surface of a critical fcc nucleus. *Phys Rev Lett* 1995;75:2714–7.
- [29] Steinhauser M, Hiermaier S. A review of computational methods in materials science: examples from shock-wave and polymer physics. *Int J Mol Sci* 2009;10:5135–216.
- [30] Anwar J, Zahn D. Uncovering molecular processes in crystal nucleation and growth by using molecular simulation. *Angew Chem Int Ed* 2011;50:1996–2013.
- [31] Frenkel D. Simulations: the dark side. *Eur Phys J Plus* 2013;128:1–21.
- [32] Li F, Josephson DP, Stein A. Colloidal assembly: the road from particles to colloidal molecules and crystals. *Angew Chem Int Ed* 2011;50:360–88.
- [33] Anderson VJ, Lekkerkerker HNW. Insights into phase transition kinetics from colloid science. *Nature* 2002;416:811–5.
- [34] Pusey PN, van Megen W. Phase behaviour of concentrated suspensions of nearly hard colloidal spheres. *Nature* 1986;320:340–2.
- [35] Hunter GL, Weeks ER. The physics of the colloidal glass transition. *Rep Prog Phys* 2012;75:066501.
- [36] Peng Y, Wang Z, Alsayed AM, Yodh AG, Han Y. *Phys. Rev. Lett.* 2010;104:205703.
- [37] Pusey PN, Zaccarelli E, Valeriani C, Sanz E, Poon WC, Cates ME. Hard spheres: crystallization and glass formation. *Philos Trans A Math Phys Eng Sci* 2009;367:4993–5011.
- [38] Borwankar AU, Dinin AK, Laber JR, Twu A, Wilson BK, Maynard JA, et al. Tunable equilibrium nanocluster dispersions at high protein concentrations. *Soft Matter* 2013;9:1766–71.
- [39] Zaccarelli E. Colloidal gels: equilibrium and non-equilibrium routes. *J Phys Condens Matter* 2007;19:323101.
- [40] Diao YY, Liu XY. Controlled colloidal assembly: experimental modeling of general crystallization and biomimicking of structural color. *Adv Func Mater* 2012;22:1354–75.
- [41] Zhang TH, Liu XY. Experimental modelling of single-particle dynamic processes in crystallization by controlled colloidal assembly. *Chem. Soc. Rev.* 2014;43:2324–47.
- [42] Böhmer M. In situ observation of 2-dimensional clustering during electrophoretic deposition. *Langmuir* 1996;12:5747–50.
- [43] Trau M, Saville DA, Aksay IA. Field-induced layering of colloidal crystals. *Science* 1996;272:706–9.
- [44] Ristenpart WD, Aksay IA, Saville DA. Electrohydrodynamic flow around a colloidal particle near an electrode with an oscillating potential. *J Fluid Mech* 2007;575:83–109.
- [45] Ristenpart WD, Aksay IA, Saville DA. Assembly of colloidal aggregates by electrohydrodynamic flow: kinetic experiments and scaling analysis. *Phys Rev E* 2004;69:021405.
- [46] Gong T, Marr DWM. Electrically switchable colloidal ordering in confined geometries. *Langmuir* 2001;17:2301–4.
- [47] Liu Y, Xie R-G, Liu X-Y. Fine tuning of equilibrium distance of two-dimensional colloidal assembly under an alternating electric field. *Appl Phys Lett* 2007;91:063105.
- [48] Ristenpart WD, Aksay IA, Saville DA. Electrically driven flow near a colloidal particle close to an electrode with a faradaic current. *Langmuir* 2007;23:4071–80.
- [49] Nadal F, Argoul F, Hanusse P, Pouligny B, Ajdari A. Electrically induced interactions between colloidal particles in the vicinity of a conducting plane. *Phys Rev E* 2002;65:061409.

- [50] Zhang K-Q, Liu XY. Controlled formation of colloidal structures by an alternating electric field and its mechanisms. *J Chem Phys* 2009;130:184901–7.
- [51] Liu XY. Gelation with small molecules: from formation mechanism to NanostructureArchitecture. In: Low molecular mass gelator. *Topics in current chemistry*, vol. 256. Springer Berlin Heidelberg; 2005. p. 1–37.
- [52] Saridakis E, Chayen NE. Imprinted polymers assisting protein crystallization. *Trends Biotechnol* 2013;31:515–20.
- [53] Zhang K-Q, Liu XY. In situ observation of colloidal monolayer nucleation driven by an alternating electric field. *Nature* 2004;429:739–43.
- [54] Fowler R, Guggenheim EA. *Statistical thermodynamics*. London: Cambridge University; 1960.
- [55] Liu XY. A new kinetic model for 3D heterogeneous nucleation. *J Chem Phys* 1999;111:1628.
- [56] Liu XY. Generic mechanism of heterogeneous nucleation and molecular interfacial effects. In: Sato K, Nakajima K, Furukawa Y, editors. *Advances in crystal growth research*. Amsterdam: Elsevier Science B.V.; 2001. p. 42.
- [57] Li J-L, Liu X-Y. Architecture of supramolecular soft functional materials: from understanding to micro-/nanoscale engineering. *Adv Func Mater* 2010;20:3196–216.
- [58] Yau S-T, Petsev DN, Thomas BR, Vekilov PG. Molecular-level thermodynamic and kinetic parameters for the self-assembly of apoferritin molecules into crystals. *J Mol Biol* 2000;303:667–78.
- [59] Thomas P. Crystallization kinetics of repulsive colloidal spheres. *J Phys Condens Matter* 1999;11:R323–60.
- [60] Galkin O, Vekilov PG. Are nucleation kinetics of protein crystals similar to those of liquid droplets? *J Am Chem Soc* 1999;122:156–63.
- [61] Fokin VM, Zanotto ED. Crystal nucleation in silicate glasses: the temperature and size dependence of crystal/liquid surface energy. *J Non-Cryst Solids* 2000;265:105–12.
- [62] Kashchiev D. *Nucleation: basic theory with applications*. Oxford: Butterworth-Heinemann; 2000.
- [63] Ostwald W. Studien über die bildung und umwandlung fester körper. *Z Phys Chem* 1897;22:289–330.
- [64] Stranski IN, Totomanow D. Rate of formation of (crystal) nuclei and the Ostwald step rule. *Z Phys Chem* 1933;163:399–408.
- [65] Lutsko JF, Nicolis G. Theoretical evidence for a dense fluid precursor to crystallization. *Phys Rev Lett* 2006;96:046102.
- [66] ten Wolde PR, Frenkel D. Enhancement of protein crystal nucleation by critical density fluctuations. *Science* 1997;277:1975–8.
- [67] Addadi L, Raz S, Weiner S. Taking advantage of disorder: amorphous calcium carbonate and its roles in biomineralization. *Adv Mater* 2003;15:959.
- [68] Beniash E, Aizenberg J, Addadi L, Weiner S. Amorphous calcium carbonate transforms into calcite during sea urchin larval spicule growth. *Proc R Soc Lond Ser B* 1997;264:461.
- [69] Navrotsky A. Energetic clues to pathways to biomineralization: precursors, clusters, and nanoparticles. *Proc Natl Acad Sci USA* 2004;101:12096–101.
- [70] Zhang TH, Liu XY. Multistep crystal nucleation: a kinetic study based on colloidal crystallization. *J Phys Chem B* 2007;111:14001–5.
- [71] Ganapathy R, Buckley MR, Gerbode SJ, Cohen I. Direct measurements of island growth and step-edge barriers in colloidal epitaxy. *Science* 2010;327:445–8.
- [72] Ehrlich G, Hudda FG. Atomic view of surface self-diffusion: tungsten on tungsten. *J Chem Phys* 1966;44:1039.

- [73] Kunkel R, Poelsema B, Verheij LK, Comsa G. Reentrant layer-by-layer growth during molecular-beam epitaxy of metal-on-metal substrates. *Phys Rev Lett* 1990;65:733.
- [74] Caspersen KJ, Stoldt CR, Layson AR, Bartelt MC, Thiel PA, Evans JW. Morphology of multilayer Ag/Ag(100) films versus deposition temperature: STM analysis and atomistic lattice-gas modeling. *Phys Rev B* 2001;63:085401.
- [75] van Dijken S, Jorritsma LC, Poelsema B. Steering-enhanced roughening during metal deposition at grazing incidence. *Phys Rev Lett* 1999;82:4038.
- [76] Yu J, Amar JG. Effects of short-range attraction in metal epitaxial growth. *Phys Rev Lett* 2002;89:286103.
- [77] Zhang TH, Liu XY. Effect of long-range attraction on growth model. *J Phys Chem C* 2007;111:1342–6.
- [78] Xie R, Liu X-Y. Controllable epitaxial crystallization and reversible oriented patterning of two-dimensional colloidal crystals. *J Am Chem Soc* 2009;131:4976–82.
- [79] Haberland H, Insepov Z, Moseler M. Molecular-dynamics simulation of thin-film growth by energetic cluster impact. *Phys Rev B* 1995;51:11061–7.
- [80] Liu X-Y, Bennema P, van der Eerden JP. Rough-flat-rough transition of crystal surfaces. *Nature* 1992;356:778–80.
- [81] Liu X-Y, van Hoof P, Bennema P. Surface roughening of normal alkane crystals: solvent dependent critical behavior. *Phys Rev Lett* 1993;71:109–12.
- [82] Liu XY. Modeling of the fluid-phase interfacial effect on the growth morphology of crystals. *Phys Rev B* 1999;60:2810–7.
- [83] Liu XY. Simulating ‘atomic’ processes of crystallization via controlled colloidal assembly. In: Wang M, Tsukamoto K, Wu D, editors. *Selected topics on crystal growth: 14th international summer school on crystal growth*. Dalian: American Institute of Physics; 2010. p. 173–220.
- [84] Kosterlitz JM, Thouless DJ. Ordering, metastability and phase transitions in two-dimensional systems. *J Phys C Solid State Phys* 1973;6:1181–203.
- [85] Zhang K-Q, Liu XY. Two scenarios for colloidal phase transitions. *Phys Rev Lett* 2006;96:105701.
- [86] Liu XY, Lim SW. Templating and supersaturation-driven anti-templating: principles of biomineral architecture. *J Am Chem Soc* 2003;125:888–95.
- [87] Hashimoto A, Suenaga K, Gloter A, Urita K, Iijima S. Direct evidence for atomic defects in graphene layers. *Nature* 2004;430:870–3.
- [88] Lee G-D, Wang CZ, Yoon E, Hwang N-M, Kim D-Y, Ho KM. Diffusion, coalescence, and reconstruction of vacancy defects in graphene layers. *Phys Rev Lett* 2005;95:205501.
- [89] Pertsinidis A, Ling XS. Equilibrium configurations and energetics of point defects in two-dimensional colloidal crystals. *Phys Rev Lett* 2001;87:098303.
- [90] Zhang TH, Liu XY. Configurations and diffusion of point defects in two-dimensional colloidal crystals. *Appl Phys Lett* 2006;89:261914.
- [91] Pertsinidis A, Ling XS. Diffusion of point defects in two-dimensional colloidal crystals. *Nature* 2001;413:147–50.
- [92] Penn RL, Banfield JF. Imperfect oriented attachment: dislocation generation in defect-free nanocrystals. *Science* 1998;281:969–71.
- [93] Li D, Nielsen MH, Lee JRI, Frandsen C, Banfield JF, De Yoreo JJ. Direction-specific interactions control crystal growth by oriented attachment. *Science* 2012;336:1014–8.
- [94] Zhang D, González-Mozuelos P, de la Cruz MO. Cluster formation by charged nanoparticles on a surface in aqueous solution. *J Phys Chem C* 2010;114:3754–62.

# Morphological Stability

R.F. Sekerka<sup>1</sup>, S.R. Coriell<sup>2</sup>, G.B. McFadden<sup>2</sup>

<sup>1</sup>CARNEGIE MELLON UNIVERSITY, PITTSBURGH, PA, USA; <sup>2</sup>NATIONAL INSTITUTE OF STANDARDS AND TECHNOLOGY, GAITHERSBURG, MD, USA

## CHAPTER OUTLINE

<b>14.1 Introduction</b> .....	<b>595</b>
<b>14.2 Elementary Considerations</b> .....	<b>597</b>
14.2.1 Elementary Theory for a Pure Melt .....	597
14.2.2 Constitutional Supercooling .....	600
<b>14.3 Linear Stability Analysis</b> .....	<b>602</b>
14.3.1 Planar Interface .....	602
14.3.1.1 TSS Approximation .....	605
14.3.1.2 Experimental Tests of Morphological Stability .....	609
14.3.1.3 Long-Wavelength Perturbations .....	609
14.3.2 Spheres and Cylinders .....	611
14.3.2.1 Circular Cylinder .....	615
14.3.3 Paraboloids, Ellipsoids, and Other Shapes .....	616
<b>14.4 Extensions of the Mullins-Sekerka Analysis</b> .....	<b>616</b>
14.4.1 Rapid Solidification .....	617
14.4.2 Other Extensions .....	618
<b>14.5 Nonlinear Analysis</b> .....	<b>620</b>
14.5.1 Weakly Nonlinear Analysis .....	620
14.5.2 Other Nonlinear Topics .....	623
14.5.2.1 Sideband Instability of the Two-Dimensional Solution .....	623
14.5.2.2 Three-Dimensional Weakly Nonlinear Solutions .....	624
<b>14.6 Concluding Remarks</b> .....	<b>626</b>
<b>References</b> .....	<b>627</b>

## 14.1 Introduction

The phenomenon of morphological stability pertains to the stability of the shape of a crystal during growth. In particular, it pertains to the stability relative to some idealized shape, the so-called unperturbed shape that is based on a reasonable simplification or

idealization of the growth conditions. It can pertain to growth from the vapor or from solution, but in this article we will concentrate on growth from the melt by means of crystallization (solidification), which has been studied extensively.

A vast literature on this subject has developed since the original papers by Mullins and Sekerka [1,2] and Voronkov [3]. Although the phenomenon became well known to members of the metallurgy and crystal growth communities, where it was reviewed by Delves [4], the review article by Langer in 1980 [5] brought the subject to the attention of the physics community which introduced new quantitative methodologies. For example, see the reviews by Kessler et al. [6] and Caroli et al. [7].

The comprehensive article in the previous edition of the *Handbook of Crystal Growth* [8] by two of the current authors contains extensive references to this literature, including other review articles. In the present article, and in the spirit of writing for a handbook, we will begin by taking a more tutorial approach with the objective of acquainting the nonexpert reader with the basic aspects of the phenomenon. In later sections, we will present a more detailed analysis of some of the more important aspects. In many cases, however, we will not repeat the account given in [8]. In the final section, Concluding Remarks, we will give a brief discussion and references to closely related topics that space limitations have precluded.

The motivation for the theory of morphological stability comes from experiments involving unidirectional solidification of dilute alloys [9] in which the solid-liquid interface would ideally be planar but is observed to deviate, under certain conditions, from planarity on a scale of typically 10–100  $\mu\text{m}$ . In particular, rapid extraction of the liquid during the solidification process often reveals a cellular structure which could only have formed if the planar interface were unstable. In growth from a pure melt, instability might be expected if the melt is supercooled because a slight projection of the solid into the supercooled liquid would reach a colder region where solidification might take place more rapidly, thus enhancing its growth. Most experiments, however, were performed on binary alloys with a positive temperature gradient in the liquid at the solid-liquid interface. In that case, such instabilities were attributed to constitutional supercooling (CS) [10], according to which the liquid ahead of the solid was supercooled with due respect to its composition. This results because an alloy melt has a different freezing point than a pure melt. In castings, especially alloy castings, one frequently encounters dendritic growth which is a more extreme morphology that results subsequent to the onset of morphological instability.

The explanation of morphological instability on the basis of the idea of supercooling was attractive and tended to explain experimental results but suffers from the fact that it did not account for the dynamics of the solidification process, which would be expected to change as a shape perturbation attempted to grow preferentially. The theory of morphological instability, on the other hand, is based on a dynamic approach in which the equations that govern heat flow, and also diffusion in the case of an alloy, are solved simultaneously while allowing for a change of shape due to a perturbation.

## 14.2 Elementary Considerations

We first give a simplified analysis of the instability of a planar interface for unidirectional solidification of a pure melt. This will introduce the reader to the methodology of a perturbation analysis of stability in a simplified setting and prepare for the stability analyses of future sections for more complicated problems. For a binary alloy, it is found experimentally that the solid–liquid interface can be unstable even for a positive temperature gradient in the liquid. We shall, therefore, review the simple idea of CS, which suggests a reason for such instability.

### 14.2.1 Elementary Theory for a Pure Melt

We analyze the stability of a crystal that is growing at constant unidirectional velocity  $V$  from a pure melt [11,12] by means of unidirectional solidification, perhaps brought about by means of a traveling furnace and heat sink. The sample is assumed to be very long and initially has a planar interface located in the moving plane  $z=0$  located far from its ends. We suppose that a steady-state exists such that constant temperature gradients  $G_S$  and  $G_L$  are maintained in the solid and liquid just behind and ahead of the moving planar interface, where the temperature is at the melting point  $T_M$ .

The situation is assumed to be one dimensional, so conservation of energy requires

$$K_S G_S - K_L G_L = L_V V \quad (14.1)$$

where  $K_S$  and  $K_L$  are thermal conductivities of solid and liquid and  $L_V$  is the latent heat per unit volume. For simplicity, we assume that the solid and liquid have equal and constant densities and forbid fluid convection in the melt. This is the idealized unperturbed solution whose stability we shall examine.

We proceed to solve the problem for a slightly perturbed interface having features of very small amplitude. The amplitude will be assumed to be sufficiently small that we can describe an arbitrary perturbation by means of normal modes, so we proceed to examine a single Fourier component of spatial wavenumber  $\omega$ . Thus the perturbed interface shape is represented by

$$z = h(x, t) = \delta(t) \cos(\omega x) \quad (14.2)$$

where  $\delta(t)$  is a small amplitude whose dependence on time remains to be determined and  $x$  is a coordinate perpendicular to  $z$ . It suffices to consider only a two-dimensional problem in this linear analysis because a perturbation of the form  $\cos(\omega_x x) \cos(\omega_y y + \phi)$  gives the same results if  $\omega \rightarrow \sqrt{\omega_x^2 + \omega_y^2}$ , as shown in Section 14.3.1.

The perturbed temperature fields  $T_S$  and  $T_L$  depend on time and satisfy time-dependent equations. However, near the onset of instability, the perturbations are expected to evolve so slowly relative to heat conduction that the temperature fields relax rapidly to steady state solutions to Laplace's equation that evolve slowly with time.

This is known as the thermal steady-state (TSS) approximation, which is valid except for perturbations of long wavelength. The unperturbed temperature fields are, therefore, given by the equations

$$T_S^{(0)} = T_M + G_S z, \quad z < 0; \quad T_L^{(0)} = T_M + G_L z, \quad z > 0 \quad (14.3)$$

and the perturbed temperatures can be taken in the form

$$T_S = T_S^{(0)} + T_S^{(1)}, \quad \text{solid}; \quad T_L = T_L^{(0)} + T_L^{(1)}, \quad \text{liquid} \quad (14.4)$$

where

$$T_S^{(1)} = A_S(t) \exp(\omega z) \cos(\omega x); \quad T_L^{(1)} = A_L(t) \exp(-\omega z) \cos(\omega x). \quad (14.5)$$

It is readily evident that the expressions in Eqn (14.5) satisfy  $\nabla^2 T_{S,L} = 0$  and decay to zero far from the interface; whereas, the amplitudes  $A_S(t)$  and  $A_L(t)$  will be determined by satisfying the boundary conditions at the interface.

At the perturbed interface, the temperature fields must be continuous and assumed to equal the temperature  $T_I(x, t)$  of that interface determined by thermodynamic considerations. Thus

$$T_S(x, h(x, t), t) = T_L(x, h(x, t), t) = T_I(x, t). \quad (14.6)$$

The temperature  $T_I(x, t)$  is given by the Gibbs–Thomson equation

$$T_I = T_M - T_M \Gamma \mathcal{K} \quad (14.7)$$

where  $\mathcal{K}$  is the interface mean curvature and  $\Gamma = \gamma/L_V$  is a capillarity length, where  $\gamma$  is the solid–liquid interfacial free energy. For our small amplitude perturbation,

$$\mathcal{K} \approx -\partial^2 h / \partial x^2 = \delta(t) \omega^2 \cos(\omega x). \quad (14.8)$$

Equation (14.6) is to be expanded to terms linear in  $h$ , which gives

$$A_S = -\delta(t)(G_S + T_M \Gamma \omega^2); \quad A_L = -\delta(t)(G_L + T_M \Gamma \omega^2). \quad (14.9)$$

The remaining boundary condition for conservation of energy at the interface can be written for perturbations of small amplitude in the form

$$L_V \left( V + \frac{\partial h}{\partial t} \right) = K_S \left( \frac{\partial T_S}{\partial z} \right)_{z=h} - K_L \left( \frac{\partial T_L}{\partial z} \right)_{z=h}, \quad (14.10)$$

where it is to be understood that the right-hand side is to be expanded to terms linear in  $h$ , consistent with former small amplitude approximations. It therefore becomes

$$L_V (V + \dot{\delta} \cos(\omega x)) = K_S (G_S + \omega A_S \cos(\omega x)) - K_L (G_L - \omega A_L \cos(\omega x)), \quad (14.11)$$

where  $\dot{\delta} = d\delta/dt$ . After simplification by using Eqn (14.1), Eqn (14.11) can be solved to give

$$\frac{\dot{\delta}}{\delta} = \frac{(K_S + K_L)}{L_V} \omega \left[ -G^* - T_M \Gamma \omega^2 \right] \quad (14.12)$$

where

$$G^* = \frac{K_S G_S + K_L G_L}{K_S + K_L} \quad (14.13)$$

is a conductivity-weighted average temperature gradient.

Equation (14.12) is a differential equation for the perturbation amplitude  $\delta(t)$  and determines whether the planar interface is stable or unstable. The left-hand side is the fractional rate of change of amplitude with time which increases with time for any values of  $\omega$  for which the right-hand side is positive. The right-hand side is sketched in Figure 14.1 as a function of  $\omega$ . It will be positive for a band of wavenumbers  $\lambda = 2\pi/\omega$  whenever

$$G^* < 0; \quad \text{instability} \quad (14.14)$$

and all wavenumbers will be stable if  $G^* > 0$ . In view of Eqn (14.1), we see that instability occurs whenever more of the latent heat is extracted into the liquid, as opposed to the solid. If Eqn (14.1) is used, Eqn (14.14) takes the form  $G_L < -LV/2K_L$ , so a sufficiently negative gradient in the liquid is required for instability. Provided that  $G^* < 0$ , we see that perturbations having wavenumber  $\omega < \omega_{00} = [-G^*/(T_M \Gamma)]^{1/2}$  are unstable and of those, the fastest growing will have wavenumber  $\omega_0 = \omega_{00}/\sqrt{3}$ , which corresponds to the maximum of curve *b* in Figure 14.1.

The previous simple analysis illustrates correctly that capillarity (the term in  $\Gamma$  in Eqn (14.12)) is always stabilizing, whereas the temperature gradient term involving  $G^*$  will be destabilizing if negative. For a given value of the right-hand side of Eqn (14.12), we see that  $\delta$  changes exponentially with time. If  $\delta$  increases exponentially with time, it will soon become so large that our linearization for small  $\delta$  will become invalid, so all that we are able to say is that the interface starts to become unstable, but then other things will happen because nonlinearities become important. It might continue to become unstable in a more complex way (e.g., dendritic growth) or stabilize into a cellular structure, all of which is beyond the scope of linear stability theory.

The present analysis breaks down for sufficiently small  $\omega$  which corresponds to very large wavelengths. For example, if a sample has a cross-sectional width  $W$ , wavelengths are essentially limited to  $\lambda < W$  which corresponds to  $\omega > W/2\pi$ . Moreover, the TSS approximation breaks down for sufficiently long wavelengths because the propagation

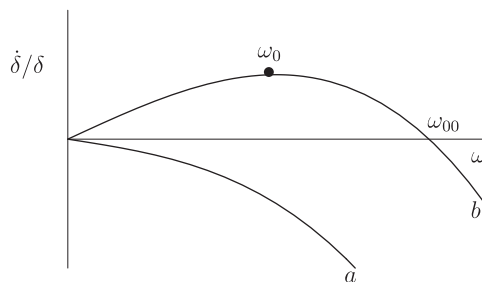


FIGURE 14.1 Sketch of Eqn (14.12) as a function of  $\omega$ . If  $\dot{\delta}/\delta$  is positive for any value of  $\omega$ , the interface is unstable to perturbations of that wavenumber. Curve *a* is for  $G^* > 0$ , stability, while curve *b* is for  $G^* < 0$ , instability.  $\omega_{00}$  is the wavenumber for marginal stability and  $\omega_0$  is the wavenumber of the fastest growing perturbation.

time for heat to diffuse over a distance  $\lambda$  is roughly  $t \sim \lambda^2/\kappa$  where  $\kappa$  is a thermal diffusivity. An improved analysis given in Section 14.3.1.3 shows that perturbations with very small  $\omega$  are stable if  $G^* > 0$  and explores conditions for which all perturbations are stable even for  $G^*$  slightly negative.

## 14.2.2 Constitutional Supercooling

Prior to the development of morphological stability theory, the instability of a planar interface during unidirectional solidification of a dilute binary alloy was explained by appealing to the concept of CS [10]. This concept is based on a steady-state solution in a moving reference frame for the solute profile in the liquid ahead of a planar solid–liquid interface that moves with constant velocity  $V$  in the  $z$  direction. For a steady state in a frame of reference that moves with velocity  $V$ , the concentration  $c(z)$  of solute in the liquid is governed by the equation

$$\frac{\partial^2 c}{\partial z^2} + \frac{V}{D_L} \frac{\partial c}{\partial z} = 0 \quad (14.15)$$

where  $D_L$  is the diffusivity in the liquid, assumed to be constant for simplicity. Diffusion in the solid is ignored because the solid diffusivity is several orders of magnitude smaller than  $D_L$ . The boundary conditions are  $c(0) = C_L$  at the solid–liquid interface and  $c = C_\infty$  far into the liquid, as  $z \rightarrow \infty$ . To achieve a steady state, the concentration in the solid must also be  $C_\infty$ . It is assumed that the alloy is dilute, so the liquidus and solidus lines of the phase diagram are straight lines. The liquidus line has a slope  $m$ , and the solidus line has a slope  $m/k$  where  $k$  is a constant known as the distribution coefficient. These lines meet at the melting point  $T_M$  of the pure solvent. There are two possible cases,  $k < 1$  and  $k > 1$ , as illustrated by the phase diagrams in Figure 14.2. The sign convention is such that  $m(k - 1) > 0$ .

During solidification, local equilibrium at that interface is assumed, so  $C_\infty = kC_L$ . Thus, the solution of Eqn (14.15), subject to the aforementioned boundary conditions, is

$$c = C_\infty \frac{1 - k}{k} \exp(-Vz/D_L) + C_\infty. \quad (14.16)$$

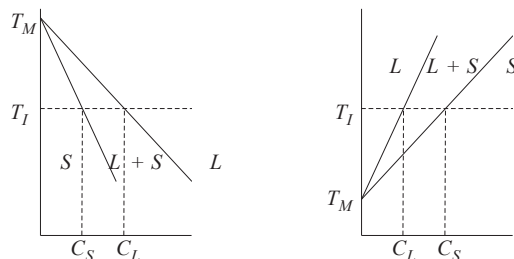


**FIGURE 14.2** Portions of idealized phase diagrams for dilute binary alloys. On the left,  $k < 1$  and  $m < 0$  and on the right  $k > 1$  and  $m > 0$ . In both cases,  $C_S = kC_L$ ,  $m(k - 1) > 0$ , and the solid–liquid interface temperature is  $T_I = T_M + mC_L = T_M + mC_S/k$ .

For  $k < 1$ , solute is rejected on freezing and builds up in a boundary layer ahead of the interface; whereas, if  $k > 1$ , solute is preferentially incorporated on freezing, so there is a depleted zone in a boundary layer ahead of the interface. The thickness of the boundary layer is roughly  $D_L/V$ . The temperature at the interface is  $T_I = T_M + mC_\infty/k$ . The temperature in the liquid is given by

$$T_L = T_M + mC_\infty/k + G_L z \quad (14.17)$$

whereas, the freezing point of the liquid ahead of the interface would be given by

$$T_F = T_M + mc = T_M + mC_\infty/k + m(k-1)(C_\infty/k)[1 - \exp(-Vz/D_L)], \quad (14.18)$$

which is sketched in [Figure 14.3](#). Recalling  $m(k-1) > 0$ , we see for  $z = 0$  that  $T_L = T_F$  as expected, but for  $z > 0$ , the liquid ahead of the interface will never be supercooled if  $G_L > (dT_F/dz)_{z=0}$ , so stability of the planar interface might be expected. On the other hand, there will be a zone of supercooled liquid if  $G_L < (dT_F/dz)_{z=0}$  and instability might be expected. We note that

$$\left(\frac{dT_F}{dz}\right)_{z=0} = m\left(\frac{dc}{dz}\right)_{z=0} \equiv mG_c = m\frac{k-1}{k}C_\infty\frac{V}{D_L} \quad (14.19)$$

This leads to the CS criterion

$$G_L > mG_c \quad \text{stability}; \quad G_L < mG_c \quad \text{instability}. \quad (14.20)$$

Note that the quantity  $mG_c$  is always positive, irrespective of whether  $k < 1$  or  $k > 1$ . To analyze experiments, one typically plots  $G_L/V$  versus  $C_\infty$  which is a straight line that passes through the origin and divides stable (large  $G_L/V$ ) from unstable regions, as shown in [Figure 14.4](#).

For typically slow crystal growth speeds, the CS criterion is roughly in agreement with experiments, considering the uncertainty of material parameters, especially  $D_L$ . Nevertheless, it is based on a comparison of temperatures before any instability takes place. We know that any perturbation that grows must release latent heat and that heat can also be conducted into the solid. Moreover, the CS criterion does not account for any stabilization due to capillarity, which essentially arises because the nonplanar interface

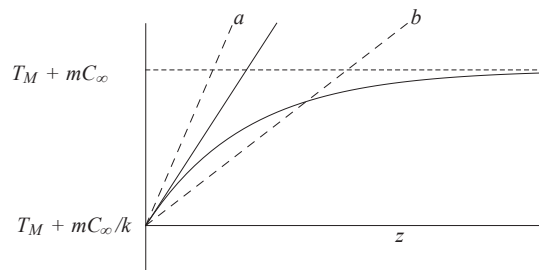


**FIGURE 14.3** Graph of temperature versus  $z$  to illustrate constitutional supercooling. The curved line is the freezing temperature  $T_F$  given by [Eqn \(14.18\)](#). The three sloping lines are possible actual temperatures with gradients  $G_L$ . Line  $a$  is for large  $G_L$  and is greater than  $T_F$ , while line  $b$  is for small  $G_L$  and cuts below  $T_F$ , resulting in a zone of liquid that is supercooled with due respect to its composition. The full line corresponds to the critical gradient for which the initial slopes are the same.

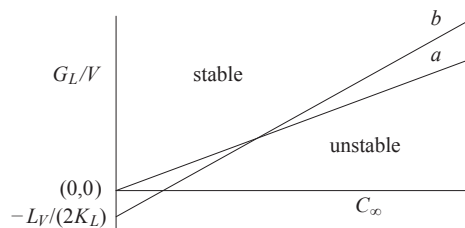


**FIGURE 14.4** Comparison of the constitutional supercooling (CS) criterion (line *a*) with the modified CS criterion (line *b*) corresponding to Eqn (14.46) below, illustrated for  $K_S = 2K_L$  and  $m' = m$ . Because of a finite latent heat, the modified CS line does not pass through the origin. Experiments are unlikely to distinguish between these two criteria unless very good materials property data are available.

will have a larger surface free energy. These are the main things that morphological stability theory seeks to correct by providing a criterion based on the dynamics of perturbation growth.

## 14.3 Linear Stability Analysis

We now turn to a systematic application of linear stability analysis for various geometries. First we treat the linear stability of a planar interface and then go on to explore other shapes such as spheres and cylinders.

### 14.3.1 Planar Interface

We first discuss the morphological stability of a planar interface during the directional solidification of a binary alloy, essentially following the original work of Mullins and Sekerka [2]. Then we discuss various extensions of that work.

For the analysis that follows immediately, we shall employ a frame of reference that moves in the  $z$  direction with constant velocity  $V$  along with the unperturbed planar interface that will be analyzed for stability. The temperature fields in the melt ( $L$ , liquid) and the crystal ( $S$ , solid) are governed by the equations

$$\nabla^2 T_L + \frac{V}{\kappa_L} \frac{\partial T_L}{\partial z} = \frac{1}{\kappa_L} \frac{\partial T_L}{\partial t}; \quad \nabla^2 T_S + \frac{V}{\kappa_S} \frac{\partial T_S}{\partial z} = \frac{1}{\kappa_S} \frac{\partial T_S}{\partial t}, \quad (14.21)$$

where  $\kappa_L$  and  $\kappa_S$  are thermal diffusivities, assumed to be constant and isotropic. Isotropy is only valid for cubic crystals. The concentrations in the liquid and solid are governed by

$$\nabla^2 c_L + \frac{V}{D_L} \frac{\partial c_L}{\partial z} = \frac{1}{D_L} \frac{\partial c_L}{\partial t}; \quad \nabla^2 c_S + \frac{V}{D_S} \frac{\partial c_S}{\partial z} = \frac{1}{D_S} \frac{\partial c_S}{\partial t}, \quad (14.22)$$

where  $D_L$  and  $D_S$  are solute diffusivities, also assumed to be constant and isotropic. We also forbid convection in the melt and assume that the densities of solid and liquid are the same and uniform. Relaxation of some of these assumptions will be discussed later. Typically,  $D_S \ll D_L$ , so we will ignore diffusion in the solid unless otherwise specified.

The unperturbed fields pertain to a steady state in the moving frame of reference, in which case the time derivatives on the right-hand sides of Eqn (14.21) and Eqn (14.22) are zero. Since we are interested in perturbing a steady-state solution and seek to understand the onset of instability, we expect the perturbations to evolve so slowly that the temperature and solute fields will relax rapidly to steady state fields that evolve slowly with time. Thus, one can make the quasi-steady-state (QSS) approximation by setting the right-hand sides to zero, even for the perturbed fields. Since we know from the CS analysis that the relevant length scale of the solute boundary layer is  $D_L/V$ , we observe that  $V/\kappa_{L,S} = (V/D_L)(D_L/\kappa_{L,S})$ . But typically,  $D_L/\kappa_{L,S} \ll 1$ . Thus, the thermal fields can be assumed to obey Laplace's equation,  $\nabla^2 T_L = 0$  and  $\nabla^2 T_S = 0$ , which we call the TSS approximation. These approximations were made in the original work of Mullins and Sekerka but here we proceed at first in more generality [13,14].

Boundary conditions at the solid–liquid interface are

$$(\mathbf{v} \cdot \hat{\mathbf{n}})L_V = (K_S \nabla T_S - K_L \nabla T_L) \cdot \hat{\mathbf{n}} \quad (14.23)$$

for conservation of energy, and

$$(\mathbf{v} \cdot \hat{\mathbf{n}})(c_L - c_S) = -D_L \nabla c_L \cdot \hat{\mathbf{n}} \quad (14.24)$$

for the conservation of solute.  $\hat{\mathbf{n}}$  is a unit vector normal to the interface and pointing into the liquid. The interface temperature is given by a modification of Eqn (14.7) to account for the presence of solute and takes the form

$$T_L = T_S = T_M + g(c_L) - T_M \Gamma \mathcal{K} \equiv T_e \quad (14.25)$$

where  $T_E = T_M + g(c_L)$  is the equation of the liquidus line of the phase diagram. The quantity  $T_e = T_E - T_M \Gamma \mathcal{K}$  is the local equilibrium temperature of a curved interface, and the solidus is given by  $c_S = k(c_L)c_L$  [14]. This is a little more general than used in Section 14.2.2 where  $g(c_L) = mc_L$  where  $m$  is a constant and  $k(c_L)$  is also a constant. Instead of the constants  $m$  and  $k$ , the linearized equations will depend on parameters  $m' = (dg/dc_L)_{c_L^0}$  and  $k' = (d[k(c_L)c_L]/dc_L)_{c_L^0} = [k + c_L(dk/dc_L)]_{c_L^0}$ , where  $c_L^0(0)$  denotes the liquid concentration at the planar interface. For simplicity hereafter, we use the symbol  $k$  to denote the value  $k(c_L^0(0))$  which results in  $c_L^0(0) = C_\infty/k$  as in our treatment of CS as well as the treatment of Mullins and Sekerka.

To do a linear stability theory, we can take the interface shape to be of the form

$$z = h(x, y, t) = \delta_0 \exp[\sigma t + i(\omega_x x + \omega_y y)] \quad (14.26)$$

where we employ complex variables to represent sinusoidal perturbations with the understanding that we can ultimately take the real part. Here,  $\delta_0 \exp(\sigma t)$  plays the role of the amplitude  $\delta(t)$  in Eqn (14.2). We recall from Eqn (14.12) that  $\delta(t)$  evolves exponentially with time. Here, we allow for the possibility that  $\sigma$  could have an imaginary part in which case one could have the more general possibility of oscillations in time with an exponential amplitude factor. In that case, the criterion for stability would require the real part of  $\sigma$  to be negative.

To proceed, it is necessary to linearize all boundary conditions in  $h$ . The fields are sums of an unperturbed part and a perturbed part, specifically  $T_L = T_L^0(z) + T_L^1(z)h$ ,  $T_S = T_S^0(z) + T_S^1(z)h$  and  $c_L = c_L^0(z) + c_L^1(z)h$ . The linearized mean curvature is  $\mathcal{K} = -\nabla^2 h = \omega^2 h$ , where  $\omega^2 = \omega_x^2 + \omega_y^2$ , so  $x$  and  $y$  are not distinguished because of the assumption of isotropy of the interfacial free energy. If we set  $f(x, y, z, t) = z - Vt - h(x, y, t)$  we find that  $\hat{\mathbf{n}} = \nabla f / |\nabla f|$ , and  $\mathbf{v} \cdot \hat{\mathbf{n}} = -\partial f / \partial t / |\nabla f|$  which can be inserted in Eqn (14.23) and Eqn (14.24) to give

$$L_V(V + \sigma h) = \left\{ K_S \frac{\partial [T_S^0(z) + T_S^1(z)h]}{\partial z} - K_L \frac{\partial [T_L^0(z) + T_L^1(z)h]}{\partial z} \right\}_{z=h} \quad (14.27)$$

and

$$(c_L - c_S)_{z=h}(V + \sigma h) = - \left\{ D_L \frac{\partial [c_L^0(z) + c_L^1(z)h]}{\partial z} \right\}_{z=h} \quad (14.28)$$

The interface temperature is given by

$$[T_L^0(z) + T_L^1(z)h]_{z=h} = [T_S^0(z) + T_S^1(z)h]_{z=h} = T_M + g(c_L^0)_{z=h} + m'c_L^1 h - T_M \Gamma \omega^2 h. \quad (14.29)$$

After evaluation at  $z = h$ , further linearization in  $h$  and subtraction of the unperturbed parts, the factors of  $h$  all cancel from Eqns (14.27)–(14.29).

By solving Eqn (14.21) for  $T_S$  and  $T_L$  and Eqn (14.22) for  $c_L$  subject to the linearized boundary conditions, one obtains the dispersion relation given by equation 36 of [8], namely

$$\sigma = \left\{ -\frac{K_L G_L}{2\bar{K}\bar{\alpha}} \left( \alpha_L - \frac{V}{K_L} \right) - \frac{K_S G_S}{2\bar{K}\bar{\alpha}} \left( \alpha_S + \frac{V}{K_S} \right) - T_M \Gamma \omega^2 + m' G_c \frac{\alpha - V/D_L}{\alpha - p'V/D_L} \right\} \times \left\{ \frac{L_V}{2\bar{K}\bar{\alpha}} + \frac{m' G_c}{V(\alpha - p'V/D_L)} \right\}^{-1}, \quad (14.30)$$

where

$$\alpha = \left( V/2D_L \right) + \left[ (V/2D_L)^2 + \omega^2 + \sigma/D_L \right]^{1/2} \quad (14.31)$$

$$\alpha_L = \left( V/2\kappa_L \right) + \left[ (V/2\kappa_L)^2 + \omega^2 + \sigma/\kappa_L \right]^{1/2} \quad (14.32)$$

$$\alpha_S = - \left( V/2\kappa_S \right) + \left[ (V/2\kappa_S)^2 + \omega^2 + \sigma/\kappa_S \right]^{1/2} \quad (14.33)$$

$$\bar{\alpha} = (K_S \alpha_S + K_L \alpha_L) / (2\bar{K}); \quad \bar{K} = (K_S + K_L) / 2 \quad (14.34)$$

$$m' = (dg/dc_L)_{C_\infty/k}; \quad k' = k + (C_\infty/k)(dk/dc_L)_{C_\infty/k}; \quad p' = 1 - k' \quad (14.35)$$

Equation (14.30) is a rather complicated equation for  $\sigma$ , which also occurs in many places on its right-hand side. It is likely to have many roots, including complex roots

$\sigma = \sigma_r + i\sigma_i$  which would correspond to solutions that oscillate with time. Its analysis can be simplified considerably if we somehow know that  $\sigma_i = 0$  at the onset of instability where  $\sigma_r = 0$ . In other words,  $\sigma = 0$  at the onset of instability, which is known as the principle of exchange of stabilities. By means of an analysis based on the Laplace transform [13], the exchange of stabilities has been shown to hold in the steady-state approximation for the thermal fields (TSS), i.e.,  $\kappa_S$  and  $\kappa_L$  are infinite. In the same approximation, exchange of stabilities was demonstrated explicitly for this problem by Wollkind and Segel [15] for vanishing latent heat. It has also been shown that there are no unstable oscillatory modes if either the thermal properties of solid and liquid are equal or if the TSS approximation is valid [16]. See Ref. [7] for an extended discussion.

#### 14.3.1.1 TSS Approximation

We proceed to make the TSS approximation, in which case  $\alpha_L = \alpha_S = \bar{\alpha} = \sqrt{\omega^2} = |\omega|$  and Eqn (14.30) becomes

$$\sigma = \mathcal{N}(\omega^2, \sigma) \left\{ \frac{L_V}{2\bar{\kappa}|\omega|} + \frac{m'G_c}{V(\alpha - p'V/D_L)} \right\}^{-1}, \quad (14.36)$$

where the numerator

$$\mathcal{N}(\omega^2, \sigma) = \left\{ -G^* - T_M\Gamma\omega^2 + m'G_c \frac{\alpha - V/D_L}{\alpha - p'V/D_L} \right\}. \quad (14.37)$$

In Eqn (14.37),  $G^*$  and  $G_c$  are the same as given by Eqn (14.13) and (14.19). The quantity  $\alpha$  still depends on  $\sigma$ , so  $c_L$  is still a solution to the full time-dependent Eqn (14.22). But in this case, we know that we have an exchange of stabilities, so at the onset of instability where  $\sigma = 0$ ,  $\alpha$  becomes  $\alpha_0 = (V/2D_L) + [(V/2D_L)^2 + \omega^2]^{1/2}$ . This is the result one would get if  $\partial c_L / \partial t = 0$  in Eqn (14.22) and amounts to the QSS approximation for  $c_L$ , which was made in the original work by Mullins and Sekerka. In that approximation, Eqn (14.36) is already solved for  $\sigma$  as a function of  $\omega$  and can be replaced by  $\hat{\delta}/\delta$  where  $\delta(t)$  is the interface amplitude that evolves exponentially.

It turns out that the onset of instability is the same, whether or not one makes the QSS approximation. This occurs because the denominator in Eqn (14.36) is positive provided that  $k' > 0$ , which will be true unless there is retrograde solubility, a possibility that has been treated [16], but one that we eliminate here. Therefore, at the onset of instability, we need

$$0 = \mathcal{N}(\omega^2, 0) = \left\{ -G^* - T_M\Gamma\omega^2 + m'G_c \frac{\alpha_0 - V/D_L}{\alpha_0 - p'V/D_L} \right\}. \quad (14.38)$$

Equation (14.38) is the same as analyzed by Mullins and Sekerka provided that  $m' = m$  and  $p' = 1 - k$  are constants corresponding to a phase diagram having straight lines for the solidus and liquidus. For  $G^* > 0$ , which would insure stability for a pure melt, analysis shows that  $\mathcal{N}(\omega^2, 0)$  begins at  $-G^*$  and either decays to  $-\infty$  as  $\omega^2$  increases or rises to a

simple maximum and then decays to  $-\infty$  as  $\omega^2$  increases. The division between these two behaviors can be found by studying the derivative

$$\frac{\partial \mathcal{N}(\omega^2, 0)}{\partial \omega^2} = -T_M \Gamma + \frac{k' V m' G_c}{2D_L} \left\{ \omega^2 + (V/2D_L)^2 \right\}^{-1/2} \{ \alpha_0 - p' V / D_L \}^{-2}. \quad (14.39)$$

This is a monotonically decreasing function of  $\omega^2$  whose value at  $\omega^2 = 0$  is given by

$$\left. \frac{\partial \mathcal{N}(\omega^2, 0)}{\partial \omega^2} \right|_{\omega^2=0} = \frac{m' G_c D_L^2}{k' V^2} (1 - \mathcal{A}); \quad \mathcal{A} = \frac{k' T_M \Gamma V^2}{m' G_c D_L^2}. \quad (14.40)$$

Thus for  $\mathcal{A} > 1$ , we see that  $\partial \mathcal{N}(\omega^2, 0) / \partial \omega^2$  begins at a negative value and continues to decrease as  $\omega^2$  increases, which means that  $\mathcal{N}(\omega^2, 0)$  begins at the negative value  $-G^*$  and decreases as  $\omega^2$  increases. Consequently, for  $\mathcal{A} > 1$ ,  $\mathcal{N}(\omega^2, 0)$  is always negative so Eqn (14.38) can not be satisfied and the planar interface is stable. This stabilization is due to strong capillarity and was called absolute stability by Mullins and Sekerka. It becomes important at large  $V$  that corresponds to small values of the characteristic length scale  $D_L / V$ .

For  $\mathcal{A} < 1$ ,  $\partial \mathcal{N}(\omega^2, 0) / \partial \omega^2$  begins at a positive value and continues to decrease to negative values as  $\omega^2$  increases. This means that  $\mathcal{N}(\omega^2, 0)$  increases from its initial value  $-G^*$ , passes through a maximum and then continues to decrease. When this maximum has the value zero, Eqn (14.38) can be satisfied. Therefore, the onset of instability occurs whenever

$$\mathcal{N}(\omega^2, 0) = 0 \quad \text{and} \quad \frac{\partial \mathcal{N}(\omega^2, 0)}{\partial \omega^2} = 0. \quad (14.41)$$

The roots of  $\partial \mathcal{N}(\omega^2, 0) / \partial \omega^2 = 0$  can be found by introducing the variable  $r = [1 + (2D_L \omega / V)^2]^{1/4}$  and solving the cubic equation [17]

$$r^3 + (2k' - 1)r - 2k' / \mathcal{A}^{1/2} = 0. \quad (14.42)$$

By graphical methods, it is easy to see that Eqn (14.42) has only one real positive root greater than one, which we designate by  $r_{cr}(\mathcal{A}, k')$ . This root can be substituted into Eqn (14.38) to get

$$\frac{G^*}{m' G_c} = 1 - 3\mathcal{A}^{1/2} r_{cr} + [1 - (1 - 2k') r_{cr}^2] \mathcal{A} / 4k' \equiv \mathcal{S}(\mathcal{A}, k'). \quad (14.43)$$

The stability function  $0 < \mathcal{S}(\mathcal{A}, k') < 1$  and has been evaluated numerically; see Ref. [11,17] for graphs of  $\mathcal{S}(\mathcal{A}, k')$  versus  $\mathcal{A}$  for various values of  $k'$ . The criterion for stability is therefore

$$\frac{G^*}{m' G_c} > \mathcal{S}(\mathcal{A}, k'). \quad (14.44)$$

For small velocities,  $\mathcal{A} \ll 1$  and  $\mathcal{S}(\mathcal{A}, k') \approx 1$ , so

$$\frac{G^*}{m' G_c} > 1; \quad \text{stability, modified CS} \quad (14.45)$$

which is known as the modified CS criterion. It resembles Eqn (14.20) except the conductivity-weighted gradient  $G^*$  replaces  $G_L$ . In terms of  $G_L$  it becomes

$$\frac{G_L}{V} > \frac{L_V}{2K_L} + \frac{K_L + K_S}{2K_L} \frac{m'(k-1)}{D_L k} c_\infty; \quad \text{stability, modified CS.} \quad (14.46)$$

This becomes the CS criterion if we set  $L_V = 0$ ,  $K_S = K_L$  and  $m' = m$ . The two criteria are sketched in Figure 14.4.

For larger velocities, the function  $S(\mathcal{A}, k')$  can be quite small, resulting in considerable stabilization due to capillarity (interfacial free energy) effects. The typical behavior can be illustrated by taking  $k' = 1/2$  which allows a simple solution of the cubic Eqn (14.42), namely  $r = \mathcal{A}^{-1/6}$ . The corresponding critical value of  $\omega$  and its associated wavelength are given by

$$\omega_{cr} = \frac{V}{2D_L} \frac{(1 - \mathcal{A}^{2/3})^{1/2}}{\mathcal{A}^{1/3}}; \quad \lambda_{cr} = 4\pi \frac{D_L}{V} \frac{\mathcal{A}^{1/3}}{(1 - \mathcal{A}^{2/3})^{1/2}} = \frac{\lambda_0}{\mathcal{A}^{2/3}(1 - \mathcal{A}^{2/3})^{1/2}}, \quad (14.47)$$

where  $\lambda_0 = 2\pi\Gamma T_M / (-mC_\infty)$ . The stability function becomes simply

$$S(\mathcal{A}, 1/2) = 1 - (3/2)\mathcal{A}^{1/2} + (1/2)\mathcal{A}. \quad (14.48)$$

Figure 14.5 shows plots of the wavelength  $\lambda_{cr}/\lambda_0$  and the stability function  $S(\mathcal{A}, 1/2)$  versus  $\log_{10}\mathcal{A}$ . For  $\mathcal{A} \ll 1$ , we observe that  $S(\mathcal{A}, 1/2) \approx 1$ , which is the region where the modified CS criterion is applicable and  $\lambda_{cr}/\lambda_0 \approx \mathcal{A}^{-2/3} \propto (D_L/V)^{2/3}$ . As  $\mathcal{A}$  increases to larger values,  $\lambda_{cr}/\lambda_0$  decreases, capillarity (interfacial free energy) becomes an important stabilizing factor, and  $S(\mathcal{A}, 1/2)$  decreases toward zero, which is the threshold of absolute stability for positive  $G^*$ .

The general behavior of the stability criterion can be illustrated in terms of the control parameters  $C_\infty$ ,  $V$ , and  $G_L$  by the log-log plots in Figure 14.6. To make such a plot, one can introduce reference values  $C_0 = kL_V D_L / [(K_S + K_L)m'(k-1)]$ ,  $V_0 = L_V D_L^2 / [k'T_M \Gamma(K_S + K_L)]$ , and  $G_0 = (D_L L_V)^2 / [2k'K_L(K_S + K_L)T_M \Gamma]$ . Then we can

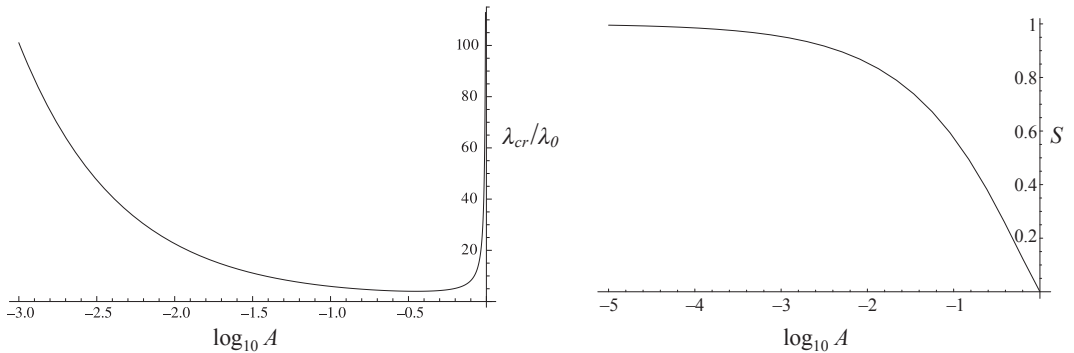
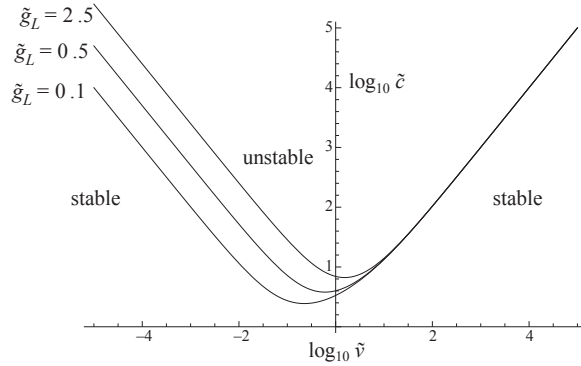


FIGURE 14.5 Plots of the critical wavelength  $\lambda_{cr}$  for instability from Eqn (14.47) and the function  $S$  from Eqn (14.48) as functions of  $\log_{10}\mathcal{A}$  for  $k' = 1/2$ . For  $\mathcal{A} \rightarrow 1$ ,  $\lambda_{cr} \rightarrow \infty$  rapidly as absolute stability sets in. For small  $\mathcal{A}$ ,  $\lambda_{cr}$  becomes proportional to  $(D_L/V)^{2/3}$ .



**FIGURE 14.6** Log–log plot for  $k' = 1/2$  of the critical dimensionless concentration,  $\tilde{c} = C_\infty/C_0$ , versus dimensionless velocity  $\tilde{v} = V/V_0$  at three values of the dimensionless temperature gradient in the liquid,  $\tilde{g}_L = G_L/G_0$ . The quantities  $C_0$ ,  $V_0$ , and  $G_0$  are given in the text for general  $k'$ . For  $\tilde{v} \ll 1$  and  $\tilde{c} \gg 1$ , the curves depend on  $\tilde{g}_L$  and are nearly straight lines with slope  $-1$ . They would be given approximately by the modified CS criterion, Eqn (14.46), which in these units is  $\tilde{g}_L/\tilde{v} = \tilde{c} - 1$ . For large  $\tilde{v}$ , the curves merge, capillary stabilization comes into play, and stabilization becomes possible for large values of  $\tilde{c}$  along the line  $\tilde{v} = \tilde{c}$  which corresponds to  $\mathcal{A} = 1$ , the threshold for absolute stability. For a fixed value of  $\tilde{c}$  above the minimum of a curve, the interface first becomes unstable with increasing  $\tilde{v}$  and then restabilizes for sufficiently large  $\tilde{v}$ .

introduce dimensionless variables  $\tilde{v} = V/V_0$ ,  $\tilde{c} = C_\infty/C_0$ , and  $\tilde{g}_L = G_L/G_0$  which allows the stability criterion to be written in the form

$$\tilde{g}_L + \tilde{v} = \tilde{v}\tilde{c}S(\mathcal{A}, k'); \quad \mathcal{A} = \tilde{v}/\tilde{c}. \quad (14.49)$$

For  $k' = 1/2$ , we can insert the value of  $S(\mathcal{A}, 1/2)$  from Eqn (14.48) to obtain a quadratic equation for  $\tilde{c}^{1/2}$  which can be solved to give

$$\tilde{c}^{1/2} = (3/4)\tilde{v}^{1/2} + \sqrt{(1/16)\tilde{v} + \tilde{g}_L/\tilde{v} + 1}. \quad (14.50)$$

For small  $\tilde{v}$  and large  $\tilde{c}$ , the lines in Figure 14.6 depend on the temperature gradient  $\tilde{g}_L$  and are nearly straight with a slope of  $-1$ . This is the region where the modified CS criterion, Eqn (14.46), applies approximately. In this region,  $\mathcal{A} = \tilde{v}/\tilde{c} \ll 1$ , so  $S \sim 1$  and  $\tilde{g}_L/\tilde{v} \sim \tilde{c} - 1$ . For large values of  $\tilde{v}$ , there is stabilization because of capillarity (interfacial free energy) and the lines coalesce into a single line, practically independent of  $\tilde{g}_L$ . That single line is given approximately by  $\tilde{c} = \tilde{v}$  which corresponds to  $\mathcal{A} = 1$ , which is the onset of absolute stability.

Incidentally, if the parameter  $G^*$  rather than  $G_L$  is used, one can make a similar plot in terms of the dimensionless parameter  $\tilde{g}^* = G^*/[2K_L G_0/(K_S + K_L)]$ . In that case, again for  $k' = 1/2$ ,  $\tilde{c}^{1/2} = (3/4)\tilde{v}^{1/2} + \sqrt{(1/16)\tilde{v} + \tilde{g}^*/\tilde{v}}$ . Now for  $\tilde{v}/\tilde{c} \ll 1$ , the curves will asymptote  $\tilde{g}^*/\tilde{v} = \tilde{c}$ .

A plot similar to Figure 14.6, but in terms of dimensional variables, is given by Coriell and McFadden [8] in their figure 3 for a germanium–silicon alloy for a temperature gradient in the liquid of 50 K/cm. They also give some analytic sufficient conditions for stability for general values of  $\mathcal{A}$  and  $k'$ .

### 14.3.1.2 Experimental Tests of Morphological Stability

The directional solidification of tin-bismuth alloys were carried out on the United States Microgravity Payload space flights USMP1 and USMP3 by using the Mephisto Bridgman furnace [18]. A comparison of the experimental results for the onset of instability with the CS and morphological stability criterion was made. Since the experiments were carried out in space, convective effects were greatly reduced. For the alloys with atomic fractions of 0.58% and 1.6%, the experimental velocities for the onset of instability were stated to be  $6.2 \pm 0.4 \mu\text{m/s}$  and  $2.25 \pm 0.1 \mu\text{m/s}$ , respectively (in terms of total uncertainties). The morphological stability criterion yields 6.8 and  $2.35 \mu\text{m/s}$ , respectively, in agreement with the experimental results. The corresponding CS criterion gives 10 and  $3.45 \mu\text{m/s}$ , respectively. For the low velocities used in these experiments, the surface tension terms in the morphological stability criterion are unimportant, and the theories differ because the conductivity-weighted temperature gradient replaces the liquid temperature gradient. An extensive discussion of the accuracy of the values of the thermophysical properties of tin-bismuth alloys was given.

### 14.3.1.3 Long-Wavelength Perturbations

As pointed out by Coriell and McFadden [8], the TSS approximation is not valid for perturbations of long wavelength which correspond to  $\omega^2$  at or near zero. This occurs because  $(V/2\kappa_{S,L})^2$  becomes comparable to  $\omega^2$  and can no longer be ignored. This can have implications for the unusual case  $G^* < 0$  which must be treated with great care. One must therefore use the full expression given by Eqn (14.30). The problem is only tractable, however, if the thermal properties of liquid and solid are the same, in which case there is an exchange of stabilities (no unstable oscillatory modes). In that case, the term  $-G^*$  in Eqn (14.37) is replaced by  $-(G_S + G_L)/2 - L_V V^2/(4\kappa_L K_L \bar{\alpha})$  and only  $\sigma = 0$  is considered, so  $\bar{\alpha} = [(V/2\kappa_L)^2 + \omega^2]^{1/2}$ . The analysis is similar to that for  $\mathcal{N}(\omega^2, 0)$  which gets replaced by  $\mathcal{R}(\omega^2, 0) = \mathcal{N}(\omega^2, 0)_{K_S=K_L} - L_V V^2/(4\kappa_L K_L \bar{\alpha})$ , which has the value  $-G_S$  at  $\omega = 0$  and becomes  $-\infty$  as  $\omega^2 \rightarrow \infty$ . Then one can examine  $\partial \mathcal{R}(\omega^2, 0)/\partial \omega^2$ , which turns out to be a monotonically decreasing function of  $\omega^2$ . It has the property

$$\left[ \frac{\partial \mathcal{R}(\omega^2, 0)}{\partial \omega^2} \right]_{\omega=0} = \frac{L_V \kappa_L^2}{K_L V} + \frac{m' G_c D_L^2}{k' V^2} (1 - \mathcal{A}), \quad (14.51)$$

which, if negative, would be a sufficient condition for stability if  $-G_S < 0$  because it would guarantee that  $\mathcal{R}(\omega^2, 0)$  would decay monotonically from a negative value to  $-\infty$ . Inserting values for  $\mathcal{A}$  and  $G_c$ , this sufficient condition for instability becomes [19]

$$V > \frac{L_V \kappa_L^2}{K_L T_M \Gamma} + \frac{D_L m'}{k' T_M \Gamma} \frac{k-1}{k} C_\infty \quad (14.52)$$

which might require unrealistically high velocities  $V$  to satisfy. This condition also turns out to be necessary if  $G_S = 0$ . Thus, if  $G_S = 0$  and  $G_L < 0$ , growth into such a supercooled

liquid would be unstable for realistic conditions. Of course for  $G_S \neq 0$  one could analyze the extrema of the function  $\mathcal{R}(\omega^2, 0)$  to obtain a necessary condition for instability, but this has not been done for the binary alloy.

For a pure material, for which  $m'G_c = 0$ , the problem is greatly simplified, and one can easily determine the necessary and sufficient conditions for stability. In that case, the stability condition becomes

$$\frac{(G_S + G_L)}{2} > \max\{\mathcal{Q}(\omega^2)\}; \quad \mathcal{Q}(\omega^2) \equiv -\frac{L_V V^2}{4K_L \kappa_L \bar{\alpha}} - T_M \Gamma \omega^2, \quad (14.53)$$

where “max” means the maximum as a function of  $\omega^2$ . We find

$$\left[ \frac{\partial \mathcal{Q}(\omega^2)}{\partial \omega^2} \right] = \frac{L_V V^2}{8K_L \kappa_L \bar{\alpha}^3} - T_M \Gamma; \quad \left[ \frac{\partial \mathcal{Q}(\omega^2)}{\partial \omega^2} \right]_{\omega^2=0} = \frac{L_V \kappa_L^2}{K_L V} - T_M \Gamma. \quad (14.54)$$

We note that  $[\partial \mathcal{Q}(\omega^2)/\partial \omega^2]$  is a monotonically decreasing function of  $\omega^2$  and define the parameter

$$\eta = (T_M \Gamma K_L V / L_V \kappa_L^2). \quad (14.55)$$

Then if  $\eta \geq 1$  we see that  $[\partial \mathcal{Q}(\omega^2)/\partial \omega^2]_{\omega^2=0} \leq 0$ , so  $\mathcal{Q}$  will decay from its value at  $\omega^2 = 0$  to negative values as  $\omega^2$  increases. Since  $\mathcal{Q}(0) = -L_V V / 2K_L$ , we will have

$$\frac{(G_S + G_L)}{2} > -\frac{L_V V}{2K_L}; \quad \text{stability } \eta \geq 1. \quad (14.56)$$

Since  $G_S - G_L = L_V V / K_L$ , we must recognize that with  $V$  specified,  $G_L$  and  $G_S$  are not independent variables. Thus Eqn (14.56) is equivalent to

$$G_S > 0 \quad \text{or} \quad G_L > -\frac{L_V V}{K_L} \quad \eta \geq 1. \quad (14.57)$$

We note that  $\eta > 1$  gives Eqn (14.52) for  $C_\infty = 0$ , so it is unlikely to be satisfied.

If  $\eta < 1$ ,  $[\partial \mathcal{Q}(\omega^2)/\partial \omega^2]_{\omega^2=0} > 0$ , so  $\mathcal{Q}(\omega^2)$  rises from  $-L_V V / 2K_L$ , passes through a negative maximum, and then decays to  $-\infty$  as  $\omega^2$  increases. This maximum occurs at  $\omega^2 = (V/2\kappa_L)^2(\eta^{-2/3} - 1)$  and has the value

$$\max\{\mathcal{Q}\} = -\frac{L_V V}{2K_L} f(\eta); \quad f(\eta) = \frac{3}{2}\eta^{1/3} - \frac{1}{2}\eta. \quad (14.58)$$

The function  $0 < f(\eta) < 1$ , so for small  $\eta$  the system will be much less stable. The stability condition becomes

$$\frac{(G_S + G_L)}{2} > -\frac{L_V V}{2K_L} f(\eta); \quad \text{stability } \eta < 1. \quad (14.59)$$

Equivalent conditions are

$$G_S > \frac{L_V V}{2K_L}(1 - f(\eta)) \quad \text{or} \quad G_L > -\frac{L_V V}{2K_L}(1 + f(\eta)) \quad \eta < 1. \quad (14.60)$$

These stability conditions are shown graphically in Figure 14.7. For small  $\eta$ , the region of stability for negative  $(G_L + G_S)/2$  becomes very small.

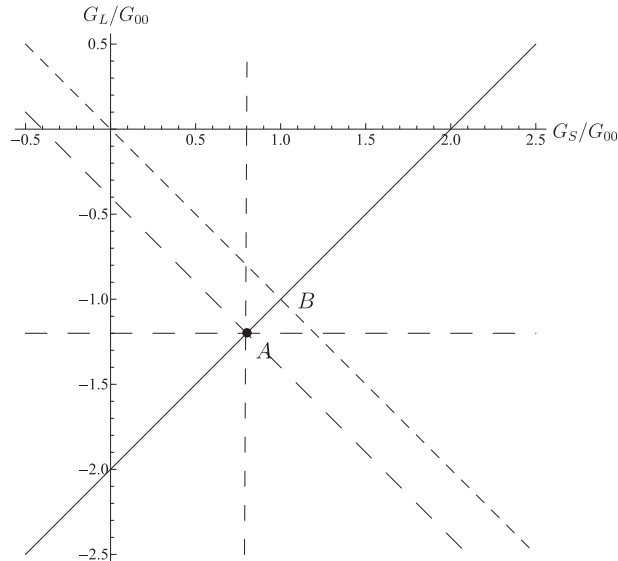


**FIGURE 14.7** Stability diagram illustrating the compatibility of stability conditions Eqn (14.59) and Eqn (14.60) for  $f(\eta) = 0.2$ . Temperature gradients  $G_S$  and  $G_L$  are plotted in units of  $G_{00} = L_V V / 2K_L$ . The dashed horizontal line  $G_L = -G_{00}(1 + f)$  meets the dashed vertical line  $G_S = G_{00}(1 - f)$  and the sloping dashed line  $(G_S + G_L)/2 = -G_{00}f$  at point A; there is stability along the solid line upward and to the right. The sloping line with small dashes that passes through the point B is  $G_S + G_L = 0$ . There is stability for negative  $(G_S + G_L)/2$  only along the solid line between A and B, a region that shrinks to zero as  $\eta \rightarrow 0$ . For  $\eta = 1$ , the intersection point A would be located at the point  $G_L = -2G_{00}$ ,  $G_S = 0$ .

### 14.3.2 Spheres and Cylinders

We present the linear stability analysis of a sphere growing from a pure supercooled melt [1], which has several complicating features compared to the planar analysis. First, the sphere itself is growing, so its radius changes and the base state we must perturb depends on time. Second, we must perturb the sphere with a compatible set of eigenfunctions, namely spherical harmonics, which are somewhat more complicated than sinusoids. The problem turns out to be tractable provided that the dimensionless supercooling is small, specifically

$$S_T = \frac{K_L(T_M - T_\infty)}{\kappa_L L_V} = \frac{T_M - T_\infty}{L_V / C_{LV}} \ll 1. \quad (14.61)$$

Here,  $T_\infty$  is the temperature of the supercooled melt (bath temperature) and  $C_{LV}$  is the heat capacity per unit volume of the liquid. The quantity  $L_V / C_{LV}$  is typically several hundred degrees K, so this inequality is satisfied for an interesting range of supercoolings. For any supercooling  $S_T < 1$ , it is possible to solve the time-dependent growth of a sphere having constant temperature  $T_M$  exactly. The sphere grows with radius  $R = \xi_0(\kappa_L t)^{1/2}$  where  $\xi_0$  satisfies a rather complicated transcendental equation

(see equation 90 of Ref. [8]). But for small  $S_T$ , the root of this equation is simply  $\xi_0 = (2S_T)^{1/2}$ , so the sphere grows according to

$$R = [(2K_L/L_V)(T_M - T_\infty)t]^{1/2}. \quad (14.62)$$

If the time-dependent equation for  $T_L$  is approximated by Laplace's equation,  $\nabla^2 T_L = 0$ , we obtain

$$T_L = T_\infty + (T_M - T_\infty)R(t)/r \quad (14.63)$$

where  $r = \sqrt{x^2 + y^2 + z^2}$ . Thus,

$$dR/dt = -(K_L/L_V)[dT_L/dr]_R = (K_L/L_V)(T_M - T_\infty)/R. \quad (14.64)$$

Multiplication of Eqn (14.64) by  $R$  and integration subject to  $R=0$  at  $t=0$  leads immediately to Eqn (14.62). Therefore, we see that the TSS approximation is valid for small dimensionless supercooling. The steady-state approximation is also valid for growth of precipitates by diffusion if the supersaturation is small [20]. Mullins and Sekerka [1] used this approximation to give a similar analysis of the stability of a spherical precipitate growing by diffusion.

Of course, the growth rate predicted by Eqn (14.62) is infinite at  $t=0$  and, therefore, unrealistic. This is easily fixed in the TSS approximation by replacing  $T_M$  by  $T_M(1 - 2\Gamma/R)$  which would be the equilibrium temperature for a sphere of mean curvature  $2/R$ . Then, by introducing the nucleation radius  $R^* = 2T_M\Gamma/(T_M - T_\infty)$ , Eqn (14.64) is replaced by

$$\frac{dR}{dt} = \frac{K_L(T_M - T_\infty)(1 - R^*/R)}{L_V R}. \quad (14.65)$$

According to Eqn (14.65),  $dR/dt < 0$  for  $R < R^*$  and  $dR/dt > 0$  for  $R > R^*$ , so the nucleation radius  $R = R^*$  is a point of unstable equilibrium. If the sphere were just slightly larger than  $R^*$ , it would start to grow, achieve a maximum velocity of  $K_L(T_M - T_\infty)/(4L_V R^*)$  at  $R = 2R^*$ , and then decay in velocity in proportion to  $1/R$  for  $R \gg R^*$ . This ability to include capillarity in the TSS approximation is essential because we know that capillarity gives rise to stabilization while a negative temperature gradient will be destabilizing. It is also possible to include linear interface kinetics in the TSS approximation, but we defer that for now. One can treat a perturbed sphere by means of a perturbation

$$R = R(t) + \delta(t)Y_{\ell m}(\theta, \varphi) \quad (14.66)$$

where  $\delta$  is a small amplitude and  $Y_{\ell m}(\theta, \varphi)$  is a spherical harmonic, with  $\theta$  and  $\varphi$  the polar and azimuthal angles of spherical coordinates. These harmonics are known to be a complete set of functions on a sphere, so by superposition one can treat an arbitrary perturbation, just as with sinusoids for the planar interface. Since we are doing linear stability, we can even use the complex spherical harmonics common to quantum mechanics, which are known to be eigenfunctions of the angular part of the Laplacian operator with eigenvalue  $-\ell(\ell + 1)$ . This is very useful because the mean curvature  $\mathcal{K}$  that appears in the interface temperature can be calculated by using the Laplacian operator, resulting in (see equation 5 of Ref. [1])

$$T_I = T_M \{1 - 2\Gamma/R - \Gamma(\delta/R^2)(\ell + 2)(\ell - 1)Y_{\ell m}(\theta, \varphi)\}. \quad (14.67)$$

One can then find a perturbed temperature containing a term in  $Y_{\ell m}(\theta, \varphi)$ , linearize all other boundary conditions, and ultimately cancel  $Y_{\ell m}(\theta, \varphi)$  from all perturbed terms to obtain

$$\dot{\delta}/\delta = \left(\dot{R}/R\right)(\ell - 1) \left[1 - (1/2)(R/R^* - 1)^{-1}(\ell + 2)(\ell + q\ell + 1)\right], \quad (14.68)$$

where  $\dot{\delta} = d\delta/dt$ ,  $\dot{R} = dR/dt$ , and  $q = K_S/K_L$ . In Eqn (14.68), the factor  $\ell - 1$  appears because a sphere perturbed with real linear combinations of the  $Y_{\ell m}$  is just a slightly translated sphere.

One can obtain a criterion for marginal instability by requiring the expression in brackets to be positive. This gives

$$\begin{aligned} R/R^* &> 1 + (1/2)(\ell + 2)(\ell + q\ell + 1) \\ &= [(1 + q)/2]\ell^2 + [(2 + 2q + 1)/2]\ell + 2; \quad \text{marginal instability.} \end{aligned} \quad (14.69)$$

For  $\ell = 2$ , instability occurs at  $R_2/R^* = 7 + 4q$  and for  $\ell = 3$ , at  $R_3/R^* = 11 + 15q/2$ . We see in general that as  $R$  increases, perturbations with larger  $\ell$  will grow.

This is not the whole story, however, because the sphere is also growing. Thus, if the relative growth rate  $\dot{\delta}/\delta$  of perturbations is smaller than the relative growth rate  $(\dot{R}/R)$  of the sphere, the change will be toward a more spherical shape. Put another way,  $(R/\delta)d(\delta/R)/dt = \dot{\delta}/\delta - \dot{R}/R > 0$  for shape change to be enhanced. The more meaningful criterion for relative instability is therefore

$$\frac{\dot{\delta}/\delta}{\dot{R}/R} > 1 \quad \text{relative instability} \quad (14.70)$$

which leads to

$$R/R^* > 1 + \frac{(\ell - 1)(\ell + 2)(\ell + q\ell + 1)}{2(\ell - 2)}; \quad \text{relative instability.} \quad (14.71)$$

In Eqn (14.71), the factor of  $(\ell - 2)$  in the denominator requires  $R/R^* = \infty$  which is at first alarming but is just a manifestation of the well-known result that a sphere perturbed by  $Y_{20}$  is an ellipsoid which also grows like  $t^{1/2}$ . Thus, the first meaningful relative instability occurs at  $\ell = 3$  for which  $(R_3/R^*)^{rel} = 21 + 15q$ , which is larger than  $R_3/R^*$  for marginal stability. This trend continues for larger  $\ell$ ; however, for very large  $\ell$ , the factor  $(\ell - 1)/(\ell - 2) \rightarrow 1$ , so the two instability criteria become the same.

We can also express the growth rate of perturbations in terms of the negative of the temperature gradient at  $r = R$ , namely  $-G_L = (T_M - T_\infty)(1 - R^*/R)/R = (L_V/K_L)\dot{R}$ . Then Eqn (14.68) becomes

$$\dot{\delta}/\delta = (K_L/L_V)[(\ell - 1)/R] [-G_L - (T_M\Gamma/R^2)(\ell + 2)(\ell + q\ell + 1)]. \quad (14.72)$$

This shows that  $G_L < 0$  is destabilizing while the capillarity term containing  $\Gamma$  is stabilizing. For large  $\ell$ , we can identify a perturbation wavelength  $\lambda \sim 2\pi R/\ell$  and thus a perturbation wavenumber  $\omega = \ell/R$  in which case Eqn (14.72) becomes

$$\dot{\delta}/\delta = (K_L/L_V)\omega [-G_L - T_M\Gamma(q + 1)\omega^2]. \quad (14.73)$$

This resembles Eqn (14.12) for a planar interface, except now  $G_S = 0$ . The important point here is the relative roles played by temperature gradient and capillarity, somewhat irrespective of the geometry of the solidifying front.

For Eqn (14.72), marginal stability occurs at  $\omega^2 = (q + 1)T_M\Gamma/(-G_L)$  which for equal thermal conductivities,  $q = 1$  corresponds to a wavelength

$$\lambda \sim 2\pi \left[ \frac{2T_M\Gamma}{-G_L} \right]^{1/2} = 2\pi \left[ 2d_0 \frac{\kappa_L}{V} \right]^{1/2} \quad (14.74)$$

where the capillary length  $d_0 = \Gamma T_M C_{LV}/L_V$ .

Langer and Müller-Krumbhaar [21,22] have used Eqn (14.73) in an effort to select the tip radius  $\rho$  in dendritic growth. For the growth of a branchless dendrite in the shape of a paraboloid of revolution, a heat flow analysis by Ivantsov [23] shows that  $\rho V/2\kappa_L$  is a function of the dimensionless undercooling  $S_T$  given by Eqn (14.61) but provides no means of determining  $V$  and  $\rho$  separately. Langer and Müller-Krumbhaar conjectured that the tip radius could be determined by a stability criterion by assuming that  $\rho \sim \lambda$  for marginal stability. Accordingly, they wrote Eqn (14.74) in the form

$$\sigma^* = \frac{2d_0\kappa_L}{\rho^2 V} = \frac{1}{(2\pi)^2} \approx 0.025. \quad (14.75)$$

Surprisingly, this result is in reasonable agreement with experiments, although the actual value of the constant  $\sigma^*$  seems to be fortuitous. Nevertheless, this result suggested that capillarity plays a significant role in dendrite tip selection and spurred much further analysis, including the very existence of a steady-state solution that includes capillarity (so-called microscopic solvability theory) as well as an essential role played by crystalline anisotropy [24–27].

Coriell and McFadden [8] allowed for departure from local equilibrium at the solid–liquid interface by means of a linear interface kinetic law, namely  $v = \mu_0(T_e - T_L)$ , where  $T_e$  is the equilibrium temperature, including capillarity, and  $T_L$  is the actual temperature at the interface. Then by using the TSS approximation, Eqn (14.65) becomes

$$\frac{dR}{dt} = \frac{K_L(T_M - T_\infty)(1 - R^*/R)}{L_V R(1 + \beta/R)}, \quad (14.76)$$

where  $\beta = K_L/\mu_0 L_V$  is a length associated with the kinetic coefficient. The factor  $(1 + \beta/R)$  has the effect of slowing down the unperturbed growth rate. But kinetics also slows down the growth rate of perturbations, and Eqn (14.68) is replaced by

$$\dot{\delta}/\delta = (\dot{R}/R)(\ell - 1) \left[ \frac{1 - (1/2)(R/R^* - 1)^{-1}(\ell + 2)(\ell + q\ell + 1)(1 + \beta/R)}{1 + (\beta/R)(\ell + q\ell + 1)} \right]. \quad (14.77)$$

Equation (14.77) is now sufficiently complicated that one must resort to numerical analysis. By scaling with a time  $\tau = L_V R^{*2}/[K_L(T_M - T_\infty)]$ , Coriell and McFadden made plots of the dimensionless quantities  $\Delta_0 = \tau \dot{R}/R$  and  $\Delta = \tau \dot{\delta}/\delta$  as functions of  $R/R^*$  for

two values of  $\beta/R^*$  and various  $\ell$ . Thus, there is relative instability whenever  $\Delta > \Delta_0$ . For  $\beta/R^* = 0$ , the curves cross at values given by Eqn (14.71). By comparison of the case  $\beta/R^* = 10$  with  $\beta/R^* = 0$  (see their figures 4 and 5) they find that instabilities are shifted by kinetics to much larger values of  $R/R^*$ . For example, for  $\ell = 4$  they are shifted from 40.5 to 100.

The role of a small anisotropy of surface free energy  $\gamma$ , and hence of  $\Gamma = \gamma/L_V$ , was investigated by Cahn [28]. The anisotropy was taken to have the form  $\Gamma = \Gamma_0 + \Gamma_{\ell m} Y_{\ell m}(\theta, \varphi)$ . The base state is no longer a perturbed sphere and the expression for  $\dot{\delta}/\delta$  in Eqn (14.72) is modified so that  $\Gamma$  in the second term in brackets is replaced by  $\Gamma_0(1 - \delta_e/\delta)$ , where  $\delta_e = \Gamma_{\ell m} R/\Gamma_0$ . This extra factor due to anisotropy is effective in triggering an instability consistent with the anisotropy, but once there is significant growth of  $\delta$  it has little effect. Of course, the actual anisotropy of  $\Gamma$  must be consistent with crystal symmetry, which would require a suitable combination of spherical harmonics to be used. The role of surface tension anisotropy for a planar interface has been discussed in Ref. [8], Section 3.2.3.

#### 14.3.2.1 Circular Cylinder

The instability of a circular cylinder was treated by Coriell and Parker [29] by using cylindrical coordinates  $r, \varphi, z$  where now  $r = \sqrt{x^2 + y^2}$  is the cylindrical radius. They conducted a linear stability analysis for a perturbed cylinder of the form

$$r = R(t) + \delta(t) \cos(n\phi) \cos(\omega z). \quad (14.78)$$

More general perturbed shapes can be obtained by superposition. They also used the steady-state approximation, although now there is a complication because the axially symmetric solution to Laplace's equation is of the form  $T_L = c_1 + c_2 \ln r$  where  $c_1$  and  $c_2$  are constants. Thus, the unperturbed solution would diverge for  $r \rightarrow \infty$ . They handled this technical problem by cutting off the solution at a large time-dependent value  $r = R_c(t)$ , where the cutoff radius  $R_c(t)$  was chosen to match the  $t^{1/2}$  growth rate of a time-dependent solution in cylindrical coordinates. Then they added capillarity, as for the sphere. Another complication is the well-known Rayleigh instability that occurs for  $n = 0$  for a perturbed cylinder with no net growth, so its volume is equal to that of the unperturbed cylinder. In that case, the total surface energy actually decreases for perturbations of wavelength greater than the unperturbed circumference. This happens because the principal radii of a perturbed cylinder with  $n = 0$  have opposite signs in certain places, so their sum, the total curvature, can be negative. For wavelengths larger than the unperturbed circumference, the total surface area actually decreases, so capillarity can actually be destabilizing. Aside from these complications, the stability analysis is similar to that for the sphere.

Hardy [30–32] conducted experiments for cylinders of ice growing from supercooled water but comparison with theory required several refinements. Instabilities with  $n$  equal to a multiple of six began to grow, apparently due to the hexagonal anisotropy of ice in the basal plane. Those with  $\omega = 0$  first began to grow and became rather large

before those with  $\omega \neq 0$  appeared. It was, therefore, necessary to develop an approximate nonlinear correction [33] for instability of a shape initially of the form  $r = R(t) + \delta_\phi(t) \cos(n\phi)$  perturbed by adding  $\delta_z \cos(n\phi) \cos(\omega z)$ . By comparison of perturbation growth rates with this theory, the interfacial energy for ice-water was calculated and found to be  $25 \text{ mJ/m}^2$ , as compared to  $29 \text{ mJ/m}^2$  measured from grain boundary groove shapes. This is quite reasonable, given the approximations of the nonlinear analysis and the difficulty of the measurements. See Ref. [8] for more detail and related experiments.

### 14.3.3 Paraboloids, Ellipsoids, and Other Shapes

The question naturally arises as to whether and how the morphological stability phenomenon applies to other shapes such as paraboloids and ellipsoids. It is hard to believe that it would not, because of the basic physics behind equations such as Eqn (14.12) and Eqn (14.73) for planes and spheres. Essentially, for supercooled melts, the temperature gradient (negative) is destabilizing, and capillarity is stabilizing, pretty much independent of geometry.

To address this question quantitatively, it is necessary to recognize that all three shapes treated so far in this article have surfaces of constant mean curvature,  $\mathcal{K}$ . Therefore, incorporating the isotropic Gibbs–Thomson effect (see Eqn (14.7) and Eqn (14.25), for example) leads to unperturbed shapes with isothermal temperatures. Such is not the case for bodies that do not have isocurvature.

To illustrate the complications that are involved, there exists an exact solution by Ivantsov [23] for a solid in the shape of an isothermal circular paraboloid at a constant temperature  $T_M$  that translates at constant velocity  $V$  into a supercooled melt. Such a body has been used as a model of a branchless dendrite. But the curvature of such a body varies over its surface, being largest at its tip and decreasing toward zero far from the tip. Temkin [34] has calculated approximate thermal fields in both solid and liquid in terms of integrals of Bessel functions for such a nonisothermal paraboloid, but was only able to satisfy the heat flux condition at the tip. However, despite these technical complications, there is no reason to believe that the correct steady-state shape of a branchless nonisothermal body is a paraboloid, or even if such a solution exists, as has been addressed by microscopic solvability theory [24–27]. Therefore, any attempt to add perturbations to the paraboloidal dendrite would first have to correct for the *shape* of the steady-state body and then give information about its stability. An attempt to do this was carried out by J.J. Xu [35–37] but is beyond the scope of this article. Similar considerations would apply to ellipsoids and other bodies that are not shapes of isocurvature.

## 14.4 Extensions of the Mullins-Sekerka Analysis

In the previous edition of this handbook [8], Coriell and McFadden discuss a number of extensions of the original Mullins-Sekerka analysis. There is little to add to these comprehensive discussions, so here we shall deal mostly with rapid solidification, which

turns out to trigger the new phenomenon of oscillatory instabilities, and then we will summarize a few more recent extensions.

### 14.4.1 Rapid Solidification

The term “rapid solidification” usually refers to growth speeds so large that there are significant departures from local equilibrium, an example being an interface temperature that is a measurable amount below the equilibrium melting point or a solute incorporation in the solid that is much closer to the liquid concentration than in equilibrium. At very high growth speeds, solute from the liquid can become trapped in the solid, and the segregation coefficient can approach unity. This requires modification of the boundary conditions at the solid–liquid interface, which is undercooled by an amount  $\Delta T = T_e - T_I$  where  $T_e$  is its local equilibrium temperature (see Eqn (14.25)) and  $T_I$  is its local actual temperature. This undercooling can be related to the local normal growth speed  $v$  by a so-called kinetic law, which we write in the form

$$v = f(\Delta T, c_I) = f(T_e - T_I, c_I). \quad (14.79)$$

Nonequilibrium segregation of solute can be handled by allowing the segregation coefficient  $k$  to also depend on  $v$ , namely

$$c_{SI} = c_I k(c_I, v). \quad (14.80)$$

One might expect large departures from local equilibrium for the unperturbed solution but for slowly growing perturbations of that solution the corresponding deviations are expected to be small. Therefore, for the perturbations we can linearize about the base state, which leads to four derivatives of the base state known as kinetic coefficients, namely

$$\mu_T = \partial f / \partial (\Delta T); \quad \mu_c = \partial f / \partial c_I \quad (14.81)$$

and

$$k_c = \partial k / \partial (c_I); \quad k_v = \partial k / \partial v \quad (14.82)$$

where these derivatives are assumed to be evaluated at the unperturbed base state.

When one carries out a linear stability analysis, the results of a linear stability analysis resemble Eqn (14.36) but with several modifications. First of all,  $m'$  is replaced by  $m^* = m + \mu_c / \mu_T$  and  $p'$  is replaced by  $p^* = p' - c_I k_c$ , but these changes are assumed to be sufficiently small that they do not result in sign changes. On the other hand, the denominator becomes [8]

$$\mathcal{D}(\omega^2, \sigma) = \left\{ \frac{L_V}{2\bar{K}\bar{\alpha}} + \frac{1}{\mu_T} + \frac{m^* G_c}{V(\alpha - p^* V/D_L)} \left[ 1 - \frac{V k_v}{1 - k} \right] \right\} \quad (14.83)$$

which involves the kinetic coefficients  $\mu_T$  and  $k_v$ . The coefficient  $\mu_T$  is positive except for very large supercoolings, so it is regarded as positive and does not result in any qualitatively new effects. On the other hand, if  $k_v / (1 - k)$  is positive, as it is for the model of Aziz and Jackson et al. [38,39], the term in square brackets can become

negative for large  $V$ . This term could cause the entire denominator  $\mathcal{D}$  to become negative, thus reversing the regions of stability and instability previously analyzed on the basis of local equilibrium.

For positive  $k_v/(1-k)$ , but still positive  $\mathcal{D}$ , the dispersion relation has been analyzed numerically [14]. The previous modes for  $\sigma=0$  are still found, but the exchange of stabilities no longer holds. For sufficiently large  $Vk_v/(1-k)$ , oscillatory modes with long wavelengths become strongly unstable. At high solidification rates, lateral diffusion of solute can only occur over short distances, but perturbations of short wavelength are strongly stabilized by capillarity. However, variations of the local normal growth speed  $v$  along the interface can result in variations of solute segregation over long wavelengths which are hardly stabilized by capillarity. This has been called the “solute pump mechanism” and is suspected to be responsible for unstable oscillatory modes [14].

Huntley and Davis [40] have used nonequilibrium kinetic laws to analyze oscillatory instabilities under more general conditions. They find that oscillatory modes can be unstable at zero wavenumber, corresponding to an oscillating planar interface. Experiments by Boettinger et al. [41] were used to study the effect of velocity on microstructure for silver–copper alloys. For copper concentrations with weight fractions of 1 and 5%, they find a fairly normal transition from a cellular to a segregation-free microstructure at respective velocities 15 and 60 cm/s, in qualitative agreement with local equilibrium theory, as illustrated in Figure 14.6. However, for higher concentrations, a banded structure occurs at velocities intermediate to those that yield cellular and segregation-free microstructure. The bands are perpendicular to the growth direction and alternate between cellular structure and segregation-free structure. This suggests some kind of oscillatory instability, but a firm connection between current theory and experiment has not been established.

### 14.4.2 Other Extensions

If the alloy concentration during directional solidification exceeds the concentration for morphological instability, the onset of instability may occur during the initial transient as the interface concentration increases from the bulk concentration  $c_\infty$  to  $c_\infty/k$ . While it is not possible to carry out a stability analysis for this time-dependent base state, the relevant differential equations and boundary conditions can be solved numerically, and the time evolution of a small perturbation can be calculated [42]. The results for the onset of instability are in good agreement with the time-independent base state theory if the instantaneous values of the interface velocity and temperature gradient are used.

Van Vaerenbergh et al. [43] have considered the effect of thermodiffusion (Soret effect) and the temperature dependence of the liquid diffusion coefficient on morphological stability during directional solidification of a tin alloy containing silver. For this alloy, the diffusion coefficient is a linear function of temperature [44]. This temperature dependence has little effect on the conditions for the onset of instability, but has a significant effect on the wavenumber at the onset of instability.

Isotropic interface kinetics does not affect the conditions for the onset of instability for the directional solidification of a binary alloy. For many metals, the interface kinetic coefficient is large; for example Rodway and Hunt [45] have measured a kinetic coefficient for lead of 28 cm/(sK) so that for a growth velocity of 10  $\mu\text{m/s}$ , the kinetic undercooling is less than 0.0001 K. The anisotropy of the kinetic coefficient for nickel has been calculated by molecular dynamics, and the values are 35.8, 25.5, and 24.1 cm/(sK) for the 100, 110, and 111 interfaces, respectively [46]. However, for materials which develop facets for specific crystallographic orientations and grow by step motion, the kinetic coefficient is a strong function of crystallographic orientation. Such materials include metals such as gallium and bismuth, many semiconductors, and crystals grown from solution. A quasistatic approximation to the diffusion field demonstrated that kinetic anisotropy gave rise to traveling waves along the interface [47]; hence, for anisotropic kinetics the principle of exchange of stability is not valid. If we consider growth in which the planar interface deviates slightly from a singular surface, then the kinetic coefficient is given by  $\mu = \mu_{st}|p|$ , where  $\mu_{st}$  is the step kinetic coefficient and  $p = \tan\theta$ , where  $\theta$  measures the deviation of the interface from a singular orientation. For silicon, the value of the step kinetic coefficient has been estimated as 50 cm/(sK) [48]. Yuferev [49] showed that anisotropic kinetics enhanced morphological stability.

For growth by motion of steps along the interface, morphological instability leads to the formation of macrosteps. Shear flows along the interface can have a large effect on stability. In experiments on the growth of ammonium dihydrogen phosphate [50] in which the direction of the shear flow was periodically reversed, a macrostep developed on the side of the hillock where the flow was down the steps and disappeared on the side where the flow was up the steps. A number of articles have analyzed morphological stability in which anisotropic kinetics is due to step motion, and the orientation of the interface is near a singular orientation (a vicinal surface) for constant velocity growth from a supersaturated solution [51,52] and for solidification [53,54]. The effect of shear flows along the interface have also been treated [55,56] and confirm the observation that flow up the steps is stabilizing and flows down the steps are destabilizing. The effects of an oscillatory shear flow on stability was calculated using Floquet theory [57] to model the experiments of Chernov et al. [50].

Morphological stability during the electrodeposition of copper in the presence of a catalyst that enhances the growth rate has been treated by McFadden et al. [58]. Both the copper ions and the catalyst satisfy diffusion equations and the catalyst coverage at the interface is governed by an adsorption equation. The growth rate is described by the Butler–Volmer equation.

Peppin et al. [59] have carried out morphological stability calculations for the freezing of water containing a hard sphere colloidal suspension. The dependence of the diffusion coefficient on concentration is treated.

Style and Worster [60] have considered the morphological stability of a solid–vapor interface. The results are applied to frost flowers, which form when ice evaporates into a cold vapor.

## 14.5 Nonlinear Analysis

Up to now, we have only considered linear stability theory according to which perturbations can decay or grow exponentially, depending on growth conditions. Several essential things are missing from such an analysis. On the one hand, perturbations that grow exponentially will soon become large, and the linear analysis will no longer be valid. For example, for a planar interface, if a sinusoidal perturbation of the form  $z = h(x, t) = \delta(t) \cos(\omega x) = \delta(t) \cos(2\pi x/\lambda)$  grows exponentially, we will soon have a situation in which  $|\delta(t)/\lambda| \sim 1$ . Also, the slope  $\partial h/\partial x = -2\pi(\delta/\lambda) \sin(\omega x)$  will no longer be small compared to unity and the denominator in the formula for the curvature, namely  $(1 + (\partial h/\partial x)^2)^{3/2}$  will no longer be nearly equal to one. Evaluation of boundary conditions, such as Eqn (14.6), at the interface could not be expanded accurately to first order in  $h$ . Superposition of solutions having different  $\omega$  would no longer be valid. Instead, Fourier modes will couple, and the time evolution of the interface will change considerably. Furthermore, for growth conditions in which a linear analysis would result in stability, a larger perturbation might actually grow.

It might also be possible for the interface to restabilize but with some nonplanar periodic shape. In two dimensions, such shapes are usually called “corrugations” or “bands.” In three dimensions, stable shapes known as “cells” or “nodes,” often in hexagonal arrays, can form. If the interface restabilizes with a nonplanar shape, steady-state crystal growth will still be possible, but for alloys there will be solute segregation, known as microsegregation, in the direction perpendicular to the growth direction. If the system does not restabilize, branching might continue, forming a dendritic (tree-like) structure with primary, secondary, and tertiary arm spacings.

### 14.5.1 Weakly Nonlinear Analysis

A fully nonlinear analysis would require repeated solution of a free-boundary problem for a variety of perturbations, which could only be accomplished in principle by numerical calculations, a formidable task. We can, however, gain more insight into nonlinearities by means of a weakly nonlinear expansion, first introduced to this problem by Wollkind and Segel [15]. The key idea is to work near the threshold of instability such that a single (fundamental) Fourier component, say  $h_1(x, t) = A(t) \cos(\omega x)$ , is the most important and use expansion techniques to develop an approximate nonlinear amplitude equation for that component. Thus, the interface would be assumed to have the form

$$h = h_1(x, t) + h_2(x, t) + h_3(x, t) + \dots \quad (14.84)$$

where  $h_2$  is of order  $A^2$ ,  $h_3$  is of order  $A^3$ , etc. Then, after expansion of all equations and boundary conditions, terms of the same order of  $A$  are equated. In doing so, however, it is necessary to treat carefully just a few other Fourier components that couple strongly to the fundamental component. For example, there will be nonlinear terms such as  $A^2 \cos^2(\omega x) = A^2 \left[ \frac{1}{2} + \frac{1}{2} \cos(2\omega x) \right]$ , but neither term would “resonate” with  $A \cos(\omega x)$ . But

a third order term such as  $A^3 \cos^3(\omega x) = A^3[3 \cos(\omega x) + \cos(3\omega x)]/4$  contains the fundamental  $\cos(\omega x)$  and would resonate and couple. See Eqns (116) and (117) of Ref. [8] for discussion of formalities of the expansion technique and solvability condition.

The result of such a weakly nonlinear analysis to lowest order is an equation of the form

$$\frac{dA}{dt} = \sigma A - a_1 A^3 \quad (14.85)$$

which is known as a Landau equation. In the lowest order term,  $\sigma$  is the same as in a linear stability analysis, so  $\sigma < 0$  corresponds to linear stability and  $\sigma > 0$  corresponds to linear instability. In the third-order term,  $a_1$  can be either positive or negative. A quadratic term in  $A$  is missing because the problem has a translational symmetry such that  $x \rightarrow x + \pi$  is the same as  $A \rightarrow -A$ . There are four possibilities, as illustrated in Figure 14.8. The most interesting ones occur if  $\sigma$  and  $a_1$  have the same sign; then one can solve  $dA/dt = 0$  to obtain a nontrivial steady solution,  $A = \pm a$  where  $a = \sqrt{\sigma/a_1}$ . Without loss of generality, we can restrict our analysis to positive  $A$  for which the four possibilities are:

*Stability*  $\sigma < 0$  and  $a_1 > 0$ ; there is stability for all  $A$ .

*Instability*  $\sigma > 0$  and  $a_1 < 0$ ; there is instability for all  $A$ .

*Subcritical bifurcation*  $\sigma < 0$  and  $a_1 < 0$ ; the system is stable for small  $A$  but becomes unstable for  $A > a$ . Thus, there is a threshold value of  $A$  needed for instability; if exceeded, instability can take place prior to conditions for linear instability. This is called a subcritical bifurcation and is illustrated in the left member of Figure 14.9. The steady-state  $A = a$  is unstable because a slightly different value of  $A$  will lead to motion away from  $a$ .

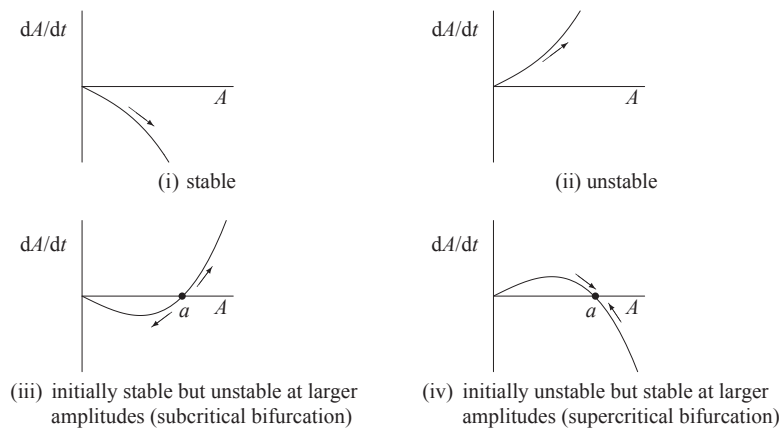


**FIGURE 14.8** Plots of  $dA/dt = A\sigma - a_1 A^3$  versus  $A$  for the four cases discussed in the text. (i)  $\sigma < 0$ ,  $a_1 > 0$ ; (ii)  $\sigma > 0$ ,  $a_1 < 0$ ; (iii)  $\sigma < 0$ ,  $a_1 < 0$ ; (iv)  $\sigma > 0$ ,  $a_1 > 0$ . The arrows along the curves point in the direction of increasing time. The states corresponding to  $A = a$  are steady states, unstable for the subcritical bifurcation for which the arrows lead away from  $a$  and stable for the supercritical bifurcation for which the arrows lead toward  $a$ .

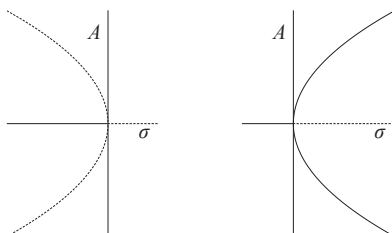


**FIGURE 14.9** Bifurcation diagrams illustrating nonplanar steady states  $A = \pm\sqrt{\sigma/a_1}$  as a function  $\sigma$  for fixed values of  $a_1$ . Dashed lines represent unstable states. The bifurcation on the left is subcritical ( $\sigma < 0$  and  $a_1 < 0$ ) because instability at finite amplitude can occur before linear instability occurs. The bifurcation on the right is supercritical ( $\sigma > 0$  and  $a_1 > 0$ ) because instability takes place according to linear stability at an infinitesimal amplitude and the system evolves to a stable nonplanar steady state.

*Supercritical bifurcation*  $\sigma > 0$  and  $a_1 > 0$ ; the system is unstable for small  $A$  but becomes stable for  $A > a$ . There is no threshold amplitude for instability, which first takes place when  $\sigma$  first becomes positive, as for linear instability. This is called a supercritical bifurcation and is illustrated in the right member of [Figure 14.9](#). The steady-state  $A = a$  is stable because a slightly different value of  $A$  will lead to motion toward the point  $a$ .

The stability of the states  $A = a$  for subcritical bifurcation and supercritical bifurcation can be analyzed by writing  $A = a + \varepsilon$  where  $|\varepsilon/A| \ll 1$  and expanding [Eqn \(14.85\)](#) to first order in  $\varepsilon$ . This results in  $d\varepsilon/dt = -2\sigma\varepsilon$ , so

$$\varepsilon = \varepsilon_0 \exp(-2\sigma), \quad (14.86)$$

where  $\varepsilon_0$  is the initial value of  $\varepsilon$ . In fact, [Eqn \(14.85\)](#) is separable and can be integrated for  $\sigma/a_1 = a^2 > 0$  to obtain a solution for all  $A$ , which can be written in the form

$$A/a = \left\{ 1 + \left[ (a/A_0)^2 - 1 \right] \exp(-2\sigma) \right\}^{-1/2}, \quad (14.87)$$

where  $A_0$  is the initial value of  $A$ .

In [Figure 14.9](#) we note the  $A \rightarrow -A$  symmetry, inherent in [Eqn \(14.85\)](#); these are known as “pitchfork bifurcations.” Small imperfections such as a grain boundary could produce bias and destroy this symmetry [\[61,62\]](#). An elementary model that illustrates this point is

$$\frac{dA}{dt} = \sigma A - a_1 A^3 + \varepsilon \quad (14.88)$$

where  $\varepsilon$  is a small quantity that will be taken as positive for the sake of illustration. Steady-state solutions will therefore satisfy

$$\sigma = a_1 A^2 - \varepsilon/A. \quad (14.89)$$

Symmetry for positive and negative  $A$  is broken, and there are no longer roots at  $A = 0$ , so solutions avoid that point and are, therefore, strongly distorted near  $\sigma = 0$ . As illustrated in [Figure 14.10](#), each pitchfork bifurcation is replaced by two continuous branches.

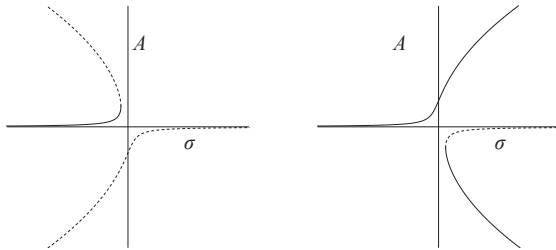


**FIGURE 14.10** Diagrams illustrating the distortion of perfect bifurcations, Figure 14.9, by imperfections. Amplitude  $A$  of nonplanar steady states is plotted as a function  $\sigma$  for fixed  $a_1 < 0$  (left) and  $a_1 > 0$  (right) for Eqn (14.89). Dashed lines represent unstable states. The transitions are now smooth, and instabilities first take place at finite amplitudes.

## 14.5.2 Other Nonlinear Topics

### 14.5.2.1 Sideband Instability of the Two-Dimensional Solution

The fundamental work of Eckhaus in 1965 [63] showed that the weakly nonlinear steady-state solution  $h(x) = A \cos \omega x$  of Eqn (14.85) can be unstable to two-dimensional perturbations with wavenumbers that are nearby to  $\omega$  (“sideband instabilities”).

Linear stability theory predicts a critical wavenumber  $\omega_c$  for a state of marginal stability with a vanishing growth rate  $\sigma$ . Near this point of marginal stability we may formally express the dispersion relation for linear stability in the functional form (cf. Ref. [8,64])

$$\sigma = \mathcal{F}(M, \omega), \quad (14.90)$$

where  $M = mG_c/G^*$  can be regarded as a dimensionless control parameter; for notational simplicity, we suppress the dependence of the growth rate on the remaining material parameters. The point of marginal stability  $\sigma = 0$  then corresponds to a critical value  $M = M_c$  and  $\omega = \omega_c$ . Owing to the quadratic nature of the dispersion relation near  $\omega_c$ , if  $M > M_c$  there is a range of unstable wavenumbers  $|\omega - \omega_c|^2 \sim (M - M_c)$  for which  $\sigma > 0$ . The question of which wavenumber, if any, the unstable system prefers can be partially addressed by considering the stability of weakly nonlinear solutions to a generalized version of the Landau Eqn (14.85) known as the Landau–Ginzburg equation,

$$\frac{\partial A}{\partial t} = sA - a_1 |A|^2 A + \kappa \frac{\partial^2 A}{\partial x^2}, \quad (14.91)$$

where  $A(x, t)$  is now a complex amplitude such that the interface has the approximate form

$$h(x, t) = \text{Re}\{A(x, t) \exp(i\omega_c x)\}. \quad (14.92)$$

Here  $\text{Re}(w)$  denotes the real part  $u$  of the complex number  $w = u + iv$ , with absolute value  $|w| = \sqrt{u^2 + v^2}$ . The coefficients  $s$  and  $\kappa$  are determined by the linear dispersion relation in Eqn (14.90), with

$$s \approx \frac{\partial \mathcal{F}}{\partial M}(M_c, \omega_c) [M - M_c], \quad \kappa \approx -\frac{1}{2} \frac{\partial^2 \mathcal{F}}{\partial \omega^2}(M_c, \omega_c) > 0, \quad (14.93)$$

and the coefficient of the cubic term  $a_1$  again determines whether the bifurcation is supercritical ( $a_1 > 0$ ) or subcritical ( $a_1 < 0$ ); here we consider the case of supercritical

instabilities. Equation (14.91) then admits a steady-state nonplanar solution of the form

$$A = A_q \exp(iqx), \quad |A_q|^2 = \frac{s - \kappa q^2}{a_1} \quad (14.94)$$

representing a perturbed interface with total wavenumber  $\omega_c + q$  that lies inside the band of linearly unstable wavenumbers, here given by  $q^2 < s/\kappa$ . It is relatively straightforward to perform a linear stability analysis of this solution (see, e.g., Ref. [65]). We write the perturbed shape in terms of a normal mode,  $A(x, t) = A_q + B_p \exp(\lambda t) \exp(i(q + p)x)$ , and find an instability ( $\lambda > 0$ ) when  $(3q^2 - s/\kappa - p^2/2) > 0$ . The band of stable wavenumbers is then reduced to the range  $q^2 < s/3\kappa$  (cf. Figure 4.3 of Ref. [64]).

By considering an appropriate two-dimensional version of the Landau–Ginzburg equation, it is also possible to test the stability of the one-dimensional solution  $A_q$  to normal modes that depend on both lateral coordinates  $x$  and  $y$ . One then finds conditions for a “zig-zag” instability of a banded structure with periodic wiggles in the transverse direction [66,67].

#### 14.5.2.2 Three-Dimensional Weakly Nonlinear Solutions

As discussed in Section 14.3.1 the linear stability of the planar solution to a three-dimensional perturbation with wavenumbers  $\omega_x$  and  $\omega_y$  in the transverse directions will depend only on their magnitude  $\omega = \sqrt{\omega_x^2 + \omega_y^2}$  in the absence of anisotropic effects. This leads to a number of possible small amplitude nonplanar solutions with different interface shapes that share a common value of  $\omega$ . Consider, for example, an interface of the form

$$z = h(x, y, t) = A(t) \left\{ \cos \omega x + \cos \omega \left[ -\frac{x}{2} + \frac{\sqrt{3}y}{2} \right] + \cos \omega \left[ -\frac{x}{2} - \frac{\sqrt{3}y}{2} \right] \right\}, \quad (14.95)$$

representing the superposition of three two-dimensional interfaces with wavenumbers of equal magnitude but differing in direction by  $120^\circ$ . In the terminology of Morris and Winegard [68], a solution of this type corresponds to a hexagonal array of “cells” ( $A > 0$ ) or “nodes” ( $A < 0$ ). To study the stability of solutions of this type, Sriranganathan et al. [69] considered interfaces having the general form

$$h(x, y, t) = A(t) \cos(\omega x) + B(t) \cos(\omega x/2) \cos(\sqrt{3}y/2), \quad (14.96)$$

for which the solution in Eqn (14.95) is a special case with  $B(t) = 2A(t)$ . They derived a coupled set of amplitude equations for  $A$  and  $B$  of the form

$$\frac{dA}{dt} = \sigma A - a_0 B^2 - A(a_1 A^2 + a_2 B^2), \quad (14.97)$$

$$\frac{dB}{dt} = \sigma B - 4a_0 AB - B \left[ 2a_2 A^2 + \frac{1}{4}(a_1 + 2a_2) B^2 \right], \quad (14.98)$$

to describe the evolution of the system near marginal stability ( $\sigma = 0$ ). Here the coefficients  $a_0$ ,  $a_1$ , and  $a_2$  depend on the material parameters in the system, and

determine the amplitude and stability of the nonplanar solutions. For example, the “band” solutions correspond to  $B=0$  and  $A^2 = \sigma/a_1$ , and the hexagonal solutions satisfy  $(a_1 + 4a_2)A^2 + 4a_0A - \sigma = 0$  and  $B=2A$ . There is also a more general rectangular solution that connects these two branches of solutions. The stability of these solutions can be determined by performing a linear stability analysis of the amplitude equations, whose results are cataloged by Sriranganathan et al. [69]. This two-mode analysis has also been extended by Wollkind et al. [70] to a more general six-mode analysis with independent complex amplitudes for each of the three basic wavenumbers. The set of weakly nonlinear solutions is basically unchanged, but their stability is modified upon consideration of this broader class of perturbations. One can also consider Eckhaus instabilities of hexagonal interfaces [71]. An extension to the case of a surface energy with cubic anisotropic for growth along two-, three-, or four-fold axes of symmetry has also been considered [72]. Finite amplitude numerical computations have been performed that complement weakly nonlinear analyses. Examples of interface shapes and their associated solute fields are shown in Figure 14.11 and can be compared to the experimental results obtained by Morris and Winegard (Ref. [68]; see also Ref. [70]).

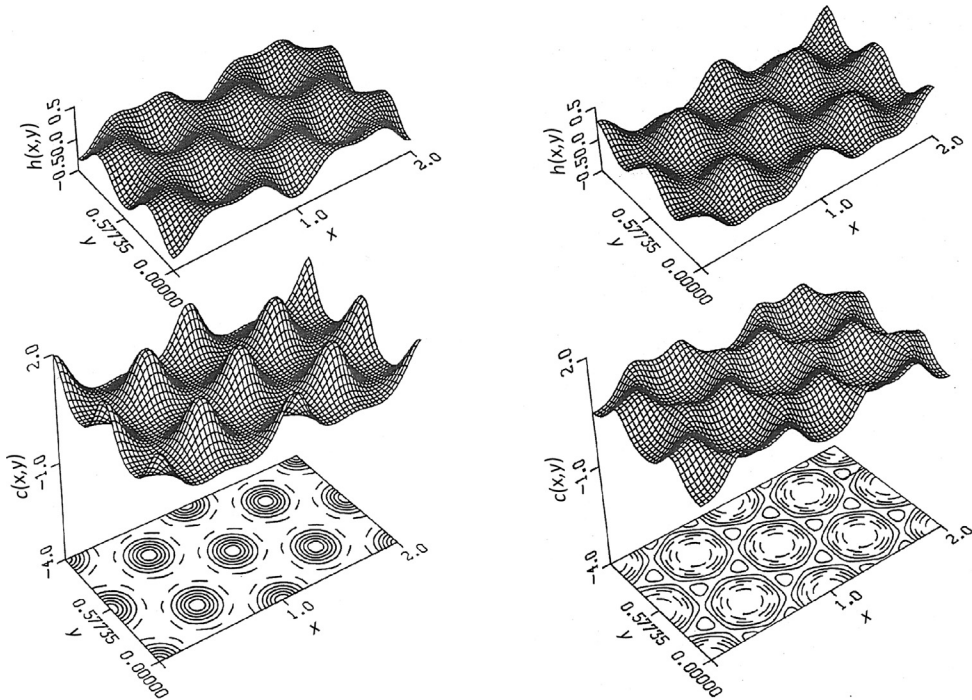


**FIGURE 14.11** The solute field (lower plots) in the crystal at the crystal–melt interface for the interface shape (upper plots)  $z = A[\cos(x) + 2 \cos(x/2) \cos(\sqrt{3}y/2)]$  with distribution coefficient  $k = 0.4$  [73]. Left: For  $A = -0.1$  the solute field corresponds to “nodes.” Right: For  $A = 0.1$  the solute field corresponds to “cells.”

In certain parameter regimes, the critical wavelength becomes large compared to other lengths in the system, and it is possible to obtain large-amplitude evolution equations for the interface shape that allows an extended analysis of nonplanar solutions. A number of such longwave evolution equations have been obtained by Davis and colleagues, as described in Ref. [64], Section 4.2. For a treatment in the context of dissipative systems, see the book by Pismen (Ref. [74], Chapters 2–4).

## 14.6 Concluding Remarks

Convection in the fluid, which has not been treated here due to space limitations, can have significant effects on morphological stability. This huge subject was treated extensively by Davis [75] in Chapter 13, Vol. 1b of the previous edition of this handbook. The central difference from convection in regions with fixed boundaries is that interfaces can deform by means of phase transformation, and this can greatly enhance fluid dynamical instabilities. For example, for free convection of a pure fluid between vertical concentric cylinders, deformation by phase transformation of the inner cylinder can reduce the critical Grashof number by a factor of more than 10 and result in spiral instabilities. Similarly, phase transformation can increase greatly the critical Taylor number for instability in Taylor-Couette flow. Generally speaking, convection in the melt can help to homogenize the concentration, thus enhancing morphological stability somewhat, but morphological modes and fluid-dynamical modes can couple, so forced convection can easily promote morphological instability in certain directions. See also the book on solidification by Davis (Ref. [64], Chapters 9 and 10) and the book by Johns and Narayanan (Ref. [76], Chapter 7) on interfacial instability for further information and references to the original literature.

Another important topic that is not treated here is phase field theory, which provides important information about growth subsequent to morphological instability. According to phase field theory, the sharp interface between phases is replaced by a diffuse interface described by a continuous phase field variable that changes rapidly over a thin layer. This subject is being treated in the present edition of this handbook by Plapp [77]. In order to get the phase field model to agree with the sharp interface model, it is necessary to modify the phase field equations by extra terms that insure that the basic physics is the same. This was first done by McFadden et al. [78] for pure materials and later by Echebarria et al. [79] for alloys in which the additional terms alleviate solute trapping. But the real power of the phase field model is that it enables the computation of growth forms in the strongly nonlinear regime subsequent to morphological stability. An example of the morphology of cells computed from an early alloy phase field model [80] is shown in Figure 14.12. Note especially the secondary instability showing droplets of solute-rich liquid in the cell grooves. Such droplets have been observed in directional solidification of thin samples of transparent organics, but it remains for more refined phase field models to determine whether they are artifacts of the model.

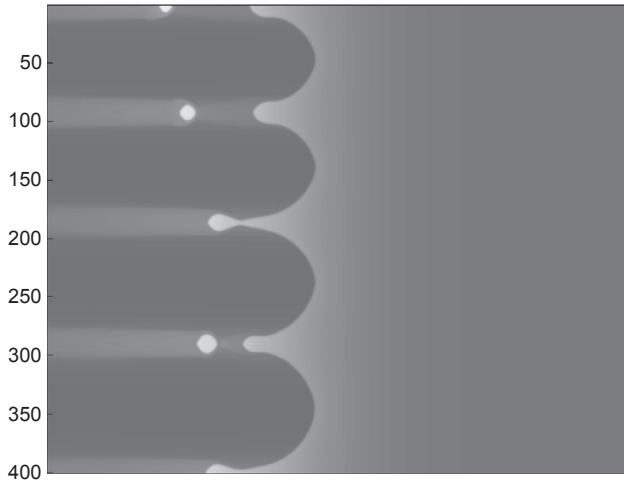


**FIGURE 14.12** Cellular interface computed by Bi [81] from the phase field model for directional solidification of a binary alloy. The light regions show solute ( $k < 1$ ) segregation in the liquid and in the cell grooves. A secondary instability in the cell grooves leads to the encapsulation of liquid droplets.

The general aspects of pattern formation subsequent to morphological stability of alloys has been reviewed in an article by Billia and Trivedi [82] contained in Chapter 14, Vol. 1b of the previous edition of this handbook. This review contains the results of extensive experiments that were analyzed by theory and scaling analysis. It is shown that the transition from cellular to dendritic arrays occurs as velocity is increased during directional solidification; the cell spacing first decreases and then abruptly increases just prior to the transition to a dendritic array, suggesting that some cells go on to become dendrites, and those in between them cease to grow. A detailed experimental study of individual dendrites and comparison with theory by Glicksman [83] is contained in Chapter 14, Vol. 1b of the previous edition of this handbook, but an updated review that also addresses nearly convection-free dendritic growth in microgravity may be found in the present edition of this handbook [84].

## References

- [1] Mullins WW, Sekerka RF. *J Appl Phys* 1963;34:323.
- [2] Mullins WW, Sekerka RF. *J Appl Phys* 1964;35:444.
- [3] Voronkov VV. *Sov Phys Solid State* 1965;6:2378.
- [4] Delves RT. In: Pamplin BR, editor. *Crystal growth*. Oxford: Pergamon Press; 1974. p. 40.
- [5] Langer JS. *Rev Mod Phys* 1980;52.
- [6] Kessler DA, Koplik J, Levine H. *Adv Phys* 1988;37:255.
- [7] Caroli B, Caroli C, Roulet B. In: Godreche C, editor. *Solids far from equilibrium*. Cambridge: Cambridge University Press; 1992. p. 155.
- [8] Coriell SR, McFadden GB. Morphological stability. Chapter 12. In: Hurle DTJ, editor. *Handbook of crystal growth*, vol. 1b. Elsevier; 1993. p. 785.

- [9] Rutter JW, Chalmers B. *Can J Phys* 1953;31:15.
- [10] Tiller WA, Jackson KA, Rutter JW, Chalmers B. *Acta Metall* 1953;1:428.
- [11] Sekerka RF. In: Bever MB, editor. *Encyclopedia of materials science and engineering*. Oxford: Pergamon; 1986. p. 3486.
- [12] Sekerka RF. In: Müller G, Métois JJ, Rudolph P, editors. *Crystal growth – from fundamentals to technology*. Amsterdam: Elsevier; 2004. p. 55.
- [13] Sekerka RF. In: Peiser HS, editor. *Crystal growth*. Oxford: Pergamon; 1967. p. 691.
- [14] Coriell SR, Sekerka RF. *J Cryst Growth* 1983;61:499.
- [15] Wollkind DJ, Segal LA. *Philos Trans R Soc London A* 1970;268:351.
- [16] Coriell SR, McFadden GB, Voorhees PW, Sekerka RF. *J Cryst Growth* 1987;82:295.
- [17] Sekerka RF. *J Appl Phys* 1965;36:264.
- [18] Garandet JP, Boutet G, Lehmann P, Drevet B, Camel D, Rouzaud A, et al. *J Cryst Growth* 2005;279:195.
- [19] Trivedi R, Kurz W. *Acta Metall* 1986;34:1663.
- [20] Zener C. *J Appl Phys* 1949;20:950.
- [21] Langer JS, Müller-Krumbhaar H. *J Cryst Growth* 1977;42:11.
- [22] Langer JS, Müller-Krumbhaar H. *Acta Metall* 1978;26:1681. 1978;26:1689; 1978;26:1697.
- [23] Ivantsov GP. *Dokl Akad Nauk SSSR* 1947;58:567; translation by G. Horvay, General Electric Research Report No. 60-RL-2511M (1960).
- [24] Kessler D, Koplik J, Levine H. *Phys Rev A* 1986;34:4980.
- [25] Kessler D, Koplik J, Levine H. *Adv Phys* 1988;37:255.
- [26] Langer JS. In: Souletie J, Vannimenus J, Stora R, editors. *Chance and matter*. North-Holland; 1987. p. 629.
- [27] Langer JS. *Science* 1989;243:1150.
- [28] Cahn JW. In: Peiser HS, editor. *Crystal growth*. Oxford: Pergamon Press; 1967. p. 681.
- [29] Coriell SR, Parker RL. *J Appl Phys* 1965;36:632.
- [30] Hardy SC, Coriell SR. *J Cryst Growth* 1968;3(4):569.
- [31] Hardy SC, Coriell SR. *J Cryst Growth* 1970;7:147.
- [32] Hardy SC, Coriell SR. *J Cryst Growth* 1973;20:292.
- [33] Coriell SR, Hardy SC, Sekerka RF. *J Cryst Growth* 1971;11:53.
- [34] Temkin DE. *Dokl Akad Nauk SSSR* 1960;132:1307.
- [35] Xu JJ. *Phys Rev E* 1996;53:5051.
- [36] Xu JJ, Yu DS. *J Cryst Growth* 1998;187:314.
- [37] Xu JJ, Yu DS. *J Cryst Growth* 2001;222:399.
- [38] Jackson KA, Gilmer GH, Leamy HJ. In: White CW, Peercy PS, editors. *Laser and electron beam processing of materials*. New York: Academic Press; 1980. p. 104.
- [39] Aziz MJ. *J Appl Phys* 1982;53:1158.
- [40] Huntley DA, Davis SH. *Acta Metall Mater* 1993;41:2025.
- [41] Boettinger WJ, Shechtman D, Schaefer RJ, Biancaniello FS. *Met Trans* 1984;15A:55.
- [42] Coriell SR, Boisvert RF, McFadden GB, Brush LN, Favier JJ. *J Cryst Growth* 1994;140:139–47.

- [43] Van Vaerenbergh S, Coriell SR, McFadden GB. *J Cryst Growth* 2001;223:565.
- [44] Bruson A, Gerl M. *Phys Rev* 1980;B21:5447.
- [45] Rodway GH, Hunt JD. *J Cryst Growth* 1991;112:554.
- [46] Sun DY, Asta M, Hoyt JJ. *Phys Rev B* 2004;69:024108.
- [47] Coriell SR, Sekerka RF. *J Cryst Growth* 1976;34:157.
- [48] Voronkov VV. *Sov Phys Cryst* 1973;17:807.
- [49] Yuferev VS. *Phys Chem Mech Surf* 1983;2:1916.
- [50] Chernov AA, Kuznetsov Yu G, Smol'sky IL, Rozhansky VN. *Sov Phys Cryst* 1986;31:705.
- [51] Chernov AA, Coriell SR, Murray BT. *J Cryst Growth* 1993;132:405.
- [52] Coriell SR, Chernov AA, Murray BT, McFadden GB. *J Cryst Growth* 1998;183:669.
- [53] Coriell SR, Murray BT, Chernov AA. *J Cryst Growth* 1994;141:219.
- [54] Chernov AA, Coriell SR, Murray BT. *J Cryst Growth* 1995;149:120.
- [55] Coriell SR, Murray BT, Chernov AA, McFadden GB. *J Cryst Growth* 1996;169:773.
- [56] Coriell SR, Murray BT, Chernov AA, McFadden GB. *Metall Mater Trans* 1996;27A:687.
- [57] Murray BT, Coriell SR, Chernov AA, McFadden GB. *J Cryst Growth* 2000;218:434.
- [58] McFadden GB, Coriell SR, Moffat TP, Josell D, Wheeler D, Schwarzacher W, et al. *J Electrochem Soc* 2003;150:C591.
- [59] Peppin SSL, Worster MG, Wettlaufer JS. *Proc R Soc A* 2007;463:723.
- [60] Style RW, Worster MG. *Proc R Soc A* 2010;466:1005.
- [61] Ungar LH, Brown RA. *Phys Rev* 1984;B30:3993.
- [62] Yeh SY, Chen CC, Lan CW. *J Cryst Growth* 2011;324:296.
- [63] Eckhaus V. *Studies in nonlinear stability theory*. New York: Springer; 1965.
- [64] Davis SH. *Theory of solidification*. Cambridge: Cambridge University Press; 2001.
- [65] Tuckerman LS, Barkley D. *Phys D* 1990;46:57.
- [66] Newell AC, Whitehead JA. *J Fluid Mech* 1969;38:279.
- [67] Segel LA. *J Fluid Mech* 1969;38:203.
- [68] Morris LR, Winegard WC. *J Cryst Growth* 1969;5:361.
- [69] Sriranganathan R, Wollkind DJ, Oulton DB. *J Cryst Growth* 1983;62:265.
- [70] Wollkind DJ, Oulton DB, Sriranganathan R. *Phys D* 1984;12:215.
- [71] Sushchik MM, Tsimring LS. *Phys D* 1994;74:90.
- [72] McFadden GB, Coriell SR, Sekerka RF. *J Cryst Growth* 1988;91:180.
- [73] McFadden GB, Boisvert RF, Coriell SR. *J Cryst Growth* 1987;84:371.
- [74] Pismen LM. *Patterns and interfaces in dissipative systems*. New York: Springer; 2006.
- [75] Davis SH. Effects of flow on morphological stability. Chapter 13. In: Hurler DTJ, editor. *Handbook of crystal growth*, vol. 1b. Elsevier; 1993. p. 859–97.
- [76] Johns LE, Narayanan R. *Interfacial instability*. New York: Springer; 2002.
- [77] Plapp M. Phase Field Theory. In: Nishinaga T, editor. *Handbook of Crystal Growth*, Vol. 1A. Elsevier; 2014.
- [78] McFadden GB, Wheeler AA, Anderson DM. *Phys D* 2000;144:154.
- [79] Echebarria B, Folch R, Karma A, Plapp M. *Phys Rev E* 2004;70:061604.

- [80] Bi Z, Sekerka RF. *Phys A* 1998;261:95.
- [81] Bi Z. Directional solidification of a binary alloy using the phase field model [Ph.D. thesis]. Carnegie Mellon University; 2001.
- [82] Billia B, Trivedi R. Pattern formation in crystal growth. Chapter 14. In: Hurle DTJ, editor. *Handbook of crystal growth*, vol. 1b. Elsevier; 1993. p. 899–1073.
- [83] Glicksman ME, Marsh SP. The dendrite. Chapter 15. In: Hurle DTJ, editor. *Handbook of crystal growth*, vol. 1b. Elsevier; 1993. p. 1075–122.
- [84] Glicksman ME. Dendritic Growth. In: Nishinaga T, editor. *Handbook of Crystal Growth*, Vol. IA. Elsevier; 2014.

# Phase-Field Models

Mathis Plapp

*PHYSIQUE DE LA MATIÈRE CONDENSÉE, ÉCOLE POLYTECHNIQUE, CNRS, PALAISEAU, FRANCE*

## CHAPTER OUTLINE

<b>15.1 Introduction</b> .....	<b>631</b>
<b>15.2 Order-Parameter Models: The “Bottom-Up” View</b> .....	<b>633</b>
<b>15.3 Diffuse Interfaces at Equilibrium</b> .....	<b>639</b>
<b>15.4 Free-Boundary Problems: The “Top-Down” View</b> .....	<b>645</b>
<b>15.5 Phase-Field Models for Solidification</b> .....	<b>650</b>
15.5.1 Pure Substance .....	650
15.5.2 Anisotropy and Dendritic Growth.....	652
15.5.3 Binary Alloy.....	655
15.5.4 Antitrapping Current.....	657
15.5.5 Multiphase and Multicomponent Solidification .....	659
<b>15.6 Conclusions and Open Questions</b> .....	<b>664</b>
<b>References</b> .....	<b>666</b>

## 15.1 Introduction

Crystal growth can generate a huge variety of different morphologies. A visit to a good minerals collection or the observation of frost and snowflakes in winter will motivate any curious spirit to ask the question by which set of fundamental mechanisms this wealth of shapes is created. There are also some practical reasons that call for a precise understanding of pattern formation in crystal growth: many manmade materials are crystalline, and their properties depend on their microstructure. Hence, which patterns form for given processing conditions is a question of both fundamental and practical interest.

Fundamentally, crystal growth can be divided into two stages: new material has to be transported to the surface of the growing crystal, and it has to find its place in the structure of the growing crystal. Which of these is the rate-limiting step depends on the structure of the crystal interface at the atomistic scale. For crystals that have a microscopically rough interface (atoms can easily attach to and detach from the surface, microscopic fluctuations of the interface structure are large), growth is mainly controlled by bulk transport. This is generally the case for metals. In this case, morphological

instabilities occur, simple growth shapes are unstable, and complex microstructures develop, such as dendrites (tree-like, branched structures). In contrast, for crystals whose interfaces are smooth on an atomic scale, growth is mainly controlled by the kinetics of incorporation, which depends on the density of surface defects such as steps, kinks, and dislocation outcrops. Generally, this growth mode leads to the emergence of strongly faceted shapes, such as found in many minerals.

Historically, the problem of transport-limited crystal growth was first formulated as a *free-boundary problem* [1,2]: the interface is represented by a mathematical surface without thickness, and its local growth velocity is proportional to the flux of heat and/or matter that arrives at the crystal surface. The temperature and concentrations at the surface obey thermodynamic boundary conditions, and fluxes of heat and matter follow the appropriate transport laws inside the volume of both phases. While this formulation is simple and intuitive, free-boundary problems are known to be extremely hard to solve, both analytically and numerically.

Since about 30 years ago, the phase-field method has been established as a new approach to the modelling of transport-limited crystal growth. Surfaces and interfaces are described implicitly by one or several scalar fields, the so-called phase fields that describe the local state of matter. The equations of motion for these fields are rooted in the physics of phase transitions and can be obtained from the laws of out-of-equilibrium thermodynamics. They are coupled to the transport equations for heat and chemical constituents. The advantage of the phase field approach is that an explicit tracking of the evolving interfaces is avoided, which makes it possible to implement phase-field models with the standard mathematical methods used for any set of coupled partial differential equations. The phase-field method has been extremely successful in the description of crystal growth; in particular, it has had a tremendous impact on the understanding of solidification microstructures.

The phase-field method is also used in many other fields, such as, for example, solid-state phase transformations [3] and hydrodynamics [4], and it has become one of the standard methods for the modelling of moving interfaces. Therefore, the available literature is abundant. There are several pedagogic reviews [5–8], an introductory book [9], and several recent papers that review various applications in crystal growth and solidification [10–14]. Therefore, in the present contribution I will not attempt to be exhaustive, but instead present some essential concepts, “bricks” and ingredients that are needed to construct efficient phase-field models for crystal growth. Some of the material is fairly basic, but a thorough understanding of some fundamentals is necessary to appreciate the differences between the various models found in the literature, which are sometimes subtle, but can have important consequences for the performance in simulations. One of the difficulties for a review of phase-field models is that the notations, conventions, and definitions are not standardized and differ between various “schools.” Sometimes, I will attempt to quote several different formulations, but an exhaustive panorama would be too lengthy. I will restrict the presentation to phase-field models for solidification; it will be assumed in the following that the reader is familiar

with the fundamentals of solidification science [15–17]. Phase-field models for step-flow growth during molecular beam epitaxy are briefly reviewed by W. Miller in Chapter 12 of Vol. IA of this book.

For the understanding of phase-field models, it is useful to take two complementary perspectives: a “bottom-up” and a “top-down” view. On the one hand, order-parameter models have originally been developed as a continuum description of phase transitions. They can therefore be obtained, by a coarse-graining procedure, from microscopic models (as described in Section 15.2), which provides one of the centerpieces of phase-field models, namely, a mesoscopic free energy functional. This description naturally yields *diffuse interfaces*, some properties of which will be reviewed in Section 15.3. On the other hand, phase-field models can be seen as a numerical tool for the solution of free-boundary problems; in this “top-down” perspective, the diffuse interfaces are a mathematical regularization of a sharp-interface problem (Section 15.4). These two viewpoints are combined in Section 15.5 to construct phase-field models for a variety of solidification phenomena. Finally, Section 15.6 will present a brief conclusion and a selection of open problems.

## 15.2 Order-Parameter Models: The “Bottom-Up” View

The roots of the phase-field method can be found in the continuum description of phase transitions. A characteristic feature of first-order phase transitions is the coexistence of two thermodynamic phases. This implies the existence of interfaces that delimit the domains occupied by each phase. Seen on a macroscopic scale, these interfaces appear as surfaces of discontinuity in an otherwise continuous medium. However, on the microscopic scale, interfaces have a finite width and an internal structure. The first theory for a phase transition with *diffuse interfaces* was formulated by van der Waals for the liquid–vapor transition in a one-component fluid (pure substance) [18]. Later on, this description was connected to the general theory of phase transitions by Ginzburg and Landau. The first application to materials science was the Cahn-Hilliard equation for the evolution of composition in binary mixtures [19].

In this approach, the spatial structure and time evolution of a heterogeneous system is described by a continuous field that is identified with a physical quantity—the *order parameter* of Landau theory. The time evolution of this field is then given by the laws of out-of-equilibrium thermodynamics, taking into account the nature of the order parameter (scalar, vector, or tensor), its conservation laws, and the symmetries of the problem.

In principle, the evolution equations can also be obtained directly from a microscopic description using the method of *coarse-graining*. While this procedure can in general not be carried out explicitly without drastic approximations, it provides insights into numerous properties of order-parameter models. Therefore, it seems useful to outline, as an example, the principal steps that need to be taken in order to obtain diffuse-interface equations for two simple lattice models, the Ising model for the

ferromagnetic to paramagnetic transition and a binary lattice alloy model; more details can be found in [5].

In its simplest version, the microscopic Hamiltonian of the Ising model is given by

$$\mathcal{H} = -J \sum_{\langle i,j \rangle} S_i S_j - h \sum_i S_i. \quad (15.1)$$

Here,  $i$  and  $j$  denote points on a lattice, which for simplicity is assumed to have periodic boundary conditions and to be large enough for finite-size effects to be negligible. The “spin variables” (magnetic moments)  $S_i$  can take the values  $\pm 1$ , the first sum runs over the pairs of nearest neighbor sites, and the constant  $J$  is positive, such that parallel alignment of neighboring spins is favored. The second term describes the interaction of the spins with the external magnetic field  $h$ .

The thermodynamic (Helmholtz) free energy  $F$  is obtained from the standard formula

$$F = -k_B T \ln Z, \quad (15.2)$$

where  $k_B$  is Boltzmann’s constant,  $T$  is the (fixed) temperature, and the partition function is given by

$$Z = \sum_{\mathcal{C}} \exp\left(-\frac{\mathcal{H}(\mathcal{C})}{k_B T}\right), \quad (15.3)$$

where the sum runs over all possible configurations  $\mathcal{C}$ , that is, all possible sets of spin values  $\{S_i\}$ .

With these definitions,  $F$  is a function of temperature  $T$  and magnetic field  $h$ . In order to describe inhomogeneous systems, some information about the spatial distribution of spin values needs to be retained. To this end, space is divided in “cells,” say cubes of  $\ell^d$  lattice sites, where  $d$  is the space dimension. Then, in each cell (labeled by capital indices), a local magnetization is defined by

$$m_I = \frac{1}{\ell^d} \sum_{i \in I} S_i. \quad (15.4)$$

The calculation of the partition function can now be split in two steps:

$$Z = \sum_{\{m_I\}} \sum_{\mathcal{C}/\{m_I\}} \exp\left(-\frac{\mathcal{H}(\mathcal{C})}{k_B T}\right). \quad (15.5)$$

The idea is that the same set of cell magnetizations can, in general, be obtained by many different microscopic configurations; the second sum in Eqn (15.5) runs over all the microstates that are compatible with the “imposed” set of cell magnetizations. A free energy can then be defined by the logarithm of just the second sum,

$$\mathcal{F}(\{m_I\}) = -k_B T \ln \sum_{\mathcal{C}/\{m_I\}} \exp\left(-\frac{\mathcal{H}(\mathcal{C})}{k_B T}\right). \quad (15.6)$$

This *mesoscopic* free energy depends on the set of  $m_I$  and, therefore, on the spatial structure of the magnetization field. The thermodynamic free energy can then be

obtained by summation over the cell variables, which corresponds to the outer sum in Eqn (15.5).

It is generally impossible to evaluate explicitly these formulas. To make further progress, the standard path is to use mean-field approximations for the coarse-grained free energy. The local magnetization variables are hence replaced by local average values. Furthermore, under the assumption that the magnetization varies slowly on the scale of a coarse-graining cell, the magnetization values in the individual cells can be interpolated by a continuous magnetization field, and the first sum in Eqn (15.5) can be replaced by an integral. As a result, the coarse-grained free energy takes the Ginzburg-Landau form

$$\mathcal{F} = \int_V \left[ \frac{1}{2} \tilde{K} (\nabla m)^2 + f(m) \right] dV, \quad (15.7)$$

where integration is over the volume of the system,  $f(m)$  is the local free energy density (the free energy calculated for a single coarse-graining cell), and the gradient term arises from the interactions between neighboring coarse-graining cells (the constant  $\tilde{K}$  is proportional to the interaction energy  $J$  and to the number of lattice bonds between neighboring cells). For the Ising model, the free energy density in the mean-field approximation takes the form

$$f(m) = \frac{1}{a^d} \left\{ -\frac{zJ}{2} m^2 - hm + k_B T \left[ \left( \frac{1+m}{2} \right) \ln \left( \frac{1+m}{2} \right) + \left( \frac{1-m}{2} \right) \ln \left( \frac{1-m}{2} \right) \right] \right\} \quad (15.8)$$

where  $a$  is the lattice spacing and  $z$  the coordination number of the lattice (number of first neighbors). The first two terms inside the braces represent the spin-spin interactions and the interaction with the external magnetic field, respectively; the third term represents the contribution of the configurational entropy to the free energy. An expression that is easier to handle analytically is obtained by a Taylor expansion around the *critical point* ( $T = T_c = zJ/k_B$ ,  $m = 0$ ), which yields (up to a constant that can be omitted)

$$f(m) = \frac{1}{a^d} \left\{ \frac{1}{2} k_B (T - T_c) m^2 + \frac{1}{12} k_B T_c m^4 - hm \right\}. \quad (15.9)$$

This free energy density is plotted in Figure 15.1 for temperatures above and below the critical temperature. For  $T > T_c$ , the system is *paramagnetic*: the free energy has a single minimum, the location of which is shifted by the application of a magnetic field. For  $T < T_c$ ,  $f(m)$  has a double-well structure. For zero magnetic field, the two minima are equivalent, which corresponds to the coexistence of two phases with opposite spontaneous magnetizations: the system is *ferromagnetic*. The transition from the paramagnetic to the ferromagnetic state is of second order (the equilibrium magnetization varies continuously with temperature). Below  $T_c$ , there is a first-order transition when the magnetic field is varied: the magnetization jumps discontinuously from one minimum to the other when the magnetic field crosses zero. For a range of magnetic fields around  $h = 0$ , there are still two minima, but with different

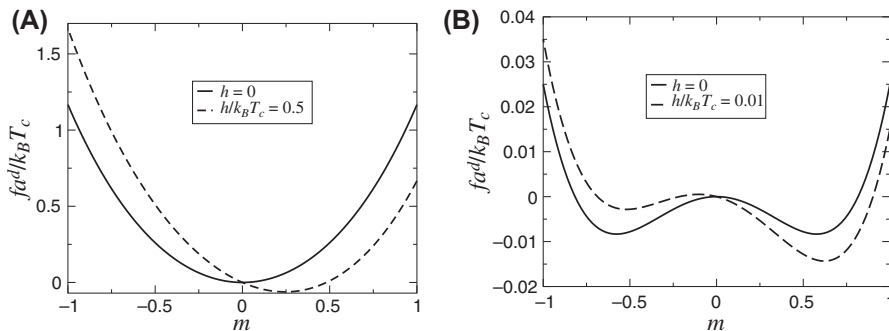


FIGURE 15.1 The free energy density given by Eqn (15.9) for (A)  $T = 2T_c$  and (B)  $T = 0.9T_c$ .

values of the free energy density; the higher one of the two corresponds to a meta-stable phase.

There are several methods to obtain an equation of motion for this model. We will follow here standard arguments of irreversible thermodynamics. Equilibrium is reached when the total free energy is minimal; therefore, an equation which implies a decrease in the free energy will drive the system towards (global or local) equilibrium. The time derivative of the total free energy is

$$\frac{d\mathcal{F}}{dt} = \int_V \frac{\delta\mathcal{F}}{\delta m(\vec{x})} \frac{\partial m(\vec{x}, t)}{\partial t} d\vec{x}, \quad (15.10)$$

where  $\delta\mathcal{F}/\delta m(\vec{x})$  denotes the functional derivative of the free energy functional with respect to the magnetization at the point  $\vec{x}$ , and we have used the chain rule for differentiation. It is easy to see that we always have  $d\mathcal{F}/dt \leq 0$  if we choose

$$\frac{\partial m}{\partial t} = -\Gamma \frac{\delta\mathcal{F}}{\delta m(\vec{x})}, \quad (15.11)$$

where  $\Gamma$  is a positive constant: this expression makes the integrand on the right-hand side of Eqn (15.10) negative or zero. The quantity  $\delta\mathcal{F}/\delta m$ , that is, the variation of the free energy with the local magnetization, can be interpreted as a thermodynamic force, and  $\Gamma$  as a mobility. The local magnetization is a nonconserved quantity, since it can change by simple flips of the spins inside a coarse-graining cell. Equation (15.11) thus simply expresses that the rate of change of the magnetization is proportional to the thermodynamic driving force. It can be shown by statistical mechanics methods (linear response theory) that this proportionality is always valid for small enough driving forces and for systems in which the time evolution results from the superposition of numerous microscopic processes.

Let us now consider a binary lattice alloy model. Lattice sites are occupied by atoms A or B (no vacancies), and atoms interact only when they are on nearest neighbor sites, with atoms of the same kind contributing a negative energy. It can be shown through a simple change of variables that the microscopic Hamiltonian is then completely

equivalent to the one of the Ising model, with “up spins” corresponding to A atoms, and “down spins” to B atoms. As a consequence, the coarse-grained free energy functional is also equivalent. It is usually written in terms of the composition, or local fraction of B atoms (the number of B atoms in a coarse-graining cell divided by the number of lattice sites in the cell), which is related to the magnetization  $m$  by

$$c \leftrightarrow \frac{1+m}{2}. \quad (15.12)$$

The phase transition is now from a miscible to a phase-separated mixture: for  $T > T_c$ , the system is miscible (all compositions are stable). For  $T < T_c$ , a miscibility gap exists: for a range of composition, the system separates into an A-rich and a B-rich phase.

There is one decisive difference between the two systems: whereas the local magnetization can change by a simple flip of a spin, an A atom cannot transform into a B atom. The number of B atoms in a cell can therefore only change if atoms are exchanged between neighboring cells; the composition  $c$  obeys a *conservation law*:

$$\frac{\partial c}{\partial t} + \vec{\nabla} \cdot \vec{J} = 0, \quad (15.13)$$

where  $\vec{J}$  is the exchange current of A and B atoms. Under this constraint, the time derivative of the free energy becomes

$$\frac{d\mathcal{F}}{dt} = \int_V \frac{\delta\mathcal{F}}{\delta c(\vec{x})} \frac{\partial c(\vec{x}, t)}{\partial t} d\vec{x} = - \int_V \frac{\delta\mathcal{F}}{\delta c(\vec{x})} \vec{\nabla} \cdot \vec{J} d\vec{x}. \quad (15.14)$$

Integration by parts yields for a closed system (no mass currents through the system boundaries)

$$\frac{d\mathcal{F}}{dt} = \int_V \vec{J} \cdot \vec{\nabla} \frac{\delta\mathcal{F}}{\delta c(\vec{x})} d\vec{x}. \quad (15.15)$$

A decrease in the free energy can thus be guaranteed by the choice

$$\vec{J} = -M \vec{\nabla} \frac{\delta\mathcal{F}}{\delta c(\vec{x})} = -M \vec{\nabla} \tilde{\mu}, \quad (15.16)$$

with  $M$  a positive constant. Again, this equation has a direct microscopic interpretation. The variation  $\delta\mathcal{F}/\delta c$  (designated by  $\tilde{\mu}$  in the second equality of the right-hand side of Eqn (15.16)) is the change in free energy with composition; the system can therefore lower its energy if B atoms flow to regions where  $\tilde{\mu}$  is lower, and A atoms in the opposite direction. The gradient of  $\tilde{\mu}$  hence drives the mass currents that correspond, on a microscopic level, to exchange processes between A and B atoms. The quantity  $\tilde{\mu}$  is sometimes called “chemical potential,” sometimes “diffusion potential;” it is given by

$$\tilde{\mu} = \rho(\mu_B - \mu_A), \quad (15.17)$$

where  $\mu_i = \partial F / \partial N_i|_{T, V, N_j}$  are the “standard” chemical potentials of A and B atoms, and  $\rho$  is the density of lattice sites (in other words,  $\rho = \mathcal{N}_A / V_m$ , with  $\mathcal{N}_A$  the Avogadro number and  $V_m$  the molar volume of the mixture). Equation (15.16) again is the product of a

thermodynamic driving force (the gradient of diffusion potential) and a mobility  $M$ . The combination of Eqns (15.13) and (15.16) yields the Cahn-Hilliard equation,

$$\frac{\partial c}{\partial t} = \vec{\nabla} \cdot \left[ M \vec{\nabla} \frac{\delta F}{\delta c} \right]. \quad (15.18)$$

At this point, it is useful to make a number of general comments:

- We have obtained the evolution equations for the magnetization and the composition in the canonical ensemble (fixed temperature), with the free energy as the thermodynamic potential. The introduction of a Ginzburg-Landau free energy functional that has the form of an integral over a local free energy density implies the assumption that the individual coarse-graining cells are large enough to make the evaluation of local partition functions and statistical averages meaningful. In this case, the equivalence between statistical ensembles applies, and the evolution equations can also be formulated in other thermodynamic ensembles. Many authors have started from an entropy functional (microcanonical ensemble, see for example Ref. [20]), and used the condition that the local entropy production must always be positive. Grand-canonical approaches have also been used more recently [21–23].
- The mobilities introduced in Eqns (15.11) and (15.16) can depend on local state variables, on space and/or time, as long as they remain positive.
- We have obtained the evolution equations by thermodynamic arguments. It is also possible to derive them from microscopic models, which often makes it possible to obtain expressions for the mobility functions. Lattice models are very naturally simulated by the Monte Carlo method, which defines a microscopic stochastic process. The microscopic master equation can then be used to describe the evolution of local averages. In a kinetic mean-field approximation, it is possible to obtain evolution equations of the form of Eqns (15.11) and (15.18) for simple spin-flip and particle-exchange models, respectively (see Ref. [24] for a review).
- The definition of a coarse-grained free energy functional implies the choice of a coarse-graining length (in the above example, the cell size  $\ell$ ). Obviously, the free energy density as well as the gradient energy coefficient  $\tilde{K}$  depend on this choice, since the number of microscopic configurations inside a coarse-graining cell and the interaction strength between neighboring cells both depend on  $\ell$ . This dependence on  $\ell$  disappears in the mean-field approximation, but is present in more accurate evaluations of the partition functions, which is perfectly natural since the mesoscopic functional  $\mathcal{F}$  can contain only the free energy of all fluctuations on length scales below  $\ell$ . The complete free energy is obtained by the outer summation in Eqn (15.5). In the dynamic Eqns (15.11) and (15.18), these large-scale fluctuation modes can be included by additional stochastic noise terms, which transforms them into Langevin equations. Indeed, it is clear that under a given microscopic dynamics (for example, a Monte Carlo process), the cell variables exhibit fluctuations with an amplitude that depends on the coarse-graining size.

Therefore, the noise amplitude has to be consistent with the free energy functional. More detailed investigations of these questions in the context of solid-state diffusion can be found in Refs [25,26]. Some further issues concerning the addition of noise are discussed in Refs [22,27].

- Whereas coarse-graining is conceptually simple and intuitive, it generally cannot be performed rigorously. It relies on strong assumptions about scale separation: on the one hand, the coarse-graining cells must be large enough to justify the use of local thermodynamic identities; on the other hand, the cells must remain small enough to be considered homogeneous, that is, they must remain smaller than the correlation length. For solid–liquid interfaces in metals, the typical width of the microscopically rough interface is about half a nanometer, which corresponds to only a few atomic distances [28]. Therefore, there exists no intermediate scale between the size of an atom and the thickness of the interface on which coarse-graining could be rigorously performed. In the vicinity of a critical point, where the correlation length diverges, the fluctuations also diverge such that mean-field approximations break down. Therefore, direct quantitative results for the thermodynamic description of specific systems cannot be expected from mesoscopic free-energy functionals, which should rather be seen as a phenomenological description.
- The Taylor expansion that leads from Eqns (15.8) and (15.9) is an example for a Landau expansion. The idea of Landau theory is that for *any* phase transition there exists a suitable order parameter that can distinguish between the different phases. Around a critical point, the free energy density can always be expanded in a polynomial form that only depends on the structure of the order parameter and the symmetries of the considered problem. First-order phase transitions can also be phenomenologically described by such free-energy densities, despite the fact that they may not exhibit a critical point. As a consequence, it is straightforward to write down order-parameter models for a large variety of phenomena: it is sufficient to identify the suitable order parameters and their conservation laws. The Landau expansion, together with gradient square terms, yields the free energy functional, and the conservation laws determine the form of the equations of motion. A classification of the simplest possible models was given by Hohenberg and Halperin [29]. In this list, Eqn (15.11) (one nonconserved order parameter) is called model A, and Eqn (15.18) (one conserved order parameter) model B; model C has one nonconserved and one conserved order parameter and was the original starting point for phase-field models of solidification [30–32]; finally, a model that includes hydrodynamics is called model H. It describes the liquid–vapor transition of a one-component fluid, taking into account conservation of mass, momentum, and energy.

### 15.3 Diffuse Interfaces at Equilibrium

Two-phase coexistence implies the existence of interfaces. Their properties can readily be obtained from the Ginzburg-Landau free energy functional introduced in the

preceding section. This will first be illustrated for the simple example of the Ising model, and then discussed in more generality.

Let us consider a ferromagnetic state of the Ising model ( $T < T_c$ ) without magnetic field ( $h = 0$ ). The local free energy density given by Eqn (15.9) has two minima for

$$f'(m) = 0 \leftrightarrow m = \pm m_{\text{eq}} \quad m_{\text{eq}} = \sqrt{6 \frac{(T_c - T)}{T_c}}. \quad (15.19)$$

In terms of  $\psi = m/m_{\text{eq}}$ , the free energy can be rewritten as

$$\mathcal{F} = \int \frac{1}{2} K (\vec{\nabla} \psi)^2 + H f_{\text{dw}}(\psi), \quad (15.20)$$

with  $K = \tilde{K} m_{\text{eq}}^2 / a^d$ ,  $H = k_B T_c m_{\text{eq}}^4 / (3a^d)$  and the double-well function (with minima at  $\psi = \pm 1$ )

$$f_{\text{dw}}(\psi) = -\frac{\psi^2}{2} + \frac{\psi^4}{4}. \quad (15.21)$$

In this formulation, all the physical parameters are contained in the two constants  $K$  and  $H$ . They have a dimension of energy per unit length and energy per unit volume, respectively. From this, we can immediately deduce fundamental scaling relations for the thickness  $\xi$  of the interface (a length) and its surface free energy  $\gamma$  (energy per unit surface),

$$\xi \sim \sqrt{\frac{K}{H}}, \quad (15.22)$$

$$\gamma \sim \sqrt{KH} \sim H\xi. \quad (15.23)$$

To understand these relations, observe that the first term in the integral of Eqn (15.20) is minimized by a flat profile (with zero gradients), whereas the second one favors values of  $\psi$  close to  $\pm 1$  and is thus minimized by a step function. Therefore, the finite interface thickness results from the competition between the two terms in the functional. Moreover, inside the interface, the field  $\psi$  takes values in between the two minima, such that the interface contributes an extra free energy density of order  $H$  (from the ‘‘potential’’  $Hf_{\text{dw}}$ ) across a space region of thickness  $\xi$ .

For a more rigorous derivation of these relations, consider the equation for an equilibrium interface,  $\delta F / \delta \psi = 0$ , for a planar interface oriented normal to the  $x$  direction, with a profile  $\psi(x)$ . The evaluation of the functional derivative (see Eqn (15.60) below for the precise definition of this procedure) yields

$$-K \partial_{xx} \psi + H f'_{\text{dw}}(\psi) = 0, \quad (15.24)$$

where  $\partial_{xx} \psi$  is shorthand for  $\partial^2 \psi / \partial x^2$ , and  $f'_{\text{dw}}$  denotes the derivative of  $f_{\text{dw}}$  with respect to  $\psi$ . We introduce the dimensionless coordinate  $\tilde{x} = x/W$  with  $W = \sqrt{K/H}$ . After a change of variables from  $x$  to  $\tilde{x}$  and division by  $H$ , Eqn (15.24) becomes

$$-\partial_{\tilde{x}\tilde{x}} \psi + f'_{\text{dw}}(\psi) = 0. \quad (15.25)$$

Therefore, the interface profile  $\psi_{\text{eq}}(\tilde{x})$  is determined by the double-well function; only its length scale depends on the physical parameters.

Far away from the interface, the magnetization tends to its equilibrium values  $m = \pm m_{\text{eq}}$  ( $\psi = \pm 1$ ), and the bulk free energy density is  $Hf_{\text{dw}}(\pm 1)$ . For definiteness, let us suppose that  $\psi(-\infty) = 1$  and  $\psi(\infty) = -1$ . The surface energy  $\gamma$  is defined as the excess free energy (per surface area) due to the presence of an interface. This can be expressed as

$$\begin{aligned}\gamma &= \int_{-\infty}^{\infty} \left\{ \frac{1}{2} K (\partial_x \phi)^2 + H [f_{\text{dw}}(\psi(x)) - f_{\text{dw}}(\pm 1)] \right\} dx \\ &= \sqrt{KH} \int_{-\infty}^{\infty} \left\{ \frac{1}{2} (\partial_{\tilde{x}} \psi)^2 + [f_{\text{dw}}(\psi(\tilde{x})) - f_{\text{dw}}(\pm 1)] \right\} d\tilde{x}.\end{aligned}\quad (15.26)$$

This integral can be simplified with the help of a relation that is obtained from Eqn (15.25) by multiplying both sides with  $\partial_{\tilde{x}} \psi$  and integrating from  $-\infty$  to  $\tilde{x}$ , which yields

$$\frac{1}{2} (\partial_{\tilde{x}} \psi)^2 = f_{\text{dw}}(\psi(\tilde{x})) - f_{\text{dw}}(\pm 1). \quad (15.27)$$

This result can be used to eliminate either one of the two terms in the integral of Eqn (15.26); after the elimination of the square gradient term and a change of integration variable from  $\tilde{x}$  to  $\psi$ ,  $\gamma$  can be evaluated as

$$\gamma = \sqrt{KH} \int_{-1}^1 \sqrt{2[f_{\text{dw}}(\psi) - f_{\text{dw}}(\pm 1)]} d\psi = \sqrt{KH} I \quad (15.28)$$

where  $I$  (the value of the integral) is defined by the second equality. For the fourth-order polynomial given by Eqn (15.21),  $I = 2\sqrt{2}/3$ , and the interface solution is given by

$$\psi(x) = -\tanh\left(\frac{x - x_0}{\sqrt{2}W}\right) \quad (15.29)$$

for an interface centered at  $x_0$ .

Again, several general remarks can be made:

- The fourth-order polynomial given by Eqn (15.21) is the most popular choice for a double-well function, both because it is the lowest-order double-well function that appears in a Landau expansion and because of the existence of a closed-form analytic solution for the interface. However, any other double-well function yields a similar interface shape (that is, a sigmoid curve) because of Eqn (15.25): the modulus of the slope is highest in the center of the interface, where  $\psi$  is “on the top” of the potential barrier.
- The definition of the interface thickness  $\xi$  is somewhat arbitrary, and many different conventions have been used in the literature. One choice that works for arbitrary potentials is to define  $\xi$  as the inverse of the maximum slope,  $\xi = 1/\max(|\partial\psi/\partial x|)$ , which yields  $\xi = \sqrt{2}W$  for the fourth-order polynomial.
- The above results can be used to rewrite the free energy in two different forms, which both have been used in the literature. In the first, the coefficient  $H$  of the

double-well potential is pulled out of the integral, and the definition  $W^2 = K/H$  is used to obtain [33]

$$\mathcal{F} = H \int_V \frac{1}{2} W^2 (\vec{\nabla} \psi)^2 + f_{\text{dw}}(\psi). \quad (15.30)$$

The ratio  $\mathcal{F}/H$  is sometimes called “dimensionless free energy,” although it is the free energy *density* (the integrand) which is dimensionless. Therefore, when the prefactor  $H$  is absorbed in the definition of  $\mathcal{F}$ , the latter acquires the dimension of a volume, and the surface free energy becomes a length [33]. The advantage of this convention is that a rescaling of all lengths by  $W$  yields equations that do not contain any coefficients, such as Eqn (15.25). Another possibility to rewrite the free energy is to eliminate the coefficients  $K$  and  $H$  in the functional in favor of  $\xi$  and  $\gamma$ . The result for the fourth-order polynomial is

$$\mathcal{F} = \int_V \frac{3}{8} \gamma \left[ \xi (\vec{\nabla} \psi)^2 + \frac{f_{\text{dw}}(\psi)}{\xi} \right]; \quad (15.31)$$

both the square gradient and the potential term have to be modified if the interface thickness is to be changed at constant surface energy.

Let us now generalize these results for other interfaces. Consider a mixture of  $K$  different components in which two phases are in coexistence (elastic effects are not included here for simplicity; for a detailed discussion of stress effects on interface thermodynamics, see for example Ref. [34]). The extensive thermodynamic quantities are energy  $E$ , entropy  $S$ , and the number  $N_i$  of particles of species  $i$ , with volume densities  $e$ ,  $s$ , and  $\rho_i$ , respectively. The conjugate intensive variables for  $S$  and  $N_i$  are the temperature  $T$  and the chemical potentials  $\mu_i$ . Since there is an equilibrium between two phases which can exchange energy and particles, all the intensive variables must be equal in the two phases, and uniform in inhomogeneous systems (and, thus, in diffuse interfaces). In contrast, the densities of the extensive quantities can be different in the two phases, and vary through the interface region in a continuous manner, as in the example of the magnetization seen above. Macroscopic thermodynamic properties can be assigned to such profiles through the classic Gibbs construction, illustrated in Figure 15.2: in a system of total length  $L$  that contains an interface normal to the  $x$  direction, the total amount of an extensive quantity of density  $y(x)$  is compared to a macroscopic two-phase system with an interface at position  $x_{\text{int}}$ , and the difference is assigned to the interface,

$$y_{\text{int}} = \left[ \int_0^L y(x) dx \right] - [y_\alpha x_{\text{int}} + y_\beta (L - x_{\text{int}})], \quad (15.32)$$

where  $y_\alpha$  and  $y_\beta$  are the bulk densities of  $y$  in the two phases. If  $y_\alpha \neq y_\beta$ , the value of the interface excess depends on the choice of the interface position  $x_{\text{int}}$ . Therefore, it is always possible to *define* the interface position such that the interface excess is zero. However, when several extensive quantities exhibit variations through the interface, only

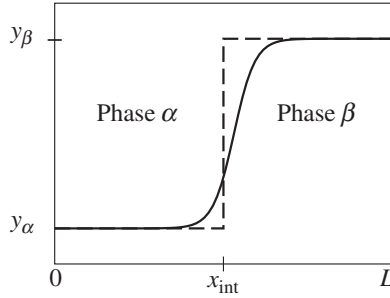


**FIGURE 15.2** Illustration of the Gibbs construction: thermodynamic properties and a position on a macroscopic scale can be assigned to a diffuse interface by comparing the total content of an extensive quantity  $y(x)$  with the one of a step function, localized at the position  $x_{\text{int}}$ , between the macroscopic values of  $y$  in the two phases.

one of the corresponding excess quantities can be made zero by the choice of the interface position, except in the presence of special symmetries.

The interface free energy is the interface excess of the relevant thermodynamic potential, which is often quite loosely called “free energy” without further precisions. “Relevant” means that this potential must have the same value in the two phases; otherwise, the surface energy cannot be defined unambiguously since it would depend on the choice of the interface position. Since the coarse-grained description is based on volume integrals, we will consider a system of fixed total volume  $V$ . In that case, the relevant potential is the grand potential. In contrast, if a fixed pressure is assumed, the relevant potential is the Gibbs free energy. See Ref. [35] for a detailed discussion on how to define interface excesses in this case. For constant volume, the pressure is not an independent variable, but is equal to the negative of the grand potential density,  $-P = e - Ts - \sum_{i=1}^K \mu_i \rho_i$ . The equality of the pressures in the two phases therefore implies

$$e_\alpha - Ts_\alpha - \sum_i \mu_i \rho_i^\alpha = e_\beta - Ts_\beta - \sum_i \mu_i \rho_i^\beta, \quad (15.33)$$

where  $\rho_i^\nu$  are the equilibrium number densities of component  $i$  in phase  $\nu$ .

Two special cases merit further discussion. For a pure substance ( $K=1$ ) in which both phases have equal number densities ( $\rho_\alpha = \rho_\beta$ ), Eqn (15.33) reduces to  $e_\alpha - Ts_\alpha = e_\beta - Ts_\beta$ , that is,  $f_\alpha = f_\beta$ , with the free energy densities  $f_\nu = e_\nu - Ts_\nu$ . Therefore, the surface free energy is given by the excess of the Helmholtz free energy. Note that we have already used this fact in the definition of  $\gamma$  for the magnetic model, Eqn (15.26), in which the two phases are related by the up-down symmetry of the spins. For a binary mixture ( $K=2$ ) of A and B particles with constant number density (or, equivalently, constant molar volume),  $\rho_A + \rho_B = \rho$ ,  $f_\alpha - (\mu_B - \mu_A)\rho_B^\alpha = f_\beta - (\mu_B - \mu_A)\rho_B^\beta$ . Using that the composition  $c = \rho_B/\rho = \rho_B V_a$ , with  $V_a = V_m/\mathcal{N}_A$  the volume occupied by an atom, we find

$$f_\alpha - \bar{\mu}c_\alpha = f_\beta - \bar{\mu}c_\beta = \omega_{\text{eq}}, \quad (15.34)$$

where  $\tilde{\mu} = (\mu_B - \mu_A)/V_a$  is the diffusion potential introduced in Eqn (15.16). The surface free energy is the interface excess of  $\omega = f - \tilde{\mu}c$  with respect to its equilibrium value  $\omega_{\text{eq}}$ ,

$$\gamma = \int_{-\infty}^{\infty} [f - \tilde{\mu}c - \omega_{\text{eq}}] dx. \quad (15.35)$$

Let us now introduce the *phase field*. This name was coined at the beginning of the 1980s when the first diffuse-interface models for solidification were formulated [30–32]. The phase field is a scalar field that specifies the state of matter (solid or liquid). One may ask why such a field is needed, although the thermodynamics of *any* system can be expressed in the traditional thermodynamic variables  $e$ ,  $s$ , and  $\rho_i$ ; indeed, the solid and liquid phases generally have different values for all of these quantities. Why not choose one of them as a marker to distinguish between solid and liquid? The answer to this question lies in the particular nature of the solid–liquid transition, which does not have a critical point, contrary to the other phase transitions that have been discussed so far. Indeed, for a phase-separating mixture, there are two distinct phases at low temperature, which means that not all values of the composition are accessible; however, at high temperature the system becomes completely miscible. This means that there is a unique free energy function  $f(c, T)$  which can describe all possible states of the system. The same holds for the liquid–gas transition and its free energy  $f(\rho, T)$ . For the solid–liquid transition, there is no continuous thermodynamic path that connects solid and liquid, which means that these two phases must be described by separate free energy curves. Therefore, an additional parameter is needed to interpolate between these curves.

A physical interpretation can be given to the phase field as the order parameter of the solid–liquid transition, which can be defined even if there is no critical point for this transition. A pure solid and its liquid are distinguished by the long-range order present in the crystal, which can be probed by diffraction experiments. Order parameter functions can be defined that locally detect crystalline order in the data of molecular dynamics simulations [36,37]. In classical density functional theory, the fundamental field is the probability of presence of an atom at a particular position. Whereas this probability density is uniform in a liquid, for a solid it exhibits peaks around the equilibrium positions of the atoms in the lattice. This means that in reciprocal space the amplitude of certain “density waves” is finite for a solid, but zero for a liquid. Therefore, the amplitudes of density waves can be used as order parameters [38]. If this amplitude is allowed to vary in space on a scale much larger than the lattice spacing, in the spirit of amplitude equations, the free energy for solid–liquid coexistence takes a Ginzburg-Landau form, with a double-well potential and square gradient terms for the amplitude [39]. Therefore, the assumption of a Ginzburg-Landau form for the contribution of the phase field to the free energy is well justified.

The phase field  $\phi$  is usually defined as the normalized order parameter, that is,  $\phi = 0$  in the liquid and  $\phi = 1$  in the solid. All the formulas derived so far for the dimensionless magnetization field  $\psi$  are also valid for the phase field, with the change of variables

$\phi = (1 + \psi)/2$ ; the standard double-well potential used for  $\phi$  is  $f_{\text{dw}} = \phi^2(1 - \phi)^2$ . The phase field  $\phi$  exhibits a variation through the interface, just like the extensive thermodynamic quantities. However, there is no intensive variable that is conjugate to the phase field. The phase field can be related to the volume fraction of solid: in a system of volume  $V$ , the latter is given by  $(1/V)\int_V \phi(\vec{x})$ , and a time evolution of the phase field corresponds to a relaxation of the volume fraction of solid towards its equilibrium value. Since the crystalline order can change locally by short-range motion of the atoms into or out of the equilibrium positions in a crystal lattice, the phase field is a nonconserved quantity and, therefore, must satisfy an equation of the type of Eqn (15.11). However, the evolution of the phase field (interpreted as a volume fraction) depends on the values of the local thermodynamic state variables and, therefore, the equations for  $\phi$ , the temperature, and the composition are intrinsically coupled, as will be detailed below.

## 15.4 Free-Boundary Problems: The “Top-Down” View

In Section 15.2, we have seen how mesoscopic free-energy functionals and equations of motion for the associated order parameters can be obtained by coarse-graining, that is, by averaging over the small length and time scales of the microscopic dynamics. Now, we will take the opposite, “top-down” view and see how phase-field models can be obtained by introducing supplementary small scales into a macroscopic problem.

The starting point are *free-boundary problems*, introduced by Stefan [1,2] for the growth of ice layers at a water surface in contact with cold air. In free-boundary problems, partial differential equations (usually for transport phenomena) need to be solved in domains that evolve with time in response to the fluxes at the boundaries. The time evolution of the domain boundaries is thus a part of the problem solution.

As a simple example, let us consider the freezing of a pure substance (the growth of a one-component pure crystal from its melt). We suppose that the density of solid and liquid are equal and that the melt is quiescent, such that no hydrodynamic flow needs to be taken into account. Under these circumstances, crystal growth is limited by the diffusion of heat: upon solidification, the latent heat is set free and has to be evacuated for crystal growth to continue. This problem can be formulated as a set of equations for the temperature field  $T(\vec{x}, t)$  defined on domains of solid and liquid that are separated by a sharp interface:

$$\frac{\partial T}{\partial t} = D_\nu \vec{\nabla}^2 T \quad (\nu = l, s) \quad (15.36)$$

$$V_n L = \hat{n} \cdot [C_s D_s \vec{\nabla} T|_s - C_l D_l \vec{\nabla} T|_l] \quad (15.37)$$

$$T_{\text{int}} = T_m - \frac{\gamma T_m}{L} \mathcal{K} - \frac{V_n}{\mu_k}. \quad (15.38)$$

The first equation describes the diffusion of heat in the two phases (liquid and solid), with  $D_s$  and  $D_l$  the associated heat diffusion coefficients. The second equation (Stefan condition) expresses the conservation of energy at the interface that advances with normal

velocity  $V_n$ ;  $L$  is the latent heat per unit volume,  $\hat{n}$  the unit normal vector to the interface pointing into the liquid, and  $C_s$  and  $C_l$  the specific heats per unit volume in solid and liquid. Finally, Eqn (15.38) gives the boundary condition for the temperature at the interface, which differs from the bulk melting temperature  $T_m$  by the Gibbs–Thomson effect (capillary shift of the melting temperature), where  $\mathcal{K}$  is the interface curvature, and by interface dissipation due to the finite time of attachment of new atoms to the surface, with  $\mu_k$  being the interface mobility (for more details, see for example Ref. [17]). Equation (15.38) also implies that the temperature is continuous at the interface.

For future reference, let us restate this set of equations in terms of a dimensionless temperature field

$$u = \frac{T - T_m}{L/C_l}. \quad (15.39)$$

The Equations (15.36)–(15.38) become

$$\frac{\partial u}{\partial t} = D_\nu \vec{\nabla}^2 u \quad (\nu = l, s) \quad (15.40)$$

$$V_n = \hat{n} \cdot \left[ (C_s/C_l) D_s \vec{\nabla} u|_s - D_l \vec{\nabla} u|_l \right] \quad (15.41)$$

$$u_{\text{int}} = -d_0 \mathcal{K} - \beta V_n. \quad (15.42)$$

Here,  $d_0 = \gamma T_m C_l / L^2$  is the thermal capillary length and  $\beta = C_l / (\mu_k L)$  is the kinetic coefficient. A particularly simple case that has been widely employed is the *symmetric model*, in which  $C_s = C_l$  and  $D_s = D_l$  are assumed.

The free-boundary formulation is appealing because it directly corresponds to our intuition about the motion of macroscopic domains—the finite thickness of the interfaces is hidden from our eyes or even the standard means of observation (for example, optical microscopes). Of course, this very fact is also the reason why sharp-interface models are an excellent description: there is a scale separation of several orders of magnitude between the thickness of the interface and the characteristic length scales of the macroscopic problem, such that the internal structure of the interfaces has no detectable effect on the macroscopic evolution.

However, free-boundary problems are notoriously difficult to solve. In *front-tracking methods*, the interface is represented explicitly, for example by marker points that are located on the interface (Figure 15.3). Boundary conditions and fluxes are then evaluated at this boundary, and the velocity of the points is computed. Problems arise, however, if the length of the interface increases (by ramification, for example) or if topological changes such as pinch-off or coalescence occur, because the interfaces need to be frequently remeshed in order to maintain a desired precision. The alternative idea of *front-capturing methods* is to use an additional scalar field to implicitly represent the interface by one of its level sets. Since the level set changes when the field evolves, the laws of motion for the interface need to be translated into an evolution equation for the new field that takes into account the correct boundary conditions. The most well-known method of this type is probably the level-set method [40]. The phase-field

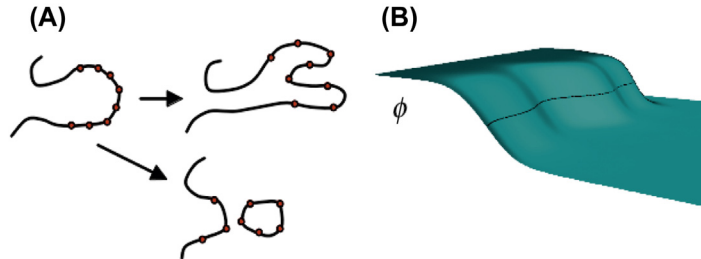


**FIGURE 15.3** (A) Illustration of interface tracking versus interface capturing methods: in interface tracking, the interface is represented *explicitly*, for example by marker points. (B) In interface capturing, it is treated *implicitly* as a level set of a function that evolves with time (black line on the blue surface).

method can be seen as another member of this family, with the additional advantage that its thermodynamic construction implies that number of boundary conditions at the interface, as well as the important conservation laws, are “automatically” incorporated. In this perspective, the phase field is seen as a mathematical tool for the computation of the interface evolution, and its equation of motion only needs to reproduce, on a large scale, the desired free-boundary problem.

Mathematically, this view of the phase field corresponds to a *regularization* of the free-boundary problem. Indeed, [Eqns \(15.36\)–\(15.38\)](#) implicitly contain singularities: the material’s properties (specific heat, diffusion coefficient) exhibit jumps at the interface, and the latent heat is released at the infinitely thin interface, which corresponds to a singular heat source term. Formally, this can be made apparent by rewriting [Eqns \(15.40\)–\(15.42\)](#) in terms of distributions: the domain occupied by the solid is represented by an indicator function,  $\theta_s(\vec{x})$ , which equals one inside the solid, and zero outside. The interface location can then be described by a Dirac  $\delta$  function that is related to the derivative of  $\theta_s$ ,  $\nabla\theta_s = -\delta(\vec{x} - \vec{x}_{\text{int}})\hat{n}$ , where  $\hat{n}$  is again the unit normal to the interface pointing into the liquid, and  $\vec{x}_{\text{int}}$  is any point located on the interface. Detailed discussions about this procedure can be found in [\[17,41–44\]](#).

The numerical treatment can be simplified by smoothing out these singularities. The smoothed indicator function of the solid domain can directly be identified with the phase field. In this spirit, the thickness of the smooth interfaces is not linked to any physical quantity, but is a mathematical parameter that can be freely chosen as long as the necessary scale separation is maintained. As a simple example, reconsider [Eqn \(15.31\)](#) for the surface free energy with  $\xi$  as a free parameter. It can be seen, on the one hand, that in the limit  $\xi \rightarrow 0$  the free energy excess is concentrated in an infinitely thin layer (while keeping a constant value), which corresponds to the sharp-interface formulation. On the other hand, an interface with a given free energy can be represented by a profile of arbitrary thickness  $\xi$  if the two terms in the interfacial free energy density are properly rescaled, as expressed by [Eqn \(15.31\)](#).

The smoothing of a sharp interface as described by [Eqn \(15.31\)](#) is exact for a stationary planar interface. When the interface is curved and/or in motion, the smoothing

(which corresponds to the introduction of the additional length scale  $\xi$ ) induces errors with respect to the original free-boundary problem, which need to be quantified if the method is to be used as a reliable simulation tool. This can be accomplished by the method of *matched asymptotic expansions*, often also called boundary-layer calculations. The main steps of such a formal calculation are the following.

1. Define two different coordinate systems. The first one corresponds to the sharp-interface problem (“outer scale”), characterized by a macroscopic scale  $l$  specific to the considered problem (for example, the tip radius in the case of dendritic growth). The second (“inner scale”) is attached to the interface, and scaled by the interface thickness  $\xi$ . The ratio  $\varepsilon = \xi/l$  defines a small parameter.
2. Formally expand the relevant fields as a power series in the parameter  $\varepsilon$  on the two different scales, which gives an outer expansion and an inner expansion.
3. Solve the equations of the phase-field model perturbatively order by order in  $\varepsilon$  in each region, using the relevant coordinate system.
4. Match the two expansions order by order using the condition that the limit of the inner expansion far from the interface must coincide with the limit of the outer expansion when the interface is approached.
5. The results of this procedure are boundary conditions for the relevant fields on the outer scale which are determined by the equations on the inner scale. In general, these boundary conditions also take the form of a power series in  $\varepsilon$ .

The explicit calculation of the matched asymptotics is quite tedious and has been presented in detail in several publications [8,33,45,46]. Therefore, here only an example for a particular model will be reviewed: the celebrated phase-field model of Karma and Rappel [33]. It consists of two coupled equations for a phase field  $\psi$  that varies between +1 (solid) and  $-1$  (liquid) and the dimensionless temperature field  $u$ , defined in Eqn (15.39),

$$\partial_t \psi = W^2 \nabla^{-2} \psi + \psi - \psi^3 - \lambda u (1 - \psi^2)^2, \quad (15.43)$$

$$\partial_t u = D \nabla^{-2} u + \frac{1}{2} \partial_t \psi. \quad (15.44)$$

Here,  $W$  is the interface thickness as introduced in Eqn (15.30), and  $\lambda$  is a dimensionless constant. Details about the derivation of this model will be given in Section 15.5 below. In order to illustrate the procedure of asymptotic matching, we consider a planar interface of a solid that grows towards the positive  $x$  direction into a melt of initial dimensionless temperature  $u(\infty) = -1 - \Delta$  with  $0 < \Delta \ll 1$ . It is easy to verify that the free-boundary problem has a steady-state solution: an interface propagating with a constant velocity  $V = \beta\Delta$  and the temperature given by  $u = -\Delta$  for  $x < x_{\text{int}}$  and  $u = -1 - \Delta + \exp[-(x - x_{\text{int}})V/D]$  for  $x > x_{\text{int}}$ . The numerical solution of the phase-field model given by Eqns (15.43) and (15.44) is plotted in Figure 15.4 on the two relevant scales. On the outer scale (given by the diffusion length  $l = D/V$ ), the phase-field profile appears as a sharp step, and the slope of the temperature field has an apparent discontinuity at the

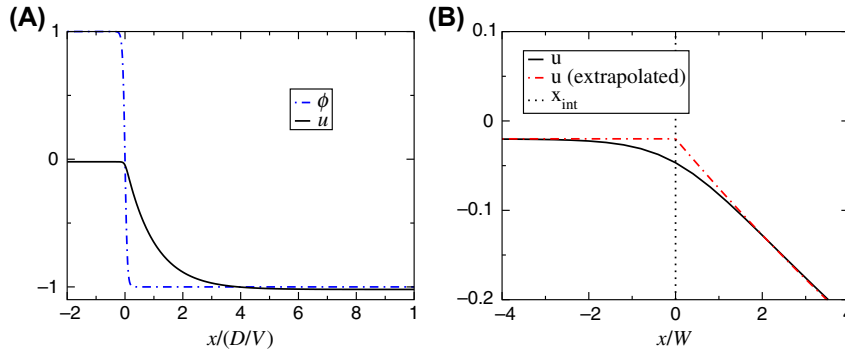


**FIGURE 15.4** Steady-state solution of Eqns (15.43) and (15.44) for  $\Delta = 0.02$  and  $\lambda = 1$ , plotted on the scale of the diffusion length  $l = D/V$  in (A) and on the scale of the interface thickness  $W$  in (B).

interface, as prescribed by the Stefan condition, Eqn (15.41). On the inner scale  $W$ , the slope of the temperature field changes slowly and continuously, since the source of latent heat is not concentrated in a single point, but “smeared out” over the entire interface region.

The two dash-dotted lines in Figure 15.4(B) are fits to the asymptotes of the inner solution far from the interface, extrapolated to the interface position (the point where  $\phi = 0$ ). This is an illustration of the matching condition between inner and outer fields: the boundary conditions for the field  $u$  “seen” on the outer scale correspond to the values of these asymptotes at the interface. Note that (1) the two asymptotes reach the same value at the interface position, so that the temperature is continuous on the outer scale, and (2) that the value of  $u$  at the intersection point (that is, the boundary condition on the outer scale) does not correspond to any value of the actual field  $u$  taken inside the interface.

The main result of the asymptotic calculations is that the system of Eqns (15.43) and (15.44) is equivalent to the symmetric model of solidification, with

$$d_0 = a_1 \frac{W}{\lambda} \quad (15.45)$$

$$\beta = a_1 \left[ \frac{\tau}{\lambda W} - a_2 \frac{W}{D} \right], \quad (15.46)$$

where  $a_1 = 5\sqrt{2}/8$  and  $a_2 = 0.6267$  are numbers of order unity. The first of these equations describes the Gibbs–Thomson effect, and is “naturally” built into the phase-field model, as will be described below. The second deserves some more comments.

Equation (15.46) contains two terms. The first one is obtained if the temperature field is assumed to be constant inside the interface, and describes the dissipation due to a homogeneous undercooling of the interface. The second term is due to the inhomogeneities of the temperature field inside the interface, which are illustrated in Figure 15.4(B). After what has been said above, it may seem surprising that this contribution plays an important role: the characteristic scale for the variations of the

temperature field is the diffusion length and, therefore, an inhomogeneity on the scale of the interface should be unimportant if  $WV/D$  is small enough. However, this reasoning neglects the heat source term in Eqn (15.44): this term varies on the scale of  $W$  and thus always creates contributions to the diffusion field on that scale; therefore, the second term of Eqn (15.46) is important even for small velocities [33].

The expression of the kinetic coefficient given by Eqn (15.46) is of crucial importance. Since there are two contributions of opposite sign, it is possible to choose  $\beta = 0$ , that is, to simulate interfaces in local equilibrium, with arbitrary interface thickness. The choice is limited, of course, by the convergence of the asymptotic matching procedure, which requires a sufficient separation between inner and outer scales. In practice, good convergence can often be obtained even with a scale ratio as large as 0.1. In order to appreciate the gain in computational time that can be achieved by this procedure, it is sufficient to remark that the smallest grid spacing needed to resolve a diffuse-interface model is proportional to the interface thickness. Therefore, being able to “upscale” the interface thickness with respect to its physically realistic value permits the use of larger grid spacings and, therefore, also of larger time steps. For a simple explicit algorithm on a regular grid, the number of numerical operations scales as  $1/W^{d+2}$  [33], and thus an increase of the interface thickness by a factor of 100 provides a gain of  $10^{10}$  in the computation time in three dimensions ( $d = 3$ )!

## 15.5 Phase-Field Models for Solidification

The construction of a few elementary phase-field models for solidification will now be reviewed. In this exposition, the “bottom-up” and thermodynamic viewpoint is taken as a guideline, but repeated use of the “top-down” philosophy is also made in order to obtain efficient models that can be used to calculate solidification microstructures for realistic parameters.

### 15.5.1 Pure Substance

Microstructure formation in a pure substance is mainly of academic interest. The growth of a dendritic monocrystal is a paradigmatic problem of pattern formation and has attracted an enormous amount of attention over many decades. It comes, therefore, as no surprise that this was also one of the first test beds for the accuracy of phase-field models.

Let us consider the symmetric model of solidification, introduced in Section 15.4, and choose the free energy as the thermodynamic potential (canonical ensemble). The free energy functional is written in terms of a phase field  $\phi$  that takes the values  $\phi = 1$  in the solid and  $\phi = 0$  in the liquid as

$$\mathcal{F} = \int_V f_{\text{int}}(\phi, \vec{\nabla}\phi) + g(\phi)f_s(T) + (1 - g(\phi))f_l(T). \quad (15.47)$$

Here,  $f_{\text{int}}$  represents the surface energy contribution and is of the form of Eqn (15.20), with  $f_{\text{dw}} = \phi^2(1 - \phi)^2$ ,  $f_s(T)$  and  $f_l(T)$  are the free energy densities of solid and liquid, respectively, and  $g(\phi)$  is an interpolation function that satisfies

$$g(0) = 0 \quad g(1) = 1 \quad g'(0) = g'(1) = 0. \quad (15.48)$$

The two choices that are most frequently used in the literature are the polynomials  $g(\phi) = 3\phi^2 - 2\phi^3$  and  $g(\phi) = 10\phi^3 - 15\phi^4 + 6\phi^5$ . The motivation for Eqn (15.47) is easily understood: both of the quoted expressions for  $g(\phi)$  are monotonous in  $\phi$  and, therefore,  $g(\phi(\vec{x}))$  is an approximation for the step function  $\theta_s(\vec{x})$  and  $g(\phi)f_s(T) + (1 - g(\phi))f_l(T)$  approximates the bulk free energy in the sharp-interface formulation. Moreover, the first term, when integrated across the interface, yields the surface free energy, so that the volume integral of  $f_{\text{int}}$  is an approximation of the surface tension times the interfacial area.

The last condition in Eqn (15.48),  $g'(0) = g'(1) = 0$ , ensures that the bulk equilibrium values of the phase field are always equal to 0 or 1. Indeed, the phase field follows a nonconserved equation with mobility  $\Gamma$ ,

$$\frac{1}{\Gamma} \partial_t \phi = - \frac{\delta \mathcal{F}}{\delta \phi} = K \vec{\nabla}^2 \phi - H f'_{\text{dw}}(\phi) - g'(\phi) [f_s(T) - f_l(T)]. \quad (15.49)$$

For a homogeneous system ( $\vec{\nabla} \phi = 0$ ), since  $g'(0) = g'(1) = 0$ , the two fixed points of this equation are  $\phi = 0$  and  $\phi = 1$ , even when  $T \neq T_m$  and thus  $f_s \neq f_l$ .

The equation for the temperature can be obtained with the help of thermodynamic identities. First, we exploit the fact that the variation of the free energy with respect to the temperature is the opposite of the entropy density,

$$\frac{\delta \mathcal{F}}{\delta T} = -s(T, \phi) = -s_s(T)g(\phi) - s_l(T)[1 - g(\phi)], \quad (15.50)$$

where  $s_v = -\partial f_v(T)/\partial T$  are the entropy densities of liquid and solid. Next, we use that at constant density  $de = T ds$ , and find

$$de = T \frac{\partial s}{\partial T} dT + T \frac{\partial s}{\partial \phi} d\phi \quad (15.51)$$

with the help of the chain rule. Finally, we divide this equation by  $dt$ , combine it with the conservation law for the internal energy density,

$$\partial_t e = \vec{\nabla} \cdot (C D \vec{\nabla} T), \quad (15.52)$$

and use that the specific heat  $C = T \partial s / \partial T$  and the latent heat  $L = T[s_l(T) - s_s(T)]$ . The result is

$$C(\phi, T) \partial_t T = \vec{\nabla} \cdot (C(\phi, T) D \vec{\nabla} T) + L g'(\phi) \partial_t \phi. \quad (15.53)$$

In the case of the symmetric model,  $C$  is independent of  $\phi$ . Since, in addition, we are interested in a limited range of temperatures around the melting point, we may approximate the values of  $C$ ,  $s_s$ ,  $s_l$ , and  $L$  by their values at the melting point. Then, we obtain the simple equation,

$$\partial_t T = \vec{\nabla} \cdot (D \vec{\nabla} T) + \frac{L}{C} g'(\phi) \partial_t \phi, \quad (15.54)$$

which is very intuitive: the temperature changes by heat diffusion in the bulk and by the release of latent heat at the interface. The equation for the phase field can also be simplified by expanding the free energies in the right-hand side around the melting temperature, which yields

$$\frac{1}{\Gamma} \partial_t \phi = K \nabla^2 \phi - H f'_{\text{dw}}(\phi) - g'(\phi) \frac{L}{T_m} (T - T_m). \quad (15.55)$$

The model of Karma and Rappel can now be obtained from these equations by the following steps:

1. Choose the fifth-order polynomial for  $g(\phi)$  and the standard fourth-order polynomial for  $f_{\text{dw}}$ .
2. Replace the function  $g(\phi)$  by another function  $h(\phi)$  in the equation for the temperature. This function describes how the latent heat is released inside the interface and should, therefore, satisfy  $h(0) = 0$  and  $h(1) = 1$ . If  $h(\phi) \neq g(\phi)$ , the model is no longer variational; however, it has been shown in Ref. [33] that more efficient models can be obtained with this additional freedom. In Eqn (15.44),  $h(\phi) = \phi$ .
3. Change variables from  $\phi$  to  $\psi = (1 + \phi)/2$  and from  $T$  to the dimensionless field  $u$ . Divide the equation for the phase field by the constant  $H$  contained in  $f_{\text{int}}$ , define the phase-field relaxation time by  $\tau = 1/(\Gamma H)$ , and combine all constants and numerical prefactors in the last term on the right-hand side in the parameter  $\lambda$ . The expression for  $\lambda$  that results from these steps is identical to Eqn (15.45). This shows that the Gibbs–Thomson effect is naturally present in the phase-field model through its thermodynamic construction.

## 15.5.2 Anisotropy and Dendritic Growth

All equations discussed so far have been *isotropic*. It is clear that such equations cannot describe the phenomenon of dendritic growth since a dendrite has well-defined privileged growth directions that are set by the crystallographic axes of the solid. According to microscopic solvability theory, two different effects linked to the crystallographic structure have a decisive influence on the selection of the dendrite operating state: the anisotropies of the interface free energy and of the interface mobility.

The static (capillary) anisotropy leads to a dependence of the interface free energy on the interface orientation. The coordinate system is attached to the crystallographic axes of the growing monocrystal, and the surface free energy is expressed as a function of the interface normal  $\hat{n}$  as

$$\gamma(\hat{n}) = \bar{\gamma} a_c(\hat{n}), \quad (15.56)$$

where  $\bar{\gamma}$  is the mean surface free energy and  $a_c(\hat{n})$  is a dimensionless function. Similarly, the interface mobility  $\mu_k$ , or equivalently the kinetic coefficient  $\beta$  of Eqn (15.42), may depend on the orientation as

$$\beta(\hat{n}) = \bar{\beta} a_k(\hat{n}). \quad (15.57)$$

These anisotropies lead to a modification of the Gibbs–Thomson boundary condition in the sharp-interface problem. Equation (15.42) is replaced by

$$u_{\text{int}} = -d_0 \sum_{i=1,2} \left[ a_c(\hat{n}) + \frac{\partial^2 a_c(\hat{n})}{\partial \theta_i^2} \right] \frac{1}{R_i} - \beta(\hat{n}) V_n, \quad (15.58)$$

where the capillary length  $d_0$  is now evaluated using the mean surface free energy  $\bar{\gamma}$ ,  $R_i$  are the local principal radii of curvature of the interface, and  $\theta_i$  are derivatives with respect to the angle along the corresponding principal directions. The new terms arise from the fact that now the interface energy can change in two ways, by a change in the surface area or by a rotation with respect to the crystallographic axes.

Since the phase-field methodology is based on a free energy functional, it is straightforward to incorporate capillary anisotropy by letting the surface free energy contribution  $f_{\text{int}}$  in Eqn (15.47) depend on the interface orientation. In view of the general scaling relation for the surface free energy given by Eqn (15.23), there are several possibilities to achieve this. Historically, the first idea was to make the coefficient of the square gradient term depend on orientation [47–49]. In the formalism of Eqn (15.30) (dimensionless free energy density), it is sufficient to replace  $W$  by

$$W(\hat{n}) = \bar{W} a_c(\hat{n}). \quad (15.59)$$

The kinetic anisotropy can then be incorporated by choosing the orientation-dependent phase-field relaxation time by Eqn (15.46), which remains valid for anisotropic interfaces if  $W$  is replaced by its orientation-dependent value [33].

This method works well for weak anisotropy. However, Eqn (15.59) implies that there is also a variation of the interface thickness with orientation, which may lead to numerical problems for strong anisotropy. This can be avoided by using the formulation of Eqn (15.31), which directly makes  $\gamma$  and  $\xi$  appear in the free energy functional, and by replacing  $\gamma$  by  $\gamma(\hat{n})$  at constant  $\xi$ . This form of the functional was found to perform well for strong anisotropy [50].

In both cases, the equation for the phase field has to be modified. The correct equation is “automatically” generated by the evaluation of the functional derivative. For a free energy of the form  $\mathcal{F} = \int_V f(\phi, \nabla \phi)$ , where  $f(\phi, \nabla \phi)$  is the total free energy density (with local and square gradient terms), the general formula for the functional derivative is

$$\frac{\delta \mathcal{F}}{\delta \phi} = \frac{\partial f}{\partial \phi} - \sum_{i=1}^d \frac{\partial}{\partial x_i} \frac{\partial f}{\partial (\partial_i \phi)}, \quad (15.60)$$

where  $d$  is the dimension of space,  $x_i$  are the (Cartesian) coordinates, and  $\partial_i \phi$  denotes the  $i$ th component of  $\vec{\nabla} \phi$ . The outward unit normal vector is expressed in terms of the phase field as

$$\hat{n} = - \frac{\vec{\nabla} \phi}{|\vec{\nabla} \phi|}. \quad (15.61)$$

Since  $a_c$  is a function of  $\hat{n}$  and thus of  $\vec{\nabla}\phi$ , the derivatives of the free energy density with respect to the gradient components generate the derivatives of  $a_c$  appear with respect to the orientation in Eqn (15.58). This straightforward incorporation of surface energy anisotropy is one of the major advantages of the phase-field model with respect to sharp-interface methods. Indeed, the curvatures, directions, and angles that appear in Eqn (15.58) are contained in the functional derivative of the phase field and do not need to be evaluated explicitly.

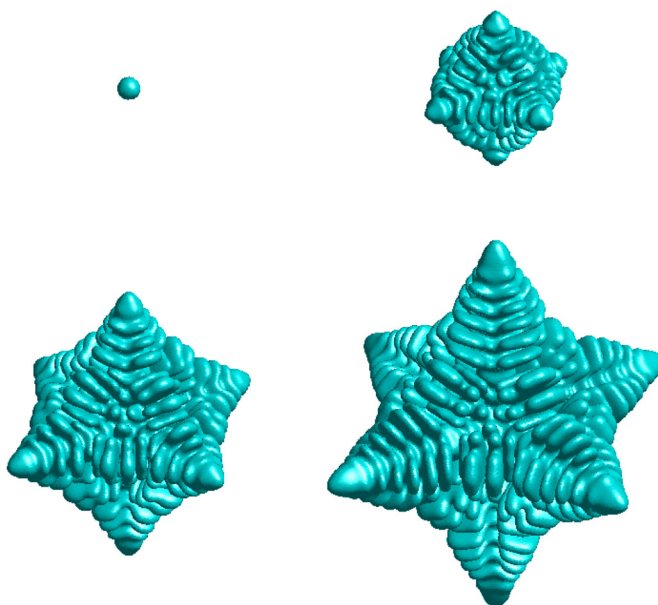
The anisotropy function that has been most extensively used is the “standard” cubic anisotropy given by

$$a_c(\hat{n}) = 1 + \varepsilon_c \left[ 4(n_x^4 + n_y^4 + n_z^4) - 3 \right], \quad (15.62)$$

where  $\varepsilon_c$  is the anisotropy strength; an equivalent expression holds for the kinetic anisotropy. In two dimensions, the interface orientation is described by a single angle  $\theta$ , with  $\hat{n} = (\cos \theta, \sin \theta)$ , and we have simply  $\gamma(\theta) = \bar{\gamma}[1 + \varepsilon_4 \cos(4\theta)]$ . Simulations of dendritic growth have been carried out using this form of the anisotropy, and the results are in good agreement with solvability theory both at high [33,51] and low undercooling [52]. An example for such a dendrite is shown in Figure 15.5. Good agreement with experiments has also been achieved concerning the anisotropic shape of the dendrite tip at low undercooling [52,54] and the growth velocity of nickel dendrites at high undercooling [55]. This proves that a quantitative description of dendritic growth in a pure substance can be obtained with the help of the phase-field method.

It should also be mentioned that for anisotropies that are strong enough to generate *forbidden orientations*, the phase-field model has to be amended. Indeed, in this

**FIGURE 15.5** Growth of a dendrite simulated with the anisotropic version of the phase-field model for a pure substance, given by Eqns (15.43) and (15.44), with an anisotropy of the surface free energy given by Eqn (15.62) with  $\varepsilon_c = 0.00625$ , and isotropic (vanishing) kinetics ( $\beta(\hat{n}) = 0$ ). The dimensionless undercooling is  $\Delta = 0.1$ , that is, the initial and boundary values of  $u = -0.1$ . The simulation is carried out with the multiscale algorithm described in Ref. [53].



situation, there exist orientations in which an interface is unstable with respect to the formation of hill-and-valley structures [56]; for interfaces in these orientations, the equations outlined above become ill-posed, and the model has to be regularized, either by a “convexification” of the anisotropy function [57] or by the addition of higher-order derivatives (such as the square of the Laplacian, or the square of the local interface curvature) in the free-energy functional. See Ref. [50] for a more detailed discussion of these issues and the various models that have been proposed.

### 15.5.3 Binary Alloy

Alloy solidification is obviously of great practical importance. Whereas “real” alloys used in metallurgy usually have multiple components, binary alloys offer the simplest setting in which to develop the methods that can later be extended to multicomponent systems. Therefore, let us come back to the model system of a binary alloy, which is assumed to have constant total number density  $\rho$  (or, equivalently, constant molar volume). The new variable with respect to the pure substance is the composition  $c = \rho_B/\rho$ .

The earliest attempts to formulate models for binary alloys just extended the formalism for a pure substance presented above (to be more precise, they were not exactly formulated as presented below, but they can easily be brought into this form) [58,59]. The free energy densities  $f_s$  and  $f_l$  of the functional given by Eqn (15.47) are now functions of both  $T$  and  $c$ , and the equation of motion for the variable  $c$  (a conserved quantity) is obtained by the standard procedure,

$$\partial_t c = -\vec{\nabla} \cdot \vec{J} = \vec{\nabla} \cdot \left( M \vec{\nabla} \frac{\delta \mathcal{F}}{\delta c} \right). \quad (15.63)$$

While this model is a viable representation of the physical system if the thickness of the phase field interface has its natural (atomistic) width, it is difficult to use it with “upscaled” interfaces. The reason is that the interface properties intrinsically depend on the bulk thermodynamics in this model. This can be understood in several manners. As already found in Eqn (15.34) in Section 15.3, equilibrium between solid and liquid in a mixture implies that the function  $\omega_\nu = f_\nu - \tilde{\mu}c_\nu$  takes the same values  $\omega_{\text{eq}}$  for liquid and solid ( $\nu = l, s$ ). Since the composition of solid and liquid in an alloy differ, this implies that there are two extensive quantities ( $f$  and  $c$ ) which vary across the interface, in addition to the phase field  $\phi$ . If Gibbs dividing surfaces are constructed by the condition of zero interface excesses for  $c$ ,  $\phi$ , and  $f$  following the procedure outlined in Section 15.3, the positions of the three surfaces will, in general, not coincide, which implies that the interface thermodynamics is nontrivial [34]. The profiles of  $\phi$  and  $c$  at equilibrium are actually related, because the condition that the diffusion current vanishes yields

$$\frac{\delta \mathcal{F}}{\delta c} = g(\phi) \frac{\partial f_s}{\partial c} + (1 - g(\phi)) \frac{\partial f_l}{\partial c} = \tilde{\mu}_{\text{eq}} = \text{constant}. \quad (15.64)$$

This equation relates  $c$  and  $\phi$ , and at a given point  $x$  within the interface,  $g(\phi(x))f_s(c(x)) + (1 - g(\phi(x)))f_l(c(x)) - \tilde{\mu}c(x)$  generally differs from  $\omega_{\text{eq}}$ . According to Eqn (15.35), this

gives a contribution to the interface excess free energy  $\gamma$ . This fact was detected for the first time in Ref. [60].

Another way to reach the same insight is to write down the equilibrium condition for the phase field across a planar interface. It reads

$$0 = -\frac{\delta\mathcal{F}}{\delta\phi} = K\partial_{xx}\phi - Hf'_{\text{dw}}(\phi) + g'(\phi)[f_s(c, T) - f_l(c, T)]. \quad (15.65)$$

For a pure substance, the free energy densities of solid and liquid are equal; this is not the case for alloys. Therefore, in the interface (where  $g'(\phi) \neq 0$ ), a driving force acts on the phase field that competes with the terms proportional to  $K$  and  $H$  to shape the interface profile. As a consequence, the surface free energy does not follow the simple scaling of Eqn (15.23), but also depends on the choice of the bulk free energies.

Different solutions have been developed to overcome this problem and to obtain models in which the interface width can be more easily adjusted. The first idea was to start from a “phase-superposition” picture that is based on the general principles of volume-averaged transport equations for multiphase systems [61]. Solid and liquid are seen as two independent macroscopic phases, with two separate composition fields  $c_s$  and  $c_l$ , which overlap in the diffuse interface region. Since there is, in reality, only one global composition, the additional degree of freedom has to be removed by a supplementary condition. In the case of a dilute binary alloy, one may use the partition relation  $c_s = kc_l$ , where the partition coefficient  $k$  is a constant. With the help of this relation,  $c_s$  can be eliminated, and the model can be completely written in terms of  $c_l$  [43,62]. In the general case, the relation between the two compositions results from the equilibrium between the solid and liquid phases,

$$\tilde{\mu}_s = \left. \frac{\partial f_s(c, T)}{\partial c} \right|_{c_s} = \tilde{\mu}_l = \left. \frac{\partial f_l(c, T)}{\partial c} \right|_{c_l}. \quad (15.66)$$

The “true” composition is then obtained as

$$c = c_s g(\phi) + c_l [1 - g(\phi)] = c_l [1 - (1 - k)g(\phi)], \quad (15.67)$$

where the second equality is valid only for a dilute alloy. It is immediately clear, that with this convention, the combination  $f - \tilde{\mu}c$  is a constant through the interface, and thus, there is no interface excess energy associated with bulk thermodynamics. The equations of motion for the composition and the phase field are given in Ref. [60]; the combination  $f - \tilde{\mu}c$  appears as the thermodynamic driving force for the phase field.

A completely equivalent formulation of this model can be given, in which the connection to the model for a pure substance is more straightforward [63]. It starts from the functional

$$\Omega = \int_V \omega_{\text{int}} + \omega_s(\tilde{\mu}, T)g(\phi) + \omega_l(\tilde{\mu}, T)[1 - g(\phi)]. \quad (15.68)$$

Here,  $\omega_{\text{int}}$  has the same form as  $f_{\text{int}}$ , and  $\omega_v = f_v - \tilde{\mu}c$  are Legendre transforms of the free energy densities, which means that they depend on the diffusion potential instead of the

composition. This functional has been called “grand potential functional,” although the correct expression for the grand potential of a binary mixture is  $f - \mu_A \rho_A - \mu_B \rho_B$ ; however, in the case of constant molar volume, the function  $\omega$  satisfies exactly the same thermodynamic relations as the grand potential of a pure substance if the chemical potential is replaced by the diffusion potential. In particular,

$$\frac{\partial \omega_v}{\partial \tilde{\mu}} = -c_v. \quad (15.69)$$

The equations of motion for the variables  $\phi$  and  $\tilde{\mu}$  can now be obtained in a straightforward way. The equilibrium equation for the phase field is equivalent to Eqn (15.65), with the difference  $f_s - f_l$  replaced by  $\omega_s - \omega_l$ . Since the latter is zero at equilibrium, the interface profile is determined by  $\omega_{\text{int}}$  alone, and the scaling of Eqn (15.23) applies, as desired.

The variation of  $\Omega$  with respect to  $\tilde{\mu}$  yields an expression for the local composition,

$$\frac{\delta \Omega}{\delta \tilde{\mu}} = \frac{\partial \omega_s}{\partial \tilde{\mu}} g(\phi) + \frac{\partial \omega_l}{\partial \tilde{\mu}} [1 - g(\phi)] = -c(\tilde{\mu}, \phi). \quad (15.70)$$

It can easily be seen using Eqn (15.69) that this expression is actually identical to Eqn (15.67). By taking the time derivative of  $c(\tilde{\mu}, \phi)$  and using mass conservation,  $\partial_t c = \nabla \cdot (M \nabla \tilde{\mu})$ , one obtains an equation for the diffusion potential,

$$\chi(\tilde{\mu}, T, \phi) \partial_t \tilde{\mu} = \nabla \cdot (M \nabla \tilde{\mu}) + (c_l - c_s) g'(\phi) \partial_t \phi, \quad (15.71)$$

with

$$\chi(\tilde{\mu}, T, \phi) = \chi_s(\tilde{\mu}, T) g(\phi) + \chi_l(\tilde{\mu}, T) [1 - g(\phi)] \quad \chi_v = \frac{\partial^2 \omega_v}{\partial \tilde{\mu}^2} \quad (15.72)$$

being a generalized susceptibility [5]. The structure of this equation is perfectly equivalent to the one of Eqn (15.53) for the temperature, with  $\chi$  playing the role of the specific heat  $C$ , and  $c_l - c_s$  in place of  $s_l - s_s$ . Of course, this just expresses the thermodynamic equivalence of the intensive variables  $T$  and  $\tilde{\mu}$  and the extensive variables  $s$  and  $c$ . The major difference, however, with the case of a pure substance is that  $\chi$  is generally quite different for liquid and solid, so that the dependence of  $\chi$  on  $\phi$  cannot be neglected.

### 15.5.4 Antitrapping Current

The model outlined above, as well as the models of Refs [43,60] are still not suitable for the quantitative modelling of solidification microstructures with upscaled interfaces. The reason is the phenomenon of *solute trapping*, which occurs during the solidification of alloys at sufficiently high velocity. Since liquid and solid have different compositions, the composition of a piece of matter has to change during the solidification process; some components are rejected into the liquid, others are incorporated into the solid. Generally, solute (impurities) has to be rejected during solidification. When the driving force for solidification (provided, for example, by rapid cooling) is high, the interface advances at such a high velocity that these redistribution processes cannot be

completed, and the solid remains at a composition that differs from the equilibrium one. As a simple criterion for the occurrence of solute trapping, one may compare the time that an interface needs to propagate by a distance equal to its intrinsic thickness,  $\xi/V$ , to the characteristic time of diffusion through the same interface,  $\xi^2/D$ , where  $D$  is the solute diffusivity within the interface. If the ratio of the two,  $\xi V/D$ , is much smaller than unity, the solute atoms have enough time to escape from the advancing solid; in the opposite limit, they are *trapped*. This means that the solid does not grow at the composition that corresponds to the thermodynamic equilibrium with the liquid, but at a higher solute content. In other words, the diffusion potential does not have the same value at the two sides of the interface: there is a jump in this intensive quantity across the interface.

Although, under such circumstances, the hypothesis that local equilibrium is established on the scale of a coarse-graining cell breaks down (recall that we had supposed that intensive quantities are constant within a cell, which is not the case any more for the diffusion potential), phase-field models can describe solute trapping quite well [64]: the transition from growth in local equilibrium to complete solute trapping with increasing growth velocity is well reproduced when the parameter  $\xi V/D$  is varied. The problem for quantitative simulations is now obvious: since this effect depends on the thickness of the interface, its magnitude is greatly exaggerated if the interface thickness is upscaled in simulations. This means that solute trapping will appear for solidification velocities that are much smaller than those for which it is really observed in experiments. For accurate simulations, it has hence to be eliminated from the model.

A way to accomplish this was developed in Ref. [65] for isothermal solidification, and in Ref. [46] for directional solidification: an *antitrapping current* is added to the model. This is an additional contribution to the solute current which counteracts solute trapping. For this purpose, it should be proportional to the interface thickness and to the growth velocity, and it should be directed from the solid to the liquid in order to assist solute redistribution. Concretely, the solute current is written as

$$\vec{J} = -M\vec{\nabla}\mu + \vec{J}_{\text{at}}, \quad (15.73)$$

with the antitrapping current

$$\vec{J}_{\text{at}} = -a(\phi)(c_l - c_s)\xi\partial_t\phi\hat{n}, \quad (15.74)$$

where  $a(\phi)$  is a dimensionless function of  $\phi$  that depends on the details of the model, and  $c_l - c_s$  is the composition jump between the phases, taken at equilibrium. For the models of Refs [46,65] that describe the solidification of binary alloys, the function  $a(\phi)$  is actually just a constant, the value of which has to be determined by matched asymptotic expansions. The details of this procedure can be found in Ref. [46].

These works were the first examples of a successful interface upscaling in phase-field modelling of alloy solidification; since then, this methodology has been used to explore dendritic and cellular solidification, and convincing quantitative agreement between simulations, theories, and experiments has been achieved [66–69]. The antitrapping

methodology has also been extended to other alloy models [13,23,63,70]. Furthermore, the models for pure substance and alloy have been combined to build a model for crystal growth limited simultaneously by heat and solute diffusion [71], which has then been used to explore dendritic growth in this regime [72].

### 15.5.5 Multiphase and Multicomponent Solidification

Many solidification phenomena involve multiple phases. The simplest example is the solidification of eutectic alloys, during which two different solids with distinct compositions are formed from the liquid. For such situations, models with more than one order parameter are needed in order to distinguish between phases. In the earliest attempts to formulate such models, one phase field and the composition field [73,74] or two phase fields [75] were used, with free energies in the form of simple Landau expansions. While these models were capable of describing the basic features of eutectic growth, their generalization to different alloy phase diagrams or a larger number of phases is not straightforward.

A general approach was provided by the *multiphase-field method*, first introduced in Ref. [76]. One phase field is associated to each thermodynamic phase that is present in the system and interpreted as local volume fraction, which implies

$$\sum_{i=1}^N \phi_i(\vec{x}) = 1 \quad \forall \vec{x} \quad (15.75)$$

for  $N$  phases. With this constraint, there are obviously only  $N - 1$  independent fields, and one variable could immediately be eliminated. However, it is advantageous to keep all the degrees of freedom for the formulation of the free energy functional because this gives rise to particularly simple and symmetric functional forms. The constraint can be taken into account at the end with the help of a Lagrange multiplier.

A multiphase system contains multiple types of interfaces and, therefore, a generalization of the interface free energy density  $f_{\text{int}}$  is needed in terms of the multiple phase fields. The extensions of the square gradient terms that are most commonly used are  $\sum_{\alpha\beta} K_{\alpha\beta} \nabla\phi_\alpha \cdot \nabla\phi_\beta$  or  $\sum_{\alpha\beta} K_{\alpha\beta} |q_{\alpha\beta}|^2$  with  $q_{\alpha\beta} = \phi_\alpha \nabla\phi_\beta - \phi_\beta \nabla\phi_\alpha$ . Both expressions are sums over pairwise terms that are zero everywhere except in  $\alpha$ - $\beta$  interfaces or multijunctions. For the local free energy density, we need a multiwell potential function over the  $N - 1$ -dimensional state space of the phase field configurations (taking into account the sum constraint), with  $N$  distinct minima that describe the possible phases.

The choice of the gradient terms and the potential function presents some new nontrivial issues that are illustrated in Figure 15.6 for the case of three phases. The state space for the three phase fields, taking into account the sum constraint, can be conveniently visualized in the standard simplex, an equilateral triangle in which each corner represents a pure phase (one of the fields equals 1, all others 0). The free energy density must have a minimum on each corner to generate the correct number of phases, with potential barriers in between (for an example, see Figure 15.7). Interfaces between phases correspond to trajectories in the state space that go from one minimum to

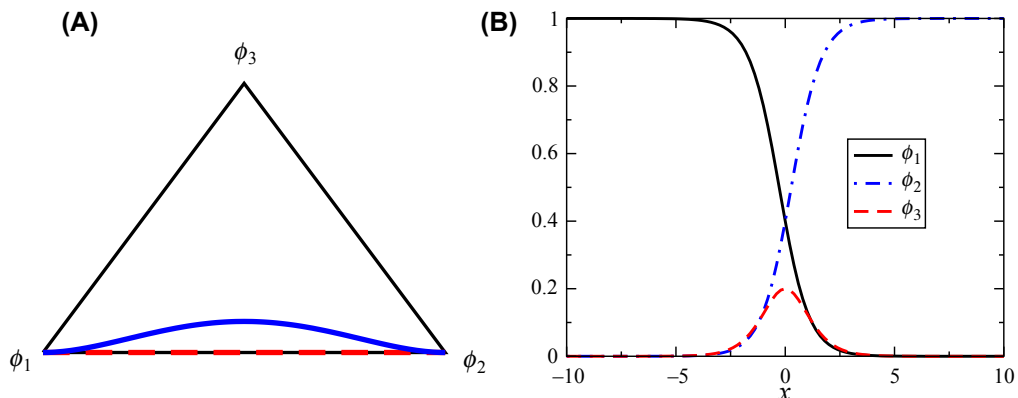


**FIGURE 15.6** Left: representation of the state space of a multiphase-field model with three phases ( $\phi_1 + \phi_2 + \phi_3 = 1$ ) in a simplex. Each corner corresponds to a pure phase. The two lines represent different interfaces between phases 1 and 2. Along the red dashed line,  $\phi_1 + \phi_2 = 1$ . Along the full blue line, the phase fields vary as depicted in the graph to the right for an interface along the  $x$  direction.

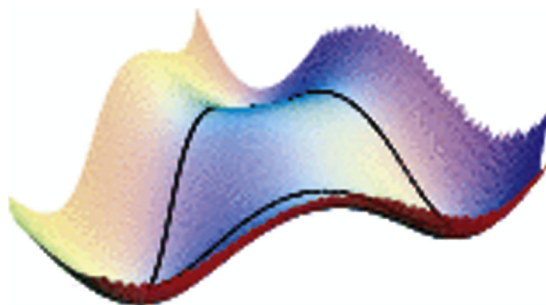


**FIGURE 15.7** Triple-well potential of the three-phase model detailed in Ref. [77], plotted over the three-phase simplex (black lines). This multiwell potential,  $\sum_{i=1}^3 [\phi_i^2 (1 - \phi_i)^2]$ , generates interfaces that run along the edges of the simplex.

another. The properties of the interface are determined by this trajectory, which is influenced both by the shape of the potential landscape and the gradient terms (see Ref. [78] for a detailed illustration and discussion of this point in a specific model).

Since a precise control of the interface properties is mandatory for interface upscaling, one would like, in particular, to have “clean” two-phase interfaces. That is, in a system in which only bulk phases  $\alpha$  and  $\beta$  are present, the interface between these phases should be free of the presence of any other phase, that is, one requires to have  $\phi_\alpha + \phi_\beta = 1$  instead of Eqn (15.75). In the simplex of Figure 15.6, this corresponds to a perfectly straight line along one of the edges (the dashed red line). In contrast, if the trajectory travels inside the simplex (full blue line), this corresponds to the presence of additional phases inside the interface, and thus to “third-phase adsorption.” This phenomenon (which could be present in real systems) makes the analytic solution of

interface equations and the calculations of asymptotic matching impossible. For a quantitative modelling of solidification, the presence of such additional phases in the interfaces must therefore be avoided.

For a smooth free-energy functional, this requirement imposes nontrivial conditions on the potential landscape and the gradient terms. A formulation that allows for a complete control of the interface properties in three-phase systems (for example, one liquid and two solids) has been given in Ref. [77] and extensively benchmarked against sharp-interface models and experiments [79]. The potential landscape is shown in Figure 15.7, plotted over the three-phase simplex. Unfortunately, a generalization of this approach to more than three phases is not straightforward. This task is simplified by the use of the *multiobstacle potential*. In the “double-obstacle potential,” the double-well function for a simple phase field,  $f_{\text{dw}}(\phi)$ , is replaced by

$$f_{\text{do}}(\phi) = \begin{cases} H\phi(1-\phi) & \text{if } 0 < \phi < 1 \\ \infty & \text{otherwise} \end{cases} \quad (15.76)$$

which can be seen as the limit of zero temperature of Eqn (15.8). In practice, when the simulation code yields a value of the phase field lower than 0 or larger than 1,  $\phi$  is just set back to the limit of the allowed interval with the help of an “if” instruction. The advantage of this formulation is that it yields an evolution equation for  $\phi$  that is linear and has as equilibrium solution a simple sine profile. Moreover, since the derivative of the potential at the (cusp-like) minima is finite, there is always a finite force that drives the phase field to its bulk values. For multiple phase fields, the configuration space is restricted to the simplex defined by  $\phi_\nu > 0 \forall \nu$ ,  $\sum_\nu \phi_\nu \leq 1$ . The finite slope of the potential landscape at the borders of this simplex “pushes” the interface solution against the “walls” (obstacles), which provides the desired “clean” interfaces. In summary, a simple version of the interface energy can be written as

$$f_{\text{int}} = \sum_{\alpha,\beta=1}^N [K_{\alpha\beta} \vec{\nabla} \phi_\alpha \cdot \vec{\nabla} \phi_\beta + H_{\alpha\beta} \phi_\alpha (1 - \phi_\beta)]. \quad (15.77)$$

The surface free energy for each interface can then be controlled as in the case of a single phase field with the help of the constants  $K_{\alpha\beta}$  and  $H_{\alpha\beta}$ . If these values are strongly different for different interfaces, higher-order terms (products of more than two phase fields) may need to be added in order to avoid third-phase adsorption.

The free energy functional is completed by the thermodynamic part, that is, the contribution of the bulk phases. This is straightforward: since each phase  $\nu$  occupies a certain spatial domain described by a specific phase field  $\phi_\nu$ , the indicator function is approximated by  $g(\phi_\nu)$ , and the bulk contribution to the free energy is written as

$$f_{\text{bulk}} = \sum_{\nu=1}^N g(\phi_\nu) f_\nu(c, T). \quad (15.78)$$

One can see that Eqn (15.47) is a special case of this expression for two phases. Also, it is clear that in order to obtain a model with good upscaling properties, either the

phase-superposition approach has to be generalized to multiple phases (with the introduction of a separate composition field for each phase) [62], or a grand-canonical approach has to be used [23].

Let us now come to the equation of motion for the multiple phase fields. Since the phase fields can still be seen as nonconserved order parameters, they should obey the relaxation dynamics of Eqn (15.11). If one such equation is written down for each field, only  $N - 1$  mobility coefficients can be specified, whereas there are in total  $N(N - 1)/2$  different types of interfaces in an  $N$ -phase system (the number of possibilities to choose two different phases out of  $N$ ). At first glance it, therefore, seems that the kinetic properties of each interface cannot be controlled separately. However, there are several possibilities to circumvent this difficulty. Either, the evolution equation can be made nonlinear by making the mobilities depend on the phase fields, which gives the possibility to give the mobility the desired value on each interface [77]. Or, the principles of out-of-equilibrium thermodynamics may be used, which stipulate that the time evolution of any state variable can depend on *all* the thermodynamic driving forces in the system. Therefore, the general evolution equation for the phase fields reads

$$\partial_t \phi_\alpha = - \sum_{\beta=1}^N \Gamma_{\alpha\beta} \frac{\delta \mathcal{F}}{\delta \phi_\beta}. \quad (15.79)$$

Furthermore, the Onsager symmetry principles imply that  $\Gamma_{\alpha\beta} = \Gamma_{\beta\alpha}$ . Since there are only  $N - 1$  independent fields, there are only  $N(N - 1)/2$  independent coefficients in the matrix  $\Gamma_{\alpha\beta}$ , which precisely corresponds to the number of independent interfaces. A particularly intuitive manner of rewriting the above equation is

$$\partial_t \phi_\alpha = \sum_{\beta \neq \alpha} \tilde{\Gamma}_{\alpha\beta} \left( \frac{\delta \mathcal{F}}{\delta \phi_\beta} - \frac{\delta \mathcal{F}}{\delta \phi_\alpha} \right). \quad (15.80)$$

In this form, the rate of transformation of phase  $\alpha$  is decomposed in the same manner as for a network of chemical reactions, in which a substance  $\alpha$  can transform into various other chemicals by different reaction pathways. The coefficients  $\tilde{\Gamma}_{\alpha\beta}$  directly control the rate of transformation from phase  $\alpha$  to  $\beta$  and, therefore, the kinetics of the  $\alpha\beta$  interfaces.

Let us finally briefly touch upon the subject of multicomponent systems, which is a whole area of research in itself; here, only the aspects that are important for the construction of phase-field models will be very briefly mentioned. In a system with a total number of  $K$  components, the composition fields  $c_i$  give the molar fractions of component  $i$  and satisfy

$$\sum_{i=1}^K c_i = 1. \quad (15.81)$$

It is customary to designate one of the components (in principle, the majority component, say component  $K$ ) as the “solvent,” and to eliminate its composition field to obtain

$K - 1$  independent variables. The conjugate intensive variables are the  $K - 1$  diffusion potentials  $\tilde{\mu}_i = (\mu_i - \mu_K)/V_a$ , where  $\mu_i$  are the chemical potentials and  $V_a$  the atomic volume. The diffusion current of component  $i$  is then written as

$$\vec{J}_i = - \sum_{j=1}^{K-1} M_{ij} \vec{\nabla} \tilde{\mu}_j \quad (15.82)$$

with a matrix of mobility coefficients  $M_{ij}$ . Each component obeys a separate conservation law,

$$\partial_t c_i = - \vec{\nabla} \cdot \vec{J}_i. \quad (15.83)$$

The driving force for phase transformations that appears in the equation of motion for the phase fields also has to be generalized. It now involves the difference between the functions

$$\omega_\nu = f_\nu - \sum_{i=1}^{K-1} \tilde{\mu}_i c_i \quad (15.84)$$

taken for two phases  $\alpha$  and  $\beta$ . The evolution equation for the phase fields can be written down either in the phase-superposition approach, in which the driving force is evaluated in terms of separate concentration fields for each phase and component [13,80], or in the grand-canonical approach, in which the functions  $\omega$  are used to construct a generalization of the functional  $\Omega$  of Eqn (15.68), and a change of variables from the compositions  $c_i$  to the diffusion potentials  $\tilde{\mu}_i$  is made [23]. Several generalizations of the antitrapping current to multiphase and multicomponent systems have also been proposed [13,23,70,77]. Therefore, in principle, all the elements needed for a quantitative modelling of solidification in multicomponent and multiphase systems are available.

As an example for the use of multiphase-field models, Figure 15.8 shows simulations of microstructures obtained during the directional solidification of a binary eutectic alloy. In such an alloy, a liquid of composition close to the eutectic point can solidify in two different solids of distinct compositions, and the solidification process generally results in a composite in which the crystals of the two phases are intertwined in complex patterns. The two most frequent morphologies are regular lamellae and rods, but more

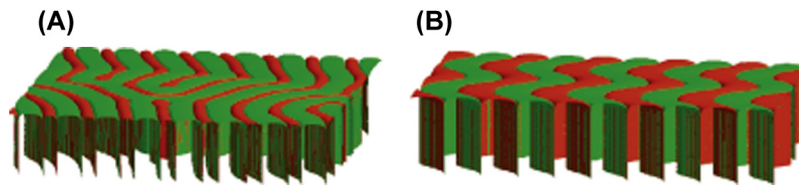


**FIGURE 15.8** Simulations of eutectic microstructures, carried out with the multiphase-field model of Ref. [77]. The solid grows upward in a temperature gradient, and the liquid (transparent) solidifies into two solid phases. Disordered labyrinths (A) and zig-zag structures (B) have been obtained [81], in good agreement with experimental observations [82].

complicated patterns have recently been observed in real time in situ observations of transparent eutectic alloys [82], among which are disordered labyrinths and zig-zag patterns, which are both well reproduced by the model [81].

## 15.6 Conclusions and Open Questions

The models described in this chapter represent developments that have spanned more than three decades. During this period, enormous progress has been made both in model development and in the understanding of the solidification phenomena that have been studied with their help. Nevertheless, there is still a large number of open questions. I have not touched at all the coupling of phase-field models to mechanics (both hydrodynamics and elasticity), which could be the subject of a review on its own, and which presents important and exciting research opportunities. I will conclude this chapter by commenting on some active and open research questions in diffusion-limited crystal growth, within the areas that are covered in the preceding sections.

- **Asymptotics.** The asymptotic matching described in Section 15.4 has made it possible to perform accurate and efficient simulations in two important special cases: the symmetric model (equal diffusivities in both phases) and the one-sided model (no diffusion in the solid). There is, presently, no generalization for arbitrary diffusion coefficients in the two phases. Attempts have been made to formulate such models by generalizing the antitrapping concept [13,83], but these models work well only in cases in which the current arriving at the interface is zero (or at least small) in one of the phases [22]. In the general case, there always remain some thin-interface corrections that make an accurate interface upscaling impossible. A solution to this problem would be of great interest.
- **Anisotropy.** Surprising results have recently been obtained when the effect of interface anisotropy was explored with functional forms that go beyond the simple expressions given by Eqn (15.62). For instance, “hyperbranched” dendrites can be obtained by combining two different cubic harmonics [84]; a “dendrite–orientation transition” is also observed in alloys of substances that have different crystal structures [85]. Finally, anisotropy effects also play an important role for the selection of cellular microstructures [67]. All these results show that there is a lot left to understand concerning the relation between anisotropy and structure selection.
- **Junctions.** In multiphase-field models, trijunctions, triple lines, and multijunctions naturally appear. The equilibrium properties of these singularities conform to the well-known Young–Laplace law, which is implied by the thermodynamic construction of the model. However, much remains to be learned about nonequilibrium behavior. It has already been shown [77] that the dynamics of trijunctions in phase-field models is slightly different from the assumptions usually made in sharp-interface models. Moreover, the energetics of such junctions can be

controlled in phase-field models by adding suitable higher-order terms (products of three or more phase fields) to the free-energy functional. This possibility has been explored little so far.

- Growth and diffusion kinetics. Up to now, attention has been mostly focused on models that permit maintaining local equilibrium at the interfaces. However, in many cases, it is necessary to introduce strong interface kinetics or departure from equilibrium between the two sides of an interface in a well-controlled way, for example if slowly diffusing species are present in multicomponent systems. In a recent line of works, several authors have formulated phase-field models that contain new coupling terms between the phase field and the diffusion equation [86–88], which lead to discontinuities in intensive fields at the interface. This approach also yields an interesting new derivation of the antitrapping current. Moreover, the “phase-superposition” approach has been generalized, replacing the equilibrium condition of Eqn (15.66) between the phases by a kinetic equation for the individual phase compositions [89,90]. Both of these approaches could considerably extend the domain of applicability of phase-field models and should be further pursued.
- Polycrystals. Monocrystals are actually quite rare in nature; most crystal growth processes lead to the spontaneous emergence of *polycrystals*, that is, solids that consist of multiple grains of the same thermodynamics phase, separated by grain boundaries. Two very different phase field approaches have been pursued to model polycrystals. The first is an application of the multiphase-field concept: each grain is represented by a different phase field, but with identical free energy densities [78,91,92]. The second is the orientation-field approach, in which a single phase field is combined with an orientation field that indicates the local direction of the crystallographic axes. Whereas the validity of the evolution equation for the orientation can actually be questioned [22], these models were successful in describing a large variety of polycrystalline growth structures [93,94]. It is highly interesting from a conceptual point of view to further explore the possibilities of such models and their eventual relation to crystal plasticity.
- Multicomponent systems. As already mentioned, several models have been proposed and used for multicomponent and multiphase systems. They differ in various choices for the free energy functionals, the interpolation schemes, and the mobility functions. Only in very few cases have rigorous asymptotics been carried out. Therefore, there is still a need for comprehensive benchmarking in order to thoroughly assess their reliability. This task is made difficult by the fact that multicomponent multiphase systems are inherently complex, and thus the definition of useful and accessible benchmark problems is far from simple. However, the large practical impact of such modelling tools is expected to provide an important driving force for future developments in this area.

## References

- [1] Stefan J. Sitzungsberichte der Österreichischen Akademie der Wissenschaften Mathematisch-Naturwissenschaftliche Klasse, Abteilung 2, Mathematik, Astronomie, Physik, Meteorologie und Technik. vol. 98; 1889. p. 965–83.
- [2] Stefan J. *Ann Phys Chem* 1891;42:269–86.
- [3] Chen L-Q. *Annu Rev Mater Res* 2002;32:113.
- [4] Anderson DM, McFadden GB, Wheeler AA. *Annu Rev Fluid Mech* 1998;30:139.
- [5] Langer JS. In: Godrèche C, editor. *Solids far from equilibrium*. Edition Aléa Saclay. Cambridge (UK): Cambridge University Press; 1991. p. 297–363.
- [6] Boettinger WJ, Warren JA, Beckermann C, Karma A. *Annu Rev Mater Res* 2002;32:163–94.
- [7] Plapp M. In: Wang M, Tsukamoto K, Wu D, editors. *Selected topics on crystal growth – 14th international summer school on crystal growth*. AIP conference proceedings, vol. 1270. Melville; 2010. p. 247–54.
- [8] Plapp M. In: Mauri R, editor. *Multiphase microfluidics: the diffuse interface model*. Wien: Springer; 2012. p. 129–75.
- [9] Provatas N, Elder K. *Phase-field methods in materials science and engineering*. Weinheim: Wiley-VCH; 2010.
- [10] Plapp M. *J Cryst Growth* 2007;303:49–57.
- [11] Singer-Loginova I, Singer HM. *Rep Prog Phys* 2008;71:106501.
- [12] Emmerich H. *Adv Phys* 2008;57:1–87.
- [13] Steinbach I. *Model Simul Mater Sci Eng* 2009;17:073001.
- [14] Steinbach I. *Annu Rev Mater Res* 2013;43:89–107.
- [15] Langer JS. *Rev Mod Phys* 1980;52:1.
- [16] Kurz W, Fisher DJ. *Fundamentals of solidification*. Zurich (Switzerland): Trans Tech Publications; 1998.
- [17] Dantzig JA, Rappaz M. *Solidification*. Lausanne: EPFL Press; 2009.
- [18] Rowlinson JS. *J Stat Phys* 1979;20:197–244.
- [19] Cahn JW, Hilliard JE. *J Chem Phys* 1958;28:258–67.
- [20] Penrose O, Fife PC. *Phys D* 1990;43:44–62.
- [21] Conti M. *Phys Rev E* 2001;64:051601.
- [22] Plapp M. *Philos Mag* 2011;91:25–44.
- [23] Choudhury A, Nestler B. *Phys Rev E* 2012;85:021602.
- [24] Gouyet J-F, Plapp M, Dieterich W, Maass P. *Adv Phys* 2003;52:523–638.
- [25] Bronchart Q, Bouar YL, Finel A. *Phys Rev Lett* 2008;100:015702.
- [26] Garnier T, Finel A, Bouar YL, Nastar M. *Phys Rev B* 2012;86.
- [27] Karma A, Rappel W-J. *Phys Rev E* 1999;60:3614–25.
- [28] Hoyt JJ, Asta M, Karma A. *Mat Sci Eng R* 2003;41:121.
- [29] Hohenberg PC, Halperin BI. *Rev Mod Phys* 1977;49:435–79.
- [30] Langer JS. In: Grinstein G, Mazenko G, editors. *Directions in condensed matter physics*. Singapore: World Scientific; 1986. p. 165–86.
- [31] Fix GJ. In: Fasano A, Primicerio M, editors. *Free boundary problems: theory and applications*. Boston: Piman; 1983. p. 580.

- [32] Collins JB, Levine H. *Phys Rev B* 1985;31:6119–22.
- [33] Karma A, Rappel W-J. *Phys Rev E* 1998;57:4323–49.
- [34] Nozières P. In: Godrèche C, editor. *Solids far from equilibrium*. Edition Aléa Saclay. Cambridge (UK): Cambridge University Press; 1991. p. 1–154.
- [35] Cahn JW. In: Carter WC, Johnson WC, editors. *The selected works of John W. Cahn*. Warrendale: The Minerals, Metals, and Materials Society; 1998. p. 379.
- [36] Steinhardt PJ, Nelson DR, Ronchetti M. *Phys Rev B* 1983;28:784–805.
- [37] Hoyt JJ, Asta M, Karma A. *Phys Rev Lett* 2001;86:5530–3.
- [38] Ramakrishnan TV, Yussouff M. *Phys Rev B* 1979;19:2775–94.
- [39] Wu K-A, Karma A, Hoyt JJ, Asta M. *Phys Rev B* 2006;73:094101.
- [40] Sethian JA. *Level set methods and fast marching methods: evolving interfaces in computational geometry, fluid mechanics, computer vision, and materials science*. Cambridge: Cambridge University Press; 1999.
- [41] Bedeaux D, Albano AM, Mazur P. *Physica A* 1975;82:438–62.
- [42] Caroli B, Caroli C, Roullet B. In: Godrèche C, editor. *Solids far from equilibrium*. Edition Aléa Saclay. Cambridge (UK): Cambridge University Press; 1991. p. 155–296.
- [43] Beckermann C, Diepers H-J, Steinbach I, Karma A, Tong X. *J Comput Phys* 1999;154:468.
- [44] Sun Y, Beckermann C. *Phys D* 2004;198:281.
- [45] Almgren RF. *SIAM J Appl Math* 1999;59:2086–107.
- [46] Echebarria B, Folch R, Karma A, Plapp M. *Phys Rev E* 2004;70:061604.
- [47] Caginalp G, Fife P. *Phys Rev B* 1986;34:4940–3.
- [48] McFadden GB, Wheeler AA, Braun RJ, Coriell SR, Sekerka RF. *Phys Rev E* 1993;48:2016–24.
- [49] Kobayashi R. *Phys D* 1993;63:410–23.
- [50] Torabi S, Lowengrub J, Voigt A, Wise S. *Proc R Soc A* 2009;465:1337–59.
- [51] Karma A, Rappel W-J. *J Cryst Growth* 1997;174:54–64. 10th American conference on crystal growth/ 9th International conference on vapor growth and epitaxy. Vail (CO); August 04–09, 1996.
- [52] Karma A, Lee YH, Plapp M. *Phys Rev E* 2000;61:3996–4006.
- [53] Plapp M, Karma A. *J Comput Phys* 2000;165:592.
- [54] LaCombe JC, Koss MB, Fradkov VE, Glicksman ME. *Phys Rev E* 1995;52:2778–86.
- [55] Bragard J, Karma A, Lee YH, Plapp M. *Interface Sci* 2002;10:121–36.
- [56] Herring C. *Phys Rev* 1951;82:87–93.
- [57] Eggleston JJ, McFadden GB, Voorhees PW. *Phys D* 2001;150:91–103.
- [58] Wheeler AA, Boettinger WJ, McFadden GB. *Phys Rev A* 1992;45:7424–39.
- [59] Caginalp G, Xie W. *Phys Rev E* 1993;48:1897–909.
- [60] Kim SG, Kim WT, Suzuki T. *Phys Rev E* 1999;60:7186–97.
- [61] Ni J, Beckermann C. *Met Trans B* 1991;22:349–61.
- [62] Tiaten J, Nestler B, Diepers H-J, Steinbach I. *Phys D* 1998;115:73–86.
- [63] Plapp M. *Phys Rev E* 2011;84:031601.
- [64] Ahmad NA, Wheeler AA, Boettinger WJ, McFadden GB. *Phys Rev E* 1998;58:3436.
- [65] Karma A. *Phys Rev Lett* 2001;87:115701.

- [66] Greenwood M, Haataja M, Provatas N. *Phys Rev Lett* 2004;93:246101.
- [67] Gurevich S, Karma A, Plapp M, Trivedi R. *Phys Rev E* 2010;81:011603.
- [68] Echebarria B, Karma A, Gurevich S. *Phys Rev E* 2010;81:021608.
- [69] Bergeon N, Tourret D, Chen L, Debierre J-M, Guérin R, Ramirez A, et al. *Phys Rev Lett* 2013;110:226102.
- [70] Kim SG. *Acta Mater* 2007;55:4391–9.
- [71] Ramirez JC, Beckermann C, Karma A, Diepers H-J. *Phys Rev E* 2004;69:051607.
- [72] Ramirez JC, Beckermann C. *Acta Mater* 2005;53:1721–36.
- [73] Karma A. *Phys Rev E* 1994;49:2245–50.
- [74] Elder KR, Drolet F, Kosterlitz JM, Grant M. *Phys Rev Lett* 1994;72:677–80.
- [75] Wheeler AA, McFadden GB, Boettinger WJ. *Proc Roy Soc A* 1996;452:495–525.
- [76] Steinbach I, Pezzolla F, Nestler B, Seeßelberg M, Prieler R, Schmitz GJ, et al. *Phys D* 1996;94:135–47.
- [77] Folch R, Plapp M. *Phys Rev E* 2005;72:011602.
- [78] Moelans N, Blanpain B, Wollants P. *Phys Rev B* 2008;78:024113.
- [79] Perrut M, Parisi A, Akamatsu S, Bottin-Rousseau S, Faivre G, Plapp M. *Acta Mater* 2010;58:1761–9.
- [80] Eiken J, Böttger B, Steinbach I. *Phys Rev E* 2006;73:066122.
- [81] Parisi A, Plapp M. *Acta Mater* 2008;56:1348.
- [82] Akamatsu S, Bottin-Rousseau S, Faivre G. *Phys Rev Lett* 2004;93:175701.
- [83] Ohno M, Matsuura K. *Phys Rev E* 2009;79:031603.
- [84] Haxhimali T, Karma A, Gonzales F, Rappaz M. *Nat Mater* 2006;5:660–4.
- [85] Dantzig JA, Napoli PD, Friedli J, Rappaz M. *Met Mat Trans A* 2013;44A:5532–43.
- [86] Brener EA, Boussinot G. *Phys Rev E* 2012;86.
- [87] Boussinot G, Brener EA. *Phys Rev E* 2013;88.
- [88] Fang A, Mi Y. *Phys Rev E* 2013;87.
- [89] Steinbach I, Zhang L, Plapp M. *Acta Mater* 2012;60:2689–701.
- [90] Zhang L, Steinbach I. *Acta Mater* 2012;60:2702–10.
- [91] Fan D, Chen L-Q. *Acta Mater* 1997;45:611–22.
- [92] Kim SG, Kim DI, Kim WT, Park YB. *Phys Rev E* 2006;74:061605.
- [93] Granasy L, Pusztai T, Börzsönyi T, Warren JA, Douglas JF. *Nat Mater* 2004;3:645–50.
- [94] Gránásy L, Pusztai T, Tegze G, Warren JA, Douglas JF. *Phys Rev E* 2005;72:011605.

# Dendritic Growth

Martin E. Glicksman

FLORIDA INSTITUTE OF TECHNOLOGY, COLLEGE OF ENGINEERING, MELBOURNE,  
FLORIDA, USA

## CHAPTER OUTLINE

<b>16.1 Introduction and Background</b> .....	<b>670</b>
16.1.1 Early History of Dendrites .....	671
16.1.2 Dendrites: Both Useful and Deleterious .....	672
<b>16.2 Observations and Simulation of Dendritic Growth</b> .....	<b>676</b>
16.2.1 Initiation of Dendrites .....	678
16.2.2 Alloy Dendrites .....	679
16.2.3 Castings .....	679
<b>16.3 Dendritic Growth Theories</b> .....	<b>681</b>
16.3.1 Background .....	681
16.3.2 Transport Theory .....	681
16.3.2.1 Key Assumptions and Boundary Conditions .....	683
16.3.2.2 Solution Parameters .....	684
16.3.3 Transport Solution .....	685
16.3.3.1 Dendrite Thermal Field .....	685
16.3.3.2 Supercooling Limits .....	686
16.3.3.3 Other Steady-State Transport Solutions .....	688
16.3.4 Tests of Transport Theory .....	689
16.3.5 Boundary Layers and Diffusion Interactions .....	691
16.3.5.1 Small Péclet Numbers .....	693
16.3.5.2 Large Péclet Numbers .....	694
16.3.6 Interface Physics .....	695
16.3.6.1 Tip Characteristics .....	695
16.3.6.2 Marginal Stability .....	697
16.3.6.3 Estimating $v$ and $R_{\text{tip}}$ .....	700
16.3.7 Numerical Methods .....	701
16.3.8 Other Kinetic Limitations .....	702

<b>16.4 Branching</b> .....	<b>704</b>
16.4.1 Stochastics .....	704
16.4.2 Deterministic Branching .....	706
16.4.2.1 Background .....	706
16.4.2.2 Interface Energy Conservation .....	707
16.4.2.3 Time Scales .....	709
16.4.2.4 Interface Capillarity .....	709
16.4.2.5 Local Equilibrium .....	710
16.4.3 Interfacial Gradients and Fluxes .....	711
16.4.4 Bias Field .....	713
16.4.4.1 Dynamic Responses .....	713
16.4.4.2 Dendritic Branching .....	715
<b>16.5 Summary</b> .....	<b>716</b>
<b>Acknowledgment</b> .....	<b>717</b>
<b>References</b> .....	<b>717</b>

## 16.1 Introduction and Background

Dendrites, a descriptive word derived from the Greek, “dendron” (*δενδρον*—a tree) are tree-like crystalline objects, more formally described as fine, ramified, single crystals that grow by diffusion-limited heat and mass transfer. Dendrites typically exhibit morphological features that include constrained directionality, i.e., crystallographically-related, straight primary stems, which periodically branch laterally into secondary “side arms.” The side arms, in turn, often branch into tertiary, or even higher-order, arms. This cascade of multiple branching exhibits a progression of crystalline stems growing in the surrounding space, obeying crystallographically-related angles, each displaying symmetries that appropriately reflect the underlying lattice structure of the material. Sharp asperities growing in crystallographically selected directions enhance locally the thermal- and mass-diffusion fields that surround them. This insures locally intense heat and mass transfer to and from the surrounding phase, which may be a melt, solution, or vapor. For example, many cubic materials (e.g., both face-centered and body-centered) develop similar looking dendrites, with each order of branching developing orthogonally to the prior order along one of the six equivalent  $\langle 100 \rangle$  cube-edge directions. In this respect, dendrites make efficient use of their available growth space to transform their parent fluid phase into crystalline matter.

Other associated thermodynamic and kinetic factors, derived from the underlying crystalline fields and liquid-state properties of the melt or solution from which dendrites form, include interfacial energy anisotropy, and directional preferences for easy molecular attachment. These kinetic mobility and energy anisotropy factors further modify the morphology and growth characteristics of dendritic crystals. The multiplicity of physical factors influencing the shapes and growth characteristics of dendrites accounts

for the fact that there are at present only a few definitive rules for predicting the features of dendritic structures for different substances crystallizing at different rates under different supersaturations. For example, the interplay of thermal and solutal fields with capillarity induces temperature and concentration changes that affect the dendritic kinetics. Absent, however, are fundamental rules for predicting details of dendritic morphologies. Nonetheless, rapid, kinetically unhindered, attachment of molecules from a surrounding supercooled or supersaturated melt or solution are considered the most important general requirement for inducing dendritic growth forms. Details of such mechanisms will be discussed later in this chapter.

### 16.1.1 Early History of Dendrites

Snow flakes and hoar frost are the most common natural examples of dendritic growth. Snow flakes evolve individually from microscopic ice nuclei born at high altitudes that grow, and, eventually, fall through a water-saturated cold atmosphere. Frost patterns appear where ground-level moisture condenses, supercools, and then freezes dendritically in contact with cold surfaces. Indeed, snow flakes, the iconic symbol of winter the world over, are recognized by their distinctive six-fold intricate patterns. Such patterns reflect the underlying arrangement of hydrogen-bonded  $\text{H}_2\text{O}$  molecules arranged in the rhombohedral crystal structure of water-ice, yet exhibit endlessly elaborate geometries [1–3]. See Figure 16.1.

Indeed, dendritic snow-flake patterns have drawn the attention of astute observers of nature, including such notables as Johannes Kepler, (the German mathematician and astronomer who seldom ever looked downward) but in 1611 published his essay, “Strena

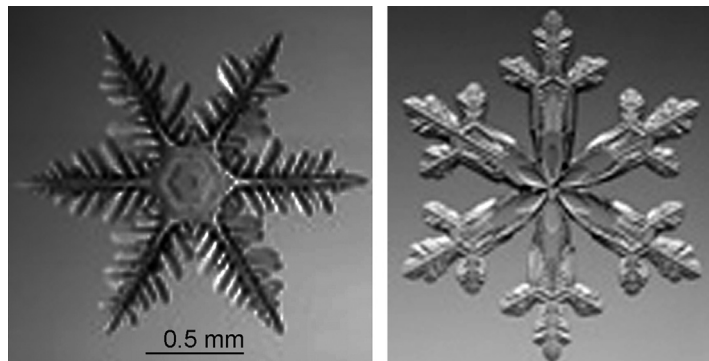


**FIGURE 16.1** Magnified images of snow flakes ( $\text{H}_2\text{O}$  ice-vapor dendrites) as viewed on the basal plane. Their striking “snow-flake” symmetry arises from ice’s rhombohedral crystal structure, which is 6-fold symmetric about its  $\langle 100 \rangle$  direction. Inspection of these snow flakes reveals three levels of dendritic branching. One notes, however, that despite the apparent—but only approximate—hexagonal symmetry, each main branch, or primary stem, remains unique in its detailed form, exhibiting fine-scale features only imperfectly mirrored by the remaining stems. This is evidence for random disturbances affecting dendritic patterns. *Photos adopted from the work of K. Libbrecht [5].*

Seu De Nive Sexangula.”<sup>1</sup> More than two centuries later, similar comments were elicited from Henry David Thoreau—the famous 19<sup>th</sup> century American philosopher/naturalist—who noted in his journal, “How full of the creative genius in the air in which these [snow flakes] are generated!”

Many different natural crystalline materials develop dendritic structures besides water-ice, including native copper (face-centered cubic), and a multitude of mineral compounds that exhibit strongly preferred low-index growth directions for their primary stems, plus crystallographically related branches determined by their individual underlying lattice and point-group symmetries. In technology, dendritic crystalline forms appear in melt-grown and electro-deposited metallic crystals, many of which facet readily, including elemental diamond-cubic silicon and germanium, and trigonal bismuth and antimony, as well as vapor-grown snow flakes that form even more intricate faceted dendritic structures. Dendrites may in addition exhibit “hopper-like” facets, fins, and internal twins, combined with non-faceted primary tips. Faceting in dendritic structures also depends on such factors as their anisotropic interfacial energy, kinetic mobility, and the crystallographic ability to form low-energy twin variants.

### 16.1.2 Dendrites: Both Useful and Deleterious

Dendrites may be viewed as the fully evolved “end-state” attending unstable crystal growth. In this regard, dendrites represent crystalline structures that have evolved via a series of morphogenic changes from a simpler starting geometry initiated at nucleation. Figure 16.2 shows a series of interfacial patterns observed by Losert, Shi, and Cummins in a binary organic alloy [6]. The sequence starts with a featureless planar interface and evolves toward a dendritic state.

Complex dendritic morphologies, in fact, are clearly undesirable in most crystal growth processes, especially those developed to produce nearly perfect, homogeneous, stress-free, bulk crystals. The appearance of dendrites in these important products must be avoided wherever possible. It is their geometrically complicated, indeed, nearly fractal character, that is responsible for the onset of chemical microsegregation, sub-boundary defects, non-equilibrium phase distributions, void formation, and inclusions in dendritically ‘contaminated’ single crystals [10]. Such deleterious aspects during bulk crystal growth degrade chemical and structural uniformity, and are harmful in crystals for which inhomogeneities in chemical, electrical, magnetic, or optical properties would diminish their quality and possibly compromise device performance.

The challenge to contemporary crystal growers is the necessity to avoid, at acceptable cost, the appearance during crystal growth of dendrites, or the onset of other unstable growth forms, such as interfacial cells that can cause similar problems. This can be accomplished in practice by adopting specific precautions and strategies to be discussed

<sup>1</sup>Kepler’s title, *Strena Seu De Nive Sexangula*, translates to “A New Year’s Gift of Hexagonal Snow,” a commentary on how complex and beautiful patterns emerge mysteriously from “thin air” [4].

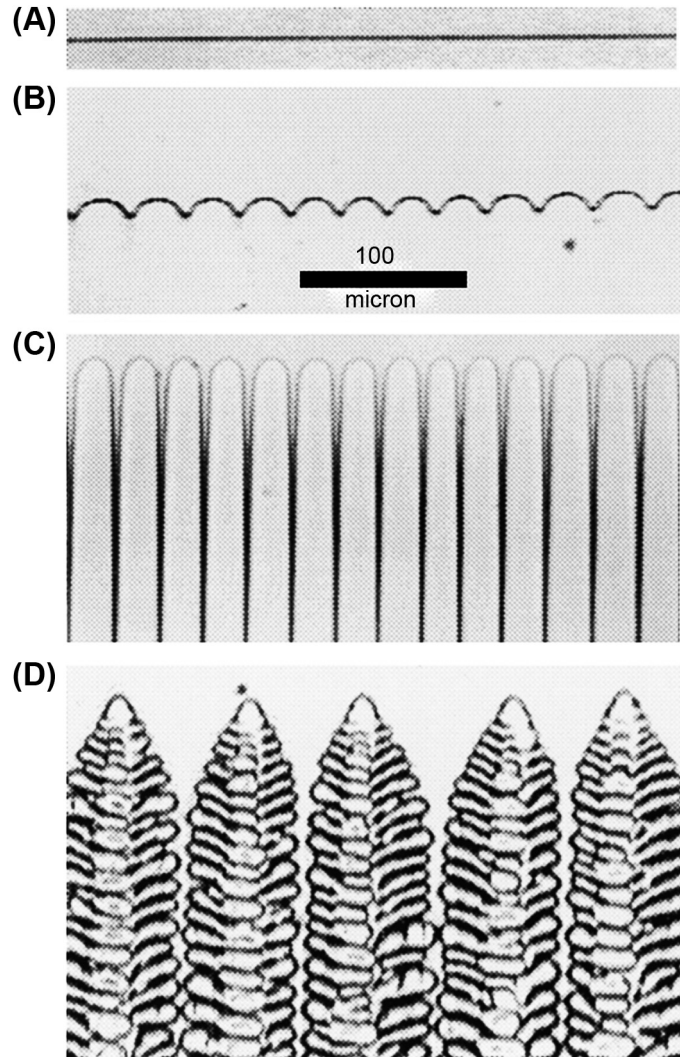


**FIGURE 16.2** Steady-state crystallization fronts observed in a dilute organic alloy, showing three major interfacial morphologies as the growth speed normal to the interface is increased step-wise from slowest, panel (A) Plane front; (B) Periodically rippled; (C) Deep cells; to fastest, panel (D) Aligned three-dimensional dendrites. Adapted from Ref. [6].

later in this chapter. The “cost” of avoiding dendrites and other forms of interfacial instability accompanying bulk crystal growth involves either reducing rates of crystal growth—i.e., diminished productivity—and/or accepting the application of higher, more technically difficult, and potentially defect-inducing, temperature gradients. As mentioned above, avoiding cellular breakdown and dendritic growth at a growing crystal interface is far more preferable than attempting amelioration of their detrimental effects on single crystal quality and performance by resorting to post-growth processing.

In the industrial important sectors of primary metals production, alloy casting, and welding, dendritic growth modes during solidification are unavoidable, and their potentially negative impact on the properties of cast and fusion-welded materials must be dealt with by foundry and welding engineers. For example, in casting metallurgy, dendrites determine the difficulty of melt flow to “feed” remote areas within a solidifying casting, and often dictate the distance scales over which chemical microsegregation occurs as well as the time-scales to eradicate chemical segregation by annealing. Dendrites also determine a material’s as-cast solidification texture, porosity, and grain size, all of which collectively influence the mechanical and chemical properties of cast materials. Such practical considerations dictate the need and added expense for downstream processing to reduce chemical segregation, lower residual stresses, and improve as-cast mechanical properties to meet engineering requirements.

On the positive side, for example, dendrites proved essential in an industrial crystal growth process developed in the early to mid-1960s by R. Seidensticker and his associates at Westinghouse Semiconductor Division [7, 8]. Known as “web-silicon,” this crystal growth process produced electronic-grade single-crystal ribbons of Si directly from the melt. Dendritic ribbons were grown for the commercial purpose of producing high-efficiency, inexpensive solar cells. Web silicon crystal growth employs pairs of widely-spaced growing dendrites, between which is stretched a thin film of molten Si that is withdrawn from the bulk melt and steadily crystallized as a continuous single crystal ribbon or sheet. The dendrites maintain strict crystallographic integrity and high structural perfection throughout the entire crystal, even after many meters of continuous ribbon growth.

A commercially successful example of controlled dendritic crystal growth is manufacturing near-net-shape superalloy single crystals for jet engines—currently a multi-billion dollar world-wide technology for aircraft engines and their refurbishment. The process of directional dendritic growth was developed in the 1960s by F. Versnyder and A. Giamei, both research metallurgists at Pratt & Whitney Aircraft Corporation [9]. One could claim that it was the development of directional dendritic growth of superalloys that allows today’s cost-effective, safe, efficient, high-speed air travel. The development and broad adoption of directionally solidified (DS) single-crystal shaped castings for civil jet aircraft represents one of the most important materials improvement in producing high-temperature turbine-blades for manufacturing reliable jet aircraft engines, as well as for developing efficient high-temperature turbomachinery now used in large-scale, land-based, electrical energy production.

As in the web-silicon process, it is the preferred growth orientations of dendritic primary stems during directional solidification that allow crystallographic orientation to overcome thermally induced uncontrolled flows in the melt, and to resist other random disturbances encountered during crystal growth. Proprietary DS casting methods, which were vastly improved over the past half-century by Pratt & Whitney, GE, Siemens, and Rolls Royce, impose sufficient crystallographic coherency of processed superalloys that leads to well-aligned dendritic textures even in large (circa 1 m long) geometrically complex castings, such as turbine airfoils. Controlled DS castings qualify as “single

crystals,” with their specified (001) dendritic zone axis aligned to withstand maximum service stresses in the part. Shaped dendritic castings are devoid of grain boundaries, and therefore are technically considered monocrystals, notwithstanding their occasional, unavoidable, low-angle sub-boundaries and second phase precipitates, or troublesome “freckle” defects that occur near sharp cross-section changes [9]. DS processed dendritic crystals also suffer from a distribution of small rotational misorientations about the controlled primary growth axis.

A simple example of crystallizing a seeded DS dendritic crystal in the form of a shaped airfoil is shown in Figure 16.3. The impressive degree of structural alignment of the component dendrites achieved by industrial DS processing is also suggested in Figure 16.3, in which is inserted a scanning electron (SEM) micrograph of a small region in a decanted superalloy casting. The dense “forest” of aligned dendrites is evident in this SEM micrograph, with all the (001) primary stems pointing upward (antiparallel) to the maximum heat flow direction maintained during solidification. In addition, one notes that all the dendrites within the SEM’s field of view have the four {010} lateral branching sheets in strict alignment, indicating that single crystallinity was achieved throughout this region of the casting.

Dendrites, of course, also dominate the as-cast microstructures of more commonplace polycrystalline alloy castings produced via numerous industrial methods,

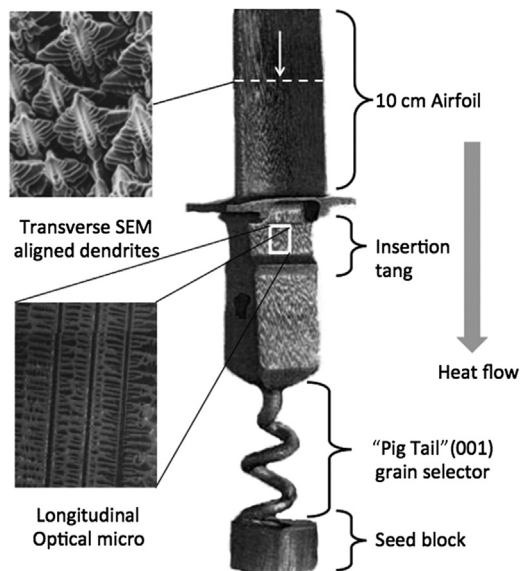


**FIGURE 16.3** Directionally solidified (DS) superalloy “single crystal,” shown macroetched. DS dendritic technology was developed through the 1960s at Pratt & Whitney Aircraft [10]. Strong directional heat flow, augmented by a grain selector, aligns a fast growing (001) dendritic direction with the blade’s centrifugal stress axis. Single crystal airfoils resist cracking much better than do polycrystalline ones, provide excellent creep and rupture life, and represent an enormous metallurgical step forward in the engineering of reliable high-temperature turbomachinery. Adapted from Refs [7,11,12].

including sand- and permanent-mold casting, poured ingots, continuous casting, directional casting, spray casting, die casting, and fusion welding. In fact, the study, understanding, and, ultimately, the control of crystalline dendrites gain additional importance where this mode of freezing is not only ubiquitous but unavoidable. Dendrites appear under most industrial solidification conditions where commodity ferrous and non-ferrous foundry alloys are cast rapidly under relatively uncontrolled, multidirectional, low temperature gradients. Such conventional casting methods represent both expedient and cost effective manufacturing of shaped parts.

Finally, beside their obvious importance in metals processing, dendrites are also encountered and affect the production and quality of pharmaceuticals, many of which are manufactured in industrial-scale batch crystallizers, and of commodity chemicals, such as fertilizers and pesticides, which are crystallized by the kilotonne using high-throughput prilling towers [13,14].

## 16.2 Observations and Simulation of Dendritic Growth

Dendrites of many pure substances and alloys are capable of growing relatively rapidly (0.1–1 mm/s) even under moderate cooling rates and shallow thermal gradients, or at small melt supercooling or supersaturation. The growth rate of dendritic crystals in *pure* substances, such as molten Ni, was found to be limited primarily by the thermal conductivity of the melt and its supercooling [15,16]. J. Walker, and independently, G. Colligan, who were among the earliest researchers on rapid dendritic growth in bulk metallic melts, successfully supercooled, by several hundred Kelvins, specimens of molten Ni encapsulated in a protective flux. The specimens used by Walker and Colligan had relatively large volumes, in the range of 10–50 cm<sup>3</sup>. Walker and Colligan reported dendritic growth speeds exceeding 10 m·s<sup>-1</sup>, often accompanied by a burst of acoustic emission [17]. In the case of highly supercooled metallic melts, dendrites can achieve impressive axial growth rates approaching 30 m·s<sup>-1</sup> [18,19].

Later, a variety of droplet techniques was developed to supercool a much wider range of metals and alloys far below their melting points or liquidus temperatures. Droplet techniques include fine droplet flux dispersion used in nucleation experiments [20], and “containerless” solidification methods, including drop tubes, and electromagnetic or electrostatic levitation [21–23]. This remarkable feature of high-speed dendritic growth is directly related to the fact that the size scale of dendritic tips and stems is *inversely* related to their growth speed. The tip-size/speed relationship for dendrites remains an important theoretical issue for this mode of crystal growth, and will be discussed in more detail in Section 16.3.

An early optical growth sequence photographed *in situ* is shown in Figure 16.4. These photo frames show details of a metallic dendrite growing on the surface of its slightly supercooled melt. The series of photos was taken over equal time intervals. The crystalline and molten surfaces of pure, elemental Sn, a body-centered tetragonal (BCT) crystal were protected by a thin transparent layer of molten anhydrous SnCl<sub>4</sub>, which acts

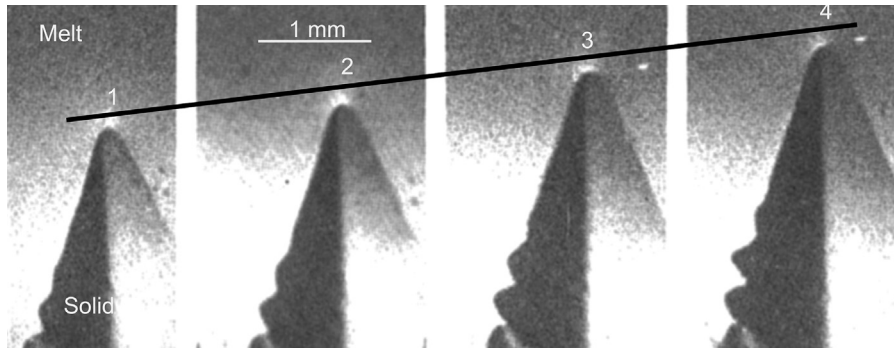


**FIGURE 16.4** *In situ* photo-sequence of BCT Sn dendrites actively crystallizing on the surface of supercooled pure molten Sn. The melt is protected from contamination by an immiscible layer of a transparent molten flux ( $\text{SnCl}_4$ ). The four micrographs of this thermal dendrite reveal its “steady-state” features: the unchanging curved tip and the uniform rate of advance; as well as the periodic emission of branches. Adapted from Ref. [24].

as a protective flux capable of dissolving any oxide films. These early micrographs show an actively growing Sn crystal periodically developing side branches, behind what appears to be a steadily advancing curved tip that preserves its contour over time. It will be shown later in this chapter, however, that the “steady-state” aspects of dendritic crystal shapes—a feature often claimed in conventional theories of dendritic growth—is perhaps more apparent than real.

A great deal of progress has been made over the past decade both in understanding the fundamentals of dendritic growth, and in achieving improved engineering control of dendritic crystallization. For example, Figure 16.5(A), shows an example of a synchrotron x-ray image extracted from a video of an Fe–Si dendrite growing from its continuously

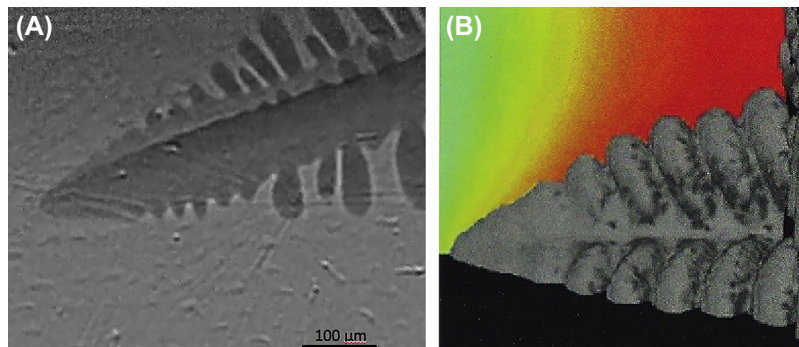


**FIGURE 16.5** (A) Synchrotron X-ray image of an iron-silicon dendrite growing from a high-temperature melt of Fe-5.3 At% Si cooled through its liquidus temperature at 2K/min. (Image extracted from synchrotron video data provided by Professor B. Billia, University of Marseille, France, 2010.) (B) Computer simulation of a Ni-alloy dendrite growing from a mold wall in a 5-component melt (Ni–Al–Cr–Ta–W). Color scale indicates the melt’s thermal field into which the dendrite advances. This simulation was used to advertise commercially available software, according to which computational thermodynamics (THERMO-CALC<sup>®</sup>) and multicomponent diffusion simulations (DICTRA<sup>®</sup>) were combined with a phase-field microstructure evolution code (MICRESS<sup>®</sup>). Simulation image adapted from Ref. [26].

cooled melt at 1500 C. Comparisons of x-ray images of metals solidifying dendritically at high temperatures with earlier optical micrographs of transparent plastic crystals crystallizing near ambient temperatures show extremely good correlation of their morphologies and speed with the melt properties. Such observations provide confidence that dendritic morphologies, and even dendritic kinetic behavior, have several “universal” features that are substantially material independent.

Dendritic crystal growth may now be simulated by numerical computation, even for cases of multicomponent melts that approach the compositional complexity of a modern superalloy [25]. Computational thermodynamics and multicomponent diffusion data bases, combined with microstructure evolution simulated using phase-field models, now yield reasonably realistic results. Figure 16.5(B) shows the computed image of a 5-component Ni-base alloy dendrite with its associated thermal field growing in its melt. Thermodynamic and kinetic data bases are now available to simulate solidification of tool steels, superalloys, semiconductors, ceramics, as well as numerous non-ferrous casting alloys based on Al, Ti, Mg, and Zr [26]. (See chapter on phase-field models.)

### 16.2.1 Initiation of Dendrites

The result of a heterogeneous nucleation event occurring within the volume of a transparent supercooled melt is shown in Figure 16.6(A). Here one sees the initial growth of a dendrite of high-purity succinonitrile (SCN)<sup>2</sup>. Plastic crystalline behavior is, of

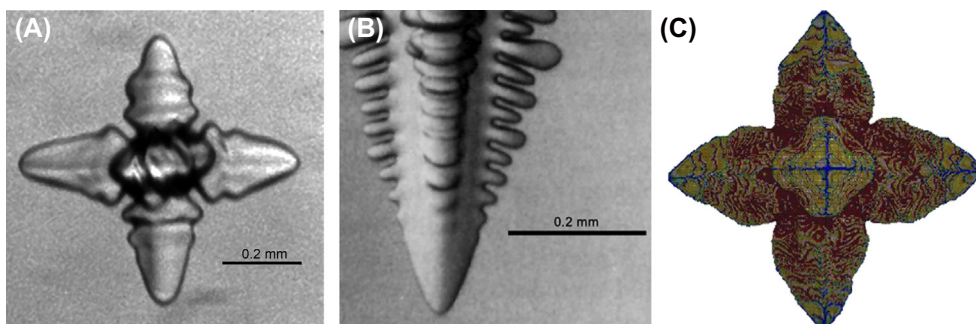


**FIGURE 16.6** (A) Photomicrograph of the early stages in the growth of an equiaxed dendritic crystal of SCN. This crystal displays initial development of primary stems extending in the six cube-edge,  $\langle 100 \rangle$ , directions—with four growing in the plane of the photograph, and two growing normal to the page. The six dendrite tips form the vertices of an octahedron in the available melt space, which is the cubic analog to the hexagonal snow flakes shown in Figure 16.1. Appearance of secondary branches is just beginning on each stem behind the advancing tips. (B) Dendritic SCN crystal at a more advanced stage, showing development of initially periodic side arms along a downward-pointing primary stem. Other arms grow in the four equivalent  $\{100\}$  planes, forming “sheets” consisting of parallel side branches. Mature branches compete in a coarsening process caused by their polydispersity in curvature distributions. (C) Kinetic Monte Carlo simulation of the initiation of a dendritic crystal using  $10^6$  voxels in the computation. Color scale related to the local temperature gradients acting on the growing crystal. Courtesy of T.P. Schultze [27].

<sup>2</sup>Succinonitrile ( $N_2(CH_4)_2N_2$ ) is a transparent, BCC, “plastic crystal.” Plastic crystallinity allows such compounds to be used as convenient analogs for *in situ* studies of dendritic crystal growth [28].

course, common in metals, but relatively rare among organic compounds. SCN is easily purified, transparent, freezes at 58.08 C, and proves convenient for studying the detailed morphology and evolution of dendritic crystals. [Figure 16.6\(A\)](#) was photographed normal to the {100} plane, with two of the six primary  $\langle 100 \rangle$  growth directions oriented normal to the page. Again, hints of incipient side-branch growth may be observed near the base of the four projecting stem tips. [Figure 16.6\(B\)](#) shows the later stage morphology of a  $\langle 100 \rangle$  primary stem. Fully developed secondary branching ‘sheets’ extend outward with side-arms in the {100} planes of this cubic crystal. An interesting simulation of dendrite initiation in a supercooled melt using kinetic Monte Carlo numerical techniques is displayed in [Figure 16.6\(C\)](#). Comparison of this simulation with the early-stage dendrite photomicrograph shown in the adjacent left-hand panel reflects key features of dendrite initiation. These include the formation of six primary  $\langle 100 \rangle$  stems and faint indication of their incipient branches. The pattern’s correspondence with reality is remarkable, considering how few “molecules” (circa 1 million voxels) actually participated in this simulation.

### 16.2.2 Alloy Dendrites

Alloy dendrites, for which transport of rejected components away from the interface is the limiting transport process governing growth, develop and grow spontaneously during directional solidification (DS), without any thermal supercooling of the melt. The driving force for growth is “constitutional supercooling” near the tip, a concept introduced in the mid-1950s by B. Chalmers [29]. Pure substances will not form dendrites under DS control—as constitutional supercooling does not develop without the presence of some solute or impurity; thermal supercooling of the melt is thus required. It should be noted, however, that even minute levels of impurities, which are present even in nominally “pure” materials, can initiate dendrites under DS conditions, providing the imposed growth speed is sufficiently high to induce constitutional supercooling.

[Figure 16.7\(A\)](#) shows an array of aligned [100] dendrites of SCN + 0.1 vol% acetone growing steadily with a uniform tip shape and well-developed, regular, primary stem spacings. Here the heat of solidification was conducted back through the already-formed solid. [Figure 16.7\(B\)](#) is a video frame of directionally solidifying low-carbon steel, freezing under a steep applied thermal gradient. Alloy dendrites are non-equilibrium structures with fine branches that have a large interfacial area per unit mass, with a corresponding large excess free energy stored in the branched microstructure.

### 16.2.3 Castings

Castings usually solidify under low, relatively uncontrolled thermal gradients. Dendrites in castings often grow in multiple directions as they crystallize without benefit of directional heat transfer. Individual dendrites, of course, remain single crystals with their primary stems along a  $\langle 100 \rangle$  zone axis in cubic materials. [Figure 16.8](#) shows some well-resolved dendrites in a partially solidified Al–Cu alloy, imaged with scanning electron microscopy (SEM) on a decanted portion of the casting’s equiaxed zone [33].

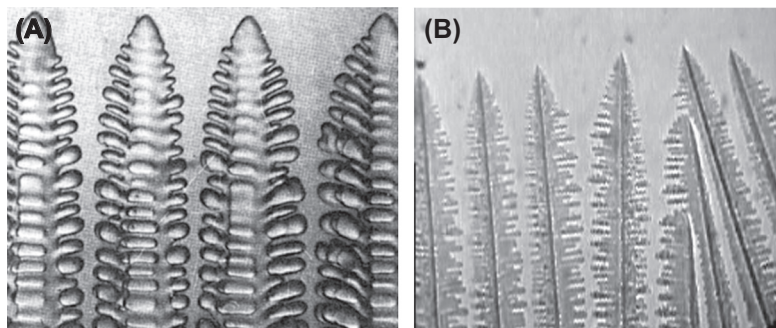


**FIGURE 16.7** (A) *In situ* micrograph of slow directional solidification (DS) of SCN+acetone alloy forming aligned primary dendritic stems. The heat of fusion is extracted through a heat sink located below the bottom of the photo, so the melt is constitutionally supercooled. See Reference [30] for a complete discussion of constitutional supercooling during DS processing. Note the uniform stem spacings and tip shapes, displaying well-developed secondary arms, the spacing of which sets the scale of microsegregation. Adapted from [31]. (Size scale not available.) (B) Frame from an X-ray video of directionally solidifying low-carbon steel (Fe-0.11 wt.% C), advancing at 1 cm/s in an applied thermal gradient of 100 K/mm. Two partially solidified grains, consisting of aligned dendrites, compete for space as they advance through the melt. A misorientation of  $17^\circ$  occurs between the dendrite's [100] preferred growth directions, which, when fully solidified, will result in the formation of a high-angle grain boundary. (Size scale not available.) Adapted from [32].

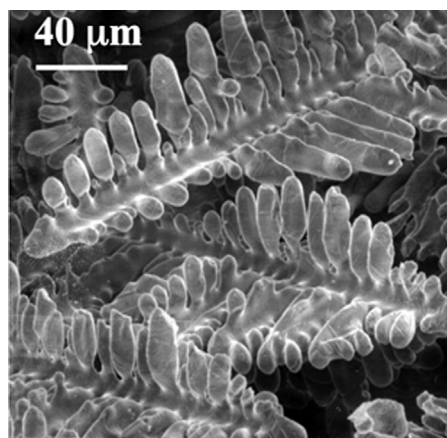


**FIGURE 16.8** SEM image of dendrites from the equi-axed zone of an Al-Cu alloy casting. Note how the proximity of these crystals causes foreshortened side branches to develop on the upper dendrite in the SEM. Side-branch foreshortening is caused by local melt convection and so-called “soft collisions,” caused by overlap of the thermal fields. Here latent heat released from the lower dendrites causes the melt (removed here by decanting) to become hotter and more buoyant, thereby slowing the growth of branches on the upper dendrite. Such local heat-transfer effects profoundly influence the microstructures of conventionally cast alloys [33].

## 16.3 Dendritic Growth Theories

### 16.3.1 Background

As discussed in [Section 16.1.2](#), dendritic crystalline forms appear commonly in nature and throughout important technologies such as metal casting and crystal growing. Analytical transport theories were initially sought to predict dendritic speed and size relationships, and later, a variety of microscopic hypotheses involving the crystal-melt interface were introduced, as transport theory alone was recognized as insufficient to solve the dendrite pattern problem. Combining macroscopic transport concepts with various microscopic theories became the approach used during the 1970s and 1980s to provide fundamentally-based estimates of dendritic growth direction, speed, tip size, and, less successfully, dendritic morphology. These characteristics of dendritic crystals were considered significant in materials applications where their control is important.

Theories of dendritic growth originally consisted of two distinct components: (1) classical transport theory, describing steady-state heat conduction and mass diffusion from the moving interface into the surrounding melt phase; and (2) “microscopic” considerations at the crystal-melt interface involving capillarity (curvature and excess interfacial energy) and/or details of the liquid-to-solid phase transformation (usually concerned with the ease of molecular attachment and interface mobility). The interested reader should also consult references [\[34\]](#) and [\[35\]](#) for more comprehensive reviews and commentary on the extensive literature published on these subjects.

Contemporary crystal growth theories, discussed in [Section 16.3.7](#), evolved over the past 20 years with the rapid development of efficient computational methods in materials science, which are now capable of solving energy and matter transport while evolving and up-dating the interfacial form separating the phases. These computations are accomplished by numerically solving coupled sets of partial differential equations that track relevant thermodynamic energies, mass conservation, and entropy changes. The interested reader should consult the monograph on phase-field analysis by H. Emmerich for basic details of the method [\[36\]](#).

### 16.3.2 Transport Theory

In 1947, G. Ivantsov published an exact mathematical solution to the steady-state temperature field surrounding an isothermal branchless dendrite growing in the form of a paraboloid of revolution [\[37\]–\[39\]](#). This particular shape approximates the tip shape of dendritic crystals, and was suggested by experimental observations made by A. Papapetrou [\[40\]](#).

[Figure 16.9\(A\)](#) shows the tip region of a steadily-advancing SCN dendrite. The vertical line separates the dendrite’s “steady-state” tip region from its time-dependent branching region. The separation of these regions is actually arbitrary, as will be shown in [Section 4](#), and proves more apparent than real. The time-independent form of a paraboloidal dendrite, as adopted in Ivantsov’s theory, is shown in the adjacent panel, [Figure 16.9\(B\)](#),

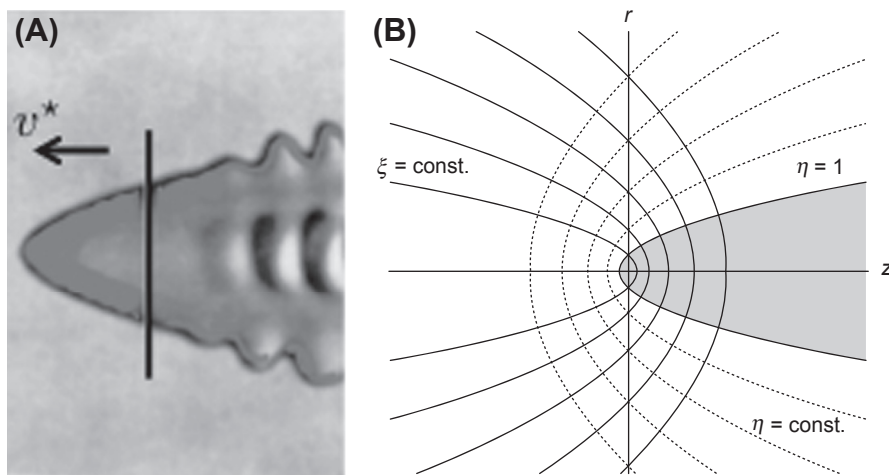


**FIGURE 16.9** (A) Photomicrograph of an advancing SCN dendrite. To the left of the vertical black bar is the “steady-state” region, which approximates a smooth body of revolution with its tip growing at a speed  $v^*$ . To the right of the vertical bar appears the time-dependent region, as a regular sequence of growing side-branches. The branching region is *not* included in Ivantsov’s steady-state analysis. (B) Branchless model used by Ivantsov to formulate the diffusion field surrounding a paraboloid of revolution. Heat flow surfaces,  $\xi = \text{const.}$ , and isotherms,  $\eta = \text{const.}$ , are indicated on this projection onto the plane  $\varphi = 0$ . The three-dimensional steady-state thermal field,  $T_i(\eta, \xi, \varphi)$ , is co-moving with the paraboloid’s tip with radius,  $R_{\text{tip}}$ , advancing at speed  $v$  in the  $+z$ -direction. The crystal-melt interface is the coordinate surface  $\eta = 1$ . Alternative  $(r, z, \varphi)$  cylindrical coordinates are also included here, as the model’s temperature field is assumed to be axisymmetric. Adapted from [41].

along with associated, co-moving coordinate systems  $(\eta, \xi, \varphi)$  and  $(r, z, \varphi)$  used to solve the steady-state transport problem. Orthogonal isotherms,  $\eta = \text{constant}$ , and heat flow surfaces,  $\xi = \text{constant}$ , in the surrounding melt are easily portrayed with confocal paraboloidal coordinates, a planar projection of which ( $\varphi = 0$ ) is also included on the diagram [42, 43].

The solid and its melt (at a uniform hydrostatic pressure) are assumed to be pure phases in local equilibrium at their melting temperature,  $T_m$ . The melting temperature is taken as a constant everywhere along the interface. The effect of curvature and interfacial energy on the melting point (the Gibbs–Thomson effect) [44], are not included in Ivantsov’s analysis. Of course, a real dendrite, as shown in Figure 16.9(A), displays a more complex time-dependent morphology than is suggested by the steady-state tip shape assumed in this analysis. Despite overlooking time-dependent aspects of dendrites, steady-state heat flow analysis correctly captures several important features of the thermal conduction process surrounding a dendrite tip. Thermal conduction alone, in fact, controls the important relationship between a dendrite’s axial propagation speed,  $v$ , and its tip radius,  $R$ .

Time-dependent morphological features, such as the trailing wake of side branches, remain of great practical importance, because side branches are responsible for the occurrence of spatial variations of chemical concentration (microsegregation) in

dendritically crystallized alloys. The presence of side branches has only a moderate effect on thermal or solutal diffusion around the tip region, which accounts, in part, for the success of Ivantsov's theory describing transport fields surrounding dendritic crystals. Indeed, the tip region of dendrites in weakly anisotropic crystals, as exemplified in Figure 16.9(A), is well approximated as a paraboloid of revolution, although other more complex dynamic shapes occur that are flattened, finned, or cruciform.

Ivantsov solved two steady-state thermal transport equations: one that holds everywhere within the "infinite" supercooled melt phase, and one valid within the evolving dendritic crystal. These equations are written in a Galilean coordinate system that removes the explicit time-dependence by moving at the steady-state speed of the advancing dendrite tip,  $v$ . These equations do not include any advective effects in the melt induced by the small mass density change accompanying crystallization. McFadden and Coriell showed that melt advection accompanying the density change on crystallization typical for most substances has minor effects on the kinetics of dendritic growth [45].

The *steady-state* energy equations that describe the temperature fields within the crystal ( $i = s$ ) and the melt ( $i = \ell$ ), written in coordinates co-moving with the velocity,  $\vec{v}$ , of the dendrite tip are:

$$\frac{\partial T_i}{\partial t} = \nabla^2 T_i + \frac{\vec{v}}{\alpha_i} \cdot \nabla T_i = 0 \quad (i = s, \ell), \quad (16.1)$$

where  $\alpha_i = \frac{k_i \Omega_i}{C_i^p}$  is the thermal diffusivity in the  $i^{\text{th}}$  phase.

### 16.3.2.1 Key Assumptions and Boundary Conditions

The following physical assumptions and boundary conditions establish the basis for Ivantsov's steady-state solution for paraboloidal dendrites:

1. The  $+z$ -coordinate is aligned with the primary growth direction of the dendrite. For cubic crystals, this axis aligns with the  $\langle 100 \rangle$  cube-edge direction. Dendrites in cubic materials exhibit four-fold symmetry about their  $\langle 100 \rangle$  zone axis, not the radial symmetry assumed in Ivantsov's treatment. For low anisotropy crystals i.e., for crystals with small interfacial energy variations, the tip region of a dendrite is well approximated as a body of revolution.
2. Solute diffusion becomes inoperative when crystallizing pure materials. Ivantsov's solution, when applied to such pure materials, describes only the conduction of latent heat from the moving crystal-melt interface into the surrounding supercooled melt, as described by equation (1).
- 3 The melt is initially uniformly supercooled by an amount  $\Delta T = T_m - T_\infty$ , permitting dendritic crystallization to occur spontaneously via thermal conduction. The melt at points remote from the growing dendrite ( $r \rightarrow \infty$ ) remains at its initial supercooled temperature,  $T_\infty < T_m$ .
4. The temperature at the interface equals the equilibrium (bulk) freezing point,  $T_m$ . The influence on the equilibrium temperature caused by interfacial curvature and crystal-melt energy is ignored. This simplification is equivalent to assuming that

the interfacial energy is zero. In addition, interfacial isothermality at  $T_m$  implies that molecular transfer from the melt and subsequent attachment to the crystal lattice, plus *all* other microscopic kinetic processes, occur easily, i.e., with negligible dissipation of free energy. The latter assumption is tantamount to assuming ‘infinite’ interfacial mobility.

5. The steady temperature field,  $T_\ell(\zeta, \rho)$ , developed in the melt surrounding the moving dendrite may be found by solving Eqn (16.1) in co-moving coordinates, non-dimensionalizing the results by using the (unknown) tip radius,  $R_{tip}$ , as the length scale for physical distances in the problem, namely,  $\zeta = z/R_{tip}$ , and  $\rho = r/R_{tip}$ .
6. The temperature field,  $T_s(\zeta, \rho)$ , developed at steady-state within the isothermal crystal is the trivial solution to Eqn (16.1), namely,  $T_s(\zeta, \rho) = T_m$ . The temperature variable itself is usually non-dimensionalized by scaling the thermal field by the material’s so-called “characteristic temperature”,  $\Delta H_f/C_p$ , where  $\Delta H_f$  and  $C_p$  are the molar latent heat of freezing and the molar specific heat of the melt, respectively.

### 16.3.2.2 Solution Parameters

The following parameters and equations appear in Ivantsov’s transport analysis:

1. As mentioned in Section 16.3.2.1, item 6, the thermal scale for non-dimensionalizing the transport field is set by the material’s characteristic temperature,  $\Delta H_f/C_p$ . Specifically,  $\vartheta(\zeta, \rho)$  is the dimensionless temperature, or thermo-potential, throughout the melt space, the field for which is defined here as,

$$\vartheta(\zeta, \rho) \equiv \frac{T_\ell(\zeta, \rho)}{\Delta H_f/C_p}. \quad (16.2)$$

2. The growth Péclet number,  $P$ , is the main dependent variable which describes key aspects of the dendritic kinetics, specifically the dendrite’s speed and tip radius. The Péclet number is defined as the dimensionless parameter,

$$P \equiv \frac{vR_{tip}}{2\alpha_\ell}. \quad (16.3)$$

The Péclet number becomes the unknown to be found by solving the dimensionless transport equation and its boundary conditions.

3. The growth Péclet number, defined in equation (16.3), may also be used for solute diffusion transport that describes dendritic growth in alloy melts, by simply substituting the melt’s solute diffusivity,  $D_\ell$ , for its thermal diffusivity,  $\alpha_\ell$ . Thus, the Péclet number may be thought of in pure substances as the ratio of the dendrite’s tip radius,  $R_{tip}$ , to its ‘thermal conduction length’ in the melt,  $2\alpha_\ell/v$ , or, in the case of alloys, the ratio of the dendrite’s tip radius to its ‘diffusion length’,  $2D_\ell/v$ . These dimensionless ratios have a direct influence on the nature of the conduction/diffusion boundary layer that develops adjacent to the crystal-melt interface, which will be discussed in Section 3.5.

The growth Péclet number, for thermal- or solutal-limited crystal growth conveniently non-dimensionalizes Eqn (16.1), and yield at a specified supersaturation, or supercooling, much finer, but slower, alloy dendrites.

4. The steady-state energy equation for the melt, Eqn (16.1), may be scaled for distances and temperatures (or, equivalently, concentrations, for alloys) to yield the linear, nondimensional, convecto-diffusion equation,

$$\nabla^2 \vartheta + 2P\nabla\vartheta = 0, \quad (16.4)$$

where in Eqn (16.4) the Laplacian,  $\nabla^2[ ]$ , and the gradient,  $\nabla[ ]$ , both represent scalar operators taken with respect to the non-dimensional distance coordinates in the melt region,  $(\zeta, \rho)$ .

5. The inner boundary condition for the melt is given as the *constant* dimensionless interface temperature,

$$\vartheta_{int} = \frac{T_m}{\Delta H_f / C_p}, \quad (16.5)$$

and its outer boundary condition, or far-field melt temperature, is the dimensionless initial melt temperature,

$$\vartheta_{\infty} = \frac{T_{\infty}}{\Delta H_f / C_p}. \quad (16.6)$$

6. The scaled temperature difference between the outer and inner melt boundaries,  $\vartheta_{\infty} - \vartheta_{int}$ , provides the independent variable that acts as the thermodynamic “driving force” for dendritic growth, namely the dimensionless “supercooling”,  $\Delta\vartheta$ , defined as<sup>3</sup>

$$\Delta\vartheta \equiv \vartheta_{int} - \vartheta_{\infty}, \quad (0 \leq \Delta\vartheta \leq 1), \quad (16.7)$$

where the unitary range of dimensionless supercooling is specified in Eqn (16.7) to obtain a unique transport solution<sup>4</sup>.

## 16.3.3 Transport Solution

### 16.3.3.1 Dendrite Thermal Field

Ivantsov obtained an analytic expression for the steady-state temperature field surrounding a paraboloidal dendrite. His transport solution allows application of energy

<sup>3</sup>The dimensionless supercooling, or supersaturation used here in this discussion of dendritic growth theory is also referred to as the Stefan number,  $St$ , in heat transfer theory for solidification free boundary problems [46]–[48]. The Stefan number also proves to be a convenient parameter for comparing the kinetic behavior of dendrites at different melt supercooling or supersaturation.

<sup>4</sup>Exceeding the upper-bound for supercooling,  $\Delta\vartheta_{max} \geq 1$ , in Eqn (16.7) and (16.8) leads to the condition of “hypercooling,” where dendritic growth can continue to total crystallization without additional transfer of latent heat from the melt to its surroundings. If a melt is hypercooled, the crystal-melt interface must depart from local equilibrium, and its temperature is no longer determined by capillarity alone [49]. Hypercooling require additional kinetic information about the melt’s viscosity, the ease or difficulty of rapid molecular attachment, and defect creation. See Section 16.3.8 for additional details on hypercooling and associated non-equilibrium behavior during dendritic growth from deeply supercooled melts.

conservation to the heat-emitting interface to establish the relationship between the dimensionless supercooling,  $\Delta\vartheta$ , the independent variable, and the growth Péclet number,  $P$ , the dependent variable.

Specifically, a “characteristic equation” that connects these parameters of the transport problem is derived using energy (or mass) balance between the gradient field at the crystal-melt interface, which is responsible for heat conduction (or mass diffusion), and the corresponding release rates of latent heat (or rejected solute) during crystallization.

$$\Delta\vartheta = P e^P E_1(P) \equiv \mathcal{I}v(P), \quad (16.8)$$

where  $E_1(P)$ , is the 1<sup>st</sup> exponential integral, a tabulated function defined as,

$$E_1(P) \equiv \int_P^\infty \frac{e^{-u}}{u} du. \quad (16.9)$$

Ivantsov’s result, Eqn (16.8), may be written formally as  $\Delta\vartheta = \mathcal{I}v(P)$ , which notation implies that the dimensionless supercooling is a unique function of the growth Péclet number. In most crystal growth processes, however, the *independent* variable is not the Péclet number, but rather the melt supercooling or supersaturation. Thus, the Péclet number would normally be chosen as the *dependent* variable, and the inverse to Eqn (16.8) would offer a better form for the desired transport solution.

An analytic inverse to Eqn (16.8), however, does not exist in “closed form”. That is, a combination of a finite number of elementary functions cannot represent the inverse Ivantsov solution. Instead, one may express the inverse transport solution symbolically, as  $P = \mathcal{I}v^{-1}(\Delta\vartheta)$ , where the notation  $\mathcal{I}v^{-1}()$  represents the formal mathematical inverse. If presented as a graph or table of the solution characteristic, the inversion may be accomplished numerically, by merely plotting the supercooling, or supersaturation, as the abscissa, or independent variable. Eqn (16.8) is plotted in this manner on double-logarithmic coordinates in Figure 16.10 to show the nature of Ivantsov’s “inverted” transport solution.

### 16.3.3.2 Supercooling Limits

At large supercoolings, see again Figure 16.10, the growth Péclet number derived from transport theory increases rapidly, and as  $\Delta\vartheta \rightarrow 1$ , or, equivalently, as  $\Delta T \rightarrow \Delta H_f/C_p$ , a divergence occurs in the transport solution, and  $P \rightarrow \infty$ . The divergence of Ivantsov’s solution at large supercooling implies that if the dimensionless supercooling exceeds unity, so  $\Delta\vartheta \geq 1$ , a condition termed “hypercooling” occurs, and the kinetics of dendritic growth would no longer be transport-limited [49, 50]. The reason heat transport no longer controls interface speed is that beyond the onset of hypercooling the interfacial thermal gradient developed at the tip of a dendrite, assuming constant molar latent heat and specific heat of the melt, is given by the ratio of the material’s characteristic temperature,  $\Delta H_f/C_p^\ell$ , divided by its limiting boundary layer thickness,  $\alpha/v$ . [See explanation in Section 16.3.5.2 associated with Eqn (16.24)], namely,

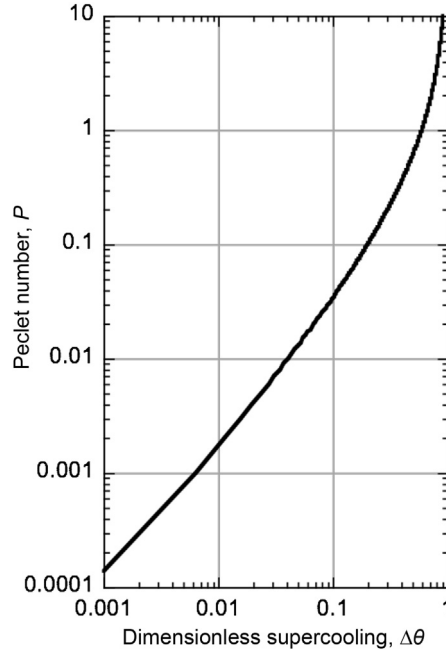


**FIGURE 16.10** Plot on double-logarithmic coordinates of Ivantsov's characteristic Eqn (16.8). The growth Péclet number becomes singular ( $P \rightarrow \infty$ ), and diverges as the dimensionless supercooling,  $\Delta\vartheta$ , approaches unity. Over a portion of the range of supercooling shown here, viz.,  $0.001 < \Delta\vartheta < 0.05$ , the (log) Péclet number is almost linear with log supercooling. It may be approximated as the power law, Eqn (16.13).

$$\text{Grad}(T_\ell)_{tip} = -\frac{\left(\frac{\Delta H_f}{C_p^\ell}\right)}{\frac{\alpha}{v}}. \quad (16.10)$$

The precise definition of the hypercooled state must take into account the fact that the molar specific heat of a melt,  $C_p^\ell$ , usually increases with supercooling [51]. The melt supercooling,  $T_m - T_{hyp}$ , at which hypercooling begins is given by the integral expression,

$$\Delta H_f = \int_{T_{hyp}}^{T_m} C_p^\ell dT. \quad (16.11)$$

Eqn (16.11) also indicates that for small molar latent heat, or for melts with nearly constant specific heat, hypercooling occurs when

$$St = 1 \approx \frac{T_m - T_{hyp}}{\Delta H_f / C_p^\ell}. \quad (16.12)$$

Thus, when the melt supercooling (approximately) equals the material's characteristic temperature, some additional kinetic barrier, or barriers, to crystallization, other than latent heat conduction, must intercede to limit the speed of the interface. Heat flow,

per se, no longer sets the speed limit. The condition of hypercooling has been reported in a variety of diverse crystallizing melts, including metals and alloys [52, 53], organics [54], and ceramics [55].

The Péclet number becomes nearly linear on log-log coordinates in the range of small dimensionless supercooling (or supersaturation) and low growth rates encountered in crystal growth. Ivantsov's solution can be approximately as the power law,

$$Pe \approx 0.647 \Delta \vartheta^{1.27} \quad (\Delta \vartheta \ll 0.1). \quad (16.13)$$

Substituting the definition of the Péclet number, Eqn (16.3), into the formal inverse provides a hyperbolic relationship between the growth speed,  $v$ , and the tip radius,  $R_{tip}$ . Specifically, Ivantsov's solution predicts that

$$vR_{tip} = 2\alpha_\ell \mathcal{I}v^{-1}(\Delta \vartheta). \quad (16.14)$$

Although transport theory yields a steady-state relationship, Eqn (16.14), connecting all the dendritic parameters, viz.,  $v$ ,  $R_{tip}$ ,  $\alpha_\ell$  and  $\Delta \vartheta$ , the *unique* steady-state solution, or kinetic “operating state” of the dendrite,  $(v^*, R_{tip}^*)$ , that one expects to observe at a specified melt supercooling remains elusive. The reason, of course, is that Eqn (16.14) contains two unknown quantities,  $v$  and  $R$ , and, consequently, is incapable of predicting the unique velocity and radius of the dendrite for a given supercooling. Thus, an additional equation *independent* of energy transport—to be developed later in this discussion—must be introduced to solve the steady-state dendritic growth problem. To accomplish this, one usually appeals to the microscopic physics of dendritic growth.

Figure 16.11 shows the hyperbolic relationship established between  $v$  and  $R_{tip}$  by transport theory, via Ivantsov's solution, Eqn (16.14). Results are plotted for several values of the supercooling for a fixed value of the melt's thermal diffusivity,  $\alpha_\ell$ . One notes that blunt-tipped thick dendrites grow slowly relative to sharp-tipped slender ones that grow more rapidly. The general tendency for slowly growing dendrites to have large tips, whereas rapidly growing ones to have small tips, is referred to as the “point effect”—a well-known effect of geometry in diffusion field theory [56].

### 16.3.3.3 Other Steady-State Transport Solutions

Analytic solutions of the steady-state diffusion equation have been found for other families of dendritic shapes that vary from cylindrical sheets to elliptical paraboloids [57]. All such solutions involve finding the characteristic equations that lead to different relationships between the growth Péclet number and the supercooling. Suffice it to say, however, that the dynamic shapes of dendrite tips are determined by several additional factors affecting the growth kinetics, none of which are included in Ivantsov's analysis. These additional factors include the anisotropies of the interface energy [58] and mobility, both of which introduce non-linear effects on the tip shape. LaCombe et al. studied the steady-state tip morphologies of pure pivalic anhydride dendrites. These investigators found that the tips differed markedly from paraboloids of revolution, which are well approximated at small anisotropies [59]. Pivalic anhydride freezes as a non-faceting FCC

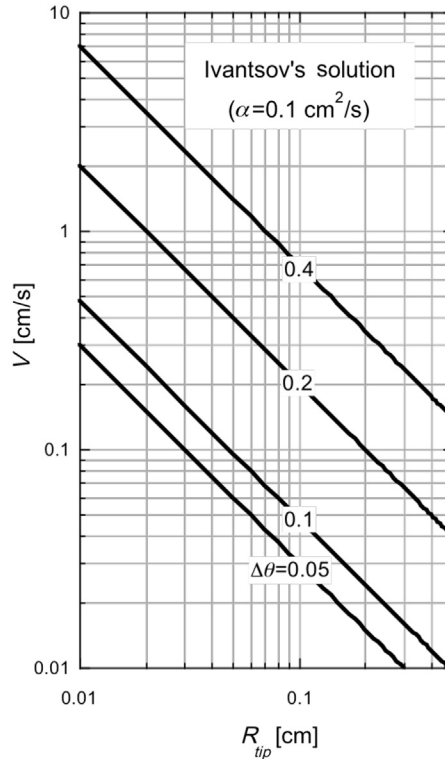


**FIGURE 16.11** Double logarithmic coordinate plot of Ivantsov's transport solution, displaying as straight lines the hyperbolic relationships between growth velocity,  $v$ , and tip radius,  $R_{tip}$ , for several values of the dimensionless supercooling,  $\Delta\vartheta$ . The thermal diffusivity is arbitrarily selected as  $\alpha = 0.1 \text{ cm}^2/\text{s}$ . The general trend is that transport of heat (or solute) from a dendrite tip is a more efficient process at smaller tip radii, the larger curvature of which increases the local gradient field, fluxes, and tip speed. Thus, fast growing dendrites usually exhibit finer scale features, and slower dendrites are coarser.

crystal, but has a relatively large 3–4% anisotropy in its crystal-melt interfacial energy [60]. Dendritic growth theory was expanded to include solute diffusion in alloy melts by Lipton and co-workers [61, 62]. When steady-state tip shapes remain unknown, due to the presence of these and other factors, numerical methods are needed to solve the associated transport equations, and to evolve the correct interface shape dynamically. Numerical techniques used to simulate dendritic growth will be discussed briefly in Section 16.3.7.

### 16.3.4 Tests of Transport Theory

Pure diffusion-limited dendritic growth was carefully measured in the mid-1990s in a series of microgravity experiments carried out on NASA's United States Microgravity Payload missions (USMP) aboard the shuttle *Columbia* [63, 64]. Three missions, USMP-2, 3, and 4, flown by NASA in 1994, 1996, and 1997 carried the *Isothermal Dendritic Growth Experiment* (IDGE), the purpose of which was to observe the kinetics and

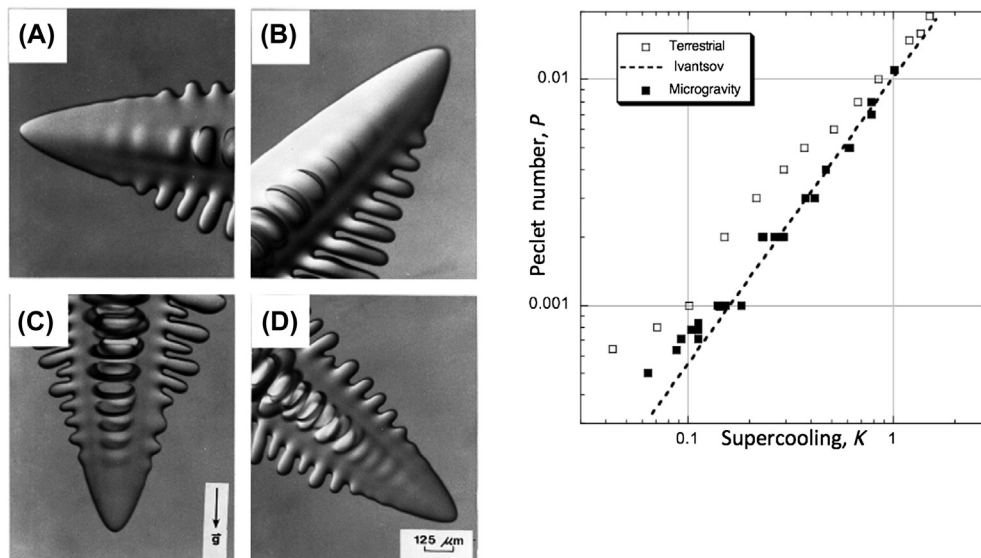


**FIGURE 16.12** Left: Dendrites growing at various angles with respect to earth's gravity,  $\vec{g}$ . The orientation to gravity affects the convective melt-flow pattern adjacent to the crystal-melt interface, which changes heat transfer rates, growth velocities, and the morphology. In panel (A), the dendrite grows normal to the gravity vector and exhibits foreshortened upper branches. In panel (B), the dendrite grows at an oblique angle to gravity, and secondary branches fail to appear along its upper interface. In panel (C), where the primary growth axis is parallel to the gravity vector, the dendrite exhibits the balanced, four fold symmetry expected for a cubic crystal. Panel (D) shows that moderate angular deviations from growth parallel to gravity have small effects on the morphology. Right: Plots of Péclet number,  $P = vR_{tip}/2\alpha_l$ , versus supercooling. All data points shown were measured with the IDGE either under terrestrial conditions,  $\square$ , or in microgravity  $\blacksquare$ . These experimental data and the Ivantsov diffusion transport solution, (dashed line) Eqn (8), provide a critical zero-parameter check of dendritic transport theory. Note that the data obtained in supercooled melts in microgravity,  $0.003 \leq \Delta\vartheta \leq 0.08$ , show broad agreement with Ivantsov's analysis, whereas terrestrial data agree only where  $\Delta T \geq 1$  K, above which thermal conduction finally becomes stronger than convective heat transfer in the presence of earth's gravity.

photograph the morphologies of diffusion-limited dendritic growth, free of gravity-induced convection.<sup>5</sup>

Figure 16.12 (A) shows four SCN dendrites growing under terrestrial conditions at various angles with respect to the earth's gravity vector,  $\vec{g}_0$  [66]. The growth orientation to terrestrial gravity alters the buoyancy-induced melt-flow patterns, which convectively modify local heat transfer at the crystal-melt interfaces [67, 68] and influence the growth rate and morphology. Melt convection, if strong, precludes comparison of observed dendritic growth with predictions made on the basis of diffusion transport theory presented in Section 16.3.2. When dendrites grow without the presence of gravity,<sup>6</sup> as they

<sup>5</sup>For a recent review of crystal growth research conducted in microgravity, the reader is directed to reference [65].

<sup>6</sup>The quasi-static acceleration levels for all the IDGE experiments in low-Earth orbit was circa  $10^{-7} \times |\vec{g}_0|$ , where  $|\vec{g}_0| \approx 9.8 \text{ m}\cdot\text{s}^{-2}$  [69,70]. As such, melt convection all but disappears in microgravity, save for weak advective flows caused by the mass density change at the crystal-melt interface.

do in low-Earth orbit, buoyancy-mediated convection in the melt disappears, and interfacial heat transfer during dendritic growth occurs by thermal conduction and radiation. As shown by the data in Figure 16.12(B), the observed growth speed and dendritic tip radii may be combined as the growth Péclet number, and predicted from the supercooling by using transport theory. Only convection-free dendritic growth results in a predicted growth Péclet number that agrees with transport theory. See again Eqn (16.3).

Transport theory alone is, however, incapable of predicting the *unique* combination of variables,  $(v^*, R_{tip}^*)$ , that would be observed if one sets the supercooling level and conducts a solidification experiment. The dendrite’s “operating state” thus remains beyond the predictive power of transport analysis alone, which is not a surprising outcome given that Eqn (16.14) is one equation in two unknowns, viz.,  $v^*$  and  $R_{tip}^*$ . Clearly additional physics is needed to provide an independent equation connecting these unknowns. The choice of such physics will be discussed in Section 16.3.6.1 in order to determine the operating steady-state of a dendrite.

Before adding the required interfacial physics, several useful engineering concepts concerning thermal and solutal boundary layers will be discussed, to help make clear how dendritic crystals interact among themselves and with their environment during growth.

### 16.3.5 Boundary Layers and Diffusion Interactions

Figure 16.9(A) shows a sketch of a branchless dendrite growing in a melt at a speed  $v^*$  in the  $+z$  direction. As suggested by the right panel, the total diffusion field,  $\vartheta_\ell(\xi, \eta)$ , surrounding the crystal-melt interface at  $\eta = 1$  extends, in principle, to infinity. In practice, however, a thermal or solutal boundary layer of thickness  $\Delta z$  extends a short distance outward from the advancing interface, capturing the “meaningful,” or active region over which the transport field extends and exerts physical influences. Boundary layers represent estimates of the important distances within which are contained the gradient fields primarily responsible for transferring heat or solute to the bulk melt. When dendrites develop during crystallization they can interact with and influence their neighbors, or be affected themselves by the local crystal growth environment. For example, boundary layer thicknesses indicate the proximity at which significant interactions between a growing interface and nearby walls, probes, or baffles. Thus, dendritic boundary layers provide engineering estimates of the effective size scale of these crystals and their transport fields, denoting the physically significant extent of their “active” thermal or solutal fields.

Besides providing practical estimates of the spatial extent of transport fields during crystal growth, thermal and solutal boundary layers also help identify the system parameters upon which these fields depend. As mentioned, boundary layers have finite thicknesses, in contrast with the “infinite” extent of the (mathematically predicted) transport field, or the “infinitesimal” character of the ‘sharp’ interface model. For

example, the thickness of a *thermal* boundary layer,  $\Delta Z_{th}$ , may be defined in a pure system as the estimated distance over which the temperature falls substantially from the melting point,  $T_m$ , at the crystal–melt interface, to the supercooled temperature,  $T_\infty$ , located at some distance from that interface. Similarly, a solute boundary layer thickness may be defined as the distance,  $\Delta Z_{sol}$ , over which the equilibrium solubility in the melt,  $\widehat{C}_\ell$ , immediately adjacent to the interface, falls (or rises) to the nominal melt composition,  $C_0$ , at some distance ahead of an advancing interface.

First, we consider thermal boundary layers. Local energy conservation yields a thermal flux balance at any arbitrary point on the crystal–melt interface, requiring that the latent heat released at each location is conducted away into the nearby supercooled melt via the local normal temperature gradient. This net zero sum of the latent heat released and the heat conducted through the melt represents the local form of Stefan’s energy balance, which may be expressed as,

$$\frac{\Delta H_f}{\Omega} (\vec{v} \cdot \vec{n}) = -k_\ell \vec{\nabla} T \cdot \vec{n}, \quad (16.15)$$

where  $\vec{n}$  is the unit normal vector on the solid–liquid interface pointing toward the melt,  $k_\ell$  is the thermal conductivity of the melt, and  $\Omega$  is the molar volume. If the right-hand side of Eqn (16.15) is applied to thermal conduction conditions prevailing at the dendrite tip,  $r=0$ , the local normal vector,  $\vec{n}$ , aligns with the  $+z$ -axis. The magnitude of the thermal gradient vector at the dendrite tip,  $|\nabla T|_{tip}$ , may be *estimated* as the total temperature drop ahead of the tip, viz.,  $T_\infty - T_m$ , divided by the thermal boundary layer thickness,  $\Delta Z_{th}$ . The steady-state heat flux leaving the advancing tip is,

$$\frac{\Delta H_f}{\Omega} (\vec{v} \cdot \vec{n}) \approx k_\ell \left( \frac{T_m - T_\infty}{\Delta Z_{th}} \right). \quad (16.16)$$

Eqn (16.16) defines a boundary layer thickness at the dendrite tip,  $\Delta Z_{th}$ .

Solving Eqn (16.16) for  $\Delta Z_{th}$ , and recalling the definition of the dimensionless supercooling,  $\Delta\vartheta \equiv (T_m - T_\infty)C_p/\Delta H_f$ , one finds that the thermal boundary layer thickness at a dendrite tip is

$$\Delta Z_{th} = \frac{k_\ell \Omega \Delta\vartheta}{C_p v}. \quad (16.17)$$

Dividing both sides of Eqn (16.17) by the dendritic tip radius,  $R_{tip}$ , then multiplying the numerator and denominator of the right-hand side by 2, and recalling the definitions of the thermal diffusivity of the melt,  $\alpha_\ell \equiv k_\ell \Omega / C_p$ , and the Péclet number,  $P = vR_{tip}/2\alpha_\ell$ , Eqn (16.3), yields the ratio of the boundary layer thickness to the dendritic tip radius,

$$\frac{\Delta Z_{th}}{R_{tip}} = \frac{\Delta\vartheta}{2P}. \quad (16.18)$$

If the Ivantsov solution, Eqn (16.8) is now substituted for the dimensionless supercooling,  $\Delta\vartheta$ , on the right-hand side of Eqn (16.18), one obtains an expression for this ratio in terms of the growth Péclet number,

$$\frac{\Delta Z_{th}}{R_{tip}} = \frac{e^P E_1(P)}{2}. \quad (16.19)$$

Not surprisingly, the boundary layer thickness is also a sensitive function of the melt supercooling or supersaturation. Figure 16.13 displays the thermal boundary layer thickness,  $\Delta Z_{th}$ , in units of the dendritic tip radius,  $R_{tip}$ , plotted as a function of the growth Péclet number in accord with Eqn (16.19). Approximations appropriate at ‘small’ and ‘large’ growth Péclet numbers are also included for comparison in figure 13. These boundary-layer approximations are discussed next.

### 16.3.5.1 Small Péclet Numbers

Many dendritic growth and casting processes operate at small growth Péclet numbers,  $P \ll 1$ . One may substitute the well-known expansions that follow for each of the corresponding functions that appear in the characteristic equation, Eqn (16.8), and thereby simplify both the transport solution and the boundary layer expression, Eqn (16.19), at low Péclet numbers:

- i.  $e^P = 1 + P + (P)^2/2 + \dots$ ,  
 ii.  $E_1(P) = -(\ln P + \gamma_E) + P - (P)^2/4 + \dots$ , where  $\gamma_E = 0.57721\dots$  is Euler's constant.

One obtains an approximation for  $\Delta\vartheta$  in elementary functions by inserting these expansions into the characteristic Eqn (16.8) if  $Pe \ll 1$ :

$$\Delta\vartheta \approx P(1 + P) (P - \ln P - \gamma_E). \quad (16.20)$$

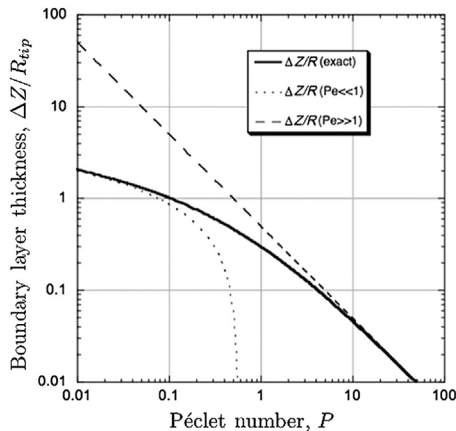


**FIGURE 16.13** Ratio of the dendritic boundary layer thickness to the tip radius,  $\frac{\Delta Z_{th}}{R_{tip}}$ , versus growth Péclet number. Asymptotic approximations for the boundary layer thickness at low and high Péclet numbers are included (dotted and dashed curves, respectively) that show their respective ranges of validity. Note that the exact transcendental relationship (solid curve), Eqn (16.19), is required over the intermediate range of growth Péclet numbers,  $0.1 < P < 10$ , where large errors would occur using asymptotic boundary layer approximations.

Using the low Péclet number expansion developed for  $\Delta\vartheta$  in Eqn (16.20) and dropping higher-order terms, yields the ratio of the thermal boundary layer width to the tip radius for small Péclet numbers,

$$\frac{\Delta Z_{th}}{R_{tip}} \approx - \left[ \ln \sqrt{P} + \gamma_E \right] \quad (P \ll 1). \quad (16.21)$$

### 16.3.5.2 Large Péclet Numbers

Ivantsov's solution is also easily approximated in the limit of large Péclet numbers, where  $P \gg 1$ . Large Péclet numbers are encountered both in the crystallization of deeply supercooled pure melts, or in cast alloys, where  $\Delta\vartheta$  also represents the dimensionless solute supersaturation of the melt, defined as the solute concentration,  $C$ , divided by the width of the phase diagram's tie-line,  $\widehat{C}_\ell - \widehat{C}_s$ , at the crystal growth temperature. Analogy with Ivantsov's thermal transport solution shows that the solutal growth Péclet number is given by  $P_{sol} = \nu R_{tip} / 2D_\ell$ , where  $D_\ell$  is the solute diffusivity in the melt.

Substituting expansions *i.* and *ii.*, given above, into the characteristic equation, Eqn (16.8), yields for high Péclet numbers the approximation,

$$\Delta\vartheta \approx 1 - \frac{1}{P} \quad (P \gg 1). \quad (16.22)$$

If a flux balance is applied to the tip of the dendrite, and the procedures outlined for Eqn (16.16–16.21) are followed—excepting the use of expansion Eqn (16.22) instead of Eqn (16.20)—one obtains the ratio of the solutal boundary layer thickness to the tip radius in the limit  $P \gg 1$  as

$$\frac{\Delta Z_{sol}}{R_{tip}} \approx \frac{1}{2} \left( \frac{1}{P} - \frac{1}{P^2} \right). \quad (16.23)$$

Given that Eqn (16.23) is valid only when  $P$  is large, so  $1/P \ll 1$ , the solutal boundary layer thickness in the case of alloys is given by,

$$\Delta Z_{sol} \approx \frac{R_{tip}}{2P} = \frac{D_\ell}{\nu}. \quad (16.24)$$

Thus, at high dimensionless supersaturations the solutal boundary layer thickness at the tip of a dendrite equals the diffusion length,  $D_\ell/\nu$ , ahead of a *planar* front moving at the same speed. Solutal boundary layers can be much smaller than the tip radius itself. Equivalently, at high supercoolings, approaching the hypercooling point of a melt, the thermal boundary layer thickness at the tip of a pure dendrite equals its thermal diffusion length,  $\alpha_\ell/\nu$ . Eqn (16.19) and its approximations at low and high Péclet numbers confirm that the ratio of the boundary layer thickness to the physical tip radius depends only on the relevant Péclet number. Eqn (16.19), moreover, predicts *both* thermal and solute boundary layers in dendritic growth, because their corresponding thermal and solute transport solutions are mathematical equivalents. One merely uses  $\Delta\vartheta$  to represent either the supercooling for the thermal boundary layer, or the supersaturation for

the solutal boundary layer. Solute Péclet numbers at the tip region of a dendrite in a pure material, as already mentioned, are usually much larger than the thermal Péclet numbers because of the disparity (about 4-orders of magnitude) between values for the thermal and solutal diffusivities in most melts. Consequently, solute boundary layers tend to be much thinner than are thermal boundary layers. Boundary layer analysis also teaches that dendrites only interact with each other and their environment at close proximity, corresponding to just a few tip radii; consequently, dendrites grow nearly independently, and therefore develop surprising uniformity in their tip shapes and branching sequences even in densely populated cast microstructures.

### 16.3.6 Interface Physics

As mentioned in Section 16.3.3, transport theory alone is incapable of predicting the operating state of a dendritic crystal for a given level of supercooling or supersaturation. Numerous hypotheses were posed over the intervening 60 years since Ivantsov's work, each attempting to add the elusive "missing" interface physics. Among the early suggestions for improving the kinetic theory of dendritic growth (See, for example, Ref. [71]) was the *ad hoc* notion that dendrites ought to grow at the maximum rate permitted by transport theory, and could do so by reducing their tip radii to just twice the critical nucleation radius, as set by the melt supercooling [72]. Experiments eventually showed, however, that dendrites grow with their tip radii almost 100 times larger than their nucleation radii, and achieve growth rates that are only a small fraction of this "theoretical" hypothesized maximum [66].

Others thought that dendrites grow so their entropy production rates are minimized [73], or even maximized! Xu and co-workers, using slender-body analysis and other mathematical techniques, showed that "trapped-wave" eigenstates are possible in dendritic crystals, which could account for deterministic branching [74–76]. Another now broadly accepted theory evolved from a self-consistent analysis of steady-state dendritic growth [77, 78]. Known as "microscopic solvability," this theoretical approach to model dendritic growth asserts that the allowed operating state, found through sophisticated mathematical analysis, is the fastest (steady-state) speed compatible with the anisotropy of the interfacial energy, and maintaining a smoothly-shaped tip [79–81]. Despite the remarkable diversity of theoretical approaches, none of the analytic theories developed to date have been verified experimentally, despite careful attempts to check them [60].

#### 16.3.6.1 Tip Characteristics

Some theoretical treatments of dendritic growth apply concepts of dynamic morphological stability, which were developed during the early 1960s by Mullins and Sekerka [82–84] and independently by Voronkov [85]. Interface stability theories alone will be detailed further in this chapter, because of their compelling physical and mathematical simplicity, and their success in providing scaling laws for dendrites.

Stability-based dendritic growth theories, moreover, originated more than 40 years ago with the numerical studies reported by W. Oldfield [86], whose findings were among the first computational approaches applied to the study of dendritic growth. Specifically, Oldfield suggested that dendritic crystals develop a “dynamic balance” between the stabilizing influences of interface capillarity and the destabilizing effects of solute diffusion or thermal conduction. His numerical work was soon followed by several analytical tip stability models [87, 88], in which steady-state behavior could be captured by the same interesting scaling law discovered numerically by Oldfield: viz., that the volumetric rate of freezing at a dendrite’s tip,  $v R_{tip}^2$ , remains constant, *independent* of supercooling. Transport theory, as discussed in Section 16.3.3, shows that  $v$  and  $R_{tip}$  are both sensitive functions of supercooling, so the dendritic scaling law,  $v R_{tip}^2 = \text{const.}$ , derived from linear stability-based theories, indeed suggests a surprising aspect of their kinetic behavior.

The analysis of dendritic tip stability was proposed first by J. Langer and H. Müller-Krumbhaar [89,90] and is now known as marginal stability theory. That analysis was influenced by contemporary experimental progress based on several quantitative *in situ* observations of steady-state dendritic growth [91, 92]. Examples drawn from these experimental studies are presented in Figure 16.14, where tip-speed data for pure substances were obtained over wide dynamic ranges of the supercooling. The tip-speed data contained in Figure 16.14—although not recognized at the time they were reported—were affected by (unavoidable) gravitationally-induced melt convection, a transport mechanism already mentioned in Section 16.3.4. Nevertheless, these dendritic growth experiments provide at least semi-quantitative agreement with predictions based on stability-based dendritic growth theories. Eventually, other prominent theories, such as microscopic solvability, were carefully re-checked during the 1990s, using a combination of terrestrial [60] and microgravity experiments [93, 94]. These later experiments show convincingly that solvability theories yield relatively poor estimates of observed dendritic growth behavior, and thus the detailed interfacial physics used to formulate them remains in doubt.

Marginal stability, to be detailed in the next section, encouraged additional accurate experiments [95, 96], which confirmed quantitatively that the spacing of side branches and a dendrite’s corresponding tip radii were *not* independent features, linked by the marginal stability hypothesis.<sup>7</sup> That is, the proportionality between branch spacings and tip radii, which was assumed heuristically in marginal stability theory, indeed held true, despite the fact that dendritic side branches are time-dependent features, whereas the tip shape itself was assumed to be at steady-state. See again Figure 16.9 (A) for the questionable distinction drawn between the so-called “steady-state” and “time-dependent” growth regions of the crystal-melt interface in dendrites.

<sup>7</sup>This peculiarity is resolved later in Section 16.4.2, as the tip region of a dendrite does *not* actually grow in a truly steady-state mode, but as suggested by Xu’s trapped-wave analysis [97], and by independent dynamic studies by Lowengrub and Li [98], undergoes faint oscillations as side branches initiate extremely close to the tip.

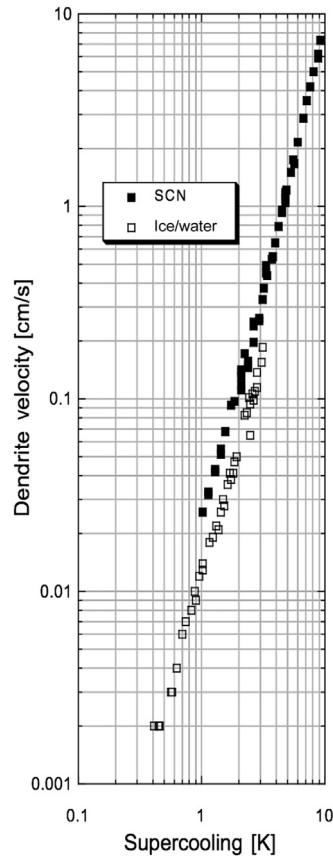
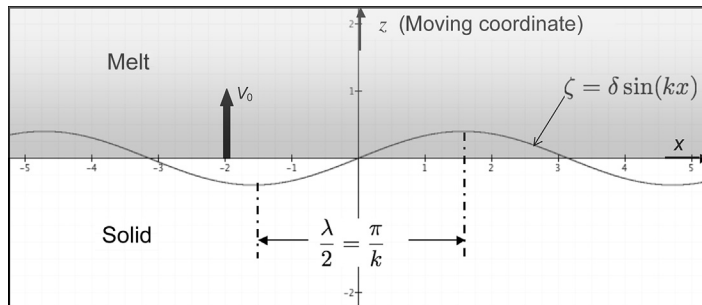


**FIGURE 16.14** Free dendritic growth velocity versus melt supercooling (log–log). The four-decade correlation shown by these free dendritic growth data suggested that a consistent kinetic mechanism operates in dendritic growth over wide dynamic ranges, even for very different crystals, such as SCN, a BCC organic plastic crystal, and H<sub>2</sub>O-ice I, a rhombohedral hydrogen-bonded crystal. Experimental results such as these helped to stimulate theories to explain this ubiquitous form of crystal growth.

### 16.3.6.2 Marginal Stability

Consider a pure crystal-melt system with a planar interface advancing into its supercooled melt at a velocity  $v_0$  in the  $+z$  direction. The interface is subject to random perturbations, or disturbances, each comprised of small-amplitude sinusoidal distortions. The Fourier-components of the disturbance have wavenumbers  $k = \frac{2\pi}{\lambda}$ , where  $\lambda$  is the wavelength of each independent component, which exhibits a small, time-dependent amplitude,  $\delta(k, t) \ll 1$ . The question addressed by linear perturbation theory is, Among all possible wavenumbers,  $0 \leq k \leq \infty$ , what is the critical, or smallest wavenumber,  $k^*$ , to which the interface could be subjected without destabilizing it? Stability requires the evolving amplitudes to decay, and eventually vanish, whereas instability allows the amplitudes to increase exponentially in time. Note that the curved dendritic tip being tested is rather loosely treated here, by analyzing its shape stability

**FIGURE 16.15** Sinusoidal perturbation,  $\zeta(x, t)$ , of an interface advancing in the  $+z$  direction at a speed  $v_0$ . This interface is of infinite extent in the  $\pm x$  directions. A moving coordinate,  $Z$ , travels with the planar interface, which only roughly approximates the stability conditions at a curved tip.



either as a *planer* interface [87] or as a *spherical* interface [96]. The conclusions reached concerning marginal dendritic tip stability, however, differ only slightly with the particular choices of the interface shape being analyzed.

Figure 16.15 shows the general conditions prevailing near a perturbed planar interface. The stability function (a complex exponent) for this interface when perturbed by its marginal (minimum) wavenumber,  $k^*$ , is found to be  $\mathcal{F}(k^*)$ , the real part of which reduces to zero, allowing the amplitude of tip perturbations to remain constant. The linear dynamical condition found for *marginal stability* is

$$\mathcal{F}(k^*) = 0 = -T_m \Gamma k^{*2} - \frac{G_s + G_\ell}{2}. \quad (16.25)$$

The first term on the right-hand side of Eqn (16.25) contains the microscopic capillary length,  $\Gamma = \gamma_{sl}\Omega/\Delta H_f$ , which accounts for the *stabilizing* influence of interfacial energy,  $\gamma_{sl}$ , that resists the growth of fine-scale ripples with high wavenumbers, whereas the second term accounts for the *destabilizing* negative thermal gradient present ahead of the advancing interface that favors the growth of ripples with high wavenumbers. Note, these countervailing effects of capillarity and thermal gradients are what Oldfield originally suggested from his numerical analysis of dendritic growth [86].

Specifically, the solid phase thermal gradient,  $G_s$ , in Eqn (16.25), is zero, because the interior of the dendrite remains isothermal and is gradient-free. Thus, the *average* gradient on the right-hand side of Eqn (16.25),  $\bar{G} = -G_\ell/2$ , depends solely on the thermal gradient developed in the melt at the advancing tip. Inserting the average thermal gradient into Eqn (16.25) and solving for the critical wavenumber,  $k^*$ , yields the result,

$$k^* = \sqrt{\frac{-G_\ell}{2T_m\Gamma}}. \quad (16.26)$$

Ivantsov's transport solution yields the non-dimensional thermal gradient,  $\hat{G}_\ell$  in the melt just ahead of the dendrite's tip as,

$$\hat{G}_\ell = -2Pe. \quad (16.27)$$

The dimensional thermal gradient  $G_\ell$ , may be recovered from Eqn (16.27) by using the characteristic thermal gradient,  $\Delta H_f/(C_p R_{tip})$ , and substituting the definition of the

growth Péclet number,  $Pe \equiv vR_{tip}/(2\alpha_l)$ . These steps yield the steady-state thermal gradient in the melt at the dendrite tip as,

$$G_\ell = -\left(\frac{\Delta H_f}{\alpha_l C_p}\right)v. \quad (16.28)$$

Inserting Eqn (16.28) into Eqn (16.26) provides an important relationship defining the marginal wavenumber and wavelength,

$$k^\star = \frac{2\pi}{\lambda^\star} = \sqrt{\frac{v\Delta H_f}{2\alpha_l C_p T_m \Gamma}}. \quad (16.29)$$

Solving for  $\lambda^\star$ , and grouping some of the material constants, yields the central result of marginal stability theory, namely that

$$\lambda^\star = 2\pi\sqrt{\frac{2\alpha_l d_0}{v}}, \quad (16.30)$$

where the length scale,  $d_0$ , has been introduced into Eqn (16.30) that is proportional to the capillary length<sup>8</sup>  $\Gamma$ . This branching length is defined as,

$$d_0 \equiv \frac{C_p T_m \Gamma}{\Delta H_f}. \quad (16.31)$$

If both sides of Eqn (16.30) are squared, and the terms rearranged, a scaling law for dendritic growth results, which is similar to that discussed in Section 16.3.6.1, namely,

$$v\lambda^{\star 2} = 4\pi^2(2\alpha_l d_0) = \text{const.} \quad (16.32)$$

Langer and Müller-Krumbhaar suggested that a dendrite tip operates just within the margin of stability, whereas the remainder of the dendritic interface grows in an unstable, time-dependent manner, producing waves that amplify into side arms, or branches. As their stability analysis is linear, and approximates the tip shape as a plane, issues such as branch location and spacing, and their growth rate are not addressed.

Eqn (16.32) predicts that the speed of the dendrite tip multiplied by the square of the marginally stable wavelength is a constant, independent of the supercooling. Langer and Müller-Krumbhaar's idea that the tip of a dendrite operates at the margin of stability suggests that the tip grows as large as possible without experiencing instability, or splitting. Their hypothesis for the dendritic operating state is one of "noise-mediated" stability and provides a basis for their guess that  $R_{tip} \approx \lambda^\star$ . The approximation symbol applied here between the *observable* tip radius,  $R_{tip}$ , and the *unobservable* marginal wavelength,  $\lambda^\star$ , helps underscore an important fact: namely, linear morphological stability analysis was developed to test initially simple interfacial "basis shapes" (i.e., planes, spheres, and cylinders) that can become cellularly unstable, and *not* for dendrites

<sup>8</sup>The small variation of the magnitude of  $d_0$  among materials as diverse as metals, semiconductors, ceramics, and polymers, also suggests that dendritic crystals tend to exhibit similar morphological characteristics among different materials classes.

that evolve as non-linear dynamic structures that pass through several stages of shape changes.

Nevertheless, by accepting, tentatively, that marginal stability selects an accurate dynamic state for a dendrite tip, also allows the scaling law, Eqn (16.32), to be restated in terms of the volumetric crystal growth rate at the dendrite tip,

$$\frac{2\alpha_\ell d_0}{\nu R_{tip}^2} = \frac{1}{4\pi^2} \cong 0.025. \quad (16.33)$$

The dendritic scaling law,  $\nu R^2 = \text{const.}$ , has several useful applications. It permits estimates to be made of the spatial scales for chemical segregation in cast microstructures, and can help relate cast materials properties to several key solidification variables, including pouring temperature, cooling rate, and alloy composition.

The selection, or stability, constant,  $1/4\pi^2$ , that appears in Eqn (16.33) is usually designated  $\sigma^*$  in the literature. The approximate theoretical value for  $\sigma^*$  varies from about  $0.0192 \pm 0.005$  to  $0.0253 \pm 0.005$ , depending on details of the stability analysis. Experimental checks of  $\sigma^*$  show, however, that its value is *not* a constant for a given test material, but falls slowly with increasing melt supercooling, as confirmed by experimental measurements of steady-state dendritic growth carried out under microgravity conditions [99–100].<sup>9</sup>

### 16.3.6.3 Estimating $\nu$ and $R_{tip}$

Ivantsov's transport solution, Eqn (16.14) and Eqn (16.33)—the scaling law derived from marginal stability theory—are sufficient to predict an operating state of a steady-state dendrite. One can summarize these independent equations as follows:

$$\text{Dendritic transport theory : } \nu R_{tip} = 2\alpha_\ell \mathcal{I} \nu^{-1}(\Delta\vartheta), \quad (16.34)$$

$$\text{Linear interface stability : } \nu R_{tip}^2 = 2\alpha_\ell \sigma^* d_0. \quad (16.35)$$

Solving Eqns (16.34) and (16.35) simultaneously for the values of the dendrite's operating velocity,  $\nu^*$ , and radius,  $R_{tip}^*$ , gives

$$\nu^* = \frac{2\alpha_\ell}{\sigma^* d_0} [\mathcal{I} \nu^{-1}(\Delta\vartheta)]^2, \quad (16.36)$$

and

$$R_{tip}^* = \frac{\sigma^* d_0}{\mathcal{I} \nu^{-1}(\Delta\vartheta)}. \quad (16.37)$$

The operating state (tip speed and radius as a function of supercooling) of a dendrite growing in a pure melt can be expressed in their dimensional form as,

<sup>9</sup>Experimental support for the scaling law given by Eqn (16.33) does not, however, test all the important elements of dendritic growth theory that are based on selective noise amplification. This scaling law verifies only that heat and mass diffusion and interface capillarity comprise significant aspects of the physics of dendritic growth, which are broad conclusions that seem to be valid, provided that the melt supercooling is not large.

$$v^* \cong 0.018 \left( \frac{\alpha_\ell T_m \Delta S_f^2}{c_p \gamma_{sl} \Omega} \right) \Delta\vartheta^{2.5}, \quad (16.38)$$

and

$$R_{tip}^* \cong 55 \left( \frac{c_p \gamma_{sl} \Omega}{T_m \Delta S_f^2} \right) \Delta\vartheta^{-1.25}. \quad (16.39)$$

Equations (16.38) and (16.39) remain valid for values of the dimensionless supercooling,  $\Delta\vartheta$ , over which most free dendritic growth experiments are carried out ( $0.01 \leq \Delta\vartheta \leq 0.3$ ). At values of  $\Delta\vartheta \ll 0.01$ , stability theory reduces to a pair of linked power laws:  $v^* = K_v \Delta\vartheta^2$ , and  $R_{tip}^* = K_R \Delta\vartheta^{-1}$ , so the scaling law, Eqn (16.35), still holds, viz.,  $v \times R_{tip}^{*2} = K_v K_R^2 = \text{const}$ . As a practical matter, however, the thermal boundary layer surrounding a slowly growing dendrite at low supercooling widens sufficiently that the crystal's growth kinetics becomes extremely sensitive to even minor convective motions in the melt. Such dendrites, observed in any realistic experimental setting, would no longer be considered as “freely growing” and “isolated” from their environment.

### 16.3.7 Numerical Methods

Analytic models of crystal growth are more and more supplanted by computer simulations capable of including many more kinetic and thermodynamic factors. Simulations yield graphical displays and numerical outputs that provide great versatility and convenience for foundry engineers and crystal growers analyzing the process. Moreover, advances in simulation methods, as well as major improvements in machine speed and memory—some accomplished just over the past decade—now allow credible simulation of alloy casting. Compare the realistic simulations exhibited in Figure 16.5 with the simplified analytical model sketched in Figure 16.9. Microstructure simulations employ sophisticated algorithms, currently offered through continuum level set and phase-field methods, as well as by cellular automata and finite elements. Even discrete molecular dynamics captured by Monte Carlo methods, as shown Figure 16.6, prove useful for modeling dendritic growth. Commercial solidification codes are now applied routinely in foundries to improve vastly the detail and accuracy of many kinds of simulated solidification processes. Such codes are becoming increasingly capable of making useful and accurate predictions down to the grain-scale of cast microstructures, but do not yet capture details of the dendritic structure.

Phase-field models solve coupled partial differential equations describing the kinetics of crystal growth [127–132]. Although phase-field approaches remain fundamentally-based continuum calculations [25, 36], and offer seemingly boundless capability to incorporate time-dependent complexities, such as dendritic branching and coarsening, their impressive and realistic-looking results are not always straightforward to interpret mechanistically. This difficulty arises firstly from the abstract potentials and parameters required to carry out phase-field and level-set computations, which do not always identify easily with commonly known macroscopic system parameters, including latent

heat, interfacial energy density, thermal diffusivity, etc. In addition, phase field simulations require demanding algorithmic trade-offs that are made to achieve acceptable resolution of the wide spatial scales to be captured that include a dendrite's macroscopic form, along with adequate temporal resolution of the motion of its molecularly thin solid-liquid interface. All that and avoiding excessive computational cost are afforded by continuum phase-field models, which certainly place them among the leading choices as future microstructural models of complex crystal growth and solidification processes.

Increased computational speed, parallel processing, and massive memory storage, also combine to permit practical application of statistical mechanical models, such as employing kinetic Monte Carlo methods to simulate dendritic growth, “atom by atom,” so to speak. For example, a kinetic Monte Carlo model, developed by T. P. Schulze, uses a million ‘atoms’ (voxels) to simulate earlystage *microscopic* processes associated with dendritic growth, including nucleation, interface formation and organization, lattice fields and anisotropy, surface diffusion and side-branching [133,134]. These fundamental modeling efforts will doubtless help contribute knowledge about the microscopic physics of dendritic crystal growth at yet smaller length scales than have been probed to date.

### 16.3.8 Other Kinetic Limitations

At large supercooling and supersaturation—i.e., at values of  $\Delta\vartheta$  approaching or exceeding unity—the assumption of local equilibrium at a dendrite's crystal-melt interface fails, and may no longer be used as an approximation in formulating growth theories at large supercooling. Dendritic growth enters the kinetic realm of “far-from-equilibrium” solidification, where crystal growth processes based on such large departures from local equilibrium are termed rapid solidification processing (RSP). Rapid solidification and deep melt supercooling are crystal growth situations accompanied by a variety of interesting non-equilibrium kinetic phenomena, many aspects of which depend sensitively on the chemistry of the melt and details of the resultant crystal structure. For more comprehensive reviews of rapid solidification, deep supercooling of melts, and detailed discussions on rapid crystallization concepts and techniques see references [102–108].

Kinetic processes induced by rapid interface motion during dendritic growth of highly supercooled metallic melts, or even by crystals growing more slowly from viscous, covalently- or anisotropically-bonded network melts cooled to temperatures low enough to approach their glass transitions [109], behave in ways quite different from near-equilibrium crystal growth described thus far. Crystal-melt interfaces under extreme supercooling continue to dissipate some of the available melt free energy, first by producing entropy needed to transport the heat and solute rejected from the crystal-melt interface, by transport processes already described in Section 16.3.2. Such far-from-equilibrium interfaces also “re-allocate” a portion of the available free energy into other modes sequestered, or “stored”, within the growing crystal. Free-energy storage via line and surface defects, or excess monovacancies raises the chemical potential of the

resultant metastable crystalline structure above that of its equilibrium phase, and correspondingly lowers its solidus temperature.

Stored free energy induced by rapid dendritic freezing may variously appear in the form of lattice dislocations; stacking faults; sub-boundaries; solute trapping; excess vacancy concentrations and lattice disorder; and even quasi-crystal and glass-phase formation [110]. These interesting non-equilibrium effects were studied experimentally from the mid-1980s to the present by D. Herlach and co-workers, using drop tubes and other containerless melting and crystallization devices to access deep supercooling. Their investigations include most of the major non-equilibrium kinetic effects discovered during rapid dendritic growth of metallic [22], semiconductor [111], and glass-forming alloys subject to extreme supercooling [112–121]. Laser and electron beam melting experiments, as alternatives to form thin supercooled films that crystallize rapidly, also contributed much useful kinetic information on solute trapping and other far-from-equilibrium processes; however, thin film crystallization studies fall outside the scope of the present chapter.

To date only a few elements have been reported as successfully crystallized beyond the onset of hypercooling. Two early examples of hypercooled melts include 1)  $\alpha$ -white phosphorus,  $P_4$ , ( $\Delta T_{hyp} = 25.1$  K) that forms a melt consisting of  $P_4$  molecules, which crystallizes to a complex  $\alpha$ -manganese cubic phase [49], and 2) small drops (0.15 g) of molten Ga that were hypercooled with respect to both gallium's  $\beta$ -phase ( $\Delta T_{hyp} = 88$  K) [122], and to its  $\alpha$ -phase ( $\Delta T_{hyp} = 189$  K) [123]. Herlach also confirmed that hypercooling was achieved in large drops of molten transition metals, including Mo ( $\Delta T_{hyp} = 585$  K), Fe ( $\Delta T_{hyp} = 311$  K), and Ni ( $\Delta T_{hyp} = 480$  K) [22]. Perepezko and coworkers, using fine droplet dispersions of pure metals in fluxes to suppress surface nucleation, reported the onset of hypercooling in Hg ( $\Delta T_{hyp} = 79$  K) and In ( $\Delta T_{hyp} = 105$  K) [124]. A few alloy melts have been successfully hypercooled, including Pb-Bi and Zr-Cu [125], but many alloy melts when cooled rapidly to the supercooled state, especially those exhibiting deep eutectic valleys in their phase diagrams, are prone to glass formation with, or without, partial crystallization [126].

Two examples of experimental studies of hindered molecular attachment caused by fast dendritic growth in non-network (simple molecular) melts, coupled with the onset of increasing melt viscosity from deep supercooling, are presented together in Figure 16.16. Both of these kinetic effects dissipate much of the available free energy during crystallization. They also can add sufficient interfacial “drag”, or resistance, inhibiting crystal growth to the point where the growth speed slows even at increasing supercooling! Such effects are more commonly observed in polymer melts and oxide glasses, but are seldom seen in simple molecular melts or metallic alloys that crystallize congruently.

The dendritic growth speeds of  $\alpha$ - $P_4$ , and equimolar Zr-Cu, an alloy melt which freezes congruently, are plotted together in Figure 16.16 as functions of their dimensionless melt supercooling,  $\Delta\vartheta$ , or Stefan number. Despite the much lower thermal diffusivity of  $P_4$ , its dendrites achieve speeds above  $350 \text{ cm}\cdot\text{s}^{-1}$ , whereas molten metallic Zr-Cu, with its much higher thermal conductivity, exhibits dendritic growth speeds

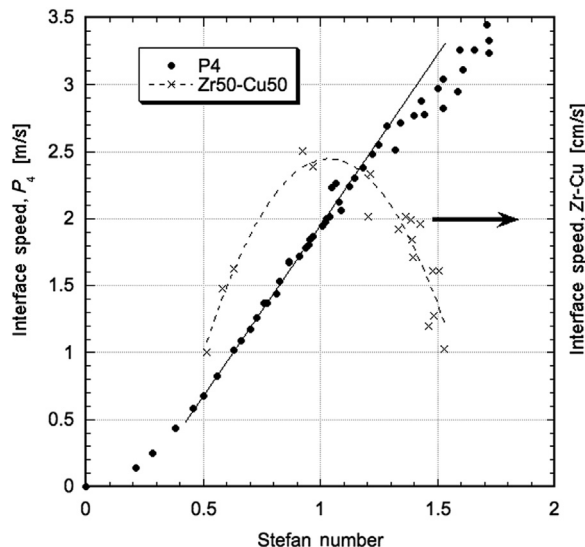


**FIGURE 16.16** Dendritic growth speed versus supercooling for (cubic)  $\alpha$ -P<sub>4</sub> [49] and equimolar Zr-Cu alloy, reference [111]. Supercooling is expressed here dimensionlessly as the Stefan number,  $St = \frac{\Delta T}{\Delta H_f / C_p}$ . Hypercooling occurs when  $St \geq 1$ . Interface speeds up to  $350 \text{ cm}\cdot\text{s}^{-1}$  were observed for  $\alpha$ -P<sub>4</sub>, which forms a melt with low thermal diffusivity, compared to a maximum growth speed of only  $2.5 \text{ cm}\cdot\text{s}^{-1}$  in Zr-Cu, which has a much higher (metallic) thermal diffusivity. Data here suggest that the combined dissipative kinetics of hindered molecular attachment, plus latent heat transport to the melt, operate continuously for  $\alpha$ -P<sub>4</sub> over the supercooling range  $0.5 \leq St \leq 1.5$ . Beyond  $St = 1.5$ , a fall-off is observed from the linear behavior between speed and supercooling as the P<sub>4</sub> melt viscosity rises gradually with supercooling. By contrast, dendrites crystallizing from equimolar Zr-Cu, ( $\Delta T_{hyp} = 202 \text{ K}$ ), show a precipitous drop in speed beyond  $St = 1$  from the rapid increase in its melt viscosity as its glass-transition is approached.

limited to only  $2.5 \text{ cm}\cdot\text{s}^{-1}$ . The thermal gradients developed at the crystal-melt interface in molten  $\alpha$ -P<sub>4</sub>, supercooled beyond its onset of hypercooling at  $\Delta T \geq 25.1 \text{ K}$ , are enormous, exceeding  $2 \times 10^6 \text{ K/cm}$ . Clearly, this example of rapid dendritic crystal growth is removed so far from the condition of local equilibrium that estimates of its kinetic behavior based on conventional transport theory would be misleading.

## 16.4 Branching

### 16.4.1 Stochastics

Branching is a basic morphological characteristic of dendrites that seems well described theoretically by various analytical and numerical growth models [135–137]. Yet, dendritic branching still remains curiously uncertain from a deeper mechanistic standpoint, despite its historical utility in correlating cooling rates in cast alloys using the secondary side-branch spacing [138]. The reason for uncertainty in the branching mechanism is that models for dendritic growth, such as marginal stability, described in Section 16.3.6.2, consistently consider branching as a randomly induced, noise-related phenomenon. In

the specific case of marginal stability, the crystal-melt interface is tested for stability by applying linear perturbation theory, wherein the interface reacts dynamically to a broad spectrum of small-amplitude sinusoidal disturbances. Recall that the marginal wavenumber,  $k^*$ , is selected as it separates higher wavenumber interfacial perturbations that decay uneventfully, from lower wavenumber disturbances that result in instability. Thus, wave-like interfacial branches on dendrites are assumed to be “selectively-amplified” interfacial noise. For visualization of dynamic instability at a planar crystal-melt interface undergoing first cellular instability, then dendritic growth, see again the sequence shown in [Figure 16.2](#). The notion of a stochastic origin for dendritic branching is also reinforced by the fact that some numerical models of dendritic growth actually require the addition of noise—either numerical, thermodynamic, or extrinsic in origin—to stimulate the growth dynamics and produce side branches that resemble those in experiments.

Study of morphological stability using non-linear analyses [139–141], augmented by accurate non-linear numerical simulations [142,143] seem well-grounded in their explanation of the onset of stages of *cellular* instabilities from low-amplitude perturbations at growing crystal-melt interfaces to deep cell formation [144]. As a cautionary note, however, it was also demonstrated experimentally over 40 years ago [145] that some interfacial structures arise as instabilities during crystal growth that are not stimulated by noise and random fluctuations, but depend instead on *persistent* disturbances caused by the presence of crystalline imperfections interacting with the interface. Examples of such “persistent disturbances” include the initial network of grooves marking the traces of sub-boundary intersections with the interface, as well as localized shallow pits, or dimples, from individual dislocation cores threading through the interface.

Other experimental observation relevant to dendritic branching and stability were made in the late 1970s by studying the precise forms of free dendrites [95,96]. S.C. Huang and the present author found that dendrite tips for a given substance behaved self-similarly: that is, their steady-state profiles are identical, except for scale, and remain so independent of the melt supercooling. Self-similarity did not, however, also hold for the adjacent branching and coarsening that occur behind the advancing tip, as would be otherwise suggested by stability models based on amplification of selected noise. More specifically, [Figure 16.17](#) shows a series of micrographs of SCN dendrites photographed while growing from their melt over a wide (20-fold) range of supercooling and a 500-fold range of tip speeds. The magnification of these micrographs is adjusted in [Figure 16.17](#) so the tip radii appear to be identical, i.e., display self-similarity. Were branching induced through selective amplification of noise acting under the *single* transport field surrounding each dendrite, then the subsequent branching sequence should also scale self-similarly, as do the tips themselves. Instead, one notes that at progressively higher supercooling side branches make their initial appearance closer and closer to the tip, by amplifying faster—which is a non-self-similar behavior, suggestive of a causal mechanism different from that acting at the tip.

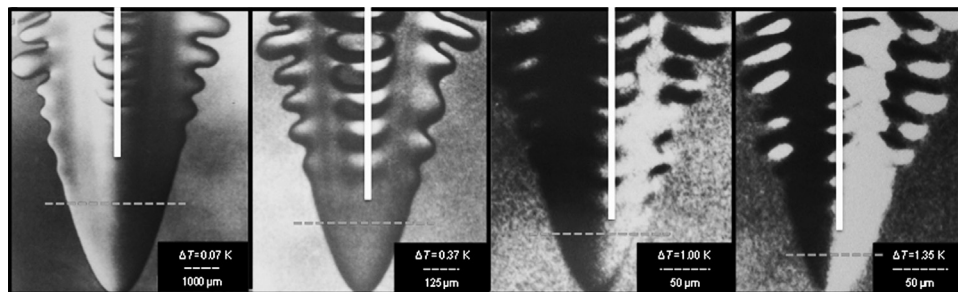


**FIGURE 16.17** Branch amplification on SCN dendrites growing at different supercoolings. Self-similar branching, at the *same* relative locations, would be expected if branching were caused by selective amplification of noise. Horizontal dashed lines indicate the observed locations for the first discernible branches on the plan view. Vertical white bars show locations of the first discernible branches that are growing normal to the plane of these micrographs. Both observations show incursion of branching.

As will be discussed in the next section, dendritic branching appears instead to be stimulated by a *persistent* interfacial perturbation that travels along with the tip, and not by random noise selectively amplified over differing wavenumber ranges by the exterior (Ivantsov) field. The origin of these persistent perturbations was not recognized until recently [146–148].

## 16.4.2 Deterministic Branching

### 16.4.2.1 Background

About ten years ago, a numerical model capable of accurately computing complex diffusion-limited microstructures patterns was developed by J. Lowengrub and his collaborators [149–153]. Their numerical model solves Laplace's equation in two- or three-dimensions for a crystal growing in a melt, under some prescribed far-field temperature or flux. Their numerical code accurately tracks the evolution of a sharp interface, by summing, as integral equations, the field responses produced by a dense distribution of Green function heat sources distributed along the interface. Capillarity and interface attachment kinetics were included in their model.

What proved especially interesting for our purposes using Lowengrub and Li's dynamic numerical model is that it is virtually noise free. Their model, devoid of any significant noise, and with zero interfacial energy anisotropy, simulated complex patterns evolving from simple starting shapes, similar to those observed when two fluids of differing viscosity interpenetrate in Hele-Shaw cells [154–156]. When interfacial anisotropy was introduced into their model, it simulated noise-free dendritic crystals growth patterns. As demonstrated in Figure 16.18, Lowengrub and Li showed that their model evolves noise-free dendritics in two dimensions from simple starting shapes, including circles and ellipses, or in three dimensions from spheres, *providing* that some anisotropy was included either in the crystal-melt interfacial energy density, or the interface mobility [157]. These noise-free simulation data were related back to earlier

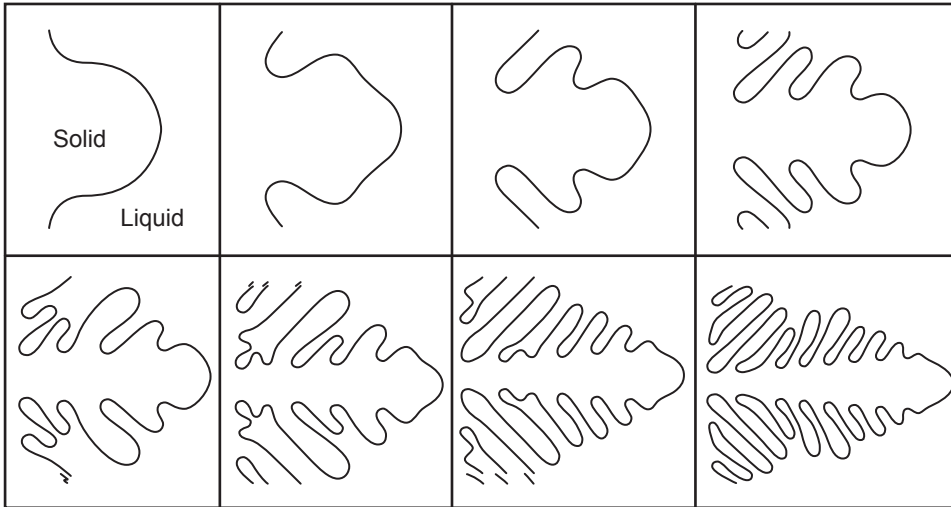


**FIGURE 16.18** Dynamic evolution of a dendrite in two dimensions ( $\mathbb{R}^2$ ) from a projecting “bump” (upper row, left), simulated by Lowengrub and Li using their integral equation solver in a *noise-free* numerical environment. Computational results such as these raised questions concerning the broadly accepted view that dendritic branching is a result of selective amplification of noise impressed on the interface.

experimental observations of capillary-induced shape changes in the melting of small ellipsoidal crystals in microgravity [158], which were eventually shown to be relevant to the same mechanism of persistent perturbations stimulating dendritic branching [159].

#### 16.4.2.2 Interface Energy Conservation

The origin of persistent perturbations that induce dendritic branching may be identified by a general analysis of energy conservation for a two-phase crystal-melt domain containing a curved, time-dependent, interface,  $S(t)$ . This analysis follows, by analogy, a mass conservation model developed by Spencer et al. [160] to track surface diffusion of mobile species during solid-state phase transformation.

Total time differentiation of all the energies contained within a two-phase crystal-melt domain, both those within the phase volumes and their interface, yields a form of the Leibniz-Reynolds energy transport theorem [161,162]. The bi-phase domain is subject to “contraction”, a procedure that excludes the volumetric energies, but retains surface energies on the evolving crystal-melt interface,  $S(t)$ , around which the surrounding phases *remain in local equilibrium*.

Energy conservation applied to the crystal-melt interface,  $S(t)$ , is expressed by the following integral, which reveals four rates of energy change that collectively cancel at every point along the evolving interface:

$$\iint_{S(t)} \left[ - \left( k_s \vec{\nabla}[T_s]_{S(t)} + k_\ell \vec{\nabla}[T_\ell]_{S(t)} \right) \cdot \vec{\mathbf{n}} + \frac{\Delta H_f}{\Omega} \vec{\mathbf{v}} \cdot \vec{\mathbf{n}} + \gamma(\varphi) \mathcal{H}(\varphi) \vec{\mathbf{v}} \cdot \vec{\mathbf{n}} + \sum_{m=1}^2 \vec{\nabla}_m \cdot \mathbf{J}_m \right] dA = 0. \quad (16.40)$$

The terms appearing in the integrand of Eqn (16.40) are as follows:

1.  $-(k_s \vec{\nabla}[T_s]_{S(t)} + k_\ell \vec{\nabla}[T_\ell]_{S(t)}) \cdot \vec{\mathbf{n}}$  is the sum of heat flux components normal to the interface that are conducted to, or from, the adjacent solid (s) and liquid (l) by their respective thermal gradients,  $k_i \vec{\nabla}[T_i]_{S(t)}$ .
2.  $\frac{\Delta H_f}{\Omega} \vec{\mathbf{v}} \cdot \vec{\mathbf{n}}$  is the rate of latent heat released, or absorbed, from crystallization or melting, at an interface point moving at speed  $\vec{\mathbf{v}} \cdot \vec{\mathbf{n}}$ . Here  $\vec{\mathbf{v}}$  is the local interface velocity, and  $\vec{\mathbf{n}}$  is the unit normal vector at that point on the interface, directed toward the melt.
3.  $\gamma(\varphi)\mathcal{H}(\varphi) \vec{\mathbf{v}} \cdot \vec{\mathbf{n}}$  is the rate of interfacial “stretching,” which accounts for the rate that energy is stored or released, as interfacial regions with mean curvature  $\mathcal{H}(\varphi)$  either increase or decrease their areas, respectively.
4.  $\sum \vec{\nabla}_m \cdot \mathbf{J}_m$  is the scalar sum of the surface divergences of capillary-mediated tangential heat fluxes on an interface. These fluxes are directed along each surface coordinate,  $m = 1, 2$ , containing the principal curvatures,  $\kappa_m$ . Note that for “ruled” interfaces, to be considered shortly, only one (in-plane) curvature,  $\kappa$ , exists.

We also note that term 3, the interface stretching (storage) rate, remains small provided the interface is not too irregular. This restriction remains valid for typical mesoscale structures such as dendrites. Once multiple branching or splitting occur, however, the interface becomes rumped, and energy storage by “stretching” could make a non-trivial contribution to the local energy balance.

Now, limiting Eqn (16.40) to just the remaining three rates of energy exchange, i.e., terms 1, 2, and 4, the Stefan energy balance reduces to

$$-\left(k_s \vec{\nabla}[T_s]_{S(t)} + k_\ell \vec{\nabla}[T_\ell]_{S(t)}\right) \cdot \vec{\mathbf{n}} + \frac{\Delta H_f}{\Omega} \vec{\mathbf{v}} \cdot \vec{\mathbf{n}} + \sum_{m=1}^2 \vec{\nabla}_m \cdot \mathbf{J}_m = 0, \quad (16.41)$$

The “standard” Stefan energy balance used in theories of crystal growth contains only the first two terms appearing in Eqn (16.41), where term 1, heat conduction to or from the bulk phases, balances term 2, the latent heat release [46, 163]. The last term in Eqn (16.41), as revealed by the Leibniz-Reynolds theorem, also affects the local Stefan balance, as a persistent perturbation. We designate this term as the capillary *bias field*, which represents a weak, capillary-mediated source of energy that derives from the surface divergence of the *tangential* thermal fluxes along principal curvature directions on the interface. Tangential fluxes, such as  $\mathbf{J}_m$ , are normally dismissed as “unimportant,” insofar as they do not contribute to the *net* rate of phase transformation. Although this statement remains true, one finds that the surface divergences of the tangential fluxes provide additional rates of energy release, or withdrawal, along the interface. We now proceed to show that the scalar bias field affects the local interface velocity without affecting the global, or net, transformation rate over the total interface. This energetic interaction provides the perturbative mechanism that induces interfacial branching.

### 16.4.2.3 Time Scales

The capillary bias field,  $\mathcal{E}(\varphi) = \vec{\nabla}_m \cdot \mathbf{J}_m$ , as shown in the next section, derives straightforwardly from classical capillarity, combining with the rate of latent heat release to modulate the local interface motion. Both the capillary bias field and latent heat release involve extremely fast microscopic processes occurring at the molecular level, on or adjacent to the interface: i.e., 1) the capillary bias field derives from gradients in the Gibbs-Thomson-Herring potential (discussed in detail in [Section 16.4.2.5](#)) that reflect *local* interfacial equilibrium established by molecules exchanging across the interface, and 2) the latent heat results from molecular phase transition events, as melt molecules arrive and join the growing crystal. By contrast, thermal conduction, the first term in the Stefan balance, [Eqn \(16.41\)](#), changes relatively slowly in time, as it requires long-range macroscopic diffusion over many millions of molecules. The large disparity in the time scales for heat conduction, compared to the fast generation of latent heat, allows the capillary bias field and phase change energy to combine on short time scales as a *total* local energy rate. This total energy release rate is balanced by the more slowly varying macroscopic heat conduction term. The effect of this energetic combination—latent heat modified by capillary energy—is to perturb the interface at special points where the bias field changes sign.

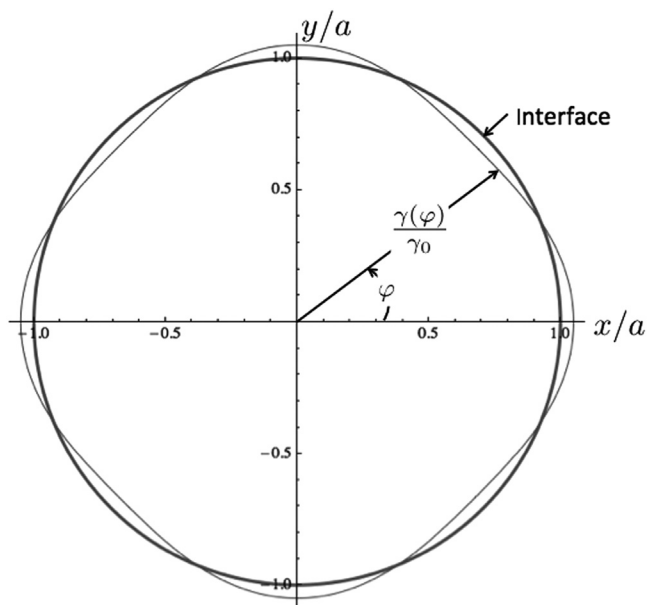
Consequently, if the bias field, responding to the local interface shape and orientation, results in a positive deposition of energy that adds to the latent heat term, with the latter proportional to the interface speed, then the interface slows slightly to satisfy the Stefan energy balance, which is dominated by the slowly changing thermal conduction field. Vice versa, if the bias field results in energy removal, and reduces the total heat release, then the interface accelerates slightly to boost the latent heat and interface speed and allow energy balance with the conduction term. In summary, the bias field tracks the fast-changing GTH equilibrium potential distribution. Its energy rate, which may be positive or negative, perturbs the latent heat production rate by modulating the interface normal speed. In this manner, microscopic and macroscopic processes always remains in balance.

Even more importantly, where the bias field changes sign, it establishes a *persistent* “disturbance” that induces branching by inflecting the interface. The details of this deterministic branching mechanism will be explained next. Thus, it is capillarity that provides coupling of fast-changing rates of energy, linking the local interface configuration with the interface speed and latent heat release. This critically important perturbative interaction occurs during dendritic growth, but is overlooked in conventional crystal growth theory, despite the fact that careful thermodynamic analyses of interfaces [\[173,164\]](#) had already clearly identified all the terms appearing in [Eqns \(16.40\) and \(16.41\)](#).

### 16.4.2.4 Interface Capillarity

The surface energy density of a crystal-melt interface is normally anisotropic, as it reflects the directional molecular fields established by the underlying crystal lattice

**FIGURE 16.19** A circular crystal-melt interface (thick curve on Cartesian axes)  $x^2 + y^2 = a^2$ , where  $a$  is the crystal's initial radius, and the corresponding convex polar plot (thin curve) of the 4-fold interfacial energy density, Eqn (16.42). This initially circular crystal, which is growing, is *not* the Wulff shape required at *global* equilibrium, and thus the initial interface depicted here, and its subsequent evolved dynamic shapes, achieve only *local* equilibrium via the Gibbs–Thomson–Herring temperature distribution. The quantity  $\frac{\gamma(\varphi)}{\gamma_0}$ , plotted on polar coordinates, is the anisotropic interfacial energy density,  $\gamma(\varphi)$ , scaled to its angular average, or modulus,  $\gamma_0$ . Were the crystal not forced to grow, it would relax toward its equilibrium Wulff form, which is a shape congruent with the pedal transform of the convex gamma-plot shown here (light polar contour).



[165–167]. We treat the simple example of a circular interface in two dimensions enclosing a growing crystal. This crystal is subject to anisotropic surface energy density, but as it is growing, the interface may not relax toward its full equilibrium Wulff form—which represents the sole circumstance under which the GTH interface potential becomes uniform. Instead it evolves dynamically. See Figure 16.19. The anisotropy of the crystal's interfacial energy density is described by  $\gamma(\varphi)$ , where the normal angle,  $\varphi = 0$ , aligns with the positive  $x$ -axis, which orients the interface normals,  $\mathbf{n}$ , to the crystalline axes. The energy density,  $\gamma(\varphi)$ , is chosen, again for simplicity, as a two-dimensional convex graph, with 4-fold harmonics and pairs of maxima aligned along the circle's  $x$ - and  $y$ -axes. These maxima are located at corresponding interface orientations  $\varphi = (0, \pi)$  and  $\varphi = \left(\frac{\pi}{2}, \frac{3\pi}{2}\right)$ , respectively. The anisotropic energy density is, therefore, chosen as

$$\gamma(\varphi) = \gamma_0(1 + \varepsilon \cos 4\varphi), \quad (16.42)$$

where  $\gamma_0$  is the modulus, or angularly averaged energy density over the interface. The amount, or strength, of 4-fold anisotropy, is specified by  $\varepsilon$ . To avoid concerns about “missing” orientations i.e., jumps in the normal vectors caused by equilibrium faceting, the energy densities allowed for the purposes of this discussion are restricted to convex graphs [168,169], which limit the maximum amplitude of 4-fold anisotropy to  $\varepsilon \leq 1/15$ .

#### 16.4.2.5 Local Equilibrium

The chief assumption employed in this model of deterministic dynamic branching is that local—not global—equilibrium prevails along the interface, which contacts the

surrounding melt at uniform pressure. Local equilibrium will prevail if, and only if, the interfacial temperature follows the Gibbs–Thomson–Herring (GTH) equilibrium condition [165, 166]. Global equilibrium, by contrast, requires minimization of the system’s free energy, a process which is precluded here by dynamic crystal growth. The GTH condition, a necessary, but insufficient, condition for global equilibrium [167–169], derives from the Euler–Lagrange variational principle [170, 171]. Thus, the local interfacial temperature,  $T_{int}(\varphi, t)$ , is prescribed at each point by the GTH condition through the local interface curvature,  $\kappa(\varphi)$ , and its orientation-dependent energy density,  $\gamma(\varphi)$ . As such, the GTH temperature distribution along the interface depends only on its shape and local crystallographic orientation,  $\mathbf{n}(\varphi)$ , as

$$T_{int}(\varphi, t) = T_m - \frac{T_m \gamma_0 \Omega}{\Delta H_f} \left( \frac{\gamma(\varphi) + \gamma_{\varphi,\varphi}}{\gamma_0} \right) \kappa(\varphi, t). \quad (16.43)$$

The term  $T_m$ , appearing on the right-hand side of Eqn (16.43), denoted the equilibrium temperature on a planar crystal–melt interface at the same melt pressure; the term  $\gamma_{\varphi,\varphi}$  is the second derivative of the interfacial energy density,  $\gamma(\varphi)$ , with respect to the normal angle. Rearrangement of Eqn (16.43) leads to the definition of the dimensionless GTH thermal potential along the interface,

$$\vartheta(\varphi, t) \equiv \frac{T_{int}(\varphi, t) - T_m}{T_m} = \frac{\lambda_c}{a} \left( \frac{\gamma(\varphi) + \gamma_{\varphi,\varphi}}{\gamma_0} \right) \widehat{\kappa}(\varphi, t), \quad (16.44)$$

where  $\frac{\lambda_c}{a} = \frac{\gamma_0 \Omega}{a \Delta H_f}$  is the system’s capillary constant, and  $\widehat{\kappa}(\varphi) \equiv a \kappa(\varphi)$  is the dimensionless curvature of the interface, where  $a$  is the radius of the initial circular interface.

Our choice of 4-fold interfacial anisotropy, Eqn (16.42), and the GTH equilibrium constraint, Eqn (16.44), may be combined to yield the harmonic form for the thermodynamic potential existing momentarily along the evolving circular interface, namely,

$$\vartheta(\varphi; \varepsilon) = \frac{\lambda_c}{a} [15\varepsilon \cos(4\varphi) - 1] \quad (t = 0). \quad (16.45)$$

The anisotropy strength appearing in the interfacial energy density,  $\varepsilon$ , as already explained in Section 16.4.2.4, is limited here to values less than 1/15. This choice avoids possible formation of equilibrium facets.

### 16.4.3 Interfacial Gradients and Fluxes

Gradients of the GTH temperature field, or thermal potential, always occur along a curved crystal–liquid interface, save for two related exceptions representing *global* equilibrium: 1) circular interfaces with isotropic interfacial energy, or 2) So-called “Wulff shapes” evolved with their corresponding anisotropic energy densities [169]. We choose the case of a circular interface of radius  $a$ , with 4-fold anisotropic energy,  $\varepsilon \neq 0$ , to demonstrate the action of bias-field effects. Consequently, the spatially varying equilibrium temperature along such a circular interface supports the presence of tangential interfacial gradients. Temperature continuity between the crystal and the

adjacent melt also imply identical tangential gradients impressed on the bulk phases where they meet.

The general form for the tangential thermal gradient,  $\vec{\mathbf{G}}_{\tau}(\varphi)$ , induced by capillarity is found by differentiating the GTH thermal field, either Eqn (16.43) or (16.44), with respect to the interfacial arc length,  $s(\varphi)$ . The interfacial temperature gradient in the positive i.e., anti-clockwise  $\varphi$ -direction may be found conveniently by first differentiating the GTH temperature field with respect to its normal angle,  $\varphi$ , and then applying the chain rule by multiplying that derivative by  $\partial\varphi/\partial s = \kappa(\varphi)$ . Carrying out these operations sequentially on Eqn (16.44) yields the tangential thermal gradient along any smoothly curved crystal-melt interface in  $\mathbb{R}^2$ ,

$$\vec{\mathbf{G}}_{\tau}(\varphi) = \frac{\lambda_c T_m}{a^2} \widehat{\kappa}(\varphi)^2 \left[ \left( \frac{\gamma_{\varphi} + \gamma_{\varphi,\varphi}}{\gamma_0} \right) + \left( \frac{\gamma(\varphi) + \gamma_{\varphi,\varphi}}{\gamma_0} \right) \frac{\widehat{\kappa}_{\varphi}}{\widehat{\kappa}(\varphi)} \right] \vec{\tau}. \quad (16.46)$$

Here  $\vec{\tau}$  is a unit tangent vector pointing in the anti-clockwise direction along the interface, with crystal located on the left, and melt located on the right, and the subscripted  $\varphi$ -notation indicating the various orders of differentiation with respect to the normal angle.

The tangential thermal flux,  $\vec{\mathbf{J}}_{\tau}(\varphi)$ , associated with this interfacial gradient field may be calculated from Eqn (16.46) by applying Fourier's law of heat conduction to the interfacial region, namely,

$$\vec{\mathbf{J}}_{\tau}(\varphi) = -k_{int} \vec{\mathbf{G}}_{\tau}(\varphi). \quad (16.47)$$

The crystal-melt interface is modeled as a smoothly curved surface with a non-zero thermal conductivity,  $k_{int}$ , which bears units of [J/K-s], so as to be compatible with the units of the corresponding tangential energy fluxes that are [J/m-s]. The interfacial conductivity is a "composite" transport property reflecting the passage of thermal energy through the region where the crystalline and melt phases meet. Few details are known at present about this interfacial transport property, except that one might estimate it as an average response by the bulk phases to a gradient impressed along their respective surfaces. By contrast, surface diffusion coefficients for mobile species diffusing over crystalline interfaces have been measured and reported for more than a century [172]. Their thermal analogy,  $k_{int}$ , although seldom discussed, has been exposed by careful analyses of interface thermodynamics, e.g., Caroli et al. [173], and clearly implied by analogy in kinetic studies of surface evolution by Mullins [174] and Spencer et al. [160].

Application of the tangential flux expression, Eqn (16.47), to the specific case of a circular interface subject to 4-fold anisotropic interfacial energy density gives its tangential energy flux as

$$\vec{\mathbf{J}}_{\tau}(\varphi) = -60 \left( \frac{k_{int} T_m \lambda_c}{a^2} \right) \varepsilon \sin 4\varphi \vec{\tau}. \quad (16.48)$$

A tangential flux, such as  $\vec{\mathbf{J}}_{\tau}(\varphi)$ , cannot alter the overall, or net, transformation rate of the initial circular crystal, because its net rate of growth is determined solely by its surrounding transport field, which provides normal thermal gradients that conduct away

the latent heat to the surrounding melt. Nevertheless, the surface divergence of the vector tangential flux,  $\vec{\nabla}_\tau \cdot \vec{\mathbf{J}}_\tau(\varphi)$ , which equals (minus) the scalar bias field, locally deposits and removes energy from the interface, causing, as already explained in [Section 16.4.2.3](#), perturbation of the local interface speed *without* altering the crystal's overall growth rate. This feature is another interesting attribute of the capillary bias field: it modulates local growth rates without affecting the overall growth rate. The bias field, even for non-circular shapes, remains a net zero energy field, and thus only perturbs the interface dynamics locally.

### 16.4.4 Bias Field

We now analyze the exact *initial* forms of the capillary bias field,  $\mathfrak{E}(\varphi, 0)$ , acting on a circular interface, to predict the early stages of pattern evolution, namely, where branching initiates on a circular crystal exhibiting 4-fold anisotropy.

The bias field can be determined analytically by taking the surface divergence of (minus) the vector tangential flux, [Eqn \(16.48\)](#). This is accomplished by differentiating the tangential flux field with respect to its normal angle,  $\varphi$ , and again applying the chain rule by multiplying that result by  $\partial\varphi/\partial s = \kappa(\varphi)$ . That procedure yields an analytic expression for the initial bias field, acting on the circular interface at  $t = 0$ , namely,

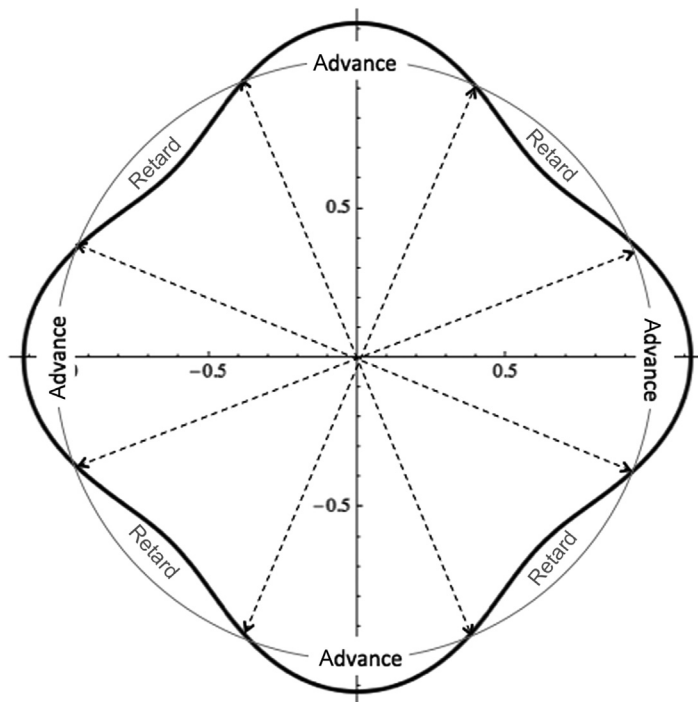
$$\mathfrak{E}(\varphi, 0) = -\vec{\nabla}_\tau \cdot \vec{\mathbf{J}}_\tau(\varphi) = 240 \left( \frac{k_{int} T_m \lambda_c}{a^3} \right) \varepsilon \cos 4\varphi. \quad (16.49)$$

Inspection of the Stefan balance, [Eqn \(16.41\)](#), shows that if the conduction term is momentarily considered as constant (at least for the brief interval needed to establish local equilibrium) then the algebraic sum of the bias field energy rate plus the latent heat release rate also remains constant. If the bias field were positive at a point on the interface (contributing energy) the latent heat term would be decreased by slightly lowering the local interface speed,  $\mathbf{v} \cdot \vec{\mathbf{n}}$ . Conversely, if the bias field energy rate were negative (removing energy) the local interface speed would increase commensurately to balance the (momentarily constant) conduction term with a slightly larger release of latent heat.

#### 16.4.4.1 Dynamic Responses

[Figure 16.20](#) shows a polar plot of the analytically predicted initial interface response to the bias field, equation [Eqn \(16.49\)](#), for a small anisotropy,  $\varepsilon = 0.005$ , acting on the circular interface. Recalling that the interface accelerates slightly where  $\mathfrak{E}(\varphi, 0) < 0$ , and is retarded where  $\mathfrak{E}(\varphi, 0) > 0$ , one predicts a total of eight initial inflection points that develop around the circular interface, each separating interfacial segments where outward acceleration switches to retardation. Precisely the same behavior is noted dynamically in [Figure 16.21](#), where the predicted four branches (eight inflection points) appear in the first two video panels displayed on the top row. These two panels represent the initial circle (Frame 001), and an early stage of its dynamically evolved shape is observed seventy-five frames later (Frame 76), where four prominent bumps form, as predicted analytically from the bias field mechanism.

**FIGURE 16.20** Local effects of capillary-mediated bias field on an initially circular crystal-melt interface (thin unit circle). The initial distortions of a circular interface with anisotropy are actually independent of the anisotropy strength,  $\epsilon$ , and consist of local segments of interfacial acceleration and retardation, separated by the eight roots of the bias field function, Eqn (16.49). Compare the analytical branching predictions (thick curve) with dynamic results displayed in Figure 16.21, top row, first two frames from left (dynamic video frames 001 and 076).



As time increases, the roots of the bias field drift outward toward the tips of the initial four bumps, where another sixteen inflections occur, causing eight new bumps to develop, as shown in the third video panel of the top row (Frame 94). Later, as the dynamic shape becomes increasingly ramified, it couples more strongly with the exterior transport field and accelerates the process of branching. The initial four bumps have by now clearly evolved into primary stems, and sixteen more inflections, and eight new side bumps form along the extending tips at positions where the roots of the bias field stimulate additional inflections of the interface. The second panel on the lower row shows that the tips of the primary stems no longer exhibit semi-circular tip profiles, as they did along the top row, but are beginning to look more like parabolic tips. That important change is evident in the last panel, where a distinctly parabolic tip begins “sprouting” periodic side branches. Still not understood is the dynamic synchronization of the bias field roots with the tip motion, which leads to a branching pattern suggestive of a periodic “limit cycle,” which produces the classical dendritic morphology [144].

One means to check quantitatively the bias-field analysis developed here is to compare its predictions against dynamic simulations of the same starting shape. Accurate measurements of the inflection points developed in the early dynamic pattern allow retrospective analysis by measuring their drift *backward in time* toward the starting shape. This procedure independently tests the analytical estimate of the early

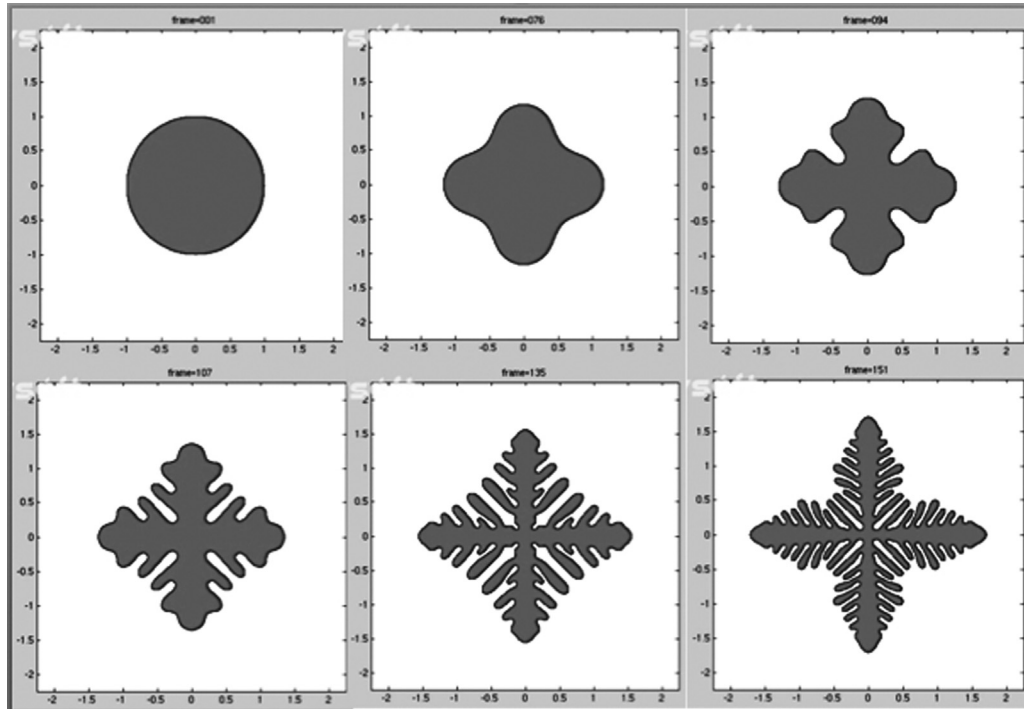


**FIGURE 16.21** Progression of noise-free dynamic frames showing pattern evolution of an initially circular crystal, in local equilibrium, with a weak 4-fold anisotropy ( $\varepsilon = 0.005$ ). The total pattern area (black pixels) developed in this simulation are kept constant in time for ease of comparison. Analytical results, shown in [Figure 16.20](#), are in agreement with the simulated sequence shown in the first two panels on the top row. The lower row of frames, taken later in the simulation, produce a progression of branches that appear eventually to synchronize with the advancing (parabolic) tip and establish a “limit cycle.” Video data for dynamic frame extractions produced by J. Lowengrub and S. Li [175].

pattern evolution using several arbitrary initial shapes. In this manner one reveals the dynamic interface perturbations that autonomously modified the initial form into its time-sequence of dynamic shapes. Convergence to a few tenths of a percent of the numerical and analytical procedures for several elliptical shapes (not detailed here) reveal that capillary-mediated bias fields are the likely deterministic cause of branching in dendrites.

#### 16.4.4.2 Dendritic Branching

Zeros, or roots, of the bias energy field are especially important near dendrite tips, as they designate interfacial locations where the local change in the interface speed also undergoes a sign change. As local acceleration in interface speed boosts curvature, whereas local retardation in interface speed decreases curvature, an inflection, or “twist” develops. [Figure 16.22](#) shows quantitatively how deposition and removal of bias field energy induce interface inflection over time. The adjacency along the interface of

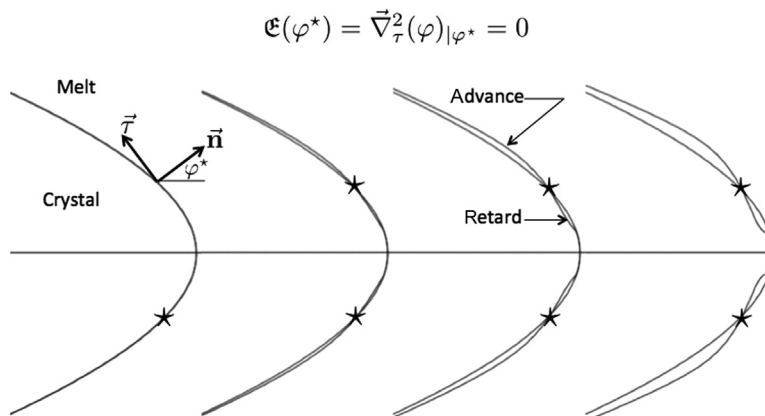


**FIGURE 16.22** Initiation of deterministic branching near a hyperbolic tip with weak 4-fold anisotropy ( $\epsilon=0.005$ ). The zeros,  $\mathfrak{E}(\varphi^*) = 0$ , locate the positions on the interface where the sign of the bias energy changes. Bias field zeros induce inflection, or “twisting”, of the interface by retarding the interface where  $\mathfrak{E} \geq 0$ , and advancing the interface where  $\mathfrak{E} \leq 0$ . The persistent negative field aft of the roots produces small humps on the interface that develop over time into side branches.

simultaneous retardation and acceleration of the local normal velocity stimulates inflection and branching. The examples shown here in [Figure 16.22](#) is a hyperbolic protuberance, with a bias field that has a small 4-fold anisotropy.

## 16.5 Summary

This chapter reviewed selected areas of the history, applications, and scientific state of knowledge concerning the field of dendritic crystal growth—a crystalline form of considerable scientific and technological importance. Dendrites that appear in crystalline materials as diverse as snow flakes, minerals, casting alloys, chemicals, and superalloys, are broadly the result of diffusion-limited crystal growth that leads to complex, and often beautiful tree-like forms. As discussed and developed in this chapter, theoretical descriptions of dendritic growth generally entail a combination of transport theory, i.e., heat conduction, melt convection, and species diffusion—all, incidentally, well understood subjects—with microscopic interfacial processes that include capillarity, molecular interface attachment, and viscosity-limited melt mobility, which remain as subjects of active, ongoing materials research. As pointed out with specific industrial successes, such as directional freezing of alloys, single crystal castings, and large-scale crystallization of commodity chemicals, our limitations in the scientific understanding of growth kinetics and pattern formation has neither stifled technological progress, nor limited innovation in materials processing that involve dendritic growth at some stage of their production or use. That scientific progress will accelerate in the near term is virtually assured, especially with constant improvements and maturation of numerical simulation techniques, which include phase field, as well as other continuum

models, quantum-level molecular dynamics, and, recently, statistical methods realized through large-scale kinetic Monte Carlo calculations. The next decade of scientific and technological progress in this area of crystal growth may yet prove to be the most impressive. This author looks forward to seeing those anticipated scientific advances and associated technological improvements unfold in time.

## Acknowledgment

The author is indebted to his colleagues, Professors John Lowengrub and Shuwang Li for access to their ongoing dynamic studies on dendritic branching, and to Professor Andrew Mullis, University of Leeds, UK, and Professor Paulo Rangel Rios, Universidade Federal Fluminense Escola de Engenharia Industrial Metalúrgica de Volta Redonda, Brazil, for their encouragement in my pursuing the mechanism of microstructure pattern development. My heartfelt thanks go to Professor Markus Rettenmayr, Friedrich Schiller University, Jena, Germany, for his thorough critique of the penultimate draft of this chapter, and for many useful suggestions made for improving its clarity. Finally, appreciation is noted for Professor T.P. Schultze, University of Tennessee, Knoxville, TN; Professors Dieter Herlach and Ivan Egry, German Space Agency (DLR), Köln-Portz; and Professor John Perepezko, University of Wisconsin, Madison, WI; for their individual assistance in up-dating my knowledge of significant research progress in several key areas involving dendritic growth.

## References

- [1] Bentley WA. *Snowflakes in photographs*. Mineola (NY): Dover Publications; 2000. Originally published as *Snowcrystals*, McGraw-Hill, New York, 1931.
- [2] Nakaya U. *Snow crystals: natural and artificial*. Cambridge (MA): Harvard University Press; 1954.
- [3] Furukawa Y. Ice crystal growth. In: Nishinaga T, Rudolph P, Kuech T, editors. *Handbook of crystal growth*. 2nd ed. Amsterdam: Elsevier; 2014. IB, Chapter 25.
- [4] Janner A. *Acta Cryst* 1997;53:615.
- [5] Libbrecht KG. *The snowflake: winter secret beauty*. Stillwater (MN): Voyageur Press; 2003. 112.
- [6] Losert W, Shi BQ, Cummins HZ. *Proc Nat Acad Sci USA* 1998;95:431.
- [7] Seidensticker RG, Hopkins RH. *J Cryst Growth* 1980;50:221–35.
- [8] Seidensticker RG. *Crystals* 1982;8:145–72.
- [9] Lalena JN, Cleary DA, Carpenter E, Dean NF. *Inorganic materials synthesis and fabrication*. Hoboken (NJ): John Wiley & Sons; 2008. 251.
- [10] Chung FH, Smith DK. *Industrial applications of X-ray diffraction*. New York (NY): Marcel Dekker, Inc; 2000. 134 Chapter 6.
- [11] Blackford J. *Engineering of superalloys*. 2002. <http://www.cmse.ed.ac.uk/AdvMat45/superEng.pdf>.
- [12] Courtesy of David S, Boatner L. Oak Ridge National Laboratory. Private communication (1995).
- [13] Mersmann A. *Crystallization technology handbook*. Boca Raton (FL): CRC Press; 2001. 69.
- [14] Mullin JW. *Crystallization*. 4th ed. Butterworth-Heinemann; 2001. 403 Chapter 9.
- [15] Walker JL. In: Chalmers B, editor. *Principles of solidification*. New York: J. Wiley & Sons; 1964. p. 114.

- [16] Colligan GA, Bayles BJ. *Acta Metall* 1962;8:895.
- [17] Glicksman ME. *Acta Metall* 1965;13:1231–46.
- [18] Wu Y, et al. *Metall Mat Trans A* 1987;18:915.
- [19] Klein S, et al. *Phys Rev B* 2009;80:212202.
- [20] Perepezko J, Andersen I. Synthesis and properties of metastable phases. In: Machlin ES, Rowland TJ, editors. *The metallurgical society of AIME*; 1980. p. 31.
- [21] Willnecker R, Herlach DR, Feuerbacher B. *Phys Rev Lett* 1989;62:2707–10.
- [22] Herlach DM. *Annu Rev Mater Sci* 1991;21:23.
- [23] Schwarz M, et al. *Phys Rev Lett* 1994;73:1380.
- [24] Glicksman ME, Schaefer RJ. *Acta Metall* 1966;14:1226.
- [25] Plapp M. Phase field theory. In: Nishinaga T, Rudolph P, Kuech T, editors. *Handbook of crystal growth*. 2nd ed. Amsterdam: Elsevier; 2014. IB, Chapter 15.
- [26] THERMO-CALC<sup>®</sup> software, a product of Thermo-Calc AB, Stockholm (Sweden). Applications brochure, TMS Annual Mtg., Seattle (WA); 2010.
- [27] Schultze TP. Private comm. Los Angeles: Institute for Pure and Applied Mathematics, University of California; 2012.
- [28] Glicksman ME, Schaefer RJ, Ayers JD. *Metall Trans A* 1976;7:1747.
- [29] Chalmers B. *Trans AIME* 1956;200:519.
- [30] Glicksman ME. Principles of solidification. New York: Springer; 2010. 221–234 Chapter 9.
- [31] Esaka H, Kurz W. *Z Metall* 1985;76:127.
- [32] <http://www.msm.cam.ac.uk/phase-trans/phase.field.models/movies2.html>.
- [33] Glicksman ME. Principles of solidification. New York: Springer; 2010. 299 Chapter 12.
- [34] Glicksman ME, Marsh SP. The dendrite. In: Hurler DTJ, editor. *Handbook of crystal growth*. Amsterdam: Elsevier Science Publishers; 1993. p. 1075.
- [35] Jackson KA. Kinetic processes: crystal growth, diffusion, and phase transitions in materials. Weinheim: Wiley-VCH; 2004.
- [36] Emmerich H. *Phase Field Methods*. Springer: Berlin; 2003.
- [37] Ivantsov GP. *Dokl Akad Nauk USSR* 1947;58:567.
- [38] Ivantsov GP. *Dokl Akad Nauk USSR* 1951;81:179.
- [39] Ivantsov GP. *Dokl Akad Nauk USSR* 1952;83:573.
- [40] Papapetrou A. *Z F Kristallogr* 1935;92:89.
- [41] Chen Y-Q, Tang X-X, Xu J-J. *Chin Phys B* 2009;18:671.
- [42] Morse PM, Feshbach H. *Methods of theoretical physics, part I*. New York: McGraw-Hill; 1953. 664.
- [43] Moon P, Spencer DE. *Field theory handbook, including coordinate systems, differential equations, and their solutions*. 2nd ed. New York Berlin: Springer-Verlag; 1988. 47.
- [44] Glicksman ME. Principles of solidification. New York: Springer; 2010. 199–203 Chapter 8.
- [45] McFadden GB, Coriell SR. *J Cryst Growth* 1986;74:507–12.
- [46] Carslaw HS, Jaeger JC. *Conduction of heat in solids*. 2nd ed. Oxford: Clarendon Press; 1984.
- [47] Alexiades V, Solomon AD. *Mathematical modeling of melting and freezing processes*. Washington (DC): Hemisphere Publishing Co; 1993.
- [48] Crank J. *Free and moving boundary problems*. Oxford: Clarendon Press; 1984.

- [49] Glicksman ME, Schaefer RJ. *J Cryst Growth* 1967;1:297–310.
- [50] Glicksman ME. *Principles of solidification*. New York: Springer; 2010. 429–434 Chapter 17.
- [51] Perepezko JH, Paik JS. *J Non-Cryst Solids* 1984;61/62:113–8.
- [52] Perepezko JH. *Mater Sci Engr* 1984;65:125.
- [53] Perepezko JH, et al. In: fine ME, Starke EA, editors. *Rapidly solidified powder aluminum alloys: a symposium*. W. Conshohocken (PA): ASTM International; 1986.
- [54] Ludwig A. *Scr Mat* 1996;34:597.
- [55] Li M, Kuribayashi K. *Acta Mat* 2004;52:3639.
- [56] Glicksman ME. *Diffusion in solids*. New York: John Wiley & Sons; 2000.
- [57] Horvay G, Cahn JC. *Acta Met* 1961;9:695.
- [58] Singh NB, Glicksman ME. *Thermochim Acta* 1990;159:93.
- [59] LaCombe JC, Koss MB, Glicksman ME. *Metall Mat Trans A* 2007;38A:116–26.
- [60] Muschol M, Liu D, Cummins HZ. *Phys Rev A* 1992;46:1038.
- [61] Lipton J, Kurz W, Trivedi R. *Acta Metall* 1987;35:957.
- [62] Lipton J, Kurz W, Trivedi R. *Acta Metall* 1987;35:965.
- [63] Glicksman ME, Koss MB, Winsa EA. *Phys Rev Lett* 1994;73:573.
- [64] Glicksman ME, Koss MB, Bushnell LT, LaCombe JC, Winsa EA. *Adv Space Res* 1995;16:181.
- [65] Glicksman ME, “Solidification Research in Microgravity”, *ASM Handbook*, vol. 15 (2008) 398-401, American Society for Materials, Materials Park, OH. <http://dx.doi.org/10.1361/asmhba0005228>
- [66] Glicksman ME, Huang S-C. *Adv Space Res* 1981;1:25.
- [67] Glicksman ME, Coriell SR, McFadden GB. *Ann Rev Fluid Mech* 1986;18:307.
- [68] McFadden GB, Wheeler AA, Braun RJ, Coriell SR, Sekerka RF. *Phys Rev E* 1993;48:2016.
- [69] Curreri PA. *Low-gravity effects during solidification*. *ASM handbook, casting* 1988;15:147–58.
- [70] Glicksman ME. *Solidification research in microgravity*. In: *ASM handbook, 15, casting*. Materials Park (OH): ASM International; 2009.
- [71] Temkin DE. *Dokl Akad Nauk SSSR* 1960;132:1307.
- [72] Bolling GF, Tiller WA. *J Appl Phys* 1961;32:2587.
- [73] Sekhar JA. *J Mater Sci* July 2011. <http://dx.doi.org/10.1007/s10853-011-5688-0>. published on-line, Springer, ISSN 0022-2461.
- [74] Xu JJ. *Dynamics of dendritic growth interacting with convective flow—global instabilities and limiting state selection*. *Adv Mech Math* 2002;1:113. Springer, New York.
- [75] Chen XJ, Chen YQ, Xu JP, Xu JJ. *Front Phys China* 2008;3:1.
- [76] Chen YQ, Tang XX, Xu JJ. *Chin Phys B* 2009;18:686.
- [77] Nash GE, Glicksman ME. *Acta Metall* 1974;22:1283.
- [78] Nash GE, Glicksman ME. *Acta Metall* 1974;22:1291.
- [79] Kessler D, Levine H. *Phys Rev B* 1986;33:7867.
- [80] Kessler D, Levine H. *Phys Rev Lett* 1986;57:3069.
- [81] Kessler D, Levine H. *Acta Metall* 1987;36:2693.
- [82] Mullins WW, Sekerka RF. *J Appl Phys* 1963;34:323.
- [83] Mullins WW, Sekerka RF. *J Appl Phys* 1964;35:444.

- [84] Sekerka RF. Morphological stability. In: Nishinaga T, Rudolph P, Kuech T, editors. Handbook of crystal growth. 2nd ed. Amsterdam: Elsevier; 2014. IB, Chapter 14.
- [85] Voronkov VV. Sov Phys Solid State 1964;6:2278.
- [86] Oldfield W. Mater Sci Eng 1973;11:211.
- [87] Langer JS, Müller-Krumbhaar H. J Cryst Growth 1977;42:11.
- [88] Doherty RD, Cantor B, Fairs S. Metall Trans A 1978;9:621.
- [89] Langer JS, Muller-Krumbhaar H. Acta Met 1978;26:1681.
- [90] Langer JS. Rev Mod Phys 1980;52:1.
- [91] Glicksman ME, Schaefer R.J. Acta Metall 1966;14:1226.
- [92] Fujioka T, Sekerka RF. J Cryst Growth 1974;24–25:84.
- [93] Koss MB, Tennenhouse LA, LaCombe JC, Glicksman ME, Winsa EA. Metall Mat Trans A 1999;30A:3177.
- [94] LaCombe JC, Koss MB, Fradkov VE, Glicksman ME. Phys Rev E 1995;E52:2778.
- [95] Huang SC, Glicksman ME. Acta Metall 1981;11:701.
- [96] *ibid.*, 717.
- [97] Xu JJ. Introduction of dynamical theory of solidification interfacial instability. Beijing: Chinese Academy Press; 2007.
- [98] Lowengrub J, Li S. Private communication. 2006.
- [99] Glicksman ME, Koss MB, Bushnell LT, Lacombe JC, Winsa EA. Iron Steel Inst Jpn Int 1995;35:604.
- [100] Koss MB, Glicksman ME, Winsa EA. J Met 1995;47:49–54.
- [101] Glicksman ME, Koss MB, Bushnell LT, LaCombe JC, Winsa EA. Mat Sci Forum 1996;215-216:179–90.
- [102] Kelton KF, Greer AL. J Non-Cryst Solids 1986;79:295.
- [103] Duwez P, Willens RH, Klement W. J Appl Phys 1960;31:1136.
- [104] Hirth JP. Met Trans A 1978;9a:401–4.
- [105] Perepezko JP, Rasmussen DH. Met Trans A 1978;9A:1490–2.
- [106] Cahn JW, Coriell SR, Boettinger WJ. In: White CW, Peercy PS, editors. Laser and electron beam processing of materials. New York (NY): Academic Press; 1980. p. 8.
- [107] Boettinger WJ, Aziz MJ. Acta Metall 1989;37:3379.
- [108] Glicksman ME. Principles of solidification. Chapter 17. New York: Springer; 2010. 427–446.
- [109] Ediger MD, Harrowell P, Yu L. J Chem Phys 2008;128:034709.
- [110] Holland-Moritz D, Herlach DM, Urban K. Phys Rev Lett 1993;71:1196–9.
- [111] Li D, Herlach DM. Phys Rev Lttrs 1996;77:1801.
- [112] Wilnecker R, Herlach DM, Feuerbacher B. Appl Phys Lett 1986;49:1339–41.
- [113] Schleip E, Herlach DM, Feuerbacher B. Europhys Lett 1990;11:751–5.
- [114] Eckler K, et al. Phys Rev B 1992;45:5019–22.
- [115] Schwarz M, Karma A, Eckler K, Herlach DM. Phys Rev Lett 1994;73:1380–4.
- [116] Barth M, Wei B, Herlach DM. Phys Rev B 1995;51:3422–8.
- [117] Li D, Herlach DM. Phys Rev Lett 1996;77:1801–4.
- [118] Arnold CB, Aziz MJ, Schwarz M, Herlach DM. Phys Rev B 1999;59:3324–43.

- [119] Schroers J, Holland-Moritz D, Herlach DM, Urban K. *Phys Rev B* 2000;61:14500–6.
- [120] Reutzel S, Hartmann H, Galenko PK, Schneider S, Herlach DM. *Appl Phys Lett* 2007;91:041913. p.1, p.3.
- [121] Hartmann H, Holland-Moritz D, Galenko PK, Herlach DM. *Europhys Lett* 2009;87:40007. p.1, p.6.
- [122] Bosio L, Cortes R, Defrain A. *J Chim Phys Physico-Chim Biol* 1973;70:357–9.
- [123] Perepezko J. Private comm. 2013.
- [124] Perepezko J. Crystallization of undercooled liquid droplets. In: Mehrabian R, Kear BH, Cohen M, editors. *Rapid solidification processing: principles and technologies II*. Baton Rouge: Claitor's Publishing Division; 1980. p. 56–67.
- [125] Wang Q, et al. *Phys Rev B* 2011;83:014202. p.1, p.5.
- [126] Turnbull D, Cech RE. *J Appl Phys* 1950;21:804.
- [127] Provatas N, Goldenfeld N, Dantzig J, LaCombe JC, Lupulescu A, Koss MB, et al. *Phys Rev Lett* 1999; 82:4496.
- [128] Spencer BJ, Huppert HE. *J Cryst Growth* 1995;148:305.
- [129] Karma A, Rappel W-J. *J Cryst Growth* 1997;174:54.
- [130] Penrose O, Fife PC. *Phys D* 1990;43:44.
- [131] Wheeler AA, Murray BT, Schaefer RJ. *Phys D* 1993;66:243.
- [132] Murray BT, Wheeler AA, Glicksman ME. *J Cryst Growth* 1995;154:386.
- [133] Schulze TP. *J Comp Phys* 2008;227:2455–62.
- [134] Schulze TP. *Phys Rev E* 2008;78. Art. no. 020601.
- [135] Pieters R, Langer J. *Phys Rev Lett* 1986;56:1948.
- [136] Kessler DA, Levine H. *Phys Rev A* 1986;34:4908.
- [137] Pelce P. *Dynamics of curved fronts*. New York: Academic Press; 1988.
- [138] Bower TF, Brody HD, Flemings MC. *Trans AIME* 1966;236:624.
- [139] Warren JA, Langer JS. *Phys Rev A* 1990;42:3518.
- [140] Warren JA, Langer JS. *Phys Rev E* 1993;47:2702.
- [141] Riley D, Davis SH. *IMA J Appl Math* 1990;45:267.
- [142] McFadden GB, Boisvert RF, Coriell SR. *J Cryst Growth* 1987;84:371.
- [143] McFadden GB, Coriell SR. *Phys D* 1984;12:253.
- [144] Glicksman ME. *Principles of solidification*. Chapter 11. New York: Springer; 2010. 263–272.
- [145] Schaefer RJ, Glicksman ME. *Metall Trans A* 1970;A1:1973.
- [146] Glicksman ME. *J Phys* 2011;327. <http://dx.doi.org/10.1088/1742-6596/327/1/0120>. Conf. Series: 012001.
- [147] Glicksman ME. *Met Mat. Trans A* 2012;43A:391–404.
- [148] Glicksman ME. *Mat Sci Engr* 2012;33. <http://dx.doi.org/10.1088/1757-899X/33/1/012097>. IOP Conf. Series: 012097.
- [149] Li S, Lowengrub J, Leo P, Cristini V. *J Cryst Growth* 2004;267:703–13.
- [150] Li S, Lowengrub J, Leo P, Cristini V. *J Cryst Growth* 2005;277:578–92.
- [151] Glicksman M, Lowengrub J, Li S. In: Gandin CA, Bellet M, editors. *Modelling of casting, welding and adv. solid. processes XI*; 2006. p. 521.
- [152] Li S, Lowengrub J, Leo P. *J Comp Phys* 2007;225:554–7.

- [153] Cristini V, Lowengrub J. *Crystal Growth* 2004;266:552–67.
- [154] Hele Shaw HJS. *Nature* 1898;58:34.
- [155] Saffman PG. *J Fluid Mech* 1986;173:73.
- [156] Paterson L. *J Fluid Mech* 1981;113:513.
- [157] Glicksman ME, Lowengrub J, Li S. *J Met* 2007;59:27.
- [158] Glicksman ME, Lupulescu A, Koss MB. *J Thermophys Heat Transf* 2003;17:69.
- [159] Glicksman ME. *J Phys* 2011. Conf. Series, Proc. of the 4th International Conference on Physical Science in Space, Bonn-Bad Godesburg, Germany.
- [160] Spencer BJ, Voorhees PW, Tersoff J. *Phys Rev B* 2001;64(235318):1–31.
- [161] Leal LG. *Advanced transport phenomena: fluid mechanics and convective transport processes*. Cambridge (UK): Cambridge University Press; 2007. 912.
- [162] Lin CC, Segel LA. *Mathematics applied to deterministic problems in the natural sciences*. New York: SIAM; 1995. 484485.
- [163] Glicksman ME. *Principles of solidification*. NewYork (USA): Springer; 2011. 69–97 Chapter 4.
- [164] Davi F, Gurtin ME. *J Appl Math Phys* 1990;41:782.
- [165] Herring C. In: Kingston WE, editor. *Physics of powder metallurgy*. New York: McGraw-Hill; 1951. p. 143.
- [166] Herring C. The use of classical macroscopic concepts in surface-energy problems. In: Gomer R, Smith CS, editors. *Structure and properties of solid surfaces*. University of Chicago Press; 1953. p. 5–72.
- [167] Mullins WW. Solid surface morphologies governed by capillarity. In: *Metal surfaces: structure, energetics, and kinetics*. Materials Park (OH): American Society for Metals; 1963. p. 17–66.
- [168] Voorhees PW, Coriell SR, McFadden GB, Sekerka RF. *J Cryst Growth* 1984;67:425–40.
- [169] Gurski KF, McFadden GB. *Proc Roy Soc Lond Ser A* 2003;459:2575–98.
- [170] Morse PM, Feshbach H. *The variational integral and the euler equations, in methods of theoretical physics, part I*. New York: McGraw-Hill; 1953. 276–280.
- [171] Gelfand IM, Fomin SV. In: Silverman RA, editor. *Calculus of variations*. Mineola (NY): Dover Publications, Inc.; 1991. p. 42.
- [172] Ehrlich G, Stolt K. *Ann Rev Phys Chem* 1980;31:603–37.
- [173] Caroli B, Caroli C, Roulet B. *J Cryst Growth* 1984;66:575.
- [174] Mullins WW. *JAppl.Phys* 1957;28:333–9.
- [175] Li S, Lowengrub J. *Private Comm* 2009.

# Grain Growth in the Melt

Kozo Fujiwara

*INSTITUTE FOR MATERIALS RESEARCH, TOHOKU UNIVERSITY, SENDAI, MIYAGI, JAPAN*

## **CHAPTER OUTLINE**

<b>17.1 Introduction</b> .....	<b>723</b>
<b>17.2 Kinetics of Nucleation–Growth</b> .....	<b>724</b>
17.2.1 Time Relations for Nucleation–Growth [1].....	725
17.2.2 KJMA Theory .....	726
17.2.2.1 Geometric Approach of Johnson/Mehl and Avrami.....	727
17.2.2.2 Probabilistic Approach of Kolmogorov .....	729
<b>17.3 Growth Rate of Crystal Grains in Melt Growth [11,12]</b> .....	<b>731</b>
17.3.1 Wilson-Frenkel Formula.....	731
17.3.2 Heat Conduction Process.....	734
17.3.3 Growth of Crystals Containing Twin Boundaries .....	736
<b>17.4 Grain Growth during Unidirectional Growth of Polycrystalline Ingot</b> .....	<b>742</b>
<b>17.5 Concluding Remarks</b> .....	<b>747</b>
<b>References</b> .....	<b>747</b>

## 17.1 Introduction

Grain growth is an important phenomenon in the solidification of silicon for photovoltaic applications. In the photovoltaic market, solar cells made of polycrystalline Si (commonly called multicrystalline Si, or mc-Si) are the main products both now and potentially in the future because of their production cost, storage of raw materials, safety, reliability, and energy conversion efficiency of solar cells. The crystal structure of an mc-Si ingot obtained by casting based on a unidirectional solidification technique is markedly different from that of an Si single crystal (sc-Si) grown by the Czochralski (CZ) method. The formation of grain boundaries and the distribution of crystallographic orientations prevent the realization of high-efficiency solar cells. A reduction of grain boundary density can significantly improve the energy conversion efficiency of solar cells because some grain boundaries serve as recombination centers of photocarriers. Once an mc-Si ingot is obtained by casting, it is hard to drastically change its grain size in the solid state. Therefore, it is necessary to control grain size during the solidification process. For this reason, fundamental studies of grain growth have attracted attention recently.

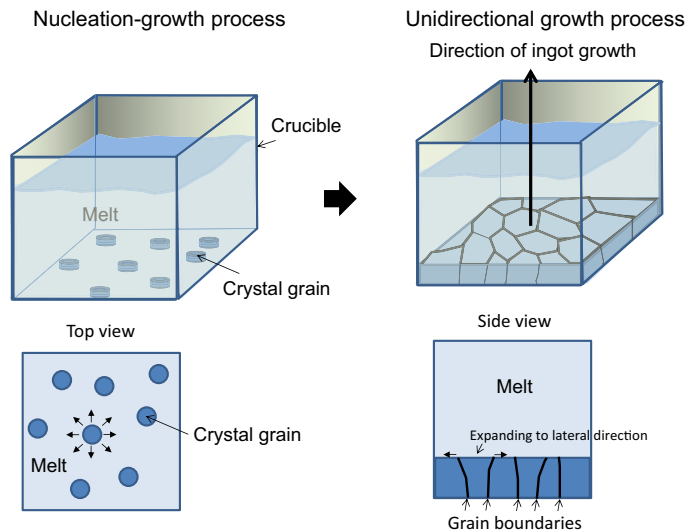


Figure 17.1 Growth of a polycrystalline ingot.

Generally, there are two processes for crystal grains to propagate themselves during the growth of an ingot, as schematically shown in Figure 17.1: nucleation–growth, which occurs on the bottom wall of the crucible in the earlier stage of growth, and unidirectional growth, which occurs after the formation of the bottom part of the ingot. In the former, each crystal grain can grow after nucleation on the crucible wall until it impinges on other crystal grains; in the latter, some crystal grains competitively grow laterally in the direction of ingot growth until the completion of unidirectional solidification.

In this chapter, the grain growth phenomenon during the growth of a bulk polycrystalline ingot will be described, with a focus on the growth of an mc-Si ingot. To understand the kinetics of phase transformation from the liquid phase to solid phase from a macroscopic viewpoint, the Kolmogorov-Johnson-Mehl-Avrami equation will be explained first. Next, a general expression of the growth rate of a crystal grain in melt growth and the growth mechanism of a faceted dendrite, which is often observed in the growth of an mc-Si ingot, will be described. Finally, grain growth phenomena during unidirectional growth will be introduced. The growth mode on the atomic scale related to surface kinetics, such as step advancement, two-dimensional nucleation–growth, or spiral growth, will not be described in this chapter to avoid overlapping with other chapters.

## 17.2 Kinetics of Nucleation–Growth

In the early stage of the growth of a polycrystalline ingot, nucleation–growth occurs on the bottom wall of the crucible, as shown in Figure 17.1 (left). First, we should consider this phase transformation from the macroscopic viewpoint. Göler and Sachs

theoretically studied nucleation–growth for the first time in the 1930s [1]. Then, Kolmogorov [2], Johnson and Mehl [3], and Avrami [4–6] developed the kinetics of this phase transformation. They obtained a similar result, which we now express with the Kolmogorov-Johnson-Mehl-Avrami theory (KJMA theory). Their general ideas, including the historical background of the development of the kinetics of the phase transformation, were explained in detail by Koiwa [7–10]. In this section, derivations of the KJMA theory will be shown, following the explanation described in Refs. [7,9,10].

### 17.2.1 Time Relations for Nucleation–Growth [1]

Nucleation occurs when a melt is cooled to a temperature  $T$  below the melting point  $T_M$ , and small crystal grains grow with the advancement of the crystallization front, as shown in Figure 17.2. For simplicity, we consider the case of a constant nucleation frequency and a constant crystal growth rate. When a nucleus formed at time  $\tau$  isotropically grows at a constant rate  $R$ , the volume of the crystal  $v$  at time  $t$  is given as

$$v(t, \tau) = \left(\frac{4\pi R^3}{3}\right)(t - \tau)^3. \quad (17.1)$$

Because the nucleation occurs only in the remaining melt  $V_0 - V(t)$ , the total volume of the crystal  $V(t)$  is

$$V(t) = \int_0^t v(t, \tau) N_v [V_0 - V(\tau)] d\tau, \quad (17.2)$$

where  $N_v$  is the nucleation frequency per unit volume and unit time.

When the total volume is normalized as  $V_0 = 1$ , the volume of the remaining melt  $U(t)$  is given as

$$U(t) = 1 - V(t), \quad (17.3)$$

and

$$U(t) = 1 - \left(\frac{4\pi N_v R^3}{3}\right) \int_0^t U(\tau)(t - \tau)^3 d\tau. \quad (17.4)$$

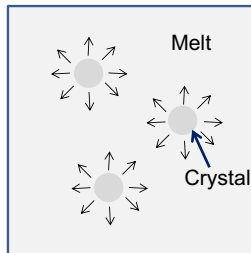


Figure 17.2 Early stage of nucleation–growth.

The solution of the integral equation Eqn (17.4) is given as

$$U(t) = \cosh pt \cdot \cos pt, \quad (17.5)$$

$$V(t) = 1 - U(t) = 1 - \cosh pt \cdot \cos pt, \quad (17.6)$$

$$p^4 = 2\pi N_v R^3. \quad (17.7)$$

This solution has physical significance at  $0 \leq t \leq t_r$  ( $\equiv \pi/2p$ ) because the crystallization finishes when  $U(t) = 0$  and  $V(t) = 1$  at  $t = t_r$ .

Figure 17.3 shows the time dependence of  $V(t)$  obtained by Eqn (17.6). For comparison, the result based on Eqn (17.8) derived by the KJMA theory, which will be explained in the next section, is also shown in Figure 17.3. In the above treatment, the impingement of growing crystals was not considered. Therefore, Eqn (17.6) correctly represents only the very early stage of crystallization; thus, the difference of both results in Figure 17.3 becomes remarkable in the later stage. The problem of such impingement was independently studied by Kolmogorov, Johnson and Mehl, and Avrami.

## 17.2.2 KJMA Theory

As shown in Figure 17.4, the main problem of the impingement of growing crystal grains is how to treat the overlapping of two or more crystal grains. For this problem, the theoretical approaches by Kolmogorov [2], Johnson and Mehl [3], and Avrami [4–6] gave one and the same solution, which is described as

$$V = 1 - \exp(-Kt^n). \quad (17.8)$$

Equation (17.8) was individually derived by the geometrical approach of Johnson and Mehl [3] and Avrami [4–6] and by the probabilistic approach of Kolmogorov [2]. In the following, these derivations of Eqn (17.8) will be described.

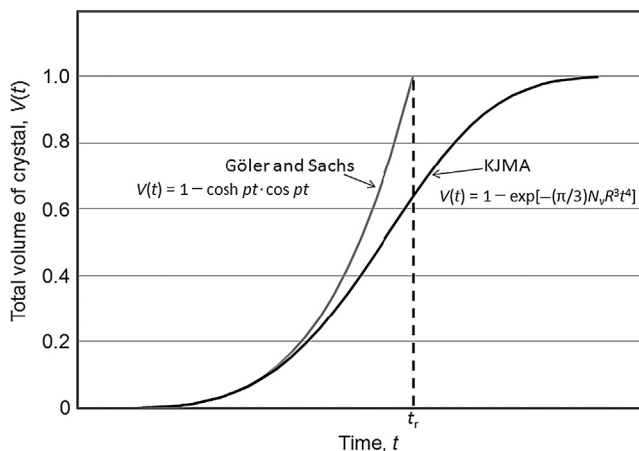


Figure 17.3 Progress of crystallization. Comparison of the result based on Eqn (17.6) and on the KJMA theory expressed as the form of Eqn (17.8). KJMA, Kolmogorov-Johnson-Mehl-Avrami.

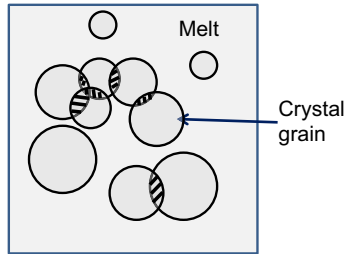


Figure 17.4 Overlapping of growing crystal grains [4].

### 17.2.2.1 Geometric Approach of Johnson/Mehl and Avrami

We consider the overlapping of crystal grains, as shown by the shadowed areas in Figure 17.4, and assume that there is no interaction among growing crystals. Now, the extended-volume  $V_{\text{ex}}$  (as expressed by Avrami), which is the volume at which the phase transformation finished, is considered as follows: In the calculation of  $V_{\text{ex}}$ , the volume of the shadowed region is counted in response to the number of overlapping crystals. When two crystals overlap, the volume of the shadowed region is counted twice. When  $n$  crystals overlap, it will be counted  $n$  times.

Now, let us consider the relationship between  $dV_{\text{ex}}$  and  $V$ , where  $dV_{\text{ex}}$  is the variation in  $V_{\text{ex}}$  between the time  $t$  and  $t + dt$ , and  $V$  is the volume at which the phase transformation finished. When we choose one point inside the total volume, the probability that the chosen point is the point in the region where the phase transformation is not finished is  $(1 - V)$ . Therefore, if  $dV_{\text{ex}}$  appears in the entire range of total volume with equivalent probabilities, the following relationship is established:

$$dV = (1 - V)dV_{\text{ex}}. \quad (17.9)$$

$dV_{\text{ex}}$  always appears as spherical shells surrounding spherical crystals, as shown in Figure 17.5.

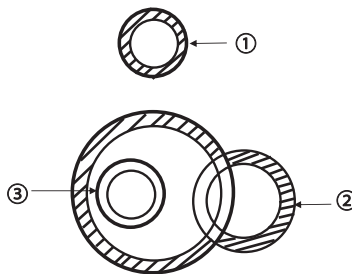


Figure 17.5 Impingement of crystal grains in nucleation-growth. The rings represent the increase in volume in time  $dt$ : in ring ①, all of the increase is effective; in ring ③, none of the increase is effective; in ring ②, only the part of the increase (hatched area) lying outside all other grains is effective. From the appendix in Ref. [3].

Johnson and Mehl considered that, if we calculate the extended volume  $V_{\text{ex}}$  by permitting the assumption that nucleation occurs not only in the untransformed region but also in the transformed region (assuming a phantom nucleus), the completely randomized condition will be satisfied. Thus, we can use

$$V_{\text{ex}} = \int_0^t v(t, \tau) N(\tau) d\tau \quad (17.10)$$

instead of Eqn (17.2).  $N(\tau)$  is the nucleation frequency.

The integration of Eqn (17.9) gives

$$V = 1 - \exp(-V_{\text{ex}}). \quad (17.11)$$

When the nucleation rate  $N_v$  and the growth rate  $R$  are constant,  $V_{\text{ex}}$  is described as Eqn (17.12) from Eqn (17.10):

$$V_{\text{ex}} = \left(\frac{\pi}{3}\right) N_v R^3 t^4. \quad (17.12)$$

Therefore,

$$V = 1 - \exp\left(-\frac{\pi}{3} N_v R^3 t^4\right). \quad (17.13)$$

Equation (17.13) was derived by Johnson and Mehl.

Avrami also used Eqns (17.10) and (17.11) to derive the relationship between  $V_{\text{ex}}$  and  $V$ , similarly to Johnson and Mehl. However, the treatment of the time dependence of the nucleation rate differed between them; Johnson and Mehl assumed a constant nucleation rate as above, whereas Avrami considered that the nucleation rate is dependent on time. Avrami assumed that there are “germ nuclei” that serve as the basis of the growth, and that these nuclei are consumed as the reaction proceeds. When we neglect the case in which germ nuclei are swallowed up by growing crystal grains during transformation, the number of germ nuclei is given by  $N_0 \exp(-nt)$ ; thus, the nucleation rate at the unit untransformed volume and unit time is given by  $nN_0 \exp(-nt)$ . In this case, the relationship between  $V_{\text{ex}}$  and  $V$  is derived as follows.

When we use  $\tau = nt$  instead of time  $t$  and the constant growth rate  $R$  for simplicity, the extended volume is described as

$$V_{\text{ex}} = \sigma \alpha^3 N_0 \int_0^\tau (\tau - z)^3 e^{-z} dz \quad (17.14)$$

where  $\alpha \equiv R/n$  and  $\sigma$  is a constant related to the shape of the crystal grain. The integration of Eqn (17.14) is

$$V_{\text{ex}} = \frac{6\sigma R^3 N_0}{n^3} \left[ e^{-\tau} - 1 + \tau - \frac{\tau^2}{2!} + \frac{\tau^3}{3!} \right] \equiv \beta_3 E_3(-\tau) \quad (17.15)$$

where

$$\begin{aligned}\beta_3 &\equiv 6\sigma N_0 (R/n)^3 \\ E_m(-x) &= \frac{1}{m!} \int_0^x (x-z)^m e^{-z} dz \\ &= (-1)^{m+1} \left[ e^{-x} - 1 + x \cdots (-1)^{m+1} \frac{x^m}{m!} \right].\end{aligned}\quad (17.16)$$

In the case of two-dimensional grains (e.g., platelike grains with a very small thickness),  $m = 2$ . For one-dimensional grains (e.g., fine lines),  $m = 1$ .

Here,  $e^{-\tau}$  is developed as

$$e^{-\tau} = 1 - \tau + \tau^2/2! - \tau^3/3! + \tau^4/4! + \cdots \quad (17.17)$$

Therefore, when  $\tau$  is very small,

$$V_{\text{ex}} \approx \beta_3 \tau^4 / 4! = \sigma R^3 N_0 n t^4 / 4. \quad (17.18)$$

When  $\tau$  becomes larger, the term  $\tau^3$  becomes more dominant than the terms  $e^{-\tau}$ ,  $\tau$ , and  $\tau^2$ ; then,

$$V_{\text{ex}} \approx \beta_3 \tau^3 / 3! = \sigma R^3 N_0 n t^3. \quad (17.19)$$

Therefore, the transformation proceeds with time as

$$V = 1 - \exp(-V_{\text{ex}}) = 1 - \exp(-kt^n). \quad (17.20)$$

When  $\tau$  is small and the nucleation rate is constant, Eqn (17.20) corresponds to Eqn (17.13) derived by Johnson and Mehl.

The values of  $n$  are  $4 \sim 3$  for three-dimensional growth,  $3 \sim 2$  for two-dimensional growth, and  $2 \sim 1$  for one-dimensional growth.

#### 17.2.2.2 Probabilistic Approach of Kolmogorov

Kolmogorov's paper [2] was published in 1937, before Johnson and Mehl [3] and Avrami [4–6]. However, it was difficult for many people to read it because it was published in Russian. Here, we summarize Kolmogorov's approach on the basis of the explanations in Refs. [10,11].

Here, we consider the probability  $q(t)$  that an arbitrarily chosen point P in the melt has not crystallized at time  $t$ . If nucleation occurs at another point P' at time  $\tau$  ( $\tau < t$ ), the radius of the nucleus becomes  $R(t - \tau)$  at time  $t$  when the growth rate is  $R$ . The point P is included in the crystallized region at  $R(t - \tau) > \overline{PP'}$ . Thus, if nucleation occurs at time  $t'$  ( $\tau < t' < t$ ) in the spherical region around P, P is included in the crystallized region at time  $t$ , as shown in Figure 17.6. The volume of the spherical region around P is described as  $v(\tau) = (4\pi/3)R^3(t - \tau)^3$ . Now, the probability that at least one nucleus will form in the time interval  $\Delta\tau$  in the volume  $v(\tau)$  is given by  $N_v v(\tau) \Delta\tau$ , and the probability that a nucleus will not form in  $\Delta\tau$  in  $v(\tau)$  is given by  $1 - N_v v(\tau) \Delta\tau$ .

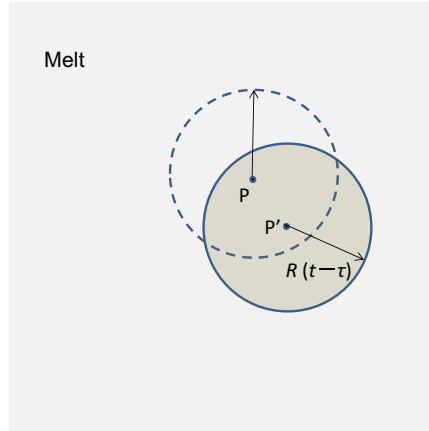


Figure 17.6 Calculation of the probability of finding an arbitrarily chosen point  $P$  in a crystallized region.

$\Delta\tau$ . The probability for  $P$  to be outside a crystallized region at time  $t$  from the beginning of the process is given by

$$q(t) = \prod_{i=1}^n (1 - N_v v(i\Delta\tau) \Delta\tau), \quad (17.21)$$

where  $t = n\Delta\tau$  and  $\tau_i = i\Delta\tau$ . Taking the logarithm of Eqn (17.21) yields

$$\ln q(t) = \sum_{i=1}^n \ln (1 - N_v v(i\Delta\tau) \Delta\tau) = - \sum_{i=1}^n N_v v(i\Delta\tau) \Delta\tau = -N_v \int_0^t v(\tau) d\tau = -N_v \Omega. \quad (17.22)$$

$$\Omega = \int_0^t v(\tau) d\tau = \frac{4\pi}{3} R^3 \int_0^t (t - \tau)^3 d\tau = \frac{\pi}{3} R^3 t^4.$$

The volume of the remaining melt  $U(t)$  is given as

$$U(t) = q(t) = e^{-N_v \Omega} = \exp\left(-\frac{\pi}{3} N_v R^3 t^4\right). \quad (17.23)$$

Therefore, the transformed volume  $V(t)$  is

$$\begin{aligned} V(t) &= 1 - q(t) \\ &= 1 - \exp\left[-\frac{\pi}{3} N_v R^3 t^4\right]. \end{aligned} \quad (17.24)$$

Equation (17.24) is in agreement with Eqn (17.13) derived by Johnson and Mehl.

As described above, the kinetics of phase transformation during nucleation–growth were individually derived by Kolmogorov, Johnson and Mehl, and Avrami. Their approaches were different but the equations they obtained were similar. These equations led to the KJMA equation.

Finally, let us introduce the simplest derivation of Eqn (17.11) by Hillert, which was also introduced by Koiwa [7,10] as follows.

We consider the case that the phase transformation proceeds in the system with a total volume  $V$ . The ratio at which phase transformation was completed is expressed by  $f$ . Suppose there are spherical particles of volumes  $v_1, v_2$ , etc. at time  $t$ . We assume that, even if the impingement of these particles occurs, they will maintain their volume with the same shape as when they grow without impingement. The probability that a certain point is outside the volume  $v_1$  is  $1 - v_1/V$ . The probability that it is outside all the volumes is  $1 - f$ , but also

$$\prod \left(1 - \frac{v_i}{V}\right).$$

When each nodule is much smaller than the total system  $V$ , we obtain

$$\ln(1 - f) = \sum \ln(1 - v_i/V) \cong - \sum \frac{v_i}{V}. \quad (17.25)$$

If the number of nuclei is  $N$  at  $t = 0$ , then

$$\sum v_i/V = N \cdot \frac{4\pi}{3} r^3 V = \frac{N}{V} \cdot \frac{4}{3} \pi R^3 t^3; \quad (17.26)$$

If the nucleation rate is constant  $N_v$ , then

$$\sum v_n/V = \int \frac{N_v}{V} \cdot \frac{4\pi}{3} R^3 (t - \tau)^3 d\tau = \frac{N_v}{V} \cdot \frac{4}{3} \pi R^3 t^4. \quad (17.27)$$

Here,  $\sum v_n = V_{\text{ex}}$ : thus, we immediately obtain

$$f = 1 - \exp(-V_{\text{ex}}). \quad (17.28)$$

Again, Eqn (17.28) corresponds to Eqn (17.13).

The time relations for the nucleation–growth process considered by Kolmogorov, Johnson and Mehl, and Avrami show that this process is expressed in the form of Eqn (17.8).

In the unidirectional growth of an mc-Si ingot, the phenomenon treated in this section appears in the earlier stage at the bottom wall of the crucible, as shown in the left of Figure 17.1. In actuality, the total time taken for this process is dependent on the growth rate of crystal grains, which will be considered in the next section.

## 17.3 Growth Rate of Crystal Grains in Melt Growth [11,12]

The kinetics of phase transformation during nucleation–growth were described from the macroscopic viewpoint in the previous section. Here, we consider the growth rate  $R$  of each crystal grain during melt growth. The growth of a crystal grain containing twin boundaries, the so-called faceted dendrite, is also described, which often appears in the melt growth of silicon and germanium.

### 17.3.1 Wilson-Frenkel Formula

When the melt temperature  $T$  is reduced to below the melting point  $T_M$ , a crystal grain born from a melt grows until it impinges on another crystal grain [11,12]. The grain

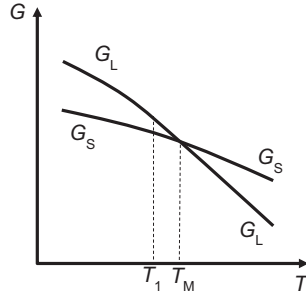


**Figure 17.7** Gibbs free energies of liquid ( $G_L$ ) and solid ( $G_S$ ) phases at constant pressure  $p$  as functions of temperature  $T$ .

growth is driven by the second law of thermodynamics to minimize the Gibbs free energy  $G$  at a given temperature  $T_1$  and a pressure  $p$ .

At the melting point  $T_M$ , the Gibbs free energies of the liquid ( $G_L$ ) and solid ( $G_S$ ) phases cross each other, as shown in [Figure 17.7](#):

$$G_S(T_M, p) = G_L(T_M, p), \quad (17.29)$$

$$H_S(T_M, p) - T_M S_S(T_M, p) = H_L(T_M, p) - T_M S_L(T_M, p), \quad (17.30)$$

where  $H$  and  $S$  are the enthalpy and entropy, respectively. The latent heat  $L$  generated at the melting point corresponds to the enthalpy difference between the liquid and solid phases as  $L = H_L(T_M, p) - H_S(T_M, p)$ ; thus,  $L$  is proportional to the entropy difference  $\Delta S = S_L(T_M, p) - S_S(T_M, p)$ :

$$L = H_L - H_S = T_M \Delta S. \quad (17.31)$$

Because  $S$  is the temperature derivative of Gibbs free energy as  $S = -(\partial G / \partial T)_p$ , [Eqn \(17.31\)](#) is written as

$$\left( \frac{\partial G_L}{\partial T} \right)_p - \left( \frac{\partial G_S}{\partial T} \right)_p = -\frac{L}{T_M}. \quad (17.32)$$

[Equation \(17.32\)](#) shows that the phase transition with a latent heat is associated with the discontinuity in the slope of Gibbs free energy.

The growth of crystal grains in a melt occurs below the melting point to minimize Gibbs free energy; thus, the driving force of grain growth is the difference in Gibbs free energy between the melt and the crystal:  $\Delta G = G_L(T, p) - G_S(T, p)$ . When the undercooling  $\Delta T = T_M - T$  is small, the driving force is approximately described as

$$\Delta G \approx \left( \frac{\partial G_L}{\partial T} \right)_p (T - T_M) - \left( \frac{\partial G_S}{\partial T} \right)_p (T - T_M) = L \frac{\Delta T}{T_M}. \quad (17.33)$$

Now, we consider the ideal growth rate  $R$  of a crystal grain, where we neglect the temperature increase at the crystal/melt interface induced by the latent heat of crystallization as well as by the roughness of the crystal surface at the crystal/melt interface. To grow a crystal grain, atoms or molecules in the melt must be incorporated into the

crystal grain at the crystal/melt interface. Now, we consider how atoms in the melt become crystals. The density of a melt is not markedly different from that of a crystal—that is, the numbers of atoms or molecules in a certain volume are not markedly different between the melt and the crystal at the crystal/melt interface. In the case of silicon or germanium, the density of the melt is higher than that of the crystal. In such a situation, atoms change their positions mainly with a vibration of frequency  $\nu$ . To change the configuration, atoms have to overcome the energy barrier  $E_d$ , and this probability is expressed by  $\exp(-E_d/k_B T)$  at a temperature  $T$ , where  $k_B$  is the Boltzmann constant. Therefore, the rate of crystallization is given as  $\nu \exp(-E_d/k_B T)$ . Considering the probability of melting at the crystal/melt interface, the growth rate of crystal grains is given as

$$R = av \exp\left(-\frac{E_d}{k_B T}\right) \left[1 - \exp\left(-\frac{\Delta\mu}{k_B T}\right)\right], \quad (17.34)$$

where  $a$  is the height of an atom and  $\Delta\mu$  is the difference in chemical potential between the liquid and solid phases. Using the Einstein–Stokes relation [13],

$$a^2 \nu \exp\left(-\frac{E_d}{k_B T}\right) = D = \frac{k_B T}{6\pi\eta a}, \quad (17.35)$$

where  $\eta$  and  $D$  are the liquid viscosity and diffusion constant, respectively.  $R$  is given as

$$R = \frac{k_B T}{6\pi a^2 \eta} \left[1 - \exp\left(-\frac{\Delta\mu}{k_B T}\right)\right] = K \left[1 - \exp\left(-\frac{\Delta\mu}{k_B T}\right)\right]. \quad (17.36)$$

Equations (17.34) and (17.36) are called the Wilson-Frenkel formula [14,15] for melt growth, and  $K = k_B T / 6\pi a^2 \eta$  in Eqn (17.36) is called the kinetic coefficient. At a small undercooling  $\Delta T$ ,  $R$  is approximated by

$$R \approx K \frac{\Delta\mu}{k_B T} \approx K_T \Delta T, \quad (17.37)$$

where  $K_T = Kl/k_B T T_M$ , with  $l = L/N$  being the latent heat per atom. Equation (17.37) shows that the ideal growth rate of crystal grains is proportional to  $\Delta T$  when the undercooling of a melt is small.

In the above consideration, we did not consider any rate-determining processes in crystallization. Generally, there are three processes that control the growth rate of crystal grains [11,12]:

1. Surface kinetics: the process in which atoms in the melt are incorporated in the crystal at the crystal/melt interface
2. Chemical diffusion: the process in which atoms in the melt are transported to the crystal/melt interface
3. Heat conduction: the process in which latent heat released by crystallization is transported away from the crystal/melt interface.

The ideal growth rate given by Eqn (17.37) is realized if all processes are sufficiently fast. When one process is particularly slow, the growth rate of crystal grains is governed by the slowest process. In actuality, the conduction of latent heat must govern the

growth rate of crystal grains in melt growth. The surface kinetics at the crystal/melt interface is also important in the melt growth of silicon or germanium, which has anisotropic crystal/melt interfacial energies. The surface kinetics at an atomically smooth crystal/melt interface and an atomically rough crystal/melt interface must be different. However, such a difference related to the growth mode will not be treated in this chapter; a detailed explanation is provided in Chapter 9 of Volume IA.

### 17.3.2 Heat Conduction Process

As shown in Eqn (17.37), the growth of crystal grains occurs in an undercooled melt at a temperature  $T_1$ . The latent heat  $L$  is released at the growth front with grain growth. The growth of crystal grains is driven by the difference between the Gibbs free energies of the crystal and melt:

$$\Delta G = G_L - G_S = L \frac{T_M - T_1}{T_M}, \quad (17.38)$$

where  $G_L$  and  $G_S$  are the Gibbs free energies per volume of the melt and crystal, respectively, and  $L$  is the latent heat per volume. However, in actuality, the temperature at the crystal/melt interface increases to a temperature  $T_i$  by the release of the latent heat, as schematically shown in Figure 17.8. Therefore, the driving force of crystal growth at the crystal/melt interface reduces to  $\Delta G_i = L(T_M - T_i)/T_M$ . If the crystal surface at the crystal/melt interface is rough, the growth rate is proportional to  $\Delta G_i$  following the Wilson-Frenkel formula:

$$R_v = K_T(T_M - T_i), \quad (17.39)$$

with  $K_T$  as the kinetic constant.

The heat flow  $J$  should be proportional to the temperature gradient  $\nabla T$  as

$$J = -k\nabla T, \quad (17.40)$$

where  $k$  is the thermal conductivity. The temperature change at a certain position is

$$C_p \frac{\partial T}{\partial t} + \nabla \cdot J = 0, \quad (17.41)$$

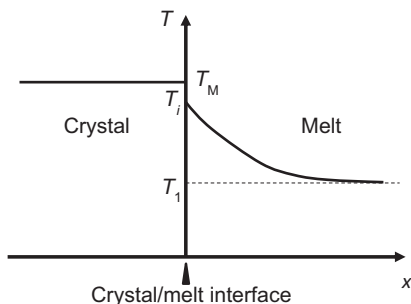


Figure 17.8 Temperature field around the crystal/melt interface of growing crystal grains.

where  $C_p$  is the specific heat per volume. From Eqns (17.12) and (17.13), the thermal diffusion equation is given as

$$\frac{\partial T}{\partial t} = D_T \nabla^2 T. \quad (17.42)$$

Here,  $D_T = k/C_p$  is called the temperature conductivity. Although it is considered here that the heat is transported only in the melt for simplicity, heat transport also occurs in the crystal.

When the crystal grain is growing at  $R_x$ , the latent heat released per unit area in unit time is  $LR_x$ . This heat is transported by heat flow in the  $x$ -direction as

$$LR_x = -k(\mathbf{x} \cdot \nabla)T \equiv -k\partial_x T. \quad (17.43)$$

Now, consider that a crystal grain with a flat crystal/melt interface grows along the  $x$ -direction, which is vertical to the interface plane ( $y$ - $z$  plane) at a constant rate  $R$ . In this case, the temperature is a function expressed as  $x' = x - Rt$ . Therefore, the temperature change and position change with time are

$$\frac{\partial T(x')}{\partial t} = \frac{dT}{dx'} \frac{\partial x'}{\partial t} = -R \frac{dT}{dx'}, \quad (17.44a)$$

and

$$\frac{\partial T(x')}{\partial x} = \frac{dT}{dx'} \frac{\partial x'}{\partial x} = \frac{dT}{dx'}, \quad (17.44b)$$

respectively. From the thermal diffusion equation Eqn (17.42),

$$-R \frac{dT}{dx'} = D_T \frac{d^2 T}{dx'^2}. \quad (17.45)$$

The solution of Eqn (17.45), which satisfies both conditions that the temperature at the crystal/melt interface is  $T_i$  and that the temperature far from the interface ( $x \rightarrow \infty$ ) is  $T_1$ , is

$$T(x, y, z, t) = T_i + (T_1 - T_i)(1 - e^{-R(x-Vt)/D_T}). \quad (17.46)$$

Here, the diffusion length  $l_D$  is defined as

$$l_D = \frac{2D_T}{R}. \quad (17.47)$$

The heat flow  $J$  at the crystal/melt interface is

$$J = -k \left. \frac{\partial T}{\partial x} \right|_{x=Vt} = -kV \frac{T_\infty - T_i}{D_T} = -C_p V (T_\infty - T_i). \quad (17.48)$$

As latent heat is transported by this heat flow, Eqn (17.43) becomes

$$LR = -C_p R (T_\infty - T_i). \quad (17.49)$$

Therefore, the temperature at the crystal/melt interface is  $T_i = T_\infty + L/C_p$ . From the Wilson-Frenkel formula, growth rate is described as

$$R = K_T (T_M - T_\infty - L/C_p). \quad (17.50)$$

The thermal field shown in Figure 17.8 is maintained when a growing crystal is surrounded by an undercooled melt with a sufficiently large area. However, when a growing crystal grain encounters another growing crystal grain, the thermal fields in front of the crystal/melt interface overlap; thus, the temperature at the crystal/melt interface increases, which leads to a decrease in the growth rate of crystal grains.

### 17.3.3 Growth of Crystals Containing Twin Boundaries

In this section, we consider the grain growth of a crystal containing twin boundaries. Currently, it is recognized that many twin boundaries exist in an mc-Si ingot grown by casting, which is widely used for solar cells. Silicon and germanium are typical faceted materials with an anisotropic crystal/melt interfacial energy. Therefore, it seems that a silicon or germanium crystal grain is bounded by  $\{111\}$  facet planes during its growth, when a growing crystal grain is surrounded by a sufficiently undercooled melt. Twin boundaries are often generated in a growing crystal because the grain boundary energy of twin boundaries with a  $\{111\}$  boundary plane is quite low in silicon (i.e.,  $30 \text{ mJ/m}^3$ ) [16]. Many models of twin boundary formation have been proposed, as summarized in Ref. [17]. When at least two  $\{111\}$  twin boundaries with a narrow spacing are generated in a growing crystal, the crystal initially grows with a dendritic shape, which is the so-called faceted dendrite. The unique growth behavior of a faceted dendrite was found in germanium by Billig in 1955 [18]. To clarify the growth mechanism, we directly observed the growth process of faceted dendrites from silicon melt by using an in situ observation system consisting of a furnace and a microscope. Figure 17.9 shows one of our in situ observation systems. A silicon sample was set in a crucible. The inside of the furnace was evacuated using a rotary pump and then filled with argon gas. A temperature gradient was formed in the furnace by setting the temperatures of the two heaters at different

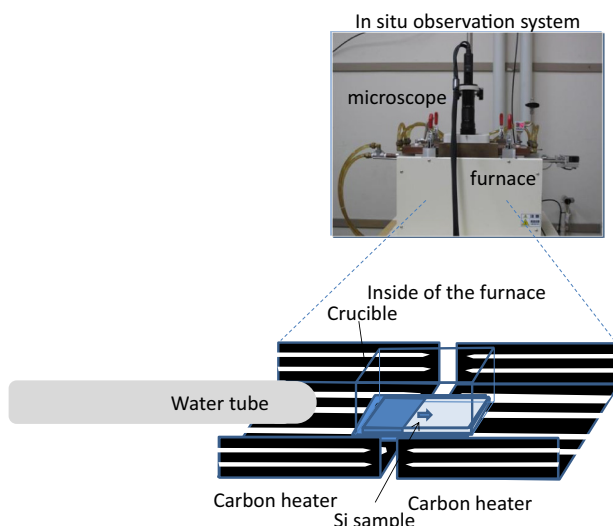
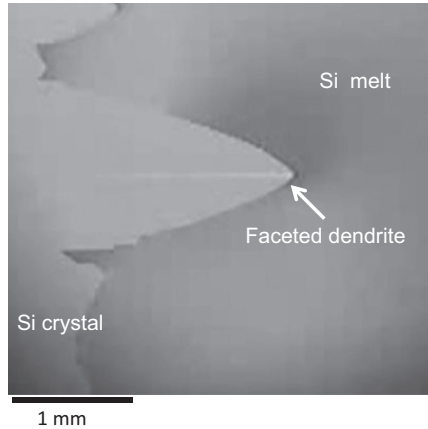


Figure 17.9 In situ observation system.



**Figure 17.10** Observation of growing faceted dendrite.

values during the heating and cooling processes. It is also able to promote the unidirectional growth by inserting a water tube. Crystallization processes were recorded on videotape or computer. We could clearly observe the growth process of faceted dendrite, as shown in [Figure 17.10](#). The features of a faceted dendrite are different from dendrites of metallic alloys in terms of the following [19–27]:

1. Its surface is bounded by  $\{111\}$  facet planes.
2. At least two parallel  $\{111\}$  twin boundaries exist at its center.
3. Its preferential growth direction is  $\langle 112 \rangle$  or  $\langle 110 \rangle$ . (Hereafter, dendrites with these growth directions will be expressed as  $\langle 112 \rangle$  and  $\langle 110 \rangle$  dendrites, respectively.)

The growth rate of a faceted dendrite is much higher than that of a crystal with no twin boundaries, as shown in [Figure 17.10](#).

The growth model of  $\langle 112 \rangle$  dendrites was proposed in 1960 [20,21]; it was improved on the basis of observations of the growth of  $\langle 112 \rangle$  and  $\langle 110 \rangle$  dendrites [28,29]. [Figure 17.11](#) shows the growth shapes of  $\langle 112 \rangle$  and  $\langle 110 \rangle$  dendrites observed from  $\langle 110 \rangle$  or  $\langle 112 \rangle$  direction (upper figures) and  $\langle 111 \rangle$  direction (lower figures). The features of growth shapes of  $\langle 112 \rangle$  and  $\langle 110 \rangle$  dendrites were clarified by observations of growing dendrites from the direction perpendicular to the  $\{111\}$  twin boundaries:

- Triangular corners with an angle of  $60^\circ$  are formed at the tip of faceted dendrites.
- The direction of the  $60^\circ$  corners alternately changes from outward to forward in the direction of growth.
- The tip of  $\langle 112 \rangle$  dendrites becomes wider during their growth, whereas that of  $\langle 110 \rangle$  dendrites remains narrow.

Before considering the growth mechanism of faceted dendrites, let us consider the effect of twin boundaries on crystal growth. Crystals bounded by  $\{111\}$  facet planes containing no twin boundaries and one twin boundary are shown in [Figure 17.12](#) [20].

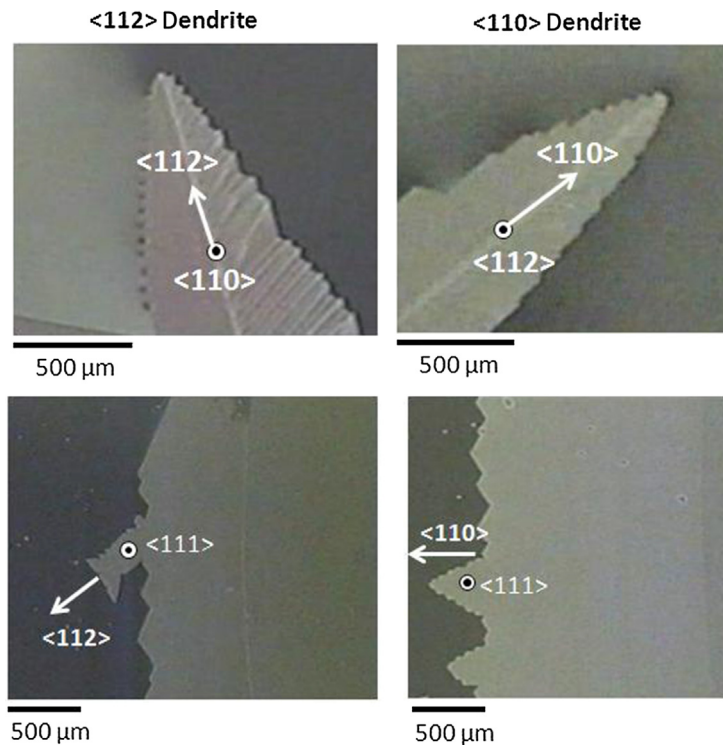


**Figure 17.11** Difference in the growth shape of  $\langle 112 \rangle$  and  $\langle 110 \rangle$  dendrites [29].

When a twin boundary is formed in the growing crystal, reentrant corners with an angle of  $141^\circ$  are formed at the growth surface, as shown in [Figure 17.12](#) (upper right).

Now, the difference between the incorporation of atoms in a melt to a crystal at a reentrant corner and that at a flat  $\{111\}$  surface should be considered. Each atom in a silicon or germanium crystal has four bonds connected to neighboring atoms. We can consider that an adatom becomes a “crystal” when half of its bonds are connected to other atoms at the crystal/melt interface. When a crystal grows on a  $\{111\}$  surface (left panel of [Figure 17.13](#)), three adatoms are required to form half of their bonds with each other and the underlying crystal surface. On the other hand, a pair of adatoms can satisfy half of their bonds with each other and the underlying crystal surface at the reentrant corner at a  $\{111\}$  twin boundary (right panel of [Figure 17.13](#)). Therefore, it seems that the rapid growth in the  $\langle 112 \rangle$  direction occurs at a reentrant corner. When the rapid growth occurs at a reentrant corner, triangular corners are formed eventually, as shown in [Figure 17.12](#) (lower right). At this moment, the reentrant corner disappears from the growth surface, and thus the rapid growth of the crystal ceases. Therefore, continuous rapid growth like dendrite growth does not occur in crystals containing only one twin boundary.

On the other hand, when a crystal contains at least two twin boundaries, the crystal can continue its rapid growth (faceted dendrite growth). The growth scheme of the crystal with

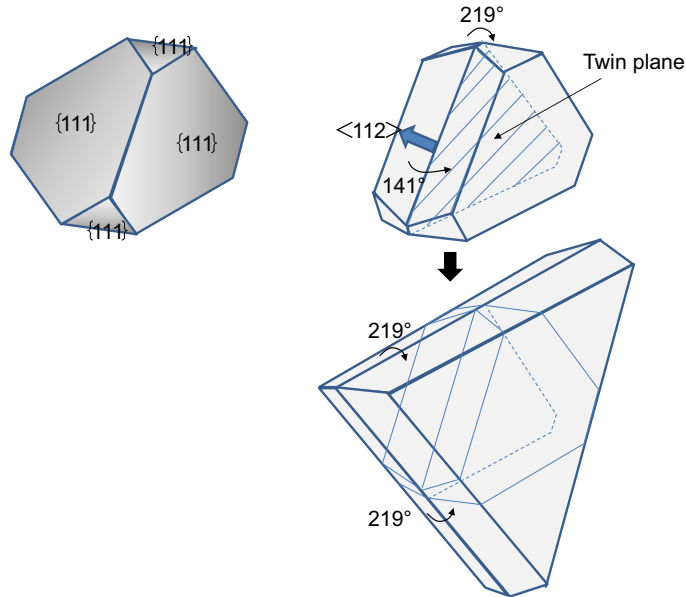


**Figure 17.12** Crystals containing no twin boundaries (left) and one twin boundary (right) bounded by  $\{111\}$  facet planes. Rapid growth at a reentrant corner with an angle of  $141^\circ$  will lead to the formation of a triangular corner at the growth tip (lower right) [20].

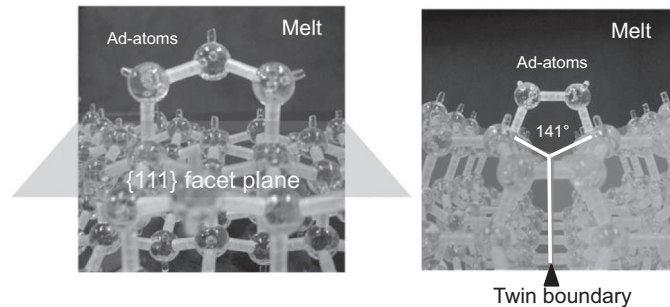


**Figure 17.13** Atomic incorporation at  $\{111\}$  facet plane (left) and reentrant corner (right).

two twin boundaries is described in Figure 17.14 [28–30]. The top views of the crystal during growth are also shown in Figure 17.14. Figure 17.14-1 shows the equilibrium shape of a crystal containing two twin boundaries of distance  $d$ . The crystal is bounded by  $\{111\}$  facet planes. We consider that this crystal unidirectionally grows in the  $\langle 112 \rangle$  direction for simplicity. A reentrant corner with an angle of  $141^\circ$  is formed at an upper-side twin boundary, whereas a cone with an angle of  $219^\circ$  is formed at a lower-side twin boundary. The rapid growth occurs at the reentrant corner at a rate of  $R_{\text{twin}}$ . The detailed growth kinetics at the reentrant corner, including the kinetic constant, has not been clarified yet. The rapid growth at the reentrant corner at the upper-side twin boundary leads to the

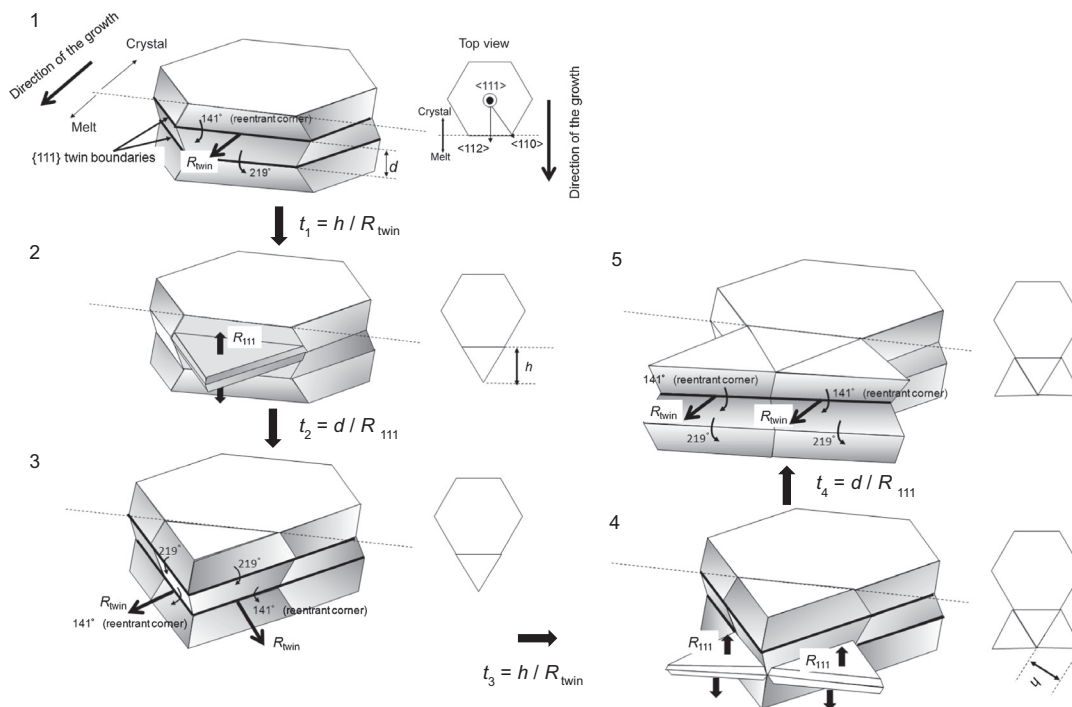


**Figure 17.14** Growth scheme of  $\langle 112 \rangle$  dendrites [28,29]. 1: Equilibrium shape of a crystal containing two twin boundaries, which is bounded by  $\{111\}$  facet planes. 2: A triangular crystal is formed due to the rapid growth at an upper-side twin boundary. Crystal growth can continue on the  $\{111\}$  flat surface, although the rapid growth is inhibited because of the disappearance of a reentrant corner with an angle of  $141^\circ$ . 3: When the triangular crystal propagates across the lower-side twin boundary, reentrant corners are formed at the lower-side twin boundary. 4: Rapid growth occurs at reentrant corners formed at lower-side twin boundary. 5: The reentrant corner is formed at the upper-side twin boundary when the triangular crystals propagate across the upper-side twin boundary.

formation of a triangular corner with an angle of  $60^\circ$ , and the reentrant corner disappears from the crystal/melt interface (Figure 17.14-2). When the length required to form a triangular corner is  $h$ , the time consumed in this process is  $t_1 = h/R_{\text{twin}}$ . Although the rapid growth is inhibited, the crystal grows continuously on a  $\{111\}$  flat surface at a rate of  $R_{111}$ . When the triangular crystal propagates across the lower-side twin boundary with a consumed time of  $t_2 = d/R_{111}$ , reentrant corners are newly formed at the lower-side twin boundary (Figure 17.14-3). Again, rapid growth occurs there until the formation of a triangular corner ( $t_3 = h/R_{\text{twin}}$ ), and then a crystal grows continuously on a  $\{111\}$  flat surface (Figure 17.14-4). The reentrant corner is formed at the upper-side twin boundary, again when the triangular crystal propagates across the upper-side twin boundary with a consumed time of  $t_4 = d/R_{111}$  (Figure 17.14-5). After that, this cycle (from Figure 17.14-1 to 17.14-5) is repeated for the growth of the  $\langle 112 \rangle$  dendrite. Figure 17.12 shows that the tip of  $\langle 112 \rangle$  dendrites becomes wider with further crystal growth, which was experimentally confirmed by in situ observation [28,29]. The time consumed and growth length in this

cycle are  $2(h/R_{\text{twin}} + d/R_{111})$  and  $h$ , respectively. Indeed, the growth on a  $\{111\}$  flat surface always occurs during this cycle. Therefore, the growth rate of a faceted dendrite preferentially grown in the  $\langle 112 \rangle$  direction  $R_{\langle 112 \rangle}$  is given as

$$R_{\langle 112 \rangle} = \frac{h}{2(h/R_{\text{twin}} + d/R_{111})} + R_{111}. \quad (17.51)$$

Equation (17.51) shows that the growth rate of dendrites is dependent on the twin boundary spacing  $d$ . We could observe three dendrites grown in the same orientation at the same solid/liquid interface, as shown in Figure 17.15 [30]. The growth rate of dendrites was  $d_1 > d_2 > d_3$ . The parallel twins observed at the center of  $d_1$ ,  $d_2$ , and  $d_3$  were measured by EBSP (Electron Back Scatter Diffraction Patterns) after crystallization, and it was found that the twin boundary spacing was  $d_3 > d_2 > d_1$ , as also shown in Figure 17.15. These experimental results supported the prediction that the growth velocity of dendrites depends on the twin boundary spacing.

Figure 17.16 shows the calculation results of the twin boundary spacing  $d$  dependence of the growth rate of  $\langle 112 \rangle$  dendrites,  $R_{\langle 112 \rangle}$ , using Eqn (17.51). In the calculation,  $h$  and  $R_{111}$  were fixed at 1 and 1  $\mu\text{m/s}$ , respectively, and  $R_{\text{twin}}$  of 5  $\mu\text{m/s}$  or 1000  $\mu\text{m/s}$  was used. It is shown that the growth rate of the dendrites abruptly increases with a decrease in twin boundary spacing. On the other hand, when twin boundary spacing becomes larger, the growth rate of the dendrites approaches the growth rate of the  $\{111\}$  facet plane. It is often observed that the growth rate of faceted dendrites is more than 10 times larger than that of normal crystals in experiments. This suggests the higher growth rate at a reentrant corner. The growth rate at a reentrant corner,  $R_{\text{twin}}$ , and the  $\{111\}$  facet plane,  $R_{111}$ , should depend on the growth mode. For the growth on the  $\{111\}$  facet plane, the two-dimensional nucleation growth mode or step flow growth mode has been considered [31–33]; however, studies of this growth mode in melt growth remain limited.

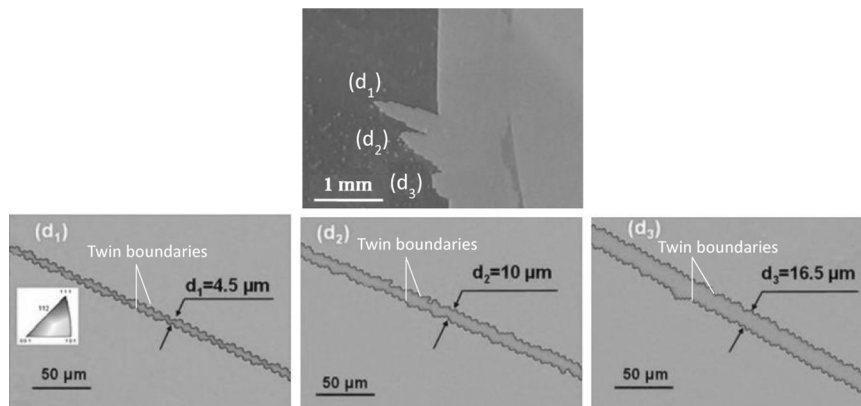


**Figure 17.15** Observation of three dendrites grown from the same interface at the same time (upper). Twin boundary spacing in those dendrites was measured by EBSP (lower) [30].

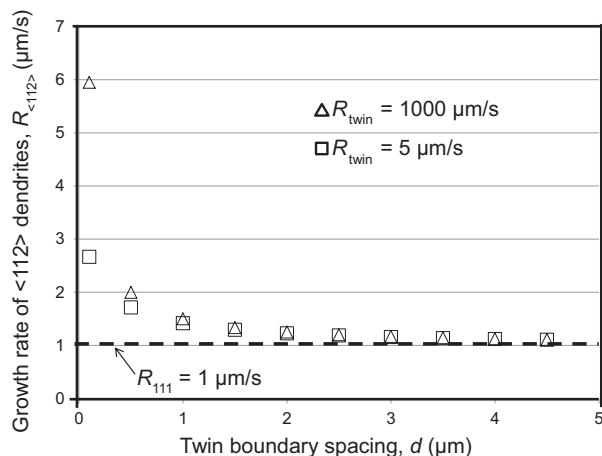


Figure 17.16 Calculation of growth rate of  $\langle 112 \rangle$  dendrites as functions of twin spacing.

Therefore, the general consideration on the kinetics at the reentrant corner and  $\{111\}$  face plane in melt growth seems worthy of study.

The growth scheme of faceted dendrites preferentially grown in the  $\langle 110 \rangle$  direction is also established by a similar growth scheme, and the shape of  $\langle 110 \rangle$  dendrites grown with a narrow tip is also represented, as shown in Figure 17.17 [29,30]. Note that reentrant corners always appear at both twin boundaries simultaneously in the growth of  $\langle 110 \rangle$  dendrites, although the reentrant corner alternately appears at each twin boundary in the growth of  $\langle 112 \rangle$  dendrites, as shown in Figure 17.14.

The fast growth of faceted dendrites will continue when the melt temperature in front of the growth tip remains sufficiently lower than the melting point. However, when a dendrite crystal grows along the crucible wall during nucleation–growth in the early stage of unidirectional solidification, as in the situation given in the left panel of Figure 17.1, the growing dendrite will encounter other crystal grains. Before the impingement of the dendrite crystal and another crystal, their thermal fields formed by the latent heat of solidification, shown in Figure 17.8, will overlap, and then the melt temperature in front of the growth tip will increase. Therefore, the fast growth of the faceted dendrite is suppressed and its tip flattens, as shown in Figure 17.18.

## 17.4 Grain Growth during Unidirectional Growth of Polycrystalline Ingot

In the previous section, the grain growth behaviors that are mainly observed during nucleation–growth were considered. In this section, the grain growth in the unidirectional growth of a polycrystalline ingot after forming the bottom structures of the ingot, as shown in Figure 17.1 (right panel), is considered. Generally, for example, in the growth

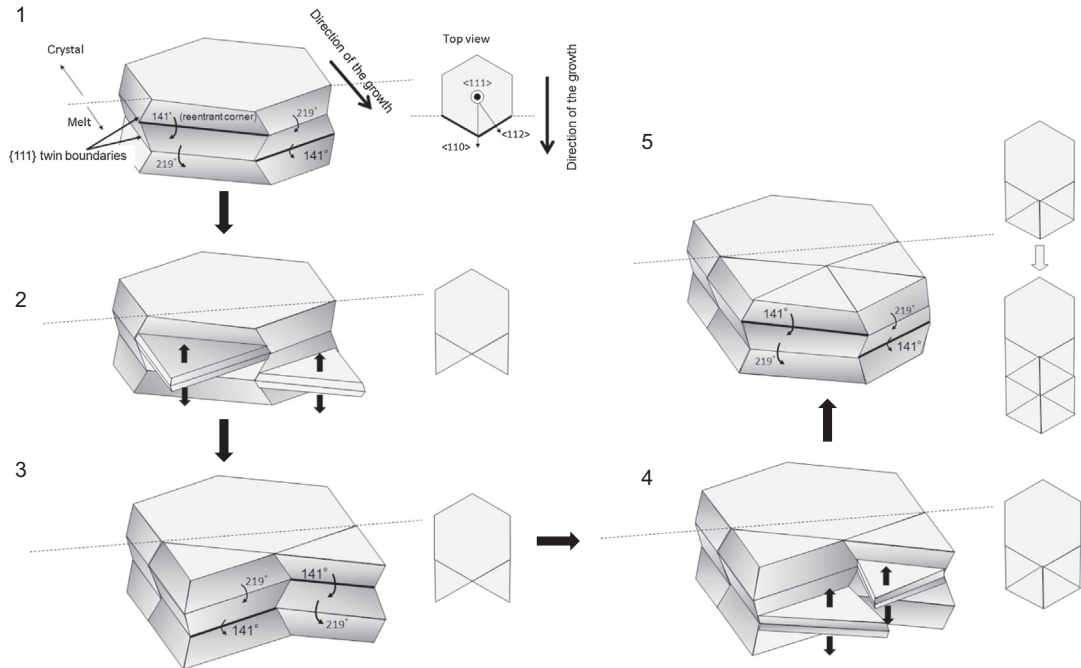


**Figure 17.17** Growth scheme of  $\langle 110 \rangle$  dendrites [29]. 1: Equilibrium shape of crystal containing two twin boundaries. It is considered that the crystal is growing only in the  $\langle 110 \rangle$  direction. Reentrant corners with an angle of  $141^\circ$  appear at both twin boundaries. 2: Triangular crystals are formed due to the rapid growth at both twin boundaries. Crystal growth can continue on the  $\{111\}$  flat surface, although the rapid growth is inhibited because of the disappearance of a reentrant corner with an angle of  $141^\circ$ . 3: When the triangular crystals propagate across another twin boundary, two reentrant corners are newly formed at both twin boundaries. 4: Rapid growth occurs at the two twin boundaries again, and triangular crystals are formed. 5: After propagation of the triangular crystals, reentrant corners are formed at the both twin boundaries.

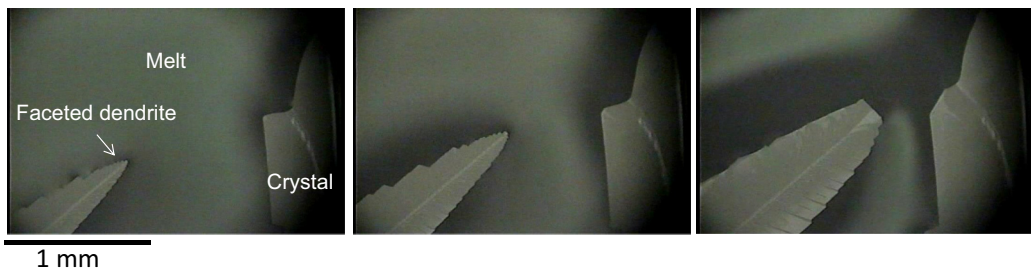


**Figure 17.18** Impingement of growing dendrite and crystal grain.

of multicrystalline Si ingots for solar cells, the melt at a crucible bottom is crystallized at the beginning of the growth. Nucleation-growth occurs on the bottom wall of the crucible. After the entire bottom wall of the crucible is covered by crystal grains, the crystallization is promoted in the upper direction, as shown in the right panel of Figure 17.1.

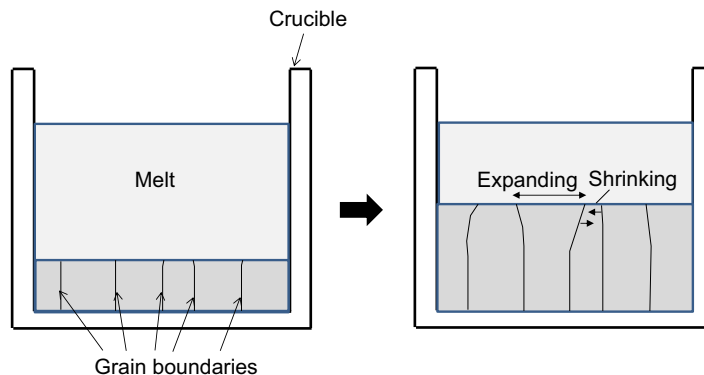


Figure 17.19 Grain growth (shrinkage) during unidirectional growth.

In this unidirectional growth, some of the characteristics, such as grain orientation and grain boundary characteristics, of crystal grains formed at the bottom will be transferred to upper part of the ingot. On the other hand, structural changes also occur during unidirectional growth; that is, various defects are generated and the nucleation of new crystal grains occurs at the crystal/melt interface. Grain growth and grain shrinkage are also observed in this process, as schematically shown in Figure 17.19. Some of the grains expand in the lateral direction of ingot growth, and adjacent grains shrink with unidirectional growth. For this phenomenon, studies are being conducted from both experimental and theoretical viewpoints [34–36]. Here, only the simplest case will be considered.

We consider the unidirectional growth of two crystal grains with one grain boundary between them, as shown in the left panel of Figure 17.20. One crystal grain has the  $\{111\}$  surface, which is an atomically smooth facet plane ( $\langle 111 \rangle$  grain), and the other has the  $\{100\}$  surface, which is an atomically rough plane ( $\langle 100 \rangle$  grain), at the crystal/melt interface. Both of the crystal/melt interfaces are flat macroscopically at the beginning. Now, two simple cases are considered. In the first case, the temperature gradient in the melt at the crystal/melt interface is negative (i.e.,  $dT/dz < 0$ ). In the second case, the temperature gradient in the melt at the crystal/melt interface is positive (i.e.,  $dT/dz > 0$ ), as indicated in the right panel of Figure 17.20. First, let us consider the case of the growth in the negative temperature gradient (Figure 17.20, upper right). When the melt temperature  $T_1$  is lower than the temperature at the crystal/melt interface,  $T_i$ , the perturbation introduced into the flat interface is amplified at the  $\{100\}$  crystal/melt interface owing to interface instability [37,38], and a zigzag interface bounded by  $\{111\}$  facet planes is established finally. The interface instability of a flat interface, the so-called Mullins-Sekerka instability [39,40], will be described in detail in another chapter. Such morphological transformation observed at the  $\{100\}$  crystal/melt interface does not occur at the  $\{111\}$  crystal/melt interface; thus, a flat interface is maintained. The zigzag crystal/melt interface of  $\langle 100 \rangle$  grain is located forward from the flat crystal/melt interface

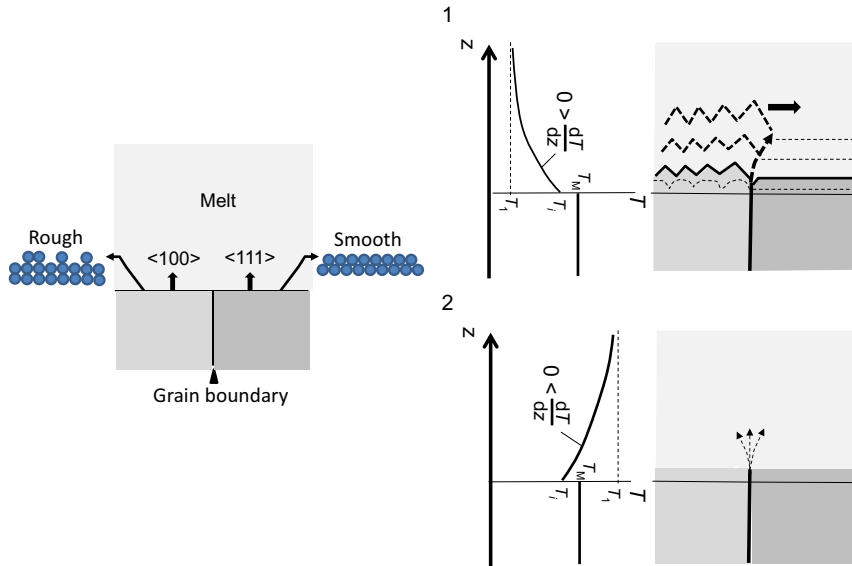


Figure 17.20 Consideration of grain growth behavior during unidirectional growth.

of  $\langle 111 \rangle$  grain at this moment. Therefore, the  $\langle 100 \rangle$  grain can grow faster in a larger amount of undercooling melt with a larger driving force, and it can also expand in the lateral direction covering the  $\langle 111 \rangle$  grain during unidirectional growth, as shown in Figure 17.20 (upper right).

We next consider the second case, where the melt temperature  $T_1$  is higher than the temperature at the crystal/melt interface,  $T_i$ . This situation is more similar to the real unidirectional growth of ingots (Figure 17.19, lower right). Let us assume that the growth rates of  $\langle 100 \rangle$  and  $\langle 111 \rangle$  grains are almost the same, and both crystal/melt interfaces are located at the same position. Interface instability does not occur at the  $\{100\}$  crystal/melt interface, owing to the positive temperature gradient. In this case, how does the grain growth during unidirectional growth occur? If the crystal/melt interface is completely straight for the two crystal grains, grain growth might not occur. However, a significant groove is formed at the grain boundary, as shown in Figure 17.21. The groove shape at the triple junction—that is, the grain-grain-melt—has been theoretically explained by Duffar and Nadri [41,42]. One can imagine that groove shape affects the temperature field at the crystal/melt interface, which determines which grain will expand during unidirectional growth, as suggested by the simulation results [36].

The phenomena shown in Figure 17.20 were experimentally observed by in situ observations [34]. In this experiment, two seed crystals of Si (100) and Si (111) were set in parallel together with Si wafer chips in the crucible, as shown in Figure 17.22(A). The sample was heated in the furnace of Figure 17.9. During the melting process, the wafer chips and part of both seed crystals were melted by controlling the temperature gradient. Before the seed crystals were completely melted, the sample was cooled at a steady rate

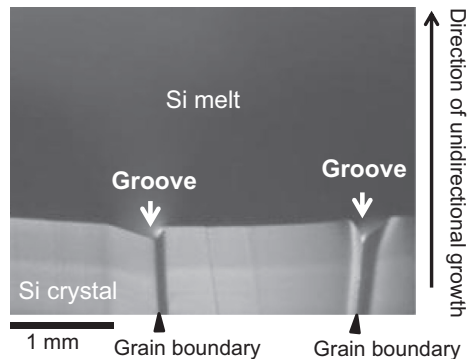


Figure 17.21 Observation of grain boundary grooves at the crystal/melt interface of mc-Si.

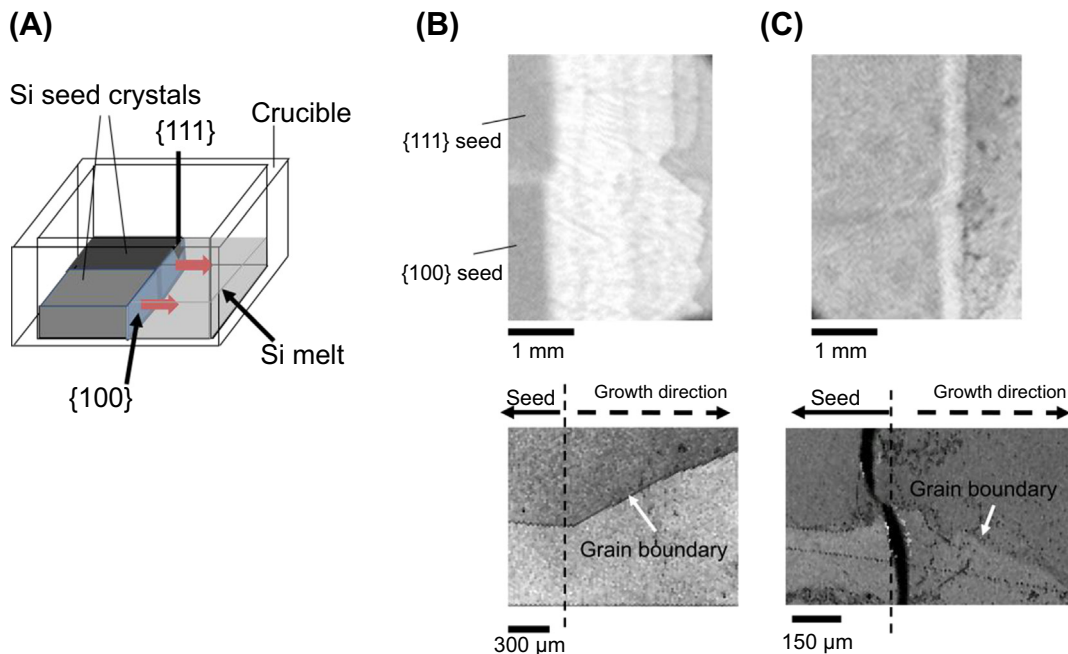


Figure 17.22 (A) Experimental setup of the sample for the growth at two seed crystals. (B) Crystal/melt interface during unidirectional growth (upper) and an SEM image after crystallization (lower) of the sample cooled at 30 K/min. (C) Crystal/melt interface during unidirectional growth (upper) and an SEM image after crystallization (lower) of the sample cooled at 1 K/min [34].

and the crystal growth started at both seed crystals. One sample was cooled at 30 K/min and the other was cooled at 1 K/min during the crystallization. Figure 17.22(B) and (C) show the crystal/melt interfaces during crystal growth and scanning electron microscopy (SEM) images after crystallization of the samples cooled at 30 K/min and 1 K/min, respectively.

From [Figure 17.22\(B\)](#), it was found that the (100) crystal/melt interface became a zigzag-faceted shape, whereas the (111) interface remained a flat shape at a larger cooling rate. It was also found that the growth rate of (100) crystal was higher than that of (111) grain. The SEM image in [Figure 17.22\(B\)](#) shows that the (100) grain gradually extended to the lateral direction, covering the (111) grain. On the other hand, both interfaces of (100) and (111) were flat and the growth rates of both grains were almost the same in the sample cooled at 1 K/min, as shown in [Figure 17.22\(C\)](#). The SEM image in [Figure 17.22\(C\)](#) showed that the (111) grain gradually extended to the lateral direction, which was the opposite result of the sample cooled at 30 K/min.

Phase field simulations by Chen et al. [35] and Cantù et al. [36] showed that the shape of the grain boundary groove at the crystal/melt interface influenced the grain growth behaviors. It was also shown that the shape of the grain boundary groove at the crystal/melt interface in mc-Si varies according to the orientations of grain boundary and crystal/melt interface [34–36,41–45]. Further accumulation of experimental/theoretical evidence on the relationship between the grain boundary groove shape and grain growth behavior is expected to increase the understanding of the grain growth phenomena at the crystal/melt interface.

## 17.5 Concluding Remarks

The study of the crystal growth of Si single crystals has a long history involving the Czochralski method and floating zone melting method. Now, high-quality Si single crystals for LSI (Large Scale Integration) and solar cells are commercially provided. On the other hand, there is a lot of room left for improvement of the crystal quality of mc-Si ingot grown by casting. The control of the macro- and micro-structures, such as grain size, grain orientation, grain boundary characteristics, dislocation/subgrain boundaries, and impurity distribution, is required during the solidification processes. Grain growth, as discussed in this chapter, is one of the phenomena that will affect the macro- and micro-structures of the mc-Si ingot. Fortunately, studies on melt growth of mc-Si have been undertaken recently. It is expected that the accumulation of fundamental studies will lead to the establishment of a technology for producing high-quality mc-Si ingots.

## References

- [1] Göler FV, Sachs G. *Z Phys* 1932;77:281.
- [2] Kolmogorov AN. *Izv Acad Sci USSR (Otd Phys Math Nauk)* 1937;1:355.
- [3] Johnson WA, Mehl RF. *Trans Am Inst Min Metall Eng* 1939;135:416.
- [4] Avrami M. *J Chem Phys* 1939;7:1103.
- [5] Avrami M. *J Chem Phys* 1940;8:212.
- [6] Avrami M. *J Chem Phys* 1941;9:177.
- [7] Koiwa M. *Mater Jpn (in Japanese)* 1986;25:640.
- [8] Koiwa M. *Mater Jpn (in Japanese)* 1989;28:294.

- [9] Koiwa M. *Mater Jpn* (in Japanese) 2011;50:55.
- [10] Koiwa M, private communication.
- [11] Markov IV. *Crystal growth for beginners*. Singapore: World Scientific; 1995.
- [12] Saito Y. *Statistical physics of crystal growth*. Singapore: World Scientific; 1996.
- [13] Einstein A. *Ann Phys (Leipzig)* 1905;17:549 [in *Investigation on the theory of Brownian movement*, (Dover, New York, 1956) p. 1–18.].
- [14] Wilson PE. *Philos Mag* 1900;50:238.
- [15] Frenkel J. *Phys Z Sowjetunion* 1932;1:498.
- [16] Kohyama M, Yamamoto R, Doyama M. *Phys Status Solidi B* 1986;138:387.
- [17] Duffar T. *Recent Res Dev Cryst Growth* 2009;5:61.
- [18] Billig E. *Proc R Soc A* 1995;229:346.
- [19] Bennett AI, Longini RL. *Phys Rev* 1959;116:53.
- [20] Hamilton DR, Seidensticker RG. *J Appl Phys* 1960;31:1165.
- [21] Wagner RS. *Acta Metall* 1960;8:57.
- [22] Albon N, Owen AE. *J Phys Chem Solids* 1963;24:899.
- [23] O'Hara S, Bennett AI. *J Appl Phys* 1964;35:686.
- [24] Barrett DL, Myers EH, Hamilton DR, Bennett AI. *J Electrochem Soc* 1971;118:952.
- [25] Lau CF, Kui HW. *Acta Metall Mater* 1991;39:323.
- [26] Li D, Herlach DM. *Phys Rev Lett* 1996;77:1801.
- [27] Nagashio K, Kuribayashi K. *Acta Mater* 2005;53:3021.
- [28] Fujiwara K, Maeda K, Usami N, Nakajima K. *Phys Rev Lett* 2008;101:055503.
- [29] Fujiwara K, Fukuda H, Usami N, Nakajima K, Uda S. *Phys Rev B* 2010;81:224106.
- [30] Yang X, Fujiwara K, Gotoh R, Maeda K, Nozawa J, Koizumi H, et al. *Appl Phys Lett* 2010;97:172104.
- [31] Beatty KM, Jackson KA. *J Cryst Growth* 2000;211:13.
- [32] Buta D, Asta M, Hoyt JJ. *Chem Phys* 2007;127:074703.
- [33] Miller W. *J Cryst Growth* 2011;325:101.
- [34] Fujiwara K, Obinata Y, Ujihara T, Usami N, Sazaki G, Nakajima K. *J Cryst Growth* 2004;266:441.
- [35] Chen P, Tsai YL, Lan CW. *Acta Mater* 2008;56:4114.
- [36] Cantù G, Popescu A, Miller W. *Acta Mater* 2012;60:6755.
- [37] Tokairin M, Fujiwara K, Kutsukake K, Usami N, Nakajima K. *Phys Rev B* 2009;80:174108.
- [38] Fujiwara K, Gotoh R, Yang XB, Koizumi H, Nozawa J, Uda S. *Acta Mater* 2011;59:4700.
- [39] Mullins WW, Sekerka RF. *J Appl Phys* 1964;35:444.
- [40] Langer JS. *Rev Mod Phys* 1980;52:1.
- [41] Duffar T, Nadri A. *Scr Mater* 2010;62:955.
- [42] Duffar T, Nadri A. *C R Phys* 2013;14:185.
- [43] Fujiwara K, Ishii M, Maeda K, Koizumi H, Nozawa J, Uda S. *Scr Mater* 2013;69:266.
- [44] Tandjaoui A, Mangelick-Noël N, Reinhart G, Billia B, Guichard X. *C R Phys* 2013;14:141.
- [45] Tandjaoui A, Mangelick-Noël N, Reinhart G, Billia B, Lafford T, Baruchel J. *J Cryst Growth* 2013;377:203.

# Growth of Semiconductor Nanocrystals

Katsuhiko Tomioka<sup>1,2,3</sup>, Takashi Fukui<sup>1,2</sup>

<sup>1</sup>GRADUATE SCHOOL OF INFORMATION SCIENCE AND TECHNOLOGY, HOKKAIDO UNIVERSITY, SAPPORO, JAPAN; <sup>2</sup>RESEARCH CENTER FOR INTEGRATED QUANTUM ELECTRONICS (RCIQE), HOKKAIDO UNIVERSITY, SAPPORO, JAPAN; <sup>3</sup>JAPAN SCIENCE AND TECHNOLOGY AGENCY (JST), PRESTO, KAWAGUCHI, JAPAN

## CHAPTER OUTLINE

<b>18.1 Overview</b> .....	<b>750</b>
<b>18.2 Selective-Area Epitaxy</b> .....	<b>753</b>
18.2.1 Microchannel Epitaxy .....	753
18.2.2 Selective-Area Growth.....	758
18.2.2.1 Facets in Selective-Area Growth.....	758
18.2.2.2 Control of Facets with SAG.....	760
18.2.2.3 Formation of Polygonal Shapes Due to Facet Growth.....	764
<b>18.3 Quantum Dots</b> .....	<b>767</b>
18.3.1 Self-assembled Growth of Quantum Dots.....	767
18.3.2 Selective-Area Growth of Quantum Dots.....	768
<b>18.4 Formation of III-V Nanowires</b> .....	<b>772</b>
18.4.1 Selective-Area Growth of III-V Nanowires.....	774
18.4.1.1 GaAs Nanowires.....	776
18.4.1.2 InAs Nanowires.....	777
18.4.1.3 InP Nanowires.....	778
18.4.1.4 InGaAs Nanowires.....	778
18.4.1.5 GaP Nanowires.....	778
18.4.1.6 InGaP Nanowires.....	778
18.4.2 Twinning Growth Model.....	781
18.4.3 Coherent Growth of Nanowire Heterostructure .....	786
<b>References</b> .....	<b>789</b>

## 18.1 Overview

The technology for semiconductor nanostructures has been progressing since Dr Richard P. Feynman made a presentation entitled “There’s Plenty of Room at the Bottom” in 1959 [1]. It is no exaggeration to say that the progress made with nanostructures and their technologies followed advances in methods of crystal growth. Tremendous advances in crystal growth methods have brought about rapid progress in device applications, such as solid-state lighting (SSL) and electronics.

The advances in epitaxy in SSL led to the realization of blue light-emitting diodes (LEDs), multicolored (from infrared to ultraviolet) light sources, and high-brightness LEDs. White LEDs using blue LEDs have recently been commercialized in displays and lighting, and SSL now needs more advanced materials that are low-cost and low-power, and that achieve high levels of brightness with epitaxial techniques. Enlarged active layers are required for high levels of power in planar LED architectures to high-brightness LEDs. However, high-brightness LEDs with low levels of power need many chips to be integrated because the intensity of LEDs is low, and this approach results in high cost. Planar LED architectures will reach a limit because these demands on epitaxial growth techniques are conflicting issues. Therefore, new architectures and nanocrystals are being explored as building blocks for future low-cost, low-power, high-brightness SSL because recent advances in epitaxial techniques have enabled low-dimensional semiconductor nanocrystals to be formed. These semiconductor nanostructures achieve high-density integration of SSL at low costs with less power consumption. Moreover, the nanostructures can achieve thresholdless lasing emissions [2,3].

The specific miniaturization of field-effect transistors (FETs) in electronic circuits is now faced with serious problems in terms of huge power consumption because of inherent issues they pose, such as an increased off-state current and enhanced short-channel effects. In this regard, Si-based FET technologies are expected to change their gate structures [4–6] and channel materials [7–9] to reduce power consumption in nanoelectronic circuits while avoiding these inherent issues in the gate length of the 8-nm node. However, the technologies to achieve miniaturization have yet to be developed for mass-produced, small Si-based transistors (gate transistors <8 nm-length). Advances in epitaxial techniques, such as heteroepitaxy on silicon platforms, are urgently needed in this field to integrate nanometer-scale channels. Non-Si materials, such as III-Vs and Ge, have higher carrier mobilities than that of Si. Several semiconductor nanostructures attained by advances in epitaxy, such as selective-area epitaxy, would be suitable for state-of-the-art FETs.

One of main reasons that Si has been the conventional material used for mass-producing transistors since the invention of the transistor in 1947 is that it has allowed excellent contact to be made between the interfaces of SiO<sub>2</sub>/Si. Therefore, superior metal-oxide-semiconductor (MOS) junctions can be created in terms of electrical properties. III-V compound semiconductors typified by GaAs, on the other hand, have no useful oxides for fabricating MOS-type transistors. Mainstream semiconductor

technology has been broadly divided due to this situation into three aspects: Si-based large-scale integrations (LSIs), optical devices that use III-V compound semiconductors, and emerging devices, such as high electron mobility transistors (HEMTs), resonant tunneling diodes (RTDs), and single electron transistors (SETs) using heterostructures in the semiconductors, which is so-called band engineering. Of these three branches, the latter two have progressed with the development of growth techniques such as molecular beam epitaxy (MBE) and metal-organic vapor phase epitaxy (MOVPE). It is now easy to fabricate superlattices (SLs), which was predicted by Esaki and Tsu [10], with these growth techniques. Expressed simply, these advances are directly related to the development of methods of fabrication to produce III-V semiconductor nanostructures.

Semiconductor nanostructures are generally categorized into three types of nanostructures: two-dimensional (2D) nanostructures (e.g., quantum wells (QWs)), one-dimensional (1D) nanostructures (quantum wires (QWRs) and nanowires (NWs)), and zero-dimensional (0D) nanostructures (quantum dots (QDs)), as shown in Figure 18.1. QW structures have become the best established of these nanostructures since their discovery by Esaki and Tsu in the 1970s [10]. They confine the motion of electrons or holes in one dimension and allow free propagation in two dimensions when the quantum well thickness is shrunk to the order of the de Broglie wavelength. In addition, they can be used in band engineering by combining them with several semiconductor QW structures. The applications of QWs have been commercialized in LEDs and HEMTs.

Studies on QDs have been rapidly expanding since it was found that self-organized InAs quantum dots were formed in the Stranski-Krastanow (S-K) mode [11]. This structure has a three-dimensional (3D)-confined density of states when dimensions are

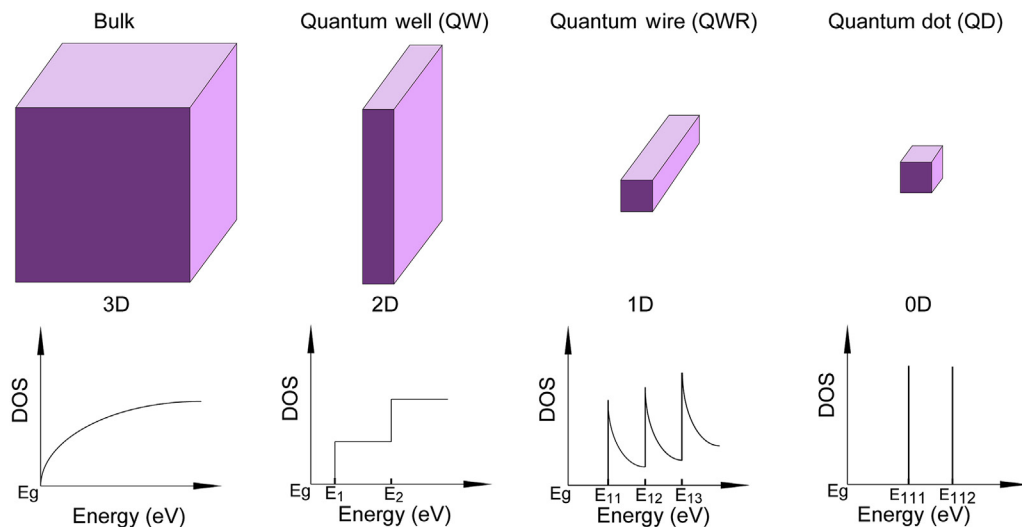


**FIGURE 18.1** Illustration for bulk, quantum wells (QWs), quantum wires (QWRs), and quantum dots (QDs) and schematics for density of states (DOSs) for bulk, QWs, QWRs, and QDs.

shrunk to the order of the de Broglie wavelength. Because QDs are zero-dimensional, they have a sharper density of states than higher-dimensional structures [2]. As a result, they have superior transport and optical properties and are being researched for use in laser diodes [3], solar cells [12], and biological sensors.

There are two approaches to the application of QDs: the first is to create high-density QDs and the second is to create single QDs at arbitrary positions. The former is an approach to gain high-intensity luminescence from QDs. Sb-irradiation has been found to achieve high-density QDs [13]. However, this approach achieves a single-photon emission device [14] and single-electron tunneling (SET) using entangled QDs. Position-controlled growth of InAs QDs is required to apply single QDs to applications.

Some approaches have aimed at forming single QDs in arbitrary positions. Fukui et al. pioneered the field of position-controlled QD growth by using selective-area MOVPE [15]. Their method used a combination of top-down and bottom-up approaches. In addition, a single-photon emitter has been reported that uses a single QD [16], as formed with a top-down approach. The high-temperature operation of a single-photon emission of GaN QDs has also been reported [17].

Studies on 1D nanostructures are more mature than those on other dimensional nanostructures. Wagner and Ellis investigated Si-whisker growth [18] in 1964. When the dimensions of structures reach the de Broglie wavelength, the motion of electrons or holes is confined in two spatial dimensions, which allows free propagation in the third dimension. The potential and advantages of one-dimensional nanostructures used in electronics and photonics have been evolving since the 1980s. Sakaki proposed in 1980 that 2D would improve the ballistic transport of electrons, which was related to the shrinking of the other two dimensions of structures [19]. In addition, the conversion from indirect bandgap to direct bandgap has been confirmed for Si 1D nanostructures formed by anodization [20] in terms of the properties of matter.

1D nanostructures have greater flexibility for shaped dimensions because their structures have both 2D and 0D nanostructures in their dimensions. In fact, 1D nanostructures can be used as a constructive tray for other nanostructures. The early investigations into 1D nanostructures focused on QWRs. Kapon demonstrated the formation of QWRs via a self-assembling process in the late 1980s and developed a high-quality QWR laser using V-grooves [21,22]. This laser involved the application of QWs in a 1D nanostructure. The controlled formation of QWRs, in addition to V-grooves, was demonstrated on vicinal surfaces. Hara et al. [23] and Miller et al. [24] pioneered controlled epitaxial growth on vicinal surfaces to create different compositions directed at different stripes—that is, theoretically to a fraction of the step length that occurred from the miscut angle of vicinal surfaces. This led to the demonstration of vertical QWs and band engineering for string-shaped superlattice structures.

The method of fabricating 1D nanostructures that was previously described is the so-called bottom-up approach. The top-down approach has also been used for a long time. One of the most intensively studied top-down approaches has been demonstrated on 1D-0D-1D resonant tunneling devices and single-electron devices. The target of these

kinds of devices has been to accomplish resonant tunneling, in which the emitter and collector use a 1D nanostructure and the active regions or core parts of the device use QDs. Reed et al. pioneered these types of devices [25] in the late 1980s, and Kita et al. more recently reported Coulomb-blockades in single-electron devices [26]. The progress made in 1D nanocrystals and their applications has been focused on so-called NWs in addition to the developments achieved in QWRs. Although the basic concept underlying NWs is the same as that behind the other 1D nanostructures previously mentioned, NWs have an advantage in terms of electronic and optical functionality.

The primary issues in the growth of semiconductor nanocrystals, such as 1D and 0D nanostructures, are to form uniform sizes and to arrange these structures at arbitrary positions. This is not only to use device applications but also to characterize the optical and electronic properties of the nanocrystals. Progress in selective-area epitaxy (SAE) based on pure crystallographic properties is expected to play an important role in this regard to resolve these issues. This chapter mainly focuses on the selective-area growth (SAG) of semiconductor nanostructures and their applications.

## 18.2 Selective-Area Epitaxy

SAE is a kind of template method that involves a combination of bottom-up (epitaxial growth) and top-down (lithography) approaches. The most common feature of SAE is that all epitaxial methods can be implemented such as liquid-phase epitaxy (LPE), MOVPE, and MBE to grow epitaxial thin film. This enables nanostructures to be fabricated with lithographically defined positioning. The masks used with SAE are usually amorphous films, such as SiO<sub>2</sub> and SiN<sub>x</sub>. The SAE technique was developed in the early 1960s and was first used for Si-integrated circuits [27]. Tausch et al. were the first to investigate the SAE of GaAs [28] in 1965, and Rai-Choudhury investigated the SAE of GaAs by using a metal-organic source [29]. Then, Jones reported the SAE of GaAs by using lithography-defined native oxide patterns [30].

SAE was divided into two main types for specific purposes after its introduction. The first was to screen for the propagation of dislocations due to lattice mismatches in the epitaxial layer by using template film and opening patterns, whereas the second was to form polygonal structures under faceting mechanisms. The former is so-called microchannel epitaxy (MCE) and the latter is SAG, which specifies the formation of semiconductor nanocrystals. MCE and SAG are summarized in this section.

### 18.2.1 Microchannel Epitaxy

Microchannel epitaxy is a combination of SAE and epitaxial lateral overgrowth (ELO). ELO has a long history in semiconductor epitaxy; its name was proposed by Jastzebski [31]. Both ELO and MCE use template masks, such as amorphous and metal films. Tsaur et al. first reported in 1982 that the heteroepitaxy of GaAs on a Ge/Si substrate by ELO had a dislocation density of  $10^4 \text{ cm}^{-2}$  in the epitaxial layer [32]. They unintentionally

reduced dislocation with ELO. In contrast to ELO, MCE intentionally suppresses the propagation of dislocation networks in the epitaxial layer while transferring lattice information. This is because amorphous films eliminate the propagation of defect information and the openings in amorphous films transfer lattice information. Nishinaga et al. reported the MCE of GaAs on GaAs [33]. Ujiie et al. reported a GaAs layer on Si grown by ELO and first found that a wide dislocation-free area could be formed by MCE outside the dislocated area above the seed [34].

MCE is categorized by two methods: horizontal and vertical. Defect information on substrate and lattice information are simultaneously transferred into the epitaxial layer in conventional epitaxy with defects, as can be seen from Figure 18.2(A). The main purpose of MCE is to transfer lattice information on the substrate through a small opening while preventing defect information from being transferred into the epitaxial layer [35]. The horizontal MCE in Figure 18.2(B) blocks defects from being propagated with an amorphous layer, and lattice information is transferred through the openings. Therefore, a defect-free layer could be grown by ELO. The vertical MCE in Figure 18.2(C) constructs an epitaxial layer vertically from small openings. This method can be used to stop dislocations from propagating and move them out of the side surface by choosing proper substrate orientations. This vertical MCE is related to faceting growth by SAG. An amorphous mask is deposited on the epitaxial substrate in the practical process flow of MCE and openings (microchannels) are formed in the amorphous mask. Then, epitaxial growth occurs in the direction of lateral growth in the openings as seeds. The dislocation area is restricted within the region over the seeds in the openings and a dislocation-free area can be formed. Sakawa et al. achieved a dislocation-free area in a GaAs epitaxial layer on Si [36], and Naritsuka et al. formed a defect-free region in an InP layer on Si [37] with MCE. Suzuki et al. investigated MCE-grown Si layers on an Si substrate [38] with homoepitaxy, and Zhang et al. reported a GaP layer grown on a GaP substrate by MCE [39]. MCE-grown GaN films on sapphire substrates were investigated by Usui et al. [40], and Sakai et al. grew a 120  $\mu\text{m}$ -thick GaN layer [41]. Dobosz et al. reported GaSb heteroepitaxial growth on a GaAs substrate [42].

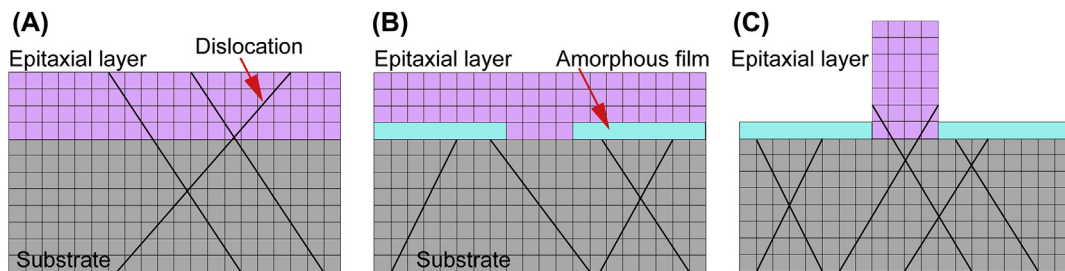


FIGURE 18.2 Concept underlying micro-channel epitaxy (MCE): (A) conventional epitaxy, (B) lateral MCE, and (C) vertical MCE.

It is important to enhance ELO to carry out horizontal MCE by using large anisotropy in epitaxial growth, in which anisotropy originates from the difference in the growth rates on a facet and on the atomically roughened surface. More lateral overgrowth (LOG) should be obtained than that of vertical growth after the initial growth or nucleation in the openings. Although the growth rate on the atomically roughened surfaces indicates a linear increase as interface supersaturation is increased, growth on the facet does not occur until 2D nuclei are generated under the high interface supersaturation. By using the difference in the growth rates, ELO is enhanced and an epitaxial layer is grown on amorphous films.

A large area for the MCE layer on amorphous films that eliminates defect information should be achieved when ELO is relatively more enhanced than vertical growth. This method effectively works on the heteroepitaxy of III-V compound semiconductors on Si substrates. There are several problems due to the mismatches in lattice and crystal structures between group-IV materials and III-V compound semiconductors, including lattice mismatches, differences in thermal expansion coefficients, and antiphase domains (or boundaries) due to polarity. These mismatches form misfit dislocations and threading dislocations, which degrade device performance. Therefore, epitaxial techniques to overcome these mismatches have been investigated since the 1980s. Thus far, the use of buffer layer growth [43] to relax strains that have resulted from lattice mismatches and two-step growth [44] to suppress the formation of antiphase domains have been proposed. There are no epitaxial techniques that can completely overcome these dislocations, although heteroepitaxial techniques have been applied to GaN growth on Si and blue LEDs [45]. The lowest dislocation density obtained with the conventional epitaxial technique is  $10^6 \text{ cm}^{-2}$ , which is too high to fabricate laser diodes.

A dislocation-free area on an Si(111) substrate by MCE was first achieved in 1989 by Ujiie and Nishinaga [34], who reported that they had formed an MBE-grown GaAs buffer layer with a huge number of dislocations and had used an amorphous mask to eliminate the propagation of dislocation networks in the buffer layer (see Figure 18.3). They grew the MCE-GaAs layer with LPE because LPE makes it difficult to obtain a smooth interface between GaAs/Si. Because Si is aggressively attacked by Ga atoms, GaAs cannot be directly grown on Si with LPE. Thus, they formed a GaAs buffer layer with MBE. Figure 18.4 has high-resolution transmission electron microscopy (TEM) image of GaAs grown by MCE on Si(111) after collusive etching. No etch pits can be observed outside the openings in the figure. The number of cracks would be increased if the buffer layer were thicker due to the difference in the thermal expansion coefficients between GaAs and Si. The lowest data thus far obtained have been a thickness of  $12 \mu\text{m}$  and a width of  $200 \mu\text{m}$  [46].

Figure 18.5 shows a TEM images of the GaAs MCE layer on the GaAs-buffer layer/Si(111) substrate, where the GaAs buffer layer was grown by metal-organic chemical vapor deposition (MOCVD). We can see some dislocation propagated on {111} planes through the openings in this figure, while defect-free regions were formed on the amorphous film. It was important to enhance ELO while suppressing vertical growth to

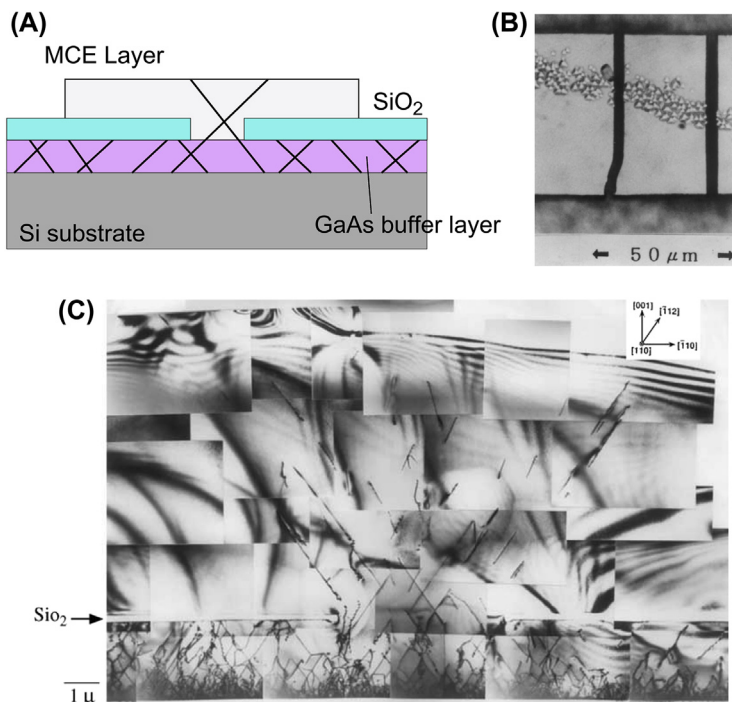


**FIGURE 18.3** (A) Illustration of micro-channel epitaxy (MCE) GaAs on Si substrate with GaAs thin buffer layer. (B) Optical microscopic image of GaAs grown by MCE on Si(111) substrate. (Adapted from Ref. [46]) (C) Cross-sectional TEM image of GaAs MCE layer on GaAs-coated Si substrate. Adapted from Ref. [34].

obtain a large defect-free area with MCE because the dislocation area expanded as growth thickness increased on the amorphous film [34]. Figure 18.5 is a cross-sectional TEM image showing a part near the SiO<sub>2</sub> mask and GaAs buffer layer interface. Propagation of dislocation stopped at the interface between SiO<sub>2</sub> and the GaAs buffer layer, and no dislocation were observed in the epitaxial layer on the SiO<sub>2</sub> mask.

The best approach for large dislocation-free areas with MCE is to achieve uniform nucleation in the initial stages of growth and to enhance ELO on the amorphous mask while suppressing the vertical growth rate. These two distinct features are mutually connected and enable a smooth MCE layer to be obtained. Initial growth in the openings should be uniform to obtain a smooth MCE layer. Deura et al. investigated the growth of InGaAs on Si with MCE and found that multinucleation affects the growth morphology [47]. When multinucleation and coalescence occurred in the early stages of growth inside the openings, the MCE layer had a hillock-like morphology. This is because coalescence formed huge numbers of adsorption sites, such as kinks and steps, and the growth rate became isotropic. Then, the morphology maintained the information of nucleation. Thus, the formation of uniform nuclei in the openings is an important parameter for MCE.

We next enhanced ELO by using a specific substrate orientation, such as (111), growth temperatures, and a growth method. A detailed description of the use of (111) surface

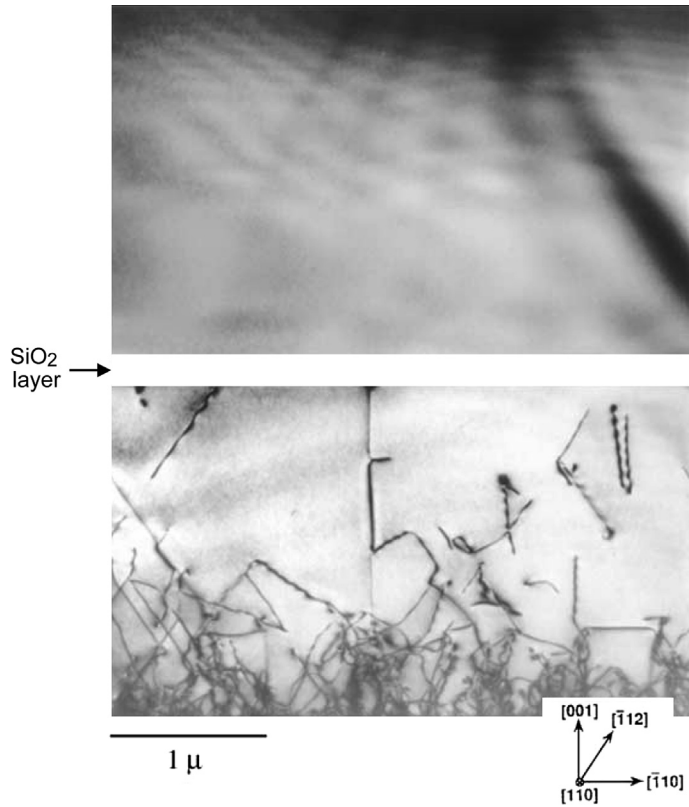


**FIGURE 18.4** High-resolution TEM image of GaAs micro-channel epitaxy layer near SiO<sub>2</sub> and GaAs buffer layer. Adapted from Ref. [35].

orientation will be given in Section 18.2.2, where the preferential direction of growth can

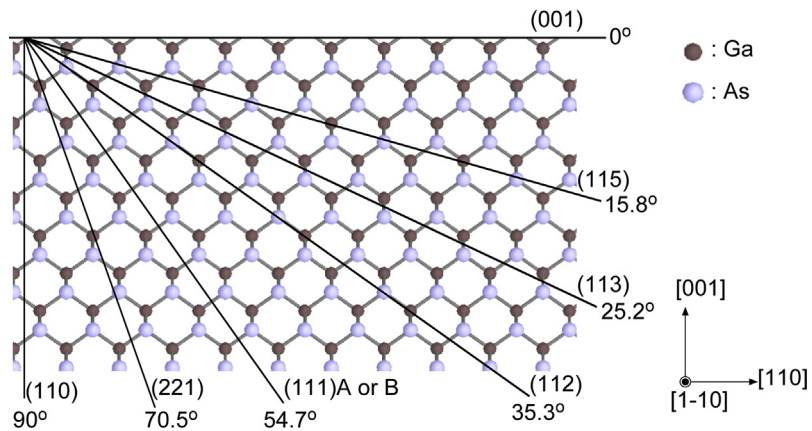


**FIGURE 18.5** Schematic of atomic arrangement viewed from the [1-10] direction and definition of facets.

be changed by the growth conditions on the (111)-oriented substrate. Another approach is to use the coalescence of MCE layers. A wide area for the MCE layer is obtained when the layer continues growth until two laterally growing layers coalesce. Zhang et al. reported this coalescence in a GaP/GaP system [39], and Nagal et al. and Banhart et al., investigated an Si/Si system by using LPE-ELO on SiO<sub>2</sub> [48,49]. Furthermore, no etch pits appeared in the coalesced area in InP/InP [50] or GaAs/GaAs systems [51]. Baccin et al. used low-angle incidence MBE, also called low-angle incidence MCE (LAIMCE), to enhance ELO with MCE. The fluxes of precursors with low angles enhanced selectivity and increased ELO in an MBE system. Umeno et al. achieved a wide area for an MCE layer with very thin MCE (~70 nm) by using LAIMCE [52].

MCE is an effective approach to form dislocation-free heteroepitaxial layers. MCE layers with less dislocation density have recently been used in optical and electronics applications on Si platforms. Naritsuka investigated the fabrication of AlGaAs-related laser diodes grown by MCE on Si [53], and Deura et al. reported a dislocation-free InGaAs MCE layer on Si toward III-V MISFET metal-insulator-semiconductor (MIS) FET applications [54]. Furthermore, MCE was practically used in laser diode applications to enhance the lifetime of devices [55] and has continuously been investigated to reduce dislocation networks in GaN free-standing films [56].

## 18.2.2 Selective-Area Growth

### 18.2.2.1 Facets in Selective-Area Growth

Equilibrium crystal shapes have a polygonal morphology surrounded by close-packed planes with low surface energy. The low surface energy results in a stable surface with a slow growth rate. Thus, crystal shapes surrounded by stable crystal planes are formed by faceting growth. This trend appears prominently in SAG. The grown structure is surrounded by low-index planes with slow growth rates. The origin of faceting in the SAG can simply be explained by the difference in the surface chemical potential of the planes (i.e., the number of dangling bonds). This is because the growth rate roughly depends on the number of dangling bonds of the surface. The planes are formed as facets normal to the vectors of the surface potential due to Wulff's construction theorem [57]. Figure 18.6 illustrates the atomic arrangement of GaAs from the <1-10> direction. For example, the tilted angles formed by the joining of (113), (111), and (110) with (001) planes correspond to 25.7°, 54.7°, and 90°. Some low-index planes are arranged on the (001) planes. Interestingly, one of the family of {110} planes, the {1-10} planes, are arranged normally to the (111)A or (111)B planes in this illustration. Fukui et al. demonstrated the formation of vertical {1-10} facets on the (111) B-oriented surface [58]. These facets can be controlled by growth conditions. The control of facets and their crystal shape using facets will be explained in this section.

The identification of crystallographic facets is one of the top priorities in investigating and understanding the nature of SAG. It should be noted that there are six {110} cleavage planes that are 30° apart, perpendicular to any {111} facets, as the basis of the orientation of facets. We can identify the orientation of crystallographic facets of grown structures on the

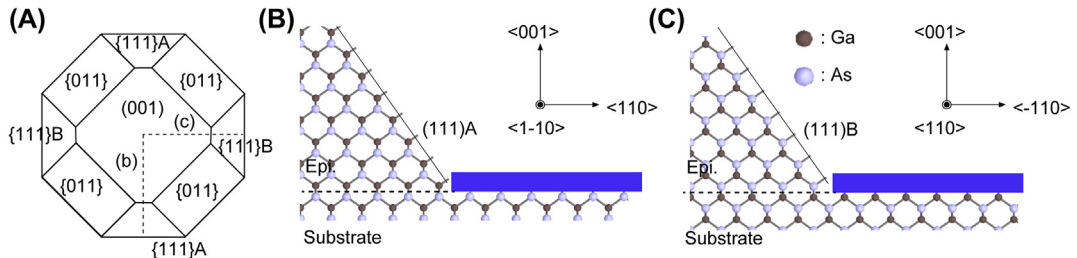


**FIGURE 18.6** (A) Illustration of the relationship between low-index facets that can exist in faceting growth on (001) surface. Schematics of relationship between edge direction and orientation of facets, and atomic arrangement viewed from (B)  $\langle -1-10 \rangle$  and (C)  $\langle 110 \rangle$  directions.

basis of six  $\{110\}$  cleavage planes of grown substrates. The upward sloping facets of grown structures (facet X) can be distinguished by the difference in contrast from the (111) top surface from the top view of grown substrates. The angle between facet X and the (111)B surface can be determined by tilting the substrate and calculating the angle from the difference in the apparent area of facet X. The angle between normal to the planes  $(h_1k_1l_1)$  and  $(h_2k_2l_2)$ ,  $\theta$ , is given by Eqn (18.1) for the dot product of the two appropriate vectors as

$$\cos \theta = \frac{h_1h_2 + k_1k_2 + l_1l_2}{(h_1^2 + k_1^2 + l_1^2)^{1/2} (h_2^2 + k_2^2 + l_2^2)^{1/2}} \quad (18.1)$$

Referring to Eqn (18.1), facet X, approximately  $35^\circ$  to (111)B, appears to correspond to  $\{110\}$ , and the facet at  $55^\circ$  appears to correspond to  $\{100\}$ .

Each facet can be controlled by the shape and direction of the openings on the masked substrate as well as the growth conditions. Figure 18.7 has a schematic of the relationship between the edge direction, the type of facet, and the atomic arrangement for  $\{111\}$ B viewed from  $[110]$ , and the  $\{110\}$  facet viewed from  $[100]$ . For example,  $\{110\}$  facets have a fourfold symmetry, so pyramidal structures can be formed with only four  $\{110\}$  facets as the sidewalls. Growth occurred under group-V atom excess conditions such as high group-V source supply rates and/or low growth temperatures ( $T_G$ ) due to the surfaces of  $\{110\}$  and  $\{111\}$ A in Figure 18.7(B) and (C). The  $\{111\}$  facets are polarity surfaces for III-V compound semiconductors. The  $\{111\}$ A planes have group-III atoms as outermost atomic arrangements. There are group-III atoms on the surface of  $\{111\}$ A  $[(111), (-1-11), (1-1-1), \text{ and } (-11-1)]$ , which are the growth conditions. Group-V atoms are revealed as the outermost surface on the  $\{111\}$ B-oriented surfaces  $[(-1-1-1), (-111), (1-11), \text{ and } (11-1)]$ . Figure 18.8 plots the relationship between low index planes that can exist in facet growth on (111)A- and (111)B-oriented surfaces. The growth rate of the facets is not isotropic, but they strongly depend on the surface coverage of group-V atoms and surface reconstructions. Thus, the shapes of grown structures can be changed by growth conditions, such as  $T_G$  and supply materials. The use of these facets enables various geometries of structures to be fabricated with SAG.

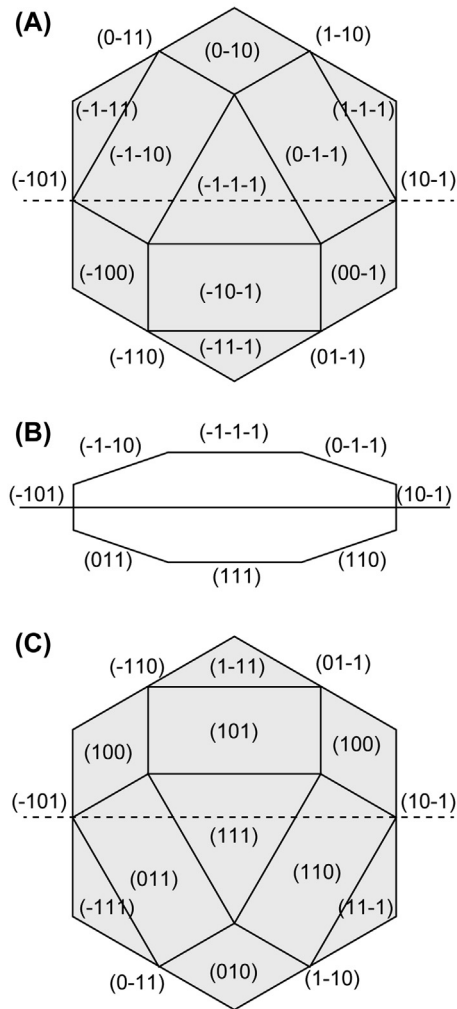
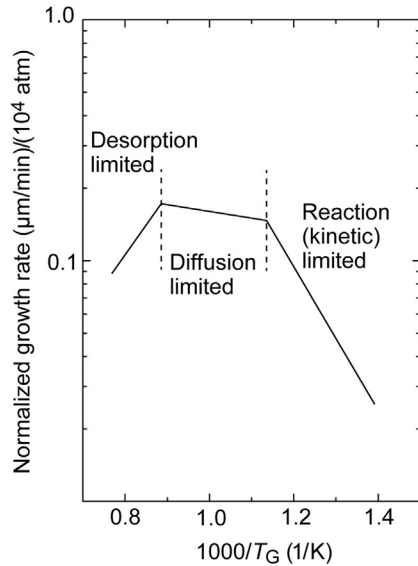


FIGURE 18.7 Illustrations of low-index facets that can exist in faceting growth on (111)A and (111)B surfaces.

### 18.2.2.2 Control of Facets with SAG

Low-index planes, whose growth rate is minimum, can appear as facets during SAG. The low-index planes are  $\{100\}$ ,  $\{110\}$ ,  $\{111\}$ A, and  $\{111\}$ B, and the growth rates of  $\{110\}$  and  $\{111\}$ B planes tend to be slow during III-V growth. Show investigated the order of growth rates for GaAs growth during vapor-phase epitaxy (VPE):  $\{111\}$ A  $>$   $\{100\}$   $>$   $\{110\}$   $>$   $\{111\}$ B [61]. Jones et al. reported the order of growth rate for GaAs growth during MOVPE:  $\{100\}$   $>$   $\{111\}$ A  $>$   $\{110\}$   $>$   $\{111\}$ B [62]. Interestingly, the growth rates of  $\{111\}$ A and  $\{100\}$  traded places with each other for VPE and MOVPE, while the growth rates of  $\{111\}$ B and  $\{110\}$  tended to be slower for both growth methods. Growth for VPE was limited due to the reaction limited regime. However, growth by MOVPE was limited by the



**FIGURE 18.8** Growth rate as a function of substrate temperature indicating three distinct growth regimes for typical III-V compound semiconductors in MOVPE. Adapted from Refs [59,60].

mass-transport limited regime. Figure 18.9 plots the growth rate of GaAs during MOVPE with variations in the growth temperature. Leys reported the dependence on temperature on the GaAs(001) substrate [59]. There were three distinct regimes: the reaction (kinetics)-limited regime, mass-transport-limited regime, and desorption-limited regime. The reaction-limited regime was below 600 °C, the mass-transport-limited regime ranged from 600 to 850 °C, and the desorption-limited regime was above 850 °C for GaAs by MOVPE. The growth rate in the mass-transport-limited regime was

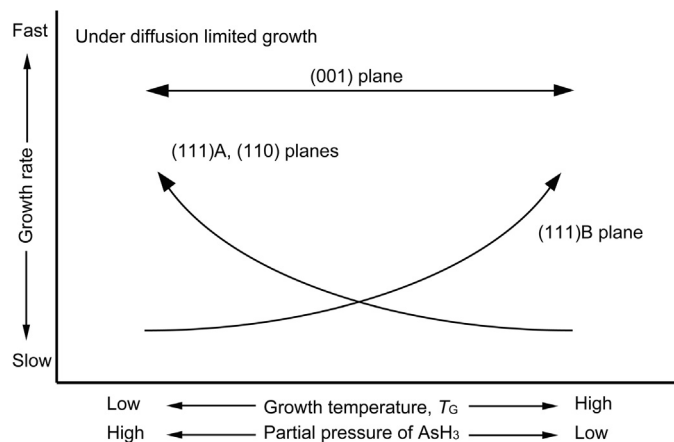


**FIGURE 18.9** Typical behaviors in growth rates of GaAs with various growth parameters under diffusion-limited regimes.

independent of the temperature. However, the growth rates of other surface orientations had different dependencies than those of the (001)-oriented surface.

The growth rate of the GaAs (001) surface was independent of variations in  $T_G$  and the partial pressure of  $\text{AsH}_3$  ( $[\text{AsH}_3]$ ) due to diffusion-limited growth. However, the growth rates of the GaAs (110), (111)A, and (111)B surfaces tended to vary with  $T_G$  and  $[\text{AsH}_3]$ , as can be seen from Figure 18.10. The growth rates of GaAs (111)A and (110) surfaces increased more than those of (111)B planes under low  $T_G$  and high  $[\text{AsH}_3]$ . This was because the As-trimers that formed on the (111)B surface suppressed nucleation on the GaAs (111)B surface. However, the growth rates of GaAs (001) and (111)B surfaces increased more than those of the GaAs (011) and (111)A surfaces at high  $T_G$  and low  $[\text{AsH}_3]$ .

The four key processes in typical MOVPE during growth have been summarized by Stringfellow as mass transport, the physical process, chemical reactions, and thermodynamics [60]. The mass-transport process is related to the boundary (stagnant) layer above the growth surface, which is formed by the laminar flow of vapor in the reactor. The growth pressure and gas flow velocity define the thickness of the boundary layer. The physical process involves the physics of adatoms on the growth surface. Growth is simply described by the Kossel model (terrace-step-kink model) [63]. Surface reconstruction as energetic stable atomic configurations should be simultaneously considered. Chemical reactions must be taken into account for a more detailed description of the growth process. The chemical processes in MOVPE have very complex radical reactions, including decomposition and desorption processes. Thermodynamics defines the deviation from equilibrium and thus the driving force for growth. The facets in SAG can mutually appear due to a combination of these distinct processes.

The growth rate of the (111)B surface will be changed by  $T_G$  and the V/III ratio in the mass-transport limited regime of GaAs during MOVPE, whereas the growth rate of the (100) surface is constant. Ando et al. investigated the growth rate of AlGaAs on (001) and (111)B with variations in  $T_G$  and the V/III ratio [64]. The growth of the (111)B surface was beyond the mass-transport-limited regime in this report and the growth rate was increased with increasing  $T_G$ , and decreased with an increasing V/III ratio. The reduced growth rate of the (111)B surface under low  $T_G$  and higher  $[\text{AsH}_3]$  resulted from higher As coverage ( $\theta_{\text{As}}$ ). The excess As atoms under higher As coverage formed As-trimers, and the trimers suppressed the crystal growth process. The formation of As-trimers was first observed by Biegelsen et al. in an MBE system [65]. Nishida et al. reported a similar formation of As-trimers during MOVPE with the method of surface photoabsorption [66]. As-trimers are sensitive to  $T_G$  and start to desorb with higher  $T_G > 700$  °C. This is because  $\theta_{\text{As}}$  decreases with higher  $T_G$ .

The  $\theta_{\text{As}}$  affects the growth rate of {110} planes. Asai investigated growth rates in the  $\langle 110 \rangle$ ,  $\langle 1-10 \rangle$ , and  $\langle 001 \rangle$  directions on a GaAs(001) substrate with variations in  $T_G$  and the V/III ratio [67]. The [110] growth rate was higher than that of  $\langle -110 \rangle$  with low  $T_G$  and higher  $[\text{AsH}_3]$  in this report, whereas the  $\langle 110 \rangle$  growth rate decreased as  $[\text{AsH}_3]$  decreased and the  $\langle -110 \rangle$  growth rate remained almost constant. Both the  $\langle 110 \rangle$  and  $\langle -110 \rangle$  growth rates increased linearly with the partial pressure of the group-III

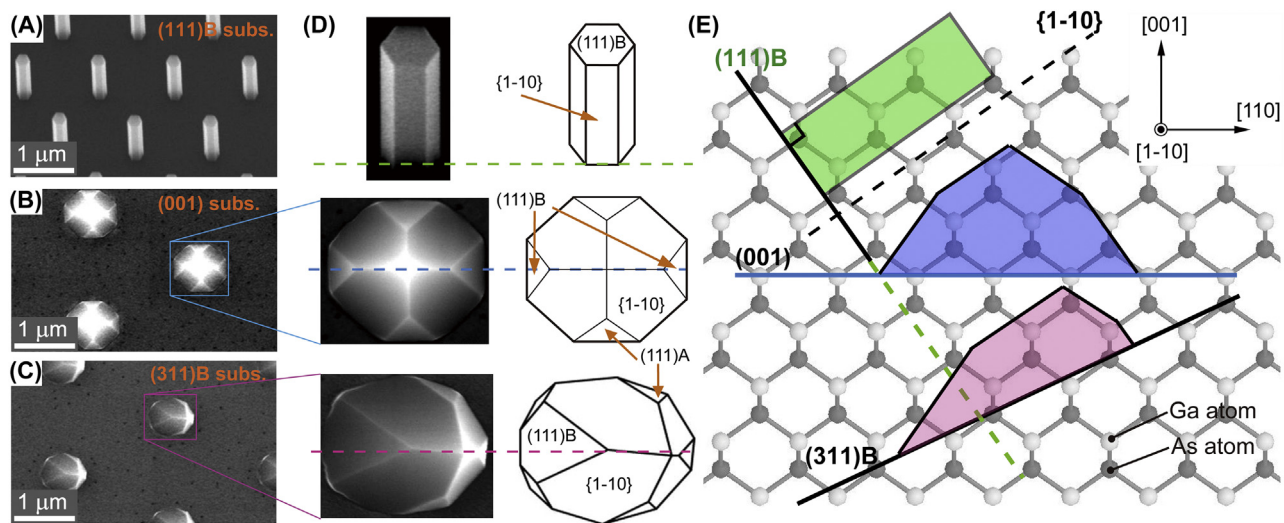


**FIGURE 18.10** Selective-area growth of GaAs on (A) GaAs(111)B substrate, (B) GaAs(001) substrate, and (C) GaAs (311)B substrate. Images summarize structures grown at high  $T_G$  and low  $[\text{AsH}_3]$ . (D) SEM images and schematics of crystal shapes on GaAs (111)B, (001), and (311)B. Schematic of GaAs crystal structure with injection of [1-10] direction. Green, blue, and red solid lines correspond to (111)B, (001), and (311)B surface orientations of GaAs. Illustrations indicate cross-sections of structures in (D). Dashed line indicates family of {1-10} planes. These planes are normal to the (111)A or (111)B surface.

precursor, which was similar to that of  $\langle 001 \rangle$ , and they reduced as  $T_G$  decreased. Chang et al. systematically investigated the growth rate in the  $\langle -110 \rangle$  direction by using the SAG of GaAs on the GaAs (111)B substrate [68]. They used stripe-patterned openings on the GaAs(111)B substrate to characterize lateral overgrowth in the  $\langle -110 \rangle$  direction under various growth conditions. The growth rate in the  $\langle -110 \rangle$  directions (i.e., LOG) increased as  $T_G$  decreased and  $[\text{AsH}_3]$  increased in their characterizations. The growth rate of (111)B, on the other hand, was suppressed with low  $T_G$  and high  $[\text{AsH}_3]$  due to the formation of As-trimers. The growth rate in the  $\langle -110 \rangle$  direction with low  $T_G$  was 23 times faster than that in the [111]B direction. The difference in the growth rate along the  $\langle -110 \rangle$  directions occurred under similar conditions to those of the (111)B surface. This is because  $\theta_{\text{As}}$  changed in the same way as that for the (111)B surface.  $\theta_{\text{As}}$  is expressed by Lagmuir's adsorption isotherm [69] as

$$\theta_{\text{As}} = BP_{\text{As}} / (1 + BP_{\text{As}}), \quad (18.2)$$

where  $B$  is the adsorption coefficient of As atoms and  $P_{\text{As}}$  is the partial pressure of As. When we described  $B$  by using the adsorption energy ( $E_{\text{As}}$ ),  $B$  and  $\theta_{\text{As}}$  are expressed as

$$B = b \cdot \exp(E_{\text{As}}/kT) \quad \text{and} \quad (18.3)$$

$$\theta_{\text{As}} = \frac{b \cdot P_{\text{As}} \exp(E_{\text{As}}/kT)}{\{1 + b \cdot P_{\text{As}} \exp(E_{\text{As}}/kT)\}}. \quad (18.4)$$

$E_{\text{As}}$  depends on the number of dangling bonds on the growth surface [67]. According to Eqn (18.4),  $\theta_{\text{As}}$  depends on  $T_G$  and  $[\text{AsH}_3]$ . Thus,  $\theta_{\text{As}}$  decreases at high  $T_G$  and low  $[\text{AsH}_3]$ . Crystal growth can proceed by suppressing the evaporation of adatoms because group-III atoms diffusing from the vapor phase are adsorbed with three dangling bonds of As atoms on the (-110) surface with high  $\theta_{\text{As}}$ . Because adsorbed As atoms on the (-110) surface can easily desorb on the surface with low  $\theta_{\text{As}}$ , the time to adsorb group-III atoms decreases. Thus, the [-110] growth rate slows at high  $T_G$  and low  $[\text{AsH}_3]$ . The GaAs polygonal shape surrounded by facets during SAG uses the difference in growth rates that originate from  $\theta_{\text{As}}$  and the formation of As-trimers.

### 18.2.2.3 Formation of Polygonal Shapes Due to Facet Growth

The SAG enables polygonal-shaped structures to be formed, surrounded by facets with precise positioning. Polygonal nanostructures surrounded by  $\{1-10\}$ , (111)B, and (111)A planes are formed on GaAs (111)B, (001), and (311)B substrates in this way, as shown in Figure 18.10. Also, tetrahedral structures surrounded by (111)A surfaces are formed at high  $T_G$  and low  $[\text{AsH}_3]$ . Interestingly, the crystal shape of GaAs on (111)B-oriented surfaces become hexagonal pillars surrounded by vertical  $\{1-10\}$  facets. This is because the family of  $\{-110\}$  planes is vertically arranged from the (111)B surface.

Furthermore, semiconductor nanocrystals with various carrier confinements can be formed by combining SAG and heterostructures. For example, Ando and Fukui reported the formation of GaAs/AlGaAs by SAG [58,64]. They used stripe patterns with a [110] direction in their research and grew GaAs at lower  $T_G$  and higher  $[\text{AsH}_3]$  to form a

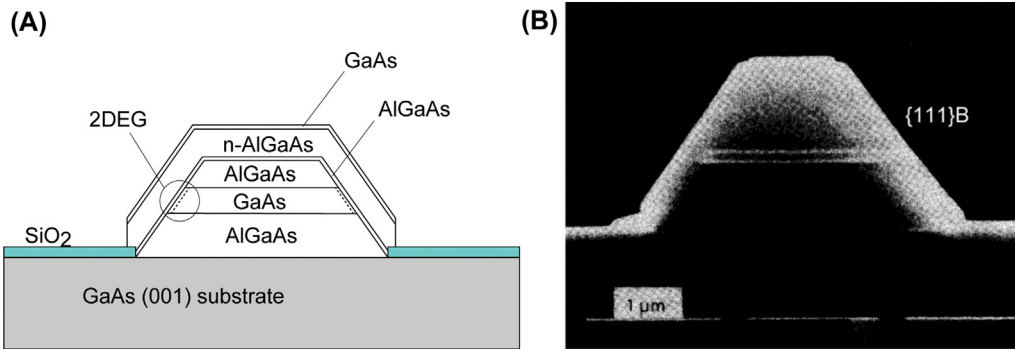


**FIGURE 18.11** (A) Illustration of GaAs/AlGaAs quantum wire structure produced by selective-area growth. (B) Cross-sectional SEM image of structure. 2DEG, two-dimensional electron gas. Adapted from Refs [58,64].

trapezoidal structure. The grown structure was surrounded by (111)B facets, which is shown in Figure 18.11. Ando et al. systematically investigated the formation of a trapezoidal structure surrounded by uniform (111)B facets [64] by growing GaAs/AlGaAs heterostructures under the same conditions. They then changed the growth conditions to form heterostructures on the (111)B inclined facets. They grew the AlGaAs/n-AlGaAs/GaAs heterostructures at high  $T_G$  and lower  $[\text{AsH}_3]$ . Carriers were confined in the GaAs/AlGaAs interface as the two-dimensional electron gas (2DEG) in Figure 18.11 due to a modulation doping effect. The width of carrier confinement in this structure could be defined by the thickness of the first GaAs layer. This method could avoid process-induced damage in the channel layer. The line-width for carrier confinement could be simply controlled by the thickness of the epitaxial layer. Thus, these are promising to characterize the carrier transport and carrier scattering mechanisms [58].

Fukui et al. demonstrated lateral QWRs achieved by SAG [70]. They grew GaAs rectangular-shaped GaAs structures surrounded by vertical  $\{-110\}$  and (111)B surfaces on a GaAs(111)B substrate at higher  $T_G$  and lower  $[\text{AsH}_3]$ . Then, a GaAs/n-AlGaAs heterostructure was formed on  $\{-110\}$  side facets under lower  $T_G$  and higher  $[\text{AsH}_3]$ . Ando et al. investigated the formation of uniform  $\{-110\}$  facets [71]. A modulation-doped heterostructure-based GaAs/n-AlGaAs/GaAs structure was formed on a vertical  $\{-110\}$  facet under specific growth conditions, as shown in Figure 18.12. Because the carrier concentration of contamination and impurities increases at higher  $T_G$  during MOVPE, the first rectangular GaAs structure was doped with oxygen to form a semi-insulating structure. The depletion layer in this structure should have taken into account the channel width of 2DEG. They characterized the effective thickness of 2DEG by magnetoresistance oscillation at 4.2 K [72], and then found that the net thickness of 2DEG was thinner than that of the grown thickness because the depletion layer could be dispersed on both sides of the (111)B surface (top (111)B and bottom (111)B surface on  $\text{SiO}_2$ ).

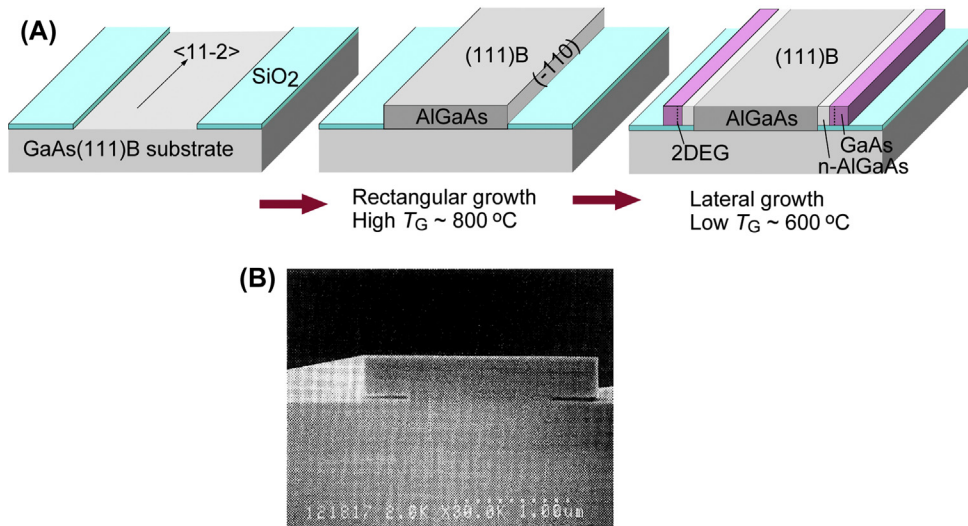


**FIGURE 18.12** (A) Fabrication flow for lateral quantum wires (QWRs) by selective-area growth. (B) Cross-sectional SEM image of lateral QWR. 2DEG, two-dimensional electron gas. Adapted from Refs [70,71].

The use of the direction of vertical preferential growth at higher  $T_G$  and lower  $[AsH_3]$  enabled QWRs to be fabricated that consisted of vertical-stacked double heterostructures (DHs), such as GaAs/AlGaAs DHs. Figure 18.13 illustrates a DH. The main advantage of this faceting growth is that the Fabry-Pérot cavity structure with crystal facet mirrors could be fabricated by only using crystal growth. Moreover, the length of the cavity could be changed by using lithographically defined opening patterns. Ando et al. reported short-cavity laser diodes fabricated with SAG and they characterized optically pumped laser oscillations with variations in cavity length [73]. Another approach to form laser cavity structures by crystal growth is to use prepatterned V-groove structures. Bhat et al. first reported the fabrication of GaAs/AlGaAs DH structures and achieved electrically pumped laser emissions by using crystal facet cavities [74].

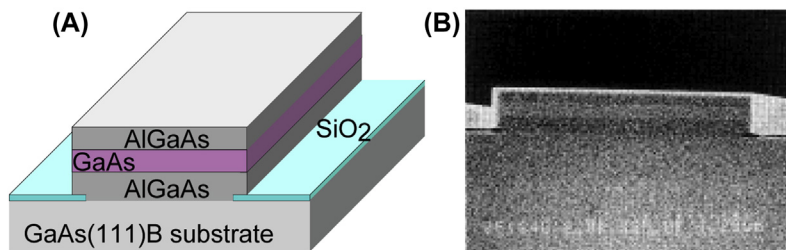


**FIGURE 18.13** (A) Illustration of GaAs/AlGaAs double heterostructure grown by selective-area growth on GaAs(111)B substrate. (B) Cross-sectional SEM image of structure. Adapted from Ref. [73].

## 18.3 Quantum Dots

### 18.3.1 Self-assembled Growth of Quantum Dots

A well-known method of growing quantum dots (QDs) is to use the Stranski-Krastanow mode in heteroepitaxial systems [11]. Lattice mismatch between the epitaxial layer and the substrate contributes to their growth modes as well as the formation of misfit dislocations in heteroepitaxial systems. There are typically three growth modes, as characterized in Figure 18.14: the Frank-van der Merwe (F-M), the Stranski-Krastanow (S-K), and the Volmer-Weber (V-W) modes. Thin film in the F-M mode in Figure 18.14(A) is atomically stacked layer by layer from the formation of 2D nuclei in the early stages of growth. The S-K mode in Figure 18.14(B) is a combination of layer-by-layer growth in the early stages of growth and 3D island growth. The transition from the layer-by-layer growth to the 3D island growth occurs across a critical thickness for the lattice to relax lattice strain due to lattice mismatch. The V-W mode in Figure 18.14(C) is only 3D island growth in the early stages of growth.

The use of the S-K growth mode enables QDs to be formed regardless of the kinds of defects under critical thickness [75]. Strain-induced roughening and the formation of defects and their propagation were suppressed in very small nanostructures during the transition from 2D nuclei to 3D island growth in the S-K mode. Eaglesham et al. reported a dislocation-free S-K growth mode in Ge/Si and SiGe/Si systems [76]. The S-K growth mode is independent of materials systems and growth methods such as VPE, MBE, and MOVPE. One of the most widely studied QDs in the S-K mode has been the growth of InAs QDs on GaAs substrates [77], where the lattice mismatch was 7.2% and 3D islands started to form from the critical thickness of 1.7 monolayer (ML).

The growth mode in a lattice-mismatched system is changed by the interface free energy and lattice mismatch. The formation of 3D islands is driven by interface energy ( $\gamma_{12}$ ) and the epitaxial layer's surface energy ( $\sigma_2$ ). If the substrate surface energy ( $\sigma_1$ ) is lower than ( $\gamma_{12} + \sigma_2$ ), thin-film growth proceeds according to the S-K or V-W modes. The variations in ( $\gamma_{12} + \sigma_2$ ) therefore drive the transition from the F-M to the V-M mode or misfit dislocations are introduced underneath the islands to relax the stain. When the adatoms interact more strongly than adatom-surface bonds,  $\sigma_2$  reaches large fractions.

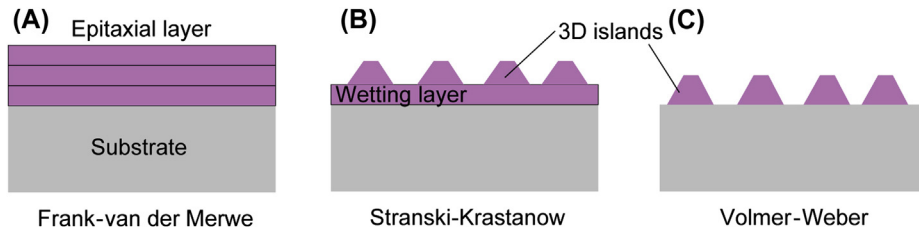
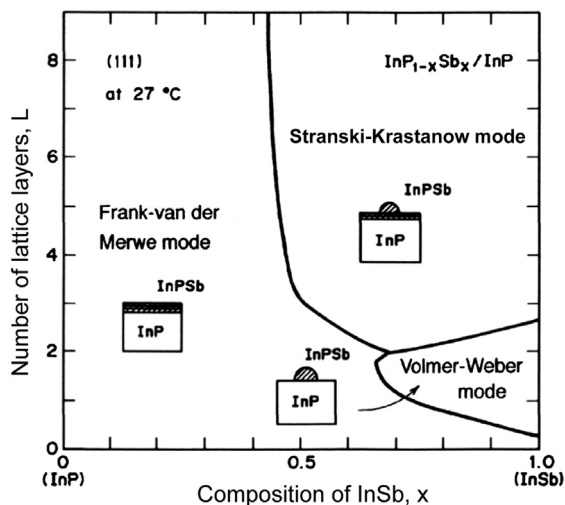


**FIGURE 18.14** Illustration of growth modes in heteroepitaxy. (A) Frank-van der Merwe, (B) Stranski-Krastanow, and (C) Volmer-Weber modes.

**FIGURE 18.15** Phase diagram of thickness-composition of Frank-van der Merwe, Stranski-Krastanow, and Volmer-Weber modes for a InPSb/InP(111) structure. Adapted from Ref. [78].



Thus, the V-W mode occurs. The S-K growth mode appears for systems with small  $\gamma_{12}$  with large lattice mismatches. Nakajima systematically characterized the free energy of these three modes in III-V ternary systems and found that the diagram of thickness-composition phases for these growth modes was determined by the balance of free energy, which is plotted in Figure 18.15 [78].

### 18.3.2 Selective-Area Growth of Quantum Dots

The SAG can synthesize QD structures by using facet growth.  $\{110\}$  facets can be formed under specific growth conditions, as was explained in Section 18.2.2. Moreover,  $\{-110\}$  and  $\{-1-10\}$  facets are distinctly controlled by changing growth conditions and shapes of mask openings. Ando et al. investigated the formation of vertical  $\{-110\}$  facets and inclined  $\{-1-10\}$  facets of GaAs SAG on (111)B-oriented substrates by changing  $T_G$  and  $[\text{AsH}_3]$  [79]. The tetrahedral structures surrounded by  $\{-1-10\}$  facets and the hexagonal structures surrounded by vertical  $\{-110\}$  facets were distinctly formed by  $T_G$  and  $[\text{AsH}_3]$ , as seen in Figure 18.16. This distinct morphology is defined by the growth rate of the (111)B surface. The growth rate of the (111)B surface was faster than that of the  $\{-1-10\}$  surface at lower  $T_G$  and higher  $[\text{AsH}_3]$ , where 35°-tilted  $\{-1-10\}$  facets were formed by SAG. The growth rate of (111)B, on the other hand, was minimal for low index planes at higher  $T_G$  and low  $[\text{AsH}_3]$  due to the formation of As-trimers, where vertical  $\{-110\}$  facets were formed rather than  $\{-1-10\}$  facets. These growth modes could be used to form QDs with lithographically defined positioning.

Fukui et al. demonstrated the formation of pyramidal structures surrounded by the  $\{-1-10\}$  facets [80], where they used triangular opening masks for SAG. Each side of the openings was parallel to the  $\langle -1-10 \rangle$  direction. First, they grew a trapezoidal AlGaAs

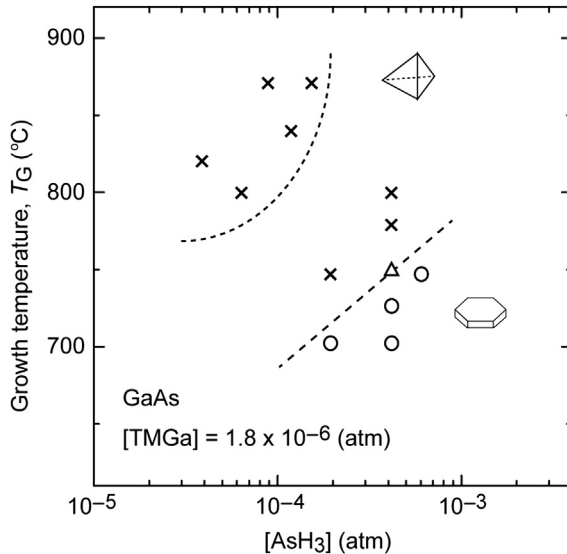


**FIGURE 18.16** Phase diagram for facet growth characteristics on the (111)B surface at various combinations of  $T_G$  and  $[AsH_3]$ . Adapted from Ref. [9].

structure surrounded by  $\{-1-10\}$  facets and the (111)B surface. The  $\{-1-10\}$  facets were tilted by  $35.26^\circ$  to the (111)B surface. Next, they stacked GaAs layers on the (111)B top surface. Then, they covered the structure with an AlGaAs layer (Figure 18.17). The GaAs layers in this structure acted as QDs. The main advantage of the SAG is that it could be used to precisely control the QD size because the surface area of the (111)B could be defined by the thickness of the first layer (Figure 18.17). Moreover, conventional thin-film growth, such as that for QWs, can be used to form QDs regardless of lattice mismatches, misfit dislocations, or lattice strain in the S-K growth mode. The quantum size effect for a GaAs QD is 20 times stronger than that of a single QW. This is because the effective quantum size effect in the GaAs pyramidal structure is close to the internal spherical shape of a pyramid and the size is approximated to the diameter of the inner ball. This formation of QDs with SAG was applied to the GaN-based QD structure [17].

The SAG enables the positions of growth of nanostructure to be controlled, such as QDs. Another interesting approach to form QDs is the combination of the S-K growth mode with SAG. Many efforts have been expended to fabricate site-controlled QDs with the S-K mode. For example, Watanabe et al. investigated dense site-controlled QDs by using inverted pyramids, or so-called V-grooves [81], where the (111)B GaAs substrates

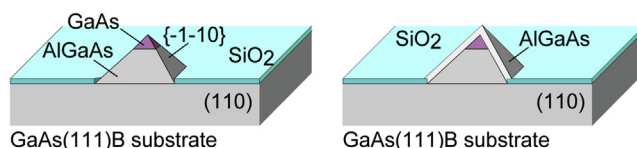
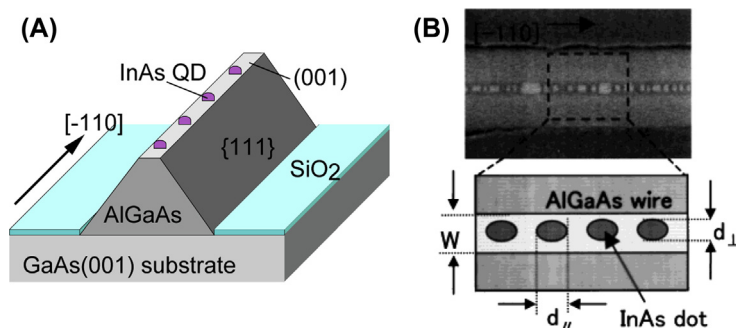


**FIGURE 18.17** Schematics of tetrahedral quantum dot based GaAs/AlGaAs obtained by selective-area growth [80].

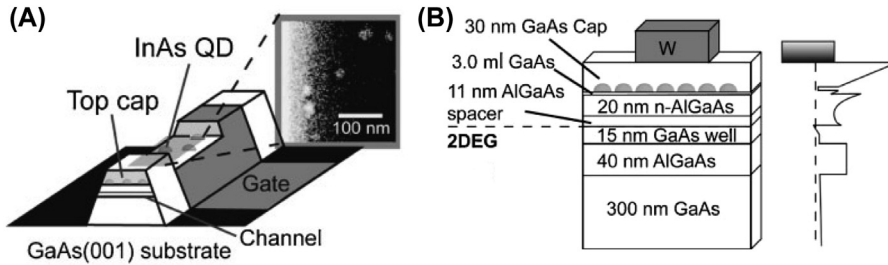
were patterned prior to growth with hexagonal arrays of inverted pyramids that consisted of three equivalent smooth (111)A facets. They formed these V-grooves with anisotropic wet etching. Then, GaAs/InGaAs/GaAs heterojunctions were grown by MOVPE. The InGaAs QDs were formed at the bottom of inverted pyramid structures because higher In-module fractions segregated into the bottom, and this formed a deeper potential well to confine carriers. They observed single-photon emissions from QDs in V-grooves [82]. Furthermore, Kitamura et al. reported the formation of InGaAs QDs aligned on GaAs multiatomic steps [83] and Tatebayashi et al. formed area-controlled InAs QDs [84]. The combination of SAG and the S-K mode has enabled the formation of site-controlled QDs regardless of any damage and etching. Kusuha et al. reported the formation of InAs QDs on AlGaAs ridge QWR structures [85].

Figure 18.18 outlines the formation of InAs QDs on ridge wire structures. InAs QDs are only formed on the (001) top facet, and the QDs across the wires are limited by the surface area of the top (001) facet. In addition, Kim et al. reported the SAG of InGaAs QDs on vicinal substrates [86]. They formed single- or double-row aligned InGaAs QDs on GaAs structures grown by SAG using the step-bunching effect. InGaAs QDs were selectively grown on the step edge of a (001) top terrace that was affected by the dissimilar bunching effect of the GaAs layer due to the misoriented angle of the substrate.

Self-assembled QDs formed by the epitaxial S-K mode have attracted a great deal of attention in device applications as well as studies on the fundamental physics in low-dimensional systems. Most investigations have concentrated on optical devices such as LEDs [2], single-photon sources [87], and photodetectors [88]. The possibilities of designing electron memory devices using QD structures have recently been expected for low-power consumption. QD memories generally consist of a QD layer to store electrons and a channel in close proximity to sense their charged states. InAs QD memories fabricated by combining SAG and the S-K mode not only enable the channel width to be reduced due to the formation of facets, but also InAs QDs to be controlled on facet surfaces. Ooike et al. fabricated a QD memory structure grown by combining SAG and



**FIGURE 18.18** (A) Illustration of InAs quantum dots (QDs) grown on top facet of AlGaAs tetrahedral structure on GaAs(001) substrate. (B) Representative SEM image of InAs QDs on AlGaAs tetrahedral structure. Adapted from Ref. [85].



**FIGURE 18.19** (A) Illustration of a memory device structure of SAG-grown InAs quantum dots (QDs). (B) Schematic of grown structure and energy-band diagram. Dashed line plots Fermi level. Adapted from Ref. [89].

the S-K modes (as shown in Figure 18.19) [89]. They grew a GaAs/AlGaAs structure including 2DEG by facet growth (Figure 18.19(B)) after they formed the stripe-patted openings along the [110] direction on the SiO<sub>2</sub>-mask. Then, InAs QDs were formed on the top (001) facets with the S-K growth mode. They characterized memory operations and found that a strong confinement effect was required for memory operation at room temperature (RT).

Numbers and position-controlled QDs are required to achieve low-power operation and uniform electrical properties. Ooike et al. further advanced the combination of SAG and the S-K mode to form single QDs. They used specific opening patterns coupled with two direction wires for the [100] and [110] directions in Figure 18.20. A GaAs saddle structure is formed in this mask pattern by facet growth and a self-limited growth mode

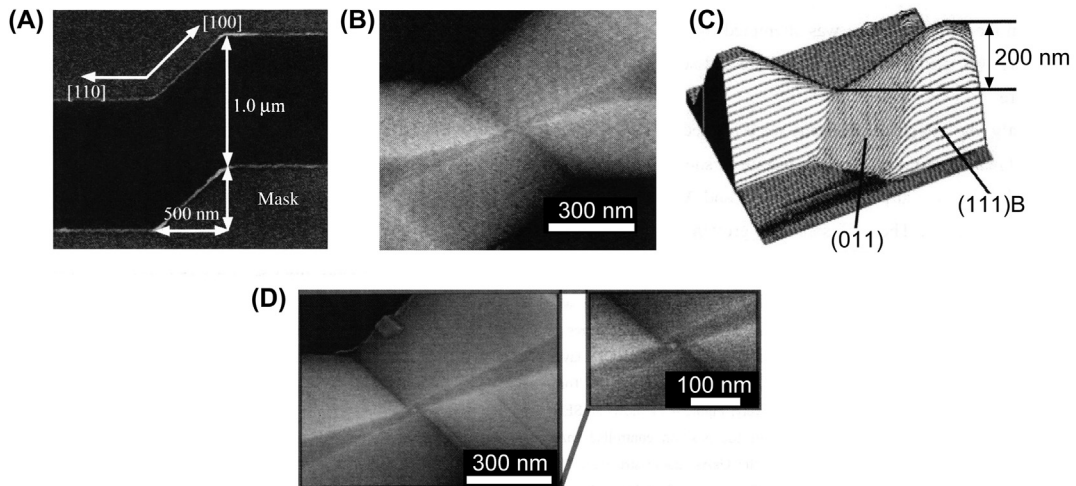


**FIGURE 18.20** (A) SEM image of mask pattern that indicates a mask openings correspond to dark part, which has structure coupled with two directional wires for [100 and 110]. (B) SEM image of GaAs saddle structure grown on mask opening. (C) Surface profile image obtained by AFM. (D) SEM image of position-controlled InAs quantum dots (QDs) on GaAs saddle structure. InAs QDs were formed self-assembled at bottom of saddle structure. Adapted from Ref. [90].

(see [Figure 18.20\(B\)](#) and [\(C\)](#)). The top (001) terrace is restricted to a small region. Then, S-K growth occurs to form a single QD. [Figure 18.20\(D\)](#) reveals how a single InAs QD is formed [\[90\]](#).

## 18.4 Formation of III-V Nanowires

Semiconductor nanowires (NWs) have attracted a great deal of attention for use in future nanometer-scale electronic and optical devices [\[91–96\]](#) because they have small diameters and large surface areas that enable high-density integration of active devices on various platforms and the fabrication of various kinds of functional devices through the use of heterostructures. The surface area to grow radial heterostructures enables core-shell (CS) or core multishell (CMS) NWs to be formed. Moreover, top surfaces with small diameters enable the formation of axial heterostructures regardless of lattice mismatches. The use of CS or axial NWs gives some functionality to NW-based applications.

The main approach to grow NWs is based on the vapor-liquid-solid (VLS) mechanism, which uses catalysts and the liquid phase underneath metal particles for crystallization. Wagner and Ellis reported the mechanism responsible for forming Si whiskers [\[18\]](#) in 1964. Small Au particles were placed on an Si substrate in the VLS growth of Si whiskers and they were heated above the eutectic temperature. Au formed small droplets that catalyzed the growth of Si whiskers through the liquid phase at the interface of droplets and Si grown material.

A typical procedure for VLS growth is illustrated in [Figure 18.21](#). Precursor atoms prefer to adsorb on the surface of droplets to form an alloy when a supply gas containing the growth materials flows over the grown substrate. Precursor atoms prominently incorporate into the liquid phase of the droplets and increase supersaturation of the grown precursors in the liquid phase. Consequently, crystal growth appears at the solid-liquid interface and NW-growth starts. Thus, this method can be used to control

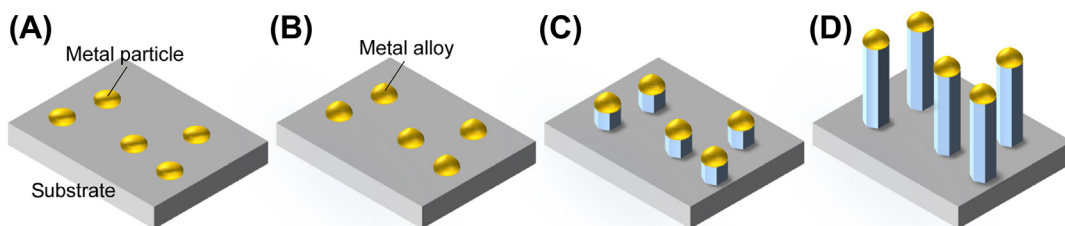


**FIGURE 18.21** Growth process flow of catalyst-assisted vapor-liquid-solid growth of nanowires (NWs). (A) Metal seed particles were formed and deposited onto substrate. (B) Sample was heated to required growth temperature and growth materials were introduced, which are allowed with the particles. (C) When appropriate, supersaturation of growth materials was achieved; nucleation occurred at the particle-crystal interface. (D) NW growth occurred at the particle-wire interface.

the NW diameter on a nanometer scale by changing the size of droplets. Droplets in most cases remain at the top of the NWs, which can be seen in [Figure 18.21\(D\)](#).

A key feature of the VLS growth mechanism is that equilibrium-phase binary diagrams can be used as guidelines to optimize catalyst and growth conditions, thereby rationalizing the synthesis of new NW materials. Therefore, optimum  $T_G$  for NW synthesis can be chosen according to binary phase diagrams between catalyst metals and target materials. For example, the pseudobinary phase diagram of Au-Si indicates that an Au-Si liquid and an Si solid are in the principle phase above 363 °C in the Si-rich region. This implies that Au can serve as a catalyst to grow Si NWs above this temperature due to the VLS mechanism. However, it is difficult to control the unintentional positions of Au droplets created by annealing Au thin films or depositing Au nano-particles. Position controlled epitaxial NWs have been studied using lithographically position-defined metal seed particles. Sato et al. reported site-controlled GaAs NWs by using an SiO<sub>2</sub> mask substrate [97]. Moreover, Ohlsson et al. synthesized size-selected III-V NWs grown on a crystalline substrate [98]. They used size-selected Au aerosol particles and controlled the whisker diameter with the size of Au particles. In addition, they demonstrated nanometer-scaled manipulation of Au aerosol atoms by atomic force microscopy (AFM) [99].

The VLS-grown III-V compound semiconductor nanowhiskers were investigated in the early 1990s [91]. The potential of NWs to be applied to future electronics and photonics was demonstrated in the early 2000s after this pioneering work [92–96]. Since then, VLS has become exceedingly common because it can be used to synthesize almost all semiconductor NWs, even oxides and metals, through rather simple procedures. Metal catalysts, however, often act as unintended impurities inside NWs [100] and form deep levels that could degrade the performance of NW-based devices. Au is the most frequently used catalyst metal for NW growth with the VLS mechanism. However, the incorporation of Au is known to result in deep-level defects near the mid-gap state of Si, which drastically degrade minority carrier lifetimes. In fact, high-angle annular dark-field (HAADF) scanning TEM images (STEM) of Si NWs have indeed provided evidence of Au particles being incorporated into Si NWs [101]. HAADF-STEM has revealed that there are more Au atoms than those expected from simple extrapolation of bulk solubility to low  $T_G$ . It should be noted that the incorporation of Au is not only a problematic issue for Si NWs, but also for the NWs of any materials, such as those for III-V compound semiconductors.

The self-catalyzed method has recently been investigated to grow NWs regardless of unintended impurities [102]. NWs can be grown with the so-called self-catalytic mechanism without Au or other metals, where the grown material itself acts as a catalyst. Morral et al. reported the formation of GaAs NWs by Ga-self catalyzed VLS and formed GaAs/AlGaAs CS NWs [103]. Heiss et al. demonstrated the formation of GaAs/InGaAs axial heterostructure NWs grown by Ga-droplet VLS [104]. Furthermore, they changed the V/III ratio for Ga self-catalyzed VLS growth to form pn-junctions [105]. In addition, one constituent of the wire material formed the catalytic droplets, enabling VLS growth

on top of NWs. Mandl et al. systematically investigated the formation of Au-free epitaxial growth of III-V NWs [106,107]. Kim et al. demonstrated catalyst-free Si and Ge NWs for group-IV NWs [108]. These methods were based on the VLS mechanism but were not concerned with contamination due to the catalyst materials.

### 18.4.1 Selective-Area Growth of III-V Nanowires

Another approach to grow NWs is catalyst-free SAG. Selective-area metal-organic vapor phase epitaxy (SA-MOVPE) is a kind of template method, which involves a combination of bottom-up (epitaxial growth) and top-down (lithography) approaches. This approach uses partially masked templates with lithographically defined opening patterns. Position-controlled polygonal nanostructures surrounded by several facets can be formed inside the openings, because crystal continues to grow through the mechanism of faceting growth. Because the direction of preferential growth for III-V NWs is  $\langle 111 \rangle_A$  or  $\langle 111 \rangle_B$ , the use of III-V (111)A or B substrates enables vertically aligned hexagonal pillars to be formed surrounded by  $\{-110\}$  vertical sidewalls. These position-controlled NWs have been achieved in III-V compound semiconductors, such as GaAs [109–112], InP [113,114], InAs [115,116], InGaAs [117–120], and GaAsP [121], as well as nitrides [122] and oxides [123]. Position-controlled AlGaAs/GaAs [124], InAs/InP [124], and GaAsP/GaAs [125] CS NWs, and InP/InAs/InP CMS [126] NWs have been reported by using SA-MOVPE. The position-controlled growth of InGaAs/GaAs [127,128], InAsP/InP [129], and AlGaAs/GaAs axial [130] heterostructured NWs has also been investigated.

The actual growth procedure to form NWs with SAG is outlined in Figure 18.22. After the substrate is degreased, SiO<sub>2</sub> films with a thickness of 10–30 nm are formed by radiofrequency (RF) sputtering, plasma-enhanced chemical vapor deposition (PECVD), or thermal oxidation (Figure 18.22(A)). Thermal oxidation is usually used to form SiO<sub>2</sub> where III-V NWs are grown on Si because of the thermal tolerance of the film. Next, circular openings with a regular pitch are formed on the amorphous films by using electron-beam (EB) lithography and wet chemical etching. The circular openings are arranged in a triangular lattice with a pitch of 0.4–3.0  $\mu\text{m}$ . The opening diameter,  $d_0$ , ranges from 20 to 400 nm. The  $d_0$  is around 70–300 nm when NWs are used in optical

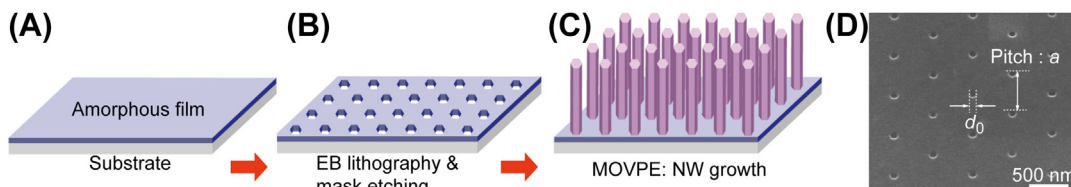


**FIGURE 18.22** (A) Fabrication process to grow nanowires (NWs) with selective-area growth. After amorphous film was deposited, hole openings were formed by lithography and etching. NWs were grown with MOVPE. (B) SEM image of the patterned substrate. EB, electron beam.

applications. Reactive-ion etching (RIE) is occasionally used. There is a scanning electron microscopy (SEM) image of the masked substrate in [Figure 18.22\(D\)](#). Finally, NWs were grown by MOVPE. The (111)B or (111)A-oriented surfaces were used to grow NWs with SA-MOVPE because III-V NWs preferentially grew in  $\langle 111 \rangle$ A or  $\langle 111 \rangle$ B directions. The (111)A surface had its topmost layer arranged by group-III atoms, and the (111)B surface had topmost layer arranged by group-V atoms.

Therefore, hexagonal III-V NWs surrounded by  $\{1-10\}$  vertical facets could be formed on the (111)B-oriented surface because these tendencies in the SAG of GaAs have commonly been in other III-V compound semiconductors, except for InP. It should be noted that vertical InP NWs have been formed on (111)A-oriented surfaces in SAG [\[113\]](#). This is because the direction of preferential growth for InP NWs is in the  $\langle 111 \rangle$ A direction and phosphorous trimers can be formed on the InP (111)A surface [\[131\]](#). The growth rate of GaAs (111)A and (110) surfaces, on the other hand, increases more than that on (111)B planes under low  $T_G$  and high  $[\text{AsH}_3]$ . This is because the As-trimers formed on the (111)B surface suppress nucleation on the GaAs (111)B surface [\[65\]](#). Controlling the growth conditions enables the CS NWs to be formed.

The formation of facets was further confirmed by their dependence on growth conditions. The  $\langle 111 \rangle$ B-growth for GaAs was considerably suppressed under low  $T_G$  with high  $[\text{AsH}_3]$ . As-trimers were formed due to high  $\theta_{\text{As}}$  on the (111)B under these conditions and these trimers suppressed adsorption and nucleation processes. The rapid reduction in the  $\langle 111 \rangle$  growth rate was mentioned in [Section 18.2.2](#). Similar suppression of the growth rate of the (111)B surface was observed on grown structures on (001)- and (311)B-oriented mask substrates, in which the area of (111)B facets was enlarged (see [Figure 18.23\(B\)](#)). Moreover, the growth rate of (111)A facets increased and the (111)A surface eventually disappeared on the grown structure in [Figure 18.23](#). The growth rate along the  $\langle 110 \rangle$  direction on the (110)-oriented substrate was enhanced under low  $T_G$  with high  $[\text{AsH}_3]$ . These enhancement in growth on the (111)A and  $\{110\}$  surfaces can be explained by the increments of adsorbed Ga sites at high  $\theta_{\text{As}}$ .

We can see typical results for III-V NWs grown with SAG in [Figure 18.24](#). [Figure 18.24\(A\)](#) has GaAs NWs grown on a GaAs(111)B substrate. The NWs are 70 nm in diameter and 3  $\mu\text{m}$  high. [Figure 18.24\(B\)](#) shows InAs NWs grown on an InP(111)B substrate with a diameter of 20 nm and a height of 400 nm. [Figures 18.24\(C\) and \(D\)](#) have InP NWs grown on InP(111)A under different growth conditions [\[113,114\]](#). The diameters of NWs in [Figure 18.24](#) were equal to the diameters of openings. The edges of the openings in [Figure 18.24\(B\)](#) were tapered due to isotropic etching by the HF solution. The diameters of the InAs NWs in [Figure 18.24\(B\)](#) corresponded to those of the bottom windows of the openings. Position-controlled III-V NWs were successfully grown on III-V(111)B or (111)A substrates. Nanometer-scale growth with SAG has enabled III-V NWs to be formed on lattice-mismatched substrates regardless of lattice mismatching [\[132–136\]](#). The optimum conditions to form III-V NWs by SAG will not change in these heteroepitaxial systems. We will next briefly summarize the optimum conditions and typical behaviors to grow these III-V NWs with SAG.

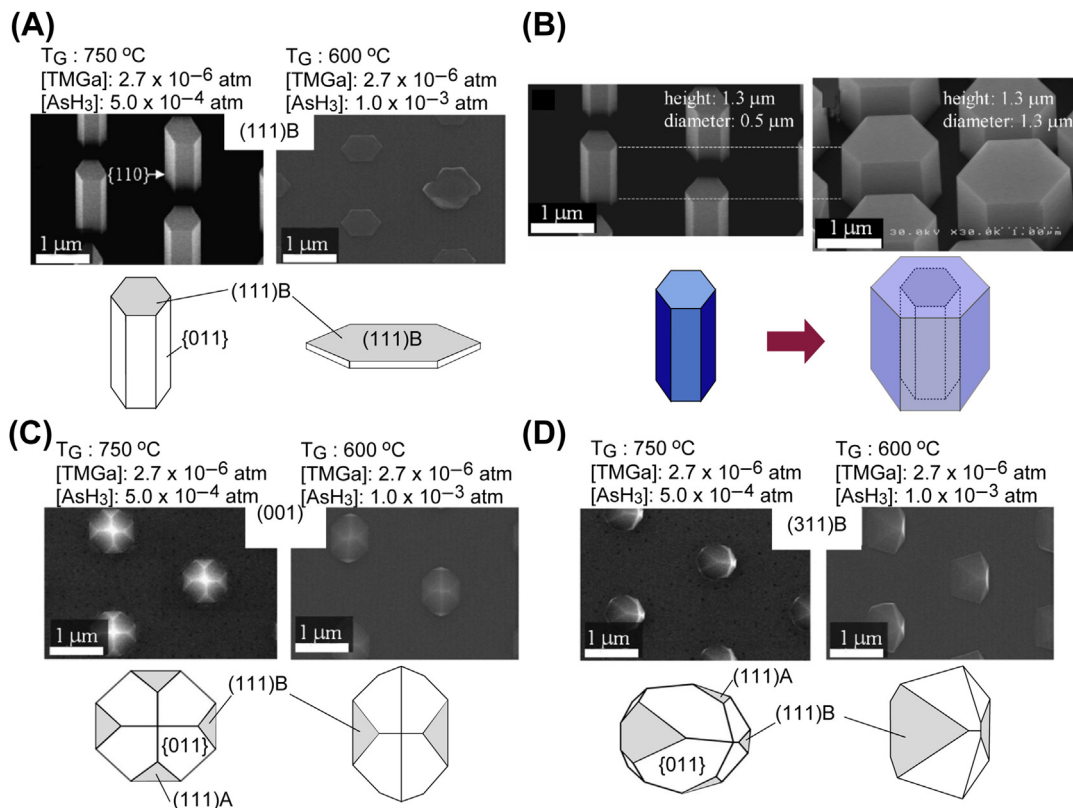


**FIGURE 18.23** SEM image of GaAs growth. (A) (111)B, (C) (001), and (D) (311)B substrates. Images summarize structures grown under high  $T_G$  and low  $[\text{AsH}_3]$  conditions (figure at left) and those grown at low  $T_G$  and high  $[\text{AsH}_3]$  (figure at right). (B) SEM image of selectively grown GaAs on (111)B with one step (left) and two-step (right) conditions. Adapted from Ref. [111].

#### 18.4.1.1 GaAs Nanowires

The optimum  $T_G$  window ranges from 700 to 750 °C [109–112]. The metal-organic (MO) sources were TMGa and  $\text{AsH}_3$ . Tertiarybutyl arsine (TBA) is sometimes used to grow NWs [137]. The GaAs NWs were formed under a V/III ratio of 100–250. The optimum  $T_G$  window for GaAs NWs was the boundary between the formation of As-trimers and the desorption of adatoms on the (111)B surface. The As-trimer forming on the (111)B surface became dominant below the optimum  $T_G$ , and their formation suppressed GaAs growth on the (111)B surface. Here, LOG along the  $\langle 1-10 \rangle$  direction was dominant because the growth rate of {1-10} sidewalls was faster than that of the (111)B surface. However, the desorption of adatoms was enhanced above the optimum  $T_G$  because desorption-limited growth occurred in these temperature ranges. LOG was almost suppressed above the optimum  $T_G$ , where the growth rate of GaAs NWs decreased because of desorption. Moreover, the growth rate of {1-10} sidewalls was suppressed due

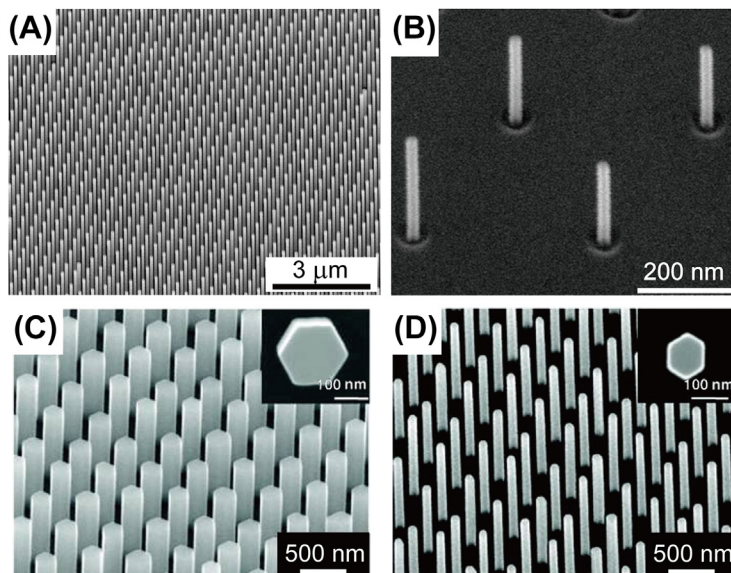


**FIGURE 18.24** Typical results for III-V nanowires (NWs) grown by SA-MOVPE. (A) GaAs NWs with diameter of 70 nm and height of 3  $\mu\text{m}$ . Substrate is GaAs(111)B. (B) InAs NWs with diameter of 20 nm and height of 400 nm. Substrate is InP(111)B. (C) InP NWs grown at 600  $^{\circ}\text{C}$  and V/III ratio of 55. (D) InP NWs grown at 660  $^{\circ}\text{C}$  and V/III ratio of 18.

to desorption of group V-atoms. The use of optimum growth conditions for GaAs enabled growth of the highly uniform NW arrays shown in [Figure 18.24\(A\)](#). GaAs NWs can also be grown on Si(111) substrates [133].

The height of GaAs NWs was inversely proportional to the opening diameter of the mask [112]. This suggests that the migration of growth species on the NW sidewalls played a major role in the SAG of GaAs NWs.

#### 18.4.1.2 InAs Nanowires

[Figure 18.24\(B\)](#) shows InAs NWs grown on an InP(111)B substrate (lattice mismatch is 3.3%). Very thin InAs NWs with a diameter of 20 nm were grown on an InP(111)B substrate that was patterned with lithography. The optimum  $T_G$  window ranged from 540 to 580  $^{\circ}\text{C}$  [115]. This optimum  $T_G$  window is typical for  $\text{H}_2$  carrier gas. The  $T_G$  window changes from 650 to 700  $^{\circ}\text{C}$  for nitrogen carrier gas [116]. The MO sources were TMIIn and  $\text{AsH}_3$ . The InAs NWs were formed under a V/III ratio of 250 with SAG. LOG was enhanced below the optimum  $T_G$ , and the growth rate for InAs NWs was reduced above the optimum  $T_G$  [115]. The mechanism for these behaviors was the same as that for the GaAs NWs with SAG. The height of the InAs NWs was inversely proportional to the square of the opening diameter of the mask [115]. This means that the surface diffusion of growth species on the  $\text{SiO}_2$  and NW sidewalls played a major role in NW growth. We confirmed that InAs NWs could be grown on (111)B-oriented and Si(111) substrates [115,132].

#### 18.4.1.3 *InP Nanowires*

The optimum  $T_G$  window ranged from 600 to 660 °C [124]. The MO sources were TMIIn and tertiarybutyl phosphine (TBP). The InP NWs were formed under a V/III ratio of 15–60 with SAG. The direction of preferential growth was  $\langle 111 \rangle_A$ . Thus, vertical InP could be formed on the (111)A substrate. LOG was enhanced below the optimum  $T_G$  and high [TBP]. The most distinct features of InP NWs are their different morphologies and crystal structures. The morphology of InP NWs achieved a straight and cylindrical structure at low  $T_G$  and a high V/III ratio, as seen in Figure 18.24(C), and a tapered structure was formed at high  $T_G$  and a low V/III ratio, as seen in Figure 18.24(D). We found that these differently shaped InP NWs had dissimilar crystal structures. The tapered InP NWs exhibited wurtzite structure with few stacking faults, and the straight InP NWs exhibited a twin-included zincblende structure [125].

#### 18.4.1.4 *InGaAs Nanowires*

The optimum  $T_G$  to form InGaAs NWs on InP(111)B ranged from 630 to 670 °C [117–120], and the  $T_G$  to form InGaAs NWs on GaAs(111)B ranged from 650 to 700 °C [120]. Moreover, the In/Ga composition varied with the NW pitch due to the migration of growth species on SiO<sub>2</sub> and NW sidewalls. For instance, the Ga composition of InGaAs NWs changed from 62% to 80% with decreasing pitch from 6 to 0.6 μm [119]. The MO sources were TMIIn, TMGa, and AsH<sub>3</sub>. The height of InGaAs NWs was inversely proportional to the square of the opening diameter of the mask [119]. This was because the surface migration of In atoms was dominant during InGaAs NW growth.

#### 18.4.1.5 *GaP Nanowires*

The pyramidal structures surrounded by {111}B surfaces for GaP were formed on GaP(111)A. Hexagonal GaP NWs, on the other hand, were formed on the GaP(111)B surface. The direction of preferential growth was in the  $\langle 111 \rangle_B$  direction. The optimum  $T_G$  window ranged from 770 to 790 °C. The MO sources were TMGa and TBP. The GaP NWs were formed with a V/III ratio of 200–250 with SAG.

#### 18.4.1.6 *InGaP Nanowires*

The SAG of InGaP NWs was reported by Ishizaka et al. [138]. They investigated the SAG of In-rich InGaP NWs on an InP(111)A substrate. The  $T_G$  was fixed at 650 °C. There was an issue regarding the preferential growth direction for ternary InGaP NWs with variations in the In composition. The preferential growth direction for In-rich InGaP was  $\langle 111 \rangle_A$ , which was similar to that of InP NWs fabricated by SAG. However, the preferential growth direction changed to  $\langle 111 \rangle_B$  for Ga-rich InGaP NWs, which was similar to that of GaP NWs fabricated by SAG. Furthermore, the optimum  $T_G$  for ternary InGaP NWs would depend on the In/Ga composition of the ternary. In fact, the LOG of InGaP NWs with a Ga-supply of 10% was enhanced more than that of InGaP NWs with a Ga-supply of 5%. This indicates that the increment of Ga composition of InGaP NWs changed the optimum  $T_G$  for NW growth regardless of LOG.

**Table 18.1** Stacking Fault Energy of Si, GaAs, InAs, and InP

Materials	Optimum $T_G$ for nanowires ( $^{\circ}\text{C}$ )	Melting point $T_C$ ( $^{\circ}\text{C}$ )	TG/(TG + TC)
GaAs	700–750	1238	0.36–0.37
InAs	540–580	943	0.36–0.38
InP	600–660	1070	0.36–0.38
InGaAs	630–670	–	–
GaP	770–790	1467	0.34–0.35
InGaP	650	–	–

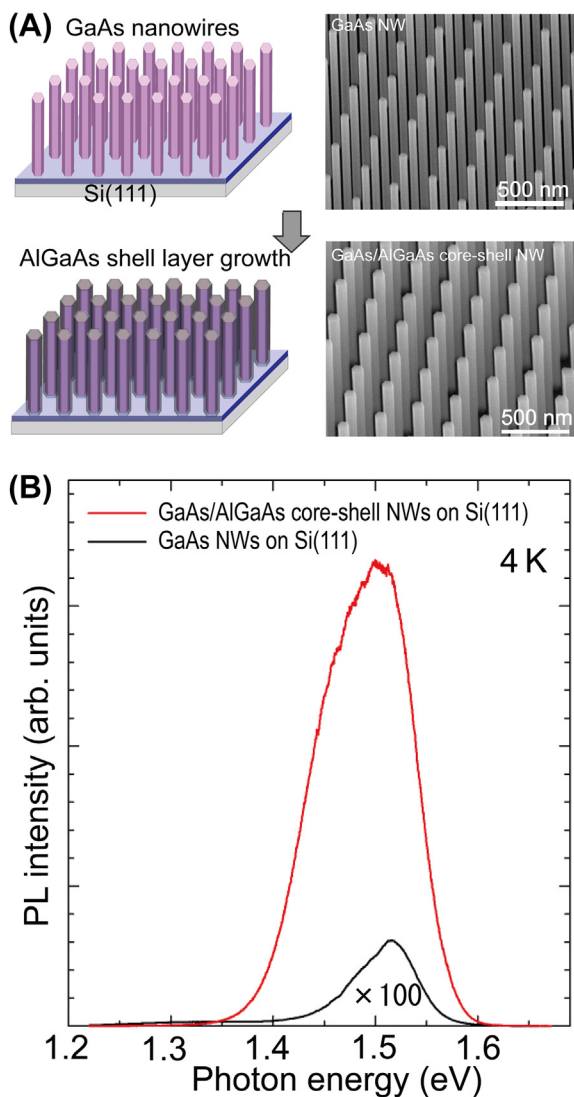
Table 18.1 summarizes the optimum  $T_G$  of III-V NWs obtained through SAG and the melting point ( $T_C$ ). Interestingly, the optimum  $T_G/(T_G + T_C)$  for SAG growth of III-V NWs, regardless of the coincidence of LOG, was around 0.34–0.38 of the melting point. Although this tendency is a trivial coincidence, it could be a guideline for the SAG growth of NWs with unknown materials, such as other IV, III-V, and II-VI materials.

The most distinctive feature of SAG for NWs growth is the isolation of LOG and NW growth modes by  $T_G$  or the V/III ratio. For example, low  $T_G$  enhanced the LOG of GaAs without any NW growth after GaAs NWs were grown under optimum  $T_G$  [111]. The diameter of GaAs NWs increased more than that of the mask opening without NW growth. This is because the growth rate of the  $\{-110\}$  sidewall increased due to the suppressed desorption process on these same  $\{-110\}$  sidewalls. Ikejiri et al. systematically investigated the controllability of LOG of GaAs by using  $T_G$  [111]. They grew GaAs NWs at high  $T_G$  with low  $[\text{AsH}_3]$  and then grew GaAs at low  $T_G$  with high  $[\text{AsH}_3]$ .

Figure 18.23(B) shows micrographs and a schematic of the growth results. The GaAs NWs were 1.3  $\mu\text{m}$  high and 500 nm in diameter after the first GaAs growth. The diameter of the GaAs NWs increased to 1.3  $\mu\text{m}$  while the NW height remained constant. This further confirmed that GaAs only grew on (111)B-oriented facets at high  $T_G$  with low  $[\text{AsH}_3]$ , and only on  $\{-110\}$ -oriented facets at low  $T_G$  and high  $[\text{AsH}_3]$ . The importance of the formation of facets during SAG is illustrated in Figure 18.24. This tendency was similarly observed in other materials. Phosphorous (P) coverage ( $\theta_P$ ) governed by  $T_G$  and [TBP] was found to similarly strongly influence the direction of InP growth [113] for InP NWs. Although relatively lower  $\theta_P$  induced axial growth, higher  $\theta_P$  was altered, and competing growth of the top (111)A surface and the (110) sidewall facets occurred, making it possible to accurately define the growth direction by precisely optimizing growth conditions.

The use of this property to grow heterostructures enabled us to form CS or CMS NWs, such as GaAs/AlGaAs CS NWs [139]. Figure 18.25(A) has schematics and micrographs of GaAs/AlGaAs CS NWs grown on an Si substrate [133]. LOG of the AlGaAs shell layers only occurred on the sidewalls of the GaAs NWs because the height of the NWs was the same before and after the AlGaAs shell layer were grown. The number of surface states of NWs could be increased more than that with planar III-V because the NWs had large surface areas on the NW sidewalls. These surface states degraded the

**FIGURE 18.25** (A) Illustration of growth of GaAs/AlGaAs core-shell (CS) nanowires (NWs) and SEM images of GaAs NWs and GaAs/AlGaAs CS NWs on Si substrates. (B) photoluminescence (PL) spectra of GaAs NWs and GaAs/AlGaAs CS NWs at 4.2 K. Adapted from Ref. [133].



optical properties of III-V NWs and device performance through a nonradiative recombination process. The CS structures effectively passivated these surface states of NWs. The shell layers were also more stable in the atmosphere compared to sulfur passivation [138]. GaAs/AlGaAs CS NWs improved photoluminescence (PL) intensity up to 490-fold due to the reduction in surface states plotted in Figure 18.25(B) [133]. The ability to control the growth mode is promising for the formation of NWs with complex structures, such as heterostructures and pn-junctions. Except for simple GaAs/AlGaAs CS or CMS NWs, InAs/InP/InAs CMS heterostructures [124], GaAs/GaAsP radial/axial

heterostructures [125], InP CS with radial pn-junctions [140], and GaAs/AlGaAs CMS with radial pn-junctions [141] have been fabricated by controlling the growth direction during SAG. These growth techniques have further been used to demonstrate NW-LEDs using GaAs/AlGaAs CS [141], GaAs/InGaAs CMS NWs [142], NW-solar cells using GaAs CS [105,143], GaAs/GaAsP (or InGaP) CMS NW [144,145], InP/AlInP CS NW [146], NW-FETs using InAs/InAlAs CMS [147], InGaAs/InAlAs CS [136,148], and InGaAs/InP/InAlAs/InGaAs CMS NWs [136].

### 18.4.2 Twinning Growth Model

The unit cell of diamond or zincblende (ZB) crystal structures is the same and is cubic with a side length of  $a_0$ , called the lattice parameter. The diamond unit cell can be described as a one face-centered cubic (fcc) unit cell interlaced with another translated by  $a_0/4$  along all three axes. The two fcc sublattices contain different species of atoms in the ZB structure. One sublattice of III-V consists of group-III atoms and the other of group-V atoms. Figure 18.26 outlines the atomic arrangement of the ZB structure in the  $\langle 1-10 \rangle$ -viewing direction. The cubic ZB structure in the  $[111]$  direction consists of three distinct atomic bilayers stacked [...ABCABCABC...]. The atomic stack in the  $\langle 111 \rangle$  direction of the ZB structure creates specific defects, such as rotational twins. The crystal structure of GaAs NWs, whose growth direction is  $\langle 111 \rangle_B$ , is basically that of cubic ZB, which contains rotational twins around the  $\langle 111 \rangle$  growth axis (Figure 18.26). The stacking sequence for the ZB structure in the  $\langle 111 \rangle$  direction is expressed as ...ABCACBA... Thus, the ZB structure in the  $[111]$  direction consists of three distinct atoms in bilayer stacking. However, the stacking sequence for the rotational twins is ...ABC/A/CBA..., where the slash denotes the twin boundary (dashed square in Figure 18.26). The structure model of the rotational twin is illustrated in Figure 18.26. As the sequence of group-III and -V layers at the rotational twin boundary is not changed, the  $(111)_B$  surface is maintained after twinning, while the crystal axis along the  $\langle 111 \rangle_B$  direction is rotated by  $60^\circ$ .

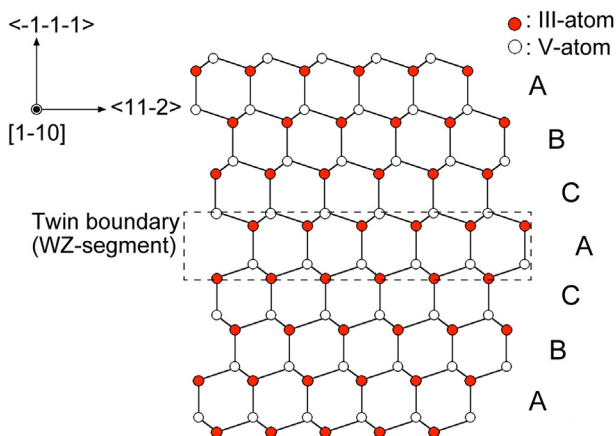


**FIGURE 18.26** Atomistic model of zincblende structure with rotational twin viewing from  $[1-10]$  and twin boundary.

Nucleation of twin planes, such as the B plane on top of ABC in ZB resulting in ABCB, occurs under typical NW growth conditions. The extra interface energy associated with this is the twin energy, which has been approximated by half the stacking fault energy in Table 18.2 [149]. Ikejiri et al. discussed a comparison of changes in the Gibbs free energy of nucleation related to critical size in the early stages of NW growth [112]. The Gibbs free energy of nucleation was calculated for tetrahedral and hexagonal structures as a function of the base length of the tetrahedron shown in Figure 18.28. The diffusion/surface migration of the growth species and gas were neglected in nucleation growth. For simplicity, they assumed that the base length of the tetrahedron was equal to the diameter of the hexagon (NW diameter) and that both shapes grew to an equal volume.

The Gibbs free energy change is expressed as

$$G = (\text{surface energy change}) - (\text{chemical potential change}). \quad (18.5)$$

The chemical potential change per mole of nucleation is calculated as

$$\Delta\mu = (RT) \left\{ P_{\text{III}} \log_e \left( P_{\text{III}}/P_{0\text{III}} \right) + P_{\text{V}} \frac{\log_e(P_{\text{V}}/P_{0\text{V}})}{P_{\text{III}} + P_{\text{V}}} \right\}, \quad (18.6)$$

where  $R$  is the gas constant,  $T$  is the absolute temperature,  $P_{\text{III}}$  and  $P_{\text{V}}$  are the partial pressures of III and V sources, and  $P_{0\text{III}}$  and  $P_{0\text{V}}$  are the equilibrium vapor pressures of III and V atoms on the solid III-V surface at temperature  $T$ . The  $[\text{AsH}_3]$  for GaAs growth in forming NWs with SAG was two orders of magnitude higher than that of  $[\text{TMGa}]$  under the experimental conditions. Therefore, this approximated Eqn (18.7) as

$$\Delta\mu \approx (RT) \log_e \left( P_{\text{As}}/P_{0\text{As}} \right), \quad (18.7)$$

where  $\Delta\mu$  is calculated by using two source gas pressures of  $5.03 \times 10^{-4}$  and  $5.03 \times 10^{-7}$  atm. The different pressures correspond to the assumption that TMGa is 100% effective and AsH<sub>3</sub> is 0.1% effective at nucleation. The surface energy was calculated for the entire surface of the tetrahedron or hexagon except for the bottom face.

**Table 18.2** Optimum Growth Temperature  $T_G$ , and Melting Points of GaAs, InAs, InP, InGaAs, GaP, and InGaP

		Substrate/Lattice Constant at 300 °K (Å)							
		Si	Ge	AlP	AlAs	GaP	GaAs	InP	InAs
Lattice Mismatch		5.43	5.66	5.46	5.66	5.45	5.65	5.87	6.06
Epitaxial layer	Si	–	4.0%	0.6%	4.1%	0.4%	3.9%	7.5%	10.4%
	Ge	4.2%	–	3.6%	0.0%	3.8%	0.1%	3.6%	6.6%
	AlP	0.6%	3.4%	–	3.5%	0.2%	3.4%	6.9%	9.8%
	AlAs	4.2%	0.0%	3.6%	–	3.8%	0.1%	3.5%	6.6%
	GaP	0.4%	3.7%	0.2%	3.7%	–	3.6%	7.1%	10.0%
	GaAs	4.1%	0.1%	3.5%	0.1%	3.7%	–	3.7%	6.7%
	InP	8.1%	3.7%	7.4%	3.7%	7.7%	3.8%	–	3.1%
	InAs	11.6%	7.1%	10.9%	7.0%	11.1%	7.2%	3.2%	–

There were (-1-10), (0-1-1), and (-10-1) facets for tetrahedral GaAs structures that have a three-fold symmetry around the  $\langle 111 \rangle$  axis in Figure 18.27. All three facets were  $35.3^\circ$  off the (111)B substrate surface. They were also equivalent to the (1-10) side facet of hexagonal GaAs. The surface energy was related to the density of dangling bonds on the crystal surface, and the surface energy of the (1-10) facet was about 23% higher than that of (111) [150]. The total surface energies for tetrahedrons and hexagons were obtained by using the surface energy density of  $0.482 \text{ J/m}^2$  for the (1-10) [151]. The Gibbs free energy change ( $\Delta G$ ) for tetrahedral growth in Figure 18.27 indicates that  $\Delta G$  reached maximum at the critical size of  $a = 3.6 \text{ nm}$  as an increase from zero, but it rapidly decreased after maximum for the source gas pressure of  $5.03 \times 10^{-7} \text{ atm}$ . The maximum energy was reduced and shifted to the smaller critical size of  $a = 1.0 \text{ nm}$  as the source gas pressure was increased by three orders of magnitude.  $\Delta G$  for hexagonal NW growth reached maximum at  $a = 5.7 \text{ nm}$  as an increase from zero, but it decreased after the peak for the source gas pressure of  $5.03 \times 10^{-7} \text{ atm}$ . Maximum energy was reduced and the critical condition occurred at  $a = 1.5 \text{ nm}$  for the source gas pressure of  $5.03 \times 10^{-4} \text{ atm}$ . The critical size for hexagons was 50–60% greater than that for tetrahedrons at the same source gas pressure. Note that the maximum energy for tetrahedrons was 1/3 to 1/4 that for hexagons under the same conditions. This means that the nucleation of tetrahedral shapes was energetically favorable.

Figure 18.28 shows the initial growth of GaAs with a mask opening diameter of  $100 \text{ nm}$  under NW growth condition. The grown crystal had facets with threefold symmetry of (-1-10), (0-1-1), and (-10-1) facets, as shown in the upper left of Figure 18.28 [152]. There were two kinds of tetrahedral structures, in which one of the three corners was pointed

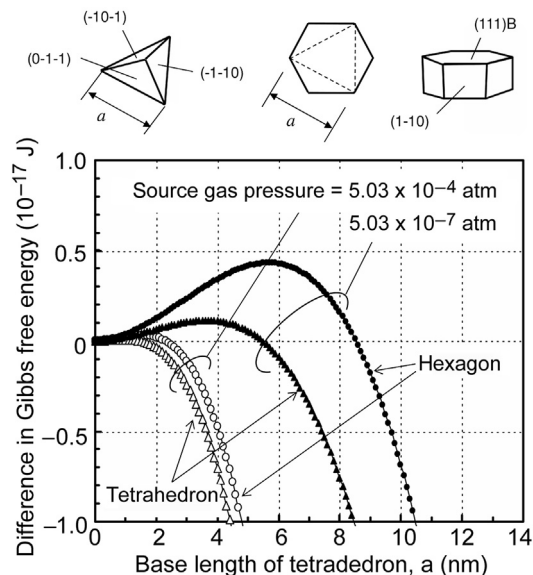
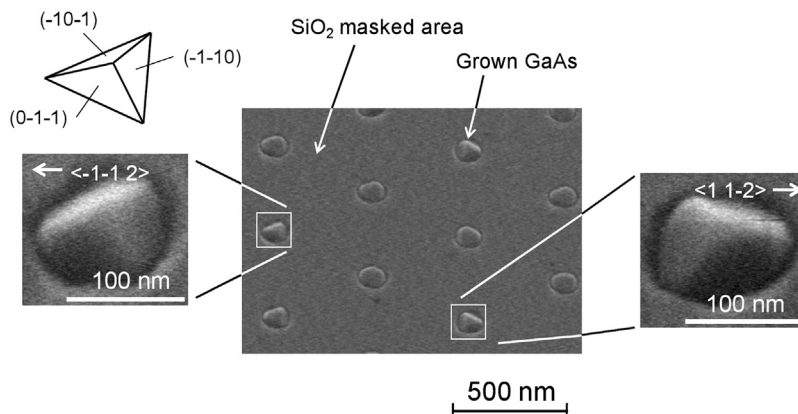


FIGURE 18.27 Difference in change on Gibbs free energy calculated as a function of tetrahedron base length (hexagon diameter). Adapted from Ref. [112].



**FIGURE 18.28** SEM images of GaAs substrate surface after MOVPE for growth time of 1 min at 750 °C. Mask window diameter is 100 nm and pitch is 500 nm. Schematic of tetrahedron at the upper left above depicts threefold symmetry facets (-1-10), (-1-10), and (0-1-1), which correspond to grown crystal in enlarged SEM image below. Adapted from Ref. [112].

toward the  $\langle -1-12 \rangle$  or  $\langle 11-2 \rangle$  directions. It is uncertain which of the two directions the corner was likely to take because of the threefold symmetry of the (111)B surface of the substrates. Tetrahedral structure, which had threefold symmetry having three inclined (-1-10) facets with respect to the (111)B surface, were obtained with decreasing  $[\text{AsH}_3]$  or increasing  $T_G$ . This is consistent with the report by Ando et al. [73]. Hexagonal NWs, on the other hand, which have sixfold symmetry and are surrounded by six (-110)-equivalent vertical facets with respect to the (111)B substrate, were grown within a small mask opening at lower  $T_G$  and higher  $[\text{AsH}_3]$ . Therefore, whether GaAs grew as tetrahedral or hexagonal shapes depended on the three parameters of  $T_G$ ,  $[\text{AsH}_3]$ , and opening size.

There may be another explanation for the difference in the morphologies (tetrahedral or hexagonal shapes) due to difference in surface reconstructions. Surface reconstruction in GaAs(111)B has been studied both during MBE and MOVPE and is known to depend on  $\theta_{\text{As}}$ —that is, on  $T_G$  and  $[\text{AsH}_3]$ . A  $2 \times 2$  structure whose unit cell consists of As-trimers appears at low  $T_G$  or higher  $[\text{AsH}_3]$ . However, a  $\sqrt{19} \times \sqrt{19}$  reconstruction, which consists of an array of As-capped hexagonal rings, appears at low  $[\text{AsH}_3]$  or high  $T_G$  under vacuum conditions [153–156]. Nishida et al. revealed the behavior of surface reconstruction on the GaAs (111)B surface during MOVPE determined from surface photoabsorption measurements [66]. A phase transition from  $2 \times 2$  to  $\sqrt{19} \times \sqrt{19}$  takes place in this phase diagram, where the  $[\text{AsH}_3]$  is decreased or  $T_G$  is increased. The solid lines A, B, and C denote the borders of the previously mentioned GaAs (111)B surface reconstructions as functions of  $1/T_G$  and  $[\text{AsH}_3]$ . Ando et al. also reported that GaAs grew into tetrahedral or hexagonal shapes depending on  $[\text{AsH}_3]$  and  $T_G$  by using MOVPE [73]. According to these reports, similar dependencies in the same graph as functions of  $[\text{AsH}_3]$  and  $1/T_G$  can be plotted in Figure 18.29. The border between hexagonal and tetrahedral structures is indicated by dashed line D in Figure 18.29. Interestingly, the slopes of lines A–D are almost the same,

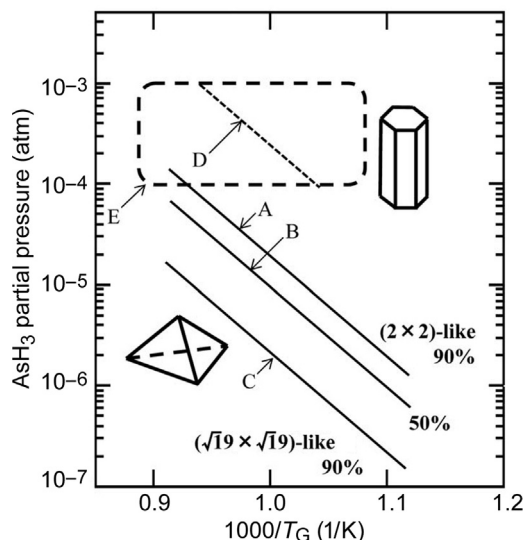


**FIGURE 18.29** Phase diagram where hexagons or a tetrahedrons exist as functions of  $[\text{AsH}_3]$  and  $1/T_G$ . Solid lines on the map denote boundary lines of GaAs surface reconstruction as functions of  $[\text{AsH}_3]$  and  $1/T_G$  reported by Nishida et al. (Adapted from [66].) Solid line A denotes condition where  $(2 \times 2)$ -like surface reconstruction occurs with 90% probability. Solid bold line B indicates border of  $(2 \times 2)$  and  $\sqrt{19} \times \sqrt{19}$  structures. Solid line C indicates condition where  $\sqrt{19} \times \sqrt{19}$  like surface reconstruction occurs with 90% probability. Broken line D indicates another border where tetrahedral and hexagons occur with equal probability under selective-area growth (SAG) conditions. Dashed line enclosed by E denotes region for SAG experimental conditions. Adapted from Ref. [152].

even though the experiments were carried out using different growth methods. The optimum growth conditions for GaAs NWs by SAG are within dashed rectangle E in Figure 18.29. Chen et al. reported that there were GaAs tetrahedral structures and twins existing in the transition region between the  $2 \times 2$  and  $\sqrt{19} \times \sqrt{19}$  reconstructed surface during MBE. When they increased  $T_G$ , the twins completely disappeared while tetrahedral structures remained. They also found that higher substrate temperature and a low  $[\text{AsH}_3]$  produced a tendency to decrease twin density with various growth methods [112].

Ikejiri et al. proposed a model for the evolution of crystal shapes of III-V NWs with SAG that was called the “twinning growth model” [112]. Selectively grown GaAs initially takes a truncated tetrahedral shape, forming inclined (110) facets with respect to (111)<sub>B</sub> at an initial stage in this model. It then develops into a hexagonal shape with (110) vertical facets through several atomic layers being stacked up on one another along the  $\langle 111 \rangle_B$  direction, with rotational twins sandwiched in between. This model implies a strong relationship between the twins and formation of GaAs NW growth. A hypothetical growth model of how the GaAs shape changes from triangular to hexagonal in the early stages of growth is shown in Figure 18.30. The SEM images above or next to the illustrations correspond to the crystal shapes for the respective stages. The crystal at growth stage (A) has an inverse mesa shape. Inverse mesas have a high growth rate in the lateral threefold symmetrical directions of  $\langle 11\bar{2} \rangle$ ,  $\langle 1\bar{2}1 \rangle$ , and  $\langle \bar{2}11 \rangle$ . Triangular crystal grows into a

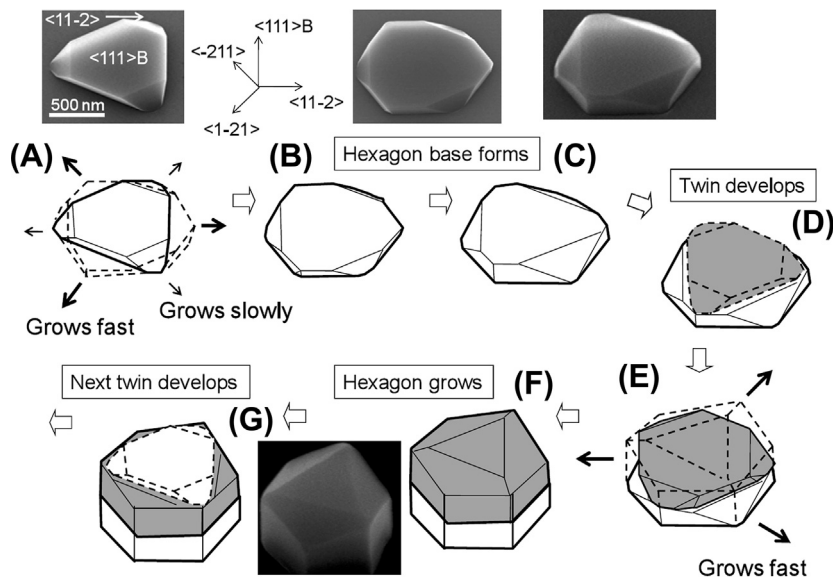


**FIGURE 18.30** Estimated evolution of GaAs hexagons featuring lateral growth and twin development from triangular crystal. Illustrations (A)–(G) partly connected with SEM images depicting how crystal shape changed during growth. Crystal twins have been shaped and whitened for clarity.

hexagonal base in (C) and then grows thicker to reach stage (D). A twin plane develops on the triangular (111)B top surface at stage (E). Three inverse mesa facets are formed in this way and fast lateral growth is again promoted toward the threefold symmetry directions of  $\langle -1-12 \rangle$ ,  $\langle -12-1 \rangle$ , and  $\langle 2-1-1 \rangle$ , as schematically indicated in (B) to (F). When stage (G) is reached, the next twin develops at stage (H). Therefore, a hexagonal pillar grows along the  $\langle 111 \rangle$ B direction by twins being piled up one after another.

### 18.4.3 Coherent Growth of Nanowire Heterostructure

Heteroepitaxy enables advances in optoelectronics using semiconductor heterostructures. The heteroepitaxy of semiconductors, however, inherently forms defects due to mismatches in lattice constants, thermal expansion, and polarity. Conventional heteroepitaxial thin-film growth is especially affected by the formation of misfit dislocations due to lattice mismatches. The lattice mismatch between two materials is given as

$$\epsilon \approx \frac{a_{\text{epi}} - a_{\text{sub}}}{a_{\text{sub}}}, \quad (18.8)$$

where  $a_{\text{epi}}$  is the lattice constant of the epitaxial layer and  $a_{\text{sub}}$  is that of the host substrate. For instance, a lattice with Si for GaAs and InP is 4.1% for the former and 8.1% for the latter. The lattice constants are summarized in [Table 18.3](#).

A serious problem in heteroepitaxy with large lattice mismatches is the quality of interfaces with high misfit dislocation density. The formation of misfit dislocation occasionally changes the growth mode of two-dimensional thin-film growth (F-M mode)

**Table 18.3** Lattice Mismatches in Two Materials

Materials	Stacking Fault Energy (mJ/m <sup>2</sup> )
Si	55 ± 7
GaAs	45 ± 7
InAs	30 ± 7
InP	518 ± 7

rather than degrades interface quality. Defects, in this regard, act as preferred sites for impurity atoms, high diffusivity paths of dopants, and nonradiative recombination centers. These sites degrade electrical or optical properties. Matthews and Blakeslee introduced a general model for the critical thickness of lattice relaxation due to lattice mismatches for the formation of misfit dislocations [157]. This model was based on the assumption of a condition for mechanical equilibrium and represented an elasticity approach. The epitaxial layers in this model relax when defects are forming when the layer reaches a certain critical thickness, which limits the dislocation-free thickness of strained layers [157]. People and Bean modeled the critical thickness of heteroepitaxial films by using elastic energy in dislocation, which was based on energy equilibrium and its balance between epitaxial film and the host material [158].

As the requirement for lattice matching is relaxed in heterostructure NWs during NW growth due to small footprints, NWs exhibit surface-strain relaxation without the formation of defects usually observed in a highly lattice mismatched system, such as III-V heteroepitaxy on Si. Thus, NWs are usually single-crystalline, which indicates a highly crystalline structure. The nanometer-scale footprint in NW structures achieves coherent growth regardless of misfit dislocations. Ertekin et al. and Glas modeled the critical diameter for the coherent growth mode in NW growth using equilibrium analysis as a function of lattice mismatch [159,160]. The critical diameter decreases as lattice mismatch increases, as shown in Figure 18.31. For instance, no defects are formed at the heterointerface in 200-nm diameter NWs with as much as 3% mismatch [159]. Björk et al. demonstrated InP/InAs axial NWs regardless of misfit dislocations using the VLS method [161].

Selective-area growth can systematically change the diameter of interfaces by changing the opening diameter. Tomioka et al. first achieved coherent growth of GaAs NWs on an Si substrate with SAG [133]. They reduced the opening diameter to less than 20 nm and grew very thin GaAs NWs on Si. TEM observations and strain analysis of the heterointerface of GaAs/Si revealed that the heterointerface had no misfit dislocations instead of the strained layer at the interface. They reported the formation of misfit dislocations in InAs NW/Si heterojunctions in highly lattice mismatched systems, such as InAs on Si [132,133], where they observed the periodicity of misfit dislocation was enlarged more than that of planar lattice mismatch (11.6%). Tomioka et al. systematically investigated the formation of lattice mismatches in III-V NW/Si interfaces as a function of the diameter of

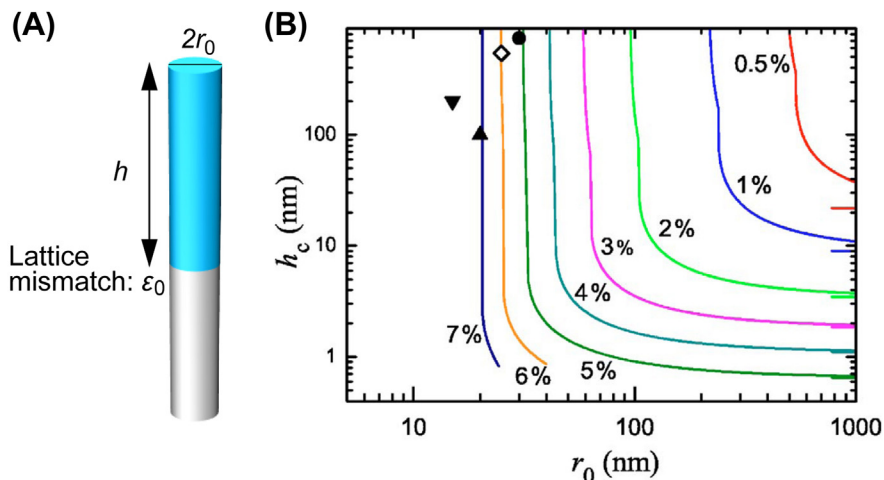


**FIGURE 18.31** (A) Schematic of nanowire (NW) geometry with lattice-mismatched heterostructures. (B) Variations in critical thickness of misfit layer growing on top of NWs as a function of radius ( $r_0$ ), for various values of lattice mismatch ( $\epsilon_0$ ), given in percent near each curve and Poisson's ratio of  $1/3$ . Adapted from Ref. [160].

heterointerfaces [162]. They fabricated a number of heterointerfaces made with InAs (11.6%),  $\text{In}_{0.7}\text{Ga}_{0.3}\text{As}$  (8.1%), and GaAs NWs (4.1%) on Si (see in Figure 18.32). InAs NW/Si and InGaAs NW/Si had larger lattice mismatches of 11.6% for the former and 8.1% for the latter, but the effective lattice mismatch of these III-V NWs on Si decreased as the diameter decreased. For example, the number of misfit dislocations for InGaAs NWs with a diameter of 18 nm was the same as those for GaAs/Si (4.1%: dashed curve in Figure 18.32). These plots predict the critical diameter for coherent growth regardless of misfit dislocations in the heteroepitaxy of III-V NWs with various lattice mismatches.

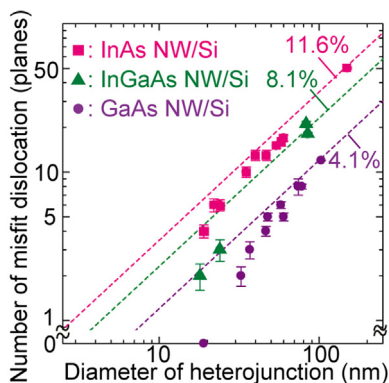


**FIGURE 18.32** Numbers of misfit dislocations at III-V nanowire (NW)/Si heterojunctions with variations in diameters of heterointerfaces. Dashed lines are calculated values from lattice mismatches. Closed squares (InAs NW/Si), triangles (InGaAs NW/Si), and circles (GaAs NW/Si) are experimental data obtained from mapping and TEM images. Adapted from Ref. [161].

## References

- [1] Feynman RP. There's plenty of room at the bottom. In: American physical society annual meeting. California: California Institute of Technology; 1959.
- [2] Arakawa Y, Sakaki H. *Appl Phys Lett* 1982;40:939.
- [3] Arakawa Y, Sakaki H, Nishioka M, Okamoto H, Miura N. *Jpn J Appl Phys* 1983;22:L804.
- [4] Huang X, Lee W-C, Kuo C, Hisamoto D, Chang L, Kedzierski J, et al. *IEEE IEDM Tech Dig* 1999; 67.
- [5] Ferrain I, Colinge AA, Clinge J-P. *Nature* 2011;479:310.
- [6] Takato JH, Sunouchi K, Okabe N, Nitayama A, Hieda K, Horiguchi F, et al. *IEEE Trans Electron Dev* 1991;38:573.
- [7] del Alamo JA. *Nature* 2011;479:317.
- [8] Pillarisetty R. *Nature* 2011;479:324.
- [9] Radosavljevic M, Chu-Kung B, Corcoran S, Dewey G, Hudait MK, Fastenau JM, et al. *IEEE IEDM Tech Dig* 2009;319.
- [10] Esaki L, Tsu R. *IBM J Res Dev* 1970;14:61.
- [11] Stranski IN, Krastanow L. *Abh Math – Naturwissenschaftlichen Klasse Iib* 1938;146:797.
- [12] Martí A, López N, Antolín E, Cánovas E, Luque A. *Appl Phys Lett* 2007;90:233510.
- [13] Ohta M, Kanto T, Yamaguchi K. *Jpn J Appl Phys* 2006;45:3427.
- [14] Yuan Z, Kardynal BE, Stevenson RM, Shields AJ, Lobo CJ, Cooper K, et al. *Science* 2002;295:102.
- [15] Fukui T, Ando S, Tokura Y, Toriyama T. *Appl Phys Lett* 1991;58:2018.
- [16] Ward MB, Farrow T, See P, Yuan ZL, Karimov OZ, Bennett AJ, et al. *Appl Phys Lett* 2007;90:063512.
- [17] Kako S, Santori C, Hoshino K, Götzinger S, Yamamoto Y, Arakawa Y. *Nat Mat* 2006;5:887.
- [18] Wagner RS, Ellis WC. *Appl Phys Lett* 1964;4:89.
- [19] Sakaki H. *Jpn J Appl Phys* 1980;19:L735.
- [20] Canham LT. *Appl Phys Lett* 1990;57:1046.
- [21] Bhat R, kapon E, Hwang DM, Koza MA, Yun CP. *J Cryst Growth* 1988;93:850.
- [22] Kapon E, Hwang DM, Bhat R. *Phys Rev Lett* 1989;63:430.
- [23] Hara S, Ishizaki J, Motohisa J, Fukui T, Hasegawa H. *J Cryst Growth* 1994;145:692.
- [24] Miller MS, Pryor CE, Weman H, Samoska LA, Kroemer H, Petroff PM. *J Cryst Growth* 1991; 111:323.
- [25] Reed MA, Randall JN, Aggarwal RJ, Matyi RJ, Moore TM, Wetsel AE. *Phys Rev Lett* 1988;60:535.
- [26] Kita T, Chiba D, Ohno Y. *Appl Phys Lett* 2007;91:232101.
- [27] Joyce BD, Baldrey JA. *Nature* 1962;195:485.
- [28] Tausch FW, Lapierre AG. *J Electrochem Soc* 1965;112:706.
- [29] Rai-Choudhury P. *J Electrochem Soc* 1969;116:1745.
- [30] Jones SH, Lau KM. *J Electrochem Soc* 1987;134:3149.
- [31] Jabstzebski L, Corboy JF, McGinn JT, Pogliar Jr R. *J Electrochem Soc* 1983;130:1571.
- [32] Tsauer B-Y, McClelland RW, Fan JCC, Gale RP, Salerno JP, Vojak BA, et al. *Appl Phys Lett* 1982;41:347.
- [33] Nishinaga T, Nakano T, Zhang S. *Jpn J Appl Phys* 1988;27:1964.
- [34] Ujiie Y, Nishinaga T. *Jpn J Appl Phys* 1989;28:L337.

- [35] Nishinaga T. *J Cryst Growth* 2002;237-239:1410.
- [36] Sakawa S, Nishinaga T. *Jpn J Appl Phys* 1992;31:L359.
- [37] Naritsuka S, Nishinaga T. *Jpn J Appl Phys* 1995;34:L1432.
- [38] Suzuki Y, Nishinaga T. *Jpn J Appl Phys* 1989;28:440.
- [39] Zhang S, Nishinaga. *Jpn J Appl Phys* 1990;29:545.
- [40] Usui A, Sunakawa H, Sakai A, Yamaguchi AA. *Jpn J Appl Phys* 1997;36:L899.
- [41] Sakai A, Sunakawa H, Usui A. *Appl Phys Lett* 1998;73:481.
- [42] Dobož D, Zytkeiwicz ZR. *Int J Mater Prod Tech* 2005;22:50.
- [43] Takagi Y, Yonezu H, Samonji K, Tsuji T, Ohshima N. *J Cryst Growth* 1998;187:42.
- [44] Akiyama M, Kawarada Y, Kaminishi K. *Jpn J Appl Phys* 1984;23:L843.
- [45] Egawa T, mooku T, Ishikawa H, Ohtsuka K, Jimbo T. *Jpn J Appl Phys* 2002;41:L663.
- [46] Chang YS, Naritsuka S, Nishinaga T. *J Cryst Growth* 1998;192:18.
- [47] Deura M, Kondo Y, Takenaka M, Takagi S, Nakano Y, Sugiyama M. *J Cryst Growth* 2010;312:1353.
- [48] Nagel N, Barnhart F, Phillip F, Czeck E, Silier I, Bauser E. *Appl Phys A* 1993;57:249.
- [49] Bernhart F, Negel N, Czeck E, Silier I, Phillip F, Bauser E. *Appl Phys A* 1993;57:441.
- [50] Yan Z, Namaoka Y, Naritsuka S, Nishinaga T. *J Cryst Growth* 2000;212:1.
- [51] Huang WD, Nishinaga T, Naritsuka S. *Jpn J Appl Phys* 2001;40:5357.
- [52] Baccin G, Nishinaga T. *J Cryst Growth* 2000;208:1.
- [53] Naritsuka S, Mochizuki Y, Motodohi K, Ohya S, Ikeda N, Sugimoto Y, et al. *J Res Inst Meijo Univ* 2002;1:77.
- [54] Deura M, Ikuhara Y, Yamamoto T, Hoshii T, Takenaka M, Takagi S, et al. *Appl Phys Exp* 2009;2:011101.
- [55] Nakamura S, Senoh M, Nagahama S, Iwasa N, Yamada T, Matsushita T, et al. *Jpn J Appl Phys* 1998;37:L309.
- [56] Motoki K, Okahisa T, Matsumoro N, Matsushima M, Kimura H, Kasai H, et al. *Jpn J Appl Phys* 2001;40:L140.
- [57] Dobrusin RL, Kotechy R, Shlosman S. *Wulff construction: a global shape from local interactions*. American Mathematical Society, Providence; 1993.
- [58] Fukui T, Ando S. *Electron Lett* 1989;25:410.
- [59] Leys MR, Veenvliet H. *J Cryst Growth* 1981;55:145.
- [60] Stringfellow GB. *Organometallic vapor-phase epitaxy: theory and practice*. 2nd ed. Academic Press, Inc.; 1999.
- [61] Show DW. *2nd Int Symp GaAs Tech Dig* 1968;50.
- [62] Jones SH, Seidel LK, Lau KM, Harold M. *J Cryst Growth* 1991;108:73.
- [63] Kossel W. *Nach Ges Wiss Gottingen* 1927;143.
- [64] Ando S, Fukui T. *J Cryst Growth* 1989;98:646.
- [65] Biegelsen DK, Bringans RD, Northrup JE, Swartz L-E. *Phys Rev Lett* 1990;65:452.
- [66] Nishida T, Uwai K, Kobayashi Y, Kobayashi N. *Jpn J Appl Phys* 1995;34:6326.
- [67] Asai H. *J Cryst Growth* 1987;80:425.
- [68] Chang SS, Ando S, Fukui T. *Surf Sci* 1992;267:214.

- [69] Lagmuir I. *J Am Chem Soc* 1918;40:1361.
- [70] Fukui T, Ando S, Fukai Y. *Appl Phys Lett* 1990;57:1029.
- [71] Ando S, Chang SS, Fukui T. *J Cryst Growth* 1991;115:69.
- [72] Fukai Y, Yamada S, Asai H, Ando S, Fukui T. *JSAP SSDM Tech Dig* 1988;631.
- [73] Ando S, Kobayashi N, Ando H. *J Cryst Growth* 1998;37:L105.
- [74] Bhat R, Kapon E, Hwang DM, Koza MA, Yun CP. *J Cryst Growth* 1988;93:850.
- [75] Seifert W, Carlsson N, Miller M, Pistol ME, Samuelson L, Wallenberg LR. *Prog Cryst Growth Char* 1996;33:423.
- [76] Eaglesham DJ, Cerullo M. *Phys Rev Lett* 1990;64:1943.
- [77] Leonard D, Pond K, Caroff PM. *Phys Rev B* 1994;50:11687.
- [78] Nakajima K. *Jpn J Appl Phys* 1999;38:1875.
- [79] Ando S, Kobayashi N, Ando H. *J Cryst Growth* 1994;145:302.
- [80] Fukui T, Ando S, Tokura Y, Toriyama T. *Appl Phys Lett* 1991;58:2018.
- [81] Watanabe S, Pelucchi E, Dwir B, Baier MH, Leifer K, Kapon E. *Appl Phys Lett* 2004;84:2907.
- [82] Juska G, Dimastrodonato V, Mereni LO, Gocalinska A, Pelucchi E. *Nat Photo* 2013;7:527.
- [83] Kitamura M, Nishioka M, Oshinowo J, Arakawa Y. *Jpn J Appl Phys* 1995;34:4378.
- [84] Tatebayashi J, Nishika M, Someya T, Arakawa Y. *Appl Phys Lett* 2000;77:3382.
- [85] Kusuhara T, Nakajima F, Motohisa J, Fukui T. *Jpn J Appl Phys* 2002;41:2508.
- [86] Kim HJ, Motohisa J, Fukui T. *Nanotechnology* 2004;15:292.
- [87] Ryzhill V. *Semicond Sci Tech* 1996;11:759.
- [88] Michler P, Kiraz A, Becher C, Schoenfeld WV, Petroff PM, Zhang L, et al. *Science* 2000;290:2282.
- [89] Ooike N, Motohisa J, Fukui T. *Jpn J Appl Phys* 2007;46:4344.
- [90] Ooike N. *Fabrication and electrical characterization of GaAs base quantum dot memories [Ph.D. thesis]. University of Hokkaido; 2007.*
- [91] Hiruma K, Yazawa M, Katsuyama T, Ogawa K, Haraguchi K, Koguchi M, et al. *J Appl Phys* 1995;77:447.
- [92] Huang Y, Duan X, Cui Y, Lauhon LJ, Kim K-H, Lieber CM. *Science* 2001;294:1313.
- [93] Huang MH, Mao S, Feick H, Yan H, Wu Y, Kind H, et al. *Science* 2001;292:1897.
- [94] Gudixsen MS, Lauhon LJ, Wang J, Smith DC, Lieber CM. *Nature* 2002;415:617.
- [95] Lauhon LJ, Gudixsen MS, Wang D, Lieber CM. *Nature* 2002;420:57.
- [96] Johnson JC, Choi H-J, Knutsen KP, Schaller RD, Yang P, Saykally RJ. *Nat Mat* 2002;1:106.
- [97] Sato T, Hiruma K, Shirai M, Tominaga K, Haraguchi K, Katsuyama T, et al. *Appl Phys Lett* 1995;66:159.
- [98] Ohlsson BJ, Björk MT, Magnusson MH, Deppert K, Samuelson L, Wallenberg LR. *Appl Phys Lett* 2001;79:3335.
- [99] Junno T, Deppert K, Montelius L, Samuelson L. *Appl Phys Lett* 1995;66:3627.
- [100] Yan ZX, Milnes AG. *J Electrochem Soc* 1982;129:1353.
- [101] Allen JE, Hemesath ER, Perea DE, Lensch-Falk JL, Li ZY, Yin F, et al. *Nat Nanotech* 2008;3:168.
- [102] i Morral AF, Colombo C, Abstreiter G, Arbiol J, Morante JR. *Appl Phys Lett* 2008;92:063112.
- [103] i Morral AF, Spirkoska D, Arbiol J, Heigoldt M, Morante JR, Abstreiter G. *Small* 2008;4:899.

- [104] Heiss M, Gustafsson A, Conesa-Boj S, Peiro F, Morante JR, Abstreiter G, et al. *Nanotechnology* 2009;20:075603.
- [105] Colombo C, Heiß M, Gratzel M, i Morral AF. *Appl Phys Lett* 2009;94:173108.
- [106] Mandl B, Stangl J, Mårtensson T, Mikkelsen A, Eriksson J, Karlsson LS, et al. *Nano Lett* 2006;6:1817.
- [107] Mandl B, Stangl J, Hilner E, Zakharov AA, Hilletich K, Dey AW, et al. *Nano Lett* 2010;10:4443.
- [108] Kim B-S, Koo T-W, Lee J-H, Kim DS, Jung YC, Hwang SW, et al. *Nano Lett* 2009;9:864.
- [109] Motohisa J, Noborisaka J, Takeda J, Inari M, Fukui T. *J Cryst Growth* 2004;272:180.
- [110] Noborisaka J, Motohisa J, Fukui T. *Appl Phys Lett* 2005;86:213102.
- [111] Ikejiri K, Noborisaka J, Hara S, Motohisa J, Fukui T. *J Cryst Growth* 2007;298:616.
- [112] Ikejiri K, Sato T, Yoshida H, Hiruma K, Motohisa J, Hara S, et al. *Nanotechnology* 2008;19:265604.
- [113] Mohan P, Motohisa J, Fukui T. *Nanotechnology* 2005;16:2903.
- [114] Kitauchi Y, Kobayashi Y, Tomioka K, Hara S, Hiruma K, Fukui T, et al. *Nano Lett* 2010;10:1699.
- [115] Tomioka K, Mohan P, Noborisaka J, Hara S, Motohisa J, Fukui T. *J Cryst Growth* 2007;298:644.
- [116] Akabori M, Sladek K, Hardtdegen H, Schöoers Th, Grützmacher D. *J Cryst Growth* 2009;311:3813.
- [117] Akabori M, Takeda J, Motohisa J, Fukui T. *Nanotechnology* 2003;14:1071.
- [118] Sato T, Motohisa J, Noborisaka J, Hara S, Fukui T. *J Cryst Growth* 2008;310:2359.
- [119] Sato T, Kobayashi Y, Motohisa J, Hara S, Fukui T. *J Cryst Growth* 2008;310:5111.
- [120] Yoshimura M, Tomioka K, Hiruma K, Hara S, Motohisa J, Fukui T. *Jpn J Appl Phys* 2010;49:04DH08.
- [121] Fujisawa S, Sato T, Hara S, Motohisa J, Hiruma K, Fukui T. *Jpn J Appl Phys* 2011;50:04DH03.
- [122] Sekiguchi H, Kishino K, Kikuchi A. *Appl Phys Lett* 2010;96:231104.
- [123] Kim Y-J, Lee C-H, Hong YJ, Yi G-C, Kim SS, Cheong H. *Appl Phys Lett* 2006;89:163128.
- [124] Mohan P, Motohisa J, Fukui T. *Appl Phys Lett* 2006;88:013110.
- [125] Hua B, Motohisa J, Kobayashi Y, Hara S, Fukui T. *Nano Lett* 2009;9:112.
- [126] Mohan P, Motohisa J, Fukui T. *Appl Phys Lett* 2006;88:133105.
- [127] Yang L, Motohisa J, Takeda J, Tomioka K, Fukui T. *Nanotechnology* 2007;18:105302.
- [128] Shapiro JN, Lin A, Wong PS, Scofield AC, Tu C, Senanayake PN, et al. *Appl Phys Lett* 2010;97:243102.
- [129] Sasakura H, Humano K, Suemune I, Motohisa J, Kobayashi Y, van Kouwen M, et al. *J Phys Conf Ser* 2009;193:012132.
- [130] Hayashida A, Sato T, Hara S, Motohisa J, Hiruma K, Fukui T. *J Cryst Growth* 2010;312:3592.
- [131] Li CH, Sun Y, Law DC, Visbeck SB, Hicks RF. *Phys Rev B* 2003;68:085320.
- [132] Tomioka K, Motohisa J, Hara S, Fukui T. *Nano Lett* 2008;8:3475.
- [133] Tomioka K, Kobayashi Y, Motohisa J, Hara S, Fukui T. *Nanotechnology* 2009;20:145302.
- [134] Tomioka K, Tanaka T, Hara S, Hiruma K, Fukui T. *IEEE J Sel Top Quantum Electron* 2011;17:1112.
- [135] Hertenberger S, Rudolph D, Bichler M, Findley JJ, Abstreiter G, Koblmüller G. *J Appl Phys* 2010;108:114316.
- [136] Tomioka K, Yoshimura M, Fukui T. *Nature* 2012;488:189.
- [137] Sladek K, Klinger V, Wensorra J, Akabori M, Hardtdegen H, Grützmacher D. *J Cryst Growth* 2010;312:65.
- [138] Ishizaka F, Ikejiri K, Tomioka K, Fukui T. *Jpn J Appl Phys* 2013;52. UNSP 04CH05.
- [139] Noborisaka J, Motohisa J, Hara S, Fukui T. *Appl Phys Lett* 2005;87:093109.

- [140] Goto H, Nosaki K, Tomioka K, Hara S, Hiruma K, Motohisa J, et al. *Appl Phys Exp* 2009;2:035004.
- [141] Tomioka K, Motohisa J, Hara S, Hiruma K, Fukui T. *Nano Lett* 2010;10:1639.
- [142] Chen R, Tran T-TD, Ng KW, Ko WS, Chuang LC, Sedgwick FG, et al. *Nat Photo* 2011;5:170.
- [143] Mariani G, Wong PS, Katzenmeyer AM, Léonard F, et al. *Nano Lett* 2011;11:2490.
- [144] Mariani G, Scofield A, Hung C-H, Huffaker DL. *Nat Comm* 2013;4:1497.
- [145] Nakai E, Yoshimura M, Tomioka K, Fukui T. *Jpn J Appl Phys* 2013;52. UNSP 055002.
- [146] Yoshimura M, Nakai E, Tomioka K, Fukui T. *Appl Phys Lett* 2013;6:052301.
- [147] Tomioka K, Tanaka T, Fukui T. *ECS Trans* 2011;41:61.
- [148] Tomioka K, Fukui T. *IEEE IEDM Tech Dig* 2011;773.
- [149] Takeuchi S, Suzuki K. *Physica State Solidi (A)* 1999;171:99.
- [150] Jaccodine RJ. *J Electrochem Soc* 1963;110:524.
- [151] Hurle DTJ. *J Cryst Growth* 1995;147:239.
- [152] Yoshida H, Ikejiri K, Sato T, Hara S, Hiruma K, Motohisa J, et al. *J Cryst Growth* 2009;312:52.
- [153] Thornton JMC, Woolf DA, Weighman P. *Appl Surf Sci* 1998;123–124:115.
- [154] Rajkumar KC, Chen P, Madhukar A. *J Appl Phys* 1991;69:2219.
- [155] Woolf DA, Westwood DI, Williams RH. *Appl Phys Lett* 1993;61:1370.
- [156] Chen P, Rajkumar KC, Madhukar A. *Appl Phys Lett* 1991;58:1771.
- [157] Matthews JW, Blakeslee AE. *J Cryst Growth* 1974;27:118.
- [158] People B, Bean JC. *Appl Phys Lett* 1985;47:322.
- [159] Ertekin E, Greaney PA, Chrzan DC, Sands TD. *J Appl Phys* 2005;97:114325.
- [160] Glas F. *Phys Rev B* 2006;74:121302.
- [161] Björk MT, Ohlsson BJ, Sass T, Persson AI, Thelander C, Magnusson MH, et al. *Appl Phys Lett* 2002;80:1058.
- [162] Tomioka K, Yoshimura M, Fukui T. *Nano Lett* 2013;13:5822.

# Nucleation and Growth Mechanisms of Protein Crystals

Peter G. Vekilov

DEPARTMENT OF CHEMICAL AND BIOMOLECULAR ENGINEERING, AND DEPARTMENT OF  
CHEMISTRY, UNIVERSITY OF HOUSTON, HOUSTON, TEXAS, USA

## CHAPTER OUTLINE

<b>19.1 Introduction</b> .....	<b>796</b>
<b>19.2 Proteins and Protein Crystals</b> .....	<b>798</b>
19.1.1 The Protein Molecules .....	798
19.1.2 Intermolecular Contacts in Crystals .....	800
19.1.3 Solution Trapped in the Intermolecular Space .....	802
<b>19.3 The Thermodynamics of Protein Crystallization</b> .....	<b>802</b>
19.2.1 Definitions .....	802
19.2.2 Molecular Processes Underlying the Thermodynamics of Protein Crystallization .....	803
19.2.3 The Crystallization Driving Force .....	806
19.2.4 The Phase Diagram: Dense Liquid Phases, Crystalline Polymorphs, Gelation, Spinodals .....	807
<b>19.4 Methods of Protein Crystallization</b> .....	<b>810</b>
<b>19.5 The Role of Nonprotein Solution Components and the Intermolecular Interactions in     Solution</b> .....	<b>813</b>
19.5.1 Types of Interaction between Protein Molecules in Solution .....	814
19.5.2 Deviations from the Simple Colloid Approach .....	817
19.5.3 Buffers, Salts and Organic Molecules and the Water Structure .....	819
19.5.3.1 Buffers .....	819
19.5.3.2 Salts .....	821
19.5.3.3 Organic Molecules .....	823
<b>19.6 Crystal Nucleation</b> .....	<b>825</b>
19.6.1 The Classical Nucleation Theory .....	825
19.6.1.1 Thermodynamics .....	825
19.6.1.2 The Rate of Crystal Nucleation .....	827

19.6.2	Experimental Data on the Nucleation Kinetics.....	828
19.6.2.1	<i>Evolution of Aggregate Sizes</i> .....	828
19.6.2.2	<i>The Rate of Crystal Nucleation</i> .....	828
19.6.3	the Nucleus Size and Solution-Crystal Spinodal .....	830
19.6.4	The Classical Theory Overestimates the Crystal Nucleation Rate by 10 Orders of Magnitude .....	832
19.6.5	The Two-step Mechanism of Nucleation of a Crystal in Solution .....	833
19.6.6	Dense Liquid Clusters in the Homogenous Region of the Phase Diagram .....	836
19.6.7	The Rate Law for the Two-step Mechanism of Crystal Nucleation .....	839
19.6.8	The Rate Determining Step in the Two-step Nucleation Mechanism .....	841
19.6.9	The Role of Heterogeneous Nucleation Substrates .....	842
19.6.10	Other Systems for Which the Two-step Nucleation Mechanism Applies.....	843
19.6.11	A General Perspective on the Nucleation of Protein Crystals.....	845
<b>19.7</b>	<b>Mechanisms of Growth of Crystals .....</b>	<b>846</b>
19.7.1	Rough and Smooth Interfaces.....	846
19.7.2	Generation of Steps.....	847
19.7.3	Step Propagation .....	848
19.7.4	The Step Kinetic Coefficient .....	849
19.7.5	Generation of Kinks.....	850
19.7.6	The Barrier for Incorporation into Kinks.....	853
19.7.7	The Molecular Pathway from the Solution into a Growth Site.....	855
<b>19.8</b>	<b>Concluding Remarks .....</b>	<b>857</b>
	<b>References.....</b>	<b>857</b>

## 19.1 Introduction

In the early days of materials science, it was assumed that crystals such as those of diamond, quartz, or calcite were only a property of the mineral world, and that no living organism would contain them. The first protein crystals, of hemoglobin, were discovered accidentally in 1840, in dried earthworm blood. In the following years, by 1871, crystals of hemoglobin from nearly 50 species had been reported. By the end of the nineteenth century, crystals of numerous other proteins of both plant and animal origin had been obtained. Crystal formation was considered a criterion for purity of the protein preparation. In the further discussions of the nature of proteins, their ability to form crystals was one of the major arguments supporting their molecular nature and refuting the hypothesis, common at that time, that proteins are colloid particles of disordered matter [1].

Currently, protein crystals are of interest for several fields of science and technology. Their formation underlies several human pathological conditions. An example is the crystallization of hemoglobin C, illustrated in [Figure 19.1](#), and the polymerization of

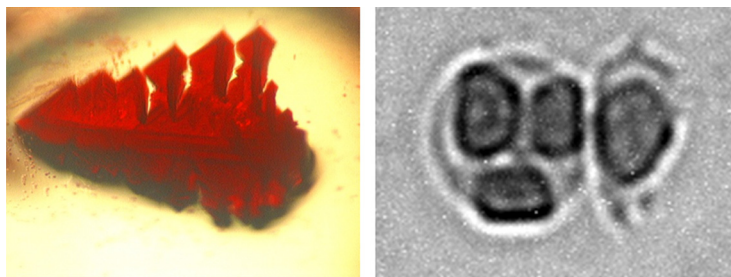


**FIGURE 19.1** Crystals of human hemoglobin C, a relatively rare mutant associated with CC disease. Right: a crystal of about  $300\ \mu\text{m}$  in width grown in the laboratory and imaged with bright field microscopy. Left: two red blood cells containing crystals of hemoglobin C; diameter of cell to the right is about  $7\ \mu\text{m}$ ; imaging by differential interference contrast microscopy.

hemoglobin S that cause, respectively, the CC and sickle cell diseases [2–5]. The formation of crystals and other protein condensed phases of the so-called crystallines in the eye lens underlies the pathology of cataract formation [6,7]. A unique example of benign protein crystallization in humans and other mammals is the formation of rhombohedral crystals of insulin in the islets of Langerhans in the pancreas. The suggested function of crystal formation is to protect the insulin from the proteases present in the islets of Langerhans and to increase the degree of conversion of the soluble proinsulin [8].

Another area which relies on protein crystals is pharmacy: the slow crystal dissolution rate is used to achieve sustained release of medications, such as insulin, interferon- $\alpha$ , or the human growth hormone [9–13]. Work on the crystallization of other therapeutically active proteins, e.g., antibodies for foreign proteins, which can be dispensed as a microcrystalline preparation, is underway. If the administered dose consists of a few equidimensional crystallites, steady medication release rates can be maintained for longer periods than for doses comprising many smaller crystallites.

Traditionally, protein crystals have been used for the determination of the atomic structure of protein molecules by X-ray crystallography [14], illustrated in Figure 19.2; this method contributes  $\sim 87\%$  of all protein structures solved, with the majority of the other determinations carried out by Nuclear Magnetic Resonance (NMR) spectroscopy [15].

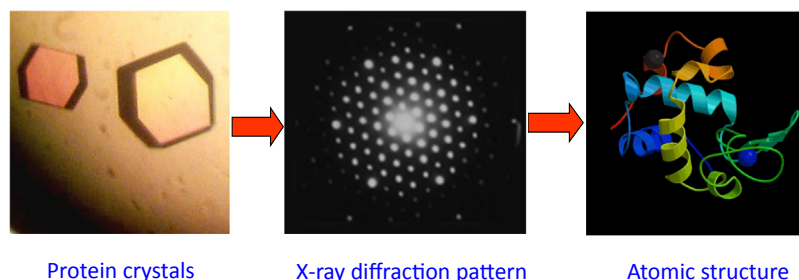


**FIGURE 19.2** Crystallography is the main route to structure determination of proteins. The preparation of diffraction-quality crystals of soluble and membrane proteins is the bottleneck in this process.

The last 30 years have seen the Golden Age of protein crystallization research. The field has greatly benefited from the adoption of concepts and methods from physics, chemistry, and life sciences. Physics contributed the theory of phase transitions, the understanding and control of intermolecular interactions, and the mechanism of nucleation and crystal growth. Chemistry came in with the notions of solvent structuring, hydration and hydrophobicity, and salt bridges and ionicity. Biochemistry and molecular biology brought about the ideas of molecular patches, the role of amino acid residues, homologs, and mutations to enhance crystallizability.

In turn, protein crystallization has enriched many of these fields not only with additional examples of the applicability of established theories, but also by assisting the development of new concepts and mechanisms. A few examples include the role of molecular anisotropy for the thermodynamics and kinetics of phase transitions [16,17], direct imaging of crystallization processes at the molecular level, determination of molecular level parameters [18–22], clarification of defect formation mechanisms [23], and novel mechanisms of crystallization [24,25]. Particularly important was a contribution to nucleation theory: the two-step nucleation mechanism. In contrast to classical theory, which envisions that solute molecules form crystal nuclei directly as they assemble into a high-concentration cluster, this mechanism posits that the first step of crystal nucleation is the formation of disordered protein-rich clusters of mesoscopic size [24,26–28]. The second step is the formation of crystal nuclei inside the clusters [29,30]. In all these works, the pursuit of informative results has been facilitated by the large sizes of the protein molecules. In addition, proteins proved convenient for monitoring and manipulating because their molecular interactions can be influenced by a variety of methods that include mutations, varying solution ionic strength, and the use of co-solutes.

In this chapter, we review the advances in the understanding of the processes of nucleation and growth of crystals obtained with proteins and their relevance to the broad fields of crystal growth and protein crystallization.

## 19.2 Proteins and Protein Crystals

### 19.1.1 The Protein Molecules

The protein molecules are heteropolymers of only 20 amino acids linked by the so-called peptide bond into linear chains, [Figure 19.3](#). One protein chain may contain up to several 100 amino acid residues. In these 20 amino acids the amine group is attached at  $\alpha$ -positions, i.e., it is separated by one methylene group from the carboxyl residue. The amino acids differ by the side chain attached to the same  $\alpha$  position: the 20 side chains vary from a single hydrogen atom in glycine to the bulky arginine, in which a three-carbon aliphatic chain is capped by a complex guanidinium group. Counting the amine group, the side chain, the carboxyl group, and remaining hydrogen atom, the  $\alpha$ -carbon atom has four different ligands and is chiral. In all proteins in nature, this

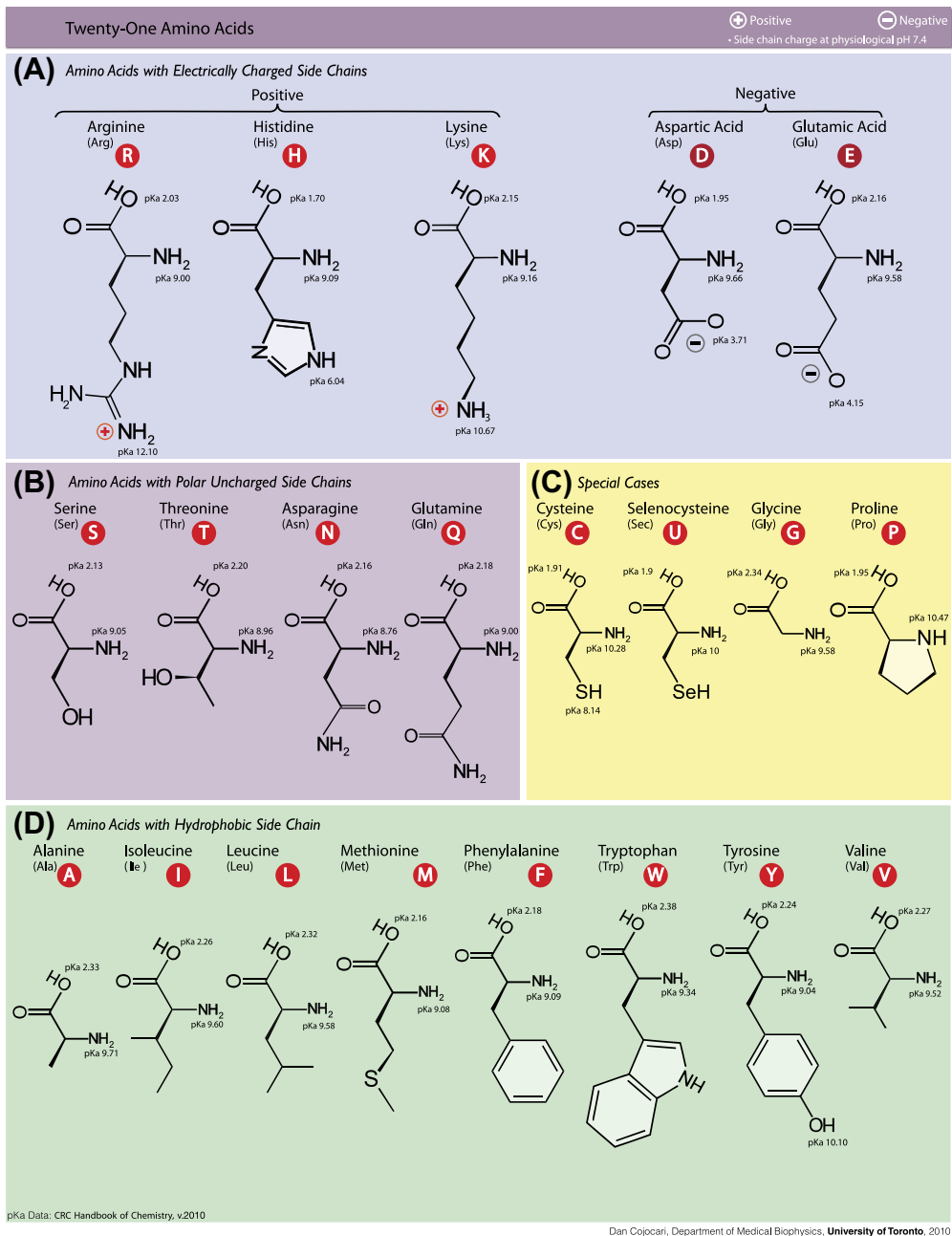


**FIGURE 19.3** The structure of the biological amino acids and selenocysteine. *From Wikipedia commons.* ©Dan Cojocari, 2010.

carbon atom is in the L-conformation so that all naturally existing amino acids are  $\alpha$ -L- amino acids. The amino acid residues can be classified according to their polarity as nonpolar, polar, and positively or negatively charged, [Figure 19.3](#). The nonpolar residues consist of straight or branched aliphatic chains and may contain aromatic rings; the polar ones contain alcohol or amide groups. The positive side chains contain one or more extra amino groups which associate a positive hydrogen ion in acidic solutions. The negative amino acids contain an extra carboxylic group, which may dissociate and form an anion in basic solutions.

In their native environments, the protein chains do not exist as random coils but fold into compact structures. The structures are unique and representative for every protein. The folded chain is not fixed in place, and considerable dynamics exist. These dynamics are crucial for the understanding of many aspects of protein behavior and function: the binding to substrates and to nucleic acids, resistance to aggregation and proteolysis, and others. In the folded protein molecules, the hydrophobic nonpolar residues are tucked inside and are mostly in contact with other such residues from the same molecule. The charged and the polar residues are mostly on the outside and ensure favorable interactions with water and protein solubility. The amino and carboxyl groups in the side chain are weak bases or acids and have  $pK_a$  values in a broad range, from 4.0 for glutamic acid to 12.48 for arginine [\[31\]](#). Hence, at a set pH value some of the surface residues are charged and others neutral. In this way, the pH of the environment in which a protein exists and functions regulates its charge.

The proteins are divided into two big classes: globular and transmembrane. The globular proteins are water soluble and are present in the cytosol of live cells and in the intracellular and body fluids such as blood, stomach juice, etc. The transmembrane proteins are embedded in the cellular membranes and serve to transmit signals between the cellular environment and the cytosol, to transfer nutrition into cells and waste out, to strengthen and control the membrane, and others. To be able to perform these functions, the transmembrane proteins are structured as a hydrophobic midriff capped with two hydrophilic plates: one facing the cytosol and the other the cellular environment.

### 19.1.2 Intermolecular Contacts in Crystals

For each set of crystallization conditions, i.e., protein, precipitant, buffer concentrations, pH, and temperature, the bonds between molecules in the crystal are directionally specific. If this specificity is missing, crystals would grow preserving only the translational but not the orientational order of molecules. The translational order leads to faceted and optically birefringent crystals, which do not yield crystalline X-ray diffraction patterns; a case in point is thermolysin [\[32\]](#).

Each specific intermolecular contact between neighbor molecules includes several hydrogen bonds between reciprocal basic and acidic side chains, several water-mediated hydrogen and ionic bonds, and several van der Waals bonds between hydrophobic side

chains, all sitting on the surfaces of the contacting molecules. The contacts between adjacent protein molecules in the crystal lattice are often categorized in terms of patches of several amino acid residues. A patch often covers only a few percent of the whole molecular surface so that all contacts may cover less than half of it.

An example in Figure 19.4 shows in red the contact areas between molecules of the thermophilic tRNA synthetase in orthorhombic and monoclinic polymorphs [33]. This

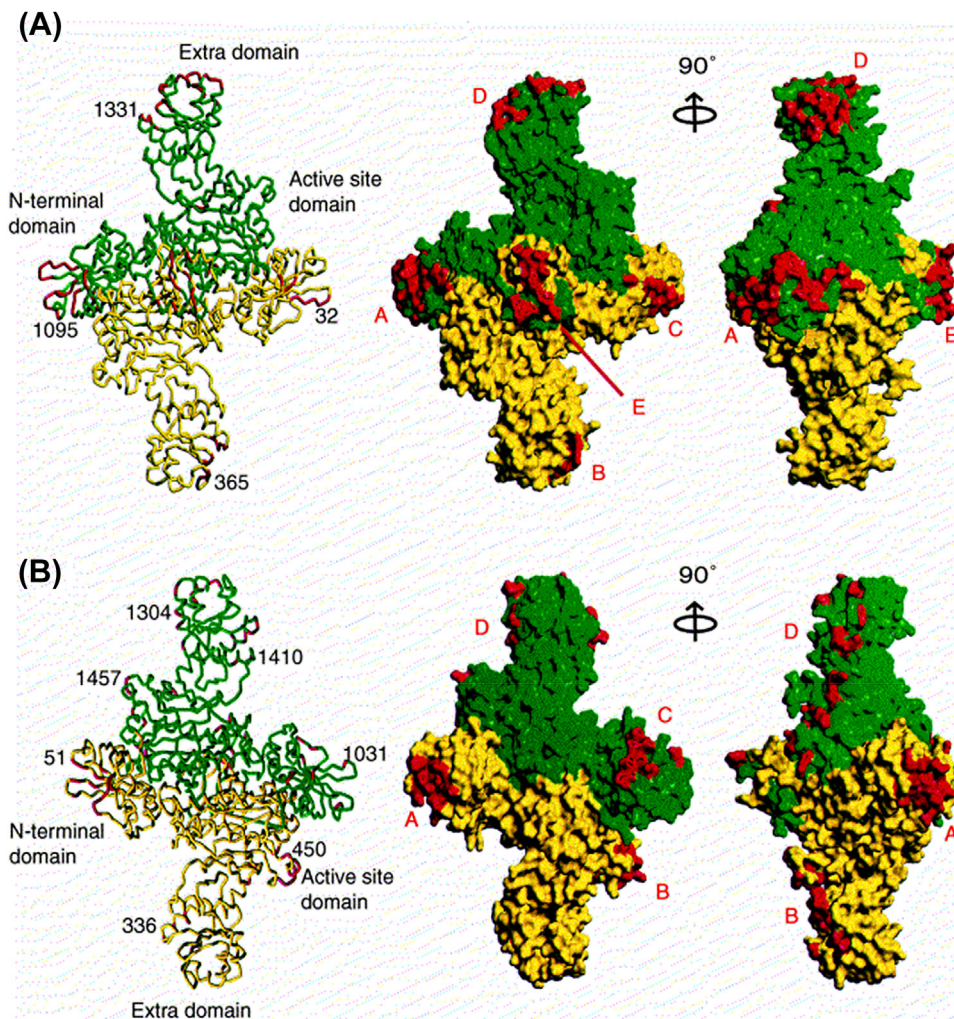


**FIGURE 19.4** Molecule of the aspartyl-tRNA synthetase consists of two firmly bound domains shown in green and yellow. Molecular structure was found to be identical when found from orthorhombic (A) and monoclinic (B) crystalline modifications. Areas (patches) involved in the intermolecular contacts within these two different polymorphs are shown in red. In (A) and (B), all the patches occupy 14.4 and 7.8% of the whole molecular surface, respectively. *With permission from Ref. [33].*

enzyme is responsible for attachment of amino acids to their cognate tRNA in translating genetic information in protein synthesis. Each molecule ( $Mw = 132$  kDa) is a homodimer of two firmly bound subunits interrelated by the two fold symmetry axis. In the orthorhombic case (Figure 19.4, row A), all six contact patches cover 14.4% ( $7040 \text{ \AA}^2$ ) of the total molecular surface. The largest macro contact takes 7.2% ( $3540 \text{ \AA}^2$ ) of the total solvent-accessible molecular area, the other two take 4.2% and 4%. Out of 51 amino acid residue bonds, there are 38 hydrophobic and 13 are ionic and hydrogen bonds. In the monoclinic polymorph, the same molecule has not six but eight nearest neighbors involved in contacts (Figure 19.4, row B). These eight patches cover only 7.8% of the molecular surface. Among the 53 contacts between surface residues, there are 35 van der Waals and 18 ionic and hydrogen bonds. The general conclusions emerging from this and other similar analyses of the intermolecular contacts in protein crystals are that (1) the contact patches occupy a low fraction of the molecular surface, and (2) that different amino acids are selected to partake in the intermolecular contacts in different crystal polymorphs of the same protein molecule.

### 19.1.3 Solution Trapped in the Intermolecular Space

In solutions and crystals of small molecules, the size of the molecules or ions is comparable to the range of the molecular forces, 2–3 Å, or less. In macromolecular systems, the size of the macromolecules ranges from 20 to 2000 Å. The consequences of this difference in size are discussed in detail below [34]. One trivial observation is that, because of this size disparity between solute and solvent, a significant amount of solvent is trapped in the void space between the protein molecules in the crystals.

The solvent filling the intermolecular voids between protein molecules occupies 30% and 70% of the crystal volume. Much of the water, buffer, and other solvents molecules in the interstices are free to diffuse in and out of the crystal. This property is extensively used in protein structure determinations to infuse a ready crystal with heavy metal ions that have higher X-ray contrast and, in this way, their presence facilitates the determination of the structure. On the other hand, the hydrophilicity of the protein surfaces results in 20–30% of the total trapped water being structurally fixed.

## 19.3 The Thermodynamics of Protein Crystallization

### 19.2.1 Definitions

In correspondence to the typical physiological, laboratory, and industrial conditions, protein phase transitions are typically considered under constant temperature and pressure. With such constraints, the transfer of protein molecules from solution to the crystal is driven by the change of Gibbs free energy [35]. The change in Gibbs free energy of crystallization  $\Delta G_{cryst}^0$  at constant temperature  $T$  is the sum of the contributions of the

enthalpy  $\Delta H^{\circ}_{cryst}$  and entropy  $\Delta S^{\circ}_{cryst}$ :  $\Delta G^{\circ}_{cryst} = \Delta H^{\circ}_{cryst} - T\Delta S^{\circ}_{cryst}$ . The associated crystallization equilibrium constant,

$$K_{cryst} \equiv \exp\left(-\Delta G^{\circ}_{cryst}/RT\right), \quad K_{cryst} = C_e^{-1}, \quad (19.1)$$

in which  $C_e^{-1}$  is the protein solubility with respect to the studied crystalline form,  $R$  is the universal gas constant, and  $T$  is the absolute temperature.

## 19.2.2 Molecular Processes Underlying the Thermodynamics of Protein Crystallization

In the last few years, chemists and physicists working in the area of protein solutions realized that the molecular-level processes in protein solutions operate on two distinct microscopic length scales: a finer scale, determined by the size of water and other solvent molecules, and a coarser one, corresponding to the size of the significantly larger protein molecules [16,36,37]. Whereas some features of the mechanisms of protein crystallization can be reasonably well understood on the coarser length scale of the protein molecules, understanding of principles that govern molecular recognition and the thermodynamic driving forces leading to or preventing crystallization requires consideration of the finer length scale of the solvent [38,39]. Various techniques have shown that a several ångstrom thick solvent layer exists around protein molecules [40–44]. Within this biological layer [44,45], the water molecules are in either of two states, between which a dynamic equilibrium exists: directly attached to the protein surface, and free, Figure 19.5. Another equilibrium exists between the biological layer

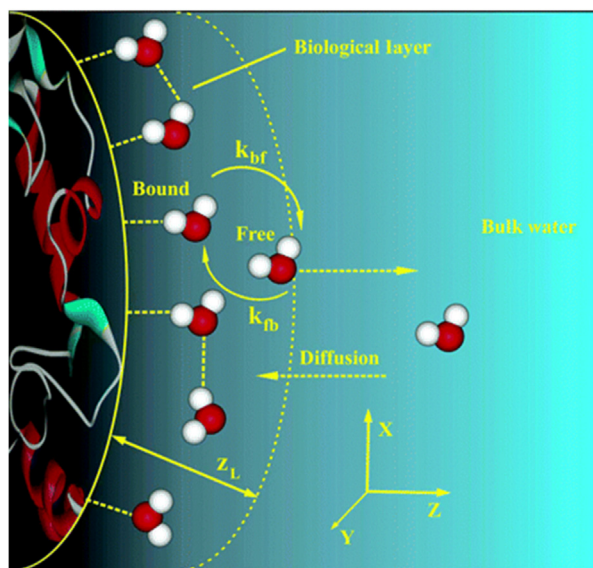


**FIGURE 19.5** Schematic of exchange of waters within a biological layer and between this layer and solution bulk. Hydrogen bonds are shown as dashed lines. There are also free water molecules that are not directly hydrogen bonded to the protein. Solid curved arrows indicate the dynamical exchange between free and bound water. Free water molecules diffuse into the layer from the bulk, and this represents a feedback mechanism of layer hydration.  $z_L$ , width of hydration layer,  $k_{bf}$  and  $k_{fb}$ , kinetic constants of exchange between the free water and bound water molecules in the hydration layer. *With permission from Ref. [44].*

and the bulk solution water [44]. This layer affects enzyme-substrate and deoxyribonucleic acid (DNA)-drug binding [46,47], and is natural to expect a similar effect on the protein-protein interactions involved in protein crystallization.

Although the existence of this layer is necessary for the protein's conformational stability [48], it may interfere thermodynamically with protein function (DNA or substrate binding, or other) and assembly. This potential conflict is resolved by the fact that in contrast to the classically envisioned iceberg structure [48], the solvent layer is not rigid, and the water molecules are constantly exchanged between the different states [44,45]. Below, we show that the enthalpy and entropy contributions from the biological solvent layer largely determine the thermodynamics of crystallization.

A number of recent molecular dynamics (MD) studies of model mesoscopic solutes: colloid particles, graphene sheets, protein molecules, etc., were aimed at quantification of the intermolecular interaction potentials on the length scales of a water molecule [40–44,49–57]. As expected, these studies demonstrate in these potentials a primary attractive minimum, mostly due to the van der Waals interactions. The MD results also indicate that in addition to this minimum, there exist relatively shallow secondary and tertiary minimums, Figure 19.6. These extra minimums correspond to one and two water layers between the solutes. Three key observations are in order: (1) The extra minimums have depth of several units of the thermal energy  $k_B T$ . (2) They are present independent of whether the solutes are hydrophilic or hydrophobic, and whether the bare solutes attract or repel [52–54,56–58]. (3) The secondary and tertiary minimums are at distances significantly greater than the typical binding distances between small molecules.

Several analyses of protein crystallization thermodynamics have shown that the standard free energy change for crystallization  $\Delta G_{cryst}^o$  is only moderately negative; this makes the crystallization process sensitive to even the slightest changes in the

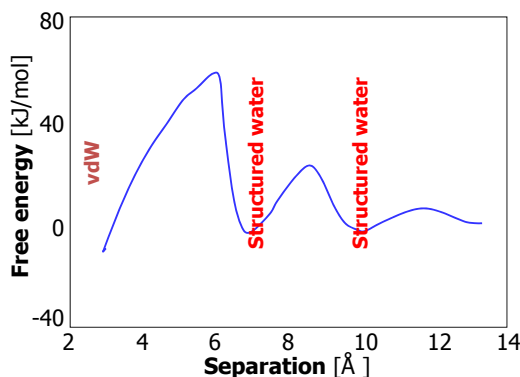


**FIGURE 19.6** The potential of mean force for interaction in water between two graphene sheets, each consisting of 60 carbon atoms, which imitate the interactions between the hydrophobic amino acid groups on the surface of protein molecules. Separation is measured from the centers of the C-atoms. *vdW* indicates the deepest minimum due to van der Waals attraction between bare C atoms, the other two minimums, and all three local maximums are due to water structured at the surfaces of the graphene sheets. *With permission from Ref. [53].*

experimental conditions. Intuitively, it appears that crystallization is prohibitively disfavored by a massive negative change in entropy as three-dimensional (3D) order is imposed on the molecules in the crystal lattice. Indeed, this entropy cost consists of the loss of six translational and rotational degrees of freedom per protein molecule, and is only fractionally compensated by the newly created vibrational degrees of freedom [59,60]. Theoretical models suggest that the balance should yield an average entropy loss of about  $-100 \text{ J mol}^{-1} \text{ K}^{-1}$  [59,61] although it may be as high as  $-280 \text{ J mol}^{-1} \text{ K}^{-1}$ , as predicted for insulin [60]. This negative entropy contributes to a positive  $\Delta G^{\circ}_{cryst}$  and, unless it is compensated, no crystallization will occur. The compensation may come from a negative  $\Delta H^{\circ}_{cryst}$  or from the entropy of accompanying processes.

In those few cases where accurate measurements were made, the crystallization enthalpy  $\Delta H^{\circ}_{cryst}$  varied within a broad range, from  $-70 \text{ kJ mol}^{-1}$  for lysozyme [62], through  $\sim 0 \text{ kJ mol}^{-1}$  for ferritin, apoferritin, and lumazine synthase [63–65], to  $155 \text{ kJ mol}^{-1}$  for hemoglobin C [66,67]. Thus, enthalpy effects are unlikely to rationalize crystallization in a general sense, and in many cases are also unfavorable.

To understand entropy effects, we consider the two distinct microscopic length scales significant for protein solutions. Experimental studies of crystallization of such proteins as apoferritin, ferritin, hemoglobin C, lysozyme, insulin and lumazine synthase allowed estimates of the enthalpy, entropy, and the standard free energy change for crystallization as functions of the temperature and of the composition of the respective solutions [63,66–68]. These thermodynamic determinations indicate that upon incorporation into a crystal lattice, some of the structured water/solvent molecules, bound to the protein molecule in solution, are released or, conversely, additional water/solvent molecules may be trapped, as schematically depicted in Figure 19.7. Both phenomena would have a significant entropy effect: the analogous transfer of water from clathrate, crystal hydrate, or other ice-like structures leads to an entropy gain of  $\sim 22 \text{ J mol}^{-1} \text{ K}^{-1}$  [61,69]. Considering the complexity and importance of the entropy effects, the solvent and protein entropy changes during crystallization have been distinguished:

$$\Delta G^{\circ}_{cryst} = \Delta H^{\circ}_{cryst} - T(\Delta S^{\circ}_{protein} + \Delta S^{\circ}_{solvent}). \quad (19.2)$$

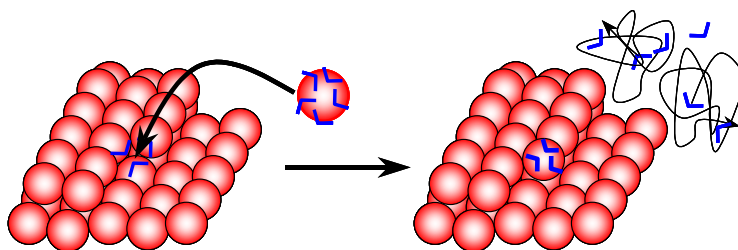


**FIGURE 19.7** A schematic illustration of  $\Delta S_{solvent} > 0$ . The protein molecules in solution and its incorporation site are coated with water molecules, which are released upon attachment of the protein molecules to the crystal. If, alternatively, additional water molecules are trapped upon attachment of a protein molecule,  $\Delta S_{solvent} < 0$  would ensue.

A more negative  $\Delta G_{cryst}^o$  is favored by a positive sum ( $\Delta S_{protein}^o + \Delta S_{solvent}^o$ ). In some cases it has been possible to estimate the value of  $\Delta S_{protein}^o$  [34,63,67,70,71–75]. As expected, the resulting value of  $\Delta S_{protein}^o$  is in the range  $-15$  to  $-100$  J mol<sup>-1</sup> K<sup>-1</sup>. This negative contribution is overcome by a significantly positive  $\Delta S_{solvent}^o$  Refs. [34,38,39]: the experimentally determined values of  $\Delta S_{solvent}^o$  range from 100 J mol<sup>-1</sup> K<sup>-1</sup> to more than 600 J mol<sup>-1</sup> K<sup>-1</sup> for different proteins. With the above value of the entropy gain for the release of one water molecule, this corresponds to the release of  $\sim 5$ –30 water or solvent molecules upon the incorporation of a protein molecule into a crystal [39,67]. Thus, it appears that in most cases the structuring of the water around the protein molecules is the main thermodynamic driving force for crystallization [39,67]. (An important exception is lysozyme crystallization, for which  $\Delta S_{solvent}^o$  is estimated as  $-70$  J mol<sup>-1</sup> K<sup>-1</sup> indicating the trapping of three or four water molecules; in this case the negative crystallization enthalpy  $\Delta H_{cryst}^o$  is the main driving force for crystallization.)

Although the above thermodynamic considerations yield considerable insight into the driving forces of protein crystallization, they are oversimplified: although assigning microscopic properties to the solvent, they do not consider the microscopic properties of the protein surface structure, its dynamics, and the associated entropy, enthalpy, and free-energy factors, as well as the associated kinetic consequences. The protein molecules are viewed as rigid spheres, ignoring the chemical specificity of their surfaces. A better model for the protein molecules is a rigid body enveloped by the sheath of conformationally variable, high-entropy side chains, the chemical nature of which affects the water structure. Thus, the protein's microscopic surface properties will have a critical impact on the thermodynamics and kinetics of crystallization. This opens a possibility of rational engineering of proteins to enhance their crystallization potential [75,76].

There have been a few preliminary, still qualitative attempts to address the role of individual amino acid residues on the surface of a protein molecule in protein crystallization. These approaches focus on the change, upon crystallization, of the configurational entropy of lysine, glutamate, and arginine residues on the protein crystal surface [77–79].

### 19.2.3 The Crystallization Driving Force

Crystal formation occurs in supersaturated solutions, in which the concentration  $C$  is higher than the solubility  $C_e$ . Accordingly, the chemical potential of the solute  $\mu$  in the solution is greater than the one at equilibrium  $\mu_e$ , which in turn is equal to the chemical potential of the crystallizing material in the crystal,  $\mu_e = \mu_{crystal}$ . The chemical potential  $\mu = \mu_0 + RT \ln \gamma C$  and  $\mu_e = \mu_0 + RT \ln \gamma_e C_e$ , in which  $\gamma$  and  $\gamma_e$  are the activity coefficients of the solute in the crystallizing solution and in a solution with equilibrium concentration  $C_e$ , respectively, and  $\mu_0$  is the chemical potential in a standard solution. Then the nucleation driving force  $\Delta\mu = \mu - \mu_e = RT \ln(\gamma C / \gamma_e C_e)$ . Often, it is assumed that  $\gamma = \gamma_e$  so that  $\Delta\mu = RT \ln(C/C_e)$ .

Because  $\gamma$  is a function of concentration, if  $C \gg C_e$ , the assumption  $\gamma = \gamma_e$  is unjustified. In protein solutions, the activity coefficients are evaluated from the relation  $\ln \gamma \cong 2A_2C$ , in which  $A_2$  is the second osmotic virial coefficient, discussed in depth in Section 19.5.1 below.

This definition of  $\Delta\mu = \mu - \mu_e = \mu - \mu_{crystal}$  accepted in the fields of phase transformations, nucleation and crystal growth, contradicts the standard definition of the change of a thermodynamic variable in a physical or chemical process. In the standard definition,  $\Delta$  signifies the difference between the final and initial states, whereas in the above definition, the crystal is the final state and the solution the initial. Hence, the two definitions of  $\Delta\mu$  differ in sign.

### 19.2.4 The Phase Diagram: Dense Liquid Phases, Crystalline Polymorphs, Gelation, Spinodals

The thermodynamics of the formation of protein condensed phases, i.e., the regions in the phase diagram of stability, metastability, and coexistence of the respective phases, the driving forces, and the underlying processes occurring at the level of protein and solvent molecules are by now relatively well understood [80]. The phase diagram in the temperature, concentration ( $T$ ,  $C$ ) plane of the solution of the protein lysozyme, a favorite model in protein physical chemistry, is shown in Figure 19.8.

The phase diagram in Figure 19.8 contains the liquidus or solubility lines, which denote the concentration of a solution in equilibrium with a crystal phase, the lines

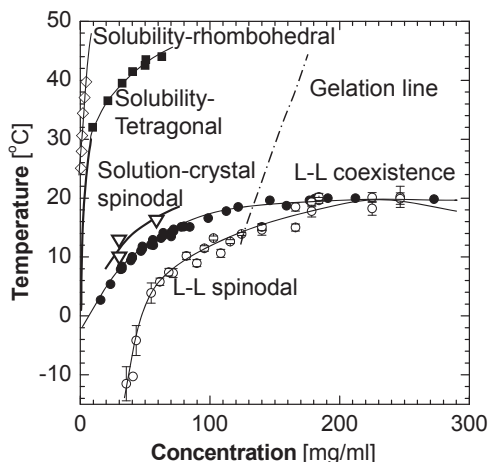


**FIGURE 19.8** The phase diagram of a lysozyme solution determined experimentally in 0.05 M Na acetate buffer at pH = 4.5% and 4.0% NaCl. Liquidus, or solubility lines—from Refs. [116,305], liquid-liquid (L-L) coexistence and respective spinodal, from Ref. [95], solution-crystal spinodal, from Ref. [224], gelation line, from Refs. [94,95]. Solidus line is at  $\sim 800 \text{ mg ml}^{-1}$  and is calculated from the density of the crystals of  $1.3 \text{ g cm}^{-3}$  and water content of 33% [306].

characterizing the dense liquid phase, and a gelation line. A crucial feature of the protein phase diagrams, also seen in [Figure 19.8](#), is that the liquid–liquid (L–L) coexistence line (also called binodal) is submerged below the lines of liquid–solid equilibrium [\[6,37,81,82\]](#); this is in contrast to the phase diagrams of binary mixtures of small molecules. The reason for the lowering of the L–L binodal is that the characteristic ranges of all types of interactions between protein molecules in solution are shorter than the sizes of the respective protein molecules by several nanometers: the ranges of the hydration and hydrophobic interactions are a few water molecular diameters, i.e., up to 10 Ångstroms [\[41,83,84\]](#); the ionic or other bridges have an even shorter range of a few Ångstroms [\[85,86\]](#); the van der Waals forces extend to about the same distances [\[87,88\]](#); the electrostatic range is defined by the so-called Debye length, which is about eight Ångstroms in solutions of the physiological ionic strength of  $\sim 0.3$  M and even shorter at the higher ionic strengths used in laboratory and industrial processing of proteins [\[89,90\]](#).

Like all other liquid–liquid separations [\[91\]](#), the formation of the dense protein liquid phase is characterized with two phase lines: the coexistence line and a spinodal, below which the formation of the dense liquid proceeds without a nucleation barrier [\[92,93\]](#). Experimentally, the L–L binodal is detected by direct microscopic observation of the formation of dense liquid droplets and their dissolution in a protein solution; these are sometimes referred to as clouding and de-clouding [\[29,94\]](#). The temperature of the spinodal is determined for a given solution composition by static light scattering by extrapolating the temperature dependence of the reciprocal intensity  $I^{-1}$  of the scattered light to the temperature at which  $I^{-1}$  reaches zero [\[92,93,95\]](#). Because light is scattered by the concentration fluctuations,  $I^{-1} \rightarrow 0$  and  $I \rightarrow \infty$  correspond to a diverging amplitude of these fluctuations. The spinodal and binodal touch at the so-called critical point for liquid–liquid separation: the highest temperature at which the coexistence of two liquid phases is possible. In [Figure 19.8](#), the critical point is at  $T = 19$  °C and the  $C = 231$  mg ml $^{-1}$ .

If more than one solid phase is possible in a solution of certain composition, the phase diagram will contain a respective number of solubility lines. In the lysozyme case depicted in [Figure 19.8](#), these are the solubilities of the tetragonal and rhombohedral crystals. The presence of two solubilities highlights the fact that the solubility is a property of the solution–crystal equilibrium and not of the protein alone, as sometimes presented in the biochemical literature. The two respective solidus lines, denoting the concentration of protein material in these two crystal forms, would be at concentrations about 800 mg ml $^{-1}$ , which are outside of the range of the concentration axis in [Figure 19.8](#). Because little is known about the temperature dependence of the protein crystal density, the solidus is typically drawn as a vertical line [\[6,65\]](#).

At higher protein concentrations the protein solution may gel, even if the temperature is above the critical temperature for liquid–liquid separation [\[29,94\]](#). Protein gelation is still relatively poorly understood; some recent theories attribute it to the action of

additional, long-range attractive forces [96–98]. A recent hypothesis links gelation to the formation of weak, limited-lifetime networks of protein molecules [99].

Both the L–L coexistence boundary and the solubility can be shifted to higher or lower temperatures by varying the acidity and ionicity of the solution [94,100], or the use of other modifiers of the protein intermolecular interactions, e.g., nonadsorbing polymers [29,101].

The lysozyme phase diagram in Figure 19.8 is an example of normal temperature dependence: the solubilities of the crystal phases and the concentration of the solution in equilibrium with the dense liquid decrease as temperature is lowered. This dependence indicates that the condensed phases are favored at low temperature. Opposite examples, in which crystallization or liquid–liquid separation are favored at high temperature, exist: hemoglobin C has the so-called retrograde temperature dependence of the solubility, whereby the solubility increases at low temperature [66,102]; dense liquid appears in solutions of several hemoglobin variants upon temperature increase [103,104].

In crystallographic practice, only limited control of temperature is available and experiments are carried out either at room temperature, i.e., around 22 °C, or in cold chambers at 4 °C. Hence, use is made of phase diagrams on coordinates ( $C_{\text{protein}}$ ,  $C_{\text{precipitant}}$ ), similar to the one depicted on Figure 19.9(A). In such phase diagrams, the phase areas of undersaturated solution, metastable solution, unstable solution, and precipitation are delineated. The distinction comes from empirical observations of the behavior of protein solutions in the different parts of the phase diagram. Thus, a crystal placed in an unsaturated solution would dissolve, whereas a crystal placed in a metastable solution would grow. On the other hand, spontaneous nucleation of crystals in the metastable zone is unlikely. Such spontaneous nucleation is expected to occur in the unstable zone. At very high supersaturation, precipitation of amorphous phases occurs. Although it is possible that these phases may contain amyloid fibrils, the issue is had not

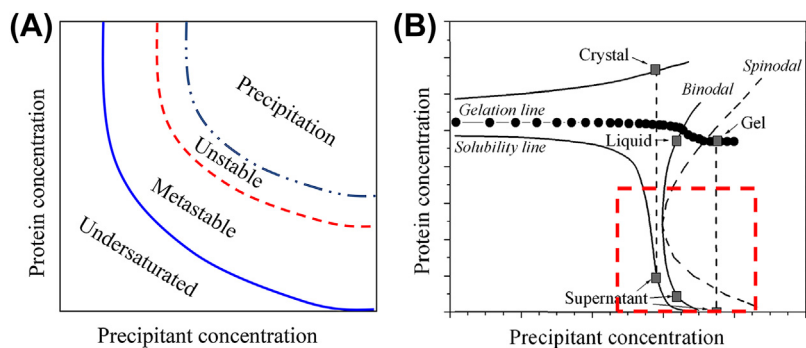


**FIGURE 19.9** The phase diagram of the protein solution in coordinates ( $C_{\text{protein}}$ ,  $C_{\text{precipitant}}$ ). (A) the empirical phase diagram used in protein crystallization work. (B) A theoretical phase diagram highlighting the analogy between higher temperature and lower precipitant concentration as determinants of the phase behavior in protein solutions. With permission from Ref. [105].

been explored because, even if this is so, they would be of little use for structure determinations.

Phase diagrams in  $(C_{\text{protein}}, C_{\text{precipitant}})$  coordinates such as the one in [Figure 19.9\(A\)](#) are used to rationalize and optimize crystallization conditions. It is considered that nucleation should occur at the boundary between the metastable and the unstable zones so that relatively few crystals would form and, the depletion of the solution due to their growth would shift the system into the metastable regime, in which these crystals would grow to advantageous sizes.

Recent theoretical work has demonstrated in most general terms that a protein solution responds to increases in precipitant concentration in the same way that it responds to lower temperature: both of these changes in external parameters drive a transition to condensed phases [105,106]. Thus, the phase diagram in coordinates  $(C_{\text{protein}}, C_{\text{precipitant}})$  in [Figure 19.9\(B\)](#) appears very similar to the one in coordinates  $(C_{\text{protein}}, T)$  in [Figure 19.8](#): the lines for the solubility, concentration of protein in the crystal, the binodal and spinodal for liquid–liquid coexistence, and even the gelation lines are present in both. It is tempting to view the empirical phase diagram in [Figure 19.9\(A\)](#) as a subsection of the diagram in [Figure 19.9\(B\)](#), highlighted by the dashed square. Indeed, it is likely that the boundary between the unsaturated and the metastable zones in [Figure 19.9\(A\)](#) is the solubility line in [Figure 19.9\(B\)](#). However, the analogy ends here: the boundary between the metastable and the unstable zones is likely not the liquid–liquid binodal, but the solution–crystal spinodal plotted in [Figure 19.8](#) and discussed in [Section 19.6.3](#) below. Furthermore, the boundary between the unstable and precipitation zones is again not the liquid–liquid binodal, but an empirical line that may be anywhere below the solution–crystal spinodal.

## 19.4 Methods of Protein Crystallization

The methods for protein crystallization account for the fact that expression, extraction, and purification of a protein are often time-consuming procedures. Hence, wide use is being made of various micro-methods of protein crystallization allowing one set of crystallization experiments in protein solution of droplets of 5–20  $\mu\text{l}$  containing only 0.1–0.5  $\mu\text{g}$  of the protein.

There are four commonly used methods for protein crystallization: dialysis, vapor diffusion, batch crystallization, and liquid–liquid diffusion [107]. Each of these methods uses a smart combination of the transport properties of the proteins and small molecule or polymer additives and elaborate control of convective flows through the size and geometry of the respective cells to achieve a gentle increase of the supersaturation and, along the way, test several combinations of protein and precipitant concentrations for their efficacy in producing crystals, [Figure 19.10](#).

There are numerous commercial cells for microdialysis. In a typical arrangement, the crystallization volume is separated into two parts by a membrane (or, in some cases, gel plug), which is impenetrable for the protein, but allows free passage of the

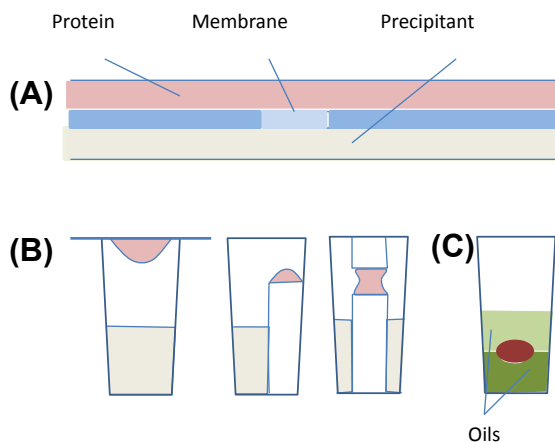


**FIGURE 19.10** Laboratory methods of protein crystallization. (A) The microdialysis method: the volumes holding the protein and the precipitant are separated by a semipermeable membrane. The crystals form in the protein volume. (B) Vapor diffusion methods: hanging drop, sitting drop, and sandwiched drop. (C) The microbatch method.

low-molecular components of the solution, [Figure 19.10a](#). The protein solution and a buffer is held on one side of the membrane and the precipitant is on the other. Crystallization occurs when a precipitant that lowers the protein solubility diffuses through the membrane into the protein-containing cell [\[108\]](#).

The vapor diffusion methods are most commonly used in protein X-ray crystallography. The protein solution is placed in a sealed container, which also hosts a greater volume of solution with a higher concentration of the some of the additives, but without protein, called a reservoir, [Figure 19.10\(B\)](#). Because of the higher additive concentration in the reservoir, the water chemical potential in it is lower and water diffuses toward it through the air space separating the two solution volumes [\[109\]](#). Depending on the geometry of the droplet and the reservoir, this method is divided into hanging drop, sitting drop, and sandwich drop. In the simplest hanging-drop cell, a drop of protein solution containing a small amount of precipitant is placed on a glass plate [\[110,111\]](#). Then the plate with the drop is turned over and placed on top of a cup containing the precipitant solution in concentration sufficient to precipitate the protein. After several days of (mainly water) vapor diffusion, the precipitant and protein concentration in the drop rises and the protein starts to crystallize. The sitting-drop technique is similar with the drop sitting on top of a pedestal rising above the solution reservoir. In the sandwiched-drop technique, the protein solution is held between two surfaces.

In the batch technique, protein and additives are mixed in the solvent at their desired concentrations and placed in an environment of controlled temperature. The containers are monitored for the appearance of crystals. In some implementations of this technique, slow evaporation of solvent is allowed to achieve gentle increase in supersaturation. Recently, a microbatch technique was proposed, illustrated in [Figure 19.10\(C\)](#), in which the protein and precipitant solutions are held between two layers of silicone, perfluorosilicone, or lipid oil [\[112,113\]](#). The water has extremely low solubility in either of

these oils, and so its escape from the solution droplet is very slow. This provides for a gentle increase in supersaturation and increases the chances of crystal formation.

In the liquid–liquid diffusion method, two solutions are loaded at the two ends of a capillary and placed in contact at the middle [114]. This method is similar to the dialysis technique in Figure 19.10(A), and differs from it by the absence of a membrane separating the volumes of the protein and precipitant solutions. One of the solutions contains the precipitant and the other one the protein. As the precipitant and protein diffuse against one another, a continuum of combinations of protein/precipitant concentration ratios is achieved. Furthermore, if a crystal is not formed at a certain location in the capillary, the concentrations of protein and precipitant continuously increase imposing higher supersaturation. On the other hand, if a crystal is formed, the local concentrations of protein and precipitant drop and the constrained geometry of the capillary provides for a gentle supply of these two components mostly through diffusion.

The crystallization conditions are usually found by trial and error, which involves screening tens or even hundreds of drops. At present, special computer-controlled installations, robots, are employed to screen thousands of protein crystallization conditions. Complete automation of all liquid handlings increases the speed, precision, and reproducibility of the experiment. Recent further advances of these methods based on microfluidics have reduced the size of the solution droplets for crystallization down to the nanoliter scale, thus reducing the amount of protein required [14,107,109].

To somewhat rationalize the trial-and-error approach, the influence of various ions on the protein solubility [115–117], dependence of growth rates of different crystal faces on the protein concentration in the solution [118–120], convection and flow rates close to the growing crystal [121–126], and epitaxy of the protein crystals [127] have all been investigated. Relatively weak interaction between the large protein molecules in solution (per unit molecular area), peculiarities of protein structure, and multicomponent composition of mother solutions make the crystallization process extremely sensitive to physical and chemical conditions. The same protein can crystallize in several crystalline forms, depending on the solution composition and pH. For instance, lysozyme crystallizes in tetragonal, monoclinic, triclinic, and orthorhombic polymorph modifications.

In their native environments, the membrane proteins are embedded in the phospholipid bilayer of the cell membrane, where they are held by their hydrophobic midribs. Two approaches to extract the membrane proteins from the membrane and make them mobile have been designed. In the first approach, illustrated in Figure 19.11(A), the membrane proteins are solubilized by coating this midriff with detergent molecules, akin to enclosing them in a detergent micelle [128]. The search for crystallization conditions of the solubilized protein is then carried out as for the water-soluble proteins. The second approach relies on the existence of three-dimensional (3D) structures in high-concentration solutions of some lipids, Figure 19.11(Bb) [129,130]. These structures consist of a lipid bilayer warped into 3D network of rods and junctions, interlaced with aqueous channels.

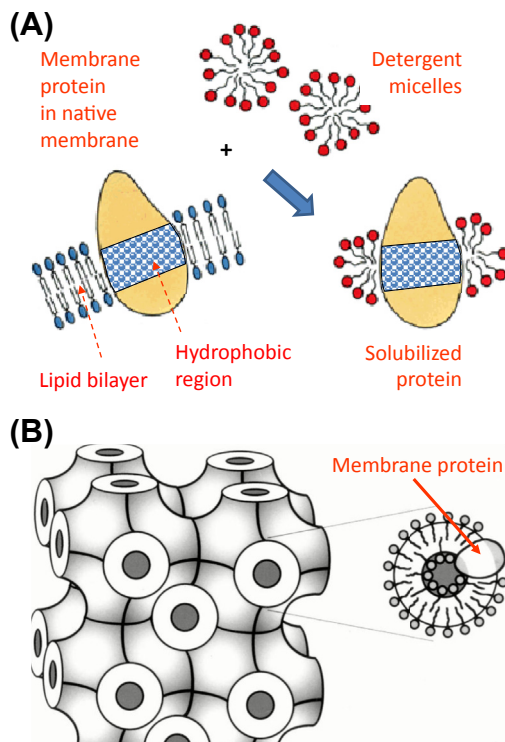


**FIGURE 19.11** Methods of crystallization of membrane proteins. (A) Solubilization by coating the hydrophobic midriff of the molecules with detergent. (B) The membrane protein molecules are embedded in lipidic cubic structures, as the one shown on the left, in which the protein molecule is in an environment resembling the one in the cell membrane.

## 19.5 The Role of Nonprotein Solution Components and the Intermolecular Interactions in Solution

In their native environment, the cytosol, soluble proteins are in a water-based environment at pH around 7.2. In the cytosol, most of the small-molecule components are at low concentrations, and the ionic strength is around 0.3 M [31]. In this environment, proteins are stable against aggregation because of positive natural selection during many years of evolution [131]. The relatively few proteins that crystallize in their native environments: insulin in mammalian pancreases [8], or gluten in grain [132], have been modified in the course of evolution to readily allow crystallization [132].

In the laboratory or an industrial facility, proteins are placed under conditions far removed from native. Even if pH is near the physiological, it is maintained by a buffer, the ions of which are a component foreign to the protein. Furthermore, inorganic, organic, or mixed salts are added and are believed to induce screening of the charges between the protein molecules and in this way facilitate attraction between them and,

eventually, crystallization. Very often, organic molecules, such as acetone, glycerol, polyethylene glycol (PEG), mono-, di-, and polyvalent alcohols and others, are also added [110,111,133]. The effects on the protein molecules of the components of a solution, and the consequences of these molecular-level effects for the complex of processes leading to protein crystals, are even now largely unclear. Below, we summarize a few recent findings in an attempt to provide some initial understanding of the effects of these additives.

Often, the effects of additives on protein crystallization are cast in the term specific interactions. In a subset of these cases, in which divalent or polyvalent additives are used, the specific interactions are bridges, in which an additive molecule binds to two adjacent protein molecules in the crystal. The role of a variety of additives in protein crystallization with two or more functional groups: di- and tri-carboxylic acids, diamine compounds, molecules bearing one or more sulfonyl or phosphate groups, and a broad range of common biochemicals, coenzymes, biological effectors, and ligands was analyzed in Refs. [85,134]. It was found that the polyvalent additives serve as bridges between protein molecules in the crystal and in this way facilitate crystallization. However, in many cases the additive molecules are monovalent and cannot serve as bridges and the term specific interactions is left as a placeholder for unclear.

A viewpoint stemming from recent experimental and theoretical results is that all of these components have one common role at the molecular level: they modify the structure of the water shell around the protein molecules to allow intermolecular contacts compatible with a crystallographic arrangement. Although the modification of the water structure may be the most significant effect common for many additives, it is not the only one: many additives may serve as intermediates in bridging interactions [85]; salts, polymers and other organic additives at concentrations commensurate to that of water (55.5 M). Thus, in a 20% w/v solution of PEG, which is about 4.5 M with respect to the  $-\text{CH}_2\text{CH}_2\text{O}-$  units, with each of them binding four molecules of water [135], PEG lowers the water activity by 18 M and may affect the activity of the bulk water, etc.

In this subsection, we examine how the added solution components: buffer ions, precipitant ions, and organic additives modify these water structures. Our objective is to provide a framework, within which the action of the additives tested by a crystallization practitioner can be rationalized and the search for additives yielding useful crystals can be accelerated.

### 19.5.1 Types of Interaction between Protein Molecules in Solution

As discussed above, protein crystals grow out of solutions containing inorganic and organic ions, as well as numerous molecular species. Traditionally, it has been assumed that electrolytes induce crystallization (or other types of solid-phase formation) by screening the electrostatic repulsion between the like-charged protein molecules.

Reference is often made to the Derjaguin, Landau, Verwey, and Overbeek (DLVO) theory of colloid stability [136,137], which is based on the balance between van der Waals attraction and electrostatic repulsion mediated by the electrolyte in the solution.

For the electrostatic part of the DLVO potential, the solution of the Poisson–Boltzmann equation for the potential energy  $U_{el}$  between two charged spheres at a distance  $r$  is [138]

$$U_{el}(r) = \frac{(z_0 e)}{\varepsilon} \frac{\exp(2\kappa a)}{(1 + \kappa a)^2} \frac{\exp(-\kappa r)}{r}, \quad (19.3)$$

in which  $z_0$  is the number of charges per protein molecule,  $e$  is the elementary charge,  $\varepsilon$  is the dielectric constant of the solvent,  $n_i$  and  $z_i$  are, respectively, the number ionic concentration and charge. The constant  $\kappa$  is the Debye–Hückel inverse screening length defined by

$$\kappa = \sqrt{\frac{4\pi e^2}{\varepsilon k_B T}} \times I, \quad I = \frac{1}{2} \sum_i n_i z_i^2 \quad (19.4)$$

in which  $k_B$  and  $T$  are the Boltzmann constant and absolute temperature, respectively, and  $I$  is the solution ionic strength.

The attractive part of the DLVO potential comes from the van der Waals dispersion interactions. In a dielectric medium, this potential is given by [138]

$$U_{vdw}(r) = -\frac{A_H}{12} \left[ \frac{1}{(r+1)^2} + \frac{1}{r^2+2r} + 2 \ln \left( \frac{r^2+2r}{(r+1)^2} \right) \right] \quad (19.5)$$

in which  $A_H$  is the Hamaker constant, independent of electrolyte type or concentration.

A common way to evaluate the interaction between protein molecules in solution is via the second osmotic virial coefficient  $A_2$  [139,140]. This  $A_2$  can be determined by light, X-ray, and neutron-scattering techniques [87,140–142]; recently, methods based on self-interaction chromatography have been developed [143,144]. Static light scattering is a reliable method for  $A_2$  determination, available in many laboratories. The method is based on recording the concentration dependence of the scattered light intensity. The Raleigh ratio  $R_\theta = I_\theta/I_0$ , in which  $I_\theta$  is the intensity scattered at angle  $\theta$ , typically,  $90^\circ$ , and  $I_0$  is the incident intensity, is plotted as a function of the protein concentration  $C$ , the so-called Debye plot [145]

$$\frac{KC}{R_\theta} = \frac{1}{M_w} (1 + 2A_2 M_w C), \quad (19.6)$$

in which  $M_w$  is the molecular mass of the protein, and  $K = 1/N_A (2\pi n_0/\lambda^2)^2 (dn/dC)^2$  is a constant,  $(dn/dC)$  is the increment of the solution refractive index with protein concentration,  $N_A$  is Avogadro's number,  $\lambda$  is the wavelength, and  $n_0$  is the refractive index of the solvent. The dimensionless form of  $A_2$  in Eqn (19.6) is

$$B_2 = \frac{3A_2 M_w^2}{4\pi N_A d_h^3}. \quad (19.7)$$

The link between the experimentally observed second virial coefficients  $A_2$  and  $B_2$  and the interaction potentials between the molecules  $U(r)$  comes from the definition of  $B_2$  [139]

$$B_2(T) = 12 \int_0^\infty \left[ 1 - \exp\left(-\frac{U(\tilde{r}, T)}{k_B T}\right) \right] \tilde{r}^2 d\tilde{r}, \quad \tilde{r} = r/2a. \quad (19.8)$$

According to Eqn (19.8),  $B_2$  is an integral characteristic of the interaction potential  $U(r)$ . Hence,  $U$  cannot be directly evaluated from data on  $B_2$ . However, by recording the dependence of  $B_2$  on external parameters of the solutions, e.g., electrolyte concentration [84,89], concentration of an additive [146], temperature [64,95], or others, valid conclusions about the role of the tested components on the intermolecular interactions can be formulated.

The second virial coefficient is one of the few thermodynamics concepts (solubility is another one) that are widely used by protein crystallographers in the interpretation of the results of crystallization trials. The reason for this is a correlation found in the early 1990s between the values of the  $A_2$  [140,147,148]. It was found that if  $A_2$  is mildly negative, corresponding to a weak average attraction between the molecules in a solution, relatively large crystals of good perfection form. If  $A_2$  is positive, crystals do not form, and strongly negative values of  $A_2$  lead to precipitation [140,147,148]. The range of values of  $A_2$  suitable for crystallization was named the crystallization window [140,148].

As justifications for this observation, two sets of theoretical observations were offered. In the first one, the nature of  $A_2$  and  $B_2$  as integral characteristics of the interactions between pairs of protein molecules was highlighted [80,82,84,86,87,90,143,144,149–155]. In the second approach, a thermodynamic correlation between the second virial coefficient and the protein solubility was derived, with heavy approximation, and in a few cases experimentally demonstrated [64,156].

In fact, there are no fundamental reasons why the second virial coefficient and the solubility or crystallizability of a protein should be correlated. The solubility is the result of the balance between the interactions between protein molecules in the solution and those in the crystal. Because of the rotational and translational mobility of the molecules, the solution interactions are averaged over all distances and angles. The interactions in the crystal only occur at the surface patches in contact with patches from other molecules. On the other hand,  $A_2$  and  $B_2$  are averaged characteristics of the interactions in the solution. This averaging masks the role of the locations of contacts in the crystal, and is the basis of the different response of  $B_2$  and the solubility to variations in solution parameters.

By now, there are numerous observations in the literature of protein crystals forming under conditions of positive  $A_2$  and of uncorrelated changes of  $A_2$  and the solubility in response to a solution parameter. An example is the crystals of lumazine synthase, depicted in Figure 19.12 Ref. [65]. Although  $A_2$  stays positive at phosphate concentrations up to 1.3 M, crystals form at any phosphate concentration higher than 0.5 M.

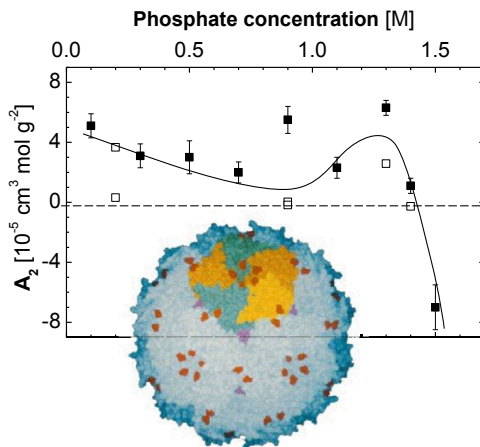


**FIGURE 19.12** The dependence of the second virial coefficient  $A_2$  on the concentration of the phosphate buffer at 20 °C. Closed and open symbols denote two independent series of determinations. Solid line is just a guide for the eye. Horizontal dashed line indicates value of  $A_2 = 3.2 \times 10^{-6} \text{ cm}^3 \text{ mol g}^{-2}$  for noninteracting hard spheres of volume and mass equal to those of the lumazine synthase molecule. (From Ref. [42].) Insert: A model of the lumazine synthase molecule. The molecule has diameter of  $\sim 15.6 \text{ nm}$  and consists 60 identical subunits. (With permission from Ref. [65].)

Furthermore, the variation of  $A_2$  in Figure 19.12 and the solubility response to  $C_{\text{phosphate}}$  from Ref. [65] are uncorrelated: the solubility decreases steeply as the phosphate concentration is increased above 0.1 M.

### 19.5.2 Deviations from the Simple Colloid Approach

There are several problems with the above interpretation of the interactions between protein molecules and of electrolyte function. At a relatively moderate ionic strength of 0.1 M, corresponding to concentrations of monovalent electrolytes, such as NaCl or  $\text{KH}_2\text{PO}_4$ , of 0.1 M, the screening length  $\kappa^{-1}$  is  $\sim 10 \text{ \AA}$  [89,157], i.e., not sufficiently longer than the size of the ions and solvent molecules to warrant the continuum approximation underlying the above theories. Even if we ignore this inconsistency and expect the theory to produce results at least qualitatively adequate to reality, we see that the predicted range of the interactions is significantly shorter than the molecular size and the typical intermolecular distances in a solution. That is, the electrostatic repulsion is already suppressed, and further increases in the electrolyte concentration should not affect the protein interactions and the resulting thermodynamics and kinetics; see, e.g., [158,159]. The threshold concentration for “suppression” of electrostatic interactions is even lower for divalent, such as  $\text{CaSO}_4$ , or trivalent, such as  $\text{Al}(\text{NO}_3)_3$ , electrolytes [137].

A related contradiction in the application of the colloid stability approach to protein solutions and protein crystallization is the assumption of isotropic interactions. Although this assumption maybe justified for relatively large colloid particles, it is

certainly a poor approximation for protein molecules: for protein molecules, the length scale of the anisotropy is the size of the surface amino acid residues,  $\sim 0.5$  nm, and this is not sufficiently smaller than the molecule size of a few nanometers to justify the isotropic assumption. On the other hand, due to the rotational diffusion of the protein molecules, the isotropic assumption may be valid for interactions at longer separations. To estimate the typical size at which the anisotropy of a protein molecule becomes insignificant for its interactions with another protein molecule, we evaluate the mean length  $\langle \Delta x^2 \rangle^{1/2}$  of translational diffusion during the mean time of molecule rotation  $\tau$ . Typical rotational diffusivities of protein molecules are on the order of  $D_{\text{rot}} \approx 10^6 \text{ s}^{-1}$ , so that  $\tau \approx 4 \times 10^{-5} \text{ s}$ . With the typical translational diffusivities of  $D_{\text{rot}} \approx 10^{-7} - 10^{-6} \text{ cm}^2 \text{ s}^{-1}$ ,  $\langle \Delta x^2 \rangle^{1/2} \approx 10^{-6} \text{ cm} = 10 \text{ nm}$ .

This estimate shows that anisotropic interactions should be considered for intermolecular separations closer than 10 nm. A simple estimate [27] shows that such separations are reached for protein solution concentrations higher than  $\sim 50 \text{ mg ml}^{-1}$ . Thus, the assumption of isotropic interactions may be adequate in discussing dilute solutions, but would fail to describe dense liquids and crystals. More importantly, the isotropy assumption would be inadequate in the description of equilibria involving dense liquids and crystals even if the other equilibrium state is the dilute solution.

Although numerous systems have displayed decreasing repulsion with increasing salt concentrations predicted by Eqns (19.3) and (19.4) [89], observations of gross deviations from the predictions of the DLVO theory even at the qualitative level abound. Thus, it was found that different salts at the same ionic strengths have different effects. These differences have been cast in the form of a ‘‘Hofmeister series’’ of co-solvent ions. However, even this empirical classification of the strength for the individual ions is not obeyed for all proteins. It appears that for an often-studied protein, lysozyme, the ‘‘reverse Hofmeister series’’ applies [117]. For other proteins, completely different relative efficacies of the individual ions have been recorded [160].

As another deviation, a careful quantification of the interaction between lysozyme molecules found that the Hamaker constant depends not only on the type, but also on the concentration of the counter ions; that at the ionic strengths employed the DLVO theory predicts complete loss of stability of the protein solution, whereas the solution is stable at significantly higher salt concentrations [89]. The unequivocal conclusion of the authors, in line with the other evidence summarized above, was that specific protein-ion binding strongly modifies the interactions included in the simple colloid model [89].

In light of these contradictions, other types of interactions have been discussed. The thermodynamic evidence, discussed in Section 19.3.2 above, favors the hydration repulsion and the hydrophobic attraction. Both of these two types of interaction are due to the structuring of water molecules on the surface of the protein molecule. Their different nature—attraction versus repulsion—is due to the different polarity of the amino acid residues at which the water molecules align: If the protein surface is polar, the water molecules are firmly attached to it and their removal, upon the approach of another protein molecule, leads to a free-energy increase [161–163]. At nonpolar protein

surfaces, water structuring is driven by the maximization of the number of hydrogen bonds per water molecule while the water molecules remain unattached to the protein. When another protein molecule approaches, these waters are set free and this leads to an entropy increase, free energy decrease, and effective attraction between the molecules [53,58]. Both the hydration and the hydrophobic interactions may be enhanced by electrolytes. Modification of hydrophobic attraction requires electrolyte concentrations of order moles per liter for noticeable effects [162–164], while the build-up of hydrated ions at polar protein molecules surface has been shown to enhance hydration repulsion even if the ion concentration is in the millimolar range [158,159]. The effects of electrolytes, present in protein solutions as buffers or salt precipitants, and of uncharged small molecules on the hydration layer around protein molecules are discussed below.

### 19.5.3 Buffers, Salts and Organic Molecules and the Water Structure

#### 19.5.3.1 Buffers

Buffers are solutions of weak acids (or, sometimes, weak bases) and their salts. They maintain the solution pH at a relatively fixed value independent of the addition of other solution components. A buffer is most effective at a pH that is near the  $pK_a$  of its component acid [31]. If a protein is placed in a solution the pH of which is fixed by a buffer, some of the protein's acidic and basic residues will have a  $pK_a$  above the set pH, whereas the  $pK_a$  of other such residues will be below this pH. Thus, some of the acidic and basic residues will be protonated; others will be neutral; whereas a third group will be deprotonated. The association of a proton,  $H^+$ , shifts the charge of the protein molecule by one elementary unit in the positive direction, whereas the dissociation of a protein shifts the charge by one unit in the negative direction. In turn, the molecular charges determine the strength of the Coulomb forces between the protein molecules. Thus, buffers set the charge of the protein molecules in solution and in this way control the electrostatic intermolecular interactions.

The possibility that buffers play an extra role and the role of buffers for the interactions between protein molecules in solutions was addressed on the example of the protein lumazine synthase [65]. This protein crystallizes in phosphate buffer at  $pH = 8.7$ . For insight into the phosphate contribution to the interactions between the lumazine synthase molecules, the dependence of the second osmotic virial coefficient  $A_2$  on the concentration of the phosphate buffer was determined, Figure 19.12 [65]. The values of  $A_2$  in Figure 19.12 at  $C_{\text{phosphate}} < 1.4$  M are significantly greater than the values for noninteracting hard spheres,  $A_2^{HS} = 4V_m M_w^{-2}$ , ( $V_m$  is the molar volume of lumazine synthase). This suggests significant repulsion between the molecules, which cannot be due to the action of electric double-layer forces [89,165]. The reason is that, at ionic strengths  $>0.25$  M (the ionic strength of a phosphate buffer at  $pH = 8.7$  is near 0.3 at  $C_{\text{phosphate}} = 0.1$  M), these forces are almost fully screened [158,159]. Hence, the repulsion reflected in Figure 19.12 must be of nonelectrostatic origin. Because the list of repulsive

forces in solution contains two items, and the first one, electrostatic, is excluded, we are left with the second source of repulsion, structuring of the solvent: water, phosphate, and cations, around the protein molecules. Such solvent structures, as discussed above, introduce a repulsive minimum at molecular separations  $\sim 1$  nm, corresponding to the thickness of a shell of several water molecules [41,44,158,159,166,167]. This intermediate-range repulsion is the likely reason for the large positive  $A_2$  values seen in Figure 19.12.

In view of the lack of correlation between the angle-averaged intermolecular interactions and the crystallization behavior, the role of buffers on the protein crystallizability should be independently examined. Figure 19.13 shows crystals of the protein lysozyme from hen egg white, grown from a 50 mM potassium phosphate buffer at pH 7.2, without the addition of other components. The crystallization times were several hours, near those typically observed with this protein. However, when the protein was placed in solution with the same pH, maintained by HEPES (N-2-Hydroxyethylpiperazine-N'-2-ethanesulfonic acid) buffer at the same concentrations of 50 mM (both phosphate and HEPES have polyvalent anions and at pH = 7.2 maintain approximately equal ionic strength), no crystals formed in any of several runs even after days of observation. It is unlikely that the crystals formed in the presence of phosphate are due to phosphate bridges between the lysozyme molecules: the crystals in Figure 19.13 are tetragonal and similar to lysozyme crystals formed with many other inorganic additives. The contrast between the actions of the two buffers indicates that the buffers affect the interactions between patches on the protein molecular surface, involved in intermolecular contacts. Because the two tested buffers maintain the same pH, the affected interactions are not electrostatic. Most likely, the buffers are involved in the formation of the water structures at the contact patches and, in this way, the nature of the buffer determines the protein crystallizability [168].

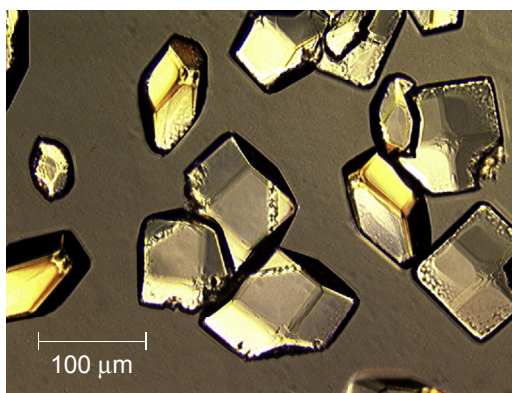


**FIGURE 19.13** Crystal of lysozyme formed at pH = 7.2 in phosphate buffer with concentration 0.05 M, corresponding to ionic strength  $\sim 0.12$  M. *W. Pan, private communication, 2007.*

## 19.4.3.2 Salts

Protein crystals grow out of solutions containing inorganic and organic ions, as well as numerous molecular species. Traditionally, it has been assumed that electrolytes induce crystallization (or other types of solid-phase formation) by screening the electrostatic repulsion between the like-charged protein molecules. In light of the contradictions between the application of the colloid stability approach to protein crystallization and the experimental observation, discussed previously, other types of interactions that may be affected by ions in the solution have been invoked. Evidence for one type of such interaction is the unusual dependence of the dimensionless second osmotic virial coefficient  $A_2$  in apoferritin solutions on the concentration of  $\text{Na}^+$  ions. This dependence exhibits a minimum at  $[\text{Na}^+]$  between 0.1 and 0.15 M, see Figure 19.14 [64,158,159]. The value of  $A_2$  at the minimum of  $\sim 4$  is equal to that expected for noninteracting hard spheres, indicating that at these  $[\text{Na}^+]$ , electrostatic repulsion is completely suppressed. The ascending branch of this dependence is a manifestation of a surprisingly strong repulsion between the molecules at electrolyte concentrations about and above 0.2 M, at which electrostatic interactions are insignificant. This strong deviation from the predictions of the DLVO theory was attributed to the water structuring, enhanced by the accumulation of hydrophilic counter ions around the apoferritin molecules, see Figure 19.15 [34,64,158,159], giving rise to hydration repulsive forces [41,164].

The addition of even 0.01 M  $\text{Cd}^{2+}$  leads to a drop of the virial coefficient in a solution with 0.2 M  $\text{Na}^+$  from the relatively large positive value typical of the hydration repulsion, to about zero [158]. Note that even these low  $\text{Cd}^{2+}$  concentrations are orders of magnitude higher than the apoferritin concentrations (in the micromolar range in a 1 mg/mL solution of this protein with  $M_w = 450,000$  Da). However, further increases of the  $[\text{Cd}^{2+}]$  up to 0.22 M = 2.5% (w/v) (the value typically used in crystallization trials) did not lower the value of  $A_2$  further and it remained around zero. We interpret the action of  $\text{Cd}^{2+}$  on the molecular interactions in the following way. The strong coordination bond

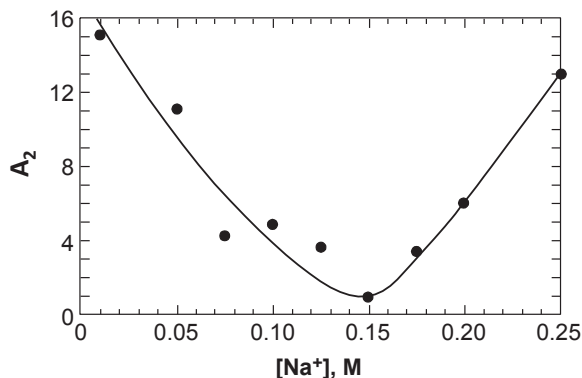
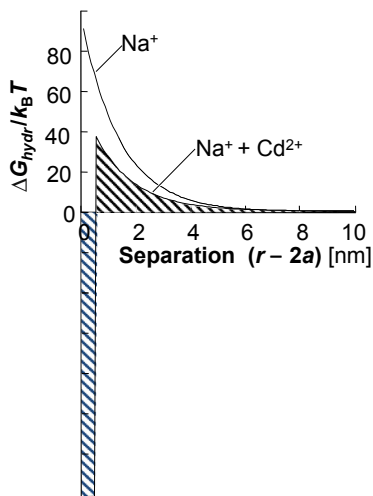


FIGURE 19.14 Dependence of the dimensionless second osmotic virial coefficient  $A_2$  on the concentration of sodium ions  $[\text{Na}^+]$ . Curve is just a guide for the eye. With permission from Ref. [159].



**FIGURE 19.15** Mean-field potential of interaction between two apoferritin molecules with diameter  $2a$  at a distance  $r$  between their centers. Upper curve: potential of hydration forces in the presence of  $0.2\text{ M Na}^+$ ; lower curve: likely potential in the presence of  $0.2\text{ M Na}^+$  and  $0.22\text{ M Cd}^{2+}$ .

that  $\text{Cd}^{2+}$  establishes between two apoferritin molecules [169–171] is reflected in the potential as a deep minimum limited to distances of about  $0.2\text{ nm}$ , i.e., comparable to the size of the  $\text{Cd}^{2+}$  ion. If, in addition to this effect,  $\text{Cd}^{2+}$  would also destroy the hydration shell around each molecule, this deep minimum would lead to highly negative  $B_2$  values. The closeness of the actual values to zero indicates that the repulsive hydration shells are present even with the  $\text{Cd}^{2+}$  in the solution. The resulting potential around an apoferritin molecule in a crystallizing solution containing  $0.2\text{ M Na}^+$  and  $0.22\text{ M Cd}^{2+}$  is schematically depicted in Figure 19.15.

The potential depicted in Figure 19.15 differs from those modeled in Figure 19.6 only in the nature of the deep minimum close to the protein molecular surface: in the system, modeled in Figure 19.6, the minimum is due to the van der Waals attraction, whereas in Figure 19.15 it reflects the  $\text{Cd}^{2+}$  mediated bond. In both cases, the local maximum at intermediate separations is due to the structuring of the solvent. A smaller difference is that in the case depicted in Figure 19.15, the solvent structures include sodium cations, whereas in Figure 19.6, only water molecules partake in the shell around the protein molecules.

Previously, we provided an example of hydration repulsion, due to the buildup of hydrated ions at the surface of the protein molecules [41,161–164]. Another type of water-structuring interactions, which has always been considered by the protein biochemists and physical chemists, is the hydrophobic attraction. It is important to note that the hydrophobic attraction is also enhanced by electrolytes, organic molecules, and other solution components [69,172,173]. Typically, it is assumed that the required concentrations of the additives needed for the engineering of the hydrophobic bonds are higher, up to moles per liter.

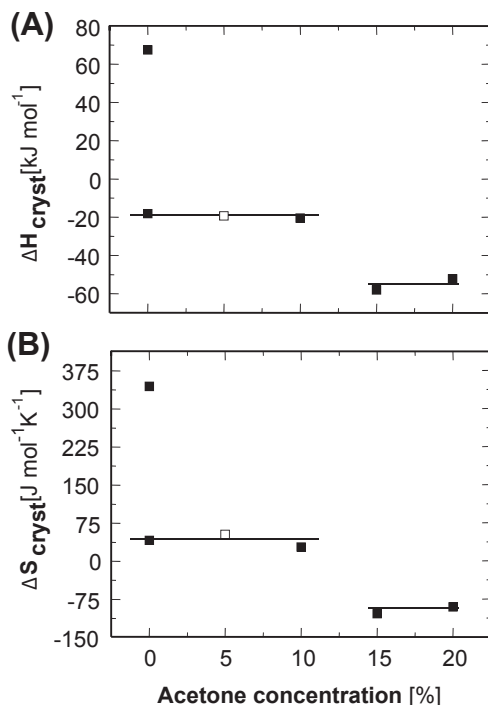


**FIGURE 19.16** Variations with acetone concentration of (A) standard crystallization enthalpy and (B) standard entropy change for crystallization of insulin. *With permission from Ref. [68].*

### 19.4.3.3 Organic Molecules

The role that small organic molecules play in the stability of protein solutions and in protein crystallization is very poorly understood. Numerous facts on the effects of molecules such as mono-, di- and polyalcohols, ketones, polymers, ethers, and others, have been cast in descriptive terms, which carry little information about the molecular mechanism of action of the respective additive and weak rationalization of its applicability to new systems.

One compound, the role of which in protein crystallization has been rationalized is PEG; it has been suggested that its presence enhances protein intermolecular attraction through the action of depletion forces [101,174–176]. This explanation is somewhat problematic: the action of the physical mechanism behind the depletion forces requires that the interacting molecules be significantly larger in size than the dimensions of the random PEG coil in solution (which has a hydrodynamic radius equal to that of a protein with about three-fold greater molecular mass), and this is not the case for many proteins for which PEG is employed [29].

For deeper insight into the mechanisms of organic additives, the action of acetone on the intermolecular interactions in insulin solutions, and on the crystallization of this protein was studied. The temperature dependence of the solubility of insulin at varying

concentration of the co-solvent acetone revealed that, as a rule, the solubility increases as temperature increases. The entropy change upon crystallization  $\Delta S_{\text{cryst}}^{\circ}$  is  $\sim 35 \text{ J mol}^{-1} \text{ K}^{-1}$  at the low-acetone-concentration range, and drops to about  $-110 \text{ J mol}^{-1} \text{ K}^{-1}$  at the higher, Figure 19.16(B) [68]. As discussed above, positive values of the crystallization entropy indicate release of solvent, mostly water, molecules structured around the hydrophobic patches on the insulin molecules' surface in the solution. As acetone concentration increases to 15% and above, unstructured acetone molecules apparently displace the waters, and their contribution to  $\Delta S_{\text{cryst}}^{\circ}$  is minimal. This shifts  $\Delta S_{\text{cryst}}^{\circ}$  to a negative value close to the value expected for tying up of one insulin molecule from the solution. The accompanying increase in  $\Delta H_{\text{cryst}}^{\circ}$  from about  $-20 \text{ kJ}\cdot\text{mol}^{-1}$  in acetone-free solutions and at low acetone concentration to about  $-55 \text{ kJ}\cdot\text{mol}^{-1}$  at acetone concentrations above 15%, Figure 19.16(A), suggests that the water structured around the hydrophobic surface moieties has a minimal enthalpy effect, likely due to the small size of these moieties [68]. The solubility is a reflection of the balance of thermodynamic variables between two states: molecules in solution and those in the crystal. Thus, the variations of the thermodynamic variable for insulin crystallization with acetone concentration reveal that acetone destroys the water structures existing in solution at the sites on intermolecular contacts in the crystal.

This conclusion is supported by the determinations of the second osmotic virial coefficient  $A_2$  from the data in Figure 19.17. Both Debye plots in Figure 19.17 yield negative values of the second osmotic virial coefficient  $A_2$ , indicating both in the presence and absence of acetone the interactions averaged over all intermolecular separations and all body angles are attractive. Insulin forms nice rhombohedral crystals in both solvents. Because the crystals formed in both solvents are identical, it is likely that the depth and width of the respective minima are also identical. Then, the lower magnitude of  $A_2$  in purely aqueous solvent indicates that a repulsive maximum exists at

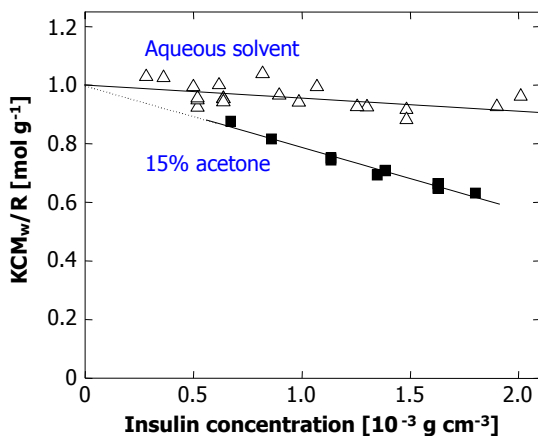


FIGURE 19.17 Determination of the second osmotic virial coefficient  $A_2$  of insulin, in crystallizing solutions in the presence and absence of acetone.  $A_2$  is the slope of the straight lines.

intermediate separations and partially compensates for the minimum in  $B_2$  value. The most likely molecular mechanism that underlies this repulsive maximum is structuring of the water molecules around the insulin molecules in purely aqueous solvents. The addition of acetone destroys this structure and leads to a lower values of  $A_2$ .

Correlating the effects of acetone on the insulin solubility to those on the second virial coefficient, we note another deviation from the general rule that lower algebraic value of  $A_2$  leads to lower solubility: as discussed above, insulin solubility in the presence of acetone is higher than in purely aqueous solvents. To understand this deviation, we note that acetone destroys the water structures both at the molecular surface sites involved in crystal contacts, which is reflected in the solubility, and over the entire surface of the molecule, reflected in  $A_2$ . The reason for the deviation from the general correlation between  $A_2$  and the solubility, despite the similarity of the action of acetone at the molecular level, are the entropy consequences of the structured water. When the water structures are destroyed, the crystallization entropy decreases, and the crystallization free energy increases, leading to higher solubility. This entropy effect on the crystallization free energy is sufficiently strong to compensate for the decrease in crystallization enthalpy in [Figure 19.16\(A\)](#). On the other hand, the destruction of the water structures is accompanied by decrease in  $A_2$ , as discussed previously.

## 19.6 Crystal Nucleation

Because of its crucial place at the start of the crystallization process, the nucleation of protein crystals determines many properties of the emerging crystalline phase. It is obvious that the nucleation selects the polymorphic form and if a different polymorph is desired, conditions at which its nucleation is faster than that of the other possible polymorphs should be sought. If nucleation is fast, many crystals form nearly simultaneously. Their growth depletes the medium of solute and may lead to cessation of nucleation at the later stages of crystallization. Thus, the majority of crystals grow to approximately identical sizes. In contrast, if nucleation is slow and fewer crystals nucleate at a time, the supersaturation in the solution drops slowly, the nucleation of new crystals continues and a population of crystals of various sizes forms. Ultimately, if nucleation is hindered everywhere in the growth container but at a few selected spots, crystals only nucleate at these spots and grow large before the solution is depleted of nutrient. Hence, control of nucleation is a means to control size, size distribution, polymorphism, and other properties of the crystals, [Figure 19.18](#).

### 19.6.1 The Classical Nucleation Theory

#### 19.6.1.1 Thermodynamics

The formation of crystals is a first-order phase transition. Accordingly, it is characterized by nonzero latent heat, the crystallization enthalpy  $\Delta H_{cryst}^0$ . More significant for the kinetics of nucleation is the second feature of first-order phase transitions: the

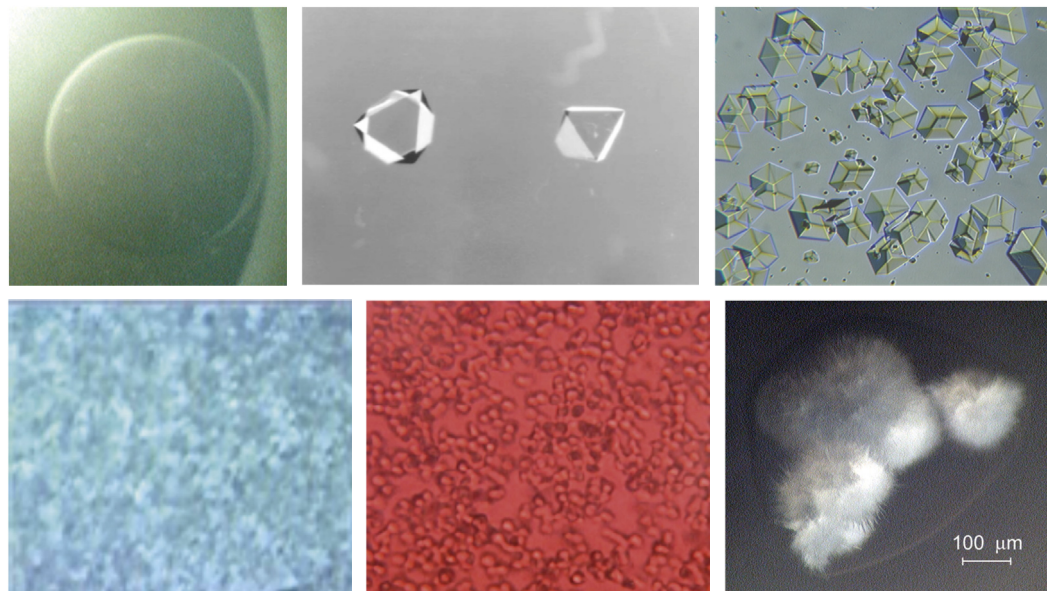


**FIGURE 19.18** Nucleation largely determines the outcome of crystallization. Examples of protein crystals and other condensed phases illustrate, at top left, the failure of nucleation, in which no crystals or other condensed phase are generated in a supersaturated lysozyme solution; and clockwise from there, the nucleation of two crystals of apoferritin, which grow to a relatively large size; the nucleation of numerous crystals of insulin, which have a broad size distribution; needle-like crystals of lysozyme; dense liquid droplets in a solution of hemoglobin A, and, at bottom left, amorphous precipitate in a supersaturated lysozyme solution. Scale bar is shown in bottom right panel.

discontinuity of the concentration at the phase boundary. Because of this discontinuity, the solution–crystal boundary possesses nonzero surface free energy. If a small piece of a condensed phase forms in a supersaturated solution, the surface free energy of the emerging phase boundary makes this process unfavorable. Thus, a very limited number of embryos of the condensed phase appear because of the few fluctuations which overcome the free-energy barrier. The first step in the formation of a new phase, in which the kinetics of the phase transformation is determined by this barrier, is called nucleation.

The thermodynamic part of the classical nucleation theory was developed by J.W. Gibbs in two papers [177,178]. We present it here with two modifications: we consider the formation of a crystal in contrast to the J.W. Gibbs' consideration of a liquid droplet, and we assume that the initial crystallite is shaped like a cube with a side  $a$  instead of assuming a spherical droplet of a certain radius. In a supersaturated solution, i.e., one in which the solute chemical potential is higher than that of molecules in the crystal so that  $\Delta\mu = \mu_{\text{solute}} - \mu_{\text{crystal}} > 0$ , the formation of such a cluster leads to a free energy loss of  $-n\Delta\mu$ . On the other hand, the creation of the phase boundary with area  $S$  and surface free energy  $\alpha$  between the cluster and the solution leads to a free energy gain  $S\alpha$ . Assuming

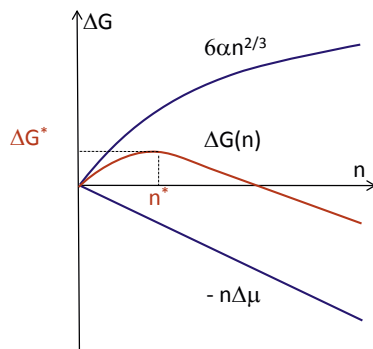


**FIGURE 19.19** Illustration of the thermodynamic effects of formation of a crystal.  $n$ : number of molecules in crystalline embryo;  $\Delta\mu$ : solution supersaturation;  $\alpha$ : surface free energy;  $\Delta G$ : free energy; \* denotes critical cluster.

that the crystal cluster is a cube,  $S = 6a^2n^{2/3}$ ; other shapes will lead to coefficients different than  $6a^2$  in this relation, but the  $2/3$  scaling with  $n$  will be preserved for all three-dimensional nuclei. Thus.

$$\Delta G(n) = -n\Delta\mu + 6a^2n^{2/3}\alpha. \quad (19.9)$$

This dependence is plotted in [Figure 19.19](#).

Differentiating  $\Delta G(n)$ , we find the cluster size  $n^*$  for which  $\Delta G$  passes through a maximum  $\Delta G^*$

$$n^* = \frac{64\Omega^2\alpha^3}{\Delta\mu^3} \quad \text{and} \quad \Delta G^* = \frac{32\Omega^2\alpha^3}{\Delta\mu^2} = \frac{1}{2}n^*\Delta\mu, \quad (19.10)$$

in which  $\Omega = a$  [3] is the volume occupied by a molecule in the crystal.

As [Figure 19.19](#) illustrates,  $\Delta G^*$  is the barrier that must be overcome to form a crystal from solute molecules. The growth of clusters smaller than  $n^*$  is associated with an increase of free energy and is unfavorable. Clusters may still grow to such sizes because of fluctuation, but because a driving force exists for the decay of these clusters, such events are rare. On the other hand, if as a result of a fluctuation a cluster reaches a size greater than  $n^*$ , its growth is accompanied by a decrease of free energy and occurs spontaneously. A cluster of size  $n^*$  has equal probabilities of growth and decay and, hence, such clusters are called critical, and they represent the nuclei of the new phase. Note that, by this definition, all nuclei are critical and the term critical nuclei is redundant [179].

### 19.6.1.2 The Rate of Crystal Nucleation

To model the nucleation rate  $J$ , i.e., the number of nuclei which appear in a unit solution volume per unit time; M. Volmer postulated—in analogy to the Arrhenius equation—that  $J = J_0 \exp(-\Delta G^*/k_B T)$ , in which  $k_B$  is the Boltzmann constant [180]. The external parameters, such as temperature, concentration, and pressure, as well as the solution supersaturation, affect the nucleation rate mostly through  $\Delta G^*$  according to [Eqn \(19.10\)](#); the effects on  $J_0$  are significantly weaker. There are numerous statistical-mechanical derivations of the nucleation rate law within the assumption of the classical nucleation

theory; for an example, see Ref. [181]. The final expression of these derivations can be represented as [182]

$$J = \nu^* Z n \exp(-G^*/k_B T) \quad (19.11)$$

in which  $\nu^*$  is the rate of attachment of monomers to the nucleus,  $Z$  is the Zeldovich factor, which accounts for the width of the free-energy profile  $\Delta G(n)$  in the vicinity of the maximum  $\Delta G^*$ , see Figure 19.19, and  $n$  is the number density of molecules in the solution. Equation (19.11) assumes that the replacement partition function of the nucleus [181,182] is equal to one. This factor accounts for the additional stabilization of the nuclei due to their translational and rotational degrees of freedom [183]. Neglecting it is a reasonable assumption for crystal nuclei suspended in a viscous solution; this would not be the case for nucleation in the gas phase.

## 19.6.2 Experimental Data on the Nucleation Kinetics

### 19.6.2.1 Evolution of Aggregate Sizes

The time evolution of the sizes of large aggregates observed by dynamic light scattering in supersaturated solutions of satellite tobacco mosaic virus (STMV) is shown in Figure 19.20 [184,185]. This figure shows that the size of these large aggregates  $R$  reaches a critical value  $R_c$ , after which the size increase is fast. The higher the STMV supersaturation in solution, the shorter the time needed to reach this critical  $R_c$ . These observations agree with the predictions of the classical nucleation theory for the nucleation of STMV crystals. The slow initial increase of  $R$  corresponds to the attempts by subcritical clusters, by fluctuations, to climb on the top of the free energy barrier in Figure 19.19. After the barrier is overcome, the addition of new molecules to the cluster brings about decrease, rather than increase, of the cluster's free energy. Thus,  $R_c$  was identified as the radius of the nucleus  $R_c = \frac{\alpha}{2} \sqrt[3]{n^*}$  (for the definition of  $n^*$ , see Eqn (19.10) above). Similar experiments were carried out with solutions of horse spleen ferritin, apoferritin, and pumpkin seed globulin. The  $R_c$  dependencies on the supersaturation  $\sigma \equiv \Delta\mu/k_B T$  are plotted in Figure 19.21 and they agree with the proportionality between  $R_c$  and  $1/\sigma$  predicted by Eqn (19.10). The values of the surface free energy of the nucleus  $\alpha$ , emerging from the data in Figure 19.21, are 0.018 erg cm<sup>-2</sup> for STMV, 0.027 erg cm<sup>-2</sup> for apoferritin, and 0.061 erg cm<sup>-2</sup> for pumpkin globulin [184,185].

### 19.6.2.2 The Rate of Crystal Nucleation

For further insights into the mechanism of nucleation of protein crystals, we turn to data on the dependence of the nucleation rate on supersaturation for crystals of the protein lysozyme, a convenient and often used model system. The dependencies of the homogeneous nucleation rate of lysozyme crystals on the thermodynamic supersaturation  $\sigma$ , at three different concentrations of the precipitant NaCl, are presented in Figure 19.22 [186–189].

Each data series in Figure 19.22 corresponds to nucleation experiments carried out at a fixed precipitant concentration and at a fixed temperature. In agreement with general

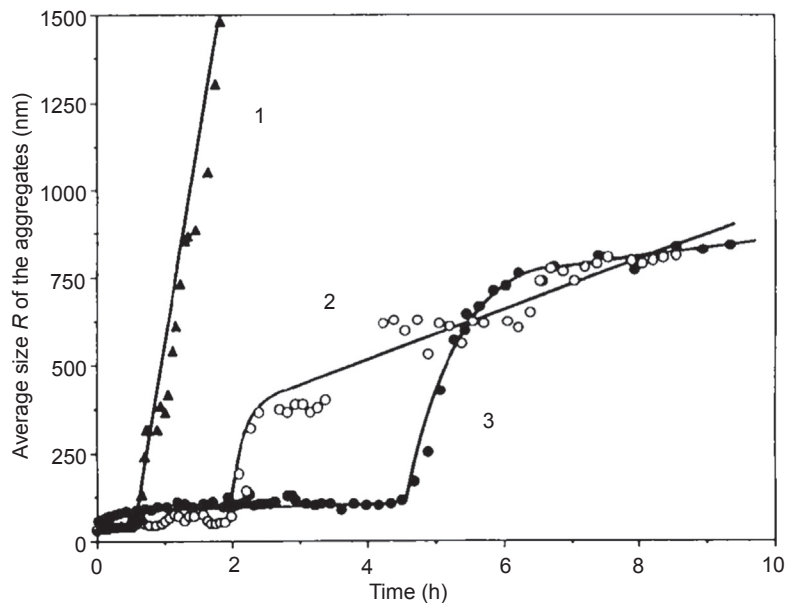


**FIGURE 19.20** Time evolution of the average radius of a satellite tobacco mosaic virus (STMV) cluster forming crystalline nucleus, obtained using dynamic light scattering from supersaturated solutions. Supersaturation rises from curve three to curve 1. *With permission from Ref. [184,185].*

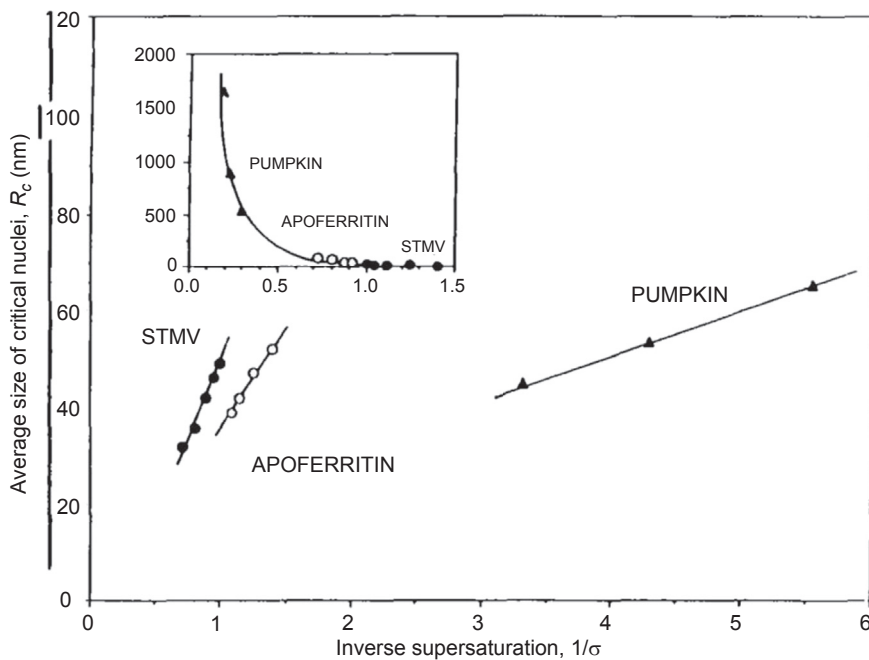


**FIGURE 19.21** The dependencies of the critical nuclear size  $R_c$  vs inverse supersaturation,  $1/\sigma$ , for pumpkin globulin, apoferritin and STMV crystallization. Insert: The supersaturation dependency of the number of protein and virus particles composing the critical nucleus. *With permission from Ref. [184,185].*

expectations and Eqn (19.3), the nucleation rate increases exponentially with supersaturation at each of the three precipitant concentrations, and, overall, is higher at higher precipitant concentrations. However, the dependencies contain four peculiarities.

1. The  $J(\sigma)$  dependence at the highest precipitant concentration,  $C_{\text{NaCl}} = 4\%$ , breaks at  $\sigma > 3.1$  and, in dramatic contrast to prediction of Eqns (19.11) and (19.10), the section above this concentration is practically steady as supersaturation increases.
2. At  $\sigma > 3.45$  in the same  $J(\sigma)$  dependence, the data scatter increases and three of the recorded points deviate significantly from the dominant trend.
3. The measured nucleation rates are on the order of  $0.1\text{--}1 \text{ cm}^{-3}\text{s}^{-1}$ , which is about 10 orders of magnitude less than the prediction of the classical nucleation theory; the estimate of  $J$  stemming from the classical nucleation theory is discussed subsequently.
4. The dependence of the nucleation rate on temperature, shown in Figure 19.23 presents another puzzling complexity: as supersaturation is increased upon lowering of temperature, the nucleation rate first increases exponentially, as expected from the classical theory, but then passes through a sharp maximum and recedes following a weaker dependence.

In the following subsections, we discuss these four peculiarities.

### 19.6.3 the Nucleus Size and Solution-Crystal Spinodal

To understand the breaking  $J(C)$  dependency, feature (1) previously, we use the nucleation theorem to determine the size of the critical nucleus for crystallization. According to Eqn (19.2), the number of molecules in the nucleus  $n^*$  largely determines the height of the free-energy barrier for nucleation  $\Delta G^*$ , and hence the nucleation rate  $J$ . The nucleation theorem [190–193], a universal, model-independent nucleation law, provides an estimate for  $n^*$  from the nucleation rate  $J$ .

$$n^* - n_0 = k_B T \frac{\partial \ln J}{\partial \Delta \mu} + \alpha_1, \quad (19.12)$$

in which  $\alpha_1$  is a correction that takes values between 0 and 1 [191].

Figure 19.22(B) indicates that at  $C_{\text{NaCl}} = 2.5\%$  and  $3\%$ ,  $n^*$  does not change throughout the respective supersaturation ranges, whereas at  $C_{\text{NaCl}} = 4\%$  the nucleus size changes abruptly at  $\sigma = 3.1$ , corresponding to  $C = 33.5 \text{ mg/ml}$ . The value of the parameter  $n_0$ , which roughly corresponds to the number of solute molecules displaced by the nucleus, can be roughly estimated as less than 1. Then the nucleus sizes  $n^* - n_0$ , extracted from the four linear segments in Figure 19.22(B), are ten, four, five and one molecules, respectively. From here we see that the breaking in the  $J(C)$  dependence at  $C_{\text{NaCl}} = 4\%$  is due to the transition of the nucleus size from five to one molecules.

Nucleus size  $n^* - n_0 = 1$  means that every molecule in the solution can be an embryo of the crystalline phase, and the growth to dimer and larger clusters occurs with a free energy gain. Thus, the free energy barrier for the formation of the crystalline phase  $\Delta G^*$  is

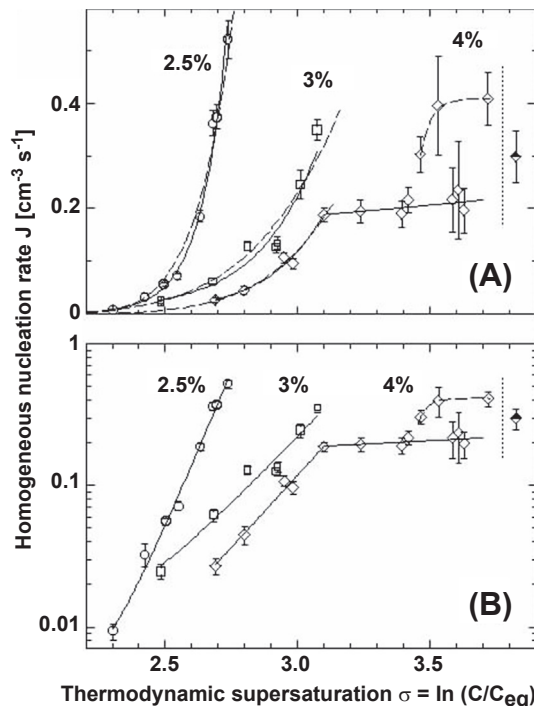


**FIGURE 19.22** The dependence of the rate of homogeneous nucleation  $J$  of lysozyme crystals of supersaturation  $\sigma \equiv \Delta\mu/k_B T$  at  $T = 12.6^\circ\text{C}$  and at the three concentrations of the precipitant NaCl indicated on the plots. Solid lines: fits with exponential functions; dashed lines fits with the classical nucleation theory expression, Eqn (11). Vertical dotted lines at  $\sigma = 3.9$  indicate the liquid–liquid coexistence boundary at this  $T$  and  $C_{\text{NaCl}} = 4\%$ ; this supersaturation corresponds to lysozyme concentration  $67\text{ mg ml}^{-1}$ . (A) Linear coordinates; (B) semi-logarithmic coordinates. With permission from Ref. [205].

below the thermal energy of the molecules. In analogy to the nucleation of a fluid within another fluid, we call spinodal the phase line at which the nucleation barrier vanishes and the rate of generation of the new phase is only limited by the kinetics of growth of its clusters. The spinodal is defined as the boundary between metastability and instability of an old phase, supersaturated with respect to a new phase [177,178,194].

The case discussed here, the solution–solid phase transition, is one for which a mean-field free energy expression encompassing both phases cannot be formulated because of different standard states. Because the inflection point in the dependence of  $\Delta G$  on the order parameter along which the phase transition occurs is typically used to define the spinodal [195–197], a thermodynamic definition of the solution–crystal spinodal is impossible [195]. The definition proposed here is a kinetic one, based on the transition to nucleus size of one molecule, i.e., to where no thermodynamic barriers for the formation of the crystalline phase exist.

In Figure 19.8, we have depicted the solution–crystal spinodal line in the  $(C, T)$  plane, determined as the concentration  $C$  at the transition to  $n^* - n_0 = 1$  from Ref. [198].

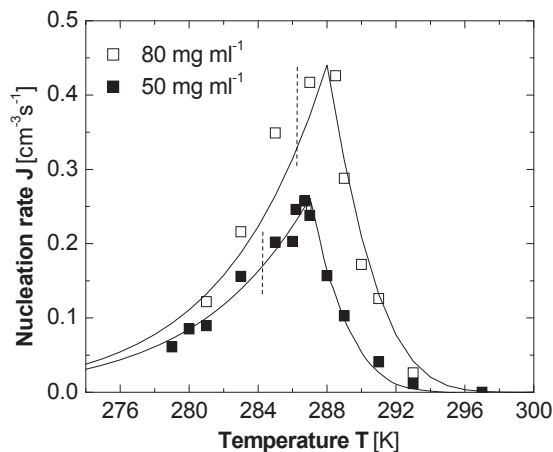


**FIGURE 19.23** The dependence of the rate of homogeneous nucleation  $J$  of lysozyme crystals on temperature  $T$  at two fixed lysozyme concentrations indicated in the plot. The temperatures of equilibrium between crystals and solution are 315 K at  $C_{\text{lys}} = 50 \text{ mg ml}^{-1}$  and 319 K at  $C_{\text{lys}} = 80 \text{ mg ml}^{-1}$ . The temperatures of L-L separation are 285 K at  $C_{\text{lys}} = 50 \text{ mg ml}^{-1}$  and 287 K at  $C_{\text{lys}} = 80 \text{ mg ml}^{-1}$  [95] and are marked with vertical dashed lines. Symbols represent experimental results from [29]. Lines are results of two-step model in Eqns (19.13)–(19.15). With permission from Ref. [199].

At concentrations and temperature below this spinodal line  $\Delta G^* \approx 0$ , the nucleation rate  $J$  does not increase as supersaturation is increased by increasing  $C$  or lowering  $T$ . This explains puzzle (1) above. The existence of a solution–crystal spinodal also helps to explain the maximums in the dependencies of the nucleation rate  $J$  on temperature in Figure 19.23, puzzle (4) above; for a further details and a theoretical model of these factors, see below.

The transition to a spinodal regime of crystal formation also explains the increased data scatter of  $J(\sigma)$  at  $\sigma > 3.45$ , puzzle (2) above. As shown in Ref. [29,199], at the point of transition from nucleation to spinodal decomposition the nucleation rate undergoes a sharp maximum: on the one side is an ascending branch due to the decrease of the size of the nucleus, and on the other side is a descending branch due to the temperature decrease and associated kinetic factors. Near this maximum, the nucleation rate is very sensitive to variations of the experimental conditions: temperature, protein and precipitant concentrations, and others. Hence, minor inconsistencies of these parameters may lead to significant variations in  $J$  [30].

#### 19.6.4 The Classical Theory Overestimates the Crystal Nucleation Rate by 10 Orders of Magnitude

To understand puzzle (3) above, we use Eqn (19.11) for an estimate of the crystal nucleation rate based on the classical nucleation theory. The rate  $\nu^*$  can be evaluated from the rate of attachment of molecules to lysozyme crystals at similar protein concentrations. As discussed in Section 19.7.1 below, the surfaces of a crystal growing in

solution are smooth and molecules only attach to growth steps that occupy about  $10^{-3} - 10^{-2}$  of the crystal surface [200]. Hence, the rate of attachment to crystals should be estimated from the velocity of step propagation rather than from the rate of growth of the crystal faces.

There are numerous determinations of the step velocities of lysozyme crystals [120,126,201]. At temperatures and concentrations similar to those during the determination of the nucleation rate in Figure 19.22 the step velocities are  $\sim 1 \mu\text{m s}^{-1}$ . This yields, with molecular size of lysozyme of 3.2 nm, attachment rate to the steps  $\sim 300 \text{ s}^{-1}$ . In contrast to that of large crystals, the nucleus surface is likely rough (because of the small size of the nucleus) and molecules can attach anywhere. Hence, we assume that  $\nu^* \approx 300 \text{ s}^{-1}$ . This estimate of  $\nu^*$  should be viewed as approximate because the configuration of molecules in a kink on the smooth crystal facet during crystal growth may be significantly different than the molecular configuration on the rough surface of a near-critical cluster. Hence, the barriers encountered by an incoming molecule may also differ. On the other hand, estimates of  $\nu^*$  from the diffusion rate of molecules in the solution would yield a significant overestimate because they would completely neglect this barrier, which can be on the order of several tens of kilojoules per mole [22,202].

The Zeldovich factor  $Z$  accounts for the width of the free energy profile along the nucleation reaction coordinate around the location of the maximum [179,181,203,204]. It is expected to be on the order of 0.1–0.01 for nucleation of any protein condensed phase [179,204,205]. The protein number density in a solution of concentration  $\sim 50 \text{ mg ml}^{-1}$  as the one used for the experiments in Figure 19.22 [93] is  $n = 2 \times 10^{18} \text{ cm}^{-3}$ . With these values for  $\nu^*$ ,  $Z$  and  $n$ , the pre-exponential factor in Eqn (19.11) is of order  $10^{19} - 10^{20} \text{ cm}^{-3} \text{ s}^{-1}$ .

The nucleation barrier  $\Delta G^*$ , determined from the slope of the dependencies in Figure 19.22(B),  $\Delta G^* \approx 10^{-19} \text{ J}$ . We can use Eqn (19.10) to evaluate the surface free energy  $\alpha$  of the interface between the dense liquid and the solution from the value of  $\Delta G^*$ . From the crystal structure,  $\Omega \cong 3 \times 10^{-20} \text{ cm}^3$  [206]. We get  $\alpha \approx 0.2 \text{ erg cm}^{-2}$  Ref. [205], which is close to determinations for number of other protein crystals [184,185], see Section 19.6.2.a above and this correspondence supports the estimate of  $\Delta G^*$  from the data in Figure 19.22.

Combining the estimate for the pre-exponential factor with this estimate for  $\Delta G^*$  we get from Eqn (19.10) a prediction for  $J \approx 10^8 - 10^9 \text{ cm}^{-3} \text{ s}^{-1}$ . This value is about 10 orders of magnitude higher than those in Figure 19.22. It is important to note that because we estimate  $\Delta G^*$  from experimental data, the difference between the experimentally determined  $J$  and the prediction of the classical nucleation theory is due to an overestimate of the preexponential factor by the classical theory.

### 19.6.5 The Two-step Mechanism of Nucleation of a Crystal in Solution

To understand puzzles (3) and (4) above, that the nucleation rate is lower by many orders of magnitude than the prediction of the classical theory and the nonmonotonic

dependence of the nucleation rate on temperature, we consider a mechanism of the nucleation of crystals, according to which the formation of crystalline nuclei occurs inside stable droplets or metastable mesoscopic clusters of dense protein liquid, as illustrated in [Figure 19.24](#).

A major assumption in the derivation of [Eqn \(19.11\)](#) is that the solute molecules exchange directly with the crystalline embryo. To understand the meaning of this assumption and why it might not apply to nucleation of crystals in solution, we need to step back and consider the distinction between a solution and a crystal.

Let us start with the phase diagram of a solution in coordinates concentration and temperature at constant pressure, as in [Figure 19.8](#). This phase diagram typically contains three equilibrium phases: a dilute solution, a dense liquid, and crystal; a higher number of phases are possible if more than one crystalline polymorph may form; kinetically arrested states, such as gels, are sometimes included in the phase diagram. Although with some solutions of small-molecule compounds the dense liquid might not be observable, the dense liquid is readily seen in protein, colloid, and some organic solutions [[81,94,95,207](#)]. To distinguish between the three phases present in the phase diagram, at least two parameters, called order parameters, are needed. Thus, the dilute solution and the dense liquid differ by the solute concentration, the dense liquid and the crystal differ by structure (there may be a slight difference in concentration), and the dilute solution and the crystal differ by both concentration and structure.

From this point of view, the formation of crystals in solution should be viewed as a transition along two order parameters: concentration and structure [[18](#)]. If a crystal nucleates not from its melt, but from a dilute solution or gas, both a concentration and a structure fluctuation are needed so that a crystalline nucleus may form, [Figure 19.24\(A\)](#). Thus, the above assumption that an ordered nucleus forms directly in the dilute solution corresponds to the assumption that the solution to crystal transformation occurs as a transition along both order parameters, density and crystallinity, simultaneously; in [Figure 19.23\(A\)](#) this pathway is represented by the arrow along the diagonal of the (Concentrations, Structure) plane. It could be argued that a more energetically favorable pathway is for the transition to proceed along the two order parameters in sequence. Such a sequential pathway would correspond to the formation of droplet of a dense liquid followed by the formation of a crystalline nucleus inside this droplet, as illustrated in [Figure 19.24\(B\)](#).

This mechanism was first suggested by simulations and analytical theory [[208–210](#)]. These theoretical efforts predicted that the density and structure fluctuations are only separated near the critical point for liquid–liquid (L–L) separation occurring in model protein solution systems [[37,92,208](#)], whereas for off-critical compositions, the fluctuations of the density and structure order parameters occur synchronously [[208](#)], similarly to the classical viewpoint.

According to the two-step mechanism, the nucleation of crystals proceeds in two steps: the formation of a droplet of a dense liquid, followed by nucleating a periodic crystal within the droplet [[29,30,211,212](#)], as schematically illustrated in [Figure 19.24](#).

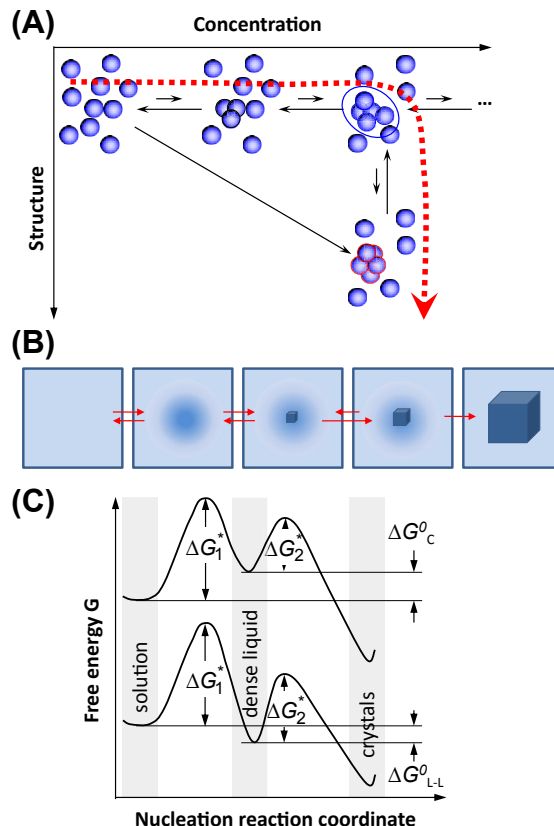


**FIGURE 19.24** Schematic illustration of the two-step mechanism of nucleation of crystals. A dense liquid cluster forms. A crystal nucleus may form inside the cluster. (A) Microscopic viewpoint in the (Concentration, Structure) plane; (B) Macroscopic viewpoint of events along thick dashed line in (A). (C) The free energy  $\Delta G$  along two possible versions of the two step nucleation mechanism. If dense liquid is unstable and  $\Delta G_{L-L}^0 > 0$  ( $\Delta G_{L-L}^0$ —standard free energy of formation of dense liquid phase), dense liquid exists as mesoscopic clusters,  $\Delta G_{L-L}^0$  transforms to  $\Delta G_c^0$ , and upper curve applies; if dense liquid is stable,  $\Delta G_{L-L}^0 < 0$ , reflected by lower curve.  $\Delta G_1^*$  is the barrier for formation of a cluster of dense liquid,  $\Delta G_2^*$  is for a formation of a crystalline nucleus inside the dense liquid.

If the dense liquid is stable with respect to the dilute solution—this case is represented by the lower curve in Figure 19.24(C)—the nucleation of crystals occurs inside macroscopic droplets of this phase. A far more common case is when the dense liquid is not stable but has a higher free energy than the dilute solution [94,95], represented by the upper curve in Figure 19.24(C). In these cases, the dense liquid is contained in metastable clusters, intriguing objects in their own right, and crystal nucleation occurs within the clusters.

Direct observations of ordered nuclei forming within the dense liquid exist, but only for the case of stable dense protein liquid, Figure 19.25 [103,213]. Such direct imaging

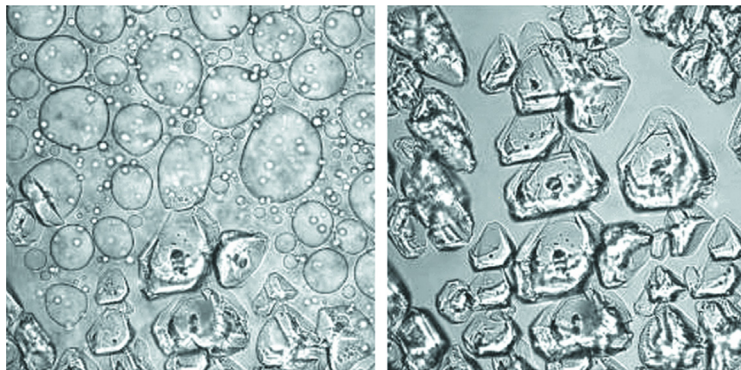


**FIGURE 19.25** Confocal scanning laser fluorescence microscopy imaging of nucleation of crystals of glucose isomerase within dense liquid droplets. Bright field imaging, PEG with molecules mass  $10,000 \text{ g mol}^{-1}$  (PEG 10,000) used to induce crystallization. The time interval between the left and right images is 380 s.  $C_{\text{protein}} = 55 \text{ mg ml}^{-1}$ ,  $C_{\text{PEG}} = 9.5\%$ ,  $0.5 \text{ M NaCl}$ ,  $10 \text{ mM Tris}$  maintaining  $\text{pH} = 7$ . The width of each image is  $326 \mu\text{m}$ . *With permission from Ref. [213].*

would be difficult or impossible for the more common case in which the dense liquid is unstable. The action of the two-step mechanism in this case is inferred from two pieces of evidence: First, we demonstrate the existence of metastable mesoscopic dense liquid clusters in solutions. Then, we analyze the complex kinetic curves for nucleation of crystals of the protein lysozyme in [Figures 19.22 and 19.23](#), propose a kinetic law for the two-step mechanism, and show that its predictions qualitatively and quantitatively agree with the experimental data. Finally, we review experimental results which demonstrate that this mechanism applies to many other proteins, to small molecule organic and inorganic compounds, including biominerals and colloids.

### 19.6.6 Dense Liquid Clusters in the Homogenous Region of the Phase Diagram

If crystallization is carried out at a point in the phase diagram where the dense liquid is unstable, all density fluctuations are expected to decay with a characteristic time on the order of the diffusion time of the protein molecules,  $10 \mu\text{s}$ , see below [\[26,27,65\]](#). Because the molecules in the region of high concentration within the fluctuation move with the same characteristic time, it would be impossible for them to probe various structures and find the right one for the crystalline nucleus. Thus, the crucial question for the understating of nucleation from dilute media is: How does the transition along the order parameter concentration occur? The answer lies in the recently discovered metastable mesoscopic clusters of dense liquid.

The evidence for metastable dense liquid clusters comes from monitoring solutions of three hemoglobin variants, oxy-HbA, oxy-HbS, and deoxy-HbS [\[26\]](#), and the proteins lumazine synthase [\[24,65\]](#) and lysozyme [\[27\]](#) by dynamic light scattering (DLS) and atomic force microscopy [\[214\]](#). [Figure 19.26\(A\)](#) shows a typical intensity correlation

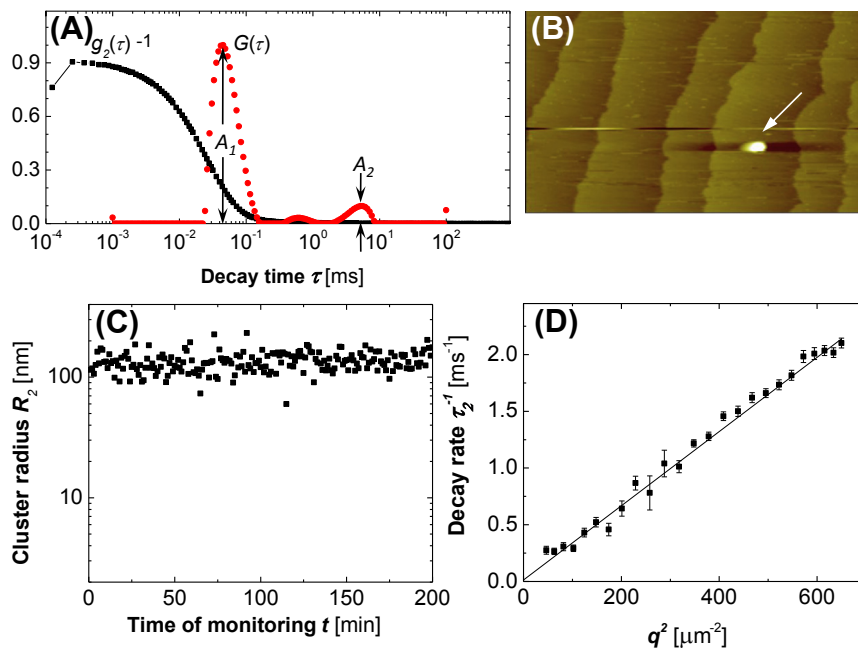


**FIGURE 19.26** Characterization of dense liquid clusters. (A) Examples of correlation function of the scattered intensity  $g_2(\tau)$  and the respective intensity distribution function  $G(\tau)$  of a lysozyme solution with  $C = 148 \text{ mg ml}^{-1}$  in 20 mM HEPES buffer; data collected at angle  $145^\circ$ . (B) Atomic force microscopy imaging of liquid cluster landing on the surface of a crystal in a lumazine synthase solution. Tapping mode AFM imaging, scan width  $20 \mu\text{m}$ . Apparent lateral cluster dimensions are misleading; cluster height is 120 nm. (With permission from Ref. [24].) (C) Time dependence of the radius of dense liquid clusters in the same lysozyme solution as in a. (D) The dependence of the decay rate  $\Gamma = \tau_2^{-1}$  [1] of the cluster peak in the correlation function on the squared wave vector  $q^2$  for a lysozyme solution as in (A).

function of a lysozyme solution in the homogeneous regions of the phase diagram. The correlation function reveals two processes: the faster process, with characteristic time  $\tau_1$  on the order of 10–100  $\mu\text{s}$ , is the Brownian motion of single lysozyme molecules; it is present at all solution concentrations. The corresponding hydrodynamic radius, determined via the Stokes–Einstein equation, is about 1.5 nm and matches well the diameter of a lysozyme molecule of 3.2 nm. The slower process has a characteristic time  $\tau_2$  on the order of milliseconds; its amplitude increases with higher lysozyme concentrations. This longer time could come from either compact lysozyme clusters suspended in the lysozyme solution, or from single lysozyme molecules embedded in a loose network structure constraining their free diffusion. Because the measured low shear viscosity of lysozyme solutions is equal to those determined using high shear rates [99], no loose networks in lysozyme molecules exist in these solutions, and we conclude that the long times in Figure 19.26(A) indeed correspond to lysozyme clusters [26]. The time-dependence of their radius is shown in Figure 19.26(C), and it shows that the clusters

appear immediately after solution preparation; their radius is relatively steady. We therefore conclude that these are clusters of dense liquid.

The number density  $n_2$  of the dense liquid clusters and the fraction of the total solution volume  $\varphi_2$  they occupy are evaluated from the amplitudes of the respective peaks in the distribution function in Figure 19.26(A) [26]. Further results on the behavior of clusters of dense liquid in solutions of hemoglobin and lumazine synthase are presented in Refs. [24,26,65]. It was found that with all studied proteins, the clusters exist in broad temperature and protein concentration ranges. The clusters occupy  $\varphi = 10^{-6} - 10^{-3}$  of the solution volume and have number densities on the order of  $10^5 - 10^{10} \text{ cm}^{-3}$  Ref. [26].

To evaluate the lifetime of the lysozyme clusters, we note that cluster decay processes contribute a  $q$ -independent component to the overall rate  $\Gamma_2 = \tau_2^{-1}$  sensed by DLS Ref. [215],  $\Gamma_2 = \Gamma_0 + D_2 q^2$ , and can be distinguished from cluster diffusion. ( $\Gamma_0$  is the rate of cluster decay,  $D_2$  is the cluster diffusion coefficient, and  $q$  is the wave-vector.) The  $q$ -dependent, diffusion component indeed dominates the DLS signal, Figure 19.26(D). Using  $\Gamma_0 \ll D_2 q^2$  with  $q^2 = 3.5 \times 10^{10} \text{ cm}^{-2}$  and  $D_2 = 2 \times 10^{-9} \text{ cm}^2 \text{ s}^{-1}$ ,  $\Gamma_0 \ll 70 \text{ s}^{-1}$ , we obtain a lower bound  $1/\Gamma_0 \approx 15 \text{ ms}$  for cluster lifetimes.

The determination of the lifetime of the clusters of lumazine synthase was more straightforward and yielded an estimated of  $\sim 10 \text{ s}$  [24,65]. In addition to detection by dynamic light scattering, clusters of lumazine synthase were directly imaged by atomic force microscopy, Figure 19.26(B) [24,65], which confirmed their macroscopic lifetimes and their size.

The lifetimes of the clusters ( $>15 \text{ ms}$  for Hb and lysozyme and  $\sim 10 \text{ s}$  for lumazine synthase) significantly exceed the equilibration times of the protein concentration at submicrometer length scales, i.e.  $\sim 10^{-5} \text{ s}$ . Thus, the compact clusters represent a metastable phase separated from the bulk dilute solution by a free energy barrier.

Attempts to rationalize the finite size of clusters have focused on a balance of short-range attraction, due to van der Waals, hydrophobic, or other forces, and screened Coulombic repulsion between like-charged species [216,217]. Although small clusters that contain about 10 particles naturally appear in such approaches, large clusters are expected only if the constituent particles are highly charged, with hundreds of elementary charges. Such high charges are feasible for micron-size colloidal particles; however, proteins in solution are known to carry less than 10 elementary charges per molecule. Hence, whereas for colloidal suspensions these theories successfully predict aggregation [218–220], or even the existence of metastable clusters [221], we conclude that a distinct mechanism is at work in protein systems, in which clusters contain as many as  $10^6$  molecules [27]. A recent study concluded that the clusters consist of a nonequilibrium mixture of single protein molecules and long-lived but ultimately unstable complexes of proteins [27]. The puzzling mesoscopic size of the clusters is determined by the lifetime and diffusivity of these complexes. Several possible mechanisms of complex formation: domain swapping, hydration forces, dispersive interactions, and other, system-specific interactions were highlighted.

### 19.6.7 The Rate Law for the Two-step Mechanism of Crystal Nucleation

A phenomenological theory was developed that takes into account intermediate high-density metastable states in the nucleation process [199]. The rate law for the dependence of the nucleation rate on protein concentration and temperature emerging from this theory is.

$$J = \frac{k_2 C_1 T \exp\left(-\frac{\Delta G_2^*}{k_B T}\right)}{\eta(C_1, T) \left[1 + \frac{U_1}{U_0} \exp\left(\frac{\Delta G_C^o}{k_B T}\right)\right]}, \quad (19.13)$$

in which the constant  $k_2$  scales the nucleation rate of crystal inside the clusters,  $C_1$  is the protein concentration inside the clusters, i.e.,  $\sim 300 \text{ mg ml}^{-1}$ ,  $D\Delta G_2^*$  is the barrier for nucleation of crystals inside the clusters,  $\eta$  is the viscosity inside the clusters,  $U_1$  and  $U_0$  are the effective rates of, respectively, decay and formation of clusters at temperature  $T$ , and  $\Delta G_C^o$  is the standard free energy of a protein molecule inside the clusters in excess of that in the solution, depicted schematically in Figure 19.24(C) Ref. [199]. Recent experimental determinations indicate that  $\Delta G_C^o$  is on the order of  $10 k_B T$  [27].

Following Ref. [222], the nucleation barrier  $\Delta G_2^*$  in the vicinity of the solution–crystal spinodal was modeled as

$$\Delta G_2^*(T) = \frac{E^*}{(T_e - T)^2} \left[1 - \frac{(T_e - T)^2}{(T_e - T_{sp})^2}\right], \quad (19.14)$$

in which  $E^*$  is a parameter,  $T_e$  is the temperature at which a solution of the studied concentration is in equilibrium with a crystal, and  $T_{sp}$  is the spinodal temperature.  $T_e$  and  $T_{sp}$  are determined from the phase diagram in Figure 19.8, and  $E^*$  is determined by fitting Eqn (19.14) to the slope of the  $J(C)$  dependencies in Figure 19.22(B).

The viscosity inside the dense liquid clusters was modeled as.

$$\eta = \eta_0 \{1 + [\eta] C_1 \exp(k_\eta [\eta] C_1)\} \exp(-E_\eta/k_B T), \quad (19.15)$$

in which  $[\eta]$  is the viscosity increment, and  $k_\eta$  and  $E_\eta$  are constants; all three viscosity parameters are determined from the known dependencies of viscosity in the studied solution on temperature and concentration.

A crucial assumption in Eqn (19.13) is that the concentration inside the dense liquid clusters  $C_1$  increases as temperature is lowered, in agreement with the phase diagram in Figure 19.8 and the likely similarity between the dense liquid in the clusters and the stable sense liquid depicted in the phase diagram [199]. As a result of this  $C_1(T)$  dependence, the viscosity  $\eta$  increases much more strongly in response to decreasing temperature  $T$  than suggested by the quasi-Arrhenius member of Eqn (19.15) with  $E_\eta$  about  $10\text{--}20 \text{ kJ mol}^{-1}$  [223].

The denominator of Eqn (19.13) offers another pathway by which decreasing temperature affects the nucleation rate  $J$ , besides the temperature dependence of the

viscosity. Because  $(U_0/U_1)\exp(-\Delta G_C^o/kBT)$  is the nonequilibrium volume fraction occupied by the clusters  $\phi_2$ , the term in the square brackets in the denominator of Eqn (19.13) is approximately  $\phi_2^{-1}$ . Because  $\Delta G_C^o > 0$ , see above, lower  $T$  leads to a greater value of the denominator, which corresponds to a lower volume of the dense liquid clusters and accordingly to lower  $J$ . This contributes about factor of five in the decrease in  $J$  as temperature is lowered from  $T_{sp}$  to the lowest values probed in Figure 19.23.

Using Eqns (19.13)–(19.15), nucleation rate data at varying temperature and protein concentrations in Figure 19.22 and Ref. [224], as well as nonmonotonic dependencies of the nucleation rate on temperature in Figure 19.23 were reproduced with high fidelity using literature values or independently determined parameters of the thermodynamic and kinetic parameters of the system [199]. The good correspondence between the model results and the experimental data supports the validity of the two-step nucleation mechanism. According to Eqn (19.13), the increasing part of the  $J(T)$  as temperature is lowered below  $T_e$  is due to the increase of the supersaturation  $\Delta\mu$  that shrinks  $\Delta G_2^*$  according to Eqn (19.10); this leads to exponential increase in the nucleation rate  $J$ . The maximum in  $J(T)$  is reached exactly at  $T = T_{sp}$ , in which  $\Delta G_2^*$  vanishes; note that  $T_{sp}$  is independently determined from plots similar to the one at 4% in Figure 19.22(B) [224]. The steep decrease in the nucleation rate as  $T$  is lowered beyond the maximum at  $T_{sp}$  is a crucial part of the proof of the validity of the two-step mechanism: within the two-step mechanism this steep decrease is explained by the smaller volume of the dense liquid clusters at lower temperature, and by the higher concentration inside them, leading to higher viscosity. Both the lower volume of the clusters and the higher viscosity lead to lower nucleation rate.

No pathway of steep decrease of nucleation rate beyond the spinodal temperature exists if one assumes one-step nucleation: nuclei forming within the dilute solution would be exposed to its viscosity, which is a weak function of temperature. Thus, the nucleation rate would decrease almost imperceptibly, by  $\sim 16\%$ , assuming  $E_\eta = 20 \text{ kJ mol}^{-1}$ , within the 5–6 K range probed. Note that the decrease in nucleation rate in glass-forming melts in response to temperature decrease, interpreted as a result of viscosity increase in the melt, occurs over 40–50 K [225]; furthermore, this response is significantly enhanced by the stronger temperature dependence of melt viscosity as compared to that of solutions.

To understand puzzle (iii) above, that the nucleation rate is lower by 10 orders of magnitude than the prediction of the classical theory, we compare the nucleation kinetic law in Eqn (19.13) to that in Eqn (19.11). We see that  $k_2\phi_2C_1T/\eta$  takes the place of the product  $\nu Zn$ . In solutions of concentration  $C$  in the range 20–60 mg ml<sup>-1</sup>, as the ones in which the nucleation rates in Figure 19.22 were measured, the cluster volume fraction  $\phi_2$ , represented by the denominator in Eqn (19.13), is on the order of  $10^{-7}$ – $10^{-6}$ . With the concentration  $C_1$  in the clusters around 300 mg ml<sup>-1</sup>, Eqn (19.15) shows that the viscosity  $\eta$  of the dense liquid in the clusters is around 100 centiPoise, or  $\sim 100$  times higher than in the normal solution. We get that the nucleation rate should

be  $\sim 10^9$  times lower than the prediction of the classical theory, which assumes nucleation in the solution bulk.

### 19.6.8 The Rate Determining Step in the Two-step Nucleation Mechanism

The derivation of Eqn (19.13) is based on the assumption that the first step in the two-step mechanism, the formation of the dense liquid clusters, is fast and that the second step, the formation of the crystal nuclei within the dense liquid clusters, is rate determining. Although the excellent agreement between the experimental data and the prediction of Eqn (19.13) in Figure 19.23 can be viewed as a support of this assumption, it should and can be tested independently.

As first evidence in favor of the fast rate of generation of the dense liquid clusters, we view data on the time dependence of three characteristics of the cluster population: average radius, number density, and volume fraction, illustrated for the case of average cluster radius in Figure 19.26(C). All of these dependencies, monitored for the proteins lumazine synthase [24,65], lysozyme [27], and three hemoglobin variants [26] reveal that the clusters appear within several seconds of solution preparation. After that, the cluster populations are stable for several hours.

For an additional test, we use the similarity between the clusters and stable droplets of dense liquid that exist below the liquid–liquid coexistence line in the phase diagram in Figure 19.8. The rate of nucleation of the dense droplets was determined by monitoring the increase in time of the number of droplets appearing in an isothermal solution supersaturated with respect to the formation of dense liquid [93]. These data yield droplet nucleation rates, which are on the order of  $10^8 \text{ cm}^{-3} \text{ s}^{-1}$ . These rates are about 10 orders of magnitude faster than the rates of crystal nucleation and support the conclusion that the nucleation of the dense liquid precursors, stable or unstable, is much faster than the rate of crystal nucleation within these precursors.

The conclusion that the rate of nucleation of crystals within the dense liquid clusters is the rate-determining step in the two-step nucleation mechanism supports the applicability of Eqn (19.13) as the rate law for this process. Another important consequence of this conclusion is related to the applicability of the nucleation theorem to the two-step nucleation mechanism. Because cluster formation is fast, the clusters can be considered in equilibrium with the solution. Then the chemical potential of the protein in the clusters is equal to the chemical potential of the protein in the solution, and  $\Delta\mu = \mu_{\text{solute}} - \mu_{\text{crystal}}$  is the supersaturation to which the crystal nuclei are exposed within the clusters. Because the cluster number is steady,  $J$  is the rate of nucleation of crystals inside the clusters. From the latter two conclusions, it follows that applying the nucleation theorem, Eqn (19.12), with the macroscopically observed nucleation rate and the external supersaturation, is equivalent to applying the nucleation theorem to the nucleation of crystals in the dense liquid. Hence, the size of the nuclei determined using the nucleation theorem refers to the crystalline nuclei within the clusters. Furthermore,

the transition to the spinodal regime occurs when the crystalline nuclei reach the size of one molecule, and this transition corresponds to  $\Delta G_2^* = 0$ .

Finally, we can resolve an apparent controversy. From the above estimate of the lowering of the nucleation rate due to the low volume fraction and the high viscosity of the dense liquid, it may appear that the selection of the two-step mechanism violates the principle of fastest increase of entropy, e.g., Ref. [226,227]. This principle governs the selection of kinetic pathways toward, in most cases, the mechanism leading to the fastest rate: faster consumption of supersaturation corresponds to faster increase of the total entropy of the universe. This is an incorrectly posed problem: the estimate of the nucleation rate above used the value of the nucleation barrier  $\Delta G^*$  extracted from the experimental data. As just demonstrated, this barrier is in fact  $\Delta G_2^*$  from Figure 19.24(C) and Eqn (19.13), i.e., the barrier for nucleation of crystals inside the clusters. Because the surface free energy at the interface between the crystal and the solution is likely significantly higher than at the interface between the crystal and the dense liquid, the barrier for nucleation of crystals from the solution would be much higher. This would lead to much slower nucleation of crystals directly from the solution than inside the clusters. Thus, the protein crystal nucleation follows the two-step nucleation mechanism because it provides for faster rate of the solution-to-crystal phase transition and in this way for faster decrease of the free energy of the system, which corresponds to faster increase of the entropy of the universe.

### 19.6.9 The Role of Heterogeneous Nucleation Substrates

Knowing that the nucleation of crystal within the dense liquid clusters is the rate-limiting step in the two-step mechanism, we can address a broader related question: Because from a general point of view, the rate of nucleation via the two-step mechanism depends on two preexponential factors,  $J_{01}$  and  $J_{02}$ , and two barriers,  $\Delta G_1^*$  and  $\Delta G_2^*$ , which of these four parameters is the most significant? From the discussion in the previous subsection, the answer should be sought between  $J_{02}$  and  $\Delta G_2^*$ . Because nucleation occurs in the vicinity of the solution–crystal spinodal,  $\Delta G_2^*$  is very small, and hence, the most important parameter is  $J_{02}$ . This is a surprising conclusion, and it sheds light on the role of heterogeneous substrates in nucleation.

Nucleation is often facilitated by heterogeneous centers [195,228]. The generally accepted mechanism of heterogeneous nucleation is that it follows the kinetic law for homogeneous nucleation but is faster due to lowering of the nucleation free energy barrier [195]. Because we now know that  $\Delta G_2^*$  is insignificant, we conclude that, in contrast to the generally accepted viewpoint, heterogeneous nucleation centers assist nucleation not by lowering  $\Delta G_2^*$ , but by assisting the growth of the ordered clusters through the factor accounted for in the preexponential factor  $J_{02}$ .

Many mechanisms exist by which a surface may facilitate the growth of the ordered clusters. The most obvious one is that the right crystal structure, i.e., the one that minimizes the free energy of the system, is similar to the structure of the surface.

Alternatively, the surface structure may stabilize a necessary intermediary en route to the right crystal structure, similar to the way enzymes stabilize the transition state, and not the final product of the catalyzed reaction [61]. Another possibility is that the surface may catalyze the formation of the intermolecular bonds in the crystal. If the structure of a substrate is similar to the structure of the growing crystal, this is referred to as templating [229,230]. Examples were found for crystallization of proteins on mineral substrates and on ordered lipid layers [127,231]. One may view the acceleration of nucleation of  $\gamma$ -glycine crystals in the bulk of a supersaturated solution by elliptically polarized light, and  $\alpha$ -glycine crystals by linearly polarized light, as examples of assisted structuring of the dense liquid by an appropriately structured electric field [232].

### 19.6.10 Other Systems for Which the Two-step Nucleation Mechanism Applies

Previously, we analyzed in detail data on the kinetics of nucleation of crystals of the protein lysozyme, which allow a rather confident conclusion about the applicability of the two-step mechanism. The evidence for the applicability of this mechanism to the nucleation of crystals of other proteins is less direct. In Ref. [233], crystals of several intact immunoglobulins were found to coexist for extended lengths of time with dense liquid droplets without the droplets generating additional crystal nuclei. The crystals that were nucleated on the droplet boundaries grew into the dilute solution, rather than into the dense liquid. This was interpreted in favor of nucleation of the crystals within dense liquid clusters suspended in the solution.

Besides the nucleation of protein crystals, the action of the two-step mechanism has recently been demonstrated for the homogeneous nucleation of HbS polymers, with metastable dense liquid clusters serving as precursor to ordered nuclei of the HbS polymer [26,234,235]. Other studies have shown that the nucleation of amyloid fibrils of several proteins and peptide fragments, such as Alzheimer-causing A- $\beta$ -peptide or the yeast prion protein, follows a variant of the two-step mechanism in which the role of the intermediate liquid state is played by a molten globule of consisting of unfolded protein chains [236,237].

The applicability of the two-step mechanism to the nucleation of crystals of urea and glycine was deduced in a series of experiments, in which high-power laser pulses were shone on supersaturated solutions [232,238]. It was found that the nucleation rate increases because of the illumination by eight to nine orders of magnitude and that by using elliptically or linearly polarized light,  $\alpha$ - or  $\gamma$ - glycine crystals could be preferentially nucleated. Because glycine does not absorb the illumination wavelength, and the electric field intensity was insufficient to orient single glycine molecules, it was concluded that the elliptically or linearly polarized pulses stabilize the structure fluctuations within the dense liquid, which lead to the respective solid phases [211,238].

Colloid systems are the ones for which the evidence in favor of the applicability of the two-step mechanism is the strongest. By tracking the motions of individual particles of the size of a few microns by scanning confocal microscopy, the nucleation of crystals in colloidal solutions was directly observed [239–241]. These experiments revealed that the formation of crystalline nuclei occurs within dense disordered and fluid regions of the solution [242].

The role of an amorphous precursor in the nucleation of crystal of biominerals has been speculated for a long time; for a historic overview, see [243]. However, it was envisioned that the precursor does not facilitate that formation of the crystalline nuclei, but only serves as a source of material for reprecipitation into a crystalline phase. Only recently, it was shown that amorphous or liquid clusters of calcium and carbonate ions are present in calcium carbonate solutions and facilitate the nucleation of calcite crystals in a manner similar to the role of the mesoscopic clusters in lysozyme crystallization discussed above [243–245]. The free energy landscape along the nucleation reaction pathway in Figure 19.24(C) was used to characterize kinetics of the process of calcite crystallization [245].

A two-step nucleation mechanism going through metastable clusters (in this case, swollen micelles) has also been theoretically predicted for a ternary system of two homopolymers and their block-copolymer [246].

Stable dense liquid was found to exist in solutions of organic materials and serve as location where crystals nucleate and grow [207]. The existence of the dense liquid in these solutions has been attributed to the same fundamental physical mechanism as the one acting in protein solutions: the size of the solute molecules is larger than the characteristic length scale of the intermolecular interactions in the solution [37]. On the other hand, unpublished evidence from the pharmaceutical industry suggests that in many other cases the stable dense liquid, referred to as oil by the practitioners in the field, is so viscous that no crystals can form in it. This is in contrast to the observations in Figure 19.25, in which crystals form in the relatively nonviscous dense protein liquid. Although this has not been tested, it is possible that the two-step mechanism operates in these organic systems by utilizing dense liquid clusters, similar to those seen in protein, colloid, and calcium carbonate solutions.

The broad variety of systems in which the two-step mechanism operates suggests that its selection by the crystallizing systems in preference to the nucleation of ordered phases directly from the low-concentration solution may be based on general physical principles. This idea is supported by two examples of physical theory: by Sear [247] and by Lutsko and Nicolis [248]. Of particular interest is the latter work. It treated a range of points in the phase diagram of two different model systems, which likely encompass a broad variety of real solutions, and demonstrated that the two-step formation of crystalline nuclei, via a dense liquid intermediate, encounters a significantly lower barrier than the direct formation of an ordered nucleus and should be faster. Interestingly, the intermediate state resulting from the theory was not stabilized and represents a just as well developed density fluctuation.

### 19.6.11 A General Perspective on the Nucleation of Protein Crystals

Recent advances in the understanding of nucleation of protein and other crystals in solution have shown that the classical nucleation theory fails to provide understanding of several features of measured kinetic curves: nucleation rates, which are orders of magnitude lower than the classical prediction; nucleation kinetics curves, which exhibit saturation, or, even more puzzling, maximums and decreasing branches, with increasing supersaturation, as well as the role of the other, stable and unstable, phases possible in solution.

These features of the nucleation kinetics reflect the action of two factors, which are unaccounted by the classical nucleation theory: the existence of a spinodal for the solution-to-crystal phase transition, and the action of a two-step nucleation mechanism. As the spinodal is reached upon supersaturation increase, the barrier for nucleation of crystals vanishes and further increases in supersaturation do not yield a faster nucleation rate. According to the two-step mechanism, the nucleation of a crystal occurs within mesoscopic clusters of dense liquid. Although the initial thought-provoking results on the nucleation kinetics were obtained for the nucleation of protein crystals, and, correspondingly, the two-step mechanism was first proposed only for these types of crystals, further investigations have shown the validity of this mechanism to several organic, inorganic, and colloid materials, including the important class of biominerals.

In general, the two possible intermediate states for the two-step mechanism, the stable dense liquid and the metastable clusters, have distinct mechanisms: the discrepancy of the length scale of the intermolecular interactions in the solution, the size of the crystallizing molecules for the stable dense liquid, and the existence of limited-lifetime complexes for the clusters. Thus, for a given system, the availability of any of these two intermediate states is independent of the other; both of them depend on the exact physicochemical characteristics of the system.

To assess the applicability of the two-step mechanism to the overwhelming majority of untested systems, we note that its action relies on the availability of disordered liquid or amorphous metastable clusters in the homogeneous solutions prior to nucleation. Although such clusters have been demonstrated for several protein systems and for calcium carbonate solutions, it is likely that not all solutions would support the existence of such clusters with properties allowing the nucleation of crystals in them. In such systems, the action of the direct nucleation mechanism might be the only option. On the other hand, an intriguing hypothesis is presented by one of the theories discussed above: that a stabilized intermediate state, as a stable dense liquid, as seen in [Figure 19.25](#), or as a metastable mesoscopic cluster, as in [Figure 19.26](#), is not needed, and the two-step mechanism will act even if the intermediate step is just a density fluctuation. Thus, the two-step mechanism may in fact operate in systems where no intermediate is independently found.

The applicability of the concept of the solution–crystal spinodal appears more straightforward: the nucleation of numerous crystals in industrial and laboratory

practice is carried out at such high supersaturations that the nucleation occurs either in the spinodal regime or in the immediate vicinity of this regime, in which the nucleus consist of just a few molecules.

## 19.7 Mechanisms of Growth of Crystals

### 19.7.1 Rough and Smooth Interfaces

The elementary act of growth of a crystal or a dense droplet is the attachment of molecules from the solution. In the case of growth of crystals, this attachment occurs at sites called kinks, in which an incoming molecule has half of the number of neighbors that it would have in the crystal bulk [249,250], Figure 19.27. The kinks were defined as special sites for growth because of two specificities of attachment there: the kinks are retained after the attachment, and the attachment does not alter the surface free energy of the crystal [250]. The rate constant of growth of a crystal is determined by two factors: the density of kinks on the interface with the growth medium, and the barriers, both entropic and enthalpic, for incorporation of a molecule into a kink.

In some cases, the kink density is high: it comprises a significant fraction, e.g., one tenth or higher, of all molecular sites at the interface. Such interfaces are called rough, and their existence is related to the low surface free energy between the growth medium and the crystal [251]. There is one example of a rough interface during the growth of protein crystals: the protein ferritin studied in Ref. [252].

Protein crystals typically exhibit smooth interfaces because of high surface free energy between the crystal and the growth medium. The smooth interfaces between crystals and solution are usually crystal planes with a high density of molecules, designated with low Miller indexes. This is because these planes are the slowest to grow: the faster growing planes taper out because of geometry and disappear from the crystal faceting. Thus, the notion that a macroscopic crystal is faceted by planes that minimize its surface free energy is a misconception, albeit a common one. In fact, the anisotropy

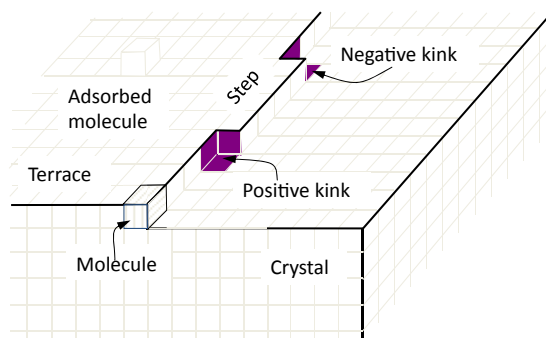


FIGURE 19.27 Schematic illustration of the structure of the surface of a faceted crystal.

of the surface free energy only affects the shape of crystals of near-equilibrium size, i.e., the size of the nucleus [253].

From the above, we see that crystals in contact with the solution are typically faceted and follow the layer growth mode. In this mode, a new lattice layer, typically one lattice spacing high, is deposited on the smooth surface of the previous lattice layer, [Figure 19.27](#). The edges of the incomplete layers are called steps. The flat terraces between the steps are the singular crystal planes. The kinks on faceted crystals are located at the steps, [Figure 19.27](#).

Experimental determinations of the step density on the surfaces of growing protein crystals have yielded numbers on the order of  $10^{-2} - 10^{-3}$  Refs. [19,20,25,63,201,254–259]. The density of the kinks along the steps is from  $10^{-2}$  to 1. This relatively low density of kinks on the surface of a growing protein crystal highlights the significance of three issues for the regulation of the crystal growth rate: the mechanism of generation of kink, the pathway of the molecules from the solution into the sparse kinks, and the kinetics of incorporation of a molecule into a kink. In turn, the issue of kink density subdivides into generation of steps and generation of kinks along the steps.

### 19.7.2 Generation of Steps

Faceted crystals grow by the generation and spreading of layers. New layers are generated only in supersaturated solutions by several mechanisms. A common layer generation mechanism is by screw dislocations, piercing the growing facet. The dislocation produces a step on the facet, which terminates and is pinned at the point where the dislocation outcrops on the surface. The step grows in a supersaturated solution and because of the pinned end, twists into a spiral around the dislocations. If step motion is isotropic, the spiral will be circular; if the velocity of step propagation is faster in some directions and slower in others, the spiral will develop edges at the faster directions and become polygonized. This mechanism was postulated by F.C. Frank in 1948 [70] and is illustrated by an image of a polygonized spiral during insulin crystallization in [Figure 19.28\(A\)](#) [255,260].

Another common layer generation mechanism is by two-dimensional (2D) nucleation of islands of new layers. This is the original layer generation mechanism put forth by Stranski and Kaischew in the 1930s [261,262]. This mechanism operates at high supersaturations and is illustrated in [Figure 19.28\(B\)](#) on the example of an apoferritin crystal.

Recently, a new mechanism of layer generation was discovered during crystallizations of the enzyme lumazine synthase. In a certain supersaturation range, below the threshold needed for 2D nucleation, droplets of dense liquid of the protein [65], several 100 nanometers in size, land on the crystal facet and transform into crystalline matter that is in perfect registry with the underlying lattice [24,254]. The island of layers, several lattice parameters thick, spreads sideways generating several new steps, [Figure 19.28\(C\)](#). These clusters were discussed above in relation to their role in the nucleation

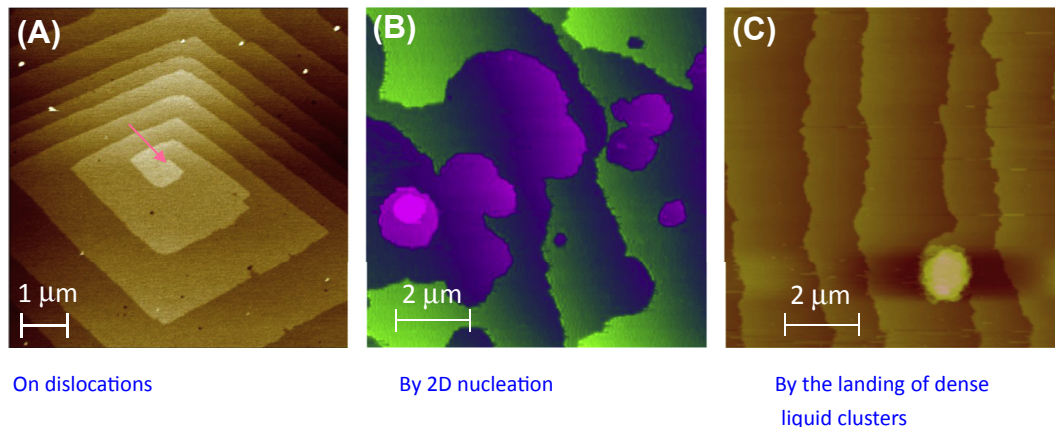


**FIGURE 19.28** Three mechanisms of generations of crystalline layers. (A) By a screw dislocation outcropping on the face; a (100) insulin face is shown. (With permission from Ref. [255].) (B) By 2D nucleation; a (111) ferritin face; red color: higher crystal layers; green color: lower layers. (With permission from Ref. [22].) (C) By the landing and subsequent crystallization of metastable clusters of dense liquid; a (0001) face of lumazine synthase crystal. (With permission from Ref. [24].)

mechanism; they are common in protein solutions [24,26,65], and, importantly, also in small-molecule solutions [263], hence, this mechanism is likely to be valid for a wide range of systems.

Other modes of layer generation discussed in literature mostly involve gross defects in the crystals: occlusions of solution, or the imperfect incorporation of microcrystals into larger growing crystals [23,252,258,264,265].

The growth rate  $R$  of a faceted crystal, measured in a direction perpendicular to the growing facet, is related to the step velocity  $v$  via the mean step density,  $h/l$ , in which  $l$  is the characteristic spacing between the steps and  $h$  is the step height, typically equal to one or two lattice parameters in the direction perpendicular to the growing face.

$$R = (h/l)v. \quad (19.16)$$

If the steps are generated by a screw dislocation, the spiral around its outcrop point forms a hillock. Because the spacing  $l$  between the steps in this spiral is constant [70,253], this hillock has constant slope  $p = h/l$  and.

$$R = pv. \quad (19.17)$$

### 19.7.3 Step Propagation

If the step contains kinks with a mean spacing  $y_0 = a\bar{n}_k$ , in which  $a$  is the molecular size or, more accurately, the lattice parameter, and  $\bar{n}_k$  is the mean number of molecules between two kinks, then [266]

$$v = a/\bar{n}_k(j_+ - j_-). \quad (19.18)$$

In this relation,  $(j_+ - j_-)$  is the net flux of molecule into a kink, the difference between the number incoming  $j_+$  and departing  $j_-$  molecules per unit time, and  $a(j_+ - j_-)$  is the rate of kink propagation along the step. The kink density  $\bar{n}_k^{-1}$  relates the 1D growth of a kink to the 2D growth of a step in the same way that the slope  $p$  relates the step propagation to the 3D growth of the crystal in Eqn (19.12).

Because the incorporation of molecules into steps is a monomolecular process and follows first-order chemical kinetics,  $v$  is proportional to  $[\exp(-\Delta\mu/k_B T) - 1]$  [267,268], in which  $\Delta\mu = \mu_{crystal} - \mu_{solution}$  is the difference in chemical potential of the crystallizing species, as defined in Section 19.3.3 above.

### 19.7.4 The Step Kinetic Coefficient

Because the molecular concentration of the crystallizing species in the solution is significantly lower than in the crystal, the coefficient of proportionality between  $v$  and  $C/C_{eq} - 1$  is divided into two, and  $v$  is written as.

$$v = \beta \Omega C_{eq} (C/C_e - 1), \quad (19.19)$$

in which  $\beta$  is the step kinetic coefficient, and  $\Omega$  is the crystal volume per molecule, so that the dimensionless product  $\Omega C_e$  accounts for the change in number density of molecules between the solution and the crystal. Derivations of Eqn (19.19) have been offered, which, however, imply a mechanism of incorporation of molecules from the solution into the crystal [266]. Thus, it is better justified to use Eqn (19.19) as a definition of  $\beta$ . This provides uniformity and the ability to compare kinetic coefficients of different systems regardless of their concrete mechanism. On the other hand, the physical meanings of  $\beta$  should be judged on the basis of additional data on the mechanism of attachment of molecules from the solution into kinks [269].

If  $C$  in Eqn (19.19) above is replaced by the concentration of the molecules in the immediate vicinity of a kink, then the kinetic coefficient  $\beta$  relates to the first-order kinetic constant for incorporation into a kink  $k$  as  $\beta = a k$  and has units of length per time.  $\beta$  is also related to the free energy barrier  $\Delta G^\ddagger$  for incorporation into a kink as

$$\beta = a \bar{n}_k^{-1} v_+ \exp(-\Delta G^\ddagger / k_B T) = a \bar{n}_k^{-1} v_+ \exp(\Delta S^\ddagger / k_B) \exp(-\Delta H^\ddagger / k_B T), \quad (19.20)$$

in which  $v = (j_+ - j_-)$  is net flux of molecules into kinks, and  $v_+$  is an effective frequency of attempts by a solute molecule to enter a kink by overcoming the barrier  $\Delta G^\ddagger$ . Because in solution the entropy, especially its contribution from the association of solvent molecules, is an important part of the thermodynamics of crystallization, see Section 19.3.2 above [20,39,67,68,76], it is likely that it contributes to the incorporation barrier via  $\Delta S^\ddagger$ . Note that typical methods of evaluation of the barrier heights in chemical kinetics, via determinations of  $\beta$  as a function of  $T$  and plotting the data in Arrhenius coordinates, would only yield the enthalpy part  $\Delta H^\ddagger$  of the barrier.

Equations (19.20) show that the kinetic coefficient  $\beta$  and thus the step velocity  $v$ , and, to a large extent, the crystal growth rate  $R$ , are determined by the kink density  $\bar{n}_k^{-1}$  and the incorporation barrier  $\Delta G^\ddagger$ . The kink density  $\bar{n}_k^{-1}$  is determined by the mechanism of

generation of kinks, whereas  $\Delta G^\ddagger$  is determined by the mechanism of incorporation of molecules into kinks and the chemical interactions between solute and solvent and crystal surface and solvent. The concentration of molecules in the immediate vicinity of a kink is determined by the pathways of the molecules from the solution to the steps. These three factors are discussed subsequently.

### 19.7.5 Generation of Kinks

In general, kinks along the steps are generated by one of three mechanisms: thermal fluctuations of the step edge, 1D nucleation of new molecular rows, and association of 2D clusters preformed and diffusing on the terraces between the steps.

The suggestion that the edges of the unfinished layers, the steps, fluctuate and in this way create kinks was put forth by J.W. Gibbs [177]. Burton, Cabrera, and Frank (BCF) hypothesized that the same mechanism would apply in supersaturated solutions, and it would determine the kink density during growth of a step [70]. They derived a relation between the mean kink density  $\bar{n}_k^{-1}$  and the free energy of kinks  $\omega$ .

$$\bar{n}_k = 1/2\exp(\omega/k_B T) + 1. \quad (19.21)$$

The validity of the BCF hypothesis was demonstrated in a broad supersaturation range for the crystallization of ferritin and apoferritin: the kink density at  $C/C_e = 43$  was equal to that at equilibrium and to that at several intermediate supersaturation values [20,63]. The molecular structures of a {111} apoferritin face and of a growth step are shown in Figure 19.29. A molecule at a kink in the face-centered cubic (f.c.c.) lattice of ferritin and

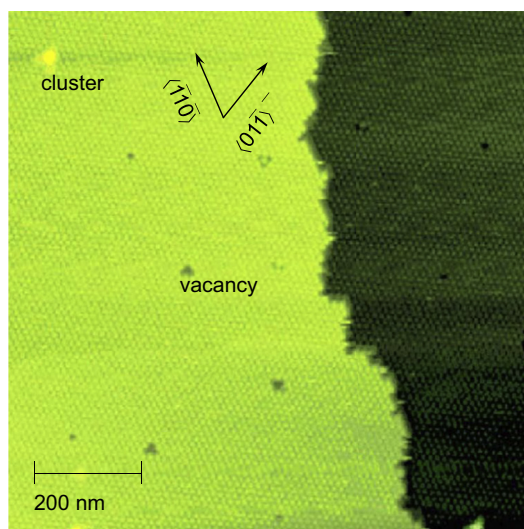


**FIGURE 19.29** Molecular structure of a growth step on an apoferritin crystal. Dark color: lower layer; light color: advancing upper layer. Adsorbed impurity clusters and surface vacancies are indicated. The kinks are the ends of the unfinished rows of molecules at the step edge. *With permission from Ref. [63].*

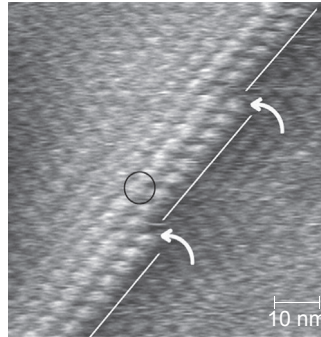


**FIGURE 19.30** Structure of steps on {100} faces of insulin crystals at supersaturations  $(C/C_e - 1) < 0.05$ . AFM image of typical structure of steps on a (100) face of insulin crystals at low supersaturations. A step with two kinks (curved arrows) is highlighted with white lines. An insulin hexamer is encircled in black. *With permission from Ref. [25].*

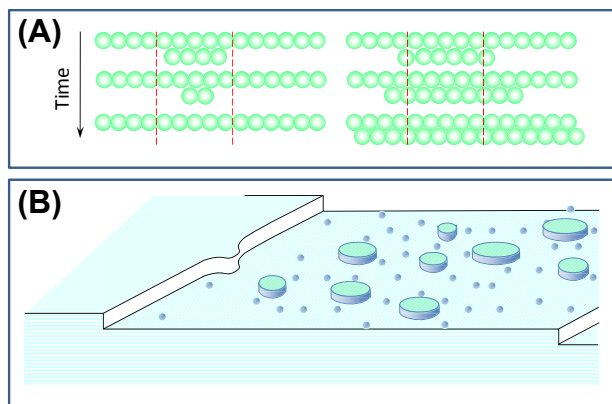
apoferritin has six neighbors, which is half of the total number of adjacent molecules in this lattice. Out of the six neighbors in a kink, three molecules belong to the underlying layer, and three molecules are from the step. From Figure 19.29 and other similar images, the distribution of the number of molecules between two kinks,  $n_k$ , was determined yielding  $\bar{n}_k = 3.5$  [270]. From the value of  $\bar{n}_k$  in Figure 19.29 and Eqn (19.21), we get  $\omega = 1.6 k_B T$ . If we assume first-neighbor interactions only, we can evaluate the intermolecular bond energy,  $\phi$ . When a molecule is moved from within the step on a (111) face of an f.c.c. crystal to a location at the step, four kinks are created. For this, seven bonds (four in the top layer and three with molecules from the underlying layer) are broken, and five are formed. Then,  $\omega = \phi/2$  and  $\phi = 3.2 k_B T \cong 7.8 \text{ kJ/mol}$ .

According to Eqn (19.17), on materials for which the energy of the bonds between the molecules is such that  $\omega$  becomes higher than  $(1-2)k_B T$ , the distance between kinks will exponentially increase. One example of such high kink energy is crystallization of insulin, illustrated in Figure 19.30. At low supersaturations, near equilibrium, the step contains only single-molecule kinks. From Figure 19.30 and other similar images at low supersaturations, it was found that  $\bar{n}_k = 5.6$ , corresponding to a kink density  $\bar{n}_k^{-1} = 0.18$ .

Several other cases of such steps have been studied and it was found that instead of growing with correspondingly low velocity, the steps use additional mechanisms of kink generation: by one-dimensional (1D) nucleation of new molecular rows or by the association with the steps of clusters pre-formed on the terraces. In contrast to 3D and 2D nuclei, a 1D nucleus cannot be defined thermodynamically. However, a 1D nucleus can be defined kinetically, as a molecular row of length such that its probability to grow is equal to its probability to dissolve [271], Figure 19.31(A). Analyses [271] yielded that if new rows are generated by 1D nucleation, the mean distance between kinks increases with supersaturation from its equilibrium value  $\bar{n}_{k,0}$ .

$$\bar{n}_k = \bar{n}_{k,0} (C/C_e)^{1/2}, \quad (19.22)$$

**FIGURE 19.31** (A) Schematic illustration of kink generation by 1D nucleation of new molecular rows. Rows shorter than a critical length, denoted with vertical dashed lines, dissolve, as shown at left. Rows longer than this critical length, grow. (B) The association of 2D clusters preformed on the terraces to the steps, yields protrusions (one such protrusion is shown), rich in kinks. The protrusions spread sideways and promote the step forward.



and

$$v \propto a v_+ (C/C_e)^{1/2} (C/C_e - 1). \quad (19.23)$$

Equation (19.23) assumes that the kinks generated by 1D nucleation are still relatively few and the kink density does not reach its limit. However, the kink density is limited by geometry to 0.5, and, if one accounts for kink stabilization due to their mobility, the upper bound of the kink density should be even lower. Thus, if, upon supersaturation increase, this maximum kink density is reached,  $v$  can only increase linearly with supersaturation. The total dependence of  $v$  on  $(C/C_e - 1)$  then consists of a linear part at  $(C/C_e - 1) < \bar{n}_{k,0}^{-1}$ , an accelerating part at  $(C/C_e - 1) > \bar{n}_{k,0}^{-1}$ , and a second linear part at  $(C/C_e - 1) \gg \bar{n}_{k,0}^{-1}$ .

An example of a protein crystal with low kink density is the crystallization of the orthorhombic form of lysozyme, for which it was found that  $\omega = 7.4 k_B T$  [272]. This high value leads to an extremely low kink density with  $\bar{n}_k$  as high as 400–800, and step propagation limited by the rate of kink generation [272].

A novel mechanism of kink generation was demonstrated for the crystallization of insulin [270,273]: 2D clusters of several insulin molecules, preformed on the terraces between steps, associate with the steps, as schematically depicted in Figure 19.31(B). This mechanism operates at moderate and high supersaturations, whereas, as discussed above, at low supersaturations, only kinks generated by thermal fluctuations exist. The mobility of clusters of several molecules is not surprising; see discussion, theory, and experimental examples in Refs. [274,275]. This mobility prevents identification of their structure prior to their association. They might be ordered or disordered, akin to a 2D liquid formed in the pool of insulin hexamers adsorbed on the terraces: examples of liquid phases in 2D systems [276] have been discussed [277]. A 3D analog of this process would be layer generation by the landing of dense liquid droplets on the surface of an existing crystal [24], discussed above and seen in Figure 19.28(C).

Rhombohedral crystals of Zn-insulin hexamers form in the islets of Langerhans in the pancreatic  $\beta$ -cells of mammals [8,278–280]. The likely biological function of insulin crystallization *in vivo* is to protect the insulin from further proteolysis (after conversion from proinsulin) while it is stored until regulated secretion into the blood serum [8,279]. It has also been suggested that crystal formation increases the degree of conversion from soluble proinsulin [8,281]. Either of the two functions of crystallization requires that the rate of growth of the crystals be fast and readily responsive to inevitable fluctuations in the rate of conversion. The mechanism of kink generation by the association of 2D clusters preformed on the terraces provides an understanding of the fast growth rates and nonlinear acceleration of the rates of insulin crystallization.

### 19.7.6 The Barrier for Incorporation into Kinks

Given the crucial role of structured water in the thermodynamics of crystallization and for the interactions between protein molecules in solution, discussed in Sections 19.3.2 and 19.5 previously, it is natural to hypothesize that the water structuring plays a major role in crystal growth kinetics. It was shown that the rate of the elementary step of crystallization, the attachment of a molecule from the solution to an existing growth site on the crystal surface, is determined by the rate of diffusion over a repulsive barrier [34,38,202,282]. Within the mechanism of the role of water structures in the kinetics of crystallization, this barrier would be the repulsive maximum depicted in Figure 19.6 and 19.15.

Critical tests of this hypothesis were carried out with the protein insulin. In laboratory conditions, this protein crystallizes in the presence and absence of an organic co-solvent, acetone. Thermodynamic analyses revealed that acetone destroys the shell of structured water around the insulin molecules in solution [68]. Figure 19.32 shows that this leads to faster kinetics of crystallization and a five times greater kinetic coefficient  $\beta$  [255]. When transport limitations were overcome by using the edges of larger crystals, around which buoyancy-driven convection is faster [122,124], or by forced solution flow [126],  $\beta$  in the presence of acetone reached  $0.4 \text{ mm s}^{-1}$ , comparable to these of small molecular

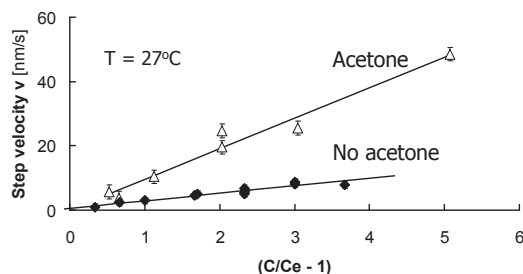


**FIGURE 19.32** Step velocity on the (100) face of insulin as a function of supersaturation ( $C/C_e - 1$ ), in the presence and the absence of acetone. Lines are regression fits to the respective sets of data. *With permission from Ref. [255].*

**Table 19.1** Kinetic Coefficients,  $\beta$ , Diffusivities,  $D$ , Effective Molecular Diameter  $a$ , Point Symmetry Group of Molecule  $G$ , Order of Symmetry Group  $Z$ , for Protein and Inorganic Systems

Protein	$\beta$ , $10^{-4}$ (cm s $^{-1}$ )	$D$ , $10^{-6}$ (cm $^2$ s $^{-1}$ )	$a$ [284]	$G$	$Z$	Source
Insulin			6.5	$\bar{3}$	6	257
No acetone	90	0.79				
~5% acetone	420					
Apoferritin	6	0.32	13	432	24	65
Ferritin	6	0.32	13	432	24	204
Canavalin, R3 form	5.8–26	0.4	3.5–8	3	3	121
Lumasine synthase	3.6	0.16	18	m5	60	24
Catalase	0.32	n.a.	11.5	222	4	292
Hemoglobin C	0.2	0.5	5.5	2	2	293
Lysozyme {101}		0.73	3	1	1	
Typical	2–3					294
No step bunching	22–45					128
Lysozyme {110}	2–3					120
STMV	4–8	0.2	16	m5	60	19
Thaumatococcus	2	0.6	4.0	1	1	295
Various inorganic systems (ADP, KDP, alums, etc.)	~100–1000	~1–5	0.5	1, 2, $\bar{2}$ , m, etc.	1, 2	34

compounds [283]. Thus, the destruction of the water shell correlates with faster kinetics, supporting the important role of structured water for the kinetics of incorporation.

The destruction of the water shell around solute molecules is likely the main component of the barrier for incorporation in kinks not only for protein but also for other materials. For evidence of this hypothesis, these barriers were determined for about 10 diverse substances and were found to fit into an unusually narrow range of  $28 \pm 7$  kJ mol $^{-1}$ , Table 19.1 [285]. The chemical nature of these substances ranges from inorganic salts, through organic molecular compounds, to proteins and viruses. Hence, the narrow range of the activation barriers is unexpected if the barriers should reflect the chemical variety of the crystallizing compounds. On the other hand, if the barrier in all cases reflects a high-energy state of partial destruction of the water structures around the solute molecules and at the kinks, the consistency of the barrier is natural. This magnitude of the barrier corresponds to the energy of one or two hydrogen bonds, i.e., one can think that the high-energy state is when these bonds have been broken and the new bonds that exist in the crystal have not formed. Although the participation of one or two hydrogen bonds in the association of small molecules and ions to kinks is expected, one may wonder why the barriers are not higher for a protein crystal, in which a greater number of hydrogen bonds may be broken. However, as discussed in Section 19.2.2 above, the large protein molecules have relatively limited areas of intermolecular contact in the crystal lattice [286], in which only a few hydrogen bonds exist.

Clearly, the barrier for incorporation, which is due to the water structuring, contains a large entropy component, which, as the entropy of crystallization, splits into entropy due to solvent and entropy due to the solute molecules. The solvent component may be both positive and negative, depending on whether additional molecules of water are trapped in the transition state, or some of those associated with the solute molecules are released. The contribution of the solute molecules to the activation entropy is due to the necessity to orient the molecule in a way suitable for association with the kink [266,287]. There have been estimates that the protein reorientation may slow crystallization kinetics of large molecules by as much as 1000 times. The estimates of this contribution are based on the following line of thought: With the typical translational diffusivities of the protein molecules on the order of  $10^{-7} \text{ cm}^2 \text{ s}^{-1}$ , see Table 19.1, a protein molecule spends  $\sim 10^{-7} \text{ s}$  travelling through the last  $10 \text{ \AA}$  prior to incorporation. During that time, with the typical rotational diffusivities of  $10^6 \text{ s}^{-1}$ , the molecule could rotate by  $\sim 0.3 \text{ rad}$ . Because an incorrectly aligned molecule would not be able to form the necessary bonds with the kink and will be rejected, only  $0.3/4\pi \approx 0.02$  of all attempts of incorporation will succeed, decreasing by 50 times the kinetic coefficient. Because the rotational diffusivity scales as  $a^{-3}$  Ref. [288], and the translational diffusivity scales as  $a^{-1}$  Ref. [289], the slowing down is significantly stronger for larger molecules.

To evaluate the significance of this contribution, in Table 19.1 we compare the step kinetic coefficients  $\beta$  of about a dozen proteins, protein complexes and viri, as well as some inorganic substances [19,24,34,63,118,119,126,202,255,290–293]. The  $\beta$ 's for the large molecules fit in the range  $(0.2\text{--}420) \times 10^{-4} \text{ cm s}^{-1}$ . The molecular symmetry groups of these large molecules have orders ranging from 1, through 3, to 24 for the ferritin and apoferritin, and 60 for the viri and lumazine synthase. No correlation exists between higher molecular symmetry and higher kinetic coefficients.

This lack of correlation once again suggests that in the case of solution growth the activated state is not a classical one with stretched bonds, but rather is a state in which the water shell is slowly destroyed, while the molecule retains rotational freedom. The slow destruction of the water shell prolongs significantly, by a factor of  $\sim \exp(28,000/RT) \approx 1 \times 10^5$  the time for the approach of a molecule to the kink. During this extended approach time, the incoming molecule tests different orientations and finds the right one. With some inaccuracy, it could be said that the overcoming of the barrier due to the water shells is the rate-limiting step in the association with a kink, whereas the selection of the proper orientation is significantly faster and does not affect the kinetics.

### 19.7.7 The Molecular Pathway from the Solution into a Growth Site

During crystal growth from solution, the solute molecules have two possible pathways between the solution and the kinks: they can be directly incorporated [70,253], as schematically illustrated in Figure 19.33(A), or they can first adsorb on the terraces between the steps, diffuse along them, and then reach the steps [70,180,294], Figure 19.33(B).

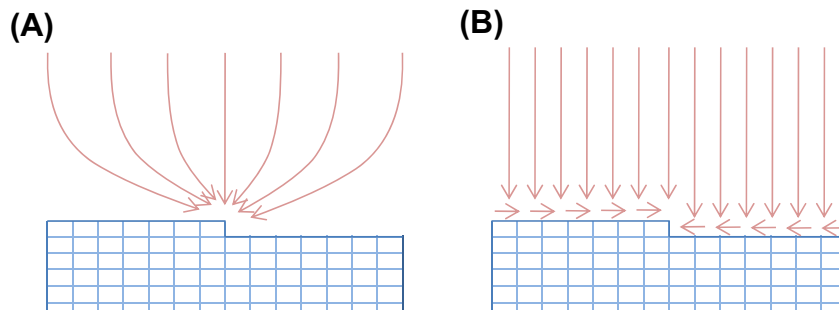


**FIGURE 19.33** Schematic illustration of the two pathways of a molecule from the solution into a step. Left: Direct incorporation from the solution. Right: Adsorption on the surface followed by surface diffusion and incorporation into a step.

If a crystal grows by the direct incorporation mechanism, the competition for supply between adjacent steps is mild [253,295]. On the contrary, competition for supply confined to the adsorption phase is acute [295,296]; it retards step propagation and acts as a strong effective attraction between the steps. This dramatically affects the stability of the step train, the appearance and evolution of step bunches [297–300], and ultimately the crystal quality and utility [298,301].

The two mechanisms can be directly discerned by monitoring the adsorbed solute molecules on the crystal surface. Direct imaging of the diffusion of fluorescently labeled lysozyme molecules along the surface of a growing crystalline faces was monitored in elaborate recent experiments [201,302]. Electron microscopy of flash-frozen samples has in several cases revealed the presence of adsorbed solute molecules on the crystal surface [303].

Indirect evidence for the growth mechanism of several systems has been sought by comparing the velocities of isolated steps to those of closely spaced steps. Slower growth of dense step segments was interpreted in favor of the surface diffusion mechanism for the proteins lysozyme [304] and canavalin [119].

A study of the growth processes of crystals of the proteins ferritin and apoferritin at the molecular level compared the fluxes of molecules entering the steps to those leaving the steps,  $j_+$  and  $j_-$  from Eqn (19.19) [269]. Comparing Eqns (19.19) and (19.20), it is relatively straightforward to show that in the case of direct incorporation, the ratio of these two fluxes should be equal to the ratio of the concentration to the solubility,  $j_+/j_- = C/C_e$  [38,269]. However, it was found that at  $C/C_e = 2$  or 3, the upper bound for the ratio  $j_+/j_-$  was 1.1. This and other pieces of evidence for this system allowed the conclusion that during the growth of ferritin and apoferritin crystals, the molecules from the solution enter the steps via a state of adsorption on the terraces between steps.

Although further tests may reveal direct incorporation of solute molecules into kinks for a studied crystallization system, such a finding appears unlikely. First, in all cases in which critical tests have been carried out, the action of the surface diffusion mechanism has been unambiguously demonstrated. Furthermore, estimates of the barrier for

incorporation of a molecule from the solution directly into a kink suggest that this barrier should be  $\sim 2$  times any of the barriers of the subsequent steps in the surface diffusion mechanism. Because the typical barriers for any of these steps is on the order of  $30 \text{ kJ mol}^{-1}$ , this enhanced barrier for incorporation would lead to slower incorporation by a factor of  $\sim 10^5$ . This higher barrier may be the general reason for the selection of the surface diffusion mechanism in solution growth, including solution growth of protein crystals.

## 19.8 Concluding Remarks

In this chapter, we have provided a summary of the physical principles underlying the crystallization of proteins. Although the basic laws of crystallization work well for the proteins, their large size and the sensitivity of their surfaces to the solution chemistry adds new features to the protein crystals and their formation. We cannot overemphasize that whereas it is very important to know the physical principles of the processes, it is equally important to realize the importance of the biochemical specificity of the proteins—that in many cases the physics will be masked by the biological and chemical features of the process. On the other hand, one should not make the opposite mistake: because of the huge difference between the proteins, draw the conclusion that the physics are unimportant, and cannot help in any way. The integration of the biochemical understanding of the specificity of each protein into the current crystal growth models is the challenge that the field now faces.

## References

- [1] Tanford C, Reynolds JA. *Nature's robots: a history of proteins*. Oxford University Press; 2001.
- [2] Charache S, Conley CL, Waugh DF, Ugoretz RJ, Spurrell JR. Pathogenesis of hemolytic anemia in homozygous hemoglobin C disease. *J Clin Invest* 1967;46:1795–811.
- [3] Hirsch RE, Raventos-Suarez C, Olson JA, Nagel RL. Ligand state of intraerythrocytic circulating HbC crystals in homozygote CC patients. *Blood* 1985;66:775–7.
- [4] Eaton WA, Hofrichter J. Sick cell hemoglobin polymerization. In: Anfinsen CB, Edsal JT, Richards FM, Eisenberg DS, editors. *Advances in protein chemistry*, vol. 40. Academic Press; 1990. p. 63–279.
- [5] Vekilov P. Sick cell haemoglobin polymerisation: is it the primary pathogenic event of sickle-cell anaemia? *Brit J Haematol* 2007;139:173–84.
- [6] Berland CR, Thurston GM, Kondo M, Broide ML, Pande J, Ogun O, Benedek GB. Solid-liquid phase boundaries of lens protein solutions. *Proc Natl Acad Sci USA* 1992;89:1214–8.
- [7] Asherie N, Pande J, Pande A, Zarutskie JA, Lomakin J, Lomakin A, Ogun O, Stern LJ, King J, Benedek GB. Enhanced crystallization of the Cys18 to Ser mutant of bovine gammaB crystallin. *J Mol Biol* 2001;314:663–9.
- [8] Dodson G, Steiner D. The role of assembly in insulin's biosynthesis. *Curr Opin Struct Biol* 1998;8: 189–94.
- [9] Brange J. *Galenics of insulin*. Springer; 1987.

- [10] Long ML, Bishop JB, Nagabhushan TL, Reichert P, Smith GD, DeLucas LJ. Protein crystal growth in microgravity review of large scale temperature induction method. *J Cryst Growth* 1996;168:233–43.
- [11] Matsuda S, Senda T, Itoh S, Kawano G, Mizuno H, Mitsui Y. New crystal form of recombinant murine interferon- $\beta$ . *J Biol Chem* 1989;264:13381–2.
- [12] Peseta S, Langer JA, Zoon KC, Samuel CE. Interferons and their actions. In: Richardson CC, Boyer PD, Dawid IB, Meister A, editors. *Annual review of biochemistry*, vol. 56; 1989. p. 727–78. *Annual Reviews*.
- [13] Reichert P, et al. *Metal-interferon-alpha crystals*. US Patent 5,441,734. 1995.
- [14] McPherson A. *Introduction to macromolecular crystallography*. John Wiley; 2009.
- [15] Berman HM, Westbrook J, Feng Z, Gilliland G, Bhat TN, Weissig H, Shindyalov IN, Bourne PE. The Protein Data Bank. *Nucleic Acids Research* 2000;28:235–42.
- [16] Lomakin A, Asherie N, Benedek G. Aelotopic interactions of globular proteins. *Proc Natl Acad Sci USA* 1999;96:9465–8.
- [17] Fusco D, Charbonneau P. Crystallization of asymmetric patchy models for globular proteins in solution. *Phys Rev E* 2013;88.
- [18] Durbin SD, Carson WE, Saros MT. In situ studies of protein crystal growth by atomic force microscopy. *J Phys D Appl Phys* 1993;26:B128–32.
- [19] Malkin AJ, Land TA, Kuznetsov YuG, McPherson A, DeYoreo JJ. Investigation of virus crystal growth mechanism by in situ atomic force microscopy. *Phys Rev Lett* 1995;75:2778–81.
- [20] Yau S-T, Thomas BR, Vekilov PG. Molecular mechanisms of crystallization and defect formation. *Phys Rev Lett* 2000;85:353–6.
- [21] Yau S-T, Vekilov PG. Quasi-planar nucleus structure in apoferritin crystallization. *Nature* 2000;406:494–7.
- [22] Vekilov PG. What determines the rate of growth of crystals from solution? *Cryst Growth Des* 2007;7:2796–810.
- [23] Malkin AJ, Thorne RE. Growth and disorder of macromolecular crystals: insights from atomic force microscopy and X-ray diffraction studies. *Methods* 2004;34:273–99.
- [24] Gliko O, Neumaier N, Pan W, Haase I, Fischer M, Bacher A, Weinkauff S, Vekilov PG. A metastable prerequisite for the growth of lumazine synthase crystals. *J Amer Chem Soc* 2005;127:3433–8.
- [25] Georgiou DK, Vekilov PG. A fast response mechanism for insulin storage in crystals may involve kink generation by association of 2D clusters. *Proc Natl Acad Sci USA* 2006;103:1681–6.
- [26] Pan W, Galkin O, Filobelo L, Nagel RL, Vekilov PG. Metastable mesoscopic clusters in solutions of sickle cell hemoglobin. *Biophys J* 2007;92:267–77.
- [27] Pan W, Vekilov PG, Lubchenko V. The origin of anomalous mesoscopic phases in protein solutions. *J Phys Chem B* 2010;114:7620–30.
- [28] Sleutel M, Van Driessche AE. Role of clusters in nonclassical nucleation and growth of protein crystals. *Proceedings of the National Academy of Sciences of the United States of America* 2014; 111(5):E546–53.
- [29] Galkin O, Vekilov PG. Control of protein crystal nucleation around the metastable liquid-liquid phase boundary. *Proc Natl Acad Sci USA* 2000;97:6277–81.
- [30] Vekilov PG. Dense liquid precursor for the nucleation of ordered solid phases from solution. *Cryst Growth Des* 2004;4:671–85.
- [31] Nelson DL, Cox MM. *Lehninger's principles of biochemistry*. 3rd ed. W.H. Freeman; 2000.

- [32] Sasaki G, Ooshima H, Kato J, Harano Y, Hirokawa N. Mechanism of crystallization of enzyme protein thermolysin. *J Cryst Growth* 1993;130:357–67.
- [33] Charron C, Sauter C, Zhu DW, Ng JD, Kern D, Lorber R, Giege R. Packing contacts in orthorhombic and monoclinic crystals of aspartyl-tRNA synthetase favor the hydrophobic regions of the protein. *J Cryst Growth* 2001;232:376–86.
- [34] Vekilov PG, Chernov AA. The physics of protein crystallization. In: Ehrenreich H, Spaepen F, editors. *Solid state physics*, vol. 57. Academic Press; 2002. p. 1–147.
- [35] Prausnitz J, Foose L. Three frontiers in the thermodynamics of protein solutions. *Pure Appl Chem* 2007;79:1435–44.
- [36] Lomakin A, Asherie N, Benedek GB. Monte Carlo study of phase separation in aqueous protein solutions. *J Chem Phys* 1996;104:1646–56.
- [37] Asherie N, Lomakin A, Benedek GB. Phase diagram of colloidal solutions. *Phys Rev Lett* 1996;77:4832–5.
- [38] Vekilov PG. Microscopic, mesoscopic, and macroscopic lengthscales in the kinetics of phase transformations with proteins. In: De Yoreo JJ, Lui XY, editors. *Nanoscale structure and assembly at solid-fluid interfaces*. vol. II: assembly in hybrid and biological systems. Kluwer Academic Publishers; 2004. p. 145–200.
- [39] Vekilov PG. Solvent entropy effects in the formation of protein solid phases. In: Carter Jr CW, Sweet RM, editors. *Methods in enzymology volume 368: macromolecular crystallography, Part C*. Academic Press; 2003. p. 84–105.
- [40] Svergun DI, Richard S, Koch MH, Sayers Z, Kuprin S, Zaccai G. Protein hydration in solution: experimental observation by x-ray and neutron scattering. *Proc Natl Acad Sci USA* 1998;95:2267–72.
- [41] Leckband D, Israelachvili J. Intermolecular forces in biology. *Quart Rev Biophys* 2001;34:105–267.
- [42] Raviv U, Klien J. Fluidity of bound hydration layers. *Science* 2002;297:1540–3.
- [43] Ball P. Chemical physics: how to keep dry in water. *Nature* 2003;423:25–6.
- [44] Pal SK, Zewail AH. Dynamics of water in biological recognition. *Chem Rev* 2004;104:2099–124.
- [45] Bhattacharyya SM, Wang Z-G, Zewail AH. Dynamics of water near a protein surface. *J Phys Chem B* 2003;107:13218–28.
- [46] Chalikian TV, Plum GE, Sarvazyan AP, Breslauer KJ. Influence of drug binding on DNA hydration: acoustic and densimetric characterizations of netropsin binding to the poly(dAdT)·poly(dAdT) and poly(dA)·poly(dT) duplexes and the poly(dT)·poly(dA)·poly(dT) triplex at 25°C. *Biochemistry* 1994;33:8629–40.
- [47] Chalikian TV, Völker J, Srinivasan AR, Olson WK, Breslauer KJ. The hydration of nucleic acid duplexes as assessed by a combination of volumetric and structural techniques. *Biopolymers* 1999;50:459–71.
- [48] Kauzmann W. Some forces in the interpretation of protein denaturation. In: Anfinsen CB, Anson ML, Bailey Kenneth, Edsall John T, editors. *Advances in protein chemistry*, vol. 14. Academic Press; 1959. p. 1–63.
- [49] Lounnas V, Pettitt BM, Findsen L, Subramanian S. A microscopic view of protein solvation. *J Phys Chem* 1992;96:7157–8.
- [50] Lounnas V, Pettitt BM, Phillips NG. A global model of the protein-solvent interface. *Biophys J* 1994; 66:601–14.
- [51] Makarov VA, Pettitt BM, Feig M. Solvation and hydration of proteins and nucleic acids: a theoretical view of simulation and experiment. *Acc Chem Res* 2002;35:376–84.

- [52] Choudhury N, Pettitt BM. Dynamics of water trapped between hydrophobic solutes. *J Phys Chem B* 2005;109:6422–9.
- [53] Choudhury N, Pettitt BM. Enthalpy-entropy contributions to the potential of mean force of Nanoscopic hydrophobic solutes. *J Phys Chem B* 2006;110:8459–63.
- [54] Choudhury N, Pettitt BM. The dewetting transition and the hydrophobic effect. *J Am Chem Soc* 2007;129:4847–52.
- [55] Lu L, Berkowitz ML. Hydration force between model hydrophilic surfaces: computer simulations. *J Chem Phys* 2006;124:101101.
- [56] Zangi R, Hagen M, Berne BJ. Effect of ions on the hydrophobic interaction between two plates. *J Am Chem Soc* 2007;129:4678–86.
- [57] Bresme F, Wynveen A. On the influence of solute polarizability on the hydrophobic interaction. *J Chem Phys* 2007;126:044501.
- [58] Choudhury N, Pettitt BM. On the mechanism of hydrophobic association of nanoscopic solutes. *J Am Chem Soc* 2005;127:3556–67.
- [59] Finkelstein A, Janin J. The price of lost freedom: entropy of bimolecular complex formation. *Protein Eng* 1989;3:1–10.
- [60] Tidor B, Karplus M. The contribution of vibrational entropy to molecular association. The dimerization of insulin. *J Mol Biol* 1994;238:405–14.
- [61] Fersht A. *Structure and mechanism in protein science*. W.H. Freeman; 1999.
- [62] Schall C, Arnold E, Wiencek JM. Enthalpy of crystallization of hen egg White lysozyme. *J Cryst Growth* 1996;165.
- [63] Yau S-T, Petsev DN, Thomas BR, Vekilov PG. Molecular-level thermodynamic and kinetic parameters for the self-assembly of apoferritin molecules into crystals. *J Mol Biol* 2000;303:667–78.
- [64] Petsev DN, Thomas BR, Yau S-T, Tsekova D, Nanev C, Wilson WW, Vekilov PG. Temperature-independent Solubility and Interactions between Apoferritin Monomers and Dimers in Solution. *J Cryst Growth* 2001;232:21–9.
- [65] Gliko O, Pan W, Katsonis P, Neumaier N, Galkin O, Weinkauff S, Vekilov PG. Metastable liquid clusters in super- and undersaturated protein solutions. *J Phys Chem* 2007;111:3106–14.
- [66] Vekilov PG, Feeling-Taylor AR, Petsev DN, Galkin O, Nagel RL, Hirsch RE. Intermolecular Interactions, Nucleation and Thermodynamics of Crystallization of Hemoglobin C. *Biophys J* 2002;83:1147–56.
- [67] Vekilov PG, Feeling-Taylor AR, Yau S-T, Petsev DN. Solvent entropy contribution to the free energy of protein crystallization. *Acta Crystallogr Sect D* 2002;58:1611–6.
- [68] Bergeron L, Filobelo L, Galkin O, Vekilov PG. Thermodynamics of the hydrophobicity in crystallization of insulin. *Biophys J* 2003;85:3935–42.
- [69] Tanford C. *The hydrophobic effect: formation of micelles and biological membranes*. John Wiley & Sons; 1980.
- [70] Burton WK, Cabrera N, Frank FC. The growth of crystals and equilibrium structure of their surfaces. *Phil Trans Roy Soc Lond Ser A* 1951;243:299–360.
- [71] Swartzentruber BS, Mo Y-W, Kariotis R, Lagally MG, Webb MB. Direct determination of site and kink energies of vicinal Si(001). *Phys Rev Lett* 1990;65:1913–6.
- [72] Dunitz JD. The entropic cost of bound water in crystals and biomolecules. *Science* 1994;264:670.
- [73] Giesen M, Schulze Icking-Konert G, Stapel D, Ibach H. Step fluctuations on Pt(111) surfaces. *Surf Sci* 1996;366:229–38.

- [74] Kuipers L, Hoogeman M, Frenken J. Step dynamics on Au(110) studied with a high-temperature, high-speed scanning tunneling microscope. *Phys Rev Lett* 1993;71:3517–20.
- [75] Derewenda Z. Rational protein crystallization by mutational surface engineering. *Struct (Camb)* 2004;12:529–35.
- [76] Derewenda ZS, Vekilov PG. Entropy and surface engineering in protein crystallization. *Acta Crystallogr Sect D* 2006;62:116–24.
- [77] Mateja A, Devedjiev Y, Krowarsch D, Longenecker K, Dauter Z, Otlewski J, Derewenda Z. The impact of Glu→Ala and Glu→Asp mutations on the crystallization properties of RhoGDI: the structure of RhoGDI at 1.3 Å resolution. *Acta Crystallogr D Biol Crystallogr* 2002;58:1983–91.
- [78] Czepas J, et al. The impact of Lys→Arg surface mutations on the crystallization of the globular domain of RhoGDI. *Acta Crystallogr D Biol Crystallogr* 2004;60:275–80.
- [79] Derewenda Z. The use of recombinant methods and molecular engineering in protein crystallization. *Methods* 2004;34:354–63.
- [80] Dumetz AC, Chockla AM, Kaler EW, Lenhoff AM. Protein phase behavior in aqueous solutions: crystallization, liquid-liquid phase separation, gels, and aggregates. *Biophysical J* 2008;94:570–83.
- [81] Broide ML, Berland CR, Pande J, Ogun OO, Benedek GB. Binary liquid phase separation of lens proteins solutions. *Proc Natl Acad Sci USA* 1991;88:5660–4.
- [82] Grigsby JJ, Blanch HW, Prausnitz JM. Cloud-point temperatures for lysozyme in electrolyte solutions: effect of salt type, salt concentration and pH. *Biophysical Chem* 2001;91:231–43.
- [83] Paliwal A, Asthagiri D, Abras D, Lenhoff AM, Paulaitis ME. Light-scattering studies of protein solutions: role of hydration in weak protein-protein interactions. *Biophysical J* 2005;89:1564–73.
- [84] Kuehner DE, Heyer C, Ramsch C, Fornefeld UM, Blanch HW, Prausnitz JM. Interactions of lysozyme in concentrated electrolyte solutions from dynamic light-scattering measurements. *Biophys J* 1997;73:3211–24.
- [85] McPherson A, Cudney B. Searching for silver bullets: an alternative strategy for crystallizing macromolecules. *J Struct Biol* 2006;156:387–406.
- [86] Dumetz AC, Snellinger-O'Brien AM, Kaler EW, Lenhoff AM. Patterns of protein – protein interactions in salt solutions and implications for protein crystallization. *Protein Sci* 2007;16:1867–77.
- [87] Velev OD, Kaler EW, Lenhoff AM. Protein interactions in solution characterized by light and neutron scattering: comparison of lysozyme and chemotrypsinogen. *Biophys J* 1998;75:2682–97.
- [88] Song XY, Zhao XF. The van der Waals interaction between protein molecules in an electrolyte solution. *J Chem Phys* 2004;120:2005–9.
- [89] Muschol M, Rosenberger F. Interaction in undersaturated and supersaturated lysozyme solutions: static and dynamic light scattering results. *J Chem Phys* 1995;103:10424–32.
- [90] Coen CJ, Newman J, Blanch HW, Prausnitz JM. Electrostatic protein-protein interactions: comparison of Point-Dipole and finite-length dipole potentials of mean force. *J Colloid Interface Sci* 1996;177:276–9.
- [91] Atkins P, DePaula J. *Physical chemistry*. 7th ed. Freeman; 2002.
- [92] Thomson JA, Schurtenberger P, Thurston GM, Benedek GB. Binary liquid phase separation and critical phenomena in a protein water solution. *Proc Natl Acad Sci USA* 1987;84:7079–83.
- [93] Shah M, Galkin O, Vekilov PG. Smooth transition from metastability to instability in phase separating protein solutions. *J Chem Phys* 2004;121:7505–12.
- [94] Muschol M, Rosenberger F. Liquid-liquid phase separation in supersaturated lysozyme solutions and associated precipitate formation/crystallization. *J Chem Phys* 1997;107:1953–62.

- [95] Petsev DN, Wu X, Galkin O, Vekilov PG. Thermodynamic functions of concentrated protein solutions from phase equilibria. *J Phys Chem B* 2003;107:3921–6.
- [96] Noro MG, Kern N, Frenkel D. The role of long range forces in the phase behavior of colloids and proteins. *Eurpophys Lett* 1999;48:332–8.
- [97] Sear RP. Phase behaviour of a simple model of globular proteins. *J Chem Phys* 1999;111:4800–6.
- [98] Kulkarni AM, Dixit NM, Zukoski CF. Ergodic and non-ergodic phase transitions in globular protein suspensions. *Faraday Discuss* 2003;123:37–50. discussion 75–97, 419–421.
- [99] Pan W, Filobelo L, Pham NDQ, Galkin O, Uzunova VV, Vekilov PG. Viscoelasticity in Homogeneous Protein Solutions. *Phys Rev Lett* 2009;102:058101.
- [100] Broide ML, Tominc TM, Saxowsky MD. Using phase transitions to investigate the effects of salts on protein interactions. *Phys Rev E* 1996;53:6325–35.
- [101] Tardieu A, Bonnete F, Finet S, Vivares D. Understanding salt or PEG induced attractive interactions to crystallize biological macromolecules. *Acta Crystallogr Sect D* 2002;58:1549–53.
- [102] Feeling-Taylor AR, Banish RM, Hirsch RE, Vekilov PG. Miniaturized scintillation technique for protein solubility determinations. *Rev Sci Instr* 1999;70:2845–9.
- [103] Galkin O, Chen K, Nagel RL, Hirsch RE, Vekilov PG. Liquid-liquid separation in solutions of normal and sickle cell hemoglobin. *Proc Natl Acad Sci USA* 2002;99:8479–83.
- [104] Chen Q, Vekilov PG, Nagel RL, Hirsch RE. Liquid-liquid separation in hemoglobins: distinct aggregation mechanisms of the  $\beta 6$  mutants. *Biophys J* 2004;86:1702–12.
- [105] Foffi G, McCullagh GD, Lawlor A, Zaccarelli E, Dawson KA, Sciortino F, Tartaglia P, Pini D, Stell G. Phase equilibria and glass transition in colloidal systems with short-ranged attractive interactions: Application to protein crystallization. *Phys Rev E* 2002;65:031407.
- [106] Dumetz AC, Chockla AM, Kaler EW, Lenhoff AM. Effects of pH on protein-protein interactions and implications for protein phase behavior. *BBA-Proteins Proteomics* 2008;1784:600–10.
- [107] Chayen NE, Helliwell JR, Snell EH. *Macromolecular crystallization and crystal perfection*. IUCr monographs on crystallography, 24. Oxford University Press; 2010.
- [108] Chao WC, et al. Control of concentration and volume gradients in microfluidic droplet arrays for protein crystallization screening. *Conf Proc IEEE Eng Med Biol Soc* 2004;4:2623–6.
- [109] Bergfors T. *Protein crystallization*. 2nd ed. La Jolla, CA: International University Line; 2009.
- [110] McPherson A. *Preparation and analysis of protein crystals*. Wiley; 1982.
- [111] McPherson A. *Crystallization of biological macromolecules*. Cold Spring Harbor Laboratory Press; 1999.
- [112] Chayen NE. A novel technique for containerless protein crystallization. *Protein Eng* 1996;9:927–9.
- [113] Chayen NE. Crystallization with oils: a new dimension in macromolecular crystal growth. *J Cryst Growth* 1999;196:434–41.
- [114] Garcia-Ruiz JM, Gonzalez-Ramirez LA, Gavira JA, Otalora F. Granada crystallization box: a new device for protein crystallization by counter-diffusion techniques. *Acta Crystallogr D Biol Crystallogr* 2002;58:1638–42.
- [115] Cacioppo E, Munson S, Pusey ML. Protein solubilities determined by a rapid technique and modifications of the technique to a micro method. *J Cryst Growth* 1991;110:66–71.
- [116] Cacioppo E, Pusey ML. The solubility of the tetragonal form of hen egg white lysozyme from pH 4.0 to 5.4. *J Cryst Growth* 1991;114:286–92.
- [117] Ries-Kautt MM, Ducruix AF. Relative effectiveness of various ions on the solubility and crystal growth of lysozyme. *J Biol Chem* 1989;264:745–8.

- [118] Vekilov PG, Rosenberger F. Dependence of lysozyme growth kinetics on step sources and impurities. *J Cryst Growth* 1996;158:540–51.
- [119] Land TA, DeYoreo JJ, Lee JD. An in-situ AFM investigation of canavalin crystallization kinetics. *Surf Sci* 1997;384:136–55.
- [120] Malkin AJ, Kuznetsov YG, McPherson A. In situ atomic force microscopy studies of surface morphology, growth kinetics, defect structure and dissolution in macromolecular crystallization. *J Cryst Growth* 1999;196:471–88.
- [121] Pusey M, Witherow W, Naumann R. Preliminary investigation into solutal flow about growing tetragonal lysozyme crystals. *J Cryst Growth* 1988;90:105–11.
- [122] Lin H, Petsev DN, Yau S-T, Thomas BR, Vekilov PG. Lower incorporation of impurities in ferritin crystals by suppression of convection: modeling results. *Cryst Growth Des* 2001;1:73–9.
- [123] Lin H, Rosenberger F, Alexander JID, Nadarajah A. Convective-diffusive transport in protein crystal growth. *J Cryst Growth* 1995;151:153–62.
- [124] Lin H, Vekilov PG, Rosenberger F. Facet morphology response to non-uniformities in nutrient and impurity supply. II. Numerical modeling. *J Cryst Growth* 1996;158:552–9.
- [125] Vekilov PG, Rosenberger F. Protein crystal growth under forced solution flow: experimental setup and general response of lysozyme. *J Cryst Growth* 1998;186:251–61.
- [126] Vekilov PG, Thomas BR, Rosenberger F. Effects of convective solute and impurity transport on protein crystal growth. *J Phys Chem B* 1998;102:5208–16.
- [127] McPherson A, Shlichta P. The use of heterogeneous and epitaxial nucleants to promote the growth of protein crystals. *J Cryst Growth* 1988;90:47–50.
- [128] McPherson A. A brief history of protein crystal growth. *J Cryst Growth* 1991;110:1–10.
- [129] Landau EM, Rosenbusch JP. Lipidic cubic phases: a novel concept for the crystallization of membrane proteins. *Proc Natl Acad Sci USA* 1996;93:14532–5.
- [130] Landau EM. Crystallization of membrane proteins in lipidic cubic phases. In: Iwata S, editor. *Methods and results in crystallization of membrane proteins*, vol. 39–55. International University Line; 2003.
- [131] Doye JPK, Louis AA, Vendruscolo M. Inhibition of protein crystallization by evolutionary negative design. *Phys Biol* 2004;1:9–13.
- [132] Doye JPK, Poon WCK. Protein crystallization in vivo. *Curr Opin Colloid Interface Sci* 2006;11:40–6.
- [133] Ducruix A, Giege R. *Crystallization of nucleic acids and proteins. A Pract Approach*. Oxford: IRL Press; 1992.
- [134] Sauter C, Ng JD, Lorber B, Keith G, Brion P, Hossieni MW, Lehn J-M, Giege R. Additives for the crystallization of proteins and nucleic acids. *J Cryst Growth* 1999;196:365–76.
- [135] Harris JM. *Poly(ethylene)glycol chemistry: biotechnical and biomedical applications*. New York: Plenum; 1992.
- [136] Derjaguin BV. *Theory of stability of colloids and thin films*. Plenum; 1989.
- [137] Verwey EJW, Overbeek JTG. *Theory of stability of lyophobic colloids*. Elsevier; 1948.
- [138] Petsev DN, Denkov ND. Diffusion of charged colloidal particles at low volume fraction: theoretical model and light scattering experiments. *J Colloid Interface Sci* 1992;149:329–44.
- [139] McQuarrie DA. *Statistical mechanics*. Harper & Row; 1976.
- [140] George A, Wilson WW. Predicting protein crystallization from a dilute solution property. *Acta Crystallogr Sect D* 1994;50:361–5.
- [141] Tardieu A, Finet S, Bonnete F. Structure of macromolecular solutions that generate crystals. *J Cryst Growth* 2001;232:1–9.

- [142] Tardieu A, Verge AL, Malfois M, Bonnette F, Finet S, Ries-Kaut M, Belloni L. Proteins in solution: from x-ray scattering intensities to interaction potentials. *J Cryst Growth* 1999;196:193–203.
- [143] Tessier PM, Vandrey SD, Berger BW, Pazhianur R, Sandler SI, Lenhoff AM. Self-interaction chromatography: a novel screening method for rational protein crystallization. *Acta Crystallogr D Biol Crystallogr* 2002;58:1531–5.
- [144] Tessier PM, Lenhoff AM. Measurements of protein self-association as a guide to crystallization. *Curr Opin Biotechnol* 2003;14:512–6.
- [145] Zimm BH. The scattering of light and the radial distribution function of high polymer solutions. *J Chem Phys* 1948;6:1093–9.
- [146] Liu W, Cellmer T, Keerl D, Prausnitz JM, Blanch HW. Interactions of lysozyme in guanidinium chloride solutions from static and dynamic light-scattering measurements. *Biotechnol Bioeng* 2005;90:482–90.
- [147] Wilson WW. Monitoring crystallization experiments using light scattering: assaying and monitoring protein crystallization in solution. *Methods* 1990;1:110–7.
- [148] Guo B, Kao S, McDonald H, Wilson WW, Asanov A, Combs LL. Correlation of second virial coefficients and solubilities useful in protein crystal growth. *J Cryst Growth* 1999;196:424–33.
- [149] Rosenbaum DF, Zamora PC, Zukoski CF. Phase behavior of small attractive colloid particles. *Phys Rev Lett* 1996;76:150–3.
- [150] McClurg RB, Zukoski CF. The electrostatic interaction of rigid, globular proteins with arbitrary charge distributions. *J Colloid Interface Sci* 1998;208:529–42.
- [151] Kokkoli E, Zukoski CF. Effect of solvents on interactions between hydrophobic self-assembled monolayers. *J Colloid Interface Sci* 1999;209:60–5.
- [152] Rosenbaum DF, Kulkarni A, Ramakrishnan S, Zukoski CF. Protein interactions and phase behavior: sensitivity to the form of the pair potential. *J Chem Phys* 1999;111:9882–90.
- [153] Neal BL, Asthagiri D, Lenhoff AM. Molecular origins of osmotic second virial coefficients of proteins. *Biophys J* 1998;75:2469–77.
- [154] Neal BL, Asthagiri D, Velev OD, Lenhoff AM, Kaler EW. Why is the osmotic second virial coefficient related to protein crystallization? *J Cryst Growth* 1999;196:377–87.
- [155] Anderson CO, Niesen JF, Blanch HW, Prausnitz JM. Interactions of proteins in aqueous electrolyte solutions from fluorescence anisotropy and circular-dichroism measurements. *Biophys Chem* 2000;84:177–88.
- [156] Haas C, Drenth J, Wilson WW. Relation between the solubility of proteins in aqueous solutions and the second virial coefficient of the solution. *J Phys Chem B* 1999;103:2808–11.
- [157] Shchukin ED, Pertsov AV, Amelina EA. *Colloid chemistry*. Moscow University Press; 1982.
- [158] Petsev DN, Thomas BR, Yau S-T, Vekilov PG. Interactions and aggregation of apoferritin molecules in solution: effects of added electrolytes. *Biophys J* 2000;78:2060–9.
- [159] Petsev DN, Vekilov PG. Evidence for non-DLVO hydration interactions in solutions of the protein apoferritin. *Phys Rev Lett* 2000;84:1339–42.
- [160] Carbonnaux C, Ries-Kautt M, Ducruix A. Relative effectiveness of various anions on the solubility of acidic *Hypoderma lineatum* collagenase at pH 7.2. *Protein Sci* 1995;4:2123–8.
- [161] Israelachvili J, Pashley R. The hydrophobic interaction is long range decaying exponentially with distance. *Nature* 1982;300:341–2.
- [162] Israelachvili JN. *Intermolecular and surface forces*. Academic Press; 1995.
- [163] Pashley RM, Israelachvili JN. DLVO and hydration forces between mica surfaces in  $Mg^{2+}$ ,  $Ca^{2+}$ ,  $Sr^{2+}$  and  $Ba^{2+}$  chloride solutions. *J Colloid Interface Sci* 1984;97:446–52.

- [164] Israelachvili J, Wennerstrom H. Role of hydration and water structure in biological and colloidal interactions. *Nature* 1996;379:219–25.
- [165] Bonneté F, Finet S, Tardieu A. Second virial coefficient: variations with lysozyme crystallization conditions. *J Cryst Growth* 1999;196:403–14.
- [166] Paunov V, Kaler E, Sandler S, Petsev D. A model for hydration interactions between apoferritin molecules in solution. *J Colloid Interface Sci* 2001;240:640–3.
- [167] Manciu M, Ruckenstein E. Long range interactions between apoferritin molecules. *Langmuir* 2002;18:8910–8.
- [168] Vekilov PG. What is the molecular-level role of the solution components in protein crystallization? *Cryst Growth Des* 2007;7:2239–46.
- [169] Lawson SE, Oakley S, Smith NA, Bareford D. Red cell exchange in sickle cell disease. *Clin Lab Haematol* 1999;21:99–102.
- [170] Harrison PM, Arosio P. The ferritins: molecular properties, iron storage function and cellular regulation. *Biochim Biophys Acta* 1996;1275:161–203.
- [171] Hempstead PD, Yewdall SJ, Fernie AR, Lawson DM, Artymiuk PJ, Rice DW, Ford GC, Harrison PM. Comparison of the three dimensional structures of recombinant human H and horse L ferritins at high resolution. *J Mol Biol* 1997;268:424–48.
- [172] Eisenberg D, Kauzmann W. The structure and properties of water. University Press; 1969.
- [173] Eisenberg D, Crothers D. Physical chemistry with applications to life sciences. The Benjamin/Cummins; 1979.
- [174] Asakura S, Oosawa F. Interaction between particles suspended in solutions of macromolecules. *J Polym Sci* 1958;33:183–92.
- [175] Kulkarni AM, Chatterjee AP, Schweitzer KS, Zukoski CF. Depletion interactions in the protein limit: effects of polymer density fluctuations. *Phys Rev Lett* 1999;83:4554–7.
- [176] Kulkarni AM, Zukoski CF. Depletion interactions and protein crystallization. *J Cryst Growth* 2001;232:156–64.
- [177] Gibbs JW. On the equilibrium of heterogeneous substances, first part. *Trans Connect Acad Sci* 1876;3:108–248.
- [178] Gibbs JW. On the equilibrium of heterogeneous substances (concluded). *Trans Connect Acad Sci* 1878;3:343–524.
- [179] Kashchiev D. Nucleation. Basic theory with applications. Butterworth, Heinemann; 2000.
- [180] Volmer M. Kinetik der Phasenbildung. Steinkopff; 1939.
- [181] Mutaftschiev B. Nucleation theory. In: Hurlé DTJ, editor. Handbook of crystal growth, vol. I. Elsevier; 1993. p. 189–247.
- [182] Vekilov PG, Monaco LA, Thomas BR, Stojanoff V, Rosenberger F. Repartitioning of NaCl and protein impurities in lysozyme crystallization. *Acta Crystallogr Sect D* 1996;52:785–98.
- [183] Lothe J, Pound GM. On the statistical mechanics of nucleation theory. *J Chem Phys* 1966;45:630–4.
- [184] Malkin AJ, McPherson A. Light scattering investigations of protein and virus crystal growth: ferritin, apoferritin and satellite tobacco mosaic virus. *J Cryst Growth* 1993;128:1232–5.
- [185] Malkin AJ, McPherson A. Light scattering investigation of the nucleation processes and kinetics of crystallization in macromolecular systems. *Acta Crystallogr Sect D* 1994;50:385–95.
- [186] Bhamidi V, Varanasi S, Schall CA. Measurement and modeling of protein crystal nucleation kinetics. *Cryst Growth Des* 2002;2:395–400.
- [187] Dixit NM, Kulkarni AM, Zukoski CF. Comparison of experimental estimates and model predictions of protein crystal nucleation rates. *Colloids Surfaces A* 2001;190:47–60.

- [188] Dixit NM, Zukoski CF. Crystal nucleation rates for particles experiencing short-range attractions: applications to proteins. *J Colloid Interface Sci* 2000;228:359–71.
- [189] Vekilov PG, Galkin O. On the methods of determination of homogeneous nucleation rates of protein crystals. *Colloids Surfaces A* 2003;215:125–30.
- [190] Kashchiev D. On the relation between nucleation work, nucleus size, and nucleation rate. *J Chem Phys* 1982;76:5098–102.
- [191] Oxtoby DW, Kashchiev D. A general relation between the nucleation work and the size of the nucleus in multicomponent nucleation. *J Chem Phys* 1994;100:7665–71.
- [192] Ford JJ. Nucleation theorems, the statistical mechanics of molecular clusters, and a revision of classical nucleation theory. *Phys Rev E* 1997;56:5615–29.
- [193] Schmelzter JN. Comments on the nucleation theorem. *J Colloid Interface Sci* 2001;242:354–72.
- [194] van der Waals JD. The equation of state for gases and liquids. In: Nobel lectures, physics 1901–1921, 254. Elsevier Publishing Company; 1910.
- [195] Debenedetti PG. *Metastable liquids*. Princeton Univ Pr; 1996.
- [196] Cahn JW, Hilliard JE. Free energy of a nonuniform system. I. interfacial free energy. *J Chem Phys* 1958;28:258–67.
- [197] Langer JS. Spinodal decomposition. In: Riske T, editor. *Fluctuations and instabilities in phase transitions*. Plenum; 1975. p. 19–42.
- [198] Filobelo L. *Kinetics of phase transition in protein solutions on microscopic and mesoscopic length scales* [PhD thesis], University of Houston, 2005.
- [199] Pan W, Kolomeisky AB, Vekilov PG. Nucleation of ordered solid phases of protein via a disordered high-density state: phenomenological approach. *J Chem Phys* 2005;122:174905.
- [200] Vekilov PG. Incorporation at kinks: kink density and activation barriers. In: Skowronski M, DeYoreo JJ, Wang CA, editors. *Perspectives on inorganic, organic and biological crystal growth: from fundamentals to Applications: AIP conference proceedings*. AIP conference series, vol. 916. AIP; 2007. p. 235–67.
- [201] Van Driessche AES, Otalora F, Sasaki G, Sleutel M, Tsukamoto K, Gavira JA. Comparison of Different Experimental Techniques for the Measurement of Crystal Growth Kinetics. *Crystal Growth & Design* 2008;8:4316–23.
- [202] Petsev DN, Chen K, Gliko O, Vekilov PG. Diffusion-limited kinetics of the solution-solid phase transition of molecular substances. *Proc Natl Acad Sci USA* 2003;100:792–6.
- [203] Zel'dovich YB. Theory of new phase formation: Cavitation. *Acta Physicochim URSS* 1943;18:1–22.
- [204] Kashchiev D. Nucleation. In: van der Eerden JP, Bruinsma OSL, editors. *Science and technology of crystal growth*. Kluwer Academic Publishers; 1995. p. 53–6.
- [205] Galkin O, Vekilov PG. Are nucleation kinetics of protein crystals similar to those of liquid droplets? *J Amer Chem Soc* 2000;122:156–63.
- [206] Steinrauf LK. Preliminary X-ray data for some crystalline forms of  $\beta$ -lactoglobulin and hen egg-white lysozyme. *Acta Crystallogr* 1959;12:77–8.
- [207] Bonnett PE, Carpenter KJ, Dawson S, Davey RJ. Solution crystallization via a submerged liquid-liquid phase boundary: oiling out. *Chem Commun* 2003:698–9.
- [208] ten Wolde PR, Frenkel D. Enhancement of protein crystal nucleation by critical density fluctuations. *Science* 1997;277:1975–8.
- [209] Talanquer V, Oxtoby DW. Crystal nucleation in the presence of a metastable critical point. *J Chem Phys* 1998;109:223–7.

- [210] Soga KG, Melrose JM, Ball RC. Metastable states and the kinetics of colloid phase separation. *J Chem Phys* 1999;110:2280–8.
- [211] Oxtoby DW. Crystals in a flash. *Nature* 2002;420:277–8.
- [212] Anderson VJ, Lekkerkerker HNW. Insights into phase transition kinetics from colloid science. *Nature* 2002;416:811–5.
- [213] Vivares D, Kaler E, Lenhoff A. Quantitative imaging by confocal scanning fluorescence microscopy of protein crystallization via liquid-liquid phase separation. *Acta Crystallogr D Biol Crystallogr* 2005;61:819–25.
- [214] Vekilov PG, Pan W, Gliko O, Katsonis P, Galkin O. Metastable mesoscopic phases in concentrated protein solutions. In: Franzese G, Rubi M, editors. *Lecture notes in physics*, vol. 752: aspects of physical biology: biological water, protein solutions, transport and replication. Springer; 2008. p. 65–95.
- [215] Uzgiris EE, Golibersuch DC. Excess scattered-light intensity fluctuations from hemoglobin. *Phys Rev Lett* 1974;32:37–40.
- [216] Sciortino F, Mossa S, Zaccarelli E, Tartaglia P. Equilibrium cluster phases and low-density arrested disordered states: the role of short-range attraction and long-range repulsion. *Phys Rev Lett* 2004; 93:055701.
- [217] Groenewold J, Kegel WK. Anomalously large equilibrium clusters of colloids. *J Phys Chem B* 2001; 105:11702–9.
- [218] Liu Y, Chen W-R, Chen S-H. Cluster formation in two-Yukawa fluids. *J Chem Phys* 2005;122: 044507.
- [219] Mossa S, Sciortino F, Tartaglia P, Zaccarelli E. Ground-state clusters for short-range attractive and long-range repulsive potentials. *Langmuir* 2004;20:10756–63.
- [220] Stradner A, et al. Equilibrium cluster formation in concentrated protein solutions and colloids. *Nature* 2004;432:492–5.
- [221] Hutchens SB, Wang Z-G. Metastable cluster intermediates in the condensation of charged macromolecule solutions. *J Chem Phys* 2007;127:084912.
- [222] Kashchiev D. Thermodynamically consistent description of the work to form a nucleus of any size. *J Chem Phys* 2003;118:1837–51.
- [223] Fredericks WJ, Hammonds MC, Howard SB, Rosenberger F. Density, thermal expansivity, viscosity and refractive index of lysozyme solutions at crystal growth concentrations. *J Cryst Growth* 1994; 141:183–92.
- [224] Filobelo LF, Galkin O, Vekilov PG. Spinodal for the solution-to-crystal phase transformation. *J Chem Phys* 2005;123:014904.
- [225] Chernov AA. *Modern Crystallography III, crystal growth*. Springer; 1984.
- [226] Lauffer MA. Entropy—driven processes in biology. *Mol Biol Biophys* 1975;20:1–264.
- [227] Hill A. Entropy production as the selection rule between different growth morphologies. *Nature* 1990;348:426–8.
- [228] Walton AG. Nucleation in liquids and solutions. In: Zettlemoyer AC, editor. *Nucleation*. Marcel Dekker; 1969. p. 225–307.
- [229] Hollingsworth MD. Crystal engineering: from structure to function. *Science* 2002;295:2410–3.
- [230] Lee JS, Lee Y-J, Tae EL, Park YS, Yoon KB. Synthesis of zeolite as ordered multicrystal arrays. *Science* 2003;301:818–21.
- [231] Hemming SA, Bochkarev A, Darst SA, Kornberg RD, Ala P, Yang DS, Edwards AM. The mechanism of protein crystal growth from lipid layers. *J Mol Biol* 1995;246:308–16.

- [232] Garetz B, Matic J, Myerson A. Polarization switching of crystal structure in the nonphotochemical light-induced nucleation of supersaturated aqueous glycine solutions. *Phys Rev Lett* 2002;89:175501.
- [233] Kuznetsov YG, Malkin AJ, McPherson A. The liquid protein phase in crystallization: a case study intact immunoglobins. *J Cryst Growth* 2001;232:30–9.
- [234] Galkin O, Nagel RL, Vekilov PG. The kinetics of nucleation and growth of sickle cell hemoglobin fibers. *J Mol Biol* 2007;365:425–39.
- [235] Galkin O, Pan W, Filobelo L, Hirsch RE, Nagel RL, Vekilov PG. Two-step mechanism of homogeneous nucleation of sickle cell hemoglobin polymers. *Biophys J* 2007;93:902–13.
- [236] Lomakin A, Chung DS, Benedek GB, Kirschner DA, Teplow DB. On the nucleation and growth of amyloid b-protein fibrils: detection of nuclei and quantitation of rate constants. *Proc Natl Acad Sci USA* 1996;93:1125–9.
- [237] Krishnan R, Lindquist SL. Structural insights into a yeast prion illuminate nucleation and strain diversity. *Nature* 2005;435:765–72.
- [238] Aber JE, Arnold S, Garetz BA. Strong DC electric field applied to supersaturated aqueous glycine solution induces nucleation of the polymorph. *Phys Rev Lett* 2005;94:145503.
- [239] Leunissen ME, Christova CG, Hynninen A-P, Royall CP, Campbell AI, Imhof A, Dijkstra M, van Roij R, van Blaaderen A. Ionic colloidal crystals of oppositely charged particles. *Nature* 2005;437:235–40.
- [240] Savage JR, Dinsmore AD. Experimental evidence for two-step nucleation in colloidal crystallization. *Phys Rev Lett* 2009;102:198302.
- [241] Zhang TH, Liu XY. Multistep crystal nucleation: a kinetic study based on colloidal crystallization. *J Phys Chem B* 2007;111:14001–5.
- [242] Kawasaki T, Tanaka H. Formation of a crystal nucleus from liquid. *Proc Natl Acad Sci* 2010;107:14036–41.
- [243] Gower LB. Biomimetic model systems for investigating the amorphous precursor pathway and its role in biomineralization. *Chem Rev* 2008;108:4551–627.
- [244] Pouget EM, Bomans PHH, Goos JACM, Frederik PM, de With G, Sommerdijk NAJM. The Initial Stages of Template-Controlled CaCO<sub>3</sub> Formation Revealed by Cryo-TEM. *Science* 2009;323:1455–8.
- [245] Gebauer D, Volkel A, Colfen H. Stable prenucleation calcium carbonate clusters. *Science* 2008;322:1819–22.
- [246] Wang JF, Muller M, Wang ZG. Nucleation in A/B/AB blends: Interplay between microphase assembly and macrophase separation. *J Chem Phys* 2009;130.
- [247] Sear RP. Nucleation via an unstable intermediate phase. *J Chem Phys* 2009;131:074702.
- [248] Lutsko JF, Nicolis G. Theoretical evidence for a dense fluid precursor to crystallization. *Phys Rev Lett* 2006;96:046102.
- [249] Kossel W. *Nachr Ges Wiss Göttingen* 1928:135–8.
- [250] Stranski IN. Zur theorie des Kristallwachstums. *Z Phys Chem* 1928;136:259–78.
- [251] Jackson KA. Interface structure. In: Doremus RH, Roberts BW, Turnbull D, editors. *Growth and perfection of crystals*. Chapman and Hill; 1958. p. 319–23.
- [252] Malkin AJ, Kuznetsov YG, Land TA, DeYoreo JJ, McPherson A. Mechanisms of growth of protein and virus crystals. *Nat Struct Biol* 1996;2:956–9.
- [253] Chernov AA. The spiral growth of crystals. *Sov Phys Uspekhi* 1961;4:116–48.

- [254] Gliko O, Neumaier N, Pan W, Haase I, Fischer M, Bacher A, Weinkauff S, Vekilov PG. Dense liquid droplets as a step source for the crystallization of lumazine synthase. *J Cryst Growth* 2005;275: e1409–16.
- [255] Reviakine I, Georgiou DK, Vekilov PG. Capillarity effects on the crystallization kinetics: insulin. *J Am Chem Soc* 2003;125:11684–93.
- [256] Kuznetsov YG, Malkin AJ, Land TA, DeYoreo JJ, Barba AP, Konnert J, McPherson A. Molecular resolution imaging of macromolecular crystals by atomic force microscopy. *Biophys J* 1997;72: 2357–64.
- [257] Malkin AJ, Kuznetsov YG, Glanz W, McPherson A. Atomic force microscopy studies of surface morphology and growth kinetics of thaumatin crystallization. *J Phys Chem* 1996;100:11736–43.
- [258] Malkin AJ, McPherson A. Probing of crystal interfaces and the structures and dynamic properties of large macromolecular ensembles with in situ atomic force microscopy. In: De Yoreo JJ, Lui XY, editors. *From fluid-solid interfaces to nanostructural engineering. Assembly in hybrid and biological systems*, vol. 2. Plenum/Kluwer Academic; 2004. p. 201–38.
- [259] Yip CM, Brader ML, DeFelippis MR, Ward MD. Atomic force microscopy of crystalline insulins: the influence of sequence variation on crystallization and interfacial structure. *Biophys J* 1998;74: 2199–209.
- [260] Gliko O, Reviakine I, Vekilov PG. Stable equidistant step trains during crystallization of insulin. *Phys Rev Lett* 2003;90:225503.
- [261] Stranski IN, Kaischew R. Über den Mechanismus des Gleichgewichtes kleiner Kriställchen. I *Z Phys Chem* 1934;B 26:100–13.
- [262] Kaischew R. Zur Theorie des Kristallwachstums. *Z Phys* 1936;102:684–90.
- [263] Jacob J, Anisimov MA, Sengers JV, Oleinikova A, Weingartner H, Kumar A. Novel phase-transition behavior near liquid/liquid critical points of aqueous solutions: Formation of a third phase at the interface. *Phys Chem Chem Phys* 2001;3:829–31.
- [264] Malkin AJ, Kuznetsov YG, McPherson A. Defect structure of macromolecular crystals. *J Struct Biol* 1996;117:124–37.
- [265] Malkin AJ, Kuznetsov YG, McPherson A. Incorporation of microcrystals by growing protein and virus crystals. *Proteins: Struct Funct Genet* 1996;24:247–52.
- [266] Chernov AA, Komatsu H. Topics in crystal growth kinetics. In: van der Eerden JP, Bruinsma OSL, editors. *Science and technology of crystal growth*. Kluwer Academic; 1995. p. 67–80.
- [267] Eyring H, Lin SH, Lin SM. *Basic chemical kinetics*. John Wiley and Sons; 1980.
- [268] Houston PL. *Chemical kinetics and reaction dynamics*. McGraw-Hill Higher Education; 2001.
- [269] Chen K, Vekilov PG. Evidence for the surface diffusion mechanism of solution crystallization from molecular-level observations with ferritin. *Phys Rev E* 2002;66:021606.
- [270] Yau S-T, Thomas BR, Galkin O, Gliko O, Vekilov PG. Molecular mechanisms of microheterogeneity-induced defect formation in ferritin crystallization. *Proteins: Struct Funct Genet* 2001;43:343–52.
- [271] Voronkov VV. The movement of an elementary step by means of the formation of one-dimensional nuclei. *Sov Phys Crystallogr* 1970;15:8–13.
- [272] Chernov AA, Rashkovich LN, Yamlinski IV, Gvozdev NV. Kink kinetics, exchange fluxes, 1D “nucleation” and adsorption on the (010) face of orthorhombic lysozyme crystals. *J Phys:Condens Matter* 1999;11:9969–84.
- [273] Hooks DE, Yip CM, Ward MD. Nanoconfined electrochemical nucleation of crystalline molecular monolayers on graphite substrates. *J Phys Chem B* 1998;102:9958–65.

- [274] Kellogg GL. Oscillatory behavior in the size dependence of cluster mobility on metal surfaces: Rh on Rh(100). *Phys Rev Lett* 1994;73:1833–6.
- [275] Sholl DS, Skodje RT. Diffusion of clusters of atoms and vacancies on surfaces and the dynamics of diffusion-driven coarsening. *Phys Rev Lett* 1995;75:3158–61.
- [276] Lyuksyutov I, Naumovets AG, Pokrovsky V. Two-dimensional crystals. Academic Press; 1992.
- [277] Schwartz DK. Mechanisms and kinetics of self-assembled monolayer formation. *Annu Rev Phys Chem* 2001;52:107–37.
- [278] Howell S, Tyhurst M. The insulin storage granule. In: Poisner, Trifaro, editors. *The secretory granule*. Elsevier; 1982. p. 155–72.
- [279] Halban P, Mutkoski R, Dodson G, Orci L. Resistance of the insulin crystal to lysosomal proteases: implications for pancreatic B-cell crinophagy. *Diabetologia* 1987;30:348–53.
- [280] Baker EN, Blundell TL, Cutfield JF, Cutfield SM, Dodson EJ, Dodson GG, Crowfoot-Hodgkin DM, Hubbard RE, Isaacs NW, Reynolds CD, Sakabe K, Sakabe N, Vijayan NM. The Structure of 2Zn Pig Insulin Crystals at 1.5Å Resolution. *Phil Trans R Soc Lond* 1988;B319:369–456.
- [281] Carroll RJ, Hammer RE, Chan SJ, Swift HH, Rubenstein AH, Steiner DF. A Mutant Human Proinsulin is Secreted from Islets of Langerhans in Increased Amounts Via an Unregulated Pathway. *PNAS* 1988;85:8943–7.
- [282] Vekilov PG. Kinetics and mechanisms of protein crystallization at the molecular level. In: Vo-Dinh T, editor. *Methods in molecular biology*, vol. 300: protein nanotechnology, protocols, instrumentation, and applications. Humana Press; 2005. p. 15–52.
- [283] Georgiou DK. Phase transitions in insulin solutions and possible implications in living organisms, PhD Dissertation. (University of Houston, 2006).
- [284] Yamashita M, Wesson L, Eisenman G, Eisenberg D. Where metal ions bind in proteins. *PNAS* 1990; 87:5648–52.
- [285] De Yoreo JJ. Eight Years of AFM: What has it taught us about Solution Crystal Growth. In: 13 International conference on Crystal Growth, T. Hibiya, J.B. Mullin, & M. Uwaha, editors. Elsevier.
- [286] Oki H, Matsuura Y, Komatsu H, Chernov AA. Refined structure of orthorhombic lysozyme crystallized at high temperature: correlation between morphology and intermolecular contacts. *Acta Crystallogr Sect D* 1999;55:114–21.
- [287] Chernov AA, Komatsu H. Principles of crystal growth in protein crystallization. In: van der Eerden JP, Bruinsma OSL, editors. *Science and technology of Crystal growth*. Kluwer Academic; 1995. p. 329–53.
- [288] Doi M, Edwards SF. *The theory of polymer dynamics*. Clarendon Press; 1986.
- [289] Berry PS, Rice SA, Ross J. *Physical chemistry*. 2nd ed. Oxford University Press; 2000.
- [290] Malkin A, Kuznetsov Y, McPherson A. An in situ AFM investigation of catalase crystallization. *Surf Sci* 1997;393:95–107.
- [291] Feeling-Taylor AR, Yau S-T, Petsev DN, Nagel RL, Hirsch RE, Vekilov PG. Crystallization Mechanisms of Hemoglobin C in the R State. *Biophys J* 2004;87:2621–9.
- [292] Vekilov PG. Elementary processes of protein crystal growth. In: Komatsu H, editor. *Studies and concepts in Crystal growth*. Pergamon; 1993. p. 25–49.
- [293] Kuznetsov YG, Konner J, Malkin AJ, McPherson A. The advancement and structure of growth steps on thaumatin crystals visualized by atomic force microscopy at molecular resolution. *Surf Sci* 1999;440:69–80.
- [294] Gilmer GH, Ghez R, Cabrera N. An analysis of combined volume and surface diffusion processes in crystal growth. *J Cryst Growth* 1971;8:79–93.

- [295] Vekilov PG, Kuznetsov YG, Chernov AA. Interstep interaction in solution growth; (101) ADP face. *J Cryst Growth* 1992;121:643–55.
- [296] Vekilov PG, Kuznetsov YG. Growth kinetics irregularities due to changed dislocation source activity; (101) ADP face. *J Cryst Growth* 1992;119:248–60.
- [297] Williams ED, Bartelt NC. Thermodynamics of surface morphology. *Science* 1991;251:393–400.
- [298] Bauser E. Atomic mechanisms in semiconductor liquid phase epitaxy. In: Hurlé DTJ, editor. *Handbook of crystal growth*, vol. 3b. North Holland; 1994. p. 879–911.
- [299] Vekilov PG, Alexander JID, Rosenberger F. Nonlinear response of layer growth dynamics in the mixed kinetics-bulk transport regime. *Phys Rev E* 1996;54:6650–60.
- [300] Uwaha M, Saito Y, Sato M. Fluctuations and instabilities of steps in the growth and sublimation of crystals. *J Cryst Growth* 1995;146:164–72.
- [301] Vekilov PG, Rosenberger F. Intrinsic kinetics fluctuations as cause of growth inhomogeneity in protein crystals. *Phys Rev E* 1998;57:6979–81.
- [302] Sazaki G, Okada M, Matsui T, Watanabe T, Higuchi H, Tsukamoto K, Nakajima K. Single-Molecule Visualization of Diffusion at the Solution; Crystal Interface. *Cryst Growth & Design* 2008;8:2024–31.
- [303] Braun N, Tack J, Fischer M, Bacher A, Bachmann L, Weinkauff S. Electron microscopic observations on protein crystallization: adsorption layers, aggregates and crystal defects. *J Cryst Growth* 2000; 212:270–82.
- [304] Vekilov PG, Monaco LA, Rosenberger F. Facet morphology response to non-uniformities in nutrient and impurity supply. I. Experiments and interpretation. *J Cryst Growth* 1995;156:267–78.
- [305] Howard SB, Twigg PJ, Baird JK, Meehan EJ. The solubility of hen-egg-white lysozyme. *J Cryst Growth* 1988;90:94–104.
- [306] Steinrauf LK. Preliminary X-ray data for some new crystalline forms of -lactoglobulin and hen-egg-white lysozyme. *Acta Cryst B* 1959;12:77–9.

# Biological Crystallization

Jaime Gómez-Morales<sup>1</sup>, Giuseppe Falini<sup>2</sup>, Juan Manuel García-Ruiz<sup>1</sup>

<sup>1</sup>LABORATORIO DE ESTUDIOS CRISTALOGRAFICOS, INSTITUTO ANDALUZ DE CIENCIAS DE LA TIERRA, CSIC-UNIVERSIDAD DE GRANADA, GRANADA, SPAIN; <sup>2</sup>DIPARTIMENTO DI CHIMICA "G. CIAMICIAN," ALMA MATER STUDIORUM UNIVERSITÀ DI BOLOGNA, BOLOGNA, ITALY

## CHAPTER OUTLINE

<b>20.1 Introduction</b> .....	<b>874</b>
<b>20.2 The Mechanisms of Biological Crystallization</b> .....	<b>875</b>
20.2.1 Biological Control at Nucleation Level .....	875
20.2.2 Biological Control at Growth Level.....	883
20.2.3 Biological Control at Constructional Level .....	885
<b>20.3 Crystallization Techniques to Study Biological Crystallization</b> .....	<b>886</b>
20.3.1 Batch Crystallization .....	886
20.3.2 Vapor Diffusion .....	887
20.3.3 Gel Crystallization .....	888
20.3.4 In vivo Induced Mineralization.....	889
<b>20.4 The Role (Function) of Biological Crystallization</b> .....	<b>890</b>
20.4.1 Crystals to Support and Protect the Organism's Body: Exoskeletons and Endoskeletons.....	890
20.4.2 Crystals to Control Water Flow: Lipids in the Epidermis .....	890
20.4.3 Crystals to Chew: The Teeth .....	892
20.4.4 Crystals to Hear and Balance: The Otoliths.....	894
20.4.5 Crystals to Orient and Navigate .....	895
20.4.6 Organisms to Produce Engineered Biological Crystallization.....	897
20.4.7 Crystals to Packaging: Eggshells—The Protein Containers.....	897
20.4.8 Undesired Crystallization: Pathological Mineralization .....	899
20.4.9 Crystals to Manipulate Light.....	900
20.4.10 Induced Biological Crystallization .....	901
<b>20.5 Current Trends and the Future of Biological Crystallization</b> .....	<b>903</b>
<b>Acknowledgments</b> .....	<b>905</b>
<b>References</b> .....	<b>905</b>

## 20.1 Introduction

Life is a geological force [1]. Since life appeared on our planet, most probably more than 3.5 billion years ago (a date still under discussion [2]), it has continuously and dramatically affected the geochemical evolution of the planet. At the beginning, unicellular organisms were only able to modify their neighborhood, for instance by increasing the local pH and triggering the precipitation of magnesium and calcium carbonates. Their organic surfaces also acted in many cases as a substrate for heterogeneous nucleation, reducing the free energy required for mineralization. The sticky extracellular polymeric substances secreted by these organisms served to adsorb mineral particles and to build large complex mineral rocks called microbialites [3]. All of these mechanisms by which life rather passively favors mineral precipitation are called biologically induced mineralization. However, living organisms started to govern control over nucleation and crystal growth after the appearance of the first multicellular organisms perhaps 1.5 billion years ago (another date under discussion [4]) and certainly after the explosion of diversity that took place 540 million years ago [5,6]. These multicellular organisms managed to control precipitation in order to build mineral structures required to support the increasing volumes and weight of their organisms. But they also created mineral devices of complex patterns to see, to hear, to balance, to orient and navigate, to color, to eat (chew), as well as for transpiration or to protect their embryo. This kind of sophisticated biomineralization in which organisms play an active role is called biologically controlled mineralization.

After so many millions of years of Darwinian evolution, it is not a surprise that biological crystallization is a ubiquitous phenomenon in nature that accounts not only for the formation of both inorganic and organic compounds by organisms but also for the crystallization of biological macromolecules such as proteins, lipids, keratins, chitins, etc. Many organisms from diverse phyla have developed the ability to precipitate various minerals [7], exploring distinctive pathways to use these minerals to build sophisticated structural architectures for different purposes [8]. Most of these processes take place under physiologic conditions, at lower temperatures than those required to precipitate their inorganic counterparts [9], therefore with a highly efficient use of energy for the construction of such architectures. Under strict biological control of the nucleation, growth, and organization of the crystals, organisms are able to build sophisticated structures with hierarchical order and physical properties in many cases as yet unparalleled by their synthetic counterparts. Even in those cases in which organisms crystallize minerals abnormally, so-called pathological crystallization, in some specific cases (e.g., kidney stones) the deposits can show a structure with a hierarchical organization with their morphological and textural features strongly linked to the organization of nanocrystals at the mesoscopic level [10].

There are several excellent textbooks, dedicated volumes, and reviews where the subject of biomineralization is described more extensively than in this chapter (e.g., [7,8,11–17]) or that deal with specific biomineralization problems in more detail (e.g.,

eggshell [18,19], bone [20,21], enamel [22,23], dentin [24,25], pathological calcification [10], etc. to cite a few examples). We have decided to review different crystalline devices made by organisms, first from the point of view of their function and then the formation mechanism of these structures. Therefore, we will cover the current knowledge on the biological control of nucleation, growth, and organization of inorganic or organic crystalline structures for a number of functional composite inorganic/organic biominerals such as mollusk shells, echinoderm spines, bones, teeth, otoliths, eggshells, magnetosomes, pearls, stromatolites, proteins, and pathological crystallizations. We will also cover purely organic structures such as the mammalian stratum corneum, reptilian molts, fish scales, or butterfly wings where the crystalline order is mesoscopic and not always translational. The minerals precipitated by biological induction do not usually have a function. Consequently, this chapter does not deal much with biologically induced mineralization processes, except for the interesting case of microbialites. Note that we have titled this chapter “Biological Crystallization” instead of the more classical “Biomineralization” or “Biological Mineralization” because this chapter deals with many structures that are not made by minerals but by organic molecules such as carbohydrates, polysaccharides, proteins, and biopolymers in general, and we are more interested in the formation and growth of the crystals than in the structure itself. It is not clear whether this term will stand in the future, but we believe it is worthwhile to use it.

The chapter is organized into four main sections. After this introduction, in [Section 20.2](#) we review the mechanisms of biological crystallization, including how living organisms control nucleation, growth, and texture. Then, in [Section 20.3](#) we discuss several crystallization techniques used to study and in some cases to mimic the problem of biological crystallization in vitro. In [Section 20.4](#), we revise the different roles played by devices made by biological crystallization. Finally, we conclude with the current trends and some considerations of future challenges in this fascinating crystallization topic.

## 20.2 The Mechanisms of Biological Crystallization

After hundreds of millions of years of evolution, organisms are able to grow many different minerals, but the mechanisms of nucleation and crystal growth have been reasonably studied only for a few of them. This section provides an overview of the strategies adopted by organisms in the control of nucleation, growth, and construction of their mineralized regions, with a focus on a few examples for which enough information is available.

### 20.2.1 Biological Control at Nucleation Level

In biological crystallization, heterogeneous nucleation is ubiquitous. Thus, a central question is how organized organic surfaces can control the nucleation of inorganic materials by geometric, electrostatic, and stereochemical complementarity between nuclei and functionalized substrates. Nucleation is the initial appearance of a new phase

during a first-order phase transition when the nuclei that have formed within a supersaturated solution overcome the nucleation barrier. In other words, small crystal nuclei form spontaneously in supersaturated solutions, but unless their size exceeds a critical value—the so-called critical nucleus—they will redissolve instead of growing [26–28].

The crystal nucleation rate,  $J_n$ , depends exponentially on the nucleus size, from which comes a nucleation free-energy barrier [29].

$$J_n = Ae^{(-B\gamma^3/\sigma^2)} \quad (20.1)$$

where  $A$  is a kinetic preexponential factor that depends on many parameters (viscosity of the solution, the molecular charge, the molecular volume, and the density of the solution) and the coefficient  $B$  comprises all the factors (temperature, molar volume) other than interfacial energy ( $\gamma$ ) and supersaturation ( $\sigma$ ) [29]. Eqn (20.1) shows that the height of the nucleation free-energy barrier depends on interfacial energy and supersaturation.

In general, the effect of the organic substrate is to lower the interfacial energy [30]. Moreover, the equilibrium crystal phase is controlled by the depths and shapes of the energy minima [30]. By varying the height of the energy barrier, the growth kinetics can be controlled and nonequilibrium final or intermediate states can be selected [15].

The nucleation process has been well described by classical theories [29], but numerous recent observations in biological crystallization studies strongly suggest that this view of nucleation is not appropriate. The discovery of stable prenucleation clusters (PNCs) [31] has defined nonclassical nucleation, which represents the basis of nonclassical crystallization theory [32].

Accordingly, during the nucleation of biominerals, the relevant species are not ions but PNCs that encode distinct structures before precipitation takes place [33,34]. In this novel view of the nucleation process, the crystallization phase diagram is analogous to that of atomic and molecular systems and can be described under the laws of classical nucleation theory [35].

The earliest events of homo/heterogeneous nucleation from an initial supersaturated solution are pivotal in order to address the knowledge of biological crystallization strategies. Direct observation of nucleation is very difficult because once crystal nuclei have grown to an observable size, they are already beyond the critical stage [36]. Even in the light of nonclassical crystallization theory in which PNCs are involved, the factors that control the formation and stabilization of the PNCs and their transformation in the crystalline phase are still unclear.

In biomineralization, the organic matrix, composed of proteins, polysaccharides, and lipid assemblies, is the key to triggering nucleation. The organic matrix is the major control factor for PNC formation, maturation, and transformation [37–39]. Indeed, it has been shown that organic matrix proteins play an important role in the nucleation process and can work as “mineral enzymes” in manipulating the PNCs pathway [31,33,40]. The catalytic role that proteins have in the nucleation stage during a biomineralization process is beginning to be understood, and it is likely that over time mechanistic insights will emerge [41]. The nucleation pathway to the final crystalline

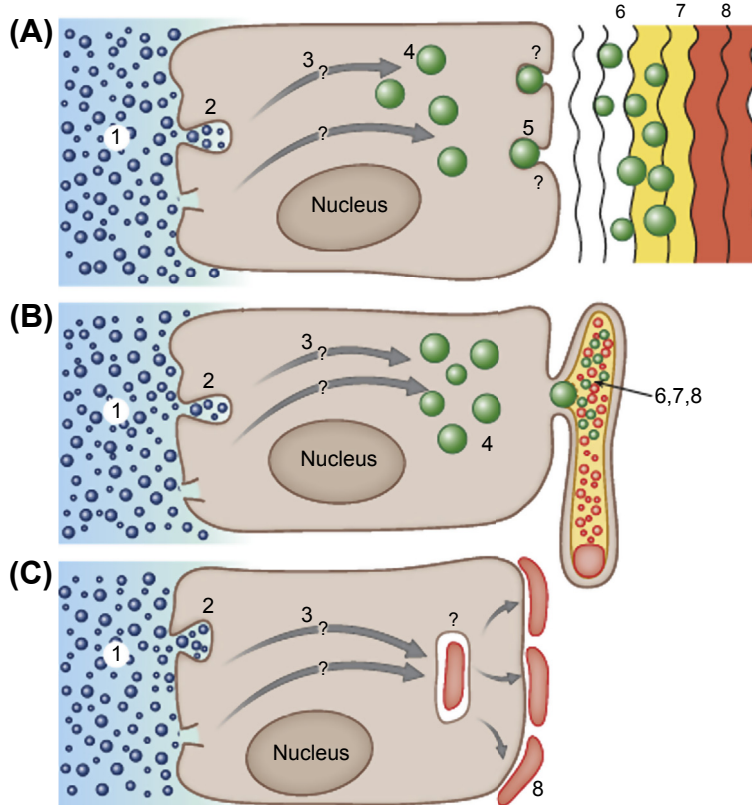


**FIGURE 20.1** Crystallization pathways. Schematic diagrams of generalized crystallization pathways involving (A) an extracellular matrix, (B) a vesicle-confined space (syncytium), and (C) the formation of mature mineralized elements within a vesicle inside the cell. (1) The medium from which the ions are derived (seawater or body fluids). (2) The ion-sequestering process: endocytosis of seawater droplets and/or ion channels and/or transporters. (3) Transport within the cell to specialized vesicles. (4) Specialized vesicles in which the formation of the first disordered mineral phase occurs. (5) Transport of the mineral-bearing vesicles and their contents into the extracellular environment or into the syncytium. (6) The translocation of the disordered phase to the crystallization front. (7) Transformation of the initial disordered phase into more ordered phases. (8) The mature mineralized tissue. In the case of the crystallization pathway shown in panel c, the mature mineralized product may remain within the cell (e.g., guanine crystals in fish skin) or may be transported to the cell surface (e.g., Coccolithophoridae and miliolid foraminifera). Very little is known about transient precursor phases in the crystallization pathway shown in panel c. *Figure 20.6 from [43] with permission.*

state seems to pass through several stable states of increasing stability (Figure 20.1) [26,27,35,42,43].

The first reported example of this process is the teeth of the chiton (see also *crystal to chew* section) [44]. The outer layer of the tooth contains magnetite, a hard magnetic mineral. It forms from a disordered ferrihydrite (hydrous ferric oxyhydroxide) precursor phase [45]. The inner layer of the tooth contains carbonated apatite, the same mineral present in bone. This inner layer forms by way of an amorphous calcium phosphate precursor phase [46]. In the years following these discoveries, it was shown that

ferrihydrate is a precursor phase of magnetite formation in magnetotactic bacteria [47]. Recently, the use of pulsed-laser atom-probe tomography has unveiled the three-dimensional chemical maps of organic fibers, which have a diameter of 5–10 nm and surround nanocrystalline magnetite in the tooth. Most fibers co-localize with either sodium or magnesium ions, and the clustering of these cations in the fiber indicates a structural level of hierarchy in which individual organic fibers probably have different functional roles in controlling fiber formation and matrix–mineral interactions [48]. The important role of precursors and organic matrix molecules in the formation of magnetite has recently been reexamined. Cryogenic transmission electron microscopy has shown that the nucleation and growth of magnetite proceeds through the rapid agglomeration of nanometric primary particles and, in contrast to the nucleation of other minerals, no intermediate amorphous bulk precursor phases are involved [49].

The spines of echinoderms represent another example of biomineralization control over nucleation that has been extensively investigated (Figure 20.2). These single crystals [50] form inside a syncytium [51], a membrane envelope produced by many cells. The cells provide the necessary raw materials for constructing the growing crystals [52,53]. The crystal grows out of an aqueous solution saturated with calcium carbonate [54]. Insights into the nucleation of these crystals have been gained from studies of calcitic spicule formation in sea urchin larvae [55]. The larval spicules grow on a single calcite crystal seed by the transformation of a transient amorphous calcium carbonate (ACC) phase [56]. ACC is apparently fed into the syncytium by cells in the form of ACC-containing vesicles [57]. Thus, packages of ACC are delivered to the crystal deposition site and then transform in a controlled manner into calcite single crystals. Moreover, there is no discernible aqueous phase around the growing spicule [57]. Most of the information on spine formation was gained taking advantage of the fact that sea urchins are able to regenerate spines that break. Spine regeneration begins with the epidermis reconstruction around the broken spine. Within this space, a new syncytium is formed by sclerocytes in contact with the stump of the old spine. The regenerated and old spines together diffract X-rays as one single crystal [50]. The regeneration process is thus considered to be very similar to the original spine growth. Following this approach

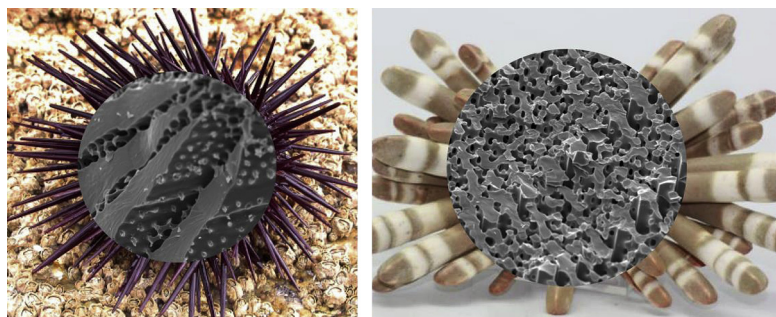


**FIGURE 20.2** SEM images of fractured spine from sea urchin *Paracentrotus lividus* (left) and *Heterocentrotus mammillatus* (right). On the background a camera picture of the two coral species is shown.

it was observed that calcium carbonate is first deposited as hydrated ACC, which then dehydrates prior to or concomitant with crystallization. ACC is introduced into the syncytium as an isotropic noncrystalline solid and can thus be molded into any shape. The solid itself is clearly a very concentrated source of ions. The subsequent transformation of the amorphous phase into a composite crystalline solid with much better mechanical properties [58] leads to a functional skeleton. The mechanism of transformation is complex—the transforming spine does not display a well-defined crystallization front. In fact, there are three distinct mineral phases: a short-lived, presumably hydrated ACC phase; an intermediate transient form of ACC; and the biogenic crystalline calcite phase. The amorphous and crystalline phases are placed side by side, often appearing in adjacent sites. Thus, the amorphous-crystal transformation may propagate following a winding path through preexisting amorphous units [59]. The co-orientation of the nanoparticles in the polycrystalline matrix occurs via solid-state secondary nucleation, propagating out from the previously formed fibers and plates into the amorphous precursor nanoparticles [60]. During this process, a residual surface layer of ACC and/or macromolecules remains around the crystalline nanoparticle units and contributes to the conchoidal fracture behavior [61].

Nacre represents one of the most studied mineralized tissues (more than 600 published papers in the last 10 years, WoK source). It consists of a brick-and-mortar-like structure in which hard aragonite tablets are glued together with soft organic materials to form tiles (Figure 20.3). Different models have been proposed to describe the mechanisms of nacre nucleation. Weiner et al. [62–64] suggested a structural relationship between organic macromolecules and the tablet-like aragonite crystals, where the organic sheets template aragonite tablet orientation by heteroepitaxy. This model is supported by in vitro experiments that show how the nacre-extracted organic molecules induce aragonite deposition rather than the more stable calcite [65–67]. By doing

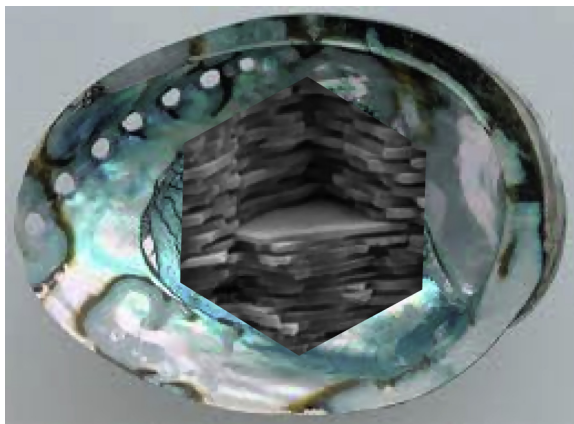


**FIGURE 20.3** Scanning electron microscope of the cross-section of the nacreous layer (in the hexagon) from the shell of Abalone *rufescens* (in background).

histochemical assays, Nudelman et al. hypothesized that each tablet crystal nucleates independently by a single, well-defined macromolecule arrangement in the organic matrix sheet, resulting in a peculiar pattern of functional groups highly conserved across species [68]. Schäffer et al. [69] observed the presence of “mineral bridges” through pores in the organic sheets, which is in agreement with the connected tablet model by which no new nucleation events occur at each tablet [70]. The presence of pores in the organic matrix has been repeatedly questioned as an effect caused by the sample preparation [71]. Nonetheless, in recent studies, Checa et al. [72] have shown that the mineral bridges of several mollusk species do not connect tablets; they are interrupted by organics, and the crystals across interruptions are not co-oriented. Olson et al. [73] proposed a mechanism in which there is one mineral bridge at the center of each organic tablet site of nucleation, which looks like a donut with a hole at its center. In a recent study, stacks of co-oriented aragonite tablets arranged into vertical columns or staggered diagonally were found [74]. Overgrowing nacre tablet crystals were most frequently co-oriented with the underlying spherulitic aragonite or with another tablet, connected by mineral bridges. Therefore, aragonite crystal nucleation in nacre is epitaxial or near-epitaxial. The presence of one mineral bridge per tablet was proposed [74], and that “bridge-tilting” was a possible mechanism to introduce small, gradual, or abrupt changes in the orientation of crystals within a stack of tablets as nacre grows.

There are three main hypotheses to explain the nucleation mechanism of individual nacre tablets, that is (1) single crystal growth, (2) a coherent agglomeration of nanograins, and (3) phase transformation from ACC to stable aragonite. Nassif et al. [75] discovered that the aragonite tablets in nacre are covered with a continuous layer of ACC. Rousseau et al. [76] provided evidence of nanocrystals within the aragonite tablet. Qia in Qiao et al. [77] reported *in vitro* crystal growth on a nacre surface, by monitoring in real time the growth process of nacre-like tablets and layers on the fresh nacre surface. The formation of nacre-like tablets was a complex and multistep process, from an ACC layer, to iso-oriented nanostacks, to hexagonal tablets. Zhang and Xu [78] observed that the early immature tablet consists of closely packed colloidal nanoparticles, which contain nanocrystals surrounded by ACC. The nanocrystals were generally different in shape, size, and orientation. In this work, it is shown that the immature tablet grew via oriented attachment instead of a transformation of the ACC phase; and with growth, the colloidal nanoparticles gradually increased in crystallinity and size until fully crystallized and fused together, leading to a mature tablet that is a monolithic single crystal of aragonite.

Other interesting examples of biological control of nucleation are apatite nucleation during the formation of bone and enamel. Bone has a particular hierarchically structured architecture, unique mechanical properties, and remodeling capabilities. Weiner and Wagner [21] have observed seven levels of hierarchy in bone structure, ranging from the nanoscale to the macroscopic scale (Figure 20.4). At the most elementary level, bone composition includes molecular and crystalline components such as collagen, apatite, water, and the rest of molecules, while the second level is a description of the bone nanostructure composed of mineralized collagen fibrils.

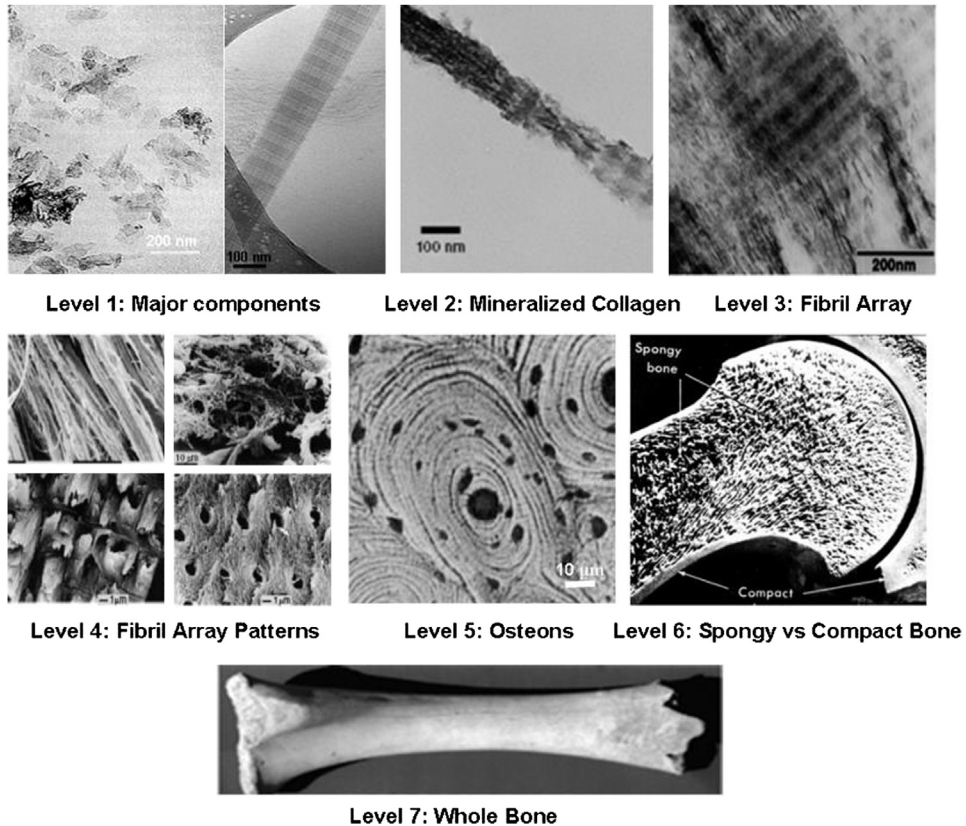


**FIGURE 20.4** The seven hierarchical levels of bone organization. Reprinted with permission from [85]. Copyright Dove Medical Press Ltd, 2010.

Different arrays of mineralized collagen fibrils, different patterns of fibril arrays, and cylindrical structures called osteons constitute the third, fourth, and fifth levels, respectively. The sixth level is composed of spongy (trabecular or cancellous) or compact (cortical) bone tissues, while the seventh one is the whole bone. The nucleation, growth, and orientation of the biological crystals of apatite take place in the second level of bone hierarchy. Type I collagen molecules assemble their tropocollagen units giving rise to holes and overlapping areas that can be observed as a periodic banding pattern along the 67-nm repeat and a less dense 40-nm-long gap zone (when stained for observation by TEM), the so-called D-band pattern (Figure 20.5). In the gap zone the first crystalline units of apatite nucleate. For many years there has been controversy over whether it is collagen or noncollagenous proteins (NCPs) [79] that initiate intrafibrillar mineral nucleation, and over the mechanisms producing it at molecular level. It was thought that NCPs, while bonded to collagen fibers, could act as promoters of intrafibrillar nucleation. Such a hypothesis was supported by reports showing that NCPs appear during the formation of new bone in a very specific

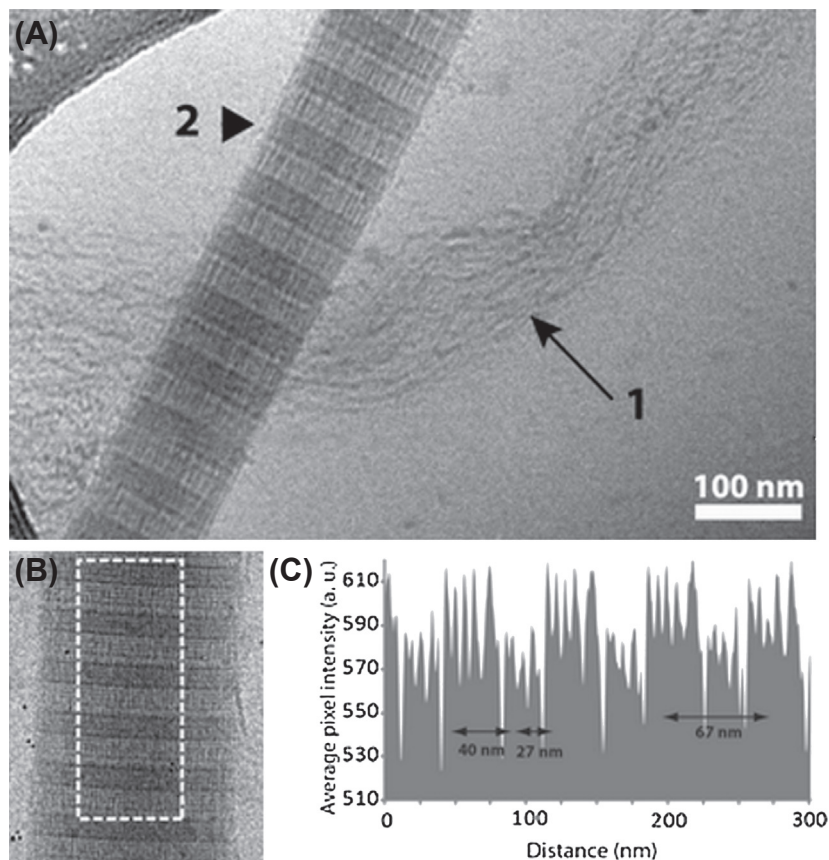


**FIGURE 20.5** Cryo-TEM images of (A) loosely packed collagen bundle (arrow, 1) and assembled fibril (arrowhead, 2) at pH 7.4. (B) Assembled fibril showing clear D-band pattern. The dashed rectangle indicates the area used to calculate the profiles depicted in (C). (C) Intensity profile of the collagen fibril along the long axis, showing D-band pattern. Reprinted with permission from [86]. Copyright Royal Society of Chemistry, 2011.

spatiotemporal time line [80] and also that type-I collagen alone, dissociated from NCPs, is unable to produce bone mineralization [81]. On the other hand, it has been proven that some NCPs, when they are dissociated from collagen, are inhibitors of calcium phosphate nucleation in solution [82]. Price et al. [83] proposed a mechanism for fibril mineralization based on inhibitor exclusion, in which macromolecular inhibitors of apatite growth favor fibril mineralization by selectively inhibiting apatite crystal growth in the solution outside the fibril. These authors tested this mechanism by using fetuin, a 48-kDa inhibitor of apatite nucleation. In the absence of fetuin, mineral formation occurs primarily in the solution outside bone collagen, whereas in the presence of fetuin, mineral forms almost exclusively within bone collagen. In 2010, Sommerdijk and coworkers [84] used cryo-TEM and cryogenic electron tomography to show that collagen functions in synergy with inhibitors of apatite (polyaspartic acid or

fetuin instead of NCPs) nucleation to actively control mineralization by a mechanism of electrostatic interactions.

Enamel formation, or amelogenesis, is a highly regulated process involving physiological and chemical events, including protein secretion, protein assembly, mineral growth, and protein degradation. The major structural protein is amelogenin, which accounts for more than 90% of the total organic matrix. Other secreted proteins are ameloblastin, enamelin, and amelotin. In short, during the initial stage of enamel formation, the secretion and self-assembly of the extracellular matrix occurs in a stepwise and programmed manner with the crystals growing along the *c*-axis, forming long thin ribbons [23]. During the formation of enamel [87], these ribbon-like crystals co-align their *c*-axis and form parallel arrays. In the maturation stage, the matrix is rapidly degraded by resident proteases whilst mineral ribbons grow rapidly in thickness and width, resulting in a hypermineralized tissue containing >97% w/w mineral, and only 1–2% of protein and water, with a structural organization of the enamel crystals established during the secretory stage [88]. Over the last 40 years, significant progress has clearly been made to elucidate the mechanism by which proteins control mineralization and organization of crystals in enamel tissue. It was suggested that a function of amelogenin is stabilizing the amorphous calcium phosphate phase (ACP), in control of apatite crystal morphology and orientation, and in control of enamel thickness [22,89–91]. One of the roles of enamelin in cooperation with amelogenin is the control of mineral nucleation and elongated growth [92,93], while ameloblastin is involved in biological events such as cell adhesion, control of cell differentiation, and keeping the rod integrity [94]. However, the complete mechanism of enamel formation remains unknown.

## 20.2.2 Biological Control at Growth Level

One of most striking features of many biologically formed crystals is the remarkable morphology. Organisms can produce single crystals with complex shapes and curved surfaces. They have developed mechanisms that override the basic growth form of a crystal. They have crystals whose overall morphologies often bear no relationship with the symmetry of the crystal lattice. Biological control over the growth is mainly exerted by: (1) interaction of growing crystals with soluble additives, which can be occluded within biominerals; (2) physical constraints of the compartment in which mineralization takes place; and (3) changes in the activity or positioning of ion pumps and channels during mineralization that may lead to crystal growth in preferred directions.

The morphological influence of additives was first described in general crystal growth theory [95], and Weiner and Addadi were the first to suggest its potential applicability to biomineralization [96]. Since then, it has been widely demonstrated that many additives can alter the morphology of calcite crystals and other biologically relevant minerals, e.g., [97,98]. This was shown to occur by adsorption onto specific crystallographic faces. Atomic force microscopy (AFM) studies suggest that this specificity in binding may

actually be occurring at the growing step edges and not the flat crystal faces [99,100]. The “sculpted” nonequilibrium morphologies observed in various biominerals were supposed to result from the stereospecific interactions with the soluble organic matrix. The evidence to support this mechanism was partly based on in vitro crystal growth experiments in the presence of additives, including proteins extracted from the biomineral, e.g., [66,101–103]. These experiments show that proteins influence crystal growth and often produce the expression of new crystal faces, which, although rough, have been correlated to the crystallographic planes expressed on the corresponding biomineral. This argument was also supported by the analysis of biomineral crystallographic textures, which arose from anisotropic intercalation of proteins after they had adsorbed to specific crystallographic faces [104–106]. In addition to biological macromolecules, moderately sized organic molecules [98,107] and small inorganic molecules [108,109] may influence mineralization kinetics and energetics as well as the shapes of crystals [110].

Crystals with unusual morphologies and curved surfaces are typically found within vesicles (e.g., calcite produced by coccoliths and sea urchin larval spicules) [16]. Vesicles have well-defined shapes, and crystals grow until they impinge upon the vesicle, which effectively acts as a mold. The size and shape of the vesicle may be altered during the crystal growth process. Soft organic membranes also impose a form on a crystal. The growth of biogenic single crystals of calcite may also occur inside the cell, and the final morphology is determined by the cell membrane. The coccolith (from the algae *Emiliania huxleyi*) comprises about 30–40 units organized in a ring to give a double-rimmed structure. The formation of coccoliths begins with the assembly of vesicles along the rim of an organic baseplate scale. Nucleation then occurs within the vesicles to generate a proto-coccolith ring of interlinked calcite crystals. The crystals initially form as 40 nm thick rhombohedral plates that are inclined to the plane of the ring. The plates grow up to a height of 100 nm, and radial outgrowth along the c-axis from the top and bottom faces generates a Z-shape. These units become interlinked by selective growth along the inside rim, and further radial growth from the base and top of the element produces the proximal and distal shield elements.

In contrast to this, there are additives, inorganic or organic, that can modify the crystallization process by transforming the conventional crystal growth into an amorphous precursor process. Notably, the organic–inorganic interactions that lead to shape regulation in this case occur prior to the formation of any crystal structure and, therefore, do not require interactions specific to crystal lattice arrangements. These process-directing agents can have a pronounced effect on crystal morphology, as well as other crystal properties, and thus provide an alternative explanation for the morphogenesis of biominerals [111].

Bone apatites are calcium-deficient (and hydroxide-) nanocrystals whose size varies depending on the technique used: length (20–50 nm), width (15–30 nm), and thickness (1.5–4 nm) [7,112,113]. They are doped with ionic substituents, typically 4–6 wt% carbonate, 0.9 wt% Na, 0.5 wt% Mg, and other minor elements. Bone apatite also presents a

typical plate-like morphology and poor crystallinity. Synthetic nanocrystalline apatites present a hydrated surface layer that becomes progressively transformed into the more stable apatitic lattice upon maturation in aqueous media. As this layer has a strong ability for ion exchange and adsorption of organic molecules, it is thought that in bone apatite this layer might actively participate in homeostasis [114]. It is generally assumed that the very small particle size and the nonstoichiometry are features that presumably bestow the mineral phase with the solubility needed for resorption of the bone by osteoclasts, while their small thickness favors the mechanical properties, likely preventing crack propagation. Using advanced solid-state NMR spectroscopy, Hu et al. [115] have revealed that a small carboxylate molecule, the citrate, accounts for about 5.5 wt% of total bone organic matrix and is strongly bound to apatite surfaces (1 molecule per every 2 nm<sup>2</sup>). These researchers proposed this molecule as responsible for the inhibition of crystal thickening and also for the stabilization of nanocrystals within the collagen matrix. The role of citrate ions leading to the platy morphology during ACP to apatite transformation, therefore breaking the hexagonal crystal apatite symmetry, was further confirmed by using synchrotron X-ray total scattering combined with AFM [116].

### 20.2.3 Biological Control at Constructional Level

The impressive complexity of mineralized biological structures arises from the controlled construction of hierarchical architectures that involves the assembly of mineral-based building blocks into a series of progressively more highly ordered structures. This concept has evolved to the definition of mesocrystals [32]. Mesocrystals are three-dimensional registered nanocrystals, which diffract X-rays as a single crystal does. The shape and structural organization of these nanocrystals is controlled by specific macromolecules that cover this double function. The shape of nanocrystals is controlled by specific molecular adsorption, as described above. Even more intriguing is the capability of these macromolecules to induce the alignment of the nanocrystals. In this case, the process seems to be driven by specific functional groups' interactions. It cannot be excluded that the register may also imply phenomena of pseudo-epitaxy, as reported for nacre. Indeed, although it has been demonstrated that large molecules, such as proteins, are incorporated within a biogenic single crystal, the locations have been found by measure of the coherence length and domain spread. The three-dimensional mapping of the distribution of imperfections of sets of biogenic calcite single crystals of very different shapes (sea urchin spines and larval spicules, five different kinds of calcareous sponge spicules, single prisms from mollusk shells and two kinds of foraminifera shells) has revealed a striking correspondence with macroscopic crystal shape [104,105,117]. This observation can be explained by assuming an accurate, nanometer-scale controlled delivery of the proteins onto the growing crystals. Protein intercalation is also mirrored by the mechanical properties. Microindentation carried out on spicules results in anisotropic crack propagation along the same unique direction where proteins are not intercalated [97]. When crystal morphology matches crystal symmetry, it may be

sufficient to exploit the recognition capabilities of the (glyco)proteins for specific crystal motifs.

The biological “prevail” of the inherent nature of the crystal protein interactions raises the question of whether or not it has the functional purpose of producing a more isotropic material in terms of defect distributions.

## 20.3 Crystallization Techniques to Study Biological Crystallization

Biological crystallization involves the precipitation of inorganic crystals under strict control of the nucleation and growth mechanism. This process is mediated by biological “additives,” i.e., soluble macromolecules, templates, membranes, or vesicles that act as isolated compartments. In many cases, these processes are produced in biological media whose viscosity and physicochemical features resemble those of a hydrogel-like media. The kinetics in biological crystallization are slower in comparison to “typical” crystallization. Thus, in order to mimic these processes, the primary goal has been to adapt or develop suitable techniques such as those presented in this section: batch, vapor diffusion, and gel crystallization. Moreover, crystallization may also be manipulated by using microorganisms for specific applications, a technique that is here described as “in vivo induced mineralization.”

### 20.3.1 Batch Crystallization

The easiest way to test the effect of an additive on the crystallization of a given mineral phase is to use a batch method. Batch methods are commonly used in the chemical and pharmaceutical industry to prepare a wide variety of crystalline products. To study biomineral formation at laboratory scale, the most useful method is reactive crystallization, a process in which supersaturation is achieved by a chemical reaction between two soluble reactants. The decrease of supersaturation is accompanied by the precipitation of a sparingly soluble compound. A wide variety of electrodes allow us to monitor several reaction parameters such as temperature, pH, conductivity, and ionic concentration, all of them carrying information on the evolution of the supersaturation as well as on the effect of the additives. Most inorganic counterparts of biominerals found in nature can be precipitated in batch, such as calcium carbonates [118] or nanocrystalline carbonate-apatites [119].

Different arrangements can be adopted either to keep the supersaturation and/or the pH constant, the best known being the so-called “constant composition method” [120,121] and/or the “pH-stat method.” The effect of an additive on the mineral nucleation and growth can be studied by means of unseeded or seeded experiments [122]. The advantages of the technique are speed and simplicity; the disadvantage is that only one condition is tested in each run. Scaling down the precipitation processes using

plates, microdroplets, or microfluidic devices, whilst increasing the possible number of batches for each experiment, can reduce the consumption of biological additives.

### 20.3.2 Vapor Diffusion

A longstanding method employed by the biomineralization community to precipitate calcium carbonate is the slow diffusion of vapor released from ammonium carbonate sources [66,123]. The method is essentially based on the diffusion of  $\text{NH}_3(\text{g})$  and  $\text{CO}_2(\text{g})$  released from  $(\text{NH}_4)_2\text{CO}_3$  into a  $\text{Ca}^{2+}$  solution bearing the additive. The experiment is carried out inside a closed system (usually a desiccator). The released  $\text{NH}_3(\text{g})$  diffuses through a few mL of the  $\text{Ca}^{2+}$  solution, increasing its pH while the  $\text{CO}_2(\text{g})$  reacts to form  $\text{CO}_3^{2-}$  species, eventually leading to the precipitation of  $\text{CaCO}_3$ .

To reduce the consumption of biological additives, the experiment can be performed in microdroplets (around 40  $\mu\text{L}$ ) using an innovative microdevice called a “crystallization mushroom.” In addition to its reduced volume, this setup offers the advantage of good reproducibility due to the possibility of running numerous batches of crystals for each experiment. Hernández-Hernández et al. [124] used the crystallization mushroom to reveal the dramatic effect of myoglobin and  $\alpha$ -lactalbumin in selecting calcite as the preferred precipitating polymorph in contrast to the additive-free experiment, which yielded a precipitate composed of 63% calcite, 15% aragonite, and 22% vaterite. The effect of these proteins in selecting the polymorph calcite was more pronounced as the protein concentration was higher.

Apart from  $\text{CaCO}_3$ , the vapor diffusion method has been adapted to crystallize biomimetic calcium phosphates [125–127]. Iafisco et al. [126] and Gómez-Morales et al. [125] carried out calcium phosphate crystallization experiments using a modified “mushroom” (Figure 20.6) by diffusing vapors of  $\text{NH}_4\text{HCO}_3$  through aqueous droplets containing a  $\text{Ca}(\text{CH}_3\text{COO})_2/(\text{NH}_4)_2\text{HPO}_4$  mixed solution. Thus, in additive-free experiments performed over 1 week [126], ACP was obtained at the early stages, then it

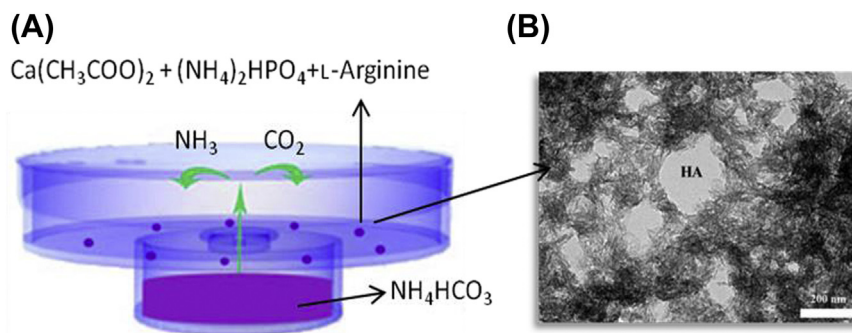


**FIGURE 20.6** (A) Crystallization mushroom setup. (B) Carbonate-apatite nanocrystals precipitated in sitting droplets containing  $\text{Ca}(\text{CH}_3\text{COO})_2 + (\text{NH}_4)_2\text{HPO}_4 + \text{L-Arginine}$ . The  $\text{NH}_3(\text{g})$  and  $\text{CO}_2(\text{g})$  slowly diffuse from the  $\text{NH}_4\text{HCO}_3$  reservoir to the droplets through the small hole located in the bottom of the upper chamber.

transformed to octacalcium phosphate ( $\text{Ca}_8\text{H}_2(\text{PO}_4)_6 \cdot 5\text{H}_2\text{O}$ , OCP) and carbonate-apatites nanocrystals whose sizes oscillated between 60 nm and 120 nm. However, when the experiment was performed in the presence of amino acids with different isoelectric points, namely L-aspartic acid (L-asp, iep = 2.77), L-alanine (L-ala, iep = 6.00), and L-arginine (L-arg, iep = 10.76) at different concentrations, irrespective of the nature and concentration of the amino acid used, the early stage in the precipitation consisted in the formation of a white viscous suspension of ACP spherulites. After 1 week, at the higher concentration of L-aspartic acid, brushite ( $\text{CaHPO}_4 \cdot 2\text{H}_2\text{O}$ , DCDP) platelets and a few needle-like carbonate-apatite crystals were found. In the presence of L-alanine, the precipitate was composed of both OCP platelets and needle-like carbonate-apatite, and in the presence of L-arginine, carbonate-HA nanocrystals (shown in [Figure 20.6](#)) of 20–40 nm and a few OCP crystals [125]. These experiments illustrate the crucial role of biological additives in calcium phosphate precipitation.

### 20.3.3 Gel Crystallization

A remarkable feature of gels is that they suppress convection and sedimentation [128], thus creating a diffusive scenario for the transport of reactant species during the crystallization process. Crystal growth in gels and, in particular, the counterdiffusion technique, has attracted the interest of many researchers as a method for optimizing crystal size and crystalline quality [129–133], to simulate microgravity environments [133], or to produce crystals analogous to those formed in geological environments [134].

Very recently, this technique has emerged as a powerful platform for mimicking crystal deposition in biomineralization processes [135–139]. The main motivation behind this approach has been that many processes take place in a gel-like organic matrix, which is an assembly of proteins, polysaccharides, and/or glycoproteins. These matrices provide the structural framework that serves as a source of functional groups to direct the nucleation and growth of inorganic minerals [135,140,141]. Among the many different minerals, most noteworthy is the employment of this technique to crystallize calcium phosphates [136,142] and calcium carbonates [138,143,144] along with the study of the effects of inorganic and organic additives on the crystallization processes of these substances [143,144].

In a typical counterdiffusion experiment, two reacting solutions are allowed to diffuse against each other from two reservoirs separated by a gel column. This setup generates a continuous gradient of concentrations of both reagents in the gel column, and thus a continuous variation in space and time of the ionic activity product and supersaturation [145,146]. Therefore, precipitation will occur at the time and location of the gel column where the critical supersaturation value for nucleation is reached for the first time [29,146–149]. Under the counterdiffusion configuration, the supersaturation threshold to trigger nucleation is a function of the rate of development of supersaturation [146–149], and, at the same time, the equivalence rule must be satisfied in addition to reaching the supersaturation threshold [29,146,148,149].

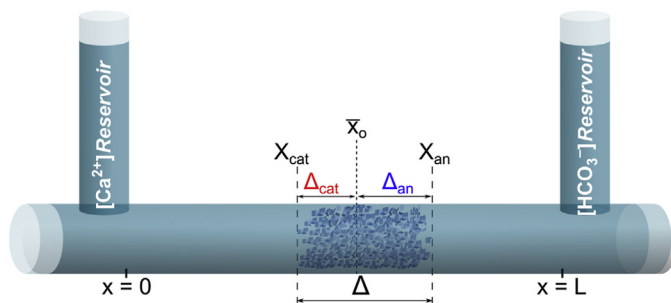


**FIGURE 20.7** Schematic diagram showing a U-tube setup for counterdiffusion experiments.

Figure 20.7 illustrates the precipitation of  $\text{CaCO}_3$  in a high viscous agarose sol, i.e., hydrogel with a low degree of entanglement. In the U-tube setup, three main parameters can be estimated: the waiting time ( $t_w$ ) or elapsed time from the onset of the experiment up to the appearance of the first precipitate; the starting point of precipitation ( $x_o$ ) or distance from the cationic reservoir to the place where the first crystals appear; and the crystal growing space ( $\Delta$ ) or length within the column gel where precipitates are observed at the end of the experiment. The boundaries of  $\Delta$ ,  $x_{\text{cat}}$ , and  $x_{\text{an}}$  represent, respectively, the places where the activity of anions in the zone close to the cationic reservoir and the activity of cations in the zone close to the anionic one are the lowest to still sustain nucleation and growth of crystals.

Two examples of the use of this setup can be found in references [150,151]. The effect of charged polypeptides entrapped in an agarose sol on the crystallization of  $\text{CaCO}_3$ , mimicking the role of acidic macromolecules on a model biomineralization process [150], or the role of a soluble organic matrix extracted from *Balanophyllia europaea* (a zooxantellated coral) and *Leptopsammia pruvoti* (an azooxantellated one) entrapped on the agarose, have been assessed by analyzing their impact on the above-defined crystallization parameters.

### 20.3.4 In vivo Induced Mineralization

In recent years, considerable interest has been aroused by the use of microorganisms (bacteria) that have the ability to induce the extracellular deposition of a wide range of minerals, for purposes as diverse as strengthening and consolidation of soils, protection and repair of concrete and cement structures, or protection and consolidation of decayed ornamental stones. Bacteria can influence the chemistry of the environment where they grow as a result of their metabolic activity. They can therefore actively create conditions of supersaturation to induce the precipitation of a given mineral phase. Bacteria may also act in a passive manner, by serving as a nucleation site for mineral deposition [152]. There is a wide variety of bacteria capable of inducing the precipitation of carbonates [153], oxides [154], sulfates [155], and phosphates [156]. It is noteworthy that those bacteria are able to induce the precipitation of calcium carbonate used in conservation and restoration of ornamental limestone [157–159]. Rodríguez-Navarro et al. [159] tested a bacterial conservation method based on the use of *Myxococcus*

xanthus, a gram-negative, nonpathogenic, common soil bacterium belonging to the  $\delta$  subdivision of the proteobacteria. Depending on the culture media, this bacterium is able to induce the formation of phosphates (struvite, schertelite, newberyite), carbonates (calcite, Mg-calcite, vaterite) and sulfates (barite, taylorite). This capability for biomineralization is of particular importance because it may be used to consolidate a wide spectrum of materials.

## 20.4 The Role (Function) of Biological Crystallization

### 20.4.1 Crystals to Support and Protect the Organism's Body: Exoskeletons and Endoskeletons

The exoskeleton and the endoskeleton are the hardest part of the body of vertebrates and invertebrates, respectively. In popular usage, some of the larger kinds of exoskeletons are known as "shells." Examples of exoskeleton organisms include insects such as grasshoppers and cockroaches, and crustaceans such as crabs and lobsters. The shells of the various groups of shelled mollusks, including those of snails, clams, tusk shells, chitons, and nautiluses, are also exoskeletons. Exoskeletons contain rigid and resistant components that fulfill a set of functional roles including protection, excretion, sensing, support, feeding, and acting as a barrier against desiccation in terrestrial organisms. Exoskeletons have an important role in defense from pests and predators, in support, and in providing an attachment framework for musculature. The types of minerals forming exoskeletons, the sites of deposition, and the organizational motifs in which they are found are all extremely diverse [7]. Endoskeleton is constituted of bones, rigid organs that fulfill important mechanical and biological functions, the most important of which are to support, move, and protect the various organs of the body as well as to produce red and white blood cells and store minerals [160]. From a material science point of view, bone can be described as an organic-inorganic composite material, where the organic fraction (basically type-I collagen, noncollagenous proteins, signaling molecules, and minor organic molecules) represent about 25 wt%; the mineral phase, composed of nanocrystalline apatite, represents about 65 wt%; and the rest is water, which acts as a plasticizer [7,21].

### 20.4.2 Crystals to Control Water Flow: Lipids in the Epidermis

The primary function of the skin is to act as a barrier against unwanted influences from the environment. The barrier function of the skin is located in its outermost layer, the *stratum corneum*, which consists of dead cells filled with keratin and water, and embedded in lipid regions. The latter are the only continuous structure in the *stratum corneum* and represent the main barrier component. Small-angle X-ray diffraction studies have revealed the biological crystallization of lipids in two lamellar phases in the human *stratum corneum*: one with a short periodicity of approximately 6 nm and a long one of approximately 13 nm [161].

In the plane perpendicular to the direction in which the lamellar phases are defined, the lipids are arranged in a liquid phase, a hexagonal phase, or an orthorhombic phase. The orthorhombic phase is the most densely packed. It has been shown that there is a correlation in the content of the orthorhombic lateral packing that is present in the *stratum corneum* and the transepidermal water loss value [162], a measure for the skin barrier activity. This demonstrates the relevance of the orthorhombic lateral packing in the skin barrier function.

Recently, it has been observed that water permeability in snake molt drastically varies among species living in different climates and habitats. The analysis of molts from four snake species—tiger snake, Gabon viper, rattlesnake, and grass snake—revealed correlations between the molecular composition and the structural crystalline organization of the lipid-rich mesos layer with control in water exchange as a function of temperature (Figure 20.8). It was shown that this control is generated from the change in size and phase distribution of crystalline domains of specific lipid molecules as a function of temperature. The content of lipids in orthorhombic lateral packing was the discriminating factor. This research also revealed that these lipid structures can protect the snakes from water loss even at temperatures higher than those of their usual habits, showing the relevance of this biological crystallization [163].

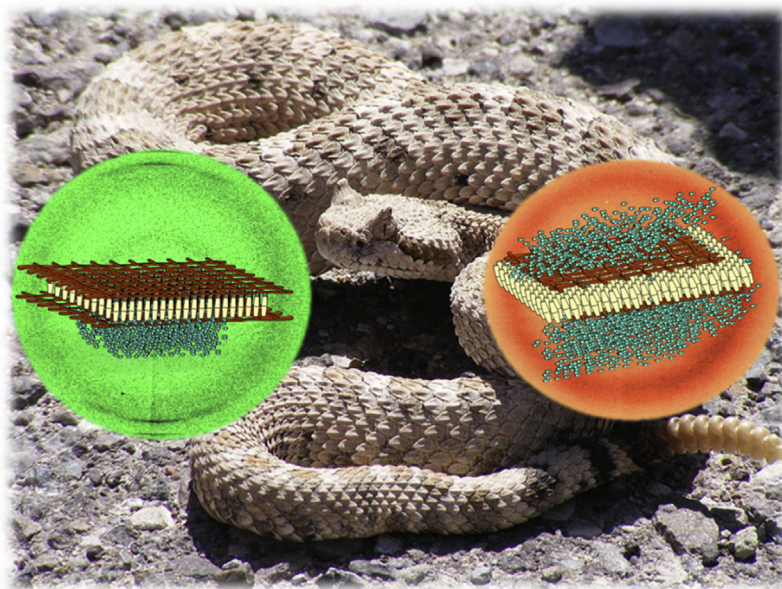


**FIGURE 20.8** The picture shows the details of 3D structures concerning snake molt, consisting of mesos layer (shown as vertical cylinders) sandwiched between keratin layers (the brown net). The two models (based on micro-XRD data) show how the change in the crystalline structure (due to temperature) controls the water (shown as blue molecules) passage through the molt. Beyond the 3D models, which concerns the structure at 298 K (green bowl) and 333 K (red bowl), it is possible to see the corresponding micro-XRD spectra.

### 20.4.3 Crystals to Chew: The Teeth

Diamonds are known as the best material for grinding, but have a high cost and show a lack of adaptation [164]. Organisms, on the other hand, produce cheap and functional, highly performing teeth to grind and bite using diverse content and types of crystals formed into specific organic matrices. Two representative case studies are the mammalian tooth enamel and the radula teeth.

Teeth are composed of a bulk of dentin covered with enamel on the crown and cementum on the root surface [165]. Dentin is similar to bone in inorganic content (about 70 wt% carbonate-apatite), crystal size, crystallinity, and organic composition, including a type-I collagen matrix [166,167]. Enamel, by contrast, is a highly mineralized tissue that protects teeth from external physical and chemical damage. Mature enamel is an almost completely inorganic structure (>97 wt% apatite with about 1–2 wt% proteins and water) composed of extremely long and narrow crystals (50–70 nm width, 20–25 nm thick and aspect ratios higher than 500 [168]). When compared to hydroxyapatite mineral, however, enamel has a higher elastic modulus and hardness, as well as much better fracture toughness. Additionally, the dentin–enamel junction provides additional mechanical support that prevents enamel deformation, which might otherwise result from the high external forces involved in chewing. Unlike other biomineralized tissues, mature enamel is acellular and does not resorb or remodel.

A complex architecture is present in enamel—on the nanoscale, a highly organized array of hydroxyapatite (HA) crystallites that grow preferentially along the *c*-axis in the amelogenin matrix [22,169–171]. At the mesoscale, rod and interrod are present as main structural components. The rods are bundles of aligned crystallites that are organized into intricate architectures (3–5  $\mu\text{m}$  in diameter). The individual nanoscale crystallites contained within the rods of mature human enamel are approximately 30 nm thick and 60 nm wide [172] and vary among species on the order of millimeters in length [173]. The interrod (or interprismatic) enamel, which surrounds and packs between the rods, is the second structural component of the enamel matrix. The rod and the interrod differ in the orientation of HA crystals; the former contains aligned crystallites, whereas in the latter they are less ordered. These structures coalesce to form the tough tissue of enamel (shown in Figure 20.9), which can withstand high forces and resist damage by crack deflection [23,168,172,174–176].

Chitons and limpets feed by rasping macro- and microalgae from the rocks on which they live through the use of a radula. The radula has been coined as a conveyor belt of continuously developing teeth, replaced by new teeth as they are worn and lost. These biologically crystallized teeth of chitons are sophisticated composite structures resulting in highly efficient, self-sharpening, feeding implements ideally suited to their function. These biologically optimized tools possess many of the desirable features of a perfect knife.

In both limpets and chitons, newly formed teeth consist of a  $\alpha$ -chitin matrix with associated proteins [177]. In limpet teeth, mineralization begins with the formation of

### Hierarchical Structure of Mammalian Tooth

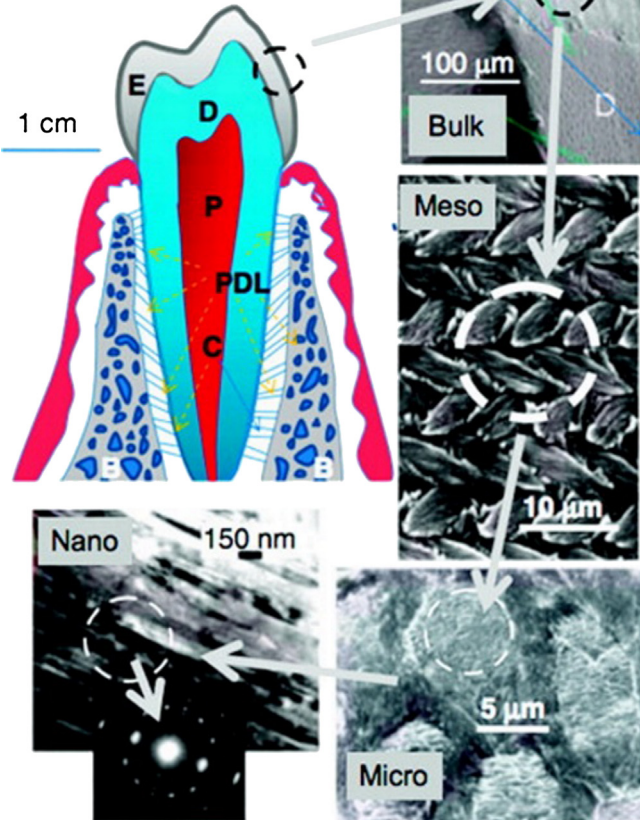


**FIGURE 20.9** Hierarchical architecture of mammalian enamel. Enamel (E) is the outermost layer at the crown of the tooth and resides above the dentin (D). The pulp (P) contains nerves and blood vessels, while the cementum (C) is the outermost layer of mineralized tissue surrounding the root of the tooth, allowing the tooth to be anchored to the jawbone through the periodontal ligament (PDL). The bulk image depicts the E organ, the transition across the D-E junction, and the D below. On the mesoscale level, prismatic E consisting of the weaving of rods (or prisms) that range from 3 to 5  $\mu\text{m}$  in diameter can be visualized. Upon further magnification, the micrometer scale shows the composition of a single rod. The nanometer scale reveals a highly organized array of individual HA crystallites (approximately 30 nm thick, 60 nm wide, and several millimeters in length), which are preferentially aligned along the c-axis. Adapted from [254]. Copyright 2008 Materials Research Society.

elongated crystals of goethite ( $\alpha\text{-FeOOH}$ ) [44] closely associated to the organic matrix [178]. At later stages, further toward the mouth, the space between goethite crystals is impregnated with a hydrated amorphous silica phase ( $\text{SiO}_2 \cdot n\text{H}_2\text{O}$ ) [179,180]. The particular arrangement of the goethite crystals determines the fracture and wears characteristics of the tooth [181]. The orientations of goethite crystals in the tooth are controlled by the chitin fibers of the organic matrix [178,180]. By using cryotechniques, it has been observed that the unmineralized matrix is formed by relatively well-ordered, densely packed arrays of chitin fibers, with only a few nanometers between adjacent fibers. The first-formed mineral phase within the chitin matrix is goethite, which nucleates on the chitin fibers that control the orientation of the crystals. Contrariwise, crystal growth is only influenced by the matrix [182,183] (Figure 20.10).

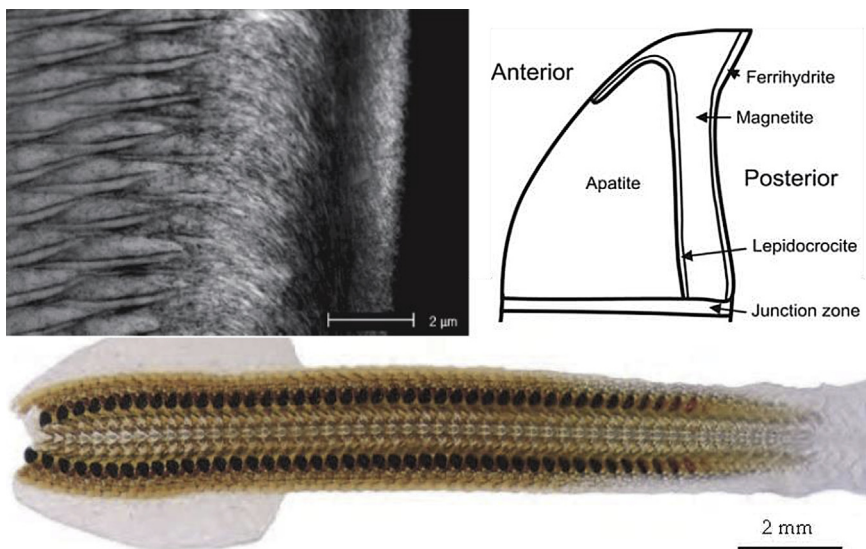


**FIGURE 20.10** (bottom) Light micrograph of the radula of the chiton *Acanthopleura gaimardi* showing the progressive stages of radular tooth development. From the clear unmineralized teeth, comprised of a chitinous organic matrix on the right, to the black, fully mineralized, working teeth on the left. (top left) Images of the organomineral interactions in the magnetite region of the tooth cusps of *Acanthopleura echinata*, showing the fish scale appearance of the rod and trough structures, viewed with an environmental scanning electron microscope. (top right) Diagram depicting the various regions in the tooth cusp. Adapted from [184].

#### 20.4.4 Crystals to Hear and Balance: The Otoliths

The basic principle of gravity perception by organisms is that downward gravity forces exerted by specially formed heavy bodies are detected by the surrounding tissues. The movement of the whole organism realigns these tissues relative to the forces of gravity exerted by the heavy bodies, and it is this movement that is detected and interpreted in terms of a change in orientation [185]. The quantity of minerals used by organisms for gravity perception is extraordinary, with many different specific gravities ranging from 2.2 in gypsum to 4.5 in barite. Most of the minerals formed by animals for gravity perception are calcium salts.

The hearing and body balance in fish are two different sensations initiated by a common mechanism [186]. The inner ear contains three otolith organs that contain macular sensory hair cells coupled with an otolith, a biomineralized ear stone composed of calcium carbonate and proteins. The otolith acts as an inertial mass, and sound- and head movement-evoked acceleration produces relative displacement between the otolith and the coupled hair cells due to the difference in their inertia. This displacement mechanically deflects the hair bundles and opens mechanotransduction channels, which can subsequently produce a receptor potential [187]. Behavioral studies that eliminated the otolith organ in fish revealed the functional differences between the three otolith organs the saccule (S) and lagena (L) are necessary for auditory perception, and the utricle (U) is

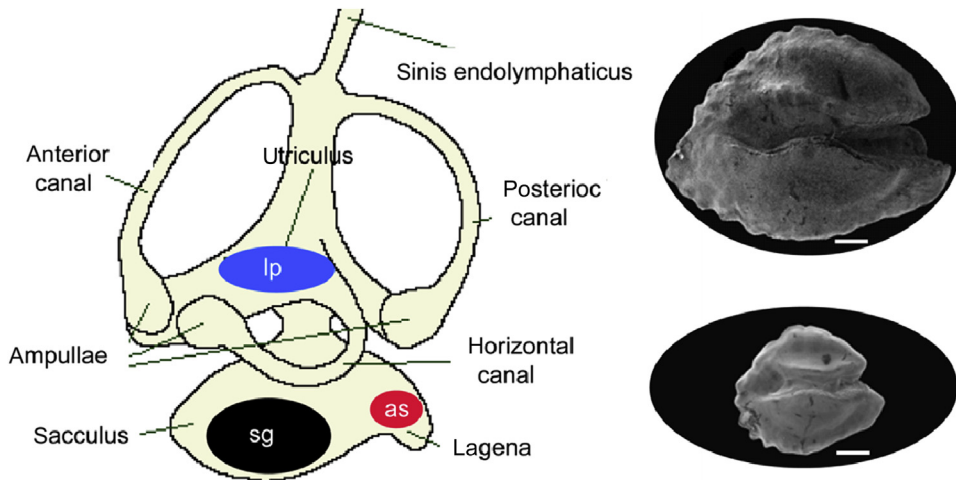


**FIGURE 20.11** Schematic illustration (left) of the inner ear of teleost fish showing terminology. The labyrinth includes three connected semicircular canals and three otolith organs consisting of the sacculus, utricle, and lagena, each of which contains an otolith called sagitta (sg), asteriscus (as), and lapillus (lp), respectively. The asteriscus and lapillus are usually millimeter sized, but the sagitta can range from millimeter to centimeter size. As sagittae are the largest otoliths, they have been widely utilized in teleost growth rate and age assessment studies. Crystals of otoliths, once deposited, are metabolically inert, except under extreme stress. Thus, the otolith can potentially retain the variation in crystalline structure due to variation in the organic matrix or in the crystallization environment. The two scanning electron microscopy images (right) show the sagitta from *Aspitrigla cuculus* in juvenile and adult age. Scale bar 500  $\mu$ m.”

essential for postural equilibrium [188,189]. The mechanisms underlying their functional differentiation, however, remain unclear. Interestingly, the otoliths removed from maculae, especially the S otoliths, did not grow as large as otoliths that remained in their normal environment. This indicated that otolith growth occurred in a region-specific manner that is specific to each macula. This shows that components of the otolithic membrane, and proteins secreted by macular hair cells and supporting cells, are important for otolith development. Thus, the growth of the S otolith is tightly regulated during development so that the otolith grows to an appropriate size for acoustic sensory transduction [190] (Figure 20.11). The biological crystallization of otoliths occurs from the same endolymphatic fluid. In this process the presence of specific macromolecules is able to control the shape and, eventually, the polymorphisms of the otoliths [102]. The biosynthesis of the polymorphism regulating macromolecules is controlled at genetic level. It was reported that a gene, *starmaker*, is required in zebrafish for otolith morphogenesis. Reduction of *starmaker* caused a change in the otolith polymorphism and morphology [191].

#### 20.4.5 Crystals to Orient and Navigate

One of the most sophisticated functions of biological crystallization is the detection of the earth's magnetic field using magnetite, as performed by the magnetotactic bacteria,

discovered by Blakemore [192] in 1975. Magnetotactic bacteria form linear chains of magnetite crystals, each one of which is sheathed and held together by a lipid bilayer admixed with proteins [193]. The entire structure is called magnetosome (Figure 20.12). The crystals have various shapes in the size range of 0.1  $\mu\text{m}$  and are considered single crystalline domains. This way the entire magnetosome acts as a single bar magnet. The function of the magnetosome is to align the bacterium along magnetic field lines, in such a way that using the flagellae it propels itself in this referred direction. Magnetotaxis is the process by which magnetotactic bacteria orientate themselves within Earth's geomagnetic field. Thus, magnetotactic bacteria in the northern hemisphere are north seeking while those in the southern hemisphere are south seeking. Iron is not only used as the element forming magnetite but is an essential element for all living organisms, though potentially toxic, for which reason it needs to be stored safely. For these purposes, many organisms use ferritin. Ferritin is formed by an inner core containing iron minerals and a multisubunit protein shell with a diameter of 12.5 nm [194].

Magnetotactic bacteria are typically divided into three groups according to the type of magnetic nanocrystal that they synthesize: (1) magnetite ( $\text{Fe}_3\text{O}_4$ ); (2) greigite ( $\text{Fe}_3\text{S}_4$ ) or a combination of greigite and pyrite ( $\text{FeS}_2$ ); and (3) a combination of magnetite and greigite [195–197]. Magnetotactic bacteria that synthesize iron sulfide minerals can

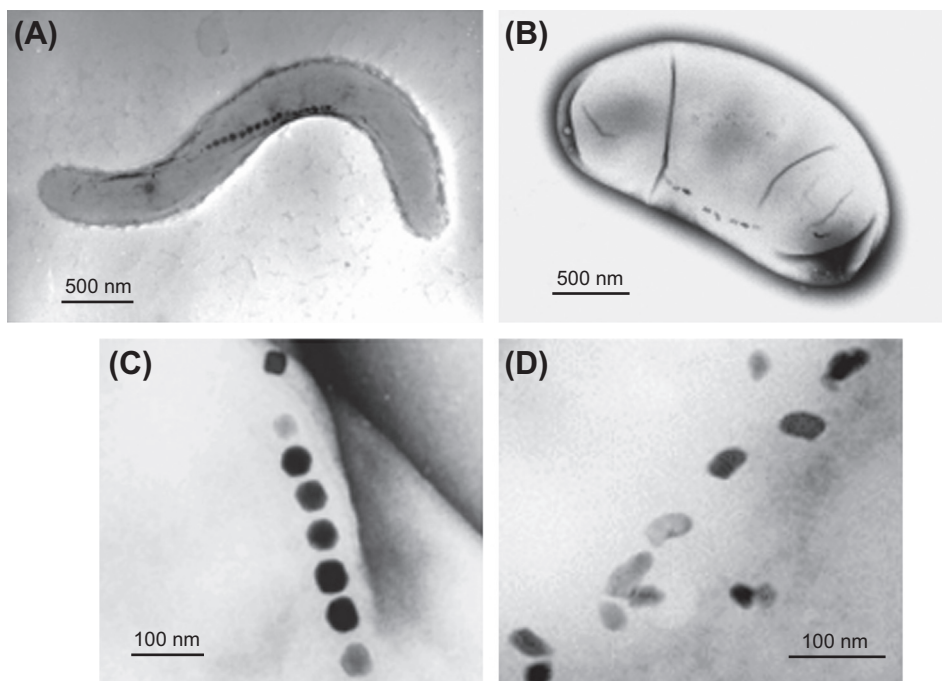


**FIGURE 20.12** TEM images of magnetotactic bacteria. (A) *Magnetospirillum magneticum* strain AMB-1 and (B) *Desulfovibrio magneticus* strain RS-1. BacMPs of (C) the AMB-1 strain and (D) the RS-1 strain. Figure from [194], with permission. Copyright 2008 Materials Research Society.

sequester a large amount of sulfur and may therefore exert significant effects on the biogeochemical cycling of sulfur, in addition to iron, on Earth [198].

It has been observed that biomineralization in magnetotactic bacteria provides highly uniform magnetite crystals with narrow size distributions (an average diameter of 50–100 nm; [197]). Furthermore, magnetite crystals in magnetosomes are of high chemical purity [199,200]. The size, type, and morphology of magnetic crystals vary from species to species but are highly conserved within the same bacterial species or genus [201]. The three most common magnetic crystal morphologies are elongated prismatic, roughly cuboidal, and tooth shaped [192,195,197]. In contrast, magnetite crystals produced by abiotic mineralization have low crystallinity and broad size distributions.

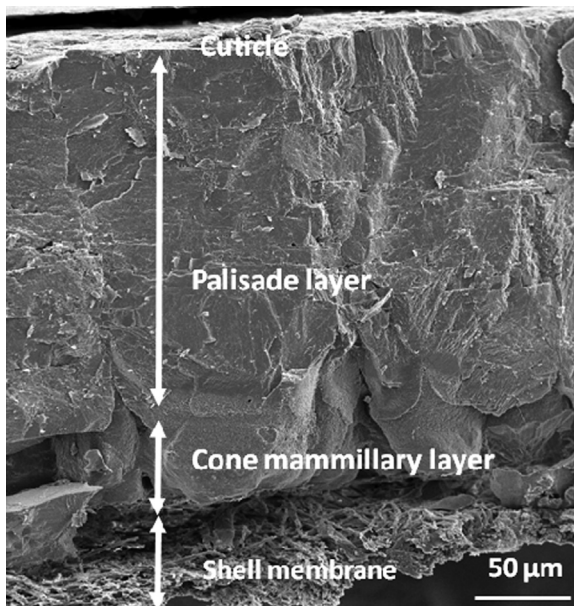
#### 20.4.6 Organisms to Produce Engineered Biological Crystallization

Sometimes biological crystallization is triggered in organisms trying to protect themselves from foreign bodies. Pearls are formed in mollusks by this mechanism. To protect themselves, mollusks secrete  $\text{CaCO}_3$  aragonite and proteins to envelop the irritant body. The result is the formation of a pearl. Depending on how aragonite is arranged, the pearl may have a high luster (nacre, or mother-of-pearl) or a more porcelain-like surface. Pearls may be of a variety of colors, including white, pink, and black. Any mollusk can form a pearl, although some of them are pearl oysters, including species in the genus *Pinctada*. The species *Pinctada maxima* produces pearls known as South Sea pearls. Black pearls are grown by *Pinctada margaritifera* [202], an oyster extremely abundant in Polynesian waters, whose shells have been used in the button industry. The pearls produced by the *P. margaritifera* vary in color from pearly white to nearly black and include purple, gray, champagne, and greenish colors. There are no pearls that are completely black in color like an onyx.

#### 20.4.7 Crystals to Packaging: Eggshells—The Protein Containers

Eggshell formation represents one of the most intriguing and beautiful examples of biomineralization and a source of inspiration for material scientists aiming to design and construct a perfect container for biological material. Eggshell is a porous composite material containing about 95% of calcite as mineral phase, 3.5% of organic phase and 1.5% of water. It possesses remarkable mechanical properties. In hens, the shell resists up to 30 N in static compression for a mean thickness of 0.33 mm. This structure is crucial for the protection of its biological content against the microbial environment, in the control of water and gases through the pores of the shell during the embryonic development, in protection against predators, and in the birth of the chick. The eggshell is composed of six layers (Figure 20.13). The innermost two layers are the noncalcified inner and outer shell membranes made of a network of organic fibers (mainly collagen). The inner calcified layer (cone layer) is composed of the basal parts of calcified column that penetrates the outer eggshell membranes. The palisade layer starts when the columns amalgamate to form a compact shell. The pores are formed when columns are not

**FIGURE 20.13** Scanning electron micrograph showing a cross-section through a fully formed eggshell that reveals the eggshell membranes, the cone mammillary layer, the palisade layer, and the cuticle.



amalgamated. The thin vertical crystal layer is deposited on the surface of the palisade layer. The cuticle is the most external layer of the shell and is constituted of organic matter and eggshell pigments.

The process of shell mineralization takes place in the uterine fluid, an acellular milieu whose calcium concentration,  $\text{CO}_2$  partial pressure, and organic composition change through its three main stages [19,203]: (1) the initial stage when the first calcite crystals are deposited around the mammillary knobs to form the cone layer; (2) the active growth phase when there is a rapid mineral deposition during the formation of the palisade layer; and (3) the terminal phase (the last 2 h of the egg formation process) when there is an arrest of shell calcification and the deposition of the most external layer, the cuticle.

The eggshell structure and, consequently, its mechanical properties are most probably the result of, on one hand, a competitive crystal growth mechanism by which crystals growing from adjacent sites compete for the available space [204] and, on the other hand, from the influence of matrix molecules on the nucleation and growth of the crystals [19,205–207]. During the last decade, much effort has been made to identify the different organic macromolecules in the crystallization milieu (uterine fluid) and in the shell. The identified matrix protein components can be divided into three distinctive groups: (1) “egg white” proteins such as ovalbumin [208], lysozyme [209] and ovotransferrin [210]; (2) ubiquitous proteins that are found in many other tissues such as osteopontin, a phosphorylated glycoprotein also present in bone and other hard tissues [211], and clusterin, a widely distributed secretory glycoprotein that is also found in chicken egg white [212]; and (3) matrix proteins unique to the shell calcification process

that are secreted by specific regions of the oviduct where eggshell mineralization is initiated and takes place (red isthmus and uterus). Ovocleidin-17 (OC-17) was the first eggshell protein purified from the shell [213]. Ovocleidin-116 (OC-116), another eggshell-specific protein, was the first eggshell matrix protein to be cloned [214]. A more recent proteomic survey of the acid-soluble organic matrix of the calcified chicken eggshell layer has allowed the identification of several hundred proteins in the shell [215]. The number of these organic components and their concentration change in the uterine fluid along the different stages of eggshell deposition in a well-defined way [203]. In each stage, specific organic components are expressed at a given concentration. Also, these organic components are secreted at specific times and locations in the oviduct and incorporated at specific substructural regions of the eggshell. On the other hand, *in vitro* precipitation tests show that some of these components influence calcium carbonate precipitation. In particular, they affect the nucleation frequency, the polymorph selection, the crystal size, and the morphology [206,207].

#### 20.4.8 Undesired Crystallization: Pathological Mineralization

When talking about pathological crystallization many readers think of the formation of kidney stones or urinary calculi; however, several major diseases such as cancer and cardiovascular abnormalities may be linked to the pathological deposition of minerals or organic compounds in various tissues.

In particular, pathological calcifications due to the ubiquity of calcium and the wide presence of carbonate, phosphate, oxalate, or other anions, may occur in various organs or locations in the body [10], namely joints, brain, breast, cartilage, cardiac valves, middle ear, gallbladder, gastric system, heart, intestine, kidney, larynx, liver, lungs, pancreas, prostate, saliva, tendons, testicle, tooth, thyroid, and artery and vessels. Even calcifications of medical devices made of polyurethane, silicone, and hydrogels have been reported [216]. Different minerals or organic compounds have been identified on these microcalcifications. To cite a few examples, calcium pyrophosphate dihydrate ( $\text{Ca}_2\text{P}_2\text{O}_7 \cdot 2\text{H}_2\text{O}$ ), octacalcium phosphate (OCP), carbonated apatite ( $\text{CO}_3\text{-Ap}$ ), tricalcium phosphate ( $\text{Ca}_3(\text{PO}_4)_2$ ), and whitlockite  $\text{Ca}_9\text{Mg}(\text{HPO}_4)(\text{PO}_4)_6$  have been described as occurring in joints [167]; apatite and weddellite (calcium oxalate dehydrate, COD,  $\text{CaC}_2\text{O}_4 \cdot 2\text{H}_2\text{O}$ ) were found in breasts [217]; different calcium and magnesium phosphates including  $\text{CO}_3\text{-Ap}$ , OCP, brushite, whitlockite and struvite, calcium oxalates monohydrate, dihydrate and trihydrate (COM, COD and COT), anhydrous uric acid, monohydrate and dehydrate, different urate salts and amino acids such as cysteine, leucine, tyrosine, etc. formed kidney stones [218]; cholesterol, calcium bilirubinates,  $\text{CO}_3\text{-Ap}$ , amorphous carbonated calcium phosphates, and calcium carbonate anhydrous polymorphs (aragonite, vaterite, calcite) were found in the liver [219]; calcium carbonate polymorphs in the pancreas [220]; whitlockite and  $\text{CO}_3\text{-Ap}$ , in the aorta [221];  $\text{CO}_3\text{-Ap}$  in skin and muscle [222]; and so on.

Pathological crystallization (basically calcifications) includes four families of biominerals of medical interest [10]. First, *concretions*, formed by precipitation from supersaturated mineralized fluids, as for example urine found in the kidney, to form stones. Second and third are *metastatic* and *dystrophic calcifications*, unexpected mineralizations occurring in soft tissues. In the case of the metastatic, they are associated with systemic mineral imbalance. The fourth group is composed of those *physiological calcifications*, such as bone mineralization, that become pathological with diseases such as arthrosis or osteoporosis.

Biological calcified entities may have hierarchical structural organizations, which are the morphological characteristics strongly linked to nanocrystal organization at the mesoscopic level, and can be related to the clinical history of the patient [10]. Thus, two different morphologies of whewellite kidney stones originate from hyperoxaluria type 1, a rare inherited disease, or by an alimentation disorder. The different levels of organization are the result of an aggregation process of microcrystals, where each microcrystal appears formed by primary nanocrystals, typically of several hundreds of nanometers. The formation of these entities is related to the solubility of the different mineral phases, nucleation, growth, and aggregation phenomena as well as to the presence of proteins, organic substances, or ions acting as crystallization promoters or inhibitors. Epitaxial growth is also important in the formation of different types of calcifications [223,224]. Due to the complex environments where they form, which, in the case of urine, for example, has a variable flow rate, pH, and chemical composition, although supersaturation must be reached for the precipitation of a given phase, it alone does not predict stone formation.

### 20.4.9 Crystals to Manipulate Light

Apparently more sophisticated than other uses—but just another finding of evolution—is the ability of living organisms to precipitate crystalline structures with textural patterns that allow them to handle light with different purposes. For instance, cystoliths are ACC bodies that form in the leaves of some plant families. They are regularly distributed in the epidermis and protrude into the photosynthetic tissue, the mesophyll. In some cases, ACC is replaced by calcium oxalate druses. It has been demonstrated that in both cases they act as light scatterers and improve the efficiency of the distribution of the light flux more evenly inside the leaf [225]. The compound eyes of extinct Paleozoic arthropods named trilobites have lenses made of calcite [226]. The calcite crystals self-assemble to be co-oriented with their three-fold axes parallel toward the light flow, thus avoiding optical birefringence.

Among the most fascinating devices developed by living organisms are those created with the purpose of coloring themselves, either to avoid visual predators or to attract partners or symbiotic species [227]. In many cases, the color of bird feathers, butterfly wings, and the carapaces or some fruits and leaves are not produced by pigments or dyes. They are actually the product of the interaction of visible light with mineral structures organized at nanoscale, so they are properly called structural colors, which are

more intense, lasting, and brighter than colors produced by pigments and dyes. In fact, these nanopatterns are nothing other than what is known nowadays as photonic structures, a kind of novel structure of great technological interest that life started to create about 600 million years ago [228–230]. Unlike for exo- and endoskeletons, the materials used by organisms to build these photonic crystals are not inorganic minerals but organic macromolecules such as keratin, cellulose, collagen, or chitin. The photonic structures are either one-dimensional, two-dimensional, or three-dimensional quasi-order structures. For a detailed analysis and classification of crystalline structures in biological photonic crystals, see the work of Hyde and Schroder-Turk [231].

There are many studies correlating the optical properties with the mesoscale crystalline patterns. For instance, the colors of the wings of *Chrysidia rhipheus* arise from coherent scattering and interference of light by the microstructure of the ribbon-like scales made of chitin-air [232]. In other cases, the wing scales carry assemblies of chitin-air multilayers with perforated chitin layers [233]. By studying five butterfly species from *Papilionidae* and *Lycaenidae* families, with small-angle X-ray scattering (SAXS), Saranathan and coworkers [234] have shown that the chitin-air 3-D photonic nanostructures are actually single network gyroid (I4<sub>1</sub>32) photonic crystals, that is, 3D cubic crystals with a lattice parameter in the range of hundreds of nm, rather than a 2D film.

Noticeably, these patterns are not the result of classical nucleation and crystal growth mechanisms but of self-assembly processes in many cases not yet properly understood. To continue with the example of the butterfly, it has been shown that the hard porous chitin wing-scale material is templated by an extant soft lipid–protein matrix that is itself self-assembled. It has been shown that the complex chitin matrix seen in mature wing scales in butterfly pupae is produced by the gradual polymerization of chitin oligomers within a water matrix defined by the bounding lipid membrane that spontaneously form a gyroid structure [235], i.e., they are the result of the self-assembly of biological lipid-bilayer membranes. These butterfly photonic nanostructures initially develop a double gyroid nanostructure that is later transformed into a single gyroid network through the deposition of chitin in the extracellular space. It is interesting to note the suggestion that the butterflies develop the thermodynamically favored double gyroid precursors as a route to the optically more efficient single gyroid nanostructures [234]. Many more studies are required to fully understand their formation mechanism and how biology controls with precision the self-assembly of the lipidic mesophases and their filling by the ending material. The increasing technological interest in photonic crystals means that whether there is anything to learn from biomimesis, not only in the structure of the devices but in the way they are grown in life, will soon be explored in more detail.

## 20.4.10 Induced Biological Crystallization

Beyond the sophisticated mineral skeletons described above, living organisms are able to induce the formation of complex mineral structures without having a direct and active role in precipitation. For instance, benthic microbial communities have the ability to

create organosedimentary deposits by inducing mineral precipitation by different mechanisms. One of these is the change in physicochemical conditions of the local environment by their metabolism or degradation [236], for instance by increasing the pH to trigger the nucleation of calcium carbonate. A second is achieved by facilitating heterogeneous nucleation, offering calcium binding negatively charged surface groups such as carboxylate, phosphate, and sulfate as passive substrate for nucleation [237]; and a third, as binders of nano and microparticles of minerals through their extracellular polymeric substances (EPS). The results of this passive effect of living organisms are structures called microbialites [238], which can be made from one or more different mineral phases, including carbonates, phosphates, sulfates, arsenates, oxides-hydroxides, silica, chlorides, fluorides, or metals, and certainly by organic crystals [239,240].

One of the most interesting examples of biologically induced crystallization is the so-called stromatolites, laminated structures made from the trapping, binding, and cementation of mineral microparticles by microbial mats [241]. The morphology of these accretionary structures varies from simple semispherical balls, called trombolites, to large columns with mushroom-like morphologies, such as those found in the hypersaline seawaters of Shark Bay in Western Australia (Figure 20.14). Stromatolites are found in modern environments, including hypersaline waters, but also in fresh water, whether marine or continental. However, they are very scarce compared to ancient times. As seen from the geological record, petrologic structures strongly reminiscent of modern stromatolites appear widely distributed during the Precambrian [242,243] time, and they started to decline upon the emergence of grazing animals, about 600 million years ago. These stromatolitic structures are important pieces in the search for primitive life on this planet because they are the most frequent remnants of life for a period of 2 billion years. Indeed, as some stromatolitic-like structures are thought to date back as far as about 3.5 Gy [244–246], their possible biotic origin would have profound consequences for our current views on how and when life began on Earth.



**FIGURE 20.14** Left: calcium carbonate stromatolites photographed at low tide in Shark Bay, Western Australia. The height of the rocks on the pictures is 40 cm in average. Right: 2.7 Gy old stromatolitic structure from the Andalusian Hill, Tumbiana Formation, (Hammersley Basin, Western Australia, Australia). The height of the sample is 22 cm.

Modern stromatolites are undoubtedly organosedimentary structures induced by living organisms. Actually, their construction results from a combination of roles of different microbial mats, which explains the layering but also the growth features such as pro-gravity growth. Thus, each layer of the stromatolithic structures is formed first by filamentous cyanobacteria whose extracellular polymeric substances (EPS) bind mineral particles. This is followed by a thin biofilm of heterotrophic bacteria that favors calcium carbonate precipitation preserving the underlying particles, and finally another film of endolithic cyanobacteria that tunnels the minerals and fills the holes with EPS, where aragonite is precipitated (see [239]). Complex and sophisticated as this life-induced morphogenetic process can be, it does not necessarily mean that petrological structures reminiscent of stromatolites formed in Archean times also necessarily have a biological origin [247–249].

However, while complex mineral microstructures with continuous curvature mimicking primitive life remnants have been produced in the laboratory under plausible geochemical conditions [250], stromatolite-like laminated structures are really difficult to produce either by laboratory analogous [249] or by computer simulation [251]. Those stromatolithic structures that have overall fingering morphology or mushroom-like structure are difficult to explain abiotically, especially when the curvature creates flaps areas where the gravity vector and the growth vector are parallel or pseudoparallel. There is one possible inorganic explanation for the formation of stromatolithic structures made of gypsum such as those found in small ponds named Los Puquíos in the Salar de Llamara, north of Atacama Desert in Chile (Figure 20.15). There the water is near saturation for gypsum, and therefore precipitation is linked to evaporation versus refilling with underground water. The biological diversity is very broad in these communities, but the mechanism of gypsum growth and dissolution seems to be governed by physicochemistry. The mushroom shape of these structures can be explained by the strong dependence of growth and dissolution of gypsum on NaCl concentration (Figure 20.15 bottom right). The water is saturated in gypsum, and, when the water level is rather high, gypsum precipitates as semispherical radial layered structures. However, when the evaporation flux is high enough to decrease the level of water below the height of the hemispherical ball and to increase the concentration of salt beyond nucleation threshold, gypsum becomes unstable and the lower part of the hemisphere dissolves. Upon several cycles of growth and dissolution, the structure takes the form of a mushroom by decreasing the size of its lower part, creating the “foot” of the mushroom.

## 20.5 Current Trends and the Future of Biological Crystallization

To lose the field notes or laboratory notebook of an entire working year would be a real disaster. Then why lose not 1 but 600 million years of continuous experimentation in the fabulous laboratory of trial and error that is life? Thousands of species populate the

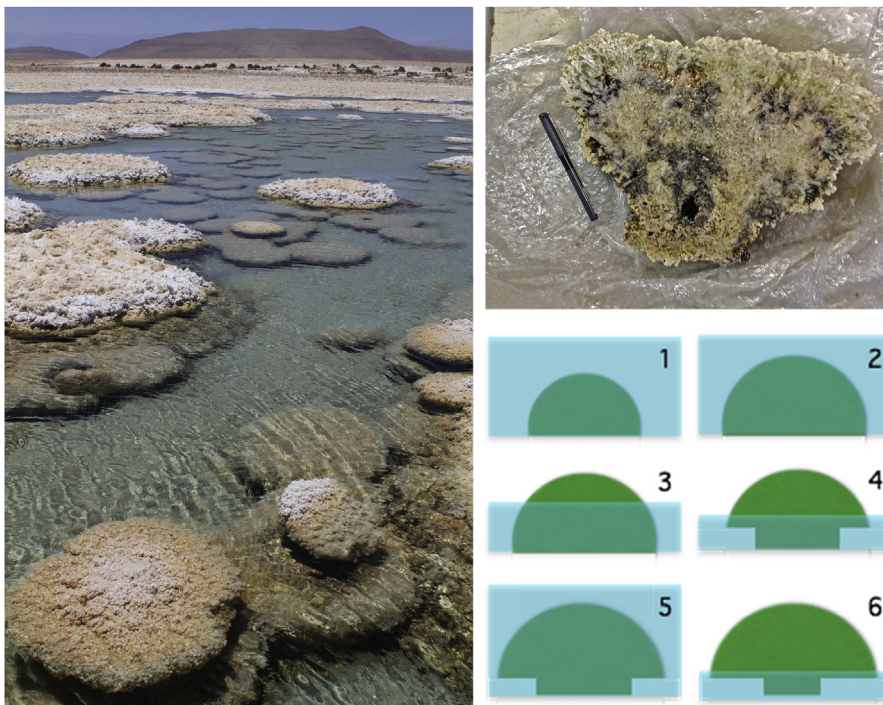


**FIGURE 20.15** Left: Gypsum stromatolitic structures from los Puquios de Llamara (Atacama, Desert, Chile). Top right: Cross-section of one of the stromatolitic structures. Bottom right: An abiotic explanation of the mushroom shape of the gypsum stromatolitic structures.

planet carrying on and/or in their bodies a broad but distinguished list of materials and devices made to fit the needs of different ecosystems and different functions. In the laboratory of life, millions of crystallization experiments have produced patterned materials at the mesoscale and nanoscale that have fabulous physical and chemical properties, and they do so at low energy cost and using clean “technology.” In many cases, these devices developed by life are years ahead of the best device imagined by our “inorganic” technology. Therefore, one of the main trends in the future will be to reinforce the detailed study of the chemistry of materials and textures and the physics of devices seeking inspiration in biology.

Actually, what is really important in biomimetic or bio-inspired studies are not the devices themselves but to understand the mechanisms that life uses to produce them. The reason is that living organisms do not design ad hoc materials or procedures to manufacture their bodies. Life, as we have said above, works by trial and error, and is always producing new models, which are tested and selected by an external medium with relentless adaptability criteria. Therefore, the molecular machinery and its products are not necessarily models of excellence (although sometimes they could look like models because of their exquisite performance), and thus they can be improved. Moreover, any biologically inspired crystallization taking advantage of the synthetic

strategies developed by organisms will not be constrained to the use of nontoxic elements but potentially may have any chemical composition.

While the study of classical nucleation and crystal growth processes will continue to yield interesting information on kinetics and on textural and morphological control, the main interest will soon shift toward self-assembly. In the opinion of the authors, in the coming years there will be an increasing interest in the studying of self-organized, autocatalytic processes leading to the complex structures recently found in many organisms, including, for instance, 3D mesophases. Understanding the pathway that life uses to produce these sophisticated structures with precision at the nanometer scale, at low cost and at low temperature, will be invaluable for the development of high-tech materials. Conversely, knowledge obtained from pattern formation of self-assembled complex materials synthesized in the laboratory (for instance, inorganic biomorphs [252,253]) will be very useful to understand possible morphogenetic and textural pathways found by life.

Another subject that will be explored in the future is the detailed study of biologically induced mineralization. This low-cost route that life has explored for about 3 billion years may conceal very useful information for sustainability technologies, including CO<sub>2</sub> sequestration, biomining, and industrial reutilization of waste materials. In a very advanced era, wise from the environmental point of view, this aspect will be of ever-increasing interest.

## Acknowledgments

This review has been carried out within the framework of projects of Spanish MINECO co-funded with FEDER: CGL2010-16882, MAT2011-28543 and the Consolider-Ingenio 2010 “Factoría de Cristalización” CSD2006-00015. G.F. gratefully thanks the European Research Council under the EU FP7/2007-2013Program (ERC grant agreement no. 249930 – CoralWarm: Corals and global warming: the Mediterranean versus the Red Sea) and the Consorzio Interuniversitario di Ricerca della Chimica dei Metalli nei Sistemi Biologici (CIRC MSB) for the support.

## References

- [1] Westbroek P. *Life as a geological force*. New York, London: W.W. Norton & Co; 1991. 240.
- [2] Carnerup AM, Christy AG, García-Ruiz JM, Hyde ST, Larsson AK. In: Seckbach J, editor. *Life as we know it*. Dordrecht: Springer; 2006. p. 237.
- [3] Evans LV, editor. *Biofilms: recent advances in their study and control*. CRC Press; 2000. p. 490.
- [4] Albani EL, Bengtson S, Canfield DE, Bekker A, Macchiarelli R, Mazurier A, et al. *Nature* 2010;466:100.
- [5] Knoll AH. *Rev Min Geochem* 2003;54:329.
- [6] Leadbetter BSC, Riding R, editors. *Biom mineralization in lower plants and animals. The systematics association, Sp. vol. 30*. Oxford: Clarendon Press; 1986.
- [7] Lowenstam HA, Weiner S. *On biomineralization*. Oxford, UK: Oxford University Press; 1989.

- [8] Weiner S, Dove PM. *Rev Min Geochem* 2003;54:1–29.
- [9] Wang L, Hamilton MN. *Front Biol.* 2013;8:234.
- [10] Bazin D, Daudon M, Combes C, Rey C. *Chem Revs* 2012;112:5092.
- [11] Banfield JF, Tyson GW, Allen EE, Whitaker RJ. In: Banfield JF, Cervini-Silva J, Neelson KH, editors. *Molecular geomicrobiology*, vol. 59; 2005. p. 1–7. *Revs Miner. Geochem, Miner Soc Am.*
- [12] Baeuerlein E, editor. *Handbook of biomineralization: the biology of biomineral structure formation*, vol. 1. Springer; 2007.
- [13] Behrens P, Baeuerlein E, editors. *Handbook of biomineralization, biomimetic and bioinspired chemistry*. Weinheim: Wiley-VCH; 2009.
- [14] Carter JG, editor. *Skeletal biomineralization, patterns, processes and evolutionary trends*. New York: Van Nostrand Reinhold and Company; 1990.
- [15] De Yoreo JJ, Vekilov PG. *Biomineralization*. In: Dove PM, De Yoreo JJ, Weiner S, editors. *Revs Miner Geochem*, vol. 54. Washington, DC: The Mineralogical Society of America; 2003. p. 57–94.
- [16] Mann S. *Biomineralization: principles and concepts in bioinorganic materials chemistry*. New York: Oxford University Press; 2001.
- [17] Simkiss K, Wilbur KM. *Biomineralization: cell biology and Mineral deposition*. New York: Academic Press; 1989.
- [18] Hincke MT, Nys Y, Gautron J, Mann K, Rodriguez-Navarro AB, McKee MD. *Front Biosci* 2012;17:1266.
- [19] Nys Y, Gautron J, Garcia-Ruiz JM, Hincke MT, Palevol CR. 2004;3:549.
- [20] Olszta MJ, Cheng X, Jee SS, Kumar R, Kim YY, Kaufman MJ, et al. *Mater Sci Eng R* 2007;58:77.
- [21] Weiner S, Wagner HD. *Annu Rev Mater Sci* 1998;28:271.
- [22] Du C, Falini G, Fermani S, Abbott C, Moradian-Oldak J. *Science* 2005;307:1450.
- [23] Fincham AG, Moradian-Oldak J, Simmer JP. *J Struct Biol* 1999;126:270.
- [24] Boskey AL. *Crit Rev Oral Biol Med* 1991;2:369.
- [25] Kinney JH, Marshall SJ, Marshall GW. *Crit Rev Oral Biol Med* 2003;14:13.
- [26] Auer S, Frenkel D. *Nature* 2001;409:1020.
- [27] Auer S, Frenkel D. *Nature* 2001;413:71.
- [28] Liu XY. In: Liu XY, De Yoreo JJ, editors. *From solid–fluid interface to nanostructure engineering*. New York: Plenum/Kluwer; 2004.
- [29] Garcia Ruiz JM. *J Struct Biol* 2003;142:22.
- [30] Mann S, Archibald DD, Didymus JM, Douglas T, Heywood BR, Meldrum FC, et al. *Science* 1993; 261:1286–92.
- [31] Gebauer D, Völkel A, Cölfen H. *Science* 2008;322:1819.
- [32] Cölfen H, Antonietti M. *Mesocrystals and nonclassical crystallization*. Chichester: John Wiley & Sons Ltd.; 2008.
- [33] Demichelis R, Raiteri P, Gale JD, Quigley D, Gebauer D. *Nat Comm* 2011;2(590):1.
- [34] Gebauer D, Gunawidjaja PN, Ko JP, Bacsik Z, Aziz B, Liu LJ, et al. *Angew Chem Int Ed* 2010;49:8889.
- [35] Habraken WJEM, Tao J, Brylka LJ, Friedrich H, Bertinetti L, Schenk AS, et al. *Nat Comm* 2013;4:1507.
- [36] Kimura Y, Niinomi H, Tsukamoto K, García-Ruiz JM. *J Am Chem Soc* 2014;136:1762.
- [37] Addadi L, Raz S, Weiner S. *Adv Mater* 2003;15:959.

- [38] Politi Y, Batchelor DR, Zaslansky P, Chmelka BF, Weaver JC, Sagi I, et al. *Chem Mater* 2010; 22:161.
- [39] Shechter L, Glazer S, Cheled E, Mor S, Weil A, Berman S, et al. *Proc Natl Acad Sci USA* 2008;105:7129.
- [40] Cartwright JHE, Checa AG, Gale JD, Gebauer D, Sainz-Diaz CI. *Angew Chem Int Ed* 2012;51:11960.
- [41] Zhang G, Fang X, Guo X, Li L, Luo R, Xu F, et al. *Nature* 2012;490:49.
- [42] Weiner S, Sagi I, Addadi L. *Science* 2005;309:1027.
- [43] Weiner S, Addadi L. *Annu. Rev Mater Res* 2011;41:21.
- [44] Lowenstam HA. *Science* 1962;137:279.
- [45] Towe KM, Lowenstam HA. *J Ultrastruct Res* 1967;17:1.
- [46] Lowenstam HA, Weiner S. *Science* 1985;227:57.
- [47] Kirschvink JL, Jones DS, MacFadden BJ, Mann S. In: Kirschvink JL, Jones DS, MacFadden BJ, editors. *Magnetite biomineralization and magnetoreception in organisms*. New York: Plenum; 1985. p. 311–32.
- [48] Gordon L, Joester D. *Nature* 2011;469:194.
- [49] Baumgartner J, Dey A, Bomans PHH, Le Coadou C, Fratzl P, Sommerdijk NAJM, et al. *Nat Mater* 2013;12:310.
- [50] Dubois PH, Chen C. *Calcification in echinoderms*. In: Jangoux MJ, Lawrence JM, editors. *Echinoderm studies*, vol. 3. Rotterdam: Balkema; 1989. p. 109–78.
- [51] Okazaki K. *Embryol (Nagoya)* 1960;5:283.
- [52] Markel K, Roser U. *Zoomorphology* 1983;103:25.
- [53] Pilkington JB. *J Mar Biol Assoc UK* 1969;49:857.
- [54] Markel K, Roser U, Stauber M. *Zoomorphology* 1989;109:79.
- [55] Wilt FH. *Zool Sci* 2002;19:253.
- [56] Beniash E, Aizenberg J, Addadi L, Weiner S. *Proc R Soc Lond B Biol Sci* 1997;264:461.
- [57] Beniash E, Addadi L, Weiner S. *J Struct Biol* 1999;125:50.
- [58] Berman A, Addadi L, Weiner S. *Nature* 1988;331:546.
- [59] Politi Y, Metzler RA, Abrecht M, Gilbert B, Wilt FH, Sagi I, et al. *Proc Natl Acad Sci USA* 2008;105: 17362.
- [60] Killian CE, Metzler RA, Gong YUT, Olson IC, Aizenberg J, Politi Y, et al. *J Am Chem Soc* 2009;131: 18404.
- [61] Seto J, Ma YR, Davis SA, Meldrum FC, Gourrier A, Kim Y-Y, et al. *Proc Natl Acad Sci USA* 2012; 109(10):3699.
- [62] Weiner S, Traub W. *FEBS Lett* 1980;111:311.
- [63] Weiner S, Traub W, Parker SB. *Phil Trans R Soc Lond B Biol Sci* 1984;304:425.
- [64] Weiner S, Lowenstam H. *Crit Rev Biochem Mol Biol* 1986;20:365.
- [65] Belcher AM, Wu XH, Christensen RJ, Hansma PK, Stucky GD, Morse DE. *Nature* 1996;381:56.
- [66] Falini G, Albeck S, Weiner S, Addadi L. *Science* 1996;271:67.
- [67] Metzler RA, Evans JS, Killian CE, Zhou D, Churchill TH, Appathurai NP, et al. *J Am Chem Soc* 2010; 132:6329.
- [68] Nudelman F, Gotliv AB, Addadi L, Weiner S. *J Struct Biol* 2006;153:176.
- [69] Schäffer TE, Ionescu-Zanetti C, Proksch R, Fritz M, Walters DA, Almqvist N, et al. *Chem Mater* 1997;9:1731.

- [70] Wada K. *Biom mineralisation* 1972;6:141.
- [71] Kalisman YL, Falini G, Addadi L, Weiner S. *J Struct Biol* 2001;135:8.
- [72] Checa G, Cartwright JHE, Willinger MG. *J Struct Biol* 2011;176:330.
- [73] Olson IC, Kozdon RH, Valley JW, Gilbert PUPA. *J Am Chem Soc* 2012;134:7351.
- [74] Olson IC, Blonsky AZ, Tamura N, Kunz M, Pokroy B, Romao CP, et al. *J Struct Biol* 2013;184:454.
- [75] Nassif N, Pinna N, Gehrke N, Antonietti M. *Proc Natl Acad Sci USA* 2005;102:12653–5.
- [76] Qiao L, Feng Q, Lu S. In vitro growth of nacre-like tablet forming: From amorphous calcium carbonate, nanostacks to hexagonal tablets. *Cryst. Growth Des* 2008;8:1509.
- [77] Rousseau M, López E, Coute A. *J Struct Biol* 2005;149:149.
- [78] Zhang G, Xu J. *J Struct Biol* 2013;182:36.
- [79] Gericke A, Qin C, Spevak L, Fujimoto Y, Butler WT, Sorensen ES, et al. *Calcif Tiss Int* 2005;77:45.
- [80] Ingram RT, Clarke BL, Fisher LW, Fitzpatrick LA. *J Bone Min Res* 1993;8:1019.
- [81] Takano-Yamamoto T, Takemura T, Kitamura Y, Nomura S. *J Histochem Cytochem* 1994;42:885.
- [82] Boskey AL, Doty SB, Kudryashov V, Mayer-Kuckuk P, Roy R, Binderman I. *Bone* 2008;42:1061.
- [83] Price PA, Toroian D, Lim JE. *J Biol Chem* 2009;284:17092.
- [84] Nudelman F, Pieterse K, George A, Bomans PHH, Friedrich H, Brylka LJ, et al. *Nat Mater* 2010;9:1004.
- [85] Roveri N, Iafisco M. *Nanotechnol Sci Appl* 2010;3:107.
- [86] Sanders H, Iafisco M, Pouget EM, Bomans PHH, Nudelman F, Falini G, et al. *Chem Comm* 2011;47:1503.
- [87] Travis DF, Glimcher MJ. *J Cell Biol* 1964;23:447.
- [88] Robinson C, Kirkham J. Dynamics of amelogenesis as revealed by protein compositional studies. In: Butler WT, editor. *The chemistry and biology of mineralized tissues*. Birmingham: EBSCO Media; 1985. p. 248.
- [89] McDougall M, Simmons D, Gu TT, Forsman-Semb K, Mardh CK, Mesbah M, et al. *Eur J Oral Sci* 2000;108(4):303.
- [90] Prakash SK, Gibson CW, Wright JT, Boyd C, Cornier T, Sierra R, et al. *Calcif Tiss Int* 2005;77(1):23.
- [91] Lyngstadaas SP, Risnes S, Sproat BS, Thrane PS, Prydz HP. *EMBO J* 1995;14(21):5224.
- [92] Akita H, Fukae M, Shimoda S, Aoba T. *Arch Oral Biol* 1992;37:953.
- [93] Fan D, Iijima M, Bromley KM, Yang X, Mathew S, Moradian-Oldak J. *Cells Tiss Org* 2011;194(2–4):194.
- [94] Hu JC, Hu Y, Smith CE, McKee MD, Wright JT, Yamakoshi Y, et al. *J Biol Chem* 2008;283:1085.
- [95] Buckley HE. *Crystal growth*. London: Chapman Hall; 1951.
- [96] Weiner S, Addadi L. *J Mater Chem* 1997;7:689.
- [97] Jiménez-López C, Rodríguez-Navarro A, Domínguez-Vera JM, García-Ruiz JM. *Geochim Cosmochim Acta* 2003;67:1667.
- [98] Orme CA, Noy A, Wierzbicki A, McBride MY, Grantham M, Dove PM, et al. *Nature* 2001;411:775.
- [99] DeYoreo JJ, Wierzbicki A, Dove PM. *Cryst Eng Comm* 2007;9:1144.
- [100] Teng HH, Dove PM, DeYoreo JJ. *Geochim Cosmochim Acta* 1999;63:2507.
- [101] Bouropoulos N, Weiner S, Addadi L. *Chem Eur J* 2001;7:1881.
- [102] Falini G, Fermani S, Maritic M, Vanzo S, Zaffino G. *Eur J Inorg Chem* 2005;1:162.

- [103] Marchegiani F, Cibej E, Tosi G, Fermani SP, Vergni P, et al. *J Cryst Growth* 2009;311:4219.
- [104] Aizenberg J, Hanson J, Koetzle TF, Leiserowitz L, Weiner S, Addadi L. *Chem Eur J* 1995;1:414.
- [105] Berman A, Hanson J, Leiserowitz L, Koetzle TF, Weiner S, Addadi L. *Science* 1993;259.
- [106] Weiner S, Addadi L, Wagner D. *Mater Sci Eng C* 2000;11(1):1.
- [107] Qiu R, Wierzbicki A, Orme CA, Cody AM, Hoyer JR, Nancollas GH, et al. *Proc Natl Acad Sci USA* 2004;101:1811.
- [108] Davis KJ, Dove PM, De Yoreo JJ. *Science* 2000;290:1134.
- [109] Touryan LA, Lochhead MJ, Marquardt BJ, Vogel V. *Nat Mater* 2004;3:239.
- [110] De Yoreo JJ, Dove PM. *Science* 2004;306:1301.
- [111] Pouget M, Bomans PHH, Goos JACM, Frederik PM, de With G, Sommerdijk NAJM. *Science* 2009;323:1455.
- [112] Currey JD. *Osteoporos Int* 2003;14:29.
- [113] Jackson SA, Cartwright AG, Lewis D. *Calcif Tiss Res* 1978;25:217.
- [114] Rey C, Combes C, Drouet C, Sfihi H, Barroug A. *Mater Sci Eng C* 2007;27:198.
- [115] Hu YY, Rawal A, Schmidt-Rohr K. *Proc Natl Acad Sci USA* 2010;107:22425.
- [116] Delgado-López JM, Frison R, Gómez-Morales J, Cervellino A, Guagliardi A, Masciocchi N. *Adv Funct Mater* 2014;24:1090.
- [117] Aizenberg J, Addadi L, Hanson J, Leiserowitz L, Koetzle TF, Weiner S. *FASEB J* 1995;9:262.
- [118] Falini G, Reggi M, Fermani S, Sparla F, Goffredo S, Dubinsky Z, et al. *J Struct Biol* 2013;183:226.
- [118] Delgado-López JM, Iafisco M, Rodríguez Ruiz I, Tampieri A, Prat M, Gómez-Morales J. *Acta Biomater* 2012;8:3491.
- [120] Beck R, Seierste M, Andreassen JP. *J Cryst Growth* 2013;380:187.
- [121] Kazmleerczak TF, Tomson MB, Nancollas GH. *J Phys Chem* 1982;86:103.
- [122] López-Macipe A, Gómez-Morales J, Rodríguez-Clemente R. *J Cryst Growth* 1996;166:1015.
- [123] Aizenberg J, Lambert G, Addadi L, Weiner S. *Adv Mater* 1996;8:222.
- [124] Hernández-Hernández A, Rodríguez-Navarro AB, Gómez-Morales J, Jiménez-López C, Nys Y, García-Ruiz JM. *Cryst Growth Des* 2008;8(5):1495.
- [125] Gómez-Morales J, Delgado-López JM, Iafisco M, Hernández-Hernández A, Prat M. *Cryst Growth Des* 2011;11(11):4802.
- [126] Iafisco M, Gómez-Morales J, Hernández-Hernández A, García Ruiz JM, Roveri Norberto. *Adv Eng Mater* 2010;12:218.
- [127] Nassif N, Martineau F, Syzgantseva O, Gobeaux F, Willinger M, Coradin T, et al. *Chem Mater* 2010;22:3653.
- [128] García-Ruiz JM, Novella ML, Moreno R, Gavira JA. *J Cryst Growth* 2001;232:165.
- [129] Fernández-Díaz L, Astilleros JM, Pina CM. *Chem Geol* 2006;225:314.
- [130] García-Ruiz JM. *Key Eng Mat* 1991;88:87.
- [131] García-Ruiz JM, Novella ML, Otálora F. *J Cryst Growth* 1999;196:703.
- [132] Henisch HK. *Crystal growth in gels and Liesegang rings*. Cambridge: Cambridge University Press; 1988.
- [133] Otálora F, Gavira JA, Ng JD, García-Ruiz JM. *Prog Biophys Mol Biol* 2009;101:26.
- [134] Putnis A, Fernández-Díaz L, Prieto M. *Nature* 1992;358:743.

- [135] Asenath-Smith E, Li H, Keene EC, Seh ZW, Estroff LA. *Adv Funct Mater* 2012;22:2891.
- [136] Dorvee JR, Boskey AL, Estroff LA. *Cryst Eng Comm* 2012;14:5681.
- [137] Geckil H, Xu F, Zhang X, Moon S, Demirci U. *Nanomedicine* 2010;5:469.
- [138] Kosanović C, Falini G, Kralj D. *Cryst Growth Des* 2011;11:269.
- [139] Silverman L, Boskey AL. *Calcif Tiss Int* 2004;75:494.
- [140] Falini G. *Int J Inorg Mater* 2000;2:455.
- [141] Meldrum C, Cölfen H. *Chem Rev* 2008;108:4332.
- [142] Iafisco M, Marchetti M, Gómez-Morales J, Hernández-Hernández A, M García-Ruiz J, Roveri N. *Cryst Growth Des* 2009;9:4912.
- [143] Sánchez-Pastor N, Gigler AM, Cruz JA, Park S-H, Jordan G, Fernández-Díaz L. *Cryst Growth Des* 2011;11:3081.
- [144] Fernández-Díaz L, Putnis A, Prieto M, Putnis CV. *J Sediment Res* 1996;66:482.
- [145] Henisch HK. *Crystal growth in gels*. University Park, PA: Pennsylvania State University Press; 1970.
- [146] Henisch HK, García-Ruiz JM. *J Cryst Growth* 1986;75:195.
- [147] Prieto M, Putnis A, Fernández-Díaz L, López-Andrés S. *J Cryst Growth* 1994;142:225.
- [148] Putnis A, Prieto M, Fernández-Díaz L. *Geol Mag* 1995;132:1.
- [149] García-Ruiz JM. *Estud Geol* 1982;38:209.
- [150] Sancho-Tomás M, Fermani S, Durán Olivencia MA, Otalora F, Gómez-Morales J, Falini G, et al. *Cryst Growth & Des* 2013;13:3884.
- [151] Sancho-Tomás M, Fermani S, Goffredo S, Dubinsky Z, Garcia-Ruiz JM, Gómez-Morales J, et al. *Cryst Eng Comm* 2014;16:1257.
- [152] Chafetz HS, Buczynski C. *Palaios* 1992;7:277–93.
- [153] Chekroun KB, Rodriguez-Navarro C, Gonzalez-Muñoz MT, Arias JM, Cultrone G, Rodríguez-Gallego M. *J Sediment Res* 2004;74:868.
- [154] Coates JD, Anderson RT, Woodward JC, Phillips EJP, Lovley DR. *Environ Sci Technol* 1996;30(9):2784–9.
- [155] Jerden Jr JL, Sinha AK. *Appl Geochem* 2003;18:823.
- [156] Smith W, Streckfu J, Vogel J, Ennever J. *J Dent Res* 1971;50(3):777.
- [157] Castanier S, Le Métayer-Levrel G, Orial G, Loubière J-F, Pethuisot J-P. In: Ciferri O, et al., editors. *Of microbes and art: the role of microbial communities in the degradation and protection of cultural heritage*. New York: Plenum; 2000. p. 203–18.
- [158] Rodriguez-Navarro C, Rodriguez-Gallego M, Ben Chekroun K, Gonzalez-Muñoz MT. *Appl Environ Microbiol* 2003;69:2182.
- [159] Rodriguez-Navarro C, Jroundi F, Schiro M, Ruiz-Agudo E, González-Muñoz MT. *Appl Environ Microbiol* 2012;78:4017.
- [160] Loveridge N. *J Anim Sci* 1999;77:190.
- [161] Bouwstra JA, Gooris GS, van der Spek JA, Bras W. *J Invest Dermatol* 1991;97:1005.
- [162] Damien F, Boncheva M. *J Invest Dermatol* 2010;130:611.
- [163] Torri C, Mangoni A, Teta R, Fattorusso E, Alibardi L, Fermani S, et al. *J Struct Biol* 2014;185:99.
- [164] Weinkamer R, Dunlo JWC, Brechet Y, Fratz P. *Acta Mater* 2013;61:880.
- [165] Kawasaki K. *Dev Genes Evol* 2009;219:147.
- [166] Butler WT, Ritchie H. *Int J Dev Biol* 1995;39:169.

- [167] Nguyen C, Ea HK, Bazin D, Daudon M, Lioté F. *Arthritis Rheum* 2010;62:2829.
- [168] Moradian-Oldak J. *Front Biosci* 2013;17:1996.
- [169] Kirkham J, Zhang J, Brookes SJ, Shore RC, Wood SR, Smith DA, et al. *J Dent Res* 2000;79:1943.
- [170] Wen HB, Moradian-Oldak J, Fincham AG. *J Dent Res* 2000;79:1902.
- [171] Wen X, Lei YP, Zhou YL, Okamoto CT, Snead ML, Paine ML. *Cell Mol Life Sci* 2005;62:1038.
- [172] Wang RZ, Weiner S. *J Biomech* 1998;31:135.
- [173] Robinson C, Kirkham J, Shore R, editors. *Dental enamel formation to destruction*. Boca Raton FL: CRC Press; 1995.
- [174] Eastoe JE. *Nature* 1960;187:411.
- [175] Paine ML, White SN, Luo W, Fong H, Sarikaya M, Snead ML. *Matrix Biol* 2001;20:273.
- [176] White SN, Paine ML, Luo W, Sarikaya M, Fong H, Yu ZK, et al. *J Am Ceram Soc* 2000;83:238.
- [177] Liddiard KJ, Hockridge JG, Macey DJ, Webb J, van Bronswijk W. *Molluscan Res* 2004;24:1–11.
- [178] Mann S, Perry CC, Webb J, Luke B, Williams RJP. *Proc R Soc Lond B* 1986;227:179.
- [179] Lowenstam HA. *Science* 1971;171:487.
- [180] van der Wal P. *J Ultrastruct Mol Struct Res* 1989;102:147.
- [181] van der Wal P, Giesen HJ, Videler JJ. *Mater Sci Eng C* 2000;7:129.
- [182] Saunders M, Kong C, Shaw JA, Macey DJ, Clode PL. *J Struct Biol* 2009;167:55.
- [183] Sone SED, Weiner S, Addadi L. *J Struct Biol* 2007;158:428.
- [184] Brooker LR, Shaw JA. The Chiton radula: a unique model for biomineralization studies. In: Seto J, editor. *Advanced topics in biomineralization*. InTech; 2012, ISBN 978-953-51-0045-4.
- [185] Ross MD. *Adv Space Res* 1983;3:179.
- [186] Hudspeth J. *Annu Rev Neurosci* 1983;6:187.
- [187] Popper AN, Fay RR. *Hear Res* 2011;273:25.
- [188] Bianco IH, Ma L-H, Schoppik D, Robson DN, Orger MB, Beck JC, et al. *Curr Biol* 2012;22:1285.
- [189] Riley B, Moorman SJ. *J Neurobiol* 2000;43:329.
- [190] Inoue M, Tanimoto M, Oda Y. *Sci Reports* 2013;3:2114.
- [191] Sollner C, Burghammer M, Busch-Nentwich E, Berger J, Schwarz H, Riekel C, et al. *Science* 2003;302:282.
- [192] Blakemore RP. *Science* 1975;190:377.
- [193] Gorby YA, Beveridge TJ, Blakemore RP. *J Bacteriol* 1988;170:834.
- [194] Arakaki A, Nakazawa H, Nemoto M, Mori T, Matsunaga T. *J R Soc Interface* 2008;5:977.
- [195] Bazylini DA, Frankel RB, Heywood BR, Mann S, King JW, L Donaghay P, et al. *Appl Environ Microbiol* 1995;61:3232.
- [196] Frankel RB, Blakemore RP, Wolfe RS. *Science* 1979;203:1355.
- [197] Mann S, Sparks NHC, Frankel RB, Bazylini DA, Jannasch HW. *Nature* 1990;343:258.
- [198] Faivre D, Schüler D. *Chem Rev* 2008;108:4875.
- [199] Arakaki A, Webb J, Matsunaga T. *J Biol Chem* 2003;278:8745.
- [200] Bazylini DA, Frankel RB. *Rev Min Geochem* 2003;54:217.
- [201] Bazylini DA, Frankel RB. *Nat Rev Microbiol* 2004;2:217.

- [202] Arnaud-Haond S, Goyard JE, Vonau V, Herbaut C, Prou J, Saulnier D. *Mar Biotechnol* 2007;9:113.
- [203] Gautron J, Hincke MT, Nys Y. *Connect Tiss Res* 1997;36:195.
- [204] García-Ruiz JM, Rodríguez-Navarro A. Competitive crystal growth: the avian eggshell model. In: Allemand D, Cuif J-P, editors. *Biom mineralization*, vol. 93. Monaco: Musée Oceanographique; 1994. p. 85–94.
- [205] Fernández MS, Moya A, López L, Arias JL. *Matrix Biol* 2001;19:793.
- [206] Hernández-Hernández A, Vidal ML, Gómez-Morales J, Rodríguez-Navarro AB, Labas V, Gautron J, et al. *J Cryst Growth* 2008;310:1754.
- [207] Hernández-Hernández A, Gómez-Morales J, Rodríguez-Navarro AB, Gautron J, Nys Y, García-Ruiz JM. *Cryst Growth Des* 2008;8:4330.
- [208] Hincke MT. *Connect Tiss Res* 1995;31:227.
- [209] Hincke MT, Gautron J, Panhéleux M, Garcia-Ruiz JM, McKee MD, Nys Y. *Mat Biol* 2000;19:443.
- [210] Gautron J, Hincke MT, Panhéleux M, García-Ruiz JM, Boldicke T, Nys Y. *Connect Tiss Res* 2001;42:255.
- [211] Pines M, Knopov V, Bar A. *Matrix Biol* 1995;14:765.
- [212] Mann K, Gautron J, Nys Y, McKee MD, Bajari T, Schneider WJ, et al. *Matrix Biol* 2003;22:397.
- [213] Hincke MT, Tsang CPW, Courtney M, Hill V, Narbaitz R. *Calcif Tiss Int* 1995;56:578.
- [214] Hincke MT, Gautron J, Tsang CPW, McKee MD, Nys Y. *J Biol Chem* 1999;274:32915.
- [215] Mann K, Macek B, Olsen JV. *Proteomics* 2006;6:3801.
- [216] Shen M, Lajos PS, farge D, Daudon M, Carpentier S, Chen L, et al. *Ann Thorac Surg* 1998;66(5):S236.
- [217] Kopans D, Gavenonis S, Halpern E, Moore R. *Breast J* 2011;17:638.
- [218] Stephens AD. *J Inherit Metab Dis* 1989;12:197.
- [219] Ropion-Michaux H, Mathias J, Bruot O, Ganne PA, Laurent V, Régent D. *J Radiol* 2010;91:759.
- [220] Matsuda I, Hao H, Zozumi M, Koishi M, Matsumoto T, et al. *Pathol Res Pract* 2010;206:372.
- [221] Reid D, Andersen ME. *Atherosclerosis* 1993;101:213.
- [222] Mommers X-A, Henault B, Aubriot M-H, Trost O, Malka F, Zwetyenga N. *Rev Stomatol Chir Maxillo-Faciale* 2012;113(1):53.
- [223] Boistelle R, Rinaudo C. *J Cryst Growth* 1981;53:1.
- [224] Pak CYC. *J Cryst Growth* 1981;53:202.
- [225] Gal A, Brumfeld V, Weiner S, Addadi L, Oron D. *Adv Mater* 2012;24:OP 77.
- [226] Clarkson E, Levi-Setti R, Horváth G. *Arthropod Struct Dev* 2006;35:247.
- [227] Kinoshita S. *Structural colors in the realm of nature*. Singapore: World Scientific Publishing; 2008. 345.
- [228] Parker AR. *J Opt A* 2000;2:R15.
- [229] Parker AR. *J R Soc Interface* 2005;2:1.
- [230] Vukusic P, Sambles JR. *Nature* 2003;424:852.
- [231] Hyde ST, Schroder-Turk GE. *Interface Focus* 2012;2:529.
- [232] Prum RO, Quinn T, Torres RH. *J Exp Biol* 2006;209:748.
- [233] Bálint Z, Kertész K, Piszter G, Vértesy Z, Biró LP. *J R Soc Interface* 2012;9:1745.

- [234] Saranathana V, Osujib CO, Mochrie SGJ, Noh H, Narayanan S, Sandy A, et al. PNAS 2010;107:11676.
- [235] Ghiradella H. *Microsc Res Tech* 1994;27:429.
- [236] Bosak T, Newman DK. *Geology* 2003;31:577.
- [237] Braissant O, Cailleau G, Dupraz C, Verrecchia EP. *J Sediment Res* 2003;73:485.
- [238] Riding R. In: Reitner J, V.Thiel, editors. *Enciclopedia of geobiology*. Springer; 2011. p. 635.
- [239] Dupraz C, Reid RP, Visscher PT. In: Reitner J, Thiel V, editors. *Enciclopedia of geobiology*. Springer; 2011. p. 617.
- [240] Weiner S, Addadi L. *Science* 2002;298:375.
- [241] Riding R. *Lethaia* 2007;32:321.
- [242] Awramik SM. *Nature* 2006;441:700.
- [243] Grotzinger JP, Knoll AH. *Annu Rev Earth Planet Sci* 1999;27:313.
- [244] Allwood C, Walter MR, Kamber BS, Marshall CP, Burch IW. *Nature* 2006;441:714.
- [245] Van Kranendonk MJ. Earth's oldest rocks. In: Van Kranendonk MJ, Smithies RH, Bennet V, editors. *Developments in precambrian geology*. Amsterdam: Elsevier; 2007. p. 855.
- [246] Walter MR, Buick R, Dunlop JSR. *Nature* 1980;248:443.
- [247] Grotzinger JP, Rothman DR. *Nature* 1996;383:423.
- [248] Lowe DR. *Geology* 1994;22:387.
- [249] McLoughlin N, Wilson LA, Brasier MD. *Geobiology* 2008;6:95.
- [250] García-Ruiz JM, Hyde ST, Carnerup AM, Christy AG, Van Kranendonk MJ, Welham NJ. *Science* 2003;302:1194.
- [251] Cuerno R, Escudero C, García-Ruiz JM, Herrero MA. *J R Soc Interface* 2012;9:1051.
- [252] Kellermeier M, Cölfen H, García-Ruiz JM. *Eur J Inorg Chem* 2012:5123–44.
- [253] Kellermeier M, Glaab F, Melero-García E, García-Ruiz JM. Experimental techniques for the growth and characterization of silica biomorphs and silica gardens. In: De Yoreo James, editor. *Methods in enzymology*. Research methods in biomineralization science, vol. 532. Burlington: Academic Press; 2013. p. 225–56.
- [254] Bull MRS, Tamerler C, Sarikaya M. *MRS Bull*. Copyright 2008 Materials Research Society 2008;33:504.

# Crystallization of Pharmaceutical Crystals

S. Veesler<sup>1</sup>, F. Puel<sup>2</sup>

<sup>1</sup>CINaM-CNRS, Aix-Marseille Université, Marseille, France; <sup>2</sup>LAGEP UMR CNRS 5007, UNIVERSITÉ DE LYON, ESCPE LYON, VILLEURBANNE CEDEX, LYON, FRANCE

## CHAPTER OUTLINE

<b>21.1 Introduction</b> .....	<b>916</b>
<b>21.2 Crystallization from Solution</b> .....	<b>917</b>
21.2.1 The Crystallization Medium .....	917
21.2.2 Solubility, Supersaturation, and Phase Diagrams .....	917
21.2.3 Crystal Nucleation .....	920
21.2.3.1 Primary Nucleation.....	920
21.2.3.2 Secondary Nucleation .....	922
21.2.4 Crystal Growth.....	923
21.2.5 Dissolution .....	925
21.2.6 Phases .....	925
21.2.6.1 Solubility and Ostwald Rules.....	926
21.2.6.2 Phase Transition.....	927
21.2.7 Ripening .....	928
<b>21.3 Crystallization Methods</b> .....	<b>929</b>
21.3.1 Temperature .....	930
21.3.2 Solvent Evaporation.....	930
21.3.3 Chemical Composition .....	932
21.3.4 Chemical Reaction.....	934
21.3.5 Co-crystallization .....	935
<b>21.4 Development of a Batch Crystallization Process at the Laboratory Scale</b> .....	<b>937</b>
21.4.1 Prerequisite .....	937
21.4.2 Screening of Crystallization Conditions and Phases.....	937
21.4.3 Determination of Operating Conditions .....	938
21.4.3.1 Solvent Selection .....	938

21.4.3.2 Seeding Strategy.....	938
21.4.3.3 Cooling Strategy.....	940
21.4.3.4 Crystallizer Hydrodynamics (Mixing).....	941
<b>21.5 Conclusion.....</b>	<b>943</b>
<b>References.....</b>	<b>943</b>

## 21.1 Introduction

Crystallization is a popular research topic for the pharmaceutical industry, because it offers the opportunity to purify, improve, and tailor physicochemical properties of pharmaceuticals. When a new active pharmaceutical ingredient (API) is launched on the market, it is essential to have a thorough knowledge of its different solid phases and to respect the Good Manufacturing Practice Guide for APIs (<http://www.ich.org/products/guidelines/quality/quality-single/article/good-manufacturing-practice-guide-for-active-pharmaceutical-ingredients.html>). For instance, recent history in the pharmaceutical industry [1] has shown that the emergence of a new phase can seriously compromise the intended process and potentially the patient's life. S.R. Chemburkar of Abbott Laboratories, who dealt with the ritonavir case in the 1990s, drew the following conclusion known as the 7P rule: "Dealing with Polymorphism is Potentially Precarious Practice and the Proper way to Play this game is with Patience and Perseverance" [2]. Moreover, product quality characteristics are also related to crystal morphology, habit, and size distribution (CSD). That is why, early in the development of a process to produce an API or an intermediate, crystallization conditions and the phase to be produced must be defined. This prerequisite means determining the system thermodynamics and kinetics, that is, the phase diagram (the number of polymorphs and/or phases and their relative thermodynamic stability) and the phase transition kinetic. Thus, it is necessary to develop an experimental strategy in order to study the respective influence of temperature, supersaturation, medium (chemical conditions), and hydrodynamics on the API or intermediate crystallization.

Moreover, depending on whether the chemical composition of the crystal is monocomponent or multicomponent, different terminologies are used. An API or an intermediate can be crystallized as different phases [3] (e.g., polymorphs or solvates) or as pure enantiomer, racemate, or conglomerate [4]. API can also be crystallized as a salt [5] or a co-crystal [6]. This is for technological reasons (i.e., increasing solubility (in water) and improving the dissolution profile, bioavailability, stability, and compressibility) or for economic reasons such as patent protection. The final objective is a robust crystallization process producing a crystallized solid with the desired properties.

In the previous chapters of this volume, the following aspects were treated: nanocrystal growth from solution, protein crystal growth, biological crystallization, organic crystal growth, and growth of chiral molecules. In this chapter, we treat pharmaceutical crystallization. First, the basic concepts are illustrated with examples. Second,

crystallization methods used in the laboratory are described. Lastly, we look at how a batch crystallization process is developed in the laboratory.

## 21.2 Crystallization from Solution

Producing pharmaceutical crystals raises the same problems regardless of whether it is for biology, opto-electronics, or nanomaterials, because in all these cases crystal growth mechanisms are the same. That is to say, macromolecules and small organic or mineral molecules follow the same crystallization rules [7], even though each material exhibits specific characteristics. In the specific case of pharmaceutical crystallization, it is important to control the physicochemical properties, which are related to the phase, the morphology, the habit, and the size of the crystals.

### 21.2.1 The Crystallization Medium

The crystallization medium is defined by the chemical composition of the medium used for crystallization. Note that crystallization is a purification process; thus, the solvent is considered as an impurity. In pharmaceutical crystallization, the crystallization medium is composed of the solvent (either pure or a mixture) and/or other species such as byproducts, isomers, or enantiomers.

In order to obtain any nucleation or growth, it is necessary to dissolve the API in a good solvent. In crystallization, a good solvent is defined by high solubility of material, easy control of nucleation, and/or fast growth of crystals exhibiting the appropriate properties. Dissolution of the solute occurs via the creation of solvent–solute interactions. What is the best solvent for a given crystal? Boistelle [9] proposed following the old rule according to which like dissolves like. That is to say, the choice of the solvent is directed by the solute to be dissolved. Solvents are classified into nonpolar, polar aprotic, and polar protic solvents (Table 21.1). For instance, chlorides, sulfates, and phosphates are more soluble in polar protic solvents than in polar aprotic solvents. The anions are dissolved by ion–dipole interactions (polar solvents), with some additional hydrogen bonding (protic solvents).

### 21.2.2 Solubility, Supersaturation, and Phase Diagrams

Once the material is in solution, this solution must be supersaturated in order to observe nucleation or growth. The solution is supersaturated when the solute concentration exceeds its solubility, namely, the concentration at which crystals and solution are at equilibrium. Supersaturation is the driving force for nucleation and growth. Supersaturation is the difference between the chemical potential of the solute molecules in the supersaturated state ( $\mu$ ) and in the saturated state ( $\mu_s$ ). For one molecule, the expression of this difference is:

$$\Delta\mu = \mu - \mu_s = kT\ln\beta \quad (21.1)$$

**Table 21.1** Classification of Organic Solvents

Type of Solvent	Chemical Species	Low Boiling Point	High Boiling Point
Polar protic	Alcohol–water	Methanol	n-butanol
		Ethanol	Benzyl alcohol
Polar aprotic	Ketone Nitrogen compound Amino compound Ester Ether Chlorinated compound Aromatic chlorinated compound	Acetone	Methyl-isobutyl-ketone
		Acetonitrile	Propionitrile, dimethylformamide
		Ethyl acetate	N-methyl-2 pyrrolidone
		Diethyl-ether, methyl-tert-butyl-ether	Isopropyl acetate, butyl acetate
		Dichloromethane	Dibutyl-ether
		Monochlorobenzene	Ortho-dichlorobenzene
Nonpolar	Alkane Aromatic	Pentane, hexane	Decane
		Toluene, xylene	

Reprinted with permission from Ref. [8]. Copyright 2009 American Chemical Society.

where  $k$  (J/K) is the Boltzmann constant; and  $T$  (K) is the temperature. For the sake of simplicity, supersaturation is usually defined as a ratio  $\beta$ , and considering activities equal to the concentrations,  $\beta$  can be written here without specifying the units:

$$\beta = C/C_s \quad (21.2)$$

where  $C$  is the concentration of the solute in solution; and  $C_s$  is its saturated or equilibrium concentration. Another dimensionless ratio  $\sigma = \beta - 1$  is also used in the literature:

$$\sigma = (C - C_s)/C_s \quad (21.3)$$

Moreover, if  $\beta > 1$ , the crystal grows; if  $\beta < 1$ , the crystal dissolves; and, if  $\beta = 1$ , crystals and solution are at equilibrium. It is also worth noting that supersaturation is sometimes defined as the difference between  $C$  and  $C_s$ . In this case, its value depends entirely on the concentration units. However, this may conceal the specific influence of the concentration (and medium) on crystallization. As an example, let us consider the case of carbamazepine (phase III), whose solubility in different solvents is known [10] (Figure 21.1). Thus, a supersaturation,  $\beta = 2$ , can be achieved in different solvents: for instance, in methanol, where solubilities are high (109.3 g/L at 311.4 K); or in 2-propanol, where solubilities are lower (18.9 g/L at 311.4 K). In these cases, the mass of solute crystallized is either 109.4 g/L or only 18.9 g/L, respectively. Consequently, despite the same  $\beta$  value, nucleation and growth will be favored in methanol.

API molecules that exhibit acidic and/or basic functions are a special case. These API can be crystallized in either their neutral or salt forms. The neutral form is poorly soluble in water. Conversely, the salt form is much more soluble and is very often preferred for therapeutic use. In water, these acidic and/or basic functions can be partially dissociated when they are weak. The consequence is that these molecules present a pH-dependent solubility profile.

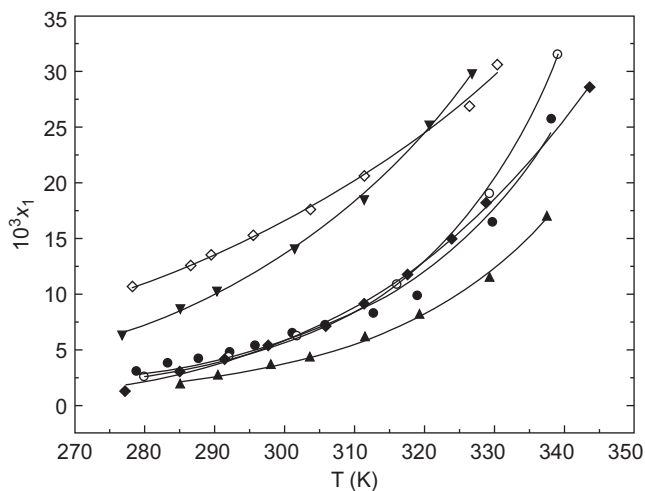


**FIGURE 21.1** Mole fraction solubility of carbamazepine (phase III),  $x_1$ , in different solvents:  $\blacktriangledown$ , methanol;  $\bullet$ , ethanol;  $\circ$ , 1-propanol;  $\blacktriangle$ , 2-propanol;  $\blacklozenge$ , 1-butanol;  $\diamond$ , tetrahydrofuran. Reprinted with permission from Liu et al. [10]. Copyright 2008 American Chemical Society.

For a weakly acidic API, at  $\text{pH} < \text{pK}_a - 2$  (with  $\text{pK}_a$  the acid ionization constant), the molecule is mainly in its undissociated form (99%), namely, free acid, with the remaining 1% being in its dissociated form. The crystal is composed of the free acid molecule, and its intrinsic solubility concentration  $C_s$  can be measured by titration of the saturated solution. The supersaturation definitions (21.2) and (21.3) for undissociated compounds can be applied. Conversely, at  $\text{pH} > \text{pK}_a + 2$ , the molecule is almost completely dissociated (99%), and the remaining 1% is undissociated, with a counter-ion in solution that ensures electroneutrality. The salt form crystallizes above a precise pH called  $\text{pH}_{\text{max}}$ .  $\text{pH}_{\text{max}}$  differs from  $\text{pK}_a$ , being dependent on the cation associated with an acid anion [11]. Like sparingly soluble electrolytes, the supersaturation ratio  $\beta$  is expressed as [12,13]:

$$\beta = \frac{[A^{a-}]^x [B^{b+}]^y}{K_s} \quad \beta = \frac{[A^{a-}]^x \cdot [B^{b+}]^y}{K_s} \quad (21.4)$$

where  $[A^{a-}]$  and  $[B^{b+}]$  are the concentrations of the dissociated acid and its counter-ion, respectively;  $K_s$  is the concentration solubility product;  $x$  and  $y$  are the stoichiometric factors; and  $a$  and  $b$  are the valencies of the ions.

For a weakly basic API,  $A^{a-}$  is the counter anion and  $B^{b+}$  is the protonated base. For  $\text{pH} > \text{pH}_{\text{max}}$ , the free base form is crystallized, and the supersaturation definition (21.4) can be applied. Conversely, the salt form is crystallized at a pH lower than  $\text{pH}_{\text{max}}$ , and the supersaturation expression (21.4) needs to be used.

Lastly, there is another class of multicomponent crystals named co-crystals, which are composed of an API with its co-crystallizing agent, the two species forming a building block in the crystalline lattice. Although co-crystals are not ionic compounds (the species remains neutral), the supersaturation of co-crystals can be evaluated by

considering the solubility product [14,15]. The supersaturation definition (21.4) can be applied and expressed as:

$$\beta = \frac{[\text{API}]^X \cdot [\text{B}]^Y}{K_S} \quad (21.5)$$

where [API] and [B] are the concentrations of the API and its co-crystallizing agent, respectively;  $K_S$  is the concentration solubility product of the co-crystal  $\text{API}_X\text{B}_Y$ ; and X and Y are the stoichiometric factors of the two species in the building block. For the moment, most of the referenced co-crystals are equimolar ( $X = 1:Y = 1$ ); however, there are also ternary and quaternary co-crystals [16]. Note that the solvent affects the composition of the stoichiometric solid phase nucleated [17].

The phase diagram is the map of the experimental domain, in which the stability domains of the solid and liquid phases are located. Polymorphs are crystals of a chemical compound that have the same composition but different crystal structures. In contrast, different crystal phases are crystals of a compound that have both different compositions and different crystal structures. Moreover, in the phase diagram, there is a region where two coexisting liquids can be observed, which corresponds to a miscibility gap in the phase diagram. The phase diagram describes the thermodynamics of the system and thus does not include the kinetics, but we will see in the following how important the phase diagram is to the understanding, control, and design of crystallization experiments.

### 21.2.3 Crystal Nucleation

When a solution is supersaturated, the solid phase forms more or less rapidly depending on crystallization conditions: the temperature, supersaturation and concentration of solute, nature and concentration of impurities, hydrodynamics (crystallizer geometry and stirring), and presence of solid particles. This phase transition is called nucleation.

#### 21.2.3.1 Primary Nucleation

Primary nucleation occurs in a solution that is clear, without crystals. It is called homogeneous nucleation if the nuclei form in the bulk of the solution. It is called heterogeneous nucleation if the nuclei preferentially form on substrates such as the walls of the crystallizer or solid particles such as dust particles. Conversely, secondary nucleation is induced by crystals of the same phase present in the slurry, either resulting from primary nucleation or introduced as seeds by the operator.

Until recently, primary solution nucleation has been described solely by classical nucleation theory (CNT), a theory derived from nucleation of droplets in the bulk of pure supersaturated vapors. It considers that once a cluster has reached the critical size  $r^*$ , given by the Gibbs–Thomson equation (Eqn (21.6)), nucleation starts.

$$r^* = \frac{2\Omega\gamma}{kT\ln\beta} \quad (21.6)$$

where  $\gamma$  is the crystal–solution interfacial free energy ( $\text{J/m}^2$ ); and  $\Omega$  is the volume of a molecule inside the crystal ( $\text{m}^3$ ). Note that the larger the supersaturation, the smaller the critical nuclei, and thus the easier the nucleation.

While this theory has the advantage of simplicity, some discrepancies have been observed with experiments [18,19]. Therefore, a more complicated two-step mechanism has been proposed for protein crystallization [20]: first, formation of a dense phase of clusters on the model of a liquid–liquid phase separation; and, second, organization of these clusters into structured clusters (Figure 21.2). This second step was found to be rate limiting in the case of lysozyme crystallization [19], explaining why it is often more difficult to nucleate macromolecules than small molecules.

The homogeneous nucleation rate or nucleation frequency  $J_1$  is the number of crystals that form in a supersaturated solution per unit of time and unit of volume [22–25]. Hence,  $J_1$  is proportional to  $n$  times the solubility,  $N_0$ , which is expressed as the number of molecules per unit of volume. Here, we only need to recall that (in the case of CNT):

$$J_1 = nN_0\nu \exp\left(-\frac{f\Omega^2\gamma^3}{(kT)^3 \ln^2\beta}\right) \quad (21.7)$$

where  $\nu$  ( $\text{s}^{-1}$ ) is the frequency with which nuclei of critical size  $r^*$  become supercritical by the addition of a molecule and develop into crystals; the term  $nN_0\nu$  can be simply described as a pre-exponential factor  $K_0$ ; and  $f$  is the nuclei form factor ( $16\pi/3$  for a spherical nuclei, as assumed in the CNT). Equation (21.7) shows that the frequency of nucleation depends not only on the supersaturation  $\beta$  but also on the concentration of molecules  $nN_0$ . All things being equal, including supersaturation, the higher the probability of intermolecular contact, the easier nucleation appears. Systems with high solubility meet this condition. For systems with low solubility, the solute molecules are separated by greater distances and by a greater number of solvent molecules. The probability that the molecules will come into contact and form a nucleus is thus lower. To summarize, the higher the solubility, the easier the nucleation.

Now we can introduce kinetic information: in the phase diagram, a zone where nucleation is kinetically inactive appears, bounded by the metastable zone limit (MZL). According to the definition given by Kashchiev et al. [26], the MZL is characterized by the maximum supersaturation, below which a solution can retain its metastability for a time defined according to the application (with no nucleation occurring during this time).

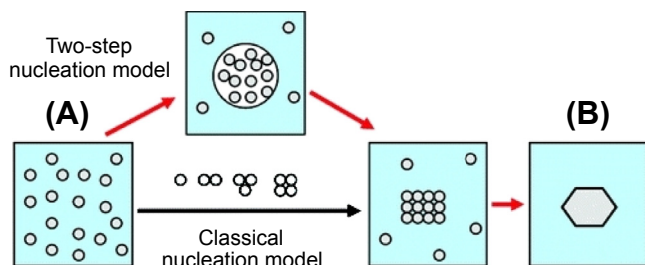


**FIGURE 21.2** Schematic representation of the different nucleation mechanisms, from (A) a supersaturated solution to (B) a crystal. Reprinted with permission from Erdemir et al. [21]. Copyright 2009 American Chemical Society.

### 21.2.3.2 Secondary Nucleation

In an industrial context, where crystallization is performed on a large scale under stirring, secondary nucleation mechanisms play a major role, as shown by Oullion et al. [27] for a plate-like organic product. Generally, the crystallization is carried out in the metastable zone. Experimental results reveal two significant secondary nucleation phenomena. First, a surface nucleation mechanism may occur on smooth, growing crystals. Secondary nuclei are formed on the crystal surface, as a preordered species, as clusters in the immediate solution vicinity, or by dendritic growth and dendritic coarsening. These nuclei and/or small dendrites can detach from the crystal surface [28]. This surface mechanism appears to be strongly dependent on the supersaturation level and on the total crystal surface area. A kinetic expression was proposed by Mersmann [28] and successfully applied to model the temporal evolution of particle size distribution during a batch operation [29].

$$J_{2,\text{surf}} = E \cdot a_c \cdot \frac{D_{AB}}{d_m^4} \cdot \exp\left(-\pi \cdot K^2 \cdot \frac{[\ln(C_C/C^*)]^2}{\ln\beta}\right) \quad (21.8)$$

where  $a_c$  is the total crystal area per cubic meter of suspension ( $\text{m}^{-1}$ );  $D_{AB}$  is the diffusion coefficient of the solute in the solution ( $\text{m}^2/\text{s}$ );  $d_m$  is the molecular diameter (m);  $C_C$  is the crystal molar density ( $\text{M}/\text{m}^{-3}$ );  $C^*$  is the solubility ( $\text{M}/\text{m}^{-3}$ ); and  $\beta$  is the supersaturation degree.  $K$  is derived from the calculation of the interfacial tension between the crystal and the solution. Nielsen [30] originally proposed a calculated value of 0.414. On the basis of numerous experimental data, the value of 0.333 was reported by Mersmann [28].  $E$  represents the fraction of crystal area that is really “efficient” in producing single nuclei. Generally,  $K$  is fixed and  $E$  tuned so as to reproduce the observed experimental behavior of the studied system.

Like primary nucleation, this surface mechanism is an activated one and decreases as supersaturation decreases in the metastable zone. Because the production of particles remains active under stirring even at rather low supersaturation levels, a contact mechanism is proposed based on micro-attrition of crystals when crystals collide with each other or with the stirrer blades and walls of the vessel [28,31]. A “standard” phenomenological kinetic equation is proposed in the literature and accounts for the dependence of the contact secondary nucleation rate upon the supersaturation level, solid concentration, and stirring power:

$$\Gamma_{N2,\text{cont}} = k_N \varepsilon \sigma^{j_A} C_S^{j_S} \quad (21.9)$$

where  $\varepsilon$  ( $\text{W}/\text{kg}$ ) is the specific stirring power dispersed per unit mass of slurry;  $\sigma$  is the relative supersaturation; and  $C_S$  is the molar concentration of solids in suspension. The kinetic parameter  $k_N$  is generally assumed to be temperature dependent, according to Arrhenius’s law. Exponent  $j_A$ , which does not depend on temperature, is commonly found to be between 0.5 and 2.5, whereas exponent  $j_S$  is generally found to be between 1 and 2, and is expected to slightly depend on temperature [32].

As a concluding remark, it should be emphasized that the objective of crystal growers is to control the crystallization process, and thus separate the nucleation and growth phases as much as possible. This task is extremely challenging because growth of crystals is optimal in the metastable zone, at low supersaturation, where primary nucleation is kinetically inactive and secondary nucleation can be controlled. To obtain reproducible operation and to avoid batch-to-batch differences, seeding is often used (see [Section 21.4.3](#) in this chapter).

### 21.2.4 Crystal Growth

Once the nuclei are formed and exceed the critical size, they become crystals and grow.

A crystal is limited by faces. The set of equivalent faces resulting from the crystal symmetry is a form<sup>1</sup>. All the forms present on a crystal represent the morphology of the crystal. However, in order to describe the external form of a crystal, morphology is not sufficient and the concept of crystal habit is needed, entailing the notion of face extension or morphological importance. But it is important to point out that the growth form of the crystal is defined by the faces with the slowest growth rates. This is shown by [Figure 21.3](#), which represents the growth in the metastable zone of a seeded monoclinic Bovine Pancreatic Trypsin Inhibitor (BPTI) crystal in Potassium Thiocyanate (KSCN) solution [33]. During the experiment, all the faces migrate parallel to themselves and cross distances proportional to their growth rates. Obviously, the growth forms are different in frames (3(A) and (C)). The slowest faces develop at the expense of the fastest faces, which entirely disappear. The growth form thus depends on kinetic factors, that is, crystallization conditions. This is the reason why changing the crystallization conditions (medium, supersaturation, or temperature) produces different crystal habits for the same crystal phase.

Because the theories of crystal growth mechanisms are extensively discussed elsewhere [34–36] and in this book, we will limit ourselves here to a brief survey. Growth kinetics and mechanisms depend on external factors (medium or chemical composition, temperature, supersaturation, and hydrodynamics) and on internal factors (structure,

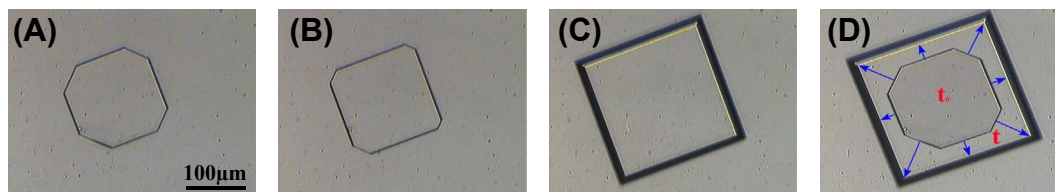


**FIGURE 21.3** Growth of a BPTI crystal in 350 mM KSCN at pH=4.9. (A)–(C) are frames of a time sequence, obtained at different temperatures, showing the evolution of the growth form as illustrated in (D), in which arrows indicate the face displacement with time. Reprinted with permission from Astier and Veesler [33]. Copyright 2008 American Chemical Society.

<sup>1</sup>Note that in the pharmaceutical literature, “different crystal forms” is often used instead of “different crystal phases” (inaccurate use of terms).

bonds, and defects). The growth medium influences the growth kinetics of the faces in different ways. First of all, the solvent is more or less adsorbed on the faces and selectively slows down their growth rates. Moreover, growth rate increases with solubility. The growth medium also influences solvation, desolvation, and complex formation [37]. Furthermore, variations in temperature produce extremely different growth rates. Lastly, hydrodynamics, the relative velocity of the solution compared to the crystal [38], is an important parameter. If the solution is quiescent, the face grows slowly at a rate determined by molecular diffusion and convection of the solute toward the crystal. The growth rate of the face increases with the flow velocity of solution to the crystal. However, there is still a diffusional limitation: this growth rate tends very quickly toward a plateau and thus reaches an upper limit determined by phenomena at the crystal surface. Note that at the laboratory scale, thermal and mass convections can be reduced using either gel as a medium of crystallization [39] or small volumes as in microfluidics experiments [40–44].

Crystallization is a purification process, and because impurities are often present in the crystallization medium, they tend to concentrate during crystallization. This increase in impurity concentration is more pronounced for evaporation-based methods. Impurities are all that is contained in the crystallization medium apart from the solute: that is, the solvent, chemical impurities coming from the solvent, byproducts, and additives. In practice, impurities adsorb on the crystal faces. Depending on the energy of the bonds between impurity and adsorption sites, adsorption is more or less reversible. Thus, while growth proceeds, there is competition between the kinetics of molecule incorporation and the kinetics of impurity adsorption and desorption. Accordingly, impurities hinder the crystallization processes so that nucleation and growth rates are sometimes drastically slowed down. When impurity adsorption selectively occurs on a crystal face, the growth rate of this face is selectively reduced and its relative development rapidly increases at the expense of the development of the other faces. Thus, this behavior induces crystal habit modification and influences the crystal characteristics [45]. When impurity adsorption takes place on all crystal faces and is irreversible (i.e., without exchanges with the surrounding solution), growth is completely inhibited. Then, the so-called growth cessation is observed. One way to overcome this difficulty is to drastically increase supersaturation, which sometimes leads to new surface nuclei, meaning that growth starts again. Another option is to start to dissolve crystals, by increasing the temperature for instance, and then recreate growth conditions, by lowering the temperature for instance. However, if the crystal surface is too energetically “poisoned” by impurities [36], 3D nucleation becomes easier than growth. Thus, the solution nucleates new crystals.

As a general rule, the habit and/or kinetic change results from impurity adsorption and not from impurity incorporation. However, impurity incorporation can take place, especially when the molecule of the impurity resembles the molecule of the crystal. This was first observed in the case of small molecules (e.g., glutamic acid incorporated into asparagine monohydrate crystals [46]) and later on in the case of biological

macromolecules (e.g., contamination of turkey-egg-white lysozyme crystallizing solutions by hen-egg-white lysozyme [47]). Consequently, pure materials are difficult to grow when impurity and crystal molecules are homologs.

Lastly, the presence of impurities can lead to the nucleation of a new phase (here, the term new phase means a phase not previously observed), as for ritonavir [48] a related compound with structural similarities was able to act as a template for nucleation of a new phase.

### 21.2.5 Dissolution

Dissolution study of API is very important in the pharmaceutical industry, because dissolution kinetics govern the bioavailability of a drug and are involved in phase transformation (part 6). Dissolution tests are generally performed on pharmaceutical dosage forms and are mainly used for quality control [49–51]. In practice, dissolution occurs when the crystal is located in an undersaturated solution. There is a loss of species (molecules, ions, or atoms, depending on the nature of the crystal) from the crystal lattice, leading to a decrease in the particle size and to an increase in solute concentration. As in the case of crystal growth, dissolution involves two main steps: (1) surface reaction and detachment of the surface species, followed by (2) mass transfer of this species toward the bulk solution across the diffusion layer that surrounds the crystals [52]. Like the crystal growth rate, the dissolution rate is controlled by the slowest step. The dissolution kinetic of a readily soluble compound is limited by mass transfer (step 2), whereas the dissolution of a sparingly soluble compound is controlled by the kinetics of the events occurring at the crystal surface (step 1). Moreover, for a mineral and an API, several authors have revealed different behaviors depending on the degree of undersaturation [53,54]. At high undersaturation, the dissolution rate was found to vary linearly with the initial undersaturation and quadratically at lower undersaturation. The authors concluded that the mechanism changed from a mass-transfer-controlled process at high undersaturation to a process controlled by a surface mechanism at lower undersaturation. Moreover, in the case of polycrystalline or aggregates, disaggregation can occur during the initial stage of dissolution, leading to an acceleration of the overall dissolution kinetics at the beginning of the dissolution process [55].

### 21.2.6 Phases

The variations in the physical properties of a solid, such as crystal habit, solubility, hardness, color, melting point, or chemical reactivity, play an essential part in the formulation of the solid and in the application of the formulated product [56]. For instance, the bioavailability of an API depends directly on its solubility, which itself depends on the phase crystallized. A drug can thus become completely ineffective if the amount of substance initially intended to enter the blood circulation system is reduced through low solubility and/or low dissolution kinetics. Moreover, if its solubility is higher than intended, the risks of side effects are increased [57,58]. Thus, the discovery or

emergence of a new phase may delay its marketing; for instance, in the case of ritonavir, “the sudden appearance and dominance of this dramatically less soluble crystal form made this formulation unmanufacturable” [48]. However, it may also extend it, as with Zantac [56]. Note that the new phase can also be a salt or a co-crystal.

### 21.2.6.1 Solubility and Ostwald Rules

Let us consider a dimorphic system, that is, one constituted by two polymorphs, I and II. At a specific temperature, polymorph II is more stable than polymorph I. The more stable polymorph has the lower free energy  $G$ ; in other words, the more stable polymorph of the two always has lower solubility, whatever the solvent in contact with the solid. This rule is not (always) true for solvates or desmotropes [59], for instance. In practice, two situations are possible for a dimorphic system (Figure 21.4). First, the system is considered as enantiotropic if the solubility curves cross each other at a lower temperature (noted  $T_r$ , or transition temperature) than the melting points of polymorphs I and II. As presented in Figure 21.4(A), polymorph II is less soluble under the transition temperature and therefore stable in this temperature range. Conversely, above the transition temperature, polymorph I is the stable form.

Second, the system is considered as monotropic if the solubility curves do not cross each other in solution. In Figure 21.4(B), polymorph II is the stable one. The temperature range of the solubility curves is often limited in solution (e.g., by the boiling temperature of the solvent).

When several phases are possible in the same solution, each of them has its own solubility so that the solution can be supersaturated with respect to several phases at the same time. Another consequence of nucleation is the occurrence, for kinetic reasons, of unstable phases, despite the fact that the supersaturation of the stable phase is higher than for the metastable phase. These unstable phases may remain in a metastable state for a few seconds or several centuries. The transformation of a metastable phase into a stable phase, corresponding to the minimal free energy of the system, is called the phase transition. Ostwald [60] established in 1897 the (kinetic) rule that a chemical system does

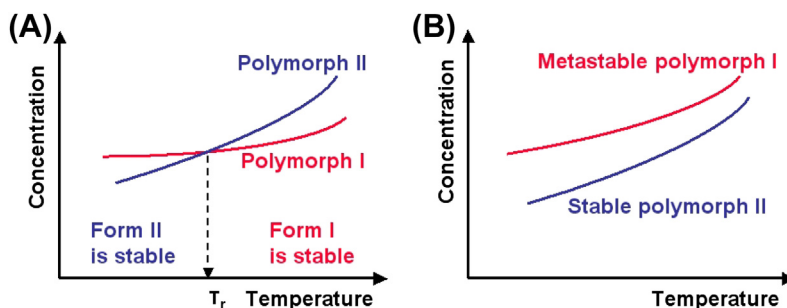


FIGURE 21.4 Solubility curves for two polymorphs, I and II, related either (A) enantiotropically or (B) monotropically. Reprinted with permission from Mangin et al. [8]. Copyright 2009 American Chemical Society.

not directly tend toward equilibrium but rather toward the closest metastable state. In other words, nature prefers to follow a sequence of nucleations, growths, and phase transitions rather than directly nucleating the most stable phase.

### 21.2.6.2 Phase Transition

Several phases or polymorphs can temporarily coexist, but all except one are subject to transformation. Metastable phases undergo a phase transition as soon as a nucleus of a more stable phase (i.e., a less soluble phase) appears. This transformation in the presence of a solvent is called a solution-mediated phase transformation (SMPT). The basic phenomena involved in SMPT have already been described [61]. For a given system, this transformation requires at least three mechanisms:

1. primary nucleation, often heterogeneous, of the more stable solid phase (this step can be replaced by a seeding of the stable solid phase) and growth of both phases until solubility of the metastable phase is reached;
2. dissolution of the metastable solid phase; and
3. growth of the more stable solid by mass transfer of solute in the solution.

These three mechanisms are either consecutive or concomitant. The primary nucleation of the stable phase, or its seeding, is thus the trigger for a phase transition in a stirred crystallizer. In most cases, heterogeneous primary nucleation occurs on the surface of a substrate, such as an impurity [48] or crystals of the metastable phase (Figure 21.5(A)) [62–68]. It can also occur by heteroepitaxy, as shown in Figure 21.5(B) [69].

Generally speaking, three types of phase diagram occur naturally, depending on the range of the molecular substance interaction [70–73]. (1) For simple hard spheres, only fluid and crystal phases are present; and (2) introducing attractive interactions results in three-phase equilibria: gas–liquid–crystal or liquid–liquid–crystal. For instance, this type of phase diagram is observed and described for the emulsification and crystallization of lauric acid in an ethanol–water mixture [74]. The nucleation of a new liquid phase is called liquid–liquid phase separation (LLPS) or demixion, also termed “oiling-out” in the industrial literature. And (3), with shorter range attractions, the gas–liquid or liquid–liquid equilibrium becomes metastable. This type of phase diagram is often observed in protein

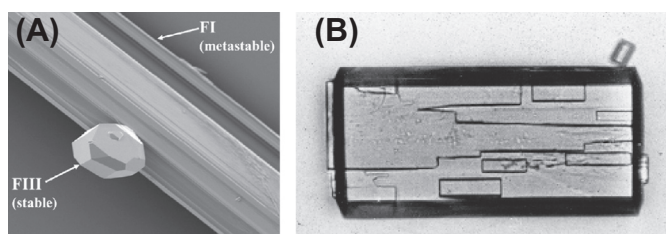


**FIGURE 21.5** (A) Carbamazepine stable phase (FIII) nucleated, in ethanol, on carbamazepine metastable phase (FI). Reprinted with permission from O’Mahony et al. [68]. Copyright 2013 American Chemical Society. (B) Uric acid monohydrate phase epitaxially grown on the anhydrous phase, after Boistelle and Rinaudo [69].

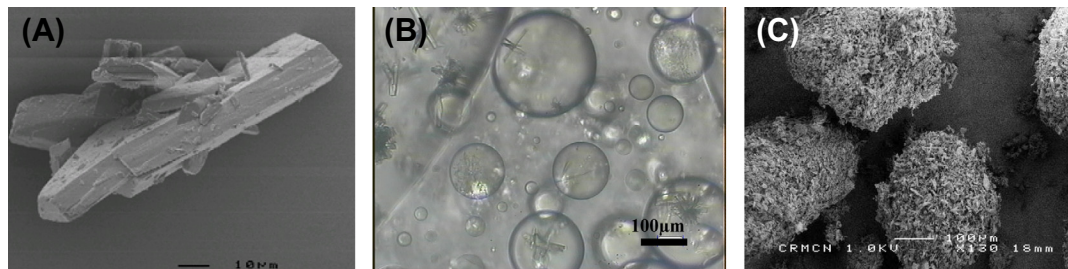


**FIGURE 21.6** (A) Crystals obtained by a classical secondary nucleation and growth experiment; (B) observation by optical microscopy of the nucleation of crystals in the droplets of the API-rich phase at 20 °C; and (C) scanning electron microscopy image of quasispherical particles obtained after crystallization in the droplets of (B). Reprinted with permission from Veesler *et al.* [93]. Copyright 2006 American Chemical Society.

systems [75–77]; however, a few cases are documented for small molecules [78–85]. When there is competition between liquid and solid phase nucleation, the nucleation of a dense liquid metastable phase is more likely than crystal nucleation (stable phase) because the excess free energy of the solution–liquid interface is considerably reduced relative to the solution–crystal interface, resulting in a lower thermodynamic barrier to LLPS than to crystallization [20,86], in agreement with the Ostwald rule of stages. This phenomenon is known to disturb the crystallization process and thus affects product quality [78,79,81–83,87]. In the example presented in Figure 21.6, the authors compared crystals of an API obtained from different experimental starting positions in the phase diagram, inside (Figure 21.6(C)) or outside the LLPS region (Figure 21.6(A)). They showed that the LLPS strongly affected crystallization. The presence of API-concentrated droplets completely alters the medium, changing from classical crystallization from solution to emulsion crystallization such as spherical crystallization [88,89]. In these experimental conditions, quasispherical agglomerates (Figure 21.6(C)) with good handling and compression properties [90] are produced.

NB: In spherical crystallization [88,89] a quasiemulsion is normally formed by adding a binary mixture of a good solvent and a solute to a poor solvent. With LLPS, the quasiemulsion is obtained as temperature-induced phase separation; it can also be obtained as composition-induced phase separation [91,92].

### 21.2.7 Ripening

After nucleation, in a batch crystallization experiment for instance, crystals of different sizes are present in suspension depending on the time at which they formed and the velocity at which they grow. We observe a decrease in supersaturation that, in theory, should reach solubility. At the end of crystallization, a decrease in the number of crystals and an increase in the crystal size can also be observed. Large crystals grow at the expense of small ones due to the fact that smaller crystals have higher solubility: this phenomenon is called Ostwald ripening [94]. From Eqn (21.10), it appears that each



**FIGURE 21.7** Kinetic ripening of  $\alpha$ -amylase crystals shown in (A), by (B) partial dissolution and (C) regrowth. Reprinted with permission from Astier and Veessler [33]. Copyright 2008 American Chemical Society.

crystal of radius  $r$  corresponds to only one concentration  $C$  for which the equation stands. Thus, the smaller the crystal size  $r$ , the greater the  $C$ .

$$r = \frac{2\Omega\gamma}{kT \ln \frac{C}{C_s}} \quad (21.10)$$

Ostwald ripening is an isothermal process that is very slow for crystals larger than  $1 \mu\text{m}$  and very fast for submicrometer crystals. In protein crystallization, this explains why sometimes crystals grow from precipitates [95]. In fact, these precipitates are composed of submicrometer crystals, the largest of which grow and the smallest of which dissolve.

In an API production process, the crystallization step has to be fast and efficient; therefore, crystallization is stopped before equilibrium is reached. Moreover, kinetics of dissolution and growth are usually (very) low in the vicinity of solubility; thus, Ostwald ripening is not very often observed in pharmaceutical crystallization. Ripening can be activated by temperature: this is the kinetic ripening method [96,97]. Temperature fluctuations in the neighborhood of the equilibrium temperature induce dissolution of the smallest crystals and growth of the largest ones. Figure 21.7 presents the complete kinetic ripening process for  $\alpha$ -amylase crystals in experiments with a wide CSD (Figure 21.7(A)). In the first stage, the temperature is increased by a few degrees. Both small and large crystals dissolve (Figure 21.7(B)), but as small crystals have less matter to be transferred, they dissolve faster and the process is stopped by a temperature decrease (second stage) before complete dissolution of the larger crystals. Finally, large crystals grow and are faceted (Figure 21.7(C)).

### 21.3 Crystallization Methods

Crystallization requires the creation of conditions where the equilibrium solubility value is lower than that of the concentration of solute in the solution. In practice, this means that the system is moved in the phase diagram from an undersaturated region to a supersaturated one. Supersaturation can be generated either by reducing solubility or by concentrating the medium. These two methods of generating supersaturation ways can also be used in concert. Five practical methods are discussed hereafter from the

commonest to the newest: (1) temperature change, (2) solvent evaporation, (3) modifying the composition of the solution by changing the solvent composition, (4) chemical reaction, and (5) adding a co-crystallizing agent.

### 21.3.1 Temperature

The most commonly used method is changing the temperature of the medium in order to reduce solubility. As discussed in the previous section, the solubility of most materials decreases with decreasing temperature, so the medium is cooled. The concentration remains constant (pathway 1 in Figure 21.8). Crystallization starts when the MZL is reached.

Conversely, solubility may decrease with increasing temperature. In this case, the temperature change necessitates heating the medium (Figure 21.9). Temperature change is useful because it allows supersaturation to be generated at constant composition, and the effect is reversible [33]. Usually, surface cooling occurs through the wall of a jacketed reactor. Another industrial procedure is to evaporate the solvent, condense it, and recycle it. The coolest part of the medium is the boiling surface rather than the reactor walls, thus avoiding fouling. Moreover, the heat transfer capacity is 10 to 20 times higher, allowing a quicker cooling rate.

### 21.3.2 Solvent Evaporation

After temperature change, partial evaporation of the solvent in isothermal conditions is the most commonly used method of generating supersaturation, because the solute

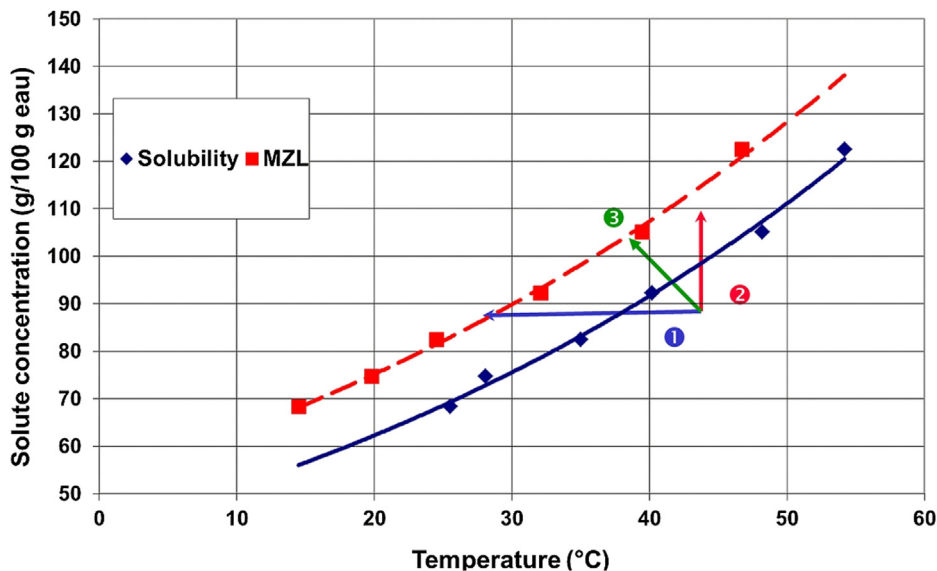
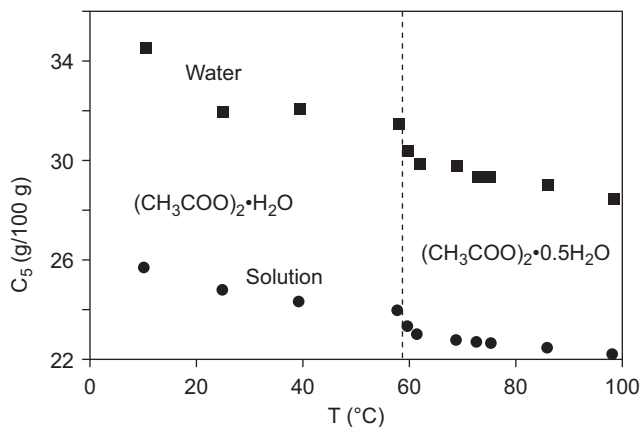
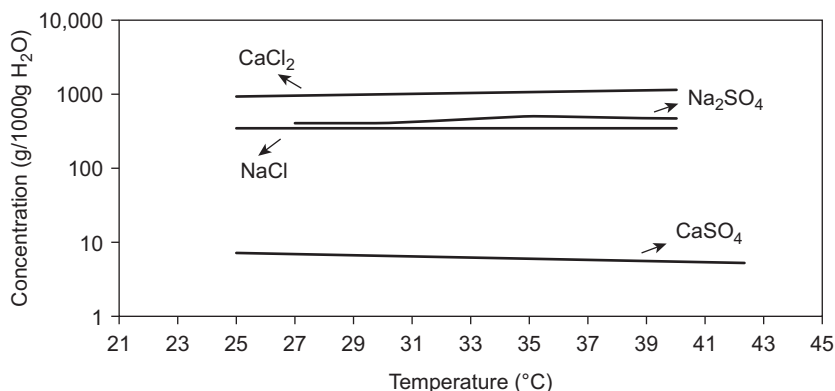


FIGURE 21.8 Solubility and metastable zone limit (MZL) of lysine monohydrochloride. (Pathway 1: cooling crystallization; pathway 2: evaporative cooling; pathway 3: adiabatic evaporative cooling.) Data from [125].



**FIGURE 21.9** Solubilities of calcium acetates, monohydrates, and hemihydrates in water versus temperature. Reprinted with permission from Saury et al. [98]. Copyright 1993 American Chemical Society.

concentration increases as the solvent is removed. The route follows a vertical line in the phase diagram (pathway 2 in Figure 21.8). As previously, the primary nucleation is triggered at the MZL, followed by the growth of nuclei. This procedure is particularly recommended when the temperature dependence of solubility is too low and when the crystallization is operated continuously. For instance, this is the case for some inorganic compounds in water (Figure 21.10). Performing such isothermal evaporation necessitates heating the crystallizer, and the solvent evaporation temperature is controlled via the pressure level in the reactor. An advantage is that it is possible to perform crystallization at high temperature, often leading to a high growth rate and sometimes to particles of millimeter size. Nevertheless, all species in the solution also concentrate, and thus impurities may hinder nucleation and crystal growth and modify API solubility in the medium. A possible deterioration of the particle habit grown in the final moments is also possible. This last point could be a major drawback.



**FIGURE 21.10** Solubilities of NaCl, Na<sub>2</sub>SO<sub>4</sub>, CaSO<sub>4</sub>, and CaCl<sub>2</sub> in water. After Ref. [99].

When the crystallization yield is not high enough during a batch operation, it is possible to combine the cooling of the medium with the evaporation of the solvent (pathway 3 in [Figure 21.8](#)). This is easily possible with an adiabatic evaporation. A progressive depressurization profile is applied in the reactor leading to a cooling profile. There is no need to heat the reactor.

### 21.3.3 Chemical Composition

The modification of the solvent composition to crystallize low-molecular-weight compounds is quite common in pharmaceutical processing, as it can often rapidly create higher supersaturation compared to cooling or evaporation. The more general term is antisolvent crystallization; the principle is dissolving the API in a good solvent (in which solubility is high) and adding an antisolvent (in which the API is sparingly soluble). The inverse procedure common in producing pharmaceuticals and fine organic chemicals, when the solution containing the solute is added to an antisolvent, is known as drowning out. If an organic solvent is added to an aqueous solution containing a salt to be crystallized, the process is termed salting out. Whatever the denominations, the fundamentals are the same [100]. Note that it is necessary to choose an antisolvent fully miscible with the solvent already present in the medium. This condition is not sufficient because an LLPS prior to the crystallization may occur (see [Section 21.2.6](#) and [Figure 21.6\(B\)](#)). This complicates the process, because a ternary medium composed of two populations of droplets and particles is formed in a continuous liquid phase. Crystals developed in this manner will likely have a poorly defined structure and be agglomerated ([Figure 21.6\(B\)](#) and [\(C\)](#)). Four types of problems may result from such a scenario: (1) a large drop of coalesced oil (dense phase) that will not disperse and can harden into a gel, and gum or stick on walls, stirrer blades, and shafts; (2) severe mixing problems due to the presence of these two dispersed phases; (3) occlusion of impurities and solvent in the solid phase, in particular if crystals agglomerate due to the preferential wettability of the oil on the particles; and (4) poorly defined structure not fully crystalline. However, this situation can, in some cases, be avoided by increasing the temperature before adding the antisolvent in order to avoid the demixion or oiling-out zone in the phase diagram before primary nucleation occurs.

The normal mode of addition is to add the antisolvent to the medium. Even though the medium is partially diluted, the supersaturation region is quickly attained because solubility declines quickly ([Figure 21.11](#)). Crystallization starts as soon as the nucleation is kinetically active, when the concentration corresponding to the MZL is reached, the addition flowrate being the operating parameter. If the demixion or oiling-out is avoided, one major advantage is that the process is often carried out at the ambient temperature, which is of paramount importance for heat-sensitive compounds. Moreover, the level of supersaturation when primary nucleation occurs is reasonably low but higher than in cooling or evaporative crystallization. If the API exhibits several polymorphs, a metastable polymorph or a mix of polymorphs, including the stable one, could be obtained

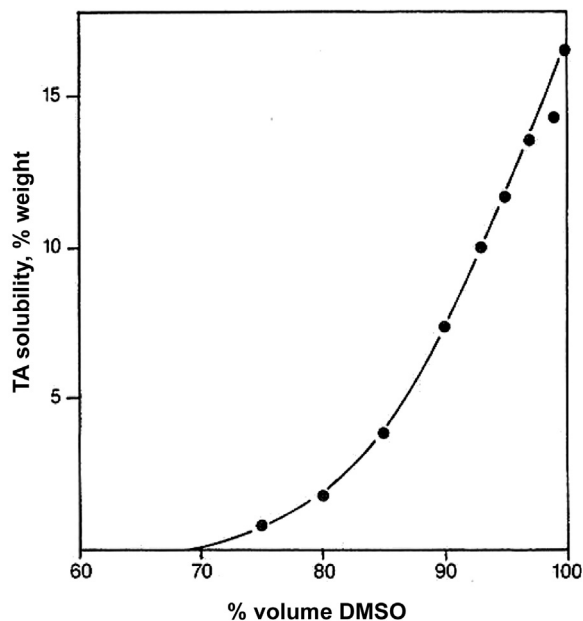


FIGURE 21.11 Solubility of terephthalic acid (TA) in dimethyl sulfoxide (DMSO)-water mixture at 25 °C. After Ref. [99].

(abecarnil [101]). A reverse addition mode consists of adding the product solution to the antisolvent. This favors very high supersaturation levels resulting in high nucleation rates, sometimes with agglomeration. This inverted mode can be used to produce small particles. Nevertheless, product purity can be compromised, because analog impurities can also crystallize in such a low-solvating and highly supersaturated medium. Moreover, the tendency for organic compounds to form a demixion with this reverse mode is higher, because high supersaturation is generated locally. However, this can be a useful way to screen the polymorphism of an API. Beckmann [101] on abecarnil API evaluates the level of supersaturation using the two addition modes (normal and reverse) and shows that the polymorph obtained differs depending on the addition mode. Using a supercritical fluid (like compressed carbon dioxide) in reverse addition mode (known in the literature as the gas antisolvent process) is also possible, leading to higher supersaturation and other polymorphs [101].

A mixture of solvents is sometimes used, producing a co-solubilizing effect that enables the initial solute concentration in the medium to be increased [102].

Adding a solvent that induces a solubility decrease can lead to different cases. In the example of Figure 21.12, the experiment starts from point ① at a concentration of 26 g/100 of solvent (paracetamol in 70–30 weight% isopropanol–water mixtures) at 40 °C; with the addition of water, the solute concentration decreases to point ②. In practice, two cases are possible. First, as in the case of Figure 21.12, point ② is undersaturated at 40 °C; therefore, to crystallize, the antisolvent addition has to be combined with cooling to

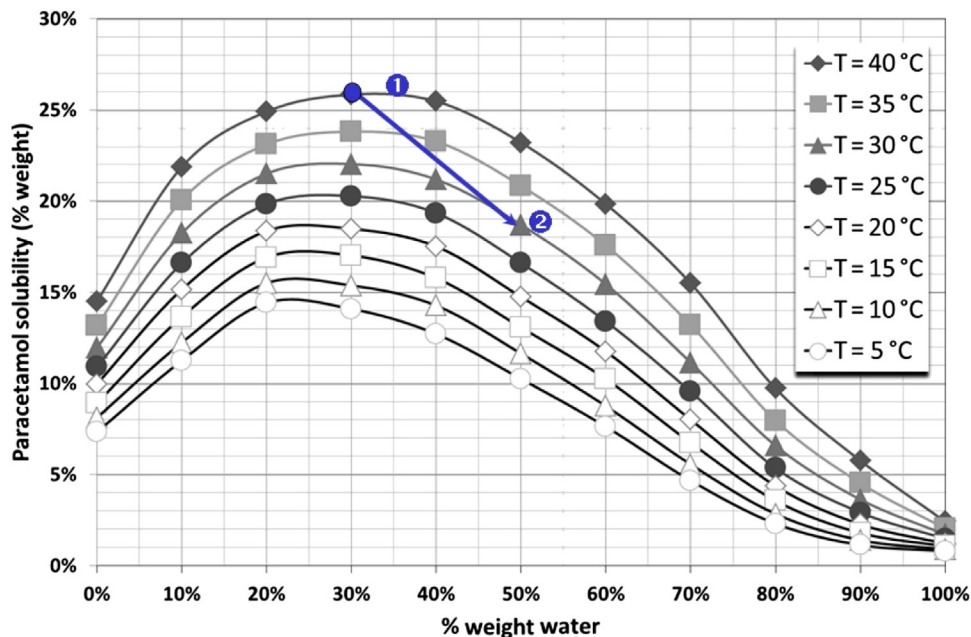


FIGURE 21.12 Solubility of paracetamol in isopropanol–water mixture. Reprinted with permission from Hojjati and Rohani [103]. Copyright 2006 American Chemical Society.

$T < 30\text{ }^{\circ}\text{C}$ . Second, after the antisolvent addition, the solution is supersaturated and crystallization starts.

### 21.3.4 Chemical Reaction

When API supersaturation is generated by a chemical reaction, the operation is termed reactive crystallization. This operation is also known as precipitation. The reaction is between two complex organic compounds mixed under stirring. The product of the reaction can exhibit a solubility several orders of magnitude lower than that of the reactants, leading to very high supersaturation, higher than that generated by antisolvent crystallization. The chemical reaction is generally fast, involving rapid mixing of the reactants. Macro- and micromixing are vital to this process [100]. This method is chosen in the fine chemicals industry to create fine particles for a wide variety of applications, including photographic chemicals, dyes, and printing inks. API molecules often have basic or acidic functions, their solubilities significantly changing as a function of pH in protic mediums. Hence, supersaturation can be achieved by varying pH. In aqueous medium, it is the neutral molecular form (also called free acid or free base) that is less soluble and is crystallized by neutralizing the salt form. Conversely, in organic medium, the neutral molecular form is much more soluble, and crystallization occurs provided salt is formed. An API can first be isolated in a solid state in a

chemically neutral form in order to purify it, and subsequently dissolved and precipitated in an organic solvent as a salt for biopharmaceutical applications. Such a strategy requires a multidisciplinary approach involving chemists, chemical engineers, and pharmacists [5]. The final CSD is determined by the balance between primary nucleation, growth, and agglomeration rates.

### 21.3.5 Co-crystallization

The co-crystallization method may appear to be a recent development, but, as Childs and Zaworotko [104] pointed out, it is actually an older method revived. Co-crystallization makes it possible to generate a multicomponent crystal containing an API when it is difficult to isolate a given API that cannot crystallize easily in its pure solid phase, in solvate, or in its salt form. Moreover, co-crystals sometimes offer better pharmaceutical properties [105] than pure API crystals. Finally, patenting co-crystal phases of API is also a new way for pharmaceutical companies to acquire extra years of patent protection for the drug substance beyond the expiry of the API molecule patent [106]. Co-crystallization allows two or more molecular species to be bounded within one crystallographic lattice without making or breaking covalent bonds, leading to a multicomponent crystal. The species interact by hydrogen bonding or other noncovalent interactions rather than by ion pairing [107]. The co-crystals differ from a salt in that the molecular species remain neutral. They also differ from solvate crystals in that both components exhibit pure crystalline phases at room temperature.

Thus, the method consists in adding a molecular species (called a co-crystallizing agent) to the crystallization medium in order to generate a molecular association between the API (the solute) and its co-crystallizing agent. The phase diagram changes drastically, and several regions appear in which only the co-crystal is the stable phase. Figure 21.13 is a broad view in the orthogonal axis of the phase diagram of carbamazepine (CBZ) and nicotinamide (NCT, the co-crystallizing agent) in isothermal condition in ethanol. It shows the solubility curves of the CBZ–NCT co-crystal, and of the monocomponent crystals of CBZ and NCT at 25 °C [108,109]. The easiest procedure is to add crystals of this co-crystallizing agent to the solution containing the solute. The concentration of the molecular association rises along the bisecting line (arrow in Figure 21.13) as these crystals dissolve until a supersaturated region is reached for the co-crystals, which nucleate and grow. Note that the choice of solvent is critical [17]. Although there is no chemical reaction, this method is conceptually close to precipitation, because it is the addition of a foreign species, which triggers crystallization. Generally, the solubility product of co-crystals is much higher than that of ionic compounds or salts, with the result that they are moderately soluble and crystallization is more progressive, without the problem of mixing reactants often encountered in precipitation. Another advantage of this method is that it is possible to increase the yield either by adjusting the amount of co-crystallizing agent introduced in the medium [14,109] or by finishing the operation with a classic cooling crystallization (if the

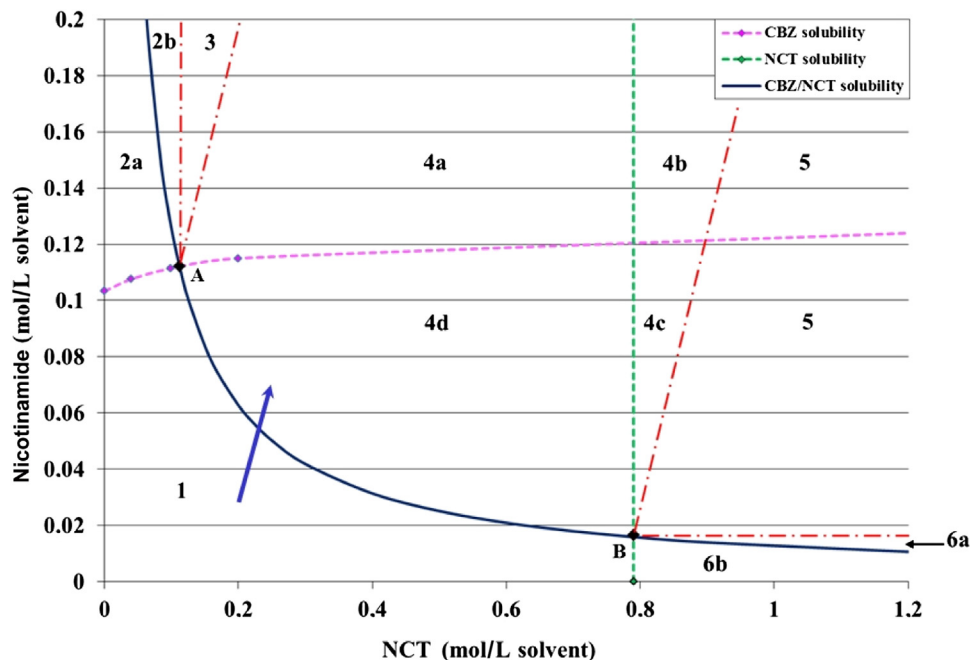


**FIGURE 21.13** Phase diagram of carbamazepine (CBZ)–nicotinamide (NCT) system in ethanol at 25 °C. Dashed lines are CBZ (horizontal) and NCT (vertical) solubility curves; solid line is CBZ–NCT co-crystal solubility curve. Reprinted with permission from Gagniere et al. [14,109].

solubility product declines with temperature). The drawback to be underlined is that the API or the co-crystallizing agent may also simultaneously crystallize in their pure form as metastable solids. This is due to the fact that the kinetic pathway crosses a region where a undesired solid phase may also nucleate [108]. Moreover, one solid phase can favor the crystallization of another phase by heterogeneous nucleation because these phases can exhibit an epitaxial relationship [108]. We recommend focusing the operation in the region of the phase diagram in which only the co-crystal phase appears, with the other solid phases remaining soluble. This zone is called the safe operating region. For co-crystallization in isothermal mode, this corresponds to region 4d in the phase diagram (Figure 21.13). When the operation is carried out in polythermal mode, this region is narrower [109,110]. If a foreign solid phase pollutes the solid phase, a reprocessing treatment can be set up by triggering an SMPT by the addition of one of the co-crystal components [109,111].

If the API is a protein, things are more complex, because almost all the parameters listed above can interact on the phase diagram of this particular class of (bio) chemical compound. Nevertheless, the crystallization methods are no different from those used on small molecules [112], and these are treated in Chapter 19, “Protein crystal growth.”

## 21.4 Development of a Batch Crystallization Process at the Laboratory Scale

### 21.4.1 Prerequisite

Generating intermediate or API crystals has three main objectives: (1) to obtain sufficient chemical product quality and purity, for instance removing traces of impurities resulting from the chemical synthesis; (2) to generate the solid phase required and to ensure uniformity from batch to batch (according to established specifications); and (3) to obtain a physical product quality such that downstream operations can be performed more easily: adequate filterability, low fine-particle concentrations, limited caking in storage, and good powder flow. Obtaining good physical properties is a real challenge that is still relevant today, whatever the chemical composition of the crystal (mono-component for pure API; multicomponent for hydrate, solvate, salt, and co-crystal).

Crystallization operations can be carried out regularly in a process having several synthetic steps in order to limit the number of different impurities and their total quantity. In practice, this is always done after the last synthetic step in order to obtain a crude product. A re-crystallization operation is often performed in order to ensure the desired chemical and physical properties. The crystallization operations are defined as follows:

- Dissolution of the crude product in a given solvent by raising temperature if necessary.
- A possible decolorizing on activated charcoal followed by filtration to remove foreign particles is then performed.
- Start of the operation by playing with one of the parameters described in [Section 21.3](#). If the primary nucleation can be avoided, a seeding procedure is recommended.
- Crystal growth starts as soon as nuclei or external seeds are present.
- Agglomeration of crystals may sometimes develop.
- Because impurities are concentrated in the liquid medium when cooling is performed, all the crystallization kinetics (secondary nucleation, growth, and agglomeration) decrease with time. The solid production rate is high in the first hours of crystallization, but the manufacturer must wait a few hours, sometimes with a final isothermal plateau, in order to let the medium reach equilibrium, thus obtaining the desired yield.

### 21.4.2 Screening of Crystallization Conditions and Phases

This first step needs to be done as early as possible, in order to guide the practitioner, chemist, or process engineer in selecting the phase to be developed and the crystallization methods. The first step is an efficient screening of all the possible solid phases (including polymorphs, solvates and hydrates, salts, and co-crystals). This step can be

carried out on a small amount of API, using experimental techniques with or without solvent, sometimes in a way far removed from the final operating conditions. These screening strategies are presented in recent reviews and textbooks [5,6,8].

The second step requires the construction of the thermodynamic phase diagram. The solid phase that will be developed is chosen based on stability, end use, and bioavailability. In terms of process development, it is preferable to select a stable phase rather than a metastable phase. The relative stability of the solid phases in solution that may be encountered in the process sometimes needs to be determined, because the appearance of another phase will alter the crystalline purity of the final solid.

### 21.4.3 Determination of Operating Conditions

To control a batch operation, the essential parameters to consider are solvent selection, seeding strategy, cooling rate, evaporation rate, or addition flowrate, depending on the crystallization method or process. Mixing methods also need to be taken into account, particularly in the case of precipitation.

#### 21.4.3.1 Solvent Selection

The selection of the solvent for a given crystallization is not always easy. In many cases, the solvent may already have been selected from the upstream operations, because a solvent used in a synthetic step or a liquid purification step (i.e., liquid extraction) may be used. From a process point of view, there are three main points to consider when a solvent is chosen:

- The solute to be crystallized should be readily soluble in the solvent. [Section 21.2.1](#) in this chapter explains how to choose a solvent able to dissolve the API. Mullin [12] defined as solvent power the mass of solute that can be dissolved by a mass of solvent at one specified temperature. This point affects crystallizer volume and crystallization yield.
- The temperature (or other process parameter) dependence of the solubility is the second point to consider, because it has a tremendous impact on crystal yield.
- There are many factors to take into account in choosing the solvent, such as its toxicity and hazard (the list of allowed solvents is becoming shorter and shorter), its chemical stability with time for all foreseeable operating conditions and absence of reaction with any of the crystallizer materials or with the solute, its viscosity (moderate viscosity may reduce solute diffusion in solution and hence crystal growth rate), its impact on crystal habit (if possible, choose a solvent that promotes an equant habit), its ease of recovery in the process by mechanical and thermal treatments, and the level of residual solvent in the dry product as well as its cost.

#### 21.4.3.2 Seeding Strategy

Seeding techniques are applied for batch crystallization in order to control the primary generation of solids during the initial stage of the run. During this period, there are very

few particles in suspension present on which the solute can nucleate. This is particularly frequent with APIs, which tend to be difficult to nucleate, and/or when homolog impurities from the synthetic steps are present in solution in sufficient quantities to prevent the formation of nuclei. Thus, high supersaturation is often reached, followed by an excessive uncontrolled primary nucleation producing very fine particles. This can also lead to incrustation and/or equipment damage. There are also some systems that are characterized by a random primary nucleation. For all these reasons, it really makes sense to control the nucleation process in order to avoid significant batch-to-batch variations [113]. Another reason is to control the solid phase by seeding with the desired phase [8,114].

Five points are critical to successful seeding:

- Seed quality: dry seed is very often used in industry, for practical reasons. However, seed particles may float on the liquid if the wettability of the solid is poor and if some air bubbles remain around the particles. Conversely, wet seed is in equilibrium with the solvent and is immediately reactive upon introduction in the solution. Wet seed can be produced at laboratory scale by mixing dry particles from a previous batch in a solvent already saturated or slightly undersaturated in order to dissolve fine particles stuck on the surface and/or to desorb impurities so as to prepare or activate the seed surface for growth and secondary nucleation [27]. In industry, seeds can either be prepared specifically in a batch or a small amount of slurry can be recycled from the previous batch.
- Seed surface area and seed quantity: if the seed area is too small, secondary nucleation and growth will be insufficient to consume the supersaturation and the MZL will be reached, resulting in spontaneous nucleation. The final CSD obtained is broad, leading to poor filterability. In practice, it is the seed quantity rather than the seed surface area that is determined. The quantity varies from 0.5% weight up to 5% weight of the total final product.
- Seed CSD and mean size: we recommend choosing calibrated particles in order to control the seed area. Nevertheless, for practical reasons, bulk particles with a broad CSD are often used, and it is mainly the smallest particles that are active in the seeding process, representing the largest part of the surface area. An alternative is to retrieve a small part of the slurry coming from a previous batch, wet mill it to generate more active seeds, and then use it as wet seeds.
- Seeding point: seeding at low supersaturation necessitates introducing the seeds close to the solubility curve. The risk of triggering a surface secondary nucleation during the seeding is almost negligible, but the quantity of seeds must be substantial in order to obtain the growth of the particles. Sometimes, the seeds start growing only if higher supersaturation is generated [115]. Seeding at higher supersaturation, quite close to the MZL, induces a burst of secondary nucleation, quite often via a surface mechanism. The number of final particles is then much higher than the number of seed particles, and the final particles are smaller [27]. The

standard recommendation is to seed at 40% of the maximum subcooling metastable zone width [100].

- Cooling profile (after seeding): the most frequent recommendation is to maintain an isothermal plateau of 1 h at least, in order to start the growth of the seed. Consequently, supersaturation decreases and can reach the equilibrium. Slow cooling is then applied and is progressively increased in order to limit the operation time.

All these points were discussed by Mersmann and Rennie [28] for inorganic compounds and Kohl et al. [116,117] for  $\beta$ -cyclodextrin in water. Note that soluble impurities in solution may interact on seeding, by modifying the solubility level and by a possible poisoning of the seed surface, limiting seed growth. This is why it is necessary to test the seeding procedure on industrial solutions if the study was primarily carried out in pure medium.

#### 21.4.3.3 Cooling Strategy

Cooling is the main operating parameter commonly used since it is easily controlled in a batch process. Let us consider a classic situation where a stirred reactor is cooled via a coolant circulating in a jacket. The difference between the external (coolant) and internal (slurry) temperatures is also limited in order to avoid fouling on the vessel walls. The initial hot solution is undersaturated. The cooling profile is critical in several ways because it strongly influences the supersaturation pathway in the phase diagram.

- The position of the MZL in the phase diagram depends on the cooling rate and the crystallizer volume and geometry, due to its kinetic nature. Fast cooling shifts the MZL to a higher supersaturation zone [99]. Consequently, the primary nucleation rate may be dramatically more intense, leading to a smaller final CSD. This is why we recommend starting an unseeded crystallization with a moderate cooling rate (from a few to 10 °C/h), and the value of the cooling rate needs to be determined according to the observed nucleation temperature.
- After primary nucleation or seeding, there are two possibilities: (1) a slow cooling rate allows the crystals to consume the solute and then to consume the supersaturation. The desupersaturation rate is higher than the cooling rate and the solute concentration pathway tends to approach the solubility curve (pathway ① in Figure 21.14). Surface secondary nucleation vanishes quickly under a supersaturation threshold, but contact secondary nucleation is still present and can produce significant quantities of crystal fragments over time. Note that impurities in solution can hinder the growth rate quite early in the operation, when a low supersaturation level is reached. Thus, concentration no longer decreases and supersaturation increases again due to the cooling rate, with the risk of an unwanted nucleation [118]. (2) With a fast cooling rate, supersaturation continues to increase because solute consumption by growth is not great enough to balance the cooling rate. The solute concentration pathway tends to the MZL until a second

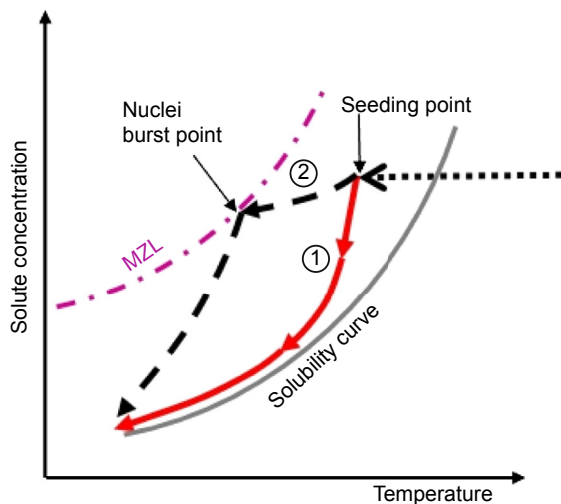


**FIGURE 21.14** Solute concentration kinetic pathway in a concentration–temperature diagram after seeding: ① slow cooling rate (solid line); and ② fast cooling rate (dashed line). MZL, metastable zone limit.

burst of nuclei occurs spontaneously (pathway ② in Figure 21.14). The return to equilibrium may be quick, but the CSD is bimodal (i.e., the population consists of large particles from the first primary nucleation or seeding and of a large quantity of finer particles). This is why the recommendation after seeding is always to start with a slow cooling rate (see the previous section about seeding strategy) and to use on-line sensors to monitor and control solution concentration throughout the crystallization [113].

Whatever the situation (seeded or unseeded batch), it is always recommended to start with a slow cooling rate as soon as particles are present in suspension and then progressively increase it as the total crystalline surface area increases. Wey and Karpinsky [98] provide a good discussion of the current state of the art in this area for industrial practitioners.

#### 21.4.3.4 Crystallizer Hydrodynamics (Mixing)

Mixing is a general term that can be broken down into two processes depending on the scale of observation. Macromixing refers to the blending of a suspension in the crystallizer with an antisolvent or a reactant when a semibatch operation is performed, and to the input flowrate.

Macromixing occurs by convection generated by the stirring system and leads to spatial uniformity of the average concentration of the solute (hence the average supersaturation) in solution, and of the solid in the slurry. Macromixing is governed by stirring intensity and affects all the mechanisms and kinetics of crystallization.

Micromixing is the mixing that occurs at molecular and near molecular scales. The local value of solute concentration (hence local supersaturation) is determined by

micromixing. Primary nucleation is the fastest of the crystallization mechanisms and the main competitor with micromixing. Changing stirring speed, stirrer, or feedstream locations will modify crystallization mechanisms and kinetics [119]. It is obvious that micromixing should only be considered if an intense primary nucleation rate occurs for a significant time. This occurs with precipitation carried out in a semibatch mode.

How mixing parameters affect crystallization carried out in a mechanically stirred vessel is treated thoroughly in detail in textbooks [119–122]. Here, we focus on five recommendations:

- A turbulent flow regime should be ensured in the suspension (except when viscosity is too high) because it eases the scale-up of the operation from the laboratory to pilot or to plant.
- Sufficient bulk turnover needs to be achieved in the reactor through a high-flow recirculation rate, in order to (1) promote sufficient heat transfer between the vessel jacket and the slurry, which also minimizes possible fouling on the vessel walls; (2) promote sufficient mass transfer of the solute from the solution to the crystallizing surface, which may counteract growth inhibition by impurities; (3) avoid particle settling in the vessel bottom (it is not necessary to uniformly disperse particles in the slurry); and (4) ensure sufficient dispersion of an anti-solvent or a chemical reactant through good macromixing. Note the possible negative effects of overmixing, resulting in crystal breakage and microattrition and/or surface nuclei detachment [123].
- The design of the crystallizer equipment plays a major role. Very often, crystallization is carried out in a multipurpose plant, and the most appropriate reactor for a crystallization operation needs to be chosen. The use of baffles even in a glass-lined vessel is essential. The stirrer must ensure a sufficient recirculation rate with reduced shear. This is achieved by using an axial flow stirrer, like a three-flat-blade propeller. A 45° pitched blade turbine (PBT45) could be an alternative because this stirrer is quite common due to its versatility for chemical reactions, liquid extraction, and crystallization operations. It offers a suitable balance between shear and pumping flow. A common arrangement involves adding a secondary radial flow impeller smaller in diameter on the stirring shaft near the bottom of the tank in order to avoid local incrustation and to ensure mixing until the slurry discharge is complete.
- The stirring rate is a practical parameter to be tuned at laboratory scale. Ensuring particle off-bottom suspension is often considered. The stirring speed is then calculated according to the well-known correlation of Zwietering [124]. Some authors prefer to choose a value of 0.3 W/kg of the specific power input (also denoted as the average energy dissipation rate in computational fluid dynamics). Generally, this last criterion is kept constant when scaling up is considered.
- The feed addition point needs to be determined if the primary nucleation interacts with micromixing. A simple test proposed by Klein and David [119] is to perform

trials at constant stirring speed, with different addition points located in zones of differing turbulence. If no significant modification of CSD is observed, then there is no influence of micromixing for this stirring rate, and the feed point location no longer needs to be taken into account. Otherwise, micromixing plays a role, and the optimum feed addition point must be located in the maximum turbulence zone characterized by the shortest mixing time. This necessitates using a subsurface addition line. For a downpumping PBT45, this point is just above the stirrer so that the input flow is rapidly mixed. For a radial flow turbine (flat blade or Rushton type), it would be directed into the discharge zone.

In practice, laboratory runs allow the effects of these parameters to be investigated. It is essential to use a scaled-down stirred vessel designed to mimic the plant crystallizer hydrodynamics as closely as possible.

## 21.5 Conclusion

This chapter introduces the fundamental physical concepts in pharmaceutical crystallization: solubility, supersaturation, nucleation, growth, phase transformation, and ripening of crystals. Above all, we believe that a thorough knowledge of the phase diagram is vital to the selection of the starting position and pathway for any crystallization experiment.

## References

- [1] Dunitz JD, Bernstein J. Disappearing polymorphs. *Acc Chem Res* 1995;28:193–200.
- [2] Chemburkar SR, Bauer J, Deming K, Spiwek H, Patel K, Morris J, et al. Dealing with the impact of ritonavir polymorphs on the late stages of bulk drug process development. *Org Process Res Dev* 2000;4:413–7.
- [3] Brittain HG. *Polymorphism in pharmaceutical solids, drugs and the pharmaceutical sciences*. New York: Marcel Dekker; 1999.
- [4] Jacques J, Collet A, Wilen SH. *Enantiomers, racemates and resolutions*. Malabar, Florida: Krieger Publishing Company; 1994.
- [5] Stahl PH, Wermuth CG. *Handbook of pharmaceutical salts*. Weinheim: Wiley-VCH; 2002. pp. 374.
- [6] Wouters J, Quéré L. *Pharmaceutical salts and co-crystals*. Cambridge: RSC; 2012.
- [7] Chernov AA. Crystal growth science between the centuries. *J Mater Sci Mater Electron* 2001;12:437–49.
- [8] Mangin D, Puel F, Veesler S. Polymorphism in processes of crystallization in solution: a practical review. *Org Process Res Dev* 2009;13:1241–53.
- [9] Boistelle R. The concepts of crystal growth from solution. In: Grunfeld JP, editor. *Advance in nephrology*. Chicago: Year Book Medical Publisher Inc.; 1986. p. 173–217.
- [10] Liu W, Dang L, Black S, Wei H. Solubility of carbamazepine (form iii) in different solvents from (275 to 343) K. *J Chem Eng Data* 2008;53:2204–6.

- [11] Pudipeddi M, Serajuddin ATM, Grant DJW, Stahl H. Solubility and dissolution of weak acids, bases, and salts. In: Stahl PH, Wermuth CG, editors. Handbook of pharmaceutical salts. Weinheim: Wiley-VCH; 2002. p. 19–39.
- [12] Mullin JW. Crystallization. 4th ed. Oxford: Butterworth-Heinemann; 2001.
- [13] Söhnel O, Garside J. Precipitation. Oxford: Butterworth-Heinemann; 1992.
- [14] Gagnière E, Mangin D, Puel F, Rivoire A, Monnier O, Garcia E, et al. Formation of co-crystals: kinetic and thermodynamic aspects. *J Cryst Growth* 2009;311:2689–95.
- [15] Rodríguez-Hornedo N, Nehm SJ, Seefeldt KF, Pagán-Torres Y, Falkiewicz CJ. Reaction crystallization of pharmaceutical molecular complexes. *Mol Pharm* 2006;3:362–7.
- [16] Desiraju GR. Pharmaceutical salts and co-crystals: retrospect and prospects. In: Wouters J, Quere L, editors. Pharmaceutical salts and co-crystals. Cambridge: RSC; 2011. p. 1–28.
- [17] Leyssens T, Springuel G, Montis R, Candoni N, Veessler S. Importance of solvent selection for stoichiometrically diverse cocrystal systems: caffeine/maleic acid 1:1 and 2:1 cocrystals. *Cryst Growth Des* 2012;12:1520–30.
- [18] Dixit NM, Kulkarni AM, Zukoski CF. Comparison of experimental estimates and model predictions of protein crystal nucleation rates. *Colloid Surf A Physicochem Eng Aspect* 2001;190:47–60.
- [19] Knezic D, Zaccaro J, Myerson AS. Nucleation induction time in levitated droplets. *J Phys Chem B* 2004;108:10672–7.
- [20] Ten Wolde PR, Frenkel D. Enhancement of protein crystal nucleation by critical density fluctuations. *Science* 1997;277:1975–8.
- [21] Erdemir D, Lee AY, Myerson AS. Nucleation of crystals from solution: classical and two-step models. *Acc Chem Res* 2009;42:621–9.
- [22] Zettlemoyer AC. Nucleation. New York: Marcel Dekker; 1969.
- [23] Abraham FF. Homogeneous nucleation theory. Amsterdam: Academic Press; 1974.
- [24] Toschev S. Homogeneous nucleation. In: Hartman P, editor. Crystal growth: an introduction. Amsterdam: North Holland; 1973. p. 1–49.
- [25] Kashchiev D. Nucleation: basic theory with applications. Oxford: Butterworth-Heinemann; 2000.
- [26] Kashchiev D, Verdoes D, Van Rosmalen GM. Induction time and metastability limit in new phase formation. *J Cryst Growth* 1991;110:373–80.
- [27] Oullion M, Puel F, Févotte G, Righini S, Carvin P. Industrial batch crystallization of a plate-like organic product. In situ monitoring and 2D-CSD modelling. Part 1: experimental study. *Chem Eng Sci* 2007;62:820–32.
- [28] Mersmann A. Crystallization technology handbook. 2nd ed. New York: Marcel Dekker; 2001.
- [29] Oullion M, Puel F, Févotte G, Righini S, Carvin P. Industrial batch crystallization of a plate-like organic product. In situ monitoring and 2D-CSD modelling. Part 2: kinetic modelling and identification. *Chem Eng Sci* 2007;62:833–45.
- [30] Nielsen AE. Electrolyte crystal growth mechanics. *J Cryst Growth* 1984;67:289–310.
- [31] Gahn C, Mersmann A. Theoretical prediction and experimental determination of attrition rates. *Chem Eng Res Des* 1997;75:125–31.
- [32] Garside J. Industrial crystallization from solution. *Chem Eng Sci* 1985;40:3–26.
- [33] Astier JP, Veessler S. Using temperature to crystallize proteins: a mini-review. *Cryst Growth Des* 2008;8:4215–9.
- [34] Burton WK, Cabrera N, Frank FC. The growth of crystals and the equilibrium structure of their surfaces. *Phil Trans R Soc* 1951;243:299–358.

- [35] Gilmer GH, Ghez R, Cabrera N. An analysis of combined surface and volume diffusion processes in crystal growth. *J Cryst Growth* 1971;8:79–93.
- [36] Chernov AA. *Modern crystallography III, crystal growth*. Berlin Heidelberg: Springer-Verlag; 1984.
- [37] Nielsen AE, Toft JM. Electrolyte crystal growth kinetics. *J Cryst Growth* 1984;67:278–88.
- [38] Rosenberger F. *Fundamentals of crystal growth I*. Berlin: Springer-Verlag; 1979.
- [39] Garcia-Ruiz JM, Novella ML, Moreno R, Gavira JA. Agarose as crystallization media for proteins: I: transport processes. *J Cryst Growth* 2001;232:165–72.
- [40] Squires TM, Quake SR. Microfluidics: fluid physics at the nanoliter scale. *Rev Mod Phys* 2005;77:977.
- [41] Li L, Mustafi D, Fu Q, Tereshko V, Chen DL, Tice JD, et al. Nanoliter microfluidic hybrid method for simultaneous screening and optimization validated with crystallization of membrane proteins. *Proc Natl Acad Sci* 2006;103:19243–8.
- [42] Shim J-U, Cristobal G, Link DR, Thorsen T, Fraden S. Using microfluidics to decouple nucleation and growth of protein. *Cryst Growth Des* 2007;7:2192–4.
- [43] Leng J, Salmon JB. Microfluidic crystallization. *Lab Chip* 2009;9:24–34.
- [44] Ildefonso M, Candoni N, Veesler S. A cheap, easy microfluidic crystallization device ensuring universal solvent compatibility. *Org Process Res Dev* 2012;16:556–60.
- [45] Weissbuch I, Leiserowitz L, Lahav M. “Tailor-made additives” and impurities. In: Mersmann A, editor. *Crystallization technology handbook*. New York: Marcel Dekker; 1995. p. 401–58.
- [46] Black SN, Davey RJ, Halcrow M. The kinetics of crystal growth in the presence of tailor-made additives. *J Cryst Growth* 1986;79:765–74.
- [47] Abergel C, Nesa MP, Fontecilla-Camps JC. The effect of protein contaminants on the crystallization of turkey egg white lysozyme. *J Cryst Growth* 1991;110:11–9.
- [48] Bauer J, Spanton S, Henry R, Quick J, Dziki W, Porter W, et al. Ritonavir: an extraordinary example of conformational polymorphism. *Pharm Res* 2001;18:859–66.
- [49] Pillay V, Fassihi R. Evaluation and comparison of dissolution data derived from different modified release dosage forms: an alternative method. *J Control Release* 1998;55:45–55.
- [50] Cammarn SR, Sakr A. Predicting dissolution via hydrodynamics: salicylic acid tablets in flow through cell dissolution. *Int J Pharm* 2000;201:199–209.
- [51] Costa P, Sousa Lobo JM. Modeling and comparison of dissolution profiles. *Eur J Pharm Sci* 2001;13:123–33.
- [52] Zhang J, Nancollas GH. Unexpected pH dependence of dissolution kinetics of dicalcium phosphate dihydrate. *J Phys Chem* 1994;98:1689–94.
- [53] Amathieu L, Boistelle R. Crystallization kinetics of gypsum from dense suspension of hemihydrate in water. *J Cryst Growth* 1988;88:183–92.
- [54] Garcia E, Hoff C, Veesler S. Dissolution and phase transition of pharmaceutical compounds. *J Cryst Growth* 2002;237–239:2233–9.
- [55] Mangin D, Garcia E, Gerard S, Hoff C, Klein JP, Veesler S. Modeling of the dissolution of a pharmaceutical compound. *J Cryst Growth* 2006;286:121–5.
- [56] Bladgen N, Davey R. Polymorphs take shape. *Chem Br* 1999:44–7.
- [57] Byrn SR. *Solid state chemistry of drugs*. New York: Academic Press; 1982.
- [58] Haleblan JK. Characterization of habits and crystalline modification of solids and their pharmaceutical applications. *J Pharm Sci* 1975;64:1269–88.

- [59] Taulelle P, Astier JP, Hoff C, Pèpe G, Veesler S. Pharmaceutical compound crystallization: growth mechanism of needle-like crystals. *Chem Eng Technol* 2006;29:239–46.
- [60] Ostwald W. Studien über die bildung und umwandlung fester körper. *Z Phys Chem* 1897;22: 289–330.
- [61] Cardew PT, Davey RJ. The kinetics of solvent-mediated phase transformation. *Proc R Soc Lond A* 1985;398:415–28.
- [62] Ferrari ES, Davey RJ, Cross WI, Gillon AL, Towler CS. Crystallization in polymorphic systems: the solution-mediated transformation of  $\beta$  to  $\alpha$  glycine. *Cryst Growth Des* 2003;3:53–60.
- [63] Cashell C, Corcoran D, Hodnett BK. Control of polymorphism and crystal size of L-glutamic acid in the absence of additives. *J Cryst Growth* 2004;273:258–65.
- [64] Ono T, Ter Horst JH, Jansens PJ. Quantitative measurement of the polymorphic transformation of l-glutamic acid using in-situ Raman spectroscopy. *Cryst Growth Des* 2004;4:465–9.
- [65] Scholl J, Bonalumi D, Vicum L, Mazzotti M, Muller M. In situ monitoring and modeling of the solvent-mediated polymorphic transformation of l-glutamic acid. *Cryst Growth Des* 2006;6:881–91.
- [66] Righini S. Polymorphic transformation of 2,6-dihydroxybenzoic acid (2,6-DHB). UMIST; 2000.
- [67] Caillet A. Etude de la transition de phase en solution d'un hydrate grâce à un suivi in-situ par spectroscopie Raman et acquisition d'images. Modélisation par bilan de population. Lyon: Université Claude Bernard Lyon 1; 2006. p. 179.
- [68] O'mahony MA, Seaton CC, Croker DM, Veesler S, Rasmuson ÅC, Hodnett BK. Investigation into the mechanism of solution-mediated transformation from FI to FIII carbamazepine: the role of dissolution and the interaction between polymorph surfaces. *Cryst Growth Des* 2013;13:1861–71.
- [69] Boistelle R, Rinaudo C. Phase transition and epitaxies between hydrated orthorhombic and anhydrous monoclinic uric acid crystals. *J Cryst Growth* 1981;53:1–9.
- [70] Asherie N, Lomakin A, Benedek GB. Phase diagram of colloidal solutions. *Phys Rev Lett* 1996;77: 4832–5.
- [71] Wolde PR, Frenkel D. Enhancement of protein crystal nucleation by critical density fluctuations. *Science* 1997;277:1975–8.
- [72] Noro MG, Kern N, Frenkel D. The role of long-range forces in the phase behavior of colloids and proteins. *Europhys Lett* 1999;48:332–8.
- [73] Anderson VJ, Lekkerkerker HNW. Insights into phase transition kinetics from colloid science. *Nature* 2002;416:811–5.
- [74] Maeda K, Aoyama Y, Fukui K, Hirota S. Novel phenomena of crystallization and emulsification of hydrophobic solute in aqueous solution. *J Colloid Interface Sci* 2001;234:217–22.
- [75] Broide ML, Tominc TM, Saxowsky MD. Using phase transitions to investigate the effect of salts on protein interaction. *Phys Rev E* 1996;53:6325–35.
- [76] Grouazel S, Perez J, Astier J-P, Bonneté F, Veesler S. BPTI liquid–liquid phase separation monitored by light and small angle X-ray scattering. *Acta Cryst* 2002;D58:1560–3.
- [77] Vivares D, Belloni L, Tardieu A, Bonneté F. Catching the PEG-induced attractive interaction between proteins. *Eur Phys J E* 2002;9:15–25.
- [78] Lafferrere L, Hoff C, Veesler S. Polymorphism and liquid–liquid demixing in supersaturated drug solution. *Eng Life Sci* 2003;3:127–31.
- [79] Bonnett PE, Carpenter KJ, Dawson S, Davey RJ. Solution crystallisation via a submerged liquid–liquid phase boundary: oiling out. *Chem Commun* 2003:698–9.
- [80] Lafferrere L, Hoff C, Veesler S. Study of liquid–liquid demixing from drug solution. *J Cryst Growth* 2004;269:550–7.

- [81] Kiesow K, Tumakaka F, Sadowski G. Experimental investigation and prediction of oiling out during crystallization process. *J Cryst Growth* 2008;310:4163–8.
- [82] Sheikh AY, Pal AE. Crystallization in the vicinity of liquid–liquid phase separation boundary. In: Ulrich MKAJ, editor. 16th international symposium on industrial crystallization. Dresden, Germany: VDI Verlag GmbH; 2005. p. 659–70.
- [83] Zhao H, Xie C, Xu Z, Wang Y, Bian L, Chen Z, et al. Solution crystallization of vanillin in the presence of a liquid–liquid phase separation. *Ind Eng Chem Res* 2012;51:14646–52.
- [84] Smith KW, Cain FW, Favre L, Talbot G. Liquid–liquid phase separation in acetone solutions of palm olein: implications for solvent fractionation. *Eur J Lipid Sci Technol* 2007;109:350–8.
- [85] Deneau E, Steele G. An in-line study of oiling out and crystallization. *Org Process Res Dev* 2005;9:943–50.
- [86] Wallace AF, Hedges LO, Fernandez-Martinez A, Raiteri P, Gale JD, Waychunas GA, et al. Microscopic evidence for liquid–liquid separation in supersaturated CaCO<sub>3</sub> solutions. *Science* 2013;341:885–9.
- [87] Lafferrere L, Hoff C, Veessler S. In situ monitoring of the impact of liquid–liquid phase separation on drug crystallization by seeding. *Cryst Growth Des* 2004;4:1175–80.
- [88] Espitalier F, Biscans B, Laguerie C. Particle design part A: nucleation kinetics of ketoprofen. *Chem Eng J* 1997;68:95–102.
- [89] Sano A, Kuriki T, Kawashima Y, Takeuchi H, Niwa T. Particle design of tolbutamide by the spherical crystallization technique. II. Factors causing polymorphism of tolbutamide spherical agglomerates. *Chem Pharm Bull* 1989;37:2183–7.
- [90] Espitalier F, Biscans B, Laguerie C. Particle design part B: batch quasi-emulsion process and mechanism of grain formation of ketoprofen. *Chem Eng J* 1997;68:103–14.
- [91] Gupta R, Mauri R, Shinnar R. Liquid–liquid extraction using the composition-induced phase separation process. *Ind Eng Chem Res* 1996;35:2360–8.
- [92] Maeda K, Nomura Y, Guzman LA, Hirota S. Crystallization of fatty acids using binodal regions of two liquid phases. *Chem Eng Sci* 1998;53:1103–5.
- [93] Veessler S, Revalor E, Bottini O, Hoff C. Crystallization in the presence of a liquid–liquid phase separation. *Org Process Res Dev* 2006;10:841–5.
- [94] Baronnet A. Ostwald ripening in solution; the case of calcite and mica. *Estud Geol* 1982;38:185–98.
- [95] Ng JD, Lorber B, Witz J, Théobald-Dietrich A, Kern D, Giegé R. The crystallization of biological macromolecules from precipitates: evidence for Ostwald ripening. *J Cryst Growth* 1996;168:50–62.
- [96] Boistelle R, Astier JP, Marchis-Mouren G, Desseaux V, Haser R. Solubility, phase transition, kinetic ripening and growth rates of porcine pancreatic alpha-amylase isoenzymes. *J Cryst Growth* 1992;123:109–20.
- [97] Hohmann HH, Kahlweit M. Ostwald ripening of crystalline precipitates in aqueous solutions at constant temperature and periodic temperature changes. *Berichte Bunsen-Gesellschaft* 1972;76:933–8.
- [98] Saury C, Boistelle R, Dalem F, Bruggeman J. Solubilities of calcium acetates in the temperature range 0–100 degree C. *J Chem Eng Data* 1993;38:56–9.
- [99] Schwartz AM, Myerson AS. Solutions and solution properties. In: Myerson AS, editor. *Handbook of industrial crystallization*. 2nd ed. Woburn: Butterworth-Heinemann; 2002. p. 1–31.
- [100] Wey JS, Karpinski PH. 10-Batch crystallization. In: Myerson AS, editor. *Handbook of industrial crystallization*. 2nd ed. Woburn: Butterworth-Heinemann; 2002. p. 231–48.
- [101] Beckmann W. Nucleation phenomena during the crystallisation and precipitation of abecarnil. *J Cryst Growth* 1999;198–199:1307–14.

- [102] Espitalier F, Biscans B, Peyrigain PS, Laguerie C. Ternary diagram: alpha-(3-benzoylphenyl)-propionic acid (ketoprofen) in acetone-water mixtures at different temperatures. Experimental data and predicted results. *Fluid Phase Equilibria* 1995;113:151–71.
- [103] Hojjati H, Rohani S. Measurement and prediction of solubility of paracetamol in water–isopropanol solution. Part I. Measurement and data analysis. *Org Process Res Dev* 2006;10:1101–9.
- [104] Childs SL, Zaworotko MJ. The reemergence of cocrystals: the crystal clear writing is on the wall introduction to virtual special issue on pharmaceutical cocrystals. *Cryst Growth Des* 2009;9:4208–11.
- [105] Schultheiss N, Newman A. Pharmaceutical cocrystals and their physicochemical properties. *Cryst Growth Des* 2009;9:2950–67.
- [106] Aaltonen J, Allesø M, Mirza S, Koradia V, Gordon KC, Rantanen J. Solid form screening – a review. *Eur J Pharm Biopharm* 2009;71:23–37.
- [107] Almarsson O, Zaworotko MJ. Crystal engineering of the composition of pharmaceutical phases. Do pharmaceutical co-crystals represent a new path to improved medicines? *Chem Commun* 2004:1889–96.
- [108] Gagniere E, Mangin D, Puel FO, Bebon C, Klein J-P, Monnier O, et al. Cocrystal formation in Solution: in situ solute concentration monitoring of the two components and kinetic pathways. *Cryst Growth Des* 2009;9:3376–83.
- [109] Gagnière E, Mangin D, Veesler S, Puel F. Co-crystallization in solution and scale-up issues. In: Wouters J, Quere L, editors. *Pharmaceutical salts and co-crystals*. Cambridge: RSC; 2012. p. 188–209.
- [110] Yu ZQ, Chow PS, Tan RBH. Operating regions in cooling cocrystallization of caffeine and glutaric acid in acetonitrile. *Cryst Growth Des* 2010;10:2382–7.
- [111] Gagnière E, Mangin D, Puel F, Valour J-P, Klein J-P, Monnier O. Cocrystal formation in solution: inducing phase transition by manipulating the amount of cocrystallizing agent. *J Cryst Growth* 2011;316:118–25.
- [112] Candoni N, Grossier R, Hammadi Z, Morin R, Veesler S. Practical physics behind growing crystals of biological macromolecules. *Protein Peptide Lett* 2012;19:714–24.
- [113] Lewiner F, Févotte G, Klein JP, Puel F. Improving batch cooling seeded crystallization of an organic weed-killer using on-line ATR FTIR measurement of supersaturation. *J Cryst Growth* 2001;226:348–62.
- [114] Beckmann W. Seeding the desired polymorph: background, possibilities, limitations, and case studies. *Org Process Res Dev* 2000;4:372–83.
- [115] Lewiner F, Klein JP, Puel F, Févotte G. On-line ATR FTIR measurement of supersaturation during solution crystallization processes. Calibration and applications on three solute/solvent systems. *Chem Eng Sci* 2001;56:2069–84.
- [116] Kohl M, Puel F, Klein JP, Hoff C, Monnier O. Investigation of the growth rate of [beta]-cyclodextrin in water during both flow-cell and batch experiments. *J Cryst Growth* 2004;270:633–45.
- [117] Kohl M, Févotte G, Klein JP, Monnier O, Hoff C. Why is seeding of organic substances in the batch-crystallization still treated as an art? In: *Proceeding of the 4th international workshop on CGOM (special event of the 6th BIWIC)*, Halle (Saale); 1997. p. 175–81.
- [118] Kubota N, Doki N, Yokota M, Sato A. Seeding policy in batch cooling crystallization. *Powder Technol* 2001;121:31–8.
- [119] Klein JP, David R. Reaction crystallization. In: Mersmann A, editor. *Crystallization technology handbook*. New York: Marcel Dekker; 2001. p. 393–474.
- [120] Green D. 8-Crystallizer mixing: understanding and modeling crystallizer mixing and suspension flow. In: Myerson AS, editor. *Handbook of industrial crystallization*. 2nd ed. Woburn: Butterworth-Heinemann; 2002. p. 181–99.

- [121] Tung H-H, Paul EL, Midler M, Mccauley JA. Mixing and crystallization. In: Crystallization of organic compounds: an industrial perspective. Wiley; 2009. p. 117–36.
- [122] Atiemo-Obeng VA, Penney WR, Armenante P. Solid–liquid mixing. In: Handbook of industrial mixing. John Wiley & Sons, Inc.; 2003. p. 543–84.
- [123] Veessler S, Boistelle R, Lamerant JM, Philipponneau G. Attrition of hydrargillite (Al(OH)<sub>3</sub>): mechanism and quantification of particle fragility by a new attrition index. Powder Technol 1993;75: 49–57.
- [124] Zwietering TN. Suspending of solid particles in liquid by agitators. Chem Eng Sci 1958;8:244–53.
- [125] Rabesiaka M, Porte C, Bonnin-Paris J, Havet J-L. An automatic method for the determination of saturation curve and metastable zone width of lysine monohydrochloride. Journal of Crystal Growth 2011;332:75–80.

# Crystallization of Chiral Molecules

Cristóbal Viedma<sup>1</sup>, Gérard Coquerel<sup>2</sup>, Pedro Cintas<sup>3</sup>

<sup>1</sup>DEPTO. DE CRISTALOGRAFÍA Y MINERALOGÍA, UNIVERSIDAD COMPLUTENSE, MADRID, SPAIN; <sup>2</sup>NORMANDIE UNIVERSITÉ, UNIVERSITÉ DE ROUEN, MONT-SAINT-AIGNAN, CEDEX, FRANCE; <sup>3</sup>DEPTO. QUÍMICA ORGÁNICA E INORGÁNICA, UNIVERSIDAD DE EXTREMADURA, BADAJOZ, SPAIN

## CHAPTER OUTLINE

<b>22.1 Introduction and Background</b> .....	<b>952</b>
22.1.1 What Chirality is and how it Works in Molecules and Crystals .....	952
22.1.2 Chirality in Crystals and Structure Determination.....	954
22.1.3 Chirality Measurements.....	956
22.1.4 Crystal Growth and Hemihedrism: Revisiting Pasteur and Early Stereochemistry .....	957
22.1.5 Industrial and Biological Significance of Chiral Substances. The Role of Crystallization .....	960
<b>22.2 Chiral Crystallization</b> .....	<b>964</b>
22.2.1 Characterization of the Racemic Composition by Using Phase Diagrams .....	964
22.2.1.1 Non-Racemizable Enantiomers .....	964
22.2.1.2 Racemizable Enantiomers in the Liquid Phase .....	967
22.2.2 Statistics about Racemic Compounds, Conglomerates, and Solid Solutions.....	968
22.2.2.1 How to Spot a Stable or a Metastable Conglomerate?.....	970
22.2.2.2 Techniques Used to Spot a Conglomerate .....	972
22.2.2.3 How to Make a Stable Conglomerate Crystallizing .....	973
22.2.2.4 Interest in Spotting Conglomerates .....	974
22.2.3 Resolution by Preferential Crystallization .....	975
22.2.4 Deracemization in Heterogeneous Systems.....	979
22.2.5 Resolution of Racemates via Diastereomeric Associations (Usually Salt Formation) .....	980
22.2.5.1 Nature of the Resolving Agent.....	980
22.2.5.2 Nature of the Solvent .....	983
22.2.5.3 Influences of Solute/Resolving Agent, Solute + Resolving Agent/Solvent Stoichiometries .....	986
22.2.5.4 Crystallization Temperature .....	990
22.2.5.5 Control of Crystal Growth .....	990

22.2.5.6 Enantiomeric Purification.....	991
22.2.5.7 Chemical Purity of the Racemic Mixture.....	991
<b>22.3 Chiral Crystallization from Achiral and Chiral Molecules.....</b>	<b>992</b>
22.3.1 Homochirality in Crystal Growth from Achiral Molecules.....	992
22.3.2 Near-Equilibrium Systems.....	993
22.3.3 Extension to Chiral Molecules.....	995
<b>Acknowledgments .....</b>	<b>998</b>
<b>References.....</b>	<b>999</b>

## 22.1 Introduction and Background

### 22.1.1 What Chirality is and how it Works in Molecules and Crystals

Chirality is a useful concept in physical and life sciences, especially when applied to a molecular level. It derives from the Greek work *cheir* meaning “hand” because, like hands, the molecules and objects in general are not superposable with their mirror images [1]. The term *chiral* was coined by Lord Kelvin in his Baltimore lectures (given in 1884 and 1893) [2], although its usage remained ignored for nearly one century, being rediscovered by the mid-1960s to define a geometrical model devoid of certain symmetry elements, with the exception of an axis of rotation.

Chirality manifests itself in both molecules and crystals, and its origin lies clearly in molecular architecture. The analogy between crystals and molecules in this context was first caught by Pasteur (vide infra, cf. Section 22.1.4), who realized that the nonidentity of the crystal (or molecule) with its mirror image was due to what he called *dissymmetry* (we would now say chirality). Although Pasteur himself conjectured on different structural arrangements, including tetrahedra, he was unaware of the tetrahedral asymmetric carbon postulated by van't Hoff and Le Bel in 1874. The two forms of a chiral molecule are called *enantiomers* and have identical physical and chemical properties, although they will rotate the plane of polarized light in opposite senses (i.e., optical activity). Two enantiomers will usually differ in reactivity in the presence of other chiral molecules, a fact of enormous significance in biology and drug discovery (Section 22.1.5).

Chiral and related words (e.g., *homochiral*, *heterochiral*) have engendered both confusion and ambiguity in the literature and, unfortunately, improper usage is not unusual. A brief, yet convenient, discussion illustrates the points. A single chiral molecule will either be right-handed or left-handed. The term *chiral* is insufficient, however, when applied to a compound or sample (i.e., a macroscopic collection of molecules), because it does not imply that we are dealing with molecules having the same sense of chirality. Introduction of homochiral or heterochiral labels are appropriate to this end. Moreover, homochiral means that the sample is made up of molecules with the same sense of chirality or handedness, which does not necessarily imply the existence of a

single enantiomer (L-alanine and L-valine are thus homochiral). Clearly, one needs to know if the sample in question is actually *racemic* (made up of equal numbers of molecules of opposite chirality within the limits of technical detection), or *nonracemic*, in which the chiral sample contains a certain excess of the major enantiomer [3]. Finally, as one would have expected for a term restricted to molecules and objects, chiral and chirality should not be employed for dynamic transformations (e.g., chiral synthesis, chiral separation, chiral amplification and so on) despite their widespread use [4]. The situation may even be more complex in crystals because a racemic crystal is not equivalent to a racemic compound in terms of molecular composition (cf. Section 22.1.2) [5]. In addition, the distinctive nature of stereoisomers in the solid state is crucial to understand the separation and resolution of enantiomers by crystallization (see Section 22.2) [6].

Chirality can be recognized at different length scales, from subatomic particles to atoms and molecules, and beyond, which includes of course crystals, polymers, and supramolecular assemblies. With the exception of elementary particles, whose inherent chirality accounts for parity violation at a cosmic scale, spontaneous resolution can actually be observed through different dimensions: enantiomorphous solids, monolayers, liquid crystals, and large noncovalent aggregates [7].

The most common structural motif encountered in chiral molecules is the chiral center (or asymmetric center in old literature), usually a carbon atom surrounded by four different substituents ( $C_{abcd}$ ). The presence of a single and configurationally stable chiral center is a sufficient condition (although not a necessary one) for the existence of chirality, i.e., the existence of a molecule that is not superposable with its mirror image like the enantiomers of the proteinogenic amino acid alanine shown in Figure 22.1.

It is often customary to allude to stereogenic center instead of chiral center, but once again, here is the stereochemical terminology to worry us. In their highly cited 1984 paper, Mislow and Siegel pointed out the misuse of this term and introduced the term *chirotopic* [8]. Since interchange of two ligands at a stereogenic center leads to a stereoisomer, stereogenic centers may be or may not be chiral (consider, for instance, achiral carbons in diastereomeric alkenes or cycloalkanes). However, all chiral centers are stereogenic. For the sake of clarity, the term *chiral center* (a carbon atom in

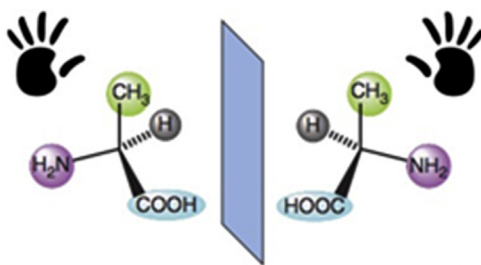
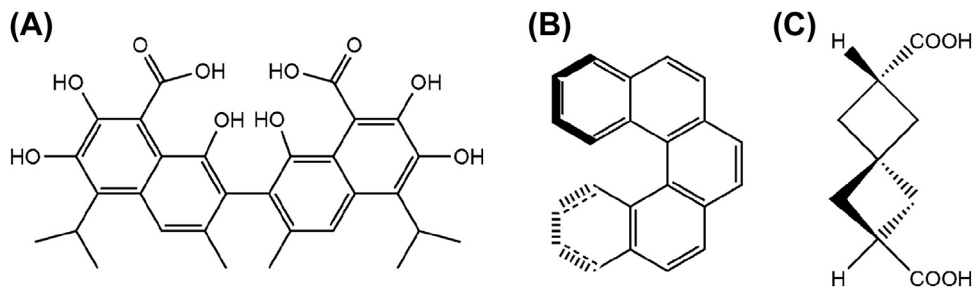


FIGURE 22.1 The two mirror-image enantiomers of the amino acid alanine behave as a pair of left- and right-hand gloves.



**FIGURE 22.2** Molecular structures of compounds displaying axial chirality: (A) gossypol (chirality not shown), (B) pentahelicene [*(P)*-(+)-isomer], and (C) Fecht acid [*(P)*- or *(S)*-configured].

particular) is strongly recommended in line with the concept embedded in van't Hoff's asymmetric carbon.

Chirality in molecules devoid of chiral centers occurs in both natural and synthetic substances, which have enormous importance as ligands in asymmetric catalysis, and some exhibit biological activity (e.g., the antifertility agent gossypol, [Figure 22.2](#)). Molecules belonging to this class of stereoisomers include biphenyls, allenes, spiranes, helicenes, cyclophanes, and molecular propellers. Unlike molecules possessing chiral centers (*central chirality*), the above examples possess chiral axes (*axial chirality*) and can also be viewed as helices, where chirality is due to molecular overcrowding. The existence of symmetry planes gives rise to achiral structures (*meso*), which lack obviously optical activity.

### 22.1.2 Chirality in Crystals and Structure Determination

Things can ostensibly be more complex when one moves to the crystal territory (as mentioned above for racemic crystals), because chiral structures require the assistance of unambiguous elucidation methods such as X-ray diffractometry. It is well established that molecules can pack into 230 space groups, which are also divided into centrosymmetric and noncentrosymmetric groups [9]. Among the noncentrosymmetric ones, there are 65 space groups lacking both reflection and inversion symmetry, and they are the only ones in which enantiopure chiral molecules can crystallize. If the crystal space group is noncentrosymmetric, then the sample will be a *conglomerate* (although rare exceptions do exist), i.e., a racemic mixture of the two enantiomers with each crystal being made up of a single enantiomer (homochiral molecules). Under such circumstances, resolution of enantiomer mixtures may be possible without the assistance of other chiral substances. An in-depth discussion is provided in [Section 22.2](#), although structure–chirality relationships are introduced herein for clarity.

Those 65 space groups include 11 pairs of enantiomorphous crystal classes. Such space groups are inherently chiral, and when one enantiomer crystallizes in one of such enantiomorphous groups, the opposite enantiomer will do it the opposite space group of the pair ([Section 22.2.2](#)).

Counterintuitively, achiral molecules can crystallize in chiral space groups, a fact recognized more than 150 years ago and observed since in numerous inorganic and organic compounds, which are not resolvable. Typical examples include minerals such as  $\alpha$ -quartz ( $P3_121$ ) or cinnabar ( $\alpha$ -HgS,  $P3_121$ ), and a wide range of achiral molecules, e.g.,  $\text{NaClO}_3$  ( $P2_13$ ),  $\text{SrSi}_2$  ( $P4_132$ ), hydrogen peroxide ( $\text{H}_2\text{O}_2$ ,  $P4_12_12$ ), benzil ( $P3_12$ ), succinic anhydride ( $P2_12_12_1$ ), glycine ( $P2_1$ ,  $P3_1$ ) or tri-*o*-thymotide ( $P3_12_1$ ). The inherent handedness in the solid state arises from screw axes constructed with helicoidal or spiral chains of achiral molecules. As noted above, a few rare cases of racemic compounds (i.e., substances existing as two enantiomers and hence potentially resolvable) also crystallize as chiral crystals (e.g., *o*-tyrosine, erythro-phenylglyceric acid or camphor oxime, all in  $P2_1$  space group).

A chiral solid is by definition optically active, and rotations can be estimated in the same way as the specific rotation in solution. Enantiomers are of course optically active molecules, and their crystals will exhibit optical rotations too; rotations can actually be greater than those observed for the pure enantiomer in solution [9]. The probability of accommodating pure enantiomers in a chiral space group varies considerably, and two space groups ( $P2_1$ , monoclinic;  $P2_12_12_1$ , orthorhombic) represent the favored arrangements. Moreover, the probability of finding hemihedral faces (rare but instrumental in Pasteur's discovery) is moderate to good in  $P2_1$  and rather poor in  $P2_12_12_1$ . The correlation between crystal structures and molecular chirality can be summarized through the flow chart shown in Figure 22.3.

The chirality sense of a molecule is denoted by its *absolute configuration*, which can be ascertained by different tools, notably diffraction and chiroptical methods. In a chiral crystal, however, the chirality sense is specified by what we call *absolute structure*, again an elusive term. Determination of structure requires the systematic use of X-ray and neutron diffraction analyses, and crystals are studied as molecular systems in controlled orientations. The issue lies beyond the scope of this article, although an in-depth, yet understandable, discussion has been provided by Flack [10]. Investigations on single

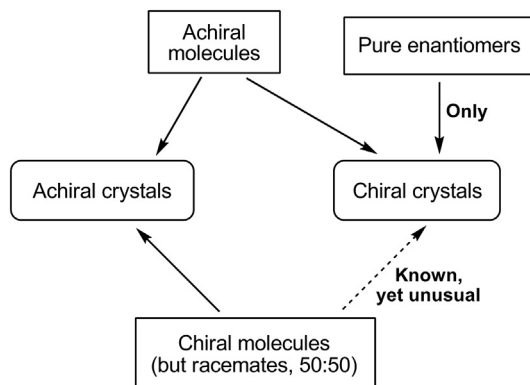


FIGURE 22.3 Molecular chirality versus chiral and achiral solids.

crystals by X-ray diffraction measurements benefit from the so-called Flack parameter, which is the molar fraction ( $x$ ) in equation  $C = (1-x)A + x\bar{A}$ , where  $C$  represents a crystal treated as a mixture of an oriented structure  $A$  and its inverted structure  $\bar{A}$  [11]. For noncentrosymmetric and achiral crystal structures,  $x$  denotes the proportions of the oriented ( $A$ ) and oriented-inverted ( $\bar{A}$ ) domain structures, which are related by rotation. For chiral structures,  $x$  describes the ratio of the two enantiomorphs in the sample. The Flack parameter thus provides a way to detect the two different hands of the chiral lattice, as well as the existence of racemic twinning. The parameter must in any case be treated as significant (larger than statistical error). A small number would point to a correct handedness by pure chance. Conversely, if  $x$  approaches to 1, one should refine the inverted structure, which will be the correct chirality sense. Flack has also wondered about crystal structures generated from nonracemic enantiomeric mixtures, which have presumably been reported, although reliable data are difficult to obtain from a direct search on the Cambridge Structural Database (CSD). Symmetry arguments tell us that only chiral structures should be permitted [10].

There are certainly some limitations regarding the application of diffraction methods (e.g., equivalence of enantiomorphous pairs in some circumstances) [12] and the Flack parameter invariably exhibits a standard uncertainty [13,14], although further protocols and improvements may overcome such hurdles [15]. Comparisons of X-ray crystal structures with *ab initio*-calculated structures appear to be crucial for accurate determinations.

### 22.1.3 Chirality Measurements

It has been reasonably argued that the number of chiral crystals in nonbiological samples could be higher than thought, a fact usually overlooked [16]. The unit cell and therefore the whole crystal may be chiral by virtue of chiral clusters of individual molecules (which may actually be interconnected by hydrogen bonds) or based on chiral conformers frozen in the unit cell. While the individual molecule retains its achirality, such clusters can adopt different symmetries.

Chirality measurements, estimated by different algorithms [17–20], can be a useful diagnostic tool as well for assessing the degree of chirality of a crystal. Among them, the continuous symmetry measures (CSM) formalism, developed by Avnir and associates, deserves consideration [18,19]. In short, one searches for the minimal distance that the atoms of a given molecule deviates from the nearest perfectly  $G$ -symmetric object. A value of  $S(G) = 0$  denotes achirality (the desired  $G$ -symmetry) and the measure increases as the object becomes more chiral. The CSM methodology is rather general and can be applied to a wide range of chiral molecules for comparative purposes and quantitative relationships. This of course includes chiral crystals and can be employed to determine the degree of helicity or, alternatively, the degree of  $C_2$ -symmetry as the  $C_2$  axis bisects the helical axis. Interestingly, the helix of quartz reaches the maximal  $S(G)$  value after one turn and a third. A straightforward application of CSM in such a case is also

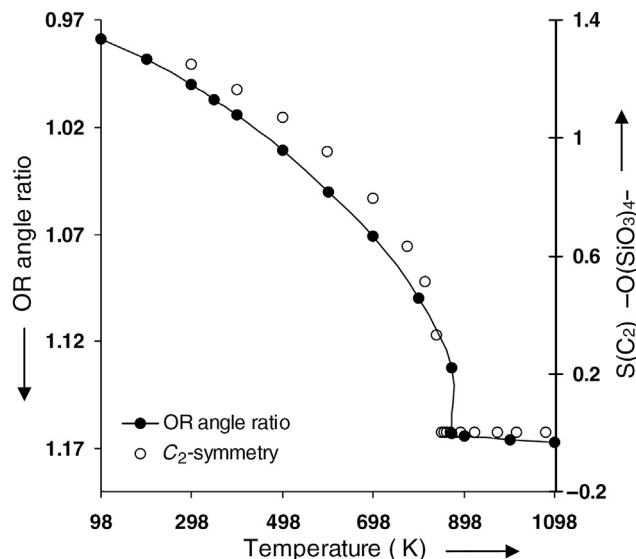


**FIGURE 22.4** Dependence of the degree of helicity (degree of  $C_2$ -symmetry) of quartz tetrahedra [ $-O(SiO_3)_4-$  helical fragment] on temperature. The Y axis denotes the optical rotation (OR) ratio. Reproduced with permission from Ref. [21]. Copyright 2006 Elsevier Ltd.

illustrated by chirality–temperature correlations [21], following the seminal observation by Le Châtelier in the late nineteenth century that the optical rotation of quartz increases with temperature; a phase transition occurs at 848 K. Figure 22.4 makes clear that an increase in temperature is associated with an increase in the degree of chirality; in other words, a decrease of  $S(C_2)$  values as shown (the helical fragment  $-O(SiO_3)_4-$  becomes closer to  $C_2$ -symmetry) [21].

#### 22.1.4 Crystal Growth and Hemihedrism: Revisiting Pasteur and Early Stereochemistry

It should be unnecessary to underline the importance of Pasteur’s experiments with tartrate crystals that led ultimately to the first example of spontaneous resolution. There are comprehensive treatments on the history of stereochemistry and Pasteur himself, although the reader is referred herein to a few authoritative and recent reviews, which summarize well Pasteur’s achievements in context [22,23]. It suffices to highlight again how instrumental the existence of hemihedrism in tartrate crystals was to achieve their manual enantioseparation. In the absence of hemihedral faces (such as  $h$  faces in Figure 22.5), the enantiomorphism of the crystals cannot be detected. Hemihedrism was a known morphological phenomenon before 1848. The French mineralogist Haüy noticed as early as 1801 the existence of hemihedrism in quartz crystals and in 1822 the British astronomer Herschel observed a relationship between the sense of optical rotation and faces inclined in one direction.

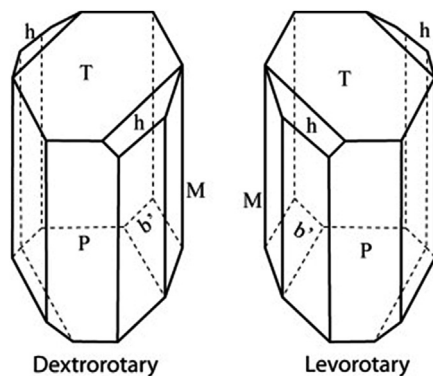


FIGURE 22.5 Schematic representation of the sodium ammonium salts of (+)- and (–)-tartaric acid crystals, which are related as an object to its mirror image.

While these observations were confined to quartz, which exhibits optical activity in the solid state only, Pasteur envisaged that, since tartrate salts showed optical activity in solution as well, there should be a correlation between crystal's handedness and molecular dissymmetry; i.e., molecules would thus bear a similar relationship of non-superposable mirror images. Since hemihedrism is certainly rare and chirality in crystals may be investigated by other methods, scientists have largely overlooked the relationship between crystal habit (of interest to crystallographers) and molecular configuration (relevant to chemists). In fact, assignments of absolute configuration linked to crystal morphology took more than one century [24].

Pasteur's notebooks contain remarkable pieces of work about other chiral substances and observations on crystal growth, polymorphism, and twinning [23]. Based on a previous synthesis of aspartic acid from a fumarate salt, Pasteur was the first in realizing that while naturally occurring and synthetic aspartic acids had identical physico-chemical properties, the synthetic sample had no optical activity. Although Pasteur's conclusions were inaccurate and confusing due in part to the poor quality of aspartic acid crystals with respect to those of tartrate salts optically active aspartic acid crystallized in a different crystal system from the synthetic sample, which is characteristic of a racemic compound. Thus, the search for a universal dissymmetric force in nature leading to optically active substances became a recurring idea in Pasteur's working hypotheses and dissertations.

By the mid-1850s, Pasteur recognized that chiral crystal structures may be generated from enantiomerically pure compounds as well as by achiral molecules. Without clear-cut knowledge of molecular structure, he concluded that for crystals formed from achiral molecules, the chirality arose from the crystalline arrangement only and had nothing to do with the corresponding molecular structure. Like in quartz, Pasteur was able to obtain both right- and left-handed crystals of strontium diformate, an achiral compound, and suggested using this substance for further studies, which were never published. Notably, Pasteur mentioned sodium chlorate ( $\text{NaClO}_3$ ) for the first time in 1856 as a compound

having achiral ions with a chiral crystal structure, although he ignored the use of such crystals in further investigations, harnessed by Kipping and Pope much later (1898; see Section 22.3).

In the context of crystal growth, Pasteur performed seminal experiments on broken and repaired crystals, mainly on malate salts, as collected in his notebooks, although most results were not published [23]. He observed that a broken crystal grew on all faces; however, growth of the broken section occurred faster than the rest, until the whole crystal reached the original morphology. By measuring the rates of growth of crystal faces, Pasteur concluded that such differential growth rates from aqueous solutions of pure enantiomers were responsible for the disappearance of the minor faces, thereby producing a chiral morphology. Regrowth of broken crystals showing achiral morphology in aqueous solutions revealed the appearance of the minor faces showing the chirality at the regrowth zone. However, the minor faces disappeared after full regrowth.

Least-known studies continued after 1860 when Pasteur turned his attention to microbiology rather than chemistry. In 1886, Italian chemist Arnaldo Piutti succeeded in separating enantiomorphous crystals of asparagine (a nonessential amino acid). Since L- and D-asparagine exhibit different taste (a fact noticed by Piutti), that separation not only represents the second recorded example of spontaneous resolution, but also the first finding of enantioselectivity at biological receptors [25].

While the study of optically active molecules and crystals is largely confined to organic compounds, this by no means excludes inorganic substances, particularly metal coordination compounds whose chirality was predicted by Alfred Werner (1866–1919), the founder of this field [26–28]. Moreover, by 1890 Werner pointed out (in a joint paper with Arthur Hantzsch) that a nitrogen atom should possess a tetrahedral geometry and could then give rise to isomers in a similar fashion to carbon atoms.

Werner enrolled in the field of coordination chemistry fascinated, like other chemists, by the curious reactivity and broad range of colored solutions shown by transition metal complexes. He soon challenged the current structural descriptions (“the chain theory”) and formulated arrangements where a central metal atom was surrounded by ligands that could be replaced by other groups. He noticed clearly the existence of stereoisomers, including nonsuperimposable mirror image structures. Werner realized that the type of isomerism was different from that of organic compounds as there is no asymmetric carbon. Surprisingly, however, it took more than one decade for the first separation of enantiomers. In collaboration with his American student Victor King, Werner succeeded in resolving  $[\text{Co}(\text{en})_2(\text{NH}_3)\text{Cl}]\text{Cl}_2$  using chiral D-bromocamphorsulfonate. While this key result was reported in 1913, it seems that the possibility of spontaneous resolution had been neglected in Werner’s group.

Reinvestigations of past events often lead to new insights and prove how useful and fascinating the marriage of history and chemistry can be. This is certainly the case in [27]. Edith Humphrey (who died in 1977 at 102) was the first woman to earn a Ph.D. degree under Werner’s guidance in 1901. She had obtained *cis* (chiral) and *trans* (achiral)

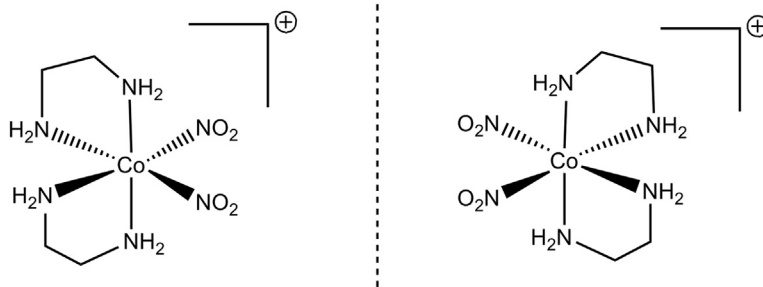


**FIGURE 22.6** Structures of the enantiomers of the bis(ethylenediamine)dinitro cobalt cation. Bromide and chloride salts crystallize as conglomerates.

isomers of bis(ethylenediamine)dinitro cobalt salts:  $[\text{Co}(\text{en})_2(\text{NO}_2)_2]\text{X}$  (Figure 22.6). Both the chloride ( $\text{X} = \text{Cl}$ ) and the bromide ( $\text{X} = \text{Br}$ ) exhibit different solubility for the racemate and pure enantiomers, and therefore spontaneous resolution might have occurred. Unfortunately, conclusive evidence on conglomerate behavior and X-ray diffraction data were reported nearly 80 years after the original publication by Werner and Humphrey. It is now clear that Werner was fully aware of conglomerate crystallizations, although enantiomer separations and identification of crystal enantiomorphism were unsuccessful, chiefly due to the small crystal size and poor quality of the samples. A collection of  $[\text{Co}(\text{en})_2(\text{NO}_2)_2]\text{Br}$  crystals, obtained by Humphrey and Werner's other students, was stored at the University of Zürich and subjected recently to Flack-parameter-based X-ray diffraction analysis and circular dichroism spectra in solution; the result was that large crystals showed no enantiomorphism. Only small crystals were enantioenriched (Figure 22.7). Other samples containing a few crystals revealed racemic, enantioenriched, and enantiopure specimens.

### 22.1.5 Industrial and Biological Significance of Chiral Substances. The Role of Crystallization

With rare exceptions in the realm of natural products [29], chiral molecules are usually produced in living organisms in enantiomerically pure form. Paradigmatic examples of life's single handedness are amino acids, nearly all being left-handed (L-configured), and most sugars belonging to the D-series. This evolutionary aspect has been associated with the origin of life itself, in the belief that key processes of molecular recognition and replication would have been extremely inefficient in a racemic world. Hypotheses and theories accounting for the origin of homochirality are diverse, and a unified frame cannot be established. Probably, some mechanisms might have occurred, often operating in a synergic manner [30]. In this context, the spontaneous resolution of conglomerates appears to be one of the most plausible mechanisms of separation of chiral molecules. During the crystallization process of conglomerates, any of the two enantiomers may crystallize preferentially, while the mirror image molecule will remain in solution.

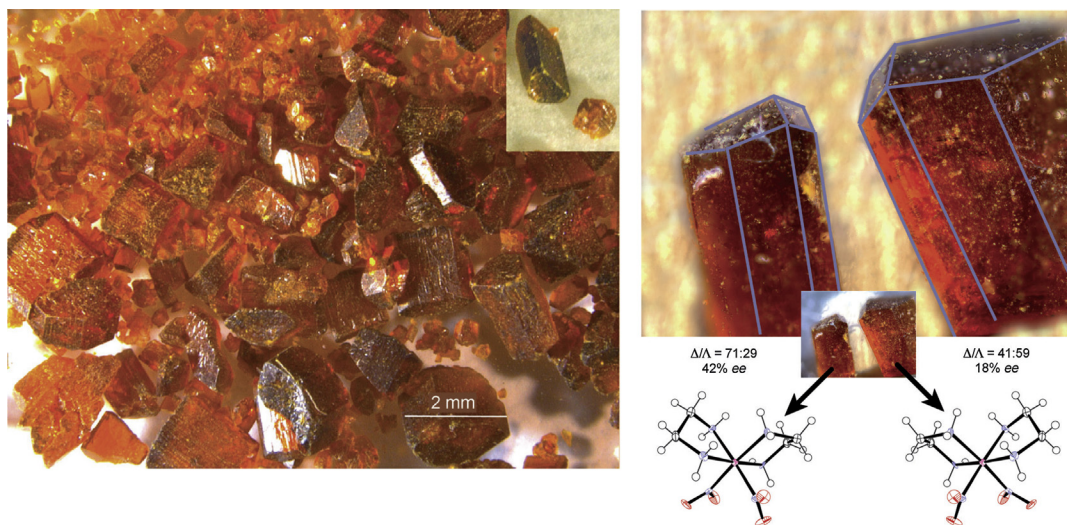


**FIGURE 22.7** Left: Humphrey's crystals of  $[\text{Co}(\text{en})_2(\text{NO}_2)_2]\text{Br}$  (inset: large crystals do not show enantiomorphism). Right: microscope images of enantiomorphous crystals. For the sake of clarity, crystal edges are shown with blue lines. The absolute structures were elucidated by X-ray diffraction analysis. *Reproduced with permission from Ref. [27]. Copyright 2011 Wiley-VCH Verlag GmbH & Co. KGaA.*

Moreover, the actions of enantiomorphous inorganic crystals and chiral surfaces present on Earth's minerals and rocks should be highlighted. Enantioselective adsorptions of primeval organic partners on such crystals might likewise have contributed to local enantioenrichment. The latter has been postulated in the case of clays or quartz, which can form chiral structures [30,31]. Centrosymmetric crystals (e.g., calcite), which are achiral as a whole, may possess faces that bear mirror image relationships and as a result, enantiomers of opposite configuration will preferentially attack one of such faces [32]. Glycine crystals grown with face orientation at the air–water interface may also discriminate the absolute configuration of  $\alpha$ -amino acids [33]. When glycine crystals grow from a solution of glycine (achiral molecule) and racemic mixtures of  $\alpha$ -amino acids, the (*R*)-enantiomers (*D*-configured) are selectively occluded into the (010) face, whereas the (*S*)-enantiomers (*L*-configured) are occluded in the opposite enantiomorphous face. If by chance one monocrystal of glycine exposes its (010) face toward the solution, the enantioselective adsorption of the (*R*)-enantiomers will cause a small imbalance of the (*S*)-amino acid in solution. Crystal growth will thus continue by orienting the (010) face to the solution, which will be enriched in one of the enantiomers. In general, these processes should neither be neglected nor overestimated in the context of chirobiogenesis. Naturally occurring chiral crystals (quartz being the typical case) are present in local niches in high enantiopurity, but the global distribution on Earth approaches a racemic state. On the other hand, the enantiomeric excesses observed during selective adsorptions are generally very small, so that a further amplification mechanism would have been required to justify the high enantiomeric excesses characteristic of biomolecules.

A practical consequence of the distinctive response of enantiomeric molecules in chiral media is the fact that essential physiological and metabolic processes involve only one of the possible enantiomers of a chiral molecule. Biological receptors (e.g., enzymes) are enantiopure substances and the two enantiomers of a drug will bind differently to the active site, which often lead to different biological effects.

The chirality of drugs has become a significant topic in the discovery, design, patenting, and marketing of new pharmaceuticals [34,35]. Until the 1990s, the market was dominated by racemates, but the advent of more sophisticated protocols and technologies, particularly the development of catalytic asymmetric syntheses and biotransformations allowed the preparation of single enantiomers in large amounts and high enantiopurity [36]. Legal regulations, particularly according to U.S. Food and Drug Administration (FDA) guidelines, have become stricter and, in general the marketing of a racemic drugs is justified only in cases where the drug in question undergoes *in vitro/in vivo* racemization or *in vivo/in vitro* stereochemical inversion, and after assessing the toxicity of each stereoisomer separately. The latter is well exemplified by the “profens” family of painkillers and anti-inflammatory agents (ibuprofen or naproxen as representative compounds), as the less active (*R*)-enantiomer converts *in vivo* (in humans) into the most active (*S*)-enantiomer. Still, administration of a single stereoisomer may prevent undesirable side effects or toxicity caused by the racemic mixture. Both enantiomers of the anesthetic agent bupivacaine do show anesthetic properties; however the levorotatory enantiomer is a safer drug than the racemate due to the cardiotoxicity of the dextrorotatory isomer. Consequently, some countries have introduced the unichiral drug in clinical practice. In addition, the patenting of a chiral molecule, either as single enantiomer or racemate, may lead to claims of invention or intellectual property. A few years ago, the oral antiplatelet chiral drug Plavix<sup>®</sup> (Clopidogrel) was under legal fire in the United States, as the original patent claimed both enantiomers and their mixture, while a later patent claimed only the (+)-enantiomer [37]. Figure 22.8 depicts the marketing evolution of chiral drugs (expressed in terms of new molecular entities), approved by the U.S. FDA and other developed countries in the past decade [38].

Clearly, crystallization currently plays a pivotal role in the preparation of chiral drugs as well as other fine chemicals [39]. Classical or dynamic resolutions represent standard procedures to obtain the pure enantiomers for pharmaceutical or industrial purposes. Given the scarce number of chiral compounds crystallizing as conglomerates (ca. 10%), spontaneous resolution has limited applicability. The resolution of a racemic compound, i.e., a homogeneous crystal form where both enantiomers are packed together in the crystal lattice, cannot be achieved by direct crystallization. A versatile and general strategy to produce pure enantiomers (even if yields are far from ideal) involves the formation of diastereomers, which can be separated by fractional crystallization. The phenomenon dates back to Pasteur’s preliminary experiments in the early 1850s [23]. He noted that some achiral compounds combined with either dextrorotatory or levorotatory tartaric acids gave rise to derivatives with identical physical and chemical properties

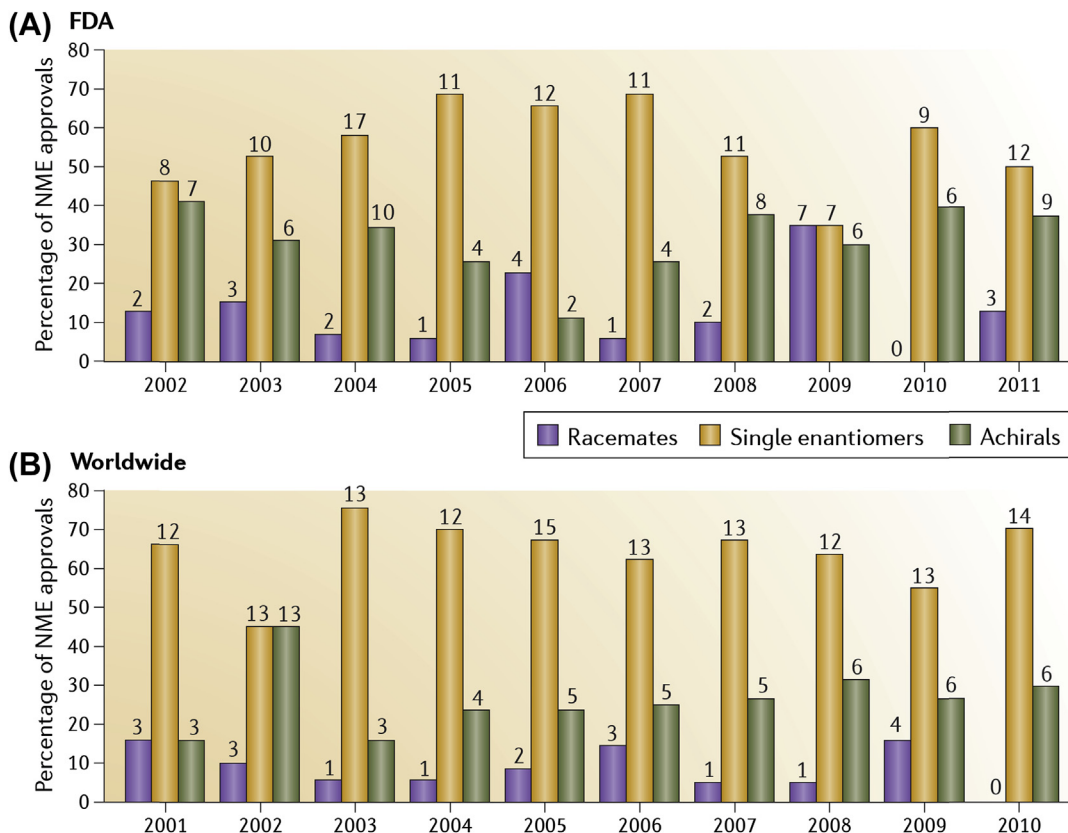


**FIGURE 22.8** Percentages (shown on the y-axis) and number (above the bars) of new molecular entities (NMEs) according to their chirality approved by (A) the U.S. Food and Drug Administration (FDA) and (B) worldwide in the periods specified. Reproduced with permission from Ref. [38]. Copyright 2012 Macmillan Publishers Ltd.

except for the sign of their optical rotation. When the achiral compound was replaced by an optically active substance (natural alkaloids such as quinine, brucine, or strychnine), two different products were obtained. Modern applications on a large scale are employed by the pharmaceutical industry. For instance, preferential crystallization and resolution of ibuprofen with (*S*)-lysine are conducted in a semibatch process from the viewpoint of the slurry concentration, but it is semicontinuous by virtue of constant supersaturation and temperature. During resolution, (*S*)-Ibu-(*S*)-Lys is grown selectively in the crystallizer while (*R*)-Ibu-(*S*)-Lys is left in the dissolver. The resolution is achieved by the appropriate control of seed and supersaturation to grow the desired diastereomer [40]. Crystallization can be combined with other methodologies such as chromatography or chemical/enzymatic preparations to recycle the unwanted enantiomer. Important drugs are thus susceptible to enantioresolution by means of tandem sequences involving chemical and physical purification [41,42].

In the next sections, we shall discuss asymmetric crystallizations in detail from the above-mentioned traditional methods of enantioseparation by direct crystallization and diastereomer formation to most innovative cases of resolutions and deracemizations.

## 22.2 Chiral Crystallization

### 22.2.1 Characterization of the Racemic Composition by Using Phase Diagrams

From a thermodynamic point of view, enantiomers make a unique situation resulting from the perfect symmetry between them. Indeed, every nonvectorial intensive property leads to the same value, e.g., density, enthalpy of melting, melting point, refractive index, etc. When vectorial properties are considered, they have the same absolute values but opposite signs, e.g., specific rotatory power ( $\alpha$ ) (which depends on the wavelength of the polarized light, the solvent, and the temperature), or the anomalous scattering effect [43].

The phase rule has to be carefully considered when dealing with enantiomers. The possible racemization has also to be taken into account. For nonracemizable enantiomers, the perfect symmetry between the two mirror image components leads to amend the Gibbs phase rule (Eqn (22.1)) [44].

$$V = \frac{n_2}{2} + n_1 + 2 - \frac{\varphi_2}{2} - \varphi_1 \quad (22.1)$$

$n_1$  and  $\varphi_1$  stand for the number of independent components and number of phases, respectively, which are not symmetrical, while  $n_2$  and  $\varphi_2$  denote, respectively, the number of independent components and number of phases that are symmetrical. It is worth noting that this relationship is applicable only if  $\varphi_2 \geq 2$  and, to date, no clear-cut experimental evidence has been found. For racemizable enantiomers in the liquid phase, the system undergoes a symmetry breaking when solid phases are considered; in other words, as if we had two symmetrical unary systems.

#### 22.2.1.1 Non-Racemizable Enantiomers

A selection of seven phase diagrams is given below as an illustration of the most probable occurrence. For every case in Figures 22.9 and 22.10, the upper monophasic domain corresponds to the liquid phase or a complete solid solution. From Figures 22.9.1–22.9.4, there is progressive homochiral recognition. Figure 22.9.1 shows a complete solid solution at low temperature; (–) and (+) enantiomers can substitute each other in the crystal lattice. Here, the chiral discrimination in the solid state is extremely poor. Figure 22.9.2 shows that below  $T_c$  the monophasic domain splits in two symmetrical solid solutions, one progressively rich in (–), the other progressively rich in (+) as temperature is lowered [45]. Figure 22.9.3 shows a miscibility gap between the two enantiomers, which has enlarged to such an extent that it creates a eutectic invariant [46,47]. In Figure 22.9.4, the domains of partial solid solutions are not detectable at any

temperature. The latter is the conglomerate without partial solid solution, and this corresponds to the best chiral discrimination in the solid state.

From Figures 22.10.1–22.10.4 there is progressive heterochiral recognition. Figure 22.10.1 shows the emergence of an intermediate monophasic domain (sss  $\gamma$ ). This nonstoichiometric racemic compound has a much higher thermal stability in Figure 22.10.2. In Figure 22.10.3, there is no partial solid solution associated with the enantiomers; in contrast, the racemic compound is still nonstoichiometric. Figure 22.10.3' shows the opposite case, where the racemic compound is stoichiometric but partial solid solutions exist on both ends of the binary system. Figure 22.10.4 shows the most popular case of supramolecular association: the racemic compound. It can be viewed as a stoichiometric co-crystal. To keep it simple, the situations described above in Figures 22.9 and 22.10 do not consider all possible impacts of polymorphism associated (or not) with solid solutions, which is quite common among organic compounds.

The relative stability of the racemic compound versus the conglomerate can be temperature dependent. In other words, at a given temperature, a conglomerate could become more stable than the racemic compound and vice versa at another temperature. Figures 22.11.1 and 22.11.2 depict such cases. The corresponding three solid phase equilibria are the peritectoid and the eutectoid invariants, respectively. It is worth mentioning that those three phase equilibria are associated with a poor heat transfer and a slow kinetics, which make them difficult to detect in the binary system, thus ternary systems (with solvents) make their detection easier [48,49]. These three phase invariants should not be confused with polymorphism [50].

Figures 22.12.1–22.12.3, supposed to be expressed in mole fraction, depict cases with stable conglomerates without solid solution but with different  $\alpha$  ratio ( $\alpha$  = molar solubility of the racemic mixture/molar solubility of the enantiomer).

Figure 22.12.1 is typically what can be obtained with a fully dissociated salt (it might be necessary to add excess of a counter-ion to observe this effect; thus, it is actually a ternary section of a quaternary system). Figure 22.12.2 corresponds to the ideal case: the solubility of one enantiomer does not influence the solubility of the other [51]. Figure 22.12.3 depicts how one enantiomer can increase the solubility of its antipode. Figure 22.12.4 shows the presence of a stable conglomerate with partial solid solutions. The tie-lines (in blue) connect the compositions of the solid phases to the compositions of the liquid phases with which they are in equilibrium [46,47,52]. Figure 22.12.5 shows the most popular situation: a stable racemic compound. Due to the symmetry of the diagram, this stable racemic compound has necessarily a congruent solubility. The conglomerate is metastable and can be observed in a limited number of cases [53,54]. Figure 22.12.6 shows the case of a stable racemic compound in the binary system (–)(+); nevertheless, at that temperature in that solvent (V), the two enantiomers crystallize as solvates whose 50:50 mixture (i.e., stable conglomerate) is more stable than the nonsolvated racemic compound. This interesting case demonstrates that conglomerate screening should not be limited to counter-ions or co-crystal formers, but it should

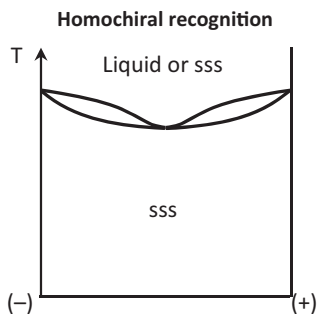


Figure 9.1

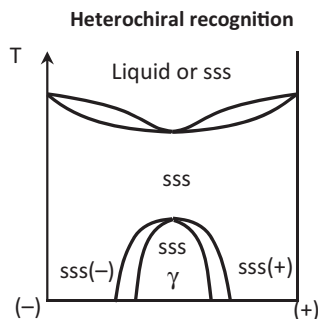


Figure 10.1

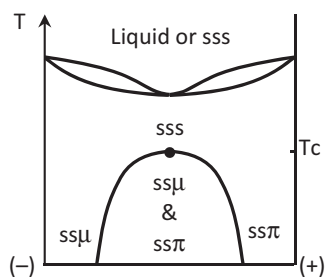


Figure 9.2

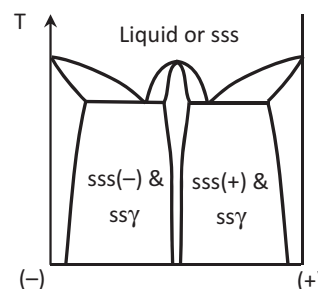


Figure 10.2

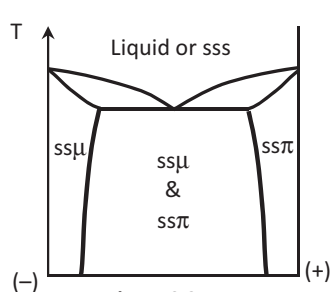


Figure 9.3

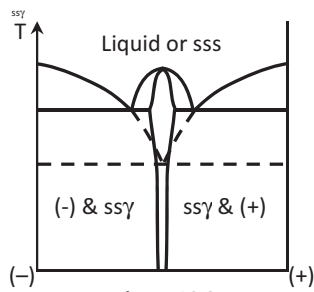


Figure 10.3

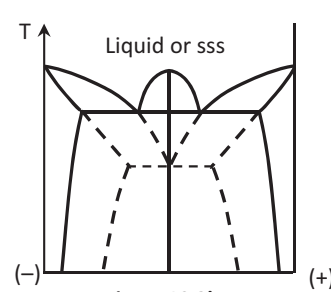


Figure 10.3'

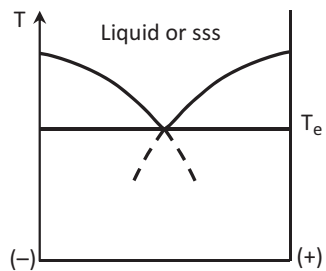


Figure 9.4

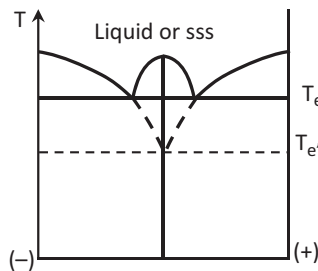
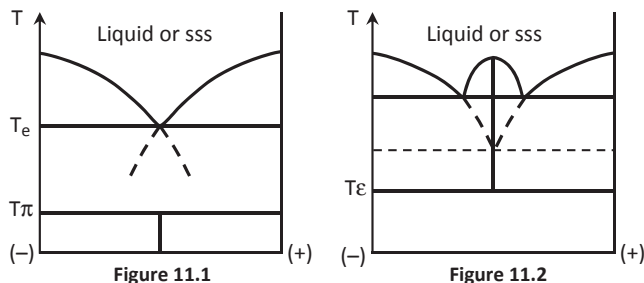


Figure 10.4

FIGURE 22.9 AND 22.10 The symbol 'sss' stands for solid solution by substitution. Figure 22.9.1 shows a complete solid solution between two enantiomers. Figure 22.9.2 shows a complete solid solution at high temperature and a miscibility gap for  $T < T_c$ . Figure 22.9.3 shows a eutectic with two symmetrical partial solid solutions, i.e., a



**FIGURE 22.11** Figure 22.11.1 shows a peritectoid invariant at  $T_\pi$ . Above that temperature the conglomerate is stable, and below that temperature the racemic compound is stable. Figure 22.11.2 shows a eutectoid invariant at  $T_e$ . Below that temperature the conglomerate is stable, and above that temperature the racemic compound is stable.

also involve a screen of solvates or heterosolvates for every partner of crystallization (counter-ion or co-crystal former).

### 22.2.1.2 Racemizable Enantiomers in the Liquid Phase

We will suppose that the racemization kinetics are almost instantaneous in the liquid phase, and there is no racemization in the solid state, at least when the molecular mobility is low ( $T < T_g$ ). Figure 22.13.1 shows that when approaching the liquid state, the kinetics associated with the formation of the  $\langle 1-1 \rangle$  heterochiral compound (i.e., the racemic compound) increase; this is symbolized by the length of the arrows. At low temperature, a full asymmetric transformation delivers a pure enantiomer that can remain enantiopure for long periods of time as long as the temperature of storage is far from the temperature of the molten state. Figures 22.13.2 and 22.13.3 correspond to conglomerates with and without partial solid solutions, respectively. After formation of the racemic mixture, the system will remain a physical mixture of mirror-related phases as long as the systems are not submitted to temperature close to fusion and/or submitted to attrition, temperature gradients, ultrasounds, temperature cycles, etc. (see Section 22.3 on deracemization). If, by contrast, the systems are stimulated by a flux of energy and/or any physical effect that facilitates the transfer of matter (e.g., introduction of a solvent), a spontaneous break of symmetry should occur (Figure 22.13.2.1 or else Figure 22.13.2.2, with partial solid solutions, and Figure 22.13.3.1 or else Figure 22.13.3.2 without partial solid solution).

Figure 22.14 displays the corresponding isotherms with racemizable enantiomers in the liquid phase.

← conglomerate with partial solid solution. Figure 22.9.4 depicts a conglomerate without solid solution.

Figure 22.10.1 shows a complete solid solution at high temperature and a nonstoichiometric racemic compound at low temperature. Figure 22.10.2 shows a nonstoichiometric compound and two symmetrical partial solid solutions. Figures 22.10.3 and 22.10.3' show partial solid solutions associated to the racemic compound and the enantiomers, respectively, and Figure 22.10.4 depicts the usual stoichiometric racemic compound.

Isotherms with different cases of conglomerates (mole fraction)

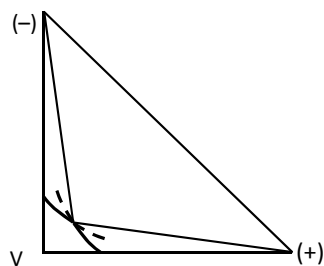


Figure 12.1

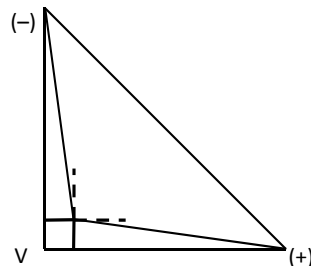


Figure 12.2

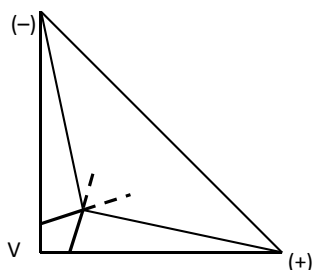


Figure 12.3

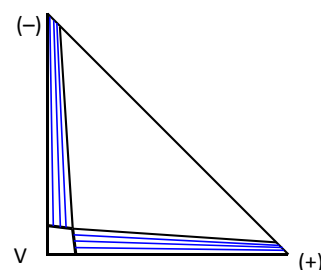


Figure 12.4

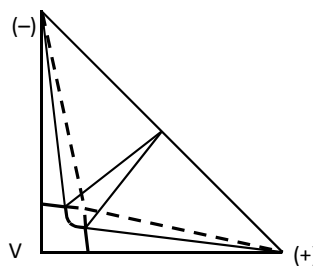


Figure 12.5

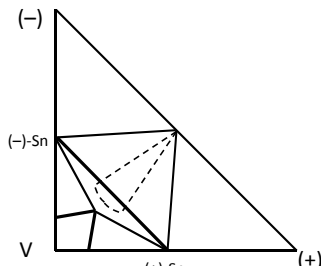


Figure 12.6

**FIGURE 22.12** Figure 22.12.1 shows a stable conglomerate with  $\alpha < 2$ ; Figure 22.12.2: stable conglomerate with  $\alpha = 2$ ; Figure 22.12.3: stable conglomerate with  $\alpha > 2$ ; Figure 22.12.4: stable conglomerate with partial solid solution; Figure 22.12.5: stable racemic compound and metastable conglomerate; Figure 22.12.6: stable conglomerate of solvates and nonsolvated metastable racemic compound.

## 22.2.2 Statistics about Racemic Compounds, Conglomerates, and Solid Solutions

A rough view on this subject leads to the following figures: racemic compounds amount to 90–95%, 5–10% for conglomerates, and a small percentage for solid solutions [9]. Nevertheless, these statistics tend to overlook the following points:

(1) There are important fluctuations in the probability to find a conglomerate-forming system. Figure 22.15 shows two series of structurally related conglomerates.

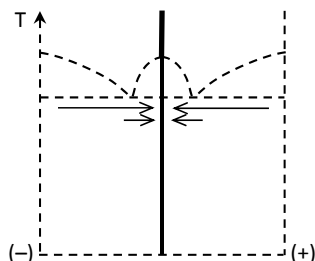


Figure 13.1

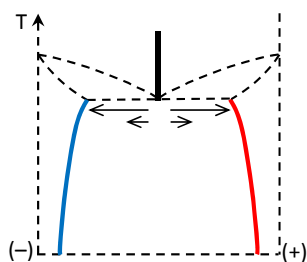


Figure 13.2

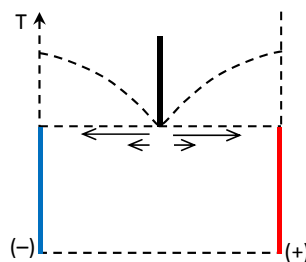


Figure 13.3

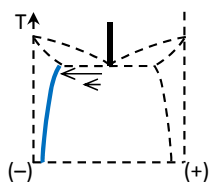


Figure 13.2.1

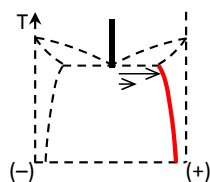


Figure 13.2.2

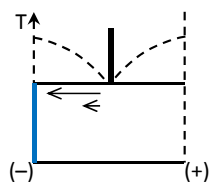


Figure 13.3.1

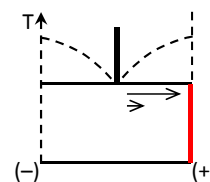


Figure 13.3.2

**FIGURE 22.13** Solid–liquid equilibria between racemizable enantiomers in the liquid state; for all of them, only the 50:50 composition is accessible in the liquid state. Figure 22.13.1 corresponds to a stable racemic compound forming system. Figures 22.13.2 and 22.13.3 show, respectively, conglomerate-forming systems with (Figure 22.13.2) and without (Figure 22.13.3) partial solid solution. On aging, or when a flux of energy crosses the system (mechanical stresses, thermal cycles or gradients), spontaneous symmetry breaking occurs, leading to either Figure 22.13.2.1 or Figure 22.13.2.2 for partial solid solutions and either Figure 22.13.3.1 or Figure 22.13.3.2 in the case of conglomerate-forming system without solid solution.

For instance, derivatives of 5-aryl-5-alkyl hydantoin and 4-aryl-triazolyl ketones constitute clusters of conglomerates.

Likewise, in the series of *trans*-cinnamate salts of 1-amino-alkan-2-ols: 1-amino-butan-2-ol, 1-amino-pentan-2-ol, 1-amino-3-methylbutan-2-ol, 1-amino-hexan-2-ol, 1-amino-4-methylpentan-2-ol, and 1-amino-2-cyclohexylethan-2-ol are all stable conglomerates [55]. This demonstrates that modulations around the developed formulae of a molecule forming a stable conglomerate increase the chance, even for salts, of observing full homochiral discrimination in the solid state. This is particularly true when nonpolar moieties, just involved in Van der Waals contacts, are “slightly” modified.

(2) When the volume of the achiral counter-ion increases, the probability of detecting at least partial solid solutions increases as well. Therefore, when the difference in volume

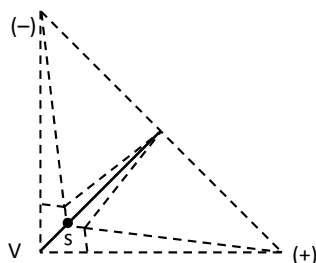
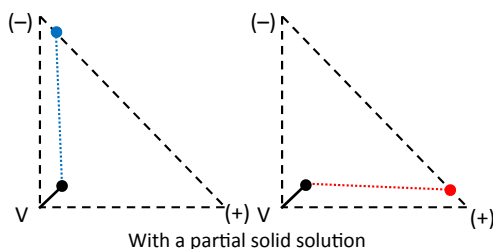


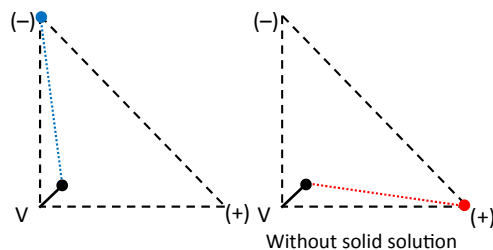
Figure 14.1



With a partial solid solution

Figure 14.2.1

Figure 14.2.2



Without solid solution

Figure 14.3.1

Figure 14.3.2

**FIGURE 22.14** In Figure 22.14.1, only the racemic line is accessible in the liquid phase and the solid phase ( $s$  represents the solubility curve of the racemic compound at the temperature of the isotherm). The following figures are associated: Figures 22.13.2.1 and 22.14.2.1, Figures 22.13.2.2 and 22.14.2.2, Figures 22.13.3.1 and 22.14.3.1, Figures 22.13.3.2 and 22.14.3.2. (red and blue).

exceeds a certain threshold, the crystal lattice of the salt will be mainly governed by the achiral ion, and both chiral species can accommodate the crystallographic site irrespective of their handedness.

#### 22.2.2.1 How to Spot a Stable or a Metastable Conglomerate?

There is a restriction of symmetries for crystal containing an enantiomeric excess. In the crystal lattice of a pure enantiomer symmetry, operators must regenerate a homochiral equivalent, and therefore any center of symmetry, mirrors and glide mirrors, inverted axes  $(-3)$ ,  $(-4)$ ,  $(-6)$  cannot exist. Out of the 230 space groups, only 65 remain compatible with a pure enantiomer. The exhaustive list is given in Table 22.1. Space

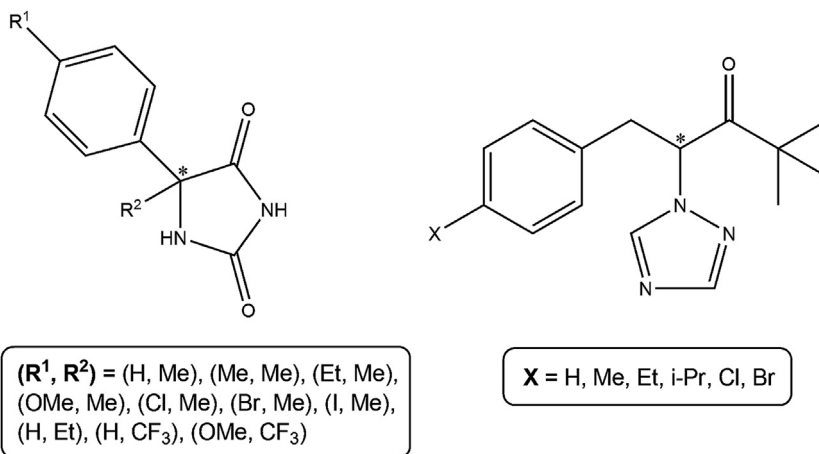


**FIGURE 22.15** Conglomerate-forming structures in hydantoin and triazolyl-ketone derivatives. The asterisk denotes the chiral center.

**Table 22.1** Space Groups Compatible with Homochiral Molecules

Systems	Point Groups	Mode	Space Groups
Triclinic	(1)	P	P1
Monoclinic	(2)	P	P2; P2 <sub>1</sub>
		C	C2
Orthorhombic	(2 2 2)	P	P222; P222 <sub>1</sub> ; P2 <sub>1</sub> 2 <sub>1</sub> 2; P2 <sub>1</sub> 2 <sub>1</sub> 2 <sub>1</sub>
		C	C222; C222 <sub>1</sub>
		I	I222; I2 <sub>1</sub> 2 <sub>1</sub> 2 <sub>1</sub>
		F	F222
Tetragonal	(4)	P	P4; [P4 <sub>1</sub> ; P4 <sub>3</sub> ]; P4 <sub>2</sub>
		I	I4; I4 <sub>1</sub>
	(422)	P	P422; P42 <sub>1</sub> 2; [P4 <sub>1</sub> 22; P4 <sub>3</sub> 22]; [P4 <sub>1</sub> 2 <sub>1</sub> 2; P4 <sub>3</sub> 2 <sub>1</sub> 2]; P4 <sub>2</sub> 22; P4 <sub>2</sub> 2 <sub>1</sub> 2
		I	I422; I4 <sub>1</sub> 22
Trigonal	(3)	P	P3; [P3 <sub>1</sub> ; P3 <sub>2</sub> ]; R3
	(32)	P	P312; P321; [P3 <sub>1</sub> 12; P3 <sub>2</sub> 12]; [P3 <sub>1</sub> 21; P3 <sub>2</sub> 21]; R32
Hexagonal	(6)	P	P6; [P6 <sub>1</sub> ; P6 <sub>5</sub> ]; [P6 <sub>2</sub> ; P6 <sub>4</sub> ]; P6 <sub>3</sub>
		P	P622; [P6 <sub>1</sub> 22; P6 <sub>5</sub> 22]; P6 <sub>3</sub> 22; [P6 <sub>4</sub> 22; P6 <sub>2</sub> 22]
Cubic	(23)	P	P23; P2 <sub>1</sub> 3
		I	I23; I2 <sub>1</sub> 3
		F	F23
		P	P432; [P4 <sub>1</sub> 32; P4 <sub>3</sub> 32]; P4 <sub>2</sub> 32
		F	F432; F4 <sub>1</sub> 32

groups in brackets are enantiomorphous in terms of symmetry operators; space groups listed in blue and italics are those that should fulfill Kleinman restrictions for SHG (second harmonic generation, vide infra) detection of noncentrosymmetry, provided that no adsorption effect exists. Note that *all chiral* space groups are noncentrosymmetric, but *the reverse is not true*.  $P2_12_12_1$  alone represents ca. 58% for chiral “small” organic molecules; this is why it is often called the “whale” [56]. The  $P2_1$  space group represents circa 30% of crystal packing observed for chiral small molecules.

Below, we shall examine some techniques used to detect mixtures of homochiral crystals and to crystallize those stable conglomerates.

#### 22.2.2.2 Techniques Used to Spot a Conglomerate

Because the probability of spotting a conglomerate is quite small, multiple efforts have been made to find techniques that are appropriate to detect them. Several of the most commonly used techniques are listed below. Some comments are added to detail the pros and cons of these techniques.

1. *Construction of the binary phase diagram between antipodes*. It is rather time consuming and useless (if the purpose is just to spot a stable conglomerate). Moreover, many organic crystals do not stand fusion, and at least one enantiomer should be available.
2. *Construction of ternary phase diagram between antipodes and a solvent* (if this is extended to a mixture of solvents, then it is just a ternary section of a higher order phase diagram). This constitutes more work than the construction of the binary system. The diagnostic will be error free, although a disproportionate amount of work will be required for the potential benefit.
3. *Prescreening by means of second harmonic generation (SHG)*. [57] Nonlinear optics teaches that when a noncentrosymmetric crystal is illuminated by powerful pulses of a laser beam (wavelength  $\lambda$ ), a part of the energy is converted into photons that have a wavelength  $\lambda/2$ . Conversely, when a powder is emitting at half of the wavelength of the illuminating beam, it can be concluded that a noncentrosymmetric material exists in this powder. This effect can be used to discard all centrosymmetric phases produced during a conglomerate screen (Table 22.2). Fortunately, the vast majority of the racemic compounds crystallize in centrosymmetric space groups such as  $P2_1/c$ ,  $P-1$ ,  $C2/c$ ,  $Pbca$ ,  $Pbcm$ , etc., which makes this technique efficient. This allows the experimenter to concentrate effort on differentiating chiral from noncentrosymmetric, nonchiral space groups. For the latter, in a subset including  $Pc$ ,  $Pca2_1$ ,  $Cc$ ,  $Pna2_1$  space groups, the 50:50 composition corresponds obviously to a racemic compound, since there is at least one inverting symmetry operation in the lattice. Thus, application of the SHG method can only constitute a prescreening, but it is still interesting because: (1) no comparison with the crystal lattice of the corresponding pure enantiomer is required; (2) it is almost instantaneous; (3) it is nondestructive; (4) a small amount of solid (often  $\sim 10$  mg is

**Table 22.2** Centrosymmetric, Chiral, and Noncentrosymmetric, Nonchiral Space Groups. The SHG Method Serves to Differentiate Centrosymmetric Space Groups (*SHG Negative*) from the Two Other Classes (*SHG Positive*)

System	Centrosymmetric Space Groups	Chiral Space Groups	Noncentrosymmetric Nonchiral Space Groups
Triclinic	1	1	–
Monoclinic	6	3	4
Orthorhombic	28	9	22
Tetragonal	26	16	26
Cubic	17	13	6
Trigonal	8	11	6
Hexagonal	6	12	9
Total	92	65	73

enough) is required; (5) it can be run in an automatic way; (6) it can operate at different temperatures [58,59], and (7) it works on suspensions, which means that efflorescent solvate conglomerates can be detected as well. On the other hand, there is also a potential drawback with the highly symmetrical space groups stemming from the (422) (622) and (432) point groups (Table 22.1). To discard centrosymmetric space groups, Kleinman relationships [60] lead to conclude that the corresponding space groups, even though chiral, should be SHG inactive. The main problem will be associated with deleting the “good” chiral space groups (e.g.,  $P4_12_12$  and  $P4_32_12$ , essentially), which are not common but not exceptional either (ca. 2–3% or lower probability among conglomerates). Fortunately, and based on our experience, these limitations do not hold because a sufficient adsorption phenomenon is present most of the time [61].

4. *Evidence of an entrainment effect.* Even if a conglomerate is metastable, it might be possible to perform preferential crystallization (vide infra for further details). The recent example of diprophylline highlights this point very well. Conversely, a stable conglomerate does not anticipate a feasible preferential crystallization [62,63].
5. *Comparison between spectroscopic data of the racemic mixture and the pure enantiomer* by means of solid-state nuclear Magnetic Resonance (SS-NMR), Infrared Spectroscopy (IR), Raman spectroscopy, X-ray powder diffraction (XRPD), or terahertz spectroscopy. Such techniques need access to the pure enantiomer, and sometimes it is difficult to differentiate spectroscopic data due to the high degree of similarity between the two crystal lattices and/or poor crystallinity.

### 22.2.2.3 How to Make a Stable Conglomerate Crystallizing

Based on the above paragraph, there are two possibilities:

1. The experimenter already knows one stable conglomerate with a well-defined structure, and it is then possible to find “around” other conglomerates by

introducing minor structural changes in the chiral molecule or its crystallization partners (counter-ions, solvent molecules, co-crystal formers).

2. It is a new chemical entity with a priori no direct relationship with any other known conglomerate. In that case, the “game” consists in adding partners with which the crystal lattice will be fully chiral discriminating. In practice, this means that a combinatorial screen will have to be implemented. It is not unusual to perform hundreds of trials, a certain number of them resulting in oils, gums, or other badly crystallized materials.

A regular screen consists in trying to crystallize solvates or heterosolvates (i.e., different solvent molecules located at different crystallographic sites in the lattice), salts, co-crystals, and all sorts of hybrids between those classes of compounds. Thus, for a particular counter-ion, it is recommended to make tests in different solvents or solvent mixtures, even checking “exotic” stoichiometries that deviate from the natural ratios between acid-base functions [64]. Moreover, these protocols may also be repeated at different temperatures.

#### 22.2.2.4 Interest in Spotting Conglomerates

A series of benefits and advantages can easily be identified:

1. *Recovery of the whole enantiomeric excess (ee).* When a resolution method or a partial asymmetric synthesis yields a mixture of enantiomers, a stable conglomerate gives the opportunity to recover the full *ee*, without loss, by a single recrystallization. Starting from a mixture M of enantiomers (Figure 22.16), a precise amount of solvent V can be used to recrystallize and ensure that the mother liquor will have no *ee* ( $ee = 0$ ). In addition, this could be employed to spot a conglomerate: Starting from a known *ee*, it is possible to observe that the concentrated suspension has no *ee*, for example, by using High Performance Liquid Chromatography (HPLC) or polarimetry.

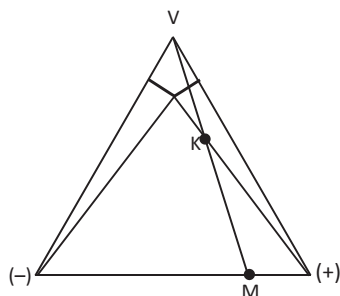


**FIGURE 22.16** This diagram shows the best composition (point K) for a quantitative purification of a mixture M of enantiomers. Point K represents the maximum amount of solvent required leading to a mother liquor without enantiomeric excess (0% *ee*).

When using diastereomeric salts for resolution (for instance, of a given amine) rather than recrystallizing the mixture of diastereomeric salts, it is often wiser to free the base (salting out) and purify the mixture of enantiomers so long as they form a stable conglomerate. In practice, this depends mainly on whether or not there is presence of a partial solid solution between the diastereomers.

2. *Recovery of the whole amount of each enantiomer* (if preferential crystallization is applicable; see next section).
3. *Induction of preferential primary nucleation* (initiated by addition of a pure enantiomer structurally related to the racemic ( $\pm$ ) solute [65]).
4. *Deracemization in the solid state by means of racemization in the liquid state and application of flux of energy* (as mentioned by means of attrition, sonication, temperature cycles, etc.). Furthermore, there is also the application of the so-called second-order asymmetric transformation (provided that crystallization and racemization in the liquid phase plus attrition can be combined under the same operating conditions).

### 22.2.3 Resolution by Preferential Crystallization

Preferential crystallization is an interesting process owing to three key arguments [66]: (1) there is no need for a chiral resolving agent; (2) it leads to an easy and quantitative enantiomeric purification of the crude products, and (3) the process itself is compatible with both batch and continuous processes. We shall first examine preferential crystallization of nonracemizable enantiomers, at least in the crystallization context (Figures 22.17–22.22).

Preferential crystallization is an alternate process that has several variants depending mainly on the seeding mode and temperature variations. The key step is a stereoselective crystallization of a single enantiomer out of a doubly supersaturated solution. The simplest mode is seeded and isothermal preferential crystallization (SIPC). Starting from point E at high temperature containing an excess of M mass units of an enantiomer (Figure 22.17), the system is cooled (Figure 22.18) and moves from equilibrium to

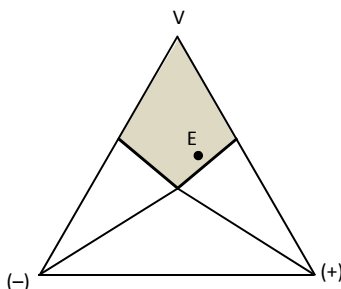


FIGURE 22.17 Equilibrium at  $T_1$  (monophasic domain in grey).

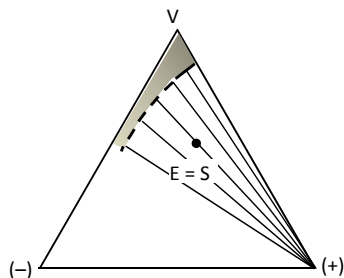


FIGURE 22.18 System out of equilibrium (as Figure 22.17) after a fast cooling.

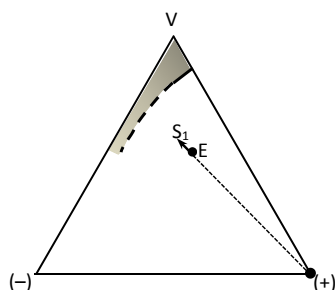


FIGURE 22.19 Preferential crystallization after selective seeding with (+)-crystal.

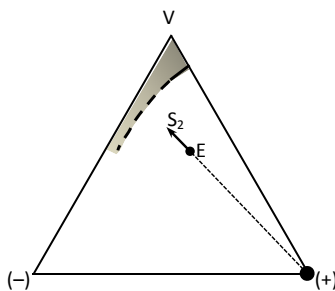
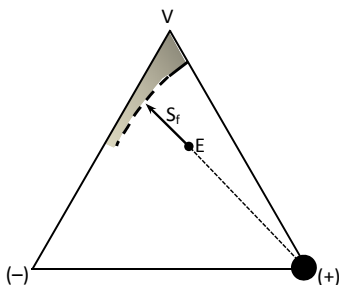
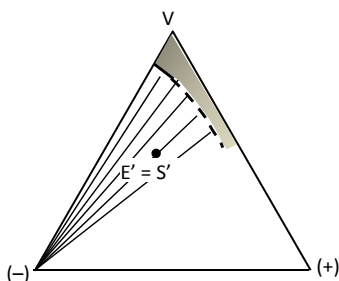


FIGURE 22.20 Preferential crystallization of (+)-enantiomer continued after stage shown in Figure 22.19.

out-of-equilibrium conditions. Upon seeding with particles containing the pure enantiomer in excess (preferably with a large surface area), the crystallization of that single enantiomer is triggered. The solution point and the overall composition point are superimposed first (Figure 22.18). Then, due to the stereoselective crystallization of the (+)-enantiomer, the solution point moves continuously along the (+)-E line toward the metastable solubility curve  $S-S_1-S_2-S_f$  (Figures 22.19–22.21). When, ideally,  $S_f$  is attained, a fast filtration is implemented, leading to a mass  $2M$  of the (+)-enantiomer and a mother liquor with  $M$  mass units of excess of the opposite (–)-enantiomer. By adding



**FIGURE 22.21** Preferential crystallization of (+)-enantiomer at the final stage; metastable equilibrium for (-)-enantiomer. The size of the black disc in Figures 22.19–22.21 is proportional to the amount of solid.



**FIGURE 22.22** Stage after filtration of previous run and reloading in racemic mixture.

2 M mass units of the racemic mixture and heating at  $T_1$  for complete homogenization and cooling down to  $T_F$ , the out-of-equilibrium system is represented by points  $E'$  and  $S'$  symmetrical to  $E = S$  in Figure 22.22 through the medium plane of the ternary system. On cooling from  $T_1$  to  $T_F$ , seeding with fine and very pure particles of the (-)-enantiomer ensures the stereoselective crystallization of the (-)-enantiomer at a point ( $S'_f$ , not represented) symmetrical to  $S_f$  through the medium plane. This second entrainment affords 2 M mass units of the (-)-enantiomer. The following steps consist simply in adding 2 M followed by these two symmetrical crystallizations.

Among the variations proposed, one should mention:

1. *Auto-seeded process* [67–69]. Here, instead of a complete dissolution, the highest temperature is adjusted so that the overall synthetic mixture is located in the biphasic domain: <+> and its saturated solution  $s$  (Figure 22.23). Thus, the starting point of the process corresponds to a suspension of a pure enantiomer and there is no need for seeding. Up to 40% of the future crops can already be present as crystals in equilibrium with their saturated solution. The same procedure is applied to the auto-seeded crystallization of the antipode. When compared to the seeded and isothermal process, the auto-seeded and polythermic preferential crystallization appears somewhat as a preferential growth because crystals are bigger (and easier

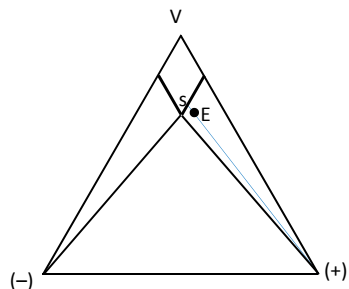


FIGURE 22.23 Location of the overall composition mixture as the starting point of the auto-seeded process.

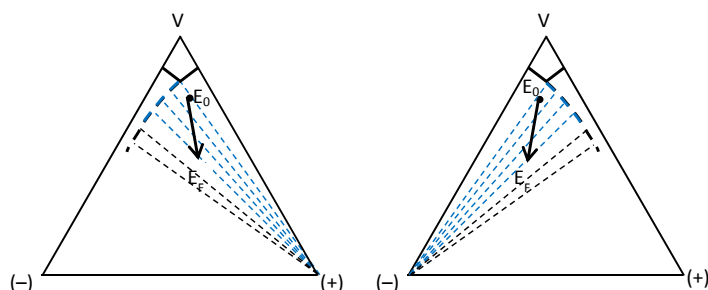


FIGURE 22.24 Pathways of the overall synthetic mixtures during resolution of the (+)-enantiomer (left) and (-)-enantiomer (right) by using ASPreCISE. The corresponding pathways of the solution points are not represented, but they can ideally be considered to move along the metastable solubility curves (in blue) at the extremities of the tie-lines.

to filtrate) [70], yields are improved, the process is usually more reproducible and robust, and it can easily be scaled up [71].

2. *Preferential crystallization induced by solvent evaporation (ASPreCISE)* [72,73]. This variation is adapted for temperature-sensitive products and/or when the solubility curve is excessively steep, i.e., the variation of solubility versus temperature is very small over a substantial range of temperature (Figure 22.24). In that case, supersaturation can be created by evaporation of a volatile solvent (or mixture of solvents) in which the solute has a sufficient solubility [73]. The evaporation can be carried out by simple distillation with or without depression or stripping by injection of an inert gas (e.g.,  $N_2$ ). This variant of preferential crystallization is compatible with auto-seeding (e.g., the evaporation starts with a suspension), and it also yields interesting results in resolutions involving temperature-sensitive molecules, as the process can be conducted without temperature cycles.
3. *Simultaneous preferential crystallization.* In this process, simultaneous crystallization with two different sizes of crystals is implemented. Ideally, this process works

with two nonoverlapping crystal size distributions. Sieving at the end of the process ensures the separation of the two enantiomers [74–76].

4. *Coupling with racemization in solution* [72]. This process, labelled SOAT for second-order asymmetric-transformation, can theoretically lead to a single enantiomer with a yield limited by the solubility of the enantiomer at the final temperature. As the preferential crystallization is progressing, the mother liquor keeps at  $ee = 0\%$  because of the racemization of the solvated enantiomers (here, we suppose that racemization in solution is faster than crystallization).

#### 22.2.4 Deracemization in Heterogeneous Systems

When two enantiomers crystallize as a stable conglomerate (a metastable conglomerate might be considered as well, but the application can be more problematic) and undergo a fast racemization in solution (or loss their chirality when solvated), a deracemization process can be implemented [77,78]. This general process is the ultimate access to homochirality and will be discussed in detail in Section 22.3, although some preliminary ideas can be introduced herein within the broad context of resolution protocols. Starting from a suspension of the racemic mixture, a flux of energy is applied through the heterogeneous system. The system, adopting different kinetic behaviors, will sooner or later evolve toward a suspension containing a single enantiomer. The energy flux can be different in nature, e.g., mechanical attrition (Viedma ripening) [79], ensured by glass beads, ultrasound with long exposure and high energy to speed up the process [80], temperature cycles, or temperature gradients [75,81,82]. They can be used as a unique source of energy or in various combinations. In general, the more powerful the flux of energy, the faster the deracemization (of course, there is an upper limit!).

If the starting material is perfectly racemic and without any chiral impurities, the evolution of the system should be perfectly stochastic. Nevertheless, those conditions are rarely fulfilled, thus the system could be “biased” so that a preferred enantiomer will be obtained. The advantage is provided by the enantiomer having the bigger particles, although if the antipode largely outnumbers, the final evolution could be toward the initial “small particles.”

When the system is not far from the above conditions, no “irreversible” evolution can be detected, even after several days. However, one can detect the presence of local fluctuations in  $ees$ . Those deviations are globally cancelling each other. In practice, a given enantiomer can be targeted; the latter being envisaged by unbalancing the initial enantiomeric excess of the solid in the slurry toward that enantiomer. A specific chiral impurity is also an alternative to “push” the evolution toward a desired enantiomer.

Several authors have tried to interpret the mechanism of this process (see Section 22.3), some proposing a model that accounts for the usual S shape of the  $ee$  (solid) versus time representation. This means that the whole process is autocatalytic. In other words, the more the solid phase deviates from the 50:50 composition, the faster the kinetics of deracemization. Even if all the authors agree with the autocatalytic character of this

phenomenon, the underlying mechanism is still a matter of debate, and synergetic effects may be involved.

### 22.2.5 Resolution of Racemates via Diastereomeric Associations (Usually Salt Formation)

To date, the resolution of racemic mixtures by diastereomeric salt formation has been the most widely used process, and the literature reveals thousands of successful applications (this includes a high proportion of patents; cf. the extensive review by Newman [83]). The advantages of this Pasteurian method are: (1) resolution is based on stable thermodynamic equilibria; (2) operational simplicity; (3) flexibility and compatibility with intermittent stages of production; and (4) easy scaling up (from mg to hundreds of tons). Nevertheless, the commonly acknowledged drawbacks of this method should likewise be highlighted: (1) a great deal of time and substantial amounts of matter might be necessary to find a productive and cost-effective process; (2) the need for a great deal of handling and time occupancy of the equipment; (3) the need for a quantitative salting out and the possible recycling of the resolution agent (additional work-up is often required); (4) traces of the resolving agent might be present in the final enantiomer, which could jeopardize the interest of the whole procedure (especially in the pharmaceutical industry); (5) both enantiomers of the resolving agent are not always available; and (6) the filterability of the crude, less soluble diastereomer can also be problematic. As for any resolving method, the racemization of the distomer (the less active enantiomer in terms of therapeutic applications) has a major impact on the economical performance of the process.

The main factors controlling the success of preparative resolutions are listed below and will be examined in the following paragraphs:

1. nature of the resolving agent
2. nature of the solvent
3. solute/resolving agent stoichiometries and solute/resolving agent/solvent stoichiometries
4. temperature of crystallization
5. control of crystal growth
6. enantiomeric purification
7. chemical purity of the racemic mixture to be resolved.

#### 22.2.5.1 *Nature of the Resolving Agent*

Despite considerable efforts to rationalize the design of optimal resolving agents for a given couple of enantiomers, it is still a matter of trial and error. Nevertheless, some empirical guidelines, based largely on experience, are commonly used as criteria for selecting a priori a resolving agent or synthesizing new resolution agents [84]. Thus, (1) the chiral center should be as close as possible to the functional group responsible for

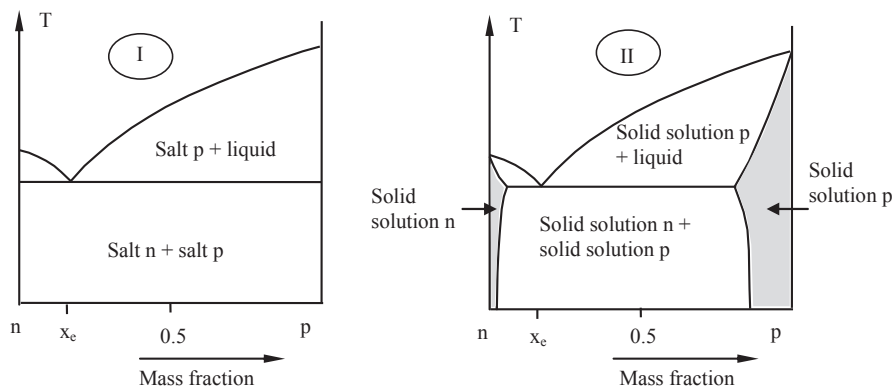


**FIGURE 22.25** Binary systems between diastereomers with (I) and without (II) partial solid solutions. NB: the composition of the eutectic liquid remains identical.

the salt formation; (2) the diastereomeric salt should have a tight rigid structure, which is usually achieved when several polar functional groups forming hydrogen bonds are readily accessible; and (3) strong acids or bases generally give better results than weak acids or bases.

Crystal structures and molecular modelling show that the differences in the physicochemical properties of the two salts lie in the 3D network of the two packings, and usually these differences are small, if not very small. Ideally, the best resolving agent, A(+) hereafter, should lead to a huge difference in solubility of the two associations A(+)B(−) (denoted salt *n* because of the sign of the two chiral species) and A(+)B(+) (i.e., salt *p*) in a simple solvent at (or near) room temperature. Provided this condition is fulfilled, the yield of the resolution could be almost quantitative. As a general statement, the yield of the resolution will depend on how far the eutectic composition departs from the 50:50 composition (examples in Figure 22.25: system I is more favorable than system II) and the absence of solid solution for, at least, the less soluble salt. When the diastereomers are nonsolvated phases, this situation is prompted by a great difference between the melting point of salts *n* and *p*; moreover, the diastereomeric salt with the highest temperature should have the highest enthalpy of fusion as well. Examples of such influences are given by the binary systems I and III (Figure 22.26) shown below.

In cases of ideal behavior with the solvent used (see Figures 22.27.1 and 22.27.2), the yield *Y* (or *Y'*) of the process is simply given by the application of the lever rule:

$$Y = \frac{1 - 2X_e}{1 - X_e} \in [0; 1] \quad \text{or} \quad Y' = \frac{0.5 - X_e}{1 - X_e} \in [0; 0.5]$$

Figures 22.27 (below) show two binary phase diagrams corresponding to *n* and *p* salts with the same melting points and the same enthalpy of melting. The difference between these two binary systems relies on the existence (or not) of domains of partial solid solution. In Figure 22.25(II), the yield of the resolution is lower than that of Figure 22.25(I). When the solvent leads to an ideal behavior, the purification of the solids

$$Y = \frac{1 - 2Xe}{1 - Xe} \in [0; 1] \text{ or } Y' = \frac{0.5 - Xe}{1 - Xe} \in [0; 0.5]$$

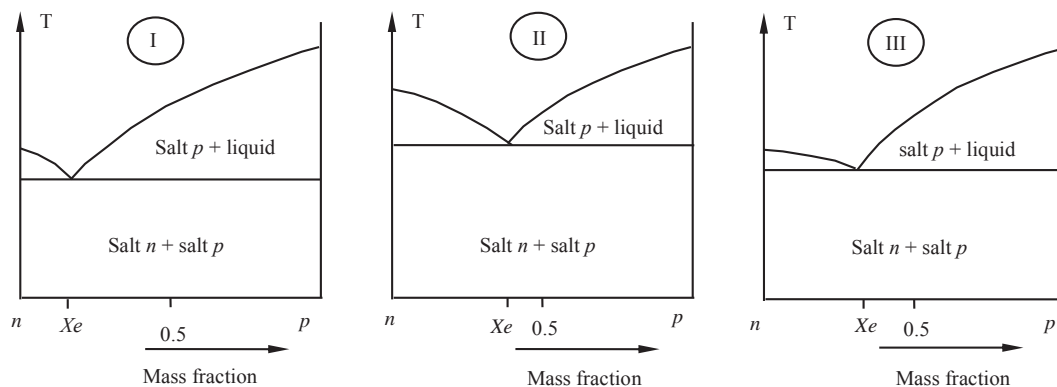


**FIGURE 22.26** Effects of differences in temperature of fusion and enthalpy of fusion of the diastereomers on the composition of the eutectic. In the three schematic cases (I, II, III), the melting temperature and the enthalpy of fusion of diastereomer *p* are kept the same. Diagrams I and II show the effect of the difference in melting temperature between the diastereomers: the greater the difference, the more deviates the diastereomeric excess of the eutectic liquid. Diagrams I and III show the effect of the melting enthalpy of the diastereomer *n* on diastereomeric excess of the eutectic liquid.

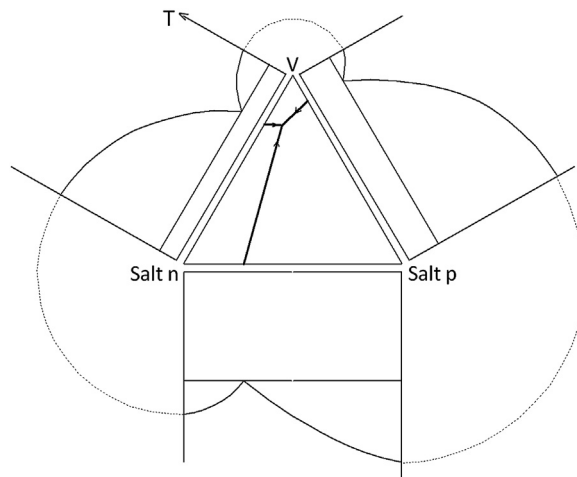


**FIGURE 22.27.1** Polythermic projection showing the monovariant lines in the ideal case.

is limited by the width of the monophasic domain and the temperature of crystallization. As a rule of thumb, the domain of solid solutions is narrow in composition if the crystal structure contains several H-bonds (directional strong bonds) between the cation and the anion.

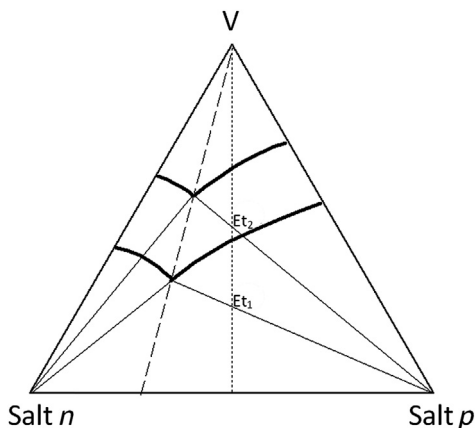


**FIGURE 22.27.2** Two isotherms are represented without partial solid solution; also neither polymorphism nor solvate. Starting from an initial 50:50 composition, the ideal composition for the best yield and purity of the salt  $p$  is denoted by  $Et_1$  at high temperature and  $Et_2$  at low temperature.

To optimize the resolution at pilot and industrial scales, several additional conditions apply to the resolving agent. (1) It should be available in the purest possible state and (2) it should be readily recoverable after completion of the crystallization step (and of course the same applies for the desired enantiomer). This recycling should give a high yield and be racemization-free even after many recoveries; in addition, it should easily be achieved by treatment with strong mineral acids or alkalis. A counter example is given by  $D(-)$  mandelic acid, which does not withstand completely the strong conditions of the free base step. (3) The resolving agent should be available as both enantiomers so that both chiral molecules can be obtained at the first crystallization step.

The formation of solid solutions can be used in a beneficial way by adding several closely related resolving agents of the same handedness: usually three is enough. The less soluble salt (we suppose here a family of acidic derivatives of resolving agents:  $RA_1$ ,  $RA_2$ , and  $RA_3$ ) usually has the following formulae:  $RA_1(1-x-y)RA_2^xRA_3^yB$ , where  $x$  and  $y$  generally depart from any simple ratios. This means that spontaneously the crystals will sort out the best composition, which builds the most stable less soluble salt. This variant of the Pasteurian resolution, called “family resolution” or “Dutch resolution,” has been found to increase the number of crystallized tests and the yield of the resolution. It also seems to have an inhibiting effect on the nucleation of the most soluble salt [85].

#### 22.2.5.2 Nature of the Solvent

In the vast majority of applications, the resolution is performed in a solvent; therefore, the selective crystallization takes place in the three-component system salt  $n$ –salt  $p$ –solvent. In some cases (see next section), the order of the system is even higher.

A few extra considerations are important too, such as deviation from ideality or the presence of a solvate. Regarding the former, starting from the results in the binary

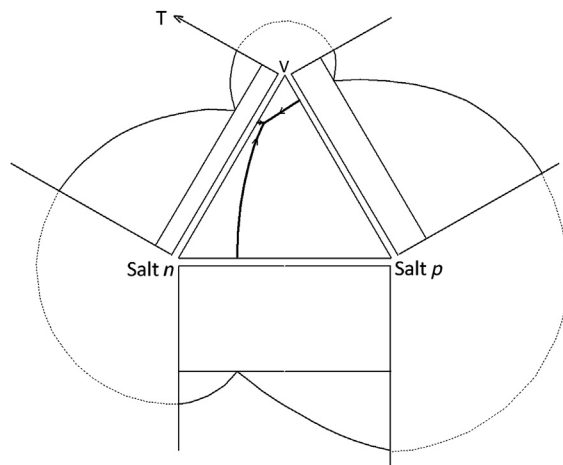


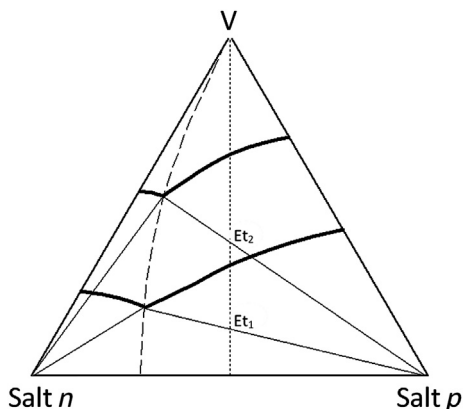
**FIGURE 22.28.1** Polythermic projection showing the monovariant lines. Departure from ideality leads to a favorable situation at low temperature.

system (see above), the solvent will be of major importance according to whether or not there is a deviation from ideality induced by the third component in the saturated solutions. Figures 27–29 illustrate the three different possibilities: (i) ideal behavior, (ii) positive deviations from ideality, and (iii) negative deviations from ideality.

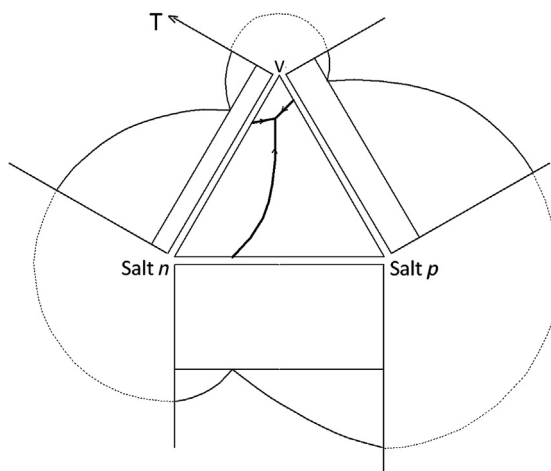
Figure 22.27.1 depicts the polythermic projection of the ternary phase diagram. Starting from the binary eutectic mixture, the monovariant line goes straight down to the ternary eutectic point; the solvent is just a physical diluent which does not introduce any deviation from the binary eutectic composition. Figure 22.27.2 shows two isothermal sections of this ideal ternary system. The best composition to perform an optimal resolution are points  $Et_1$  and  $Et_2$ , depending on the working temperature  $T_1$  and  $T_2$ , respectively [86,87]. The temperature of crystallization and filtration has an impact just on the volumic yield. The lower the temperature, the greater the amount of solvent, thus the lower the volumic yield.

Figure 22.28.1 shows the polythermic projection of the system: salt  $p$ –salt  $n$ –solvent  $V$ . By comparison to the similar ideal case (Figure 22.27.1), it is clear that the monovariant valley deviates toward the more soluble salt (salt  $n$ ) as temperature decreases. Without taking into account the effect linked to dilution—impacting on the volumic yield—the resolution should be preferably performed at low temperature. Two isotherms displayed in Figure 22.28.2 explicitly show the effect of the interactions between the solid phases and the saturated solutions at two different temperatures.

Figure 22.29.1 illustrates a negative effect of the solvent on the resolution process. The monovariant valley deviates toward the 50:50 composition plane. The yield is lowered as the temperature of crystallization/filtration is dropped. The two isothermal sections at  $T_1$  and  $T_2$  (Figure 22.29.2) clearly show that the lower the temperature, the lower the yield.



**FIGURE 22.28.2** Two isotherms are shown without partial solid solution, polymorphism, or solvate. Starting from an initial 50:50 composition, the ideal compositions for the best yield and purity of the salt *p* are denoted by  $Et_1$  at high temperature and  $Et_2$  at low temperature, the latter being the more favorable.



**FIGURE 22.29.1** Polythermic projection showing the monovariant lines. Departure from ideality leads to an unfavorable situation at low temperature.

The results of the resolution of  $\alpha$ -(2-thianaphthenyl)propionic acid demonstrate that, apart from the choice of the resolving agent, the selection of the solvent plays a decisive role [88]. It is worth noting that addition of small quantities of co-solvents can drastically modify the course of the separation. As the *n* and *p* components possess ionic bonds, water often has an important impact on the practical course of the crystallization. For example, resolution of 2-phenylpropionic acid using (+)- $\alpha$ -phenylethylamine is best carried out with propan-2-ol containing water (10%) as co-solvent [89]. By contrast, resolutions of 1-amino-alkan-2-ols are achieved in pure ethanol (the drier the better) [55]. As soon as the ethanol contains more than 0.5% of water, the process becomes more difficult to carry out and the yield decreases.

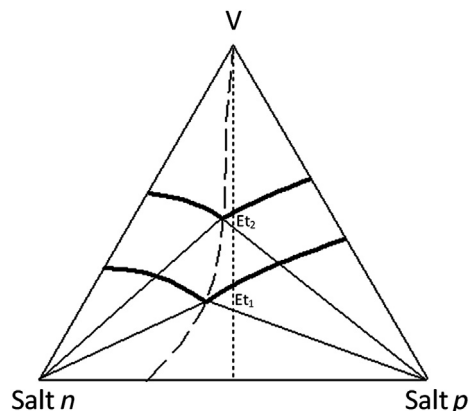


FIGURE 22.29.2 Two isotherms are shown without partial solid solution, polymorphism, or solvate. Starting from an initial 50:50 composition, the ideal compositions for the best yield and purity of the salt *p* are denoted by  $Et_1$  at high temperature and  $Et_2$  at low temperature, the former being the more favorable.

Concerning the presence of solvates, solvent molecules cannot only be the major component of the saturated solutions, and play a role in the possible deviation from ideality, but they can also be active partners in the construction of the crystal lattices. Among numerous situations, [Figures 22.30–22.32](#) illustrate situations where the presence of solvate is favorable, unfavorable, or even makes resolution impossible at low temperature. So, given these possible effects, the presence of a solvate must be systematically screened. Most of such solvates have a noncongruent melting. Some of them can lead to solid–vapor formation and decomposition (i.e., efflorescence) according to the value of the couple: temperature–partial pressure of the solvent.

### 22.2.5.3 Influences of Solute/Resolving Agent, Solute + Resolving Agent/Solvent Stoichiometries

The classical procedure involves a solute/resolving agent ratio = 1:1. Within the framework of ideality, [Figure 22.27.2](#) gives at two temperatures the best solute + resolving agent/total mass ratio. The coordinates of the total synthetic mixture are represented by  $Et_1$  at temperature  $T_1$  (the most concentrated system) and by  $Et_2$  at temperature  $T_2$  (the less concentrated system). The yields of the two processes carried out at  $T_1$  and  $T_2$  are identical and equal to:

$$Y = (0.5 - x_0) / (1 - x_0)$$

If a solvate appears at low temperature (salt *p*- $V_k$ , e.g., [Figure 22.30.2](#)) a more favorable process can be carried out at temperature  $T_2$ .

Two main modifications are occasionally applied to the classical procedure:

(1) Solute/resolving agent  $\neq 1$  [86,87]. Usually in this situation, the solute/resolving agent ratio is greater than 1, and as a result the consumption of the chiral resolving agent is reduced. The optimal ratio is determined by studying, at least, a part of the quaternary system: solvent; (+)enantiomer; (–) enantiomer; resolving agent. The resolving agent

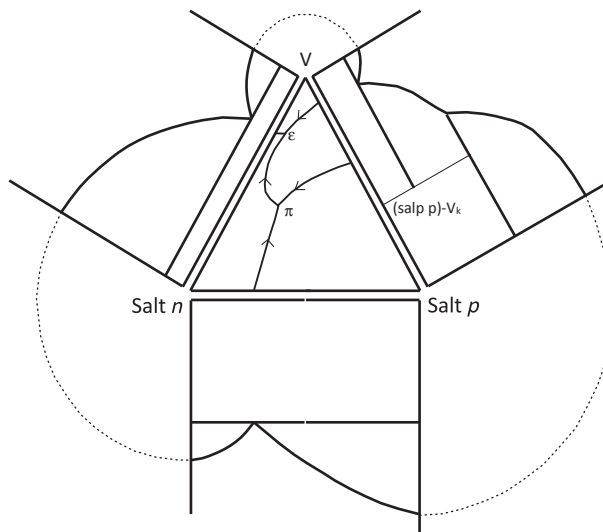


**FIGURE 22.30.1** Polythermic projection showing the monovariant lines. The presence of a stable solvate for the less soluble salt leads to a more favorable situation at low temperature.

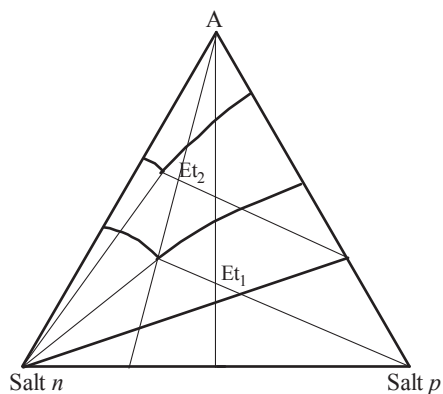


**FIGURE 22.30.2** Two isotherms are displayed with neither partial solid solution nor polymorphism, but with a solvate of the less soluble salt at low temperature. Starting from the 50:50 composition, the ideal compositions for the best yield and purity of the salt *p* are denoted by  $Et_1$  at high temperature and  $Et_2$  at low temperature, the latter being the more favorable.

added in excess can also be used so that the solute is more soluble (i.e., use as pH modifier). For instance, an excess of  $\alpha$ -methylbenzylamine can be added for resolving a racemic acid to ensure a better solubility of a poorly soluble chiral acidic molecule to be resolved [90]. In Figure 22.33 below (isotherm of the quaternary system: (+)-(–)-resolving agent-solvent), the resolving agent induces a solid solution of the less soluble salt when used in 1:1 stoichiometry. When used in default, the domain of the solid solution has been significantly reduced without impairing the diastereomeric

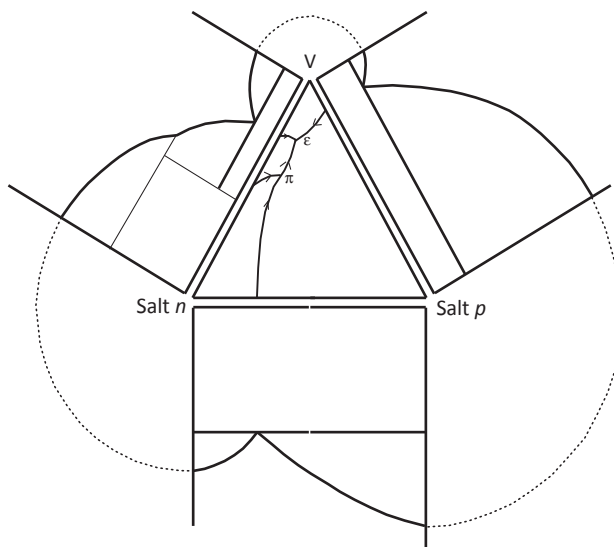


**FIGURE 22.31.1** Polythermic projection showing the monovariant lines. The presence of a stable solvate for the more soluble salt leads to an unfavorable situation at low temperature.

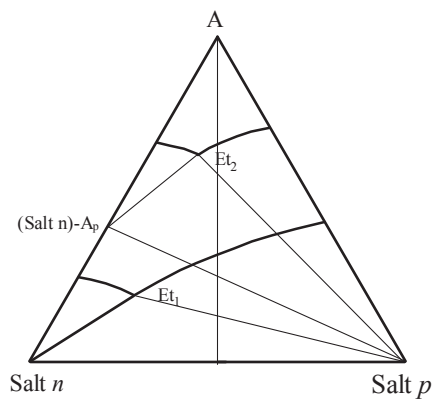


**FIGURE 22.31.2** Two isotherms are shown with neither partial solid solution nor polymorphism, but with a solvate of the most soluble salt. Starting from the 50:50 composition, the ideal compositions for the best yield and purity of the salt *p* are displayed by *Et*<sub>1</sub> at high temperature and *Et*<sub>2</sub> at low temperature, the former being the more favorable.

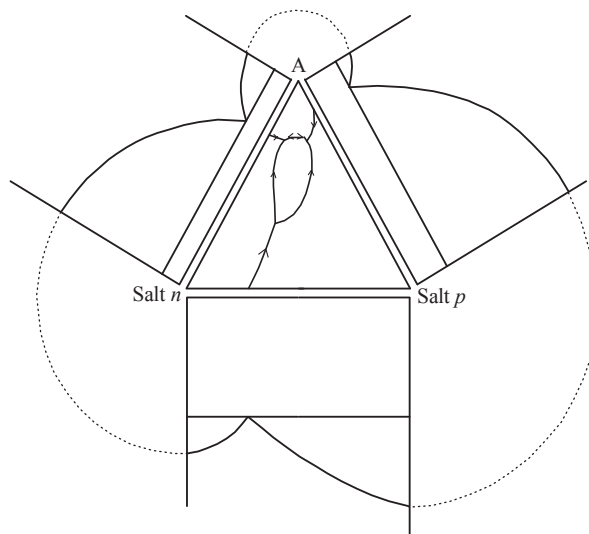


**FIGURE 22.32.1** Polythermic projection showing the monovariant lines. The existence of a stable double solvate impedes resolution at low temperature.

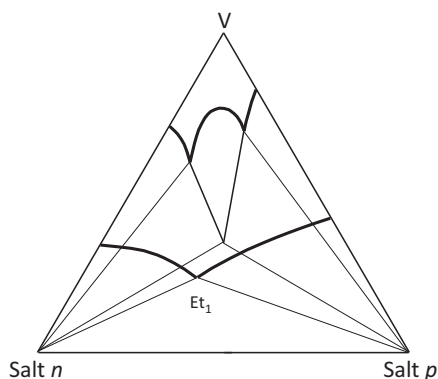


**FIGURE 22.32.2** Two isotherms are shown with neither partial solid solution nor polymorphism, but with a double solvate at low temperature. Starting from the 50:50 composition, the ideal composition for the best yield and purity of the salt *p* is denoted by  $Et_1$  at high temperature. No resolution takes place at low temperature.

discrimination (the diastereomeric excess of the invariant liquid remains unchanged). It is also worth mentioning that some anomalous salts can appear in these systems especially if, for instance, the resolving agent is a polyfunctional carboxylic acid.

(2) Addition of an achiral ion *Z* of the same ionic sign as the resolving agent [91]. The optimal composition is determined by studying part of the quinary system: solvent-(+)-(-)-resolving agent and *Z*. Usually the salts between *Z* and the solute in question are very soluble in the solvent used (or a mixture of solvents). This method helps in reducing the consumption in resolving agent [90,92].

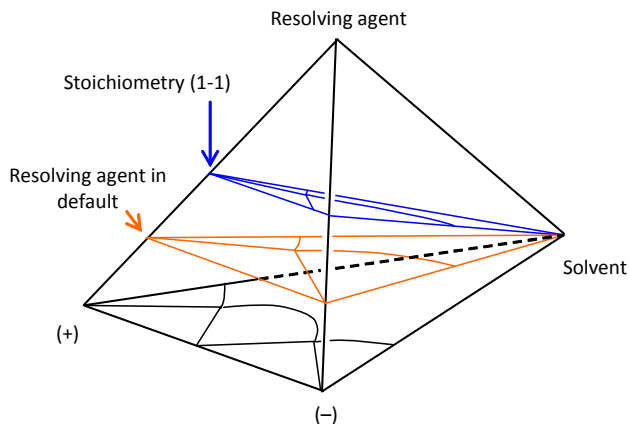


**FIGURE 22.33** Influence of the solute/resolving agent ratio on resolution performances. For 1:1 stoichiometry, the less soluble salt—with the (–)-enantiomer—has a domain of partial solid solution. In the other section where the resolving agent is in default, the domain of solid solution is almost nonexistent without changing the diastereomeric excess of the invariant liquid.

#### 22.2.5.4 Crystallization Temperature

The efficiency of the process is constant if the heterogeneous equilibrium has a quasi-ideal behavior whatever the temperature. In practice, this is not the usual rule and the yield is temperature dependent. The presence of solvate(s) and/or polymorphism constitute additional complications, which require the identification of the phases in competition as well as their domain of crystallization.

#### 22.2.5.5 Control of Crystal Growth

Despite very favorable thermodynamic conditions for resolution to occur, a process can be of low efficiency and difficult to carry out because of problems appearing during the nucleation stage and/or crystal growth of the less soluble salt and/or downstream operations such as filtration.

1. Nucleation. Because 50% of the solute is an “impurity,” the metastable Ostwald area can be enlarged to such an extent that no crystallization occurs, or when it does, the suspension (composed of the mother liquor plus the less soluble salt) is far too viscous to lead to a manageable filtration. The possible remedy to that problem is to seed the mother liquor as soon as the temperature is low enough, thereby favoring a smooth process of crystal growth of the less soluble salt at the expense of a noncontrolled primary nucleation. Another option is to perform some temperature cycling, thus favoring the growth of large crystals and to improve the crystallinity of solid particles.
2. Crystal growth. The great similarities between the two diastereomers can lead to a strong inhibiting effect on the crystal growth of the less soluble salt. The resulting

effects of these interactions at the solid–solution crystal interface are: (1) a decrease in the rate of crystallization; (2) possibility of creating inclusion among crystals, which lowers the optical purity of the crops; (3) a decrease in the crystallinity of the crop so that the presence of the counter diastereomer is possible, even beyond the thermodynamic concentration given by the equilibrium, and (4) induction of extreme shape in crystals—usually very fine platelets or elongated needle along the crystallographic axis parallel to the bonds that have the most ionic character. The last effect makes the suspension prior to filtration viscous and prompts difficulties during the separation of the crystals from their mother liquor. The above alternative methods (vide supra: [Subsection 22.2.5.3](#)) can be of great help in dealing with such difficulties. Some tailor-made additives can also constitute an option as crystal-shape modifiers. In any case, the control of the nucleation step (e.g., by means of seeding) and the implementation of a programmed cooling rate is strongly recommended in this situation.

#### 22.2.5.6 *Enantiomeric Purification*

The best strategy is to analyze carefully two ternary systems: salt *n*-salt *p*-solvent and (–)-enantiomer-(+)-enantiomer-solvent (base of the tetrahedral [Figure 22.33](#)) and to seek the best opportunity for purification purposes. Basically, there are two options:

1. Advantageous purification of the less soluble salt prior to release of the desired enantiomer (if no solid solution exists among the diastereomeric salts and/or a stable racemic compound exists between the enantiomers, or a solid solution exists in the ternary system: (–)-enantiomer-(+)-enantiomer-solvent).
2. Advantageous purification of the crude enantiomer could be performed in the ternary system: (–)-enantiomer-(+)-enantiomer-solvent (in the case of a solid solution between diastereomeric salts and/or a stable conglomerate between the enantiomers) [93]. It is worth mentioning that extreme pH values can induce (a partial) racemization. It is therefore recommended to check the stability of the enantiomer during salting out.

#### 22.2.5.7 *Chemical Purity of the Racemic Mixture*

This issue can be of prime importance when screening resolving agents and solvents. Indeed, the attempts to crystallize a diastereomeric salt can be seriously inhibited by the impurity(ies) in the racemic mixture. As a preventive action, it is recommended to purify the racemic mixture prior to any resolution effort. In a second step, when a positive “hit” has been found, the crude racemic mixture can be checked and, perhaps, the good surprise could be that the resolution is not derailed by the side product(s). If, unfortunately, the impurity(ies) has(have) a detrimental effect on the course of the resolution, a fair comparison with the purified starting racemic mixture can help in quantifying the magnitude of the problem.

## 22.3 Chiral Crystallization from Achiral and Chiral Molecules

As mentioned above, achiral molecules can crystallize in one of the 65 Sohncke space groups, although the chirality of the crystal structure arises from a particular molecular packing such as the formation of chiral helices. The two enantiomers will appear in two separate chiral crystals. It is still a matter of debate among stereochemists whether or not the latter should be denoted *spontaneous resolution* (vide supra: [Section 22.2](#) in any case) because, strictly, there is no racemate to resolve, but merely spontaneous generation of chirality.

A paradigmatic example is provided by sodium chlorate,  $\text{NaClO}_3$ . This substance is achiral, but it crystallizes as two enantiomorphous chiral solids (*l* and *d*), in the cubic chiral space group  $P2_13$  [94]. Hence,  $\text{NaClO}_3$  is achiral before crystallization, as it exists in solution as more or less dissociated ions or clusters without a definite chirality, although such species are able to generate a chiral solid. In the classical experiments by Kipping and Pope in the late nineteenth century [95],  $\text{NaClO}_3$  was crystallized by evaporation of an unstirred solution. Many crystallites were nucleated spontaneously and grew further. This experiment was systematically repeated, and in most cases equal amounts of left- and right-handed crystals were formed.

### 22.3.1 Homochirality in Crystal Growth from Achiral Molecules

It is possible to generate an enantiopure sample from an initial racemic batch of crystals through Ostwald ripening if all crystals convert into a single crystal, whereby the surface-to-volume ratio is minimum and thermodynamically more stable. In such experiments, the selection of chirality is largely stochastic and different trials will give rise to either enantiomer (vide infra for an extended discussion).

However, the whole amount of solute may be crystallized as a single enantiomer, which represents a case of symmetry breaking during crystallization. Kondepudi et al. reported the most striking example of this phenomenon when the crystallization process was performed under rapid stirring [96]. In a given experiment, crystals with the same chirality could be formed, either levorotatory or dextrorotatory, thus leading to complete symmetry breaking. Obviously, the handedness distribution in different experiments is random, and L and D crystals are obtained in different solutions ([Figure 22.34](#)).

What accounts for this symmetry breaking is clearly *secondary nucleation*. Under rapid stirring, the first chiral crystal, randomly formed, is broken by shear forces and triggers the production of a large number of secondary crystals of the same chiral sense. The growth process of such “daughter” crystals depletes the solution, avoiding supersaturation, which would lead to opposite-handed crystals by primary nucleation. Overall, this crystallization results in the generation of crystals with the same handedness in a particular batch ([Figure 22.35](#)).

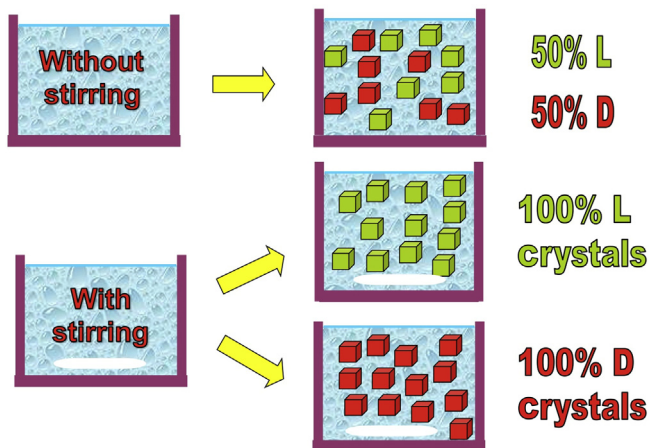


**FIGURE 22.34** Classical experiment by Kondepudi and coworkers (1990): When NaClO<sub>3</sub> was crystallized from an aqueous solution without stirring, equal numbers of *L* and *D* crystals were found. Moving the system to far-from-equilibrium conditions under stirring, a particular sample had invariably one single chirality, either *L* or *D*.

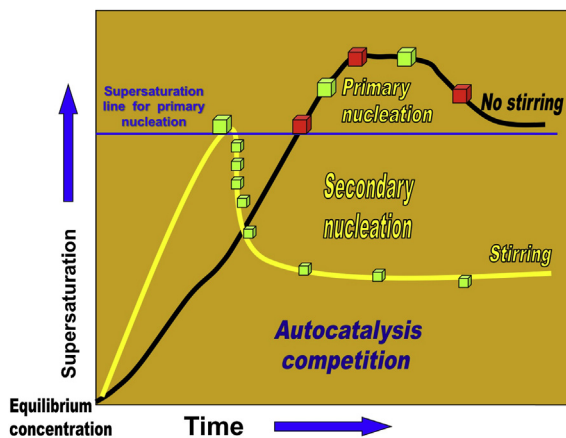


**FIGURE 22.35** Under stirring, the growth of the primary nucleus and the secondary nuclei can reduce the concentration to a level at which the rate of primary nucleation is zero. Secondary nuclei coming from a “mother” primary nucleus have the same handedness. In the absence of stirring, no (rapid) autocatalytic production of nuclei occurs, and all of them emerge from primary nucleation with random handedness.

### 22.3.2 Near-Equilibrium Systems

Viedma showed the remarkable and dramatic emergence of single chirality crystals of sodium chlorate (NaClO<sub>3</sub>) and sodium bromate (NaBrO<sub>3</sub>) in saturated suspensions of the two enantiomorphous crystals. Experiments are conducted with a racemic mixture so the system is equilibrated with an equal amount of right- and left-hand crystals in saturated aqueous solution. No new crystals nucleate under such conditions. It is demonstrated that abrasive grinding of crystals by stirring in the presence of glass beads promotes dynamic dissolution/crystallization processes that lead to a solid state of single chirality: One of the chiral populations of crystals disappears totally in an irreversible autocatalytic process that nurtures the other one. The system evolves from a similar amount of crystals of both hands to a single enantiomorphous population of crystals. The conversion takes place randomly, i.e., to the left or right hand with equal

probability. The system moves from an equilibrium stage between left- and right-handed crystals to a single chiral population of crystals promoted by grinding [79].

The first explanation of this striking observation was that attrition by glass beads produces a great number of smaller crystals, whose increase in the mixture causes in turn a slight supersaturation of  $\text{NaClO}_3$  in solution—although not enough to support primary nucleation. This is possible because, according to the Gibbs–Thomson effect, small particles have a higher solubility than large ones, therefore small crystals dissolve more readily than large crystals [97]. The latter is a direct consequence of the surface to volume ratio of the crystals as the system minimizes its total surface free energy. In a saturated solution in contact with crystals of different sizes, the phenomenon also leads to Ostwald ripening: Large crystals grow at the cost of smaller ones [98]. Thus, grinding enhances Ostwald ripening in the system and permanently generates particles of different size, therefore increasing the dissolution-growth process.

Notably, when a crystal of  $\text{NaClO}_3$  dissolves, the molecules are achiral, and they retain no memory of the previous chiral crystals, in a sort of “chiral amnesia” [99]. In this way molecules feed bigger crystals independently of their chirality: left- or right-handed crystals. Thus, a sort of recycling in this system relies on the fact that solid-phase chirality of the intrinsically achiral molecule of  $\text{NaClO}_3$  is lost upon dissolution, gaining a “second chance” at choosing its solid-phase chiral fate [99]. Ostwald ripening can reasonably be considered the driving force for the dissolution-growth process through this system (Figure 22.36).

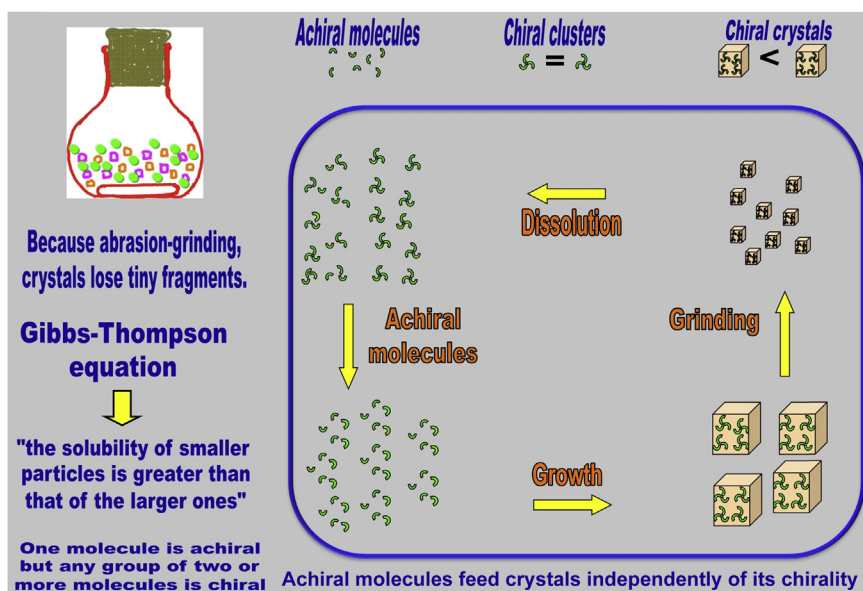


**FIGURE 22.36** Big crystals under grinding lose tiny fragments or chiral clusters that dissolve until they achieve the achiral molecular level. Such molecules or chiral clusters feed the larger crystals, thereby promoting a recycling process.

### 22.3.3 Extension to Chiral Molecules

Gratifyingly, the above premises could be extended from chiral crystals formed by achiral molecules to crystals formed by intrinsically chiral molecules. With this, we open the door to interesting applications en route to optically active and configurationally stable substances, particularly in the pharmaceutical industry [78]. The problem a priori is that chiral molecules in solution only add to chiral crystals of the same chirality: left-handed molecules add to left crystals only and right-handed molecules will add to right crystals. Obviously, under such circumstances, one cannot convert one enantiomer into the other by cycles of dissolution and growth in a mixture of enantiomorphous crystals.

Nevertheless, solution-phase racemization could satisfactorily solve that hurdle: Chiral molecules can interconvert between their left and right forms ( $L \leftrightarrow D$ ). Following this idea, Blackmond [99] and Viedma [100] suggested that evolution to a single chirality solid phase could appear in heterogeneous conglomerate systems of intrinsically chiral compounds that racemize in solution. This process allows the molecules to forget their chiral signature in solution. Racemization, essentially, plays the same role as the achiral state: Molecules lose their chiral identity, enabling the asymmetric conversion of crystals of one hand into the other (Figure 22.37). Paradoxically, molecular racemization in solution can be considered the driving force that guarantees chiral purity in the solid state from a previously solid racemic system [100].

The proof of concept could be verified experimentally for an imine derived from phenylglycine [77], aspartic acid (a proteinogenic amino acid) [101], and aldol and Mannich reaction products [102,103].

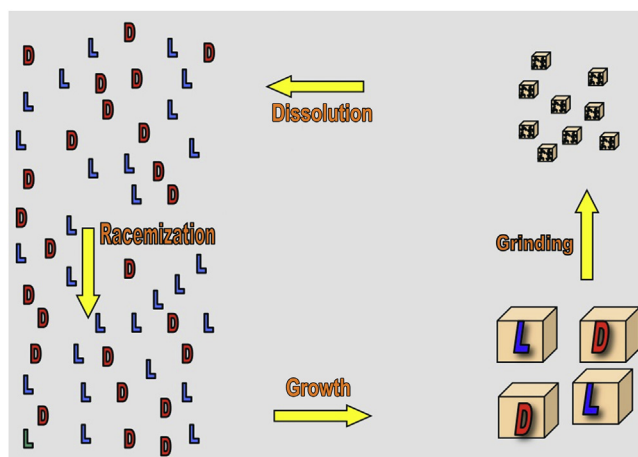


**FIGURE 22.37** The necessary recycling process for the evolution to a solid phase of single chirality can occur in heterogeneous conglomerate systems of intrinsically chiral molecules that racemize in solution.

The case of aspartic acid is noteworthy, as it represents the first example of total enantioenrichment of the solid phase for an essential amino acid mediated by solution-phase racemization. Moreover, homochiral evolution could be accomplished without mechanical energy (no glass balls), and induced only by heat. The process was studied under the Yoshioka racemizing conditions in acetic acid with a catalytic amount of salicylaldehyde [104]. Under these conditions, aspartic acid is hardly soluble and crystallizes as conglomerate [104]. The experiments start with heterogeneous solutions of racemic mixtures of L- and D-aspartic amino acid crystals in equilibrium with their solutions and the *ee* of the crystals rises inexorably over time, evolving to a single chirality solid state from any small initial imbalance in chiral crystal composition. The solid phase results in a complete solution-mediated conversion of the minor chirality into the originally more abundant crystal phase (Figure 22.38).

In principle, Ostwald ripening may account for complete homochirality of the solid phase so long as both chiral populations of crystals have different size. Different size means different solubility, and the equilibrium concentration of both molecular species in solution will not be identical. The rate constants for the forward and backward interconversion steps between D- and L-enantiomers would be different and the racemization process, proportional to the amount of enantiomers in solution, shifts toward the less soluble chiral crystals (Figure 22.39). This generates a thermodynamic disequilibrium in the system and the solution becomes supersaturated, although undersaturated for each chiral population of crystals depending on its solubility. Finally, only the less soluble enantiomer (having the biggest size) remains in solution as the system attempts to reestablish the equilibrium. This particular case has been proven experimentally for a conglomerate derivative of the amino acid phenylalanine by mixing two populations of chiral crystals with different sizes [105].

One artificial way to alter the size of crystals between two populations of chiral crystals in solution has also been proposed [106]. Thus, an enantiomerically pure solid phase can be isolated from a racemic conglomerate, even in the absence of racemization, provided that a suitable chiral additive is present during abrasive grinding. The additive stereoselectively hampers the growth of one enantiomer, and in this way

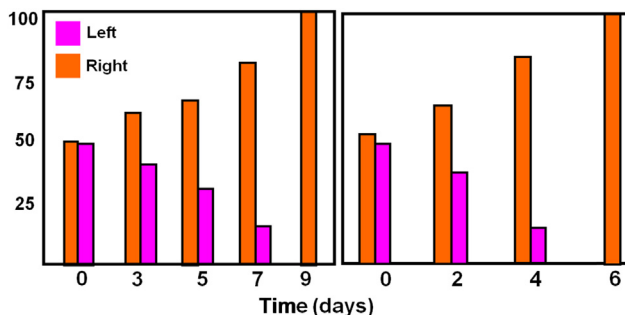
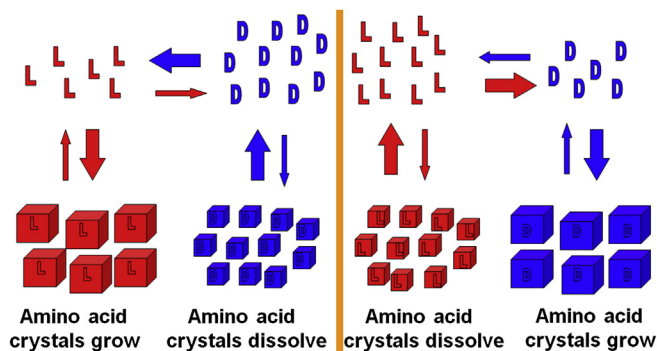
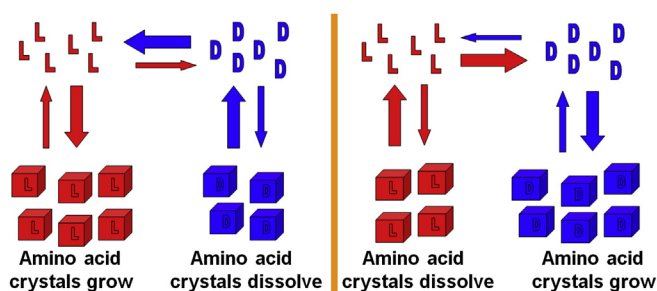


FIGURE 22.38 Evolution of solid-phase L-aspartic acid (*ees* vs time) under racemizing conditions. Different initial enantiomeric imbalances require different times to achieve homochirality.



**FIGURE 22.39** A saturated solution with chiral populations of crystals having different size (hence different solubility) shifts the racemization process toward the less soluble chiral crystals. Ostwald ripening provides a plausible rationale that justifies complete homochirality.



**FIGURE 22.40** Saturated solutions with an imbalance in the amount of solid enantiomers, but equal solubility, shift the racemization process toward the more abundant enantiomer (*vide supra*, Figure 22.39 for comparative purposes).

changes both the size and solubility between them. With this induced asymmetric bifurcation in the crystal size distribution under near-equilibrium abrasive grinding, it is possible to isolate the desired enantiomer but not to convert one enantiomer into the other. As expected, in the absence of the additive, the solid phase remained racemic.

However, an initially equal and random distribution of crystal sizes among two populations of chiral crystals, or a homogeneous distribution in size imposed by grinding, need further assumptions to justify complete homochirality. Paradoxically, the grinding process tends to avoid Ostwald ripening competition between both populations of chiral crystals because abrasion continuously standardizes crystal size distribution regardless of its chirality. Nevertheless, in all experiments, the minor chiral population of crystals dissolves and the more abundant one grows (Figure 22.40).

From a theoretical standpoint, several analyses have demonstrated that for Ostwald ripening to show exponential enantioenrichment in the solid phase, it is not sufficient to describe the crystal growth exclusively by incorporation of monomers [107]. We need an additional autocatalytic growth process to explain the observed phenomena. The first theoretical model to describe this abrasive effect was proposed by Uwaha [108]. In this model, the autocatalytic process is due to the incorporation of subcritical chiral clusters in crystals of the same handedness. Saito and Hyuga suggested that the racemization

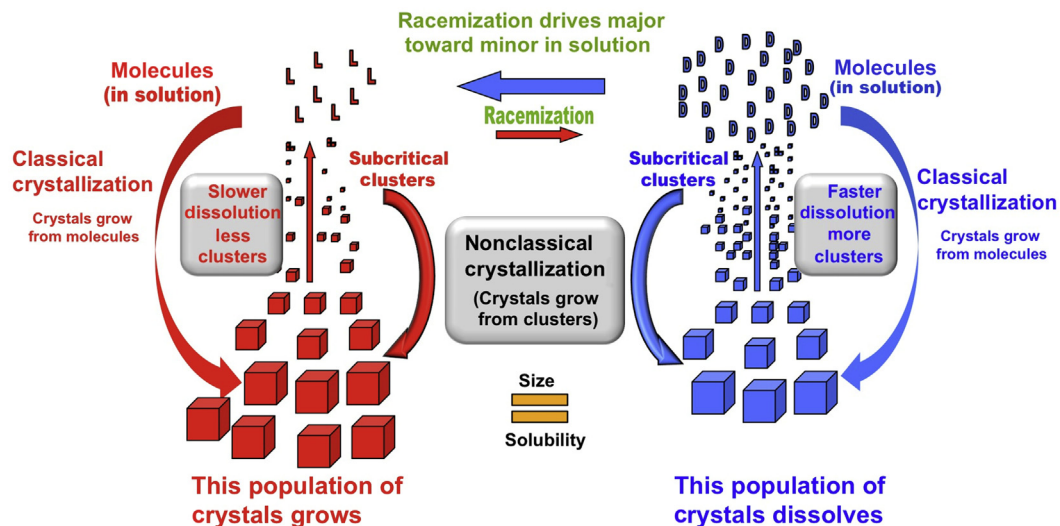


**FIGURE 22.41** During grinding, crystals are continuously fragmented into clusters. Reincorporation of chiral clusters occurs frequently for the major population of chiral crystals and, as result, a larger amount of chiral clusters of the minor population of chiral crystals dissolve.

step is enhanced at the surface of the chiral crystals [109], while Tsogoeva and associates have reported enantioenrichment in the solution of the enantiomer that forms the minor population in the solid phase during a reversible Mannich reaction [110]. These authors concluded that the chiral crystal surface enhances the racemization process.

McBride and Tully proposed that, in addition to Ostwald ripening, reincorporation of the chiral clusters to crystals of the same chirality by a sort of “nonclassical crystal growth” is required [111]. Again, this conjecture found some experimental support because, in the absence of racemization, a concentration inversion of molecules in solution exists during the grinding of a slurry of an enantioenriched racemic conglomerate [112]. The reincorporation of chiral clusters is more frequent for the major population of chiral crystals, thus a bigger amount of chiral clusters of the minor population of chiral crystals dissolve. The latter increases the concentration of molecules of the minor population in solution. Upon racemization, this difference in concentration drives molecules from the minor population to molecules of the major population. In this way, there is finally a complete conversion of the minor population of chiral crystals into crystals of the chirality that initially form the major population (Figure 22.41).

*This novel route to single chirality has been given the name Viedma ripening. [112]*

## Acknowledgments

We thank Dr. Marie-Noelle Delauney for substantial help in drawing phase diagrams.

## References

- [1] Eliel EL, Wilen SH, Doyle MP. Basic organic stereochemistry. New York: John Wiley & Sons; 2001. Ch. 1.
- [2] Kelvin Lord, Thomson W. Baltimore lectures on molecular dynamics and the wave theory of light. London: C. J. Clay & Sons; 1904.
- [3] For excellent and concise treatments of stereochemical terminology:
  - a) Mislow K. Chirality 2002;14:126–34;
  - b) Bentley R. Chirality 2010;22:1.
- [4] Cintas P. Chirality 2008;20:2.
- [5] Wallentin C-J, Orentas E, Wärnmark K, Wendt OF. Z. Krist 2009;224:607.
- [6] Eliel EL, Wilen SH. Stereochemistry of organic compounds. New York: John Wiley & Sons; 1994. p. 297–440.
- [7] Pérez-García L, Amabilino DB. Chem Soc Rev 2007;36:941.
- [8] Mislow K, Siegel J. J Am Chem Soc 1984;106:3319.
- [9] Jacques J, Collet A, Wilen SH. Enantiomers, racemates and resolutions. Malabar, FL: Krieger Publishing Co.; 1991. p. 3–31.
- [10] Flack HD. Helv Chim Acta 2003;86:905.
- [11] a) Flack HD. Acta Crystallogr 1983;A39:876;  
b) Flack HD, Bernardinelli G. Acta Crystallogr 1999;A55:908.
- [12] Ha Y, Allewell NM. Acta Crystallogr 1997;A53:400.
- [13] Flack HD, Shmueli U. Acta Crystallogr 2007;A63:257.
- [14] Thompson AL, Watkin DJ. Tetrahedron: Asymmetry 2009;20:712.
- [15] Flack HD, Bernardinelli G. Acta Crystallogr 2008;A64:484.
- [16] Dryzun C, Avnir D. Chem Commun 2012;48:5874.
- [17] Buda AB, Auf der Heyde T, Mislow K. Angew Chem Int Ed Engl 1992;31:989.
- [18] Zayit A, Pinsky M, Elgavi H, Dryzun C, Avnir D. Chirality 2011;23:17.
- [19] Petitjean M. Entropy 2003;5:271.
- [20] Bellarosa L, Zerbetto F. J Am Chem Soc 2003;125:1975.
- [21] Yogev-Einot D, Avnir D. Tetrahedron: Asymmetry 2006;17:2723.
- [22] a) Gal J. Chirality 2011;23:1;  
b) Gal J. Chirality 2008;20:1072;  
c) Gal J. Chirality 2008;20:5.
- [23] Flack HD. Acta Crystallogr 2009;A65:371.
- [24] Addadi L, Berkovitch-Yellin Z, Weissbuch I, Lahav M, Leiserowitz L. Top Stereochem 1986;16:1.
- [25] Gal J. Chirality 2012;24:959.
- [26] Ramberg PJ. Chemical structure, spatial arrangement. The early history of stereochemistry 1874–1914. Burlington, VT: Ashgate Publishing Co.; 2003. p. 277–319.
- [27] Ernst K-H, Wild FRWP, Blacque O, Berke H. Angew Chem Int Ed 2011;50:10780.
- [28] Werner H. Angew Chem Int Ed 2013;52:6146.
- [29] Finefield JM, Sherman DH, Kreitman M, Williams RM. Angew Chem Int Ed 2012;51:4802.
- [30] Guijarro A, Yus M. The origin of chirality in the molecules of life. Cambridge, UK: RSC Publishing; 2009.

- [31] Hitz T, Luisi PL. *Helv Chim Acta* 2002;85:3975.
- [32] Hazen RM, Filley TR, Goodfriend GA. *Proc Natl Acad Sci USA* 2001;98:5487.
- [33] Weissbuch I, Addadi L, Leiserowitz L, Lahav M. *J Am Chem Soc* 1988;110:561.
- [34] a) Agranat I, Caner H, Caldwell J. *Nat Rev Drug Discov* 2002;1:753;  
b) Caner H, Groner E, Levy L, Agranat I. *Drug Discov Today* 2004;9:105.
- [35] Mullard A. *Nat Rev Drug Discov* 2012;11:91.
- [36] Breuer M, Dittrich K, Habicher T, Hauer B, Kessler M, Stürmer R, et al. *Angew Chem Int Ed* 2004; 43:788.
- [37] See highlights in *Nature Rev Drug Discov* 2003;2:424.
- [38] Agranat I, Wainshtein SR, Zusman EZ. *Nat Rev Drug Discov* 2012;11:972.
- [39] Gu C-H, Grant DJW. In: Reddy IK, Mehvar R, editors. *Chirality in drug design and development*. New York: Marcel Dekker; 2004. p. 1–36.
- [40] Tung H-H, Paul EL, Midler M, McCauley JA. *Crystallization of organic compounds. An industrial Perspective*. New York: John Wiley & Sons; 2009. p. 155–166.
- [41] Polenske D, Lorenz H, Seidel-Morgenstern A. *Cryst Growth Des* 2007;7:1628.
- [42] Kaemmerer H, Horvath Z, Lee JW, Kaspereit M, Arnell R, Hedberg M, et al. *Org Process Res Dev* 2012;16:331.
- [43] Flack HD. *Acta Cryst* 2013;C69:803.
- [44] Scott RL. *J Chem Soc Faraday Trans II* 1977;3:356.
- [45] Gallis HE, Bougrioua F, Oonk HAJ, van Ekeren PJ, van Miltenburg JC. *Thermochim Acta* 1996;274:231.
- [46] Renou L, Morelli T, Coste S, Petit M-N, Berton B, Malandain J-J, et al. *Cryst Growth Des* 2007;7: 1599.
- [47] Wermester N, Aubin E, Pauchet M, Coste S, Coquerel G. *Tetrahedron: Asymmetry* 2007;18:821.
- [48] Helmreich M, Niesert C-P, Cravo D, Coquerel G, Levilain G, Wacharine-Antar S. *Pat WO2010109015 (A1)* 2010.
- [49] Druot S, Petit M-N, Petit S, Coquerel G, Chanh NB. *Molec Cryst Liq Cryst* 1996;275:271.
- [50] Coquerel G. *Enantiomer* 2000;5:481.
- [51] Meyerhoffer W. *Ber* 1904;37:2604.
- [52] Taratin NV, Lorenz H, Kotelnikova EN, Glikin AE, Galland A, Dupray V, et al. *Cryst Growth Des* 2012;12:5882.
- [53] Brandel C, Amharar Y, Rollinger J, Griesser U, Cartigny Y, Petit S, et al. *J Molec Pharm* 2013;10(10): 3850–61.
- [54] Lorenz H, von Langermann J, Sadiq G, Seaton CC, Davey RJ, Seidel-Morgenstern A. *Cryst Growth Des* 2011;11:1549.
- [55] Catroux L, Coquerel G, Combret Y. *Patent WO1998/023559* 1997.
- [56] Zorkii PM, Razumaeva AE. *Acta Cryst* 1977;A33:1001.
- [57] Galland A, Dupray V, Berton B, Morin S, Sanselme M, Atmani H, et al. *Cryst Growth Des* 2009;9: 2713.
- [58] Clevers S, Simon F, Dupray V, Coquerel G. *J Therm Anal Calorim* 2013;112:271.
- [59] Clevers S, Simon F, Sanselme M, Dupray V, Coquerel G. *Cryst Growth Des* 2013;13:3697.
- [60] Kleinman DA. *Phys Rev* 1962;128:1761.
- [61] Dailey CA, Burke BJ, Simpson GJ. *Chem Phys Lett* 2004;390:8.

- [62] Coquerel G, Perez G, Hartman P. *J Cryst Growth* 1988;88:511.
- [63] Gonella S, Mahieux J, Sanselme M, Coquerel G. *Org Process Res Dev* 2012;16:286.
- [64] Mahieux J, Gonella S, Sanselme M, Coquerel G. *Cryst Eng Comm* 2012;14:103.
- [65] Ndzié E, Cardinaël P, Petit M-N, Coquerel G. *Enantiomer* 1999;4:97.
- [66] Coquerel G. In: Sakai K, Hirayama N, Tamura R, editors. *Novel optical resolution technologies. Topics in current chemistry*, vol. 269. Berlin: Springer; 2007. p. 1–51.
- [67] Coquerel G, Bouaziz R, Petit M.-N. Patent WO1995/008522 1995.
- [68] Levilain G, Coquerel G. *Cryst Eng Comm* 2010;12:1983.
- [69] Ndzié E, Cardinaël P, Schoofs A-R, Coquerel G. *Tetrahedron: Asymmetry* 1997;8:2913.
- [70] Courvoisier L, Ndzié E, Petit M-N, Hedtmann U, Sprengard U, Coquerel G. *Chem Lett* 2001;4:364.
- [71] Coquerel G, Tauvel G, Petit M.-N. Patent WO 2009/027614 2008.
- [72] Levilain G, Coquerel G. Patent WO2011/07330 2010.
- [73] Mahieux J, Sanselme M, Harthong S, Melan C, Aronica C, Guy L, et al. *Cryst Growth Des* 2013;13:3621.
- [74] Doki N, Yokota M, Sasaki S, Kubota N. *Cryst Growth Des* 2004;4:1359.
- [75] Levilain G, Eicke MJ, Seidel-Morgenstern A. *Cryst Growth Des* 2012;12:5396.
- [76] Lorenz H, Polenske D, Seidel-Morgenstern A. *Chirality* 2006;18:828.
- [77] Noorduyn WL, Izumi T, Millemaggi A, Leeman M, Meekes H, Van Enckevort WJP, et al. *J Am Chem Soc* 2008;130:1158.
- [78] Noorduyn WL, Vlieg E, Kellog RM, Kaptein B. *Angew Chem Int Ed* 2009;48:9600.
- [79] Viedma C. *Phys Rev Lett* 2005;94:065504.
- [80] Suwannasang K, Flood A, Rougeot C, Coquerel G. *Cryst Growth Des* 2013;13:3498.
- [81] Viedma C, Cintas P. *Chem Commun* 2011;47:12786.
- [82] Hein JE, Cao BH, Viedma C, Kellog RM, Blackmond DG. *J Am Chem Soc* 2012;134:12629.
- [83] Newman P. *Optical resolution procedures for chemical compounds (volume 1: amines and related compounds)*. NY: Optical Resolution Information Center, Manhattan College: Riverdale; 1978.
- [84] Sakai K, Sakurai R, Nohira H. In: Sakai K, Hirayama N, Tamura R, editors. *Novel optical resolution technologies. Topics in current chemistry*, vol. 269. Berlin: Springer; 2007. p. 199–231.
- [85] Kellog RM, Kaptein B, Vries TR. *Novel Optical Resolution Technologies*. In: Sakai K, Hirayama N, editors. *Topics in Current Chemistry*, vol. 269. Berlin: Springer; 2007. p. 159–97.
- [86] Marckwald W. *Ber.* 1896;29:42.
- [87] Marckwald W. *Ber.* 1896;29:43.
- [88] Sjoberg B. *Ark Kemi* 1958;12:588.
- [89] Bayley CR, Vaidya NA. In: Collins AN, Sheldrake G, Crosby J, editors. *Chirality in industry: the commercial manufacture and applications of optically active compounds*. Chichester: John Wiley & Sons; 1992. Ch. 2.
- [90] Coquerel G, Petit M-N, Bouaziz R, Depernet D. *Chirality* 1992;4:400.
- [91] Pope WJ, Peachey SJ. *J Chem Soc* 1899;75:1066.
- [92] Coquerel G, Mofaddel N, Petit M-N, Bouazuiz R. *Bull Soc Chim Fr* 1991;128:418.
- [93] Marchand P, Lefèbvre L, Querniard F, Cardinaël P, Perez G, Counieux J-J, et al. *Tetrahedron: Asymmetry* 2004;15:2455.
- [94] Abrahams SC, Bernstein JL. *Acta Cryst* 1977;B33:3601.

- [95] a) Kipping FS, Pope WJ. *Nature* 1898;59:53;  
b) Kipping FS, Pope WJ. *J Chem Soc* 1898;73:606.
- [96] Kondepudi DK, Kaufman RJ, Singh N. *Science* 1990;250:975.
- [97] a) Gibbs JW. *Trans Connect Acad Sci* 1876;3:108;  
b) Gibbs JW. *Trans Connect Acad Sci* 1878;16:343.
- [98] Ostwald W. *Z Phys Chem* 1897;22:289.
- [99] Blackmond DG. *Chem Eur J* 2007;13:3290.
- [100] Viedma C. *Astrobiology* 2007;7:312.
- [101] Viedma C, Ortiz JE, De Torres T, Izumi T, Blackmond DG. *J Am Chem Soc* 2008;130:15274.
- [102] Flock AM, Reucher CMM, Bolm C. *Chem Eur J* 2010;16:3918.
- [103] Tsogoeva SB, Wei S, Freund M, Mauksch M. *Angew Chem Int Ed* 2009;48:590.
- [104] Yamada S, Hongo C, Yoshioka R, Chibata I. *J Org Chem* 1983;48:843.
- [105] Kaptein B, Noorduyn WL, Meekes H, van Enckevort WJP, Kellogg RM, Vlieg E. *Angew Chem Int Ed* 2008;47:7226.
- [106] Noorduyn WL, van der Asdonk P, Meekes H, van Enckevort WJP, Kaptein B, Leeman M, et al. *Angew Chem Int Ed* 2009;48:3278.
- [107] **For recent mathematical models:**
  - a) Skrdla PJ. *Cryst Growth Des* 2011;11:1957;
  - b) Iggländ M, Mazzotti M. *Cryst Growth Des* 2011;11:4611;
  - c) Wattis JAD. *Orig Life Evol Biospheres* 2011;41:133.
- [108] a) Uwaha M. *J Phys Soc Jpn* 2004;73:2601;  
b) Uwaha M, Katsuno H. *J Phys Soc Jpn* 2009;78:023601.
- [109] a) Saito Y, Hyuga H. *J Phys Soc Jpn* 2008;77:113001;  
b) Saito Y, Hyuga H. *J Phys Soc Jpn* 2010;79:083002.
- [110] Wei S, Mauksch M, Tsogoeva SB. *Chem Eur J* 2009;15:10255.
- [111] McBride JM, Tully JC. *Nature* 2008;452:161.
- [112] Noorduyn WL, van Enckevort WJP, Meekes H, Kaptein B, Kellogg RM, Tully JC, et al. *Angew Chem Int Ed* 2010;49:8435.

# In Situ Observation of Crystal Growth by Scanning Electron Microscopy

Yoshikazu Homma

DEPARTMENT OF PHYSICS, TOKYO UNIVERSITY OF SCIENCE, SHINJUKU, TOKYO, JAPAN

## CHAPTER OUTLINE

<b>23.1 Introduction</b> .....	<b>1003</b>
<b>23.2 Method of In Situ Imaging by SEM</b> .....	<b>1004</b>
23.2.1 Historical Background and Instrumentation .....	1004
23.2.2 Principle of Imaging.....	1007
23.2.3 Limitations of the Method.....	1009
<b>23.3 Application of In Situ SEM</b> .....	<b>1010</b>
23.3.1 Growth Mode .....	1010
23.3.1.1 Basic Picture of MBE Growth.....	1010
23.3.1.2 SE Images of 2D-Island Nucleation and Step Flow .....	1013
23.3.2 Nucleation and Growth on GaAs Surface .....	1015
23.3.2.1 GaAs(001).....	1015
23.3.2.2 GaAs(111).....	1017
23.3.3 Instability of Step-Flow Growth .....	1020
23.3.4 Graphene Growth .....	1022
23.3.4.1 Monolayer Graphene Imaging.....	1022
23.3.4.2 Multilayered Graphene .....	1024
23.3.4.3 Graphene Nucleation.....	1025
<b>23.4 Summary</b> .....	<b>1027</b>
<b>References</b> .....	<b>1028</b>

## 23.1 Introduction

Crystal growth in vapor phase is promoted by incorporation of adatoms into the kink sites of atomic steps. As a result of adatom incorporation, atomic steps advance; thus, observing the motion of atomic steps during growth provides insights into growth

physics. Atomic resolution is obtained by scanning tunneling microscopy (STM), and thus atomic processes of adatom incorporation can be observed by the state-of-the-art technology [1]. At the growth temperature of semiconducting materials, however, adatom diffusion length becomes on the order of  $10^2$ – $10^4$  nm, which is far larger than the atomic scale and is not easily accessible for atomic-resolution measurement methods. Electron microscopy is a complementary method to STM and useful to obtain wide-range information of crystal growth. Especially for III-V compound semiconductor growth, compatibility with the molecular beam epitaxy (MBE) technology is important. Thus, scanning electron probes including scanning reflection electron microscopy (SREM) and scanning electron microscopy (SEM) have been used for in situ observation of MBE processes [2–9].

The present authors have developed an atomic-step observing method based on SEM [10–12] and applied it to the in situ observation of semiconductor growth by MBE [13–25]. The advantage of SEM for observing crystal growth is that it is rather easy to combine with MBE because the SEM instrument is simple, and restriction to the geometry of molecular beam sources and the electron gun is not very strict [13,21]. Furthermore, the wide field of view in SEM is useful for observing phenomena occurring on a large scale [22–25].

This chapter describes the basics and applications of in situ SEM. Initial stages of GaAs and Si MBE processes are shown as real-space images. Different growth modes, 2D island nucleation, step propagation (step flow), and unstable step flow are observed depending on the adatom diffusion length and the terrace width on the surfaces. A recent application to graphene growth is also discussed.

## 23.2 Method of In Situ Imaging by SEM

### 23.2.1 Historical Background and Instrumentation

Ichikawa et al. used a scanning electron probe for the first time to observe MBE-grown Si surfaces [3]. They detected reflection high-energy electron diffraction (RHEED) spots to image the growing surfaces. The microprobe RHEED apparatus is shown in Figure 23.1 [2]. The primary electron beam of 20 keV was directed to the sample surface at a grazing incidence. Dark field scanning images were obtained by selecting one of RHEED spots by the aperture and optical fiber (SREM images). They demonstrated Si(111) surface topography changes corresponding to RHEED intensity oscillation during MBE growth [3].

Similar systems were attempted to be applied to the observation of GaAs and AlGaAs growth processes by Inoue et al. [4], Isu et al. [5], and Nishinaga et al. [8]. An example of an MBE system equipped with microprobe RHEED and SEM is shown in Figure 23.2 [8]. As the MBE chamber, the system has Knudsen cells and liquid nitrogen shrouds. An electron gun with differential pumping systems is mounted on top of the chamber [8] or side of the chamber [6]. To dump mechanical vibration, the whole system is set on a

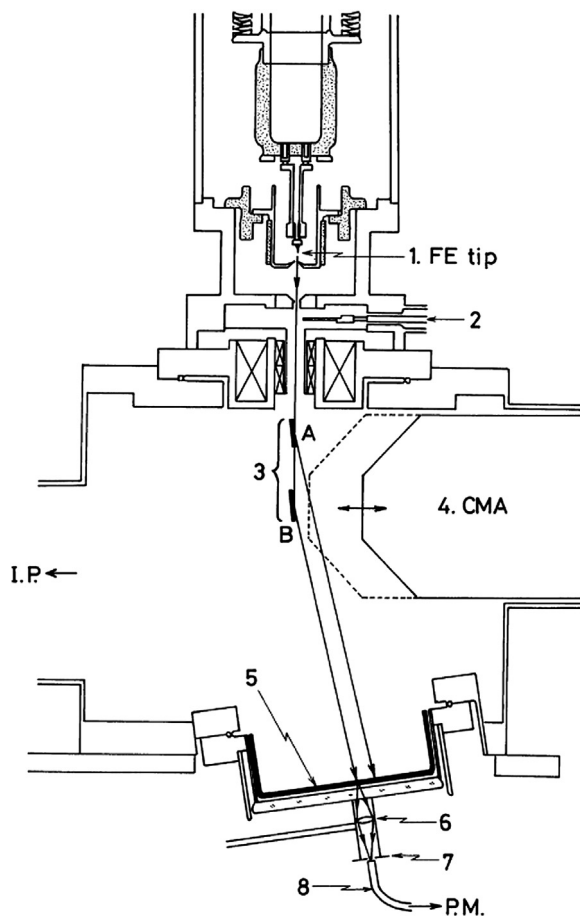


**FIGURE 23.1** Microprobe reflection high-energy electron diffraction apparatus [2]. 1. Tungsten field-emission (FE) tip, 2. variable aperture, 3. sample, 4. cylindrical mirror analyzer (CMA), 5. fluorescent screen, 6. optical lens, 7. aperture plate, 8. optical fiber.

vibration isolator. Surface diffusion lengths were analyzed from the variations of growth rate as a function of position, which were measured from intensity oscillation in the SREM images [5,9]. In addition to SREM images, secondary electron (SE) images were utilized to observe Ga droplet formation and lateral growth of Ga monolayers [7,8].

The advantage of microprobe RHEED or SREM is that structural information of the growing surfaces is obtained as real space images. However, the grazing incidence for RHEED causes extreme image foreshortening. For example, a  $2^\circ$  grazing incidence elongates the beam spot size in the beam incidence direction to about a factor of 29. Thus, when a 10-nm-diameter beam is used, the resolution in the parallel direction degrades to about 300 nm. This makes observation of small 2D islands difficult. To overcome the disadvantage of SREM, the present authors took a different approach.

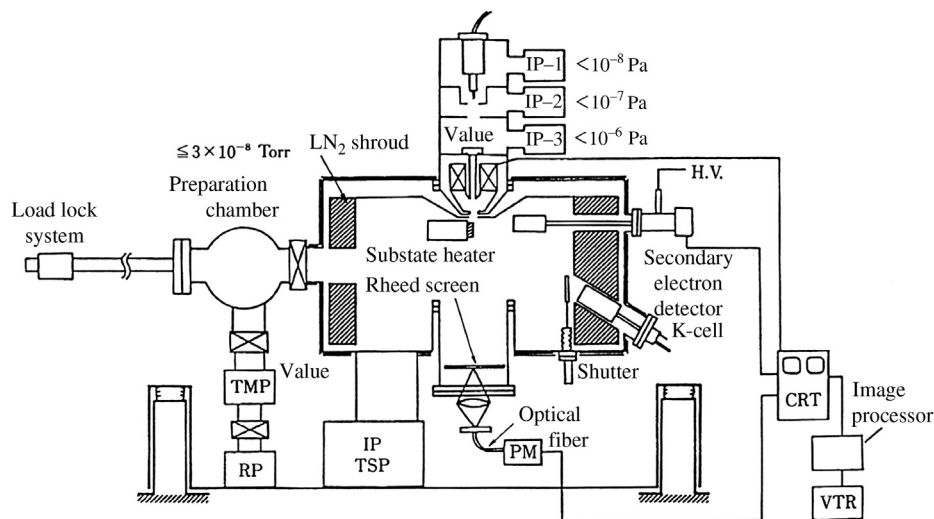


**FIGURE 23.2** Molecular beam epitaxy system equipped with scanning electron microscopy and microprobe reflection high-energy electron diffraction [8]. IP, ion pump; RP, rotary pump; TMP, turbo-molecular pump; TSP, titanium sublimation pump; VTR, videotape recorder.

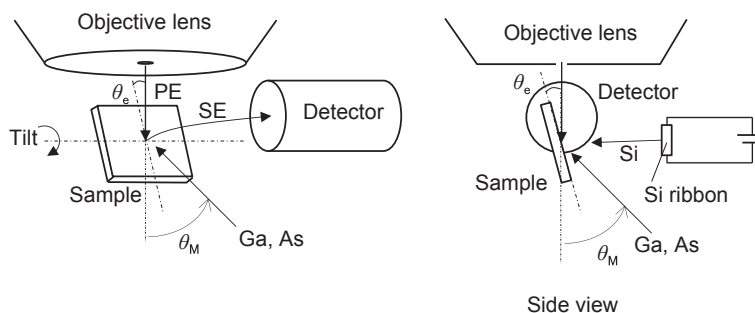


**FIGURE 23.3** Schematic illustration of the geometry around the sample in the in situ molecular beam epitaxy/scanning electron microscopy system. PE, primary electron; SE, secondary electron.

They used a moderate grazing incidence of  $10^{\circ}$ – $20^{\circ}$  and observed atomic steps and 2D islands as SE images. With a  $10^{\circ}$  incidence, the elongation of beam spot is reduced to less than a factor of 6. The apparatus was similar to the microprobe RHEED apparatus, equipped with a cold field emission electron gun, that of Hitachi S-800 modified to ultrahigh vacuum compatible, and Knudsen cells for Ga and As molecular beams. Special care was taken to reduce mechanical vibration of the sample manipulator. A schematic illustration of the geometry around the sample is shown in Figure 23.3. As a Si source, Si was evaporated by resistively heating a Si ribbon near the sample. The SE detector was a conventional Everhart–Thornley detector set near the tilt axis of the sample. For in situ SE imaging, the sample surface should be exposed to both the electron and molecular

beams. The incident angles of the electron beam and molecular beams are not independent. When the electron beam incident angle is  $\theta_e$  to the sample surface, the Ga and As molecular beams are directed upward onto the surface at  $\theta_M - \theta_e$ . With  $\theta_M \approx 45^\circ$ ,  $\theta_e$  of  $10^\circ$ – $20^\circ$  makes the molecular beam incidence of  $35^\circ$ – $25^\circ$ .

### 23.2.2 Principle of Imaging

The SE contrast of atomic steps is created by topographic effects at the step edge. The topographic contrast appears even for monatomic-high steps due to SE yield change at the step edge and anisotropy of detection efficiency of SE detector [10,11]. The behaviors of the edge contrast in terms of the relationship between electron beam incidence and step edge, and that between detector position (or detection efficiency depending on the direction of emitted SEs) and step direction are all the same for monatomic and macroscopic steps. The difference is only the total SE intensity at the steps. An example of atomic step contrast in SEM is shown in Figure 23.4. This is an atomically flat GaAs(001) surface grown in the in situ SEM/MBE combined system. There are bright and dark lines in the SE image. Those are monatomic steps on the GaAs(001) surface. Since the terrace height is lowest near the center of the image, the staircase of atomic steps goes up toward both the top and bottom of the SEM image. The primary electron beam of 25 keV was incident from the bottom to the top of the image at a grazing angle of  $10^\circ$  to the surface. Thus the electron beam goes downward to the steps for the lower half of the image and upward to the steps for the upper half. Atomic steps appear bright when

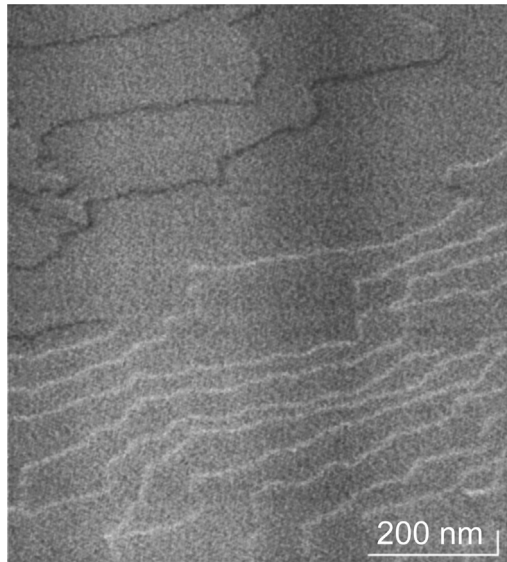


**FIGURE 23.4** Secondary electron image of atomic steps on GaAs(001) surface. The height of terrace is lowest at the center of the image. The primary electron beam of 25 keV was incident from the bottom to the top of the image at a grazing incidence of  $10^\circ$  to the surface.

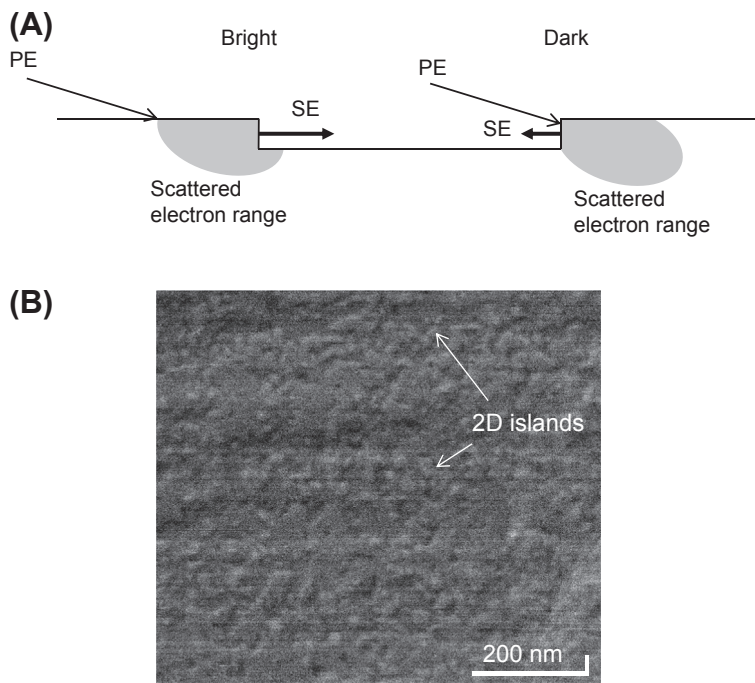


**FIGURE 23.5** (A) Schematic illustration of secondary electron (SE) emission at the step edge depending on the primary electron incident direction. (B) SE contrast of 2D islands on GaAs(001) surface. PE, primary electron.

the primary electron beam goes down the atomic step staircase, while they appear dark when the primary electron beam goes up the staircase. The difference between the step-down and step-up cases is the amount of SEs emitted from the step-riser part as shown in Figure 23.5(A). In the step-down case, a large amount of SEs is produced by forward-scattered primary electrons. Similar edge contrast can be obtained for 2D islands that are small terraces. For small islands, the bright contrast dominates as shown in Figure 23.5(B).

An entirely different type of contrast can be used for atomic step imaging on the Si(111) surface. This utilizes the surface phase contrast between the  $7 \times 7$  reconstructed domains and  $1 \times 1$  domains on the Si(111) surface. A clean Si(111) surface in ultrahigh vacuum takes a long-range ordered structure, the  $7 \times 7$  reconstruction, at below the transition temperature ( $\approx 860^\circ\text{C}$ ) [26]. In SE images, a  $7 \times 7$  domain appears brighter than a  $1 \times 1$  domain [12]. An example of  $7 \times 7$  and  $1 \times 1$  domain contrast is shown in Figure 23.6. This was observed at  $3^\circ\text{C}$  below the  $7 \times 7$ – $1 \times 1$  transition temperature. The phase transition to the  $7 \times 7$  reconstruction starts to occur at the atomic step edge. However, due to the strain energy of the  $7 \times 7$  reconstructed structure, the phase transition does not propagate to the entire terraces, and  $1 \times 1$  regions coexist at this temperature [27]. The brighter regions are  $7 \times 7$  and darker regions are  $1 \times 1$ . The origin of surface structure dependent SE emission is not well understood. The difference in the

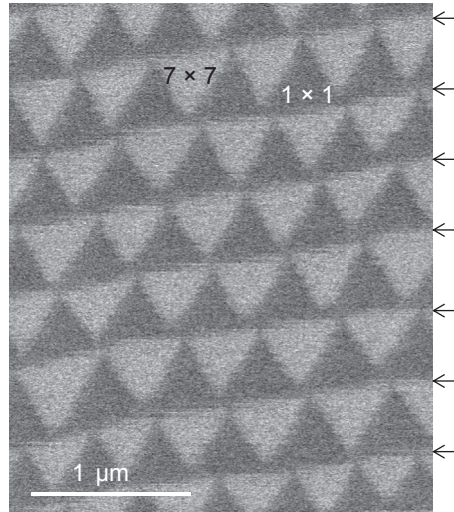


**FIGURE 23.6** Secondary electron image of Si(111) surface with  $1 \times 1$  and  $7 \times 7$  triangular domains observed at just below the  $1 \times 1$ – $7 \times 7$  phase transition temperature. The  $7 \times 7$  domains appear brighter than the  $1 \times 1$  domains. Arrows show the location of atomic steps. The primary electron beam of 25 keV was incident at  $45^\circ$  to the surface. The effect of oblique incidence was corrected by changing the aspect ratio of the image.

electronic structure or atomic scale surface roughness (e.g., corner holes in the  $7 \times 7$  structure) might be responsible for the SE yield change.

This  $7 \times 7$  and  $1 \times 1$  domain contrast is useful for step imaging on a large Si(111) terrace ( $7 \times 7$  decoration method). When the sample is rapidly quenched from above the transition temperature toward room temperature, continuous  $7 \times 7$  domains are only formed along atomic steps. On a large terrace, small  $7 \times 7$  domains nucleate but do not cover the entire terrace as shown in Figure 23.7, which shows an SEM image of Si(111) surface with a screw dislocation. Thus, atomic steps are highlighted with the bright  $7 \times 7$  lines in SE images. The width of the  $7 \times 7$  phase at step is  $\approx 1 \mu\text{m}$  [25]. This method is applicable to the observation of atomic steps on a wide terrace after MBE growth. Although this is not a real-time observation method, the effect of quenching on the step motion is negligible when large-scale phenomena are observed, and the method can elucidate the atomic step distribution at the growth temperature.

### 23.2.3 Limitations of the Method

Electron beam irradiation can cause damage of the surface if the electron current density is high. For GaAs, because the vapor pressure of As is high, As is easily desorbed from the surface by electron beam irradiation when the As flux is low or the substrate temperature is too high [16]. In such cases, monolayer holes are created on the electron beam scanned area due to evaporation of As as shown in Figure 23.8(A). The electron current density is typically on the order of  $10^{-2} \text{ A/cm}^2$  ( $10^2 \text{ A/m}^2$ ) when an area of  $1 \mu\text{m}^2$  ( $10^6 \text{ nm}^2$ ) is scanned with a beam current of  $10^{-1} \text{ nA}$ . Figure 23.8(B) shows the electron

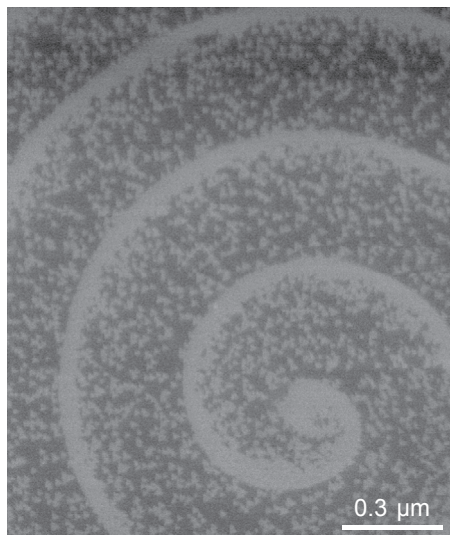


**FIGURE 23.7** Secondary electron image of  $7 \times 7$  domains on a quenched Si(111) surface. Bright lines are  $7 \times 7$  domains that decorate atomic step continuously, showing a screw-shaped distribution around a dislocation. Small triangles are individual  $7 \times 7$  domains on the terrace.

current densities and the  $\text{As}_4$  pressures, which produce beam damage at the substrate temperature of  $580^\circ\text{C}$  [16]. When the  $\text{As}_4$  pressure is less than  $1 \times 10^{-5}$  Torr and the electron current density exceeds  $1.3 \times 10^{-2}$  A/cm<sup>2</sup> (for example, at a magnification of 100,000, a scanned area of  $0.89 \times 5.1$   $\mu\text{m}$  and a beam current of 0.6 nA), surface damage occurs. Practical ways to avoid beam damage without reducing image magnification are to reduce the electron beam current or increase the  $\text{As}_4$  pressure. The electron beam current can be reduced to 0.1–0.3 nA, and the  $\text{As}_4$  pressure was usually set at  $\approx 1 \times 10^{-5}$  Torr ( $\approx 1 \times 10^{-3}$  Pa).

Another limitation comes from the scanning rate of the probe beam. The normal scanning rate of SEM is 10–40 s/frame. Because the signal/noise ratio is reduced with an increase in the scanning rate, a 10 s/frame is almost the limit for obtaining a high-contrast image of atomic steps and 2D islands. A rapid scan (TV rate) mode can be used only when the contrast of object is high enough, such as the graphene edge contrast shown in [Section 23.3.4](#).

## 23.3 Application of In Situ SEM

### 23.3.1 Growth Mode

#### 23.3.1.1 Basic Picture of MBE Growth

In the MBE growth, the growth rate is low and the surface diffusion of deposited atoms (adatoms) is the dominant process of crystal growth. Such a situation is well described with the standard model by Burton, Cabrera, and Frank [28]. In this model, the adatom

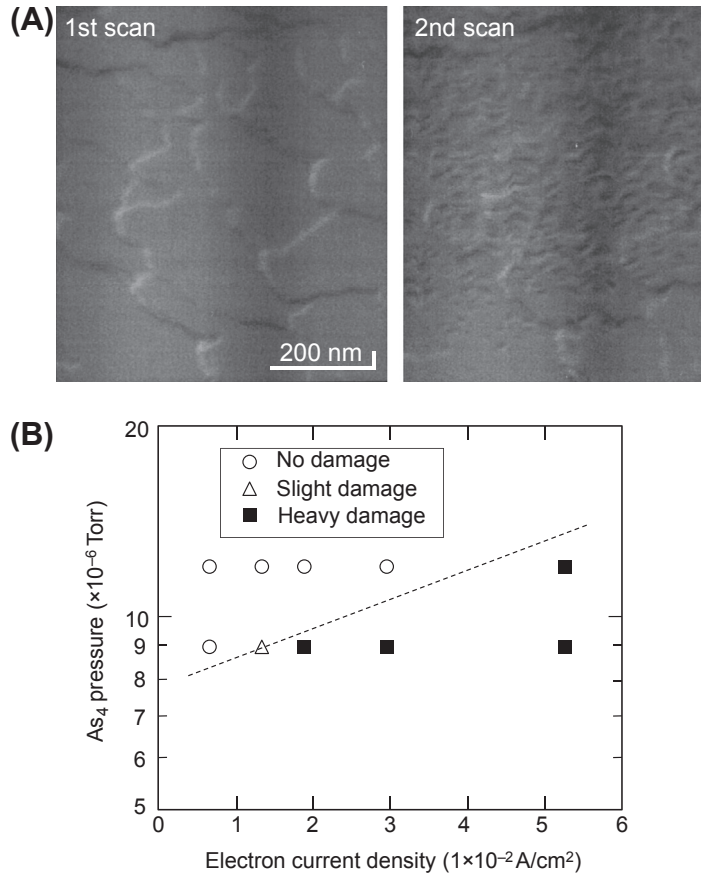


**FIGURE 23.8** (A) Electron beam damage created on GaAs surface by scanning electron microscopy observation. The surface morphology is compared between first and second electron beam scans. The beam scan area was  $0.59 \times 3.4 \mu\text{m}$ , and the beam current was 0.6 nA. (B)  $\text{As}_4$  pressure and electron current density conditions that cause electron damage on GaAs surface [16].

density  $\rho$  is determined by the surface diffusion and evaporation. The incorporation of adatoms into atomic steps is supposed to be fast enough. Then,  $\rho$  follows the diffusion equation:

$$\dot{\rho} = D_s \nabla^2 \rho - \rho/\tau + F \quad (23.1)$$

where  $D_s$  is the surface diffusion length,  $1/\tau$  is the evaporation probability of an adatom, and  $F$  is the flux of impinging atoms.  $D_s$  is related to the surface diffusion length  $\lambda_s$  as  $\lambda_s^2 = D_s \tau$ . When the rate of attachment and detachment of adatoms at the steps is much faster than that of diffusion, the adatom density at the step becomes an equilibrium value  $\rho_0$ . As the surface diffusion is much faster than the motion of steps,  $\dot{\rho} = 0$ . Then, for an isolated straight atomic step at  $x = 0$ , the solution of Eqn (23.1) is

$$\rho(x) = \rho_0 + (F\tau - \rho_0)[1 - \exp(-|x|/\lambda_s)] \quad (23.2)$$

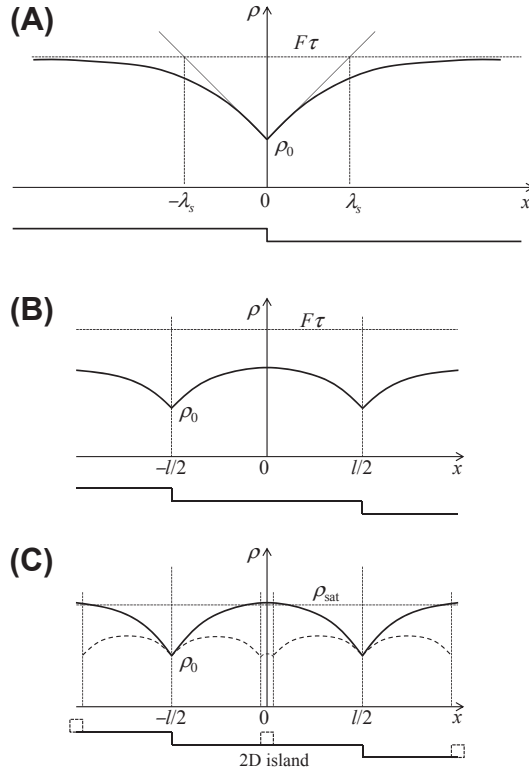


**FIGURE 23.9** Schematic illustration of adatom density distribution for (A) an isolated step, (B) steps separated by  $l$  at a low impinging flux, and (C) steps separated by  $l$  at a high impinging flux. Dashed line indicates the adatom density distribution after 2D island nucleation.

where  $F\tau$  is the equilibrium adatom density determined by the impinging and evaporation of adatoms. The adatom density distribution is schematically shown in Figure 23.9(A). The adatom diffusion flux to the atomic step is proportional to the gradient of the adatom density distribution,  $D_s d\rho/dx$ , and the resulting step velocity is

$$v_\infty = \frac{2D_s}{n_0} \left. \frac{d\rho}{dx} \right|_{x=0} = (F\tau_v - \rho_0) \frac{2\lambda_s}{n_0\tau} \quad (23.3)$$

where  $n_0$  is the density of surface sites. A factor of 2 is multiplied because both the upper and lower terraces contribute to the growth. Adatoms within  $|x| \lesssim \lambda_s$  contribute to crystal growth, and those outside the  $\approx 2\lambda_s$  region evaporate before being incorporated into atomic steps.

When the atomic step spacing  $l$  is smaller than  $\lambda_s$ , the solution of Eqn (23.1) for the terrace with atomic steps at  $x = -l/2$  and  $+l/2$  is

$$\rho(x) = F\tau_s + \frac{\cosh(x/\lambda_s)}{\cosh(l/2\lambda_s)} (\rho_0 - F\tau_s). \quad (23.4)$$

The adatom density distribution is schematically shown in [Figure 23.9\(B\)](#). For each step, adatoms on a half of the terrace contribute to the growth. For a parallel atomic step array, both the upper and lower terraces contribute to the growth. When the widths of the upper and lower terraces are  $l$  and  $l'$  and much smaller than  $\lambda_s$ , the step velocity is

$$v = \frac{v_\infty}{2\lambda_s} \frac{l+l'}{2}. \quad (23.5)$$

As seen in [Figure 23.9\(B\)](#), the adatom density is highest at the center of a terrace. When the impinging flux becomes high, the adatom density at the center can exceed the saturated adatom density  $\rho_{\text{sat}}$ . In this case, nucleation of a new terrace (2D island) occurs at the center of the terrace as depicted in [Figure 23.9\(C\)](#). If the impinging flux is very high, the effective diffusion length of adatoms becomes smaller than  $\lambda_s$  because adatoms collide with each other before evaporation. In this case, plural 2D islands nucleate on the terrace.

Thus, the growth mode changes depending on the terrace width relative to the surface diffusion length and the impinging flux. For a low impinging flux, steps propagate as the result of adatom incorporation at kink sites on the atomic steps. This growth mode is called step-flow growth. For a high impinging flux exceeding the saturated adatom density, 2D-island nucleation becomes dominant, which is called 2D-island nucleation growth. Once 2D island is formed, step-flow growth takes place until one monolayer is completed, because the adatom density decreases with a decrease in average terrace size as shown in [Figure 23.9\(C\)](#).

### 23.3.1.2 SE Images of 2D-Island Nucleation and Step Flow

As an application of in situ SE imaging, the growth modes described above will be shown with real space images. For this purpose, an ultra-large terrace on Si(111) surface is used.

Usually, the step spacing on a commercially available wafer is on the order of  $10^{-1} \mu\text{m}$ . This is because the actual wafer surface is slightly misoriented from ideal crystallographic orientation. For Si(111) wafers, the step spacing is  $0.18 \mu\text{m}$  and  $1.8 \mu\text{m}$  for the misorientation angle of  $0.1^\circ$  and  $0.01^\circ$ , respectively. On the other hand, the adatom diffusion length on the Si(111)- $1 \times 1$  surface is quite large. It reaches  $\approx 50 \mu\text{m}$  at above the  $7 \times 7-1 \times 1$  transition temperature and decreases with an increase in temperature because evaporation of adatom is enhanced [29,30]. Thus, only the step-flow growth takes place on a normal Si(111) wafer surface at high temperatures. In contrast, if we use a large crater created on a Si(111) wafer surface, it is possible to form a huge (111) terrace comparable to the diffusion length [29]. This phenomenon is schematically explained in [Figure 23.10](#). At the bottom terrace in the crater, the step-flow retraction takes place so as to expand the terrace during evaporation. Once the terrace size exceeds the adatom diffusion length, a 2D hole is created at the center of the terrace (just opposite to [Figure 23.9\(C\)](#), resulting in a concentric step distribution as shown in [Figure 23.10\(B\)](#)). Then, by increasing the diffusion length with a decrease in temperature, the bottom terrace can be expanded up to  $\sim 100 \mu\text{m}$  [31]. Such a huge terrace is useful to observe the elemental processes of crystal growth.

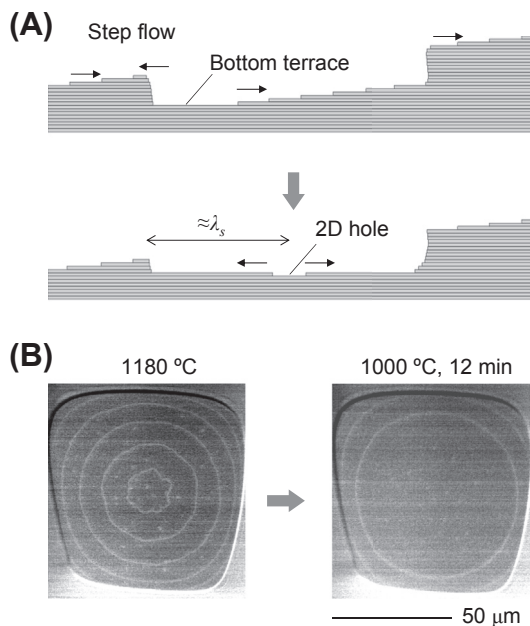


**FIGURE 23.10** (A) Schematic illustration of sublimation process of atomic layers in a crater. (B) Secondary electron images of concentric circular steps created at the bottom of a crater on Si(111). The step structures were created by annealing at 1180 °C (left image) and then annealing at 1000 °C (right image). The effect of oblique incidence (45°) was corrected by changing the aspect ratio of the image.

Figure 23.11 shows images of nucleated Si islands after 10 s growth at 880 °C with various Si deposition rates. These images were observed after quenching the sample from the growth temperature. Since the observed area was large, thermal drift due to slow cooling during observation was not a problem. When the deposition rate is high, multiple islands are created on the (111) terrace. At the deposition rate of 1.0 monolayer (ML)/s, islands cover the terrace except for  $\approx 15 \mu\text{m}$  from the edge where the adatom density has a larger concentration gradient. Step flow from the crater edge occurred as indicated by the arrow in image (A). The island size is smaller in the central area because of the higher density of islands. With decreasing the deposition rate, the number of islands decreases, and finally only one island nucleates on the terrace at the deposition rate of 0.007 ML/s as shown in image (D). The island is located at the center of the ultra-large terrace, indicating that the adatom concentration is highest at the center. This exactly corresponds to Figure 23.9(C).

Step-flow growth can be observed when the radius of the circular step is smaller than the surface diffusion length. An initial surface with a SiC particle near the center of the ultra-large terrace was prepared [22]. Growth was performed at 940 °C where the surface diffusion length was estimated to be  $51 \mu\text{m}$ . As the SiC particle acted as a nucleation site, a central 2D island was formed while outer circular steps advanced during growth as schematically depicted in Figure 23.12(A). With increasing growth time, both the central

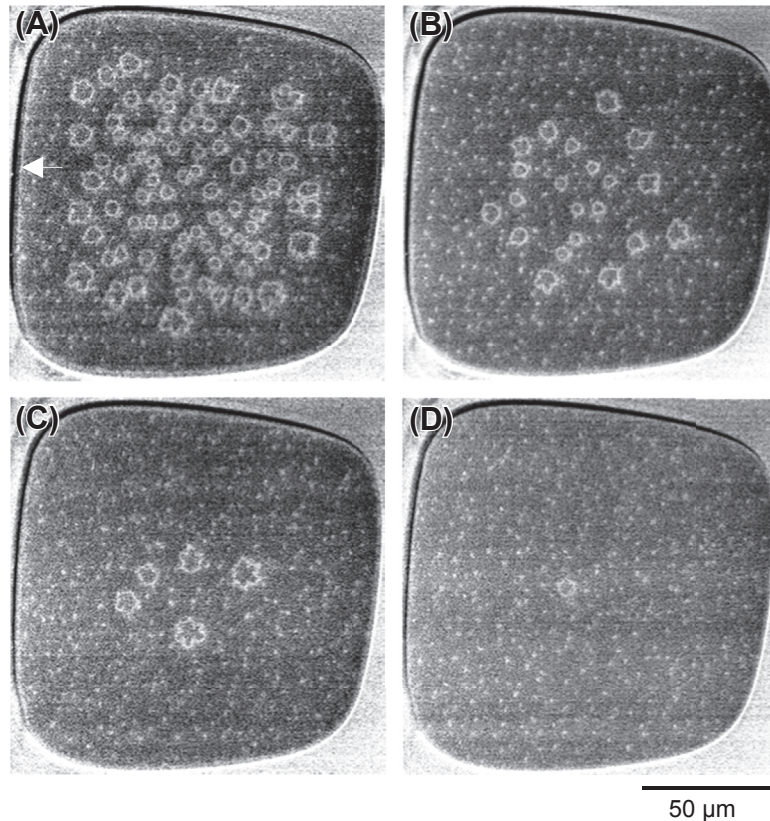


**FIGURE 23.11** Secondary electron images of 2D islands grown during 10 s growth at 880 °C on the ultra-large Si(111) terrace. The growth rate was (A) 1.0, (B) 0.2, (C) 0.06, and (D) 0.007 ML/s. The arrow in image (A) indicates the step advanced flow from the crater edge.

island and outer terraces expanded causing shrinkage of the lowest terrace as shown in [Figure 23.12\(B\)](#). The growth temperature, 940 °C, is so high that sublimation of the surface takes place when the Si flux is absent. Sublimation is the reverse process of crystal growth, which is shown in [Figure 23.12\(C\)](#). In this case, both the central island and outer terraces shrank, resulting in the expansion of the lowest terrace. The analysis of radius evolution of the island and terraces showed that growth and sublimation processes were perfectly symmetric [22].

## 23.3.2 Nucleation and Growth on GaAs Surface

### 23.3.2.1 GaAs(001)

GaAs(001) surfaces grown by MBE were observed using SEM by supplying Ga and As fluxes of  $10^{-3}$  Pa [16]. When the growth rate is low, the 2D island size becomes large enough and the initial stage of 2D island nucleation can be observed by SEM. [Figure 23.13](#) shows the initial one monolayer growth of the GaAs(001) surface [14].

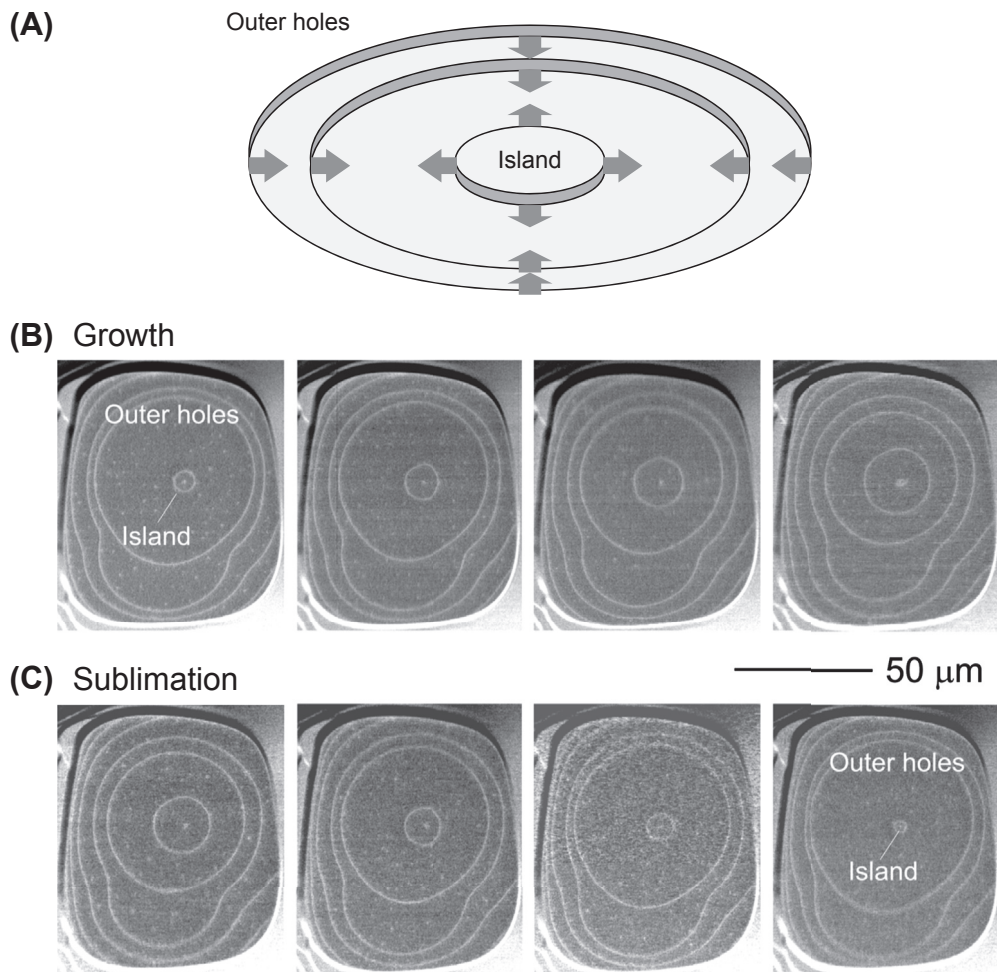


**FIGURE 23.12** Evolution of step shape on Si(111) during growth and sublimation. (A) Schematic illustration of the sample surface. Arrows indicate the step-flow direction during growth. (B) Successive secondary electron (SE) images during growth at 940 °C. (C) Successive SE images during sublimation at 940 °C. The interval of each image was about 2 min.

The growth temperature was 580 °C and the growth rate was  $\approx 50$  s/ML (0.02 ML/s). The SE image scanning rate was 80 s/frame. Thus, more than 1 ML grew during acquisition of an SE image. That is, the initial stage of 2D island nucleation and evolution is recorded on an SE image, though each stage is recorded on the different portion in the image. Growth started at the top of the image and proceeded with scanning toward the bottom. The deposited amount (not the actual coverage) is indicated at the right side of [Figure 23.13](#). In the first 0.25 ML, atomic steps are still visible, showing that the surface is almost unchanged. Then, 2D islands are seen as small bright dots. The density and size of islands increase with the growth time. Due to the increased surface roughness

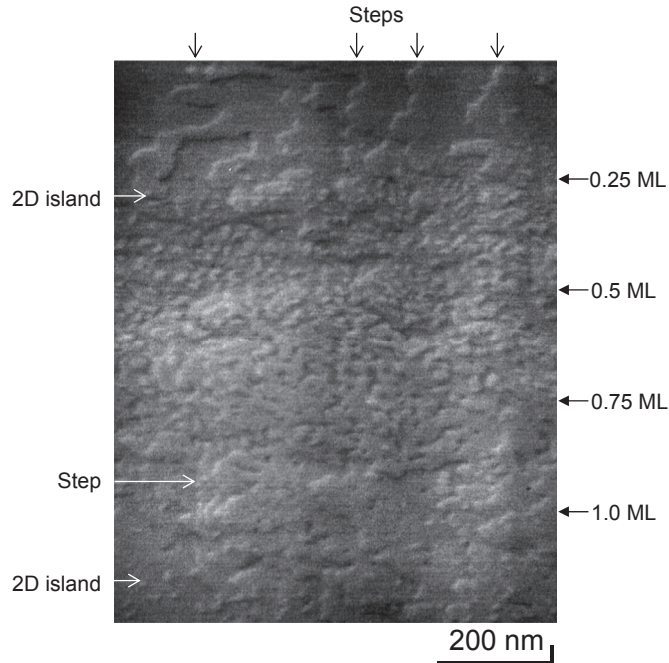


**FIGURE 23.13** Secondary electron image of GaAs(001) surface during molecular beam epitaxy growth [14]. Growth started at the top of the image.

(monolayer high), atomic steps are difficult to be discerned. With coalescence of islands, holes are left on the surface (around 0.75 ML). Finally, the first monolayer is completed at about 4/5 of the SE image. Atomic steps are visible again at this stage. The nucleation of 2D islands of second layer can be seen at near the bottom of the image.

Figure 23.14 shows an SE image recorded at a higher growth rate, 14 s/ML (0.07 ML/s) [14]. Oscillation of the surface morphology, i.e., the roughening–smoothing cycle due to 2D island nucleation and coalescence, is clearly visible. This corresponds to the RHEED oscillation [32]. It is interesting to compare the RHEED intensity oscillation with the SE image evolution, but they cannot be acquired simultaneously because of the difference in the electron beam incident angle. For comparison, the RHEED intensity separately measured at the same growth condition is shown at the right of the SEM image. In the first two cycles, the RHEED intensity and the surface morphology are clearly correlated. With an increase in the growth cycle, the surface roughness accumulates and the oscillation becomes difficult to be observed.

### 23.3.2.2 GaAs(111)

The size of 2D island depends on the nucleation density, which is governed by the effective surface diffusion length of adatoms. The effective diffusion length can be increased by decreasing the impinging molecular beam flux (see Figure 23.11), but

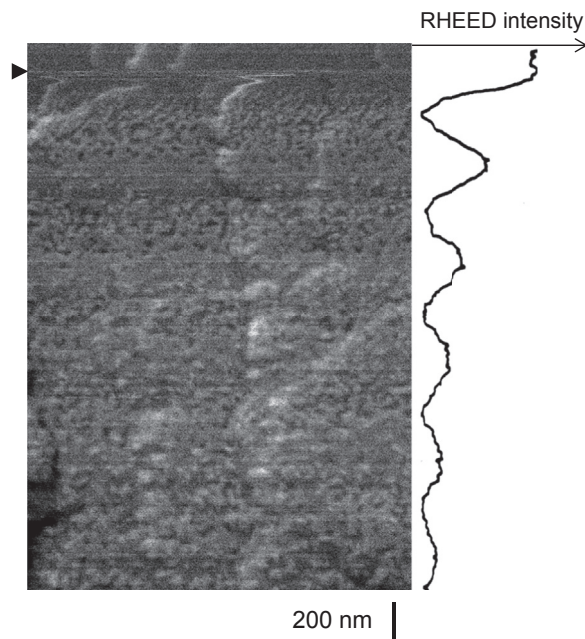


**FIGURE 23.14** Secondary electron image of GaAs(001) surface during molecular beam epitaxy growth with a higher growth rate [14]. Growth started at the position indicated by the arrowhead, and about five monolayers grew during imaging. Reflection high-energy electron diffraction (RHEED) intensity oscillation measured separately is shown at the right of the image.

is finally limited by the intrinsic diffusion length. On the GaAs(001) surface, the intrinsic diffusion length is small so that the 2D island size is limited to less than 10 nm. A larger diffusion length can be attained on the Ga-terminated GaAs(111) surface (A-surface).

Figure 23.15 shows successive SE images of a GaAs(111)A surface during MBE growth [19]. These images were observed by repeating the image scanning at 20 s/frame at the same position (because of thermal drift, imaging area was slightly shifted for each cycle). The growth temperature was 577 °C and the Ga deposition rate was 85 s/ML (0.01 ML/s). The growth rate was even lower due to desorption of Ga, and much lower than the image scanning rate. Therefore, more detailed 2D island nucleation and growth stages are recorded in an SE image. Furthermore, the 2D island size is large enough to show the triangular shape reflecting the three-holed symmetry of (111) surface. The island edges consist of  $\langle 1\bar{1}0 \rangle$  steps, and the islands expand keeping the same shape. These images clearly indicate that island growth occurs as the result of step propagation (step flow). Simultaneously, atomic steps at the edge of the terrace propagate. The diffusion length of Ga was estimated to  $\approx 100$  nm from the step velocity perpendicular to the steps based on Eqn (23.3), and was consistent with the island spacing [19]. The reason why the isolated step case (Figure 23.9(A)) can be used is that the terrace size ( $\approx 1 \mu\text{m}$ ) is larger

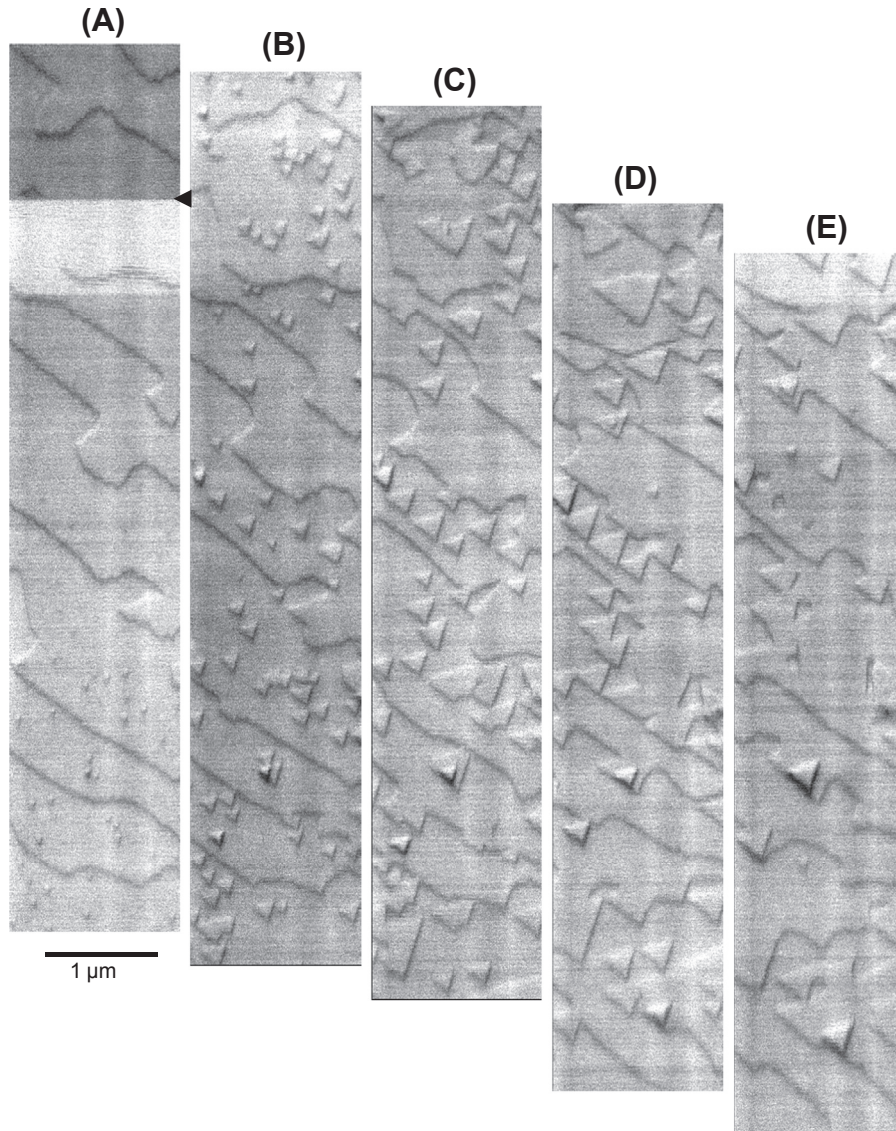


**FIGURE 23.15** Secondary electron image sequences showing the monolayer growth process of GaAs(111)A surface. Growth started at the position indicated by the arrowhead in image (A). For each image, the scanning time was about 18 s, and the interval between each image was about 8 s. The effect of oblique incidence ( $80^\circ$ ) was corrected by changing the aspect ratio of the image.

than the diffusion length. Thus, not all the deposited atoms contributed to the growth. The first monolayer is completed in image (E). The layer growth was successfully imaged in [Figure 23.15](#). Some islands show 3D (multilayered) growth, probably due to defects on the surface.

### 23.3.3 Instability of Step-Flow Growth

In [Section 23.3.1](#), we described the adatom density in one dimension. This treatment assumes straight steps. Actual MBE growth occurs on the surface, i.e., in two dimensions. Straight steps (or circular steps as shown in [Figure 23.12](#)) are not stably maintained in some situations. In this section, we will see an example of instability of step-flow growth.

Again, we use an ultra-large terrace on the Si(111) surface and observe the behavior of isolated steps. As discussed in [Section 23.3.1](#), by adjusting the deposition rate of Si, only one island nucleates at the center of the ultra-large terrace. The island growth process is observed by changing the growth time. For the observation of steps, the  $7 \times 7$  decoration method was used (see [Section 23.2.2](#)). However, quenching caused nucleation of other small islands on the surface, which hindered the observation of successive evolution of the center island. Therefore, images at different growth duration were observed by quenching the sample after each growth duration starting from the flat surface without islands.

[Figure 23.16](#) shows time evolution of island morphology [24]. Initially, the central island is circular as shown in image (A). The island shape changes to six-fold symmetry extending to  $\langle 110 \rangle$  directions as seen in images (B) and (C). The atomic step at the periphery of the crater, which is the edge of the second lowest terrace, progresses toward the center of the ultra-large terrace. This periphery step is smooth in this stage. After further growth, the periphery step becomes wandering as seen in image (D). The

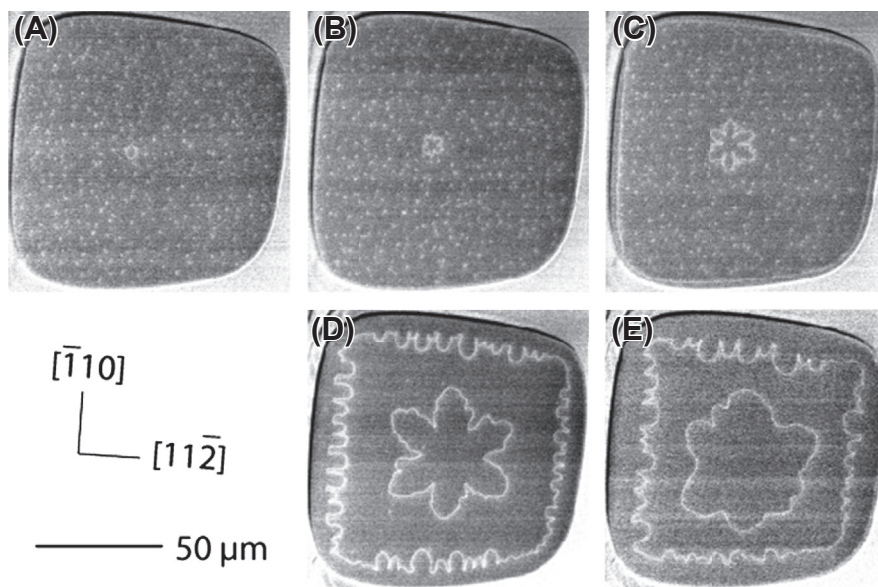


**FIGURE 23.16** Secondary electron image sequences showing the evolution of atomic step instability during growth at  $880\text{ }^{\circ}\text{C}$  on the ultra-large Si(111) terrace [24]. The images were obtained after growth of (A) 10 s, (B) 20 s, (C) 1 min, (D) 5 min, and (E) 10 min.

wandering amplitude is maximized at 0.5 ML coverage. Above this point, the wandering amplitude decreases, and the center island becomes round as seen in image (E).

The phenomenon observed in Figure 23.16 is instability of step flow [23,24]. Bales and Zangwill theoretically treated the wandering of steps in step-flow growth and showed that when the flux of adatoms from the lower terrace exceeds that from the upper terrace, the fluctuation in the atomic step is amplified, resulting in macroscale step wandering [33]. This can be understood qualitatively from simple consideration of adatom density distributions around a fluctuation (bump and dent) in a straight step as shown in Figure 23.17. Because the bump part is closer to the high adatom density region on the lower terrace, the gradient of density distribution becomes large, resulting in a larger diffusion flux from the lower terrace. Contrary to this, the diffusion flux from the upper terrace is reduced because of a smaller gradient of density distribution. For the dent, the flux from the lower terrace decreases while that from the upper terrace increases. Thus, the lower terrace contributes to enhance the fluctuation both for bump and dent, while the upper terrace contributes to reduce the fluctuation. When the lower terrace contributes more to the step flow, the instability of straight step is induced.

One of the origins of asymmetry between lower and upper terraces is the Ehrlich–Schwoebel barrier that supposes a higher energy barrier for incorporation of adatoms into a step from the upper terrace than that from the lower terrace [34,35]. However, the Ehrlich–Schwoebel barrier on the Si(111) surface at high temperatures is negligible, and this kind of step wandering is not observed for equidistant steps [22].

The origin of asymmetry between lower and upper terraces in Figure 23.16 is simply the size difference. For the growth on the ultra-large terrace, a newly grown terrace (upper terrace) is always small compared to the ultra-large terrace. Since the adatom

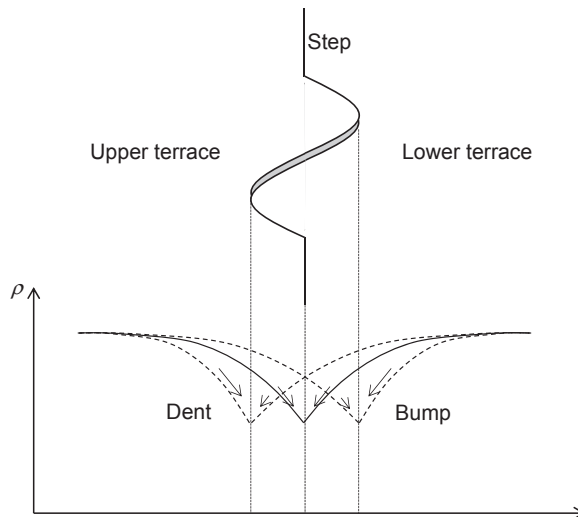


FIGURE 23.17 Schematic illustration of adatom density distributions for a fluctuated step.

diffusion flux to a step is an increasing function of the terrace width (see [Section 23.3.1](#)), the symmetry between the upper and lower terraces is broken and step instability is induced. While the shape of the center island reflects the symmetry of the Si (111) surface, the periphery step is initially smooth and then becomes wandering. This is exactly the result of step fluctuation enhancement by the large lower terrace. The decay of wandering shown in [Figure 23.16\(E\)](#) is due to the stabilization of step flow when the upper terrace becomes large. The unstable growth regime is located between stable step flow and 2D island nucleation in the phase diagram of growth mode as functions of impinging flux and step spacing.

### 23.3.4 Graphene Growth

#### 23.3.4.1 Monolayer Graphene Imaging

Graphene is a monolayer material composed of carbon honeycomb lattice. When carbon-doped Ni is slowly cooled from above 900 °C, carbon atoms segregate to the surface of Ni and form monolayer graphene [36]. This process is schematically depicted in [Figure 23.18](#). Above 900 °C, carbon atoms are dissolved in the Ni bulk. At around 900–790 °C, monolayer graphene segregates, and further segregation to form multilayer-graphene occurs below 790 °C. The segregation temperature, though, depends on the carbon concentration in Ni [37]. For lower carbon concentrations, the temperature range of monolayer graphene segregation shifts to lower temperature by  $\approx 100$  °C.

The effect of graphene on SE emission is not large except for the insulator surface where charging is compensated by the graphene overlayer [38]. On a polycrystalline surface, crystal orientation of each grain causes SE contrast due to electron channeling or work function difference, which makes recognition of few-layer graphene difficult. However, during segregation of graphene on the surface, the edge of graphene can be clearly observed by SEM [39]. Above 400 °C, the edge contrast of monolayer graphene becomes prominent, thus, monolayer graphene can be distinguished from Ni grains in SE images.

[Figure 23.19](#) shows monolayer segregation process from a polycrystalline Ni surface at around 800 °C. A Ni foil specimen  $0.5 \times 30$  mm and 0.5 mm thick (unpolished) was heated by passing direct current through it. Image (A) is the Ni surface before graphene segregation, and only Ni grain contrasts are seen. Image (B) was obtained just after nucleation of graphene islands. They extended to cover the Ni surface as shown in

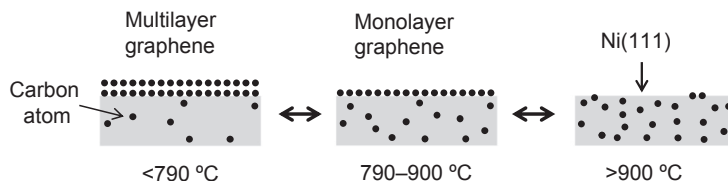


**FIGURE 23.18** Schematic illustration of graphene segregation on Ni(111) surface.

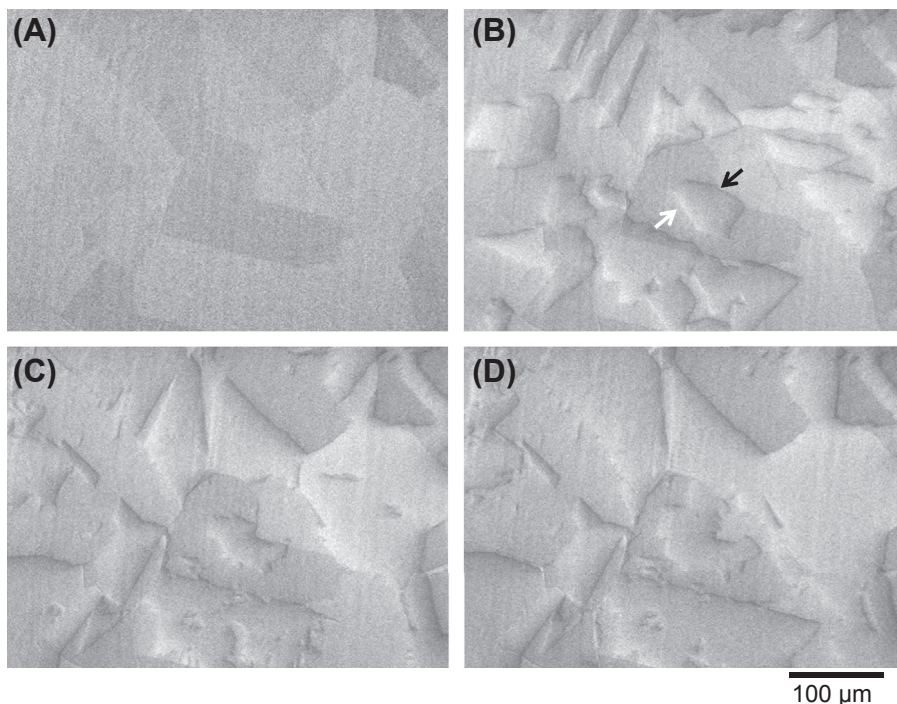


**FIGURE 23.19** In situ observation of monolayer-graphene segregation process. (A) Ni surface before graphene segregation, (B) just after graphene nucleation, (C) 3 min after graphene nucleation, and (D) 7 min after graphene nucleation. The black and white arrows in image (B) indicate the dark and bright edge contrasts, respectively. A Ni foil commercially available was used without further polishing.

images (C) and (D). Monolayer graphene islands appear as if they had steric edges due to the topographic contrast. There are two types of edge contrast as indicated by black and white arrows in image (B); dark contrast for edges facing toward top and right of the SE image; bright contrast for edges facing toward bottom and left of the SE image. Such edge contrasts are the same as those for atomic steps on Si and GaAs surfaces. In the case of graphene observation, a low voltage SEM instrument was used with normal incidence of the primary electron beam of 1.45 keV and an in-lens type SE detector that collects SEs through the objective lens [39]. Therefore, the bright and dark contrasts are due to anisotropy of detection efficiency depending on the direction of emitted secondary electrons. Note that the SE images in Figure 23.19 are obtained at low magnification, and the width of the image corresponds to 0.47 mm. Even though such a wide area is imaged, the monolayer edge contrast is extremely clear. For the observation of monatomic steps of GaAs and Si, much higher magnifications are necessary for direct imaging using the edge contrast (see Section 23.3.2). For monolayer graphene, the strength of edge contrast depends on temperature. For Ni, the edge contrast becomes prominent at around 400 °C and higher. The edge contrast is clear even on the unpolished polycrystalline surface

where the surface roughness is much larger than the monolayer graphene height. The origin of the prominent contrast and its temperature dependence is still under investigation.

#### 23.3.4.2 Multilayered Graphene

Figure 23.20 shows the successive graphene layer segregation after the monolayer graphene segregation shown in Figure 23.19 at the same temperature. The observed area was the same as that in Figure 23.19. Due to the temperature gradient in the specimen, the right side of the SE image was at lower temperature. Thus, carbon segregation first occurred at the right side. The second layer is formed at the region indicated by the arrow in image (A). Note that the edge contrast does not appear for the second layer, because the second layer segregates underneath the first layer. The second layer appears slightly darker. The third layer that is further darker appears at the right edge indicated by the arrow in image (B). The darker regions expand and the right end of the SE image becomes much darker, indicating the increase in the layer number in image (D). One-third of the surface is covered with three layers or thicker graphene layers. The

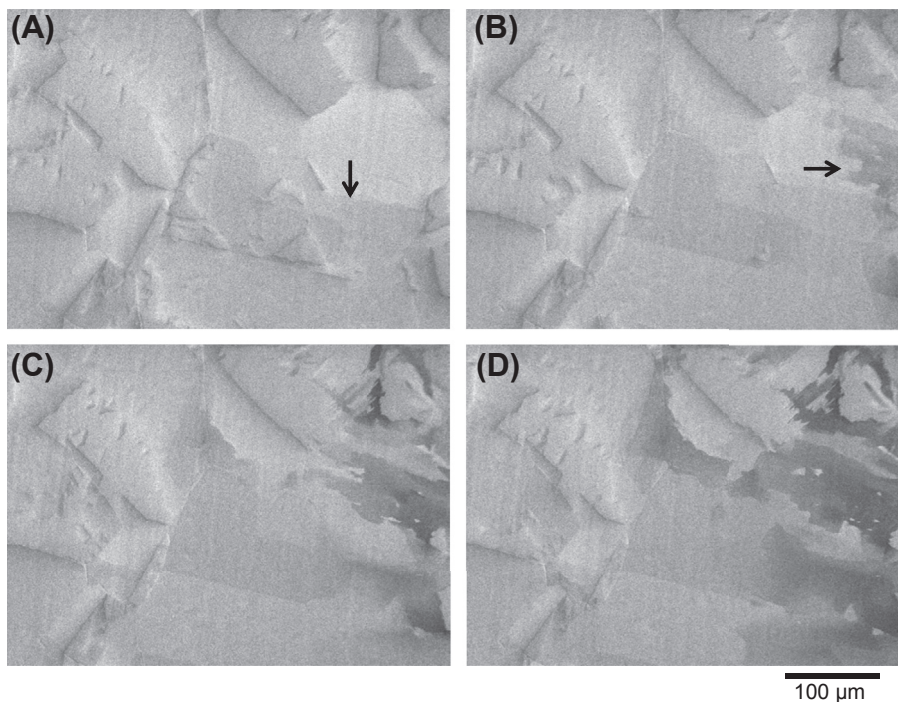


**FIGURE 23.20** In situ observation of multilayer-graphene segregation process. Those images were observed following to Figure 23.19(D). Elapsed time after graphene nucleation (Figure 23.19(B)) is: (A) 9 min, (B) 11 min, (C) 13 min, and (D) 15 min. The arrows in images (A) and (B) indicate second and third graphene layers, respectively.

contrast change depending on the number of graphene layer is attributed to the work function change and also the difference in attenuation of secondary electrons generated in Ni by graphene overlayers.

#### 23.3.4.3 Graphene Nucleation

Graphene nucleation preferentially occurs on the (111) Ni grains in the segregation case [39]. The carbon flux to the surface should be the same for all the faces when surface carbon atoms are supplied by segregation of bulk dissolved carbon atoms. However, because of the surface energy difference, the equilibrium surface concentration of carbon is higher on Ni(111) [40] and the surface atomic arrangement is commensurate to graphene on Ni(111). Thus, at a higher temperature in the monolayer graphene segregation range, graphene preferentially segregates on the (111) surface. On a mirror-polished polycrystalline Ni surface, the graphene nucleation probability by segregation of carbon is so low that a large graphene domain is formed [41]. Also, it is reported that a single-domain graphene expanded continuously in a carpet-like manner, not only over steps on the Ni surface but also over Ni grain boundaries, independent of the Miller index plane [41]. Monolayer or few-layer steps of the Ni surface have a negligible effect on the nucleation and growth of graphene. This means that Ni atomic steps are not an effective trap site of carbon atoms, different from homo-epitaxial growth of GaAs and Si.

Then, a question arises: what is the nucleation site of graphene segregation? In situ SEM is useful to investigate the nucleation processes because of the wide field of view. Observations of graphene nucleation processes on a mirror-polished polycrystalline Ni surface were performed by repeating dissolution of graphene above the segregation temperature and nucleation of graphene at the segregation temperature [42]. There were several nucleation sites where nucleation was repeatedly observed. Combining ex situ atomic force microscopy (AFM) measurement at the same areas as the SEM observation, the surface structures of nucleation sites were elucidated. Those were step-bunched structures on a Ni(111) grain. Some sites were located near the grain boundary, and others were at the center of the large (111) grain. While a grain boundary can have such a step-bunched structure, step bunches on the large (111) grain may be created by step bunching during heating.

The expansion process of the graphene island at a step-bunched structure on the large (111) grain is shown in Figure 23.21 as successive images from panel (A) to panel (F). An AFM image and line profile near the nucleation site, which is indicated with the square in the SE images, is shown in panels (G) and (H), respectively. Initially, the island expanded along the step bunch. The expansion rate perpendicular to the step bunch was low, about 1/10 of the parallel direction. Once the island edge went over the step bunch, however, it expanded rapidly as seen in panels (C)–(F), indicating slow carbon diffusion across the step bunch. The SE images of second cycle segregation are shown in panels (I) and (J). Graphene nucleated at the same area and showed similar expansion process. The step-bunched face of Ni is inclined by  $2.4^\circ$  to the (111) face [42]. The bunch consists of about 100 steps with average step spacing of 4.85 nm assuming an equidistant spacing.

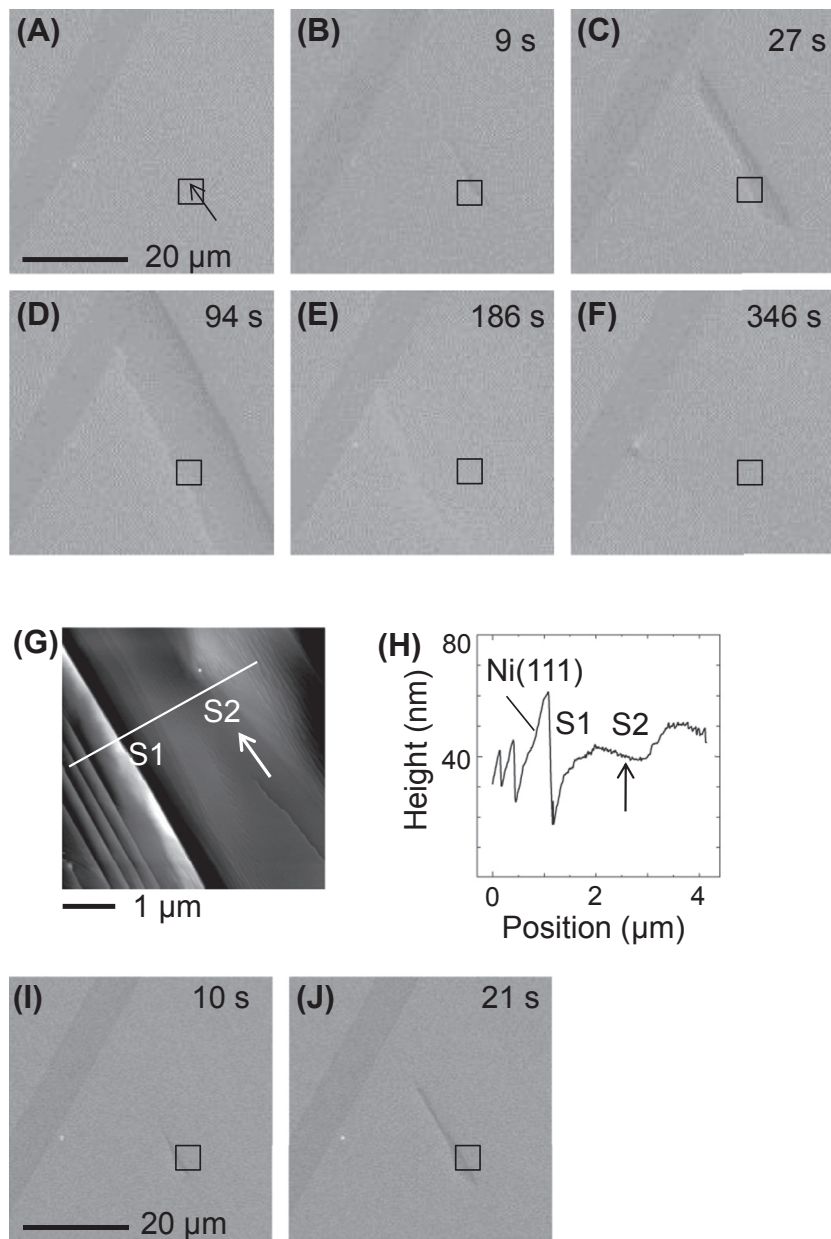


**FIGURE 23.21** (A)–(F) In situ secondary electron (SE) images of graphene nucleation and growth at a step-bunched structure. (G) Atomic force microscopy (AFM) image of the nucleation site indicated with the black square in the SE image. (H) Line profile along the line in AFM image. (I), (J) In situ SE images of graphene nucleation and growth in the second cycle. The time elapsed after graphene nucleation is indicated in the scanning electron microscopy images. A mirror-polished Ni foil was used.

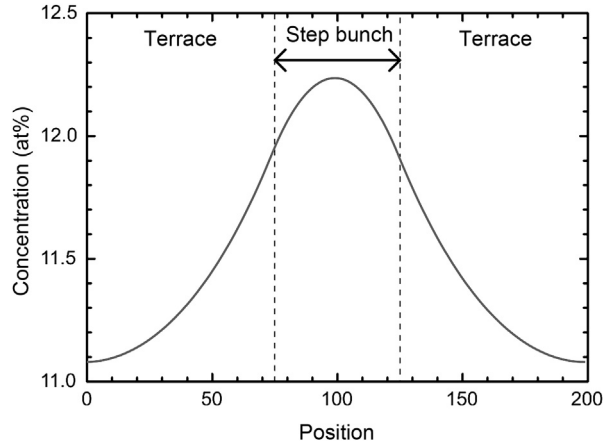


**FIGURE 23.22** Calculated steady state surface carbon concentration around a step bunch [41]. The initial carbon concentration was set  $\rho(x, 0) = 0$ . Parameters used for calculation were  $Ds = 0.1$ ,  $F = 0.1$ ,  $1/\tau(\text{terrace}) = 1$ , and  $1/\tau(\text{step bunch}) = 0.5$ .

As mentioned above, Ni atomic steps are not an effective trap site of carbon atoms. However, the equilibrium carbon concentration at the Ni step edge can be slightly higher than the terrace region, and the Ni steps can reduce carbon atom diffusion perpendicular to the steps. This situation can be expressed by assuming a smaller  $1/\tau$  at the steps compared to that on terraces in Eqn (23.1); here  $F$  represents the carbon flux segregating from the bulk instead of the impinging flux from the vapor phase. A numerical solution of Eqn (23.1) for the surface with a step-bunched region is shown in Figure 23.22, by assuming that  $1/\tau$  at the step-bunched region is twice as low as that on the terrace, and the step spacing is much smaller than  $\lambda_s$ . Although this is a simple model, and the parameters are set as examples, the result clearly shows that the surface carbon concentration at the center of the step bunch is slightly higher than that on the terrace. The higher carbon concentration enhances the nucleation probability of graphene nuclei at the step bunch. The large number of steps hinders the surface diffusion of carbon atoms and thus causes the slower growth rate of graphene island perpendicular to the step bunch. The critical step bunch size should be large enough to achieve the carbon concentration for graphene nucleation in the center of step bunch. From the results in Figure 23.21, the critical size would be 20 nm in height with 100 steps.

## 23.4 Summary

Initial stages of MBE growth have been observed by in situ SEM. On the GaAs(001) surface, a small diffusion length (on the order of 10 nm) caused 2D island growth. The monolayer growth processes, 2D island nucleation, island growth and coalescence, and completion of monolayer, were clearly imaged. On the GaAs(111)A surface, the diffusion length reached 100 nm, and 2D islands became large enough to show the symmetry of

the surface. The step flow growth following to 2D island growth could be observed. On the Si(111)- $1 \times 1$  surface, where the diffusion length was as large as 50  $\mu\text{m}$ , the motion of isolated steps was observed using the ultra-large terrace. When the terrace size was comparable to the diffusion length, unstable step-flow growth could be observed. The method was also applied to the observation of graphene segregation on a polycrystalline Ni surface. Extremely clear contrasts of monolayer graphene edges could be obtained at elevated temperatures.

It is interesting that macroscopic observations by SEM can reveal phenomena that relate to the attachment of atoms to atomic steps. Although this chapter mainly focuses on the imaging aspects, quantitative analyses have been done using those images [19,22]. The analyses showed that the MBE growth of GaAs and Si is well described with the standard model by Burton, Cabrera, and Frank [28]. That is, the surface diffusion of adatoms is the dominant process of crystal growth, and the incorporation of adatoms into atomic steps is fast enough.

## References

- [1] Bastiman F, Cullis AG, Hopkinson M. InAs/GaAs(001) molecular beam epitaxial growth in a scanning tunnelling microscope. *J Phys Conf Ser* 2010;209(012048):1–9.
- [2] Ichikawa M, Doi T, Ichihashi M, Hayakawa K. Observation of surface micro-structures by microprobe reflection high-energy electron diffraction. *Jpn J Appl Phys* 1984;23:913–20.
- [3] Ichikawa M, Doi. Observation of Si(111) surface topography changes during Si molecular beam epitaxial growth using microprobe reflection highenergy electron diffraction. *Appl Phys Lett* 1987; 50:1141–3.
- [4] Osaka J, Inoue N, Mada Y, Yamada K, Wada K. In-situ observation of roughening processes of MBE GaAs surface by scanning electron microscopy. *J Cryst Growth* 1990;90:120–3.
- [5] Hata M, Watanabe A, Isu T. Surface diffusion length observed by in situ scanning microprobe reflection high-energy electron diffraction. *J Cryst Growth* 1991;111:83–7.
- [6] Inoue N. MBE monolayer growth control by in-situ electron microscopy. *J Cryst Growth* 1991;111: 75–82.
- [7] Kanisawa K, Osaka J, Hirono S, Inoue N. Al-Ga monolayer lateral growth observed in situ by scanning electron microscopy. *Appl Phys Lett* 1991;58:2363–5.
- [8] Suzuki T, Nishinaga T. First real time observation of reconstruction transition associated with Ga droplet formation and annihilation during molecular beam epitaxy of GaAs. *J Cryst Growth* 1994; 142:49–60.
- [9] Nishinaga T, Shen XQ, Kishimoto D. Surface diffusion length of cation incorporation studied by microprobe-RHEED/SEM MBE. *J Cryst Growth* 1996;163:60–6.
- [10] Homma Y, Tomita M, Hayashi T. Secondary electron imaging of monolayer steps on a clean Si(111) surface. *Surf Sci* 1991;258:147–52.
- [11] Homma Y, Tomita M, Hayashi T. Atomic step imaging on silicon surfaces by scanning electron microscopy. *Ultramicroscopy* 1993;52:187–92.
- [12] Homma Y, Suzuki M, Tomita M. Atomic configuration dependent secondary electron emission from reconstructed silicon surfaces. *Appl Phys Lett* 1993;62:3276–8.
- [13] Homma Y, Osaka J, Inoue N. In-situ observation of monolayer steps during molecular beam epitaxy of gallium arsenide by scanning electron microscopy. *Jpn J Appl Phys* 1994;33:L563–6.

- [14] Homma Y, Osaka J, Inoue N. In situ observation of surface morphology evolution corresponding to reflection high energy electron diffraction. *Jpn J Appl Phys* 1995;34:L1187–90.
- [15] Osaka J, Inoue N, Homma Y. Delayed and continuous nucleation of islands in GaAs molecular beam epitaxy revealed by in situ scanning electron microscopy. *Appl Phys Lett* 1995;66:2110–2.
- [16] Homma Y, Osaka J, Inoue N. Secondary electron imaging of nucleation and growth of GaAs. *Surf Sci* 1996;357–358:441–5.
- [17] Homma Y, Yamaguchi H, Horikoshi Y. Direct comparison of GaAs surface morphology between migration enhanced epitaxy and molecular beam epitaxy. *Appl Phys Lett* 1996;68:63–5.
- [18] Homma Y, Yamaguchi H, Horikoshi Y. In situ observation of MEE GaAs growth using scanning electron microscopy. *J Cryst Growth* 1997;175/176:292.
- [19] Yamaguchi H, Homma Y. Imaging of layer by layer growth processes during molecular beam epitaxy of GaAs on (111)A substrates by scanning electron microscopy. *Appl Phys Lett* 1998;73:3079–81.
- [20] Yamaguchi H, Homma Y, Kanisawa K, Hirayama Y. Drastic improvement in surface flatness properties by using GaAs(111)A substrates in molecular beam epitaxy. *Jpn J Appl Phys* 1999;38:635–44.
- [21] Homma Y. In situ observation by scanning electron microscopy of III-V Growth. In: *Encyclopedia of materials: science and technology*. Elsevier; 2001. p. 3680–3.
- [22] Finnie P, Homma Y. Nucleation and step flow on ultraflat silicon. *Phys Rev B* 2000;62:8313–7.
- [23] Finnie P, Homma Y. Stability-instability transitions in silicon crystal growth. *Phys Rev Lett* 2000;85:3237–40.
- [24] Homma Y, Finnie P, Uwaha M. Morphological instability of atomic steps observed on Si(111) surfaces. *Surf Sci* 2001;492:125–36.
- [25] Homma Y, Finnie P. Step dynamics on growing silicon surfaces observed by ultrahigh vacuum scanning electron microscopy. *J Cryst Growth* 2002;237–239:28–34.
- [26] Florio JV, Robertson WD. Phase transformations of the Si(111) surface. *Surf Sci* 1970;22:459–64.
- [27] Hibino H, Homma Y, Ogino T. Triangular-tiled arrangement of  $7 \times 7$  and  $1 \times 1$  domains on Si(111). *Phys Rev B* 1998;58:R7500–3.
- [28] Burton WK, Cabrera N, Frank FC. The growth of crystals and the equilibrium structure of their surface. *Phil Trans R Soc* 1951;243:299–358.
- [29] Homma Y, Hibino H, Ogino T, Aizawa N. Sublimation of Si(111) surface in ultrahigh vacuum. *Phys Rev B* 1997;55:R10237–40.
- [30] Homma Y, Hibino H, Ogino T, Aizawa N. Sublimation of a heavily boron-doped Si(111) surface. *Phys Rev B* 1998;58:13146–50.
- [31] Finnie P, Homma Y. Motion of atomic steps on ultraflat Si(111): constructive collisions. *J Vac Sci Technol A* 2000;18:1941–5.
- [32] Harris JJ, Joyce BA. Oscillations in the surface structure of Sn-doped GaAs during growth by MBE. *Surf Sci* 1981;103:L90–6.
- [33] Bales GS, Zangwill A. Morphological instability of a terrace edge during step-flow growth. *Phys Rev B* 1990;41:5500–8.
- [34] Ehrlich G, Hudda FG. Atomic view of surface self-diffusion: tungsten on tungsten. *J Chem Phys* 1966;44:1039–49.
- [35] Schwoebel RL, Shipsey EJ. Step motion on crystal surfaces. *J Appl Phys* 1966;37:3682–6.
- [36] Shelton JC, Patila HR, Blakely JM. Equilibrium segregation of carbon to a nickel (111) surface: a surface phase transition. *Surf Sci* 1974;43:493–520.

- [37] Eizenberg M, Blakely JM. Carbon monolayer phase condensation on Ni(111). *Surf Sci* 1979;82: 228–36.
- [38] Hiura H, Miyazaki H, Tsukagoshi K. Determination of the number of graphene layers: discrete distribution of the secondary electron intensity stemming from individual graphene layers. *Appl Phys Express* 2010;3. 095101-1-3.
- [39] Takahashi K, Yamada K, Kato H, Hibino H, Homma Y. In situ scanning electron microscopy of graphene growth on polycrystalline Ni substrate. *Surf Sci* 2012;606:728–32.
- [40] Isett LC, Blakely JM. Segregation isosteres for carbon at the (100) surface of nickel. *Surf Sci* 1976;58: 397–414.
- [41] Odahara G, Hibino H, Nakayama N, Shimbata T, Oshima C, Otani S, et al. Macroscopic single-domain graphene growth on polycrystalline nickel surface. *Appl Phys Express* 2012;5. 035501-1-3.
- [42] Momiuchi Y, Yamada K, Kato H, Homma Y, Hibino H, Odahara G, et al. In situ scanning electron microscopy of graphene nucleation during segregation of carbon on polycrystalline Ni substrate. *J. Phys. D: Appl. Phys.* 2014.

# In Situ Observation of Crystal Growth and Flows by Optical Techniques

Katsuo Tsukamoto

GRADUATE SCHOOL OF SCIENCE, TOHOKU UNIVERSITY, ARAMAKI Aoba, SENDAI, JAPAN

## CHAPTER OUTLINE

<b>24.1 Introduction</b> .....	<b>1032</b>
24.1.1 Major Rate-Determining Processes.....	1032
24.1.2 Surface Observation.....	1032
24.1.3 Growth Rate versus Supersaturation Measurement .....	1033
<b>24.2 Development of Optical Techniques</b> .....	<b>1035</b>
24.2.1 Toward In situ Observation of Crystal Growth.....	1035
24.2.2 Phase-Sensitive Microscopic Techniques .....	1037
24.2.3 Observation of Monomolecular Growth Steps.....	1037
24.2.4 Measurement of Step Height by Classical Interferometry .....	1039
<b>24.3 Modern Interferometry and Microscopy for In situ Observation of Crystal Growth</b> .....	<b>1043</b>
24.3.1 Phase-Shift Interferometry .....	1043
24.3.2 Application of Modern Interferometry to In situ Observation of Crystal Growth .....	1045
24.3.3 In situ Measurement of Growth Rate by Interferometry .....	1047
24.3.4 Confocal Microscopy .....	1048
24.3.5 Laser Confocal Phase-Shift Interferometry.....	1049
<b>24.4 Three-Dimensional Observation of Flow and Concentration Field</b> .....	<b>1050</b>
24.4.1 Convection or Convection-Free Environment .....	1050
24.4.2 Importance of Computerized Tomography in Crystal Growth .....	1052
24.4.3 Interferometric Tomography .....	1053
<b>24.5 Future Developments</b> .....	<b>1055</b>
<b>Acknowledgments</b> .....	<b>1057</b>
<b>References</b> .....	<b>1057</b>

## 24.1 Introduction

We focus on the development of high-resolution optical microscopies for in situ observation of crystal growth from solution and their application to varieties of crystal growth fields with comparison to other techniques. In situ observation is needed not only in the field of fundamental crystal growth to understand crystal growth mechanisms but also in applications such as semiconductor technologies, mineralogy, space sciences, environmental problems like carbon sequestration or nuclear waste disposal underground. The range of applications has expanded from laboratories to the depth of the earth and space environments.

There is a growing interest in understanding the growth kinetics and variations in surface morphologies of a crystal growing from its aqueous solution. It has therefore been experimentally as well as theoretically established that the growth history and perfection of the growing crystal are intricately linked with its time-dependent external shape and surface morphology along with the associated heat and mass transport phenomena in the growth solution. These parameters, in conjunction with the interfacial solution temperature and the degrees of supersaturation in 2D and 3D over the crystal surface, govern the growth rates, the surface morphology, and resultant character of the growing crystals. It is therefore important to visualize these parameters during the growth process at the best possible spatial and time resolution. Since no probe needs to be introduced in the field of observation, optical visual techniques are nonintrusive and nondestructive and thus useful for in situ monitoring of the growth process and to directly understand the crystal growth mechanism.

### 24.1.1 Major Rate-Determining Processes

Crystal growth from solution is the process of mass and heat transport from the environment to the crystal surface, followed by the integration of these molecules at the crystal surface [1–3]. Among varieties of crystal growth mechanisms from liquids, crystal growth from solution differs from the crystal growth from melts, in which heat transport is the major rate-determining process. In the solution growth, coupling of mass transport of molecules in the solution and the integration of molecules at the crystal surface are the major rate-determining processes, [Figure 24.1](#). Dehydration process of molecules at the interface is also important rate-determining process as discussed later. In order to understand these processes, we have attempted to analyze each process by a variety of techniques. Observation of crystal surfaces and the growth rate measurement are the examples [3].

### 24.1.2 Surface Observation

In 1949, Frank [4] pointed out the possibility that growth of crystals at low supersaturation could take place at the emergent points of dislocations with a screw component. When growth take place on these exposed molecular terraces, the edges of these

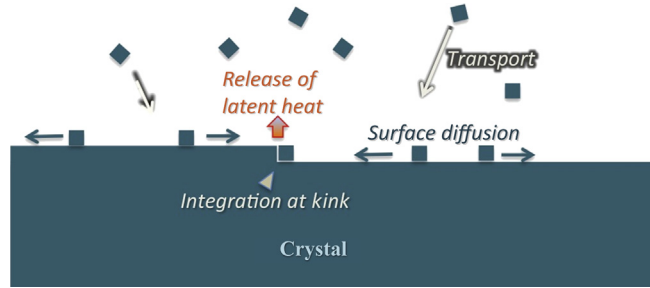


**FIGURE 24.1** Major rate-determining processes in solution growth, though dehydration process is not illustrated here.

layers develop into spirals centered on the dislocation. Griffin [5] verified the spiral growth theory by observing these monomolecular layers on the (0001) face of a natural beryl crystal and has shown by multiple-beam interferometry [6] that the height of these steps are only one unit cell high. By measuring the spiral step spacing, the authors could calculate the small degree of the supersaturation in nature at which the crystal was growing slowly.

After this observation, numerous spiral steps were observed on SiC [7], diamond [8], and natural hematite crystals [9,10], verifying the applicability of spiral theory to the growth from vapor and melt phases. However, it was not clear whether the spiral theory could be applied to aqueous solution-grown crystals. The observation of spirals on aqueous solution-grown crystals, like NaCl and KCl, was not easy because the surface was easily damaged with moisture. Surface microstructures of the (100) faces of these crystals were observed under the phase contrast and differential interference contrast microscopes after crystals were taken out from the solution. In both cases, evidence showing spiral growth was obtained for the first time in 1972 [11], Figure 24.2, followed by the observations of spirals on KDP, ADP [8,12], and protein crystals by optics [13], and by atomic force microscopy [14–16].

Numerous growth spirals have been observed on the faces of SiC [7] and measured with the aid of phase contrast microscopy [17] and multiple-beam interferometry. The surfaces were observed not only for the verification of the spiral growth theory but also for the characterization of differences in polytypes and their origins. Since spiral patterns reflect how and where the crystals grew, the observation has been important in earth sciences [9].

In the 1950s, these spirals of transparent crystals were observed by coating the crystal faces with a thin film of silver of reflectivity nearly 90% in order to reduce the reflection from inside of the crystal. This technique was used until recently when in situ observation methods and confocal techniques were developed.

### 24.1.3 Growth Rate versus Supersaturation Measurement

It was Bennema [3,18] who measured the growth rate of inorganic crystals from aqueous solution as a function of supersaturation. He pointed out the importance of the relation

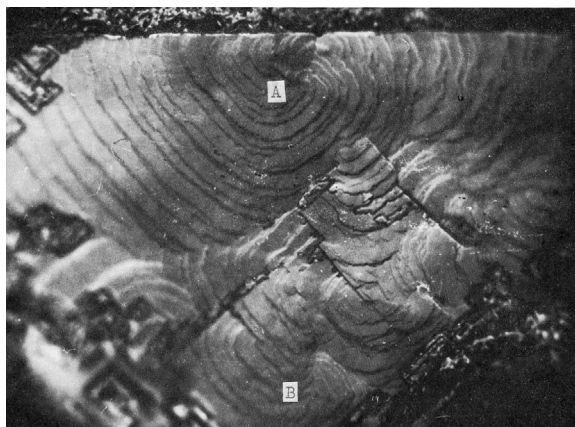


**FIGURE 24.2** Composited spiral steps from solution-grown KCl crystal, differential interference contrast microscopy. (A) and (B): spiral centers.

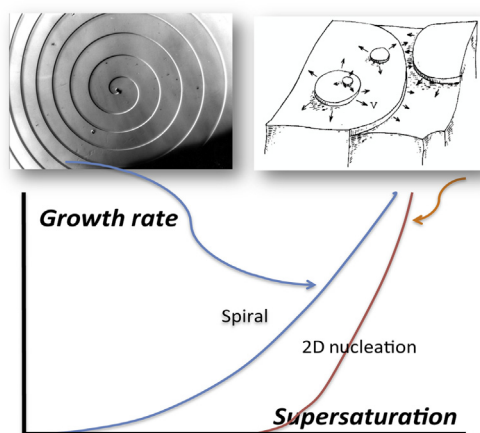


**FIGURE 24.3** Growth rate vs supersaturation that depends on growth mechanism. Spiral: spiral growth; 2D Nucleation: 2D nucleation growth.

to verify the spiral growth mechanism for growth also from solution, [Figure 24.3](#); for this experiment, he developed a fine weighing method to measure the growth rate of solution grown from extremely small supersaturation, [Figure 24.4](#). He concluded that the Burton–Cabrera–Frank (BCF) spiral theory that was developed for crystal growth from vapor could also be applied to the solution growth. This idea to measure the growth rate versus supersaturation became important for the prediction of growth mechanism. His weighing method was simple, but there were several disadvantages in its practical use. For instance, it took many hours/days to measure the growth rate at low supersaturation and the measured rate was an average values from all crystal faces. Interferometry and optical microscopies have subsequently been used to measure the

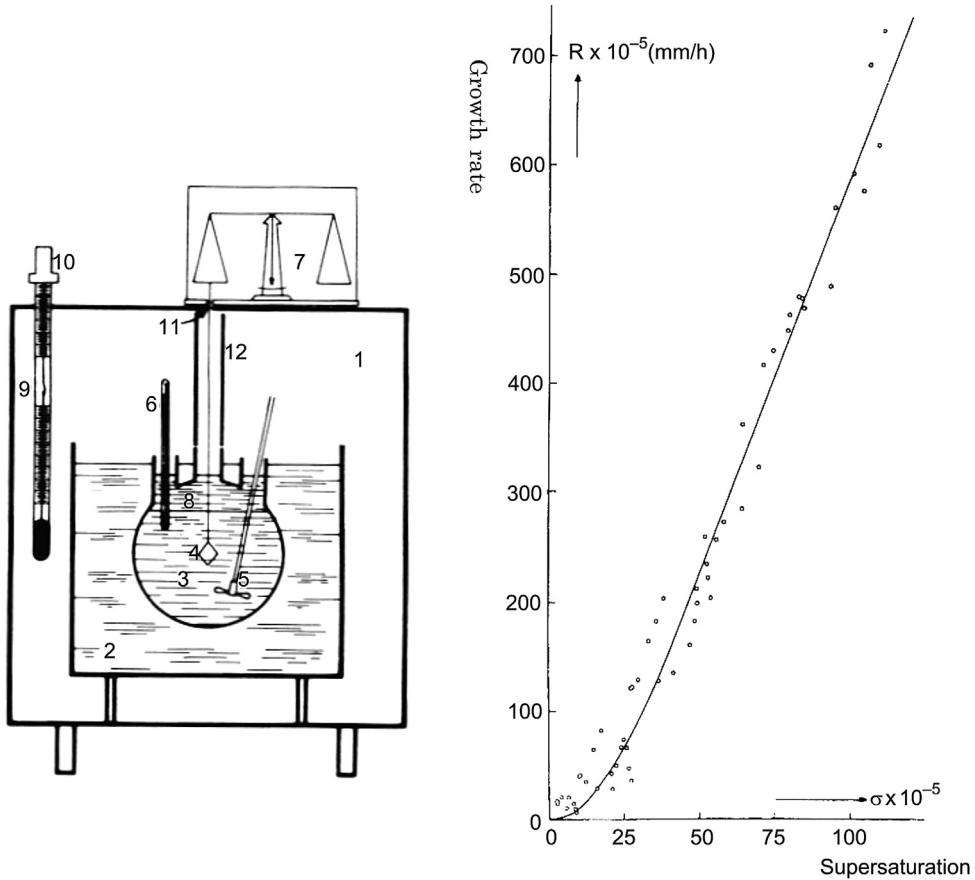


**FIGURE 24.4** The weighing method to measure the growth rate vs supersaturation. This apparatus was used by Bennema.

growth rate for much smaller growth rate measurements, details of which will be discussed in later sections.

There is wide variety of crystal growth/dissolution rate of crystals, [Figure 24.5](#). The maximum growth rate of solution-grown crystals might be several mm/s. The growth rate measured from giant gypsum crystals, [Figure 24.6](#), in Nica, Mexico, was  $10^{-5}$  nm/s [19], which is the slowest growth rate measured to date by any technique.

## 24.2 Development of Optical Techniques

### 24.2.1 Toward In situ Observation of Crystal Growth

Developments in microscopy and interferometry have resulted in a resurgence of optical imaging techniques in the field of crystal growth in the past few decades. In situ observation of the process of crystal growth is a novel and completely nondestructive

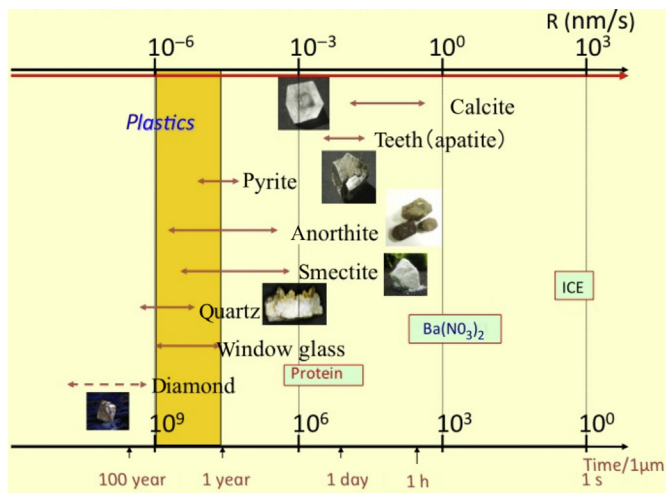


FIGURE 24.5 Wide varieties of growth/dissolution rate of crystals.



FIGURE 24.6 Giant gypsum crystal in Nica, Mexico. Some are more than 10 m long. The growth rate was measured to be  $10^{-5}$  nm/s in the laboratory by PSI.

approach for directly understanding the crystal growth mechanism. We have focused especially on observing monomolecular growth steps on the crystal surface and the concentration field adjacent to the crystal surface.

The importance of optical techniques for such applications has been highlighted primarily for two reasons. First, specially designed optical methods aid the study of

crystal growth by enabling direct observation of surface phenomena. For example, modern interferometric techniques have successfully paved the way for the observation of surface features at a resolution sufficient enough to reveal monomolecular growth steps on crystals. In fact, the vertical resolution provided by these modern techniques is comparable to that achieved with atomic force microscopy (AFM) technique. Second, with the advent of highly coherent light sources and means for faster data storage, optical methods have added a new dimension of quantitatively mapping the solution properties and related transport phenomena around a growing crystal, such as temperature and/or concentration field distribution and their gradients in the growth chamber. For example, in the case of inorganic crystal growth, the difference of 0.01 mol concentration at the surface was detected during the growth process [20–26]. A majority of optical techniques are field techniques in the sense that an entire cross-section of the physical region can be mapped. The recorded images can be interpreted as path integrals in the direction of line of sight. Three-dimensional local properties can be subsequently reconstructed by using the principles of tomography [27–29]. Moreover, they can be employed over a wide range of working temperatures, e.g., from room temperature to elevated temperatures as high as 2000 K or even more [30,31].

### 24.2.2 Phase-Sensitive Microscopic Techniques

The optical microscopic technique is one of the oldest and most popular methods for in situ observation of micromorphological features of crystal surfaces. For the observation of growth patterns on the surface of the growing crystal, a variety of optical phase-sensitive microscopes are available. Whereas surface scanning microscopic techniques, such as Atomic Force Microscope (AFM) and Scanning Tunneling Microscope (STM), have a better lateral resolution, these optical microscopic techniques have similar vertical resolution, [Figure 24.7](#). It may be surprising to learn that these optical techniques were used to observe growth steps of 0.23 nm height almost 50 years ago [10,32].

Phase contrast [33] and differential interference contrast microscopy are well-known phase-sensitive microscopic techniques that have been used for crystal surface observation [34]. Recent developments of phase-shift interferometry (PSI) [20,35–38] have changed the notion that was prevalent for the last few decades that interferometry is for measurements and microscopy is for observation. Several recent studies have shown that PSI [39] has the capability to both measure as well as observe the crystal growth surface, the details of which will be discussed later.

### 24.2.3 Observation of Monomolecular Growth Steps

[Figure 24.8](#) is an illustration of growth steps with monomolecular height,  $h$ . When an incident light illuminates the surface, a phase difference of  $2h$  appears in the reflection, though we cannot detect the phase difference but can detect intensity or color

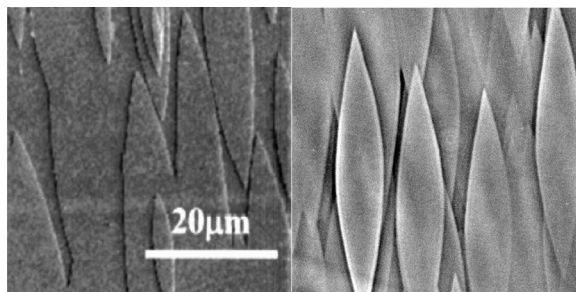


**FIGURE 24.7** Growth steps observed by AFM (left) and phase contrast microscopy (right). Note the similar vertical resolution.

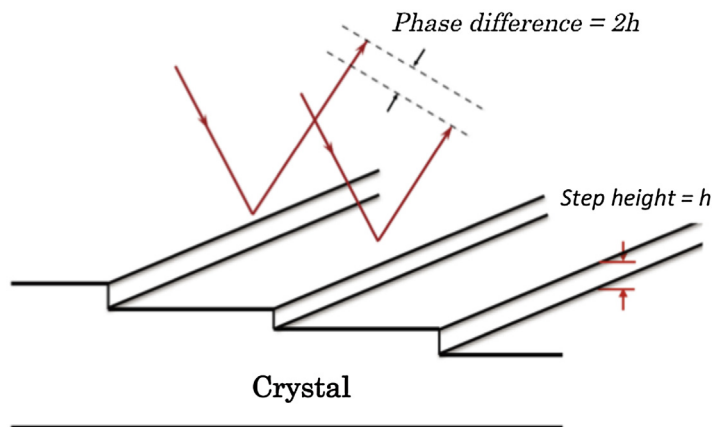


**FIGURE 24.8** Phase difference arising from growth steps with less than 1 nm height.

differences. The phase difference therefore has to be converted by phase-sensitive microscopy [33,40] or interferometry [7] to intensity or color differences if we want to observe the steps.

Two examples will illustrate the use of phase-sensitive optical microscopy for observation of the crystal surface during growth. In the case of transmission phase contrast microscopy [41], steps are observed through the crystal, solution, and glass windows of the growth cell. We need to keep in mind that normal objective lenses employed in the microscopes are made for use in air; therefore, if there is a medium other than air, which changes the phase of the images, various optical aberrations occur—in the worst case, the image will not be clear and lose the contrast. To avoid such aberrations, the total thickness of the crystal, solution, and glass windows of the growth cell along the optical path must be reduced as much as possible to reduce the optical aberrations; or alternatively, objective lenses should be

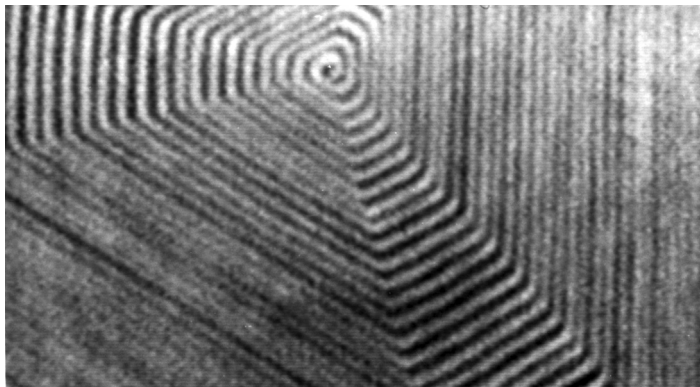


**FIGURE 24.9** Spiral steps of  $\text{CdI}_2$ , by transmission phase contrast microscopy, in situ.

designed to correct for the optical aberrations arising due to the thickness. The maximum allowable thickness depends on the magnification and on the microscopy.

Figure 24.9 shows an example of in situ observation of spiral growth steps on the surface of  $\text{CdI}_2$  crystal during its growth from aqueous solution. In this case, the total thickness of the crystal, solution, and glass windows is less than 1 mm. If reflection-type microscopy is used, the role played by the thickness of the crystal is not important; however, the optical path increase doubles due to reflection. The increase of the aberration leads to the loss of image sharpness and also considerably reduces the contrast of the image, which is important for surface observation.

Another example is shown in Figure 24.10, in which 2D islands on a protein crystal (hen-egg white lysozyme crystal), left and a spiral growth hillock, right are shown. The minimum heights of these steps are 5.6 nm and 11 nm, respectively, as described later.

#### 24.2.4 Measurement of Step Height by Classical Interferometry[41]

Among the different types of interferometers available, the Michelson interferometer has been extensively used for measuring the growth rate of crystals growing from their aqueous solution for the understanding of growth and dissolution kinetics [21,42–44]. The interferometer has also been used to observe the detailed shapes and profiles of growth hillocks during crystal growth from solution [43].

The optical configuration of a Michelson interferometer for in situ observation of crystal growth processes is schematically shown in Figure 24.11. A beam splitter is used to split a laser beam into two separate beams: test beam and reference beam. The phase of one of the interfering beams (the test beam) that is reflected from the crystal surface is shifted due to the variations in the morphology of the crystal surface. This phase variation manifests itself in the form of changes in the resultant fringe pattern in the

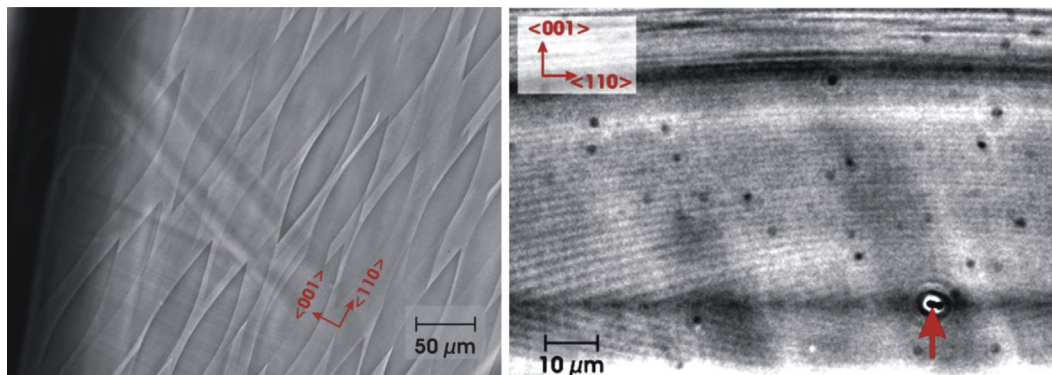


FIGURE 24.10 2D growth islands of tetragonal-lysozyme crystal (left) and spiral growth steps originating from a dislocation generated from an inclusion (indicated by an arrow) just below the surface (right) as observed using transmission phase contrast microscopy.

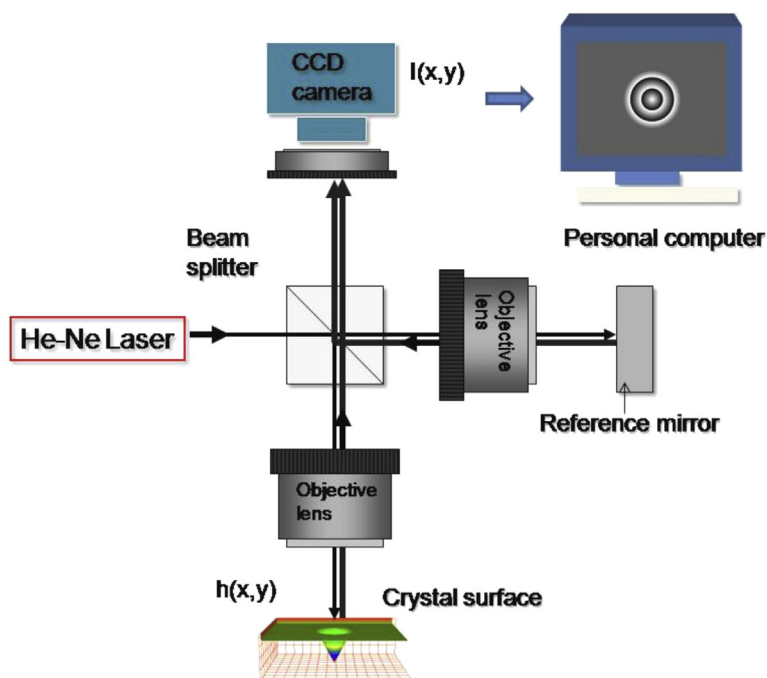


FIGURE 24.11 Schematic diagram of a standard Michelson interferometer with objective lenses for surface observation.

interferogram produced due to the interference of the two beams. Though multiple-beam interferometry after Tolansky [6] is a very sensitive method for the measurement of step height, there is a limitation for in situ observation because of a spatial configuration to use a half mirror.



FIGURE 24.12 Michelson two-beam interferogram from spiral hillocks of  $\text{Ba}(\text{NO}_3)_2$  growing in solution.

The interferograms recorded using Michelson interferometry technique are capable of providing direct qualitative as well as quantitative information about the surface morphology of a growing crystal, e.g., growth step, 2-D islands, spiral growth hillocks, etc. One such interferogram is shown in Figure 24.12 for illustration. The physical significance of the fringe pattern shown in the figure can be understood as following: The face of the growing crystal shows the presence of two large spiral hillocks and a small hillock. These growth hillocks, originated from screw dislocations, result in an interference pattern consisting of concentric fringes of almost equal inclinations.

The series of interferograms provides a time-dependent geographical description of the growing face, from which various growth kinetic parameters—such as normal growth rate  $R$ , the change of slope of the spiral growth hillock  $p$ , and the tangential growth velocity  $v$  of the steps—Figure 24.13, can be computed. The difference of height between adjacent fringe contours on a hillock can be expressed as:

$$d = \lambda/2n$$

Here  $\lambda$  is the wavelength of the laser used as the light source and  $n$  is the refractive index of the solution. Similarly, if  $D$  is the distance between the two points on a face, which lie on the adjacent fringes, then slope of the dislocation growth hillock  $p$  is:

$$p = \tan \theta = \frac{d}{D}$$

Michelson interferometry often employs laser illumination for quantitative measurements, but noncoherent white light sources can also be used to avoid laser speckle patterns that decrease lateral resolution. While making an interference pattern by laser is fairly easy, it is somewhat difficult to suppress speckle noises due to unwanted interference patterns caused by reflections from other areas of the growing crystal and/or optical components. Suppressing this noise is the key to achieving high resolution and meaningful interference fringes.

The quality of images recorded using a Michelson interferometer can be very sensitive not only to small inclusions or imperfections in the growing crystal but also to the

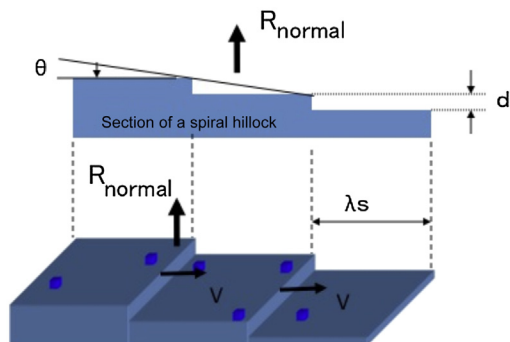


**FIGURE 24.13** Schematic step profile.  $V$ ,  $R_{\text{normal}}$ ,  $\lambda_s$ , and  $d$  are, respectively, step velocity, growth rate normal to the surface, step spacing, and step height.

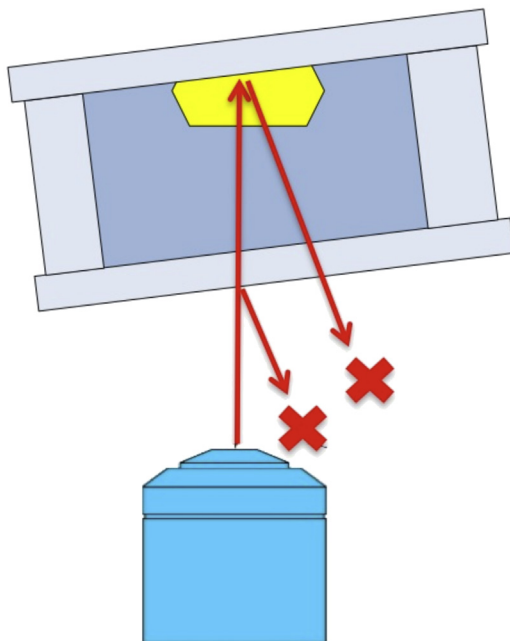


**FIGURE 24.14** Surface observation to reduce reflections from the back side, glass windows. This simple configuration considerably improves the image quality.

surface of glass windows. This aspect of imaging has been pictorially demonstrated in [Figure 24.14](#). For example, since the reflectivity of the crystal surface of, say, protein crystals is less than 1%, light scattered from inclusions, from the back side of the crystal or glass windows, leads to a considerable amount of noise in the interference images, thereby reducing the image contrast. Reflections from the surface of glass windows of

growth cells can also distort images, and it is important to slightly tilt the windows or use antireflection coating.

For the best imaging, it is also important to reduce the thickness of the glass windows and the solution above the growing crystal surface since most objective lenses are designed assuming that no medium other than air is present between the object under study and the objective lens. The presence of such media between the object and the objective lens causes optical aberration, which considerably reduces the contrast and quality of images [45].

## 24.3 Modern Interferometry and Microscopy for In situ Observation of Crystal Growth

Because of recent progress in optical microscopes [46,47] and interferometry [20,35], image quality has dramatically improved compared to when in situ observation of monomolecular growth steps began [41,48]. New cooled CCD cameras with much higher resolution, higher contrast, and low-noise specifications and high definition recording systems have contributed greatly to the improvements in the image quality. The development of optics like PSI and combination of confocal principle with DIC [46,47] have contributed extremely important improvements, too.

As mentioned previously, microscopy and interferometry developed independently, and each has respectively been employed for qualitative 2D observation of the crystal surface and quantitative growth rate measurements along the direction normal to the crystal surface. The combination of these two methods is needed to get 3D information from the surface with, for instance, spiral steps. However, this combination had not been achieved until PSI developed for in situ observation of crystal growth. This interferometry has a great advantage in sensitivity (two order of magnitude higher) but also each pixel of the image has phase information (height information) and thus each pixel possesses absolute value of height information with the accuracy of  $<1$  nm [20,35].

### 24.3.1 Phase-Shift Interferometry

Although classical interferometry is a highly sensitive measurement technique, it is still not capable of observing and measuring growth steps with monomolecular height. Therefore, the step height was calculated by counting the number of growth steps between two neighboring interference fringes, which corresponds to one-half of the wavelength of the light beam, by phase contrast microscopy, for instance [32,41].

As discussed in the previous section, in order to analyze the phase arising from the step height difference, one needs to measure the relative fringe shift from the fringe pattern obtained using conventional two-beam interferometry (e.g., Michelson interferometer). In this regard, recent developments in the field of real-time phase-shift interferometric techniques [20,39,49,50] have caused a revival in the concept of

interferometry. In PSI, the intensity of fringes is directly related to the phase that we want to measure.

The intensity  $I(x, y)$  of interference fringes from two beams  $E_1$  and  $E_2$  at  $(x, y)$  is:

$$I(x, y) = \frac{E_1^2 + E_2^2}{2} + E_1 E_2 \cdot \cos\{\phi(x, y) + 2\theta\} \quad (24.1)$$

Here  $\phi(x, y)$  and  $2\theta$  are the phase difference and the angle between two vibrations of the beams, respectively. As seen in Eqn (24.1), the measurable intensity  $I(x, y)$  is not a function of the phase alone. By a process in which the phase is successively shifted by  $\lambda/4$  wavelengths, the following three equations corresponding to the three phase-shifted values can be obtained:

$$I_1 = a + b \cdot \cos\{\phi(x, y) + 2\theta_1\} \quad (24.2)$$

$$I_2 = a + b \cdot \cos\{\phi(x, y) + 2\theta_2\} \quad (24.3)$$

$$I_3 = a + b \cdot \cos\{\phi(x, y) + 2\theta_3\} \quad (24.4)$$

where  $a = \frac{E_1^2 + E_2^2}{2}$ ,  $\theta_1 = -\frac{\pi}{4}$ ,  $\theta_2 = \frac{\pi}{4}$ ,  $\theta_3 = \frac{3\pi}{4}$  and  $b = E_1 E_2$ .

Equations (24.2) through (24.4) lead to the simple relation:

$$\phi(x, y) = \tan^{-1} \left( \frac{I_1 - I_2}{I_2 - I_3} \right) \quad (24.5)$$

The phase in Eqn (24.5) is directly related to the intensity of the interferogram at any point  $(x, y)$ , which is illustrated in Figure 24.15 for the case of a lysozyme crystal growing in its aqueous solution.

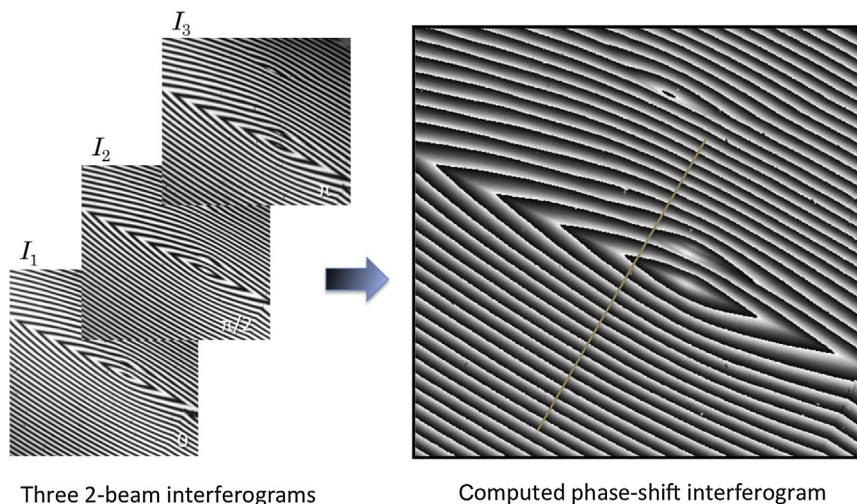


**FIGURE 24.15** Principle of PSI. By successive phase shift of  $\pi/2$ , three interferograms ( $I_1, I_2, I_3$ , left) are obtained, from which one phase-shift interferogram can be calculated (right). Note the saw-shaped intensity profile along a line in PSI. In two-beam interferogram, the profile is sinusoidal.

PSI has the advantages of microscopy as well as interferometry because the vertical resolution of this interferometry from each pixel of an image is less than 1 nm if a 8 bit A/D converter is used for the processing. This value is much less than the height of elementary steps of proteins, and therefore surface topographies with nanometer resolution can be directly measured and the microscopic image can be mapped. [Figure 24.8](#) is an example showing 2D islands of a growing lysozyme crystal with the elementary step height of 5.6 nm. Since better 12–16 bit A/D converters are available, the vertical resolution might exceed 0.1 nm in the processing. The availability of such high resolution, however, depends on the quality of original optical images and interference fringes. The key for success in the improvement is also whether they can suppress the optical aberration. Conventional lenses are made for observing objects that are placed in air and not in solution or melt, or through glasses or solution, and thus aberration appears in principle for in situ observation of crystals in solution.

### 24.3.2 Application of Modern Interferometry to In situ Observation of Crystal Growth

A two-beam interferogram and a phase-shift interferogram are compared in [Figure 24.16](#). Since PSI can directly measure the absolute height of steps, it is possible to obtain not only height of growth steps but also the images of the steps. Roughly speaking, the resolution of 2-beam interferometry is one-tenth of the wavelength of light. PSI is approximately 100 times more sensitive [39].

PSI has been applied to the growth of a protein crystal (lysozyme) to study the growth mechanism, [Figure 24.17](#). PSI image in (A) has the height information in each pixel. The height profile along  $x-x'$  is readily be seen to calculate the step height, 5.6 nm, which is exactly the same as elementary step height obtained from the crystal structure of a tetragonal hen-egg lysozyme crystal. The height information also gives a micrographic

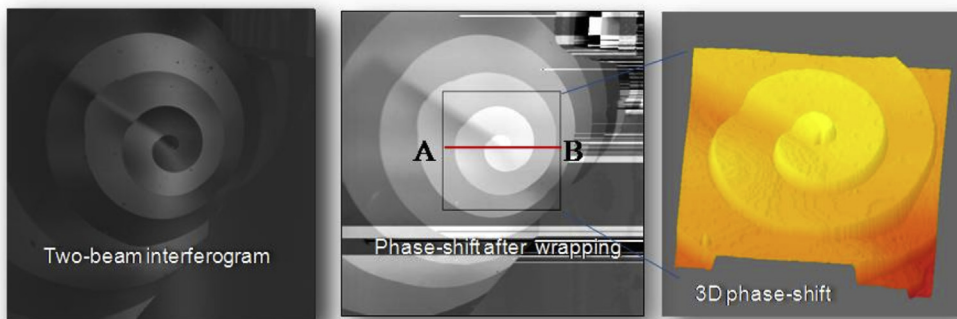


**FIGURE 24.16** Two-beam interferometry vs phase shift interferometry: ex situ observation of a SiC surface. In phase-shift interferometry (PSI), the interference fringe intensity is proportional to the height and the 3D phase-shift image can be directly obtained.

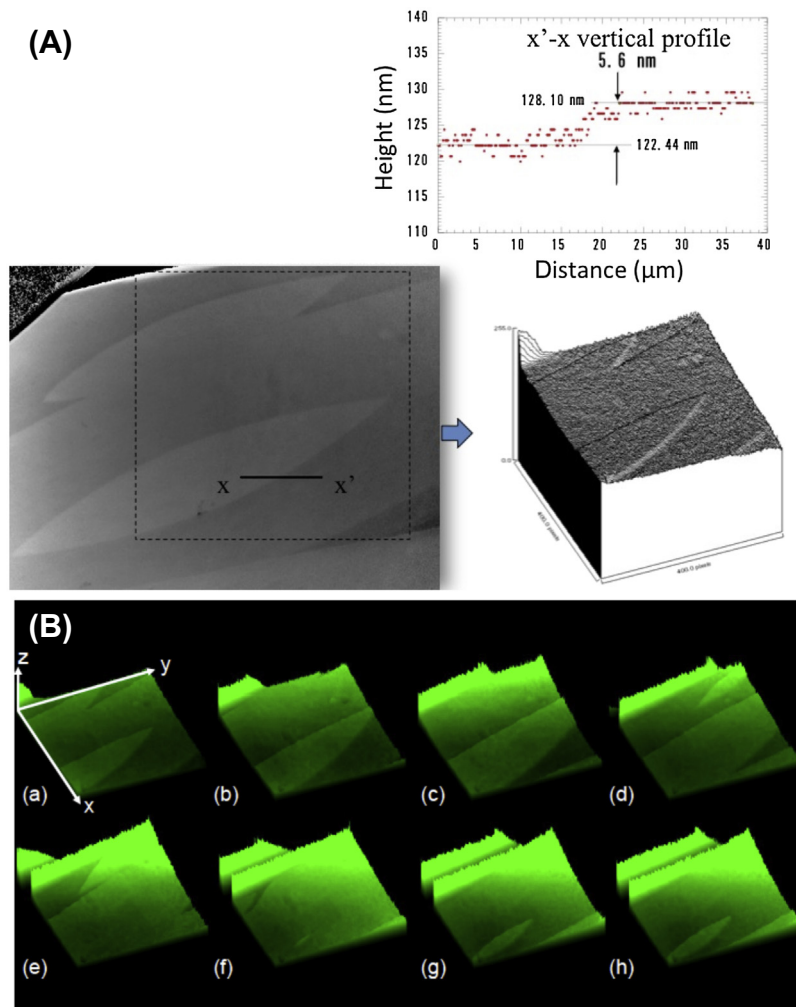


**FIGURE 24.17** Monomolecular growth steps of 2D islands, tetragonal lysozyme with 5.6 nm high by white beam PSI, unpublished (Dold and Tsukamoto). (A) The vertical resolution of PSI is less than 1 nm. Left down: a phase-shift image of 2D islands; Right down: 3D display of the 2D islands, 5.6 nm high. (B) Successive images showing how the crystal face grows by 2D nucleation and spread of the steps. Both nucleation rate and step advance rate can be measured directly.

image and a 3D image as shown below in (A). Successive phase-shift interferograms (B) are important for the measurement of frequency of 2D nucleation and step advance rate of these monomolecular steps.

This method can be applied to the dissolution of crystals with an extremely slow rate. In [Figure 24.18](#), an example of the dissolution process of a calcite crystal is shown together with an A–B profile and a 3D-surface topography of etch pits in PSI image and in a differential phase image. The latter image can be obtained by taking a derivation of

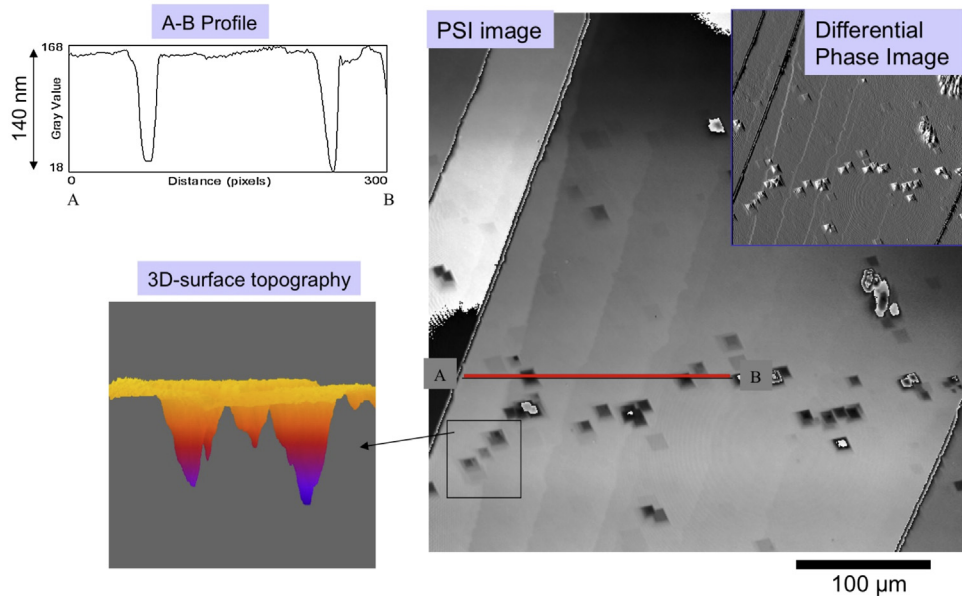


**FIGURE 24.18** Dissolution of a calcite crystal observed by PSI. Note the 3D dissolution topography being suitable for small dissolution rate. The differential phase image (right) is obtained by taking derivative of the PSI image.

the PSI image along the horizontal direction. Since the PSI image possesses height/depth information, both 3D growth and dissolution rate can be calculated precisely from desired areas. PSI could cover most of the growth/dissolution rate shown in Figure 24.5, if the rate is more than  $10^{-5}$  nm/s.

### 24.3.3 In situ Measurement of Growth Rate by Interferometry

Recently, PSI has been used to measure the growth rate of crystals in a precise way, as shown in Figure 24.19. In (A), an original phase-shift interferogram of a spiral hillock on a growing lysozyme crystal is shown. In (B), the corresponding time line along a solid line in (A) is shown. Since the vertical axis in (B) is time, the slope of the fringes in (B) is the spreading velocity of the fringes, which can be converted to the normal growth rate of the spiral hillock. Among varieties of methods of growth rate, this is probably the most sensitive and accurate way to measure crystal growth rate. The smallest growth or dissolution rate measured to date is about  $10^{-5}$  nm/s [51–54], which corresponds to a rate of only 1  $\mu\text{m}/\text{year}$ !

This sensitive method is important in environmental sciences and mineralogy because these phenomena are usually natural phenomena and thus is very slow process compared to the synthesis of crystals. The dissolution of concrete or clay barriers of the containers for nuclear radioactive waste disposal underground, dissolution or alteration of minerals or concrete [53–58], and carbon sequestration to reduce carbon dioxide in atmosphere to form calcium carbonates underground are in such a category. Since the

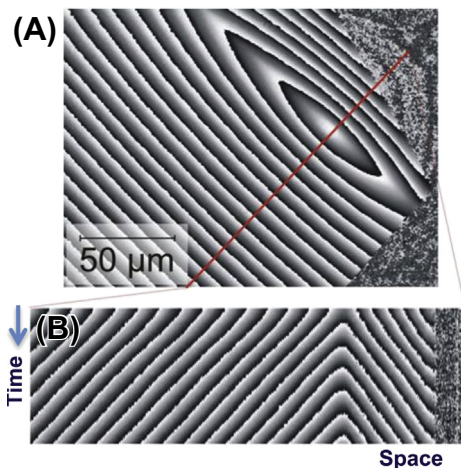


**FIGURE 24.19** Phase-shift fringes and the time line, to precisely measure the growth rate of a crystal and its fluctuation. Tetragonal-lysozyme, unpublished.

process is very slow, acceleration test by changing conditions has commonly been used. However, in situ observation techniques are capable of revealing each elementary process during the whole reaction.

PSI is a highly sensitive technique in which even the slight disturbances from airflow, mechanical stage vibration, cell expansion due to temperature inhomogeneity, voices, or slight changes in ambient conditions can severely affect measurement accuracy. For small growth rate measurements, such disturbances cause the mechanical shift of the cell much larger than the thickness increase due to growth of crystals. In order to compensate for these disturbances, a reference area on the surface of the crystal is generally prepared [51,59]. For dissolution experiments, a part of the crystal surface is masked with a thin gold foil [52–55,57].

#### 24.3.4 Confocal Microscopy

If the crystal is transparent, transmission-type phase contrast microscopy is a highly efficient method to observe monomolecular growth steps [41]. However, because of defects and inclusions in crystals or because of complex crystal morphologies, reflection-type microscopy often seems to be a better option. The method of observation of a step profile using reflection-type microscopy is schematically shown in Figure 24.14. If the crystal is opaque, there is no problem since the reflection of the incident light is strong. However, if the crystal is transparent, many problems arise due to reflections from the back side of the crystal or from inclusions within the body of the crystal. It is usually the case that the intensity of light reflected from the back side is higher than the intensity of light reflected from the top surface. This problem may be solved simply, for instance, by cutting off the back side with the angle of a few degrees from the front surface to avoid the strong reflection from back side, Figure 24.14.

The principle of confocal microscopy has been used to overcome these problems. The original idea of confocal microscopy was to get the three-dimensional profile of a relatively flat surface by using a pinhole with a scanning laser beam [60]. In order to reduce the effects caused due to unwanted reflections from the crystal back surface and inclusions, new types of microscopy and interferometry have recently been developed using of the basic principle of confocal microscopy. Laser confocal microscopy technique was coupled with differential interference contrast microscopy to produce laser confocal differential interference contrast microscopy (LCDICM) [46]. We should keep in mind, however, that confocal principle cannot improve the contrast of the images but can suppress the useless reflection that reduces the contrast or the image quality arising from inside of the crystals. This is also true for laser confocal phase-shift interferometry (LCPSI) [37,61], which is described in the following section. This, in turn, means that if you obtain good reflection from the surface, conventional differential interference microscopy (DICM) is enough for quantitative surface observation.

### 24.3.5 Laser Confocal Phase-Shift Interferometry

The recently developed LCPSI is shown in Figure 24.20. It consists of a small Michelson interferometer attached to a commercially available laser confocal microscope. Compared to white light PSI, the adjustment for in situ observation of the surface is

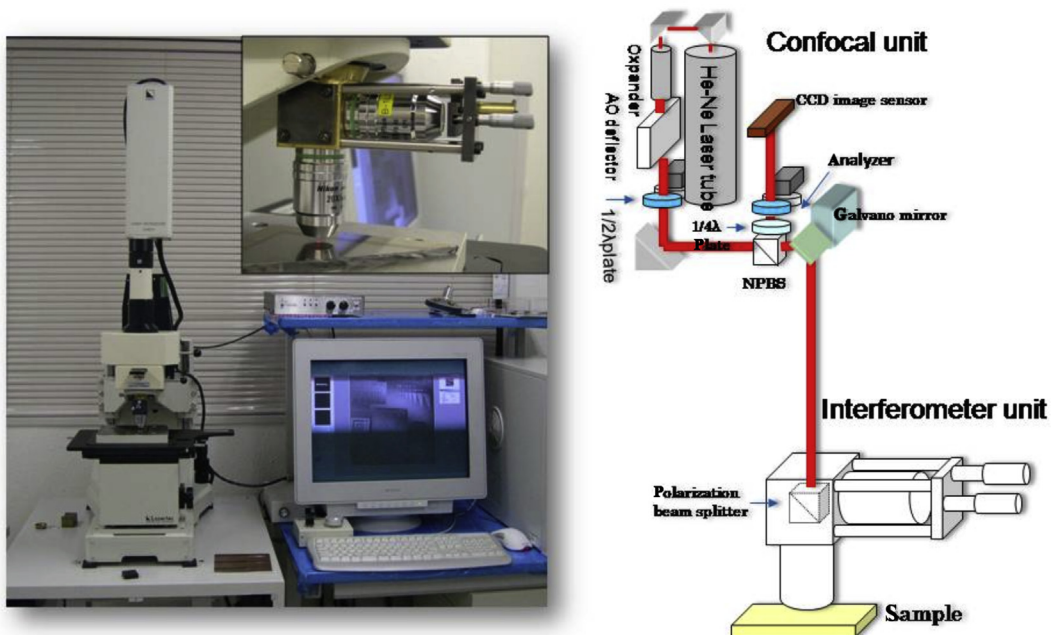
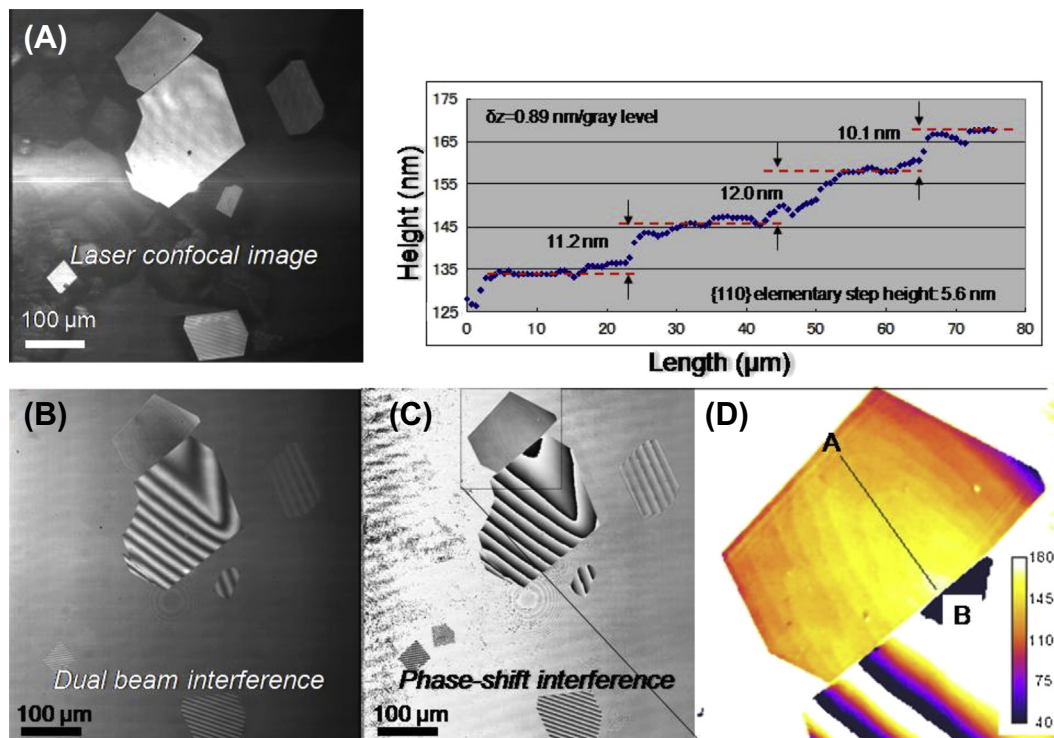


FIGURE 24.20 Configuration of laser confocal phase-shift interferometer (LCPSI) newly developed mainly for in situ observation of transparent crystals like protein crystals.



**FIGURE 24.21** In situ observation of lysozyme crystals: comparison between confocal microscopy (A), 2-beam interferometry (B) and laser confocal phase-shift interferometry (LCPSI) (C) and (D). Intensity of phase-shift interference fringes is a direct representative of the height information. The step profile is from the A–B in (D).

much easier. In [Figure 24.21](#), a confocal image, a two-beam interference image, and an LCPSI image of growing lysozyme crystals are shown in comparison. The step profile measurement of the crystal is also shown. Because the phase information is involved in the phase-shift images, the height profile along A–B in (D) can be plotted. The steps that consist of a hillock in (D) have double height of the step of 2D islands. This is attributed to the fact that the unit Burgers vector of the crystal is  $\sim 11$  nm.

## 24.4 Three-Dimensional Observation of Flow and Concentration Field

### 24.4.1 Convection or Convection-Free Environment

There has been extensive discussion as to why convection-free microgravity conditions [62], in a gel or in upside-down geometry of the growth cell [63] sometimes lead to better quality of crystals. In solution growth, the concept of forced convection has been applied for homogenizing the concentration gradients over the growing crystals to improve the

crystal quality. However, in convection-free conditions, the buoyancy-induced convection is generally suppressed, and thus a larger concentration gradient over the surface is expected, yet they have been claimed to grow better quality crystals.

In order to answer these pertinent questions, the 2D supersaturation distribution over the (100) face of a sodium chlorate crystal with/without convection under normal gravity conditions has been conducted by measuring a 3D concentration field around the crystal by using 3D interferometry [29]. Many researches have been conducted by interferometry or Schlieren method to visualize convection or concentration fields around growing crystals in solution [20,22,64,65] for the study of effects of convection or concentration gradient on the crystal quality or growth mechanisms.

These studies have aimed to measure the concentration profile over the surface. However, this is not so easy because in gravity, solutal convection cannot be avoided, which is highly complex in shape, and thus conventional 2-D interferometry to view along a single direction is not sufficient. In order to overcome these difficulties, multi-directional interferometry has been applied to reconstruct 3D-distribution images around a crystal, leading to the reconstruction of 2D distribution of supersaturation along a surface.

Although there are many reports on the measurements of concentration fields close to crystal surfaces, most of these are based on 2D observations, namely, projected optical imaging from only one direction. Therefore, the resultant concentration field is path integrated along the direction of propagation of the light beam and hence represents path-averaged information. Previous works have shown that the concentration field around a growing crystal is not uniform due to flow or convection, etc., and, as a result, the growing crystal surface deviates from the desired ideal flatness.

Although some previous studies have used 3D observations to visualize convection around the crystal [66], quantitative measurements for crystal growth studies at an appropriate resolution of the concentration field have not been reported. Srivastava and coworkers [28,67] observed the concentration surrounding a crystal by the Schlieren method.

Srivastava et al. [28] recently initiated a quantitative analysis of the concentration field around a crystal interface by using an octagonal crystal-growth cell in combination with a Mach-Zehnder interferometer, which is more sensitive in the change of concentration field. One of the advantages that interferometry-based optical imaging techniques offers is that, in addition to be an effective tool for mapping the surface features of the crystal, these techniques can simultaneously be used for in situ investigation of the associated transport phenomena in the vicinity of the growing crystal. The distribution of concentration gradients near the crystal surface-solution interface and surface concentration can provide important information in addressing the coupled effects of fluid dynamics and mass transport that are often detrimental to the crystal quality. The rate of solute transport from the solution to the crystal surfaces is primarily controlled to the concentration gradients. Hence, a higher concentration gradient would cause a higher probability of morphological instabilities [68–70],

resulting in macro steps, step bunches, and solution inclusions on the growing crystal surfaces.

### 24.4.2 Importance of Computerized Tomography in Crystal Growth

A crystal growing from its aqueous solution creates a three-dimensional solute distribution in its vicinity that is responsible for the evolution of buoyancy-driven convection currents in the growth chamber. Hence mapping of convection patterns as well as the determination of the three-dimensional concentration fields is required to fully understand the mechanism of crystal growth. With the availability of high-speed computers and means for large data storage, it is theoretically possible to record a very large number of projections of the concentration field around a growing crystal in many directions and subsequently reconstruct the original concentration field to a high degree of accuracy using the principles of tomography [71].

The ray indices, in Figure 24.22, are  $s$  and  $\theta$ , where  $s$  is the perpendicular distance of the ray from the object center and  $\theta$  is the angle of the source position (or object rotation). Here,  $z$  is a coordinate along the chord SD. In a given experiment, the optical techniques collect the projection data  $p(s, \theta)$  for various values of  $s$  and for several  $\theta$ . Usually the projection profile is measured for  $\theta$  ranging from 0 to  $\pi$ . The transformation of an object function  $f(r, \phi)$  into its projection data  $p(s, \theta)$  is called the Radon transform. The method of tomography then creates the 3D map of the field under study from a collection of 2D projection data.

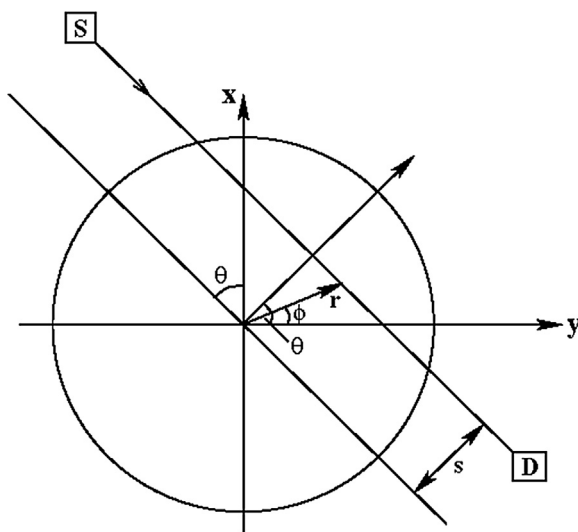


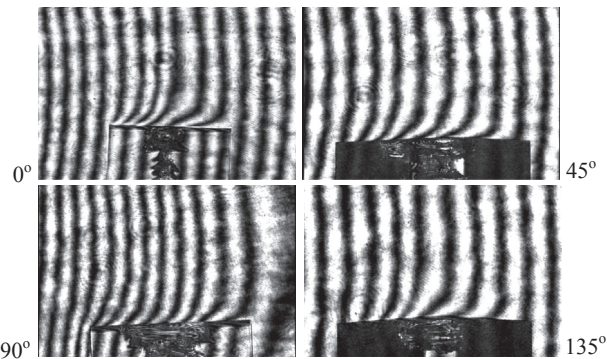
**FIGURE 24.22** Schematic drawing showing the data collection using parallel beam geometry. S: source, D: detector,  $s$ : perpendicular distance from the center of the object to the ray,  $\theta$ : view angle, and  $(r, \phi)$ : polar coordinates.

### 24.4.3 Interferometric Tomography

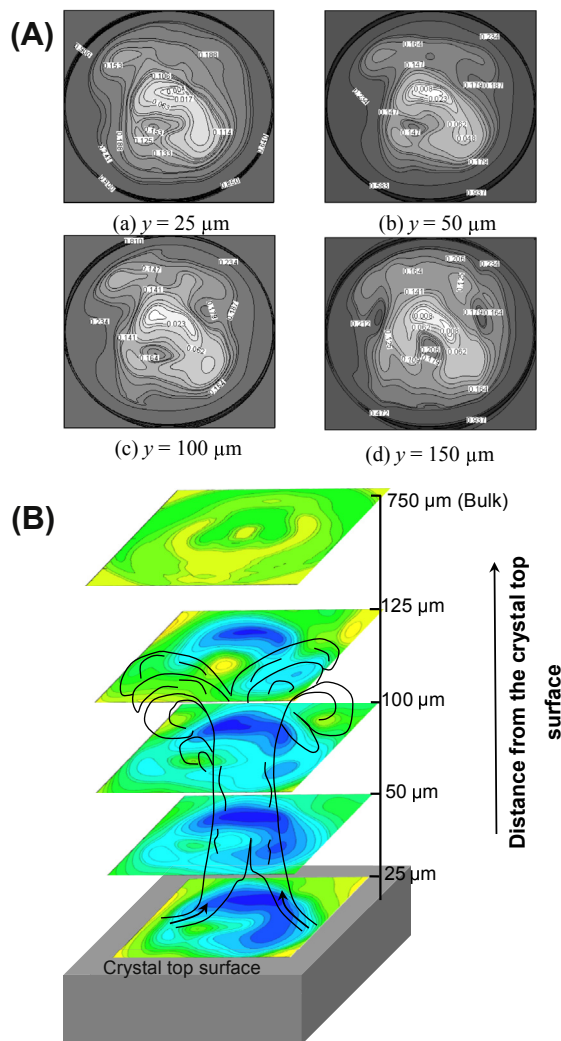
This section briefly discusses the reconstruction results of three-dimensional distribution of concentration field around a  $\text{NaClO}_3$  crystal growing from its aqueous solution using interferometric tomography technique. The crystal growth experiments have been carried out in an octagonal growth cell. Projection data of the concentration field has been recorded using a Mach–Zehnder interferometer from four different view angles— $0^\circ$ ,  $45^\circ$ ,  $90^\circ$ , and  $135^\circ$ —by slowly turning the growth chamber [28].

Figure 24.23 shows the interferograms as recorded from four view angles. Lateral dimension of the crystal is about 1 mm. Concentration gradients caused due to the deposition of salt onto the crystal surfaces are visible in the form of fringe displacements in the figure. The thickness of the solutal boundary layer can be identified as the region over which fringe displacement is seen in the interferograms. Figure 24.24(A) shows reconstructed concentration profiles at four horizontal planes above the growing crystal. Figures (A–C) in Figure 24.24(A) correspond to four planes located within the thickness of the boundary layer (at a distance of  $25\ \mu\text{m}$ ,  $50\ \mu\text{m}$ ,  $100\ \mu\text{m}$ , and  $150\ \mu\text{m}$ , respectively, from the crystal surface). In Figure 24.24(B), 3D representation of the concentration map over the crystal is shown. The stability of convection plum was reported to be related to growth rate fluctuation [45,72] but also to the formation of quasi-hopper surface, Figure 24.25, due to the large concentration gradient along the surface [73]. Such a large concentration gradient was recently investigated by 3D interferometry precisely using a cylindrical cell [29].

Murayama et al. [29] compared this result with the data from convection-free condition. It has been believed that if the convection or flows were suppressed in convection-free condition, the concentration gradient along the surface would increase due to no solution mixing effect. However, they found that the reduction of supersaturation at the middle of the surface without convection is less than 40%, the value of



**FIGURE 24.23** Interferometric images as recorded from four different view angles ( $0^\circ$ ,  $45^\circ$ ,  $90^\circ$ , and  $135^\circ$ ) using the Mach–Zehnder interferometer,  $\text{NaClO}_3$ .



**FIGURE 24.24** (A) Reconstructed concentration profiles over four horizontal planes above the top surface of the growing crystal. The coordinate  $y$  represents the vertical distance of the horizontal plane from the crystal surface. (B) Schematic representation of possible fluid movement in the vicinity of the growing crystal drawn on the basis of distribution of three-dimensional salt concentration obtained using Fourier analysis-based phase-shift interferometric tomography. Blue shade represents low salt concentration, whereas green and yellow shades correspond to relatively higher concentration of solute.

which is much smaller than the case when a convection plume is formed over the surface of a crystal. This situation is shown schematically in [Figure 24.26](#). A similar result was obtained from the comparison of crystal growth of lysozyme under microgravity [59] and in gravity.

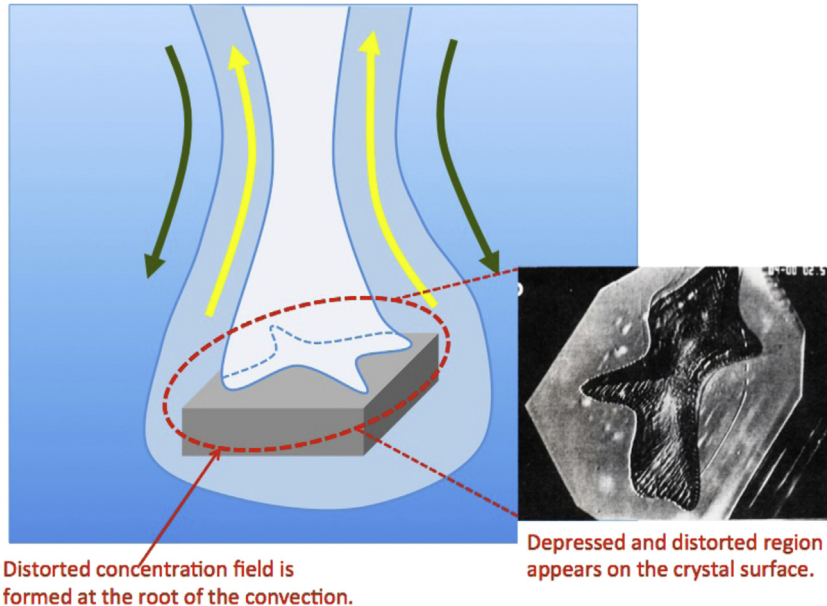


**FIGURE 24.25** Formation of quasi-hopper surface due to convection plume. This depression of the surface at the middle would result in the formation of defects, like inclusions and dislocations.

This result would give us a key to solve why crystal quality is sometimes better in convection-free microgravity condition because of improved stability of a crystal face caused by more homogeneous distribution of supersaturation over along the crystal surface [69,70]. This result will also be confirmed using the data of space experiments on lysozyme crystal growth in the International Space Station, to be published in forthcoming papers.

## 24.5 Future Developments

The contents of this chapter have emphasized the importance of recent advances made in the field of, mainly, interferometric-based imaging techniques for nanoscopic mapping of morphological features of the surface of a growing crystal and the associated hydrodynamics in the crystal vicinity. By improving optical methods, sensitivity in the phase detection, i.e., vertical resolution for the surface observation became less than 1 nm, and the growth rate of less than  $10^{-5}$  nm/s could be measured in a short time. This is a victory in the improvement of spatial resolution. Then, how about time resolution?

Time resolution is practically limited by the TV rate, and thus the maximum speed of real-time PSI [45,49] is 30 frames/s. There are many interesting phenomena in crystallization. Nucleation of crystals is such a phenomenon to be investigated by in situ methods. However, nucleation is a rapid phenomenon compared with crystal growth.

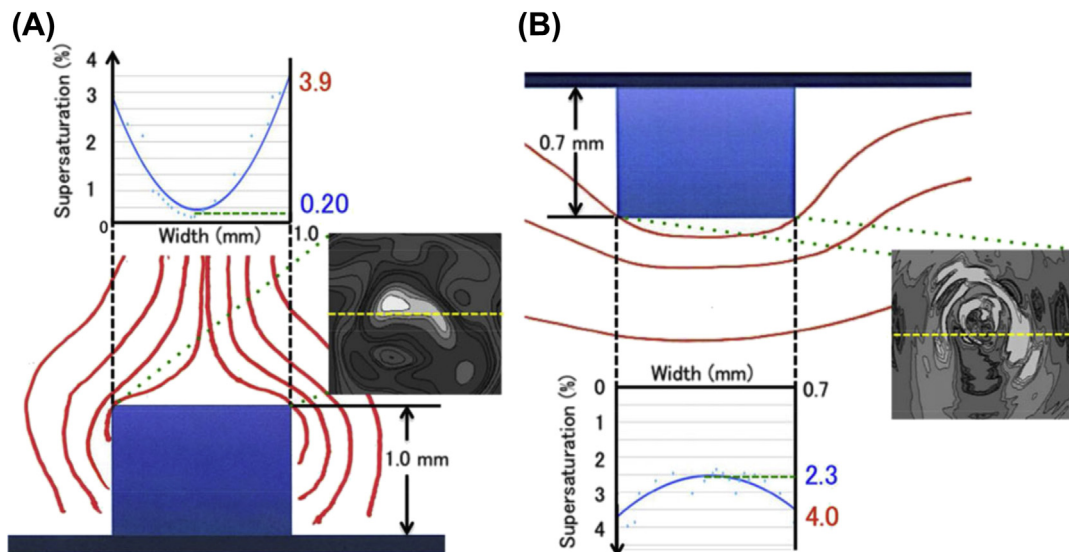


**FIGURE 24.26** Schematic summary of experimental results (A) in convective and (A) in convective-free conditions. The red lines schematically represent equal concentration in the solution. The gray contour maps are 2D supersaturation distributions over the crystal surface. The blue lines show the concentration profiles along the yellow dotted lines in the supersaturation contour maps. (A) Large reduction of supersaturation at the middle of the crystal face due to buoyancy-driven convection. (B) Quasi-microgravity condition by suppression of the convection using upside-down geometry. Note the reduction of supersaturation at the middle of the face is much smaller than the case of (A). This smaller drop of supersaturation in (B) would keep the stability of a crystal face.

We have therefore been trying to improve time resolution for the study of nucleation and some other rapid phenomena. Oxide smoke particles are our target materials [74,75]. Figure 24.27 is one example that shows the nucleation of tungsten smoke particles as observed by unpublished ultra-high speed PSI. Since the concentration of gas and the temperature are measurable, the critical supersaturation for nucleation can be calculated, so we can test whether nucleation theories can be applicable based on experimental data from in situ observation.

Finally, we emphasize the importance of coupling these optical in situ observation techniques with other independent observation methods. We have been employing frequency modulated AFM, which is capable of imaging atomic configuration of the surface [76] and even the hydration structures [77] formed over a crystal surface during crystal growth. Crystal growth proceeds via the transport of molecules from solution to the interface. This means that precious information is stored not only at the surface of the crystal but also in water molecule structures near the interface. We need to understand how molecules arrive at the surface through hydrated structures because the dehydration process is the most important rate-determining process in aqueous solution growth [78].

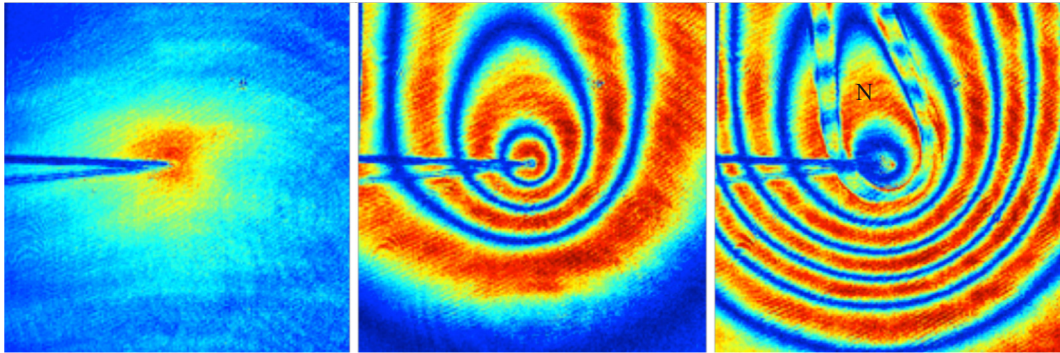


**FIGURE 24.27** Evaporation of tungsten followed by nucleation of smoke particles as observed by ultra-high speed PSI. N: nucleation area. The temperature and concentration of gas are measured so that the condition of nucleation could be measured.

## Acknowledgments

Thanks are due to Y. Nishimura, H. Satoh, P. Dold, A. Srivastava, and G. Sazaki, for their help in the development of in situ observation systems for crystal growth and discussion. Special thanks are due to Olympus Co. and Lasertech Co. for the development of new interferometers.

## References

- [1] Chernov AA. In: *Modern crystallography III. Crystal growth*. Heidelberg, New York, Tokyo: Springer-Verlag Berlin; 1984, ISBN: 3-540-11516-1. p. 517. 244 figs. Price: Cloth, DM 154.
- [2] Chernov AA. *Crystal growth and crystallography*. *Acta Crystallogr A Found Crystallogr* 1998;54:859–72.
- [3] Bennema P. Analysis of crystal growth models for slightly supersaturated solutions. *J Cryst Growth* 1967;1:278–86.
- [4] Frank FC. *Crystal growth*. *Farad Soc Discuss* 1949;5.
- [5] Griffin LJ. *Phil Mag* 1950;41:196.
- [6] Tolansky S. *Surface microtopography*. Interscience Publishers; 1960.
- [7] Amelinckx S. Growth mechanism of carborundum crystals. *Nature* 1951;168:431.
- [8] Tolansky S, Sunagawa I. Macro- and Micro-Morphology of Diamonds. *Nature* 1959;185:1526.
- [9] Sunagawa I. *Crystals: growth, morphology and perfection*. Cambridge University Press; 2005.
- [10] Sunagawa I. Mechanism of growth of hematite. *Am Mineral* 1962;47:1139–55.
- [11] Sunagawa I, Tsukamoto K. Growth spirals on NaCl and KCl crystals grown from solution phase. *J Cryst Growth* 1972;15:73–8.
- [12] Van Enckevort WJP, Janssen-van Rosmalen R, van der Linden WH. Evidence for spiral growth on the pyramidal faces of KDP and ADP single crystals. *J Cryst Growth* 1980;49:502–14.
- [13] Azuma T, Tsukamoto K, Sunagawa I. Clustering phenomenon and growth units in lysozyme aqueous solution as revealed by laser light scattering method. *J Cryst Growth* 1989;98:371–6.
- [14] Malkin AJ, Kuznetsov YG, Land TA, DeYoreo JJ, McPherson A. Mechanisms of growth for protein and virus crystals. *Nat Struct Mol Biol* 1995;2:956–9.

- [15] Durbin SD, Carlson WE. Lysozyme crystal growth studied by atomic force microscopy. *J Cryst Growth* 1992;122:71–9.
- [16] McPherson A. Current approaches to macromolecular crystallization. *Euro J Biochem* 1991;190:49–71.
- [17] Verma A. Growth mechanism of silicon carbide. *Nature* 1951;167:939.
- [18] Bennema P. Interpretation of the relation between the rate of crystal growth from solution and the relative supersaturation at low supersaturation. *J Cryst Growth* 1967;1:287–92.
- [19] Van Driessche AES, García-Ruíz JM, Tsukamoto K, Patiño-Lopez LD, Satoh H. Ultraslow growth rates of giant gypsum crystals. *Proc Natl Acad Sci* 2011;108:15721–6.
- [20] Onuma K, Tsukamoto K, Nakadate S. Application of real time phase shift interferometer to the measurement of concentration field. *J Cryst Growth* 1993;129:706–18.
- [21] Onuma K, Tsukamoto K, Sunagawa I. Dissolution kinetics of K-alum crystals as judged from the measurements of surface undersaturations. *J Cryst Growth* 1991;110:724–32.
- [22] Onuma K, Tsukamoto K, Sunagawa I. Measurements of surface supersaturations around a growing K-alum crystal in aqueous solution. *J Cryst Growth* 1989;98:377–83.
- [23] Maruyama S, Shibata T, Kozaki T. Measurement of solutal and thermal diffusion subjected to rapid cooling in microgravity by parabolic flight. In: Proc. 3rd KSME-JSME thermal engineering conference, Kyongju, Korea; 1996.
- [24] Maruyama S, Shibata T, Kozaki T. Measurement of diffusion field of solutions by real-time phase-shift interferometer and rapid heat-transfer control system. In: Proc. 4th world conference on experimental heat transfer, Brussels; 1997. p. 225–32.
- [25] Maruyama S, Shibata T, Tsukamoto K. Measurement of diffusion fields of solutions using real-time phase-shift interferometer and rapid heat-transfer control system. *Exp Therm Fluid Sci* 1999;19:34–48.
- [26] Maruyama S, Shibata T, Tsukamoto K. Measurement of solutal and thermal diffusion subjected to rapid cooling in microgravity and crystal growth. *Nihon Kikai Gakkai Ronbunshu B Hen/Transactions Jpn Soc Mech Eng Part B* 1998;64:174–81.
- [27] Srivastava A, Inatomi Y, Tsukamoto K, Maki T, Miura H. In situ visualization of crystallization inside high temperature silicate melts. *J Appl Phys* 2010;107:114907.
- [28] Srivastava A, Tsukamoto K, Yokoyama E, Murayama K, Fukuyama M. Fourier analysis based phase shift interferometric tomography for three-dimensional reconstruction of concentration field around a growing crystal. *J Cryst Growth* 2010;312:2254–62.
- [29] Murayama K, Tsukamoto K, Srivastava A, Miura H, Yokoyama E, Kimura Y. Measurement of two-dimensional distribution of surface supersaturation over a sodium chlorate crystal surface using multidirectional interferometry. *Cryst Res Technol* 2014;315–22.
- [30] Abe T, Tsukamoto K, Sunagawa I. Growth and stability of  $\text{CaAl}_2\text{Si}_2\text{O}_8$  Polymorphs. *Phys Chem Mineral* 1991;17:473–84.
- [31] Inatomi Y, Srivastava A, Satoh H, Maki T, Tsukamoto K. Real-time optical system for observing crystallization in levitated silicate melt droplets. *Rev Sci Instrum* 2010;81:073708.
- [32] Sunagawa I. Step height of sprails of natural hematite crystals. *Am Mineral* 1961;46:1216–26.
- [33] Zernike F. How I discovered phase contrast. *Science* 1955;121:345–9.
- [34] Sangwal K. Growth kinetics and surface morphology of crystals grown from solutions: recent observations and their interpretations. *Prog Cryst Growth Charact Mater* 1998;36:163–248.
- [35] Onuma K, Kameyama T, Tsukamoto K. In situ study of surface phenomena by real time phase shift interferometry. *J Cryst Growth* 1994;137:610–22.
- [36] Gliko O, Booth NA, Vekilov PG. Step bunching in a diffusion-controlled system: phase-shifting interferometry investigation of ferritin, *Acta crystallographica. Section D, Biological crystallography* 2002;58:1622–7.

- [37] Tsukamoto K, Dold P. Interferometric techniques for investigating growth and dissolution of crystals in solutions. *AIP Conf. Proc.* 2007;916:329–41.
- [38] Booth NA, Chernov AA, Vekilov PG. Characteristic lengthscales of step bunching in KDP crystal growth: in situ differential phase-shifting interferometry study. *Journal of Crystal Growth* 2002; 237–9. Part 3 1818–1824.
- [39] Tsukamoto K. In situ observation of crystal growth from solution. *Faraday Discuss* 1993;95:183–9.
- [40] Murphy D. Differential interference contrast (DIC) microscopy and modulation contrast microscopy. In: *Fundamentals of light microscopy and digital imaging*. New York: Wiley-Liss; 2001. p. 153–68.
- [41] Tsukamoto K. In situ observation of mono-molecular growth steps on crystals growing in aqueous solution. I. *J Cryst Growth* 1983;61:199–209.
- [42] Maiwa K, Tsukamoto K, Sunagawa I. Activities of spiral growth hillocks on the (111) faces of barium nitrate crystals growing in an aqueous solution. *J Cryst Growth* 1990;102:43–53.
- [43] Onuma K, Tsukamoto K, Sunagawa I. Growth kinetics of K-alum crystals in relation to the surface supersaturations. *J Cryst Growth* 1990;100:125–32.
- [44] Chernov AA, Rashkovich LN, Mkrтчan AA. Solution growth kinetics and mechanism: prismatic face of ADP. *J Cryst Growth* 1986;74:101–12.
- [45] Tsukamoto K. In situ observation of mono-molecular growth steps on aqueous solution grown crystals and the transport of molecules to the crystals. In: *NASA conference publication*; 1986. p. 233–8.
- [46] Sazaki G, Matsui T, Tsukamoto K, Usami N, Ujihara T, Fujiwara K, et al. In situ observation of elementary growth steps on the surface of protein crystals by laser confocal microscopy. *J Cryst Growth* 2004;262:536–42.
- [47] Sazaki G, et al. In situ observation of elementary growth processes of protein crystals by advanced optical microscopy. *Protein Pept Lett* 2012;19:743–60.
- [48] Tsukamoto K, Onuma K, Maruyama S, Shimizu K, Irisawa T, Furukawa Y, et al. In situ observation of crystal growth from solution in microgravity. *J Jpn Soc Microgravity Appl* 1994;11:58–70.
- [49] Tsukamoto K, Onuma K. In-situ observation of crystal growth in microgravity by high-resolution microscopies. In: *Crystal growth in space and related optical diagnostics*. San Diego (CA, USA): SPIE; 1991. p. 112–23.
- [50] Gliko O, Booth NA, Vekilov PG. Step bunching in a diffusion-controlled system: phase-shifting interferometry investigation of ferritin. *Acta Crystallogr D Biol Crystallogr* 2002;58:1622–7.
- [51] King HE, Plumper O, Putnis A. Effect of secondary phase formation on the carbonation of olivine. *Environ Sci Technol* 2010;44:6503–9.
- [52] Satoh H, Ishii T, Owada H. Dissolution of compacted montmorillonite at hyperalkaline pH and 70°C: in situ VSI and ex situ AFM measurements. *Clay Miner* 2013;48:285–94.
- [53] Satoh H, Nishimura Y, Tsukamoto K, Ueda A, Kato K, Ueta S. In-situ measurement of dissolution of anorthite in Na–Cl–OH solutions at 22°C using phase-shift interferometry. *Am Mineral* 2007;92:503–9.
- [54] Satoh H, Nishimura Y, Tsukamoto K, Ueda A, Ueta S, Kato K. Optical metrology of nano-scale mineral dissolutions using a phase-shift interference microscope. In: *2005 AGU Fall meeting program and abstract(CD-ROM)*. American Geophysical Union; 2005. V43B-1578.
- [55] Ueta S, Satoh H, Nishimura Y, Ueda A, Tsukamoto K. Dynamic and topographic observation of calcite dissolution using enhanced in-situ phase-shift interferometry. *J Cryst Growth* 2013;363:294–9.
- [56] Ueda A, Ueta S, Kato K, Tsukamoto K, Sato H, Nishimura Y. A preliminary report of development of high resolution phase shift interferometry for the assessment of nuclear waster disposal. *J Geochem Explor* 2006;88:355–7.
- [57] King H, Satoh H, Tsukamoto K, Putnis A. Nanoscale observations of magnesite growth in chloride- and sulfate-rich solutions. *Environ Sci Technol* 2013;47:8684–91.

- [58] Satoh H, Tsukamoto K, Garcia-Ruiz JM. Formation of chemical gardens on granitic rock: a new type of alteration for alkaline systems. *Eur J Mineral* 2014;26:415–26.
- [59] Yoshizaki I, Tsukamoto K, Yamazaki T, Murayama K, Oshi K, Fukuyama S, et al. Growth rate measurements of lysozyme crystals under microgravity conditions by laser interferometry. *Rev Sci Instrum* 2013;84.
- [60] Takamatsu T, Fujita S. Microscopic tomography by laser scanning microscopy and its 3-Dimensional reconstruction. *J Microsc* 1988;149:167–74.
- [61] Tsukamoto K, Srivastava A, Dold P, Wang W, Tsukamoto K, Wu D. Developments in interferometric techniques for in-situ observation of surface kinetics of crystals in solutions and three-dimensional analysis of transport phenomena. *AIP Conf. Proc.* 2010;1270:292–315.
- [62] DeLucas LJ, Smith CD, Smith HW, Vijay-Kumar S, Senadhi SE, Ealick SE, et al. Protein crystal growth in microgravity. *Science* 1989;246:651–4.
- [63] Adawy A, Rebuffet E, Törnroth-Horsefield S, de Grip WJ, van Enkevort WJP, Vlieg E. High resolution protein crystals using an efficient convection-free geometry. *Cryst Growth Des* 2013;13:775–81.
- [64] Onuma K, Tsukamoto K, Sunagawa I. Role of buoyancy driven convection in aqueous solution growth; a case study of  $\text{Ba}(\text{NO}_3)_2$  crystal. *J Cryst Growth* 1988;89:177–88.
- [65] Mamyama S, Miyagawa Y, Tsukamoto K, Aihara T. Transient simulation of double diffusive convection of crystal growth in microgravity. *Int J Fluid Mech Res* 1998;25:699–710.
- [66] Bedarida F, Zefiro L, Boccacci P, Pontiggia C. Reconstruction by multidirectional holographic interferometry of the concentration field in a supersaturated solution near a growing  $\text{NaClO}_3$  crystal. *J Cryst Growth* 1983;61:641–4.
- [67] Srivastava A, Tsukamoto K, Murayama K. Single lens-based schlieren microscope for investigation of three-dimensional buoyancy-induced convective flow fields. *J Flow Visualization Image Process* 2011;18:347–69.
- [68] Sekerka RF. Role of instabilities in determination of the shapes of growing crystals. *J Cryst Growth* 1993;128:1–12.
- [69] Yokoyama E, Toshio K. Pattern formation in growth of snow crystals occurring in the surface kinetic process and the diffusion process. *Phy Rev A* 1990;41:2038.
- [70] Chernov AA. Stability of faceted shapes. *J Cryst Growth* 1974;24-25:11–31.
- [71] Herman GT. Image reconstruction from projections. New York: Academic; 1980.
- [72] Sunagawa I, Tsukamoto K, Maiwa K, Onuma K. Growth and perfection of crystals from aqueous solution: case studies on barium nitrate and K-alum. *Prog Cryst Growth Charact Mater* 1995;30:153–90.
- [73] Onuma K, Tsukamoto K, Sunagawa I. Effect of buoyancy driven convection upon the surface microtopographs of  $\text{Ba}(\text{NO}_3)_2$  and  $\text{CdI}_2$  crystals. *J Cryst Growth* 1989;98:384–90.
- [74] Kimura Y, Tsukamoto K. Interferometric observation of temperature distributions in the smoke experiment. *J Jpn Soc Microgravity Appl* 2011;28:S9–12.
- [75] Kimura Y, Tanaka KK, Miura H, Tsukamoto K. Direct observation of the homogeneous nucleation of manganese in the vapor phase and determination of surface free energy and sticking coefficient. *Cryst Growth Des* 2012;12:3278–84.
- [76] Araki Y, Tsukamoto K, Oyabu N, Kobayashi K, Yamada H. Atomic-resolution imaging of aragonite (001) surface in water by frequency modulation atomic force microscopy. *Jpn J Appl Phys* 2012;51:08KB09.
- [77] Kimura K, Ido S, Oyabu N, Kobayashi K, Hirata Y, Imai T, et al. Visualizing water molecule distribution by atomic force microscopy. *J Chem Phys* 2010;132.
- [78] Maruyama M, Tsukamoto K, Sazaki G, Nishimura Y, Vekilov PG. Chiral and achiral mechanisms of regulation of calcite crystallization. *Cryst Growth Des* 2009;9:127–35.

# Snow and Ice Crystal Growth

Yoshinori Furukawa

INSTITUTE OF LOW TEMPERATURE SCIENCE, HOKKAIDO UNIVERSITY, HOKKAIDO, JAPAN

## CHAPTER OUTLINE

<b>25.1 Introduction</b> .....	<b>1062</b>
<b>25.2 Crystallographic Features of an Ice Crystal</b> .....	<b>1064</b>
<b>25.3 Surface Structure of an Ice Crystal</b> .....	<b>1066</b>
25.3.1 Surface Melting .....	1066
25.3.2 Experimental Evidence for Surface Melting of Ice .....	1068
25.3.3 Visualizations of QLL Behaviors on a Molecular Scale .....	1071
25.3.4 Computer Simulation Studies of Ice Surface Structures .....	1072
<b>25.4 Growth of Snow Crystals</b> .....	<b>1072</b>
25.4.1 Typical Features of the Growth Morphologies of Snow Crystals .....	1072
25.4.2 Kuroda–Lacmann Model for the Habit Change of Snow Crystals .....	1075
25.4.3 Formation of a Dendritic Pattern of a Snow Crystal .....	1077
25.4.4 Effect of Air Flow on Pattern of a Snow Crystal .....	1079
25.4.5 Twinned Snow Crystals .....	1080
25.4.5.1 Structures of Twinned Snow Crystals .....	1080
25.4.5.2 Formation Mechanism of Twinned Snow Crystals .....	1080
<b>25.5 Free Growth of an Ice Crystal in Supercooled Water</b> .....	<b>1081</b>
25.5.1 Equilibrium Forms of Ice Crystals .....	1081
25.5.2 Growth Morphologies of Ice in Free Growth .....	1082
25.5.3 Free Growth of Ice Crystals under Microgravity Conditions .....	1084
25.5.3.1 Experimental Setup .....	1084
25.5.3.2 Results of ISS–Kibo Experiments .....	1085
25.5.4 Molecular Dynamics Simulation of the Ice–Water Interface .....	1089
<b>25.6 Directional Growth of Ice Crystals</b> .....	<b>1090</b>
25.6.1 Pattern Formation at the Ice–Water Interface .....	1090
25.6.1.1 Experiments .....	1090
25.6.1.2 Morphological Instability at an Ice Interface Growing in KCl Solution .....	1091
25.6.2 Solute Distribution in Front of the Ice–Water Interface and Morphological Instability .....	1093

25.6.3 Cellular Tilting .....	1095
25.6.3.1 Tilt Angle Measurement for Cellular Patterns of Ice Crystals .....	1095
25.6.3.2 Anisotropic Interface Kinetics .....	1096
<b>25.7 Ice Crystal Growth Controlled by Biological Macromolecules.....</b>	<b>1098</b>
25.7.1 Features of Biological Macromolecules with Antifreeze Function .....	1098
25.7.1.1 Antifreeze Effect.....	1098
25.7.1.2 General Functions of Antifreeze Glycoproteins and Proteins.....	1098
25.7.2 Ice Crystal Growth and AFGP Adsorption on the Ice Interface .....	1102
25.7.2.1 Growth Behavior of Ice Crystals and AFGP Distribution .....	1102
25.7.2.2 Adsorption of AFGP Molecules on the Ice–Water Interface .....	1103
25.7.2.3 Two-Step Adsorption of AFGPs and Inhibition of the Growth of Prismatic Interfaces .....	1104
25.7.2.4 Directional Growth of Ice Crystal from AFGP Solution .....	1104
<b>25.8 Summary .....</b>	<b>1107</b>
<b>Acknowledgments .....</b>	<b>1107</b>
<b>References.....</b>	<b>1108</b>

## 25.1 Introduction

Snow and ice are the most ubiquitous materials in our daily life, associated with weather, winter sports, frozen foods, etc. They seasonally or perennially cover vast regions of our planet. Snow and ice play a central role in various natural phenomena occurring in the cryospheric regions of the earth surface and in the cold atmosphere [1–4]. In this chapter, we discuss the growth and pattern formation of these unique materials. Understanding the formation mechanisms of an ice or snow crystal, which usually occur at temperatures close to their melting point, is essential for predicting the future of the earth’s climate, geology, and life. They are also interesting in relation to crystal growth fundamentals, surface sciences, morphological instability, and pattern formation. Snow and ice crystals, while both are crystals of water, are recognized as crystals grown from supersaturated water vapor during their fall through clouds and as crystals grown from supercooled liquid water, respectively.

Snow crystals, as shown in [Figure 25.1](#), have been among the most familiar natural crystals to people living in cold-climate regions of the earth. Their natural beauty and exquisite symmetry property undoubtedly fascinate anyone observing them for the first time. Observations of natural snow crystals have a very long history, beginning in 1611 with Kepler’s [5] discussion of why snow crystals are hexagonal in his book entitled *A New Year’s Gift on the Six-cornered Snowflakes*. The historic transition of snow crystal observations has been discussed in detail by Kobayashi and Kuroda [6].

Probably the most famous publication about snow crystals is the book entitled *Snow Crystals*, which was published in 1931 by Bentley and Humphreys [7]. It includes

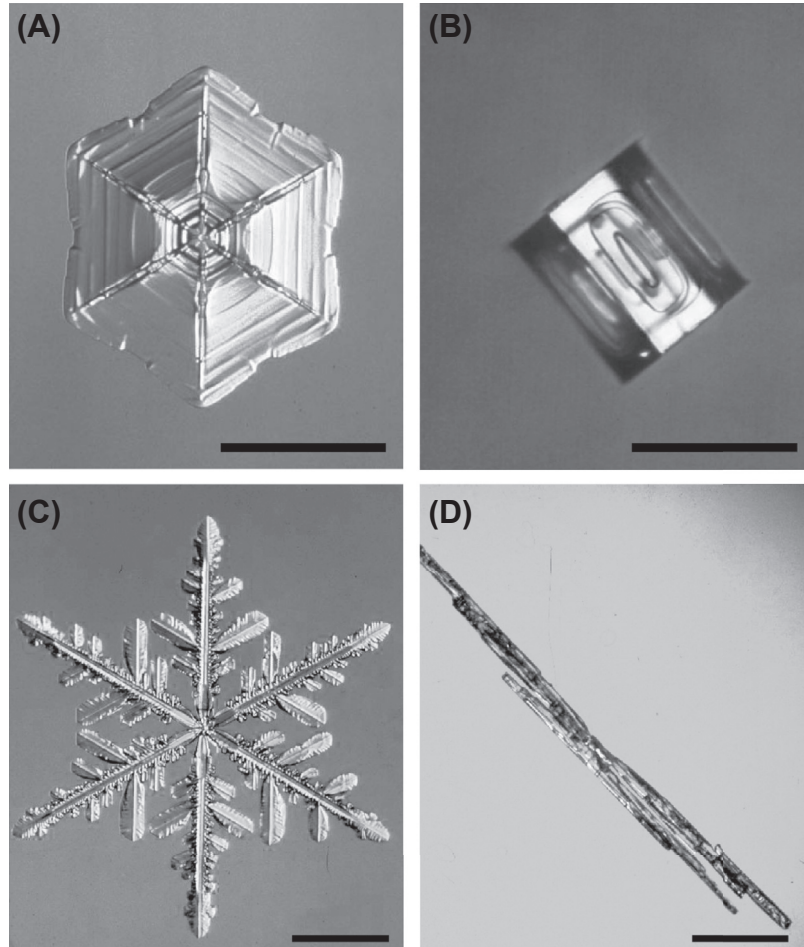


**FIGURE 25.1** Pictures of naturally occurring snow crystals taken in the mountainous area of central Hokkaido, Japan using a conventional microscope with a special illumination method. (A) Hexagonal plate (planar view), (B) hexagonal dendrite (planar view), (C) hexagonal prism (side view), and (D) needle. Scale bars indicate 0.5 mm.

approximately 2500 micrographs of natural snow crystals taken by Bentley, who was a farmer by trade, not a scientist. His pictures, however, are impressive in light of the fact that the universal hexagonal shapes and infinite number of beautiful patterns observed in snow crystals are hidden in a veil of mystery. Professor Ukichiro Nakaya of Hokkaido University, Sapporo, who had been inspired by Bentley's book, started research on snow crystals in 1932. He began by observing natural snow crystals and took more than 3000 photographs in mountainous areas of Hokkaido over a period of several years [8]. Initially, he classified the snow crystal patterns into about 40 categories of morphology. He subsequently succeeded in producing almost all natural snow crystal morphologies in the laboratory [9]. As a result, he elucidated the relationships between shapes of snow crystals and atmospheric conditions (i.e., temperature and supersaturation of the

atmosphere). He summarized his results in the form of a diagram [8], which is now referred to as the Nakaya diagram. This diagram allows one to “read” the meteorological information “written” on a snow crystal, because the weather conditions in the upper air can be inferred by observing snow crystal morphologies on the ground. In this sense, Nakaya was often quoted as referring to a snow crystal as “a letter from the sky”. He might be considered to be the first researcher who discussed snow crystals as a topic of physics prior to the emergence of the crystal growth research field [4,6].

Nakaya’s pioneering work, however, did not provide answers to basic questions, such as why the morphology of snow crystals can change drastically with only slight variations of crystal growth conditions as described in subsection 25.4.1. Although many researchers had struggled with this difficult problem over the 50 years after Nakaya’s work, they had not been able to obtain satisfactory understanding for the remarkable variety of observed snow crystal shapes, because elucidation of this fascinating mystery is strongly associated with knowledge accumulation about the crystal growth fundamentals. In the last two decades, important clues in the formation mechanisms of a variety of snow crystal shapes have been discovered.

The first in-situ observation of ice crystal growth in supercooled water was also carried out at the laboratory of Nakaya in 1952 [10,11]. Growth patterns of an ice crystal at the surface of supercooled water were photographed by the method of shadowgraphy and clearly showed the process of morphological instability at the interface between the solid and liquid. This work was carried out more than 10 years before publication of the Mullins–Sekerka instability model in 1964 as the first model of morphological instability at the crystal–melt interface [12].

Thus, crystal growth and pattern formation on snow and ice crystals include many kinds of basic subjects related to various aspects of the fundamentals of crystal growth. In this chapter, we will introduce the special features of pattern formation and morphological instability of snow and ice crystals.

## 25.2 Crystallographic Features of an Ice Crystal

Crystalline features are very important to consider the growth of a crystal. Because unusual and typical features of the crystalline structure of ice have been discussed in detail in many books [13–16] related to ice crystals, we summarize those very briefly here. When liquid water freezes under usual atmospheric conditions or water vapor is deposited at temperatures below 0 °C or above about –80 °C, the water molecules are arranged in orderly repetitive positions to form a crystalline solid with hexagonal symmetry, which is referred to as normal hexagonal ice  $I_h$ , or simply ice. Although ice  $I_h$  is just one of at least 13 polymorphs that have been observed under different conditions of pressure and temperature, it is the most important and popular phase appearing in terrestrial conditions [16]. Because we consider only the first-order phase transformations between vapor–solid phases or liquid–solid phases in this chapter, a phase diagram between ice  $I_h$  and the liquid and vapor phases around the triple point (273.16 K

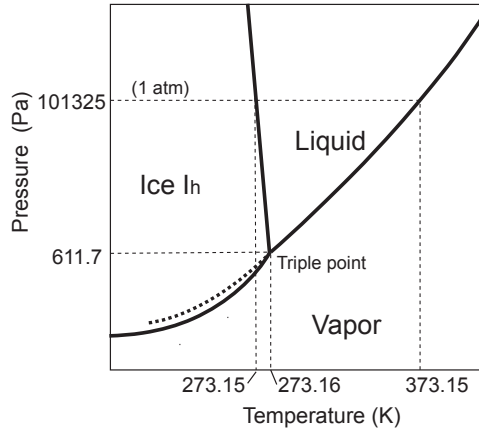


**FIGURE 25.2** Phase diagram of  $\text{H}_2\text{O}$  around the triple point (273.16 K and 611.7 Pa). Dotted line indicates the equilibrium line between vapor and supercooled water. Scales of the longitudinal and abscissa axes are not accurate but the drawing specifies the feature of phase diagram.

and 611.7 Pa) is shown in [Figure 25.2](#). It is well known as the basic feature of ice that the ice  $\text{I}_h$  melting point curve (the boundary between ice  $\text{I}_h$  and water phases) has a negative slope with increasing pressure, and the melting point reaches 273.15 K at atmospheric pressure, which is taken as the zero degree of the Celsius scale of temperature. The negative slope of the melting curve also reflects phenomena such as increase in the specific volume of ice by freezing of water and melting of pressurized ice below  $0^\circ\text{C}$ . This feature also appears on crystals of semiconductors, such as Si and Ge [17].

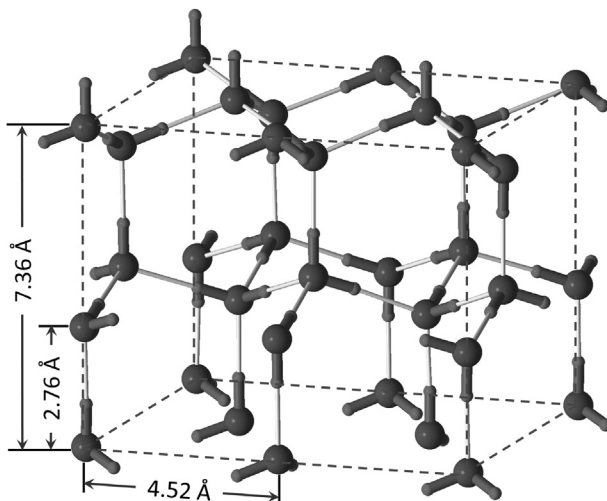


**FIGURE 25.3** Crystallographic structure of ice  $\text{I}_h$ . Each oxygen atom (indicated by large spheres) makes a water molecule with the association of two hydrogen atoms (indicated by small spheres) at the tips of bars extending from each oxygen atom and connects with four neighboring oxygen atoms by the hydrogen bond. The hydrogen atoms are disorderly arranged in ice  $\text{I}_h$ , in accordance with the Bernal-Fowler rules. Adapted from Nada [18].

Figure 25.3 shows the crystalline structure ( $P6_3/mmc$ ) of ice  $I_h$  [18]. Oxygen atoms, shown by large spheres, are arranged on a hexagonal lattice with a structure named after the mineral wurtzite. Each oxygen atom is covalently connected to the four nearest neighboring oxygen atoms located at the corners of a tetrahedron by hydrogen bonds. The hydrogen atoms, shown by small spheres, are located on two alternative sites on each bond to form  $H_2O$  molecules in the crystal lattice. A statistical model for the disordered arrangement of hydrogen atoms in the crystalline lattice of ice  $I_h$  is dominated by assumptions referred to as the ice rules (namely, Bernal–Fowler rules [19]), which are “there are two hydrogen atoms adjacent to each oxygen atom” and “there is only one hydrogen atom per bond”. As a result, completely disordered structures for the “orientations” of water molecules in three dimensions are produced, and this disordered structure remains even at the absolute zero temperature. It is called “residual entropy” or “zero-point entropy” [14,15,20]. The unusual dielectric and conductive properties of ice are strongly related to how water molecules turn round or protons flow through the crystalline lattice originating from the disordered structure of ice, rather than the molecular arrangement and lattice vibrations of an ice crystal.

The ice crystalline structure contains many kinds of point defects, dislocations, and planar defects in common with other crystalline materials [16,21]. It is well known that there are several categories for point defects in ice: molecular defects, impurity defects, electronic defects, protonic defects, and combined defects. Dislocations in the ice structure are also formed during the growth and plastic deformation of ice crystals and can be directly observed by X-ray topography [16,22]. Because the crystal structure of ice consists of basal  $\{0001\}$  planes of molecules stacked on top of one another, a stacking fault can be easily introduced as a planar defect normally lying on a basal plane. This structural feature relates to the transformation between hexagonal ice and cubic ice, which will be described in Section 25.4.5.

## 25.3 Surface Structure of an Ice Crystal

### 25.3.1 Surface Melting

Crystal growth rates strongly depend on the microscopic structures of crystal surfaces. It is well known as a basic property of ice surfaces at temperatures in a range close to the melting point that the ice surface is covered by a thin melted liquid film, a so-called quasi-liquid layer (QLL) or liquid-like layer, since Michael Faraday [23] first proposed the existence of such a layer on an ice crystal in the 1850s. The QLLs play very important roles in the slipperiness of a skating rink [24], regelation (pressure-induced change in freezing) [25], dynamics of ground freezing [26–28], evolution of the polycrystalline fabrics of great ice sheets [24], mechanism of charge transfer that drives thunderstorm electrification [29,30], icicle growth from the thin water layer [31], ozone destruction [32], and so on. However, the most interesting phenomenon related to the QLL is the pattern formation of snow crystals. In the 1980s, Kuroda and Lacmann [33] first pointed out the

relationship between the habit change of snow crystals and the anisotropic property of surface melting of ice, and Furukawa et al. [34] confirmed the existence of QLLs on both the basal  $\{0001\}$  and prismatic  $\{10\bar{1}0\}$  faces of ice and their anisotropic properties using the method of ellipsometry. This phenomenon is a kind of first-order phase transition occurring on the crystal surfaces or interfaces and is not unique to ice crystals but generally occurs on many kinds of crystals [35]. It is well known that superheating of a crystal, which is the effect opposite to supercooling of the liquid, is never observed except in the internal melting cavity, such as a Tyndall figure formed inside an ice crystal by infrared radiation [15]. The reason comes from the fact that a crystal surrounded by surfaces or interfaces can start to melt by the continuous increase in QLL thickness at the melting point [17]. That is, surface nucleation process is not required for bulk melting of a crystal.

Here, let us briefly consider the thermodynamic aspect of the QLL, because the detailed properties of a QLL based on thermodynamic consideration have been described in many previously published reports [18,35–37]. The existence of a QLL on the surface below the melting point is disadvantageous in the sense of free energy of the bulk liquid phase but is advantageous in the sense of total surface free energy. The wettability parameter, which is calculated by the equation  $\Delta\sigma_\infty = \sigma_{sv} - (\sigma_{qv} + \sigma_{sq})$ , is a judgment condition for the occurrence of surface melting, where  $\sigma_{sv}$ ,  $\sigma_{qv}$ , and  $\sigma_{sq}$  are the interface free energies at solid (s)-vapor (v), QLL (q)-vapor (v) and solid (s)-QLL (q), respectively, as shown in Figure 25.4. Namely, a QLL can exist on the surface when  $\Delta\sigma_\infty$  is positive. Although it is not easy to determine the value of  $\Delta\sigma_\infty$ , predicted values of  $\Delta\sigma_\infty$  for major elements' crystals are summarized in Ref. [35].

The total free energy,  $\sigma$ , of the vapor-QLL-crystal interface system for a unit area is given by

$$\sigma = \sigma_{sq} + \sigma_{qv} + LN \frac{\Delta T}{T_m}, \quad (25.1)$$

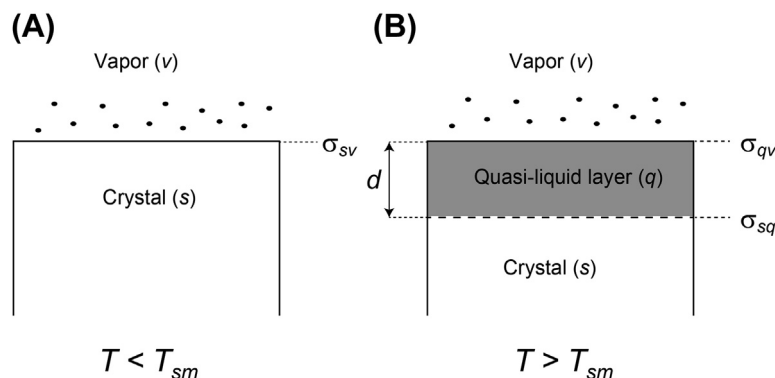


**FIGURE 25.4** Schematic illustration of ice crystal surfaces: (A) a bare surface; (B) a surface covered with a quasi-liquid layer (QLL) formed by surface melting. At a temperature,  $T$ , lower than the critical temperature,  $T_{sm}$ , of surface melting, the bare ice crystal surface is thermodynamically stable. In contrast, at  $T > T_{sm}$ , the crystal surface covered with a QLL with a thickness  $d$  becomes stable.  $\sigma_{sv}$ ,  $\sigma_{qv}$  and  $\sigma_{sq}$  show free energies at each interface.

where  $L$  is the latent heat of melting for one molecule,  $N$  is the number of molecules contained in the QLL of thickness  $d$ ,  $T_m$  is the melting temperature, and  $\Delta T = T_m - T$ . QLLs show properties that are intermediate between those of solid and bulk liquid, and more specifically, thinner QLLs receive stronger effects of substrate crystalline characteristics. Based on this equation, the equilibrium thickness of the QLL  $d_{eq}$  can be determined by minimization of the total free energy. For example, if we assume a long-range interaction between the molecules, it is given by the power function,

$$d_{eq}(T) = a \left\{ \left( \frac{T_m \Delta \sigma_\infty p N_0^{p-1}}{\Delta T L} \right)^{1/(p+1)} - 1 \right\}. \quad (25.2)$$

Here,  $N_0$  is the number of molecules on a crystal surface for a unit area, and then  $d = aN/N_0$ :  $a$  is a lattice constant of crystal, and  $p$  is the positive integer.

In the case of an ice crystal, Kuroda and Lacmann [33] clarified that the value of  $\Delta \sigma_\infty$  becomes positive just below the melting point and the crystallographic-surface dependence of  $\Delta \sigma_\infty$  is estimated to be  $\Delta \sigma_\infty(10\bar{1}0) < \Delta \sigma_\infty(0001)$  from the specific surface density of dangling hydrogen bonds and the hydrogen-bond energy estimated from latent heat of vaporization. This result indicates the relation of  $d_{eq}(10\bar{1}0) > d_{eq}(0001)$ . In addition, when we assume that long-range interaction, such as van der Waals attraction, dominates the interaction between water molecules,  $d_{eq}$  is given by Eqn (25.2) and  $p = 2$ . Because  $d_{eq}$  is proportionate to  $\Delta T^{-1/3}$ , QLL grows thick up to infinity at 0 °C, at which temperature ice and water coexist as indicated in the phase diagram.

As the thickness becomes equal to or thinner than one monomolecular layer below a critical temperature,  $T_{SM}$ , the crystal surface is no longer covered with the QLL and is regarded as a surface that is geometrically irregular. It may correspond to the case of a rough or uneven surface. The degree of this irregularity may decrease with falling temperature and become very small at another particular temperature and finally become a molecularly smooth surface. This is the so-called thermal roughening transition [38,39]. These two transition temperatures correspond to the surface melting temperature and the roughening transition temperature, respectively, and these temperature-dependent surface structures may cause critical changes in growth kinetics and eventually in growth rates, as described in Section 25.4.

### 25.3.2 Experimental Evidence for Surface Melting of Ice

The existence of QLLs on ice surfaces had been claimed by many researchers, in connection with many interesting phenomena related to the surface structures [29,40–43]. Various experimental studies on ice surfaces melting at vapor surfaces have been carried out using a variety of techniques, including optical determination [34,44,45], proton channeling [46], glancing angle X-ray scattering [47,48], atomic force microscopy [49,50], sum-frequency vibrational spectroscopy [51,52], and near-edge

X-ray absorption fine-structure spectra [53]. The existence of QLLs at grain boundaries and interfaces between the ice crystal and other substrates has been also detected by various experiments using optical determination [54], nuclear magnetic resonance [55–57], adsorption isotherms [58], X-ray diffraction pattern [59,60], Fourier transformation infrared spectroscopy [61,62], and so on. Major results for QLL thickness and properties are summarized in Table 25.1. It should be noted that experimental results for QLL have still scattered and that exact structures and dynamic properties of ice surfaces have remained unclear, as pointed out in Ref [16].

Even though all the experimental results described in Table 25.1 indicated that the ice surface is covered by a QLL, definite evidence for QLL thickness and physical properties has been obtained only by noncontact optical measurements. Beaglehole and Nason [44] and Furukawa et al. [34] used the ellipsometry method for ice surface samples placed in air-filled chambers, and Elbaum et al. [45] conducted measurements of reflectivity at the Brewster angle for samples placed in a pure water-vapor environment. Because the melting of low-index surfaces, such as basal and prismatic planes at equilibrium in clean environments, is limited to a span of only a few degrees below the melting point, particular care was taken to assure crystal surface perfection in all three studies. Beaglehole and Nason [44] used samples cut from a single crystal and then wiped with a warmed copper blade, but the surface orientations were off within  $\pm 20^\circ$  from the exact basal or prismatic planes. On the other hand, Furukawa et al. studied surfaces lumbered from “negative crystals” [34,64,65], which are cavities grown in a single ice crystal. These surfaces had exact orientations of both basal and prismatic planes and were molecularly smooth because they were formed by layer-by-layer evaporation. Elbaum et al. [45] prepared vapor-deposited surfaces on freshly cleaved mica.

The results all showed that surface melting depends on orientation; for example, the lowest temperatures at which Furukawa et al. [34] could detect liquid were  $2^\circ\text{C}$  on the basal face but  $-4^\circ\text{C}$  on the prismatic face, and the QLL thickness was larger on the former than on the latter at temperatures above  $-1^\circ\text{C}$ . In addition, the index of refraction for the QLL was also measured as 1.330, which was very close to that for the bulk water, 1.333, but slightly smaller. This was the first result suggesting that the transition layers observed on ice crystal surfaces had a physical property different from that of bulk water. In contrast, Elbaum et al. [45] found the surface melting of both basal and prismatic faces was *incomplete*, with the QLL thickness being far larger on the former than on the latter. On basal faces, QLL smoothly became thicker as it was warmed, but halted at a few hundredths of a degree below  $T_m$  and then droplets were observed on the wetted surface above this temperature. Thus, they claimed that the melted layer no longer *wetted* the bulk ice within that narrow interval below  $T_m$  [66]. Elbaum and Wettlaufer [67] found that the behavior changed to *complete* surface melting—that is, smoothly increasing to divergence at  $T_m$ , when the ice surface was placed in air. This finding is consistent with the results of earlier works [34,44] carried out in an atmosphere of humid air that showed surface melting smoothly increased all the way to  $T_m$ .

**Table 25.1** Summary of Experimental Evidence for Quasi-Liquid Layers (QLLs) on Ice Surfaces

Technique (References)	Technical Merit	Sample Preparation	Thickness of the QLL	Description for the QLL
Nuclear magnetic resonance [57]	Detects the liquid state in the solid state by nuclear resonance measurement	Ice-silica interface	~90 nm at $-1\text{ }^{\circ}\text{C}$	QLL was detected even below $-30\text{ }^{\circ}\text{C}$
Attenuated total reflectance-Fourier transform infrared spectroscopy [61,62]	Detects the liquid state in the solid state by infrared adsorption	Grain boundaries in polycrystalline ice	5 nm at $-1\text{ }^{\circ}\text{C}$	Disordered layer was detected over $-40\text{ }^{\circ}\text{C}$
X-ray diffraction pattern [59]	Detects the distribution of $\text{H}_2\text{O}$ molecules from the lattice points	Surfaces and grain boundaries		
Proton channeling [46]	Detects thermal vibration of the oxygen atoms in the QLL	Basal surface prepared by cleavage of ice-glass interface	~94 nm at $-1\text{ }^{\circ}\text{C}$	
Ellipsometry [34]	Measures the dielectric profile at the surface	Exact basal and prismatic surfaces prepared by the negative crystal method	20 nm for both basal and prismatic surfaces at $-1\text{ }^{\circ}\text{C}$	Anisotropy between basal and prismatic surfaces, and refractive index of QLL $\sim 1.330$
Optical reflectometry [45]	Measures the dielectric profile at the surface	Vapor-deposited surfaces on freshly cleaved mica	~7 nm in air and ~2 nm in pure water vapor at $-1\text{ }^{\circ}\text{C}$	Incomplete wetting in pure water vapor, but complete wetting in air
Sum-frequency vibrational spectroscopy [51,52]	Measures the degree of orientational order of the dangling OH bonds at the surface	Basal surfaces in contact with air, a hydrophobic substrate, and a hydrophilic substrate	Disordered structure was detected above 200 K and increased dramatically with temperature	
Glancing angle X-ray scattering [47,48]	Detects the disruption of the hydrogen-bonding network at the surface	Basal and prismatic surfaces	30 nm on the basal surface and ~90 nm on the prismatic surface at $-1\text{ }^{\circ}\text{C}$	
Near-edge X-ray absorption fine-structure spectra [53]	Measures the intensity of transition from O1s core state to empty states which is affected by the bonding environment of $\text{H}_2\text{O}$ molecules at the surface	Surface of polycrystalline ice	~2 nm at $-1\text{ }^{\circ}\text{C}$	
Atomic force microscopy [49,50]	Measures jump-in distance induced by capillary force from the QLL	Surface of polycrystalline ice	~20 nm at $-1\text{ }^{\circ}\text{C}$	
Laser confocal microscopy combined with differential interference microscopy [63]	Visualizes a thin layer with a height smaller than the monomolecular scale	Exact basal and prismatic surfaces epitaxially grown on the cleavage surface of AgI		Two types of QLL, namely $\alpha$ - and $\beta$ -QLL, were first observed

### 25.3.3 Visualizations of QLL Behaviors on a Molecular Scale

For experiments previously carried out for an ice crystal, uniformly covering QLLs on an ice surface had been assumed as a prerequisite for analyzing their thickness and properties, because no one had succeeded in observing the dynamic behavior of a QLL on the ice surface. Only recently, Sazaki et al. [63,68] successfully observed dynamic behaviors of QLL on basal surfaces of ice placed in a nitrogen atmosphere by using a newly developed microscope consisting of a laser confocal microscope combined with a differential interference microscope (LCM-DIM), which could directly visualize the 0.37-nm-thick elementary steps on ice crystal surfaces [69]. Figure 25.5 shows the surface morphologies of basal faces. “Elementary steps” were seen on the surfaces at temperatures below  $-0.2$  °C (Figure 25.5(A)), but rounded objects (white arrowhead) appeared at  $-0.3$  °C (Figure 25.5(B)). Then, the number and size of rounded objects both increased with a rise in temperature (Figure 25.5(C)). Although they look like droplets, analysis of interference fringes observed on the droplets

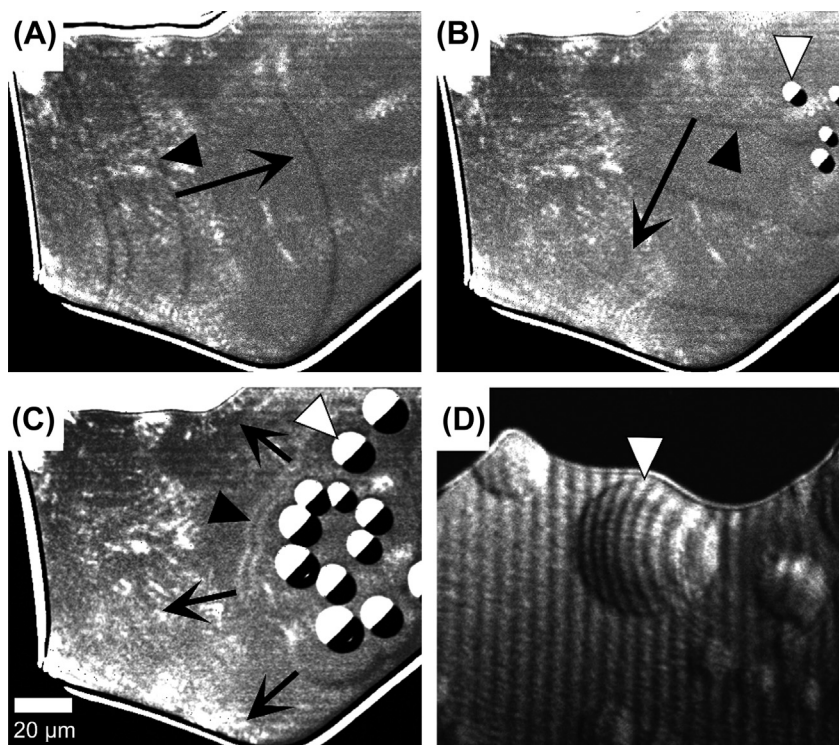


**FIGURE 25.5** Appearance of a quasi-liquid layer (QLL) with a curved surface shape ( $\alpha$ -QLL phase), indicated by white arrowheads on a basal face of an ice crystal [68]. Temperatures of ice samples were (A)  $-0.6$  °C, (B)  $-0.4$  °C, and (C)  $-0.3$  °C. Black arrowheads and black arrows indicate elementary steps and their directions of movements, respectively. (D) Interference fringes that appeared on the surface of a different ice crystal at  $-0.3$  °C. Adapted from [68].

showed that they are about 50  $\mu\text{m}$  in width and about 0.5  $\mu\text{m}$  in height (in [Figure 25.5\(D\)](#)); namely, their height/width ratios are very small (less than 1/100). At a higher temperature of  $-0.2\text{ }^{\circ}\text{C}$ , a different type of QLL, like a thin layer, newly appeared, as shown by the half-white/black arrowheads in [Figure 25.6](#). When the temperature was further increased to  $-0.1\text{ }^{\circ}\text{C}$ , a bare surface with advancing elementary steps in the left side of the observation area and a surface covered with a melted layer in the right side coexisted at the same time. The thickness of the thin layer was smaller than the detection limit of interferometry (smaller than several tens of nanometers). This result means that two types of QLLs exist on ice surfaces, and they were named  $\alpha$ -QLL and  $\beta$ -QLL, respectively. Amazingly, both types of QLLs are immiscible in spite of the fact that both QLLs are identical, and also the feature of surface melting of the ice is completely different from the traditional concept of the surface being covered by a uniform QLL with temperature-dependent thickness. In conclusion, there remain many unanswered questions regarding ice surface structures, and even the mechanisms of various natural phenomena related to the surface melting must be reconsidered in the future.

### 25.3.4 Computer Simulation Studies of Ice Surface Structures

Surface melting of an ice crystal has been a popular and attractive subject for computer simulation, especially molecular dynamics (MD) simulation, and has been treated over and over again by many researchers, depending on the advanced technological stage of computers. Weber and Stillinger [70] first found that melting of a 250-molecule hexagonal ice crystal began at the surface and proceeded inward at  $-150\text{ K}$ , and Kroes [71] also found that the onset of surface melting of the basal face began with high molecular rotational and translational mobility at about  $-40\text{ }^{\circ}\text{C}$ . However, the most important MD simulations were carried out by Nada and Furukawa, who examined the microscopic structures of ice-vapor and ice-water surfaces and their relation to growth kinetics [72–74] (see [Figure 25.7](#)). They used a newly developed potential model (six-site model) for an  $\text{H}_2\text{O}$  molecule [75] that was designed to adjust to various physical properties of both water and crystalline ice. Their simulation showed that the surface melting of basal and prismatic faces differs in onset temperature and temperature dependence of QLL thickness, consistent with the results of ellipsometry measurement [34] discussed in the previous section.

## 25.4 Growth of Snow Crystals

### 25.4.1 Typical Features of the Growth Morphologies of Snow Crystals

Even though naturally observed snow crystals include not only many types of single-crystalline patterns but also many types of twinning patterns, pictures of natural snow crystals in books or the literature are often single-crystalline types, as shown in [Figure 25.1](#). The reason for this is that taking pictures of polycrystalline snow crystals

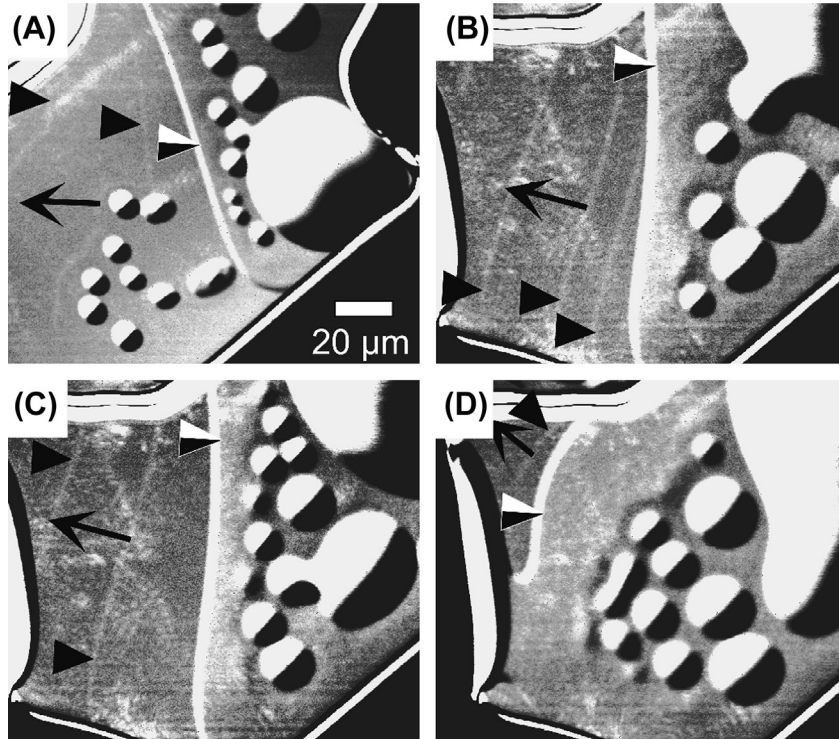


**FIGURE 25.6** Appearance of a quasi-liquid layer (QLL) in the state of a thin film ( $\beta$ -QLL phase), indicated by half-white/black arrowheads, with a rise in temperature [68]. Temperatures of ice surfaces were (A)  $-0.2$  °C and (B–D)  $-0.1$  °C. Images (B)–(D) were taken at 0, 18, and 239 s after the temperature reached  $-0.1$  °C. Other arrows and arrowheads indicate the same as those in Figure 25.5. Adapted from Sazaki (2012).

with three-dimensional structures using a microscope is very difficult compared to taking pictures of single snow crystals with planer configuration. In this section, we first describe the pattern formation of single-crystalline snow crystals and briefly describe the formation of twinned snow crystals at the end.

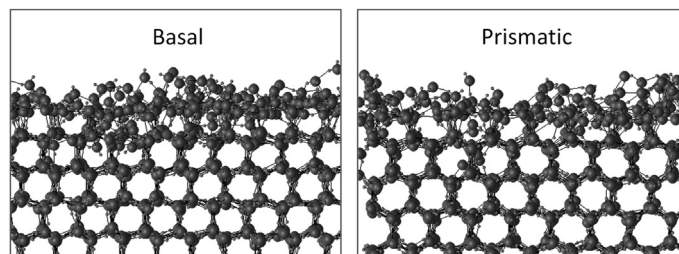


**FIGURE 25.7** Surface structures of the basal and prismatic faces of an ice crystal, obtained by a 2-ns molecular dynamics simulation at 280 K, which is very close to the melting point [18]. The six-site potential model for a water molecule [75] and the Ewald summation method for estimation of the Coulomb interaction were used in the simulation. The melting point for the hexagonal ice crystal in this model was predicted to be 289 K [76]. Adapted from Nada (2013).

As mentioned in [Section 25.1](#), the first full-fledged study on snow crystals goes back to the determination of the Nakaya diagram in the 1940s, which shows the relationship between their growth patterns and growth conditions. Since then, many researchers [77,78] have carried out experiments on the growth of artificial snow crystals. Finally, Kobayashi [79] updated the Nakaya diagram of snow crystal shapes as a function of temperature and excess vapor density by the consolidation of various experimental results (see Ref. [4] about this diagram). The most important thing indicated by this diagram is that there are two kinds of changes in snow crystal shapes [33], as shown in [Figure 25.8](#). That is, the first one shows three alternations of the basic patterns of snow crystals with falling temperature: namely, from plate to prism at  $-4^\circ\text{C}$ , to plate again at

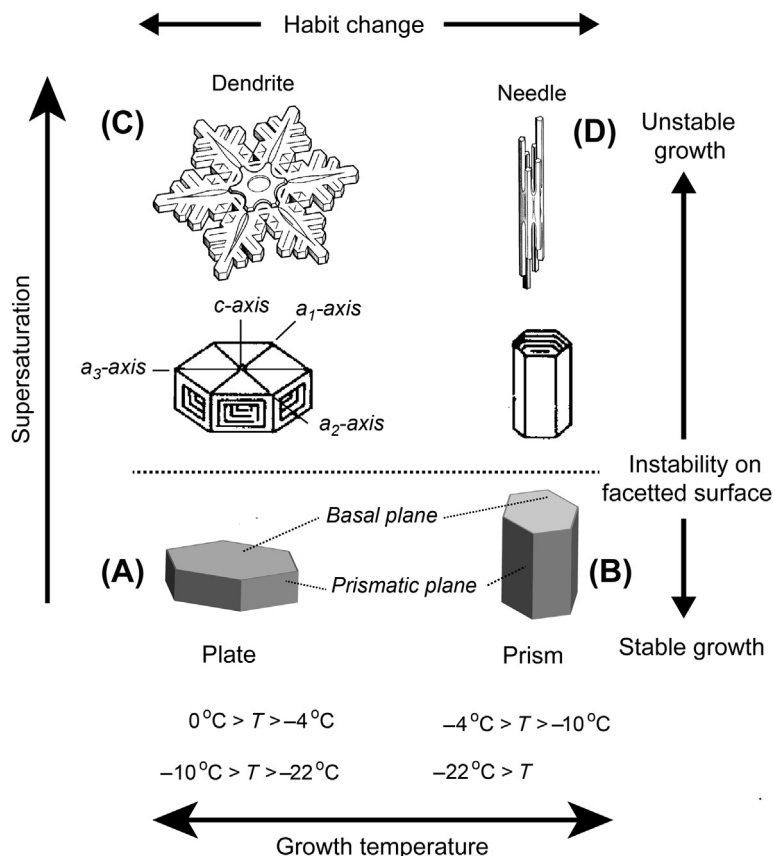


**FIGURE 25.8** An illustration showing two basic changes of snow crystal patterns. The horizontal axis indicates the temperature dependence of the habit change, and the vertical axis indicates the degree of instability for the faceted crystals as a function of supersaturation. Each pattern at the four corners, (A)–(D), indicates the basic patterns of snow crystals and corresponds to the pictures, (A)–(D), shown in [Figure 25.1](#). The diverse shapes of natural snow crystals arise from intermediate configurations among these basic patterns or combinations of these different patterns. *Modified from Ref. [33].*

–10 °C, and then to prism at –22 °C. This temperature-dependent change is the so-called habit change. The second is a change of in pattern from a simple hexagonal shape to a more complicated shape with increasing supersaturation, such as from a hexagonal plate to a sector plate and then to a hexagonal dendrite in the temperature ranges of 0 to –4 °C and –10 to –22 °C or from a hexagonal column to a skeletal crystal and then to a needle crystal in other temperature ranges. This change relates to the “instability on faceted surface” occurring during the growth of a polyhedral crystal [80]. Namely, we can claim that the shapes of snow crystals should be distinguished by only four categories, delineating the growth features of snow crystals (i.e., plate, prism (column), dendrite, and needle), which correspond to the pictures of snow crystals shown in Figure 25.1. Actually, natural snow crystals may be formed as intermediate shapes between different types and/or complete transitions from one type to another type during the growth.

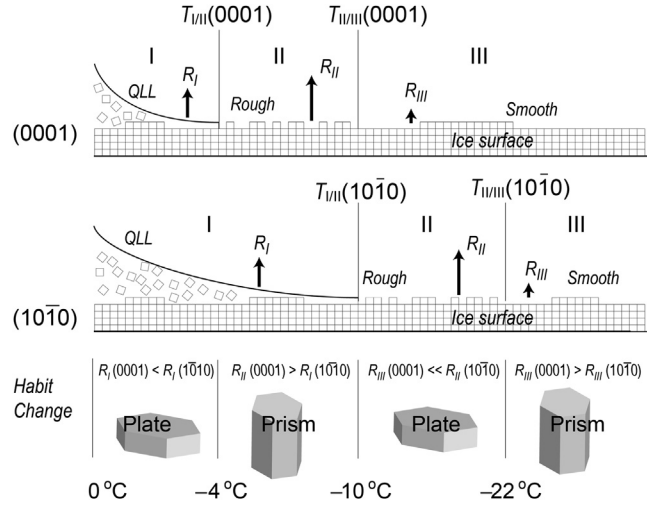
Before considering the basic pattern formation mechanisms of snow crystals, it will be very useful to consider the initial process of snow crystal formation in the cloud. Small ice particles (the origin of snow crystals) are formed in a cloud by the freezing of small cloud droplets with diameters of approximately 10  $\mu\text{m}$ . Such particles with spherical shapes start to grow in the supersaturated water vapor. Because only the crystallographic planes with the lowest growth velocities can survive during the growth, the initially spherical particles grow into hexagonal prisms with an aspect ratio of nearly unit ( $l_c/l_a \sim 1$ ). Here,  $l_c$  is the length along the  $c$ -axis and  $l_a$  is the diameter along 1120-axes. The fundamental prisms continue to grow while falling through the cloud, and their shapes change into plate-like or columnar habits. It should be noted that the habit of a snow crystal is determined as a necessary consequence of crystal growth. When the growth rate of the basal plane,  $R(0001)$ , is larger than that of the prismatic planes,  $R(10\bar{1}0)$ , the habit becomes prism-like ( $l_c/l_a > 1$ ). When the reversed relation  $R(0001) < R(10\bar{1}0)$  holds, a plate-like habit ( $l_c/l_a < 1$ ) appears. Consequently, the fundamental challenge in understanding the habit change is to clarify the alternative changes in the growth rates between the basal and prismatic planes.

#### 25.4.2 Kuroda–Lacmann Model for the Habit Change of Snow Crystals

The habit change of snow crystals is related to the temperature-dependent surface structures, as mentioned in the previous section. Here, we introduce one of the mechanisms for the habit change of snow crystal patterns based on the model proposed by Kuroda and Lacmann [33]. This model is based on the growth mechanism depending on different surface structures and anisotropic changes of surface structures on the basal and prismatic surfaces. This model is schematically shown in Figure 25.9. First, we consider the growth mechanisms of ice surfaces with different structures.

*Smooth surface (at region III below the transition temperature  $T_{III/IV}$ ):* Incident water molecules from vapor are incorporated only at the kink sites along the growth steps after diffusion along the surface. These growth steps on the ice surfaces are thought

**FIGURE 25.9** Kuroda–Lacmann model to explain the habit change of snow crystals depending on the temperature-dependent change of ice surface structures and its anisotropy between the basal and prismatic faces. Modified from Ref. [33].



to be formed by a two-dimensional nucleation mechanism, because few screw dislocations are observed in snow crystals [81]. The growth rate or nucleation rate depends on the relative supersaturation on the ice surface. Consequently, the growth rate in region III,  $R_{III}$ , is determined by the nucleation rate  $J$ , as well as the step velocity  $v$  [33]:

$$R_{III} = \delta J^{1/3} v^{2/3}, \quad (25.3)$$

where  $\delta$  is the average spacing of growth steps.

*Rough surface (at region II between the transition temperatures of  $T_{III}$  and  $T_{III/II}$ ):* Incident water molecules from vapor should be immediately incorporated after attachment to the rough surface (i.e., the adhesive growth mechanism). Consequently, the growth rate is dominantly determined by the diffusion process of water molecules in the atmosphere surrounding the growing snow crystal and the growth rate in region II,  $R_{II}$ , is given by the Hertz-Knudsen equation of

$$R_{II} = \alpha_c \frac{(p - p_i)\Omega}{(2\pi mkT)^{1/2}}, \quad (25.4)$$

where  $p$  is the actual pressure of water vapor in the atmosphere,  $p_i$  is the equilibrium vapor pressure of the ice surface,  $\Omega$  is the molecular volume,  $m$  is the mass of a water molecule, and  $\alpha_c$  is the condensation coefficient. For adhesive growth,  $\alpha_c \approx 1$ .

*Surface covered by a QLL (at region I above the transition temperature of  $T_{III}$ ):* Growth rate,  $R_I$ , is determined by the balance between the rate of incorporation of water molecules from vapor to the QLL,  $R_I^{QLL}$ , and the rate of solidification from the QLL to the crystal lattice,  $R_I^{QLL/ice}$ —namely, the V-QLL-S mechanism. For example, the former is determined by the Hertz–Knudsen equation and the latter is determined by

two-dimensional nucleation at the interface between the QLL and ice, and the two rates must be equal in a steady state:

$$R_I = R_I^{QLL} = R_I^{QLL/ice}. \quad (25.5)$$

This mechanism is basically the same as the VLS growth mechanism, which is a well-known mechanism for the growth of a eutectic system [82]. However, the driving forces for the two mechanisms are different—namely, thickness of the QLL for the former and solute concentration in the liquid for the latter.

Based on this model, Kuroda and Lacmann calculated the growth rates of ice surfaces as a function of temperature. In conclusion, the relationship of  $R_{II} > R_I \gg R_{III}$  was confirmed, and those growth rates are schematically shown by arrows in Figure 25.9. On the other hand, the transition temperatures  $T_{I/III}$  and  $T_{II/III}$  of the surface structure as well as growth mechanism depend on the surface orientation. Taking into consideration the anisotropic surface free energies, they obtained the relations of  $T_{I/II}(0001) > T_{I/II}(10\bar{1}0)$  and  $T_{II/III}(0001) > T_{II/III}(10\bar{1}0)$ . Consequently, if we assign

$$\begin{aligned} T_{I/III}(0001) &= -4^\circ\text{C}, & T_{II/III}(0001) &= -10^\circ\text{C}, & \text{and} \\ T_{I/II}(10\bar{1}0) &= -10^\circ\text{C}, & T_{II/III}(10\bar{1}0) &= -20^\circ\text{C}, \end{aligned}$$

we can divide the temperature region into four parts according to the combination of growth mechanisms of each surface, as shown in Figure 25.9. In temperature region A, both surfaces grow by the V-QLL-S mechanism, but the relation  $R(0001) < R(10\bar{1}0)$  can be expected on the basis of a detailed discussion about the step energy dependence at two-dimensional nucleation growth. In temperature range B, because the basal surface grows by the adhesive mechanism but the prismatic plane continues to grow by the V-QLL-S mechanism,  $R(0001) \gg R(10\bar{1}0)$ . In temperature range C,  $R(0001) \ll R(10\bar{1}0)$ , as is the case in range B. In range D, both surfaces grow by the two-dimensional nucleation mechanism, but  $R(0001) > R(10\bar{1}0)$  can be obtained by taking into consideration the vapor diffusion field around the crystal. In conclusion, the habit change of a snow crystal depending on growth temperature can be explained by the behavior of anisotropic surface melting.

This theoretical aspect for the habit change of a snow crystal provides an elegant solution to the problem that has alluded many researchers for a long time. To examine this model, it is important to continue to study ice crystal surfaces and growth kinetics in more depth by various methods.

### 25.4.3 Formation of a Dendritic Pattern of a Snow Crystal

Snow crystals grow from water vapor in the atmosphere, and both the diffusion process of water vapor to the growing surface and the diffusion process of heat released from the surface are important, as well as the surface kinetic process. External forms of snow crystals change remarkably during growth depending on the degree of supersaturation in addition to the atmospheric temperature. A spherical single ice crystal with a radius in

the order of 1–10  $\mu\text{m}$  is initially formed by freezing of a supercooled water droplet in a cloud, and then it grows into a hexagonal prism bounded by two basal and six prismatic faces. The hexagonal prism growing in the temperature region between  $-10$  and  $-22$   $^{\circ}\text{C}$ , for example, forms various types of plate-like snow crystals such as a hexagonal plate, sector plate, and dendrite. In this section, we summarize the simulation of pattern formation in growth of plate-like snow crystals based on the work of Yokoyama and Kuroda [83].

The formation of snow crystal patterns is mainly controlled by a diffusion process for supplying the water vapor in air toward the crystal surface and a surface kinetic process for incorporating the water molecules into the crystalline lattice. Because the growth rate is not so large, the effect of thermal diffusion of released latent heat can be ignored. Yokoyama and Kuroda treated the formation of growth patterns starting from a circular single ice crystal in two dimensions. Growth rate determined dominantly by a surface kinetic process,  $V_k$ , is generally calculated by the following equation:

$$V_k = \beta(\theta, \sigma_S)\sigma_S, \quad (25.6)$$

where  $\beta(\theta, \sigma_S)$  is the kinetic coefficient depending on the rotation angle  $\theta$  around the 0001-axis of hexagonal ice crystal and the surface supersaturation  $\sigma_S$ . The  $\theta$  dependence for  $\beta(\theta, \sigma_S)$  has six minima with respect to  $60^{\circ}$  corresponding to six prismatic planes. As is well known,  $\sigma_S$  is determined by the interaction between the diffusion process and surface kinetic process. If there is no anisotropy for the kinetic coefficient, we may still obtain circular disk forms. When the minima of anisotropic kinetic coefficients are sufficiently deep, anisotropy of growth rates also become stronger and then prismatic faces appear as facet surfaces. For an intermediate degree of anisotropy, the area of facets decreases with increase in  $\sigma_S$ . As an example of the source of anisotropic kinetics, Yokoyama and Kuroda [83] assumed that growth steps on the prismatic faces are supplied from the screw dislocations emerging at the center of six prismatic faces during the growth process from a circular disk to a perfect hexagonal plate and at the corner of hexagonal plates for further growth process.

By the condition of mass conservation, the growth rate  $V_k$  determined by the surface kinetic process must be equal to the growth rate  $V_d$  that is determined by the volume diffusion process under a steady-state condition [84], namely  $V_k = V_d$ . Furthermore, supersaturation  $\sigma$  in the region surrounding a crystal is governed by the Laplace equation for diffusion:  $\Delta\sigma = 0$ . Adding the boundary condition specified as  $\sigma = \sigma_{\infty}$ , Yokoyama and Kuroda solved the diffusion field and the pattern development of snow crystals as a function of growth time. Here,  $\sigma_{\infty}$  is the supersaturation far from the growing snow crystal.

By this analysis, Yokoyama and Kuroda obtained various patterns ranging from a circular disk to a dendritic pattern as functions of the diffusion coefficient of water vapor in air and the value of  $\sigma_{\infty}$ . Figure 25.10 shows the growth process of a snow crystal under the conditions of  $D = 0.2$   $\text{cm}^2/\text{s}$  (corresponding to the value in 1 atm air) at 258.15 K ( $-15$   $^{\circ}\text{C}$ ) and  $\sigma_{\infty} = 8.5, 17,$  and  $34\%$ . The initial circular disk changes to a hexagonal disk, and the corners start to develop, and finally dendritic patterns are formed. It should be

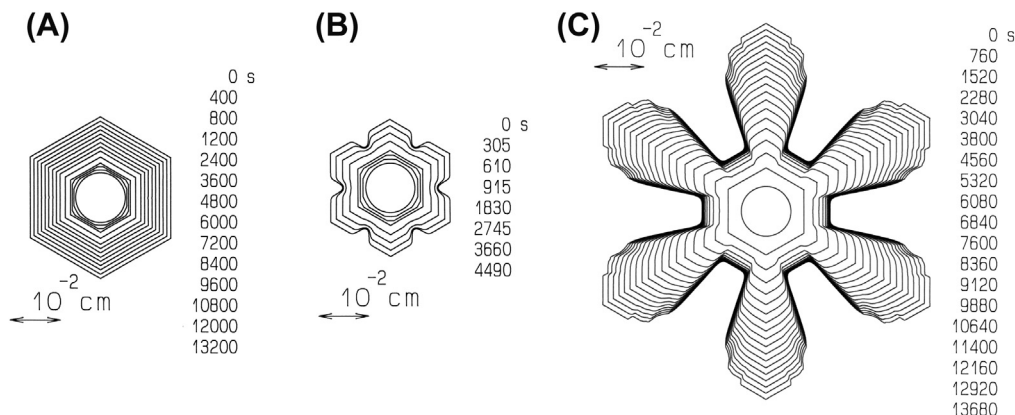


**FIGURE 25.10** Simulation results for pattern evolutions of prismatic faces surrounding snow crystals [83]. (A) Diffusion coefficient  $D = 0.2 \text{ cm}^2/\text{s}$  of water vapor in air (corresponding to 1 atm) and supersaturation  $\sigma_\infty = 8.5\%$  at a position far from the crystal. A circular crystal becomes a perfect hexagon at 1200 s by anisotropic kinetics. (B)  $D = 0.2 \text{ cm}^2/\text{s}$  and  $\sigma_\infty = 17\%$ . The onset of transition from a hexagonal pattern to a dendritic pattern. (C)  $D = 0.2 \text{ cm}^2/\text{s}$  and  $\sigma_\infty = 34\%$ . Formation of six primary branches with periodic structures at the tips was caused by bunching of monomolecular steps, which played a role in the formation of secondary branches. Modified from Ref. [83].

noted that the six primary branches have periodic structures at their tips caused by the bunching process of monomolecular growth steps. These structures may play a role in the formation of secondary branches of snow crystals, because surface supersaturation at the bunch should become a local maximum. In conclusion, Yokoyama and Kuroda showed that snow crystal patterns strongly depend on crystal size in addition to supersaturation.

#### 25.4.4 Effect of Air Flow on Pattern of a Snow Crystal

It is well known that dendrites observed in natural snow crystals always have extremely refined hexagonal symmetry, as shown in Figure 25.1. Natural snow crystals grow during their fall in the atmosphere and achieve a falling velocity of 30–100 cm/s depending on the crystal shape and size [85]. On the other hand, artificial snow crystals grown in a growth chamber usually lack symmetry, as indicated by many pictures of artificial snow crystals appearing in the literature [8,78]. Because artificial snow crystals are usually fixed on a thin fiber, this asymmetry may occur due to the lopsided supply of water vapor to the surface of the snow crystal, which is mainly caused by the convection around the growing snow crystal. Keller and Hallett [86] first carried out experiments on the growth of artificial snow crystals fixed on a fiber in a growth chamber with forced air flow; they found that both the growth forms and growth rates at the dendrite tips are strongly modified by introduction of air at a velocity of only 5 cm/s. Consequently, the reason why a natural snow dendrite has such excellent symmetry is not so trivial. At least, the symmetrical property observed on the natural snow dendrite strongly indicates that all

of the tips of the six branches are growing under exactly the same conditions, including the effect of air flow. That is, branching at the dendrite tip may occur in a *deterministic manner* for all of the dominant factors related to crystal growth but in a *random process*, as appeared on the fractal patterns.

## 25.4.5 Twinned Snow Crystals

### 25.4.5.1 Structures of Twinned Snow Crystals

Most of the snow crystals falling from the sky are twinned snow crystals. The importance of twinned snow crystals was first pointed out at the opening lecture given by Frank [87] at the Fourth International Conference on Crystal Growth held in Tokyo in 1974. Single snow crystals are in fact seldom seen among snow crystals in nature. The structures and formation mechanisms of twinned snow crystals are therefore important research issues in relation to crystal growth.

After Frank's lecture, Japanese researchers measured the angles between 0001 axes of components using natural twinned snow crystals, and they discovered the salient fact that those angles were dominantly concentrated at  $70.5\text{--}70.6^\circ$  (or  $109.4\text{--}109.5^\circ$  as degrees of their supplementary angles) and that one of the  $11\bar{2}0$  axes of one component corresponded to that of the other component [6,88–93]. Amazingly, this angle agreed completely with the angle between the {111} faces of a cubic ice structure,  $I_c$ , namely  $109.5^\circ$ . Cubic ice is usually observed in a deposited ice film from water vapor at temperatures ranging from about 130 to 150 K, but it is metastable at temperatures higher than 170 K and is easily transformed to ordinary hexagonal ice,  $I_h$  [94–96]. Even though the lowest formation temperature of natural snow crystals is not lower than about 220 K, what seems certain is that cubic ice has an important role in the twin formation.

Kobayashi and Furukawa [93] speculated that metastable cubic ice can be forced to nucleate rather than stable hexagonal ice when ice nucleation occurs in a supercooled water droplet at temperatures above 220 K. Because the surface structure of {111} faces of cubic ice is equivalent to that of basal faces of hexagonal ice, hexagonal ice can grow on {111} faces of cubic ice in a continuous manner. Finally, the water droplet will change into an ice sphere composed of eight components of hexagonal ice with 0001 axes intersecting the angle of  $109.5^\circ$ . Each component of hexagonal ice continues to grow in a manner similar to that of a single ice crystal, and finally a twinned snow crystal is formed. This phenomenon is well known as Ostwald's step rule [97]—that is, a metastable phase with higher chemical potential can appear in the run-up to the formation of a stable state with lower chemical potential in the process of phase transformation.

### 25.4.5.2 Formation Mechanism of Twinned Snow Crystals

Takahashi [98,99] theoretically investigated the possible nucleation process in a supercooled droplet by the cubic ice instead of hexagonal ice. The {111} faces of cubic ice and the basal faces of hexagonal ice have the same configuration of water molecules in the nearest neighbors but different configurations for the secondary nearest neighbors, because the cubic and hexagonal structures differ from each other only in the stacking

sequence of molecular layers. Consequently, the relationship of  $\sigma_{111} < \sigma_{0001}$  is expected. Because the unit density of the dangling bonds on prismatic faces is larger than that of basal faces, the relationship of  $\sigma_{0001} < \sigma_{10\bar{1}0}$  is also approved. Based on these relationships, Takahashi investigated the total free energies for the regular octahedron of cubic ice and the hexagonal column of hexagonal ice as a function of size. He found that the total free energy for the former was lower than that for the latter when the embryo size was smaller than a critical value, but that this magnitude relation was inverted when the sizes became larger than the critical value. Johari [100] recently pointed out that, on the basis of the enthalpy and interfacial energy of hexagonal ice and cubic ice, water droplets smaller than 15 nm in radius and films thinner than 10 nm would freeze to cubic ice in the temperature range of 160–220 K. A computer simulation study [101] also showed the formation and stability of cubic ice in a frozen water droplet.

As for evidence of the occurrence of cubic ice in the atmosphere, Whalley [102] suggested that Scheiner's halo, which occasionally occurs at  $27.46^\circ$  from the sun can be exclusively produced by light passing through regular octahedral crystals of cubic ice. Mayer and Hallbrucker [103] detected X-ray diffraction peaks coming from the structure of cubic ice at approximately 240 K for a polycrystalline ice sheet formed by freezing deposition of water droplets on a copper cold plate, and they also found that cubic ice was kept for long stretches even at this temperature. This temperature was much higher than the stable temperature range below 170 K for cubic ice formed by vapor deposition [16]. This was the first direct evidence of the formation of cubic ice by the freezing of water droplets, and various studies have since been carried out to clarify the mechanism of cubic ice formation in frozen water droplets in conjunction with cubic ice formation in the earth's atmosphere [104].

Similar phenomena have also been reported for other materials. For example, a tetrapod-like twin crystal of ZnO [105–107] or CdS [108] is formed by the successive growth of wurzite crystals on the four zinc {111} surfaces of a cubic crystallite, and its existence at the center of a tetrapod-like twin crystal was confirmed by electron diffraction. Recently, Niekawa and Kitamura [109] theoretically studied the conditions for transformation induced by heterogeneous nucleation of a stable phase on the surface of a preformed metastable phase, referred to as “epitaxy-mediated transformation” based on Ostwald's step rule, and showed that the formation of twinned crystals is dominantly formed by the transformation from the metastable phase to stable phase at the initial stage of crystallization.

## 25.5 Free Growth of an Ice Crystal in Supercooled Water

### 25.5.1 Equilibrium Forms of Ice Crystals

Pattern formation of an ice crystal during growth in supercooled water is also a very interesting subject in relation to morphological instability. When we consider this

problem, the most fundamental subject is the equilibrium form. Even though the theoretical expedition of equilibrium form is quite common, direct observation is generally difficult, with rare exceptions. In the case of ice, Maruyama and his coworkers [110,111] successfully observed equilibrium forms with the use of volume dilatation upon the freezing of water, as is well known from the phase diagram of water (Figure 25.2). Because this is a beautiful work for the equilibrium forms, it is worth introducing in this section. Maruyama and his coworkers put only one single ice crystal in a pressurized chamber completely filled with pure water and immersed the whole apparatus in refrigerant liquid, of which the temperature was kept constant below 0 °C. When the ice crystal grows in the chamber, the inside pressure increases due to volume dilatation of the ice crystal and then it conduces to melting point depression. Growth of the ice crystal is gradually suppressed and finally stops when the melting point of ice becomes equal to the ambient temperature. In this way, a complete equilibrium state at the coexistence state of a single ice crystal and water is automatically accomplished, and they found that the equilibrium form of an ice crystal is a circular disk surrounded by two flat basal faces and a rounded prismatic face above  $-16$  °C, but that it changes to a hexagonal plate surrounded by two basal and six prismatic faces. These results mean that the basal face is molecularly flat (smooth plane) even at the triple point of 0 °C, while the prismatic face transits from a molecularly flat interface to a molecularly rough interface at  $-16$  °C, indicating that the so-called thermal roughening transition [39] occurs on the prismatic interface of the ice crystal and that the anisotropy of free energies for the interfaces perpendicular to the basal plane is negligibly small at temperatures above  $-16$  °C. It should be noted that they also successfully observed the transition process between circular and hexagonal disks by artificial changes of pressure [112].

### 25.5.2 Growth Morphologies of Ice in Free Growth

In situ observations of ice crystal growth in supercooled water under atmospheric pressure conditions have been carried out by many researchers [113–115]. Figure 25.11 shows sequent pictures of a growing ice crystal in supercooled H<sub>2</sub>O water. The ice crystal shape is initially a circular disk bounded by two basal interfaces (Figure 25.11(A)), and morphological instability subsequently occurs at the periphery of the ice disk, resulting in the formation of a perturbed disk (Figure 25.11(B)). Finally, a well-developed dendrite with hexagonal symmetry is formed, as shown in Figure 25.11(F). Furukawa and Shimada [113] first analyzed the three-dimensional patterns of an ice crystal during its growth using Mach–Zehnder interferometry. They observed that the dendrite consists of a combination of two flat basal interfaces and a rounded interface, and that the tip patterns of the dendrite are not symmetric with respect to the basal plane; that is, the interface joining basal faces is not parallel to the *c*-axes. Although the observed tip shapes of ice dendrites are different from the parabolic shapes that are generally assumed in the theory of dendritic growth [116–119], the tip growth velocities shown as a

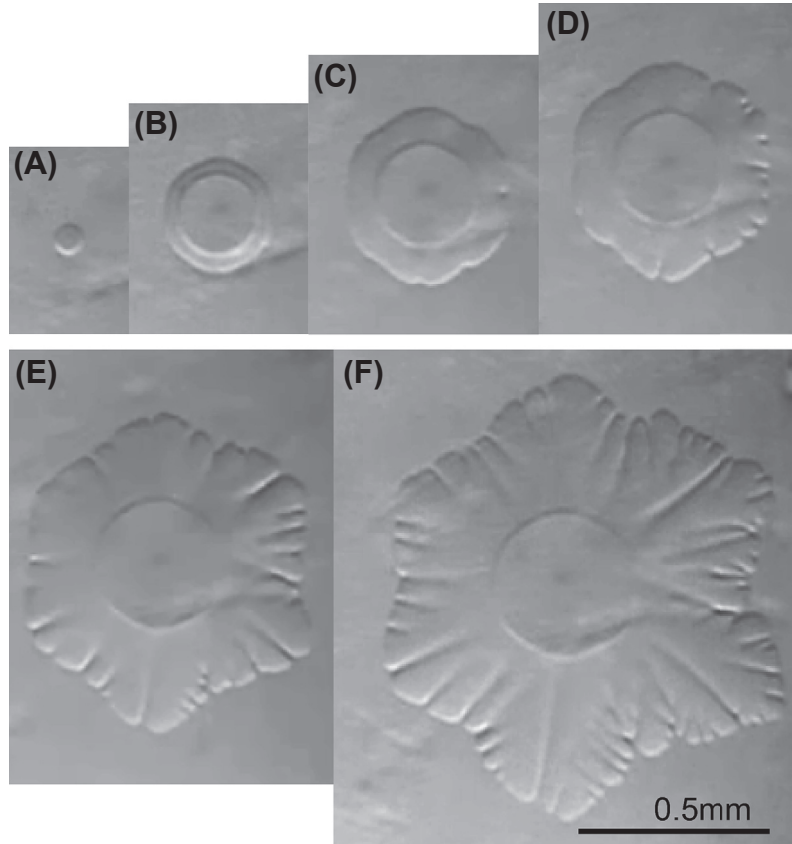


**FIGURE 25.11** Sequential pictures of an ice crystal growing in supercooled pure water in a thin circular growth cell. Time intervals were 2 s. The ice crystal initially had a circular disk shape with flat basal faces (B), and then perturbation occurred along the periphery of the ice disk (C), and a hexagonal dendrite pattern was formed (D)–(F).

function of supercooling exhibit good agreement with the theory of dendritic growth, except for the condition of low supercooling. Shimada and Furukawa [115] also showed that morphological instability occurs at the edge of the circular disk when the thickness exceeds a critical value,  $h_c$ , which is inversely proportional to the bulk supercooling,  $\Delta T$ .  $\Delta T = T_m - T_\infty$ , where  $T_\infty$  is the water temperature far from the crystal interface. This means that morphological instability is controlled by disk thickness rather than disk radius.

The first theoretical analysis of ice disk growth was carried out by Fujioka and Sekerka [120] with the assumption that the disk thickness is constant, with no growth on the basal interfaces. The experimental results of reference [115] were analyzed using phase plane analysis of an ordinary differential equation for  $h$  with respect to  $R$ , in which it was shown that the difference between the two types of disk growth corresponds to a

difference of kinetics on the basal faces between spiral growth, with the aid of a screw dislocation, and growth by two-dimensional nucleation [121]. Recently, it has been shown that the critical thickness  $h_c$  is related to the critical condition for the stable growth of a basal face, and that the difference between the growth rates of two basal faces is a possible mechanism for the appearance of an asymmetrical disk shape [122].

Sekerka [123] pointed out that the shapes of growing crystals are determined by an interplay of complex processes that include transport of energy and matter through bulk phases, capillarity-related processes that determine local equilibrium conditions at the crystal–nutrient interface, and nonequilibrium kinetic processes that take place locally at that interface. By treating the above three processes in pairs, he showed that the interplay of transport and interface kinetics leads to a consideration of facet instability, that the interplay of diffusive transport and capillarity leads to morphological instability, and that the interplay of capillarity and interface kinetics leads to a consideration of corner instability. In contrast, the determination of shapes of ice crystals growing in supercooled water must be controlled by all of these factors, different from the simple cases described in Sekerka’s paper, because the basal faces related to facet instability and the rounded side face related to morphological instability exist together in an ice crystal shape.

### 25.5.3 Free Growth of Ice Crystals under Microgravity Conditions

#### 25.5.3.1 *Experimental Setup*

The role of interaction between the flat basal faces and rounded faces in pattern formation of an ice crystal is a very interesting subject. There has, however, been no measurement of the growth rate of basal faces freely growing in supercooled water, even though the growth rates at dendrite tips have been measured under a gravity condition [113,114]. Consequently, simultaneous measurement of growth velocities, both at the dendrite tip and at the basal plane, with no convection effect is important. In this section, we present the results of experiments on free growth of ice in supercooled bulk water that were carried out in the Japanese Experiment Module (generally called “Kibo”) of the International Space Station (ISS) in the period from December 2008 to February 2009 [124–126]. The purpose of these experiments was to examine how the growth of basal faces affects the appearance of an asymmetrical disk, the morphological stability at the edge of the asymmetrical disk, and the formation of patterns of dendrites.

Figure 25.12 shows a schematic of the ice growth apparatus used in space, which is composed of two parts: a cylindrical growth cell and a disk-shaped nucleation cell. Both cells were connected with a thin glass capillary. The growth apparatus was completely filled with pure water degassed by vacuum evacuation. The temperature of each cell could be independently controlled within the accuracy of  $\pm 0.05$  °C by Peltier cooling elements. In this experiment, heavy water ( $D_2O$ ) was used as the water sample instead of  $H_2O$ , because the higher melting point of  $D_2O$  than that of  $H_2O$  could compensate for the limited power supply to the apparatus from the system of Kibo.

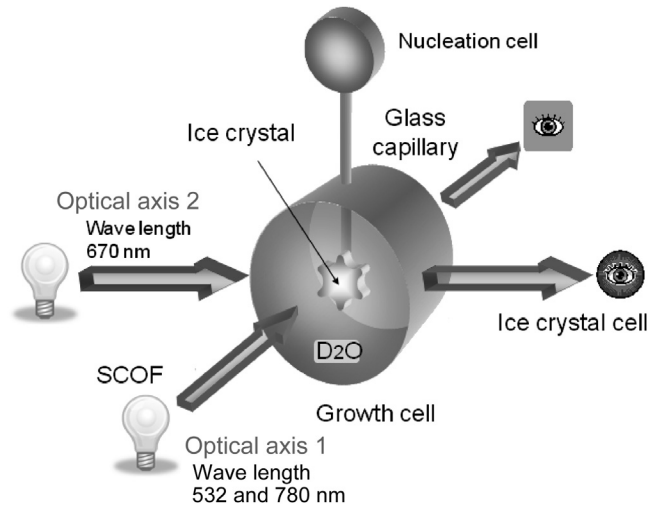


**FIGURE 25.12** Schematic illustration of an ice growth apparatus for space experiments [125]. The apparatus consisted a growth cell of 26 mm in diameter and 24 mm in length, a nucleation cell of 6 mm in diameter and 1.2 mm in thickness, and a glass capillary of 1 mm in outside diameter connecting the two cells. Inside surface of the growth cell carved out from a cube of oxygen-free high-conductivity copper was coated with a thin Teflon layer to maintain the supercooled state. The inside wall of the nucleation cell was coated with Au to promote ice nucleation. One end of the capillary was connected to the side wall of the nucleation cell, and the other end was inserted into the center of the growth cell. Observation of a growing ice crystal was carried out by using orthogonally-crossed biaxial Mach-Zehnder interferometers. Movie images of crystal growth were simultaneously downlinked from the International Space Station (ISS) in operation of space experiments. SCOF indicates the solution crystallization observation facility, which is one of the facilities equipped in “Kibo” of ISS. The SCOF has a two-wavelength interference microscope to simultaneously measure changes in morphology and growth conditions (i.e., temperature or concentration). Researchers can freely design experiment-unique cartridges.

The growth and melting processes of an ice crystal could only be controlled by setting the temperature remotely from the ground. Video images and temperature data were downloaded from ISS to the ground with a time lag of several seconds. The experimental procedure started from making a homogeneous supercooling state of the  $D_2O$  sample in the growth cell. After the complete establishment of supercooling, the nucleation cell was rapidly cooled to initiate ice nucleation. Then, nucleated ice particles continued to grow inside the capillary and compete against each other, and only one crystal could finally survive inside the capillary. Consequently, an ice crystal, with its  $c$ -axis perpendicular to the capillary axis, started to grow from the end of the capillary into the supercooled  $D_2O$ . A total of 134 experiments were successfully carried out using a single growth apparatus in the supercooling range from 0.03 to 2 K.

### 25.5.3.2 Results of ISS–Kibo Experiments

Time-sequence images of an ice crystal grown in space under the supercooling of 0.4 K, which were imported from the moving image file, are shown in Figure 25.13. The

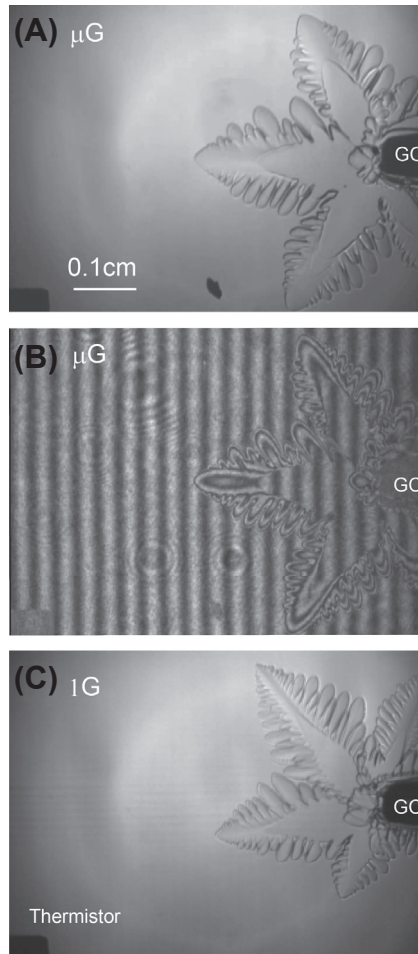


**FIGURE 25.13** An ice crystal grown in space at  $\Delta T = 0.4$  K. Bright-field image (A) and interference fringe image obtained by using Mach–Zehnder interferometer (B). The movie images were appropriately analyzed by using spatiotemporal image processing, and both the growth velocities of dendrite tips and the growth rates of basal faces were precisely analyzed [125]. An ice crystal shown in (C) was grown on the ground. GC indicates the tip of glass capillary.

growth rates,  $v_{tip}$  and  $v_{basal}$ , along the  $11\bar{2}0$ - and  $0001$ -axes, respectively, obtained in space are shown in Figure 25.14. Figure 25.14(A) plots the dimensionless tip growth velocity  $V$  as a function of dimensionless supercooling  $\Delta$ , which is defined by the equation

$$\Delta = \frac{T_M - T_\infty}{L/c_p}, \quad (25.7)$$

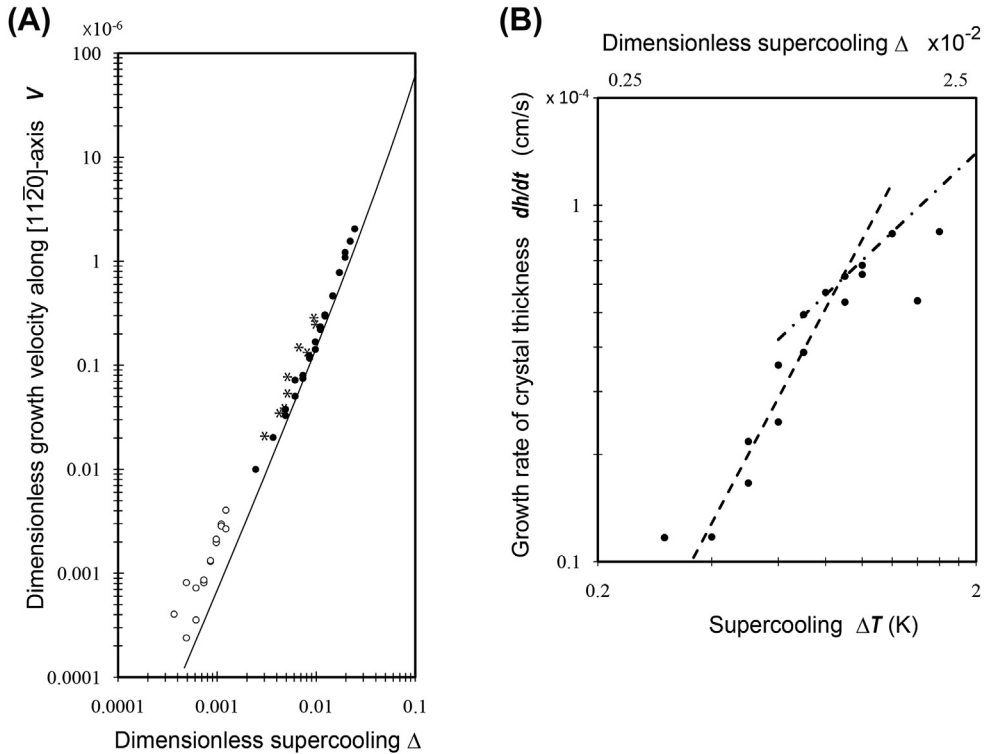


**FIGURE 25.14** Growth rates of ice crystals measured in space [125]. (A) Dimensionless tip growth velocity  $V$  as a function of dimensionless supercooling  $\Delta$ . The solid curve was obtained from the universal law proposed by LMK theory [116,117]. The open circles indicate no growth on the basal faces and the solid circles indicate the situation of growing basal faces. The star marks were obtained by ground experiments under 1G [113] (B) Rate of increase in thickness  $dh/dt (=2v_{basal})$  as a function of supercooling  $\Delta T$ .

where  $L$  is the latent heat released per unit volume of  $D_2O$  ice, and  $c_p$  is the specific heat. The tip growth velocity  $v_{tip}$  is also scaled by the ratio of capillary length  $d_0$  to thermal diffusivity  $\kappa_T$  of  $D_2O$  water, which is indicated as the equation

$$V = \frac{d_0}{\kappa_T} v_{tip}, \quad (25.8)$$

where  $d_0 = \gamma c_p T_m / L^2$ , including the isotropic surface tension  $\gamma$ . Figure 25.14(B) shows the rate increase in thickness between both-sided basal faces,  $dh/dt (\approx 2v_{basal})$ , as a function of supercooling  $\Delta T$ .

The tip growth velocities plotted as both open circles and solid circles in Figure 25.14(A) indicate the situations of no growth on the basal faces for  $\Delta < 0.002$  and growing basal faces with  $\Delta > 0.002$ , respectively. The corresponding patterns of ice crystals during no growth of basal faces were a disk shape for  $\Delta < 0.0007$ , a disk with a

perturbed periphery for  $\Delta \sim 0.0007$  and a perturbed disk having broad and short primary stalks for  $0.0008 < \Delta < 0.002$ . On the other hand, well-developed dendrites including secondary branches appeared with the start of basal face growth. The solid curve in this figure shows the theoretical prediction obtained from the universal law for dendrite tip growth proposed by Langer and Müller-Krumbhaar (LMK) [116,117], assuming no anisotropy of surface tension  $\gamma$ .

The tip growth velocities agree with the LMK theory in the region of supercooling for  $\Delta > 0.002$  (=0.16 K) when the growth on the basal face is not zero. At very low supercooling of less than 0.1 K, there is no growth on the basal face. With increase in supercooling, the basal faces start to grow and the growth rate changes as a function of supercooling with a power law, with an exponent of  $\sim 2$  from 0.2 to 0.5 K and with an exponent approaching 1 as supercooling increases to above 0.5 K. We interpret the growth on the basal face as being controlled by two-dimensional nucleation for  $\Delta T < 0.1$  K, which changes to spiral growth with the aid of screw dislocations for  $0.2 \text{ K} < \Delta T < 0.5 \text{ K}$  and then to a linear growth law with increasing supercooling for  $\Delta T > 0.5 \text{ K}$ . Because there appears to be disagreement between the theoretical curve and the tip growth velocities for  $\Delta < 0.002$  in the temperature range in which there is no growth on the basal face, we conclude that the basal face kinetics significantly affects the tip growth velocity rather than the asymmetric shape with respect to the basal plane.

Yoshizaki et al. [126] measured the tip radii of dendrites using the results of space experiments and estimated the stability factor  $\sigma^*$  defined in the LMK theory [116,117]. This value is theoretically predicted to be constant and around 0.02 for dendrite tips with the paraboloid of revolution. Figure 25.15 shows the estimated  $\sigma^*$  values as a function of supercooling. The values measured for ice crystals in space were constant against supercooling. This tendency has already been pointed out on the basis of the results of ground-based experiments conducted by Furukawa and Shimada [113], and is qualitatively supported by the results obtained in microgravity. The values obtained here ( $\sim 0.007$ ), however, are about 30 times less than the theoretical prediction (0.02), while the values measured in microgravity by Koss et al. [127] for succinonitrile (SCN) was very close to 0.02. This large discrepancy was due to the fact that the tip shape of the ice dendrite deviated from the paraboloid of revolution. As reported by Furukawa and Shimada [113], the tip of an ice dendrite has two radii,  $R_1$  and  $R_2$ , which are tip radii in the basal plane and in the direction perpendicular to the basal plane, respectively.  $R_2$  is two orders of magnitude less than  $R_1$ . In the case of SCN,  $R_1$  equals  $R_2$ . It is not appropriate to use  $R_1$  or  $R_2$  to represent the tip radius for calculating  $\sigma^*$ . The calculated value of  $\sigma^*$  with the geometric mean radius  $R_{mean}$  defined by  $\sqrt{R_1 \cdot R_2}$  is also shown in Figure 25.15, where values of  $R_2$  were estimated by the relation of  $R_2/d_0 = 425 \times \Delta^{-0.58}$  obtained by Furukawa and Shimada [113]. The value of  $\sigma^*$  calculated by using  $R_{mean}$  became about 0.013, which was nearer to theoretically predicted value, even though tip shapes of ice dendrites were far from the paraboloid of revolution. The reason for this fact has not been explained.

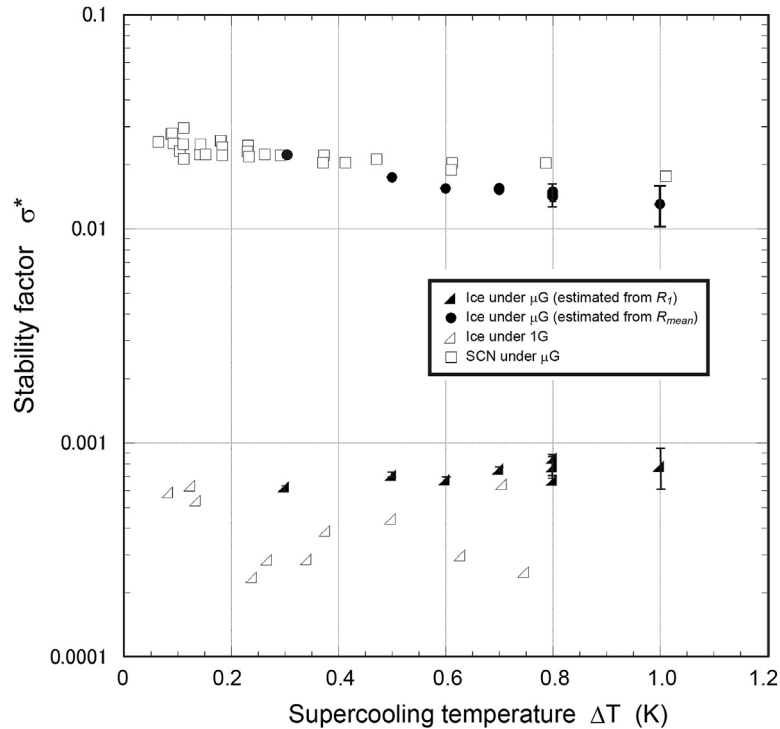


**FIGURE 25.15** Relationship between stability factor  $\sigma^*$  and supercooling [126]. The solid circles and triangles are results in microgravity using  $R_{mean}$  and using  $R_1$ , respectively. The open triangles indicate ground-based results for ice dendrites obtained from the reference [113], and the open squares indicate the results succinonitrile in microgravity [127].

#### 25.5.4 Molecular Dynamics Simulation of the Ice–Water Interface

Structural and dynamic properties at the ice–water interface near the melting point are attractive subjects for computer simulations, such as MD or Monte-Carlo simulations [18]. MD simulations for the interfacial structure at the ice–water interface under a stable condition have been carried out using a classical potential model of TIP4P [128] by Karim and Haymet [129] and by Nada and Furukawa [130–132]. The former showed that the interface of the basal plane has a diffuse structure throughout the thickness of several molecular layers ( $\sim 1$  nm). In response, the latter indicated that, although the interface thickness is larger for the basal plane than for the prismatic plane, the diffusion coefficient of  $\text{H}_2\text{O}$  molecules in water near the interface is smaller for the prismatic plane than for the basal plane. This interesting result may be related to the molecularly rough structure of the prismatic interface, which has been shown by various experiments.

Nada et al. [133,134] performed MD simulation in order to observe the growth process in the molecular scale on the interfaces of basal, prismatic, and  $\{11\bar{2}0\}$ -secondary prismatic planes using the new potential model for  $\text{H}_2\text{O}$  molecules developed by Nada

and van der Eerden [75], which is called a six-site model of rigid H<sub>2</sub>O and was developed in a reproducible fashion for both physical properties of ice crystal and liquid water. Using the simulation data, they analyzed the growth mechanism for each plane aside from the interface structure. The results indicated that the interface structure for the basal plane was molecularly flat, whereas the structures for the prismatic and  $\{11\bar{2}0\}$  planes were rough in the molecular scale, and also that the growth processes of ice crystals occurred by the arrangement of hydrogen-bonded networks of H<sub>2</sub>O molecules in water near the interface from the structures of water to ice crystal lattice. They also found that the ice crystal was grown by a layer-by-layer mode for the basal plane but by the rearrangement in three dimensions for the prismatic and  $\{11\bar{2}0\}$  planes, namely the collective incorporation of water molecules. It is notable that these results of MD simulations reproduce very well the actual anisotropy for ice growth and the interface structure, which have been described in many reports [18,113,125].

The anisotropy in the growth mechanism and the interface structure could be explained on the basis of the difference in the directions of dangling bonds, which the stable configuration has, among the planes [133]. Namely, though the stable configuration on the  $\{0001\}$  plane has seven dangling bonds, six of them are in directions parallel to the plane and the other one is normal to the interface (see Figure 25.3). This is a reason why growth occurs two-dimensionally and why the interface structure tends to be molecularly flat. On the other hand, for the other planes, all dangling bonds are in intermediate directions between parallel and normal to the plane. Consequently, growth can occur three-dimensionally in a collective manner and the interface structure also tends to be molecularly rough. Results of MD simulations using the six-site model have greatly contributed to an understanding of the growth kinetics of ice on the molecular scale [76,135,136].

## 25.6 Directional Growth of Ice Crystals

### 25.6.1 Pattern Formation at the Ice–Water Interface

#### 25.6.1.1 Experiments

One-directional growth of a single crystal in the defined temperature gradient is also a universal method for observing the morphological instability and pattern development at the growing interface [137]. This method has been applied to ice crystal growth in a solution of muriate because ice crystal growth induced by a temperature gradient condition can usually occur anywhere on the terrestrial surface, such as during ice growth by freezing of seawater on the polar sea surface. In this section, some interesting phenomena that are distinctly different from others are introduced [138–140].

A thin rectangular growth cell ( $76 \times 20 \text{ mm}^2$ ) with a gap of  $100 \mu\text{m}$ , which was filled with water containing potassium chloride (KCl), was put on each of two separately placed copper blocks, the temperatures of which were independently kept constant. Then, a linear temperature gradient ( $G$ ) was established in the orientation of the long

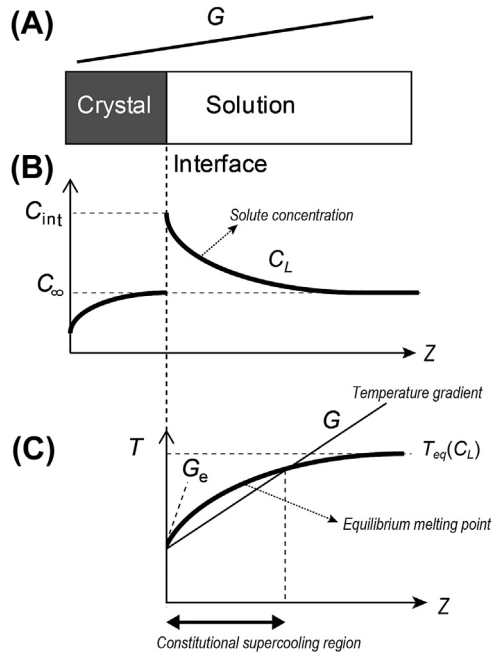


**FIGURE 25.16** Schematic illustration of the development of a constitutional supercooling region in front of the growing interface [139]. (A) Schematic configuration of one-directional growth cell. (B) The solute is rejected at the growing interface and exponentially distributed concentration field is formed in front of growing interface. (C) An equilibrium melting point corresponding to the solute concentration is estimated using a relation for molar depression of freezing point. A constitutional supercooling region is defined at the region where  $G_e$  is larger than  $G$ .

axis of growth cell ( $Z$ -direction), and a flat water–crystal interface was formed at the center of the growth cell (Figure 25.16 (A)). The growth cell could be moved transversally at an arbitrary constant velocity  $V$  using a stepping motor system, and the ice crystal was forced to grow at the same speed as  $V$  but in the opposite direction of cell movement.

The whole apparatus was placed on the stage of a microscope combined with a Mach–Zehnder interferometer, and the three-dimensional patterns of interfaces and the distribution of additives in front of the growing interface were analyzed.

### 25.6.1.2 Morphological Instability at an Ice Interface Growing in KCl Solution

Morphological instability at the interface during one-directional growth is usually promoted by constitutional supercooling, which is caused by interaction between the diffusion field of an impurity developing in front of the growing interface and the temperature gradient. Because the effect of impurity concentration works as depression of the equilibrium melting point, the kinetics of crystal growth is hardly affected by the existence of impurity molecules in the solution.

Only one single crystal with its 0001 axis perpendicular to the growth cell, namely the basal plane of the growing ice crystal being parallel to the growth cell surface, was grown

in all of the experiments. Water sample thickness of  $100\ \mu\text{m}$  and KCl concentration of 3 wt% were selected to obtain the most appropriate interference fringes, even though they were much larger than those used for conventional experiments on one-directional growth. Sequential photographs showing the development of interfacial patterns at  $V = 5\ \mu\text{m/s}$  observed by a conventional microscope are presented in Figure 25.17. Before the start of growth cell movement, the interface was completely flat and perpendicular to the direction of the temperature gradient at the position of equilibrium melting temperature. After starting to grow, it changed to an unleveled interfacial pattern at unpredictable intervals, namely the initiation of morphological instability at the interface (Figure 25.17(A)). The amplitude of its unevenness gradually increased (Figure 25.17(B)–(E)) and then cellular structures appeared (Figure 25.17(F)). Splitting

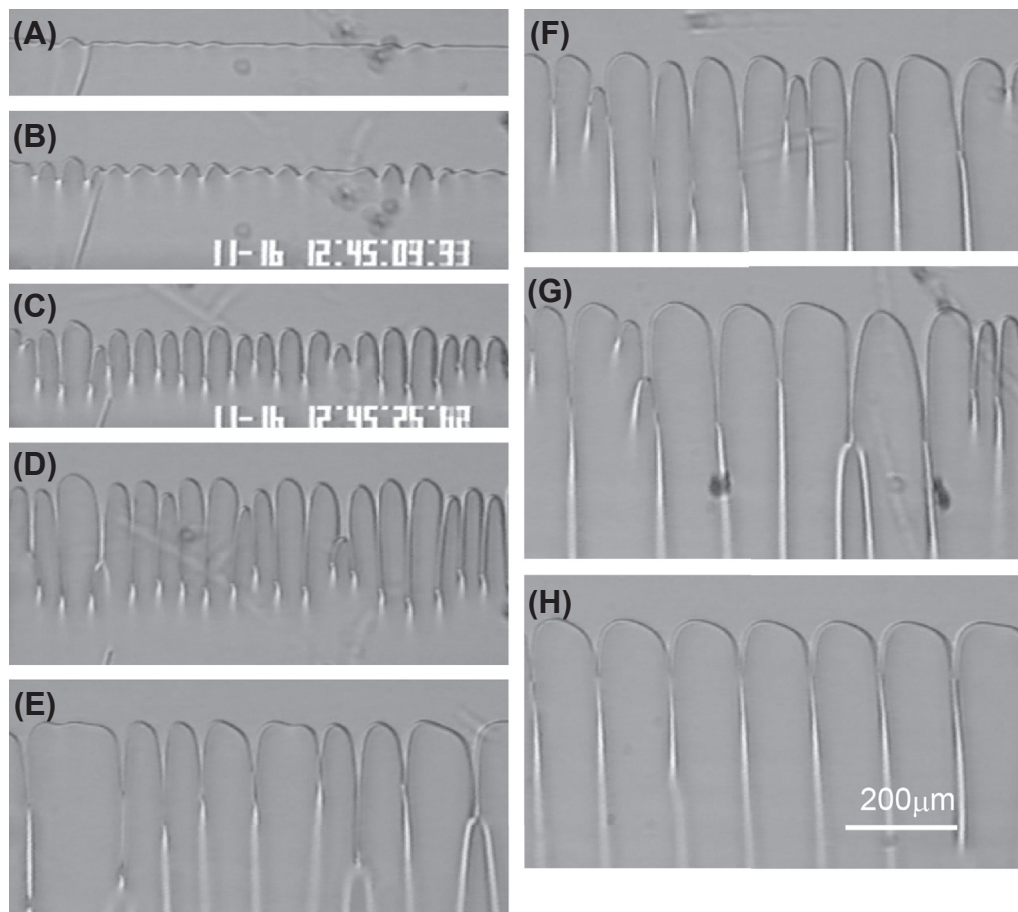


**FIGURE 25.17** Sequential pictures of the interfacial pattern observed at the interface between an ice crystal and KCl solution. The 0001 axis is perpendicular to the plane of space. Elapsed times after start of growth are (A) 180 s, (B) 193 s, (C) 215 s, (D) 245 s, (E) 377 s, (F) 443 s, (G) 829 s, and (H) 1431 s.

and coalescing continuously occurred at the tips of cellular patterns (Figure 25.17(G)), and regular cellular patterns were finally formed (Figure 25.17(H)).

Morphological instability of the interface during one-directional growth arises due to constitutional supercooling that develops in front of the interface [137,141]. Figure 25.16 schematically shows the phenomenon that occurs in the interfacial region during growth. Because the segregation coefficient  $k$  of KCl for an ice crystal is nearly equal to zero ( $k = 2.7 \times 10^{-3}$ ), the KCl solute is rejected at the growing interface and distribution of solute concentration,  $C_L$ , develops in front of the planar interface, as shown in Figure 25.16(B). An equilibrium melting point  $T_{eq}$  corresponding to  $C_L$  can be estimated using a novel relation of equilibrium temperature depression for a colligative solution. Figure 25.16(C) shows  $T_{eq}$  as a function of  $Z$ . If the equilibrium temperature gradient ( $G_e$ ) at a point of the interface is larger than  $G$ , a constitutional supercooling region is formed in the solution near the interface and causes morphological instability of the interface.

The dynamics are usually explained on the basis of Mullins-Sekerka instability [12]. The criterion for the occurrence of morphological instability during one-directional growth is generally given as the following relationship:

$$\frac{V}{G} \leq \left( \frac{mC_0}{D_L} \right) \frac{(1-k)}{k}, \quad (25.9)$$

where  $m$  is the gradient of the liquidus line in the phase diagram for a two-component solution system,  $D_L$  is the diffusion coefficient of solute in the solution, and  $k$  is the segregation coefficient. This model is very general but direct evidence of a relationship between the development of constitutional supercooling and morphological instability of the interface, to the best of my knowledge, has not been shown because it is not easy to directly observe the solute concentration distribution in front of a growing interface. In the next section, evidence for this relationship obtained in an ice growth experiment is shown.

## 25.6.2 Solute Distribution in Front of the Ice–Water Interface and Morphological Instability

Sequential pictures of interfacial fringes observed in the region around the interface growing at  $V = 5 \mu\text{m/s}$  are shown in Figure 25.18. In the initial condition of no growth, the interface was perpendicular to the  $Z$ -axis, and straight interference fringes indicate no diffusion field of solute in the solution (Figure 25.18(A)). After growth started, interference fringes also started to curve in both regions of the solution and the ice around the interface (Figure 25.18(B)–(D)). At the same time, development of perturbation at the interface began as shown in Figure 25.18(C). By analysis of the interference fringes, the solute concentration profile,  $C_L$ , in front of an advancing interface was obtained as shown in Figure 25.19(A). The figure clearly shows that a solute diffusion field started to grow from the uniform distribution of solute by the rejection of solute soon after the start of growth and continued to develop as a function of growth time. These profiles can be easily converted to equilibrium melting point profiles by estimating the colligative temperature depression generally given by the relationship

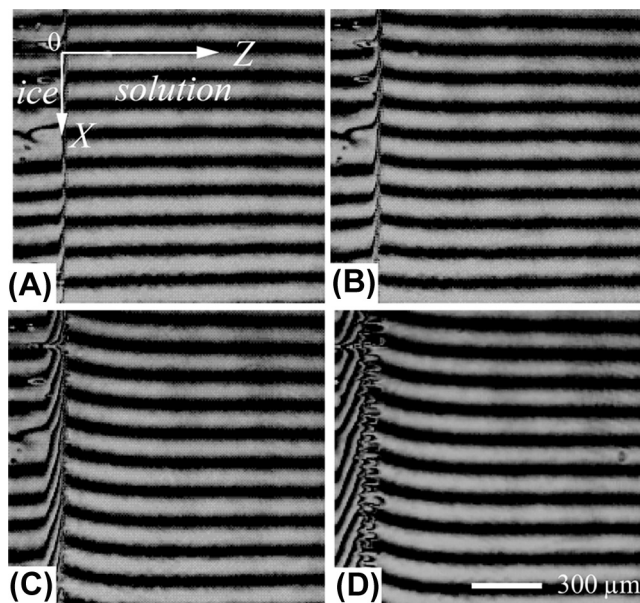


**FIGURE 25.18** Sequential pictures of the development of a diffusion field in front of a growing interface observed by using a Mach-Zehnder interference microscope [139]. Growth conditions were  $G = 2.3$  K/mm,  $C_0 = 3$  wt%, and  $V = 5$   $\mu\text{m/s}$ . (A) Flat interface in the initial condition, (B) beginning of instability, (C) appearance of a wavy pattern, and (D) development of a cellular structure. Elapsed time of each picture is 1-min interval after the start of growth at (A).

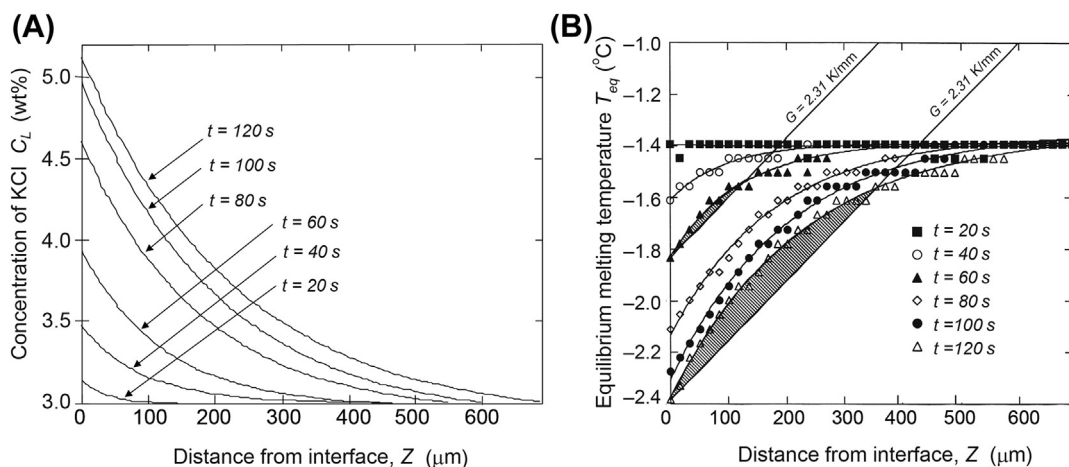


**FIGURE 25.19** Results of analysis of the development of a diffusion field in front of an interface [139]. (A) Concentration distributions  $C_L$  as a function of the distance from the interface forefront  $Z$ . Growth conditions were the same as these shown in the caption of Figure 25.18. (B) Profiles of equilibrium melting point  $T_{eq}$  estimated from  $C_L$  as shown in (A). At  $t \geq 0$  s,  $T_{eq}$  near the interface decreased due to an increase in the solute concentration, and the interface moved to a position at which the actual temperature was equal to the interface melting point. Solid lines indicate the actual temperature profiles in the solution at the elapsed times of 60 and 120 s. The hatched regions correspond to constitutional supercooling, namely the region of  $T \leq T_{eq}$ . Instability was initiated at the moment of formation of constitutional supercooling.

$T_{eq} = mC(Z)$ . For a KCl solution,  $m = -0.468$  K/wt%. In Figure 25.19(B), the profiles of equilibrium melting temperatures of ice  $T_{eq}$  versus  $Z$  are given as a function of growth time. The slope of the equilibrium temperature profile at the interface,  $dT_{eq}/dZ$  ( $Z = 0$ ), increased with time and finally exceeded the value of the actual temperature gradient determined as the experimental condition at  $t = 60$  s. Namely, a constitutional supercooling region formed in front of the interface, as shown by the hatched region at  $t = 120$  s in Figure 25.19(B). Furthermore, if we go back to Figure 25.17 again, we can know that morphological instability at the interface occurred at the moment of  $t = 60$  s, which was the beginning of constitutional supercooling. This is the first direct evidence of a relationship between morphological instability and development of constitutional supercooling.

On the other hand, the diffusion length  $l_s$  of the solute can be determined by the equation  $(C(l_s) - C_0)/(C_{int} - C_0) = 1/e$ , assuming exponential decay of the solute distribution profile. In this experiment,  $l_s$  was estimated to about 250  $\mu\text{m}$  and independent of growth time. This value is much larger than the average cell spacing at the interface (which is less than 135  $\mu\text{m}$  as shown in Figure 25.17). Consequently, the spatial fluctuation in the solute distribution might be caused by the mutual interaction among growing cellular branches through the diffusion field around each branch.

Finally, let us consider the behavior of  $C_{int}$  depending on the development of an interfacial pattern. Even though  $C_{int}$  gradually increased with advance of the interface due to the rejection of solute while the interface was flat at the initial stage, it showed a sudden decrease after morphological instability occurred on the planar interface. After a steady-state cellular structure had been attained and a stable diffusion field was maintained,  $C_{int}$  remained constant but was much lower than the critical value expected from the equilibrium segregation coefficient. Consequently, the “effective” segregation coefficient for the cellular pattern interface could be determined from this analysis. For example,  $C_{int}$  was estimated to approximately 3.7 wt% under the conditions of  $V = 10$   $\mu\text{m/s}$  and  $C_0 = 3$  wt% [139], because the solute could be incorporated into the interspaces between the neighboring cellular branches and/or the interfaces between ice crystals and glass walls.

### 25.6.3 Cellular Tilting

#### 25.6.3.1 Tilt Angle Measurement for Cellular Patterns of Ice Crystals

Although the 0001 axes of ice crystals growing by the one-directional growth method always remained in the direction perpendicular to the glass plate of the growth cell, the directions of  $11\bar{2}0$  axes were randomly allocated in the plane parallel to the glass plate. For this reason, the axes of cellular patterns could be tilted from the growth direction of the ice crystal ( $Z$ -direction) depending on the growth velocity  $V$  of ice crystal and the angle,  $\psi$ , between the  $Z$ -direction and one of the ice  $11\bar{2}0$  axes. Figure 25.20 shows pictures of cellular patterns as a function of  $V$  at  $\psi = 20^\circ$ . The tilt angle of the cellular pattern,  $\phi$ , was calculated by the relation  $\phi = \tan^{-1}(V_X/V)$  from the measurement of the

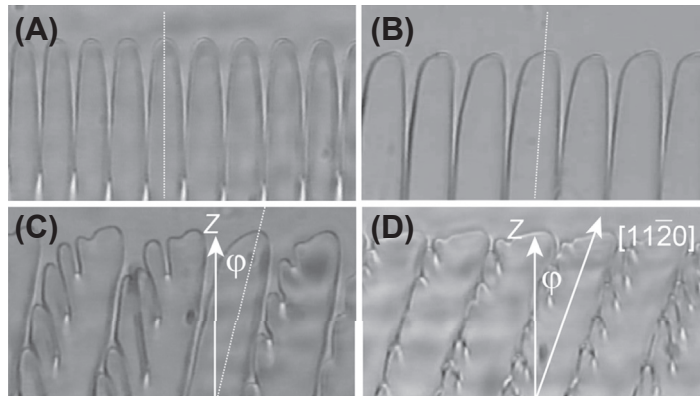


**FIGURE 25.20** Regularly arrayed cellular patterns in a steady state condition at  $\psi = 20^\circ$ . Growth velocities  $V$  were (A)  $3 \mu\text{m/s}$ , (B)  $5 \mu\text{m/s}$ , (C)  $7 \mu\text{m/s}$ , and (D)  $40 \mu\text{m/s}$  [138]. Dotted lines indicate the directions of central axes of cellular pattern.

lateral growth velocity,  $V_X$ , of cellular tips, and tilting angles for various growth velocities are shown as a function of  $\psi$  in Figure 25.21(A). It is notable that tilting of the cellular pattern was not observed at  $\psi = 30^\circ$  in this range of  $V$ . The average cell spacing for cellular patterns, which could be measured in these observations, is also important for discussion of the effects of interface kinetics, as explained in the next section.

### 25.6.3.2 Anisotropic Interface Kinetics

Analysis of tilted cellular patterns provides quantitative results concerning the anisotropic interface kinetics. Coriell and Sekerka [142] developed a linear stability model for small

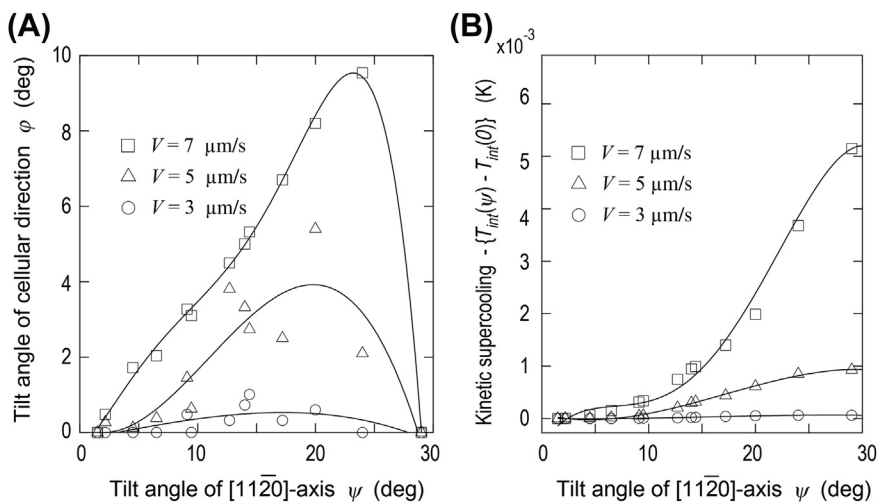


**FIGURE 25.21** (A) Tilt angles  $\phi$  of cellular patterns as a function of  $\psi$  for various values of growth velocities  $V$ . (B) Kinetic supercooling temperatures as a function of  $\psi$  [138].

perturbations on a planar interface during directional growth of binary alloys, and they analyzed both the effects of anisotropic interfacial free energy and kinetics. They showed that a translational perturbation wave can occur along the interface ( $x$ -axis) due to the effect of anisotropic interface kinetics and the anisotropic kinetic parameter,  $\mu_X/\mu_T$ :

$$V_X = -2h \left( \frac{\mu_X}{\mu_T} \right). \quad (25.10)$$

Here,  $\mu_X$  and  $\mu_T$  represent  $\partial V/\partial \varphi$  and  $\partial V/\partial(\Delta T_k)$ , respectively.  $\Delta T_k (= T_{eq} - T_{int})$  defines the kinetic supercooling at the interface, namely the difference between the equilibrium temperature,  $T_{eq}$ , which is depressed by the effects of local curvature and solute concentration at the interface, and the actual interfacial temperature,  $T_{int}$ . The parameter  $h$  is usually derived in consideration of the kinetic effect. However, because the tip growth velocities measured for free growth of dendrites completely agreed with the theoretical predictions without any kinetic effect [114,116,117,119], absolute magnitude of the kinetic effect may be negligibly small. Consequently, we may neglect the kinetic terms in the derivation of parameter  $h$ , which is given in the form of a local equilibrium condition, as follows:

$$2h = V\omega \left\{ G \frac{k_S - k_L}{k_S + k_L} + \frac{\omega m G_C}{\omega^* - \frac{V}{D}(1-k)} \right\}^{-1}, \quad (25.11)$$

where  $k_S$  and  $k_L$  represent the thermal conductivities of solid and liquid, respectively,  $m$  is the slope of the liquidus line, and  $G_C$  is the concentration gradient at a planar interface.  $\omega^*$  is given by  $(V/2D) + [(V/2D)^2 + \omega^2]^{\frac{1}{2}}$ , where  $\omega (= 2\pi/\lambda)$  is the wave number of the cellular array. At small values of  $V$ ,  $\omega^* \approx \omega + (V/2D)$ .

On the other hand, the following relationship is obtained by the solute flux balance at the interface:

$$G_C = - \left( \frac{V}{D} \right) (1-k) C_{int}. \quad (25.12)$$

Thus, the anisotropic kinetic parameter  $\mu_X/\mu_T$  is obtained by substituting Eqns (25.11) and (25.12) into Eqn (25.10) as

$$\mu_X/\mu_T = - \left( \frac{\lambda V_X}{2\pi V} \right) \left[ G \frac{k_S - k_L}{k_S + k_L} - \frac{m C_{int} V}{D} + \frac{\lambda(2k-1)}{4\pi} \right]. \quad (25.13)$$

Finally, it should be noted again that anisotropy of the kinetic effect becomes clear in Eqn (25.13). In addition, observations of cellular tilting indicate that nonzero *anisotropy* of kinetics exists for growth of an ice crystal, no matter how small the *magnitude* of the kinetic effect is.

Because the anisotropic kinetic parameter,  $\mu_X/\mu_T$ , is given as  $(\partial(\Delta T_k)/\partial\psi)_V$  from the definitions of  $\mu_X$  and  $\mu_T$ , it is possible to calculate this value with Eqn (25.13) from the results for  $V_X$  and  $\lambda$ . Furthermore, the integration of  $(\partial(\Delta T_k)/\partial\psi)_V$  with respect to interface orientation  $\psi$  at a constant velocity gives the kinetic supercooling,  $\Delta T_k(\psi) - \Delta T_k(0)$ —that is,  $-[T_{int}(\psi) - T_{int}(0)]$ .

Figure 25.21(B) shows results estimated from Figure 25.21(A) using the following values of physico-chemical parameters:  $T_m = 273.15$  K,  $k_S = 2.2$  J/msK, and  $k_L = 0.56$  J/msK for pure water and ice and  $m = -0.468$  K/wt% and  $D = 1.70 \times 10^{-9}$  m<sup>2</sup>/s for KCl solution. Because these values are proportional to the interfacial kinetic effect for growth, the degrees of anisotropy for growth kinetics in the interface parallel to the basal plane were quantitatively determined as a function of growth velocity. Namely, the preferred growth direction of an ice dendrite, which corresponds to the 11 $\bar{2}$ 0 direction, coincides with the directions with minimum effects of growth kinetics.

## 25.7 Ice Crystal Growth Controlled by Biological Macromolecules

### 25.7.1 Features of Biological Macromolecules with Antifreeze Function

#### 25.7.1.1 Antifreeze Effect

Seawater temperature underneath the sea surface covered by ice in polar or subpolar regions can drop to about  $-2$  °C by the colligative effect of salt water, namely the molar depression of equilibrium freezing point. Even in this subzero environment, many kinds of fish make their habitats. While the serum of fish living in polar seawater can carry enough salt to lower their freezing temperature to about 1 °C, it is not enough to head off a crisis of freezing death. Consequently, they must rely on another mechanism for survival in a supercooled state [143]. Elucidation of the mechanism of antifreeze effect is a crucial issue related to crystal growth controlled by biological macromolecules. In this section, we describe findings regarding the mechanism of ice crystal growth inhibition by the existence of special proteins with an antifreeze function.

The “antifreeze effect” for polar fish was first discovered by DeVries and Wohlschlag [144,145], and four types of antifreeze proteins (AFPs) and one type of glycoprotein (antifreeze glycoprotein (AFGP)) were identified in the serum of fish [143]. Some new types of AFPs, which exert a 10-times greater antifreeze effect than that of fish proteins, have been identified in the bodies of insects [146,147], plants [148], and bacteria [149]. Currently, AF(G)Ps are used in some frozen foods [150] and are known to improve the storage of rat islets and human blood platelets [151,152]. It is important from both a scientific standpoint as well as a technological one to understand the fundamental mechanism of the action of AF(G)Ps, and it has been the focus of much research to date. While it has dramatic consequences for natural biological processes and technological applications, little is known about the dynamic mechanism of ice growth inhibition [153].

#### 25.7.1.2 General Functions of Antifreeze Glycoproteins and Proteins

There exist at least five distinct classes of these proteins, ranging in structure from a short  $\alpha$ -helical rod to extended helices and even larger globular forms with distinct compositions. Yet they all have the same basic functions: inhibition of ice crystal growth

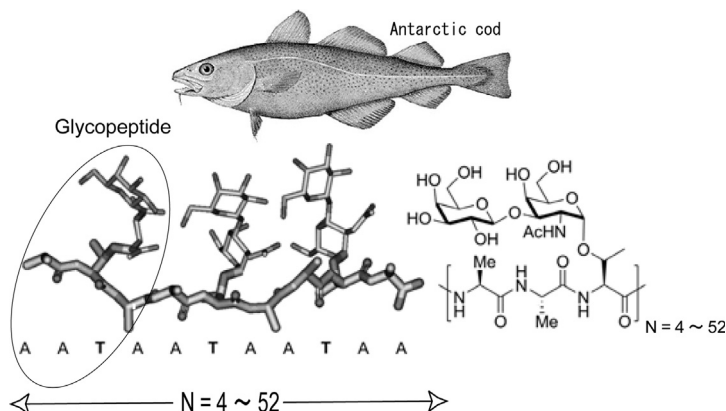


**FIGURE 25.22** An Antarctic cod (*Trematomas borchgreviki*) with antifreeze glycoprotein (AFGP) in its blood serum (top), and the molecular structure of AFGP (bottom). The peptide backbone is composed of alanine(A)-alanine(A)-threonine(T) repeating tripeptide units. The threonine peptide has a disaccharide residue. Eight distinct fractions of these proteins have been isolated from fish serum, and the difference is mostly in the number of tripeptide repeats, which change from 52 (~33 kDa) to 4 (~2.6 kDa) for bands 1–8, respectively [143].

and ice recrystallization and radical modification of growth forms [143]. Figure 25.22 shows that the molecular structure of an AFGP consists of a varying number of repeating units of alanine–alanine–threonine (*Ala–Ala–Thr*), with minor sequence variations and a disaccharide residue joined to the hydrogen oxygen of the threonine residue, varying in molecular mass from 2.6 to 33 kDa, categorized as AFGP1-8 depending on the molecular weight. Here, the characteristic functions of AFGPs that make them unique are summarized (other fish AFPs also have the similar functions as described below [143,154,155]):

1. They lower the freezing temperature ( $T_f$ ) of water by inhibiting the growth of existing ice crystals but keep the melting point ( $T_m$ ) of ice at the equilibrium melting point. As shown in Figure 25.23(A), the temperature region between  $T_m$  and  $T_f$  is called the “thermal hysteresis” region [143]. Interestingly, the amount of AFGP required for freezing inhibition is up to 500 times less than that of the colligative effect of protein solutions, and even much less for some proteins in insect serum.
2. These proteins drastically modify the growth forms of ice crystals. Figure 25.24 shows pictures of ice crystals grown in supercooled AFGP solutions with different concentrations. The ice crystals are much different from the growth forms in supercooled pure water as shown in Figure 25.11. The growth forms in AFGP solution greatly depend on the concentration of AFGP and the supercooling, but growth kinetics switches to a layer-by-layer mode, becoming highly faceted, and the  $l_c/l_a$  ratio can be greater than one at higher concentrations, namely needle-type crystals [156,157]. It should be emphasized that the crystals in AFGP solution in the

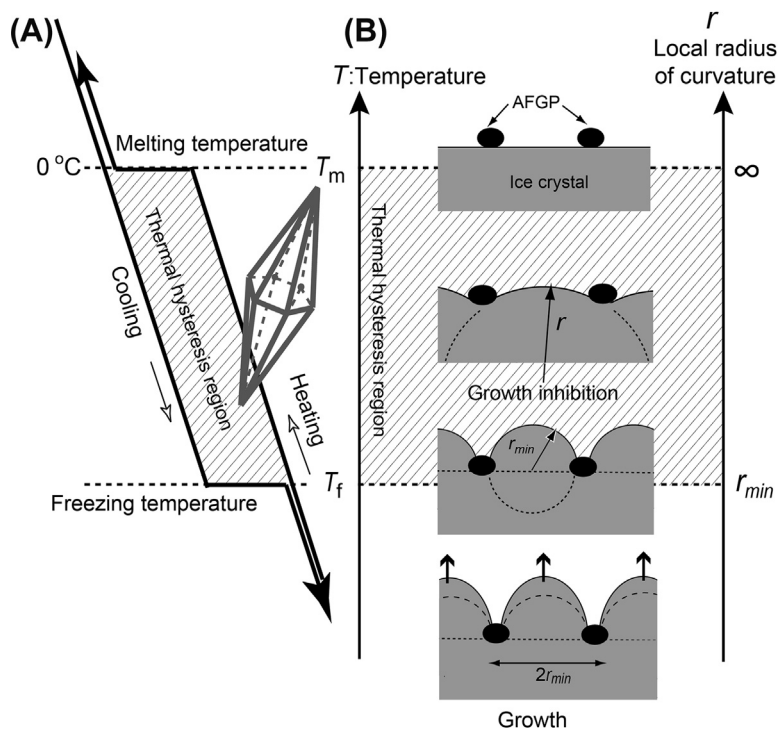


**FIGURE 25.23** Schematic illustration of thermal hysteresis and Gibbs–Thomson model for ice growth inhibition. (A) In the cooling process of antifreeze glycoprotein (AFGP) solution, ice crystals existing in the supercooled solution do not grow unless and until the solution temperature reaches the critical freezing temperature ( $T_f$ ). Melting of ice crystals during the heating process, however, can occur at the bulk melting point ( $T_m$ ). The thermal difference between  $T_f$  and  $T_m$  is the so-called *thermal hysteresis region*. Ice crystals inside this region have hexagonal bipyramidal shapes. (B) Fundamental conception of the growth inhibition mechanism (Gibbs–Thomson model). Local melting point depression is induced by local curvatures between the pinning points of adsorbed AFGP molecules, and the interface temperature equilibrates with the circumjacent supercooling temperature.

hysteresis temperature range take on hexagonal bipyramidal shapes surrounded by  $\{10\bar{1}1\}$  faces with length of a few tens of microns at most, and their growth completely stops (Figure 25.23(A));

3. The recrystallization inhibition function has emerged as perhaps the most important function due to its applicability in frozen foods [143]. It is well known that, at concentrations as low as a few  $\mu\text{g}/\text{ml}$ , AFGPs significantly reduce the recrystallization process of polycrystalline ice samples.

These special features of AF(G)Ps strongly suggest that these proteins function via some interaction with the ice–water interface, namely in a nonequilibrium way. Figure 25.23(B) shows illustrative images for pinning models based on the adsorption of AF(G)P molecules on the ice–water interfaces, first proposed by DeVries and Wohlschlag [144]. The adsorbed molecules can work as pinning points for further growth of the

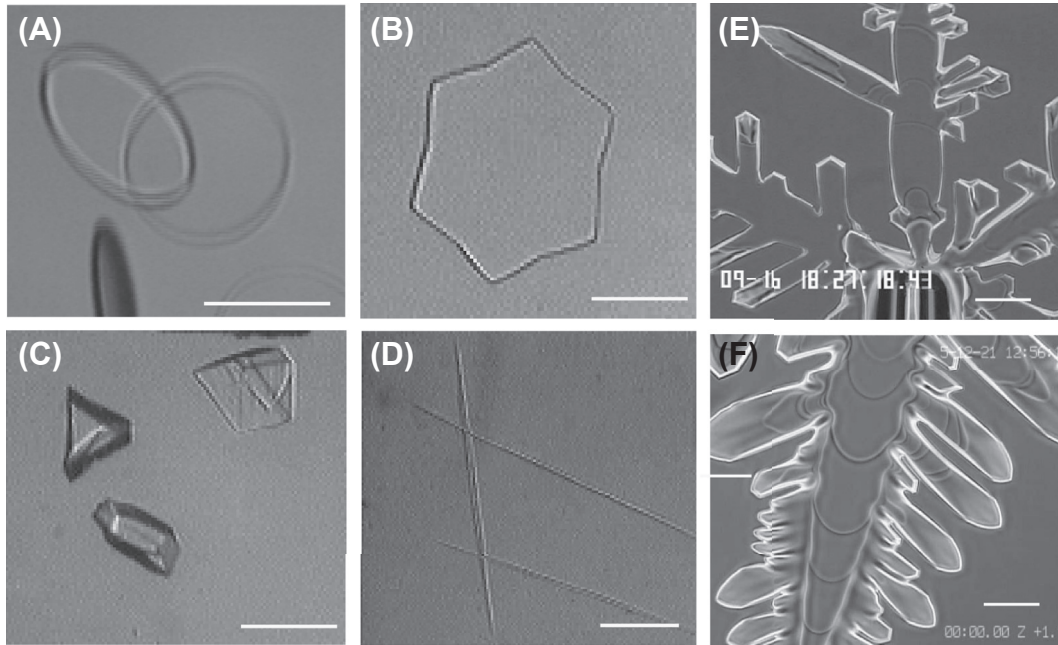


**FIGURE 25.24** Pictures of ice crystals growing in AFGP solutions with different concentrations: (A) in pure water (circular disk), (B) 10  $\mu\text{g/ml}$  (hexagonal plate), (C) 200  $\mu\text{g/ml}$  (polygonal column), (D) 5  $\text{mg/ml}$  (needle), (E) faceted dendrite of ice crystal, and (F) bunched growth steps observed on  $\{0001\}$  interfaces. Scale bars indicate 500  $\mu\text{m}$ , respectively.

crystal interface, and the interfaces between the neighboring adsorbed molecules should be forced to bulge into the supercooled water, resulting in curvature formation. Because the melting point of the curved interface changes by the amount estimated by the Gibbs–Thomson equation,

$$\Delta T = \frac{2\Omega\gamma T_m}{r\Delta H_0}, \quad (25.14)$$

the melting temperature of the curved interface equals the supercooling temperature of water in the hysteresis region. Here,  $\Omega$  is the molar volume of ice,  $\gamma$  is the interface free energy,  $\Delta H_0$  is the latent heat of fusion, and  $r$  is the radius of local curvature at the interface. Because the curvature radius of protrusions reaches half of the distance between neighboring adsorbed molecules at the lower limit,  $T_f$  of the hysteresis region, the adsorbed molecules are incorporated into the ice crystal and overgrowth of the interface is promoted.

This growth inhibition kinetics has been accepted so far by many researchers since the first idea proposed by DeVries and Wohlschlag [144]. Direct experimental evidence for the adsorption–inhibition relationship, however, has not been provided, and the exact inhibition mechanism by AF(G)P molecules therefore remains unknown. Consequently, results of recent research on the growth behavior of ice crystals and the

adsorption behavior of AF(G)P molecules themselves will be summarized in the following subsections.

## 25.7.2 Ice Crystal Growth and AFGP Adsorption on the Ice Interface

### 25.7.2.1 Growth Behavior of Ice Crystals and AFGP Distribution

To obtain direct evidence for the interaction between adsorption of proteins and ice growth inhibition, Zepeda et al. [158,159] conducted experiments on free growth of single ice crystals in supercooled water containing 5  $\mu\text{g}/\text{ml}$  of AFGP labeled by fluorescent protein molecules (fluorescein isothiocyanate). In their experiments, the supercooling temperature of the solution was kept at less than 0.05 K (i.e., just around the freezing temperature), presumably due to small temperature variations formed by heat released during growth.

Figure 25.25(A) shows a snapshot of an ice crystal growing at the tip of the glass capillary observed by a laser confocal fluorescent microscope. The ice crystal has a thin hexagonal shape surrounded by basal and prismatic faces. The contrast of this image reflects in the intensity of fluorescence emission, and the most striking feature is that the prismatic interfaces marked by 1, 3, and 4 are bordered by bright rims along the interfaces and their growth is completely inhibited, but no bright rim is seen along interface 2, which continuously grows. This observation directly confirms inhibition of

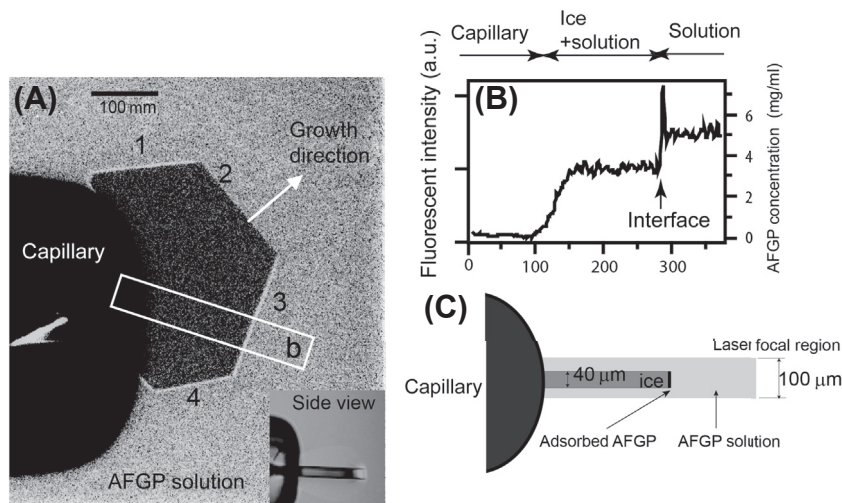


**FIGURE 25.25** Redistribuition of FITC-labeled antifreeze glycoprotein (AFGP) molecules during the growth of an ice crystal. (A) A snapshot of an ice crystal in the form of a hexagonal plate growing in AFGP solution at a concentration of 5  $\mu\text{g}/\text{ml}$  with supersaturation of 0.05 K, which was observed by a confocal and fluorescent microscope system. The small picture shows an ice disk grown in pure water. (B) AFGP concentration distribution along the longer direction of rectangular region *b* indicated in (A). (C) Schematic illustration for side view of an ice crystal. Thickness of laser focal region for confocal optical system was about 100  $\mu\text{m}$ , and the thickness of ice crystal was 40  $\mu\text{m}$ . Consequently, the fluorescent intensity at an “ice + solution” region was about 60% of that at a solution region. Modified from Ref. [159].

ice crystal growth caused by the interfacial adsorption of AF(G)P molecules. Figure 25.25(B) shows the distribution of average concentrations along the rectangle indicated as “b” in Figure 25.25(A), which was calculated from the fluorescent intensity variation. The local peak at the interface comes from the adsorbed molecules on the prismatic faces perpendicular to the basal plane. Because the fluorescent intensity observed inside the ice crystal corresponds to the number of AFGP molecules existing in the solution included in the focal depth (Figure 25.25(C)), we can conclude that AFGP molecules are never incorporated into the matrix of the ice crystal. Actually, the bright rim along the prismatic interface as shown in Figure 25.25(A) can easily fade away by some cause, and then its interface immediately starts to grow again. Namely, AFGP molecules adsorbed on the prismatic faces can easily break away from the interfaces and diffuse back into the solution.

#### 25.7.2.2 Adsorption of AFGP Molecules on the Ice–Water Interface

From detailed analysis of the fluorescence intensity profile as shown in Figure 25.25(B), the adsorption density of AFGP molecules on the prismatic interfaces could be obtained. In this particular case, the distance between the nearest neighboring molecules was estimated to be about  $21 \pm 4$  nm [159]. Because the average diameter of AFGP molecules was about 3 nm, the spacing between the neighboring AFGP molecules,  $d$ , was deduced to be about 17 nm. The Gibbs–Thomson model predicted a freezing temperature lowering of 6 °C for this open interface. This value is much lower than the solution temperature (−0.05 °C) configured as an experimental condition. This contradiction indicates that the simple static model based on the Gibbs–Thomson effect, which was introduced in the previous subsection, can no longer be used as a model to explain the antifreeze effect of AFGPs.

Meanwhile, let us consider the situation of AFGP molecules adsorbing on ice–water interfaces. The secondary structure of an AFGP molecule has been shown to be a highly flexible extended helix by precise analysis using various methods, including nuclear magnetic resonance [160], Raman [161], X-ray scattering [162] and infrared [163] spectroscopic techniques. Even though it is, in contrast, quite difficult to analyze those in the adsorbed state on the ice–water interface, Uda et al. [62] successfully analyzed the secondary structures of AFGP molecules in the adsorbed state on the ice–water interface using the method of attenuated total reflection (ATR)-Fourier transform infrared spectroscopy (FTIR) spectroscopy. As measurement samples, thin films of D<sub>2</sub>O containing AFGPs were deposited on the surface of an ATR prism and then cooled down at a constant rate. During the course of cooling, the phase change of the film from a liquid state to a supercooled state and finally to a frozen state was monitored by using the FTIR spectrum from the O–D stretching band of D<sub>2</sub>O molecules. Some liquid-state water was still observed in the frozen film below the melting point. This liquid came from the QLL formed at the grain boundaries and the interfaces between the ice crystal and the ATR prismatic surface [61], and its thickness was estimated to be 15 nm at −1 °C and it decreased with decreases in temperature. Because AFGP molecules are never

incorporated into the ice crystal lattices as shown in the previous subsection, all of the molecules included in the original liquid film should be concentrated in the QLL in the grain boundaries. In this context, the amide I band spectrum coming from AFGP molecules, which was not overlapped with any band coming from D<sub>2</sub>O molecules, was analyzed to determine the secondary structures of the molecules. As a result, a dominant increase in the  $\alpha$ -helical content of AFGP molecules was clearly detected when the film changed from the supercooled state to frozen state. The difference between  $\alpha$ -helix contents in the two states indicates that a fraction of AFGP molecules upon adsorption at the ice–water interface underwent a conformational change from the flexible extended helix to the  $\alpha$ -helix, emphasizing the importance of the structure–function relationship, even for highly flexible AFGP molecules.

#### 25.7.2.3 *Two-Step Adsorption of AFGPs and Inhibition of the Growth of Prismatic Interfaces*

Experimental results described in the previous section suggest that AFGP molecules excessively adsorb on the interface compared to the amount predicted by the classical Gibbs–Thomson model, but only a fraction of those molecules have an  $\alpha$ -helix secondary structure. Even though AFGP molecules with the original extended helix structure can be absorbed on the ice interface, their adsorption force should be weaker than that of AFGP molecules with an  $\alpha$ -helix structure, because the former do not have periodicity sufficient to fit in the ice crystal lattices, whereas the latter may fit in the crystal lattices. Actually, Nada and Furukawa [164,165] confirmed by MD simulation that  $\alpha$ -helix molecules such as AFP type I molecules can strongly adsorb if they sit only in the appropriate direction to the ice crystal lattice. We conclude that the adsorption of AFGP molecules occurs in a phased step from “weak adsorption” to “strong adsorption,” depending on the change in secondary structures. The weakly adsorbed AFGP molecules do not work as pinning points for advance of the interface and can be easily desorbed from the interface, which means reversible adsorption of AFGP molecules on the ice interfaces. The strongly adsorbed AFGP molecules, on the other hand, will be able to work as pinning points. Figure 25.26 shows the adsorption states of AFGP molecules at the ice–water interface. Only the strongly adsorbed AFGP molecules contribute to the inhibition of ice interface growth, and the others are adsorbed in the reversible manner. This behavior of AFGP molecules on prismatic interfaces is called two-step reversible adsorption, which is a crucial model to understand the adsorption-inhibition mechanism of AFGP molecules for ice prismatic interfaces.

#### 25.7.2.4 *Directional Growth of Ice Crystal from AFGP Solution*

Pattern formation at an ice–water interface during one-directional growth from a solution of AF(G)Ps is also an interesting subject in relation to anisotropy of the kinetic effect for ice growth. An experiment similar to these described in the previous section was carried out using a growth cell with inside dimensions of  $76 \times 16 \times 0.06 \text{ mm}^3$  [166]. The AFGP concentration of the solution used in that experiment was 0.2 mg/ml (i.e., 0.02 wt%).

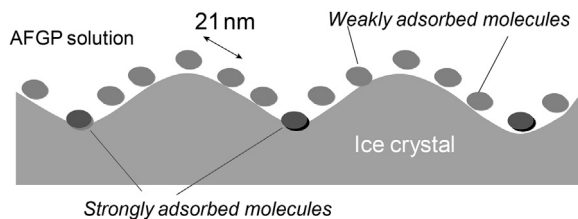


**FIGURE 25.26** A new model for inhibition of the growth of a prismatic face based on the concept of two-step reversible adsorption. Some of the antifreeze glycoprotein (AFGP) molecules on the prismatic interface adsorb strongly and can work as pinning points for advancement of the interface. The majority of AFGP molecules on the interface adsorb weakly and cannot work as pinning points. These weakly adsorbed molecules can be easily desorbed from the interface.

An ice crystal growing from the AFGP solution in the temperature gradient of  $G = 1.1 \text{ K/mm}$  was observed in the velocity range from  $V = 3\text{--}11 \text{ }\mu\text{m/s}$ . Only one single crystal was grown in the growth cell, and the 0001-axis orientation of the ice crystal was fixed in the direction perpendicular to the glass wall. **Figure 25.27** shows sequential pictures of pattern development at the ice–water interface for  $V = 5 \text{ }\mu\text{m/s}$ . The process of pattern development and the interfacial patterns in the steady state are both very different from those observed during one-directional growth from a salt solution system. The difference from the cellular patterns observed in KCl solution is the formation of regularized

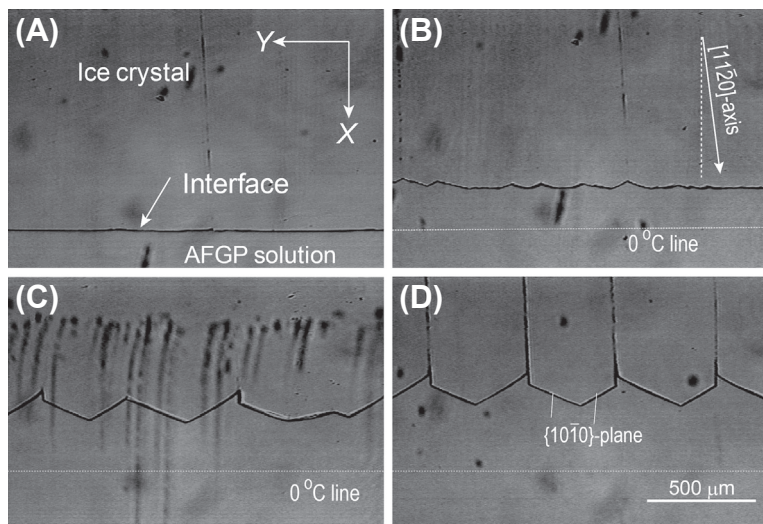


**FIGURE 25.27** Sequential pictures of pattern development at the interface between ice and antifreeze glycoprotein (AFGP) solution during one-directional growth in a thin growth cell [166]. The initial concentration of AFGP was  $200 \text{ }\mu\text{g/ml}$ , the growth velocity was  $5 \text{ }\mu\text{m/s}$  and the tilting angle of the  $11\bar{2}0$ -axis  $\psi$  was  $3^\circ$ . Positions shown by broken arrows indicate the lines of  $0^\circ\text{C}$ . The dotted lines indicate the position of interface before the start of growth, namely the position of interface in (A). Elapsed times after the start of growth are (A) 0 s, (B) 41 s, (C) 62 s, (D) 363 s, (E) 650 s, and (F) 1798 s.

patterns bounded by faceted interfaces. Because the kinetics at the growing interface have a profound effect on crystal growth in the case of ice crystal growth in an AFGP solution, the actual position of the interface may be pushed down on the line of  $T_f$  which is the freezing temperature defined in Figure 25.23.

Figure 25.28 shows pictures of interfacial patterns at  $\psi = 3^\circ$ ,  $8^\circ$  and  $28^\circ$  that were observed under a quasi-steady condition. The repetition intervals of zigzag patterns become larger with increasing  $\psi$  and finally disappear when  $\psi$  reaches  $30^\circ$ , at which point the flat interface coincides with the prismatic plane. The absolute positions of  $0^\circ\text{C}$  in the temperature gradient are indicated by the dotted lines in each picture. It should be noted that the line of  $0^\circ\text{C}$  does not coincide with the position of the flat interface at

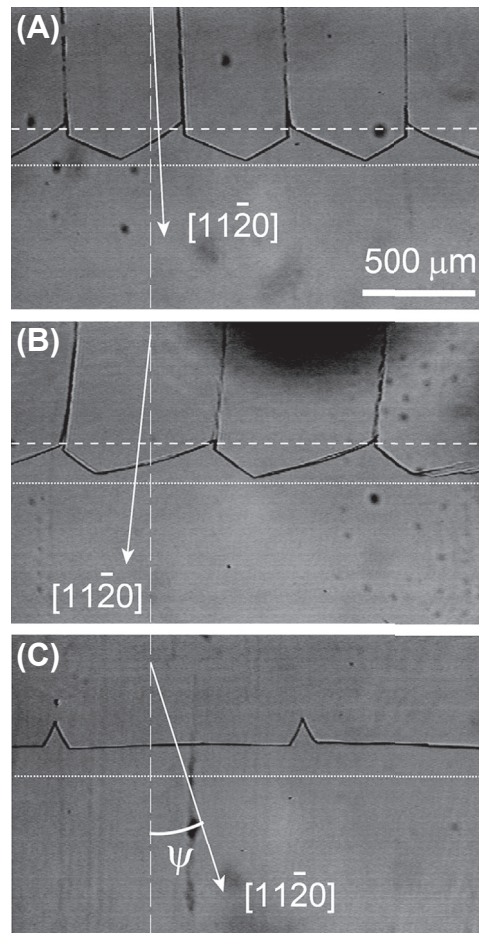


**FIGURE 25.28** Regularly arrayed zigzag patterns that are kept stationary during growth at  $V = 5 \mu\text{m/s}$  [166]. The tilting angles,  $\psi$ , were (A)  $3^\circ$ , (B)  $8^\circ$ , and (C)  $28^\circ$ . The dotted and broken lines indicate the positions of  $0^\circ\text{C}$  lines and bottom lines of zigzag patterns, respectively.

$\psi = 28^\circ$  (Figure 25.28(C)). Namely, the interfacial temperature should be equal to  $T_f$ . In this case,  $T_f = -0.2^\circ\text{C}$ . Compared with this, the lines connecting the tips and bottoms of the zigzag patterns observed at  $\psi = 3^\circ$  and  $8^\circ$  coincided with the lines of  $T_m$  and  $T_f$  respectively, as shown in Figures 25.28(A) and (B). Interestingly, this result indicates that the thermal hysteresis region  $\Delta T$  can be determined from analysis of the zigzag interface pattern.

## 25.8 Summary

In this chapter, selected topics of the scientific states of knowledge concerning crystal growth of ice from water vapor (snow crystal) and from supercooled water (ice crystal) were reviewed. Ice crystals show very interesting phenomena as diverse as morphological instability, pattern formation, morphology change, surface melting, twinning, impurity effect, and growth control by biological macromolecules. As discussed in this chapter, unique and advanced results have been obtained from theoretical, experimental, and computational studies and have attracted the attention of many researchers working in other research fields. Furthermore, because an ice crystal usually grows under a temperature condition close to the equilibrium melting point, it may be regarded as a useful test material for the melt growth of metals or semiconductors. On the other hand, ice crystals are one of the most ubiquitous materials found in the surface area of the terrestrial cryosphere. Their crystal growth phenomena commonly occur in diverse ways and play crucial roles in climate change, weather phenomena (e.g., snowing, raining, lightning), and artificially induced environmental concerns (e.g., ozone hole formation). Consequently, research on ice crystal growth constitutes the bedrock of these global problems that are crying out for solutions.

Finally, let us again place emphasis on the importance of the bilateral character of an ice crystal—that is, generality and particularity. As we already know, the former is the characteristic as one of the materials and the latter is the characteristic as the dominant material on terrestrial surfaces. This issue indicates the direction that crystal growth research should take in the near future.

## Acknowledgments

The author is indebted to Professor Etsuro Yokoyama, Gakushuin University, Tokyo, Japan and Professor Emeritus Robert F. Sekerka, Carnegie Mellon University, Pittsburgh, USA for continuous discussions about morphological instability and pattern formation of snow and ice crystals and to Professor Gen Sasaki, Hokkaido University, Sapporo, Japan for discussions about ice surface structures in the molecular scale. My heartfelt thanks go to Dr Hiroki Nada, AIST, Tsukuba, Japan for his continuous efforts in MD simulation studies related to ice surfaces and interfaces and also to my colleagues, Dr Salvador Zepeda and Dr Yukihiro Uda, for conducting experiments on antifreeze proteins. Finally, the author gives special thanks to Mr Shunichi Nakatsubo, Hokkaido University, Sapporo, Japan for his continuous technical support in research.

## References

- [1] Wettlaufer JS, Dash JG, Untersteiner N. Ice physics and the natural environment, NATO ASI series. Berlin; Tokyo: Springer; 1999.
- [2] Thorsten B-R. Nature 2013;494:27–9.
- [3] Bartels-Rausch T, Bergeron V, Cartwright JHE, Escibano R, Finney JL, Grothe H, et al. Rev Mod Phys 2012;84:885–944.
- [4] Furukawa Y, Wettlaufer JS. Phys Today 2007;60:70–1.
- [5] Kepler J. A new year's gift or on the six-cornered snowflake. In: Hardie C, editor. *Strena seu de nive sexangula*, Godfrey Tampach at Frankfort on Main. Oxford Press; 1611. p. 24.
- [6] Kobayashi T, Kuroda T. Snow crystals. In: Sunagawa I, editor. *Morphology of crystals*. Tokyo: Tera Sci. Pub. Co. & D. Reidel Pub. Co; 1987. p. 645–743.
- [7] Bentley WA, Humphreys WJ. Snow crystals. Dover: McGraw Hill; 1931.
- [8] Nakaya U. Snow crystals, natural and artificial. Cambridge: Harvard University Press; 1954.
- [9] Nakaya U. Q J Roy Meteor Soc 1938;64:619–24.
- [10] Arakawa K, Higuchi K. J Fac Sci Hokkaido Univ Ser II 1952;4:201–9.
- [11] Arakawa K. J Glaciol 1955;2:463–4.
- [12] Mullins WW, Sekerka RF. J Appl Phys 1964;35:444–51.
- [13] Eisenberg DS, Kauzman W. The structure and properties of water. London: Oxford at the Clarendon Press; 1969.
- [14] Fletcher NH. The chemical physics of ice. London: Cambridge University Press; 1970.
- [15] Hobbs PV. Ice physics. Oxford: Clarendon Press; 1974.
- [16] Petrenko VF, Whitworth RW. Physics of ice. Oxford: Oxford University Press; 1999.
- [17] Ubbelohde AR. The molten state of matter: melting and crystal structure. Chichester; New York: Wiley; 1978.
- [18] Furukawa Y, Sazaki G, Nada H. Surface of ice. In: Wandelt K, editor. *Surface and interface science*. Wiley; 2013. p. 305–48.
- [19] Bernal JD, Fowler RH. J Chem Phys 1933;1:515–48.
- [20] Pauling L, Brockway LO. J Am Chem Soc 1935;57:2684–92.
- [21] Hirth JP, Lothe J. Theory of dislocations. New York: Wiley; 1982.
- [22] Higashi A. Lattice defects in ice crystals. Sapporo: Hokkaido University Press; 1988.
- [23] Faraday M. Lecture given at Royal Institution, London; 1850.
- [24] Dash JG. Contemp Phys 1989;30:89–100.
- [25] Churaev NV, Bardasov SA, Sobolev VD. Colloid Surf A 1993;79:11–24.
- [26] Saruya T, Kurita K, Rempel AW. Phys Rev E 2013;87:032404.
- [27] Style RW, Peppin SSL, Cocks ACF, Wettlaufer JS. Phys Rev E 2011;84:041402.
- [28] Wilen LA, Dash JG. Phys Rev Lett 1995;74:5076–9.
- [29] Dash JG, Fu H, Wettlaufer JS. Rep Prog Phys 1995;58:115–68.
- [30] Mason BL, Dash JG. J Geophys Res Atmos 2000;105:10185–92.
- [31] Ogawa N, Furukawa Y. Phys Rev E 2002;66:041202.
- [32] McNeill VF, Loerting T, Geiger FM, Trout BL, Molina MJ. Proc Natl Acad Sci USA 2006;103:9422–7.

- [33] Kuroda T, Lacmann R. *J Cryst Growth* 1982;56:189–205.
- [34] Furukawa Y, Yamamoto M, Kuroda T. *J Cryst Growth* 1987;82:665–77.
- [35] Van der Veen JF, Pluis B, Denier van der Gon AW. Surface melting. In: Vanselow R, Howe RF, editors. *Chemistry and physics of solid surfaces VII*. Berlin: Springer-Verlag; 1988. p. 455–90.
- [36] Dietrich S. Wetting phenomena. In: Domb C, Lebowitz JL, editors. *Phase transitions and critical phenomena*. London; New York: Academic Press; 1988. p. 1–218.
- [37] Woodruff DP. *The solid–liquid interface*. London: Cambridge University Press; 1973.
- [38] Burton WK, Cabrera N, Frank FC. *Philos Trans R Soc Lond Ser A* 1951;243:299–358.
- [39] Chernov A. Crystallization processes. In: *Modern crystallography*. Berlin: Springer-Verlag; 1980. p. 7–232.
- [40] Dash JG. *Rev Mod Phys* 1999;71:1737–43.
- [41] Dash JG, Rempel AW, Wettlaufer JS. *Rev Mod Phys* 2006;78:695–741.
- [42] Wettlaufer JS. *Philos Trans R Soc Lond Ser A* 1999;357:3403–25.
- [43] Li Y, Somorjai GA. *J Phys Chem C* 2007;111:9631–7.
- [44] Beaglehole D, Nason D. *Surf Sci* 1980;96:357–63.
- [45] Elbaum M, Lipson SG, Dash JG. *J Cryst Growth* 1993;129:491–505.
- [46] Golecki I, Jaccard C. *J Phys C Solid State* 1978;11:4229–38.
- [47] Dosch H, Lied A, Bilgram JH. *Surf Sci* 1995;327:145–64.
- [48] Dosch H, Lied A, Bilgram JH. *Surf Sci* 1996;366:43–50.
- [49] Bluhm H, Salmeron M. *J Chem Phys* 1999;111:6947–54.
- [50] Döppenschmidt A, Butt H-J. *Langmuir* 2000;16:6709–14.
- [51] Wei X, Miranda PB, Shen YR. *Phys Rev Lett* 2001;86:1554–7.
- [52] Wei X, Miranda PB, Zhang C, Shen YR. *Phys Rev B* 2002;66:085401.
- [53] Bluhm H, Ogletree DF, Fadley CS, Hussain Z, Salmeron M. *J Phys Condens Matter* 2002;14:L227–33.
- [54] Furukawa Y, Ishikawa I. *J Cryst Growth* 1993;128:1137–42.
- [55] Kvlividz VI, Kiselev VF, Kurzaev AB, Ushakova LA. *Surf Sci* 1974;44:60–8.
- [56] Mizuno Y, Hanafusa N. *J Phys Colloq* 1987;48-C1:511–7.
- [57] Ishizaki T, Maruyama M, Furukawa Y, Dash JG. *J Cryst Growth* 1996;163:455–60.
- [58] Ocampo J, Klinger J. *J Phys Chem* 1983;87:4167–70.
- [59] Kouchi A, Furukawa Y, Kuroda T. *J Phys Colloq* 1987;48-C1:675–7.
- [60] Maruyama M, Satoi T, Taniguchi S, Kawamura M, Kodera S, Kishimoto Y, et al. *Jpn J Appl Phys* 2000;39(Part 1):6696–9.
- [61] Sadtchenko V, Ewing GE. *J Chem Phys* 2002;116:4686–97.
- [62] Uda Y, Zepeda S, Kaneko F, Matsuura Y, Furukawa Y. *J Phys Chem B* 2007;111:14355–61.
- [63] Sazaki G, Asakawa H, Nagashima K, Nakatsubo S, Furukawa Y. *Cryst Growth Des* 2013;13:1761–6.
- [64] Furukawa Y, Kohata S. *J Cryst Growth* 1993;129:571–81.
- [65] Knight CA, Knight NC. *Science* 1965;150:1819–21.
- [66] Elbaum M, Schick M. *Phys Rev Lett* 1991;66:1713–6.
- [67] Elbaum M, Wettlaufer JS. *Phys Rev E* 1993;48:3180–3.

- [68] Sazaki G, Zepeda S, Nakatsubo S, Yokomine M, Furukawa Y. Proc Natl Acad Sci USA 2012;109:1052–5.
- [69] Sazaki G, Zepeda S, Nakatsubo S, Yokoyama E, Furukawa Y. Proc Natl Acad Sci USA 2010;107:19702–7.
- [70] Weber TA, Stillinger FH. J Phys Chem 1983;87:4277–81.
- [71] Kroes G-J. Surf Sci 1992;275:365–82.
- [72] Furukawa Y, Nada H. J Phys Chem B 1997;101:6167–70.
- [73] Nada H, Furukawa Y. Appl Surf Sci 1997;121–122:445–7.
- [74] Nada H, Furukawa Y. Surf Sci 2000;446:1–16.
- [75] Nada H, van der Eerden JPJM. J Chem Phys 2003;118:7401–13.
- [76] Abascal JL, Sanz E, Garcia Fernandez R, Vega C. J Chem Phys 2005;122:234511.
- [77] Hallett J, Mason BJ. Proc R Soc Lond Ser A 1958;247:440–53.
- [78] Kobayashi T. J Met Soc Jpn 1957;75:7.
- [79] Kobayashi T. Philos Mag 1961;6:1363–70.
- [80] Chernov AA. J Cryst Growth 1974;24:11–31.
- [81] McKnight C, Hallett J. J Glaci 1978;21:397–407.
- [82] Givargizov EI. J Cryst Growth 1975;31:20–30.
- [83] Yokoyama E, Kuroda T. Phys Rev A 1990;41:2038–49.
- [84] Kuroda T, Irisawa T, Ookawa A. J Cryst Growth 1977;42:41–6.
- [85] Locatelli JD, Hobbs PV. J Geophys. Res 1974;79:2185–97.
- [86] Keller VW, Hallett J. J Cryst Growth 1982;60:91–106.
- [87] Frank FC. J Cryst Growth 1974;24–25:3–5.
- [88] Furukawa Y. J Met Soc Jpn 1982;60:535–47.
- [89] Furukawa Y, Kobayashi T. J Cryst Growth 1978;45:57–65.
- [90] Kobayashi T, Furukawa Y. J Cryst Growth 1975;28:21–8.
- [91] Kobayashi T, Furukawa Y. J Cryst Growth 1978;45:48–56.
- [92] Kobayashi T, Furukawa Y, Kikuchi K, Uyeda H. J Cryst Growth 1976;32:233–49.
- [93] Kobayashi T, Furukawa Y, Takahashi T, Uyeda H. J Cryst Growth 1976;35:262–8.
- [94] Hansen TC, Koza MM, Lindner P, Kuhs WF. J Phys Condens Matter 2008;20:285105.
- [95] Kuhs WF, Sippel C, Falenty A, Hansen TC. Proc Natl Acad Sci USA 2012;109:21259–64.
- [96] Shallcross FV, Carpenter GB. J Chem Phys 1957;26:782–3.
- [97] Ostwald W. Z. Phys Chem 1897;22:42.
- [98] Takahashi T. J Cryst Growth 1982;59:441–9.
- [99] Takahashi T, Kobayashi T. J Cryst Growth 1983;64:593–603.
- [100] Johari GP. J Chem Phys 2005;122:194504.
- [101] Murray BJ, Bertram AK. PCCP 2006;8:186–92.
- [102] Whalley E. J Phys Chem 1983;87:4174–9.
- [103] Mayer E, Hallbrucker A. Nature 1987;325:601–2.
- [104] Malkin TL, Murray BJ, Brukhno AV, Anwar J, Salzmann CG. Proc Natl Acad Sci USA 2012;109:1041–5.

- [105] Kitano M, Hamabe T, Maeda S, Okabe T. *J Cryst Growth* 1991;108:277–84.
- [106] Shiojiri M, Kaito C. *J Cryst Growth* 1981;52(Part 1):173–7.
- [107] Yoshioka T, Kawasaki M, Kitano M, Nishio K, Shiojiri M. *J Electron Microsc* 1995;44:488–92.
- [108] Kaito C, Fujita K, Shiojiri M. *J Cryst Growth* 1982;57:199–202.
- [109] Niekawa N, Kitamura M. *Cryst Eng Comm* 2013;15:6932–41.
- [110] Maruyama M. *J Cryst Growth* 2005;275:598–605.
- [111] Maruyama M, Kishimoto Y, Sawada T. *J Cryst Growth* 1997;172:521–7.
- [112] Cahoon A, Maruyama M, Wettlaufer JS. *Phys Rev Lett* 2006;96:255502.
- [113] Furukawa Y, Shimada W. *J Cryst Growth* 1993;128:234–9.
- [114] Langer JS, Sekerka RF, Fujioka T. *J Cryst Growth* 1978;44:414–8.
- [115] Shimada W, Furukawa Y. *J Phys Chem B* 1997;101:6171–3.
- [116] Langer JS, Müller-Krumbhaar H. *Acta Metall* 1978;26:1681–7.
- [117] Langer JS, Müller-Krumbhaar H. *Acta Metall* 1978;26:1689–95.
- [118] Müller-Krumbhaar H, Langer JS. *Acta Metall* 1978;26:1697–708.
- [119] Xu J-J. *J Cryst Growth* 1990;100:481–90.
- [120] Fujioka T, Sekerka RF. *J Cryst Growth* 1974;24–25:84–93.
- [121] Yokoyama E, Sekerka RF, Furukawa Y. *J Phys Chem B* 1999;104:65–7.
- [122] Yokoyama E, Sekerka RF, Furukawa Y. *J Phys Chem B* 2009;113:4733–8.
- [123] Sekerka RF. *J Cryst Growth* 1993;128:1–12.
- [124] Adachi S, Yoshizaki I, Ishikawa T, Yokoyama E, Furukawa Y, Shimaoka T. *Phys Rev E* 2011;84:051605.
- [125] Yokoyama E, Yoshizaki I, Shimaoka T, Sone T, Kiyota T, Furukawa Y. *J Phys Chem B* 2011;115:8739–45.
- [126] Yoshizaki I, Ishikawa T, Adachi S, Yokoyama E, Furukawa Y. *Microgravity Sci Technol* 2012;24:245–53.
- [127] Koss M, LaCombe J, Tennenhouse L, Glicksman M, Winsa E. *Metall Mater Trans A* 1999;30:3177–90.
- [128] Jorgensen WL, Chandrasekhar J, Madura JD, Impey RW, Klein ML. *J Chem Phys* 1983;79:926–35.
- [129] Karim OA, Haymet ADJ. *J Chem Phys* 1988;89:6889–96.
- [130] Nada H, Furukawa Y. *Jpn J Appl Phys* 1995;34:583–8.
- [131] Nada H, Furukawa Y. *J Cryst Growth* 1996;169:587–97.
- [132] Nada H, Furukawa Y. *J Phys Chem B* 1997;101:6163–6.
- [133] Nada H, Furukawa Y. *J Cryst Growth* 2005;283:242–56.
- [134] Nada H, van der Eerden JP, Furukawa Y. *J Cryst Growth* 2004;266:297–302.
- [135] Carignano MA, Shepson PB, Szleifer I. *Mol Phys* 2005;103:2957–67.
- [136] Nada H. *Cryst Growth Des* 2011;11:3130–6.
- [137] Billia B, Trivedi R. Pattern formation in crystal growth. In: Hurlé DTJ, editor. *Handbook of crystal growth*, vol. 1. Amsterdam: North-Holland; 1993. p. 899–1074.
- [138] Nagashima K, Furukawa Y. *J Cryst Growth* 1997;171:577–85.
- [139] Nagashima K, Furukawa Y. *J Phys Chem B* 1997;101:6174–6.

- [140] Nagashima K, Furukawa Y. *J Cryst Growth* 2000;209:167–74.
- [141] Glicksman ME, Marsh SP. The dendrites. In: Hurlle DTJ, editor. *Handbook of crystal growth*, vol. 1. Amsterdam; Tokyo: North-Holland; 1993. p. 1075–122.
- [142] Coriell SR, Sekerka RF. *J Cryst Growth* 1976;34:157–63.
- [143] Yeh Y, Feeney RE. *Chem Rev* 1996;96:601–18.
- [144] DeVries AL, Wohlschlag DE. *Science* 1969;163:1073–5.
- [145] DeVries AL, Komatsu SK, Feeney RE. *J Biol Chem* 1970;245:2901–8.
- [146] Graether SP, Kuiper MJ, Gagne SM, Walker VK, Jia Z, Sykes BD, et al. *Nature* 2000;406:325–8.
- [147] Liou Y-C, Tocilj A, Davies PL, Jia Z. *Nature* 2000;406:322–4.
- [148] Griffith M, Yaish MWF. *Trends Plant Sci* 2004;9:399–405.
- [149] Jia Z, DeLuca CI, Chao H, Davies PL. *Nature* 1996;384:285–8.
- [150] Wang J-H. *Cryobiology* 2000;41:1–9.
- [151] Inglis SR, Turner JJ, Harding MM. *Curr Prot Pept Sci* 2006;7:509–22.
- [152] Matsumoto S, Matsusita M, Morita T, Kamachi H, Tsukiyama S, Furukawa Y, et al. *Cryobiology* 2006;52:90–8.
- [153] Knight CA. *Nature* 2000;406:249–51.
- [154] Bar M, Celik Y, Fass D, Braslavsky I. *Cryst Growth Des* 2008;8:2954–63.
- [155] Pertaya N, Marshall CB, Celik Y, Davies PL, Braslavsky I. *Biophys J* 2008;95:333–41.
- [156] Harrison K, Hallett J, Burcham TS, Feeney RE, Kerr WL, Yeh Y. *Nature* 1987;328:241–3.
- [157] Knight CA, DeVries AL. *PCCP* 2009;11:5749–61.
- [158] Zepeda S, Nakatsubo S, Furukawa Y. *Rev Sci Instrum* 2009;80:115102.
- [159] Zepeda S, Yokoyama E, Uda Y, Katagiri C, Furukawa Y. *Cryst Growth Des* 2008;8:3666–72.
- [160] Homans SW, DeVries AL, Parker SB. *FEBS Lett* 1985;183:133–7.
- [161] Drewes JA, Rowlen KL. *Biophys J* 1993;65:985–91.
- [162] Davies PL, Hew CL. *FASEB J* 1990;4:2460–8.
- [163] Tsvetkova NM, Phillips BL, Krishnan VV, Feeney RE, Fink WH, Crowe JH, et al. *Biophys J* 2002;82:464–73.
- [164] Nada H, Furukawa Y. *J Phys Chem B* 2008;112:7111–9.
- [165] Nada H, Furukawa Y. *PCCP* 2011;13:19936–42.
- [166] Furukawa Y, Inohara N, Yokoyama E. *J Cryst Growth* 2005;275:167–74.

# Crystal Growth of Quasicrystals

An-Pang Tsai<sup>1,2</sup>, Can Cui<sup>3</sup>

<sup>1</sup>INSTITUTE OF MULTIDISCIPLINARY RESEARCH FOR ADVANCED MATERIALS, TOHOKU UNIVERSITY, SENDAI, JAPAN; <sup>2</sup>NATIONAL INSTITUTE FOR MATERIALS SCIENCE, TSUKUBA, JAPAN; <sup>3</sup>DEPARTMENT OF PHYSICS, CENTER FOR OPTOELECTRONIC MATERIALS AND DEVICES, ZHEJIANG SCI-TECH UNIVERSITY, HANGZHOU, CHINA

## CHAPTER OUTLINE

<b>26.1 Introduction to Quasicrystals .....</b>	<b>1114</b>
26.1.1 Crystal and Periodicity .....	1115
26.1.2 Restriction on Symmetry by Translation .....	1116
26.1.3 Discovery of QCs .....	1117
<b>26.2 Structures of QCs .....</b>	<b>1118</b>
26.2.1 One-dimensional Quasiperiodic Structures and the Fibonacci Sequence .....	1118
26.2.2 Two-dimensional Quasiperiodic Structures and the Penrose Pattern .....	1120
26.2.3 Three-dimensional Quasiperiodic Structures .....	1123
<b>26.3 Variations of QCs .....</b>	<b>1126</b>
26.3.1 Three-dimensional QCs .....	1126
26.3.1.1 Lattice Type .....	1126
26.3.1.2 Structure of Icosahedral Clusters .....	1127
26.3.2 Two-dimensional QCs .....	1128
26.3.3 Alloy Systems of Stable Phases .....	1129
<b>26.4 Growth Methods .....</b>	<b>1131</b>
26.4.1 Czochralski Method .....	1131
26.4.2 Bridgman Method .....	1132
26.4.3 Floating Zone Method .....	1133
26.4.4 Solution Growth (Self-Flux) Method .....	1134
<b>26.5 Selected Results .....</b>	<b>1135</b>
26.5.1 Al–Pd–Mn System .....	1135
26.5.2 Al–Ni–Co System .....	1138
26.5.3 Zn–Mg–RE System .....	1139
26.5.4 Ag–In–Yb System .....	1140
26.5.5 Cd–RE and Zn–Sc Systems .....	1142

<b>26.6 Growth Mechanism</b> .....	<b>1142</b>
26.6.1 Morphologies of QCs .....	1142
26.6.1.1 <i>Stellated Polyhedron</i> .....	1142
26.6.1.2 <i>Rhombic Triacontahedron</i> .....	1143
26.6.1.3 <i>Pentagonal Dodecahedron</i> .....	1143
26.6.1.4 <i>Decaprisism</i> .....	1145
26.6.2 Morphological Stability Theory .....	1146
26.6.3 QCs upon Rapid Solidification .....	1148
26.6.4 QCs Prepared by Classic Crystal Growth Methods .....	1149
26.6.5 Selection of Growth Direction .....	1151
<b>26.7 Concluding Remarks</b> .....	<b>1152</b>
<b>Acknowledgments</b> .....	<b>1153</b>
<b>References</b> .....	<b>1153</b>

## 26.1 Introduction to Quasicrystals

Quasicrystals (QCs) are a new form of matter, which differs from crystalline and amorphous materials by exhibiting a new ordered structure, quasiperiodicity, and symmetries that are forbidden in classic crystallography (e.g., 5-fold, 10-fold, 8-fold, 12-fold). The first diffraction pattern (Figure 26.1) of a QC was reported by Shechtman et al. in 1984 [1]. Since then, several new concepts have been employed to understand the structure and stability of QCs. Soon after the discovery in the 1980s, great progress was made by theorists in understanding the framework of atomic structure and fundamental properties in structure of QCs [2]. Progress on the experimental side was made by the discovery of a series of stable QCs [3].

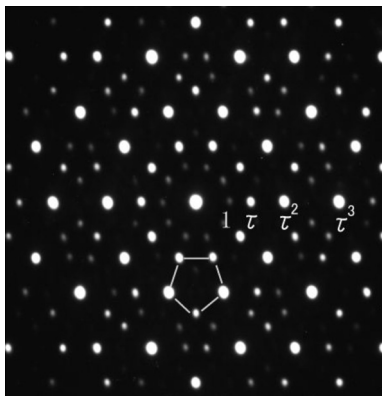


**FIGURE 26.1** Electron diffraction pattern of a rapidly solidified  $\text{Al}_{86}\text{Mn}_{14}$  alloy taken along a fivefold axis [1].

The Nobel Prize in Chemistry of 2011 was awarded to Shechtman for the discovery of QCs. This made the name “quasicrystal” more widely known among various fields in science as well as industry; nevertheless, the QC is not well understood. The difficulty of understanding QCs arises from the fact that one must figure out the structure of a QC in reciprocal space, which is not easy to imagine in real space for those outside the field of crystallography.

### 26.1.1 Crystal and Periodicity

The structures of crystals are realized by Bragg’s law, by which the atoms arrange periodically in three dimensions. Bragg’s law is shown in Eqn (26.1):

$$2d \sin \theta = n\lambda \quad (26.1)$$

where  $d$  and  $\lambda$  are the lattice spacing of a crystal and wavelength of radiation, respectively;  $\theta$  is the incident angle of radiation; and  $n$  is any integer. Because  $\lambda$  is fixed, diffraction is generated when  $\theta$  and  $d$  satisfy Bragg’s law. Equation (26.1) can be rewritten as  $\sin \theta = n\lambda/2d$ . Here,  $d$  represents a sequence of lattice planes with equidistance, which is inversely proportional to  $\sin \theta$ , implying that periodicity of atomic planes is requested for generating diffractions. Assuming the observation of crystal was performed with transmission electron microscopy (TEM) operating at an accelerating voltage at 200 kV, as shown in Figure 26.2(A),  $\lambda$  would be around 0.003 nm,

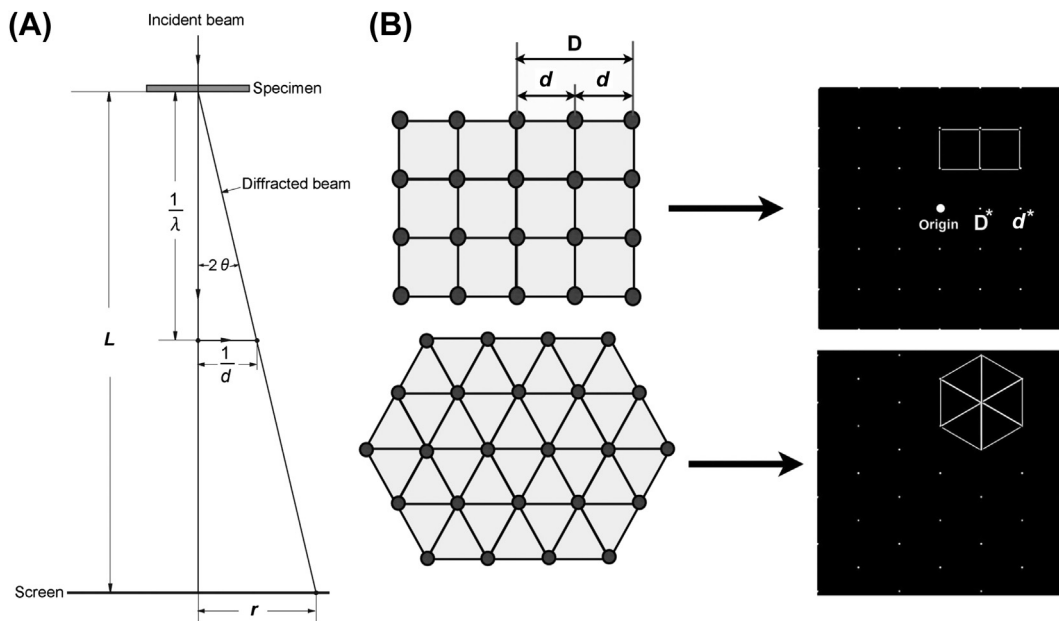


**FIGURE 26.2** (A) Schematic description of formation of diffraction pattern in transmission electron microscopy (TEM). (B) Real square and triangular lattices and their corresponding calculated diffraction patterns.

which is much smaller than  $d$ ; hence,  $\sin \theta \cong \theta$ . Then, Eqn (26.1) could be simplified to  $\theta = n\lambda/2d$ .

Note that the relationship between  $\lambda$ ,  $d$ , and  $\theta$  shown in Figure 26.2(A) satisfies Bragg's law. Therefore, it could be regarded approximately that  $\theta$  is inversely proportional to  $d$ . On the other hand, camera constant  $L$  is the distance between the specimen and the screen where diffractions are being projected, which is a constant parameter of the microscopy.  $r$  is the distance between the transmitted peak and diffraction peaks on the screen, which is measurable from the diffraction pattern. Once  $r$  is obtained, one can easily determine  $d$  or  $\theta$ . Again,  $r$  is inversely proportional to  $d$ .

With this in mind, let us consider a diffraction pattern generated from a square lattice, as shown in Figure 26.2(B). A sequence of lattice spacing  $d$  generated a diffraction of  $r = d^*$  on the diffraction pattern. Then, the other sequence of lattice spacing  $D$ , where  $D = 2d$ , would generate a diffraction of  $r = D^*$ , where  $D^* = d^*/2$ . Although the diffraction is reciprocal to the corresponding lattice spacing, both of them share the same property of periodicity. That is, the arrangement of diffractions generated by a crystal with periodic structure (real lattice) must be periodic in the diffraction pattern (reciprocal lattice). By the definition of Bragg's law, the occurrence of diffractions is equivalent to periodicity, which is another name for crystals in classic crystallography.

For a two-dimensional square lattice, the same periodic arrangement of diffractions would be observed along the vertical direction. As a result, diffractions form a square arrangement in the diffraction pattern analogy to its original lattice. A similar correlation must be observed in any three-dimensional lattice as well. An important feature inherent in this correlation is that the shape in the real lattice is preserved in the reciprocal lattice. Therefore, in Figure 26.2(B), if the real lattice is described by repetition of a square, then one must be able to find a square to describe the reciprocal lattice. The words "repetition" and "translation" have different meanings, but they are commonly used to describe the periodicity. Therefore, for a long time, "periodicity" was another name for a crystal, until the discovery of QCs.

### 26.1.2 Restriction on Symmetry by Translation

Because a crystal structure is composed of a translation of the lattice and point group of symmetry of the basis, only a number of symmetries are allowed. Restriction of symmetry due to translation is described in Figure 26.3(A). Assuming a crystal containing lattice points of A, B, C, D, and E, distances between these lattice points are commonly  $a$ . If angles between lines formed by lattice points are  $\alpha$ , then  $n\alpha = 360^\circ = 2\pi$ , where  $n$  is an integer that represents the times of symmetry. Let  $AB = b$ ; then  $b = ma$  must be approved, where  $m$  must be an integer in order to satisfy translation. The equation of  $b = 2a \cos \alpha$  could be derived, and conclusively  $\cos \alpha = m/2$ . Because  $m$  must be an integer, only a number of rotation angles are allowed, as shown in Table 26.1. Consequently, the allowed rotation symmetries  $n$  are 1, 2, 3, 4 and 6, and no rotation symmetry more than 6 is allowed. According to this derivation, fivefold

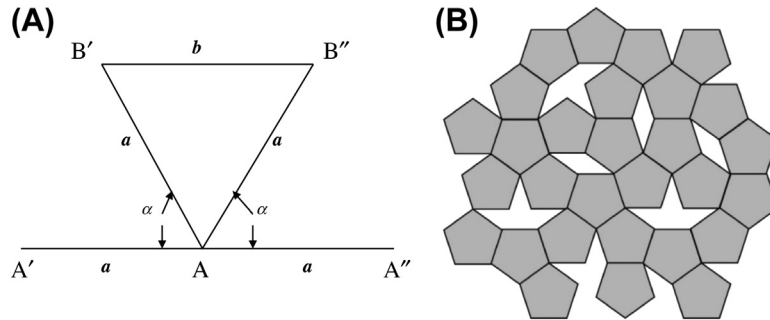


**FIGURE 26.3** Descriptions of (A) rotational symmetries compatible with lattice translation and (B) the impossibility of tiling by only using pentagons.

**Table 26.1** Rotational Symmetries Compatible with Lattice Translation

$m$	$\cos \alpha = m/2$	$\alpha$	$n = 360^\circ/\alpha$
2	1	$0, 2\pi$	1
1	$1/2$	$\pi/3$	6
0	0	$\pi/2$	4
-1	$-1/2$	$2\pi/3$	3
-2	-1	$\pi$	2

symmetry and its multiplicity are not allowed in the classic crystallography. This can also be easily understood in terms of tiling by using a pentagon, as shown in Figure 26.3(B), where the rhombus cavity would come out. In other words, a basis or a motif with fivefold symmetry is impossible to fill in a two-dimensional plane or three-dimensional space.

### 26.1.3 Discovery of QCs

The electron diffraction pattern shown in Figure 26.1 was in conflict with the definition and restriction of a crystal. The electron diffraction pattern exhibits somewhat sharp diffractions arraying with tenfold symmetry, which were forbidden in crystals as mentioned above. However, the first discovered Al-Mn icosahedral QC (IQC) shown in Figure 26.1 was prepared by rapid solidification; hence, it had a highly disordered structure as evidenced by peak broadening and shifting of diffractions, as well as low thermal stability. Two promising structural models for IQC—the icosahedral glass (IG) model [4,5] and the giant crystal model [6]—were proposed to explain the disorder. IQC structures described by the IG model or a metastable state of approximants can be interpreted within a framework of typical solid structures [7]. Therefore, new

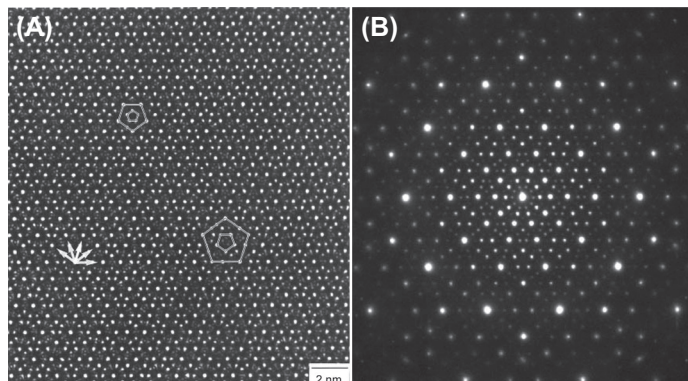


**FIGURE 26.4** (A) High-resolution transmission electron microscopy image and (B) electron diffraction pattern taken along a fivefold axis of the stable  $\text{Al}_{65}\text{Cu}_{20}\text{Fe}_{15}$  IQC [3].

structures, such as the Penrose pattern [8] or the concept of quasilattice, would have been unnecessary to describe IQC structures; hence, there was a huge controversy concerning whether IQCs really represented a new form of solid. This controversy lasted for a few years after the discovery of the first IQC. The discovery of the stable Al–Cu–Fe IQC (Figure 26.4) represented a breakthrough because its diffraction pattern and high-resolution image could not be interpreted by either the IG model or metastable states of approximants [3]. The highly ordered structure was maintained over a wide range, as large as on the order of millimeters. Consequently, stable QCs revealing sharp diffractions, as verified in a sequence of alloys, established that the QCs were a new form of solids. The International Union of Crystallography redefined the crystal in 1991 as “any solid having an essentially discrete diffraction diagram” [9]. In the new definition, the QC, which will be described next, is a crystal in high-dimensional space.

## 26.2 Structures of QCs

The question “Where are the atoms?” was asked soon after the discovery of QCs [10]. Here, we first describe the basic concept to understand the framework of structure of QCs, then provide two real examples of structures with accurate atomic decorations.

### 26.2.1 One-dimensional Quasiperiodic Structures and the Fibonacci Sequence

A one-dimensional quasilattice obtained by a cut-and-projection method [11], as shown in Figure 26.5(A), is the best example to describe how a high-dimensional crystal converts to a QC. First, let us put a square lattice in two-dimensional space.

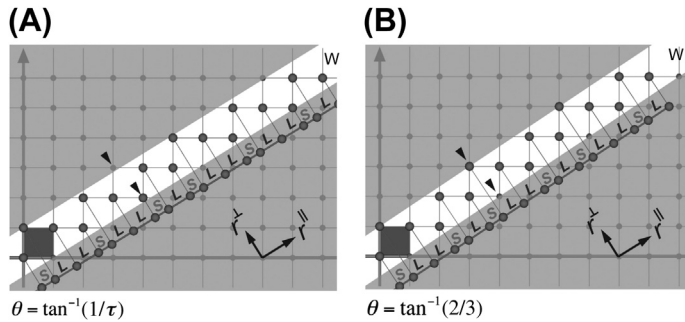


**FIGURE 26.5** Projection of a two-dimensional lattice onto a one-dimensional space with (A) an irrational slope ( $1/\tau$ ) and (B) a rational slope ( $2/3$ ) to obtain a one-dimensional quasicrystals and approximant, respectively.

Then, we introduce a set of orthogonal axes, namely  $r^{\parallel}$  and  $r^{\perp}$ , which are rotated by an angle of  $\theta$  with respect to the original coordinate system of the square lattice.  $r^{\parallel}$  and  $r^{\perp}$  are two projection axes, called the physical axis and complementary axis, respectively. Parallel to  $r^{\parallel}$ , we introduce a strip with a width of a unit square ( $\mathbf{W}$ ) along  $r^{\perp}$ . The strip is also called a “window” for projection, which contains a number of lattice points of the square lattice. The next step is let the lattice points inside the window project on to  $r^{\parallel}$ , as shown in Figure 26.5. A tiling consisting of two different lengths long ( $L$ ) and short ( $S$ ), which are the projection of two different sides of the unit square lattice, is then obtained.

If the  $\tan \alpha$  is irrational, such as in the case in Figure 26.5(A) where  $\alpha = \tan^{-1}(1/\tau) \approx 31.716^\circ$  ( $\tau = \frac{1+\sqrt{5}}{2}$  is Golden mean), a one-dimensional quasiperiodic tiling with  $L$  and  $S$  line segments is formed. Note that if a small  $\mathbf{W}$  is used, points of projection will be less dense and  $L$  and  $S$  line segments will be larger, and vice versa. The size of  $\mathbf{W}$  only changes the density of projection points or the lengths of  $L$  and  $S$ ; as long as the slope is the same, one gets the same quasiperiodic array and length ratio,  $S/L = 1/\tau$ . This is the property of self-similarity, and the factor of self-similarity for a quasiperiodic array is irrational.

If the slope of  $\mathbf{W}$ ,  $m$  ( $=S/L$ ) approached a rational number, as shown in Figure 26.5(B), such as  $m = 2/3$ , the projection points will form a periodic array with a periodicity of  $2S + 3L$ . The quasiperiodic array is a one-dimensional QC, and a periodic array derived by projection is an approximant crystal. By choosing  $m$  to be a continued-fraction approximant to  $\tau$  ( $m = 1/1, 1/2, 2/3, 3/5\dots$ ), one creates a structure with larger periods that approximate the quasiperiodic tiling (Figure 26.5, right) better and better. The sequences of  $L$  and  $S$  for the quasiperiodic structure and approximant (projected with  $m = 1/\tau$  and  $m = 2/3$ , respectively) are shown in Figure 26.5. The differences between two sequences are indicated with arrowheads, where the  $LS$  observed in quasiperiodic tiling is replaced by  $SL$  in the approximant [12]. The period of the approximant is  $LSLLS$ . The difference is due to a flipping between  $L$  and  $S$ ; with regard to QCs, this flipping is called “phason flipping,” which is a sort of defect in QCs.

Because the one-dimensional quasiperiodic structure can be derived from a two-dimensional periodic structure, as shown in [Figure 26.5](#), a QC is called a crystal in high-dimensional space. The one-dimensional quasiperiodic sequence can be obtained by a substitution rule:  $L \rightarrow LS$  and  $S \rightarrow L$ , which can be expressed by [Eqn \(26.2\)](#).

$$\begin{aligned}
 &L \\
 &LS \\
 &LSL \\
 &LSLLS \\
 &LSLLSLSL \\
 &LSLLSLLSLS \\
 &\dots
 \end{aligned} \tag{26.2}$$

Each series can be expressed as  $F_n = F_{n-1} + F_{n-2}$ , where  $\lim_{n \rightarrow \infty} \frac{F_{n+1}}{F_n} = \frac{1}{\tau}$ . The number of total  $L$  and  $S$  for each series will be 1, 2, 3, 5, 8, 13, 21, 34, 55, 89, ... This is the Fibonacci number or Fibonacci sequence. Note that a series of ratios of numbers, such as  $1/2$ ,  $2/3$ ,  $3/5$ ,  $5/8$ ... are corresponding to  $m$  and are used to obtain a series of approximant crystals.

## 26.2.2 Two-dimensional Quasiperiodic Structures and the Penrose Pattern

There are a number of two-dimensional quasiperiodic structures owning different symmetries, such as 8-fold (octagonal), 10-fold (decagonal), and 12-fold (dodecahedral) symmetries [\[13\]](#). In reality, QCs with a decagonal lattice (decagonal quasicrystals, DQC) are well studied and are stable, which allowed discussion of the mechanism of crystal growth; here, we focus on the decagonal lattice.

The typical decagonal lattice is described by the well-known Penrose pattern shown in [Figure 26.6\(A\)](#). The Penrose pattern is constructed by tiling a two-dimensional plane with two rhombic tiles, namely a “fat” tile with an angle  $\pi/5$  and a “skinny” one with an angle  $\pi/10$ . A perfect Penrose pattern is formed only when tiling is made along so-called matching rules, which are formulated using a marking of the edge. Each rhombus has single or double arrows along the edges; rhombi of the same type have identical arrow markings. Neighboring rhombi have edges in common. To make a Penrose tiling, one fits these rhombic tiles together according to the matching rule: two rhombic tiles can be placed side by side only if coinciding edges have the same type and directions of the arrows. This leads to quasiperiodicity of the tiling.

Each vertex in an infinite Penrose tiling is surrounded by one of eight combinations of tiles [\[14\]](#). In an infinite Penrose tiling, the ratio between the number of fat tiles ( $N_F$ ) and that of skinny tiles ( $N_S$ ) will approach  $\tau$ . Any vertex out of these eight combinations will be a defect and the ratio of  $N_F/N_S$  will deviate from  $\tau$ . The Penrose pattern could be obtained by the cut-and-projection method of a five-dimensional cubic lattice onto a two-dimensional space, similar to that shown in [Figure 26.5](#). In this case, instead of

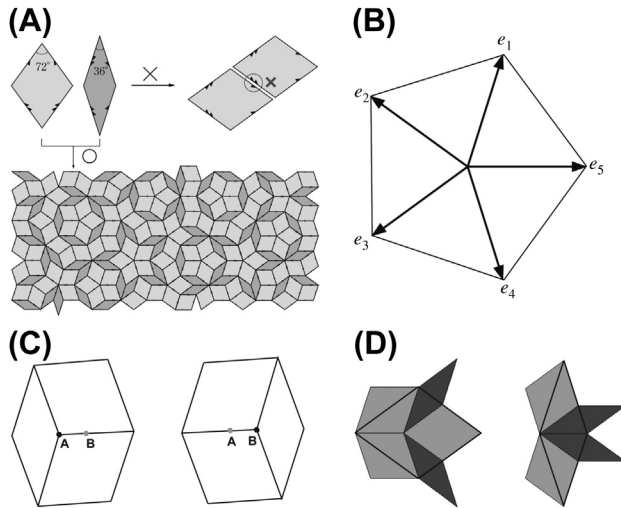


**FIGURE 26.6** (A) Description of Penrose tiling made with two rhombi. (B) Five basis vectors used to index the Penrose lattice. (C) A description of the phason flip: lattice position exchange between A and B changes the arrangement of tiles. (D) Inflation in Penrose tiling.

a strip shown in Figure 26.5, a number of polygons, namely pentagons of windows (also called occupation domains), are used. The vertex of Penrose patterns forms a two-dimensional QC, which could be assigned with five vectors:  $e_1, e_2, e_3, e_4$ , and  $e_5$ , as shown in Figure 26.6(B), with an angle of intersection of  $\pi/5$ . Because  $e_1 + e_2 + e_3 + e_4 = -e_5$ , four vectors is enough for assignment. Every spot in its diffraction pattern can be indexed with a combination of the vectors  $(\cos(2\pi j/5), \sin(2\pi j/5))/a$  [15], where  $a$  is the edge length of Penrose pattern and  $j = 1, \dots, 5$ .

A typical flipping of tiles, as shown in Figure 26.6(C) is also observed in the mismatching of Penrose tiling, which could be made from projection by a shift or change in size of  $W$ . Two hexagons have the same outline; both are made of two skinny and one fat tiles, but their arrangements are different. In terms of tiling, the flipping of tiles makes a significant difference. However, if we assume that the seven vertexes are all occupied by atoms, this flipping is simply made by a slight switching of atomic position from A to B (or B to A) at the interior of hexagons. This is phason flipping in a two-dimensional QC, which has been observed in real QC samples.

There is a self-similarity of Penrose pattern, as shown in Figure 26.6(D). By dividing the original tile with a length ratio of  $1:\tau$ , one may obtain identical tiles with a scale of  $1/\tau$  with respect to the original ones. In the Penrose pattern, a larger number of vertices reveal local fivefold symmetry, and along any direction there is no periodicity of lattice spacing. The calculated diffraction pattern of the Penrose pattern reveals 10-fold symmetry and a quasiperiodic arrangement of diffractions inflated with  $\tau$  scaling, which closely resembles that observed by Shechtman et al. Obviously, the Penrose pattern is the key to understanding the structure of QCs. It is normally used as a template for modeling the structure of two-dimensional QCs by decorating rhombic tiles with atoms.

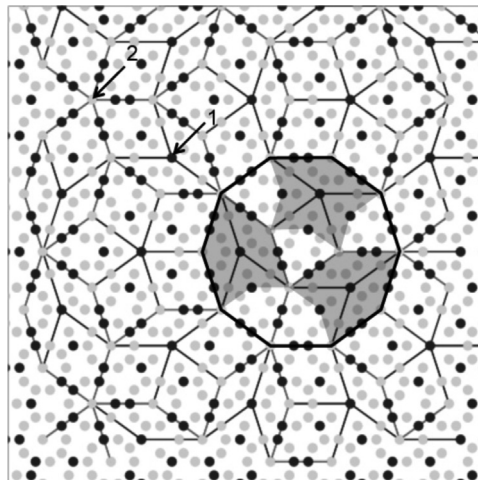


**FIGURE 26.7** Structural model of  $\text{Al}_{72}\text{Ni}_{20}\text{Co}_8$  DQC superimposed by two different atomic layers. Gray circles and black circles represent Al and transition metals (Ni or Co), respectively. A highlighted decagon composed of kites, boats, and a star is Gummelt decagon, which is used to construct the structure by overlapping rather than tiling [16].

The Penrose pattern itself is a decagonal structure with a 10-fold axis and is the simplest template to describe a DQC. A structure of a DQC, as shown in Figure 26.7 [16], is periodic along one direction and quasiperiodic in the plane perpendicular to it (i.e., the paper). Thus, it can be expressed as a periodic stacking made by different atomic layers alternatively along a decagonal axis. The period of Figure 26.7 is on the order of 0.4 nm (two different atomic layers), but it could be a multiple of this periodicity.

TEM is a powerful tool for studying DQC because it can get high-resolution images along the periodic direction, which contain symmetry and the interior atomic position of clusters. The formation of stable DQCs allows one to study the structure by means of a single-grain X-ray diffraction technique; one example is shown in Figure 26.7. The structure model with atomic decoration superimposes on the Penrose pattern for Al–Ni–Co DQC. This DQC exhibits a periodicity of 0.4 nm or two atomic layers; hence, the atomic positions shown in Figure 26.7 are a projection of two different atomic layers. High-resolution TEM studies suggested a similar structure, indicating the model is reliable [17].

It should be noted that the atomic positions in Figure 26.7 are not fully occupied and there are several partial sites in the real DQC structure. Two partial sites could be treated as one atom flipping between two too-close sites, shown in Figure 26.6(C); in terms of tiling, this is the phason flipping. There are several flipping sites in real DQCs, which are essential for forming long-range quasiperiodic structures and are the origin of the diffuse scattering observed in X-ray diffraction studies. The DQC structure can be described by the overlap of decorated decagons (Grummelt decagon) [18,19] with a diameter of 0.2 nm, as highlighted by the thick lines in Figure 26.7.

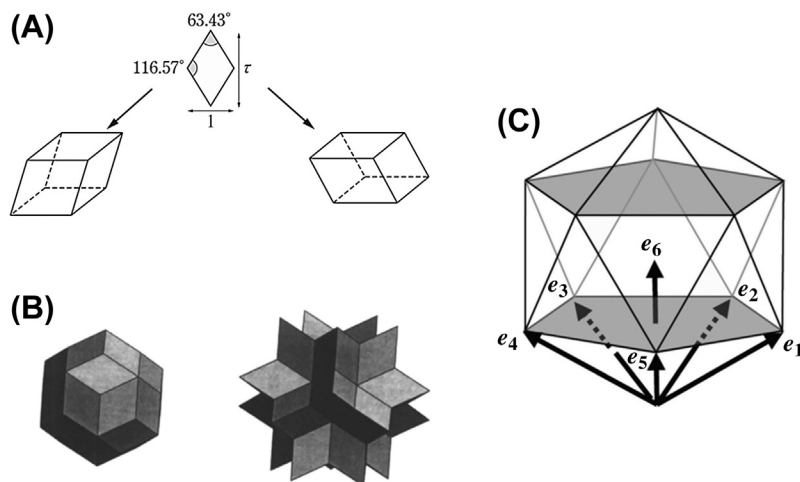


**FIGURE 26.8** (A) Acute rhombus (AR) and obtuse rhombus (OR) constructed by a so-called golden rhombus, of which the ratio of diagonals is  $\tau$ . (B) A rhombic triacontahedron constructed by 10 AR and 10 OR and a stellated dodecahedron constructed by 20 AR. (C) Six basis vectors used to index lattice of icosahedral quasicrystals, described by an icosahedron.

### 26.2.3 Three-dimensional Quasiperiodic Structures

There is only one three-dimensional quasiperiodic structure: the IQC. The simplest set of unit cells for a three-dimensional quasiperiodic structure consists of the acute and obtuse rhombohedra shown in Figure 26.8(A). These two unit cells play the same roles as the skinny and fat tiles, respectively, in the Penrose tiling. All the faces are identical rhombuses, which are a Golden rhombus with length ratio  $\tau$  for two diagonals.

As shown in Figure 26.8(B), 10 acute and obtuse rhombohedra can be packed to form a rhombic triacontahedron (RTH) and 20 acute rhombohedra can be packed to form a stellated dodecahedron. Both polyhedrons reveal icosahedral symmetry, which shows how the unit cells can be packed to fill space. Using polyhedrons as unit cells with atomic decoration, it is easy to imagine the symmetry of structure. Similar to Penrose patterns, a three-dimensional quasiperiodic structure can be obtained by a cut-and-projection method of a six-dimensional cubic lattice onto a three-dimensional space. The typical  $W$  for the projection is a rhombic triacontahedraon shape with edge length  $1/\tau^2$  times that of projected structure [14]. In the six-dimensional construction, the analog of  $W$  in Figure 26.5 is the product of a three-plane and a suitable three-dimensional cross-section. The  $L$  and  $S$  line segments correspond to acute and obtuse rhombohedra, respectively. If the vectors used to describe  $W$  are a series of  $(m, 1, 0)$  vectors, then the three-dimensional quasiperiodic structure results when  $m \rightarrow \tau$ . By taking the rational approximants  $m = 0/1, 1/1, 1/2, 2/3, \dots$ , one obtains a sequence of cubic structures with larger and larger lattice constants. Two  $1/1$  approximants have been verified in  $\alpha$ -AlMnSi [12] and  $(Al, Zn)_{49}Mg_{32}$  [20] compounds, which are

body-centered cubic (bcc) packing of icosahedral clusters with different shell structures. For simplicity, both the IQC and the approximant consist of icosahedral clusters, of which the arrangement is quasiperiodic for the former and periodic for the latter. Therefore, the approximants contain very useful information for building an initial structural model for IQCs. Lattice points of IQCs are normally assigned with six vectors expressed on an icosahedron—namely  $e_1, e_2, e_3, e_4, e_5,$  and  $e_6$ , as shown in Figure 26.8(C). A possible basis for the diffraction spots of an IQC is given by the six vectors [21]:

$$a_i^* = \frac{1}{a}(1, \tau, 0), \frac{1}{a}(-1, \tau, 0), \frac{1}{a}(0, 1, \tau), \frac{1}{a}(\tau, 0, 1), \frac{1}{a}(\tau, 0, -1), \frac{1}{a}(0, 1, -\tau) \quad (26.3)$$

where  $i = 1, \dots, 6$ .

So far, there is only one IQC, namely  $i\text{-Cd}_{5.7}\text{Yb}$  [22], whose structure has been completely solved [23]. A cubic-phase  $\text{Cd}_6\text{Yb}$  with a space group of  $Im\bar{3}$  and lattice parameter  $a = 0.156$  nm exists in the Cd–Yb phase diagram [24]. The structure of  $\text{Cd}_6\text{Yb}$  has been determined, and it was demonstrated to be a 1/1 approximant to the IQC phase. The  $i\text{-Cd}_{5.7}\text{Yb}$  is adjacent to the  $\text{Cd}_6\text{Yb}$  phase in the phase diagram. The shell structure of the icosahedral cluster deduced from  $\text{Cd}_6\text{Yb}$  is shown in Figure 26.9(A). The icosahedral cluster in  $\text{Cd}_6\text{Yb}$  approximant has the following structure: the first shell is created by four Cd atoms around the cluster center; the second shell consists of 20 Cd atoms that form a dodecahedron; the third shell is an icosahedron of 12 Yb atoms, the fourth shell is a Cd icosidodecahedron obtained by placing 30 Cd atoms on the edges of

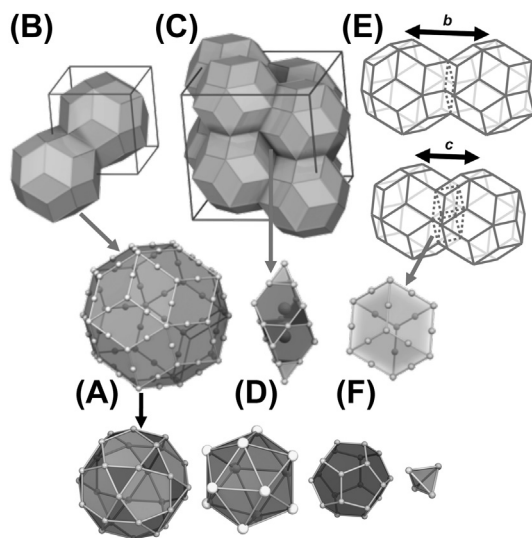


**FIGURE 26.9** (A) A rhombic triacontahedral (RTH) unit with atomic decoration used to construct (B) 1/1 and (C) 2/1 approximants in Cd–Yb system, where the structure of 1/1 approximant can be described by the RTH and structure of 2/1 approximant needs a (D) decorated acute rhombus unit in addition to the RTH. There are only two linkages between two adjacent RTH are allowed: (E) b-linkage link by sharing a rhombus unit and (F) c-linkage connected by overlapping an obtuse rhombus [23].

the Yb icosahedron, and the fifth shell is an RTH in which Cd atoms are located on 32 vertices and 60 edge centers. The  $i\text{-Cd}_{5.7}\text{Yb}$  was studied by single-grain X-ray diffraction, by which the icosahedral cluster was demonstrated to be identical to that of the  $\text{Cd}_6\text{Yb}$  approximant. The icosahedral cluster contains five atomic shells (Figure 26.9(A)) and is an RTH cluster. It is important to indicate that a well-defined chemical order presents in the RTH cluster, where Yb (only on an icosahedral shell) and Cd occupy different atomic sites.

The structure of the 1/1 approximant is a bcc packing of RTH clusters, as shown in Figure 26.9(B). Furthermore, the structure of a 2/1 approximant (Figure 26.9(C)) was solved to consist of the same RTH as the 1/1 approximant, but it needs an additional unit [25]—namely, an acute rhombohedron (Figure 26.9(D)) with suitable atomic decoration to fill the cavity. In both approximants, the RTH clusters are linked to each other (Figure 26.9(E)) along the twofold (**b**-bond) directions by sharing a rhombus face and the three-fold direction (**c**-bond) with interpenetration of an obtuse rhombohedron, as shown in Figure 26.9(F). Consequently, three fundamental building units—an RTH cluster (a), an acute rhombohedron (d), and an obtuse rhombohedron (f)—are supposed to be necessary for constructing the IQC structure.

Using the knowledge of linkage rules and building units, a precise structural model for  $i\text{-Cd}_{5.7}\text{Yb}$  was proposed (Figure 26.10), which describes the structure in terms of inflation and hierarchical packing of clusters. Figure 26.10 shows the RTH center positions and their connection on a fivefold plane. Starting from the center, it can be shown that a cluster of RTH units (icosidodecahedron) is formed. The cluster of RTH forms a

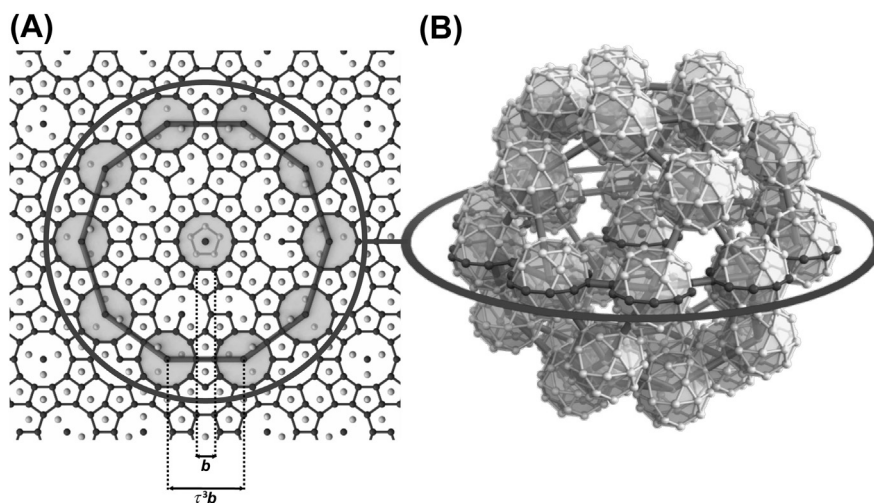


**FIGURE 26.10** Structural description of  $i\text{-Cd}_{5.7}\text{Yb}$  with rhombic triacontahedral (RTH) unit. (A) A dense plane of RTH units is seen along a fivefold axis. (B) A small ball represents an RTH unit used to construct an icosidodecahedral cluster, by which a larger icosidodecahedral cluster can be built up. Ratio of edge length between large and small icosidodecahedra is  $\tau^3$  [23].

large “cluster of a cluster,” which is also an icosidodecahedron but with a  $\tau^3$  times increase in scale. A prominent feature of the model is that almost all of the IQC structure is described by interpenetrating RTH clusters because 93.8% of the atoms belong to the RTH clusters [23]. The full structure is described by the RTH clusters, where 100% of atoms belong to the RTH clusters for the 1/1 approximant. These two structures are both described by the RTH clusters but stand at two oppositional extremes, with a difference in composition of only  $\sim 2$  at%. One interesting feature is that all approximants exist as stable phases in nature; they can be mathematically derived by a cut-and-projection scheme.

## 26.3 Variations of QCs

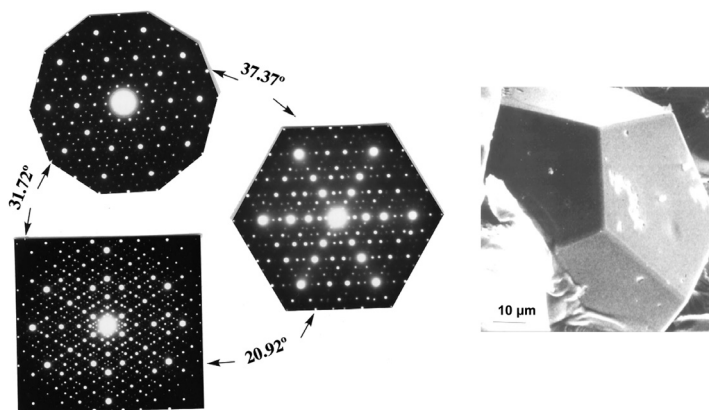
QCs can be formed through various processes and by various techniques. The structure and the intrinsic disorder of QCs are very sensitive to the process of formation. They could be stable and metastable, depending on alloys, and they reveal a number of variations in structure. QCs can be sorted by their diffraction features and symmetries, which are easily determined from diffraction patterns.

### 26.3.1 Three-dimensional QCs

#### 26.3.1.1 Lattice Type

In terms of symmetry, only one three-dimensional QC has been discovered so far—IQC. This is the QC studied most extensively among all known QCs. Figure 26.11 shows the typical selected area electron diffraction (SAED) patterns taken with incidences along fivefold, threefold, and twofold symmetry axes, as well as the morphology of a single IQC. The IQC possesses a very high symmetry with the point group  $m\bar{3}5$ . It was predicted from theory that there exist three types of Bravais lattices in three-dimensions, consistent with the icosahedral point symmetry. They correspond to primitive, body-centered,

**FIGURE 26.11** Electron diffraction patterns taken along the fivefold, threefold, and twofold axes (left) and a SEM image (right) of stable  $\text{Al}_{65}\text{Cu}_{20}\text{Fe}_{15}$  IQC [26].



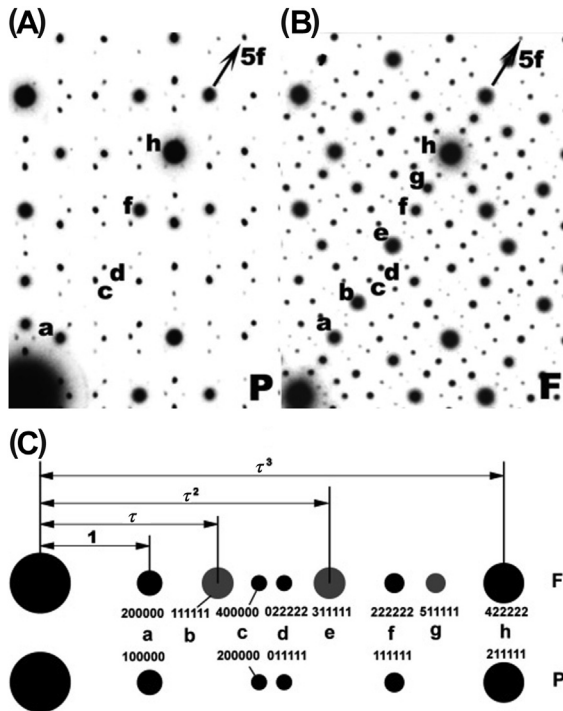


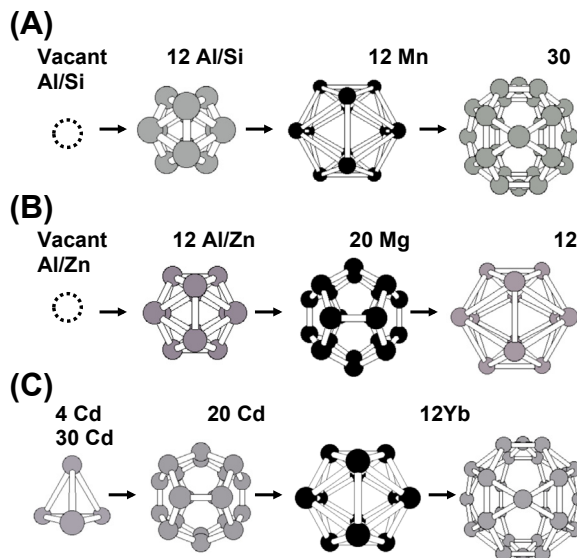
**FIGURE 26.12** Electron diffraction patterns of (A) P-type and (B) F-type IQCs and (C) indexing of diffraction spots in their corresponding fivefold axis [3].

and face-centered hypercube in a six-dimensional hyperspace. The primitive and face-centered types have been verified in real samples. These two types of IQCs can be distinguished by extinction rules of diffractions in their twofold patterns [3,13]. Figure 26.12(A) and (B) shows partial diffraction patterns taken along twofold axes for the primitive and face-centered IQCs. Indexing is given in Figure 26.13(C), where the diffraction spot arrangement is inflated by  $\tau^3$  and  $\tau$  for primitive and face-centered type lattices, respectively. Note that face-centered type lattice has odd–even parity. Most Al-based metastable IQCs should have a face-centered lattice, but it is obscured by quenched-in disorder. For stable IQCs, Al-based and Zn–Mg–RE (where RE = rare earth metals) systems have face-centered lattices and Cd–Yb groups have primitive lattices.

### 26.3.1.2 Structure of Icosahedral Clusters

IQC can be classified into three classes according to the hierarchic structures of icosahedral clusters derived from their corresponding crystalline approximants: the Al–Mn–Si class [12], the Mg–Al–Zn class [27], and the Cd–Yb class [22]. The structures of atomic shells for the three classes are shown in Figure 26.13. The three classes are also called Mackay, Bergman, and Tsai clusters, respectively. The clusters were first recognized by Henley and Elser in two compounds,  $\alpha$ -Mn<sub>12</sub>(Al,Si)<sub>57</sub> [12] and Mg<sub>32</sub>(AlZn)<sub>48</sub> [20], which are supposed to be 1/1 approximants to IQCs. The clusters have icosahedral symmetry,

**FIGURE 26.13** Atomic decoration of successive shells of atomic clusters expected in various families of icosahedral quasicrystals: (A) Mackay type, (B) Bergman type, and (C) Tsai type.



which was very useful for guessing the structure of IQCs. However, the structures of most stable IQCs have not been solved; the hierarchic structures of icosahedral clusters were not determined to belong to either of the two classes, except  $\text{Al}_{5.5}\text{Li}_3\text{Cu}$ , which revealed the same clusters as  $\text{Mg}_{32}(\text{AlZn})_{48}$ . Recently, a series of IQC and approximants were discovered in Na-containing intermetallic compounds [28], which belong to the Bergman type. More recently, the structure of an Al–Pd–Cr–Fe  $3/2$  approximant to IQC of the Al–Pd–Mn system has been solved [29], which is well described as a dense packing of two kinds of clusters: mini-Bergman and pseudo-Mackay clusters. For the group of  $\text{Zn}_{60}\text{Mg}_{30}\text{RE}_{10}$  stable IQCs, the structure of icosahedral cluster is still unknown because no appropriate approximant has been reported. Obviously, grouping the IQCs by hierarchic structures of clusters may not be clear for these two classes. On the other hand, the Tsai cluster was verified to be identical in several IQCs and approximants in Cd–Yb, Ag–In–Yb, Zn–Sc, and so on [30], as shown in Figure 26.9 and Figure 26.13(C); cluster grouping is strictly clear in this group. For convenience, the stable IQCs are grouped as Al–TM, Zn–Mg–RE, and Cd–Yb classes in this chapter.

### 26.3.2 Two-dimensional QCs

So far, there are three kinds of two-dimensional QCs: decagonal, dodecahedral, and octagonal QCs, as classified by their electron diffraction patterns. Figure 26.14 shows the typical diffraction patterns of DQC along a 10-fold axis and two characteristic twofold axes, together with an scanning electron microscopy image revealing decaprisim morphology. The 10-fold axis is the axis along which the diffractions are arranged periodically. Perpendicular to this axis is the quasiperiodic plane, in which the

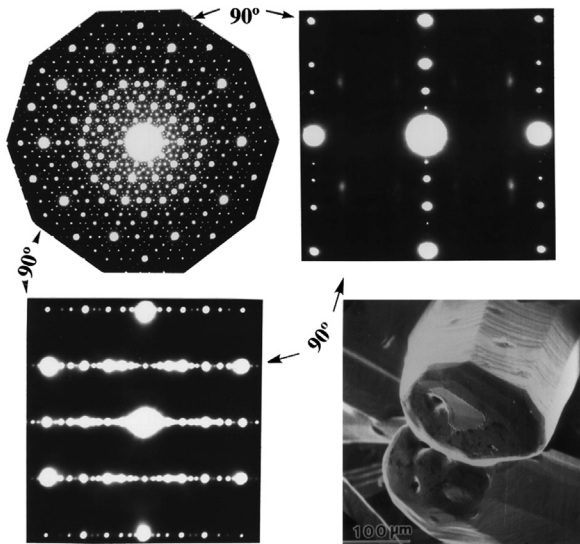


**FIGURE 26.14** Electron diffraction patterns taken along a 10-fold and two twofold axes, and an SEM image of  $\text{Al}_{72}\text{Ni}_{20}\text{Co}_8$  decagonal quasicrystal.

diffractions are arranged in a quasiperiodic array with a 10-fold symmetry. This will be 12-fold [31] and 8-fold [32] symmetries for dodecahedral and octagonal QCs, respectively, as shown in Figure 26.15. Only DQC was found to be stable in Al–Ni–Co, Al–Cu–Co, and some Al–Pd systems.

### 26.3.3 Alloy Systems of Stable Phases

Stable QCs have two inherent properties: stability and a well-ordered structure. The stability allows QCs to be grown at slow cooling rates, thus enabling large single-domain QCs with high structural orders to be produced for precise measurements. Both properties are crucial for verifying that QCs are a new form of solid that differs from both crystalline and amorphous solids. The first Al–Mn QC was prepared by rapid

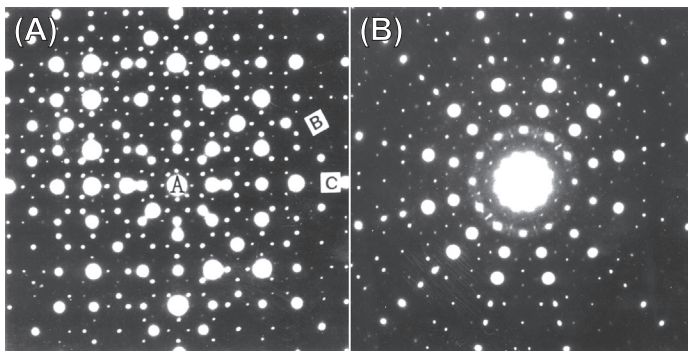


**FIGURE 26.15** Electron diffraction patterns taken along an 8-fold (A) and a 12-fold (B) from octagonal and dodecahedral quasicrystals, respectively.

solidification and hence had a high defect density and low thermal stability. QCs obtained by rapid solidification are thermodynamically metastable and thus decompose into crystalline phase(s) on heating at temperatures much lower than their melting points. Moreover, their grain sizes are a few micrometers, which is too small to precisely investigate their structures. In such samples, the structure and properties originating from their quasiperiodicity are masked by the structural disorder. This resulted in controversy regarding structural modeling for interpreting the origin of diffraction patterns observed in the early 1980s. Since 1986, several stable QCs with grain sizes as large as  $\sim 100 \mu\text{m}$  and faceted morphologies have been discovered in various alloys. This greatly increased the precision of QC measurements, enabling structural analysis and investigations of the physical properties of single QCs to be performed. The stability of stable QCs has been explained in terms of electronic structures or valance concentration ( $e/a$ : electron-atom ratio) in several articles, so we do not go into detail in this chapter.

The stable QCs alloys discovered to date are summarized in Table 26.2. Most stable QCs (especially IQC) are a new group of electron compounds as described by Hume-Rothery for intermetallic compounds in the early 1900s [33]. The  $e/a$  criterion is even stricter for IQCs than crystalline compounds because stable IQCs only form at sharp compositions with strict  $e/a$  values [34]. Unlike stable IQCs, stable DQCs only form in a few alloy systems, such as Al–Ni–Co and Al–Cu–Co systems, but their compositional ranges are much wider in each system.

A phase appears in the equilibrium-phase diagram, meaning that it is thermodynamically stable. This was first noted in the Al–Li–Cu phase diagram established in 1955 [35], of which an unknown T phase was verified to be an IQC in 1986 [36]. Revisiting the phase diagram after discovery of the stable  $i$ -Al–Cu–Fe [26], it was found that when the system being mapped in 1930s [37], the IQC was observed and labeled as the  $\psi$  phase, as shown in Figure 26.16(A). Similarly, the  $\text{Zn}_{60}\text{Mg}_{30}\text{Y}_{10}$  IQC [38] turned out to be the so-called Z-phase [39], as shown in Figure 26.16(B), which had been reported as distinct but unidentified phase in the Zn–Mg–Y system a few years before the discovery of QCs.

**Table 26.2** Alloy Systems Forming Stable Icosahedral Quasicrystals

P-Type		F-Type
Al–Mn–Al		$\text{Al}_{63}\text{Cu}_{25}\text{TM}_{12}$ (TM:Fe Ru Os)
		$\text{Al}_{70}\text{Pd}_{20}\text{TM}_{10}$ (TM:Mn Tc RE)
Zn–Mg–Al	$\text{Al}_5\text{Li}_3\text{Cu}$	$\text{Zn}_{60}\text{Mg}_{30}\text{RE}_{10}$ (RE:Y Dy Ho Gd Er Tb)
	$\text{Zn}_{70}\text{Mg}_{20}\text{RE}_{10}$ (RE:Er Ho)	$\text{Zn}_{74}\text{Mg}_{19}\text{TM}_7$ (TM:Zr Hf)
Cd–Yb	$\text{Cd}_{5.7}\text{M}$ (M:Yb Ca), $\text{Zn}_{88}\text{Sc}_{12}$ , $\text{Cd}_{88}\text{M}_{12}$ (M:Gd,Tm,Y)	
	$\text{Cd}_{65}\text{Mg}_{20}\text{M}_{15}$ (M:Yb Ca Y Ho Gd Er Tb)	
	$\text{Zn}_{80}\text{Mg}_5\text{Sc}_{15}$	
	$\text{In}_{42}\text{Ag}_{42}\text{M}_{16}$ (M:Yb Ca)	
	$\text{Au}_{60}\text{Sn}_{25}\text{M}_{15}$ (M = Yb,Ca), $\text{Au}_{51}\text{Al}_{34}\text{Yb}_{15}$	
	$\text{Zn}_{74}\text{Ag}_{10}\text{Sc}_{16}$ , $\text{Zn}_{75}\text{Pd}_9\text{Sc}_{16}$	
	$\text{Zn}_{77}\text{Fe}_7\text{Sc}_{16}$ , $\text{Zn}_{18}\text{Co}_6\text{Sc}_{16}$ , $\text{Zn}_{75}\text{Ni}_{10}\text{Sc}_{15}$	

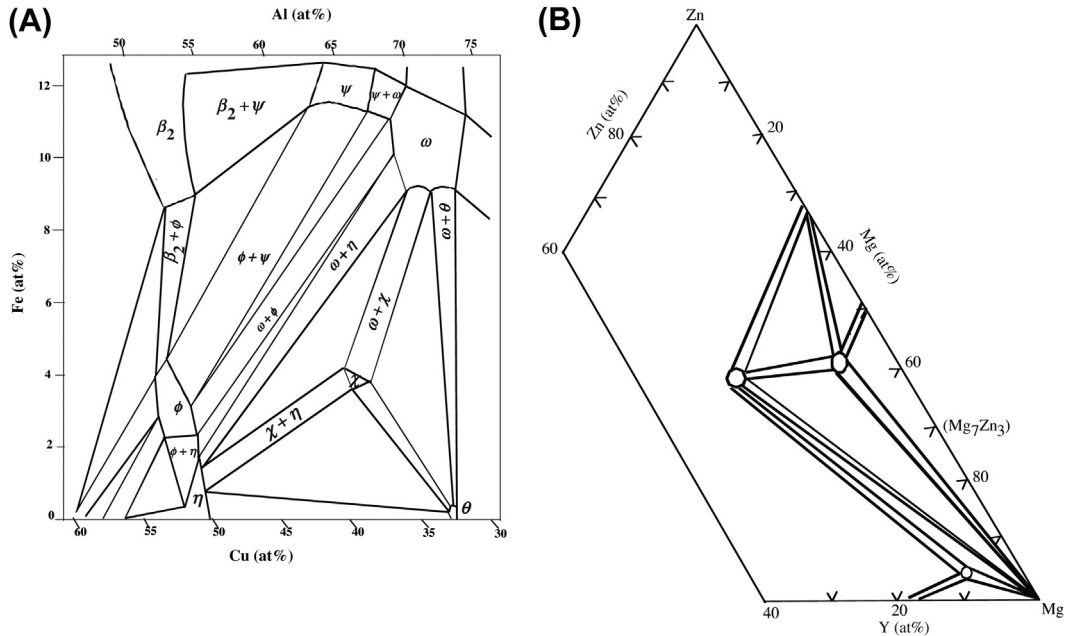


**FIGURE 26.16** Partial phase diagrams involving the icosahedral quasicrystal (IQC) phase in the (A) Al–Cu–Fe [37] and (B) Zn–Mg–Y [39] systems, where  $\psi$  and Z phases were indicated as unknown compounds and later were verified to be IQC phases.

## 26.4 Growth Methods

Many quasicrystalline phases have been discovered as stable phases in equilibrium-phase diagrams. Thus, it is possible to grow large single-grain QCs by conventional crystal growth methods for the precise measurement of crystal structure, surface structure, and physical properties.

### 26.4.1 Czochralski Method

The Czochralski method has been adopted to grow large single QCs of *i*-Al–Fe–Cu [40,41], *i*-Al–Pd–Mn [42,43], *i*-Al–Li–Cu [44], *d*-Al–Ni–Co [45–50], and *d*-Al–Cu–Co [51,52]. The crystals prepared by the Czochralski method grow from near-equilibrium conditions, so a detailed phase diagram involving the primary crystallization field of quasicrystalline phase is necessary for designing the starting composition and temperature program.

A typical setup of a Czochralski furnace is illustrated in Figure 26.17(A) [42]. As for many others materials, the necking process is applied to obtain a narrow volume for selective growth of a single nucleus and eliminate dislocations in the subsequent growth. Most QCs are ternary intermetallic compounds with incongruent solidification, so relatively slow growth rates are required for growing high-quality single QCs. The typical

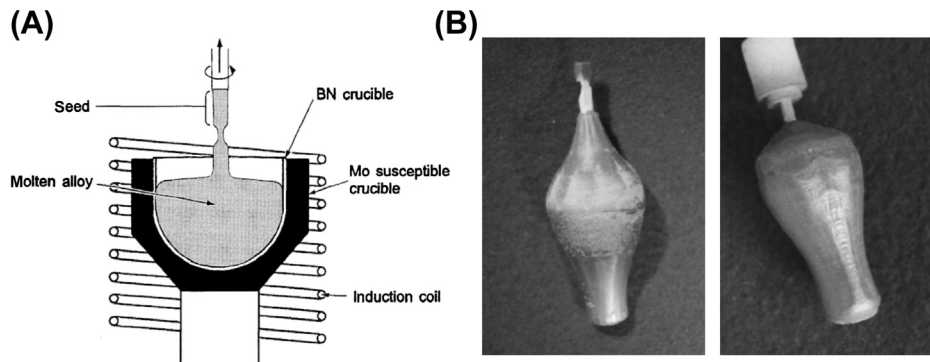


**FIGURE 26.17** (A) The schematic illustration of the Czochralski growth apparatus [42]. The crucible containing molten alloy is heated by high-frequency induction coil. A pull rod with a seed crystal is mounted axially above the crucible. (B) Single *d*-Al-Ni-Co synthesized by the Czochralski method on [00001] and [10-100] oriented seeds [50].

pulling rate for Al-based QCs is in the range of 0.1–10 mm/h. The diameter of the ingot is controlled by the temperature of molten solution, and the composition of the residual liquid melt in the crucible is varied during the growth. With the Czochralski method, a skilled researcher can grow single QCs of about 1 cm in diameter and several centimeters in length. Figure 26.17(B) shows photographs of the Czochralski *d*-Al-Ni-Co ingots [50].

### 26.4.2 Bridgman Method

In most cases of QC growth, the sample nucleates spontaneously rather than grows on a preset seed, because it is difficult to control the partial melting of the seed at the beginning of crystal growth. Therefore, the control of spontaneous nucleation at the early stage of crystal growth is of primary importance. A crucible with a cone-shape bottom is usually used to minimize the possibility of forming many nuclei (Figure 26.18). The conventional Bridgman furnace that the authors used has three temperature zones, as schematically illustrated in Figure 26.18.

To protect sample from oxidation or evaporation, the crucible with initial materials is sealed in a quartz ampoule (Figure 26.18), which is preliminarily evacuated and filled with an inert gas. At the beginning of crystal growth, the ampoule is raised into the upper zone and kept at a high temperature for a long time to get a homogeneous molten solution. Then, the ampoule is pulled down slowly in the furnace to pass the temperature gradient zone. The QC first nucleates at the bottom of the crucible and then grows upwards when the molten solution passes the liquid–solid interface. A slow pulling speed in the range of 0.1–10 mm/h is used for single QC growth. With this method, large-size, high-quality single *i*-Al-Pd-Mn [53], *i*-Ag-In-Yb [54,55], *i*-Zn-Mg-Ho [56,57], *d*-Al-Ni-Co [43,58], and *d*-Al-Cu-Co [59] have been grown. For congruent melting QCs, such as *i*-Ag-In-Yb [55], *i*-Cd-Yb, and *i*-Ag-In-Ca, the whole ingot can be a single grain when the starting material is of stoichiometry.

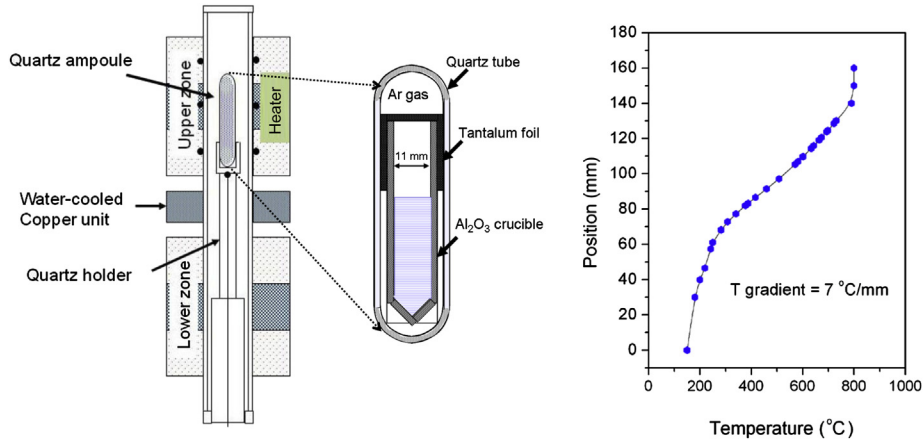


FIGURE 26.18 The schematic illustration of the Bridgman furnace (left), quartz ampoule encapsulated crucible (middle), and temperature profile in the furnace (right).

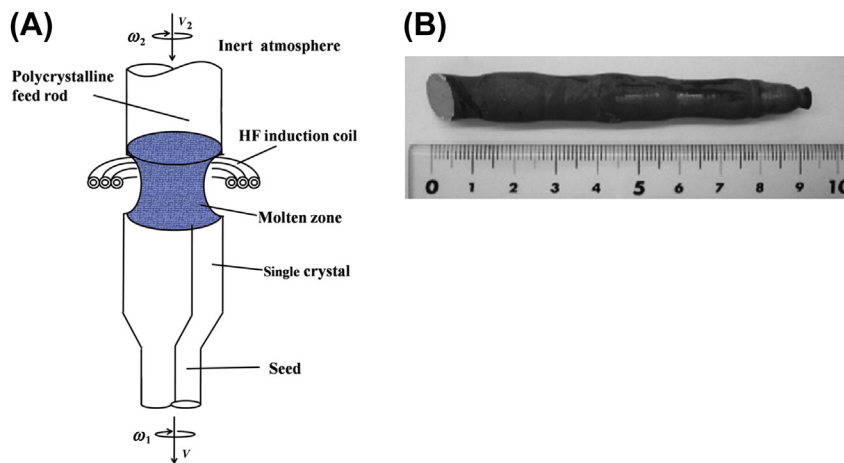


FIGURE 26.19 (A) The schematic illustration of the floating zone method. (B) A single *i*-Al-Pd-Mn grown by the floating zone method [3]. HF, high-frequency.

### 26.4.3 Floating Zone Method

The floating zone method is schematically illustrated in Figure 26.19(A). Before crystal growth, a polycrystalline feed rod with the same composition as the target QC is prepared by arc melting or the electrical induction method. The diameter of the feed rod is similar to that of the final single QC. The concept of this method is forming a molten zone (floating zone) in the feed rod using a high-frequency induction coil or infrared heater (halogen lamps mounted around the growth region) and moving the molten zone upwards at a speed around 0.5–1 mm/h. The crystal growth proceeds by moving the molten zone from the bottom to the upper part of the feed rod.

Similar to the Czochralski method, an oriented seed can be preset at the bottom of the feed rod to control the quality and direction of the single QC. Because a planar liquid–solid interface is hard to achieve due to the inhomogeneous heating in the molten zone, the feed rod and grown rods are rotated slowly in opposite directions to eliminate the composition gradient along the radial direction in the molten zone. So far, the floating zone method has been successfully used for growing large single QCs of *i*-Al–Pd–Mn [3] and *d*-Al–Ni–Co [60,61]. Figure 26.19(B) shows a photograph of the single *i*-Al–Pd–Mn produced by the floating zone method [3]. The growth direction is along a twofold axis, which is controlled by a single grain seed at the right part of the image.

#### 26.4.4 Solution Growth (Self-Flux) Method

There exists a field that the QC is in equilibrium with the melt in the phase diagrams in many QC alloys; hence, the self-flux method is applicable. It is possible to extract single grains from molten solution at high temperatures if an appropriate starting composition and a suitable decanting temperature are selected. So far, the self-flux method has been widely applied for growing single QCs of *i*-Al–Cu–Fe [62], *i*-Al–Pd–Mn [63], *i*-Al–Cu–Ru [64], *i*-Al–Pd–RE [65,66], *i*-Ag–In–Yb [67], *i*-Zn–Mg–RE (RE = Y and rare earth) [68], *i*-Zn–Sc [69], *i*-Cd–RE [70], and *d*-Al–Ni–Co [43,71] by cooling an off-stoichiometric melt that intersects the liquids associated with the QC phase.

Figure 26.20 shows a schematic illustration of process for the self-flux method applied in several QCs. Special care in the process is that a mesh fixed at a position above the alloy for decanting the melt at the end of crystal growth. Normally, the melt is homogenized at high temperatures and then cooled down slowly at a rate of 0.1–3 °C/h. In some cases, to control the nucleation process and reduce the number of nuclei, a cold finger attached at the bottom of the crucible is introduced in a modified setup [72]. At a certain temperature before a second phase solidifies, the ampoule containing the single QCs and melt is removed from the furnace and turned upside down into a centrifuge to spin off the remaining liquid phase. There is an advantage to this method, in that the QCs grown always exhibited a natural facet, as shown in Figure 26.21, which enable one to index the orientation of QC quickly.

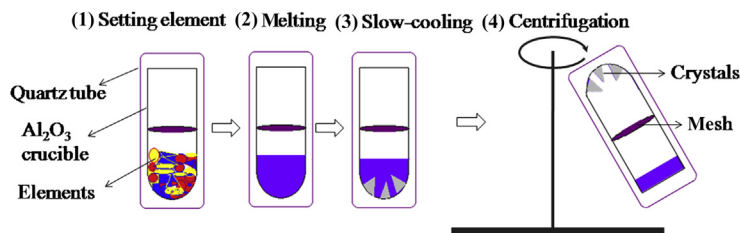


FIGURE 26.20 The schematic illustration of the self-flux method.

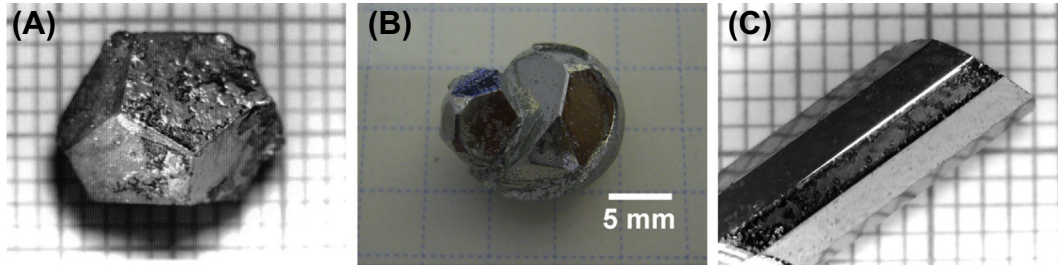


FIGURE 26.21 Single quasicrystals of (A) *i*-Al-Pd-Mn [63], (B) *i*-Ag-In-Yb [67], and (C) *d*-Al-Ni-Co [71] synthesized by the self-flux method.

## 26.5 Selected Results

As shown in Section 26.3 and Table 26.2, QCs are stable in some alloy systems and exist in the phase diagrams. Moreover, most stable QCs reveal high structural perfection, for which one may expect production of high-quality single-grain samples. However, in reality, this is still a technical challenge because of the following reasons. (1) Most stable QCs are ternary intermetallic compounds. This gives a complexity to the solute partition between melts and solids upon solidification. (2) Most QCs form through complex peritectic reactions. That is, they do not crystallize primarily in the melts. (3) Some QCs consist of elements such as Zn or Mg, which have low melting temperatures and high vapor pressures, thus creating technical difficulty in crystal growth. These problems are also inherent in many binary and ternary crystalline intermetallic compounds. Hence, the successful growth of single crystal requires applying the proper method, designating the alloy composition, and maintaining precise control of the temperature program. The single crystal growth processes developed for a number of QCs using various techniques in different alloys systems are summarized in Table 26.3 A number of cases are described in the following sections.

### 26.5.1 Al-Pd-Mn System

The temperature gap between the *L* (liquid) and IQC phase in Al-Pd-Mn system is around 20 °C, which is the smallest among Al-base QC alloys and can be easily bypassed by supercooling during crystal growth. Hence, only the single grains of *i*-Al-Pd-Mn with sizes on the order of centimeters have been easily grown by the Czochralski method [42,43], Bridgman method [53], floating zone method [3], and self-flux method [63].

Yokoyama et al. reported a partial isothermal phase diagram, in which the IQC phase precipitates as a primary phase in the range of 3–9 at% Mn and 18–25 at% Pd [42]. Based on the phase diagram, a large single IQC with diameter of 10 mm and length of 50 mm could be grown with an initial composition of Al<sub>73.5</sub>Pd<sub>19.7</sub>Mn<sub>6.8</sub> at 870 °C by the Czochralski method [42]. Gödecke and Lück [73] reported the refined phase diagram shown in Figure 26.22, where the IQC phase solidifies from melt in range of about 71–78 at% Al, 15–22 at% Pd, and 4–10 at% Mn. A vertical cut section at 20 at% Pd content

**Table 26.3** Single Crystal Growth Process Developed for a Number of Quasicrystals Using Various Techniques in Different Alloys Systems

Alloys	Techniques	Conditions (Initial Composition, Growth Temperature, Growth Rate)	Size	References
<i>i</i> -Al-Fe-Cu	Czochralski	Al <sub>57.7</sub> Cu <sub>37.7</sub> Fe <sub>3.5</sub> Si <sub>1.1</sub> , 800 °C, 0.2 mm/h	Φ = 4 mm, L = 40 mm	[40]
		Al <sub>57.7</sub> Cu <sub>37.7</sub> Fe <sub>3.5</sub> Si <sub>1.1</sub> , 800 °C, 0.18 mm/h	Φ = 2 mm, L = 100 mm	[41]
	Self-flux	Al <sub>60</sub> Cu <sub>36</sub> Fe <sub>4</sub> , cooled from 900 to 780 °C at 1 °C/h and decanted	5 mm	[62]
<i>i</i> -Al-Pd-Mn	Czochralski	Al <sub>73.5</sub> Pd <sub>19.7</sub> Mn <sub>6.8</sub> , 870 °C	Φ = 10 mm, L = 50 mm	[42]
		Al <sub>72.4</sub> Pd <sub>20.5</sub> Mn <sub>7.1</sub> , 890 °C	Φ = 8 mm, L = 50 mm	[43]
	Bridgman	0.5 °C/h	1.5 × 0.5 × 0.5 cm <sup>3</sup>	[53]
	Floating zone	Al <sub>72</sub> Pd <sub>19</sub> Mn <sub>9</sub> , 1 mm/h	Φ = 12 mm, L = 50 mm	[3]
	Self-flux	Al <sub>73</sub> Pd <sub>19</sub> Mn <sub>8</sub> , cooled from 875 °C to T <sub>d</sub> (835–870 °C) in a duration of 120 h	10 mm	[63]
<i>i</i> -Al-Li-Cu	Czochralski	Al <sub>63</sub> Li <sub>25</sub> Cu <sub>12</sub> , 600 °C, 0.3 mm/h	Φ = 1–5 mm, L = 60 mm	[44]
<i>i</i> -Al-Cu-Ru	Self-flux	Al <sub>62</sub> Cu <sub>34.5</sub> Ru <sub>3.5</sub> , cooled from 1050 to 800 °C at 2 °C/h and decanted	5 mm	[64]
<i>i</i> -Al-Pd-RE	Self-flux	Al <sub>75</sub> Pd <sub>20</sub> Re <sub>5</sub> , cooled from 1050 to 900 °C at 1 °C/h and decanted	5 mm	[65]
		Al <sub>93-x</sub> Pd <sub>x</sub> Re <sub>7</sub> (x = 15–22), cooled from 1025 to 900 °C at 0.5 °C/h and decanted	5 mm	[66]
<i>i</i> -Ag-In-Yb	Bridgman	Ag <sub>42</sub> In <sub>42</sub> Yb <sub>16</sub> , upper temperature 800 °C, 0.2 mm/h	Φ = 10 mm	[54]
		Ag <sub>42</sub> In <sub>42</sub> Yb <sub>16</sub> , upper temperature 800 °C, 0.5–0.8 mm/h	Φ = 11 mm, L = 30 mm	[55]
	Self-flux	Ag <sub>41</sub> In <sub>44</sub> Yb <sub>15</sub> , cooled from 635 to 610 °C at 1 °C/h and decanted	10 mm	[67]
<i>i</i> -Zn-Mg-RE	Bridgman	Zn <sub>46</sub> Mg <sub>51</sub> Ho <sub>3</sub> , upper temperature 680 °C, 0.2 mm/h	0.5 cm <sup>3</sup>	[56]
		Zn <sub>62.8</sub> Mg <sub>33.6</sub> Ho <sub>3.6</sub> , upper temperature 750 °C, 0.2 mm/h	1.5 × 0.8 × 0.2 mm <sup>3</sup>	[57]
	Self-flux	Zn <sub>46</sub> Mg <sub>51</sub> RE <sub>3</sub> , cooled from 650 to 480 °C at 2 °C/h and decanted	8 mm	[68]
<i>i</i> -Zn-Sc	Self-flux	Zn <sub>100-x</sub> Sc <sub>x</sub> (x = 2–4), cooled from 800 to 480 °C at 5–10 °C/h and decanted	0.5 cm <sup>3</sup>	[69]
<i>i</i> -Cd-RE	Self-flux	Cd <sub>99.2</sub> RE <sub>0.8</sub> (RE = Y, Gd–Dy) or Cd <sub>99.4</sub> RE <sub>0.6</sub> (RE = Ho–Tm), cooled from 455 to 335 °C at 2 °C/h and decanted	1 mm	[70]
<i>d</i> -Al-Ni-Co	Czochralski	Al <sub>75</sub> Ni <sub>14.5</sub> Co <sub>10.5</sub> , 7 mm/h	Φ = 8 mm, L = 30 mm	[45]
		Al <sub>83</sub> Ni <sub>9</sub> Co <sub>8</sub> , 927 °C, 1 mm/h	Φ = 1–7 mm, L = 60 mm	[46]
		Al <sub>75.6–78.5</sub> Ni <sub>11.0–14.0</sub> Co <sub>7.5–13.4</sub> , 1050 or 1100 °C, 0.2–0.5 mm/h	1 cm <sup>3</sup>	[47,48]
		Al <sub>75</sub> Ni <sub>14.5</sub> Co <sub>10.5</sub> , 1–2 mm/h	Φ = 10 mm, L = 60 mm	[49]
		Al <sub>77</sub> Ni <sub>17</sub> Co <sub>6</sub> , 0.15 mm/h	Centimeters	[50]

**Table 26.3** Single Crystal Growth Process Developed for a Number of Quasicrystals Using Various Techniques in Different Alloys Systems—cont'd

Alloys	Techniques	Conditions (Initial Composition, Growth Temperature, Growth Rate)	Size	References
	Bridgman	$\text{Al}_{77}\text{Ni}_{12.5}\text{Co}_{10.5}$ , upper temperature 1200 °C, 1 mm/h	3–4 cm <sup>3</sup>	[43]
	Floating zone	$\text{Al}_{72}\text{Ni}_{12}\text{Co}_{16}$ , 0.5 mm/h	1 cm <sup>3</sup>	[60,61]
	Self-flux	$\text{Al}_{77.0}\text{Ni}_{10.5}\text{Co}_{12.5}$ , slowly cooled from 1200 to 1000 °C and decanted	1 cm <sup>3</sup>	[71]
		$\text{Al}_{77.0}\text{Ni}_{10.5}\text{Co}_{12.5}$ , slowly cooled to 1010 °C and decanted	1–2 cm <sup>3</sup>	[43]
<i>d</i> -Al–Cu–Co	Czochralski	$\text{Al}_{63.9}\text{Cu}_{28.2}\text{Co}_{7.9}$ , 900 °C, 0.3 mm/h	$\Phi = 1\text{--}5$ mm, $L = 30$	[51]
		$\text{Al}_{66.0}\text{Cu}_{26.0}\text{Co}_{8.0}$ , 0.1 mm/h	2 g, needle shape	[52]
	Bridgman	$\text{Al}_{65}\text{Cu}_{27.5}\text{Co}_{7.5}$ , upper temperature 1100 °C, 0.2 mm/h	$\Phi = 5$ mm, $L = 10$ mm	[59]

$\Phi$ , diameter;  $L$ , length.

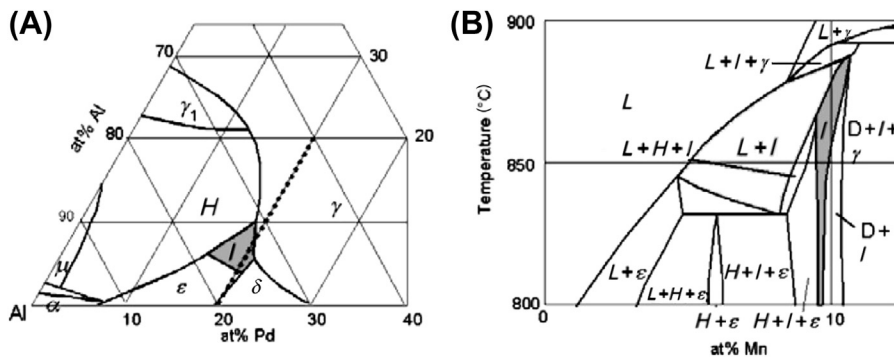


**FIGURE 26.22** (A) Phase diagram of the Al–Pd–Mn system involves the solidification area of the icosahedral quasicrystal phase. (B) A vertical cut section at 20 at% Pd content, as highlighted by the dotted line in (A) [74].

(highlighted by the dotted line in Figure 26.22(A)) is shown in Figure 26.22(B), in which the  $L + I$  refers to the area that the IQC phase is in equilibrium with liquid phase, with  $I$  being the stability range of the IQC phase.

Based on the phase diagram, Feuerbacher et al. prepared high-quality single *i*-Al–Pd–Mn from a melt of  $\text{Al}_{72.4}\text{Pd}_{20.5}\text{Mn}_{7.1}$  using the Czochralski method [43]. Single grain with twofold or fivefold orientation was used as seeds and dipped into the melt at 890 °C. After wetting the seed, the temperature of the melt was increased by about 10 °C to grow a thin neck of about 1 cm in length, followed by a decrease in temperature to increase the ingot diameter. The final temperature for constant diameter growth was about 880 °C.

Further progress for single IQC growth in a Al–Pd–Mn system was made using a self-flux method developed by Fisher et al. [63]. The optimal initial composition is  $\text{Al}_{73}\text{Pd}_{19}\text{Mn}_8$ , which is close to the composition of the IQC phase ( $\text{Al}_{71}\text{Pd}_{21}\text{Mn}_8$ ). The temperature profile is as follows: heat to 1100 °C to get a homogeneous melt, rapidly cool

down to 875 °C, slow cool (approximately 120 h) from 875 to  $T_d$  ( $835\text{ °C} < T_d < 870\text{ °C}$ ), and decant the residual liquid phase. By changing the decanting temperature, single grains with a mass of several to several tens of grams have been grown. The obtained single grains exhibited pentagonal dodecahedral faceted morphology (Figure 26.21(A)).

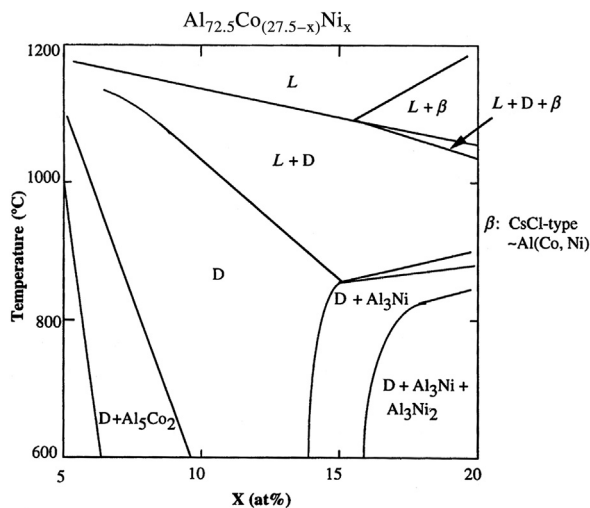
## 26.5.2 Al–Ni–Co System

Among the DQCs found to date, it is easy to grow a large single grain in *d*-Al–Ni–Co ( $\text{Al}_{72}\text{Ni}_{12}\text{Co}_{16}$ ). As shown in Table 26.3, single *d*-Al–Ni–Co grains with a size on the order of centimeters have been synthesized via the Czochralski method [45–50], Bridgman method [43], floating zone method [60,61], and self-flux method [43,71].

The phase diagram of the Al–Co–Ni alloy system has been studied by several groups [75,76]. Figure 26.23 shows a partial phase diagram along  $\text{Al}_{72.5}\text{Co}_{27.5-x}\text{Ni}_x$  ( $x = 5\text{--}20$  at%) isopleths involving the primary crystallization field of the quasicrystalline phase [75]. The *d*-Al–Ni–Co is an incongruent melting phase, existing in a large composition range compared to the IQCs in Al-based alloys.  $L + D$  shows the area that the DQC phase is in equilibrium with liquid phase and  $D$  is the stability range of DQC phase. Sato et al. were the first to grow centimeter-sized single *d*-Al–Ni–Co by the floating zone method [60]. Single grains with a volume of  $1\text{ cm}^3$  have been obtained using starting polycrystalline rods with a composition of  $\text{Al}_{72}\text{Ni}_{12}\text{Co}_{16}$  at a growth rate of 0.5 mm/h. Because the *d*-Al–Ni–Co phase is in equilibrium with the Al-enriched liquid phase in a large composition range in the phase diagram, it is easy to grow single *d*-Al–Ni–Co from Al-rich molten solution by the self-flux method. Fisher et al. [71] and Feuerbacher et al. [43] have prepared centimeter-sized single *d*-Al–Ni–Co from an initial melt of  $\text{Al}_{77.0}\text{Ni}_{10.5}\text{Co}_{12.5}$ .

The most successful growth of centimeter-sized single *d*-Al–Ni–Co has been carried out using the Czochralski method [45–50]. The details have been studied by Gille et al. [47,48,50]. With this method, high-quality single grains of centimeter size have been

**FIGURE 26.23** A partial phase diagram along  $\text{Al}_{72.5}\text{Co}_{27.5-x}\text{Ni}_x$  ( $x = 5\text{--}20$  at%) isopleths involving the primary crystallization field of the decagonal quasicrystal phase [75].



synthesized from Al-rich melts in the range of approximately 75.6–78.5 at% Al, 11.0–14.0 at% Ni, and 7.5–13.4 at% Co. During the process, the seed was dipped into the melt at 1050 °C. The crystal growth was performed using a very slow pulling rate (0.1–0.5 mm/day) as well as rotation of the crucible and the growing ingot in opposite directions. The diameter of the ingot is mainly controlled by the temperature of the melt. Thus, after having increased the diameter of the ingot to about 10–15 mm at a certain temperature, a decrease in temperature of 0.1–0.8 K/h is applied to keep the diameter constant. The morphology of the final ingot is dependent on the orientation of the seed QC. Circular cross-sections of the growing ingot were obtained when *d*-Al–Ni–Co seeds of [00001] orientation were used, whereas with other growth directions elliptical shapes of the growth interface occurred due to the anisotropic growth, with much faster growth rates along the periodic direction of the 10-fold axis. The single *d*-Al–Ni–Co grown on an oriented seed shows a clear faceting corresponding to the 10-fold or 2-fold symmetry, as shown in Figure 26.17(B). The unoriented single *d*-Al–Ni–Co has facets of 32 types, with different inclination of planes toward the 10-fold axis [50].

### 26.5.3 Zn–Mg–RE System

The *i*-Zn–Mg–RE system ( $\text{Zn}_{60}\text{Mg}_{30}\text{RE}_{10}$ , RE = Y and rare earth) is a family of stable IQCs that contains localized 4f electrons of rare earth elements, which enable intrinsic magnetism inherent in quasiperiodic lattices [39,68]. The growth of single IQCs in this system allows one to study the magnetic properties of a quasiperiodic structure. Langsdorf et al. has performed single crystal growth in a Zn–Mg–Y system using a liquid-encapsulated top-seeded solution growth method [77,78], in which a LiCl–KCl mixture was used as liquid encapsulant to prevent the evaporation of Zn and Mg components. With this method, single grains of *i*-Zn–Mg–Y with dimensions of a few millimeters in size can be obtained. Sato et al. reported the growth of a large single *i*-Zn–Mg–Ho of 0.5 mm<sup>3</sup> in volume with the Bridgman method, in which the vapor can be confined within a small closed crucible [56]. However, considering the phase diagram of the Zn–Mg–RE systems, the most suitable method for single *i*-Zn–Mg–RE growth is the self-flux method from Mg-rich melts [68].

Figure 26.24(A) shows a pseudobinary section of the Zn–Mg–Y phase diagram for the section of  $\text{Zn}_{40+2y}\text{Mg}_{60-3y}\text{Y}_y$  determined by Langsdorf et al. [77,78], in which the IQC phase is in equilibrium with the liquid in a wide range (Q + melt), being easy to grow single IQCs from molten solution via the self-flux method. Other Zn–Mg–RE systems have similar phase diagrams as that of Zn–Mg–Y. Based on the phase diagram, the optimal starting composition for crystal growth with the self-flux method has been adjusted to be  $\text{Zn}_{46}\text{Mg}_{51}\text{RE}_3$  [68,77,78]. An exception is the Zn–Mg–Tb system, in which the primary solidification surface has shifted in composition and the initial composition is set to  $\text{Zn}_{40}\text{Mg}_{57.4}\text{Tb}_{2.6}$  [68]. Ta (or Mo) tubes are used in the experiment to prevent attack from Mg and rare earth elements. A perforated Ta strainer is incorporated into the Ta tube for decanting the remaining liquid melt. Following this procedure and the temperature program shown in Ref. [68], one can produce single IQCs with pentagonal

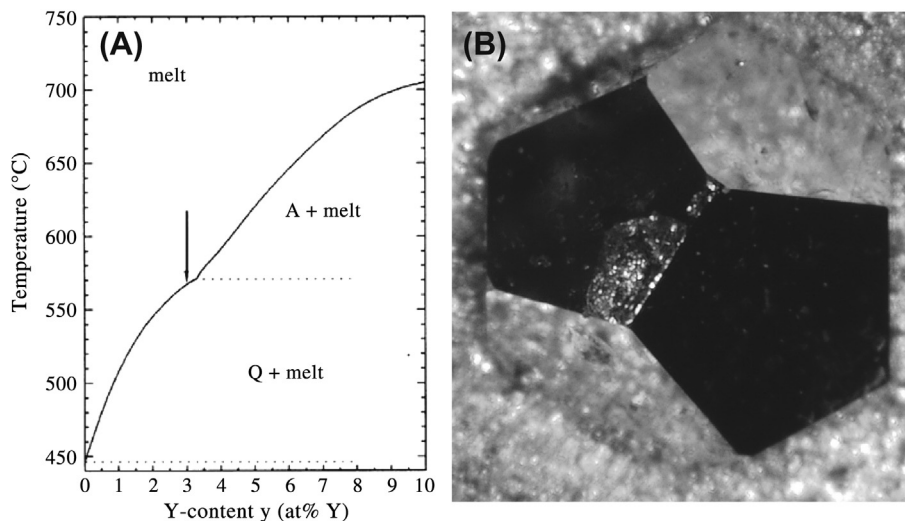


**FIGURE 26.24** (A) Pseudo-binary cut of the Zn–Mg–Y phase diagram for the section of  $Zn_{40+2y}Mg_{60-3y}Y_y$  [77,78]. The two-phase region in which the icosahedral quasicrystal phase is in equilibrium with the liquid is labeled Q + melt. The arrow shows the starting composition for crystal growth with the self-flux method. (B) Photograph of a single *i*-Zn–Mg–Dy ( $\sim 2$  mm in size) grown by self-flux method.

dodecahedral faceted morphology of up to centimeters in size (Figure 26.24(B)). The composition of the final obtained single *i*-Zn–Mg–RE is around  $Zn_{57}Mg_{34}RE_9$ .

#### 26.5.4 Ag–In–Yb System

The *i*-Ag–In–Yb system ( $Ag_{42}In_{42}Yb_{16}$ ) has been discovered based on the stable binary *i*-Cd–Yb ( $Cd_{5.7}Yb$ ) by replacing one half of the Cd with Ag and the other half of Cd with In [22,74]. In addition to the IQC phase, two kinds of periodic cubic structural approximants (the 1/1  $Ag_{40}In_{46}Yb_{14}$  approximant and 2/1  $Ag_{41}In_{44}Yb_{15}$  approximant) have also been discovered [54]. It is thus possible to carry out comparative investigation of IQC and approximants, which have similar building blocks but different long range orders [23].

The Ag–In–Yb can be regarded as a pseudo-binary system, and its partial phase diagram involving IQC phase and approximants is similar as that of the Cd–Yb system (Figure 26.25). The *i*-Ag–In–Yb is a congruently melting compound and is suitable for growing a large single grain with the Bridgman method [54,55], as shown in Figure 26.18. The sample is kept heating at 800 °C for 2 days to enable the homogeneous melting of the elements; then, the temperature of the upper zone is decreased to 627 °C for crystal growth. In the experiment, a growth rate of  $\sim 0.8$  mm/h produces high-quality single *i*-Ag–In–Yb. At a growth rate above 5 mm/h, the possibility of obtaining a polycrystalline sample increases evidently.

Figure 26.26(A) shows the macrographs of a sample grown with a starting composition of  $Ag_{42}In_{42}Yb_{16}$  at a growth rate of 0.8 mm/h. The size of the sample is 1.1 cm in diameter

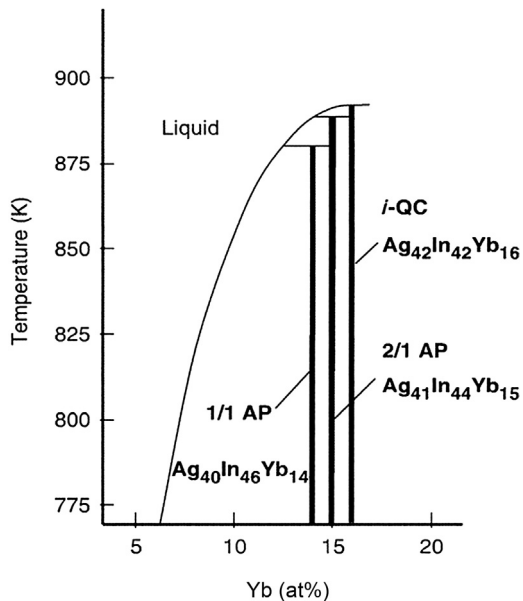


FIGURE 26.25 A partial phase diagram of the temperature-composition section along the composition line  $\text{Ag}_{26+x}\text{In}_{74-2x}\text{Yb}_x$  [54].

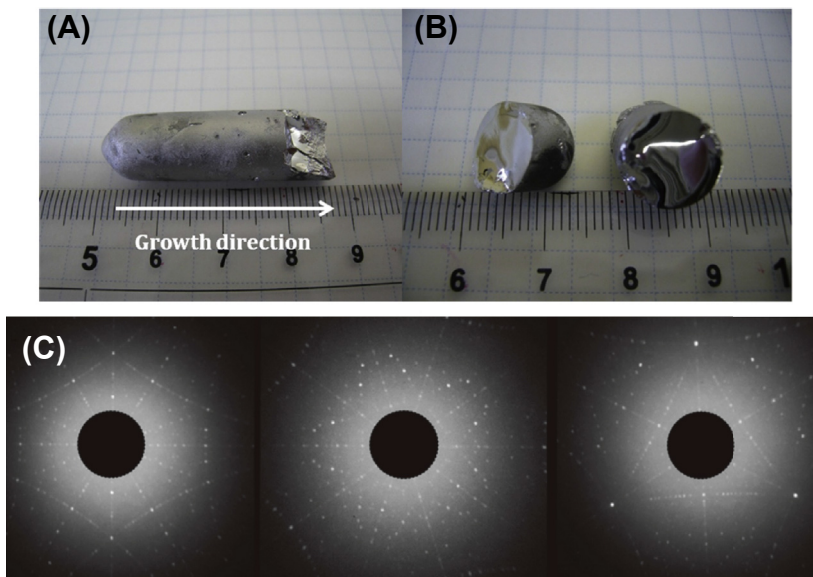


FIGURE 26.26 Macrograph of (A) appearance and (B) naturally cleaved fracture surface for the  $\text{Ag}_{42}\text{In}_{42}\text{Yb}_{16}$  sample [55]. (C) Back Laue diffraction patterns obtained from single grain of (A, B).

and over 3 cm in length. From the fragment, one can clearly observe the shiny part corresponding to the single grain region. Figure 26.26(B) shows the mirror-like naturally cleaved fracture surface of the same sample, which has luster and is smooth but not absolutely flat. The single grain is chemically homogeneous to be around  $\text{Ag}_{42}\text{In}_{42}\text{Yb}_{16}$  and structurally uniform, as confirmed by the back-reflection Laue X-ray diffraction patterns shown in Figure 26.26(C). The clear diffraction patterns with two-, three-, and fivefold symmetries indicate a highly ordered IQC structure over a long range of centimeter order. All the single-grain IQCs (about 20 samples) synthesized by the Bridgman method grew nearly along a twofold axis, according to the Laue diffraction experiment.

### 26.5.5 Cd-RE and Zn-Sc Systems

Two types of stable binary QCs—*i*-Cd-RE (RE = Gd to Tm, Y) and *i*-Zn-Sc ( $\text{Zn}_{88}\text{Sc}_{12}$ )—were discovered by Goldman and Canfield et al. via re-examination of the existing binary phase diagrams at compositions close to the approximant phase [69,70]. Both types of IQCs contain the same basic structural unit of an RTH cluster as that of *i*-Cd-Yb. However, the newly discovered *i*-Cd-RE QCs contain localized magnetic moments, which are different from the previously discovered nonmagnetic *i*-Cd-Yb. These binary QCs are obtained at compositions near the known crystalline approximants by the solution growth decanted at high temperatures and normally exhibited high disorder in structures.

## 26.6 Growth Mechanism

Because QCs are produced by both rapid and slow solidification, their morphologies and growth mechanism can be qualitatively understood in terms of classical solidification theory. However, due to the complexity of structure and phase diagrams, difficulties arose in the course of experiments. Short of structural information, there were only few reports dealing with growth mechanism. Recently, great progress on structural analysis has been made for *i*-Cd-Yb, which is helpful for understanding growth mechanism of QCs. Surface studies on QCs also provided crucial information for understanding growth morphology and stability. Indeed, understanding the stability and morphologies of QCs surfaces allows insight into the growth mechanism of QCs. Here, the morphologies of QCs will first be described; then, on the basis of the morphologies, phase diagrams, and surface studies, the growth mechanism will be discussed in terms of solidification theory.

### 26.6.1 Morphologies of QCs

#### 26.6.1.1 Stellated Polyhedron

In most of the early experiments, QCs synthesized by rapid solidification revealed highly dendritic morphologies. Visible but distorted pentagon dodecahedra around  $\sim 0.01$  mm

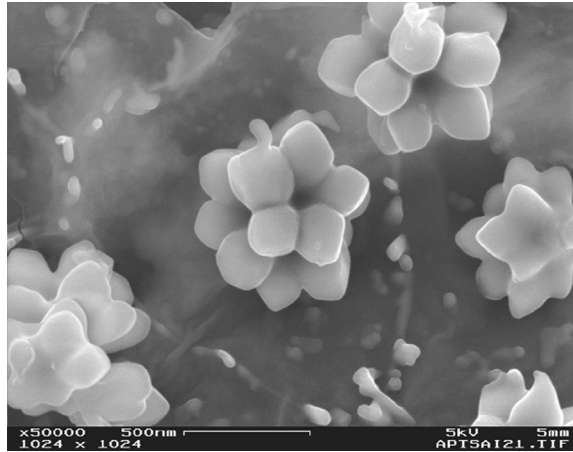


**FIGURE 26.27** An SEM image of melt-quenched  $A_{94}Mn_6$  alloy after etching treatment. Icosahedral quasicrystal reveals a stellated dodecahedral form.

were observed in melt-quenched  $AlMnSi$  [79,80]. For alloys containing lower contents of Mn (below 8 at%), a stellated polyhedron as shown in Figure 26.27 appeared, resembling one of the polyhedrons in the three-dimensional quasiperiodic lattice; this is shown in Figure 26.8(B), as composed of 20 acute rhombohedra and exhibiting icosahedral symmetry. The beautiful stellated polyhedral morphologies are only observed in low Mn-content Al alloys because of the formation of a small number of nuclei in the melt upon solidification, which allowed equiaxial growth of IQC grains. In view of the morphologies, it seems that the preferential growth direction is along the threefold direction.

#### 26.6.1.2 Rhombic Triacontahedron

One of most beautiful morphologies observed is the conventional solidification state of *i*-Al–Li–Cu ( $Al_{5.5}Li_3Cu$ ), which exhibits a form of a rhombic triacontahedron [81,82], as shown in Figure 26.28. This is the other polyhedron existing in a three-dimensional quasiperiodic lattice, which is consisted of 10 acute rhombohedra and 10 obtuse rhombohedra.

#### 26.6.1.3 Pentagonal Dodecahedron

The pentagonal dodecahedron is the morphology most often observed in IQCs. Clear morphologies were observed in conventionally solidified Al–Cu–Fe and Ga–Mg–Zn alloys. Similar morphologies with grain sizes of  $\sim 1$  mm were also observed in most stable IQCs, such as *i*-Al–Cu–Ru, *i*-Al–Pd–RE, *i*-Zn–Mg–RE, and *i*-Ag–In–Yb. As mentioned previously, except for *i*-Cd–Yb and *i*-Ag–In–Yb, all stable IQCs form through peritectic reactions at stoichiometric compositions. Figure 26.29(A) shows a faceted sphere morphological form in an as-solidified  $Al_{65}Cu_{20}Fe_{15}$  alloy. According to the phase diagram, the  $\beta$  and  $\lambda$  phases are the nucleation sites of IQC phase. It was recognized that the

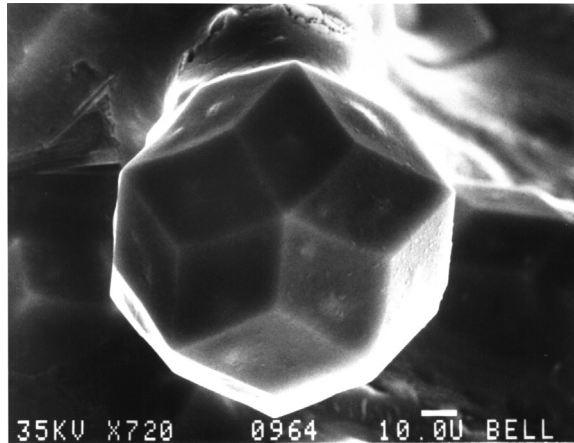


**FIGURE 26.28** An SEM image for an isolated single icosahedral quasicrystal with a rhombic tricontahedral morphology in Al-Li-Cu alloy [82].

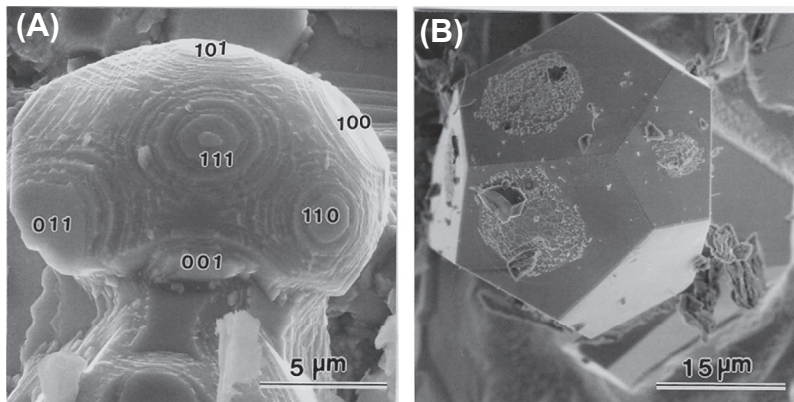


**FIGURE 26.29** (A) A faceted sphere and (B) a dodecahedral morphological forms of  $\beta$  and icosahedral quasicrystal phases in an arc-melting  $\text{Al}_{65}\text{Cu}_{20}\text{Fe}_{15}$  alloy [13].

faceted sphere is the  $\beta$  phase on which faceted planes can be indexed. Many steps surrounding the facet planes are clearly observed, which is a fingerprint of peritectic reactions. The [110] axis has been found to be coincident with one of the fivefold axes of the IQC phase. Hence, we may expect that the [110] plane would grow and the [100] and [111] would degenerate [13]. Therefore, the faceted sphere shown in Figure 26.29(A) is a midway stage of crystal growth; at a sufficiently slowing cooling rate, the  $\beta$  phase would be fully consumed to form a dodecahedral IQC phase, as shown in Figure 26.29(B). According to the morphology, it is clear that the IQCs in this case are not dendritic growth along three-fold axes. Instead, exhibition of larger and flat pentagonal planes indicates planar growth of IQCs along fivefold axes in melts upon slow cooling.

Surface studies on the *i*-Ag–In–Yb and *i*-Al–Pd–Mn show that fivefold planes have a flat structure—enough for obtaining atomic resolution [83]. This is evidence that the fivefold planes are relatively stable, terminating at planes containing relatively high concentrations of Yb (40 at%) for *i*-Ag–In–Yb (16 at% Yb) and Al (~80 at%) for *i*-Al–Pd–Mn (70 at% Al), with respect to their bulk compositions. According to structure models, the atomic densities  $\rho$  of twofold planes are highest ( $\rho_2 > \rho_5 > \rho_3$ ) in these two IQCs. However, Yb and Al, which have relatively low surface energies [84] with respect to the other two constituent elements, concentrated at fivefold planes would sufficiently lower the surface energy of fivefold planes. Especially upon crystal growth produced by solution growth process, the lower surface energies would reduce solid–liquid interfacial energies; consequently, a pentagonal dodecahedron would form.

#### 26.6.1.4 Decaprisism

Figure 26.30 shows columnar decagonal solidification morphologies of single grains in a conventionally solidified  $\text{Al}_{70}\text{Ni}_{15}\text{Co}_{15}$  alloy. The DQC phase possesses a two-dimensional quasiperiodic plane stacked periodically and the decaprisism morphology reflects the crystallographic symmetry of the DQC itself. Because the DQC forms in a wide composition range in the Al–Ni–Co system, this morphology was universally observed in several alloys. The elongated prismatic axis demonstrates that the growth is fastest along the 10-fold axis and slowest along twofold directions.

Figure 26.30(A) shows the beginning of columnar growth for DQC, where a number of grains are growing along the same 10-fold direction. The fronts of columns are basically spherical, but many facets inclined to the 10-fold axis on the fronts are visible. These facets correspond to planes relating to the periodic and quasiperiodic directions; they indicate the existence of dense atomic layers in DQC on net planes (lattice planes) inclined to the 10-fold axis and are related to strong Bragg reflections. Because they link

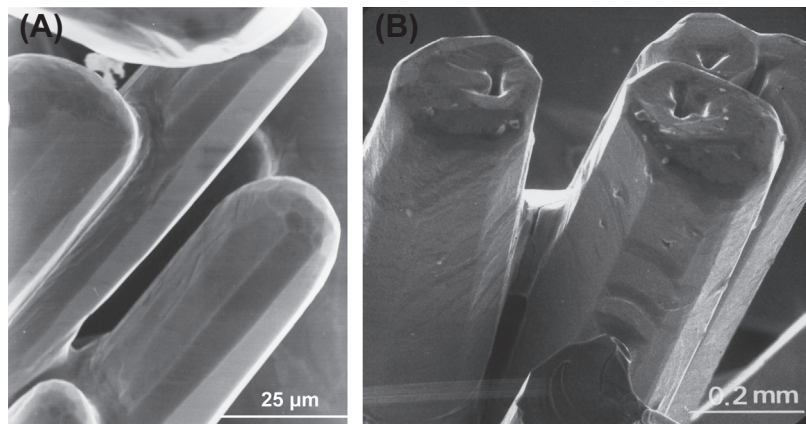


**FIGURE 26.30** A columnar decaprismatic solidification morphology of single grains of the decagonal quasicrystal in an  $\text{Al}_{70}\text{Ni}_{15}\text{Co}_{15}$  alloy. (A) A faceted column and (B) a decaprismatic solidification morphologies of single grains of decagonal quasicrystal in an  $\text{Al}_{70}\text{Ni}_{15}\text{Co}_{15}$  alloy

the quasiperiodic and periodic directions, these inclined net planes may play a crucial role in the growth and stabilization of DQC. Evidently, the atomic layers associated with these planes are not completely flat and exhibit some degree of corrugation [85]. However, this is supposed to be observed only in the very beginning of crystal growth, where the crystal is small enough and interfacial energy still works.

In Figure 26.30(B), many wrinkle-like lines are clearly seen at the twofold planes, which run across on different twofold planes along the twofold directions. This is a sign that crystal growth in DQCs is planar growth along the 10-fold axis. Surface studies on DQCs also revealed that the tenfold plane is stable because surface preparation was easy to prepare and large terraces were easy to obtain for 10-fold planes. On the other hand, there were always strong corrugations at twofold planes. One might be able to predict the morphology of decaprisms for QDCs from their surface stabilities.

## 26.6.2 Morphological Stability Theory

Because most stable QCs available for studying crystal growth are ternary alloys and have complicated phase diagrams, initial solidification processes are not easy to study. However, crystal growth for QCs could be qualitatively figured out in terms of the classical solidification theory.

According to the solidification theory, the solidification morphology of a crystalline grain is determined by the stability of the solid–liquid interface. When the interface changes from stable to unstable, the morphology of crystalline grains change from equiaxial grains with a planar interface to cellular grains, and then from cellular grains to dendritic grains on the basis of the *constitutional undercooling criterion*. Generally, the limit of constitutional undercooling can be expressed in its usual form [86]:

$$G/R > mC_0(k - 1)/D \quad (26.4)$$

where  $G$  is the interface temperature gradient,  $m$  is the liquidus slope,  $R$  is the rate of interface movement,  $C_0$  is the initial bulk solute concentration,  $k$  is the partition coefficient (the ratio of solute concentration in solid to that in liquid), and  $D$  is the diffusion coefficient. If the ratio of  $G/R$  is smaller than  $mC_0(k - 1)/Dk$ , interface instability will occur. It is clear that in a relatively low solute concentration, a high thermal gradient must be imposed in order to suppress interface instability and cellular dendritic growth.

By taking account of the interfacial energy, an absolute interface stability criterion has been derived in a dilute alloy [87].

$$A = k^2 T_m \Gamma R / (k - 1) m C_0 D \quad (26.5)$$

where  $A$  is an interface stability parameter (being 1 for a stable interface),  $\Gamma = \sigma/\Delta H$  is the surface tension constant,  $\sigma$  is the interfacial energy, and  $\Delta H$  is the latent heat. The criterion is especially available at high solidification rates. The higher the rate of interface movement, the less time there is for lateral diffusion of solute: long-wavelength perturbations at the solid–liquid interface do not have enough time to form. On the other hand, short-wavelength perturbations will be suppressed by surface tension. Thus, for a

liquid with given bulk solute concentrations, there is a solidification rate above which a planar interface is always stable. At a high solidification rate, stable planar growth can occur at concentrations far greater than those predicted by the constitutional supercooling criterion. Therefore, the absolute interface stability criterion is a good approximation at high solidification rates (e.g., the melt-quenched process), whereas the constitutional supercooling criterion is a good one at low solidification rates (e.g., normal crystal growth processes) [88]. As an illustration, a metastable equilibrium pseudo-binary phase diagram of the IQC phase and  $\alpha$ -Al face-centered cubic (fcc) phase in the Al–Mn system is shown in Figure 26.31(A) [89]. A schematic microstructure dependence on growth velocity,  $R$ , and composition,  $C_0$ , was constructed and is shown in Figure 26.31(B) [89]. At small  $C_0$  when  $R$  is small, the interface is stable and planar. This regime is represented by the lower left corner of the diagram. As the growth rate of a dendritic structure approaches that for absolute interface stability, it is anticipated that

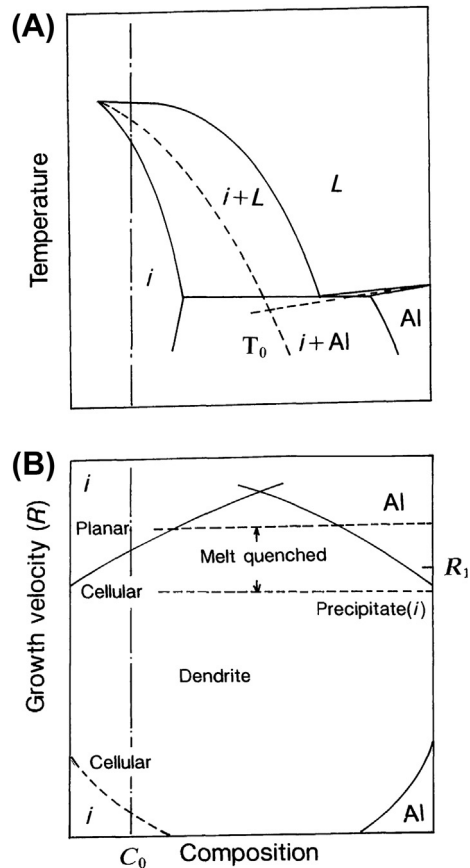


FIGURE 26.31 (A) A schematic of the metastable phase equilibria between the icosahedral quasicrystal ( $i$ ) and fcc Al phases. (B) The dependence of microstructure on the growth rate  $R$  and the composition  $C_0$  [89].

the microstructure will change from dendritic to cellular before becoming a planar front. At a very large  $R$  ( $A > 1$ ), the instability is suppressed and a planar front is retained, corresponding to the upper left corner of the diagram in [Figure 26.31\(B\)](#).

### 26.6.3 QCs upon Rapid Solidification

In earlier morphological investigations, the IQC grains were found to possess rounded outlines embedded in a matrix of fcc Al [90]. The IQC grains grew dendritically with arm directions along threefold axes. In some cases, faceted outlines with rather straight boundaries between the Al crystal and IQC phase and consequently pentagon dodecahedral morphology were found [80]. Now, the pentagonal dodecahedron as a principal morphology, found in rapidly solidified alloys as well as in most stable IQCs except Al–Li–Cu, is a consensus. However, depending on the preparation conditions, the morphology could be dendritic arms or pentagonal dodecahedra. This has been clarified by an investigation on melt-quenched Al–Pd–Cr alloy on the basis of criterion of the interface stability in alloy solidification [89]. [Figure 26.32](#) shows the TEM electron micrographs of melt-quenched  $\text{Al}_{72}\text{Pd}_{25}\text{Cr}_3$  alloy, revealing a mixed structure consisting of IQC and DQC phases. The IQC grains show an elongated columnar structure with a flat plane perpendicular to the fivefold axis; they are surrounded by the DQC phase in [Figure 26.32\(A\)](#). Here, the two IQC grains show the same twofold diffraction pattern with the same orientation, showing one of the fivefold directions that coincide with the planar growth direction (indicated with arrows) of the columnar structure. The results strongly suggest that the IQC predominantly grows along the fivefold direction during rapid solidification.

The diffraction patterns along the twofold direction taken from the regions near the interface between the IQC (A, C) and DQC (B, D) are compared in [Figure 26.32](#). One of fivefold directions of the IQC coincides with the 10-fold direction of their DQC. The angle between two adjacent 10-fold axes is  $63.43^\circ$ , which is equal to the angle

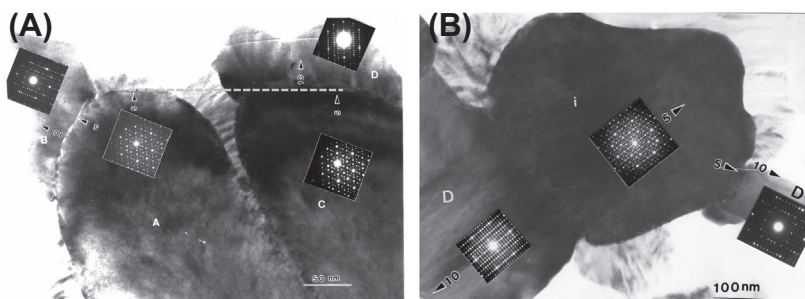


**FIGURE 26.32** Transmission electron microscopy images of a melt-quenched  $\text{Al}_{72}\text{Pd}_{25}\text{Cr}_3$  alloy taken along the coincident twofold axes of the decagonal quasicrystal (DQC) and the icosahedral quasicrystal (IQC) phases. (A) Each DQC phase grain is observed to be growing with its tenfold axis along one of fivefold axes of the parent IQC phase. (B) Two DQC grains grow with their tenfold axes along two different fivefold axes of the parent IQC phase [89].

between two fivefold axes on the twofold diffraction pattern or two adjacent fivefold axes of an icosahedron. The same orientation relationship was also confirmed in the different regions of the sample, as shown in [Figure 26.32\(B\)](#), where two DQC grains with angle of intersection of  $63.43^\circ$  nucleated from the same IQC grain. In all cases, the IQC phase grows along the fivefold direction, and the DQC nucleated out of the IQC and grow along the 10-fold direction, which coincides with one of the fivefold directions of the IQC.

The average compositions for IQC and DQC are  $\text{Al}_{67}\text{Pd}_{29}\text{Cr}_4$  and  $\text{Al}_{73}\text{Pd}_{25}\text{Cr}_2$ , respectively. IQC has higher Pd and Cr contents and, according to the phase diagrams, the solidification temperature for IQC would be higher than that of DQC. During solidification, the IQC nucleates and grows first, rejecting the excess Al into melt. This process then slows down the growth of the IQC and favors the nucleation of an Al-rich DQC. If the moving rate of the solid–liquid interface was fast enough to suppress the diffusion of Al at the interface, the formation of DQC would be suppressed and IQC with planar growth would be completed. In [Figure 26.32\(A\)](#), in the upper part, a horizon line indicates that the two IQC grains had the same front of the solid–liquid interface in the beginning, but it broke down upon solidification due to either the slow-moving rate of the interface or fast solute diffusion across the interface. Consequently, the dendritic growth would occur as shown in [Figure 26.31](#). For the same alloy but at a higher solidification rate, planar growth is still expected [89].

#### 26.6.4 QCs Prepared by Classic Crystal Growth Methods

The QCs produced by these processes have a common feature that they all revealed planar growth upon solidification. Because the solidification rates are all very small and the moving rate of the solid–liquid interface  $R$  would be small, and in terms of the constitutional supercooling criterion, planar growth occurs if the temperature gradient is not too large at the interface. This condition corresponds to the lower left part in [Figure 26.31\(B\)](#). The large pentagonal and decagonal planes observed in IQCs and DQCs prepared by the solution growth process are evidence of the planar growth. The planar growth is along the fivefold axis for the former and is along the 10-fold axis for the latter. The planar growth is also observed in several QCs prepared by the Bridgman and floating zone methods.

[Figure 26.33\(A\)](#) is a longitudinal microstructure near the solidification interface for a single DQC prepared by the floating zone method at a growth rate of 0.5 mm/h, starting with a raw material of  $\text{Al}_{72}\text{Ni}_{12}\text{Co}_{16}$  [91]. Phases aligned in the form of rods near the solidification interface consisted of fcc Al,  $\text{Al}_3\text{Ni}_2$ ,  $\text{Al}_9\text{Co}_2$ , and the DQC phase, although only the DQC was detected from the grown crystal and feed rod. These results indicate that at the steady state, a single DQC grain grows. When the heating power of the furnace is turned off, the melt starts to solidify from the solid–liquid interface, forming the four phases in the rod configurations. Therefore, the present quenching rate is high enough to preserve the solidification interface during the steady-state single crystal growth.

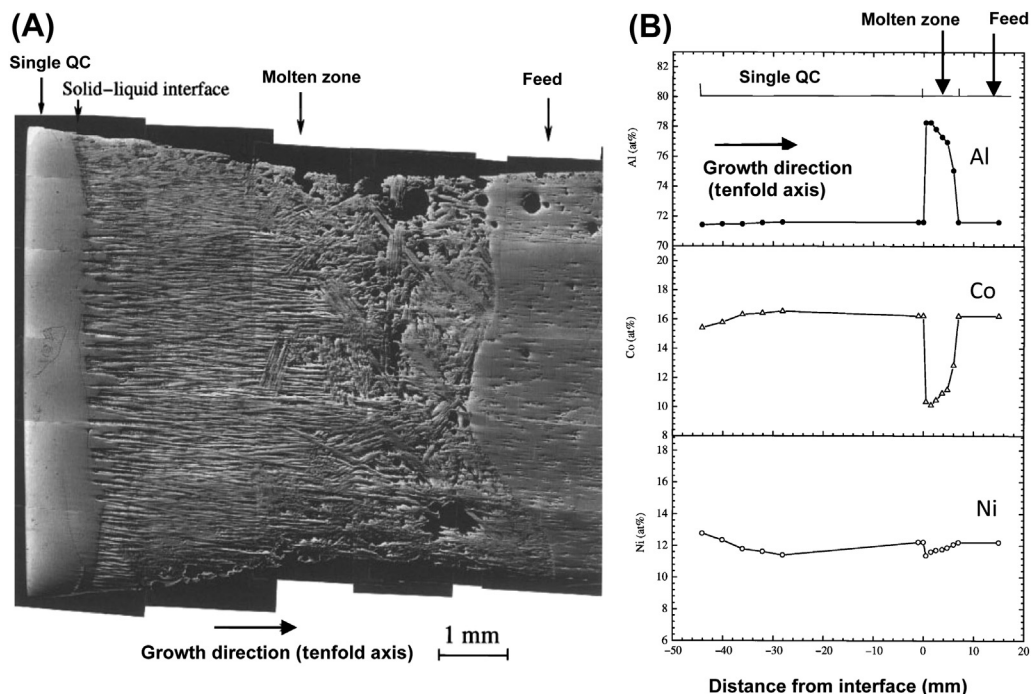


**FIGURE 26.33** (A) Optical microstructure of a longitudinal cross-section of an  $\text{Al}_{72}\text{Ni}_{12}\text{Co}_{16}$  alloy prepared by the floating zone method along the growth direction near the quenched molten zone. Note that the solidification interface is flat. (B) Composition distribution of Al, Ni, and Co along the longitudinal (growth) direction of the same sample [91].

Similar to crystalline solids, the flat quenched interface implies that planar growth proceeded, which is a prerequisite for single crystal growth of QCs.

Figure 26.33(B) shows the chemical composition distribution from the grown crystal to the feed rod through the quenched molten zone. At the initial growth stage, the crystal starts to grow, with Al and Co contents that are lower than those of the feed rod and Ni content that is the opposite. As the crystal growth proceeds, the composition becomes close to that of the feed rod and reaches the steady state. Solute redistribution at this steady state can be clearly seen at the quenched solidification interface in Figure 26.33(B). Al is significantly enriched in front of the solidification interface by 6.87 at%; conversely, Co and Ni are depleted by 5.95 at% and 0.93 at%, respectively, which indicates that the DQC is incongruent at  $\text{Al}_{72}\text{Co}_{16}\text{Ni}_{12}$ . The melt with this composition is considered to play the role of flux for the crystal growth of the incongruent alloy. Interestingly, the flux was spontaneously produced during the crystal growth. The solute partition ratios are supposed to be close to the equilibrium state. Due to significant solute redistribution, the single DQCs was only could grow at the lower growth rate,  $R$ . It is noted that spontaneous growth direction is parallel to the 10-fold axis. Similar planar growth with similar solute partition ratios was also observed for

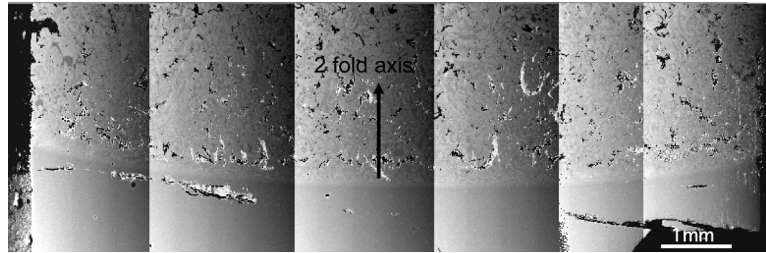


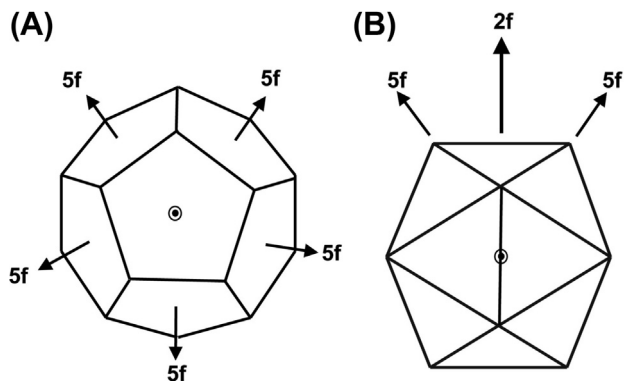
**FIGURE 26.34** Optical microstructure of a cross-section near the solidification interface of  $\text{Al}_{72}\text{Pd}_{19.5}\text{Mn}_{8.5}$  grown by the Bridgman method at a growth rate of 0.2 mm/h.

an IQC prepared by the floating zone method starting with  $\text{Al}_{72}\text{Pd}_{19.5}\text{Mn}_{8.5}$  and with a growth rate of 1.0 mm/h, in which the spontaneous growth direction was parallel to a twofold axis. Figure 26.34 is the microstructure of a cross-section across the solidification interface for a single IQC grown by the Bridgman method at 0.2 mm/h starting with  $\text{Al}_{72}\text{Pd}_{19.5}\text{Mn}_{8.5}$ . The front of solidification interface is slightly curved due to the surface tension of liquid and the effect of the crucible, but basically it is planar growth parallel to the twofold axis.

### 26.6.5 Selection of Growth Direction

The previously mentioned processes are common when using slow cooling upon solidification, but they differ in temperature gradient, growth direction, and crucible. In the floating zone, Czochralski, and solution growth process, QCs were grown in liquid without effects from the furnace; hence, they revealed different degrees of facet. In the solution growth process, because the overall furnace was cooled homogeneously, the temperature gradient at the solid–liquid interface is supposed to be very small. Isotropic growth of IQCs and anisotropic growth of DQCs in the liquids are expected according to their structure symmetries. In this case, the growth direction will be determined by the stability of atomic plane (i.e., the atomic structure of QCs themselves). According to structure models and surface studies [92,93], densities  $\rho$  of the atomic planes are in the order of  $\rho_2 > \rho_5 > \rho_3$  for  $i\text{-Ag-In-Yb}$  and  $i\text{-Al-Pd-Mn}$  (or  $i\text{-Al-Cu-Fe}$ ). Actually, the difference between  $\rho_5$  and  $\rho_2$  is very small and the concentration of elements with lower surface energies, such as Yb in  $i\text{-Ag-In-Yb}$  and Al in  $i\text{-Al-Cu-Fe}$ , are relatively higher on fivefold planes. In other words, concentration fluctuation of Yb or Al is the largest along the fivefold axis, and this scenario has been successful for interpreting the surface structures of fivefold planes for IQCs, where large terraces with nonperiodic step heights are observed [92,93]. The lower surface energy of the fivefold plane induces lower interfacial energy of the solid–liquid interface; this is a plausible reason why the fivefold plane is a steady state for growth, and consequently pentagonal dodecahedra of a few millimeters in size were observed in these two systems. This is also the case for  $i\text{-Zn-Mg-RE}$ .

**FIGURE 26.35** Schematics of (A) dodecahedrons and (B) icosahedrons used for describing the favorable direction upon unidirectional growth of icosahedral quasicrystals.



However, when temperature gradient was employed in crystal growth (e.g., floating zone and Bridgman methods) for IQCs, the growth direction was always along the direction parallel to a twofold axis. Two reasons are considerable for the conflict with the solution growth process. First, with the temperature gradient existing near the solid–liquid interface, the stability of the interface will be dominated by both solute distribution and interfacial energy. As a result, planar growth will prefer a direction with less concentration fluctuation (homogeneous) and, on an atomic plane, lower surface energy or higher atomic density. The second reason is explained by icosahedral symmetry of the IQCs. Figure 26.35 shows a schematic pentagonal dodecahedron along a fivefold axis (Figure 26.35(A)) and projection of icosahedron onto a twofold axis (Figure 26.35(B)), where twofold and fivefold axes are indicated with arrows. If there is a temperature gradient at the interface, the growth of IQCs will be constrained to unidirectional; six different fivefold planes with lower surface energy will be competitive for growth and only one of them will be selected, with the rest being suppressed (Figure 26.35(A)). With respect to this as shown in Figure 26.35(B), two adjacent fivefold planes complementarily grow; consequently, growth along a twofold axis will be energetically favored. On the other hand, due to strong anisotropy, the DQCs reveal a common feature of growth direction regardless of the crystal growth process.

## 26.7 Concluding Remarks

After a general introduction of QCs, including structural properties, structural models, and alloy systems, the crystal growth of QCs (as studied so far) was reviewed. Solidification theories, such as constitutional supercooling, and absolute interface stability criteria were employed to understand the growth mechanism of QCs. The solid–liquid interface stability and growth direction of QCs were interpreted in terms of structural models and surface studies.

It is clear now that more than a few QCs are stable and exist in the phase diagrams as equilibrium phases. All stable IQCs could be regarded as a new group of intermetallic

compounds that form at very strict compositions and normally have a special value of  $e/a$ . On the other hand, the formation of stable DQCs is more flexible in composition. For the former, the strict composition is an indication of the high structural stability, which favors crystal growth of IQCs in a given process. For the latter, flexibility in composition makes growing single grains easy, but their precise compositions are not controllable. Although the crystal structure of QCs is very complex, the quality of single grains of QC seems to be better than well-known intermetallic compounds with simple structures, as evidenced by the occurrence of a large number of sharp diffractions.

Due to the success in growing high-quality single grains of QCs, great progress in the structure, physical, and chemical properties and surfaces have been achieved. This progress can be used to understand the mechanisms of crystal growth for QCs.

## Acknowledgments

CC acknowledges the support of the National Natural Science Foundation of China (No.11074220) and Qianjiang Talent Program of Zhejiang Province (2013R10060).

## References

- [1] Shechtman D, Blech I, Gratias D, Cahn JW. *Phys Rev Lett* 1984;53:1951.
- [2] Levine D, Steinhardt PJ. *Phys Rev Lett* 1984;53:2477.
- [3] Tsai AP. *Chem Soc Rev* 2013;42:5352.
- [4] Shechtman D, Blech I. *Met Trans* 1985;16A:1005.
- [5] Stephens PW, Goldman AI. *Phys Rev Lett* 1986;56:1168.
- [6] Pauling L. *Proc Natl Acad Sci USA* 1990;87:7849.
- [7] Stephens PW, Goldman AI. *Sci Am* 1991;4:44.
- [8] Penrose R. *Bull Inst Math Appl* 1974;10:266.
- [9] International Union of Crystallography. *Acta Cryst* 1992;A48:922.
- [10] Bak P. *Phys Rev Lett* 1986;56:861.
- [11] de Bruijn NG. *Proc K Ned Akad Wet* 1981;A84:39.
- [12] Elser V, Henley CL. *Phys Rev Lett* 1985;55:2883.
- [13] Tsai AP. In: Stadnik Z, editor. *Physical properties of quasicrystal*. Springer series in solid-state science, vol. 126. Springer-Verlag Berlin Heidelberg; 1999. p5.
- [14] Henley CL. *Phys Rev B* 1986;34:797.
- [15] Yamamoto A. *Acta Cryst* 1996;A52:509.
- [16] Takakura H, Yamamoto A, Tsai AP. *Acta Cryst* 2001;A57:576.
- [17] Saito K, Tsuda K, Tanaka M, Kaneko K, Tsai AP. *Jpn J Appl Phys* 1987;36:1400.
- [18] Grummelt P. *Geometriae Dedicata* 1996;62:1.
- [19] Steinhardt PJ, Jeong HC, Saitoh K, Tanaka M, Abe E, Tsai AP. *Nature* 1998;396:55.
- [20] Henley CL, Elser V. *Philos Mag* 1986;B53:59.

- [21] Elser V. *Phys Rev B* 1985;32:4892.
- [22] Tsai AP, Guo JQ, Abe E, Takakura H, Sato TJ. *Nature* 2000;408:537.
- [23] Takakura H, Gomez CP, Yamamoto A, deBoissieu M, Tsai AP. *Nat Mater* 2007;6:58.
- [24] Palenzona A. *J Less Common Met* 1971;25:367.
- [25] Gómez CP, Lidin S. *Angew Chem Int Ed* 2001;40:4037.
- [26] Tsai AP, Inoue A, Masumoto T. *Jpn J Appl Phys* 1987;26:1505.
- [27] Bergman G, Waugh JLT, Pauling L. *Acta Cryst* 1957;10:254.
- [28] Semetana V, Lin Q, Pratt DK, Kreyssig A, Ramazanoglu M, Corbett JD, et al. *Angew Chem Int Ed* 2012;51:12699.
- [29] Fujita N, Takano H, Yamamoto A, Tsai AP. *Acta Cryst A* 2013;69:322.
- [30] Ishimasa T. In: Fujiwara T, Ishii Y, editors. *Quasicrystals: handbook of metal physics*. Elsevier; 2008. p. 49.
- [31] Wang N, Chen H, Huo KH. *Phys Rev Lett* 1987;59:1010.
- [32] Krumeich F, Conrad M, Harbrecht B. In: Jouffrey B, Colliex C, editors. *Proceedings of the 13th international congress on electron microscopy*. Les Editions de Physique Les Ulis, vol. 2A; 1994. p. 751.
- [33] Hume-Rothery W. *J Inst Met* 1926;36:295.
- [34] Tsai AP. *J Non Cryst Solids* 2004;317:334–5.
- [35] Hardy HK, Silcock JM. *J Inst Met* 1955–1956;84:423.
- [36] Ball MD, Lloyd DJ. *Scr Metall* 1985;19:1065.
- [37] Bradley AJ, Goldschmidt HJ. *J Inst Met* 1939;65:403.
- [38] Tsai AP, Niikura A, Inoue A, Masumoto T, Nishida Y, Tsuda K, et al. *Philos Mag Lett* 1994;70:169.
- [39] Padezhnova E, Melnik EV, Miliyevskiy RA, Dobotkina TV, Kinzhibalo VV. *Russ Metall (Engl Transl)* 1982;4:185.
- [40] Yokoyama Y, Fukaura K, Sunada H, Note R, Hiraga K, Inoue A. *Mater Sci Eng A* 2000;294–296:68–73.
- [41] Yokoyama Y, Matsuo Y, Yamamoto K, Hiraga K. *Mater Trans* 2002;43:762–5.
- [42] Yokoyama Y, Miura T, Tsai AP, Inoue A, Masumoto T. *Mater Trans JIM* 1992;33:97–101.
- [43] Feuerbacher M, Thomas C, Urban K. In: Trebin H-R, editor. *Quasicrystals. Structure and physical properties*. Weinheim: Wiley-VCH; 2003. p. 2–25.
- [44] Yokoyama Y, Fukaura K, Sunada H, Note R, Sato T, Hiraga K, et al. *Mater Trans JIM* 2000;41:522–6.
- [45] Feuerbacher M, Bartsch M, Grushko B, Messerschmidt U, Urban K. *Philos Mag Lett* 1997;76:369–76.
- [46] Yokoyama Y, Note R, Kimura S, Inoue A, Fukaura K, Sunada H. *Mater Trans JIM* 1997;38:943–9.
- [47] Gille P, Dreier P, Graber M, Scholpp T. *Cryst J. Growth* 1999;207:95–101.
- [48] Graber M, Barz R-U, Dreier P, Gille P. *Mater Sci Eng A* 2000;294–296:143–6.
- [49] Jeong HT, Kim SH, Kim WT, Kim DH, Inkson BJ. *J Cryst Growth* 2000;217:217–21.
- [50] Gille P, Meisterernst G, Faber N. *J Cryst Growth* 2005;275:224–31.
- [51] Yokoyama Y, Note R, Yamaguchi A, Inoue A, Fukaura K, Sunada H. *Mater Trans JIM* 1999;40:123–31.
- [52] Gille P, Dreier P, Barz R-U. *J Alloys Compd* 2002;342:7–12.
- [53] de Boissieu M, Durand-Charre M, Bastte P, Carabelli A, Boudard M, Bessiere M, et al. *Philos Mag Lett* 1992;65:147–53.

- [54] Ohhashi S, Hasegawa J, Takeuchi S, Tsai AP. *Philos Mag* 2007;87:3089.
- [55] Cui C, Tsai AP. *J Cryst Growth* 2010;312:131.
- [56] Sato TJ, Takakura H, Tsai AP. *Jpn J Appl Phys* 1998;37:663–5.
- [57] Uhrig E, Bruhne S, Sterzel R, Schropfer L, Assmus W. *Philos Mag Lett* 2003;83:265–72.
- [58] Zhang LM, Luck R, Gille P. *J Cryst Growth* 2005;275:2077–82.
- [59] Guo JQ, Abe E, Sato TJ, Tsai AP. *Jpn J Appl Phys* 1999;38:1049–51.
- [60] Sato TJ, Hirano T, Tsai AP. *J Cryst Growth* 1998;191:545–52.
- [61] Tsai AP, Sato TJ, Guo JQ, Hirano T. *J Non Cryst Solids* 1999;250–252:833.
- [62] Guo JQ, Tsai AP. *J Mater Res* 2001;16:3038.
- [63] Fisher IR, Kramer MJ, Wiener TA, Islam Z, Ross AR, Lograsso TA, et al. *Philos Mag B* 1999;79:1673–84.
- [64] Guo JQ, Hasegawa H, Tsai AP, Takeuchi S. *J Cryst Growth* 2002;236:447–81.
- [65] Guo JQ, Sato TJ, Abe E, Takakura H, Tsai AP. *Philos Mag Lett* 2000;80:495–502.
- [66] Fisher IR, Xie XP, Tudosa I, Gao CW, Song C, Canfield PC, et al. *Philos Mag B* 2002;82:1089–98.
- [67] Cui C, Tsai AP. *J Alloys Compd* 2012;536:91.
- [68] Fisher IR, Islam Z, Panchula AF, Cheon KO, Kramer MJ, Canfield PC, et al. *Philos Mag B* 1998;77:1601–15.
- [69] Canfield PC, Caudle ML, Ho CS, Kreyssig A, Nandi S, Kim MG, et al. *Phys Rev B* 2010;81:020201.
- [70] Goldman AI, Kong T, Kreyssig A, Jesche A, Ramazanoglu M, Dennis KW, et al. *Nat Mater* 2013;12:714–8.
- [71] Fisher IR, Kramer MJ, Islam Z, Ross AR, Kracher A, Wiener TA, et al. *Philos Mag B* 1999;79:425–34.
- [72] Heggen M, Feuerbacher M, Schall P, Klein H, Fisher IR, Canfield PC, et al. *Philos Mag Lett* 2000;80(3):129–36.
- [73] Gödecke T, Lück R. *Z Metallkd* 1995;86:109.
- [74] Guo JQ, Tsai AP. *Philos Mag Lett* 2002;82:349.
- [75] Fujiwara A, Inoue A, Tsai AP. In: Takeuchi S, Fujiwara T, editors. *Proceeding of the sixth international conference on quasicrystals*. Singapore: World Scientific; 1998. p. 341.
- [76] Gödecke T. *Z Metallkd* 1997;88:557.
- [77] Langsdorf A, Ritter F, Assmus W. *Philos Mag Lett* 1997;75:381.
- [78] Langsdorf A, Assmus W. *J Cryst Growth* 1998;192:152–6.
- [79] Ishimasa T, Nissen HU. *Phys Scr T* 1986;13:291.
- [80] Robertson JL, Misenheimer ME, Moss SC, Bendersky LA. *Acta Metall* 1986;34:2177.
- [81] Dubost B, Lang JM, Tanaka M, Sainfort P, Audier M. *Nature* 1986;324:48.
- [82] Kortan AR, Chen HS, Parsey Jr JM, Kimerling LC. *J Mater Sci* 1989;24:1999.
- [83] Sharma HR, Shimoda M, Tsai AP. *Adv Phys* 2007;56:403.
- [84] Vitos L, Ruban AV, Skriver HL. *J Kollar Surf Sci* 1998;411:186.
- [85] Steurer W, Cervellino A. *Acta Cryst A* 2001;57:333.
- [86] Flemings MC, editor. *Solidification process*. New York: McGraw-Hill; 1974. p. 273.
- [87] Mullins WW, Sekarka RF. *J Appl Phys* 1964;35:444.
- [88] Coriell SR, Sekarka RF. *Rapid solidification and technology II*. In: Mehrabian R, Kear BH, Cohen M, editors. *Baton Rouge, LA: Claitors; 1980. p. 35.*

- [89] Tsai AP, Chen HS, Inoue A, Masumoto T. *Jpn J Appl Phys* 1991;30:1132.
- [90] Schaefer RJ, Bendersky LA, Shechtman D, Boettinger WJ, Biancaniello FS. *Metall Trans A* 1986;17:2117.
- [91] Guo JQ, Sato TJ, Hirano T, Tsai AP. *J Cryst Growth* 1999;197:963.
- [92] Sharma HR, Fournee V, Shimoda M, Ross AR, Lograsso TA, Tsai AP, et al. *Phys Rev Lett* 2004;93:165502.
- [93] Sharma HR, Shimoda M, Sagisaka K, Takakura H, Smerdon JA, Nugent PJ, et al. *Phys Rev B* 2009;80:121401R.



# Index

*Note:* Page numbers followed by “b”, “f” and “t” indicate boxes, figures and tables respectively

## A

- AACG. *See* American Association for Crystal Growth
- Ab initio  
  calculations, 145, 395–396  
  methods, 522  
  thermodynamics, 535–537
- Ab initio-based approach, 478–479  
  computational methods, 479–484  
  GaAs, 484–492  
  GaN, 502–510
- A–B phase diagram, 112–113
- Absolute solid-on-solid model (ASOS model), 286
- ACC. *See* Amorphous calcium carbonate
- Accelerated crucible rotation technique (ACRT), 47
- Achiral molecules, 992–998
- ACP. *See* Amorphous calcium phosphate phase
- ACRT. *See* Accelerated crucible rotation technique
- Active pharmaceutical ingredient (API), 916.  
  *See also* Pharmaceutical crystallization
- Adatoms, 383, 531–533
- Adhesive growth. *See* Normal growth
- ADP. *See* Ammonium dihydrogen phosphate
- Adsorption, 533–534
- Adsorption-layer theory, 6
- Adsorption–desorption behavior, 485
- AEF. *See* Alternating electric field
- AEF-controlled 2D colloidal system, 577
- AFGP. *See* Antifreeze glycoprotein
- AFM. *See* Atomic force microscopy
- AFP. *See* Antifreeze protein
- Ag–In–Yb system, 1140–1142
- Air flow on pattern, 1079–1080
- Al<sub>72</sub>Ni<sub>20</sub>Co<sub>8</sub> DQC, 1122f
- Alanine–alanine–threonine (Ala–Ala–Thr), 1098–1100
- Al–Co–Ni alloy system, 1138
- ALD. *See* Atomic layer deposition
- ALE. *See* Atomic layer epitaxy
- Alloy dendrites, 679
- Al–Ni–Co system, 1138–1139
- Al–Pd–Mn system, 1135–1138
- Alternating electric field (AEF), 564
- Amelogenesis, 883
- American Association for Crystal Growth (AACG), 3–4
- Ammonium dihydrogen phosphate (ADP), 40
- Amorphous calcium carbonate (ACC), 878–879
- Amorphous calcium phosphate phase (ACP), 883
- Amorphous structures, 410
- Andreev field, 240
- Angular distributions, 438
- Anisotropy, 304, 664  
  growth, 652–655  
  interface kinetics, 1096–1098
- Anomalous melting, 425–427
- Anomalous X-ray scattering, 422
- Antifreeze function, 1098–1102
- Antifreeze glycoprotein (AFGP), 1098–1102  
  ice crystal  
    directional growth, 1104–1107  
    growth behavior, 1102–1103  
    molecule adsorption, 1103–1104  
    two-step adsorption, 1104
- Antifreeze protein (AFP), 1098–1102
- Antisolvent, 932
- Antitrapping current, 657–659
- API. *See* Active pharmaceutical ingredient
- Apodization technique, 419

- Aqueous solution growth, 38–41  
 Artificial epitaxy, 64–65  
 ASOS model. *See* Absolute solid-on-solid model  
 Asymmetric kinetics, 384–385  
 Asymptotics, 664  
 Atomic force microscopy (AFM), 523–524, 773, 883–884, 1025, 1036–1037  
 Atomic form factor, 407  
 Atomic layer deposition (ALD), 62  
 Atomic layer epitaxy (ALE), 62  
 Atomic-range attractions, 253–255  
 Atomically rough surfaces, diffuseness for  
   intrinsic width of step, 291  
   picture of roughening, 290–291  
   preroughening phenomena, 291–292  
 Atomistic  
   effects, 462–463  
   model, 395–396  
   scale calculations, 141–142  
 Attenuated total reflection (ATR), 1103–1104  
 Attractive step–step interaction, 250–253  
   atomic-range attractions, 253–255  
   other than  $l^2$ , 253  
   periodic ranges of separation, 255–257  
 Auto-seeded process, 977–978  
 Autocatalytic process, 979–980  
 Axial chirality, 954
- B**
- Ball and spring model, 545  
 Bands. *See* Corrugations  
 BaO–B<sub>2</sub>O<sub>3</sub> flux, 44  
 Batch crystallization, 886  
   conditions, 937–938  
   operating conditions, 938–943  
   phases, 937–938  
   prerequisite, 937  
 Batch technique, 811–812  
 BCC structure. *See* Body-centered cubic structure  
 BCF model. *See* Burton, Cabrera, and Frank model  
 BCSOS model. *See* Body-centered cubic solid-on-solid model  
 BCT. *See* Body-centered tetragonal  
 Beams production, 430  
   neutron sources, 431–433  
   X-ray sources, 430–431  
 Bernal–Fowler rules, 1066  
 Bias field, 713  
   dendritic branching, 715–716  
   dynamic responses, 713–715  
 Binary alloy, 655–657  
 Binary lattice alloy model, 636–637  
 Binodal line, 807–808  
 Biological crystallization  
   biological control, 875–886  
   controlling water flow, 890–891  
   crystals to chew, 892–893  
   Darwinian evolution, 874  
   induced, 901–903  
   light manipulation, 900–901  
   mechanisms of, 875  
   organisms, 890, 897  
   orientation and navigation, 895–897  
   otoliths, 894–895  
   pathways, 877f  
   packaging, 897–899  
   techniques, 886–890  
   undesired crystallization, 899–900  
 Biological macromolecules  
   with antifreeze function, 1098–1102  
   growth, 41–43  
 Biological receptors, 962  
 Biologically controlled mineralization, 874  
 Biomineralization, 876  
 Bloch function, 525  
 Body-centered cubic solid-on-solid model (BCSOS model), 219–220, 266–267, 285–286  
 Body-centered cubic structure (BCC structure), 285, 575–576  
 Body-centered tetragonal (BCT), 676–677  
   in situ photo-sequence, 677f  
 Boltzmann constant, 634, 732–733  
 Boltzmann factor, 396  
 Bond selection mechanism (BSM), 349–350  
 Bond-valence model, 176–177  
 Bone apatites, 884–885

- “Bottom-up” view. *See* Order-parameter models
- Boundary layers, 691–695  
calculations, 647–648
- Bovine Pancreatic Trypsin Inhibitor (BPTI), 923
- BPTI. *See* Bovine Pancreatic Trypsin Inhibitor
- Bragg-Williams statistical model, 11
- Bragg’s law, 1115–1116
- Branching  
bias field, 713–716  
deterministic, 706–707  
circular crystal-melt interface, 710f  
interface capillarity, 709–710  
interface energy conservation, 707–708  
local equilibrium, 710–711  
time scales, 709  
fluxes, 711–713  
interfacial gradients, 711–713  
stochastics, 704–706
- Bread loafing, 447–448
- Bridgman technique, 36, 1132, 1133f
- Bridgman–Stockbarger method, 25–27
- BSM. *See* Bond selection mechanism
- Buffers, 819–820
- Bulk crystals, 44–48
- Bulk diffusion, 381–382
- Bulk growth method  
chemical transport reaction, 56–57  
CVD, 58  
sublimation, 55–56
- Burst nucleation, 348
- Burton, Cabrera, and Frank model (BCF model), 269–270, 383–384, 550–551, 850, 1033–1035
- C**
- c-EMF. *See* Crystallization electromotive force
- c-LN. *See* Conventional congruent-melting LiNbO<sub>3</sub>
- c-LT. *See* Congruent LiTaO<sub>3</sub>
- Calcifications. *See* Pathological mineralization
- Calcium oxalates dihydrate (COD), 899
- Calcium oxalates monohydrate (COM), 899
- Calcium oxalates trihydrate (COT), 899
- CALCulation of PHase Diagrams (Calphad), 109
- Calogero–Sutherland model, 238
- Cambridge Structural Database (CSD), 955–956
- CaO–SiO<sub>2</sub> system, 122
- Capillarity, 599, 607
- Capillary bias field, 708
- Capillary length, 393
- Capillary nucleation theory. *See* Classical nucleation theory (CNT)
- Capillary wave, 274, 280  
Hamiltonian derivation, 307–308
- Carbamazepine (CBZ), 935–936
- Castings, 679
- Ca<sub>x</sub>Ba<sub>1-x</sub>Nb<sub>2</sub>O<sub>6</sub> (CBN), 115
- CBB. *See* Crystal building block
- Cd-RE system, 1142
- Cells, 620
- Cellular tilting  
anisotropic interface kinetics, 1096–1098  
tilt angle measurement, 1095–1096
- Central chirality, 954
- Centrosymmetric crystals, 961
- Chain theory, 959
- Chemical composition, 932–934
- Chemical potential, 181, 479–483  
of Li sites, 191  
of Li<sub>2</sub>B<sub>4</sub>O<sub>7</sub>, 185–186  
standard-state, 183, 186, 198f
- Chemical reaction, 934–935
- Chemical transport reaction method (CRT method), 56–57
- Chemical vapor deposition process (CVD process), 54, 58, 86
- Chiral crystallization  
from chiral and achiral molecules, 992–998  
conglomerates, 968–975  
deracemization in heterogeneous system, 979–980  
preferential crystallization, 975–979  
racemates resolution, 980–991  
racemic composition, 964–967  
racemic compounds, 968–975  
solid solutions, 968–975

- Chiral molecules, 953, 992–998. *See also* Chiral crystallization
- Chiral solid, 955
- Chirality, 952
- crystal growth and hemihedrism, 957–960
  - in crystals, 954–956
  - industrial and biological significance, 960–964
  - measurements, 956–957
- Classic crystal growth methods, 1149–1151
- Classical interferometry, 1039–1043
- Classical nucleation theory (CNT), 317–318, 568–573, 579, 825–828, 920–921. *See also* Nonclassical nucleation
- critical nucleus size, 319–322
  - discrepancies with observations, 575–576
  - earlier corrections, 331–335
  - energy barriers, 319–322
  - equilibrium state, 572
  - experimental verification, 574–575
  - homogeneous nucleation
    - rate of, 322–326
    - thermodynamics, 319–322
  - induction time for nucleation, 327–328
  - non-steady-state, 326–327, 573
  - nucleation
    - driving force, 318–319
    - kinetics, 572
  - steady state, 573
    - nucleation rate, 322–326
- Clausius-Clapeyron formula, 425
- Cluster potentials, 142–143
- CMS. *See* Core multishell
- CNT. *See* Classical nucleation theory
- Co-crystallization, 935–936
- Coalescence balance, 354
- Coarse-grained free energy, 635
- Coarse-graining, 633–634, 639
- COD. *See* Calcium oxalates dihydrate
- Coherence volume, 413–414, 414f
- Coherent scattering, 408–409
- Colloidal systems, 562, 563f, 844
- Colloids, 562
- COM. *See* Calcium oxalates monohydrate
- Commercial software packages, 109
- Complex crystals, 446–447
- Component, 86
- Compton scattering, 415
- Computational methods
  - chemical potential, 479–483
  - Monte Carlo simulations, 483–484
- Computerized tomography, 1052
- Concentration, 87
  - triangles, 126–127
- Configurational degeneracy factor, 139–140
- Configurational entropy, 149
- Confocal microscopy, 1048–1049
- Conglomerates, 968
  - metastable, 970–972
  - spotting, 974–975
  - stable, 970–974
  - techniques using, 972–973
- Congruent, 196–199
  - composition, 181–182
  - melting, 122–123
- Congruent LiTaO<sub>3</sub> (c-LT), 182
- Conservation law, 637
- Constant
  - composition method, 886
  - interfacial angles, 4–5
  - temperature process, 39–40
- Constituent element activities
  - conventional stoichiometric crystal in, 185–188
  - extended stoichiometric crystal in, 189–191
  - in melt and solid states, 196–199
- Constitutional supercooling (CS), 12–13, 600–602, 679
- Continuous symmetry measures (CSM), 956–957
- Continuum models, 396–397, 462–463
- Controlled colloidal assembly, 563–567
  - crystal
    - defects, 588–589
    - growth kinetics, 580–584
    - crystallite network formation, 586–588
    - interfacial structural mismatch, 586–588
    - nonclassical nucleation, 576–579
    - thermodynamic driving force for crystallization, 568–576

- Convection-free environment, 1050–1051
- Conventional congruent-melting  $\text{LiNbO}_3$  (c-LN), 185, 193
- Conventional differential interference microscopy (DICM), 1049
- Conventional sputtering, 61–62
- Conventional stoichiometric crystal, 184–188  
activities of constituent elements, 185–188
- Conventional stoichiometric  $\text{LiNbO}_3$  (s-LN), 185
- Cooling profile, 940
- Cooling strategy, 940–941
- Core multishell (CMS), 772
- Core-shell (CS), 772
- Corrugations, 620
- COT. *See* Calcium oxalates trihydrate
- Critical 2D nucleus, 371–372
- Critical nucleus size, 319–322
- Critical point, 635
- CRT method. *See* Chemical transport reaction method
- Crystal building block (CBB), 321
- Crystal defects, 588–589
- Crystal formation, 796
- Crystal growth, 16–17, 89–90, 360–361, 385–387, 580, 631, 923–925, 1003–1004, 1032. *See also* Epitaxial growth; Nonclassical nucleation; Optical techniques; Thermodynamic driving force
- barrier for incorporation, 853–855
  - cluster adsorption, 582–583
  - concentration field, 1050–1055
  - control, 990–991
  - crystals growth/dissolution rate, 1036f
  - diffusion field, 391
    - melt and solution growth, 391–394
    - planar interface growth, 394–395
  - growth rate *vs.* supersaturation measurement, 1033–1035, 1034f–1035f
  - major rate-determining process, 1032, 1033f
  - generation of steps, 847–848
  - kinks generation, 850–853
  - melt growth method, 17–38
  - molecular pathway, 855–857
  - from mother phases
    - melt growth, 365–369
    - solution growth, 369–370
    - vapor growth, 364–365
  - normal and lateral growth
    - adhesive growth on rough faces, 370–371
    - spiral growth with screw dislocations, 377–380
    - two-dimensional nucleation, 371–377
  - phase transition process, 361
    - equilibrium and transition to solid phase, 361–362
    - linear kinetics, 363
    - transport and chemical potential, 363
  - rough interface, 846–847
  - simulation models, 395
    - atomistic model and, 395–396
    - continuum models, 396–397
  - smooth interface, 846–847
  - solid state recrystallization, 70–72
  - solution growth method, 38–53
  - step kinetics, 580–582
    - step kinetic coefficient, 849–850
  - step propagation, 848–849
  - surface
    - observation, 1032–1033
    - roughening, 583–584
  - synthetic diamond crystals, 65–70
  - theories evolution, 4
    - early developments, 4–5
    - nineteenth century, 5–6
    - twentieth century, 6–16
  - three-dimensional observation of flow, 1050–1055
  - transport-limited, 632
  - vapor growth method, 53–65
- Crystal morphology, 450
- Crystal nucleation, 825, 920–923. *See also* Protein crystallization
- aggregate sizes evolution, 828
  - classical nucleation theory, 825–828
  - classical theory overestimation, 832–833
  - dense liquid clusters, 836–838
  - heterogeneous nucleation substrates, 842–843

- Crystal nucleation (*Continued*)  
 in melts, 330  
 molecular-kinetic approach, 335–338  
 nucleus size, 830–832  
 on protein crystals nucleation, 845–846  
 rate, 827–830  
 solution-crystal spinodal, 830–832  
 in solutions, 331  
 two-dimensional, 339–342  
 two-step mechanism, 833–836, 835f  
   evidence for, 843  
   principles, 844  
   rate determination, 841–842  
   rate law, 839–841  
   urea and glycine, 843
- Crystal sites  
 degrees of freedom in, 188–189  
 in oxide crystals, 179–180
- Crystal-melt interface, 276–277, 712
- Crystalline  
 imperfections, 7–8  
 polymorphs phase, 807–810
- Crystallite network formation, 586–588
- Crystallization, 562, 916, 924, 960–964  
 conditions, 812  
 driving force, 806–807  
 medium, 917  
 multistep, 578–579  
 from solution, 917–929  
 temperature, 990  
 thermodynamic driving force for, 568–576
- Crystallization electromotive force (c-EMF),  
 180, 193–196, 196f, 202–203
- Crystallizer hydrodynamics, 941–943
- Crystals equilibrium shape, 339. *See also*  
 Nucleation
- CS. *See* Constitutional supercooling;  
 Core-shell
- CSD. *See* Cambridge Structural Database
- CSM. *See* Continuous symmetry measures
- Cubic zirconia (ZrO<sub>2</sub>), 37
- Curie group, 113–115
- Cutoff energy, 526
- CVD process. *See* Chemical vapor deposition  
 process
- Cylinders, 611–616  
 circular, 615–616
- Czochralski crystal pulling method  
 invention, 20–22  
 oxide growth, 24–25  
 semiconductors, 22–24
- Czochralski method, 1131–1132
- D**
- d*-Al-Ni-Co phase, 1138
- Daltonides. *See* Line compounds
- Debye length, 807–808
- Debye plot, 815
- Debye-Hückel inverse screening length, 815
- Decagonal lattice, 1120
- Decagonal quasicrystals (DQC), 1120
- Decaprisim, 1145–1146
- Degeneracy function, 155
- Dendrites, 15, 670  
 early history, 671–672  
 steady-state crystallization fronts, 673f  
 thermodynamic and kinetic factors, 670–671  
 useful and deleterious, 672–676
- Dendritic growth, 652–655  
 alloy dendrites, 679  
 branching  
   bias field, 713–716  
   deterministic branching, 706–711  
   fluxes, 711–713  
   interfacial gradients, 711–713  
   stochastics, 704–706  
 castings, 679  
 initiation of dendrites, 678–679  
 observations and simulation, 676–679  
 theories, 681  
   boundary layers, 691–695  
   diffusion interactions, 691–695  
   interface physics, 695–701  
   kinetic limitations, 702–704  
   numerical methods, 701–702  
   transport solution, 685–689  
   transport theory, 681–685, 689–691
- Dendritic pattern formation, 1077–1079
- Dendritic snow-flake patterns, 671–672
- Dense liquid

- clusters, 836–838
- phase, 807–810
- Density functional theory method (DFT method), 145, 437–438, 522
  - ab initio thermodynamics, 535–537
  - adatoms, 531–533
  - adsorption, dissociation and diffusion, 533–534
  - basics of method, 524–529
    - order of computations, 528–529
    - surfaces, 527–528
  - binding energies, 532t
  - surface structure and reconstruction, 529–531
- Density matrix renormalization group method (DMRG method), 303
- Density-of-states (DOS), 155
- Deposition rate effect, 451–452
- Deracemization, 979–980
- DERI. *See* Droplet elimination by radical beam irradiation
- Deryagin–Landau–Verwey–Overbeek theory (DVLO theory), 563, 564f, 814–815
- Detailed balance equation, 325–326
- Deuterated potassium dihydrogen phosphate (DKDP), 40–41
- Dewetting, 452–453
- DF. *See* Downward funneling
- DFP. *See* Disordered flat phase
- DFT method. *See* Density functional theory method
- DG model. *See* Discrete Gaussian model
- Diamonds, 892
- DICM. *See* Conventional differential interference microscopy
- Differential scanning calorimetry (DSC), 101–102, 205–206
- Differential thermal analysis (DTA), 122
- Diffraction by crystal, 412–413
- Diffuse interfaces, 633
  - at equilibrium, 639–645
  - picture, 368–369
- Diffusion, 533–534
  - boundary layer, 381
  - interactions, 691–695
  - length, 395
- Diffusion-limited dendritic growth, 689–690
- Dimensionless free energy, 642
- Direct techniques, 434–435
- Directional growth, ice crystals
  - cellular tilting, 1095–1098
  - pattern formation, 1090–1093
  - solute distribution, 1093–1095
- Directional solidification (DS), 674–675, 675f, 679
  - in situ* micrograph, 680f
- Discontinuous surface tension, 300–302
- Discrete Gaussian model (DG model), 308
- Discrete order parameter, 276
- Dislocation loops, 152–153
- Disordered flat phase (DFP), 291–292
- Dispersion relation, 604, 618, 623
- Dissociation, 533–534
- Dissolution, 925
- Distinct scatterers, 408
- DKDP. *See* Deuterated potassium dihydrogen phosphate
- DLS. *See* Dynamic light scattering
- DMRG method. *See* Density matrix renormalization group method
- DOS. *See* Density-of-states
- Double differential scattering cross section, 408–409
- Downward funneling (DF), 580–581
- DQC. *See* Decagonal quasicrystals
- Driving force
  - for crystal growth, 304, 305t
  - of solidification, 362
- Droplet elimination by radical beam irradiation (DERI), 511
- Drumhead wandering, 269–270, 272–275
- “Drumhead” Hamiltonian work, 274
- DS. *See* Directional solidification
- DSC. *See* Differential scanning calorimetry
- DTA. *See* Differential thermal analysis
- DVLO theory. *See* Deryagin–Landau–Verwey–Overbeek theory
- Dynamic light scattering (DLS), 836–838
- Dynamic responses, 713–715
- Dystrophic calcifications, 900

**E**

- EBSP. *See* Electron Back Scatter Diffraction Patterns
- ECMC simulation. *See* Electron-counting Monte Carlo simulation
- ECS. *See* Equilibrium crystal shape
- Edge-defined film-fed growth (EFG), 22, 34–35
- EDIP. *See* Environment-dependent interatomic potential
- EFG. *See* Edge-defined film-fed growth
- Eggshell formation, 897–899
- EHD flow. *See* Electrohydrodynamic flow
- Ehrlich-Schwoebel barrier (ES barrier), 384–385, 452
- 8-interstitial cluster, 151
- Einstein–Stokes relation, 367, 732–733
- Elastic step–step repulsion, 297
- Elastic strain, 544–548
- Electrochemical crystal growth, 52–53
- Electrodeposition, 52
- Electrohydrodynamic flow (EHD flow), 565–567
- Electron Back Scatter Diffraction Patterns (EBSP), 741
- Electron-counting Monte Carlo simulation (ECMC simulation), 483
- Electron–electron repulsion, 524
- Electroosmotic flow (EOF), 566–567
- Elementary theory for pure melt, 597–600
- Ellingham type diagrams, 131–133
- Ellipsoids, 616
- ELO. *See* Epitaxial lateral overgrowth
- Empirical potential atomistic simulations, 142–145
- Empirical potential Monte Carlo technique (EPMC technique), 434–436
- Empirical potential structure refinement (EPSR). *See* Empirical potential Monte Carlo technique (EPMC technique)
- Enamel formation, 883
- Enantiomeric purification, 991
- Endoskeletons, 890
- Energy barriers, 319–322, 351–352
- Enthalpy, 91–94
- Entropy, 94–96, 805
- Environment-dependent interatomic potential (EDIP), 142–143
- EOF. *See* Electroosmotic flow
- Epitaxial deposits, 48
- Epitaxial growth, 484–485. *See also* Crystal growth
  - density functional theory calculations
    - ab initio thermodynamics, 535–537
    - adatoms, 531–533
    - adsorption, dissociation and diffusion, 533–534
    - basics of method, 524–529
    - surface structure and reconstruction, 529–531
  - KMC simulations, 538
    - of deposition from gas phase, 538–540
    - with elastic strain, 544–548
    - on-lattice, 540–544
    - quantum dots growth, 548–549
  - methods and goals, 522–524
  - phase field methods
    - PFC model, 551–554
    - philosophy, 550–551
- Epitaxial lateral overgrowth (ELO), 753–754
- Epitaxy-mediated transformation, 1081
- EPMC technique. *See* Empirical potential Monte Carlo technique
- EPS. *See* Extracellular polymeric substances
- Equilibrium concentrations, 141–142
- Equilibrium crystal shape (ECS), 216, 267–268
  - attractive step–step interaction, 250–253
  - first-order transitions, 245–250
  - formal results applications
    - cusps and facets, 224–225
    - sharp edges and forbidden regions, 225–227
    - Wulff plot, 227–229
  - sharp edges, 245–250
  - from surface free energies
    - formal treatment, 220–223
    - general considerations, 217–220
- Equilibrium partition coefficient, 199
- Equivalent lattice gas model, 276–277
- ES barrier. *See* Ehrlich-Schwoebel barrier
- ESS. *See* European spallation source

European spallation source (ESS), 432–433  
 Eutectic(s), 117–119  
   crystal, 15  
   system, 107–108  
 Eutectoids, 117–119  
 EXAFS. *See* X-ray absorption fine structure  
 Exchange–correlation potential, 526–527  
 Exoskeletons, 890  
 Extended stoichiometric crystal, 193  
   activities of constituent elements, 189–191  
 Extracellular polymeric substances (EPS),  
   901–903

## F

F-M mode. *See* Frank-van der Merwe mode  
 Face-centered cubic (fcc), 1146–1148  
 Facet, 363  
 Faceted dendrite, 731  
 Faceting transition, 267–268  
 fcc. *See* Face-centered cubic  
 FDA. *See* U.S. Food and Drug Administration  
 FDL. *See* Frank partial loop  
 Ferromagnetic system, 635–636  
 FET. *See* Field-effect transistor  
 FF. *See* Free fermion  
 FFM. *See* Friction force microscope  
 Fibonacci sequence, 1118–1120  
 Field-effect transistor (FET), 750  
 Film growth, 455. *See also* Monte Carlo  
   simulations (MC simulations)  
   inhibited diffusion effect, 457–458  
   smooth film growth strategy, 459  
   temperature effect, 457  
   wetting effect, 455–456  
 First-order transitions, 99, 245–250  
   phase transition, 316  
   shape transition, 298  
 First-principles calculations. *See* ab initio  
   calculations  
 Fission reactors, 432  
 Flack parameter, 955–956  
 Flame fusion method, 19  
 Floating zone technique, 32, 1133–1134  
 Flux growth method. *See* Solution growth  
   method

Fluxes, 711–713  
 Forbidden orientations, 654–655  
 45° pitched blade turbine (PBT45), 942  
 4-interstitial cluster, 149–150  
 Fourier transform infrared spectroscopy  
   (FHIR), 1103–1104  
 Frank partial loop (FDL), 152–153  
 Frank-van der Merwe mode (F-M mode), 767  
 Frank's theory, 10  
 Free energy  
   density, 635–636  
   functional, 661  
 Free fermion (FF), 237–238, 269  
 Free-boundary  
   formulation, 646  
   problem, 632, 645–650  
 Friction force microscope (FFM), 536  
 Front-capturing methods, 646–647  
 Front-tracking methods, 646–647  
 FTIR. *See* Fourier transform infrared  
   spectroscopy  
 Fugacity, 481–483

## G

Gallium arsenide (GaAs), 130–131, 484–485  
   GaAs(001) surface, 1015–1017  
   GaAs(111) surface, 1017–1019  
   growth on, 488–492  
   InAs on, 493–502  
     growth on, 496–502  
     surface structures, 493–496  
   nanowires, 776–777  
   surface, 485–488  
     growth, 1015–1019  
     nucleation, 1015–1019  
 Gallium nitride (GaN), 502–503  
   growth on, 507–510  
   InGaN on, 510–511  
     growth on, 513–515  
     surface structure, 511–513  
     surface structure, 504–506  
 $\gamma$  plot, 216–217, 221f  
 GaP nanowires, 778  
 Gas bubble nucleation, 328–329  
   crystal nucleation, 330–331

- Gas bubble nucleation (*Continued*)  
 heterogeneous nucleation, 329
- Gases, rare, 425–426
- Gel crystallization, 888–889
- Gel growth method, 43–44
- Gelation phase, 807–810
- Generalized gradient approximation (GGA),  
 145, 526–527
- Generalized Wigner distribution (GWD), 238
- Geneva Rubies, 19
- Germ nuclei, 728
- GF method. *See* Gradient freeze method
- GGA. *See* Generalized gradient approximation
- Gibbs construction, 642–643, 643f
- Gibbs energy minimization, 109
- Gibbs free energy, 96–98, 535  
 change, 782
- Gibbs phase rule, 88, 964
- Gibbs–Curie–Wulff theorem, 339
- Gibbs–Thomson  
 effect, 141, 393, 645–646, 682  
 equation, 321, 324, 920–921  
 model for ice growth, 1100f
- GMPT type. *See* Gruber–Mullins–Pokrovsky–  
 Talapov type
- Gradient freeze method (GF method), 26–27
- Grain growth, 723  
 unidirectional growth of polycrystalline ingot,  
 742–747
- Grand potential functional, 656–657
- Graphene growth, 1022–1027
- Graphene nucleation, 1025–1027
- Graphoepitaxy, 64–65
- Green’s function formalism, 545
- Ground state point defect. *See also* High  
 temperature defect thermodynamics  
 cluster thermodynamics, 147  
 large planar self-interstitial clusters,  
 152–153  
 small compact self-interstitial clusters,  
 149–151  
 vacancy clusters, 147–149
- formation properties  
 empirical potential atomistic simulations,  
 142–145  
 quantum mechanical estimation, 145–147
- Growth cessation, 924
- Growth direction selection, 1151–1152
- Growth mechanism, 1142  
 by classic crystal growth methods, 1149–1151  
 growth direction selection, 1151–1152  
 morphologies of, 1142–1148  
 rapid solidification, 1148–1149
- Gruber–Mullins–Pokrovsky–Talapov type  
 (GMPT type), 269
- Gruber–Mullins approximation, 236
- GWD. *See* Generalized Wigner distribution
- ## H
- HA. *See* Hydroxyapatite
- HAADF. *See* High-angle annular darkfield
- Half-crystal position, 335–336, 335f
- Hall process, 52
- Hartree potential. *See* Electron–electron  
 repulsion
- Heat  
 conduction process, 734–736  
 of fusion, 92–93  
 of transition, 92–93  
 of vaporization, 92–93
- Heat exchanger method (HEM), 30, 86
- Heavy water (D<sub>2</sub>O), 1084
- Height–height correlation function, 280
- Hertz–Knudsen equation, 1076–1077
- HEM. *See* Heat exchanger method
- Hemihedrism, 957–960
- HEMT. *See* High electron mobility transistor
- Hertz–Knudsen formula, 365
- Hess’s law, 93–94
- Heterogeneous nucleation, 329, 342–346, 920  
 nucleation substrates, 842–843
- High electron mobility transistor (HEMT),  
 750–751
- High pressures and temperatures (HPHT),  
 65–66
- High temperature defect thermodynamics,  
 158  
 self-interstitial clusters, 163–167  
 single vacancy, 158–159  
 vacancy clusters, 159–163

- High temperature solution growth  
 bulk crystals, 44–48  
 thin film liquid phase epitaxy, 48–49
- High-angle annular darkfield (HAADF), 773
- Hofmeister series, 818
- Homochirality, 992
- Homogeneous nucleation, 920  
 thermodynamics, 319–322
- Horizontal ribbon growth method  
 (HRG method), 35–36
- HPHT. *See* High pressures and temperatures
- HRG method. *See* Horizontal ribbon growth method
- Humble/Arai configuration, 163–164
- Hybrid functional B3LYP, 526–527
- Hydrothermal growth, 49–52
- Hydroxyapatite (HA), 892
- I**
- i*-Ag–In–Yb system, 1140
- i*-Al–Li–Cu alloy, 1143, 1144f
- i*-Cd<sub>5</sub> <sub>7</sub>Yb phase, 1124–1125, 1125f
- i*-Zn–Mg–RE system, 1139
- ICCG. *See* International Conferences on Crystal Growth
- Ice crystals, 1062. *See also* Snow crystals  
 crystallographic features, 1064–1066  
 directional growth, 1090–1098  
 free growth, 1081–1090  
 growth control, 1098–1107  
 surface structure, 1066–1072
- Ice rules. *See* Bernal–Fowler rules
- Ice surface, 1072  
 melting, 1066–1068  
 experimental evidence, 1068–1069
- Ice–water interface, 1089–1090  
 AFGP molecules adsorption, 1103–1104  
 pattern formation, 1090–1093  
 solute distribution, 1093–1095
- Icosahedral clusters, 1127–1128
- Icosahedral glass (IG), 1117–1118
- Icosahedral QC (IQC), 1117–1118
- IDGE. *See* Isothermal Dendritic Growth Experiment
- IG. *See* Icosahedral glass
- III-nitride semiconductors, 502–503
- ILL. *See* Laue-Langevin Institute
- Imaginary-path-weight random walk method  
 (IPW random walk method), 278,  
 304–306
- Imaging principle, 1007–1009
- In situ imaging method, 1004–1010
- In situ observation, 1032  
 crystal growth, 1035–1037  
 microscopy, 1043–1050  
 modern interferometry, 1043–1050
- In vivo induced mineralization, 889–890
- InAs nanowires, 777
- Incoherent scattering, 408–409
- Incongruent melting, 119–120
- Incorporation barrier, 849–850
- Induced biological crystallization, 901–903
- Induction time, 327
- Inelastic scattering, 440
- InGaAs nanowires, 778
- InGaP nanowires, 778
- Inherent Structure Landscape (ISL), 153–154  
 for defects in crystals, 155–156
- Inherent structure theory, 153–157
- InP nanowires, 778
- Interface  
 capillarity, 709–710  
 energy conservation, 707–708  
 equivalent lattice gas model, 276–277  
 existence of roughening transition  
 temperature, 275–276  
 free energy, 222, 607–608, 643  
 Ising model, 276–277  
 kinetics, 363  
 physics, 695  
 Ivantsov’s transport solution, 700–701  
 marginal stability, 697–700  
 tip characteristics, 695–696  
 tension, 277–279
- Interfacial gradients, 711–713
- Interferometric tomography, 1053–1055.  
*See also* Computerized tomography
- Intermediate compounds, 121–122
- International Conferences on Crystal Growth (ICCG), 3

- International Organization of Crystal Growth (IOCG), 3
- International Space Station (ISS), 1084
- Intrinsic point defects, 138
- Inverse roughening, 292
- Inverse techniques, 435–436
- IOCG. *See* International Organization of Crystal Growth
- IPW random walk method. *See* Imaginary-path-weight random walk method
- IQC. *See* Icosahedral QC
- Ising model, 234, 276–277
  - ferromagnetic state of, 640
  - microscopic Hamiltonian of, 634
- ISL. *See* Inherent Structure Landscape
- Isopleth sections, 127–128
- Isothermal Dendritic Growth Experiment (IDGE), 689–690
- Isotropic formalism. *See* Ball and spring model
- Isotropic interface kinetics, 619
- Isotropy, 113–115
- ISS. *See* International Space Station
- ISS–Kibo experiments, 1085–1088
- Ivantsov’s transport solution, 700–701
- J**
- Jackson  $\alpha$  factor, 11
- Jackson’s parameter, 271
- K**
- K<sub>2</sub>O flux, 46–47
- Kapitza’s method, 30–31
- Karma and Rappel model, 652
- KDP. *See* Potassium dihydrogen phosphate
- Kinetic
  - coefficient, 363, 382, 733
  - law, 617
  - limitations, 702–704
  - molecular theory, 6
  - roughening, 379
- Kinetic Monte Carlo simulations (KMC simulations), 483, 522–523
  - of deposition from gas phase, 538–540
  - with elastic strain, 544–548
  - on-lattice KMC, 540–544
- Kinks generation, 850–853
- KJMA theory. *See* Kolmogorov-Johnson-Mehl-Avrami theory
- KMC simulations. *See* Kinetic Monte Carlo simulations
- Koch–Cohn cluster, 178
- Kohn–Sham equation, 525–526
- Kolmogorov-Johnson-Mehl-Avrami theory (KJMA theory), 724–731
  - geometric approach, 727–729
  - probabilistic approach, 729–731
- Kossel-like crystal nucleus model, 350–351
- Kosterlitz–Thouless transition (KT transition), 266, 286–290
- Kröger–Vink notation, 200–201
- KT transition. *See* Kosterlitz–Thouless transition
- L**
- $l^{-1}$  repulsions, 219
- $l^{-2}$  interaction, 218–219
- LAIMCE. *See* Low-angle incidence microchannel epitaxy
- LAMMPS software, 157
- Landau theory
  - Landau equation, 621–622
  - Landau–Ginzburg equation, 623
  - order parameter, 633
- Langer and Müller-Krumbhaar method (LMK method), 614, 1087–1088
- Langmuir adsorption, 292–293
- Large planar self-interstitial clusters, 152–153
- Large-scale integration (LSI), 750–751
- Laser confocal differential interference contrast microscopy (LCDICM), 1049
- Laser confocal microscope-differential interference microscope (LCM-DIM), 1071–1072
- Laser confocal phase-shift interferometry (LCPSI), 1049–1050
- Laser diode (LD), 502–503
- Laser-heated pedestal fiber growth (LHPG), 32–33
- Lateral coherence, 413–414
- Lateral growth, 370

- Lateral overgrowth (LOG), 755  
 Lattice gas automata (LGA), 523  
 Lattice type, 1126–1127  
 Lattice-mismatched system, 767–768  
 Laue-Langevin Institute (ILL), 431  
 Layer growth. *See* Lateral growth  
 LCDICM. *See* Laser confocal differential interference contrast microscopy  
 LCM-DIM. *See* Laser confocal microscope-differential interference microscope  
 LCPSI. *See* Laser confocal phase-shift interferometry  
 LD. *See* Laser diode  
 LDA. *See* Local density approximation  
 Lead magnesium niobium-titanate (PMNT), 71–72  
 LEC method. *See* Liquid encapsulation Czochralski method  
 LED. *See* Light emitting diode  
 LEED. *See* Low-energy electron diffraction  
 Lenosky potential (LP), 142–143  
 Lever rule, 119–121  
 LGA. *See* Lattice gas automata  
 LHPG. *See* Laser-heated pedestal fiber growth  
 $\text{Li}_2\text{B}_4\text{O}_7$ . *See* Lithium borate  
 Light emitting diode (LED), 48–49, 502–503, 750  
 $\text{LiNbO}_3$ . *See* Lithium niobate (LN)  
 Line compounds, 105–106  
   stoichiometric crystal, 192  
 Linear kinetics, 363  
 Linear stability analysis, 602. *See also* Mullins-Sekerka analysis; Nonlinear analysis  
   cylinders, 611–616  
     circular cylinder, 615–616  
   ellipsoids, 616  
   linear stability theory, 623  
   paraboloids, 616  
   planar interface, 602–610  
     experimental tests of morphological stability, 609  
     long-wavelength perturbations, 609–610  
     TSS approximation, 605–608  
   spheres, 611–616  
 Liquid  
   diffractometer, 433  
   liquid-like layer, 1066–1067  
   metals, 425–426  
   semiconductors, 427  
 Liquid encapsulation Czochralski method (LEC method), 24  
 Liquid phase epitaxy (LPE), 48, 753. *See also* Selective-area epitaxy (SAE)  
 Liquid state, 402–405. *See also* Supramolecular liquid structures  
   characterizations, 436–438  
   computer simulations, 434–436  
   experimental setups, 433–434  
 Liquid–liquid (L–L), 807–808  
   coexistence line, 807–808  
   diffusion method, 812  
   separation, 834  
 Liquid–liquid phase separation (LLPS), 927–928  
 Liquidus, 106–109, 113–115  
 $\text{LiTaO}_3$ . *See* Lithium tantalate (LT)  
 Lithium borate ( $\text{Li}_2\text{B}_4\text{O}_7$ ), 184, 187  
 Lithium niobate (LN), 32–33, 101–102, 177, 179, 181, 207  
   compositions, 190f  
   MgO-doped, 201–207  
   neutral and ionic chemical species, 192f  
 Lithium tantalate (LT), 180, 207  
   compositions, 200f  
   MgO-doped, 207–210  
 L–L. *See* Liquid–liquid  
 LLPS. *See* Liquid–liquid phase separation  
 LMK method. *See* Langer and Müller-Krumbhaar method  
 LN. *See* Lithium niobate  
 Local density approximation (LDA), 145, 526–527  
 Local equilibrium, 710–711  
 LOG. *See* Lateral overgrowth  
 Long range order (LRO), 402–403  
 Long-wavelength perturbations, 609–610  
 Longitudinal coherence, 413  
 Low-angle incidence microchannel epitaxy (LAIMCE), 756–758

- Low-energy electron diffraction (LEED),  
530–531
- LP. *See* Lenosky potential
- LPE. *See* Liquid phase epitaxy
- LRO. *See* Long range order
- LSI. *See* Large-scale integration
- LT. *See* Lithium tantalate
- M**
- Mach–Zehnder interferometer, 1051
- Macromixing, 941
- Magnesium oxide (MgO), 176–177
- Magnetotactic bacteria, 896
- Magnetotaxis, 895–896
- Many-body Schrödinger equation, 524
- Marginal stability, 696–700
- Marginal wavenumber, 704–705
- Maryland notation, 218–219
- Mass crystallization, 345–346
- Master equation, 408
- Matched asymptotic expansion method,  
647–648
- MBE. *See* Molecular beam epitaxy
- MC simulations. *See* Monte Carlo simulations
- mc-Si. *See* Multicrystalline Si
- MCE. *See* Microchannel epitaxy
- MD. *See* Molecular dynamics
- MEAM. *See* Modified embedded-atom model
- Mean value of work of separation (MWS), 336
- “Mean-field” value, 240
- Meandering. *See* Step wandering
- Melt growth method, 17–18, 365–369. *See also*  
Solution growth method
- Bridgman–Stockbarger method, 25–27
- crystal grain growth, 731
- heat conduction process, 734–736
- twin boundaries, 736–742
- Wilson–Frenkel formula, 731–734
- Czochralski crystal pulling method, 20–25
- diffuse interface picture, 368–369
- Kapitza’s method, 30–31
- Nacken–Kyropoulos methods, 28–29
- nineteenth century and Verneuil process,  
18–20
- shaped growth, 33–36
- sharp interface picture, 366–368
- skull melting method, 37–38
- Stöber/heat exchanger methods, 30
- twentieth century, 20
- zone melting method, 31–33
- Membrane proteins, 812, 813f
- Memory effects, 330
- Mephisto Bridgman furnace, 609
- Mesoscopic free energy, 634
- Metal oxides, 180
- Metal-insulator-semiconductor (MIS), 758
- Metal-organic chemical vapor deposition  
(MOCVD), 544, 755–756
- Metal-organic vapor-phase epitaxy (MOVPE),  
477–478, 750–751
- Metal-oxide-semiconductor (MOS), 750–751
- Metastable equilibrium state, 379
- Metastable zone limit (MZL), 921
- Metastatic calcifications, 900
- Metropolis Monte Carlo simulation (MMC  
simulation), 483
- MgO. *See* Magnesium oxide
- MgO-doped LiNbO<sub>3</sub>, 201
- bulk crystal growth, 203–207
- crystallization electromotive force, 202–203
- melting temperature distribution, 201–202,  
202f
- temperature gradient dependence, 203f
- MgO-doped LiTaO<sub>3</sub>, 207
- bulk crystal growth, 208–210
- crystallization electromotive force, 208
- curie temperature, 208–210
- melting temperature distribution, 207–208
- Michelson interferometer, 1040f, 1041–1043
- Micro-pulling-down method ( $\mu$ -PD method),  
32–33, 86, 194f
- Microbatch technique, 811–812
- Microchannel epitaxy (MCE), 753–758
- Micromixing, 941–942
- Microscopy, 1043–1050
- models, 308
- solubility, 695
- Microstructure formation, 650
- Migration, 488–489
- MIS. *See* Metal-insulator-semiconductor

- Mixed crystal, 88
- Mixing. *See* Crystallizer hydrodynamics
- ML. *See* Monolayer
- MLEK method, 29
- MMC simulation. *See* Metropolis Monte Carlo simulation
- MOCVD. *See* Metal-organic chemical vapor deposition
- Modern interferometry, 1043–1050
- Modified embedded-atom model (MEAM), 142–143
- Molecular beam epitaxy (MBE), 60, 477–478, 523–524, 750–751, 1003–1004, 1010–1013
- Molecular crystals, size and habit evolution, 466–472
- Molecular dynamics (MD), 434–435, 522–523, 804, 1072
- sampling inherent structures, 156–157
  - simulation, 13, 156–157, 396
  - of ice–water interface, 1089–1090
- Molecular-kinetic approach, 335–338
- Monoatomic liquids, 416–419
- Monochromatic plane wave, 413
- Monolayer (ML), 767, 1014
- graphene imaging, 1022–1024
- Monotectics, 124
- Monte Carlo simulations (MC simulations), 396, 434–435, 446, 483–484, 638
- deposition on spherical crystal seed, 450
  - deposition rate effect, 451–452
  - faceting, 450–451
  - description, 448–449
  - molecular crystals, 466–472
  - nucleation of films, 452
    - inhibited diffusion effect, 454–455
    - temperature effect, 453
    - wetting effect, 452–453  - PVD, 462–466
  - step coverage, 462–466
  - texture development, 460–462
- Moore's temperature lowering method, 40
- Morphological instability, 1091–1093
- Morphological stability, 595–596
- elementary considerations, 597
  - constitutional supercooling, 600–602
  - elementary theory for pure melt, 597–600
- linear stability analysis, 602
- paraboloids and ellipsoids, 616
  - planar interface, 602–610
  - spheres and cylinders, 611–616
- Mullins-Sekerka analysis, 616–617
- extensions, 618–619
  - rapid solidification, 617–618
- nonlinear analysis, 620
- sideband instability, 623–624
  - three-dimensional weakly nonlinear solutions, 624–626
  - weakly nonlinear analysis, 620–622
- stability theory, 1146–1148
- MOS. *See* Metal-oxide-semiconductor
- Mound formation, 380
- MOVPE. *See* Metal-organic vapor-phase epitaxy
- MSC process. *See* Multistep crystallization process
- Mullins-Sekerka analysis, 616–617. *See also* Linear stability analysis; Nonlinear analysis
- extensions, 618–619
  - instability, 744–745
  - rapid solidification, 617–618
- Multicomponent
- solidification, 659–664
  - systems, 665
- Multicrystalline Si (mc-Si), 723
- Multilayered graphene, 1024–1025
- Multinucleation growth, 373, 376–377
- Multiphase solidification, 659–664
- Multiphase-field method, 659, 664–665
- Multistep crystallization process (MSC process), 579
- MWS. *See* Mean value of work of separation
- MZL. *See* Metastable zone limit
- N**
- Nacken-Kyropoulos methods, 28–29
- Nanocrystals, 880
- Nanowires (NW), 751, 772
- III-V NW formation, 772

- Nanowires (NW) (*Continued*)  
 coherent growth, 786–788  
 SAG, 774–781  
 twinning growth model, 781–786  
 VLS growth mechanism, 773
- NCP. *See* Noncollagenous protein
- NCT. *See* Nicotinamide
- NDIS. *See* Neutron diffraction with isotopic substitution
- Near-equilibrium system, 993–994
- Neutron  
 scattering, 405–416  
 sources, 431–433
- Neutron diffraction with isotopic substitution (NDIS), 421
- Next nearest-neighbor interaction (NNN interaction), 233
- Nicotinamide (NCT), 935–936
- Nodes. *See* Cells
- Non-racemizable enantiomers, 964–967
- Non-steady-state nucleation rate, 326–327
- Nonaqueous solution growth, 44
- Nonclassical nucleation, 576. *See also* Classical nucleation theory (CNT); Crystal growth  
 multistep crystallization, 578–579  
 Ostwald's rule, 579  
 structure evolution of precritical nuclei, 576–578
- Noncollagenous protein (NCP), 880–883
- Nonlinear analysis, 620  
 sideband instability, 623–624  
 weakly nonlinear analysis, 620–622  
 three-dimensional, 624–626
- Nonprotein solution components, 813.  
*See also* Protein crystallization  
 buffers, 819–820  
 organic molecules, 823–825  
 protein molecules interaction, 814–817  
 salts, 821–822  
 simple colloid approach, 817–819
- Nonreactive gases, 61
- Nonstationary time lag, 327
- Nonstoichiometry, 176
- Normal growth, 370
- Normal melting, 425–427
- Nucleation, 316, 361, 825–826, 875–876, 990.  
*See also* Classical nucleation theory (CNT)  
 barrier, 569, 570f  
 burst, 348  
 gas bubbles, 328–331  
 heterogeneous, 342–346  
 nucleation–growth kinetics, 724–725  
 KJMA theory, 726–731  
 time relations, 725–726  
 phase formation, 317f  
 probabilistic features, 347–348  
 protein crystals, 348–354  
 theorem, 346–347  
 theories, 333–335, 346–347  
 3D models of Kossel-crystals, 344f  
 in vapors, 317–328
- Nuclei saturation density, 345–346
- Nucleus size, 830–832
- Numerical methods, 701–702
- NW. *See* Nanowires
- O**
- OC-17. *See* Ovocleidin-17
- Octacalcium phosphate (OCP), 899
- Off-lattice KMC, 523
- OM precursor. *See* Organometallic precursor
- OMVPE. *See* Organometallic vapor phase epitaxy
- On-lattice KMC, 540–544
- 1/1 approximant, 1125
- One component systems. *See also* Two component systems  
 fields, 111–112  
 pressure–temperature diagrams, 110–111
- One-dimensional quasiperiodic structure, 1118–1120
- 1D nanostructures, 752–753
- Onsager symmetry principles, 662
- Optical parametric oscillator (OPO), 204–205
- Optical techniques  
 crystal growth in situ observation, 1035–1037  
 monomolecular growth steps, 1037–1039  
 phase-sensitive microscopic techniques, 1037

- standard Michelson interferometer, 1040f
- step height measurement, 1039–1043
- visualization techniques, 1032
- Order parameter, 633
  - functions, 644
- Organic
  - matrix, 876
  - molecules, 823–825
  - solvent, 932
  - solvents classification, 918t
- Organometallic precursor (OM precursor), 58–59
- Organometallic vapor phase epitaxy (OMVPE), 58–60
- Ostwald ripening, 70, 928–929
- Ostwald rules, 579, 926–927
  - step rule, 1080
- Otoliths, 894–895
- Ovocleidin-116 (OC-116), 898–899
- Ovocleidin-17 (OC-17), 898–899
- Oxide crystals. *See also* Stoichiometric crystal
  - growth characteristics
    - crystal sites in, 179–180
    - extended concept of stoichiometry, 182–191
    - partitioning behavior of ionic solutes, 180–182
    - stoichiometric composition coincident with congruent point, 200–212
    - stoichiometry and point defects, 176–179
    - vacancy clustering and cluster association, 178f
- Oxide growth, 24–25
- Oxide melt, 192–193
  - activities of constituent elements, 196–199
  - partitioning behavior of ionic solutes in, 180–182
- P**
- p-RSOS model, 300
- Pair correlation function, 403f, 404–405, 419–420
- Paraboloids, 616
- Paramagnetic system, 635–636
- Partial pair correlation functions, 424–425
- Partial structure factors, 420–423
- Partially stabilized zirconia (PSZ), 37
- Pasteur stereochemistry, 957–960
- Pathological mineralization, 899–900
- Pauli's principle, 524–525
- PBT45. *See* 45° pitched blade turbine
- PDB. *See* Protein Data Bank
- PDL. *See* Perfect dislocation loop
- Pearson, Takai, Halicioglu, Tiller potential (PHT potential), 142–143
- Péclet numbers
  - growth, 684
  - large, 694–695
  - small, 693–694
- PECVD. *See* Plasma-enhanced chemical vapor deposition
- Pedal, 216–217
- Pedestal growth method, 32
- PEG. *See* Polyethylene glycol
- PEL. *See* Potential energy landscapes
- Penrose pattern, 1120–1122
- Pentaerythritol Tetranitrate crystal (PETN crystal), 467
- Pentagonal dodecahedron, 1143–1145
- Perfect dislocation loop (PDL), 152–153
- Peritectics, 122–123
  - point, 123
- Peritectoids, 122–123
- PES. *See* Potential-energy surface
- PETN crystal. *See* Pentaerythritol Tetranitrate crystal
- PFC model. *See* Phase field crystal model
- pH-stat method, 886
- Pharmaceutical crystallization, 917
  - batch crystallization process development, 937–943
  - crystal
    - growth, 923–925
    - nucleation, 920–923
  - crystallization
    - medium, 917
    - methods, 929–936
  - dissolution, 925
  - organic solvents classification, 918t
  - phases, 917–920, 925–928
  - ripening, 928–929

- Pharmaceutical crystallization (*Continued*)  
 solubility, 917–920  
 supersaturation, 917–920
- Phase diagram, 86, 807–810, 917–920  
 analytical expressions, 106–109  
   Gibbs energy minimization, 109  
 calculation, 103–109  
 miscibility, 103–106
- Phase equilibria, 86  
 components and concentrations, 86–88  
 between condensed phases  
   one component, 110–112  
   three and more components,  
     124–129  
   two components, 112–124  
 gas phase, 129  
   Ellingham type diagrams, 131–133  
   volatile species, 130–131  
 phase transitions, 98–103  
 phases and phase rule, 88–89  
 system, 89–90  
 thermodynamic functions and potentials,  
   90–98
- Phase field crystal model (PFC model), 522,  
 551–552  
 step growth and beyond, 553–554  
 structures and defects, 551–552
- Phase-field models, 397, 632–633, 644, 701–702  
 diffuse interfaces at equilibrium, 639–645  
 free-boundary problems, 645–650  
 order-parameter models, 633–639  
 for solidification, 650  
   anisotropy and dendritic growth, 652–655  
   antitrapping current, 657–659  
   binary alloy, 655–657  
   multiphase and multicomponent  
     solidification, 659–664  
   pure substance, 650–652
- Phase-shift interferometry (PSI), 1037,  
 1043–1045, 1044f  
 in situ measurement, 1047–1048
- Phase(s), 88–89, 925–928  
 contrast microscopy, 1048  
 field, 523  
 rule, 88–89  
 transitions, 98–103, 927–928  
 temperatures, 285t
- Phason flipping, 1119, 1122
- Photoluminescence (PL), 779–781
- Physical vapor deposition (PVD), 446, 462–466
- Physical vapor transport (PVT), 86, 130
- Physiological calcifications, 900
- Piezoelectric materials, 51
- Pinctada maxima*, 897
- Pitchfork bifurcations, 622
- PL. *See* Photoluminescence
- Planar interface, 602–610  
 experimental tests of morphological stability,  
   609  
 long-wavelength perturbations, 609–610  
 TSS approximation, 605–608
- Plasma-enhanced chemical vapor deposition  
 (PECVD), 774–775
- PMNT. *See* Lead magnesium niobium-titanate
- Point defects, 139–140, 176–179  
 clusters, 140–142
- Polyatomic liquids, 420–425
- Polycrystalline microstructures, 446
- Polycrystals, 665
- Polyethylene glycol (PEG), 813–814
- Polygonal shape formation, 764–766
- Polygons, 525
- Polymorphism, 916
- Potassium chloride (KCl), 1090–1091  
 morphological instability, 1091–1093
- Potassium dihydrogen phosphate (KDP),  
 40–41
- Potassium Thiocyanate (KSCN), 923
- Potential energy landscapes (PEL), 153–157
- Potential-energy surface (PES), 508
- Precipitation. *See* Reactive crystallization
- Preferential crystallization, 975–979
- Preroughening phenomena, 291–292
- Pressure–temperature diagrams, 110–111
- Primary nucleation, 922, 941–942
- Product-wave-function renormalization group  
 (PWFRG), 240–241, 254–255, 303
- Prokrovsky-Talapov argument, 240–241
- Protein crystallization, 798, 810–812, 811f  
 crystal growth mechanisms, 846–857

- experiments, 41
  - thermodynamics, 802–810
  - Protein crystals, 796–797
    - aspartyl-tRNA synthetase, 801f
    - crystallography, 797f
    - intermolecular contacts, 800–802
    - nucleation, 348–354, 845–846
    - protein molecules, 798–800
    - solution trapping, 802
  - Protein Data Bank (PDB), 349
  - Protein(s), 798–802
    - cluster-cluster aggregation, 352–354
    - intercalation, 885
    - molecules, 798–800
      - interaction, 814–817
    - protein-rich clusters, 798
  - Pseudobinary system, 86
  - Pseudoternary system, 86
  - PSI. *See* Phase-shift interferometry
  - PSZ. *See* Partially stabilized zirconia
  - PTHT potential. *See* Pearson, Takai, Halicioğlu, Tiller potential
  - Pure phase, 109
  - Pure substance, 650–652
  - PVD. *See* Physical vapor deposition
  - PVT. *See* Physical vapor transport
  - PWFRG. *See* Product-wave-function renormalization group
- Q**
- QC. *See* Quasicrystals
  - QD. *See* Quantum dots
  - QHA. *See* Quasi-harmonic approximation
  - QLL. *See* Quasi-liquid layer
  - QMS. *See* Quadrupole mass spectroscopy
  - QSS approximation. *See* Quasi-steady-state approximation
  - Quadrupole mass spectroscopy (QMS), 487–488
  - Quantum chemical simulations, 522
  - Quantum dots (QD), 493, 548–549, 751, 751f, 767
    - SAG, 768–772
    - self-assembled growth, 767–768
  - Quantum well (QW), 751, 751f
  - Quantum wire (QWR), 751, 751f
  - Quartz, 51
  - Quasi-harmonic approximation (QHA), 160–161
  - Quasi-liquid layer (QLL), 1066–1067, 1071f, 1073f
    - experimental evidence, 1070t
    - visualizations of, 1071–1072
  - Quasi-steady-state approximation (QSS approximation), 603
  - Quasicrystals (QC), 1114
    - discovery, 1117–1118
    - electron diffraction pattern, 1114f
    - fibonacci sequence, 1118–1120
    - growth mechanism, 1142–1152
    - growth methods, 1131–1134
    - one-dimensional quasiperiodic structure, 1118–1120
    - Penrose pattern, 1120–1122
      - and periodicity, 1115–1116
      - selected results, 1135–1142
    - single crystal growth process, 1136t–1137t
    - symmetry by translation, 1116–1117
    - three-dimensional quasiperiodic structure, 1123–1126
    - two-dimensional quasiperiodic structure, 1120–1122
      - variations, 1123–1126
  - Quasielastic scattering, 440
  - Quasiperiodic array, 1119
  - QW. *See* Quantum well
  - QWR. *See* Quantum wire
- R**
- Racemates resolution, 980–991
  - Racemic
    - composition, 964–967
    - compounds, 968–975
    - mixture chemical purity, 991
  - Racemizable enantiomers, 967
  - RAD method. *See* Ribbon against drop method
  - Radial distribution function (RDF), 404
  - Radiofrequency (RF), 774–775
  - Radius of critical nucleus, 371–372
  - Rate law, 839–841

- Rayleigh instability, 615  
 RDF. *See* Radial distribution function  
 Re-crystallization operation, 937  
 Reactive crystallization, 934–935  
 Reciprocal salt pairs, 128–129  
 Reflection high-energy electron diffraction (RHEED), 487–488, 523–524, 1004, 1005f  
 Regeneration process, 878–879  
 Residual entropy, 1066  
 Resolving agent, 980–983  
 Resonant tunneling diode (RTD), 750–751  
 Restricted solid-on-solid model (RSOS model), 286  
   RSOS-I model, 308  
 Reverse Monte Carlo approach (RMC approach), 434–435  
 RF. *See* Radiofrequency  
 RHEED. *See* Reflection high-energy electron diffraction  
 Rhombic triacontahedron (RTH), 1123–1124, 1143  
 Ribbon against drop method (RAD method), 35–36  
 Ribbon to ribbon method (RTR method), 35–36  
 Ripening, 928–929  
 RKKY interaction, 256  
 RMC approach. *See* Reverse Monte Carlo approach  
 Rocking tank method, 40  
 Room temperature (RT), 770–771  
 Rough interface, 846–847  
 Rough regions near facets. *See also* Equilibrium crystal shape (ECS)  
   critical behavior  
     experiment on lead, 241–243  
     novel approach, 243–245  
     theory, 239–241  
   vicinal surfaces–entrée, 234–239  
 Rough surface, 1076  
   energy and shape relationship, 281–282  
   interface, 275–279  
   roughness of single step, 282–284  
   surface roughness, 279–281  
 Roughening, 11  
   exponent, 216–217  
   and faceting transition, 284–293  
   temperature changes  
     inverse roughening, 292  
     Langmuir adsorption, 292–293  
   transitions, 266  
 Rough–smooth transition  
   drumhead wandering, 272–275  
   entropy effect, 271–272  
   rough surface, 275–284  
     in crystal growth, 270–271  
   universal features, 266–270  
 RSOS model. *See* Restricted solid-on-solid model  
 RT. *See* Room temperature  
 RTD. *See* Resonant tunneling diode  
 RTH. *See* Rhombic triacontahedron  
 RTR method. *See* Ribbon to ribbon method
- S**  
 S-K mode. *See* Stranski-Krastanow mode  
 s-LN. *See* Conventional stoichiometric LiNbO<sub>3</sub>; Stoichiometric LiNbO<sub>3</sub>  
 s-LT. *See* Stoichiometric LiTaO<sub>3</sub>  
 SA-MOVPE. *See* Selective-area metal-organic vapor phase epitaxy  
 SAE. *See* Selective-area epitaxy  
 SAED. *See* Selected area electron diffraction  
 SAG. *See* Selective-area growth  
 Salts, 821–822  
   formation, 980–991  
 Sample environment, 433–434  
 Satellite tobacco mosaic virus (STMV), 828  
 SAXS. *See* Small-angle X-ray scattering  
 SBN. *See* Strontium barium niobate  
 Scaled surface width, 280  
 Scanning electron microscopy (SEM), 679, 774–775, 1003–1004  
   in situ imaging method, 1004–1010  
     GaAs surface nucleation and growth, 1015–1019  
     graphene growth, 1022–1027  
     growth mode, 1010–1015

- Scanning reflection electron microscopy (SREM), 1003–1004
- Scanning transmission electron microscope (STEM), 773
- Scanning tunneling microscope (STM), 237, 243, 523–524, 530, 1003–1004
- Scattering
  - neutrons, 405–416
  - spectrum, 410
  - X-rays, 405–416
- Scherrer broadening, 412–413
- Schwoebel instability, 453
- SCN. *See* Succinonitrile
- Screw dislocation, 377
- SE. *See* Secondary electron
- Second-order phase transition, 316
- Secondary electron (SE), 1004–1005, 1007–1008
  - step flow, 1013–1015
  - 2D-Island nucleation, 1013–1015
- Secondary harmonic generation (SHG), 182, 972–973
  - conversion efficiency, 206–207
- Secondary nucleation, 922–923
- Seed quality, 939
- Seeded and isothermal preferential crystallization (SIPC), 975–977
- Seeding strategy, 938–940
- Segregation, 119–121
- Selected area electron diffraction (SAED), 1126–1127
- Selective-area epitaxy (SAE), 753. *See also* Microchannel epitaxy (MCE)
- Selective-area growth (SAG), 753, 787–788
  - facets, 758–759
    - control, 760–764
    - of GaAs, 763f
    - III-V NWs formation, 774–781
    - polygonal shapes formation, 764–766
    - QD structures, 768–772
- Selective-area metal-organic vapor phase epitaxy (SA-MOVPE), 774
- Self-catalyzed method, 773–774
- Self-epitaxial nucleation-induced assembly, 586, 587f
- Self-flux method. *See* Solution growth method
- Self-interaction correction (sic), 527
- Self-interstitial clusters, 163–167
  - landscape roughness and pressure effect, 165–167
- SEM. *See* Scanning electron microscopy
- Semiconductors, 22–24
  - materials, 478
  - nanocrystals, 750–751, 753
    - III-V NWs formation, 772–788
    - QD, 767–772
    - SAE, 753–766
- Sequential layering film deposition process, 62
- SET. *See* Single electron transistor; Single-electron tunneling
- 7P rule, 916
- SFT. *See* Stacking-fault tetrahedrons
- Shadow effect, 586
- Shaped growth, 33–36
- Sharp
  - edges, 245–250
    - facet reconstruction, 245–250
  - interface
    - models, 396–397
    - picture, 366–368
- SHG. *See* Secondary harmonic generation
- Short range order (SRO), 402–403
- sic. *See* Self-interaction correction
- Sideband instability, 623–624
- Silicon, 53
  - homoepitaxial growth of, 541
- Simple colloid approach, 817–819
- Simultaneous preferential crystallization, 978–979
- Single electron transistor (SET), 750–751
- Single nucleation growth, 373
- Single vacancy, 158–159
- Single-crystal silicon, 138
- Single-electron tunneling (SET), 752
- SIPC. *See* Seeded and isothermal preferential crystallization
- Skull melting method, 37–38
- SL. *See* Superlattice
- Small compact self-interstitial clusters, 149–151

- Small-angle X-ray scattering (SAXS), 901
- Smooth free-energy functional, 661
- Smooth interface, 846–847
- Smooth surface, 1075–1076
- SMPT. *See* Solution-mediated phase transformation
- Snow crystals, 1062, 1063f. *See also* Ice crystals  
 air flow on pattern, 1079–1080  
 dendritic pattern formation, 1077–1079  
 growth morphologies, 1072–1075  
 Kuroda–Lacmann model, 1075–1077, 1076f  
 twinned snow crystals, 1080–1081
- Sodium bromate ( $\text{NaBrO}_3$ ), 993–994
- Sodium chlorate ( $\text{NaClO}_3$ ), 958–959, 992–994
- Solid solutions, 968–975
- Solid state recrystallization, 70–72
- Solid-on-solid model (SOS model), 266–267  
 interfacial model, 584
- Solid-state lighting (SSL), 750
- Solid-state physics simulations, 522
- Solidification, 595–596, 1148–1149
- Solid–liquid interfacial free energy, 598
- Solidus line, 106–109, 113–115
- Solubility, 816  
 rules, 926–927
- Solute  
 partitioning behavior, 180  
 pump mechanism, 618  
 solute/resolving agent, 986–989  
 trapping, 657–658
- Solution growth, 369–370
- Solution growth method, 38, 45–46, 369–370, 1134, 1134f. *See also* Vapor growth.  
 method  
 aqueous solution growth, 38–41  
 biological macromolecules growth, 41–43  
 electrochemical crystal growth, 52–53  
 growth from gels, 43–44  
 high temperature solution growth, 44–49  
 hydrothermal growth, 49–52  
 nonaqueous solution growth, 44
- Solution-crystal spinodal, 830–832
- Solution-mediated phase transformation (SMPT), 927
- Solvent, 983–986  
 evaporation, 930–932  
 requirements, 45  
 selection, 938
- Soret effect, 618
- SOS model. *See* Solid-on-solid model
- Spallation sources, 432–433
- Specific heat capacity, 90–91
- Spheres, 611–616
- Spherical crystallization, 928
- Spider rotating seed holder, 40
- Spinodals phase, 807–810
- Spiral growth, 377  
 facet with dislocations, 378–379  
 growth mode change, 379  
 kinetic roughening, 379  
 mound formation, 380  
 screw dislocation, 377  
 velocity of, 377–378
- Sputtering method, 61–62
- Squared surface width, 279
- SREM. *See* Scanning reflection electron microscopy
- SRO. *See* Short range order
- $\text{SrTiO}_3$ . *See* Strontium titanate
- $\text{Sr}_x\text{Ba}_{1-x}\text{Nb}_2\text{O}_6$ . *See* Strontium barium niobate (SBN)
- SSL. *See* Solid-state lighting
- Stable equilibrium, 320f
- Stable phases alloy system, 1129–1130
- Stacking-fault tetrahedrons (SFT), 493
- Static approximation, 410–412
- Stationary state. *See* Steady state
- Steady state, 573  
 energy equations, 683  
 nucleation rate, 322–326
- Stefan energy balance, 708–709
- Stellated polyhedron, 1142–1143
- STEM. *See* Scanning transmission electron microscope
- Step  
 bunching, 390–391  
 coverage, 462–466  
 free energy, 584  
 kinetic coefficient, 849–850  
 propagation, 848–849

- wandering, 388–389
- Step faceting  
 discontinuous surface tension, 300–302  
 macrostep stability, 298–300
- Step flow growth, 1013–1015  
 instability, 1020–1022
- Stillinger–Weber potential (SW potential),  
 142–143
- Stirring rate, 942
- STM. *See* Scanning tunneling microscope
- STMV. *See* Satellite tobacco mosaic virus
- Stöber/heat exchanger methods, 30
- Stoichiometric crystal growth characteristics,  
 192. *See also* Oxide crystals  
 activities of constituent elements, 196–199  
 crystallization electromotive force, 193–196  
 oxide melt, 192–193
- Stoichiometric  $\text{LiNbO}_3$  (s-LN), 182
- Stoichiometric  $\text{LiTaO}_3$  (s-LT), 182
- Stoichiometry, 182–183  
 conventional stoichiometric compositions,  
 184–188  
 extended concept, 182  
 impurities and vacancies, 188–191  
 law of multiple proportions, 184–188  
 materials, 176  
 pseudo-binary systems, 184f  
 stoichiometric-congruent composition,  
 195–196  
 thermodynamic definition, 183–184
- Strain-annealed crystal growth, 71
- Stranski-Krastanow mode (S-K mode),  
 751–752, 767
- Stratum corneum*, 890–891
- Striation, 25
- Strontium barium niobate (SBN), 115
- Strontium titanate ( $\text{SrTiO}_3$ ), 111, 528, 529f,  
 536–537
- Sublimation, 55–56, 130
- Subregular solution model, 104
- Substrate nucleation. *See* Heterogeneous  
 nucleation
- Succinonitrile (SCN), 678–679, 1088
- Supercooled water, ice crystal free growth in  
 equilibrium forms, 1081–1082  
 growth morphologies, 1082–1084  
 ice–Water interface, 1089–1090  
 microgravity conditions, 1084–1088
- Supercritical bifurcation, 622
- Superlattice (SL), 750–751
- Supersaturation, 337, 886, 917–920, 934–935
- Supersaturation-driven interfacial structural  
 mismatch nucleation, 586–588
- Supramolecular liquid structures, 438–440
- Surface  
 diffusion, 382–387  
 length, 383–384  
 free energy, 267–268  
 reconstruction, 478–480  
 surface-phase diagram calculations, 478–479  
 width calculation, 306–307
- Surface roughness  
 height–height correlation function, 280  
 microscopic models, 284  
 ASOS model, 286  
 BCSOS model, 285–286  
 RSOS model, 286  
 surface width–variance of surface height,  
 279–280  
 thin film-like surface, 281
- SW potential. *See* Stillinger–Weber potential
- Symmetric model, 646
- Syntectics, 124
- Synthetic diamonds, 65–66  
 crystals, 65–70
- T**
- Tammann’s method, 20
- Tangential flux, 712–713
- Taylor expansion, 639
- TBP. *See* Tertiarybutyl phosphine
- Teeth, 892–893, 893f
- TEM. *See* Transmission electron microscope
- Temperature  
 change, 930  
 conductivity, 735  
 effect, 453, 457
- 10-fold axis, 1128–1129

- Terrace step kink model (TSK model), 235, 269, 294–295
- Terrace-ledge-kink model (TLK model), 6–7, 269
- Terrace-width distribution (TWD), 236
- Tertiarybutyl phosphine (TBP), 778
- Texture development, 460–462
- Theory of chemical bonding, 6–7
- Thermal steady-state approximation (TSS approximation), 598, 605–608
- Thermodynamic driving force, 568. *See also*
- Crystal growth
  - CNT, 568–573
    - discrepancies with observations, 575–576
    - experimental verification, 574–575
- Thermodynamics, 825–827
- protein crystallization, 802–803
    - crystallization driving force, 806–807
    - molecular process, 803–806
    - phase diagram, 807–810
    - supersaturation, 318
- Thermomechanical analysis (TMA), 102–103
- Thin films, 48, 446
- liquid phase epitaxy, 48–49
- Third-phase adsorption, 660–661
- 3-body correlations, 437–438
- Three-dimensional quasicrystal, 1126–1128
- Three-dimensional quasiperiodic structure, 1123–1126
- Tie-line, 119–120
- Tilt angle measurement, 1095–1096
- Time-dependent morphological features, 682–683
- TLK model. *See* Terrace-ledge-kink model
- TMA. *See* Thermomechanical analysis
- TMG. *See* Trimethylgallium
- Tolman length, 331–332
- “Top-down” view. *See* Free-boundary problems
- Top-seeded solution growth method (TSSG), 46–47, 86
- Transition state, 396–397
- Transitions of first kind. *See* First-order transitions
- Transmission electron microscope (TEM), 523–524, 755, 1115–1116, 1122
- Transport solution
- dendrite thermal field, 685–686
  - steady-state, 688–689
  - supercooling limits, 686–688
- Transport theory, 681–685
- key assumptions and boundary conditions, 683–684
  - solution parameters, 684–685
  - tests, 689–691
- Transverse coherence, 413–414
- “Trapped-wave” eigenstates, 695
- Trimethylgallium (TMG), 487–488
- Trouton’s rule, 272
- TSK model. *See* Terrace step kink model
- TSS approximation. *See* Thermal steady-state approximation
- TSSG. *See* Top-seeded solution growth method
- TWD. *See* Terrace-width distribution
- Twinned snow crystals, 1080–1081
- Twinning growth model, 781–786
- Two component systems, 112
- eutectics and eutectoids, 117–119
  - intermediate compounds, 121–122
  - lever rule, 119–121
  - peritectics and peritectoids, 122–123
  - segregation, 119–121
  - syntectics and monotectics, 124
  - total miscibility in 2 phases, 113–117
- 2D circular island growth, 374–375
- 2D-Island nucleation, 1013–1015
- Two-dimensional crystal nucleation, 339–342, 340f
- Two-dimensional electron gas (2DEG), 764–765
- Two-dimensional quasicrystal, 1128–1129
- Two-dimensional quasiperiodic structure, 1120–1122
- Two-dimensional square lattice, 1116
- Two-step nucleation mechanism, 334–335, 833–836, 835f
- rate determination, 841–842
  - rate law, 839–841

**U**

U.S. Food and Drug Administration (FDA), 962  
 Unidirectional casting method, 36  
 United States Microgravity Payload missions (USMP), 689–690

**V**

V-W mode. *See* Volmer-Weber mode  
 Vacancy clusters, 147–149, 159–163  
 Vapor diffusion, 887–888  
 Vapor growth, 364–365, 382–387  
   method, 53–55  
     artificial epitaxy, 64–65  
     bulk growth method, 55–58  
     vapor phase epitaxy, 58–62  
     VLS method, 63–64  
 Vapor phase epitaxy  
   ALD, 62  
   MBE, 60  
   OMVPE, 58–60  
   sputtering method, 61–62  
 Vapor-liquid-solid technique (VLS technique), 63–64, 772–773  
 Vapor-phase epitaxy (VPE), 53–54, 478–479, 760–762  
 Vdovichenko's method, 306  
 Verneuil process, 18–20  
 Vertical elevator furnace, 26  
 Vertical gradient freeze method (VGF method), 26–27, 86  
 Vibrational entropy, 139–140  
 Vicinal face growth, 380. *See also* Crystal growth  
   bulk diffusion, 381–382  
   deformation of, 388f  
   stepped surface morphology, 387–391  
   surface diffusion, 382–387  
   vapor growth, 382–387  
 Vicinal surface  
   logarithmic behavior  
     elastic step–step repulsion, 297  
     height–height correlation function, 296–297  
   1D free-fermion universal features, 295–296  
   TSK picture, 294–295

VLS technique. *See* Vapor-liquid-solid technique

Voids, 162  
 Volatile species, 130–131  
 Vollmer–Weber growth, 546  
 Volmer-Weber mode (V-W mode), 767  
 “Vortex” spin configuration, 267  
 VPE. *See* Vapor-phase epitaxy

**W**

Water-structuring interactions, 822  
 Weakly nonlinear analysis, 620–622, 624–626  
 Web-silicon, 674  
 Wetting effect, 452–453, 455–456  
 Wetting layer (WL), 493  
 Wilson-Frenkel formula, 367, 731–734  
 “Window” for projection, 1118–1119  
 Wulff construction, 222, 222f, 467  
   2D studies, 233–234  
   thermal faceting and reconstruction, 229–230  
   type A & B, 231  
 Wulff plot, 227–229  
 Wulff's theorem, 339

**x**

X-ray  
   scattering, 405–416  
   sources, 430–431  
 X-ray absorption fine structure (EXAFS), 403, 427–430  
 X-ray absorption near edge structure (XANES regime), 427–428  
 X-rays absorption spectroscopy (XAS), 427–430  
 x–y diagrams, 124–125

**Y**

Young–Laplace equation, 316  
 Young–Laplace law, 664–665  
 Yttrium zirconia (Y CZ), 37

**Z**

Zeldovich factor, 373, 833  
 Zero-dimension (0D), 751

Zero-point entropy, 1066

Zinc oxide (ZnO), 53

Zincblende (ZB), 781, 781f

Zirconium–hafnium system, 113–115

Zn–Mg–RE system, 1139–1140

Zn–Mg–Tb system, 1139–1140

Zn–Sc system, 1142

Zonal sublimation method, 55

Zone leveling, 32

Zone melting method, 31–33